

INMATEH -

**AGRICULTURAL
ENGINEERING**

JANUARY - APRIL

No liability is assumed by the editorial staff for the content of scientific papers and opinions published in this volume. They represent the author's point of view

Managing Editorial Board - INMA Bucharest

Editor in Chief

Lucian-Ionel CIOCA, Professor, PhD.Eng., "Lucian Blaga" University of Sibiu

Executive Editor

Lucreția POPA
PhD.Eng, SR I

Assistant Editor

Nicolae-Valentin VLADUȚ
PhD.Eng, SR I
Mihai-Gabriel MATAȚHE
PhD.Eng, SR I

Logistic support, database

Virgil MURARU
PhD.Eng, SR I

Scientific Secretary

Cârdei Petre, math.

Official translator

RADU Daniela-Cristina, English

Editorial Board

- *QUENDLER Elisabeth – Austria, Vienna, Univ. of Natural Resources & Applied Life Sciences;*
- *Ir. HUYGHEBAERT Bruno – Belgia, Walloon Agricultural Research Center CRA-W;*
- *Van IMPE F.M. Jan – Belgia, KU Leuven University*
- *FABBRO Dal Inacio Maria - Brazil, Campinas State University;*
- *ATANASOV Atanas – Bulgaria, "Angel Kanchev" University of Rousse*
- *MOLINOS-SENANTE María – Chile, Pontificia Universidad Católica - Vicedecana, Escuela de Ingeniería UC*
- *BILANDZIJA Nikola – Croatia, Zagreb University, Faculty of Agriculture;*
- *KOSUTIC Silvio – Croatia, Zagreb University, Faculty of Agriculture;*
- *KOVACEV Igor - Croatia, Zagreb University, Faculty of Agriculture;*
- *GONZÁLEZ Omar – Republic of Cuba, Central University "Marta Abreu" de las Villas;*
- *KATHIJOTES Nicholas – Cyprus, University of Nicosia;*
- *HERAK David - Czech Republic, Czech University of Agriculture Prague;*
- *BORCHARD Nils – Finland, Natural Resources Institute Finland (Luke);*
- *SAUER Johannes – Germany, Technical University Munich;*
- *FENYVESI László – Hungary, Hungarian Institute of Agricultural Engineering Godollo;*
- *PEEYUSH Soni - India, Indian Institute of Technology, Kharagpur;*
- *MOHAMMADREZA Alizadeh – Iran, Department of Agricultural Engineering, Rice Research Institute of Iran (RRII);*
- *De WRACHIEN Daniele - Italy, State University of Milan;*
- *BIOCCA Marcello - Italy, Agricultural Research Council, Agricultural Engineering Research Unit;*
- *COLANTONI Andrea – Italy, University Viterbo;*
- *SARAUSSKIS Egidijus – Lithuania, Vytautas Magnus University, Faculty of Agricultural Engineering;*
- *KRIAUCIUNIENE Zita - Lithuania, Vytautas Magnus University;*
- *DUKE Mike – New Zealand, University of Waikato, Faculty of Science and Engineering;*
- *EWEMOJE Temitayo Abayomy – Nigeria, University of Ibadan, Faculty of Technology, Department of Agricultural and Environmental Engineering;*
- *SKIERUCHA Wojciech – Poland, Institute of Agro-physics Polish Academy of Sciences, Lublin;*
- *EKIELSKI Adam - Poland, Warsaw University of Life Sciences;*
- *KOT Sebastian - Poland, Czestochowa University of Technology*
- *SAVIN Lazar– Serbia, University of Novi Sad, Faculty of Agriculture, Department of Agricultural Engineering;*
- *SIMIKIC Mirko– Serbia, University of Novi Sad, Faculty of Agriculture, Department of Agricultural Engineering;*
- *MARTINOV Milan - Serbia, Faculty of Agriculture, Department of Agricultural Engineering,*
- *TURAN Jan – Slovakia, Technical University Kosice, Dept Elect & Multimedia Commun, Kosice;*
- *MADYIRA M. Daniel - South Africa, University of Johannesburg, Mechanical Engineering Science Department*
- *COZ FERNANDEZ Alberto – Spain, University of Cantabria, School of Nautical Studies, Department of Chemistry and Process & Resource Engineering;*
- *ERTEKIN Can - Turkey, Akdeniz University Antalia;*
- *KABAŞ Önder –Turkey, Antalia, Agricultural Scientific Research Institute of Batı Akdeniz;*
- *SELVI Kemal Çağatay - Turkey, Samsun, University of Ondokuz Mayıs, Faculty of Agriculture, Department of Machines for Agriculture;*
- *ÖTLEŞ Semih - Turkey, Ege University, Engineering Faculty, Food Engineering Department;*
- *MARUSCHAK Pavlo - Ukraine, Ternopil Ivan Pul'uj National Technical University, Department of Technical Mechanics and Agricultural Engineering;*
- *BULGAKOV Volodymyr – Ukraine, National University of Life and Environmental Sciences of Ukraine;*
- *PARASCHIV Gigel - Romania, Politehnica University of Bucharest;*
- *VOICU Gheorghe - Romania, Politehnica University of Bucharest;*
- *BIRIŞ Sorin - Romania, Politehnica University of Bucharest;*
- *MAICAN Edmond - Romania, Politehnica University of Bucharest;*
- *FILIP Nicolae - Romania, Technical University Cluj Napoca;*
- *COZAR Onuc-Romania, „Babes-Bolyai” University of Cluj-Napoca Romania, Faculty of Physics;*
- *VLASE Sorin - Romania, “Transilvania” University of Braşov;*
- *ȚENU Ioan - Romania, USAMV Iași;*
- *HERIŞANU Nicolae - Romania, Politehnica University of Timisoara;*
- *MARSAVINA Liviu - Romania, Politehnica University of Timisoara*
- *MARINCA Vasile - Romania, Politehnica University of Timisoara*
- *GERGEN Iosif - Romania, USAMVB Timișoara;*
- *BORDEAN Despina-Maria - Romania, USAMVB Timișoara;*
- *BUNGESCU Sorin - Romania, USAMVB Timișoara;*
- *RODINA Steliana – Romania, ICEADR, Bucharest;*
- *VOICEA Iulian - Romania, INMA Bucharest;*
- *DEAK Gyorgy - Romania, INCDFM Bucharest;;*
- *BELC Nastasia - Romania, IBA Bucharest;*
- *BUȚU Alina - Romania, INCDSB Bucharest;*
- *PAUN Mihaela - Romania, INCDSB, Bucharest*

INMATEH - Agricultural Engineering journal is indexed in the next international databases:
ELSEVIER /SciVerse SCOPUS, CLARIVATE - WEB of SCIENCE- Emerging Sources Citation Index (ESCI),
ULRICHS Web: Global Serials Directory, CABI, SCIPRO, Index COPERNICUS International, EBSCO Publishing,
Elektronische Zeitschriftenbibliothek

INMATEH - Agricultural Engineering

vol. 75, no.1 / 2025

e-ISSN: 2068-2239; p: ISSN: 2068-4215

<https://inmateh.eu/>

E-mail: inmatehjournal@gmail.com

Edited by: **INMA Bucharest**

Copyright: INMA Bucharest / Romania

National Institute for Research-Development of Machines and Installations
Designed for Agriculture and Food Industry - INMA Bucharest
6, Ion Ionescu de la Brad Blvd., sector 1, Bucharest, ROMANIA

CONTENT

		Page(s)
1.	<p>DESIGN AND OPTIMIZATION OF AIR-ASSISTED SPIRAL SEED-SUPPLY DEVICE FOR HIGH-SPEED DENSE PLANTING MAIZE SEEDER / 玉米高速密植播种机气送式螺旋供种装置设计与优化</p> <p>Wen-sheng SUN¹⁾, Shu-juan YI¹⁾, Hai-long QI²⁾, Yi-fei LI^{1,3)}, Zhi-bo DAI¹⁾, Yu-peng ZHANG¹⁾, Jia-sha YUAN¹⁾, Song WANG¹⁾</p> <p>¹⁾College of Engineering, Heilongjiang Bayi Agricultural University, Daqing/P.R.China ²⁾Heilongjiang Beidahuang Modern Agricultural Service Group Zhongrong Agricultural Machinery Co., Ltd, Harbin / P.R.China; ³⁾College of Engineering, Northeast Agricultural University, Harbin/P.R.China</p>	13
2.	<p>DESIGN AND EXPERIMENT OF GUIDANCE CAM OF AIR SUCTION GARLIC CLOVE DIRECTIONAL METERING DEVICE / 气吸式大蒜定向排种器导向凸轮的设计与试验</p> <p>Kunqiao LI, Fuhai FANG, Zhuo WANG, Yongzheng ZHANG, Mingliang ZHANG</p> <p>Shandong University of Technology, College of Agricultural Engineering and Food Science, Zibo, China</p>	26
3.	<p>RESEARCH ON THE OPTIMIZATION METHOD OF CLUTCH ENGAGEMENT TRAJECTORY IN THE TRACTOR POWER SHIFT PROCESS / 拖拉机动力换挡过程离合器接合轨迹优化方法研究</p> <p>Dongyang WANG¹⁾, Weipeng ZHANG²⁾, Jiangtao JI³⁾, Zuohua DONG⁴⁾, Hongmei ZHU¹⁾, Zhanyu LI¹⁾</p> <p>¹⁾College of Automotive and Transportation Engineering, Shenzhen Polytechnic University, Shenzhen/China; ²⁾ National Key Laboratory of Agricultural Equipment Technology, China Academy of Agricultural Mechanization Science Group Co., Ltd, Beijing / China ³⁾ College of Agricultural Equipment Engineering, Henan University of Science and Technology, Luoyang/China ⁴⁾ Changzhou Dongfeng Agricultural Machinery Group Co. Ltd., Changzhou/China</p>	35
4.	<p>DESIGN AND TEST OF A CLAMPING-SHEAR INTRA-ROW WEEDING DEVICE / 夹持剪切式株间除草装置设计与试验</p> <p>Jiacheng ZHOU, Min FU*, Jianhao CHEN, Ji CUI</p> <p>Northeast Forestry University, College of Mechanical and Electrical Engineering, Harbin / China</p>	45
5.	<p>DETECTION OF ADULT PEACH FRUIT MOTH BASED ON IMPROVED YOLOv8m / 基于改进 YOLOV8M 的桃小食心虫成虫检测方法</p> <p>Lijun CHENG^{*1)}, Yihe ZHANG¹⁾, Jianglin YAN¹⁾, Zhengkun ZHAI¹⁾, Zhiguo ZHAO^{*2)}, LinQiang DENG¹⁾</p> <p>¹⁾ College of Software, Shanxi Agricultural University, Taigu, Shanxi / China; ²⁾ College of Software, Shanxi Agricultural University, Taigu, Shanxi / China</p>	57
6.	<p>INNOVATIVE TECHNICAL SYSTEMS USED IN SERICULTURE – A REVIEW / SISTEME TEHNICE INOVATIVE UTILIZATE IN SERICULTURA – A REVIEW</p> <p>Adriana MUSCALU^{*1)}, Cătălina TUDORA¹⁾, Cristian SORICĂ¹⁾</p> <p>¹⁾ INMA Bucharest. / Romania</p>	67
7.	<p>RESEARCH ON YOLOv5-BASED VISUAL SLAM OPTIMISATION METHOD IN FARM DEPOT ENVIRONMENT / 农场仓库环境中基于 YOLOv5 的视觉 SLAM 优化方法研究</p> <p>Pengcheng LV^{1,2)}, ZhenWei LI^{2,*)}</p> <p>¹⁾ Shandong University of Technology, College of Agricultural Engineering and Food Science, Zibo, China ²⁾ Hezhou University, School of Artificial Intelligence, Hezhou, China</p>	83
8.	<p>NUMERICAL SIMULATION AND PARAMETER OPTIMIZATION OF COMBINED CUTTING AND CRUSHING FORAGE CRUSHER / 铡切揉碎组合式牧草粉碎机数值模拟与参数优化</p> <p>Tao CHEN, Shu-juan YI*, Song WANG, Wen-sheng SUN</p> <p>College of Engineering, Heilongjiang Bayi Agricultural University, Daqing/P. R. China</p>	95
9.	<p>CALIBRATION OF DISCRETE ELEMENT SIMULATION PARAMETERS FOR BUCKWHEAT SEEDS / 荞麦种子离散元仿真参数标定</p> <p>Yulong CUI^{1,2)}, Shaobo YE^{1,2)}, Shuai FENG^{1,2)}, Decong ZHENG^{1,2)}</p> <p>¹⁾ College of Agricultural Engineering, Shanxi Agricultural University, Taigu, China; ²⁾ Dryland Farm Machinery Key Technology and Equipment Key Laboratory of Shanxi Province, Taigu, China</p>	110
10.	<p>SIMULATION AND TEST OF A NEW COAXIAL COUNTER-ROTATING AGITATOR / 新型同轴异转搅拌器的仿真与试验</p> <p>Longlong REN^{1,2,3)}, Yuqiang LI¹⁾, Zhenxiang JING¹⁾, Yuepeng SONG^{1,2,3)}, Jing GUO^{1,2,3)}, Siwen SHEN⁴⁾</p> <p>¹⁾ Shandong Agricultural University, College of Mechanical and Electrical Engineering/ China; ²⁾ Shandong Provincial Key Laboratory of Horticultural Machinery and Equipment/ China; ³⁾ Shandong Provincial Engineering Laboratory of Agricultural Equipment Intelligence/ China; ⁴⁾ Shandong Electric Power Higher Specialised College, Department of Power Engineering/ China</p>	121
11.	<p>DESIGN AND EXPERIMENT OF AIR-SUCTION GARLIC SEEDING UNIT / 气吸式蒜苗单体的设计与实验</p> <p>Minghao LU¹⁾, Yazi WANG¹⁾, Tao LIU¹⁾, Chunling ZHANG^{*1)}, Ce LIU¹⁾, Gang ZHAO¹⁾</p> <p>¹⁾ Anhui Agricultural University College of Technology / China</p>	132

		Page(s)
12.	<p>A REVIEW OF THE FEED RATE DETECTION AND STABILITY CONTROL METHODS IN COMBINE HARVESTERS / 联合收割机喂入量检测与稳定控制方法研究现状与发展趋势 Xiaoyu YANG¹, Panpan LI¹, Zhihao ZHAO¹, Chaoxu LEI¹, Chengqian JIN^{*,1,2} ¹School of Agricultural Engineering and Food Science, Shandong University of Technology, Zibo, Shandong / China ²Nanjing Institute of Agricultural Mechanization, Ministry of Agriculture and Rural Affairs, Nanjing, Jiangsu / China</p>	143
13.	<p>PREDICTIVE MODELLING OF PH LEVELS FOR OPTIMIZING WATER QUALITY IN SHRIMP FARMING / การสร้างแบบจำลองการพยากรณ์ค่าความเป็นกรด-ด่างเพื่อเพิ่มประสิทธิภาพการจัดการคุณภาพน้ำในการเลี้ยงกุ้ง Thanin MUANGPOOL^{1,2}, Sanya KUANKID^{1,2}, Boonthong WASURI^{1,2}, Ouychai INTHARASOMBAT^{*1} ¹ Faculty of Science and Technology, Nakhon Pathom Rajabhat University, Nakhon Pathom / Thailand; ² Creating Innovation for Sustainable Development Research Center, Nakhon Pathom Rajabhat University, Nakhon Pathom / Thailand</p>	158
14.	<p>ANALYSIS OF VIBRATION CHARACTERISTICS AND STRUCTURAL OPTIMIZATION OF THE CHASSIS FRAME OF CRAWLER-TYPE COMBINE HARVESTER / 履带式联合收割机底盘机架振动特性分析与结构优化 Zihao ZHAO¹, Chengqian JIN^{1,2}, Guangyue ZHANG², Youliang NI², Zhenjie QIAN² ¹ School of Agricultural Engineering and Food Science, Shandong University of Technology, Zibo, Shandong / China ² Nanjing Institute of Agricultural Mechanization, Ministry of Agriculture and Rural Affairs, Nanjing, Jiangsu / China</p>	167
15.	<p>DESIGN AND EXPERIMENTAL STUDY ON TWIN-SCREW STRAW PULPING MACHINE / 稻秆双螺杆制浆机设计与试验 Huiting CHENG, Nan ZHAO, Dezhi REN, Wei WANG, Yuanjuan GONG, Wanyuan HUANG College of Engineering, Shenyang Agricultural University, Shenyang/ China</p>	178
16.	<p>STRUCTURAL DESIGN AND SIMULATION ANALYSIS OF AIR-ABSORBING VEGETABLE PRECISION SEEDER / 气吸式蔬菜精量播种机结构设计与仿真分析 ChunYan ZHANG^{1,2}, Xin HE^{1,2}, XiaoYu WANG^{1,2}, YanJun LI^{3*} ¹ Shandong Academy of Agricultural Machinery Sciences, Jinan/China; ² Key Laboratory of Intelligent Agricultural Equipment in Hilly and Mountainous Areas of Shandong Province, Jinan/China; ³School of Machinery and Automation, Weifang University, Weifang/China</p>	190
17.	<p>STRUCTURE DESIGN AND LEVELLING CONTROL SYSTEM DEVELOPMENT FOR SELF-PROPELLED SPRAYER BOOM / 自走式喷雾机喷杆结构设计与仿形调平控制系统开发 Zhenyu ZHANG¹, Jiayu CAO¹, Peijie GUO¹, MiaoYun WANG², Yu CHEN^{*1} ¹ College of Mechanical and Electronic Engineering, Northwest A&F University, Yangling, China; ² College of Intelligent Manufacturing, Shaanxi Institute of Mechatronic Technology, Baoji, China</p>	200
18.	<p>ANALYSIS OF SOIL STRESS VARIATIONS DURING THE SEEDLING PLANTING PROCESS WITH DIRECT INSERTION SEEDLING DEVICE / 直插式栽苗器栽苗过程中土壤应力变化过程分析 Fandi ZENG¹, Xinchao GAO³, Hongbin BAI², Ji CUI², Limin LIU¹, Xuying LI², Hongwei DIAO¹ ¹ Shandong Agriculture and Engineering University, College of Mechanical and Electronic Engineering, Jinan, China; ² Inner Mongolia Agricultural University, College of Mechanical and Electrical Engineering, Hohhot, China; ³ Hebei Petroleum University of Technology, Department of Mechanical Engineering, Chengde, China</p>	212
19.	<p>OPTIMIZING WALNUT SHELL MECHANICAL PROPERTIES FOR EFFICIENT SHELL-CRACKING USING HEAT TREATMENTS: A COMPARATIVE STUDY OF RADIO FREQUENCY AND HOT AIR HEATING METHODS / 通过热处理优化核桃壳力学性能以实现高效脱壳：射频和热风加热的对比研究 Yaohuo GAO¹, Jundang LU², Xiaoxi KOU^{*1} ¹ College of Mechanical and Electronic Engineering, Northwest A&F University, Yangling, Shaanxi, China; ² Shaanxi Agri-machinery Research Institute, Xianyang, Shaanxi, China</p>	221
20.	<p>EFFECTS OF MOISTURE CONTENT ON MECHANICAL CRUSHING PERFORMANCE OF SOYBEAN SEEDS AND ITS APPLICATION IN MECHANIZED HARVESTING/ 含水率对大豆种子机械破碎性能的影响及其在机械化收获中的应用 Panpan LI¹, Zheng LIU², Jin WANG², Lulu LV¹, Anqi JIANG¹, Han YAN¹, Chengqian JIN^{1,2} ¹ School of Agricultural Engineering and Food Science, Shandong University of Technology, Zibo, China; ² Nanjing Institute of Agricultural Mechanization, Ministry of Agriculture and Rural Affairs, Nanjing, China</p>	231
21.	<p>OPTIMIZATION OF TECHNOLOGICAL PARAMETERS FOR FUEL ROLL PRODUCTION USING AGRICULTURAL CROP STEM BIOMASS / ОПТИМІЗАЦІЯ ТЕХНОЛОГІЧНИХ ПАРАМЕТРІВ ДЛЯ ВИРОБНИЦТВА ПАЛИВНИХ РУЛОНІВ З ВИКОРИСТАННЯМ СТЕЛБОВОЇ БІОМАСИ СІЛЬСЬКОГОСПОДАРСЬКИХ КУЛЬТУР Svitlana YAHELIUK^{*1}, Volodymyr DIDUKH¹, Mikhalo FOMICH¹, Olexandr YAHELIUK² Tetyana KUZMINA², Galina BOIKO² ¹ Lutsk National Technical University, Ukraine; ² Kherson National Technical University, Ukraine</p>	243

		Page(s)
22.	<p>DESIGN OF A WHEELED ADAPTIVE CHASSIS LEVELING SYSTEM FOR HILLY AND MOUNTAINOUS AREAS / 丘陵山区轮式自适应底盘调平系统设计</p> <p>Yuqian ZHAO¹⁾, Wei LIU¹⁾, Shijun SONG¹⁾, Peng LIU¹⁾, Yihu WANG¹⁾, Guohai ZHANG^{1,2*)}</p> <p>¹⁾ Shandong University of Technology, Collage of Agricultural Engineering and Food Science, Zibo, China ²⁾ Shandong University of Technology, Institute of Modern Agricultural Equipment, Zibo, China</p>	253
23.	<p>DESIGN AND EXPERIMENT OF SEGMENTABLE ADJUSTABLE THRESHING DEVICE FOR RICE SEED BREEDING / 制繁种水稻分段可调脱粒装置设计与试验</p> <p>Ranbing YANG^{1,2)}, Qi LIU¹⁾, Yiren QING^{*2)}, Zhiguo PAN¹⁾, Guoying LI³⁾, Shuai WANG¹⁾, Peiyu WANG²⁾, Yalong SHU¹⁾</p> <p>¹⁾ College of Electrical and Mechanical Engineering, Qingdao Agricultural University, Qingdao / China ²⁾ College of Mechanical and Electrical Engineering, Hainan University, Haikou / China ³⁾ Qingdao Pulantech Machinery Technology Co., Ltd., Qingdao / China</p>	269
24.	<p>NON-DESTRUCTIVE DETECTION OF MOLD IN MAIZE USING NEAR-INFRARED SPECTRAL FINGERPRINTING / 基于近红外光谱指纹技术的霉变玉米籽粒无损检测</p> <p>Longbao LIU¹⁾, Qixing TANG^{1*)}, Juan LIAO¹⁾, Lu LIU¹⁾, Yujun ZHANG²⁾, Leizi JIAO³⁾</p> <p>¹⁾Anhui Agricultural University, Hefei, China; ²⁾ Key Laboratory of Environmental Optics & Technology, Anhui Institute of Optics and Fine Mechanics, Chinese Academy of Sciences, Hefei, China; ³⁾Beijing Res Ctr Intelligent Equipment Agr, Beijing Academy of Agriculture and Forestry Sciences, Beijing, China</p>	283
25.	<p>INVESTIGATION OF THE CONTROL SYSTEM FOR MAIZE SEEDER SOWING DEPTH BASED ON SOIL MOISTURE CONTENT / 基于土壤含水率的玉米播种机播深控制系统的研究</p> <p>Xianliang LIU¹⁾, Rui ZHANG^{*1)}, Yubin ZHAI¹⁾, Wenjie LI¹⁾, Haozhe WEI¹⁾</p> <p>¹⁾College of Mechanical and Electrical Engineering, Qingdao Agricultural University, Qingdao, China</p>	300
26.	<p>DESIGN AND TESTING OF DUAL-STATION HIGH EFFICIENCY WHOLE TRAY AIR-SUCTION SEEDING ASSEMBLY LINE FOR RICE SEEDLING CULTIVATION / 整盘气吸式水稻双工位高效育秧播种流水线设计与试验</p> <p>Junhui CHENG^{1,2,3,4)}, Yaoming LI^{*1,2)}, Jin CHEN^{1,2)}, Fenglei LI⁵⁾, Yanbin LIU^{1,2)}, Kuizhou JI²⁾, Hanhao WANG²⁾, Zhiwu YU²⁾, Zhiyou PEI²⁾</p> <p>¹⁾Key Laboratory of Modern Agricultural Equipment and Technology, Ministry of Education, Jiangsu University; Zhenjiang, China; ²⁾ School of Agricultural Engineering, Jiangsu University; Zhenjiang, China; ³⁾ School of Electrical and Photoelectronic Engineering, West Anhui University, Lu'an, China; ⁴⁾ Anhui Undergrowth Crop Intelligent Equipment Engineering Research Center, West Anhui University, Lu'an, China; ⁵⁾ Changzhou Fenglei Precision Machinery Co., Ltd, Chang Zhou, China</p>	309
27.	<p>A LIGHTWEIGHT MILLET DOWNY MILDEW SPORE DETECTION METHOD BASED ON IMPROVED YOLOV8S / 基于改进 YOLOv8s 的轻量化谷子白发病孢子检测方法</p> <p>Jianglin YAN¹⁾; Zhengkun ZHAI¹⁾; Zhixiang FENG¹⁾; Lijun CHENG^{*1)}; Jie YANG^{*2,3)}</p> <p>¹⁾ College of Software, Shanxi Agricultural University, Shanxi / China; ²⁾ College of Health Service and Management, Shanxi University of Traditional Chinese Medicine, Shanxi / China</p>	323
28.	<p>WORKING MECHANISM ANALYSIS AND EXPERIMENTAL STUDY OF GRASS CRUSHER / 牧草粉碎机工作机理分析与试验研究</p> <p>Tao CHEN, Shu-juan YI¹⁾, Song WANG, Wen-sheng SUN</p> <p>¹⁾College of Engineering, Heilongjiang Bayi Agricultural University, Daqing/P.R.China</p>	334
29.	<p>FARMLAND OBSTACLE RECOGNITION BASED ON IMPROVED FASTER R-CNN / 基于改进 FASTER R-CNN 的农田障碍物识别</p> <p>Xiangyu BAI^{1,2)}, Kai ZHANG²⁾, Ranbing YANG^{1,3)}, Zhiguo PAN¹⁾, Huan ZHANG¹⁾, Jian ZHANG^{*1,3)}, Xidong JING¹⁾, Shiteng GUO¹⁾, Sen DUAN¹⁾</p> <p>¹⁾ College of Electrical and Mechanical Engineering, Qingdao Agricultural University, Qingdao / China ²⁾ National Key Laboratory of Intelligent Agricultural Power Equipment, Henan / China ³⁾ College of Mechanical and Electrical Engineering, Hainan University, Haikou / China</p>	346
30.	<p>WHEAT GRAIN APPEARANCE QUALITY DETECTION BASED ON IMPROVED YOLOv8n / 基于改进 YOLOv8n 的小麦籽粒外观品质检测</p> <p>Qingzhong KONG, Na MA¹⁾</p> <p>College of Information Science and Engineering, Shanxi Agricultural University, Taigu/China</p>	356
31.	<p>EVALUATION AND OPTIMIZATION OF AGRICULTURAL MANAGEMENT CLOUD PLATFORM BASED ON AHP/FCE / 基于 AHP/FCE 的智慧农业管理云平台评价与优化</p> <p>Jiyuan SUN¹⁾, Bin QI^{*1,2)}, Xiaoming Sun^{*1,2)}, Yuanqi LIU¹⁾, Yuchao REN¹⁾, Tengyun MA¹⁾, Bohan ZHANG¹⁾, Qiong Wu³⁾</p> <p>¹⁾ College of Agricultural Engineering and Food Science, Shandong University of Technology/ China; ²⁾ School of Fine Arts and Design, Shandong University of Technology, Zibo / China; ³⁾ Zibo Normal College / China</p>	366
32.	<p>DESIGN AND EXPERIMENT OF CLAMPING AND CONVEYING DEVICE FOR TRACKED SELF-PROPELLED CHINESE CABBAGE HARVESTER / 履带自走式大白菜收获机夹持输送装置设计与试验</p> <p>Shengbo GAO^{1,2)}, Yanwei YUAN^{1,2)}, Kang NIU^{1,2)}, Bo ZHAO^{1,2)}, Liming ZHOU^{1,2)}, Chengxu LV^{1,2)}, Shenghe BAI^{1,3)}, Shuaiyang ZHANG^{1,2)}, Ran AN^{1,2)}</p> <p>¹⁾ Chinese Academy of Agricultural Mechanization Sciences Group Co., Ltd., Beijing, China; ²⁾ State Key Laboratory of Agricultural Equipment Technology, Beijing, China; ³⁾ Department of Electrical and Mechanical Engineering, College of Engineering, China Agricultural University, Beijing, China</p>	376

		Page(s)
33.	<p>HARDWARE-IN-THE-LOOP SIMULATION FOR DRIVE WHEEL SLIP CONTROL OF HIGH-POWER TRACTOR FOR PLOUGHING OPERATION / 基于硬件在环仿真的大马力拖拉机犁耕作业驱动轮滑转控制研究 Shuo ZHANG¹⁾, YanQing LUO¹⁾, Lei JIA¹⁾, JingMing WEN¹⁾, HongLing JIN¹⁾, Yu CHEN^{*1)} College of Mechanical and Electronic Engineering, Northwest A&F University, Yangling, China</p>	390
34.	<p>GLOBAL PATH PLANNING OF FARMLAND PLOTS BASED ON IMPROVED WHALE OPTIMIZATION ALGORITHM / 基于改进鲸鱼优化算法地块整体路径规划 Shiteng GUO^{1,2,3)}, Xueping ZHAO²⁾, Jian ZHANG³⁾, Zhi guo PAN¹⁾, Xiangyu BAI¹⁾, Zhuhe SHAO¹⁾, Yao Li¹⁾, Zhen LIU¹⁾, Shuai WANG¹⁾ ¹⁾ College of Electrical and Mechanical Engineering, Qingdao Agricultural University, Qingdao/ China ²⁾ National Key Laboratory of intelligent agricultural power Equipment Luoyang/China ³⁾ College of Mechanical and Electrical Engineering, Hainan University, Haikou/China</p>	403
35.	<p>INNOVATIVE PYROLYSIS REACTOR DESIGN FOR ENHANCED PERFORMANCE AND SUPERIOR BIOCHAR QUALITY / REACTOR INOVATOR DE PIROLIZĂ PENTRU O PERFORMANȚĂ ȘI O CALITATE SUPERIOARĂ ÎMBUNĂȚITĂ A BIOCHARULUI Laurentiu-Constantin VLADUTOIU ^{*1)}, Mario CRISTEA^{*1)}, Florin NENCIU ¹⁾, Valentin VLĂDUȚ ¹⁾, Mihai OLAN ¹⁾, Iulia GRIGORE ¹⁾, Cristian SORICA ¹⁾, Nicoleta VANGHELE ^{1,2)}, Oana-Diana CRISTEA ¹⁾ ¹⁾The National Institute of Research-Development for Machines and Installations Designed for Agriculture and Food Industry-INMA Bucharest / Romania; ²⁾Politehnica University of Bucharest, Bucharest / Romania</p>	414
36.	<p>DESIGN AND EXPERIMENT OF A MOREL PICKING MACHINE / 羊肚菌采摘机设计与试验 Xiaohu BAI, Xiang ZOU, Zexu WANG, Guojing DU, Chuan LI, Chonghe GAO College of Engineering, Shenyang Agricultural University, Shenyang/China</p>	423
37.	<p>STATISTICS AND ANALYSIS OF PHYSICAL PARAMETERS OF ADZUKI BEAN SEEDS / 红小豆种子物理参数统计及分析 Guoqiang DUN^{*1)}, Luhan WANG²⁾, Huiwen XUE¹⁾, Xinxin JI^{1,2)}, Quanbao SHENG²⁾, Xinming LI²⁾, Chaoxia ZHANG¹⁾, Yuhan WEI¹⁾ ¹⁾ Harbin Cambridge University, Intelligent Agricultural Machinery Equipment Engineering Laboratory, Harbin / China; ²⁾ Northeast Forestry University, College of Mechanical and Electrical Engineering, Harbin / China</p>	433
38.	<p>RESEARCH ON DETECTION OF SPARTINA ALTERNIFLORA BASED ON SA-YOLO / 基于 SA-YOLO 的互花米草识别算法研究 Chunqing WANG, Shuqi SHANG, Ruzheng WANG, Ziao YANG, Xiaoning HE, Dansong YUE Mechanical and Electrical Engineering, Qingdao Agricultural University, Qingdao, Shandong, China</p>	447
39.	<p>DETECTION AND COUNTING OF GRAZING CATTLE FROM AERIAL IMAGES USING CNN / CNN АШИГЛАН АГААРЫН ЗУРГААС БЭЛЧЭЭРИЙН МАЛЫГ ИЛРҮҮЛЭХ, ТООЛОХ Hu GEJILETU¹⁾, Hishigdalai ULAANKHUU²⁾, Bat-Erdene NYANDAG^{3*)} ^{1,3)} Department of Computer Science, School of Applied Sciences, Mongolian University of Life Sciences, Ulaanbaatar, Mongolia ²⁾ School of Business, Mongolian University of the Humanities, Ulaanbaatar, Mongolia</p>	459
40.	<p>RESEARCH ON GREENHOUSE PLANTING DENSITY OF LANDSCAPE FLOWERS IN COLD REGIONS BASED ON CFD SIMULATION / 基于 CFD 模拟的寒冷地区景观花卉温室种植密度研究 Qibeier XIE, Jie REN ¹⁾, ¹⁾ School of Architecture, Inner Mongolia University of Technology, Hohhot, China</p>	469
41.	<p>STUDY ON THE OPERATING EFFECT OF STRAW CRUSHING AND SPREADING DEVICES ON SINGLE AXIAL FLOW HARVESTERS / 单纵轴流收获机装配秸秆粉碎抛撒装置作业效果问题研究 Jiang WANG¹⁾, Longjing LI¹⁾, Weiliang SHI¹⁾, Youqiang DING²⁾ ¹⁾ College of Automotive Engineering, Zibo Vocational Institute, Zibo/China; ²⁾ Nanjing Institute of Agricultural Mechanization, Ministry of Agriculture and Rural Affairs, Nanjing/China</p>	480
42.	<p>DETERMINATION OF PHYSICAL PARAMETERS OF PELLETED RICE SEEDS AND CALIBRATION OF DISCRETE ELEMENT SIMULATION PARAMETERS / 丸粒化水稻种 254 子物性参数测定与离散元仿真参数标定 Qianshu MA, Tongjie LI, Donghan XU, Qingqing WANG¹⁾ Anhui University of Science and Technology, Bengbu, China</p>	490
43.	<p>RESEARCH ON ENVIRONMENTAL MONITORING AND COMPREHENSIVE EVALUATION SYSTEM OF PIG HOUSE BASED ON INTERNET OF THINGS TECHNOLOGY / 基于物联网技术的猪舍环境监测与综合评价系统研究 Lihong RONG¹⁾, Junling FAN¹⁾, Xiaolong GUO²⁾, Zhimin TONG¹⁾, Wenlong XU¹⁾, Yuexin PAN¹⁾, Shengzhang LI¹⁾, Weilong ZHANG¹⁾, Fang SUN¹⁾ ¹⁾ College of Electrical and Mechanical Engineering, Qingdao Agricultural University, Qingdao/ China ²⁾ Shandong Hengji Agricultural and Animal Husbandry Machinery Co., Ltd., Weifang/ China</p>	501

		Page(s)
44.	<p>PRELIMINARY THERMODYNAMIC ASSESSEMENT OF A REFRIGERATION SYSTEM WITH A PCM BASED DEFROSTING / EVALUAREA TERMODINAMICĂ PRELIMINARĂ A UNUI SISTEM FRIGORIFIC CU DEGIVRARE PE BAZĂ DE PCM</p> <p>Valentin APOSTOL¹⁾, Horatiu POP^{*1)}, Tudor PRISECARU¹⁾, Claudia IONITA¹⁾, Jamal AL DOURI¹⁾, Adrian CHIRIAC^{*1,2)}, Cornel Constantin PAVEL¹⁾</p> <p>¹⁾ Faculty of Mechanical Engineering and Mechatronics, National University of Science and Technology POLITEHNICA Bucharest / Romania. ²⁾ Academy of Romanian Scientists, Ilfov 3, 050044 Bucharest, Romania</p>	515
45.	<p>DESIGN AND EXPERIMENT OF A DOUBLE LONGITUDINAL AXIAL-FLOW CORN THRESHING DEVICE FOR LARGE FEEDING CAPACITY / 大喂入量双纵轴流玉米脱粒装置设计与试验</p> <p>Mingrui LI^{1,3)}, Yanchun YAO^{1,2,3*)}, Yongkang ZHU^{1,3)}, Xibin LI^{1,3)}, Dong YUE¹⁾, Duanyang GENG¹⁾</p> <p>¹⁾ College of Agricultural Engineering and Food Science, Shandong University of Technology, Zibo, China; ²⁾ Opening Fund of National Key Laboratory of Agricultural Equipment Technology, Beijing, China ³⁾ Institute of Modern Agricultural Equipment, Zibo, China</p>	527
46.	<p>CFD-DEM BASED DESIGN OF ELBOW LIFTING PIPE CONVEYANCE UNDER NEGATIVE PRESSURE AIRFLOW / 基于 CFD-DEM 的负压气流下弯头提升管道输送设计</p> <p>Lianglong ZHANG¹⁾, Yue SUN¹⁾, Fan Yang¹⁾, Yalin Sun¹⁾, Fangyan Wang^{1,3)}; Xin Wang²⁾</p> <p>¹⁾ College of Mechanical and Electrical Engineering, Qingdao Agricultural University, Qingdao / China. ²⁾ College of Civil Engineering and Architecture, Qingdao Agricultural University, Qingdao / China. ³⁾ Collaborative Innovation Center for Shandong s Main Crop Production Equipment and Mechanization, Qingdao / China</p>	539
47.	<p>DESIGN AND TESTING OF SMALL ELECTRIC DOUBLE-ROW LEEK HARVESTER / 小型电动双行韭菜收获机设计与试验</p> <p>Yuxin SHAN¹⁾, Yinping ZHANG^{*1)}, Hua ZHOU¹⁾, Jiasheng WANG²⁾, Qun MA³⁾</p> <p>¹⁾ College of Agricultural Engineering and Food Science, Shandong University of Technology, Zibo/China. ²⁾ College of Mechanical and Electrical Engineering, Qingdao Agricultural University, Qingdao/China. ³⁾ Shandong Dayi General Purpose Machinery Limited Company, Linyi/China.</p>	550
48.	<p>DESIGN AND SIMULATION ANALYSIS OF KEY COMPONENTS OF GRASS CRUSHER / 牧草粉碎机关键部件设计与仿真分析</p> <p>Tao CHEN, Shu-juan YI¹⁾, Song WANG, Wen-sheng SUN</p> <p>College of Engineering, Heilongjiang Bayi Agricultural University, Daqing/P.R.China</p>	560
49.	<p>DESIGN AND EXPERIMENTAL STUDY OF CLEANING DEVICE FOR WHEAT HARVESTER BASED ON CFD-DEM / 基于 CFD-DEM 的制繁种小麦收获机清选装置的设计与试验研究</p> <p>Ranbing YANG^{1,2)}, Shuai WANG¹⁾, Zhiguo PAN¹⁾, Guoying LI³⁾, Yalong SHU¹⁾, Qi LIU¹⁾, Zhen LIU¹⁾, Yihui MIAO¹⁾</p> <p>¹⁾ College of Electrical and Mechanical Engineering, Qingdao Agricultural University, Qingdao/ China ²⁾ College of Mechanical and Electrical Engineering, Hainan University, Haikou/ China ³⁾ Qingdao Pulantech Machinery Technology Co., Ltd., Qingdao/ China</p>	571
50.	<p>MASS FLOW DETECTION TECHNOLOGY FOR SEED AND FERTILISER PARTICLES AND ITS APPLICATION IN UAV-BASED SPREADING / 种肥颗粒质量流量检测技术及其在无人机播撒中的应用建议</p> <p>Yanshuang WANG^{1,2,3)}, Cancan SONG^{*1,2,3)}, Yongqi GAO^{1,2,3)}, Yubin LAN^{1,2,3)}, Guobin WANG^{1,2,3)}, Rui MING⁴⁾</p> <p>¹⁾ College of Agricultural Engineering and Food Science, Shandong University of Technology, Zibo / China; ²⁾ Shandong University of Technology Sub-center of National Center for International Collaboration Research on Precision Agricultural Aviation Pesticide Spraying Technology, Zibo / China; ³⁾ Research of Institute of Ecological Unmanned Farm, Shandong University of Technology, Zibo / China; ⁴⁾ School of Computer and Big Data, Minjiang University, Fujian Provincial Key Laboratory of Information Processing and Intelligent Control, Fuzhou / China</p>	584
51.	<p>DEVELOPMENT AND TESTING OF AN INTELLIGENT TOBACCO LEAF HARVESTING ROBOT BASED ON MACHINE VISION / 基于机器视觉的智能烟叶采摘机器人开发与测试</p> <p>YuPei LIN^{1,2)}, GuoYong YAN³⁾, Tao WANG³⁾, Tao BAI³⁾, Si TANG³⁾, JunJie CHEN^{*1,2)}, BaoLin ZHANG^{*3)}</p> <p>¹⁾ Southwest University, College of Artificial Intelligence, Chongqing, China ²⁾ National & Local Joint Engineering Research Center of Intelligent Transmission and Control Technology, Chongqing, China ³⁾ Qujing Tobacco Company of Yunnan Province, Yunnan, China</p>	600
52.	<p>OPTIMIZATION AND TESTING OF OPERATING PARAMETERS FOR THE AUTOMATIC SEEDLING PICKING DEVICE OF TOMATO POT SEEDLING TRANSPLANTER / 番茄钵苗移栽机自动取苗装置作业参数优化与试验</p> <p>Fukang ZHOU^{1,2)}, Mengqi ZHANG^{1,2)}, Weichen YAN^{1,2)}, Shijun SONG^{1,2)}, Yi NIU^{1,2)}, Tao FAN^{1,2)}, Bolong WANG^{1,2)}, Fangyuan LU^{1,2)}, Guohai ZHANG^{1,2*)}</p> <p>¹⁾ Shandong University of Technology, Collage of Agricultural Engineering and Food Science, ZiBo, China ²⁾ Shandong University of Technology, Institute of Modern Agricultural Equipment, ZiBo, China</p>	610

		Page(s)
53.	TOMATO MATURITY DETECTION BASED ON IMPROVED YOLOV8N / 基于改进 YOLOv8n 的番茄果实成熟度检测 JunMao LI, ZiLu HUANG, LingQi XIA, Hao SUN, HongBo WANG ¹⁾ College of Mechanical and Electronic Engineering, Inner Mongolia Agricultural University, Hohhot / China	619
54.	SEMI-SUPERVISED WHEAT EAR DETECTION ALGORITHM BASED ON THE MODIFIED YOLOv8 / 基于改进 YOLOv8 的半监督麦穗识别算法 Yu ZHANG ¹⁾ , Zhihui XU ¹⁾ , Fuzhong LI ¹⁾ , Xiaoying ZHANG ^{*1)} , Xiao CUI ^{*1)} ¹⁾ School of Software, Shanxi Agricultural University, Shanxi/China	630
55.	NUMERICAL SIMULATION OF AIR COOLING PROCESSES IN A POULTRY HOUSE WITH A TUNNEL-SIDE VENTILATION SYSTEM Viktor TROKHANIAK ¹⁾ , Oleksandr SYNYAVSKIY ¹⁾ , Vadym TKACHUK ¹⁾ , Tormi LILLERAND ²⁾ , Oleksandr SKLIAR ³⁾ , Yevhen IHNATIEV ^{2,3)} , Jüri OLT ²⁾ ¹⁾ National University of Life and Environmental Sciences of Ukraine, Ukraine ²⁾ Estonian University of Life Sciences, Institute of Technology, 56 Kreutzwaldi Str., Tartu, Estonia ³⁾ Dmytro Motorny Tavria State Agrotechnological University, 66 Zhukovsky Str, Zaporizhzhia, Ukraine	640
56.	EXPERIMENTAL INVESTIGATION ON THE SHEAR MECHANICAL PROPERTIES OF LICORICE ROOT / 甘草根剪切力学特性的试验研究 Bintong ZHAO ¹⁾ , Zhu ZHAO ²⁾ , Zhongnan WANG ^{*2)} , Ping ZHAO ^{*1)} ¹⁾ College of Engineering, Shenyang Agricultural University, Shenyang / China ²⁾ Liaoning Agricultural Technical College, Yingkou / China	648
57.	OPTIMIZATION AND EXPERIMENT OF CONVEYING TURNOVER DEVICE BASED ON PEANUT PLANT CHARACTERISTIC PARAMETERS / 基于花生植株特性参数的输送翻转装置优化与试验 Jiajun LIU ¹⁾ , Chenglin JIANG ¹⁾ , Penghui MAO ¹⁾ , Kuoyu Wang ¹⁾ , Shuqi SHANG ¹⁾ , Dongwei WANG ²⁾ , Ning ZHANG ^{*1)} ¹⁾ College of Mechanical and Electrical Engineering, Qingdao Agricultural University, Qingdao / China ²⁾ Yellow River Delta Intelligent Agricultural Machinery Equipment Industry Academy, Dongying / China	658
58.	MULTIPLE PARAMETER OPTIMIZATION OF A LICORICE HARVESTER BASED ON ENSEMBLE MACHINE LEARNING AND IMPROVED GENETIC ALGORITHM / 基于集成机器学习和改进遗传算法实现了甘草收获机的多参数优化 Jinyu SONG, Yonglei LI [*] , Xiaopei ZHENG, Lipengcheng WAN, Zongtian LIU China Agricultural University, College of Engineering, Beijing / China	669
59.	MILLET EAR DETECTION METHOD IN UAV IMAGES BASED ON IMPROVED YOLOX / 基于改进 YOLOX 的无人机图像谷穗检测方法 Fuming MA ¹⁾ , Shaonian LI ^{*1)} , Juxia LI ²⁾ , Yanwen LI ²⁾ , Lei DUAN ²⁾ , Linwei LI ²⁾ , Jing TAN ¹⁾ , Yifan WANG ¹⁾ ¹⁾ College of Energy and Power Engineering, Lanzhou University of Technology, Lanzhou, Gansu / China ²⁾ College of Information Science and Engineering, Shanxi Agricultural University, Jinzhong, Shanxi/ China	680
60.	OPTIMIZATION OF VIBRATION TRANSMISSION SYSTEM BASED ON IMPLICIT PARAMETRIC MODELING OF SUGARCANE HARVESTER FRAME / 基于机架梁式参数化建模的蔗杆切割损伤优化 Biao ZHANG ^{1*)} , Weimin SHEN ¹⁾ , Dan PAN ¹⁾ ¹⁾ College of Mechanical Engineering, Guangxi University, Nanning, China	691
61.	A REVIEW OF INNOVATIVE DESIGN AND INTELLIGENT TECHNOLOGY APPLICATIONS OF THRESHING DEVICES IN COMBINE HARVESTERS FOR STAPLE CROPS / 主粮作物联合收获机脱粒装置的创新设计与智能化技术应用研究综述 Fuqiang GOU ^{1,2,3)} , Jin WANG ^{1,3)} , Youliang NI ¹⁾ , Zhenjie QIAN ¹⁾ , Tengxiang YANG ¹⁾ , Chengqian JIN ^{*1,4)} ¹⁾ Nanjing Institute of Agricultural Mechanization, Ministry of Agriculture and Rural Affairs, Nanjing, Jiangsu / China ²⁾ Wenshan Advanced Technical School, Wenshan, Yunnan / China ³⁾ Graduate School of Chinese Academy of Agricultural Sciences, Beijing / China ⁴⁾ School of Agricultural Engineering and Food Science, Shandong University of Technology, Zibo, Shandong / China	706
62.	WHEAT IMPURITY DETECTION ALGORITHM BASED ON IMPROVED YOLO v8 / 基于改进 YOLO v8 的小麦杂质检测算法 Liqing ZHAO, Rui QIAN, Chuang LIU, Shuhao WANG, Junjie XIA College of Electrical and Mechanical Engineering, Qingdao Agriculture University, Qingdao / China	726
63.	RESEARCH OF THE TECHNOLOGICAL PROCESS OF GRANULATION OF BULK AGRICULTURAL MATERIALS / ДОСЛІДЖЕННЯ ТЕХНОЛОГІЧНОГО ПРОЦЕСУ ГРАНУЛЮВАННЯ СИПКИХ СІЛЬСЬКОГОСПОДАРСЬКИХ МАТЕРІАЛІВ Volodymyr BULGAKOV ¹⁾ , Adolfs RUCINS ^{*2)} , Yevhen IHNATIEV ^{3,4)} , Serhiy STEPANENKO ⁵⁾ , Lucretia POPA ⁶⁾ , Simone PASCUZZI ⁷⁾ , Ivan HOLOVACH ¹⁾ , Oleksandra TROKHANIAK ¹⁾ ¹⁾ National University of Life and Environmental Sciences of Ukraine / Ukraine; ²⁾ Latvia University of Life Sciences and Technologies / Latvia; ³⁾ Estonian University of Life Sciences / Estonia; ⁴⁾ Dmytro Motorny Tavria State Agrotechnological University / Ukraine; ⁵⁾ Institute of Mechanics and Automation of Agricultural Production of the National Academy of Agrarian Sciences of Ukraine; ⁶⁾ National Institute of Research–Development for Machines and Installations Designed for Agriculture and Food Industry–INMA, Bucharest / Romania; ⁷⁾ University of Bari Aldo Moro / Italy	737

		Page(s)
64.	OPTIMIZATION OF PARTIAL HIGH-FREQUENCY QUENCHING TECHNIQUE PARAMETERS OF ROTARY TILLING BLADES / 旋耕刀局部高频淬火工艺参数优化 Ruili WANG ¹⁾ , Xueyin BAI ¹⁾ , Fanbowen MENG ¹⁾ , Deshuai LI ¹⁾ , Zhengqing WANG ¹⁾ , Ke JIANG ¹⁾ , Wei WANG ^{*1)} , ¹⁾ College of Engineering, Shenyang Agricultural University, Shenyang, China	751
65.	DESIGN AND EXPERIMENT OF GRAIN HARVESTER YIELD MONITORING SYSTEM BASED ON MULTI-SENSOR FUSION / 基于多传感器融合的谷物收割机产量监测系统的设计与实验 Peng LIU ¹⁾ , Shijun SONG ¹⁾ , Wei LIU ¹⁾ , Yuqian ZHAO ¹⁾ , Weichen YAN ¹⁾ , Guohai ZHANG ^{1,2)} ¹⁾ Shandong University of Technology, Collage of Agricultural Engineering and Food Science, Zibo, China ²⁾ Shandong University of Technology, Institute of Modern Agricultural Equipment, Zibo, China	763
66.	RESEARCH ON A RICE FIELD METHANE DETECTION SYSTEM USING HOLLOW-CORE PHOTONIC CRYSTAL FIBRE BASED ON TDLAS TECHNIQUE / 基于 TDLAS 技术的空心光子晶体光纤稻田甲烷气体检测系统研究 Bin Li ^{*1)} , Ruotong Liu ¹⁾ , Guangfei Shang ¹⁾ , Lihui Zhang ¹⁾ , Chenghao Han ²⁾ , Yitong Huang ¹⁾ ¹⁾ School of Electrical & Computer Engineering, Jilin Jianzhu University, Changchun, China; ²⁾ School of Emergency Science and Engineering, Jilin Jianzhu University, Changchun, China	777
67.	OPTIMIZATION OF DAMAGED CORN KERNEL RECOGNITION ALGORITHM BASED ON A DUAL-LIGHT SYSTEM / 基于双光系统的破损玉米籽粒识别算法优化 Yuchao REN ¹⁾ , Bin QI ^{*1,2)} , Xiaoming SUN ^{*1,2)} , Jiyuan SUN ¹⁾ , Tengyun MA ¹⁾ , Yuanqi LIU ¹⁾ , Bohan ZHANG ¹⁾ , Qiong WU ³⁾ ¹⁾ College of Agricultural Engineering and Food Science, Shandong University of Technology/ China; ²⁾ School of Fine Arts and Design, Shandong University of Technology, Zibo City, China. ³⁾ Zibo Normal College/ China	787
68.	SEMI-PHYSICAL SIMULATION RESEARCH ON THE CONTROL SYSTEM OF COMBINE HARVESTER CUTTING TABLE / 联合收割机割台控制系统的半实物仿真研究 Yihu WANG ¹⁾ ; Guohai ZHANG ^{2*)} ; Xipeng QIAN ¹⁾ ; Qian DONG ¹⁾ ¹⁾ Shandong University of Technology, Zibo, China; ²⁾ Institute of Modern Agricultural Equipment, Shandong University of Technology, Zibo, China	797
69.	DESIGN AND PERFORMANCE EXPERIMENTS OF THRESHING AND SEPARATING DEVICE FOR HEAD-FEEDING COMBINE HARVESTER / 半喂入联合收割机脱粒分离装置设计与性能试验 Liquan TIAN ^{1*)} , Zhan SU ¹⁾ , Zhao DING ¹⁾ , ^{1*)} Corresponding author. Intelligent Manufacturing College, Jinhua University of Vocational Technology.	809
70.	RESEARCH ON HYDRAULIC DRIVE CHASSIS OF TOBACCO HARVESTER IN SOUTHERN HILLY AREA / 针对南方丘陵地区的烟叶收获机液压驱动底盘研究 Ting GUO ¹⁾ , Dandan ZHANG ²⁾ , Shuo LIN ³⁾ , Tao ZHANG ⁴⁾ , Mingduan LU ^{*5)} ¹⁾ Hunan Tobacco Company Chenzhou Branch, Chenzhou, China; ²⁾ Guangdong Tobacco Company Shaoguan Branch, Shaoguan, China; ³⁾ Anhui Tobacco Company Wannan Branch, Wannan, China ⁴⁾ Hunan Tobacco Company Changde Branch, Changde, China ⁵⁾ College of Engineering and Technology, Southwest University, Chongqing, China	819
71.	DESIGN AND EXPERIMENTATION OF ROOT-CUTTING DEVICE FOR HEAD-FORMING VEGETABLES / 结球类蔬菜切根装置设计与实验 Yanjun LI ^{1,2)} , Jianfei ZHANG ^{*1,3)} , Fuxiang XIE ^{*2)} , Yongtao YU ²⁾ ¹⁾ Key Laboratory of Modern Agricultural Equipment, Ministry of Agriculture and Rural Affairs, Nanjing/China; ²⁾ School of Machinery and Automation, Weifang University, Weifang/China; ³⁾ Nanjing Institute of Agricultural Mechanization, Ministry of Agriculture and Rural Affairs, Nanjing/China	831
72.	DESIGN OF SEMI-PHYSICAL SIMULATION PLATFORM FOR GRAIN CLEANING AND REGULATING SYSTEM / 谷物清选调控系统半实物仿真平台设计 Xipeng QIAN ¹⁾ , Yihu WANG ¹⁾ , Guohai ZHANG ^{1,2)} ¹⁾ Shandong University of Technology, Collage of Agricultural Engineering and Food Science, Zibo, China ²⁾ Shandong University of Technology, Institute of Modern Agricultural Equipment, Zibo, China	841
73.	DESIGN OF AND EXPERIMENTS WITH A CORN INTERPLANT WEEDING MACHINE BASED ON VISUAL RECOGNITION / 基于作物株距信息识别的杂草精准清除机设计与试验 JingWen ZHANG ^{1,2)} , QiangJi PENG ^{3,4)} , JianMing KANG ^{3,4)} , ZhiFeng DI ^{3,4)} , ShaoWei WANG ^{3,4)} , YingKai CHEN ^{3,4)} , YuLong CHEN ^{1,2*)} ¹⁾ School of Agricultural Engineering and Food Science, Shandong University of Technology, Zibo, China ²⁾ Institute of Modern Agricultural Equipment, Shandong University of Technology, Zibo/China ³⁾ Shandong Academy of Agriculture Machinery Sciences, Jinan, China ⁴⁾ Huang Huai Hai Laboratory of Modern Agricultural Equipment, Ministry of Agriculture and Rural Affairs, Jinan/China	852
74.	DESIGN AND TESTING OF SPIRAL CUTTER TOOTH TYPE FARMLAND STONE PICKER/ 螺旋刀齿式农田捡石机的设计与试验 Jia ZHANG ^{1,2)} , Heng QU ²⁾ , Ping XIAO ¹⁾ , Shaoteng MA ^{1,2)} , Weisong ZHAO ^{3,4*)} ¹⁾ School of Mechanical and Electrical Engineering, Xinjiang Institute of Engineering, Urumqi, Xinjiang/China ²⁾ School of Mechanical and Electrical Engineering, Xinjiang Agricultural University, Urumqi, Xinjiang/China ³⁾ Western Agricultural Research Center, Chinese Academy of Agricultural Sciences, Changji, Xinjiang/ China ⁴⁾ Nanjing Institute of Agricultural Mechanization, Ministry of Agriculture and Rural Affairs, Nanjing/China	865

		Page(s)
75.	<p>CALIBRATION AND OPTIMIZATION OF DISCRETE ELEMENT PARAMETERS FOR COTTON STALK-RUBBER BELTS INTERACTIONS / 棉秆-橡胶带相互作用的离散元参数标定与优化</p> <p>Yasenjiang BAIKELI^{1,2}, Haodong XU^{1,2}, Jiayi ZHANG^{1,2}, Rensheng XING^{1,2}, Yong YUE^{*1,2}</p> <p>¹ College of Mechanical and Electrical Engineering, Xinjiang Agricultural University, Urumqi/ China; ² Key Laboratory of Xinjiang Intelligent Agricultural Equipment, Urumqi / China</p>	878
76.	<p>THE OPPORTUNITY OF ADVANCED TECHNOLOGIES UTILIZATION FOR DETECTING BASAL STEM ROT (BSR) IN PALM OIL PLANTATION: A REVIEW / PEMANFAATAN TEKNOLOGI CANGGIH UNTUK MENDETEKSI BUSUK PANGKAL BATANG (BSR) PADA PERKEBUNAN KELAPA SAWIT: REVIEW</p> <p>Hasbi Mubarak SUUD¹, Bayu Taruna Widjaja PUTRA^{2,3,1}, Nazmi Mat NAWI⁴, Wahyu Nurkholis Hadi SYAHPUTRA^{2,3,5}</p> <p>¹ Study Program of Agricultural Science, Faculty of Agriculture, Jember, East Java, Indonesia ² Laboratory of Precision Agriculture and Geo-Informatics, University of Jember, Jember, East Java, Indonesia ³ Center of Excellence of Artificial Intelligence on Industrial Agriculture, University of Jember, Jember, East Java, Indonesia; ⁴ Universiti Putra Malaysia, Malaysia ⁵ Agrotechnology Study Program, Faculty of Agriculture, University of Jember, Jember, East Java, Indonesia</p>	888
77.	<p>DIGITAL ORCHARD CONSTRUCTION BASED ON NEURAL RADIANCE FIELD AND GEOREFERENCING TECHNOLOGY / 基于神经辐射场与地理坐标配准技术的果树三维重建</p> <p>Huiyan WANG¹); Binxiao LIU²); Jianhang WANG¹); Changkun ZHANG¹); Jinliang GONG²); Yanfei ZHANG¹)</p> <p>¹School of Agricultural Engineering and Food Science, Shandong University of Technology, Zibo / China ²School of Mechanical Engineering, Shandong University of Technology, Zibo / China</p>	903
78.	<p>HUMAN LOWER LIMB MOTION PATTERN RECOGNITION BASED ON MULTI-SENSOR FUSION / 基于多传感器融合的人体下肢运动模式识别</p> <p>Cuihong LIU¹), Yanbo HAN²), Xiangwen SONG²), Shipeng ZHANG¹), Na HAN²), Meng ZOU²), Liyan WU¹)</p> <p>¹College of Engineering, Shenyang Agricultural University, Shenyang, China; ²Key Lab for Bionics Engineering of Education Ministry, Jilin University, Changchun, China</p>	915
79.	<p>APPLICATION OF MACHINE LEARNING MODELS FOR PREDICTIVE MAINTENANCE OF BIOTECHNICAL SYSTEMS / UTILIZAREA MODELELOR DE ÎNVĂȚARE AUTOMATĂ PENTRU MENTENANȚA PREDICTIVĂ A SISTEMELOR BIOTEHNICE</p> <p>Adrian IOSIF¹), Edmond MAICAN¹), Sorin Ștefan BIRIȘ¹), Nicolae-Valentin VLĂDUȚ²)</p> <p>¹Faculty of Biotechnical Systems Engineering, University POLITEHNICA of Bucharest / Romania; ²INMA Bucharest / Romania</p>	930
80.	<p>IMPROVED YOLOV8-ALGORITHM FOR SORTING FRESH WHITE TEA: COMBINING FEATURE ENHANCEMENT AND ATTENTION MECHANISM / 改进的 YOLOv8 新鲜白茶分选算法: 将特征增强与注意力相结合</p> <p>Xuedong YU^{1,2}), Yadong NIU¹), Zhongyou ZHOU^{1,2}), Bo LU^{1,2}), Kaiqiang JIN^{1,2}), Rongyang WANG^{1,2})*</p> <p>¹ College of Intelligent Manufacturing and Elevator Technology, Huzhou Vocational and Technical College, Huzhou, China ² The Huzhou Key Laboratory of Robot System Integration and Intelligent Equipment, Huzhou, China</p>	950
81.	<p>APPLE FRUIT RECOGNITION METHOD BASED ON IMPROVED YOLOv5 / 基于改进 YOLOV5 的苹果果实识别方法</p> <p>Yang BAI¹), Shengqiao XIE²), Jian SONG^{*1}), Cunyu ZHAO¹), Fuxiang XIE¹)</p> <p>¹ School of Machinery and Automation, Weifang University, Weifang/China; ² China National Heavy Duty Truck, Jinan/China</p>	962
82.	<p>DEVELOPMENT AND PERFORMANCE EVALUATION OF A NOVEL PEELING DEVICE FOR HIGH-MOISTURE CORN COBS / 高含水率玉米果穗剥皮装置设计与试验</p> <p>Bang JI^{1,3}), Long PAN¹), Yusong XIE¹), Hao ZHOU¹), Yongkang LI¹), Pu LI²)</p> <p>¹ Hunan Agricultural University, College of Mechanical and Electrical Engineering, Changsha/China; ² Hunan Mechanical and Electrical Polytechnic, Changsha/China; ³ Hunan Key Laboratory of Intelligent Agricultural Machinery and Equipment, Changsha/China</p>	973
83.	<p>RESEARCH ON OPTIMIZING THE POWER BALANCE OF A PLOWING AGGREGATE COMPRISED OF A 180 HP TRACTOR AND A 5-MOLDBOARD PLOW / CERCETĂRI PRIVIND OPTIMIZAREA BILANȚULUI DE PUTERE AL UNUI AGREGAT DE ARAT FORMAT DINTR-UN TRACTOR DE 180 CP ȘI UN PLUG CU 5 TRUPIȚE</p> <p>Constantin LĂCĂTUȘU¹), Sorin-Ștefan BIRIȘ^{*1}), Adrian IOSIF¹), Nicolae-Valentin VLĂDUȚ²), Neluș-Evelin GHEORGHIȚĂ¹), Edmond MAICAN¹), Nicoleta UNGUREANU¹)</p> <p>¹National University of Science and Technology POLITEHNICA Bucharest, Faculty of Biotechnical Systems Engineering / Romania; ²INMA Bucharest / Romania</p>	985

		Page(s)
84.	<p>DESIGN AND EXPERIMENTAL STUDY OF HIGH-EFFICIENCY AND LOW-DAMAGE BIONIC PICKING DEVICE FOR TOBACCO LEAVES / 高效低损伤烟叶仿生采摘装置的设计与试验研究</p> <p>Chenhui ZHU¹⁾, Bingjie CHEN¹⁾, Bo LUO^{1,3)}, Wanzhang WANG¹⁾, Bingjie LIU⁴⁾, Baoshan WANG¹⁾, Liquan YANG^{*1,2)}</p> <p>¹⁾ School of Mechanical and Electrical Engineering, Henan Agricultural University, Zhengzhou, China; ²⁾ Henan Province Engineering Research Center of Ultrasonic Technology Application, Pingdingshan University, Pingdingshan, China; ³⁾ School of Intelligent Engineering, Zhengzhou College of Finance and Economics, Zhengzhou, China; ⁴⁾ College of Information and Management Science, Henan Agricultural University, Zhengzhou, China</p>	995
85.	<p>DEVELOPMENT OF A MULTI-DIMENSIONAL CLEANING SIEVE TO OPTIMIZE THRESHED OUTPUTS DISTRIBUTION AND EXPERIMENTS IN COMBINE HARVESTER / 联合收获机多维均布清选装置开发与试验</p> <p>Xiaoyu Chai¹⁾, Pengtao Zhang¹⁾, Xinting Liu²⁾, Lizhang Xu¹⁾, Liyuan Chen¹⁾, Qiang Li³⁾, Longhai Wang⁴⁾</p> <p>¹⁾ School of Agricultural Engineering, Jiangsu University, Zhenjiang, Jiangsu, China; ²⁾ Weichai Lovol Intelligent Agricultural Technology Co. Ltd, Weifang, Shangdong, China; ³⁾ Tongzhou District Agricultural Mechanization Technology Extension Station, Nantong, Jiangsu, China</p>	1015
86.	<p>LOW HEAD MICRO-HYDRO TURBINES USED FOR EFFICIENCY INCREASE OF SOLAR POWERED IRRIGATION SYSTEMS / MICRO-HIDROTURBINE DE JOASĂ CĂDERE UTILIZATE PENTRU CREȘTEREA EFICIENȚEI SISTEM DE IRIGAȚII ALIMENTATE DIN PANOURI FOTOVOLTAICE</p> <p>Rareș-Andrei CHIHAIA¹⁾, Gabriela CÎRCIUMARU¹⁾, Sergiu NICOLAIE¹⁾, Lucia-Andreea EL-LEATHEY¹⁾, Nicolae TĂNASE¹⁾, Constantin DUMITRU¹⁾</p> <p>¹⁾ National Institute for Research and Development in Electrical Engineering ICPE-CA Bucharest / Romania</p>	1027
87.	<p>STUDY ON THE CHARACTERISTICS AND DISTRIBUTION OF DAMAGE RESISTANCE ON CORN KERNEL SURFACES / 玉米籽粒表面抗损伤特性及分布研究</p> <p>Qinghao HE¹⁾, Duanxin LI¹⁾, Jianning YIN¹⁾, Yipeng CUI¹⁾, Pengxuan GUAN¹⁾, Duanyang GENG^{*1)}, Wei GU²⁾</p> <p>¹⁾ School of Agricultural Engineering and Food Science, Shandong University of Technology, Zibo/ China ²⁾ Starlight Agricultural Machinery Co., LTD, Huzhou/ China <i>Corresponding author: Corresponding author: Duanyang GENG</i></p>	1040
88.	<p>THE MULTIPLE APPLICATIONS OF INDUSTRIAL HEMP (CANNABIS SATIVA L.) IN THE CONTEXT OF SUSTAINABLE DEVELOPMENT / APLICAȚIILE MULTIPLE ALE CÂNEPII INDUSTRIALE (CANNABIS SATIVA L.) ÎN CONTEXTUL DEZVOLTĂRII SUSTENABILE</p> <p>Lorena-Diana POPA¹⁾, Simona-Florina ISTICIOAIA¹⁾, Nicolae-Valentin VLĂDUȚ²⁾, Gheorghe MATEI³⁾, Alexandra LEONTE¹⁾, Iuliana GĂGEANU²⁾, Florin NENCIU²⁾, Paula-Lucelia PINTILIE¹⁾, Andreea-Sabina PINTILIE¹⁾, Oana MILEA²⁾, Mihaela ROȘCA⁴⁾, Anca PANDA⁵⁾, Gabriel-Ciprian TELIBAN⁴⁾, Marian BURDUCEA^{4,6)}</p> <p>¹⁾ Agricultural Research and Development Station Secuieni / Romania; ²⁾ National Institute of Research-Development for Machines and Installations Designed for Agriculture and Food Industry – INMA Bucharest / Romania; ³⁾ University of Craiova / Romania; ⁴⁾ “Ion Ionescu de la Brad” Iasi University of Life Sciences / Romania; ⁵⁾ Agricultural Research and Development Station Lovrin / Romania; ⁶⁾ “Alexandru Ioan Cuza” University / Romania</p>	1051
89.	<p>TOMATO LEAVES DISEASE IDENTIFICATION MODEL BASED ON IMPROVED MobileNetV3/ 基于改进 MobileNetV3 的番茄叶片病害识别模型</p> <p>Cheng CHI^{1,2,3)}, Lifeng QIN^{*1,2,3)}</p> <p>¹⁾ College of Mechanical and Electronic Engineering, Northwest A&F University, Yangling, Shaanxi, China ²⁾ Key Laboratory of Agricultural Internet of Things, Ministry of Agriculture and Rural Affairs, Yangling, Shaanxi, China Shaanxi Key Laboratory of Agricultural Information Perception and Intelligent Service, Yangling, Shaanxi, China</p>	1072
90.	<p>DESIGN AND EXPERIMENT OF A PEANUT SEEDING DEVICE FOR SYNCHRONOUS HOLE FERTILIZATION AND DIRECTLY-ABOVE SEEDING / 花生穴施肥同步正位播种装置设计与试验</p> <p>Yi LIU¹⁾, Massoudibrahim SALEM²⁾, Haipeng YAN²⁾, Peng GUO²⁾, Chao XIA²⁾, Guangbao XIA³⁾, Ahmed F. El-Shafie^{2,4)}, Dongwei WANG^{3,*1)}</p> <p>¹⁾ College of Mechanical and Electrical Engineering, Qingdao Agricultural University, Qingdao/China ²⁾ Yellow River Delta Intelligent Agricultural Machinery Equipment Industry Academy, Dongying/China ³⁾ Industrial Research Institute of Saline and Alkaline High-Efficiency Agricultural Technology, Qingdao Agricultural University, Dongying/China; ⁴⁾ Water Relations and Field Irrigation Department, National Research Centre, Cairo/ Egypt</p>	1084
91.	<p>DESIGN AND EXPERIMENTAL STUDY OF A CONTROL SYSTEM FOR SYNCHRONIZED CORN SEEDING AND HOLE FERTILIZATION / 玉米播种和穴播施肥同步控制系统的设计与试验研究</p> <p>Ziyu WANG¹⁾, Hongchao WANG²⁾, Chunying LIANG^{*2)}, Naichen ZHAO²⁾</p> <p>¹⁾ College of Information and Electrical Engineering, Heilongjiang Bayi Agricultural University, Daqing, China; ²⁾ College of Engineering, Heilongjiang Bayi Agricultural University, Daqing/China</p>	1097

		Page(s)
92.	<p>GRAPE LEAF VARIETY RECOGNITION BASED ON THE AF-SWIN TRANSFORMER MODEL / 基于 AF-Swin Transformer 模型的葡萄叶片品种识别</p> <p>Changmei LIANG¹⁾, Jiaxiong GUAN¹⁾, Tongtong GAO¹⁾, Juxia LI^{*1)}, Yanwen LI¹⁾, Qifeng ZHAO²⁾, Pengfei WEN³⁾, Zhifeng BI⁴⁾, Fumin MA⁵⁾</p> <p>¹⁾ College of Information Science and Engineering, Shanxi Agricultural University, Jinzhong, Shanxi/ China ²⁾ Shanxi Academy of Agricultural Sciences Polomogy Institute, Jinzhong, Shanxi/ China ³⁾ College of Horticulture, Shanxi Agricultural University, Jinzhong, Shanxi/ China ⁴⁾ Department of Basic Sciences, Shanxi Agricultural University, Jinzhong, Shanxi/ China ⁵⁾ College of Energy and Power Engineering, Lanzhou University of Technology, Lanzhou, Gansu/ China</p>	1113
93.	<p>DESIGN AND EXPERIMENTAL STUDY OF A HIGH GROUND CLEARANCE WEEDING ROBOT CHASSIS / 高地隙跨垄除草机器人底盘设计与试验</p> <p>Wentao XU, Lei HAN, Yanhua MA, Tao LIU, Wen LIU</p> <p>Inner Mongolia Agricultural University, College of Mechanical and Electrical Engineering, Inner Mongolia, China</p>	1125
94.	<p>INNOVATIONS IN SMALL WIND TURBINES: A COMPREHENSIVE REVIEW OF VERTICAL AXIS DESIGN AND EXPERIMENTAL FINDINGS /</p> <p>INOVAȚII ÎN DOMENIUL TURBINELOR EOLIENE DE MICI DIMENSIUNI: O REVIZIE CUPRINZĂTOARE A PROIECTĂRII TURBINELOR EOLIENE CU AX VERTICAL ȘI A REZULTATELOR EXPERIMENTALE</p> <p>Bogdan Ovidiu DURAN[*], Adrian PANDELE, Dragos Mihail PREDA, Gheorghe VOICU[*]</p> <p>National University of Science and Technology POLITEHNICA Bucharest, Romania</p>	1135
95.	<p>RESEARCH ON ROOT PRUNING METHODS APPLIED TO ORCHARD TREES/ CERCETARI PRIVIND METODE DE TAIERE A RADACILOR POMILOR FRUCTIFERI</p> <p>Ana ZAICA, Radu CIUPERCĂ, Vasilica ȘTEFAN, Alin-Nicolae HARABAGIU, Elena-Melania CISMARU, Ștefan DUMITRU, Alexandru ZAICA</p> <p>INMA Bucharest, Romania</p>	1160
96.	<p>DESIGN AND EXPERIMENTAL STUDY OF THE SUPPLY SYSTEM FOR GRASS SEED PELLETIZATION COATING MACHINE / 草种丸粒化包衣机供给装置设计与研究</p> <p>Liyang CHEN¹⁾, Zhanfeng HOU^{*1,2,3)}, Haiyang LIU¹⁾, Bingyan LI¹⁾, Liyang BAO¹⁾, Zhimin WANG¹⁾</p> <p>¹⁾ Inner Mongolia Agricultural University, College of Mechanical and Electrical Engineering, Inner Mongolia, China ²⁾ Inner Mongolia Engineering Research Center of Intelligent Equipment for the Entire Process of Forage and Feed Production, Hohhot, China; ³⁾ Inner Mongolia Engineering Research Center for Intelligent Facilities in Prataculture and Livestock Breeding, Hohhot, China</p>	1168
97.	<p>PAME-YOLO: A MODEL FOR APPLE LEAF LESION DETECTION IN COMPLEX ENVIRONMENTS BASED ON IMPROVED YOLOv8s /</p> <p>PAME-YOLO: 一种适用于复杂环境的基于改进 YOLOv8s 的苹果叶片病斑检测模型</p> <p>Yuansheng Bing¹⁾, Xiao Yu^{*1,2)}, Zeqi Lin¹⁾, Feng Yu¹⁾</p> <p>¹⁾School of Computer Science and Technology, Shandong University of Technology, Zibo, Shandong / China ²⁾Institute of Modern Agricultural Equipment, Shandong University of Technology, Zibo, Shandong / China</p>	1179
98.	<p>POINTNET++LR3D: AN IMPROVED POINTNET++ MODEL FOR INDIVIDUAL IDENTIFICATION OF PIG BACK POINT CLOUD /</p> <p>POINTNET++LR3D: 一种改进的 POINTNET++ 模型用于猪背点云个体识别</p> <p>Yongshuai YANG¹⁾, Yaqi YAN¹⁾, Yuhang LI¹⁾, Jiarui ZHANG¹⁾, Xiaochan GAO¹⁾, Jie HU¹⁾, Juan LIU^{*2)}</p> <p>¹⁾ College of Software, Shanxi Agricultural University, Taigu, Shanxi / China; ²⁾ College of Liberal Arts and Sciences, Shanxi Agricultural University, Taigu, Shanxi / China</p>	1193
99.	<p>PATH PLANNING STUDY OF INTELLIGENT GRAIN TRANSPORTER BASED ON GRAIN DEPOT SCENARIO / 基于粮库场景下智能粮食转运车的路径规划研究</p> <p>Boqiang ZHANG¹⁾, Genliang YANG¹⁾, Liang LI²⁾, Chenglong ZHANG¹⁾, Xun ZHANG¹⁾, Xuemeng XU¹⁾, Xiaoling WU²⁾</p> <p>¹⁾ School of Mechanical and Electrical Engineering, Henan University of Technology, Zhengzhou / China; ²⁾ YUTONG BUS CO., LTD. Zhengzhou / China</p>	1207
100	<p>DESIGN OF IOT-BASED GREENHOUSE MONITORING AND CONTROL SYSTEM USING ADAPTIVE PARTICLE SWARM OPTIMIZED FUZZY PID CONTROLLER AND VISUALIZATION PLATFORM / 基于自适应粒子群优化模糊 PID 控制器和可视化平台的物联网温室监控系统设计</p> <p>Peiyu LIN^{1,2,3)}, Rui XU^{1,2,3)}, Haifang WANG⁴⁾, Jingcheng HUANG^{1,2,3)}, Zhen GUO^{1,2,3)}, Xia SUN^{1,2,3)}, Ibrahim A. DARWISH⁵⁾, Yemin GUO^{*1,2,3)}, Jicheng ZHAO^{*1,2,3)}</p> <p>¹⁾ College of Agricultural Engineering and Food Science, Shandong University of Technology, Zibo, Shandong, China; ²⁾ Shandong Provincial Engineering Research Centre of Vegetable Safety and Quality Traceability, Zibo, Shandong, China; ³⁾ Zibo City Key Laboratory of Agricultural Product Safety Traceability, Zibo, Shandong, China; ⁴⁾ Wangjing Hospital, China Academy of Chinese Medical Sciences, Beijing, China; ⁵⁾ Department of Pharmaceutical Chemistry, College of Pharmacy, King Saud University, Riyadh, Saudi Arabia</p>	1219

DESIGN AND OPTIMIZATION OF AIR-ASSISTED SPIRAL SEED-SUPPLY DEVICE FOR HIGH-SPEED DENSE PLANTING MAIZE SEEDER

玉米高速密植播种机气送式螺旋供种装置设计与优化

Wen-sheng SUN ¹⁾, Shu-juan YI ¹⁾, Hai-long QI ²⁾, Yi-fei LI ^{1,3)}, Zhi-bo DAI ¹⁾, Yu-peng ZHANG ¹⁾,
Jia-sha YUAN ¹⁾, Song WANG ¹⁾

¹⁾College of Engineering, Heilongjiang Bayi Agricultural University, Daqing/P.R.China

²⁾Heilongjiang Beidahuang Modern Agricultural Service Group Zhongrong Agricultural Machinery Co., Ltd, Harbin / P.R.China

³⁾College of Engineering, Northeast Agricultural University, Harbin/P.R.China

Tel: +86-459-13836961877; E-mail: yishujuan_2005@126.com

Corresponding author: Shu-juan Yi

DOI: <https://doi.org/10.35633/inmateh-75-01>

Keywords: maize, seed-supply device, air-assisted, spiral, CFD

ABSTRACT

In order to improve the seed supply performance of high-speed dense planting maize seeder, an air-assisted spiral seed-supply device was designed and optimized. The kinetic model of maize seeds in the migration zone was established. Based on computational fluid dynamics (CFD) simulation, the pressure and velocity distribution in the axial plane were explored when the blower pressure was 4.0, 4.5, 5.0, 5.5, 6.0 kPa, respectively. A two-factor, five-level central composite design (CCD) experiment was conducted using blower pressure and spiral shaft rotational speed as test factors while seed supply rate, coefficient of variation of seed supply rate stability and seed breakage rate were selected as seed supply performance indicators. The influence trends of the interaction terms on these performance indicators were explored. Based on the multi-objective variable optimization method, the optimal working parameter combination of the air-assisted spiral seed-supply device was determined and verified by bench experiments. The results showed that the optimal combination of working parameters was a blower pressure of 6.0 kPa and a spiral shaft rotational speed of 80 r/min. Under the verification test, the seed supply rate, the coefficient of variation of seed supply rate stability and the seed breakage rate were 2933.21 g/min, 1.87 % and 1.69 %, respectively, with a relative error of less than 5.5% compared to the optimized results. This study can provide a reference for the optimized design of seed-supply devices for high-speed dense planting seeders.

摘要

为提高玉米高速密植播种机供种环节的供种性能, 设计并优化了一种气送式螺旋供种装置。建立了玉米种子在迁移区的动力学模型。基于 CFD 仿真探究了气流送种区在风机压力分别为 4.0、4.5、5.0、5.5、6.0 kPa 时中轴面的压强与流速分布。以风机压力、螺旋轴转速为试验因素, 以供种速率、供种速率稳定性变异系数、种子破损率为供种性能指标进行了二因素五水平的中心组合设计试验, 探究了因素的交互项对供种速率、供种速率稳定性变异系数、种子破损率的影响趋势。基于多目标变量优化的方法确定了气送式螺旋供种装置的最佳工作参数组合并进行了试验验证。结果表明: 装置的最佳工作参数组合为风机压力 6.0 kPa、螺旋轴转速 80 r/min, 验证试验下该参数组合的供种速率、供种速率稳定性变异系数、种子破损率分别为 2933.21 g/min、1.87 %、1.69 %, 与参数优化结果相对误差在 5.5 % 以内。本研究可为高速密植播种机供种装置的优化设计提供参考。

INTRODUCTION

Maize is one of the most widely planted and productive food crops in the world (Tang et al., 2024; Fanigliulo et al., 2022). With the increasing demand for feed raw materials and the rapid development of deep-processing industry, the demand for maize in China has expanded rapidly (Huai et al., 2024). To improve maize yield, the dense planting pattern has gained widespread attention among agricultural workers. Maize densification planting mode (Sun et al., 2024) is based on the precision sowing technology, which can reasonably reduce the seed spacing of maize. That not only ensures the space for plant growth, but also improves the planting density and increase production and efficiency. But in the dense planting mode, the

¹Wen-sheng Sun, Ph.D.; Shu-juan Yi, Prof. Ph.D.; Hai-long Qi, bachelor degree; Yi-fei Li, Ph.D.; Zhi-bo Dai, master degree; Yu-peng Zhang, master degree; Jia-sha Yuan, master degree; Song Wang, Ph.D.

sowing quantity per unit area of soil will increase, the seed spacing will decrease, and the sowing frequency of the seeder will also be higher during high-speed operation. In addition, maize seeds are often coated before sowing, and damage to the seed coating skin should be avoided during the sowing process.

At present, the seed box of the seeder used for conventional operation is generally not provided with a seed supply control unit, and the seed is quantitatively supplied according to the outlet structure size of the seed box (Ding *et al.*, 2021). The seed supply device of the centralized pneumatic dense planting seeder is mainly controlled by machinery, and the sowing speed is generally below 10 km/h. When the seed supply device operates at a high speed (above 10 km/h), it is easy to appear the phenomenon of "lack of power" of seed supply (Wang *et al.*, 2021; Wang *et al.*, 2020). Gao Xiaojun *et al.*, (2022), explored a quantitative feeding device with a staggered symmetrical spiral groove wheel based on the discrete element method (DEM), and analyzed the effects of different inclination angles and lengths of the grooved wheels on the uniformity of maize particles flow. Yuan Hao *et al.*, (2020), designed a piezoelectric vibration seed supply device to improve the seeding performance of low seeding capacity seed-metering device for plug seedling of super hybrid rice, and explored the influence law of seed tank depth and amplitude on seed supply performance based on DEM. Lei Xiaolong *et al.*, (2017), explored the effects of dimple depth, dimple pitch and length of pressurized tube on the seed distribution and seeding uniformity during the seed supply stage of the air-assisted centralized planter, and optimized the structural parameters of the pressurized tube. Gao Xiaojun *et al.* (2018) investigated the changing rules of fluid field, coupling field, and particle field of venturi feeding tube under different nozzle mouth shrinkage angles, and optimized the constriction angle. However, there is little research on the seed-supply link of maize dense planting seeder under high-speed operation.

In order to improve the seed supply performance of seed-supplying link of high-speed dense planting seeder of maize, an air-assisted spiral seed-supply device with spiral seed relocation and airflow seed delivery was designed and optimized. The theoretical model of maize seeds in the migration zone of the device was established, and the airflow distribution of the airflow seed delivery zone under different blower pressures was explored by computational fluid dynamics (CFD) simulation. The optimal working parameter combination of the device was obtained through the central composite design (CCD) test of two factors and five levels. The seed supply performance of the device was further improved.

MATERIALS AND METHODS

Overall structure and working principle

The high-speed dense planting seeder of maize can complete the continuous operation links such as stubble cleaning, ditching, sowing, pressing and soil-covering at one time. As the seed-supply unit of the sowing link (Sun *et al.*, 2024), the air-assisted spiral seed-supply device is mainly composed of a blower, an inlet pipe, an outlet pipe, a pipe, a seed box, a spiral shaft, a sleeve, a motor, a seed-supply nozzle and other parts. The seeds in the seed box have to undergo three processes of migration, mixing and conveying in the device, which can be divided into two parts of the migration zone and the airflow seed delivery zone according to the working process. As the medium connecting the seed box and the airflow seed delivery zone, the migration zone is the core unit of the device. The spiral shaft and the sleeve are the main components of the migration zone, and the hollow part between the spiral shaft and the sleeve accommodates the migration movement of the maize seeds. The spiral shaft parameters include spiral shaft outer diameter D_1 of 56 mm, inner diameter d_1 of 19 mm, guide P_t of 56 mm, etc. The sleeve parameters include opening angle φ of 180° , sleeve length L_1 of 145 mm, sleeve axial opening L_2 of 45 mm, sleeve outer diameter D_2 of 63 mm, etc.

As shown in Fig.1, the maize seeds in the seed box fall from the seed inlet to the migration zone by gravity, and orderly migrate towards the airflow seed delivery zone under the push of the spiral blades. Following the principle of "first come, first out", they fall from the seed outlet of the migration zone to the airflow seed delivery zone. The motor drives the spiral shaft to rotate clockwise at an angular velocity of ω , and the spiral blades are left-handed. The edge of the spiral blades rises along the left arm. The migration amount of the seeds in the migration zone in unit time is adjusted by changing the rotational speed of the motor. The airflow generated by the blower flows in from the inlet pipe. The migrated seed cluster are mixed with the airflow in the seed-supply nozzle to form a gas-solid two-phase flow, and then flows into the seed-metering device through the outlet pipe and the pipe. The conveying velocity of the seeds in the airflow seed delivery zone is changed by adjusting the blower pressure. By adjusting the rotational speed of spiral shaft and the blower pressure, the aim of precisely adjustable and efficient seed-supply of the device is achieved, and the seed supply operation requirement on the device when the maize dense planting seeder operates at a high speed is met.

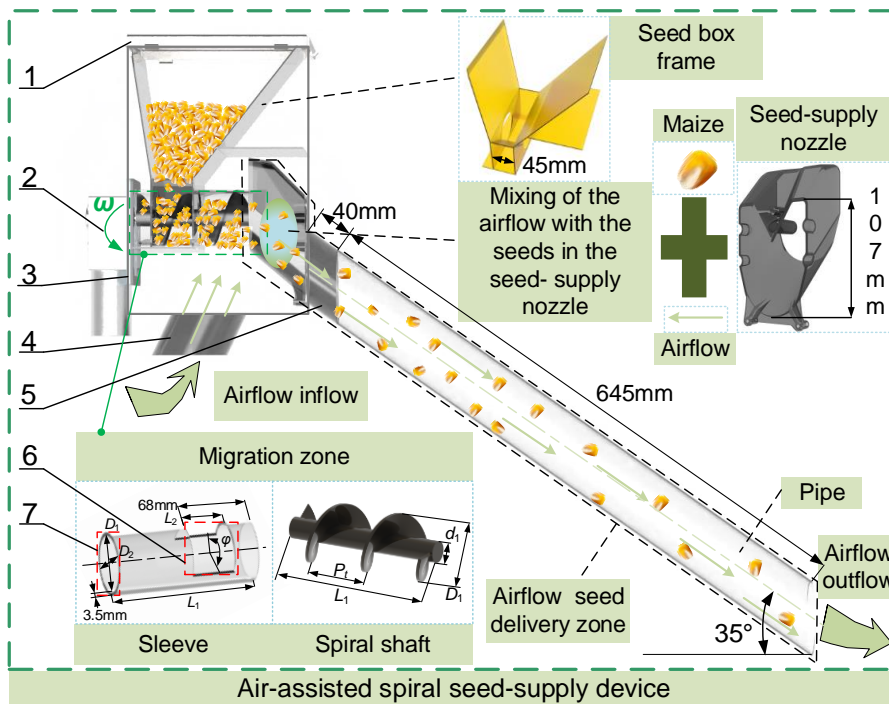


Fig. 1 - Overall structure and working principle

1. seed box cover; 2. motor; 3. seed box; 4. inlet pipe; 5. outlet pipe; 6. seed inlet of migration zone; 7. seed outlet of migration zone.

Analysis of the seed-supply process in the migration zone

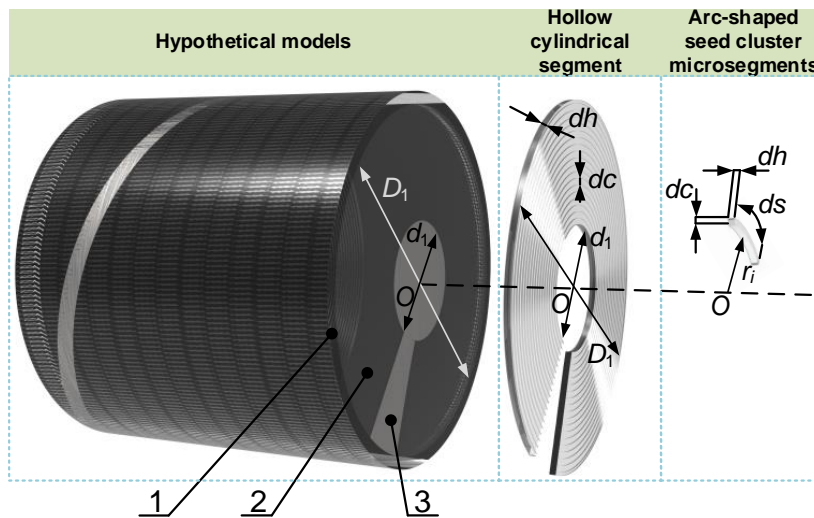


Fig. 2 - Theoretical assumptions of the seed supply process

1. sleeve; 2. seed cluster; 3. spiral shaft.

After the seeds flow into the migration zone from the seed box, they will complete the migration process in the form of bulk particles under various forces such as gravity, inertia, friction and so on. Due to the great difference in the shape and size of maize seeds, in order to facilitate the theoretical analysis of the seed cluster in the migration zone, the following motion assumptions are established for the stable seed supply process of maize seeds in the migration zone based on the infinitesimal method (Yao *et al.*, 2022):

(1) Seed cluster in the migration zone are filled completely in the hollow between the spiral shaft and the sleeve, the phenomena of separation, jumping and other like cannot occur, and the seed cluster are tightly attached to the spiral blade;

(2) Seed cluster are axially divided among the spiral blades into uniform and complete seed cluster segments, where in each segment is a hollow cylindrical segment which take the center O of a spiral shaft as a circle center, has the same inner diameter as the inner diameter of the spiral shaft, has the same outer diameter as the outer diameter of the spiral shaft and has the thickness of dh , and radially dividing each hollow cylindrical segment into arc-shaped seed cluster microsegments with the length of dc ;

(3) The arc-shaped seed cluster microsegment ds at any radius r_i on the radial section of any spiral shaft is taken as the research object, and the microsegment section is a rectangle of $dc \times dh$, as shown in Fig.2. The rotational speed of the adjacent annular seed cluster microsegments diffusely distributed in any radial direction will change.

The spiral shaft of the device is a standard single-head screw with equal guide and equal diameter. The spiral blade exerts a force on the seed cluster, which makes the seed cluster produce a migration motion, in which the rotation of the spiral shaft is induced motion, and the motion of the seed cluster relative to the spiral blade is relative motion. The seed cluster forms a complex composite motion under these two motions. A dynamic analysis is performed on the migration process of the seed cluster microsegments clinging to any radius r_i of the middle segment of the spiral blade, and a spatial rectangular coordinate system is established with the center of mass of the seed cluster microsegments as the coordinate origin, the axial direction of the spiral shaft as the z axis, the radial direction as the x axis, and the tangential direction as the y axis, as shown in Fig.3.

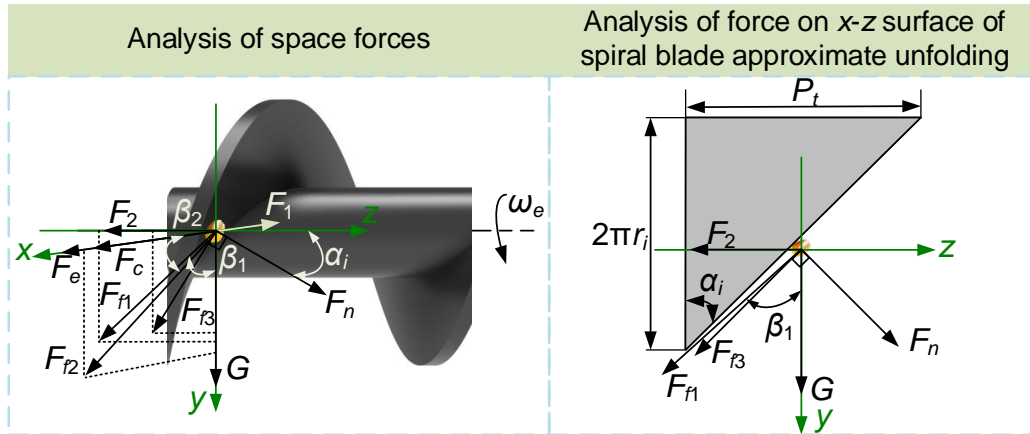


Fig. 3 - Dynamic analysis of seed cluster microsegments

The force acting on the seed cluster microsegments during the rotation of the spiral shaft can be divided into a supporting force F_n perpendicular to the spiral blade and a friction force F_{f3} between the seed and the spiral blade. In the process of seed movement, the microsegments will have the trend of moving axially to the seed outlet and radially outward. According to Newton's third law of motion-force and acceleration, the microsegments will be subjected to the interaction forces F_1 and F_2 of the adjacent seed cluster microsegments in the radial and axial directions, and at the same time, the moving microsegments will generate additional friction forces F_{f1} and F_{f2} due to the forces F_1 and F_2 . In addition, because the motion of the microsegment is a composite motion composed of relative motion and induced motion, and the induced motion is rotation, the inertial centrifugal force F_e and the Coriolis force F_c should be considered when analyzing the force model of the microsegment. According to the basic equation of particle relative motion dynamics, the microsegment dynamics equation is established as follows:

$$\left\{ \begin{array}{l} ma_r = F_e + F_c + F \\ F_e = mr_i\omega_e^2 \\ F_c = 2mr_i\omega_e\omega_r \\ \omega_a = \omega_e - \omega_r \\ F_{f1} = \mu_2F_1 \\ F_{f2} = \mu_2F_2 \\ F_{f3} = \mu_1F_n \\ G = mg \\ \tan \alpha_i = \frac{P_t}{2\pi r_i} \end{array} \right. \quad (1)$$

where: m is the mass of the microsegment, (kg); α_r is the relative acceleration of the microsegment, ($m \cdot s^{-2}$); ω_a is the absolute angular velocity of the microsegment, (rad/s); ω_e is the angular velocity of the spiral shaft, (rad/s); ω_r is the angular velocity of the microsegment relative to the spiral shaft, (rad/s); μ_1 is the friction coefficient between spiral blade and seed; μ_2 is the friction coefficient between the seeds; G is the gravity exerted on the microsegment, (N); g is the acceleration of gravity, ($m \cdot s^{-2}$); α_i is the helix angle at the position of the spiral shaft where the microsegment are located, ($^\circ$).

Projecting the relative acceleration α_r to the x-axis, y-axis and z-axis, the rectangular coordinate form of the seed relative motion differential equation is

$$\begin{cases} m \frac{d^2 r_x}{dt^2} = m \frac{dv_x}{dt} = ma_{r-x} = F_c + F_e + F_{f2} \cos \beta_2 - F_1 \\ m \frac{d^2 r_y}{dt^2} = m \frac{dv_y}{dt} = ma_{r-y} = G + F_{f1} \cos \beta_1 + F_{f3} \cos \alpha_i + F_n \sin \alpha_i + F_{f2} \sin \beta_2 \\ m \frac{d^2 r_z}{dt^2} = m \frac{dv_z}{dt} = ma_{r-z} = F_n \cos \alpha_i - F_{f3} \sin \alpha_i - F_{f1} \sin \beta_1 - F_2 \end{cases} \quad (2)$$

where:

α_{r-x} is the projection of the relative acceleration of the microsegment on the x-axis, ($m \cdot s^{-2}$); α_{r-y} is the projection of the relative acceleration of the microsegment on the y-axis, ($m \cdot s^{-2}$); α_{r-z} is the projection of the relative acceleration of the microsegment on the z-axis, ($m \cdot s^{-2}$); β_1 is the angle between the friction force F_{f1} and the gravity G , ($^\circ$); β_2 is the angle between the friction force F_{f2} and the positive x-axis, ($^\circ$).

The relative accelerations of the microsegment in the x-, y-, and z-axes are

$$\begin{cases} a_{r-x} = r_i \omega_r^2 \\ a_{r-y} = 0 \\ a_{r-z} = 0 \end{cases} \quad (3)$$

Simultaneous (1-3), available:

$$\frac{mr_i[(2\omega_e - \omega_a)^2 - 2(\omega_e - \omega_a)^2]}{F_1[1 - T\mu_2 \sin \beta_2 - \mu_2 \cos \beta_2 (T\mu_2 \cos \beta_1 - \mu_2 \sin \beta_1)] - T\mu_2 mg \cos \beta_2} = \frac{1 - T\mu_2 \sin \beta_2}{1 - T\mu_2 \sin \beta_2} \quad (4)$$

which:

$$\begin{cases} T = \frac{\mu_1 \sin \alpha_i - \cos \alpha_i}{\mu_1 \cos \alpha_i + \sin \alpha_i} \\ \sin \alpha_i = \frac{P_t}{\sqrt{P_t^2 + (2\pi r_i)^2}} \\ \cos \alpha_i = \frac{2\pi r_i}{\sqrt{P_t^2 + (2\pi r_i)^2}} \end{cases} \quad (5)$$

It can be seen from the formula (4) that the absolute angular velocity ω_a is related to the angular velocity ω_e , the radius r_i , and the guide P_t . When the angular velocity ω_e is constant, the absolute angular velocity ω_a will change with the radius r_i of the microsegment location, which is consistent with the motion assumption in the previous content. Studies have shown (Chen *et al.*, 2015; Yang *et al.*, 2020) that when the rotational speed of the spiral shaft is too fast, the seed cluster near the inner diameter of the spiral shaft will produce an additional seed-cluster-flow, which will jump and roll in the radial direction and affect the axial motion of the seed cluster. In addition, if the rotational speed is too fast, the seeds just leaving the migration zone will splash around due to the excessive inertial force. The maximum inertial centrifugal force of the seeds should be less than the gravity of the seeds to ensure a smooth transition from the migration zone to the airflow seed delivery zone:

$$m\omega_{max}^2 \frac{D_1}{2} \leq K_1 mg \Rightarrow n_{max} \leq \frac{30K_1}{\pi} \sqrt{\frac{2g}{D_1}} \quad (6)$$

where:

ω_{max} is the limiting angular velocity of the spiral shaft, (rad/s); n_{max} is the limiting rotational speed of the spiral shaft, (r/min); K_1 is the reliability coefficient.

Simulation based on CFD

The UG NX 12.0 software is used to draw the fluid domain model and import it into Space Claim software for correction. The corrected model is imported into Fluent Meshing module for meshing. The minimum and maximum values of the surface grid are set to 0.5 mm and 5 mm, respectively. After the surface grid is generated, the fluid domain is calculated using polyhedral grid to fill the body grid. The fluid domain model is shown in Fig. 4.

According to the characteristics of the gas flow in the device, the standard K-epsilon model is used as the turbulence model, the second-order upwind equation is used as the momentum equation, the first-order upwind equation is used for the turbulent kinetic energy and the turbulent dissipation rate, the turbulent intensity is set to be 5 %, the turbulent viscosity ratio is set to be 10. The Fluent time-step is 1×10^{-3} s, and the total simulation time is 2 s. The inlet pressure was set as 4.0, 4.5, 5.0, 5.5, 6.0 kPa, respectively, and the outlet pressure was set as 0 Pa to explore the airflow distribution in the airflow seed delivery zone under different blower pressures.

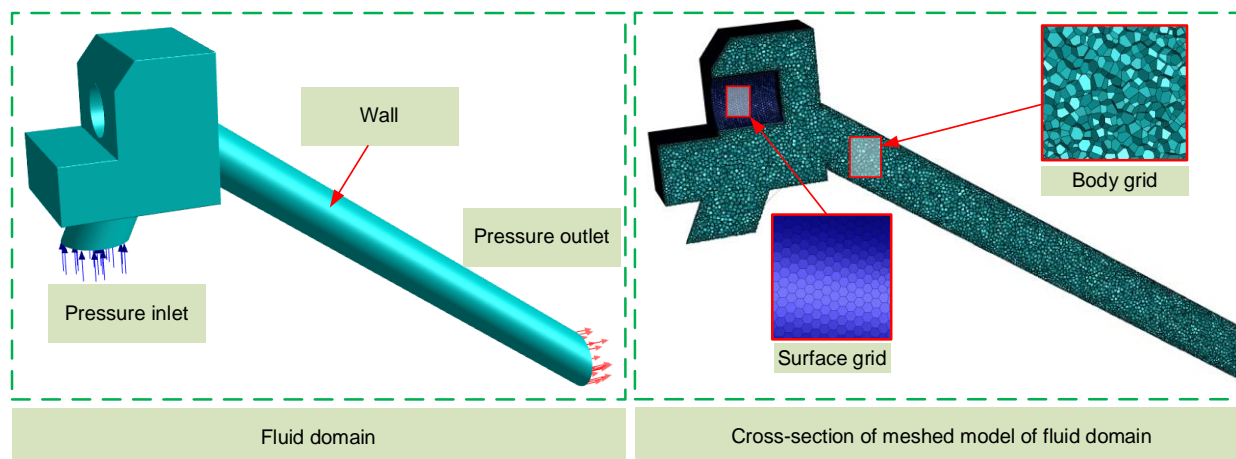


Fig. 4 - Establishment of CFD simulations

Bench test

In June 2024, the bench test of the air-assisted spiral seed-supply device was carried out in the high-speed precision seeding laboratory of the College of Engineering, Heilongjiang Bayi Agricultural University, Daqing City, Heilongjiang Province, China. The test conditions and results are shown in Fig. 5.



Fig. 5 - Bench test

1. electronic balance; 2. measuring cylinder; 3. DP2000 intelligent pressure and wind velocity air volume meter; 4. frequency converter;
5. HTB-multi-stage blower; 6. air tube; 7. switch power supply; 8. infinite speed control knob; 9. display screen; 10. motor;
11. inlet pipe; 12. seed box; 13. outlet pipe; 14. pipe; 15. seed net.

The main test equipment includes HTB-multi-stage blower, frequency converter, DP2000 intelligent pressure and wind velocity air volume meter, seed net, motor, infinite speed control knob, switch power supply, electronic balance, etc. The typical maize variety "Farley 1439" (small rounded) planted in Heilongjiang Province of China were selected as the test seeds, and the basic material characteristic parameters were shown in Table 1. The selected seeds were all coated and sorted, and the results were the average values after multiple measurements.

Table 1

Basic material characteristics of maize seed								
Variety name	Seed picture	Moisture content /%	Thousand grain weigh/g	Density /g·cm ⁻³	Pile angle/(°)	Length mm	Width mm	Thickness mm
Farley 1439 (small rounded)		12.6	296.4	1.122	20.23	8.03±0.41	7.12±0.46	6.34±0.43

In order to determine the optimal working parameters of the device and explore the interaction between the blower pressure and the rotational speed of spiral shaft on the seed-supply performance, a multi-factor experiment with two factors and five levels was carried out based on the CCD method. According to the actual test conditions, the blower pressure at 4.0 ~ 6.0 kPa and the rotational speed of spiral shaft at 50.0 ~ 80.0 r/min was set. The test factor codes are shown in Table 2, where X_1 and X_2 are the factor code values of the pressure and the rotational speed respectively.

Table 2

Experimental factors and level codes in multi-factor experiments			
Coded values	Experimental factors		
	X_1 / kPa	X_2 / r·min ⁻¹	
-1.414	4.0	50.0	
-1	4.29	54.4	
0	5.0	65.0	
1	5.71	75.6	
1.414	6.0	80.0	

Referring to GB/T 9478-2005 "Testing methods of sowing in lines", the test indexes were seed supply rate ϑ_i , coefficient of variation of the seed supply rate stability CV and seed breakage rate K_1 . Wherein, the seed supply rate is defined as the mass of the seeds flowing out of the device in unit time. The coefficient of variation of seed supply rate stability is defined as the percentage of the standard deviation of the seed supply rate to the average value of it at the same level of device parameter, measured many times to evaluate the uniformity of seed supply in the device. The seed breakage rate is defined as the percentage of the broken seed mass Z_1 out of the total seed mass Z_n flowing out of the device in given time. The evaluation index expression of seed supply performance is as follows:

$$\left\{ \begin{array}{l} \vartheta_i = \frac{\sum_{i=1}^{N_1} G_i}{N_1} \\ CV = \sqrt{\frac{\sum_{i=1}^{N_1} (G_i - \vartheta_i)^2}{N_1 - 1}} \times 100\% \\ K_1 = \frac{Z_1}{Z_n} \times 100\% \end{array} \right. \quad (7)$$

where: G_i is the seed quality of the i -th test, (g); N_1 is the number of experiments.

In the experiment, the seeds discharged from the device were collected using the seed net for 1 minute. The net weight was measured, and then the broken seeds were picked up and weighed. Each group of experiments was repeated 5 times, and the seed supply rate, the coefficient of variation of the seed supply rate stability and the seed breakage rate were calculated under different treatments.

RESULTS AND DISCUSSIONS

Simulation analysis of flow field in the airflow seed delivery zone

In order to explore the pressure distribution in the airflow seed delivery zone under different inlet pressures, the pressure nephogram in the axial plane of the fluid domain at 2 s was intercepted, as shown in Fig. 6 a ~ e. In the figure, the pressure distribution in the axial plane is similar for different inlet pressures, the pressure is higher in the area from the inlet of the inlet pipe to the inlet of the outlet pipe, the pressure in the outlet pipe and the pipe is lower, and negative pressure appears near the outlet pipe and the pipe inlet.

With the increase of the inlet pressure, the pressure range of the airflow seed delivery zone is gradually increased. The pressure ranges at 4.0, 4.5, 5.0, 5.5 and 6.0 kPa were -1271.52 ~ 3993.05, -1426.41 ~ 4558.55, -1693.46 ~ 4994.76, -1957.58 ~ 5525.13, -1950.10~5961.19 Pa, respectively.

Dividing the segment of the flow field of the axial plane in the fluid domain from the pressure inlet to the pressure outlet into Q_1Q_2 , Q_2Q_3 and Q_3Q_4 , and randomly and continuously selecting 20, 120 and 550 sample points from each segment in turn according to the arrow direction respectively. The pressure of the sample points on the line segments of 4.0, 4.5, 5.0, 5.5, and 6.0 kPa were recorded as shown in Fig. 6 f. In the process of airflow from Q_1 to Q_2 , the vertical section area of the line segment is basically unchanged. The pressure shows a downward trend, but the downward speed gradually slows down. The inlet pressure of 4.0, 4.5, 5.0, 5.5, 6.0 kPa decreased by 292.83,310.76,359.53,406.06 and 437.51 Pa, respectively, and the higher the inlet pressure, the more the pressure decreased. In the process of the airflow from Q_2 to Q_3 , the vertical sectional area of the line segment of the sample points before and after Q_2 suddenly changes from small to large. The vertical sectional area of the line segment of the sample points before and after Q_3 suddenly changes from large to small. The pressure first increases slowly, then fluctuates slowly, and finally decreases rapidly. The pressure inlet of 4.0, 4.5, 5.0, 5.5 and 6.0 kPa reached the maximum pressure of this segment at the 42nd, 48th, 54th, 54th and 48th sample points respectively, which are 2974.79, 3405.17, 3783.44, 4227.45 and 4446.06 Pa. During the process of airflow from Q_3 to Q_4 , the vertical cross-sectional area of the line segment remains basically unchanged, and the pressure first rapidly decreases to the lowest point of the entire flow field sample point. The inlet pressure of 4.0, 4.5, 5.0, 5.5, and 6.0 kPa reaches the minimum value at sample points 189, 189, 189, 184, and 185, respectively, which are -679.32, -828.05, -820.72, -1053.8, and -1153.51 Pa, and then shows an upward trend but the upward speed gradually slows down, reaching a local maximum before slowly decreasing again. Each inlet pressure at the 690th sample point is 0 Pa.

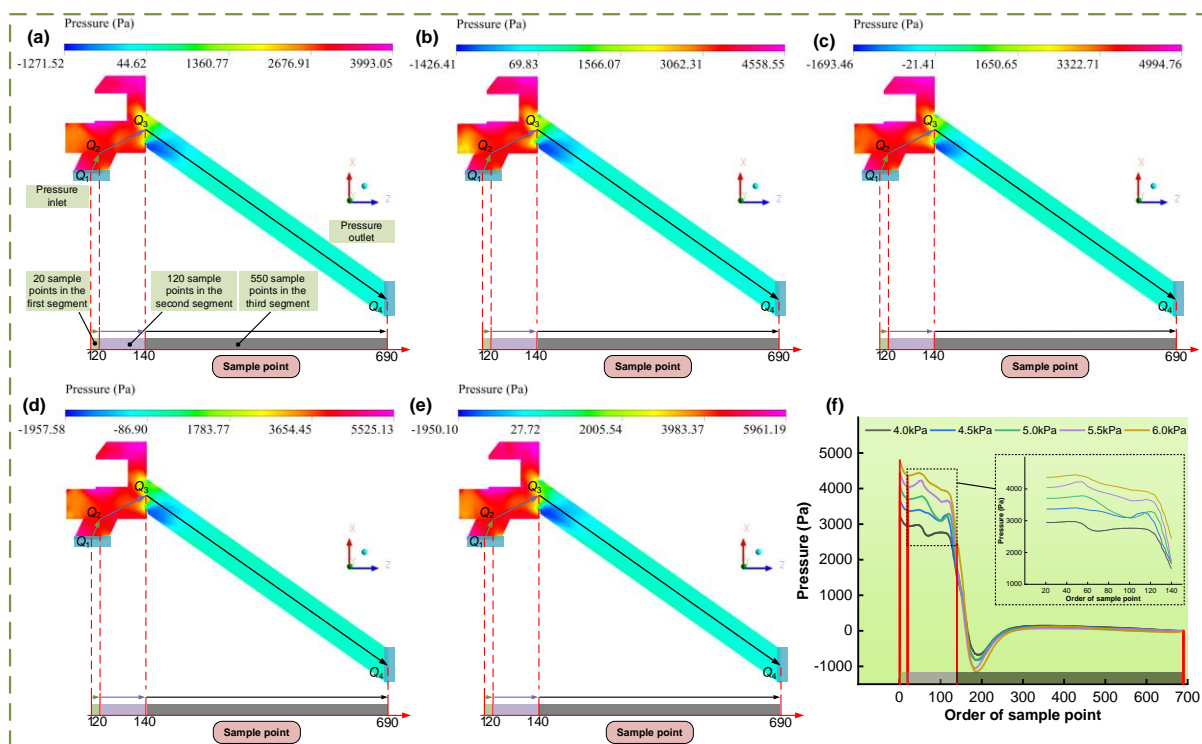


Fig. 6 - Pressure situation of the airflow seed delivery zone under different inlet pressures

a. pressure inlet=4.0 kPa; b. pressure inlet=4.5 kPa; c. pressure inlet=5.0 kPa; d. pressure inlet=5.5 kPa; e. pressure inlet=6.0 kPa; f. sample point pressure curve of different inlet pressures.

In order to explore the velocity distribution under different inlet pressures in the airflow seed delivery zone, the axial plane velocity nephogram of the fluid domain at 2 s was intercepted, as shown in Fig. 7 a ~ e. In the figure, with the increase of inlet pressure, the maximum velocity of the whole flow field shows a gradual upward trend, and the maximum velocity reaches 88.61 m/s when the inlet pressure is 6.0 kPa. There was little difference in the velocity distribution of the axial plane under different inlet pressures, and the highest velocity appeared at the outlet pipe, which was caused by the sudden decrease of the cross-sectional area of the airflow from the seed-supply nozzle to the outlet pipe.

The velocity at the sample points on Q_1Q_2 , Q_2Q_3 and Q_3Q_4 with inlet pressures of 4.0, 4.5, 5.0, 5.5, 6.0 kPa were recorded as shown in Fig. 7 f. In the process of the airflow from Q_1 to Q_2 , the vertical sectional area of the line segment is basically unchanged, and the velocity shows an upward trend, but the rising speed gradually slows down, which is completely opposite to the pressure change trend in the segment, and conforms to the relationship between the velocity and the pressure in Bernoulli's principle. The Q_1Q_2 segment reaches a maximum velocity of 51.7 m/s at the inlet pressure of 6.0 kPa. In the process of airflow from Q_2 to Q_3 , the velocity of each inlet pressure sample does not change much from the 21st to about the 50th sample points, and then it decreases rapidly. The inlet pressures of 4.0, 4.5, 5.0, 5.5, and 6.0 kPa reach the local minimal of the velocity of this segment at the 68th, 61st, 66th, 58th, and 65th sample points, respectively, which are 23.23, 19.52, 28.32, and 22.94, 29.1 m/s. After which the velocity roughly shows a trend of first rising, then falling and then rising. The inlet pressures of 4.0, 4.5, 5.0, 6.0 kPa reach the minimum velocity in this segment at the 111th, 113th, 118th, 115th sample points, respectively, which are 13.62, 16.7, 17.39, and 23.75 m/s. In the process of the airflow from Q_3 to Q_4 , the velocity first rises rapidly to the maximum of the whole flow field sample points. The inlet pressures of 4.0, 4.5, 5.0, 5.5, and 6.0 kPa reach the maximum velocity at the 168th, 164th, 168th, 168th and 168th sample points, respectively, which are 65.66, 64.71, 72.9, 78.88 and 79.4 m/s, and then decreased rapidly. Among them, the inlet pressure of 4.0 kPa and 5.0 kPa decreased relatively slowly, and the inlet pressure of 4.5 kPa was the lowest value of 16.74 m/s at the 229th sample point. The velocity of the sample points before and after the lowest value fluctuated greatly. Finally, the velocity showed an upward trend, but the rising speed gradually slowed down. The velocities at the 690th sample point were 47.68, 52.64, 60.21, 56.8 and 64.82 m/s at the inlet pressures of 4.0, 4.5, 5.0, 5.5, 6.0 kPa, respectively.

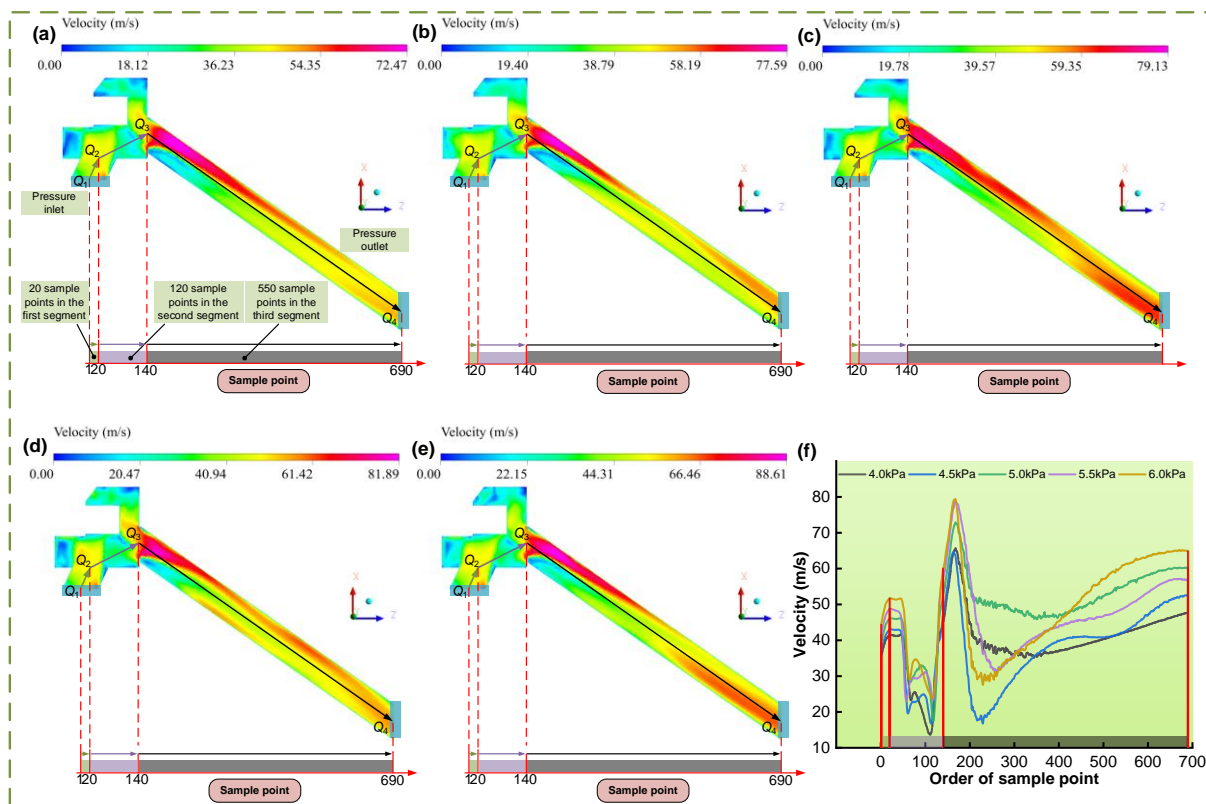


Fig. 7 - Velocity situation of the airflow seed delivery zone under different inlet pressures

a. pressure inlet=4.0 kPa; b. pressure inlet=4.5 kPa; c. pressure inlet=5.0 kPa; d. pressure inlet=5.5 kPa; e. pressure inlet=6.0 kPa; f. sample point velocity curve of different inlet pressures.

Results of the multi-factor experiments

According to the range of factors in Table 2, a multi-factor test was conducted, and the test results are shown in Table 3. In the table, X_1 , X_2 , and X_3 are coded values of seed supply rate, coefficient of variation of seed supply rate stability, and seed breakage rate, respectively. The test results were processed and analyzed by Design-Expert 12 software, and the quadratic equation variance analysis was obtained as shown in Table 4.

Table 3

Design and results of the Central-Composite experiment					
No.	Experimental factors		Experiment indexes		
	X1/ kPa	X2/ km·h ⁻¹	Y1/ g·min ⁻¹	Y2/ %	Y3/ %
1	-1	-1	1390.15	1.64	1.22
2	1	-1	2152.24	1.05	1.51
3	-1	1	1833.94	1.61	1.46
4	1	1	2676.8	1.54	1.58
5	-1.414	0	1448.44	1.94	1.3
6	1.414	0	2554.86	1.16	1.62
7	0	-1.414	1670.56	1.15	1.36
8	0	1.414	2402.78	1.89	1.56
9	0	0	2017.56	1.65	1.48
10	0	0	2007.56	1.58	1.43
11	0	0	2001.99	1.52	1.44
12	0	0	2002.98	1.59	1.47
13	0	0	2043.70	1.69	1.49
14	0	0	2030.79	1.72	1.39
15	0	0	2008.34	1.51	1.37
16	0	0	2022.48	1.71	1.42

Table 4

Variance analysis of the regression model						
Source	Seed supply rate		Coefficient of variation of seed supply rate stability		Seed breakage rate	
	Sum of squares	p-value	Sum of squares	p-value	Sum of squares	p-value
Model	1.761E+06	< 0.0001**	0.8020	0.0005**	0.1451	< 0.0001**
X1	1.256E+06	< 0.0001**	0.3886	0.0003**	0.0930	< 0.0001**
X2	5.019E+05	< 0.0001**	0.2837	0.0008**	0.0439	0.0002**
X1 X2	1630.95	0.0251*	0.0676	0.0439*	0.0072	0.0446*
X1 ²	663.32	0.1242	0.0237	0.2027	0.0005	0.5795
X2 ²	565.05	0.1524	0.0385	0.1126	0.0005	0.5795
Residual	2354.41		0.1273		0.0137	
Lack of fit	835.36	0.3523	0.0788	0.0666	0.0009	0.9134
Pure error	1519.06		0.0485		0.0128	
Cor total	1.763E+06		0.9293		0.1588	

Note: * indicates a significant impact; ** indicates a highly significant impact.

In Table 4, the p values of the regression models of seed supply rate $Y1$, Coefficient of variation of seed supply rate stability $Y2$, and seed breakage rate $Y3$ were all less than 0.01, indicating that the regression models were extremely significant. The p -values of the lack of fit test were all more than 0.05, indicating that the regression models had good fit. In the variance analysis of the $Y1$, $Y2$ and $Y3$, the blower pressure $X1$ and rotational speed of spiral shaft $X2$ showed extremely significant effects, and the interaction $X1 X2$ showed significant effects. The influence order of each factor on the $Y1$, $Y2$ and $Y3$ was: $X1$, $X2$. The quadratic regression equation of $Y1$, $Y2$ and $Y3$ is as follows:

$$\begin{cases} Y1 = -1584.37 + 567.44X1 + 0.44X2 + 2.69X1X2 - 18.21X1^2 + 0.075X2^2 \\ Y2 = 2.33 - 0.35X1 + 0.011X2 + 0.017X1X2 - 0.11X1^2 - 0.00062X2^2 \\ Y3 = -0.97 + 0.37X1 + 0.027X2 - 0.0057X1X2 + 0.015X1^2 + 0.000067X2^2 \end{cases} \quad (8)$$

In order to explore the influence trend of interaction terms of factors on the $Y1$, $Y2$ and $Y3$, the contour map is drawn as shown in Fig. 8.

In Fig. 8a, when the rotational speed is constant, the $Y1$ is positively correlated with the blower pressure. The greater the pressure, the faster the conveying velocity of maize seeds entrained by airflow, the shorter the conveying time, and the higher the seed supply rate. When the pressure is constant, the $Y1$ is positively correlated with the rotational speed. The increase of the rotational speed can improve the migration velocity of the seeds in the migration zone, thereby improving the seed supply rate of the device. When the

pressure is 5.75~6.0 kPa and the rotational speed is 75~80 r/min, the $Y1$ is relatively high, ranging from 2712.86 to 2975 g/min. In Fig. 8b, when the rotational speed is constant, the $Y2$ is negatively correlated with the pressure at the rotational speed of 50 ~ 75 r/min, and it increases slowly at first and then decreases with the increase of the pressure at the rotational speed of 75 ~ 80 r/min. When the pressure was constant, the $Y2$ increased first and then decreased with the increase of the rotational speed at the pressure of 4.0~4.6 kPa, and it was roughly positively correlated with the rotational speed at the pressure of 4.6~6.0 kPa. When the pressure is 5.75~6.0 kPa and the rotational speed is 50~52.5 r/min, the $Y2$ is relatively low, ranging from 0.53 % to 0.83 %. In Fig. 8c, when the rotational speed is constant, the $Y3$ is positively correlated with the pressure. The higher the pressure, the faster the airflow entraps the seeds in the airflow seed delivery zone, and the easier it is to cause damage to the seeds coating when the seed collides with the seed and the seed collides with the inner wall of the device. When the pressure was constant, the $Y3$ was positively correlated with the rotational speed. With the increase of the rotational speed, the disturbance effect of the spiral shaft on the seed cluster in the migration zone is more obvious. The frequency of friction between seeds and seeds, seeds and components in the migration zone is increased. At the same time, with the increase of the rotational speed, the inertia force when the seeds flow out from the migration zone also increases, and the collision between the seeds and the seed-supply nozzle is intensified under the action of airflow. When the pressure is 4.0~4.25 kPa and the rotational speed is 50~55 r/min, the $Y3$ is relatively low, ranging from 1.12 % to 1.25 %.

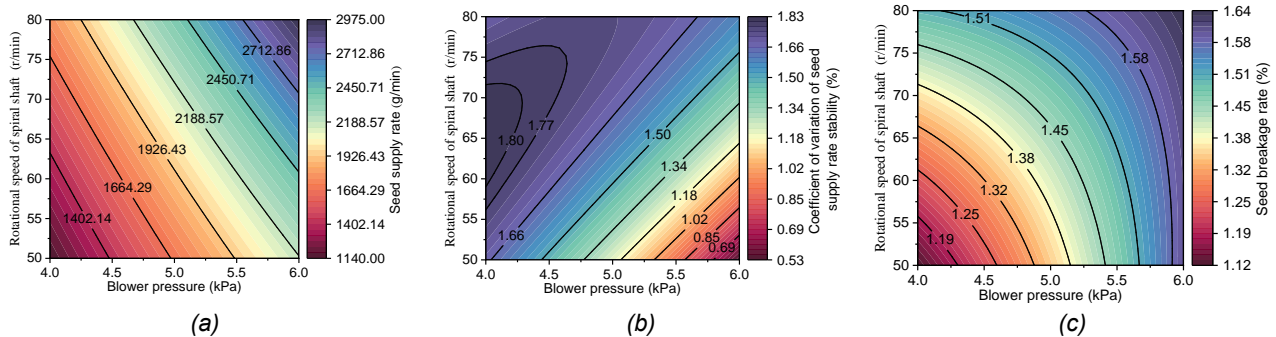


Fig. 8 - Effect of interactivity on test index

According to the results of multi-factor experiments, the optimal working parameter combination of the device was determined based on the multi-objective variable optimization method. With the highest $Y1$, the lowest $Y2$ and $Y3$ as the optimization objectives, the optimization equation is established within the range of factors and solved by Design-Expert 12 software.

The optimization equation is as follows:

$$\left\{ \begin{array}{l} \max Y1 \\ \min Y2 \\ \min Y3 \\ s. t. \left\{ \begin{array}{l} 4\text{kPa} \geq X1 \geq 6\text{kPa} \\ 50\text{r/min} \geq X2 \geq 80\text{r/min} \\ 1 \geq Y2(X1, X2) \geq 0 \\ 1 \geq Y3(X1, X2) \geq 0 \end{array} \right. \end{array} \right. \quad (9)$$

After calculation, the optimal working parameter combination for the device is: the pressure and the rotational speed are 6.0kPa and 80r/min, respectively. Under this parameter combination, the $Y1$, $Y2$, and $Y3$ are 2971.515 g/min, 1.774 %, and 1.616 %, respectively. The results were verified by bench test, and the $Y1$, $Y2$, and $Y3$ were 2933.21 g/min, 1.87 %, and 1.69 %, respectively, with the relative error of less than 5.5 % compared to the parameter optimization results. The optimized combination of working parameters makes the device achieve better test results in the bench test, and the error is small, which shows that the parameter optimization is effective.

CONCLUSIONS

In this study, according to the working process, the air-assisted spiral seed-supply device was divided into the migration zone and the airflow seed delivery zone. By establishing the kinetic model of maize seeds in the migration zone, the theoretical relationship between the absolute angular velocity ω_a of the seed cluster microsegment and the angular velocity ω_s of the spiral shaft was obtained. Based on the CFD simulation, when the inlet pressure of the airflow seed delivery zone at 2 s was 4.0, 4.5, 5.0, 5.5 and 6 kPa, the pressure range

was -1271.52 ~ 3993.05, -1426.41 ~ 4558.55, -1693.46 ~ 4994.76, -1957.58 ~ 5525.13, -1950.10 ~ 5961.19 Pa, and the maximum velocity of the airflow was 88.61 m/s. Based on the CCD, the multi-factor experiment was carried out, and the influence order of blower pressure X_1 and rotational speed of spiral shaft X_2 on seed supply rate, coefficient of variation of seed supply rate stability and seed breakage rate was: X_1 , X_2 . Based on the multi-objective variable optimization method, the optimal working parameter combination of the device was determined as the blower pressure of 6.0 kPa and the rotational speed of spiral shaft of 80 r/min. Under the verification test, the seed supply rate, the coefficient of variation of seed supply rate stability and the seed breakage rate were 2933.21 g/min, 1.87% and 1.69%, respectively. The relative error is within 5.5% compared with the result of parameter optimization. The device obtains higher seed supply performance under the optimized working parameter combination.

ACKNOWLEDGEMENT

The study was funded by the Heilongjiang Province Key Research and Development Program Major Projects, China (2022ZX05B02) and Ltd. 2023 Pilot Project on Integration of Agricultural Machinery R&D, Manufacturing, and Promotion and Application.

REFERENCES

- [1] Chen, X., Luo, X., Wang, Z., Zhang, M., Hu, L., Yang, W., Zeng, S., Zang, Y., Wei, H., & Zheng, L. (2015). Design and experiment of a fertilizer distribution apparatus with double-level screws. *Transactions of the Chinese Society of Agricultural Engineering*, Vol. 31, Issue 3, pp. 10-16. <https://doi.org/10.3969/j.issn.1002-6819.2015.03.002>
- [2] Ding, Y., Wang, K., Liu, X., Liu, W., Chen, L., Liu, W., & Du, C. (2021). Research progress of seeding detection technology for medium and small-size seeds. *Transactions of the Chinese Society of Agricultural Engineering*, Vol. 37, Issue 8, pp. 30-41. <https://doi.org/10.11975/j.issn.1002-6819.2021.08.004>
- [3] Fanigliulo, R., Grilli, R., Benigni, S., Fornaciari, L., Biocca, M., & Pochi, D. (2022). Effect of sowing speed and width on spacing uniformity of precision seed drills. *INMATEH-Agricultural Engineering*, Vol. 66, Issue 1, pp. 9-18. <https://doi.org/10.35633/inmateh-66-01>
- [4] Gao, X., Xie, G., Xu, Y., Yu, Y., & Lai, Q. (2022). Application of a staggered symmetrical spiral groove wheel on a quantitative feeding device and investigation of particle motion characteristics based on DEM. *Powder Technology*, Vol. 407, pp. 117650. <https://doi.org/10.1016/j.powtec.2022.117650>
- [5] Gao, X., Xu, Y., Yang, L., Zhang, D., Li, Y., & Cui, T. (2018). Simulation and experiment of uniformity of venturi feeding tube based on DEM-CFD Coupling. *Transactions of the Chinese Society of Agricultural Machinery*, Vol. 49, Issue S1, pp. 92-100. <https://doi.org/10.6041/j.issn.1000-1298.2018.S0.013>
- [6] Huai, H., Zhang, Q., Liu, M., & Tang, X. (2024). Changes in climate attributes and harvest area structures jointly determined spatial-temporal variations in water footprint of maize in the Beijing-Tianjin-Hebei region. *Heliyon*, Vol. 10, Issue 12, pp. E32565. <https://doi.org/10.1016/j.heliyon.2024.e32565>
- [7] Lei, X., Liao, Y., Wang, L., Wang, D., Yao, L., & Liao, Q. (2017). Simulation of gas-solid two-phase flow and parameter optimization of pressurized tube of air-assisted centralized metering device for rapeseed and wheat. *Transactions of the Chinese Society of Agricultural Engineering*, Vol. 33, Issue 19, pp. 67-75. <https://doi.org/10.11975/j.issn.1002-6819.2017.19.009>
- [8] Sun, W., Yi, S., Qi, H., Dai, Z., Zhang, Y., & Wang, S. (2024). Research progress on narrow row and dense planting delta-row seeding technology and equipment. *Agricultural Engineering*, Vol. 14, Issue 5, pp. 5-9. <https://doi.org/10.19998/j.cnki.2095-1795.2024.05.001>
- [9] Sun, W., Yi, S., Qi, H., Li, Y., Dai, Z., Zhang, Y., & Wang, S. (2024). Design and experiment of progressive seed-cleaning mechanism for air-pressure maize precision seed-metering device. *INMATEH-Agricultural Engineering*, Vol. 73, Issue 2, pp. 473-486. <https://doi.org/10.35633/inmateh-73-40>
- [10] Tang, H., Guan, T., Xu, F., Xu, C., & Wang, J. (2024). Test on adsorption posture and seeding performance of the high-speed precision dual-chamber maize metering device based on the seed characteristics. *Computers and Electronics in Agriculture*, Vol. 216, pp.108471. <https://doi.org/10.1016/j.compag.2023.108471>
- [11] Wang, L., Liao, Y., Liao, Q., Qi, T., Zhang, Q., & Wang, B. (2021). Design and test on centralized metering seed feeding device of air-assisted planter for rapeseed. *Transactions of the Chinese Society of Agricultural Machinery*, Vol. 52, Issue 2, pp.75-85. <https://doi.org/10.6041/j.issn.1000-1298.2021.02.007>

- [12] Wang, L., Liao, Y., Zhang, Q., Liu, H., Wang, B., & Liao, Q. (2020). Experiments and analysis on seeding performance of seed feeding device of rapeseed centralized metering device under lateral tilt. *Transactions of the Chinese Society of Agricultural Engineering*, Vol. 36, Issue 19, pp.1-10. <https://doi.org/10.11975/j.issn.1002-6819.2020.19.001>
- [13] Yao, L., Liao, Q., Wang, L., Liu, H., Wei, G., & Wang, B. (2022). Design and experiment of spiral seed feeding device in spinning disc high-speed metering device for rapeseed. *Transactions of the Chinese Society of Agricultural Machinery*, Vol. 53, Issue 6, pp. 78-88. <https://doi.org/10.6041/j.issn.1000-1298.2022.06.008>
- [14] Yang, W., Fang, L., Luo, X., Li, H., Ye, Y., & Liang, Z. (2020). Experimental study of the effects of discharge port parameters on the fertilizing performance for fertilizer distribution apparatus with screw. *Transactions of the Chinese Society of Agricultural Engineering*, Vol. 36, Issue 17, pp.1-8. <https://doi.org/10.11975/j.issn.1002-6819.2020.17.001>
- [15] Yuan, H., Liu, C., Song, J., Du, X., Jiang, M., & Li, W. (2020). Piezoelectric vibration seed supply device of precision metering device for plug seedling of super hybrid rice. *Transactions of the Chinese Society for Agricultural Machinery*, Vol. 51, Issue S2, pp. 31-40. <https://doi.org/10.6041/j.issn.1000-1298.2020.S2.004>

DESIGN AND EXPERIMENT OF GUIDANCE CAM OF AIR SUCTION GARLIC CLOVE DIRECTIONAL METERING DEVICE

气吸式大蒜定向排种器导向凸轮的设计与试验

Kunqiao LI, Fuhai FANG, Zhuo WANG, Yongzheng ZHANG, Mingliang ZHANG

Shandong University of Technology, College of Agricultural Engineering and Food Science, Zibo (255000), China

Tel: +86-13015557631; E-mail: jixieshiji2021@126.com

DOI: <https://doi.org/10.35633/inmateh-75-02>

Keywords: air suction type, directional metering device, guide cam, garlic, garlic clove direction

ABSTRACT

To enhance the upright orientation rate of garlic clove bud tips, an air-suction garlic clove directional metering device with a guiding cam was developed. Key parameters influencing garlic clove discharge performance were determined through mechanical analysis. After optimization, the guiding cam's thickness (D) was set at 4 mm, with the lead-in and the seeding section tilt angles (α, β) of 5° and 15° , respectively. Comparative tests were conducted using optimal parameters, focusing on seed discharge disc rotational speed (n) and negative pressure (P) as main variables, with the upright rate of seeds in the receiving hopper serving as the evaluation index. Under conditions of -11.5 kPa negative pressure and 7 rad/s rotational speed, the upright rate reached 97.2%. Results demonstrated that the addition of guiding cams significantly improved the upright rate, increasing it by over 10% compared to directional metering devices without guiding cams.

摘要

为了提高排种后蒜种芽尖向上直立率低的问题。设计了一种带有导向凸轮的气吸式定向排种器，通过完成蒜种接触导向凸轮过程的力学分析，明确了影响导向排种性能的关键参数。得出导向凸轮厚度为 4mm、导入段倾斜角度为 5° 、投种段倾斜角度为 15° 。并且接料斗最优参数组合下进行对比验证试验，排种盘转速 (n) 以及负压大小 (P) 为试验因素，落入接料斗直立率为评价指标。增设导向凸轮排种器 p 为 -11.5kPa、 n 为 7rad/s 时，落入接料斗直立率达到 97.8%。稳定吸附时，排种器直立率之差 $\Delta > 10\%$ 。因此，增设导向凸轮的直立率显著高于不安装导向凸轮。

INTRODUCTION

The metering device in sowing machinery typically performs four functions: seed filling, cleaning, guarding, and casting, with a guide mechanism ensuring uniform plant spacing. In garlic planting, maintaining an upright bud orientation is crucial (Wu et al., 2024; Liu et al., 2022; Xu et al., 2021). The garlic clove discharger must ensure uniform seed feeding in both timing and speed while discharging cloves with the bud tip upward to facilitate smooth entry into the hopper and improve seed uprightness (Babatunde et al., 2020; Chen et al., 2016).

Recent studies by both domestic and international scholars have led to advancements in seed guiding devices (Kang et al., 2022; Zhao et al., 2018; Liao et al., 2020; Liu et al., 2015). A belt-type, high-speed corn seed guiding device using a rotating clamping method to improve seed entry accuracy and stability was developed (Ma et al., 2023). A soybean precision seeding device was designed to ensure consistent grain spacing (Chen et al., 2022). A corn posture-controlled seeding device that optimizes the seed guiding trajectory to maintain constant seed placement and speed was introduced (Dong et al., 2023). A finger-driven, synchronous belt seed guiding system was developed (Liu et al., 2017). John Deere of the United States created a brush belt seed guiding device to ensure stable seed guidance at high speeds (Ji et al., 2021). The seeds discharged from the seed meter are thrown onto the partition of the conveyor belt by turning the fingers. The seeds move to the seeding port along the conveyor belt and are delivered to the seed furrow at a consistent speed (Liu et al., 2020).

The primary goal of seed guidance design is stable, accurate seeding. While prior research focuses on non-directional crops, this study introduces a fixed guide cam for air-suction garlic seeders, ensuring cloves discharge with the bud tip upward for smooth hopper entry.

MATERIALS AND METHODS

Principle and composition of the guided cam working profile

The air-suction garlic seeding device rotates at speed n , guiding suction holes through seed suction (I), directional (II), and discharge (III) areas, as shown in Figure 1. In the suction area, cloves are captured; in the directional area, they align tangentially with the suction hole's center circle, maintaining an attitude angle of -15° to 15° . In the discharge area, cloves are released with the bud tip upward. Positioning the discharge point at S (horizontal) causes instability due to height, while lowering it to P resolves this. The guide cam adjusts the deflection angle for proper orientation, making its contour and position critical.

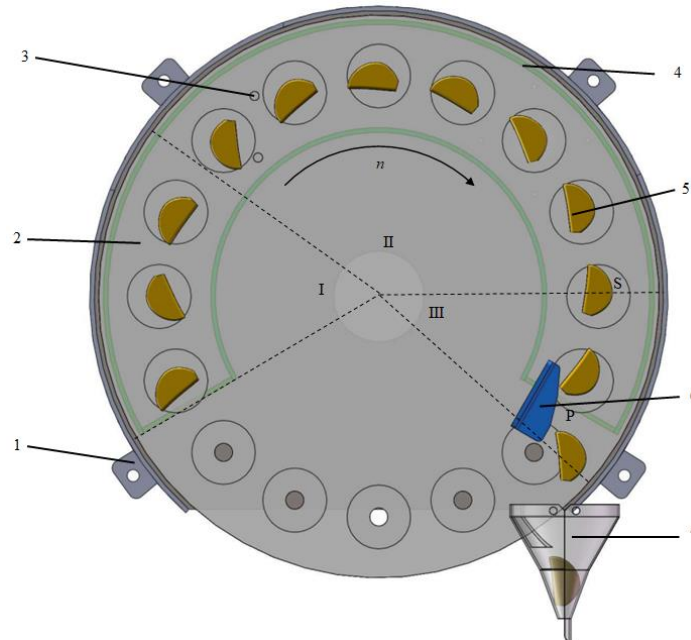


Fig. 1 - Working principle diagram of a seed tray

1 - Shell; 2 - Seed plate; 3 - Directional needles; 4 - Negative pressure chamber; 5 - Garlic clove; 6 - Guide cam; 7 - Hopper.

The guide cam's working profile comprises two curved sections, ab and bc , connected smoothly by rounded corners. In-plane projection, these sections appear as straight lines. When garlic cloves contact the ab and bc sections, their posture and deflection angles are adjusted, correcting the 30° deflection at point P observed without a guide cam. This ensures the cloves fall smoothly into the receiving bucket with the bud tip facing upward, completing the guiding and seeding process.

Guided Process Analysis

The guiding process of garlic cloves was analyzed using a plane analytical method to examine the contact torque between cloves and the guide cam. Contact types include side edge and arc surface contact. For side edge contact, the cloves' posture angle at point S ranges from -15° to 15° , with contact occurring along varying straight-line segments. A coordinate system X and Y with point b as the origin was established to analyze the garlic clove contact, as shown in Fig.2.

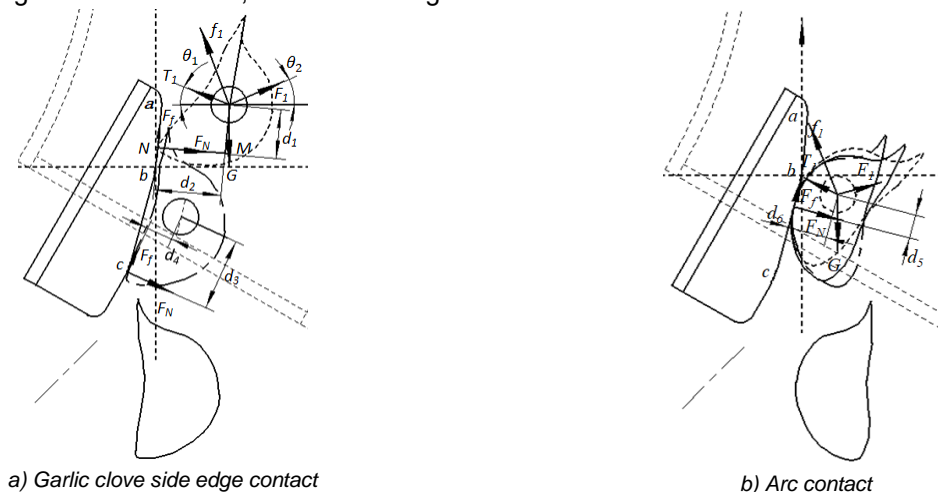


Fig. 2 - Analysis of garlic clove contact guide cam process

When the garlic clove first contacts the ab segment, as shown in Fig.2 (a), the counterclockwise torque (M_1) must exceed the clockwise torque (M_2) to meet the guidance requirements, as shown in formula (1).

$$\begin{cases} M_1 > M_2 \\ M_1 = F_N \cdot d_1 \\ M_2 = F_f \cdot d_2 \end{cases} \quad (1)$$

where: M - rotational torque of garlic clove, N·mm;

d - rotational force arm of garlic clove, mm;

F_N, F_f - the force of the guide cam relative to the garlic clove, N;

The force arm (d) is defined as the distance from the center of the suction hole to the straight line (l). The expression for the force arm is determined by solving the equations of the two straight lines.

$$\begin{cases} y_1 = \frac{1}{\tan a_t} \cdot x_1 \\ y_2 = -\tan a_t x_2 + \frac{\sqrt{x_a^2 + y_a^2}}{\cos a_t} \end{cases} \quad (2)$$

Garlic clove rotation arm(d) is obtained, as shown in formula (3):

$$d_1 = \frac{\left| \tan a_t x_b + y_b - \frac{\sqrt{x_a^2 + y_a^2}}{\cos a_t} \right|}{\sqrt{1 + \tan^2 a_t}}, \quad d_2 = \frac{\left| -\frac{1}{\tan a_t} x_b + y_b \right|}{\sqrt{-\frac{1}{\tan^2 a_t} + 1}} \quad (3)$$

where: y_1, y_2 - expression for straight line segment l_{MN}, l_{ab} ;

a_t - the lead-in section (ab) tilt angle, °;

Taking the suction hole as the origin, F_N and F_f are obtained by analyzing the force on the garlic clove.

$$\begin{cases} T_1 \cos \theta_1 = F_1 \cos \theta_2 \\ F_f = \mu F_N \\ F = \sqrt{F_N^2 + F_f^2 + 2F_N F_f \cos \theta_3} \end{cases} \quad (4)$$

where: θ_1 - angle between centripetal force (T) and horizontal direction, °;

θ_2 - angle between resultant force (F_1) and horizontal direction, °;

θ_3 - the angle between the force (F_N) and the friction force (F_f), °;

T - centripetal force on a garlic clove, N;

Substituting Formula (4), and Formula (3) into Formula (1), Formula (5) can be obtained by simplifying it:

$$\left(\sin a_t + y_b \cos a_t - \frac{\sqrt{x_a^2 + y_a^2}}{\cos a_t} \right) \cdot F_N > x_b \cos a_t + y_b \sin a_t \cdot F_f \quad (5)$$

The analysis of formula (5) reveals that counterclockwise rotation requires a relationship between a_t and contact point positions (x_a, y_a). When the garlic clove first contacts the bc segment (Figure 2b), and the adjustment angle β aligns with the clove's deflection angle, the force arm $d_3 > d_4$, making β crucial for guiding. Therefore, the parameters a_t, β , and the contour require precise design.

Determination of guide cam profile

The guide cam's position and contour were optimized using Jinshan garlic as the study object. Most cloves, measuring 27-34 mm in length and 16-23 mm in width, account for 96% of the total sample, with larger cloves contacting the guide cam earlier. For analysis, a clove length of 34 mm and width of 20 mm were selected. Initial contact scenarios were evaluated to determine the guide cam's position parameters.

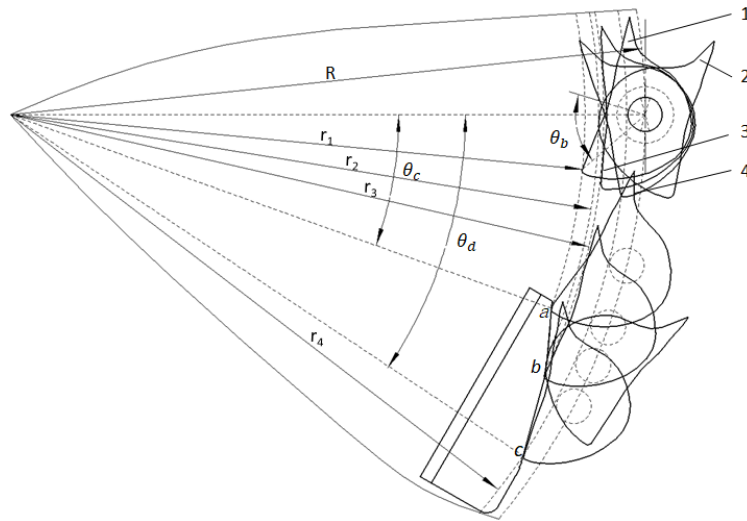


Fig. 3 - Schematic diagram of the position where the garlic clove first contacts the guide cam
 1 - Side edge contact $\theta_z = 15^\circ$; 2 - Arc contact $\theta_z = 15^\circ$; 3 - Side edge contact $\theta_z = 0^\circ$; 4 - Side edge contact $\theta_z = -15^\circ$.

The design conditions for guide cam points *a*, *b*, and *c* are as follows: First, when θ_z is 15° , the side edge contacts point *a* at a distance r_1 from the center, ensuring that cloves of various sizes make contact with the *ab* segment. Second, when θ_z is 15° , the arc surface contacts point *b* at a distance r_2 from the center, positioning the force below the suction hole. At θ_z , the side edge passes smoothly through point *b*, and at θ_z is -15° , it contacts point *c* at a distance r_4 from the center, as shown in figure 3. This design ensures garlic cloves maintain contact with the guide cam before separating from negative pressure, optimizing the guidance effect.

$$\left\{ \begin{array}{l} \tan \theta_b = \frac{L/2}{D/2} \\ r_1 = R - \frac{D}{2 \cos \theta_b} \cdot \cos 90^\circ - \theta_b \\ r_2 = R - \frac{D}{2 \cos \theta_b} \\ r_3 = R - \frac{D}{2} \\ r_4 = R - \frac{D}{2 \cos \theta_b} \cos \theta_b + 15^\circ \end{array} \right. \quad (6)$$

where: *R* - Radius from the center of the suction hole to the center of the seed plate, mm;
 θ_b - The angle between the length *L* and width *B* of the garlic clove, $^\circ$.

The dimension parameters of the guide cam *ab* segment meet the following requirements:

$$129.47\text{mm} \approx r_1 < 134.2\text{mm} \approx r_2 < r_3 < r_4 \approx 141.35\text{mm} \quad (7)$$

From formula (7), point *a* is positioned at $r_1 = 130\text{mm}$, point *b* at $r_2 = 135\text{mm}$, and point *c* at $r_4 = 140\text{mm}$.

Determination of guide cam thickness and installation position

The precise guiding of garlic cloves depends on the thickness of the guide cam and its distance from the seed plate. An improper distance can lead to ineffective contact or tipping of the garlic clove. Measurements of Jinxiang garlic cloves indicate side edge contact points (l_1) ranging from 2.6mm - 4.8mm and arc surface contact points (l_2) from 5.1mm - 7.2mm. Consequently, the distance between the guide cam's center line and the seed plate (*T*) was set at $T=5\text{mm}$. The final thickness was established at $D=4\text{mm}$, ensuring effective guidance for 98% of the cloves.

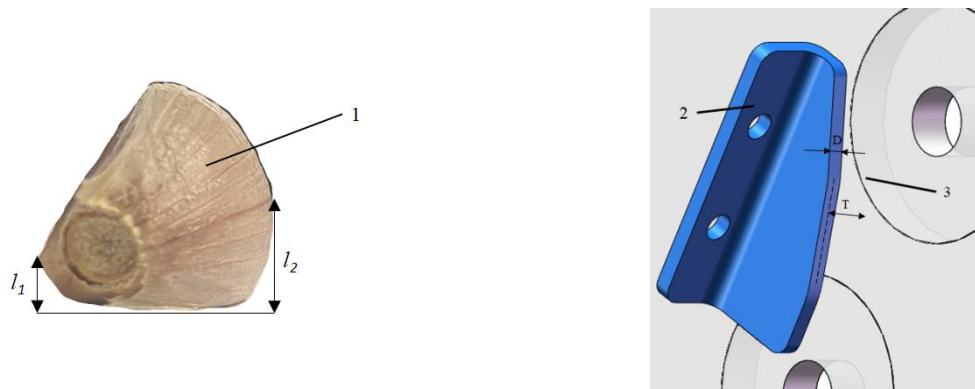


Fig. 4 - Garlic clove contact surface height
 1 - Garlic clove; 2 - Guide cam; 3 - Seed plate.

Determination of tilt angle parameters

The determination of the inclination angle of the lead-in section (α_t) and the seeding section are crucial, as it directly influences the direction of the resultant force (F). If F points toward the center, it can cause the garlic clove to move radially, resulting in jamming and reduced sowing accuracy. To prevent this, the contact between the garlic clove and point a is analyzed. Ensuring point a does not cause jamming guarantees that as the clove contacts the ab section, the angle between the force and the suction hole center increases, thus avoiding jamming. By appropriately setting the α_t angle, $\lambda_l > 0$ is maintained, ensuring smooth guidance of the garlic clove, as shown in Figure 5(a).

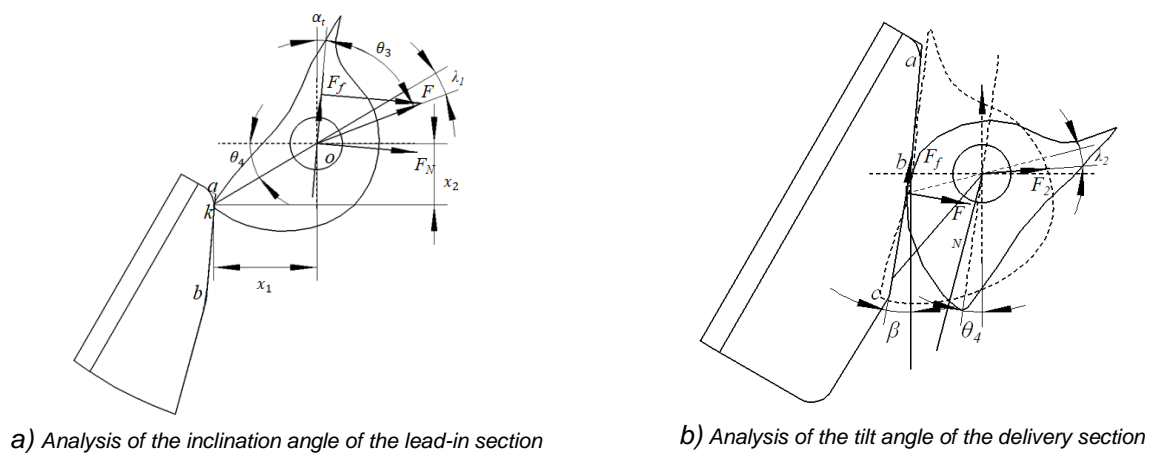


Fig. 5 - Garlic clove contact profile analysis

Geometric analysis of garlic clove contacting point a in the lead-in section:

$$\begin{cases} \tan \theta_4 = \frac{x_1}{x_2} \\ \theta_3 = \arccos \frac{F_f}{F_1} \\ \lambda_1 = \beta + \theta_4 + \theta_3 - 90^\circ \end{cases} \quad (8)$$

where: θ_4 - the angle between ok and the horizontal direction, °; λ_1 - the angle between ok and F , °; x_1, x_2 - horizontal distance and vertical distance between k and O , mm.

Experimental measurements showed that for varying size ranges x_1 and x_2 , $\theta_2 \approx 60^\circ$, and θ_3 ranged from $20.5^\circ - 25.6^\circ$. Substituting θ_2 and θ_3 into formula(13), when $\lambda_1 > 0$, the value range of α_t is $2.3^\circ - 8.6^\circ$.

If $\beta < \alpha_t$, misguidance occurs ; if $\beta > \alpha_t$, root engagement fails, altering torque. β must position the force below the suction hole while ensuring root contact, as shown in Figure 5(b). For $\lambda_2 > 0$, β ranges from 10° to 30.3° . To avoid misdirection, $\beta < 18.5^\circ$, setting the bc section's inclination between 13° and 19.5° .

Experimental materials and equipment

The JPS-12 sowing bench test, with a modified air control system, positioned the negative pressure zone and seeding point 30° below the horizontal plane, as shown in Figure 7. Garlic cloves, categorized by thickness—A (12–15 mm, 30%), B (15–18 mm, 41%), and C (18–21 mm, 25%)—covered 96% of Jinxiang samples (Li et al., 2022). The guide cam and hopper are 3D printed using resin.

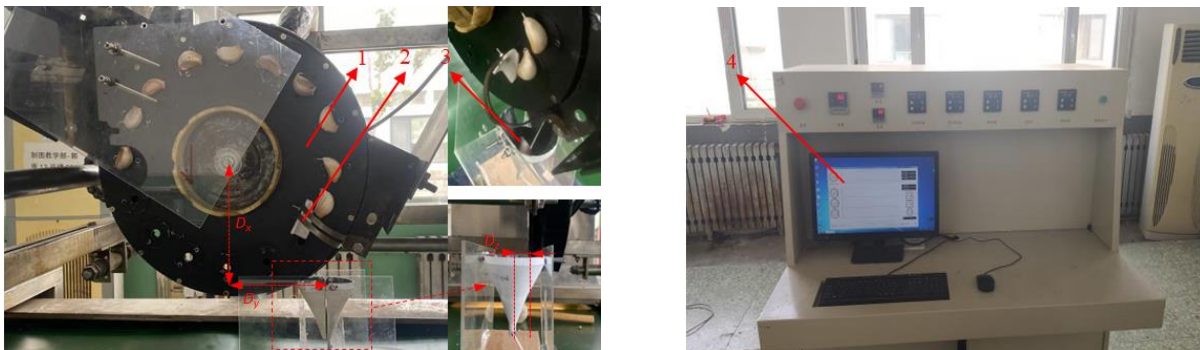


Fig. 7 – Bench testing of metering devices

1 - Metering device; 2 - Guide cam; 3 - Falling into the hopper in an upright position; 4 - Equipment Controls.

Test methods

(1) A five-factor, three-level design experiment was conducted in a stable environment with initial trials to determine α_t , β , D_x , D_y and D_z ranges. The optimal parameter combination was determined using the upright orientation rate (Y_1) as the evaluation index. The experimental structure code is shown in Table 1.

Table 1

Table of factors and levels

Level	Factors				
	Angle of the lead in section, $\alpha_t / ^\circ$	Angle of the seeding section, $\beta / ^\circ$	Lateral distance, D_x / mm	Longitudinal distance, D_y / mm	Vertical distance, D_z / mm
-1	3	13	140	125	9
0	5	15	145	130	11
1	7	17	150	135	13

(2) Based on the experiment (1), a bench high-speed operation performance comparison test was conducted on the seed meter with and without additional guides. A two-factor experiment tested negative pressure across 10 gradients (-8.5 to -13 kPa) and rotational speed at 4 levels(6–9 rad/s).

The upright orientation rate(Y_1) evaluated the guide cam's effectiveness:

$$Y_1 = \frac{m_1}{Q} \times 100\% \tag{9}$$

where: m_1 - the number of buds falling into the receiving hopper with the buds pointing upwards;

Q - total number of garlic cloves.

RESULTS

Analysis of test results

The results of the orthogonal test are shown in Table 2, where A, B, C, D, and E are structural coding values. Each group of tests was performed 4 times to obtain the average value.

Table 2

Experimental program and results

Number	Factors					Indicators	Number	Factors					Indicators
	A	B	C	D	E			Y ₁	A	B	C	D	
1	-1	-1	0	0	0	92.6	24	0	1	1	0	0	95.8
2	1	-1	0	0	0	88.6	25	-1	0	0	-1	0	91.8
3	-1	1	0	0	0	94.5	26	1	0	0	-1	0	85.6
4	1	1	0	0	0	85.4	27	-1	0	0	1	0	88.8
5	0	0	-1	-1	0	93.8	28	1	0	0	1	0	82.4

Number	Factors					Indicators Y ₁	Number	Factors					Indicators Y ₁
	A	B	C	D	E			A	B	C	D	E	
6	0	0	1	-1	0	94.6	29	0	0	-1	0	-1	93.6
7	0	0	-1	1	0	91.2	30	0	0	1	0	-1	94.2
8	0	0	1	1	0	90.2	31	0	0	-1	0	1	89.6
9	0	-1	0	0	-1	90.5	32	0	0	1	0	1	89.2
10	0	1	0	0	-1	93.4	33	-1	0	0	0	-1	88.6
11	0	-1	0	0	1	87.2	34	1	0	0	0	-1	84.5
12	0	1	0	0	1	82.6	35	-1	0	0	0	1	87.6
13	-1	0	-1	0	0	93.8	36	1	0	0	0	1	82.8
14	1	0	-1	0	0	86.1	37	0	-1	0	-1	0	92.6
15	-1	0	1	0	0	94.6	38	0	1	0	-1	0	93.8
16	1	0	1	0	0	86.8	39	0	-1	0	1	0	88.4
17	0	0	0	-1	-1	91.2	40	0	1	0	1	0	87.6
18	0	0	0	1	-1	92.4	41	0	0	0	0	0	95.6
19	0	0	0	-1	1	87.6	42	0	0	0	0	0	96.9
20	0	0	0	1	1	85.8	43	0	0	0	0	0	92.8
21	0	-1	-1	0	0	95.5	44	0	0	0	0	0	96.2
22	0	1	-1	0	0	92.6	45	0	0	0	0	0	97.4
23	0	-1	1	0	0	94.8	46	0	0	0	0	0	98.7

The test results were analyzed using Design-Expert software to establish a quadratic regression model for the upright orientation rate (Y₁). The model's significance was verified through Anova and regression coefficient tests, the results showed that the most significant factors were A, D, and E, Results are presented in Table 3. The responses between the important factors and their effects on Y₁ were analyzed by completing the response surface, as shown in Figure 8.

Table 3

Measured test data from variance analysis

Sources	Sum of Squares	Degrees of Freedom	Mean Square	F-value	P-value
Models	722.36	20	36.12	11.65	<0.0001 *
A	156.88	1	156.88	50.99	<0.0001 *
B	1.27	1	1.27	0.4082	0.5287
C	1.00	1	1.00	0.3225	0.5752
D	36.60	1	36.60	11.80	0.0021*
E	81.00	1	81.00	26.12	<0.0001 *
Lack of Fit	57.45	20	2.87	0.7154	0.7325
Pure Error	20.07	5	4.01	R²	0.9131

Note: * means extremely significant (P < 0.01)

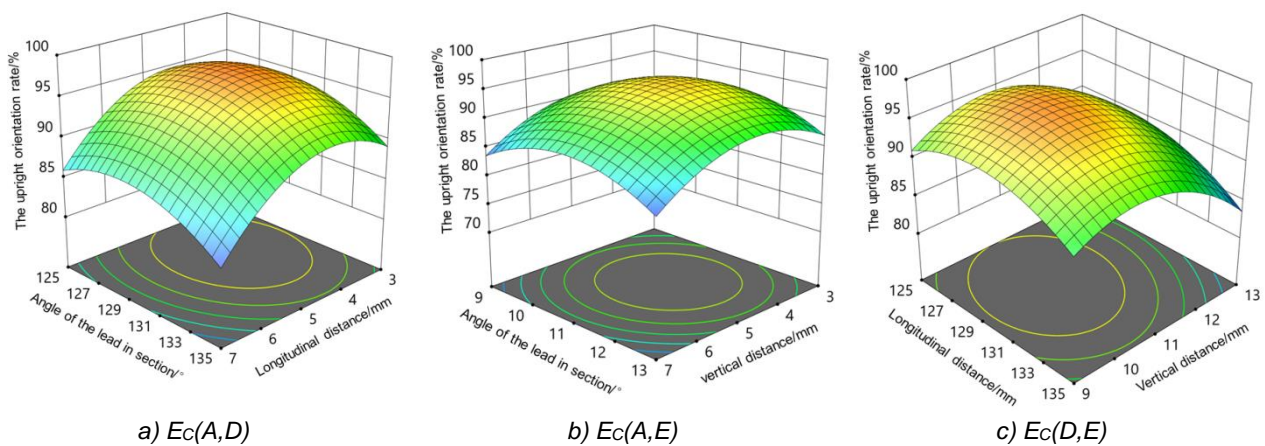


Fig. 8 – Bench testing of metering devices

Optimization of the model by parameter combination with Y₁ taking the maximum value of $\alpha_i=5^\circ$, $\beta=15^\circ$, $D_x=140\text{mm}$, $D_y=128\text{mm}$, $D_z=9\text{mm}$. Verification tests with these parameters resulted in an average uprightness of 96.8%, which was determined to be the optimal parameter.

Comparative test

Table 4 compares the performance of devices *K* and *T* under varying pressures and speeds. Device *T*'s upright rate rose and then fell with increasing pressure; low pressure caused unstable C-size clove adsorption, while high pressure impeded posture adjustment. Optimal rates (>92%) were achieved at -10 to -12 kPa. Device *K*'s upright rate stabilized at -10 kPa after an initial rise.

Table 4

Comparison of the qualified index of *K* and *T* seeding devices (Short version)

Working speed (n) / (rad/s)	-8.5 kPa			-9 kPa			-9.5 kPa			-10 kPa			-10.5 kPa		
	K	T	Δ	K	T	Δ	K	T	Δ	K	T	Δ	K	T	Δ
6	66.3	67.2	-0.9	71.2	70.2	1.0	72.2	76.4	-4.2	78.5	82.6	-4.1	82.4	88.4	-6.0
7	63.2	61.2	-2	68.8	70.6	-1.8	75.8	78.0	-2.2	79.0	83.8	-4.8	84.2	90.2	-6.0
8	54.2	58.0	-3.8	63.4	60.4	3.0	60.2	61.8	-1.6	68.3	73.0	-4.7	76.3	84.6	-8.3
9	50.3	48.6	1.7	50.2	49.4	0.8	55.2	56.4	-1.2	68.0	70.4	-2.4	70.2	78.4	-8.2
Working speed (n) / (rad/s)	-11 kPa			-11.5 kPa			-12 kPa			-12.5 kPa			-13 kPa		
	K	T	Δ	K	T	Δ	K	T	Δ	K	T	Δ	K	T	Δ
6	82.6	93.4	-10.8	86.2	95.6	-9.4	82.0	94.6	-12.6	86.5	92.8	-6.3	82.0	89.6	-7.6
7	83.5	93.5	-10.0	87.6	98.8	-11.2	88.5	97.9	-9.4	87.6	94.4	-6.8	86.2	95.2	-9.0
8	83.5	90.8	-7.3	86.4	96.6	-10.2	83.4	94.2	-10.8	84.4	91.4	-7.0	81.3	90.6	-9.3
9	82.4	91.4	-9.0	85.6	95.8	-10.2	85.4	94.0	-9.6	84.6	92.6	-8.0	83.4	92.5	-9.1

Note: *K* represents the upright rate of the bud tip without a guide cam (%), *T* represents the upright rate with a guide cam (%), and Δ is the difference between the two rates (%)

As shown in Table 4, the difference in the vertical rate (Δ) highlights the guide cam's impact on seeders *T* and *K*. Δ increases and then decreases with pressure changes. At -8.5 to -10 kPa, $|\Delta| < 5\%$, showing minimal impact. Between -10 and -12 kPa, Δ reaches up to 10%, significantly improving the vertical rate. At -11.5 kPa and 7 rad/s, the *T* seeder achieves a vertical rate of 98.8%, with Δ at -11.2%, confirming the guide cam's superior performance.

CONCLUSIONS

The traditional air-absorbing garlic clove metering device has been improved by adding a guiding cam to control the orientation of the garlic cloves so that the bud tips are discharged in an upward direction, which improves the stability of the sowing and meets the agronomic requirements. The analysis of garlic clove size and attitude determined the key parameters: introduction angle $\alpha_t = 5^\circ$, thickness $D = 4$ mm, and seeding section inclination $\beta = 15^\circ$, $D_x=140$ mm, $D_y=128$ mm, $D_z=9$ mm, enabling effective posture adjustment. Validation experiments showed the guide cam significantly improved upright rates. At -10.5kPa, the upright rate difference (Δ) exceeded 5%, reaching (Δ) to 10% at -11 to -12kPa. At -11.5kPa and 7 rad/s, the upright rate peaked at 97.2%, 11.2% higher than without the guide cam, confirming its design effectiveness.

ACKNOWLEDGEMENT

This research was supported by the Natural Science Foundation of Shandong Province (ZR2022ME103) and the 2022 Agricultural Application Technology Innovation Project of Jinan City (CX202216).

REFERENCES

- [1] Babatunde S. (2020). Design and fabrication of an electrically powered maize planter. *Journal of Engineering Studies and Research*. Vol.26, pp. 204 -211.
- [2] Chen C. (2016). *Structural design and performance test of belt-type seed guide device of precision seeder* (精量播种机带式导种装置结构设计与性能试验研究), Master's thesis Inner, Mongolia Agricultural University.
- [3] Chen Y., Han J., Lan Y., Zhang M., Jin Y., Zhang Z., Wang W. (2022). Design and experiment of the

- combined seed guiding tube for precision metering device (精密排种器组合式导种管设计与试验). *Transactions of the Chinese Society of Agricultural Engineering*, Vol. 38, pp. 14-24.
- [4] Dong J., Gao X., Zhang S., Huang Y., Zhang C., Shi J., (2023). Design and Test of Guiding Seed Throwing Mechanism for Maize Posture Control and Driving Metering Device (玉米姿控驱导式排种器导向投种机构设计与试验). *Transactions of the Chinese Society for Agricultural Machinery*, Vol.54, pp.25-34.
- [5] Ji J., Sang Y., He Z., Jin X., Wang S. (2021). Designing an intelligent monitoring system for corn seeding by machine vision and Genetic algorithm-optimized back propagation algorithm under precision positioning. *Plos One*, Vol. 16, pp. 7-10.
- [6] Kang J., Xiang Y., Zhang C., Peng Q., Zhang G. (2022). Analysis and experiments of the seed feeding performance of air-suction roller dibbler for peanuts (气吸滚筒式花生穴播器投种性能分析与试验). *Transactions of the Chinese Society of Agricultural Engineering (Transactions of the CSAE)*, Vol. 38, pp.1-11.
- [7] Liao Y., Li C., Liao Q., Wang L., (2020). Research Progress of Seed Guiding Technology and Device of Planter (播种机导种技术与装置研究进展分析). *Transactions of the Chinese Society for Agricultural Machinery*, Vol. 51, pp. 1-14.
- [8] Liu L., Yang H., (2015). 3D reverse engineering design on seed tube based on Geomagic Design software (基于 Geomagic Design 软件的导种管三维逆向工程设计). *Transactions of the Chinese Society of Agricultural Engineering*, Vol. 31, pp. 40-45.
- [9] Liu S., Jia H., Wang J., (2022). Promotion and application of mechanization technology in garlic production (大蒜生产机械化技术的推广应用). *Promotion of Agricultural Machinery Technology*, Vol. 08, pp. 17-19.
- [10] Liu Z., Xia J., Hu M., Du J., Luo C., Zheng K., (2021). Design and analysis of a performance monitoring system for a seed metering device based on pulse width recognition. *Plos One*, Vol. 16.
- [11] Li C., (2022). Experimental study on garlic air-suction seed metering device for application of image recognition and orientation technology (便于图像识别定向技术应用的大蒜气吸式排种器的试验研究). Master's thesis Inner, Shandong University of Technology.
- [12] Liu Q., (2017). *Design and experimental study of seed precision delivery mechanism of high-speed seeder* (高速播种机种子精准投送机构设计与试验研究). PhD dissertation, China Agricultural University.
- [13] Ma C., Yi S, Tao G., Li Y., (2023). Mechanism Analysis and Parameter Optimization of Corn Seeds Receiving by Rotating Clamp of Belt-type Seed Guiding Device (带式玉米高速导种装置旋夹纳种机理分析与参数优化). *Transactions of the Chinese Society for Agricultural Machinery*, Vol.54, pp. 134-143.
- [14] Wu X., Zhong Z., Tang L., (2024). Experimental study on the effects of different garlic planters and planting parameters on garlic planting efficiency (不同机型和播种参数对大蒜播种效果的影响). *Journal of Shenyang Agricultural University*, Vol. 55, pp. 474-482.
- [15] Xu H., Li C., Feng R., Song J., Xiang H., (2021). Effect of garlic planting orientation on garlic growth and yield (蒜种植方位对大蒜生长发育及产量的影响). *Journal of Chinese Agricultural University*, Vol.42, pp.74-78.
- [16] Zhao S., Chen J., Wang J., Chen J., Yang C., Yang Y., (2018). Design and Experiment on V-groove Dialing Round Type Guiding-seed Device (精量播种机V型凹槽拨轮式导种部件设计与试验). *Transactions of the Chinese Society for Agricultural Machinery*, Vol. 49, pp. 146-158.

RESEARCH ON THE OPTIMIZATION METHOD OF CLUTCH ENGAGEMENT TRAJECTORY IN THE TRACTOR POWER SHIFT PROCESS

拖拉机动力换挡过程离合器接合轨迹优化方法研究

Dongyang WANG¹⁾, Weipeng ZHANG²⁾, Jiangtao JI³⁾, Zuohua DONG⁴⁾, Hongmei ZHU¹⁾, Zhanyu LI¹⁾

¹⁾College of Automotive and Transportation Engineering, Shenzhen Polytechnic University, Shenzhen/China;

²⁾ National Key Laboratory of Agricultural Equipment Technology, China Academy of Agricultural Mechanization Science Group Co., Ltd, Beijing/ China

³⁾ College of Agricultural Equipment Engineering, Henan University of Science and Technology, Luoyang/China

⁴⁾ Changzhou Dongfeng Agricultural Machinery Group Co. Ltd., Changzhou/China

Tel: 86-15236286319; E-mail: zpt_wdy@szpu.edu.cn

DOI: <https://doi.org/10.35633/inmateh-75-03>

Keywords: Clutch, Engagement trajectories, Pseudo-spectroscopy, Optimization

ABSTRACT

To address the issue of reduced comfort and operational accuracy in tractors caused by the clutch engagement process in combination with automatic transmissions, dual-clutch transmissions, and hybrid power tractors, a new method is proposed that considers both the slipping process and synchronous instantaneous control at the moment of engagement. In this method, the optimal engagement process model of the clutch considering the clutch sliding process and synchronous instantaneous control was established, and the optimal trajectory of the clutch engagement process was solved based on the pseudo-spectral method. Then, the optimization results were compared with those obtained without considering the synchronous instantaneous. The results show that the proposed method considering the sliding process and synchronous instantaneous constraint can reduce the frictional loss of the clutch by 9%, and suppress the impact to below 10 m/s³. Finally, this method was applied to the control of tractor starting up, gear shifting and hybrid power mode switching processes. Simulation results demonstrate that this method can be effectively applied to these three operating conditions.

摘要

为解决搭配自动变速器、双离合变速器 and 混合动力拖拉机离合器接合过程导致的拖拉机舒适性和作业精度降低问题，提出了一种考虑滑摩过程和同步瞬间控制的新方法。在该方法中，建立了考虑离合器滑摩过程和同步瞬间控制的离合器最优接合过程模型，并基于伪谱法求解了离合器接合过程的最优轨迹。结果表明，考虑滑动过程和同步瞬间约束优化方法可使离合器的摩擦损耗降低 9%，并可抑制冲击降低到 10 m/s³ 以下。最后，将该方法应用于拖拉机起步、换挡和混合动力模式切换过程的控制，仿真结果表明，该方法能较好地应用于上述三种工况。

INTRODUCTION

As a key component in the tractors' driveline, the clutch has important impact on the comfort of the vehicle during start-up, shifting and mode switching of hybrid vehicles (Fig.1) (Park et al, 2021; Van Berkel et al, 2014; Lu, 2012; Li et al, 2020; Minh et al, 2012). To ensure smooth driving and prolong the service life of components, the clutch is supposed to be engaged quickly and smoothly during the start-up, shift and mode switch process of tractors equipped with automatic transmission and hybrid-driven driveline (Gavvani et al, 2016; Zhao et al. 2016; Fu et al., 2016). Researches have shown that the fast and smooth engagement can be obtained by controlling the drive and driven disc of the clutch to engage in a certain trajectory (Zhao. et al., 2016). Therefore, it is necessary to optimize the engagement trajectory of the clutch.

¹⁾ Dongyang Wang, Lecture, Ph.D. Eng; Weipeng Zhang, Senior engineer Ph.D. Eng; Jiangtao Ji, Prof. Ph.D.Eng; Zuohua Dong, Senior engineer, M.S. Eng; Hongmei Zhu, Assoc. Prof. Ph.D. Eng; Zhanyu Li, Assoc. Prof. Ph.D. Eng.

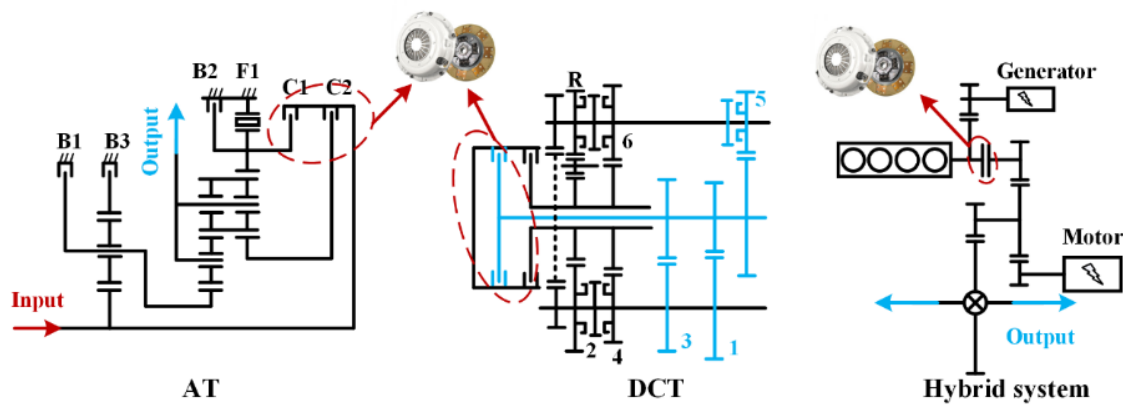


Fig. 1 - Typical driveline in the tractors

For the optimization of clutch engagement trajectory, many experts and scholars have carried out extensive and in-depth research. *Peng et al., (2009)*, proposed a clutch engagement curve correction algorithm based on optimization theory, which corrects the original curve by judging the Hamilton function on the basis of the basic structure of the original curve. However, this method only analyzed the situation of the initial speed of the driven disc as 0, they did not analyze the gear shift process and the mode switch process of hybrid vehicles. To solve the problem of the variability of clutch engagement trajectory under uncertain factors such as system parameter perturbation and external load disturbance, *Li et al., (2018)*, proposed an optimization method which take the frictional loss and jerk as the optimization goal, and solve the optimization problem by using the Pontryagin theory. The result showed that, this method can reduce the frictional loss of the clutch during its engagement process, but the method did not solve the jerk of the synchronous instantaneous of the clutch. *Li et al., (2018)*, optimized the shifting process with optimal control theory, and designed a linear quadratic optimal controller for the torque phase and the inertial phase. The results show that this method can reduce the jerk of torque phase and inertia phase during gear shifting process. To reduce the vibration during the inertial phase of the clutch engagement of shifting process, *Lu et al., (2014)*, proposed to use the model predictive control method to control the inertial phase in the shifting process, and the results show that the method reduces the inertial phase vibration in the vehicle shifting process while ensuring the minimum change of the control amount in the shifting process. *Mesmer et al. (2017, 2018)*, optimized the shifting process with the goal of minimizing the shifting time and frictional loss, and designed the optimal trajectory tracking controller for the shifting process by using the method of embedded nonlinear model predictive control, the simulation and experimental results show that the method can obtain better shifting quality, but the instantaneous synchronization of the clutch was not controlled in this study, resulting in residual oscillation on the drive shaft after clutch engagement. *Guo, (2017)*, analyzed the clutch engagement process of hybrid vehicles from pure electric mode to hybrid drive state, he divided the clutch engagement process into two stages, slipping friction phased and synchronization phase. He proposed to use the method of Laguerre function set to optimize the control process of clutch engagement in hybrid vehicles, the results show that this method can reduce the torsional vibration of the transmission system during the engine starting process of hybrid vehicles.

Making the clutch engage fast and smoothly is an important measure to improve the vehicle start-up, shifting and hybrid vehicle mode switching process (*Wurm et al., 2016, Kim et al, 2017*), in view of the problems of synchronous instantaneous jerk existing in the current research, a method combining process control and terminal constraints was proposed.

The frictional loss and jerk during the clutch engagement process were chosen as the optimization goals during the slipping phase. In addition, the same acceleration of the drive and driven clutch was set as the terminal constraint. The pseudo-spectral method was used to solve this optimization problem, and the proposed method was applied to the start-up, shifting, and mode-switching processes of the hybrid vehicle.

MATERIALS AND METHODS

Modeling the clutch engagement process

In practice, the working state of the clutch is divided into two types, engagement and disengagement. During the engagement process, the actuator pushes the clutch driven disc move to the drive disc, and the disc rubs against each other to transmit the torque, which can be illustrated in Figure 2.

Assuming that the input torque is T_{in} , the torque transmitted during slipping phase is T_c , and the resistance clutch is T_r , according to Newton's second law, the clutch engagement process can be modeled (Li, J., 2016).

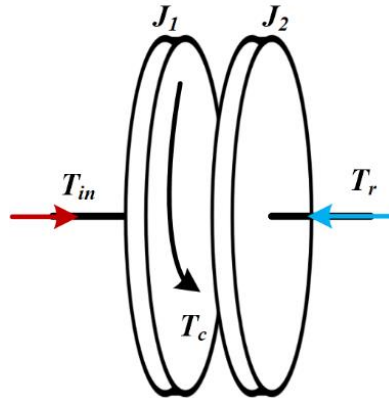


Fig. 2 - Model of clutch engagement process

$$\begin{cases} J_1 \dot{\omega}_1 = T_{in} - T_c \\ J_2 \dot{\omega}_2 = T_c - T_r \end{cases} \quad (1)$$

Take $x = [\omega_1, \omega_2, \omega_1 - \omega_2, T_{in}, T_c]^T$ as the state variable, $u = [T_{in}, T_c]^T$ as the control variable, the model of the clutch engagement process can be transferred into state space equation.

$$\begin{cases} \dot{x}_1 = \frac{1}{J_1} (x_4 - x_5) \\ \dot{x}_2 = \frac{1}{J_2} (x_5 - T_r) \\ \dot{x}_3 = x_1 - x_2 \\ \dot{x}_4 = u_1 \\ \dot{x}_5 = u_2 \end{cases} \quad (2)$$

where, J_1 is the inertia of drive disc of clutch, J_2 is the inertia of driven disc of clutch, ω_1 is the rotation speed of clutch drum and ω_2 is the rotation speed of clutch hub.

Indicators for clutch engagement process

1. Jerk. In the longitudinal dynamics of the tractor, the jerk (the change rate of longitudinal acceleration) is generally used to reflect the comfort of the tractor during acceleration. Moreover, the jerk can be represented by equation (3). When the value of the jerk is less than 10 m/s³ during clutch engagement process, the tractor can get good comfort during acceleration (Fu et al., 2016).

$$j = \frac{da}{dt} = \frac{1}{J_e} \frac{d(T_c - T_r)}{dt} \quad (3)$$

To prevent the clutch from generating a large jerk during the engagement process, it is generally necessary to control change rate of the transmitted torque T_c when the clutch engages.

2. Frictional loss. The frictional loss of the clutch during the engagement process can be measured by the slipping work, it reflects the degree of the wear of the clutch during the engagement process. Therefore, it is necessary to control its slipping work during the clutch engagement process, and the clutch slipping work can be measured with equation (4).

$$W = \int_{t_s}^{t_e} T_c |\omega_1 - \omega_2| dt \quad (4)$$

Wherein, W is the clutch slipping work, t_s is the time when the clutch starts to slip with each other, and t_e is the time when the clutch engaged totally.

During clutch slipping phase, it is generally required that the frictional loss and jerk to be as small as possible. Meanwhile, it is important to control the jerk caused by the synchronous instantaneous. According to the above requirements, the optimization goal of the clutch engagement process can be established.

$$l = \int_{t_s}^{t_e} \lambda_1 u_1^2 dt + \lambda_2 \int_{t_s}^{t_e} T_c |\omega_1 - \omega_2| dt \quad (5)$$

where, λ_1, λ_2 is the weight coefficient, u_1 is the control variable. The objective function consists of two parts. The first part is the sum of squares of the torque change rate, which represents the limit of the torque change rate during the clutch engagement process; it also represents jerk control. The second part is expressed as the frictional loss during the clutch engagement process. In addition, keeping the acceleration of the two discs at the moment of synchronous can reduce the jerk generated by the clutch engagement synchronous instantaneous.

Based on the above objective function of the clutch engagement process, the clutch engagement process can be converted into an optimization problem, which can be expressed as equation (6).

$$\begin{aligned} \min J(x(t), u(t), t) &= \int_{t_s}^{t_e} \lambda_1 u_1^2 dt + \int_{t_s}^{t_e} T_c |\omega_1 - \omega_2| dt \\ \text{st } &\begin{cases} \dot{x} = f(x, u, t) \\ x_1(t_e) - x_2(t_e) = 0 \\ \dot{x}_1(t_e) - \dot{x}_2(t_e) = 0 \\ T_{in_min} \leq T_{in} \leq T_{in_max} \\ T_{c_min} \leq T_c \leq T_{c_max} \\ x_{1_min} \leq x_1 \leq x_{1_max} \\ x_{2_min} \leq x_2 \leq x_{2_max} \end{cases} \end{aligned} \quad (6)$$

wherein, T_{in_min} is the minimum of the input torque, the T_{in_max} is the maximum of the input torque, the T_{c_min} is the minimum torque transmitted during the clutch slipping process, the T_{c_max} is the maximum torque transmitted during the clutch slipping process, the x_{1_min} is the minimum speed of the clutch drum, the x_{1_max} is the maximum speed of the clutch drum, the x_{2_min} is the minimum speed of the clutch hub, and the x_{2_max} is the maximum speed of clutch hub.

It can be seen from the above optimization problem that this problem is an optimization problem with terminal constraints, especially for the clutch synchronous moment, the constraint problem of the acceleration of the main and slave disks. For optimization problems with terminal constraints, the general analytical method is difficult to solve, therefore, this paper uses the numerical solution method to solve.

When solving optimization problems with terminal constraints, pseudo-spectral method uses global interpolation polynomials to approximate state variables and control variables on a series of discrete points, and converts differential equation constraints into algebraic constraints by introducing pseudo-spectral difference matrices similar to finite difference matrices, and then solves nonlinear optimization problems with complex constraints. According to different distribution methods, pseudo-spectral methods can be divided into Legendre pseudo-spectroscopy, Radau pseudo-spectroscopy, Gauss pseudo-spectroscopy and Chebyshe pseudo-spectroscopy (Feng et al, 2023).

Radau pseudo-spectroscopy (RPM) is a numerical solution algorithm for solving nonlinear optimization problems. The basic idea is to discretize first and then optimize. Firstly, the unknown state quantity and control quantity to be solved are discretized at a series of Legendre-Gauss-Radau (LGR) points, and then the state variables and control variables are approximated by constructing global interpolation polynomials, and the original kinetic differential equation is replaced by derivation of the state variables, the optimization problem of continuous system is discretized into a series of algebraically constrained nonlinear optimization problems, and the nonlinear optimization problem of algebraic constraint is solved by numerical solving algorithm.

Radau pseudo-spectral optimization problems can be divided into the following steps (Feng et al, 2022).

1) Time domain transformation:

To satisfy the time domain of the Legendre orthogonal polynomial, it is necessary to convert the time domain in the optimization problem to the standard time domain [-1,1], and the variable τ represents the transformed time variable.

$$\tau = \frac{2t - (t_f + t_0)}{t_f - t_0} \tag{7}$$

2) Polynomial approximation of state variables and control variables

Based on the normalized time variable, the Lagrange interpolation polynomial is used to approximate the state and control variable.

$$\begin{cases} \mathbf{x}(\tau) \approx \mathbf{X}(\tau) = \sum_{j=1}^{N+1} X_j L_j(\tau) \\ \mathbf{u}(\tau) \approx \mathbf{U}(\tau) = \sum_{j=1}^{N+1} U_j L_j(\tau) \end{cases} \tag{8}$$

wherein, $L_j(\tau)$ is the Lagrange interpolated polynomial.

$$L_j(\tau) = \prod_{\substack{i=1 \\ i \neq j}}^{N+1} \frac{\tau - \tau_i}{\tau_j - \tau_i}, \quad j = 1, \dots, N+1 \tag{9}$$

wherein, τ_1, \dots, τ_N is the root of the Legendre polynomial, and τ_{N+1} is the unconfigured node, which represents the end time.

3) Polynomial approximation of differential equations

Based on the approximation of the state quantity, the approximate state variable can be derived.

$$\frac{dX}{dt} = \frac{t_f - t_0}{2} f(\mathbf{X}(\tau), \mathbf{U}(\tau), \tau) \tag{10}$$

$$\frac{dX}{d\tau} \equiv \dot{\mathbf{X}}(\tau) = \sum_{j=1}^{N+1} X_j \dot{L}_j(\tau) \tag{11}$$

Substituting Equation 11 into 10 and discretizing at the LGR point, equation (12) is obtained.

$$\sum_{j=1}^{N+1} X_j D_{ij} - \frac{t_f - t_0}{2} f(\mathbf{X}(\tau), \mathbf{U}(\tau), \tau) = 0 \tag{12}$$

where D_{ij} is the differential matrix of the Radau pseudo-spectral method, and it can be expressed by equation (13).

$$D_{ij} = \begin{cases} \frac{\dot{h}(\tau_i)}{(\tau_i - \tau_j) \dot{h}(\tau_i)} & i \neq j \\ \frac{\ddot{h}(\tau_i)}{2\dot{h}(\tau_i)} & i = j \end{cases} \tag{13}$$

After the conversion of the above steps, the optimization problem of the clutch engagement process can be expressed by equation (14).

$$\begin{aligned} \min J &= \int_{-1}^1 l(x(\tau), u(\tau)) d\tau \\ &\begin{cases} \sum_{j=1}^{N+1} X_j D_{ij} - \frac{t_f - t_0}{2} f(\mathbf{X}(\tau), \mathbf{U}(\tau), \tau) = 0 \\ C_{eq}(x(\tau), u(\tau)) = 0 \\ C_{ieq}(x(\tau), u(\tau)) < 0 \\ \phi(x(\tau_0), u(\tau_0), x(\tau_f), u(\tau_f), \tau_0, \tau_f) = 0 \end{cases} \end{aligned} \tag{14}$$

where, $l(x(\tau), u(\tau))$ is the stage value function in the clutch engagement process. C_{eq} is the equality constraint, C_{ieq} is the inequality constraint, and ϕ is the terminal constraint.

Thus, the optimization problem of continuous system is transformed into a series of nonlinear programming problems with algebraic constraints, and the discretized algebraic optimization problem is solved by using the sequence quadratic programming (SQP).

RESULTS

To test the effectiveness of the algorithm. The Optimization results were compared with the results obtained without considering the terminal constraint case.

Case 1. With terminal constraints

In this case, the engagement of the clutch for start-up was optimized. The initial speed of the clutch hub was set to be 0 r/min, the speed of clutch drum was set to be 764 r/min. The optimization problem was solved with *GPOPS*. The optimized engagement trajectory is shown in the Figure 3 illustrating the rotation speed of the clutch drum and hub. It can be seen from this figure that the rotation speed of the clutch hub increases gradually. The rotation speed of the clutch drum is kept as low as possible to keep the speed difference between clutch drum and hub at a small value because the objective function requires the frictional loss as small as possible. The clutch drum has small fluctuation at the synchronization stage to make the acceleration of the drive and driven disc tend to be consistent. When synchronized, the acceleration of the drive and driven disc is the same, as shown in the enlarged section in Figure 3a.

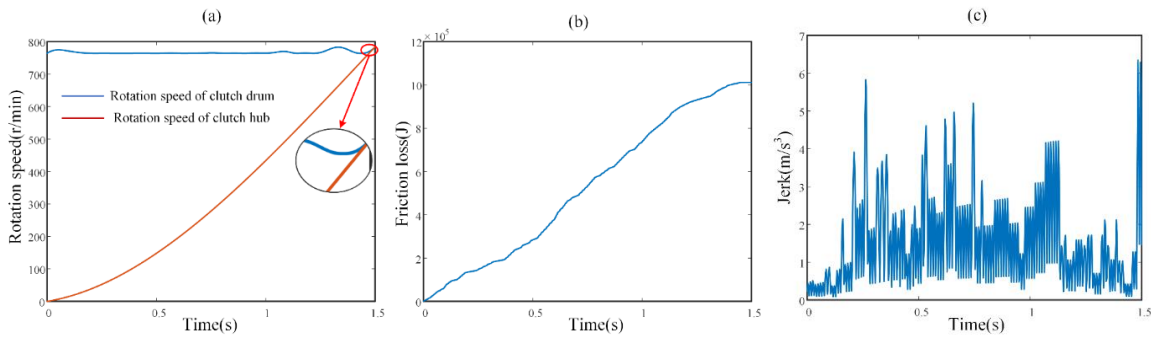


Fig. 3 - Clutch engagement trajectory optimized by pseudo-spectroscopy

Figure 3b shows the frictional loss during the engagement process. It can be seen from Figure 3b that the frictional loss is 10.12×10^5 J. Figure 3c shows the value of the jerk during the engagement process, and it can be seen from Figure 3c that the value of the jerk is less than 10 m/s^3 during the entire engagement process of the clutch, and at the moment of clutch synchronization, although the value of the jerk is larger, it is still less than 10 m/s^3 .

2. Case 2. Without terminal constraints

To check the effectiveness of the optimal problem that considers the process constraints and terminal constraints, the optimal problem without terminal constraints, which is mostly used in the optimal problem for clutch engagement process was also solved.

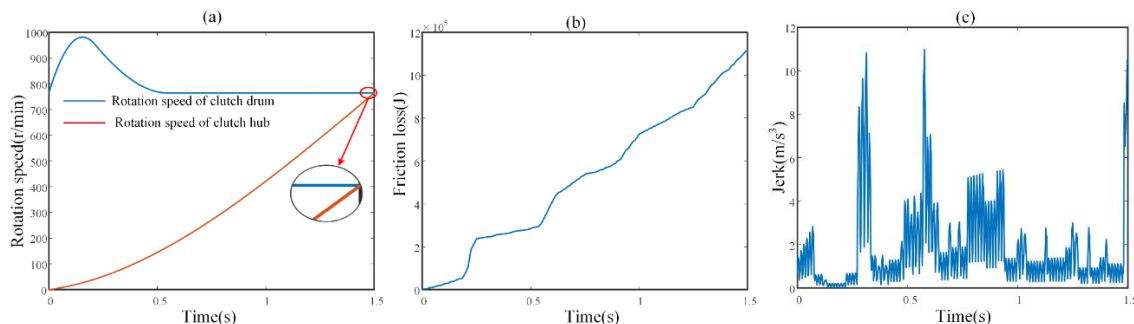


Fig.4 - Optimization results of clutch engagement process without considering terminal acceleration constraints

Figure 4 shows the results without considering the terminal constraint, Figure 4a is the rotation speed of the clutch drum and hub. It can be seen from the figure that the rotation speed of the clutch drum increases at first and then quickly decreases to the lowest value of the engine to make difference of the clutch drum and hub to be smallest during the whole engagement process. The rotation speed of the clutch drum was not adjusted at the synchronization stage, so the acceleration of the clutch drum and hub

was inconsistent, as shown in the enlarged section of the figure. Figure 4b shows the frictional loss during clutch engagement, and it can be seen from the figure that the frictional work is $11.1 \times 10^5 \text{ J}$, which is higher than the values produced by the pseudo-spectroscopy. Figure 4c shows the value of the jerk during the engagement process. It can be seen from the figure that the maximum values of jerk exceed 10 m/s^3 at 0.25 s, 0.6 s and synchronization moment. Compared with the optimization without considering terminal constraints, the frictional loss is reduced by 9%, and the jerk is less than 10 m/s^3 .

From the result of optimization with terminal constraints and without terminal constraints, it can be seen that the rotation speed of the clutch hub gradually increases, and the rotation speed of the clutch drum has been running at a lower value to keep the difference between the clutch drum and hub at a smaller value, so as to minimize the slip loss. Wherever, the rotation speed of the clutch drum was adjusted, and during the adjustment period, it resulted in two large jerks (0.25 s, 0.6 s) during the engagement process.

Meanwhile, the rate of change of the torque transmitted by the clutch is constrained in the value function, resulting in a smaller value of the jerk throughout the clutch engagement process. When the terminal constraint is considered, the process constraint and the terminal constraint are both applied, resulting in a smaller jerk during the clutch engagement process, while if only the process constraint is applied without the terminal constraint, the clutch not only experiences a larger jerk at the slip phase, but also at the moment of synchronization.

Clutch engagement trajectory optimization under different operating conditions

(1) Start-up process

In vehicles equipped with automatic transmissions, the clutch driven disc starts at zero and the rotation speed of drive disc is limited by the minimum engine speed. Therefore, the clutch engagement process during the start-up process is optimized with the condition that the initial speed of the driven disc is zero.

Figure 5 shows the optimization curve of the clutch engagement process in the vehicle start-up process. To validate different start-up situations that are often present, three different start-up times was set to be 1.5 s, 2.0 s and 2.5 s, respectively. The optimization result is shown in Figure 5. It can be seen from the figure that the rotation speed curve of the driven disc is a smooth curve, and when the clutch is about to synchronize, the acceleration of the drive and driven disc is consistent, thus ensuring that the clutch has a small jerk during the slipping process and the synchronization moment.

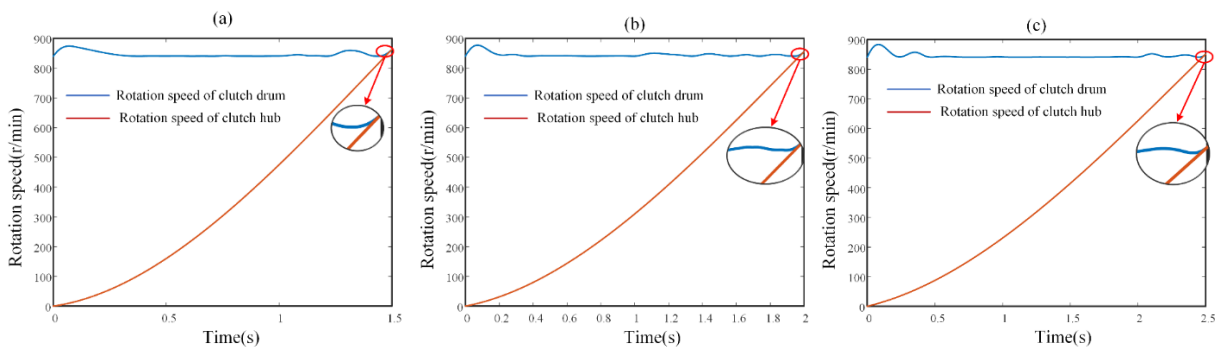


Fig. 5 - Start-up process, clutch engagement process optimized

Shift process

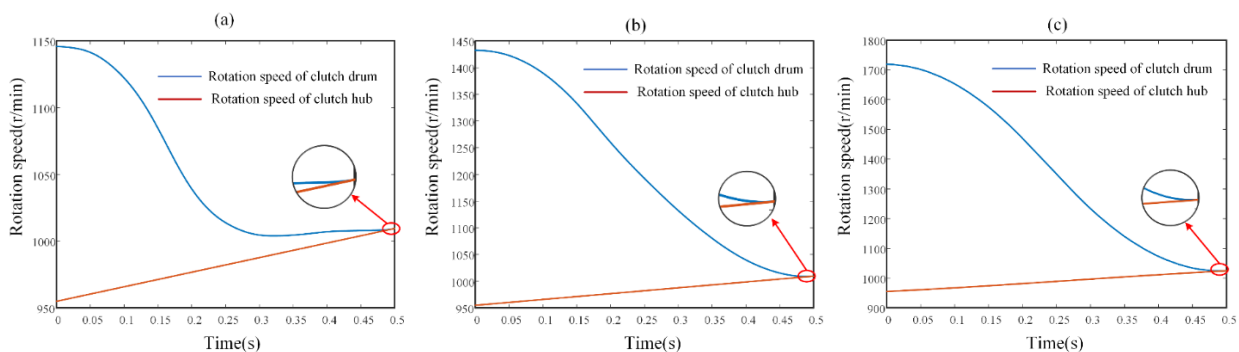


Fig. 6 - Optimal engagement curve of the clutch during the upshift process

Unlike in the vehicle starting process, the initial speed value of the clutch driven disc is not zero during the shifting process. In this study, the upshift process was taken as an example. During the upshift process, the initial speed value of the driven disc is not zero, and the speed of drive disc is higher than the speed of driven disc of the target gear.

To simulate the upshift process of different gears, the shift process time is set to 0.5 s, and three different gear values are set, the corresponding gear ratios are 1.2, 1.5, 1.8, respectively and the clutch driven disc speed value is set to 955 r/min. The optimization process of the optimal engagement path of the clutch in the upshift process under different transmission ratios is shown in Figure 6. From the figure, it can be seen that the drive disc speed decreases actively, the driven disc speed rises gradually, and at the end of the shift, the rotation speed of the drive and driven disc were consistent, and the angular acceleration value is the same at the same time.

Mode switching situation in the hybrid tractor

In parallel hybrid tractors, at high speeds, the engine is usually used to drive the vehicle directly to reduce the overall energy consumption. Parallel hybrid vehicles require clutch control when the engine intervenes to prevent sudden engine intervention and vibrations in the driveline. For the parallel hybrid vehicle, a small generator is used to drive the engine to start when the parallel hybrid vehicle engine is involved, and the speed of the engine is adjusted to be slightly higher than the speed of the clutch driven disc, meanwhile, the difference between the speed of drive and driven disc is small so that the clutch can be engaged smoothly and quickly when engaged. To verify the applicability of the method in the clutch engagement process of mode switch process, three different small speed differences were set to be 48 r/min (5 rad/s), 95 r/min (10 rad/s) and 144 r/min (15 rad/s), respectively, and the engagement time of the clutch was set to be 0.5 s, the optimization results are shown in Figure 7. It can be seen from Figure 7 (a) (b) that the rotation speed of driven disc increases gradually, the speed of the drive disc decreases gradually, and there are some fluctuations when the speed of the drive disc decreases, the reason for this fluctuation that the difference between the drive and driven disc is small, is that the engine needed to be adjusted to make the acceleration of the drive and driven disc be consistent. For the large value of the difference between the drive and driven disc, the engine speed can be smoothly reduced, which can be seen in Figure 7c, and the acceleration of drive and driven disc can still be consistent at the synchronization moment.

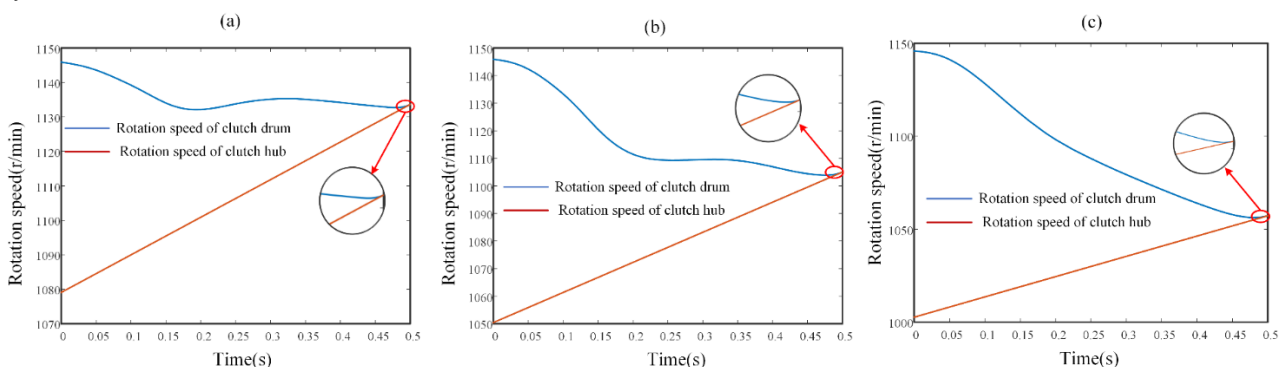


Fig. 7 - In hybrid systems, the clutch engages the optimal curve when the engine is involved

CONCLUSIONS

In this study, an optimization method that considers the slipping phase and synchronization moment of the clutch engagement was proposed. The frictional loss and jerk during the slipping phase were considered and the jerk at the moment of clutch synchronization was also considered as well, and the clutch engagement process was transformed into an optimization problem with terminal constraints. To solve this problem, the pseudo-spectral method was used and the optimization result was compared with the optimization method without considering the terminal constraints, and the results show that the frictional loss can be reduced by 9% and the jerk is lower than 10 m/s^3 by using the pseudo-spectral method considering the terminal constraint method, and this method was applied to the start-up, shift and mode switch process of the hybrid driveline. The results show that the method can ensure that the acceleration value of the clutch drum and hub tends to be consistent when the clutch is synchronized, which will reduce the residual oscillation on the drive shaft after clutch engagement (Petrescu et al, 2018).

This study optimizes the engagement trajectory of the clutch engagement process in terms of jerk and frictional loss, and solves the problem of jerk at the moment of clutch synchronization. However, the efficiency and energy consumption of the engine/motor connected to the clutch drum during its adjustment in the clutch engagement process have not been considered. In future work, the overall energy consumption of the process will be thoroughly analyzed. Additionally, a test rig will be developed to validate this method, and a novel control approach for tracking the optimal trajectory will also be explored.

ACKNOWLEDGEMENT

This work is supported by the National Key R&D Program Project of China (No.2023YFD2001102), Shenzhen Polytechnic University Research Fund (No. 6023310012K), Scientific Research Project of Shenzhen Polytechnic University (No. 6021310021K) .

REFERENCES

- [1] Feng, J., Qin, D., Liu, Y., Wang, X., & Lv, H. (2023). Pseudo-spectral optimization and model predictive control of vehicle shift process with dual clutch transmission. *Proceedings of the Institution of Mechanical Engineers, Part C: Journal of Mechanical Engineering Science*, 237(16), 3789-3806. <https://doi.org/10.1177/09544062221148040>
- [2] Feng, J., Qin, D., Liu, Y., Wang, X., & Lv, H. (2022). Pseudo-spectral optimization and data-driven control of vehicle start process with dual-clutch transmission. *Mechanism and Machine Theory*, 172, 104814. <https://doi.org/10.1016/j.mechmachtheory.2022.104814>
- [3] Fu, Y., Liu, Y., Cui, L., & Xu, X. (2016). Dynamic analysis and control strategy of wet clutches during torque phase of gear shift. *Journal of Mechanical Science and Technology*, 30, 1479-1496.
- [4] Gavgani, A. M., Sorniotti, A., Doherty, J., & Cavallino, C. (2016). Optimal gearshift control for a novel hybrid electric drivetrain. *Mechanism and Machine Theory*, 105, 352-368. <https://doi.org/10.1016/j.mechmachtheory.2016.06.016>
- [5] Guo D. (2017). *Torque-related Control Strategies for Mode Transition and Gear Shifting in Hevs (混合动力汽车模式切换及换挡的转矩控制策略研究)*. Wuhan University of Technology, Wuhan.
- [6] Kim, S., Oh, J., & Choi, S. (2017). Gear shift control of a dual-clutch transmission using optimal control allocation. *Mechanism and Machine Theory*, 113, 109-125. <https://doi.org/10.1016/j.mechmachtheory.2017.02.013>
- [7] Lu, T., Dai, F., Zhang, J., & Wu, M. (2012). Optimal control of dry clutch engagement based on the driver's starting intentions. *Proceedings of the Institution of Mechanical Engineers, Part D: Journal of Automobile Engineering*, 226(8), 1048-1057. <https://doi.org/10.1177/0954407011435465>
- [8] Li, J., Wang, Y., & Wang, Y. (2016). Optimal control for jitter suppression of clutch engagement in upshift process of electric vehicles. *Advances in Mechanical Engineering*, 8(12), 1687814016674847. <https://doi.org/10.1177/1687814016674847>
- [9] Li X.X., Wang A.L., Fan, X.C., Wu J. (2020). Optimization and tracking control of the clutch engagement process under non-stationary random cyclic conditions (非平稳随机循环工况离合器接合优化及跟踪控制). *Journal of Harbin Institute of Technology*, 52(7):52-58. DOI: [10.11918/201906001](https://doi.org/10.11918/201906001)
- [10] Li, C., Meng, F., Xi, J., & Zhai, Y. (2019). Starting shift control of heavy-duty automatic transmissions based on the optimal trajectory of turbine speed. *Mechanical Systems and Signal Processing*, 126, 490-504. <https://doi.org/10.1016/j.ymssp.2019.02.030>
- [11] Li, G., & Görges, D. (2018). Optimal control of the gear shifting process for shift smoothness in dual-clutch transmissions. *Mechanical Systems and Signal Processing*, 103, 23-38. <https://doi.org/10.1016/j.ymssp.2017.09.040>
- [12] Lu, X., Chen, H., Gao, B., Zhang, Z., & Jin, W. (2014). Data-driven predictive gearshift control for dual-clutch transmissions and FPGA implementation. *IEEE Transactions on Industrial Electronics*, 62(1), 599-610. DOI: [10.1109/TIE.2014.2312312](https://doi.org/10.1109/TIE.2014.2312312)
- [13] Minh, V.T., Mohd Hashim, F.B., & Awang, M. (2012). Development of a real-time clutch transition strategy for a parallel hybrid electric vehicle. *Proceedings of the Institution of Mechanical Engineers, Part I: Journal of Systems and Control Engineering*, 226(2), 188-203. <https://doi.org/10.1177/09596518114147>

- [14] Mesmer, F., Hentzelt, S., Szabo, T., & Graichen, K. (2017). Optimal control of dual-clutch transmissions with multiple groups. In *2017 IEEE International Conference on Advanced Intelligent Mechatronics (AIM)* (pp. 1749-1754). IEEE. DOI: [10.1109/AIM.2017.8014271](https://doi.org/10.1109/AIM.2017.8014271)
- [15] Mesmer, F., Szabo, T., & Graichen, K. (2018). Embedded nonlinear model predictive control of dual-clutch transmissions with multiple groups on a shrinking horizon. *IEEE Transactions on Control Systems Technology*, 27(5), 2156-2168. DOI: [10.1109/TCST.2018.2856191](https://doi.org/10.1109/TCST.2018.2856191)
- [16] Park, J., & Choi, S. (2021). Optimization method of reference slip speed in clutch slip engagement in vehicle powertrain. *International Journal of Automotive Technology*, 22, 55-67. <https://doi.org/10.1007/s12239-021-0007-5>
- [17] Peng, J.X., Jin, H., Chen, H.Y. (2009). Engagement Curve of Clutch Based on Optimization Theory. *Transactions of Beijing institute of Technology*, (11), 964-968.
- [18] Petrescu, R. V., Aversa, R., Apicella, A., & Petrescu, F. I. (2018). Dynamic Synthesis of a Dual-Clutch Automatic Gearboxes. *American Journal of Engineering and Applied Sciences*, 11(2), 663-679.
- [19] Van Berkel, K., Hofman, T., Serrarens, A., & Steinbuch, M. (2014). Fast and smooth clutch engagement control for dual-clutch transmissions. *Control Engineering Practice*, 22, 57-68. <https://doi.org/10.1016/j.conengprac.2013.09.010>
- [20] Wurm, A., & Bestle, D. (2016). Robust design optimization for improving automotive shift quality. *Optimization and Engineering*, 17, 421-436.
- [21] Zhao, Z., He, L., Zheng, Z., Yang, Y., & Wu, C. (2016). Self-adaptive optimal control of dry dual clutch transmission (DCT) during starting process. *Mechanical Systems and Signal Processing*, 68, 504-522. <https://doi.org/10.1016/j.ymssp.2015.06.012>

DESIGN AND TEST OF A CLAMPING-SHEAR INTRA-ROW WEEDING DEVICE

夹持剪切式株间除草装置设计与试验

Jiacheng ZHOU, Min FU*, Jianhao CHEN, Ji CUI

Northeast Forestry University, College of Mechanical and Electrical Engineering, Harbin / China;

Tel: +86 15663688203; E-mail: fumin1996@163.com

DOI: <https://doi.org/10.35633/inmateh-75-04>**Keywords:** mechanical weeding, inter-row weeding, weeding device, weeding shovel, ridge planting**ABSTRACT**

Aiming at the complexity and insufficient adaptability of current weeding devices for ridge tillage, this paper presents the design of a clamping-shear weeding device that mimics the hand-grabbing motion. Through the force analysis of the weed root system, the optimal shovel surface inclination angle is determined to be $10^{\circ}\sim 40^{\circ}$. To ensure the sliding cutting condition, the shovel blade angle is calculated and determined as 30° . Based on the Mohr-Coulomb shear theory, the shovel width is set at 50 mm. A single-factor test was conducted with the soil penetration depth of 40 mm and the clamping-shear speed of 4 cm/s, the results showed that the weed removal rate was over 85% and the crop injury rate was less than 6%. The optimal performance was observed with the shovel inclination angle of 30° .

摘要

针对现有垄作田间株间除草装置结构复杂、适应性差等问题，本文设计了一种模仿人手抓取操作的夹持剪切式除草装置。通过对杂草根系的受力分析，确定最佳铲面倾角为 $10^{\circ}\sim 40^{\circ}$ 。以满足滑切条件为原则，对铲刃倾角进行分析计算，确定铲刃角为 30° 。基于摩尔-库仑剪切理论，确定除草铲宽度为 50mm。设定入土深度 40mm、夹持剪切速度 4cm/s，进行了铲面倾角单因素试验，结果表明：除草率在 85% 以上，伤苗率在 6% 以下，当铲面倾角为 30° 时，除草性能为最优值。

INTRODUCTION

Ridge tillage is one of the important farming methods in China, cultivating numerous food crops and supporting significant benefits to society, ecology, and economy (Liang et al., 2022). However, weeds grow disorderly on the ridges and compete with crops for sunlight, water, and nutrients, resulting in a decrease in crop yield and quality, causing huge losses to the agricultural economy (Li et al., 2022; Ahmad et al., 2020). To reduce labor costs and minimize environmental pollution, mechanical weeding is considered an ideal method (Fang et al., 2022; Dilipkumar et al., 2020). According to different weed operating areas in the field, mechanical weeding can be divided into intra-row weeding and inter-row weeding (Bing et al., 2021). Since intra-row weeds are closer to crops, there is a higher risk of damaging crops when removing weeds. Therefore, intra-row weeds are more difficult to control than inter-row weeds (Longzhe et al., 2021). At present, the optimization and innovation of intra-row weeding devices have become the research and focus of many scholars.

From the perspective of function, intra-row weeding devices can be divided into those that cut weed roots, those that separate weeds from soil, and those that combine both functions. Devices that cut weed roots mainly include rotary discs (Pérez-Ruiz et al., 2011) and swing hoes (Huang et al., 2012). The rotary discs were used earlier, and the weeding blades reciprocated rotating between crops to achieve the two actions of avoiding crops and weeding. They have a simple structure, but they cannot separate weed roots from the soil, therefore, weed control is not effective. The swing hoes mainly use the reciprocating swing of the weeding blades to achieve the actions of avoiding crop and weeding. The structure of this device is relatively compact and the crop injury rate is low, but current models use the pneumatic system to drive the swing weeding shovel, and the supporting power system is complex and heavy, making it unsuitable for lightweight operations. Devices that cut weed roots offer good crop-avoidance performance and minimize the risk of crop damage. However, the roots remain in the soil, leading to incomplete weeding. Devices that separate weeds mainly include finger weeder (Riemens et al., 2007), brush weeder (Ziwen et al., 2015), torsion weeder (Cirujeda et al., 2013) and cycloid hoe (Hu et al., 2012). The first three are relatively common weeding devices, but they can only remove weeds with shallow root systems and have a high risk of damaging crops; the cycloid hoe is

also a commonly used weeding device. Research on the cycloid hoe intra-row weeding device conducted by Hu Lian et al (*Hu et al., 2012*) shows that the weeding effect is remarkable and the damage to crops is less than 8%. However, the cycloid hoe structure is complex, the maintenance cost is high, and the control is difficult. Weeding devices that separate weeds can completely remove weeds from the soil, but there is a certain risk of damaging the crops. The main hybrid weeding devices include the rotary hoe (*Qinsong et al., 2022*). This device uses the rotation of the rotary hoe, and the needle teeth penetrate the soil to cut the weed roots and take them away from the soil. The hybrid type has a better weeding effect. However, the mechanism is generally complex and the production cost is high.

In summary, most existing intra-row weeding devices suffer from complex structures, poor adaptability, high crop injury rates, and suboptimal weeding performance. To address these challenges, this paper designs a clamping and shearing intra-row weeding device tailored for corn ridge fields, particularly for operations during the 3-4 leaf stage. The design mimics the hand-grasping motion, with a parallelogram mechanism used in the finger component to reduce drive elements and simplify the device's structure. The weeding device is mounted on a six-axis robotic arm, leveraging the arm's multi-degree-of-freedom and flexibility to perform crop-avoidance and weeding tasks. This enhances the device's field adaptability and minimizes crop damage. Key parameters are designed, and the device's effectiveness is validated through tests using crop injury and weed removal rates as evaluation indexes.

MATERIALS AND METHODS

Weeding device design

Weeding field environment

Ridge tillage is the most common farming method in China, with ridge parameters varying by region. In plain areas, ridge heights (H) range from 160~350 mm, ridge spacing (D_1) from 500~1000 mm, ridge top width (W_1) about 300 mm, and ridge bottom width (W_2) about 600 mm. Taking 3~5 leaf stage corn field as an example, the intra-row ridge spacing (D_2) is about 240~300 mm, with the planting ridge parameters shown in Fig. 1. Weeds grow unorderedly on the ridges. While tillage can effectively remove weeds between rows, intra-row weeds must be removed precisely to avoid accidentally damaging crops. According to field surveys and relevant literature (*Fujun et al., 2018*), weed roots typically extend about 20 mm below the surface, while corn roots at the same depth have a radial spread of about 50 mm. To protect crop roots, the diameter of the crop protected area is set to 60 mm.

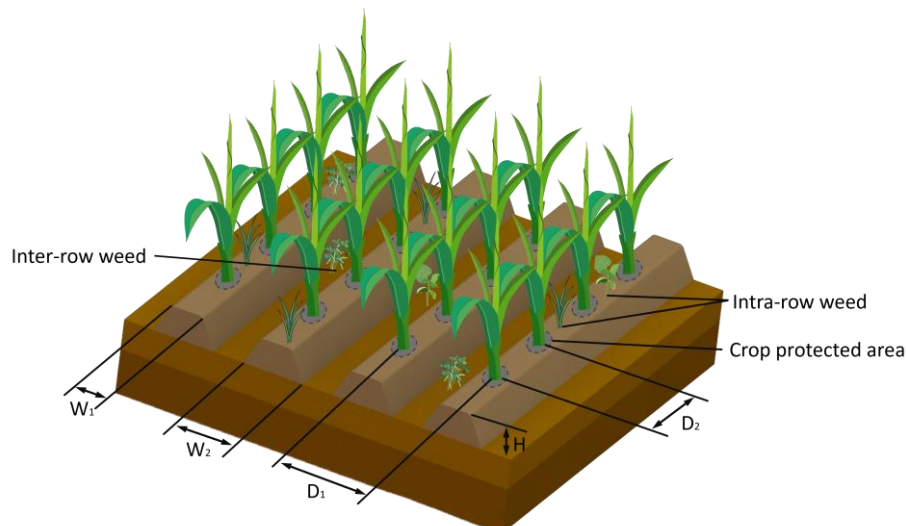


Fig. 1 - Ridge parameters

Weeding device configuration design

A human-like mechanical gripper is highly effective at grasping various objects due to its flexibility and adaptability (*Bircher et al., 2021*). Inspired by this, the weeding device in this paper is designed using the human hand as a bionic prototype. The human hand's structure primarily consists of an open kinematic chain with a series of moving and rotating joints. The configuration of the weeding device is divided into two main parts: the fingers and the palm. The fingers consist mainly of rotating joints, while the palm features moving joints. Key considerations in designing the fingers include the number and structure of the bionic fingers.

Having too many bionic fingers can complicate the structure and make control more difficult. Therefore, the number of bionic fingers should be minimized, provided the weeding function is maintained. For the palm, important factors include the connection between the palm and fingers, as well as the layout of the bionic fingers on the palm.

The configuration of the bionic weeding device designed in this paper is shown in Fig. 2. The device features four fingers, each with two degrees of freedom, comprising two joints and two connecting rods. The joints control the rotation angles of the connecting rods, allowing the fingers to bend by adjusting these angles. The fingers are symmetrically distributed on either side of the palm, which has one degree of freedom. The connection between the fingers and the palm is achieved through a slider pair, enabling the fingers to open and close.

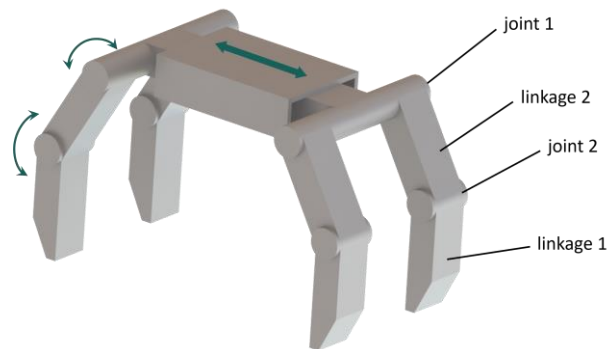


Fig. 2 - Weeding device configuration diagram

Weeding device structure design

Based on the configuration design described in the section 2.2, each finger has two degrees of freedom. To achieve full constraint, two drive elements are necessary. However, directly adding a drive element to the second joint would result in a bulky finger structure and require a large driving torque. To address this, a multi-link mechanism is employed for the single-finger design. By utilizing the characteristics of a parallelogram mechanism, a revolute pair is added to introduce a constraint, allowing the avoidance of placing drive elements at the second joint. This design makes the mechanism compact and lightweight. To further simplify the structure, the two fingers on the same side are driven synchronously by a double-head servo. The distal end of the finger, designed for weeding, is shaped like a cross-finger to closely mimic a human hand. The design model of the finger mechanism is shown in Fig. 3.



Fig. 3 - Finger design model

The design model of the palm is shown in Fig. 4. A single-head servo serves as the power source, driving the fingers at both ends of the palm. The inward and outward opening and closing movements of the fingers are achieved through a gear rack transmission mechanism.

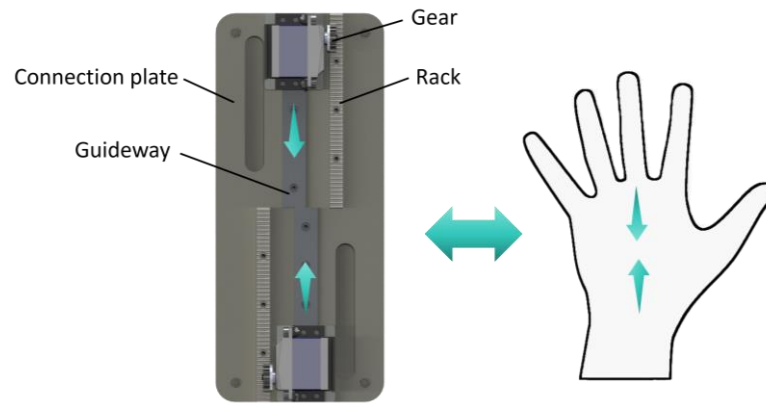


Fig. 4 - Palm design model

The overall structure of the weeding device is shown in Fig. 5. A double-head servo is connected to the second connecting rod of the two fingers on the same side, providing the necessary driving torque. This second connecting rod acts as a power arm, transmitting force to the weeding shovel via a parallelogram mechanism, allowing the shovels on both sides to mesh inward. The fingers on the same side are mounted on a shared slider, with a single-head servo driving their opening and closing along a guide rail through a gear rack transmission, thereby enabling the claw's movement.

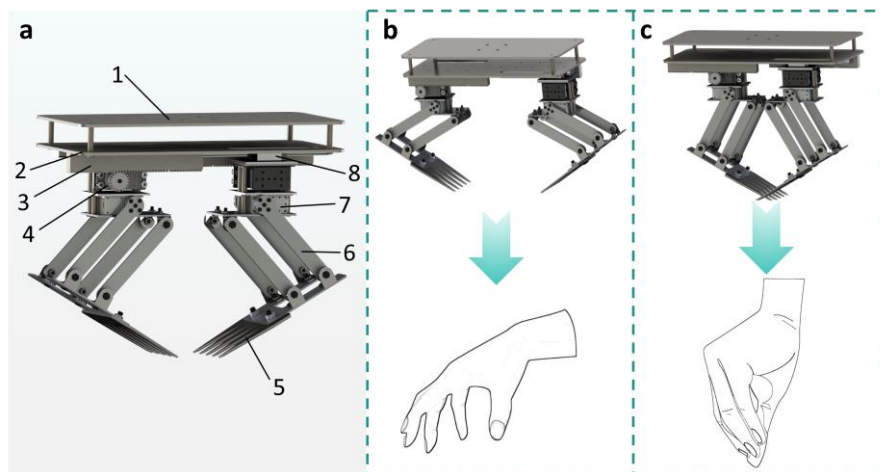


Fig. 5 - Overall structure of weeding device

(a). 3D diagram; (b). open state; (c). closed state

1.fixed plate; 2.connecting plate; 3.rack; 4.single-head servo; 5.weeding shovel; 6.connecting rod; 7.double-head servo; 8.slider

The principle of avoiding crop and weeding of the weeding device

The weeding device is mounted on a six-axis robotic arm, and the operation process is divided into the avoiding crop process and the weeding process. The weeding operation is shown in Fig. 6.

(a) When the operation begins, the visual system first detects crops and weeds. If no weeds are detected, the robotic arm positions the weeding components in the neutral position between the rows. When the visual system detects weeds, a crop protection and a weeding areas are constructed.

(b) After identifying and locating the weeds, the robotic arm, receiving signals from the control system, maneuvers the weeding device to bypass the crops and position itself over the weeding area at an appropriate height, avoiding the crops.

(c) The weeding device's two double-head servos rotate the second connecting rod, causing the weeding shovels to move toward the center. The tips of the shovels penetrate and break the soil surface, initiating the weeding process.

(d) Once the soil-breaking is completed, the double-head servos cease rotation. Then, the single-head servos engage, rotating gears on a rack that slides the two clamping claws toward the center along the guide rail. The weeding shovels advance into the field ridge at a fixed angle, continuing to break the soil. The root-soil complex is then sheared under the combined effects of gravity and soil friction, gradually lifting along the shovel surface as the shovels mesh, initially separating the weed roots from the soil. Once the shovels completely mesh and shear the weed roots, the single-head servos stop.

(e) Finally, the robotic arm lifts the weeding device, completely separating the weeds from the soil. After the weeds are clamped and removed from the soil, all servos reverse direction, returning the weeding device to its initial state, simultaneously releasing the weeds, thereby completing the weeding operation.

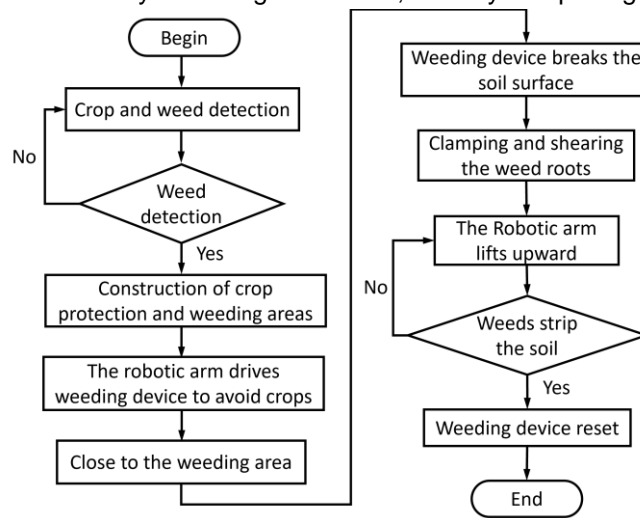


Fig. 6 - Flow chart for the weeding operation

Design of key parameters of weeding device

In order to meet the operation requirements of the weeding device, its key parameters are designed in this paper. These requirements include minimizing soil excavation during weed removal, possessing the ability to crush clay, incorporating a self-cleaning function in the weeding shovel to prevent grass and soil buildup, and ensuring excellent wear resistance.

Shovel surface inclination angle

The integrity of weeds is closely linked to the stability of their roots. Therefore, to ensure the complete removal of weeds from the soil, it is essential to disrupt the stability of the weed roots. The force analysis during the clamping and shearing process is shown in Fig. 7.

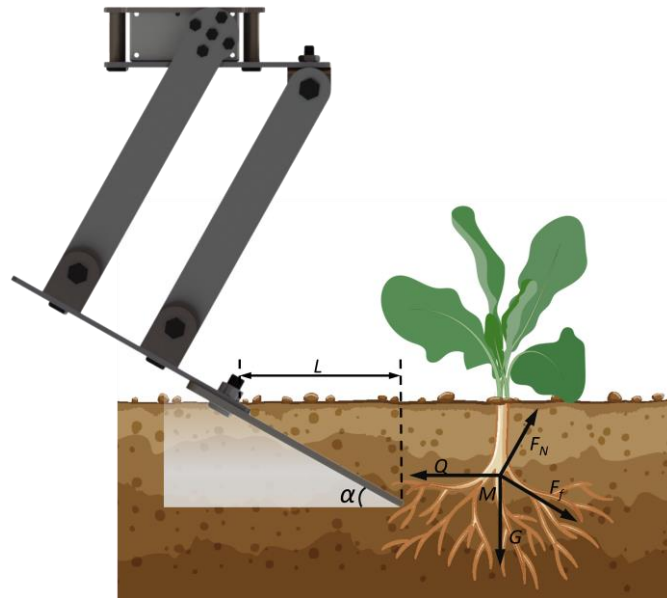


Fig. 7 - Force analysis diagram of weed root

Note: F_N is the support of weeding shovel to weed roots; F_f is the friction between root-soil complex and weeding shovel; G is the gravity of weed roots; Q is the force required to move the weed; α is shovel surface inclination angle; point M is the center of the weed roots; L is the projection length of weeding shovel in the horizontal direction

From the force analysis in Fig. 7, the force on the weed root in the X and Y directions is:

$$F_f \cos \alpha + F_N \cos(\pi / 2 - \alpha) = m_0 a_x \tag{1}$$

$$F_N \sin(\pi / 2 - \alpha) - F_f \sin \alpha - G = m_0 a_y \tag{2}$$

This is obtained from the momentum theorem:

$$\left[F_f \cos \alpha + F_N \cos(\pi/2 - \alpha) \right] \Delta t = m_0 v \quad (3)$$

where:

m_0 is the quality of weeds, kg; Δt is the time of weeding shovel acting on weeds, s; v is inward clamping-speed of weeding shovel, cm/s; a_x is acceleration of weed root moving in horizontal direction, cm/s²; a_y is acceleration of weed root moving in vertical direction, cm/s².

From Eq. (1) and (2), it is evident that a_x increases with an increase in the shovel surface inclination angle, while a_y decreases as the angle rises. Eq. (3) shows that when the clamping speed v of the weeding shovel is constant, an increase in the shovel surface inclination angle leads to a decrease in the L . This results in a shorter horizontal contact time between the weeds and the weeding shovel, increasing the impulse. Consequently, as the shovel surface inclination angle rises, the stability of the weed root system diminishes, making it easier to disrupt the roots. However, if the angle is excessively large, the resistance encountered during the clamping shear of the weeding shovel will also increase. Combined with the analysis of the operation process of the weeding shovel and the root-soil complex, the mechanical relationship between the two is obtained:

$$F_f + G \sin \alpha = Q \cos \alpha \quad (4)$$

$$G \sin \alpha + Q \sin \alpha = F_N \quad (5)$$

$$F_f = \mu_1 F_N \quad (6)$$

$$\alpha \leq \arctg \frac{Q - \mu_1 G}{\mu_1 Q + G} \quad (7)$$

where: μ_1 is the friction factor between soil and weeding shovel.

Through preliminary field tests, it was found that the force required to move the weeds was 10 N, the weight of the weed roots was 0.05 N, and the friction factor between the soil and the weeding shovel was 0.7. Applying these values to Eq. (7), it was determined that $\alpha \leq 54^\circ$. However, when $\alpha \leq 10^\circ$, the depth of the weeding shovel's penetration into the soil is insufficient, preventing complete weed removal. Based on this analysis and referencing relevant literature (Jinchuan *et al.*, 2017), the optimal range for the weeding shovel inclination angle is $10^\circ \leq \alpha \leq 40^\circ$ to ensure effective weeding while minimizing working resistance.

Shovel blade angle

During the weeding process, the weeding shovel must demonstrate effective soil penetration and a self-cleaning function for its surface. To achieve this, it is essential to ensure that the sliding cutting force of the soil on the blade exceeds the friction force between the soil and the blade. The force of the weeding shovel blade designed in this paper is shown in Fig. 8.

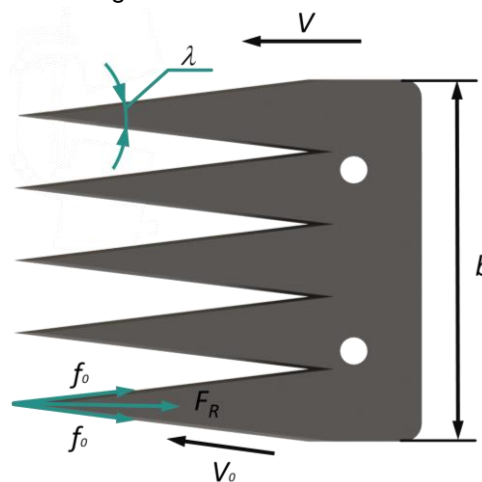


Fig. 8 - Force analysis diagram of weeding shovel blade

Note: F_R is the sliding cutting force on the blade, N; f_0 is the friction between soil and shovel blade, N; v_0 is the sliding cutting speed, cm/s.

Sliding cutting conditions should meet:

$$F_R \sin(90^\circ - \frac{\lambda}{2}) \geq f_0 \quad (8)$$

$$f_0 = \tan \varphi F_R \cos(90^\circ - \frac{\lambda}{2}) \quad (9)$$

where:

λ is shovel blade angle, ($^\circ$); φ is the friction angle between soil and weeding shovel surface, ($^\circ$).

From Eq. (8) and Eq. (9), shovel blade angle λ should be satisfied:

$$90^\circ - \frac{\lambda}{2} \geq \varphi \quad (10)$$

$$\mu_2 = \tan \varphi \quad (11)$$

where:

μ_2 is the friction factor between weed root and weeding shovel.

It can also be seen from Fig. 8 that the relationship between v and v_0 is :

$$v_0 = v \cos \frac{\lambda}{2} \quad (12)$$

Through the actual field measurements and reference to relevant literature (Jinchuan *et al.*, 2017), the friction factor between the soil and the weeding shovel is 0.569~0.718, and the friction factor between the weed root and the weeding shovel is 0.89~0.97, so it is enough to meet the friction factor between the weed root and the weeding shovel, and it can be brought into the Eqs. (10) and (11) to calculate that $\lambda \leq 120^\circ$ can meet the requirements. It can be seen from Eq. (12), that the smaller the λ , the smaller the v_0 , so the weeding shovel weeding process is more stable, however, when $\lambda < 30^\circ$, the weeding shovel strength is greatly reduced, resulting in weeding shovel wear and tear aggravated, and easy to cause the shovel surface bending, so the weeding shovel blade angle is designed for 30° .

Weeding shovel width

In order to further improve the performance of the weeding device, reduce the resistance in the weeding process, and ensure the smooth shear removal of the weed root-soil complex, the weeding shovel width is designed. In order to completely remove the weed root, the weeding shovel width should be greater than the radiation diameter of the weed root. The weeding shovel width is calculated as:

$$w \geq d + \varepsilon + n \quad (13)$$

where:

w is the weeding shovel width, mm; d is the radiation diameter of weed roots, mm; n is the weeding shovel operation deviation; ε is the standard deviation of weed root diameter.

Through relevant literatures and field research (Longzhe *et al.*, 2021), the depth of weed roots under the surface is about 20 mm, the radiation diameter is about 40 mm, the weeding shovel operation deviation is 7 mm, and the standard deviation of weed root diameter is 3 mm. Therefore, the width of weeding shovel should be $w \geq 50$ mm.

According to the shovel structure resistance model of Mohr-Coulomb soil shear theory proposed by Wheeler *et al.*, (1996), the resistance during the inward clamping process of the weeding shovel is also related to the weeding shovel width. The resistance model is shown in Fig. 9. When the weeding shovel is clamped and sheared inward at speed v , the soil in the triangular ABC area in front of the weeding shovel produces resistance P to the shovel surface, which can be divided into horizontal force F_x and vertical force F_y . In the absence of other external forces applied to the soil:

$$F_x = (\gamma h^2 N_\gamma + chN_{ca}) [w + h(m - (m-1)/3) + \gamma v^2 N_a h(w + 0.6h)] \sin(\alpha + \varphi) \quad (14)$$

$$F_y = (\gamma h^2 N_\gamma + chN_{ca}) [w + h(m - (m-1)/3) + \gamma v^2 N_a h(w + 0.6h)] \cos(\alpha + \varphi) \quad (15)$$

where:

γ is the soil volume weight, $\text{kg}\cdot\text{m}^{-3}$; c is the soil cohesion, $\text{kN}\cdot\text{m}^{-2}$; h is the depth of weeding shovel into soil, mm; m is the soil fracture width-depth ratio; N_γ is the soil gravity coefficient; N_{ca} is the soil bonding coefficient; N_a is the soil inertia coefficient.

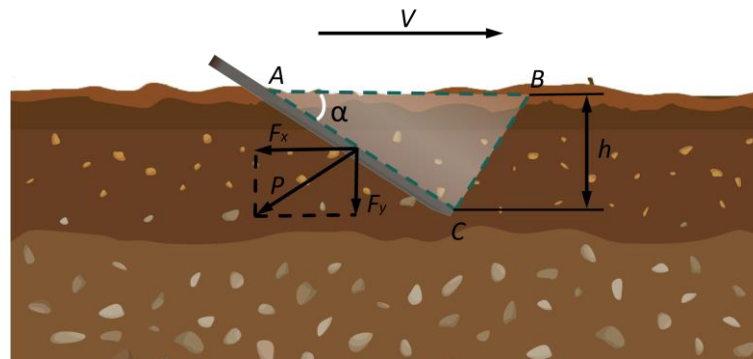


Fig. 9 - Resistance model diagram

Therefore, the resistance P is:

$$P = (\gamma h^2 N_\gamma + ch N_{ca} + \gamma v^2 h N_a) w \quad (16)$$

It can be seen from Eq. (16) that under the condition of a certain clamping speed, the resistance of the weeding shovel is linearly related to the width of the shovel surface, and the larger the width of the shovel surface, the greater the resistance of the weeding shovel. Therefore, in the case of smooth shearing and removing weeds, the weeding shovel width should be as small as possible. Combined with Eq. (13), the weeding shovel width is designed to be 50 mm, which can ensure that the weeding shovel can completely remove the weeds under the condition of small resistance.

Test and result analysis

Test condition

This test simulated the corn ridge field environment and was conducted in the Robotics Laboratory of the School of Mechanical and Electrical Engineering, Northeast Forestry University. The main test equipment includes a weeding device, AUBO-E5 robotic arm, LegionY7000P computer, mobile power supply, etc., as shown in Fig. 10. The weeding device is installed on the AUBO-E5 robotic arm test platform, and the speed of the robotic arm is adjustable.

The constructed ridge length is 3 m, the ridge distance is 600 mm, the average ridge height is 200 mm, and the soil water content is 17%~18%. The focus of this study is to verify the weeding effect of the weeding device. Therefore, in this test, the 3-4 leaf stage corps with similar sizes were used to replace the real corns and the weeds were transplanted to the weeds growing in the natural environment of the field. In order to reduce the test error, the distribution of crops and weeds in each group was as consistent as possible. The sample crop distance is 240~300 mm, and the weed density is 0.01~0.02 plants/ cm^2 .

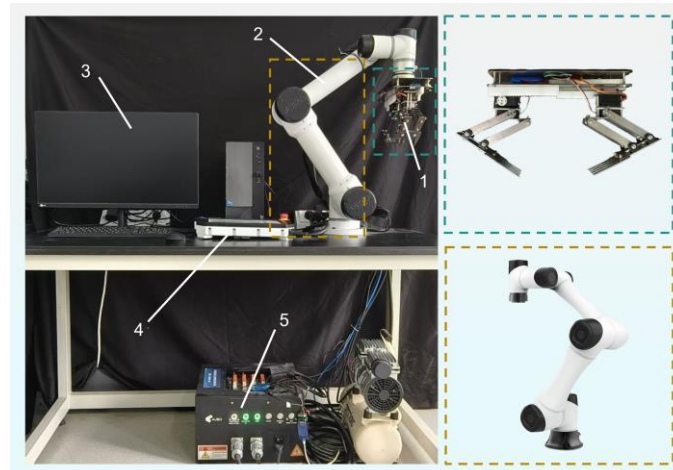


Fig. 10 - Test environment

1. weeding device; 2. robotic arm; 3. desktop computer; 4. control panel; 5. mobile power supply

Test method

Based on the determination of key parameters for the weeding components, insights from relevant literature, and field testing experience, it is evident that a small shovel surface inclination angle negatively impacts the weeding effect, while a large inclination angle increases weeding resistance. Therefore, the selected inclination angle is set to 10°~40°, and a single-factor test is conducted. The weeding operation process is illustrated in Fig. 11.

The weeding device remains in an initial state, ready for operation. The visual system identifies and locates the weeds, after which the robotic arm drives the weeding device to avoid the crops and position itself in the designated weeding area. The weeding device, powered by two sets of steering engines, performs the actions of breaking the soil and clamping and shearing the weeds roots. Once complete, the mechanical arm lifts the weeding device to separate the weeds from the soil. After the weeding operation, the mechanical arm resets the device in preparation for the next task.

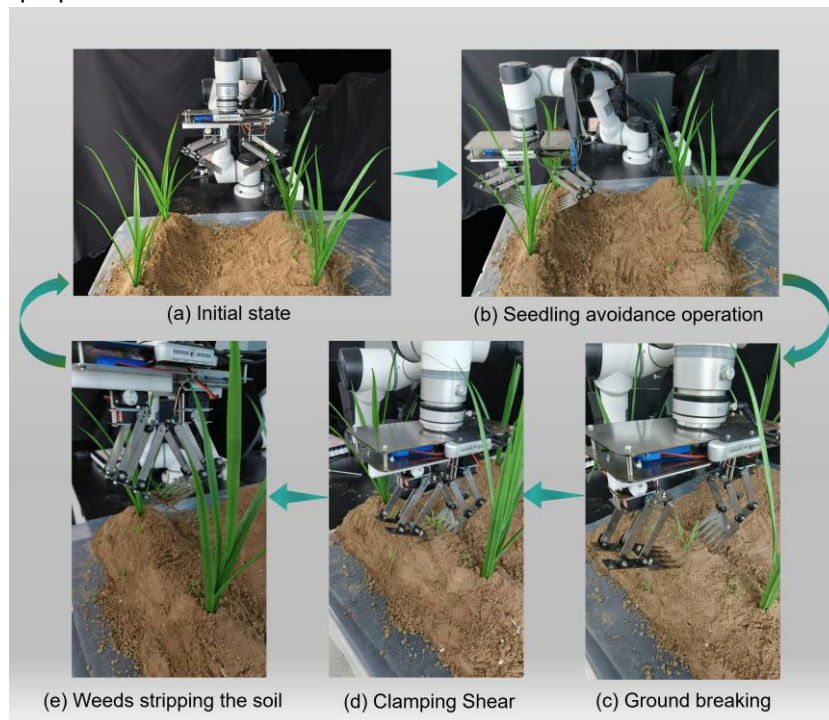


Fig. 11 - Weeding operation process

Weeding operation process

In this test, the crop injury rate and weed removal rate were used as test indexes. Successful weeding was defined by the cutting and destruction of the weeding area and the removal of soil. Due to test limitations, the corns used were at the 3-5 leaf stage. During the test, any sample crops that were uprooted or significantly displaced were considered injured. The number of injuries was counted manually. The calculation formula for the test metrics is as follows (Bao et al., 2020):

$$k = \frac{Q_z - H_z}{Q_z} \times 100\% \quad (17)$$

$$s = \frac{M_s}{M_z} \times 100\% \quad (18)$$

where:

k is weed removal rate, %; Q_z is the number of weeds before weeding in the test area; H_z is the number of weed plants after weeding in the test area; s is crop injury rate, %; M_s is the number of injured crops after weeding in test area; M_z is the number of injured crops before weeding in test area.

RESULTS

According to the previous test research, the deepest penetration depth $p=40$ mm and the clamping shear speed $v=4$ cm/s were set. According to the shovel surface inclination angle ranging from 10° to 40°, the

test was set to 7 levels of 10°, 15°, 20°, 25°, 30°, 35° and 40°. The test results are shown in Table 1, and the relationship between each performance evaluation index and the shovel surface inclination angle is shown in Figure 12.

As shown in Table 1, the weed removal rate exceeds 85%, while the crop injury rate remains below 6%. These results indicate that the weeding device has a reasonable structure and effectively meets the current needs for intra-row weeding in the field.

Table 1

Results of weeding test					
Test number	Shovel surface inclination angle (°)	Penetration depth (mm)	Clamping-shear speed (cm/s)	Weed removal rate (%)	Crop injury rate (%)
1	10	40	4	85	3
2	15	40	4	85.5	3.3
3	20	40	4	86.3	3.5
4	25	40	4	87.2	3.7
5	30	40	4	88.8	4.2
6	35	40	4	89.6	4.7
7	40	40	4	90	5.5

As shown in Fig. 13, with the increase of the shovel surface inclination angle, the weed removal rate first increased slowly, and then tended to be stable, and the crop injury rate first increased slowly and then increased sharply. When $\geq 30^\circ$, the weed removal rate tends to be stable, but the crop injury rate rises sharply. Therefore, the suitable range of the inclination angle is 10°~30°. Considering the weeding shovel penetration ability, weeding resistance and intra-row soiling effect in the process of intra-row weeding device, $\approx 30^\circ$ is the better value.

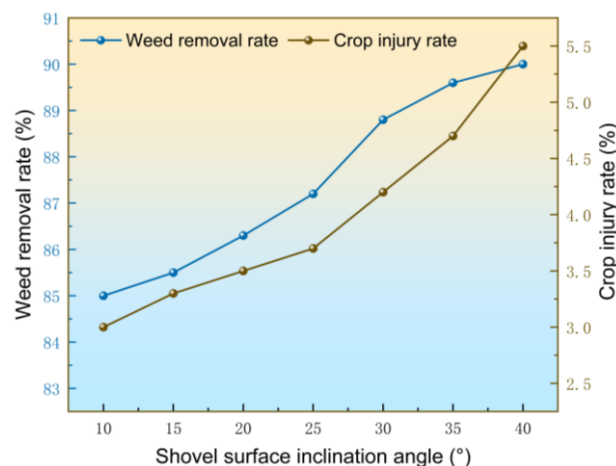


Fig. 12 - The relationship between evaluation index and the shovel surface inclination angle

CONCLUSIONS

(1) For intra-row weeding in ridge fields, a clamping-shear intra-row weeding device was designed by imitating the clamping operation of human hands. The weeding shovel part of the device adopts a parallelogram mechanism, which makes the finger mechanism compact and lightweight, effectively reduces the driving torque, and prolongs the life of the steering gear. The weeding part is mounted on the six-axis manipulator. When the visual system does not recognize the weed, the manipulator drives the weeding part to be in the neutral position between the rows. When the visual system recognizes the weed, the manipulator drives the weeding part to bypass the crop, and the weeding device is accurately moved to the weeding area for weeding.

(2) Through the analysis of the forces acting on the weeding shovel during the clamping and shearing of weeds, it was concluded that the stability of the weed root system decreases as the digging angle of the shovel increases. Consequently, the optimal inclination angle for the weeding shovel was determined to be between 10° and 40°. By analyzing and calculating the shovel blade angle, it is determined that when the blade angle is 30°, there will be no winding grass and soil in the weeding operation. Additionally, a resistance model was established based on the Mohr-Coulomb soil shear theory, leading to the determination of the weeding shovel width, which was set at 50 mm to ensure minimal resistance while completely removing weeds.

(3) On the test platform built in the laboratory, the designed weeding device was tested with the shovel inclination angle as a single factor. The test results showed that the weed removal rate of the weeding device was above 85 %, and the crop injury rate was below 6 %. Meet the requirements of intra-row weeding in the ridge field, and when the shovel inclination angle is 30°, the weeding performance of the device is optimal. The research in this paper can provide a reference for the design and improvement of intra-row weeding devices in ridge fields.

ACKNOWLEDGEMENT

This research is funded by the National Science Foundation of China (Grant No. 51975114).

REFERENCES

- [1] Ahmad, F., Qiu, B., Dong, X., Ma, J., Huang, X., Ahmed, S., & Chandio, F. A. (2020). Effect of operational parameters of UAV sprayer on spray deposition pattern in target and off-target zones during outer field weed control application. *Computers and Electronics in Agriculture*, 172, 105350.
- [2] Bao, H. A. N., Chang, G. U. O., Yingling, G. A. O., Qiao, L. I. U., Shuo, S. U. N., & Xiaowei, D. O. N. G. (2020). Design and Experiment of Soybean Intra-row Weeding Monomer Mechanism and Key Components. *Nongye Jixie Xuebao/Transactions of the Chinese Society of Agricultural Machinery*, 51(6), 112-121.
- [3] Bircher, W. G., Morgan, A. S., & Dollar, A. M. (2021). Complex manipulation with a simple robotic hand through contact breaking and caging. *Science Robotics*, 6(54), 2666.
- [4] Bing, X., Decong, Z., Jiabin, W., & Youzhi, Y. (2021). Workspace analysis of a flame intra-row weeding robot in vegetable field and numerical simulation of propane combustion. *INMATEH-Agricultural Engineering*, 65(3), 73-81. DOI: <https://doi.org/10.35633/inmateh-65-08>
- [5] Cirujeda, A., Aibar, J., Moreno, M. M., & Zaragoza, C. (2015). Effective mechanical weed control in processing tomato: Seven years of results. *Renewable Agriculture and Food Systems*, 30(3), 223-232.
- [6] Dilipkumar, M., Chuah, T. S., Goh, S. S., & Sahid, I. (2020). Weed management issues, challenges, and opportunities in Malaysia. *Crop Protection*, 134, 104347.
- [7] Fang, H., Niu, M., Xue, X., & Ji, C. (2022). Effects of mechanical-chemical synergistic weeding on weed control in maize field. *Trans. CSAE*, 38(6), 44-51.
- [8] Fujun, Z. H. O. U., Wenming, W. A. N. G., Xiaoli, L. I., & Zunfeng, T. A. N. G. (2018). Design and experiment of cam rocker swing intra-row weeding device for maize. *Nongye Jixie Xuebao/Transactions of the Chinese Society of Agricultural Machinery*, 49(1), 77-85.
- [9] Huang, X. L., Liu, W. D., Zhang, C. L., Zhang, Y., & Li, W. (2012). Optimal design of rotating disc for intra-row weeding robot. *Transaction of the Chinese Society for Agricultural Machinery*, 43(6), 42-46.
- [10] Hu, L., Luo, X., Yan, Y. A., Chen, X., Zen, S., & Zhang, L. (2012). Development and experiment of intra-row mechanical weeding device based on trochoid motion of claw tooth. *Transactions of the Chinese Society of Agricultural Engineering*, 28(14), 10-16.
- [11] Jinchuan, L., Yimin, Z., Xin, S., Song, M., & Xinpeng, S. (2017). Optimization of the angle of artichoke harvester's second-order flat shovel based on Mathematica. *Ganhan Diqu Nongye Yanjiu*, 35(2), 282-288.
- [12] Liang, Y. G., Hu, W. B., Liu, Y., Li, Y. Y., & Fang, B. H. (2022). The research progress of ridge cultivation mode in China. *Chinese Journal of Ecology*, 41(7), 1414-1422.
- [13] Li, Y., Guo, Z., Shuang, F., Zhang, M., & Li, X. (2022). Key technologies of machine vision for weeding robots: A review and benchmark. *Computers and Electronics in Agriculture*, 196, 106880.
- [14] Longzhe, Quan N., Jingyu, Zhang, Wei, Jiang, Hengda, Li, Chunjie, Yang, & Xilin, Zhang. (2021). Development and Experiment of Intra-row Weeding Robot System Based on Protection of Maize Root System. *Nongye Jixie Xuebao/Transactions of the Chinese Society of Agricultural Machinery*, 52(12), 115-123.
- [15] Pérez-Ruiz, M., Slaughter, D. C., Gliever, C. J., & Upadhyaya, S. K. (2012). Automatic GPS-based intra-row weed knife control system for transplanted row crops. *Computers and Electronics in Agriculture*, 80, 41-49.
- [16] Qinsong, X., Suming, D., Xinyu, X., Longfei, C., Feixiang, L., & Yinghang, L. (2022). Research on the development status of intelligent field weeding robot. *Journal of Chinese Agricultural Mechanization*, 43(8), 173.

- [17] Riemens, M.M., Groeneveld, R.M.W., Lotz, L.A. P., & Kropff, M.J. (2007). Effects of three management strategies on the seedbank, emergence and the need for hand weeding in an organic arable cropping system. *Weed Research*, 47(5), 442-451.
- [18] Wheeler, P.N., & Godwin, R.J. (1996). Soil dynamics of single and multiple tines at speeds up to 20 km/h. *Journal of Agricultural Engineering Research*, 63(3), 243-249.
- [19] Ziwen, C., Nan, L., Zhe, S., Tao, L., Chunlong, Z., & Wei, L. (2015). Optimization and experiment of intra-row brush weeding manipulator based on planetary gear train. *Nongye Jixie Xuebao/Transactions of the Chinese Society of Agricultural Machinery*, 46(9).

DETECTION OF ADULT PEACH FRUIT MOTH BASED ON IMPROVED YOLOv8m

/ 基于改进 YOLOV8M 的桃小食心虫成虫检测方法

Lijun CHENG^{*1)}, Yihe ZHANG¹⁾, Jianglin YAN¹⁾, Zhengkun ZHAI¹⁾, Zhiguo ZHAO^{*2)}, LinQiang DENG¹⁾¹⁾ College of Software, Shanxi Agricultural University, Taigu, Shanxi / China;²⁾ College of Software, Shanxi Agricultural University, Taigu, Shanxi / ChinaCorresponding authors: Lijun Cheng; Tel: +86-13835441585; E-mail: cljzyb@sxau.edu.cnZhiguo Zhao; Tel: +86-15034664518; E-mail: nice2me@126.comDOI: <https://doi.org/10.35633/inmateh-75-05>**Keywords:** YOLOv8m; pest detection; down sampling; CPCA attention mechanism; Inner-WIoU**ABSTRACT**

The peach fruit moth was a fruit-eating pest and one of the major pests of fruit trees in China, Korea, Japan, and Australia. Due to long-term problems such as improper control methods, low technical quality, and untimely treatment, the yield and efficiency of fruit products were greatly affected, which constrained the development of the fruit industry. This paper developed a method for detecting adult peach fruit moths based on an improved YOLOv8m to address the challenging problem of manually detecting peach fruit moths. To increase the Receptive Field of the model, v7Down Sampling was introduced in its backbone network. Then, the channel-prioritized Convolutional Attention Mechanism Module (CPCA), which dynamically allocated the spatial attention weights on each channel, reducing the noise and the algorithm's complexity, was incorporated. Finally, the inner-WIoU loss function was introduced to enhance the convergence and generalization of the bounding box. The precision (P) of the improved model increased by 3.4 percentage points compared to YOLOv8m. The recall (R) improved by 2.1 percentage points, and the mAP improved by 1.2 percentage points. The single-category precision (AP) for peach fruit moth detection improved by 2.4 percentage points. Moreover, the weight size, number of model parameters, and computational volume were reduced by 3.6MB, 1.8M, and 1.7G, respectively. This achieved an improvement in the model's effectiveness in detecting adult peach fruit moths without increasing the model's complexity. The results provided strong technical support for the subsequent real-time monitoring of the peach fruit moth.

摘要

桃小食心虫是一种食果害虫，也是中国、韩国、日本、澳大利亚等果树的主要害虫之一。因为长期的防治方法不当、技术素质低、处理不及时等问题，使果品的产量和效益都受到很大影响，制约果业的发展。本文针对人工检测桃小食心虫困难问题，开发了一种基于改进 YOLOv8m 的桃小食心虫成虫检测方法。我们在其主干网络引入 v7Down Sampling，增加模型的感受野。然后引入通道优先卷积注意力机制模块（CPCA），动态分配各个通道上的空间注意力权重，减少了噪声及算法的复杂度。最后引入 Inner-WIoU 损失函数，增强了边界框的收敛和泛化能力。改进后模型的精确度 P 相较 YOLOv8m 提高了 3.4 个百分点。召回率 R 提高了 2.1 个百分点。mAP 提高了 1.2 个百分点。桃小食心虫单类别精度 AP 上提高了 2.4 个百分点。并且权重大小、模型参数量和计算量分别减少了 3.6MB、1.8M、1.7G。实现了在不增加模型复杂度的同时提高模型对桃小食心虫成虫的检测效果，其结果可为后续桃小食心虫的实时监测提供有力的技术支撑。

INTRODUCTION

The peach fruit moth (*Carposina sasakii* Matsumura), is a fruit-eating pest of the genus Peach Fruit Moth in the family Lepidoptera. It is widely distributed and has a serious infestation in China, Japan, Korea, Russia, Australia, and other countries (Kim et al., 2000). The peach fruit moth had a wide range of host plants, with the Rosaceae, Rhamnaceae, and Pomegranateaceae being the primary ones. When the damage was severe, it caused worm droppings and rotten fruits, which directly affected the yield and quality of fruits and resulted in significant economic losses (Fang et al., 2022). Prediction could prevent the occurrence of the pest in advance based on the dynamic patterns of its emergence. At present, the detection and counting of adult peach fruit moths relied on visual discrimination. From 2021 to 2022, Zhang Xiaowei monitored the population size of adult pear fruit moths and peach fruit moths in pear orchards in Shanxi Province. This study was conducted manually for two consecutive years, using pear orchards in Shanxi Province as monitoring sites. It provided a theoretical basis for the prediction and integrated management of these two types of pear fruit moths (Zhang et al., 2024).

This manual method of detecting and counting peach fruit moths was time-consuming and inefficient. Moreover, the number of adult peach fruit moths was high during the peak incidence period, and accurate counting was challenging due to the wide range of infested fruit species (Zhang *et al.*, 2023). These difficulties seriously hindered the accurate control of peach fruit moths.

In recent years, the level of agricultural intelligence gradually increased, and deep learning detection algorithms were applied to the field of agricultural pest detection (Yue *et al.*, 2024). Min Dai *et al.*, (2023), proposed an improved plant pest detection method based on YOLOv5m. Experimental results showed that the improved YOLOv5m achieved 95.7% accuracy, a 93.1% recall rate, a 94.38% F1 score, and a 96.4% mean average precision (mAP). Li Bin proposed an improved YOLOv5 rice pest detection method, and the mAP value of the improved model was 1.49 percentage points higher than that of YOLOv7 and 12.89 percentage points higher than that of Faster R-CNN (Li *et al.*, 2024). Ma Pan *et al.*, (2023), proposed a cotton aphid image detection algorithm based on the YOLO neural network and integrated it into software. The average time for cotton aphid image detection was 4.1 seconds, and the counting accuracy for both live and dead cotton aphids exceeded 93%. The use of deep learning algorithms could enable the rapid detection of peach fruit moths, significantly improving detection efficiency. Therefore, this study aimed to use a YOLO series of algorithms to address the problems of difficult target recognition and low detection accuracy caused by background clutter and overly dense samples in the peach fruit moth dataset. The base model was optimized and improved to provide a model basis for the detection of peach fruit moths.

MATERIALS AND METHODS

Data set establishment

The adult peach fruit moth dataset used in this study was obtained from the Institute of Fruit Tree Research, Shanxi Agricultural University, Taigu District, Jinzhong City, Shanxi Province, China. In this study, triangular traps were hung on fruit trees 1.2-1.5 m above the ground in pear and apple orchards from May to October 2023 -2024. The traps consisted of a triangular trap frame, white sticky boards, and peach fruit moth traps (Zhao *et al.*, 2023). 2-3 days later, the white sticky boards were removed and images of the dataset were captured with a Nikon D7000 camera from different angles. A total of 1781 images in JPG format were taken in this study, as shown in Fig. 1.

The 1781 original data were randomly divided into a training set (1068), a validation set (356), and a test set (357) in the ratio of 6:2:2 to ensure that the training set and validation set were completely independent and not duplicated. To improve the generalization ability and robustness of the model during the training process, this study first uses Open Computer Vision Library (OpenCV) and randomly selects Gaussian fuzzy, adding noise, rotation, brightness change, flipping panning, and other methods for data enhancement of the divided training set. A dataset containing 4982 images was finally obtained, of which 4269 were for the training set, 356 for the validation set, and 357 for the test set. In the process of data collection, it was found that in addition to peach small heartworms, many pear small heartworms and Chinese pear louse also appeared on the white sticky board. Therefore, in this experiment, adult pear small heartworm and Chinese pear louse were added to the data categories, and the data set was labelled with the software Labellmg. The labelling was divided into “*Carposina lipogenesis*”, “*Psylla chinensis*” and “Oriental Fruit Moth”.



Fig. 1 -Collection environment and collection device for peach fruit moth datasets

Improved YOLOv8m target detection algorithm

The improved YOLOv8m model structure in this paper is shown in Fig. 2. Firstly, the v7Down Sampling (v7DS) from YOLOv7 was added to the backbone network of YOLOv8. Then, the Channel-Prior Convolutional Attention Mechanism Module (CPCABlock) was incorporated into the backbone section. Finally, the Inner-WIoU loss function was introduced.

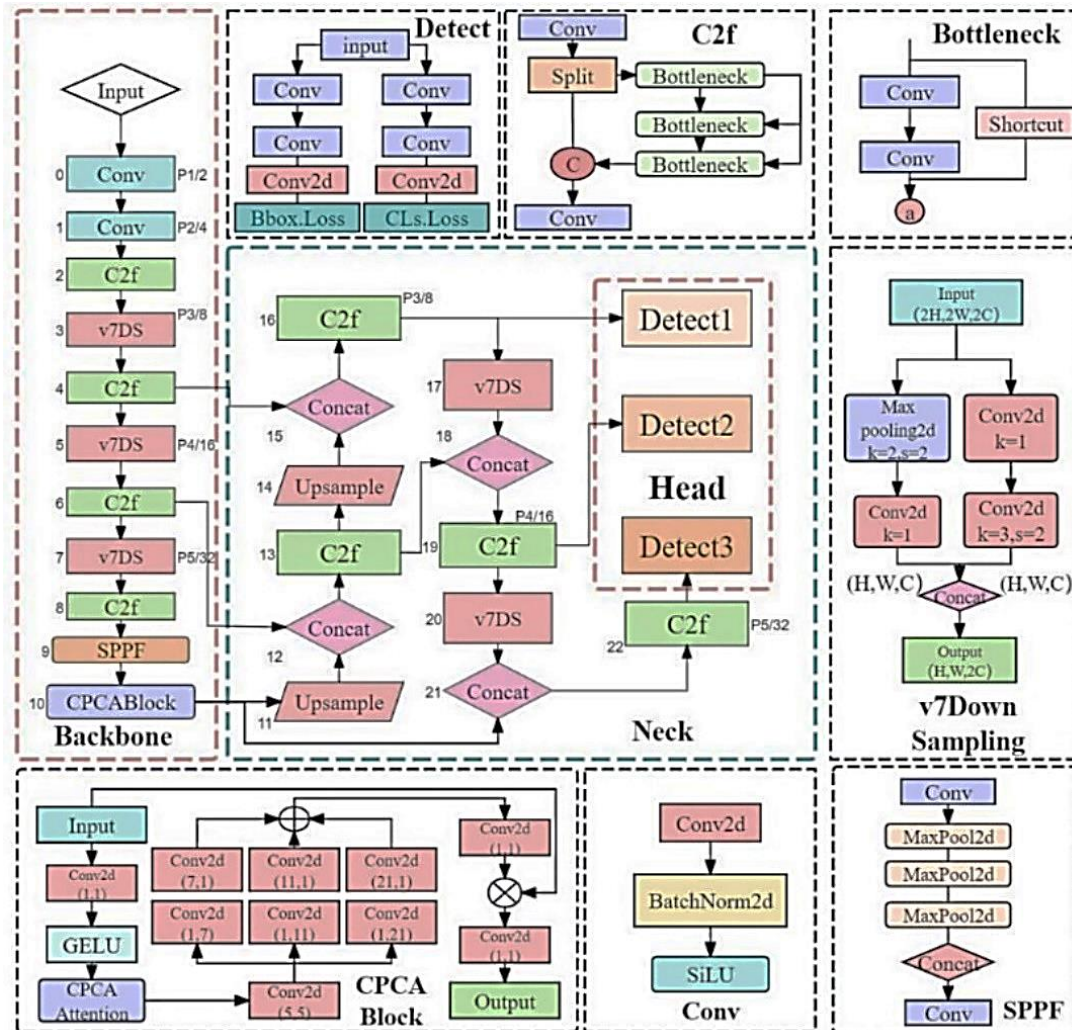


Fig. 2 - Improved YOLOv8m model structure diagram

Conv is convolution, V7DownSampling is the YOLOv7 downsampling module, SPPF is the spatial pyramid pooling module, CPCABlock is the channel-first convolutional attention mechanism module, Contact is the feature connection module, Upsample is upsampling module, Detect is detection head, Bbox. Loss and Cls. Loss is bounding box loss and classification loss, Split is the slice operation, Bottleneck is the bottleneck layer, SiLU is the activation function, MaxPooling is the maximum pooling operation, Maxpool2d is the maximum pooling, Conv is the convolution, Contact is the feature connection module and Bbox. Loss and Cls. The Losses are bounding box losses and classification losses, respectively.

Downsampling Module v7DS

Downsampling is a commonly used image processing method in image detection. It can shrink the image without altering its effective content, reduce the image resolution, decrease the amount of data computation, and generate a downsampling map corresponding to the image. This helps extract high-level semantic features from the image and increases the model's Receptive Field, thereby enhancing the model's ability to detect targets (Lin et al., 2023).

The downsampling v7DS of YOLOv7 utilizes the Spatial Pyramid Pooling (SPP) structure. It produces a feature map with the number of output channels equal to the number of input channels and reduces the spatial resolution by a factor of two. The structure is shown in Figure 3 below. By reducing the size and resolution of the input image and the computational load of the model, the network can better capture features in the image, process detailed information of the input image, and handle large image data more efficiently (Wang et al., 2022).

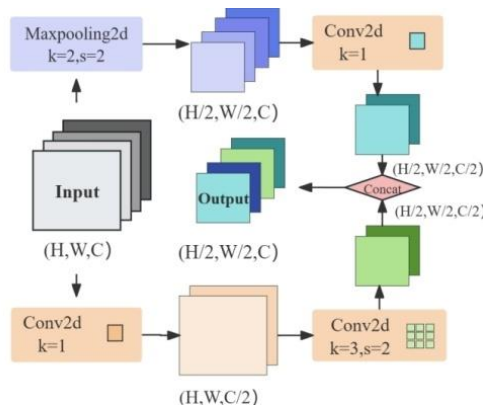


Fig. 3 -v7DS model structure diagram

Channel Prioritized Convolutional Attention Mechanism Module

The peach fruit moth dataset was collected in an open-air environment and was characterized by a cluttered background and fuzzy samples, which required the model to have the ability to judge target objects more accurately. The attention mechanism can suppress the expressive ability of non-essential features on the feature map and enhance the expressive ability of main features, effectively weakening the influence of the cluttered background on the detection results during the detection process.

The Channel-Prior Convolutional Attention Mechanism (CPCA), proposed by Hejun Huang et al. (Huang et al., 2024), combines channel attention and spatial attention. It reduces noise and algorithm complexity while achieving dynamic allocation of spatial attention weights on each channel. CPCA is a lightweight yet high-performance attention mechanism that can alleviate computational burden. The model structure is shown in Figure 4 below.

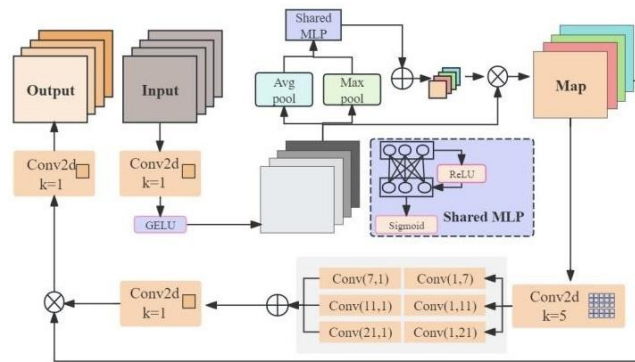


Fig. 4 -CPCABlock module structure diagram

Channel Attention Module of CPCA: The input feature maps are subjected to global average pooling and global maximum pooling respectively to obtain new feature maps, then the weight coefficients are obtained through the σ function, and the weight coefficients are multiplied with the new feature maps to finally obtain the output feature maps, which is calculated as in equation (1).

$$CA(F)=\sigma\left(MLP(AvgPool(F_m))+MLP(MaxPool(F_m))\right) \tag{1}$$

where: σ is the Sigmoid function, *AvgPool* is the global average pooling, and *MaxPool* is the global maximum pooling (Wang et al., 2024).

Spatial Attention Module for CPCA: Utilizing depth-separable convolution to capture spatial relationships between features, a multi-scale structure is used to enhance the ability of the convolution operation to capture spatial relationships, which is calculated as in equation (2).

$$SA(F)=Conv_{1\times 1}\left(\sum_{i=0}^3 Branch_i(DwConv(F))\right) \tag{2}$$

where: *DwConv* denotes the depth convolution. *Branch_i*, $i\in\{0,1,2,3\}$ denotes the *i*-th branch. *Branch₀* is the identity connection.

Inner-WIoU loss function

The peach fruit moth dataset has problems such as high sample density and different target scales, *Inner-WIoU* implements the similarity calculation by considering the scale difference between the auxiliary

border and the actual border, which is suitable for the situation that needs to adjust the loss of focus dynamically and meets the needs of this experiment. As shown in Fig. 5.

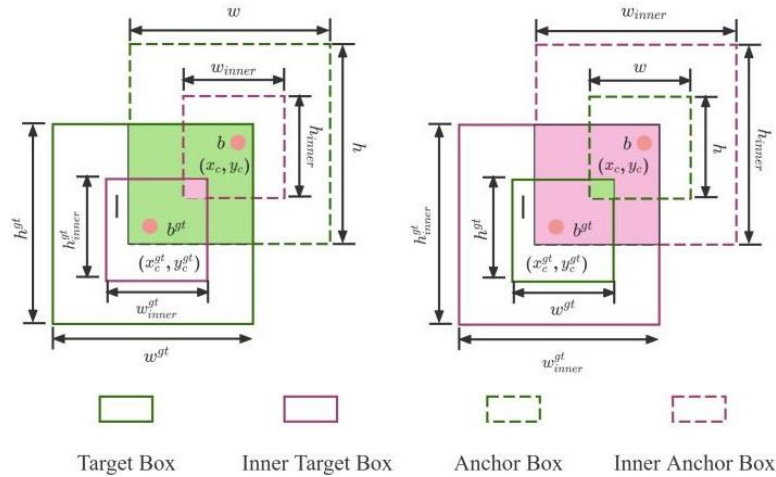


Fig. 5 -Description of Inner-WIoU

Inner-IoU is a combination of loss functions such as *EIoU* and *WIoU* using the idea of Inner. It controls the scale size of the auxiliary bounding box for calculating the loss by introducing the scale factor ratio, which can simultaneously take into account the convergence of the high *IoU* samples and the regression of the low *IoU*, and overcomes the limitations of the existing methods in terms of generalization ability (Zhang et al., 2023). *WIoU* is a kind of bounding box loss based on the dynamic non-monotonous focusing mechanism, whose loss function is shown in Eq. (3):

$$L_{WIoU} = r \times R_{WIoU} \times L_{WIoU}, R_{WIoU} \in [0, 1] \quad (3)$$

where: the distance focusing mechanism is used to amplify the ordinary moderate anchor frame L_{IoU} , and the non-monotonic focusing coefficient r is used to focus the ordinary quality anchor frame, which provides better target frame regression loss to improve the performance of the target detector. *WIoU* removes the aspect ratio penalty term in *CIoU*, and also balances the effects of high and low-quality anchor frames on the regression of the model, which enhances the model's generalization ability, and improves the model's overall performance (Tong et al., 2023).

The *Inner-IoU* is applied to the existing *WIoU*-based marginal regression loss function defined as in equation (4):

$$L_{Inner-WIoU} = L_{WIoU} + IoU - IoU^{inner} \quad (4)$$

Experimental Platform

The main parameters of the AutoDL server platform used in this experiment are as follows: 12 vCPU Intel(R) Xeon(R) Silver 4214R CPU with 2.40 GHz, 90 GB of RAM, and an RTX 3080 Ti (12 GB) GPU. The experiments were conducted on the Linux operating system, and the PyTorch deep learning framework was used for model building, training, and evaluation. The model was built, trained, and evaluated using PyTorch version 1.13.1, Python version 3.8.6 (Ubuntu 20.04), and CUDA version 11.7.

Training Parameter Settings

The image input size was set to 640×640, the batch size was set to 16, and multithreading was configured to 8. The Stochastic Gradient Descent (SGD) optimizer was selected, and the training rounds were set to 200 with YOLOv8m's early stopping mechanism applied. The initial learning rate was 0.01, and the final learning rate was 0.001. The momentum parameter was set to 0.937, and the weight decay parameter was set to 0.0005. The random seed was fixed at 0.

Evaluation Metrics

To evaluate the performance of the model's detection results on the peach fruit moth dataset, the following evaluation criteria were chosen: precision (P), recall (R), mean average precision (mAP@0.5), mAP@0.5:0.95, single-category precision for peach fruit moth (**Carposina sasakii** AP%), number of parameters (Params), model weights (Weight), and computational volume (FLOPs). These metrics were used to assess the model's effectiveness in detecting peach fruit moths and to compare its performance with other models.

RESULTS

Ablation Experiments

Ablation experiments were conducted for different improvement points, and the results are shown in Table 1. YOLOv8m-A introduced v7DS for downsampling in the backbone network, which improved the single-category accuracy of the peach fruit moth by 3.1 percentage points. YOLOv8m-B introduced the CPCA attention mechanism in the backbone network, which significantly reduced model weights and computational load. It reduced the weights by 45.52 MB and the computational volume by 70.3 G, respectively, compared to YOLOv8m. YOLOv8m-C introduced the Inner-WIoU loss function in the backbone network, which improved the all-category precision (P) by 1.6 percentage points over the original model. Both YOLOv8m-D and YOLOv8m-E showed improved performance compared to YOLOv8m. However, the YOLOv8m-VCI model, which incorporated all three improvement points, demonstrated even more significant enhancements. It achieved a 3.4 percentage point improvement in precision (P) compared to YOLOv8m. The recall (R) improved by 2.1 percentage points, and the mAP improved by 1.2 percentage points. The single-category precision (AP) for peach fruit moth detection improved by 2.4 percentage points. Additionally, the weight size, the number of model parameters, and the computational volume were reduced by 3.6 MB, 1.8 M, and 1.7 G, respectively. These improvements enhanced the model's detection effectiveness for adult peach fruit moths without increasing the model's complexity.

Table 1

Ablation test results for different improvement points.

Model	v7DS	CPCA	Inner-WIoU	P	R	mAP@0.5	AP	Weight	Params	FLOPs
				[%]	[%]	[%]	[%]	[MB]	[M]	[G]
YOLOv8m	—	—	—	84.8	84.4	85.6	92.2	52	25.8	78.7
YOLOv8m-A	√	—	—	85.6	84.5	86.3	95.3	47.2	23.4	76.2
YOLOv8m-B	—	√	—	85.0	84.1	85.6	94.4	6.5	31.	8.4
YOLOv8m-C	—	—	√	86.4	84.0	86.4	94.1	52	25.8	78.7
YOLOv8m-D	√	√	—	85.7	85.3	86.0	93.6	48.4	24.0	77.0
YOLOv8m-E	√	—	√	88.0	83.2	87.0	93.6	47.2	23.4	76.2
YOLOv8m-VCI	√	√	√	88.2	86.5	86.8	94.6	48.	24.0	77.0

Note: √ indicates that the module is used; — indicates that the module is not used

Detection results of YOLOv8m-VCI

(1) The improved YOLOv8m-VCI achieved 88.2% precision, 86.5% recall, and 86.8% mAP. The single-class precision (AP) for peach fruit moth detection reached 94.6%. The detection results of YOLOv8m-VCI are visualized in Fig. 6. YOLOv8m incorporates an early-stopping mechanism to prevent model overfitting. The experiment was automatically halted when the optimal performance was achieved at 100 training epochs. The training curve of YOLOv8m-VCI stabilized in the later stages of the training process, exhibiting minimal fluctuations.

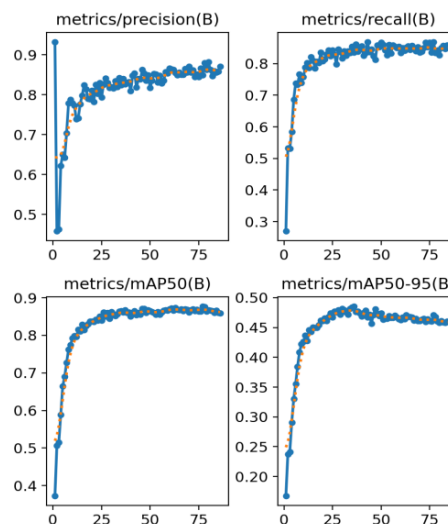


Fig. 6 -YOLOv8m-VCI curves during the training period

(2) In order to examine the improved model more closely, the P-R curves and F1-Confidence Curve for different categories are observed, as shown in Fig.7. The P-R curve, also known as the precision-recall curve, is a comprehensive representation of the model's performance. The more convex the P-R curve is, and the closer it is to the upper-right corner of the coordinate system, the better the model's performance. The more convex the P-R curve is and the closer it is to the right corner of the coordinate system, the better the model performance. Analysing the P-R curve, it can be seen that YOLOv8m-VCI is 98.5% effective in detecting the adult peach small heartworm. The mAP for the whole category reached 86.7%. The F1-Confidence Curve demonstrates the relationship between the F1 scores and different confidence thresholds. The F1 score is the harmonic mean of Precision and Recall, ranging from 0 to 1, with larger values indicating better model performance. Analysing the F1-Confidence Curve shows that YOLOv8m-VCI is the best for detecting the adult peach small heartworm. The F1 score for the whole category reaches 84% when the confidence threshold is 0.304.

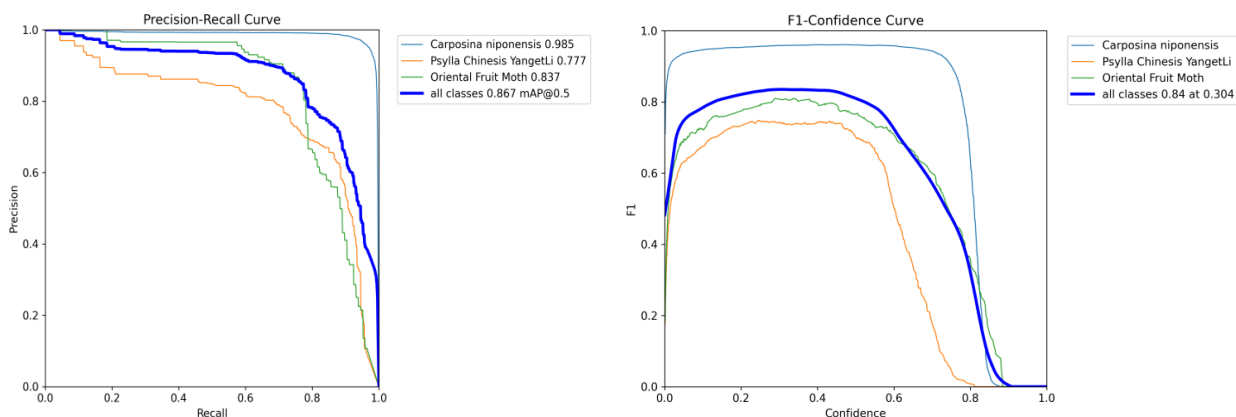


Fig. 7 - P-R curves and F1-Confidence Curve for YOLOvm-VCI during training

Performance Comparison of Different Target Detection Models

(1) In this experiment, seven mainstream target detection models—YOLOv5s, YOLOv5n, YOLOv7, YOLOv7-tiny, YOLOv8m, YOLOv8l, and YOLOv9c—were compared. The improved model, YOLOv8m-VCI, was also introduced for comparison. The results are presented in Table 2.

Table 2

Comparison of detection effects of different models

Model	P	R	mAP@0.5	mAP@.5 .95	Weight	Params	FLOPs
	[%]	[%]	[%]	[%]	[MB]	[M]	[G]
YOLOv5s	83.6	86.5	83.8	43.8	14.4	7.02	15.8
YOLOv5n	83.	85.7	84.8	44.7	3.8	1.76	4.1
YOLOv7	83.3	85.4	84.3	41.9	71.3	37.2	105.1
YOLOv7-tiny	81.7	87.0	85.1	44.5	11.7	6.02	13.2
YOLOv8m	84.8	84.4	85.6	45.7	52.0	25.8	78.7
YOLOv8l	85.6	83.0	85.7	45.9	87.6	43.6	164.8
YOLOv9c	85.5	83.1	85.1	44.9	102.8	51.0	237.7
YOLOv8m-VCI	88.2	86.5	86.8	45.2	48.4	24.0	77.0

As can be seen from Table 2, YOLOv8m-VCI is optimal in terms of precision, which is also 2.7 percentage points better than YOLOv9c. It is only 0.5 percentage points lower than YOLOv7-tiny in recall, which is better than other models. It improves by 3 percentage points over YOLOv5s in mAP and is optimal. mAP50-95 reaches 45.2%. In addition, the model is lower than YOLOv8m in terms of weight, number of parameters, and computational effort. YOLOv8m-VCI meets the requirements for real-time detection of peach fruit moths in real environments.

(2) The detection effects of the improved YOLOv8m-VCI model and the YOLOv8m model are shown in Fig. 8. In (1a), the peach fruit moth was wrongly detected as peach fruit moth, and in (1b), it was detected correctly and with an accuracy P of 66%; in (2a), the YOLOv8m model in the lower-right corner of the figure omitted the detection of the peach fruit moth, and in (2b) the improved YOLOv8m-VCI model detected it correctly. The accuracy P of the improved YOLOv8m-VCI model for detecting peach fruit moth in (3b) is higher

than the accuracy of the YOLOv8m model in (3a). It can be seen that compared with the original model, the improved YOLOv8m-VCI model has improved the misdetection and omission of peach fruit moth, and the accuracy P has been significantly improved.

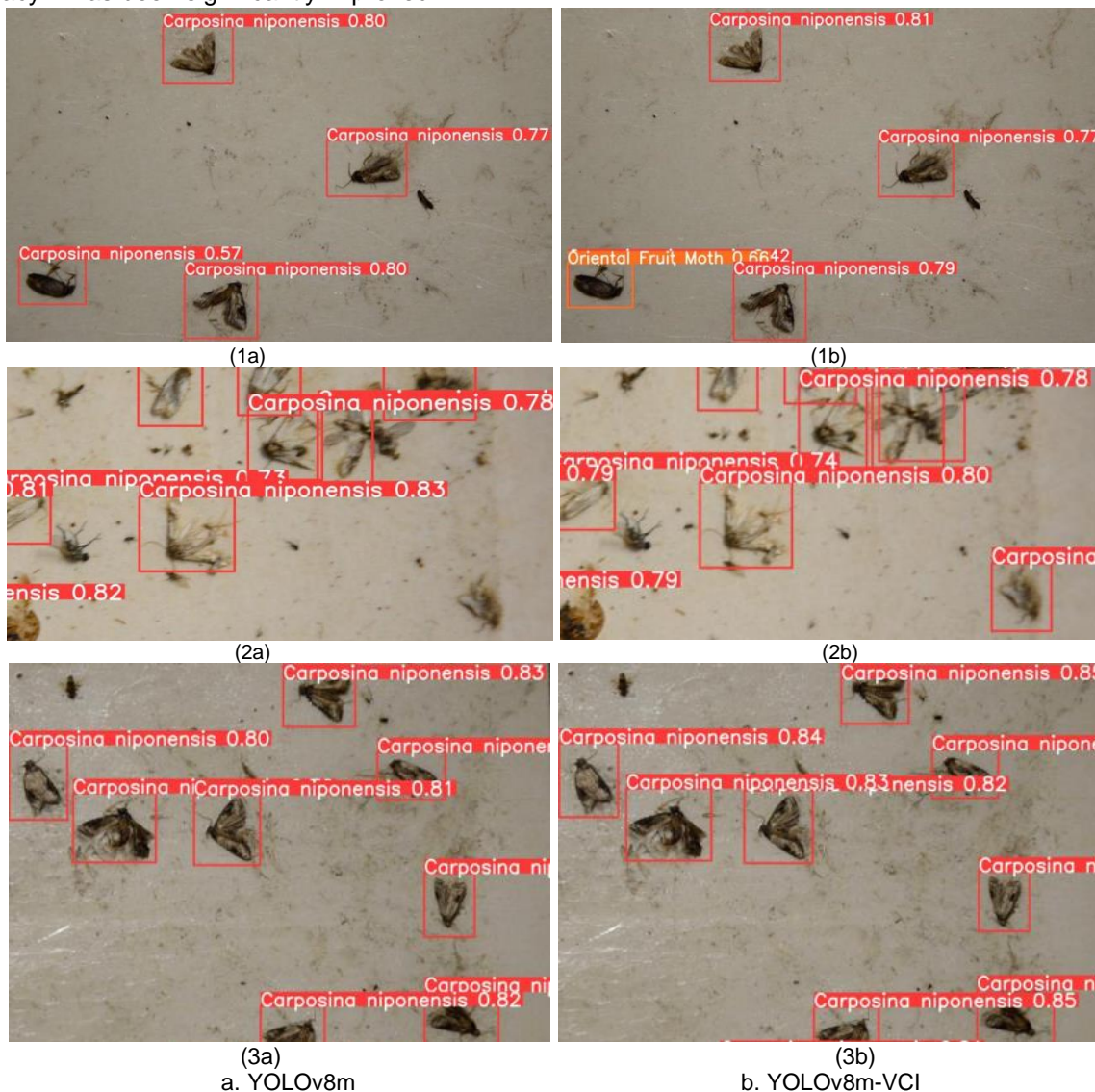


Fig. 8 - Comparison of detection effect of YOLOv8m-VCI model and YOLOv8m model

The Peach Fruit Moth Detection System

The Peach Fruit moth identification application utilized the PyQt framework of Python for front-end interface development. PyQt combined the concise syntax of Python with the powerful functionalities of Qt. It offered a rich library of controls, facilitating users in constructing interfaces, and also achieved cross-platform compatibility, ensuring the consistency and stability of the user interface across different operating systems. The QtDesigner tool of PyQt allowed for a more intuitive and rapid design of the program interface, enhancing the development speed of the program, and separating the program interface from its logic, which made it easier to maintain in the later stages. As shown in Figure 9.

The application primarily implemented the following four functions:

1) Pest image file import function. This section provided four methods for importing image files: importing a single image, an entire file, a video file, and real-time detection via a camera.

2) Detection results display function. This section was responsible for displaying the detection data to the user, including the time taken for detection, the number of targets detected, the type of targets, confidence levels, and the location of targets. Additionally, it offered a target selection feature to meet the user's need to view the detection results of a single target.

3) Detection results and target location information display function. This section generated a list after the detection was completed. The list included the target serial number, file path, category, confidence level, and coordinate location.

4) Operation function. This section provided two operations that users could perform on the system. These were the save and exit functions.

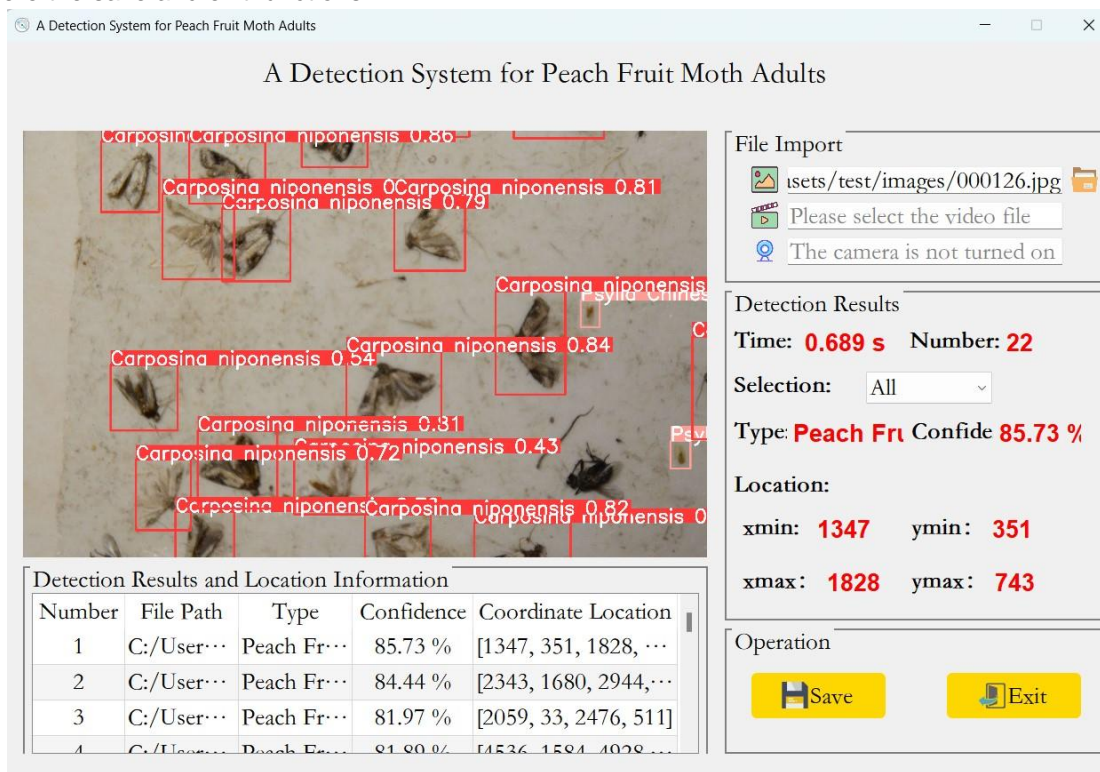


Fig. 9 - The Peach Fruit Moth Detection System

CONCLUSIONS

By introducing v7Down Sampling, CPCA Attention Mechanism, and Inner-WIoU Loss Function in the backbone network of YOLOv8m, the precision P is improved by 3.4 percentage points compared to YOLOv8m. Recall R improved by 2.1 percentage points. mAP improved by 1.2 percentage points. Peach fruit moth single-category precision AP improved by 2.4 percentage points. The size of weights, the number of model parameters, and the computational volume were reduced by 3.6MB, 1.8x106M, and 1.7G, respectively, which realized the improvement of the model's detection effect on adult peach fruit moth without increasing the model's complexity. The detection effect was better than the other seven YOLO series models compared.

The datasets of this study were collected outdoors, taking into account the real application scenarios of the model, and the real background was retained in the image processing, which is conducive to the model's ability to accurately detect small peach fruit moths even when the background is cluttered.

Follow-up research can expand the collection area of the dataset to broaden the scope of application of the model.

In the process of data collection, it was found that there was still a lot of Pear small heartworm and Chinese pear louse on the sticky boards with the addition of small peach fruit moth cores, so the two were added to the study together. However, the proportion of peach fruit moth, pear small heartworm, and Chinese pear louse samples in the actual dataset differed greatly, and there was the problem of sample imbalance. The detection accuracy of the single category of peach fruit moth with more sample data was high, while the detection accuracy of Pear small heartworm and Chinese pear louse with less sample data was low, thus affecting the detection effect of the whole category. In future research, the peach fruit moth and Chinese pear woodlouse can also be taken as research objects to increase the number of samples of the two, which can nearly improve the detection accuracy of the model for these three pests and enhance the detection efficiency.

Follow-up research can deploy the model on mobile terminals, deploy cameras in triangular traps in orchards, and utilize Internet of Things (IoT) technology to connect cameras and mobile terminals to realize real-time monitoring of peach fruit moth and improve the detection efficiency of peach fruit moth.

ACKNOWLEDGEMENT

This research was supported by the Teaching Reform Innovation Project of Higher Education Institutions in Shanxi Province (J20220247) and the Youth Scientific Research Project of the Basic Research Program of Shanxi Province (NO.202303021222039).

REFERENCES

- [1] Dai, M., Dorjoy, M.M.H., Miao, H., & Zhang, S. (2023). A new pest detection method based on improved YOLOv5m. *Insects*, 14(1), 54.
- [2] Fang, S.S., Qiao, X. F., Su, S., Jian, C.Z., & Chen, M.H. (2022). Advance of Research in Damage and Control of *Carposina sasakii* Matsumura (桃小食心虫的危害及其防治研究进展). *Shaanxi Journal of Agricultural Sciences*, 68(07):77-82.
- [3] Haishi, T., Koizumi, H., Arai, T., Koizumi, M., & Kano, H. (2011). Rapid detection of infestation of apple fruits by the peach fruit moth, *Carposina sasakii* Matsumura, larvae using a 0.2-T dedicated magnetic resonance imaging apparatus. *Applied magnetic resonance*, 41, 1-18.
- [4] Kim, D.S., Lee, J.H., & Yiem, M.S. (2000). Spring emergence pattern of *Carposina sasakii* (Lepidoptera: Carposinidae) in apple orchards in Korea and its forecasting models based on degree-days. *Environmental Entomology*, 29(6), 1188-1198.
- [5] Kotani, S., & Suzuki, Y. (2013). Development of an X-ray penetration imaging system for detecting peaches injured by the peach fruit moth. *Journal of the Japan Society for Precision Engineering*, 79(11), 995-998.
- [6] Li, B., & Fan, J. (2024). Classification of Rice Pests Based on YOLO v5 (基于YOLO v5的水稻害虫分类). *Jiangsu Agricultural Sciences* (02), 175-182.doi:10.15889/j.issn.1002-1302.2024.02.025.
- [7] Ma, P., Yang, Z. H., Wan, H., He, S., Huang, Y., & Xu, S.Y. (2023) A new cotton aphid image recognition algorithm and software based on YOLOv8 (基于YOLOv8网络的棉蚜图像识别算法及软件系统设计). *Journal of Intelligent Agricultural Mechanization (in Chinese and English)*, 4(03):42-49.
- [8] Zhang, X.W., Ding, W.Y., Wang, W.L., Jia Y.J., Zhu, G.F., Zhao, P., Wang Y.P, Zhang, S.D., Li, Z., &Liu, X.X. (2024). The occurrence and population dynamics of adult *Grapholita molesta* and *Carposina sasakii* in two pear orchards in Shanxi Province (山西梨园梨小食心虫和桃小食心虫成虫种群发生动态研究). *Chinese Journal of Applied Entomology*, 61(4).
- [9] Zhang, L.Y., Liu, A. H., Kong, T. T., Sheng, Z.H., & Zhu, Z.F. (2023). Progress in the study of *Carposina sasakii* Matsumura (桃小食心虫研究进展). *China Plant Protection* (12),20-26.
- [10] Yue, X. S., (2024). Research progress of deep learning in crop disease identification (深度学习在农作物病害识别中的研究进展). *Anhui Agricultural Science Bulletin* (06), 100-103.doi:10.16377/j.cnki.issn1007-7731.2024.06.027.
- [11] Zhao, W.H., Liu, X.K., Aertzguli, R.Z., Fu, K.Y., Ding, X.H., Jia, Z.Z., Adili, A.H.M.T., & Guo, W.C. (2023). Evaluation of the trapping effect of different types and densities of traps on the peach fruit moth (不同类型和密度的诱捕器对桃小食心虫诱捕效果评价). *Xinjiang Agricultural Sciences*, 60(12).
- [12] Li, M., Xiao, Y.Y., Zong, W.Y., & Song, B. (2024). Detecting chestnuts using improved lightweight YOLOv8 (基于改进YOLOv8模型的轻量化板栗果实识别方法). *Transactions of the Chinese Society of Agricultural Engineering*, 40(1).
- [13] Terven, J., Córdova-Esparza, D. M., & Romero-González, J. A. (2023). A comprehensive review of yolo architectures in computer vision: From YOLOv1 to YOLOv8 and YOLO-NAS. *Machine Learning and Knowledge Extraction*, 5(4), 1680-1716.
- [14] Lin, L. H, Lin, S. L., Lu, B. J., Lin, Z. X. & Guo T. L. (2024). Remote Sensing Image Target Detection Algorithm Based on Spatial Feature Fusion Down-sampling Convolution (基于空间特征融合下采样卷积的遥感图像目标检测算法). *Infrared Technology*, 1-8.2024, 54(2):1-8.
- [15] He, K., Zhang, X., Ren, S., & Sun, J. (2015). Spatial pyramid pooling in deep convolutional networks for visual recognition. *IEEE transactions on pattern analysis and machine intelligence*, 37(9), 1904-1916.
- [16] Wang, C. Y., Bochkovskiy, A., & Liao, H. Y. M. (2023). YOLOv7: Trainable bag-of-freebies sets new state-of-the-art for real-time object detectors. In *Proceedings of the IEEE/CVF conference on computer vision and pattern recognition*. pp. 7464-7475.
- [17] Huang, H., Chen, Z., Zou, Y., Lu, M., Chen, C., Song, Y., ... & Yan, F. (2024). Channel prior convolutional attention for medical image segmentation. *Computers in Biology and Medicine*, 178, 108784.
- [18] Wang, Q., Feng, W., Zhao, H., Liu, B., & Liu, S. (2024). VALNet: Vision-Based Autonomous Landing with Airport Runway Instance Segmentation. *Remote Sensing*, 16(12), 2161.
- [19] Zhang, H., Xu, C., & Zhang, S. (2023). Inner-loU: more effective intersection over union loss with auxiliary bounding box. *arxiv preprint arxiv:2311.02877*.
- [20] Tong, Z., Chen, Y., Xu, Z., & Yu, R. (2023). Wise-loU: bounding box regression loss with dynamic focusing mechanism. *arxiv preprint arxiv:2301.10051*.

INNOVATIVE TECHNICAL SYSTEMS USED IN SERICULTURE – A REVIEW

/

SISTEME TEHNICE INOVATIVE UTILIZATE IN SERICULTURA – A REVIEW

Adriana MUSCALU*¹⁾, Cătălina TUDORA¹⁾, Cristian SORICĂ¹⁾

¹⁾ INMA Bucharest. / Romania

Tel: 0726234242; E-mail: amuscalis@yahoo

DOI: <https://doi.org/10.35633/inmateh-75-06>

Keywords: silkworm, temperature, humidity, mulberry, IoT, machine learning, sustainable agriculture

ABSTRACT

Silk is a biomaterial with remarkable properties, used in various fields: the textile industry, aeronautics, medicine, etc. Sericulture is the practice of raising silkworms to obtain silk threads. This activity provides an opportunity to improve economic and social status, especially for rural populations. The high demand for labor, along with technical progress, has led to the necessity to implement technical solutions and modern activities in sericulture farms. This paper presents a brief analysis of the current state of research on some innovative technical solutions applied in sericulture sectors and activities, aimed at increasing silk thread production.

REZUMAT

Mătasea este un biomaterial cu proprietăți deosebite, utilizat în diverse domenii: industria textilă, aeronautică, în medicina, etc. Sericicultura se ocupa cu creșterea viermilor de mătase pentru obținerea firelor. Aceasta activitate oferă posibilitatea de creștere a statutului economic și social, mai ales pentru populația rurală. Consumul ridicat de forță de muncă, precum și progresul tehnic au impus implementarea unor soluții tehnice și activități moderne în fermele sericicole. Aceasta lucrare prezintă o scurtă analiză a stadiului actual al cercetărilor privind unele soluții tehnice inovative aplicate în sectoarele și activitățile din sericicultură, în vederea sporirii producției de fire de mătase.

INTRODUCTION

Sericulture is a science (a branch of zootechnics) that focuses on the breeding and multiplication of silkworms for the purpose of obtaining cocoons intended for processing. In 2022, UNESCO inscribed "Sericulture and traditional production of silk for weaving" (17.COM) on the Representative List of the Intangible Cultural Heritage of Humanity (<https://ich.unesco.org/en/RL/sericulture-and-traditional-production-of-silk-for-weaving-01890#video>).

According to the ISC (*International Sericultural Commission*) statistics for 2022, the total silk production was 91,319 metric tons, produced by 22 countries, with 8 of them being the main producers, accounting for 99.9% of the total production. China, which holds the lead, contributed over half of the world's production (approximately 55%), followed by India, which provided 40%. 90% of the silk was obtained from the mulberry silkworm, while the remaining 10% was non-mulberry silk, produced by silkworm species that feed on plants other than mulberry (<https://inserco.org/en/statistics>). These species include: *Antheraea mylitta*, *Antheraea assamensis*, and *Samia ricini*, producing types of silk such as Tasar, Eri, and Muga. Only India produces all these commercial types of silk, which are also classified based on the number of generations of silkworms in a year: univoltine, bivoltine, and multivoltine (*Taufique and Hoque, 2021; Gautam et al., 2022; Kaviraj et al., 2021*). The mulberry silkworm (*Bombyx mori* L.), a moth in the order Lepidoptera, is monophagous and survives only on mulberry leaves. It is the only domesticated insect since ancient times, in China between 2600 and 2700 BC, for silk fiber production. The finest silk, known as "The Queen of Textiles," is obtained from it, characterized by its glossy shine, softness, elegance, and durability (*El-Shewy and Elgizawy, 2017; Hailu, 2016*). Silk threads are known for their extraordinary biocompatibility with the human body, along with a range of exceptional properties: elasticity, high strength, and hardness. Additionally, these animal-origin threads are eco-friendly and biodegradable compared to synthetic fibers, which are polluting (*Popescu et al., 2024; Baci et al., 2021*). They are produced by the silk glands of mature larvae in the fifth stage. They are a natural polymer of silk proteins, consisting of fibroin and sericin, produced in PSG (posterior silk gland) and, respectively, MSG (middle silk gland). Fibroins are the basic fibrous proteins and are hydrophobic, while sericins surround the fibroins and are hydrophilic. The anterior silk gland (ASG) is the third division of the silk gland in silkworms, where the liquid silk protein is assembled into silk fibers (*Saikia and Saikia, 2022; Zhu et al., 2022*).

Sericulture has the advantage of being practiced profitably both on a small, artisanal scale and on an industrial scale, capable of scalable production (Altman and Farrell, 2022). This rural and ecological industry comprises three interconnected sectors: sericulture, which deals with the cultivation of mulberry (*Morus sp.*) to provide food for the silkworms (*Bombyx mori*), which form the protective cocoon, from which raw silk threads are obtained through various processes in the post-cocoon sector (Chanotra and Bali, 2019). The goal is to produce high-quality cocoons with the highest silk content, with current efforts focusing on the most efficient use of this precious material. Beyond traditional uses related to fashion (clothing, shoes, bags, wallpapers, etc.), technological progress has made silk indispensable for medicine, nanotechnology, biotechnology, optical industry, etc. The entire activity of producing primary products represented by natural fibers generates various by-products and waste, which are aimed to be utilized as efficiently as possible (Reizabal et al., 2023; Hăbeanu et al., 2023; Lujerdean et al., 2022; Jaiswa et al., 2021; Pop et al., 2018). The use of by-products (such as silkworm pupae) for animal feed, food, cosmetics, vermiculture, biogas production, artisanal products, etc., by promoting circular economy supply chains, represents new trends in sericulture. Additionally, all these applications and activities reduce environmental impact, increase employment in certain rural areas, and raise their socio-economic level (Seo et al., 2023; Ekka and Bais, 2023; Tassoni et al., 2022; Sharma et al., 2022; Barcelos et al., 2021).

Since sericulture involves multiple sectors and activities, mechanization in sericulture refers to: agricultural tools, machines, and equipment for mulberry cultivation (land preparation, crop maintenance), harvesting mulberry leaves and proper storage, systems for silkworm rearing, and machinery for the post-cocoon sector. Machinery is important for increasing land and labor productivity, helping manage activities that must be performed within specific time frames. It is also indispensable for the actual production of silk fabrics, with the quantity and quality of the silk depending on it (Karthick Mani Bharathi et al., 2024; da Silva et al., 2018).

Silkworms are very sensitive to their diet, specifically the quantity and quality of the food, as well as to environmental factors such as temperature, humidity, light, and air. Silkworm rearing is strongly influenced by the rearing techniques adopted, including feeding, cleaning, spacing, etc. An unsuitable environment negatively impacts the growth of silkworms, and consequently, the quantity and quality of the cocoons (Gupta and Dubey, 2021; Andadari et al., 2021). Immediately after collection, silkworm cocoons undergo several operations. They are steamed/dried (to destroy the butterfly pupa) after being pre-sorted, with undeveloped or double cocoons removed. The goal is to preserve their quality for long-term storage. Properly conditioned cocoons can undergo further operations to obtain silk threads: final sorting, cleaning of impurities, scalding, reeling, etc. A wide range of machinery has been studied and optimized for these operations (Safarov et al., 2019; Angel et al., 2018; Alim et al., 2016).

It is important for improved silkworm rearing technologies to be known and adopted by farmers in the field. Enhancing competence in sericulture depends on investment, promotion of technologies, and advancements in professional training. Modern agricultural technologies and production systems have the potential to increase efficiency and open new opportunities for various agricultural methods (Vlăduț and Ungureanu, 2024; Hajam et al., 2021; Singh et al., 2021).

The paper provides a brief overview of the current state of research on innovative technical solutions applied to mulberry shoot cutting, monitoring/control of silkworm growth factors, and the post-cocoon sector, aiming to reduce labor and energy consumption, thereby improving the efficiency of operations and the final quality of silk.

MATERIALS AND METHODS

The quality and nutritional composition of mulberry leaves influence the growth performance of silkworms (Gheorghe et al., 2023). In sericulture, obtaining these leaves is a major issue. Mulberry branches are cut individually, which requires significant time and labor. Cutting can be done with a hydraulic shear or other cutting tools/machines. Therefore, research has been conducted to reduce the physical effort exerted by the operator. A device was developed for this operation, featuring a mobile arm and a rotating saw (fig. 1). The cut branches are collected in a tray specifically designed for this purpose. Figure 2 shows the block diagram of the device's operation (Kumar et al., 2021).

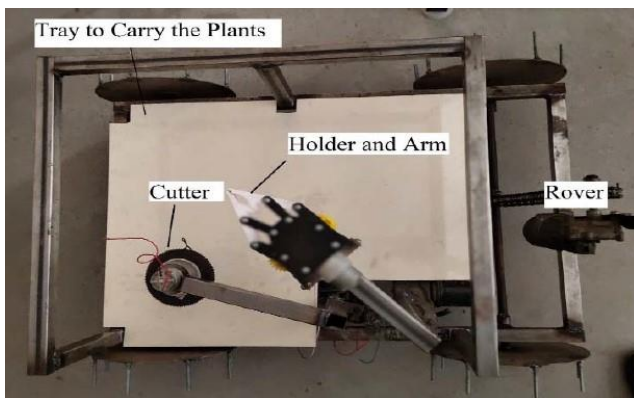


Fig.1 - Mulberry Branch Cutting Device
(Kumar et al., 2021)

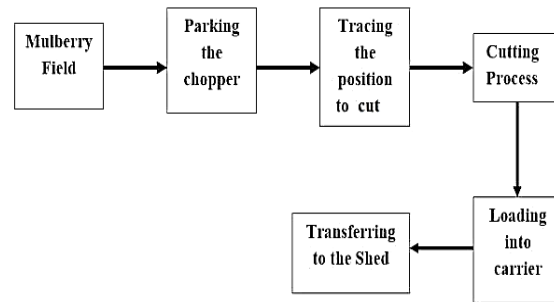


Fig.2 - Block diagram
(Kumar et al., 2021)

The arm is attached to a rod driven by a DC motor (like those used in windshield wipers), allowing the arm to move in the desired direction, meaning its opening and closing are controlled. The circular saw is also powered by a DC motor, but with high torque for effective cutting. The cutting device is manually moved to the position of the branch that needs to be cut. The automatic module is activated, and the control system manages and monitors the sequence of operations:

- The support holding the arm opens so that the arm can extend outward to grasp the branch, then it closes.
- The open-source Arduino Uno platform immediately activates the cutting system, and the arm extends to cut the branch.
- After cutting, the arm holding the mulberry branch retracts, loosening its grip. This sequence is controlled by the controller and relay.
- Finally, the branch is discharged into the storage tray, and the cycle repeats (Kumar et al., 2021).

In China, several research efforts have focused on developing mulberry leaf harvesting equipment, including piston-type, spiral-type, semi-automatic, and multi-degree-of-freedom devices. However, these innovations have not eliminated manual labor, although they have reduced the physical effort required by operators and improved the efficiency of the picking operation. As a result, research has been initiated to develop intelligent mulberry leaf harvesting techniques. The first stage involves locating the picking points. Using appropriate infrastructure, researchers began by identifying and segmenting the harvesting nodes area through the development of a Mask R-CNN model, which classifies nodes based on their shape ("Y" or "rectangle"). This model was then optimized to enhance recognition accuracy. Finally, a method was devised to obtain the picking points of the mulberry leaf nodes, along with visual information for intelligent harvesting (Zeng et al., 2023). Mask R-CNN is a Convolutional Neural Network (CNN) and represents the state-of-the-art in image segmentation. This Deep Neural Network variant detects objects in an image and generates high-quality segmentation masks for each instance. Researchers developed Mask R-CNN based on the original Faster R-CNN, a Region-Based Convolutional Neural Network, by extending it with an additional branch and using existing detection to predict the target in parallel (Hassan et al., 2022).

Other researchers have used neural networks to develop early detection models for mulberry leaf diseases, aiming to combat these diseases and prevent the use of affected leaves as feed for silkworms, as they negatively impact their health and development (Nahiduzzaman et al., 2023).

In agriculture, robots are often mobile platforms, which have seen remarkable development over the past decade (Shamshiri et al., 2018). Research has been conducted to expand their use in sericulture, particularly for handling large frames used in the rearing process of silkworms. For a stacking device, a model of a mobile transport platform was designed (fig. 3), focusing on making it: compact, capable of movement along two axes, with reduced construction and functional complexity, thus resulting in a low production cost while still achieving high efficiency in handling and placing the frames. The mobile platform (fig. 3) includes: (1) electric drive motors, (2) rack-and-pinion transmission for movement along the X axis (horizontal), (3) rack-and-pinion transmission for movement along the Z axis (vertical), (4) frame gripping system for silkworm frames (not described in this work). Additionally, (5) the main frame of the device supports the mobile transport platform. For movement along the X axis, the pinion of the rack-and-pinion transmission receives motion from the electric motor via a straight-toothed gear mounted on its shaft, forming a cylindrical gear system.

The pinion shaft is supported by two sliding bearings located on either side. The bearings are mounted on the mobile platform, which slides. Thus, Figure 4 shows: (1) the mobile platform, (2) the cylindrical gear system, (3) the rack, (4) the guide, (5) the pinion shaft for the rack-and-pinion transmission, (6) the roller bearings. For movement along the Z axis, the pinion of the rack-and-pinion transmission receives motion from the electric motor via a bevel gear system (fig. 5). On the shaft of the electric motor (5), a bevel pinion engages with the bevel gears (4) which transmit motion to the pinion (2) through a common shaft supported by bearings (3) mounted on the mobile platform (1). The pinion (2) moves along the rack (6) (Jiang et al. 2024).

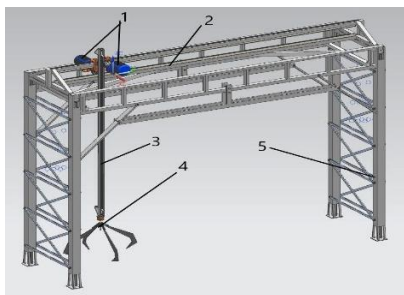


Fig.3 - Mobile Transport Platform
(Jiang et al., 2024)

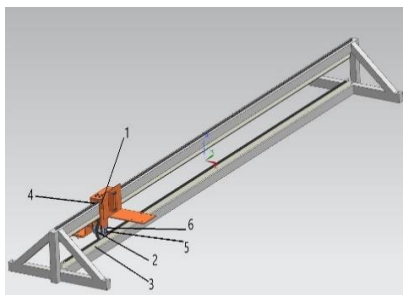


Fig.4 - Movement Transmission of the Mobile Platform along the X Axis (Jiang et al., 2024)

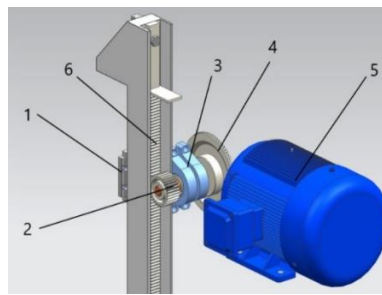


Fig.5 - Movement Transmission of the Mobile Platform along the Z Axis (Jiang et al. 2024)

Considering the dimensions of the frames (1000mm x 1500mm), the stacking height of these frames in a group (2000 mm), the distance between the platform and the frame gripping system (500 mm), as well as the horizontal distances that need to be maneuvered, the height of the main frame was established as 3000 mm, and the length of the transverse beam as 4000 mm. For the pinion shafts of the rack-and-pinion transmissions, made of quality carbon steel (with 0.45% C content), a strength check was conducted using simulated modal analysis (Jiang et al., 2024).

To avoid losses in sericulture, in addition to diet, monitoring environmental factors and the health status of silkworms is critically important (Bekkamov and Samatova, 2023; Chopade et al., 2021). Numerous research efforts have been undertaken, resulting in various automated systems or methods (experimental or prototypes) designed to be as efficient, cost-effective, and interactive for farmers as possible. Although these systems aim for the same goal, they differ in their components and technologies used.

Thus, a system was developed that utilizes a microcontroller combined with a GSM module to offer tracking and automatic control features. The automated system, with the architecture shown in Figure 6, detects temperature, light intensity, humidity, and gases (LPG, carbon dioxide) in the sericulture farm environment. These represent the inputs, and when threshold values are exceeded, information is transmitted to the user via a wireless network, with the microcontroller taking necessary actions (e.g., correcting temperature, humidity, air quality, light intensity, etc.) to avoid losses due to silkworm deaths. The system communicates with the user via the GSM module to perform tasks such as feeding the silkworms. The system can be divided into: a detection part and an action part (Gunasheela et al., 2018).

In another study, a similar embedded system was developed (fig.7) for close monitoring and regular control of environmental parameters in the silkworm rearing chamber/enclosure. The system maintains temperature, humidity, light intensity, and CO₂ concentration. It is equipped with a fire alarm, and also ensures the distribution of food and medicine for the silkworms.

The system consists of sensors, an Arduino controller, and actuators (cooling fan, food dispenser, medication sprayer). The sensors circuit comprises four analog sensors: temperature, humidity, light, and CO₂ sensors, and a digital fire sensor. The Arduino is programmed with threshold values and the capacity to monitor and control the system. The system comprises both software and hardware components (Manjunatha and Neelagar, 2018).

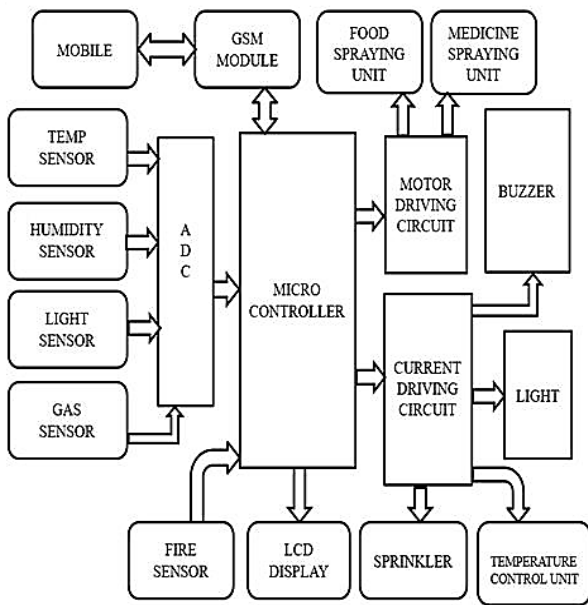


Fig.6 - Architecture of the Automated System
(Gunasheela et al., 2018)

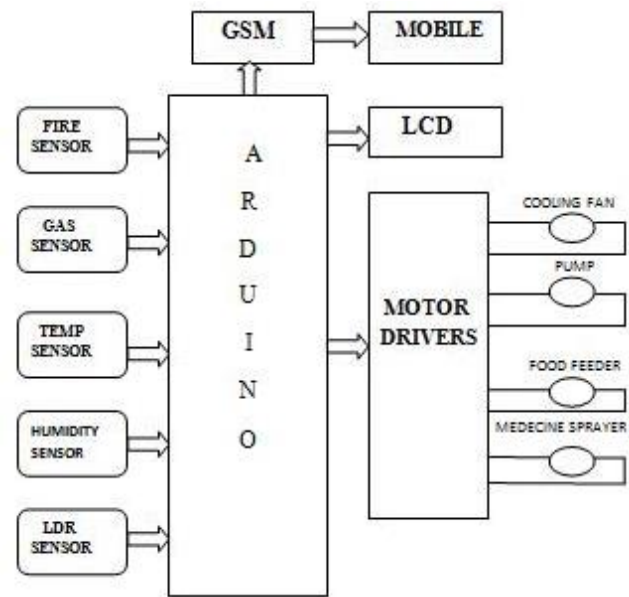


Fig.7 - Embedded System Diagram
(Manjunatha and Neelagar, 2018)

For a silkworm incubator (fig.8), a monitoring system was used that employs an open-source, low-cost data acquisition and transmission system. This system utilized an embedded platform with cloud remote monitoring through the Google Drive file hosting service and the Internet of Things. The proposed conceptual model (fig.9) includes: sensor readings, communication channel, and data storage in the cloud. Several sensors record environmental parameters (humidity, temperature, and light) in a silkworm incubator. The information is uploaded to the Google Drive cloud via Wi-Fi. With a username and password, information can be accessed from any device that can access Google Drive. The system is highly flexible, with possibilities for expansion or adaptation. The monitoring system was used in the silkworm incubator (*Incubapremium Columbia type*) equipped with 9 trays with metal mesh (food-grade aluminum) to allow air circulation, for 200 silkworms, continuously for 25 days. The trays for silkworms (1x0.6m) are arranged on shelves, spaced 15 cm apart. (Duque-Torres et al., 2018).



Fig.8 - Silkworm incubator
(Duque-Torres et al., 2018)

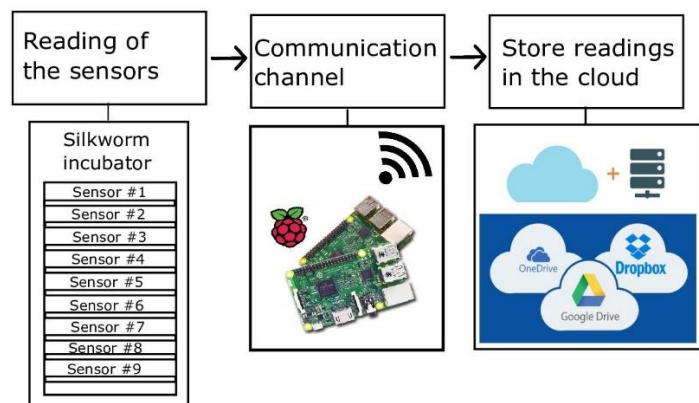


Fig.9 - Silkworm incubator monitoring system conceptual model
(Duque-Torres et al., 2018)

The temperature in the chamber is controlled by a heating system based on an electric heater, and a humidifier placed in the lower part of the incubator controls the humidity. For monitoring, DTH22 sensors were used. Silkworms are photosensitive and do not like light that is too strong or too weak. For light measurement, the APDS-9301 sensor was used due to its high accuracy and low energy consumption. For the prototype of the monitoring system, a Raspberry Pi version 3 (RPi3) controller was used due to its technical and economic advantages (Duque-Torres et al., 2018).

In another study, an advanced monitoring and control system for ecological conditions in a silkworm incubator was proposed (fig.10), based on the use of an Arduino Uno microcontroller due to its numerous capabilities. To ensure favorable conditions for silkworm development in the incubator, temperature and humidity are the primary factors to be controlled. Their estimation is done continuously. The threshold levels for temperature and humidity can be easily set and modified remotely from a portable device. When the temperature falls below the set value, the microcontroller is programmed to activate the heater loop. When the humidity falls below the threshold value, the humidifier is activated. Temperature and humidity can be checked remotely (Kokila et al., 2021).

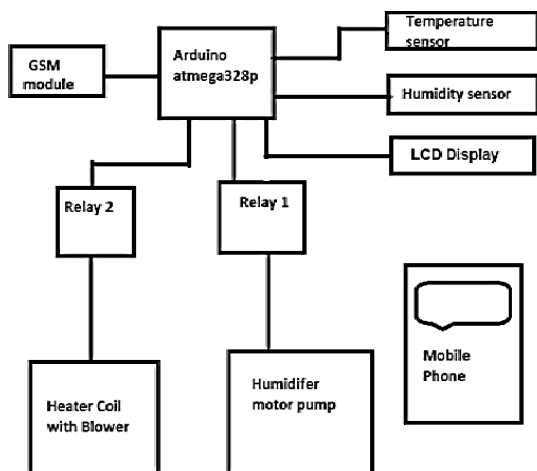


Fig.10 - Block diagram of advance silkworm incubator with environment control
(Kokila et al. 2021)

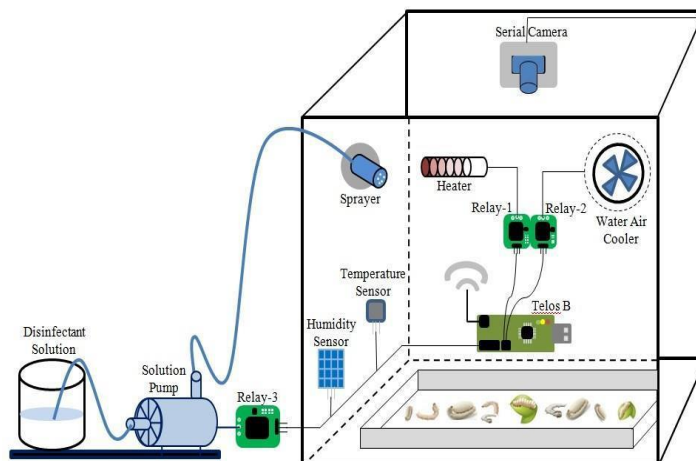


Fig.11 - IoT based Block Representation of the Sericulture Monitoring and Actuation System
(Arun et al., 2019)

To prevent unfavorable conditions and actions affecting the development of silkworms (such as temperature variation, humidity, lack of food, disease occurrence, etc.), an Automated Smart Sericulture System has been developed. Figure 11 shows the proposed system architecture for a silkworm rearing chamber, based on IoT, consisting of temperature and humidity sensors, a camera, actuating devices (electric heater, cooler, digital image processing, sprayer) connected to smart nodes, with wireless communication. Based on real-time data provided by the sensors, the smart nodes will make decisions and perform actions. Raw images from the camera are digitally processed to extract improved versions and additional information. For visualization, application development (using various built-in signal processing algorithms), and numerical calculations, MATLAB will be used (Arun et al., 2019).

In another study, for classifying silkworms as healthy or unhealthy, CNN neural network archives were used due to their proven high accuracy for less complex elements. The proposed system consists of two parts: Hardware and Software. For these, widely available component parts, open-source software such as Arduino IDE and Rest API, and commercial software MATLAB for image processing techniques were utilized (Yogeshraj et al., 2022).

Regarding post-cocoon operations, two methods (infrared drying and combined drying) were investigated and compared for their effectiveness in killing and drying silkworm cocoons. Fresh cocoons stored in the refrigerator were maintained at room temperature for 15 minutes before drying. The cocoons were spread out in a single layer on stainless steel trays of the drying equipment used. The entire sample was weighed every 30 minutes to trace the drying curves. An infrared laboratory dryer of type "ASIA," with a power of 750 W, incorporating three 250 W infrared emitters, and an experimental dryer with a 50 Hz ultrasonic frequency and 1000 W IR radiation power were used. Drying temperatures for both experiments were set at 60°C, 65°C, and 70°C, with an ultrasonic exposure time of 10 seconds. Initial material moisture, instantaneous moisture, and drying rate for a specific time interval Δt were calculated. Experimental data were processed using statistical analysis programs (Samandarov et al., 2023).

During the life cycle of silkworms, gender classification of cocoons is important for ensuring the perpetuation and preservation of genetic material through egg production, as well as for post-cocoon operations. A non-destructive multi-sensor system for gender classification and separation of silkworm cocoons was developed, with the schematic and prototype shown in Figures 12 and 13.

The machine consists of the vertical conveyor module (VCM) that individually picks up cocoons from the hopper at a constant speed without causing physical damage, and then transfers them to the feature extraction module (FEM). Here, each cocoon is analyzed, extracting data related to its shape and weight. Using dedicated software running on an autonomous workstation, a digital image is obtained. The image characteristics and weight information are combined into an input feature vector, analyzed by a pre-trained pattern recognition classifier for making decisions regarding gender classification/sorting. The final module is a horizontal conveyor (HCM) that directs individual cocoons to be physically sorted and blown into designated baskets (male or female) (Raj et al., 2019).

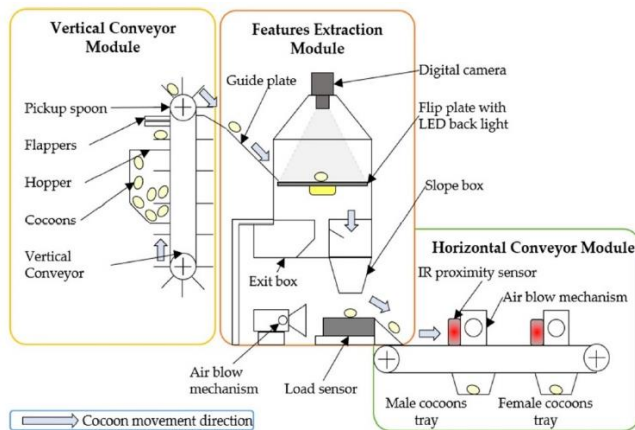


Fig. 12 - The scheme of the machine for separating cocoons by gender (Raj et al. 2019)

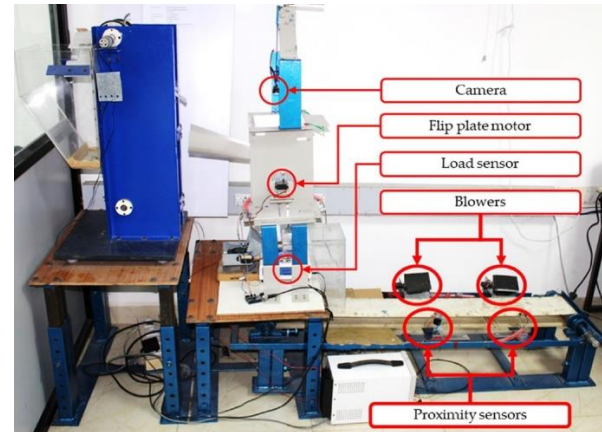


Fig.13 - The prototype of the machine for separating cocoons by gender (Raj et al., 2019)

VCM is a vertical belt conveyor driven by an electric motor (12V, 10 rpm). On the belt, which has a speed of 6.3 cm/s, 16 special, concave pockets shaped like spoons are mounted equidistantly by riveting. Two rows of flaps help remove excesses, so each pocket only holds one cocoon. FEM consists of a support frame with a mount for a 5-megapixel digital camera, an inclined feed chute, an output chute, a detachable load sensor, and a blowing system. Image processing and cocoon weight measurement provide information sent to a binary classifier to determine gender. Under the camera, there is a tilting acrylic plate that, through a shaft driven by a servomotor, can be positioned in three directions (horizontal 0°, 90° clockwise, -90° counterclockwise). The tilting plate receives cocoons from the VCM in the horizontal position. A square LED panel light (18 W), directed from back to front, is used to capture the hard shell silhouette of the cocoon, allowing precise area calculation through image threshold techniques. The cocoon is transferred to the load sensor after the image is acquired. The falling speed of the cocoon is dampened by moving across multiple inclined planes. Cocoon weight data is acquired with an error of 0.01 g and transferred to the workstation after reaching the load sensor surface. The cocoon is transferred to the HCM using a blowing system, which consists of a blower and a pivoting "U" shaped cover that stops the air flow. One side of the cover is coupled to a servomotor, while the other rotates freely relative to the wall via a cylindrical pin joint. Normally, the cover is closed, and no airflow is directed towards the cocoon. Once weight data is acquired, the system sends a command to the servomotor, and the pivoting arm opens for 2 seconds to allow cocoon transfer. The power requirement for FEM is 25 W. HCM consists of a horizontal belt conveyor, 2 infrared proximity sensors (IR) paired with 2 blowing units, all placed along the conveyor. The positions were empirically determined to ensure the workstation has the necessary time for classification index calculation and provision. Based on this, the blowers in each pair are activated/deactivated to transfer the cocoon to the appropriate tray (Raj et al., 2019).

The quality and lighting of the image were aimed to be optimized to obtain the best experimental conditions, so the Otsu Method was used for processing. Thus, this algorithm performs thresholding for image binarization on the acquired image. In the FEM module, an image is obtained and sent to the workstation, where shape characteristics (area, perimeter, major axis length, minor axis length, etc.) are calculated. The area of the cocoon from the binarized image is compared with an empirical threshold value. If the threshold is exceeded, excess cocoons are ejected by rotating the tilting plate counterclockwise, moving them out of the module through the output box to return to the feed hopper. If only one cocoon is on the tilting plate, the binarized image area does not exceed the threshold.

The microcontroller is signaled to rotate the tilting plate clockwise, and the cocoon reaches the load sensor, where its weight is acquired and transmitted to the workstation.

Shape and weight characteristics are combined and sent to a pre-trained SVM (Support Vector Machine), assigning an index and gender label stored in the workstation. The air blowing system moves the cocoon from the sensor to the HCM. As it moves, the cocoon reaches the first proximity sensor (IR), which sends a signal to another microcontroller. This retrieves the classification label of the current cocoon to control the blowers. If the designated label is “male,” the first blower is activated, pushing the cocoon onto the “male cocoon tray.” Conversely, if the cocoon's label is “female,” the second blower is activated, pushing the cocoon onto the “female cocoon tray.” The prototype of the machine for separating cocoons by gender was tested on two silkworm races, CSR2 and Pure Mysore, provided by an industry partner (*Raj et al., 2019*).

Additionally, to further optimize the sorting operation, which can be done before drying cocoons and before spinning, a prototype was developed based on a patent No. IT201900016208A1. Unlike the previously mentioned equipment that uses one camera and several sensors, this one relies on three cameras and image algorithms that identify the shape, size, and external spots of cocoons, along with a custom light sensor and an AI model to remove dead cocoons. The equipment (Fig. 14), which practically embodies a patented invention, is an opto-electrical machine, with cocoon selection occurring through three zones, each with different functions (*Vasta et al., 2023, Assirelli et al., 2019*).

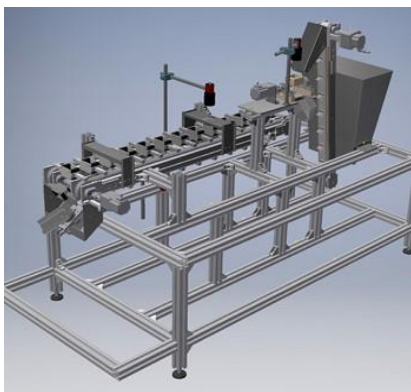


Fig. 14 - 3D CAD render of the prototype (*Vasta et al., 2023*)

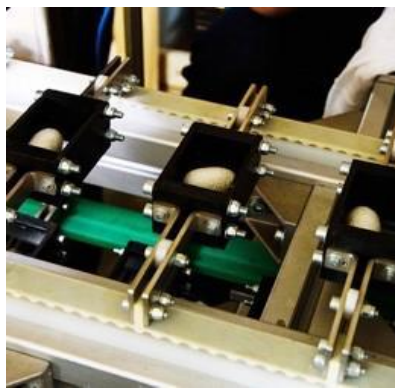


Fig. 15 - Custom-made conveyor belt (*Vasta et al., 2023*)



Fig.16 - Screenshot of GUI written in Java (*Vasta et al., 2023*)

The equipment was built around a conveyor belt (Fig. 15) driven by a stepper motor, with all mechanical movement systems controlled by a programmable PLC. It also controls the solenoid valves that activate the pneumatic actuators for initial and final selection (Fig. 16). The frame of the equipment was made from aluminum profiles, and the horizontal conveyor, having a special construction, was custom-made. The feeding is done with a vertical feeding system that directs the cocoons to an inclined feeding chute at 45° (Fig. 14). The first camera was placed at the end of this chute, and the two pneumatic actuators, mounted perpendicular to its direction, serve to remove cocoons that are unsuitable in shape. Those approved in shape fall into small capsules placed on the horizontal conveyor. Due to the horizontal movement of the belt, each capsule with a cocoon inside reaches the next two specialized cameras for spot selection, one providing an image from bottom to top and the other from top to bottom. This way, both faces of the same sample are captured to reduce any possible reading error. The last selection zone was dedicated to distinguishing between live and dead pupae inside the cocoons. For this, a complex sensor based on photodiodes was used, for which a PCB (Printed Circuit Board) and dedicated software were designed. At the end of sorting, based on different quality grades, the cocoons were directed into different containers with the help of a pneumatic device placed at the end of the belt (*Vasta et al., 2023*).

The three cameras installed on the prototype were connected to a main personal computer (PC) via an Ethernet cable, each receiving trigger signals to take pictures at a specific moment. The preliminary operations performed before the acquisition process were managed with a GUI (Graphical User Interface) designed and managed in the Java programming language. Using the GUI, various parameters were monitored: the number of photos taken, the status of the cameras, the status of the analog-to-digital converter (ADC), etc., as well as starting or stopping data acquisition. Multi-threading programming techniques were used for the main PC to perform all tasks while simultaneously storing all synchronized images from the cameras and raw data received from the sensor.

Synchronization between the PC, the custom light sensor, and the PLC was achieved using the Modbus Ethernet communication protocol, which was implemented on the Arduino Portenta H7 using the corresponding software library. Based on this protocol, the hierarchy can be summarized as a client (PC) and two servers (Arduino and PLC). To coordinate the movement of all mechanical parts, a Boolean data exchange between the PC and PLC was designed. The correlation between the light sensor and the computer allowed Boolean data to manage the timing of acquisition. To transmit raw data to the Modbus registers of the computer, the same bus was subsequently used (Vasta et al., 2023).

RESULTS

The performance of the intelligent mulberry branch cutting device was analyzed in comparison with existing methods, which involve manual cutting using a cutter-type tool. Thus, the operation durations and associated costs are presented comparatively in Figures 17 and 18 (Kumar et al., 2021).

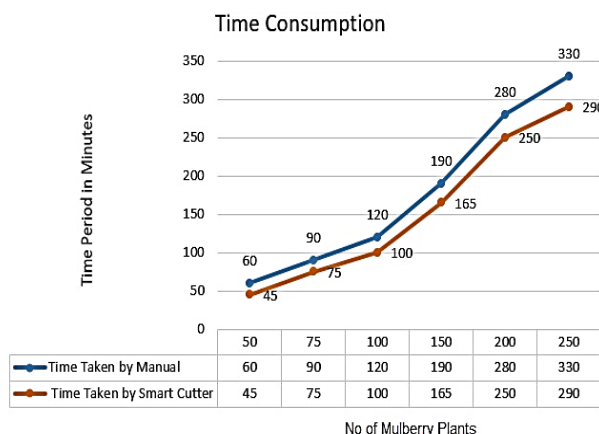


Fig. 17 - The time consumed for performing the cutting operation for a number of mulberry plants (shoots) (adapted from Kumar et al., 2021)

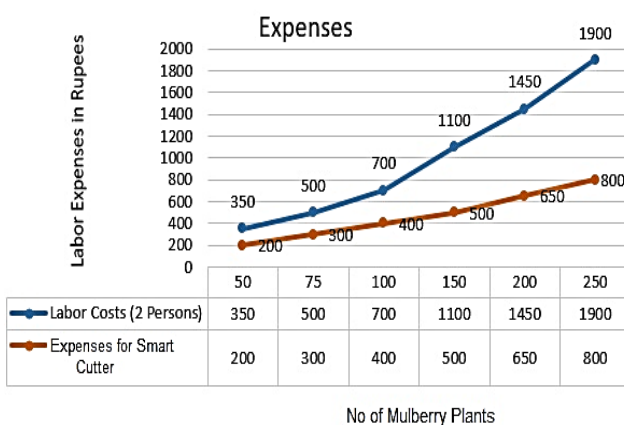


Fig. 18 - The expenses for the cutting operation for a number of mulberry plants (shoots) (adapted from Kumar et al., 2021)

The intelligent cutting device is operated by a single person, and the results obtained constitute an important premise for increasing productivity and reducing the labor required for feeding silkworms.

For the development of intelligent harvesting, Zeng et al. (2023) improved the detection capability of the mulberry leaf node area by replacing the ResNet network with an enhanced ResNeXt network, adding a bottom-up fusion path, as well as a multi-scale regional suggestion network. The optimization efficiency was evaluated through: precision rate (P), recall rate (R), average precision (AP), and F1 score (Table 1). The final detection precision improved by 2.8%, and the F1 score increased by 3.5% compared to the non-enhanced model. The method used in this study can accurately locate the harvesting point, with the leaf nodes obtained through segmentation (Zeng et al., 2023).

Table 1

Evaluation results of the model before and after improvement (Zeng et al. 2023)

	Precision rate (P)	Recall rate (R)	Average precision (AP)	Scor (F1)
	[%]	[%]	[%]	[%]
Model Mask R-CNN	84,2	63,2	86,3	72,2
Improved Model Mask R-CNN	86,7	67,1	89,1	75,5

In the study by Nahiduzzaman et al. (2023), a PDS CNN model based on XAI (Explainable Artificial Intelligence) was proposed to classify mulberry leaves into categories of healthy, rust-affected, and spotty leaves using a newly created database containing 764 original images, selected by experts. These images were preprocessed into 6000 synthetic images, with an additional 218 and 109 images for testing and validation, respectively. The PDS-CNN model is a unique, parallel, depth-separable CNN (Conventional Neural Network) developed by applying depth-separable convolutional layers to reduce parameters, layers, and size, while enhancing classification performance. The model achieved an accuracy of $95.05 \pm 2.86\%$ for three-class classifications and $96.06 \pm 3.01\%$ for binary classifications with 0.53M parameters, 8 layers, and 6.3 MB in size. Thus, promising classification performance was achieved, with model interpretability induced by SHAP (Shapley Additive Explanations) and confirmed by sericulture experts.

Due to its specific features, the developed model can be accessible to a wide range of users in sericulture (both professionals and ordinary farmers). Early identification of mulberry leaf diseases leads to significant production savings and benefits for farmers.

In the study by *Jiang et al. (2024)*, considering all the necessary elements for using modal analysis in a simulated regime to verify the durability of pinion transmission trees with rack, it was found that they meet the durability requirements. The development of a cheap mobile transport platform that helps handle the frames/trays used in sericulture would substantially reduce labor consumption, improving work efficiency in this field.

The system designed in the study by *Gunasheela et al. (2018)* has a configuration that responds to any climatic changes occurring inside the silkworm rearing enclosure, efficiently responding to stimuli. If the user closes the phone or if the signal strength is low, causing disruptions in the GSM network, the system does not respond adequately. Solutions applied to eliminate these disadvantages include automating the farm so that operations are performed in a timely manner and enabling call redirection. Thus, the system can send messages to a specified alternative number by placing the GSM module in an area where full signal strength is available for communication.

Manjunatha and Neelagar (2018) developed an embedded system model for monitoring and controlling environmental parameters in the silkworm rearing unit, which was tested. The preliminary test demonstrated that the model can work progressively to monitor conditions within the enclosure. Its actuators operate only when necessary, reducing the need for human intervention. The system was implemented smartly, using cost-effective and energy-efficient components. As the system can be relatively easily realized, it is expected to be optimized by using broadband/Wi-Fi and Internet of Things (IoT) for matching processes and securing information.

The system monitoring environmental conditions during the process conducted in a silkworm incubator, as described in the study by *Duque-Torres et al., (2018)*, was tested in real time. Data were exported from RPi3 into a simple .txt file (in a Google Drive account). This provided the date, time, temperature measurements from sensor one to sensor nine, humidity measurements from sensor one to sensor nine, and light intensity measurements. Uniformity of environmental conditions inside the incubator is essential. However, the analysis of automatically recorded data revealed the generation of microclimates between the levels of the incubator, highlighted by temperature variation (Fig. 19) and humidity variation (Fig. 20). Besides its low cost, the developed system also features portability, and data visualization and analysis can be performed remotely. Additionally, it is directly programmable, based on open-source codes, which enhances its flexibility compared to commercial tools that only offer predetermined functions.

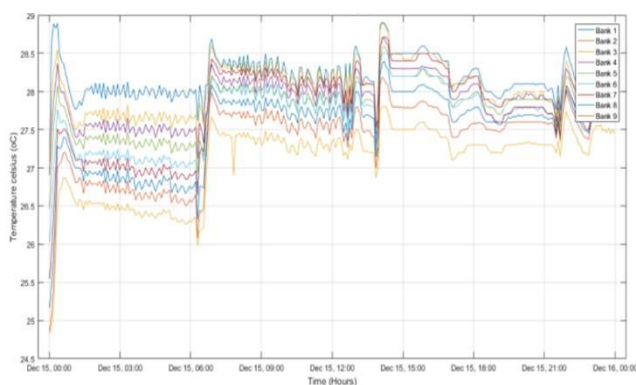


Fig. 19 - Temperature variance graphic
(*Duque-Torres et al., 2018*)

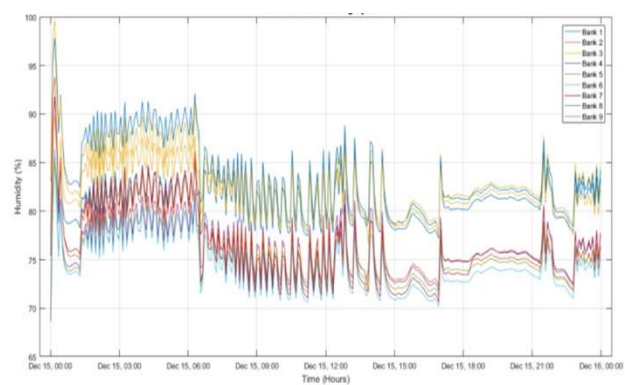


Fig. 20 - Humidity variance graphic
(*Duque-Torres et al., 2018*)

Using the advanced ecological monitoring and control system in a silkworm rearing incubator proposed by *Kokila et al., (2021)*, the egg hatching to larvae occurred between 10-11 days, and the production of silkworm cocoons from larvae lasted 25-30 days. Additionally, productivity was high due to the low mortality rate. Thus, by using this system, farmers have the opportunity to achieve 12-15 iterations of silk production in a year, with reduced labor consumption. Being easy to use and maintaining temperature and humidity with ease, its application scope is expected to expand in the future.

The preliminary test for the Automated Smart Sericulture System from the study by *Arun et al., (2019)*, showed that it is capable of successfully monitoring and controlling established state parameters in real time.

These parameters can be monitored remotely, with automation handling the creation of suitable conditions inside. In addition to temperature and humidity sensors, many other sensors for different parameters can be interfaced with this system. Furthermore, image capture can be performed wirelessly, making it more compatible and intelligent. The system's optimization prospects involve deploying the sensor network for sericulture based on CoAP and connecting it to the IPv6 framework for real-time internet monitoring.

The system developed by *Yogeshraj et al. (2022)* can monitor environmental factors (temperature and humidity) and control them using heating systems and fans. Image processing algorithms were used to successfully resize images by detecting edges and performing maximum grouping (Fig. 21). The processed images (Fig.22) allowed differentiation between healthy and unhealthy silkworms, with sick ones being detected. The convolutional neural network-based classification introduced in the proposed scheme improved accuracy and reduced computation time.



Fig. 21 - Worm resized images
(*Yogeshraj et al., 2022*)



Fig. 22 - Output the healthy and unhealthy silkworms are detected
(*Yogeshraj et al., 2022*)

The effects of drying mulberry silkworm cocoons in an infrared (IR) device at temperatures of 60, 65, and 70°C, and durations of 15, 12, and 10 minutes, are presented in the figures below (Fig. 23, 24, 25) (*Samandarov et al., 2023*).

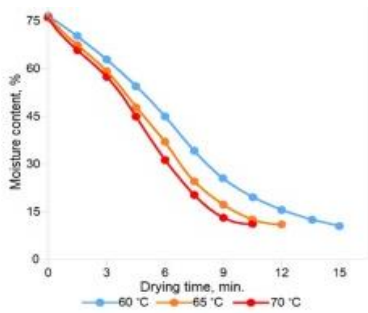


Fig. 23 - Variation in humidity (IR)
(*Samandarov et al., 2023*)

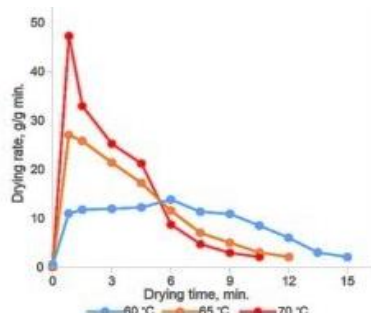


Fig. 24 - Variation in drying speed (IR)
(*Samandarov et al., 2023*)

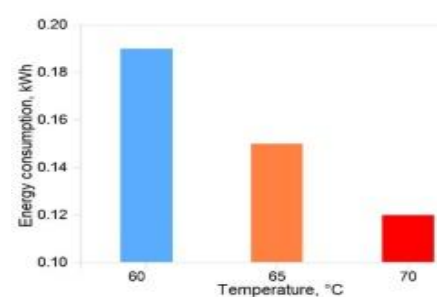


Fig.25 - Variation in energy consumption (IR)
(*Samandarov et al., 2023*)

For the drying of mulberry silkworm cocoons under the same conditions (IR), with the addition of exposure to ultrasonic (US) waves, the effects are presented in Figures 26, 27, 28 (*Samandarov et al., 2023*).

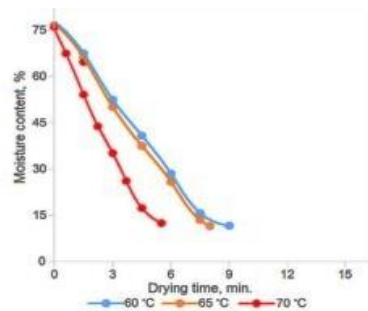


Fig. 26 - Variation in humidity (IR+US)
(*Samandarov et al., 2023*)

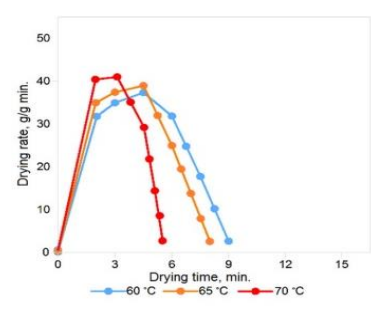


Fig. 27 - Variation in drying speed (IR+US)
(*Samandarov et al., 2023*)

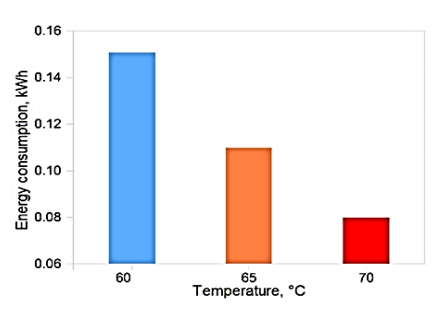


Fig. 28 - Variation in energy consumption (IR+US)
(*Samandarov et al., 2023*)

Combining the two methods (Infrared IR and Ultrasound US) results in faster and more efficient drying, reducing energy consumption, as ultrasound can affect the microstructure of mulberry cocoons. Thus, the optimal drying conditions were determined to be: temperature 70 °C, ultrasound frequency 50 Hz, and exposure time of approximately 5 minutes (Samandarov *et al.*, 2023).

The performance of the prototype machine for separating cocoons by gender is evaluated based on accuracy, robustness, and speed. Table 2 shows the performance metrics calculated, namely: Accuracy, True Male Rate (TMR), True Female Rate (TFR), Male Predictive Rate (MPR), and Female Predictive Rate (FPR), with reference to both training and test phases for CSR2 and Pure Mysore cocoons (Raj *et al.*, 2019).

Table 2

Performance metrics (PM) obtained for CSR2 and pure Mysore cocoons from SVM

(Raj *et al.* 2019)

Performance metrics (PM)	Training		Testing	
	CSR2	Pure Mysore	CSR2	Pure Mysore
Accuracy	0.9259	0.9778	0.8649	0.9355
True Male Rate (TMR)	0.9642	1.000	0.8947	0.9286
True Female Rate (TFR)	0.8846	0.9583	0.8333	0.9412
Male Predictive Rate (MPR)	0.9000	0.9545	0.85	0.9286
Female Predictive Rate (FPR)	0.9583	1.000	0.8824	0.9412

During the gender separation operation, a cocoon moves from the VCM module of the machine to the FEM module in an average time of approximately 4.6 seconds. It remains there for about 2.2 seconds, consuming 1 second to acquire shape characteristics and 1.2 seconds for weight characteristics. It then reaches the collection tray through the HCM in approximately 3.6 to 4.1 seconds. Thus, a cocoon moves from the hopper to the collection tray in approximately 10.9 seconds. The machine can classify about 5.5 cocoons per minute, which translates to about 330 cocoons per hour, or approximately 2640 cocoons per shift (8 hours). With an average cocoon weight of 1.3 grams, the machine can classify about 3.4 kg of cocoons per shift, with an accuracy of approximately 86.48% to 93.54% and a repeatability of 88%. The results demonstrate the machine's potential to enhance the productivity of gender classification of cocoons in silk farming centers, as well as in the industry. The cocoon gender sorting machine, which does not damage the casing, represents a significant step forward in reducing human intervention and automating operations in sericulture (Raj *et al.*, 2019).

The performance of the automated prototype for *Bombyx Mori* cocoon sorting varied depending on the selection parameters considered. Following the tests and improvements in both software and hardware, the equipment achieved a maximum sorting frequency of 80 cocoons per minute. The equipment also achieved optimal performance for oversized cocoons, but performance for undersized cocoons was lower due to their tendency to be positioned vertically in the capsule (Fig. 29), which affected the accurate image capture for identification (Vasta *et al.*, 2023).

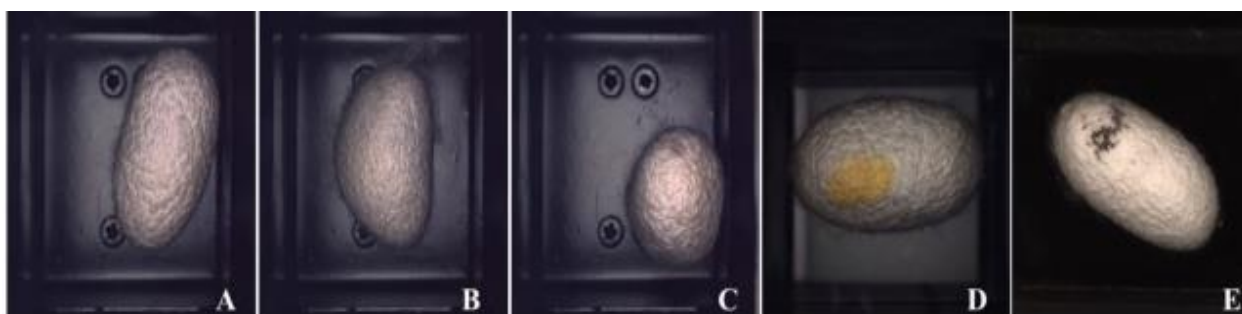


Fig. 29 - The position of cocoons inside their housing (Vasta *et al.*, 2023).

A - regular cocoon; B - defective shape; C - incorrect size due to positioning; D - stained at the top (large orange spot); E - stained at the bottom (black spot)

The performance regarding the dimensional selection of cocoons is presented in Table 3 (Vasta *et al.*, 2023).

Table 3

The equipment performances (defective cocoons marked as such) (Vasta et al. 2023)

Parameters	True Positive Percentage [%]
Oversized cocoons (larger than 450 mm ²)	87.8
Undersized cocoons (smaller than 300 mm ²)	29.6
Undersized cocoons with no vertically positioned ones	90.0

The performance metrics of the prototype in dead-cocoon selection based on the logistic regression model from the photodiode matrix were: classification ratio and cross-validation accuracy. The correct classification ratio achieved for dead-cocoon selection was 81.5% on the training set and 78.4% on the test set. Cross-validation with 100 steps was also performed, yielding an average accuracy of 80.7% for training and 81.6% for testing. The development and testing of the equipment allowed for a detailed study of the patented idea. Additionally, its encouraging performance contributed to identifying various aspects, especially practical ones, that should be optimized and could be the subject of further research (Vasta et al. 2023).

CONCLUSIONS

This paper provides a synthesis of recent research on innovative technical solutions across various sectors related to sericulture. Generally, in agriculture, the use of modern machinery, equipment, and production systems ensures sustainability and enhances both production and quality. Technological innovations play a crucial role in the employment opportunities offered by sericulture.

Despite a global decline in cocoon and silk production, current trends make natural silk fibers highly favored in the fashion and textile industries, as well as in numerous other fields, due to their unique characteristics.

The technical solutions presented are highly accessible to users, aiming to minimize human intervention in silk production or increase the productivity of operations that cannot maintain consistent performance levels when done manually. They also focus on implementing innovative ideas or smart applications to enhance the added value of sericulture products. These innovative solutions provide a significant basis for future research aimed at developing and modernizing specific technologies and revitalizing or resuming sericulture activities in geographic areas where they were once intensively practiced in the past century.

ACKNOWLEDGEMENT

This paper was supported: by Ministry of Research, Innovation and Digitalization one funding source the NUCLEU Program, Contract 9N/01.01.2023, Project PN 23 04 02 05 "Innovative technology for the superior use of inflorescences and seeds of medicinal plants" and by a grant of the Romanian Ministry of Agriculture and Rural Development, Funding contract no. 24.1.3/ 17.07.2023, project ADER 24.1.3 "Research on the development of new systems and technologies for the sustainable management of genetic resources in the sericulture field and the identification of new paths for the valorization of main and secondary products with economic and social impact".

REFERENCES

- [1] Alim, A., Hossain, S., & Islam, S. (2016). Study on comparative reeling performance of multi-end reeling machine and cottage basin reeling machine for qualitative and quantitative improvement of raw silk production *Elixir Applied Chemistry*, 95, 41180-41183, ISSN 2229-712X
- [2] Altman, H.G., & Farrell, D. B. (2022). Sericulture as a sustainable agroindustry, *Cleaner and Circular Bioeconomy*, 2, 100011, 1-9, <https://doi.org/10.1016/j.clcb.2022.100011>
- [3] Andadari, L., Minarningsih, & Suwandi (2021). The effect of feeding various species of mulberry (*Morus* spp.) on the growth of silkworm and quality of cocoon hybrid BS 09, *IOP Conf. Series: Earth and Environmental Science*, 914, 012017 IOP Publishing, doi:10.1088/1755-1315/914/1/012017
- [4] Angel, L.C.B., Afuyog, M.T., & Cadao, J.B. (2018). Design, fabrication, and performance evaluation of a motorized cocoon deflossing machine, *Mountain Journal of Science and Interdisciplinary Research MJSIR*, 78(2), 9-20, ISSN 2619-7855
- [5] Arun, R., Sandhya, P., Kiran, D. L., Monika, S. G., & Chiranjeevi, S. (2019). Automated smart sericulture system, *Journal of Emerging Technologies and Innovative Research*, 6(5), 682-685, ISSN-2349-5162

- [6] Assirelli, A., Cabassi, G., Cappellozza, S., Costa, C., Figorilli, S., Marinoni, L., Pallottino, F., & Saviane, A. (2019). *Procedimento e Apparecchiatura per la Cernita Automatizzata di Insetti*. Patent No. IT201900016208A1, Italy.
- [7] Barcelos, D. B. M. S., Salvador, R., Barros, V. M., de Francisco, A. C., & Guedes, G. (2021). Circularity of Brazilian silk: Promoting a circular bioeconomy in the production of silk cocoons, *Journal of Environmental Management*, 296, 113373, <https://doi.org/10.1016/j.jenvman.2021.113373>
- [8] Baci, G. M., Cucu, A. A., Moise, A. R., & Dezmiorean, D. S. (2021). Applicability of honey on silkworms (*Bombyx mori*) and quality improvement of its biomaterials. *Applied Sciences*, 11(10), 4613, <https://doi.org/10.3390/app11104613>
- [9] Bekkamov, Ch., & Samatova, S. (2023). Impact of temperature variations in worm containers and nutrition amount on silk glands and silk productivity, *IOP Conf. Series: Earth and Environmental Science*, 1142, 012065, doi:10.1088/1755-1315/1142/1/012065
- [10] Chanotra, S., & Bali, K. (2019). Importance of mechanization in sericulture industry, *Journal of Pharmacognosy and Phytochemistry*, 8(6), 912-914, E-ISSN 2278-4136, P-ISSN 2349-8234
- [11] Cheng, C., Fu, J., Su, H., & Ren, L. (2023). Recent advancements in agriculture robots: benefits and challenges. *Machines*, 11(1), 48, <https://doi.org/10.3390/machines11010048>
- [12] Chopade P., Raghavendraa, C. G., Mohana Kumar, S. B., & Bhaskar, R. N. (2021). Assessment of diseases in bombyx mori silkworm – A survey, *Global Transitions Proceedings*, 2(1), 133-136, <https://doi.org/10.1016/j.gltip.2021.01.019>
- [13] da Silva, A. V., da Silva C. M., Soares Pessoa, W. R. L., Vaz, M. A., Matos de Oliveira, K., & dos Santos F. S. R. (2018). Agricultural mechanization in small rural properties in the State of Piauí, Brazil, *African Journal of Agricultural*, 13(33), 1698-1707, DOI: 10.5897/AJAR2018.13304
- [14] Duque-Torres, A., Rodriguez-Pabon, C., Ruiz-Rosero, J., Zambrano-Gonzalez, G., Almanza-Pinzon, M., Rendon, O.M.C., & Ramirez-Gonzalez, G. (2018). A new environmental monitoring system for silkworm incubators, *F1000Research*, 7:248, 1-7, doi: 10.12688/f1000research.13633.1
- [15] El-Shewy, A.M., & Elgizawy, K. KH. (2017). Effect of alternative plants on physiological and biological characteristics of silkworm *Bombyx mori* L., *Middle East Journal of Agriculture Research*, 6(4), 1268-1272, <https://www.curreweb.com/mejar/mejar/2017/1268-1272.pdf>
- [16] Ekka, V., & Bais, P. (2022). Sericulture as a Livelihood Option in Raigarh, Chhattisgarh. *Critical Issues, Opportunities and Experiments in Sustainable Development of Society, Industrial Development, Material, Energy and Environment*, 1(5), 1–7, ISBN: 978-93-94819-10-8, <https://doi.org/10.5281/zenodo.7109711>
- [17] Gautam, M. P., Singh, D.K., Singh, S. N., Singh, S. P., Kumar M. & Singh, S. (2022). A review on silkworm (*Bombyx mori* Linn.) an economic important insect, *Biological Forum – An International Journal* 14(4a): 482-491, ISSN (Print): 0975-1130, ISSN (Online): 2249-3239
- [18] Gheorghe, A., Hăbeanu, M., Mihălcea, T., & Diniță, G. (2023). Artificial diet as an alternative in silkworm (*Bombyx mori* L.) feeding - A review, *Scientific Papers. Series D. Animal Science*. LXVI(1), 76-86, ISSN 2285-5750; ISSN CD-ROM 2285-5769; ISSN Online 2393-2260; ISSN-L 2285-5750
- [19] Gunasheela, T. J., Renuka V. T., Prathiba, S. N., & Shilpa, A. P. (2018). Implementation of sericulture farm automation using sensor Network and GSM technology, *International Journal of Pure and Applied Mathematics*, 119(14),13-20, ISSN: 1314-3395 (on-line version)
- [20] Gupta, S. K., & Dubey, R. K. (2021). Environmental factors and rearing techniques affecting the rearing of silkworm and cocoon production of *Bombyx mori* Linn, *Acta Entomology and Zoology* 2(2), 62-67, e-ISSN: 2708-0021, P-ISSN: 2708-0013, DOI:[10.33545/27080013.2021.v2.i2a.46](https://doi.org/10.33545/27080013.2021.v2.i2a.46)
- [21] Hailu, A. (2016) Assessment of Growth and Performance of Silk Worms (*Bombyx mori* L.) on Mulberry Leaves at Jimma, South West Ethiopia, *Journal of Biology, Agriculture and Healthcare* 6(9), 10-16, ISSN 2224-3208 (Paper) ISSN 2225-093X (Online)
- [22] Hajam, O.A., Qadri, S. F. I, Malik M. A., Dar, M. A., & Malik F. A. (2021). A study on the knowledge and adoption level of improved sericulture technologies by the farmers of Kothar area of Anantnag district of Kashmir, *Journal of Entomology and Zoology Studies*, 9(1), 267-271, E-ISSN: 2320-7078, P-ISSN: 2349-6800
- [23] Hassan E., El-Rashidy, N., & Talaat F. (2022). Review: Mask R-CNN Models, *Nile Journal of Communication & Computer Science*, 3(1), 1-10, DOI:[10.21608/njccs.2022.280047](https://doi.org/10.21608/njccs.2022.280047)

- [24] Hăbeanu, M., Gheorghe, A., & Mihalcea, T. (2023). Silkworms pupae as protein source for pigs—A review, *Scientific Papers. Series D. Animal Science*, LXVI(2), 116-125, ISSN 2285-5750; ISSN CD-ROM 2285-5769; ISSN Online 2393-2260; ISSN-L 2285-5750
- [25] Jaiswal, K.K., Banerjee, I., & Mayookha, V. P. (2021) Recent trends in the development and diversification of sericulture natural products for innovative and sustainable applications, *Bioresource Technology Reports*, 13, 100614, <https://doi.org/10.1016/j.biteb.2020.100614>
- [26] Jiang, J., Sun, J., Huang, Z., Liang, H., Huang, Zf., & Li, C. (2024) Silkworm frame stacking system based on two axis motion platform, *International Journal of Frontiers in Engineering Technology*, 6(3), 135-142, ISSN 2706-655X, DOI: 10.25236/IJFET.2024.060317
- [27] Karthick mani Bharathi, B., Susikaran, S., Parthiban, K. T., Vasanth, V., Navaneetha Krishnan, S., Ramya Harika, K., Garai I., Ashwin Niranjana, M., Vijay S., & Gajjala Nitish (2024). Mechanization in moriculture, *International Journal of Zoology and Applied Biosciences*, 9(3), 46-50, ISSN: 2455-9571, <https://doi.org/10.55126/ijzab.2024.v09.i03.008>
- [28] Kaviraj, M., Kumar, U., Chatterjee S. N., Swain, S. L., Singh, M., & Nandi, K. (2021). Comparative performance analysis of mulberry silkworm (*Bombyx mori* L.) races for integration of superior yield and maximize profit in West Bengal, *bioRxiv*, CC-BY-ND 4.0 International license, 1-34, doi:<https://doi.org/10.1101/2021.03.22.436391>
- [29] Kokila, K. S., Praveena, K. P., Sanjay, M., Tejas Kumar, N. K., & Tejas, R. (2021). Advance Silkworm Incubator with Environment Control, *International Research Journal of Engineering and Technology*, 8(7), 2131-2134, e-ISSN: 2395-0056, p-ISSN: 2395-0072
- [30] Kumar, R. R., Navinkumar T. M., Aravindh, P., Kavinesh, T., Sathyanarayanan Y., & Sedhumaadhavan P. (2021). Smart Mulberry Plant Cutter, *IOP Conf. Series: Materials Science and Engineering* 1055, 012037, 1-8, doi:10.1088/1757-899X/1055/1/012037
- [31] Lujerdean, C., Baci, G. M., Cucu, A. A., & Dezmirean, D. S. (2022). The Contribution of Silk Fibroin in Biomedical Engineering. *Insects*, 13(3), 286, <https://doi.org/10.3390/insects13030286>
- [32] Manjunatha M., & Neelagar M. (2018). Arduino Based Automated Sericulture System, *International Journal of Computer Science and Mobile Computing* 7(7), 88-95, ISSN 2320-088X
- [33] Nahiduzzaman, M., Chowdhury, M. E. H., Salam, A., Nahid, E., Ahmed, F., Al-Emadi, N., Ayari, M. A., Khandakar, A., & Haider, J. (2023). Explainable deep learning model for automatic mulberry leaf disease classification. *Frontiers in Plant Science*, 14, 117551, 1-19, doi: 10.3389/fpls.2023.1175515
- [34] Pop, L. L., Mărghițaș A. L., Dezmirean D., Bobis O., Moise A., & Pasca C. (2018). Sericulture industry in Romania - analysis on current situation and prospects of development, *Scientific Papers. Series D. Animal Science*, LXI(1), 251-258, ISSN 2285-5750; ISSN CD-ROM 2285-5769; ISSN Online 2393-2260; ISSN-L 2285-5750
- [35] Popescu, A., Șerban, V., & Ciocan H. N. (2024). New trends in the global silk production in the period 2011-2022, *Scientific Papers Series Management, Economic Engineering in Agriculture and Rural Development*, 24(1), 775-786, PRINT ISSN 2284-7995, E-ISSN 2285-3952
- [36] Raj, A. J. N., Sundaram, R., Mahesh, V. G. V., Zhuang, Z., Simeone, A. (2019) A multi-sensor system for silkworm cocoon gender classification via image processing and support vector machine, *Sensors* 2019, 19, 2656; doi:10.3390/s19122656
- [37] Reizabel, A., Costa, C. M., Pérez-Álvarez, L., Vilas-Vilela J. L., & Lanceros-Mendez, S. (2023). Silk fibroin as sustainable advanced material: material properties and characteristics, processing, and applications, *Advanced Functional Materials*, 33(3), 2210764, 1-25, DOI: 10.1002/adfm.202210764
- [38] Safarov, J. E., Sultanova, Sh. A., & Samandarov, D. I. (2019). Method for primary processing of here silkworm cocoons by using infrared radiation and elastic waves, *Technical science and innovation*, Vol. 2018(3), 30-36, DOI: <https://doi.org/10.51346/tstu-01.18.2.-77-0010>
- [39] Saikia S., & Saikia M. (2022). Physical and chemical properties of Indian silk fibres, *The Pharma Innovation Journal*, 11(3), 732-738, ISSN (E) 2277- 7695, ISSN (P) 2349-8242
- [40] Samandarov, D., Sultanova, S., Safarov, J, Pulatov M., & Jumaev, B. (2023). Theoretical and experimental study of primary cocoon processing, *BIO Web of Conferences* 105, 01019, IV International Conference on Agricultural Engineering and Green Infrastructure for Sustainable Development, 1-6, <https://doi.org/10.1051/bioconf/202410501019>
- [41] Seo, S. J., Das, G., Shin, H. S., & Patra, J. K. (2023). Silk Sericin Protein Materials: Characteristics and Applications in Food-Sector Industries. *International Journal Molecular Science*, 24(5), 4951, <https://doi.org/10.3390/ijms24054951>

- [42] Singh, T., Nigam, A., & Kapila, R. (2021). Innovations in Silkworm Rearing and Importance: Recent Advances, *Journal of the Textile Association*, 82(2), 87-90
- [43] Shamshiri, R. R., Weltzien, C., Hameed, I. A., Yule, I. J., Griff, T. E., Balasundram, S. K., Pitonakova, L., Ahmad, D., & Chowdhary G. (2018). Research and development in agricultural robotics: A perspective of digital farming, *International Journal of Agricultural and Biological Engineering*, 11(4), 1-14, <https://doi.org/10.25165/ijabe.v11i4.4278>
- [44] Sharma, P., Bali, K., Sharma A., Gupta R. K., & Attri, K. (2022). Potential use of sericultural by products: A review, *The Pharma Innovation Journal*, 11(8), 1154-1158, ISSN (E) 2277- 7695, ISSN (P) 2349-8242
- [45] Tassoni, L., Cappelozza, S., Dalle Zotte A., Belluco, S., Antonelli, P., Marzoli, F., & Saviane, A. (2022). Nutritional Composition of *Bombyx mori* Pupae: A Systematic Review, *Insects*, 13(7), 644, <https://doi.org/10.3390/insects13070644>
- [46] Taufique, M., Hoque, A. (2021) Current scenario of sericulture production in India: a spatio-temporal analysis, *IRJEdT 02 (04), August 2021*, pp.12-23, ISSN2581-7795
- [47] Vasta, S., Figorilli, S., Ortenzi, L., Violino, S., Costa, C., Moscovini, L., Tocci, F., Pallottino, F., Assirelli, A., Saviane, A., & Cappelozza S. (2023). Automated prototype for *Bombyx mori* cocoon sorting attempts to improve silk quality and production efficiency through multi-step approach and machine learning algorithms, *Sensors*, 23, 868, <https://doi.org/10.3390/s23020868>
- [48] Vlăduț, N. V., & Ungureanu, N. (2024). Beyond Agriculture 4.0: Design and development of modern agricultural machines and production systems, *Agriculture*, 14, 991, <https://doi.org/10.3390/agriculture14070991>
- [49] Yogeshraj, N. S., Thamilarasi, N., Sailaja, S., Poonguzhali, C., & Kannagi, S. (2022). Smart automated sericulture based on image processing technique and embedded system, *Journal of University of Shanghai for Science and Technology*, 24(1), 327-331, ISSN: 1007-6735
- [50] Zeng, S., Yingchun, H., & Qin, S. (2023). Location of Mulberry Leaf Picking Points Based on Improved Mask RCNN, *ICAIE 2023, AHCS 15*, pp. 337–344, https://doi.org/10.2991/978-94-6463-242-2_42
- [51] Zhu, L., Lin, J.; Pei, L., Luo, Y., Li, D., & Huang, Z. (2022). Recent advances in environmentally friendly and green degumming processes of silk for textile and non-textile applications, *Polymers*, 14, 659. <https://doi.org/10.3390/polym14040659>
- [52] *** International Sericulture Commission – ISC, <https://inserco.org/en/statistics>
- [53] *** UNESCO Representative List of the Intangible Cultural Heritage of Humanity <https://ich.unesco.org/en/RL/sericulture-and-traditional-production-of-silk-for-weaving-01890#video>

RESEARCH ON YOLOv5-BASED VISUAL SLAM OPTIMISATION METHOD IN FARM DEPOT ENVIRONMENT

农场仓库环境中基于 YOLOv5 的视觉 SLAM 优化方法研究

Pengcheng LV ^{1,2)}, ZhenWei LI ^{2,*})

¹⁾ Shandong University of Technology, College of Agricultural Engineering and Food Science, Zibo, China

²⁾ Hezhou University, School of Artificial Intelligence, Hezhou, China

Tel: +86 18077508818; E-mail: lizhenwei0511@163.com

Corresponding author: ZhenWei LI

DOI: <https://doi.org/10.35633/inmateh-75-07>

Keywords: Dynamic environments; YOLOv5; Synchronized positioning and mapping; Robustness

ABSTRACT

Conventional simultaneous localization and mapping (SLAM) systems for agricultural robots rely heavily on static rigidity assumptions, which makes it susceptible to the influence of dynamic target feature points in the environment thus leading to poor localization accuracy and robustness of the system. To address the above issues, this paper proposes a method that utilizes a target detection algorithm to identify and eliminate dynamic target feature points in a farm depot. The method initially employs the YOLOv5 target detection algorithm to recognize dynamic targets in the captured warehouse environment images. The detected targets are then integrated into the feature extraction process at the front end of the visual SLAM. Next, dynamic feature points belonging to the dynamic target part are eliminated from the extracted image feature points using the LK optical flow method. Finally, the remaining feature points are used for location matching, map construction and localization. The final test on the TUM dataset shows that the enhanced vision SLAM system improves the localization accuracy by 91.47% compared to ORB-SLAM2 in highly dynamic scenes. This improvement increases the accuracy and robustness of the system and outperforms some of the best SLAM algorithms while maintaining high real-time performance. These features make it more valuable for mobile devices.

摘要

农业机械人的传统同步定位和地图构建 (SLAM) 系统在很大程度上依赖于静态刚性假设, 这使得它很容易受到环境中动态目标特征点的影响从而导致系统的定位精度和鲁棒性变差。针对上述问题, 本文提出了一种利用目标检测算法来识别和消除农场库房中动态目标特征点的方法。该方法最初采用 YOLOv5 目标检测算法来识别采集库房环境图像中的动态目标。然后将检测到的目标整合到视觉 SLAM 前端的特征提取过程中。接着, 使用 LK 光流方法从提取的图像特征点中剔除属于动态目标部分的动态特征点。最后, 剩余的特征点用于位置匹配、地图构建和定位。在 TUM 数据集上的最终测试表明, 在高动态场景中, 增强型视觉 SLAM 系统与 ORB-SLAM2 相比, 定位精度提高了 91.47%。这一改进提高了系统的准确性和鲁棒性, 并在保持高实时性的同时超越了一些优秀的 SLAM 算法。这些特点使其对移动设备更有价值。

INTRODUCTION

With the development of autonomous mobile robot platforms, agricultural robots have been widely used in agricultural production and warehousing services, such as farm management, orchard inspection, fruit picking, and automation of warehousing tasks. In these scenarios, robots need to understand the entire area and the precise location of the target objects in the map to accomplish autonomous navigation. In order to realize autonomous navigation, mobile robots need to accomplish two tasks: attitude estimation and map construction. Simultaneous localization and mapping (SLAM) refers to the robot in an unknown environment, which through its own matching sensors estimates its own position and build the environment map (He et al., 2020). SLAM according to the different sensors are mainly divided into two categories. One is SLAM equipped with LiDAR, which is a mature system with small computation and accurate ranging, but the cost of LiDAR is high and not easy to maintain, so it is not commonly used in indoor robots. The other category is the camera-equipped vision SLAM, which is characterized by low cost, high cost-effectiveness, and the ability to obtain rich environmental information, so it has become a hot spot of attention in the field of robotics research.

Currently, visual SLAM can be classified into two kinds according to the methods used: the feature point method with FAST corner points as feature extraction and BRIEF descriptors as identity information matching, which can be used for sparse point cloud building; and the direct method with the information of the image gray value to directly judge the camera motion, which can be used for dense point cloud building, but with certain assumptions on the gray invariance. ORB-SLAM2 is considered to be one of the most complete one of the visual SLAM frameworks and also represents the feature point method (*Mur et al., 2017*), but its results are not satisfactory in highly dynamic working environments, which leads to the low applicability of SLAM systems in real-world scenarios. The implementation of the direct method is based on the assumption of constant gray scale, but the light in the environment changes from time to time, and the assumption is difficult to be completely valid, so the SLAM system based on the direct method has poor robustness. In indoor dynamic environments, the feature points extracted from irregularly changing moving objects will seriously affect the accuracy of the camera position evaluation. *Engel et al., (2014)*, proposed LSD-SLAM, which utilizes gray values to achieve localization and construct semi-dense point cloud stacks. *Wang et al., (2017)*, contributed DSO-SLAM based on the sparse direct method is superior to LSD-SLAM in terms of robustness, accuracy, and speed, but it does not include the loopback detection function, which is an incomplete SLAM algorithm.

Among the approaches relying on deep learning, *Bescos et al., (2018)*, proposed the DynaSLAM algorithm, which utilizes a priori information for segmenting dynamic targets by means of a deep learning neural network, Mask R-CNN, which was first proposed by *He et al., (2017)*, and *Liu et al., (2018)*, utilized semantic segmentation to identify the a priori dynamic regions of an image, and tracking and mapping using static feature points. *Yu et al., (2018)*, proposed a DS-SLAM algorithm that combines a SegNet real-time semantic segmentation network with motion consistency detection to reduce the impact of dynamic targets on the system and reduce the localization accuracy in dynamic scenes compared to ORB-SLAM2. Compared with ORB-SLAM2, the localization accuracy in dynamic scenes is improved by one order of magnitude, but the semantic segmentation is time-consuming and fails to meet the real-time requirements. RDS-SLAM proposed by *Liu et al., (2021)*, adds semantic tracking threads and optimization threads on the basis of the ORB-SLAM3 system and eliminates the outliers of the tracking threads by using the data correlation algorithm. The RTD-SLAM proposed by *Wang et al., (2023)*, adds YOLOV5-based parallel semantic threads and optical flow modules to the tracking threads to eliminate dynamic feature points, which improves the system's localization accuracy and real-time performance. Based on the ORB-SLAM3 system, the semantic segmentation thread is added to improve the camera localization accuracy in dynamic scenes, but the dynamic feature points of potential dynamic targets (e.g., books held by people) are detected as static feature points, which are used in the tracking thread for feature matching and camera pose computation, resulting in a decrease in the system localization accuracy (*Law et al., 2018*).

In summary, the SLAM system's positioning accuracy may be affected by dynamic objects in the complex environment, leading to poor real-time performance. To tackle these issues, this paper selects YOLOv5 as the target detection network. Then, it combines the optical flow method in the tracking thread of the SLAM system to eliminate feature points that do not meet the requirements. Finally, only the processed feature points are utilized for estimating the camera position. Experiments were conducted on the TUM dataset and compared with ORB-SLAM2 and other dynamic SLAM algorithms. The results showed that the localization accuracy of the improved visual SLAM system was 91.47% higher than that of ORB-SLAM2. Compared to ORB-SLAM2, the improved visual SLAM system demonstrated a 91.47% increase in localization accuracy in highly dynamic scenes. This enhancement effectively improves the system's robustness and localization accuracy, while also providing higher real-time performance on mobile devices. As a result, the system has greater application value.

MATERIALS AND METHODS

ORB-SLAM2 system

ORB-SLAM2 is a feature-point based SLAM system that enables simultaneous localization and map construction using camera-captured image data. It is highly stable, operates quickly, and is easy to implement. Currently, it is the most widely used system in the field of vision SLAM. The system contains three main threads: tracking, local map construction, and closed-loop detection. Figure 1 shows the system framework.

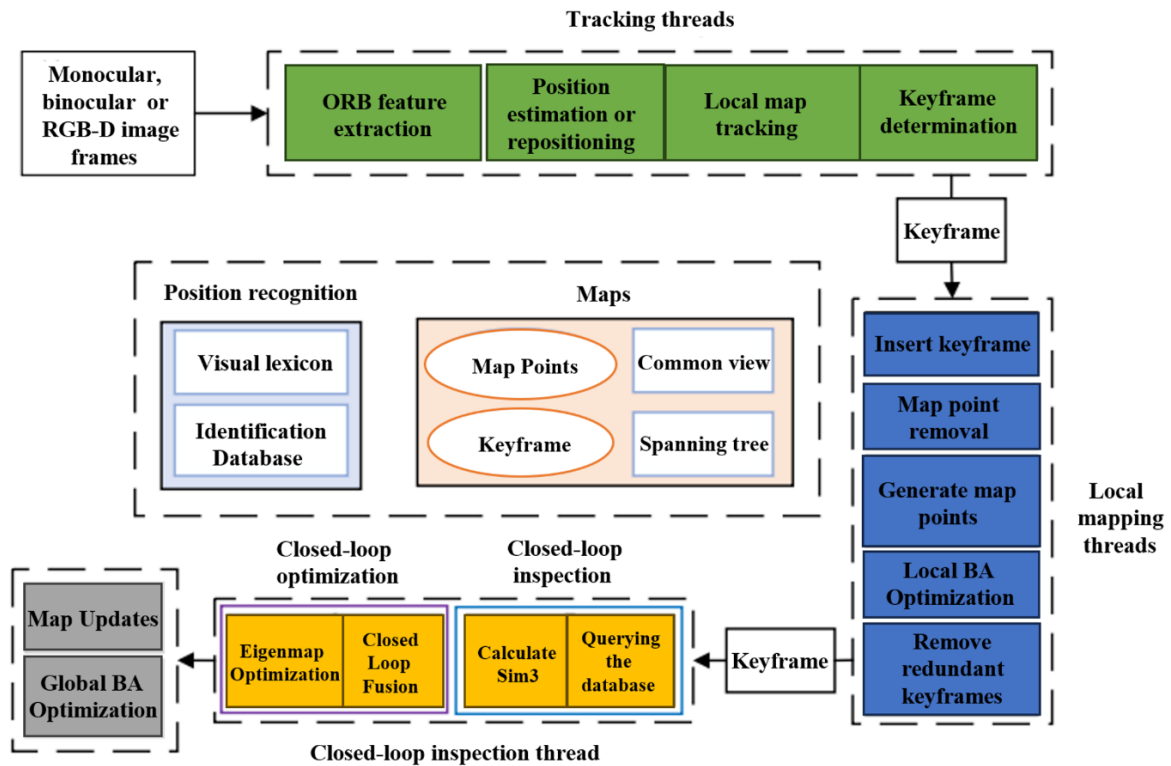


Fig. 1 – ORB-SLAM2 algorithm system framework

Improved SLAM system

The ORB feature points extracted from dynamic objects in the traditional tracking thread can accumulate errors when matching positions, resulting in reduced position evaluation accuracy or even localization failure (Liang et al., 2022). To minimize the impact of dynamic objects on the system and improve positioning accuracy, this paper proposes a method that combines target detection and optical flow algorithms to reject dynamic feature points in the scene (Liang et al., 2022). A target detection module and a dynamic feature point rejection module have been added to the tracking thread of the ORB-SLAM2 framework, as shown in Figure 2. A new detection thread has been included in the front-end, and the tracking and detection threads share information (Placed et al., 2022). When the system receives the image frames, they are processed by the tracking and detection thread. The process involves two threads: tracking and detection. The tracking thread extracts ORB feature points from the image and uses the optical flow method to track and match the remaining feature points. The detection thread recognizes the object based on a priori information, such as the screen, chair, and human, and calculates the frame position of each category. The tracking thread then divides the frames into dynamic and static categories based on the returned frame information and categories, and calculates the basis matrix. The system's robustness and positioning accuracy are improved by matching the remaining static points with features to estimate their position, which reduces the influence of dynamic objects in the environment (Khan et al., 2022; Wang et al., 2022; Tian et al., 2023; Engel et al., 2017).

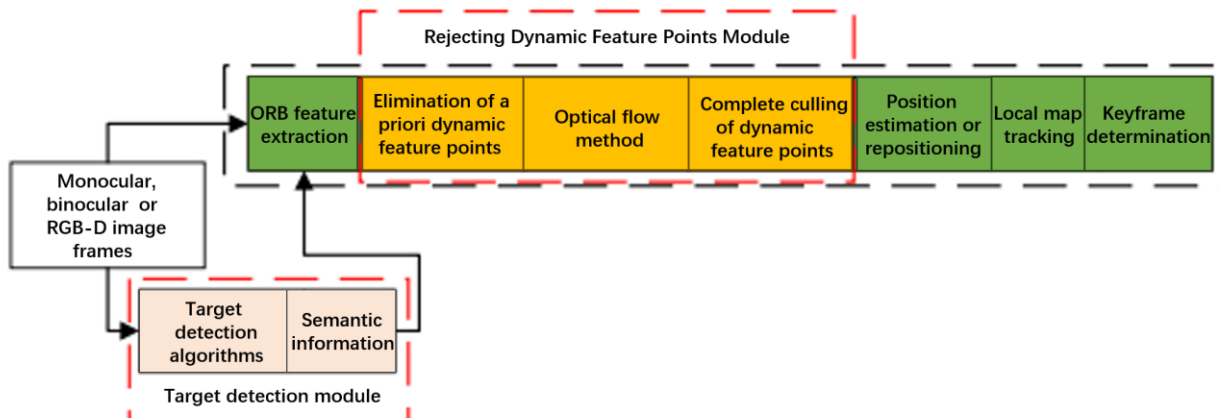


Fig. 2 – Improved trace threads

Feature tracking and matching based on the LK optical flow method

The optical flow method can be used for computer vision tasks by comparing the change in brightness values of corresponding pixels in two images to infer the direction and magnitude of the pixel's motion in the image. This method can track the motion process of a stationary pixel and a dynamic target's same pixel in the image (Xu et al., 2021). The two types of optical flow are sparse optical flow, which describes the motion state of some pixels in the image, and dense optical flow, which describes the motion state of all pixels (Shen et al., 2023). The Hom-Schunck optical flow represents the dense optical flow, while the Lucas-Kanade optical flow, also known as LK optical flow, dominates the sparse optical flow (Zou et al., 2022).

In this paper, the purpose is to reduce computation by computing only the optical flow field of the ORB feature points extracted by the visual odometry of the SLAM system. Therefore, the LK optical flow is used (Fang et al., 2009).

The LK optical flow is founded on 3 assumptions:

1. For a moving target in a grayscale image, the luminance (gray scale) of its pixel points does not change between adjacent frames.
2. Time continuity or motion is small enough that there is no drastic change in the target position due to time change in each computation, and the change in the corresponding position of pixel points of a moving target between adjacent frames is relatively small.
3. Spatial consistency, the vicinity of feature points All neighboring pixel points move similarly.

As shown in Fig. 3, the gray scale of an image can be regarded as a function of time: at moment t , the gray scale of an ORB feature point located at (x, y) in the image can be written as $I(x, y, t)$. According to the gray scale invariance assumption of the optical flow method, the gray scale value of the same feature point is fixed in each image. For a feature point located at (x, y) at time t , it will move to $(x+dx, y+dy)$ at time $(t+dt)$ (Zhang et al., 2020).

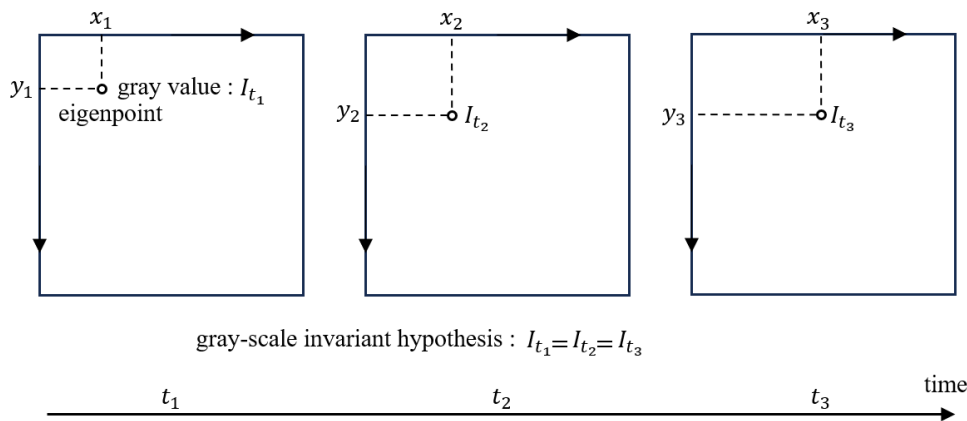


Fig. 3 – Schematic diagram of LK optical flow method

The following mathematical formula is obtained based on the assumption of gray scale invariance:

$$I(x+dx, y+dy, t+dt) = I(x, y, t) \tag{1}$$

A Taylor expansion of the left-hand side of the equal sign of Eq. (1), retaining the first-order terms yields Eq. (2):

$$I(x+dx, y+dy, t+dt) \approx I(x, y, t) + \frac{\partial I}{\partial x} dx + \frac{\partial I}{\partial y} dy + \frac{\partial I}{\partial t} dt \tag{2}$$

According to the gray scale invariance assumption, the gray scale values of the feature points at moments t and $t+dt$ are equal, which can be obtained:

$$\frac{\partial I}{\partial x} dx + \frac{\partial I}{\partial y} dy + \frac{\partial I}{\partial t} dt = 0 \tag{3}$$

Both sides are obtained by dividing by dt at the same time:

$$\frac{\partial I}{\partial x} \frac{\partial x}{\partial t} + \frac{\partial I}{\partial y} \frac{\partial y}{\partial t} = - \frac{\partial I}{\partial t} \tag{4}$$

In Eq. (4) dx/dt is the motion velocity of the feature point on the X -axis and dy/dt is the velocity on the Y -axis, which are denoted as u and v , respectively (Kundu et al., 2009).

$\partial I/\partial x$ is the gradient of the image in the X -axis direction at the point, and $\partial I/\partial y$ is the gradient in the Y -axis direction, which are denoted as I_x and I_y , respectively (Migliore et al., 2009). The amount of change in the grayscale of the feature point with respect to the time is denoted as it. It is written in the form of a matrix, as shown in Eq. (5) as follows (Lin et al., 2010):

$$\begin{bmatrix} I_x & I_y \end{bmatrix} \begin{bmatrix} u \\ v \end{bmatrix} = -I_t \quad (5)$$

According to Eq. (5), additional constraints need to be introduced to find the velocity vector of a pixel (Zou et al., 2012). In the LK optical flow, a 6×6 window is assumed with the feature point as the center, and according to Assumption 3, the 36 pixels inside have the same motion, and the equation is transformed into a super-definite linear equation about u , v . The equation is transformed into a hyper-definite linear equation about, and solved by the least squares method (Du et al., 2020). Since in the actual application scenario, the static part of the image generates optical flow vectors due to the movement of the camera, the average optical flow vectors of the static part of the image are calculated according to Equation (6) (You et al., 2023).

$$\begin{bmatrix} U \\ V \end{bmatrix} = \frac{1}{N} \sum_{k=1}^N \begin{bmatrix} u_k \\ v_k \end{bmatrix} \quad (6)$$

The feature points are filtered using equation (6) to determine whether the feature points are dynamic or not (Xiao et al., 2019).

$$\sqrt{(u-U)^2 + (v-V)^2} > z \quad (7)$$

where z is the threshold value for determining whether the feature point is a dynamic feature point, which is generally twice the static mean optical flow vector. If it is greater than this value, it is judged to be a dynamic feature point, and vice versa for a static feature point (Zhong et al., 2018).

Dynamic property setting for indoor targets

The YOLO algorithm is a neural network-based object recognition and localization tool that is fast and can be used in real-time systems. It is currently one of the most widely used single-stage target detection algorithms. The YOLOv5 version contains five models: YOLOv5n, YOLOv5s, YOLOv5m, YOLOv5l, and YOLO5x. The detection accuracy of the YOLOv5 model gradually increases from YOLOv5n to YOLO5x, while the detection speed gradually decreases. YOLOv5 employs mosaic data enhancement technology to enhance the generalization of the model by synthesizing multiple images into one large image. Secondly, it performs adaptive optimization in anchor point and image scaling processing to improve the performance of the model. For the backbone layer, YOLOv5 combines Focus and CSP structures to extract more representative features. The neck network introduces FPN and PAN structures to realize multi-scale feature fusion and improve detection accuracy. Finally, in the head output layer, the loss function GIOU_Loss and the predictive frame filtering GIOU_nms are improved to increase the accuracy and recall of the model. (Wu et al., 2021; Redmon et al., 2016; Redmon et al., 2017; Redmon et al., 2018).

This paper selects the widely used YOLOv5s network for dynamic target detection due to its better balance between accuracy and speed. YOLOv5s is only 27MiB in size and has a fast inference speed, meeting the real-time detection requirements of the visual system when compared to YOLOv4 (Liu et al., 2016; Lin et al., 2017; Bochkovskiy et al., 2020).

The data structure of the YOLOv5 detection frame is output in the format (X , Y , W , H , class, confidence), where X and Y represent the X and Y coordinates of the center point of the detection frame, respectively, W and H represent the width and height of the frame, class represents the category, and confidence represents the confidence level. In order to facilitate reading in the SLAM system, it is necessary to transform the first 4 position information into the coordinates under the original image. The conversion formula is as follows:

$$\begin{cases} X_1 = \left(X - \frac{W}{2} \right) \times L \\ X_2 = \left(X + \frac{W}{2} \right) \times L \\ Y_1 = \left(Y + \frac{H}{2} \right) \times D \\ Y_2 = \left(Y - \frac{H}{2} \right) \times D \end{cases} \quad (8)$$

The current approach defines dynamic and static boxes based on given coordinates and image dimensions. Where (X_1, Y_1) and (X_2, Y_2) denote the upper left and lower right coordinates of the detection frame, and L and D denote the width and height of the image respectively. The detection frame for the human body is defined as dynamic, while the detection frames for other objects are tentatively defined as static. Once the ORB feature points are extracted, the tracking thread receives the detection data from YOLOv5 and traverses the feature points in the detection frame. The feature points are categorized according to the definition of different frames. Figure 4 depicts the schematic diagram of feature points. To determine whether a feature point is dynamic or static when two boxes overlap, check if it is located inside the dynamic box and outside the static box. If the condition is met, the feature point is considered dynamic. If not, it is considered static (Girshick et al., 2014; Borrego et al., 2018; Ren et al, 2015).

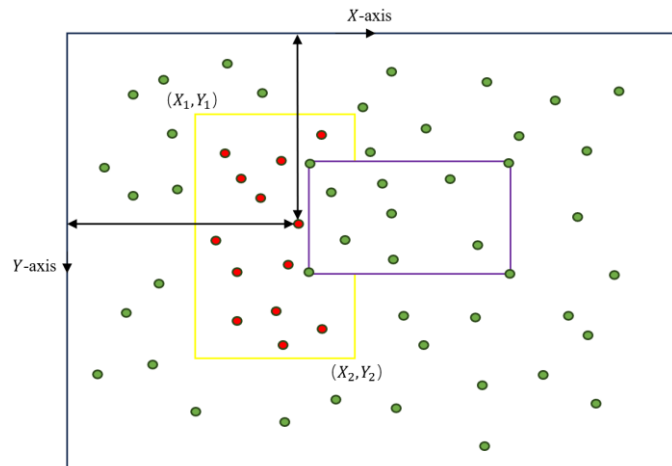


Fig. 4 – Schematic diagram of feature points

The current strategy for rejecting dynamic feature points necessitates the dynamic detection of all feature points within the target detection anchor frame. While this approach can improve localization accuracy in low dynamic sequences, it negatively impacts the system's real-time performance. To address this issue, this paper proposes a new dynamic feature point rejection strategy. This strategy employs a priori knowledge to classify targets. For instance, frequently moving targets like people, animals, and sweeping robots are classified as dynamic targets, while targets like tables and chairs that may move due to human movement are classified as potential dynamic targets.

Table 1

Dynamic property setting for indoor targets

Target objects	Target category	Target objects	Target category
Human	a	Desk	b
Dog	a	Chair	b
Cat	a	Water cup	b
Bird	a	Book	b
Pig	a	Laptop	b

Table 1 displays the categorization of common indoor targets, where 'a' denotes a dynamic target and 'b' denotes a potential dynamic target. Based on these classifications, feature points located in the anchor frame of dynamic targets are classified as dynamic feature points, feature points located in the anchor frame of potentially dynamic targets are classified as potentially dynamic feature points, and the remaining feature points are classified as static feature points. Assuming that the set of dynamic feature points in an image frame is Z , the set of potential dynamic feature points is Q , and the set of static feature points is P , the number of feature points that need to be dynamically detected can be reduced. This improves the real-time performance of the system.

Using Fig. 5 as an example, the tracking thread of the SLAM system extracts feature points while employing the YOLOv5s target detection network for target detection. Feature points in the anchor frames of dynamic targets (e.g. people in the two figures) are placed in set Z . Feature points in the anchor frames of potentially dynamic targets (e.g. the computer screen and chair in the figure) are placed in set Q , and the remaining feature points are placed in set P .

Calculate the optical flow vectors of the feature points in sets Q and P using the Lucas-Kanade optical flow method. The optical flow vectors of the feature points in set P are used as the optical flow vectors of the static region and are substituted into Equation (6) to calculate the average optical flow vectors. The optical flow vectors of the feature points in set Q are substituted into Equation (7) to make a judgment. If they are less than the threshold value, it means that the feature point is a static feature point and is then moved into set P of the static feature points. Finally, the feature points in set P are retained for feature matching and camera pose estimation, and the remaining feature points are rejected.

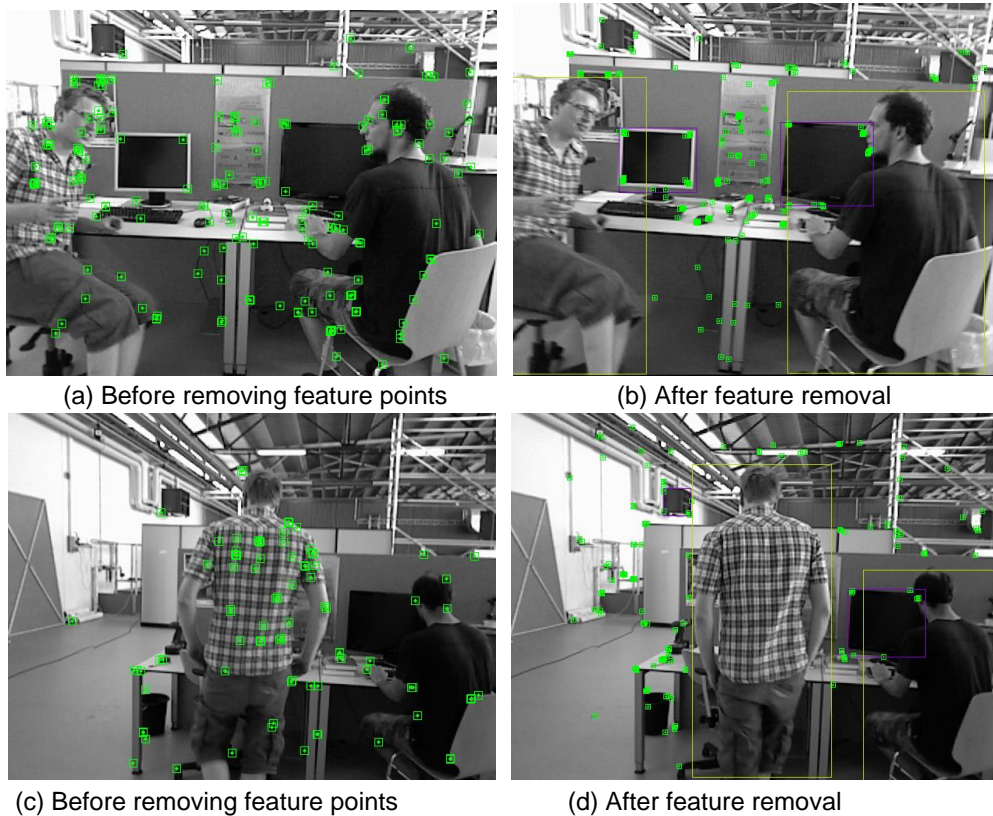


Fig. 5 – Dynamic feature point rejection effect comparison

Our strategy utilizes the LK optical flow method to determine whether a feature point is affected by a dynamic target, rather than simply removing all feature points in the target detection frame. An optical flow vector threshold is set; if the optical flow vector is less than this threshold, it indicates that the feature point is not affected by the dynamic target and can be added to the set P. Increasing the number of feature point matches can further improve the localization accuracy and robustness of the system. The effect of dynamic feature point rejection is demonstrated in Fig. 5. The algorithm rejects feature points on the person as dynamic and retains feature points on the computer anchor frame that overlap with the person's anchor frame, provided that the optical flow vector is less than the threshold. Feature points on the chair's anchor frame portion are also rejected as dynamic due to the person's movement. This strategy enables more accurate rejection of dynamic feature points, resulting in improved system stability and accuracy.

RESULTS

Experiment details

To evaluate the effectiveness of the improved ORB-SLAM2 algorithm, experiments and tests using the TUM dataset were conducted. This dataset consisted of synchronized RGB images and depth images of an indoor warehouse scene captured by a robot equipped with a Kinect sensor. It became one of the most widely used evaluation datasets in the field of SLAM for comparing the performance of different algorithms. This paper tested six sequences from the TUM dataset, including sitting_xyz, sitting_static, walking_halfsphere, walking_rpy, walking_static, and walking_xyz. The sitting_xx sequence was a low-dynamic scenario, while the walking_xx sequence was a high-dynamic scenario. Generally, SLAM algorithm evaluation considered aspects such as time consumption, complexity, and accuracy.

Accuracy evaluation was often the most important, and it involved metrics such as absolute and relative trajectory errors. This paper used root mean square error (RMSE) and standard deviation (STD) to evaluate these metrics. To reduce the impact of tracking failures in dynamic sequences during experiments, each sequence was run fifty times and the average value was recorded as the experimental data.

The experimental equipment used for the experiment was a Shenzhou laptop, its CPU model was I7-12650H, memory was 16G, the graphics chip was NVIDIA Geforce GTX4060, the system environment was Ubuntu20.04, and the deep learning framework PyTorch 1.9.0 was loaded in the virtual environment of Anaconda. The target detection experiment running software was Visual Studio Code. The target detection network was written in Python3.6, and the SLAM part was written in C++.

Analysis of experimental results

Since the system in this paper is an improvement on the ORB-SLAM2 system, the improved system with the ORB-SLAM2 system is compared and the evo tool is used to compare the bitwise trajectories estimated by the algorithm in this paper and the ORB-SLAM2 algorithm with the real trajectory map groundtruth.txt given by the dataset to quantify the effect of the algorithm in this paper on the improvement effect of the SLAM algorithm.

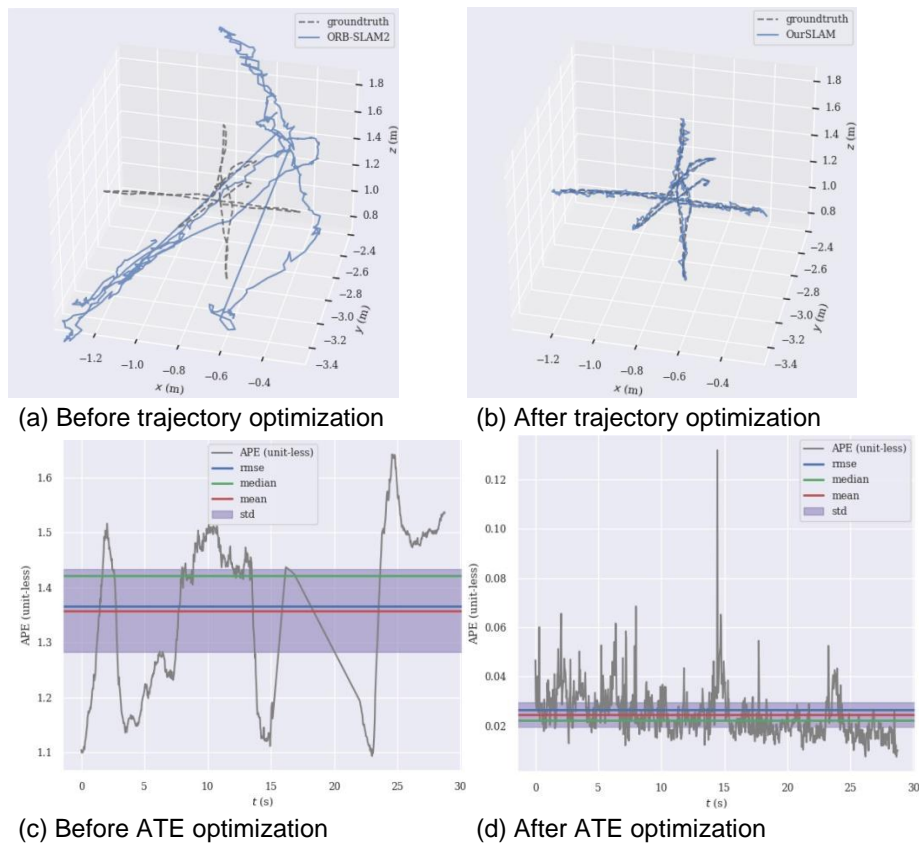


Fig. 6 – Comparison of trajectories and errors of datasets on walking_xyz

Figures 6 and 7 compare and analyze the camera trajectories evaluated by ORB-SLAM2 and this algorithm on the walking_xyz and walking_halfsphere datasets, respectively. The dotted line represents the real trajectory, while the solid line represents the camera trajectory evaluated by ORB-SLAM2 and this algorithm. The absolute trajectory error is denoted as (ATE). Figures 6 and 7 demonstrate the algorithm's accuracy by showing the similarity between its trajectories and the real trajectories. Additionally, the improved algorithm (Figures 6(d) and 7(d)) significantly reduces various types of error values compared to the unimproved algorithm.

To verify the effectiveness of the experimental design, ablation experiments were conducted on the TUM dataset. ORB-SLAM2 served as the base group, and the base group + YOLOv5s (ORB+YOLO) and the base group + LK optical flow method (ORB+LK), as well as the improved algorithm proposed in this paper, were tested.

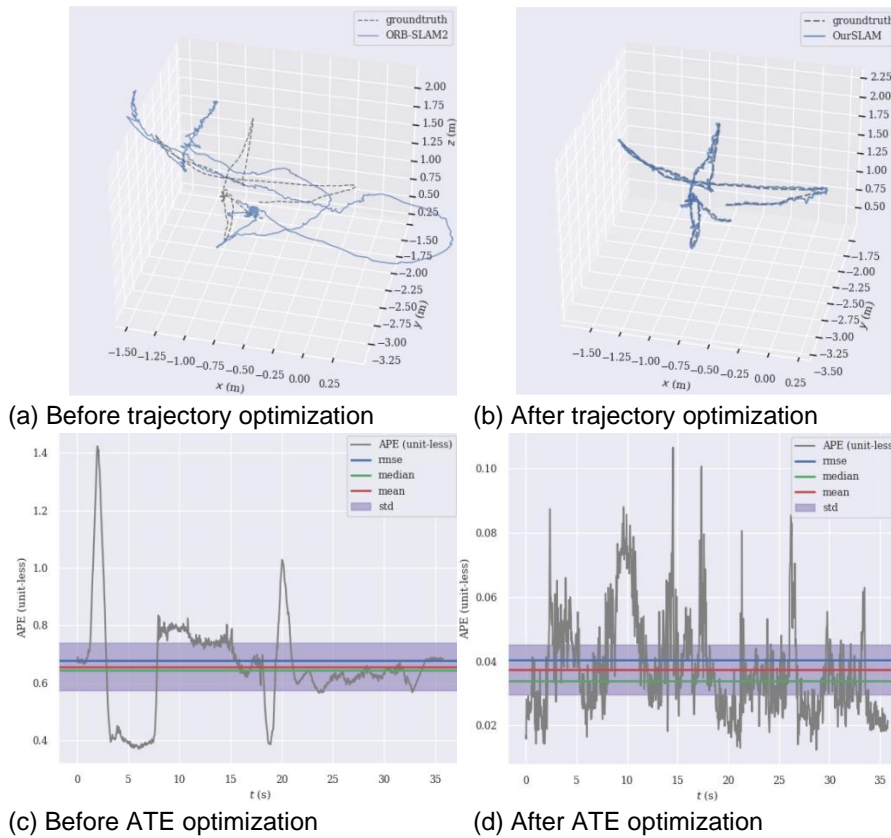


Fig. 7 – Comparison of trajectories and errors of datasets on walking_halfsphere

The comparison results are presented in Table 2, which demonstrate the superior effectiveness of the improved algorithm.

Table 2

Comparison results of ablation experiments

Data set	ORB-SLAM2		ORB + YOLO		ORB + LK		Ours	
	Rmse	STD	Rmse	STD	Rmse	STD	Rmse	STD
walking_xyz	0.2991	0.1186	0.0197	0.0116	0.1894	0.0752	0.0185	0.0092
walking_halfsphere	0.4754	0.1676	0.0411	0.0327	0.0752	0.0436	0.0381	0.0161
walking_static	0.0925	0.0714	0.0098	0.0087	0.0168	0.0114	0.0094	0.0082
walking_rpy	0.3575	0.2364	0.0468	0.0359	0.0748	0.0367	0.0349	0.0249
sitting_xyz	0.0153	0.0068	0.0161	0.0052	0.0151	0.0067	0.0134	0.0052
sitting_static	0.0122	0.0043	0.0124	0.0051	0.0097	0.0048	0.0082	0.0030

In this paper, the algorithm is simulated on six datasets in high and low dynamic environments, and the improvement degree of the improved algorithm over ORB-SLAM2 is calculated as shown in Eq. (9), which visually expresses the optimization effect.

$$\rho = \frac{\mu - \gamma}{\mu} \times 100\% \tag{9}$$

In the formula: ρ is the degree of improvement; μ is the result data of ORB-SLAM2 algorithm; γ is the result data of this paper's algorithm.

Table 3 and Table 4 show that the improved algorithm has an average improvement rate of RMSE and STD of less than 25% for the two sitting datasets in low dynamic scenarios, which is suboptimal. In datasets with dynamic objects, the removal of portrait feature points has little effect on the system's normal operation in low dynamic scenarios. However, in high dynamic scenarios, the algorithm presented in this paper shows an average improvement of 91.47% in the RMSE of four dynamic datasets compared to the ORB-SLAM2 algorithm. This indicates that the algorithm in this paper provides better localization accuracy in high dynamic scenarios.

Table 3

Comparison of absolute trajectory errors between ORB-SLAM2 and our algorithm

Data set	ORB-SLAM2		Ours		Relative uplift rate/%	
	Rmse	STD	Rmse	STD	Rmse	STD
walking_xyz	0.2991	0.1186	0.0185	0.0092	93.815	92.243
walking_halfsphere	0.4754	0.1676	0.0381	0.0161	91.986	90.394
walking_static	0.0925	0.0714	0.0094	0.0082	89.838	88.515
walking_rpy	0.3575	0.2364	0.0349	0.0249	90.238	89.467
sitting_xyz	0.0153	0.0068	0.0134	0.0052	12.418	23.529
sitting_static	0.0122	0.0043	0.0082	0.0030	32.787	30.233

In recent years, scholars have presented numerous cases using the fusion of deep learning and optical flow methods. This paper compares the reliability of the algorithm with recent domestic and international dynamic vision SLAM algorithms, as shown in Table 5. The compared algorithms include DynaSLAM, DS-SLAM, and RDS-SLAM, with the root-mean-square error of the absolute trajectory path as the comparative data. The comparison data is the root mean square error of the absolute trajectory path. To eliminate the influence of other factors, such as hardware equipment, this paper calculates the relative improvement rate. This directly illustrates the improvement rate of the enhanced algorithm compared to the original SLAM algorithm under the same experimental conditions. The DynaSLAM algorithm and the algorithm proposed in this paper have shown the best results. However, the DynaSLAM algorithm's use of a semantic segmentation algorithm for dynamic feature point rejection consumes a lot of time, making it unsuitable for real-time requirements. In contrast, this paper's algorithm has demonstrated relatively impressive localization accuracy in highly dynamic scenes, confirming its reliability.

Table 4

Comparison of relative trajectory errors between ORB-SLAM2 and our algorithm

Data set	ORB-SLAM2		Ours		Relative uplift rate/%	
	Rmse	STD	Rmse	STD	Rmse	STD
walking_xyz	0.2107	0.1079	0.0163	0.0088	92.264	91.844
walking_halfsphere	0.3247	0.1642	0.0274	0.0142	91.561	91.352
walking_static	0.0372	0.0612	0.0042	0.0063	88.710	89.706
walking_rpy	0.3547	0.4665	0.0351	0.0462	90.104	90.096
sitting_xyz	0.0167	0.0062	0.0162	0.0061	2.994	1.613
sitting_static	0.0114	0.0018	0.0111	0.0017	2.632	5.556

Table 5

Comparison of ATE analysis between the improved algorithm and other dynamic SLAM algorithms

Data set	DynaSLAM	RDS-SLAM	DS-SLAM	Ours
walking_xyz	92.74/%	91.27/%	90.56/%	93.82/%
walking_halfsphere	94.28/%	90.74/%	89.38/%	91.99/%
walking_static	87.78/%	86.54/%	83.34/%	89.84/%
walking_rpy	92.67/%	90.13/%	86.52/%	90.24/%

CONCLUSIONS

This paper proposes a method that uses a target detection algorithm to identify and exclude feature points of dynamic targets in a farm depot. The method first utilizes the YOLOv5 target detection algorithm to identify dynamic targets in the acquired environment images. The recognized targets are then integrated into the visual SLAM front-end for feature extraction. Next, an LK optical flow method is used to eliminate dynamic feature points that belong to the dynamic target portion of the extracted image feature points. The remaining feature points are then utilized for bit matching and map construction to determine the location of the feature points. Tests were also conducted on the TUM dataset to evaluate the performance of the proposed method. The experimental results show that the enhanced visual SLAM system improves the localization accuracy by 91%. In highly dynamic scenes, the system effectively improves the localization accuracy and robustness by 47% over ORB-SLAM2. In addition, compared with other excellent SLAM algorithms, the system has significantly improved localization accuracy and higher real-time performance, so it is more suitable for the application of mobile devices on agricultural robots, which will promote the development of smart agriculture.

ACKNOWLEDGEMENT

The project supported by the R&D of low-speed unmanned autonomous navigation controller Project under Grant (No.2022TSGC1175).

REFERENCES

- [1] Bescos B, Fácil JM, Civera J. (2018). DynaSLAM: Tracking, mapping, and inpainting in dynamic scenes. *IEEE Robotics and Automation Letters*, 3(4):4076-4083. <https://doi.org/10.1109/LRA.2018.2860039>
- [2] Bochkovskiy A, Wang CY, Liao HYM, (2020). Yolov4: Optimal speed and accuracy of object detection. *arXiv preprint arXiv:200410934*, . <https://doi.org/10.48550/arXiv.2004.10934>
- [3] Borrego J, Figueiredo R, Dehban A. (2018). A generic visual perception domain randomization framework for gazebo. *2018 IEEE International Conference on Autonomous Robot Systems and Competitions (ICARSC)*, p.237-242. <https://doi.org/10.1109/ICARSC.2018.8374189>
- [4] Du ZJ, Huang SS, Mu TJ. (2020). Accurate dynamic slam using CRF-based long-term consistency. *IEEE Transactions on Visualization and Computer Graphics*, 28(4):1745-1757. <https://doi.org/10.1109/TVCG.2020.3028218>
- [5] Engel J, Koltun V, Cremers D. (2017). Direct sparse odometry. *IEEE transactions on pattern analysis and machine intelligence*, 40(3):611-625. <https://doi.org/10.1109/TPAMI.2017.2658577>
- [6] Engel J, Schöps T, Cremers D. (2014). LSD-SLAM: Large-scale direct monocular slam. *European conference on computer vision*, p.834-849. https://doi.org/10.1007/978-3-319-10605-2_54
- [7] Fang Y, Dai B. (2009). An improved moving target detecting and tracking based on optical flow technique and Kalman filter. *2009 4th International Conference on Computer Science & Education*, p.1197-1202. <https://doi.org/10.1109/ICCSE.2009.5228464>
- [8] Girshick R, Donahue J, Darrell T. (2014). Rich feature hierarchies for accurate object detection and semantic segmentation. *Proceedings of the IEEE conference on computer vision and pattern recognition*, p. 580-587. <https://doi.org/10.48550/arXiv.1311.2524>
- [9] He G, Yuan X, Zhuang Y. (2020). An integrated GNSS/LiDAR-SLAM pose estimation framework for large-scale map building in partially GNSS-denied environments. *IEEE Transactions on Instrumentation and Measurement*, 70:1-9. <https://doi.org/10.1109/TIM.2020.3024405>
- [10] He K, Gkioxari G, Dollár P. (2017). Mask R-CNN. *Proceedings of the IEEE international conference on computer vision*, p.2961-2969. <https://doi.org/10.48550/arXiv.1703.06870>
- [11] Khan MU, Zaidi SAA, Ishtiaq A. (2021). A comparative survey of lidar-slam and lidar based sensor technologies. *2021 Mohammad Ali Jinnah University International Conference on Computing (MAJICC)*, p.1-8. <https://doi.org/10.1109/MAJICC53071.2021.9526266>
- [12] Kundu A, Krishna KM, Sivaswamy J, 2009. Moving object detection by multi-view geometric techniques from a single camera mounted robot. *(2009) IEEE/RSJ Inter-national Conference on Intelligent Robots and Systems*, p.4306-4312. <https://doi.org/10.1109/IROS.2009.5354227>
- [13] Law H, Deng J. (2018). CornerNet: Detecting objects as paired keypoints. *Proceedings of the European conference on computer vision (ECCV)*, p.734-750. <https://doi.org/10.1007/s11263-019-01204-1>
- [14] Liang T, Bao H, Pan W. (2022). Traffic sign detection via improved sparse R-CNN for autonomous vehicles. *Journal of Advanced Transportation*, 2022:1-16. <https://doi.org/10.1155/2022/3825532>
- [15] Liang T, Bao H, Pan W. (2022). DetectFormer: category-assisted transformer for traffic scene object detection. *Sensors*, 22(13):4833. <https://doi.org/10.3390/s22134833>
- [16] Lin KH, Wang CC. (2010). Stereo-based simultaneous localization, mapping and moving object tracking. *2010 IEEE/RSJ International Conference on Intelligent Robots and Systems*, p.3975-3980. <https://doi.org/10.1109/IROS.2010.5649653>
- [17] Lin TY, Goyal P, Girshick R. (2017). Focal loss for dense object detection. *Proceedings of the IEEE international conference on computer vision*, p.2980-2988. <https://doi.org/10.48550/arXiv.1708.02002>
- [18] Liu W, Anguelov D, Erhan D. (2016). SSD: Single shot multibox detector. *Computer Vision–ECCV 2016: 14th European Conference, Amsterdam, The Netherlands, October 11–14, 2016, Proceedings, Part I 14*, p.21-37. https://doi.org/10.1007/978-3-319-46448-0_2
- [19] Liu Y, Miura J. (2021). RDS-SLAM: Real-time dynamic slam using semantic segmentation methods. *IEEE Access*, 9:23772-23785. <https://doi.org/10.1109/ACCESS.2021.3050617>
- [20] Migliore D, Rigamonti R, Marzorati D. (2009). Use a single camera for simultaneous localization and mapping with mobile object tracking in dynamic environments. *ICRA Workshop on Safe navigation in open and dynamic environments: Application to autonomous vehicles*, p.12-17.

- [21] Mur-Artal R, Tardós JD. (2017). ORB-SLAM2: An open-source SLAM system for monocular, stereo, and RGB-D cameras. *IEEE transactions on robotics*, 33(5):1255-1262. <https://doi.org/10.1109/TRO.2017.2705103>
- [22] Placed JA, Strader J, Carrillo H. (2023). A survey on active simultaneous localization and mapping: State of the art and new frontiers. *IEEE Transactions on Robotics*, . <https://doi.org/10.1109/TRO.2023.3248510>
- [23] Redmon J, Divvala S, Girshick R. (2016). You only look once: Unified, real-time object detection. Proceedings of the *IEEE conference on computer vision and pattern recognition*, p.779-788. <https://doi.org/10.48550/arXiv.1506.02640>
- [24] Redmon J, Farhadi A. (2017). Yolo9000: better, faster, stronger. Proceedings of the *IEEE conference on computer vision and pattern recognition*, p.7263-7271. <https://doi.org/10.48550/arXiv.1612.08242>
- [25] Redmon J, Farhadi A, 2018. YoloV3: An incremental improvement. *arXiv preprint arXiv:180402767*, . <https://doi.org/10.48550/arXiv.1804.02767>
- [26] Ren S, He K, Girshick R. (2015). Faster R-CNN: To-wards real-time object detection with region proposal networks. *Advances in neural information processing systems*, 28. <https://doi.org/10.1109/TPAMI.2016.2577031>
- [27] Shen S, Kerofsky L, Yogamani S. (2023). Optical flow for autonomous driving: Applications, challenges and improvements. *arXiv preprint arXiv:230104422*, . <https://doi.org/10.48550/arXiv.2301.04422>
- [28] Tian C, Liu H, Liu Z. (2023). Research on multi-sensor fusion SLAM algorithm based on improved Gmapping. *IEEE Access*, 11:13690-13703. <https://doi.org/10.1109/ACCESS.2023.3243633>
- [29] Wang K, Yao X, Ma N. (2023). Real-time motion removal based on point correlations for RGB-D SLAM in indoor dynamic environments. *Neural Computing and Applications*, 35(12):8707-8722. <https://doi.org/10.1007/s00521-022-07879-x>
- [30] Wang R, Schworer M, Cremers D. (2017). Stereo DSO: Large-scale direct sparse visual odometry with stereo cameras. Proceedings of the *IEEE International Conference on Computer Vision*, p.3903-3911. <https://doi.org/10.48550/arXiv.1708.07878>
- [31] Wang S, Huang Y, Yue P. (2022). Research progress on visual slam for dynamic environments. *International Workshop of Advanced Manufacturing and Automation*, p.108-115. https://doi.org/10.1007/978-981-19-9338-1_14
- [32] Wu W, Liu H, Li L. (2021). Application of local fully convolutional neural network combined with YOLO v5 algorithm in small target detection of remote sensing image. *PLOS One*, 16(10):e0259283. <https://doi.org/10.1371/journal.pone.0259283>
- [33] Xiao L, Wang J, Qiu X. (2019). Dynamic-slam: Semantic monocular visual localization and mapping based on deep learning in dynamic environment. *Robotics and Autonomous Systems*, 117:1-16. <https://doi.org/10.1016/j.robot.2019.03.012>
- [34] Xu Z, Rong Z, Wu Y. (2021). A survey: which features are required for dynamic visual simultaneous localization and mapping? *Visual Computing for Industry, Biomedicine, and Art*, 4(1):1-16. <https://doi.org/10.1186/s42492-021-00086-w>
- [35] You M, Luo C, Zhou H. (2023). Dynamic dense CRF inference for video segmentation and semantic slam. *Pattern Recognition*, 133:109023. <https://doi.org/10.1016/j.patcog.2022.109023>
- [36] Yu C, Liu Z, Liu XJ. (2018). DS-SLAM: A semantic visual slam towards dynamic environments. *2018 IEEE/RSJ international conference on intelligent robots and systems (IROS)*, p.1168-1174. <https://doi.org/10.1109/IROS.2018.8593691>
- [37] Zhang T, Zhang H, Li Y. (2020). FlowFusion: Dynamic dense RGB-D SLAM based on optical flow. *2020 IEEE International Conference on Robotics and Automation (ICRA)*, p.7322-7328. <https://doi.org/10.1109/ICRA40945.2020.9197349>
- [38] Zhong F, Wang S, Zhang Z. (2018). Detect-SLAM: Making object detection and SLAM mutually beneficial. *2018 IEEE Winter Conference on Applications of Computer Vision (WACV)*, p.1001-1010. <https://doi.org/10.1109/WACV.2018.00115>
- [39] Zou L, Huang Z, Yu X. (2022). Automatic detection of congestive heart failure based on multiscale residual UNet++: From centralized learning to federated learning. *IEEE Transactions on Instrumentation and Measurement*, 72:1-13. <https://doi.org/10.1109/TIM.2022.3227955>
- [40] Zou D, Tan P, (2012). CoSLAM: Collaborative visual SLAM in dynamic environments. *IEEE transactions on pattern analysis and machine intelligence*, 35(2):354-366. <https://doi.org/10.1109/TPAMI.2012.104>

NUMERICAL SIMULATION AND PARAMETER OPTIMIZATION OF COMBINED CUTTING AND CRUSHING FORAGE CRUSHER

铡切揉碎组合式牧草粉碎机数值模拟与参数优化

Tao CHEN¹⁾, Shu-juan YI^{*1)}; Song WANG¹⁾, Wen-sheng SUN¹⁾

College of Engineering, Heilongjiang Bayi Agricultural University, Daqing/P. R. China

Tel: +86-459-13836961877; E-mail: yishujuan_2005@126.com;

Corresponding author: Shu-juan Yi

DOI: <https://doi.org/10.35633/inmateh-75-08>

Keywords: forage; kneading machine; discrete element method; numerical simulation; parameter optimization

ABSTRACT

The lack of effective visualization research methods for the crushing process of grass kneading has restricted the development of grass kneading machine to a certain extent. In this paper, the hay kneading process was numerically simulated by using the discrete element method, the stem movement rule, the mechanical characteristics of the stem particle group and the power consumption of the kneading were analyzed, and the motion and breaking mechanism of the grass in the hay kneading machine were defined. The effects of motor output speed and feed rate on the spinning rate and power consumption were studied. The regression equation between test factors and evaluation indexes was established. With the goal of maximizing the silk rates and minimizing the power consumption, the motor output speed and feeding amount are optimized and solved. The optimal parameter combination is determined as follows: when the output speed of the motor is 282.88 r/min and the feeding amount is 1.86 kg/s, the knead verification test shows that the silk rates is 92.88% and the power consumption is 3.68 kJ. The research results provide a reference for realizing high efficiency and low power consumption of grass kneading and parameter optimization of kneading device.

摘要

针对牧草揉丝破碎过程缺乏有效可视化研究方法，在一定程度上制约了牧草揉丝机发展进程的问题。本文以铡切揉碎协同式牧草揉丝机为研究对象，采用离散元方法对牧草揉丝过程进行数值模拟，对牧草茎秆运动规律、茎秆颗粒群力学特性、揉丝功耗进行分析，明确了牧草在揉丝机内运动和破碎机理。进行了台架多因素性能试验，研究了电机输出转速和喂入量对丝化率和功耗的影响，构建了试验因素和评价指标之间的回归方程。以丝化率最大化和功耗最小化为目标，对电机输出转速和喂入量进行优化求解，确定最优参数组合为：电机输出转速为282.88r/min、喂入量为1.86kg/s时，揉丝验证试验表明，丝化率为92.88%、功耗为3.68kJ。研究结果为实现牧草高效、低功耗揉丝和揉丝装置参数优化提供参考。

INTRODUCTION

The kneading machine is a machine for processing and crushing forage grass (Wu et al., 2022; Wang et al., 2017; Fan et al., 2021). After kneading, the forage grass is filamentous with exposed internal nutrients (Kang et al., 2021; Tang, 2023), which can not only improve palatability, but also increase the contact area with the gastric juices of livestock, shorten the time of rumination and chewing, reduce the energy required for chewing of livestock, and have a better taste, which is convenient for the feeding and digestion of ruminant livestock (Li et al., 2023; Wang et al., 2017; Pei et al., 2023).

The contact between agricultural machinery and various agricultural materials and its impact on the design of agricultural machinery are important contents and difficulties in the digital design of modern agricultural equipment (Shi et al., 2022). As a computer numerical simulation method based on the discontinuity hypothesis, discrete element method can be used to simulate and analyze the interaction between agricultural materials and mechanical equipment, shorten the research and development cycle, and provide a means for the digital design of modern agricultural equipment, which has been widely used in the field of agricultural engineering (Zeng et al., 2021).

¹ Tao Chen, Ph.D.; Shu-juan Yi, Prof. Ph.D.; Song Wang, Ph.D.; Wen-sheng Sun, Ph.D.

Aiming at the problem of the lack of effective numerical simulation methods for the kneading and crushing process of corn stem, *Zhang Fengwei et al. (2019)* established a corn stem simulation model based on the discrete element method, and checked the parameters of the corn stem bonding contact model through the combination of physical and virtual tests, and finally conducted the crushing simulation and test verification for the corn stem discrete element model. *Geng Duanyang et al. (2021)* established a silage corn straw bonding model based on discrete element method, and carried out a silk kneading simulation test using EDEM to explore the effects of the number of teeth, two-roll differential ratio, the number of gap spiral turns and the driving roll speed on the silk ratio of straw. The relative error between the simulation test and the bench test results was 3.03%. *Zhang Tao et al. (2018)* used EDEM software to simulate the influence of the rotor speed of the hammer straw crusher on the straw conveying performance and the impact force of the straw, as well as the movement process of straw particle groups in the kneading chamber under different rotor speeds, providing a basis for the rotor speed optimization of the crusher. At present, the numerical simulation of forage crushing is mainly focused on crop straw, and rarely involves the research of forage. Therefore, it is necessary to further expand the research methods of forage crushing, and realize the visualization of forage crushing process by using convenient and economical research methods, so as to facilitate parameter optimization and control.

In this paper, the cooperative forage kneading machine for cutting and kneading was taken as the research object (*Chen et al., 2024*). The flexible alfalfa stem was established through the Hertz-Mindlin with Bonding contact model in EDEM software, the working process of the kneading machine was numerically simulated, and the movement rule of alfalfa stem in the kneading machine was observed. The mechanical properties of stem particle groups and the power consumption of kneading were studied under different working parameters. The research results can provide a reference for expanding the research methods of grass crushing, and solve the problem that the traditional physical method is difficult to visualize the material movement in the kneading machine.

MATERIALS AND METHODS

Structure and working principle

Cutting and kneading cooperative grass kneading machine is mainly composed of feeding conveyor belt, conveyor chain plate, feeding mechanism, screening mechanism, kneading mechanism, cutting mechanism and other parts. The structure is shown in Fig.1.

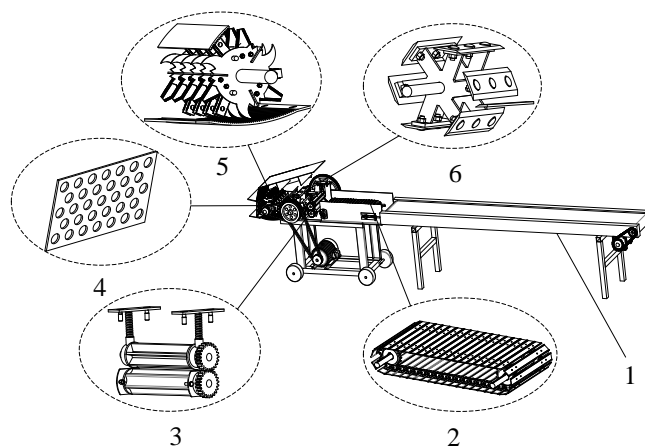


Fig. 1 – Structural diagram of cutting and crushing cooperative forage kneader

1. Feeding conveyor belt; 2. Conveyor chain plate; 3. Feeding mechanism;
4. Screening mechanism; 5. Kneading mechanism; 6. Cutting mechanism

The kneading operation is mainly divided into the following stages: feeding stage, the whole grass is transported to the conveyor chain plate through the feeding conveyor belt, and the grass enters the cutting chamber by rotation of the feed roller. In the cutting stage, the grass is cut into a certain length under the shearing action of the rotating motion of the grass knife and the fixed knife, and the cut grass is pushed to the kneading chamber under the rotation of the grass knife. In the kneading stage, the grass section is broken into filaments under the synergistic action of the hammer and serrated knife, the kneading and tearing between the hammer and serrated knife and the kneading tooth plate, the impact and friction between the sieve plate, etc.

In the screening and sending stage, the broken grass that meets the kneading length is thrown to the outside of the kneading machine through the screen plate under the combined action of the air flow generated by the rotation of the kneading rotor and the centrifugal force. The broken grass that is larger than the kneading length needs is kneaded in the kneading chamber for the next time, and further broken through the same crushing method as the last kneading until the length meets the kneading demand.

Determination of alfalfa stem intrinsic parameters and establishment of discrete element model
Determination of intrinsic parameters

The alfalfa used in the experiment was taken from the grass planting base in Duerbert County, Daqing City, Heilongjiang Province. The collected alfalfa was free from pests and diseases and there was no obvious mechanical damage. The average moisture content of alfalfa was determined by random sampling to be 78.4%. The stems were divided into root, middle and neck, and 100 mm stems were randomly intercepted as test materials. The diameter and length of the sample were measured using a digital display vernier caliper with an accuracy of 0.01 mm, and the distribution of stem samples and diameters was shown in Fig. 2.

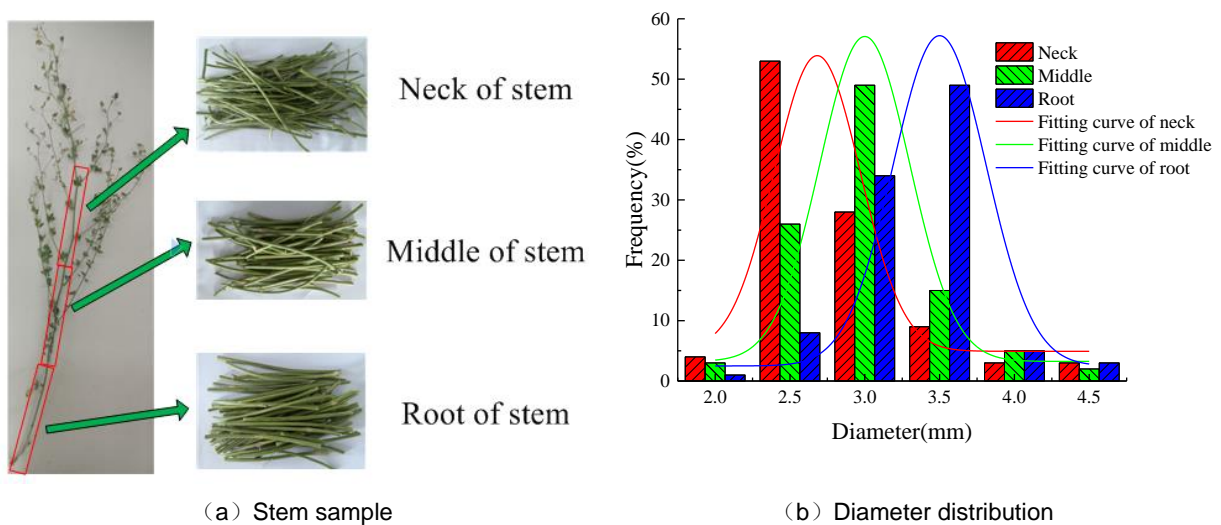


Fig. 2 - The sample and diameter distribution of alfalfa stem

The average diameter and length of alfalfa stem root were 3.24 mm and 128.47 mm respectively. The average diameter in the middle is 3.13 mm and the length is 142.73 mm. The average diameter of the neck is 2.87 mm and the length is 151.12 mm.

Contact model

In this study, the discrete element simulation model of alfalfa stem adopts the Hertz-Mindlin with bonding contact model. In this model, two adjacent particles are connected by Bonding bond, and both ends of the bond are fixed on the connected spherical particles. The end of the bond can be deformed with the movement of the spherical particle, such as elongation, bending and torsion (Wang et al., 2020; Zhang et al., 2023; Xie et al., 2023; Liu et al., 2022). In the simulation, the fracture of bond was used to simulate the breaking process of alfalfa stem. The established alfalfa stem discrete element flexible model is shown in Fig. 3.

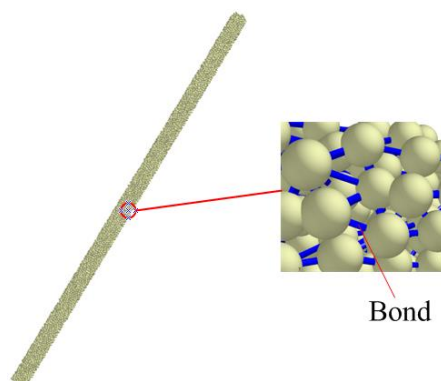


Fig. 3 - Alfalfa stem discrete element flexible model

Simulation parameter

According to the team's previous research results (*Chen et al., 2023*), the discrete element simulation parameters of alfalfa stem are shown in Table 1.

Table 1

Simulation parameters of alfalfa stem

Parameter class	Name	Numerical value
Intrinsic parameters	Poisson ratio of alfalfa stem	0.45
	Poisson's ratio of steel plates	0.30
	Clover stem shear modulus / MPa	17.5
	Shear modulus of steel plate / Pa	7.94×10^{10}
	Alfalfa stem density / ($\text{kg} \cdot \text{m}^{-3}$)	996
	Steel plate density / ($\text{kg} \cdot \text{m}^{-3}$)	7850
Contact parameter	Alfalfa stem - alfalfa stem collision recovery coefficient	0.44
	Alfalfa stem - alfalfa stem static friction factor	0.39
	Alfalfa stem - alfalfa stem rolling friction factor	0.13
	Collision recovery coefficient of alfalfa stem and steel plate	0.5
	Static friction factor of alfalfa stem and steel plate	0.5
	Alfalfa stem and steel plate rolling friction factor	0.2
Bonding parameter	Normal contact stiffness / ($\text{N} \cdot \text{m}^{-1}$)	3.57×10^9
	Tangential contact stiffness / ($\text{N} \cdot \text{m}^{-1}$)	4.01×10^8
	Critical normal stress / Pa	3.5×10^6
	Critical tangential stress / Pa	2.95×10^6
	Bonding radius / mm	0.5

Numerical simulation of kneading and crushing process

Simulation model

The 3D model of the kneading device was established in SolidWorks software. In order to improve the simulation efficiency, the simplified kneading device mainly includes feeding conveyor belt, conveying chain plate, feeding roller, cutting mechanism, kneading mechanism, screen plate, etc., which was saved as igs format and imported into EDEM 2020 software. The simulation model is shown in Fig. 4.



Fig. 4 - Simulation model of guillotine cutting and crushing cooperative forage kneading machine

RESULTS AND DISCUSSIONS

Analysis of movement state of alfalfa stem

The motion state of alfalfa stem during the kneading process in the simulation model was analyzed. At 0.3 s, the stems begin to be transported to the conveyor chain plate of the kneading machine, as shown in Fig. 5 (a). At 0.5 s, the stems begin to be transferred to the feed roller, as shown in Fig. 5 (b). At 0.8 s, the stem begins to be transported to the cutting chamber, as shown in Fig. 5(c). At 1.4 s, the cut alfalfa segment begins to be pushed to the kneading chamber, as shown in Fig. 5 (d). At 2 s, stems that meet the kneading length are thrown out of the body through the sieve plate, as shown in Fig. 5(e). At 2.6 s, the stems are all fed into the kneading machine, as shown in Fig. 5 (f).

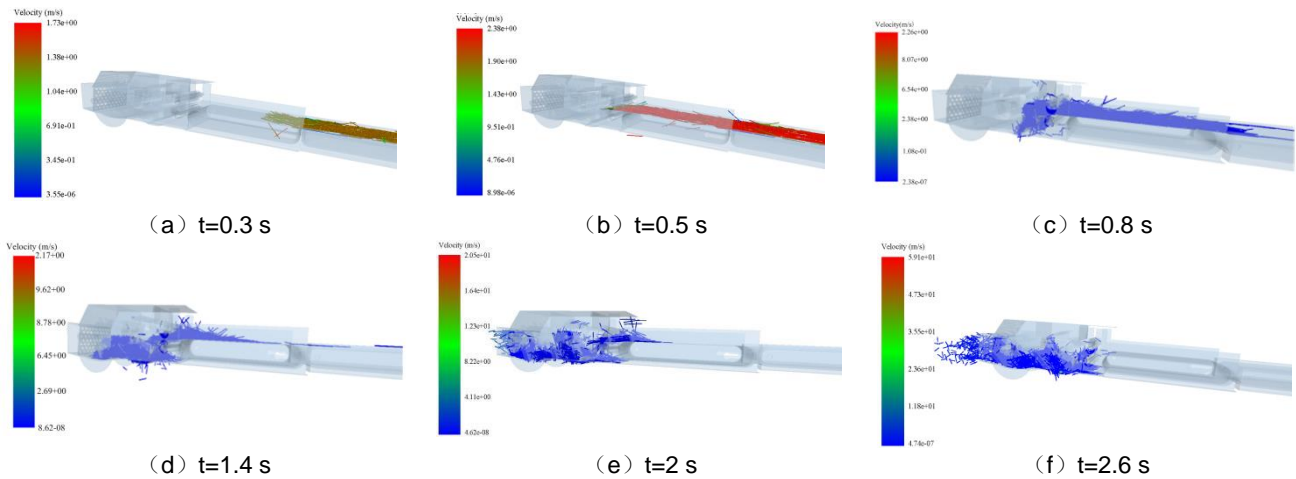


Fig. 5 - Alfalfa stem movement at different time

Change analysis of bond quantity

When the alfalfa stem model is broken, the bond between particles will be damaged and disconnected (Liu et al., 2019; Leblicq T. et al., 2016; Liu et al., 2020). At present, it is difficult to make quantitative statistics on the length of the material and the number of bonds contained after kneading. Therefore, this paper evaluated the effect of kneading machine crushing alfalfa stem by calculating the change of the number of all bonds in the domain.

In order to study the influence of rotor speed on the kneading effect, simulation was carried out under the motor output speed of 100 r/min, 200 r/min, 300 r/min, 400 r/min and 500 r/min respectively. According to the transmission ratio designed by the machine, the corresponding cutting shaft speed is 47 r/min, 94 r/min, 141 r/min, 188 r/min, 235 r/min; kneading shaft speed is 130 r/min, 260 r/min, 390 r/min, 520 r/min, 650 r/min; The effect of rotor speed on the number of bonds is shown in Fig. 6.

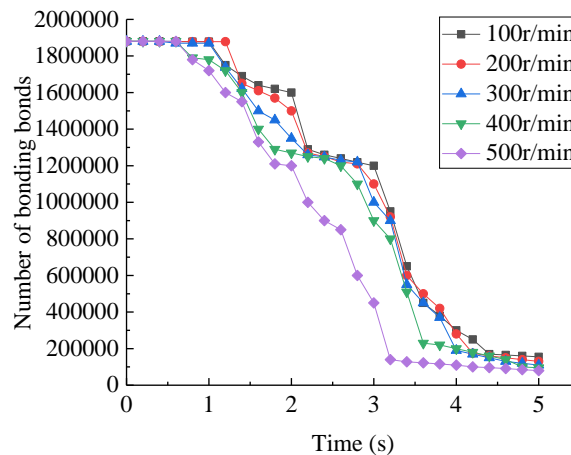


Fig. 6 - The number of bonds varies under different motor output speed

It can be seen from the Figure 6, that when $t=0\sim 0.5$ s, the stem is in the transport process, and the number of bonds remains unchanged. When $t=0.5\sim 1.5$ s, the stem is in the stage of cutting, and the bond gradually decreases at each speed, and the number of bonds decreases faster the higher the speed. From $t=1.5\sim 4$ s, the number of bonds began to decrease sharply at each speed, indicating that the stem entered the kneading chamber and began to be kneaded. At this stage, the speed has a great influence on the change of the bond, and the obvious difference can be seen. The material in the kneading chamber is stable for $4\sim 5$ s, and the number of bonds basically remains unchanged. Through the analysis of the change of the number of bonds at different rotational speeds, it can be seen that with the increase of rotational speed, the kneading efficiency will also accelerate.

Material quantity analysis in kneading machine

In the EDEM software, three monitoring areas (I , II , III) were established, as shown in Fig. 7, and the total number of alfalfa stems flowing through each interval was recorded, so as to calculate the change of the amount of materials at the cutting chamber, the kneading chamber and the discharge port with time at different rotating speeds.

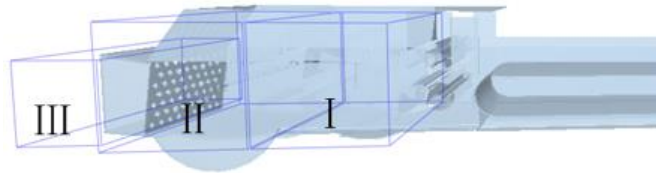


Fig. 7 - Material quantity monitoring area

Guillotine cutting chamber

The change of stem quantity in the cutting chamber under different rotation speed of the cutting shaft is shown in Fig. 8.

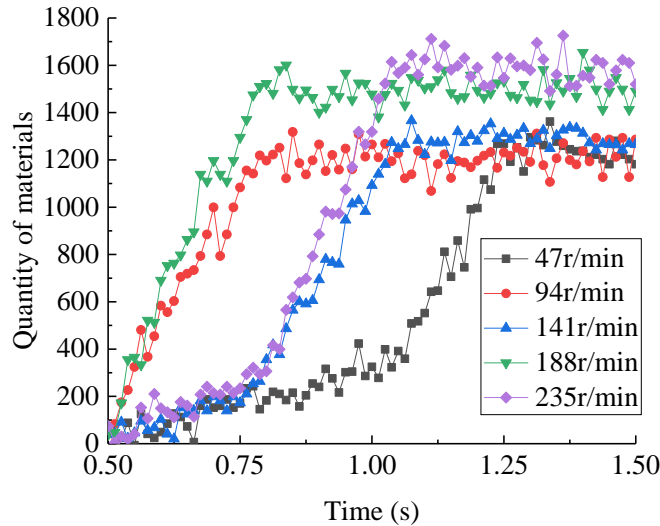


Fig. 8 – The number of stem in the cutting chamber with time

It can be seen from the figure that the number of stem in the cutting chamber under different cutting shaft speeds increases rapidly and shows a stable trend. After the number of stems was stabilized, the average number of stems in the knead chamber with the rotating speed of 47 r/min, 94 r/min, 141 r/min, 188 r/min and 235 r/min was 1085, 1170, 1224, 1532 and 1621, respectively, and then began to fluctuate around this number. The results showed that with the increase of the rotation speed of the cutting shaft, the number of stem cut in the cutting chamber in unit time also increased.

Kneading chamber

The changes in the amount of materials in the kneading chamber under different kneading shaft speeds are shown in Fig. 9.

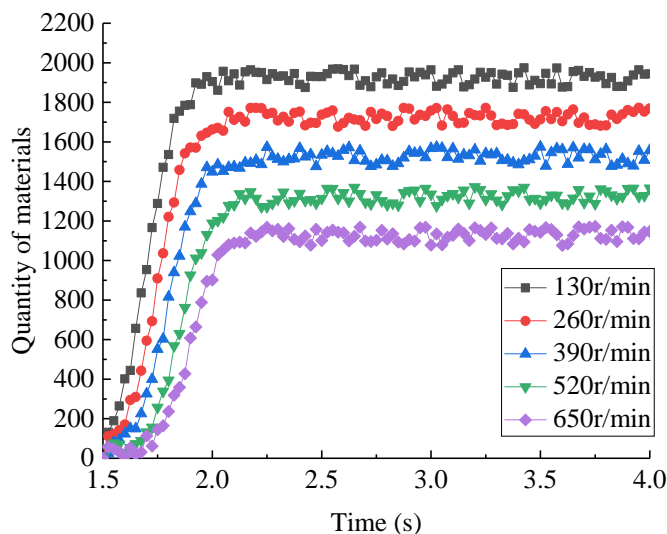


Fig. 9 - The number of stems in the kneading chamber changes with time

It can be seen from Fig. 9 that the number of stems in the kneading chamber increases rapidly and then shows a stable trend under different kneading shaft rotation speeds. After the number of stems was stabilized, the average number of stems in the knead chamber at 130 r/min, 260 r/min, 390 r/min, 520 r/min and 650 r/min were 1168, 1252, 1435, 1652 and 1836, respectively, and then began to fluctuate around this number. The results show that the amount of kneading machine per unit time increases with the increase of the rotational speed of the kneading shaft. The movement trajectory of the stem in the kneading chamber is shown in Fig. 10.

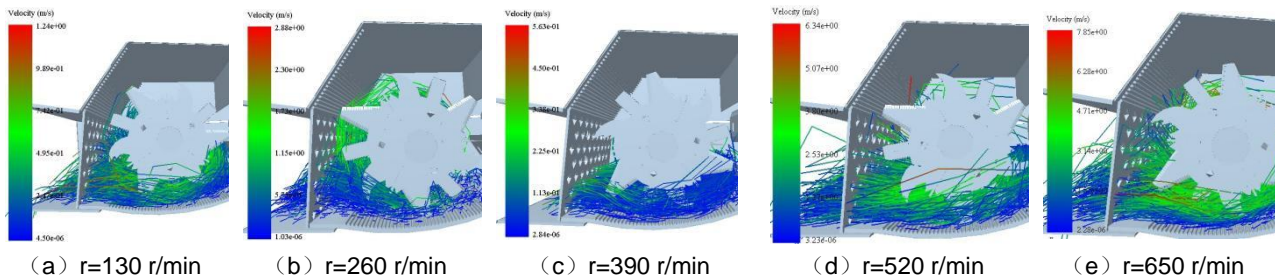


Fig. 10 - Stem movement trajectory in the kneading chamber

Discharge gate

The change of the number of broken stems at the discharge port over time is shown in Fig. 11.

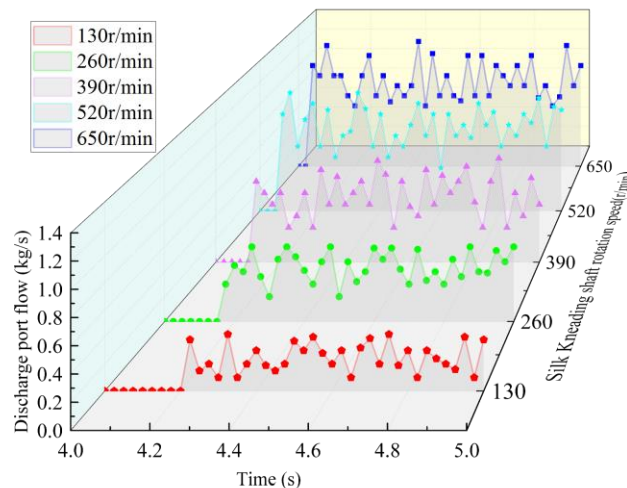


Fig. 11 - Changes in the quantity of materials at the discharge port over time

As can be seen from the figure, as the rotational speed of the kneading shaft increases, the number of broken stems at the discharge port also increases. When the rotational speed is lower than 260 r/min, due to the low interaction frequency between the stems and the kneading parts in unit time, the number of stems entering the kneading chamber in unit time is less, and the stems cannot be fully kneaded in a short time and cannot be timely screened, so the number of broken stems at the discharge port is less.

At 390 r/min, the stems can be broken in time, and there is almost no secondary kneading and circulation phenomenon. The silked stems can be stable and pass through the sieve, so the number of broken stems at the discharge port increases. When the rotational speed is higher than 520 r/min, due to the large centrifugal force on the stem, some of the longer stems that have not been fully kneaded are also directly discharged at the discharge port, so the amount of material at the discharge port increases significantly.

Mechanical analysis of stem particle group

Because there is only shear breakage for the alfalfa stem in the cutting chamber, the stress of the stem is relatively simple. However, in the kneading chamber, the stems are broken in various forms such as hitting, rubbing and impact, and the stress situation of the stems is more complicated (Hu et al., 2020; Zhu et al., 2022). Therefore, it is necessary to analyze the stress situation of the stem particle groups in the kneading chamber.

Analysis of stem energy change

The stem energy includes stem kinetic energy and potential energy. The influence of rotating speed of kneading axis on average stem energy is shown in Fig. 12.

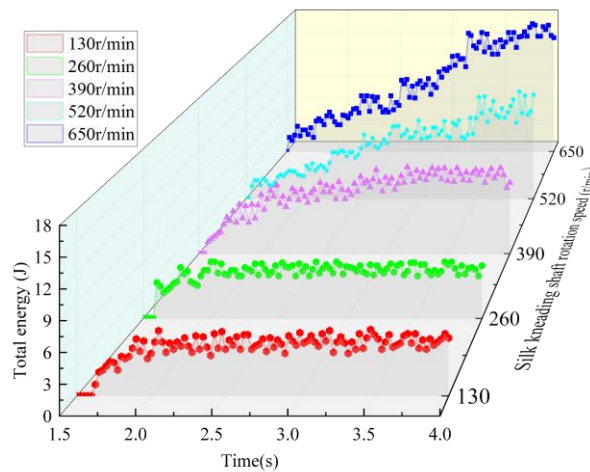


Fig. 12 - Effect of rotating speed of kneading shaft on average energy of stem

As can be seen from the figure, the average stem energy in the kneading chamber showed a trend of fluctuation and increase with the increase of the rotational speed of the kneading shaft. The average stem energy did not change significantly when the spindle speed increased from 130 r/min to 260 r/min. The average stem energy increased significantly when the spindle speed increased from 260 r/min to 650 r/min. The difference between the mean energy of stems at 390 r/min and that at 520 and 650 r/min increased with time.

Mean stem to stem interaction force

The influence of rotating speed of the kneading shaft on the average force between stems is shown in Fig.13.

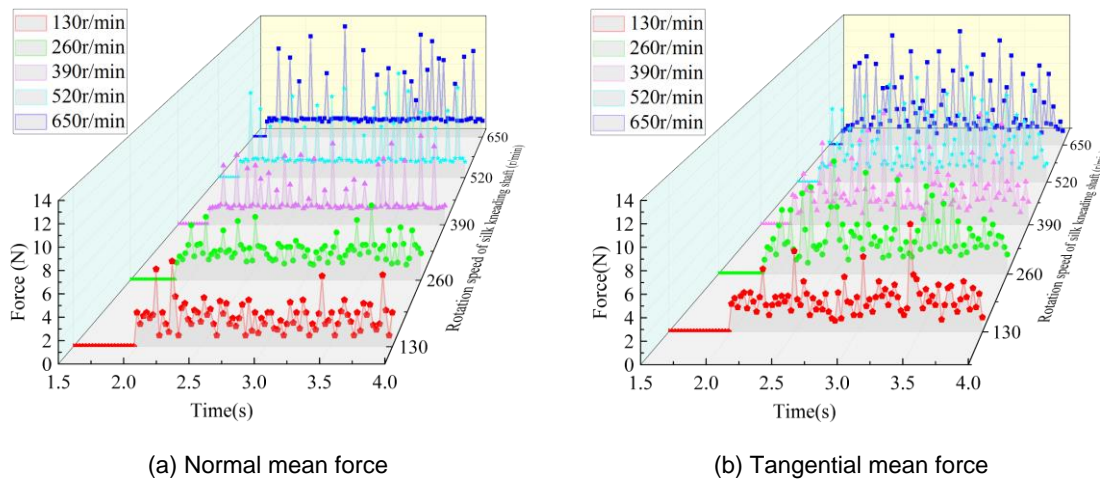


Fig. 13 - Effect of rotating speed of kneading shaft on average stem to stem force

As can be seen from the figure, the average stem to stem interaction force fluctuated sharply, and the fluctuation amplitude increased with the increase of the rotational speed of the kneading shaft. When the rotating speed of the kneading shaft was 130 r/min, 260 r/min, 390 r/min, 520 r/min and 650 r/min, the maximum normal forces of stem to stem could reach 7.2 N, 7.5 N, 9.3 N, 11.8 N and 13.5 N respectively. The maximum tangential mean force can reach 9.6 N, 10.9 N, 11.6 N, 12.9 N and 13.6 N respectively. The fluctuation of the average stem to stem interaction force is related to the random movement of a large number of stems in the kneading chamber, and the collision between the stems has a great influence on the movement of the stems in the kneading chamber. On the other hand, the increase of the rotational speed of the kneading shaft increases the energy of the stem, leading to the intensification of the collision between the stem, thus accelerating the energy loss of the stem itself, which is not conducive to the smooth screening of the stem.

Mean stem to sieve plate interaction

The influence of the rotating speed of the kneading shaft on the average force of the stem to sieve plate is shown in Fig. 14.

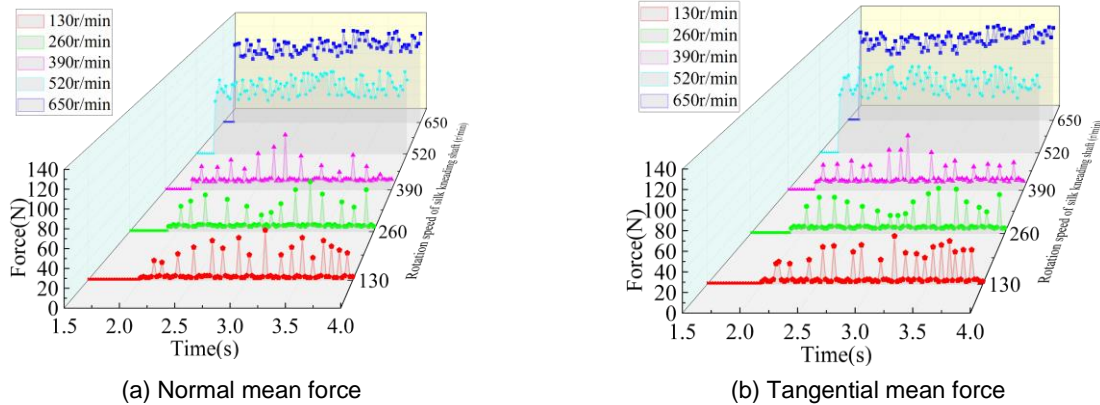


Fig. 14 - Effect of the rotational speed of the wire kneading shaft on the average force between the crushing rod and sieve plate

As can be seen from the figure, the average force of stem to sieve plate at different kneading shaft speeds all showed a fluctuating state after increasing from zero to a certain range. At 130 r/min, 260 r/min, 390 r/min, the mean interaction force of stem and sieve plate fluctuated sharply, and the maximum normal interaction force reached 53, 57, 68 N, and the maximum tangential interaction force reached 49, 50, 65 N, respectively. The fluctuation intensity of the average interaction force at 520 and 650 r/min is smaller than that at 130~390 r/min, and the maximum normal average interaction force can reach 110 and 130 N, and the maximum tangential average interaction force can reach 110 and 129 N, respectively. The increase of the rotational speed of the kneading shaft intensifies the collision between the stem and the sieve plate, resulting in a large amount of loss of the stem energy in the collision. Therefore, the rotational speed of the kneading shaft is not easy to be too fast under the premise of satisfying the quality of the kneading wire. The high-speed rotating hammer collides with the alfalfa section, thus providing the power for the alfalfa section to move. However, the collision between the alfalfa segment and the kneading chamber shell will consume the kinetic energy of the alfalfa segment. Therefore, in this paper, a serrated knife is installed on the kneading rotor of the cooperative grass kneading machine, which forms a staggered arrangement with the hammer in the axis to improve the distribution density of the kneading parts, so that it covers more kneading space in the work, and increases the frequency of interaction between the stem and the kneading parts per unit time. In order to increase the collision between the alfalfa segment and the kneading parts, and reduce the collision between the alfalfa segment and the kneading chamber shell, it is more beneficial to the movement of the alfalfa segment.

Influence of different parameters on power consumption

Effect of rotational speed on power consumption

The influence of rotation speed on power consumption is shown in Fig. 15.

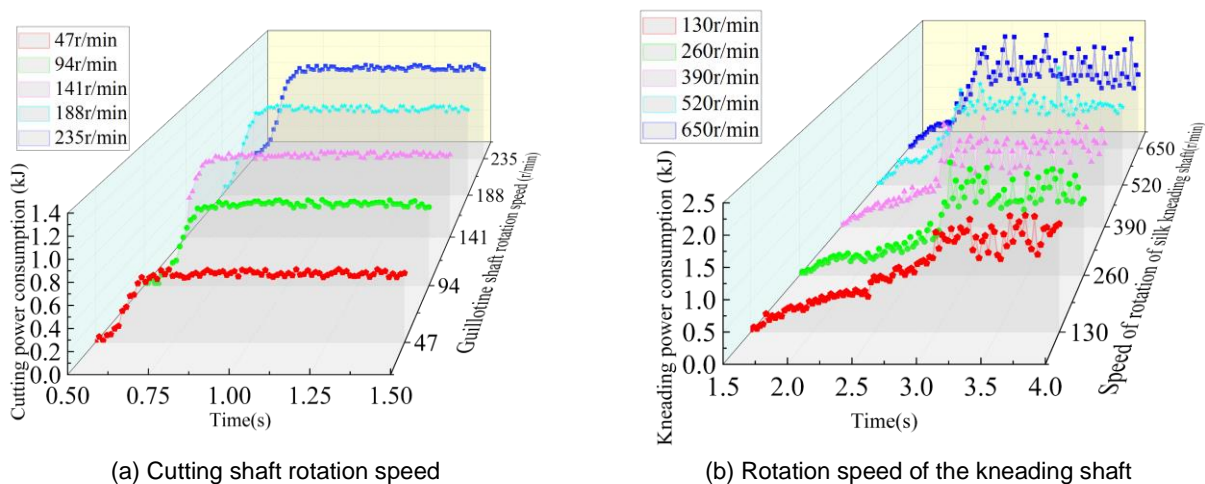


Fig. 15 - Influence of rotational speed on power consumption

As can be seen from the figure, the fluctuation of the kneading power consumption is more severe than the cutting power consumption. Cutting power consumption and kneading power consumption are increased with the increase of rotor speed, the reason is that the speed increases, the number of interactions between the mechanical parts and the stem per unit time increases, and the power consumption increases. When the speed of the kneading shaft is lower than 260 r/min, the power consumption increases slowly, and when the speed reaches 390 r/min, the power consumption increases sharply, because the stem and the rotor rotate at the same speed, forming a material circulation layer, and the torque required for high speed is also greater. When the cutting shaft speed is 47, 94, 143, 188, 235 r/min, the average power consumption is 0.56, 0.71, 0.84, 0.94, 1.08 kJ, and the maximum is 0.66, 0.84, 0.91, 1.02, 1.14 kJ, respectively. When the rotating speed of the kneading shaft is 130, 260, 390, 520 and 650 r/min, the average power consumption of the kneading shaft is 1.39, 1.54, 1.76, 1.89 and 2.05 kJ, respectively, and the maximum power consumption is 1.89, 1.98, 2.06, 2.38 and 2.46 kJ, respectively.

Influence of feeding amount on power consumption

The influence of feeding amount on power consumption is shown in Fig. 16.

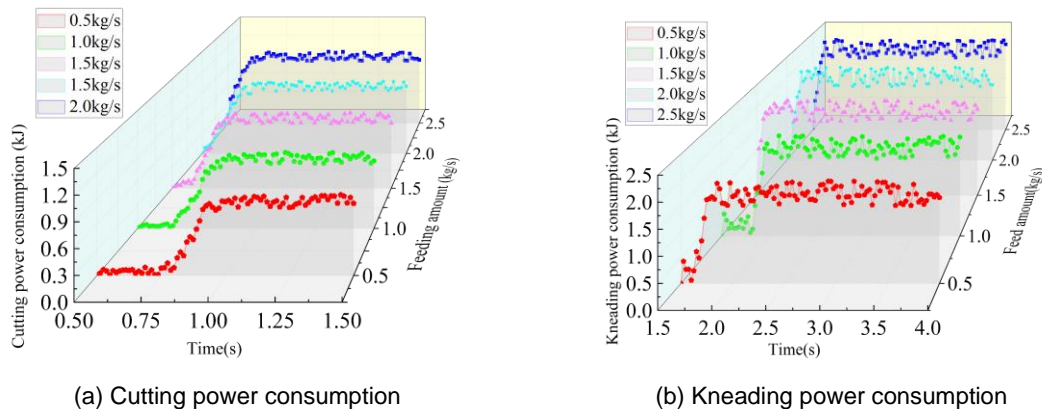


Fig. 16 - Influence of feeding amount on power consumption

It can be seen from the figure that with the increase in the amount of feeding, the cutting power consumption and kneading power consumption are increased, the reason is that with the increase in the amount of feeding, the number of stems in the cutting chamber increases, the density of the stems in the cutting chamber and the kneading chamber increases, the impact force increases, the impact resistance of the cutting knife and the hammer increases, the friction between the stems leads to an increase in resistance, the number of collisions increases, resulting in an increase in power consumption. When the feeding amount is the same, the fluctuation of the kneading power consumption is more severe than that of the guillotine power consumption. When the feeding amount is 0.5, 1.0, 1.5, 2.0, 2.5 kg/s, the average power consumption of cutting is 0.57, 0.68, 0.81, 0.88, 0.99 kJ, and the maximum power consumption is 0.94, 0.97, 1.03, 1.06, 1.12 kJ, respectively. The average power consumption of kneading is 1.60, 1.61, 1.87, 1.98, 2.09 kJ, and the maximum power consumption is 1.97, 2.10, 2.13, 2.25, 2.32 kJ, respectively.

Bench test

The bench performance test was carried out on the self-developed kneading test bench, and the test was carried out in the crop harvest Laboratory of Heilongjiang Bayi Agricultural University, as shown in Fig. 17.



Fig. 17 - Test site

1. Power consumption test device 2. Kneading machine 3. Feeding conveyor belt

Experimental design

The evaluation indicators are calculated as follows:

Silk rates

Samples were collected at the outlet, at the same time interval for 3 times, each time no less than 200 g. All samples were mixed and weighed. Qualified alfalfa silk was screened and weighed, and its silk rate was calculated as:

$$W_h = \frac{m_1}{m_0} \times 100\% \quad (1)$$

where: m_1 is quality of alfalfa silk in the sample, g; m_0 is alfalfa sample quality, g.

Power consumption

The power consumption is determined by the DYN-200 torque power sensor installed on the motor spindle. After each group of tests, the instantaneous torque, power and required time measured by the sensor are derived through the torque measurement system, and the instantaneous power of the effective working period is calculated to obtain the kneading power consumption. The calculation formula is as follows:

$$W_z = \int P(t) dt_z \quad (2)$$

where: W_z is kneading power consumption, kJ; $P(t)$ is instantaneous power, kW; t_z is kneading time, s.

Test results and analysis

In the range of output speed 100~500 r/min and feed rate 0.5~2.5 kg/s, two-factor and five-level quadratic rotation orthogonal combination tests were carried out. The regression equation and optimization model between test factors and evaluation indexes are established by using Design-Expert 12.0 software. Factor coding is shown in Table 2. x_1 and x_2 are factor coding values, and the values in brackets in the table are rounded results according to actual operation requirements.

Table 2

Coding	Factor	
	Motor output speed x_1 (r/min)	Feeding quantity x_2 (kg/s)
1.414	500	2.5
1	441.44 (440)	2.21 (2.2)
0	300	1.5
-1	158.56 (160)	0.79 (0.8)
-1.414	100	0.5

The test scheme and results are shown in Table 3.

Table 3

Test scheme and results				
Number	Motor output speed x_1 (r/min)	Feeding quantity x_2 (kg/s)	Silk rate W_h (%)	Power consumption W_z (kJ)
1	-1	-1	90.49	3.31
2	1	-1	90.31	2.99
3	-1	1	97.27	4.26
4	1	1	91.97	3.88
5	-1.414	0	91.36	3.92
6	1.414	0	90.96	3.16
7	0	-1.414	89.67	3.37
8	0	1.414	96.37	4.21
9	0	0	92.26	3.38
10	0	0	92.18	3.35
11	0	0	91.07	3.36
12	0	0	91.28	3.26
13	0	0	91.41	3.48

The results of variance analysis of silk rate and power consumption are shown in Table 4 and Table 5 respectively.

Table 4

Analysis of variance of silk rate

Source of variance	Sum of squares	Degree of freedom	Mean sum of squares	F	P
Model	56.04	5	11.21	16.73	0.0009**
x_1	4.57	1	4.57	6.82	0.0348*
x_2	40.12	1	40.12	59.89	0.0001**
x_1x_2	6.55	1	6.55	9.78	0.0167*
x_1^2	0.13	1	0.13	0.19	0.6766
x_2^2	4.4	1	4.4	6.56	0.0374*
Residual error	4.69	7	0.67		
Lack of fit	3.51	3	1.17	3.95	0.1089
Error	1.18	4	0.3		
Sum total	60.73	12			

As can be seen from the table, the silk rate regression model ($P=0.0009$) is significant, while the loss of fit term ($P=0.1089$) is not, indicating that the model has a good degree of fitting and no loss of fit phenomenon occurs. The determination coefficient $R^2=0.9228$, the correction determination coefficient $R_{adj}=0.8676$, which is very close to 1, and the coefficient of variation is 0.89%, indicating that the test data is reliable. There is a significant relationship between the predicted value of the regression equation and the actual value obtained through the analysis of the test results. The regression equation of each factor and evaluation index obtained is shown as follows:

$$W_h = 91.64 - 0.76x_1 + 2.24x_2 - 1.28x_1x_2 - 0.14x_1^2 + 0.8x_2^2 \tag{3}$$

Table 5

Analysis of power consumption variance

Source of variance	Sum of squares	Degree of freedom	Mean sum of squares	F	P
Model	1.83	5	0.37	25.25	0.0002**
x_1	0.39	1	0.39	27.16	0.0012**
x_2	1.15	1	1.15	79.06	< 0.0001**
x_1x_2	0.0009	1	0.0009	0.062	0.8104
x_1^2	0.037	1	0.037	2.57	0.1526
x_2^2	0.27	1	0.27	18.86	0.0034**
Residual error	0.1	7	0.014		
Lack of fit	0.077	3	0.026	4.14	0.1018
Error	0.025	4	0.006		
Sum total	1.93	12			

As can be seen from the table, the power regression model ($P=0.0002$) is significant, while the loss of fit term ($P=0.1018$) is not, indicating that the model has a good degree of fitting and no loss of fit phenomenon occurs. The determination coefficient $R^2=0.9475$, the correction determination coefficient $R_{adj}=0.9099$, which is very close to 1, and the coefficient of variation is 2.99%, indicating that the test data is reliable. There is a significant relationship between the predicted value of the regression equation and the actual value obtained through the analysis of the test results. The regression equation of each factor and evaluation index obtained is shown as follows:

$$W_z = 3.87 - 0.22x_1 + 0.38x_2 - 0.02x_1x_2 - 0.07x_1^2 + 0.2x_2^2 \tag{4}$$

Parameter optimization and test verification

Design-Expert 12.0 software Optimization module was used to optimize the model with the goal of maximizing the silk rate and minimizing the power consumption, and the optimization mathematical model was established through the analysis.

$$\begin{cases} \max W_h(x_1, x_2) \\ \min W_z(x_1, x_2) \\ s.t. \begin{cases} -1.414 \leq x_1 \leq 1.414 \\ -1.414 \leq x_2 \leq 1.414 \end{cases} \end{cases} \quad (5)$$

The optimal parameter combination of the kneading machine is obtained as follows: when the output speed of the motor is 282.88 r/min and the feeding amount is 1.86 kg/s, the spinning rate is 93.13% and the power consumption is 3.63 kJ. At this time, the maximum value of the comprehensive evaluation index is 0.474, which is the optimal parameter combination, and the comprehensive evaluation response surface is shown in Fig. 18.

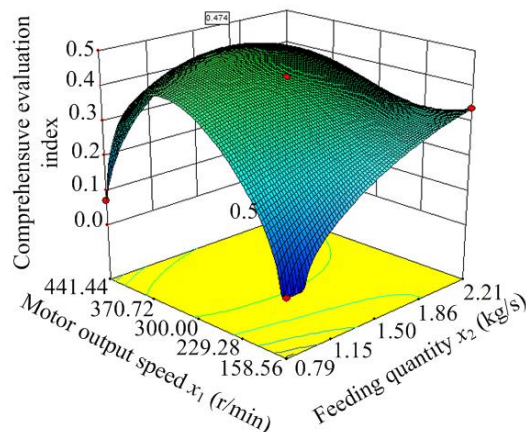


Fig. 18 - Comprehensive evaluation response surface

The bench verification test was carried out according to the optimal parameter combination obtained from the response surface analysis. In order to reduce the error, the test was repeated five times to take the average value, and the test results were as follows: the silk ratio was 92.88%, the power consumption was 3.68 kJ, and the difference between the actual test value and the software analysis value was 0.27% and 1.38%, respectively. The experimental results are close to the optimized values, which proves that the optimized results are accurate and reliable.

CONCLUSIONS

(1) EDEM discrete element simulation software was used to simulate the working process of the kneading machine in different working parameters, and the law of stem movement, mechanical characteristics of stem particle groups and power consumption were analyzed, and the motion and crushing mechanism of the forage in the kneading machine were defined.

(2) The multi-factor test of bench performance was carried out, and the regression model of the spinning rate and power consumption was established. The variance analysis showed that the main and secondary factors affecting the spinning rate and power consumption were the feeding amount and the output speed of the motor.

(3) With the goal of maximizing the silk rate and minimizing the power consumption, the output speed and feeding amount of the motor were optimized by multi-objective solution, and the optimal parameter combination was obtained as follows: when the output speed of the motor was 282.88 r/min and the feeding amount was 1.86 kg/s. The verification test shows that the silk rate is 92.88% and the power consumption is 3.68 kJ, which meets the requirement of high moisture content alfalfa silk kneading.

ACKNOWLEDGEMENT

This work was supported by National Natural Science Foundation of China (52275246) and Heilongjiang Bayi Agricultural University Graduate Innovative Research Project (YJSCX2023-Z02).

REFERENCES

- [1] Chunyong. T. (2019). Effects of different cutting lengths on Whole plant silage corn silage quality and beef cattle weight gain. *Sichuan Animal Husbandry and Veterinary Science*. Vol. 50, Issue 10 pp. 27-29.

- [2] Decheng, W., Changbin, H., Hongjian, W., Yong, Y., & Guanghui, W. (2017). Review of Alfalfa Full-mechanized Production Technology. *Transactions of the Chinese Society for Agricultural Machinery*, Vol. 48, Issue 8, pp. 1-25.
- [3] Defu, W., Mo, W., & Liqiao, L. (2017). Mechanism Analysis and Parameter Optimization of Hammer Mill for Corn stem. *Transactions of the Chinese Society for Agricultural Machinery*, Vol. 48, Issue 11 pp. 165-171.
- [4] Duanyang, G., Xiaodong, M., Yancheng, S., Yangmeng, Z., Huabiao, L., & Huixin, J. (2021). Simulation and Test of Silage Corn Screw Notched Sawtooth Type Crushing Roller. *Transactions of the Chinese Society for Agricultural Machinery*, Vol. 52, Issue 12 pp. 134-141.
- [5] Fengwei, Z., Xuefeng, S., Xuekun, Z., Fangyuan, Z., Wancheng, W. & Fei, D. (2019). Simulation and experiment on mechanical characteristics of kneading and crushing process of corn straw. *Transactions of the CSAE*, Vol. 35, Issue 9, pp. 58-65.
- [6] Gang, P., Zhiping, Z., Yuezheng, L., & Suchuan, S. (2023). Analysis of Coupling Motion Characteristics of Material and Airflow in Multi-function Forage Kneading Machine. *Transactions of the Chinese Society for Agricultural Machinery*, Vol. 54, Issue s2, pp. 156-163.
- [7] Guoqiang, F., Zhongyu, W., Baoxing, W., Jinxing, W., Heyin, D., & Jian, H. (2021). Design and Experiment of Rotary Feed Tube Hammer Grinder. *Transactions of the Chinese Society for Agricultural Machinery*, Vol. 52, Issue 12 pp. 43-53.
- [8] Haijun, Z., Yi, Q. & Haiqing, T. (2024). Design and Experimental Optimization of V-shaped Hammer for Hammer Mill. *INMATEH-Agricultural Engineering*, Vol. 73, Issue 2, pp.191-200.
- [9] Hongcheng, L. (2023). *Study on Influence Mechanism and Optimization of the Hammer Mill Grinding Performance*. WuHan: Huazhong Agricultural University.
- [10] Huibin, Z., Xian, W., Lizhen, B., Cheng, Q., Haoran, Z., & Hui, L. (2022). Development of the biaxial stubble breaking no-tillage device for rice stubble field based on EDEM-ADAMS simulation. *Transactions of the CSAE*, Vol. 38, Issue 19, pp. 10-22.
- [11] Jianping, H., Jun, Z., Haoran, P., Wei, L., & Xingsheng, Z. Prediction (2020). Model of Double Axis Rotary Power Consumption Based on Discrete Element Method). *Transactions of the Chinese Society for Agricultural Machinery*, Vol. 51, Issue s1 pp. 9-16.
- [12] Leblicq T., Smeets B., Vanmaercke S. (2016). A discrete element approach for modelling bendable crop stems. *Computers and Electronics in Agriculture*, 124:141-149.
- [13] Peng, L., Jin, H., Zhiqiang, Z., Caiyun, L., Zhenguo, Z., & Han, L. (2020). Kinematic Characteristic Analysis and Field Test of Chopped stem in Straw Retention Machine Based on CFD-DEM Coupling Simulation Method. *Transactions of the Chinese Society for Agricultural Machinery*, Vol. 51, Issue s1, pp. 244-253.
- [14] Qirui, W., Hanping, M., & Qinglin, L. (2020). Simulation of Vibration Response of Flexible Crop Stem Based on Discrete Element Method. *Transactions of the Chinese Society for Agricultural Machinery*, Vol. 51, Issue 11 pp. 131-137.
- [15] Ruijie, S., Fei, D., Wuyun, Z., Fengwei, Z., Linrong, S., & Junhai, G. (2022). Establishment of Discrete Element Flexible Model and Verification of Contact Parameters of Flax Stem. *Transactions of the Chinese Society for Agricultural Machinery*, Vol. 53, Issue 10, pp. 146-155.
- [16] Tao, C., Shujuan, Y., Yifei, L., Guixiang, T., Shanmin, Q., & Rui, L. (2023). Establishment of Discrete Element Model and Parameter Calibration of Alfalfa Stem in Budding Stage. *Transactions of the Chinese Society for Agricultural Machinery*, Vol. 54, Issue 5 pp. 91-100.
- [17] Tao, C., Shujuan, Y., Yifei, L., Guixiang, T., Xin, M., & Shanmin, Q. (2024). Design and Test of Cutting and Crushing Cooperative Silk Kneading Machine. *Transactions of the Chinese Society for Agricultural Machinery*, Vol. 55, Issue 5 pp. 149-159.
- [18] Tao, Z., Fei, L., Manquan, Z., Qi, F., & Peng, Y. (2018). The Motion Law of Indoor Straw Swarm at Different Rotational Speeds Based on Discrete Element Method. *Agricultural Mechanization Research*, Vol. 40, Issue 9, pp. 195-19.
- [19] Wei, X., Lei, P., Pin, J., Dexin, M., & Xiushan, W. (2023). Discrete Element Model Building and Optimization of Double-layer Bonding of Rape Shoots Stems at Harvest Stage. *Transactions of the Chinese Society for Agricultural Machinery*, Vol. 54, Issue 5, pp. 112-120.
- [20] Weigang, L. (2019). Analysis of straw crushing characteristics and optimization of crushing equipment structure. Guiyang: Guizhou University.

- [21] Xirui, Z., Xuhang, H., Junxiao, L., Youming, Y., & Yue, L. (2023). Calibration and Verification of Bonding Parameters of Banana Straw Simulation Model Based on Discrete Element Method. *Transactions of the Chinese Society for Agricultural Machinery*, Vol. 54, Issue 5, pp. 121-130.
- [22] Yanbin, L., Yaoming L., & Tao Z. (2022). Effect of concentric and non-concentric threshing gaps on damage of rice straw during threshing for combine harvester. *Biosystems Engineering*, Vol. 219, pp.1-10.
- [23] Yonggang, K., Yunqiong, L., & Guangqin, Z. (2021). Effects of kneaded Corn Straw microstorage on Growth Performance, Organ index and Blood Biochemical Indexes of Xuhuai Goats. *China Feed*, Vol. 17, pp.129-134.
- [24] Zhiwei, Z., Xu, M., Xiulong, C., Zehua, L., & Xicheng, W. Critical (2021). Review of Applications of Discrete Element Method in Agricultural Engineering. *Transactions of the Chinese Society for Agricultural Machinery*, Vol. 52, Issue 4, pp. 1-20.

CALIBRATION OF DISCRETE ELEMENT SIMULATION PARAMETERS FOR BUCKWHEAT SEEDS

荞麦种子离散元仿真参数标定

Yulong CUI^{1,2)}, Shaobo YE^{1,2)}, Shuai FENG^{1,2)}, Decong ZHENG^{1,2)}

¹⁾ College of Agricultural Engineering, Shanxi Agricultural University, Taigu 030801, China;

²⁾ Dryland Farm Machinery Key Technology and Equipment Key Laboratory of Shanxi Province, Taigu 030801, China

Corresponding author: Shaobo Ye

Tel: +86-152-3435-5087; E-mail: yes@sxau.edu.cn

DOI: <https://doi.org/10.35633/inmateh-75-09>

Keywords: Buckwheat; Parametric calibration; Discrete element; Angle of repose

ABSTRACT

To address the challenge of parameter accuracy in discrete element method (DEM) simulations of buckwheat seeds within a seed metering device, this study characterized the physical properties of buckwheat seeds and subsequently calibrated the simulation model parameters. Initially, physical experiments were conducted to determine the triaxial dimensions, angle of repose, and static friction coefficients of buckwheat seeds against stainless steel surfaces. A three-dimensional model of the buckwheat seeds was then generated using Inventor and it was imported into EDEM to simulate the seed stacking process, with the angle of repose quantified via image processing techniques. Employing a Plackett-Burman design, initial parameters were screened, identifying the static friction coefficient between buckwheat seeds, the rolling friction coefficient between buckwheat seeds, and the static friction coefficient between buckwheat seeds and stainless steel as significant factors influencing the angle of repose. The optimal range for these significant parameters was determined through a steepest ascent experiment, and a second-order regression model was developed using Box-Behnken experimental results to optimize the angle of repose and the identified parameters. The optimized parameter set comprised a static friction coefficient between buckwheat seeds and stainless steel of 0.448, a rolling friction coefficient between buckwheat seeds of 0.038, and a static friction coefficient between buckwheat seeds of 0.372. Validation through both simulations and physical experiments revealed a relative error of 1.08%, confirming the reliability of the calibrated parameters for simulating buckwheat seed sowing machinery.

摘要

针对荞麦种子在排种器中进行离散元排种仿真模拟试验缺乏准确参数的问题,本研究对荞麦种子进行物性参数测定及仿真模型参数标定。首先,通过物理试验测定荞麦种子的三轴尺寸,休止角以及荞麦种子与不锈钢板间静摩擦系数。其次,运用 Inventor 绘制荞麦种子的三维模型,并导入到 EDEM 中建立荞麦离散元模型,来模拟荞麦种子的堆积过程,通过图像处理技术,获得准确的休止角。通过 Plackett-Burman 试验对初始参数进行筛选,得出荞麦间静摩擦系数、荞麦间滚动摩擦系数、荞麦-不锈钢之间的静摩擦系数对颗粒堆休止角影响显著。最后在最陡爬坡试验确定显著性参数最优值区间的基础上,根据 Box-Behnken 试验结果建立了休止角与显著性参数的二阶回归模型并对其进行优化,得到显著性参数的最佳组合。通过试验得出荞麦-不锈钢静摩擦系数为 0.448、荞麦间滚动摩擦系数为 0.038、荞麦间静摩擦系数为 0.372。通过仿真与物理试验对比验证,得到二者相对误差为 1.08%,标定参数可为荞麦播种机械仿真提供数据依据。

INTRODUCTORY

Buckwheat is one of the small grains native to China, planted area of about 850,000 hm², accounting for approximately one-third of the world's planted area. The average annual production is about 980,000 tons, ranking second globally (Wu L.G. et al., 2018). Buckwheat is valued for its unique functional components and high nutritional value, attracting increasing global attention. However, the level of mechanization in buckwheat sowing remains relatively low worldwide. In China's alpine and hilly regions, where buckwheat planting is extensive, mechanized harvesting is limited. Available models are scarce, and harvest quality is poor. Even in northern regions with higher mechanization levels, temporary modifications of other crop sowing machines are commonly used. These adaptations complicate interactions between seeds, seed dischargers, and machine components. Analysis using the discrete element method (DEM) allows for a detailed understanding of these interactions and facilitates the design and optimization of related equipment and process parameters (Zeng Z.W. et al., 2021).

Previous studies have calibrated DEM parameters for materials such as coal dust, cereal seeds, corn, potatoes, and garlic. *Zhang Rui et al., (2017)*, calibrated the contact parameters of sand and soil using standard and non-standard ball methods, and investigated whether different quality of sand and soil with different calibration methods would affect the results of stacking angle as well as the contact parameters. *Li Yong Xiang and others, (2019)*, simplified irregularly shaped wheat flour particles into soft spherical ones and scaled them, selected the “Hertz - Mindlin with JKR” contact model, and used the angle of repose to calibrate the contact parameters. *Wang Chengjun et al., (2012)*, determined the elastic properties of wheat and investigated the effects of collision material, material thickness, drop height and wheat moisture content on the coefficient of recovery of wheat, and determined the significance ranking of the effects of each factor on the coefficient of recovery of wheat for Q235 collision material. *Wu Jia Sheng et al., (2019)*, used the cylinder stacking method with EDEM simulation and combined with image processing technology to determine the stacking angle of forenut seeds, and calibrated the physical parameters of forenut seeds based on the response surface optimization method, *Liu Wen Zheng et al., (2018)*, optimized and calibrated potato parameters by combining physical and simulation tests. *González-Montellano et al., (2012)* studied maize and olive and obtained large CV (coefficient of variation) values for seeds at different collision velocities by means of a collision recovery test, which showed that in most cases the CV values were determined by the nature of the seeds themselves. In summary, it can be seen that most of the discrete element simulation calibration are powder, corn, seeds and large objects, and there is little content on the determination and calibration of discrete element simulation parameters of buckwheat grains.

This study combines physical and simulation tests to calibrate nine parameters for buckwheat grains. Physical test values were used as input ranges for Plackett-Burman, steepest climb, and Box-Behnken experiments. The results provide data support for future DEM simulations of buckwheat sowing machinery, enhancing simulation accuracy.

MATERIALS AND METHODS

Static friction angle measurement test

The static friction coefficient of buckwheat seeds represents the maximum static friction force divided by the normal force during contact. Seed surface roughness primarily determines this coefficient—greater roughness increases the coefficient and reduces seed movement tendency. The test apparatus is shown in Fig. 1. The oblique plane method was used to measure the static friction coefficient. The angle θ was gradually increased until the seeds began to slide, at which point θ was recorded.

The static friction coefficient μ was calculated using Eq. 1 (*Li et al., 2023*).

$$\mu = \frac{f}{N} = \frac{mg\sin\theta}{mg\cos\theta} = \tan\theta \quad (1)$$

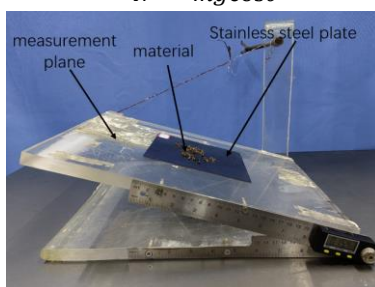


Fig. 1 - Static friction measurement

Based on the measured data, the angle of static friction between the buckwheat seeds and the stainless steel plate can be derived, and the static friction factor was calculated as 0.275.

Stacking Experiment

The methods of angle of repose measurement include gravitational equilibrium method and internal collapse method. Based on the experimental conditions of our institute, the funnel method was adopted to measure the angle of repose. The funnel apparatus is illustrated in Fig.2, with a large diameter (a_1) of 140 mm, a small diameter (a_2) of 25 mm, and a height (h_1) of 170 mm. The height of the funnel above the platform (h_2) is 100 mm, and the diameter of the frustum (a_3) is 100 mm. During the experiment, the distance between the bottom of the funnel and the frustum below (h_3) was adjusted and buckwheat seeds were uniformly added

into the funnel at a constant rate. The seeds gradually formed a conical pile, with the angle between the slope of the conical pile and the plane of the frustum representing the angle of repose (θ), as shown in Fig.3.

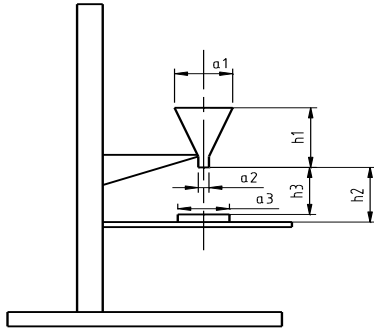


Fig. 2 - Schematic diagram of the funnel device



Fig. 3 - Buckwheat seed pile

In order to reduce human error in measurement, the computer image processing method Matlab is used here for image processing of buckwheat rest angle. As shown in Fig.4. First use the camera perpendicular to the side of the buckwheat pile to take a picture, to obtain the original image, as shown in Fig.4 (a).

The image is converted into a gray-scale image by Matlab processing as shown in Fig.4 (b), and then the image is binarized to obtain the binarized image, followed by extracting the curve data in the picture to obtain the boundary as shown in Fig.4 (c).

Subsequently the calibration between the picture and the curve is performed to obtain the unprocessed scatter plot. The scatter points are converted into useful curves and the scanned curves are shown in Fig.4 (d). Finally, the extracted data were fitted and the fitted curve was obtained as shown in Fig.4 (e). For each experiment, the repose angle of the buckwheat pile was measured in four directions: front, back, left, and right. The experiment was repeated twice to obtain an average value. The calculated repose angle α for the buckwheat in the actual experiment was found to be 27.65° .

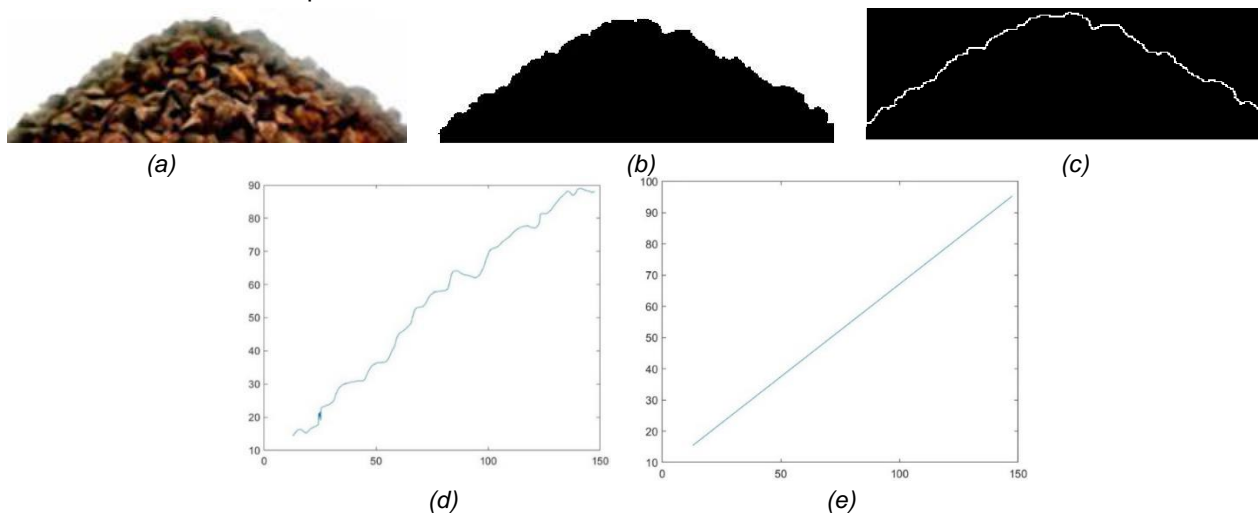


Fig. 4 - Angle of repose image processing

Establishment of discrete elemental model and parameter calibration of buckwheat

The discrete element model needs to roughly match the appearance of the actual object. In the discrete element simulation parameter settings, different input values give different results. Therefore, the physical test values are used as a target for the optimization of individual contact parameters (Xu B et al., 2021).

Model building

The three-axis dimensions of buckwheat were determined using a calliper, with the measurement results being presented in Table 1. This experiment focused on laboratory-cultivated bitter buckwheat and measurements were taken ten times to calculate the average value. Then, Inventor was used to draw the three-dimensional model of buckwheat, which was saved in STL format and imported into EDEM. Relevant literature shows that for the simulation modeling, smaller shape errors have less impact on the simulation results, and smaller errors between the size and shape of the actual particles and the discrete element model can be allowed. Therefore, the measured and statistical buckwheat shape dimensions were filled as shown in Fig. 5.

Table 1

Buckwheat triaxial size

	Length	Width	Height
maximum values /mm	6.15	4.92	4.58
average value /mm	6.01	4.13	4.09
minimum value /mm	5.84	4.02	3.96

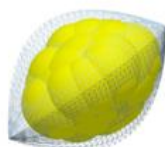


Fig. 5 - Discrete metamodel of buckwheat

Modeling of the funnel

The material chosen for the funnel is Q235 to model the discrete element of the funnel, where the diameter of the large end of the funnel is 140 mm, the diameter of the small end is 25 mm, and the height of the funnel is 170 mm. There is also a circular table with a diameter of 100 mm and a height of 7 mm (Chen G et al., 2024).

Formation of particle stacks

After the funnel model was established, it was imported into EDEM, and the dynamic particle generation method was used to establish a particle plane at the upper end of the funnel, the buckwheat seeds were discharged from the buckwheat grain container at a consistent rate, and eventually the grains would form a stable conical particle pile on the circular table. The whole process of seed grain formation is shown in Fig.6 (Lei et al., 2023).

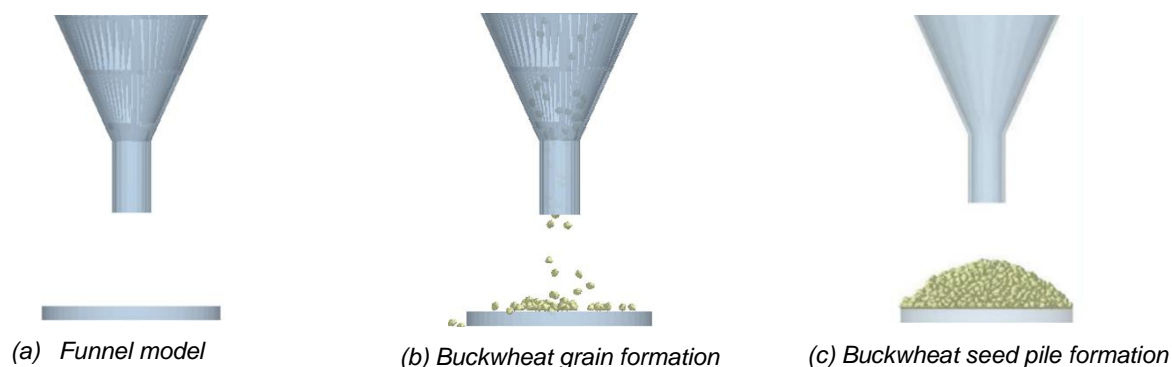


Fig. 6 - Simulated formation process of buckwheat kernels

Simulation model parameter calibration test

● **Plackett-Burman test**

Design-Expert software was applied to design the Plackett-Burman test, using the angle of repose of buckwheat seed drop test as the response value, and the simulation parameters with significant influence on the response value were screened out. It was combined with the previous physical tests and related literature to determine the individual simulation parameters in this study. The collision recovery coefficient for buckwheat ranges from 0.2 to 0.5, while the static friction coefficient is between 0.3 and 0.61. The rolling friction coefficient for buckwheat falls within 0.01 to 0.1. In interactions between buckwheat and stainless steel, the collision recovery coefficient is observed to be between 0.1 and 0.508, the static friction coefficient ranges from 0.2 to 0.7, and the dynamic friction coefficient is between 0.043 and 0.1. Simulation experiments were conducted to optimize nine parameters labelled A-I, selecting the upper and lower limits of two values to establish high and low levels, resulting in a total of 12 test groups, as detailed in Table 2 (Rittisak et al., 2023; Xu et al., 2023).

Table 2

Buckwheat simulation parameters

Symbol	Parameters	Levels	
		-1	+1
A	Buckwheat Intercollision Recovery Coefficient	0.2	0.5
B	Coefficient of static friction between buckwheat seeds	0.3	0.61
C	Coefficient of rolling friction between buckwheat seeds	0.01	0.1
D	Buckwheat seeds-stainless steel dynamic collision recovery coefficient	0.1	0.508
E	Buckwheat seeds-stainless steel coefficient of static and dynamic friction	0.2	0.7
F	Buckwheat seeds-stainless steel coefficient of kinetic friction	0.043	0.1
G	Buckwheat Poisson's ratio	0.3	0.5
H	Buckwheat density	1034	1250
J	Buckwheat shear modulus	1E+06	3.43E+06

- **Plackett-Burman experimental design**

Utilizing the Plackett-Burman design, the fundamental contact parameters influencing the buckwheat seed drop test as a variable factor were assessed, with each test yielding an average angle of repose of approximately 2. The experimental findings are presented in Table 3.

Table 3

Plackett-Burman experimental design

Test No.	A	B	C	D	E	F	G	H	J	Angle of repose / (°)
1	0.2	0.61	0.1	0.508	0.2	0.043	0.3	1250	1E+06	21.67
2	0.2	0.61	0.1	0.1	0.7	0.1	0.5	1034	1E+06	38.62
3	0.2	0.3	0.01	0.508	0.2	0.1	0.5	1034	3.43E+06	12.94
4	0.5	0.61	0.01	0.508	0.7	0.1	0.3	1034	1E+06	26.42
5	0.2	0.61	0.01	0.508	0.7	0.043	0.5	1250	3.43E+06	28.02
6	0.2	0.3	0.01	0.1	0.2	0.043	0.3	1034	1E+06	11.63
7	0.5	0.3	0.01	0.1	0.7	0.043	0.5	1250	1E+06	20.36
8	0.2	0.3	0.1	0.1	0.7	0.1	0.3	1250	3.43E+06	29.99
9	0.5	0.61	0.01	0.1	0.2	0.1	0.3	1250	3.43E+06	14.90
10	0.5	0.3	0.1	0.508	0.2	0.1	0.5	1250	1E+06	15.88
11	0.5	0.3	0.1	0.508	0.7	0.043	0.3	1034	3.43E+06	31.80
12	0.5	0.61	0.1	0.1	0.2	0.043	0.5	1034	3.43E+06	24.11

Analysis of variance was performed on the test data and the results of the Plackett-Burman test were used to identify significant effects using the Lenth method, which yielded a half-normal probability effects plot for the standardized effects of the factors as shown in Fig.7 (a) as well as a Pareto chart for the standardized effects of the factors as shown in Fig.7 (b). As can be seen from Fig.7 (a), the standardized effect points of factors B, C and E are farther away from the fitted line, so they are significant factors ($P < 0.05$), that is, the significant factors affecting the angle of repose are the coefficient of static friction between buckwheat seeds, the coefficient of rolling friction between buckwheat seeds, the coefficient of static friction between buckwheat seeds - stainless steel, and the standardized effect points of the other factors are smaller. The Pareto chart of standardized effects, shown in Fig.7 (b), further determines the magnitude and significance of the effect, factors B, C, and E exceeded the t-value as a significant factor.

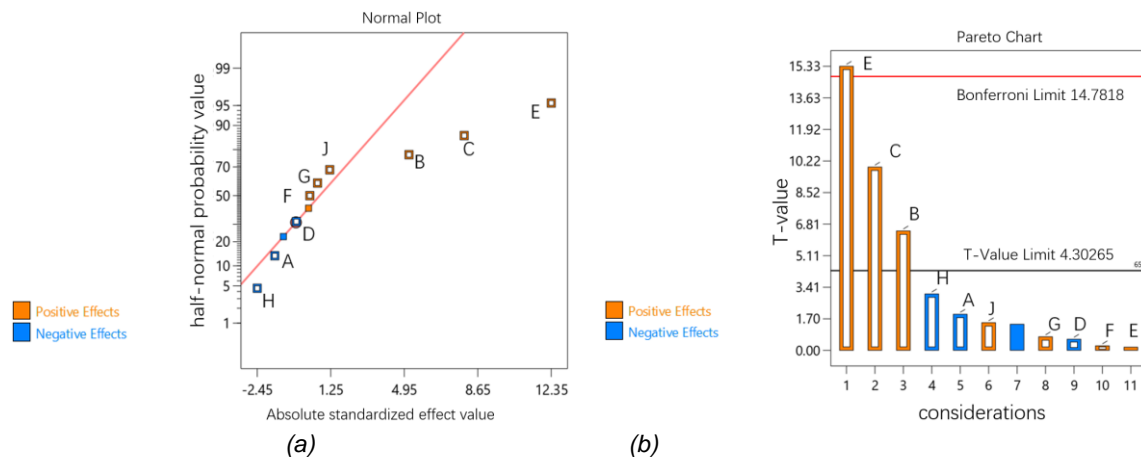


Fig. 7 - Half-normal probability effect plot for standardized effects and Pareto chart of standardization effects

A: Buckwheat Intercollision Recovery Coefficient; B: Coefficient of static friction between buckwheat seeds; C: coefficient of rolling friction between buckwheat seeds; D: Buckwheat seeds-stainless steel crash recovery coefficient; E: Buckwheat seeds-stainless steel static friction coefficient; F: Buckwheat seeds-stainless steel coefficient of kinetic friction; G: Buckwheat Poisson's ratio; H: Buckwheat density; J: Buckwheat Shear Modulus

As can be seen in Table 4, the p-value of the model is $0.0018 < 0.05$, which indicates significance, so the design is reliable and well fitted over the entire regression area of the study; the complex correlation coefficient $R^2=0.9644$, which indicates good correlation; and the corrected coefficient of determination $R^2_{adj}=0.9216$, which indicates that 92.16% of the variability of the experimental data can be accounted for by this regression model (Dun G et al., 2024).

Table 4

Plackett-Burman test factors, levels and significant analysis

Source	Square sum	Degrees of freedom	Mean square	F-value	P-value	
mould	760.04	9	84.45	43.38	0.0227	statistically significant
A	7.36	1	7.36	3.78	0.1914	
B	80.78	1	80.78	41.50	0.0233	
C	190.36	1	190.36	97.79	0.0101	
D	0.6984	1	0.69	0.36	0.6100	
E	457.38	1	457.38	234.96	0.0042	
F	0.1151	1	0.11	0.06	0.8306	
G	1.03	1	1.03	0.53	0.5427	
H	18.00	1	18.00	9.24	0.0933	
J	4.31	1	4.31	2.22	0.2750	
Residual	3.89	2	1.95			
Aggregate	763.93	11				

Typically, a lower coefficient of variation (CV) indicates greater reliability and accuracy of the test. In this case, a CV of 10.13% suggests that the Plackett-Burman test has acceptable reliability and accuracy. Additionally, precision, defined as the ratio of effective signal to noise, is considered reasonable when it exceeds 4.0. The precision of this test is 14.5784, confirming its reliability.

● **Steepest Climb Test**

By fitting a multiple regression equation to the data, the regression equation was obtained: $Y = 23.03 - 0.7829A + 2.59B + 3.98C - 0.2412D + 6.17E + 0.0979F + 0.2929G - 1.22H + 0.5996J$ (2)

From the formula, it can be seen that the partial regression coefficient of factor B is 2.59, indicating that factor B has a positive effect on the angle of repose; as factor B increases, the angle of repose will also increase. Factors C and E also exhibit positive effects.

As can be seen from Figure 7(a), the standardized effect points of factors B, C, and E are far from the fitting line, indicating that they are significant influencing factors. Furthermore, Figure 7(b) further determines the magnitude and importance of these effects, and factors B, C, and E all exceed the critical t-values as significant factors. Therefore, only these three factors are considered.

Since the most significant factor is E, E is used as the unit of climb.

Step E

$$\frac{0.7 - 0.2}{2} = 0.25 \tag{3}$$

Step C

$$\frac{3.98}{6.17} * \frac{0.1 - 0.01}{2} = 0.029 \tag{4}$$

Based on the experimental results, a value of 0.03 was utilized.

Step B

$$\frac{2.59}{6.17} * \frac{0.61 - 0.3}{2} = 0.065 \tag{5}$$

Based on the experimental results, a value of 0.07 was utilized.

The rest of the test parameters were buckwheat seeds collision recovery coefficient of 0.3, buckwheat seeds - stainless steel collision recovery coefficient of 0.5, buckwheat seeds - stainless steel coefficient of kinetic friction of 0.1, buckwheat Poisson's ratio of 0.3, buckwheat density of 1250, buckwheat shear modulus of 3.43E + 06. The results of the experimental design are shown in Table 5.

Table 5

Results of the steepest climb test design

A: Buck wheat Inter-collision Recovery Coefficient	B: Coefficient of static friction between buckwheat seeds	C: Coefficient of rolling friction between buckwheat seeds	D: Buckwheat seeds - stainless steel crash recovery coefficient	E: Buckwheat seeds - stainless steel static friction coefficient	F: Buckwheat seeds - stainless steel coefficient of kinetic friction	G: Buckwheat Poisson's ratio	H: Buckwheat density / (kg/m ³)	J: Buckwheat shear modulus / Pa	Angle of repose / (°)		
0.3	0.3	0.01	0.5	0.2	0.1	0.3	1250	3.43E+06	12.41	11.4	11.91
0.3	0.37	0.04	0.5	0.45	0.1	0.3	1250	3.43E+06	27.51	27.18	27.35
0.3	0.44	0.07	0.5	0.7	0.1	0.3	1250	3.43E+06	32.49	30.58	31.54
0.3	0.51	0.1	0.5	0.95	0.1	0.3	1250	3.43E+06	38.05	36	37.02
0.3	0.58	0.13	0.5	1.2	0.1	0.3	1250	3.43E+06	41.87	41.11	41.49
0.3	0.65	0.16	0.5	0.45	0.1	0.3	1250	3.43E+06	43.05	43.69	43.37

The steepest climb test was performed to calculate the relative error between the steepest climb test rest angle β and the physical test rest angle α using the formula Y. Y=(|β-α|)/α*100%. From the relative error, it can be seen that test 2 can be used as the centre point of the response surface test.

● Response surface methodology tests

According to the steepest climb test, the Box-Behnken test was implemented with test 2 as the centre point, and three factors of static friction coefficient between buckwheat seeds, rolling friction coefficient between buckwheat seeds and static friction coefficient between buckwheat seeds and buckwheat seeds-stainless steel were selected as the independent variables, and a three-factor, three-level test was established according to the Box-Behnken design with the angle of repose as the response value. The experimental design is shown in Table 6 (Jyoti et al., 2019; Zhang et al., 2015).

Table 6

Level	Considerations	Coefficient of static friction between buckwheat seeds	Coefficient of rolling friction between buckwheat seeds	Buckwheat seeds-stainless steel static friction coefficient
1		0.36	0.03	0.44
2		0.37	0.04	0.45
3		0.38	0.05	0.46

RESULTS

● **Box-Behnken test data processing**

The experimental results of the Box-Behnken test are shown in Table 7.

Table 7

Box-Behnken experimental design and its results

Test number	Coefficient of static friction between buckwheat seeds	Coefficient of rolling friction between buckwheat seeds	Buckwheat seeds-stainless steel static friction coefficient	Angle of repose / (°)
1	0.37	0.04	0.45	27.87
2	0.36	0.03	0.45	27.19
3	0.38	0.04	0.46	32.53
4	0.37	0.03	0.46	29.27
5	0.36	0.05	0.45	30.03
6	0.38	0.05	0.45	31.73
7	0.37	0.03	0.44	28.68
8	0.38	0.03	0.45	30.16
9	0.38	0.04	0.44	31.22
10	0.37	0.04	0.45	27.67
11	0.37	0.05	0.46	32.1
12	0.37	0.04	0.45	27.72
13	0.37	0.04	0.45	27.56
14	0.37	0.04	0.45	27.28
15	0.37	0.05	0.44	30.38
16	0.36	0.04	0.44	29.53
17	0.36	0.04	0.46	30.16

A quadratic polynomial equation was obtained by fitting a quadratic multiple regression to the data:

$$Y = 27.62 + 1.09A + 1.12B + 0.5313C - 0.3175AB + 0.1700AC + 0.2825BC + 1.45A^2 + 0.7025B^2 + 1.79C^2 \quad (6)$$

The multivariate correlation coefficient of the equation is R2=0.9948, which indicates that the model fits well to the actual situation, and the experimental results can be analysed by the equation, and the results of the ANOVA of the response surface test are shown in Table 8.

Table 8

Box-Behnken experimental design quadratic model ANOVA

Source	Square sum	Degrees of freedom	Mean square	F-value	P-value	
Mould	49.46	9	5.50	148.16	< 0.0001	significant
A-buckwheat static friction	9.53	1	9.53	256.86	< 0.0001	significant
B-roll friction between buckwheat	9.99	1	9.99	269.36	< 0.0001	significant
C-buckwheat-stainless steel static friction	2.26	1	2.26	60.88	0.0001	significant
AB	0.4032	1	0.4032	10.87	0.0132	significant
AC	0.1156	1	0.1156	3.12	0.1208	
BC	0.3192	1	0.3192	8.61	0.0219	significant

Source	Square sum	Degrees of freedom	Mean square	F-value	P-value	
A ²	8.91	1	8.91	240.33	< 0.0001	significant
B ²	2.08	1	2.08	56.02	0.0001	significant
C ²	13.42	1	13.42	361.71	< 0.0001	significant
residual	0.2596	7	0.0371			
incoherent	0.0654	3	0.0218	0.4492	0.7316	insignificant
inaccuracies	0.1942	4	0.0485			
CV (%)	0.6534					
			R2	0.9948	R2adj	0.9881

As can be seen from Table 8, the model is highly significant ($P < 0.05$) while the out-of-fit term is not significant ($P > 0.05$), the model correlation coefficient $R^2 = 0.9948$ and the correction coefficient $R^2_{adj} = 0.9881$, which indicates that the model fit is better, and the model can explain 98.81% of the variation of the response value, and the angle of repose can be analysed and predicted using this model. From the results in Table 8, it can be seen that the factors primary terms A, B and C have significant effect on the angle of repose; the interaction terms AB, BC have significant effect on the angle of repose and AC has insignificant effect; the secondary terms A², B², C² have significant effect on the angle of repose. This indicates that the relationship between the factors and the response value is not a simple linear relationship, the degree of influence of the factors is: $B > A > C$, i.e., rolling friction between buckwheat seeds > static friction between buckwheat seeds > buckwheat seeds - stainless steel static friction.

The angle of repose was predicted using the regression model, and in order to facilitate the observation of the model prediction results, the correlation graph between the model predicted values and the experimental values was plotted. From Fig. 8, it can be found that the sample points are all in the vicinity of the 45° diagonal, indicating that the model's prediction of the angle of repose under each factor is highly correlated with the experimental values, and the difference between the two is relatively small. Figure 9 illustrates the distribution of the model's prediction error. A reliable model typically requires that the prediction error for most samples remains within the $\pm 2SD$ range.

As shown in Figure 9, all sample points lie within this range, with no anomalies observed. This indicates that the model has high prediction accuracy and is suitable for analysing the angle of repose.

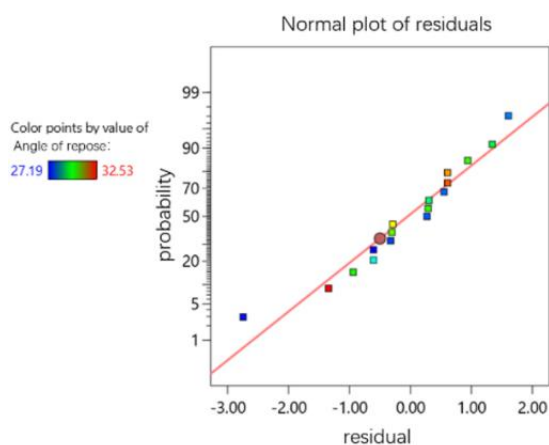


Fig. 8 - Correlation of model predicted values with experimental values

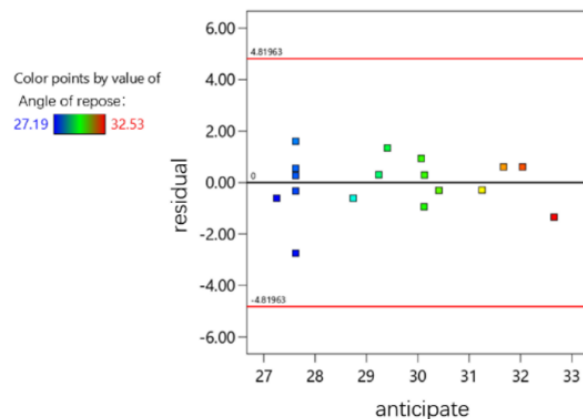


Fig. 9 - Plot of residuals on model predicted walks

Based on the regression equation, the response surface analysis was plotted using Design-expert and the results are shown in Figure 10. The three-dimensional plot of the response surface can be clearly seen through the range of tests performed including the area where the minimum value is located.

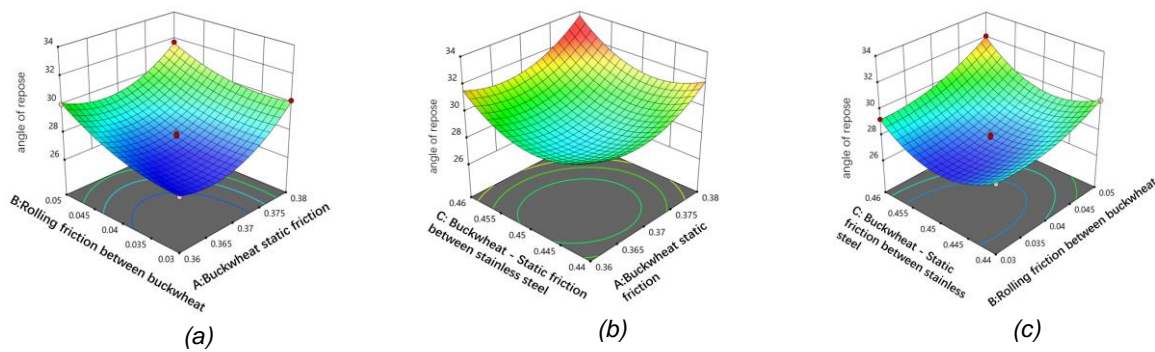


Fig. 10 - Response surface analysis plot

Response surface analysis plotted using Design-expert shows that static friction between buckwheat seeds and rolling friction interaction between buckwheat seeds-stainless steel have a significant effect on the angle of repose.

● Determination of optimal combination parameters and validation results

Based on the optimization module in the Design-Expert software, the regression model was optimized and solved with the target value of 27.65° of the physical test, and parameters similar to those of the physical test were obtained: the coefficient of static friction between buckwheat seeds was 0.372, the coefficient of rolling friction between buckwheat seeds was 0.038, and the coefficient of static friction between buckwheat seeds-stainless steel was: 0.448.

CONCLUSIONS

(1) A simulation model for the stacking angle of repose of buckwheat seeds was developed using EDEM software. MATLAB image processing technology was employed to linearly fit the edge contour of the angle of repose, providing an accurate response value. The results of the Plackett-Burman test indicate that the static friction coefficient between buckwheat seeds, the rolling friction coefficient between buckwheat seeds, and the static friction coefficient between buckwheat seeds and stainless steel significantly influence the angle of repose;

(2) Based on the results of the Box-Behnken response surface test, a quadratic regression model was developed to describe the relationship between significant parameters and the angle of repose. The analysis of variance revealed that the primary terms (static friction coefficient between buckwheat seeds, rolling friction coefficient between buckwheat seeds, and static friction coefficient between buckwheat seeds and stainless steel), the interaction terms (static friction coefficient and rolling friction coefficient between buckwheat seeds, as well as rolling friction coefficient and static friction coefficient between buckwheat seeds and stainless steel), and the quadratic terms of these coefficients significantly affect the angle of repose.

(3) By optimizing the regression equation to find the optimal solution, the following values were obtained: a static friction coefficient of 0.372 for buckwheat, a rolling friction coefficient of 0.038 for buckwheat, and a static friction coefficient of 0.448 for the buckwheat-stainless steel interaction. The remaining parameters were set to their intermediate levels. The relative error between the physical test results and the simulation outcomes was 1.08%, indicating that the contact parameters and the contact model parameters are both accurate and reliable.

ACKNOWLEDGEMENT

This research was funded by the Shanxi Province Basic Research Program (No.202203021212417). Shanxi Agricultural University Academic Restoration Project (No.2023XSHF2). Central guidance for local scientific and technological development funding projects (No. YDZJSX20231C009);

REFERENCES

- [1] Chen G. (2024). Parameter calibration and experiment of discrete element simulation of spherical-like soybean based on DEM. (基于 DEM 的类球型大豆离散元仿真参数标定与试验). *INMATEH - Agricultural Engineering*, Vol.74, Issue 03, pp.303-315.

- [2] Dun G. (2024). Simulation of soybean seed physical properties on filling performance (大豆种子物理特性对充种性能影响的仿真研究). *INMATEH - Agricultural Engineering*, Vol.74, Issue 03, pp.95-104.
- [3] González-Montellano, C, (2012). Determination of the mechanical properties of maize grains and olives required for use in DEM simulations. *Journal of Food Engineering*, Vol.111, Issue 4, pp. 553-562.
- [4] Jyoti G. (2019). Optimization of esterification of acrylic acid and ethanol by Box-Behnken design of response surface methodology. *Indian Journal of Chemical Technology*, Vol. 26, Issue 1, pp. 89-94;
- [5] Lei X. (2023). Determination of Material and Interaction Properties of Granular Fertilizer Particles Using DEM Simulation and Bench Testing. *Agriculture*, Vol.13, Issue 9, pp. 1704;
- [6] Li Y.X. (2019). Discrete meta-parameter calibration of wheat flour based on particle scaling (基于颗粒缩放的小麦粉离散元参数标定). *Journal of Agricultural Engineering*, Vol.35, Issue 16, pp. 320-327;
- [7] Li G. (2023). Establishment and Calibration of Discrete Element Model for Buckwheat Seed Based on Static and Dynamic Verification Test. *Agriculture*, Vol.13, Issue 5;
- [8] Liu W.Z. (2018). Parameter calibration for micro potato simulation based on discrete elements (基于离散元的微型马铃薯仿真参数标定). *Journal of Agricultural Machinery*, Vol.49, Issue 05, pp. 125-135+142;
- [9] Rittisak S. (2023). Application of the Plackett-Burman design for screening and optimisation of factors affecting the aqueous extract for total anthocyanin content of broken riceberry rice. *International Food Research Journal*, Vol.30, Issue 3, pp. 649-655;
- [10] Wang C J, (2012). Determination of the coefficient of recovery in a wheat grain collision model (小麦籽粒碰撞模型中恢复系数的测定). *Journal of Agricultural Engineering*, Vol.28, Issue 11, pp. 274-278, Huainan / P.R.C.;
- [11] Wu J.S. (2019). Determination of Physical Properties of Qianhu Seeds and Calibration of Parameters of Discrete Element Simulation Model (前胡种子物性参数测定及其离散元仿真模型参数标定). *Journal of Gansu Agricultural University*, Vol.54, Issue 04, pp. 180-189;
- [12] Wu L.G. (2018). Buckwheat Nutritional and Functional Properties and Related Food Development Research Progress (荞麦营养功能特性及相关食品开发研究进展). *Grain, Oil and Food Science and Technology*, Vol.26, Issue 03, pp. 41-44;
- [13] Xu B. (2021). Construction of a discrete element model of buckwheat grain and calibration of parameters. *INMATEH - Agricultural Engineering*, Vol 64, Issue 2 , pp. 175-184;
- [14] Xu T. (2023). Ellipsoidal seed modeling and simulation parameter selection based on the discrete element method. *Materials Today Communications*, Vol. 37;
- [15] Zeng Z.W. (2021). Current status and perspectives of the application of discrete element method in agricultural engineering research (离散元法在农业工程研究中的应用现状和展望). *Journal of Agricultural Machinery*, Vol.52, Issue 04, pp. 1-20.
- [16] Zhang R, (2017). Research on calibration method of sand parameters in discrete element simulation (离散元模拟中沙土参数标定方法研究). *Journal of Agricultural Machinery*, Vol.48, Issue 03, pp. 49-56;
- [17] Zhang Y-j. (2015). Optimization of one-step pelletization technology of Biqu granules by Plackett-Burman design and Box-Behnken response surface methodology. *China journal of Chinese materia medica*, Vol.40, Issue 22, pp. 4406-4410.

SIMULATION AND TEST OF A NEW COAXIAL COUNTER-ROTATING AGITATOR

/ 新型同轴异转搅拌器的仿真与试验

Longlong REN ^{1,2,3}, Yuqiang LI ¹, Zhenxiang JING ¹, Yuepeng SONG ^{1,2,3*}, Jing GUO ^{1,2,3}, Siwen SHEN ⁴⁾¹¹ Shandong Agricultural University, College of Mechanical and Electrical Engineering/ China;² Shandong Provincial Key Laboratory of Horticultural Machinery and Equipment/ China;³ Shandong Provincial Engineering Laboratory of Agricultural Equipment Intelligence/ China;⁴ Shandong Electric Power Higher Specialised College, Department of Power Engineering/ China;

E-mail: renlonglong123@126.com

DOI: <https://doi.org/10.35633/inmateh-75-10>**Keywords:** water-fertiliser integration; coaxial counter-rotating agitator; flow field analysis; orthogonal test**ABSTRACT**

Addressing the issues of water resource wastage, low fertilizer utilization efficiency, and uneven water-fertilizer mixing in current irrigation and fertilization practices, a new type of coaxial counter-rotating agitator was designed. Based on computer numerical simulation technology, this paper simulated and analysed the agitator's modes and flow field distribution, establishing the law that governed the variation of velocity distribution within the agitator's internal flow field with changes in rotational speed. An orthogonal experimental design was employed, utilizing stirring speed, stirring duration, and submerged depth as the experimental variables, and the outcomes were subsequently analysed utilizing Design-Expert software. The findings indicated that optimal fertilizer solubility was achieved when the stirring speed was 400 r/min, the stirring time was 5 minutes, and the stirring depth was 660 mm. This study provided a theoretical basis for the design and application of the coaxial counter-rotating agitator and aided in guiding parameter selection and optimization for practical applications.

摘要

针对目前灌溉施肥中存在的水资源浪费、肥料利用率较低以及水肥混合不均匀的问题,设计了一种新型同轴异转搅拌器。本文基于计算机数值模拟仿真技术,对搅拌器的模态、流场分布进行模拟分析,确定了搅拌器内部流场的速度分布随转速变化的规律;以搅拌转速、搅拌时间和潜液深度为试验因素设计正交试验,使用 Design-Expert 软件对结果进行分析,结果表明:当搅拌速度 400 r/min、搅拌时间 5 min、搅拌深度 660 mm 时,肥料溶解度最优。本研究为新型同轴异转搅拌器的设计和运用提供了理论依据,并有助于指导实际应用中的参数选择和优化。

INTRODUCTION

Currently, agriculture accounts for more than 60% of the country's total water consumption (Dali Fang et al., 2024), and traditional irrigation techniques such as flood irrigation and manual fertilization led to inefficient water and fertilizer use, with an average fertilizer utilization rate of only 33%, which not only increased the production cost, but also exacerbated the environmental pollution problem (Yuan Hongbo et al., 2016; He Weiyuan et al., 2020). Water-fertilizer integration technology could significantly improve the simultaneous efficiency of irrigation and fertilization by delivering nutrient solution directly to plant roots through drip irrigation system (Ma Martínez Gimeno et al., 2020), and the water-fertilizer mixing efficiency was directly correlated with the utilization rate of water-soluble fertilizers (Jin Zhou et al., 2020). Inadequate dissolution of fertiliser could easily lead to clogging of irrigation pipes, and such clogging was not only difficult to remove, but also time-consuming and labour-intensive to replace the pipes, as well as significantly increasing the cost of irrigation. Therefore, it was crucial to improve the efficiency of fertiliser dissolution and to ensure that the water and fertiliser were evenly mixed.

The application of large quantities of chemical fertilizers in agricultural production raised the risk of environmental pollution, Liu Shufeng et al., (2022), investigated the effects of different solid-liquid mixing ratios, agitator forms and mixing speeds on the mixing effect, and optimized the operating parameters of the agitator and fertilizer pumps to improve the homogeneity of fertilizer mixing. Mechanical agitation was an important method to promote the homogeneity of solid-liquid mixtures. Li Tianhua et al., (2023), analysed the

¹ Longlong Ren Lecturer Ph.D. Eng.; Yuqiang Li, M.Sc. Stud. Eng.; Zhenxiang Jing, M.Sc. Stud. Eng.; Yuepeng Song, Prof. Ph.D. Eng.; Jing Guo, Prof. Ph.D. Eng.; Siwen Shen, Lecturer M.Sc. Eng.;

hydrodynamic characteristics of different fertilizer mixing modes through numerical simulation of the mixing operation of different types of fertilizers, and designed a fertilizer mixing device combining unloading reflux and mechanical agitation to realize the mixing operation of different types of fertilizers. Different forms of agitators could produce different flow fields and agitation energies, thus realizing diversified mixing effects. *Tian Yongjian, (2024)*, designed a portable air agitator, which could agitate the sediment and fix impurities at the bottom of the storage tank while blowing them to improve the homogeneity of solid-liquid mixing. *Liu Wenliang et al., (2022)*, focused on improving the uniformity of fertilizer mixing, optimized and improved the fertilizer mixing components, and made use of the mixer's own structure to make the water and fertilizer fully mixed. *Zhang Shuai et al., (2018)*, designed a high-efficiency fertilizer mixer to analyse the flow field distribution diagram of different mixing speeds, and the fertilizer mixer produced more disturbed and turbulent flow inside the fertilizer mixer when the mixing speed was greater than the critical mixing speed, which could effectively improve the effect of fertilizer mixing. *Li Lei., (2024)*, designed an energy-saving axial flow mixer by setting the paddles in a circular arc shape and the arc side set diagonally downward, which enhanced the degree of turbulence in the axial and radial directions, so as to make the mixing effect better. When designing a mixing and blending device for fertilizers, it was crucial to ensure dissolution efficiency and mixing homogeneity of the fertilizers, and rational design of the mixing device was the key to achieving this goal (*Dang Lingui et al., 2013*).

This paper evaluated a newly designed mixer with a novel shape, explored the velocity distribution of the flow field inside the agitator with the change of rotational speed through computer simulation, compared with the coaxial co-rotating agitator, verified the superiority of the design of the fertilizer mixer, and obtained the optimal operating parameters of the agitator through design experiments and parameter optimization.

MATERIALS AND METHODS

Structural design of the fertilizer mixing unit

Selection of fertilizer mixing drum with an inner diameter of 600 mm and a height of 1,000 mm. According to the relevant literature and the requirements of the mechanical design of mixing equipment, combined with the relevant design specifications and empirical formulas, through the calculation of the overall size of the agitator, the relevant values were obtained:

$$d = (0.2 \sim 0.5)D \quad (1)$$

$$h = 0.02 d \quad (2)$$

$$S = 0.66 D \quad (3)$$

where: D - inner diameter of fertilizer mixing drum, mm; d - diameter of mixing paddle, mm; h - thickness of mixing paddle, mm; S - agitator submergence depth; mm;

By calculating the dimensional parameters of the agitator through the above formula, the diameter of the stirring paddle was set to 200 mm, the thickness of the stirring paddle was 4 mm, and the submerged depth of the agitator was 660 mm. Common agitators on the market are single-steering single-paddle axial-flow agitators, which have mediocre mixing effect and cannot form a turbulent field to dissolve fertilizers very well. Therefore, based on the shortcomings of the existing agitator, a new type of coaxial counter-rotating agitator was designed by making the stirring direction bidirectional and incorporating double paddles. A three-bladed propeller agitator paddle was used, providing improved mixing efficiency and enhanced hydrodynamic characteristics. The three-blade paddle could produce uniform radial and axial flow, improved mixing efficiency and reduced dead zone, while balancing the mechanical vibration in the mixing process and enhancing the stability of the system. The inclination angle of the agitator designed for 30° could be adapted to most of the equipment structure requirements of the water and fertilizer integration machine, under the condition of the same power consumption, small diameter, high speed agitator, the power was mainly consumed in the turbulent pulsation, which was conducive to the microscopic mixing.

The upper mixing paddle of the coaxial counter-rotating agitator was connected to the outer sleeve, and the lower mixing paddle was connected to the centre shaft, which was designed to be easy to install and prevent relative sliding in the working process. The upper and lower mixing paddles were connected by C-type coupling. When the mixer was working, the upper bevel gear and the lower bevel gear were synchronized to rotate in the reverse direction, which made the upper and lower mixing paddles rotate in the reverse direction coaxially. Realizing the effect of a composite cyclonic flow field in a single device could create a larger turbulence distribution during mixing and improve the homogeneity of mixing and blending (*Hua Jian et al., 2023*), the final design is shown in Fig. 1. Fig. 2 shows the overall structural diagram of the fertilizer mixer, and Fig. 3 shows the structure of the mixing paddle.



Fig. 1 - Coaxial counter-rotating agitator

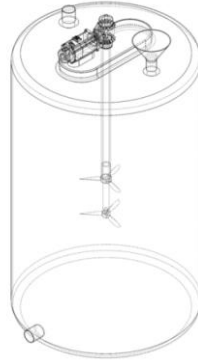


Fig. 2 - Overall structure of the fertilizer mixer

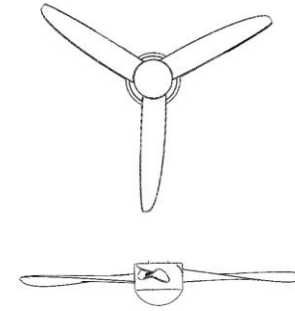


Fig. 3 - Mixing paddle

Calculation of critical stirring speed of the agitator

Agitation had a limited effect on the mass transfer coefficient, mainly by promoting the suspension of solid particles to increase the solid-liquid interface, and thus improved the mass transfer efficiency. When the complete suspension of particles was achieved, it was no longer obvious to increase the stirring intensity to improve the mass transfer efficiency. For the process of dissolving solids, the bottom of the particles can be suspended, without the need to achieve a complete uniform distribution of the liquid phase. In view of this, it was crucial to determine the critical stirring speed of the mixing equipment, which depended on the density difference between the solid and liquid phases, the liquid density, the solids concentration, the liquid viscosity, the physical properties such as particle size, and the geometrical relationship between the mixing vessel and the agitation device. Based on the formula for calculating the critical stirring speed published by Zwietering, it was possible to determine the appropriate stirring speed, avoiding unnecessary energy consumption:

$$N_c = Kd^{-0.85} \nu^{0.1} d_p^{0.2} \left| g \frac{\rho_p - \rho}{\rho} \right|^{0.45} \left| 100 \times \frac{\rho_p \phi_v}{\rho(1 - \phi_v)} \right|^{0.13} \quad (4)$$

where: N_c - critical RPM; K - equation constant, the propeller impeller is approximately $2.57 \sim 3.19(D/d)0.80 \sim 0.86$; D - inner diameter of fertilizer mixing drum, m; d_p - solid particle diameter, m; ϕ_v - solid volume fraction; ρ - density of liquids, kg/m^3 ; ρ_p - density of solid particles, kg/m^3 ; ν - kinematic viscosity of liquids, m^2/s ; d - diameter of mixing paddle, m; g - gravitational acceleration, m/s^2 ;

The majority of the parameters in the above equation were determined by the calculation of the specific dimensions of the mixer in the paper, and according to the study of *Yang Xiaozhen et al., (2014)*, it was known that the density of the water-fertiliser mixing liquid was 1150 kg/m^3 and its kinematic viscosity was $0.0016 \text{ m}^2/\text{s}$. The data provided by *Guo Shanming et al., (2017)*, pointed out that the particle diameter of the general-purpose water-soluble fertilisers was 2 mm , and its density was 1335 kg/m^3 . Based on these parameters, the critical stirring speed (N_c) was calculated to be approximately 398.28 r/min . The critical stirring speed (N_c) of the fertiliser mixer was calculated to be approximately 398.28 r/min , and this result was informative for subsequent comparative class studies.

Simulation modelling and meshing of agitator

In computer simulation analysis, meshing was crucial because proper meshing could improve simulation accuracy and reduce the time required for computation (*Zhang Yubin et al., 2018*).

Through COMSOL Multiphysics software, the simulation model used a tetrahedral mesh and the rotating part of the agitator was refined to ensure higher simulation accuracy (*An Bo et al., 2023*). The histogram of the mesh quality showed a normal distribution, ensuring uniformity and proper size distribution of the mesh. Figure 4 shows the grid details of the flow field analysis of the agitator and fertilizer mixing tank.

After the meshing was completed, the quality of the grid was viewed through the statistical information under the grid (mesh) component, where the agitator grid diagram in Figure 3 had a cell count of $187,122$, and the fertilizer mixing tank grid diagram had a cell count of $850,624$ for the statistical information of the domain cells.



Fig. 4 -Agitator grid figure; flow field analysis grid diagram of fertilizer mixing tank

Modal analysis of coaxial counter-rotating agitator

The high speed of rotation during agitator operation led to vibration. To ensure the stability of the equipment, modal analysis was essential to reveal the vibration characteristics. Modal analysis was designed to identify the inherent vibration modes of an object based on a fixed structural shape and constraints. Based on the established model and constraints imposed (Liu Shuangxi et al., 2020), modal analysis could be performed to obtain the first six modal frequencies of the agitator, the first six orders of modal diagrams were shown in Fig. 5.

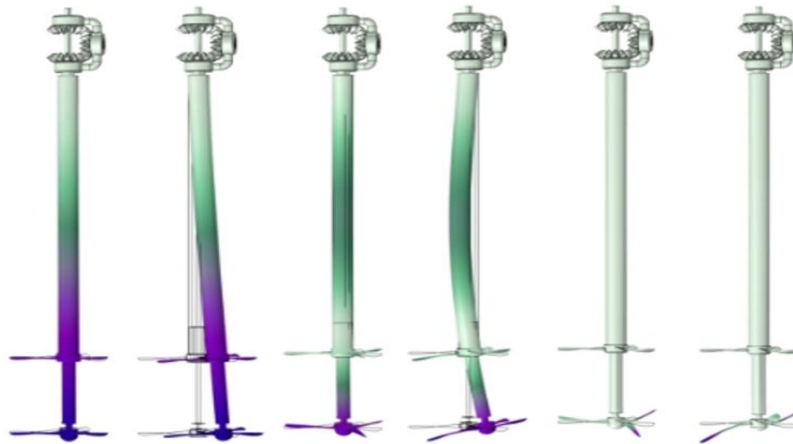


Fig. 5 - First six modes

Simulation analysis of the flow field of a coaxial counter-rotating agitator

In the study of fluid dynamics, velocity vector diagram was an important tool to reveal the dynamic trend, state and change of flow direction of the fluid in the flow field (Jin Yu et al., 2023). In this study, numerical simulation was used to simulate the flow at different rotational speeds, specifically analysing the velocity field distribution in the central profile of the fertilizer mixer at rotational speeds of 200, 300, 400 and 500 r/min, respectively.

The spatial distribution characteristics of the flow velocity could be observed visually through the generated velocity clouds. Comprehensive comparison of these velocity cloud maps enabled this study to explore in depth the law of the velocity distribution of the flow field inside the agitator as a function of the rotational speed, and to determine the optimal operating rotational speed accordingly.

Prototyping and design of experiments

In this paper, through mechanical design as well as simulation analysis, the coaxial counter-rotating agitator was designed and the prototype object was machined, as shown in Fig. 6. The main components of the agitator, such as the active teeth, motor, coupler, outer sleeve, lower stirring paddle, upper stirring paddle, lower follower teeth, centre shaft, upper follower teeth, etc., are indicated in the figure. The overall size and length of the agitator was consistent with the previous design model, while the structure was compact and the components had good working stability. In the actual production process, in order to save production costs, a fixed-speed motor with defined parameters could be chosen, which could effectively meet the production requirements and would not require frequent adjustment of the agitator's stirring speed.

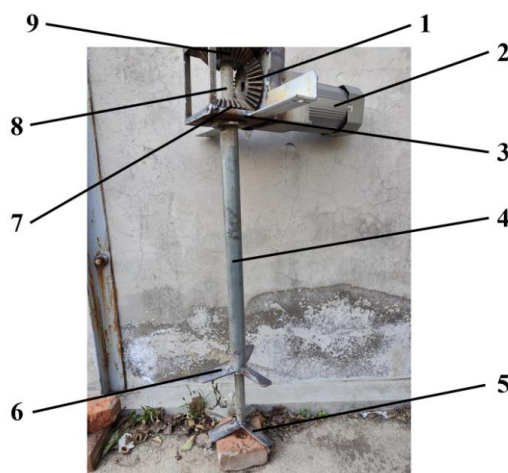


Fig. 6 -New coaxial counter-rotating agitator

1. Driving teeth, 2. Motor, 3. Coupler, 4. Outer sleeve, 5 down stirring paddle, 6. Upper stirring paddle, 7. Lower driven teeth, 8. Centre shaft, 9. Upper driven teeth

In this study, in order to determine the optimal agitation conditions, the Box-Behnken design method was used with stirring speed, stirring time and submergence depth as independent variables and electrical conductivity (EC) as the response variable. By implementing a three-factor, three-level orthogonal experimental design, it was aimed to find the optimal combination of stirring speed (A, a), stirring time (B, b) and agitator submergence depth (C, c). The experimental conditions were designed as follows: the N, P, and K ratio of the mixed fertilizer was 20% ~ 20% ~ 20%. For the test, 1000 g of fertilizer was selected and mixed with 100 L of aqueous solution under different test conditions. After the mixing was completed, 200 ml of the fertilizer aqueous solution was taken out and its concentration was determined using a portable PH/EC tester. In this case, electrical conductivity (EC value) was used as a measure of the solubility of the fertilizer. Fig.7 shows the physical picture of the composite fertilizer and Fig. 8 shows the test site.



Fig. 7 - Physical Map of Fertilizer



Fig. 8- Pilot test site

The experimental range of stirring speed was set at 300 to 500 r/min, based on the results of previous hydrodynamic simulations. The stirring time was selected from 3 to 7 minutes to ensure adequate dissolution of the fertilizer and reasonable energy consumption. The submerged depth of the agitator was set between 610 and 690 mm based on previous calculations. Table 1 demonstrated the experimental factors with their corresponding coded values. This experimental design and parameter selection was devoted to evaluate the effectiveness of the new coaxial counter-rotating agitator in the fertilizer mixing process, so as to provide theoretical and experimental support for the optimization of the fertilizer mixing process.

Table 1

Correspondence between Test Factor Level and Coded Value in Stirring Process

Coded value	Stirring speed A / (r/min)	Stirring time B / min	Agitator submergence depth C / mm
-1	300	3	610
0	400	5	650
1	500	7	690

RESULTS

Analysis of agitator simulation results

According to the results of the modal analysis in Table 2, the fundamental frequency of the agitator was 38.57 Hz, which was the lowest among all modes. Considering that the operating frequency interval of the speed-regulated motor was 0-500 r/min, this corresponded to a vibration frequency of 0-8.34 Hz. Since this frequency was much lower than the first order modal frequency of the agitator, the effect of other external excitation frequencies on the fertilizer mixing tank could be neglected. Literature indicates that the lower order modes had a more significant effect on the vibration of the equipment, while the effect of the higher order modes gradually decreases (Liu Shuangxi et al., 2020). In summary, the highest frequency of external excitation was significantly lower than the lowest mode of the mixer, which means that the agitator had good anti-vibration performance and would not enter into resonance due to external excitation, meeting the design specification requirements.

Table 2

Sixth-order mode of blender						
ORDER	1	2	3	4	5	6
FREQUENCY / Hz	38.57	41.11	250.42	256.28	449.16	449.41

Fig. 5 showed that the vibration pattern of the agitator was mainly divided into the vibration of the stirring rod and the vibration of the stirring paddle, in which the vibration pattern corresponding to the first, second, third and fourth order modes was mainly the left and right oscillation of the stirring rod. The vibration mode corresponding to the fifth and sixth order modes was mainly the up and down swinging of the agitator paddle, while the agitator was mainly operated by the central shaft and outer sleeve rotating around the centre with the same direction and speed. The vibration characteristics of the agitator were mainly expressed as torsional vibration in the direction of the central axis, which was different from the transverse and vertical vibration modes.

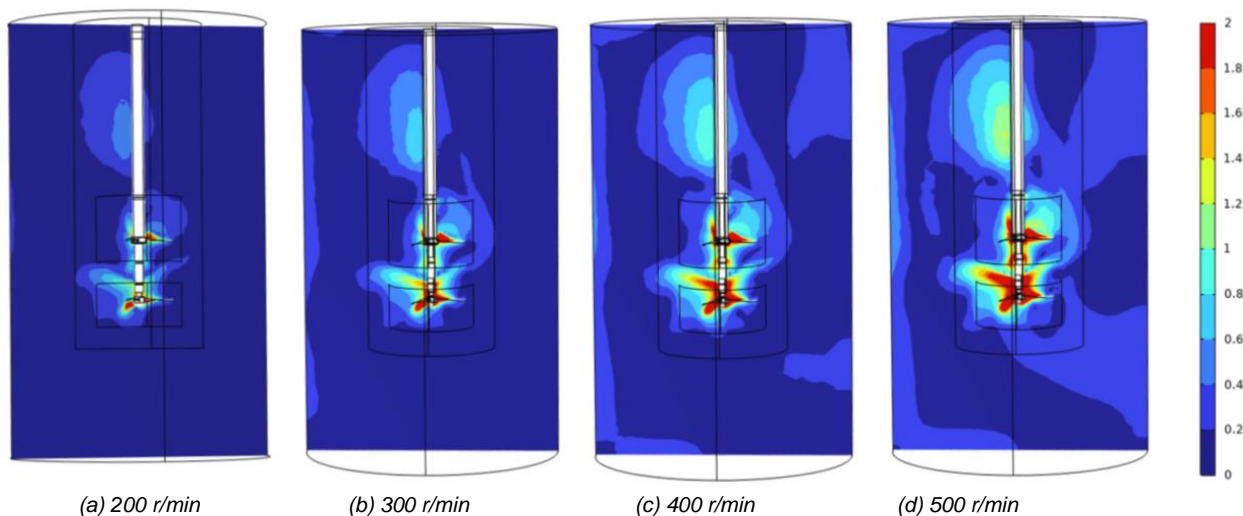


Fig. 9 - Speed cloud picture of agitator at different speeds

From Fig. 9, it could be observed that at critical speeds lower than 400 r/min, the velocity was higher near the rotating paddle and lower at the periphery away from the rotor. The velocity distribution in this region was more uniform and lacked a significant velocity gradient, resulting in a weakening of the interlayer flow, which was not conducive to the development of turbulence, thus affecting the dissolution and mixing efficiency of the fertilizer.

When the rotational speed was higher than the critical rotational speed of 400 r/min, it was observed that the overall velocity cloud map showed a similar pattern, with a larger value of velocity in the rotating region of the agitator's stirring paddles, and the overall velocity in the fertilizer mixing drum showed the distribution characteristics of the middle being the highest, the edge the second highest, and the mezzanine being the lowest, which formed an obvious middle-low-high velocity distribution. This velocity distribution effectively enhanced the relative motion between the liquid layers, and this frequently changing medium-low-high velocity distribution formed a complex flow field distribution, which promoted turbulence and was conducive to the dissolution of the fertilizer.

Analysing the velocity clouds under different speed conditions, it could be seen that: under the condition of lower than critical agitation speed, the flow field of the agitator showed a single flow pattern, and the turbulence distribution was restricted, which limited the dissolution efficiency of the fertilizer.

In contrast, when the speed was higher than the critical agitation speed, the distribution of the flow field became more complex, the value of the velocity in the rotating area of the agitator's mixing paddles was larger, and the overall velocity in the fertiliser mixing drum showed the distribution characteristics of the highest in the middle, the second on the edge, and the lowest in the mezzanine layer, which phenomenon improved the shear action and circulation characteristics inside the fluid and thus accelerated the dissolution mechanism of the fertilisers. With the increase of velocity, the velocity vector field and velocity isosurface map mainly reflect the growth of velocity amplitude, while the overall distribution pattern of velocity was kept relatively consistent with the trend of vector change.

Therefore, after the speed exceeded the critical stirring speed, increasing the rotational speed had less effect on the distribution of the flow field, but the velocity value would increase. After comparison and analysis, both 400 r/min and 500 r/min speed could meet the requirements. Considering the overall power consumption, the rotational speed should be reduced as much as possible to improve the energy efficiency while generating a good flow field distribution. Therefore, 400 r/min is finally selected as the optimum speed for the new coaxial counter-rotating agitator.

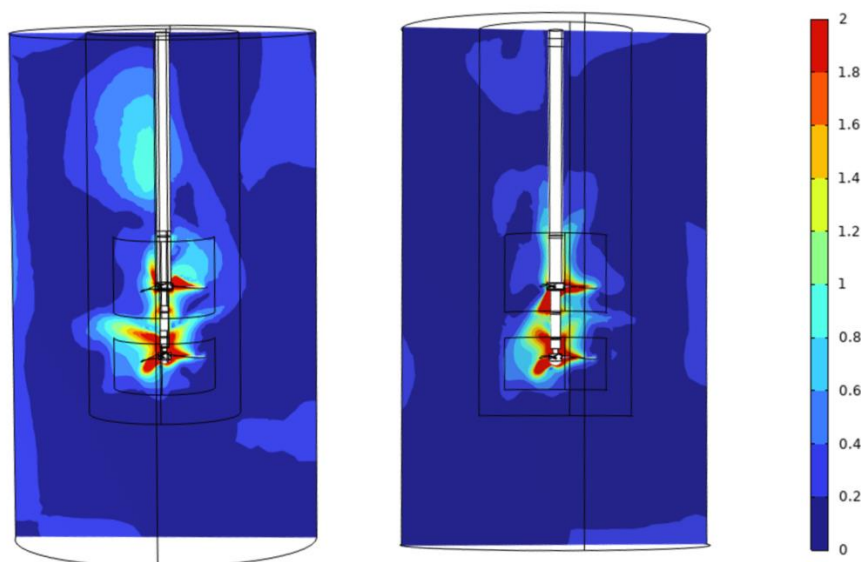


Fig. 10 - Velocity distribution at 400 r/min under coaxial differential rotation and coaxial simultaneous rotation

The simulation results in Fig. 10 showed that the overall flow velocity distribution of the coaxial counter-rotating agitator was significantly better than that of the coaxial co-rotating agitator when the rotational speed was 400 r/min. Due to the fact that the stirring blades of the coaxial co-rotating stirrer rotated in the same direction, it resulted that the flow velocity in the flow field was concentrated in the rotating region of the stirring blade, and the mobility was insufficient. Therefore, this situation was not conducive to the dissolution of fertiliser and other processes. The coaxial counter-rotating agitator produced stronger vortex and turbulence effects due to the opposite direction of rotation of the agitator paddles. Such flow characteristics were conducive to diffusion and mixing, making the process of dissolving fertiliser more complete and rapid.

Through numerical simulation analysis, the multi-dimensional flow field structure produced by the coaxial counter-rotating agitator could promote the effective contact between the fertiliser particles and the solvent, which increased the surface area of dissolution, and was conducive to improving the dissolution rate and efficiency

Regression modelling and analysis of variance

An important indicator for assessing the results of the working parameters was the electrical conductivity (EC value) of the fertilizer solution, which was obtained by removing 200 ml of aqueous fertilizer solution from the fertilizer mixing drum after mixing and measuring its concentration using a portable PH/EC tester. In accordance with the principles of Box-Behnken experimental design, 17 sets of experiments on fertilizers were executed in this study and the corresponding data were collected. The experimental program and its results were summarized in Table 3.

Table 3

Fertilizer Mixing Test Scheme and Result				
No	Stirring speed A/(r/min)	Stirring time B/min	Agitator submergence depth C/mm	Fertiliser EC M/(us/cm)
1	0	1	1	10840
2	0	0	0	11430
3	0	-1	-1	10380
4	0	0	0	11480
5	0	-1	1	10240
6	1	-1	0	10620
7	-1	0	1	10110
8	0	0	0	11450
9	-1	-1	0	9780
10	1	0	-1	10940
11	0	0	0	11460
12	0	0	0	11430
13	-1	1	0	10480
14	1	1	0	11090
15	0	1	-1	10920
16	1	0	1	10710
17	-1	0	-1	10060

Note: m_1 , m_2 and m_3 are the corresponding coded values of M_1 , M_2 and M_3 , the same as below.

A quadratic regression model was obtained as a result of analysing and processing the experimental data shown in Table 3 by entering them into the Design Expert software. The model describes the relationship between the electrical conductivity (EC value) of the water-soluble fertilizer obtained after dissolving the fertilizer and the coded values of the three variables: agitation speed, agitation time, and agitator submergence depth. The quadratic regression equations obtained from the EC value of the water fertilizer solution and the coded values of the three influencing factors, stirring speed, stirring time and agitator submergence depth, respectively, were:

$$M = 11450 + 366.25a + 288.875b - 49.875c - 57.5ab - 70ac + 15.25bc - 548.875a^2 - 408.625b^2 - 446.125c^2 \quad (5)$$

The results obtained from the analysis of variance (ANOVA) of the regression equation for fertilizer solubility using Design Expert software showed that the P-values of all the factors in the model were significantly below the 0.05 threshold. And the P-values of three variables, namely, agitation speed, agitation time and submerged depth of agitator were well below 0.01, which characterizes the regression model as being extremely statistically significant. The magnitude of the F-statistic further indicated the importance of these variables in the model, manifesting their impact on the amount of fertilizer dissolved. A larger F value implies a stronger influence. Accordingly, among the factors examined, agitation speed had the most significant effect on fertilizer solubility, followed by agitation time, and then submerged depth of the agitator.

Table 4

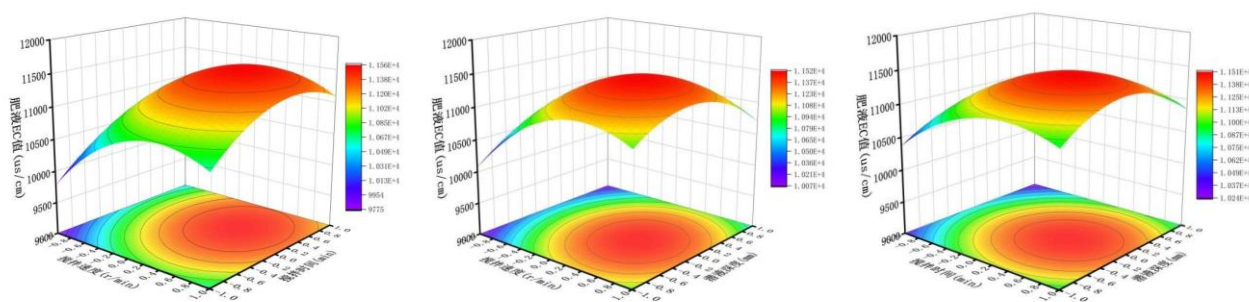
Analysis of variance						
Source of variance	Square sum	Degrees of freedom	Mean square	F-value	P-value	Significance
Model	4.927e6	9	5.474e5	1735.75	< 0.0001	**
a	1.073e6	1	1.073e6	3402.46	< 0.0001	**
b	6.676e5	1	6.676e5	2116.69	< 0.0001	**
c	19900.13	1	19900.13	63.10	< 0.0001	**

Source of variance	Square sum	Degrees of freedom	Mean square	F-value	P-value	Significance
ab	13225.00	1	0.023	41.93	0.0003	**
ac	19600.00	1	0.01	62.14	0.0001	**
bc	930.25	1	0.016	2.95	0.1296	
a2	1.268e6	1	1.268e6	4021.90	< 0.0001	**
b2	7.031e5	1	7.031e5	2229.12	< 0.0001	**
c2	8.38e5	1	8.380e5	2657.04	< 0.0001	**
residual	2207.75	7	315.39			
lost proposal	407.75	3	135.92	0.3020	0.8236	
errors	1800.00	4	450.00			
sum	4.929e6	16				

Note: *means significant, $p < 0.05$; **means significant, $p < 0.01$

Two-factor interaction effect analysis and parameter optimization

Based on the results obtained from the analysis of the above regression equation, the effect of the remaining factors on the solubility of the fertilizer will be further investigated by arbitrarily selecting the level of one of the factors to be zero. By applying Design Expert software, the response surface for the interaction effects was derived as shown in Fig. 11.



(a) stirring speed versus stirring time response surface (b) stirring speed versus submerged liquid depth response surface (c) stirring time versus submerged liquid depth response surface

Fig. 11- Corresponding surfaces for the effect of interacting factors on test metrics

When observing the images, it was found that the two-factor response surface morphology of different fertilizers showed remarkable consistency, and there was also an essential similarity in the influence pattern of each factor. First of all, through Figure 11a it was noticed that the solubility of fertilizers tended to increase with the increase of time under the condition that the stirring speed was kept constant. However, the effect on the solubility gradually decreased with the continuous increase of time. In the case where the stirring time was kept constant, the solubility of the fertilizer tended to increase as the stirring speed increased. The effect on solubility gradually decreased as the speed was increased to a certain level. Observation of Fig. 11c reveals a similar pattern, which also showed a tendency of decreasing and then increasing as the depth of the submerged liquid increased.

Finally, observation of Figure 11b reveals that the solubility of the fertilizer tended to increase as the stirring speed increased while the depth of the submerged liquid was kept constant, but once the speed was increased to a certain level, its effect on the solubility gradually diminished. The effect of stirring time also showed a similar pattern. Therefore, the above analysis showed that the effects of stirring time, stirring speed and submerged liquid depth on the solubility of fertilizers had similar regular trends. Under well-mixed conditions, continuing to increase the stirring speed made a decreasing contribution to the dissolution of the fertilizer, consistent with the simulation data. Therefore, optimizing the stirring speed can reduce energy consumption while ensuring mixing efficiency. Similarly, the increase in dissolution rate by extending the agitation time had a marginal effect and was limited by the inherent solubility of the fertilizer.

Selecting the appropriate stirring time was a key factor in reducing energy consumption and improving operational efficiency.

The depth of submerged liquid had a significant effect on the solubility of fertilizer, showing a non-linear relationship. The undissolved amount of fertilizer decreased and then increased as the submerged depth increased. This phenomenon would be due to the fact that too deep a submerged depth would result in the flow field generated by agitation at the bottom of the container, although it was ideal, but its effect could not be effectively extended to the upper layer of the liquid; and when the submerged depth was insufficient, the flow field could not reach the bottom of the container adequately.

Therefore, optimizing the submerged liquid depth was a key factor to improve the efficiency of fertilizer dissolution.

Combining the above factors, global multi-objective optimization was carried out, and the fertilizer solubility was taken as the objective function, and the stirring speed, stirring time and submerged liquid depth were optimally designed. The best combination of each parameter was available through the optimization mathematical model equation, according to the optimization mathematical equation :

$$\begin{cases} \max M = f_1 & A, B, C \\ s.t. \begin{cases} A \in 300, 500 \\ B \in 3, 7 \\ C \in 610, 690 \end{cases} \end{cases} \quad (6)$$

where: A, B, and C were the actual values corresponding to stirring speed, stirring time, and agitator submergence depth, respectively.

In order to obtain the optimal parameter combinations, Design expert software would be applied to solve the optimization. Finally, Table 5 would present the optimal operating parameter combinations of the agitator.

Table 5

Type	Optimum stirring speed / (r/min)	Optimum stirring time /min	Optimum Submersible Depth /mm
Theoretical	394.3	5.31	651.64
Actual value	400	5	660

To ensure the feasibility of the theoretically optimized values in practical applications, rounding was performed and experimentally verified. The results showed that the optimal agitation parameters were 400 r/min, 5 min stirring time, and 660 mm agitator submerged liquid depth.

CONCLUSIONS

(1) A new type of coaxial counter-rotating agitator was designed and the results of modal analysis showed that the agitator had good vibration performance and did not cause equipment resonance, which was in line with the design expectations.

(2) The field simulation analysis showed that when the stirring speed exceeded the critical agitation speed threshold, the fluid flow was complicated, the speed in the agitation zone was higher, and the velocity distribution in the fertilizer mixing drum was characterized as the highest in the middle, the second highest at the edge, and the lowest in the mezzanine. In order to improve energy efficiency, 400 r/min was finally determined as the optimal speed.

(3) The Box-Behnken design method was used to optimize the working parameters, and quadratic regression analysis was used to investigate the effects of stirring speed, time and agitator submerged depth on the solubility of fertilizers, and it was found that the solubility of fertilizers increased with the increase of stirring speed and time, but the positive effect was weakened beyond the specific threshold, and the relationship between the submerged depth of the agitator and the solubility showed a nonlinear correlation. The optimal working parameters were stirring speed of 400 r/min, stirring time of 5 min, and submerged depth of 660 mm.

ACKNOWLEDGEMENT

We are very grateful to all the authors for their support and contribution with the manuscript. This work is partly supported by: Key R&D Program of Shandong Province, China" (2024TZXD045, 2024TZXD038);

Innovation Team Fund for the Fruit Industry of Shandong's Modern Agricultural Technology System (SDAIT-06-12); The State Key Laboratory of Mechanical System and Vibration (Grant No. MSV202002), and the Modern Agriculture Coarse Grain Industry Technology System Project of Shandong Province (SDAIT-15-05).

REFERENCES

- [1] An, B., Meng, X. Y., Yang, S. J., Sang, W. M., (2023). Study of local mesh refinement LBM algorithm for non-uniform rectangular grids. *Journal of Mechanics*, vol.55(10), pp. 2288-2296.
- [2] Dang, L G., Guo, S X., Wang, D. B., Zhang, S. G., Cao, H. L., (2013). Numerical study of agitation characteristics of different combined paddle agitators, *Journal of Zhengzhou University: Engineering Edition*, vol.34 (03), pp. 59-62.
- [3] Fang, D. I., Wang, J., Liu, J. J., Lou, Y. Z., (2024). Spatial and Temporal Differentiation of Agricultural Water Use Efficiency and Its Influencing Factors Under the Combination of Multiple Models. *Water Saving Irrigation*, pp. 105-113.
- [4] Guo, S. M., Liu, J. P., (2017). Commonly used fertilisers and scientific fertilization technology for greenhouse vegetables, *Agriculture and Technology*, vol.37 (24), pp. 32-32.
- [5] Hua, J., Li, W., Lu, Z. P., Zhan, L. B., Huang, T. C., (2023). Study on solid-liquid mixing uniformity in double-layer paddle mixing tank [J]. *Science, Technology and Engineering*, vol.23 (28), PP. 80-90.
- [6] Jin, Z., Zhang, J., Guo H. Y., Hu, Y. M., Chen, X. Y., Huang, H., Wang, H. Y., (2020). Development and testing of intelligent sensing and precision proportioning system of water and fertilizer concentration. *Smart Agriculture*, vol.2 (2), pp. 82-93.
- [7] Jin, Y., Zhao, L. X., Xu, B. R., Zhang, X. G., et al., (2023). Flow field characteristics of a cyclone separation column under vibration conditions. *Chemical Engineering*, vol.51(11);
- [8] Li, L., (2024). Energy-saving axial flow mixer. Patent. CN202410985251.3 CHINA Li, T. H., Zhang, S. Q., Zhang, C. F., et al., (2023). Research and experiment on efficient mixing modes of different forms of water and fertilizer. *INMATEH Agricultural Engineering*, vol.70 (2), pp. 278-298.
- [9] Liu, S. F., Lu, Z. Q., Shi, X. P., et al., (2022). Analysis and design of solid-liquid mixed fertilizer device for organic fertilizer on solid-liquid two-phase flow. *INMATEH Agricultural Engineering*, vol.66 (1), pp. 167-181.
- [10] Liu, S. X., Xu, C. B., Zhang H. J., Zhang, C. F., Liu, X. M., (2020), Optimised design and test of orchard open furrow fertiliser machine frame. *Journal of Agricultural Machinery*, vol.51 (S1), pp. 113-122.
- [11] Liu, W. L., Yang, R. B., Pan, Z. G., et al., (2025). Design and experimental study of water-fertilizer integrated fertilizer mixer in large fields. *Journal of Agricultural Mechanization Research*, vol.47 (2), pp. 139-145.
- [12] Martínez-Gimeno M A., Jiménez-Bello M A., Lidón A, Manzano J., Badal E., Pérez-Pérez J G., Bonet L., Intrigliolo D S and Esteban A., (2020). Mandarin irrigation scheduling by means of frequency domain reflectometry soil moisture monitoring. *Agricultural Water Management*, vol.235, issue.5, pp. 234-241.
- [13] Song, Y. P., Zhang, S., Li, T. H., Gao, D. S., Fan, G. J., (2018). Design and numerical simulation analysis of orchard fertilizer mixer. *Transactions of the Chinese society for Agricultural Machinery*, vol.49 (S1), pp. 181-188.
- [14] Tian, Y. J., Hui, T., Li, X. J., Zhang, A., Bai, Y. J., (2024). *A portable air agitator*. Patent. CN202323497341.8. China
- [15] Wang, F. H., Zhang, C. H., Wang, G. Q., Jiang, L. Y., Liu, H., (2024). Numerical simulation and performance analysis of granular fertilizer agitator in greenhouse. *Journal of Agricultural Mechanization Research*, vol.45 (10), pp. 60-68.
- [16] Wu, X. B., Gong, F., Ye, Y., (2023). Regional differences and convergence of green efficiency of agricultural water use in China. *China Rural Water Conservancy and Hydropower*, vol.6, pp.196-201.
- [17] Yuan, H.B., Li, L., Wang, J.H., Wang, H. H., N. A. Sigrimis., (2016). Design and testing of greenhouse water-fertiliser-integrated nutrient solution control equipment. *Journal of Agricultural Engineering*, vol.32, issue 8, pp.27-32.
- [18] Zhang, Y., Zhang, N., Wang, Y. Q., Liu, X. H., (2014). Effects of drip irrigation on the growth, yield and quality of watermelon in greenhouse, *Journal of Agricultural Engineering*, vol.30 (7), pp. 109-118.
- [19] Zhang, Y. B., Wei, Z. Y., Hu, Y., (2018), Design and numerical simulation of water-fertiliser mixer, *Agricultural Mechanisation Research*, vol. 40 (3), pp. 33-36.

DESIGN AND EXPERIMENT OF AIR-SUCTION GARLIC SEEDING UNIT

气吸式蒜苗单体的设计与实验

Minghao LU¹⁾, Yazhi WANG¹⁾, Tao LIU¹⁾, Chunling ZHANG^{*1)}, Ce LIU¹⁾, Gang ZHAO¹⁾¹⁾ Anhui Agricultural University College of Technology / ChinaTel: 0551-65786317; E-mail: zhangcl@ahau.edu.cn

*Corresponding author: Chunling Zhang

DOI: <https://doi.org/10.35633/inmateh-75-11>**Keywords:** Garlic seeding unit, Air-suction, Garlic seed sowing, the bud reversing device.**ABSTRACT**

Based on the requirements for hybrid garlic seed sowing, the overall structure of an air-suction garlic seeding unit was designed, and its working principle was described. The adsorption pressure required for the seed metering device was determined to be -5 kPa. One hopper was selected for the bud reversing device, with an angle of 24.5°, and the perimeter of the insertion device measured 600 mm. The optimal combination of parameters for sowing involved a negative pressure of -5 kPa and a forward speed of 1 km/h at the third level. Under these conditions, the qualified rate of individual sowing reached 84.26%, while the missed sowing rate was 7.12%, meeting the agronomic requirements for garlic seed sowing. Field experiments validated the theoretical analysis and bench tests, providing a solid foundation for the future production and promotion of garlic sowing units.

摘要

根据杂交大蒜种子的播种要求, 设计了吸气式大蒜播种单体的整体结构, 并描述了其工作原理。确定种子计量装置所需的吸附压力为-5 KPa。为磷芽交换装置选择了一个料斗, 角度为24.5°, 插入装置的周长为600 mm。播种的最佳参数组合为负压-5 KPa, 前进速度为1 km/h, 设定在三级档位。在此条件下, 单粒播种的合格率达到了84.26%, 漏播率为7.12%, 满足了大蒜种子播种的农艺要求。田间试验验证了理论分析和台架试验的准确性, 为大蒜播种单体的未来生产和推广奠定了基础。

INTRODUCTION

Garlic can be consumed as both garlic head and garlic sprouts and can also be used as a seasoning. Garlic has the effects of disinfection, swelling relieving, insecticidal, and dysentery stopping (Jia-feng et al., 2021). Garlic polysaccharides extracted from garlic have a specific lipid-lowering effect, which can improve human intestinal microbiota, reduce liver burden, and may reduce the risk of metabolic syndrome (Chan-yuan et al., 2020). In 2020, the global garlic planting area was 1.68 million hectares, with a garlic production of 32 million tons. Its planting area, production, and foreign trade export volume ranked first globally (Xiang-yuan et al., 2017; Bin-bin et al., 2019). At present, the cultivation of garlic in China is still mainly artificial (Jia-lin et al., 2018). However, due to the high planting cost and long planting cycle, the mechanization of garlic planting should be strengthened. At present, Minghao Lu from Anhui Agricultural University, one of the article's author, has designed an anti-seed tooth assisted air suction garlic seeder. Chun-ling Zhang et al., (2021), designed an electric hydraulic mixed regulation garlic seeder. Xiang et al., (2023), from Nanjing Vocational and Technical University of Technology have designed a self-propelled garlic sowing and fertilization integrated machine. Internationally, Türkiye DEMSAN Company has designed a traction garlic planter (Zhao-guo et al., 2021). Italian company SPAPPERI has also designed a mechanical garlic seeder that can sow a single seed, avoiding situations where there is multiple or no garlic seeds at once (Shuang-xi et al., 2015). French company ERME has designed three different series of garlic seeders (Dong et al., 2020).

Garlic seeders on the market still mainly use mechanical seed picking and metering. People used metering components similar to the spoon chain type (Ai-jun et al., 2018), which cannot adapt well to different garlic sizes and may cause congestion. At the same time, there will be significant vibration when sowing in the field, making the efficiency of the mechanical seeder low (Yu-xiang et al., 2022). The pneumatic type relies on the negative pressure provided by the fan to tightly adsorb garlic onto the seed tray, meeting the requirements of garlic seeds of different sizes and ensuring the stability of single seed picking (Xin-peng et al., 2022; Han et al., 2023).

Zaidi *et al.*, (2019), invented a pneumatic planter for peas planting. However, current research is still limited to seeders, and it is necessary to study a garlic seeding unit to solve the seeding problem (Yu-dao and Xue-zhen, 2020).

To increase the single seed rate of garlic seeding, a kind of air-suction garlic seeding unit was designed in this paper. It mainly includes an air-suction garlic seeder, an upright planting mechanism, a pneumatic system, and a profiling mechanism. It can achieve the functions of single seed picking and upright planting of garlic seeds, meeting the agronomic requirements of garlic planting.

MATERIALS AND METHODS

The air-suction garlic sowing unit mainly consists of components such as an air-suction garlic seeder, a bracket, a profiling rod, a ground wheel, a seed guide device, a bud reversing device, and an upright insertion device, as shown in Figure 1. The unit body adopts a traction type and is connected to the tractor through a three-point suspension. The bracket mainly consists of square, tubular, and fixed brackets. The front end of the tubular support is fixedly connected with a three-point suspension hanger, the upper part of the tubular support is fixedly connected with a negative pressure fan, and the tubular support is fixedly connected with fixed support. The two sides of the fixed support are connected with four profiling rods through shaft hinges, and the other end of the four profiling rods is hinged with the square frame through another pair of shafts. The rear end of the negative pressure fan is fixedly connected to the belt pulley on the PTO (Power Take-Off) device through a belt, forming a mechanical structure with belt transmission. The belt pulley serves as the driving wheel, and the shaft at the rear end of the fan serves as the driven shaft. Through a hose, the fan is connected to the negative pressure pipe of the suction garlic seeder to form a closed channel, and the fan provides stable negative pressure for the air chamber of the seeder.

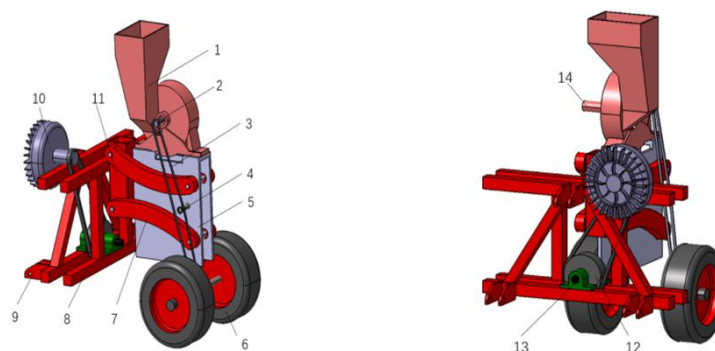


Fig. 1 - Schematic Diagram of the Air-Suction Garlic Sowing Unit Structure

(1) Air suction garlic seeder; (2) Seeding shaft; (3) Chain; (4) Tensioning wheel; (5) Square bracket; (6) Ground wheel; (7) Profiling rod; (8) Pipe bracket; (9) Three-point suspension hanger; (10) Negative pressure fan; (11) Fixed bracket; (12) Belt pulley; (13) PTO device; (14) Negative pressure pipe

Inside the square bracket, a seed guide device is fixedly connected below the seed discharge port of the air-suction garlic seed metering device. A bud reversing device is fixedly connected below the seed guide device. A vertical insertion device is fixedly connected below the bulb-reversing device. A tensioning wheel is fixedly connected to the outer surface of the square bracket and meshes with the chain to help adjust its tension. A ground wheel is fixedly connected to the rear of the vertical insertion device below the square bracket.

The suction-type garlic sowing unit provides negative pressure adsorption of garlic seeds on the seeding tray through a negative pressure fan and rotates regularly with the seeding tray. Subsequently, the hybrid garlic seeds are discharged from the seed discharge port of the seeder and then enter the bulb-reversing device. Finally, they enter the vertical insertion device in an upright posture. With the insertion device standing upright, they are planted in the soil, and the air-suction garlic sowing unit achieves a single seed sowing operation.

Structure of the bud-reversing device

Below the seed guide device is a bud reversing device, mainly composed of a conical hopper, connecting rod, gear, and other components, as shown in Figure 2. The apex of the conical hopper faces downwards. When the garlic seed falls into the conical hopper, it leans against the side wall. After the garlic seed stabilizes in the hopper, the hopper opens from the top of the cone, it leans against the side wall.

After the garlic seed stabilizes in the hopper, the hopper opens from the height of the cone, and the garlic seed that tends to be upright at this time falls out in this posture. The movement process of the hopper is shown in Figure 3. In this upright state, the hybrid garlic seeds enter the insertion device to achieve the goal of upright sowing.

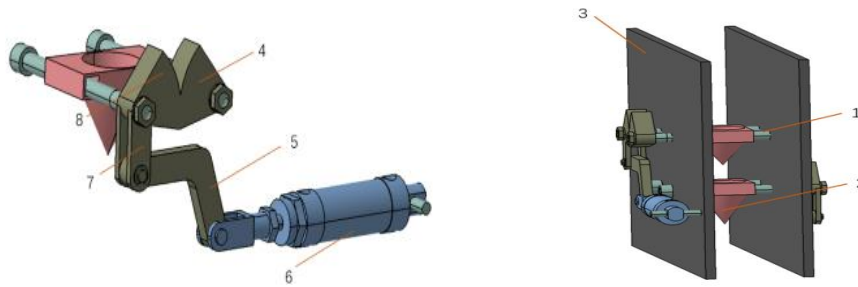


Fig. 2 - Schematic diagram of the structure of the bud-reversing device:

(1) Rotary shaft; (2) Conical hopper; (3) Square frame; (4) Right gear; (5) Obtuse angle connecting rod; (6) Cylinder; (7) Straight connecting rod (8) Left gear

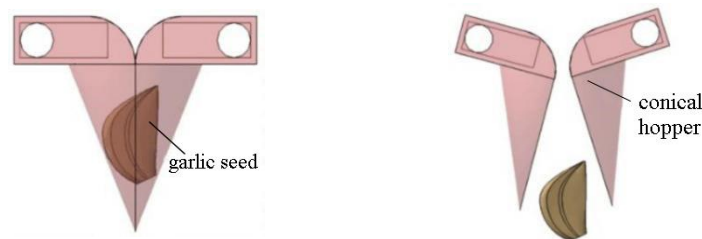


Fig. 3 - Working process of conical hopper

For the opening and closing of the conical hopper, the principle is controlled by the motion of the connecting rod mechanism. A pair of rotating shafts with gears connected to the surface are symmetrically fixed near the conical top surface of the hopper. The two gears mesh together, and a straight connecting rod is fixedly connected below the left gear. Its lower hinge is hinged with an obtuse angle connecting rod, and a small cylinder is hinged with it below this obtuse angle connecting rod. The small cylinder relies on an electromagnetic valve to control the extension of the piston, which causes the left gear to rotate clockwise, driving the right gear and its corresponding rotating shaft to rotate, making the hopper open and close. After some time, the piston rod retracts, and similarly, the hopper becomes tightly closed.

For the design of a conical hopper size, the following conditions must be met, as shown in the formula (1) (Rong-jiang et al., 2022).

$$\begin{cases} D_Z > h_{\max} \\ D_1 > t_{\max} \\ D_1 > w_{\max} \\ H_Z > h_{\text{avg}} \end{cases} \quad (1)$$

$$k = \frac{D_1}{2H_Z} \quad (2)$$

where:

D_Z is the top diameter of the seed dropping and D_1 is the stabilizing zones of the conical hopper, [mm]; H_Z is the height of the stabilizing zone, [mm]; h_{\max} is the maximum length of the hybrid garlic seed, 34.1 mm; t_{\max} is its maximum thickness, 19.8 mm; w_{\max} is the maximum width of the hybrid garlic seed, 21.8 mm; h_{avg} is the average length of the hybrid garlic seed, 29.6 mm. k is the slope of the generatrix of the conical hopper.

Therefore, the seed falling area of the conical hopper is designed to be 40 mm, the diameter of the stable area is not less than 21.8 mm, and the height of the stable area is not less than 29.6 mm. According to formula (2), the slope of the hopper generatrix can be obtained.

Support and profiling mechanism

In the design of the air suction garlic sowing unit, a square bracket is set up with a U-shaped side view. Above, it is used to place an air-suction garlic seeder, and a groove is opened for the seeder to drop seeds at the seed discharge port. Two profiling rods are hinged on the square frame's outer side. During the movement of the air suction seeding unit, the relative position of the fixed bracket remains unchanged and is only affected by the traction of the tractor. The components behind the fixed bracket will fluctuate with the fluctuation of the ground.

For the contour line of the profiling rod, a certain degree of curvature is used to ensure that the rod can withstand internal and external pressure during stationary and moving processes. One side of the four rods is hinged on a fixed bracket, and the other is hinged on a square bracket (Safari et al., 2019; Patel and Prajapati, 2018).

In order to carry the garlic seeder with a bottom length of 405 mm and a width of 88.5 mm, accommodate the bud reversing device, and reduce weight, volume, and cost; its length is designed as 410 mm, and its width is designed as 120 mm. For the design of the profiling rod, the parallelogram profiling mechanism, known for its parallelogram movement characteristics, is widely used in corn seeders to ensure consistent sowing depth during operation and enhance the overall stability of the machine (Patel and Prajapati, 2018).

The profiling rod is in contact with the square bracket, so the lateral width of the profiling rod is designed to be 120 mm, the length is designed to be 250 mm, and the profiling rod is designed to be parallel to the profiling rod, as shown in Figure 4.

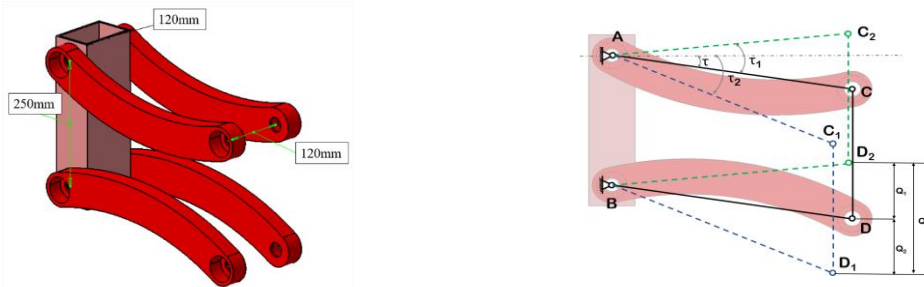


Fig. 4 - Schematic Diagram and Dimensional Drawing of the Profiling Rod

The calculation formula for the upper and lower profiling quantities (Shu-hong et al., 2013) is shown below.

$$Q = L[\sin(\tau + \tau_2) + \sin(\tau_2 - \tau)] \tag{3}$$

$$L = \frac{Q_2}{\sin \tau + \sin(\tau_2 - \tau)} \tag{4}$$

$$Q_1 = L[(\tau + \tau_1) - \sin \tau] \tag{5}$$

where:

Q is the total profiling displacement, [mm]; Q_1 is the upper profiling displacement, [mm]; Q_2 is the lower profiling displacement, [mm]; L is the length of the line connecting the hinge points on both sides of the profiling rod, [mm]; τ is the traction angle, [°]; τ_1 is the upper profiling angle, [°]; and τ_2 is the lower profiling angle, [°].

According to the formula, when the upper and lower profiling quantities are the same, the shorter the profiling rod L , the greater the variation of τ . Therefore, it is necessary to reduce the variation range of τ appropriately while ensuring that the machine's overall size and center of gravity are reasonable. Referring to the work Ji-guo et al., (2022), substituting formula (6) yields $L_{AC} = 413.4$ mm, taken as $L_{AC} = 410$ mm, and substituting formula (5) yields $Q_2=99.2$ mm, satisfying the condition.

Performance analysis of air-suction garlic sowing unit operation

The angle of the conical hopper is set to the intermediate value of 24.5° , and simulation experiments are conducted on 1, 2, and 3 hoppers, as shown in Figure 5. The statistical test results show the effect of the number of conical hoppers on the rate of bulb erection. Set each hopper's opening and closing times to 10 times, and each particle factory drops seeds ten times. After repeating the experiment at three levels five times, statistically analyze the number of garlic seeds with upright scales and record the upright rate of scales, as shown in Table 1. The maximum upright rate of scale buds is 92.09%, the minimum is 90.83%, and the difference is 1.26%. Therefore, the number of conical hoppers has little effect on whether the scale buds of hybrid garlic seeds can stand upright. Therefore, one is selected as a component of the bud-reversing device in selecting the number of conical hoppers.



Fig. 5 - Simulation process diagram of the effect of the number of hoppers on the upright scale of hybrid garlic seeds

(a) 2-stage conical hopper (b) 3-stage conical hopper

Analysis of the influence of conical hopper angle

When the number of conical hoppers is 1, a single-factor experiment is conducted on the angle of the conical hopper to analyze the influence of its angle on the vertical rate of the scales.

Seven levels, 18.5° , 20.5° , 22.5° , 24.5° , 26.5° , 28.5° , and 30° , were set as hopper angles. Each hopper's opening and closing times were set to 10 times, and each particle factory dropped ten times. After repeating the experiment five times at the three levels, the vertical rate of the experimental evaluation index was statistically analyzed. The specific experimental plan and results are shown in Table 2.

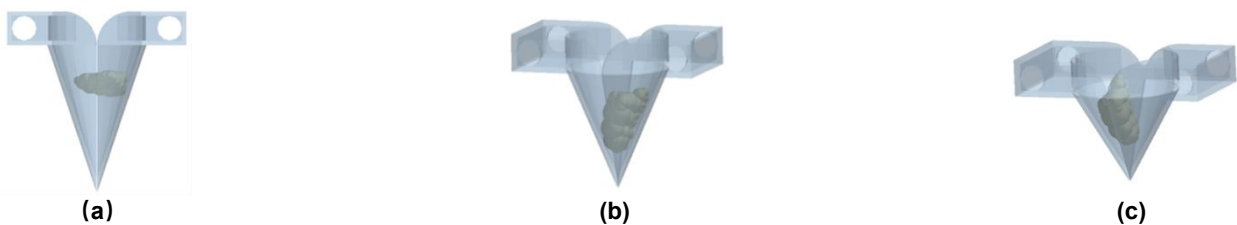


Fig. 6 - Simulation process diagram of the effect of hopper angle on the upright scale of hybrid garlic seeds

(a) 18.5° conical hopper (b) 24.5° conical hopper (c) 30° conical hopper

Analysis of Vertical Insertion Performance

As the final step in the sowing process of hybrid garlic seeds, the performance of the vertical sowing device directly affects the sowing results. In the previous section, the angle of the conical hopper was determined to be 24.5° . In order to make the seeding depth meet the requirements, a cone with the same top diameter and a height of 50 mm is designed on the external surface of the inserter, as shown in Figure 7(a).

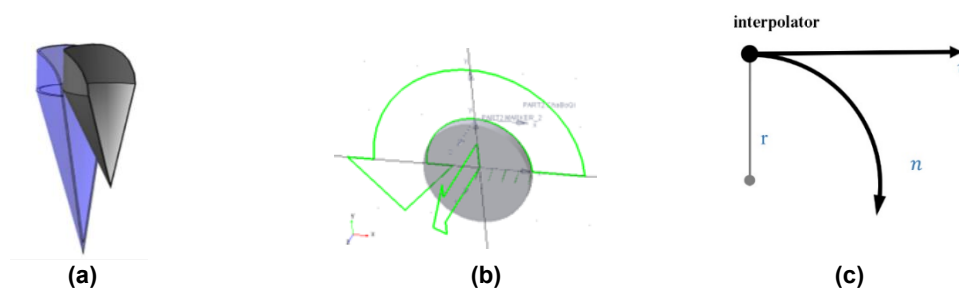


Fig. 7 - Schematic diagram of the structure and motion principle of the insertion device

The movement of the planting mechanism is composed of the horizontal movement of the air-suction garlic planting unit and the planting motion of the planting device. Using the Adams virtual prototype analysis software, a dynamic simulation analysis of the planting mechanism was conducted. The planting device model was simplified to a circular cam, and the planting mechanism was simplified to a marked point on the edge of the cam. In the simulation software, it was assumed that there is no gravity, as shown in Figure 7 (b).

Conduct dynamic analysis on the insertion device, where the insertion device is located at the highest position relative to the ground, the initial position of movement, and moves in a circular direction while also moving horizontally with the tractor, as shown in Figure 7 (c).

Set the distance between the marked point and the axis of the circular convex block as r , and as time passes, the coordinates (x, y) of the marked point will continuously change, as shown in the following equation.

$$x = vt + r \cos 2\pi nt \quad (6)$$

$$y = 2r - \sin 2\pi nt \quad (7)$$

where: x is the horizontal displacement component of the seeding unit, [m]; y is the vertical displacement component of the seeding unit, [m]; v is the forward speed of the machine unit, [m/s]; n is the rotational speed of the seeding unit, [r/s]; r is the radius of the seeding unit, [m].

In general, during actual sowing operations, the forward speed of the unit is 0.5~1.5 km/h, and the spacing of garlic seeds is 10 cm. Therefore, when the insertion device rotates around the axis to the next insertion device and comes into contact with the ground, the arc length is 10 cm. The relationship between the perimeter of the insertion device, the number of insertion devices installed on the insertion mechanism, and the rotation speed of the insertion device is shown below.

$$C = 0.1u \quad (8)$$

$$C = 2\pi r \quad (9)$$

$$n = \frac{v}{C} \quad (10)$$

where: C is the circumference of the seeding unit, [m]; u is the number of seeding unit; v is the forward speed of the machine unit, [m/s].

From the above equation, it can be concluded that the circumference of the insertion device is only related to the number of insertion devices. Once the circumference is determined, the size of the rotational speed can be determined.

Field trials

This article tests the sowing performance of air-suction garlic seeders by GB/T 6973-2005 “Test Methods for Single Grain (Precision) Planters”. A field experiment was conducted in the Agricultural Cuiyuan of Anhui Agricultural University in April 2023, with a temperature of 15-22°C. Before sowing, rotary tillage was performed on the soil.

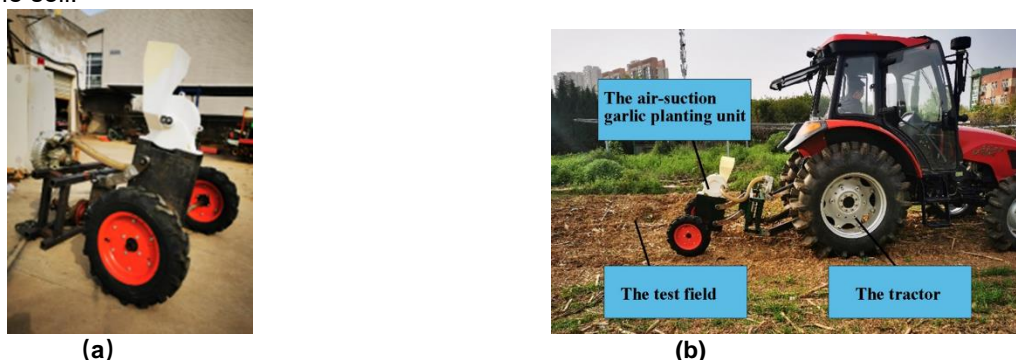


Fig. 9 - Field Experiment

As shown in Figures 9(a) and 9(b), the sowing unit includes a frame, profiling rod, seed guide, scale bud reversing device, vertical planting device, pneumatic system, and transmission system. The tractor powers the fan to supply negative pressure for the air-suction metering device, allowing stable discharge of garlic seeds. Hybrid garlic seeds, separated from low-quality seeds, served as the experimental material, with an average length, width, thickness, and sphericity of 29.6 mm, 16.9 mm, 15.1 mm, and 66.3%, respectively.

The seeds were spot-sown at 100 mm intervals, with a 30-40 mm depth and 45-52 plants/hm² density. The air-suction seeder operated under a -5 kPa pressure and at forward speeds of 0.5, 1, and 1.5 km/h.

After each sowing, record the number of holes without garlic seeds as the missed seeding count, and record the number of holes with a single garlic seed as the qualified seeding count. The formulas for calculating the missed seeding rate and qualified seeding rate are as follows:

$$A = \frac{a}{S} \times 100\% \quad (11)$$

$$B = \frac{b}{S} \times 100\% \quad (12)$$

where: A is the missed seeding rate, [%]; a is the number of holes without garlic seeds; S is the total number of hybrid garlic seeds counted; B is the qualified seeding rate, [%]; b is the number of holes with a single garlic seed.

RESULTS

The effect of the number of conical hoppers on the rate of bulb erection

After repeating the experiment at three levels five times, statistically analyze the number of garlic seeds with upright scales and record the upright rate of scales, as shown in Table 1. The maximum upright rate of scale buds is 92.09%, the minimum is 90.83%, and the difference is 1.26%. Therefore, the number of conical hoppers has little effect on whether the scale buds of hybrid garlic seeds can stand upright. Therefore, one is selected as a component of the bud-reversing device in selecting the number of conical hoppers.

Table 1

The effect of the number of hoppers (1, 2, 3) on the uprightness rate of garlic seeds, including the standard deviation and coefficient of variation of the experimental results

Number of conical hoppers X_1 (piece)	Scale bud upright rate (%)	Average (%)	Standard deviation (%)	Coefficient of variation (%)
1	91.62	91.54	0.39	0.43
	92.09			
	91.76			
	91.31			
	90.94			
2	90.98	91.26	0.37	0.40
	90.83			
	91.37			
	91.21			
	91.89			
3	91.38	91.60	0.28	0.31
	91.95			
	91.53			
	91.21			
	91.88			

The influence of single-factor hopper angles on the upright scale of hybrid garlic seeds

After repeating the experiment five times at the three levels, the vertical rate of the experimental evaluation index was statistically analyzed. The specific experimental plan and results are shown in Table 2.

The simulation process diagram shows the influence of single-factor hopper angles on the upright scale of hybrid garlic seeds. Seven angle levels were set in the experiment, and the diagram only displays three different conical hopper designs.

Table 2

Results of single factor test on the effect of hopper angle on hybrid garlic seed upright rate

Hopper angle (°)	Upright rate of hybrid garlic seeds (%)				
	1	2	3	4	5
18.5	84.31	84.87	85.09	85.01	84.62
20.5	87.56	86.57	87.43	86.96	87.02
22.5	90.03	90.14	89.94	91.24	90.53
24.5	91.98	92.65	91.44	91.88	91.32
26.5	90.26	89.42	89.57	88.79	89.36
28.5	86.01	85.71	86.47	85.71	86.39
30.0	84.12	85.21	84.01	84.98	85.62

Note: In the single-factor experiment, the number of hoppers was set to 1.

By analyzing the trend of changes in the upright rate of the bulb, it can be concluded that when the number of conical hoppers is 1, the upright performance of the bulb reversing device first increases and then decreases with the increase of hopper angle. When the angle of the conical hopper is 24.5°, the upright effect of the bulb is the best. The upright rate of hybrid garlic seeds is 91.85%, which can meet the requirements for the upright rate of garlic seeds.

The influence of the insertion device perimeter on the trajectory of the inserter

Draw a trajectory map of the inserter with a 400-900 mm circumference, as shown in Figure 8. Observe the trend of changes in the trajectories of each graph. The point corresponding to the end of the vertical axis is the lowest point of the inserter. Moving 50 mm above the vertical axis is the trajectory of the inserter entering and exiting the soil.

As the inserter's perimeter increases, the inserter's trajectory entering the soil tends towards a vertical line. However, considering the position relationship of the insertion device and the size of the individual machine, 600 mm is selected as the perimeter of the insertion device, which means there are six insertion devices, and the rotation speed of the insertion device is 0.463 rad/s.

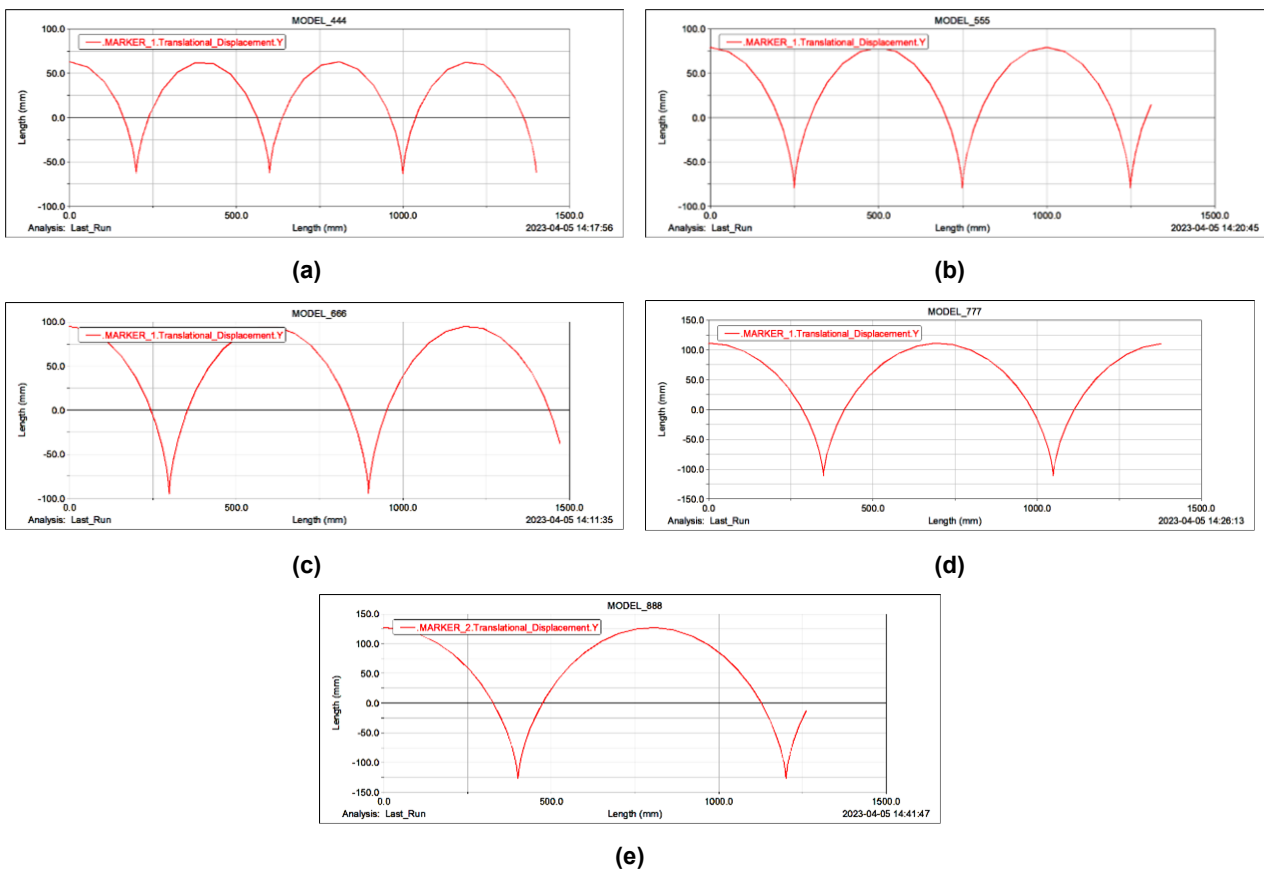


Fig. 8 - Spooler trajectory diagram

(a) 400 mm perimeter trajectory; (b) 500 mm perimeter trajectory; (c) 600 mm perimeter trajectory; (d) 700 mm perimeter trajectory; (e) 800 mm perimeter trajectory

Field trials results

The experiments were conducted under the specified conditions, and the following results were obtained. Statistical analysis revealed the effect of the unit's forward speed on the seeding qualification rate and missed seeding rate. Each experiment was repeated three times, with the average values calculated and presented in Table 3.

Table 3

Impact of three-level unit forward speed on garlic seeding qualification and missed seeding rates

Level	Forward speed of the unit (km/h)	Seeding qualification rate (%)	Missed seeding rate (%)
1	0.5	81.12	11.33
2	1	84.26	7.12
3	1.5	79.29	9.54

Table 3 shows that when the negative pressure remains constant, and the unit advances at a speed of 1 km/h, it is the level with the highest qualified seeding rate and the lowest missed seeding rate among the three levels.

The forward speed of the unit is set to 1 km/h, and three levels of negative pressure (-4, -5, and -6 kPa) were applied to regulate the metering devices in the seeding unit. Each experiment is repeated three times. Calculate the average of the test results and record the results as shown in Table 4.

Table 4

Impact of three-level negative pressure on garlic seeding qualification and missed seeding rates

Level	Negative pressure (kPa)	Seeding qualification rate (%)	Missed seeding rate (%)
1	-4	80.39	9.33
2	-5	84.26	7.12
3	-6	82.86	7.83

When the negative pressure is -5kPa, the qualified rate of sowing reaches the highest among the three levels, and the missed rate reaches the lowest among the three levels.

CONCLUSIONS

This study proposes an air-suction garlic seeding unit. This unit allows the garlic to be stably planted upright in the soil. The unit adsorbs garlic seeds onto the seeding tray through negative pressure and delivers the seeds to the seed guide device at zero speed. Finally, it enters the vertical planting device upright and is planted in the soil. Therefore, it meets the agronomic requirements of garlic seeds to achieve single-seed sowing and erect scales during the mechanical sowing process.

According to the requirements of hybrid garlic seed sowing, the overall structure of the air-suction garlic sowing unit is designed, and its working principle is explained. For the principle analysis and theoretical calculation of the critical components of the seeding unit, the adsorption pressure required for the seed metering device is -5kPa, the number of hoppers used for the bulb seed changing device is selected as 1, the angle is selected as 24.5 °, and the perimeter of the insertion device is selected as 600 mm. These data provide support for subsequent field experiments.

When conducting a three-level field experiment, the optimal parameter combination for sowing results is negative pressure of -5kPa and a forward speed of 1 km/h at the three-level. The qualified rate of individual sowing can reach 84.26%, and the missed sowing rate is 7.12%, which meets the agronomic requirements for garlic seed sowing. Field experiments have verified the accuracy of theoretical analysis and bench tests, laying the foundation for the future production and promotion of garlic sowing units.

ACKNOWLEDGEMENT

Scientific Research Program of Anhui Province Higher Education Institutions: Research on the Annular Airflow Guiding Mechanism for No-till Corn Sowing Based on the Seed Collision Mechanism in the Seed Guide Tube and the Mechanism of Uniform Plant Spacing (No: 2022AH050897); Anhui Province Agricultural Machinery Equipment Application Industry Technology System Project.

REFERENCES

- [1] Ai-jun G., Xiao-yu L., Jia-lin H., Zhi-long Z., Ji & C.jun Z., (2018), Design and experiment of automatic directing garlic planter. *Transactions of the Chinese Society of Agricultural Engineering*, 34(11), 17-25. <https://doi.org/10.11975/j.issn.1002-6819.2018.11.003>
- [2] Bin-bin Y., Yi-xiang Z., Bang-hong Z., (2019), Measurement of the international competitiveness of China's garlic industry and it is influencing factors. *Agricultural Outlook*, 15(10),113-117+126.
- [3] Chan-yuan X., Wei G., Xue L., Shuang-shuang L., Yee C.F., (2020), Study on the hypolipidemic properties of garlic polysaccharide in vitro and normal mice as well as its dyslipidemia amelioration in type2 diabetes mice. *Food Bioscience*, 47. <https://doi.org/10.1016/j.fbio.2022.101683>
- [4] Chun-ling Z., Xiao-qing W., Dong-bou X., (2021), Design and experiment of electro-hydraulic mixed garlic planter. *Transactions of the Chinese Society of Agricultural Engineering*, 52(10), 166–174. <https://doi.org/10.6041/j.issn.1000-1298.2021.10.017>
- [5] Dong Z., Dong-mei C., Li-xiang Q., (2020), Design and experiment of modularized garlic combine harvester. *Transactions of the Chinese Society of Agricultural Engineering*, 51(4),95-102. <https://doi.org/10.6041/j.issn.1000-1298.2020.04.011>
- [6] Han T., Fu-dong X., Chang-su X., Jia-le Z., W. Yi-jia, (2023), The influence of a seed drop tube of the inside-filling air-blowing precision seed-metering device on seeding quality. *Computers and Electronics in Agriculture*, 204, 107555. <https://doi.org/10.1016/j.compag.2022.107555>
- [7] Jia-feng L., Mahmood M.S., Abbas R.Z., Dillawar A., Nawaz Z., Luqman M., Abbas A., Rafique A., (2021), Therapeutic appraisal of ethanolic and aqueous extracts of clove (*syzygium aromaticum*) and garlic (*allium sativum*) as antimicrobial agent. *Pakistan Journal of Agricultural Sciences*, 58(1), 245-251. <https://doi.org/10.21162/PAKYA/21.650>
- [8] Jia-lin H., Sheng-Hai H., Zi-ru N., Yan-qiang W., (2018), Mechanism analysis and test of adjusting garlics upwards using two duckbill devices. *Transactions of the Chinese Society of Agricultural Engineering*, 9(11), 87–96. <https://doi.org/10.6041/j.issn.1000-1298.2018.11.010>
- [9] Patel S.S., Prajapati J.M., (2018), Experimental investigation of surface roughness and kerf width during machining of blanking die material on wire electric discharge machine. *International Journal of Engineering*, 31(10), 1760-1766.
- [10] Rong-jiang C., Xiao-yu W., Jia-cheng X., Liang S., Chang-yu W., (2022), Design and test of arc duck-billed garlic seed planter. *Transactions of the Chinese Society of Agricultural Engineering*, 23(11),120-130.
- [11] Safari M., Joudaki J., Ghadiri Y., (2019), A comprehensive study of the hydroforming process of metallic bellows: investigation and multi-objective optimization of the process parameters. *International Journal of Engineering*, 32(11),1681-168.
- [12] Shuang-xi L., Jin-xing W., Hua-wei M., Lian-xaing F., Sheng-hui F., Z. Chang-wen, (2015), Design and experiment of moving along ridge control system for tobacco picking machine. *Transactions of the Chinese Society of Agricultural Engineering*, 33(s2), 83–87. <https://doi.org/10.11975/j.issn.1002-6819.2015.z2.012>
- [13] Shu-hong Z., En-chen J., Yi-xun Y., Yue-qian Y., Bai-liang T., (2013), Design and motion simulation of opener with bidirectional parallelogram linkage profiling mechanism on wheat seeder. *Transactions of the Chinese Society of Agricultural Engineers*, 29(14), 26-32.
- [14] Xiang D., Hai-chao S., Lin-hui Y., Xiaoping Z., Jin-jun M., (2023), Optimized design and experiment of the self-propelled garlic drilling and fertilizing integrated machine. *Journal of Chinese Agricultural Mechanization*, 44(7),16–25. <https://doi.org/10.13733/j.jcam.issn.2095-5553.2023.07.003>
- [15] Xiang-yuan L., Ai-jun G., Jia-lin H., Ji Z., Zhi-liang Z., (2017), Research status and prospects of garlic seeders. *Farm Machinery*, 2,105–107.
- [16] Xin-peng Z., Le Z., Fugui Z., (2022), Review of domestic pneumatic precision seed disperser research. *Agricultural Equipment & Vehicle Engineering*, 60(9), 93-97+113.
- [17] Yu-dao L., Xue-zhen S., (2020), Design and experimental study of a combined pneumatic plot seed-metering device for cotton. *International Journal of Engineering*, 33(8), 1652-1661. <https://doi.org/10.5829/IJE.2020.33.08B.24>

- [18] Yu-xiang H., Peng L., Jian-xin D., Xu-hui C., Shi-lin Z., Yan L., (2022), Design and experiment of side-mounted guided high-speed precision seed metering device for soybean. *Transactions of the Chinese Society of Agricultural Engineering*, 53(10), 44-53+75. <https://doi.org/10.6041/j.issn.1000-1298.2022.10.005>
- [19] Zaidi M.A., Amjad N., Mahmood H.S., Shah S.S., (2019), Performance evaluation of pneumatic planter for peas planting. *Pakistan Journal of Agricultural Sciences*, 56: 237-244. <https://doi.org/10.21162/PAKJAS/19.2125>
- [20] Zhao-guo Z., Yan -bin L., Hai-yi W., (2021), Research progress on key technology and equipment of potato mechanized harvest. *Journal of Yunnan Agricultural University (Natural Science)*, 36(6), 1092-1103

A REVIEW OF THE FEED RATE DETECTION AND STABILITY CONTROL METHODS IN COMBINE HARVESTERS

联合收割机喂入量检测与稳定控制方法研究现状与发展趋势

Xiaoyu YANG¹⁾, Panpan LI¹⁾, Zhihao ZHAO¹⁾, Chaoxu LEI¹⁾, Chengqian JIN^{*,1,2)}

¹⁾ School of Agricultural Engineering and Food Science, Shandong University of Technology, Zibo, Shandong / China

²⁾ Nanjing Institute of Agricultural Mechanization, Ministry of Agriculture and Rural Affairs, Nanjing, Jiangsu / China

Corresponding author: Chengqian JIN

Tel: +8615366092900; E-mail: 412114402@qq.com

DOI: <https://doi.org/10.35633/inmateh-75-12>

Keywords: Combine harvester, feed rate detection, noise removal, automatic control, research progress

ABSTRACT

The feed rate is an important index for evaluating the performance of a combine harvester. Determining how to accurately reflect the feed rate during harvesting and establishing a reliable detection model is a major focus of current research and an important basis for the next step of feed rate stable control. This paper provides an overview of feed rate detection methods and stable control techniques for combine harvesters. It reviews methods that estimate the feed rate based on the inclined conveyor extrusion pressure, header power, and threshing unit energy consumption. Additionally, it introduces machine learning-based methods that incorporate multiple influencing factors to predict the feed rate. A comparison of different noise reduction techniques used in feed rate detection is also presented, analyzing their effectiveness. Furthermore, this study examines feed rate control methods in combine harvesters, discussing various control approaches with an emphasis on methods that stabilize the feed rate by adjusting header height and harvester forward speed. In response to the current issues of inadequate detection accuracy in feed rate monitoring, limited adaptability, and instability in control systems, it is pointed out that future research needs to innovate in developing advanced sensor technology, optimizing automatic control algorithms as well as data fusion and analytical methodologies.

摘要

喂入量是衡量联合收割机性能的重要指标，通过何种方式将收获时机的喂入量反应出来并建立可靠的检测模型是当前研究的重点，也是下一步稳定控制喂入量的重要依据。该文概述了联合收割机喂入量检测方法以及喂入量稳定控制方法的研究现状，综述了基于过桥挤压力、割台功率、脱粒元件功耗等反应收割机喂入量的方法，介绍了利用机器学习结合多种影响喂入量的因素预测喂入量的方法，并对比了喂入量检测中不同降噪方法的降噪效果的优劣，接着对联合收割机喂入量控制方法进行了梳理，探讨了不同控制策略，着重分析了通过调节喂入量高度、收割机前进速度使喂入量保持稳定的方法。结果表明现阶段喂入量检测方法均能在一定程度上反映出喂入量变化情况，但普遍存在稳定性差、检测精度不高等问题。通过控制喂入量有效减少了收获损失率，但控制误差易受田间环境影响、波动大。针对上述问题，指出今后研究需要在发展先进传感器技术、优化自动控制算法、数据融合与分析等方面开拓创新。

INTRODUCTION

A combine harvester is a field operation machinery that integrates cutting, threshing, separation, and cleaning functions. Its introduction has significantly reduced the labor intensity of farmers and enhanced production efficiency in agricultural settings (Pingali, 2007). As the crucial mechanical equipment in the grain harvesting process, the harvesting quality and efficiency of the combine harvester have always been the indicators of user's concern, and also the focus of research by scholars. Crop feeding process is the front-end operation of combine harvester, affecting the machine threshing, cleaning and other subsequent operations. The feed rate has always been an important indicator for evaluating the performance of the harvester. Both excessive or insufficient feed rate can lead to a decrease in the efficiency of the harvester (Fan et al., 2022). Therefore, it is beneficial for the harvester to keep the best working condition by monitoring the real-time data of the feed rate and stabilizing feed rate during field harvesting (Chen et al., 2011).

At present, scholars at home and abroad have conducted a series of studies on the feed rate and its stable control methods, and have made some progress. Overseas research focuses on the height and density of feeding crops, estimating the feed rate indirectly by calculating the crop density in front of the harvester. Domestic research on feed rate detection methods mainly focuses on the following three aspects: estimating the feed rate by detecting grain flow rate; predicting the feed rate by measuring the squeezing force on inclined conveyor during crop feeding; establishing a feed rate detection model through analyzing the power consumption of major threshing components (*Tang et al., 2023; Zhang, 2019; Wang et al., 2019; Abdeen et al., 2022*).

In terms of feed rate control, mature feed rate control systems have been widely applied on large combine harvesters abroad, while most domestic research in China remains at the experimental stage, with a certain gap between research and practical application.

This review aims to present the research status of feed rate detection and stability control methods in combine harvesters. It summarizes common feed rate detection methods, feed rate signal denoising methods, feed rate stability control methods, highlights the problems and limitations of existing approaches, and proposes future research directions for improving feed rate detection and control methods.

RESEARCH PROGRESS ON FEED RATE DETECTION METHODS IN COMBINE HARVESTERS

The feed rate of the combine harvester refers to the total mass of all materials fed into the thresher body within a unit of time. It is closely related to header cutting width, operation speed, yield per mu, grain-straw ration, etc. Real-time monitoring and controlling the feed rate is crucial for the combine harvester to achieve optimal working efficiency (*Jie, 2009*).

Since the 1970s, many experts have conducted research on feed rate detection and have achieved certain results. In *Cao Chongwen, (1975)*, many parameters that were considered as the basic for adjusting the feed rate were summarized, including the torque of several important transmission shafts such as cutter drive shaft and screw conveyor shaft, the speed of threshing cylinder and the pressure of concave plate, etc. (*Cao, 1975*).

Jie Zhan et al. (1990) began researching quantitative measuring techniques for feed rate, using two methods of measuring pressure and displacement, and conducting a rice bench simulation experiment. By utilizing the principle that the sensor can convert the feed rate into electrical signals, the study explored the correlation between feed rate and electrical signals, and respectively summarized the fitting equations between pressure sensor voltage and feed rate, and displacement sensor voltage and feed rate. The error calculation results showed that the test accuracy of the pressure sensor is better than that of the displacement sensor. In order to improve the detection accuracy, the pressure sensor was calibrated. Firstly, the sensor was statically calibrated through weight loading, and after obtaining the static calibration regression equation, dynamic calibration was conducted through bench testing (*Jie et al., 1990*).

In 2009, a mathematical model for feed rate testing was established (*Jie et al., 2009*). The force-electric sensor was installed on the bottom plate of the inclined conveyor to conduct real-time analysis and processing of feed rate signals. The regression curves were established for the preset feed rate data group and the signal mean, as well as the signal change value. Due to random errors caused by factors such as the state of the feed-in material, placement factors and conveying factors, the repeatability of the feed rate data was poor. Although the stability and reliability of this system have been greatly improved, it still did not meet the technical requirements for telemetry of feed rate in field experiments.

Tang Zhong et al. (2012) analyzed the power consumption of the longitudinal flow threshing-separation process, and deduced the relationship between the feeding rate and the net threshing power consumption of the longitudinal-flow threshing cylinder in wheat harvesting. The field test results showed that the net threshing power consumption of the longitudinal-flow threshing cylinder could accurately predict the feed rate (*Tang et al., 2012*).

Lu Wentao et al. (2011) designed a hydraulic infinitely variable speed system for threshing cylinder of grain combine harvester and installed a pressure sensor in hydraulic to measure oil pressure. This oil pressure was used to represent the feed rate. By analyzing the data of oil pressure, threshing cylinder and engine speed under different feed rate, the fitting equation of oil pressure and feed rate was established. However, the feed rate model established by this method can be valid only when the combine harvester is operating stably, the physical properties of the crop are consistent and the feeding is uniform, which is an ideal condition (*Lu et al., 2011*).

Liang Xuexiu et al. (2013) analyzed the flow rate of grains, the torque and the speed of the threshing cylinder, corrected and calculated the formula for the feed rate, and designed a set of field online monitoring system for the feed rate (Liang et al., 2013).

Liu Yuanyuan et al. (2017) analyzed the power and dynamic model of the header auger conveyor, and designed a power consumption monitoring system for the auger conveyor. The location of the sensor is shown in Figure 1. This monitoring system was installed on the Guwang TB60 combine harvester for field experiments. Through linear fitting of the power of the header screw conveyor and the feed rate data, it was found that there is a linear relationship between the two, with a correlation coefficient $R^2=0.9099$, indicating that the method of predicting the feed rate based on monitoring the power of the auger conveyor is feasible (Liu et al., 2017).

Yin Yanxin et al. (2018) designed a chain wheel torque speed sensor based on the feeding auger structure characteristics, and constructed a multi-information acquisition system for combine harvester based on the distributed data collection, transmission and processing system of CAN bus (Fig 2). This system can synchronously obtain online parameter information such as the power output of the header lifting, auger conveyor, inclined conveyor, and threshing cylinder of the combine harvester, providing reliable data for predicting the feed rate and operation quality of the grain combine harvester (Yin et al., 2018).

Zhang Zhenqian et al. (2019a) designed a feed rate monitoring system, which obtains the header drive shaft torque signal through a wireless torque sensor, and measures the header drive shaft speed signal with a Hall sensor to predict the feed rate (Zhang et al., 2019).

Sun Yifan et al. (2020) selected the feed rate detection method based on the power of the header active shaft and the power of the inclined conveyor to design the text system, and compared the detection accuracy of the two methods. After processing and analyzing the field text data, the linear regression equations between the torque voltage signal of the header's driving shaft, the inclined conveyor's power shaft torque voltage signal and actual feed rate were respectively established by the least square method. Although this method simplifies the calculation process for the feed rate model, it cannot reflect the relationship between feed rate and power at different shaft speeds (Sun et al., 2020).

At present, the related research results of feed rate detection method based on traditional mathematical model are shown in Table 1.

Table 1

Research on the detection method of combine harvester feed rate				
Detection method	Sensor type	Installation position	Grain type	Error
Inclined conveyor extrusion pressure	Force-electric sensor	Inclined conveyor bottom plate	Rice	Bench test error $\leq 8\%$.
Power consumption of threshing element	Torque sensor	Threshing cylinder active shaft	Wheat	Bench test error $\leq 0.89\%$
	Oil pressure sensor	Threshing cylinder hydraulic stepless variable speed system oil circuit	Rice	
Header power	Torque sensor	Header auger conveyor active shaft	Wheat	$R^2=0.9099$
	Torque sensor	Header active shaft	Wheat	$R^2=0.8520$
	Torque sensor	Header drive shaft	Wheat	$R^2=0.8325$
Combined type	Torque sensor; Pressure sensor	Between the threshing cylinder power source and the load; Between the grain elevator and the grain outlet	Rice	Error $\leq 5\%$
	Chain wheel torque speed sensor	Header auger active shaft; Inclined conveyor drive shaft; Threshing cylinder active shaft	Rice	Error $\leq 2\%$

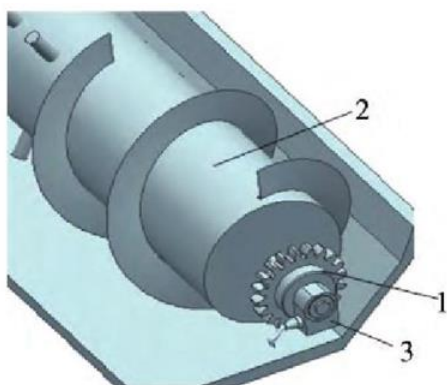


Fig. 1 - Installation diagram of torque sensor
 (Liu Yuanyuan et al., 2017)
 1. Torque sensor; 2. Header screw conveyer;
 3. Signal convertor torque sensor

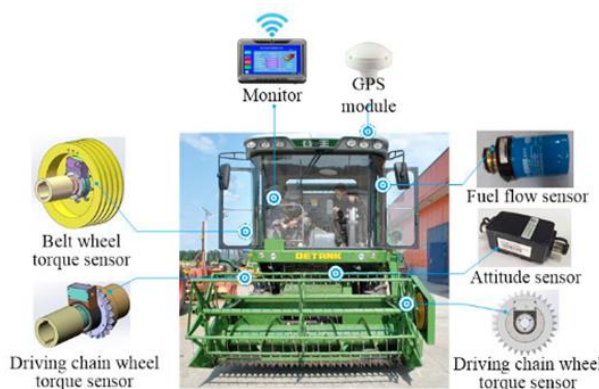


Fig. 2 - The scheme of the system layout and sensors installation sites of the system
 (Yin Yanxin et al., 2018)

With the development of computer science, more and more scholars use machine learning models such as fuzzy neural networks and convolutional neural networks to predict the feed rate (Dorokhov et al., 2019). Lu Wentao (2014) considered that when the physical characteristics of the grain changed, the one-to-one correspondence between the feed rate and the oil pressure was not established. In this condition, it was difficult to obtain the accurate feed rate by using the theoretical equation, so they used a neural network to establish the model for the feed rate. Through the orthogonal test, it was concluded that the feed rate, material humidity and grain-straw ration had significant effects on the oil pressure, so the oil pressure, material humidity and grain-straw ration were taken as the three neurons of the input layer, and the feed rate was taken as the neuron of the output layer. A feed rate neural network model was established by processing and analyzing the experimental data. Comparing the training results of the network model with the multiple linear regression function, it was concluded that the network model is superior to the regression equation. This method can reduce the impact of the changes in physical characteristics of the feed material on the accuracy of the feed rate detection (Lu et al., 2014).

Sun Yifan (2022) used rice as the harvest object and designed a feeding monitoring system that could simultaneously monitor the header height, rice moisture content and the torque changes of the header's power shaft. In order to accurately calculate the feed rate, he established a three-layer BP neural network with 12 neurons in the hidden layer, with header height, grain moisture content and header's power shaft torque as input layers, and the feed rate as the output layer. The structure of the neural network is shown in Fig. 3. To prevent the neural network from getting stuck in local minima during the fitting process, the particle swarm optimization algorithm was introduced to optimize the initial value and threshold of BP network. The average absolute percentage error of the optimized feed rate model decreased from 8.42% to 7.62% (Sun et al., 2022). The neural network prediction method of feed rate is summarized as shown in table 2.

Table 2

Neural network prediction method of feed rate		
Model	Input layer signal	Effect
Fuzzy neural network	Crop density deviation, Crop density deviation change rate	
BP neural network	Oil pressure, material humidity, grain-straw ration	SSE=0.769
	Header height, grain moisture content, header's power shaft torque	MAE=7.69%
Convolutional neural network		Accuracy=86.7%

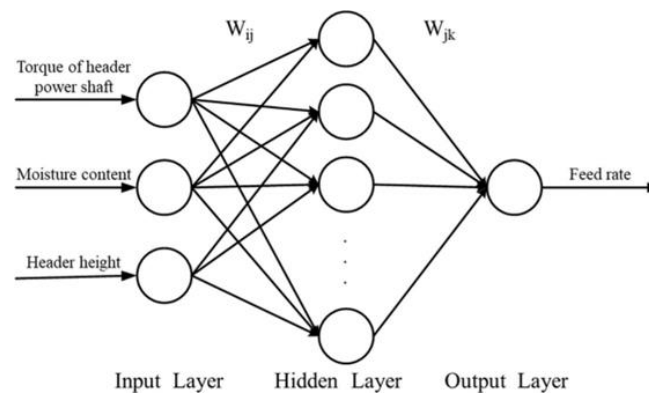


Fig. 3 - Structure of the BP neural network
(Sun et al., 2022)

In response to the issue of insufficient interpretability of processing results in machine learning prediction models, some scholars have begun to predict the feed rate model through grey relational analysis and association rule analysis. Grey relational analysis is an analytical method based on grey system theory, mainly used to deal with incomplete information or uncertainty. Compared to traditional machine learning methods, grey relational analysis places more emphasis on evaluating the degree of correlation and establishing correlation models. Zhang Yawei et al (2018) studied the factors affecting the feed rate of combine harvester based on the grey correlation analysis. The feed rate, crop attributes and harvesting conditions were regarded as a grey system with some information being clear and some unclear. Combined with the data of crop attributes and the feed rate, the grey relational analysis was used to find out the correlation between factors such as operating speed, crop density, torque and speed of the feeding auger and the inclined conveyor, torque and speed of threshing cylinder and the feed rate. It was concluded that in the actual field harvesting, the correlation degrees of operation speed and the feed rate were the highest, followed by the torque of the threshing cylinder. Based on this, a prediction model of feed rate detection error based on grey prediction was proposed, using the product of operating speed and crop density, feeding auger torque, inclined conveyor and threshing cylinder torque as inputs to establish the feed rate detection model (Zhang et al., 2018). Liu Yehong et al (2023) incorporated the torque and speed of the threshing cylinder, grain, grain augers and tailing augers into the feed rate monitoring. He proposed using association rules to explore the relationship between each parameter and the feed rate (Liu et al., 2023).

In addition to detecting the feed rate by measuring the power, pressure and other key components of the combine harvester during operation, many scholars have studied the crop growth status at the front end of the harvester, proving reference basis for subsequent feed rate detection and control. Ji Binbin (2005) designed a combine harvester feed rate prediction system based on fuzzy neural network. According to the crop density deviation and the change rate of crop density deviation measured by the combine harvester grain feeding amount sensor at time t , the actual crop density deviation of $t + \Delta t$ was predicted. Fuzzy neural networks combine the advantage of fuzzy logic and neural networks and can overcome the shortcomings of traditional neural networks in handling fuzzy and uncertain information. This combination can help in dealing with fuzzy inputs, outputs and rules, making the network more adaptable to problems involving fuzzy concepts (Ji, 2005).

Saeyns et al. (2009) used two types of light detection and ranging sensor and different online processing methods to estimate the crop density in front of the combine harvester. They proposed a new method for estimating crop volume by fitting thin plate splines to ground and ear points to calculate the volume between ground profiles and crop profiles (Saeyns et al., 2009; Blanquart et al., 2020).

Pan Jing et al (2010) used computer image processing technology to fit the 2R+G color feature value extracted by image processing with the actual measured feed density image, and established relevant model coefficients. The feed density of the combine harvester was obtained in real time to predict the feed rate of the harvester (Pan et al., 2010). Zhang Shuqi (2021) used machine vision to measure the height of rapeseed in the field, and built a convolutional neural network model to predict the density of rapeseed in the field, which was used as the basis for detecting the feed rate. Based on obtaining accurate feed rate detection results, an adaptive control strategy was used to achieve a scientific match between the forward speed and the rotation speed of the reel wheel (Zhang, 2021).

SIGNAL NOISE REDUCTION PROCESSING METHODS IN FEED RATE DETECTION

The working environment of the combine harvester is special. The terrain fluctuates in the field making it impossible to maintain a consistent flatness. The density and height of the harvested crops also vary. Moreover, the combine harvester itself has a complex system and harsh operation conditions. During operation, noise caused by the machine's vibrations and bumps inevitably interferes with sensor signals. In order to improve the accuracy of feed rate prediction, it is necessary to denoise the signal collected by the sensors.

Zhang Zhenqian (2019b) performed double threshold filtering on the torque signal of the header drive shaft collected by the sensor for edge detection and segmentation, and then used piecewise linear interpolation to obtain more detailed information to remove singular values. He made a comparison on the noise reduction effects of Butterworth low-pass filtering, FIR low-pass filtering, moving average filtering and adaptive filtering on the torque signal. After error analysis, it was found that the adaptive filtering had the best noise reduction effect (Zhang et al., 2019).

Sun Yifan et al. (2020) performed Fourier transform on the collected data, converting the data from the time domain to the frequency domain, providing clearer frequency domain information for filtering processing, and then using Butterworth band-pass filter to filter the torque signal (Sun et al., 2020). The denoising framework is shown in Figure 4.

In order to solve the signal noise issue in the feed rate monitoring system, Tao Jiang et al. (2022) first performed Fast Fourier Transform on the torque of the auger conveyor drive shaft during the no-load rotation of the harvester to obtain the noise frequency domain information. Since the signal during the harvester's loaded operation is a non-stationary process, Fourier transform has limitations in that it can only determine the frequency components contained in a segment of the signal overall, without knowledge of when each component appears. Therefore, it cannot determine the changes in signal frequency during feeding, nor can it filter out noise in the signal. In response to this situation, wavelet transform was applied to the torque signal obtained during the harvester loaded operation, followed by denoising using a fixed threshold estimation method to reduce errors in the relationship between torque and the feed rate (Jiang et al., 2022). The denoising framework is shown in Figure 5.

Fengzhu Wang et al. (2023) studied a feed rate detection method based on multi-component power monitoring, effective data automatic screening and multivariate data fusion regression. The Mann-Kendall algorithm was used to detect the boundary points of field harvest data. The Grubbs standard was used to validate the data, and outliers were rejected one by one at a confidence level of 0.05. The correlation of the established regression model was verified by Pearson algorithm, and multi-parameter calibration and fusion feeding amount detection were realized (Wang et al., 2023).

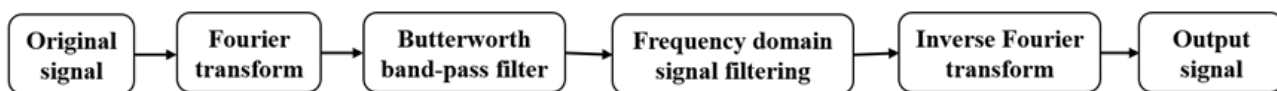


Fig. 4 - Fourier transform denoising framework (Sun Yifan et al., 2020)

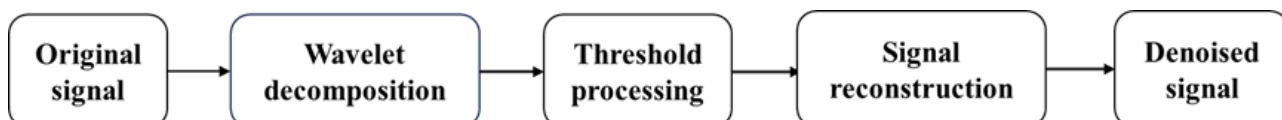


Fig. 5 - Wavelet method denoising framework (Wang et al., 2023)

RESEARCH PROGRESS ON THE FEED RATE CONTROL METHOD IN COMBINE HARVESTERS

The application of automatic control technology in agricultural machinery has a breakthrough impact on modern agricultural production, which is conducive to the intelligent and sustainable development of agricultural equipment in production operations. Currently, research on the automatic control of combine harvesters mainly focuses on controlling the rotational speed of the threshing drum, the concave screen clearance, the height of the header, the forward speed etc. (Ivan et al., 2015).

Alabushev et al. (2020) explored the factors influencing the binding force of winter wheat grains and ears and established a regression model to provide a basis for intelligent control of threshing process (Alabushev et al., 2010). Xu Baoyan et al. (2020) conducted experiments by setting different concave plate clearances and drum speeds, and derived the relationships among concave plate clearance, drum speed, and

threshing quality. Based on a type - 2 fuzzy logic controller, they designed a threshing controller with a low loss rate (Xu et al., 2020). Fan Chenglong et al. (2022) designed a guide vane inclination adjustment mechanism with a hydraulic cylinder as the driving source under the monitoring of the feed rate (Fan et al., 2022). Li Ying et al. (2021) designed a frequency subsection regulation system for the combine harvester header cutter. By constructing the cutter trajectory equation, they analyzed the relationship between the forward speed of the harvester and the cutting frequency, as well as the impact on the cutting area, and determined the optimal cutting frequency range at different operating speeds (Li et al., 2021). In view of the shortcomings of current combine harvester research, such as the focus on single-device control, inaccurate feedback information, and poor adaptability of control models, Li Yang et al. (2024) regarded the threshing cylinder device as an integrated control object. They designed an electric adjustment mechanism for the main operating parameters of the threshing and cleaning devices. Based on the fusion method of particle swarm optimization and wavelet neural network, they conducted system identification on the state - space model and the NARMAX model to explore their applicability and obtain the optimal model. They adopted the model predictive control method to adjust the threshing and cleaning parameters and carried out the control process simulation in Simulink, achieving good results (Li et al., 2022; Li et al., 2024). Yang Yu et al. (2024) designed an electric control adjustment device for threshing clearance based on a crank - rocker mechanism, proposed a control method for threshing clearance based on a fuzzy neural network PID, and established relevant models and determined parameters (Yang et al., 2024).

Controlling the feed rate within a stable range during the operation of a combine harvester is beneficial for the machine to achieve optimal performance and reduce grain loss. The feed rate cannot be directly controlled. Zhang Yawei et al. (2018) found through grey relation analysis that the forward speed during harvesting has the highest correlation with the feed rate, followed by the correlation between the threshing cylinder torque and the feed rate (Zhang et al., 2018). At present, there are two main methods for controlling the feed rate: one is to control the forward speed of the harvester to control the feed rate, and the other is to achieve stable control of the feed rate by adjusting the height of the header (Maertens and Baerdemaeker, 2004).

The CR90.90 combine harvesters developed by Case New Holland Company use two ultrasonic sensor to detect the feed rate of threshing cylinder. When an excessive feed rate is detected, the machine's overload anti-spitting device can automatically adjust. The machine is equipped with the AFS advanced precision agriculture system, which effectively combines and analyzes data from several key stages of cultivation, providing users with personalized agricultural solutions (Cheng et al., 2018; Wang, 2021).

Huang Zhigen (2010) designed a multi-signal acquisition system for combine harvester, which can detect the rotation speed, feeding rate and grain loss signal during the operation. In order to obtain a stable feeding rate, he designed an automatic speed control mechanism for the combine harvester. The main control unit based on ARM was used to control the stepper motor and then control the angle of the hydraulic stepless transmission joystick to control the forward speed of the combine harvester. In addition, a load feedback automatic control system of the combine harvester was established, utilizing fuzzy control technology to create a multi-information fuzzy control model (Huang, 2010).

Fuzzy control system is a control method based on fuzzy logic theory, which simulates human thinking and decision-making process, and can deal with the problems of uncertainty and fuzziness.

Mahmoud Omid et al. (2010) designed a fuzzy logic control system combined with human expert knowledge, which integrates human expert knowledge into the learning process, and finds the best technical parameters of the harvester through continuous trial and error based on expert knowledge and relevant experience. It provided a reference for the design of combine harvester control system in the future (Omid et al., 2010). You Huiyuan et al. (2015) used PLC to establish a fuzzy control system for feed rate, and controlled the working speed of the combine harvester to keep the feed rate within a stable range. The actuator adopts an electronically controlled hydrostatic system, which changed the speed of the hydraulic motor by altering the current signal and the swashplate angle of the variable pump to adjust the travel speed (You et al., 2015).

Wang Li et al. (2021) designed an intelligent control test bench for combine harvesters. The designed double - closed - loop PD controller can effectively and dynamically adjust the control parameters according to the changes in the driving speed of the harvester. The motor module was utilized to simulate the rotational speeds of rotating components such as the combine drum, conveyor through, and header screw conveyor of the combine harvester, while the simulation module was used to simulate the feeding and loss processes. The intelligent control algorithm for the forward speed of the test bench was tested, achieving good results (Wang et al., 2021).

He Yongqiang *et al.* (2024) proposed a control algorithm that combines the Pose Vector Method (PVM) and the Support Vector Regression (SVR) model. They designed a research platform for traveling control adapted to different Paddy Ground Conditions (PGCs), and used the Real - Time Kinematic Global Navigation Satellite System (RTK - GNSS) to measure information such as the pose of the combine harvester. The PVM was proposed to determine the steering radius online, and the SVR model was used to predict the error - correction factor for the steering trajectory radius. A feedforward compensation control method was designed based on the steering control model. This study provided new ideas for enhancing the online perception of the motion state of crawler combine harvesters and improving the adaptive control performance (He *et al.*, 2024).

Because the combine harvester is a complex system with nonlinear time-varying and time delay and has numerous and complex working components and changeable working environment, the traditional control theory was difficult to be applied to the harvester control system (Pan *et al.* 1999).

Fuzzy control considers fuzzy and imprecise input and output, making the system more adaptable to fuzzy, uncertain, or difficult to model situations. In the past two decades, it has been widely used in the design of combine harvester control system. However, fuzzy control has low interpretability, complex calculation, and lack of global optimization. Many scholars have begun to try to combine fuzzy control with some algorithms such as adaptive control to make the system more adaptable to complex environments and changes (Wang *et al.*, 2014.; Randal *et al.*, 2005).

Chen Jin *et al.* (2014) designed a fuzzy adaptive control system of forward speed for combine harvester based on model reference, as shown in Figure 6. Compared with the traditional fuzzy control, the adaptive fuzzy control system introduces self-adaptability. The system can dynamically adjust the reference fuzzy rules and member functions according to real-time feedback to adapt the changes of the system. The control system received input and loss signals collected by sensors, and then calculated the change of the forward speed of the combine harvester through the model reference fuzzy adaptive control algorithm, and outputted the control signal to drive the actuator to adjust the forward speed (Chen *et al.*, 2014).

Ning Xiaobo *et al.* (2015) conducted a comprehensive dynamic analysis of the motion mechanism of the combine harvester, and designed a fuzzy logic controller, with the speed deviation of the threshing cylinder and the rate of change of the speed deviation as input variable, and the rotation angle of the stepping motor as the output variable. If the input variable exceeded the range of change, the controller would adjust the forward speed of the harvester by controlling the hydraulic infinite transmission based on the output variable (Ning *et al.*, 2015).

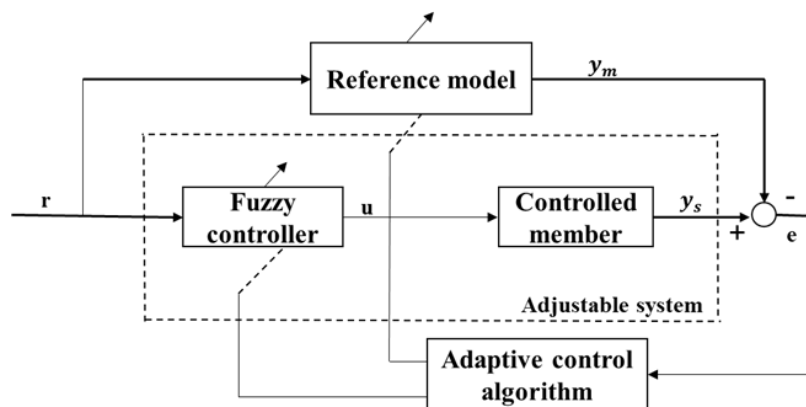


Fig. 6 - Structure diagram of model reference fuzzy adaptive control system (Chen *et al.*, 2014)

Because fuzzy control requires more professional knowledge to model the system, and the design process is more complex and subjective, some scholars began to use optimization algorithms to help adjust the parameters of fuzzy controllers to improve system performance.

Ning Xiaobo (2015) further used a multi-objective genetic algorithm to optimize the influence factors of each parameter in the constructed multi-parameter fuzzy control system, such as the speed of the tangential cylinder. By comparing the simulation test with the model before optimization, it can be seen that the overall performance of the harvester is improved (Ning, 2015). In addition, Ning Xiaobo, Chen Jin *et al.* (2016) used association rule knowledge to evaluate the weight factor of association rules between each operating parameter of the harvester and the feed rate and loss rate, studied the principle of adaptive fuzzy control, constructed the adaptive control model of the whole domain operating speed of combine harvester and designed the adjustable factor fuzzy controller (Ning *et al.*, 2016).

In 2017, *Chen Jin (2017)* proposed a multi-parameter fuzzy control strategy for the forward speed of the combine harvester based on Knowledge Discovery in Databases (KDD). She found the optimal trade-off point between the auger conveyor, the inclined conveyor and the threshing cylinder, and used MATLAB to establish a multi-parameter control model based on KDD (*Chen et al., 2017*).

Hou Ankang (2021) designed the control system of header module, threshing module, grain tank and travel module of combine harvester, and established the speed control model of each component of the combine harvester. The core idea was to control the feed rate to be constant, and this was achieved by controlling the flow rate of the hydraulic valve (*Hou, 2021*). *Li Xiaoyu et al. (2023)* designed the automatic control algorithm of corn grain harvester, with a travel system using closed-loop hydrostatic drive. They proposed an improved particle swarm optimization that combines the cuckoo search algorithm's local wandering strategy, and built a PSO-CS-Fuzzy PID control model based on MATLAB Simulink. This algorithm was beneficial for addressing the issue of traditional particle swarm algorithms easily getting stuck in local minima, and achieved good control effects in subsequent simulation experiments (*Li et al., 2023*).

Sun Yifan et al. (2023) established a model for detecting the change of feed rate during the operation of the combine harvester. The harvester operation speed was taken as the control object, and the stable control of feed rate was taken as the control target. The model prediction method was used to simulate and control the feed rate. The grey wolf optimization algorithm was used to optimize the weight matrix to reduce the control error of the output feed rate (*Sun et al., 2023*). Table 3 summarized the research on the stable control strategy of feed rate with the control target of controlling the forward speed of harvester.

Table 3

Research on the stable control strategy of feed rate		
Control strategy	Optimistic algorithm	Advantage
Fuzzy control		The rules are intuitive in form, adaptable and flexible.
MSIFC		Control precision and robustness are improved.
AFC	Association rules analysis	The extraction of fuzzy rules is more accurate, and the control system is more interpretable.
FRAMFC		The system response speed and modeling accuracy are improved.
MPFC	MOGA	The global optimization ability is improved, and the multi-parameter coordinated optimization is improved.
	KDD	Parameter optimization is more targeted.
PID control	PSO-CS	Avoid falling into local optimal value
MPC	GWO	The convergence speed is faster and adapts to the multivariable complex system.

In addition to controlling the forward speed of the combine harvester, another effective way is to adjust the height of the header to control the feed rate. By raising or lowering the header, the cutting position of the crop can be changed, and this flexible control method can more finely adjust the feed rate (*Cheng et al., 2018; Tai et al., 2020; Wang et al., 2024*).

Chen Jin et al. (2018) designed a key electric controlled adjustment device for header parameters with PLC as main controller, which can realize the key electric controlled of header height, reel height and reel speed. The actuator of the header was controlled by hydraulic pressure, and the components were three-position four-way solenoid directional valve and proportional solenoid valve. The speed control model of the reel was established, and the fuzzy control and PID control were combined to realize the real-time control of the system. Effective header height control is helpful to improve the stability of feed rate and reduce the load fluctuation of each link of the whole machine (*Chen et al. 2018*).

Zhuang Xiaobo and Li Yaoming (2020) analyzed the dynamics of the header and established the model. According to the hydraulic motion equation, the state space model of the header height hydraulic system was established. They proposed a height control strategy of combine harvester header based on robust feedback linearization, which could make the header height follow the ground fluctuation. They designed a controller and compared it with the PID controller in experiments. The results showed that under the same simulation conditions, the error under the control of this method was smaller than that under the PID control (*Zhuang et al., 2020*).

Ni Youliang *et al.* (2021) developed a height adjustment system for soybean harvester header. They designed a profiling mechanism and a hydraulic drive system based on existing soybean harvesters, and designed a header height self-adaptive adjustment system, and established an evaluation index for the height adjustment system of the soybean harvester header (Ni *et al.*, 2021; Liu *et al.*, 2023).

Ji Kuizhou *et al.* (2022) proposed a multi-sensor data fusion technique based on a backpropagation (BP) neural network. This method integrates ultrasonic sensors for ground height detection, infrared sensors for monitoring crop lodging status, and pressure sensors for real-time measurement of header load. By adaptively adjusting the weighting of data from various sensors through the neural network, the system optimizes the self-adaptive regulation of header height in combine harvesters (Ji *et al.*, 2022).

Ruan Mingjian *et al.* (2019) designed an automatic control system for the header height of a combine harvester. They established a relational model between the header height of the combine harvester and the sensor signals, and adopted the grey prediction PID algorithm to reduce the hysteresis of the header height control model. Good results were achieved in the field experiments (Ruan *et al.*, 2022).

CONCLUSIONS AND RECOMMENDATIONS

In summary, at present, researchers have made a lot of achievement in the research of combine harvester feed rate detection and stability control methods. However, the existing methods still have certain limitations, and there is still a considerable gap in the application of combine harvester design. The main problems are as follows:

(1) The current feed rate detection method is difficult to adapt to the complex environmental changes during the operation of the harvester, and the detection accuracy is not high. The mainstream detection method is to establish the relationship between the feed rate and the power consumption of the main working components such as the header and the threshing cylinder during the harvester operation. However, it is difficult to avoid the fluctuation of land and the change of crop density when the harvester is working, which can lead to insufficient stability of sensors, and noise interference from driveline torsional vibration, bending moment, and engine vibration can affect the signals collected by the sensors. The filtering method is difficult to completely eliminate noise and can only reduce noise to a certain extent.

(2) The stability of the control system is low, and research on the speed control algorithms remains limited. Currently, widely used fuzzy rules mainly depend on expert experience. Some improved methods are also based on fuzzy rule control, making it difficult to dynamically adjust weight factors and other relevant parameters for different situations. Additionally, combine harvesters exhibit significant time delays during operation, yet current research rarely considers factors such as actuator delays, resulting in control effects that fail to meet expected performance levels.

In response to the current issues, the future research on the feed rate detection and stability control of combine harvester is supposed to focus on the following aspects:

(1) Advanced sensing technology. In view of the limitations of current sensors, research is being conducted on more advanced and stable sensor technology to improve detection accuracy in complex environments and adapt to changes in land topography and crop density.

(2) Data fusion and analysis. Introducing big data technology to conduct more comprehensive and real-time analysis on data collected by sensors. Utilizing data fusion technology, combined with machine learning algorithms, to establish more accurate feed rate models.

(3) Advanced control algorithms. By studying more advanced speed control algorithms, including model predictive control, adaptive control etc., it is possible to better cope with complex environments and time-delay characteristics and improve the stability of the control system.

(4) Delay compensation technology. The control algorithm considering the delay of the harvester actuator is studied to adapt to the time delay of the harvester.

The future development of combine harvesters will move towards the application of intelligent technology, modular design, and autonomous driving technology. By utilizing advanced sensors, machine learning, and artificial intelligence technology, the harvester will be able to better adapt to different field condition, and modular design will enhance the flexibility of machine applications. It is necessary to accelerate research and innovation in the detection and stable control of the feed rate of combine harvesters to align with the development trend.

ACKNOWLEDGEMENT

We greatly appreciate the careful and precise reviews by the anonymous reviewers and editors. This research was funded by the National Key Research and Development Plan project (2021YFD2000503) and the National Natural Science Foundation of China (No. 32171911), and the National Natural Science Foundation of China (No. 32272004).

REFERENCES

- [1] Abdeen, M.A., Xie, G., Salem, A.E., Fu, J., Zhang, G. (2022). Longitudinal axial flow rice thresher feeding rate monitoring based on force sensing resistors. *Scientific Reports*, Vol. 12, pp. 1369. Wuhan/China. <https://doi.org/10.1038/s41598-021-04675-w>
- [2] Alabushev, A. V., Buryanov, A. I., Pakhomov, V. I., Kolinko, A. A., Chervyakov, I. V. (2020). Development of a method to control threshing process based on properties of harvested crop variety and external factors. *IOP Conference Series: Earth and Environmental Science*, Vol. 422, pp. 012005. Voronezh/Russian. <https://iopscience.iop.org/article/10.1088/1755-1315/422/1/012005/meta>
- [3] Blanquart, J.-E., Sirignano, E., Lenaerts, B., Saeys, W. (2020). Online crop height and density estimation in grain fields using LiDAR. *Biosystems Engineering*, Vol. 198, pp.1–14. Leuven/Belgium. <https://doi.org/10.1016/j.biosystemseng.2020.06.014>
- [4] Cao, C. (1975). Automatic adjustment of grain combine harvester (谷物联合收割机的自动调节). *Machinery for Cereals Oil and Food Processing*, Vol. 975, pp. 75–90+97. Henan/China.
- [5] Chen, D., Wang, S., Kang, F., Zhu, Q., Li, X. (2011). Mathematical model of feeding rate and processing loss for combine harvester (联合收割机喂入量与收获过程损失模型). *Transactions of the Chinese Society for Agricultural Engineering*, Vol.27, pp. 18–21. Beijing/China. <https://doi.org/10.3969/j.issn.1002-6819.2011.09.004>
- [6] Chen, J., Ning, X., Li, Y., Yang, G., Wu, P., Chen. S. (2017). A fuzzy control strategy for the forward speed of a combine harvester based on KDD. *Applied Engineering in Agriculture*, Vol. 33, pp. 15–22. Jiangsu/China. <https://doi.org/10.13031/aea.11299>
- [7] Chen, J., Ning, X., Li, Y., Yang, G., Wu, P. (2014). Fuzzy adaptive control system of forward speed for combine harvester based on model reference (联合收获机前进速度的模型参考模糊自适应控制系统). *Transactions of the Chinese Society for Agricultural Machinery*, Vol. 45(10), pp. 87-91+86. Jiangsu/China. <https://doi.org/10.6041/j.issn.1000-1298.2014.10.014>
- [8] Chen, J., Wang, S., Lian, Y. (2018). Design and test of header parameter keys electric control adjusting device for rice and wheat combined harvester (稻麦联合收获机割台参数按键电控调节装置设计与试验). *Transactions of the Chinese Society for Agricultural Engineering*, Vol. 34(16), pp. 19–26. Jiangsu/China. <https://doi.org/10.11975/j.issn.1002-6819.2018.16.003>
- [9] Cheng, N., Hu, Y., Miao, Y. (2018). Research on fuzzy control of harvester header height (收割机割台高度的模糊控制策略研究). *Mechatronics*, Vol. 24, pp. 17-22. Shanghai/China. <https://doi.org/10.16413/j.cnki.issn.1007-080x.2018.04.003>
- [10] Dorokhov, A.S., Sibirev, A.V., Aksenov, A.G. (2019). Dynamic systems modeling using artificial neural networks for agricultural machines. *INMATEH-Agricultural Engineering*, Vol. 58 / No.2, pp. 63-74. Bucharest / Romania. <https://doi.org/10.35633/INMATEH-58-07>
- [11] Fan, C., Zhang, D., Yang, L., Cui, T., He, X., Zhao, H., Dong, J. (2022). Development and performance evaluation of a guide vane inclination automatic control system for corn threshing unit based on feedrate monitoring. *Computers and Electronics in Agriculture*, Vol. 194, pp.106745. Beijing/China. <https://doi.org/10.1016/j.compag.2022.106745>
- [12] Fan, C., Zhang, D., Yang, L., Cui, T., He, X., Dong, J. (2022). Power consumption and performance of a maize thresher with automatic gap control based on feed rate monitoring. *Biosystems Engineering*, Vol. 216, pp.147–164. Beijing/China. <https://doi.org/10.1016/j.biosystemseng.2022.02.015>
- [13] Hou, A. (2021). Design of control system for full-feeding combine harvester (全喂入式联合收割机控制系统设计) (Master's thesis). *Shanghai Jiao Tong University*. Shanghai/China.
- [14] Huang, Z. (2021). Multi-signal processing method research of combine harvester load feedback system (联合收割机负荷反馈系统多信号处理方法的研究) (Master's thesis). *Jiangsu University*. Zhenjiang/China.

- [15] Ivan, Gh., Vlăduț, V., Ganea I. (2015). Improving threshing system feeding of conventional cereal harvesting combine, *Proceedings of the 43 International Symposium on Agricultural Engineering "Actual Tasks on Agricultural Engineering"*, pp. 431-440, Opatija/Croatia.
- [16] Ji, B. (2005). Research of predictive system for feed quality of combine based on fuzzy neural network (基于模糊神经网络的联合收割机喂入量预测系统研究) (Master's thesis). *Jiangsu University*. Zhenjiang/China.
- [17] Ji, K., Li, Y., Zhang, T., Xia, S., Cheng, J. (2022). Technology of Adjusting the Header Height of The Harvester by Multi-Sensor Data Fusion Based on BP Neural Network. *INMATEH-Agricultural Engineering*, pp.91–98. <https://doi.org/10.35633/inmateh-68-09>
- [18] Jiang, T., Guan, Z., Li, H., Mu, S., Wu, C., Zhang, M., Wang, G., Chen, X. (2022). A feeding quantity monitoring system for a combine harvester: Design and experiment. *Agriculture*, Vol. 12, pp. 153. Nanjing/China. <https://doi.org/10.3390/agriculture12020153>
- [19] Jie, Z. (2009). Prospect of test method of grain random loss rate in China (我国谷物随机损失率测试展望). *Journal of Agricultural Mechanization Research*, Vol. 31, pp. 5–9. Henan/China. <https://doi.org/10.13427/j.cnki.njji.2009.07.007>
- [20] Jie, Z., Luo, S., Zhou, X. (2009). LabVIEW-based telemetering experiments of rice feed quantity for combined harvester (基于 LabVIEW 的联合收割机水稻喂入量遥测试验). *Transactions of the Chinese Society for Agricultural Engineering*, Vol. 25, pp. 87–91. Henan/China. <https://doi.org/10.3969/j.issn.1002-6819.2009.2.z018>
- [21] Jie, Z., Zhou, X. (2001). Study on mathematical model of feed quantity sensor measuring (喂入量传感器测试模型研究). *Transactions of the Chinese Society for Agricultural Machinery*, Vol. (5), pp. 53–55. Henan/China.
- [22] Jie, Z., Zhu, Y., Li, Z., Wu, C., Shi, Q. (1990). Study on quantitative measuring technique for random feed quantity of grain (谷物随机喂入量定量测试技术研究). *Journal of Luoyang Institute of Technology*, Vol. 11, pp. 43–48. Henan/China.
- [23] Li, X., Du, Y., Liu, L., Mao, E. (2023). Design and experiment of the automatic control system for low damage corn grain direct harvesters (玉米低损籽粒直收机自动控制系统设计与试验). *Transactions of the Chinese Society for Agricultural Engineering*, Vol. 39, pp. 34–42. Beijing/China. <https://doi.org/10.11975/j.issn.1002-6819.202210210>
- [24] Li, Y., Guan, Z., Chen, Y. (2021). Development and Test of Frequency Subsection Regulation System for Combine Harvester Header Cutter. *INMATEH-Agricultural Engineering*, pp.283–292. <https://doi.org/10.35633/inmateh-65-30>
- [25] Li, Y., Xu, L., Lv, L., Shi, Y., Yu, X. (2022). Study on Modeling Method of a Multi-Parameter Control System for Threshing and Cleaning Devices in the Grain Combine Harvester. *Agriculture*, Vol. 12, pp.1483. Zhenjiang/China. <https://doi.org/10.3390/agriculture12091483>
- [26] Liang, X., Chen, Z., Zhang, X., Wei, L., Li, W., Che, Y. (2013). Design and experiment of on-line monitoring system for feed quantity of combine harvester (联合收获机喂入量在线监测系统设计与试验). *Transactions of the Chinese Society for Agricultural Machinery*, Vol. 44, pp. 1–6. Beijing/China. <https://doi.org/10.6041/j.issn.1000-1298.2013.S2.001>
- [27] Liu, G., Ni, Y., Yang, T., Qi, Y., Chen J. (2023). Design and experiment of header height automatic control system for soybean harvester (大豆收获机割台高度自动控制系统设计与试验). *Journal of Chinese Agricultural Mechanization*, Vol. 44, pp. 155–160. Nanjing/China. <https://doi.org/10.13733/j.jcam.issn.2095-5553.2023.06.022>
- [28] Liu, Y., Dai, D., Tang, C., Wang, X., Wang, S. (2023). Discriminating Feed Rate of Combine Harvester by Using Association Rule Mining. *ELEKTRON ELEKTROTECH*, Vol. 29, (3): pp.4–10. Beijing/China. <https://doi.org/10.5755/j02.eie.33859>
- [29] Liu, Y., Liu, H., Yin, Y., An, X. (2017). Feeding assessment method for combine harvester based on power measurement (基于功率监测的联合收割机喂入量预测方法). *Journal of China Agricultural University*, Vol. 22, pp. 157–163. Beijing/China. <https://doi.org/10.11841/j.issn.1007-4333.2017.11.18>
- [30] Lu, W., Liu, B., Zhang, D., Li, J. (2011). Experiment and feed rate modeling for combine harvester (谷物联合收获机喂入量建模与试验). *Transactions of the Chinese Society for Agricultural Machinery*, Vol. 42, pp. 82–85. Henan/China.

- [31] Lu, W., Zhang, L., Zhang, D., Li, J. (2014). The research situation of monitoring and controlling system of combine harvester (谷物联合收获机喂入量神经网络模型建立). *Journal of Agricultural Mechanization Research*, Vol. 36, pp. 12–16. Henan/China. <https://doi.org/10.13427/j.cnki.njyi.2014.10.003>
- [32] Maertens, K., De Baerdemaeker, J. (2004). Design of a virtual combine harvester. *Mathematics and Computers in Simulation*, Vol. 65, pp. 49–57. Leuven/Belgium. <https://doi.org/10.1016/j.matcom.2003.09.007>
- [33] Ni, Y., Jin, C., Chen, M., Yuan, W., Qian, Z., Yang, T., Cai, Z. (2021). Computational model and adjustment system of header height of soybean harvesters based on soil-machine system. *Computers and Electronics in Agriculture*, Vol. 183, pp. 105907. Nanjing/China. <https://doi.org/10.1016/j.compag.2021.105907>.
- [34] Ning, X. (2016). Whole-range self-adaptive control system of combine harvester operating speed based on association rules (基于关联规则联合收获机全论域作业速度自适应控制系统) (Doctoral dissertation). *Jiangsu University*. Zhenjiang/China.
- [35] Ning, X., Chen, J., Li, Y., Wang, K., Wang, Y., Wang, X. (2015). Kinetic model of combine harvester threshing system and simulation and experiment of speed control (联合收获机脱粒系统动力学模型及调速控制仿真与试验). *Transactions of the Chinese Society for Agricultural Engineering*, Vol. 31, pp. 25–34. Jiangsu/China. <https://doi.org/10.11975/j.issn.1002-6819.2015.21.004>
- [36] Ning, X., Chen, J., Li, Y., Yang, G., Wu, P., Chen, S. (2015). Multi-objective genetic algorithm optimization of forward speed of fuzzy control system for combine harvester (联合收获机前进速度模糊控制系统多目标遗传优化). *Transactions of the Chinese Society for Agricultural Machinery*, Vol. 46, pp. 68–74. Jiangsu/China. <https://doi.org/10.6041/j.issn.1000-1298.2015.05.011>
- [37] Omid, M., Lashgari, M., Mobli, H., Alimardani, R., Mohtasebi, S., Hesamifard, R. (2010). Design of fuzzy logic control system incorporating human expert knowledge for combine harvester. *Expert Systems with Applications*, Vol. 37, pp. 7080–7085. Karaj/Iran. <https://doi.org/10.1016/j.eswa.2010.03.010>
- [38] Pan, J., Shao, L., Wang, K. (2010). Detection method on feed density for rice combine (水稻联合收割机喂入密度检测方法). *Transactions of the Chinese Society for Agricultural Engineering*, Vol. 26(8), pp. 113–116. Anhui/China. <https://doi.org/10.3969/j.issn.1002-6819.2010.08.019>
- [39] Pan, X., Qiu, B., Wang, G. (1999). Exploration on the fuzzy logic control of combine (联合收割机的模糊控制探讨). *Journal of Jiangsu University of Science and Technology (Natural Science)*, Vol.4, pp. 27–29.
- [40] Pingali, P. (2007). Agricultural Mechanization: Adoption Patterns and Economic Impact. In R. Evenson, & P. Pingali (Eds.), *Handbook of Agricultural Economics*, Vol. 3, pp. 2779–2805. Elsevier. Rome/Italy. [https://doi.org/10.1016/S1574-0072\(06\)03054-4](https://doi.org/10.1016/S1574-0072(06)03054-4)
- [41] Ruan, M., Jiang, H., Zhou, H., Ye, J., Hu, J. (2022). Design and Test of Automatic Control System for Header Height of Combine Harvester. *INMATEH-Agricultural Engineering*, pp.569–578. <https://doi.org/10.35633/inmateh-68-56>
- [42] Saeys, W., Lenaerts, B., Craessaerts, G., Baerdemaeker, J.D. (2009). Estimation of the crop density of small grains using LiDAR sensors. *Biosystems Engineering*. Leuven/Belgium. <https://doi.org/10.1016/j.biosystemseng.2008.10.003>.
- [43] Sun, Y., Liu, R., Li, S., Zhang, M., Li, H. (2023). Research on operation speed control method and simulation experiment of combine harvester based on GWO-MPC (基于 GWO-MPC 的联合收获机喂入量控制方法与仿真实验). *Transactions of the Chinese Society for Agricultural Machinery*, pp. 1–11. Beijing/China. <https://doi.org/10.6041/j.issn.1000-1298.2023.11.008>
- [44] Sun, Y., Liu, R., Ou, H., Zhang, Z., Zhang, M., Li, H. (2020). Analysis and comparison of feed rate detection methods of combine harvester based on power detection (基于功率测量的联合收获机喂入量检测方法研究). *Transactions of the Chinese Society for Agricultural Machinery*, Vol. 5, pp. 118–123. Beijing/China. <https://doi.org/10.6041/j.issn.1000-1298.2020.05.012>
- [45] Sun, Y., Liu, R., Zhang, M., Li, M., Zhang, Z., Li, H. (2022). Design of feed rate monitoring system and estimation method for yield distribution information on combine harvester. *Computers and Electronics in Agriculture*, Vol. 201, pp. 107322. Beijing/China. <https://doi.org/10.1016/j.compag.2022.107322>
- [46] Tai, J., Li, H. T., Du, Y. F., Mao, E. R., Zhang, J. N., Long, X. J. (2020). Rapid design of maize ear harvester header based on knowledge engineering. *INMATEH-Agricultural Engineering*, Vol. 61/No.2, pp. 263-272. <https://doi.org/10.35633/inmateh-61-29>

- [47] Tang, L., Wei, X., Tong, H., Li, C., Wu, S. (2023). Research on the detection method of combine harvester feeding rate (联合收割机喂入量检测方法研究). *Journal of Agricultural Mechanization Research*, Vol. 45, pp.37–42. Zhenjiang/China. <https://doi.org/10.13427/j.cnki.njji.2023.05.003>
- [48] Tang, Z., Li, Y., Xu, L., Pang, J., Li, H. (2012). Experimental study on wheat feed rate of tangential-axial combine harvester (切纵流联合收获机小麦喂入量预测的试验研究). *Transactions of the Chinese Society for Agricultural Engineering*, Vol. 28, pp. 26–31. Zhenjiang/China. <https://doi.org/10.3969/j.issn.1002-6819.2012.05.005>
- [49] Taylor, R. K., Hobby, H. M., Schrock, M. D. (2005). Evaluation of an automatic feed rate control system for a grain combine. In *American Society of Agricultural and Biological Engineers Conference*, Tampa, FL, July pp. 17-20. St. Joseph/Michigan. <https://doi.org/10.13031/2013.18870>
- [50] Wang, F., Wang, J., Ji, Y., Zhao, B., Liu, Y., Jiang, H., Mao, W. (2023). Research on the measurement method of feeding rate in silage harvester based on components power data. *Agriculture*, Vol. 13, pp. 391. Beijing/China. <https://doi.org/10.3390/agriculture13020391>
- [51] Wang, J., Gou, F., Qian, Z., Ni, Y., Jin, C. (2024). A Review of Intelligent Header Technology for Grain Combine Harvester. *INMATEH-Agricultural Engineering*, pp.731–744. <https://doi.org/10.35633/inmateh-73-62>
- [52] Wang, L., Li, S., Lv, D., Ekhlo, G. (2021). Multi-Sensor Signal Acquisition and Data Processing Analysis of Combine Harvester. *INMATEH-Agricultural Engineering*, pp.335–344. Bucharest/Romania; <https://doi.org/10.35633/inmateh-63-34>
- [53] Wang, S., Hu, Z., Wu, F., Yu, Z., Cao, M., Gao, X. (2019). Modeling and experiment of feeding rate for full-feed peanut pickup harvester (全喂入花生捡拾收获机喂入量建模与试验). *Transactions of the Chinese Society for Agricultural Engineering*, Vol. 35, pp. 29–36. Nanjing/Chian. <https://doi.org/10.11975/j.issn.1002-6819.2019.23.004>
- [54] Wang, X., Fu, H., Wang, S., Cui, Z., Chen, L. (2012). Robust optimal design of multi-objective control model of working speed for combine harvester (收割机作业速度多目标控制模型的鲁棒优化设计). *Transactions of the Chinese Society for Agricultural Engineering*, Vol. 28, pp. 27–33. Beijing/China. <https://doi.org/10.3969/j.issn.1002-6819.2012.20.004>
- [55] Wang, Z. (2021). Research on speed control system of combine harvester based on feed quantity forecast (基于喂入量预测的联合收获机作业速度控制系统研究) (Master's thesis). *Jiangsu University*. Zhenjiang/China. <https://doi.org/10.27170/d.cnki.gjsuu.2021.001590>
- [56] Xu, B., Ni, X., Wang, Y., Wang, Y., Liu, Y., Wang, X. (2020). Optimization of threshing quality control strategy based on type-2 fuzzy logic controller. *Elektronika ir Elektrotechnika*, Vol. 26, pp. 15-23. Beijing/China. <https://doi.org/10.5755/j01.eie.26.2.25924>
- [57] Yang, L., Li, X., Yao, L., Liya, L., Maolin, S. (2024). Modeling and control methods of a multi-parameter system for threshing and cleaning in grain combine harvesters. *Computers and Electronics in Agriculture*, Vol. 225, pp.109251. Changzhou/China. <https://doi.org/10.1016/j.compag.2024.109251>
- [58] Yin, Y., Zhang, Y., Meng, Z., Du, C., Qin, W., Guo, S. (2018). Design and experiment of multi-information collection system for grain combine harvesters. *IFAC-PapersOnLine*, Vol. 51, pp. 855–860. Beijing/China. <https://doi.org/10.1016/j.ifacol.2018.09.247>
- [59] You, H., Lu, W. (2015). Fuzzy control system for feed quality of combine harvester (联合收割机喂入量模糊控制系统研究). *Journal of Northwest A&F University* (Nat. Sci. Ed.), Vol. 43, pp. 229–234. Henan/China. <https://doi.org/10.13207/j.cnki.jnwafu.2015.05.018>
- [60] Yu, Y., Cheng, Y., Fan, C., Chen, L., Wu, Q., Qiao, M., Zhou, X. (2024). Automatic Control System for Maize Threshing Concave Clearance Based on Entrainment Loss Monitoring. *Processes*. Vol. 13, pp.58. Zhenjiang/China. <https://doi.org/10.3390/pr13010058>
- [61] Zhang, S. (2021). A dissertation submitted to Nanjing University for the professional degree of Master of Control Engineering (基于机器视觉的油菜收获喂入量及品质监测) (Master's thesis). *Nanjing University*. Nanjing/China. <https://doi.org/10.27235/d.cnki.gnjj.2021.000752>
- [62] Zhang, Y. (2019). Mechanisms and control strategies research on threshing and separating quality of combine harvester (联合收割机脱粒分离质量影响机理及控制策略研究) (Doctoral dissertation). *China Agricultural University*. Beijing/China
- [63] Zhang, Y., Chen, D., Yin, Y., Wang, X., Wang, S. (2018). Experimental study of feed rate related factors of combine harvester based on grey correlation. *IFAC-PapersOnLine*, Vol. 51, pp. 402–407. Beijing/China. <https://doi.org/10.1016/j.ifacol.2018.08.188>

- [64] Zhang, Z., Peng, C., Sun, Y., Liu, R., Zhang, M., Li, H. (2019). Signal analysis and processing of combine harvester feed rate monitoring system (联合收获机喂入量监测系统信号分析与处理). *Transactions of the Chinese Society for Agricultural Machinery*, Vol. 50, pp. 73–78. Beijing/China. <https://doi.org/10.6041/j.issn.1000-1298.2019.S0.012>
- [65] Zhang, Z., Sun, Y., Liu, R., Zhang, M., Li, H., Li, M. (2019). Design and test of feed rate monitoring system for combine harvester (联合收获机喂入量监测系统设计与试验). *Transactions of the Chinese Society for Agricultural Machinery*, Vol. 50, pp. 85–92. Beijing/China. <https://doi.org/10.6041/j.issn.1000-1298.2019.06.009>
- [66] Zhuang, X., Li, Y. (2020). Header height control strategy of harvester based on robust feedback linearization (基于鲁棒反馈线性化的联合收获机割台高度控制策略). *Transactions of the Chinese Society for Agricultural Machinery*, Vol. 51, pp. 123–130. Zhenjiang/China. <https://doi.org/10.6041/j.issn.1000-1298.2020.11.013>

PREDICTIVE MODELLING OF PH LEVELS FOR OPTIMIZING WATER QUALITY IN SHRIMP FARMING

การสร้างแบบจำลองการพยากรณ์ค่าความเป็นกรด-ด่างเพื่อเพิ่มประสิทธิภาพการจัดการคุณภาพน้ำในการเลี้ยงกุ้ง

Thanin MUANGPOOL ^{1,2)}, Sanya KUANKID ^{1,2)}, Boonthong WASURI ^{1,2)}, Ouychai INTHARASOMBAT ^{*1)}

¹⁾ Faculty of Science and Technology, Nakhon Pathom Rajabhat University, Nakhon Pathom / Thailand;

²⁾ Creating Innovation for Sustainable Development Research Center, Nakhon Pathom Rajabhat University, Nakhon Pathom / Thailand

Tel: +66 86 089 9945; E-mail: ouychai@npru.ac.th

DOI: <https://doi.org/10.35633/inmateh-75-13>

Keywords: pH Prediction, Water Quality Management, Water Monitoring System, Shrimp Farming

ABSTRACT

Water quality is a critical factor in shrimp farming, directly influencing the growth, reproduction, and survival of shrimp. pH is one of the key parameters that affect water quality, with deviations from the optimal range (5.5–8.5) leading to stress, weakened immune responses, and potential infections in shrimp. This research presents the development of an automated pH monitoring and forecasting system aimed at improving water quality management in shrimp farms. The system uses a moving average algorithm to predict future pH levels based on real-time data collected by a pH sensor. The predicted and real-time values are transmitted to a cloud database, and farmers receive alerts via the Line application if pH levels deviate from the acceptable range. The system's performance was evaluated through six experiments, using different data collection intervals and durations. The most accurate forecasting results were achieved with 10-minute data collection intervals over a 2-hour period, yielding a mean squared error (MSE) of 0.003050 and a root mean square error (RMSE) of 0.038628. The system also demonstrated its ability to send real-time alerts to the farmer, ensuring prompt corrective action in the event of critical pH values.

บทคัดย่อ

คุณภาพน้ำเป็นปัจจัยสำคัญในอุตสาหกรรมการเลี้ยงกุ้ง ซึ่งส่งผลโดยตรงต่อการเจริญเติบโต การสืบพันธุ์ และอัตราการรอดชีวิตของกุ้ง โดยค่า pH เป็นหนึ่งในตัวแปรสำคัญที่มีผลต่อคุณภาพน้ำ หากค่า pH เบี่ยงเบนจากช่วงที่เหมาะสม (5.5–8.5) จะทำให้กุ้งเกิดความเครียด ภูมิคุ้มกันอ่อนแอลง และเสี่ยงต่อการติดเชื้อ งานวิจัยนี้นำเสนอการพัฒนาระบบตรวจสอบและพยากรณ์ค่าความเป็นกรด-ด่าง (pH) แบบอัตโนมัติที่มีวัตถุประสงค์เพื่อปรับปรุงการจัดการคุณภาพน้ำในฟาร์มกุ้ง ระบบนี้ใช้เทคนิคการพยากรณ์แบบค่าเฉลี่ยเคลื่อนที่ (Moving Average Algorithm) เพื่อทำนายค่าความเป็นกรด-ด่างในอนาคต โดยอิงจากข้อมูลแบบเรียลไทม์ที่เก็บรวบรวมจากเซ็นเซอร์ตรวจวัดค่า pH ข้อมูลค่าที่ทำนายและค่าที่วัดได้ในปัจจุบันจะถูกส่งไปยังฐานข้อมูลบนคลาวด์ และเกษตรกรจะได้รับการแจ้งเตือนผ่านแอปพลิเคชัน Line หากค่าความเป็นกรด-ด่างเบี่ยงเบนออกจากช่วงที่เหมาะสม ประสิทธิภาพของระบบได้รับการประเมินผ่านการทดลอง 6 ครั้ง โดยใช้ช่วงเวลาและระยะเวลาการเก็บข้อมูลที่แตกต่างกัน ผลการพยากรณ์ที่แม่นยำที่สุดได้รับการเก็บข้อมูลทุก ๆ 10 นาทีเป็นระยะเวลา 2 ชั่วโมง ซึ่งให้ค่า MSE (Mean Squared Error) เท่ากับ 0.003050 และค่า RMSE (Root Mean Square Error) เท่ากับ 0.038628 นอกจากนี้ระบบยังแสดงความสามารถในการส่งการแจ้งเตือนแบบเรียลไทม์ไปยังเกษตรกร ทำให้สามารถดำเนินการแก้ไขได้อย่างทันท่วงทีเมื่อเกิดค่าความเป็นกรด-ด่างที่ผิดปกติ

INTRODUCTION

Shrimp farming is an important sector of Thailand's economy, providing significant income to cultivators. However, the success of shrimp farming is highly dependent on various environmental factors that affect shrimp growth, reproduction, and survival rates. Among these factors, water quality plays a critical role. Factors such as pH levels, oxygen concentration, and salinity directly influence the health and productivity of shrimp (Komarudin et al., 2021; Hsieh et al., 2021; Kim et al., 2024). Maintaining optimal water quality is essential to ensure the long-term sustainability of shrimp farming operations (Ariadi et al., 2020; de los Santos et al., 2020; Tarunamulia et al., 2024).

One of the most important indicators of water quality is the potential of hydrogen ions (pH), which measures the acidity or alkalinity of the water. The pH scale ranges from 0 to 14, with a value of 7 considered neutral. Water with pH levels below 7 is acidic, while levels above 7 indicate alkalinity (Gambin *et al.*, 2021). In shrimp farming, maintaining pH levels between 5.5 and 8.5 is essential to minimize stress, promote healthy growth, and prevent infections in shrimp (Yu *et al.*, 2020; Ariadi *et al.*, 2023). Extreme fluctuations in pH can lead to stress, poor growth, and susceptibility to diseases, impacting the overall productivity of shrimp farms (Supriatna *et al.*, 2023).

Fluctuations in water pH are primarily caused by natural processes such as photosynthesis and respiration in aquatic environments. During the day, photosynthesis by phytoplankton reduces carbon dioxide (CO₂) levels in the water, causing a decrease in acidity and a rise in pH. At night, the respiration of aquatic organisms increases CO₂ levels, resulting in higher acidity and a drop in pH (Qiao *et al.*, 2020). Such fluctuations can disrupt the balance of microorganisms and chemical parameters in the water, making pH monitoring essential for effective water management in shrimp farming (Durai *et al.*, 2021; Shirly-Lim *et al.*, 2024).

Given the importance of pH stability, predictive systems that can forecast pH levels in advance are valuable tools for shrimp farmers. By anticipating changes in pH, cultivators can implement timely interventions to maintain water quality and optimize shrimp production. Previous studies have successfully applied predictive models to monitor and forecast water quality parameters in aquaculture. For example, Mirsanjari and Mohammadyari (2018) used time series models to predict groundwater quality, while Monteiro and Costa (2018) evaluated statistical models to forecast dissolved oxygen concentrations in river water. Similarly, Thai-Nghe *et al.* (2020) developed an IoT-based system for real-time water quality monitoring and prediction using deep learning techniques.

Building upon this body of knowledge, the present study introduces a predictive model aimed at forecasting pH levels in shrimp farming systems. By utilizing historical pH data, this model seeks to anticipate fluctuations and alert shrimp farmers to potential deviations from optimal water quality conditions. The development of such a model is expected to contribute significantly to improving water management strategies in shrimp farming, ultimately enhancing shrimp health, growth rates, and overall farm productivity.

MATERIALS AND METHODS

This research was conducted in shrimp farm of Mr. Prasopchoke Somsua, a shrimp cultivator from Donka district, Bangpae province, Rachaburi city, Thailand. The experiments were performed during January to March 2024. The experimented farm consisted of 4,000 square meters with 120 population of shrimps per square meter. The method used in this research were as followed.

System Infrastructure Design

The system developed for this study consists of four key components that are an automatic water quality measurement system, a processing and reporting system, a cloud-based database, and an automatic notification system. Figure 1 illustrates the overall infrastructure of the pH forecasting system.

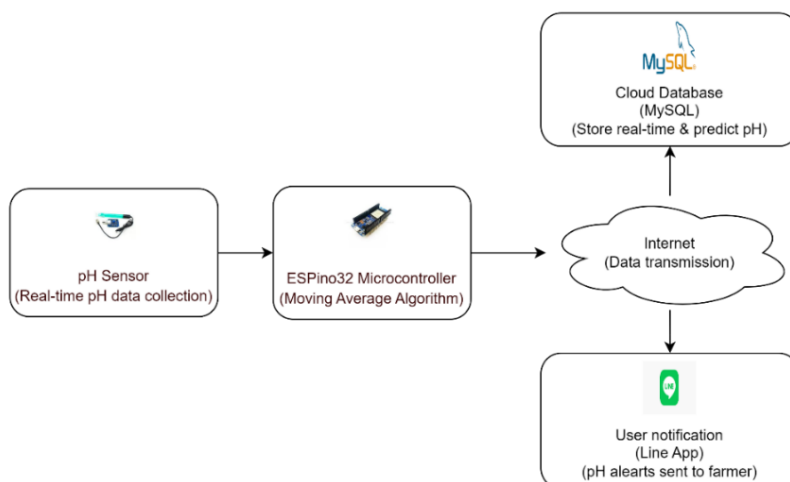


Fig. 1 - Infrastructure of the pH forecasting system for shrimp farms

- Automatic Water Quality Measurement System, a pH sensor was used to continuously monitor the water's pH level. This sensor was connected to an ESPino32 microcontroller, which collected real-time pH data.

- Processing and Reporting System, the collected pH values were processed using a moving average model to predict future pH levels. The predictions were then reported to the cloud database and the user's mobile device via the Line application.

- Cloud-Based Database, all collected and predicted pH data were stored in a MySQL cloud database for easy access and management. This cloud-based system allowed the data to be accessed remotely by the shrimp farmer at any time.

- Automatic Notification System, the system was configured to automatically notify the user via the Line application if the pH level deviated from the acceptable range (5.5–8.5). Both real-time pH values and predicted future pH values were sent to the farmer's device, allowing for immediate corrective actions if necessary.

pH Monitoring and Forecasting System

The pH monitoring and forecasting system operates in a sequential manner to ensure real-time data collection, analysis, and predictive capabilities. The process begins with the collection of pH values from the shrimp pond and continues through data processing, forecasting, and notification to the farmer. The system's workflow is outlined as follows.

1. Data Collection

The system initiates by collecting real-time pH values from the shrimp pond using a pH sensor. This data serves as the basis for both immediate evaluation and predictive modelling.

2. Data Processing

Once the pH value is collected, the system processes the data to assess its validity and determine whether further action is required. The collected pH data is first evaluated against a predefined range of acceptable values (5.5–8.5), which represents the optimal water conditions for shrimp growth and health.

3. Critical Value Detection, the system then checks if the collected pH value exceeds the acceptable thresholds.

3.1 If the pH value is either higher than 8.5 or lower than 5.5, the system identifies this as a critical value. In this case, an alert is triggered to notify the shrimp farmer via a mobile application (Line notification). This notification prompts immediate corrective action to prevent potential harm to the shrimp population.

3.2 If the pH value is within the acceptable range, the system proceeds to the next step, bypassing the alert stage.

4. pH Forecasting

For pH values that fall within the acceptable range, the system uses a moving average algorithm to predict future pH values. This forecasting process is essential for identifying potential trends that could lead to unfavorable water conditions if left unaddressed. The forecasting model uses historical pH data collected over time to generate accurate predictions of future pH fluctuations.

5. Current and Future pH Reporting: The system outputs both the current pH value and the forecasted future pH value. These values are then stored in a cloud-based database (MySQL) for further analysis and record-keeping. The availability of historical and predicted data allows for long-term monitoring and provides insights into water quality trends.

6. Database Integration

The pH data, both real-time and forecasted, is stored in the system's cloud database. This storage provides a centralized platform for accessing and analyzing pH data, enabling the farmer to review historical water quality data and respond proactively to changes in water conditions.

7. System Termination

The system completes the workflow after storing the pH data and either alerting the farmer or completing the forecasting process. The system continuously loops, allowing for ongoing real-time monitoring of water quality.

Experimental Setup

During the first quarter of 2024, the experiments were conducted in the shrimp farm at Donka district, Bangpae province, Rachaburi city, Thailand. The experiment was conducted under six different data collection configurations to evaluate the performance of the pH prediction model. The configurations were as follows:

1. pH data collection every 10 minutes for 2 hours
2. pH data collection every 10 minutes for 4 hours
3. pH data collection every 10 minutes for 6 hours
4. pH data collection every 30 minutes for 2 hours
5. pH data collection every 30 minutes for 4 hours
6. pH data collection every 30 minutes for 6 hours

For each configuration, the collected pH data was used to generate predictions using the moving average model. The accuracy of the predictions was evaluated using the mean squared error (MSE) and root mean square error (RMSE) metrics. These metrics provided an objective measure of the model's predictive performance, with lower MSE and RMSE values indicating higher accuracy.

Accuracy Evaluation

Time series forecasting is a technique which solely depends on past collected data to predict future value of the collected data. It is based on the assumption that the future data can be predicted through the existing data. This research is conducted relied on moving average (MA) which is one of the three average value forecasting techniques, including, Naïve approach, constant model, and moving average. The MA equation is as shown in equation (1) (Ivanovski *et al.*, 2018; Amali *et al.*, 2022; Huriati *et al.*, 2022).

$$MA = \frac{\sum(actual)}{n} \quad (1)$$

In this research, the accuracy of the predicted result is measured through mean squared error (MSE) and root mean square error (RMSE). The best result is selected from the predicted value with the lowest MSE and RMSE out of six calculation schemes. The selected result is considered the most accurate prediction since it has the least different value from the real data. The equations of MSE and RMSE are as shown in equations (2) and (3), respectively (Hu *et al.*, 2019; Eze *et al.*, 2021; Ardiansah *et al.*, 2021; Ensafi *et al.*, 2022).

$$MSE = \frac{\sum(actual-forecast)^2}{n} \quad (2)$$

$$RMSE = \sqrt{\frac{\sum(actual-forecast)^2}{n}} \quad (3)$$

RESULTS

The developed pH monitoring and forecasting system was tested in a shrimp farm to evaluate its performance in predicting water quality and ensuring real-time alerts in cases of critical pH values. The system collected pH data at regular intervals, processed the data, and generated both real-time and forecasted pH values, which were subsequently compared to the observed values.

Hardware Design

The hardware component, as shown in Figure 2, including the pH sensor (number 2) combined with a probe head (number 3) and the ESPino32 microcontroller (number 1), functioned reliably throughout the experimental period. Data collection was performed at 10-minute intervals over a 2-hour period, and the sensor demonstrated consistent accuracy in capturing real-time pH levels. The data was transmitted to the cloud database without notable communication delays or data loss, ensuring smooth operation across all components.

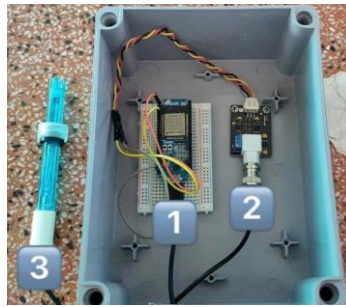


Fig. 2 - Hardware design of the pH forecasting

Prediction Accuracy

To assess the accuracy of the pH forecasting model, six experiments were conducted with varying data collection intervals and durations, ranging from 10-minute to 30-minute intervals, and covering periods of 2, 4, and 6 hours. For each experiment, the system generated both current and forecasted pH values. The accuracy of the forecasts was evaluated based on the mean squared error (MSE) and root mean square error (RMSE) metrics.

The experiment that collected pH data every 10 minutes over a 2-hour period produced the most accurate predictions, with an MSE of 0.003050 and an RMSE of 0.038628 (Figure 3a). In contrast, the experiment with 30-minute intervals over a 6-hour period yielded higher error values, with an MSE of 0.003307 and an RMSE of 0.042485 (Figure 3f). Table 1 presents the results of the forecasting accuracy for each experimental setup.



Fig. 3 - The results of six experiments for the pH forecasting

Real-Time pH Monitoring

During the experiment, the system continuously monitored the real-time pH values in the shrimp pond. Whenever the pH value deviated from the acceptable range (5.5–8.5), the system immediately triggered an alert. As shown in Figure 4, the system successfully notified the farmer via the Line application whenever the pH level fell below or exceeded the threshold, allowing the farmer to take prompt corrective actions. This immediate response helped maintain optimal water quality and minimized potential stress on the shrimp.



Fig. 4 - The result of system notification whenever the pH level fell below or exceeded the threshold

Predictive pH Analysis

The predictive analysis component of the system proved effective in forecasting pH values during the first quarter of 2024. The experiment as shown in Figure 5 was conducted, the shrimp pond was 4,000 square meters with 120 density of shrimps per square meter. The pH values were collected every 10 minutes within 2 hours for further prediction calculation. The monthly average collected pH, predicted pH, MSE and RMSE are as shown in Table 1.

The average deviation between the forecasted and actual pH values remained low across all months, with the lowest MSE (0.000225) observed in March 2024, demonstrating the robustness of the moving average algorithm in predicting pH fluctuations.

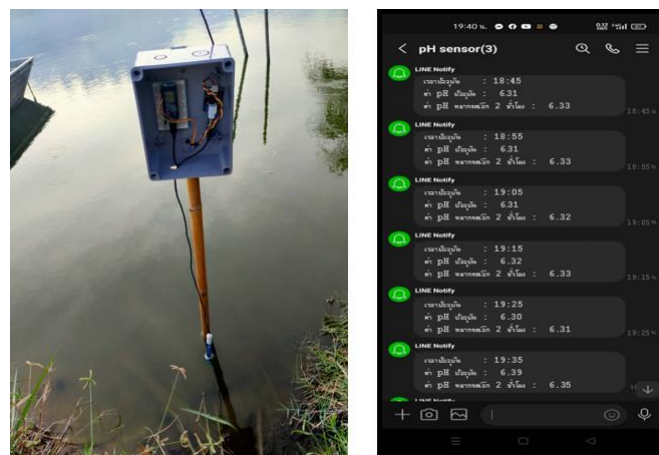


Fig. 5 - The experiment and the notification of current pH and predicted pH

Table 1

Results in actual pH, forecast pH, MSE and RMSE during the first quarter of 2024

Month	Actual average pH value	Forecast average pH value	MSE	RMSE
January 2024	7.85	7.83	0.000434	0.020833
February 2024	7.83	7.83	0.000711	0.026667
March 2024	7.83	7.83	0.000225	0.015000

Notifications and Data Storage

The system's notification functionality performed as expected, sending timely alerts to the farmer when critical pH levels were detected. Both real-time and forecasted pH values were successfully stored in the cloud-based MySQL database, ensuring that the data could be accessed at any time for further analysis or reporting purposes. The database provided a comprehensive record of water quality data, including historical trends and predictive insights, facilitating long-term water quality management.

Overall, the pH monitoring and forecasting system demonstrated a high level of accuracy and reliability in both real-time monitoring and predictive analysis. The system effectively maintained water quality within the acceptable range, reduced the risk of pH-related stress on the shrimp population, and provided the farmer with timely notifications of potential issues. These results suggest that the system is a valuable tool for improving the management of water quality in shrimp farming environments.

CONCLUSIONS

This research presents the development and evaluation of an automated pH monitoring and forecasting system for shrimp farming, designed to enhance water quality management. The system integrates real-time pH data collection, predictive analysis using a moving average algorithm, and automated notifications to alert shrimp farmers when critical pH values are detected.

The experimental results demonstrate that the system performs reliably in both monitoring and forecasting pH levels. The hardware components, including the pH sensor and ESPino32 microcontroller, consistently captured and transmitted pH data, ensuring stable system operation. Moreover, the cloud-based storage of real-time and forecasted data facilitates easy access to historical and predictive water quality data for future reference. The pH forecasting model, evaluated through multiple experiments, exhibited high accuracy in predicting future pH values. The experiment utilizing 10-minute intervals over a 2-hour period produced the lowest MSE and RMSE, indicating the effectiveness of the model in short-term pH forecasting. These predictions provided shrimp farmers with valuable insights into potential future fluctuations in water quality, allowing for timely interventions to prevent adverse conditions.

In addition, the system's automated notification feature performed as expected, sending immediate alerts to the farmer via the Line application whenever the pH values fell outside the acceptable range (5.5–8.5). This real-time feedback ensured that the farmer could promptly respond to changes in water quality, reducing the risk of pH-related stress on the shrimp population and improving overall farm productivity.

While the system has demonstrated effectiveness in monitoring and predicting pH levels, future enhancements could include the integration of additional water quality parameters, such as dissolved oxygen (DO) and salinity. This would provide a more comprehensive tool for managing water conditions in shrimp farming. Moreover, the use of advanced predictive algorithms, including machine learning techniques, may further improve the accuracy of the forecasts, particularly over longer time periods.

ACKNOWLEDGEMENT

This research was made possible with the research budget support from the Research and Development Institute of Nakhon Pathom Rajabhat University, and Creating Innovation for Sustainable Development Research Center, Nakhon Pathom Rajabhat University, Nakhon Pathom, Thailand, which supported laboratories, equipment and tools used for research. Finally, we would like to express our deepest appreciation to Mr. Prasopchoke Somsua, a shrimp cultivator from Donka district, Bangpae province, Rachaburi city, Thailand, for providing experimenting location for this research.

REFERENCES

- [1] Amali, Pranoto, G. T. & Darwis, M. (2022). Forecasting with weighted moving average method for product procurement stock. *Jurnal Sistem Informasi dan Sains Teknologi*, 4(2).
- [2] Ariadi, H., Wafi, A. & Supriatna. (2020). Relationship between water quality and FCR values in vannamei shrimp intensive aquaculture (*Litopenaeus vannamei*). *Samakia: Fisheries Science Journal*, 11(1), 44-50.
- [3] Ariadi, H., Azril, M. & Mujtahidah, T. (2023). Water quality fluctuations in shrimp ponds during dry and rainy seasons. *Croatian Journal of Fisheries*, 81, 127-137. <https://doi.org/10.2478/cjf-2023-0014>

- [4] Ardiansah, I., Adiarsa, I. F., Putri and Pujiyanto, T. (2021). Application of Time Series Analysis in Organic Product Sales Forecasting using Moving Average and Exponential Smoothing Methods. *Jurnal Teknik Pertanian Lampung*, 10(4), 548-559.
- [5] de los Santos, C. B., Olive, I., Moreira, M., Silva, A., Freitas, C., Luna, R. A., Quental-Ferreira, H., Martins, M., Costa, M. M., Silva, J., Cunha, M. E., Soares, F., Pousao-Ferreira, P. & Santos, R. (2020). Seagrass meadows improve inflowing water quality in aquaculture ponds. *Aquaculture*, 528, 735502.
- [6] Deepradit, S. & Prompes, C. (2022). The forecasting of horticulture monthly price using individual and top-down hierarchical methods. *Kasem Bundit Engineering Journal*, 12(1).
- [7] Durai, V., Alagappan, M. and Yuvarajan, P. (2021). Importance of Water Quality Management in Whiteleg Shrimp. *Penaeus vannamei Farming. AgriCos e-Newsletter*, 2(9), 7-20.
- [8] Ensafi, Y., Amina, S. H., Zhang, G. & Shah, B. (2022). Time-series forecasting of seasonal items sales using machine learning -A comparative analysis. *International Journal of Information Management Data Insights*, 2.
- [9] Eze, E., Halse, S. & Ajmal, T. (2021). Developing a Novel Water Quality Prediction Model for a South African Aquaculture Farm. *Water*, 13. <https://doi.org/10.3390/w13131782>
- [10] Gambin, Á. F., Angelats, E., Gonzalez, J. S., Miozzo, M. & Dini, P. (2021). Sustainable Marine Ecosystems: Deep Learning for Water Quality Assessment and Forecasting. *IEEE Access*, 9, 121344-121365
- [11] Hsieh, H-H., Weerathunga, V., Weerakkody, W.S., Huang, W-J., Muller, F.L.L., Benfield, M.C. and Hung, C-C. (2021). The effects of low pH on the taste and amino acid composition of tiger shrimp. *Scientific Reports*, 11, 21180. <https://doi.org/10.1038/s41598-021-00612-z>
- [12] Hu, Z., Zhang, Y., Zhao, Y., Xie, M., Zhong, J., Tu, Z. & Liu, J. (2019). A Water Quality Prediction Method Based on the Deep LSTM Network Considering Correlation in Smart Mariculture. *Sensors*, 19. <https://doi.org/10.3390/s19061420>
- [13] Huriati, P., Erianda, A., Alanda, A., Meidelfi, D., Rasyidah, Defni, & Suryani, A. I. (2022). Implementation of the Moving Average Method for Forecasting Inventory in Cv. Tre Jaya Perkasa. *International Journal of Advanced Science Computing and Engineering*, 4(2), 67-75
- [14] Ivanovski, Z., Milenkovski, A. & Narasanov, Z. (2018). Time series forecasting using a moving average model for extrapolation of number of tourist. *UTMS Journal of Economics*, 9(2), 121–132.
- [15] Kim C-W, Lee J-W, Kang S-W, Kang H-S. (2024). Study on Ferritin Gene Expression to Evaluate the Health of White Leg Shrimp (*Litopenaeus vannamei*) Postlarvae Due to Changes in Water Temperature, Salinity, and pH. *Water*. 2024; 16(11):1477. <https://doi.org/10.3390/w16111477>
- [16] Komarudin, M., Septama, H. D., Yulianti, T., Yudamson, A., Hendri, J. & Arafat, M. A. D. (2021). Multi node sensors for water quality monitoring towards precision aquaculture. *IOP Conf. Series: Earth and Environmental Science*, 739, 012026
- [17] Lin, Q., Yang, W., Zheng, C., Lu, K., Zheng, Z., Wang J. & Zhu, J. (2018). Deep-learning based approach for forecast of water quality in intensive shrimp ponds. *Indian J. Fish.*, 65(4), 75-80, 2018, <https://doi.org/10.21077/ijf.2018.65.4.72559-09>
- [18] Mirsanjari, M. M. & Mohammadyari, F. (2018). Application of Time-series Model to Predict Groundwater Quality Parameters for Agriculture: (Plain Mehran Case Study). *IOP Conf. Series: Earth and Environmental Science*, 127, 012012, <https://doi.org/10.1088/1755-1315/127/1/012012>
- [19] Mohammadyari, F., Zarandian, A. & Beigmohammadi, F. (2022). Modeling Ground-Water Quality using time Series Models (A Case Study: Dehloran Plain, Ilam). *Irrigation Sciences and Engineering*, 45(2), 81-97
- [20] Monteiro, M. & Costa, M. (2018). A Time Series Model Comparison for Monitoring and Forecasting Water Quality Variables. *Hydrology*, 5(3). <https://doi.org/10.3390/hydrology5030037>
- [21] Qiao, L., Chang, Z., Li, J. & Chen, Z. (2020). Phytoplankton community succession in relation to water quality changes in the indoor industrial aquaculture system for *Litopenaeus vannamei*. *Aquaculture*, 527, 735441
- [22] Shirly-Lim, Y.L., Rahmah, S., Ghaffar, M.A., Liang, L.Q., Chang, Y.M., Chisti, Y., Lee, M. and Liew, H.J. (2024). Pacific whiteleg shrimps compromise their physiological needs to cope with environmental stress. *Environmental Advances*, 15(2024), 100492, <https://doi.org/10.1016/j.envadv.2024.100492>
- [23] Supriatna, M., Darmawan A. and Maizar A. (2023). Pathway analysis of pH in whiteleg shrimp, *Litopenaeus vannamei* concrete pond intensifies in Banyuwangi East Java. *IOP Conf. Series: Earth and Environmental Science*, 1191, 012015, <https://doi.org/10.1088/1755-1315/1191/1/012015>

- [24] Tarunamulia, Ilnam, M., Sammut, J., Paena, M., Basir, Kamariah, Taukhid, I., Asaf, R., Athirah, A., Akmal and Syaichudin, M. (2024). Impact of soil and water quality on the sustainable management of mangrove-compatible brackish water aquaculture practices in Indonesia. *IOP Publishing Environmental Research Communications*, 6(2024), 085013. <https://doi.org/10.1088/2515-7620/ad6caa>
- [25] Thai-Nghe, N., Thanh-Hai, N. & Ngon, N. C. (2020). Deep Learning Approach for Forecasting Water Quality in IoT Systems. *International Journal of Advanced Computer Science and Applications*, 11(8), 686-693
- [26] Yu, Q., Xie, J., HUang, M., Chen, C., Qian, D., Qin, J. G., Chen, L., Jia, Y., Li, E. (2020). Growth and health responses to a long-term pH stress in Pacific white shrimp *Litopenaeus vannamei*. *Aquaculture Reports*, vol. 16, 100280

ANALYSIS OF VIBRATION CHARACTERISTICS AND STRUCTURAL OPTIMIZATION OF THE CHASSIS FRAME OF CRAWLER-TYPE COMBINE HARVESTER

履带式联合收割机底盘机架振动特性分析与结构优化

Zihao ZHAO¹⁾, Chengqian JIN^{1,2)}, Guangyue ZHANG²⁾, Youliang NI²⁾, Zhenjie QIAN²⁾

¹⁾ School of Agricultural Engineering and Food Science, Shandong University of Technology, Zibo, Shandong / China

²⁾ Nanjing Institute of Agricultural Mechanization, Ministry of Agriculture and Rural Affairs, Nanjing, Jiangsu / China

Corresponding author: Chengqian JIN

Tel: +8615366092900; E-mail: jinchengqian@caas.cn

DOI: <https://doi.org/10.35633/inmateh-75-14>

Keywords: vibration characteristics; chassis; static analysis; vibration velocity

ABSTRACT

To investigate the vibration characteristics of the Thinker Agricultural Machinery 4LZ-2.0 crawler-type combine harvester under operational conditions, vibration tests were conducted on the chassis frame at three different engine speeds: 2700 r/min, 1500 r/min, and 800 r/min. A static analysis was initially performed to identify regions of significant stress and deformation on the chassis frame, which guided the placement of measurement points for collecting vibration acceleration data. Subsequent processing of the acceleration data in the frequency domain revealed the variation in vibration velocity at each measurement point on the chassis frame. It was found that as the engine speed increased, the excitation frequencies from the vibrating screen and cutting platform appeared as dominant resonance frequencies at nine out of twelve measurement points on the chassis frame. By referencing the international standard ISO 20816, it was determined that most of these measurement points fell into Class D, indicating a high level of vibration severity. To mitigate the vibration of the chassis frame, two measures were implemented: enhancing the structural rigidity of the frame and reducing the area of the center of mass trajectory of the vibrating screen. Following these modifications, re-testing showed that the average vibration intensity at the three maximum vibration measurement points of the chassis in the high engine speed condition successfully decreased by 34.57% compared to the original structure.

摘要

为了解收割机运行状态下底盘机架振动特性，以星光农机 4LZ-2.0 型履带式联合收割机为研究对象，在发动机处于 2700r/min, 1500r/min, 850r/min 三种不同转速下对其底盘机架进行振动测试。首先通过静力分析找到底盘机架应力与变形较大的区域，并以此在其表面布置测点，采集振动加速度数据。通过在频域内对加速度数据进行处理得到底盘机架各测点振动速度变化情况。发现随发动机转速提升，振动筛与割台的激励频率在收割机底盘机架 12 个测点中 9 个测点作为主振频率出现。结合国际标准 ISO 20816，发现这些测点大多处于振动等级最大的 D 级，振动强度过大。为减小收割机底盘机架振动，采取增强机架结构、减小振动筛质心运动轨迹面积两种措施。经重新测试，发动机高转速状态下底盘 3 个振动最大测点各方向平均振动强度较原结构成功降低 34.57%。

INTRODUCTION

The chassis is the primary load-bearing component of a tracked combine harvester, subject to complex external excitations. Variations in the working environment and the machine's operational state can significantly affect its vibration characteristics, leading to considerable discrepancies in vibrational responses. Excessive vibrations not only impact the comfort of the operator (Biriş et al., 2022; Viăduț et al., 2023; Dimitriadis et al., 2023; Marin et al., 2024) but also increase the risk of fatigue failure at structurally weak points, thereby posing a serious threat to the overall reliability of the machine (Zhou et al., 2023; Noh et al., 2024). Consequently, it is crucial to investigate the vibrational characteristics of the combine harvester chassis.

Currently, research on the vibrations of harvesters, both domestically and internationally, primarily focuses on the cutting platform, chassis, and operator comfort (Ma et al., 2020; Jiang et al., 2017; Sun et al., 2014; Xie et al., 2019). Various methodologies, including dynamic simulation and analysis, experimental modal analysis, and test rig design, have been employed to obtain the vibrational characteristics of these

components. Wang *et al.* (2021) designed an intelligent control test bench for combine harvesters, which is capable of regulating the forward speed of the combine harvester based on data processing results. Additionally, the system can classify and handle faults, as well as transmit and print stored data via serial communication. This design not only enhances the intelligence level of combine harvesters but also provides reliable technical support for fault diagnosis and performance optimization. By integrating data processing and automatic control functions, the test bench serves as a significant experimental platform and research foundation for the intelligent development of agricultural machinery. Comparing the results of the different methods for vibration and sound datasets, Karagiovanidis *et al.* (2023) found that classification accuracy showed that in the case of vibration, the detection of cavitation in real conditions is possible. Rabbani *et al.* (2011) constructed a dynamic three-dimensional model for a half-track tractor, incorporating its bounce, pitch, and roll motions, to elucidate the tractor's vibration characteristics. Driving experiments were conducted to validate the effectiveness of the motion equations derived from the proposed dynamic model. Pang *et al.* (2019) measured and analyzed the time-domain and frequency-domain characteristics of the cutting platform's vibrational response, designing a rubber-sleeved nut that successfully reduced the vibrations transmitted to the operator's seat. Chen *et al.* (2020) assembled the combine harvester's chassis and threshing frame into a complete structure, deriving its vibrational response under multi-source excitations to provide a reference for further improvements to the chassis. Tang *et al.* (2021) conducted finite element modal analysis and vibration testing on the threshing cylinder and frame, designing support beams based on test results to mitigate vibrations generated during the threshing process.

In summary, the vibration characteristics of agricultural machinery systems have garnered considerable attention from numerous scholars (Yao *et al.*, 2017; Li *et al.*, 2023; Ding *et al.*, 2022; Zhang *et al.*, 2023). However, analyses regarding the impact of the engine, vibrating screen, and cutting mechanism on the chassis of tracked combine harvesters during operational conditions remain limited. This study primarily employs digital signal processing, complemented by finite element analysis and multi-body dynamic simulation, to explore this issue further.

MATERIAL AND METHODS

SOURCES OF CHASSIS FRAME VIBRATION AND INTRODUCTION TO CHASSIS STRUCTURE

The study focuses on the 4LZ-2.0 tracked combine harvester produced by Xingguang Agricultural Machinery, with its chassis frame primarily subjected to excitations from the engine, cutting platform, threshing drum, vibrating screen, and screw conveyor (Zhang *et al.*, 2021; Gao *et al.*, 2017; Zhang *et al.*, 2001). The spatial distribution of these components is illustrated in Figure 1.

Research on the excitatory conditions affecting the chassis is based on its structural design, as depicted in Figure 2. The chassis measures 2.75 m in length, 1.87 m in width, and 0.6 m in height. Constructed from carbon structural steel, the components are connected via welding. The orange section represents the chassis frame, with a steel pipe cross-section parameter of 40 x 60 x 3 mm. This frame directly connects to the engine, elevator, threshing drum, vibrating screen assembly, cutting platform, and the hydraulic support rods for the conveyor trough, while being anchored to two longitudinal beams (blue structure) that play a major load-bearing role.

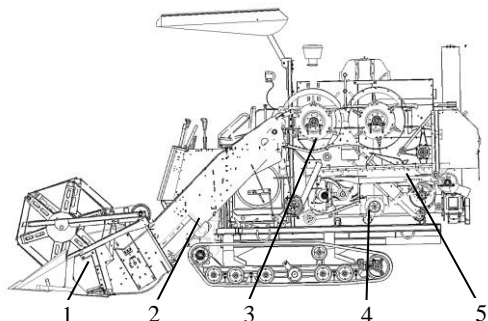


Fig. 1 - Sources of excitation for the chassis frame
1. Cutter bar; 2. Conveying trough; 3. Threshing drum;
4. Auger; 5. Vibrating screen

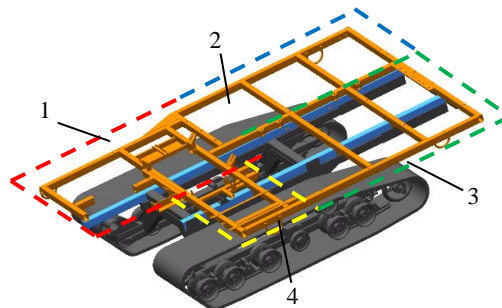


Fig. 2 - The chassis structure of the 4LZ-2.0 crawler-type combine harvester
1. Engine and cab area; 2. Grain bin area; 3. Threshing drum and vibrating screen area; 4. Cutter bar and conveying trough area

The longitudinal beams utilize steel pipes with a cross-section parameter of 50 × 70 × 3 mm, welded and fixed in place by two transverse beams with a cross-section parameter of 70 × 70 × 3 mm. These transverse beams are strategically located beneath the chassis frame at the front and middle sections, with each transverse beam linked to a truss structure. The loads borne by the chassis frame are transmitted through the truss to the track bearing wheel assembly, ultimately transferring the forces to the ground.

The structural simplification of the chassis model for the 4LZ-2.0 tracked combine harvester involves removing through-holes with diameters less than 10 mm and fillets with radii less than 5 mm, which have minimal impact on structural strength. Small flat surfaces are merged before importing the model into the finite element analysis software Ansys for static analysis. To enhance computational efficiency, the track components are excluded, and the track bearing wheel assembly is fixed as a boundary condition.

The connection methods between structures utilize the software's default settings, with structural steel selected as the material. The element size is set to 10 mm, resulting in a total of 1111691 nodes and 387396 elements. Based on manufacturer-provided parameters, the total mass of the machine is 2870 kg, with the chassis mass being 1318 kg. A vertical load of 15520 N is applied downward on the chassis frame's upper plane to simulate its stress condition in a static state, allowing for the calculation of total deformation and equivalent stress, as shown in Figure 3.

The static analysis results indicate that the chassis frame experiences the maximum deformation in the regions of the vibrating screen and threshing drum, which are farthest from the truss support. The grain tank area exhibits the next highest deformation. Stress and strain concentrations are most significant near the support points, highlighting these areas as relatively weak points in the overall frame that warrant close attention.

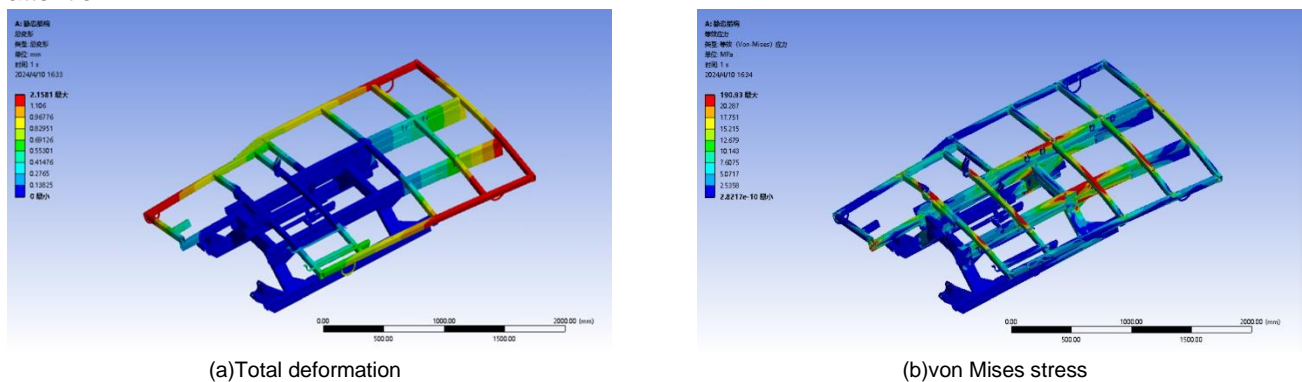


Fig. 3 - The static analysis results of the chassis

TESTING OF CHASSIS VIBRATION CHARACTERISTICS

The current international standard ISO 20816 provides guidelines for evaluating mechanical vibrations on non-rotating components based on the root mean square (RMS) vibration velocity. Vibrational intensity is categorized into four levels—A, B, C, and D—ranging from low to high. Given the differing operational characteristics of various types of machinery, the boundaries for each level are presented as fuzzy intervals, allowing users to make determinations based on their specific contexts. The boundary intervals are detailed in Table 1. In this study, each vibration level is defined by its maximum value as the boundary. Due to the large size of vibration velocity sensors, which makes them impractical for installation on the harvester chassis, vibration data is collected using acceleration sensors. This data is subsequently integrated to obtain the vibration velocity.

Vibration testing of the entire machine and the chassis frame was conducted using the Donghua Testing DH5902 data acquisition and analysis system, along with a portable computer and 12 tri-axial piezoelectric accelerometers (1A314E). This accelerometer captures acceleration amplitudes in the mutually orthogonal x, y, and z directions, with a measurement range of 500 m·s⁻² and a frequency acquisition range of 0.5 to 7000 Hz, set at a sampling frequency of 1000 Hz.

In conjunction with the static analysis results, 12 measurement points were selected on the chassis frame, evenly distributed across areas of significant deformation or stress, as shown in Figure 4. Measurement points 1, 2, 8, and 10 are located in the regions of the vibrating screen and threshing drum, points 3, 4, 5, and 11 in the grain tank area, points 6 and 12 near the engine, and points 7 and 9 in the cutting platform and conveyor trough areas.

Table 1

Boundary Intervals of Vibration Levels		
AB Boundary / mm•s ⁻¹	BC Boundary / mm•s ⁻¹	CD Boundary / mm•s ⁻¹
0.71-4.5	1.8-9.3	4.5-14.7

Table 2
The Vibration Frequencies of the Main Excitation Sources of the Harvester at Different Engine Speeds

Excitation source	Main excitation frequency /Hz		
	Low speed	Medium speed	High speed
Engine	28.33	50.00	90.00
Cutter drive shaft	2.83	5.00	9.00
Vibrating screen	2.37	4.17	7.50
Threshing drum	7.08	12.50	22.50
Screw conveyor	1.01	1.79	3.21

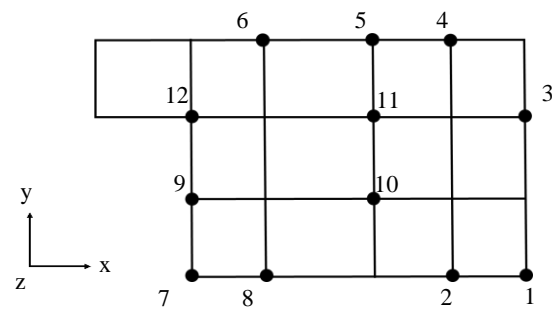


Fig. 4 - Distribution of measurement points

The vibration acceleration information in the x, y, and z directions was collected at various engine speeds: low (850 r/min), medium (1500 r/min), and high (2700 r/min). The time-domain information was analyzed, and the primary excitation frequencies associated with each source at different engine speeds are summarized in Table 2. The main excitation frequency of the engine is primarily determined by its second-order ignition frequency (Wu, et al., 2020; Hu, et al., 2015), The main vibration frequency f is calculated using the formula:

$$f = \frac{n}{60} \times \frac{c}{2} \tag{1}$$

where: n is the engine speed in revolutions per minute (r/min),

- c is the number of cylinders in the engine.

This formula provides the primary excitation frequency related to the engine's operational characteristics.



Fig. 5 – Tri-axial piezoelectric accelerometers (1A314E) at measurement point-2



Fig. 6 - Complete machine vibration testing

RESULTS

Calculation of Vibration Velocity at Each Measurement Point

To obtain the vibration velocity at each measurement point on the combine harvester chassis, the collected vibration acceleration data must be integrated. However, the velocity data obtained from direct time-domain integration is significantly affected by factors such as zero drift of the accelerometer and disturbances from other low-frequency signals, leading to noticeable trends in the results, as illustrated in Figure 6.

To eliminate these influences, it is necessary to fit the integration results and remove the trend components. However, fitting each group of signal data during large-scale signal processing can consume significant computational resources. Additionally, filtering out low-frequency components from the signal can also achieve a similar effect to detrending after integration (Wei, et al., 2018) Therefore, this study processes the data in the frequency domain to obtain velocity information while analyzing the primary sources of vibration at each measurement point.

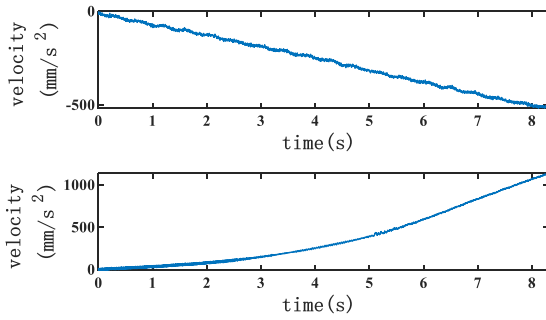


Fig. 6 - Velocity variation chart obtained by integrating untreated time-domain data from some measurement points

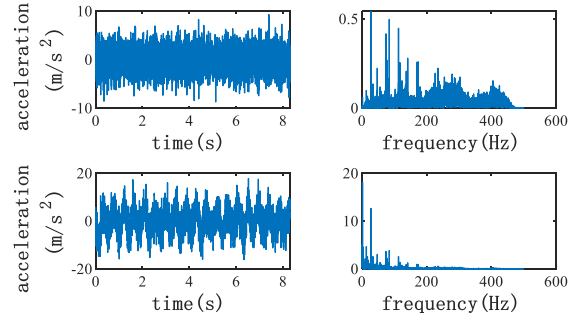


Fig. 7 - Time-domain and frequency-domain feature plot for measurement point 1

The Fast Fourier Transform (FFT) is used to convert the time-domain discrete signals collected by the accelerometers into the frequency domain. FFT is a computationally efficient method that simplifies the Discrete Fourier Transform (DFT) for faster calculations. While they are fundamentally equivalent, both methods perform the transformation of the time-domain signal as described in the following equation:

$$X(k) = \sum_{n=0}^{N-1} x(n)e^{-j\frac{2\pi}{N}kn} \quad (k=0,1,2\dots N-1) \quad (2)$$

In the context of FFT or DFT transformation, the symbols can be defined as follows:

- $X(k)$: Represents the frequency-domain signal in its complex form after FFT or DFT transformation.
- $x(n)$: Represents the discrete time-domain signal.
- $e^{-j\frac{2\pi}{N}kn}$: Describes the unit circle in the frequency domain, as defined by Euler's formula.
- k : Represents the frequency-domain signal sequence.
- N : Represents the total number of data points in the time-domain signal.
- j : Represents the imaginary unit.

The relationship between the time-domain integral of a digital signal and its corresponding representation in the frequency domain can be expressed by the following equation:

$$\mathcal{F} \left[\int_{-\infty}^t f(\tau) d\tau \right] = \frac{F(\omega)}{j\omega} + \pi F(0)\delta(\omega) \quad (3)$$

In the equation provided, the following symbols represent specific concepts:

- \mathcal{F} : Represents the Fourier transform.
- $\int_{-\infty}^t f(\tau) d\tau$: Indicates the time-domain integration of the digital signal.
- $F(\omega)$: Represents the frequency-domain value of the digital signal.
- $F(0)$: Represents the DC component.
- $\delta(\omega)$: Denotes the unit impulse function, an idealized narrow pulse with an area equal to 1.
- t : Represents the maximum time point of the selected time interval.
- ω : Represents the frequency-domain variable.

For the discrete data collected during the experiment, $F(\omega) = X(k)$ and $j\omega = jk$.

In general, the DC component is the primary factor causing trends in integration results; therefore, $F(0)$ is set to 0. To obtain the time-domain integral of the digital signal, it is sufficient to divide its frequency-domain data by $j\omega$ and then perform the inverse Fourier transform (IFT).

The process involves using the Fast Fourier Transform (FFT) to convert the acceleration signals from each measurement point into frequency-domain form. After processing the data in the frequency domain, the velocity is obtained through the inverse Fourier transform.

For example, the time-frequency characteristics of the acceleration and velocity at measurement point 1 are illustrated in Figure 7, demonstrating how the transformation and processing effectively capture the vibrational behavior of the chassis.

Analysis of Vibration Velocity at Measurement Points

After performing frequency domain integration on the vibration acceleration data collected from various measurement points of the engine under low-speed conditions, it was found that the vibration velocity does not exhibit a periodic variation exceeding 2 seconds in the time domain. To improve computational efficiency while ensuring the completeness of frequency domain information, acceleration data collected over 2 seconds at mid to high engine speeds, characterized by shorter periods, were selected for processing. It is assumed that this data contains velocity and acceleration information encompassing more than one cycle, thereby excluding frequency domain data below 0.5 Hz. The frequency characteristics of the first three modes of vibration velocity in different directions at various engine speeds (high, medium, and low) for all measurement points are presented in Table 3.

Due to the resolution limitations of frequency domain data and the fact that the engine speed remains at a specific value near the preset rotation speed, the experimentally measured vibration frequencies of excitation sources exhibit minor deviations from their theoretical values. As indicated in Tables 1 and 3, under low-speed conditions, the vibrations at measurement points on the chassis frame are influenced comparably by excitations from engine cylinder ignition, cutter drive shaft, and vibrating sieve, with their respective frequencies contributing comparably to the observed vibration spectra. However, at medium and high rotation speeds, except for measurement points 5 and 6 near the engine - which predominantly exhibit a dominant vibration frequency of 91.8 Hz in the z-direction (closely matching the engine excitation frequency) - other measurement points primarily demonstrate vibration frequencies adjacent to those generated by the vibrating sieve and cutter drive shaft. This characteristic is particularly pronounced in the x- and y-directions. These findings suggest that the reciprocating motions of the header and vibrating sieve progressively surpass engine-induced excitations as rotation speed increases, ultimately emerging as the predominant excitation sources affecting the chassis frame. This phenomenon highlights the speed-dependent evolution of excitation dominance in harvester dynamic responses.

Table 3

Frequencies of the First Three Orders of Vibration Velocity									
Measurement Points	Fundamental Frequency/Hz (Velocity /m•s ⁻¹)								
	Low Speed			Medium Speed			High Speed		
	x	y	z	x	y	z	x	y	z
Measurement Points 1	28.32 (18.1)	28.81 (3.7)	28.32 (18.2)	4.88 (77.9)	4.88 (41.2)	3.91 (63.8)	7.32 (150.0)	8.79 (75.5)	7.32 (80.5)
Measurement Points 2	28.32 (17.8)	2.93 (4.9)	2.44 (17.1)	4.88 (78.5)	4.88 (11)	3.91 (57.5)	7.32 (151.5)	1.46 (60.2)	7.32 (97.8)
Measurement Points 3	2.44 (17.8)	28.81 (2.7)	47.85 (19.1)	4.88 (83.6)	4.88 (26.1)	3.91 (66.8)	7.32 (156.8)	8.79 (56.7)	7.32 (154.5)
Measurement Points 4	3.42 (4.8)	28.32 (5.2)	28.32 (40.3)	4.88 (13.9)	4.39 (28.7)	30.27 (22.2)	8.30 (55.9)	8.79 (69.8)	7.32 (45.1)
Measurement Points 5	3.42 (2.6)	56.64 (4.0)	28.32 (14.6)	30.27 (15.6)	4.39 (14.4)	30.27 (15.7)	8.30 (69.4)	8.79 (12.3)	91.80 (43.5)
Measurement Points 6	2.44 (17.4)	2.44 (9.3)	2.44 (34.7)	4.88 (35.5)	4.39 (24.4)	3.91 (30.1)	8.30 (105.5)	8.79 (48.0)	7.32 (62.5)
Measurement Points 7	28.32 (6.8)	28.32 (3.2)	1.95 (5.7)	28.32 (6.8)	4.39 (16.7)	28.32 (4.8)	4.39 (17.5)	8.79 (30.8)	3.91 (15.3)
Measurement Points 8	28.32 (17.0)	2.93 (1.3)	28.32 (9.2)	3.91 (21.1)	4.88 (8.3)	28.81 (8.9)	8.30 (49.9)	8.79 (4.0)	7.32 (54.7)
Measurement Points 9	47.85 (6.6)	28.32 (2.9)	1.95 (24.5)	4.88 (13.3)	3.91 (31.3)	3.91 (15.0)	8.30 (89.5)	7.32 (69.9)	7.32 (32.4)
Measurement Points 10	47.85 (12.5)	1.95 (7.7)	84.96 (8.4)	4.88 (13.3)	3.42 (5.2)	3.91 (10.1)	8.30 (76.4)	1.46 (126.1)	7.32 (41.7)
Measurement Points 11	2.93 (14.9)	28.32 (4.2)	28.32 (43.9)	3.91 (18.3)	4.88 (16.7)	29.30 (19.9)	8.30 (43.2)	7.32 (38.8)	34.67 (48.8)
Measurement Points 12	2.44 (13.6)	28.32 (2.6)	1.46 (7.8)	4.88 (20.9)	4.88 (21.9)	3.91 (19.7)	8.30 (97.7)	7.32 (46.3)	7.32 (42.3)

At medium and high speeds, the reciprocating motion of the cutting platform and vibrating screen increasingly affects the chassis frame as the speed rises. Only measurement points 5 and 6, close to the engine, exhibit a principal vibration frequency of 91.8 Hz in the z-direction at high speeds, closely aligning with the engine excitation frequency. Consequently, in 30 out of the 36 data sets from the 12 measurement points, the primary vibration frequencies align more closely with the excitation frequencies from the vibrating screen and cutting platform, indicating a shift in the primary excitation source from the engine to these components. Since the cutting platform and vibrating screen are located on the left side between the chassis frames, their reciprocating motions generate inertial forces that also apply torsional moments to the chassis frame. This could explain why measurement points in the x and y directions are significantly influenced by the cutting platform and vibrating screen.

The root mean square (RMS) values of the vibration velocities for each measurement point were calculated and are presented in Figure 8. Overall, at low engine speeds, the vibration velocities in the x, y, and z directions at most measurement points are close to the boundaries of vibration levels A and B. At medium speeds, the vibration intensities at most points do not significantly change from low speeds; however, measurement points 1, 2, and 3—located at the rear of the chassis frame and far from the support structure—exhibit significantly higher vibration intensities across all three testing directions, reaching vibration levels C and D.

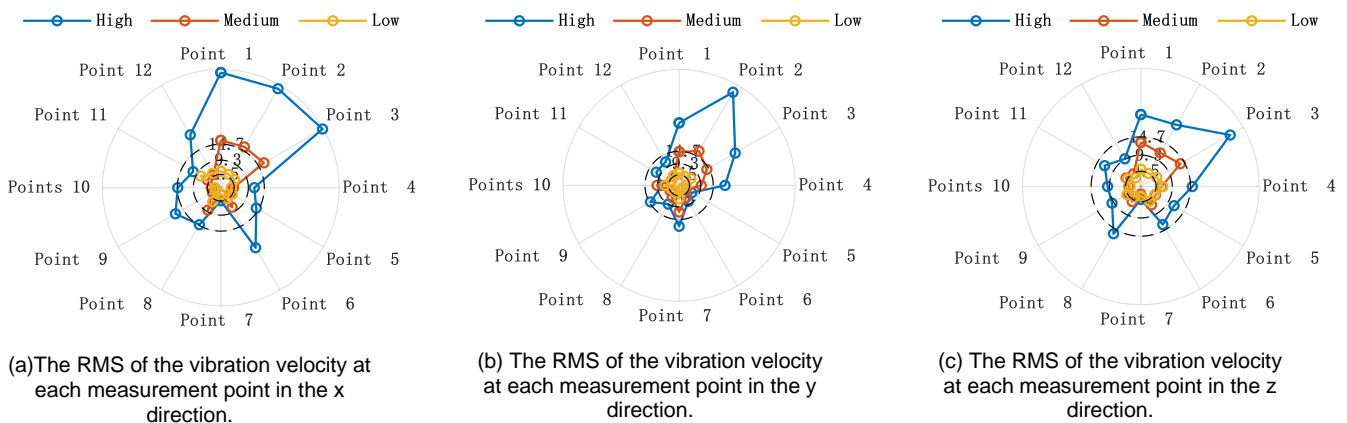


Fig. 8 - The vibration status of each measurement point

At high speeds, the vibration levels at all measurement points increase noticeably. Points that already displayed higher vibrations at medium engine speeds exhibit even greater intensities at high speeds. This suggests that, at medium engine speeds, the structural strength of the chassis frame, particularly away from the support locations, is beginning to fail under the demands of excitation from the vibrating screen and cutting platform, and this phenomenon becomes more pronounced at high engine speeds.

STRUCTURAL OPTIMIZATION OF THE COMBINE HARVESTER

To reduce the vibrations in the chassis frame of the combine harvester, improvements are made from two aspects: enhancing the structural strength of the frame and reducing excitation. First, structural reinforcements are applied to the regions at the rear of the chassis frame, specifically near measurement points 1, 2, and 3, which are far from the support points, as illustrated in Figure 9.

To decrease the excitation experienced by the chassis frame, vibration-damping pads are added at the connections between the cutting platform's hydraulic cylinders and the vibrating screen's drive shaft bearings. Additionally, given the inherent characteristics of the vibrating screen, achieving complete balance while ensuring the proper operation of other components is unrealistic. Instead, measures can be taken to reduce the area of the overall center of mass movement trajectory of the vibrating screen, thereby lowering its excitation on the chassis frame (Wang *et al.*, 2012; Zhang *et al.*, 2012; Li *et al.*, 2016).

Considering the principles of dynamic balance and the structural features of the vibrating screen and its nearby components, the decision was made to modify the center of mass of the vibrating screen's drive pulley and add eight cast iron counterweights, as depicted in Figure 10. A three-dimensional model of the vibrating screen was created, and simulations of its motion characteristics were conducted using Adams software to calculate the trajectory of the vibrating screen system's center of mass. The changes in the center of mass before and after implementing the dynamic balance design are shown in Figure 11.

After adding the counterweights, the area of the center of mass movement trajectory for the vibrating screen system was reduced, and it also moved closer to the coordinates of the drive shaft center (-1000, 0). Theoretically, this adjustment successfully weakens the inertial forces caused by the movement of the vibrating screen's center of mass.

Following these structural modifications, the vibration testing of the chassis frame was conducted again using the previously described methods. The results indicated that the vibration intensities at various measurement points were reduced to varying degrees. For example, at the more vibrationally intense measurement points 1, 2, and 3, the changes in vibration intensity at different engine speeds are summarized in Table 4.

At low engine speeds, the excitation experienced by the chassis frame is relatively low, resulting in minimal changes in vibration intensity compared to the mid and high-speed conditions. As the engine speed increases, the excitation on the chassis frame rises continuously, highlighting the advantages of the optimized structure. At high engine speeds, the average vibration intensity at the three measurement points decreased by 34.57% in different directions. Notably, the vibration velocity at measurement point 3 in the x-direction decreased from 42.67 mm·s⁻² to 11.51 mm·s⁻², shifting the vibration level from D to C, indicating a significant reduction in vibration intensity.



(a) Enhancement of horizontal structural integrity.



(b) Enhancement of vertical structural integrity.

Fig. 9 - Partial structural reinforcement locations



Fig. 10 - Vibration sieve motion balance design

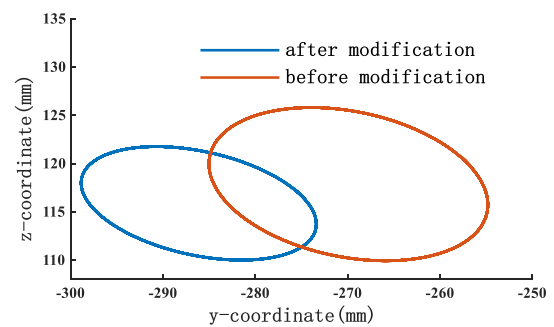


Fig. 11 - Motion trajectory of the centroid of the vibration sieve

Table 4

The root mean square of vibration velocity for selected measurement points on the chassis frame before and after structural optimization

Measurement Points		Low Speed / mm·s ⁻²			Medium Speed / mm·s ⁻²			High Speed / mm·s ⁻²		
		x	y	z	x	y	z	x	y	z
Measurement Points 1	before modification	6.01	6.02	5.36	17.88	15.20	14.40	41.94	30.51	21.43
	after modification	4.11	5.68	7.19	9.91	11.88	10.12	20.13	18.83	19.84
Measurement Points 2	before modification	5.59	4.76	4.85	17.89	7.65	12.40	41.60	17.20	21.46
	after modification	4.17	3.33	6.66	9.51	5.40	9.24	19.52	22.17	16.95
Measurement Points 3	before modification	5.82	4.46	6.32	18.97	14.64	14.51	42.67	29.40	31.84
	after modification	3.15	5.09	5.03	5.15	6.36	11.90	11.51	13.49	18.77

CONCLUSIONS

Static Analysis: Finite element analysis of the combine harvester's chassis frame revealed that the areas farthest from the support structure, particularly around the vibrating screen and threshing cylinder, experienced the greatest deformation. The maximum stress and strain were located near the support points, indicating these are relatively weak regions of the frame.

Vibration Velocity Measurement: Frequency-domain processing of the measured vibration acceleration data successfully provided the vibration velocities at various measurement points. According to the international standard ISO 20816, the original vibration levels of all points in the chassis frame were classified as the highest D level under high engine speeds.

Influence of Components: An analysis of the principal vibration frequencies at different engine speeds revealed that the impact of the vibrating screen and cutting platform on the chassis frame increased with engine speed. At high speeds, 30 out of 36 sets of data showed principal frequencies closely aligned with the excitation frequencies of the vibrating screen and cutting platform drive shafts.

Mitigation Measures: To reduce vibration intensity at various measurement points, enhancements to the chassis structure were implemented, vibration-damping pads were added at the connections between the excitation sources and the chassis, and the area of the vibrating screen's center of mass movement trajectory was minimized. Testing indicated an average vibration intensity reduction of 34.57% at the three previously most affected measurement points under high engine speeds.

Although the structural enhancements have successfully diminished the vibration intensity, the levels remain relatively high. Further research is necessary to analyze the effects of other factors, such as the center of mass of the combine harvester and support points on the chassis frame vibrations.

ACKNOWLEDGEMENT

This research was funded by the National Natural Science Foundation of China (32171911) and the National Key Research and Development Program of China (2021YFD2000503).

REFERENCES

- [1] Biriş S.Şt, Constantin A-M., Anghelache D., Găgeanu I., Cujbescu D., Nenciu F., Voicea I., Matei Gh., Popa L-D., Duțu M.F., Ungureanu N., Żelaziński T., Perișoară L., Fodorean G. (2022). Considerations regarding the vibrations transmitted to the operator by an axial flow harvester combine, *INMATEH – Agricultural Engineering*, Vol. 68 (3), pp. 747-756, <https://doi.org/10.35633/inmateh-68-74>
- [2] Chen S.R., Zhou Y P, Tang Z, Lu S N. (2020). Modal vibration response of rice combine harvester frame under multi-source excitation [J]. *Biosystems Engineering*, Vol. 194, pp. 177-195. <https://doi.org/10.1016/j.biosystemseng.2020.04.002>
- [3] Dimitriadis C., Kateris D., Xyradakis P., Gialama A., Gialamas T. (2023). Vibration assessment of tractor driver based on vibration signals, *INMATEH – Agricultural Engineering*, Vol.71 (3), pp.776-784, <https://doi.org/10.35633/inmateh-71-68>
- [4] Ding H.T., Chen S.R., Zhou W.W., Liang R.Z. (2022). A Mechanism analysis of combine harvester's vibration characteristics under feeding interference (喂入量扰动下联合收获机振动特性机理研究) [J]. *Transactions of Chinese Society for Agricultural Machinery*, Vol.53 (S2), pp.20-27+51. <https://doi.org/10.6041/j.issn.1000-1298.2022.S2.003>
- [5] Gao Z.P., Xu L.Z., Li Y.M., Wang Y.D., Sun P.P. (2017). Vibration measure and analysis of crawler-type rice and wheat combine harvester in field harvesting condition (履带式稻麦联合收获机田间收获工况下振动测试与分析) [J]. *Transactions of the Chinese Society of Agricultural Engineering*, Vol.33(20), pp.48-55. <https://doi.org/10.11975/j.issn.1002-6819.2017.20.006>
- [6] Hu Y.M., Zhou Y.J., Zhu H., Chen X.L., Sun J.M., Pi Y.J. (2015). Integration algorithm based on trend-control of error in frequency domai (基于趋势项误差控制的频域积分算法研究与应用) [J]. *Journal of Vibration and Shock*, Vol. 34 (02), pp. 171-175. <https://doi.org/10.13465/j.cnki.jvs.2015.02.030>
- [7] Jiang Y.J., Liao Y.T., Qin C., Guan Z.H., Liao Q.X. (2017). Vibration Analysis and Improvement for frame of 4SY-2.9 typed rape windrow (4SY-2. 9 型油菜割晒机架振动分析及改进) [J]. *Transactions of the Chinese Society of Agricultural Engineering*, Vol.33 (09), pp.53-60. <https://doi.org/10.11975/j.issn.1002-6819.2017.09.007>

- [8] Karagiovanidis M., Pantazi X.E., Papamichail D., Fragos V. (2023). Early Detection of Cavitation in Centrifugal Pumps Using Low-Cost Vibration and Sound Sensors. [J]. *Agriculture.*, Vol.13 (8), 1544, <https://doi.org/10.3390/agriculture13081544>
- [9] Li G., Wang C., Li Y.C., Fang M.H. (2016). Investigation on Inertial Force Balancing of Slider -crank Type Cleaning Sieve (曲柄滑块式清选筛机构惯性力平衡研究) [J]. *Journal of Agricultural Mechanization Research*, Vol. 38 (08), pp. 24-30+35. <https://doi.org/10.13427/j.cnki.njyi.2016.08.005>
- [10] Li J.Y., Li X.Q., Li Y.D., Zhang Y.X.M., Yang X.K., Xu P.X. (2023). A new method of tractor engine state identification based on vibration characteristics [J]. *Processes*, Vol.11 (2), pp.303. <https://doi.org/10.3390/pr11020303>
- [11] Ma L.N., Wei J.Y., Huang X.M., Song W.Y., Zhan G.C. (2020). Analysis of Harvesting Losses of Rapeseed Caused by Vibration of Combine Harvester Header during Field Operation (油菜联合收获机割台振动对田间收获落粒影响分析). [J]. *Transactions of Chinese Society for Agricultural Machinery*, Vol. 51 (S2), pp. 134-138+201. <https://doi.org/10.6041/j.issn.1000-1298.2020.S2.016>
- [12] Marin, E., Cârdei, P., Vlăduț, V., Biriș, S.Șt., Ungureanu, N., Bungescu, S.T., Voicea, I., Cujbescu, D., Găgeanu, I., Popa, L-D., Isticioaia, S., Matei, Gh., Boruz, S., Teliban, G., Radu, C., Kabas, O., Caba, I., Maciej, J. (2024). Research on the influence of the main vibration-generating components in grain harvesters on the operator's comfort, *INMATEH Agricultural Engineering*, Vol. 74 (3), pp. 808-823, <https://doi.org/10.35633/inmateh-74-71>
- [13] Li Wang, Li Shou, Lv Dianji, Ekhlo Ghay (2021). Multi-sensor signal acquisition and data processing analysis of combine harvester, *INMATEH – Agricultural Engineering*, Vol.63 (1), pp.335-344, <https://doi.org/10.35633/inmateh-63-34>
- [14] Noh J.H., Kim P., Yoon Y.J. (2024). Competitive advantages of a bistable vibration isolator: Cut-off frequency and operational safety near harmful resonance [J]. *Journal of Sound and Vibration*, Vol. 570 (03). <https://doi.org/10.1016/j.jsv.2023.118004>
- [15] Pang J., Li Y.M., Ji J.T., Xv L.Z. (2019). Vibration excitation identification and control of the cutter of a combine harvester using triaxial accelerometers and partial coherence sorting [J]. *Biosystems Engineering*, Vol. 185, pp. 25- 34. <https://doi.org/10.1016/j.biosystemseng.2019.02.013>
- [16] Rabbani M.A., Tsujimoto T., Mitsuoka M., Inoue E., Okayasu T., (2011). Prediction of the vibration characteristics of half-track tractor considering a three-dimensional dynamic model [J]. *Biosystems Engineering*, Vol. 110 (2), pp.178-188. <https://doi.org/10.1016/j.biosystemseng.2011.07.013>.
- [17] Sun Z., Wang L., Pan Z. (2014). Analyses of vibration characteristics of power fan for the 4ztl-1800 pneumatic conveying combine stripper harvester [J]. *Transactions of the ASABE*, Vol. 57 (3), pp. 693-699. <https://doi.org/10.13031/trans.57.10317>
- [18] Tang Z., Zhang B., Wang M.L., Zhang H.T. (2021). Damping behaviour of a prestressed composite beam designed for the thresher of a combine harvester [J]. *Biosystems Engineering*, Vol. 204, pp.130-146. <https://doi.org/10.1016/j.biosystemseng.2021.01.020>
- [19] Vlăduț V., Biriș S.Șt., Paraschiv G., Ungureanu N., Bungescu S.T., Voicea I., Cujbescu D., Găgeanu, I., Laza E., Popa L-D., Matei Gh., Atanasov At. (2023). Considerations regarding the effects of shocks and vibrations on operators of self-propelled agricultural equipment, *INMATEH –Agricultural Engineering*, Vol. 71 (3), pp. 843-856, <https://doi.org/10.35633/inmateh-71-74>
- [20] Wang L., Li S., Lv D., Ekhlo G. (2021). Ulti-sensor signal acquisition and data processing analysis of combine harvester, *INMATEH – Agricultural Engineering*, Vol. 63(1), pp.335-344, <https://doi.org/10.35633/inmateh-63-34>
- [21] Wang Q., Luo K., Yang J., Jiang L.B. (2012). Research on inertial force balance of a shaker in a combine harvester (联合收割机振动筛机构惯性力平衡的研究) [J]. *Mechanical Research & Application*, No.06, pp.36-39.
- [22] Wei C.C., Xu L.Z., Wang J.T., Li Y.M. (2018). Inertial force balance and ADAMS simulation of the oscillating sieve and return pan of a rice combine harvester [J]. *International Journal of Agricultural and Biological Engineering*, Vol.11 (01), pp. 129-137. <https://doi.org/10.25165/j.ijabe.20181101.2978>
- [23] Wu L.M., Bi Y.H., Wu B., Lei J.L., Shen L.Z. (2020). Analysis of influence of piston secondary motion on vibration and noise of non-road high pressure common rail diesel engine (活塞二阶运动对非道路高压共轨柴油机振动及噪声影响分析) [J]. *Journal of Vibration and Shock*, Vol. 39(11), pp. 193-200. <https://doi.org/10.13465/j.cnki.jvs.2020.11.026>

- [24] Xie H.R., Jin C.Q., Yin X., Qian Z.J., Teng Y.J., Yv C.X. (2019). Vibration Measurement and Analysis of Tracked Soybean Combine Harvester (履带式大豆联合收获机振动测试与分析) [J]. *Journal of Agricultural Mechanization Research*, Vol. 41(08), pp. 158-163+174. <https://doi.org/10.13427/j.cnki.njyi.2019.08.027>
- [25] Yao Y.C., Song Z.H., Du Y.F., Zhao X.Y., Mao E.R., Liu F. (2017). Analysis of vibration characteristics and its major influenced factors of header for corn combine harvesting machine (玉米收获机割台振动特性及其主要影响因素分析) [J]. *Transactions of the Chinese Society of Agricultural Engineering*, Vol. 33 (13), pp.40-49. <https://doi.org/10.11975/j.issn.1002-6819.2017.13.006>
- [26] Zhang H.T. (2012). Research on the Kinematics and inertial force balance of the vibrating screen (振动筛机构的运动分析和惯性力平衡研究) [D]. Cheng Du: School of Mechanical Engineering, Xihua University.
- [27] Zhang H.T. (2021). Research on Disturbed Vibration Characteristics of Combine Harvester Threshing Cylinder and Vibration Isolation Method (水稻联合收获机脱粒滚筒受扰振动特性及隔振方法研究), [D]. College of Agricultural Engineering, Zhen jiang: Jiangsu University. <https://doi.org/10.27170/d.cnki.gjsuu.2020.000176>
- [28] Zhang L.J., Zhou H., Yu Z.P., Jin X.X. (2001). Research on Control of Car Interior Noise due to Engine Vibration (发动机振动引起的车内噪声控制研究) [J]. *Journal of Vibration, Measurement & Diagnosis*, No. 01, pp. 61-66+76. <https://doi.org/10.16450/j.cnki.issn.1004-6801.2001.01.012>
- [29] Zhang M.J., Jin J.F., Chen Y.Y., Chen T.K. (2023). Vibration symmetry characteristics of wheeled tractor structure (轮式拖拉机对称结构的振动特性) [J]. *Journal of Jilin University (Engineering and Technology Edition)*, Vol. 53 (07), pp. 2136-2142. <https://doi.org/10.13229/j.cnki.jdxbgxb.20220313>
- [30] Zhou Y., Wang X., Hou Y., Que H.B., Guo R.B., Lin X.H., Jin S.Q., Wu C.P. (2023). Test study on vibration behavior and bearing load characteristics of high-speed train gearbox under internal excitation(内部激励下高速列车齿轮箱振动行为及轴承载荷特性实验研究) [J]. *Journal of Vibration and Shock*, Vol. 42 (13), pp. 242-250. <https://doi.org/10.13465/j.cnki.jvs.2023.13.029>

DESIGN AND EXPERIMENTAL STUDY ON TWIN-SCREW STRAW PULPING MACHINE

稻秆双螺杆制浆机设计与试验

Huiting CHENG, Nan ZHAO, Dezhi REN, Wei WANG, Yuanjuan GONG, Wanyuan HUANG¹

College of Engineering, Shenyang Agricultural University, Shenyang/ China

Tel: +86-15909822656; E-mail: 2022500013@syau.edu.cn

Corresponding author: Huang Wanyuan

DOI: <https://doi.org/10.35633/inmateh-75-15>

Keywords: rice straw; finite element analysis; $Ab-T_{10}$ breakage model; twin-screw; biomechanical pulping

ABSTRACT

Despite the abundance of agricultural straw as a renewable resource, its low utilization efficiency remains a significant challenge due to inadequate mechanical processing methods. To solve the problem, the ANSYS finite element simulation software was employed to simulate and analyze two screw configurations (parallel and staggered arrangement) and four compression zone designs. The optimal coupling breaking method was determined to be the parallel type with a 2-2-2 compression zone combination for the twin-screw system. Based on the simulation results, a twin-screw straw pulping machine was constructed. The test factors included screw speed, thread pitch, and straw moisture content, with straw breaking rate as the test index. Simulation test was conducted to optimize the structural parameters of the twin-screw straw pulping machine, followed by a verification test. The results indicated that at a screw speed of 120 r/min, a thread pitch of 203 mm, and a straw moisture content of 60%, the straw breaking rate was the highest at 79.9%. The verification test results were consistent with the simulation results, with less than 5% deviation, confirming the reliability of the simulation model and optimization outcomes. This paper provides a basis for the design and optimization of twin-screw pulping machines and offers theoretical support for the high-value utilization of agricultural waste through enhanced mechanical processing technologies.

摘要

尽管农业秸秆作为一种可再生资源非常丰富，但由于机械加工方法不足，其利用效率低下仍然是一个重大挑战。为了解决这个问题，采用 ANSYS 有限元仿真软件，对并列型与错列型 2 种螺杆配置和 4 种压缩区设计进行模拟分析，确定最佳耦合碾压破碎方式为并列型 2-2-2 压缩区组合的双螺杆，根据仿真结果试制稻秆双螺杆制浆机。以螺杆转速、螺纹间距和稻秆含水率为试验因素，以秸秆破碎率为试验指标，通过仿真试验对稻秆双螺杆制浆机进行结构参数优化，并进行验证试验。试验表明：螺杆转速为 120r/min，螺纹间距为 203mm，秸秆含水率为 60%时，秸秆破碎率最高为 79.9%；验证试验结果与仿真结果具有一致性，误差小于 5%，仿真模型和优化结果具有可靠性。本文为双螺杆制浆机的设计和优化提供了依据，为通过强化机械加工技术实现农业废弃物的高值化利用提供了理论支持。

INTRODUCTION

China has an abundant production of straw, and the raw materialization of straw is an important direction for its high-value utilization. However, the utilization rate of raw materialization is only 2.1%, which is one of the main factors constraining the improvement of the comprehensive utilization rate of straw (Hirani et al., 2018). Currently, straw pulping is one of the emerging methods for straw raw material utilization (Subramaniyan et al., 2022). The annual production of rice straw exceeds 200 million tons, accounting for about 22.74% of the total agricultural straw production, and the production is only less than that of corn straw (Gong et al., 2019). Therefore, the study of rice straw pulping is of great significance for improving the comprehensive utilization rate of straw, promoting sustainable agricultural development, alleviating the current shortage of pulp, and reducing the dependence on foreign trade in pulp.

Cheng Huiting, Ph.D. Stud. Eng.; Zhao Nan, MS. Stud. Eng.; REN Dezhi, Lec. Ph.D. Eng.; Wang Wei, Prof. Ph.D. Eng.; Gong Yuanjuan, Prof. Ph.D. Eng.; Huang Wanyuan, Lec. Ph.D. Eng.

Chemical pulping, mechanical pulping, and two-stage pulping are the principal pulping methods currently (Li *et al.*, 2023). The traditional chemical pulping method is technologically mature but poses significant environmental challenges.

The mechanical pulping method is mainly applicable to wood pulping, when used in agricultural straw and other non-wood raw materials pulping, the obtained pulp often exhibits inferior quality and cannot meet industry standards. The two-stage pulping method combines chemical or biological pre-treatment with mechanical refining post-treatment in the pulping process. Pulp obtained from non-wood raw materials using this method is of better quality than that produced by mechanical pulping, making the two-stage pulping method suitable for pulping agricultural straw and other non-wood raw materials. The two-stage pulping method is mainly divided into chemical mechanical pulping (CMP) and biological mechanical pulping (BMP). The BMP method is more environmentally friendly in terms of reduced chemical usage and lower wastewater generation.

With the emergence of BMP technology, scholars have conducted extensive research on the biological pre-treatment processes of non-wood raw materials such as rice straw (Guan *et al.*, 2018), corn straw (Qing *et al.*, 2017), and wheat straw (Kang *et al.*, 2021). However, significant challenges remain in the preparation stage of non-wood bio-mechanical pulp, highlighting the need for specialized equipment development to advance BMP technology. Twin-screw pulping machines have emerged as the primary choice for pulping equipment due to their high breaking efficiency and fibrillating capacity (Arthur and Rahmanian, 2024), yet research in this area in China is still in its infancy. Kowalski *et al.* used MDT software to design and analyze co-rotating twin-screw extruders for food applications (Kowalski *et al.*, 2018); Düphans applied CAD/CAE technology for the design and simulation of twin-screw pulping machinery (Düphans *et al.*, 2024). These studies are limited to the design of twin-screw components and have not yet addressed the complete machine design and optimization of twin-screw pulping machines. Fleur utilized Ludovic simulation software to optimize the twin-screw pulping machine, improving the production efficiency of cellulose nanofibrils and reducing energy consumption through the simulation and optimization of screw profiles (Rol *et al.* 2020). The physical and chemical properties and the matched twin-screw pulping machine are different from the BMP method for the pretreatment of wooden raw materials and the pulping raw materials produced by the chemical method. Therefore, it is of great significance to design and optimize a twin-screw pulping machine with BMP pulping technology for rice straw as raw material to promote the comprehensive utilization of straw. Rol optimized the twin-screw extrusion process through simulation software, achieving efficient production of high-quality cellulose nanofibrils (CNF), demonstrating the feasibility of simulation design in the field of pulping machinery design and optimization (Rol *et al.*, 2019).

In this paper, ANSYS finite element simulation software is used to determine the flow channel structure and the combination of compression zones of the twin-screw device, designing and constructing a twin-screw pulping machine. Based on the previously calibrated Ab-T10 breaking model, the Rocky discrete element simulation software is employed to simulate the breaking process of straw particles. Through a three-factor quadratic orthogonal rotational combination simulation test, the effects of screw speed, thread pitch, and straw moisture content on the breaking rate of rice straw were investigated to optimize the working and structural parameters of the twin-screw pulping machine, thereby increasing the breaking rate of rice straw. The accuracy and reliability of the model are verified by comparing the results of the simulation with those of the validation tests.

MATERIALS AND METHODS

Twin screw pulping machine design

Structure and Working Principle

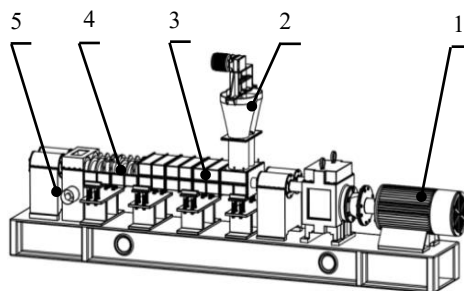


Fig. 1 - Three-dimensional model of the twin-screw pulping machine of rice straw

1 - Motor; 2 - Material feeding device; 3 - Grinding device; 4 - Grinding twin screw; 5 - Discharging device

The structure of the twin-screw pulping machine is shown in Figure 1, which mainly consists of a grinding device, an electric motor, a material feeding device, and a discharge device. During operation, rice straw is placed into the feed opening of the material feeding device at a uniform speed and in appropriate amounts to avoid blockages. The straw first enters the pulping machine through the feeding device, and after being crushed, sheared, and broken by the twin-screw grinding device, it is sent to the discharge device, where the broken pulp is collected.

Selection and design of threaded elements

The cross-section of screw elements is typically rectangular or serrated. The asymmetry of serrated screw elements enhances the mixing of materials, promotes the dispersion of fibers, and refines the pulp, thereby improving the pulping quality. Compared to the traditional rectangular cross-section, serrated screw elements are more suitable for the compression and homogenization stages of the pulping process. The shearing action can effectively improve the flowability of the material, reduce retention phenomena, and enhance uniformity and efficiency. Therefore, screw elements with a serrated cross-section were used, as shown in Figure 2.

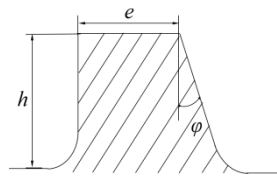


Fig. 2 - Thread cross-section shape

The screw diameter directly affects the material processing capacity and the power consumption of the device, while the screw length is related to the residence time of the material within the screw, which in turn affects the pulping efficiency (Lyashuk *et al.*, 2022). Screw elements are commonly selected in sizes of 180 mm, 240 mm, 300 mm, 350 mm, etc. Based on the laboratory equipment conditions, screw elements with an outer diameter of 180mm were chosen. The optimal diameter range of 60-200 mm ensures efficient material conveying, mixing and processing capabilities while maintaining compatibility with existing equipment (Delvar *et al.*, 2025).

$$h = (0.02 \sim 0.2)D_e \quad (1)$$

$$e = (0.08 \sim 0.12)D_e \quad (2)$$

where: h is the groove depth, mm; e is the width of normal screw prong, mm; D_e is the outer diameter of the screw, mm.

Design of thread pitch

The pitch of the screw thread affects the fill rate of the material in the screw and its flow characteristics. A smaller pitch can increase the fill rate of the material, but may lead to hindered material flow and increased screw wear, affecting the shearing action of the screw on the material. A larger pitch can provide stronger shearing forces, which is beneficial for material mixing and the disruption of the cellulose structure, but it also increases the wear on the screw. According to the transport rate of solid materials and the theory of pulp flow, the thread lift angle φ should be designed between 17° and 30° to ensure effective transport and mixing of the material within the screw. Based on equations (3) and (4), the range of pitch values can be calculated to be 172~326 mm.

$$S = \pi \cdot D_e \tan \varphi \quad (3)$$

where: S is the lead, mm; φ is the thread rising angle, $^\circ$.

$$S = pz \quad (4)$$

where: p is the thread pitch, mm; z is the number of threads, $z=1$.

Design of structural clearance

During pulping, the pulping raw materials exhibit the characteristics of soft solids, hence the clearances can be selected to be on the larger side.

$$\delta_a = (0.01 \sim 0.03)D_e \quad (5)$$

According to equation (5), the range of values for the gap σ_a between the top of the screw prong and the shaft were calculated as 1.8~5.4 mm. The smaller the σ_a , the less the leakage flow and the higher the conveying efficiency, but the mixing effect is reduced. Therefore, σ_a was chosen to be 3 mm.

At this clearance value, the equipment can maintain a certain conveying efficiency while keeping pressure fluctuations and friction between the screw and barrel moderate, thus avoiding excessive energy consumption.

$$\delta_b = (0.01 \sim 0.02)D_e \quad (6)$$

According to equation (6), the range of the gap between the twin screws δ_b was calculated as 1.8~3.6 mm. The smaller the δ_b , the higher the manufacturing precision required for the twin screws. Therefore, δ_b was chosen to be 3 mm. With this clearance, material flows stably between the twin screws, allowing sufficient time for mixing and shearing without over-pressurization or excessive residence time, which could cause overheating or degradation, thus enhancing pulp quality consistency.

$$C_L = D_e + \delta_b \quad (7)$$

Therefore, according to equation (7), the center distance C_L between the twin screws was calculated to be 180.3 mm, which ensures a moderate gap between the screws, avoiding material residue and ensuring efficient shearing and mixing effects.

$$D_s = D_e + 2\delta_a \quad (8)$$

From equation (8), the internal diameter D_s of the shaft was calculated to be 180.6 mm.

TWIN-SCREW COUPLING SIMULATION DESIGN

By integrating numerical computation and finite element simulation methods (Zhang *et al.* 2023), the two established flow channel models were simulated under various conditions by ANSYS 2022 R1. By comparing the pressure field distribution of the two flow channels, the coupling method for the twin-screw straw pulping machine was selected. Using the finite element simulation method and the selected twin-screw coupling method, the four established compression zone models were simulated under various conditions. By comparing the flow of material between the screws, the compression zone combination method for the twin-screw straw pulping machine was selected.

Model Establishment

(1) Flow Channel Model Establishment

The screws of twin-screw pulping machines are often designed in a modular fashion, allowing the installation of thread elements on the core shaft as needed, with single-start threads commonly used (Gu *et al.*, 2019). The coupling forms between thread elements are divided into parallel and staggered types, as shown in Figure 3(a). Based on the uniform continuous mixing and transportation mechanism (Düphans *et al.*, 2024), the parallel thread element coupling model used single-start thread screws; based on the shear dispersion uniformization mechanism (Kolomiets and Jirout, 2021), the staggered thread element coupling model used a 180° staggered configuration of single-start thread elements. With the Boolean operation modeling capabilities of SolidWorks software, the flow channel structure models corresponding to the two types of twin-screw coupling models were constructed, as shown in Figure 3(b).

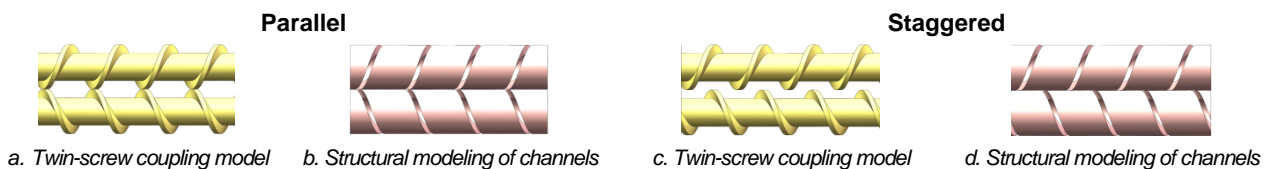


Fig. 3 - The model of twin-screw and flow channel

(2) Compression Zone Model Establishment

Positive threads have the function of conveying and compressing material, while reverse threads have the function of blocking material and increasing pressure. When the material was pushed from the positive thread to the reverse thread to the next thread area, the material was compressed and sheared under the extrusion of the positive and reverse threads. The flow channel area formed by the positive and reverse threads is a compression zone. A twin-screw device generally have three compression zones, and each segment of thread elements forming the compression zone should have 2-3 threads.

The compression zones are combined with two types, positive threaded element-reverse threaded element (referred to as 1) and reverse threaded element-positive threaded element (referred to as 2). Using SolidWorks software, four types of compression zone combination models were established as shown in Figure 4.

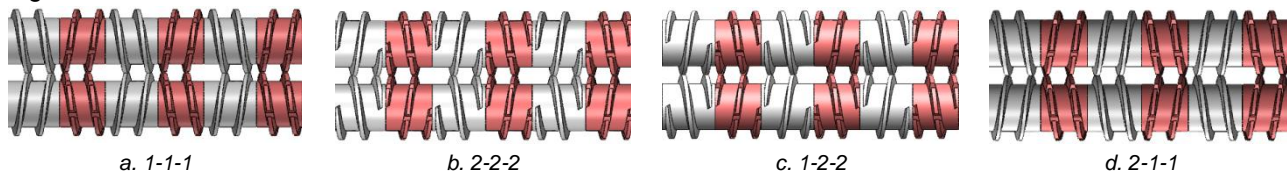


Fig. 4 - Compression zone combination model

Meshing and Simulation Parameter Settings

The model was imported into Ansys software (Xiao *et al.* 2024), and hexahedral meshing was used to optimize computational efficiency and accuracy. Local mesh refinement was performed on complex areas of the screws and flow channels to analyze the flow characteristics of the material within the channels. The rheological model of the straw pulp was set to the power-law fluid model to describe its non-Newtonian characteristics (Liu *et al.* 2019). The material properties of the rice straw pulp were shown in Table 1, Twin-screw material parameters were shown in Table 2.

Table 1

Physical parameters of straw pulp

Parameter	Value	Parameter	Value
Straw pulp consistency	682	density	232.3 kg/m ³
Power law index	0.49	specific heat capacity	6.585 J/(kg·K)
Temperature coefficient	0.042 K ⁻¹	heat transfer coefficient	0.2 W/(m·K)
Reference temperature	373.15 K		

Table 2

Twin-screw material parameters

Part	Material	Density/kg·m ⁻³	Elastic modulus/MPa	Poisson's ratio
Shaft core	42CrMo	7850	2.06×10 ⁵	0.28
Threaded element	A ₂ tool steel	7860	2.06×10 ⁵	0.28

The twin-screw rotation speed was set to 120 r/min, the entrance velocity of the rice straw pulp was set to 1 m/s, and a pressure outlet boundary condition was used. The inner wall was set to a no-slip boundary condition, using the no-slip option in Ansys-Fluent to ensure no relative sliding between the pulp and the device walls. The initial temperature was set to 25° C, the initial pressure was set to 101325 Pa, the time step was set to 0.01 seconds, the number of iterations was set to 500, and the relaxation factor was set to 0.7 to accelerate convergence. The Euler multiphase flow model was used to simulate the motion of the mixed phase of the straw pulp, capturing the flow characteristics of the straw pulp in the twin-screw device.

Dynamic Solution of Straw Pulp

To accurately analyze the dynamic characteristics of straw pulp within the crushing flow channel, the following assumptions were made: the effects of gravity and inertia forces in the flow field were neglected; the straw pulp was assumed to move in a laminar flow within the crushing device, completely filling the device and behaving as an incompressible fluid; the straw pulp was assumed to move without slippage within the cavity of the crushing device. Based on the constitutive equations of fluid dynamics and the rheological properties of the fluid, numerical simulation and analysis of the flow of straw pulp under isothermal and non-isothermal conditions were performed.

To describe the changes in the volumetric flow rate of straw pulp and the dynamic relationship between fluid density and velocity field, the conservation of straw pulp phase material during the crushing process was captured according to the continuity equation, as shown in equation (9). This equation demonstrates the conservation of mass of the straw pulp and its flow behavior within the channel during the crushing process by considering the vector velocity and density.

$$\nabla \cdot (\rho \vec{v}) + \frac{\partial \rho}{\partial t} = 0 \quad (9)$$

where: \vec{v} is the vector velocity of straw pulp, m/s; ρ is the straw pulp density, kg/m³.

The internal momentum transfer mechanism of straw pulp during the crushing process was described by the Navier-Stokes equation, as shown in equation (10). The equation reveals the mechanism of internal momentum transfer and transformation within the straw pulp during the crushing phase and enables the prediction of the flow patterns of the pulp based on relevant parameters.

$$\rho\left(\frac{\partial \vec{v}}{\partial t} + (\vec{v} \cdot \nabla) \vec{v}\right) = -\nabla p + \nabla \cdot \vec{\tau} + \vec{f}_v \quad (10)$$

where: p is the static pressure on straw pulp, Pa; $\vec{\tau}$ is the stress tensor of straw pulp, Pa; \vec{f}_v is the Volumetric force of straw pulp, N/m³.

Energy conservation equation expresses the thermodynamic behavior of straw pulp through changes in internal energy, heat exchange with the environment, and energy loss due to fluid flow, as shown in equation (11). This equation quantifies the change in internal energy of the straw pulp during crushing, taking into account the energy alterations caused by molecular thermal motion and interactions, thereby analyzing the energy trajectory of the straw pulp throughout the crushing process.

$$\rho C_p \left(\frac{\partial T}{\partial t} + \vec{v} \cdot \nabla T \right) = \nabla \cdot (k \nabla T) + \frac{\vec{\tau}}{\nabla \vec{v}} \quad (11)$$

where: C_p is the specific heat capacity, J/(kg·K); T is the temperature, K. ∇T is the temperature gradient, K/m; $\nabla \vec{v}$ is the velocity gradient tensor, s⁻¹; k is the heat transfer coefficient, W/(m·K).

Straw pulp conform to the characteristics of pseudoplastic fluids (Terashima et al., 2022). Under isothermal conditions, power-law model is used to describe rheological behavior as shown in equation (12). This equation illustrates the variation in the flow characteristics of straw pulp under different shear rates in an isothermal environment.

$$\eta = m \dot{\gamma}^{(n-1)} \quad (12)$$

where: η is the straw pulp viscosity, Pa·s; m is the straw pulp consistency, Pa·sⁿ; n is the power law index of straw pulp; $\dot{\gamma}$ is the shear rate tensor of straw pulp, s⁻¹.

Under non-isothermal conditions, the rheological behavior of straw pulp is significantly affected by temperature, and is represented by a temperature-dependent rheological model (Gienau et al., 2018). Equation (13) describes the relationship between the apparent viscosity (η) of straw pulp and the shear rate ($\dot{\gamma}$) as well as temperature. The function $H(T)$ is temperature-dependent, serving to adjust the viscosity to reflect the effects of temperature variations.

$$\eta = m \dot{\gamma}^{(n-1)} \cdot H(T) \quad (13)$$

$$H(T) = \exp[-\beta(T - T_\alpha)] \quad (14)$$

where: T is the temperature, K; β is the temperature coefficient of straw pulp, K⁻¹; T_α is the reference temperature for straw pulp, K.

SIMULATION ANALYSIS AND OPTIMIZATION OF RICE STRAW PARTICLE BREAKING

Test factors and indicators

Rice straw pre-treated by biological method was selected as the test material. In accordance with the requirements of the "HJ/T 340-2007 Clean Production Standard for the Papermaking Industry" standard, pretreated rice straw was made into oven dried pulp with a moisture content of 10%, followed by the testing samples with different moisture contents prepared using biofungal liquid and drying method.

To optimize the working performance of the rice straw twin-screw pulping machine, based on preliminary design and pretesting, the thread pitch, screw speed, and rice straw moisture content were taken as the test factors. Based on the previous section on design, the range of thread pitch was 172~326 mm; the range of screw speed was 100~140 r/min (Jiang et al., 2024); considering the characteristics of rice straw material, the moisture content range for rice straw was taken as 50~70% (Cheng et al., 2022). Based on the function of the rice straw twin-screw pulping machine, the rice straw breaking rate was chosen as the evaluation index of its working performance, and the calculation formula is as follows:

$$P = \frac{m_b}{m_t} \times 100\% \quad (15)$$

where: m_b is the mass of broken particles, g; m_t is the total mass of particle sample, g.

Test Design

The discrete element model of rice straw particles established by Jiang and others, along with the parameter calibration results of the Ab-T10 crushing model (Jiang et al., 2024), and the mechanical model constructed in this paper were imported into the Rocky DEM 4.5 to simulate the crushing process of rice straw particles and conduct a three-factor quadratic orthogonal central composite simulation test, and the factor level coding table is shown in the table 3. The screen aperture diameter x_1 , pitch x_2 , and blade and shell clearance x_3 are the actual values of the factors.

Table 3

Coding table			
Code	Screw speed (x_1)/r/min	Thread pitch (x_2)/mm	Moisture content (x_3)/%
-1.682	100	172	50
-1	108	203	54
0	120	249	60
+1	132	295	66
+1.682	140	326	70

RESULTS

Simulation results and analysis

Simulation results and analysis of twin-screw channel characteristics

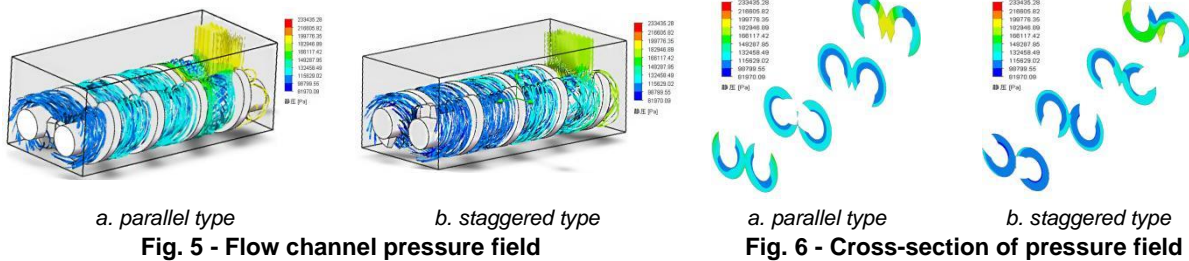


Figure 5(a) showed a mirror symmetry in the pressure gradients of the left and right flow channels, with the maximum pressure difference being less than 0.5 MPa. This symmetry was particularly evident in the screw engagement area, where symmetrical High-Pressure Ridges formed, and peak pressures were concentrated at the thread top clearance. The symmetric pressure field suppressed the lateral exchange of materials through the force equilibrium, indicating a lateral flow velocity of less than 0.1 m/s, which aligned with the flow characteristics dominated by laminar flow, where the Reynolds Number is approximately 120 (Saldana et al., 2024). The symmetric high-pressure area created a uniform shear stress field of about 450 kPa, which continuously acted on the straw particles through viscous dissipation, promoting the uniform delamination of cellulose microfibrils.

Figure 5(b) showed a significantly higher pressure peak in the left flow channel compared to the right. Local pressure discontinuities greater than 3 MPa/mm occurred at the thread top clearance and engagement area, leading to a substantial lateral pressure difference. This asymmetry triggered secondary flows, increasing the lateral flow velocity to 0.6 m/s and inducing vortices, with the flow state exhibiting transitional turbulence characteristics, where the Reynolds Number is about 450. The high pressure difference drove fibers to undergo bending-shear coupled damage in the engagement area. However, the local peak shear stress exceeded the yield strength of the straw fibers, and the uneven stress distribution resulted in a mixture of over-pulverized particles and unbroken coarse grains.

Figure 6(a) showed a cross-sectional pressure distribution that decreased in a concentric circular pattern, aligning with the predicted trend of the Generalized Herschel-Bulkley Model. Near the wall, the shear rate was synchronized with the compression-relaxation cycle of the thread clearance, forming periodic stress loading that facilitated the progressive disintegration of fibers.

Figure 6(b) showed a cross-sectional pressure field with a left-high and right-low gradient, generating a normal pressure component that compelled fibers to migrate along an inclined path, increasing the likelihood of collisions with the flight flanks. A low-pressure vortex area appeared at the bottom of the right flow channel, increasing the average residence time for some fibers and intensifying the risk of thermal degradation.

The simulation results showed that the pressure distribution of the left and right channels of the parallel type is almost symmetric in the twin-screw, keeping the material transfer and pressure state in the channel uniform. Such symmetric pressure distribution reduced the cross exchange of straw particles in the engaging area, which made the material flow more stable and continuous.

It is more favorable to destroy the structure of cellulose, hence the parallel type has more uniform effect on the grinding and shearing action of the material. The pressure distribution in the left and right flow channels with staggered thread element coupling exhibited asymmetry, especially at the screw crests and in the meshing zone. The asymmetric pressure distribution created a transverse pressure difference across the grooves, causing the shearing force experienced by straw fibers in the meshing zone to be uneven, leading to an uneven crushing and breaking effect on the straw particles.

Consequently, to ensure the pulping effect and quality of the twin-screw pulping machine, the twin-screw with parallel thread element was selected as the core breaking element of the breaking device in the twin-screw pulping machine.

Compression zone simulation results and analysis

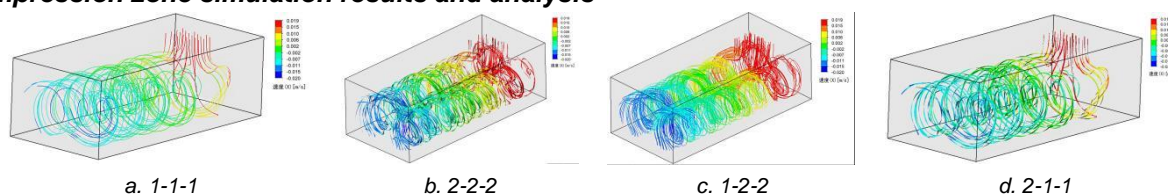


Fig. 7 - Compression zone combination velocity field

The simulation results of the four compression zones were shown in Figure 7. From Figure (a), the flow field of the 1-1-1 configuration exhibited a low-gradient uniform distribution. No significant velocity shear layer was formed between the twin screws, leading to a lower shear rate. The analysis of the flow lines indicated that the material primarily moved axially in the engagement area, with a low rate of lateral migration. Due to insufficient shear strength, the straw fibers underwent only limited disintegration, resulting in a higher retention of fiber length and a lower proportion of hydrogen bonds being broken, which caused uneven dispersion of the fiber bundles.

From Figure (b), it was observed that in the engagement area of the 2-2-2 twin screw configuration, symmetrical "V" shaped high-speed shear zones were formed. Within this region, uniform velocity gradients led to the generation of uniform shear layers, with the flow field symmetry index reaching as high as 0.92. The velocity components of the material in the axial and radial directions approached a ratio of 1:1, promoting three-dimensional mixing. The preliminary shearing action in the "V" shaped area, in conjunction with the reverse shearing action in the inverted "V" shaped area, created a cyclic loading mechanism. This mechanism significantly enhanced the efficiency of hydrogen bond breaking, effectively increased the fiber surface area, and resulted in a concentrated particle size distribution, achieving efficient crushing and dispersion. Additionally, this velocity field had good stability, which could effectively reduce the material residence time, making it the optimal configuration.

From Figure (c), the 1-2-2 configuration exhibited an asymmetric velocity distribution, with the peak velocity in the left flow channel being higher than that in the right, creating an inclined shear zone. The generation of localized vortices enhanced mixing, but the distribution of shear rates was uneven. The reverse shearing in the inverted "V" region led to a coupling of fiber bending and tearing, which reduced the proportion of coarse fibers but resulted in over-pulverization.

From Figure (d), the 2-1-1 configuration resulted in velocity dead zones between the screws, with the primary shear area being confined near the thread clearance. The streamlines indicated that the material circulated and lingered within these dead zones, leading to localized temperature increases and thermal degradation. The efficiency of fiber disintegration was relatively low, and the particle size distribution exhibited a bimodal pattern, indicating a coexistence of insufficient fragmentation and over-pulverization.

As shown in Figure 7, the 2-2-2 and 1-2-2 compression zone combinations created strong shear zones, enhancing the shearing and mixing of straw particles between the twin screws and improving their breaking efficiency. Under the action of the twin screws, straw particles entered the "V" shaped area and underwent pre-shearing, where fibers begin to separate. After entering the inverted "V" shaped area, straw particles were subjected to reverse shear forces, further breaking the hydrogen bonds between fibers, increasing the surface area of the fibers, and promoting the effective dispersion of fiber bundles. The 2-2-2 configuration demonstrated superior symmetry in the velocity distribution field compared to the 1-2-2 combination, ensuring more uniform transport of rice straw material through the flow channel and reducing flow instability caused by uneven pressure distribution.

The movement of rice straw in the 2-2-2 flow channel was more stable, and the shearing action was more uniform, which is conducive to the destruction of the cellulose structure and the dispersion of fiber bundles. Therefore, the twin-screw with the in-line 2-2-2 compression zone combination was used as the core breaking element of the breaking device in the twin-screw pulping machine.

Simulation Results and Analysis of the Crushing Process

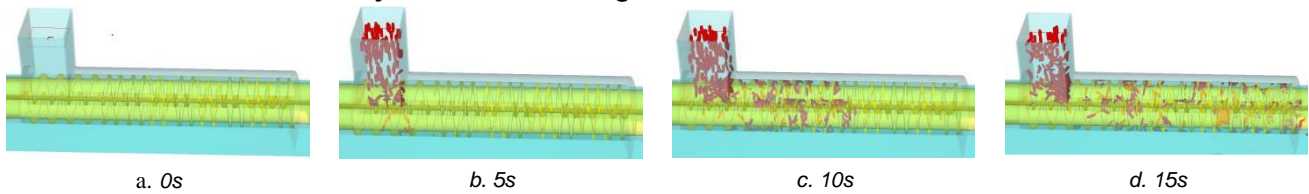


Fig. 8 - Simulation of straw particles crushing process in pulping machine

The Rocky simulation software was utilized to simulate and analyze the breaking process of straw particles from the feeding side to the crushing side, as shown in Figure 8.

Test results and analysis

The simulation results of the breaking process for rice straw particles are shown in Table 4, where A, B, and C were the factor encoding values. The experimental data were analyzed using Analysis of Variance (ANOVA) to determine the significance of the factors affecting the rice straw breaking rate. The ANOVA was conducted using the Design-Expert software, which provided a comprehensive analysis of the variance components and their corresponding F-values and P-values. The regression equation for the rice straw breaking rate (P_c) was derived from the ANOVA results, and the significance of each term in the equation was assessed. The optimization of the process parameters was performed using the Response Surface Methodology (RSM) in Design-Expert software, which allowed for the determination of the optimal screw speed, thread spacing, and straw moisture content to maximize the breaking rate. The results of the ANOVA was presented in Table 5.

Table 4

Test design and results

No.	Screw speed (A)/r/min	Thread Pitch (B)/mm	Moisture content (C)/%	Breaking rate (P_c)/%
1	1	1	1	48
2	1	1	-1	54.5
3	1	-1	1	54.25
4	1	-1	-1	56.75
5	-1	1	1	52.3
6	-1	1	-1	55.6
7	-1	-1	1	62.75
8	-1	-1	-1	51.25
9	1.682	0	0	52.75
10	-1.682	0	0	61
11	0	1.682	0	64.5
12	0	-1.682	0	51.75
13	0	0	1.682	51.25
14	0	0	-1.682	70.75
15	0	0	0	68.25
16	0	0	0	72.25
17	0	0	0	70.75
18	0	0	0	70.5
19	0	0	0	70
20	0	0	0	70.5
21	0	0	0	75
22	0	0	0	70.75
23	0	0	0	74

Table 5

Analysis of variance

Source	SS	Freedom	MS	F-value	P-value
Model	1492.76	9	165.86	7.03	0.0010
A	36.33	1	36.33	1.54	0.0064
B	3.43	1	3.43	0.1455	0.0090
C	82.65	1	82.65	3.51	0.0038
AB	0.7200	1	0.7200	0.0305	0.0040
AC	36.98	1	36.98	1.57	0.0325
BC	44.18	1	44.18	1.87	0.1942
A ²	540.49	1	540.49	22.92	0.0004
B ²	461.69	1	461.69	19.58	0.0007
C ²	303.99	1	303.99	12.89	0.0033
Residual	66.54	13	6.58		
Lack of fit	71.79	5	9.36	12.51	0.1013
Error	34.75	8	4.34		
Total value	1799.30	22			0.0010

From Table 5, it is known that the regression equation model has a P-value less than 0.01, indicating a highly significant result. The lack of fit item has a P-value of 0.1013, which suggests a good fit of the equation. The thread pitch, screw speed, rice straw moisture content, interaction terms AB, and the quadratic terms A²,

B^2 , C^2 have a highly significant effect on the rice straw crushing rate ($P < 0.01$). The interaction terms AC and BC have a significant effect on the rice straw breaking rate ($P < 0.05$). Under the interaction effects, the order of influence of each factor on the rice straw breaking rate is moisture content > thread pitch > screw speed. After eliminating the non-significant terms, the regression model for the encoded values of the rice straw breaking rate (P_c) is:

$$P_c = 71.41 - 1.63A + 0.5012B - 2.46C - 0.3000AB - 2.15AC - 2.35BC - 5.83A^2 - 5.39B^2 - 4.37C^2 \quad (16)$$

The optimal working parameters were obtained using the Optimization Numerical module of Design-Expert 8.0.6 software and based on Equation 16. When the screw speed was 120 r/min, the thread pitch was 203 mm, and the rice straw moisture content was 60%, the rice straw breaking rate reached its highest value of 79.9%.

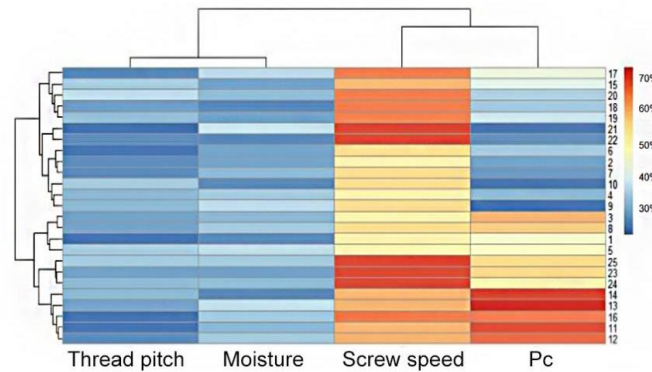


Fig. 9 - The influence of screw speed, thread pitch and straw moisture content on straw pulp rate

As shown in Figure 9, the screw speed has a significant impact on the rice straw breaking rate. When the screw speed is less than 120 r/min, the rice straw breaking rate tends to increase, and it begins to decrease after exceeding 120 r/min. This phenomenon can be attributed to the enhancement of mixing and shearing of the material by the screw as the speed increases (Fan et al., 2023). When the speed exceeds 120 r/min, the residence time of the material in the screw is shortened, reducing the breaking of the material, leading to a decrease in the breaking rate. The effect of rice straw moisture content on the rice straw breaking rate is relatively smaller. The rice straw breaking rate increases with the increase of moisture content until it reaches 60% and then begins to decrease. The expansion degree of the rice straw material increases with the increase of moisture content, leading to an increase in hardness and viscosity, a decrease in the filling density of the material in the screw, and a reduction in contact and shearing between the materials, which reduces the breaking effect. The effect of screw thread pitch on the rice straw crushing rate is the least significant. When the thread pitch is less than 203 mm, the rice straw breaking rate tends to increase, which is attributed to the increased contact frequency between the rice straw and the screw, thereby enhancing the shearing and breaking effects. When the thread pitch reaches 203 mm, the rice straw breaking rate decreases, which may be due to the overly wide pitch reducing the effective contact and shearing of the material. The effective contact and shearing of rice straw between the screws are reduced, lowering the local pressure and shearing force.

Test bench test verification



a. Rice straw twin-screw pulping machine



b. Rice straw particle grinding and breaking process

Fig. 10 - Verification test of rice straw particle breakage

Rice straw was prepared into test samples with a moisture content of 60% according to the methods previously described. Based on the simulation optimization results, the twin-screw rotation speed was set to 120 r/min, and the thread pitch was set to 203 mm. Under the optimal parameter combination, a validation test on the breaking of rice straw particles was conducted using the rice straw twin-screw pulping machine, as shown in Figure 10. To reduce random error, five replicate tests were performed.

The test values of the rice straw breaking rate were 82.7%, 78.6%, 83.4%, 81.3%, and 84.1%, with an average of 82.02% and an error value of 2.6%. The error between the simulation test results and the actual test results was less than 5%, indicating that the results of the simulation optimization are accurate. Furthermore, the proposed model demonstrates significant potential for broader applicability across diverse straw material systems (e.g., wheat, corn, and barley straws), while also providing a method to explore the intricate chemical reactions during pulping, thereby revealing the pulping mechanism.

CONCLUSIONS

(1) The ANSYS analysis software was used to conduct simulation analysis on two flow channel structures and four compression zone combinations. ANSYS analysis software was used to simulate two flow channel structures and four compression zone combinations. Results showed that the parallel 2-2-2 compression zone combination in the twin-screw design offered significant advantages in mixing and extruding rice straw material, providing a more uniform force environment compared to the staggered coupling, which performed poorly in the same speed range. This finding provides a practical basis for optimizing pulping equipment design, enabling the selection of efficient structural configurations for industrial-scale straw processing, thereby enhancing production efficiency and reducing energy consumption.

(2) Based on the simulation analysis results and the characteristics of rice straw material, a rice straw twin-screw pulping machine was designed with a screw outer diameter of 180 mm, a thread pitch range of 172–326 mm, a clearance of 3 mm between the top of the screw thread and the shaft, a clearance of 3 mm between the twin-screws, and a barrel inner diameter of 180.6 mm. This design enables industrial-scale rice straw pulping, supporting sustainable development in straw-based industries.

(3) The calibrated Ab-T₁₀ breaking model and Rocky simulation software were used to perform a three-factor quadratic orthogonal central composite simulation experiment, and a validation test was conducted using the rice straw twin-screw pulping machine. The simulation results showed that the order of influence on the straw breaking rate was: moisture content > thread pitch > screw speed. When the screw speed was 120 r/min, the thread pitch was 203 mm, and the straw moisture content was 60%, the maximum rice straw breaking rate was 79.9%. The validation test results indicated that the error between the simulation and actual test results was 2.6%, and the simulation results basically matched the actual situation, confirming the reliability of the optimization results for the rice straw twin-screw pulping machine. These findings provide a practical foundation for the design and optimization of industrial-scale pulping equipment, promoting the high-value utilization of agricultural waste.

ACKNOWLEDGEMENT

This research was funded by the Project supported by the National Natural Science Foundation of China (32171900) .

REFERENCES

- [1] Arthur T.B., & Rahmanian N., (2024). Process Simulation of Twin-Screw Granulation: A Review. *Pharmaceutics*, Vol.16, no.6, pp.706, Switzerland. DOI:10.3390/pharmaceutics16060706
- [2] Cheng H.T., Gong Y.J., Zhao N., Zhang L.J., Lv D.Q., Ren D.Z., (2022). Simulation and Experimental Validation on the Effect of Twin-Screw Pulping Technology Upon Straw Pulping Performance Based on Tavares Mathematical Model. *Processes*, Vol.10, no.11, pp.2336, Switzerland. DOI:10.3390/pr10112336
- [3] Delvar E., Oliveira I., Brito M.S.C.A., Silva C.G., Santamaria-Echart A., Barreiro M.F., Santos R.J., (2025). Literature Review on Single and Twin-Screw Extruders Design for Polymerization Using CFD Simulation. *Fluids*, Vol.10, no.1, pp.9, Switzerland. DOI:10.3390/fluids10010009
- [4] Düphans V., Kimmel V., Messing L., Schaldach G., Thommes M., (2024). Experimental and Numerical Characterization of Screw Elements Used in Twin-Screw Extrusion. *Pharmaceutical Development and Technology*, Vol.29, no.7, pp.675-683, England. DOI:10.1080/10837450.2024.2378323
- [5] Fan Z.P., Ma Z., Wang H.B., Yu Z.H., (2023). Optimization of Screw Conveying of Kneaded Corn Stalks Based on Discrete Element Method. *INMATEH Agricultural Engineering*, Vol.69, no.1, pp.626-634, Romania. DOI:10.35633/inmateh-69-60
- [6] Gienau T., Kraume M., Rosenberger S., (2018). Rheological Characterization of Anaerobic Sludge from Agricultural and Bio-Waste Biogas Plants. *Chemie Ingenieur Technik*, Vol.90, no.7, pp.988-997, Germany. DOI:10.1002/cite.201700102

- [7] Gong Y.J., Deng N., Bai X.W., Huang W.Y., Liu D.J., (2019). Detection of Corn Straw Components by Fourier Transform Infrared Spectroscopy (玉米秸秆组分的傅里叶红外光谱检测). *Taiyangneng Xuebao/Acta Energiæ Solaris Sinica*, Vol.40, no.6, pp.1664-1671, China. DOI:10.19912/j.0254-0096.2019.06.024.
- [8] Gu B.J., Dhumal G.S., Wolcott M.P., Ganjyal G.M., (2019). Disruption of Lignocellulosic Biomass Along the Length of the Screws with Different Screw Elements in a Twin-Screw Extruder. *Bioresource Technology*, Vol.275, pp.266-271, England. DOI: 10.1016/j.biortech.2018.12.033
- [9] Guan R.L., Li X.J., Wachemo A.C., Yuan H.R., Liu Y.P., Zou D.X., Zuo X.Y., Gu J.Y., (2018). Enhancing Anaerobic Digestion Performance and Degradation of Lignocellulosic Components of Rice Straw by Combined Biological and Chemical Pretreatment. *Science of The Total Environment*, Vol.637-638, pp.9-17, Netherlands. DOI:10.1016/j.scitotenv.2018.04.366
- [10] Hirani A.H., Javed N., Asif M., Basu S.K., Kumar A., (2018). A Review on First- and Second-Generation Biofuel Productions. *Biofuels: Greenhouse Gas Mitigation and Global Warming: Next Generation Biofuels and Role of Biotechnology*, pp.141–154, India. DOI:10.1007/978-81-322-3763-1_8
- [11] Jiang S.Y., Ren D.Z., Ma F., Chen Z.Y., Che Y.M., (2024). Parameter Calibration of Rice Straw Particle–Crushing Model. *Engenharia Agrícola*, Vol.44, pp.e20240063, Spain.
- [12] Kang Y.R., Su Y., Wang J., Chu Y.X., Tian G., He R., (2021). Effects of Different Pretreatment Methods on Biogas Production and Microbial Community in Anaerobic Digestion of Wheat Straw. *Environmental Science and Pollution Research*, Vol.28, no.37, pp.51772-51785, DOI: 10.1007/s11356-021-14296-5
- [13] Kolomiets A., Jirout T., (2021). Analysis of the Dispersion of Viscoelastic Clusters in the Industrial Rotor-Stator Equipment. *Processes*, Vol.9, no.12, pp.2232, Switzerland. DOI: 10.3390/pr9122232
- [14] Kowalski R.J., Hause J.P., Joyner H., Ganjyal G.M., (2018). Waxy Flour Degradation – Impact of Screw Geometry and Specific Mechanical Energy in a Co-Rotating Twin Screw Extruder. *Food Chemistry*, Vol.239, pp.688-696, England. DOI: 10.1016/j.foodchem.2017.06.120
- [15] Li P.W., Xu Y.P., Yin L., Liang X.L., Wang R.M., Liu K.Q., (2023). Development of Raw Materials and Technology for Pulping—a Brief Review. *Polymers*, Vol.15, NO.22, pp.44-65, Switzerland. DOI:10.3390/polym15224465
- [16] Liu Y.Q., Chen J.J., Song J., Hai Z., Lu X.H., Ji X.Y., Wang C.S., (2019). Adjusting the Rheological Properties of Corn-Straw Slurry to Reduce the Agitation Power Consumption in Anaerobic Digestion. *Bioresource Technology*, Vol.272, pp.360-369, England. DOI: 10.1016/j.biortech.2018.10.050
- [17] Lyashuk O.L., Hevko I.B., Hud V.Z., Tkachenko I.G., Hevko O.V., Sokol M.O., Tson O.P., Kobelnyk V.R., Shmatko D.Z., Stanko A.I., (2022). Research of Non-Resonant Oscillations of the Telescopic Screw - Fluid Medium System. *INMATEH Agricultural Engineering*, Vol.68, no.3, pp.499-510, Romania. DOI:10.35633/inmateh-68-49
- [18] Qing Q., Zhou L.L., Guo Q., Gao X.H., Zhang Y., He Y.C., Zhang Y., (2017). Mild Alkaline Presoaking and Organosolv Pretreatment of Corn Stover and Their Impacts on Corn Stover Composition, Structure, and Digestibility. *Bioresource Technology*, Vol.233, pp.284-290, England.
- [19] Rol F., Vergnes B., El Kissi N., Bras J., (2020). Nanocellulose Production by Twin-Screw Extrusion: Simulation of the Screw Profile to Increase the Productivity. *ACS Sustainable Chemistry & Engineering*, Vol.8, no.1, pp.50-59, Washington. DOI: 10.1021/acssuschemeng.9b01913
- [20] Saldana M., Gallegos S., Gálvez E., Castillo J., Salinas-Rodríguez E., Cerecedo-Sáenz E., Hernández-Ávila J., Navarra A., Toro N., (2024). The Reynolds Number: A Journey from Its Origin to Modern Applications. *Fluids*, Vol.9, no.12, pp.299, Switzerland. DOI: 10.3390/fluids9120299
- [21] Subramaniyan S.K., Rajkumar J., Santhanam S.S., Raja K., Lakshmanan G., (2022). Preliminary Studies on the Production of Paper from Millet Husk and Rice Straw. *Environmental Engineering and Management Journal*, Vol.21, no.9, pp.1545-1555, Romania. DOI: 10.30638/eemj.2022.137
- [22] Terashima M., Kotegawa Y., Sun M., Liu B., Yasui H., (2022). Modeling Thixotropic Break-Down Behavior of Dense Anaerobically Digested Sludge. *Applied Rheology*, Vol.32, no.1, pp.1-7, Poland. DOI:10.1515/arh-2022-0121
- [23] Xiao W.S., Niu P., Wang P., Xie Y.j., Xia F., (2024). Simulation Analysis and Optimization of Soil Cutting of Rotary Blade by Ansys/Ls-Dyna. *INMATEH Agricultural Engineering*, Vol.72, no.1, pp.22-32, Romania. DOI:10.35633/inmateh-72-02
- [24] Zhang F.K., Shao W.X., Zhao S.J., Zhu J.K., Li P., (2023). Simulation Test and Verification of Material Conveying for Small and Medium-Sized Air Suction Jujube Picking Machine Based on CFD-DEM Coupling. *INMATEH Agricultural Engineering*, Vol.71(3), pp.535-547, DOI: 10.35633/inmateh-71-46

STRUCTURAL DESIGN AND SIMULATION ANALYSIS OF AIR-ABSORBING VEGETABLE PRECISION SEEDER

气吸式蔬菜精量播种机结构与仿真分析

ChunYan ZHANG^{1,2)}, Xin HE^{1,2)}, XiaoYu WANG^{1,2)}, YanJun LI^{3*)}

¹⁾ Shandong Academy of Agricultural Machinery Sciences, Jinan/China;

²⁾ Key Laboratory of Intelligent Agricultural Equipment in Hilly and Mountainous Areas of Shandong Province, Jinan/China

³⁾ School of Machinery and Automation, Weifang University, Weifang/China;

Correspondent author: Yanjun LI;

E-mail: 1047996083@qq.com

DOI: <https://doi.org/10.35633/inmateh-75-16>

Keywords: vegetable seeds, small size, seed metering device, structural design

ABSTRACT

Aiming at the problems such as low seeding qualification rate of vegetable precision seeder, this paper designs a kind of air-absorbing precision seeder. The device is mainly composed of chassis part, seed discharge device, power unit, fan, gearbox and transmission device. ADAMS software is used to simulate the kinematics and dynamics of the air-absorbent seed discharger, and the simulation results show the movement and falling process of the seeds inside the seed discharger, and at the same time analyze the movement and force of the whole machine. By building a test bench, the seeding qualified rate under different factors is obtained to meet the requirements, which verifies the rationality of the machine design.

摘要

针对蔬菜精量播种机播种合格率低等问题, 本文设计了一种气吸式精量播种机。该装置主要由底盘部分、排种装置、动力装置、风机、变速箱以及传动装置等组成。利用 ADAMS 软件对气吸式排种器进行运动学和动力学仿真, 仿真结果显示了种子在排种器内部运动及下落过程, 同时对整机的运动及受力情况进行分析。通过搭建试验台, 得到不同因素下的播种合格率均满足要求, 验证了整机设计的合理性。

INTRODUCTION

With the gradual increase in the demand for vegetables in China, which caused the increase in the area of vegetable planting, under this trend, the research on vegetable seeding device to improve the performance of the seeding device has an important value (Tian et al., 2023; Zhao et al., 2020; Yang et al., 2018). In mechanized seeding, the seed discharger is the core component in the mechanical seeder. The seed discharging performance of the seed discharger will directly affect the seeding quality and seeding efficiency (Biocca et al., 2023). Currently, the domestic seeder is mainly used for sowing corn, wheat, grains, soybeans and other common large grain size crops. Seeding devices for small-sized vegetables such as carrots are rarely developed and studied, and are still in the initial stage of development (Zhang et al. 2021; Huang et al., 2022).

Common mechanical seed dischargers are prone to scratching and damaging vegetable seeds in the seed discharge process, making the efficiency and quality of seed sowing unsatisfactory. In contrast, pneumatic seed dischargers can well prevent the phenomenon of damage to the outer skin of vegetable seeds in the seed discharge process (Li et al., 2023). Pneumatic precision seed dischargers began to appear in some foreign countries with advanced science and technology in the 1950's (Zhang et al., 2022). Arzu Yazgi et al., (2007) in order to solve the problem of poor uniformity of seed discharge in pneumatic precision seed dischargers, applied the response surface methodology to optimize the parameters of pneumatic precision seed dischargers, and came up with the optimal parameters of the working combination of the dischargers. Karayl et al., (2004), optimized the structure and parameters of the pneumatic seed expeller on the basis of the physical properties of seeds, and at the same time established a vacuum model to improve the seed discharge performance of the discharger.

Onal *et al.*, (2012), developed the Noetherian model to explain the mechanism of the seeds relying on the principles of fluid and aerodynamics, in response to the phenomenon of the instability of the seed suction generated in the airflow field of the pneumatic seed discharger.

Li Qichao., (2020), of Northeast Agricultural University established a stable critical transport model for non-regular small-grained vegetable seeds through a technical study on the adaptation of a variety of small-grained vegetable seeds, and clearly resolved the mechanism of seed population separation and transport.

This study aims to design and analyze an innovative air absorbing precision seeder, using ADAMS software for kinematic and dynamic simulations and conducting experimental evaluations of its performance to provide a reference basis for the research and development of vegetable precision seeder.

MATERIALS AND METHODS

Overall design of the seeder

Composition of the whole machine

The seeder is mainly composed of two parts, the first part is the chassis movement part, the second part is the seeder sowing part, the specific structure is shown in Figure 1. The machine consists of a frame platform carried by four wheels as well as an engine drive module, the motor output power is transmitted to the gearbox, after the gearbox speed change, a part of the power is transmitted to the gears of the rear wheels of the chassis in order to drive the total device forward, which can be adjusted by adjusting the transmission ratio to control the forward speed of the machine. The seeding device adopts air-absorbing seed discharge disk, which is powered by another part of the gearbox. The suction holes on the vertical disk in the seed discharge disk use the negative pressure formed on both sides of the disk to suck the seeds. As the seed discharge disk rotates, it reaches a certain angle where the differential pressure no longer exists, causing the suction to disappear. At this moment, the seeds previously held on the seed discharge disk fall.

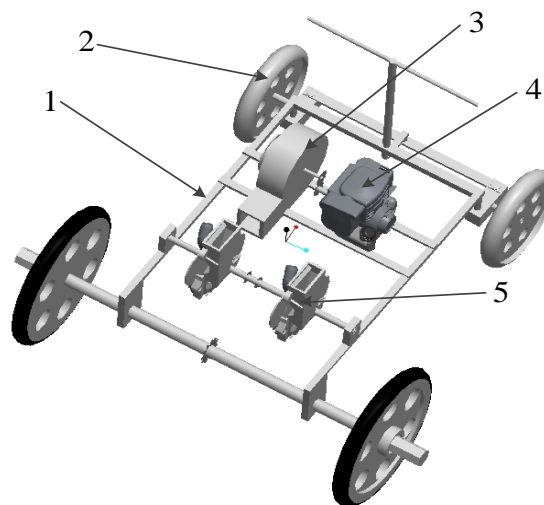


Fig. 1 - Overall structure of seeder

1.chassis; 2.tire; 3.fan; 4.gear box; 5.precision seed-metering device

Working principle

At working, the fan starts and gets a certain angular rotation speed. At the same time, the air inside the seed discharge disk sucked out. Thus, there is a certain pressure difference between the inside and outside of the two sides of the formation of suction on the seeds. The seeds in seed box fall because of gravity. At the same time, the seeds are sucked by suction onto the holes in the seed discharging disk and rotate with the disk. And in a certain range of angles, the negative pressure has always existed. This process is called seed taking and seed carrying process. When the seed discharge disk rotates at a certain angle, the negative pressure disappears, and the seeds fall back to the seed chamber or are discharged under the action of self-weight, vibration and friction. This process is called seed clearing and seed discharge process (Li *et al.*, 2024). The seed discharger keeps doing circular motion, and this process is continuously circulated to complete the seeding operation, and different specifications of seed discharging disk can be selected according to the different vegetable crops sown.

Adams virtual experiment

The kinematics and dynamics simulation is mainly carried out for the seeder in the model to analyze the influence of the rotational speed of the seed discharge disk on the trajectory of the seed drop, as well as the changes of the seed velocity, angular velocity and the force situation, to validate the stability of the rotation of the seed discharge disk (Yu *et al.*, 2024; Li *et al.*, 2021).

The model of air-aspirated vegetable precision seeder created in SolidWorks was imported into ADAMS. According to the size of the model, adjust the size and density of the grid. According to past experience, in order to get more accurate simulation results, set the range of grid activity in the X, Y direction at 6000 mm and 5000 mm, respectively. The grid size in the X, Y direction is 50 mm. The units were chosen according to the standard MMKS. The Cartesian coordinate system is selected as the ground coordinate system. After the model is imported into ADAMS, the attributes of each component should be defined, including the component name, material properties, etc. (Shi *et al.*, 2019). ADAMS can automatically calculate the mass and center of gravity position of each component, and the frame is 87 kg, and the seed discharger is 20.8 kg.

According to the connection between the components of the seeder, the corresponding fixed joint, moving joint, cylindrical joint, etc. were created in turn. Mainly create the motion joint of the internal structure of the seed discharger. The seed discharger and the frame are the fixed joint, the rotary disk inside the seed discharger and the seed discharger shell are the rotary joint; the seed inside the seed discharger and the shell are the contact joint. The specific constraints are shown in Fig. 2.

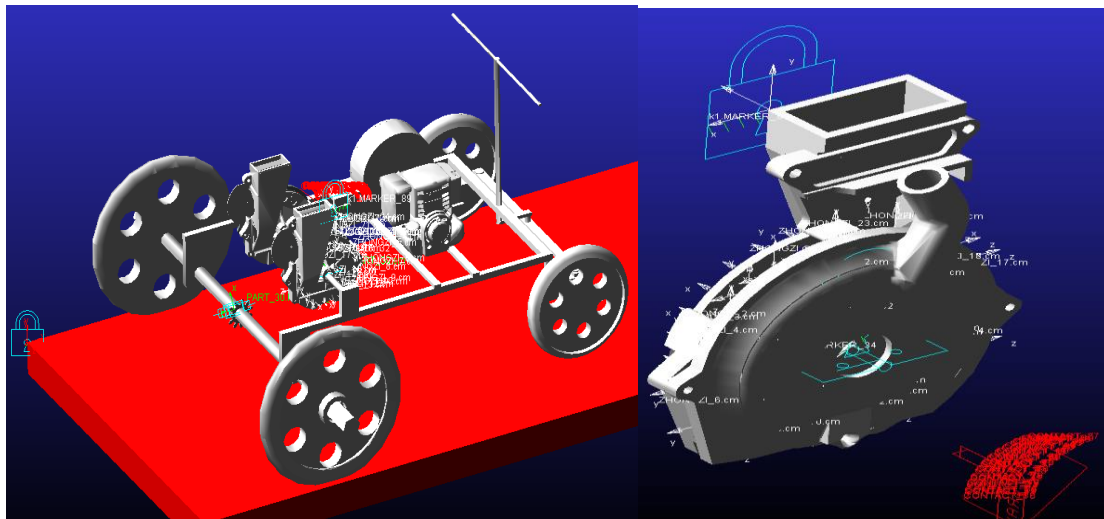


Fig. 2 - The constraints of hoisting system

Applied load and drive: This study primarily examines the relationship between the seed discharger and the speed of the seeding machine, considering two key factors: the speed of the seeder and the seed discharge rate at a given rotational speed of the seed discharger. The relationship between these factors is analyzed through simulation. The drive is applied to the mobile joint of the planter, while the rotary drive is applied to the rotational joint of the seed discharger. The traveling speed of the machine relative to the seeding speed is considered uniform. The main calculations for several operational groups are shown in Table 1.

Table 1

Working conditions of each group		
operation	rotational speed of the seed discharger	speed of the seeder
1	30 d/s	0.3 m/s
2	30 d/s	0.2 m/s
3	30 d/s	0.1 m/s
4	60 d/s	0.1 m/s

Verification test of carrot seeder

Yellow Sword No. 1 pelletized carrot seeds of Shouhe Company with less than 8% moisture content were used as the test material in the experiment (Wang *et al.*, 2015).

The whole test bench is shown in Fig. 3, which is mainly powered by a 190F gasoline engine with a continuous output of 7.0 kw. Other test supporting pieces of equipment are a rotational speed tester (3402, TACHO Hi Tester, Japan), wind pressure tester, camera, stopwatch, and meter scale.



Fig. 3 -Test bench of air-suction carrot seeder

1.chassis; 2.precision seed-metering device; 3.gear box; 4.fan; 5.petrol engine; 6.tire

Test indexes and test methods

Precision seeder adopts the national standard GB/T 6973-2005. The adoption of this standard can make the test results of different types of single grain (precision) seeders comparable. In in this standard, the three major performance indexes of precision seeders are the qualified rate of seeding, the miss-seeding rate, and the reseeding rate.

Test design

The key components of the air-absorbent seeder lie in the structure and installation position of the seeder, etc. However, there are various factors affecting the seeding of the seeder, among which the key influencing factors are the vacuum degree of the air chamber produced by the fan, the rotational speed of the seeding disk driven by the engine, the seeding height, the thickness of the seeder and the angle of the seeder when it is installed, and the number, size, layout and so on of each suction hole of the seeding disk when it is designed (Abdolazare *et al.*, 2018). Since the minimum size of the triaxial dimensions of the carrot seeds for sowing is greater than 2 mm, the diameter of the suction holes in the clock discs designed during the test was 2 mm. Using the control variable method, the pitching height was adjusted separately while keeping all other conditions unchanged. Several groups of different test results were recorded, and the obtained data were processed to determine the average value for the air-absorbent carrot planter. The study examined the effects of three factors—the vacuum degree of the air chamber, the rotational speed, and the pitching height—on the performance of seed placement. The test factor levels are shown in Table 2.

Table 2

Factors and level of orthogonal test

Level	Factors		
	A. Vacuum degree pa	B. Rotational speed of the seeding disk r/min	C. seeding height mm
1	2000	36	20
2	3000	60	30
3	4000	96	40

Through the simulation test, the trajectory and speed of the seed can be obtained, while the bench test provides data on the seed discharge performance of the seeder. Combining both methods allows for a comprehensive analysis of the seeder's operational performance.

RESULTS AND DISCUSSION

Simulation results analysis

Seed movement trajectory analysis

When the seeder is in operation, the seeds make a circumferential motion in the seed discharger and are finally discharged in a certain form of motion. The trajectory of the seed i.e. the actual curve of the seed falling on the ground. The dynamics of the seed movement is simulated using the ADAMS/ view module with a simulation time of 10 s and a simulation step count of 200 steps. The trajectory curves of the seeds under different working conditions are shown in Figure 4-7.

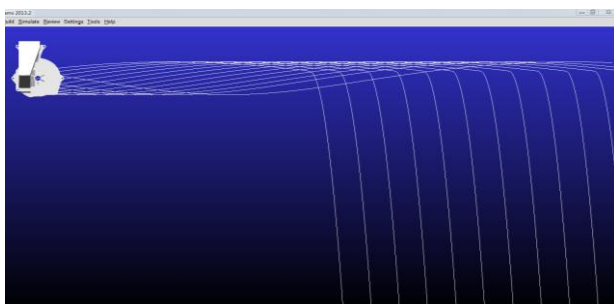


Fig. 4 - The trajectories of seeds in operation 1

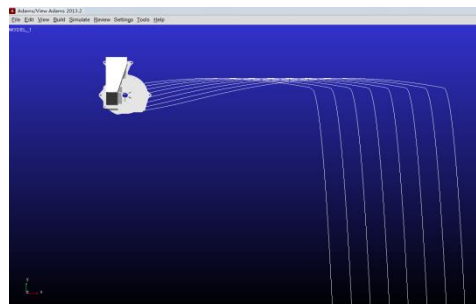


Fig. 5 - Trajectory of seeds in operation 2

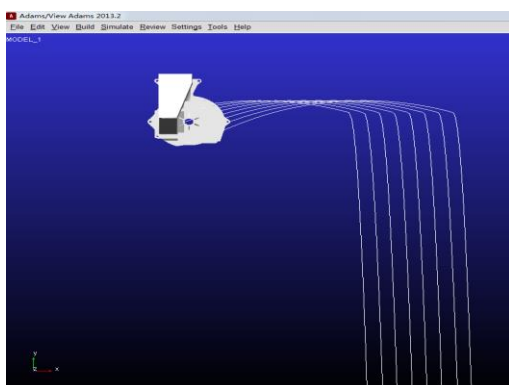


Fig. 6 - Trajectory of seeds in operation 3

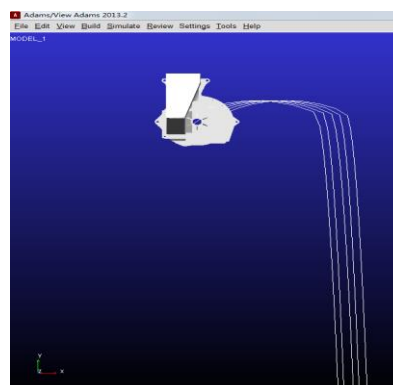


Fig. 7 - Trajectory of seeds in operation 4

In case of operation 1, the landing distance of the seeds is 100 mm, in case of operation 2, the landing distance of the seeds is 150 mm, in case of operation 3, the landing distance of the seeds is 200 mm, in case of operation 4, the landing distance of the seeds is 250 mm, and the results of the statistical calculations are shown in Table 3.

Table 3

Calculations			
Operation	Rotational speed of the seed discharger	Seeder speed	Sowing spacing
1	30 d/s	0.3 m/s	100 mm
2	30 d/s	0.2 m/s	150 mm
3	30 d/s	0.1 m/s	200 mm
4	60 d/s	0.1 m/s	250 mm

By simulating the situation of seeding spacing under different operating conditions, the ideal seeding distance can be determined. The desired seeding spacing can be obtained by adjusting the self-propelled speed of the whole machine and the speed of the upper shaft of the seed discharger.

Simulation result curve of seed under virtual prototype

In the case of the seed discharger under working operation 1, i.e., the speed of the seeder is 0.3 m/s and the rotational speed of the seed discharger is 30 d/s, the curves of the seed velocity changes during sowing are shown in Fig. 8, and the angular velocity changes of different seeds are shown in Fig. 9.

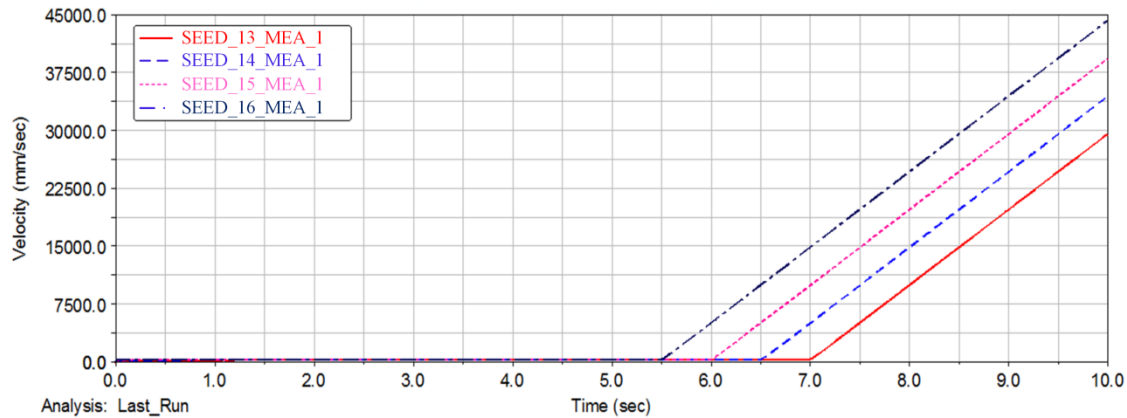


Fig. 8 - Velocity map of four seeds

As can be seen from the seed velocity change curve in Fig. 8, the seeder sequentially releases seeds from the seed discharge tray, after which they accelerate downward with constant acceleration during sowing. The time interval between the fall of every two seeds was approximately 0.5 s. The time interval between the fall of each seed is roughly the same, which shows that the seed discharger is installed more firmly. There is a small vibration which has a negligible effect on it. The simulation was carried out under ideal conditions, without the influence of external wind speed, etc. In addition, there is friction to be taken into account, but compared to the traditional coated seed, this seed is adsorbed on the seed discharging disk, and friction also has a small effect on it. Therefore, based on the time interval between seed falls, it can be concluded that the seeds are sown at relatively uniform spacing, and the emergence of the seedling is neat and tidy.

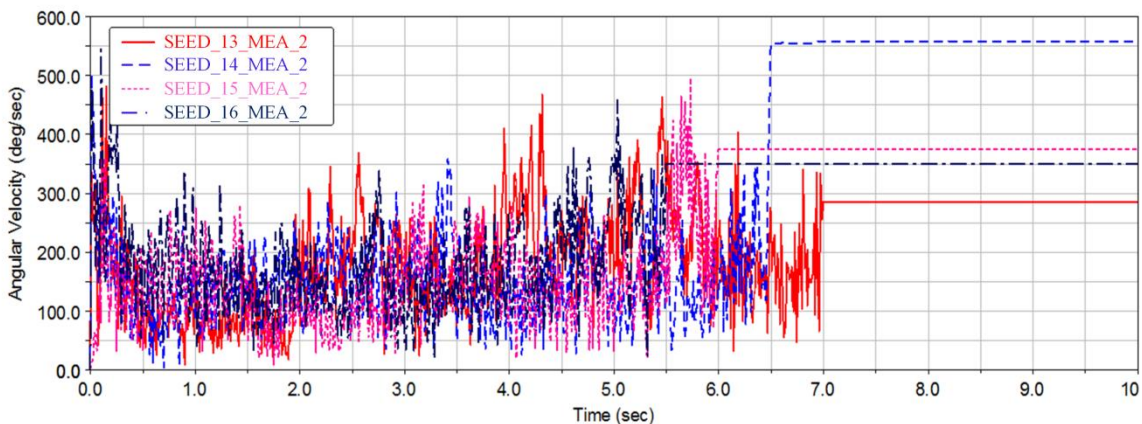


Fig. 9 - Angular velocity diagram of four seeds

Through the angular velocity of different seeds in Fig. 9, it can be seen that the seeds inside the seed discharger are rotating together with the seed discharger, and finally detach from the seed discharger from the seed casting mouth due to their own gravity and the seed scraping device. There is a certain fluctuation of the seeds inside the seed discharger, which is caused by the vibration of the whole machine and its own movement due to the seed discharger being installed on the rear axle of the frame. The angular velocity of all the seeds is basically the same as the angular velocity of the seed discharging disk, and when the seeds are discharged from the seed discharger, they will complete the later work with constant angular velocity.

Analysis of bench test results

Effect of air chamber vacuum on seeding performance

For different vegetable crop seeds, the required vacuum pressure is different, in general, the larger the vacuum degree of the air chamber, the stronger the seeds are adsorbed, and it is not easy to cause missing sowing phenomenon, but the large pressure difference inside the air chamber causes the seed discharge tray to adsorb more than one seed in one type of hole, and the phenomenon of reseeding is obvious, which makes it difficult to realize the precision sowing. Therefore, this experiment was conducted to study the effect of different vacuum degrees on the performance, to find the optimal vacuum degree and range. The wind pressure generated by the fan at work was 2000 Pa, 3000 Pa, 4000 Pa, and the grain spacing under different vacuum degrees was measured and calculated when the traveling speed of the seeder was stable. The results are shown in Table 4.

Table 4

Effect of vacuum degree in air chamber on seeding performance					
Test No.	Vacuum degree of air chamber (pa)	Qualification rate (%)	Reseeding rate (%)	Miss-seeding rate (%)	Average seed spacing (mm)
1	2000	61.25	12.71	27.62	8.4
2	3000	80.71	8.01	12.34	10.1
3	4000	71.44	14.27	15.71	22.6

From Table 4, it can be concluded that as the vacuum degree inside the seed chamber increases, the qualified seed rate rises, the reseeding rate increases, and the miss-seeding rate decreases. In this test, increasing the vacuum degree of the air chamber led to a higher qualified rate; however, it also inevitably resulted in a higher reseeding rate. Considering these three performance indexes comprehensively, the air pressure in the seed chamber should be controlled within the range of 3000–4000 Pa. When the vacuum degree in the seed chamber is at the minimum setting of 2000 Pa, the seed discharge performance is the worst—the qualified rate is relatively low, and the occurrence of empty holes is severe. However, as the air pressure increases, various performance indexes gradually improve. Once the vacuum in the seed chamber reaches a certain level, further increasing the air pressure no longer enhances the qualified rate, while the reseeding phenomenon becomes more pronounced.

Effect of seeding disk's rotational speed on seeding performance

The rotational speed of the seeding disk is another important factor affecting seeding performance. If the rotational speed is too high or too low, it may result in inefficient seeding. Therefore, when selecting the seeding disk's rotational speed, it is essential to ensure that the three key seeding performance indexes remain optimal. This test quantitatively examines the impact of the seeding disk's rotational speed on these three major performance indexes. The rotational speeds were set at 36 r/min, 60 r/min, and 96 r/min, respectively. The seed spacing at different rotational speeds was measured under stabilized conditions, and the results are presented in Table 5.

Table 5

Effect of seeding disk's rotational speed on seeding performance					
Test No.	Seeding disk's rotational speed (r/min)	Qualification rate (%)	Reseeding rate (%)	Miss-seeding rate (%)	Average seed spacing (mm)
1	36	65.20	17.49	5.52	7.8
2	60	77.02	9.14	3.48	15.3
3	96	88.74	7.48	2.73	40.3

From Table 5, it can be seen that the rotational speed and the qualified rate have a non-linear relationship. When the rotational speed is constantly increasing, the qualified rate of the seed discharger first increases and then decreases, and when it increases to a certain peak, the re-seeding rate decreases, but the miss-seeding rate increases. This occurs because when the rotational speed increases, the linear velocity of the seed discharging disk increases continuously, and the time for the seeds to be adsorbed in the seed chamber becomes shorter, resulting in the phenomenon of empty cavities, which leads to the increase of the leakage rate. When the rotational speed is 60-96 r/min, the three major performance indexes of the seed discharger are higher.

Effect of seeding height on seeding performance

Seeding height (the distance between the falling position of the seed and the furrow) is also an important parameter that has a great influence on the seeding performance, and it is an important factor in achieving precision seeding. Due to the light weight of carrot seeds, air resistance during the falling process cannot be ignored. Additionally, friction and collisions within the seed guide tube cause deviations in the falling trajectory, preventing the seeds from following the expected path precisely. Therefore, when selecting the seeding height, the optimal working height should be determined while ensuring that the three major seed discharge performance indexes remain within a reasonable range. This study quantitatively examines the effect of seeding height on these performance indexes. The selected seeding heights were 20 mm, 30 mm, and 40 mm. Once the seed falling process stabilized, grain spacing was measured, and the performance indexes within the grain spacing were calculated. The results are presented in Table 6.

Table 6

Effect of seeding height on seeding performance					
Test No.	Seeding height (mm)	Qualification rate (%)	Reseeding rate (%)	Miss-seeding rate (%)	Average seed spacing (mm)
1	20	87.35	16.49	2.75	69.7
2	30	78.62	10.62	3.47	90.3
3	40	70.28	9.13	5.53	105.4

From Table 6, it can be observed that seeding height and the qualified rate exhibit a generally linear relationship. As seeding height increases, both the qualified rate and reseeding rate of the seed discharger gradually decrease, while the miss-seeding rate increases. When the seeding height is 20 mm, the three major performance indexes show the best results. The reason is that a lower seeding height results in a shorter seed drop distance, reducing the impact of wind on the seeds. Thus, the following conclusion can be drawn: the higher the seeding height, the greater the seed drop distance, leading to increased influence from wind, inter-seed friction, collisions, and other external factors, ultimately reducing seeding accuracy. To ensure optimal seed discharge, the seeding height should be minimized as much as possible to reduce the falling distance of the seeds.

In summary, as the vacuum inside the chamber increases, the seed spacing gradually decreases, indicating a reduction in the miss-seeding rate. This occurs because an increase in vacuum pressure leads to more carrot seeds being adsorbed onto the disk, thereby increasing the number of discharged seeds and reducing seed spacing. However, if the vacuum pressure becomes too high, multiple seeds may be discharged simultaneously, leading to an increased reseeding rate. When the rotational speed of the seed discharge disk increases, the seed spacing increases. However, at very low rotational speeds, the increase in seed spacing is slower, whereas at higher rotational speeds, seed spacing increases more significantly. The reason for this phenomenon is that at higher speeds, the seed discharge disk has less time to properly adsorb enough seeds, resulting in larger seed spacing and a higher miss-seeding rate. When the seeding height is increased, seed spacing also increases, leading to a higher miss-seeding rate. This occurs because carrot seeds are very lightweight, and as the seed discharge height increases, seeds fall a greater distance and are more affected by wind, causing uneven seed distribution. Therefore, when determining the installation height of the seed discharger, it should be kept as low as possible while ensuring it does not come into contact with uneven ground.

CONCLUSIONS

(1) An air-absorbing precision seeder was designed, and its overall structure was developed. The device mainly consists of a chassis, seed discharging device, power unit, fan, gearbox, and transmission system. The working principle of the entire machine and the four seed discharge processes of the seed discharger were introduced, providing a theoretical basis for subsequent simulations to analyze the trajectory and movement process of seeds.

(2) Using ADAMS software, kinematic and dynamic simulations of the air-absorbing seed discharger were conducted. The seeding process was simulated, and the seeding speed curve was generated. The simulation results illustrate the movement and falling process of seeds within the seed discharger, while also analyzing the motion and forces acting on the entire machine.

(3) The influence of three factors—vacuum degree of the air chamber, rotational speed, and seeding height—on seed discharge performance was investigated through a test bench. The reasons for variations in test results were explained by analyzing the data. The effects of different factor levels on seed discharge performance were determined, verifying the validity and reliability of the test results.

ACKNOWLEDGEMENT

The authors were funded for this project by the Shandong Province Key R&D Program (Major Science and Technology Innovation Project)-Research and Development of High-Efficiency Production Equipment for Specialty Vegetables-2022CXGC010612 and Promotion of Agricultural Machinery in Shandong Province (Grant No. NJYTHSD-202321) and the Shandong Provincial Key R&D Program (Major Scientific and Technological Innovation Project)-Project (2024CXGC010902).

REFERENCES

- [1] Abdolazare, Z., Mehdizadeh, S. (2018). Real time laboratory and field monitoring of the effect of the operational parameters on seed falling speed and trajectory of pneumatic planter. *Computers and Electronics in Agriculture*, Vol. 145, pp. 187-198, Ramin Agr/Nat Resources Univ Khuzestan;
- [2] Arzu, Y., Adnan, D. (2007) Optimization of the seed spacing uniformity performance of a precision seeder using Spherical Materials and response surface methodology. *Bio-systems Engineering*, Vol. 97, no.3, pp. 347-356, Pittsburgh/Pennsylvania;
- [3] Biocca M., Fanigliulo, R., Pochi, D., & Gallo, R. (2019). Dust drift mitigating devices applied on precision pneumatic seed drills: a mini-review. *INMATEH - Agricultural Engineering*, Vol. 58, no.2, pp. 273-284, Bucharest / Romania; DOI:<https://doi.org/10.35633/inmateh-58-30>
- [4] Huang, Y., Li, P., Dong, J., Chen, X., Zhang, S., (2022). Design and test of high-speed precision soybean metering device with side guide (大豆高速播种机侧置导引式精量排种器设计与试验). *Journal of Agricultural Machinery*, Vol.53, no.10, pp. 44-53, 75, Shanxi/China;
- [5] Karayel D., Barut Z., Zmerzi A. (2004). Mathematical Modelling of Vacuum Pressure on a Precision Seeder, *Bio-systems Engineering*, Vol. 87, no.4, pp. 437-444, Antalya/Turkey;
- [6] Li, Q., (2020). *Mechanism Analysis and Experimental Study on Scoop Type Precision Seed Metering Device for Small Size Vegetable Seeds* (舀勺式小粒径蔬菜种子精量排种器机理分析与试验研究). [PhD dissertation], Northeast Agricultural University, Harbin/China;
- [7] Li, Y., Bai, Y., Zhang, X., Xie, F., (2023). Structural Design and Simulation Analysis of a Dual-row Pneumatic Vegetable Precision Planter. *Processes*, Vol. 11, no.6, pp. 1803, Shandong/China;
- [8] Li, Y., Ning, Y., Xie, F., Bai, Y., (2024). Seed discharge performance test of air suction seed discharger for small vegetable seeds. *INMATEH-Agricultural Engineering*, Vol.73, no.2, pp.721-730, Bucharest / Romania; DOI: <https://doi.org/10.35633/inmateh-73-61>
- [9] Li, Z., He, S., Zhong, J., Han, J., Chen, Y., Song, Y. (2021). Parameter optimization and experiment of the disturbance pneumatic plate hole metering device for rapeseed (油菜扰动气力盘式穴播排种器参数优化与试验). *Transactions of the Chinese Society of Agricultural Engineering*, Vol. 37, no.17, pp. 1-11, Anhui/China;
- [10] Onal, I., Degirmencioglu, A., Yazgi, A. (2012). An evaluation of seed spacing accuracy of a vacuum type precision metering unit based on theoretical considerations and experiments. *Turkish Journal of Agriculture and Forestry*, Vol. 36, no.2, pp. 133-144, Izmir/Turkey;
- [11] Shi, S., Zhou, J., Liu, H., Fang, H., Jian, S., Zhang, R. (2019). Design and Experiment of Pneumatic Precision Seed-metering Device with Guided Assistant Seed-filling (驱导辅助充种气吸式精量排种器设计与试验). *Journal of Agricultural Machinery*, Vol. 50, no.5, pp. 64-70, Shandong/China;
- [12] Tian, Y., Li, Y., Jiang, J., Li, C., Xie, F., (2023). Experimental study on seed compression characteristics of Pak choi (青梗小白菜种子压缩载荷试验研究). *Agricultural Mechanization Research*, Vol. 45, no.6, pp. 152-158, Shandong/China;
- [13] Wang, L., (2015). *Design and test paper of spherical vegetable seed precision seeder*(类球形蔬菜种子精量播种机设计与试验). [PhD dissertation], Huazhong Agricultural University, Wuhan/China;

- [14] Yang, M., Tang, B., Xu, Y., Wei, D., Peng, X. (2018). Experimental study on physical properties of vegetable seed (蔬菜种子物理特性试验研究). *Journal of Chinese Agricultural Mechanization*, Vol. 39, no.9, pp. 48-50, Sichuan/China;
- [15] Yu, J., Tao, Z., Xiao, L., Liu, J., Chen, X., Liu, M., Huang, N., Dong, W. (2024). Design and experiment of swing type synchronous mulching for rice direct seeder. *INMATEH-Agricultural Engineering*, Vol. 72, no.1, pp. 569-578, Bucharest / Romania; DOI: <https://doi.org/10.35633/inmateh-72-50>
- [16] Zhang, K., Ma, G., Li, J., Zhao, X., (2022). Material characteristics of vegetable seeds with small grain size and design of seed metering device. *INMATEH-Agricultural Engineering*, Vol. 68, no.3, pp. 789-797, Bucharest / Romania; DOI: <https://doi.org/10.35633/inmateh-68-78>
- [17] Zhang K., Zhang L., Ding, Y., Liu, X., Zhao, X., (2021). Design and test of air-suction pepper seed metering device based on air supply and quantitative seed supply. *INMATEH-Agricultural Engineering*, Vol. 64, no.2, pp. 345-354, Bucharest / Romania. DOI: <https://doi.org/10.35633/inmateh-62-34>
- [18] Zhao, G., Dai, Q., Wang, J., Li, Y. (2020). Experimental study on physical characteristics of typical small-sized vegetable seeds (典型小籽粒蔬菜种子物理特性试验研究). *Journal of Qingdao Agricultural University (Natural Science)*, Vol. 37, no.3, pp. 225-229, Qingdao/China.

STRUCTURE DESIGN AND LEVELLING CONTROL SYSTEM DEVELOPMENT FOR SELF-PROPELLED SPRAYER BOOM

自走式喷雾机喷杆结构与仿形调平控制系统开发

Zhenyu ZHANG¹, Jiayu CAO¹, Peijie GUO¹, MiaoYun WANG², Yu CHEN^{*1}

¹ College of Mechanical and Electronic Engineering, Northwest A&F University, Yangling, 712100, China;

² College of Intelligent Manufacturing, Shaanxi Institute of Mechatronic Technology, Baoji, 721001, China;

Tel: +86 17795759790; E-mail: jdx73@nwfau.edu.cn

DOI: <https://doi.org/10.35633/inmateh-75-17>

Keywords: Self-propelled sprayer, spray boom, levelling control system, adjustment threshold, ultrasonic distance sensor, performance experiment

ABSTRACT

To address the issues of poor boom stability and inconsistent spray quality due to harsh field conditions and varying boom height relative to the target, a five-section planar truss boom capable of height adjustment, overall tilt adjustment, and unilateral tilt adjustment was designed. A contour levelling control system for the boom was developed based on the STM32F103 platform. The levelling system uses ultrasonic distance sensors to detect the distance between the boom's ends and the target in real-time. The limit average filtering method is employed to eliminate sudden signal interference and process feedback data. The control system then drives electric actuators to adjust the boom's posture in real-time. Field and spray tests were conducted using a small electric self-propelled sprayer as the test platform. The results indicate that the best levelling performance was achieved with overall height adjustment, overall tilt adjustment, and unilateral tilt adjustment thresholds set to 30 mm, 30 mm, and 40 mm, respectively. The field spray tests showed minimal relative errors in droplet deposition coverage and density on both sides. The coefficient of variation CV of deposition along the boom direction was less than 15%, ensuring good spray distribution uniformity. These findings provide valuable references for the design and optimization of sprayer booms.

摘要

本文设计了一种可实现高度调节、整体倾斜调节、单侧倾斜调节功能的平面五段式桁架喷杆。基于STM32F103平台设计了喷杆仿形调平控制系统，调平系统采用超声波测距传感器实时检测喷杆两侧末端与目标物之间距离，利用限幅平均滤波法以排除突变信号的干扰并对反馈数据进行计算处理，控制系统驱动各机构电动推杆伸缩对喷杆姿态进行实时调整。以小型电动自走式喷雾机为试验平台，分别进行了场地试验及田间喷雾试验，场地试验结果表明当设定整体高度调节阈值为30mm、整体倾斜调节阈值为30mm、单侧倾斜调节阈值为40mm时调平效果最佳，田间喷雾试验结果表明两侧雾滴沉积覆盖率及沉积密度相对误差较小，沿喷杆向上的沉积量变异系数CV小于15%，可以保证较好的喷雾分布均匀性，研究成果为喷雾机喷杆的设计与优化提供了参考。

INTRODUCTION

Self-propelled boom sprayers are widely used in field pest and disease control due to their high operational efficiency and excellent spray quality (Dou et al., 2021; Baltazar et al., 2021; Lin et al., 2022). However, harsh field conditions often cause the sprayer to pitch, roll, and yaw, leading to boom imbalance relative to the ground, and in severe cases, the boom ends may even touch the ground (Ali et al., 2023; Li et al., 2023; Lipiński et al., 2022). Furthermore, to ensure spray quality, the boom should maintain an optimal and nearly parallel distance to the crop canopy. Therefore, the boom height must automatically adjust in real-time according to changes in crop canopy height and terrain to ensure uniform spray distribution and operational safety (Dou et al., 2021; Dou et al., 2021; Bayat et al., 2018). To this end, researchers both domestically and internationally have conducted studies on boom levelling control. Llica et al. (2018) studied boom height measurement methods and developed an automatic height adjustment control algorithm to maintain a constant

¹ Yu CHEN, Prof. Ph.D. Eng; Zhenyu ZhANG, M.R. Stud. Eng; Jiayu CAO, M.R. Stud. Eng; Peijie GUO, M.R. Stud. Eng;

² MiaoYun WANG, M.S. assistant, Eng.

distance between the nozzle tip and the target area (soil or canopy), enhancing the sprayer's application efficiency. Okamoto et al. integrated multiple sensors to detect the boom's posture, providing precise detection methods for the boom adjustment system (Okamoto et al., 2015). An Jiahao et al., (2022), designed a boom levelling mechanism based on the pendulum suspension principle, allowing the boom to swing left and right between -20° and 20° relative to the vehicle body. Based on this principle, they developed a boom levelling control system. Sun Xing et al., (2020), used a weighted average algorithm to integrate data from inclination sensors and ultrasonic sensors, and based on this, designed an expert-controlled boom height adjustment system. Zhang Meng et al., (2019), designed an automatic boom levelling control system using inclination sensors based on MEMS inertial navigation technology to achieve real-time boom posture adjustments.

This study focuses on the boom of a small electric sprayer, aiming to enhance boom operational stability and spray uniformity by designing a boom structure capable of ground contour following. Based on its working principle, ultrasonic sensors are used to detect the distance between the boom and the spraying target. The limit average filtering method is employed to eliminate sudden signal changes, and the boom contour levelling control is achieved by controlling the forward and reverse rotation and extension of electric actuators in each mechanism.

MATERIALS AND METHODS

Overall structure of the boom

The boom contour levelling system is designed based on our team's independently developed small self-propelled electric sprayer, with the overall boom structure shown in Fig. 1. The boom uses a five-section planar truss structure (left small boom, left large boom, middle boom, right small boom, right large boom), the small booms are connected to the large booms via small boom folding mechanisms, and the large booms are connected to the middle boom via unilateral tilt mechanisms and large boom folding mechanisms, the middle boom is connected to the boom mounting frame through an overall tilt mechanism, while the boom mounting frame is connected to a parallelogram lifting mechanism for height adjustment. The parallelogram lifting mechanism is connected to the chassis to secure the entire boom.

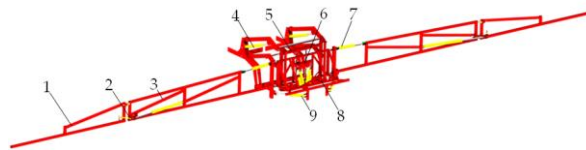


Fig. 1 - High clearance self-propelled sprayer test platform

1 – Small boom; 2 – Small boom folding mechanism; 3 – Large boom; 4 – Parallelogram lifting mechanism; 5 – Boom mounting frame; 6 – Overall tilt mechanism; 7 – Unilateral tilt mechanism; 8 – Middle boom; 9 – Large boom folding mechanism

Design of key mechanisms

(1) Design of the parallelogram lifting mechanism

The parallelogram lifting mechanism primarily consists of a boom mounting frame, upper link, lower link, boom bracket, and height-adjusting push rod, as shown in Fig. 2. The boom bracket is bolted to the sprayer chassis through pre-set bolt holes, securing the entire parallelogram lifting mechanism to the sprayer frame. The boom bracket and boom mounting frame are connected via the upper and lower links, which are of equal length and remain parallel during height adjustment. This forms a double parallelogram linkage. The double link structure enhances structural strength and prevents deformation during height adjustment.

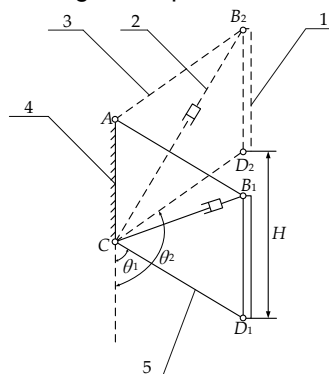


Fig. 2 - Operating principle of the parallelogram lifting mechanism

1 – Boom mounting frame; 2 – Height-adjusting push rod; 3 – Upper link; 4 – Boom bracket; 5 – Lower link

In Fig. 2, quadrilateral AB1CD1 represents the lowest position of the parallelogram lifting mechanism, and AB2CD2 represents the highest position. l_{AB} is the length of the upper link, l_{CD} is the length of the lower link, l_{AC} is the length of the fixed end of the boom bracket, θ_1 and θ_2 are the angles between the lower link and the vertical direction at the extreme positions of the boom. H denotes the maximum height adjustment distance of the boom.

As shown in Fig. 2, the maximum range of boom height adjustment is:

$$H = |l_{CD} (\cos \theta_2 - \cos \theta_1)| \tag{1}$$

The minimum length of the height-adjusting electric push rod is:

$$L_{\min} = \sqrt{l_{AB}^2 + l_{AC}^2 - 2l_{AB}l_{AC} \cos \theta_1} \tag{2}$$

The maximum length of the height-adjusting electric push rod is:

$$L_{\max} = \sqrt{l_{AB}^2 + l_{AC}^2 - 2l_{AB}l_{AC} \cos \theta_2} \tag{3}$$

If h_1 is the minimum distance from the fixed end of the boom bracket to the ground, and h_2 is the distance from the lower link hinge point of the parallelogram lifting mechanism to the bottom of the boom, then the minimum adjustable height of the boom is,

$$h = h_1 - l_{AB} \cos \theta_1 - h_2 \tag{4}$$

(2) Design of the overall inclination mechanism

The working principle of the overall inclination mechanism is shown in Fig. 3. Figures 3(a), (b), and (c) represent the left limit, horizontal, and right limit states of the spray boom. When the overall tilt angle range is set to -5° to 5° , the angles between the tilt link and the overall tilt push boom at their left and right limit positions are:

$$\theta_L = \arcsin \frac{l_a}{l_b \sin \delta} + 5^\circ, \theta_R = \arcsin \frac{l_a}{l_b \sin \delta} - 5^\circ \tag{5}$$

The length of the overall tilt push boom is:

$$l_a^2 + (l - l_L)^2 - 2l_a(l - l_L) \cos \theta_L = l_b^2, l_a^2 + (l + l_R)^2 - 2l_a(l + l_R) \cos \theta_R = l_b^2 \tag{6}$$

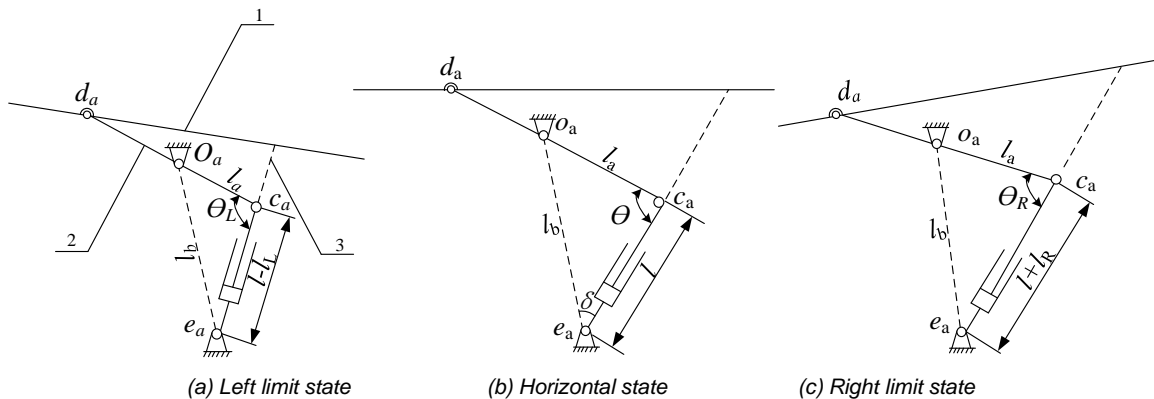


Fig. 3 - Working principle of the overall inclination mechanism
 1 – Central spray boom; 2 – Inclined link rod; 3 – Integrated inclined push rod

As shown in Fig. 4, the three-dimensional model of the integrated tilting mechanism allows relative rotation among the inclined link rod, the welded inclined plate, and the central spray boom. Additionally, the relative rotation is possible between the inclined link rod and the fixed column. By controlling the extension and retraction of the electric push rod, the overall inclination of the spray boom can be achieved. When the small-range height adjustment push rod remains stationary, shortening the integrated inclined push rod causes the right end of the inclined link rod to rotate around its center, transferring thrust to the fixed column at the left end. Since the fixed column is welded to the central spray boom, this results in a clockwise rotation and inclination of the spray boom. Conversely, when the integrated inclined push rod extends, the spray boom rotates counterclockwise. When both the small-range height adjustment push rod and the integrated inclined push rod extend or retract simultaneously at the same speed, the welded inclined plate, inclined link rod, central spray boom, and guide plate move together along the guide tube, achieving small-range height adjustment of the spray boom.

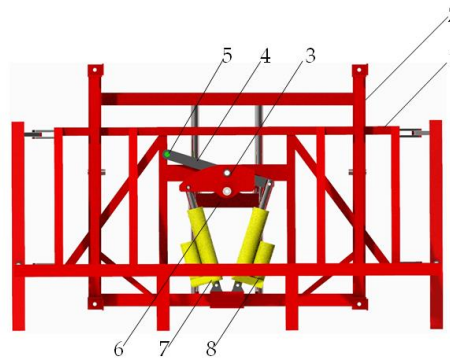


Fig. 4 - Overall inclination mechanism

1 – Central spray boom; 2 – Spray boom mounting bracket; 3 – Welded inclined plate; 4 – Inclined link rod; 5 – Fixed column; 6 – Guide plate; 7 – Small-range height adjustment push rod; 8 – Integrated inclined push rod

(3) Design of the unilateral tilting mechanism

Taking the right spray boom as an example, the working principle of the unilateral tilting mechanism is shown in Fig.5. One end of the unilateral tilting push rod is hinged to the fixed rod of the large arm spray boom, while the other end is hinged to the large arm spray boom itself. The unilateral tilting rotating block is connected to the pin shaft below the fixed rod of the large arm spray boom, the large arm spray boom can rotate at a certain angle around the fixed rod through the rotating block. When the unilateral tilting push rod contracts, it drives the large arm spray boom to rotate clockwise, when the unilateral tilting push rod extends, it drives the large arm spray boom to rotate counter clockwise, thereby achieving the tilting adjustment of the unilateral spray boom.

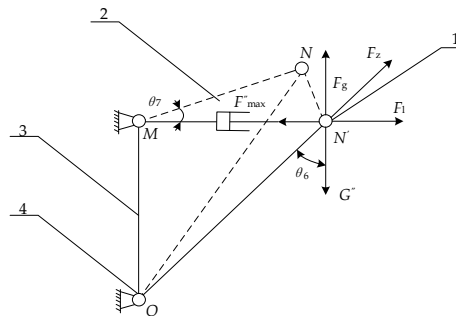


Fig. 5 - Working principle of the unilateral inclination mechanism

1 – Large arm spray boom; 2 – Unilateral inclination push rod; 3 – Large arm spray boom fixing rod; 4 – Unilateral inclination rotating block

The length of the unilateral inclination push rod at the extreme rotation position of the spray boom is,

$$l_{MN'} = l_{MN} \cos \theta_7 \tag{7}$$

The support force provided by the pin to the main arm spray boom is,

$$F_z = F_g / \cos \theta_6 \tag{8}$$

$$F_g = G'' \tag{9}$$

The maximum thrust required by the single-sided inclined push rod is,

$$F_{max}^* = F_1 = F_z \cos(90^\circ - \theta_6) \tag{10}$$

Design of the boom profiling and levelling system

(1) Working principle of the system

Currently, boom levelling systems primarily use distance sensors to detect boom height or tilt sensors to measure boom inclination (Li et al., 2020; Wang et al., 2019; Fu et al., 2020; Zürey et al., 2020; Burgers et al., 2021). Tilt sensors can measure the entire boom's tilt angle in dynamic environments and are widely used in small drones, intelligent agricultural equipment, and automobiles (Li et al., 2023; Shi et al., 2020; Yan et al., 2021). However, the boom designed in this paper is divided into five sections during profiling and levelling, allowing for separate control of the overall boom and the two sides. The use of tilt sensors alone cannot meet control requirements, so ultrasonic distance sensors are selected for real-time boom height detection.

The working principle of the boom contour levelling system is shown in Fig. 6. An ultrasonic distance sensor is installed at the end of each small arm on both sides of the boom, measuring the height of the side

booms and the overall boom above the ground. The controller processes the sensor feedback data to drive height adjustment, overall tilt, and single-side tilt electric push rods to adjust the height of each boom section, ensuring precise levelling for various terrains. To avoid repetitive adjustments near the target height during levelling, a height adjustment threshold is set. When the real-time collected boom height falls within the threshold range, the system automatically stops the levelling action.

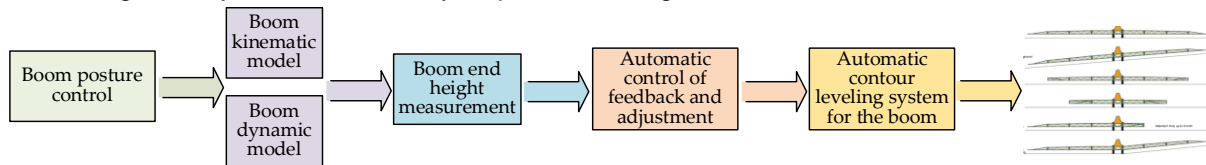


Fig. 6 - The working principle of the boom contour levelling system

The boom contour levelling control system is designed with an STM32 micro-controller as its core, with its hardware structure shown in Fig. 7. The system uses two ultrasonic distance sensors to accurately measure the ground clearance on both sides of the boom, and the detected data is input into the microprocessor for filtering and evaluation. Based on the levelling requirements, the microprocessor generates corresponding control signals to operate the H-bridge module, driving the appropriate electric actuators to adjust the boom's height or angle, thus providing real-time posture adjustments. The distance sensors are HY200P4C ultrasonic sensors with built-in temperature compensation, having a detection range of 100-2000 mm. The communication protocol used is RS485, which supports high-speed and long-distance data transmission, making it suitable for wide boom sprayers. The response time is 40 ms, with a repeat accuracy of 0.3%. The data conversion module is the GN-15 RS485-TTL module, which supports a wide voltage range (3.0-33V) and baud rates of 110-460800 BPS. The motor drive module uses the GZ-PMDC-120A7T H-bridge L298 logic speed controller, with an input voltage of 12-27V and a rated output current of 7A. Fast recovery diodes are used to prevent the control section from being damaged by large counter-electromotive forces during motor startup. The microprocessor selected is the STM32F103ZET6 based on the Cortex-M3 core, featuring 112 I/O ports, 5 UART communication ports, and 1 CAN communication port.

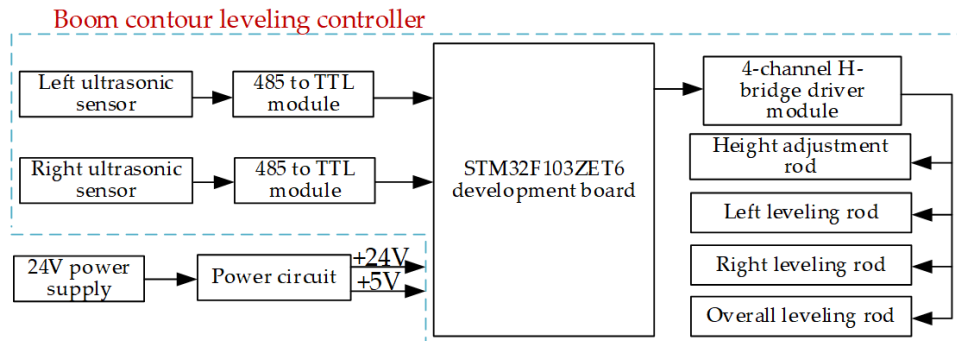


Fig. 7 - The hardware structure for boom contour levelling

(2) Information acquisition and processing of ultrasonic distance sensors

When the sprayer operates in the field, ultrasonic distance sensors are used to send measurement signals to the crop canopy. However, the spacing between crops may cause the signals to pass through gaps and reach the ground, resulting in abrupt changes in measurement values and leading to erroneous judgments by the control system. To ensure the accuracy of height information, it is necessary to apply filtering to exclude interference from sudden signal changes during data collection. After comparing various filtering techniques, the amplitude-limited averaging filter method was selected for processing the sensor signals. This method effectively eliminates deviations caused by occasional pulse interference and provides good signal smoothing (Li et al., 2022). The filtering principle is as follows: based on the plant height at different application stages, the maximum allowable deviation value A between two successive samples is determined. If the difference between the current sample value and the previous one is less than or equal to A , the current sample value is accepted; otherwise, it is discarded, and the previous value is used instead.

The filtering algorithm, shown in Equation (11), averages 20 samples that meet the criteria. If the deviation exceeds the pressed height range, the output signal drives the electric actuator to adjust the boom position.

$$y'(k) = \begin{cases} y(k), & |y(k) - y(k-1)| \leq A \\ y(k-1), & |y(k) - y(k-1)| > A \end{cases} \quad (11)$$

In the equation, $y(k)$ represents the k -th sample value, $y(k-1)$ represents the $k-1$ -th sample value, A is the maximum allowable deviation between two successive sample values, and $y'(k)$ denotes the signal value after the k -th filtering process.

(3) Control logic of the contour levelling system

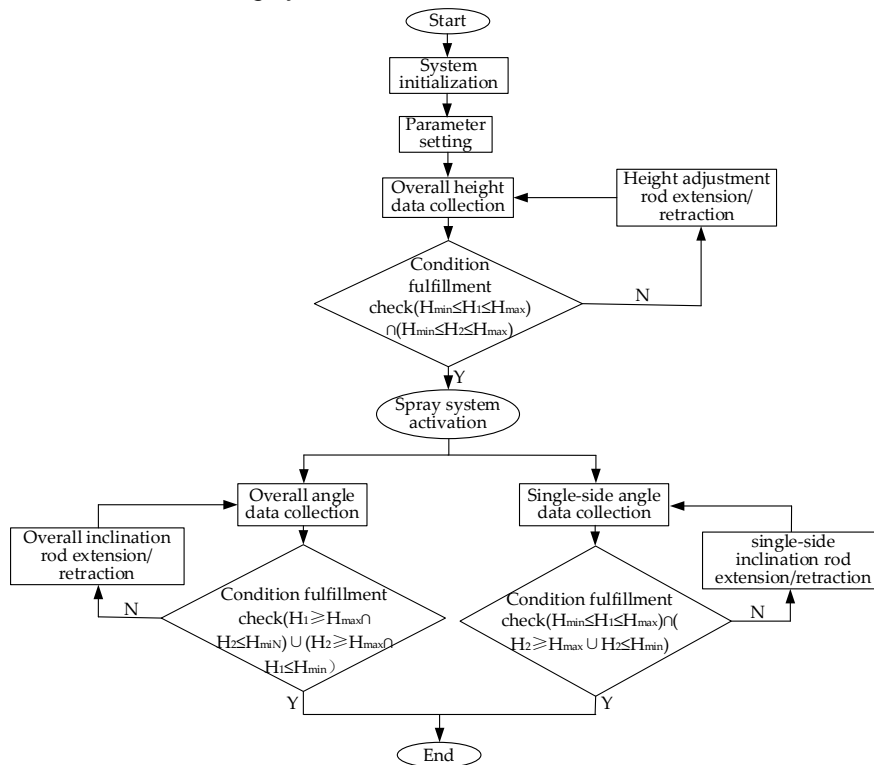


Fig. 8 - The terrain following levelling process

When the sprayer enters the field, the boom is fully extended, operator activates the ground contour levelling control system, upon entering the main program, the overall height of the crop canopy is first adjusted. If the heights on both sides do not fall within the preset range, the height adjustment rod drives the parallelogram lift mechanism to adjust the overall height of the boom. When both sides meet the preset height requirements, the spraying system is activated, and the sprayer enters the boom angle adjustment program. Angle adjustment includes both overall and single-side adjustments. If one side is below the minimum preset height and the other side is above the maximum preset height, an overall angle adjustment is performed, with the inclination rod adjusting the overall boom angle. If one side meets the preset height range while the other does not, a single-side angle adjustment is performed, with the inclination rod adjusting the angle of the single side. After adjustment, the system returns to the angle adjustment program for continuous monitoring. After spraying is completed, the ground contour levelling control system is turned off, the booms are adjusted to their initial extended state, and the booms are folded for transport.

(4) Experimental methods and procedures

The terrain in the field during the operation of the sprayer is complex and variable. To simulate the imbalance of the spray boom caused by field undulations, a stepped test site and a single-sided inclined surface were designed. To simulate the wheat plant height at different growth stages, the optimal preset distance between the spray boom and the crop canopy was adjusted. These three sets of experiments were used to verify the effectiveness of the spray boom ground contour levelling control system. After comparing the data from each experiment, the optimal threshold parameters for the control system were selected. To verify the designed spray boom's performance, spray tests were conducted in a wheat field. The spray boom ground contour levelling test methods and procedures are shown in Fig. 9.

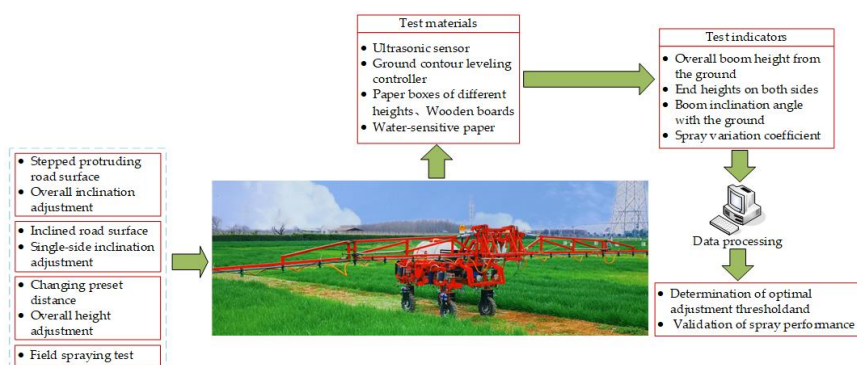


Fig. 9 - Spray boom ground contour levelling test methods and procedures

Experimental methods and condition settings

(1) Spray boom overall height adjustment experiment

During the wheat growth cycle, plant height changes continuously. If the spray boom height is not adjusted, excessive spray overlap can lead to over-spraying or missed areas. The overall ground clearance of the spray boom can be adjusted using a parallel four-bar lifting mechanism. However, due to the difficulty of altering wheat plant height, the performance of spray boom height adjustment was validated by changing the preset height of the spray boom relative to the wheat canopy. Before the test, the spray boom was fully extended and its initial ground clearance was adjusted. Controller parameters were modified to set the target height of the spray boom above the crop canopy at 400, 500, and 600 mm, with height adjustment thresholds set at 20, 30, 40, and 50 mm. After setting these parameters, the sprayer was driven at a constant speed in a straight line, and the ground contouring control system was activated. Once the spray boom height stabilized, the control system was turned off and the overall height of the spray boom was recorded.

(2) Stepwise field experiment

During field operations, undulations in the ground surface prevent the boom from maintaining a nearly parallel state relative to the application target. To simulate the inclination of the boom relative to the target during sprayer operation, a stepwise test surface was designed, as shown in Fig. 10.

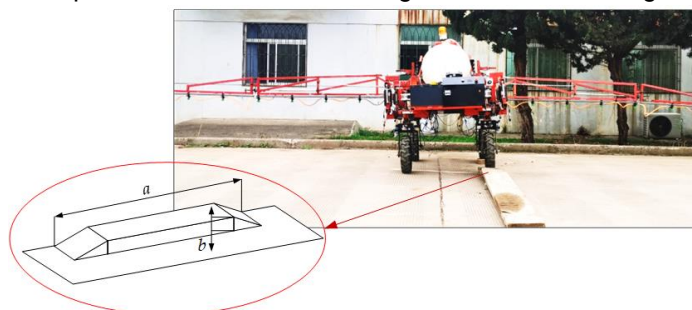


Fig. 10 - Stepwise field experiment

The designed boom has a maximum spray width of 9000 mm, and the sprayer's wheel track is 1200 mm. If the height b of the stepwise surface is set to 50 and 100 mm, and the length a is set to 5000 mm, the maximum tilt angle of the boom relative to the ground can reach 4.8° , causing a maximum displacement of 400 mm at the boom's end. To prevent collisions between the boom and the ground, the boom height was set to 700 mm, and adjustment thresholds were set to 20, 30, 40, and 50 mm. After stabilizing the boom height using the ground contour levelling system, the sprayer was driven over the stepwise surface at a constant speed of 8 km/h for four adjustment thresholds. After the front and rear right-side tires completely entered the highest point and the boom height stabilized, the control system was turned off. The heights of the boom ends on both sides and the tilt angle of the boom relative to the ground were recorded.

(3) Single-side inclination adjustment experiment

During field operations, the sprayer boom may encounter asymmetrical terrain within its coverage area. As shown in Figure 11(a), after overall tilt levelling, one side of the boom meets the spraying requirements, but the other side still fails to remain parallel to the application target. However, single-side tilt levelling can independently control the boom's posture on each side, as illustrated in Figure 11(b), enabling the boom to follow asymmetric terrain changes and maintain the optimal spraying height.

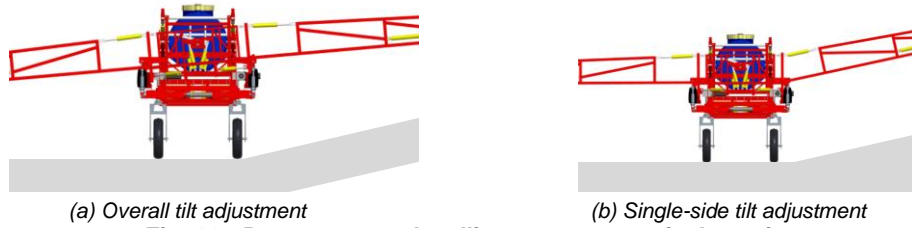


Fig. 11 - Boom contour levelling on asymmetrical terrain

The single-sided tilt adjustment test setup is shown in Fig.12, where a 10° tilted road surface was constructed beneath the right spray bar using wooden boards and cloth.



Fig. 12 - Single-sided inclination adjustment test

To prevent the spray bar from scraping against the tilted road surface, the height of the spray bar was set to 900 mm before the experiment. The adjustment thresholds were set to 20, 30, 40, and 50 mm, respectively. After stabilizing the height of the spray bar using the ground simulation levelling system, the sprayer was driven at a constant speed of 8 km/h over the tilted road surface at each of the four adjustment thresholds. Forward movement was stopped when the ultrasonic sensor detected the tilted road surface. After the spray bar height stabilized, the control system was shut down, and the angle of the right spray bar was recorded.

(4) Field spraying experiment

Water-sensitive papers were fixed to wheat plants at 25 cm intervals along the transverse direction of the spray bar to collect droplets (excluding the central 2 m of the road where the sprayer passes without wheat crops, totaling 24 water-sensitive papers). The spraying system was activated in advance to ensure that each nozzle reached the rated pressure when passing over the water-sensitive paper strip. The sprayer moved through the wheat field at a constant speed of 8 km/h. The power was turned off after the rear spray bar completely passed the water-sensitive paper strip. Once the water-sensitive papers dried naturally, they were collected into sealed bags (Liu et al., 2022). The droplet information was analyzed using the software ImagePy-master on the scanned water-sensitive papers. The experimental process is shown in Fig. 13.



Fig. 13 - Field spray test

RESULTS

The results of spray boom overall height adjustment experiment

The test results of spray boom overall height adjustment experiment are shown in Table 1.

Table 1

Results of the spray boom overall height adjustment test /mm

Target height	Adjustment threshold	Final stable height	Target height	Adjustment threshold	Final stable height	Target height	Adjustment threshold	Final stable height
/400	50	438	/500	50	531	/600	50	640
	40	420		40	517		40	626
	30	404		30	509		30	614
	20	instability		20	instability		20	instability

As shown in Table 1, when the height adjustment threshold is set between 30-50 mm, the boom profiling levelling control system stabilizes the boom height near the target value. As the adjustment threshold decreases, the overall boom height gradually approaches the target spraying height. However, when the adjustment threshold is set to 20 mm, overshoot occurs, causing the height adjustment rod to extend and retract repeatedly, failing to maintain a stable height. This instability is primarily due to the delay in the control system's input and output. The height adjustment rod maintains its previous action until it receives the next adjustment signal, leading to overshoot. Therefore, the adjustment threshold should be set to 30 mm for overall boom height adjustment.

The results of stepwise field experiment

The results of stepwise field experiment are shown in Table 2.

Table 2

Results of the stepwise field experiment

Step height/mm	Adjustment threshold/mm	Left end height/mm	Right end height/mm	Boom inclination angle/°
50	50	742	664	0.5
	40	729	675	0.35
	30	710	688	0.15
	20	/	/	/
100	50	746	670	0.5
	40	721	683	0.25
	30	714	684	0.2
	20	/	/	/

As shown in Table 2, the boom ground contour levelling control system effectively reduces the boom inclination caused by step surfaces. With different adjustment thresholds, the boom's inclination angle relative to the ground decreases as the threshold decreases. When passing over a 100 mm step surface, the boom inclination angle can be reduced to approximately 0.2°. However, with an adjustment threshold of 20 mm, an overshoot phenomenon occurs, causing the overall tilt push rod to repeatedly extend and retract, making it difficult for the boom to stabilize. The primary factor is the latency in the control system's input-output response, causing the overall tilt adjustment rod to maintain the previous adjustment action until the next signal is received, leading to overshoot. Therefore, the adjustment threshold should be set to 30 mm for the overall tilt adjustment of the boom.

The results of single-side inclination adjustment experiment

The results of Single-side inclination adjustment experiment are shown in Table 3.

Table 3

Results of the single-sided spray boom inclination adjustment test

Pavement inclination Angle /°	Adjustment threshold /mm	Right spray boom inclination angle /°	Relative error /%
10	50	9.2	8
	40	9.4	6
	30	9.6	4
	20	/	/

As shown in Table 3, the ground-following levelling control system for the spray bar effectively reduces single-sided spray bar inclination caused by uneven pavement. At different adjustment thresholds, the spray bar's inclination angle relative to the ground decreases as the adjustment threshold is reduced. When traversing a pavement with a 10° inclination angle, the single-sided spray bar can adjust to approximately 9.6°. However, when the adjustment threshold is set to 20 mm, the system experiences an overshoot phenomenon, causing repeated extensions and retractions of the single-sided tilt rod, making it difficult for the single-sided spray bar to achieve a stable state. To prevent instability caused by single-sided tilt adjustments after overall tilt adjustments, the single-sided tilt adjustment threshold is set to 40 mm.

The results of field spraying experiment

The results of the treatment of 24 water-sensitive papers were statistically analyzed. The papers on the left and right sides near the center of the road were labelled as Left 1 and Right 1, respectively. The results of the field spray test are shown in Tables 4 and 5.

Table 4

The results of the field spray test on the left side

Label	Droplet deposition coverage rate / %	Droplet deposition density / (Grain /cm ²)	Deposition amount / (μL/cm ²)
Left 1	33.44	179.33	1.26
Left 2	31.59	164.13	1.23
Left 3	35.63	172.64	1.21
Left 4	37.42	180.69	1.30
Left 5	38.71	175.38	1.25
Left 6	33.87	167.74	1.29
Left 7	39.64	181.42	1.35
Left 8	31.37	174.26	1.34
Left 9	35.79	183.97	1.27
Left 10	36.54	167.69	1.31
Left 11	34.46	171.56	1.26
Left 12	32.00	180.53	1.30

Table 5

The results of the field spray test on the right side

Label	Droplet deposition coverage rate / %	Droplet deposition density / (Grain /cm ²)	Deposition amount / (μL/cm ²)
Right 1	36.15	180.23	1.20
Right 2	34.20	168.19	1.26
Right 3	31.29	176.75	1.25
Right 4	35.49	184.46	1.31
Right 5	34.13	172.91	1.27
Right 6	34.85	183.10	1.29
Right 7	33.48	174.66	1.30
Right 8	35.69	178.43	1.29
Right 9	32.28	167.52	1.24
Right 10	37.51	171.67	1.32
Right 11	31.28	175.41	1.25
Right 12	30.66	180.42	1.34

Statistical processing was conducted on the spray test data from both sides of the nozzle to calculate the average fog droplet deposition coverage rate, the average fog droplet deposition density along the direction of the nozzle, and the coefficient of variation (CV) of deposition quantity. The results are shown in Table 6.

Table 6

Field spray test results			
Area	Average deposition coverage rate / %	Average deposition density / (Grain /cm ²)	Deposition variation coefficient (CV) / %
Left side	35.04%	174.90	3.1
Right side	33.92%	176.51	

As shown in Table 6, the average droplet deposition coverage rates on the left and right sides of the boom were 35.04% and 33.92%, respectively, and the average droplet deposition densities were 174.9 and 176.51 particles/cm², respectively. The relative errors in droplet deposition coverage and density between the two sides were minimal. The coefficient of variation (CV) of deposition along the boom direction was 3.1%, indicating that the sprayer exhibited good stability during field operations. The overall oscillation of the boom was minimal, ensuring uniform spray distribution.

CONCLUSIONS

(1) To ensure the optimal spraying height between the boom and the crop canopy, thereby improving spray quality, a five-section boom capable of ground contour following was designed. It includes a parallelogram lift mechanism, an overall tilt mechanism, and a single-side tilt mechanism. The boom height adjustment range is 360-1160 mm, the overall boom tilt angle range is -5° to 5°, and the single-side boom tilt angle range is 0° to 11°.

(2) A boom ground-following levelling control system was designed with the STM32F103ZET6 microprocessor at its core. This system employs ultrasonic distance sensors to detect the distance between the boom ends and the target objects in real-time. The microprocessor utilizes a limited amplitude averaging filter method to eliminate sudden signal interference and processes the feedback data to drive the electric actuators of each mechanism, thus adjusting the boom's position in real-time.

(3) A small electric self-propelled sprayer was used as the test platform to evaluate the performance of the boom ground-following levelling control system through various field tests. The results showed that the system performed best when the overall height adjustment threshold was set to 30 mm, the overall tilt adjustment threshold to 30 mm, and the single-side tilt adjustment threshold to 40 mm. The spray uniformity was assessed through field spray tests, which indicated that the relative error in droplet deposition coverage and density on both sides of the boom was minimal, and the coefficient of variation (CV) for deposition along the boom direction was less than 15%, ensuring good spray distribution uniformity.

ACKNOWLEDGEMENT

The research was funded by the Key R&D projects in Shaanxi Province (2024NC-YBXM-202, 2024NC-YBXM-244, 2023-YBNY-241).

REFERENCES

- [1] Ali B., Medet İ., Barış, Ö. Ö. (2023). Development and Assessment of A Novel Servo-controlled Spraying System for Real Time Adjustment of the Orientation Angle of the Nozzles of A Boom Sprayer. *Pest management science*, 79(11), 4439-4450. <https://doi.org/10.1002/ps.7644>.
- [2] An J. (2022). *Attitude Control Method and Test of Spray Rod of High Ground Clearance Pesticide Applicator*. Zibo: Shandong University of Technology.
- [3] Baltazar, A.R., Santos, F.N.D., Moreira, A. P., Valente, A., Cunha, J.B. (2021). Smarter Robotic Sprayer System for Precision Agriculture. *Electronics*, 10(17), 2061. <https://doi.org/10.3390/electronics10172061>.
- [4] Bayat, A., Itmec, M., Bolat, A. (2018). Modal Analysis of Field Sprayer Boom Design for Different Materials. *Scientific Papers-Seriesa-Agronomy*, LXI (6), 434-437.
- [5] Burgers, T. A., Gaard, J. D., Hyronimus, B. J. (2021). Comparison of Three Commercial Automatic Boom Height Systems for Agricultural Sprayers. *Applied Engineering in Agriculture*, 37(2), 287-298. <https://doi.org/10.13031/aea.14346>.
- [6] Dou, H., Zhai, C., Chen, L., Wang, X., Zou, W. (2021). Comparison of Orchard Target-Oriented Spraying Systems Using Photoelectric or Ultrasonic Sensors. *Agriculture*, 11(8), 753. <https://doi.org/10.3390/agriculture11080753>.

- [7] Dou, H., Zhai, C., Chen, L., Wang, S., Wang, X. (2021). Field Variation Characteristics of Sprayer Boom Height Using a Newly Designed Boom Height Detection System. *IEEE Access*, 9, 17148-17160. <https://doi.org/10.1109/access.2021.3053035>.
- [8] Dou, H., Wang, S., Zhai, C., Chen, L., Wang, X., Zhao, X. (2021). A LiDAR Sensor-Based Spray Boom Height Detection Method and the Corresponding Experimental Validation. *Sensors*, 21(6), 3390.
- [9] Fu, J., Chen, C., Zhao, R., Ren, L. (2020). Accurate Variable Control System for Boom Sprayer Based on Auxiliary Antidrift System. *Journal of Sensors*, 2020, 8037046. <https://doi.org/10.1155/2020/8037046>.
- [10] Lipiński, A. J., Lipiński, S., Burg, P., Sobotka, S. M. (2022). Influence of the Instability of the Field Crop Sprayer Boom on the Spraying Uniformity. *Journal of Agriculture and Food Research*, 10(9), 100432. <https://doi.org/10.1016/j.jafr.2022.100432>.
- [11] Li, J., Nie, Z., Chen, Y., Ge, D., Li, M. (2023). Development of Boom Posture Adjustment and Control System for Wide Spray Boom. *Agriculture*, 13(11), 2162. <https://doi.org/10.3390/agriculture13112162>.
- [12] Li, F., Bai, X., Su, Z., Tang, S., Wang, Z., Li, F., Yu, H. (2023). Development of a Control System for Double-Pendulum Active Spray Boom Suspension Based on PSO and Fuzzy PID. *Agriculture*, 13(9), 1660. <https://doi.org/10.3390/agriculture13091660>.
- [13] Li, F., Bai, X., Li, Y. (2020). A Crop Canopy Localization Method Based on Ultrasonic Ranging and Iterative Self-Organizing Data Analysis Technique Algorithm. *Sensors*, 20(3), 818.
- [14] Li, L., Hu, Z., Liu, Q., Yi, T., Han, P., Zhang, R., Pan, L. (2022). Effect of Flight Velocity on Droplet Deposition and Drift of Combined Pesticides Sprayed Using An Unmanned Aerial Vehicle Sprayer in A Peach Orchard. *Frontiers in Plant Science*, 13, 10129. <https://doi.org/10.3389/fpls.2022.981494>.
- [15] Liu, L., Liu, Y., He, X., Liu, W. (2022). Precision variable-rate spraying robot by using single 3D lidar in orchards. *Agronomy*, 12(10), 2509. <https://doi.org/10.3390/agronomy12102509>.
- [16] Li, C., Wu, J., Pan, X., Pan, X., Dou, H., Zhao, X., Gao, Y., Yang, S., Zhai, C. (2023). Design and Experiment of a Breakpoint Continuous Spraying System for Automatic-Guidance Boom Sprayers. *Agriculture*, 13(12), 2203. <https://doi.org/10.3390/agriculture13122203>.
- [17] Lin J., Xin W. (2022). Spray Deposition and Distribution on Rice as Affected by a Boom Sprayer with a Canopy-Opening Device. *Agriculture*, 13(1), 94. <https://doi.org/10.3390/agriculture13010094>.
- [18] Li, W., Yang, F., Mao, E., Shao, M., Sui, H., Du, Y. (2022). Design and verification of crab steering system for high clearance self-propelled sprayer. *Agriculture*, 12(11), 1893.
- [19] Llica, A., Boz, A. (2018). Design of a nozzle-height control system using a permanent magnet tubular linear synchronous motor. *Journal of Agricultural Sciences*, 24(3): 374-385. <https://doi.org/10.15832/ankutbd.456662>.
- [20] Okamoto, Y., Kameari, A., Fujiwara, K., Tsuburaya, T., Sato S. (2015). Fast Nonlinear Finite Element Analysis Using Newton-Raphson Method Implemented by Krylov Subspace Method with Relaxed Convergence Criterion. *COMPEL: The International Journal for Computation and Mathematics in Electrical and Electronic Engineering*, 34(5), 1537-1552.
- [21] Sun, X., Yang, X., Dong, X., Zhang, T., Yan, H., Wang, Z. (2020). Spray Boom Height Intelligent Adjustment System Based on Expert Control. *Transactions of the CSAM*, 32(S2), 275-282. <https://doi.org/10.3390/agriculture13091660>.
- [22] Shi, Y., Shu, X., Jiang, P., Hu, W., Lin, W., Dong, C. (2020). Design and Experimental Study on Automatic Levelling System of High Ground Gap Plant Protection System Chassis. *International Journal of Applied Systemic Studies*, 9(1), 11-25. <https://doi.org/10.1504/IJASS.2020.108656>.
- [23] Wang, G., Lan, Y., Yuan, H., Qi, H., Chen, P., Ouyang, F., Han, Y. (2019). Comparison of Spray Deposition, Control Efficacy on Wheat Aphids and Working Efficiency in the Wheat Field of the Unmanned Aerial Vehicle with Boom Sprayer and Two Conventional Knapsack Sprayers. *Applied Sciences*, 9(2), 218. <https://doi.org/10.3390/app9020218>.
- [24] Yan, J., Xue, X., Cui, L., Ding, S., Gu, W., Le, F. (2021). Analysis of Dynamic Behavior of Spray Boom Under Step Excitation. *Applied Sciences*, 11(21), 10129. <https://doi.org/10.3390/app112110129>.
- [25] Zhang, M., Hu, L., Ke, X., Tang, L., Meng, S., Du, P., Zhou, H., He, J. (2019). Design and Test of Automatic Levelling System for Spray Rod of Paddy Field Self-propelled Sprayer. *Agricultural Mechanization Research*, 41(10), 45-51.
- [26] Zürey, Z., Balci, S., Sabancı, K. (2020). Automatic Nozzle Control System with Ultrasonic Sensor for Orchard Sprayers. *European Journal of Technique*, 10(2), 264-273. <https://doi.org/10.36222/ejt.715015>.

ANALYSIS OF SOIL STRESS VARIATIONS DURING THE SEEDLING PLANTING PROCESS WITH DIRECT INSERTION SEEDLING DEVICE

直插式栽苗器栽苗过程中土壤应力变化过程分析

Fandi ZENG¹⁾, Xinchao GAO³⁾, Hongbin BAI²⁾, Ji CUI²⁾, Limin LIU¹⁾, Xuying LI²⁾, Hongwei DIAO¹⁾

¹⁾ Shandong Agriculture and Engineering University, College of Mechanical and Electronic Engineering, Jinan, China;

²⁾ Inner Mongolia Agricultural University, College of Mechanical and Electrical Engineering, Hohhot, China;

³⁾ Hebei Petroleum University of Technology, Department of Mechanical Engineering, Chengde, China;

E-mail: lixuy2000@imau.edu.cn

DOI: <https://doi.org/10.35633/inmateh-75-18>

Keywords: Greenhouse transplantation, Seedling planter, Contact stress distribution, Peak resistance

ABSTRACT

To explore the change law of contact stress distribution in the process of planting seedlings, the greenhouse transplanting equipment was developed to reduce labor intensity and improve the mechanization level of facility horticulture. This paper takes the direct insertion seedling planter as the research object, adopts the pressure distribution measurement system to study the soil stress distribution rule of different cross-section, digging depth and types of seedling planter. Both horizontal and longitudinal sections were obtained to show an increasing and then decreasing trend. The stress distribution is basically consistent at different digging depths, and the peak contact stress is roughly located at the center position. With the increasing of digging depths, the soil disturbance increases by the seedling planter and the hole tray seedlings, and the peak contact stress also shows a gradually increasing trend, leading to a gradual increase in the peak resistance of the seedling planter. The peak contact stress of the four opening seedling plant was higher than that of the three opening seedling plant. The main reason was that the soil disturbance of the four opening seedling plant increased, the peak contact stress distribution increased, and the peak resistance also increased. This study provides a basis for designing the greenhouse transplanters.

摘要

为探明栽苗过程中接触应力分布变化规律, 研制温室移栽机具, 降低劳动强度, 提高设施园艺机械化水平。本文以直插式栽苗器为研究对象, 采用压力分布测量系统研究了不同截面、不同入土深度和不同类型栽苗器的接触界面土壤应力分布变化规律。通过分析不同截面土壤应力的变化规律, 得出横向截面和纵向截面均是呈现先增加后减小的趋势。不同入土深度下接触应力分布基本一致, 接触应力峰值大致位于中心位置。随着入土深度的逐渐增加, 栽苗器、穴盘苗对接触界面土壤的扰动增加, 高应力区域占比逐渐增大, 接触应力峰值也呈现逐渐增加的趋势, 导致栽苗器的峰值阻力也呈现逐渐增大的趋势。四开口栽苗器的峰值接触应力大于三开口的栽苗器, 主要原因是由于栽苗过程中四开口栽苗器的土壤扰动量增加, 峰值接触应力分布增大, 导致峰值阻力也增大。该研究为温室移栽机具的设计提供参考。

INTRODUCTION

Seedling transplantation technology is beneficial for mitigating the impact of seasons on crops, making full use of light and heat resources, improving land use efficiency, and increasing the index of multiple cropping. With the development of seedling transplanting technology, the demand for automated greenhouse transplanting equipment is also increasing (Khadatkar et al., 2018; Jiang, 2017; Zhao et al., 2009).

At present, the change law of contact stress distribution during seedling planting is not clear, and the shape, size and operation parameters of seedling planter directly affect the contact stress distribution, and ultimately affect the planting quality. The research of greenhouse plant-transplanter has been reported abroad, mainly focusing on the effects of different seedling claws on transplantation efficiency and adaptability. These studies provide guidance for the development of greenhouse transplantation equipment (Kutz et al., 1987; Kutz, 1985; Paradkar et al., 2021; Ting et al., 1990).

Developed countries such as Japan, the United States, and Australia have developed greenhouse transplanting equipment, but its cost is high, the structure is complex, and the maintenance cost is high. It is not compatible with China's seedling cultivation technology and transplanting auxiliary operations, making it difficult to adapt to the Chinese market (Brewer *et al.*, 1994; Choi *et al.*, 2002; Simonton *et al.*, 1991; Rahul *et al.*, 2019).

In recent years, domestic scholars have also strengthened their research on greenhouse transplanting equipment. For example, Zhou *et al.*, (2009), designed an oblique wedge lever end effector, with a transplanting success rate of 76.11%. It designed a light and simple automatic transplanting machine, using two fingers and four pins to take seedlings, and transplanting experiments on 72 and 128 hole trays, respectively. The transplanting efficiency reached 1025 and 1221 plants/h, respectively, and the average transplanting success rate was 90.7% (Han *et al.*, 2016; Han *et al.*, 2015).

Cui *et al.*, (2022), designed an adjustable seedling end effector based on cylindrical cam, which can adapt to various transplanting operations with different spacing between hole trays. The success rate of transplanting is 93.33%, and the transplanting efficiency is 22 plants/min.

Tian *et al.*, (2010), designed a transplanting machine with four rows of seedling claws. The transplanting efficiency is 1800-2400 plants/h, and the transplanting success rate is 81.2%.

Yu *et al.*, (2023), designed an 8-row synchronous seedling picking mechanism with a success rate of 95% for transplantation.

Meng, 2021, developed a small space secondary clamping claw for taking seedlings, the average efficiency of transplanting was 4320 plants/h, and the success rate of transplanting could reach 97.22%.

Zhang *et al.*, (2023), designed a seedling end effector based on the principle of top clamp seedling picking, and achieved a success rate of 93.25% in seedling feeding. The pot has good integrity and meets the requirements for automatic transplanting and seedling retrieval of leafy vegetables in dry land.

In order to improve the mechanization level of facility horticulture, it is also urgent to study the change law of seedling planter, hole tray seedling and soil during the seedling planting process. Therefore, it is of great significance to study the change law of contact stress distribution in planting process to reduce planting resistance and improve planting efficiency.

The direct insertion seedling planter can quickly complete the planting of the hole tray seedlings and reduce the labor intensity. During the seedling planting process, there is an impact load between the seedling planter, hole tray seedlings, and the soil. Different soil physical properties, the structural parameters of the seedling planter, and specifications of the hole tray seedlings can affect the distribution of contact stress. It is difficult for the contact stress of soil in the theoretical state to accurately describe the stress in the complex field environment. The pressure distribution measurement system developed by the Tekscan in the United States is widely used to detect contact points and areas, contact interface shapes, and contact stresses (Komarnicki *et al.*, 2017; Stopa *et al.*, 2018). In this paper, the pressure distribution measuring system was used to carry out transplanting experiment with the direct insertion seedling plant, and the change law of soil stress distribution at the contact interface was studied under different factors. This study provides a basis for designing a greenhouse transplanter, reducing labor intensity, and improving the mechanization level of facility horticulture.

MATERIALS AND METHODS

Basic structure and motion analysis of the direct insertion seedling planter

The direct insertion seedling planter primarily consists of a tension spring, planting cylinder, pulling hook, and planting claw, as shown in Figure 1.

The planter has a height of 900 mm, a diameter of 76 mm. The planting claw opening is 140 mm in length. Its working principle involves the planting claw impacting the soil, while the puller drives the pulling hook to move the connecting ring upward. This motion causes the lower pulling hook to drive the planting claw, thereby facilitating the breakthrough of the soil. Once the seedling tray sinks to the bottom, the planting claw opens to release the seedling. The planter is then withdrawn, and the soil automatically backfills, completing the transplanting process.

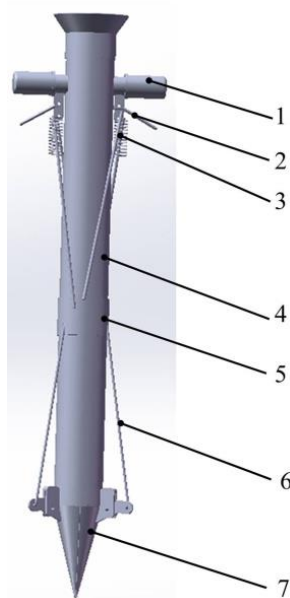


Fig. 1 – The 3D model of the direct insertion seedling planter.

1. Rubber handle. 2. Puller. 3. The tension spring. 4. Planting cylinder. 5. Connecting ring. 6. Pulling hook. 7. Planting Claw.

Sensor deployment

The pressure distribution measurement system primarily consists of the 3150 flexible thin-film network tactile pressure sensor, along with handles, computers, and other components. The core of the system is the 3150 flexible thin-film grid sensors, as shown in Figure 2. This sensor is based on a matrix that incorporates a large number of horizontal and longitudinal conductors, intersecting to form an array of stress-sensing points (Hunston. 2002; Yang *et al.*, 2018; Li. 2020). The sensing area is 435.9 mm × 368.8 mm in length × width and 0.1 mm in thickness, with a thickness of 0.1 mm. The sampling frequency of the sensor is 0~100 Hz.

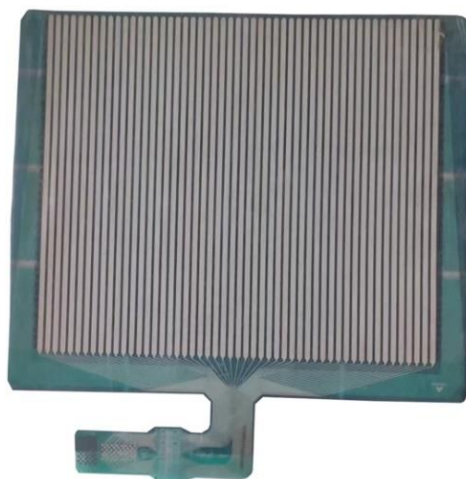


Fig. 2 - 3150 Flexible thin-film network tactile pressure sensor

To ensure the testing system records accurate data, the sensor is first calibrated. As shown in Figure 3, the sensor was placed in the middle of the black rubber pad and the transparent plastic sheet (L×W×H of 470 mm × 450 mm × 1 mm) before the test started. An acrylic frame is then placed on top. Soil is added to the acrylic frame (L × W × H of 470 mm × 450 mm × 170 mm) above the measurement system and compacted. The sensors are zeroed in preparation for the planting test.

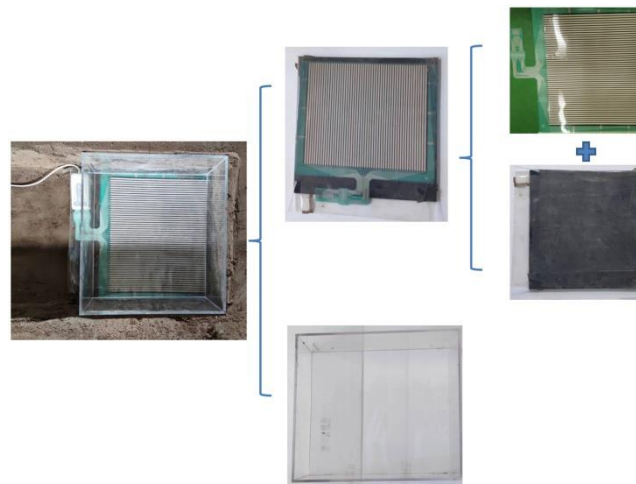


Fig. 3 - Installation of sensor

Test materials and equipment

The experiment was conducted in collaboration with Inner Mongolia Heyuan Agricultural Technology Co., Ltd., which cultivated 72 hole tray seedlings. The seedling substrate consisted of grass charcoal, vermiculite and perlite with a mass ratio of 3:1:1. The age of the seedlings was 30 d. The moisture content of the seedlings was measured between 58.78% and 62.47% using the DHG-9245A blower dryer. To study the soil stress distribution during the planting process of the direct insertion seedling planter, a contact stress distribution test bench was developed, as shown in Figure 4. The test stand mainly consists of a seedling planter, a pressure distribution measurement system, a computer and an acrylic frame. The test soil was a sandy loam and the measured soil moisture content ranged from 6.42% to 8.15%. The sensor needs to be calibrated before the test was started. The sensors were laid out in a fixed area, sieved for foreign matter such as clods and stones, and the completed sieved soil was filled into an acrylic frame and levelled off. Before testing, the sensor was calibrated, and sensors were laid out in a fixed area. The soil was sieved to remove foreign matter such as clods and stones, then filled into the acrylic frame and leveled. The sensor was zeroed before starting the test. At the end of the experiment, soil stress and pressure distribution data were retrieved from the I-Scan system. By analyzing the data at various moments and positions, the pressure distribution changes during the seedling planting process were examined. The soil compactness inside the acrylic frame was measured before each test, yielding values of 0-10 N/cm² at a depth of 100 mm.

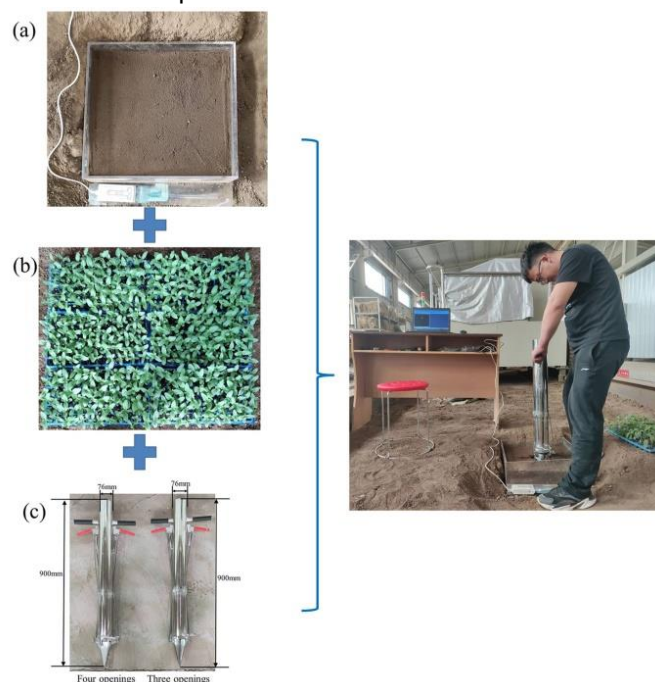


Fig. 4 - Soil stress distribution test at the contact interface during seedling planting process. (a) Sensor deployment; (b) Hole tray seedlings; (c) Different types of seedling planters

Test methods

This study investigates soil stress distribution during the seedling planting process by varying the soil depth within the acrylic frame and changing the type of seedling planter (three openings, four openings). Using a pressure distribution measurement system, peak contact stress and peak resistance pressure data were collected to analyze how soil stress distribution changes with different soil depths and planter types. The test factors and levels are shown in Table 1.

Table 1

Factors	Three axis dimensions of peanut seeds		
	Level		
	1	2	3
Digging depth[mm]	60	80	100
Type of seedling planter	Three openings		Four openings

RESULTS

Changing law of soil stress distribution in different cross sections during seedling planting process

The direct insertion seedling planter, configured with three openings and a 100 mm planting depth, was lowered at a constant speed during the planting test. A pressure distribution measurement system was used to monitor changes in soil stress at the contact interface. Low-stress areas are indicated by dark blue, high-stress areas by red, and areas with zero contact stress are colorless. Peak contact stress (Pmax) was obtained through the I-Scan system, with test results shown in Figure 5. When the soil depth of the seedling planter is 100 mm, its peak contact stress Pmax = 68 kPa. Due to the presence of a large number of horizontal and longitudinal conductors inside the sensor, it is necessary to analyze the changes in soil stress distribution during the seedling planting process in order to thoroughly study the changes in soil stress distribution at the horizontal and longitudinal sections. Both horizontal and longitudinal sections were obtained to show an increasing and then decreasing trend.

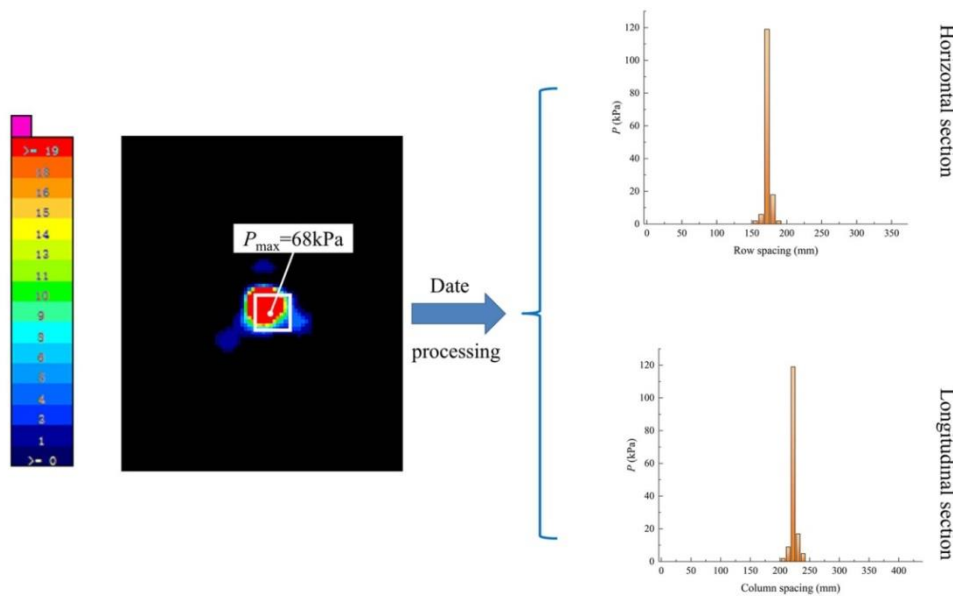


Fig. 5 - Variation of soil stress distribution in different cross sections

Effect of the contact stress distribution at different digging depths

The direct insertion seedling planter used in the experiment had three openings, with digging depths set to 60 mm, 80 mm, and 100 mm. The planter was lowered at a fixed rate during the planting tests. After the experiment, the data were processed using the I-Scan system, and the results are shown in Figure 6. The contact stress distribution remained largely consistent across different digging depths, with the peak contact stress (Pmax) generally occurring at the center.

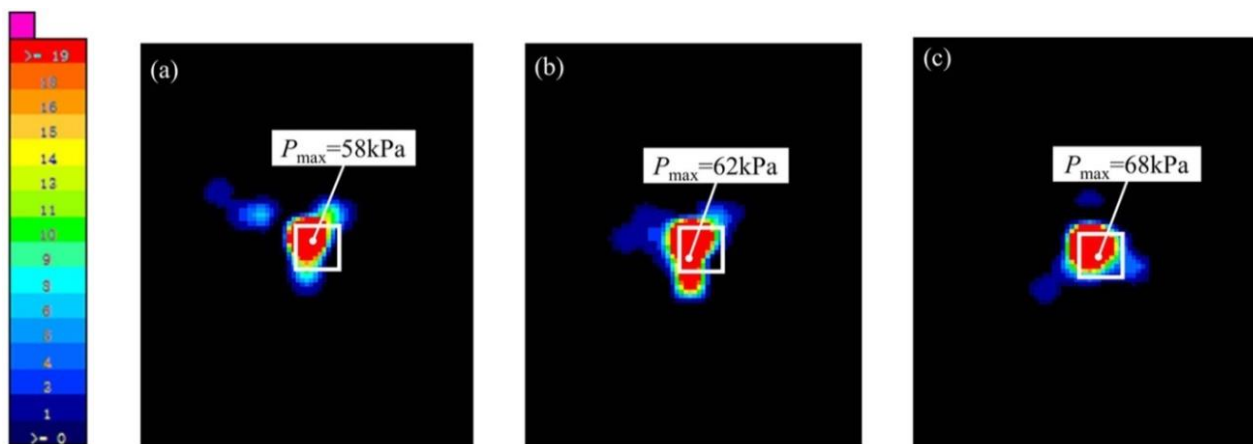


Fig. 6 - Variation of soil stress distribution at the digging depth. (a) Digging depth 60 mm; (b) Digging depth 80 mm; (c) Digging depth 100 mm

The direct insertion seedling planter compresses and shears the soil, causing soil particles to shift. At the same time, the planter experiences a reaction force from the soil, which represents the resistance encountered during planting. To further investigate the contact stress distribution, the variation in peak resistance at different digging depths was examined, as shown in Figure 7. As the digging depth of soil increases, the soil disturbance and the seedlings increases, the contact area gradually increases, and the peak resistance also shows a gradually increasing trend.

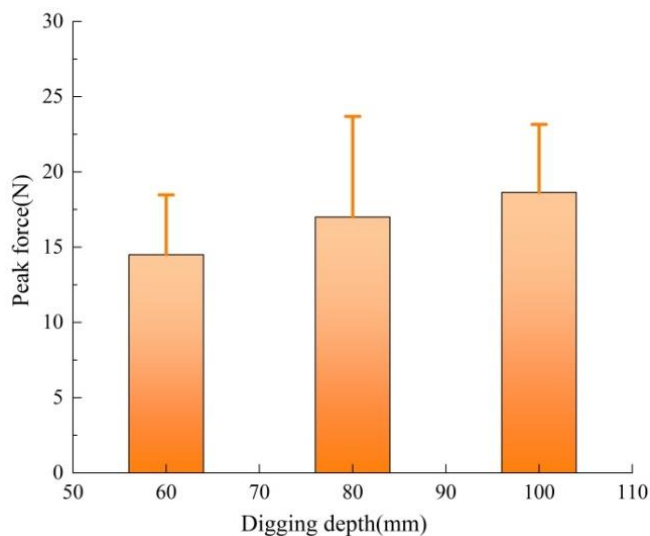


Fig. 7 - Variation changes of peak resistance at the digging depth.

Influence of contact stress distribution in different types of seedling planters

The digging depth of the direct insertion seedling planter is 80 mm, and the types of seedling planters are three or four openings. The planter is lowered at a fixed speed for seedling planting experiments. A pressure distribution measurement system was used to track changes in soil stress distribution. The experimental results are shown in Figure 8. The contact stress distribution in different types of seedling planters is basically consistent, and the peak contact stress (P_{max}) is roughly located at the center, with high stress areas occupying the main area. The peak contact stress of the four opening seedling planter is greater than that of the three opening seedling planter. The main reason is that the four opening seedling planter has more planting claws than the three opening seedling planter, which increases the soil disturbance, leading to an increase in the distribution of peak contact stress.

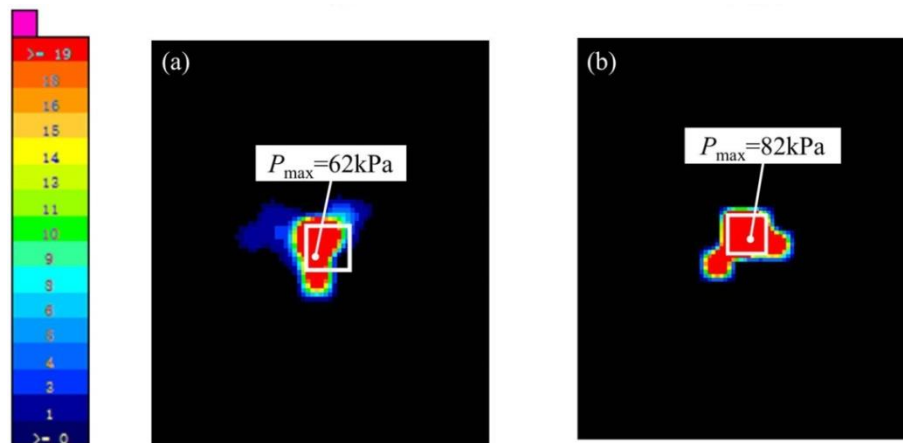


Fig. 8 - Variation of soil stress distribution in different types of seedling planters. (a) Seedling planter with three openings; (b) Seedling planter with four openings

To further study the contact stress distribution, it is necessary to study the variation of peak resistance of different types of seedling planters, as shown in Figure 9. The peak resistance of the four opening seedling planter is greater than that of the three opening seedling planter, mainly due to the increased soil disturbance caused by the four opening seedling planter during the seedling planting process, which increases the distribution of peak stress and leads to an increase in peak resistance.

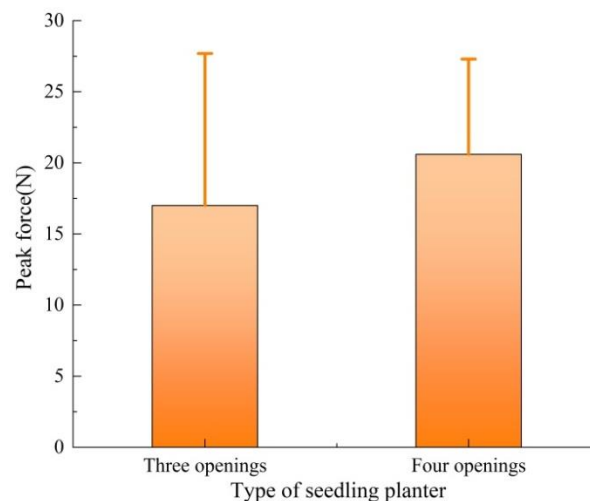


Fig. 9 - Variation changes of the peak resistance in different types of seedling planters

Discussion

This paper takes the direct insertion seedling planter as the research object, adopts the pressure distribution measurement system to study the soil stress distribution rule of different cross-section, digging depth and types of seedling planter. Both horizontal and longitudinal sections were obtained to show an increasing and then decreasing trend. The stress distribution is basically consistent at different digging depths, and the peak contact stress is roughly located at the center position. With the increasing of soil depth, the soil disturbance increases by the seedling planter and the hole tray seedlings, and the peak contact stress also shows a gradually increasing trend, leading to a gradual increase in the peak resistance of the seedling planter. The peak contact stress of the four opening seedling planter was higher than that of the three opening seedling planter. The main reason was that the soil disturbance of the four opening seedling planter increased, the peak contact stress distribution increased, and the peak resistance also increased. However, the labor intensity of the direct insertion seedling planter is still relatively high, and there are problems such as uneven depth during the actual seedling planting process, resulting in significant changes in the experimental data of soil stress distribution. Therefore, it is reasonable to choose the type of seedling planter and design the greenhouse direct insertion transplanter to reduce labor intensity and improve the mechanization level of facility horticulture.

CONCLUSIONS

This paper takes the direct insertion seedling planter as the research object, adopts the pressure distribution measurement system to study the soil stress distribution rule of different cross-section, digging depth and types of seedling planter. The main conclusions are as follows:

1) Both horizontal and longitudinal sections were obtained to show an increasing and then decreasing trend. The stress distribution is basically consistent at different digging depths, and the peak contact stress is roughly located at the center position. With the increasing of digging depth, the soil disturbance increases by the seedling planter and the hole tray seedlings, and the peak contact stress also shows a gradually increasing trend, leading to a gradual increase in the peak resistance of the seedling planter.

2) The peak contact stress of the four opening seedling planter was higher than that of the three opening seedling planter. The main reason was that the soil disturbance of the four opening seedling planter increased, the peak contact stress distribution increased, and the peak resistance also increased.

ACKNOWLEDGEMENT

This project was funded by National Natural Science Foundation of China (NSFC) (32160423) and Shandong Agriculture and Engineering University Start-Up Fund for Talented Scholars (2024GCCZR-05). We also appreciate the work of the editors and the reviewers of the paper.

REFERENCES

- [1] Brewer, H. L. (1994). Conceptual modeling automated seedling transfer from growing trays to shipping modules. *Transactions of the ASAE*, 37(4), 1043-1051.
- [2] Choi, W. C., Kim, D. C., Ryu, I. H., & Kim, K. U. (2002). Development of a seedling pick-up device for vegetable transplanters. *Transactions of the ASAE*, 45(1), 13.
- [3] Cui, Y. J., Wei, Y. Z., Ding, X. T., Cui, G. P., He, Z., & Wang, M. H. (2022). Design and experiment of adjustable spacing end-effector based on cylindrical cam(基于圆柱凸轮的株距可调式取苗末端执行器设计与试验). *Transactions of the CSAM*, 53(01), 104-114+122.
- [4] Han, L. H., Mao, H. P., Yan, L., Hu, J. P., Huang, W. Y., & Dong, L. L. (2015). Pincette-type end-effector using two fingers and four pins for picking up seedlings (穴盘育苗移栽机两指四针钳夹式取苗末端执行器). *Transactions of the chinese society for agricultural machinery*, 46(07), 23-30.
- [5] Han, L. H., Mao, H. P., Hu, J. P., Xu, J. Y., Zhao, Z. R., & Ma, G. X. (2016). Design and test of automatic transplanter for greenhouse plug seedlings (温室穴盘苗自动移栽机设计与试验). *Transactions of the Chinese Society for Agricultural Machinery*, 47(11), 59-67.
- [6] Hunston, M. (2002). Innovative thin-film pressure mapping sensors. *Sensor Review*, 22(4), 319-321.
- [7] Jiang, Z. H. (2017). *Optimal design if automatic transplanter in greenhouse and force analysis for transplanting process* (温室钵苗移栽机的优化设计及移栽过程力学分析) [Doctor's thesis], Zhejiang University.
- [8] Khadatkar, A., Mathur, S., & Gaikwad, B. (2018). Automation in transplanting. *Current science*, 115(10), 1884-1892.
- [9] Komarnicki, P., Stopa, R., Kuta, Ł., & Szyjewicz, D. (2017). Determination of apple bruise resistance based on the surface pressure and contact area measurements under impact loads. *Computers and electronics in agriculture*, 142, 155-164.
- [10] Kutz, L., Miles, G., Hammer, P., & Krutz, G. (1987). Robotic transplanting of bedding plants. *Transactions of the ASAE*, 30(3), 586-0590.
- [11] Kutz, L. J. (1985). *Robotic transplanting of bedding plants: simulation and validation (application, greenhouse, computer-aided design)* [Doctor's thesis], Purdue University.
- [12] Li, X. (2020). Based on the high-speed photography technique, the motion analysis and experiment of the seedling feeding mechanism for casting holes and discs (基于高速摄影技术的喂苗机构抛投穴盘苗运动分析与试验) [Master's thesis], Inner Mongolia Agricultural University.
- [13] Meng, Q. X. (2021). *Design and experiment of variable spacing transplanting equipment for hydroponic leafy vegetable seedlings* (水培叶菜种苗变间距移植装备设计与试验) [Master's thesis], Zhejiang Sci-Tech University.

- [14] Paradkar, V., Raheman, H., & Rahul, K. (2021). Development of a metering mechanism with serial robotic arm for handling paper pot seedlings in a vegetable transplanter. *Artificial Intelligence in Agriculture*, 5, 52-63.
- [15] Rahul, K., Raheman, H., & Paradkar, V. (2019). Design and development of a 5R 2DOF parallel robot arm for handling paper pot seedlings in a vegetable transplanter. *Computers and electronics in agriculture*, 166, 105014.
- [16] Simonton, W. (1991). Robotic end effector for handling greenhouse plant material. *Transactions of the ASAE*, 34(6), 2615-2621.
- [17] Stopa, R., Szyjewicz, D., Komarnicki, P., & Kuta, Ł. (2018). Limit values of impact energy determined from contours and surface pressure distribution of apples under impact loads. *Computers and electronics in agriculture*, 154, 1-9.
- [18] Tian, S. B., Qiu, L. C., Kondo, N. S., & Yuan, T. (2010). Development of automatic transplanter for plug seedling. *IFAC Proceedings Volumes*, 43(26), 79-82.
- [19] Ting, K. C., Giacomelli, G. A., Shen, S. J., & Kabala, W. P. (1990). Robot workcell for transplanting of seedlings part II-end-effector development. *Transactions of the ASAE*, 33(3), 1013-1017.
- [20] Yang, L. J., Zhang, Y., Liu, D. H., Xu, B. P., & Liu, C. X. (2016). Early recognition for dairy cow lameness based on pressure distribution measurement system(基于压力分布测量系统的奶牛跛行早期识别). *Transactions of the CSAM*, 47(S1), 426-432.
- [21] Yu, G. H., Wang, X. L., Liu, J. G., Ye, B. L., Li, X., & Zhao, X. (2023). Design and experiment of multi row seedling taking mechanism for dense planting and transplanting of vegetable pot seedlings(蔬菜钵苗密植移栽机多行取苗机构设计与试验). *Transactions of the Chinese Society for Agricultural Machinery*, 54(01), 94-103.
- [22] Zhao, Y. S., & Yu, H. Y. (2009). The Current Situation and Inspiration of Industrialized Seedling Cultivation in Foreign Countries. *World Agriculture*, (12), 47-48.
- [23] Zhou, T., Wang, X. C., Wang, C. Q., Zheng, L., Li, X. B., Qiao, X. J., & Wang, C. (2009). Design and simulation analysis of greenhouse cavity tray seedling transplanter. *Mechanical Design and Research*, 25(02), 121-124.
- [24] Zhang, X. D., Liu, L. J., Ning, Y. C., Kong, D. H., Liu, Y. Q., & Wu, H. H. (2023). Design and Experiment of End Effector of Seedling Taking by Jacking and Clamping of Vegetable Transplanter(蔬菜移栽机顶夹式取苗装置末端执行器设计与试验). *Transactions of the Chinese Society for Agricultural Machinery*, 54(S1), 115-124+134.

OPTIMIZING WALNUT SHELL MECHANICAL PROPERTIES FOR EFFICIENT SHELL-CRACKING USING HEAT TREATMENTS: A COMPARATIVE STUDY OF RADIO FREQUENCY AND HOT AIR HEATING METHODS

通过热处理优化核桃壳力学性能以实现高效脱壳：射频和热风加热的对比研究

Yaohuo GAO¹⁾, Jundang LU²⁾, Xiaoxi KOU^{*1)}

¹⁾ College of Mechanical and Electronic Engineering, Northwest A&F University, Yangling, Shaanxi 712100, China;

²⁾ Shaanxi Agri-machinery Research Institute, Xianyang, Shaanxi 712099, China

Tel: +86-2987092319; E-mail: kouxiaoxi@nwfau.edu.cn

Corresponding author: Xiaoxi Kou

DOI: <https://doi.org/10.35633/inmateh-75-19>

Keywords: Walnut shell-cracking, Radio frequency heat treatment, Mechanical properties, Moisture content, Compression tests

ABSTRACT

The mechanical properties of walnuts play an influential role in the process of walnut shell-cracking. To determine the optimal mechanical properties of walnuts, the effect of moisture content (MC) on the mechanical properties of walnuts was investigated. The results showed that Rupture force (F), Rupture displacement (D), and Rupture energy (E) of walnuts decreased proportionally with a reduction in the MC. To select an optimal pre-treatment for enhancing the mechanical properties of walnuts prior to shell-cracking, the effects of radio frequency (RF) and hot air (HA) heating treatment to change the mechanical properties of the walnuts were examined. The results indicated that the heating treatments of walnuts could lead to a brittle and easily breakable shell, with the F decreasing from 231.99 ± 34.31 N to 174.73 ± 24.89 N, the D decreasing from 1.68 ± 0.18 mm to 1.36 ± 0.13 mm, and the E decreasing from 207.31 ± 44.29 mJ to 119.47 ± 25.99 mJ. The mechanical properties of walnut shells are optimized to the best condition with the application of either a 2-minute RF treatment, a 3-minute RF treatment, or an 8-minute HA treatment. Notably, RF heating is significantly more time-efficient compared to the HA treatment. Quality evaluation indicated that there were no significant ($p > 0.05$) changes in color values, hardness, and brittleness between the heat-treated walnut kernels and the untreated walnut kernels. Overall, the results obtained from this study demonstrate that RF heating treatment is an effective method for optimizing the mechanical properties of walnuts prior to shell-cracking, and the results may provide guidance for the design and improvement of walnuts shell-cracking processes.

摘要

核桃的力学性能是影响核桃破壳效果的重要因素。为了获取最优的力学性能，研究了含水率对核桃力学性能的影响。结果表明，核桃的破壳力、破壳位移和破壳能均随着含水率的降低而降低。为了确定核桃破壳之前最佳的预处理方法，研究了射频(RF)加热处理和热风(HA)加热处理对核桃力学性能的影响。结果表明，加热处理使核桃壳变脆易碎， F 从 231.99 ± 34.31 N 降至 174.73 ± 24.89 N， D 从 1.68 ± 0.18 mm 降至 1.36 ± 0.13 mm， E 从 207.31 ± 44.29 mJ 降至 119.47 ± 25.99 mJ；其中，在 RF 2min、RF 3min、HA 8min 三种加热处理方法下，核桃的力学性能达到最优；并且与 HA 加热处理相比，RF 加热处理大大缩短了加热时间。品质分析结果表明，加热处理后的核桃和未处理的核桃仁的颜色值、硬度和脆性没有显著变化 ($p > 0.05$)。本研究的结果表明，RF 加热处理是优化核桃力学性能的有效方法，此研究结果可为核桃破壳工艺的设计和改进行提供指导。

INTRODUCTION

Walnuts (*Juglans regia* L.) are cultivated worldwide, with the global production of in-shell walnuts reaching approximately 3.87 million metric tons in 2022 (FAOSTAT, 2022). Walnut kernels, renowned for their significant medicinal value, are rich in a variety of unsaturated fatty acids, which have been shown to effectively reduce serum cholesterol, blood pressure, and the risk of heart disease (Guasch-Ferré, et al., 2017; Turek & Wszolek, 2021). The process of walnut shell-cracking is a pivotal step in the primary processing of walnuts, directly influencing the quality of the end product (Liu et al., 2021). There is a substantial price disparity among walnut kernels, with whole walnuts significantly outpricing their fragmented counterparts. This price gap is primarily attributed to the integrity of the walnut kernels; intact kernels fetch a higher market price due to their

superior quality and strong consumer demand. However, the task of cracking walnut shells presents a challenge, as they are predominantly composed of lignin and hemicellulose, which make them hard and resistant to breakage (Antreich *et al.*, 2019; Shi *et al.*, 2023). Moreover, the minimal gap between the shells and kernels complicates the separation process, hindering the achievement of a high whole kernel yield (Zhang *et al.*, 2022; Wang *et al.*, 2023).

Current studies on walnut shell-cracking methods primarily include multi-point extrusion (Zhang *et al.*, 2022), impact (Cao *et al.*, 2017), combined force (Wang *et al.*, 2024), and flexible-belt shearing extrusion (Liu *et al.*, 2016), among others. It is also possible to adjust parameters such as speed, angle and spacing to optimize the adaptability of the machine to different types and sizes of walnuts (Liu, *et al.*, 2021). However, the current technology for obtaining whole walnut kernels is not satisfactory and people continue to rely on manual labor to extract whole walnut kernels. Manual walnut shell-cracking methods are fraught with issues, including low processing efficiency, high costs, and concerns over food hygiene. Therefore, there is an urgent need for the development of equipment and methods that can achieve a high whole kernel yield.

Moisture content (MC) is a critical parameter in nut production, with studies demonstrating its significant impact on the rupture force, rupture energy, specific deformation, and elastic modulus of nut shells (Altuntas & Erkol, 2011; Maghsoudi *et al.*, 2012). In conventional engineering, heat treatment is a convenient, economical, and swift method to modify MC. Common heat treatment methods for agricultural products include hot air (HA) heating (Chen *et al.*, 2020), radio frequency (RF) heating (Mao *et al.*, 2021), microwave heating (Wang *et al.*, 2022), and other thermal processes.

RF energy, a non-ionizing form of electromagnetic waves ranging from 3 kHz to 300 GHz, generates heat through the frictional interaction of polarized molecules and charged ions within a product in response to RF fields (Ling *et al.*, 2023). As an emerging technology based on electromagnetic waves, RF heating possesses advantages such as high heating rates, volumetric heating, selective heating, and energy efficiency (Kou *et al.*, 2019; Zuo *et al.*, 2022). For tree nuts, such as hazelnuts and walnuts, RF heating has been applied for various purposes, including pasteurization (Zhang Ma, & Wang, 2021), disinfestation (Wang *et al.*, 2007), and drying (Wang, Tang, & Zhao, 2021). Concurrently, heat treatment can alter the mechanical properties of materials (Gao, Li, & Chen, 2023; Hao, *et al.*, 2021; Wang, *et al.*, 2020). Therefore, the effect of RF heating on the mechanical properties of walnuts warrants investigation and comparison with conventional HA heating.

Therefore, the objectives of this study were to (1) compare the effects of different MC on the mechanical properties of walnuts, (2) compare the changing in mechanical properties of walnuts under different heating treatments, and (3) evaluate walnut kernel quality under different heating treatments.

MATERIALS AND METHODS

Pre-Experiments Investigating the Impact of MC on Walnut Mechanical Properties

Walnut samples were procured from the Xinjiang Production and Construction Corps, with the cultivar selected being Wen 185. To mitigate moisture loss and damage to the walnuts, the green walnuts underwent drying and compression tests following the removal of the green husk and washing. The initial MC of the walnut shells was $31.30 \pm 2.14\%$ following the AOAC Official Method 925.40 (AOAC, 2002). A drying treatment was processed for the walnuts to obtain samples at different MC, then followed by compression tests to study the effect of MC on mechanical properties of walnuts.

For each HA drying experiment, the preset temperature was set at 60°C to ensure kernel quality (Man, *et al.*, 2024). Based on the experiments conducted on the relationship between MC and HA drying time, walnuts with HA drying times of 0, 4, and 10 hours were selected for compression experiments. After each HA drying session of the walnuts was completed, they were cooled to room temperature and compression tests were carried out immediately, with each test group repeated five times. The walnuts were dried to approximately 8% MC, placed in ziplock bags, and stored in a dry room for use in the subsequent part of the study.

Compression test and mechanical parameters

An electronic universal testing machine (DDL10, Changchun, China) was used for the compression test with an effective force range of 0–10 KN and a loading speed range of 0.01–1000 mm/min (Fig 1). The compression system mainly consists of a computer, a compression structure, and sensors. Upon commencement of the actual compression process, the deformation of the specimen induces varying forces. The sensors are capable of detecting these force and displacement changes, subsequently conveying this data to the computer for analysis.

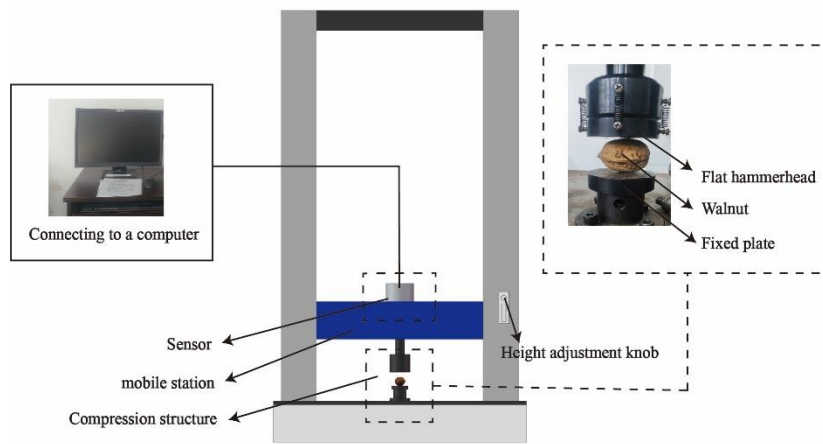


Fig. 1 – Schematic diagram of Mechanical Compression System

As depicted in Fig. 1, the compression experiment was conducted along the thickness direction of the walnuts. A flat hammer head was chosen for the compression, and the compression speed was set at 10 mm/min. Fig. 2 shows a typical force-displacement curve for compressed walnuts. It is evident from Fig. 2 that the compressive deformation process of the walnuts can be bifurcated into two distinct stages: an initial elastic deformation stage, prior to rupture, followed by a crack expansion stage post-rupture. The mechanical properties of walnut kernels are predominantly characterized by three parameters: rupture force (F), rupture displacement (D), and rupture energy (E). F (N) and D (mm) represent the force and displacement at the point of fracture, respectively, obtained from the data points exported from the electronic universal testing machine. The E (mJ) was determined from the chart by measuring the area under the force-deformation curves (Koyuncu, Ekinci, & Savran, 2004). By numerically integrating the force and displacement data points in the 0-D compression range derived from the electronic universal testing machine using the compound trapezoidal formula, the value of E can be derived as follows (Sauer, 2011):

$$E = \int_0^D f(x) dx \approx \frac{h}{2} \left(y_0 + y_m + 2 \sum_{i=1}^{m-1} y_i \right) \tag{1}$$

where:

D (mm) is the transverse coordinate of the rupture point, the value of m is the number of data points minus 1 in the 0-D interval for each set of compression tests, $h = D/m$, y_i (N) are the values of the longitudinal coordinates of each data point.

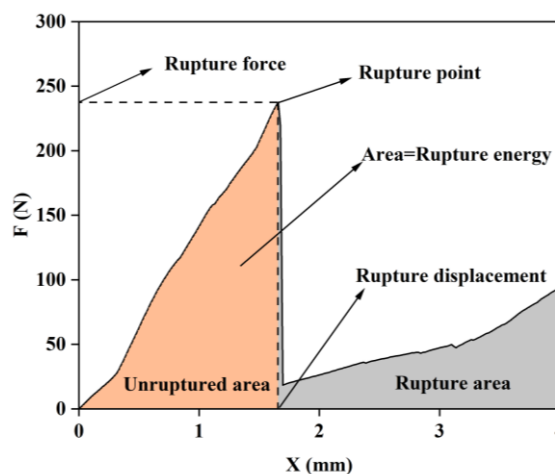


Fig. 2 – The classic force-displacement diagram of a walnut, showing the definitions of Rupture force (N), Rupture displacement (mm), and Rupture energy (mJ)

RF heating treatment

A 6 kW, 27.12 MHz free-running oscillator RF system (SO6B, Strayfield International, Wokingham, UK) associated with a HA system supplied by a 6 kW electric heater (Fig. 3) was used to heat walnuts (Wang *et al.*, 2010).

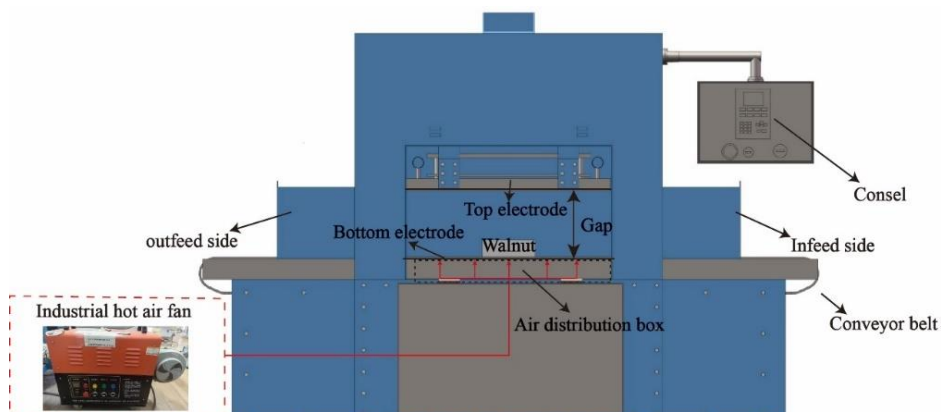


Fig. 3 – Schematic diagram of RF system

Approximately 750 g of the walnut samples were placed in a plastic container (300 mm × 250 mm × 80 mm) made of PP (Fig. 4a), which had a perforated bottom wall to allow HA to pass through the sample from the bottom, effectively expelling water vapor during the process. Before each heat treatment, the walnuts underwent a brief surface wetting procedure to clean and maintain them in the same initial conditions. According to the method proposed by Jiao *et al.* (2012), the electrode gap of 100 mm was selected for improve the evaporation of the water on the walnut surface. To obtain the optimum heating effect, the RF treatment time was carried out for 1, 2, and 3 min, respectively. To evaluate the effect of RF heating on the mechanical properties of walnuts, 15 walnuts were used in the compression test and labelled to occupy one quarter of the plastic container (Fig. 4b).

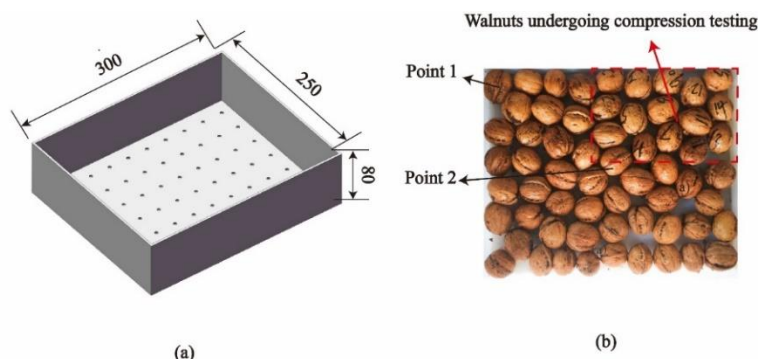


Fig. 4 – Arrangement of heat-treated walnut and fiber optic insertion point (a), shape and size of box (b) (mm)

Two methods were used to record the temperature during the heating process. Two probes of a six-channel fiber-optic temperature sensor system (HQ-FTS-D120, Heqi Technologies Inc., Xian, China) were inserted into two walnuts in the center of the vessel through pre-drilled holes in the walnut shells (Fig. 4b). The samples were photographed with an infrared thermographic camera (A300, FLIR System, NH, U.S.) to obtain the temperature distribution on the walnuts surface. After the walnuts had completed the RF heating, the samples were quickly removed from the RF chamber. The heated 15 labelled walnuts were then quickly transferred to an electronic universal testing machine for compression testing (approximately 15 minutes).

HA heating treatment

To evaluate the effect of HA heating on the mechanical properties of walnuts and compare it with RF heating treatment, an electrically heated blast heater (DGG-AGG-9030A, Shanghai, China) was used to heat the walnuts (Fig. 5). The temperature of 60°C was selected in the HA heating test same as the HARF heating (Zhang *et al.*, 2016). The walnuts were placed in plastic containers and the containers were placed in an electric radiation drying oven (Fig 5a).

The temperatures of the kernel and shell of walnuts were measured separately using a six-channel fiber-optic temperature sensor system and an infrared camera. Based on the thermal characteristics of HA heating, 8 minutes (the average temperature of walnut shells was not significantly different from that of RF heating for 2 minutes) was selected as the experimental temperature for comparison with the optimal treatment of RF heating. Similar to the RF heating treatment, 15 walnuts used for the compression experiment were placed in a quarter of the plastic container (Fig. 4b). When the HA heating of the walnuts was completed, the walnuts were quickly transferred to the electronic universal testing machine to complete the compression test (approximately 15 min).

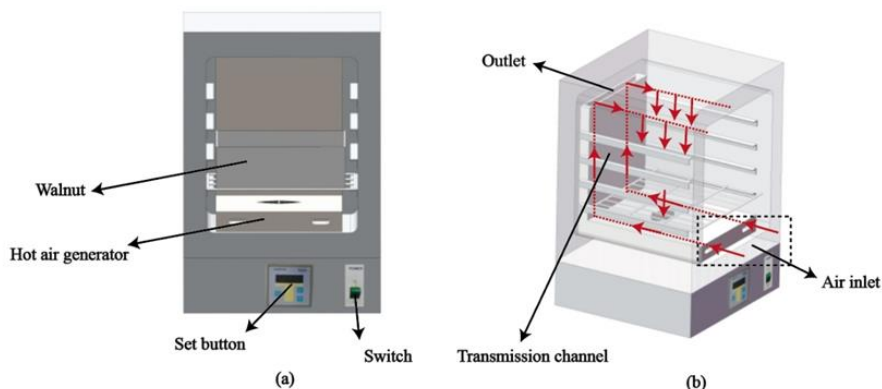


Fig. 5 – Schematic diagram of HA heating system

Evaluation of walnut kernels quality

The color of walnut kernel samples was measured with a computer vision system (CVS) reported before (Tang *et al.*, 2008). Photographs of the samples taken by the camera were utilized to capture the values of L^* , a^* , and b^* of samples as follows (Hou, Ling, & Wang, 2015; Kong *et al.*, 2007):

$$L^* = \frac{L}{2.5} \quad (2)$$

$$a^* = \frac{240}{250} a - 120 \quad (3)$$

$$b^* = \frac{240}{250} b - 120 \quad (4)$$

where:

L^* denote the brightness values of walnut kernels, a^* stand for the red-green values of walnut kernels, and b^* indicate the blue-yellow values of walnut kernels. The color values of walnut kernels from untreated, RF 1min, RF 2min, RF 3min, and HA 8min walnuts were measured using the aforementioned method on five separate occasions.

Hardness and brittleness of walnut kernels were determined using a texture analyzer (TA.XTC-18, Baosheng Industrial Development Co., Ltd., Shanghai, China) fitted with a TA/2 cylindrical probe (Jiao *et al.*, 2022). A quarter of the walnut kernels were placed on a flat surface, a compression test was applied using a cylinder probe, and a test speed of 1.0 mm/s. Texture properties were measured and calculated by the given software.

RESULTS AND DISCUSSION

Effect of water content

The changes in MC of walnut shells after HA drying are shown in Fig 6. The MC of walnut shells decreased as the drying time increased, with the drying rate gradually decreasing, which was in accordance with the typical drying curves of food and agricultural materials (Chen *et al.*, 2020). Walnuts were selected for compression tests with the MC of $31.30 \pm 2.14\%$, $14.27 \pm 1.99\%$, and $6.49 \pm 0.46\%$, corresponding to the drying time of 0, 4, and 10 hours, respectively. The results showed that the values of F, E, and D decreased significantly as the MC decreased (Fig. 7). This observation indicates that when the MC is high, the shell has a greater resistance to cracking. The lower MC tends to result in walnut shells with reduced mechanical properties, making them more susceptible to breakage. However, there was no significant changes between

the D and E values when the MC was below $14.27 \pm 1.99\%$. It can be concluded that the mechanical properties of walnuts do not change significantly at a certain level of MC and that further reduction of the MC of walnuts will only increase the cost.

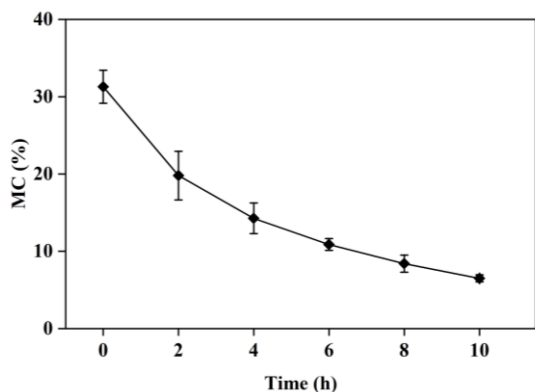


Fig. 6 –Drying curve of the sample (mean \pm SD of two replicates)

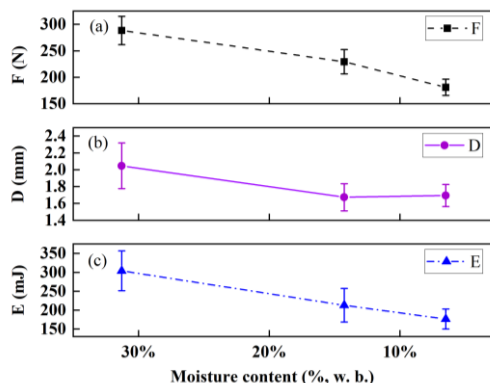


Fig. 7 –Samples rupture force-MC (a), rupture displacement-MC (b) and rupture energy-MC (c) (mean \pm SD of five replicates)

Evaluation of RF heating treatment

Fig. 8 illustrates the heating profiles of walnuts at both the edge and center positions. The heating rate of the walnut at the edge is higher than at the center due to the edge effect of RF heating, which is consistent with the findings of other researchers (Dong *et al.*, 2023; Hou, Zhang, & Wang, 2021). After three minutes of heating, the highest temperature inside the walnut only reached $57.95^{\circ}\text{C} \pm 2.33^{\circ}\text{C}$, which helps to preserve the quality of the walnut kernels. From Fig. 9, it is evident that the *F* value significantly declined, whereas the alterations in *D* and *E* are less discernible, when the heating time is 1 min. This observation can be explained by the minimal water evaporation (approximately 46.77%) and the low surface temperature (approximately 44.06°C) of the walnut shells during the heating process. Consequently, the mechanical properties of the walnut shell remain largely unaltered. As shown in Fig. 9 (b) and Fig. 9 (c), the *D* value of walnuts were 1.66 ± 0.16 mm, 1.36 ± 0.13 mm and 1.39 ± 0.14 mm, and the *E* value of walnuts were 152.51 ± 40.81 mJ, 119.47 ± 25.99 mJ and 120.45 ± 29.28 mJ, subjected to the heating time of 1, 2, and 3 min, respectively. The mechanical properties of walnuts show no significant changes after more than 2 minutes of RF treatment. This may be due to the fact that the water on the surface of the walnuts was almost evaporated after 2 minutes (approximately 82.25%, no significant from the time of 3 min), and longer heating time did not significantly affect the mechanical properties of the walnuts. As shown in Figure 10, after 1 minute of RF treatment, the walnut surfaces displayed multiple low-temperature zones, indicating residual unevaporated water. As the treatment duration extended to 2 minutes, these low-temperature areas became inconspicuous, suggesting that the water on the walnut surfaces had substantially evaporated. This observation underscores the effectiveness of RF treatment in accelerating the evaporation process, efficiently removing water from the walnut surfaces.

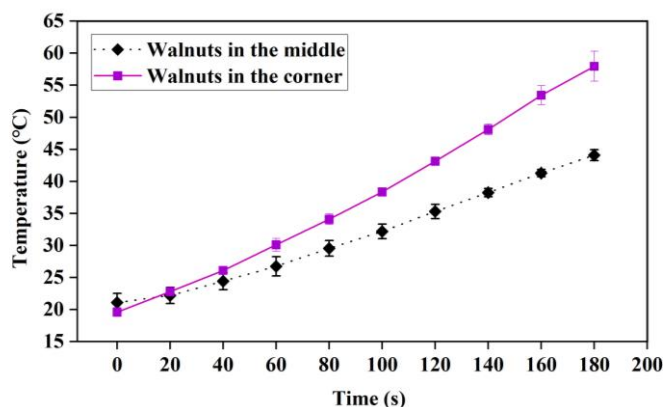


Fig. 8 – Heating curves of the interior of walnuts located in the edges and middle of the box (mean \pm SD of two replicates)

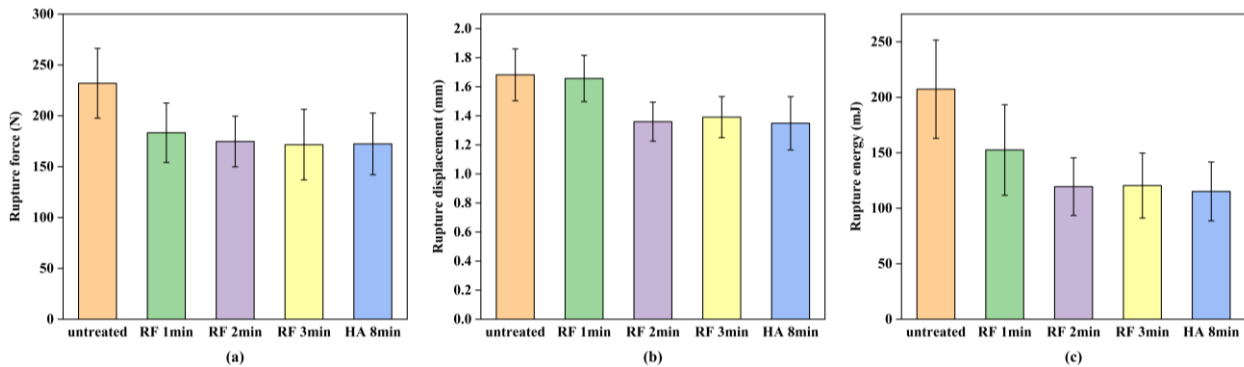


Fig. 9 – Changes in rupture force (a), rupture displacement (b) and rupture energy (c) after heating treatment (mean ± SD of fifteen replicates)

Comprehensive evaluation of HA heating and RF heating

In Fig. 8 and Fig. 11 it is demonstrated that RF heating achieves a higher heating rate compared to HA heating. The HA heating process requires 8 minutes to raise the average temperature of the walnut shell to about 50°C, whereas RF treatment accomplishes this in just 2 minutes. Table 1 shows the effect of different heating times for RF and HA on the mechanical properties of walnuts. According to the different mechanical properties of the walnuts, the walnuts were classified into three grades: A, B and C. Grade A (RF 2min, RF 3min, HA 8min): The mechanical properties of the walnut shells have been optimized to the greatest extent possible, resulting in a brittle and easily breakable shell. Grade B (RF 1min): An initial improvement in the mechanical properties of the walnut shells is observed, indicated by a significant reduction in F; however, there is no significant reduction in D, which is the factor most associated with kernel damage. Grade C (untreated): The walnuts remain untreated, resulting in tough shells that are difficult to break open to extract the kernels. Consequently, utilizing RF heating for 2 min represents the optimal pre-treatment strategy prior to the process of walnut shell-cracking.

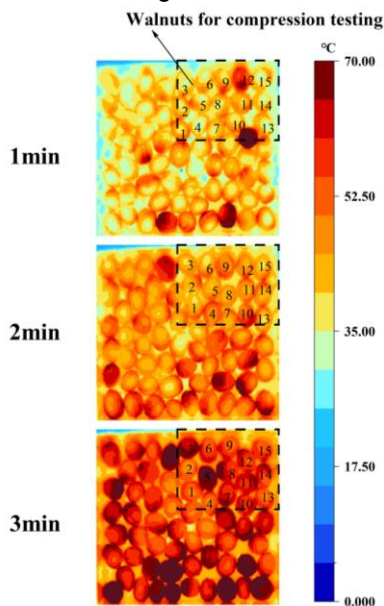


Fig. 10 – Temperature distribution of walnut surface after different RF treatment times

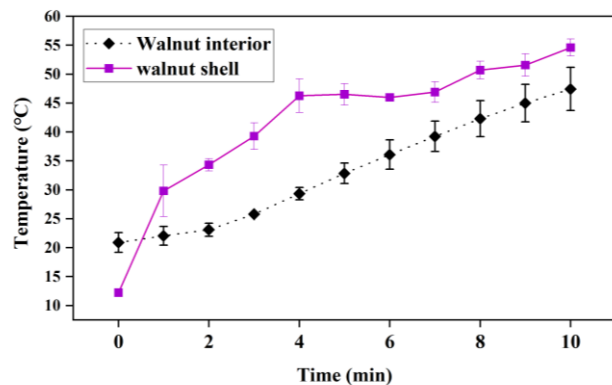


Fig. 11 – Heat-up curves of walnut shell and kernel under 60°C HA heating (mean ± SD of two replicates)

Table 1

Mechanical properties of walnuts under different heating treatments (mean ± SD of fifteen replicates)					
Variable	untreated	RF 1 min	RF 2 min	RF 3min	HA 8min
<i>F</i> (N)	231.99±34.31 ^{a#}	183.35±29.18 ^b	174.73±24.89 ^b	171.60±34.72 ^b	172.39±30.28 ^b
<i>D</i> (mm)	1.68±0.18 ^a	1.66±0.16 ^a	1.36±0.13 ^b	1.39±0.14 ^b	1.35±0.18 ^b
Mechanical properties of walnuts under different heating treatments (mean ± SD of fifteen replicates)					

Variable	untreated	RF 1 min	RF 2 min	RF 3min	HA 8min
<i>E</i> (mJ)	207.31±44.29 ^a	152.51±40.81 ^a	119.47±25.99 ^b	120.45±29.28 ^b	115.14±26.52 ^b
Grade	C	B	A	A	A

(#Different lower-case letters within a row indicate that means are significantly different at $P < 0.05$ among different treatments.)

Quality evaluation

The quality of walnut kernels was analyzed. As demonstrated in Table 2, there was no significant effect on the hardness, brittleness, and color values of the walnuts ($p > 0.05$), when RF treatment was applied for 1, 2, and 3 minutes, or HA treatment for 8 minutes. This is because the heating time is short (less than 8 min) and the heating temperature is low (not exceed 60°C). RF heat treatment, which changes the mechanical properties of the shell, does not affect the quality of the kernel while changing the mechanical properties of the shell. This process is suitable for industrial applications.

Table 2
System irrigation test Quality parameters of walnut kernel samples treated by under different heating treatments (mean ± SD of five replicates)

variable	untreated	RF 1 min	RF 2 min	RF 3min	HA 8min
Hardness (gf)	1043.71±256.22 ^a #	1001.54±179.73 ^a	1099.31±79.35 ^a	1204.64±251.07 ^a	1058.73±218.28 ^a
Frangibility (gf)	761.53±124.92 ^a	757.58±170.46 ^a	816.97±154.45 ^a	664.31±88.10 ^a	790.28±172.24 ^a
<i>L</i> *	45.39±3.16 ^a	46.37±2.43 ^a	48.89±3.76 ^a	47.87±1.03 ^a	48.33±2.77 ^a
<i>a</i> *	5.91±1.00 ^a	6.31±0.90 ^a	5.44±0.97 ^a	5.51±0.27 ^a	5.87±0.67 ^a
<i>b</i> *	26.47±1.24 ^a	25.94±0.78 ^a	25.55±1.19 ^a	25.22±1.58 ^a	26.91±0.83 ^a

(#Different lower-case letters within a row indicate that means are significantly different at $P < 0.05$ among different treatments.)

CONCLUSIONS

The objective of this paper was to propose a method for optimizing the mechanical properties of walnut shells by a heating treatment. The results of the heating treatment experiments demonstrated that 2-minute RF, 3-minute RF, and 8-minute HA heating treatments were effective in reducing the *F*, *D*, and *E* values of walnuts. Among them, under 2-minute RF treatment, *F* decreased from 231.99±34.31 N to 174.73±24.89 N, *D* decreased from 1.68±0.18 mm to 1.36±0.13 mm, and *E* decreased from 207.31±44.29 mJ to 119.47±25.99 mJ, which will help to crack the walnut shells. Moreover, 2-minute RF can significantly reduce time costs compared to other methods, making it the optimal treatment process for walnut shell-cracking. The results of the quality analysis demonstrated that the 2-minute RF process had no significant ($p > 0.05$) effects on the hardness, brittleness and color values of walnut kernels, making it suitable for industrial application. Future research may be conducted to investigate the impact of RF heating on the performance of walnut shell-cracking machinery.

REFERENCES

- [1] Altuntas, E., & Erkol, M. (2011). The effects of moisture content, compression speeds, and axes on mechanical properties of walnut cultivars. *Food and Bioprocess Technology*, 4(7), 1288-1295. <https://doi.org/10.1007/s11947-009-0283-y>
- [2] Antreich, S., Xiao, N., Huss, J. C., Horbelt, N., Eder, M., Weinkamer, R., & Gierlinger, N. (2019). The puzzle of the walnut shell: a novel cell type with interlocked packing. *Advanced Science*, 6(16), 1900644. <https://doi.org/10.1002/advs.201900644>
- [3] AOAC. (2002). *Official methods of analysis of AOAC international*. Maryland: Gaithersburg.

- [4] Chen, C., Venkatasamy, C., Zhang, W., Deng, L., Meng, X., & Pan, Z. (2020). Effect of step-down temperature drying on energy consumption and product quality of walnuts. *Journal of Food Engineering*, 285, 110105. <https://doi.org/10.1016/j.jfoodeng.2020.110105>
- [5] Cao, C., Sun, S., Ding, R., Li, B., & Wang, S. (2017). Experimental study on mechanical characteristics of nut rupturing under impact loading. *International Journal of Agricultural and Biological Engineering*, 10(1), 53-60. <https://doi.org/10.3965/ij.ijabe.20171001.2331>
- [6] Dong, J., Kou, X., Liu, L., Hou, L., Li, R., & Wang, S. (2021). Effect of water, fat, and salt contents on heating uniformity and color of ground beef subjected to radio frequency thawing process. *Innovative Food Science & Emerging Technologies*, 68, 102604. <https://doi.org/10.1016/j.ifset.2021.102604>
- [7] FAO STAT. (2022). Food and agriculture organization. <https://www.fao.org/faostat/zh/#home>
- [8] Gao, Y. Q., Li, L., & Chen, Y. (2023). Adding gaseous ammonia with heat treatment to improve the mechanical properties of spruce wood. *Holzforschung*, 77(6), 416-425. <https://doi.org/10.1515/hf-2022-0179>
- [9] Guasch-Ferré, M., Liu, X., Malik, V. S., Sun, Q., Willett, W. C., Manson, J. E., Rexrode, K. M., Li, Y., Hu, F. B., & Bhupathiraju, S. N. (2017). Nut consumption and risk of cardiovascular disease. *Journal of the American College of Cardiology*, 70(20), 2519-2532. <https://doi.org/10.1016/j.jacc.2017.09.035>
- [10] Hao, X. M., Wang, Q. Y., Wang, Y. H., Han, X., Yuan, C. L., Cao, Y., Lou, Z. C., & Li, Y. J. (2021). The effect of oil heat treatment on biological, mechanical and physical properties of bamboo. *Journal of Wood Science*, 67(1), 26-40. <https://doi.org/10.1186/s10086-021-01959-7>
- [11] Hou, L., Ling, B., & Wang, S. (2015). Kinetics of color degradation of chestnut kernel during thermal treatment and storage. *International Journal of Agricultural and Biological Engineering*, 8(4), 106-115. <https://doi.org/10.3965/ij.ijabe.20150804.1477>
- [12] Hou, L. X., Zhang, S., & Wang, S. J. (2021). Numerical analysis of disinfesting and quality of chestnuts during combined radio frequency and hot air heating based on single particle approach. *Postharvest Biology and Technology*, 171, 111340. <https://doi.org/10.1016/j.postharvbio.2020.111340>
- [13] Hussain, S. Z., Ammatullah, B., Kanojia, V., Reshi, M., Naseer, B., & Naik, H. R. (2018). Design and development of technology for walnut cracking. *Journal of Food Science and Technology*, 55(12), 4973-4983. <https://doi.org/10.1007/s13197-018-3435-0>
- [14] Jiao, Q., Lin, B., Mao, Y., Jiang, H., Guan, X., Li, R., & Wang, S. (2022). Effects of combined radio frequency heating with oven baking on product quality of sweet potato. *Food Control*, 139, 109097. <https://doi.org/10.1016/j.foodcont.2022.109097>
- [15] Jiao, S., Johnson, J. A., Tang, J., & Wang, S. (2012). Industrial-scale radio frequency treatments for insect control in lentils. *Journal of Stored Products Research*, 48, 143-148. <https://doi.org/10.1016/j.jspr.2011.12.001>
- [16] Kong, F. B., Tang, J., Rasco, B., Crapo, C., & Smiley, S. (2007). Quality changes of salmon (*Oncorhynchus gorbuscha*) muscle during thermal processing. *Journal of Food Science*, 72(2), S103-S111. <https://doi.org/10.1111/j.1750-3841.2006.00246.x>
- [17] Kou, X., Li, R., Zhang, L., Ramaswamy, H., & Wang, S. (2019). Effect of heating rates on thermal destruction kinetics of *Escherichia coli* atcc25922 in mashed potato and the associated changes in product color. *Food Control*, 97, 39-49. <https://doi.org/10.1016/j.foodcont.2018.10.019>
- [18] Koyuncu, M. A., Ekinici, K., & Savran, E. (2004). Cracking characteristics of walnut. *Biosystems Engineering*, 87(3), 305-311. <https://doi.org/10.1016/j.biosystemseng.2003.11.001>
- [19] Ling, B., Ramaswamy, H. S., Lyng, J. G., Gao, J., & Wang, S. (2023). Roles of physical fields in the extraction of pectin from plant food wastes and byproducts: A systematic review. *Food Research International*, 164, 112343. <https://doi.org/10.1016/j.foodres.2022.112343>
- [20] Liu, M., Li, C., Cao, C., Wang, L., Li, X., Che, J., Yang, H., Zhang, X., Zhao, H., He, G., & Liu, X. (2021). Walnut fruit processing equipment: academic insights and perspectives. *Food Engineering Reviews*, 13(4), 822-857. <https://doi.org/10.1007/s12393-020-09273-6>
- [21] Liu, M. Z., Li, C. H., Zhang, Y. B., Jia, D. Z., Yang, M., & Hou, Y. L. (2016). Semi-theoretical analyses on mechanical performance of flexible-belt shearing extrusion walnut shell crushing. *Applied Engineering in Agriculture*, 32(4), 459-467. <https://doi.org/10.13031/aea.32.11269>
- [22] Maghsoudi, H., Khoshtaghaza, M. H., Minaei, S., & Dizaji, H. Z. (2012). Fracture resistance of unsplit pistachio (*Pistacia vera* L.) nuts against splitting force, under compressive loading. *Journal of Agricultural Science and Technology*, 14(2), 299-310. <http://jast.modares.ac.ir/article-23-1391-en.html>

- [23] Man, X., Li, L., Fan, X., Zhang, H., Lan, H., Tang, Y., & Zhang, Y. (2024). Drying kinetics and mass transfer characteristics of walnut under hot air drying. *Agriculture*, 14(2), 182-197. <https://doi.org/10.3390/agriculture14020182>
- [24] Mao, Y., Wang, P., Wu, Y., Hou, L., & Wang, S. (2021). Effects of various radio frequencies on combined drying and disinfestation treatments for in-shell walnuts. *LWT-Food Science & Technology*, 144, 111246. <https://doi.org/10.1016/j.lwt.2021.111246>
- [25] Sauer, T. (2011). *Numerical Analysis* (2nd ed.). Upper Saddle River, NJ: Pearson.
- [26] Shi, Q., Wang, W., Zhang, H., Bai, H., Liu, K., Zhang, J., Li, Z., & Zhu, W. (2023). Porous biochar derived from walnut shell as an efficient adsorbent for tetracycline removal. *Bioresource Technology*, 383, 129213. <https://doi.org/10.1016/j.biortech.2023.129213>
- [27] Tang, Z., Mikhaylenko, G., Liu, F., Mah, J.-H., Pandit, R., Younce, F., & Tang, J. (2008). Microwave sterilization of sliced beef in gravy in 7-oz trays. *Journal of Food Engineering*, 89(4), 375-383. <https://doi.org/10.1016/j.jfoodeng.2008.04.025>
- [28] Turek, K., & Wszolek, M. (2021). Comparative study of walnut and camelina sativa oil as a functional components for the unsaturated fatty acids and conjugated linoleic acid enrichment of kefir. *LWT-Food Science & Technology*, 147, 111681. <https://doi.org/10.1016/j.lwt.2021.111681>
- [29] Wang, L., Xu, P., Yin, H., Yue, Y., Kang, W., Liu, J., & Fan, Y. (2023). Fracture resistance biomechanisms of walnut shell with high-strength and toughening. *Advanced Science*, 10(27), 2303238. <https://doi.org/10.1002/adv.202303238>
- [30] Wang, M., Tang, Z., Zhang, B., & Li, Y. (2022). Differences in breaking behavior of rice leaves under microwave and naturally drying processes. *International Journal of Agricultural and Biological Engineering*, 15(1), 89-100. <https://doi.org/10.25165/j.ijabe.20221501.6400>
- [31] Wang, S., Monzon, M., Johnson, J. A., Mitcham, E. J., & Tang, J. (2007). Industrial-scale radio frequency treatments for insect control in walnuts II: Insect mortality and product quality. *Postharvest Biology and Technology*, 45(2), 247-253. <https://doi.org/10.1016/j.postharvbio.2006.12.020>
- [32] Wang, S., Tiwari, G., Jiao, S., Johnson, J. A., & Tang, J. (2010). Developing postharvest disinfestation treatments for legumes using radio frequency energy. *Biosystems Engineering*, 105(3), 341-349. <https://doi.org/10.1016/j.biosystemseng.2009.12.003>
- [33] Wang, W., Tang, J., & Zhao, Y. (2021). Investigation of hot-air assisted continuous radio frequency drying for improving drying efficiency and reducing shell cracks of inshell hazelnuts: The relationship between cracking level and nut quality. *Food and Bioprocess Processing*, 125, 46-56. <https://doi.org/10.1016/j.fbp.2020.10.013>
- [34] Wang, X. Z., Cheng, D. L., Huang, X. N., Song, L. L., Gu, W. L., Liang, X. Y., Li, Y. J., & Xu, B. (2020). Effect of high-temperature saturated steam treatment on the physical, chemical, and mechanical properties of Moso bamboo. *Journal of Wood Science*, 66(1), 9-20. <https://doi.org/10.1186/s10086-020-01899-8>
- [35] Wang, Y., Wang, Z., Liu, M., Wan, S., & Zhang, C. (2024). Design and evaluation of pneumatic impact-twisting combined walnut fixed posture shell-breaking mechanism. *Journal of Food Process Engineering*, 47(2), e14553. <https://doi.org/10.1111/jfpe.14553>
- [36] Zhang, B., Zheng, A., Zhou, L., Huang, Z., & Wang, S. (2016). Developing hot air-assisted radio frequency drying for in-shell walnuts. *Emirates Journal of Food and Agriculture*, 28(7), 459-467. <https://doi.org/10.9755/ejfa.2016-03-286>
- [37] Zhang, H., Liu, H., Zeng, Y., Tang, Y., Zhang, Z., & Che, J. (2022). Design and performance evaluation of a multi-point extrusion walnut cracking device. *Agriculture*, 12(9), 1494. <https://doi.org/10.3390/agriculture12091494>
- [38] Zhang, L., Ma, H., & Wang, S. (2021). Pasteurization mechanism of *S. aureus* ATCC 25923 in walnut shells using radio frequency energy at lab level. *LWT-Food Science & Technology*, 143, 111129. <https://doi.org/10.1016/j.lwt.2021.111129>
- [39] Zuo, Y., Zhou, B., Wang, S., & Hou, L. (2022). Heating uniformity in radio frequency treated walnut kernels with different size and density. *Innovative Food Science & Emerging Technologies*, 75, 102899. <https://doi.org/10.1016/j.ifset.2021.102899>

EFFECTS OF MOISTURE CONTENT ON MECHANICAL CRUSHING PERFORMANCE OF SOYBEAN SEEDS AND ITS APPLICATION IN MECHANIZED HARVESTING

含水率对大豆种子机械破碎性能的影响及其在机械化收获中的应用

Panpan LI¹, Zheng LIU², Jin WANG², Lulu LV¹, Anqi JIANG¹, Han YAN¹, Chengqian JIN^{1,2}

¹ School of Agricultural Engineering and Food Science, Shandong University of Technology, Zibo, Shandong, China;

² Nanjing Institute of Agricultural Mechanization, Ministry of Agriculture and Rural Affairs, Nanjing, Jiangsu, China

Tel: +8615366092900; E-mail: jinchengqian@caas.cn

DOI: <https://doi.org/10.35633/inmateh-75-20>

Keywords: Soybean Seeds, Moisture Content, Mechanical Properties, Breakage Rate, Mechanized Harvesting

ABSTRACT

This study addresses the issue of grain crushing during the mechanical harvesting of soybeans, systematically analyzing the effect of moisture content on its mechanical crushing characteristics. Single-factor and multi-factor orthogonal experimental methods were employed to record the grain crushing process through compression tests combined with high-speed camera technology, enabling a quantitative analysis of moisture content, loading speed, compression direction, and their interactions. Field experiments were conducted in five different planting areas. The results confirmed that when the moisture content was controlled within the range of 13% to 17%, the grain crushing force could be maintained at a stable level between 137 N and 182 N. Simultaneously, the crushing rate was reduced to a minimum value of $2.15\% \pm 0.43\%$, generally remaining within a favorable range of 1.09% to 3.34%. The research findings provide a necessary theoretical basis for improving the design of key components of harvesting machinery.

摘要

本研究针对大豆机械收获过程中的籽粒破碎问题，系统分析含水率对其力学破碎特性的影响，采用单因素试验和多因素正交试验方法，通过压缩试验并结合高速摄像技术记录籽粒破碎过程，对含水率、加载速度、压缩方向及其交互作用进行定量分析。在五个不同种植区域开展田间试验，结果验证当含水率控制在 13%-17% 范围内时，籽粒压破力能够保持在 137N~182N 之间的稳定水平，此时破碎率降至最低值 $2.15\% \pm 0.43\%$ ，总体维持在 1.09%~3.34% 的良好范围内。研究结果为改进收获机械关键部件的设计提供了重要的理论依据。

INTRODUCTION

Soybeans are a vital global source of oil and protein, holding an indispensable role in modern agriculture and the food industry (Anderson et al., 2019; Mariashibu et al., 2013). In 2023, the area dedicated to soybean cultivation in China reached 10.47 million hectares, yielding a total of 20.84 million tons. However, this production is insufficient to meet domestic demand, leading to substantial annual imports of 99.409 million tons (National Bureau of Statistics, 2024; Wang, 2024; National Agricultural and Rural Economic Operation, 2024). As global demand continues to increase, large-scale mechanized harvesting has become essential for enhancing efficiency and reducing costs.

Nevertheless, high seed breakage rates during mechanical harvesting significantly impact both harvest efficiency and product quality (Gao et al., 2010; Liu et al., 2017; Fernando et al., 2004). Research has demonstrated that seed moisture content is a critical factor influencing breakage, as it affects the mechanical properties of seeds and, consequently, their integrity during harvest (Chen et al., 2010; Krishnan et al., 2014). Therefore, improving soybean harvest quality, reducing seed breakage rates, and minimizing harvest losses to decrease import dependency have become particularly crucial objectives. Theoretically, lowering seed breakage rates is an effective strategy to enhance harvest quality, with current domestic mechanized harvesting exhibiting an approximate 5% breakage rate, highlighting an urgent need for optimization.

Domestic and international scholars have conducted extensive research that has yielded significant findings regarding the relationship between seed moisture content and mechanical properties. Waelti et al. (1969) pioneered the quantification of moisture content's impact on breakage rates through mathematical relationships, establishing a foundation for subsequent research. Chowdhury et al. (1975), in corn kernel studies, demonstrated that seed breakage rates increase significantly with rising moisture content, indicating

¹ Panpan Li, MS. Stud. Eng; Zheng Liu, Ph.D. Eng; Jin Wang, MS. Stud. Eng; Lulu Lv, MS. Stud. Eng; Anqi Jiang, MS. Stud. Eng; Han Yan, Stud. Eng; Chengqian Jin, Prof

that variations in moisture directly influence seed mechanical behavior. *Zhang et al. (2017)* further revealed that the chemical composition and moisture content of soybeans significantly affect their hardness, with moisture levels playing a crucial role in mechanical properties and breakage characteristics. Additionally, *Resende et al. (2013)* investigated the mechanical properties of brown rice and paddy under varying moisture contents, finding enhanced compression resistance at higher moisture levels, which highlights the key role of moisture content in determining the compression resistance of different crops. *Kang et al. (2021)* conducted compression tests to analyze the influence of moisture content on breakage rates across various soybean varieties, further expanding the application of moisture content in soybean harvesting processes. In other crop studies, *Dong et al. (2009)* discovered a negative correlation between moisture and mechanical properties within specific moisture ranges during mechanical tests on rice, providing valuable insights into understanding seed breakage behavior at different moisture contents. *Yang et al. (2015)* studied the friction characteristics of millet seeds, while *Qiu et al. (2019)* explored the effects of millet variety and moisture content on mechanical properties. *Teng et al. (2020)* investigated the influence of external factors on the mechanical characteristics of different soybean varieties. These research outcomes have enriched theories and provided a solid theoretical foundation.

Building on these research foundations, this study employs soybean seed moisture content as the primary experimental variable. Through systematic compression experiments, high-speed imaging technology is innovatively utilized to record seed breakage processes in real time, comprehensively analyzing the effects and interactions of moisture content, loading speed, and force direction on seed breakage rates. Furthermore, by combining field trial data from multiple cultivation regions, the practical impact of moisture content on seed breakage rates is verified, key mechanical properties are identified as evaluation indicators, and ultimately the optimal moisture content range is determined for minimizing breakage rates. Results indicate that controlling moisture content between 13% to 17% can reduce seed breakage rates to $2.15\% \pm 0.43\%$, which is significantly better than the current mechanized harvesting level of approximately 5%. This research provides a scientific basis for optimizing soybean mechanical harvesting parameters and improving harvest quality, while also offering important theoretical support and engineering references for enhancements in harvesting machinery component design. Ultimately, it achieves the goals of reducing seed breakage rates, minimizing harvest losses, and enhancing soybean harvest quality, contributing to a decreased dependency on soybean imports.

MATERIALS AND METHODS

Experimental Protocol

This study systematically investigates the effects of moisture content, loading speed, and force direction on the breakage characteristics of soybean seeds. Six distinct moisture content levels (8%, 10%, 14%, 19%, 23%, and 27%) were precisely prepared using drying and spray humidification methods. In the compression tests, moisture content, loading speed, and direction were established as experimental variables to comprehensively analyze seed breakage characteristics, with compression failure force serving as the evaluation index. Notably, high-speed imaging technology was employed to capture and record real-time dynamic changes during seed breakage, providing direct evidence for an in-depth analysis of seed breakage characteristics under varying conditions.

To ensure the scientific validity and reliability of experimental data, moisture content adjustments and measurements strictly adhered to the national standard "Grain and Oilseed Inspection - Moisture Determination Method" (GB/T 5497-1985) (*State Administration of Grain and Reserve, 1985*). Additionally, mechanical testing procedures followed to the American Society for Testing and Materials (ASTM) "Standard Practices for Force Calibration and Verification of Testing Machines" (ASTM E4-24) (*ASTM International, 2024*). During the moisture adjustment process, the amount of water to be added or removed was precisely calculated using the equation (1) (*Faryal Fatima et al., 2025*).

$$W = m \times \frac{M_t - M_i}{1 - M_t} \quad (1)$$

where: W represents the target water quantity to be added or removed; m represents the initial sample mass; M_t represents the target moisture content; M_i represents the initial moisture content.

Experimental Equipment

In this experiment, the PM-8188-A moisture meter, manufactured by KETT Corporation, USA (as shown in Figure 1(a)), was utilized to measure the moisture content of the samples. This device maintains a measurement error within $\pm 0.3\%$, ensuring precise moisture content measurements. To further enhance the reliability and representativeness of the data, each sample was measured five times, and the average value was recorded as the final result.

The mechanical testing system utilizes the Instron 3340 Series single-column tabletop universal testing machine, manufactured by Instron Corporation, USA, as illustrated in Figure 1(b). This equipment provides load and strain measurement accuracy within $\pm 0.5\%$, ensuring reliable support for the precise acquisition of mechanical data. The testing machine system primarily consists of the following core components: a Force Sensing System that measures the force applied to the sample, equipped with a built-in Force Sensor for accurate force data collection; a Controller that precisely adjusts the loading rate and monitors the entire testing process; and the Computer-Aided Data Acquisition and Display Unit, located on the left side of Figure 1(b), which facilitates real-time data acquisition, display, and storage, thereby making the experimental process and results more intuitive and manageable.

To achieve high-precision recording of the dynamic fracture behavior of soybean grains under applied force, the testing system incorporates a Phantom series high-speed camera manufactured by Vision Research Inc. (VRI), USA, as illustrated on the right side of Figure 1(b). This camera offers a high resolution of 1280×800 pixels and a maximum frame rate of up to 76,000 frames per second, ensuring comprehensive capture of the grain's transient fracture process. Furthermore, the system is equipped with specialized power source and control components to ensure stable operation of the entire setup and facilitate reliable data acquisition.

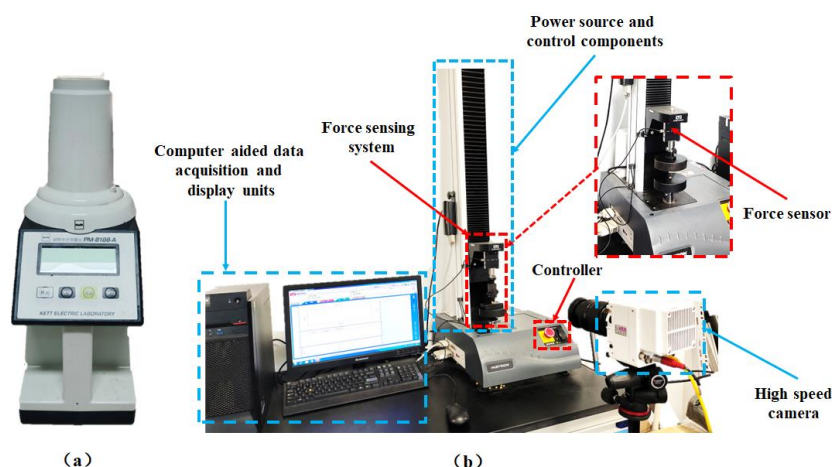


Fig. 1 - Composition of experimental equipment and testing system

(a) PM-8188-A Moisture Meter; (b) Instron 3340 Series Universal Testing Machine and Phantom High-Speed Imaging System.

Experimental Methods and Procedures

In the soybean grain compression test, the stable loading and precise stopping of the upper indenter and fixed platform must be carefully controlled to ensure the reliability of the test data. As illustrated in Figure 2, soybean grains are positioned horizontally at the center of the fixed platform. Through precise manual adjustment, the upper indenter is gradually lowered until the gap between the indenter and the soybean grain is less than 5 mm. This predetermined gap helps form a stable contact surface at the beginning of loading, effectively reducing stress fluctuations caused by rapid loading. During compression, the high-speed camera's angle and position are adjusted to clearly capture the complete fracture process of the soybean grain under compression. This image capture technique not only records the progressive deformation characteristics of the soybean grain but also provides reliable, visual data support for subsequent force analysis and fracture mechanism studies. When irreversible morphological changes in the soybean grain (such as cracking or fracturing) are observed, the downward movement of the upper indenter is immediately stopped to prevent excessive fracturing from interfering with experimental data.

Figure 2 illustrates the force application on soybean grains from different directions, covering three typical modes of compression force application: (a) Vertical Compression, where the upper indenter applies force vertically onto the grain; (b) Lateral Compression, which simulates horizontal lateral compression acting on the grain; and (c) Symmetrical Horizontal Compression, achieving symmetric loading on the grain in the horizontal direction. For each compression mode, the deformation process of the soybean grain between the upper indenter and the fixed platform is visually presented using corresponding mechanical schematic diagrams. The design of these three different loading modes facilitates a comprehensive analysis of the fracturing behavior of soybean grains under various force conditions encountered during actual harvesting. This approach provides systematic experimental support for a multi-perspective analysis of the mechanical properties of soybean grains.

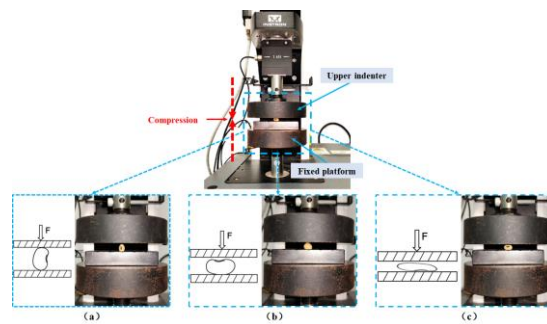


Fig. 2 - Schematic diagram of soybean grain compression loading
 (a) Vertical Compression; (b) Lateral Compression; (c) Symmetrical Horizontal Compression.

RESULTS

Analysis of the Single-Factor Effect on Crushing Force

In this experiment, the moisture content of soybean grains, machine loading speed, and compression orientation were selected as the primary test factors, with the crushing force of the grains serving as the evaluation metric. A systematic analysis was conducted to observe the variation patterns of crushing force under different conditions. A single-factor analysis approach was adopted, meaning that while keeping two other test factors constant, the working parameters of the factor under study were adjusted to perform compression tests. This approach enabled an investigation into each test factor's influence on the soybean grains' crushing force.

Based on the Compression Force-Displacement curve in Figure 3 and the staged images of a compression fracture in Figure 4, this study systematically analyzes soybean grains' force variation and fracturing behavior during the Symmetrical Horizontal compression process. High-speed imaging technology was used to fully capture the entire process from initial loading to final fracture, providing an intuitive basis for an in-depth exploration of the compression fracture mechanism of soybean grains. Figure 3 quantitatively displays the changes in crushing force with displacement across different stages. In contrast, Figure 4 presents the morphological evolution and internal structural changes of the grains at five critical moments, making the physical process of compression fracture more visually accessible.

The compression fracture process of soybean grains can be distinctly divided into five characteristic stages. In the initial non-contact stage (0–0.2 mm, Stage 1), as shown in Figure 4(a), the upper platen has not yet made contact with the grain, and the crushing force remains zero. Upon entering the initial contact stage (0.2–0.6 mm, Stage 2), as shown in Figure 4(b), the force-displacement curve exhibits slight fluctuations, and preliminary indentations appear on the grain surface. In the subsequent linear deformation stage (0.6–1.4 mm, Stage 3), as depicted in Figure 4(c), the force continues to increase, minor cracks form within the grain, and the force-displacement relationship shows a significant linear trend, indicating that the grain retains substantial structural rigidity. Upon reaching the unloading stage (1.4–1.6 mm, Stage 4), as illustrated in Figure 4(d), the applied force reaches a critical value (approximately 130–140 N), with prominent internal cracks developing, and localized collapse and separation occur. The crushing force begins to decrease, indicating a gradual loss of the grain's load-bearing capacity. In the final irreversible stage (1.6–1.8 mm, Stage 5), as shown in Figure 4(e), continuous pressure causes internal cracks to expand further, ultimately leading to complete structural failure. The force-displacement curve stabilizes, indicating that the grain has fully entered an irrecoverable fractured state. This process vividly illustrates the complete mechanical behavior of soybean grains, transitioning from elastic deformation to final fracture.

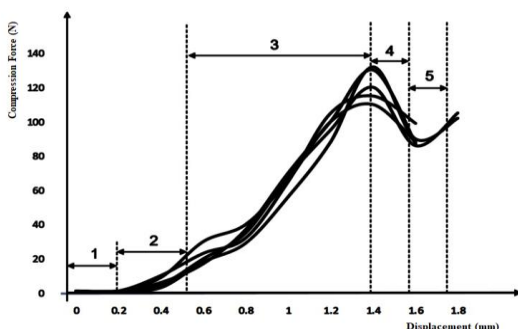


Fig. 3 - Compression Force-Displacement Curve of Soybean Grain

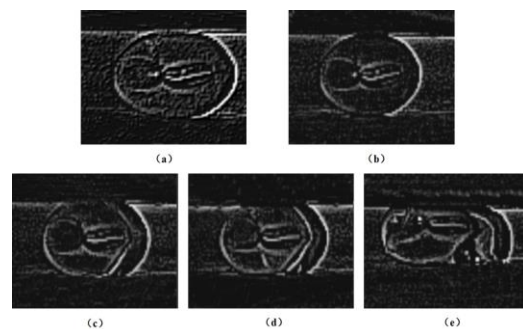


Fig. 4 - Staged images of Soybean Grain Compression Fracture Process

Effect of Moisture Content on Crushing Force

This experiment systematically investigated the impact of six different moisture content levels (8%, 10%, 14%, 19%, 23%, and 27%) on the crushing force of soybean grains, with the loading direction set to Symmetrical Horizontal compression and the loading speed maintained at a constant 30 mm/min. The Moisture Content-Crushing Force curve, is shown in Figure 5, visually depicting the trend in crushing force as moisture content varies. The curve reveals that, under low moisture content (8%), the crushing force reaches approximately 160 N, indicating a denser and harder internal structure with strong brittleness. Consequently, cracks propagate rapidly during compression, requiring a higher crushing force. As the moisture content rises to around 13%, the crushing force peaks at roughly 190 N, before dropping significantly to around 80 N as the moisture content continues to increase to 28%, exhibiting an initial increase followed by a decrease.

This trend is primarily due to changes in the internal structure of the grains caused by increasing moisture content. At lower moisture levels (8%-13%), moderate moisture increases the bonding force between cell walls, enhancing the overall strength of the grain. However, when moisture content rises beyond 13%, excessive water increases the grain's flexibility, leading to more plastic deformation under compression and thus a notable reduction in crushing force. This observation highlights the critical regulatory role of moisture content on the physical properties and compressive strength of soybean grains, offering a theoretical basis for determining optimal moisture levels for harvesting and processing.

Effect of Compression Orientation on Crushing Force

In this experiment, with the moisture content of soybean grains maintained at 14% and a loading speed of 30 mm/min, the influence of three different compression directions—Lateral Compression, Symmetrical Horizontal Compression, and Vertical Compression—on the crushing force was systematically studied. The Compression Direction-Crushing Force curve, plotted shown in Figure 6, clearly illustrates the trend in crushing force according to the compression orientation. From the curve, it can be observed that the crushing force is highest under Symmetrical Horizontal compression (approximately 186 N), followed by Lateral compression (approximately 175 N), and lowest under vertical compression (approximately 162 N). This demonstrates that variations in compression direction significantly impact the compressive strength and mechanical behavior of soybean grains.

The observed differences in crushing force are primarily due to the unique force characteristics and structural properties of soybean grains under each compression orientation. Under Symmetrical Horizontal compression, the platen applies force perpendicular to the cotyledon surfaces, with the direction of force aligned with the cotyledon's bonding interface. The large contact area and even distribution of force require a higher crushing force to induce fracture. In the Lateral compression state, the compression force directly acts on the cotyledon bond, causing cracks to initiate in the middle area of the cotyledons, leading to localized damage between the seed coat and cotyledons and thus requiring a relatively lower crushing force. In vertical compression, the force is concentrated at the top of the cotyledon bond, leading to a highly localized stress point that results in stress concentration near the embryo, making fracture easier and thus yielding the lowest crushing force.

Effect of Loading Speed on Crushing Force

In this experiment, with the moisture content of soybean grains fixed at 14% and the compression direction set to horizontal, the effect of three different loading speeds (10 mm/min, 30 mm/min, and 45 mm/min) on the crushing force was systematically studied. The Loading Rate-Crushing Force curve, shown in Figure 7, clearly illustrates the trend in crushing force with changes in loading speed. From the curve, it can be observed that at a loading speed of 10 mm/min, the crushing force is the lowest (approximately 140 N), indicating that at slower loading speeds, internal stress propagation within the grain is slower, making the structure more susceptible to damage under sustained pressure, thereby showing lower compressive strength.

As the loading speed increases to 30 mm/min, the crushing force significantly rises to around 185 N, an increase of 32.1%. This indicates that a higher loading rate accelerates stress transmission within the grain, requiring the grain to withstand greater pressure before fracturing. However, when the loading speed is further increased to 45 mm/min, the crushing force slightly decreases (to about 182 N), suggesting that at very high loading speeds, the grain's load-bearing stress reaches a stable limit, and further increases in loading speed do not significantly enhance crushing force. This finding reveals an optimal range of loading speed for maximizing crushing force: excessively low loading speeds reduce the grain's compressive performance, while excessively high speeds fail to further increase crushing force.

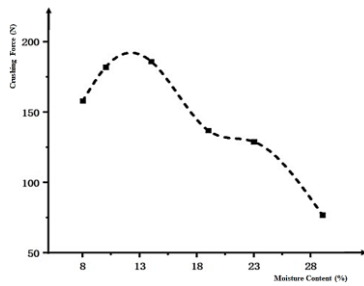


Fig. 5 - Moisture Content-Crushing Force Curve for Soybean Grain

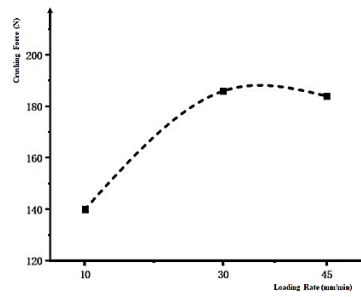


Fig. 6 - Compression Direction-Crushing Force Curve for Soybean Grain

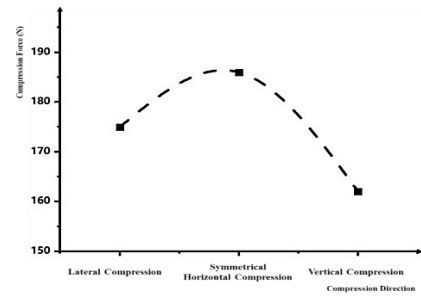


Fig. 7 - Loading Rate-Crushing Force Curve

Interaction Analysis of Multiple Factors Affecting Crushing Force

To investigate the interactive effects of moisture content, compression orientation, and loading speed on the crushing force of soybean grains, a three-factor, three-level regression orthogonal experimental design was adopted in this study, with crushing force Y_1 as the evaluation index. As shown in Table 1, the experiment selected moisture content (A), loading speed (B), and compression orientation (C) as the main influencing factors, each set at three levels: -1, 0, and 1. Specifically, moisture contents were set at 8%, 14%, and 23%; loading speeds at 10 mm/min, 30 mm/min, and 45 mm/min; and compression orientations included vertical compression (2), symmetrical horizontal compression (3), and lateral compression (4). Each experiment was repeated five times, and the average value was used as the final result to ensure data reliability.

Table 2 provides the specific orthogonal experimental scheme and results, comprising 17 test combinations. From the results, it is evident that crushing force Y_1 varies significantly across different combinations of factor levels: the minimum value recorded was 43 N (Test No. 6, with high moisture content, medium loading speed, and vertical compression), while the maximum reached 198 N (Test No. 14, with all factors at the medium level). A comparison of the center point replicates (Test Nos. 13-17) shows that when all three factors are at the 0 level, the crushing force is relatively stable, fluctuating between 176 N and 198 N, with an average of 185.6 N. This suggests that under moderate parameter conditions, soybean grains exhibit good mechanical stability. Furthermore, the results reveal an important pattern: moisture content has the most significant effect on crushing force, followed by loading speed, with compression orientation having a comparatively minor impact. Under low moisture content conditions (-1 level), the crushing force remains generally high regardless of changes in loading speed and compression orientation. As moisture content increases to the 1 level, the crushing force significantly decreases, consistent with the results from the single-factor experiments.

Table 1

Experimental Factor Levels			
Level	Factor		
	Moisture Content [%]	Loading Speed [mm/min]	Compression Orientation
-1	8	10	2
0	14	30	3
1	23	45	4

Note: The numbers 2, 3, and 4 represent Vertical compression, Symmetrical Horizontal compression, and Lateral compression, respectively.

Table 2

Orthogonal Experimental Design and Results				
Experimental Number	A	B	C	Y_1
1	-1	-1	0	152
2	1	1	0	195
3	-1	0	-1	64
4	1	0	-1	43
5	-1	0	1	89
6	0	1	-1	184
7	0	-1	1	132

Experimental Number	A	B	C	Y_1
8	0	1	1	196
9	0	0	0	186
10	0	0	0	198
11	0	0	0	180

Note: A represents moisture content (%), B represents loading speed (mm/min), C represents compression orientation, and Y_1 represents crushing force (N).

Based on the experimental results in Table 2, variance analysis of crushing force was conducted using Design-Expert 10.0 software. The analysis results indicate that moisture content (A), loading speed (B), compression orientation (C), and their interactions significantly influence the crushing force of soybean grains ($P < 0.0001$), demonstrating that the established model has strong statistical significance. The second-order polynomial model obtained through regression analysis is shown in Equation (2):

$$Y_1 = 185.6 + 31.00 * A - 7.75 * B + 11.00 * C + 26.00 * AB + 1.50 * AC - 2.00 * BC - 63.30 * A^2 + 25.20 * B^2 - 54.80 * C^2 \quad (2)$$

where: A^2 , B^2 and C^2 are the quadratic terms of each factor; and AB , AC , and BC are the interaction terms between factors.

From the analysis of the regression coefficients, it can be observed that, in terms of linear effects, the coefficient of moisture content (A) is the largest (31.00) and positive, indicating that moisture content has the strongest positive influence on crushing force. The loading speed (B) coefficient is -7.75, showing a negative correlation with crushing force, while the compression orientation (C) coefficient is 11.00, suggesting a moderate positive impact on crushing force. In terms of interaction effects, the interaction coefficient between moisture content and loading speed ($AB = 26.00$) is the largest, showing a significant synergistic effect between the two. The interaction between moisture content and compression orientation ($AC = 1.50$) is weaker, while the interaction effect between loading speed and compression orientation ($BC = -2.00$) shows a slight antagonistic effect. For the quadratic terms, the absolute value of the moisture content's quadratic coefficient ($A^2 = -63.30$) is the largest, followed by compression orientation ($C^2 = -54.80$), with loading speed ($B^2 = 25.20$) being relatively smaller. This suggests the existence of optimal value points for moisture content and compression orientation concerning their effect on crushing force. This conclusion is corroborated by the specific experimental data.

Table 3

Analysis of Variance (ANOVA) for the Regression Model					
Crushing Force (N)					
Variance Source	Sum of squares	degree of freedom	mean square	F value	P value
Model	44476.06	9	4941.78	78.67	< 0.0001***
A	7688.00	1	7688.00	122.39	< 0.0001***
B	480.50	1	480.50	7.65	0.0279*
C	968.00	1	968.00	15.41	0.0057**
AB	2704.00	1	2704.00	43.05	0.0003***
AC	9	1	9.00	0.14	0.7163
BC	16.00	1	16.00	0.25	0.6293
A ²	16871.12	1	16871.12	268.59	< 0.0001***
B ²	2673.85	1	2673.85	42.57	0.0003***
C ²	12644.38	1	12644.38	201.30	< 0.0001***
Lack of Fit	156.50	3	52.17	0.74	0.5825

Note: *** indicates $P < 0.001$ (extremely significant), ** indicates $P < 0.01$ (highly significant), and * indicates $P < 0.05$ (significant).

The ANOVA results in Table 3 show that the factors of moisture content (A), compression orientation (C), and loading speed (B) all have a significant effect on the crushing force of soybean grains. From the F-values in the ANOVA, the overall F-value for the model is 78.67 ($P < 0.0001$), which is far above the critical value required for significance, indicating that the model has a high degree of reliability.

The F-values for the main effects are as follows: moisture content (A) is 122.39 ($P < 0.0001$), compression orientation (C) is 15.41 ($P = 0.0057$), and loading speed (B) is 7.65 ($P = 0.0279$), aligning with their influence on crushing force in the order of moisture content $>$ compression orientation $>$ loading speed. Among the interaction effects, the interaction between moisture content and loading speed (AB) is the most significant, with an F-value of 43.05 ($P = 0.0003$, extremely significant). In contrast, the interactions between moisture content and compression orientation (AC) and between loading speed and compression orientation (BC) are weaker, with F-values of 0.14 ($P = 0.7163$) and 0.25 ($P = 0.6293$), respectively, neither reaching significance ($P > 0.05$).

Examining the sum of squares from the variance sources, the total sum of squares for the model is 44,476.06 with 9 degrees of freedom, and a mean square of 4,941.78, indicating that the model effectively explains the major portion of the variability in crushing force. F-value analysis of the quadratic terms shows that A^2 has the highest F-value (268.59, $P < 0.0001$), followed by C^2 (201.30, $P < 0.0001$) and B^2 (42.57, $P = 0.0003$), all reaching extreme significance levels ($P < 0.001$), demonstrating the strong nonlinear effects of these three factors on crushing force. Specifically, the sum of squares for moisture content (A) is 7,688.00, and the sum of squares for A^2 is 16,871.12, further confirming the significant impact of moisture content on crushing force. The lack of fit sum of squares is 156.50 with 3 degrees of freedom, a mean square of 52.17, and an F-value of 0.74 ($P = 0.5825 > 0.05$), indicating that the lack of fit is not significant, which further validates the reliability of this regression model.

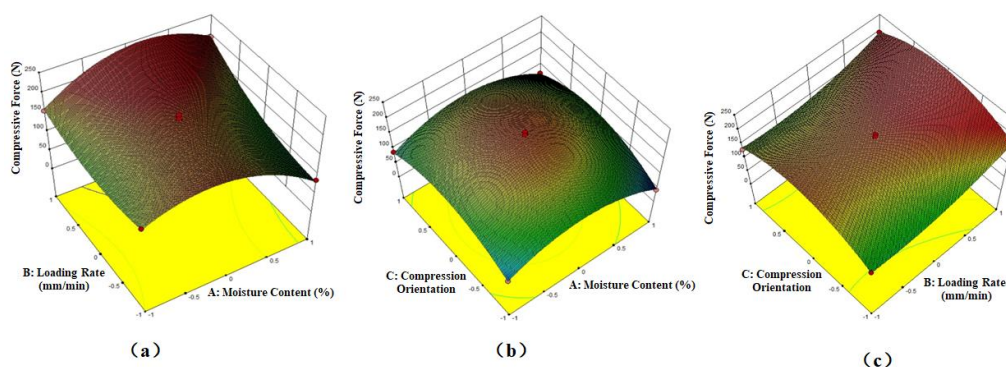


Fig. 8 - Interaction Response Surface of Soybean Seed Crushing Force

(a) Interaction between moisture content and loading speed; (b) Interaction between moisture content and compression orientation; (c) Interaction between compression orientation and loading speed.

Figure 8(a) illustrates the interaction effect between moisture content (A) and loading speed (B) on the crushing force of soybean seeds. When moisture content is fixed, the crushing force of seeds increases gradually with the rise in loading speed (B). This phenomenon can be reasonably explained by the increase in kinetic energy as the loading speed enhances, which in turn raises the crushing force. With a constant loading speed, an increase in moisture content alters the internal structure of the seed, making it softer, which leads to a trend where crushing force first increases and then decreases. As loading speed shifts from high to low levels while moisture content rises, the crushing force initially increases and then decreases noticeably. The response surface plot clearly shows that the maximum crushing force occurs at around 14% moisture content, indicating that a moderate moisture level helps preserve the structural integrity of the seeds. This significant interaction reflects the combined effect of moisture content and loading speed on crushing force.

Figure 8(b) demonstrates the interaction between moisture content (A) and compression orientation (C) on seed crushing force. At a low compression orientation level, an increase in moisture content leads to a decrease in crushing force, which is more pronounced than the effect of loading speed. As compression orientation shifts from a low to a high level, crushing force exhibits a trend of initially increasing and then decreasing. The undulations in the response surface indicate a nonlinear interaction between moisture content and compression orientation, with the interaction effect most evident at a medium compression orientation level. However, variance analysis reveals that this interaction has an F-value of only 0.14 ($P = 0.7163 > 0.05$), suggesting that although a trend is observable on the response surface, its impact is not statistically significant.

Figure 8(c) illustrates the interaction between compression orientation (C) and loading speed (B) on seed crushing force. When the compression orientation is at the 0 level, an increase in loading speed enhances the impact force, thereby increasing the crushing force. When both loading speed and compression orientation

reach high and low levels, respectively, the crushing force reaches its peak, as the machine's kinetic energy is maximized under high loading speed, with compression force primarily applied to the cotyledon surface, significantly increasing the crushing force. The response surface's overall shape suggests that compression orientation's effect becomes more prominent in high-loading-speed regions, highlighting a more significant interaction between the two factors under high-speed conditions. However, variance analysis shows that this interaction's F-value is only 0.25 ($P = 0.6293 > 0.05$), indicating that while observable on the response surface, it lacks statistical significance.

FIELD EXPERIMENT

Field Experiment Design and Preparation

The field experiment was conducted in strict accordance with national standards GB8097-2008 "Test Methods for Harvest Machinery Combine Harvesters" and GB/T 35488-2017 "Monitoring System for Combine Harvesters," ensuring compliance with regulatory requirements. The experiment site was selected at the high-standard soybean farmland testing base in Suixi County, Anhui Province (Figure 9 (b)). This site features fertile soil, well-developed irrigation facilities, and organized field plots, providing ideal conditions for the experiment. As shown in the images, the test plots are well-leveled, with uniform soybean growth and well-supported infrastructure, all contributing to the reliability of the experimental data.

For this experiment, the Lovol Gushen GM80 (4LZ-8M5) grain combine harvester was selected (Figure 9(a)). This model demonstrates strong adaptability and reliable operational performance. As shown in the image, the harvester is well-maintained, with a clean appearance and fully functional operation components.



Fig. 9 - Field Experiment Images

(a) GM80 combine harvester used in the experiment; (b) High-standard soybean farmland test base

Field Experiment Procedure

In this field experiment, the experimental area was first divided into five sections, each 10 meters long. On the first day of the experiment, soybean samples were collected from these sections at 8:00, 10:00, 12:00, 14:00, and 16:00, and the moisture content of each sample was manually measured. After that, a harvester was used to harvest the soybeans in each section at a speed of 4.4 km/h. Three groups of samples were randomly taken from the harvested soybeans and placed in sealed bags to prevent moisture changes, as shown in Figure 10, where (a) shows the experimental samples placed in sealed bags, ensuring the representativeness and sealing of the samples. Subsequently, the total mass of the soybean samples in each sealed bag was weighed one by one, and the corresponding weight data was recorded. The breakage rate analysis was conducted for each group of samples, manually selecting the broken soybean seeds from each group (as shown in Figure (b)), and weighing the mass of the broken parts. Figure (c) shows the weighing process of the broken seeds, ensuring the accuracy and reliability of the data. Finally, to determine the crushing condition for each sample group, the crushing rate was calculated using Equation (3) (Liu *et al.*, 2021) based on the actual data for each sample:

$$n = \frac{N}{M} \quad (3)$$

where: n represents the crushing rate of the seeds, N denotes the weight of the damaged seeds in the sample, and M is the total weight of the seeds in the sample. By analyzing the crushing rate of samples collected from various sections and time points, along with the sample total weight measurement process shown in Figure 10(d), a large amount of empirical data was obtained. This provides reliable foundational data to support the optimization of soybean harvesting processes and equipment, which is of significant practical importance in reducing seed damage during the harvesting process.

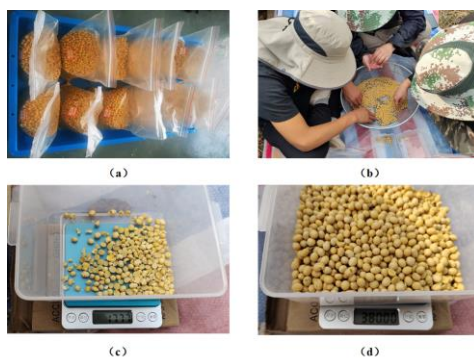


Fig. 10 - Seed Crushing Processing Images

(a) Experimental samples; (b) Selection of damaged seeds; (c) Weighing of damaged seeds; (d) Weighing of samples

Field Experiment Data Analysis and Results

Table 4

Partial Field Experiment Data				
NO	Calibrated Moisture Content [%]	Damaged Soybean Mass [g]	Sample Mass [g]	Crushing Rate [%]
1	15.52	3.87	356.61	1.09
2	14.45	6.23	406.54	1.53
3	16.02	9.62	412.65	2.33
4	17.58	8.43	252.36	3.34
5	18.61	16.23	414.62	3.91
6	22.51	17.13	335.24	5.11
7	20.63	17.77	380	4.68
8	16.53	8.84	361.64	2.44
9	20.49	8.19	382.19	2.14
10	19.64	9.03	330.24	2.73
11	16.31	9.97	397.41	2.51
12	15.58	8.05	351.33	2.29

Analysis of the experimental data in Table 4 reveals that moisture content significantly affects seed breakage during mechanized harvesting. When the moisture content exceeds 17%, the breakage rate increases notably. For example, samples numbered 5, 6, and 7 have moisture contents of 18.61%, 22.51%, and 20.63%, with corresponding breakage rates of 3.91%, 5.11%, and 4.68%. In contrast, when moisture content is in the range of 13%-17%, the breakage rate remains low. For instance, samples numbered 1, 2, and 3 have moisture contents of 15.52%, 14.45%, and 16.02%, with breakage rates of only 1.09%, 1.53%, and 2.33%. Furthermore, the total mass of samples ranged from 252.36g to 414.62g, ensuring the reliability and representativeness of the experimental results, providing valuable data support for moisture content control in soybean mechanized harvesting.

In summary, to effectively reduce seed breakage during mechanical harvesting and minimize soybean harvest losses, it is recommended to enhance field environment monitoring before harvest. Harvest timing should be carefully managed, especially during humid weather or when rain is forecasted. Regular monitoring of seed maturity and weather conditions is advised to maintain the moisture content of harvested seeds within the 13%-17% range. Coupled with appropriate harvester settings and precise operating methods, this will significantly reduce the breakage rate, thereby improving harvest quality and reducing post-harvest processing losses.

CONCLUSIONS

Field trials confirm that the optimal moisture content range for harvest is 13%-17%, resulting in the lowest seed breakage rate (2.15% ± 0.43%). To ensure high harvest quality, it is recommended to operate in the afternoon on sunny days, maintain a harvesting speed of 3-5 km/h, keep the drum speed at 400-450 r/min, and regulate the feed rate at 4-6 kg/s. Considering regional differences, the recommended moisture content for southern regions is 14%-16%, while northern regions can maintain a range of 15%-17%. Field trials further

verify the significant impact of moisture content on seed breakage rates during mechanical harvesting. Tests conducted across different regions show that seeds with moisture content between 13%-17% exhibit lower breakage rates (1.09%-3.34%). These optimized parameter recommendations provide practical guidance for improving mechanized harvest quality, enhancing efficiency, and reducing harvest losses.

ACKNOWLEDGEMENT

This research was funded by the National Key Research and Development Plan project (2021YFD2000503), the National Natural Science Foundation of China (No. 32171911), the National Soybean Industry Technology System (CARS-04), and the CAAS Center for Science in Smart Agriculture and Equipment (CAAS-SAE-202301), the authors thank relevant scholars for their assistance in the literature.

REFERENCES

- [1] Anderson, E. J., Ali, M. L., Beavis, W. D., Chen, P., Clemente, T. E., Diers, B. W., Graef, G. L., Grassini, P., Hyten, D. L., McHale, L. K., Nelson, R. L., Parrott, W. A., Patil, G. B., Stupar, R. M., & Tilmson, K.J. (2019). Soybean [*Glycine max* (L.) Merr.] breeding: history, improvement, production and future opportunities. *Advances in Plant Breeding Strategies*. 7: 431–516. https://doi.org/10.1007/978-3-030-23400-3_1.
- [2] Chen, F. L., Wei, Y. M., Zhang, B., & Ojokoh, A. O. (2010). System Parameters and Product Properties Response of Soybean Protein Extruded at Wide Moisture Range. *Journal of Food Engineering*. 96, no. 2: 208–213. <https://doi.org/10.1016/j.jfoodeng.2009.07.014>.
- [3] Chowdhury, M. H., & Buchele, W. F. (1975). Effects of the Operating Parameters of the Rubber Roller Sheller. *Transactions of the ASAE*. 18, no. 3: 482–490.
- [4] Dong, R., Lu, Z., Liu, Z., Nishiyama, Y., & Cao, W. (2009). Moisture Distribution in a Rice Kernel During Tempering Drying. *Journal of Food Engineering*. 91, no. 1: 126–132. <https://doi.org/10.1016/j.jfoodeng.2008.08.012>.
- [5] Faryal Fatima, Ehsan Khalid, Irfan Afzal, Muhammad Usman, Muhammad Ather Nadeem, Muhammad Kamran, (2025) Evaluation of cotton (*Gossypium hirsutum* L.) seed longevity and deterioration: Physiological and biochemical aspects in relation to moisture contents during storage in different module systems. *Journal of Stored Products Research*, Volume 111, 2025,102553, ISSN 0022-474X, DOI:[10.1016/j.jspr.2025.102553](https://doi.org/10.1016/j.jspr.2025.102553)
- [6] Fernando, S., Hanna, M., & Mesquita, C. (2004). Soybean Threshing Mechanism Development and Testing. *Transactions of the ASAE*. 47, no. 3: 599–605. <https://doi.org/10.13031/2013.16089>.
- [7] Gao, L., Li, X.F., Jie, X., Na, X.J., & Zhang, Y.L. (2010). Investigation on Characteristics and Ratio of Soybean Kernel Mechanical Damage. *Journal of Shenyang Agricultural University*. 41, no. 1: 55–58.
- [8] Jiayuan, L., Qianqian, L., & Xiang, C. (2021) Diversity and influencing factors of kernel breakage tolerance of different maize cultivars, *Journal of China Agricultural University*. 26, no. 12, 207-220. [10.11841/j.issn.1007-4333.2021.12.20](https://doi.org/10.11841/j.issn.1007-4333.2021.12.20)
- [9] Kang, Y., Guo, H., Jin, C., Yin, X., & Li, Q. (2021). Experiments and Studies on the Suitability of Different Varieties of Soybean for Harvest in Huang Huai Hai Area. *Journal of Agricultural Mechanization Research*. 43, no. 6: 150–159. <https://doi.org/10.13427/j.cnki.njyi.2021.06.027>.
- [10] Krishnan, P., Singh, R., Verma, A. P. S., Joshi, D. K., & Singh, S. (2014). Changes in Seed Water Status as Characterized by NMR in Developing Soybean Seed Grown Under Moisture Stress Conditions. *Biochemical and Biophysical Research Communications*. 444, no.4: 485–490. <https://doi.org/10.1016/j.bbrc.2014.01.091>.
- [11] Liu, J., Jin, C., Liang, S., & Ni, Y. (2017). The Research of Soybean Harvested by Machine. *Agricultural Mechanization Research*. 39, no. 7: 1–9, 15. <https://doi.org/10.13427/j.cnki.njyi.2017.07.001>.
- [12] Mariashibu, T.S., Anbazhagan, V.R., Jiang, S.Y., Ganapathi, A., & Ramachandran, S. (2013). In vitro regeneration and genetic transformation of soybean: Current status and future prospects. A Comprehensive Survey of International Soybean Research—Genetics, Physiology, *Agronomy and Nitrogen Relationships*, no. 5. <https://doi.org/10.5772/54268>.
- [13] Qiu, S., Yuan, X., Guo, Y., Cui, Q., Wu, X., & Zhang, Z. (2019). Effects of Variety and Moisture Content on Mechanical Properties of Millet. *Transactions of the Chinese Society of Agricultural Engineering*. 35, no.24: 322–326. <https://doi.org/10.11975/j.issn.1002-6819.2019.24.038>.

- [14] Resende, O., Corrêa, P. C., de Oliveira, G. H. H., Goneli, A. L. D., & Jarén, C. (2013). Mechanical Properties of Rough and Dehulled Rice During Drying. *International Journal of Food Studies*. 2: 158–166.
- [15] Tao, Z, Fengwei, Z, Wei, S, & Bugong, S. (2017). Modeling of Chemo-Mechanical Properties for Soybean Seed. *Transactions of the Chinese Society of Agricultural Engineering*. 33, no.5: 264–271. <https://doi.org/10.11975/j.issn.1002-6819.2017.05.038>.
- [16] Teng, Y. J., Jin, C. Q., Yin, X., Ni, Y. L., Xie, H. R., Chen, Y. P., Guo, F. Y., & Liu, P. (2020). Experiment and Research on Mechanical Properties of Soybean During Threshing. *Journal of Agricultural Mechanization Research*. 42, no. 12. <https://doi.org/10.13427/j.cnki.njyi.2020.12.022>
- [17] Waelti, H., & Buchele, W. F. (1969). Factors Affecting Corn Kernel Damage Combine Cylinders. *Transactions of the ASAE*: 55–59.
- [18] Wang, Guirong. (2024). The Overall Situation of Agricultural Economy in 2023 Is Good. *China Information News*, 2024-01-19, no. 002. <https://doi.org/10.38309/n.cnki.nzgxx.2024.000146>.
- [19] Yang, Z., Sun, J., & Guo, Y. (2015). Effect of Moisture Content on Compression Mechanical Properties and Frictional Characteristics of Millet Grain. *Transactions of the Chinese Society of Agricultural Engineering*. 31, no. 23: 253–260. <https://doi.org/10.11975/j.issn.1002-6819.2015.23.034>.
- [20] Zhang, T., Zhang, F., Sun, W., Sun, B., Wang, T., & Wu, J. (2017). Gray Relation Degree and Constitutive Modeling of Chemo-Mechanical Properties for Soybean Seed. *Transactions of the Chinese Society of Agricultural Engineering*. 33, no.5: 264–271. <https://doi.org/10.11975/j.issn.1002-6819.2017.05.038>.
- [21] Zhumadian Municipal Market Supervision Administration. (2019). DB4117/T 267-2019 Management Guide for Agricultural Product Laboratory Samples and Testing Records. *National Standard Information Public Service Platform*. <https://std.samr.gov.cn>.
- [22] ***ASTM International. (2024). ASTM E4-24: Standard Practices for Force Calibration and Verification of Testing Machines. *ASTM International*. <https://www.astm.org/e0004-24.html>
- [23] ***National Agricultural and Rural Economic Operation. (2024). Ministry of Agriculture and Rural Affairs of the People's Republic of China. https://www.moa.gov.cn/ztl/nybrl/rlxx/202401/t20240123_6446367.htm.
- [24] ***National Bureau of Statistics. (2024). Statistical Bulletin of National Economic and Social Development of the People's Republic of China (2023). *People's Daily*, 2024-03-01, no. 010. <https://doi.org/10.28655/n.cnki.nrmrb.2024.002126>.
- [25] ***State Administration of Grain and Reserve. (1985). GB/T 5497-1985 Inspection of Grain and Oilseeds—Determination of Moisture Content. *National Standard Information Public Service Platform*. <https://std.samr.gov.cn/gb/search/gbDetailed?id=71F772D79696D3A7E05397BE0A0AB82A>.

OPTIMIZATION OF TECHNOLOGICAL PARAMETERS FOR FUEL ROLL PRODUCTION USING AGRICULTURAL CROP STEM BIOMASS

ОПТИМІЗАЦІЯ ТЕХНОЛОГІЧНИХ ПАРАМЕТРІВ ДЛЯ ВИРОБНИЦТВА ПАЛИВНИХ РУЛОНІВ З ВИКОРИСТАННЯМ СТЕЛБОВОЇ БІОМАСИ СІЛЬСЬКОГОСПОДАРСЬКИХ КУЛЬТУР

Svitlana YAHELIUK^{*1)}, Volodymyr DIDUKH¹⁾, Mikhalo FOMICH¹⁾, Olexandr YAHELIUK²⁾
Tetyana KUZMINA²⁾, Galina BOIKO²⁾

¹⁾ Lutsk National Technical University, Ukraine;

²⁾ Kherson National Technical University, Ukraine

*Corresponding author's E-mail: cler2010@gmail.com

DOI: <https://doi.org/10.35633/inmateh-75-21>

Keywords: Fuel Rolls, Agricultural Crop Stem Biomass, flax, density, compaction pressure, Variable-volume Pressing Chamber

ABSTRACT

The paper develops a regression model to predict the density of Fuel Rolls produced from Agricultural Crop Stem Biomass. The study evaluates the influence of Variable-volume Pressing Chamber pressure (P , MPa), biomass volume per linear meter (V , m^3), and flax stem content (m , %) on Fuel Roll density (ρ). The goal is to optimize these parameters to ensure the desired density of Fuel Roll. A regression analysis combined with response surface methodology was employed. The optimal parameters for Fuel Rolls production include Variable-volume Pressing Chamber pressure of 0.45–0.55 MPa, biomass volumes of 0.65–0.75 m^3/m and flax stem content 75%. These technological parameters enable the production of fuel rolls with required density of 110–130 kg/m^3 . The results show that increasing pressure in the Variable-volume Pressing Chamber enhances Fuel Roll density, while larger biomass volumes lead to lower densities. Additionally, higher flax stem content improves cohesion and compaction, resulting in higher densities. These findings emphasize the importance of fine-tuning technological parameters to optimize Fuel Roll production. Utilizing agricultural crop stems for biofuel production offers significant environmental benefits, including reduced agricultural waste and lower combustion emissions.

РЕЗЮМЕ

У статті розроблено регресійну модель для прогнозування щільності паливних рулонів, вироблених із біомаси стебла сільськогосподарських культур. Дослідження оцінює вплив тиску камери пресування змінного об'єму (P , МПа), об'єму біомаси на погонний метр (V , m^3) і вмісту стебла льону (m , %) на щільність рулону палива (ρ). Мета полягає в тому, щоб оптимізувати ці параметри для забезпечення бажаної щільності паливного рулону. Було використано регресійний аналіз у поєднанні з методологією поверхні відгуку. Оптимальними параметрами для виробництва паливних рулонів є тиск у камері пресування змінного об'єму 0,45–0,55 МПа, об'єм біомаси 0,65–0,75 m^3/m і вміст стебла льону 75%. Ці технологічні параметри дозволяють виготовляти паливні рулони необхідної щільності 110–130 kg/m^3 . Результати показують, що збільшення тиску в камері пресування зі змінним об'ємом збільшує щільність паливного ролика, тоді як більші об'єми біомаси призводять до зниження щільності. Крім того, більш високий вміст стебла льону покращує когезію та ущільнення, що призводить до більшої щільності. Ці висновки підкреслюють важливість точного налаштування технологічних параметрів для оптимізації виробництва паливних роликів. Використання стебел сільськогосподарських культур для виробництва біопалива забезпечує значні переваги для навколишнього середовища, включаючи зменшення сільськогосподарських відходів і менші викиди в результаті згоряння.

INTRODUCTION

According to data (FAOSTAT, n.d.), approximately 400 million tons of agricultural plant stems are burned annually worldwide.

This practice leads to the emission of harmful substances such as solid particles (soot), nitrogen oxides, various carcinogens, and carbon monoxide, which contribute significantly to air pollution and degradation of the surface ozone layer. These pollutants exacerbate global climate change. That has been examined in depth by international researchers (Lan et al, 2022; Amann M., 2017, Milton Halder et al., 2023). To mitigate these negative effects, many scholars propose efficient methods for utilizing agricultural residues (Gatkal, N.R. et al, 2024; Kashytskyi V.P. et al, 2023). However, among the most effective solutions is the conversion of plant biomass into biofuels (Marian Gregory, 2016, Gageanu I. et al, 2022). Fossil fuels represent a limited energy resource that will eventually be exhausted. Over the past several years, the significance of environmentally sustainable biofuels has become increasingly apparent. Crop Stem Biomass is a potential renewable energy source, offers notable energy content per unit mass, albeit lower than that of fossil fuels (C.F.N, n.d.). Its utilization as a sustainable energy alternative is a growing focus of interest among researchers. (Mehmood Ali, et al., 2019, Jiang Y., et al, 2019). Although significant research has been conducted on the use of agricultural biomass for energy, there is still a lack of comprehensive studies addressing the specific technical challenges associated with compacting agricultural residues into small, high-density fuel rolls (FRs).

Solid biofuels not only address the disposal problem of agricultural residues but also serve as an eco-friendly energy source. A particularly economical and straightforward approach is the production of small-sized Fuel Rolls (FRs), designed for use in modern solid-fuel heating boilers (Yaheliuk et al., 2020). The biomass of various crops, including flax, corn, sunflower, and grain stems, can be effectively utilized for this purpose (Yaheliuk et al., 2021).

The property of crop stem biomass plays a critical role in its efficient conversion into biofuels. Key characteristics to consider include Elasticity, Strength, Viscosity, Moisture Content, Density, etc. (Hajlis G. 2004, Ibrahim Ayman, 2008, Goudenhoft C., 2018). Analyzing and accounting for these properties allow for the optimization of equipment settings, improving processing efficiency and the quality of the biofuel produced. Reducing the elastic properties of agricultural stems is an important step in improving the efficiency of biomass processing for biofuel production. High elasticity in stems can hinder effective compaction during the production of FRs or briquettes, as the material resists deformation and may spring back after compression. Didukh, V. suggested strategy to solve this issue (Didukh V. et al., 2022). This research continues this work by focusing on optimizing the pressing chamber design to minimize elasticity-related losses and ensure consistent compaction of small-sized FRs.

Despite significant achievements, there remains a clear research gap in the development of efficient technologies for converting Agricultural Crop Stem Biomass into high-quality solid biofuels. Existing research has mainly focused on large-scale pellet or briquette production, with limited attention to the specific challenges of producing small-sized FRs for decentralized energy systems. There is a lack of research on designing pressing chambers that can sustainably produce small-sized, high-density FRs and determining rational parameters for processing different types of stem biomass.

The determining quality indicators for small-sized FR are the twisting density of stem biomass and the dimensions of the roll. It is advisable to use a specially designed variable volume chamber for the production of small-sized FRs. In this case, the twisting density of the stem biomass depends on the pressure created by the rollers and the volume of a linear meter of the stem biomass tape that is fed into the Variable-volume Pressing Chamber.

The aim of this study is to investigate the effect of pressing parameters on the density of small-sized FRs and determine the optimal operating conditions for a variable volume pressing chamber to ensure high fuel efficiency.

The production of small-sized Fuel Rolls represents a promising direction for sustainable biomass utilization. By addressing existing technological gaps, this research seeks to improve the viability of biofuel production, contributing to cleaner energy solutions and reducing the environmental impact of agricultural plant residues.

MATERIALS AND METHODS

Experimental equipment was designed for research. It is a Variable-volume Pressing Chamber (VPC). The formation of small-sized FRs from the Agricultural Crop Stem Biomass (ACSB) and the determination of rational technological modes for obtaining small-sized FRs of the required density was studied with its help. The scheme of the Variable-volume Pressing Chamber for studying the impact of the compression force on the density of the obtained small-sized FRs is presented in Fig.1, a, the general view in Fig.1, b.

The ACSB (1) enters the VPC between the press rollers (2), which compress the material into a denser form. The tension springs (3) ensure that the rollers apply consistent pressure while the drive belt (5), powered by the engine (7), rotates the rollers. With each rotation of the compacting rollers (8), the action of the spring (3) increases. This allows obtaining a roll of a required density. The tension roller (6) ensures the drive belt stays taut, minimizing slippage and maximizing efficiency.

The result is compacted biomass in the form of FRs, suitable for use as biofuel. This design efficiently solves issues such as reducing elasticity in plant stems, achieving consistent compaction, and producing high-density FR. The density of the formed small-sized FR is determined by the force exerted on the biomass. Two tension springs are positioned to control compaction force (Fig. 1). The lower roller axis is mounted on the frame (4), ensuring stability and alignment during operation.

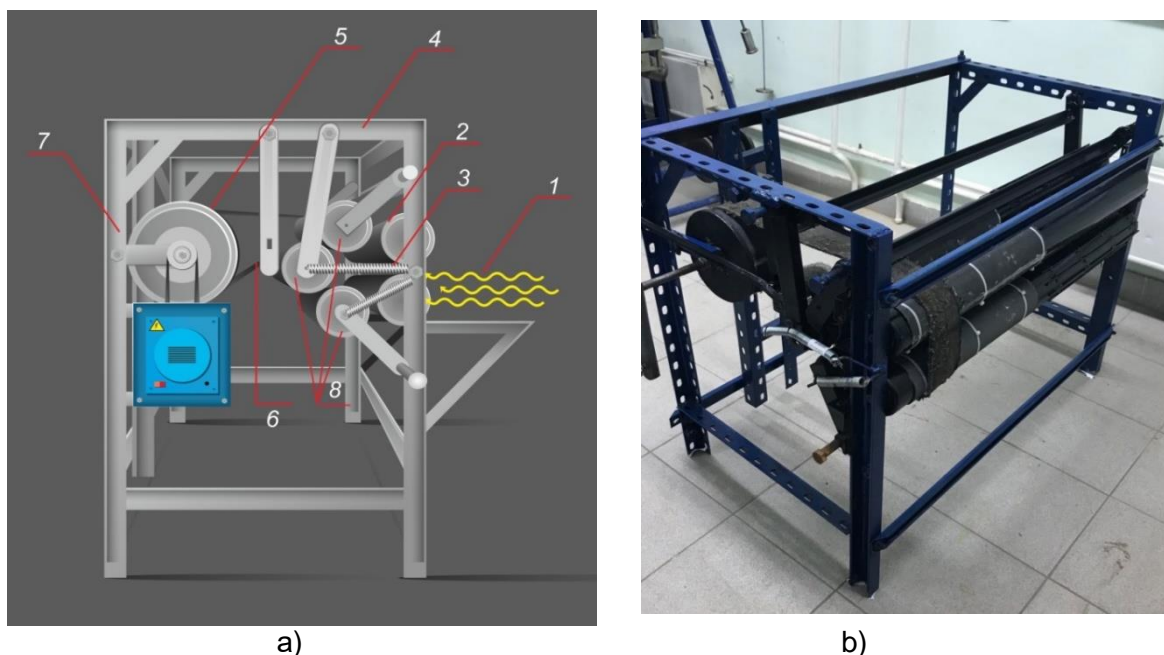


Fig. 1 – The Variable-volume Pressing Chamber (VPC) for the formation of small-sized Fuel Roll (FR) from the Agricultural Crop Stem Biomass (ACSB)

a – scheme, b – natural appearance:

1 – biomass of agricultural crop stems; 2 – press rollers; 3 – tension springs; 4 – frame; 5 – drive belt; 6 – tension roller; 7 – engine; 8 – compacting rollers.

The advantages of the VPC are:

1. Efficient Biomass Compaction. The system effectively addresses the challenge of reducing elasticity in plant stems, creating compact, dense small-sized FRs.
2. Adjustable Density. The tension springs provide flexibility to control the compaction force, allowing the production of rolls with required density.
3. Early Roll Formation. The minimum free space between the rollers at the beginning of twisting allows to form a roll from the first turns of rollers.

It was investigated (Yaheliuk *et al.*, 2019) that the operation of forming FR from the ACSB has such phases (Fig. 2):

- Initial Phase. The pressing rollers (2) compact the stem biomass (1) to form the base or "seed" of the FR. This phase has the shortest duration, as its purpose is simply to establish a FR starting point.
- Intermediate Phase (Roll Formation). The FR grows as layers of biomass are continuously wound and compacted in the pressing chamber. During this phase, the biomass is pressed further to achieve an intermediate level of density.
- Final Phase (Maximum Density). The tension springs (3) enable the compacting rollers (4) to adjust their position as the FR grows in size and density. The biomass is wound tightly to ensure maximum density, with the rollers continuously applying pressure. The springs allow the compacting rollers to move outward as the radius of the FR increases, maintaining consistent pressure throughout the process.

The rollers are designed to move outward to accommodate the increasing size of the FR, thanks to the flexibility provided by the tension springs (3).

For the production of FR, the biomass of wheat, rye, flax stems (ACSB) were used in different proportions as a raw material (Table 1). The stems were destroyed before twisting (*Didukh V. et al, 2022*). The initial relative humidity of the crop stem biomass material was 8.5-15%.

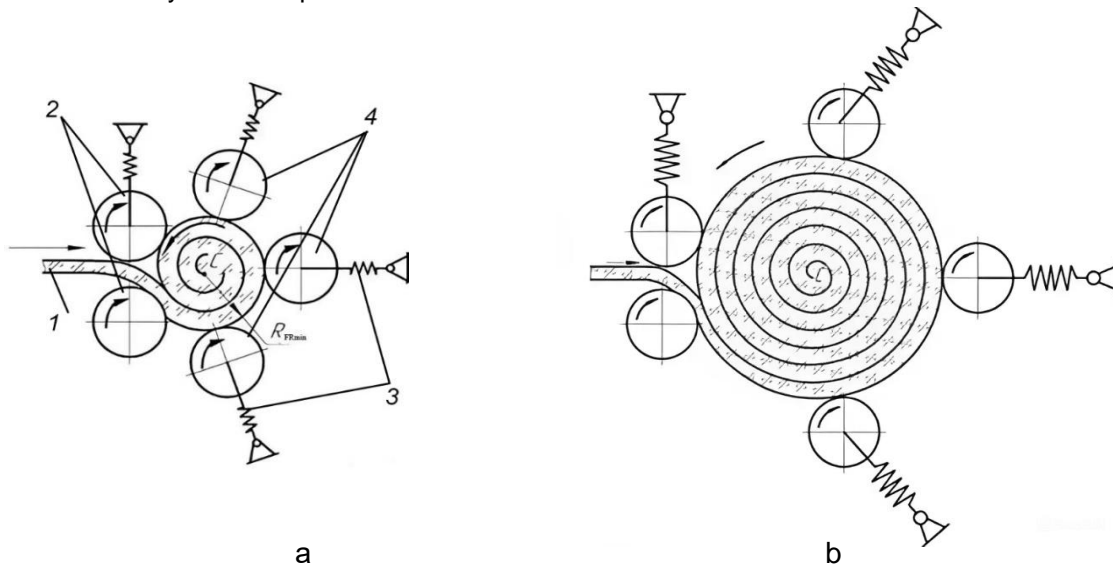


Fig. 2 – The scheme of the formation of FR from the ACSB in the VPC
a - the Initial Phase of the formation of the FR, b - the Final Phase of the formation of the FR:
 1 – biomass of agricultural crop stems; 2 – press rollers; 3 – tension springs; 4 –compacting rollers

The complexity of forming rolls from ACSB is associated with the elastic properties of plants. The stem mass obtained after the separation of seeds is not destroyed much under the action of the threshing machine. Therefore, its elastic properties are high. To preserve the shape of the roll, it is necessary to use binding agent (rope). But this is not permissible for small-sized FRs. Therefore, it is necessary, besides other, to use fiber stem materials, as flax stems, for the production of FRs.

Table 1

Content of flax stems in the Agricultural Crop Stem Biomass (ACSB)

ACSB	FR75/25	FR50/50	FR25/75
Flax stems, %	75	50	25
Wheat, rye, %	25	50	75



Fig. 3 – The FRs from biomass of agricultural plants stem:
 1 – FR25/75; 2 –FR75/25; 3– FR50/50

Density is a determining indicator of quality for FR. It affects the calorific value of FR, their transportation and storage.

The following technological parameters were determined to influence the density of FR: the pressure created by the rollers in the Variable-volume Pressing Chamber (P , MPa), the volume of a linear meter of ACSB fed into the VPC (v , m³), the content of flax stems in the ACSB fed into the VPC on the density of the obtained FR (m , %).

The study of the influence of the pressure in the pressing chamber of variable volume and the volume of a linear meter of the stem biomass of agricultural plants entering the pressing chamber on the density of the FR was carried out by the method of mathematical planning of the experiment. (Box G.E.P., Behnken D.W., 1960; Aziz R.A., Aziz S.A., 2018).

The purpose of the experiment was to determine the density of the formed FR while varying the technological parameters: the pressure created by the rollers in the VPC (P , MPa), the volume of a linear meter of the Agricultural Crop Stem Biomass, which is fed into the VPC (v , m³) and the content of flax stems in the ACSB fed into the VPC on the density of the obtained FR (m , %) (Table 2).

Table 2

Variables and Their Levels in Box-Behnken Design

Levels of variation	X, pressure P (MPa)	X2, volume of a linear meter ACSB V, (m ³)	X3, content of flax stems m, (%)
Upper (+1)	0.60	0.8	75
Main (0)	0.55	0.7	50
Lower (-1)	0.50	0.6	25
Range of variation	0.05	0.1	25

Table 3 shows the planning matrix of the three-factor experiment according to the Box-Behnken design (Box G.E.P., Behnken D. W., 1960). Matrix is presented in a coded format. The order of experiments was determined using a table of random numbers.

Table 3

Design of experiment

Run	Pressure P (MPa)	Volume of a linear meter ACSB V (m ³)	Content of flax stems m, (%)
1	1	1	0
2	-1	1	0
3	1	-1	0
4	-1	-1	0
5	1	0	1
6	-1	0	1
7	1	0	-1
8	-1	0	-1
9	0	1	1
10	0	-1	1
11	0	1	-1
12	0	-1	-1
13	0	0	0
14	0	0	0
15	0	0	0

The response function, representing the density of the FR, is expressed in the factor space as a nonlinear regression equation (1):

$$Y = b_0 + b_1 X_1 + b_2 X_2 + b_3 X_3 + b_{12} X_1 X_2 + b_{13} X_1 X_3 + b_{23} X_2 X_3 + b_{11} X_1^2 + b_{22} X_2^2 + b_{33} X_3^2 \quad (1)$$

where:

Y is the response (density of the FR, ρ), and X_1, X_2, X_3 are the coded variables for P, V , and m .

RESULTS AND DISCUSSION

As a result of the research (Table 4) data have been obtained on the density of the Fuel Roll (FR), ρ , kg/m^3 , that depends on the pressure created by the rollers in the Variable-volume Pressing Chamber (VPC), (P , MPa), the volume of a linear meter of the Agricultural Crop Stem Biomass (ACSB), which is fed into the VPC (v , m^3) and the flax stem content in the ACSB (m , %).

Table 4

Box-Behnken design scheme and the density of the FR response values

Run	P (MPa)	V (m^3)	m (%)	ρ (kg/m^3)
1	0.60	0.8	50	119.067
2	0.50	0.8	50	107.167
3	0.60	0.6	50	124.933
4	0.50	0.6	50	113.233
5	0.60	0.7	75	128.167
6	0.50	0.7	75	115.133
7	0.60	0.7	25	112.533
8	0.50	0.7	25	103.100
9	0.55	0.8	75	122.300
10	0.55	0.6	75	127.233
11	0.55	0.8	25	106.100
12	0.55	0.6	25	112.067
13	0,55	0.7	50	119.400
14	0,55	0.7	50	119.200
15	0.55	0.7	50	118.900

The experiment conducted according to the Box-Behnken design enabled the development of a mathematical model describing the dependence of FR density on technological parameters in the form of a regression equation. The results of three-factor experiments were processed according to a second-order, three-level design using a program developed in the Mathcad environment. The Box-Behnken experimental design allowed for an efficient investigation of the influence of three independent variables (technological parameters) on the response variable (density of the formed FR) (Montgomery C. Douglas, 2013). The regression model in coded factors is presented as follows (2):

$$\rho = 119.2 + 5.8X_1 - 2.8X_2 + 7.4X_3 + 0.9X_1X_3 - 2.6X_1^2 - 1.8X_3^2 \quad (2)$$

The homogeneity of the variance series was evaluated using the Cochran criterion. The calculated value $G_{res} = 0.19$ was compared to the tabular value $G_{tab} = 0.335$ (for $\alpha = 0.05$, $f_1 = 10$, $f_2 = 3$) and an alternative tabular value of 0.373. Since $G_{res} < G_{tab}$ it can be concluded that the experimental process is reproducible. The adequacy of the regression equation (2) was verified using Fisher's F -test. The calculated F -statistic value was $F_{res} = 16.196$, based on the variance of inadequacy $S_{nead}^2 = 1.026$ and the variance of reproducibility $S_y^2 = 0.063$. The tabular value of the Fisher statistic at a 5% significance level ($\alpha = 0.05$) with degrees of freedom $f_1 = 2$, $f_2 = 7$ was $F_{table} = 19.4$. Since $F_{res} < F_{tab}$ the regression model was confirmed to be adequate.

Using the given central levels ($P_0=0.55$ MPa, $V_0=0.7$ m^3 , $m_0=50$ %) and the corresponding ranges of variation ($\Delta P=0.05$, $\Delta V=0.1$, $\Delta m=25$), the regression equation in coded factors was converted into natural variables. The resulting equation, expressed in natural factors P (pressure, MPa), V (volume of a linear meter ACSB, m^3), and m (content of flax stems, %), is as follows (3):

$$\rho = -224.4 + 1240P - 28.5V + 0.19m + 0.72P * m - 1038.2P^2 - 0.003m^2 \quad (3)$$

This equation accounts for the scaling and centering of the factors, ensuring the model is directly applicable to the original experimental conditions. The regression coefficients reflect the influence of the natural variables on the response (density of the FR, ρ), making the equation suitable for practical interpretation and optimization. The response surfaces (Fig.4, a and Fig.5, a) and their contour plots (Fig.4, b and Fig.5, b) are constructed using the regression equation (3).

The response surface (Fig.4a) and contour plot (Fig.4b) illustrate the relationship between the density of FR and two variables: the pressure applied by rollers in the (P , MPa) and the volume of a linear meter of ACSB (V , m³) fed into the chamber. The response surface shows a clear trend where increasing the pressure in the pressing chamber (P) leads to a significant increase in the density of the FR.

This is evident from the upward slope of the surface as pressure values increase. Conversely, increasing the volume of biomass (V) tends to decrease the density, as represented by the downward slope of the surface in the direction of larger biomass volumes. This interplay indicates that higher pressure compresses the material more effectively, while larger volumes of biomass tend to resist compression, leading to lower densities.

The contour plot (Fig.4b) provides a detailed view of how combinations of pressure and biomass volume influence density. The interaction between pressure and biomass volume indicates that maintaining a moderate biomass volume (around 0.6–0.7 m³) while increasing pressure to values near 0.58–0.6 MPa yields the highest density. This is important for achieving FR with structural integrity, as density directly correlates with combustion efficiency and energy potential.

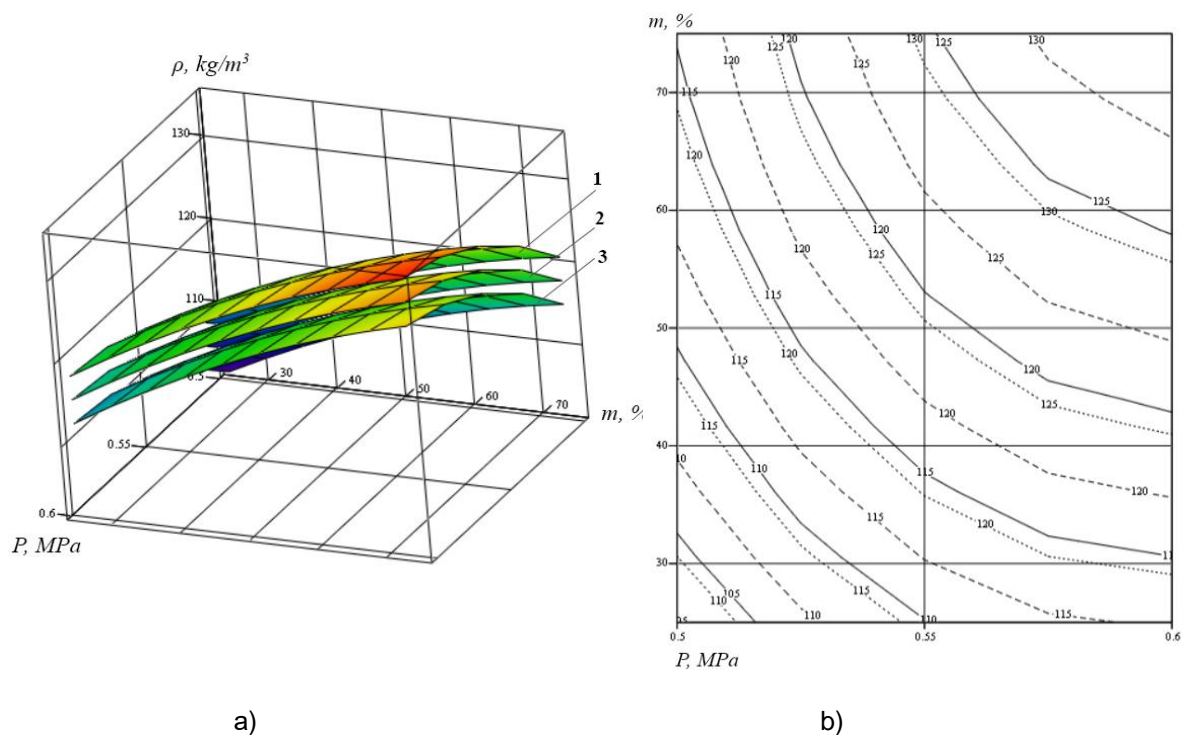


Fig. 4 - The results of the study of the dependence of the FR density on the pressure created by the rollers in the VPC (P , MPa) and the volume of a linear meter of the ACSB (V , m³)

*a – response surface; b - contour plot of the response surface:
 1 – $V=0.6$ m³; 2 – $V=0.7$ m³; 3 – $V=0.8$ m³*

The images (Fig. 5 a, b) showcase visualization of a study analyzing the dependence of FR density (ρ) on the pressure (P , MPa) exerted by rollers in a VPC and the flax stem content in FR (m , %) for three different material compositions: FR75/25, FR50/50, and FR25/75. For all material compositions, the density increases with higher rollers pressure (P). The FR75/25 composition, which has a higher proportion of flax stems, results in higher densities compared to FR50/50 and FR25/75 under similar conditions. This is due to the fibrous nature of flax, which enhances material cohesion during compression.

The contour plot (Fig.5 b) provides a top-down view of the response surface, showing density lines as a function of P and V . These contours clearly illustrate how the density changes within the defined parameter space. The spacing of the contour lines suggests that the effect of increasing P on ρ becomes less pronounced at higher pressures, indicating at a potential saturation point in compaction efficiency.

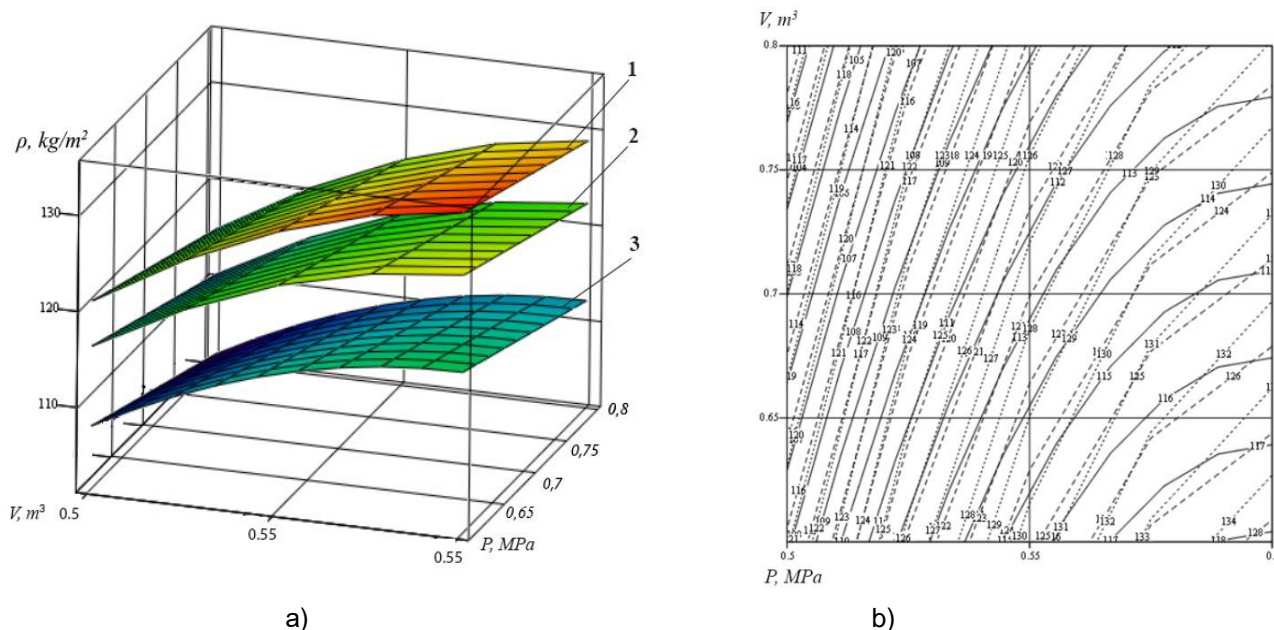


Fig. 4 - The results of the study of the dependence of the FR density on the pressure created by the rollers in the VPC (P , MPa) and content of flax stems (m , %)
a – response surface; *b* – contour plot of the response surface:
 1 – FR75/25, 2 – FR50/50, 3 – FR25/75

The studied (*C.F.N, n.d.*) data show (Table 5) that flax stems are a good source of biomass energy with an energy potential of 18 MJ/kg. Compared to traditional fossil fuels such as coal (22 MJ/kg) or fuel oil (37 MJ/kg), this is less. However, such an energy potential of flax stems makes it possible to compare flax-based FR with wood fuels (16-20.5 MJ/kg).

Flax and wheat straw are structurally similar and possess the same energy value, making them compatible for mixing. This compatibility ensures uniform energy production, which is critical for efficient combustion. Additionally, their fibrous nature enhances mechanical properties such as cohesion and density when compressed into fuel rolls. The abundant availability of these materials as by-products of agricultural processes provides economic and environmental benefits, as their use for energy production reduces waste while offering a sustainable energy source.

Table 5

The energy potential of various types of sources (*C.F.N, n.d.*)

Sources	Traditional sources of energy		Agriculture biomass							Wood biomass			
	Hard coal	Fuel oil	Corn	Flax stem	Wheat straw	Sunflower stem	Rape pomace	Sunflower husks	Cotton stems	Basket willow	Poplar	Beech	Fir
Energy potential, MJ/kg	22	42	15	18	15	15	19	18	17,5	18,5	16	18	20,5

The study presents a regression model for predicting the density of fuel rolls (FRs) produced from agricultural crop stem biomass (ACSB). To ensure efficient production of FRs from ACSB, the following technological parameters are recommended:

1. Compaction Pressure in the Variable-Volume Pressing Chamber (VPC). Recommended pressure ranges for different blends are:

- FR75/25 (75% flax stems, 25% other materials): 0.50–0.55 MPa;
- FR50/50 (50% flax stems, 50% other materials): 0.45–0.55 MPa;
- FR25/75 (25% flax stems, 75% other materials): 0.40–0.50 MPa.

Higher flax stem content requires slightly higher pressures to achieve uniform density due to its fibrous structure. Within these pressure ranges, densities of 110–130 kg/m³ can be achieved, meeting mechanical stability and energy performance requirements.

2. The volume of a linear meter of the Agricultural Crop Stem Biomass. Optimal biomass volumes for achieving the required density without compromising material cohesion or creating excessive porosity are:

- FR75/25: 0.7–0.75 m³;
- FR50/50: 0.65–0.7 m³;
- FR25/75: 0.65–0.7 m³.

By maintaining compaction pressures of 0.45–0.55 MPa, biomass volumes of 0.65–0.75 m³ of a linear meter of the ACSB, and rational blending ratios of flax stems with complementary biomass, fuel rolls can achieve densities of 110–130 kg/m³ and energy potentials of 16–18 MJ/kg. These optimized parameters ensure a balance of mechanical strength, energy efficiency, and resource sustainability, positioning flax-based FR as a competitive and eco-friendly option for bioenergy production.

CONCLUSIONS

The study highlights the significant potential of agricultural crop stem biomass (ACSB) as a sustainable and environmentally friendly resource for biofuel production. By optimizing technological parameters, it is possible to produce small-sized Fuel Rolls (FRs) with high density and substantial energy potential. Regression analysis indicates that achieving densities between 110 and 130 kg/m³ requires compaction pressures of 0.40–0.55 MPa and feed volume of 0.65–0.75 m³ of a linear meter of the Agricultural Crop Stem Biomass depending on the blending ratio of flax stems with other biomass materials. Higher flax stem content, due to its fibrous properties, demands increased pressure to ensure uniform density and material cohesion.

Flax-based FRs have energy potentials of 16–18 MJ/kg, comparable to wood fuels and sufficient for modern solid-fuel heating systems. The introduction of the Variable-Volume Pressing Chamber (VPC) successfully addressed challenges such as stem elasticity, allowing for efficient compaction and consistent density throughout production. These findings underscore the importance of integrating rational compaction pressures, biomass volumes, and blending ratios to achieve a balance between energy efficiency, mechanical strength, and sustainability.

By converting agricultural residues into biofuels, the study provides a practical solution to mitigate environmental pollution from residue burning, reduce waste, and promote renewable energy. Fuel rolls represent a competitive and sustainable alternative to traditional fossil fuels, contributing to cleaner energy solutions and advancing the global transition towards more sustainable energy practices.

REFERENCES

- [1] Amann, M., Gomez-Sanabria, A., Klimont, Z., Maas, R., Winiwarter, W. (2017). Measures to address air pollution from agricultural sources. *Report for International Institute for Applied Systems Analysis*. Available at: <https://previous.iiasa.ac.at/web/home/research/researchPrograms/air/policy/SR11-AGRICULTURE-FINAL.pdf>
- [2] Aziz, R.A., Aziz, S.A. (2018) Application of Box Behnken Design to Optimize the Parameters for Kenaf-Epoxy as Noise Absorber, *IOP Conf. Ser.: Mater. Sci.*, Vol. 454 (1), pp 1-11, DOI:10.1088/1757-899X/454/1/012001
- [3] Box G.E.P., Behnken D.W., (1960). Some New Three Level Designs for the study of Quantitative Variables, *Technometrics*, Vol. 2(4), pp. 455-475,
- [4] Didukh, V., Yaheliuk, S., Artyukh, T., Albota, D., Holiy, O. (2022) Decrease of elastic properties of oleanginous flax residues by decortication. *INMATEH-Agricultural Engineering*, Vol. 67(2), 285–292 <https://doi.org/10.35633/inmateh-67-29>
- [5] Freund, R.J., Wilson, W.J., Mohr, D.L. (2010). Data and Statistics. Statistical Methods. *Academic Press*, 1–65. doi: <https://doi.org/10.1016/b978-0-12-374970-3.00001-9>
- [6] Gageanu, I., Cujbescu, D., Persu, C., Gheorghe, G. (2022) Research on the validation of mathematical models for biomass powder compaction using a ring die pelleting equipment. *INMATEH-Agricultural Engineering*, Vol.66(1), 211–218, <https://doi.org/10.35633/inmateh-66-21>
- [7] Gatkal, N.R., Nalawade, S.M., Sahni, Walunj, A.A., Kadam, P.B., Bhanage, G.B., Rahul, D. (2024) Present trends, sustainable strategies and energy potentials of crop residue management in India: A review, *Heliyon*, 10 (21), e39815, <https://doi.org/10.1016/j.heliyon.2024.e39815>

- [8] Goudenhooff, C.; Siniscalco, D.; Arnould, O.; Bourmaud, A.; Sire, O.; Gorshkova, T.; Baley, C. (2018) Investigation of the Mechanical Properties of Flax Cell Walls during Plant Development: The Relation between Performance and Cell Wall Structure. *Fibers*, Vol. 6 (1), 6. <https://doi.org/10.3390/fib6010006>
- [9] Hajlis, G. (2004). *Plant material mechanics. (Механіка рослинних матеріалів)*. Lutsk State Technical University, Lutsk, 301, Ukraine;
- [10] Ibrahim, Ayman. (2008). Physical and mechanical characteristics for some agricultural residues. *Misr J . Ag. Eng.*, 25. 121-147. https://www.researchgate.net/publication/271012949_PHYSICAL_AND_MECHANICAL_CHARACTERISTICS_FOR_SOME_AGRICULTURAL_RESIDUS
- [11] Jiang, Y., Havrysh, V., Klymchuk, O., Nitsenko, V., Balezentis, T., & Streimikiene, D. (2019). Utilization of Crop Residue for Power Generation: The Case of Ukraine. *Sustainability*, 11(24), 7004. <https://doi.org/10.3390/su11247004>
- [12] Kashytskyi V.P., Sadova O.L., Yanchuk S.L. (2023). Intensification of the formation process of sodium sulfate-modified biocomposite materials based on the glutinous matrix. *Funct. Mater.*, Vol.30 (1), pp. 35-42. <https://doi.org/10.15407/fm30.01.35>
- [13] Lan, R., Eastham, S.D., Liu, T., Norford, L.K., Barrett S. (2022) Air quality impacts of crop residue burning in India and mitigation alternatives. *Nat Commun* 13, 6537 <https://doi.org/10.1038/s41467-022-34093-z>
- [14] Marian, Gregory. (2016) Solid biofuels: producer and property: Manual for the use of solid biofuel producers, Government Rep. Moldova, *Progr. United Nations Development*. Chisinau: S. n., 172 p.
- [15] Mehmood Ali, Muhammad Saleem, Zakir Khan, Ian A. Watson (2019) *The use of crop residues for biofuel production*, In Woodhead Publishing Series in Composites Science and Engineering, Biomass, Biopolymer-Based Materials, and Bioenergy, Woodhead Publishing, pp.369-395, <https://doi.org/10.1016/B978-0-08-102426-3.00016-3>
- [16] Milton Halder, Shahnewaz Jim Ahmad, Tanvir Rahman, Jagadish Chandra Joardar, Md.Abu Bakar Siddique, Muhammad Saiful, Islam, Mahbub Ul Islam, Shuai Liu, Sheikh Rabbi, Xinhua Peng (2023) Effects of straw incorporation and straw-burning on aggregate stability and soil organic carbon in a clay soil of Bangladesh, *Geoderma Regional*, Vol.32, e00620 <https://doi.org/10.1016/j.geodrs.2023.e00620>
- [17] Montgomery C. Douglas. (2013). *Design and Analysis of Experiments*. John Wiley & Sons, Inc. 757 p. file:///C:/Users/Sasha/Downloads/Douglas-C.-Montgomery-Design-and-Analysis-of-Experiments-Wiley-2012%20(1).pdf
- [18] Yaheliuk S., Didukh V., Tom'yk V., (2019), Justification of the new Technology of Processing Residues of Flax Stem Mass in Western Polissya. *Teka Commission of Motorization and Energetic in Agriculture*. 19(1), 5-12;
- [19] Yaheliuk, S. Didukh, V., Busnyuk, V., Boyko, G., Shubalyi, O. (2020) Optimization efficient combustion process of small-sized fuel rolls made of oleaginous flax residues. *INMATEH-Agricultural Engineering*, Vol.62(3), pp.361–368. <https://doi.org/10.35633/inmateh-62-38>
- [20] Yahelyuk, S., Fomych, M., Golii, O. (2021) Identification and classification of crop residues for further use. *Agricultural machinery*. 47, 95-101
- [21] Energy content for various biomass (n.d.) C.F.N https://cfnielsen.com/faq/what-is-the-calorific-value-of-wood/?utm_source=chatgpt.com
- [22] FAOSTAT. (n.d.). Compare Data. Retrieved October, 15, 2024, from <https://www.fao.org/faostat/en/#compare>

DESIGN OF A WHEELED ADAPTIVE CHASSIS LEVELING SYSTEM FOR HILLY AND MOUNTAINOUS AREAS

丘陵山区轮式自适应底盘调平系统设计

Yuqian ZHAO¹⁾, Wei LIU¹⁾, Shijun SONG¹⁾, Peng LIU¹⁾, Yihu WANG¹⁾, Guohai ZHANG^{1,2*)}

¹⁾ Shandong University of Technology, Collage of Agricultural Engineering and Food Science, Zibo, China

²⁾ Shandong University of Technology, Institute of Modern Agricultural Equipment, Zibo, China

Tel: +8615668066520; E-mail: guohaizhang@sdut.edu.cn

Corresponding author: Guohai Zhang

DOI: <https://doi.org/10.35633/inmateh-75-22>

Keywords: chassis for hilly and mountainous areas; leveling strategy; control system; chassis.

ABSTRACT

The cultivated land in hilly and mountainous areas of China accounts for a high proportion. However, the complex terrain makes it extremely difficult for traditional agricultural machinery to operate. There is a high risk of rollover, and the operation effect is not satisfactory. Achieving agricultural mechanization in these areas faces huge challenges. This study is dedicated to designing a four-wheel adaptive chassis suitable for hilly and mountainous areas to solve the stability problem of agricultural machinery during operation. The research adopts the leveling strategy of tracking the lowest fixed point plane in the four-point leveling method. By constructing the chassis coordinate system and analyzing the coordinate transformation matrix, the motion relationships of each support point are determined, and precise leveling is achieved based on this. In the system design, the hydraulic system is crucial. According to the preset vehicle parameters, various parameters of the hydraulic cylinder are accurately calculated, and a suitable gear pump is selected to ensure stable operation under different working conditions. The control system calculates the height errors of each point based on the body tilt angle data collected by the biaxial sensor, and then controls the action of the hydraulic valve to achieve automatic leveling of the chassis. The MATLAB/Simulink platform is used to simulate different tilt angle conditions, verifying the effectiveness of the control system. The experimental results show that the chassis can achieve rapid leveling within the range of -12° to 12° in the transverse direction and -8° to 8° in the longitudinal direction, and the leveling time is within two seconds. The leveling process is stable, without shaking and insufficient stroke problems. This indicates that the leveling strategy and system design of the chassis are reasonable and effective, which can significantly improve the stability and safety of agricultural machinery during operation in hilly and mountainous areas, providing important technical support for promoting agricultural mechanization in hilly and mountainous areas.

摘要

中国丘陵山区耕地占比高，但地形复杂致使传统农机作业困难重重，翻车风险大且作业效果不佳，实现农业机械化面临巨大挑战。本研究致力于设计一种适用于丘陵山区的四轮自适应底盘，以解决农机作业的稳定性问题。研究采用四点调平中的最低点不动面追逐调平策略，通过构建底盘坐标系和分析坐标变换矩阵，确定各支撑点的运动关系，以此为基础实现精准调平。在系统设计上，液压系统是关键，根据预设的车辆参数，精确计算液压缸的各项参数，选用合适的齿轮泵，确保在不同作业工况下都能稳定运行。控制系统依据双轴传感器采集的车身倾斜角度数据，计算各点高度误差，进而控制液压阀动作，实现底盘自动调平。利用 MATLAB/Simulink 平台对不同倾斜角度工况进行仿真，验证了控制系统的有效性。实验结果显示，该底盘在横向 -12° 至 12° 、纵向 -8° 至 8° 范围内可实现快速调平，且调平时间在两秒以内，调平过程平稳，无晃动和行程不足问题。这表明底盘的调平策略和系统设计合理有效，能显著提升农机在丘陵山区作业的稳定性和安全性，为推动丘陵山区农业机械化发展提供了重要技术支持¹。

INTRODUCTION

China has a vast territorial area and complex and diverse terrains. Among them, the cultivated land area in hilly and mountainous areas with a slope exceeding 2 degrees accounts for 38% of the country's total cultivated land area.

YuQian Zhao, M.S. Stud. Eng.; Wei Liu, M.S. Stud. Eng.; ShiJun Song, M.S. Stud. Eng.; Peng Liu, M.S. Stud. Eng.; YiHu Wang, M.S. Stud. Eng.; Guohai Zhang Prof. Ph.D. Eng.

The southwestern region is a typical representative of hilly and mountainous areas in China, and the area of hilly and mountainous areas in its major provinces generally exceeds 70% of the total area. Specifically, the area of hilly and mountainous areas in Sichuan Province accounts for 94.1% of the total area, 92.5% in Guizhou Province, 88.8% in Yunnan Province, 85.3% in Chongqing City, and the proportion of the area of hilly and mountainous areas in the Guangxi Zhuang Autonomous Region also reaches 76.1% (Luo, 2019). Due to the undulating terrain, fragmented plots and relatively large slopes in hilly and mountainous areas, conventional agricultural machinery is faced with the predicament of "difficulty in accessing and poor stability". If this problem is not properly solved, rollover accidents are highly likely to occur during the operation of agricultural machinery, resulting in irreparable losses. In addition, as the terrain is sloping, the chassis of agricultural machinery often fails to remain level during operation. Coupled with the rugged and uneven terrain, the operation effect of agricultural machinery, especially that of harvesting operations, is significantly affected. Therefore, achieving the full mechanization in hilly and mountainous areas has always been a difficult problem that urgently needs to be solved (Wang *et al.*, 2024; Sun *et al.*, 2023; Mou *et al.*, 2024; Li *et al.*, 2019).

In recent years, the international and domestic academic communities have conducted extensive research on the adaptive performance of agricultural machinery chassis. For example, the Tri-star II robot developed by the National Space Development Agency of Japan (NASDA), as a typical representative of three-wheeled all-terrain mobile robots, adopts a suspension structure design with three components arranged at equal angles (Liu *et al.*, 2005). This design significantly improves the robot's performance in obstacle crossing and adaptation to diverse terrain environments. The SHRIMP robot, developed by the Swiss Automation and Systems Laboratory (SASL), is a representative six-wheeled all-terrain mobile robot (Hussain *et al.*, 2005). This robot adopts six-wheel drive technology and has the ability to overcome obstacles with a height up to twice the diameter of its wheels. The bipedal robot Atlas, developed by Boston Dynamics, needs to be controlled by algorithms to simulate human walking movements and has the working ability in complex environments (Kuindersma *et al.*, 2016). In China, remarkable progress has also been made in relevant fields in recent years. For example, Wu *et al.*, (2021), designed an electromechanical automatic leveling system based on STM32, which achieves multi-point leveling by controlling the speed of different leg servo motors, avoiding mutual coupling caused by step-by-step adjustment of legs, and combining sensor technology to solve the problem of virtual legs. Finally, an experimental platform was built according to the design scheme to prove the feasibility of the leveling method and control system. Jian *et al.*, (2023), aimed to solve the problems of easy tipping and poor trafficability of tractors in hilly and mountainous areas. In this study, the virtual prototype technology was applied. A three-dimensional simplified model of the chassis was established by SolidWorks. The roll stability and obstacle-crossing performance were analyzed under simulated working conditions in ADAMS/View, and the finite element analysis was carried out on key components using ANSYS Workbench. The results show that the maximum roll stability angle of the tractor chassis meets the standard, the obstacle-crossing performance is good, the stress and deformation displacements of key components all meet the requirements, and the whole machine is within the safe range of use and can meet the operation requirements in hilly and mountainous areas. Yin Xiang *et al.*, (2021), and the research team developed an automatic leveling system for the spray boom of high-clearance pesticide applicators. This system utilizes the incremental PID algorithm. By calculating and outputting control signals to the solenoid valve, it further controls the movement of the leveling cylinder to achieve real-time adjustment of the spray boom's posture.

This research aims to design an adaptive wheeled chassis suitable for the terrain characteristics and working environment of hilly and mountainous areas. This chassis can achieve precise stability adjustment to solve the problems of excessive adjustment amplitude and insufficient stability that occur during the adjustment process of existing adaptive chassis. Through the chassis design proposed in this study, it is expected to significantly improve the overall operational stability of agricultural machinery and the safety during its movement.

MATERIALS AND METHODS

Construction of the Motion Model for the Leveling Strategy

Under the classification of support structures, leveling systems can mainly be divided into three types: three-point leveling, four-point leveling, and six-point leveling. The advantages of three-point leveling are its simple structure, absence of virtual legs, and simple control. However, due to the small number of support points, it has poor stability and cannot bear heavy loads, and is suitable for occasions with small slopes and light loads. Four-point leveling, as the most widely used method in practical applications, can maintain balance

both longitudinally and transversely compared with three-point leveling, ensuring stability during the operation process. Six-point leveling, due to the large number of support points and complex control process, is usually applied in large machinery (Skrickij *et al.*, 2024). Based on this, this research chooses to adopt the four-point leveling method.

According to the differences in leveling methods, they can mainly be classified into two major categories: position leveling and angle leveling. The position error leveling method mainly adopts the "tracking" leveling strategy, which can be further subdivided into four ways: the highest point remaining fixed, the lowest point remaining fixed, the center point remaining fixed, and the specified point remaining fixed. The core of the tracking leveling method lies in using the highest point, the lowest point, the center point or the specified point as the reference and achieving precise leveling through continuous adjustment (Peng *et al.*, 2018). This method performs well in terms of leveling speed and accuracy, but its control algorithm is relatively complex. In this design, the tracking leveling strategy with the lowest point remaining fixed was adopted. Given that harvesting machinery has a relatively large mass when fully loaded, using other leveling methods may lead to mechanical tilting or shaking. Therefore, choosing the tracking leveling strategy based on the lowest point is aimed at improving the stability of agricultural machinery during operation and ensuring the high efficiency of agricultural machinery operations. The angle leveling method detects the tilt angle through an angle sensor and adjusts the length of each support leg accordingly to reach the preset minimum angle threshold and complete the calibration process. This calibration technique is often applied in two-point calibration scenarios. Its algorithm structure is simple and avoids complex coupling calculations. However, this method has certain limitations in calibration time.

In practical application scenarios, the lowest point adjustment method within the position adjustment methods can be further subdivided into the conventional lowest point fixed leveling method, the lowest point fixed line tracking leveling method, and the lowest point fixed plane tracking leveling method. During the four-point leveling process, the conventional lowest point tracking leveling method may lead to chassis tilting or large movement amplitudes, thus having a negative impact on the operation effect. Comparatively, the lowest point edge tracking leveling method, that is, leveling by connecting two points and taking the lowest point as the target, is more suitable for the application of three-point leveling. Given that this research adopts the four-point leveling technique, this research has adopted the plane tracking leveling mode within the lowest point fixed leveling method (Che *et al.*, 2023). This mode constructs three adjustment points into a plane and conducts posture adjustment based on the lowest point to achieve the adjustment goal.

Fig.1 illustrates the schematic diagram of the rotation of the chassis coordinate system. A biaxial sensor is installed at the center of the chassis to measure the tilt angles of the chassis relative to the X - axis and Y - axis. Taking the plane ABCD as the coordinate plane of the chassis, OXYZ represents the chassis coordinate system. In this coordinate system, the center point of the chassis remains fixed, while the XY - axis will tilt at specific angles according to different terrains, forming the plane $OX_1Y_1Z_1$. Nevertheless, the position of the center point O remains unchanged. The tilt angles θ and δ of the X - axis and Y - axis can be measured by the sensor located at the center of the chassis.

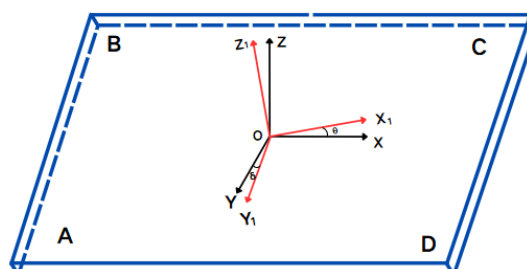


Fig. 1 – Schematic Diagram of the Rotation of the Chassis Coordinate System

Based on the rotation angles θ and δ detected by the sensor, and in combination with the transformation scenarios in different sequences, the following situations can be distinguished:

1. The moving coordinate system rotates by an angle θ around the X-axis of the reference coordinate system, and then rotates by an angle δ around the Y-axis. Since the operations in the back are performed first when multiplying, the transformation matrix is obtained as follows:

$$\begin{aligned}
 F_1 &= \text{Robot}(Y, \delta)\text{Robot}(X, \theta) \\
 &= \begin{bmatrix} \cos\delta & 0 & \sin\delta \\ 0 & 1 & 0 \\ -\sin\delta & 0 & \cos\delta \end{bmatrix} \cdot \begin{bmatrix} 1 & 0 & 0 \\ 0 & \cos\theta & -\sin\theta \\ 0 & \sin\theta & \cos\theta \end{bmatrix} \\
 &= \begin{bmatrix} \cos\delta & \sin\theta\sin\delta & \sin\delta\cos\theta \\ 0 & \cos\theta & -\sin\theta \\ -\sin\delta & \sin\theta\cos\delta & \cos\theta\cos\delta \end{bmatrix}
 \end{aligned} \tag{1}$$

2. The moving coordinate system rotates by an angle δ around the Y-axis of the reference coordinate system first, and then rotates by an angle θ around the X-axis, and the transformation matrix is obtained as follows:

$$\begin{aligned}
 F_2 &= \text{Robot}(X, \theta)\text{Robot}(Y, \delta) \\
 &= \begin{bmatrix} 1 & 0 & 0 \\ 0 & \cos\theta & -\sin\theta \\ 0 & \sin\theta & \cos\theta \end{bmatrix} \cdot \begin{bmatrix} \cos\delta & 0 & \sin\delta \\ 0 & 1 & 0 \\ -\sin\delta & 0 & \cos\delta \end{bmatrix} \\
 &= \begin{bmatrix} \cos\delta & 0 & \sin\delta \\ \sin\theta\sin\delta & \cos\theta & -\sin\theta\cos\delta \\ -\sin\delta & \sin\theta & \cos\theta\cos\delta \end{bmatrix}
 \end{aligned} \tag{2}$$

Since the tilt angles during the agricultural machinery operation can basically be regarded as small angles, it can be obtained that:

$$\sin\delta \approx \delta, \sin\theta \approx 0, \sin\theta\sin\delta \approx 0, \cos\theta \approx \cos\delta \approx 1 \tag{3}$$

It can be derived that:

$$F_1 = F_2 \approx \begin{bmatrix} 1 & 0 & \delta \\ 0 & 1 & -\theta \\ -\delta & \theta & 1 \end{bmatrix} \tag{4}$$

Therefore, regardless of whether the rotation occurs first around the X - axis or the Y - axis, under the condition that the tilt angles are small, the matrices are the same. When the chassis is horizontal, the coordinate system coincides with the moving coordinate system. Suppose point N is a certain point on the chassis when it is horizontal. Fix point N where the moving coordinate system coincides with the chassis. Thus, $N_{Z1}=0$. When the platform rotates by an angle δ relative to the Y - axis and by an angle θ relative to the X - axis, and the coordinates of point N in the reference coordinate system are (N_x, N_y, N_z) , can be obtained that:

$$\begin{bmatrix} N_x \\ N_y \\ N_z \end{bmatrix} = F \cdot \begin{bmatrix} N_{x1} \\ N_{y1} \\ N_{z1} \end{bmatrix} \tag{5}$$

$$N_z = -\delta \cdot N_{x1} + \theta \cdot N_{y1} + N_{z1} \tag{6}$$

Among them, with $N_{z1} = 0$, then $N_z = -\delta \cdot N_{x1} + \theta \cdot N_{y1}$, and the coordinate positions of each support point on the Z - axis can be calculated.

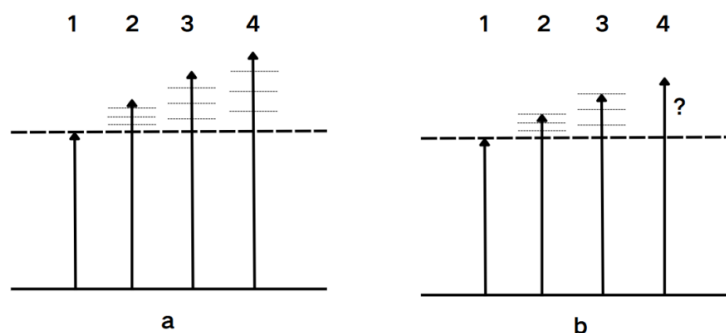


Fig. 2 -The leveling process of tracking the lowest point plane

The core of the leveling strategy in this study lies in dividing the four legs into four levels according to their height differences: the highest point, the second - highest point, the second - lowest point, and the lowest point. By subdividing the vertical height error of each leg relative to the lowest point into three intervals, during the initial adjustment stage, the displacement distances of the second - highest point and the second - lowest point relative to the lowest point are both equal to one - third of the distance of the lowest point. The lowest

point, the second - lowest point, and the second - highest point form a plane. During this process, the highest point needs to track the plane formed by the lowest point, the second - lowest point, and the second - highest point.

Assume that the coordinates of the four support points in the reference coordinate system are $a(X_a, Y_a, Z_a)$, $b(X_b, Y_b, Z_b)$, $c(X_c, Y_c, Z_c)$, and $d(X_d, Y_d, Z_d)$. According to the different positions of the four points, the following three cases can be summarized (as shown in Fig.3).

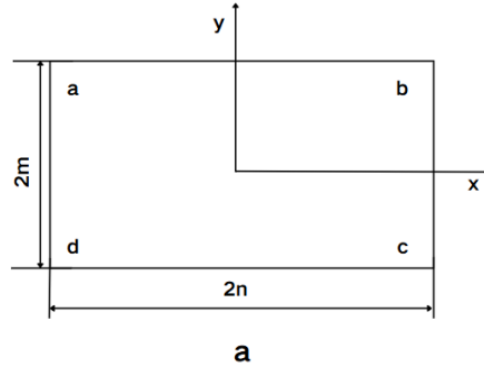


Fig. 3 - Basic Situation of the Chassis Plane

Assume that point **a** is the lowest point, point **b** is the second - lowest point, point **c** is the second - highest point, and point **d** is the highest point.

Determine the normal vector of the plane passing through points **a**, **b**, and **c**.

$$n = \begin{vmatrix} i & j & k \\ x_c - x_a & y_c - y_a & z_c - z_a \\ x_b - x_a & y_b - y_a & z_b - z_a \end{vmatrix} \tag{7}$$

$$= [y_c - y_a)\Delta z_b - (y_b - y_a)\Delta z_c]i - [(x_c - x_a)\Delta z_b - (x_b - x_a)\Delta z_c]j + [(x_c - x_a)(y_b - y_a) - (x_b - x_a)(y_c - y_a)]k$$

$$\Delta z_i = z_a - z_i = \delta(x_i - x_a) + \theta(y_a - y_i) \quad (i = a, b, c, d) \tag{8}$$

The normal vector of the plane formed by points **a**, **b**, and **c** in Figure 3 is:

$$n = -4mn\delta i + 4mn\theta j - 4mnk \tag{9}$$

Therefore, the equation of the plane is:

$$\delta(x - x_a) + \theta(y - y_a) - (z - z_a) = 0 \tag{10}$$

Assume that the moving speeds of points **b** and **c** are k ($i=b,c$). After the moving time t , the vertical position errors of points **b** and **c** relative to the lowest point are:

$$\Delta z_i(t) = \Delta z_i - tk\Delta z_i = (1 - tk)\Delta z_i \tag{11}$$

At this point, the plane determined by points **a**, **b**, **c** is:

$$-\delta(1 - tk)(x + x_a) + \theta(1 - tk)(y + y_a) - (z + z_c) = 0 \tag{12}$$

By substituting the x - and y - coordinates of point **d** into the formula of the plane formed, the z - coordinate of point **d** can be obtained.

$$z_d(t) = z_a - 2n\theta(1 - tk) \tag{13}$$

Therefore, the rising distance of **d** within time t is:

$$s_d = z_d(t) - z_d = 2n\theta tk \tag{14}$$

The rising speed of point **d**.

$$v_d = \frac{s_d}{t} = 2nek \tag{15}$$

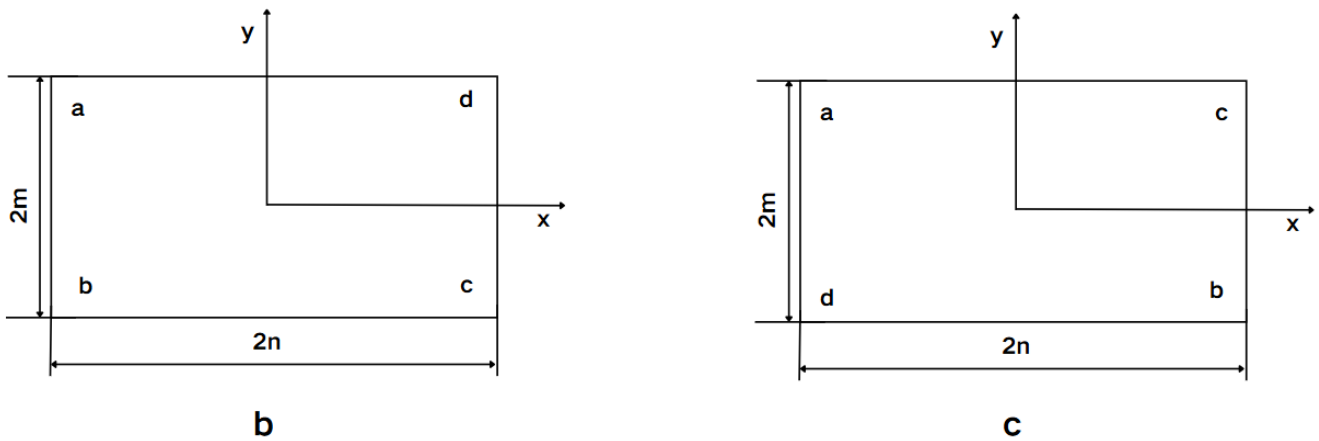


Fig. 4 - The other two basic situations

Similarly, the ascending speed of point **d** in Figure 4b $v_d=2n\delta k$, the ascending speed of point **d** in Figure 4c $v_d=(2m\delta + 2n\theta) k$ can be known.

Through predictive calculations for a variety of different situations, it was found that:

- (1) When the projected distance between points **a** and **d** on the horizontal plane is 2 m, the ascending speed of point **d** is the same as that in Figure 4a, that is, $v_d=2n\theta k$.
- (2) When the projected distance between points **a** and **d** on the horizontal plane is 2n, the ascending speed of point **d** is the same as that in Figure 4b, that is, $v_d=2n\delta k$.
- (3) When the projected distance between points **a** and **d** on the horizontal plane is equal to the diagonal distance of the plane, that is, $(2\sqrt{m^2 + n^2})$, the ascending speed of point **d** is the same as that in Figure 4c, that is, $v_d=(2m\delta + 2n\theta)$.

Therefore, it is only necessary to detect and process to calculate the positional relationship between the highest point and the lowest point, and then the movement speed of the lowest point can be determined.

Hydraulic System

The leveling system in this study consists of a detection system, a leveling mechanism, and a control system. The detection system is a dual - axis sensor. The dual - axis sensor is installed at the center point of the chassis and is used to detect the tilt angles of the chassis in the front - rear and left - right directions. The leveling mechanism is composed of a hydraulic system, which includes suspension hydraulic cylinders and direction valves respectively equipped at the four wheels.

As the core power source for adjusting the chassis attitude, the hydraulic system realizes the leveling function of the vehicle body through the telescopic movement of the hydraulic cylinders. In this study, the design of the chassis is mainly based on preset parameters, according to table 1.

Table 1

Preset Parameters	
Item	Parameter
Overall Vehicle Length	6000 mm
Entry 2	2400 mm
Wheelbase	2800 mm
Track Width	1400 mm
Predetermined Net Body Mass	5500 kg
Predetermined Full Load Mass of the Grain Bin	1500 kg

The hydraulic system mainly consists of key components such as the oil tank, filter, hydraulic pump, relief valve, two - position two - way solenoid valve, three - position four - way solenoid valve, one - way throttle valve, and hydraulic cylinder. The chassis designed in this research for the agricultural machinery field has a preset net vehicle body mass of 5500 kg. If it is applied to the harvesting machinery field, the additional weight when fully loaded with grains needs to be considered, and this load is estimated to be approximately 1500 kg.

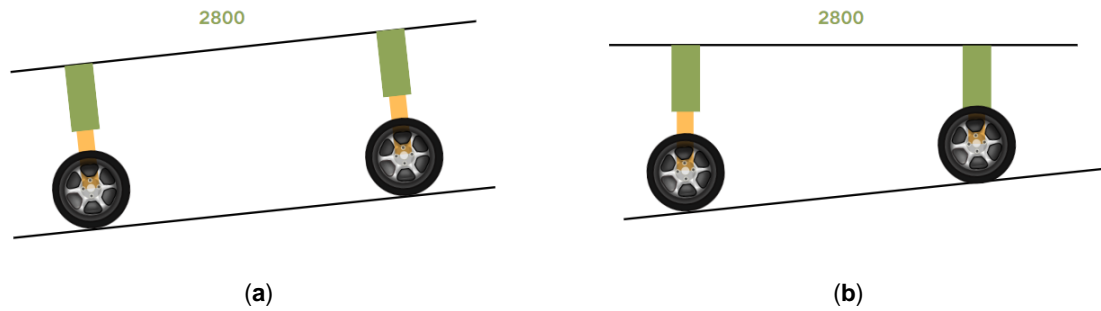
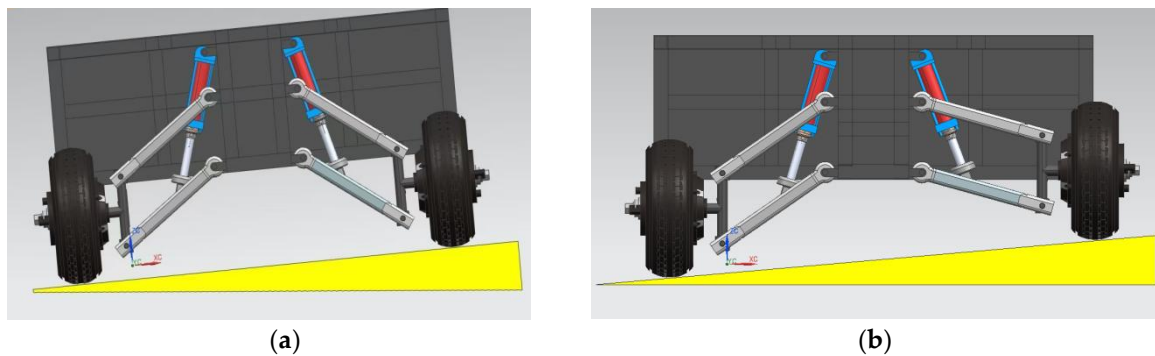


Fig. 5 - Schematic diagram of the leveling process in the longitudinal direction

During the actual operation of agricultural machinery, there are mainly four single - direction tilting conditions, namely forward tilt, backward tilt, left tilt, and right tilt, as well as four compound tilting conditions, including left - rear tilt, right - rear tilt, left - front tilt, and right - front tilt. Since the leveling is carried out in a way of tracking the plane formed by the four lowest points, regardless of the tilting condition, it only needs to determine the lowest point, the second - lowest point, the second - highest point, and the highest point. Taking Figure 5 as an example, in the case of backward tilt, the rear wheels are the lowest points. Then, the two front wheels need to track the rear wheels, and the hydraulic cylinders perform a retracting motion to lower the front part of the vehicle body, thus leveling the vehicle body. The same principle can be applied to other single - direction tilting situations.

Fig. 6-



Schematic diagram of the leveling process in the transverse direction

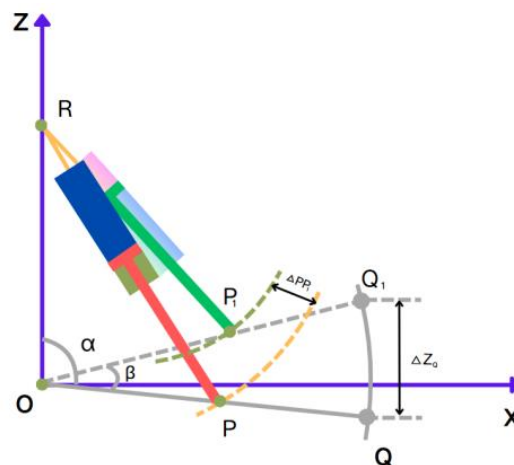


Fig. 7 - Schematic diagram of the leveling hydraulic mechanism

When there is a left - front tilt, the right - rear wheel is the lowest point and the left - front wheel is the highest point. During the leveling process, the distances between the other two wheels and the right - rear wheel are calculated. Subsequently, the hydraulic cylinders perform a retracting motion. The hydraulic cylinder of the left - front wheel retracts to track the plane formed by the other three points, reducing the distance between the vehicle body and the wheel, thus ensuring a stable leveling process. The same method can be applied to other compound - direction tilting situations.

The cosine law in triangle ORP.

$$\cos\alpha = \frac{|\overline{OR}|^2 + |\overline{OP}|^2 - |\overline{RP}|^2}{2|\overline{OR}||\overline{OP}|} \tag{16}$$

$$\alpha = \arccos \frac{|\overline{OR}|^2 + |\overline{OP}|^2 - |\overline{RP}|^2}{2|\overline{OR}||\overline{OP}|} \tag{17}$$

OQ₁ is obtained by rotating OQ around point O. Let the coordinates of point Q be (X_Q, Z_Q), and the coordinates of point Q₁ be (X_{Q1}, Z_{Q1}), where:

$$X_Q = \cos\left(\alpha - \frac{n}{2}\right) = |\overline{OQ}| \sin\alpha \tag{18}$$

$$Z_Q = |\overline{OQ}| = \sin\left(\alpha - \frac{n}{2}\right) = |\overline{OQ}| \cos\alpha \tag{19}$$

Derived from the rotation matrix:

$$Q_1 = (X_{Q1}, Z_{Q1}) = \begin{bmatrix} \cos\beta & \sin\beta \\ -\sin\beta & \cos\beta \end{bmatrix} \begin{bmatrix} X_Q \\ Z_Q \end{bmatrix} = \begin{bmatrix} \cos\beta & \sin\beta \\ -\sin\beta & \cos\beta \end{bmatrix} \begin{bmatrix} |\overline{OQ}| \sin\alpha \\ |\overline{OQ}| \cos\alpha \end{bmatrix} \tag{20}$$

Among them, the coordinate of point Q₁ in the Z-axis direction can be obtained by adding the required lifting amount to the coordinate of point Q in the Z-axis direction:

$$Z_{Q1} = Z_Q + \Delta Z_Q = |\overline{OQ}| \cos\alpha + \Delta Z_Q = -|\overline{OQ}| \sin\alpha \sin\beta + |\overline{OQ}| \cos\alpha \cos\beta \tag{21}$$

It can be simplified to obtain:

$$\cos\alpha + \frac{\Delta Z_Q}{|\overline{OQ}|} \cos\alpha \cos\beta - \sin\alpha \sin\beta = \cos(\alpha + \beta) \tag{22}$$

Thus, the size of the rotation angle β can be obtained as follows:

$$\beta = \alpha - \arccos\left(\cos\alpha + \frac{\Delta Z_Q}{|\overline{OQ}|}\right) \tag{23}$$

Based on the angles α and β as well as the lengths of sides OR and OQ₁ in triangle ORQ₁, according to the cosine theorem, the length of side RQ₁, which is the length of the hydraulic cylinder after extension and contraction, is:

$$|\overline{RP}_1| = \sqrt{|\overline{OR}|^2 + |\overline{OP}_1|^2 - 2|\overline{OR}||\overline{OP}_1| \cos(\alpha - \beta)} \tag{24}$$

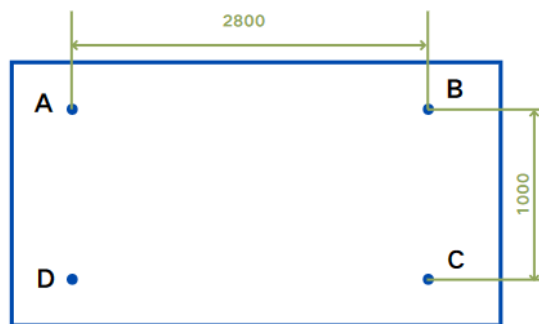


Fig. 8 - Schematic diagram of the chassis plane

As shown in the figure, the total length of the chassis in this paper is 6500 mm, and the width is 2400 mm. Among them, A, B, C, and D are hydraulic cylinders. The horizontal spacing between A and D is 1000 mm, and the longitudinal distance between A and B is 2800 mm.

This design simulates the maximum longitudinal leveling angle of ±8° and the maximum transverse leveling angle of ±12°.

1. Calculation of the Stroke of the Hydraulic Cylinder.

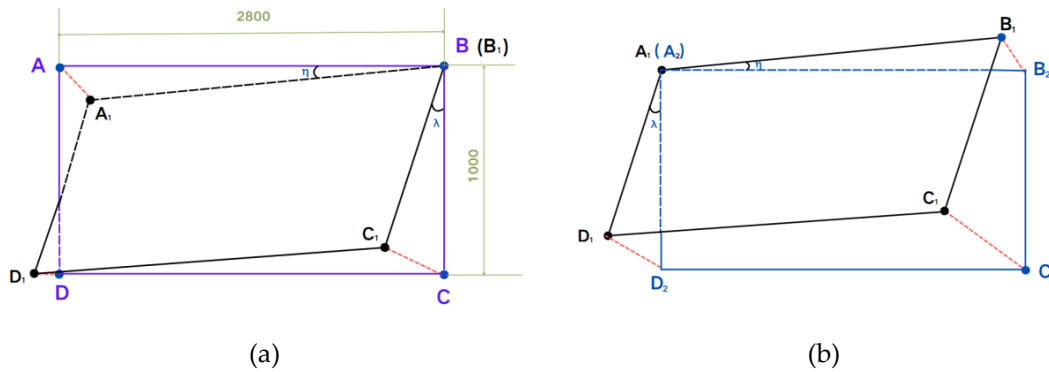


Fig. 9 - Schematic diagram of the chassis leveling process

As shown in the figure, plane ABCD is the placement diagram of the chassis in the default state. A₁B₁C₁D₁ is the placement diagram of the chassis after tilting when encountering an obstacle, and A₂B₂C₂D₂ is the result after leveling by means of the lowest point surface tracking method.

Point C is the highest point, and point A is the lowest point:

$|\overline{C_1C_2}| = |\overline{AA_1}| + |\overline{CC_1}| = 389\text{mm} + 208\text{mm} = 597\text{mm}$. Therefore, in order to achieve leveling with a longitudinal angle of 8° and a transverse angle of 12°, it is necessary to take mm.

Based on the schematic diagram of the motion model, with a value of $|\overline{OR}| = 500$ mm, the default length of the hydraulic cylinder being $|\overline{RP}| = 534$ mm, the default position being $|\overline{OP}| = 150$ mm, and α being $\alpha = 95^\circ$, by substituting the above data into the formula of the motion model, a value of $\Delta PP_1 = 162$ mm can be obtained. In order to achieve a leveling of 8° in the longitudinal direction and a left-right leveling of the hydraulic cylinder with a stroke not less than 12° in the transverse direction, the stroke should be approximately 162 mm. Therefore, the stroke of the hydraulic cylinder is set to 200 mm.

In this design, the mass of the vehicle body is 1500 kg, the preset full load weight is 5500 kg, and the total load mass is 7000 kg. Since the chassis coordinate system is located at the position of the center of gravity of the chassis, and the distances from the four support points to the center of gravity are basically the same, the loads on the four hydraulic cylinders are also basically the same, each being one-fourth of the total load on the chassis, that is, 1750 kg.

$$\sin \lambda = \frac{|\overline{CC_1}|}{|\overline{BC}|} = \frac{208}{1000} \tag{25}$$

$$\sin 12^\circ \approx 0.208 = \frac{|\overline{CC_1}|}{1000} \tag{26}$$

$$|\overline{CC_1}| = 208 \tag{27}$$

$$\sin \eta = \frac{|\overline{AA_1}|}{|\overline{AB}|} = \frac{|\overline{AA_1}|}{2800} \tag{28}$$

$$\sin 8^\circ \approx 0.139 = \frac{|\overline{AA_1}|}{2800} \tag{29}$$

$$|\overline{AA_1}| = 389 \tag{30}$$

$$G = mg \tag{31}$$

Substituting the load of a single hydraulic cylinder into the above formula, $G = 17.15$ KN is obtained.

In addition, the preset system pressure is 10 MPa, the back pressure is 0.5 MPa, and the mechanical efficiency is 0.8. By referring to the table, the speed ratio can be obtained as 1.33. When the speed ratio is 1.33, the ratio of the inner diameter of the cylinder barrel (the diameter of the rodless cavity) of the hydraulic cylinder to the diameter of the plunger rod of the hydraulic cylinder is 0.5. Through calculation, the inner diameter of the cylinder barrel of the hydraulic cylinder is 53.38 mm, and the diameter of the piston rod is 21.35 mm. According to the reference to GB/T 2348 - 1993, the inner diameter of the cylinder barrel of the hydraulic cylinder is 63 mm, and the diameter of the piston rod is 25 mm.

Table 2

Hydraulic Cylinder Dimension Diagram	
Item	Parameter
hydraulic cylinder travel	200mm
inner diameter of the hydraulic cylinder barrel	63mm
diameter of the piston rod	25mm

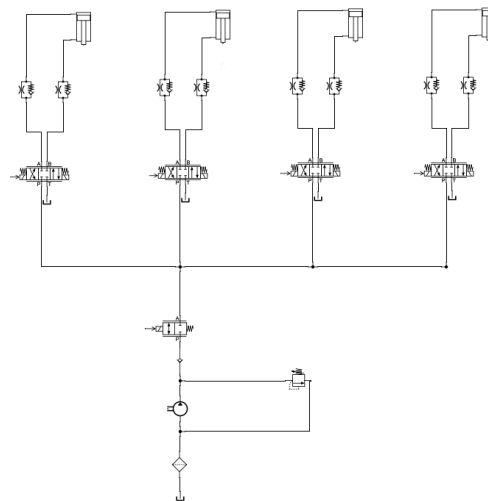


Fig. 10 - Hydraulic Schematic Diagram

1. When the vehicle body is stationary or leveling is not required, the two-position two-way solenoid valve is in the right position and in a cut-off state. Meanwhile, all four three-position four-way solenoid valves are in the middle position, the oil circuits are cut off, and none of the four hydraulic cylinders will operate.

2. When the hydraulic system enters the leveling working state: take the process where point a on the vehicle body is the highest point and point c is the lowest point as an example. At this time, after the two-position two-way solenoid valve is energized, it will be in the left position, and the main hydraulic oil circuit will be connected. Subsequently, the three-position four-way solenoid valves corresponding to **A**, **B**, and **D** are all energized and in the left position. Then, the hydraulic oil enters the rod chambers, and the hydraulic oil in the rodless chambers flows back to the oil tank. At this moment, the hydraulic cylinders **A**, **B**, and **D** perform contraction movements, and the vehicle body translates downward to achieve the leveling effect. Afterwards, if the vehicle body drives onto a flat ground and point C becomes the highest point while point A becomes the lowest point, then the three-position four-way solenoid valves corresponding to **A**, **B**, and **D** are all energized and in the right position. The hydraulic oil then enters the rodless chambers, and the hydraulic oil in the rod chambers flows back to the oil tank. At this time, the hydraulic cylinders **A**, **B**, and **D** perform extension and contraction movements, and the vehicle body translates upward to achieve the default balanced state.

Design and Simulation of the Control System

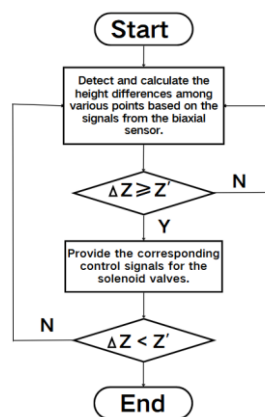


Fig. 11 - Control System Flowchart

The leveling logic of the control system is as follows:

① When the leveling starts, the dual-axis sensor collects the inclination angles of the vehicle body in the X-axis and Y-axis directions. And according to the above formula, the height of each point and the height position error in the vertical direction of the Z-axis from the lowest point are calculated.

② Judge the positional relationship between the highest point and the lowest point, and compare the relationship between ΔZ and Z' (where ΔZ represents the vertical height difference between the highest point and the lowest point, and Z' represents the threshold value for determining whether to carry out the leveling movement). If $\Delta Z \geq Z'$, the controller will send signals to each control valve to control the corresponding hydraulic cylinders to move. If $\Delta Z < Z'$, then return to the first step, and the dual-axis sensor will collect signals again to detect the position error among each point.

In order to verify the reliability and effectiveness of the adaptability of the chassis leveling parameters, this research uses the Simulink platform of MATLAB simulation software to conduct simulations and build simulation models according to the leveling strategy.

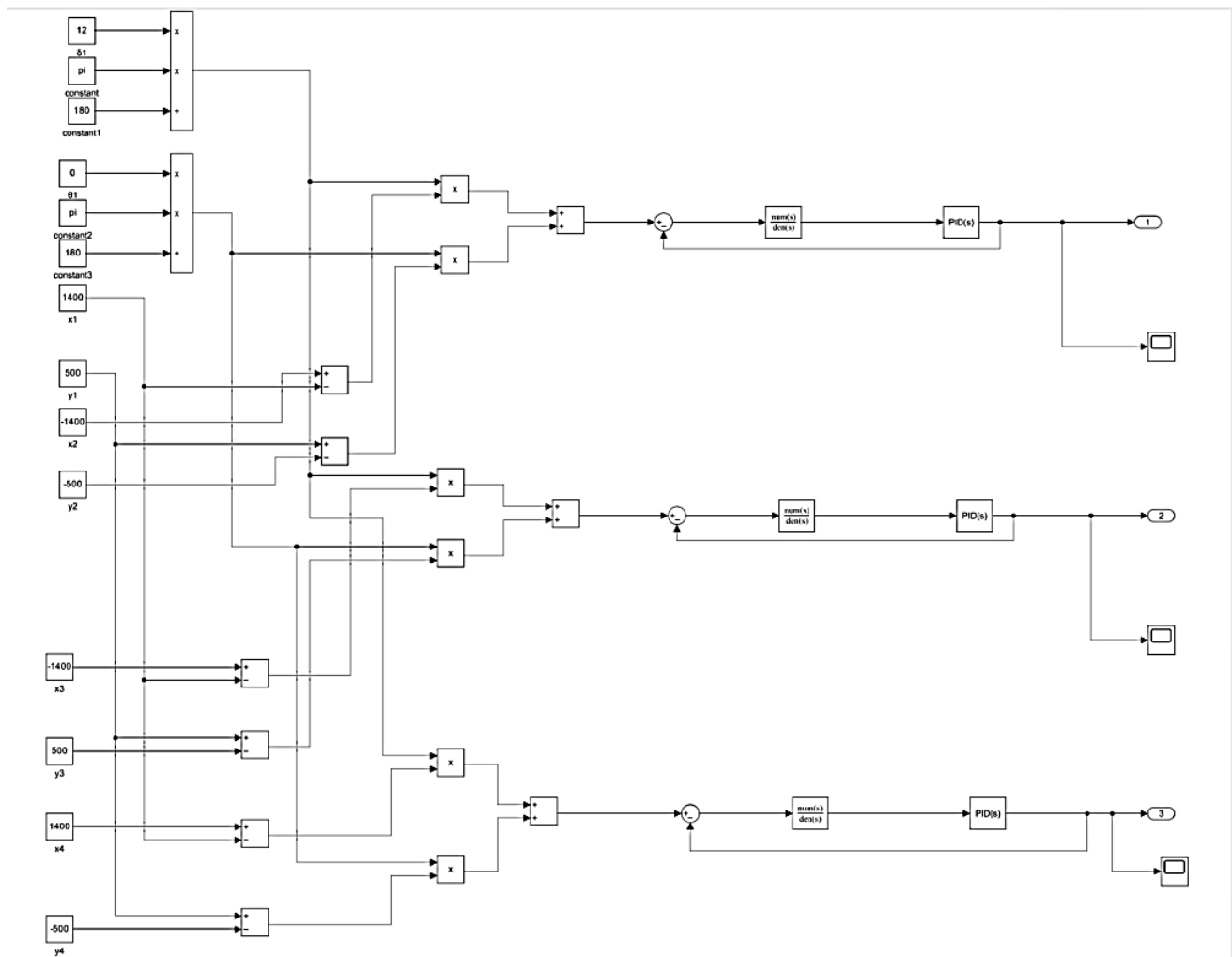


Fig. 12 - Simulation diagram on the Simulink platform

To preliminarily verify the correctness of the leveling control system, simulations will be carried out for different situations next.

1. When $\theta=8^\circ$ and $\delta=0^\circ$.

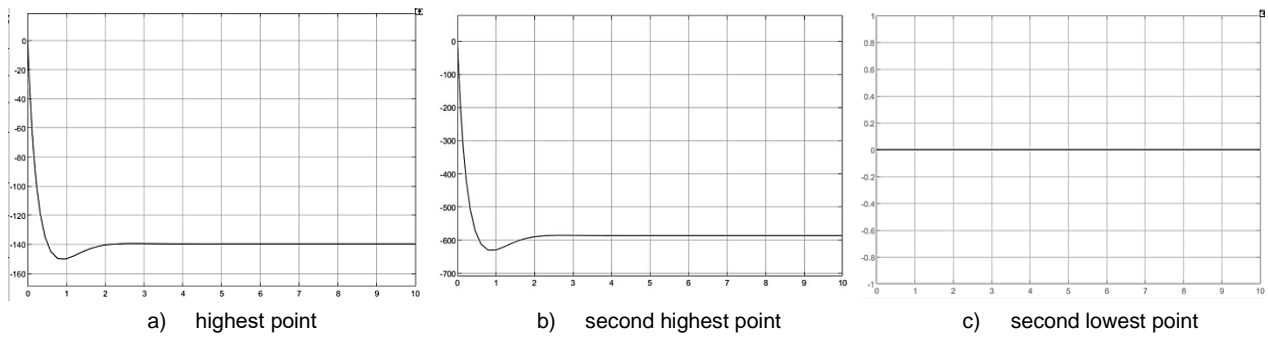


Fig. 13 - Simulation diagram on the Simulink platform

When $\theta = 8^\circ$ and $\delta = 0^\circ$, unilateral inclination occurs. The heights that need to be adjusted for the highest point and the second highest point are the same, and the heights of the lowest point and the second lowest point are the same. At this time, it is only necessary for the higher side to approach the lower side.

2. When $\theta=0^\circ$ and $\delta=12^\circ$.

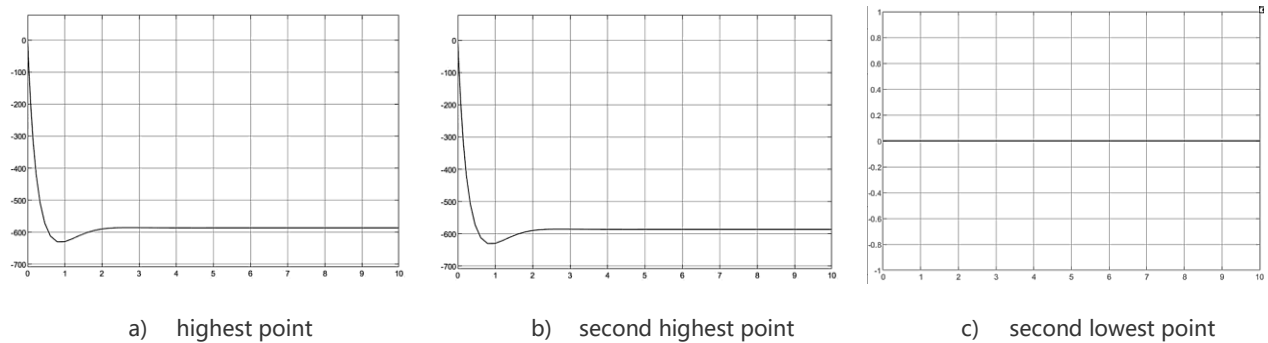


Fig. 14 - Simulation diagram on the Simulink platform

When $\theta = 0^\circ$ and $\delta = 12^\circ$, unilateral inclination occurs. The heights that need to be adjusted for the highest point and the second highest point are the same, and the heights of the lowest point and the second lowest point are the same. At this time, it is only necessary for the higher side to approach the lower side.

3. When $\theta=8^\circ$ and $\delta=12^\circ$.

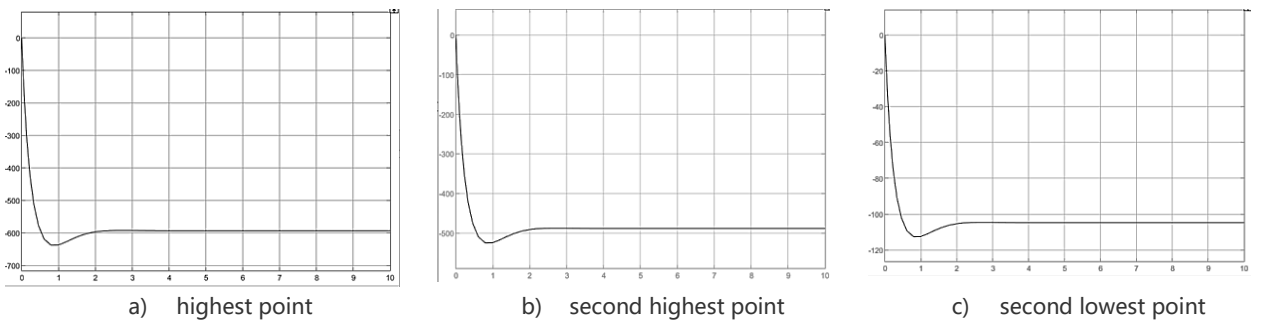


Fig. 15 - Simulation diagram on the Simulink platform

When $\theta = 8^\circ$ and $\delta = 12^\circ$, the highest point, the second highest point and the second lowest point appear. At this time, these three points approach the lowest point to complete the chassis leveling action.

4. When the angle is negative, the lowest point changes. Therefore, the simulation results are the same as when the angle is positive.

Simulation experiments on six angle conditions of inclination angles were carried out through MATLAB/Simulink. The experimental results show that each sub-process of the leveling control can work normally. The maximum range of the inclination angles is $\theta = -8^\circ$ to 8° , and $\delta = -12^\circ$ to 12° .

RESULTS

The effect of adaptive attitude adjustment will influence the performance of the whole machine during operation. Therefore, it is necessary to verify the chassis strategy and design through experiments.



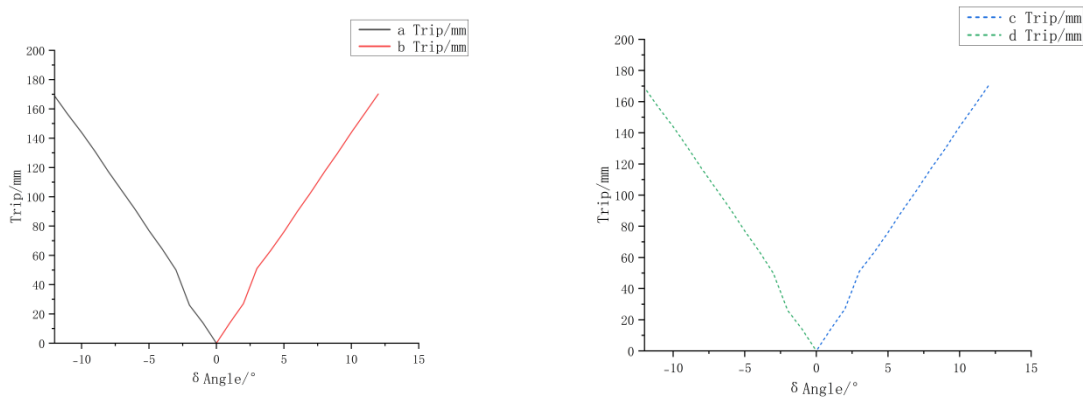
Fig. 16 - Experimental site diagram

To test the working performance of the chassis' attitude adjustment structure and attitude adjustment control system more accurately, four experiments will be carried out, and each experiment will be repeated three times. The average value will be taken and recorded.

Experiment One

Set the δ angle to incline in sequence as -12° , -10° , -8° , -6° , -4° , -2° , 0° , 2° , 4° , 6° , 8° , 10° , 12° , that is, add obstacle slopes on the left or right side according to the angles one by one to achieve the inclination of the target value of the chassis δ angle. Then immediately record the extension and contraction amounts of the attitude adjustment mechanism. Each experiment will be carried out three times to avoid contingency.

Fig. 17 -



(a) (b)
Experiment One: transversal direction tilt the stroke of each hydraulic cylinder

Experiment Two

Set the θ angle to incline in sequence as -8° , -6° , -4° , -2° , 0° , 2° , 4° , 6° , 8° , that is, add obstacle slopes in front of or behind the chassis according to the angles one by one to achieve the inclination of the chassis θ angle. Then immediately record the extension and contraction amounts of the attitude adjustment mechanism. Each experiment will be carried out three times to avoid contingency.

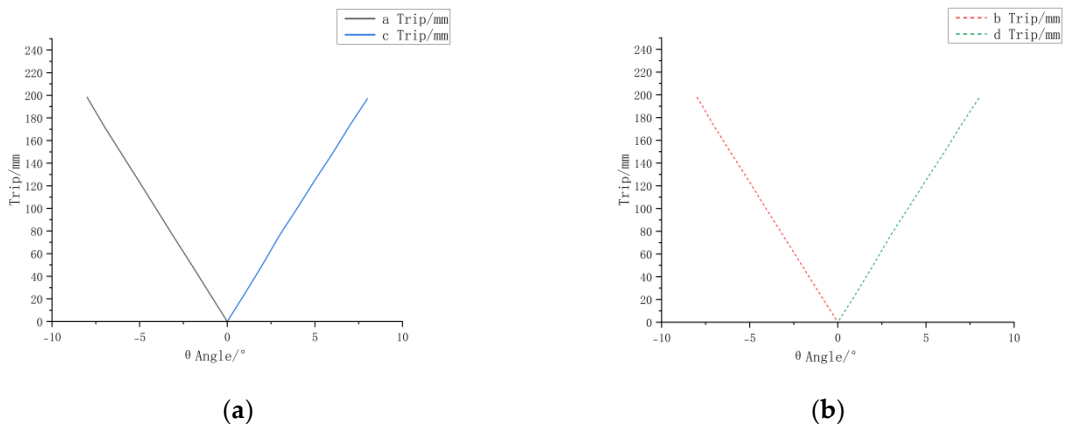


Fig. 18 - Experiment Two: longitudinal direction tilt the stroke of each hydraulic cylinder

Experiment Three:

Set the θ angle to incline in sequence as $-8^\circ, -6^\circ, -4^\circ, -2^\circ, 0^\circ, 2^\circ, 4^\circ, 6^\circ, 8^\circ$ and the δ angle to incline in sequence as $-12^\circ, -9^\circ, -6^\circ, -3^\circ, 0^\circ, 3^\circ, 6^\circ, 9^\circ, 12^\circ$ simultaneously, that is, add obstacle slopes according to the angles one by one to achieve the simultaneous inclination of the chassis θ and δ angles. Then immediately record the extension and contraction amounts of the attitude adjustment mechanism. Each experiment will be carried out three times to avoid contingency.

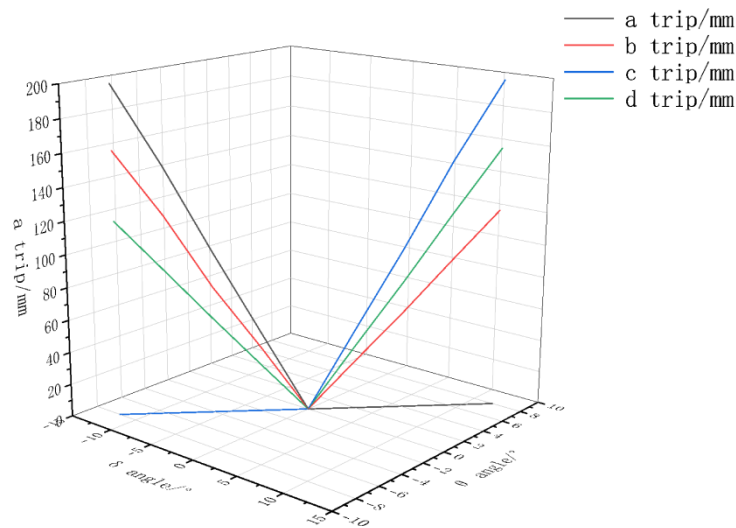


Fig. 19 - Experiment Three: The Moving Amount of Each Hydraulic Cylinder Stroke under Different Inclination Angles

Experiment Four:

Set the θ angle to incline in sequence as $8^\circ, 6^\circ, 4^\circ, 2^\circ, 0^\circ, -2^\circ, -4^\circ, -6^\circ, -8^\circ$ and the δ angle to incline in sequence as $-12^\circ, -9^\circ, -6^\circ, -3^\circ, 0^\circ, 3^\circ, 6^\circ, 9^\circ, 12^\circ$ simultaneously, that is, add obstacle slopes according to the angles one by one to achieve the simultaneous inclination of the chassis θ and δ angles. Then immediately record the extension and contraction amounts of the attitude adjustment mechanism. Each experiment will be carried out three times to avoid contingency.

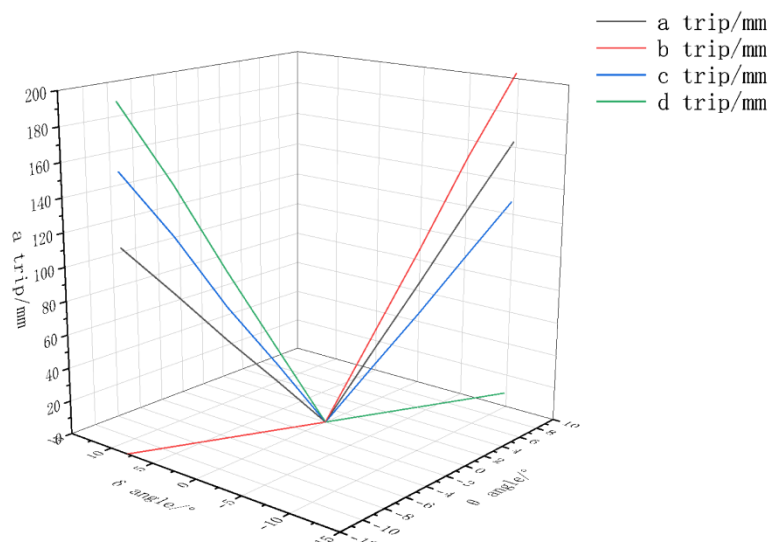


Fig. 20 - Experiment Four: The Moving Amount of Each Hydraulic Cylinder Stroke under Different Inclination Angles

CONCLUSIONS

The experimental results show that the chassis can perform leveling motion in the transverse direction within the range of $[-12^\circ, 12^\circ]$ and in the longitudinal direction within $[-8^\circ, 8^\circ]$. During the experiment, there was no instance of insufficient stroke in the hydraulic cylinder. Due to the implementation of the surface track leveling strategy, the chassis exhibited good stability throughout the leveling process, with no shaking or jolting. The chassis strategy and hydraulic cylinder stroke effectively meet the design requirements.

ACKNOWLEDGEMENT

This article was supported by a grant from the Development of High Efficiency and Low Loss Single Longitudinal Axial Flow Threshing and Separation Technology and Intelligent Flexible Threshing Device Project, Grant No. 2021YFD200050204.

REFERENCES

- [1] Che, G., Liu, W., Wan, L., Yi, S., Liu, H., Design and Experiment of Automatic Leveling System for Rice Seedling Shed and Bed Precision Leveling Machine (水稻秧棚苗床精平机自动调平系统设计与实验). *Transactions of the Chinese Society of Agricultural Engineering*, Vol. 39, Heilongjiang/China.
- [2] Hussain, Azhar, Amina Malik, Mohammed U Halim, Aslankhani Mohammad Ali., (2014). The Use of Robotics in Surgery: A Review. *International journal of clinical practice*, Vol. 68, pp. 1376-1382, Kobe/Japan.
- [3] Jian, H., Zhang, J., Liu, Y., Zheng, D., Li, Z., Virtual design and simulation analysis of adaptive hilly and mountainous tractor (自适应丘陵山地拖拉机虚拟设计及仿真分析). *Journal of Shanxi Agricultural Sciences*, Vol. 51, Shanxi/China.
- [4] Kuindersma, Scott, Robin Deits, Maurice Fallon, Andrés Valenzuela, Hongkai Dai, Frank Permenter, Twan Koolen, Pat Marion, and Russ Tedrake. (2016), Optimization-Based Locomotion Planning, Estimation, and Control Design for the Atlas Humanoid Robot. *Autonomous robots*, Vol. 40, pp. 429-55, New York/America.
- [5] Li, Z., Fan, G., Zhang, H., Qin, F., (2024). Analysis on the Present Situation and Tendency of Automatic Leveling in Agricultural Machinery (农机具自动调平现状及趋势分析). *Journal of Chinese Agricultural Mechanization*, Vol. 40, pp. 4-48, Shandong/China.
- [6] Liu, J., Wang, Y., Ma, S., Li, B., (2005). Analysis of stairs-climbing ability for a tracked reconfigurable modular robot. *IEEE International Safety, Security and Rescue Robotics, Workshop*, pp. 36-41, Shenyang/China.

- [7] Luo, X., (2011). Thoughts on the Development of Agricultural Mechanization in Hilly and mountainous Areas (对发展丘陵山区农业机械化的思考). *Agriculture Machinery Technology Extension*, Vol. 2, pp. 17-20, Guangdong/China.
- [8] Mou, X., Yang, F., Duan, L., Liu, Z., Song, Z., (2024). Research Advances and Development Trend of Mountainous Tractor Leveling and Anti-Rollover System (丘陵山地拖拉机调平与防翻关键技术研究现状与发展趋势). *Smart Agriculture*, Vol. 6, pp. 1, Shanxi/China.
- [9] Peng, H., MA, W.X., Zhao, E.P., Lu, X.Q. Feng, X. (2018). Design and physical model experiment of body leveling system for roller tractor in hilly and mountainous region (丘陵山地轮式拖拉机车身调平系统设计及物理模型试验). *Transactions of the Chinese Society of Agricultural Engineering*, Vol. 34, Jilin/China.
- [10] Skrickij V., P. Kojis, E. Sabanovic, B. Shyrokau, and V. Ivanov. (2024). Review of Integrated Chassis Control Techniques for Automated Ground Vehicles. *Sensors*, Vol. 24,10223 Vilnius/Lithuania
- [11] Sun, Q., Zang, J., Yang. M., Zhang, C., Li, Z., (2023). Stability Analysis of Three-Point Leveling Mechanism of Hilly Mountain Tractor (丘陵山地拖拉机底盘三点调平机构稳定性分析). *Agricultural Engineering*, Vol. 13, pp. 91-97, Shanxi/China.
- [12] Wang, B., Zhu, J., Chai, X., Liu, B., Zhang, G., Yao, W., (2024). Research status and development trend of key technology of agricultural machinery chassis in hilly and mountainous areas. *Computers and Electronics in Agriculture*, Vol. 226, Hebei/China.
- [13] Wu, H., Zhu, S., Zhang, F., (2021), Design of Automatic Leveling Control System for Electromechanical Support Platform. *Journal of Shandong University of Technology (Natural Science Edition)*, Vol. 35, pp. 29-35, Shandong/China.
- [14] Yin, X., An, J.H., Wang, Y.L., Wang, X., Li, J.Q., Jin, C.Q., (2021). Design and Test of Automatic Beam Leveling System for High-Clearance Sprayer. *Transactions of the Chinese Society for Agricultural Machinery*, Vol. 53, pp. 98-105,115, Shandong/China.

DESIGN AND EXPERIMENT OF SEGMENTABLE ADJUSTABLE THRESHING DEVICE FOR RICE SEED BREEDING

制繁种水稻分段可调脱粒装置设计与试验

Ranbing YANG^{1,2}, Qi LIU¹, Yiren QING^{*2}, Zhiguo PAN¹, Guoying LI³,
Shuai WANG¹, Peiyu WANG², Yalong SHU¹

¹ College of Electrical and Mechanical Engineering, Qingdao Agricultural University, Qingdao / China

² College of Mechanical and Electrical Engineering, Hainan University, Haikou / China

³ Qingdao Pulantech Machinery Technology Co., Ltd., Qingdao / China

Tel: +8618851400010; E-mail: Jsuyirenq@163.com

Corresponding author: Yiren Qing

DOI: <https://doi.org/10.35633/inmateh-75-23>

Keywords: Seed breeding, Concave screen, Threshing clearance, Low loss

ABSTRACT

In response to the current challenges in the harvesting process of hybrid rice, where the threshing gap cannot adequately adapt to the varying threshing requirements, leading to high grain breakage rates, loss rates, and frequent clogging of the drum, a new threshing device for hybrid rice was designed by adjusting the gap of the concave screen. The concave screen was divided into a low-loss threshing section and a low-damage threshing section, with the addition of a hydraulic system to enable the adjustment of the threshing gap. A dynamic analysis of the rice at the spiral feeding inlet and within the threshing drum was conducted, determining that the adjustable range of the threshing gap is between 10 and 20 mm. A prototype of the low-loss threshing device for hybrid rice was built, and bench tests were performed with feed rate, drum speed, and threshing gap as influencing factors, while cleaning rate and breakage rate were used as response indicators in an orthogonal experiment to determine the optimal parameter combination. The optimal threshing performance was achieved at a threshing gap of 14.19 mm, a drum speed of 460.12 r/min, and a feed rate of 2.13 kg/s, resulting in a cleaning rate of 97.67% and a breakage rate of 0.295%. Subsequent verification tests under the optimal combination showed a cleaning rate of 96.2% and a breakage rate of 0.36%, meeting the harvesting standards for hybrid rice. This research provides theoretical support for the development of mechanized harvesting equipment for hybrid rice.

摘要

针对目前制繁种水稻收获过程中脱粒间隙无法很好的适应不同条件下水稻脱粒需求，脱粒过程中水稻籽粒破碎率、损失率及滚筒易堵塞等问题，从调节凹板筛脱粒间隙的角度出发，设计了一种制繁种水稻脱粒装置。将凹板筛设计为低损失脱粒段与低损伤脱粒段，通过加入液压系统能够实现脱粒间隙调节。对水稻在螺旋喂入口和脱粒滚筒内进行动力学分析，确定了脱粒间隙可调范围为10~20mm。试制了制繁种水稻低损失脱粒装置试验台，进行台架试验，以喂入量、滚筒转速、脱粒间隙作为影响因素，以脱净率和破损率作为响应指标进行正交实验，确定最优组合参数，获得脱粒装置在脱粒间隙14.19mm、滚筒转速460.12r/min、喂入量2.13kg/s的组合参数下脱粒效果最优，脱净率为97.67%，破损率为0.295%，并在最优组合下验证试验，结果表明脱净率为96.2%，破损率为0.36%，满足水稻制繁种收获标准，该研究可为制繁种水稻机械化收获装备的研制提供理论支持。

INTRODUCTION

Rice, as one of China's important food and economic crops, had a planting area of 28,949 thousand hectares and a yield of 206.6 million tons in 2023, according to statistics from the National Bureau of Statistics (Wei Li et al., 2024; Tian L. et al., 2020; Guo L. et al., 2024). The widespread adoption of rice harvesting machines has saved labor and resources, improved the efficiency of rice harvesting, and played an important role in grain harvesting. In seed breeding, an important aspect of agricultural production, the requirements for seed vitality and grain threshing are more stringent compared to regular rice harvesting during the rice harvesting process. Currently, common field rice-wheat combine harvesters are widely used for rice seed breeding harvesting, which often leads to high threshing losses and severe seed breakage.

Threshing, as an indispensable process, may result in increased loss and breakage rates when working parameters are poorly configured due to changes in feed rate, making it difficult to meet threshing requirements under different conditions (Teng, Y. et al., 2020). Therefore, reducing grain loss and breakage rates during rice seed breeding harvesting has become an urgent issue.

In recent years, researchers both domestically and abroad have conducted numerous studies aimed at reducing grain loss and breakage rates. Vlăduț N.V. et al., (2022), presented a mathematical model to characterize the threshing and separation process in an axial-flow thresher. Their paper aimed to provide a theoretical foundation for optimizing thresher design and performance. Bergkamp et al., (2015), designed a constant-pressure concave screen that, by incorporating a hydraulic cylinder to adjust the piston rod extension, achieved the effect of manually adjusting the threshing clearance, preventing situations where grain loss occurs due to excessive feed rates, and concluded that the constant-pressure concave screen is superior to traditional concave screens. Vlăduț N.V. et al., (2023), found that the loss (p_{ev}) is affected by the threshing rotor speed (n), implicit rotor peripheral speed (v_p), material feed speed (v_a), the space between the rotor and the counter - rotor (δ), material feed flow (Q), material density (ρ), and the length of the threshing device (L). Since ρ and L remain constant, they analyzed the variation of the loss with respect to v_p , Q , ρ , and v_a . By changing two parameters of the loss function (presented graphically), the study aimed to minimize the loss. Ivan Gh. et al., (2015), demonstrated that by optimizing the feeding process, the capacity of the tangential threshing system can be enhanced. This is achieved when the system can guide more materials carried by the feeder house conveyor during a full rotation of the threshing cylinder. The research indicates that to improve the feeding capacity of the threshing system in conventional cereal harvesters, it is necessary to match the speed, quantity, and spacing of the feeder house conveyor slats with the number of rods on the threshing cylinder and the speed of the tangential threshing cylinder. Matousek et al., (2017), designed a three-section combined adjustable concave screen, composed of three small concave screens as a whole, with the movement of the three small concave screens controlled by rotating connecting shafts, concluding that adjusting the threshing clearance can reduce loss rates. Miu, P.I. & Kutzbach et al, (2007) analyzed the movement trajectory of rice in the threshing device, established a kinematic mathematical model based on crop position and movement speed, determined the movement laws of rice in the threshing device, providing a theoretical basis for analyzing the proportion of grains and extraneous matter in the threshing device. Osueke et al, (2011), analyzed the effects of grain threshing force, threshing clearance, feed rate, and drum speed on the threshing process, optimizing the threshing analysis model and concluding that the threshing clearance and grain threshing force are the main factors affecting threshing quality. Dai, F. et al, (2011), designed a vertical axis flow cone-type threshing device by adding a conical short bar-tooth plate structure on the drum, concluding that this method accelerates the axial transport speed of breeding wheat and is less prone to blockages. Lian Y. et al, (2020), designed an adaptive control system for the threshing system of a rice-wheat combine harvester, concluding that the operational parameter control system effectively improves harvesting efficiency by studying the adaptive control system and comparing harvesting tests with and without controllers. Zhang Lu Ke et al, (2022), proposed a rice threshing and separating device blockage monitoring and diagnostic system, effectively preventing grain loss caused by drum blockages. Liu Wanru et al, (2023), established an impact mechanics model for collisions between rice grains and different threshing elements, concluding that the optimized curved rod tooth drum effectively reduces the power consumption of the drum and enhances the threshing performance. Teng Yuejiang et al, (2020), designed a segmented vertical flow threshing and separating device, providing a reference for the improvement and optimization of the threshing device of vertical flow rice harvesters through multi-objective optimization experiments aimed at problems such as high breakage rates, incomplete threshing, and inadequate separation.

In conclusion, current research on rice threshing devices primarily focuses on adjusting the overall threshing clearance of the device through the drum and concave screen. However, the inability to simultaneously meet the threshing conditions at the front and rear ends of the threshing device due to differences in grain density inside the device caused by feed rates hinders the reduction of grain loss and breakage rates. Therefore, in response to issues such as grain loss and breakage during rice seed breeding harvesting, this paper proposes the design of a threshing device for rice seed breeding, analyzes the movement patterns of rice during threshing, and, based on single-factor and multi-factor experiments, identifies the optimal operating parameters, aiming to provide a reference for the development of harvesting equipment for rice seed breeding trials.

MATERIALS AND METHODS

Overall Structure

The overall structure of the harvesting and threshing device for hybrid rice is shown in Figure 1. It mainly consists of a material transport device, material feeding port, cover plate, concave screen, threshing drum, backing plate, hydraulic cylinder, motor, and power transmission device, among others. The main parameters of the device are presented in Table 1.

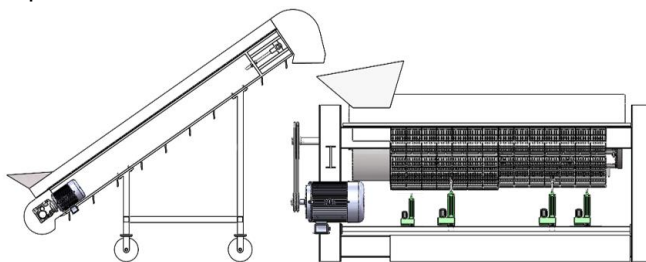


Fig. 1 – The overall structure of the segmented adjustable threshing device for hybrid rice harvesting

Table 1

The main parameters of the segmented adjustable threshing device for rice harvesting	
Parameter	Numerical value
Test bench dimensions (Length × Width × Height) / (m × m × m)	2.2×1.1×1.5
Length of concave screen (m)	1.8
Engine power (kW)	103
Type of concave screen	Grid type
Threshing gap adjustment range (mm)	5~10

When the threshing device begins to operate, rice is transported through the material conveying device into the spiral feeding inlet. From the spiral feeding inlet, it enters the threshing device for threshing, using a radial feeding and discharging method. The motor provides power to drive the power transmission device, which in turn drives the threshing drum to rotate and supports the concave screen's extension and retraction with the hydraulic cylinder. Under the combined action of the threshing drum and the concave screen, the rice undergoes multiple forces such as gravity, impact force, friction force, and centrifugal force to achieve the separation of grains from the stalks. Sensors within the threshing device are used to detect the feeding amount and grain density inside the drum, controlling the extension and retraction of the hydraulic cylinder to drive the two parts of the concave screen to move independently, adjusting the threshing gap. Ultimately, the rice grains fall into the grain bin, while impurities are discharged outside the threshing device, completing the threshing process.

Design and selection of key components

The threshing device of traditional rice harvesting machines has a fixed concave screen that is not adjustable, which cannot better meet the threshing requirements under different working conditions. When the feeding amount is too large, the grain density inside the threshing device increases, causing the rice material in the threshing drum to spiral forward in the feeding direction. As a result, the grain density in the front half of the threshing device is greater than that in the rear half, leading to a situation where an excessively large threshing gap reduces the cleaning rate, while an excessively small threshing gap increases the damage rate. To address this issue, a hydraulic system is introduced to support the concave screen and divide it into a low-loss threshing segment and a low-damage threshing segment, allowing for independent control of the two sections. This enables the adjustment of the appropriate threshing gap based on the varying grain densities, thus solving the problems of reduced cleaning rates and increased damage rates caused by uneven grain density within the threshing drum.

Dynamic analysis of rice at the helical feeding inlet

The spiral feed inlet serves as the starting point for rice entering the threshing device (Xu L., Li Y., & Ding L. et al, 2008), enabling the stable transport of rice into the threshing drum. To prevent blockages in the drum and grain loss caused by excessive feeding, a dynamic analysis of the rice is conducted at any point along the spiral feed inlet. As shown in Figure 2, the rice plant is treated as a particle O for the dynamic analysis within the spiral feed inlet. To ensure that the material moves along the spiral feed inlet and smoothly enters the threshing drum, the following conditions must be met:

$$T \cos \alpha > F_b \sin \alpha \tag{1}$$

$$F_b = f_1 T = T \tan \beta \tag{2}$$

In the formula, f_1 is the coefficient of friction between the material and the spiral feed inlet.

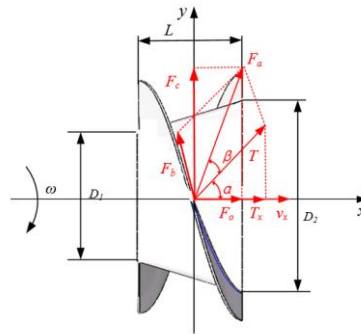


Fig. 2 – Kinetic analysis of rice at the screw feed inlet

where: ω is the angular velocity of rotation of the threshing drum, rad/s; D_1 is the diameter of the front end of the screw feeding inlet, cm; L is the length of the screw feeding inlet, cm; D_2 is the diameter of the rear end of the screw feeding inlet, cm; F_b is the friction between the rice and the screw feed inlet, N; T is the conveying force of the screw feed inlet to the rice, N; T_x is the component of T on the x-axis, N; F_a is the resultant force of F_b and T , N; F_o is the component of F_a on the x-axis, N; F_c is the component of F_a on the y-axis, N; v_x is the axial feeding speed of rice, m/s; α is the friction angle between the rice and the screw feed inlet, °; β is the helix angle of the screw feed inlet, °.

From equations (6) and (7), it can be concluded that to ensure the material moves axially along the spiral feed inlet, the axial thrust force must exceed the axial resistance, that is:

$$\cot \alpha > \tan \beta \tag{3}$$

Therefore, the β between the helix angle and the friction angle α should meet:

$$\alpha < \frac{\pi}{2} - \beta \tag{4}$$

As the main influencing factor of rice feeding speed v_x (Zeng, S., Zeng, L. et al, 2022), the helix angle β decreases when the β increases, the axial component T_x of T decreases, the feeding power P increases, the feeding speed decreases, and the feeding efficiency decreases. When β decreases, the axial component T_x of T increases, the feeding speed increases, and the feeding efficiency increases. In order to select the appropriate helix angle β , prevent the drum from clogging, and improve the feeding efficiency, the following are required:

$$P = T_x v_x \tag{5}$$

$$v_x = \omega r \tag{6}$$

In the formula, ω is the angular velocity of the drum, in rad/s; r is the radius of the drum, in mm.

Upon measurement, the friction α is 48.3°. According to equations (4), (5), and (6), the helical angle β is set to 35°.

Parameter design of the threshing drum

The structure of the threshing drum is shown in Figure 3. The threshing of rice is mainly accomplished through the cooperation between the rods and teeth of the threshing drum and the concave sieve. Considering that the moisture content of southern rice is relatively high, which can easily lead to damage during threshing, this paper selects cylindrical threshing rods to reduce the contact area with the rice, thereby lowering the damage rate. The length of the rods is 78 mm, and the distance between adjacent rods is 82 mm.

The diameter of the threshing drum determines the threshing trajectory. A smaller drum diameter reduces the threshing line speed, decreases the threshing capacity, and lowers the clean threshing rate of the rice. Conversely, a larger drum diameter increases the threshing line speed, enhances the threshing capacity, and raises the damage rate of the rice. Based on domestic standards for cylindrical threshing drums, the diameter D of the threshing drum is determined to be 500 mm.

The length L_l of the threshing drum is designed as:

$$L_l = \frac{q}{q_1} \tag{7}$$

In the formula, q is the feed rate, in kg/s, and q_1 is the threshing capacity of the drum per unit volume, in kg/(s·m).

The threshing device uses cylindrical rods, with q_1 set at 1 to 1.5 kg/(s·m) and q set at 2.5 kg/s. The length of the threshing drum is determined to be 2200 mm using formula (7).

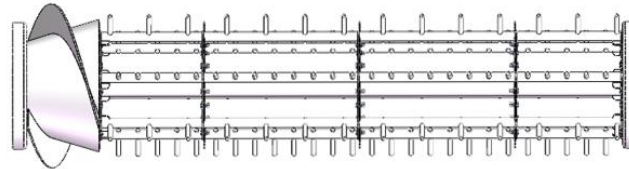


Fig. 4 – Structure diagram of threshing drum

Kinematic analysis of rice in the threshing drum

Due to the complex forces acting on rice during the threshing process, a dynamic analysis of rice threshing is conducted at low speeds to select an appropriate range for the threshing gap and drum rotational speed, thereby reducing damage to the rice grains. A coordinate system (xoy) is established with the center of gravity of the rice as the origin to analyze the force distribution on the rice, as shown in Figure 4.

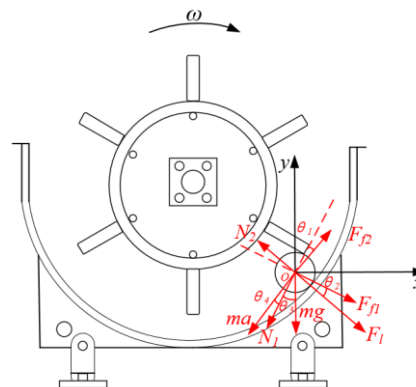


Fig. 5 – Kinetic analysis of rice in threshing drum

where: ω is the angular velocity of the threshing drum, in rad/s; N_1 is the impact force of the threshing rod teeth on the rice, in N; N_2 is the supporting force of the concave sieve on the rice, in N; F_{f1} is the frictional force between the threshing rod teeth and the rice, in N; F_{f2} is the frictional force between the concave sieve and the rice, in N; F_i is the centrifugal force acting on the rice, in N; m is the mass of the rice, in g; g is the gravitational acceleration, in N/kg⁻¹; a is the acceleration of the rice, in m/s²; θ_1 is the angle between the impact force N_1 and the frictional force F_{f2} , in degrees; θ_2 is the angle between the frictional force F_{f1} and the centrifugal force F_i , in degrees; θ_3 is the angle between the gravitational force mg and the impact force N_1 , in degrees; θ_4 is the angle between the direction of the rice’s acceleration and the impact force N_1 , in degrees.

According to Figure 5, the force analysis of rice during the threshing process is shown in formulas (8) and (9).

$$N_1 + ma \cos \theta_4 + mg \cos \theta_3 + F_i \sin \theta_2 = F_{f2} \cos \theta_1 + N_2 \sin \theta_2 \tag{8}$$

$$F_{f1} + F_i \cos \theta_2 + mg \sin \theta_3 + F_{f2} \sin \theta_1 = N_2 \cos \theta_2 + ma \sin \theta_4 \tag{9}$$

$$F_i = mr\omega^2 \tag{10}$$

$$F_{f1} = \mu_1 N_1 \tag{11}$$

$$F_{f2} = \mu_2 N_2 \tag{12}$$

In the formulas, r represents the rotation radius of the rice, in mm. μ_1 and μ_2 are the coefficients of friction between the rice and the threshing rod teeth and concave sieve, respectively, with $\mu_1 = 0.59$ and $\mu_2 = 0.54$.

Kinematic analysis of rice in the threshing drum

Before threshing the grains, the threshing device must first separate the rice from the straw. The grains are rubbed and peeled by passing through the threshing drum and concave sieve, then they enter the cleaning device through the concave sieve. Under the influence of the threshing drum and the flow guide plate, the straw moves forward in a spiral manner and is eventually discharged from the end of the threshing device (Chen L. et al, 2023; Chen J. et al., 2024; Wang J. et al., 2021).

To explore the motion laws of the material within the threshing device and ensure that the material moves axially within the threshing drum, preventing blockages and allowing for smooth discharge, an xoy coordinate system is established with the center of mass of the straw as the origin, as shown in Figure 6.

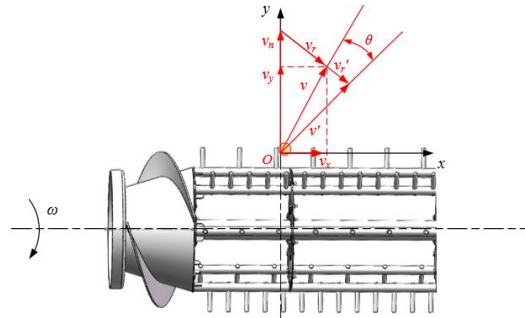


Fig. 6 – Kinematics analysis of straw in threshing device

where:

ω is the angular velocity of the threshing drum, in rad/s; v is the actual motion speed of the straw, in m/s; v_x is the component of speed v along the x-axis, in m/s; v_y is the component of speed v along the y-axis, in m/s; v_n is the pulling speed under the influence of the flow guide plate, in m/s; v_r is the sliding speed of the straw relative to the flow guide plate, in m/s; v_r' is the sliding speed in the absence of friction, in m/s; v' is the motion speed in the absence of friction, in m/s; θ is the angle of change in speed due to the action of friction, in degrees.

As shown in Figure 6, the velocity decomposition of the rice straw within the threshing device is represented by equations (15) and (16).

$$v_x = \frac{dn \left(\mu_3 + \frac{d}{2\pi r} \right)}{60 \left[1 + \left(\frac{d}{2\pi r} \right)^2 \right]} \tag{15}$$

$$v_y = \frac{dn \left(1 - \frac{\mu_3 d}{2\pi r} \right)}{60 \left[1 + \left(\frac{d}{2\pi r} \right)^2 \right]} \tag{16}$$

where: d is the pitch of the guide plate, in mm; n is the rotational speed of the drum, in rad/s; μ₃ is the coefficient of friction between the straw and the guide plate, where μ₃ = 0.18; r is the radius of the drum, in mm.

From equations (15) and (16), it can be seen that the motion speed of the straw is related to the pitch of the guide plate, the rotational speed of the drum, and the radius of the drum. When the central axis of the drum is fixed and the radius of the drum increases while the length of the threshing rod teeth remains unchanged, it can be approximated that the threshing gap increases. In this paper, the change in the radius of the drum is used to represent the change in the threshing gap.

When the drum rotational speed n increases, v_x and v_y also increase. This can be interpreted as an enhanced ability to separate grains from straw with the increasing drum speed, resulting in an increase in the instantaneous speed of the straw and a faster axial movement. When the radius of the drum r increases, the threshing gap enlarges, causing v_x and v_y to decrease, which can be explained as a reduction in the ability to separate rice grains from straw due to the enlargement of the threshing gap. When the pitch of the guide plate d increases, v_x and v_y decrease, which can be interpreted as a reduced conveying capacity for the straw with the increase in pitch, making it easier for the drum to become clogged.

In summary, to prevent the drum from clogging and to ensure the smooth progress of the threshing process, the drum rotational speed should be set between 260 and 660 r/min, and the threshing gap should be set between 10 and 20 mm.

Design of the concave plate sieve

During the threshing process, the concave plate sieve works in cooperation with the threshing drum to achieve the preliminary separation of rice grains and broken materials (Teng Y. *et al*, 2020). Traditional rice harvesters often have fixed structures for the concave plate sieve, and the fixed threshing gap cannot adapt to different working conditions, which can easily cause damage to the rice grains. Therefore, a segmented adjustable concave plate sieve has been designed, as shown in Figure 7. Based on the existing dimensions of the threshing segment of the threshing drum, this paper selects a bar-type concave plate sieve to increase grain passage, reduce collision intensity, and lower the damage rate. The length of the concave plate sieve is set at 2100 mm, divided into two parts, each measuring 1050 mm (Di Q. *et al*, 2021). The bars are made of steel plates that are 1010 mm long and 22 mm wide, with a wrap angle of 190°.

Two pads are installed in each part to connect the hydraulic cylinder with the concave plate sieve. When there are many grains, increasing the gap of the concave plate can effectively reduce the collision intensity between the concave plate sieve and the rice grains, while providing enough space for high-density rice to be threshed. Increasing the threshing gap not only improves the passage of grains but also reduces the damage caused by the squeezing of grains due to the clogging of the threshing device.

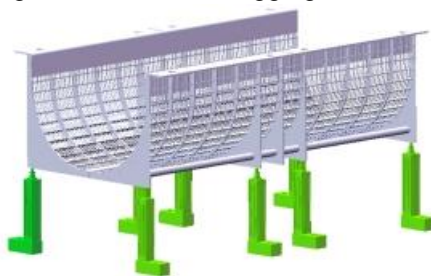


Fig. 7 – Structure diagram of concave plate screen

The hydraulic system, serving as the power device for adjusting the threshing gap, is designed with two oil inlets and sixteen oil outlets, ensuring simultaneous supply to four hydraulic cylinders with an error margin of less than 2%. When there is a need to adjust the threshing gap, the hydraulic system directs hydraulic oil into the hollow hydraulic cylinders through hydraulic rotary joints, with one side featuring a piston rod. By controlling the flow of hydraulic oil, the piston rod extends and retracts, thereby driving the movement of the concave plate sieve to modify the size of the threshing gap. When adjustment of the threshing gap is unnecessary, the hydraulic oil flow ceases, maintaining the piston rod of the hydraulic cylinder in a stationary state. The hydraulic system also remains static, ensuring that the position of the concave plate sieve does not change, thus guaranteeing a constant threshing gap.

The design of the adjustable hydraulic system allows for precise control when there is a need to modify the threshing gap, while maintaining stability when no adjustments are required.

Bench test and result analysis

To verify the working effect of the segmented adjustable threshing device, a test stand was fabricated for conducting bench tests. The test subjects selected were Shuyou No. 9 rice from the rice planting base in Xinlong Town, Dongfang City, Hainan Province, with basic parameters shown in Table 2.

Table 2

Parameters of basic physical characteristics of rice	
Parameter	Numerical value
Moisture content of rice grains / %	23.1
Moisture content of rice straw / %	74.4
Height of rice plant / cm	103.6
Thousand grain weight / g	27.1
Number of grains per ear	154

Experimental method

This experiment combines the design analysis of key component parameters, selecting threshing gap A, drum speed B, and feeding amount C as experimental factors, and selecting cleaning rate y_w and damage

rate y_p as evaluation indicators. Based on GB/T 5982-2017 "Test Methods for Threshers" and DB37/T2878.2-2016 "General Technical Requirements for Agricultural Product Harvesting Machinery", an orthogonal experiment is conducted.

The calculation formulas for cleaning rate y_w and damage rate y_p are as follows:

$$y_w = \frac{m_w}{m} \times 100\% \quad (17)$$

In the formula,

y_w is the cleaning rate, %; m_w is the weight of threshed grains, g; m is the total grain mass, g.

$$y_p = \frac{m_p}{m} \times 100\% \quad (18)$$

In the formula,

y_p is the damage rate, %; m_p is the weight of damaged grains, g; m is the total grain mass, g.



Fig. 8 – Test bench of segmented adjustable threshing device for rice harvesting

Single-factor experiment

Before conducting the orthogonal experiment, single-factor experiments should be carried out on the threshing gap A, drum speed B, and feeding amount C to determine the reasonable range of factor levels and the influence patterns of each factor on the threshing performance. Based on preliminary trials and the adjustable range of the device, the single-factor experimental ranges are set as follows: threshing gap A is 10–20 mm, drum speed B is 260–660 r/min, and feeding amount C is 1–3 kg/s.

When the threshing gap A is fixed at 15 mm, the drum speed B is set at 450 r/min, and the feeding amount ranges from 1 to 3 kg/s, the effects of feeding amount C on the cleaning rate y_w and damage rate y_p during the threshing process are shown in Figure 9. As illustrated in Figure 9, when the feeding amount is between 1–2 kg/s, both the cleaning rate and damage rate increase significantly with the rise in feeding amount; the cleaning rate rises from 93.1% to 99.2%, while the damage rate increases from 0.18% to 0.59%. However, when the feeding amount is between 2–3 kg/s, the cleaning rate shows a downward trend, decreasing from 99.25% to 94.5%. An excessively high feeding amount results in the threshing device being unable to effectively thresh the rice, leading to a decline in threshing efficiency, while the damage rate slowly increases from 0.59% to 0.8%. To ensure effective threshing, the selected feeding amount range is 1.5–2.5 kg/s.

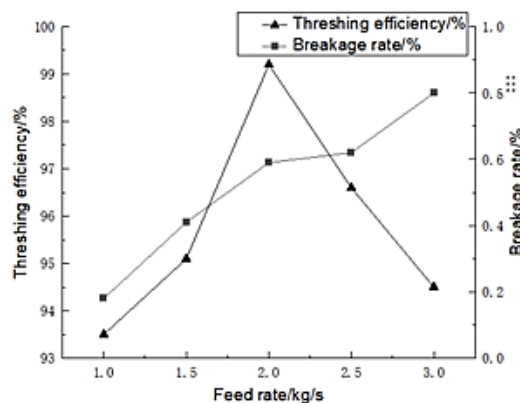


Fig. 9 – The impact of feed rate on threshing efficiency and damage rate

When the threshing gap A is fixed at 15 mm, the drum speed B ranges from 260 to 660 r/min, and the feeding amount is 2 kg/s, the effects of drum speed B on the cleaning rate y_w and damage rate y_p during the threshing process are shown in Figure 10. As illustrated in Figure 10, with the continuous increase in the drum speed, both the cleaning rate and loss rate show an overall upward trend. When the drum speed increases from 450 r/min to 550 r/min, the cleaning rate rises from 94.2% to 99.4%, indicating a significant upward trend. During this process, as the drum speed increases, the impact force on the rice becomes more pronounced, resulting in effective threshing. However, when the drum speed increases from 550 r/min to 660 r/min, the cleaning rate drops from 99.4% to 98.7%. The excessively high drum speed fails to achieve optimal threshing results, leading to grain loss. To ensure effective threshing, the selected drum speed range is set at 450–550 r/min.

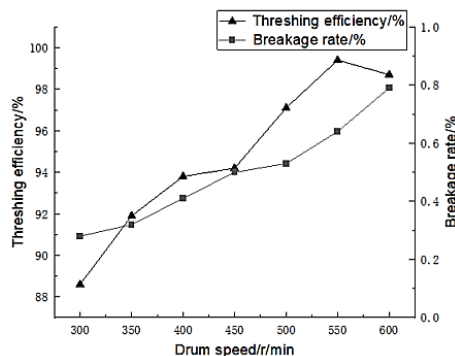


Fig. 10 – The impact of roller speed on cleaning rate and damage rate

When the threshing gap A is set between 10–20 mm, the drum speed B ranges from 260 to 660 r/min, and the feeding amount is 2 kg/s, the effects of threshing gap A on the cleaning rate y_w and damage rate y_p during the threshing process are illustrated in Figure 11. As shown in Figure 11, when the threshing gap is between 10–15 mm, the cleaning rate exhibits an upward trend, increasing from 95.5% to 99.6%. A good threshing gap allows the threshing rod teeth to fully contact the rice and effectively rub off the husk, thereby improving the threshing effect. At the same time, it reduces the collisions between the rice grains and the concave screen, with the damage rate decreasing from 0.95% to 0.32%. However, when the threshing gap is between 15 mm and 20 mm, the cleaning rate shows a downward trend, dropping from 99.6% to 94.3%. A larger threshing gap is unable to efficiently complete the threshing of rice, resulting in some rice not being fully rubbed and husked, which causes losses. Additionally, this leads to insufficient contact and collisions between the rice grains and the concave screen, causing the damage rate to further drop from 0.32% to 0.08%. To ensure effective threshing, the selected threshing gap range is set at 12–18 mm.

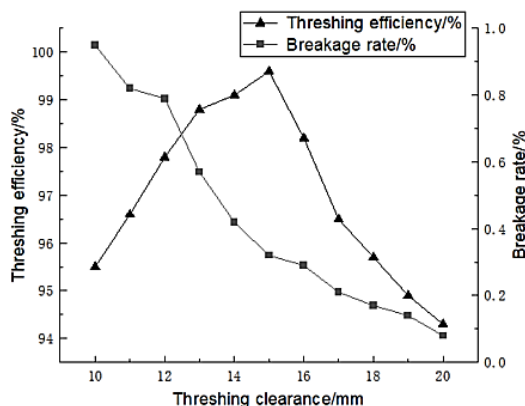


Fig. 11 – The impact of threshing gap on threshing purity and damage rate

RESULTS AND ANALYSIS

The experiment utilized a quadratic orthogonal design (Yang, R. et al., 2024), with the experimental factors being threshing gap A, drum speed B, and feeding amount C. The experimental indicators were the cleaning rate y_w and damage rate y_p . Based on the analysis of the previous experimental results, the value ranges for each experimental factor were determined: the threshing gap A is set at 12–18 mm, the drum speed B at 450–550 r/min, and the feeding amount C at 1.5–2.5 kg/s. The coding table for the levels of the experimental factors is shown in Table 3, and the experimental plan and results are presented in Table 4.

Table 3

Factor level coding table			
Material	Threshing gap A	Drum speed B	Feeding amount C
-1	12	450	1.5
0	15	500	2
1	18	550	2.5

Table 4

Test protocol and results					
Experiment number	Threshing gap A	Drum speed B	Feeding amount C	Cleaning rate / %	Damage rate / %
1	12	550	2	94.89	0.45
2	15	450	1.5	99.51	0.22
3	18	500	1.5	97.69	0.15
4	15	500	2	98.25	0.33
5	15	500	2	98	0.3
6	15	550	2.5	97.18	0.37
7	12	450	2	95.05	0.33
8	18	450	2	97.99	0.17
9	18	500	2.5	96.61	0.15
10	15	500	2	98.98	0.31
11	12	500	2.5	95.24	0.41
12	15	500	2	98.69	0.29
13	15	450	2.5	96.69	0.24
14	15	550	1.5	95.9	0.3
15	15	500	2	98.1	0.28
16	18	550	2	96.48	0.17
17	12	500	1.5	95.74	0.32

Using Design-Expert software, a quadratic regression analysis and multiple regression fitting were performed on the experimental data (Tian L. et al., 2020), along with variance analysis and significance testing of the experimental factors. As shown in Table 5, the experimental results indicate that the overall model for cleaning rate y_w and damage rate y_p is significant ($P < 0.01$), and the regression equation model for cleaning rate y_w and damage rate y_p is highly significant. Factors A, B, BC, and A^2 have a highly significant effect on cleaning rate y_w ($P < 0.01$), while factors C and B^2 have a significant effect on cleaning rate y_w ($0.01 \leq P < 0.05$). Factors AB, AC, and C^2 have no significant effect on cleaning rate y_w ($P \geq 0.05$). Similarly, factors A, B, BC, and A^2 have a highly significant effect on damage rate y_p ($P < 0.01$), while factors C and B^2 have a significant effect on damage rate y_p ($0.01 \leq P < 0.05$). Factors AB, AC, and C^2 have no significant effect on damage rate y_p ($P \geq 0.05$). The insignificant factors were included in the residual term, resulting in the regression equations for cleaning rate y_w and damage rate y_p as follows:

$$y_w = 8.99 + 7.15A + 0.2B - 12.89C + 0.041BC - 0.18A^2 - 0.26 \times 10^{-3} B^2 \tag{19}$$

$$y_p = -1.88 + 0.17A + 0.22 \times 10^{-2} B + 0.36C - 0.2 \times 10^{-3} AB - 0.015AC - 0.26 \times 10^{-2} \tag{20}$$

As shown in Table 5, the cleaning rate y_w and damage rate y_p have $P < 0.01$, indicating that the regression model is highly significant; the lack of fit term $P_w = 0.5313$ and $P_p = 0.5063$ ($P > 0.1$) are not significant. The regression equation fits well for both the cleaning rate and damage rate, with no other major factors affecting the experimental indicators. The quadratic relationship is significant, and the analysis results are reasonable.

Table 5

Analysis of variance (ANOVA) of decontamination rate and breakage rate										
Source	Cleaning Rate					Damage Rate				
	Sum of Squares	Deg. of Freedom	Mean Square	F Value	P Value	Sum of Squares	Deg. of Freedom	Mean Square	F Value	P Value
Model	31.63	9	3.51	21.60	0.0003	0.1229	9	0.0137	38.17	<0.00001
A	7.70	1	7.70	47.34	0.0002	0.0946	1	0.0946	264.39	<0.00001
B	2.87	1	2.87	17.63	0.0040	0.0136	1	0.0136	38.04	0.0005
C	1.22	1	1.22	7.48	0.0291	0.0040	1	0.0040	11.32	0.0120
AB	0.46	1	0.46	2.80	0.1382	0.0036	1	0.0036	10.06	0.0157
AC	0.084	1	0.084	0.52	0.4955	0.0020	1	0.0020	5.66	0.0490

Source	Cleaning Rate					Damage Rate				
	Sum of Squares	Deg. of Freedom	Mean Square	F Value	P Value	Sum of Squares	Deg. of Freedom	Mean Square	F Value	P Value
BC	4.20	1	4.20	25.83	0.0014	0.0006	1	0.0006	1.75	0.2279
A ²	11.47	1	11.47	70.52	0.0001	0.0023	1	0.0023	6.50	0.0382
B ²	1.78	1	1.78	10.96	0.0129	0.0415	1	0.0415	0.03	0.8753
C ²	0.79	1	0.79	4.86	0.0634	0.0019	1	0.0019	5.19	0.0568
Residual	1.14	7	0.1627			0.0025	7	0.0019		
Deviance	0.45	3	0.1487	0.8583	0.5313	0.0010	3	0.0003	0.9234	0.5063
Total Sum	32.77	16				0.1254	16			

Response surface methodology

To observe the effects of threshing gap, drum speed, and feeding rate on the cleaning rate and damage rate of hybrid rice grain harvested, this study fixes the level of one factor and investigates the interaction between the other two factors.

Through interaction response surface analysis (Ge Y. et al., 2015), the first figure in Figure 12 shows the response cloud of the cleaning rate (y_w) under the interaction of drum speed and feeding rate. It can be seen from the figure that when the threshing gap is 15 mm, as the drum speed and feeding rate increase, the cleaning rate begins to rise. This phenomenon can be attributed to the fact that the increase in drum speed enhances the force exerted by the threshing elements on the rice, allowing for successful threshing and consequently leading to an increase in the cleaning rate. From this interaction response cloud, it can be concluded that the effect of drum speed on the cleaning rate is significantly greater than that of feeding rate on the cleaning rate.

Similarly, through interaction response surface analysis, the second figure in Figure 12 shows the response cloud of the damage rate (y_p) under the interaction of threshing gap and drum speed. It can be observed that when the feeding rate is 2 kg/s, as the threshing gap and drum speed increase, the damage rate decreases. This phenomenon can be explained by the fact that the increase in threshing gap enlarges the internal space of the threshing device, reducing the force at the contact point between the grains and the concave screen under the action of the threshing drum, thereby leading to a decrease in the damage rate of the grains. However, with the increase in drum speed, the damage rate increases due to the greater force exerted on the rice when it contacts the threshing elements, which may cause damage to the grains if the drum speed is too high during threshing. The interaction response cloud indicates that the effect of threshing gap on the damage rate is clearly greater than that of drum speed on the damage rate.

Through interaction response analysis, the third figure in Figure 12 shows the response cloud of the damage rate (y_p) under the interaction of threshing gap and feeding rate.

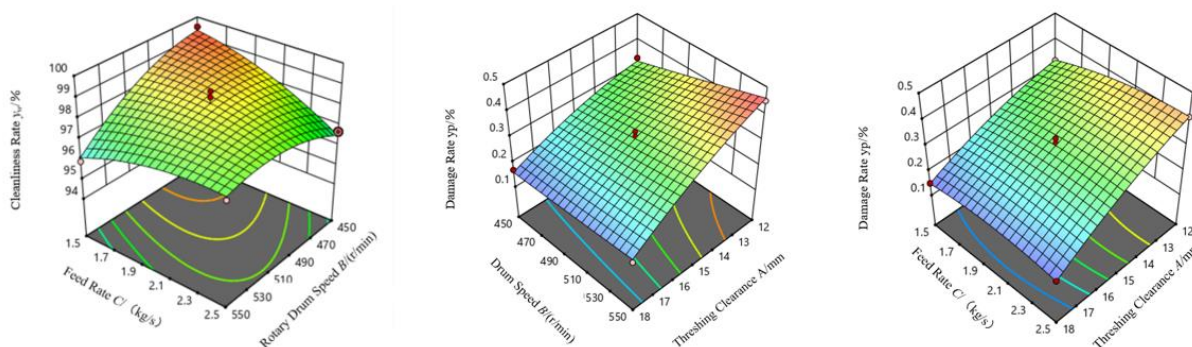


Fig. 12 – Interaction Response Plot

It can be seen that when the drum speed is 500 r/min, as the threshing gap and feeding rate increase, the damage rate decreases. This phenomenon can be explained by the fact that the increase in threshing gap enlarges the internal space of the threshing device, reducing the force at the contact point between the grains and the concave screen under the action of the threshing drum, thus leading to a decrease in the damage rate of the grains. As the feeding rate increases, the damage rate rises slightly, but the change is not significant, which can be attributed to the increased material density within the threshing device and the greater interaction

force between materials, resulting in slight damage. Therefore, it is evident that the impact of the threshing gap on the damage rate is significantly greater than that of the feeding rate on the damage rate.

Determination of optimal parameters

To increase the cleanliness rate (y_w) and reduce the damage rate (y_p), the maximization of cleanliness rate and minimization of damage rate are set as optimization objectives, seeking the best operating parameters, as shown in equation (19):

$$\begin{cases} \max y_w(A, B, C) \\ \min y_p(A, B, C) \\ 12 < A < 18 \\ 450 < B < 550 \\ 1.5 < C < 2.5 \end{cases} \quad (19)$$

Through optimization, the optimal parameters obtained are: threshing clearance of 14.19 mm, rotary drum speed of 460.11 r/min, and feed rate of 2.13 kg/s, resulting in a cleanliness rate of 97.67% and a damage rate of 0.295%, which meet the relevant threshing standards.

The adjusted parameters for the platform are: threshing clearance of 14.2 mm, rotary drum speed of 460 r/min, and feed rate of 2.1 kg/s. Experimental results indicate a cleanliness rate of 96.2% and a damage rate of 0.36%, with a relative error of less than 2 percentage points compared to the model optimization results.

CONCLUSIONS

(1) In response to the current challenges in the harvesting process of hybrid rice, where the threshing clearance cannot adequately adapt to the threshing requirements under different conditions, issues such as grain breakage rate, loss rate, and drum clogging during threshing are addressed. A threshing device for hybrid rice is designed from the perspective of adjusting the threshing clearance of the concave screen.

(2) A kinematic analysis of the threshing process is conducted. By analyzing the forces acting on the rice at the spiral feeding inlet and within the threshing drum, the selection of the concave screen and threshing drum is determined, aiming to reduce grain damage during threshing. Additionally, single-factor experiments are performed to establish the threshing clearance range of 12 to 18 mm, the drum speed range of 450 to 550 r/min, and the feed rate range of 1.5 to 2.5 kg/s.

(3) Using threshing clearance, drum speed, and feed rate as experimental factors, and cleanliness rate and damage rate as response indicators, an orthogonal experiment is conducted to establish a regression model for the relationship between threshing clearance, drum speed, feed rate, cleanliness rate, and damage rate. The results indicate that at a threshing clearance of 14.19 mm, a drum speed of 460.11 r/min, and a feed rate of 2.13 kg/s, the cleanliness rate is 97.67% and the damage rate is 0.295%. Verification through platform experiments shows that the cleanliness rate is 96.2% and the damage rate is 0.36%, with a relative error of less than 2% compared to the model optimization results. This demonstrates that this parameter combination can effectively improve the cleanliness rate of rice grains and significantly reduce the damage rate of rice grains.

ACKNOWLEDGEMENT

The authors were funded for this project by the National Key R&D Program of China, Research and Development of Low-loss and High-Purity Intelligent Harvesting Technology and Equipment for Rice Production and Multiplication (Project No. 2023YFD2000404-3) and Key R&D Project of Hainan Province (Project No. ZDYF2024XDNY181) and National Natural Science Foundation of China - Youth Science Foundation Project (Project No.52305252)

REFERENCES

- [1] Bergkamp, A., Regier. (2015). *Constant pressure concave assembly in a combine harvester processing system* (U.S. Patent No. 9220200B2).
- [2] Chen, J., Hao, S., Wang, C., Tang, Z., & Gu, X. (2024). Design of state monitoring and fault diagnosis system for combine harvester (联合收割机脱粒状态监测及故障诊断系统设计). *Journal of Agricultural Mechanization Research*, 46(07), 115–120.

- [3] Chen, L., Li, Y., Su, Z., Liu, Y., & Yin, Q. (2023). Design and test of a single-action variable-diameter threshing drum with rack (一种齿杆单动变直径脱粒滚筒的设计与试验). *Journal of Agricultural Mechanization Research*, 45(05), 43–48.
- [4] Dai, F., Gao, A., Sun, W., Zhang, F., Wei, H., & Han, Z. (2011). Design and experiment on longitudinal axial conical cylinder threshing unit (纵轴流锥型滚筒脱粒装置设计与试验). *Transactions of the Chinese Society for Agricultural Machinery*, 42(01), 74–78.
- [5] Di, Q. (2021). *Analysis and optimization design of threshing device for combine harvester (联合收割机脱粒装置分析及优化设计)* Xi'an University of Technology.
- [6] Ge, Y., Liang, Q., & Wang, G. (2015). *Experimental design method and Design-Expert software application (试验设计方法与 Design-Expert 软件应用)* Harbin: Harbin Institute of Technology Press.
- [7] Guo, L., Zhu, B., Han, Z., & Zhou, Q. (2024). Development status and suggestions of rice mechanized harvesting loss reduction technology (水稻机械化收获减损技术发展现状与建议). *Agricultural Equipment Technology*, 50(2), 4-6+9.
- [8] Ivan, Gh., Vlăduț, V., Ganea, I. (2015). Improving threshing system feeding of conventional cereal harvesting combine, *Proceedings of the 43 International Symposium on Agricultural Engineering "Actual Tasks on Agricultural Engineering"*, pp. 431-440, Opatija / Croatia.
- [9] Lian, Y. (2020). *Study on adaptive control system of operating parameters for threshing device of rice wheat combine harvester (稻麦联合收割机脱粒装置作业参数自适应控制系统研究)*. Jiangsu University.
- [10] Liu, W., Zhou, Y., Xu, H., Fu, J., Zhang, N., Xie, G., & Zhang, G. (2023). Optimization and experiments of the drum longitudinal axial threshing cylinder with rod tooth for rice (水稻鼓形纵轴流脱粒滚筒杆齿优化与试验). *Transactions of the Chinese Society of Agricultural Engineering*, 39(15), 34–45.
- [11] Matousek, R. A., & Claerhout, R. (2017). *Three section threshing concave configuration and adjustment mechanism for an agricultural harvesting combine* (U.S. Patent No. 20170164559A1).
- [12] Miu, P.I., & Kutzbach, H.D. (2007). Mathematical model of material kinematics in an axial threshing unit. *Computers and Electronics in Agriculture*, 58, 93–99.
- [13] Osueke, E. (2011). Simulation and optimization modeling of performance of a cereal thresher. *International Journal of Engineering & Technology*, 11(3), 143–152.
- [14] Teng, Y., Jin, C., Chen, Y., Liu, P., Yin, X., Wang, T. (2020). Design and optimization of segmented threshing device of combine harvester for rice and wheat (稻麦联合收割机分段式脱粒装置设计与优化). *Transactions of the Chinese Society of Agricultural Engineering*, 36(12), 1-12.
- [15] Tian, L., Li, H., & Hu, H. (2020). Design and experiment on coaxial double speed threshing for combine harvester (同轴双滚筒联合收割机设计与试验). *Transactions of the Chinese Society for Agricultural Machinery*, 51(S2), 139-146.
- [16] Tian, L., Zhang, Z., Lü, M., Jin, R., & Xiong, Y. (2020). Design and performance experiments of new threshing and separating device for head feeding combine harvester (半喂入联合收割机双速回转脱分装置设计与性能试验) *Journal of Chinese Agricultural Mechanization*, 41(09), 8-15.
- [17] Vlăduț, N.V., Biris, S.St., Cârdei, P., Găgeanu, I., Cujbescu, D., Ungureanu, N., Popa, L.D., Perișoară, L., Matei, G., Teliban, G.C. (2022). Contributions to the Mathematical Modeling of the Threshing and Separation Process in An Axial Flow Combine, *Agriculture*. 12 (10), 1520. <https://doi.org/10.3390/agriculture12101520>;
- [18] Vlăduț, N.V., Ungureanu, N., Biris, S.St., Voicea, I., Nenciu, F., Găgeanu, I., Cujbescu, D., Popa, L.D., Boruz, S., Matei, G., Ekielski, A., Teliban, G.C. (2023). Research on the identification of some optimal threshing and separation regimes in the axial flow apparatus, *Agriculture*. 13(4), 838, DOI: 10.3390/agriculture13040838, agriculture-2301663;
- [19] Wang, J., Wang, X., Li, H., He, J., Lu, C., & Liu, D. (2021). Design and experiment of rice straw chopping device for agitation sliding cutting and tearing (水稻秸秆激荡滑切与撕裂两级切割粉碎装置设计与试验). *Transactions of the Chinese Society for Agricultural Machinery*, 52(10), 28–40.
- [20] Wei, L. (2024). Analysis on the application of rice harvesting loss reduction technology (水稻机收减损技术应用分析) *South China Agricultural Machinery*, 55(08), 57-59+80
- [21] Xu, L., Li, Y., & Ding, L. (2008). Contact mechanics analysis of the collision process between rice grains and threshing elements (水稻谷粒与脱粒元件碰撞过程的接触力学分析). *Transactions of the Chinese Society of Agricultural Engineering*, (06), 146–149.

- [22] Yang, R., Wang, W., Pan, Z., Qing, Y., Zhang, J., & Qi, S. (2024). Analysis and experimental study of single plant stability of potato harvesting in breeding experiment (育种马铃薯单株收获根系稳定性分析与试验). *Transactions of the Chinese Society of Agricultural Engineering*, 40(13), 25-35.
- [23] Zeng, S., Zeng, L., Liu, W., Wei, S., Tu, Q., & Chen, H. (2022). Design and experiment of rigid-flexible coupling rod tooth threshing device of harvester for ratooning rice (再生稻收割机刚柔耦合杆齿脱粒装置的设计与试验). *Journal of South China Agricultural University*, 43(5), 61–69
- [24] Zhang, L. (2022). *Research on monitoring and diagnosis system of longitudinal axial flow rice threshing and separating device* (纵轴流水稻脱粒分离装置堵塞监控及诊断系统研究). Huazhong Agricultural University.

NON-DESTRUCTIVE DETECTION OF MOLD IN MAIZE USING NEAR-INFRARED SPECTRAL FINGERPRINTING

基于近红外光谱指纹技术的霉变玉米籽粒无损检测

Longbao LIU¹⁾, Qixing TANG¹⁾, Juan LIAO¹⁾, Lu LIU¹⁾, Yujun ZHANG²⁾, Leizi JIAO³⁾

¹⁾Anhui Agricultural University, Hefei 230061, China;

²⁾ Key Laboratory of Environmental Optics & Technology, Anhui Institute of Optics and Fine Mechanics, Chinese Academy of Sciences, Hefei 230031, China;

³⁾ Beijing Res Ctr Intelligent Equipment Agr, Beijing Academy of Agriculture and Forestry Sciences, Beijing 100097, China

Tel: +86-511-13637080689; E-mail: qxtang@ahau.edu.cn

DOI: <https://doi.org/10.35633/inmateh-75-24>

Keywords: Mold infection, Feature wavelength, Machine learning, Precision classification

ABSTRACT

Mold contamination of stored maize can cause significant economic losses, and it is crucial to effectively classify maize kernels without destroying their original structure. But existing studies have found it difficult to distinguish moldy maize. In this paper, a method for non-destructive detection of mold in maize using near-infrared spectral fingerprinting is proposed. The spectral raw data are initially acquired using a handheld near-infrared spectrometer. To enhance the signal quality, preprocessing is conducted, and a classification model is developed for full-band spectral data. In order to further optimize the model and enhance the classification accuracy, the feature wavelengths were extracted from the spectral data with effective preprocessing techniques in the full-band model. Finally, the maize kernel mold classification model is constructed. The classification accuracy of SG+SNV-SVM-ISFLA model can reach up to 97.22%, and the accuracy for the identification of asymptomatic moldy maize is 96.30%, which can realize the accurate grading of moldy maize and can well distinguish asymptomatic moldy maize. This work may significantly control the spread of molds in the food industry while improving storage economics and safety.

摘要

仓储玉米受到霉菌污染会造成重大经济损失, 因此在不破坏玉米原有结构的情况下对玉米进行有效分类至关重要。但现有研究发现, 轻微霉变玉米难以区分。本文提出了一种利用近红外光谱指纹的玉米霉变无损检测的方法。最初使用手持式近红外光谱仪获取光谱原始数据。为了提高信号质量, 进行了预处理, 并为全波段光谱数据建立分类模型。为了进一步优化模型并提高分类准确率, 对预处理后的数据进行特征提取。最后, 构建了玉米霉变分类模型。结果表明 SG+SNV-ISFLA-SVM 模型的分类准确率高达 97.22%, 对无症状霉变玉米的识别准确率为 96.30%, 可实现对玉米霉变的准确分级, 并能很好地区分无症状霉变玉米。这项工作可大大控制霉菌在食品工业中的传播, 同时提高贮藏的经济性和安全性。

INTRODUCTION

Maize, as an important crop, causes huge economic losses every year due to maize mold problems (Long et al., 2022a). Maize itself contains starch, proteins, sugar, amino acids and other nutrients for the reproduction of mold which provides the necessary nutritional conditions, while the temperature and humidity and other external factors in the storage room will also accelerate the reproduction of mold. The process of maize mold mainly produces aflatoxin, Deoxynivalenol (DON), fumonisins and other harmful substances. According to the estimation of the Food and Agriculture Organization (FAO) of the United Nations and a recent validation report, more than 25% of food crops are contaminated with mycotoxins due to the occurrence of molds (Long et al., 2022b; Zhang et al., 2020). In order to prevent and control the occurrence of molds in food, there is a need for the efficient identification of molds in maize kernels (Kang et al., 2022). Existing mold identification methods are difficult to distinguish asymptomatic moldy maize. Therefore, researching non-destructive mold identification methods while being able to accurately detect asymptomatic moldy maize is a key technical challenge currently being faced.

Traditional methods of identifying mold in crops are divided into physical and chemical methods. The physical methods mainly identify the degree of mold by observing their color, odor and touch, which are simple to operate, but are affected by subjective factors and cannot be accurately quantified (Milićević et al., 2010; Oyebanji et al., 1999).

The chemical methods are used to quantitatively analyze mold by preparing sample solution, which are highly sensitive and quantitative, but this method have high complexity and high demands for operators (Paraginski *et al.*, 2019). Visible light computer vision has been used by scholars for mold identification, which has the advantages of non-contact, high efficiency, rapidity and automation, but this technology cannot effectively identify asymptomatic moldy maize (Fei *et al.*, 2018; Qiang *et al.*, 2014; Sun *et al.*, 2022). The rapid development of spectroscopic technology provides a new method for quality detection of crops, and the identification of moldy maize by spectroscopy offers the possibility of effective identification of healthy maize and asymptomatic moldy maize (Bai *et al.*, 2020).

Near-infrared spectroscopy is often used for crop quality detection because of the fast analysis and high efficiency of the measurement process. Currently, the application of NIR spectroscopy to the detection of crop composition and diseases has achieved great results. The combined and multiplied frequencies of hydroxyl groups, such as O-H, N-H, C-H, and S-H, and C-O, are also in the NIR band (Cui *et al.*, 2019). Hydroxyl and single bond hydroxyl groups are the main groups that make up organic compounds, including oils, proteins, and sugars. Therefore, the light absorption of organic compounds in the near-infrared region is mainly the absorption of light with the multiplicative or combined frequency of hydroxyl groups. Jiahui Dai *et al.* (2024) used near infrared spectroscopy to quantitatively analyze the main active components of betel nut, and the results showed that R^2 values were close to 1, and the corresponding RPD values were all less than 3. Jiangming Jia *et al.* (2022) developed quantitative prediction models for sensory quality scores, total catechins and caffeine of different quality grades of Yuezhou Longjing tea using near-infrared spectroscopy. The results showed that the best prediction models for sensory scores, total catechins and caffeine were VCPA-IRIV + SVR, VCPA-IRIV + RF, and CARS + SVR. The relative percentage deviation (RPD) values were 2.485, 2.584 and 2.873, respectively. Jiahui Zhang *et al.* (2023) used a handheld miniature near-infrared spectrometer and applied 24 preprocessing methods in combination with a support vector machine (SVM) and a boosting algorithm. The results showed that the model exhibited high accuracy and stability during parameter tuning, with precision and F1 scores greater than 0.8 and a Kappa coefficient around 0.7. These findings confirm the feasibility of using near-infrared spectroscopy (NIRS) for the rapid identification of 'Dangshan' pear Mianhua reaction diseases. Pauline Ong *et al.* used visible and near infrared spectroscopy combined with a novel wavelength selection method called Modified Flower Pollination Algorithm (MFPA) to identify sugarcane diseases. The simplified SVM model developed utilized the MFPA wavelength selection method to obtain the best performance with an accuracy value of 0.9753, a sensitivity value of 0.9259, a specificity value of 0.9524 and an accuracy of 0.9487 (Ong *et al.*, 2023). Minhui An *et al.* (2023) used NIR to establish a prediction model for walnut mold and developed Support Vector Machine (SVM) and Extreme Learning Machine (ELM) with an accuracy of 100% for the identification of walnut mol. Hui Jiang *et al.* (2023) quantified aflatoxin B1 in moldy peanuts using two-dimensional convolutional neural network in NIR and the results showed that $R^2=0.99$, $RPD=8.3$, $RPIQ=9.3$. All of the above studies have validated the feasibility of NIR spectroscopy for crop composition analysis and disease detection as well as mold detection, but there is little research on early mold detection in maize, especially in healthy maize and asymptomatic mold.

Therefore, to address the challenge of distinguishing healthy maize from asymptomatic moldy maize, this paper proposes a method that utilizes SVM, PLS-DA, RF, KNN, and BP neural networks to analyze and determine the optimal classification model. By comparing the accuracy and F1 scores of these models, the most effective model-building approach is identified to achieve accurate classification of moldy maize. Additionally, this method enables the efficient detection of asymptomatic moldy maize, meeting the requirements of maize warehousing while enhancing its economic benefits.

MATERIALS AND METHODS

Samples

The samples for this experiment were taken from the same variety of maize that had been inoculated with molds in the breeding laboratory of Anhui Agricultural University and had been classified into four grades of moldy maize (grade 1, 2, 3, and 4), i.e., healthy maize, asymptomatic moldy maize, moderately moldy maize, and severely moldy maize, according to the method of LS/T 6132-2018, "Inspection of grain and oils—Storage fungal examination—Enumeration spores of fungi". A total of 683 maize kernel samples meeting the criteria were collected. This included 200 samples of grade 1, 153 samples of grade 2, 261 samples of grade 3, and 68 samples of grade 4. In accordance with an 8:2 ratio, all samples were randomly divided into a train set and a test set for the classification modeling study.

Near-infrared spectrum instrument

The instrument utilized to collect spectral data in this experiment is the handheld portable miniature near-infrared spectrometer "NIR-R210" created by Shenzhen Pynect Technology Co., Ltd. (Shenzhen, China). The spectral wavelength range spans from 900 nm to 1700 nm, comprising 228 bands for spectral detection, with a resolution of 3.89 nm and a signal-to-noise ratio (SNR) of 6000:1. The spectral data are collected by connecting the data line of the spectrometer to the computer. Prior to each measurement, the NIR spectrometer must undergo calibration using a black and white plate. Spectral data were acquired using the ISC-NIRScan-GUI (Windows v3.9.8-win64), supplied with the device.

Spectral data acquisition

For maximum measurement accuracy, the spectrometer underwent a 30-minute warm-up before measurement. The endosperm of each maize kernel was scanned with the endosperm side down, as illustrated in Fig. 1. Each sample underwent 5 scans, and the average of these 5 samples was considered as the final data. Each data file was named based on the sample number. Following the completion of spectral data acquisition, all files were imported. The data in each file included intensity, wavelength, absorbance, and reflectance. The absorption spectral data from the average of 5 scans were used as raw modeling spectral data.

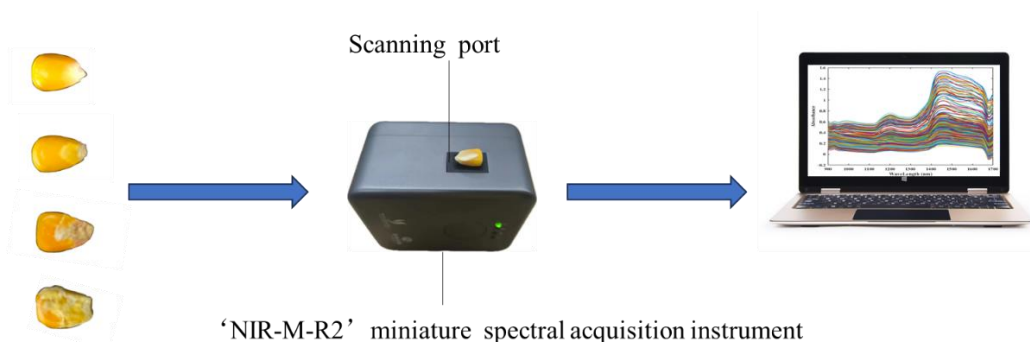


Fig. 1 - Spectral Data Scanning

RGB data acquisition

Due to the limitations of visible light cameras and the naked eye, detecting mold on asymptomatic moldy maize is challenging. Therefore, this paper adopts an electron microscope modeled as "HY-500BL" produced by Shenzhen HAYEAR Electronics Co., Ltd. to take pictures of moldy maize. It can find molds on the surface of asymptomatic moldy maize, as shown in Fig. 2. The collected microscopic photographs provide evidence that asymptomatic moldy corn is observable and allow for a secondary check of the classification results for asymptomatic mold.

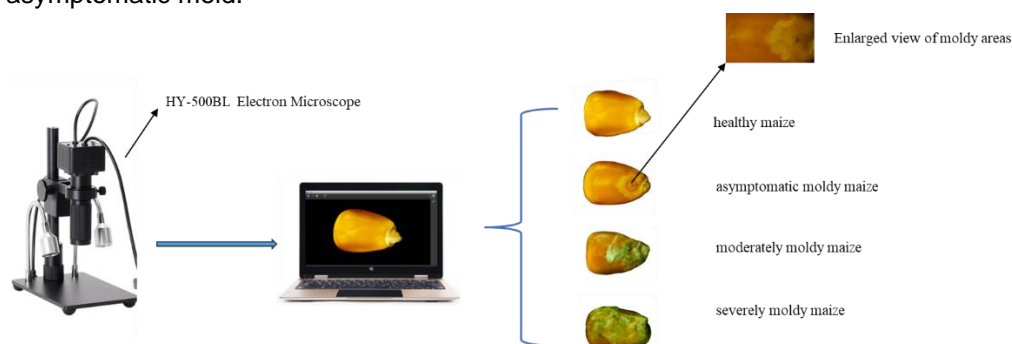


Fig. 2 - Plot of the extent of mold on maize under an electron microscope

Spectral processing method and feature wavelength extraction

During spectral data acquisition, certain disturbing factors unrelated to spectral information acquisition inevitably arise, such as the background noise of the experimental platform (Liu *et al.*, 2023). This leads to some irrelevant information in the raw spectral data. Studies have demonstrated that data preprocessing is effective in mitigating invalid information in spectral curves, enhancing the utilization rate of spectrally valid information, improving SNR of NIR, and subsequently enhancing the accuracy and stability of the regression

model established at a later stage (Xu et al., 2008). In this paper, Baseline Correction (BC) (Li et al., 2020), Multiplicative Scatter Correction (MSC) (Sun et al., 2019), Standard Normal Variate Transform (SNV) (Malavi et al., 2024), and Savitzky-Golay convolution smoothing (SG) (Lanjewar et al., 2024) were employed. Additionally, a combination of SG + SNV, SG + MSC, and SG + BC, constituting two single preprocessing algorithms, was explored to determine the optimal preprocessing method.

Specifically, BC eliminates the influence of the baseline by finding the flatter and more stable parts of the spectral data, and then subtracting or cancelling the resulting baseline from the original spectral signal by fitting the shape and position of the baseline, thus making the spectral signal features more prominent and clearer. As shown in Equation (1).

$$\begin{aligned} Y(\lambda) &= X(\lambda) - B(\lambda) \\ B(\lambda) &= a_0 + a_1\lambda + a_2\lambda^2 + \dots + a_n\lambda^n \end{aligned} \quad (1)$$

where:

$X(\lambda)$ represents the original spectral data, $B(\lambda)$ represents the fitted baseline, and $Y(\lambda)$ represents the corrected spectral data.

MSC selects a set of representative spectral data as a benchmark, averages all the spectral data of the benchmark to obtain the average spectrum, then compares each spectral data with the average spectral data, calculates the scaling factor, i.e., the scaling factor at each wavelength point, and applies the obtained scaling factor to the original sample spectral data, to obtain the scaling-corrected spectral data. As shown in Equation (2).

$$\begin{aligned} \bar{X} &= \frac{1}{N} \sum_{i=1}^N X_i \\ X_{ij} &\approx a_i \cdot \bar{X}_j + b_i \\ Y_{ij} &= \frac{X_{ij} - b_i}{a_i} \end{aligned} \quad (2)$$

where: \bar{X} represents the mean spectrum, N is the number of samples, X_i is the spectrum of the i -th sample, X_{ij} denotes the absorbance value of sample X_i at the j -th wavelength point, \bar{X}_j denotes the absorbance value of the reference spectrum at the j -th wavelength point, a_i is the slope, b_i is the intercept, Y_{ij} represents the corrected spectrum.

SNV is centered by calculating the average of the spectral intensities at each wavelength for each sample, and then subtracting the average of the corresponding wavelengths for each sample, which ensures that the average spectral intensity at each wavelength is zero. For each wavelength point, the standard deviation of the spectral intensities of all samples at that wavelength point was calculated, and for each wavelength point, the spectral intensities of all samples were divided by the standard deviation of the corresponding wavelength point. This ensured that the variance of the spectral data was relatively consistent for the purpose of standardization, as shown in Equation (3).

$$\begin{aligned} \bar{X}_i &= \frac{1}{n} \sum_{j=1}^n X_{ij} \\ \sigma_i &= \sqrt{\frac{1}{n-1} \sum_{j=1}^n (X_{ij} - \bar{X}_i)^2} \\ Y_{ij} &= \frac{X_{ij} - \bar{X}_i}{\sigma_i} \end{aligned} \quad (3)$$

where: \bar{X}_i represents the mean of the samples, n is the total number of wavelength points in the spectrum, X_{ij} denotes the absorbance value of the i -th sample at the j -th wavelength point, σ_i represents the standard deviation, and Y_{ij} represents the standardized data.

Finally, SG determines the order of the polynomial by choosing the size of the smoothing window, i.e. the number of neighboring data points to be processed at a time, and then determines the order of the polynomial, which determines the complexity of the polynomial to be fitted. The selected window is slid over the data from the first data point to the last data point and within each window polynomial fitting and smoothing of the data is done. Polynomial fitting is done by finding a polynomial by least squares that is as close as possible to all the data points within the window. Smoothing of the data is done by using the fitted polynomial to estimate the value of the window centroid i.e., the value of the smoothed data point, and the above operation is repeated until all the data points are processed, as shown in Equation (4).

$$P(x) = a_0 + a_1x + a_2x^2 + \dots + a_kx^k \quad (4)$$

$$Y_i = P(x) \cdot X_i$$

where: $P(x)$ represents the fitted polynomial, a_0, a_1, \dots, a_k denotes the coefficients of the fitted polynomial, and Y_i represents the smoothed data.

Following the preprocessing of spectral data, various feature extraction algorithms, including the Successive Projection Algorithm (SPA), Competitive Adaptive Reweighted Sampling (CARS), and Improved Shuffled Frog Leaping Algorithm (ISFLA), are utilized to identify characteristic wavelengths meeting the prediction criteria in the full-wavelength model. Subsequently, a model based on these extracted characteristic wavelengths is constructed to identify characteristic wavelengths. The model is further optimized to enhance accuracy.

The SPA algorithm first randomly selects a feature from the dataset as the initial feature. It then projects the remaining features onto the orthogonal complementary space of the already selected features, removing the influence of the selected features on the remaining ones. Afterward, the algorithm selects the feature that contributes the most to the model from the projected features. Finally, the newly selected feature is added to the set of selected features. Repeat the projection and selection steps until a predetermined number of features are selected, and the final set of selected features is representative and uncorrelated (Pang *et al.*, 2022; Vallese *et al.*, 2023).

CARS algorithm first randomly generates multiple feature subsets, each of which contains a random subset of the original features. For each feature subset, a PLS regression model is built and the regression coefficients are calculated for each feature. Based on the absolute value of the regression coefficients, weights are assigned to each feature. The larger the weight, the higher the importance of the feature to the model. Subsequently, a weighted sampling method was used to sample the features based on their weights. Features with higher weights have a higher probability of being retained. The relationship between the number of retained features and the prediction error in each iteration is calculated and a 'U' curve is plotted. Select the subset of features with the smallest prediction error, repeat the above process, continuously reduce the number of features, and recalculate the weights and feature selection in each round of iteration, and stop iterating when the predetermined number of iterations is reached or the selected subset of features is stable, and finally output the subset of features that contributes the most to the predictive ability of the model (Tang *et al.*, 2021; Xing *et al.*, 2021).

ISFLA algorithm starts by randomly generating a certain number of frogs, each frog representing a possible solution, which form the initial population. The frogs are sorted by fitness value and divided into subpopulations, each containing a number of frogs. A local search is then performed to determine the optimal frog and the worst frog in each subpopulation. The solution of the optimal frog is the best solution in the current subpopulation, and the solution of the worst frog is the worst solution in the subpopulation. The worst frog updates its position based on the solution of the optimal frog. Specifically, the worst frog moves closer to the optimal frog to increase its fitness value. If the updated position is better than the previous position, the position is accepted; otherwise, further attempts are made to update based on the global optimal solution. After all subpopulations complete the local search, all frogs are remixed to break the local optimum among subpopulations. After mixing, the subgroups are reclassified to continue the next round of local search. In order to avoid the local search from falling into local optima, ISFLA introduces an adaptive step-size adjustment strategy, which dynamically adjusts the step-size of the frogs' jumps based on the feedback during the search process. In some iterations, a more exploratory global search strategy is used to increase the ability of the algorithm to jump out of the local optimum. The local and global search processes are repeated until the stopping condition is satisfied, and the solution of the optimal frog in the whole frog population, i.e., the selected optimal wavelength, is finally output (Hsu and Wang, 2021; Kongsorot *et al.*, 2022).

Modeling method

The modeling methods utilized in this study comprise Support Vector Machines (SVM), Partial Least Squares Discriminant Analysis (PLS-DA), K Nearest Neighbor (KNN), Random Forest (RF), and Back Propagation Neural Network (BP).

The goal of SVM is to find a hyperplane that maximizes the interval between classes in order to classify the data. Specifically, a straight line (hyperplane) is computationally found to separate several classes of data while maximizing the distance between two classes of data points and the hyperplane. The closest data points to the hyperplane, known as support vectors, determine the position and direction of the hyperplane. The hyperplane is then adjusted to maximize the distance from the support vectors to the hyperplane. Finally, for new data points, their class is determined based on their position relative to the decision boundary (hyperplane) (Khairunniza-Bejo et al., 2021).

PLS-DA is a supervised learning method that combines Partial Least Squares Regression (PLS) and Linear Discriminant Analysis (LDA), and is commonly used for classification tasks, especially in high-dimensional, small-sample datasets. PLS-DA maximizes the variance of the samples on these variables by searching for latent variables, and minimizes the confounding between different classes, thereby achieving the classification purpose. Specifically, the input dataset X and the corresponding category labels Y are searched for a set of latent variables, T , so that these variables explain the maximum covariance between X and Y . Through an iterative approach, the weight vector W is computed to derive the latent variables $T = XW$, and a linear regression model of the latent variables T to the category labels Y is built, thus transforming the classification problem into a regression problem. Solve for the regression coefficient B so that $Y \approx TB$. Finally, use the results of the regression model to classify the new sample. The new sample is projected into the latent variable space and its category is determined based on the output of the regression model (Daniels et al., 2021).

KNN A simple and intuitive supervised learning algorithm mainly used for classification and regression tasks. KNN selects the nearest K neighbors by calculating the distances between the samples to be classified and the training samples, and then determines the class of the samples to be classified by the class information of these neighbors. Specifically, the input data consists of a feature matrix X and corresponding labels Y , where X is a sample dataset containing multiple features, and Y is the category label corresponding to each sample, and the Euclidean distance metric Manhattan distance, etc. are chosen to compute the distances between the samples. For the to-be-classified sample, calculate its distance from all the samples in the training set and select the nearest K samples as its neighbors. Finally, based on the categories of these K neighbors, the categories of the samples to be classified are decided by voting, and the category with the highest frequency of occurrence is selected as the final classification result (Cunningham and Delany, 2021). In this study, Euclidean distance is utilized to calculate the distances between points in the feature space. Cross-validation is employed to determine the optimal score of K (Uddin et al., 2022).

RF does this by generating multiple decision trees, each trained independently on a subset of the data, and then combining the predictions of these trees by majority voting. Specifically, the input dataset X and corresponding labels Y are input, multiple subsample sets are randomly selected from the original dataset with putback (i.e., Bootstrap sampling), each of which is used to train a decision tree, and during the construction of each tree, for each node split, a portion of the features are randomly selected to determine the optimal split thus increasing the diversity of the tree and reducing overfitting. Each decision tree is trained on the corresponding Bootstrap sample set to generate multiple different decision tree models, and finally, for new data points, the classification results of each decision tree are voted on and the category with the most votes is selected as the final prediction (Wang et al., 2021).

BP is a training algorithm for multilayer perceptron (MLP) which adjusts the network weights by calculating the errors and back propagating them so that the network is able to learn and approximate complex nonlinear functions. BP neural network consists of an input layer, a hidden layer, and an output layer, and each layer consists of a number of neurons. The core idea is to adjust the weights and bias of the network through the back propagation algorithm to minimize the error between the predicted output and the actual output, in which the input layer receives the input data, the hidden layer performs a linear transformation of the input data through the weights and bias, and then performs a nonlinear transformation through the activation function (e.g., sigmoid, ReLU, etc.), and the output layer performs a transformation of the output again through the weights and bias and through the activation function to get the final predicted output. The predicted output of the output layer is compared with the actual output (labels) and the error is calculated.

Starting from the output layer, the gradient of the error with respect to each weight and bias is calculated. By chain rule, forward propagation is performed layer by layer, calculating the gradient of each layer, and using gradient descent, the weights and biases of each layer are adjusted according to the calculated gradient to reduce the error. The process of forward propagation, error calculation and back propagation is performed repeatedly until the error converges to a preset threshold or the maximum number of iterations is reached (Wang *et al.*, 2023).

In this paper, spectral data were processed and modelled and analyzed using MATLAB 2023b.

Evaluation criteria

For the multi-class classification task of corn kernel quality detection, average evaluation metrics are more suitable. Therefore, this study uses accuracy, average recall, average precision, and average F1 score as evaluation metrics.

Acc is the ratio of the number of correctly classified samples to the total number of samples.

$$Acc = \frac{TP + TN}{TP + TN + FP + FN} \quad (5)$$

where:

TP and TN represent the true prediction of the positive sample and the true prediction of the negative sample, respectively. FP and FN represent the false prediction of the positive sample and the false prediction of the negative sample, respectively.

P is the arithmetic mean of the precision (P) of each category, which is defined in the following:

$$P = \frac{1}{k} \sum_i^k P_i = \frac{1}{k} \sum_i^k \frac{TP_i}{TP_i + FP_i} \quad (6)$$

where:

i represents the target classes, k is set to 4, as four types of corn kernels are classified, P is the proportion of the predicted positive samples that are actually positive.

R is the arithmetic mean of the recall (R) of each category. It is defined as follows:

$$R = \frac{1}{k} \sum_i^k R_i = \frac{1}{k} \sum_i^k \frac{TP_i}{TP_i + FN_i} \quad (7)$$

$F1$ is the weighted harmonic average of P and R scores, which is defined as follows:

$$F1 = \frac{1}{k} \sum_i^k \frac{2 \cdot P_i \cdot R_i}{P_i + R_i} \quad (8)$$

RESULTS

Analysis of original spectral curve

The spectral raw data were obtained using the experimental setup described above, as shown in Fig. 3(a). The overall shapes of the spectral curves of all the maize seed samples were similar. From Fig. 3(b), it can be clearly seen that there are obvious peaks at 930 nm, 1210 nm and 1460 nm, and clear troughs at 910 nm, 1220 nm and 1300 nm. The 930 nm peak corresponds to water absorption, associated with the first multiplicative frequency of the O-H bond stretching vibration in relevant carbohydrates. The 1210 nm peak corresponds to the first multiplicative frequency of the C-H bond stretching vibration in fats and oils within maize kernels, particularly fatty acids. The 1460 nm peak corresponds to C-H bond changes in fibers and polysaccharides inside the maize kernel.

Fig 3(c) shows that the absorbance of maize kernels with different degrees of mold is different, which is mainly due to aflatoxin, erythromycin, vomitoxin and other molds, which will change the hydroxyl (OH), hydrocarbon (CH) and carbonyl (C=O) groups of maize kernels. Because of the complex compounds contained in the maize kernels, the spectral profiles are more complicated and correspond to the octave and frequency information of different chemical bond vibrations, which is the main reason for the different spectral profiles of different molded maize. It was also verified that it is feasible to use microscopy to observe asymptomatic moldy maize.

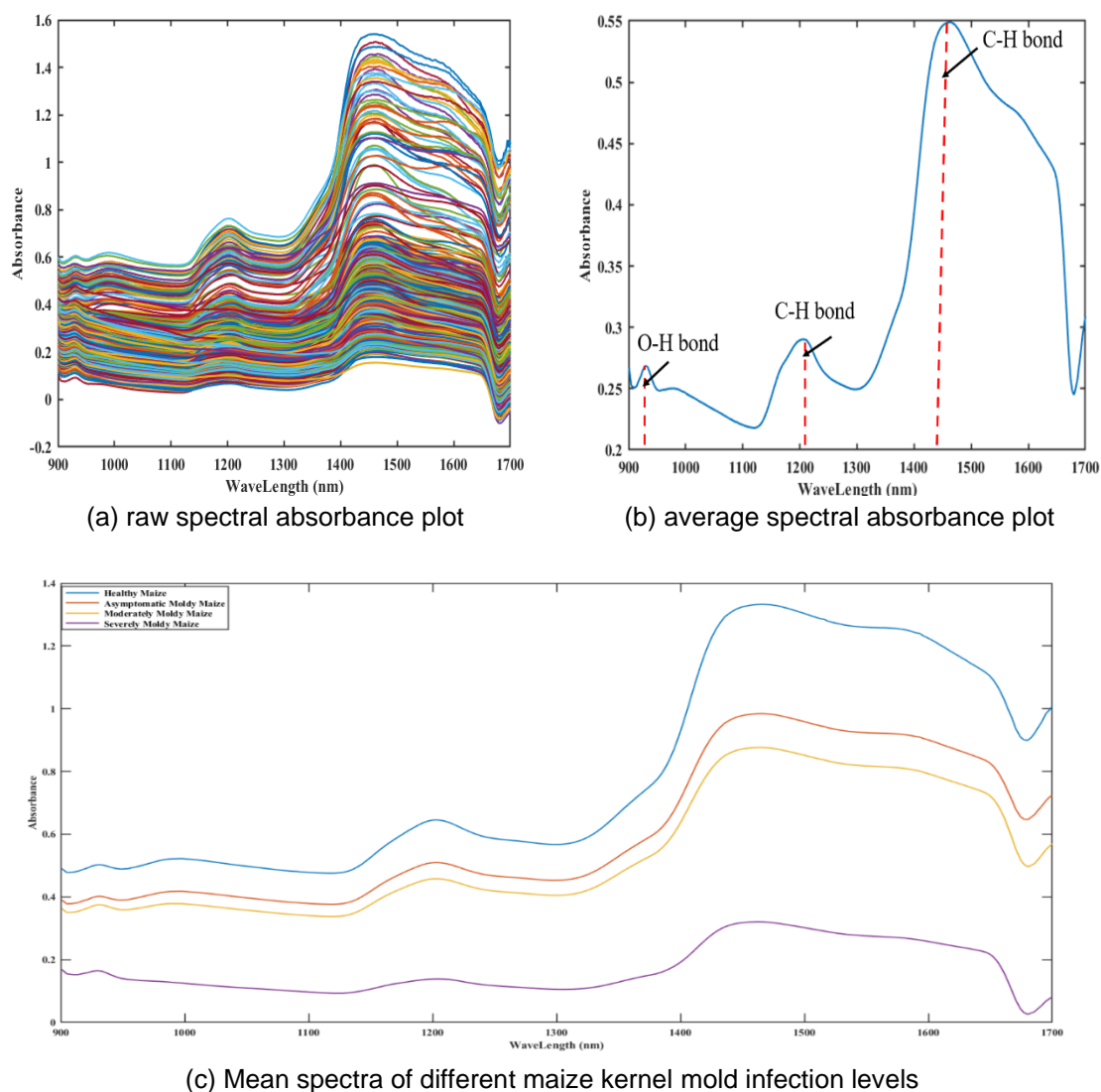
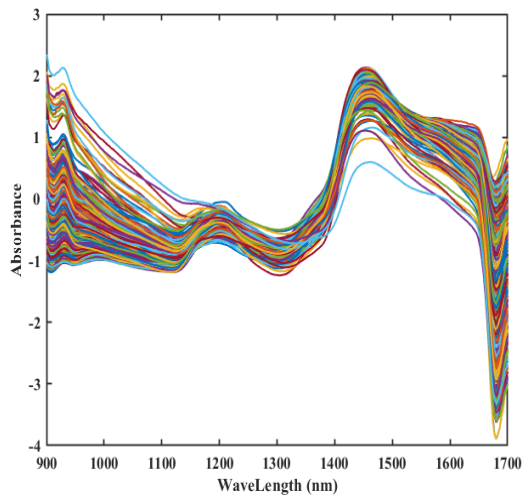


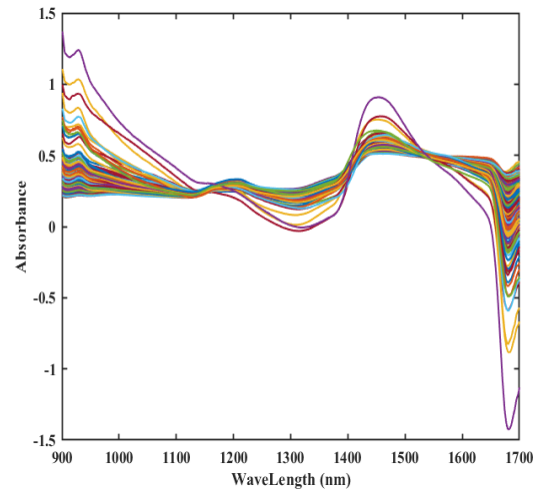
Fig. 3 - (a) raw spectral absorbance plot, (b) average spectral absorbance plot for all maize kernel samples and (c) Mean spectra of different maize kernel mold infection levels

Analysis of spectral data preprocessing results

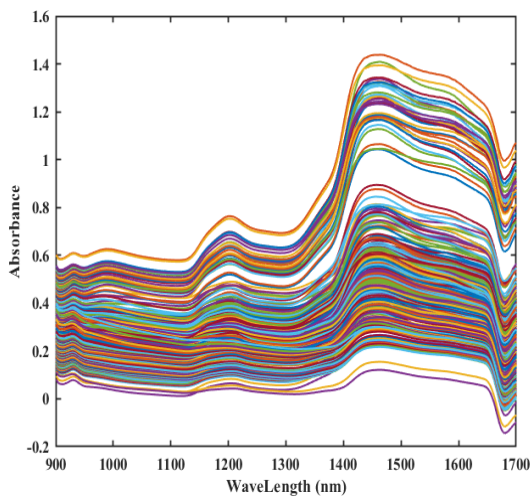
Preprocessing methods and combinations play a crucial role in reducing the interference of irrelevant information. The spectral data underwent preprocessing using SNV, MSC, SG, BC, SG+SNV, SG+MSC, and SG+BC. To ensure consistency in the observed sample data after applying different preprocessing methods, the resulting spectra were compared. The spectral curves resulting from the seven preprocessing methods are presented in Fig. 4, clearly demonstrating their distinct effects. From Fig. 4(a) and Fig. 4(b), it is evident that the spectral curves resulting from the SNV and MSC processing exhibit no significant or fluctuating trends. These methods, both belonging to the scattering processing category, effectively mitigate the scattering effect during spectral data acquisition. They enhance the signal-to-noise ratio of the spectral data, correct the spectral baseline shift, and do not impact the corresponding absorption data. The primary objective of SNV is to mitigate the scattering effect and eliminate optical range changes in the spectra. In contrast, MSC intends to correct the scattering effects due to uneven particle distribution and varied particle sizes on the sample surface. Fig. 4(c) illustrates the spectral curves obtained by applying the SG convolution smoothing method to the original spectral data. This method removes irrelevant noise from the spectra and results in a smoother curve than the original image. Fig. 4(d) displays the outcomes of BC baseline correction, revealing that the baseline drift of the spectral image improves significantly after correction. Additionally, the peaks and shapes of the spectral image are better aligned than those in the original image. This section analyses the relevance of the data preprocessing results. To evaluate the advantages and disadvantages of various preprocessing methods in this experiment, the next step is to model the preprocessed data.



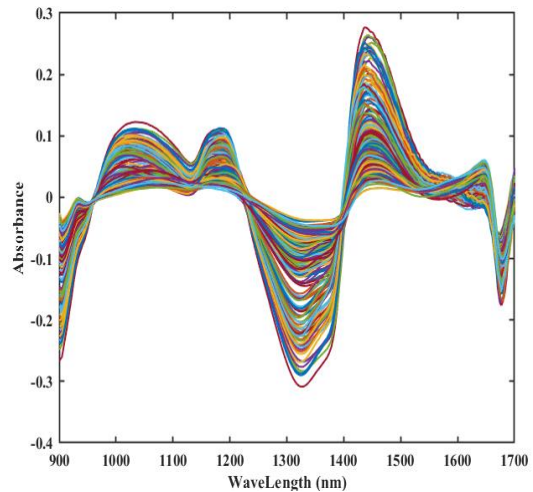
(a) spectrum with the SNV method



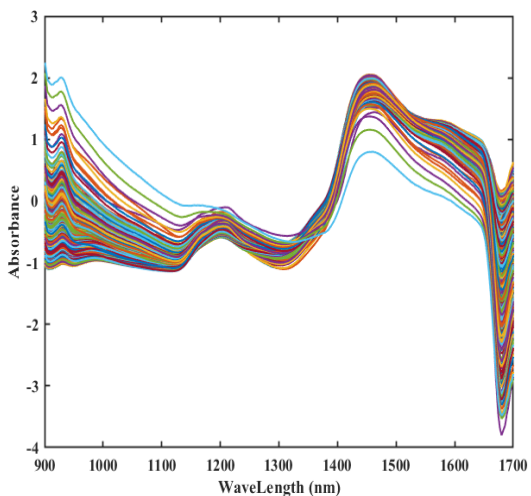
(b) spectrum with the MSC method



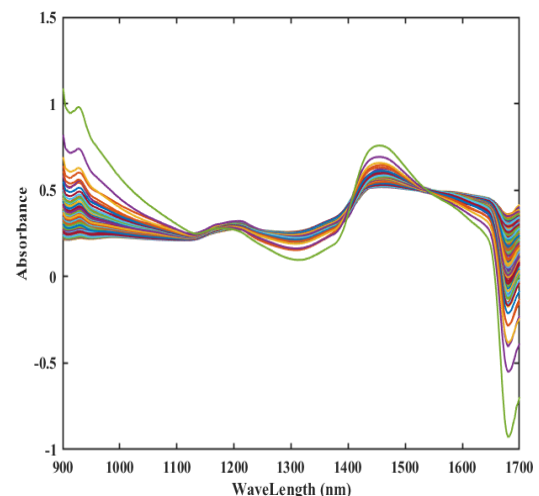
(c) spectrum with the SG method



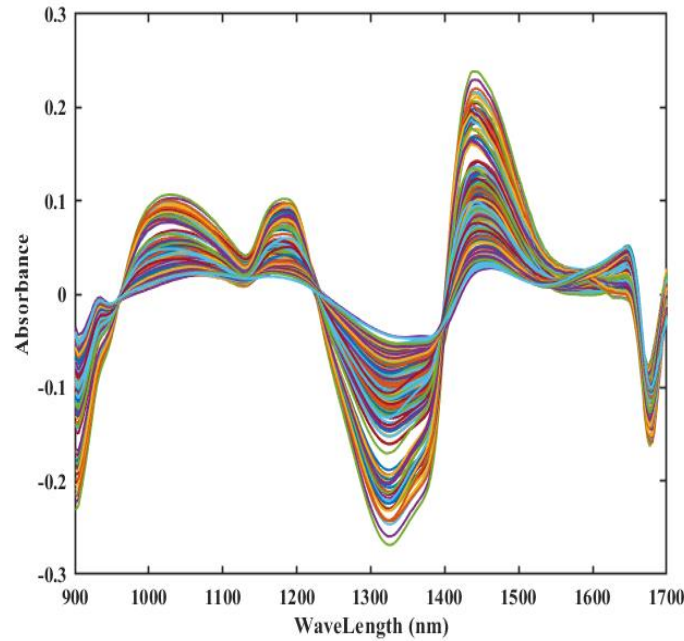
(d) spectrum with the BC method



(e) spectrum with the SG+SNV method



(f) spectrum with the SG+MSC method

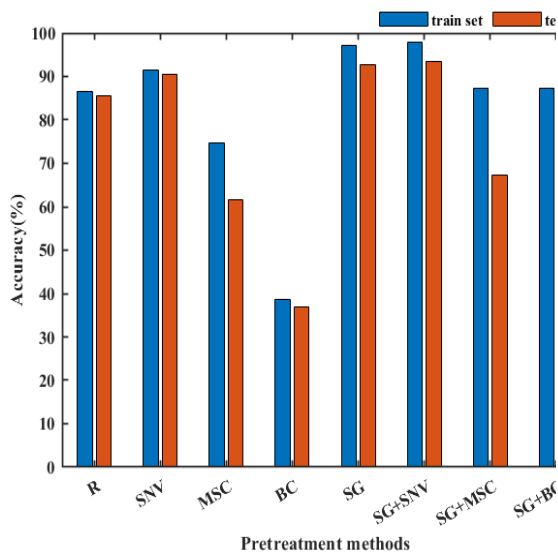


(g) spectrum with the SG+BC method

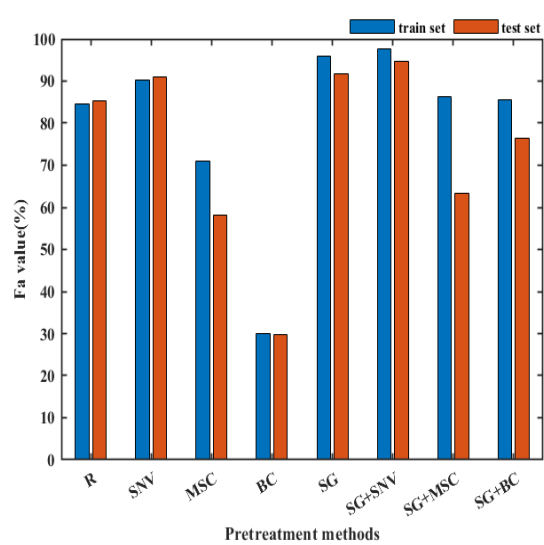
Fig. 4 -Spectral graphs after transformation based on different preprocessing methods

Full-band based modeling

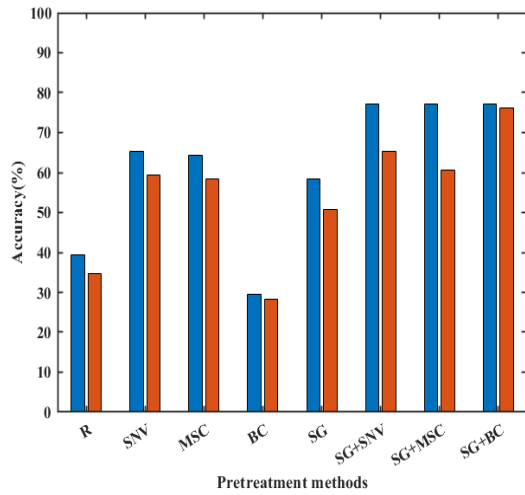
In this paper, five methods, SVM, PLS-DA, RF, KNN and BP, are used to model and analyze the spectral data after different preprocessing. Fig. 5 shows the comparison of accuracy and F1 value of each model with different preprocessing methods. From Fig. 5, it can be clearly seen that, except for the BP neural network and PLS-DA, the preprocessing effect of BC on the other models is poorer. This may be because the baseline and the signal sometimes overlap, leading to the removal of some real information during the BC process. On the other hand, the overall effect of the model after SG processing is better, mainly because SG removes high-frequency noise from the signal, making the spectral curves smoother and highlighting their key characteristics. In addition, for different models, SG+SNV, SG+MSC and SG+BC preprocessing methods all achieve good results, which indicates that the superposition of preprocessing methods is feasible.



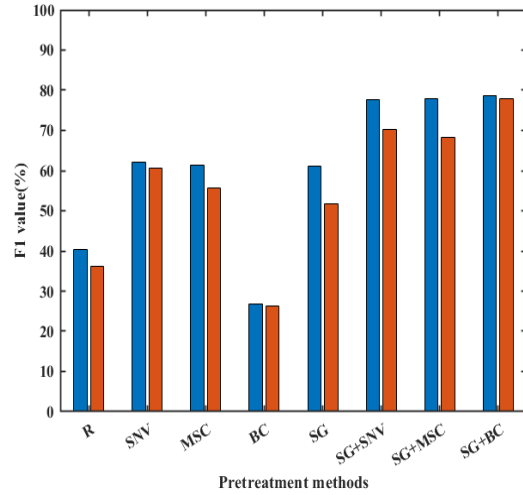
(a) Accuracy of SVM



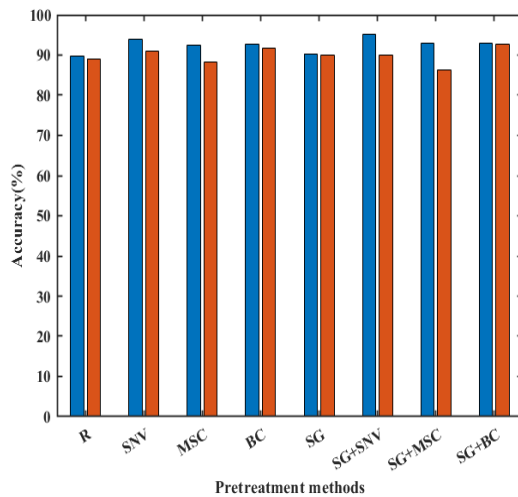
(b) F1 of SVM



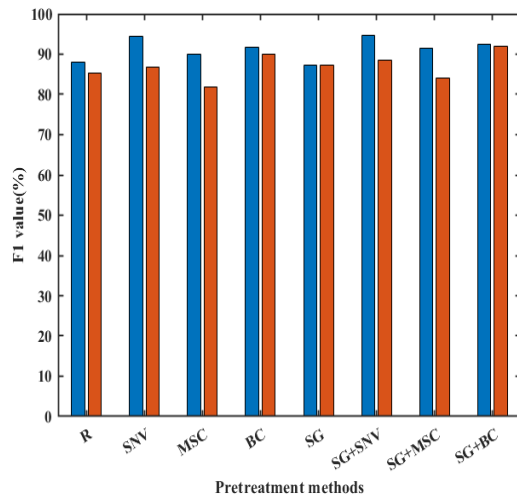
(c) Accuracy of KNN



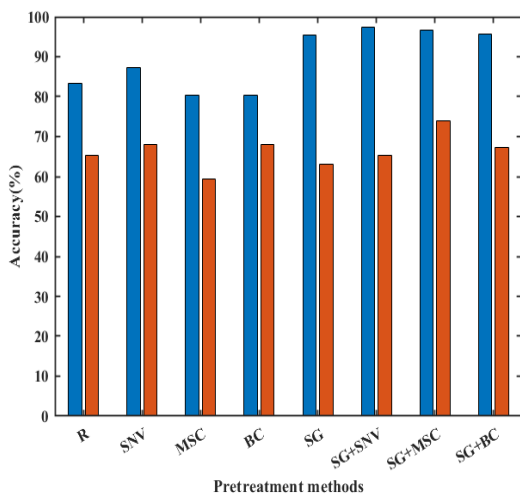
(d) F1 of KNN



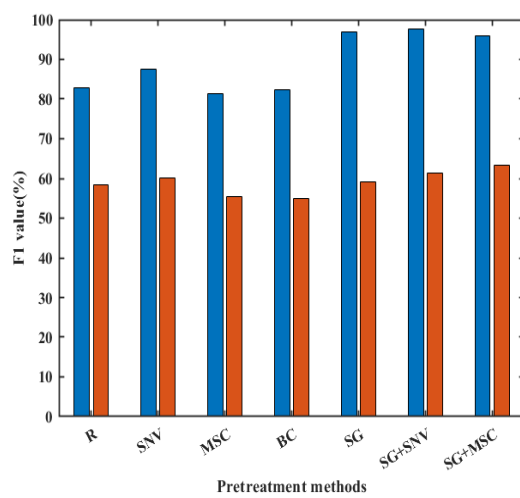
(e) Accuracy of BP



(f) F1 of BP



(g) Accuracy of PLS-DA



(h) F1 of PLS-DA

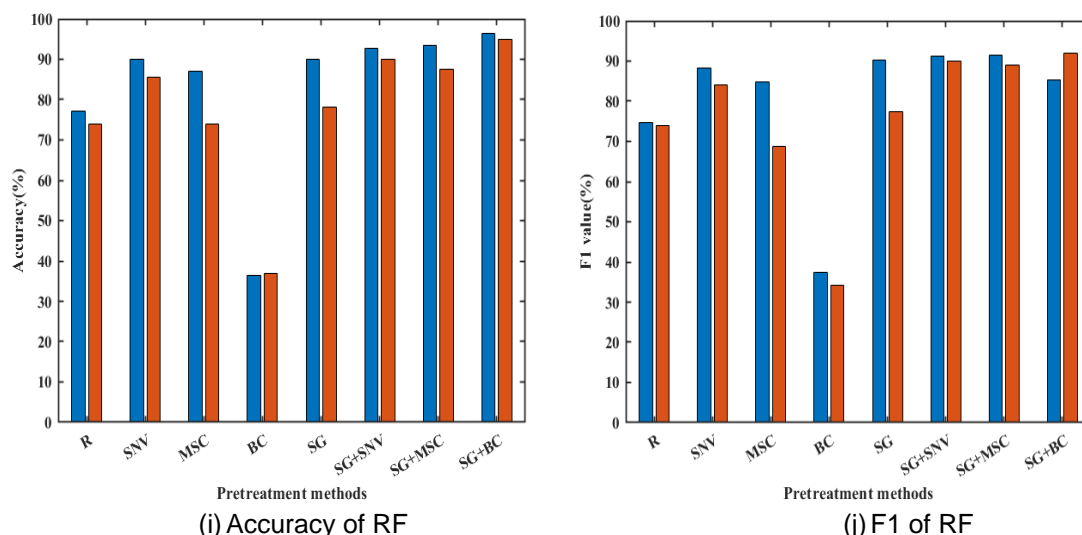


Fig. 5 - Accuracy and F1 with the testing dataset

As shown in Table 1, regarding the accuracy and F1 of each model, SVM and RF consistently outperformed PLS-DA, KNN, and BP in classifying the extent of mold in maize kernels. The best results obtained by SVM were based on spectral data after SG+SNV preprocessing with 97.98% accuracy and 97.55% F1 value for the training set, 93.48% accuracy and 94.63% F1 value for the validation set, and 88.57% identification accuracy for asymptomatic moldy maize, and the best results obtained by RF were based on spectral data after SG+BC preprocessing that the training set accuracy is 96.33% with F1 value of 95.43% and the validation set accuracy is 94.50% with F1 value of 94.98% and the recognition accuracy for asymptomatic moldy maize is 91.43%, which is slightly higher than the SVM modeling, and both models have high discriminative ability. For the identification of asymptomatic moldy maize, the SG+SNV-SVM model incorrectly identified four asymptomatic moldy maize as three healthy maize and one moderately moldy maize. The SG+BC-RF model incorrectly identified three asymptomatic moldy maize as one healthy maize and two moderately moldy maize, which due to the fact that the surface of the asymptomatic moldy maize is similar to that of the healthy maize, but its internal chemical composition is similar to that of moderate moldy maize, which can easily lead to model misidentification.

Despite PLS-DA achieving high accuracy and F1 values in the training set (97.44% for SG+SNV, 96.71% for SG+MSC, and 95.61% for SG+BC), PLS-DA's performance in the validation set was subpar (65.22% for SG+SNV, 73.83% for SG+MSC, and 67.25% for SG+BC). This disparity arises from the limitations of PLS-DA in handling highly correlated independent variables and category imbalances. On the other hand, KNN demonstrated overall lower effectiveness in modeling both raw and preprocessed data, reaching a maximum accuracy of only 77.25% for SG+BC in the training set and 76.48% in the validation set, significantly below the anticipated performance. This inefficiency is attributed to KNN's inapplicability to data with high dimensionality and unbalanced feature weights. For maize mold samples, SVM, RF and BP gave better classification results due to their robustness and good handling of non-linear and large-scale datasets.

Table 1

Classification results based on the SVM, PLS-DA, RF, KNN and BP models									
Models	Preprocessing Methods	Training Set				Testing Set			
		Accuracy	P	R	F1	Accuracy	P	R	F1
SVM	RAW	86.47%	85.23%	84.08%	84.50%	85.51%	85.06%	86.63%	85.23%
	SNV	91.59%	91.51%	89.36%	90.31%	90.58%	92.87%	89.59%	91.02%
	MSC	74.59%	74.48%	67.92%	71.05%	61.59%	68.51%	66.24%	58.25%
	BC	38.57%	37.62%	25.00%	30.04%	36.96%	36.45%	25.00%	29.66%
	SG	97.06%	96.45%	95.34%	95.86%	92.75%	90.44%	94.24%	91.78%
	SG+SNV	97.98%	98.35%	96.87%	97.55%	93.48%	95.01%	94.73%	94.63%
	SG+MSC	87.34%	91.42%	83.82%	86.32%	67.39%	70.94%	71.46%	63.34%
	SG+BC	87.34%	91.72%	83.64%	85.47%	78.99%	86.33%	78.70%	76.35%

Models	Preprocessing Methods	Training Set				Testing Set			
		Accuracy	P	R	F1	Accuracy	P	R	F1
PLSDA	RAW	83.36%	81.54%	88.51%	82.79%	65.22%	63.65%	50.00%	58.52%
	SNV	87.20%	87.31%	88.24%	87.62%	68.12%	68.23%	53.68%	60.09%
	MSC	80.45%	80.37%	84.16%	81.34%	59.42%	60.35%	51.23%	55.42%
	BC	80.27%	81.35%	85.98%	82.30%	68.12%	67.25%	53.26%	59.45%
	SG	95.42%	96.70%	97.22%	96.85%	63.04%	64.59%	48.08%	54.97%
	SG+SNV	97.44%	98.41%	96.96%	97.61%	65.22%	64.89%	54.33%	59.14%
	SG+MSC	96.71%	96.54%	94.83%	95.68%	73.83%	72.56%	53.21%	61.40%
	SG+BC	95.61%	94.58%	97.67%	95.90%	67.25%	66.57%	60.54%	63.41%
KNN	RAW	39.31%	46.14%	49.53%	40.38%	34.78%	41.52%	44.65%	36.20%
	SNV	65.25%	62.24%	67.74%	62.15%	59.42%	60.41%	65.61%	60.54%
	MSC	64.35%	62.62%	62.20%	61.38%	58.41%	52.93%	58.76%	55.69%
	BC	29.62%	28.76%	25.00%	26.75%	28.26%	27.56%	25.00%	26.22%
	SG	58.32%	62.79%	66.26%	61.07%	50.72%	50.72%	58.53%	51.85%
	SG+SNV	77.15%	77.19%	83.38%	77.75%	65.22%	66.92%	74.04%	70.30%
	SG+MSC	77.15%	77.49%	82.40%	77.92%	60.58%	65.00%	71.75%	68.21%
	SG+BC	77.25%	81.00%	84.44%	78.76%	76.23%	75.34%	80.58%	77.87%
RF	RAW	77.06%	76.01%	73.73%	74.57%	73.91%	74.52%	74.57%	73.89%
	SNV	89.91%	92.72%	85.40%	88.23%	85.51%	87.64%	82.07%	84.17%
	MSC	87.16%	87.88%	82.71%	84.80%	73.92%	72.36%	65.39%	68.70%
	BC	39.45%	38.36%	36.57%	37.44%	36.96%	34.86%	33.58%	34.21%
	SG	89.91%	89.82%	90.67%	90.16%	78.26%	79.77%	80.10%	77.43%
	SG+SNV	92.66%	92.39%	90.41%	91.33%	89.86%	90.90%	90.93%	89.82%
	SG+MSC	93.58%	93.36%	89.85%	91.37%	87.56%	89.73%	88.25%	88.98%
	SG+BC	96.33%	96.02%	94.96%	95.43%	94.50%	94.05%	96.24%	94.98%
BP	RAW	89.68%	87.77%	88.30%	87.95%	89.09%	84.88%	86.82%	85.37%
	SNV	94.04%	94.59%	94.51%	94.36%	90.91%	86.69%	87.56%	86.87%
	MSC	92.43%	88.85%	91.28%	89.94%	88.18%	81.48%	84.27%	81.97%
	BC	92.66%	93.59%	90.20%	91.66%	91.82%	89.68%	90.73%	90.12%
	SG	90.37%	91.20%	85.09%	87.25%	90.09%	87.13%	87.36%	87.17%
	SG+SNV	95.18%	95.44%	94.18%	94.72%	90.09%	88.26%	89.26%	88.48%
	SG+MSC	92.89%	91.44%	92.01%	91.57%	86.36%	83.37%	85.74%	84.17%
	SG+BC	92.89%	94.46%	90.66%	92.52%	92.73%	93.48%	90.88%	91.88%

Characteristic wavelength extraction

Based on the results of the established full-band model it can be seen that the model classification under SG+SNV and SG+BC preprocessing is better, so SPA, CARS, and ISFLA were used to extract the feature wavelengths from the spectral data after SG+SNV and SG+BC preprocessing. In the case of SG+SNV, three feature wavelength extractions were performed, yielding 107, 113, and 32 feature wavelengths, respectively. For SG+BC, 107, 109, and 33 wavelengths were extracted. As shown in Fig 6, the feature extraction wavelengths for SG+BC-SPA were concentrated in the range of 1150 nm-1250 nm and 1300 nm to 1700 nm, while those for SG+BC-CARS were mainly concentrated in the range of 980 nm-1220 nm and 1410 nm-1650 nm. For the SG+BC-ISFLA method, a reduced number of feature wavelengths were identified, yet they predominantly clustered within the spectral ranges of 1100nm-1300nm and 1300nm-1650nm. These findings suggest that the maize kernel mold-related compounds associated with these feature wavelengths are consistently concentrated within their respective mentioned ranges. Although the specific values of the extracted feature wavelengths may vary across spectral curves, the observed similarity in their distribution ranges underscores the consistent concentration of these compounds in the aforementioned spectral intervals.

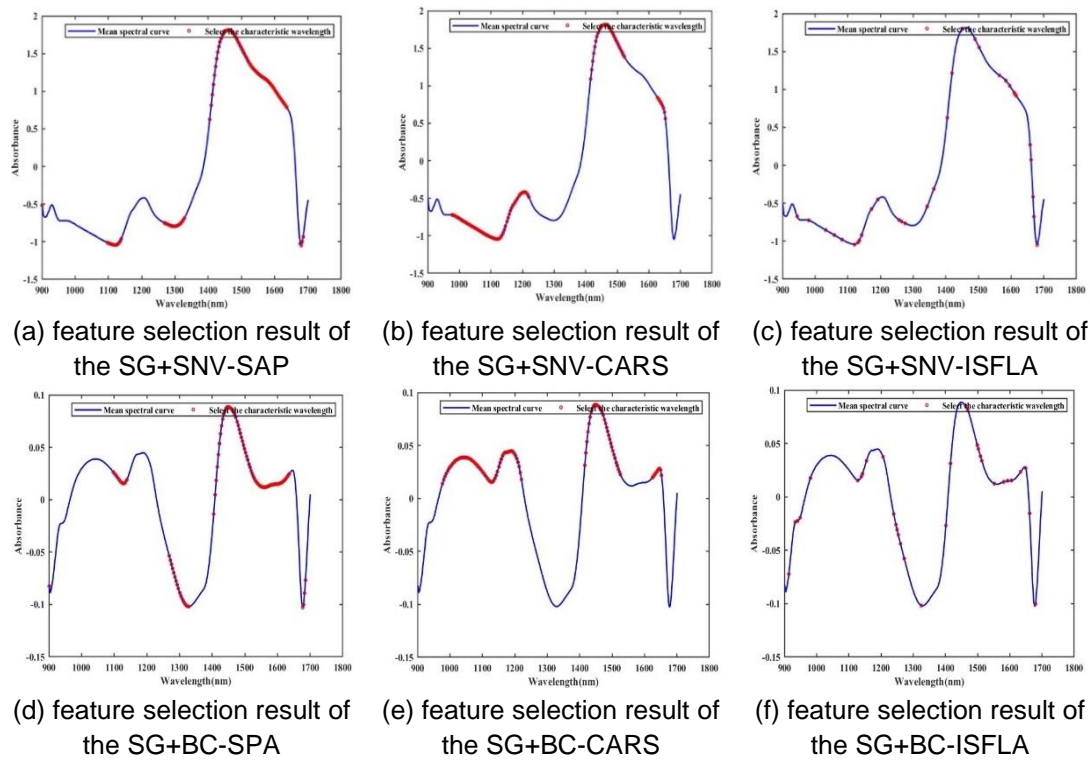


Fig. 6 -Feature extraction results

Modeling of characteristic wavelengths

According to Table 2, the models constructed after feature extraction demonstrate improvements in prediction accuracy and F1 value (Zhang et al., 2022). Specifically, for the SG+SNV-SVM model, ISFLA feature extraction yields the best results with an F1 value of 97.79%, indicating a 3.16% improvement over the pre-feature extraction performance. Conversely, SPA feature extraction shows the least favorable outcome for the SG+SNV-SVM model, resulting in a 0.63% increase compared to pre-extraction. In the case of the SG+BC-RF model, ISFLA feature extraction is the most effective, achieving an F1 value of 96.91% and a 1.93% improvement over the pre-extraction F1 value. However, SPA feature extraction for the SG+BC-RF model shows a minimal improvement of 0.09%, representing the least effective method. Finally, for the SG+BC-BP model, ISFLA feature extraction stands out with the highest F1 value of 95.20%, demonstrating a 3.32% improvement over pre-feature extraction. SPA feature extraction for SG+BC-BP achieves a 2.31% improvement compared to the other two methods. SG+SNV-SVM-ISFLA had the highest classification ability for moldy maize, with an F1 value of 97.22%. The recognition accuracy for asymptomatic moldy maize reached 96.30%, and this sample is a biological sample of high complexity, and the classification index of SG+SNV-SVM-ISFLA model is acceptable in this study.

In summary, while different feature extraction methods exhibit varying effects on the models, there is an overall enhancement in accuracy. This underscores the capability of the feature extraction process to eliminate irrelevant wavelengths and preserve information-rich features, thereby improving the predictive performance of the model.

Table 2

Modeling of maize grain mildew degree under different feature extraction methods.

Models	Characteristic Wavelength Extraction Method	Train set				Test set			
		Accuracy	P	R	F1	Accuracy	P	R	F1
SG+SNV-SVM	SPA	97.25%	97.49%	96.48%	96.91%	97.10%	97.12%	98.08%	97.54%
	CARS	97.61%	98.11%	97.81%	97.96%	97.08%	97.49%	97.87%	97.68%
	ISFLA	98.16%	98.86%	97.04%	97.94%	97.22%	98.03%	97.56%	97.79%
SG+BC-RF	SPA	98.17%	97.15%	97.15%	97.15%	95.63%	95.03%	95.12%	95.07%
	CARS	98.17%	98.89%	95.45%	96.93%	96.35%	95.90%	96.65%	96.13%
	ISFLA	96.33%	97.83%	96.37%	97.09%	96.30%	97.77%	96.43%	96.91%
	SPA	96.78%	97.20%	95.59%	96.25%	95.41%	95.47%	93.61%	94.19%

Models	Characteristic Wavelength Extraction Method	Train set				Test set			
		Accuracy	P	R	F1	Accuracy	P	R	F1
SG+BC-	CARS	97.47%	97.41%	96.09%	96.67%	95.41%	96.05%	93.92%	94.97%
BP	ISFLA	97.93%	98.23%	96.84%	97.46%	96.33%	96.71%	94.31%	95.20%

CONCLUSIONS

The aim of this paper is to investigate the use of near-infrared spectral fingerprints to classify moldy maize while at the same time accurately identifying asymptomatic moldy maize thereby reducing the probability of early mass infection of stored maize. Firstly, different preprocessing methods are used for comparative analysis, and the results show that the modeling effect of the spectral data after a series of preprocessing methods, such as SNV, MSC, SG, etc., is better than that of the original data, and better results can be obtained by using a combination of multiple preprocessing methods to deal with the original spectra, among which the SG+SNV and SG+BC are the most effective. Secondly, the full-band spectral data classification model was constructed, and the experimental results showed that the accuracy of the SG+BC-RF model for moldy maize classification could reach 94.50%. Then, feature extraction is performed on the different preprocessed data. Finally, the data after feature extraction were modelled, and the experimental results showed that the SG+SNV-SVM-ISFLA model could classify moldy maize with an accuracy of up to 97.22%, and identify asymptomatic moldy maize with an accuracy of up to 96.30%, which meets the identification requirements. This work provides new perspectives and ideas for the classification of moldy maize and the identification of asymptomatic moldy maize, as well as new ideas for early mold safety monitoring of stored maize.

ACKNOWLEDGEMENT

Project of National Natural Science Foundation of China (52105539), Anhui Natural Science Foundation (2108085QD179), National Engineering Technology Research Center (2005DP173065- 2022 - 01);

REFERENCES

- [1] An M., Cao C., Wang S., Zhang X., (2023), Analysis, Non-destructive identification of moldy walnut based on NIR. *Journal of Food Composition and Analysis*, Vol. 121, pp. 105407, China.
- [2] Bai X., Zhang C., Xiao Q., He Y., (2020), Application of near-infrared hyperspectral imaging to identify a variety of silage maize seeds and common maize seeds. *RSC advances*, Vol. 10, pp. 11707-11715, China.
- [3] Cui Y., Ge W., Li J., Zhang J., An D., (2019), Screening of maize haploid kernels based on near infrared spectroscopy quantitative analysis. *Computers and electronics in agriculture*, Vol. 158, pp. 358-368, China.
- [4] Cunningham P., Delany S.J., (2021), Delany, k-Nearest neighbour classifiers-A Tutorial. *ACM computing surveys (CSUR)*, Vol. 54, Issue 6, pp. 1-25, Ireland.
- [5] Dai J., Tang W., Zhan, J., Kang X., Dai W., Ji J., (2024), Determination and quality evaluation of active ingredients in areca nut using near-infrared rapid detection technology. *Microchemical Journal*, Vol. 196, pp. 109586, China.
- [6] Daniels A. J., Poblete-Echeverría C., Nieuwoudt H. H., Botha N., (2021), Classification of browning on intact table grape bunches using near-infrared spectroscopy coupled with partial least squares-discriminant analysis and artificial neural networks. *Frontiers in Plant Science*, Vol. 12, pp. 768046, South Africa.
- [7] Hsu H.P., Wang C.N., (2021), A Hybrid Approach Combining Improved Shuffled Frog-Leaping Algorithm With Dynamic Programming for Disassembly Process Planning. *Ieee Access*, Vol. 9, pp. 57743-87756, China.
- [8] Jia J., Zhou X., Li Y., Wang M., Liu Z., (2022), Establishment of a rapid detection model for the sensory quality and components of Yuezhou Longjing tea using near-infrared spectroscopy. *LWT*, Vol. 164, pp. 113625, China.
- [9] Jiang H., Deng J., Zhu C., (2023), Quantitative analysis of aflatoxin B1 in moldy peanuts based on near-infrared spectra with two-dimensional convolutional neural network. *Infrared physics & technology*, Vol. 131, pp. 104672, China.
- [10] Kang Z., Huang T., Zeng S., Li H., Dong L., (2022), A Method for Detection of Corn Kernel Mildew Based on Co-Clustering Algorithm with Hyperspectral Image Technology. *Sensors*, Vol. 22, Issue 14, pp. 5533.

- [11] Khairunniza-Bejo S., Shahibullah M.S., Azmi A.N.N., (2021), Non-destructive detection of asymptomatic *Ganoderma boninense* infection of oil palm seedlings using NIR-hyperspectral data and support vector machine. *Applied Sciences*, Vol. 11, Issue 22, pp. 10878, Malaysia.
- [12] Kongsorot Y., Musikawan P., Muneesawang P., (2022), An enhanced fuzzy-based clustering protocol with an improved shuffled frog leaping algorithm for WSNs. *Expert Systems with Applications*, Vol. 198, pp. 116767, Thailand.
- [13] Lanjewar M. G., Morajkar P. P., Parab J. S., (2024), Portable system to detect starch adulteration in turmeric using NIR spectroscopy. *Food Control*, Vol. 155, pp. 110095, India.
- [14] Li Y., Pan T., Li H., Chen S., (2020), Non-invasive quality analysis of thawed tuna using near infrared spectroscopy with baseline correction. *Journal of Food Process Engineering*, Vol. 43, Issue 8, pp. 13445, China.
- [15] Liu L., Zhang H., Wu L., Gu S., Xu J., Jia B., (2023), An early asymptomatic diagnosis method for cork spot disorder in 'Akizuki'pear (*Pyrus pyrifolia* Nakai) using micro near infrared spectroscopy. *Food Chemistry: X*, Vol. 19, pp. 100851, China.
- [16] Long Y., Huang W., Wang Q., (2022), Integration of textural and spectral features of Raman hyperspectral imaging for quantitative determination of a single maize kernel mildew coupled with chemometrics. *Food Chemistry*, Vol. 372, pp. 131246, China.
- [17] Long Y., Wang Q., Tian X., (2022), Screening naturally mildewed maize kernels based on Raman hyperspectral imaging coupled with machine learning classifiers. *Journal of Food Process Engineering*, Vol. 45, Issue 11, pp. 14148, China.
- [18] Malavi D., Nikkhah A., Alighaleh P., Einafshar S., Raes K., (2024), Detection of saffron adulteration with *Crocus sativus* style using NIR-hyperspectral imaging and chemometrics. *Food Control*, Vol. 157, pp. 110189, Belgium.
- [19] Milićević D., Nikšić M., Baltić T., (2010), Isolation, characterization and evaluation of significant mycoflora and mycotoxins in pig feed from Serbian farms. *World Journal of Microbiology and Biotechnology*, Vol. 26, pp. 1715-1720, Serbia.
- [20] Ong P., Jian J., Li X., Zou C., Yin J., (2023), New approach for sugarcane disease recognition through visible and near-infrared spectroscopy and a modified wavelength selection method using machine learning models. *Spectrochimica Acta Part A: Molecular and Biomolecular Spectroscopy*, Vol. 302, pp. 123037, China.
- [21] Oyebanji A O., Efiuvwevwere B.J.O., (1999), Growth of spoilage mould and aflatoxin B1 production in naturally contaminated or artificially inoculated maize as influenced by moisture content under ambient tropical condition. *International biodeterioration & biodegradation*, Vol.44, Issue 4, pp. 209-217, Nigeria.
- [22] Pang L., Wang L., Yuan P., Yan L., (2022), Rapid seed viability prediction of *Sophora japonica* by improved successive projection algorithm and hyperspectral imaging. *Infrared Physics & Technology*, Vol. 123, pp. 104143, China.
- [23] Paraginski R.T., Colussi R., Dias A.R.G., da Rosa Zavareze E., Elias M. C., (2019), Physicochemical, pasting, crystallinity, and morphological properties of starches isolated from maize kernels exhibiting different types of defects. *Food Chemistry*, Vol. 274, pp. 330-336, Brazil.
- [24] Shen F., Wei Y., Zhang B., Shao X., (2018), Rapid detection of harmful mold infection in rice by near infrared spectroscopy. *Spectroscopy and Spectral Analysis*, Vol. 38, pp. 3748-3752, China.
- [25] Sun J., Zhou X., Hu Y., Wu X., Zhang X., (2019), Visualizing distribution of moisture content in tea leaves using optimization algorithms and NIR hyperspectral imaging. *Computers and Electronics in Agriculture*, Vol. 160, pp. 153-159, China.
- [26] Sun K., Zhang Y.J., Tong S.Y., Tang M.D., (2022), Study on rice grain mildewed region recognition based on microscopic computer vision and YOLO-v5 model. *Foods*, Vol. 11, Issue 24, pp. 4031, China.
- [27] Tang N., Sun J., Yao K., Zhou X., Tian Y., Cao Y., (2021), Identification of *Lycium barbarum* varieties based on hyperspectral imaging technique and competitive adaptive reweighted sampling-whale optimization algorithm-support vector machine. *Journal of Food Process Engineering*, Vol. 44, Issue 1, pp. 13603, China.
- [28] Uddin S., Haque I., Lu H., Moni M. A., (2022), Comparative performance analysis of K-nearest neighbour (KNN) algorithm and its different variants for disease prediction. *Sci Rep 12*, Vol. 12, pp. 6256, Australia.
- [29] Vallese F. D., Paoloni S. G., Springer V., de Sousa Fernandes D. D., (2023), Analysis, Exploiting the successive projections algorithm to improve the quantification of chemical constituents and

- discrimination of botanical origin of Argentinean bee-pollen. *Journal of Food Composition and Analysis*, Vol. 126, pp. 105925, Argentina.
- [30] Wang L., Huang Z., Wang R., (2021), Discrimination of cracked soybean seeds by near-infrared spectroscopy and random forest variable selection. *Infrared Physics & Technology*, Vol. 115, pp. 103731, China.
- [31] Wang X., Jiang Z., Ji R., Han Y., Bian H., Yang, Y., (2003), Detection of Ningnanmycin Using Fluorescence Spectroscopy Combined with BP Neural Network. *Combinatorial Chemistry & High Throughput Screening*, Vol. 26, pp. 1414-1423, China,
- [32] Xing Z., Du C., Shen Y., Ma F., (2021), A method combining FTIR-ATR and Raman spectroscopy to determine soil organic matter: Improvement of prediction accuracy using competitive adaptive reweighted sampling (CARS). *Computers and Electronics in Agriculture*, Vol. 191, pp. 106549, China.
- [33] Xu L., Zhou Y. P., Tang L.J., Wu H.L., Jiang J.H., (2008), Ensemble preprocessing of near-infrared (NIR) spectra for multivariate calibration. *Analytica chimica acta*, Vol. 616, Issue 2, pp. 138-143, China.
- [34] Zhang G., Tuo X., Zhai S., Zhu X., Luo L., (2022), Near-infrared spectral characteristic extraction and qualitative analysis method for complex multi-component mixtures based on TRPCA-SVM. *Sensors*, Vol. 22, Issue 4, pp. 1654, China.
- [35] Zhang J., Liu L., Chen Y., Rao Y., Zhang X., (2023), The Nondestructive Model of Near-Infrared Spectroscopy with Different Pretreatment Transformation for Predicting “Dangshan” Pear Woolliness Disease. *Agronomy*, Vol. 13, Issue 5, pp. 1420, China.
- [36] Zhang Q., Liu C., Sun J., Cui Y., Li Q., Rapid non-destructive detection for molds colony of paddy rice based on near infrared spectroscopy. *Journal of Northeast Agricultural University (English Edition)*, Vol. 21, Issue 4, pp. 54-60, China.
- [37] Zhang Y., Gao W., Cui C., Zhang Z., He L., Zheng J., (2020), Development of a method to evaluate the tenderness of fresh tea leaves based on rapid, in-situ Raman spectroscopy scanning for carotenoids. *Food Chemistry*, Vol. 308, pp. 125648, China.

INVESTIGATION OF THE CONTROL SYSTEM FOR MAIZE SEEDER SOWING DEPTH BASED ON SOIL MOISTURE CONTENT

基于土壤含水率的玉米播种机播深控制系统的研究

Xianliang LIU¹⁾, Rui ZHANG^{*1)}, Yubin ZHAI¹⁾, Wenjie LI¹⁾, Haozhe WEI¹⁾

¹⁾College of Mechanical and Electrical Engineering, Qingdao Agricultural University, Qingdao 266109, China;

Tel: +86-19905421696; E-mail: 19905421696@163.com

Corresponding author: Rui Zhang

DOI: <https://doi.org/10.35633/inmateh-75-25>

Keywords: Sowing depth; Downforce; Moisture content; PLC controller; Proportional directional valve; Mamdani fuzzy control

ABSTRACT

To ensure the stability of seeding depth for a corn planter unit under different soil moisture conditions, a control system was designed to adjust the seeding depth of the unit based on soil moisture content. Using a PLC controller as the control foundation, the system employs a hydraulic system as its actuator. Soil moisture content is detected by moisture sensors, and the PLC controller processes the analog signals from the sensors. The controller then adjusts the forward and reverse rotation and speed of one motor via a variable frequency drive, thereby controlling the vertical displacement of the depth-limiting wheel to regulate the seeding depth. At the same time, a pressure sensor provides feedback to the PLC controller to control the switching time of the solenoid directional valve, driving the hydraulic cylinder stroke. The profiling mechanism connected to the hydraulic system moves the depth-limiting wheel accordingly, achieving stability in the planter's seeding depth. The control system is further optimized using the Mamdani fuzzy PID algorithm. Experimental results demonstrate that the designed seeding depth control system is stable and reliable, accurately adjusting the seeding depth according to different soil moisture levels. When the unit operates at speeds of 8~10 km/h, the stability of the seeding depth reaches 90%, significantly improving the stability of the unit's seeding depth.

摘要

为了使玉米播种机单体在不同含水率土壤播种工作时保持播种深度的稳定性,设计了一种根据土壤含水率控制播种单体播种深度的控制系统。以 PLC 控制器为控制基础,系统采用液压系统作为其执行机构,通过水分传感器检测土壤含水率,PLC 控制器分析处理传感器检测所获得的模拟信号后,控制器通过控制变频器调节电机正反转和转速,实现对限深轮的上下位移,完成对播种深度的控制。同时压力传感器将信号反馈给 PLC 控制器控制电磁换向阀的开断时间来驱动液压缸行程,与之相连接的仿形机构带动限深轮一同运动,实现对播种机播深的稳定性调节。利用 Mamdani 模糊 PID 算法对控制系统进行优化。实验结果表明,所设计的播种深度控制系统稳定可靠,能根据不同土壤含水率精确控制播种深度,单体作业速度在 8~10 km/h 时,播深稳定性达到 90%,系统提高了单体的播种深度稳定性。

INTRODUCTION

At present, precision seeding technology is one of the important measures to save and increase efficiency of dry farming, reduce production cost and increase economic income for modern agriculture (Xu et al., 2023). There are many factors affecting the sowing quality of precision sowing, among which soil moisture content, pressure and sowing depth are one of the many factors, among which suitable and consistent sowing depth can effectively improve the yield of corn crops (Zhu et al., 2019; Fu, 2022).

Since the middle of the last century, countries began to study the control of sowing depth. Through a series of basic theoretical and experimental studies, a variety of excellent performance of sowing machines and tools have been developed (Li et al., 2018). Jia et al., (2018), designed an adaptive tillage depth monitoring system, which used the surface adaptive swing arm and optical encoder to measure the rotation of the swing arm, and then converted the measured angle into the tillage depth through a formula.

Xianliang LIU, M.S. Stud. Eng.; Rui ZHANG*, Prof. Ph.D. Eng.; Yubin ZHAI, M.S. Stud. Eng.; Wenjie LI, M.S. Stud. Eng.; Haozhe WEI, M.S. Stud. Eng.;

Nielsen *et al.*, (2018), designed two kinds of depth measurement systems based on angle sensor, linear displacement sensor and ultrasonic sensor and a set of electro-hydraulic control system. Ultrasonic detection technology was adopted and ultrasonic detector was installed on the trencher to complete real-time detection of the trench depth (Du *et al.*, 2021; Fu *et al.*, 2019). A CAN bus monitoring and evaluation system for down pressure and sowing depth of multi-row seeder were designed (Gao *et al.*, 2019; Romaneckas, 2022). A measuring device for sowing depth and sowing pressure with angle and shaft pin sensors was adopted, the design of hydraulic drive and zonal controlled pneumatic drive device was optimized, and real-time monitoring and quality evaluation of sowing pressure and sowing depth in precision sowing operations were achieved (Rao A.S., 2023; Suomi, 2024).

At present, new progress has been made in the development of precision sowing devices in China. However, the comprehensive effects of soil moisture content, sowing depth and soil compaction on seed emergence were less studied (Xu Bing *et al.*, 2023; Hao *et al.*, 2023; Wang *et al.*, 2023). Therefore, this paper proposes an automatic control system for sowing depth of corn seeder based on soil moisture content. PLC is used as the main controller of the control system, and water content sensor and pressure sensor are used as signal input, the three-phase motor and hydraulic cylinder as the actuator realize the real-time control of the sowing depth and the downforce, so as to realize the precise control of the sowing depth of the single seeder.

MATERIALS AND METHODS

System structure and working principle

The system is composed of PLC controller, moisture content sensor, pressure sensor, seeding monomer, proportional reversing valve, hydraulic cylinder, frequency converter and AC motor, as shown in Figure 1.

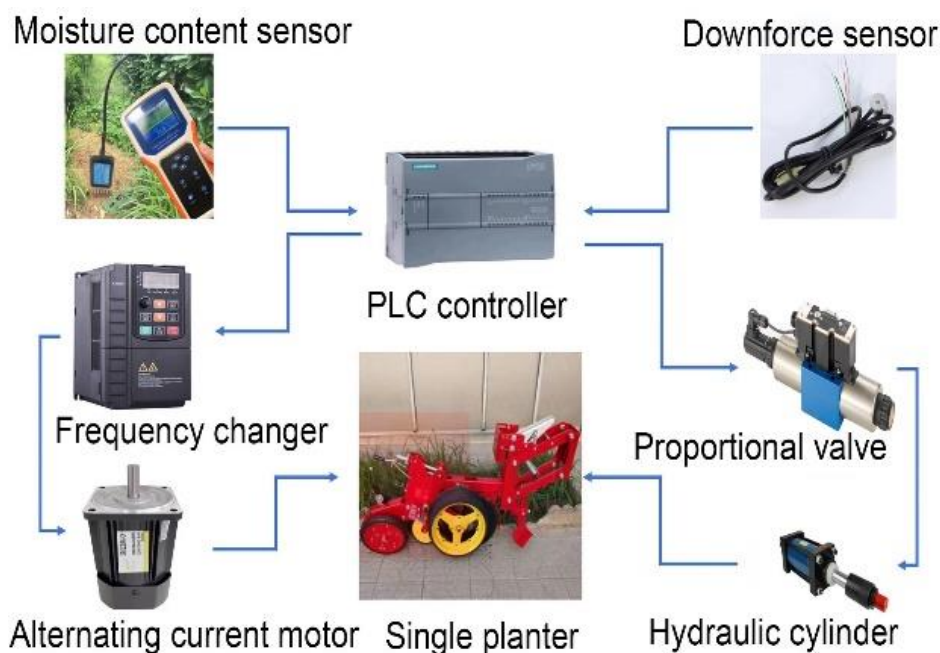


Fig. 1 - Composition of control system

The working process is as follows: PLC as the core processor of the system, equipped with analog input/output module, can collect the value of the moisture content sensor and pressure sensor, analyze and process the output control signal to the actuator, namely the frequency converter and solenoid valve. The adjustment mechanism of the system is divided into sowing depth adjustment and hydraulic feedback adjustment. The former collects soil moisture content through static moisture content sensor before the test starts, and the signal is output to the inverter after PLC processing, and the inverter controls the motor action, thus controlling the sowing depth of the seeder. The latter is to collect the signal of the lower pressure sensor, after the PLC controller analysis and processing, the result is output to the proportional valve, the proportional valve according to the signal range to control the hydraulic oil flow rate and flow, so as to control the expansion and stroke of the hydraulic cylinder, to achieve the real-time feedback action of the lower pressure, so as to achieve the stability control of the sowing depth.

PLC Controller

Siemens S7-1200PLC controller, model 6ES7214-1AG40-0XB0 is used. The controller comes with 24 digital I/O points, including 14 input points and 10 output points. In addition to the switching signal, it is necessary to use the input and output of the analog signal to control the acquisition of the sensor signal and the adjustment of the proportional valve. The control cabinet is shown in Figure 2. At the same time, TIA Portal V18 software was used for PLC configuration and programming. The Ethernet protocol was used to communicate with third-party devices, and I/O assignments are shown in Table 1.

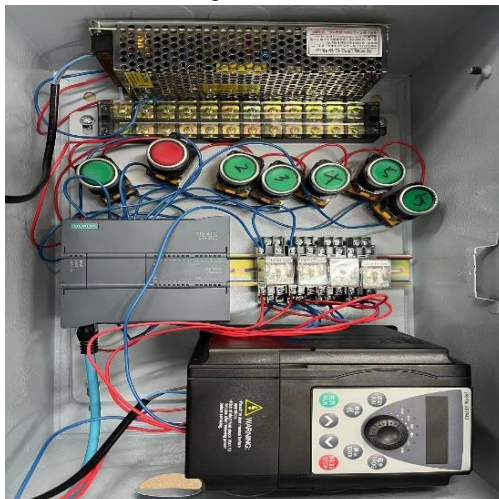


Fig. 2 - Electrical control cabinet

Table 1

PLC I/O distribution table			
Input	Feature	Output	Feature
I0.0	activate	Q1.0	Solenoid valve 1 action
I0.1	stop	Q1.1	Solenoid valve 2 action
I0.2	Solenoid valve 1 opens	Q1.2	Forward motor rotation
I0.3	Solenoid valve 2 opens	Q1.3	Motor reversal
I0.4	Measuring pressure	Q0.5	Flicker time
I0.5	Forward motor rotation	QW96	Pressure output value
I0.6	Motor reversal		
I0.7	Starting PID		
IW96	Water content input		
IW98	Pressure input		

Design of depth control system

First of all, the depth limiting wheel is used as a farming reference component, and the relative height difference between it and the trenching plate directly corresponds to the sowing depth. RS485 soil moisture content sensor is used as the detection mechanism, the measurement range is 0-100%, the accuracy is ±3%, the sampling frequency is 1Hz, and the PLC analog input module is connected. The actuator is a combination of frequency converter and three-phase motor, while the three-phase motor and the monomer are connected through a coupling, and their rotation can drive the movement of the monomer. The frequency converter is selected from Instar AE200 model (input 220VAC/50Hz, output 0-400Hz), and the motor is selected from Matsuoka three-phase 220V asynchronous motor (rated torque 5.2Nm).



Fig. 3 - Installation of frequency converter and motor

By observing the pressure sensor signal installed in the groove of the depth limiting wheel arm to reflect the change of pressure on the depth limiting wheel, the pressure sensor is directly connected to the PLC analog input module, and the pressure signal is fed back to the PLC controller. The output end of the PLC controller is connected to the proportional reversing valve. By receiving the voltage signal transmitted by the PLC controller to control the flow rate and direction of the oil in the solenoid valve, the hydraulic cylinder connected with it moves with the change of the position of the valve core, driving the parallel four-link copying mechanism to complete the upward and downward movement, controlling it to reach the predetermined pressure, and realizing the stable control of the depth. The stress analysis diagram of the pressure sensor is shown in Figure 4. The force analysis formula is shown in equation (1).

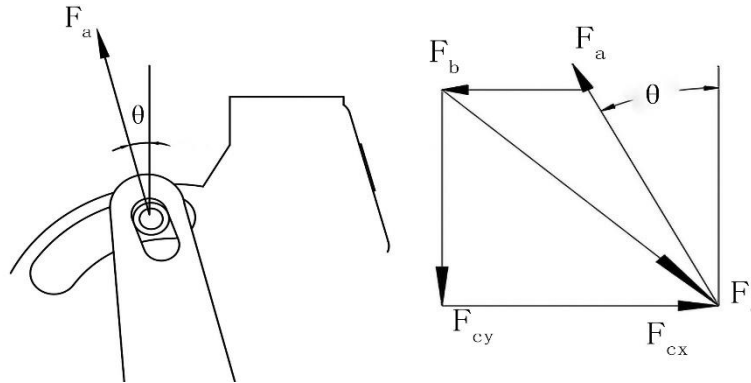


Fig. 4 - Force analysis diagram of pressure sensor

$$\begin{aligned} F_{cx} &= F_a \sin \theta + F_b \\ F_{cy} &= F_a \cos \theta \end{aligned} \quad (1)$$

where:

F_a - Reaction force of the depth limiting arm on the depth limiting block, N; F_b - Force of single frame on depth limiting block, N; F_c - Sensor force on depth limiting block, N; θ - the Angle between the depth limiting arm and the sowing unit frame, ($^\circ$); F_{cx} - F_c component in the horizontal direction, N; F_{cy} - F_c in the vertical direction, N.

The installation position of the force sensor is the limit pin of the depth limiting wheel, which does not rotate itself, and the force stability is limited only by the reaction force in the vertical direction of the deep wheel arm. Therefore, the sensor uses a high-precision micro-pressure sensor, the selected model is DYHW-108, the force range is 0 ~ 2000 N, the output voltage range is 0 ~ 10 V, and the working voltage is 15 ~ 30 V.

According to the weight of the single unit of the corn planter, the hydraulic cylinder of model MOB40X100 was selected. The inner diameter of the hydraulic cylinder D is 40 mm, the diameter of the piston rod is 20 mm, the maximum pulling force is 6.59 kN and the maximum thrust is 8.80 kN. The hydraulic cylinder can satisfy the motion control of the monomer. The installation position of hydraulic cylinder is shown in Figure 5. The oil source of the system adopts the hydraulic output after the tractor, and its output rated flow rate is generally 36 L/min, the rated working pressure is 12 MPa, and the safe working pressure is 15 MPa. Therefore, the pilot relief valve integrated block is used to stabilize the oil pressure in the cylinder, the rated flow rate is 36 L/min, the maximum pilot flow rate is 60 L/min, and the pressure range is 0 ~ 50 bar.



Fig. 5 - Installation position of hydraulic cylinder

Fuzzy PID control

In order to obtain more rapid and stable control effect, based on the traditional PID control theory, fuzzy control theory is introduced into the traditional PID control with the help of MATLAB. Fuzzy PID control has the characteristics of short response time, small overkill and good dynamic performance. According to the corresponding relationship between the pressure of the monomer and the displacement of the hydraulic cylinder, the pressure control of the monomer of the planter is transformed into the displacement of the hydraulic cylinder. After the fuzzy control algorithm processes the deviation between the given value and the output value of the system and the deviation change rate of the two through the proportion, integral and differential coefficients, the control system can get more accurate control effect.

A fuzzy PID controller suitable for the system was optimized and designed. A Mamdani dual-input-three-output fuzzy controller was constructed with the deviation e and the deviation change rate ec as inputs and the three PID control parameters k_p , k_i and k_d as outputs. e , ec , k_p , k_i and k_d are replaced by 5 fuzzy subsets respectively, namely, large positive deviation (NB), small positive deviation (NS), zero deviation (Z), small negative deviation (PS) and large negative deviation (PN). According to the actual situation, the argument domain of parameter change was set as $\{-6, -5, -4, -3, -2, -1, 0, 1, 2, 3, 4, 5, 6\}$. The input of the fuzzy controller is Gaussian membership function and the output is trigonometric membership function.

According to the parameter function of PID controller and expert experience, the fuzzy rules suitable for control system are optimized. The fuzzy rules of k_p , k_i and k_d are designed, as shown in Table 2~4.

Table 2

Kp fuzzy rules

e/ec	NB	NS	Z	PS	PB
NB	PB	PS	PS	PS	Z
NS	PS	PS	PS	Z	NS
Z	PS	PS	Z	NS	NS
PS	PS	Z	NS	NS	NS
PB	Z	NS	NS	NS	NB

Table 3

Ki fuzzy rules

e/ec	NB	NS	Z	PS	PB
NB	NB	NS	NS	NS	Z
NS	NB	NS	NS	Z	PS
Z	NS	NS	Z	PS	PS
PS	NS	Z	PS	PS	PB
PB	Z	PS	PS	PS	PB

Table 4

Kd fuzzy rules

e/ec	NB	NS	Z	PS	PB
NB	PS	NB	NB	NB	PS
NS	Z	NS	NS	NS	Z
Z	Z	NS	NS	NS	Z
PS	Z	Z	Z	Z	Z
PB	PB	PS	PS	PS	PB

Through the fuzzy rule table formulated by MATLAB software analysis and reasoning, the relationship diagram of input parameters e and ec and output parameters k_p , k_i and k_d is obtained, as shown in Figure 6.

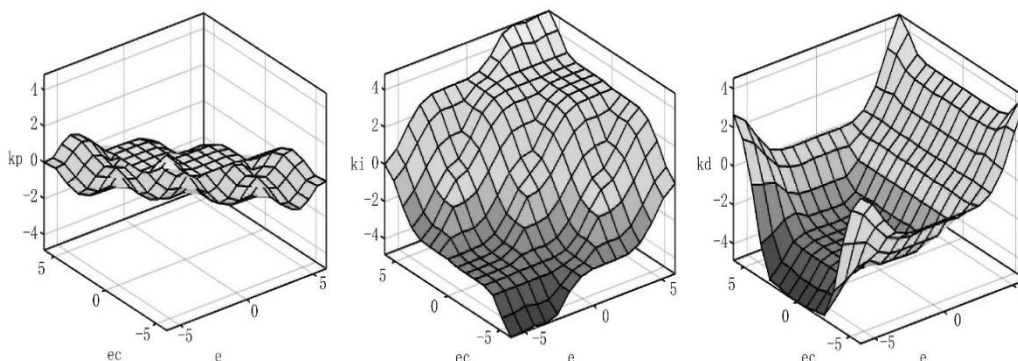


Fig. 6 - Fuzzy control relation surface

In order to verify the optimization effect of fuzzy PID control, a fuzzy controller model was built on Simulink simulation software, as shown in Figure 7. The simulation model of the pressure control system was established, as shown in Figure 8.

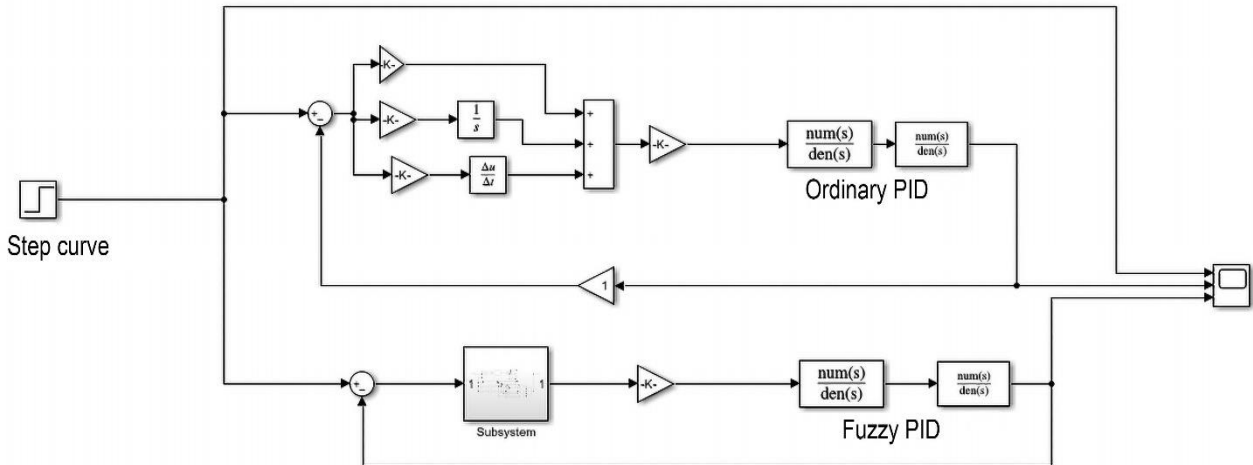


Fig. 7 - Fuzzy controller model

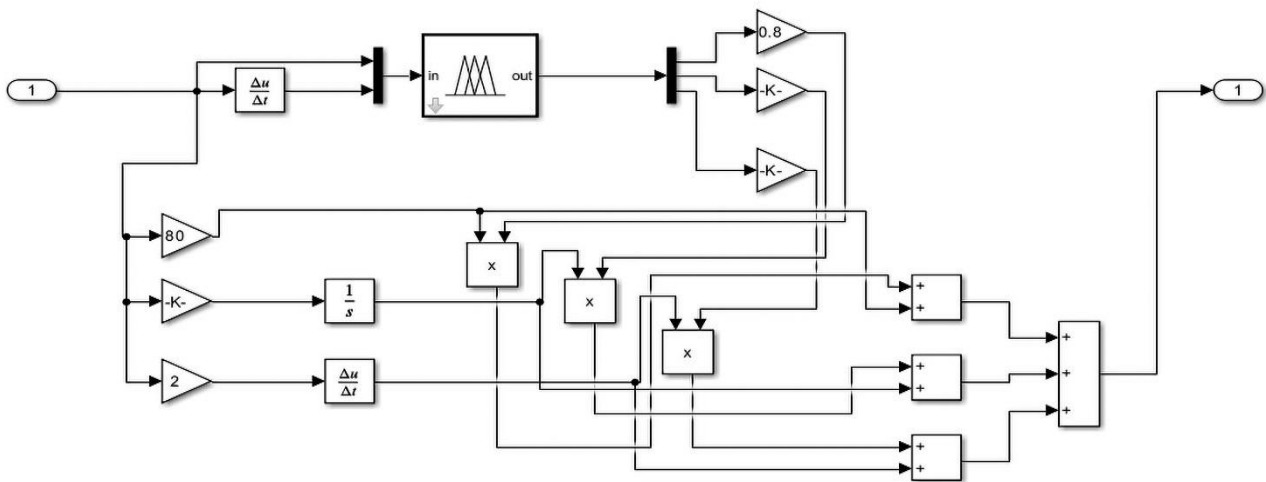


Fig. 8 - Simulation model of downforce control system

The above model is simulated by MATLAB software and the simulation results are observed through the scope window, as shown in Figure 9. As can be seen, compared to the traditional PID controller, the adjustment time of the system increases by 2.572s and the overshoot is reduced from 27% to 14% when using fuzzy PID control instead of the ordinary PID control. Fuzzy PID control can shorten the system response time to a certain extent on the premise of reducing system fluctuations, and the system control effect is significantly improved. This approach meets the stability requirements for sowing depth control.

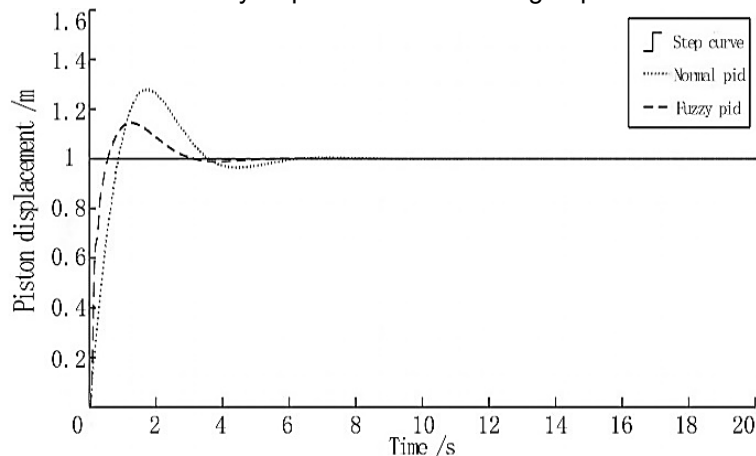


Fig. 9 - Step response curve of the system

RESULTS

A pre-experiment of soil moisture content was carried out before the field experiment. Three groups of variables (moisture content, pressure and sowing depth) were designed, and three levels were set for each group of variables. Without considering the interaction between the variables, the optimal values corresponding to the sowing depth and downforce under each group of moisture content interval were solved to achieve the highest corn emergence rate (The emergence rate is calculated by multiplying the ratio of the actual number of seedlings to the sowing amount by 100%). Multiple sets of data were measured through experiments and the emergence rate was obtained, as shown in Table 5. These results will be used as reference for subsequent tests of the control system.

Table 5

Soil moisture pretest				
number	Moisture content(%)	Downforce(N)	Sowing depth(cm)	Emergence rate(%)
1	16 ~ 18	250	5	61
2	16 ~ 18	500	6	79
3	16 ~ 18	750	7	86
4	18 ~ 20	250	5	82
5	18 ~ 20	500	6	92
6	18 ~ 20	750	7	74
7	20 ~ 22	250	5	88
8	20 ~ 22	500	6	65
9	20 ~ 22	750	7	77

The results showed that the optimal value of the lower pressure and the sowing depth were 750 N and 7 cm respectively in the range of 16% ~ 18% moisture content. The optimal value of the water content was in the range of 18% ~ 20% corresponding to the lower pressure of 500 N, the optimal value of the sowing depth was 6 cm. In the range of 20% ~ 22%, the optimal value of the lower pressure was 250 N, and the optimal value of the sowing depth was 5 cm.

In order to test the sowing depth control performance of the control system under different moisture content, the performance test was conducted in the test soil tank of Qingdao Agricultural University in the summer of 2024, as shown in Figure 10. The field environment of the soil tank was measured before the test. The measured soil volume density of 3 ~ 7 cm depth was 1.2 g/cm³, the average seed bed firmness was 2.5 kg/cm². The control system was installed in Weifang Letian Company's Grand stamping no-tillage seeder. The mechanical parallel four-link copying system was used in the control test, and the depth of the trencher was adjusted to the corresponding sowing depth according to the soil moisture content.



Fig. 10 - Soil tank test diagram

The standard operation speed of tractors in the field was 8 ~ 10 km/h. Two groups of controlled experiments were conducted. The first group adopted the sowing depth control system and added fuzzy control method, while the control group adopted ordinary mechanical copying. The corresponding relationship of different sowing depth was set according to the different moisture content of the earlier sowing data and each group of experiments was repeated six times to reduce errors. According to the agricultural industry standard NY/T 1768-2009 "Technical Specification for Quality Evaluation of no-till seeder", the average sowing depth, the qualified rate of sowing depth and the coefficient of variation of sowing depth were calculated. The test results are shown in Table 6 ~ 8.

Table 6

Consistency test results of sowing depth at different speeds (16% ~ 18% moisture content)				
Argument	Regulation mode	Tractor operating speed/(km/h)		
		8	9	10
Average sowing depth /mm	Control system	71	69	72
	Mechanical copying	65	62	63
Pass rate of sowing depth /%	Control system	96	95	93
	Mechanical copying	72	66	62
Coefficient of variation of sowing depth /%	Control system	10.4	12.3	13.4
	Mechanical copying	14.8	15.6	17.6

Table 7

Consistency test results of sowing depth at different speeds (18% ~ 20% moisture content)				
Argument	Regulation mode	Tractor operating speed/(km/h)		
		8	9	10
Average sowing depth /mm	Control system	62	58	63
	Mechanical copying	56	54	52
Pass rate of sowing depth /%	Control system	97	96	92
	Mechanical copying	75	68	65
Coefficient of variation of sowing depth /%	Control system	9.8	11.8	12.2
	Mechanical copying	14.1	15.4	16.9

Table 8

Consistency test results of sowing depth at different speeds (20% ~ 22% moisture content)				
Argument	Regulation mode	Tractor operating speed/(km/h)		
		8	9	10
Average sowing depth /mm	Control system	49	52	53
	Mechanical copying	53	57	62
Pass rate of sowing depth /%	Control system	95	94	93
	Mechanical copying	71	64	62
Coefficient of variation of sowing depth /%	Control system	10.5	12.5	13.6
	Mechanical copying	14.6	16.1	18.6

From Table 6 ~ 8, it can be seen that the qualified rate of sowing depth control system is higher than 90% at different speeds, and the qualified rate of sowing depth control system is obviously better than that of mechanical copying device. In summary, compared with ordinary mechanical copying device, the automatic sowing depth control system can maintain the stability of sowing depth at different operating speeds and with different compatibility. According to different moisture content, the monomer can be accurately controlled to reach the predetermined sowing depth, and the sowing depth control system has reliable performance.

CONCLUSIONS

Field tests on sowing depth control were conducted for three soil moisture content ranges of 16% ~ 18%, 18% ~ 20% and 20% ~ 22%. When the moisture content was within the range of 18% ~ 20% and the sowing depth was set at 60 mm, the qualification rate of sowing depth was the highest when the vehicle speed of the control system was 6 km/h. The qualified rates of the corresponding control system and mechanical profiling were 97% and 75%, respectively. Compared with the mechanical profiling mechanism, the sowing depth control system increased by 22 percentage points. Thus, the sowing depth control system is obviously superior to the traditional mechanical profiling device.

ACKNOWLEDGEMENT

This research received financial support from the National Key Research and Development Program of China (No. 2023YFD2000402-2) and Open Project of Collaborative Innovation Center for Mechanized Production Equipment of Major Crops in Shandong Province, China. Thanks to the International Field Test Mechanization Association for providing us with the research foundation and platform.

REFERENCES

- [1] Du M., (2022). Design and test analysis of corn planter based on PLC (基于 PLC 的玉米播种机设计与试验分析). *Modern Agricultural Machinery*, Vol.2, pp. 62-73, China.
- [2] Fu W., (2019). Research on Key technologies of quality control for precision seeding of maize without tillage (玉米免耕精准播种质量控制关键技术研究). *China Agricultural University*, China.
- [3] Fu Y., (2022). Design and experimental study of real-time monitoring system for sowing depth of maize no-till seeder (玉米免耕播种机播种深度实时监测系统的设计与试验研究). *Heilongjiang Bayi Agricultural University*, China.
- [4] Gao, Y., Z, Chan., Y, S., (2019). Research on CAN Bus Monitoring and Evaluation System for Down Pressure and sowing Depth of Precision planter (精密播种机下压及播种深度 CAN 总线监测评估系统研究). *Transactions of the Chinese Society for Agricultural Machinery*, Vol.51, pp. 15-28, China.
- [5] Guo, Y., Liu, P., (2019). Design and application of a small planter controlled by PLC (PLC 控制的小型播种机的设计与应用). *Agricultural Mechanization Research*, Vol.43, pp. 107-138, China.
- [6] Hao N., (2023). Research on depth detection and control system based on multi-sensor data fusion (基于多传感器数据融合的深度检测与控制系统研究). *Heilongjiang Bayi Agricultural University*, China.
- [7] Li, M., Xu, X., Zheng, L., (2018). Intelligent sowing depth adjustment system for no-till seeder based on Flex sensor and Mamdani fuzzy model (基于柔性传感器和 Mamdani 模糊模型的免耕播种机播种深度智能调节系统). *Journal of Agricultural Engineering and Technology*, Vol.42, pp.18-24, China.
- [8] Jia, H., Guo, M., Yu, H., (2016). An adaptable tillage depth monitoring system for tillage machine (一种自适应播种深度监测系统). *Biosystems Engineering*, Vol.151, pp. 187-199, China.
- [9] Nielsen, S., Munkholm, L., La, E., (2018). Seed drill depth control system for precision seeding (用于精密播种的播种机深度控制系统). *Computers and Electronics in Agriculture*, Vol.144, pp.174-180, China.
- [10] Romaneckas, K., Steponavicius, D., (2022). How to Analyze, Detect and Adjust Variable Seedbed Depth in Site-Specific Sowing Systems: A Case Study. *Agronomy-Basel*, Vol.12, pp. 5-8, Lithuania.
- [11] Rao, AS., Mounika, S., (2023). Development of Low-cost Automatic Sowing Depth Measurement Unit for Groundnut Planter. *Agricultural mechanization in Asia, Africa and Latin America*, Vol.54, pp. 4-9, India.
- [12] Suomi, Pasi., Oksanen, Timo., (2024). Automatic working depth control for seed drill using ISO 11783 remote control messages. *Computers and Electronics in Agriculture*, Vol.116, pp. 30-35, Germany.
- [13] Wang C H., (2023). Research on Electrical Control System of planter based on PLC technology (基于 PLC 技术的播种机电气控制系统研究). *Agricultural Mechanization Research*, Vol.45, pp. 140-143, China.
- [14] Xue, B., Zhou L., Niu, K., (2023). Research on fuzzy adaptive PID Control System for sowing depth of Wheat seed (小麦播种深度模糊自适应 PID 控制系统的研究). *Transactions of the Chinese Society for Agricultural Machinery*, Vol.12, pp. 42-49, China.
- [15] Xu H W., (2023). Design of sowing depth control system for no-tillage seeder (免耕播种机播种深度控制系统设计). *Agricultural Machinery Use and Maintenance*, Vol.07, pp. 26-28, China.
- [16] Zhang W., (2021). Application of PLC Technology in Electrical Control of Agricultural Machinery (PLC 技术在农机电气控制中的应用). *Modern Agricultural Machinery*, Vol.05, pp. 120-121, China.

DESIGN AND TESTING OF DUAL-STATION HIGH EFFICIENCY WHOLE TRAY AIR-SUCTION SEEDING ASSEMBLY LINE FOR RICE SEEDLING CULTIVATION

整盘气吸式水稻双工位高效育秧播种流水线设计与试验

Junhui CHENG^{1,2,3,4}, Yaoming LI^{*1,2}, Jin CHEN^{1,2}, Fenglei LI⁵, Yanbin LIU^{1,2}, Kuizhou JI²,
Hanhao WANG², Zhiwu YU², Zhiyou PEI²

¹Key Laboratory of Modern Agricultural Equipment and Technology, Ministry of Education, Jiangsu University; Zhenjiang 212013, China;

²School of Agricultural Engineering, Jiangsu University; Zhenjiang 212013, China;

³School of Electrical and Photoelectronic Engineering, West Anhui University, Lu'an 237012, China;

⁴Anhui Undergrowth Crop Intelligent Equipment Engineering Research Center, West Anhui University, Lu'an 237012, China;

⁵Changzhou Fenglei Precision Machinery Co., Ltd, Chang Zhou 213100, China

Tel: 0511-88780175; E-mail: ymli@ujs.edu.cn

Corresponding author: Yaoming Li

DOI: <https://doi.org/10.35633/inmateh-75-26>

Keywords: rice, precision measurement, whole tray air-suction, dual-station

ABSTRACT

To address the high efficiency and precision seeding requirements for rice factory seedling cultivation, a whole tray air-suction dual-station high efficiency seedling cultivation and seeding assembly line was designed. Based on the whole-tray air-suction principle, the study focused on the design of a dual-suction seed tray dual-station precision hole-to-hole seeding device, a transverse seedling tray conveying device, and an automatic seed replenishment device. Nan Jing 46, Nan Jing 5055, and Koshihikari rice seeds were used for seeding performance experiments on the assembly line. The impact of workstation configuration and production efficiency on the empty hole rate, reseeding rate, damage rate, and seeding precision was analyzed. Experimental results showed that the dual-station precision seeding method significantly improved seeding efficiency. When the seeding efficiency reached 2000 trays per hour, the seeding rate of 1-3 seeds per hole was 90.1%, while the damage rate, empty hole rate and reseeding rate were 0.38%, 0.84%, 9.06% respectively. This study shows that combining the whole tray air-suction principle with transverse seedling tray conveying device, dual-station precision hole seeding device, and automatic seed addition device can significantly enhance the seeding efficiency while ensuring the seeding accuracy, achieving a seeding efficiency of over 2000 trays per hour. This study provides an important reference for further improving the seeding accuracy and efficiency of precision rice seedling cultivation and seeding assembly line.

摘要

针对水稻工厂化育秧的高效率精量播种需求, 本文设计了一种整盘气吸式双工位高效育秧播种流水线。基于整盘气吸式原理, 重点设计了双吸种盘双工位精量对穴播种装置、横向秧盘输送装置及自动加种装置。南粳 46、南粳 5055 及越光稻种子被用于流水线播种性能试验, 分析了工位配置和生产效率对合格率、损伤率、空穴率和重播率的影响。试验结果表明, 双工位精量对穴播种方式显著提高了播种效率。当播种效率达到 2000 盘/h 时, 每穴 1-3 粒的合格率为 90.1%, 损伤率、空穴率、重播率分别为 0.38%、0.84%、9.06%。该研究表明, 将整盘气吸式原理与横向秧盘输送装置、双工位精量对穴播种装置及自动加种装置相结合, 能够在保证播种效果的同时显著提升播种效率, 达到超过 2000 盘/小时的播种效率。这一研究为进一步提高水稻精量育秧播种流水线的播种精度和效率提供了重要参考。

INTRODUCTION

As one of the world's major food crops, improving rice production efficiency and yield was of great strategic significance for ensuring food security, coping with population growth and other key issues (Zang et al., 2024). Factory-based rice seedling cultivation was a modern agricultural technology that transferred the seedling cultivation process to a controlled factory environment, achieving a high degree of standardization and automation of sowing, growth, and management, thereby effectively improving the survival rate and quality of rice seedlings (Hou et al., 2020; Zhang et al., 2023; Karayel D., 2022). As an important equipment for factory-based rice seedling cultivation, the seeding assembly line for rice seedling cultivation could complete tray feeding, subsoil laying, hole pressing, seeding, watering, topsoil covering, tray stacking all at once (Singh R.C., 2005), which could significantly improve the production efficiency and quality of rice seedling cultivation (Sun et al., 2021; Ding et al., 2021).

Currently, scholars and enterprises accomplished a series of research progress in the field of factory-based seeding assembly line for rice seedling cultivation (Yang *et al.*, 2021). The mechanical groove wheel seeding method was applied in Japan's Kubota 2BZP-800 rice seedling cultivation and seeding assembly line (Cao *et al.*, 2021). It is suitable for flat seedling trays and could reach a seeding efficiency of 800 trays per hour. The mechanical drum seeding method was applied in the 2BD-300 and 2BD-600 rice seedling cultivation and seeding assembly line produced by Changzhou Yamike Company (Yuan *et al.*, 2020). It was suitable for bowl seedling trays, and the highest seeding efficiency could reach 600 trays per hour. The radial outer groove wheel seeding method was applied in Zoomlion's 2BP-780C rice seedling cultivation and seeding assembly line (Ma *et al.*, 2018; Zhang *et al.*, 2015). It was suitable for bowl seedling trays and the seeding efficiency could reach 780 trays per hour (Hou *et al.*, 2015). The precision seeding assembly line and automatic stacking device was designed by Ma Xu *et al.* for rice seedling cultivation, while the seeding efficiency could reach 800 trays per hour (Ma *et al.*, 2019). The air-suction drum rice seed metering device designed by Han Bao *et al.* had realized the functions of automatic seed filling in the sockets and pneumatic assisted seed suction, which greatly improved the uniformity of seeding and seed integrity (Han *et al.*, 2009).

However, traditional mechanical seeding equipment had problems such as low efficiency, easy seed damage, poor adaptability, and difficulty in accurately controlling the seeding amount and position, which affected the consistency of the seeding effect (Li *et al.*, 2021; Xing *et al.*, 2020; Li *et al.*, 2009). Seed metering device based on the principles of air suction rollers and air suction needles have rarely been applied in rice seedling cultivation and seeding. These methods exhibit low working efficiency and struggle to meet the requirements for large-scale promotion and application (Li *et al.*, 2008).

In view of the above problems, a rice seeding assembly line for rice seedling cultivation based on the whole-tray air suction principle was proposed, and its key components such as the tray sending device, seed metering device and tray stacking device were optimized and improved. Under the premise of ensuring seeding accuracy, the production efficiency of rice seedling cultivation and seeding had been greatly improved, providing a new technical path for the development of precise and high-efficiency rice factory-based seedling cultivation and seeding equipment.

MATERIALS AND METHODS

OVERALL STRUCTURE AND WORKING PRINCIPLE

The whole tray air-suction seeding assembly line for rice precision seedling cultivation was mainly composed of horizontal tray delivery device, bottom soil laying device, dual-station high-efficiency seeding device, sprinkler device, topsoil covering device, horizontal tray stacking device, automatic seed adding device, seed tray high pressure fan, electric control box and frame, as shown in Fig.1.

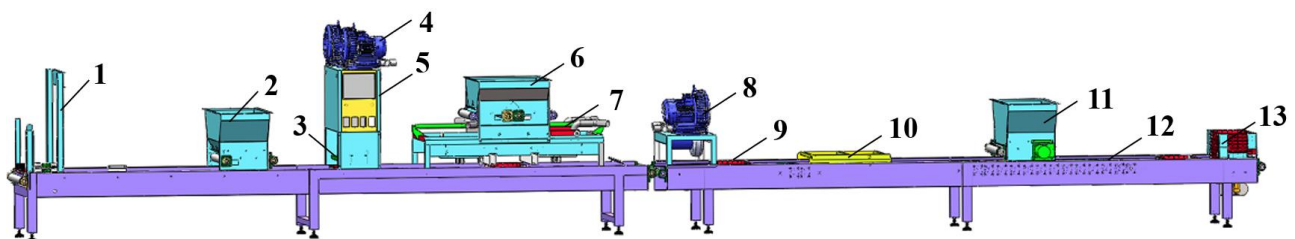


Fig.1 - Schematic diagram of the overall structure of the whole tray air-suction seeding assembly line for rice precision seedling cultivation

1. Horizontal tray delivery device
2. Bottom soil laying device
3. Hole pressing device
4. Left seed tray high pressure fan
5. Electric control box
6. Automatic seed adding device
7. Dual-station high-efficiency seeding device
8. Right seed tray high pressure fan
9. Seedling tray
10. Sprinkler device
11. Topsoil covering device
12. Frame
13. Horizontal tray stacking device

When the seed metering device was working, the power of the seeding assembly line was turned on to ensure that the air compressor and high-pressure fan were in normal working condition. Subsequently, the seedling trays were stacked on the horizontal tray delivery device. The start button on the electric control box was pressed, and then a group of seedling trays (including No. 1 seedling tray and No. 2 seedling tray) were continuously transported through the conveyor belt. When the seedling tray moved to the bottom soil laying device, the conveyor belt driven by the motor spread the nutrient soil evenly on the bottom of the seedling tray. Next, the seedling tray reached the hole pressing device, where it underwent a hole pressing process to form seed holes. Afterwards, when the seedling tray entered the dual-station high-efficiency seeding position, the cross-intermittent seeding method was used for whole-tray precision hole seeding.

Specifically, when the No. 1 seedling tray reached the seeding position, the left suction tray would discharge the seeds, and the right suction tray would suck the seeds. The No. 1 seedling tray moved forward after seeding, while the No. 2 seedling tray reached the seeding position. The right seed suction tray discharged seeds, and the left seed suction tray sucked seeds, thus completing the seeding of a group seedling trays. After the seeding operation, the seedling trays were watered, covered with topsoil and stacked in sequence, and finally the seedling trays that had been sown were removed. The above operation process was repeated to realize the continuous tray delivery - bottom soil laying - hole pressing - seeding - water sprinkling - topsoil covering - trays stacking operation of the seeding assembly line for rice seedling cultivation. The main design parameters of the seeding assembly line for rice seedling cultivation designed in this paper are shown in Table 1.

Table 1

Main design parameters of seeding assembly line		
Parameters	Unit	Values
working principle	/	whole tray air-suction
efficiency	tray/h	2000
qualification rate	%	≥85
empty hole rate	%	≤2
reseeding rate	%	≤15
damage rate	%	≤2
delivery method	/	horizontal tray delivery

KEY COMPONENTS DESIGN

Design of horizontal tray delivery and stacking device

(1) Design of horizontal tray delivery device

To ensure the seeding effect of the seed metering device, there was usually a limit to the speed of the seeding tray and the seeding assembly line. The highest efficiency of the traditional seedling cultivation and seeding assembly line could only reach 1000 trays/h. This paper proposed a horizontal tray delivery method, which adjusted the traditional vertical tray delivery method to a horizontal tray delivery method. The seedling tray delivery method is shown in Fig. 2.

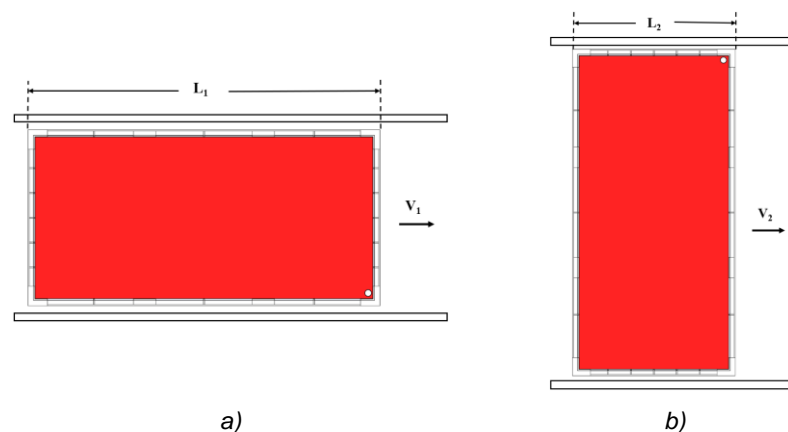


Fig. 2 - Seedling tray delivery method
 (a) horizontal delivery; (b) vertical delivery

The time t required for a single seedling tray to move was

$$t = \frac{L}{v} \tag{1}$$

Among them, L was the moving distance of the seedling tray, and v was the moving speed of the seedling tray.

The standard seedling tray size of 300mm*600mm was used in this experiment, that is, $L_1 = 2L_2$, $v_1 = v_2$.

Therefore:

$$t_1 = 2t_2 \tag{2}$$

When the horizontal tray delivery method was applied in the seeding assembly line for rice seedling cultivation, the seeding assembly line efficiency was doubled when the moving speed of the seedling tray remained unchanged.

The horizontal tray delivery device was composed of frame, upper cylinder, lower cylinder and chuck, as shown in Fig. 3. During operation, the upper cylinders on both sides extended out and the chuck was inserted between the two lowest seedling trays. The lower cylinders on both sides retracted, so that the lowest seedling tray automatically fell onto the conveyor belt of the assembly line, completing the automatic tray delivery. Then the lower cylinders on both sides extended out, the upper cylinders on both sides retracted, and the seedling tray fell on the chuck connecting the lower cylinders on both sides. Then the upper cylinders on both sides extended out, and the lower cylinders on both sides retracted to complete the next tray delivery operation.

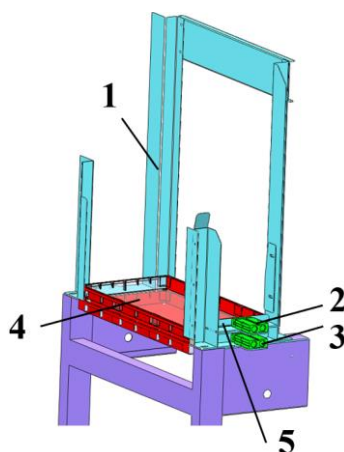


Fig. 3 - Horizontal tray delivery device

1. Frame; 2. Upper cylinder; 3. Lower cylinder; 4. Seedling tray; 5. Chuck

(2) Design of horizontal tray stacking device

The horizontal stacking device was composed of cylinder, frame, tray, and stacking chuck, as shown in Fig. 4. During operation, when the seedling tray reached the stacking position, the two stacking cylinders extended synchronously to move the seedling tray upward, and the stacking chuck was retracted into the through groove driven by the seedling tray. When the seedling tray moved to the upper side of the stacking tray chuck, the stacking tray chuck returned to the initial open state under the action of the spring. Then, the two cylinders retracted at the same time, and the seedling tray moved downward under its own weight and fell on the stacking tray chuck. When the next seedling tray was transported to the tray position, repeated the above process to complete the automatic stacking operation of seedling trays. The horizontal stacking device adjusted the stacking interval time according to the efficiency of the assembly line operation, and completed the automatic stacking operation.

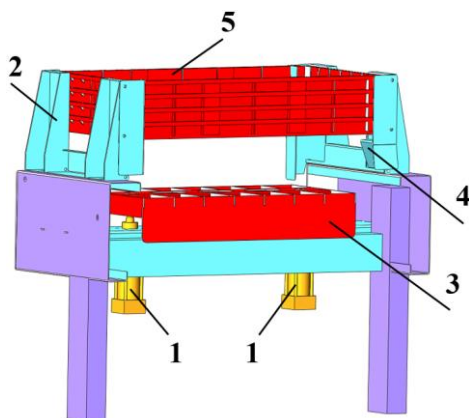


Fig. 4 - Horizontal tray stacking device

1. Stacking cylinder 2. Frame 3. Tray 4. Seedling tray 5. Stacking chuck

Design of dual-station high-efficiency seeding device and automatic seed adding device

Dual-station high-efficiency seeding device and automatic seed adding device are shown in Fig. 5. The dual-station high-efficiency seeding device realized interactive seeding with double suction seed trays, and the automatic seed adding device added seeds to the seed tray according to actual needs.

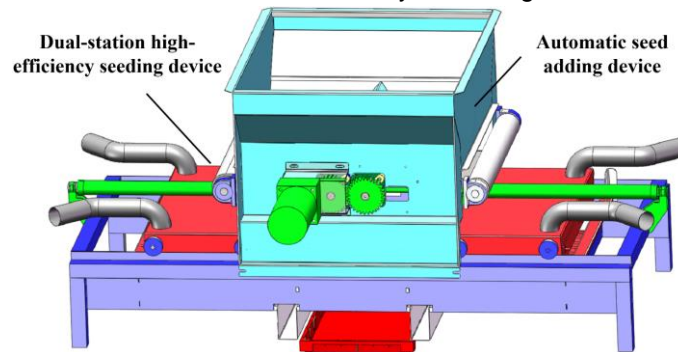


Fig. 5 - Dual-station high-efficiency seeding device and automatic seed adding device

(1) Design of dual-station high-efficiency seeding device

Dual-station high-efficiency seeding device is shown in Fig.6. The dual-station high-efficiency seeding device was mainly composed of seed suction station 1, seed suction station 2 and seeding station.

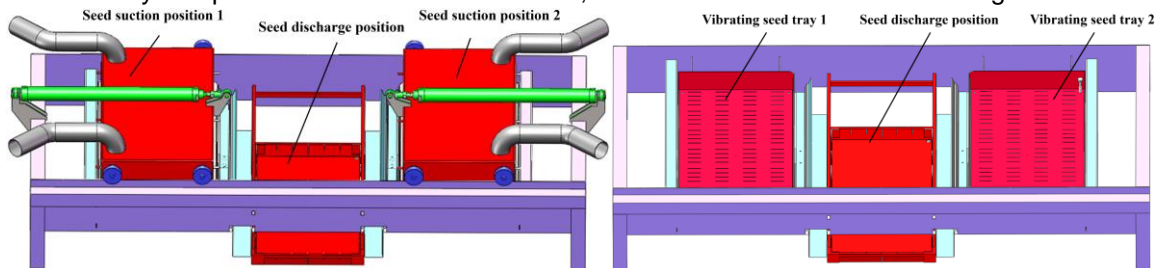


Fig. 6 - Structure diagram of the dual-station high-efficiency seeding device

In the horizontal single-station working mode, seeding work was completed by 1 seed suction tray, 1 seed suction position and 1 seed discharge position. While in the horizontal dual-station working mode, 2 seed suction trays cooperated with 2 seed suction positions and 1 seed discharge position to complete the interactive seeding work. The comparison of operation time under different working modes is shown in Fig.7.

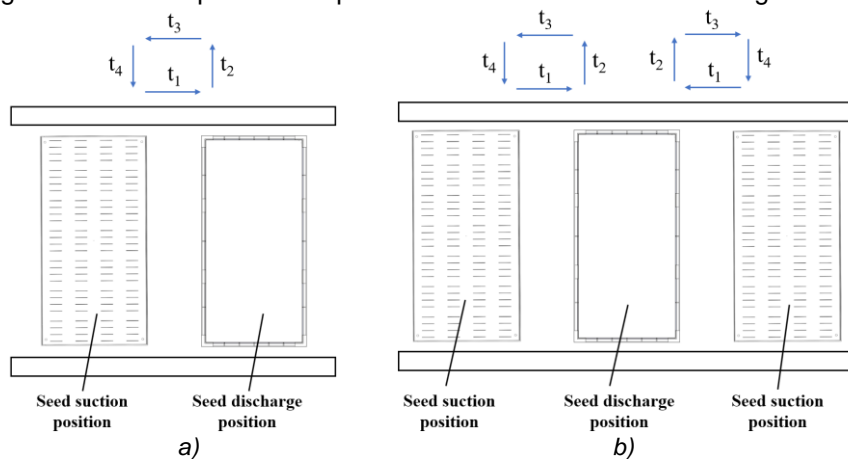


Fig. 7 - Comparison of operation time under different working modes

(a) Horizontal single-station;

(b) Horizontal dual-station

In the horizontal single-station working mode, the time required to complete the seeding of one seedling tray is T_s .

$$T_s = t_1 + t_2 + t_3 + t_4 \tag{3}$$

where t_1 is the time required for the seed suction position to move to the seed discharge position, t_2 and t_4 are the time required to complete seed discharge, t_3 is the time required for the seed discharge position to move to the seed suction position.

In the horizontal dual-station working mode, the time to complete the seeding of seedling tray No. 1 and seedling tray No. 2 when working independently was $2T_s$. When working interactively, the seeding position is shared, and only the seeding time t_2 does not overlap. When $t_1 + t_3 + t_4 \geq t_2$, the time required to complete the seeding for a set of seedling trays (two trays) is $T'_d = T_{d1} + T_{d2} = t_1 + t_2 + t_3 + t_4 = T_s$. Therefore, the time T_d required to complete one seedling tray seeding could be shown as Eq.(4).

$$T_d = T'_d = \frac{1}{2}T_s \tag{4}$$

During operation, the dual-station high-efficiency seeding device worked sequentially in reset state 1 → seeding state 1 → reset state 2 → seeding state 2. This process repeated itself to achieve interactive seeding of seed suction tray 1 and seed suction tray 2. The working principle diagram of dual-station high efficiency seeding is shown in Fig. 8.

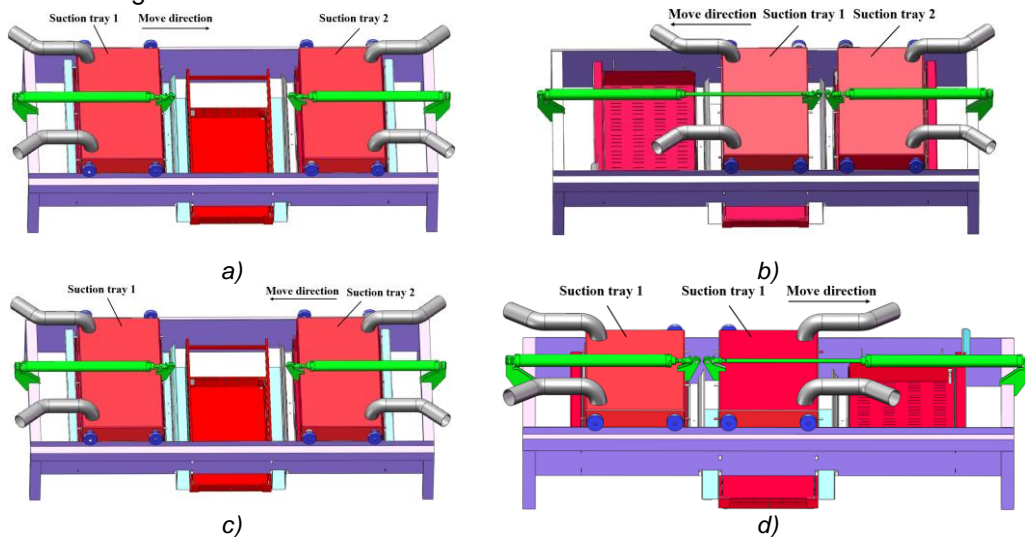


Fig. 8 - Working principle diagram of dual-station high efficiency seeding
 (a) Reset state 1; (b) Seeding state 1; (c) Reset state 2; (d) Seeding state 2

The physical object of dual-station high efficiency seeding device is shown in Fig. 9.

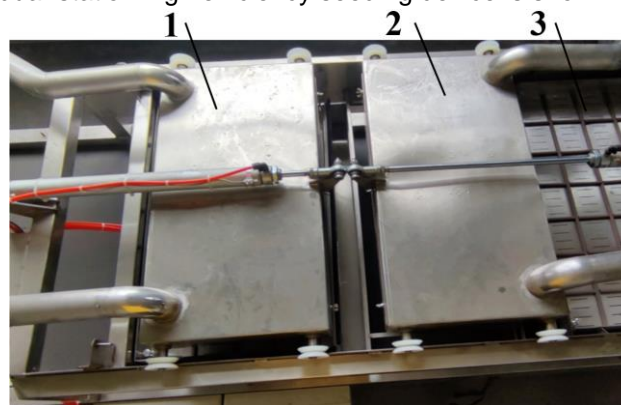


Fig. 9 - Physical object of dual-station high efficiency seeding device
 1. Seed suction tray 1; 2. Seed suction tray 2; 3. Vibrating seed tray 1

(2) Design of automatic seed adding device

The automatic seed adding device was located directly above the seeding station of the seeding frame and was connected to the dual-station high efficiency seeding device, as shown in Fig.10.

When the assembly line was working, seeds were manually placed into the seed box in advance (Liu et al., 2021). The seeds in the seed tray were continuously consumed during the operation (Wang et al., 2021). When receiving the seed addition command, the stepper motor drove the conveyor belt to move and deliver the seeds in the seed adding box to the vibrating seed tray at a preset rate, achieving automatic seed replenishment.

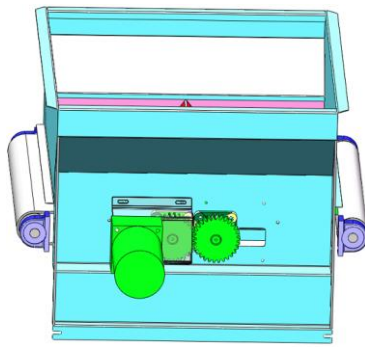


Fig. 10 - Automatic seed adding device

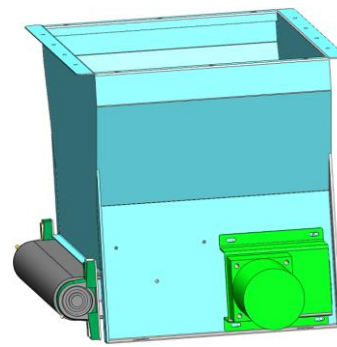


Fig. 11 - Soil laying device

Design of soil laying device

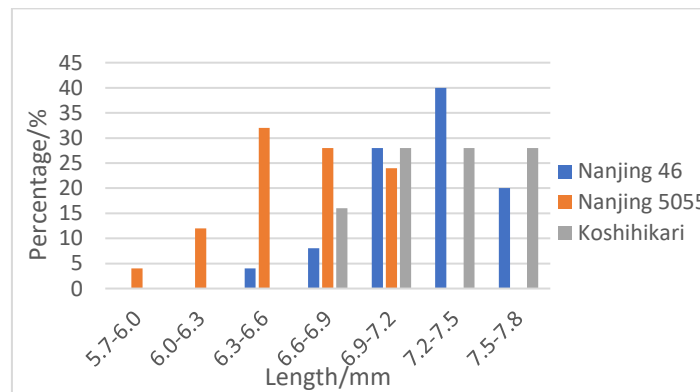
The soil laying device is shown in Fig.11. According to the difference in soil laying type for seedling tray, it could be divided into bottom soil laying device and topsoil covering device. When the seedling tray reached below the soil laying device, the stepper motor drove the conveyor belt on the soil spreading device through the reduction gear. The soil in the soil spreading device was added to the seedling tray along the conveyor belt to achieve uniform soil spreading. The soil thickness was determined by the opening of the outlet baffle and the speed of the stepper motor. According to the actual soil thickness requirements, the relevant parameters were adjusted to achieve uniform soil spreading on the seedling tray.

RESULTS

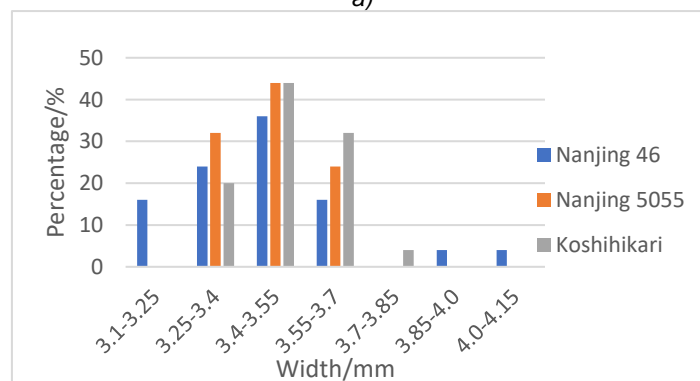
EXPERIMENT AND ANALYSIS OF SEEDING ASSEMBLY LINE

Experimental Materials

In order to verify the operating effect of this design, seeding performance tests and parameter optimization of the seeding assembly line for rice seedling cultivation were carried out. Three rice seeds varieties, namely Nanjing 46, Nanjing 5055, and Koshihikari, suitable for planting along the Yangtze River in Jiangsu Province, were used as experimental materials. 200 seeds of each variety were randomly selected, and the length, width and thickness of each seed were measured by a vernier caliper with an accuracy of 0.01 mm. The average of three times was taken to obtain the final size of the rice seeds. The rice seed size distribution is shown in Fig.12.



a)



b)

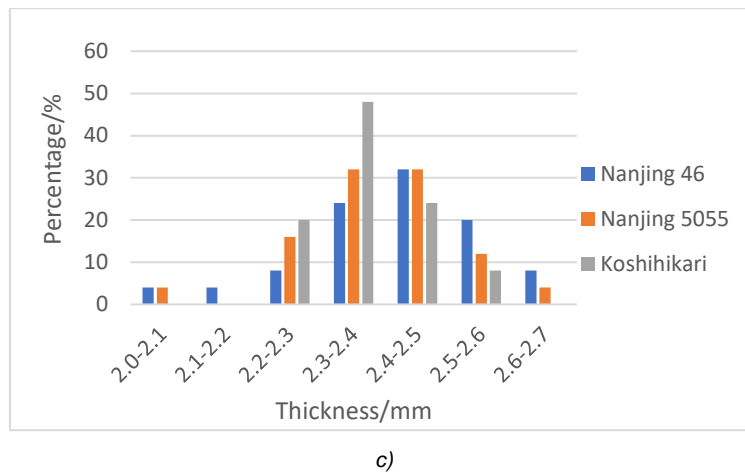


Fig. 12 - Distribution of different rice seed sizes
 (a) Length size distribution; (b) Width size distribution; (c) Thickness size distribution

Experimental Equipment

The experiment was carried out on the whole tray air-suction dual-station high efficiency seedling cultivation and seeding assembly line designed in this paper. 434-hole seed suction flat plate, 2-needle suction needle, and 434-hole standard seedling tray were used in this experiment. The physical product of the whole tray air-suction dual-station high efficiency seedling cultivation and seeding assembly line is shown in Fig.13.

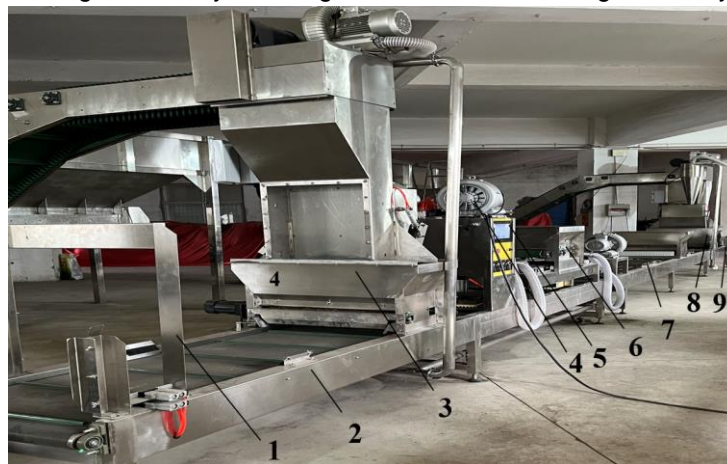


Fig. 13 - The physical product of the whole tray air-suction dual-station high efficiency seedling cultivation and seeding assembly line
 1. Horizontal tray delivery device 2. Frame 3. Bottom soil laying device 4. High pressure fan 5. Electric control box
 6. Dual-station high-efficiency seeding device 7. Sprinkler device 8. Topsoil covering device 9. Horizontal tray stacking device

The main control interface and parameter setting interface are shown in Fig.14 and Fig.15 respectively. The main control interface could realize switching between five interfaces: automatic, manual, query, precision seeding, and setting.



Fig. 14 - Main control interface



Fig. 15 - Parameter setting interface

At the same time, the main control interface could display the cumulative and current completed number of seedling trays. When a failure or emergency occurred, real-time alarm could be realized. Production efficiency could be displayed in real time and adjusted through a visual interface. The setting of vibration times, seeding times, seed scraping times and seed adding times could be realized by the parameter setting interface. At the same time, the functions of tray delivery, bottom soil laying, hole pressing, seeding, topsoil covering, precision seeding, water spraying 1, water spraying 2, automatic subsoil feeding and topsoil feeding could be enabled and disabled.

Test performance evaluation indicators

The production efficiency, qualification rate, reseeding rate and empty hole rate were taken as the main performance evaluation indicators of this equipment. The specific definition and calculation method are as follows:

(1) Production efficiency

Production efficiency refers to the number of seedling trays that can be seeded per hour on a stable seeding assembly line for rice seedling cultivation. During the experiment, seeding assembly line for rice seedling cultivation is started, and the time is measured by a stopwatch with an accuracy of 0.01 s, to obtain the number of seedling trays E_1 within 1 minute (Wang et al., 2023). Thus, the seeding efficiency of the assembly line is calculated from Eq.(5).

$$E=60 E_1 \quad (5)$$

where the unit of E is trays/h.

(2) Qualification rate

The qualification rate specified in this article is the percentage of holes with 2 ± 1 seeds per hole to the total number of holes in the seedling tray (Liu et al., 2021). Thus, the qualification rate P_1 is calculated from Eq.(6).

$$P_1 = \frac{N_1}{N_0} \times 100\% \quad (6)$$

where N_1 is the number of holes with 2 ± 1 seeds/hole, and N_0 is the total number of holes in the seedling tray.

(3) Reseeding rate

The reseeding rate specified in this article is the percentage of holes with 4 or more seeds per hole to the total number of holes in the seedling tray (Ni et al., 2022). Thus, the reseeding rate P_2 is calculated from Eq.(7)

$$P_2 = \frac{N_2}{N_0} \times 100\% \quad (7)$$

where N_2 is the number of holes with 4 or more seeds.

(4) Empty hole rate

The empty hole rate specified in this article is the percentage of holes with 0 seeds per hole to the total number of holes in the seedling tray (Hu et al., 2021). Thus, the empty hole rate P_3 is calculated from Eq.(8).

$$P_3 = \frac{N_3}{N_0} \times 100\% \quad (8)$$

where N_3 is the number of holes with 0 seeds.

Experiment on the whole tray air-suction seeding assembly line for rice precision seedling cultivation

Considering the similar seed sizes shown in Fig. 12, Nanjing 5055 rice seeds were used to conduct the experiment. Before the experiment, awns, deflated grains, and rice awns were removed from the seeds. The seeds were then soaked one day in advance to allow the buds to emerge. Two hours before the experiment, the seeds were taken out and evenly dried in a cool and dry place to remove moisture from the surface of the seeds. In order to verify that double-station sowing could promote the improvement of work efficiency. The experiment was divided into two groups, namely the single-station seeding mode and the dual-station high-efficiency seeding mode.

(1) Single-station seeding mode

Only part of the equipment of the double-station high-efficiency seeding device was started, which consisted of suction seed tray 1, vibrating seed tray 1 and seeding position (Liang et al., 2022). Before the experiment, preliminary experiments showed that the highest seeding efficiency could reach 1200 trays per hour (Hu et al., 2021). Therefore, seeding experiments were carried out sequentially at production efficiencies of 500, 600, 700, 800, 900, 1000, 1100, and 1200 trays per hour.

During the experiment, the seeds were evenly distributed in the seed boxes, the production efficiency was set, and the assembly line was started. When the assembly line was working stably, the seedling tray was placed on the horizontal tray delivery device to complete the seeding experiment (Ding et al., 2022).

Then, three consecutive seedling trays were randomly selected to obtain seeding effect data. The experimental results of different production efficiencies under the single-station seeding mode are shown in Table 2.

Table 2

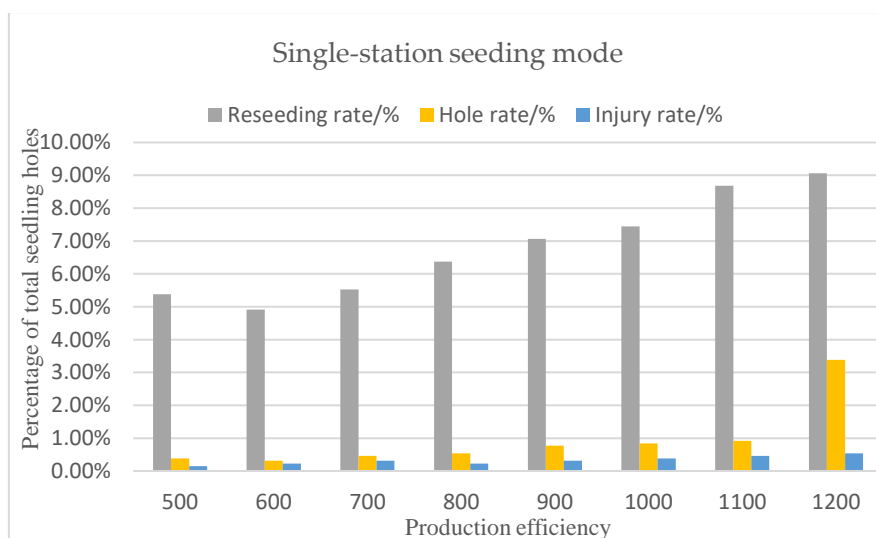
Experimental results of different production efficiencies under single-station seeding mode

No.	Production efficiency	Qualified rate (2±1) /%	Reseeding rate / %	Empty hole rate / %	Damage rate / %
1	500	94.24%	5.38%	0.38%	0.15%
2	600	94.78%	4.91%	0.31%	0.23%
3	700	94.01%	5.53%	0.46%	0.31%
4	800	93.09%	6.37%	0.54%	0.23%
5	900	92.16%	7.07%	0.77%	0.31%
6	1000	91.71%	7.45%	0.84%	0.38%
7	1100	90.40%	8.68%	0.92%	0.46%
8	1200	87.56%	9.06%	3.38%	0.54%

The changing trend of the operation effect in the single-station seeding mode is shown in Fig.16.



a)



b)

Fig. 16 - The changing trend of the operation effect in the single-station seeding mode

a) Qualified rate; (b) Reseeding rate, empty hole rate, damage rate

(2) Dual-station high-efficiency seeding mode

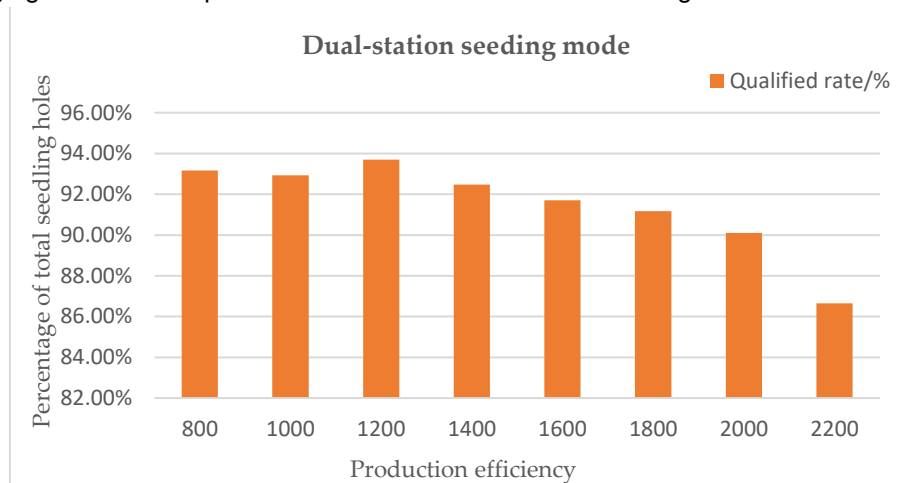
The seed suction tray 1, the vibrating seed tray 1, the seed suction tray 2 and the vibrating seed tray 2 of the dual-station high-efficiency seeding device worked together to realize interactive seeding and complete the entire seeding process (Khizhnyak V.I., 2021; Ramesh B., 2015). Before the experiment, preliminary experiments showed that the highest seeding efficiency could reach 2200 trays per hour. Therefore, seeding experiments were carried out sequentially at production efficiencies of 800, 1000, 1200, 1400, 1600, 600, 1800, 2000 and 2200 trays per hour (Sial F.S., 1984). The experiment was carried out again according to the above method and relevant results were obtained. The experimental results of different production efficiencies under the dual-station seeding mode were shown in Table 3.

Table 3

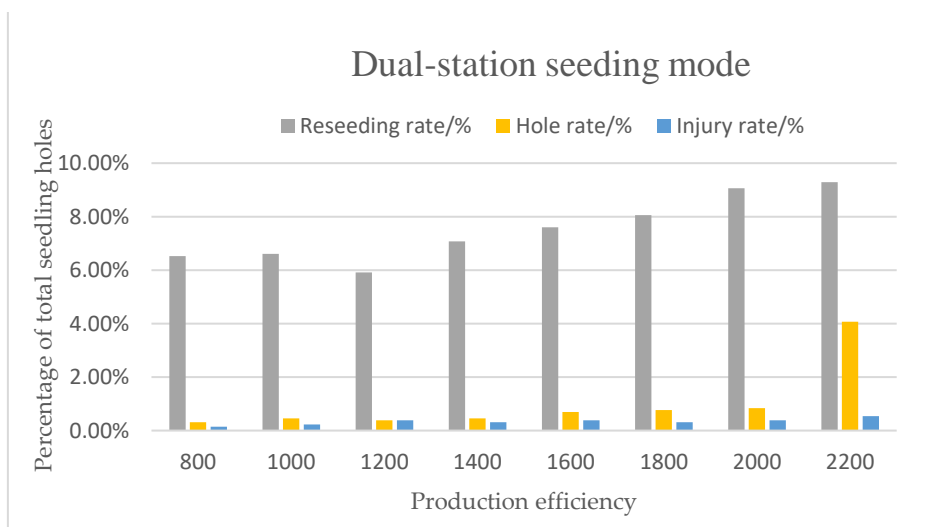
Experimental results of different production efficiencies under dual-station seeding mode

NO.	Production efficiency	Qualified rate (2±1) %	Reseeding rate %	Empty hole rate/%	Damage rate/%
1	800	93.16%	6.53%	0.31%	0.15%
2	1000	92.93%	6.61%	0.46%	0.23%
3	1200	93.70%	5.92%	0.38%	0.38%
4	1400	92.47%	7.07%	0.46%	0.31%
5	1600	91.71%	7.60%	0.69%	0.38%
6	1800	91.17%	8.06%	0.77%	0.31%
7	2000	90.10%	9.06%	0.84%	0.38%
8	2200	86.64%	9.29%	4.07%	0.54%

The changing trend of the operation effect in the dual-station seeding mode is shown in Fig.17.



a)



b)

Fig. 17 - The changing trend of the operation effect in the dual-station seeding mode
 (a) Qualified rate; (b) Reseeding rate, empty hole rate, damage rate

In the single-station seeding mode and the dual-station seeding mode, the experimental results showed the changing trends of the qualified rate, reseeding rate, empty hole rate and damage rate with the operation efficiency as shown in Table 2, Table 3, Figure 16 and Figure 17. In both working modes, the overall pass rate gradually decreased with the improvement of production efficiency. When the efficiency exceeded 1100 trays per hour (single-station mode) or 2000 trays per hour (dual-station mode), the pass rate would drop significantly. The reseeding rate and empty hole rate showed a gradual upward trend with the improvement of production efficiency, but the changes were not significant. When the number of trays per hour exceeded 1,100 (single-station mode) or 2,000 (double-station mode), the void rate would increase significantly and failed to meet the requirements for rice seedling cultivation and seeding. The principle of air suction seeding ensured that the damage rate did not change significantly with the increase of production efficiency.

Therefore, the dual-station seeding mode could improve operational efficiency while ensuring seeding accuracy. When the seeding efficiency reached 2000 trays per hour, the seeding rate of 1-3 seeds per hole was 90.1%, while the damage rate, empty hole rate and re-seeding rate were 0.38%, 0.84%, 9.06% respectively. It could meet the accuracy requirements of precision rice seedling cultivation and seeding.

CONCLUSIONS

Aiming at the common problems of low qualified rate of precision seeding and limited operation efficiency of rice seeding production line, this paper innovatively proposed the collaborative operation mode of "horizontal tray delivery—dual-station seeding". A whole tray air suction dual-station high-efficiency seeding device was designed, which adopted two sets of seed suction trays to work alternately with vibrating seed trays, combined with the optimization of the horizontal tray delivery mechanism, to compress the seeding tray movement time by 50%, and successfully achieved a breakthrough in seeding efficiency of 2000 trays/h. The experiment results showed that under the dynamic working condition of 800-2000 trays per hour, the qualified rate of 2±1 seeds/hole was more than 90.1%, and the hole rate and damage rate were kept within 0.84% and 0.38% respectively. Compared with the single-station mode, the dual-station interactive strategy improved efficiency by 81.8% while ensuring seeding accuracy. The integrated assembly line design realized the coordination of the processes of tray feeding, subsoil laying, hole pressing, seeding, watering, topsoil covering, tray stacking. It had been verified by Nanjing 46, Nanjing 5055 and Koshihikari rice seeds that it could meet the agronomic requirements of factory-based seedling cultivation and seeding of different rice varieties.

The research results have significantly improved the efficiency of mechanized rice planting. Through precision seeding, the amount of seeds used per acre will be reduced, and the rice yield per acre is expected to increase, providing technical support for ensuring food security. The proposed horizontal tray delivery mechanism and dual-station dynamic compensation strategy provide a transferable solution for the modular design of dryland seedling equipment for vegetables, flowers, etc. The interactive operation mode provides a new path to solve the problem of improving efficiency in the field of precision seeding, and has important reference significance for promoting the intelligent upgrading of precision agricultural equipment.

ACKNOWLEDGEMENTS

This work was supported by National Natural Science Foundation of China (31871528); Anhui Province University Outstanding Young Talents Support Project (gxyq2022064); University Natural Science Research Project of Anhui Province (2023AH052640, 2022AH010091); The Open Fund of Anhui Undergrowth Crop Intelligent Equipment Engineering Research Center (AUCIEERC-2022-01, AUCIEERC-2022-09); Jiangsu graduate research and Practice Innovation Program (KYCX22_3680); The Open Fund of Key Laboratory of Modern Agricultural Equipment and Technology, Ministry of Education (MAET202308).

REFERENCES

- [1] Cao X., Ma X., Li H., Weng Z., Li Z., Wang X., (2021). Design and experiment of air-suction drum precision seed meter for rapeseed seedling (气吸滚筒式油菜穴盘育苗精密排种器设计与试验). *Transactions of the Chinese Society of Agricultural Engineering*, Vol. 37, pp. 51-60, Beijing/China.
- [2] Ding B., Liang Z., Qi Y., Ye Z., Zhou J., (2022). Improving Cleaning Performance of Rice Combine Harvesters by DEM–CFD Coupling Technology. *Agriculture*, Vol.12, pp. 1-19, Switzerland.
- [3] Ding L., Yang L., Zhang D., Cui T., Zhang K., Zhong X., (2021). Analysis of the influence of adsorption posture of air-suction corn seed meter on seeding performance (气吸式玉米排种器吸附姿态对播种性能的影响分析). *Transactions of the Chinese Society of Agricultural Machinery*, Vol. 52, pp. 40-50, Beijing/China.

- [4] Han B., Wu W., Wang H., (2009). Automatic clearing and seeding device for rice seedlings in rice trays(水稻机摆钵育苗气吸滚筒式自动清堵排种器). *Transactions of the Chinese Society of Agricultural Engineering*, Vol. 25, pp. 96-99, Beijing/China.
- [5] Hou C., Hu J., Guo K., Zhao Z., (2015). Design and experiment of air suction plate type precision seeding device for super rice (气吸板式超级稻精密排种器设计与试验). *Transactions of the Chinese Society of Agricultural Engineering*, Vol. 31 (S1), pp. 14-20, Beijing/China.
- [6] Hou Z., Qiu Y., Chen Z., Chen L., Shao Z., (2020). Numerical simulation and experimental study on pelleting motion law of agropyron seeds under vibration force field. *INMATEH Agricultural Engineering*, Vol. 62, pp. 299-308, Romania.
- [7] Hu Y., Chen Y., Wei W., Hu Z., Li P., (2021). Optimization design of spray cooling fan based on CFD simulation and field experiment for horticultural crops. *Agriculture*, Vol.11, pp. 1-18, Switzerland.
- [8] Karayel D., Güngör O., & Šarauski E. (2022). Estimation of optimum vacuum pressure of air-suction seed-metering device of precision seeders using artificial neural network models. *Agronomy*, Vol.12, pp. 1-11, Switzerland.
- [9] Khizhnyak V.I., Shchirov V.V., Nesmiyan A.Y., Avramenko F.V., & Kochergin A.S. (2021). Evaluation of the efficiency of row-crop seeders using vacuum and extrabaric seed metering methods. *IOP Conference Series Earth and Environmental Science*, 659(1), 012045.
- [10] Ma G., (2018). Design of air suction drum type precision seeding line (气吸滚筒式穴盘精量播种流水线设计). *Journal of Zhejiang University (Agriculture and Life Sciences)*, Vol. 44, pp. 476-480, Hangzhou/China.
- [11] Li J., Lai Q., Zhang H., Zhang Z., Zhao J., Wang T., (2021). Suction force on high-sphericity seeds in an air-suction seed-metering device. *Biosystems Engineering*, Vol. 211, pp. 125-140, England.
- [12] Li Y., Zhao Z., Chen J., Xu L., (2009). Discrete element analysis of seed population movement in the seed tray of air-suction vibration seeding device (气吸振动式排种器种盘内种群运动的离散元分析). *Transactions of the Chinese Society of Agricultural Machinery*, Vol. 40, pp. 56-59+76, Beijing/China.
- [13] Li Y., Zhao Z., Chen J., Xu L., (2008). Numerical simulation and experiment on seed suction performance of air-suction vibration seeding device (气吸振动式排种器吸种性能数值模拟与试验). *Transactions of the Chinese Society of Agricultural Machinery*, Vol. 39, pp. 95-99+104, Beijing/China.
- [14] Liang Z., Xu L., De B., Li Y., Saeyes W., (2020). Optimisation of a multi-duct cleaning device for rice combine harvesters utilising CFD and experiments. *Biosystems Engineering*, Vol. 190, pp. 25-40, England.
- [15] Liu W., Hu J., Yao M., Zhao J., Lakhari I. A., Lu C., Wang W., (2021). Magnetic field distribution simulation and performance experiment of a magnetic seed-metering device based on the combined magnetic system (组合磁系磁控排种器磁场分布仿真及性能试验). *International Journal of Agricultural and Biological Engineering*, Vol. 14, pp. 108-117, Beijing/China.
- [16] Liu Z., Zhang M., Han J., Zhuang, Y., Lan Y., Chen Y., (2021). Effect of seed filling and releasing angles on the performance of compound vacuum seed metering device. *INMATEH Agricultural Engineering*, Vol. 65, pp. 153-162, Romania.
- [17] Lu F., Ma X., Qi L., Xing X., Li H., Guo L., (2018). Mechanism analysis and experiment of vibration rice precision seeding device (振动式水稻精密播种装置机理分析与试验). *Transactions of the Chinese Society of Agricultural Machinery*, Vol. 49, pp. 119-128+214, Beijing/China.
- [18] Ni J., Dong J., Ullah I., Mao H., (2022). CFD simulation of sucrose flow field in the stem of greenhouse tomato seedling (温室番茄幼苗茎内蔗糖流场的 CFD 模拟). *International Journal of Agricultural and Biological Engineering*, Vol. 15, pp. 111-115. Beijing/China.
- [19] Ramesh B., Reddy B.S., Veerangoud M., Anantachar M., & Shanwad U.K. (2015). Properties of cotton seed in relation to design of a pneumatic seed metering device (वायवीय बीज मापन उपकरण के डिजाइन के संबंध में कपास के बीज के गुण) . *Indian Journal of Dryland Agricultural Research & Development*, 30(1), 69-76, India.
- [20] Sial F.S., & Persson S.P. (1984). Vacuum nozzle design for seed metering. *Transactions of the ASAE*, 27(3), 688-696, America.
- [21] Singh R.C., Singh G., & Saraswat D.C. (2005). Optimisation of design and operational parameters of a pneumatic seed metering device for planting cottonseeds. *Biosystems engineering*, 92(4), 429-438, England.

- [22] Sun H., Guo G., Tang S., Xue J., Ling X., Li Q., (2021). Improvement of pressure-hole roller device and control system design for vegetable seedling and sowing production line (蔬菜育苗播种流水线压穴滚筒装置改进与控制系统设计). *Transactions of the Chinese Society of Agricultural Engineering*, Vol. 37, pp. 41-48, Beijing/China.
- [23] Wang Y.B., Li H.W., Wang Q.J., He J., Lu C.Y., Yang Q.L., Liu P. (2021). Experiment and parameters optimization of seed distributor of mechanical wheat shooting seed-metering device, *INMATEH Agricultural Engineering*, Vol. 63, pp. 29-40, Romania.
- [24] Wang Y., Su W., Lai Q., Lin Y., Li J., (2023). Simulation and measurement of the suction force on ellipsoidal seeds in an air-suction seed-metering device. *Biosystems Engineering*, Vol. 232, pp. 97-113, England.
- [25] Xing H., Wang, Z., Luo, X., He, S., Zang, Y., (2020). Mechanism modeling and experimental analysis of seed throwing with rice pneumatic seed metering device with adjustable seeding rate. *Computers and Electronics in Agriculture*, Vol. 178, pp. 1-16, England.
- [26] Yang W., Kan C., Zhang X., Wu C., Lin Q., Pan W., (2021). Design and experiment of air-suction precision seed meter for Panax notoginseng seedling sowing (气吸式三七育苗播种精密排种器设计与试验). *Transactions of the Chinese Society of Agricultural Machinery*, Vol. 52, pp. 95-105, Beijing/China.
- [27] Yuan H., Liu C., Song J., Du X., Jiang M., Li W., (2020). Research on piezoelectric vibration seed supply device of precision seed meter for super hybrid rice seedling (超级杂交稻穴盘育苗精量排种器压电振动供种装置研究). *Transactions of the Chinese Society of Agricultural Machinery*, Vol. 51, pp. 31-40, Beijing/China.
- [28] Zang Y., Huang Z., Qin W., He S., Qian C., Jiang Y., Tao W., Zhang M., Wang Z., (2024). Research and development of single-grain air-suction hybrid rice seeding device (气吸式杂交稻单粒排种器研制). *Transactions of the Chinese Society of Agricultural Engineering*, Vol. 40, pp. 181-191, Beijing/China.
- [29] Zhang M., Jiang Y., He S., Huang Z., Qin W., Qian C., Tao W., Zang Y., (2023). Design and experiment of air-suction wheel precision seeding device for vegetables (蔬菜气吸轮式精量排种器设计与试验). *Transactions of the Chinese Society of Agricultural Engineering*, Vol. 39, pp. 98-109, Beijing/China.
- [30] Zhang S., Zhao Z., Chen S., (2015). Design and experiment of non-missing seeding nozzle of vibration air suction disk type precision seeding device for seedling cultivation (振动气吸盘式穴盘育苗精密排种器无漏播吸嘴的设计与试验). *Journal of Chinese Agricultural Mechanization*, Vol. 36, pp. 22-26+57, Nanjing/China.

A LIGHTWEIGHT MILLET DOWNY MILDEW SPORE DETECTION METHOD BASED ON IMPROVED YOLOv8s

基于改进 YOLOv8s 的轻量化谷子白发病孢子检测方法

Jianglin YAN¹⁾; Zhengkun ZHAI¹⁾; Zhixiang FENG¹⁾; Lijun CHENG^{*1)}; Jie YANG^{*2 3)}

¹⁾ College of Software, Shanxi Agricultural University, Shanxi / China;

²⁾ College of Health Service and Management, Shanxi University of Traditional Chinese Medicine, Shanxi / China;

³⁾ National International Joint Research Center for Molecular Chinese Medicine, Shanxi Key Laboratory of Chinese Medicine Encephalopathy, Shanxi University of Chinese Medicine, Shanxi / China;

Correspondent authors: Lijun CHENG: Tel: 13835441585; E-mail: clizyb@sxau.edu.cn;

Jie YANG: Tel: 13623620021; E-mail: yjsxctcm@sxctcm.edu.cn

DOI: <https://doi.org/10.35633/inmateh-75-27>

Keywords: Deep learning, millet downy mildew, spores, target detection, YOLOv8s

ABSTRACT

This paper proposes a lightweight spore detection method for millet downy mildew based on an improved YOLOv8s, aiming to enhance the accuracy and efficiency of spore detection. First, the backbone network of the YOLOv8s model was modified by replacing the original backbone with EfficientViT. The substitution of the EfficientViT backbone enables global receptive field and multi-scale learning, which helps to reduce computational costs. While maintaining high performance, this modification significantly improves computational efficiency. Second, a Frequency-Adaptive Dilated Convolution (FADC) module was added to the neck of the model. By adaptively adjusting the receptive field of dilated convolution, the FADC module optimizes the detection of different frequency information. It improves the detection of small objects without adding extra computational burden. Finally, the detection head was optimized to better adapt to the task of detecting millet downy mildew spores, resulting in enhanced detection speed and accuracy. The improved algorithm, named EFP-YOLOv8s, maintains the same mAP50 as the original YOLOv8s model while reducing the number of parameters by 37.8% and computational cost by 58.5%. By balancing high performance with reduced computational resource demands, the model achieves lightweight design, making it more deployable and scalable in practical applications.

摘要

本文提出了一种基于改进 YOLOv8s 的轻量化谷子白发病孢子检测方法，旨在提高孢子检测的准确性和效率。首先，针对 YOLOv8s 模型的主干网络进行了改进，将原有的主干网络替换为 EfficientViT。通过替换主干网络 EfficientViT 实现全局感受野和多尺度学习，有助于降低计算成本。在保持高性能的同时，显著提高了计算效率。其次，在模型的颈部添加了 FADC (Frequency-Adaptive Dilated Convolution) 模块，通过自适应地调整膨胀卷积的感受野，针对不同频率的信息进行优化。在不增加额外计算量的同时改善小目标的检测效果。最后，对检测头进行了优化，使其更加适应谷子白发病孢子的检测任务，提高了检测速度和准确性。改进后的算法 EFP-YOLOv8s 相比原 YOLOv8s 模型 mAP50 保持不变，参数量下降 37.8%，计算量下降 58.5%。该模型在保持高性能的同时，也降低了计算资源的需求，实现轻量化，更易于在实际应用中部署和推广。

INTRODUCTION

Millet downy mildew is a soil-borne and seed-borne systemic disease caused by **Sclerospora graminicola* (Wang et al., 2024). This disease affects the normal growth of cereal leaves and aggravates the tendency of leaf rot. It usually occurs at the 3-leaf stage of seedlings, and at the early stage of the disease, white spots are produced on the adaxial surface of the leaves, accompanied by a moldy layer on the dorsal surface with a grayish-white color, and the diseased grains show a leaflet shape (Cheng et al., 2020). During different growth stages after millet is infected, the disease manifests symptoms such as gray back, white tip, spear-like stalk, white hair, and hedgehog head. The brown powdery substance observed in these symptoms is the oospores of the downy mildew fungus (Yan et al., 2019). These oospores can rapidly multiply and infect plants under suitable conditions, leading to a significant decrease in grain yield and even causing crop failure (Yue et al., 2021). Therefore, timely and accurate detection of cereal white disease spores is of great significance in preventing and controlling the spread of the disease and ensuring the stability and safety of cereal production.

In the early stage, spore detection and counting mainly relied on manual observation and counting, such as hemocyte counting method and plate colony counting method (Li *et al.*, 2006). Although these methods can reflect the number of spores to a certain extent, they are cumbersome, time-consuming and laborious to operate, and the operation error between different personnel is large, which makes it difficult to meet the demand for high-precision and high-volume detection. To overcome these limitations, researchers began to explore more efficient and accurate counting methods. Spore counting methods based on PCR technology are highly accurate, but the operation is complicated, costly and also time-consuming (Wang *et al.*, 2024). In recent years, spore detection and counting methods based on emerging technologies such as fluorescent labeling, flow cytometry, and molecular chemistry have emerged (Liu *et al.*, 2023; Ren *et al.*, 2022; Aguayo *et al.*, 2018). These techniques not only significantly improve the sensitivity and specificity of spore detection, but more importantly, they are able to achieve high-precision quantification of spore counts, providing more reliable data support for scientific research and practical applications.

With the rapid development of computer vision and deep learning technology, image-based target detection methods show great potential in the field of plant disease detection. In 2018, the K-means clustering algorithm was used for image segmentation, image preprocessing, identification of contacted downy spores based on shape factor and area of the spores, and contacted downy spore outline segmentation based on the combination of concavity and contour segmentation. This approach aimed to achieve accurate and automatic detection and counting of spores (Lei *et al.*, 2018). In 2020, an improved U-Net architecture was proposed, reaching a segmentation rate of 91.4%. The new network architecture achieved a higher segmentation rate in the segmentation task of the wheat powdery mildew spore image dataset (Liang *et al.*, 2020). In 2023, a spin-up UNet++ feature extraction network was constructed, with an average recognition accuracy of 99.03%, which improved the segmentation rate by 10.35 percentage points compared to the original CenterNet model (Zhou J. *et al.*, 2023). In 2024, microscopic image processing and machine learning techniques were used to help identify spores of a fungus that can be used to infect pathogens. The method extracted texture, color and shape features of the spores and classified them using Random Forest algorithm with an accuracy of 95.38% (Nezhad *et al.*, 2024).

The YOLO (You Only Look Once) series of algorithms, with its high efficiency and accuracy, has achieved remarkable results in real-time target detection tasks. In 2020, it was proposed for Yolov3 algorithm to join the traditional morphological processing of spore recognition method in microscope images. The accuracy of the spore recognition algorithm increased to more than 94%, and the detection rate was more than 82% (Li X. *et al.*, 2020). In 2023, the number of parameters and computation of the model were reduced by incorporating FasterNet and NAM attention mechanism module into the base model YOLOv5m. It effectively improved the speed and accuracy of spore detection of cucumber downy mildew fungus (Qiao C. *et al.*, 2023). In addition, the Ghost convolution of CBAM attention mechanism was introduced to replace the CSP structure, improving the feature fusion network and utilizing a finer-grained mesh for the detection of dense and sticky small targets. The loss function was enhanced by assigning different weights to various output feature maps, and DIoU_NMS was used instead of NMS (Li M. *et al.*, 2023). In 2024, a small target detection layer was added to the original Yolov8 model, incorporating the focal attention mechanism and WIoU loss function. The average detection accuracy mAP @ 0.5 in the spore data set reached 96.8 % (Zhang D. *et al.*, 2024). Additionally, the backbone network of the original YOLOv8 model was replaced with PP-LCNet, the EMA attention mechanism module was introduced in the neck network, and the bounding box loss function was replaced with WIOU. These modifications reduced the number of floating-point operations per second while maintaining higher detection accuracy (Luo B. *et al.*, 2024).

Traditional deep learning models often suffer from high computational complexity, large number of parameters, and slow inference speed, making it difficult to meet the demand for real-time detection and mobile deployment in agricultural scenarios. Therefore, it is of great practical significance to improve the YOLO series of algorithms in a lightweight way. In 2024, the CG module was added to the original backbone of YOLOv5s along with the HS-FPN module, resulting in a significant reduction in the number of model parameters and accurate detection of various types of pathogen spores. YOLOv8s optimized feature extraction capability compared to YOLOv5, improving detection accuracy while maintaining a relatively lightweight structure (Cheng *et al.*, 2024). Additionally, by introducing GhostConv to replace standard convolution, constructing the LightC3 module, adopting BiFPN instead of the Concat operator, and integrating the SE attention mechanism, the computational burden and the number of model parameters were significantly reduced while maintaining high detection accuracy (Meng F. *et al.*, 2024).

A study for wheat grain counting achieved efficient detection and counting in complex scenarios by improving the YOLOv8's neck network into a BiFPN structure, further validating the effectiveness of the lightweight design (Ma N. *et al.*, 2024).

Given the characteristics of small, dense, and clustered targets in millet downy mildew spore images, as well as the relatively high computational costs and parameter counts of the aforementioned improved networks that hinder deployment, this study develops a lightweight detection model for millet downy mildew spores by integrating an EfficientNet-ViT backbone, a C2f_FADC neck module, and an optimized detection head. This model not only achieves excellent detection performance but also enables accurate identification of pathogen spores while maintaining high efficiency. It is anticipated that the findings of this study will provide robust support for the prevention and control of millet downy mildew and contribute to the advancement of intelligent and precise agriculture.

MATERIALS AND METHODS

Image Data Acquisition

First, millet plants with typical symptoms of downy mildew were selected from the field. The mature diseased panicles were excised using sterile scissors as samples. These samples were then filtered through a 0.04 mm mesh sieve to remove large particulate impurities from the suspension. Next, the collected diseased tissue sample was placed into a centrifuge tube containing an appropriate amount of sterile water, and the spores were fully shaken using a vortex shaker to disperse the spores in suspension as evenly as possible. Finally, an appropriate amount of spore suspension droplets was added to the microscope slide, and the coverslip was placed under the microscope, and the number of oospores in the field of view was observed under the microscope at 10×10 times the microscope. A total of 2042 images were obtained, with a resolution of 1800 pixels × 1350 pixels, in jpg format.

Image Preprocessing

The acquired spore images showed significant dense distribution and adhesion characteristics, which posed a challenge to the subsequent spore identification and counting work. In this paper, the methods of randomly adjusting saturation, adding Gaussian noise and changing brightness are used to simulate the complex and changeable environmental conditions in the field and various lighting conditions, shooting angles and noise interference factors that may be encountered in the actual detection scene, aiming to expand the data set from multiple dimensions. A total of 6126 images were obtained after expansion. The dataset was divided into a training set of 4926 sheets and a validation set of 1200 sheets according to the ratio of 8:2.

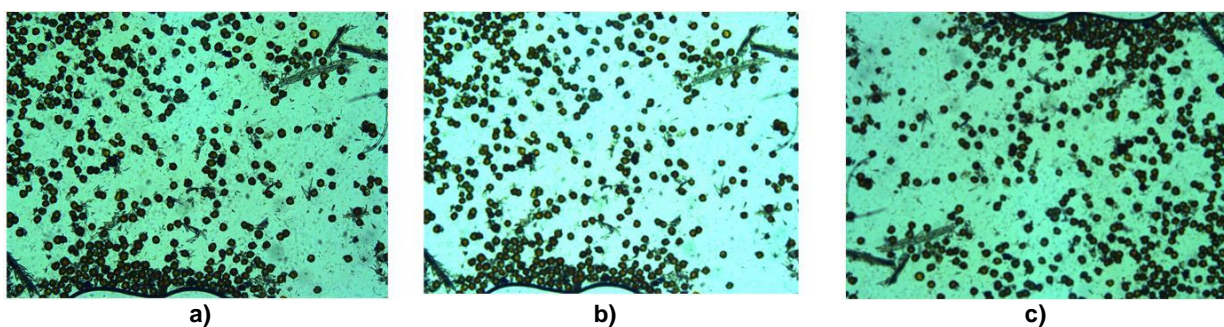


Fig. 1 - Microscopic images of millet downy mildew spores

a) Original image; b) Adjusted saturation and brightness; c) Adding Gaussian noise and flipping

YOLOv8s model structure

YOLOv8 is a YOLO target detection and image segmentation model developed by Ultralytics (Redmon J. *et al.*, 2016). YOLOv8 introduces an Anchor-Free detection head, a new loss function, and a Task-AlignedAssigner positive and negative sample allocation strategy to improve the detection accuracy and speed of the model. In addition, YOLOv8 provides models with different scales, such as Nano, Small, Medium, Large and ExtraLarge, where YOLOv8x is the most accurate but runs the slowest with the largest model size, and YOLOv8n is the fastest with the smallest model size. Considering the accuracy and speed requirements of spore detection in real scenarios, YOLOv8s in YOLOv8 is chosen as the benchmark model for improvement.

Improvement of YOLOv8s model

First, the backbone network of the YOLOv8s model was improved by replacing the original backbone network with EfficientViT. EfficientViT combines the advantages of convolutional neural network (CNN) and Transformer, which has stronger feature extraction capability and higher computational efficiency, thus enhancing the accuracy of spore detection. Secondly, the FADC module is added to the neck of the model, which enhances the model's ability to learn spore features by introducing the attention mechanism, further improving the accuracy of detection. Finally, the detection head was optimized to better adapt to the task of detecting millet downy mildew spores, resulting in improved detection speed and accuracy.

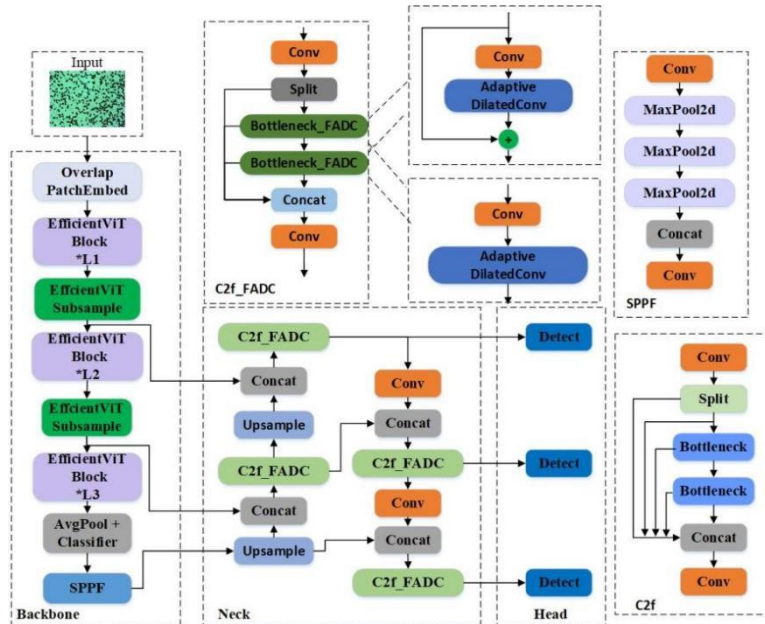


Fig. 2 - EFP-YOLOv8 model

EfficientViT

EfficientViT consists of three phases, each containing a number of sandwich structures, which are composed of 2N DWConv (spatially localized communication) and FFN (channel communication) as well as cascaded packet attention (Liu et al., 2023). Compared with the traditional Multi-Headed Self-Attention (MHSA), CGA performs head segmentation of the features before generating the query (Q), key (K) and value (V). This change not only improves the efficiency of computation, but also allows each head to focus on a different subset of features, thus enhancing the diversity and expressiveness of the model. To further enhance the model capacity, EfficientViT sums the output of each head with the input of the next head, realizing the effective transfer and fusion of feature information. Eventually, the outputs of multiple heads are stitched together and mapped through a linear layer to obtain the final output features.

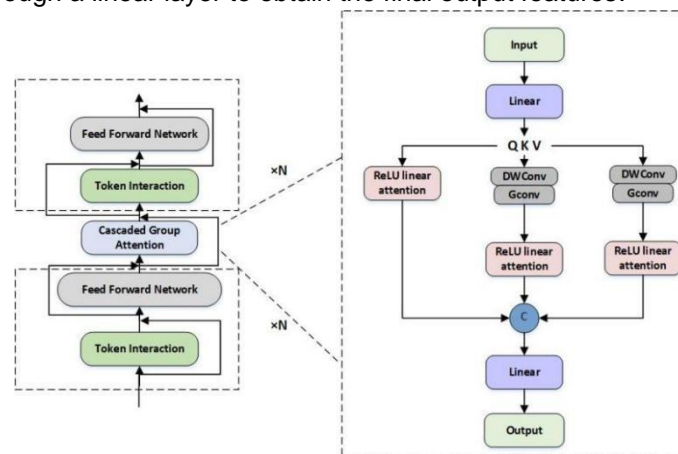


Fig. 3 - EfficientViT network structure diagram

In the Cascaded Grouped Attention (CGA) approach, the model splits the complete feature into multiple parts and provides these parts to each head separately for processing. This way of partitioning features not only saves computation, but also makes the attention computation more efficient.

Each head focuses on processing a different subset of features, which improves the diversity and robustness of the model. The computational formulas are shown in Eq. (1) to Eq. (3).

$$\tilde{X}_{mn} = \text{Attn}(X_{mn}Y_{mn}^Q, X_{mn}Y_{mn}^K, X_{mn}Y_{mn}^V) \tag{1}$$

$$\tilde{X}_{m+1} = \text{Con}[\tilde{X}_{mn}]_{n=1:h} Y_m^P \tag{2}$$

$$X'_{mn} = X_{mn} + \tilde{X}_{m(n-1)}, 1 < n \leq h \tag{3}$$

X_{mn} is the n -th partition of the input feature X_m , $X_m = [X_{m1}, X_{m2}, \dots, X_{mh}]$, $1 < n \leq h$, is the total number of heads, Y_{mn}^Q , Y_{mn}^K , and Y_{mn}^V are projection layers that partition the input features into different subspaces and Y_m^P is a linear layer that projects the connected output features with the same dimension as the input. X'_{mn} is the residual connection of the m -th head output and input.

C2F_FADC

The C2f module in YOLOv8 realizes the fusion of feature maps at different scales and improves the target detection performance by introducing the ELAN attention mechanism and Bottleneck design. The C2f_FADC module further introduces the attention mechanism and the deep convolution based on this foundation, which optimizes the computational efficiency of the model and enhances the focus on the key regions, improving the accuracy and robustness of the model in the complex scenario of the detection performance in complex scenes.

Frequency Adaptive Dilation Convolution (FADC) consists of three strategies: adaptive dilation rate (AdaDR), adaptive kernel (AdaKern), and frequency selection (FreqSelect) (Chen L. et al., 2024). AdaDR adjusts the dilation rate spatially, AdaKern operates on the convolution kernel weights, and FreqSelect directly balances the frequency power of the input features in order to encourage the acceptance of domain expansion.

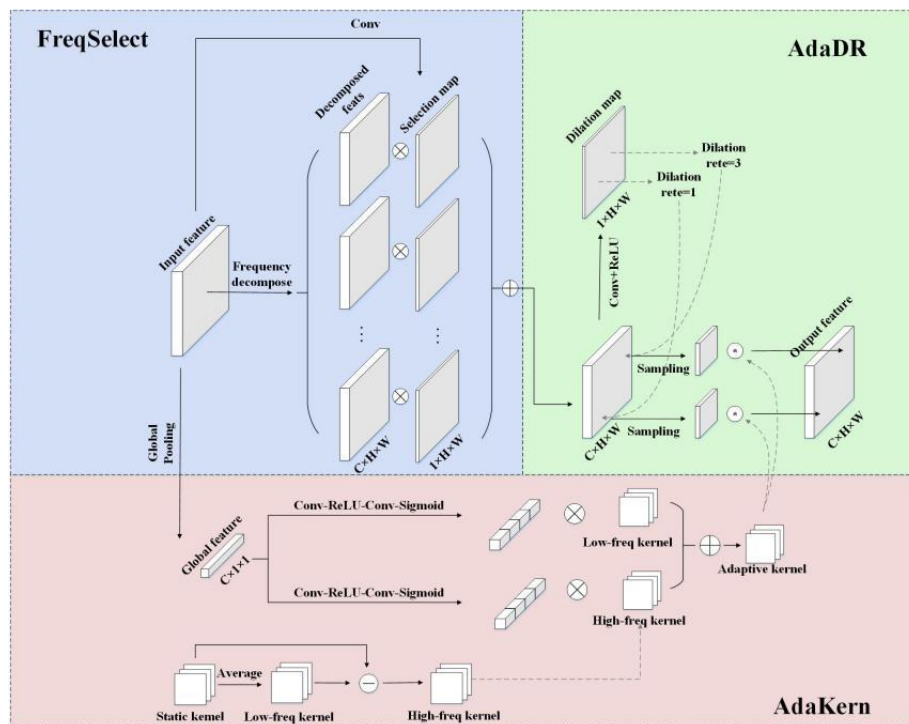


Fig. 4 - FADC network structure diagram

Adaptive Dilation Rate (AdaDR): Unlike the traditional fixed dilation rate, FADC can dynamically adjust the dilation rate according to the frequency characteristics of different image regions. In high-frequency regions, the FADC selects a smaller expansion rate to capture more detailed edge information, while in low-frequency regions, a larger expansion rate can be selected to expand the sensory field.

Adaptive Kernel (AdaKern): This module decomposes the convolutional weights into low-frequency and high-frequency components and dynamically adjusts the ratio between these components on a per-channel basis. By increasing the high-frequency portion of the convolutional weights, AdaKern is able to capture more high-frequency components, thereby increasing the effective bandwidth.

FreqSelect: The FreqSelect module optimally balances high-frequency and low-frequency components in the feature representation by re-weighting the spatial variance. It suppresses high-frequency components in the background to encourage the FADC to learn larger expansions, thereby expanding the range of the receptive field.

Detection head improvements

The main function of the detection head is to process the input feature map to detect targets in the image. It integrates and analyzes features of different levels and scales through techniques such as multi-scale feature fusion, thus adapting to the detection of targets of different sizes. In order to further reduce the number of model parameters without decreasing the detection accuracy, this paper introduces a local convolutional neural network PConv, so that the two convolutional branch inputs of the detection head share the same PConv and the output feature maps of the 1x1 Conv, which achieves the reduction of computational redundancy, and at the same time facilitates the effective sharing and utilization of features among different branches to optimize the performance and efficiency of the detection head.

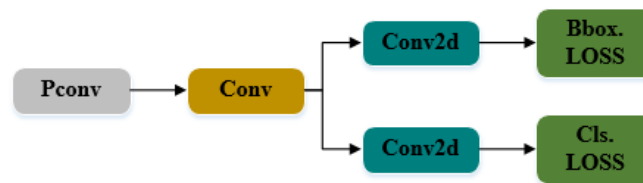
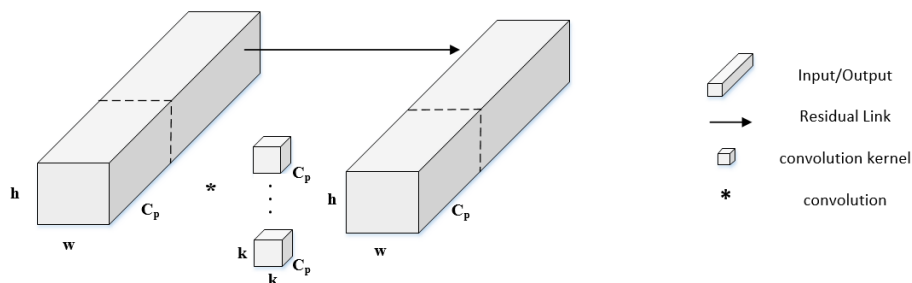


Fig. 5 -Detect structure diagram

PConv optimizes performance by reducing redundant memory accesses. When dealing with continuous or regular memory accesses, PConv can selectively apply a convolutional kernel that performs spatial feature extraction for only a portion of the input channel and leaves the remaining channels unchanged. This strategy significantly reduces memory accesses.



$$FLOPS = h \times w \times k_2 \times C_p^2$$

Fig. 6 - PConv structure diagram

The number of floating point operations FLOPs for PConv convolution is:

(6)

where h represents the height of the feature map; w represents the width; k represents the size of the convolution kernel; and C_p represents the number of channels. the number of floating-point operations for PConv convolution is only 1/16 of that for regular Conv convolution.

RESULTS

Parameter Configuration and Evaluation Indicators

For the hardware environment configuration, the CPU is Intel(R)Core(TM)i9-9900KFCPU@3.60GHz, the GPU model is Quadro P5000, the host memory is 125GB, and the video memory is 16GB. For the software environment setup, the 64-bit Linux operating system is used, and the programming language used is Python3.8. CUDA11.0 was used to complete the computational acceleration, and the deep learning framework Pytorch1.8.1 was used for training. The specific training parameters in the experiment are set as follows, the

resolution of the input image (image_size) is 640×640 pixels, the initial learning rate (learning_rate) is set at 0.01, the batch size (batch_size) is set at 16, and the number of iterations (epochs) is 100.

In this paper, the accuracy rate (Precision, P), meanAveragePrecision (mAP), the size of model parameters (Parameters), and the amount of model computation (GFLOPS) are used to evaluate the performance of the model.

The formula for each metric is as follows:

$$P = \frac{TP}{TP+FP} \quad (7)$$

$$R = \frac{TP}{TP+FN} \quad (8)$$

$$AP = \int_0^1 P(R) dr \quad (9)$$

$$mAP = \frac{1}{n} \sum_{i=1}^n AP_i; mAP = \frac{1}{n} \sum_{i=1}^n AP_i \quad (10)$$

In the formula TP is the number of spores correctly detected; FP is the number of background impurities mistakenly detected as spores; FN is the number of spores identified as impurities; R is the value of the recall rate under the current accuracy rate, which refers to the proportion of spores detected by the model to all actual spores; the area under the P - R curve plotted using the precision rate P and the recall rate R represents the average precision AP value of the category. The higher the AP value, the better the detection performance of the algorithm is considered to be.

Backbone network comparison test

In order to evaluate the advantages of replacing the backbone network with EfficientViT, three lightweight models, namely, Efficientnet, GhostNet, and MobileNetV3, are selected as the backbone network of the original model of YOLOv8s for the comparison experiments. The specific experimental results are shown in Table 1.

Table 1

Comparative experiments of different backbone networks

Model	Parameters /MB	GFLOPS	P/%	mAP50/%
YOLOv8s	11.1	28.4	97.1	97.6
YOLOv8s+Efficientnet	10	22.0	97.4	97.1
YOLOv8s+GhostNet	6.3	16.3	95.3	96
YOLOv8s+MobileNetV3	6.6	16.3	96	96.9
YOLOv8s+EfficientViT	8.4	20.4	96.9	97.1

From the analysis in Table 1, replacing the backbone network with GhostNet based on the YOLOv8s model reduces the computation and number of parameters by 4.8 and 12.1, respectively, but the $mAP50$ decreases by 1.8 percentage points. mobileNetV3 decreases in the number of parameters and computation, but decreases in P , $mAP50$, and R . EfficientNet network model has a 9.9% decrease in the number of parameters, a 22.5% decrease in computation, a 0.3 percentage point increase in precision, and decreases in both $mAP50$ and R . EfficientViT has faster detection with a very small decrease in precision, where the number of parameters decreases by about 24.3%, the computation decreases by about 28.2%.

Comparative experiments with different convolutions of the neck

From the analysis in Table 1, the experimental results show that C2f_FADC proposed in this paper performs better in terms of accuracy improvement. The number of C2f_Star_CAA parameters and the computation amount are increased compared to the base model. The introduction of C2f_RFACnv detection accuracy decreases and the computational amount rises, which is not in line with the experimental purpose of

this paper. In summary, the introduction of C2f_FADC not only realizes the lightweighting of the network, but also improves the detection accuracy of the model on the image target to achieve the purpose of the model optimization, which proves the validity of the improved method in this paper.

Table 2

Comparison experiment on different convolutions in neck				
Model	Parameters / MB	GFLOPS	P / %	mAP50/%
YOLOv8s+EfficientViT	8.4	20.4	96.9	97.1
YOLOv8s+EfficientViT+C2f_Star_CAA	9.4	22.6	96.6	97.2
YOLOv8s+EfficientViT+C2f_Faster_EMA	7	17.8	96.6	97.4
YOLOv8s+EfficientViT+C2f_RFACConv	8.4	20.6	96.2	96.9
YOLOv8s+EfficientViT+C2f_FADC	8.4	18.7	96.9	97.5

Optimized Detection Head Comparison Experiment

To further achieve lightweighting, PConv, RepConv, EMSConvP, and RepConv are used to improve the detection head, respectively. As can be seen from Table 3, the number of EMSConvP parameters decreases by 19.8%, and the computational volume decreases by 46.1%. the number of RepConv parameters rises, and the computational volume decreases by a small amount. The method using PConv to optimize the detection head compares the base model accuracy and mAP changes are not obvious, but the number of parameters decreases by 37.8% and the computation amount decreases by 58.5%, which is the best lightweight effect in the comparison experiments. The lightweight detection head in this paper has great advantages in model deployment ability and small target detection ability, and has high accuracy and fast calculation speed in grain powdery mildew spore detection.

Table 3

Improved detection head comparison experiment				
Model	Parameters / MB	GFLOPS	P / %	mAP50 / %
YOLOv8s	11.1	28.4	97.1	97.6
YOLOv8s+EfficientViT+C2f_FADC	8.4	18.7	96.9	97.5
YOLOv8s+EfficientViT+C2f_FADC+PConv	6.9	11.8	96.8	97.6
YOLOv8s+EfficientViT+C2f_FADC+EMSConvP	8.9	15.3	96.8	97.4
YOLOv8s+EfficientViT+C2f_FADC+RepConv	12.6	22.1	96.8	97.5

Comparison of different models

To further validate the advantages of the EFP-YOLOv8s model proposed in this paper for the detection of millet downy mildew spores, the improved model was compared with YOLO v5s, YOLO v6s, YOLO v8s, YOLOv9s, YOLOv10s, and the final results of the comparison are shown in Table 4. According to the experimental results, it can be seen that the accuracy rate and mAP50 value of each model are relatively close to each other, among which the base model YOLOv8s has the highest accuracy rate of 97.1%, but the number of parameters and the amount of calculation are too large. The improved model EFP-YOLOv8s decreased the accuracy rate by 0.3 percentage points compared with the original model, and the mAP remained unchanged, but the number of parameters decreased by 37.8% and the computational volume decreased by 58.5%. Compared with YOLOv5s, YOLOv6s, YOLOv9s, and YOLOv10s, EFP-YOLOv8s has the best combined accuracy and mAP, and the computational and parametric quantities are lower than the other models.

Table 4

Comparative experiments with different models				
Model	Parameters /MB	GFLOPS	P/%	mAP50/%
YOLOv5s	9.1	23.8	96.8	97.5
YOLOv6s	16.3	44	96.9	97.7
YOLOv8s	11.1	28.4	97.1	97.6

YOLOv9s	7.1	26.7	96.7	97.5
YOLOv10s	7.2	21.4	96.7	96.5
EFP-YOLOv8s	6.9	11.8	96.8	97.6

SPORE DETECTION AND TRAINING SYSTEM FOR FOXTAIL MILLET DOWNY MILDEW

In this study, a *Sporisorium scitamineum* spore detection system based on PyQt5 was developed, which comprises two main functional interfaces: the spore detection and counting interface, and the model training interface.

Spore detection and counting interface

This interface is designed to provide a convenient tool for efficient detection and precise counting of *Sporisorium scitamineum* spores. Users can select and upload spore image files stored locally through the interface to the system. The system utilizes deep learning algorithms to automatically recognize and label the spores in the images, displaying the labeled images in real-time on the interface. Upon completion of the detection, the interface automatically tallies the number of spores and presents the results clearly in the result display area. Additionally, users have the option to save the labeled images locally.

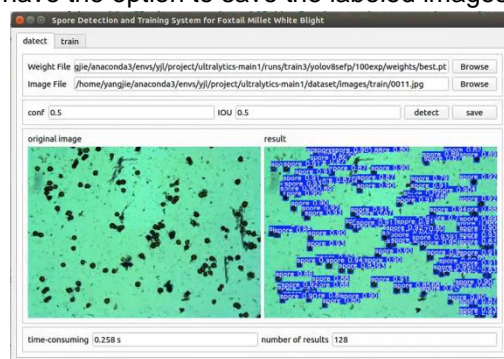


Fig. 7 - Spore detection and counting interface

Model training interface

This interface allows users to import customized spore image datasets for training or optimizing deep learning models. Users can flexibly set training parameters through this interface, such as learning rate, batch size, and number of training epochs, to enhance model performance. During the training process, the interface displays real-time training logs, aiding users in intuitively monitoring the model's training status. Additionally, the interface supports model saving and loading functionalities, enabling users to save trained models locally for direct use in subsequent detection tasks.

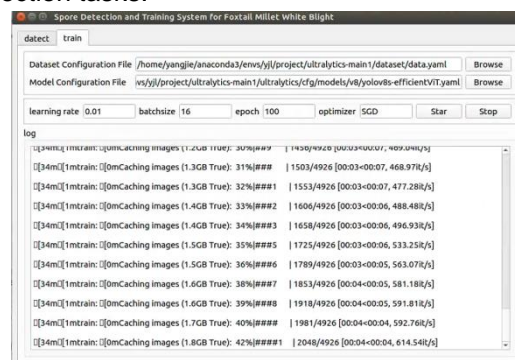


Fig. 8 - Model training interface

CONCLUSIONS

In this paper, a lightweight YOLOv8s model is proposed to replace the backbone network, introduce C2f_FADC and improve the detection head. Through comparative experiments, it is verified that the improved model maintains high precision detection accuracy compared to YOLOv8s while the number of parameters decreases by 37.8% and the computational amount decreases by 58.5%. The improved mAP50 is 97.6% and P reaches 96.8%, which gives certain advantages to the EFP-YOLOv8s model proposed in this paper compared with mainstream target detection networks.

This research result not only provides a new technical means for the prevention and control of cereal leucosis, but also provides ideas and methods that can be used for the detection of disease spores in other crops.

In the future, more advanced lightweight technology and optimization strategies will continue to be explored to further improve the detection performance and practicality of the model, and to promote the continuous development and application of intelligent technology in agriculture.

ACKNOWLEDGEMENT

This research was supported by the Teaching Reform Innovation Project of Higher Education Institutions in Shanxi Province (J20220247) and the Youth Scientific Research Project of the Basic Research Program of Shanxi Province (NO.202303021222039).

REFERENCES

- [1] Aguayo, J., Fourrier-Jeandel, C., Husson, C., Ios, R., (2018). Assessment of Passive Traps Combined with High-Throughput Sequencing to Study Airborne Fungal Communities. *Applied and environmental microbiology*, Vol. 84, United States.
- [2] Chen, L., Gu, L., Zheng, D., & Fu, Y., (2024). Frequency-Adaptive Dilated Convolution for Semantic Segmentation. *Proceedings of the IEEE/CVF Conference on Computer Vision and Pattern Recognition*, pp. 3414-3425, United States.
- [3] Cheng, F., Wang, H., Han, Y., Han, Y., (2020). Research Advances on Downy Mildew of Foxtail Millet in China (我国谷子白发病研究进展). *Journal of Shanxi Agricultural Sciences*, Vol. 48, pp. 263-267, Shanxi / China.
- [4] Cheng, T., Zhang, D., Gu, C., Zhou, X., Qiao, H., Guo, W., & Yang, X., (2024). YOLO-CG-HS: A lightweight spore detection method for wheat airborne fungal pathogens. *Computers and Electronics in Agriculture*, Vol. 227, Netherlands.
- [5] Nezhad, S. F., Rahnama, K., Javidan, M. S., & Vakilian, A. K., (2024). Application of microscopic image processing and artificial intelligence detecting and classifying the spores of three novel species of Trichoderma. *Discover Applied Sciences*, Vol. 6, Switzerland.
- [6] Redmon, J., Divvala, K. S., Girshick, B. R., & Farhadi, A., (2015). You Only Look Once: Unified, Real-Time Object Detection. *CoRR*, United States.
- [7] Lei, Y., Yao, Z., He, D., (2018). Automatic detection and counting of urediniospores of *Puccinia striiformis* f. sp. *tritici* using spore traps and image processing. *Scientific Reports*, Vol. 8, pp. 1-11, England.
- [8] Li, A., Yue, S., Ma, H., (2006). Correlativity of three counting methods of fungal spore (真菌孢子三种计数方法相关性的探讨). *Journal of Microbiology*, pp. 107-110, Liaoning/China.
- [9] Li, M., Ding, Z., Zhao, J., Chen, S., Li, W., Yang, X., (2023). Detection method for cucumber downy mildew sporangia in a solar greenhouse based on improved YOLOv5s (基于改进 YOLOv5s 的日光温室黄瓜霜霉病孢子囊检测计数方法). *Journal of Chinese Agricultural Mechanization*, Vol. 44, pp. 63-70, Jiangsu/China.
- [10] Li, X., Zhao, L., Shao, B., Wang, D., (2020). A new method for spore identification in microscope images based on morphology and Yolov3 algorithm (一种新的基于形态学与 Yolov3 算法的显微镜图像中孢子识别方法). *Intelligent Computer and Applications*, Vol. 10, pp. 30-34+38, Heilongjiang/China.
- [11] Liang, X., Wang, B., (2023) Wheat Powdery Mildew Spore Images Segmentation Based on U-Net. *Proceedings of the 2nd International Conference on Artificial Intelligence and Computer Science (AICS 2020)*, pp.529-534, Faculty of Information Technology, Beijing University of Technology.
- [12] Liu, J., Zhang, M., Ren, S., Wang, Y., Ma, J., Quan, J... & Li, Z., (2023). Genetic Diversity of *Pyricularia oryzae* Based on SRAP Molecular Markers (利用 SRAP 分子标记分析谷瘟病菌遗传多样性). *Acta Agriculturae Boreali-Sinica*, Vol. 38, pp. 179-187, Hebei/China.
- [13] Liu, X., Peng, H., Zheng, N., Yang, Y., Hu, H., Yuan, Y., (2023). EfficientVit: Memory efficient vision transformer with cascaded group attention. *Proceedings of the IEEE/CVF Conference on Computer Vision and Pattern Recognition*, pp. 14420-14430, United States.
- [14] Luo, B., Li, J., Zhou, Y., Pan, D., Huang, S., (2024). Lightweight Rice Blast Spores Detection Method Based on Improved YOLOv8 (基于改进 YOLOv8 的轻量化稻瘟病孢子检测方法). *Transactions of the Chinese Society for Agricultural Machinery*, Vol. 55, pp. 32-38, Beijing/China.

- [15] Ma, N., Li, Z., Kong, Q., (2024). Wheat grains automatic counting based on lightweight YOLOv8. *INMATEH - Agricultural Engineering*, Vol. 73, pp. 592-602, Romania.
- [16] Meng, F., Yan, C., Yang, Y., Xing, R., Zhu, D., Zhang, A., & Liao, J., (2024). A lightweight improved YOLOv5s model-based rice blast detection method and mobile deployment. *INMATEH - Agricultural Engineering*, Vol. 74, pp. 771-786, Romania.
- [17] Qiao, C., Han, M., Gao, W., Li, K., Zhu, X., Zhang, L., (2023). Quantitative Detection of Cucumber Downy Mildew Spores at Multi-scale Based on Faster-NAM-YOLO (基于 Faster-NAM-YOLO 的黄瓜霜霉病菌孢子检测). *Transactions of the Chinese Society for Agricultural Machinery*, Vol. 54, pp. 288-299, Beijing/China.
- [18] Ren, A., Chen, S., Liu, K., Zhao, J., Yang, X., Li, M., (2022). Counting of cucumber downy mildew sporangia based on flow cytometry (基于流式细胞术的黄瓜霜霉病菌孢子囊计数研究). *Acta Phytopathologica Sinica*, Vol. 52, pp. 841-848, Beijing/China.
- [19] Wang, A., Shang, Z., Zhang, M., Wang, G., Hu, X., Xu, F... & Zhou, Y., (2024). Dynamic monitoring of aerial conidia and disease estimation models for wheat powdery mildew in fields using pathogen spore traps coupled with real-time PCR technique (基于病菌孢子捕捉和 real-time PCR 技术的田间空气中小麦白粉病菌孢子动态监测及病情估计模型研究). *Plant Protection*, Vol. 50, pp. 49-56+72, Beijing/China.
- [20] Wang, Y., Li, H., Tian, G., Liu, X., Liu, H., & Wang, Z., (2024). Problems and Improvement Measures of Foxtail Millet Production in Shanxi Province (山西谷子生产问题及改进措施). *China Seed Industry*, pp. 46-48+55, Beijing/China.
- [21] Yan, Y., Xu, Y., He, Z., Gao, J., (2019). Isolation and Identification of the Mycoparasite on Oospores from Sclerospora graminicola (谷子白发病菌卵孢子重寄生真菌的分离与鉴定). *Journal of Shanxi Agricultural Sciences*, Vol. 47, pp. 891-894+907, Shanxi/China.
- [22] Yue, J., Wang, P., Han, Y., Gao, J., (2021). Isolation and Identification of Heavy Parasitic Fungi from the Oospores of Sclerospora graminicola (Sacc.) Schroet (谷子白发病卵孢子重寄生真菌的分离鉴定). *Journal of Shanxi Agricultural Sciences*, Vol. 49, pp. 82-86+104, Shanxi/China.
- [23] Zhang, D., Gao, Y., Cheng, T., Hu, G., Yang, X., Qiao, H... & Gu, C., (2024). Detection of wheat scab spores in dense scene based on YOLOv8-FECA (基于 YOLOv8-FECA 的密集场景下小麦赤霉病孢子目标检测). *Transactions of the Chinese Society of Agricultural Engineering*, Vol. 40, pp. 127-136, Beijing/China.
- [24] Zhou, J., Chen, P., Lei, Y., Huang, L., Zhao, J., & Liang, D., (2023). Automatic detection of urediniospores method for wheat stripe rust pathogen based on spin UNet++ network (基于自旋式 UNet++网络的小麦条锈病菌夏孢子自动检测方法). *Journal of Nanjing Agricultural University*, Vol. 46, pp. 1004-1010, Jiangsu/China.

WORKING MECHANISM ANALYSIS AND EXPERIMENTAL STUDY OF GRASS CRUSHER

牧草粉碎机工作机理分析与试验研究

Tao CHEN¹, Shu-juan YI¹*, Song WANG¹, Wen-sheng SUN¹)

¹College of Engineering, Heilongjiang Bayi Agricultural University, Daqing/P.R.China

Tel: +86-459-13836961877; E-mail: yishujuan_2005@126.com

Corresponding author: Shu-juan Yi

DOI: <https://doi.org/10.35633/inmateh-75-28>

Keywords: Hammer; Crusher; Mechanism analysis; Experimental study

ABSTRACT

In order to clarify the working mechanism of forage crusher, the combined cutting and crushing forage crusher was taken as the research object, the mechanical analysis was carried out on the cutting and crushing process of alfalfa stalk, the dynamic model was established, and the relationship between the shear force and the relevant parameters of the cutting mechanism was defined. It was found that the cutting Angle, the installation Angle and the wedge Angle had important effects on the cutting effect and power consumption. The force of alfalfa stem in the grinding chamber is mainly related to the speed of the grinding shaft, the gap between the hammer and the rolling plate. With the output speed of motor, feeding amount, screen diameter and water content as test factors, productivity, silking rate, power consumption and average crushing length as evaluation indicators, the single factor test was carried out to determine the influence of each test factor on the evaluation indicators. The research results can provide reference for the optimization design of grass crusher.

摘要

为明确牧草粉碎机工作机理，以切割粉碎组合式牧草粉碎机为研究对象，对苜蓿茎秆切割和粉碎过程进行了力学分析，建立了动力学模型，明确了剪切力与切割机构相关参数的关系，得到动刀遇角、安装后角和楔角对切割效果和功耗具有重要影响；苜蓿茎秆在粉碎室内受力主要与粉碎轴转速、锤片和揉搓板间隙有关。以电机输出转速、喂入量、筛孔直径、含水率为试验因素，生产率、丝化率、功耗、平均粉碎长度为评价指标，进行了单因素试验，确定了各试验因素对评价指标的影响规律，研究结果可为牧草粉碎机的优化设计提供参考。

INTRODUCTION

Animal husbandry is an important part of agriculture and plays an important role in the national economy of our country (Zhang et al., 2021; Jiang et al., 2019). The production and supply of forage is the basis of the development of animal husbandry, which affects the scale and speed of animal husbandry development. China's grass planting area is close to 15 million mu, accounting for 8.2% of the arable land. The total annual output of forage is 90 billion kg, and the total output value is 12 billion US dollars (Chen et al., 2023; Wu et al., 2022; Wu et al., 2018).

Grass processing can be divided into cutting processing, crushing processing and kneading processing according to the crushing form (Wang et al., 2021; Zhao et al., 2019; Xu et al., 2020). The corresponding models are cutting mill, hammer mill and so on. The cutting mill breaks the grass by cutting, but the broken grass after processing is mostly round stem, and there are hard joints, which will lead to indigestion and palatability of livestock, which is not conducive to digestion and absorption of livestock (Li, 2023; Wang et al., 2024; Liu et al., 2019).

The hammer mill first pulverizes the grass to a certain extent through the impact of the hammer, and then throws the grass at a faster speed to the kneading board and the sieve plate in the crushing room, and is further crushed by the collision of the kneading board and the rubbing of the sieve plate, which has high crushing efficiency and wide adaptability (Ma et al., 2016; Wang et al., 2017; Liu et al., 2011).

¹Tao Chen, Ph.D.; Shu-juan Yi, Prof. Ph.D.; Song Wang, Ph.D.; Wen-sheng Sun, Ph.D.;

Because the forage with high water content has strong toughness, the force required when it is broken by blows and other effects is greater, and the whole forage is easy to wind the rotor when it is crushed, resulting in blockage (Fan et al., 2021; Wang et al., 2021; Jia et al., 2014). Therefore, the existing grinder still has some problems, such as low efficiency, poor crushing quality, and not being suitable for forage with large water content.

To solve the above problems, our team designed a cutting and crushing combined grass crusher, which preprocessed the grass before crushing, and cut it into small segments of a certain length by cutting. However, its working mechanism is not clear. This study conducted a theoretical analysis of the cutting and crushing process, explored the crushing mechanism of the crusher on grass, identified the factors influencing crushing quality, and performed an experimental study using these factors to analyze their impact on the crushing effect.

MATERIALS AND METHODS

Structure and working principle

Cutting and crushing cooperative grass kneading machine is mainly composed of feeding conveyor belt, conveyor chain plate, feeding mechanism, screening mechanism, kneading mechanism, cutting mechanism and other parts. The structure is shown in Fig. 1.

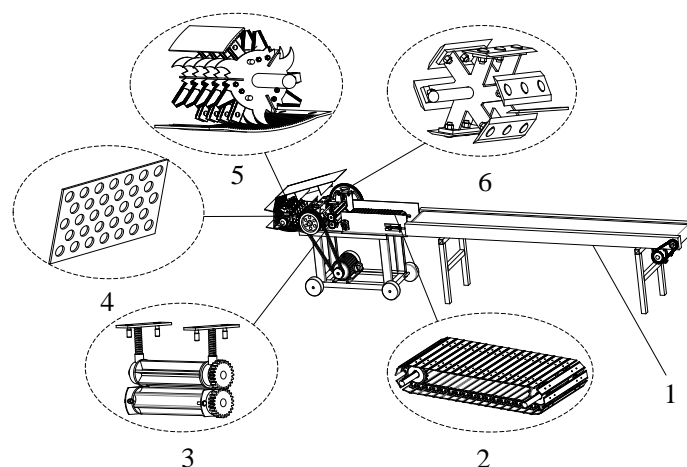


Fig.1 – Structural diagram of cutting and crushing cooperative forage kneader

1. Feeding conveyor belt; 2. Conveyor chain plate; 3. Feeding mechanism;
4. Screening mechanism; 5. Kneading mechanism; 6. Cutting mechanism

The kneading operation is mainly divided into the following stages: feeding stage, the whole grass is transported to the conveyor chain plate through the feeding conveyor belt, and the grass enters the cutting chamber by rotation of the feed roller. In the cutting stage, the grass is cut into a certain length under the shearing action of the rotating motion of the grass knife and the fixed knife, and the cut grass is pushed to the kneading chamber under the rotation of the grass knife. In the kneading stage, the grass section is broken into filaments under the synergistic action of the hammer and serrated knife, the kneading and tearing between the hammer and serrated knife and the kneading tooth plate, the impact and friction between the sieve plate, etc.

In the screening and sending stage, the broken grass that meets the kneading length is thrown to the outside of the kneading machine through the screen plate under the combined action of the air flow generated by the rotation of the kneading rotor and the centrifugal force. The broken grass that is larger than the kneading length needs is kneaded in the kneading chamber for the next time, and further broken through the same crushing method as the last kneading until the length meets the kneading demand.

Mechanical analysis of cutting process

The cutting process is realized by the combination of cutting knife and fixed knife, and the shear force generated on the stem and the thrust generated by the feed roller act on the stem together (Wu et al., 2022; Jiang et al., 2019; Wu et al., 2018). In order to facilitate the force analysis of the whole system, the following assumptions are made: the shape of alfalfa stalk is cylinder, the whole organization is uniform and continuous; the shear of the stem is balanced at every moment; the force analysis is based on a single shear. Consider alfalfa layer as a whole; the compression and deformation of the feeding roller on alfalfa were ignored.

The stress of alfalfa stem and tool in the cutting process was analyzed, as shown in Fig. 2.

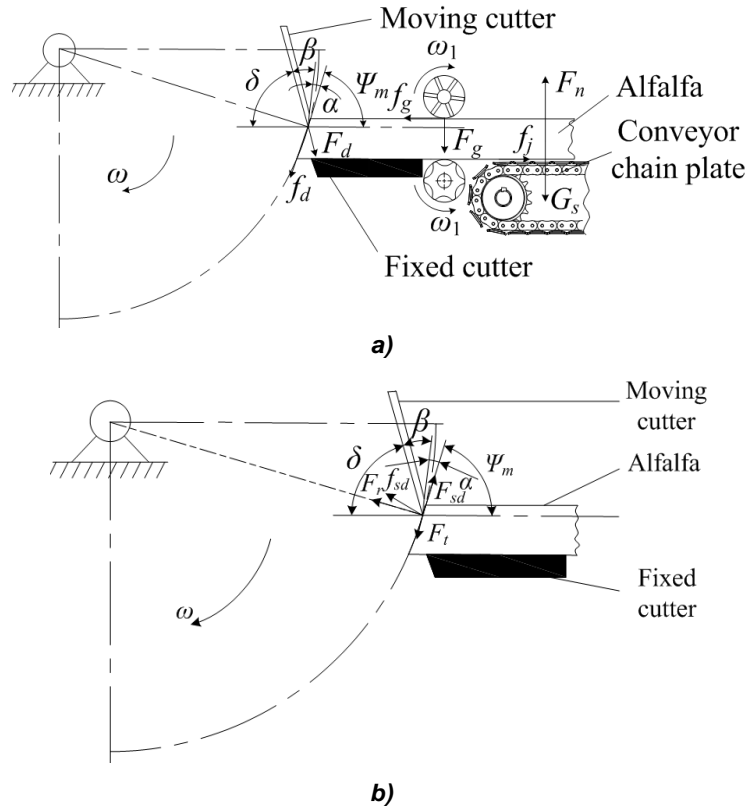


Fig. 2 – Force analysis of the chopping mechanism

a) Stress analysis of alfalfa stalk cutting process; b) Force analysis of the knife

In the process of cutting, the main forces on the stalk are: (1) the positive pressure F_d of the knife facing the stalk, the direction is perpendicular to the knife face down; (2) the friction force f_d of the knife facing the stalk, the direction is consistent with the direction of the knife movement; (3) the supporting force F_n of the feed tank and the fixed tool on the stalk, the direction is always perpendicular to the bottom surface of the feed tank and the fixed tool; (4) the direction of the pressure F_g and friction force f_g of the feeding roller on the stalk are vertically downward and consistent with the direction of the stalk feed, respectively; (5) the direction of gravity G_s on the stalk and friction f_j on the bottom of the feed tank facing the stalk are vertical downward and opposite to the direction of feed, respectively; (6) the tool is subjected to the force F_t and F_r provided by the cutting shaft, and the directions are respectively the tangential direction and the center direction of the tool moving path; (7) the tool is subjected to the friction F_{sd} of the stalk, and the direction is opposite to the direction of the knife movement; (8) the tool is subject to the supporting force f_{sd} provided by the stalk, and the direction is perpendicular to the tool face.

According to the horizontal force balance of alfalfa stalk, it can be obtained:

$$F_d \sin \delta = f_g + f_j + f_d \cos \delta \tag{1}$$

From the vertical force balance of the stem, it can be obtained:

$$F_d \cos \delta + G_s + F_g + f_d \sin \delta = F_n \tag{2}$$

With the cutting edge of the knife as the fulcrum, the moment of the stalk is balanced:

$$F_g L_1 + G_s L_3 + f_g (f - H_m) = F_n L_2 + f_j H_m \tag{3}$$

The horizontal component of F_d under the positive pressure of the blade facing the stalk is:

$$F_{d2} = f_g + f_j + f_d \cos \delta \tag{4}$$

The vertical component of F_d under the positive pressure of the blade facing the stalk is:

$$F_{d1} = F_n - G_s - f_d \sin \delta \tag{5}$$

The encounter angle of knife is:

$$\psi_m = 90^\circ - \sigma \tag{6}$$

The angle between the back cutter face and the horizontal direction is:

$$\delta = 180^\circ - \alpha - \beta - \psi_m \tag{7}$$

The shear force of cutting action on the stalk causing the stalk to break is:

$$\tau_s = \frac{F_n - G_s - F_g - f_d \sin(180^\circ - \alpha - \beta - \psi_m)}{S} \tag{8}$$

where: S is cross-sectional area of alfalfa stalk, m^2 ; α is installation rear angle of the tool, ($^\circ$); β is wedge angle of the knife, ($^\circ$); ψ_m is knife angle, ($^\circ$); H_m is vertical distance from any point on the knife path to the bottom of the feed tank, mm; L_1 is horizontal distance between the feed roll and the tool, mm; L_2 is the horizontal distance between the center of gravity of the alfalfa stem and the tool, mm.

Mechanical analysis of crushing process

Smashing process

The force analysis of alfalfa stem in the attack and breaking process is shown in Fig.3.

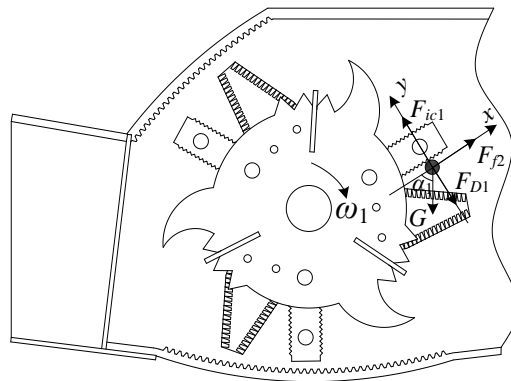


Fig. 3 – Force analysis of alfalfa stem during crushing

Alfalfa stems are mainly subjected to the combined action of four forces, namely gravity G , the striking force F_{D1} of the hammer on the alfalfa stalk, the friction force F_{f1} of the hammer on the alfalfa stalk and the Coriolis inertia force F_{ic1} of the alfalfa stalk. The center of the stalk is regarded as the center of mass, and all external forces act on the center of mass.

According to D'Alembert's principle, the balance equation of the impact force on alfalfa stalk can be obtained as follows:

$$\begin{cases} \sum F_x = 0, & F_{f1} - G \cos \alpha_1 = 0 \\ \sum F_y = 0, & F_{D1} - G \sin \alpha_1 - F_{ic1} = 0 \end{cases} \tag{9}$$

where:

$$\begin{cases} F_{f1} = \mu m_1 g \sin \alpha_1 \\ F_{ic1} = -m_1 a_c = -2m\omega_e v_{r1} \end{cases} \tag{10}$$

By combining equations (9) and (10), the following is obtained:

$$F_{D1} = 2m_1 \omega_e v_{r1} - m_1 g \sin \alpha_1 \tag{11}$$

where: F_{D1} is striking force of alfalfa stalk by hammer, N; G is alfalfa stem gravity, N; m_1 is alfalfa stalk mass, kg; F_{f2} is the friction force of alfalfa stem against the hammer, N; F_{ic1} is Coriolis inertia force, N; μ_1 is friction coefficient between alfalfa stem and sieve plate; ω_1 is angular velocity of the rotor, rad/s; v_{r1} is linear velocity at the end of the hammer, m/s; α_1 is the angle between alfalfa stem gravity and the X-axis, ($^\circ$).

According to Formula (11), when the internal structure of the kneading machine remains unchanged, the impact force F_{D1} of the alfalfa stem under the hammer is mainly affected by the angular velocity ω of the kneading rotor and the linear velocity v_{r1} of the hammer end. The greater the angular velocity of the kneading rotor ω_1 and the linear velocity of the end of the hammer piece v_{r1} , the greater the impact force on the alfalfa stalk, and the change of the two sizes depends on the change of the speed of the crushing shaft.

Impact crushing

The force analysis of alfalfa stems during impact crushing is shown in Fig. 4.

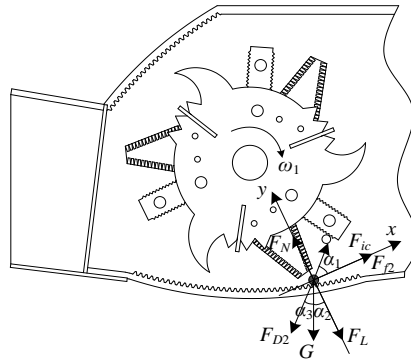


Fig.4 – Force analysis of alfalfa stem impact crushing process

According to D'Alembert's principle, the equilibrium equation of the impact force on alfalfa stalk can be obtained:

$$\begin{cases} \sum F_x = 0, & F_{D2} \sin(\alpha_2 + \alpha_3) - F_{ic2} \cos \alpha_4 - F_{f2} = 0 \\ \sum F_y = 0, & F_L + G \cos \alpha_2 + F_{D2} \cos(\alpha_2 + \alpha_3) - F_N - F_{ic2} \sin \alpha_4 = 0 \end{cases} \quad (12)$$

where:

$$\begin{cases} F_{ic2} = -2m_2\omega_{e1}v_{r1} \\ F_{f2} = \mu_2 \frac{m_2g}{\cos \alpha_2} \\ F_L = m_2 \frac{n^2}{r_1} \end{cases} \quad (13)$$

By combining equations (12) and (13) the following is obtained:

$$F_{D2} = \frac{(2\omega_{e1}v_{r1} \sin \alpha_4 - n^2) \cos \alpha_2 - r_1g(1 - \cos \alpha_2)}{\cos(\alpha_2 + \alpha_3)} \quad (14)$$

where:

F_{D2} is impact force on alfalfa stem, N; F_{f1} is friction force on alfalfa stem kneading plate, N; F_{ic2} is Coriolis inertia force, N; F_L is centrifugal force on alfalfa stem, N; n is spindle speed, r/min; r_1 is distance between the center of mass of alfalfa stem and the center of rotor, m; μ_2 is friction coefficient between alfalfa stem and kneading plate; α_2 is the angle between alfalfa stem and impact force, (°); α_3 is the angle between the alfalfa stem and the impact force (°); α_4 is angle between Coriolis inertia force and X-axis, (°); g is acceleration of gravity, m/s².

Rubbing crushing

The force analysis of alfalfa stems during rubbing and crushing is shown in Fig. 5.

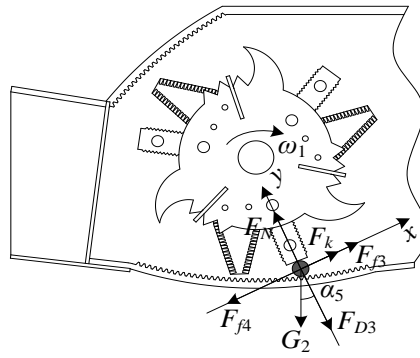


Fig. 5 – Stress analysis of alfalfa stem kneading and crushing process

According to the law of conservation of momentum:

$$Mv = Mv_1 + m_3v_2 \tag{15}$$

$$\begin{cases} v = \frac{\pi n_1 D}{60} \\ v_1 = \frac{\pi n_2 D}{60} \end{cases} \tag{16}$$

By combining equations (15) and (16), it is obtained:

$$v_2 = \frac{\pi MD(n_1 - n_2)}{60m_3} \tag{17}$$

where: M is weight of hammer, kg; v is linear velocity at the end of the hammer, m/s; v_1 is velocity after the hammer hits the alfalfa stalk, m/s; v_2 is alfalfa stalk speed after being hit, m/s; n_1 is rotational speed before the hammer hits the alfalfa stalk, r/min; n_2 is rotational speed after the hammer hits the alfalfa stalk, r/min.

According to D'Alembert's principle, the balance equation of kneading-force on alfalfa stems can be obtained as follows:

$$\begin{cases} \sum F_x = 0, & G \sin \alpha_5 + F_{f4} - F_k - F_{f3} = 0 \\ \sum F_y = 0, & F_{D3} + G \cos \alpha_5 - F_{ic3} = 0 \end{cases} \tag{18}$$

where:

$$\begin{cases} F_{f3} = \mu F_{D3} \\ F_{f4} = \mu m \frac{v^2}{D + \delta} = \mu \frac{m^2 \pi^2 D^2 (n_1 - n_2)^2}{3600(D + \delta)} \\ F_{ic3} = 2m\omega v_r \\ F_k = \frac{1}{2} C \rho S v_{r2} \end{cases} \tag{19}$$

By combining equations (18) and (19), it is obtained:

$$F_{D3} = \mu_2 \frac{M^2 \pi^2 D^2 (n_1 - n_2)^2}{3600m(D + \delta)} \tag{20}$$

where: F_{D3} is kneading force on alfalfa stem, N; F_{f3} is friction of the end of the hammer against alfalfa stalk, N; F_{f4} is friction of kneading board on alfalfa stalk, N; F_k is air resistance, N; F_{ic3} is Coriolis inertia force, N; δ is hammer plate clearance, m; C is air resistance coefficient; ρ is air density, kg/m³; S is alfalfa stem windward area, m²; v_{r2} is relative velocity of material to air, m/s

According to formula (20), the extrusion rubbing force on alfalfa stems is mainly affected by the rotational speed n_1 before the hammer hits the alfalfa stalk, the rotational speed n_2 after the hammer hits the alfalfa stalk, rotor diameter D , and the gap δ between the hammer and the kneading board.

It can be seen from the above analysis that the main factors affecting the kneading effect of alfalfa stem in the kneading room are the rotating speed of the kneading shaft and the gap between the hammer and the kneading board.

RESULTS AND DISCUSSIONS

The performance test of the designed crusher was carried out. Alfalfa was processed and collected in Duerbert County, Daqing City, Heilongjiang Province. The collected alfalfa was cut in full field at the bud stage, and there was no obvious mechanical damage. The average density of alfalfa was 996 kg/m^3 after many measurements and calculations. The experiment was conducted in the crop harvesting Laboratory of Heilongjiang Bayi Agricultural University, and the test site was shown in Fig. 6.



Fig. 6 –Test Site

1. Power consumption test device; 2. Crusher; 3. Feeding conveyor belt

According to the theoretical analysis results and in order to check the grinding effect of the machine on high water content alfalfa, productivity, silking rate, average crushing length and power consumption were selected as performance indexes, and a single factor test was carried out with motor rotation speed, screen diameter, feeding amount and water content as test factors. Alfalfa with required moisture content was obtained by natural drying. The evaluation indexes were calculated as follows:

Productivity

Feed the weighed alfalfa, record the feeding test time, weigh the output sample quality, and calculate the productivity:

$$y_1 = \frac{m}{t} \times 3600 \quad (21)$$

where: m is quality of alfalfa for testing; t is test time, s.

The test time t is short. In order to meet the test accuracy, the working time of this test is obtained from the data analysis of the torque-time curve of DYN-200 torque sensor.

Silk rates

Samples were collected at the outlet, at the same time interval for 3 times, each time no less than 200 g. All samples were mixed and weighed. Qualified alfalfa silk was screened and weighed, and its silk rate was calculated as:

$$y_2 = \frac{m_1}{m_0} \times 100\% \quad (22)$$

where: m_1 is quality of alfalfa silk in the sample, g; m_0 is alfalfa sample quality, g.

Average crushing length

By weighing 500 g samples of broken materials for measurement and classification: below 30 mm, 30~40 mm, 40~50 mm, 50~60 mm, 60~70 mm, 70~80 mm and above 80 mm, the average length of broken stems and the corresponding mass m_i between each grade are measured, weighed and measured 3 times, and the average value is taken. The average crushing length is calculated as:

$$\ln \bar{L} = \frac{\sum_{i=1}^n m_i \ln \bar{L}_i}{\sum_{i=1}^n m_i} \quad (23)$$

Power consumption

The power consumption is determined by the DYN-200 torque power sensor installed on the motor spindle. After each group of tests, the instantaneous torque, power and required time measured by the sensor are derived through the torque measurement system, and the instantaneous power of the effective working period is calculated to obtain the kneading power consumption. The calculation formula is as follows:

$$W_z = \int P(t) dt_z \quad (24)$$

where: W_z is kneading power consumption, kJ; $P(t)$ is instantaneous power, kW; t_z is kneading time, s.

Test results and analysis

According to the pre-test and the adjustable range of the machine, the rotation speed of the motor ranges from 150 to 600 r/min, the sieve diameter from 12 to 22 mm, and the feeding amount from 0.5 to 2.5 kg/s. According to the different water content requirements of the post-harvest processing of alfalfa, the water content of the single factor test ranges from 10% to 80%.

(1) Effect of motor rotation speed on performance evaluation index

The influence of motor rotation speed on performance evaluation index is shown in Fig. 7 (Sieve diameter is 16 mm, feeding amount is 1.5 kg/s, moisture content is 80%).

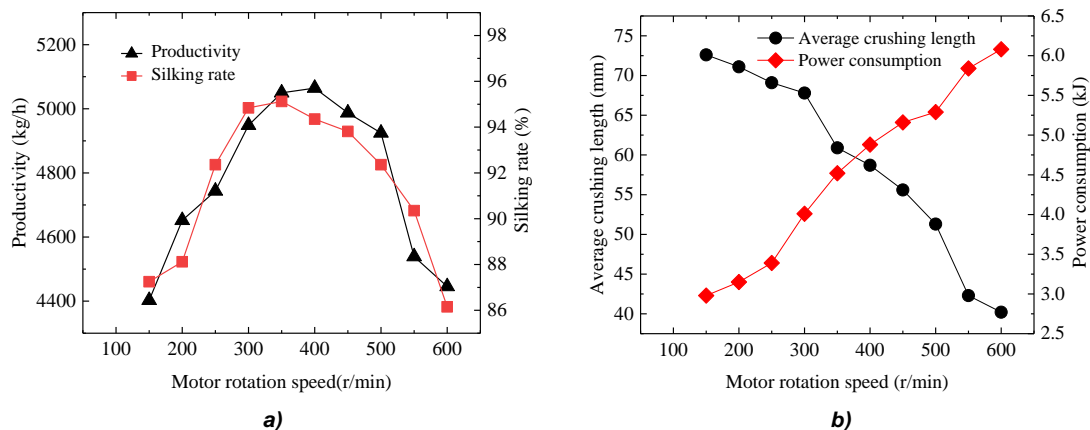


Fig. 7 – Influence of motor rotation speed on performance evaluation index

It can be seen from the figure, that with the increase of the motor rotation speed, the productivity and silking rate both increase first and then decrease, the average crushing length decreases, and the power consumption increases. The reason is that with the increase of the motor rotation speed, the chopping and crushing rotor speed will be accelerated, and the interaction frequency between alfalfa and the crushing parts can be increased per unit time, so the productivity and silk rate increase. The increase of interaction frequency also reduces the length of the stalk crushing and increases the power consumption. When the motor rotation speed is too large, the broken grass will rotate along with the crushing rotor, forming a circulation, which cannot be thrown out of the body through the screen in time through the centrifugal force, and will cause excessive crushing, and the silked alfalfa is too fine, so the productivity and silking rate show a decreasing trend. The motor rotation speed is in the range of 250~500 r/min, the productivity and the silk rate are at a high level, when the motor rotation speed exceeds 500 r/min, the productivity and the silk rate drop sharply, the average crushing length decreases sharply, and the power consumption rises sharply, so the motor rotation speed should not exceed 500 r/min. Considering the performance evaluation index comprehensively, the grinding performance is better in the range of 250~500 r/min.

(2) Effect of sieve diameter on performance evaluation index

The influence of sieve diameter on performance evaluation index is shown in Fig. 8 (motor rotation speed is 350 r/min, feeding amount is 1.5 kg/s, water content is 80%).

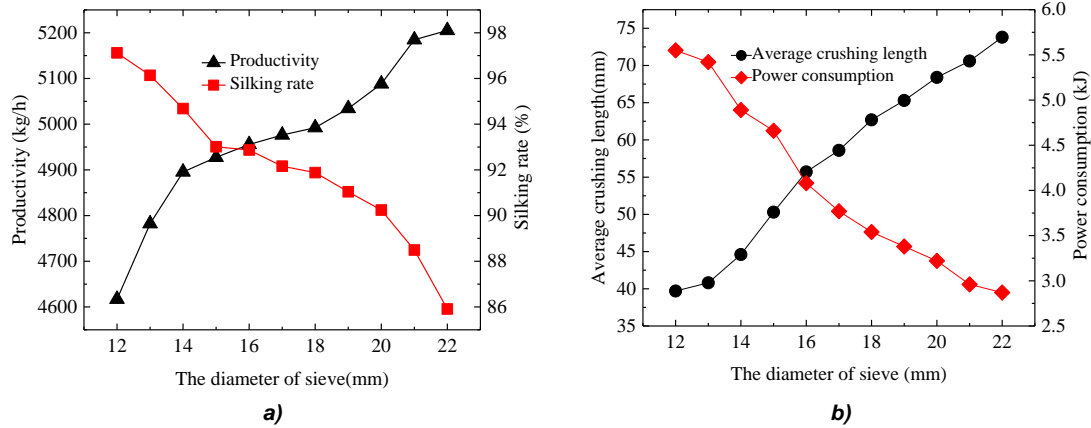


Fig. 8 – Influence of sieve diameter on performance evaluation index

It can be seen from the figure that with the increase of the screen diameter, the productivity and average crushing length show an increasing trend, while the silk rate and power consumption show a decreasing trend. The reason is that the larger the diameter of the sieve hole, the lower the limit of broken grass passing through the sieve hole, the longer the length of the stalk that can pass through the sieve, the more alfalfa can be fed in the same time, the higher the discharge efficiency, and the higher the number of crushing per unit time, so the productivity increases and the power consumption decreases.

However, some alfalfa whose length is longer than the requirement of crushing will pass through the sieve, resulting in a decrease in the silking rate and an increase in the average crushing length. When the sieve diameter is less than 14 mm, the broken grass through the sieve is more limited, so the productivity is low, the silk rate is high, the average crushing length is short, and the power consumption is large. When the screen diameter exceeds 20 mm, although the productivity is on the rise, the power consumption is low, but the silk rate drops sharply, and the average crushing length exceeds the crushing requirements. Therefore, the screen diameter should not exceed 20 mm. Considering the performance evaluation index comprehensively, the screen diameter ranges from 14 to 20 mm, the productivity and silk rate are relatively stable, and at a high level, the average crushing length is close to the crushing requirements, the power consumption is at a moderate level, and the crushing performance is better.

(3) Effect of feeding volume on performance evaluation indexes

The influence of feeding amount on performance evaluation index is shown in Fig. 9 (motor rotation speed is 350 r/min, screen diameter is 16 mm, water content is 80%).

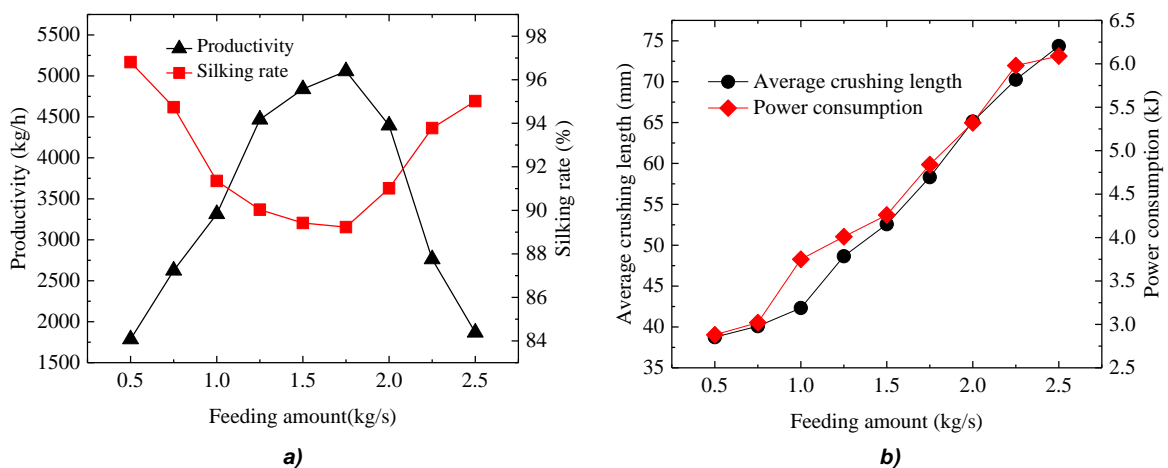


Fig. 9 – Influence of feeding amount on performance evaluation index

As can be seen from the figure, with the increase of feeding amount, the production first increased and then decreased, the silk first decreased and then increased, and the average crushing length and power consumption showed an increasing trend.

When the feeding amount is 0.5~1.75 kg/s, the feeding mechanism has self-adjustment ability, alfalfa can enter the machine smoothly, and the alfalfa in the cutting bin and crushing bin increases, so the productivity increases, the power consumption increases, the interaction frequency between a single alfalfa and the crushing parts decreases, so the silking rate decreases, and the average crushing length increases. When the feeding amount is greater than 1.75 kg/s, the self-adjustment ability of the feeding mechanism is weakened, part of alfalfa begins to accumulate at the feeding outlet, and the alfalfa in the cutting and crushing bin decreases, so the productivity decreases, and the interaction frequency between a single alfalfa and the crushing parts increases, so the silking rate increases. When the feeding amount exceeds 2 kg/s, the productivity begins to drop sharply. Considering the performance evaluation index comprehensively, the crushing performance is better in the range of 1~2 kg/s.

(4) Effect of moisture content on performance evaluation index

The influence of water content on performance evaluation index is shown in Fig. 10 (motor rotation speed is 350 r/min, screen diameter is 16 mm, feeding amount is 1.5 kg/s).

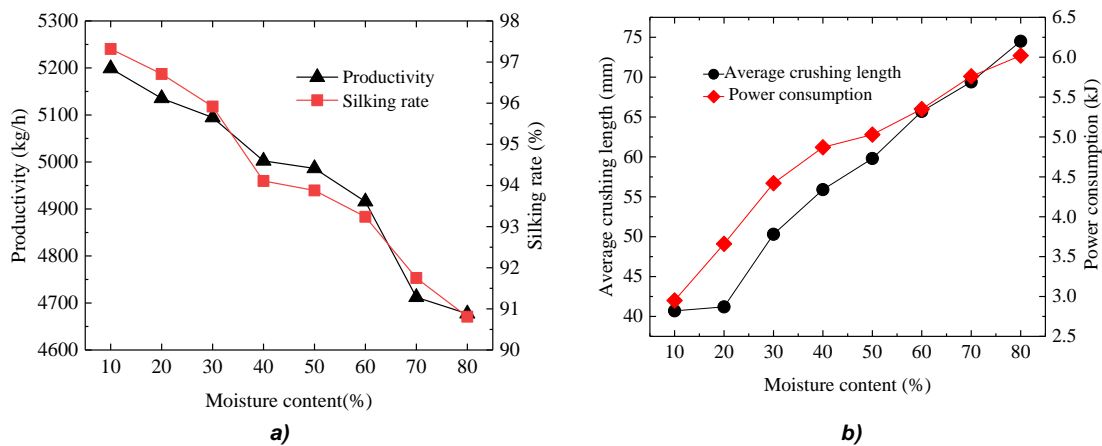


Fig. 10 – Influence of moisture content on performance evaluation index

As can be seen from the figure, with the increase of water content, both productivity and silking rate showed a downward trend. The average pulverizing length and power consumption are on the rise. The reason is that when the moisture content of alfalfa stems is low, it is brittle and easy to break, so the productivity is high and the power consumption is low. With the increase of moisture content, the toughness of alfalfa is greater, the adhesion between the internal components of the stems is enhanced, and the crushing force required is greater, and it requires multiple strikes, rubbing and impact to meet the requirements of crushing length, so the productivity and silking rate are gradually reduced. The average crushing length is long and the power consumption is large. However, the silking rate is always greater than 90%, which reflects that the machine can crush alfalfa with different moisture content.

CONCLUSIONS

(1) Dynamic analysis was carried out on the cutting process of alfalfa stalk, a dynamic model was established, and the relationship between shear force and relevant parameters of the cutting mechanism was defined. It was found that the cutting Angle, installation Angle and wedge Angle had important effects on the cutting effect and power consumption. The dynamic analysis of the grinding process of alfalfa stalk in the grinding chamber shows that the force of alfalfa stalk in the grinding chamber is mainly related to the rotation speed of the grinding shaft, the gap between the hammer and the kneading board.

(2) Through the single factor test, the influence law of motor output speed, sieve diameter, feeding amount and moisture content on productivity, silking rate, average length of silk kneading and power consumption are respectively explored. The test results show that with the increase of the output speed of the motor, the productivity and the spinning rate increase first and then decrease, the average length of the spinning wire decreases gradually, and the power consumption increases gradually. With the increase of the screen diameter, the productivity and the average length of the yarn increase gradually, and the silk rate and power consumption decrease gradually. With the increase of feeding amount, the production increases first and then decreases, the silk decreases first and then increases, and the average kneading length and power consumption increase gradually. With the increase of water content, the productivity and silking rate gradually decrease, and the average length and power consumption of the kneading wire gradually increase.

ACKNOWLEDGEMENT

This work was supported by Heilongjiang Bayi Agricultural University Graduate Innovative Research Project (YJSCX2023-Z02).

REFERENCES

- [1] Bao, L., Li, Z., & Dongxing, Z. (2011). Force and motion state of hammer in hammer mill during no-load operation (锤片式粉碎机空载运行中锤片的受力及运动状态) [J]. *Transactions of the Chinese Society of Agricultural Engineering*, Vol.27, Issue 7, pp. 123-128. Henan/China.
- [2] Defu, W., Mo, W., & Liqiao, L. (2017). Mechanism Analysis and Parameter Optimization of Hammer Mill for Corn Stalk (锤片式粉碎机粉碎玉米秸秆机理分析与参数优化) [J]. *Transactions of the Chinese Society for Agricultural Machinery*, Vol.48, Issue 11, pp. 165-171. Heilongjiang / China.
- [3] Fudi, Z., Siming, W., & Wenming, H. (2019). Analysis of mechanization utilization and development path of corn straw (玉米秸秆机械化利用情况与发展途径分析) [J]. *Agricultural Machinery Use and Maintenance*, Vol.51, Issue 7, pp. 48. Heilongjiang/China.
- [4] Guoqiang, F., Zhongyu, W., Baoxing, W., Jinxing, W., Heyin, D., & Jian, H. (2021). Design and Experiment of Rotary Feed Tube Hammer Grinder (旋筒供料锤式饲草粉碎机设计与试验) [J]. *Transactions of the Chinese Society for Agricultural Machinery*, Vol.52, Issue 12, pp.43-53. Shandong/China.
- [5] Hongcheng, L. (2023). Study on Influence Mechanism and Optimization of the Hammer Mill Grinding Performance (锤片式粉碎机工作性能影响机理与优化研究). Hubei/China.
- [6] Hongyang, X. (2020). Mechanization treatment of corn stalk and its development characteristics (玉米秸秆的机械化处理方式与发展特点) [J]. *Agricultural Machinery Use and Maintenance*, Issue 4, pp.101. Heilongjiang/China.
- [7] Kun, W., & Yuepeng, S. (2022). Research Progress Analysis of Crop Stalk Cutting Theory and Method (农作物茎秆切割理论与方法研究进展分析) [J]. *Transactions of the Chinese Society for Agricultural Machinery*, Vol.53, Issue 6, pp. 1-20. Shandong / China.
- [8] Qian, M., Fei, L., & Manquan, Z. (2016). Working mechanism and structure optimization of hammer of rubbing machine (揉碎机揉碎机理分析及锤片结构优化)[J]. *Transactions of the Chinese Society of Agricultural Engineering*, Vol.32, Issue S2, pp. 7-15. Inner Mongolia/China.
- [9] Shan., W. (2021). *Design and Experiment of orchard branch crusher (果园树枝粉碎机的设计与试验)*. Northwest A&F University. Heilongjiang/China.
- [10] Songhua, J. (2014). Research on Virtual Rotor Design of Compound Straw shredder (复合式秸秆粉碎机转子虚拟设计研究) [J]. *Chinese Journal of Agricultural Mechanization*, Vol. 35, Issue 2, pp. 164-166+182. Jiangsu/China.
- [11] Tao, C., Shujuan, Y., Yifei, L., Guixiang, T., Shanmin, Q., & Rui, L. (2023). Establishment of Discrete Element Model and Parameter Calibration of Alfalfa Stem in Budding Stage (苜蓿现蕾期茎秆离散元模型建立与参数标定) [J]. *Transactions of the Chinese Society for Agricultural Machinery*, Vol. 54, Issue 5, pp. 91-100. Heilongjiang/China.
- [12] Tao, W., & Xizhen., C. (2018). Dynamic Analysis of Rotary Cutting System of Straw Crusher (秸秆粉碎机旋切系统的动力学分析) [J]. *Southern Agricultural Machinery*, Vol. 49, Issue 7, pp. 29-30+32. Jiangsu/China.
- [13] Tiejun, W., Tieliang, W., Hongguang, C., Yuanjuan, G., Subo, T., & Ruili, W. (2021). Design and Experiment of Adjustable Feeding Straw Bale-breaking and Rubbing Filament Machine (喂入调节式秸秆破包揉丝机设计与试验)[J]. *Transactions of the Chinese Society for Agricultural Machinery*, Vol.52, Issue 6, pp. 148-158. Liaoning / China.
- [14] Xiaoqing, Z., Zifan, W., Muyou, C., Haihua, B., & Na, T. (2021). Analysis of current situation of crop straw yield and comprehensive utilization in China (中国农作物秸秆产量及综合利用现状分析). *Journal of China Agricultural University*, Vol.26, Issue 9, pp. 30-41. Inner Mongolia/China.
- [15] Xudong, L. (2019). Portable forest residues crusher of theoretical analysis and experimental research (移动式林间剩余物粉碎机理论分析与试验研究). Northeast Forestry University. Heilongjiang/China.
- [16] Yajun, J., Yitao, L., & Qingxi, L. (2019). Design and Experiment on Cylinder-type Chopping Device of Harvester for Fodder Rapeseed in Winter and Spring (冬春鲜喂饲用油菜收获机滚刀式切碎装置设计与试验) [J]. *Transactions of the Chinese Society for Agricultural Machinery*, Vol.50(2), pp.102-111. Hubei/China.

- [17] Zheng, W., Zhanhua, S., Ping, L., Yinfu, Y., Yang, L., Longlong, R., & Yuepeng, S. (2024). Development and Experiment of Crop Feeding Angle Parameter Model in Chopping Roll of Hay Cutter (铡草机切碎辊作物喂入角参数模型建立与试验) [J]. Transactions of the Chinese Society for Agricultural Machinery, Vol. 55, Issue 7, pp. 200-211. Shandong/China.

FARMLAND OBSTACLE RECOGNITION BASED ON IMPROVED FASTER R-CNN

/ 基于改进 FASTER R-CNN 的农田障碍物识别

Xiangyu BAI^{1,2}, Kai ZHANG², Ranbing YANG^{1,3}, Zhiguo PAN¹, Huan ZHANG¹, Jian ZHANG^{*1,3},
Xidong JING¹, Shiteng GUO¹, Sen DUAN¹

¹) College of Electrical and Mechanical Engineering, Qingdao Agricultural University, Qingdao/ China

²) National Key Laboratory of Intelligent Agricultural Power Equipment, Henan/ China

³) College of Mechanical and Electrical Engineering, Hainan University, Haikou/ China

Tel: +8618561879013; E-mail: zhangjian_qau@163.com

Corresponding author: Jian Zhang

DOI: <https://doi.org/10.35633/inmateh-75-29>

Keywords: Obstacle detection, Multi-scale detection, ResNet50, ROI Align

ABSTRACT

For the accurate detection of obstacles in complex farmland environments, ResNet50 is adopted as the backbone feature extraction network, feature pyramid network (FPN) is utilized to enhance the multi-scale feature fusion capability, and the region of interest alignment (ROI Align) strategy is introduced to improve the candidate box localization precision. The experimental results show that the precision, recall, and mean accuracy (mAP) of the improved model are 91.6%, 89.7%, and 93.8%, respectively, which are improved by 2.7, 2.3, and 3.1 percentage points compared with the original base network, and provide a technical reference for navigation and obstacle avoidance of unmanned agricultural machinery.

摘要

针对复杂农田环境中障碍物的准确检测, 采用 ResNet50 作为骨干特征提取网络, 利用特征金字塔网络 (FPN) 提升多尺度特征融合能力, 并引入感兴趣区域对齐 (ROI Align) 策略提高候选框定位精度。实验结果显示, 改进模型的精度、召回率和平均精度 (mAP) 分别为 91.6%、89.7% 和 93.8%, 相比于原基础网络, 提升了 2.7、2.3 和 3.1 个百分点, 为无人农业机械的导航避障提供了技术参考。

INTRODUCTION

Driven by the rapid development of agricultural machinery intelligence and automation, unmanned agricultural machinery has made significant progress. In order to ensure that these unmanned agricultural machines can operate safely and efficiently during operation and effectively avoid collision with obstacles such as utility poles, trees, buildings, etc., it is necessary to carry out accurate and fast identification of obstacles in the field. In farmland obstacle detection, deep learning detection algorithms have higher detection accuracy, stronger generalization ability and better adaptability than other detection algorithms, and can more accurately identify complex and changing obstacles in farmland, while maintaining stable detection performance under different light, climate and crop growth conditions.

Deep learning-based detection algorithms are divided into two categories: single-stage object detection algorithms (such as SSD and YOLO series) and two-stage object detection algorithms (such as Sparse R-CNN and Faster R-CNN). The latter, although more complex in process and relatively slower in speed, demonstrates higher accuracy. Research on obstacle detection in the field of machine vision has made significant progress.

He et al., (2022), improved the recognition accuracy by enhancing Mask R-CNN, employing Swin-Le Transformer for feature extraction and ME-PAPN for feature fusion. They integrated a multi-scale enhancement method to boost the detection capability of small targets, achieving a mean Average Precision (mAP) of 91.3% and an average detection time of 4.2 frames per second (FPS).

Rahman et al., (2022) implemented a transfer learning model based on the convolutional neural network MobileNetV2, which can be used on low-configured devices while maintaining a balance between detection speed and processing efficiency. The accuracy of obstacle detection reached 97.00%.

Xue et al., (2022) improved the Faster R-CNN object detection algorithm to identify obstacles in agricultural fields, effectively enhancing the speed of obstacle recognition while reducing false positives and missed detections. This improvement meets the real-time detection requirements for low-speed operations of tractors.

Du *et al.*, (2024), proposed an optimized obstacle detection method based on an improved YOLOv8. By removing the P5 layer and introducing DCNv2 to optimize the bottleneck, the model enhances the detection capability for small and irregular obstacles. The improved model achieved a 3.4% increase in mAP50, a 34.5% reduction in GFLOPs, a 77.4% decrease in parameters, and a 73% reduction in model size.

Han *et al.*, (2024) investigated an autonomous driving obstacle avoidance method based on YOLOv5 monocular vision. This approach combines a deep reinforcement learning path planning algorithm to dynamically generate safe driving paths. By introducing a monocular vision obstacle avoidance aggregation network, the MMA obstacle avoidance method is developed, achieving an accuracy that fluctuates between 78.76% and 88.26%.

Zhao *et al.*, (2024), proposed a real-time high-precision railway obstacle detection model based on a lightweight CNN and an improved Transformer (RH-Net). This model includes a Lightweight Feature Extraction Module (LEM) to minimize computational load, an Improved Transformation Module (IFM) that enhances the capability of extracting global contextual information, and an Enhanced Multi-Scale Feature Fusion Module (EFM) that optimizes the detection of obstacles of varying sizes.

Yang *et al.*, (2025) proposed the YOLO-Region model to solve the problem of oversensitive obstacle detection in unmanned electric locomotives in underground coal mines, the model backbone adopts the InceptionNeXt block and the NSPP module, extends the FPN+PAN architecture with the Impro-TSCODE header and introduces the repulsion loss to enhance the detection of occluded targets.

Researchers have made significant progress in the field of obstacle recognition, confirming the feasibility of target detection technology for obstacle detection. However, in today's era of unmanned farming, there is relatively little research on using drone equipment to capture images of agricultural fields for obstacle recognition. To address this gap, this paper selects the second-stage detection algorithm Faster R-CNN, which offers higher detection accuracy, for detecting obstacles in farmland. Given the complexity of agricultural environments, directly applying Faster R-CNN to unstructured agricultural scenes for obstacle detection may lead to decreased model accuracy, particularly under complex and variable weather conditions, where the effectiveness of obstacle detection can be significantly weakened. Therefore, this paper conducts targeted optimization based on the Faster R-CNN model, aiming to address the current issues of insufficient accuracy and poor robustness in deep learning models for obstacle detection in agricultural fields.

MATERIALS AND METHODS

Acquisition of images of farmland obstacles

This study adopts a combined ground and airborne acquisition of the dataset, i.e., combining ground-based cell phone acquisition with airborne UAV acquisition, as shown in Figure 1. Ground-based acquisition can obtain detailed and accurate information about obstacles, including the shape, size, and material of obstacles, which is suitable for complex terrain and dense obstacle areas, and can capture details that may be missed by aerial acquisition. Aerial acquisition can quickly cover a large area and improve acquisition efficiency, and it has unique advantages for high-altitude obstacles or areas that are difficult to reach on the ground. The combination of the two can result in a more complete and accurate obstacle dataset, which is useful for subsequent application and analysis.

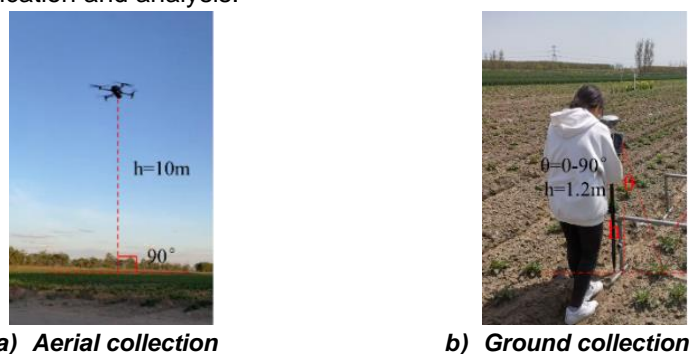


Fig. 1 – Data collection method

The dataset was collected from March to June 2023 through aerial photography and mobile imaging in Hebei and Shandong provinces, under varying lighting conditions during the morning, afternoon, and evening. The drone used was a DJI Mavic 3, which captured vertical aerial shots of the plots at an altitude of 10 meters and a flight speed of 7 m/s.

The drone automatically collected images at predetermined intervals along a designated flight path. Both longitudinal and lateral overlap rates were set at 70%. Each flight generated approximately 200 images. Simultaneously, mobile phones and cameras were employed to capture multi-angle views of the field obstacles, as illustrated in Figure 2. The types of obstacles were diverse, specifically including buildings, high-voltage power towers, trees, telegraph poles, water wells, personnel, and agricultural machinery, categorized into seven main groups.

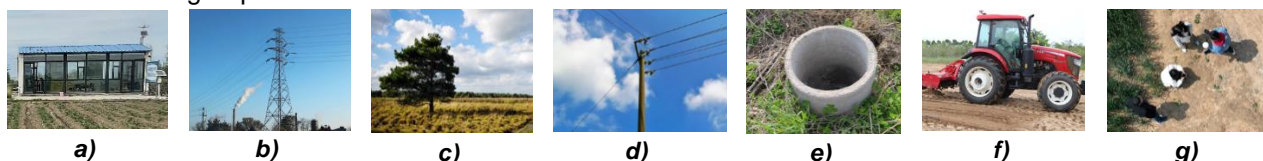


Fig. 2 – Example of dataset image

a) building; b) high-voltage power towers; c) tree; d) telegraph pole; e) water well; f) agricultural machinery; g) person

Data expansion

To improve the robustness and generalization performance of the dataset, an image enhancement strategy is implemented. As shown in Fig. 3, data enhancement includes random brightness adjustment to simulate different lighting environments, Gaussian noise addition, horizontal flip, and vertical flip to simulate diverse shooting angles. These methods not only increase the number of images, but also effectively reduce the overfitting problem during model training, and finally an expanded dataset containing 7707 obstacle images is obtained.

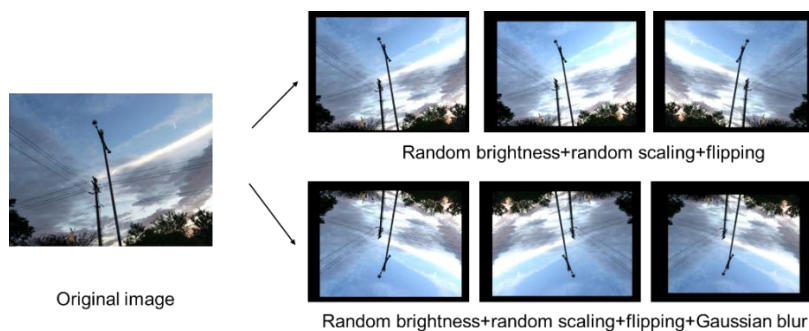


Fig. 3 – Data enrichment

Image annotation and dataset construction

Using the Labellmg image annotation tool, obstacles were annotated on the processed images. The dataset comprises 7,707 images with a total of 11,578 annotation tasks for obstacles. The training data was organized into the standard PASCAL VOC 2007 format. From the entire dataset, 6,823 images were randomly selected as the training set for model learning and parameter tuning, while 884 images were designated as the validation set to monitor the performance of the model in real-time during training, allowing for timely adjustments to the training strategy. A separate test set was established for the final evaluation of the model's recognition accuracy and generalization capability. This division ensures both the thorough utilization of the dataset and the objectivity and accuracy of the evaluation results.

Faster R-CNN model

Faster R-CNN, as a two-stage detection algorithm, has a more complex process and relatively slower running speed compared to one-stage algorithms such as the YOLO series and SSD (Single Shot MultiBox Detector), but it demonstrates a higher level of detection accuracy. Faster R-CNN consists of a feature extraction layer, a Region Proposal Network (RPN), and an RoI Pooling layer (Region of Interest Pooling). The detection process of Faster R-CNN is summarized as follows: First, the training images are resized to a uniform dimension and input into the network, where feature maps are generated via the feature extraction layer; second, the RPN network generates a series of anchor boxes on the feature map based on predefined Intersection over Union (IoU) thresholds; then, the anchor boxes produced by the RPN are combined with the feature map and sent to the RoI Pooling layer to obtain fixed-size (7x7) feature representations of the anchor boxes; finally, these feature representations are input into the classification and regression layers for bounding box regression predictions and object detection classification, resulting in accurate detection outcomes. The entire detection process is illustrated in Figure 4.

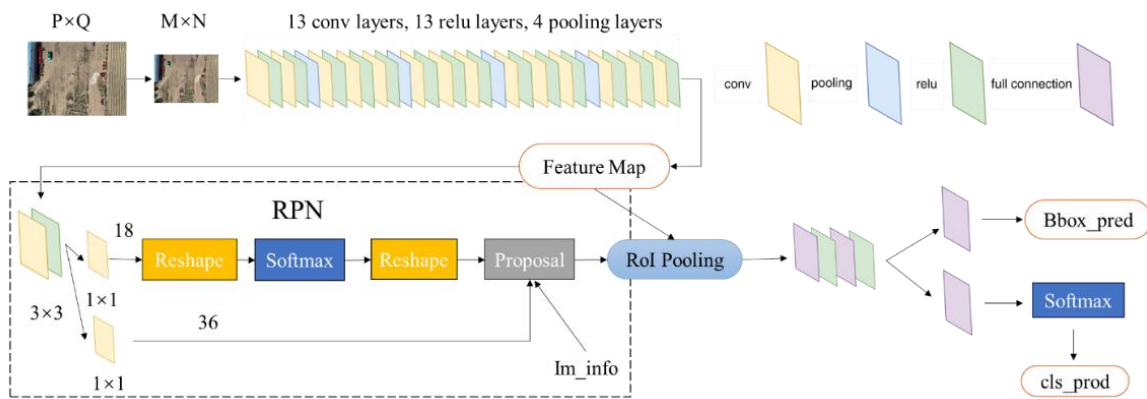


Fig. 4 – Faster R-CNN Detection Flowchart

Improved Faster R-CNN model

To enhance the obstacle detection capability of the Faster R-CNN model in complex agricultural environments, this study implemented the following key improvements: first, the original VGG16 feature extraction backbone used in Faster R-CNN was replaced with the more efficient ResNet50. Second, by introducing a Feature Pyramid Network (FPN), the fusion of high-level and low-level features was achieved, thereby enriching the information content of the feature maps. Finally, the ROI Align strategy was adopted to replace the original ROI Pooling layer, which improved the model's accuracy in candidate box localization. The architecture of the improved Faster R-CNN model is illustrated in Figure 5.

ResNet50 backbone network

To address the hardware resource limitations in agricultural environments, and to significantly enhance the feature extraction capability of the obstacle detection model while optimizing the deployment of the network model in practical production operations, this study adopted ResNet50 as a replacement for the original VGG16, serving as the new backbone network. The ResNet50 network effectively resolves the degradation problem in deep neural networks by introducing residual units. Its architecture, as shown in Figure 5, consists of five core components: conv1, conv2_x, conv3_x, conv4_x, and conv5_x. The conv1 component includes only one convolutional layer and one max pooling layer, which can be considered as the preprocessing stage of the network. The remaining four components (from conv2_x to conv5_x) are structurally similar, consisting of repeated stacks of residual structures such as ReB1 and ReB2.

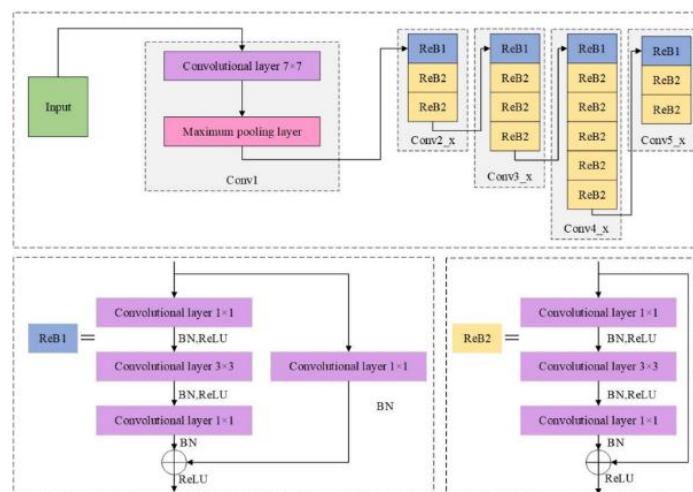


Fig. 5 – ResNet50 structure diagram

Feature pyramid network

Aiming at the problem of complex background and diverse scales of obstacle images jointly captured by UAVs and cell phones, this paper adopts the feature pyramid network FPN to improve the Faster R-CNN model. As shown in Figure 6, FPN fuses the rich semantic information of the high-level feature map with the rich spatial details of the shallow feature map to generate a richer and more accurate feature representation.

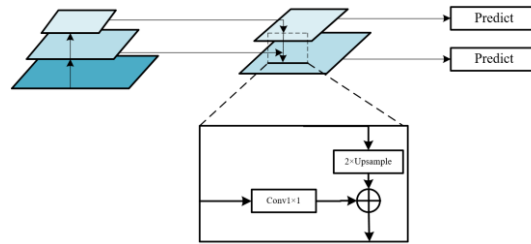


Fig. 6 – Feature pyramid network architecture

The structure combining the FPN network with the ResNet50 network is illustrated in Figure 7. First, the ResNet50 network performs bottom-up convolution operations to extract feature maps of varying scales and different channel numbers, denoted as {C2, C3, C4, C5}. Subsequently, these feature maps are fused through a top-down pathway. During the fusion process, the feature maps are first adjusted using 1x1 convolution operations, resulting in a new set of feature maps {M1, M2, M3, M4}. Then, adjacent feature maps M are fused using upsampling, followed by processing with 3x3 convolution operations, ultimately generating the feature map P. To control computational complexity, this paper only selects four feature maps of different scales for output during the feature extraction phase, namely {P2, P3, P4, P5}. Finally, all feature maps generated by the FPN are input into the Region Proposal Network (RPN), thus achieving effective fusion of high-level and low-level features, further enhancing the model's feature extraction capability.

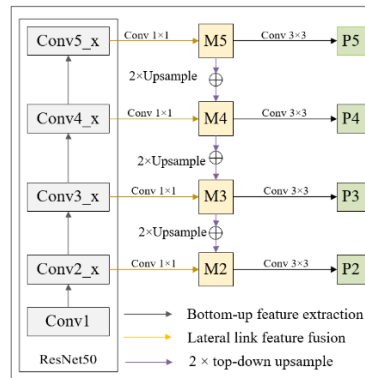


Fig. 7 – Feature pyramid network architecture

ROI Align

The operational process of ROI Align is illustrated in Figure 8. First, the predicted candidate regions are accurately mapped to the corresponding feature levels and thoroughly traversed. At this stage, each candidate region is meticulously divided into $k \times k$ uniform small grids, while ensuring the precision of boundary coordinates, effectively avoiding potential errors introduced during the quantization process. Subsequently, within each small grid, the specific values of four key sampling points are accurately calculated using bilinear interpolation. These values are then used as the basis for performing the maximum pooling operation, which determines the comprehensive feature representation of each grid. By integrating the ROI Align strategy, the model is not only able to flexibly adapt to uniform input size requirements when processing candidate regions but also achieve more precise and detailed localization, significantly enhancing the model's object recognition capability.

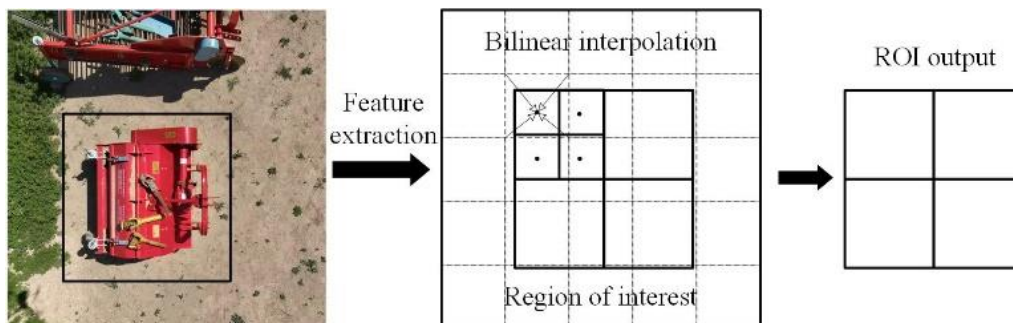


Fig. 8 – ROI Align Principle

The Faster R-CNN model architecture after the above improvements is shown in Fig. 9.

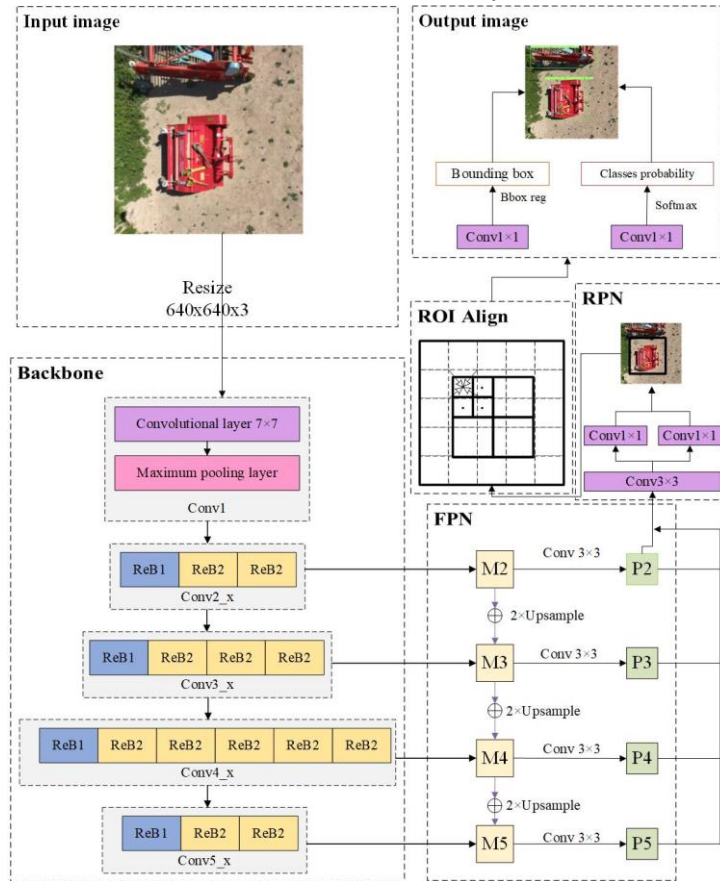


Fig. 9 – Improved Faster R-CNN model architecture

RESULTS AND ANALYSIS

Test environment

The experiments were conducted in the Anaconda environment under the Windows 10 operating system, utilizing the PyTorch framework for development and programming within PyCharm. The hardware setup included an AMD Ryzen 7 4800H processor, a Radeon Graphics 2.0GHz graphics card, an Nvidia GeForce RTX 2060 GPU, and 6GB of RAM.

Test evaluation indicators

In order to test the correctness of the algorithm, Precision (P), Recall (R), mean average precision (mAP) are used as model evaluation metrics. In terms of model complexity, the key factors considered are the parameter and FPS. Parameter indicates the computational memory resources consumed by the model, and FPS indicates the number of images that the model can process per second. The calculation formula is as follows.

$$P = \frac{T_p}{T_p + F_p} \tag{1}$$

$$R = \frac{T_p}{T_p + F_n} \tag{2}$$

$$AP = \int_0^1 P(R) dR \tag{3}$$

$$mAP = \frac{\sum_{i=1}^N AP_i}{N} \tag{4}$$

$$Parameters = r^2 \times a \times v + v \tag{5}$$

In the formula, *TP* denotes the number of samples where the positive class is predicted to be positive, *FP* denotes the number of samples where the negative class is predicted to be positive, *FN* denotes the number of samples where the positive class is predicted to be negative, *a* is the input size, *r* is the size of the convolution kernel, and *v* is the output size.

Comparative test analysis of different algorithms

To validate the effectiveness of the improved Faster R-CNN model used in this study for detecting obstacles in agricultural fields, comparative experiments were conducted under the same training environment and hyperparameter settings, contrasting the improved model with single-stage models in the deep learning domain (SSD, YOLOv8n) and two-stage models (Sparse R-CNN, Cascade R-CNN).

Table 1

Different model experiment results

Models	Precision/%	Recall/%	mAP@0.5%	Parameters/MB	FPS/(img/s)
Faster R-CNN	88.9	87.4	90.7	41.36	8.3
SSD	81.2	82.1	82.7	25.6	4.6
YOLOv8n	86.4	83.4	87.9	2.51	10.5
Sparse R-CNN	87.7	84.5	88.2	43.01	7.8
Cascade R-CNN	87.5	84.8	87.9	40.12	7.1
Our	91.6	89.7	93.8	41.45	8.7

According to the data in Table 1, Faster R-CNN demonstrates the highest accuracy, recall, and mean Average Precision (mAP) when compared to both single-stage and two-stage models, providing a solid foundation for further optimization of subsequent models. The improved Faster R-CNN model surpasses SSD, YOLOv8n, Sparse R-CNN, and Cascade R-CNN in mean Average Precision by 11.1, 5.9, 5.6, and 5.9 percentage points, respectively. In terms of accuracy, it also outperforms these models by 10.4, 5.2, 3.9, and 4.1 percentage points, respectively. Additionally, the improved Faster R-CNN exhibits excellent recall, exceeding these models by 7.6, 6.3, 5.2, and 4.9 percentage points. These data conclusively demonstrate that the improved Faster R-CNN model excels in extracting effective features and accurately predicting the coordinates and category information of obstacles.

Ablation test analysis

To evaluate the specific improvements in the performance of the basic Faster R-CNN model achieved by using ResNet50 as the backbone network, the Feature Pyramid Network, and the Region of Interest Align (ROI Align) strategy, ablation experiments were designed while keeping the dataset and experimental parameters consistent.

Table 2

Results of ablation experiment

Test	ResNet50	FPN	ROI Align	P/%	R/%	mAP@0.5%	Parameters/MB	FPS
1	×	×	×	88.9	87.4	90.7	41.36	8.1
2	√	×	×	89.5	88.1	91.9	41.14	8.3
3	√	√	×	90.7	88.5	93.2	41.14	8.7
4	√	√	√	91.6	89.7	93.8	41.25	8.7

As shown in Table 2, in Experiment 2, ResNet50 was used to replace the original VGG16 as the backbone network. Benefiting from the residual structure of ResNet50, the improved backbone network not only increased the number of convolutional layers but also achieved improvements of 0.6%, 0.7%, and 1.2% in accuracy, recall, and mean Average Precision (mAP), respectively, while reducing the number of parameters. In Experiment 3, the introduction of the Feature Pyramid Network (FPN) for multi-scale feature fusion allowed the feature maps to integrate high-level semantic information and low-level spatial information, thereby enhancing the model's capabilities in multi-scale and small object detection. This improvement resulted in increases of 1.2%, 0.4%, and 1.3% in accuracy, recall, and mean Average Precision, respectively. In Experiment 4, ROI Align was used to replace the original ROI Pooling. ROI Align improved the overall regression performance of the predicted bounding boxes, making them more precise when detecting obstacles. This enhancement led to increases of 0.9%, 1.2%, and 0.6% in accuracy, recall, and mean Average Precision, respectively. Overall, the results of the ablation experiments indicate that these improvements played a positive role in enhancing obstacle detection accuracy. Compared to the original Faster R-CNN model, the improved model not only reduced the number of model parameters and increased detection speed but also achieved increases of 2.7%, 2.3%, and 3.1% in accuracy, recall, and mean Average Precision, respectively.

Test results of different obstacles

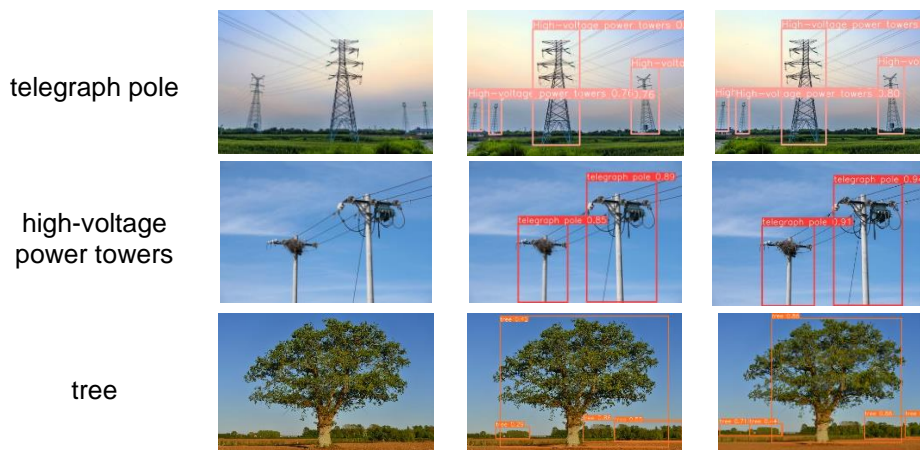
To clearly present the differences in performance between the original model and the improved model in detecting various categories of obstacles, the test results of both models were compared and the comparison results were displayed in Figure 10. Additionally, the mean Average Precision (mAP) of the obstacle detection results during the training process were statistically analyzed and they are listed in Table 3.

According to the data analysis in Table 3, the improved Faster R-CNN model, compared to its original version, shows only a slight improvement in agricultural machinery detection tasks, while achieving a significant increase in mean Average Precision (mAP) for other obstacle detection tasks. This improvement is reflected not only in the overall optimization of detection performance but also in the notable enhancement of specific obstacle detection. Taking utility pole detection as an example, the mAP@0.5 of the original model was only 82.1%, whereas after adopting the improved YOLOv8 model, the mAP@0.5 for utility pole detection increased to 89.8%. Although there remains a certain gap in detection accuracy for utility poles compared to other obstacles such as vehicles and pedestrians, the improved model has made significant progress compared to the original model. As shown in Figure 10, the improved Faster R-CNN model not only reduces the instances of missed detections and false positives compared to the original model, but it also enhances the confidence level of obstacle detection.

Table 3

Types of obstacles	mAP@0.5/%	
	pre-optimization	post-optimization
telegraph pole	82.1	89.8
high-voltage power towers	92.7	94.5
tree	91.3	93.8
building	92.5	94.6
person	89.4	93.7
agricultural machinery	95.1	95.2
water well	92.0	94.8
all	90.7	93.8

According to the data analysis in Table 3, the improved Faster R-CNN model, compared to its original version, shows only a slight improvement in agricultural machinery detection tasks, while achieving a significant increase in mean Average Precision (mAP) for other obstacle detection tasks. This improvement is reflected not only in the overall optimization of detection performance but also in the notable enhancement of specific obstacle detection. Taking utility pole detection as an example, the mAP@0.5 of the original model was only 82.1%, whereas after adopting the improved YOLOv8 model, the mAP@0.5 for utility pole detection increased to 89.8%. Although there remains a certain gap in detection accuracy for utility poles compared to other obstacles such as vehicles and pedestrians, the improved model has made significant progress compared to the original model. As shown in Figure 10, the improved Faster R-CNN model not only reduces the instances of missed detections and false positives compared to the original model, but it also enhances the confidence level of obstacle detection.



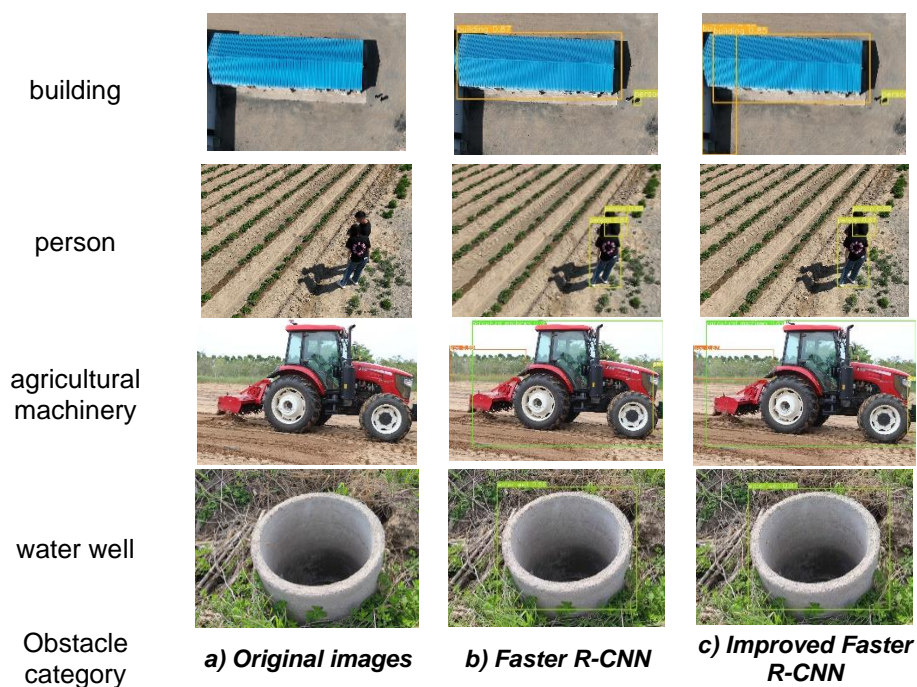


Fig. 10 –Comparison of Faster R-CNN and Improved Faster R-CNN Detection Results

As shown in Figure 10, the improved Faster R-CNN model not only reduces the instances of missed detections and false positives compared to the original model, but it also enhances the confidence level of obstacle detection.

CONCLUSIONS

This study developed a farmland obstacle detection model based on an improved Faster R-CNN model. Validation using the same obstacle dataset showed that the improved model achieved a recognition accuracy of 91.6% and a recall rate of 93.8%. In practical applications, the model's recognition rate for static obstacles such as utility poles, high-voltage towers, trees, buildings, agricultural machinery, and wells exceeded 90%. Simultaneously, the model's recognition rate for dynamic obstacles, such as people walking at a speed of 0.8 m/s, also remained at 90%, with an average detection frame time of 108 ms, meeting the requirements for real-time detection.

ACKNOWLEDGEMENT

The author has been supported by the National Key R&D Program Project (2023YFD2000904), National Modern Agricultural Industrial Technology System Project (CARS-09-P32), Natural Science Foundation of Shandong Province (ZR2022ME306), National Natural Science Foundation of China (32460445), Qingdao Science and Technology Demonstration Special Project for the Benefit of the People (23-2-8-xdny-2-nsh).

REFERENCES

- [1] Adiuku, N., Avdelidis, N. P., Tang, G., & Plastropoulos, A. (2024). Improved Hybrid Model for Obstacle Detection and Avoidance in Robot Operating System Framework (Rapidly Exploring Random Tree and Dynamic Windows Approach). *Sensors*, 24(7), 2262.
- [2] Ahuja, U., Singh, S., Kumar, M., Kumar, K., & Sachdeva, M. (2023). COVID-19: Social distancing monitoring using faster-RCNN and YOLOv3 algorithms. *Multimedia Tools and Applications*, 82(5), 7553-7566.
- [3] Balasundaram, A., Shaik, A., Prasad, A., & Pratheepan, Y. (2024). On-road obstacle detection in real time environment using an ensemble deep learning model. *Signal, Image and Video Processing*, 1-14.
- [4] Chen, J., Li, D., Qu, W., & Wang, Z. (2024). A MSA-YOLO Obstacle Detection Algorithm for Rail Transit in Foggy Weather. *Applied Sciences*, 14(16), 7322.
- [5] Cui, J., Zhang, X., Zhang, J., Han, Y., Ai, H., Dong, C., & Liu, H. (2024). Weed identification in soybean seedling stage based on UAV images and Faster R-CNN. *Computers and Electronics in Agriculture*, 227, 109533.

- [6] Dai, X., Mao, Y., Huang, T., Qin, N., Huang, D., & Li, Y. (2020). Automatic obstacle avoidance of quadrotor UAV via CNN-based learning. *Neurocomputing*, 402, 346-358.
- [7] Dev, U., Singh, T., Babu, T., Mandal, A. K., Sharma, M., & Mandal, A. (2025). Enhancing Blood Platelet Counting through Deep Learning Models for Advanced Diagnostics. *SN Computer Science*, 6(1), 1-10.
- [8] Du, Z., Feng, X., Li, F., **an, Q., & Jia, Z. (2024). A Lightweight UAV Visual Obstacle Avoidance Algorithm Based on Improved YOLOv8. *Computers, Materials & Continua*, 81(2).
- [9] EL MALLAHI, I., RIFFI, J., Tairi, H., & Mahraz, M. A. (2024). Efficient Vehicle Detection and Classification Algorithm Using Faster R-CNN Models. *Journal of Automation, Mobile Robotics and Intelligent Systems*, 86-93.
- [10] Han, L., Jiang, Y., Qi, Y., & Altangerel, K. (2024). Monocular visual obstacle avoidance method for autonomous vehicles based on YOLOv5 in multi lane scenes. *Alexandria Engineering Journal*, 109, 497-507.
- [11] He, D., Qiu, Y., Miao, J., Zou, Z., Li, K., Ren, C., & Shen, G. (2022). Improved Mask R-CNN for obstacle detection of rail transit. *Measurement*, 190, 110728.
- [12] Jafri, R., Campos, R. L., Ali, S. A., & Arabnia, H. R. (2017). Visual and infrared sensor data-based obstacle detection for the visually impaired using the Google project tango tablet development kit and the unity engine. *IEEE Access*, 6, 443-454.
- [13] Li, C. J., Qu, Z., Wang, S. Y., & Liu, L. (2021). A method of cross-layer fusion multi-object detection and recognition based on improved faster R-CNN model in complex traffic environment. *Pattern Recognition Letters*, 145, 127-134.
- [14] Nie, J., Zhang, G., Lu, X., Wang, H., Sheng, C., & Sun, L. (2024). Obstacle avoidance method based on reinforcement learning dual-layer decision model for AGV with visual perception. *Control Engineering Practice*, 153, 106121.
- [15] Park, J., Je, Y., Lee, H., & Moon, W. (2010). Design of an ultrasonic sensor for measuring distance and detecting obstacles. *Ultrasonics*, 50(3), 340-346.
- [16] Rahman, F. U., Ahmed, M. T., Hasan, M. M., & Jahan, N. (2022). Real-time obstacle detection over railway track using deep neural networks. *Procedia Computer Science*, 215, 289-298.
- [17] Shahi, T. B., Xu, C. Y., Neupane, A., & Guo, W. (2022). Machine learning methods for precision agriculture with UAV imagery: a review. *Electronic Research Archive*, 30(12), 4277-4317.
- [18] Starostin, I. A., Eshchin, A. V., Godzhaev, T. Z., & Davydova, S. A. (2024). Conceptual directions for the development of driverless agricultural mobile power units. *Tractors and Agricultural Machinery*, 91(1), 23-38.
- [19] Xue Jinlin, Li Yuqing, & Cao Xinjian. (2022). Obstacle Detection Based on Deep Learning for Blurred Farmland Images (基于深度学习的模糊农田图像中障碍物检测技术). *Transactions of the Chinese Society for Agricultural Machinery*, (03), 234-242.
- [20] Yang, T., Guo, Y., Li, D., & Wang, S. (2025). Vision-Based obstacle detection in dangerous region of coal mine driverless rail electric locomotives. *Measurement*, 239, 115514.
- [21] Zhang, Y., Tian, K., Huang, J., Wang, Z., Zhang, B., Zhang, B., Xie, Q. (2024). Field Obstacle Detection and Location Method Based on Binocular Vision. *Agriculture*, 14(9), 1493.
- [22] Zhao, Z., Kang, J., Sun, Z., Ye, T., & Wu, B. (2024). A real-time and high-accuracy railway obstacle detection method using lightweight CNN and improved transformer. *Measurement*, 238, 115380.

WHEAT GRAIN APPEARANCE QUALITY DETECTION BASED ON IMPROVED YOLOv8n

基于改进 YOLOv8n 的小麦籽粒外观品质检测

Qingzhong KONG, Na MA¹⁾

College of Information Science and Engineering, Shanxi Agricultural University, Taigu/China

Tel: +86-13834188480; E-mail: manasxau@163.com

DOI: <https://doi.org/10.35633/inmateh-75-30>

Keywords: Wheat grains, machine vision, YOLOv8n, attention mechanism, DWR module

ABSTRACT

Wheat grains are a common type of cereal variety, and due to their large quantity and high demand, traditional manual quality inspection requires a significant amount of labor with potentially inadequate results. To address this issue, this study focuses on intact, damaged, moldy, and shriveled wheat grains, and establishes a YOLO-wheat automatic wheat grain appearance quality detection model. First, a large number of wheat grain sample images were collected, preprocessed, and annotated. Next, YOLOv5n, YOLOv8n, and YOLOv10n wheat grain object detection models were established, and the optimal model YOLOv8n was selected as the base model for automatic wheat grain appearance quality detection. To further improve wheat grain detection performance, the Dilation-wise Residual (DWR) module was integrated into the YOLOv8n network structure to enhance feature extraction from the expandable receptive field in the higher layers of the network. Additionally, the TripletAttention attention mechanism was introduced, and this improved network was named YOLO-wheat. Experimental results showed that YOLO-wheat achieved an mAP value of 91.3% in wheat grain appearance quality detection, representing a 4.3% improvement compared to the previous version. This study provides technical support for automatic wheat quality detection.

摘要

小麦籽粒是一种常见的谷物类品种，且由于其数量多需求量大，在传统人工品质检测时耗费大量精力而效果不见得足够好。为解决上述问题，本研究以小麦完善粒、破损粒、发霉粒和干瘪粒为研究对象，建立 YOLO-wheat 小麦籽粒外观品质自动检测模型。首先，采集了大量小麦籽粒样本图像，并进行了数据预处理和标注整理。其次，建立了 YOLOv5n、YOLOv8n、YOLOv10n 小麦籽粒目标检测模型，从中选取最优模型 YOLOv8n 为小麦籽粒外观品质自动检测基础模型。为了进一步提升小麦籽粒检测性能，在 YOLOv8n 网络结构中使用 Dilation-wise Residual(DWR) 模块加强从网络高层的可扩展感受野中提取特征，并引入了 TripletAttention 注意力机制，将此网络命名为 YOLO-wheat。实验结果表明 YOLO-wheat 在小麦籽粒外观品质检测中 mAP 值为 91.3%，较改进前提升 4.3%。该研究可为小麦品质自动检测提供技术支持。

INTRODUCTION

In daily life, wheat is one of the most demanded and high-quality food products for human consumption (Zahra et al., 2023; Shewry et al., 2023), requiring both high quantity and quality standards. However, due to its large volume and the difficulty in distinguishing quality categories, traditional manual inspection methods are highly complex, time-consuming, and labor-intensive, often leading to unsatisfactory results. With the development of machine vision and deep learning technologies, the use of computers to achieve automated analysis of target detection images (Dhanya et al., 2022) has become a powerful tool to solve this problem, improving production efficiency and reducing labor costs. Therefore, machine learning and deep learning techniques can be utilized in combination with large datasets of labeled wheat grain samples to perform target detection on wheat grains through automated and intelligent methods, promoting the modernization and intelligent development of the agricultural industry. Furthermore, this can later be integrated with robotics to achieve intelligent agriculture (Soori et al., 2024).

Target detection tasks based on deep learning have been widely applied in agricultural production due to their high precision and rapid detection capabilities. In 2021, Wang Qiu jin et al., (2021), developed a wheat fusarium head blight grain recognition model based on feature band fusion images and deep learning algorithms. By comparing recognition accuracy, the optimal deep learning model was selected, enabling real-time online detection of fusarium-infected wheat grains.

In 2023, Wang Ling *et al.*, (2023), proposed a wheat grain counting method based on the YOLOv7-ST model. The YOLOv7-ST model accurately and quickly detected issues such as grain occlusion and adhesion under varying degrees of dispersion, significantly improving the efficiency of wheat seed testing. In 2024, Yu Zhaofu *et al.*, (2024) proposed a genetic algorithm-based optimizer designed for the YOLOv8 network, addressing the challenge of optimizing complex networks through intelligent algorithms, thus providing a better method for soybean grain recognition. Tomáš Zoubek *et al.*, (2024), conducted a comparative study of YOLO models for weed and crop recognition. By adjusting different parameters, the model was fine-tuned to address weed recognition challenges, and it was determined that different models showed improved performance for specific feature detection problems. In 2024, Ma *et al.* (2024), focused on wheat grains and proposed an improved YOLOv8-based wheat grain detection and counting method. Today, the applications of deep learning in agriculture are not limited to crop recognition. Yue *et al.*, (2024), proposed a lightweight pest detection method based on an improved YOLOv8 model, capable of identifying dynamic pests affecting crops. This method enhanced YOLOv8's feature extraction capabilities, addressing issues like low precision in small-object detection and improving the model's suitability for embedded deployment, providing valuable insights for the lightweight model in this study. In addition, YOLO models can be repeatedly modified to make them better suited for specific detection scenarios. For instance, Liu *et al.*, (2024), proposed a Fusion Transformer YOLO-based model for grape disease detection. Sangaiah *et al.*, (2024), developed UAV T-YOLO-Rice, an efficient and lightweight rice leaf disease detection model; and Ren *et al.*, (2024), introduced the FPG-YOLO model for detecting pollination stamens of "Yulu Fragrant" pears in unstructured environments. These studies demonstrate that target detection algorithms show excellent performance in agricultural modernization, especially in crop localization and recognition. Beyond agriculture, YOLOv8n-based models have also been improved for various applications. For instance, Li Bohao *et al.*, (2024), proposed an improved UAV aerial small-object detection algorithm model based on YOLOv8n. Qin *et al.*, (2024), developed a cable switch fault diagnosis model based on YOLOv8n; and Yang Ruijun *et al.*, (2024), designed a lightweight remote sensing image detection algorithm for military aircraft using YOLOv8n. These applications highlight that visual detection using the YOLOv8n base model has found use across diverse fields, providing inspiration for this study. However, research on detecting wheat grains of varying qualities remains relatively scarce, with low recognition accuracy. Therefore, this study focuses on detecting the quality of wheat grains, specifically intact grains, damaged grains, moldy grains, and shriveled grains, using deep learning methods for intelligent quality detection.

First, a large dataset of wheat grain images was collected and annotated using labeling. The detection performance of YOLOv5n, YOLOv8n, and YOLOv10n was compared, and the YOLOv8n model was ultimately selected as the base model. To further enhance the detection accuracy of the model, the Dilation-wise Residual (DWR) module, which is more suitable for small-object detection, and the TripletAttention attention mechanism were integrated into the YOLOv8n model. The enhanced model, named YOLO-wheat, was developed to achieve automated detection of wheat grain appearance quality.

MATERIALS AND METHODS

Data Acquisition and Pre-processing

In this study, a total of 684 images of intact grains, damaged grains, moldy grains, and shriveled grains were collected (Zhixiao *et al.*, 2020). These images included various scenarios such as white backgrounds, black backgrounds, different shooting angles, varying lighting conditions, different rotation degrees, and scattered stacking, aiming to realistically replicate various situations that may occur in practical application scenarios. Figure 1 shows some of the collected wheat grain images.



(a) White Background



(b) Black Background

Fig. 1 - Partial Data Collection

The images were annotated using labeling in the YOLO format. During annotation, the mouse was used to accurately draw bounding boxes on the images, ensuring that no wheat grains were missed. Each grain in the images was labeled according to its appearance quality, categorized into four classes: intact grains (denoted as "w"), damaged grains (denoted as "p"), moldy grains (denoted as "f"), and shriveled grains (denoted as "g"). The annotation results were then saved for subsequent operations.

Since images captured in a laboratory environment cannot fully reflect real-world scenarios, data augmentation techniques were applied to enrich the dataset. The collected images were further processed with random rotations, noise addition, brightness adjustments, and other image enhancement methods. These techniques were randomly combined to simulate various situations that might be encountered in practical algorithm application scenarios. Figures 2 and 3 show a comparison between the original wheat grain images and the augmented images under different backgrounds.



Fig. 2 - Comparison of Data Augmentation Effects for Wheat Grains on a Black Background



Fig. 3 - Comparison of Data Augmentation Effects for Wheat Grains on a White Background

The images were divided into a training set, validation set, and test set in a ratio of 7:2:1. The specific distribution is shown in Table 1. The dataset is categorized into two types: black background and white background. There are 348 images with a white background and 336 images with a black background. Among the white background images, the training set, validation set, and test set contain 243, 70, and 35 images, respectively. For the black background images, the training set, validation set, and test set contain 235, 67, and 34 images, respectively.

Table 1

Comparison of Experimental Parameters for Each Model					
Augmented dataset	White Background	Black Background	Augmented dataset	White Background	Black Background
Training Set	243	235	Training Set	243	235
Validation Set	70	67	Validation Set	70	67
Test Set	35	34	Test Set	35	34
Total	348	336	Total	348	336

YOLOv8n Model

The YOLO algorithm series has a long history of development (Jiang et al., 2020; Terven et al., 2023). Among them, YOLOv8n is a state-of-the-art, lightweight object detection model capable of processing images in real-time and identifying various objects within them. It demonstrates superior performance in addressing the issues designed in this study. For instance, in real-world application scenarios, it can provide rapid feedback, allowing operators sufficient time to address problems identified after detection. This makes it highly practical in terms of both usability and accuracy.

The YOLOv8n network model primarily consists of three components: the Backbone, the Neck, and the Head. In deep learning-based object detection algorithms, these three major components have distinct roles. The Backbone is mainly responsible for increasing the feature depth and level of abstraction of the input image, transforming it into feature maps that contain various information such as the location and shape of objects in the image. The Neck is primarily designed to aggregate feature information from different levels and is situated between the Backbone and the Head. The Head is used to predict the categories and locations of objects,

including their bounding boxes. The basic structure of a deep learning-based object detection algorithm follows the sequence: Input → Backbone → Neck → Head → Output.

DWR (Dilation-wise Residual) Model

The DWR module acts as a tool for extracting features at different scales in the higher layers of the network, significantly improving the algorithm's accuracy, its structure as shown in Figure 4. First, a multi-branch structure is used to expand the receptive field, where each branch employs a dilated depthwise convolution with different dilation rates. Second, a specially designed Simple Inverted Residual (SIR) module is used to extract features from the lower layers of the network. This module has only a small receptive field of 3x3 and adopts an inverted bottleneck structure to expand the number of channels, ensuring stronger feature extraction capability. Finally, based on the combination of the DWR module and the SIR module, the network DWRSeg was constructed. In this network, the decoder adopts a simple structure similar to FNC. The decoder uses strong semantic information from the last two stages to directly upsample the feature maps and then concatenate them with feature maps from earlier stages for the final prediction.

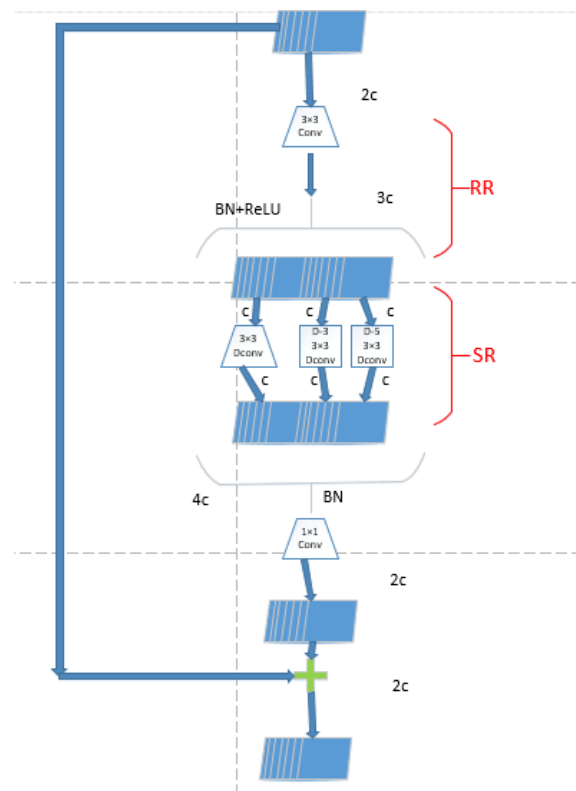


Fig. 4 - Diagram of the DWR Module

In summary, the introduction of the DWR (Dilation-wise Residual) module in the YOLO algorithm plays a crucial role in improving the accuracy of object detection. Its efficiency lies in the following key aspects: (1) Powerful receptive field expansion capability: The DWR module leverages the characteristics of dilated convolution to expand the receptive field of the convolution operation on the input image. This helps the network capture more extensive spatial information in the image. By expanding the receptive field, the model can better understand object features such as position, size, and shape, thereby improving the accuracy of object detection. (2) Multi-scale feature fusion: The DWR module introduces a residual connection mechanism to fuse feature information at different scales, enabling the network to comprehensively utilize feature representations from multiple levels. Through residual connections, the model can better learn semantic information across different scales, enhancing its ability to detect objects in complex scenes and small targets. (3) Enhanced network representation capability and learning efficiency: By incorporating residual connections and dilated convolution, the DWR module improves the network's representation capacity and learning efficiency. Residual connections help mitigate the vanishing gradient problem, accelerate the network's convergence process, and improve the model's learning efficiency.

Meanwhile, dilated convolution enhances the network's ability to learn contextual information from the image, enabling it to better understand global information in the image, thereby improving object detection accuracy. The introduction of this module allows the YOLO algorithm to achieve better performance in object detection tasks and demonstrates greater potential for practical applications.

TripletAttention Model

The Triplet Attention mechanism (Triplet Attention) refers to a mechanism in the field of deep learning that enables models to focus on multiple specific regions. It is a specialized attention mechanism designed for processing sequential data, extending the traditional bidirectional attention mechanism. It allows the model to simultaneously consider the past, present, and future information when calculating attention weights.

The YOLOv8-ALTE bridge crack detection algorithm proposed by *Yang et al. (2024)* incorporates the Triplet Attention mechanism into the shallow layers of the backbone feature extraction module. In the traditional bidirectional attention mechanism, the model generates attention weights based on the current input and achieves a more specific and detailed understanding of the context by comprehensively considering a series of historical and future information. The Triplet Attention mechanism introduces the representation of future information, enabling the model to balance the importance of past, current, and future information when calculating attention weights. Specifically, the Triplet Attention mechanism consists of three independent attention weight vectors, which represent the importance of past, present, and future information, respectively. These three attention weights are then combined to produce the final attention weight.

This mechanism is often applied to tasks such as image segmentation and object detection to help models better focus on important regions of the image, thereby improving model performance and accuracy.

In the field of deep learning, attention mechanisms are typically used to help models focus on important parts of the input when processing sequential data or images. By weighting and integrating information from different parts, attention mechanisms enhance the model's ability to process input effectively. Multi-head attention, on the other hand, learns multiple sets of different attention weights in various subspaces, allowing for a more comprehensive capture of the complex features of the input data. Triplet Attention combines these two mechanisms to help the model focus on three important regions in an image.

By learning three sets of different weight parameters, the model can independently focus on these three regions and better integrate their information to understand the image. This mechanism improves the model's ability to locate and recognize objects, thereby enhancing the performance of tasks such as object detection. The Triplet Attention mechanism offers several advantages, including a comprehensive understanding of context, reduced risk of information leakage and overfitting, and improved predictive performance. Therefore, this study primarily improves the YOLOv8n algorithm based on the Triplet Attention mechanism.

Improvement Method in This Study

The shape of wheat grains is inherently small, and factors such as adhesion further increase the difficulty of wheat grain detection. To enhance the model's ability to extract features of small objects, this study incorporates a Dilation-wise Residual (DWR) module into the C2F module of the YOLOv8n backbone network. In C2F module, the feature aggregation functionality is mainly implemented by the Bottleneck module. Therefore, in the process of algorithm improvement in this paper, the Bottleneck module is replaced with the DWR module to achieve a shift in the feature aggregation direction. This modification shifts the detection focus toward the feature extraction of small objects, strengthening the network's ability to extract features of wheat grains and improving the network's capability to learn image details and contextual information. This ultimately enhances the accuracy and robustness of the detection results. Additionally, the Triplet Attention mechanism is integrated into the YOLOv8n model after the 9th-layer SPPF module. This enables the network to focus more on multiple specific regions and capture the minute features of wheat grains, thereby enhancing the network's effectiveness in handling complex target scenes.

This makes the model's feature extraction and recognition capabilities more precise and reliable. The improved network is named YOLO-wheat (as shown in Figure 5). The YOLO-wheat model comprehensively understands the context, reduces the risks of information leakage and overfitting, and improves prediction performance, ultimately enhancing the recognition results.

From the above analysis, it is evident that the core parameters of YOLOv8n are superior, resulting in better detection outcomes. Therefore, this study adopts YOLOv8n as the baseline model and optimizes it further to achieve efficient detection of wheat grain quality.

Table 2

Model	P	R	mAP	mAP0.5:0.95	GFLOPs
YOLOv10n	72.7	76.2	81	65.5	6.5
YOLOv8n	79.7	79.7	87	66.3	7.6
YOLOv5n	73.7	82.7	85.5	65.9	7.1

Detection Results of the Improved Algorithm

To evaluate the effectiveness of the improved algorithm, experiments were conducted on the wheat grain dataset using the improved YOLO-wheat model and the baseline YOLOv8 model. The results are shown in Table 3. In the table, "w" represents the "intact" category, "p" represents the "damaged" category, "f" represents the "moldy" category, and "g" represents the "shriveled" category. As seen in the table, after applying the improved algorithm, the mAP value for the "intact" category increased from 93.3% to 95.6%, with an improvement of 2.3%. For the "damaged" category, the mAP value increased from 89.9% to 93.4%, with an improvement of 3.5%. For the "moldy" category, the mAP value increased from 84.2% to 87.5%, with an improvement of 3.3%. For the "shriveled" category, the mAP value increased from 80.2% to 88.9%, with an improvement of 8.7%. Overall, the mAP value for all categories improved from 87% to 91.3%, showing an increase of 4.3%. The mAP@0.5:0.95 metric improved from 66.3% to 75.8%. These results demonstrate that the proposed YOLO-wheat model achieves better detection performance for different categories of wheat grains.

Table 3

Model	Category	P	R	mAP	mAP0.5:0.95
YOLOv8n	w	85.9	87.1	93.9	74.4
	p	81.7	84.1	89.9	68.6
	f	77.4	75.1	84.2	61.2
	g	73.8	72.7	80.2	60.9
	all	79.7	79.7	87	66.3
YOLO-wheat	w	88.8	90	95.6	81.5
	p	90.3	87.3	93.4	77.5
	f	81.4	78.6	87.5	71.4
	g	84	74.7	88.9	72.9
	all	86.1	82.7	91.3	75.8

Ablation Experiment

As shown in Table 4 of the ablation experiment results, the baseline YOLOv8n algorithm achieves an mAP of 87%. After adding the DWR module to YOLOv8n, the mAP increases to 90%. When only the Triplet Attention is added, without the DWR module, the mAP reaches 89.1%. Finally, when both DWR and Triplet Attention are incorporated together, the model achieves the best recognition performance: Precision increases to a maximum of 86.1%, Recall rises to a maximum of 82.7%, and mAP reaches a peak of 91.3%. The experimental results demonstrate that adding either DWR or Triplet Attention individually enhances the network's feature extraction capability, but the performance is optimal when both are incorporated into the network.

Table 4

Baseline	DWR	Triplet Attention	P	R	mAP
√	×	×	79.7	79.7	87
√	√	×	84.6	81.8	90
√	×	√	82.3	82.7	89.1
√	√	√	86.1	82.7	91.3

Overall, YOLO-wheat has the following advantages over the original YOLOv8 model: With the addition of the Triplet Attention mechanism, the model can better and more accurately capture important information in images, improving the precision and performance of object detection, particularly for detecting the appearance and types of wheat grains. It also enhances the handling of both global and local information. The DWR module allows the algorithm to provide better feature extraction for complex and small objects by expanding the receptive field. In other words, the Triplet Attention mechanism helps balance the attention given to global and local information, making the model more effective at handling targets of different scales. The DWR module, on the other hand, offers better adaptability to complex backgrounds and higher precision for small targets.

Experimental results with different backgrounds

In real-world application scenarios, different backgrounds may be encountered. Therefore, during the data collection phase, wheat grains were collected with both white and black backgrounds to explore the impact of background color on the algorithm's accuracy. The detection results of wheat grains with different backgrounds using the YOLO-wheat algorithm established in this paper are shown in Table 5. From Table 5, it can be observed that compared to the white background, the Precision of wheat grains with the black background increased by 14.4%, and the mAP improved by 7.8%. Specifically, the mAP for intact grains increased by 3.1%, the mAP for damaged grains increased by 5.2%, the mAP for moldy grains increased by 12.7%, and the mAP for shriveled grains increased by 10.2%. This suggests that background color has a certain impact on wheat grain detection, with a more significant improvement in target detection when using a black background. In practical applications, setting the background to black would yield the best detection results.

Table 5

Detection results under different backgrounds					
Background	Category	P	R	mAP	mAP0.5:0.95
White background	w	84.3	94.4	92.1	71.8
	p	75.1	89.1	91.9	68.8
	f	75.9	73.9	82.2	59.2
	g	70.7	77.8	83.6	64.1
	all	76.5	83.3	87.5	66
Black background	w	96.9	83.3	95.2	65.9
	p	92.9	89.9	97.1	61.9
	f	88.5	88.6	94.9	61.7
	g	85.6	86.8	93.8	65.3
	all	90.9	87.2	95.3	63.7

Visualization of detection results

The trained YOLO-wheat model was used to validate the wheat grain dataset, and the detection results are shown in Figure 6. It can be observed that the improved algorithm in this study performs well in detecting both dispersed and clustered wheat grains under black and white backgrounds.

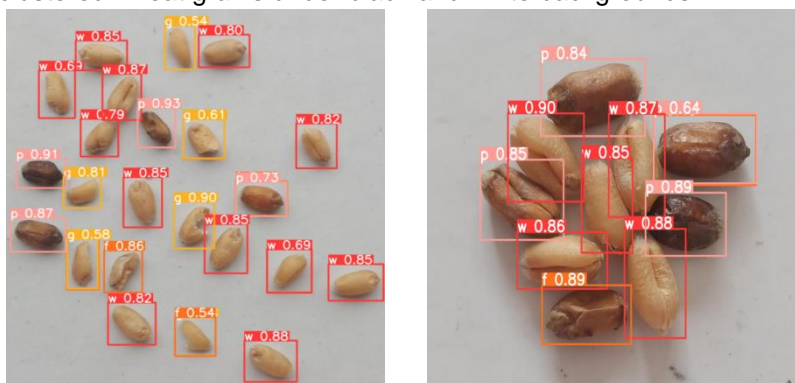




Fig. 6 - Visualization of detection results

CONCLUSIONS

With the development of machine learning and deep learning technologies, machine vision has become increasingly widespread in the agricultural sector. This study successfully developed an improved object detection model based on YOLOv8n, named YOLO-wheat, which aims to precisely locate the position and recognize the appearance quality of wheat grains. It provides technical support for intelligent wheat harvesting and recognition, as well as data collection for wheat yield analysis, making it suitable for related production environments.

(1) The dataset used in this study was constructed with black and white backgrounds as templates, incorporating image processing techniques such as random rotation, noise addition, and brightness adjustment. The goal was to simulate real-world environmental conditions and provide optimal templates for real detection environments. For example, detection should ideally be performed in a black background setting.

(2) This study employed the DWR module and the Triplet Attention module to enhance the recognition performance. YOLOv8n was used as the base model, with the DWR module placed in the C2F (Cross Feature Fusion) layer, and the Triplet Attention mechanism added after the SPPF (Spatial Pyramid Pooling Fast) layer to further improve the accuracy of the YOLOv8n model. The improved model achieved a mean Average Precision (mAP) of 91.3% for wheat grain quality detection, a 4.3% improvement over the original YOLOv8n model. This demonstrates that the proposed improvement enhances accuracy for small object detection.

This study focused on the appearance quality detection of a single type of wheat grain. However, the quality detection of multiple wheat varieties remains limited, highlighting the need for a more comprehensive dataset to increase sample diversity and improve the model's generalization capability. Finally, as this experiment is still in the algorithm research phase, further research and design of lightweight models or optimized algorithms for high-real-time scenarios may be needed before applying this in actual automated classification tasks.

ACKNOWLEDGEMENT

This research, titled "Wheat Grain Appearance Quality Detection Based on Improved YOLOv8n", was funded by The College Students Innovation Training Program of Shanxi Agricultural University (202410113026) and the Basic Research Program of Shanxi Province (202303021212115).

REFERENCES

- [1] Dhanya V.; Subeesh A.; Kushwaha N.; Vishwakarma D.; Nagesh K.; Ritika G.; Singh A. (2022). Deep learning based computer vision approaches for smart agricultural applications. *Artificial Intelligence in Agriculture*, 6, 211-229.
- [2] Jiang P.; Ergu D.; Liu F.; Cai Y.; Ma B. (2022). A Review of Yolo algorithm developments. *Procedia computer science* 199: 1066-1073.
- [3] Li B.; Li Z. (2024). UAV Aerial Small Target Detection Algorithm Based on Improved YOLOv8n [J]. *Intelligent Computer and Applications*, 1-9.
- [4] Liu Y.; Yu Q.; Geng S. (2024). Real-time and lightweight detection of grape diseases based on Fusion Transformer YOLO. *Frontiers in Plant Science*, 15, 1269423.
- [5] Ma N.; Li Z.; Kong Q. (2024). Wheat grains automatic counting based on lightweight YOLOv8. *INMATEH-Agricultural Engineering*, 73(2).

- [6] Qin X.; Li A.; Wang C. (2024). Fault Diagnosis of X-DR Cable Switch Based on Lightweight SGG-YOLOv8n [J]. *Journal of Changsha University of Science and Technology (Natural Science Edition)*, 1-1.
- [7] Ren R.; Sun H.; Zhang S.; Zhao H.; Wang L.; Su M.; Sun T. (2024). FPG-YOLO: A detection method for pollenable stamen in 'Yuluxiang' pear under non-structural environments. *Scientia Horticulturae*, 328, 112941.
- [8] Sangaiah A.; Yu F.; Lin Y.; Shen W.; Sharma A. (2024). UAV T-YOLO-rice: An enhanced tiny YOLO networks for rice leaves diseases detection in paddy agronomy. *IEEE Transactions on Network Science and Engineering*, 11(6), 5201-5216.
- [9] Shewry P. (2023). Wheat grain proteins: Past, present, and future. *Cereal chemistry*, 100(1), 9-22.
- [10] Soori M.; Arezoo B.; Dastres R. (2023). Artificial intelligence, machine learning and deep learning in advanced robotics, a review. *Cognitive Robotics*, 3, 54-70.
- [11] Terven J.; Esparza C.; González R. (2023). A comprehensive review of yolo architectures in computer vision: From yolov1 to yolov8 and yolo-nas. *Machine Learning and Knowledge Extraction*. 5.4: 1680-1716.
- [12] Wang L.; Zhang Q.; Feng T.; Wang Y.; Li Y.; Chen D. (2023). Research on Wheat Grain Counting Method Based on YOLO v7-ST Model [J]. *Transactions of the Chinese Society of Agricultural Machinery*, 54(10): 188-197.
- [13] Wang Q. (2021). Research on Wheat Fusarium Head Blight Grain Recognition Method and Online Detection System Based on Deep Learning [D]. *Nanjing Agricultural University*.
- [14] Yang R.; Zhang H.; Cheng Y. (2024). Lightweight Remote Sensing Image Military Aircraft Detection Algorithm Based on Improved YOLOv8n [J]. *Electronic Measurement Technology*, 1-12.
- [15] Yang W.; Fang H.; Tang X. (2024). Lightweight YOLOv8-ALTE Algorithm for Bridge Crack Disease Detection [J]. *Journal of Traffic and Transportation Engineering*, 1-17.
- [16] Yu Z. (2024). Construction of Genetic Algorithm Optimizer and Its Application in Soybean Grain Recognition Based on YOLO Algorithm [D]. *Wuhan University of Light Industry*.
- [17] Yue G.; Liu Y.; Niu T.; Liu L.; An L.; Wang Z.; Duan M. (2024). Glu-yolov8: An improved pest and disease target detection algorithm based on yolov8. *Forests*, 15(9), 1486.
- [18] Zahra N.; Hafeez M.; Wahid A.; Al M.; Ullah A.; Siddique K.; Farooq M. (2023). Impact of climate change on wheat grain composition and quality. *Journal of the Science of Food and Agriculture*, 103(6), 2745-2751.
- [19] Yang Z.; Fan Y.; Zheng Q. (2020). Study on the time-varying characteristics of appearance quality of stored wheat. *Journal of Henan University of Technology (Natural Science Edition)* 41.5: 116-120.
- [20] Tomáš Z.; Roman B.; Jean D.; Miroslav S.; Martin F.; František Š.; Petr B. (2025). Advancing precision agriculture with computer vision: A comparative study of YOLO models for weed and crop recognition. *Crop Protection* 107076-107076.

EVALUATION AND OPTIMIZATION OF AGRICULTURAL MANAGEMENT CLOUD PLATFORM BASED ON AHP/FCE

基于 AHP/FCE 的智慧农业管理云平台评价与优化

Jiyuan SUN¹⁾, Bin QI ^{*1,2)}, Xiaoming Sun^{*1,2)}, Yuanqi LIU¹⁾, Yuchao REN¹⁾, Tengyun MA ¹⁾, Bohan ZHANG¹⁾, Qiong Wu³⁾

¹⁾ College of Agricultural Engineering and Food Science, Shandong University of Technology/ China;

²⁾ School of Fine Arts and Design, Shandong University of Technology, Zibo City / China.

³⁾ Zibo Normal College / China

Tel: +86-15966964198; E-mail: sduid@163.com

DOI: <https://doi.org/10.35633/inmateh-75-31>

Keywords: Smart Agricultural Management Cloud Platform; Analytic Hierarchy Process (AHP); Fuzzy Comprehensive Evaluation (FCE); UI Design

ABSTRACT

UI design and user interaction optimization of smart agricultural management cloud platforms are key research directions for enhancing the overall value of the system. However, there is still room for improvement in terms of functionality and visibility of the platform interface. This study constructs a UI design evaluation model by combining the Analytic Hierarchy Process (AHP) and Fuzzy Comprehensive Evaluation (FCE), systematically evaluating and optimizing three UI design schemes of the platform. First, AHP was used to allocate weights to design factors, and then FCE was applied for comprehensive evaluation of each scheme, ultimately selecting the optimal one. Based on user heatmap data, the visual design of high-click areas was further optimized, improving the platform's score from 80.524 to 86.927. The study demonstrates that the combined AHP and FCE method has significant effects on UI design evaluation and optimization, providing scientific evidence and practical guidance for enhancing user experience in other smart agricultural management cloud platforms.

摘要

智慧农业管理云平台的 UI 设计与用户交互优化是提升系统整体价值的关键研究方向。然而，目前平台界面在功能性与可视性方面仍有改进空间。本研究通过结合层次分析法 (AHP) 与模糊综合评价法 (FCE) 构建了 UI 设计评价模型，对平台的三种 UI 设计方案进行了系统评估与优化。首先，采用 AHP 对设计因素进行权重分配，然后运用 FCE 对各方案进行综合评价，最终筛选出最优方案。基于用户热力图数据，进一步优化了高点击区域的视觉设计，使平台评分从 80.524 提升至 86.927。研究表明，AHP 与 FCE 结合的方法在 UI 设计评价与优化中具有显著效果，为其他智慧农业管理云平台的用户体验提升提供了科学依据和实践指导。

INTRODUCTION

With the integration of the Internet of Things (IoT) and big data technologies, smart agricultural management cloud platforms have emerged as the "brain" of agricultural production, enabling precise allocation of energy resources and driving industrial upgrades. The platform integrates multi-source data such as smart irrigation, greenhouse energy consumption, and agricultural machinery operations, achieving real-time monitoring of the entire agricultural production process. It provides data analysis and decision support, helping practitioners improve efficiency, reduce costs, and promote green, sustainable development.

The user interface (UI) design of the platform plays a crucial role in connecting users with the system. A high-quality UI design can enhance the user experience and ensure the efficient operation of the platform; whereas poor design can lead to operational difficulties, decision-making errors, and decreased platform effectiveness. Therefore, using scientific methods to evaluate and optimize UI design has become a key research focus in the field of smart agriculture. The interface design adheres to principles of simplicity, vitality, liveliness, and fashion, and must integrate users' functional, psychological, and interactive needs through icons, colors, and interactions. Continuously improving the design will further promote the development of smart agriculture (Huijun et al., 2020).

Jiyuan SUN, M.S.Agr; Bin QI, Assoc. Prof. Ph.D. Eng; Xiaoming Sun, M.S. Eng, Lecturer; Yuanqi LIU, M. S.Agr; Yuchao REN, M. S.Agr; Tengyun MA, M. S.Agr; Bohan ZHANG, M. S.Agr; Qiong Wu, Senior Art and Craft Specialist.

The methodological landscape has evolved through successive innovations in decision-making frameworks, beginning with the development of the Analytic Hierarchy Process (AHP) as a transformative tool for quantifying qualitative challenges (Yongfeng et al., 2012). Subsequent advancements emerged through the integration of grey relational analysis with fuzzy mathematical principles to create comprehensive product evaluation systems (Guodong et al., 2009), followed by the application of TOPSIS techniques for human-computer interface assessment (Huiliang et al., 2016). Recent technological implementations demonstrate enhanced sophistication, particularly in ergonomic evaluations combining AHP-fuzzy comprehensive methods with TRIZ-based optimization for agricultural drone controllers (Shuxing et al., 2022). Concurrent developments in consumer product research achieved breakthroughs through multimodal methodologies blending sensory analytics, morphological deconstruction, and fuzzy AHP for automotive seat design (Qinglan et al., 2025). The methodological frontier further expanded through hybrid architectures integrating AHP-entropy weighting with fuzzy assessment systems, establishing multi-criteria evaluation frameworks for micro-irrigation filtration technologies (Feng et al., 2025). This progression reflects three paradigm shifts: increased hybridization of classical decision tools, domain-specific framework adaptation, and theoretical-practical integration across engineering disciplines.

Traditional UI design evaluation methods often rely on user feedback and expert judgment, which makes it difficult to systematically and comprehensively reflect the strengths and weaknesses of the design. To address this issue, this paper introduces the combination of the Analytic Hierarchy Process (AHP) and Fuzzy Comprehensive Evaluation (FCE) to construct a scientific and objective evaluation model. AHP determines the weight of each evaluation indicator through expert scoring, while FCE uses fuzzy mathematics to handle the uncertainties and ambiguities in the evaluation process. This enables a comprehensive evaluation of the UI design for the smart agricultural management cloud platform, providing theoretical support and practical guidance for the development and improvement of the platform.

MATERIALS AND METHODS

Analytic Hierarchy Process (AHP)

The Analytic Hierarchy Process (AHP) was developed in the 1970s by the American operations researcher (Saaty et al., 2008). It is a scientific method that combines qualitative and quantitative approaches by determining weight factors, which decompose complex evaluation problems into quantifiable evaluation objects that can then be synthesized. By combining AHP with fuzzy mathematics, it is possible to better handle the uncertainty inherent in the UI design process of a smart agricultural management cloud platform, ultimately leading to the optimal design solution. The evaluation method and process are shown in Figure 1.

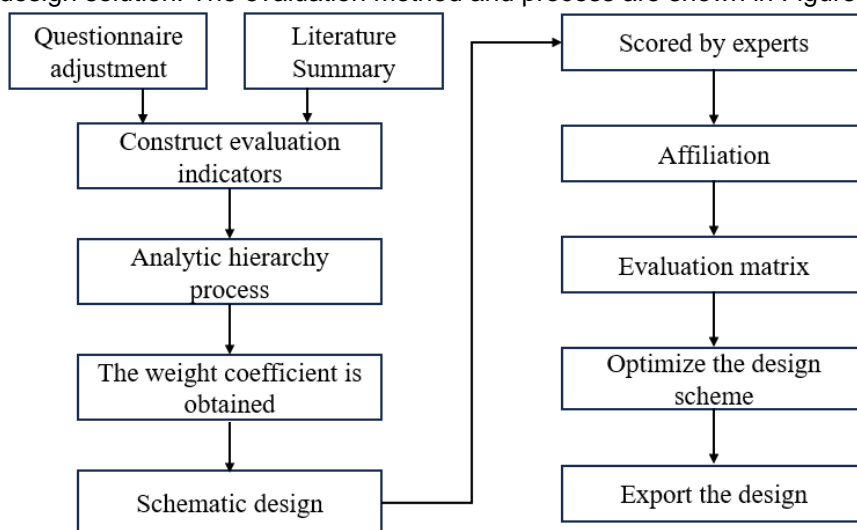


Fig. 1– Evaluation Method and Process

Hierarchical Structure Model of Agricultural Management Cloud Platform

The objectives, influencing factors, and analysis objects that need to be evaluated using the Analytic Hierarchy Process (AHP) are categorized into the highest, middle, and lowest levels according to their interrelationships. A hierarchical structure diagram is drawn (Tongxin et al., 2019).

The smart agricultural management cloud platform is placed at the goal level, with functionality experience and appearance as the criterion layer of the evaluation system (Xiangsheng et al., 2019). The criterion layer is further subdivided into seven indicator layers, as shown in Figure 2.

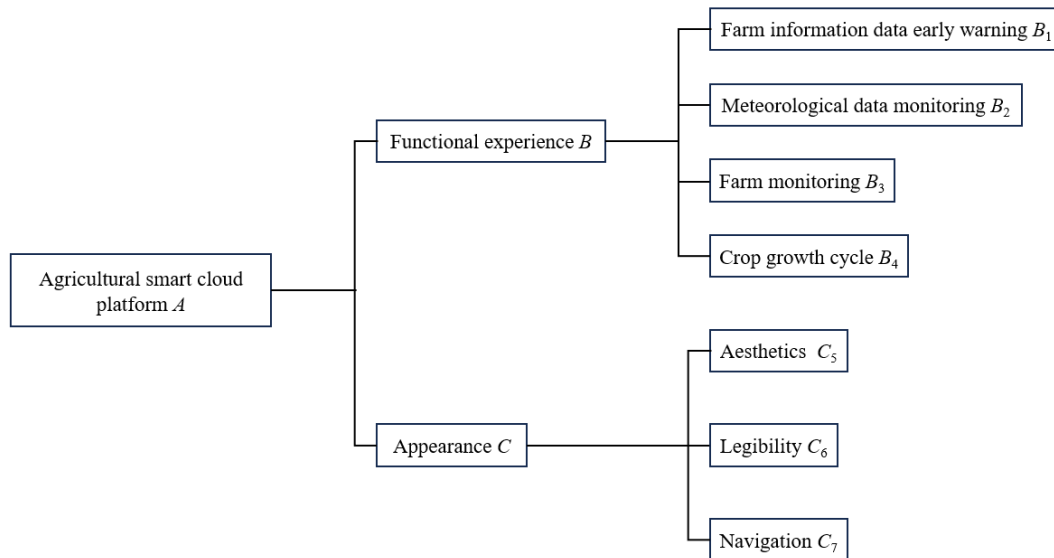


Fig. 2 – Design demand indicators for agricultural management cloud platform

Based on the design elements, the 9-point scale method can be used to construct a judgment matrix. The judgment matrix is used to compare pairwise relationships between indicators at the same level, with comparisons made at both the criterion layer and sub-criterion layer. A relative scale from 1 to 9 is assigned to each comparison, with the values reflecting the relative importance of the design elements. An example of the judgment matrix scale table is shown in Table 1 (Lin et al., 2024; Haibiao et al., 2019; Hui, 2019; Yimin et al., 2017; Qianrong et al., 2017).

Table 1

Judgment Matrix Scale		
Relative Importance Assignment (i/j)	Implication	Scaling instructions
1	Equal Importance	Indicator <i>i</i> is equally important as Indicator <i>j</i>
3	Slightly More Important	Indicator <i>i</i> is slightly more important than Indicator <i>j</i>
5	Strongly More Important	Indicator <i>i</i> is noticeably more important than Indicator <i>j</i>
7	Very Strongly More Important	Indicator <i>i</i> is strongly more important than Indicator <i>j</i>
9	Extremely Important	Indicator <i>i</i> is extremely more important than Indicator <i>j</i>
2, 4, 6, 8	The Intermediate Value of Two Adjacent Judgments	The importance is determined based on adjacent scale values
$A_{ij}=1/a_{ij}$	Reciprocal	

Arithmetic averaging is used to find weights

Based on the constructed judgment matrix, the arithmetic mean method is used to calculate the weight of each element. The steps are as follows:

- 1) Normalize each column of the judgment matrix so that the elements in each column are comparable in terms of their relative proportions. That is:

$$\bar{x}_{ij} = \frac{x_{ij}}{\sum_{i=1}^n x_{ij}} \quad (i = 1, 2, 3, \dots, n) \tag{1}$$

- 2) Sum the rows of the processed matrix to obtain the total sum of the elements in each row, and then calculate the average value of the relative weights of each element, that is,

$$\tilde{w}_i = \sum_{i=1}^n \bar{x}_{ij} \quad (i = 1, 2, 3, \dots, n) \tag{2}$$

3) Process the results after summation, and then the weight vector can be obtained.

$$w_i = \tilde{w}_i/n \tag{3}$$

Consistency Test

After obtaining the relative weights of each design element, a consistency test is required. Firstly, calculate the maximum eigenvalue of the judgment matrix based on these weights, and obtain the consistency index CI through this eigenvalue. Then, use the standard RI values in Table 2 to calculate the consistency test coefficient of the judgment matrix. This process aims to evaluate the consistency level among the various elements in the judgment matrix and ensure the reliability of the weight relationships.

1) The maximum eigenvalue of the judgment matrix.

$$\lambda_{max} = \sum_{i=1}^n \frac{(Aw)_i}{(nw)_i} \tag{3}$$

2) The consistency test values of each indicator.

$$V_{CI} = \frac{\lambda_{max}}{n-1} \tag{5}$$

3) The test coefficient of the judgment matrix

$$C_{CR} = \frac{V_{CI}}{V_{RI}} \tag{6}$$

In the formula:

n—Order of Judgment Matrix;

w—Eigenvector of the Normalized Judgment Matrix;

Aw—It is the product of matrix A and vector w, and the resulting new vector.

Table 2

Standard Value of RI

N	1	2	3	4	5	6	7	8	9
RI	0.00	0.00	0.52	0.89	1.12	1.26	1.36	1.41	1.46

Judgment matrix

Questionnaires were distributed to five experts. In accordance with the rules of the 9-point scale method, the experts were invited to evaluate and score each design element. Based on the scoring results provided by the experts, a judgment matrix was constructed, which reflects the experts' judgments on the relative importance among different elements. This judgment matrix will serve as the basis for weight calculation and consistency testing, supporting the systematic decision-making analysis process.

The judgment matrix of the intelligent agricultural management cloud platform is:

A	B	C
B	1	1/2
C	2	1

The judgment matrix among the various indicators of the functional experience criterion layer is:

B	B ₁	B ₂	B ₃	B ₄
B ₁	1	2	5	8
B ₂	1/2	1	3	4
B ₃	1/5	1/3	1	3
B ₄	1/8	1/4	1/3	1

The judgment matrix among the various indicators of the appearance - criterion layer is:

C	C ₅	C ₆	C ₇
C ₅	1	2	5
C ₆	1/2	1	4
C ₇	1/5	1/4	1

Results of Weights and Consistency Tests

Based on the calculations of Formulas (1) - (6), the weights of each evaluation indicator in the design of the intelligent agricultural management cloud platform were obtained, and the specific values are shown in Table 3. Through this weight distribution, it is possible to have a more comprehensive understanding of the contribution degree of each indicator to the design of the intelligent agricultural management cloud platform, so as to optimize the design in a more targeted manner (Ying et al., 2024).

Table 3

Index Weights of the Design Evaluation System for the Smart Agricultural Management Cloud Platform

Criterion layer	Weights of the Criterion Layer	Indicator layer	Weights of the Indicator Layer	Comprehensive Weight	λ_{max}	CR
Functional Experience B	0.3783	Farm Information Data Warning B1	0.5394	0.2040	4.0684	0.0256 < 0.1
		Meteorological Data Monitoring B2	0.2823	0.1067		
		Farm Monitoring B3	0.1206	0.0456		
		Crop Growth Cycle B4	0.0576	0.0217		
Appearance C	0.6217	Aesthetics C5	0.5695	0.3540	3.0246	0.0236 < 0.1
		Readability C6	0.3331	0.2070		
		Navigability C7	0.0974	0.0605		

The consistency ratio (CR) values in Table 3 are all less than 0.1, indicating that the judgment matrices have passed the consistency test and the data used are valid.

Design Scheme of the Smart Agricultural Management Cloud Platform

Based on the weight ranking of each item in the above text, a fuzzy comprehensive evaluation is conducted on the design scheme of the smart agricultural management cloud platform. Three different schemes are designed as evaluation objects, as shown in Figure 3 - Figure 5.



Fig. 3 – Preliminary Design Scheme 1 of the Smart Agricultural Management Cloud Platform



Fig. 4 – Preliminary Design Scheme 2 of the Smart Agricultural Management Cloud Platform



Fig. 5 – Preliminary Design Scheme 3 of the Smart Agricultural Management Cloud Platform

Fuzzy Comprehensive Evaluation of the Smart Agricultural Management Cloud Platform

The Fuzzy Comprehensive Evaluation Method is suitable for the comprehensive evaluation of multiple indicators and elements. It can reduce the problem of uncertainty in evaluation results caused by subjective factors, handle fuzzy information better, and enhance the effectiveness of decision-making results. The Fuzzy Comprehensive Evaluation Model is shown in Figure 6. The specific operation process is as follows:

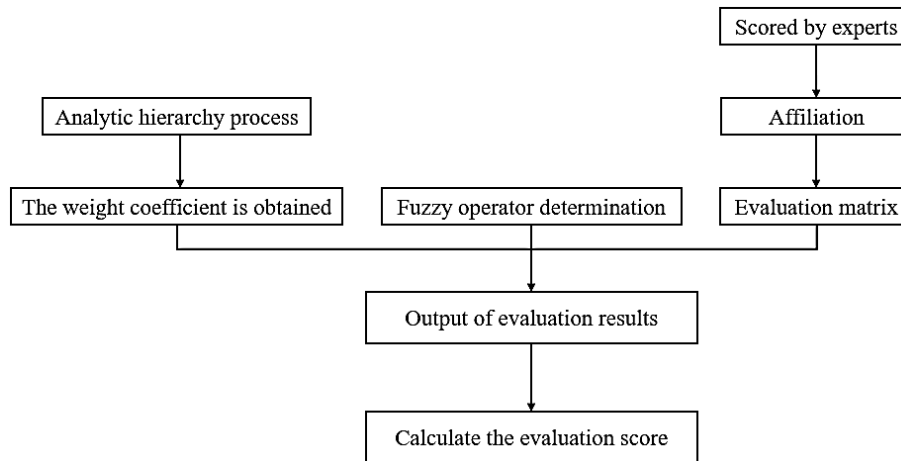


Fig. 6 – Fuzzy Comprehensive Evaluation Model

1) In this study, the UI design of the smart agricultural cloud platform is taken as the overall goal, with the goal layer being the UI design of the smart agricultural cloud platform. The evaluation is conducted from two sub-aspects, namely, functionality and appearance design, which form the criterion layer of the evaluation system. The criterion layer is further subdivided into seven indicator layers, as shown in Table 4.

2) The evaluation objects are categorized based on the various possible states, $M = \{M_1, M_2, M_3, \dots, M_N\}$, corresponding to four evaluation levels: 'Excellent', 'Good', 'Average', and 'Poor'. Then, corresponding numerical values are assigned to each evaluation grade, resulting in the value set $\{90, 80, 60, 50\}^T$. The score range and grade division criteria are as follows: Excellent for scores above 90, Good for scores between 80 and 89, Average for scores between 60 and 79, and Poor for scores below 69. These standards allow the evaluation objects to be assessed and assigned corresponding grades.

3) Weights reflect the relative importance of each indicator within the evaluation system, and the setting of these weights will directly influence the scientific validity of the final evaluation results. In this study, the AHP method is used to determine the weights for the evaluation system. As shown in Table 3, the weight for the criterion layer is $w_A = (0.3783, 0.6217)$, while the weight vector for the indicator layer is $w_B = (0.5394, 0.2823, 0.1206, 0.0576)$, and $w_C = (0.5695, 0.3331, 0.0974)$.

4) The fuzzy comprehensive evaluation matrix is composed of the degree of membership between each evaluation indicator and the evaluation set. For the three design schemes, fuzzy comprehensive evaluation matrices are established based on the scores provided by 20 experts for the criterion layer and indicator layer.

Table 4

Membership Degree of Indicators				
Scheme 1 R_{F1}	0	0.20	0.35	0.45
	0.05	0.10	0.45	0.40
	0	0.15	0.55	0.30
	0.05	0.15	0.40	0.40
Scheme 1 R_{F2}	0	0.20	0.55	0.25
	0.05	0.25	0.25	0.45
	0	0.35	0.35	0.30
Scheme 2 R_{S1}	0.15	0.35	0.25	0.25
	0.10	0.45	0.15	0.30
	0.15	0.30	0.25	0.30
	0.10	0.20	0.30	0.40
Scheme 2 R_{S2}	0.10	0.40	0	0.50
	0.10	0.30	0.15	0.45
	0.15	0	0.50	0.35
Scheme 3 R_{T1}	0.10	0.75	0.15	0
	0.25	0.50	0.15	0.10
	0.30	0.60	0.05	0.05
	0.10	0.75	0.10	0.05
Scheme 3 R_{T2}	0.25	0.65	0.10	0
	0.20	0.60	0.10	0.10
	0.30	0.55	0.15	0

After obtaining the fuzzy comprehensive evaluation matrix for each factor, the next step is to synthesize the matrix by combining the weights of each indicator w_i with the corresponding fuzzy comprehensive evaluation matrix, thus constructing a first-level evaluation matrix.

First-level Fuzzy Evaluation of Each Scheme

1. Scheme 1:

$$B_{B1} = R_{F1} \cdot w_B = [0.0170 \ 0.1628 \ 0.4052 \ 0.4149]$$

$$B_{C1} = R_{F2} \cdot w_C = [0.0167 \ 0.2313 \ 0.4306 \ 0.3215]$$

2. Scheme 2:

$$B_{B2} = R_{S1} \cdot w_B = [0.1330 \ 0.3635 \ 0.2246 \ 0.2788]$$

$$B_{C2} = R_{S2} \cdot w_C = [0.1049 \ 0.3277 \ 0.0987 \ 0.4687]$$

3. Scheme 3:

$$B_{B3} = R_{T1} \cdot w_B = [0.1665 \ 0.6613 \ 0.1350 \ 0.0371]$$

$$B_{C3} = R_{T2} \cdot w_C = [0.2382 \ 0.6236 \ 0.1049 \ 0.0333]$$

The first-level fuzzy evaluations of Scheme 1, Scheme 2, and Scheme 3 are as follows:

$$R_F = \begin{bmatrix} 0.0170 & 0.1628 & 0.4052 & 0.4149 \\ 0.0167 & 0.2313 & 0.4306 & 0.3215 \end{bmatrix}$$

$$R_S = \begin{bmatrix} 0.1330 & 0.3635 & 0.2246 & 0.2788 \\ 0.1049 & 0.3277 & 0.0987 & 0.4687 \end{bmatrix}$$

$$R_T = \begin{bmatrix} 0.1665 & 0.6613 & 0.1350 & 0.0371 \\ 0.2382 & 0.6236 & 0.1049 & 0.0333 \end{bmatrix}$$

Second-level Fuzzy Rating of the Smart Agricultural Management Cloud Platform

The second-level fuzzy evaluations of Scheme 1, Scheme 2, and Scheme 3 are as follows:

$$B_F = [0.0168 \ 0.2054 \ 0.4210 \ 0.3568]$$

$$B_S = [0.1155 \ 0.3381 \ 0.1463 \ 0.3969]$$

$$B_T = [0.2111 \ 0.6379 \ 0.1163 \ 0.0347]$$

Finally, the percentage scores for Scheme 1, Scheme 2, and Scheme 3 are 68.822, 71.498, and 80.524, respectively. The evaluation levels of Scheme 1 and Scheme 2 are "Average," while the evaluation level of Scheme 3 is "Good." Therefore, Scheme 3 is the best scheme.

RESULTS

Optimization of Evaluation Results

The evaluation level of the smart agricultural cloud platform is the result of the combined effect of the indicator layer weights and the scheme scores. In summary, by analyzing the indicator layer weights, two key indicators, 'Aesthetics' and 'Readability,' were identified as needing optimization. This provides a clear direction for UI optimization of the smart agricultural cloud platform. By combining actual user heatmaps, high-frequency click areas can be analyzed, and visual enhancements can be made in these areas to improve the platform's aesthetics and readability. The optimized interface will be re-evaluated using the fuzzy comprehensive evaluation system to verify the effectiveness of the improvements, ultimately yielding the optimized evaluation level. This method not only scientifically quantifies the improvement in user experience but also provides data support and practical guidance for future UI design optimization.

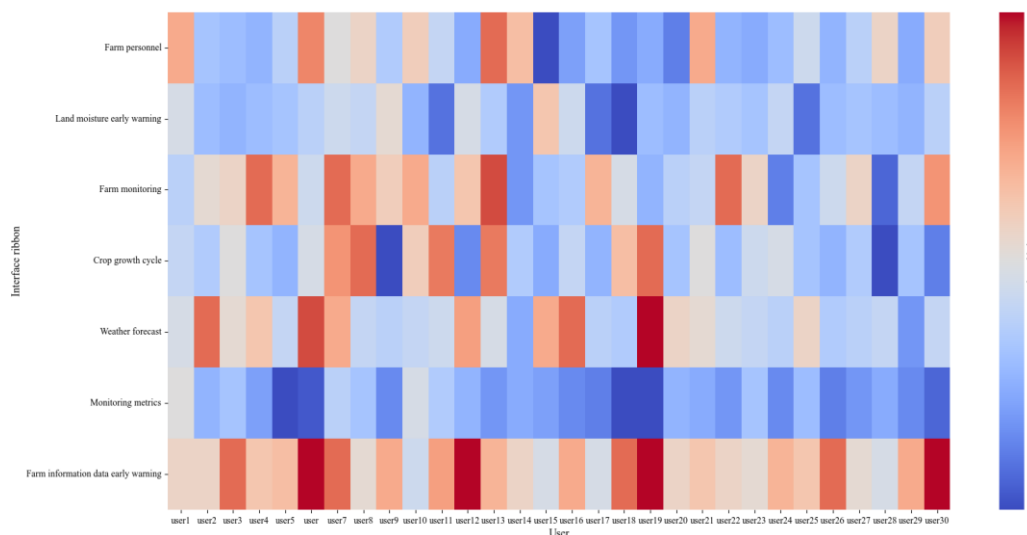


Fig. 7 – User Click Heatmap

Based on the analysis of the click heatmap in Figure 7, the area with the highest click frequency was identified as the "Farm Information Data Warning" section, while the area with the lowest click frequency was the "Land Use" section. In response to these high-click areas, improvements were proposed for the UI interface's "Aesthetics" and "Readability" indicators.

To further optimize the overall user interface (UI) effect, this study implemented a series of targeted improvements. Firstly, a visual optimization was applied to the functional area background by brightening the background tone, creating a fresher and more open visual experience, effectively enhancing operational convenience. At the same time, the interface at the top of the Smart Agricultural Management Platform dynamically displays weather scenes based on real-time weather conditions, not only enriching the interface's information but also greatly enhancing its visual appeal.

In terms of font design, to meet users' needs for information clarity, the font was adjusted to a bold style to ensure that users can quickly grasp the information while browsing, reducing visual fatigue and improving information retrieval efficiency. For the high-click area "Farm Information Data Warning," its design details were optimized. The alarm icon and related text colors were changed to prominent red, and the font size was increased and made bolder, creating a clear contrast with other information, highlighting the importance of the warning information, and making the key data in this area clearer and more readable. This ensures that users can quickly detect anomalies and take timely actions.

Considering the differences in user attention to different information modules, the low-click frequency "Regulatory Indicators" module was replaced with the "7-Day Weather Forecast." In this module design, a color-coding strategy was adopted to distinguish state information, with abnormal weather conditions highlighted in red text, helping users quickly identify key weather changes and enhancing the practicality and convenience of the information. Additionally, the "Farm Monitoring" module was subdivided into "Farm Greenhouse Monitoring" and "Farm Field Monitoring," with the display method of various farm information data optimized in the interface layout to increase visibility. Through reasonable layout and highlighting key data, users can quickly and accurately access the detailed farm information they need. The improved UI design interface is shown in Figure 8.



Fig. 8– Optimized Interface of Scheme 3

By using the established UI design evaluation system, the optimized UI of the smart agricultural management cloud platform was re-assessed, with the overall score increasing from 80.524 to 86.927, nearing the excellent level. This study focused on optimizing two key indicators: "Aesthetics" and "Readability." The optimization yielded ideal results, verifying the feasibility of this method in improving the human-computer interaction experience of the platform. In future optimization stages, the smart agricultural cloud platform can refer to this process and prioritize gradual improvements on the indicators that have the greatest impact on the final evaluation results.

CONCLUSIONS

Through the AHP method, the weights of interface design factors were quantified, and a comprehensive evaluation model was established using FCE. This model was used to compare and analyze three UI design schemes, ultimately selecting the optimal one. Based on this, the selected UI design was further optimized using user heatmap data and indicator layer weights. The following conclusions can be drawn:

1) During the UI design optimization process, the font size and color of the high-click areas were adjusted based on user click heatmaps, significantly improving the data visualization and user experience. This optimization not only simplified the operational workflow but also enhanced the overall operational efficiency and energy management efficiency. In particular, the optimization of the "Farm Information Data Alerts" section improved the clarity and readability of information in this area, thereby enhancing the functionality and real-time capabilities of the system.

2) The UI design score of the optimized smart agricultural management cloud platform increased from 82.396 to 87.471, demonstrating the scientific validity and effectiveness of the AHP/FCE method in evaluating the UI design of the platform and providing a reference for future smart agricultural management cloud platform designs.

3) The UI design evaluation and optimization system developed in this study provides valuable reference points for the decision-making stage of UI design. It helps identify and optimize deficiencies in design and offers data support and practical experience for future UI design improvements.

ACKNOWLEDGEMENT

This work was supported by the Shandong Province Science and Technology Minor Enterprises Innovation Ability Promotion Project (Project number: 2023TSGC1014), General Program of China Higher Education Association (23NL0406) and the Key Project of Undergraduate Teaching Reform Research in Shandong Province (Z2022263).

REFERENCES

- [1] Feng W., Xingjie G., Songmei Z., (2025). Fuzzy comprehensive evaluation of micro-perfusion filter based on analytic hierarchy process and entropy weight method (基于层次分析法和熵权法的微灌过滤器模糊综合评价). *Mechanical design*, ISSN1007-4929, China.

- [2] Guodong X., Xiao L., Ming X., (2009). Evaluation of human-machine interfaces based on ease of use (基于易用性的人机界面评价). *Journal of Southwest Normal University (Natural Science Edition)*. Vol. 34, ISSN 2097-3586, pp. 98-102, China.
- [3] Huiliang Z., Lin H., Li L., (2016). Evaluation of Digital Human-Machine Interface Experience Based on TOPSIS (基于 TOPSIS 的数字化人机界面体验度量评价). *Mechanical design*. Vol. 33, ISSN1001-2354, pp.120-123, China.
- [4] Huijun Y., Yuding Z., Baoying D., (2020). Research on the design of agricultural product service cloud platform based on "Internet +". (基于“互联网+”的农产品服务云平台设计研究). *Southern Agricultural Machinery*. Vol. 51, ISSN1672-3872, pp.58-89+67, China.
- [5] Haibiao W., Wenjing X., (2019). Evaluation of emergency management of earthquake safety communities based on AHP-entropy matter elements (基于 AHP-熵物元的地震安全社区应急管理评价). *Science and Technology of Work Safety in China*. Vol. 15, ISSN1673-193X, pp.55-60, China.
- [6] Hui R., (2019). Research on the location of education and training institutions based on fuzzy logic and AHP (基于模糊逻辑和 AHP 的教育培训机构选址研究). *Geospatial information*. Vol. 17, ISSN1672-4623, pp.85-88, China.
- [7] L. Saaty T., (2008). Decision Making with the Analytic Hierarchy Process. *International Journal of Services Sciences*. Vol. 1, ISSN 1753-1454, pp.83-98, American.
- [8] Lin G., Junkai Y., Hao W., (2024). Research on Situation Assessment of Industrial Control Network Based on Analytic Hierarchy Process (基于层次分析法的工控网络态势评估研究). *Journal of Xi'an University of Technology*. Vol. 40, ISSN1006-4710, pp.260-268, China.
- [9] Qinglan W., Yueqin W., (2025). Research on the texture design of automobile leather seats based on perceptual engineering and fuzzy analytic hierarchy process (基于感性工学和模糊层次分析法的汽车皮革座椅肌理设计研究). *Leather Science & Engineering*. Vol. 35, ISSN 1004-7964, pp.98-106, China.
- [10] Qianrong L., Qian Yue D., Dexian Z., (2018). Site selection of prefabricated building PC component factory based on fuzzy analytic hierarchy process (基于模糊层次分析法的装配式建筑 PC 构件厂选址). *Journal of Civil Engineering and Management*. Vol. 35, ISSN2095-0985, pp.111-117,123, China.
- [11] Shuhang Z., Bi Q., Li W., (2022). Human-machine evaluation and optimization of plant protection UAV remote control based on AHP/FCA/TRIZ (基于 AHP/FCA/TRIZ 的植保无人机遥控器人机评价与优化). *Journal of Shandong University of Technology (Natural Science Edition)*. Vol. 36, ISSN1672-6197, pp.46-51, China.
- [12] Tongxin Z., Liu Dan., Baoxing W., (2019). Improve the application of fuzzy analytic hierarchy process in workshop layout evaluation (改进模糊层次分析法在车间布局评价中的应用). *Combined machine tools and automated machining technology*. Vol. 06, ISSN1001-2265, pp.145-148, China.
- [13] Xiangsheng W., Zaiming C., (2019). The open-pit mine mining and drainage scheme based on AHP-GRAP method is optimized (基于 AHP-GRAP 法的露天矿采排方案优选). *Coal engineering*. Vol. 51, ISSN1671-0959, pp.62-67, China.
- [14] Yimin W., Jixing G., Linsheng L., (2017). Evaluation of subgrade condition during highway operation period based on analytic hierarchy process (基于层次分析法的公路运营期路基状况评价). *Journal of South China University of Technology (Natural Science Edition)*. Vol. 45, ISSN1000-565X, pp.37-43,51, China.
- [15] Yongfeng L., Liping Z., (2012). Evaluation Method of Product Usability Based on Fuzzy Analytic Hierarchy Process (基于模糊层次分析法的产品可用性评价方法). *Journal of Mechanical Engineering*. Vol. 48, ISSN0577-6686, pp.183-191, China.
- [16] Ying X., Tan T., Wenfei Z., (2024). Research on usability evaluation of HM-I design of intelligent vehicles based on AHP-FCE (基于 AHP-FCE 的智能汽车 HM-I 设计可用性评价研究). *Packaging Engineering*. Vol. 45, ISSN1001-3563, pp.144-151, China.

DESIGN AND EXPERIMENT OF CLAMPING AND CONVEYING DEVICE FOR TRACKED SELF-PROPELLED CHINESE CABBAGE HARVESTER

履带自走式大白菜收获机夹持输送装置设计与试验

Shengbo GAO^{1,2)}, Yanwei YUAN^{1,2)}, Kang NIU^{1,2)}, Bo ZHAO^{1,2)}, Liming ZHOU^{1,2)}, Chengxu LV^{1,2)},
Shenghe BAI^{1,3)}, Shuaiyang ZHANG^{1,2)}, Ran AN^{1,2)}

¹⁾ Chinese Academy of Agricultural Mechanization Sciences Group Co., Ltd., Beijing 100083, China;

²⁾ State Key Laboratory of Agricultural Equipment Technology, Beijing 100083, China;

³⁾ Department of Electrical and Mechanical Engineering, College of Engineering, China Agricultural University, Beijing 100089, China

Tel: +86-15694469045; E-mail: gaoshengbo95@163.com; correspondent author: Yanwei YUAN

DOI: <https://doi.org/10.35633/inmateh-75-32>

Keywords: Chinese cabbage, Mechanical harvesting, Clamping and conveying device, Design optimization, Finite element simulation test

ABSTRACT

To effectively solve the problem of high damage rates and low operating efficiency of clamping and conveying in the mechanized harvesting of Chinese cabbage, a "vertical clamping+flexible conveying" system was developed. Based on the measurement and analysis of the basic physical characteristics and static compression mechanical properties of Chinese cabbage, the "vertical clamping + flexible conveying" method was applied to arrange the clamping conveyor belts longitudinally. A combination of flexible feeding and soft clamping was used to achieve low-damage transportation. A dynamics coupling simulation model of the Chinese cabbage harvesting components was established. By adjusting the structural and operational parameters of the harvesting components, a simulation test of the Chinese cabbage harvesting operation was conducted to determine the kinematic and dynamic principles of the harvesting process. The designed and developed clamping conveyor device is installed on a cabbage harvester for field performance test verification. Field test results show that the field productivity of the cabbage harvester is 0.12 hm²/h, the average value of the clamping and conveying success rate is 96.38%, and the average value of the harvesting damage rate is 7.43%. The developed clamping and conveying device can effectively meet the requirements of high efficiency, and low energy consumption, low damage during harvesting, while also enhancing adaptability to Chinese cabbages of varying head diameters.

摘要

为提高大白菜机械化收获装备的作业性能,有效解决大白菜机械化收获过程中夹持输送损伤大、作业效率低的问题,研制了一种“立式夹持+柔性输送”夹持输送系统。基于测定分析大白菜基本物理特征参数和静载压缩力学特性,采用“立式夹持+柔性输送”方式对夹持输送带进行纵向排布,利用挠性喂入与柔性夹持的配合作业方法实现低损输送。建立大白菜株体-采收部件动力学耦合仿真模型,通过改变采收部件的结构参数和工作参数等,进行大白菜收获作业仿真试验,探明大白菜采收过程运动学、动力学规律。最后,将设计开发的夹持输送装置配置在大白菜收获机上进行田间性能试验验证。结果表明,夹持输送装置采用“立式夹持+柔性输送”的方式,可以实现对大白菜的高效低损输送,提高对不同球径大白菜的采收适应性。通过利用离散元法建立动力学耦合仿真模型,发现夹持输送过程大白菜所受合力大小呈现波动态势,表明夹取过程大白菜与夹持皮带的相互作用力呈动态变化。田间试验结果表明,大白菜收获机田间生产率为0.12hm²/h,夹持输送成功率均值为96.38%,采收破损率均值为7.43%,说明设计开发的夹持输送装置有效地满足高效、低能耗、低损伤的收获要求,提高了对不同球径白菜收获的适应性。

INTRODUCTION

Chinese cabbage (*Brassica pekinensis* (Lour.) Rupr.) is one of the vegetables with the largest planting area in China, accounting for about 15% and 19% of the total sown area and total output of vegetables in China (Hu et al., 2022; Liu et al., 2020). It has distinctive planting characteristics, because it has a high unit yield, storage, and transportation, long supply period, it is nutrient rich and has other advantages. In China to maintain the supply of vegetables, regulating market prices, and other aspects play a vital role (Ding et al., 2021). Chinese cabbage production methods are relatively rudimentary with low levels of mechanized harvesting and industrialization.

Currently, harvesting operations still rely entirely on manual labor, resulting in low efficiency, high labor intensity, and high operating costs. Additionally, the quality and efficiency of manual harvesting are difficult to control (Zhou *et al.*, 2023; Zhao *et al.*, 2018).

The countries that focus on cabbage harvester-related technology and equipment are mainly Japan, China, South Korea, and other countries. Most of the early cabbage harvester structures first used the spiral extraction device for extraction, and then a fixed single disk knife to complete the root-cutting harvesting, but extraction and root-cutting damage was relatively large (Park *et al.*, 2021). In order to reduce the extraction and root-cutting damage, Japan Yanmar and Osada Nouki jointly developed a tracked self-propelled cabbage harvester, which ensures the stability of the clamping and conveying process as well as the consistency of the root cutting, but the overall structure is more complex and the manufacturing cost is higher (Xu *et al.*, 2009). Researchers from Chungnam University in South Korea, Kim & Yeongsoo, (2020), developed a small tracked self-propelled cabbage harvester that demonstrated effective pulling and harvesting performance. However, its integrated pulling and conveying device, along with a complex conveyor mechanism, resulted in poor adaptability to different cabbage varieties (Park *et al.*, 2021). To enhance conveyance efficiency and stability during harvesting while reducing manufacturing costs, efforts have been made to optimize and improve the design of a tractor-mounted cabbage harvesting system (Ali *et al.*, 2019). Han *et al.* developed a tractor-mounted cabbage harvester, utilizing two tilt-mounted notched disks instead of a screw plucking device. This design proved highly efficient and well-suited for large-scale cabbage planting in northern China. However, the harvester required relatively high supporting power (Han *et al.*, 2021). Myat *et al.* designed a four-row cabbage harvester that employed a pulling shovel to extract the cabbages, followed by root transportation and cutting using V-shaped clamping belt and a single serrated disk. However, the harvesting process experienced issues such as root slanting cuts and missed cuts, leading to a high vegetable damage rate (Myat *et al.*, 2021).

Due to the tender leaves of cabbage, the clamping conveyor device will cause extrusion damage to the cabbage when clamping, so it is necessary to study the extrusion characteristics of cabbage before designing the conveyor device and design a flexible and adaptive clamping conveyor device to prevent excessive clamping. The most common types of clamping and conveying devices are double screw type and conveyor belt type (Li *et al.*, 2017; Ji *et al.*, 2023; Ding *et al.*, 2022). The double screw rod-type clamping and conveying device consists of a pair of counter-rotating screw rods. After the extraction device removes the cabbage, it is transferred to the double screw rods, where it is clamped and lifted through spiral motion (Ding *et al.*, 2018; Toncheva *et al.*, 2017). Conveyor belt-type clamping and conveying device mainly consists of two conveyor belts, with a spring tensioning mechanism designed inside the belts. This mechanism allows for secure clamping and transportation of cabbages of varying sizes (Zhou *et al.*, 2024). Shandong Agricultural University has developed a self-propelled cabbage harvester with broad adaptability. This harvester adopts a conveyor belt-type conveying and lifting system, utilizing an elastic tensioning mechanism to automatically adjust to cabbages with different physical characteristics (Zhang *et al.*, 2022).

It is necessary to improve and optimize the structural parameters of the clamping and conveying mechanism of the cabbage harvester, explore the interactions during the clamping and conveying process, and develop a low-damage, high-efficiency, and automated cabbage harvesting technology. The main objectives of this study are: (1) To determine and analyze the basic physical parameters and static load compression mechanical properties of cabbage; (2) To conduct kinematic and dynamic analysis of the cabbage clamping and conveying process, optimize the structural parameters, and complete the design of the clamping and conveying mechanism; (3) To establish a dynamically coupled simulation model of the Chinese cabbage harvesting components and analyze the kinematics and dynamics of the harvesting process; (4) To validate the machine prototype through field trials, verifying its actual field performance and identifying an optimized low-loss, high-efficiency, automated harvesting technology.

MATERIALS AND METHODS

Experimental materials and equipment

Chinese cabbage is the primary focus of harvesting machinery. Studying its basic physical characteristics and mechanical properties is essential for establishing a meaningful statistical scale model, providing a design basis and theoretical foundation for the development of cabbage harvesting equipment. Cabbages that had reached maturity and met harvesting standards were selected as test samples. To ensure reliability, only cabbages with an undamaged appearance and intact roots were chosen based on the principle of randomization and five-point sampling.

The test instruments and types of equipment used to measure the basic physical characteristic parameters of cabbage mainly include a tape measure, electronic digital display vernier caliper, electronic balance, beaker, measuring cylinder, and so on. Fifty plants were randomly selected for the measurement of basic physical characteristics and statistics. First of all, the electronic digital display vernier caliper was used to determine the total height of the cabbage plant, head height, head diameter, and other dimensions. Then, an electronic balance and electronic scales were used to measure the physical parameters of each sample three times, and the average value and standard deviation were calculated. These samples were placed horizontally between two rigid parallel plates, with 30 randomly selected cabbages tested using a GHS2000 universal testing machine under a specific loading rate. The instruments and equipment used for determining the basic physical characteristics and static compression properties of cabbage are listed in Table 1.

Table 1

Test equipment and instruments				
Equipment Name	Model Specification/Unit	Range	Accuracy	
Electronic Balance	CZ3002/g	0-300g	0.01	
Electronic Universal Testing Machine	GHS2000/N	0-2000	0.001	
Electronic Weigher	/kg	0-10kg	0.01	
Tape Rule	/m	0-3m	1	
Three-key Digital Vernier Calipers	SF2000/mm	0-200mm	0.1	

Physical and mechanical characteristics of Chinese cabbage

● Research on the physical characteristics of cabbage cultivation soil

Soil firmness was measured directly by a soil firmness meter, soil water content was measured by the drying method, and soil bulk weight was determined by the ring knife method. Soil physical properties were selected as evaluation indexes, including soil compactness, soil water content, and soil bulk density. Ten soil samples were randomly collected from the field using the five-point sampling method.



Fig. 1 - Research on soil compactness and soil water content testing

● Determination of basic physical characteristics of Chinese cabbage

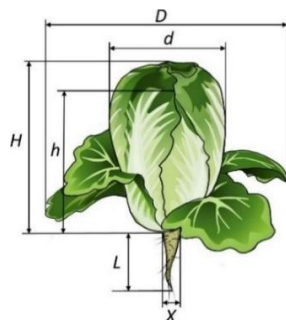


Fig. 2 - Terminology for the determination of basic physical properties of Chinese cabbage

D-Spread; d-Ball Diameter; H-Total Height; h-Nodule Height; X-Root Diameter; L-Root Length

After excluding immature and decayed cabbages from the experimental field, 50 cabbages were selected based on the principles of random sampling, diagonal sampling, and classification. In accordance with the design requirements of the cabbage harvesting equipment, the following parameters were chosen as evaluation indicators for the study of cabbage physical characteristics: total height of the whole cabbage plant (mm), nodule height (mm), spread (mm), nodule diameter (mm), total mass (kg), taproot diameter (mm) and taproot height (mm). The terminology used for determining the basic physical characteristics of cabbage is illustrated in Fig. 2, while the data collection process for these parameters is shown in Fig. 3.



Fig. 3 - The process of collecting basic physical characteristic parameters of Chinese cabbage

● **Determination of static load compression mechanical properties of Chinese cabbage**

This test was conducted to examine the radial static load compression mechanical properties of cabbage. The extrusion probe was applied to three different sections of the cabbage: the head, waist, and bottom, forming three test groups (Zhang et al., 2020; Du et al., 2019). To ensure test accuracy, the stress relaxation test of the cabbage required minimal deformation. A static measurement method was used, and the extrusion speed of the probe was set to 20 mm/min to apply pressure to the test samples.

The first group of Chinese cabbage samples (a total of 10) was placed horizontally on the fixed plate, and the bottom was fixed with a small amount of hot-melt adhesive, and the extrusion probe of the universal testing machine was placed squarely on the head of the test samples. Then, the test was carried out immediately using the GHS2000 universal testing machine at a lower loading rate of 20 mm/min. After the head-loading test was completed, the same method as described above was used to place the second group of samples (a total of 10). After the completion of the head loading test, the second group of samples (10 in total) was tested by the same method as described above, with the waist facing the extrusion probe of the universal testing machine to complete the test at a lower loading rate of 20 mm/min. Finally, the bottom of the third group of test samples was subjected to static loading compression test in the same way. When the first breakage of the exterior of the cabbage was observed, the loading was stopped, and the extrusion pressure on the test specimens was recorded to investigate the minimum extrusion pressure required for the cabbage to reach the breakage condition. Loading then continued until the cabbage was completely broken, at which point loading was stopped. This process aimed to examine the crack shape and direction in different parts of the cabbage under compression. The static compression mechanical properties test of the cabbage is shown in Fig. 4.



Fig. 4 - Static load compression mechanical characterization of Chinese cabbage plants

Structure and working principle of the whole machine

The current level of mechanization in cabbage harvesting is extremely low, mainly relying on manual labor. Additionally, harvested cabbage must not only meet agronomic production quality requirements but also minimize mechanical damage during the harvesting process to ensure a neat and visually appealing appearance (Sarkar et al., 2024; Kim et al., 2020).

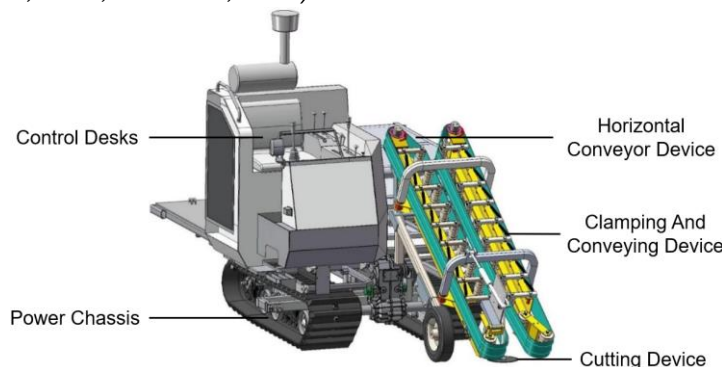


Fig. 5 - Schematic diagram of the single-row crawler-driven Chinese cabbage harvester structure

Based on the demand for mechanized harvesting of Chinese cabbage, the advantages and disadvantages of existing harvesting methods were comprehensively analyzed. The harvesting method selected for this study involves cutting the roots first, followed by clamping and conveying, and finally transporting the cabbage to the collection device. This study combines cabbage planting agronomy and harvesting requirements, developed a self-propelled cabbage harvester equipped with 52 kW engine. Through the design of well-matched root cutting device, clamping and conveying mechanism and lateral conveying device, the cabbage harvesting process can be completed in a single operation. The structure of the self-propelled cabbage harvester is shown in Fig.5.

During the working process of the harvester, the clamping conveyor device is first adjusted to an inclination angle of 20°~30° relative to the ground. The cutting device, driven by a hydraulic motor, completes the cutting of the cabbage roots. After the roots are cut, the cabbages are transferred through the clamping conveyor device to the lateral conveyor device, and finally, they are manually screened and loaded into baskets. The working process of the cabbage harvester is shown in Fig. 6. The main technical parameters of the harvesting machine are presented in Table 2.

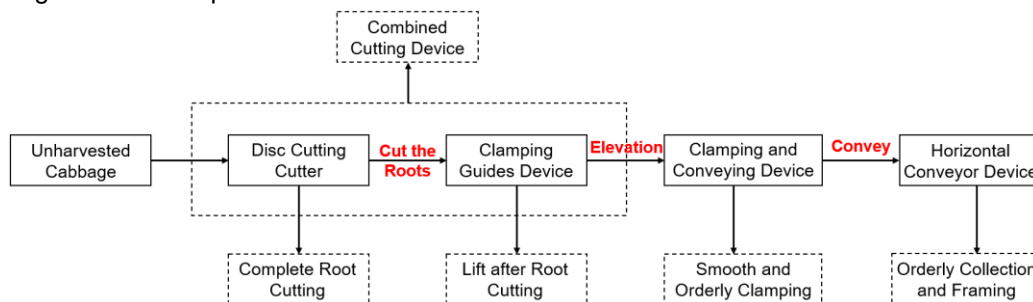


Fig. 6 - The working process of the cabbage harvester

Table 2

Main technical parameters of Chinese cabbage harvester

Technical Parameters	Numerical Value
Structural Form	Crawler-driven
Overall Dimensions /mm	4100×2000×2300
Auxiliary Power/kW	52
Output Speed/(r/min)	2500
Forward Speed/(m/s)	0-2
Number of Rows Harvested	1
Harvest Row Spacing/mm	400-500
Working Width/mm	550
Distance between Plants/mm	350-450
Machine Weight/kg	1520

Design and analysis of clamping conveyor device

Cabbage is transported using a horizontal parallel conveyor belt that clamps the top, which has poor adaptability to the uneven sizes of cabbage. Additionally, compression mechanical properties tests indicate that the radial clamping force on cabbage is relatively small, making it less likely to cause significant deformation or damage. Therefore, this design utilizes a pair of vertically arranged clamping belts, relying on friction to securely clamp the radial surface of the cabbage.

Due to the fragility of cabbage leaves, they are prone to mechanical damage. Therefore, based on the operating environment and the biological characteristics of cabbage. The structure of the clamping and conveying device designed in this program is shown in Fig.7.

The clamping and conveying device mainly consist of clamping belt, active pulley, driven pulley, tensioning pulley and driving hydraulic motor. The two active pulleys are symmetrically installed at the end of the clamping and conveying device. The driving hydraulic motor is installed on the frame above the active pulley and is connected to the driving shaft of the active pulley through a coupling. The driven pulley is suspended and installed at the front of the frame, positioned at the front end of the cutting disk, ensuring that the position of the pulleys remain in the same plane. The tensioning pulleys are installed on both side beams of the frame, with tensioning springs ensuring constant contact with the clamping belt, pushing it outward to

maintain proper tension. During operation, two independent hydraulic motors drive the active pulleys, effectively clamping the cabbage between the flexible clamping belts arranged longitudinally. The distance between the clamping belts allows the cabbage head to pass through, while the elastic tensioning wheel ensures that the flexible clamping belt adapts to cabbages of different sizes.

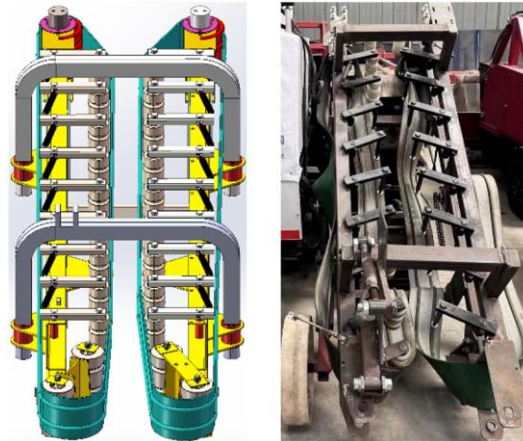


Fig. 7 - The structure of the clamping and conveying device

When the clamping position coincides with the center of gravity, the clamping stability reaches its maximum and the clamping effect is optimal. Therefore, the height of the clamping belt must be appropriately set to ensure compatibility with the cutting disk knife. The drive direction of the clamping belt has an inclination angle relative to the forward direction, which directly affects the accuracy of cabbage clamping and conveying. Based on existing research data, the optimal inclination angle range is determined to be 15° ~ 20°.

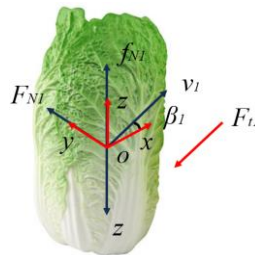


Fig. 8 - Chinese cabbage clamping conveying process force analysis

The force analysis of the cabbage in the clamping and conveying process is shown in Fig. 8. According to Fig. 8, the condition prevents the cabbage from tilting during the clamping and conveying process is:

$$\begin{cases} f_{N1} \geq mg \\ f_{N1} = F_{N1}\mu_{N1} \end{cases} \quad (1)$$

where: f_{N1} is the friction force; F_{N1} is the clamping force; μ_{N1} is the coefficient of static friction between the clamping belt and the cabbage; m is the mass of the cabbage.

The greater the clamping force and friction force provided by the clamping conveyor belt, the less likely it is to produce tilting and falling. However, excessive clamping force on the conveyor belt is likely to lead to clogging and exacerbate mechanical damage to the cabbage. To prevent excessive clamping force from damaging the outer leaves, the clamping force F_{N1} must remain below the maximum compression damage threshold. Based on the cabbage's external dimensions and weight parameters the average mass of a cabbage is set at $m = 2.3$ kg, and the static friction coefficient μ_{N1} is 0.57, resulting in a minimum required clamping force F_{N1} of at least 87.20 N.

To avoid slippage of the clamping conveyor belt, the initial tension F_0 after tensioning of the clamping belt is:

$$\begin{cases} F_0 = 500 \frac{P_c}{z v_1} (K_\alpha^{2.5} - 1) + q v_1^2 \\ P_c = (F_{t1} - F_{t2}) v_1 \end{cases} \quad (2)$$

where: F_0 is the initial tension of the clamping belt; P_c is the conveying power; z is the number of belt roots; K_α is the correction coefficient of the wrapping angle; v_1 is the linear velocity of the clamping belt; q is the mass of the clamping belt per unit length; F_{t1} , F_{t2} are the tensions of the tight and loose sides of the clamping belt, respectively.

In order to prevent cabbage from piling up and clogging at the feed opening, the clamping belt line speed v_1 should be greater than the forward speed of the harvester v_{m1} :

$$\begin{cases} v_1 \geq \frac{v_{m1}}{\cos\beta_1} \\ v_1 = \frac{\pi n_t D_1}{60} \end{cases} \quad (3)$$

where: v_{m1} is the forward speed of the harvester; β_1 is the angle between the clamping belt and the horizontal plane; D_1 is the diameter of the active pulley, mm; n_t is the rotational speed of the active pulley.

If the forward speed of the harvester v_{m1} is greater than the speed of the clamping conveyor, the cabbage will accumulate due to delayed conveyance, leading to clogging at the feed inlet. Conversely, if the forward speed of the harvester is lower than the speed of the clamping conveyor, clogging will not occur, ensuring smooth operation. As the speed of the active pulley n_t increases, the linear velocity v_1 of the clamping conveyor belt also increases, which enhances the efficiency of the clamping conveyor. However, to prevent cabbage accumulation and clogging at the feed inlet, the forward speed v_m of the harvester can be appropriately reduced and the inclination angle β_1 of the clamping conveyor belt can be adjusted accordingly.

In order to adapt to the main cultivar of cabbage “Si Jin” in Yucheng, Shandong Province, the maximum adjustable center spacing of the clamping and conveying device designed is set to 240 mm. The spacing of the feeding mechanism is set within the range of 140~200 mm, ensuring smooth passage for cabbages of varying ball diameters. Additionally, the following parameters are set: q is 0.25 kg/m, z is 1, K_a is 0.92, and β_1 is 15°, so that under non-blocking conditions, the active roller speed n_t is no less than 282.6 r/min, the linear speed of the clamping belt v_1 is no less than 1.72 m/s, the power of a single belt P_c is about 0.42 kW, and the minimum initial tension of the clamping belt F_0 is 212.76 N. The maximum adjustable center spacing of cabbage is 240 mm, while the feeding mechanism spacing is set within the range of 140~200 mm to ensure the smooth passage of cabbages of varying ball sizes.

Simulation and analysis of EDEM-based clamping conveying device

SolidWorks 3D design software was used to construct and simplify the harvesting component model. The three-dimensional model of Chinese cabbage was imported into EDEM for particle filling to determine the fixation mode of Chinese cabbage plant and soil. Harvesting simulation tests were conducted by modifying structural and working parameters.

The Chinese cabbage was simplified into two parts: the sphere and the rhizome. SolidWorks was used to create a 3D model of the cabbage, with parameter calibration based on real cabbage conditions. According to cabbage planting agronomy, a ridge soil ditch model was established, featuring a ridge top width of 650 mm and a plant spacing of 400 mm.

Table 3

Simulation model material parameters			
Materials	Densities/(kg/cm ³)	Poisson's Ratio	Shear Modulus/MPa
Chinese Cabbage	880	0.30	4.06
Soil	1360	0.40	1
Disk Cutting Cutter	7850	0.28	8.20×10 ⁴
Clamping Conveyor Belt	4000	0.25	1×10 ⁴

Table 4

Simulation model contact parameters			
Contact Type	Coefficient of Restitution	Coefficient of Static Friction	Coefficient of Kinetic Friction
Soil - Soil	0.20	0.40	0.30
Chinese Cabbage - soil	0.40	0.30	0.28
Chinese Cabbage - Chinese Cabbage	0.42	0.46	0.04
Soil - Disk Cutting Cutter	0.30	0.40	0.05
Disk Cutting Cutter - Chinese Cabbage	0.43	0.67	0.05
Clamping Conveyor Belt - Cabbage	0.50	0.50	0.01

The harvester model was simplified, retaining only the disk knife, clamping device, and traveling device. Based on the study of the basic physical parameters and mechanical properties of Chinese cabbage, the material parameters and contact parameters of the model were set. The working parameters of the cabbage harvesting components are shown in Fig. 9 and Table 5. The initial forward speed of the harvester was set to 0.1 m/s, the rotational speed of the disk knife to 100 r/min, and the speed of the conveyor belt to 100 r/min.

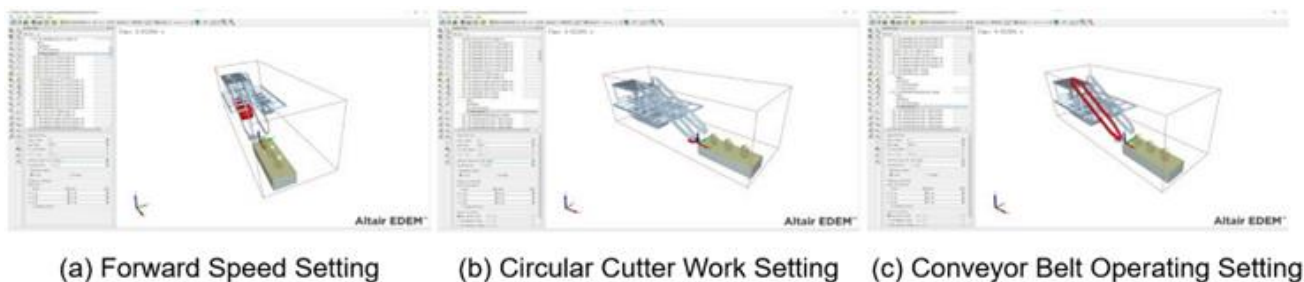


Fig. 9 - Working parameterization of Chinese cabbage harvesting components

Table 5

Simulation model working parameters setting			
Experiment No.	Forward Speed (m/s)	Cutter Speed (r/min)	Conveyor Belt Speed (r/min)
1	0.1	100	100
2	1.0	100	100
3	1.5	100	100
4	0.1	200	100
5	0.1	300	100
6	0.1	100	150
7	0.1	100	200

Arrangements for field experiment

● Experiment object

The developed self-propelled Chinese cabbage harvester was field-tested on November 18, 2024, at the planting demonstration base of Yatai Farm in Yucheng City, Dezhou City, Shandong Province. The experimental site followed a monoculture two-row open-field planting pattern. The agronomic parameters for cabbage planting were row spacing of 450 mm, plant spacing of 400 mm, and row top width of about 650 mm. The test subject was the Shandong Yucheng staple cabbage variety "Si Jin", with a total mature cabbage height ranging from 380 to 420 mm. The ball height varied from 270 to 290 mm, the spreading degree from 450 to 480 mm and the ball diameter from 160 to 180 mm. The total weight ranged between 2.1 and 2.5 kg. Additionally, soil firmness was measured at 13.46 MPa and soil moisture content was recorded at 24.75%.

● Indicators for the evaluation of experiment results

The field productivity, clamping and conveying success rate and the harvest damage rate were taken as the evaluation indexes of the performance of cabbage harvesting equipment.

(1) Field productivity

Chinese cabbage field productivity refers to the actual operating area covered by the harvesting equipment per unit time. Measurements should be taken in each test area, and the final value should be calculated as the average.

$$E = 3.6BV \quad (4)$$

where, E represents the field operation rate; B is the operating width of the cabbage harvesting equipment; V is the operating speed of the cabbage harvesting equipment.

(2) Clamping and Conveying Success Rate

The clamping and conveying success rate refers to the proportion of cabbages in the test area that were successfully cut at the roots, smoothly drawn into the clamping and conveying device, and transported without clogging, falling, or root loss due to cutting errors. The number of effectively clamped cabbages should be recorded during the test.

$$Q_p = \frac{N_p}{N} \times 100\% \quad (5)$$

In the formula, Q_P indicates the success rate of cabbage clamping and transportation; N_P is the number of effectively clamped and transported cabbages; N is the total number of harvested cabbages.

(3) Harvest Damage Rate

Harvest damage rate is the number of heavily damaged outer leaves and large deviations in cut root position as a proportion of the total harvest. $N_o = \frac{N_s}{N} \times 100\%$ (6)

In the formula, N_o represents the cabbage harvesting damage rate; N_s is the number of damaged cabbages during harvesting; N is the total number of harvested cabbages.

RESULT AND DISCUSSION

Measurement of physical and mechanical properties of Chinese cabbage

The measured soil compactness was (11.16 ± 3.20) kg/cm², soil water content was $(25.69 \pm 4.11)\%$, and soil bulk weight was (1.41 ± 0.26) g/cm³. The parameters of soil physical properties are detailed in Table 6. For Chinese cabbage, the total height H was (403.51 ± 22.05) mm, nodule height h was (277.32 ± 9.65) mm, spread d was (481.15 ± 33.10) mm, and nodule diameter d was (169.52 ± 9.05) mm. The total mass was (2.31 ± 0.18) kg, root diameter X was (28.78 ± 4.63) mm, and root length L was (103.76 ± 10.39) mm. The results of the basic physical characteristics of cabbage are presented in Table 7.

Table 6

Parameters of soil physical properties			
Test Indicators	Soil Compactness / kg·cm ⁻²	Soil Water Content /%	Soil Bulk Weight / g·cm ⁻³
Maximum Value	14.70	29.82	1.75
Minimum Value	8.30	21.61	1.24
Mean	11.16	25.69	1.41
Standard Deviation	1.63	2.07	0.14
Coefficient of Variation	0.15	0.08	0.10

Table 7

Basic physical characteristic parameters of Chinese cabbage							
Test Indicators	Total Height/mm	Nodule Height / mm	Spread / mm	Ball Diameter / mm	Total Mass / kg	Root Diameter/mm	Root Length / mm
Maximum Value	425.6	283.6	523.7	523.7	2.5	32.7	112.5
Minimum Value	381.5	264.3	457.5	457.5	2.1	23.4	91.8
Mean	403.5	277.3	481.2	481.2	2.3	28.8	103.8
Standard Deviation	13.6	5.4	16.7	16.7	0.2	2.6	6.1
Coefficient of Variation	0.03	0.02	0.03	0.03	0.06	0.08	0.06

In the static load compression mechanical properties test, cabbage samples were subjected to compression using an extrusion probe applied to the head, waist, and bottom of the cabbage. The resulting damage is illustrated in Fig. 10. By analyzing the crack direction after compression, the role of the clamping and conveying device in handling the cabbage can be determined, providing a theoretical basis for its design. The characteristic curves of squeezing force and displacement are shown in Fig. 11.



(a) Head Compression Results (b) Lumbar Compression Results (c) Bottom Compression Results

Fig. 10 - Damage diagram for static load compression test of Chinese cabbage plants

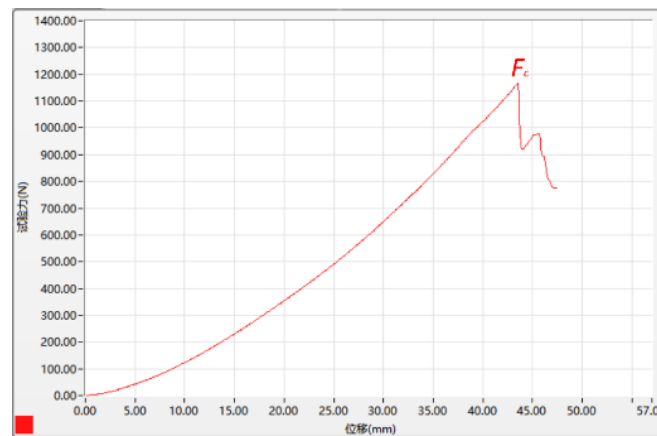


Fig. 11 - Characteristic curves of squeezing force and displacement

From the fitted curve graph, it can be seen that the cabbage strain rupture occurs when the compression displacement reaches 43.6 mm. The maximum compressive breaking force was 1166.1 N. The equation of the fitted curve for the shear characteristic test is:

$$F_p = 0.62x^2$$

where, F_p is the extrusion pressure on the cabbage strain; x is the displacement of the extrusion probe.

Simulation of Chinese cabbage harvesting process

Through the EDEM simulation interface, it can be observed that the disk cutter completes the root-cutting process at the moment when the cabbage is clamped at the front end of the clamping conveyor. The cabbage is then transported upward through the clamping conveyor, completing the entire harvesting process. From the test results, it can be seen that when the forward speed is 0.1~0.3 m/s, the rotational speed of the disk cutter is 100~300 r/min, and the rotational speed of the conveyor belt is 100~200 r/min, the cabbage root-cutting and clamping conveyor process can be successfully completed.

The harvesting process forces are shown in Figure 12. Test groups 1, 3, 5 and 7 were selected as controls. The maximum value of the combined force on the cabbage was 105.7 N. When the forward speed of the harvesting component, the rotational speed of the disk knife and the speed of the conveyor belt changed, the force on the cabbage also changed. The simulation test verified the rationality of the design of the harvesting components of the cabbage harvester. The rationality of the structural design of the device and the actual harvesting effect are further verified through subsequent field tests.

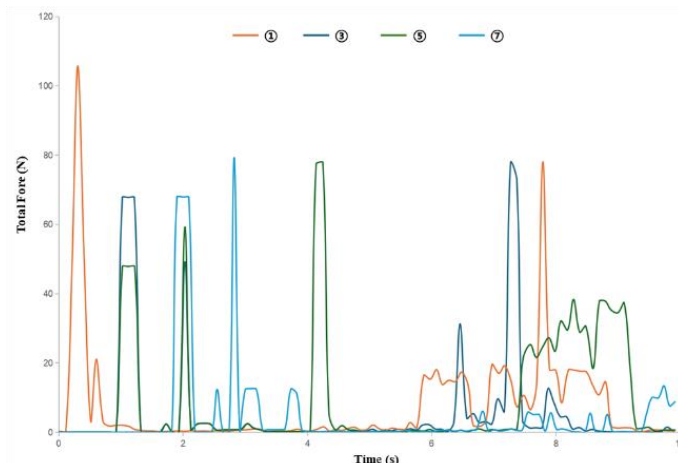


Fig. 12 - Analysis of the force results of the simulation test of Chinese cabbage

Results and analysis of the multifactorial test

Through preliminary theoretical analysis, the main influencing factors on the harvest performance index and their range of values were determined. A three-factor, five-level quadratic regression orthogonal rotary combination test was designed. The cutter speed, forward speed, and clamping belt speed were selected as the influencing factors, while the clamping and conveying pass rate was chosen as the evaluation index. The study aimed to determine the influence of factor interactions on the work performance index.

According to Table 9, the regression model for the clamping and conveying pass rate Q_p has a P -value < 0.0001 , indicating that the model is highly significant. The P -value for the lack-of-fit term is $0.2491 > 0.05$, and the correlation coefficient R^2 of the multiple regression equation is 0.9872 , demonstrating that the fitting accuracy of this regression equation is high. The effects of X_1 , X_2 , X_3 , X_{12} , X_{22} and X_{32} on the clamping qualification rate in the model are highly significant. It can be concluded that the order of influence of each factor on Q_p is: forward speed, cutter speed, and clamping belt speed.

Table 8

Test results				
Test Number	Cutter Speed (r/min)	Forward Speed (km/h)	Clamping Belt Speed (r/min)	Clamping and Conveying Pass Rate (%)
1	200	0.2	120	97.62
2	250	0.2	120	91.32
3	200	0.5	120	92.46
4	250	0.5	120	96.73
5	200	0.2	180	95.39
6	250	0.5	180	96.86

Table 9

Variance analysis of clamping and conveying pass rate					
Name	Square Sum	Degrees of Freedom	Mean Square	F-value	P-value
Model	436.48	9	46.79	101.79	< 0.0001
X_1	12.34	1	11.96	26.34	0.0002
X_2	17.62	1	16.78	37.46	< 0.0001
X_3	8.77	1	8.72	19.72	0.0006
X_1X_2	4.36	1	3.96	8.96	0.011
X_1X_3	3.43	1	3.72	7.37	0.0159
X_2X_3	12.37	1	12.49	25.49	0.0002
X_{12}	53.16	1	53.71	65.36	< 0.0001
X_{22}	248.46	1	249.25	55.47	< 0.0001
X_{32}	58.72	1	58.66	24.92	0.0002
Residuals	6.46	13	0.4736		
Incoherent	3.15	5	0.5997	1.49	0.2491
Error Term	2.79	8	0.46		
Total Error	419.91	22			

Field harvesting performance experiments

Before conducting the field test, the test area was pre-cleared of dead, immature, and otherwise unsuitable cabbages for harvesting. A laser digital tachometer was used to calibrate key operating parameters of each component. The harvester’s cutting device parameters were set as follows: a cutter inclination angle of 11° , a cutter rotational speed of 215 r/min, and a working speed of 0.28 m/s for the cabbage harvesting test. The cabbage harvesting performance test included a total of five groups, with approximately 60 cabbages in each test area. The field test site operation is shown in Fig. 13.



Fig. 13 - Field experiments of Chinese cabbage harvester

During the field performance test of the harvester prototype, the overall performance remained stable. Each component functioned properly, causing minimal mechanical damage to the cabbage. The harvester demonstrated a high harvest integrity rate and met the required harvesting standards. Following the prototype test method, key operational evaluation indexes - including field productivity, clamping and conveying success rate, and harvesting pass rate - were calculated for each test area. The average of five test results was taken. The prototype achieved an average field productivity of 0.12 hm²/h, an average clamping and conveying success rate of 96.38%, and an average harvest breakage rate of 7.43%, meeting the design requirements for the cabbage harvesting model.

Discussion

- ***Experimental analysis of physical and mechanical properties of Chinese cabbage***

The cabbage samples used in this study for physico-mechanical property tests were produced in Shandong Province, located north of the Yangtze River. The cabbage plants were relatively tall, with most leaf bulbs being tightly packed. The overall bulb height ranged from 380 to 425 mm, the mid-diameter ranged from 158 to 177 mm, the average mass distribution was between 2.1 to 2.5 kg, and the plant height exceeded 260 mm. The physical and morphological parameters of cabbage exhibited significant variations in size and quality. Therefore, to enhance the versatility and adaptability of the harvesting machinery, it is essential to incorporate a floating adjustable feeding device and a clamping device structure.

- ***Experimental analysis of Chinese cabbage harvesting process simulation***

During the clamping and conveying process, the clamping belt exerts pressure on the cabbage, leading to deformation of the belt. The combined force exerted on the cabbage during the clamping process fluctuates, indicating that the interaction force between the cabbage and the clamping belt is dynamically changing. This fluctuation is primarily influenced by the flexible deformation of the clamping belt during contact.

- ***Experimental analysis of harvesting performance in the field***

Cabbage harvesting damage is mainly attributed to the following factors: cutting damage caused by variations in individual cabbage sizes and uneven soil conditions, leading to inconsistencies in the cutting position; handling damage - occurring when cabbage collides or is compressed in the collection box after being harvested. To minimize post-harvest losses, efforts should be made to retain 2-3 outer leaves of the cabbage during harvesting. Minor root and surface damage has minimal impact on subsequent sales. Therefore, the cabbage loss rate during harvesting is acceptable within a certain range.

CONCLUSIONS

This study focused on the structural design and analysis of the clamping and conveying device of a cabbage harvester, considering the basic physical properties of cabbage and the mechanical properties of static load compression. The discrete element method (DEM) was employed to simulate and analyze the clamping and conveying process. Additionally, field harvesting performance tests and practical feasibility analyses were conducted to verify the rationality and accuracy of the clamping and conveying device design. The main conclusions are as follows

- 1) To enhance the versatility and adaptability of cabbage harvesting machinery, a floating adjustable feeding device and a clamping conveyor structure were implemented to improve the harvester's adaptability.
- 2) The clamping and conveying device adopts a longitudinal arrangement, utilizing flexible feeding and flexible clamping to achieve low-loss conveying, thereby improving its adaptability to cabbages with different ball diameters.
- 3) A dynamic coupling simulation model of cabbage harvesting components was established, allowing for the analysis of kinematic and dynamic characteristics through cabbage harvesting process simulations.
- 4) The cabbage harvester developed in this study underwent field performance tests, and the results confirmed that the harvester meets the design requirements for the mechanized harvesting of Chinese cabbage.

ACKNOWLEDGEMENT

The work was sponsored by the National Key R&D Program Project of China (2022YFD2001502).

REFERENCES

- [1] Ali, M.; Lee, Y.S.; Kabir, M.S.N.; Kang, Taegyong; Lee, S.H.; Chung, S.O. (2019). Kinematic Analysis for Design of the Transportation Part of a Tractor-Mounted Chinese Cabbage Collector. *Journal of Biosystems Engineering*, 44, 226-235, doi:10.1007/s42853-019-00033-x.
- [2] Ding, A.L.; Peng, B.L.; Yang, K.; Zhang, Y.H.; Yang, X.X.; Zou, X.G.; Zhu, Z.Q. (2022). Design of a Machine Vision-Based Automatic Digging Depth Control System for Garlic Combine Harvester. *Agriculture-Basel*, 12, doi:10.3390/agriculture12122119.
- [3] Ding, J.; Li, S.E.; Wang, H.S.; Wang, C.Y.; Zhang, Y.X.; Yang, D.N. (2021). Estimation of Evapotranspiration and Crop Coefficient of Chinese Cabbage Using Eddy Covariance in Northwest China. *Water*, 13, doi:10.3390/w13192781.
- [4] Du, X.; Yang, X.; Ji, J.; Jin, X.; Chen, L. (2019). Design and test of a pineapple picking end-effector. *Applied Engineering in Agriculture*, 35, 1045-1055, doi:10.13031/aea.13405.
- [5] Han, K.M.; Mohammad, A.L.I.; Swe, K.M.; Islam, S.; Sun Ok, C.; Kim, D.G. (2021). Fabrication and field performance test of a tractor-mounted 6-row cabbage collector. *Korean Journal of Agricultural Science*, 48, 141-149, doi:10.7744/kjoas.20210008.
- [6] Hu, S.Y.; Sun, Y.C.; Li, Z.R.; In, L.J. (2022). The Research on Technical Efficiency and Influence Factors of Chinese Cabbage Production in China. *Journal of Korea Academia-Industrial cooperation Society*, 23, 383-394, doi:10.5762/kais.2022.23.3.383.
- [7] Ji, K.Z.; Li, Y.M.; Ji, B.B.; Liang, Z.W.; Du, T. (2023). Discrete element method used to analyze the operating parameters of the cutting table of crawler self-propelled reed harvester. *Inmateh-Agricultural Engineering*, 71, 345-355, doi:10.35633/inmateh-71-30.
- [8] Kim, H.J.; Yeongsoo, C. (2020). Pulling Performance of a Self-Propelled Chinese Cabbage Harvester and Design of a Preprocessing Unit. *Journal of Agriculture & Life Science*, 54, 99-108, doi:10.14397/jals.2020.54.1.99.
- [9] Li, W.; Qin, J.H.; Deng, C.Y. (2017). Design of Key Components on LS-Type Spiral Conveyor Body. In *Proceedings of the International Conference on Green Energy and Sustainable Development (GESD)*, Chongqing, PEOPLES R CHINA, May 27-28.
- [10] Liu, W.P.; Liu, Y.X.; Kleiber, T. (2021). A review of progress in current research on chinese flowering cabbage. *Journal of Elementology*, 26, 149-162, doi:10.5601/jelem.2020.25.4.2076.
- [11] Myat, S.K.; Nafiul, I.M.; Milon, C.; Mohammad, A.L.I.; Sandah, W.; Hyeonjong, J.; SangHee, L.; SunOk, C.; DaeGeon, K. (2021). Theoretical Analysis of Power Requirement of a Four-Row Tractor-Mounted Chinese Cabbage Collector. *Journal of Biosystems Engineering*, 46, 139-150, doi:10.1007/s42853-021-00094-x.
- [12] Park, S.J.; Lee, S.Y.; parkwoojun; Yang, K.W.; Mohammad, A.L.I.; Joo, K.H. (2021). Preliminary Tests for Chinese Cabbage Harvesting with Harvesting Simulator. *Journal of Korea Academia-Industrial cooperation Society*, 22, 470-479, doi:10.5762/kais.2021.22.12.470.
- [13] Park, Y.; Jun, J.; Son, H.I. (2021). Three-axis Attitude Control of Chinese Cabbage Harvester Cutting Device Based on Sensor Fusion. *Journal of Institute of Control, Robotics and Systems*, 27, 277-284, doi:10.5302/j.lcros.2021.20.0201.
- [14] Sarkar, P.; Raheman, H. (2024). Development of an electric cabbage harvester: an eco-friendly solution for mechanical harvesting of cabbage. *Clean Technologies and Environmental Policy*, doi:10.1007/s10098-024-02868-1.
- [15] Tian, Y.; Yuan, P.P.; Yang, F.; Gu, J.H.; Chen, M.M.; Tang, J.Y.; Su, Y.L.; Ding, T.X.; Zhang, K.L.; Cheng, Q. (2018). Research on the Principle of a New Flexible Screw Conveyor and Its Power Consumption. *Applied Sciences-Basel*, 8, doi:10.3390/app8071038.
- [16] Toncheva, N.; Samsonov, A.; Yegorov, V.; Lebedev, V. (2017). Results of laboratory studies of device for transporting heads to the elevator of cabbage harvest machine. In *Proceedings of the 16th International Scientific Conference on Engineering for Rural Development*, Latvia Univ Agr, Fac Engn, Jelgava, Latvia, May 24-26; pp. 212-216.
- [17] Xu, L.M.; Yao, H.L. (2009). Research on Shear Characteristics of Chinese Cabbage Rootstalk. *Ama-Agricultural Mechanization in Asia Africa and Latin America*, 40, 30-34.
- [18] Zhang, J.F.; Cao, G.Q.; Jin, Y.; Tong, W.Y.; Zhao, Y.; Song, Z.Y. (2022). Parameter Optimization and Testing of a Self-Propelled Com-bine Cabbage Harvester. *Agriculture-Basel*, 12, doi:10.3390/agriculture12101610.

- [19] Zhang, X.J.; Yin, L.X.; Shang, S.Q.; Chung, S.O. (2022). Mechanical properties and microstructure of Fuji apple peel and pulp. *International Journal of Food Properties*, 25, 1773-1791, doi:10.1080/10942912.2022.2107006.
- [20] Zhao, X.L.; Du, X.Y.; Xu, J.C.; Chen, J.T.; Chen, Z.S. (2018). Empirical Test on Economic Benefit of Promoting the Industrialization of Chinese Cuisine under Strategy of Rural Revitalization-Taking Zengcheng Area as an Example. *In Proceedings of the International Symposium on Social Science and Management Innovation (SSMI)*, Xian, Peoples R China, Dec 15-16; pp. 628-634.
- [21] Zhou, L.M.; Zeng, Y.F.; Niu, K.; Yuan, Y.W.; Bai, S.H.; Chen, K.K. (2023). Analysis on root cutting mechanism of self-propelled chinese cabbage harvester and optimisation of device parameters. *In-mateh-Agricultural Engineering*, 71, 70-82, doi:10.35633/inmateh-71-05.
- [22] Zhou, P.; Sun, L.; Zhou, G.B.; Ma, T.B.; Wang, H.R.; Bi, W.Y.; Ma, G.Q.; Wang, W.; Yan, X.D. (2024). A New Embedded Condition Monitoring Node for the Idler Roller of Belt Conveyor. *Ieee Sensors Journal*, 24, 10335-10346, doi:10.1109/jsen.2024.3363905.

HARDWARE-IN-THE-LOOP SIMULATION FOR DRIVE WHEEL SLIP CONTROL OF HIGH-POWER TRACTOR FOR PLOUGHING OPERATION

基于硬件在环仿真的大马力拖拉机犁耕作业驱动轮滑转控制研究

Shuo ZHANG¹, YanQing LUO¹, Lei JIA¹, JingMing WEN¹, HongLing JIN¹, Yu CHEN^{*1}

College of Mechanical and Electronic Engineering, Northwest A&F University, Yangling 712100, China

Tel: +86 17795759790; E-mail: jdx73@nwfau.edu.cn

DOI: <https://doi.org/10.35633/inmateh-75-33>

Keywords: high-power tractor, ploughing operation, slip control, SMVSC, HILS

ABSTRACT

To address the issue of increased fuel consumption and reduced efficiency caused by excessive slip of the drive wheels during tractor ploughing operations, this paper considered the time-varying, uncertain, and highly nonlinear characteristics of the tractor-operating unit. A nonlinear dynamic model was constructed and a nonlinear slip control method for the drive wheels was designed using sliding mode variable structure control (SMVSC). The method was validated and tested on both the MATLAB/Simulink platform and a hardware-in-the-loop (HIL) simulation platform based on dSPACE. The HILS results indicated that, compared to the fuzzy PID algorithm, under varying soil specific resistance pulses, the mean absolute deviation of slip rate was reduced by 0.013, and the response time decreased by approximately 1.3 seconds with the SMVSC method. In case of pulse variation in slip rate, the SMVSC method reduced the tracking response time by approximately 0.8 seconds and the average control overshoot by about 0.03. Under both experimental conditions, the SMVSC method demonstrated superior control performance, ensuring more stable tractor operation. These findings provide valuable insights for drive slip control in tractor ploughing operations.

摘要

为解决拖拉机犁耕作业时驱动轮过度滑转引起燃油消耗量增加和效率降低的问题, 本文考虑拖拉机作业机组时变、不确定和强非线性特征, 构建了非线性动力学模型并结合滑模变结构控制设计了驱动轮滑转非线性控制方法, 分别在 MATLAB/Simulink 平台以及基于 dSPACE 搭建的硬件在环仿真平台进行验证测试。硬件在环测试结果表明, 相比模糊 PID 算法, 在土壤比阻脉冲变化时, SMVSC 方法下滑转率的平均绝对值偏差减少了 0.013, 响应时间减少了约 1.3s; 在滑转率脉冲变化时, SMVSC 方法的跟踪响应时间减少了约 0.8s, 平均控制过冲减少了约 0.03。两种试验条件下, SMVSC 的控制效果更佳且能够使拖拉机保持较稳定的作业状态, 对于拖拉机犁耕作业中的驱动防滑控制具有一定的参考意义。

INTRODUCTION

With the intelligent and intensive development of modern agriculture (Giller *et al.*, 2015), the heavy tractors have become important tools for efficient operation in field planting (Janulevičius *et al.*, 2019). However, excessive slip of the drive wheels during ploughing operations can significantly reduce the field operation efficiency of heavy tractor unit and negatively affect soil quality (Rahmati *et al.*, 2020). With the deepening of the concept of "Green Agriculture" and the continuous improvement of soil protection requirements (Wang *et al.*, 2020; Holthusen *et al.*, 2018), the introduction and enhancement of intelligent slip control for tractor drive wheels will substantially improve tillage efficiency and optimize soil conditions.

At present, the research on the slip rate is mainly focusing on the measurement and identification method, mathematical modelling, control algorithm, etc. For example, there are relative researches on real-time monitoring of slip rate but not involving automatic control (Pranav *et al.*, 2010), and the traction resistance is adjusted by changing the plough depth at the level of force to meet the purpose of controlling slip rate within a certain range, that it is mainly used by PID, fuzzy control and other methods (Zhang *et al.*, 2016). In the process of mathematical modelling, most of the existing researches employ linearization methods to approximate the nonlinear characteristics of tractor, electro-hydraulic hitch system or operating unit.

¹ Shuo Zhang, Associate professor, Ph.D. Eng.; YanQing Luo, M.S. Stud. Eng.; Lei Jia, M.S. Stud. Eng.; JingMing Wen, M.S. Stud. Eng.; HongLing Jin, Associate professor, Ph.D. Eng.; Yu Chen, Associate professor, Ph.D. Eng.

Although there have been some further researches on more accurate drive anti-slip control, the strong nonlinear characteristics of the large complex inertial system are not completely considered (Watanabe M. and Sakai K., 2019), resulting in limited accuracy. Sliding mode variable structure control (SMVSC) is a control method which can solve the nonlinear problem. It is mainly used in the field of agricultural machinery automatic control, such as tractor automatic steering (He et al., 2023), path tracking control (Ji et al., 2023) and trajectory tracking considering slip (Zhang et al., 2022; Ding et al., 2022).

In the research on heavy tractor control, the experimental method is also an important part. Due to the difficulty in verifying the real-time execution capability of controllers through offline simulations, field experiments are often relied upon. However, these experiments are influenced by factors such as seasonality and crop growth cycles. Hardware-in-the-loop simulation (HILS), which runs simulation models on real-time processors, can simulate dynamic changes under various experimental conditions and evaluate the performance of control systems and controllers (Li et al., 2007; Paksoy et al., 2020). Now it is gradually trying to provide test solutions for special equipment in the agricultural field. Raikwar et al., (2019), developed a set of HILS test platform based on the automatic test of tractor embedded system to detect and evaluate the faults or defects of tractor electronic control units and control functions. Wu et al., (2019), developed a hardware-in-loop test platform using digital space as a tool to test and verify the efficiency of the power system management unit of electric tractor. Xu et al., (2021), proposed a layered multi-loop robust control architecture (LMLRC) for tractor path following control, and built a hardware-in-the-loop simulation platform with MicroAutoBox, PXI hardware, LabVIEW and other tools, based on which the dynamic effectiveness of the proposed controller was verified. Zhang et al., (2023), tested the proposed active torque distribution control strategy on the dSPACE hardware-in-the-loop simulation platform, demonstrating the controller's obvious advantages in reducing tractor slip, improving traction energy efficiency, and reducing motor energy consumption.

Based on the research of the "tractor-tool-soil" system, this paper has developed a dynamic model of a high-power tractor with electro-hydraulic hitch system during ploughing operations. A slip rate control strategy has been proposed based on this model and the SMVSC theory. Finally, offline simulations and hardware-in-the-loop tests have been conducted on the MATLAB/Simulink and dSPACE platforms, respectively, using a fuzzy PID control method for comparison. The experimental results of both methods have been compared, leading to the optimization of the anti-slip control for the drive wheels of high-power tractors.

MATERIALS AND METHODS

Description of the HILS

The HILS test platform is composed of two parts: software and hardware. The software part encompasses the mathematical model of a half-vehicle, the control algorithm, and the MATLAB-Simulink software. On the hardware side, the platform is equipped with a dSPACE DS1007 serving as the main processor, along with a power supply, an AD conversion board DS2002, a DA conversion board DS2103, a CAN module DS4302, and a controller based on the Freescale MC9S12XS128MAL. The schematic diagram of the entire system is presented in Figure 1.

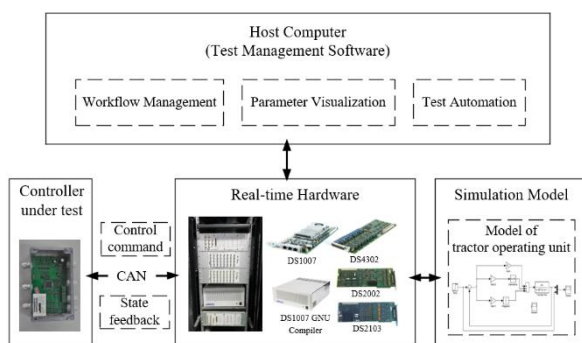


Fig. 1 - Schematic diagram of HILS

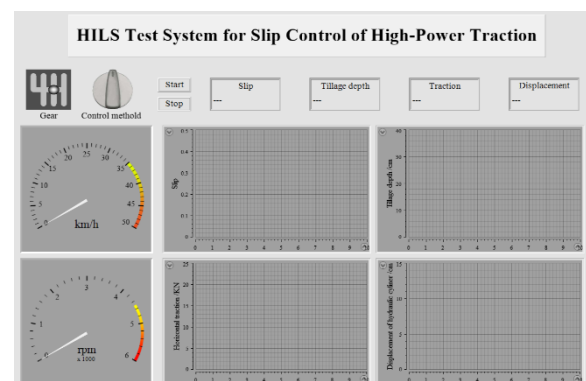


Fig. 2 - The human-machine interface of HILS

The specific functions of the system are as follows: the Tractor simulation model runs in the dSPACE real-time operating environment to simulate the dynamic response characteristics of the tractor under different working conditions; the test management software based on ControlDesk runs in the PC environment of the host computer to provide a good human-computer interaction interface, which can monitor system running state and controller performance in real time, display and dynamically modify system model parameters, and

realize workflow management and test automation. The dSPACE real-time processor interfaces with the controller through I/O interface (CAN bus) to realize the signal communication between the real-time model of tractor and the actual controller. In addition, the human-machine interface (as shown in figure 2) is designed based on the ControlDesk, including the functions of adjusting control parameters, displaying the status of the control system (tractor slip rate, tillage depth, etc.), tracking process response curve, etc.

The half-tractor model

In the mathematical modelling of heavy tractor electro-hydraulic hitch operation units, it is considered that the tractor works in the field mostly in a straight-line motion, and the field road environment is relatively flat. Therefore, the tractor's motion is simplified to linear motion in the longitudinal plane along the tractor's forward direction, ignoring the lateral movements such as sideslip and roll during forward movement. As shown in figure 3, the centre point of the rear axle is used as the coordinate origin to establish the x_0 - O - y_0 motion coordinate of the tractor's electro-hydraulic hitch operation units.

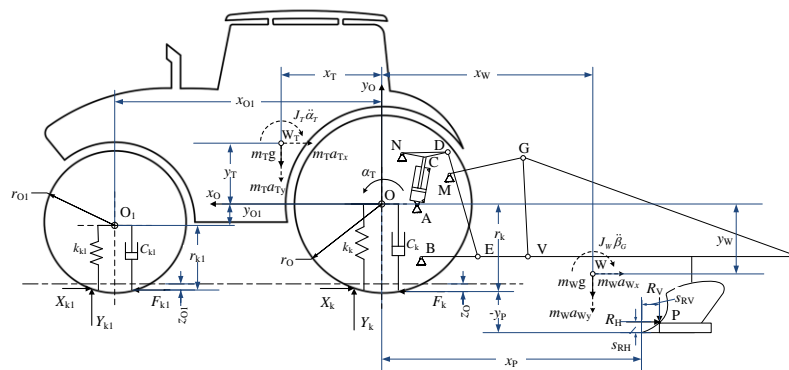


Fig. 3 - Simple diagram of kinematic and dynamic analysis for heavy tractor

● **Kinematics analysis**

The motion of the heavy tractor electro-hydraulic hitch operation unit is simplified into two parts: one is the tractor's translational motion in the forward direction with the base point O , the other is the rotational motion of the tractor's linkage around the base point O in the longitudinal plane, and the relative position relationship of the tractor's main points is expressed by the tractor's relative position relationship when driving on the flat ground. According to the basic theory of kinematics, for each main node of tractor and its linkage, its velocity can be expressed as the velocity projection component of the point and the base point O in the line direction, and its acceleration can be expressed as the vector sum of the acceleration of the base point O and the rotational acceleration of the point around the point O .

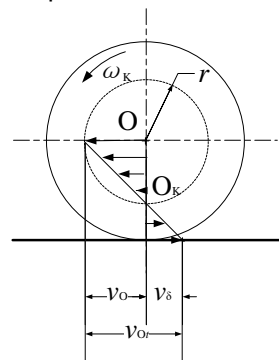


Fig. 4 - Rolling kinematics model with wheels slipping

When the tractor is ploughing, it has the characteristics of approximately constant speed linear operation, so its motion state is generally a rolling motion state with slip, as shown in figure 4. Assuming that during the movement, the instantaneous centre point of the speed of the tractor drive wheel is always above the soil ground in the field, the wheel slip rate of the rear-wheel drive tractor can be expressed as by equation (1):

$$\delta_k = \frac{v_{Or} - v_O}{v_{Or}} = \frac{r_O \omega_k - r_k \omega_k}{r_O \omega_k} = 1 - \frac{r_k}{r_O} \tag{1}$$

where: V_{O_i} and V_O are respectively the theoretical speed and instantaneous speed of the drive wheel in the forward direction, m/s; r_O and r_K are respectively the geometric radius and dynamic radius of the drive wheel, m; ω_K is the angular speed of the drive wheel, rad/s.

As shown in Fig. 5, based on the analysis of the geometric relationship model between the piston displacement of the lifting hydraulic cylinder and the position of hitch pole with changes of the farm tools' depth, the relationship between above three can be approximately obtained. On the basis of abovementioned geometric relation, the displacement of lifting hydraulic cylinder is $x_L=x_{LD}$ when the farming tool is in the predetermined tillage depth. The first-order and second-order differential relation of the angle and movement displacement of each member can be derived. Due to space limitations, the differential equations are no longer listed here.

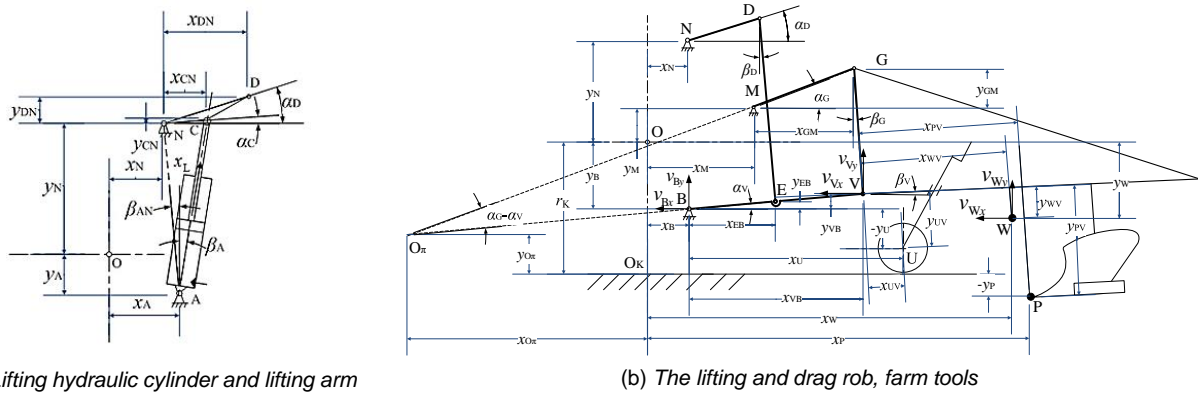


Fig. 5 - Simple diagram of kinematic and dynamic analysis for heavy tractor

NCD is the lifting arm; DE is the lifting rod; MG is the drag rob; BV is the horizontal bar; G and V are the hitch points connecting the upper and lower pull rods and farm tools; W is centroid of farm tools; x_L is the displacement of hydraulic cylinder piston; x_w, y_w are the horizontal and vertical distances from the rear wheel axis O to the centroid, m; $\alpha_c, \alpha_d, \alpha_v, \alpha_g, \beta_A, \beta_D, \beta_G$ are the angles between the corresponding member and the horizontal direction, rad; $\beta_A, \beta_D, \beta_G$ are the angles between the corresponding member and the horizontal direction, rad.

● **Dynamic analysis**

In Figure 3, the force analysis of the tractor's electro-hydraulic hitch operation unit shows that the external forces received by the tractor (including the hitch mechanism) mainly include: the tractor's gravity $m_T g$, the farm tools' gravity $m_W g$, the front wheels' vertical ground reaction Y_{K1} , the horizontal rolling resistance X_{K1} and the corresponding driving force F_{k1} , the rear wheels' vertical ground reaction Y_K , the horizontal rolling resistance X_K and the corresponding driving force F_K , and the farm tools' soil resistance R_H and R_V , the force F_G, F_{vx} and F_{vy} of the tool on the linkage at the upper and lower hitch points. Therefore, with the point O as the centre, the force and moment balance equations in the horizontal and vertical directions have been set up, as shown in equation (2).

$$\begin{cases} Y_K + Y_{K1} - R_V = m_T (g + a_{Ty}) + m_W (g + a_{Wy}) \\ F_K + F_{K1} - X_K - X_{K1} - R_H = m_T a_{Tx} + m_W a_{Wx} \\ R_H (r_K - y_P - s_{RH}) - R_V (x_P + s_{RV}) - (F_K + F_{K1}) r_K + X_{K1} y_{O1} - Y_{K1} x_{O1} \\ + m_T (g + a_{Ty}) x_T - m_T a_{Tx} y_T - m_W (g + a_{Wy}) x_W + m_W a_{Wx} y_W = J_T \ddot{\alpha}_T + J_W \ddot{\beta}_G \end{cases} \quad (2)$$

According to the above relevant kinematics and dynamics analysis, and referring to the previous research results and modelling methods, the kinematics and dynamics equations of each subsystem such as the tractor body, wheels, hitch mechanism and agricultural tools are brought into equation (2). The dynamic differential equations of tractor electro-hydraulic hitch ploughing unit are obtained, as shown in formula (3). In this formula, Y_K and $Y_{\Delta K}$ are intermediate variables; s_{O1} and s_o are respectively the compression deformation of front and rear tires, m; z_{o1} and z_o are respectively the soil subsidence caused by vertical load of front and rear tires, m; A_{K1} and A_K are the grounding area of front and rear tires, m^2 ; B_{K1} and B_K are respectively the grounding width of front and rear tires, m. The coefficients such as $m_{x_L e}, i_{x_L y_K}, J'_{x_L \alpha_L e}, l_{\alpha_T F_K}$ are respectively the intermediate equivalent mass, equivalent moment of inertia and other equivalent coefficients appearing in the process of solving the equation system, which can be expressed as expressions of known variables or constants. This study based on the author's previous work, utilizing the key dimensions and structural parameters of the tractor operating unit as outlined in reference (Zhang et al., 2020). Due to space constraints, further details are omitted.

$$\begin{cases}
 \ddot{x}_L = \frac{1}{m_{x_{1e}}} \left[p_L A_L + i_{x_{1F_K}} (F_K + F_{K1}) + i_{x_{1R_H}} R_H - i_{x_{1Y_K}} Y_K - i_{x_{1Y_{K1}}} Y_{K1} - i_{x_{1R_V}} R_V - m_{x_{1g}} g - J'_{x_{1\alpha_L}} a_T^2 - m_{x_{1\alpha_L}} \dot{x}_L \dot{a}_T - m'_{x_{1e}} \dot{x}_L^2 \right] \\
 \dot{\delta}_K = (1 - \delta_K) \left(\frac{\dot{\omega}_K}{\omega_K} - \frac{\dot{s}_O}{r_O - s_O} \right) + \frac{1}{\omega_K (r_O - s_O) (m_T + m_W)} \left\{ \frac{m_{x_{0x_L}}}{m_{x_{1e}}} p_L A_L + \left(i_{x_{0R_H}} + i_{x_{1R_H}} \frac{m_{x_{0x_L}}}{m_{x_{1e}}} \right) R_H + \left(i_{x_{0Y_K}} - i_{x_{1Y_K}} \frac{m_{x_{0x_L}}}{m_{x_{1e}}} \right) Y_K \right. \\
 + \left(i_{x_{0Y_{K1}}} - i_{x_{1Y_{K1}}} \frac{m_{x_{0x_L}}}{m_{x_{1e}}} \right) Y_{K1} + \left(l^{-1} y_T m_T - m_{x_{1g}} \frac{m_{x_{0x_L}}}{m_{x_{1e}}} \right) g - \left(i_{x_{0F_K}} - i_{x_{1F_K}} \frac{m_{x_{0x_L}}}{m_{x_{1e}}} \right) (F_K + F_{K1}) - \left(i_{x_{0R_V}} + i_{x_{1R_V}} \frac{m_{x_{0x_L}}}{m_{x_{1e}}} \right) R_V \\
 \left. + \left(m'_{x_{0x_L}} - m'_{x_{1e}} \frac{m_{x_{0x_L}}}{m_{x_{1e}}} \right) \dot{x}_L^2 - \left(J_{x_{0\alpha_T}} + J'_{x_{1\alpha_L}} \frac{m_{x_{0x_L}}}{m_{x_{1e}}} \right) a_T^2 + \left(m_{x_{0\alpha_T}} - m_{x_{1\alpha_L}} \frac{m_{x_{0x_L}}}{m_{x_{1e}}} \right) \dot{x}_L \dot{a}_T \right\} \\
 \ddot{y}_K = \ddot{y}_{OR} + \frac{1}{m_T + m_W} \left\{ \frac{m_{y_{0x_L}}}{m_{x_{1e}}} p_L A_L - \left(i_{y_{0R_H}} - i_{x_{1R_H}} \frac{m_{y_{0x_L}}}{m_{x_{1e}}} \right) R_H - \left(i_{y_{0Y_K}} + i_{x_{1Y_K}} \frac{m_{y_{0x_L}}}{m_{x_{1e}}} \right) Y_K - \left(i_{y_{0Y_{K1}}} + i_{x_{1Y_{K1}}} \frac{m_{y_{0x_L}}}{m_{x_{1e}}} \right) Y_{K1} \right. \\
 + \left(i_{y_{0F_K}} + i_{x_{1F_K}} \frac{m_{y_{0x_L}}}{m_{x_{1e}}} \right) (F_K + F_{K1}) + \left(i_{y_{0R_V}} - i_{x_{1R_V}} \frac{m_{y_{0x_L}}}{m_{x_{1e}}} \right) R_V + \left(m_{y_{0g}} - m_{x_{1g}} \frac{m_{y_{0x_L}}}{m_{x_{1e}}} \right) g + \left(m'_{y_{0x_L}} - m'_{x_{1e}} \frac{m_{y_{0x_L}}}{m_{x_{1e}}} \right) \dot{x}_L^2 \\
 \left. + \left(J_{y_{0\alpha_T}} - J'_{x_{1\alpha_L}} \frac{m_{y_{0x_L}}}{m_{x_{1e}}} \right) a_T^2 + \left(m_{y_{0\alpha_T}} - m_{x_{1\alpha_L}} \frac{m_{y_{0x_L}}}{m_{x_{1e}}} \right) \dot{x}_L \dot{a}_T \right\} \quad (3) \\
 \ddot{y}_{AK} = \ddot{y}_{OR} - \ddot{y}_{O1R} + \frac{x_{O1}}{J_{\alpha_T}} \left\{ \frac{m_{\alpha_T}}{m_{x_{1e}}} p_L A_L - \left(l_{\alpha_T R_H} - i_{x_{1R_H}} \frac{m_{\alpha_T}}{m_{x_{1e}}} \right) R_H - \left(l_{\alpha_T Y_K} + i_{x_{1Y_K}} \frac{m_{\alpha_T}}{m_{x_{1e}}} \right) Y_K - \left(l_{\alpha_T Y_{K1}} + i_{x_{1Y_{K1}}} \frac{m_{\alpha_T}}{m_{x_{1e}}} \right) Y_{K1} \right. \\
 + \left(l_{\alpha_T F_K} + i_{x_{1F_K}} \frac{m_{\alpha_T}}{m_{x_{1e}}} \right) (F_K + F_{K1}) + \left(y_T m_T + m_{x_{1g}} \frac{m_{\alpha_T}}{m_{x_{1e}}} \right) g + \left(l_{\alpha_T R_V} - i_{x_{1R_V}} \frac{m_{\alpha_T}}{m_{x_{1e}}} \right) R_V + \left(m'_{\alpha_L} - m'_{x_{1e}} \frac{m_{\alpha_T}}{m_{x_{1e}}} \right) \dot{x}_L^2 \\
 \left. + \left(J_{\alpha_T \alpha_T} + J_{\alpha_T} \frac{y_{O1}}{x_{O1}} - J'_{x_{1\alpha_L}} \frac{m_{\alpha_T}}{m_{x_{1e}}} \right) a_T^2 + \left(m_{\alpha_T \alpha_T} - m_{x_{1\alpha_L}} \frac{m_{\alpha_T}}{m_{x_{1e}}} \right) \dot{x}_L \dot{a}_T \right\} \\
 \dot{s}_O = \frac{1}{f_K} \left[A_K (k_c / B_K + k_\phi) z_O^n - k_K s_O \right] \\
 \dot{s}_{O1} = \frac{1}{f_{K1}} \left[A_{K1} (k_c / B_{K1} + k_\phi) z_{O1}^n - k_{K1} s_{O1} \right] \\
 z_O = y_K - s_O \\
 z_{O1} = y_K - y_{AK} - s_{O1}
 \end{cases}$$

Slip Rate Controller Design

Through the analysis of the movement characteristics of the heavy tractor ploughing unit, it can be seen that when the soil conditions change suddenly, the tractor slip rate changes greatly, which will seriously affect the tractor's traction performance. Therefore, in view of the nonlinear characteristics of the heavy tractor electro-hydraulic hitch unit, considering the tractor traction efficiency, according to the slip rate control requirements under different ploughing conditions and considering the uniformity of ploughing depth, a slip rate control method with the optimal slip rate $\delta_{opt}=0.2$ as the control target was designed in this paper. The operation principle of the slip rate control system based on the optimal target is shown in figure 6. In this paper, the sliding mode variable structure control method is used to study, and the fuzzy PID control method is added to compare.

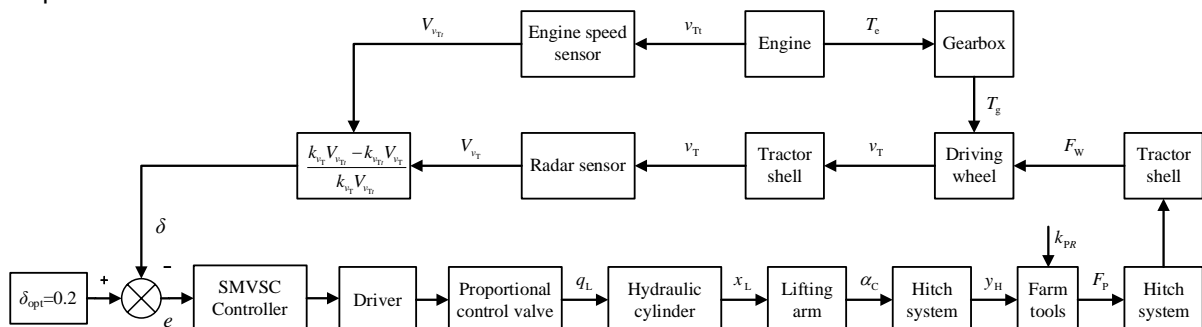


Fig. 6 - Diagram of control system working principle

● **Research on the SMVSC algorithm**

Because there are a lot of physical parameters and uncertainties which are difficult to obtain accurately in the tractor dynamics model, and the system equation has strong nonlinearity, the sliding mode variable structure control method is a nonlinear control method which adapts to the strong nonlinearity and is insensitive to the external disturbance, and has better robustness and higher reliability.

First, the output error is defined as:

$$e = \delta_K - \delta_{opt} \tag{4}$$

According to the sliding mode variable structure control theory, the switching function is defined as:

$$s(t) = Ce = C(\delta_K - \delta_{opt}) \tag{5}$$

where:

C is the sliding mode coefficient, and $C > 0$, setting $C = 1$.

The design of the sliding mode variable structure controller consists of two main aspects: on the one hand, it needs to be ensured that any position in the phase plane can reach the switching function $s=0$ in a finite time, and on the other hand, it needs to be ensured that it can converge to an equilibrium point on the switching function. According to the defined switching function and the basic principle of SMVSC, in the phase plane composed of the slip rate and the derivative of the slip rate, the switching line is a straight line with a slope of $-C$ and passing through $(\delta_{opt}, 0)$. The basic idea of SMVSC is to select an appropriate control variable, so that during the operation of the tractor, its phase trajectory $(\delta_K, \dot{\delta})$ continuously slides along the switching line to the control target $(\delta_{opt}, 0)$ by a predetermined control law. Derivation of equation (5) gives:

$$\dot{s}(t) = C\dot{e} = \dot{\delta}_K \tag{6}$$

Based on the requirement that points in the state space need to be allowed finite time to reach the termination point on the switching function $s=0$, the following conditions must be satisfied when designing the controller: when $s(t) > 0$,

$$\dot{s}(t) = C\dot{e} = \dot{\delta}_K < 0 \tag{7}$$

When $s(t) < 0$,

$$\dot{s}(t) = C\dot{e} = \dot{\delta}_K > 0 \tag{8}$$

Substituting the first-order differential equation expression of the slip rate that has been derived from the dynamic model into equation (6) gives:

$$\begin{aligned} \dot{s}(t) = (1 - \delta_K) & \left(\frac{\dot{\omega}_K}{\omega_K} - \frac{\dot{s}_O}{r_O - s_O} \right) + \frac{1}{\omega_K (r_O - s_O) (m_T + m_W)} \left\{ \frac{m_{x_O x_L}}{m_{x_L e}} p_L A_L + \left(i_{x_O R_H} + i_{x_L R_H} \frac{m_{x_O x_L}}{m_{x_L e}} \right) R_H \right. \\ & - \left(i_{x_O R_V} + i_{x_L R_V} \frac{m_{x_O x_L}}{m_{x_L e}} \right) R_V - \left(i_{x_O F_K} - i_{x_L F_K} \frac{m_{x_O x_L}}{m_{x_L e}} \right) F_K + \left(i_{x_O Y_K} - i_{x_L Y_K} \frac{m_{x_O x_L}}{m_{x_L e}} \right) Y_K + \left(i_{x_O Y_{K1}} - i_{x_L Y_{K1}} \frac{m_{x_O x_L}}{m_{x_L e}} \right) Y_{K1} \\ & \left. - m_{x_L g} \frac{m_{x_O x_L}}{m_{x_L e}} g + \left(m'_{x_O x_L} - m'_{x_L e} \frac{m_{x_O x_L}}{m_{x_L e}} \right) \dot{x}_L^2 + \left(m_{x_O \alpha_T x_L} - m_{x_L \alpha_T e} \frac{m_{x_O x_L}}{m_{x_L e}} \right) \dot{x}_L \dot{\alpha}_T - \left(J_{x_O \alpha_T} + J'_{x_L \alpha_T e} \frac{m_{x_O x_L}}{m_{x_L e}} \right) \dot{\alpha}_T^2 \right\} \tag{9} \end{aligned}$$

In order to ensure the stability of the sliding mode motion and the working quality, the dynamic effect of the convergence motion is improved by using the exponential approach law, and constant velocity approaches law is introduced to determine the convergence speed to be a certain non-zero speed when $s(\delta)$ continuously approaching 0, which ensures that the control system arrives at the switching manifold as soon as possible with this speed. The exponential approach law used is shown in equation (10).

$$\dot{s}(t) = -\varepsilon \operatorname{sgn}(s(t)) - ks(t) \tag{10}$$

where:

ε represents the law of constant velocity approach of the moving point, and $\varepsilon > 0$; k represents the law of exponential approach, and $k > 0$; $\operatorname{sgn}(s(t))$ represents the sign function.

Combine the vertical (9) and (10), and select the piston pressure $p_L A_L$ in the oil chamber of the lifting hydraulic cylinder as the equivalent control quantity, and get:

$$\begin{aligned}
 p_L A_L = & \omega_K (r_O - s_O) (m_T + m_W) \frac{m_{x_L e}}{m_{x_O x_L}} (-\varepsilon \operatorname{sgn}(s(t)) - ks(t)) - \omega_K (r_O - s_O) (m_T + m_W) \frac{m_{x_L e}}{m_{x_O x_L}} (1 - \delta_K) \left(\frac{\dot{\omega}_K}{\omega_K} - \frac{\dot{s}_O}{r_O - s_O} \right) \\
 & - \left(i_{x_L R_H} + i_{x_O R_H} \frac{m_{x_L e}}{m_{x_O x_L}} \right) R_H + \left(i_{x_L R_V} + i_{x_O R_V} \frac{m_{x_L e}}{m_{x_O x_L}} \right) R_V + \left(i_{x_O F_K} \frac{m_{x_L e}}{m_{x_O x_L}} - i_{x_L F_K} \right) F_K + \left(i_{x_L Y_K} - i_{x_O Y_K} \frac{m_{x_L e}}{m_{x_O x_L}} \right) Y_K \\
 & + \left(m'_{x_O x_L} \frac{m_{x_L e}}{m_{x_O x_L}} - m'_{x_L e} \right) \dot{x}_L^2 - \left(m_{x_O \alpha_T x_L} \frac{m_{x_L e}}{m_{x_O x_L}} - m_{x_L \alpha_T e} \right) \dot{x}_L \dot{\alpha}_T + \left(J_{x_O \alpha_T} \frac{m_{x_L e}}{m_{x_O x_L}} + J'_{x_L \alpha_T e} \right) \dot{\alpha}_T^2
 \end{aligned} \tag{11}$$

It can be seen from equation (11) that the expression is extremely complex. According to the dynamic characteristics of the motion of the electro-hydraulic hitch system and the characteristics of the sliding mode variable structure control theory, it is assumed that the tractor ploughing operation in the field is approximately constant speed operation, that is, the slip rate is kept near the optimal value with small fluctuation. Assume that the tractor engine speed is constant. Assuming that the tractor's pitching motion in the forward longitudinal plane is small, it is considered that the hydraulic cylinder push rod extends at a nearly uniform speed. Through simulation analysis and calculation, it can be further simplified:

$$p_L A_L = k_1 * (-\varepsilon \operatorname{sgn}(s(t)) - ks(t)) + k_2 v_O + k_3 R_H + k_4 R_V + k_5 F_K + k_6 Y_K + k_7 Y_{K1} \tag{12}$$

where: $k_1, k_2, k_3, k_4, k_5, k_6$ and k_7 are the coefficients related to tractor structural parameters, which are specifically expressed as follows:

$$\begin{aligned}
 k_1 = & \omega_K r_K (m_T + m_W) \frac{m_{x_L e}}{m_{x_O x_L}}, \quad k_2 = r_K \dot{s}_O \frac{m_{x_L e}}{m_{x_O x_L}} (m_T + m_W), \quad k_3 = -i_{x_L R_H} - i_{x_O R_H} \frac{m_{x_L e}}{m_{x_O x_L}}, \\
 k_4 = & i_{x_L R_V} + i_{x_O R_V} \frac{m_{x_L e}}{m_{x_O x_L}}, \quad k_5 = i_{x_O F_K} \frac{m_{x_L e}}{m_{x_O x_L}} - i_{x_L F_K}, \quad k_6 = i_{x_L Y_K} - i_{x_O Y_K} \frac{m_{x_L e}}{m_{x_O x_L}}, \quad k_7 = i_{x_L Y_{K1}} - i_{x_O Y_{K1}} \frac{m_{x_L e}}{m_{x_O x_L}}.
 \end{aligned}$$

The Lyapunov function is constructed based on the positive definite function to test the stability of the system employing the exponential convergence rate, and the Lyapunov function is:

$$V = \frac{1}{2} s^2 \tag{13}$$

Derivatives can be obtained:

$$\dot{V} = \frac{1}{2} \frac{d}{dt} s^2 = s \dot{s} < -\varepsilon |s| < 0 \tag{14}$$

where: $\varepsilon > 0$.

According to Lyapunov stability theory, it can be concluded that the designed control system is stable.

When the system enters the sliding mode motion and continuously switches along the sliding mode surface, in order to suppress the system "shaking" as much as possible, the continuous saturation function $sat(s)$ is used instead of the traditional constant velocity approach rate discontinuous symbol function $sgn(s)$, which is defined as follows:

$$sat(s) = \begin{cases} 1, & s > \psi \\ s/\psi, & |s| \leq \psi \\ -1, & s < -\psi \end{cases} \tag{15}$$

where: ψ is the thickness of the boundary layer.

The expression of the equivalent control variable $p_L A_L$ has been derived. The self-developed threaded plug-in proportional control valve was used for indoor testing. Based on the dynamic and static characteristics of the proportional control valve, the opening pressure of the proportional relief valve connected to the oil outlet of the proportional control valve was adjusted. The pressure difference between the load pressure of the proportional lowering control valve and the return oil pressure was controlled to maintain approximately 4 MPa and 9 MPa, respectively. By varying the input voltage of the proportional amplifier (driver), the steady flow of the proportional lowering valve under different driving voltages was obtained. Similarly, the steady flow of the proportional poppet under different driving voltages was measured. Through regression analysis and fitting of the test results, the relationship between control voltage and output flow was determined as follows:

$$U_{up} = \begin{cases} \frac{Q_{up}}{0.475\sqrt{\frac{2}{\rho}\Delta p}} + 3.87, & 0 \leq \frac{Q_{up}}{\sqrt{\frac{2}{\rho}\Delta p}} \leq 0.312 \\ \frac{Q_{up}}{0.475\sqrt{\frac{2}{\rho}\Delta p}} + 4.27, & \frac{Q_{up}}{\sqrt{\frac{2}{\rho}\Delta p}} > 0.312 \end{cases} \quad (16)$$

$$U_{down} = \begin{cases} 1.73 - \frac{Q_{down}}{0.48\sqrt{\frac{2}{\rho}(p_L - p_0)}}, & 0 \leq \frac{Q_{down}}{\sqrt{\frac{2}{\rho}(p_L - p_0)}} \leq 0.304 \\ 1.27 - \frac{Q_{down}}{0.48\sqrt{\frac{2}{\rho}(p_L - p_0)}}, & \frac{Q_{down}}{\sqrt{\frac{2}{\rho}(p_L - p_0)}} > 0.304 \end{cases} \quad (17)$$

where: U_{up} is the driving voltage of proportional poppet, V; U_{down} is the driving voltage of the proportional lowering valve, V; Q_{up} is the flow of hydraulic oil from the proportional lift valve into the hydraulic cylinder during the lifting process of the hydraulic cylinder, m³/s; Q_{down} is the flow from the hydraulic cylinder into the proportional descent control valve during the descent of the hydraulic cylinder, m³/s; Δp is the pressure difference between the two ends of the proportional directional valve, and the value has been set 1.5MPa; p_L is the load pressure of the hydraulic cylinder, Pa; p_0 is the return oil pressure, value 0 Pa; ρ is the density of hydraulic oil, kg/m³.

The flow continuity equation of hydraulic cylinder is shown in equation (18):

$$\dot{p}_L = \frac{\beta_e}{V_L} (q_L - A_L \dot{x}_L - C_{iL} p_L) \quad (18)$$

q_L can be obtained by combining equation (12) and equation (18). When the poppet valve is open, $q_L = q_{up}(U)$; when the drop valve is open, $q_L = -q_{down}(U)$. From the equations (16) and (17), the control voltage U of the electro-hydraulic proportional control valve can be obtained to implement the control.

● Incremental fuzzy PID control method

In order to highlight the advantages of SMVSC, PID control algorithm which is widely used in control field is selected for comparison. The fuzzy PID controller can improve the robustness of the system in the control process, taking the deviation e and the deviation change rate e_c of the slip rate as the input, and the three parameter correction quantities ΔK_P , ΔK_I and ΔK_D of the PID as the output. The domains of e and e_c are taken as [-0.6, 0.6], and the output variables ΔK_P , ΔK_I , ΔK_D are set according to experience as [-5, 5]. The tuning principles of PID controller parameters are:

(1) When e is larger and e_c is larger, in order to reduce the system response time and avoid system integral saturation, increase K_P and decrease K_I ;

(2) When e decreases gradually, in order to shorten the dynamic adjustment time, reduce overshoot and steady-state oscillation, K_P is reduced and K_I is increased;

(3) When the system begins to approach the target and enters steady-state, in order to obtain a good steady state, improve the ability to resist disturbance, increase K_D .

The fuzzy subsets of e , e_c , ΔK_I and ΔK_D are taken as {NB, NM, NS, ZO, PS, PM, PB}, representing {negative big, negative middle, negative small, zero, positive small, positive middle, positive big}, and the membership functions of all subsets are Gauss membership functions. Use MATLAB's fuzzy inference toolbox to build a fuzzy inference system and edit the membership of input and output variables.

RESULTS AND ANALYSIS

Offline simulation and analysis of control algorithm

According to the established system dynamics model and the designed control algorithm, the corresponding simulation model of slip rate control system is established in MATLAB/Simulink, and the entire system is analysed by off-line simulation. During the simulation process, the disturbance rejection characteristics of the sliding rate control system, that is the change of soil specific resistance input, and the dynamic response characteristics of the control target when the input setting value changes, are mainly

concerned. After several adjustments, the parameters of SMVSC are determined as $\varepsilon=1.2$, $k=0.01$, $\psi=0.01$, and the initial parameters of fuzzy PID controller are $K_P=12$, $K_I=0.5$, $K_D=1.5$. The initial conditions of the simulation are set as follows: the tractor gear is B2 gear, the initial displacement of the hydraulic cylinder piston rod is 8.83 cm, the initial ploughing depth of the tractor operation is 20 cm, and the simulation time is 50 seconds.

● **Soil specific resistance with pulse change**

The simulation takes $\delta_{opt}=0.2$ as the control target, takes the change of soil specific resistance as the external disturbance input, and sets the steady-state value of the soil specific resistance to 30000 N/m². At the beginning of the simulation, the soil specific resistance is added as a pulse signal with an amplitude of 8000 N/m², a period of 10s and a duty cycle of 50%. When the soil specific resistance changes, the simulation results are shown in Figure 7.

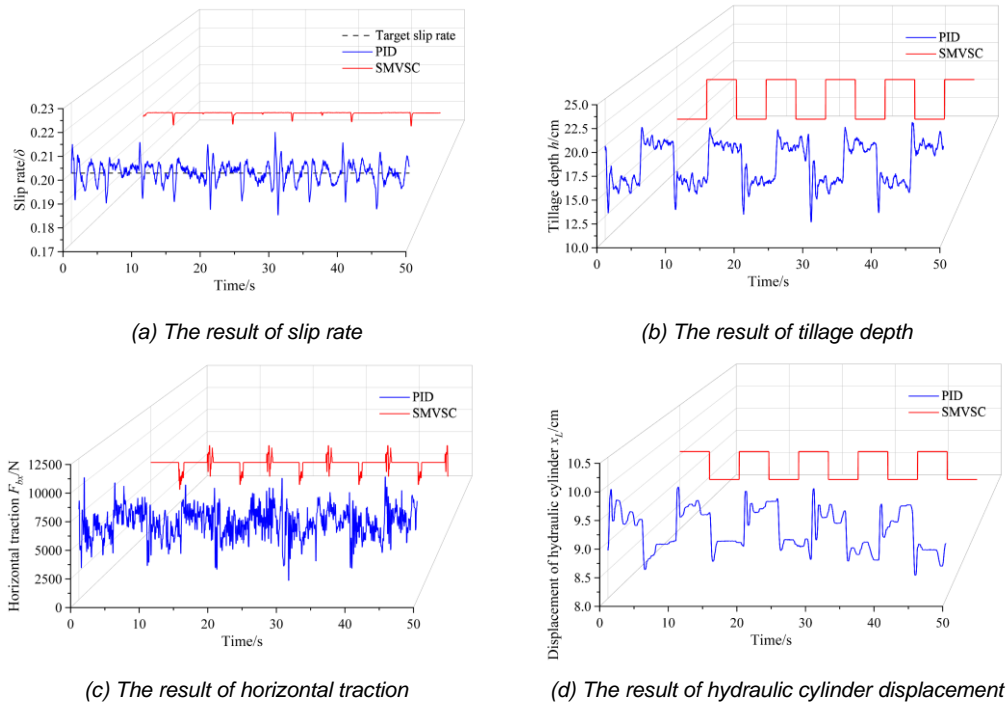


Fig. 7 - Simulation results of soil specific resistance with pulse change

According to Fig. 7 (a), when the specific resistance of soil changes step by step every 5 seconds, through the fuzzy PID control method, after a response time of about 1.5s, the slip rate can be basically controlled around 0.2, but the fluctuation is large, and the maximum error reaches 0.02. The results by the SMVSC method show that the sliding rate can be well controlled at 0.2, and the response time is very short, there is almost no overshoot at the beginning of the control. And the same time, the control target can be continuously and stably tracked in the control process, which can better resist the influence of soil specific resistance disturbance. In addition, when the specific resistance of soil is within 30000N cycle, the dynamic performance of tractor will be affected by random road excitation disturbance, so the fuzzy PID control algorithm can be adjusted according to the magnitude of deviation at any time. The slip rate has been near the target value of 0.2 by large steady-state error. But the SMVSC method has been proven to have a low steady-state error and better robustness against external disturbance, maintaining stability at 0.2 with almost no overshoot. The simulation results showed that when the soil conditions were changing, compared with the fuzzy PID control method, the SMVSC method had better disturbance rejection characteristics and faster response to the external disturbance, which verified the effectiveness and superiority of its control.

● **Control target value with pulse change**

In order to further understand the tracking performance of the control algorithm for the control target, the control target value input by the control system is varied under fixed soil conditions, and the dynamic response characteristics of the control system are analysed when the input undergoes a pulse change. The soil specific resistance is set to 30000 N/m², the initial value of the slip rate control target is 0.2, the control target change amplitude is 0.1, the period is 10s, and the pulse signal has a 50% duty cycle. The simulation results are shown in Figure 8.

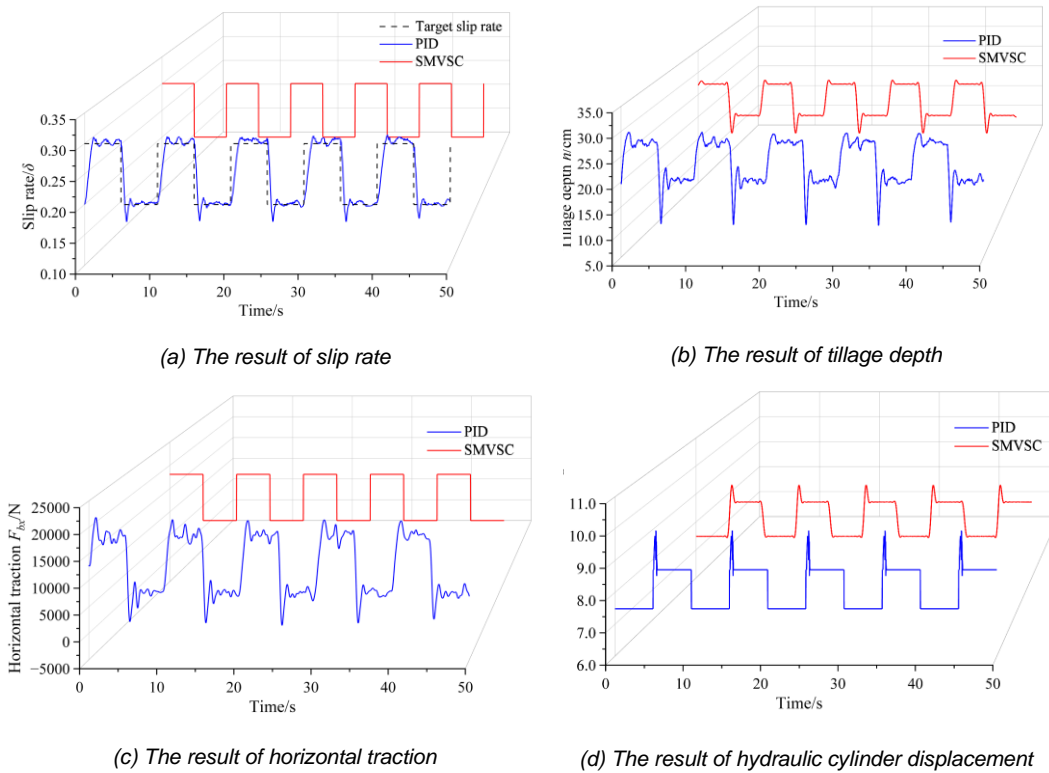


Fig. 8 - Simulation results of control target value with pulse change

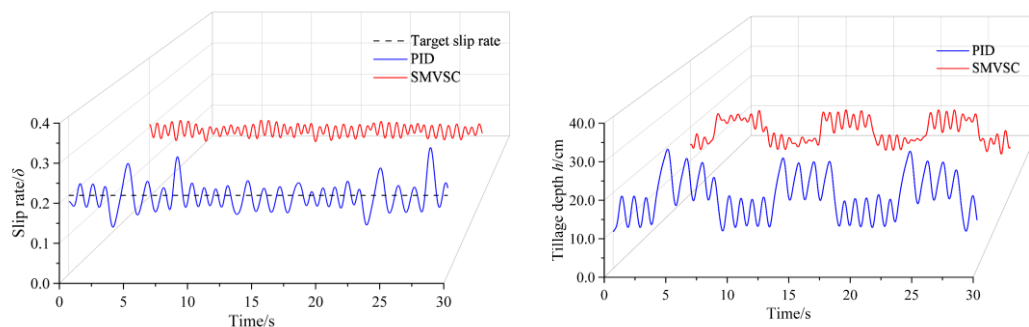
In the control process, the response time of fuzzy PID control was about 1.8s, and the maximum overshoot was 0.05, with a steady-state control error of about 0.01; there was almost no overshoot and steady-state control error by the SMVSC method. When the control target changed periodically between 0.2 and 0.3, the results showed that it reached the control target more quickly by the SMVSC method, the tracking performance of the control target is faster, and the error is smaller. It can be seen that, under certain conditions of the soil without external disturbance, when the control target changes, the dynamic tracking performance to the control target of the SMVSC is better, the response time is shorter than the fuzzy PID control, and there is almost no steady-state error, further proving the SMVSC method superiority.

HILS test and analysis of control algorithm

The HILS test system is used to experimentally investigate the slip rate control for a half-tractor model. According to the test conditions of off-line simulation, based on the HILS real-time simulation test platform, two different algorithms by SMVSC and fuzzy PID control are respectively carried out in the hardware-in-the-loop simulation test, corresponding to the analysis of the sliding rate control when the soil specific resistance pulse changes and the sliding rate control when the control target pulse changes.

● **Soil specific resistance with pulse change**

Setting the same test conditions as the offline simulation, the test duration is 30s, and the results are shown in figure 9.



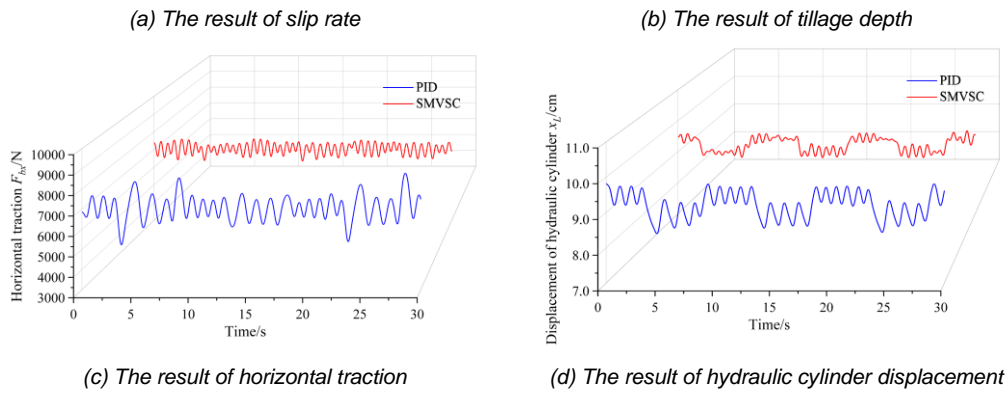


Fig. 9 - HILS results of soil specific resistance with pulse change

The absolute value deviation and variance of the mean value are used as the measurement indicators to evaluate the control effect of the slip rate, and to compare control accuracy of the two different control methods. At the same time, in order to better reflect the status of the ploughing operation under the control of slip rate, the data statistics of ploughing depth, hydraulic cylinder displacement and horizontal traction force were analysed. The analysis results are shown in table 1.

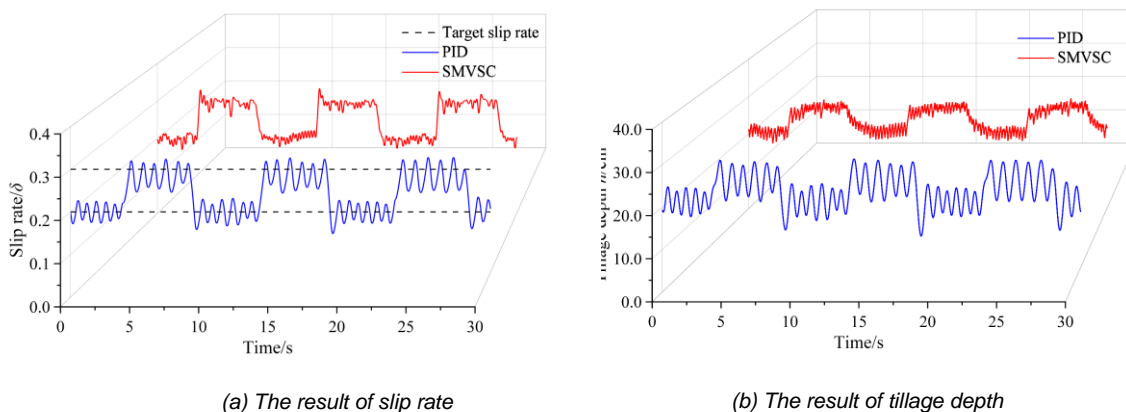
Table 1

Analysis about HILS results								
Methods	Slip rate		Tillage depth		Displacement		Horizontal traction	
	Mean Absolute Deviation	Variance	[cm]		[cm]		[N]	
			Max	Min	Max	Min	Max	Min
SMVSC	0.014	0.0002	25.22	11.92	9.67	8.81	7067.78	6350.24
PID	0.027	0.0011	31.46	9.70	9.81	8.40	8783.37	5224.83

By the SMVSC method, the maximum deviation of the slip rate control is 0.041, the mean absolute deviation is 0.014, and the slip rate variance is 0.0002. And by the fuzzy PID control method, the maximum deviation of the slip rate control is 0.121, the average absolute deviation is 0.027, and the slip rate variance is 0.0011. Although the slip rate was controlled around 0.2 through both algorithms, the deviation of the slip rate average absolute value under the SMVSC algorithm is reduced by 48%, the response time is reduced by about 1.3s, and the control deviation is smaller, and the fluctuation amplitude is far smaller than the fuzzy PID control algorithm. In addition, by the SMVSC, the adjustment change of plough depth is 5.26 cm, which is far less than 7.21 cm of fuzzy PID control, reducing about 27%; the adjustment change of hydraulic cylinder displacement is 1.15 cm, which is far less than 1.8 cm of fuzzy PID control, which is about 36%; the adjustment change of horizontal traction force is 1293.35 N, which is less than 2217 N of fuzzy PID control, which is about 42%. When the tractor realizes the optimal value control of slip rate, the adjustment amount is small, which makes the tractor keep in a more stable working state.

● Control target value with pulse change

The test conditions are set as above, and the results are shown in figure 10.



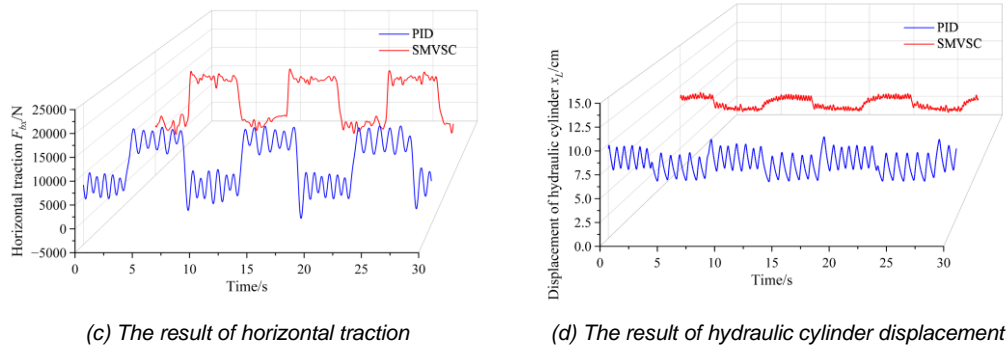


Fig. 10 - HILS results of control target value with pulse change

When the slip rate control target changes between 0.2 and 0.3, both algorithms can effectively track the dynamically changing slip rate target value, but the tracking response time of SMVSC method is reduced by about 0.8s less than that of fuzzy PID control, the average control overshoot is reduced by about 0.03, and the control deviation and fluctuation range are also significantly reduced. At the same time, the results by the SMVSC method show that, the displacement of the tractor hydraulic lift cylinder and the adjustment depth of the ploughing depth are significantly smaller than those obtained by the fuzzy PID control, and the fluctuation range of the horizontal traction force is also significantly reduced.

Compared with the integrated traction-slip ratio control method previously proposed by our team (Zhang *et al.*, 2016), the slip ratio control strategy developed in this study achieved superior target slip ratio tracking performance while maintaining minimal fluctuations in tillage depth and traction force. The proposed SMVSV method demonstrated significant improvements over existing slip ratio control approaches (Bai *et al.*, 2012; Soylyu *et al.*, 2021), reducing the system response time to within 1 second, decreasing the mean absolute deviation of slip ratio to 0.014 under soil specific resistance with pulse change, and significantly minimizing slip ratio overshoots along with fluctuations in tillage depth and traction force during target slip ratio adjustments with pulse change.

It can be seen that the method based on SMVSC has shorter response time, smaller control overshoot, and better dynamic tracking performance in the slip control process. As a robust control method, the control process of SMVSC method is independent of the state of the system and external disturbances, it has the advantages of parameter disturbance insensitivity and simple implementation. In view of the strong nonlinear and complex coupling characteristics of heavy tractor ploughing unit, SMVSC method has certain control advantages and better control effect than fuzzy PID control. While controlling the slip rate to the target value, the adjustment amount is smaller, which can maintain a more stable tractor field working condition.

CONCLUSIONS

(1) For the ploughing operation conditions, considering the nonlinear characteristics of the complex coupling system of the "tractor-tools-soil", a time-varying nonlinear dynamic model of the tractor's electro-hydraulic hitch system was developed, and the nonlinear motion characteristics of the system were clarified.

(2) Based on the theory of Sliding Mode Variable Structure Control (SMVSC), considering the strong nonlinearity, time-variability, and uncertainty characteristics of the dynamic system, the piston pressure in the hydraulic cylinder was selected as the control variable. A slip control algorithm for the tractor's drive wheels was designed, with a fuzzy PID algorithm used as a comparative benchmark. Simulations and analyses were conducted in MATLAB/Simulink.

(3) A hardware-in-the-loop simulation (HILS) test platform was developed to overcome the limitations of field experiment and to evaluate the real-time execution capabilities of the control algorithm. The results indicated that the SMVSC algorithm effectively achieved optimal slip rate control and a more stable operational state within the electro-hydraulic hitch system, characterized by reduced adjustment amplitudes. This advancement is significant for minimizing energy consumption and enhancing the quality of ploughing activities during operations.

ACKNOWLEDGEMENT

This research was supported by the National Natural Science Foundation of China (No.32201677), the Shaanxi Key Research Development Project (2023-ZDLNY-62, 2024NC-YBXM-202, 2024NC-YBXM-244).

REFERENCES

- [1] Bai X., Lu Z., Chang J., Li H., Zhou W. (2012) Fuzzy Control Algorithm Simulation of Automatic Control of Tilling Depth for Tractor Based on Slip Rate. *Transactions of the Chinese Society for Agricultural Machinery*. Vol. 43, pp. 6–10. China.
- [2] Ding C., Ding S., Wei X., Mei K. (2022) Composite SOSM Controller for Path Tracking Control of Agricultural Tractors Subject to Wheel Slip. *ISA Transactions*, Vol. 130, pp. 389–398. China.
- [3] Giller K.E., Andersson J.A., Corbeels M., Kirkegaard J., Mortensen D., Erenstein O., Vanlauwe B. (2015). Beyond Conservation Agriculture. *Frontiers in Plant Science*, Vol. 6. Netherlands.
- [4] Holthusen D., Brandt A.A., Reichert J.M., Horn R., Fleige H., Zink A. (2018). Soil Functions and in Situ Stress Distribution in Subtropical Soils as Affected by Land Use, Vehicle Type, Tire Inflation Pressure and Plant Residue Removal. *Soil & Tillage Research*, Vol. 184, pp. 78–92. Brazil.
- [5] He Z., Song Z., Wang L., Zhou X., Gao J., Wang K., Yang M., Li Z. (2023). Fasting the Stabilization Response for Prevention of Tractor Rollover Using Active Steering: Controller Parameter Optimization and Real-Vehicle Dynamic Tests. *Computers and Electronics in Agriculture*, Vol. 204, 107525. China.
- [6] Janulevičius A., Šarauskis E., Čiplienė A., Juostas A. (2019). Estimation of Farm Tractor Performance as a Function of Time Efficiency during Ploughing in Fields of Different Sizes. *Biosystems Engineering*, Vol. 179, pp. 80–93. Republic of Lithuania.
- [7] Ji X., Ding S., Wei X., Cui B. (2023) Path tracking of unmanned agricultural tractors based on a novel adaptive second-order sliding mode control. *Journal of the Franklin Institute*, Vol. 360(8), pp. 5811-5831.
- [8] Li S., Wang J., Li K. (2007). Design and Development of the Monitoring System for Hardware-in-the-Loop Simulation Test Bench. *Systems Engineering Procedia*, Vol. 19(16), pp. 3684–3687. China.
- [9] Pranav P.K., Pandey K.P., Tewari V.K. (2010). Digital Wheel Slipmeter for Agricultural 2WD Tractors. *Computers and Electronics in Agriculture*, Vol. 73, pp. 188–193. India.
- [10] Paksoy M. (2020). Nonlinear Adaptive Semiactive Control of a Half-Vehicle Model via Hardware in the Loop Simulation. *Turkish Journal of Electrical Engineering and Computer Sciences*, Vol. 28, pp. 1612–1630. Turkey.
- [11] Raikwar S., Jijyabhau Wani L., Arun Kumar S., Sreenivasulu Rao M. (2019). Hardware-in-the-Loop Test Automation of Embedded Systems for Agricultural Tractors. *Measurement*, Vol. 133, pp. 271–280.
- [12] Rahmati M., Eskandari I., Kouselou M., Feiziasl V., Mahdavinia G.R., Aliasgharzad N., McKenzie B.M. (2020). Changes in Soil Organic Carbon Fractions and Residence Time Five Years after Implementing Conventional and Conservation Tillage Practices. *Soil & Tillage Research*, 200, 104632.
- [13] Soylu S. , Arman K. . (2021). Fuzzy logic based automatic slip control system for agricultural tractors. *Journal of Terramechanics*, Vol. 95(7), pp. 25-32. Turkey.
- [14] Watanabe M., Sakai K. (2019). Impact Dynamics Model for a Nonlinear Bouncing Tractor during Inclined Passage. *Biosystems Engineering*, Vol. 182, pp. 84–94. Japan.
- [15] Wu Z., Xie B., Li Z., Mitsuoka M., Inoue E., Okayasu T., Hirai Y. (2019). dSPACE Based Hardware in the Loop Testing Platform for Powertrain Management Unit of Electric Tractor. *Journal of the Faculty of Agriculture, Kyushu University*, Vol 64, pp. 309–317. China.
- [16] Wang Y., Chen S., Zhang D., Yang L., Cui T., Jing H., Li Y. (2020). Effects of Subsoiling Depth, Period *Journal of Integrative Agriculture*, Vol. 19, pp. 1596–1608. China.
- [17] Xu G., Chen M., He X., Pang H., Miao H., Cui P., Wang W., Diao P. (2021). Path Following Control of Tractor with an Electro-Hydraulic Coupling Steering System: Layered Multi-Loop Robust Control Architecture. *Biosystems Engineering*, Vol 209, pp. 282–299. China.
- [18] Zhang S., Du Y., Zhu Z., Mao E., Liu J., Shi J. (2016). Integrated control method of traction & slip ratio for rear-driving high-power tractors. *Trans. Chinese Society of Agricultural Engineering*, Vol. 32(12), pp. 47-53. China.
- [19] Zhang S., Wu Z., Chen J., Li Z., Zhu Z., Song Z., Mao E. (2020). Control method of driving wheel slip rate of high-power tractor for ploughing operation. *Transactions of the Chinese Society of Agricultural Engineering*, Vol 36(15), pp. 47-55. China.
- [20] Zhang T., Jiao X., Lin Z. (2022) Finite Time Trajectory Tracking Control of Autonomous Agricultural Tractor Integrated Nonsingular Fast Terminal Sliding Mode and Disturbance Observer. *Biosystems Engineering*, Vol. 219, pp. 153–164. China.
- [21] Zhang S., Wen C., Ren W., Luo Z., Xie B., Zhu Z., Chen Z. (2023). A Joint Control Method Considering Travel Speed and Slip for Reducing Energy Consumption of Rear Wheel Independent Drive Electric Tractor in Ploughing. *Energy*, Vol. 263, 126008. China.

GLOBAL PATH PLANNING OF FARMLAND PLOTS BASED ON IMPROVED WHALE OPTIMIZATION ALGORITHM

基于改进鲸鱼优化算法地块整体路径规划

Shiteng GUO^{1,2,3}, Xueping ZHAO², Jian ZHANG³, Zhi guo PAN¹, Xiangyu BAI¹, Zhuhe SHAO¹, Yao LI¹, Zhen LIU¹, Shuai WANG¹

¹) College of Electrical and Mechanical Engineering, Qingdao Agricultural University, Qingdao/ China

²) National Key Laboratory of intelligent agricultural power Equipment Luoyang/ China

³) College of Mechanical and Electrical Engineering, Hainan University, Haikou/ China

Tel: +8615318715305; E-mail: peter_panzg@163.com

Corresponding author: Zhiguo Pan

DOI: <https://doi.org/10.35633/inmateh-75-34>

Keywords: Path planning, Grid method, Improved whale optimization algorithm, Optimal traversal order

ABSTRACT

Path planning is crucial for agricultural machinery navigation. To address the issue of operational path planning in fields with obstacles, this paper proposes a method for obstacle avoidance path planning in farmland by combining an improved whale optimization algorithm with Dijkstra's algorithm. The population initialization is conducted using Tent mapping and a nonlinear convergence factor α^* is introduced to reduce the oscillation and instability of the traditional whale optimization algorithm. By using the grid method to model the environment of the target field, the field is divided into multiple regular subplots. The improved whale optimization algorithm is employed to determine the optimal traversal order of these subplots. Subsequently, Dijkstra's algorithm is applied to find the shortest path connecting the subplots, achieving global obstacle avoidance path planning for farmland. Taking a rectangular plot of land in Jiaolai Town, Jiaozhou City, Qingdao as the target area for this study, the experimental results indicate that this method achieves a coverage rate of 100% in the plot coverage path experiment. Additionally, the path redundancy rate is 4.87%, which represents a reduction of 1.63% compared to traditional algorithms. This research method is applicable to regular plots, but it still has limitations for irregular plots or those with curved boundaries.

摘要

路径规划是农机导航的关键。针对地块中存在障碍物的作业路径规划问题，本文旨在提出一种基于改进鲸鱼优化算法与 Dijkstra 算法相结合的农田避障路径规划的方法。本文通过利用 Tent 映射进行种群初始化，以及引入非线性收敛因子 α^* ，降低传统鲸鱼优化算法的振荡性以及不稳定性。通过栅格法对目标地块进行环境建模，将地块分成多个规则子地块，通过改进鲸鱼算法求解子地块最佳遍历顺序，再利用 Dijkstra 算法进行子地块之间连接最短路径，实现农田全局避障路径规划。以青岛市胶州市胶莱镇的一块矩形地块为本次研究目标地块，实验结果表明：本方法在目标地块覆盖路径实验中，地块覆盖率达到 100%，路径重复率为 4.87%，路径重复率较传统算法减少 1.63%。该研究方法适用于规则地块，对于不规则或边界为曲线的地块还存在局限性。

INTRODUCTION

Path planning is one of the key technologies for achieving autonomous navigation operations in agricultural machinery (Deng H et al., 2023). The rationality and efficiency of path planning directly impact the accuracy and quality of agricultural machinery operations. The presence of structured obstacles in fields, such as utility poles, buildings, and irrigation devices, poses a significant challenge in avoiding these obstacles and achieving comprehensive coverage in path planning for agricultural machinery navigation. For the problem of full coverage path planning in agricultural fields, there are currently two main approaches: local path planning and global path planning methods. Local path planning refers to the process of obtaining real-time information about obstacles surrounding the working path through perception sensors in situations where the field environment is unknown, with an emphasis on the safety and timeliness of the path (Chakraborty, S et al, 2022). Global path planning refers to the process of planning a global path when the environmental information of the field is known, aiming to achieve full coverage of the target area.

Currently, there is limited research on path planning for agricultural machinery both domestically and internationally. Regarding local path planning, Wang Zhen, (2023), utilized an improved ant - colony algorithm with embedded genetic operators to solve for the optimal path of virtual nodes. Taking the transportation cost and time cost of agricultural robots as the objective function, the effectiveness of the optimization model and the improved ant - colony algorithm was verified through case analysis. Li Fan, (2023), classified obstacles based on the relationship between the size of field obstacles and the working width of agricultural machinery. They proposed a method for obstacle avoidance using polyline techniques to bypass small obstacles by segmenting and merging the field. In 2023, someone proposed a method for constructing the shortest tangent obstacle avoidance path, which can quickly plan an obstacle avoidance path in the case of static obstacles (Huo Yinghui et al., 2023). For global path planning, Nilsson et al., (2020), represented the coverage trajectory of farmland as a virtual road network diagram consisting of main working area trajectories, headland passages, and turning trajectories. Finally, coverage path planning was conducted based on this diagram. Experimental results demonstrate that this method is applicable to various types of single fields; however, it is not suitable for fields with obstacles. Yakoubi et al., (2016), addressed the problem of complete coverage for cleaning robots using a genetic algorithm. They iteratively optimized the path length as the fitness function and employed genetic operators such as crossover and mutation to enhance fitness. This algorithm achieved complete coverage in simple environments; however, its drawbacks include low search efficiency in the later stages and poor convergence. Le proposed an algorithm for complete coverage path planning based on a spiral generation tree, utilizing genetic algorithms (GA) and ant colony optimization to solve the Traveling Salesman Problem (TSP). However, a notable drawback of this approach is the occurrence of dead zones in areas with a high density of obstacles. Additionally, the resulting path length and the number of turns are relatively unsatisfactory (Le et al., 2020).

In summary, regarding the path planning problem in plots with obstacles, both local path planning and full coverage paths have certain deficiencies. For example, existing local path planning methods often adopt the shortest tangent method and polyline method, where the obstacle avoidance strategies are overly simplistic, considering only a single obstacle, and lack universality in situations where multiple obstacles are present in the plot. The research on global path planning faces issues such as low algorithm efficiency, poor convergence performance, and an inability to handle areas with multiple obstacles. To address the above issues, this paper proposes a path planning method for obstacle-laden plots based on an improved whale optimization algorithm. Firstly, the target plot is modeled using a grid method. Then, the plot is segmented and merged based on the obstacles present, dividing it into multiple sub-plots that are free of obstacles. An intelligent algorithm is used to determine the traversal order of the sub-plots, while Dijkstra's algorithm is employed for path planning between the sub-plots. This ultimately achieves full coverage path planning for the entire plot.

MATERIAL AND METHODS

Construction of Operational Model

Grid Modeling of the Plot

In this study, a grid modeling method is utilized to create a representation of the target plot. This method defines the grid size based on key parameters such as the length, area, and obstacle information of the target plot, using the operational range of smart agricultural machinery as a reference. The entire environment is then divided into several square cells, referred to as grids, where each grid represents a specific area within the environment. These grids effectively capture obstacle information and clearly illustrate features of free space and other environmental characteristics, thereby simplifying the complex environmental data into a manageable set of two-dimensional grid representations (Deng et al., 2023).

The target plot is a farmland located in Jiaolai Town, Jiaozhou City, Qingdao, Shandong Province, with coordinates at 36.43°N latitude and 120.05°E longitude. The digital elevation model (DEM) data indicates that the plot has a total area of 130,040 square meters and a perimeter of 1.443 kilometers. The contour feature points of the field and the obstacles within the farmland have been marked (as shown in Figure 1). In this paper, based on the information of the target plot and the working range of the agricultural robot, a 20×20 grid model is constructed in MATLAB R2023a. The white grids represent the workable grids, the black grids represent the obstacle grids. A grid that contains obstacles but is not completely filled is defined as a partial - obstacle grid; a grid that is completely filled with obstacles is called a full - obstacle grid (as shown in Fig. 3).

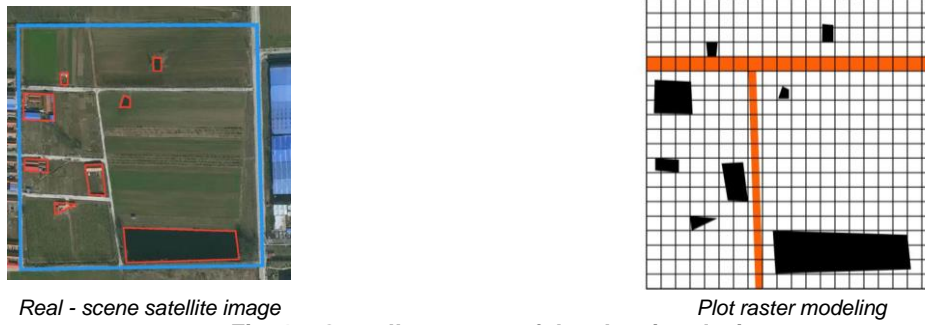


Fig. 1 – Overall structure of the cleaning device

Expansion of Obstacle Grids

Considering the varying shapes and sizes of obstacles in the field, some obstacles cannot fully occupy an entire grid cell, which increases the difficulty of algorithmic planning. Obstacles can also lead to path planning becoming trapped in local optima. Therefore, it is necessary to expand certain obstacles. When irregular obstacles do not occupy a full grid cell, their boundaries should be extended outward until the obstacles completely fill the grid cell they are in, thereby reducing the planning complexity. The specific rules for expanding obstacles are illustrated by the variations presented in Figure 2. According to these rules, the grid map in Figure 3 undergoes obstacle expansion, with the results shown in Figure 3.

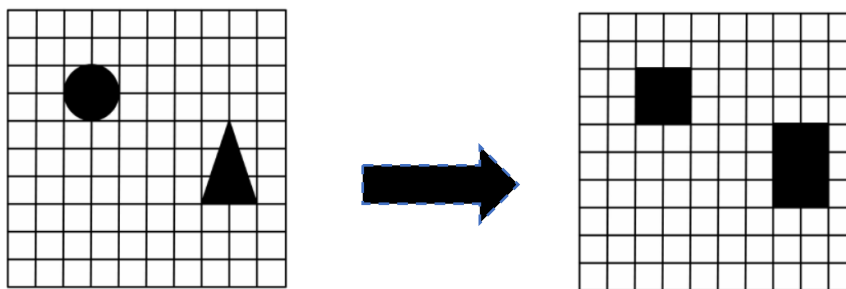


Fig. 2 – Obstacle Expansion Before and After

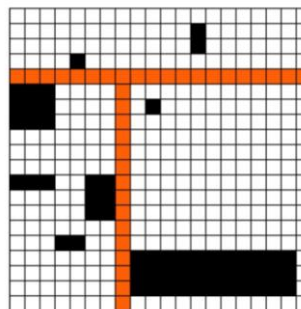


Fig. 3 – Obstacle Expansion Grid Map

Plot Division and Merging

This paper addresses obstacle avoidance path planning in farmland by partitioning the plots. The area decomposition method is employed to achieve this segmentation (*Tang et al., 2021*). Due to the presence of obstacles, the farmland is divided into multiple subplots, which can lead to an increased frequency of turns and lower coverage rates during agricultural operations. By utilizing the unit decomposition method, the farmland plots are segmented into multiple obstacle-free subplots (*Wang L. et al., 2024*).

The division of plots should be based on the grid map expanded above the obstacles. For each obstacle grid, parallel boundary lines to the X-axis and Y-axis are drawn from the two vertices at the bottom of the obstacle grid. These boundary lines extend outward until they encounter the next obstacle grid, and by repeating this process, the entire grid map can be segmented into multiple regular subplots. To reduce the operational redundancy and improve efficiency, adjacent subplots that have the same height or width should be merged to maximize the rectangular plots, thereby decreasing the number of subplots. The results of the plot division and merging are shown in Figure 4.

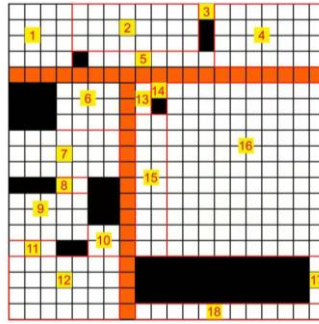


Fig. 4 – The results of the sub-plot division diagram

Sub-plot Traversal Order Planning

To achieve path planning for agricultural robots and reduce the rate of traversal duplication, it is essential to ensure that each defined sub-plot is planned exactly once in the global traversal path. This can be transformed into solving the Traveling Salesman Problem (TSP). The shortest path solution to the TSP corresponds to the optimal traversal order of the defined sub-plots. This study employs an improved whale optimization algorithm to determine the optimal traversal order among the sub-plots.

Traditional whale optimization algorithms

The whale optimization algorithm is a novel bio-inspired swarm intelligence algorithm, inspired by the foraging strategies of humpback whales (*Nadimi-Shahraki et al., 2023*). Within the framework of the whale optimization algorithm, each whale represents a feasible solution, and position updates are performed through encircling prey, bubble-net attacking, and random search.

(1) Encircling prey

In the encircling prey phase, it is assumed that the current best candidate is the target prey or an optimal solution close to the target prey (*Wei F. et al., 2023*). Once the best candidate solution is determined, all other whales will swim towards the direction of the best candidate solution, updating their positions in the process. The mathematical model for this process is as follows:

$$X(t + 1) = X_{best}(t) - A \cdot D \quad (1)$$

$$D = |C \cdot X_{best}(t) - X(t)| \quad (2)$$

In the formula, t represents the current iteration number; $X_{best}(t)$ denotes the position vector of the current best candidate solution, and $X(t)$ is the position vector of the current whale. The coefficients A and C are vector coefficients, which are calculated as follows:

$$A = 2ar - a = a(2r - 1) \quad (3)$$

$$C = 2r \quad (4)$$

$$a = 2 - \frac{2t}{T} = 2(1 - \frac{t}{T}) \quad (5)$$

In the formula, a is the convergence coefficient; r is a random vector within the range of $[0, 1]$, and T is the maximum number of iterations.

(2) Bubble Net Attack

Bubble net feeding is a unique predation behavior of humpback whales, which can be simulated using the following two mathematical models.

Constricting encirclement mechanism

The bubble net feeding technique is a unique foraging behavior of humpback whales used to capture prey, which can be simulated using the following two mathematical models.

Spiral position update

During this stage, the whales swim upstream in a spiral pattern, releasing bubble nets of varying sizes to capture prey. The mathematical model for this process is as follows:

$$X(t + 1) = D_{best} \times e^{bL} \times \cos(2\pi L) + X_{best}(t) \quad (6)$$

$$D_{best} = |X_{best}(t) - X(t)| \quad (7)$$

In this equation, D_{best} represents the distance between the current search individual and the current optimal solution; b is the spiral shape parameter; and L is a random number uniformly distributed in the range of $[-1, 1]$.

Assuming that humpback whales have an equal probability of adopting these two behaviors when attacking prey, this can be expressed using the following formula (8).

$$X(t + 1) = \begin{cases} X_{best}(t) - A, & p < 0.5 \\ D \cdot e^{bL} \cdot \cos(2\pi L) + X_{best}(t), & p \geq 0.5 \end{cases} \quad (8)$$

In the equation, P represents the probability of the predation mechanism, which is a random number within the range of $[0, 1]$.

(3) Searching for prey

To ensure that all humpback whales can thoroughly explore the solution space, they conduct random searches based on their relative positions (Yan Z. et al, 2023). When $|A| \geq 1$, the whales perform a global search, and the mathematical model is as follows:

$$D_{rand} = |C * X_{rand}(t) - X(t)| \quad (9)$$

$$X(t + 1) = X_{rand}(t) - A \cdot D \quad (10)$$

In this formula, D_{rand} represents the distance between the current search agent and a random agent, while X_{rand} denotes the position of the random agent at the current time.

Improve the whale optimization algorithm

Compared with traditional optimization algorithms and early meta-heuristic algorithms, the whale optimization algorithm has its main advantages in strong local search capability, a simple structure, and fewer required tuning parameters (Yang W. et al., 2023). However, the traditional whale optimization algorithm also faces issues such as getting easily trapped in local optima and premature convergence. Considering the advantages and disadvantages of the whale optimization algorithm, this paper aims to improve the initialization phase and the convergence factor.

(1) Improve the initialization phase

During the initialization phase, the quality of the whale population directly influences the performance of the algorithm. However, the whale optimization algorithm employs a random and uncertain strategy to generate the initial population, which fails to ensure the diversity of the population. This lack of diversity in the initial population negatively impacts the overall effectiveness of the algorithm. This paper proposes to incorporate Tent mapping into the initialization phase of the whale optimization algorithm. Tent mapping is characterized by its regularity, randomness, and strong traversability, making it an effective solution to the quality issues of the initial population in the traditional whale optimization algorithm. The Tent mapping formula is as follows:

$$X(t + 1) = \{\mu \cdot X(t), \quad 0 < X(t) < 0.5 \quad (11)$$

Assuming the initial whale population size is M , the population is represented as $X = \{X(t), 1, 2, 3, 4, \dots, M\}$. where $\mu \in (0,2)$ is the chaos parameter, and the chaotic effect is directly proportional to its value—the larger the value, the better the chaotic effect. When $\mu = 2$ the population exhibits good ergodicity and algorithmic solving speed, allowing for a more comprehensive search of a larger space within a certain range. This enables the selection of outstanding individuals from the current population as initial solutions, thereby improving the quality of the population and the performance of the algorithm.

(2) Incorporate the nonlinear convergence factor

To address the issues of the whale optimization algorithm easily falling into local optima and premature convergence, an analysis of the operational logic of three search mechanisms reveals that the efficiency of global and local search in the algorithm is determined by the magnitude of the vector coefficient $|A|$ (Chen X. et al., 2020). In the whale optimization algorithm, the convergence factor α exhibits a linearly decreasing trend. Therefore, when the number of iterations exceeds half of the maximum iteration count, $\alpha < 1$. In the iterative process, if the vector coefficient decreases prematurely to a low value, it increases the likelihood of the algorithm falling into a local optimum. To better balance the global search and local search capabilities of the algorithm, this study introduces a nonlinear convergence factor α^* , as shown in the following formula:

$$\alpha^* = 2 - \frac{2}{e^{-0.2 \cdot (t-T/2)}} \quad (12)$$

Let the maximum number of iterations be $T = 80$. The convergence factor curve is illustrated in the figure below. In the iteration data graph, during the early and mid-stages of the iteration process, the value of α^* remains at a high level to ensure the global search ability of the algorithm. In the later stages of the iteration, α^* rapidly decreases to ensure that the algorithm focuses on local search. The improved workflow of the Whale Optimization Algorithm is illustrated in Figure 6.

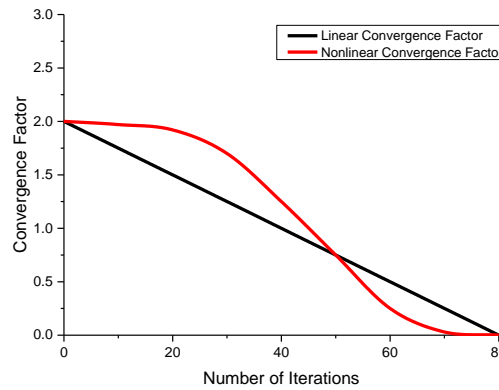


Fig. 5 – Convergence Factor Curve Graph

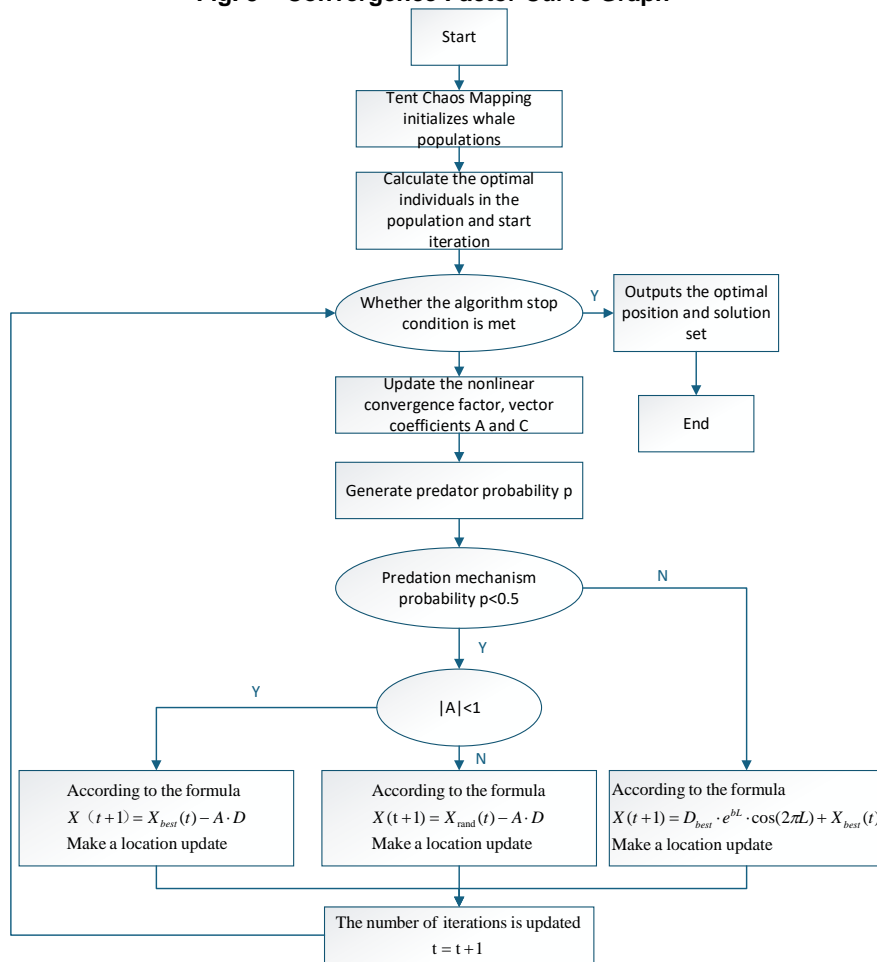
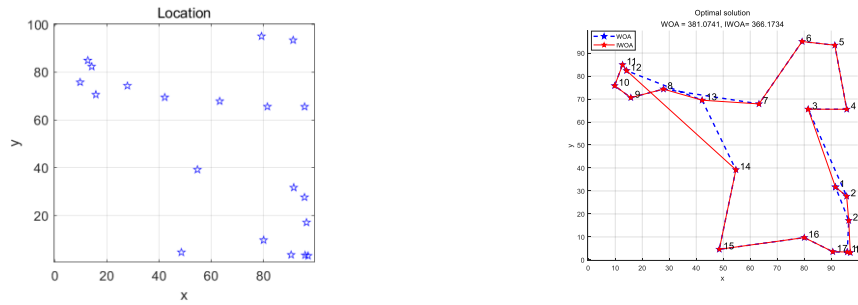


Fig. 6 – Algorithm Technical Roadmap

Improved simulation experiment of whale optimization algorithm

To demonstrate the superiority and advanced nature of the improved Whale Optimization Algorithm in solving the Traveling Salesman Problem (TSP), a comparative experimental method is employed. Both the traditional Whale Optimization Algorithm and the improved Whale Optimization Algorithm are utilized simultaneously to solve the TSP. This allows for a direct comparison of their performance and effectiveness in finding optimal or near-optimal solutions. Randomly generate coordinates for 20 cities and use the path length as the fitness value.

Figure 7a) shows the randomly generated coordinates of 20 cities, while Figure 7b) presents a comparison of the optimal traversal paths obtained using the improved whale optimization algorithm and the traditional whale optimization algorithm. This simulation was carried out in MATLAB R2023a on a Lenovo Legion Y7000 device.



a) Location
b) Traversal Path Comparison
Fig. 7 –Results of WOA and IWOA in Solving the TSP Problem

From Figure 7, it can be observed that the best fitness values for the Whale Optimization Algorithm (WOA) and the Improved Whale Optimization Algorithm (IWOA) are 381.0741 and 366.1734, respectively, indicating a reduction in fitness of approximately 3.9%. Based on the simulation results, it is evident that the solution obtained using the improved whale optimization algorithm for solving the Traveling Salesman Problem (TSP) with respect to the traversal order is significantly better than the results obtained using the traditional whale optimization algorithm.

Determine the optimal traversal order of the target sub-block

After validating the superiority of the improved whale optimization algorithm in addressing the traveling salesman problem, it is necessary to apply the improved whale optimization algorithm to the path planning for complete coverage of target plots. Based on the results of subplot division shown in Figure 4, for the convenience of planning the traversal order of regular subplots, the center coordinates of regular subplots will represent each subplot, and coordinate parameters will be used to indicate the specific locations of the subplots. Input the coordinates of the central points for each subplot; determine the optimal traversal order among the 18 subplots. The optimal traversal order between the target subplots is determined using both the traditional whale optimization algorithm and the improved whale optimization algorithm. The results are shown in the figure 8.

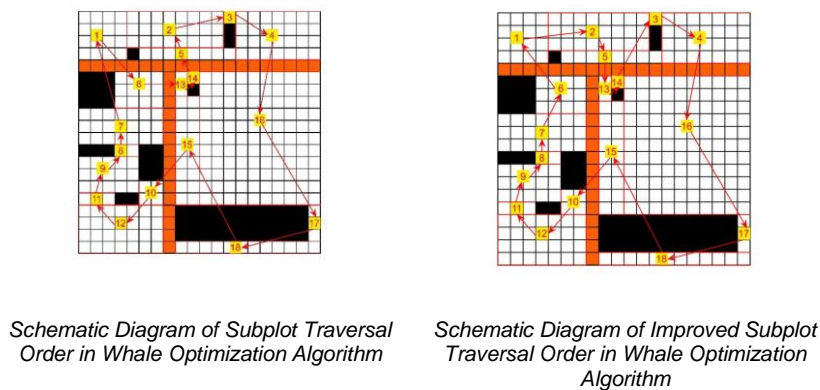
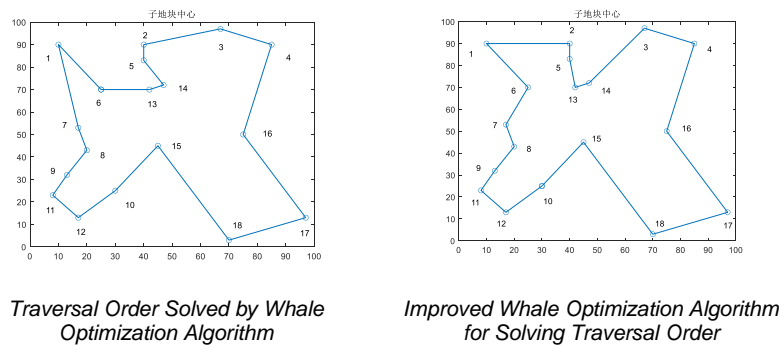


Fig. 8 –Comparison of traversal order results of subplots

Table 1

Comparison of traversal results from different algorithms		
The name of the algorithm	Traversal order	Fitness value
WOA	6-13-14-5-2-3-4-16-17-18-15-10-12-11-9-8-7-1-6	403
IWOA	16-17-18-15-10-12-11-9-8-7-6-1-2-5-13-14-3-4-16	401

According to the observations from Figure 8 and Table 1, the optimal traversal order obtained by the traditional whale optimization algorithm for the subplots is: 6-13-14-5-2-3-4-16-17-18-15-10-12-11-9-8-7-1-6, with a shortest distance of 403 meters. In contrast, the optimal traversal sequence derived from the improved whale optimization algorithm is: 16-17-18-15-10-12-11-9-8-7-6-1-2-5-13-14-3-4-16, resulting in a shortest distance of 401 meters.

Path Planning within Agricultural Subplots

Based on the grid layouts and the presence of obstacles, the plots are divided into multiple regular subplots that are free of obstacles. While irregular subplot structures are simpler, effective path planning for the regular subplots requires selecting appropriate agricultural machinery operating methods to achieve optimal results. Currently, the primary coverage methods for operations in regular plots include reciprocating and inward spiral traversal techniques, as shown in Figure 9. The objective of path planning is to enhance operational efficiency, reduce cost waste, and minimize issues such as re-tilling and missed tilling.

The inward spiral traversal method for path planning typically involves frequent turns, making it inconvenient to connect with adjacent subplots. This can lead to increased energy consumption and reduced operational efficiency. Therefore, this study opts for the reciprocating method for path planning of the subplots to enhance land utilization and reduce occurrences of re-tilling and missed tilling. The specific steps for reciprocating traversal are as follows: (1) Choose a starting point and set the coordinates of the starting point as (x_0, y_0) ; (2) Define the two edges of the rectangular plot as A and B ; (3) Determine the lengths of edges A and B , using the longer edge as the starting edge, with edge A aligned along the X-axis and edge B along the Y-axis. (4) If edge A is longer, the coordinates of the next point will be $(x_0 + 1, y_0)$. (5) If edge B is longer, the coordinates of the next point will be $(x_0, y_0 + 1)$.

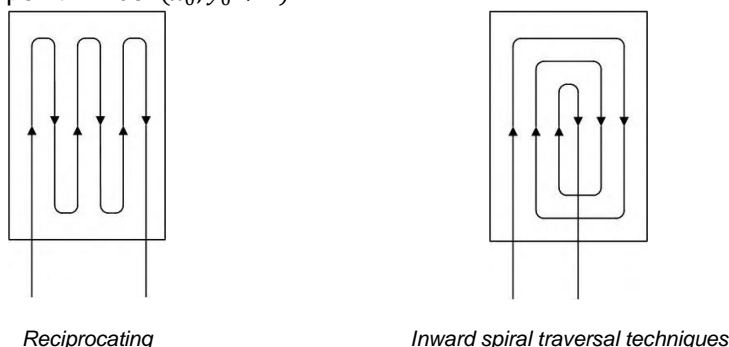


Fig. 9 – Coverage-Based Path Planning Method for Regular Plots

Subplot Connectivity Path Planning

After dividing the land into multiple subplots, agricultural robots complete traversal tasks within a single subplot area. They need to move from the current rectangular subplot to the next subplot based on the sequence of all subplots. In the path planning for connecting these two subplots, this study employs Dijkstra's algorithm for shortest path planning to reduce the redundancy of traversal paths and improve overall efficiency. The specific operational steps for using Dijkstra's algorithm for shortest path planning between points are as follows: First, read the data, set the source point a and the target point b , then mark the source point a and set $d_a = 0$, with $p_b = 0$; Subsequently, examine the distances between all marked points k and unmarked points h , and update $d_k = [d_k, d_k + m_{kh}]$. Here, m_{kh} represents the distance between points k and h . Select the unmarked point i with the smallest d_h , then find the point h^* among the marked points that is directly connected to i , and set $i = h^*$, followed by marking i . Continue this process in a loop until all points are marked. The algorithm can accurately generate the optimal path between two points, specifically achieving the shortest path from the starting point to the target point for agricultural robots.

RESULTS

Simulation of Path Planning for the Entire Agricultural Plot

All the experiments presented in this paper were conducted on a dedicated server operating under the Windows 11 system. The server is powered by an Intel(R) Core(TM) i5 - 9300H CPU, featuring a base clock frequency of 2.40 GHz and paired with 16 GB of RAM. For graphics processing, an NVIDIA GeForce RTX 4060 graphics card with 6 GB of video memory was employed. The programming and simulation tasks were accomplished using MATLAB R2023a as the development language.

In the previous sections, the traversal order between the target plot and its subplots has been determined using both the traditional whale optimization algorithm and the improved whale optimization algorithm. The starting point is determined within the initial plot, and a reciprocating planning approach is employed for the subplots of the initial plot. Subsequently, the next working area is accessed from the current regular subplot. The shortest path planning is performed using the aforementioned Dijkstra algorithm, facilitating the determination of the shortest, collision-free walking path from the traversal endpoint of the previous regular plot to the traversal starting point of the next regular plot. This process is repeated in a loop, ultimately achieving a complete coverage path planning for the entire farmland plot. The final results are compared as shown in the figure10.

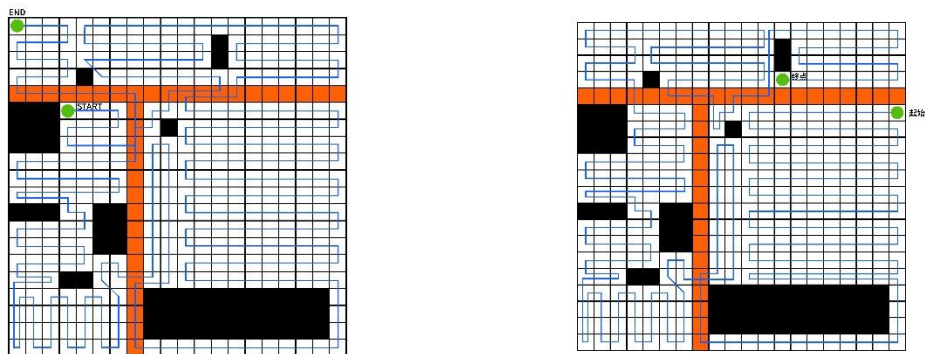


Diagram of Traditional Whale Optimization Algorithm for Path Planning

Diagram of Improved Whale Optimization Algorithm for Path Planning

Fig. 10 – Path Planning Comparison Diagram

Table 2

Comparison Diagram of Path Planning		
Path Planning Methods	Number of Covered Grids	Number of Duplicate Grids
Traditional Whale Optimization Algorithm and Dijkstra Algorithm	308	20
Improved Whale Optimization Algorithm and Dijkstra Algorithm	308	15

According to the observations from Figure 10 and Table 2, the entire grid consists of 20x20 cells, where black obstacles occupy 57 cells and roads occupy 35 cells, resulting in 308 free cells. The comparison shows that both algorithms achieve a coverage rate of 100%. Among them, the traditional whale optimization algorithm traverses 20 repeated cells, resulting in a traversal path redundancy rate of 6.5% and a path length of 4920 m. In contrast, the improved whale optimization algorithm traverses 15 repeated cells, achieving a traversal path redundancy rate of 4.87% and a path length of 4845 m. With the same coverage rate, the improved whale optimization algorithm reduces the path redundancy rate by 1.63% compared to the traditional algorithm. The experimental results indicate that the proposed method can effectively reduce path length, thereby validating the effectiveness of the research approach presented in this paper.

CONCLUSIONS

(1) This study proposes a stepwise path planning method for the entire agricultural plot area, which integrates an improved whale optimization algorithm with Dijkstra's algorithm. The method first employs the improved whale optimization algorithm to plan the traversal order of the segmented subplots, in order to determine the optimal traversal sequence for the subplots.

(2) To address the issues of local optimum entrapment and premature convergence commonly associated with the traditional whale optimization algorithm, this study utilizes Tent mapping for population initialization and introduces a nonlinear convergence factor. This approach balances the algorithm's global and local search capabilities, effectively mitigating local optima and significantly reducing search time. Experimental results using MATLAB indicate that, with 18 subplots, the improved whale optimization algorithm achieves a 4.07% reduction in average shortest path length and a 74.28% reduction in average iteration count compared to the traditional whale optimization algorithm.

(3) Using the path planning algorithm proposed in this study for full coverage of the target plots, MATLAB experiments reveal that the coverage rate of the paths generated by the improved whale optimization algorithm is 100%, with a repetition rate of 4.87%. This represents a reduction of 1.63% in repetition rate compared to the traditional whale optimization algorithm, thereby validating the effectiveness of the proposed method.

ACKNOWLEDGEMENT

The author has been supported by the "National Key R&D Program of China" (Project number: 2023YFD2000904), the "Industry Technology System of Modern Agriculture" (Project number: CARS-09-P32), and the "Qingdao Science and Technology Huimin Demonstration Project" (Project number: 23-2-8-xdny-2-nsh).

REFERENCES

- [1] Chakraborty, S., Elangovan, D., Govindarajan, P. L., ELnaggar, M. F., Alrashed, M. M., & Kamel, S. (2022). A comprehensive review of path planning for agricultural ground robots. *Sustainability*, 14(15), 9156.
- [2] Chen, X. (2020). Research on new adaptive whale algorithm. *IEEE Access*, 8, 90165-90201.
- [3] Deng, H., Liu, L., Fang, J., Qu, B., & Huang, Q. (2023). A novel improved whale optimization algorithm for optimization problems with multi-strategy and hybrid algorithm. *Mathematics and Computers in Simulation*, 205, 794-817.
- [4] Fan, L. (2023). Agricultural UAV crop spraying path planning based on PSO-A* algorithm. *INMATEH-Agricultural Engineering*, 71(3), pp.625-636. DOI: <https://doi.org/10.35633/inmateh-71-54>
- [5] Han, J., Li, W., Xia, W., & Wang, F. (2024). Research on Complete Coverage Path Planning of Agricultural Robots Based on Markov Chain Improved Genetic Algorithm. *Applied Sciences*. 2076-3417, 14(21).
- [6] Le, A. V., Nhan, N. H. K., & Mohan, R. E. (2020). Evolutionary algorithm-based complete coverage path planning for tetraiamond tiling robots. *Sensors*, 20(2), 445.
- [7] Nadimi-Shahraki, M. H., Zamani, H., Asghari Varzaneh, Z., & Mirjalili, S. (2023). A systematic review of the whale optimization algorithm: theoretical foundation, improvements, and hybridizations. *Archives of Computational Methods in Engineering*, 30(7), 4113-4159.
- [8] Nilsson, R. S., & Zhou, K. (2020). Method and bench-marking framework for coverage path planning in arable farming. *Biosystems engineering*, 198, 248-265.
- [9] Pour Arab, D., Spisser, M., & Essert, C. (2023). Complete coverage path planning for wheeled agricultural robots. *Journal of Field Robotics*, 40(6), 1460-1503.
- [10] Tang, G., Tang, C., Zhou, H., Claramunt, C., & Men, S. (2021). R-DFS: A coverage path planning approach based on region optimal decomposition. *Remote Sensing*, 13(8), 1525.
- [11] Wang, L., Zhuang, X., Zhang, W., Cheng, J., & Zhang, T. (2024). Coverage Path Planning for UAVs: An Energy-Efficient Method in Convex and Non-Convex Mixed Regions. *Drones*, 8(12), 776.
- [12] Wei, F., Li, J., & Zhang, Y. (2023). Improved neighborhood search whale optimization algorithm and its engineering application. *Soft Computing*, 27(23), 17687-17709.
- [13] Yakoubi, M. A., & Laskri, M. T. (2016). The path planning of cleaner robot for coverage region using genetic algorithms. *Journal of innovation in digital ecosystems*, 3(1), 37-43.

- [14] Yan, Z., Zhang, J., Zeng, J., & Tang, J. (2022). Three-dimensional path planning for autonomous underwater vehicles based on a whale optimization algorithm. *Ocean engineering*, 250, 111070.
- [15] Yang, L., Li, P., Wang, T., Miao, J., Tian, J., Chen, C., Tan, J. & Wang, Z. (2024). Multi-area collision-free path planning and efficient task scheduling optimization for autonomous agricultural robots. *Scientific Reports*, 14(1), 18347. <https://www.nature.com/articles/s41598-024-69265-y>
- [16] Yang, W., Kewen, X., Fan, S., Wang, L., Li, T., Zhang, J., & Feng, Y. (2022). A multi-strategy whale optimization algorithm and its application. *Engineering Applications of Artificial Intelligence*, 108, 104558.
- [17] Zhen, W., Keqing, Q., Xiaoli, Z., Xinyu, H., Xinran, L. I. (2023). Analysis on handling path optimization of agricultural robots based on improved ant colony algorithm. *INMATEH-Agricultural Engineering*, 70(2), pp.455-167. DOI: <https://doi.org/10.35633/inmateh-70-44>

INNOVATIVE PYROLYSIS REACTOR DESIGN FOR ENHANCED PERFORMANCE AND SUPERIOR BIOCHAR QUALITY

REACTOR INOVATOR DE PIROLIZĂ PENTRU O PERFORMANȚĂ ȘI O CALITATE SUPERIOARĂ ÎMBUNĂȚITĂ A BIOCHARULUI

Laurentiu-Constantin VLADUTOIU ^{*1}, Mario CRISTEA^{*1}, Florin NENCIU ¹, Valentin VLĂDUȚ ¹, Mihai OLAN ¹, Iulia GRIGORE ¹, Cristian SORICA ¹, Nicoleta VANGHELE ^{1,2}, Oana-Diana CRISTEA ¹

⁽¹⁾The National Institute of Research-Development for Machines and Installations Designed for Agriculture and Food Industry-INMA Bucharest, Ion Ionescu de la Brad -6, Sector 1, Bucharest, 013813 Romania

⁽²⁾Politehnica University of Bucharest, Splaiul Independentei no. 313, sector 6, Bucharest, 060042, Romania

E-mail: laurentiuVladutoiu82@gmail.com

DOI: <https://doi.org/10.35633/inmateh-75-35>

Keywords: *pyrolyzer, biochar, organic waste, carbon capture*

ABSTRACT

The three high-valuable products generated by the pyrolysis process are the biochar, the syngas, and the pyrolysis oil. The proportions of these products are influenced by several factors such as temperature, heating rate, and feedstock type. This research aimed to develop an innovative and improved pyrolysis reactor design, that can enhance both the quality and yield of biochar produced in thermochemical processes. The main objective was to enable the rapid conversion of various organic wastes, such as agricultural byproducts, wood chips, and other plant-based materials, into high-quality biochar. The experimental pyrolyzer model was designed with precise temperature control to optimize biochar properties and an intelligent process control system, which minimize emissions and maximize energy efficiency. This equipment not only contributes to sustainable waste management but also supports soil improvement by enhancing soil fertility and carbon sequestration in agricultural practices. The experimental results showed a high efficiency in obtaining a quality biochar within a short production time. Additionally, the biochar exhibited a water retention potential of up to 150% relative to the pre-treated biomass mass, while the energy consumption was estimated to be up to 15% lower compared to conventional methods.

REZUMAT

Cele trei produse de mare valoare generate de procesul de piroliză sunt biocharul, gazul de sinteză și uleiul de piroliză. Proporțiile acestor produse sunt influențate de mai mulți factori, cum ar fi temperatura, viteza de încălzire și tipul de materie primă. Prezenta cercetare a avut ca scop dezvoltarea unui proiect inovator de reactor de piroliză îmbunătățit, care poate îmbunătăți atât calitatea, cât și randamentul biocharului generat în procesele termochimice. Obiectivul principal a fost acela de a permite conversia rapidă a diferitelor deșeuri organice, cum ar fi produse secundare agricole, așchii de lemn și alte materiale pe bază de plante, în biochar de înaltă calitate. Modelul experimental de pirolizator este proiectat cu un control precis al temperaturii pentru a optimiza proprietățile biocharului și un sistem inteligent de control al procesului, care minimizează emisiile și maximizează eficiența energetică. Acest echipament nu numai că contribuie la gestionarea durabilă a deșeurilor, dar oferă și o îmbunătățire a solului, îmbunătățind fertilitatea solului și captarea carbonului în practicile agricole. Rezultatele experimentale au arătat o eficiență ridicată în obținerea unui biochar de calitate, într-un timp scurt de producție. Rezultatele experimentale au arătat o eficiență ridicată în obținerea unui biochar de calitate, cu un potențial de înmagazinare a apei de pana la 150% raportat la masa de tulpina înainte de tratare și un consum de energie estimat cu pana la 15% mai mic.

INTRODUCTION

Pyrolysis is a thermochemical process. It allows a controlled combustion of biomass in an oxygen-limited environment, generating both thermal energy and sterilized biochar (Amalina et al. 2023; Nenciu et al., 2024). Usually, upon completion of the thermochemical process, a significant amount of fixed carbon results in the form of biochar (between 10-20% of the initial mass), which can be used as an agricultural amendment. The gases generated during the process can be used to produce the thermal energy necessary to heat protected spaces or fruit dryers.

The industrial pyrolysis process offers a competitive alternative for the exploitation of numerous renewable energy sources, but also for the treatment and energy recovery of municipal, industrial or medical waste from various polluting industrial branches. The pyrolysis process is considered the most environmentally friendly thermochemical process, compared to combustion and incineration processes, because it has low emissions (Farag et al., 2024).

Biochar is an organic product resulting from the pyrolysis process of plant materials such as sawdust, straw or other agricultural waste. A common example of the use of pyrolysis is the conversion of plastic waste or biomass into liquid or gaseous fuels that can be used in various industrial or energy applications (Tomczyk et al., 2020; Wang et al., 2021). This process takes place at high temperatures, usually between 300 and 700 degrees Celsius, in an oxygen-limited environment (Amalina et al., 2022; Sun et al., 2017; Buss W, 2021). The resulting biochar has a porous structure and is considered a valuable soil amendment (Salma et al., 2024). Biochar contains approximately 98% carbon, which gives it chemical stability and the ability to retain nutrients in the soil. This composition makes it an effective amendment for improving soil quality (Woolf et al., 2010; Yang et al., 2021; El-Naggar et al., 2019).

The role of Biochar is to maintain moisture and stimulate beneficial microorganisms in the soil. These microorganisms are essential for plant health, as they contribute to the decomposition of organic matter and the availability of nutrients (Nidheesh et al., 2021). Among the most used materials are wood waste (Ahmad et al., 2017), agricultural residues (Zhang et al., 2022, Voicea et al., 2024), vegetable waste, manure (Wang et al., 2021; Jang et al., 2022; Nenciu et al. 2023), or industrial waste. Each of these raw materials has different characteristics that influence the final quality of the biochar produced. For example, the chemical composition and physical structure of biomass will determine the levels of fixed carbon and its ability to retain nutrients and water in the soil (Feng et al., 2021; Issaka et al., 2022; Oprescu et al. 2022).

The use of these raw materials not only helps create a valuable product such as biochar, but also contributes to the sustainable management of natural resources by recycling organic materials that might otherwise end up in landfills (Neogi et al., 2022; Voicea et al., 2024). The versatility of biochar highlights high potential in various industries, from agriculture and water treatment to animal husbandry. In a context where economic and commercial factors influence market dynamics, continuous innovation and research are essential to keep the biochar industry at the forefront of technological progress (Nenciu et al., 2024; Popescu et al., 2022).

Biochar has a complex porous network, which facilitates water absorption and retention, the size and distribution of the pores influence the water storage capacity, allowing it to retain moisture in the soil. It has many benefits such as: improving soil fertility (helps maintain moisture, which is essential for plant growth), reducing irrigation needs (by retaining water, biochar can reduce the frequency and amount of water needed for irrigation), stabilizing nutrients (preventing nutrient loss through leaching, thus maintaining a favorable environment for plants). Factors that influence the water storage potential are: the type of biomass used, pyrolysis conditions and interaction with the soil (Liu et al., 2015; Lone et al., 2015).

The objective of this work was to realize an improved design of a reactor for increasing the quality of biochar used in agricultural activities. After designing and building an Experimental Model of the equipment, it was tested for the treatment of plant waste from hemp and bamboo crops, in order to highlight the qualities of the obtained biochar and analyze the energy consumption.

MATERIAL AND METHODS

Experimental model design, customized for the pyrolysis of lignocellulosic biomass

This paper introduces an Experimental biochar production equipment designed and produced by the National Institute of Research - Development for Machines and Installations Designed for Agriculture and Food Industry - INMA Bucharest (Romania), distinguished by a series of innovative constructive elements. These advancements include enhancements in thermal efficiency, precise temperature control systems, and optimized batch management processes, all aimed at improving the quality and consistency of the resulting biochar. The equipment leverages smart control technologies for real-time monitoring and adjustment of critical parameters. This experimental setup is presented in figure 1.

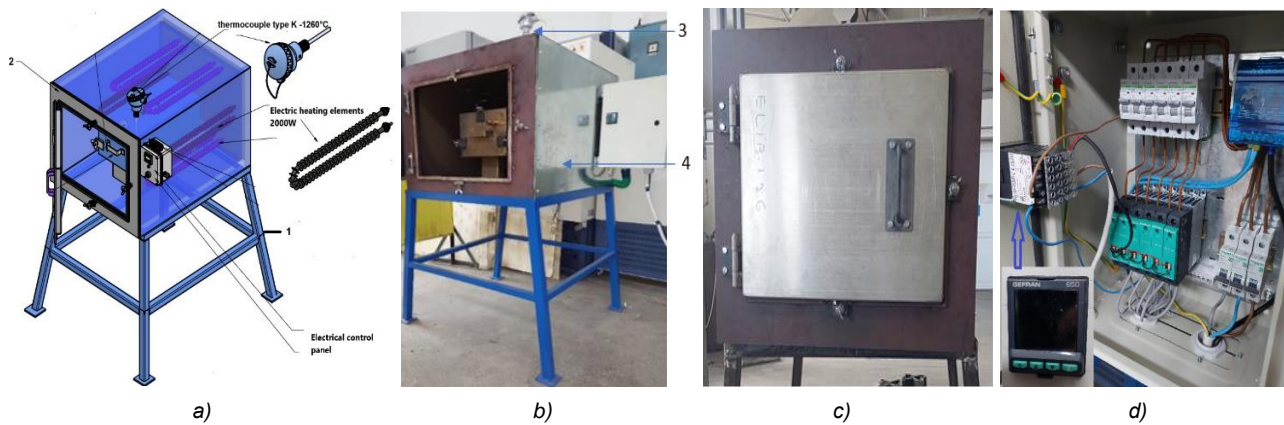


Fig. 1 – Experimental model for biochar production-general assembly

a) experimental model for biochar production; b) retort; c) equipment case; d) electrical control panel

The experimental model (figure 1-a) is customized for processing vegetable waste, consisting of a support (1) that supports a housing (2) with the actuation and control elements. This equipment features an automated system for managing the thermal process within a low-oxygen environment. The system incorporates an advanced electrical control panel (figure 1 d) that precisely regulates the combustion process, significantly reducing the time required to produce the biochar. To further enhance efficiency, the design allows for rapid replacement of the retort after each batch. By utilizing the residual high temperature within the enclosure from the initial production cycle, the new retort minimize downtime between batches. The casing (figure 1-c) is made of two galvanized tanks, suitable for corrosive industrial environments. The two casings are mounted concentrically and are insulated from each other with a ceramic fiber resistant to very high temperatures (up to 1260°C), in order to eliminate thermal energy losses. On the casing bottom and ceiling there are six electric resistances mounted around the retort (2000 W each). An overpressure valve and a high temperature thermocouple (3) are also mounted on the casing. The working temperatures are 300-500 °C for straw and other vegetable residues and 600 °C for forestry residues. The retort, illustrated in figure 2 (a), is constructed from high-temperature-resistant stainless steel (17 255 CSN, AISI 310). This material ensures durability and performance under intense thermal conditions. The retort is equipped with a discharge opening, featuring a frame (figure 2 -b) that supports three eye bolts (figure 2 -a) for securely attaching the biochar lid. For ease of handling and transportation, a handle is mounted on both the upper casing and the lid. With a capacity of 19 liters, the retort is designed to accommodate significant quantities of raw material, enhancing batch efficiency and overall productivity. The electrical resistances are presented in figure 2 b, c.

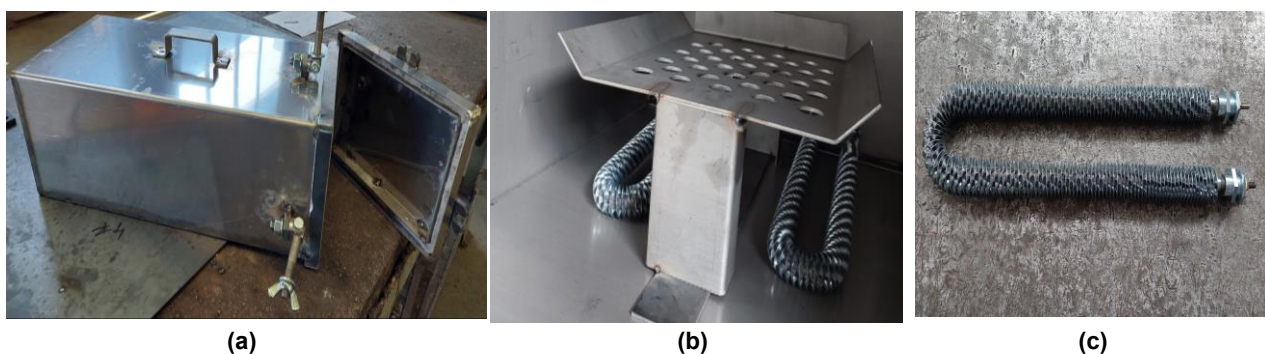


Fig. 2 - Heat treatment of organic material using a retort and electrical resistance

a) retort; b) retort support; c) electric resistances

The present experiment evaluated hemp and bamboo stems. Their high lignocellulosic content makes them well-suited for this process, yielding porous biochar with excellent water retention properties. Hemp and bamboo are fast-growing and renewable resources that may serve as sustainable feedstocks for biochar production. The stems were harvested in August, being sectioned at 1 meter in length and stored in a dry room, as can be seen in figure 3.



Fig. 3 - Hemp and bamboo stems harvested for pyrolysis processing operations
(a) Hemp stalks and (b) bamboo stems

The stem pre-processing involved cutting the plants to a maximum length of 7 cm using a circular saw. The average moisture content of the bamboo and hemp was then determined using the oven-drying method. In this process, a sample was weighed (Figure 4a and b), dried in an oven at 105°C for 24 hours (Figure 4c), cooled in a desiccator, and then reweighed.



Fig. 4 - Raw material processing
a) hemp; b) bamboo; c) drying of the raw material

Thermochemical processing method of plant materials using pyrolysis

The processing method involves opening the upper lid of the retort and loading the shredded raw material, which was shredded to a length of approximately 7 cm, for a faster processing. Once the material is loaded, the electric resistance is activated in order to initiate heating. The thermic process begins for a period that varies depending on the granulation and moisture content of the raw material, typically ranging from 30 to 120 minutes. This approach ensures efficient pyrolysis tailored to the characteristics of the raw input material. To prevent biochar oxidation, the retort was cooled by immersion in cold water for 30 minutes, then extracted and temporarily stored in a desiccator to maintain its stability until further experimental analysis.

Assessing the Water Retention Capacity of Biochar

Biochar derived from different biomass sources exhibits varying water retention properties. To evaluate these characteristics, the water storage capacity of biochar produced from bamboo and hemp was analyzed. The biochar samples were placed in a vessel, weighed (Fig.5), and then immersed in water for 2 minutes. After this interval, the excess water was drained, and the samples were weighed again. This procedure was repeated five times to ensure accuracy, for 24 hours. This approach provided a comprehensive understanding of the water retention capabilities of biochar over different timeframes.





Fig. 5 - Different phases during the experiments to evaluate the water storage potential in biochar

In order to determine the dry biochar density, a 1000 ml vessel was filled with bamboo biochar and then weighed. This process was repeated 10 times for each type of material to ensure accuracy and account for potential variations in particle arrangement and compaction. The average values were then calculated to provide a more reliable density measurement, using equation (1).

$$\rho = \frac{m}{v} \tag{1}$$

where ρ is the density (kg/L), m is the biochar mass (Kg) and v is the biochar volume (L)

RESULTS

Given that the moisture content of hemp and bamboo varies along the stem length, three representative sections were analyzed for each feedstock: the lower, middle, and upper parts of the stem. Table 1 presents the moisture content of bamboo and hemp stems, from different plant parts, after being stored for three months following harvest.

Table 1

Plant part	Stem moisture average content %	
	Bamboo plant	Hemp plant
Lower part of the stem	17	21
Middle part of the stem	18	23
Upper part of the stem	15	22

The temperature during the pyrolysis process was carefully adjusted to minimize the loss of organic matter through gasification. This controlled approach aimed to optimize the conversion efficiency, ensuring a higher yield of biochar while preserving key carbon fractions. Figure 6 illustrates the temperature increase rate during the experiment, using the pyrolysis experimental model. This evaluation was particularly useful for equipment calibration when using organic materials that present different densities.

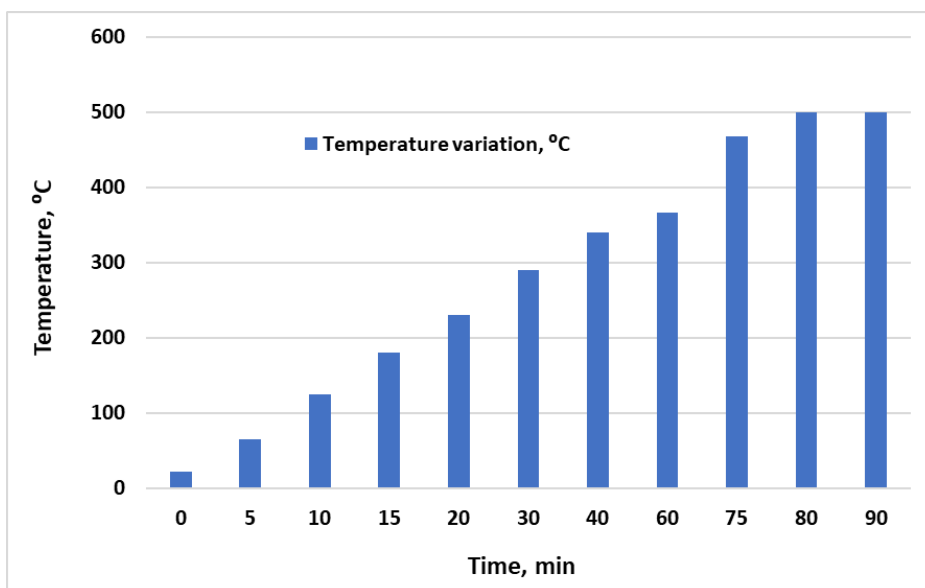


Fig. 6 - Temperature variation over time during pyrolysis equipment operation

The evaluation of biochar density after the completion of the process revealed a density for bamboo biochar of 0.2315 kg/L, while the density of hemp biochar was 0.0985 kg/L.

The cooled biochar was then weighed to evaluate the loss of material through gasification of organic material. It can be observed that the biochar obtained from bamboo lost 68.89% of its weight and the biochar obtained from hemp lost 81.96% of its weight. Hemp and bamboo stems were selected due to the shape of the stem, which has an inner hole that has a larger contact surface and allows a faster absorption of water (table 2).

Table 2

Feedstocks mass variation induced by the biochar production process

No.	Feedstocks for biochar production	Unprocessed material (kg)	Processed material (biochar) (kg)	Difference (%)
1	Bamboo biochar	0.8045	0.2503	68.89
2	Hemp biochar	0.4496	0.0811	81.96

Energy consumption per unit of time

In 1.4 hours needed to fully process the stems through pyrolysis, energy consumption reached 16.8 kWh. Based on average energy costs in Romania, this corresponds to approximately 4.1 EUR per batch. However, due to differences in plant density, the biochar yield per batch was 0.400 kg for hemp and 0.900 kg for bamboo.

Daily Productivity Calculation of Equipment

Considering that the equipment is fitted with two retorts (allowing for continuous operation without interruptions), the maximum productivity per hour is 0.29 kg/h for hemp and 0.64 kg/h for bamboo. Over an 8-hour workday, the total output reaches 2.29 kg for hemp and 5.12 kg for bamboo. Figure 7 illustrates the water storage capacity of the biochar mass, after it was immersed in water for 24 hours. The aim of the experiment was to evaluate the maximum water storage capacity within the biochar structure, simulating moisture retention in the soil.

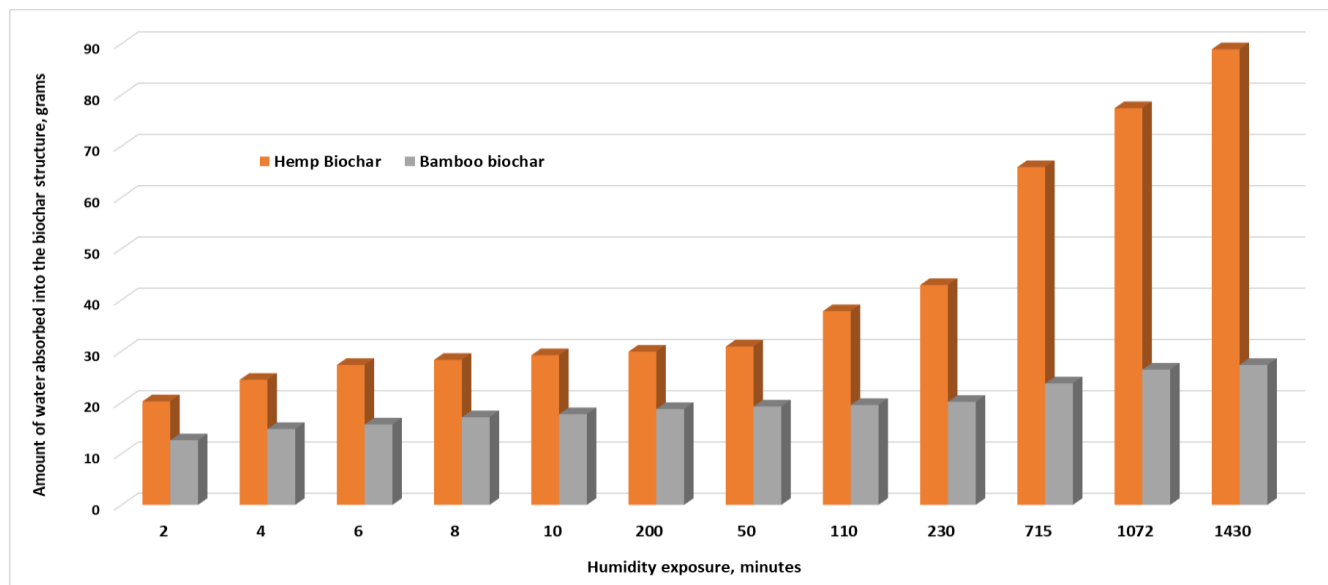


Fig. 7 - Water storage potential in biochar depending on water soaking time

Table 3 shows the water storage potential over time, the bamboo biochar stored a quantity of 27.3 grams in the 1430 min, that is 47.80%, and the hemp biochar stored a quantity of 88.9 grams, that is 150.17%.

An important indicator to consider is the percentage of water that each type of heat-treated material can retain relative to its own mass.

The stem fiber used to produce the biochar was found to play a crucial role in water storage capacity. Table 3 presents the water storage rate relative to the initial mass of each experimental plant. This analysis helps identify which structure offers the most effective storage solution.

Table 3

Water storage rate relative to the initial plant-mass

No.	Biochar type	Dry mass of biochar (gram)	Water storage potential as a percentage of biochar dry mass (%)									
			2 min	4 min	6 min	8 min	10 min	20 min	50 min	110 min	230 min	1430 min
1	Bamboo biochar	132.6	34.12	41.22	46.11	47.80	49.32	50.51	52.20	63.85	72.47	150.17
2	Hemp biochar	59.2	10.86	13.11	14.68	15.22	15.70	16.08	16.61	20.32	23.06	47.80

Discussions

Following the process of pyrolysis the material in the retort for biochar production, a significant difference was observed in the weight losses of the materials used. After cooling the biochar obtained from bamboo, it showed a weight loss of 68.89%, indicating that a considerable proportion of the original material was transformed into gases and vapors during the pyrolysis process. On the other hand, the biochar obtained from hemp had an even higher loss of 81.96%, thus suggesting that the gasification process was more pronounced for the latter. These results underline not only the efficiency of different biomasses in biochar generation, but also their high potential in the context of biochar production from organic waste. Analyzing these processes can provide valuable information for the optimization of biochar production and the efficient use of available resources.

Hemp biochar demonstrated a significantly higher water storage capacity compared to the bamboo biochar, having a better water storing potential (150.17% calculated in relation to the initial processed mass). These results suggest that hemp biochar could be more effective in improving soil water retention, which could be beneficial for agriculture, especially in arid conditions.

CONCLUSIONS

- The equipment allows a very fine adjustment of the temperatures, depending on the vegetable material, in order to customize the pyrolysis processes according to the structure of the vegetable waste. Thus, pyrolysis is improved for treating a variety of vegetable materials, keeping the high characteristics of biochar and avoiding overheating.

- The equipment consumes little energy compared to other equipment. On the one hand, this energy saving results from the advanced temperature regulation system (PLC and sensors) and on the other hand, due to the very good insulation of the thermal chamber-reactor. The circular arrangement of the electrical resistances also helps in efficient heating of the material.

- The retort type system helps to maintain a larger amount of biochar in the solid phase at the expense of gases and oils. Therefore, it is a better constructive design for the management of vegetable waste, for the purpose of use in agriculture. Constructive variants that maximize biogas and oils are more efficient for energy and industrial applications, but the proposed objective was to obtain a larger amount of biochar.

- All the adjustment of the equipment manages to increase the porosity, so that the biochar managed to store up to 150% water for bamboo (relative to the mass of the stem before treatment) and 47% water for hemp.

- The reduction in mass by 68.89% for bamboo stalks and 81.96% for hemp stalks is important because it reduces the costs of transporting the biochar from the farm to the agricultural land where it is applied.

- *The obtained biochar offers multiple benefits in agriculture and for the environment, such as:*

- Improving soil fertility: Biochar can retain nutrients and water in the soil, which improves soil fertility. It can also reduce nutrient loss through runoff.

- Reduction of carbon emissions: The production process of biochar involves the capture and storage of carbon from organic materials, due to its chemical stability, biochar can store long-term carbon in the soil.

- Improving soil structure: Biochar can improve soil structure, favoring the development of plant roots and improving its drainage.

- Remediation of degraded soils: Biochar can be used to remediate degraded soils, such as those that are saline or those affected by pollution.

- Promoting sustainability in agriculture: The use of biochar in agricultural practices can contribute to greater sustainability of agricultural systems, reducing reliance on chemical fertilizers and pesticides.

- Improving water retention: Biochar has the ability to retain water in the soil, which can be beneficial in water-scarce areas or during periods of drought. Adding biochar to sandy soils reduces irrigation requirements by up to 40%.
- Reduction of greenhouse gas emissions: By sequestering carbon in the soil and reducing methane and nitrous oxide emissions, biochar can help reduce greenhouse gas emissions from the soil.
- Improved plant health: Soils treated with biochar can support healthier crops that are more resistant to diseases and pests.

ACKNOWLEDGEMENT

This work was funded by the Ministry of Research, Innovation and Digitalization, within the NUCLEU Program, through Project 9N/ 01.01.2023 "Technology for valorization of plant residues in the form of biochar for improving soil quality" and by the Ministry of Agriculture and Rural Development (MADR), ADER Program - Contract ADER 25.3.1/20.07.2023 "Technology for valorization of poultry manure by obtaining biofertilizers rich in phosphorus".

REFERENCES

- [1] Buss W. (2021). Pyrolysis solves the issue of organic contaminants in sewage sludge while retaining carbon-making the case for sewage sludge treatment via pyrolysis. *ACS Sustain Chem Eng*, 9:10048–10053.
- [2] Farag H.A., El-kholy M.M., Okasha M., Azab, A.E., Khater, A.E., Kamel R.M. (2024). Development and Evaluation of a Continuous Flow Biochar Unit Using Rice Husk Biomass, *INMATEH Agricultural Engineering*, pp.33-44. <https://doi.org/10.35633/inmateh-72-03>
- [3] Feng D., Guo D., Zhang Y., Sun S., Zhao Y., Chang G., Guo Q., Qin Y. (2021). Adsorption-enrichment characterization of CO₂ and dynamic retention of free NH₃ in functionalized biochar with H₂O/NH₃·H₂O activation for promotion of new ammonia-based carbon capture. *Chem Eng J.*, 409:128193, <https://doi.org/10.1016/j.cej.2020.128193>.
- [4] Liu, W-J., Jiang, H., & Yu, H-Q. (2015). Development of biochar-based functional materials: toward a sustainable platform carbon material. *Chem. Rev.* 115(22), 12251–12285. <https://doi.org/10.1021/acs.chemrev.5b00195>
- [5] Lone, A.H., Najar, G.R., Ganie, M.A., Sofi, J.A., & Ali, T. (2015). Biochar for Sustainable Soil Health: A Review of Prospects and Concerns. *Pedosphere* 25(5), 639–653. [http://dx.doi.org/10.1016/S10020160\(15\)30045-X](http://dx.doi.org/10.1016/S10020160(15)30045-X)
- [6] Nenciu, F., Paraschiv, M., Kuncser, R., Stan, C., Cocarta, D., Vladut, V.N. (2022). High-Grade Chemicals and Biofuels Produced from Marginal Lands Using an Integrated Approach of Alcoholic Fermentation and Pyrolysis of Sweet Sorghum Biomass Residues. *Sustainability*, 14, 402, <https://doi.org/10.3390/su14010402>.
- [7] Nenciu, F., Fatu, V., Arsenoiaia, V., Persu, C.; Voicea, I.; Vladut, N.-V.; Matache, M.G.; Gageanu, I.; Marin, E.; Biris, S.-S.; et al. (2023). Bioactive Compounds Extraction Using a Hybrid Ultrasound and High-Pressure Technology for Sustainable Farming Systems. *Agriculture*, 13, 899, <https://doi.org/10.3390/agriculture13040899>.
- [8] Nenciu, F., Voicea, I., Stefan, V.; Nae, G., Matache, M., Milian, G., Arsenoiaia, V.N. (2022), Experimental research on a feed pelletizing equipment designed for small and medium-sized fish farms. *INMATEH Agric. Eng.*, 67, 374–383, <https://doi.org/10.35633/inmateh-67-38>.
- [9] Nidheesh PV, Gopinath A, Ranjith N, Praveen Akre A, Sreedharan V, Suresh Kumar M (2021) Potential role of biochar in advanced oxidation processes: a sustainable approach. *Chem Eng J.*, 405:126582, <https://doi.org/10.1016/j.cej.2020.126582>.
- [10] Opreacu M.R., Biris S.-S., Nenciu F. (2023), Novel Furrow Diking Equipment-Design Aimed at Increasing Water Consumption Efficiency in Vineyards. *Sustainability*, 15, 2861. <https://doi.org/10.3390/su15042861>
- [11] Popescu E., Nenciu F., Vladut V., (2022), A new strategic approach used for the regeneration of soil fertility, in order to improve the productivity in ecological systems. *Scientific Papers-Series E-Land Reclamation Earth Observation & Surveying Environmental Engineering*, Vol.11, 277-284.
- [12] Wang X., Chang V.W., Li Z., Chen Z., Wang Y. (2021), Co-pyrolysis of sewage sludge and organic fractions of municipal solid waste: synergistic effects on biochar properties and the environmental risk of heavy metals. *J Hazard Mater*, 412:125200, <https://doi.org/10.1016/j.jhazmat.2021.125200>.

- [13] Woolf D., Amonette J.E., Street-Perrott F.A., Lehmann J., Joseph S. (2010), Sustainable biochar to mitigate global climate change. *Nat Commun.* <https://doi.org/10.1038/ncomms1053>.
- [14] Yang Q., Zhou H., Bartocci P., Fantozzi F., Masek O., Agblevor F.A., Wei Z., Yang H., Chen H., Lu X., Chen G., Zheng C., Nielsen C.P., McElroy M.B. (2021), Prospective contributions of biomass pyrolysis to China's 2050 carbon reduction and renewable energy goals. *Nat Commun*, 12:1698. <https://doi.org/10.1038/s41467-021-21868-z>.
- [15] Zhang X, Yang X, Yuan X, Tian S, Wang X, Zhang H, Han L (2022) Effect of pyrolysis temperature on composition, carbon fraction and abiotic stability of straw biochars: correlation and quantitative analysis. *Carbon Res.*, 1:00017. <https://doi.org/10.1007/s44246-022-00017-1>.
- [16] Ahmad M., Lee, SS., Lee, SE., Al-Wabel, M.I., Tsang, DCW., Ok, YS. (2017) Biochar-induced changes in soil properties affected immobilization/mobilization of metals/metalloids in contaminated soils, *J. Soils Sediments*, 17:717–730. <https://doi.org/10.1007/s11368-015-1339-4>.
- [17] Amalina F., Razak, ASA., Krishnan, S., Sulaiman, H., Zularisam, AW., Nasrullah, M. (2022) Biochar production techniques utilizing biomass waste-derived materials and environmental applications—a review. *J Hazardous Mater Adv.*, 7:100134. <https://doi.org/10.1016/j.hazadv.2022.100134>.
- [18] Amalina F., Krishnan, S., Zularisam, AW., Mohd Nasrullah, M., (2023) Biochar and sustainable environmental development towards adsorptive removal of pollutants: Modern advancements and future insight, *Process Safety and Environmental Protection*, Vol 173, pp 715-728, <https://doi.org/10.1016/j.psep.2023.03.069>.
- [19] El-Naggar A., Lee, SS., Rinklebe, J., Farooq, M., Song, H., Sarmah, AK., Zimmerman, AR., Ahmad, M., Shaheen, SM., Ok, YS., (2019) Biochar application to low fertility soils: a review of current status, and future prospects. *Geoderma*, 337:536–554. <https://doi.org/10.1016/j.geoderma.2018.09.034>.
- [20] Issaka E., Fapohunda, FO., Amu-Darko, JNO., Yeboah, L., Yakubu, S., Varjani, S., Ali, N., Bilal, M., (2022) Biochar-based composites for remediation of polluted wastewater and soil environments: challenges and prospects. *Chemosphere*. 297:134163. <https://doi.org/10.1016/j.chemosphere.2022.134163>.
- [21] Jang E.S., Ryu D.Y., Kim D., (2022), Hydrothermal carbonization improves the quality of biochar derived from livestock manure by removing inorganic matter. *Chemosphere* 305:135391. <https://doi.org/10.1016/j.chemosphere.2022.135391>.
- [22] Neogi S., Sharma V., Khan N., Chaurasia D., Ahmad A., Chauhan S., Singh A., You S., Pandey A. and Bhargava, P.C. (2022) Sustainable biochar: A facile strategy for soil and environmental restoration, energy generation, mitigation of global climate change and circular bioeconomy. *Chemosphere*, 293, 133474, doi: 10.1016/j.chemosphere.2021.133474.
- [23] Salma A., Fryda, L., and Djelal, H., (2024), Biochar: A Key Player in Carbon Credits and Climate Mitigation, *Journal: Resources* 2024, <https://www.mdpi.com/2079-9276/13/2/31>
- [24] Sun J., He, F., Pan, Y., Zhang, Z., (2017) Effects of pyrolysis temperature and residence time on physicochemical properties of different biochar types. *Acta Agric Scand Sect B Soil Plant Sci.*, 67:12–22. <https://doi.org/10.1080/09064710.2016.1214745>.
- [25] Tomczyk A., Sokołowska, Z., Boguta, P., (2020) Biochar physicochemical properties: pyrolysis temperature and feedstock kind effects. *Rev Environ Sci Bio/Technol.*, 19:191–215. <https://doi.org/10.1007/s11157-020-09523-3>.
- [26] Voicea I., Nenciu F., Vlăduț N.-V., Matache M.-G., Persu C., Cujbescu D. (2024). Exploring a Self-Sufficiency Approach within a Sustainable Integrated Pisciculture Farming System. *Sustainability*, 16(18):8055. <https://doi.org/10.3390/su16188055>.
- [27] Voicea I., Nenciu F., Vlăduț N.V., Matache, M.G., Persu C., Cujbescu D. (2024). Exploring a Self-Sufficiency Approach within a Sustainable Integrated Pisciculture Farming System. *Sustainability*, 16(18), 8055. <https://doi.org/10.3390/su16188055>
- [28] Zhang X.S., Zhu D.Q., Xue K., Lanlan Li, Zhu J., Zhang S., Liaol J., (2021), Parameter optimization and experiment of slider-hole-wheel seed-metering device based on discrete element method, *INMATEH-Agricultural Engineering*, 65(3):410-420.

DESIGN AND EXPERIMENT OF A MOREL PICKING MACHINE

羊肚菌采摘机设计与试验

Xiaohu BAI, Xiang ZOU, Zexu WANG, Guojing DU, Chuan LI, Chonghe GAO

College of Engineering, Shenyang Agricultural University, Shenyang/China

E-mail: baixiaohu@syau.edu.cn

DOI: <https://doi.org/10.35633/inmateh-75-36>**Keywords:** *Robotic arm, Picking claw, Blade length, Simulation, Morel***ABSTRACT**

To address the challenges of high labour intensity and expensive manpower in morel harvesting, a specialized morel picking machine was designed. It is capable of performing the tasks of grasping, cutting, and collecting morels. A three-degree-of-freedom robotic arm was incorporated to ensure precise positioning of the picking claw. The kinematic model of this arm was established to determine the operational radius for effective picking. A three-finger picking claw was developed, with the synchronous opening and closing of the three fingers through a wire-pulling mechanism and a four-bar linkage. Buffer elastic material was installed on the picking fingers, and cutting blades were placed at the fingertips. Simulation analyses were conducted to study the movement of the robotic arm's end, the forces acted on the picking arm, the hinge between the upper and lower arms, and the hinge at the lower arm's end, as well as the velocity of the picking claw's end. Single-factor experiments were employed to investigate the effects of the blade length of the picking finger on the picking success rate, the damage rate of mature morels, and the damage rate of immature morels. The results demonstrated that with a blade length set at 15mm, the picking success rate reached 96.2%, while the damage rates of mature and immature morels were 8.6% and 6.8%, respectively. These findings indicate that the machine can effectively meet the operational requirements for morel picking.

摘要

为解决羊肚菌采摘劳动强度大、人工成本高的问题,设计了一种羊肚菌采摘机,可以完成抓取、切断、收集作业。采用三自由度机械臂实现采摘爪的精确定位,建立了机械臂的运动学模型,确定了采摘作业半径。设计了三指结构采摘爪,通过拉线驱动与四杆机构实现三指同时闭合和松开。采摘手指上安装缓冲弹性材料,末端装有切割刀片。对机械臂末端运动、机械臂受力、大臂与小臂铰链处作用力、小臂末端铰链处作用力、采摘爪末端速度进行了仿真分析。通过单因素试验,研究了采摘手指刀片长度对采摘成功率、羊肚菌损伤率、未成熟羊肚菌损伤率的影响。结果表明,当刀片长度为15mm时,采摘成功率为96.2%,采摘损伤率为8.6%,未成熟羊肚菌损伤率为6.8%,基本满足羊肚菌采摘的作业要求。

INTRODUCTION

Morel mushrooms are rich in nutrients and trace elements, and are widely cultivated in China (Huang *et al.*, 2022; Liu *et al.*, 2017; Zhao *et al.*, 2009). Due to the unique growth environment of morels, their fragile texture, and significant variations in individual morphology, traditional manual harvesting methods are labour-intensive and inefficient (Huang *et al.*, 2023). As labour costs rise and the demand for high-quality picking increases, developing equipment that is suitable for the characteristics of morels is crucial for enhancing the economic benefits of the morel industry and increasing farmers' incomes.

Currently, numerous studies focus on the end effectors and grasping mechanisms of fruit and vegetable picking machinery; however, there are relatively few reports on morel picking machinery (Li *et al.*, 2014; Safeea *et al.*, 2019; Wang *et al.*, 2016; Gu *et al.*, 2012; Ding *et al.*, 2013). Yang developed a mushroom picking machine that achieved autonomous movement and stopping through a mobile platform. This machine collected mushroom data using a visual system and controlled the actuator to pick and load the mushrooms (Yang, 2020). Zhang investigated a portabella picking robot, which features a mobile lifting platform, adjustable guide rails, picking arms, flexible picking claws, as well as a visual recognition and positioning system, along with a measurement and control system (Zhang, 2019). Wang studied a morel harvesting machine that consists of a storage box, an air tube, a cutting device, and a blower fan. After the stem of the morel is cut off, it is sucked into the box.

Although the machine has a simple structure and high picking efficiency, it is prone to damaging the morels, and the fan consumes a significant amount of energy (Wang *et al.*, 2021). Wang developed a morel harvesting device that includes a sleeve and two blades. Through the interaction of the blades, the morels can be extracted from the soil, while the soil attached to the morels is expelled through holes in the blades (Wang, 2021). Yu designed a morel harvesting tool featuring scissors mounted on a support frame. The scissors are operated by an electric push rod, and a conveyor belt transports the morels into a receiving bucket (Yu, 2022). Additionally, Wang created a morel picking device equipped with a cylindrical component and a blade, with the blade affixed to the bottom of the cylindrical component and operated by a handle (Wang, 2019).

In this paper, to address the challenges of high labour intensity, susceptibility to damage, and high labour costs associated with morel harvesting, a morel picking machine that performs the functions of grasping, cutting, and collecting morels was designed. This machine not only ensures efficient harvesting operations but also effectively minimizes damage to the morels.

MATERIALS AND METHODS

Structure of the machine

Figure 1 illustrates the overall structure of the morel picking machine. It primarily consists of driving wheels, driven wheels, a mobile platform, a robotic arm rotation mechanism, an upper arm, a lower arm, electric push rods, and a picking claw, among other components. The mobile platform is powered by two DC motors, which allow the machine to move forward and backward during operation. The robotic arm is designed to achieve precise positioning of the picking claw, thereby facilitating the actions of picking, conveying, and collecting.

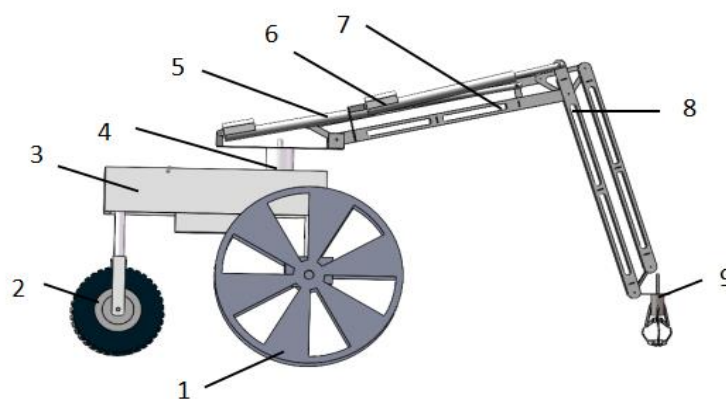


Fig. 1 - Schematic of the morel picking machine

1-driving wheels; 2-driven wheels; 3-mobile platform; 4-robotic arm rotation mechanism; 5-electric push rod for upper arm; 6- electric push rod for lower arm; 7- upper arm; 8- lower arm; 9- picking claw

Working principle of the machine

The machine is operated using a manual remote control. Once the machine is positioned for work, the rotating mechanism of the robotic arm is activated. The electric push rods of both the upper and lower arms facilitate the rotation of the arms, positioning the picking claw over the morels to be harvested. When the fingers of the picking claw close, a blade located at the tips of the fingers severs the stem of the morel, allowing it to be captured by the claw. Subsequently, the electric push rod for the upper arm contracts, elevating the upper arm. Meanwhile, the electric push rod for the lower arm rotates it by a specified angle, positioning the picking claw above the collection box. The fingers of the picking claw then open, depositing the picked morel into the collection box.

Design of the robotic arm

During the picking operation, the movement of the picking claw is simultaneously influenced by the trajectories of both the upper and lower arms (Jun, *et al.*, 2021; Zhang *et al.*, 2015; Zhang, 2019). To further analyse the angular and motion relationships among the upper arm, lower arm, and picking claw, the three-degree-of-freedom robotic arm was simplified, as illustrated in Figure 2 (Zhou, *et al.*, 2012; Yoshida *et al.*, 2022).

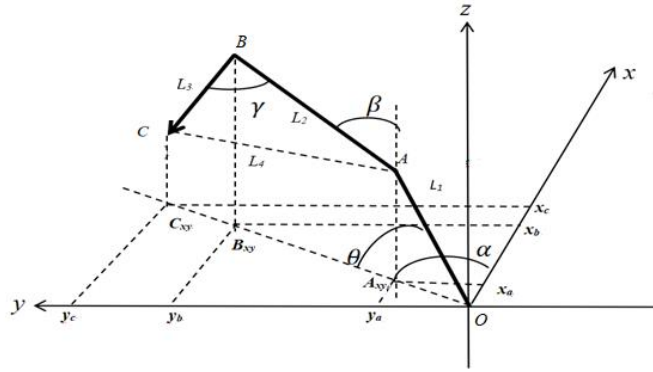


Fig. 2 - Simplified model of the robotic arm

In order to enable the picking claw at the end of the robotic arm to reach the designated picking range, the length of the upper arm was selected to be 800 mm, while the length of the lower arm was set at 650 mm, taking into account the overall structural dimensions of the machine. Using a right-handed coordinate system, the base of the robotic arm coincides with the xOy plane, and the centre of rotation for the robotic arm base is determined as the coordinate origin. The remaining components are arranged on the positive side of each coordinate axis (Zhang et al., 2020). OA represents the robotic arm rotation mechanism mounted on the base, enabling the arm to rotate around the z -axis. The length of OA is 400 mm. AB represents the upper arm, while BC represents the lower arm. θ is the angle between the robotic arm rotation mechanism OA and the xOy plane, α is the angle between the plane in which the robotic arm is situated and the xOz plane, β is the angle between the upper arm AB and the vertical direction, and γ is the angle between the lower arm BC and the upper arm AB .

Based on the geometric relationships illustrated in Figure 2, the following expression can be derived:

$$L_{OC_{xy}} = L_1 \cos \theta + L_2 \sin \beta + L_3 \sin(\gamma - \beta) \tag{1}$$

where:

$L_{OC_{xy}}$ represents the length of the projection of OC onto the xOy plane; L_1 represents the length of OA ; L_2 represents the length of AB ; L_3 represents the length of BC .

The coordinates of point A can be determined as follows:

$$\begin{cases} x_a = L_1 \cos \theta \cos \alpha \\ y_a = L_1 \cos \theta \sin \alpha \\ z_a = L_1 \sin \theta \end{cases} \tag{2}$$

The coordinates of point C can be expressed as follows:

$$\begin{cases} x_c = [L_1 \cos \theta + L_2 \sin \beta + L_3 \sin(\gamma - \beta)] \cos \alpha \\ y_c = [L_1 \cos \theta + L_2 \sin \beta + L_3 \sin(\gamma - \beta)] \sin \alpha \\ z_c = \sqrt{L_4^2 - (x_c - L_1 \cos \theta \cos \alpha)^2 - (y_c - L_1 \cos \theta \sin \alpha)^2} + L_1 \sin \theta \end{cases} \tag{3}$$

where, L_4 represents the length of AC .

According to the equations presented above, it can be concluded that when θ is 50° , α is 64° , β is 50° , and γ is 80° , the length of OC_{xy} is 1194 mm, which satisfies the requirement for a working radius greater than 1000 mm.

Motion simulation of the robotic arm

The motion trajectory of the robotic arm's end was simulated by importing the robotic arm model into Adams software, as shown in Figure 3.

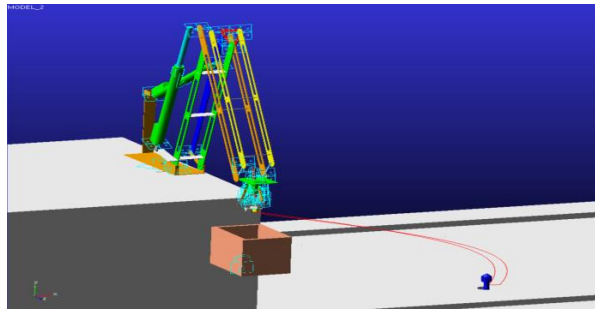


Fig. 3 - Simulation of the motion trajectory of the robotic arm's end

The variation in the mass centre coordinates of the robotic arm's end is shown in Figure 4. The labels "end.CM_Coordinate.X", "end.CM_Coordinate.Y", and "end.CM_Coordinate.Z" represent the coordinates of the centre of mass along the x, y, and z axes respectively. The label "end.CM_Coordinate.Mag" represents the distance from the robotic arm's end to the coordinate origin.

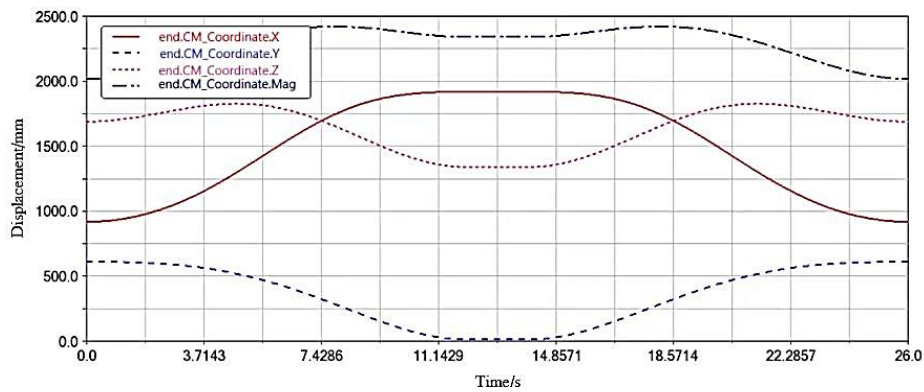


Fig. 4 - Variation in the mass centre coordinates of the robotic arm's end

The robotic arm's end is initially positioned above the collection box, with the y-axis coordinate of its centre of mass at 612.34 mm. Within 12 seconds, the end effector is manoeuvred to the picking position via the robotic arm rotation mechanism, the upper arm, and the lower arm. From 12 to 13 second, the robotic arm remains stationary while performing the picking action. At this moment, the y-axis coordinate of the mass centre of the robotic arm's end is 0.54 mm, indicating that the picking claw is nearly close to the ground. From 13 to 25 second, the robotic arm's end returns to its initial position, completing the collection action.

Force simulation of the robotic arm

An electric push rod with a stroke length of 400 mm and a thrust capacity of 1000 N was selected as the driving unit for the upper arm, while a push rod with the same stroke length of 400 mm and a thrust capacity of 480 N was chosen for the lower arm. The force acted on the robotic arm and the hinges at each connection were analysed using Adams software. Figure 5 illustrates the variation in the support force on the robotic arm. The labels "arm.Support_Force.X", "arm.Support_Force.Y", and "arm.Support_Force.Z" represent the component force along the x, y, and z axes respectively. The label "arm.Support_Force.Mag" represents the resultant force. As shown in Figure 5, the maximum support force reaches 493.76 N at 14 seconds.

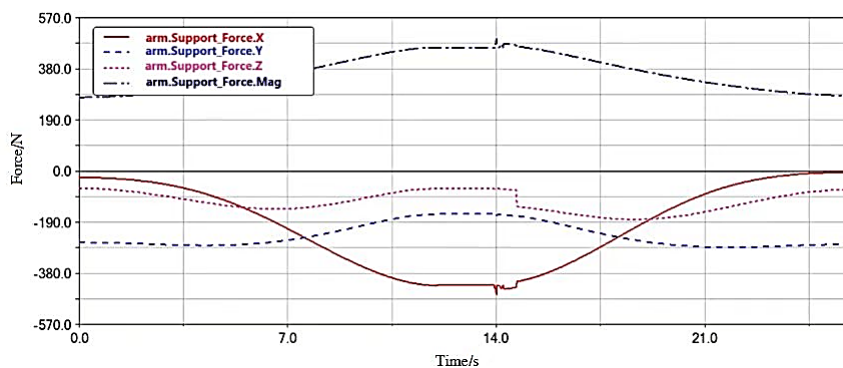


Fig. 5-Variation in the support force on the robotic arm

Figure 6 shows the variation in the force on the hinge connecting the upper arm and the lower arm. The labels “hinge.Force.X”, “hinge.Force.Y” and “hinge.Force.Z” represent the component forces along the x, y, and z axes respectively. The label “hinge.Force.Mag” represents the resultant force. As shown in Figure 6, the resultant force reaches its maximum value of 272.67 N at 26 seconds. The maximum force in the x-axis direction is 65.5 N at 18.2 seconds, the maximum force in the y-axis direction is 264.33 N at 26 seconds, and the maximum force in the z-axis direction is 54.28 N at 4.2 seconds.

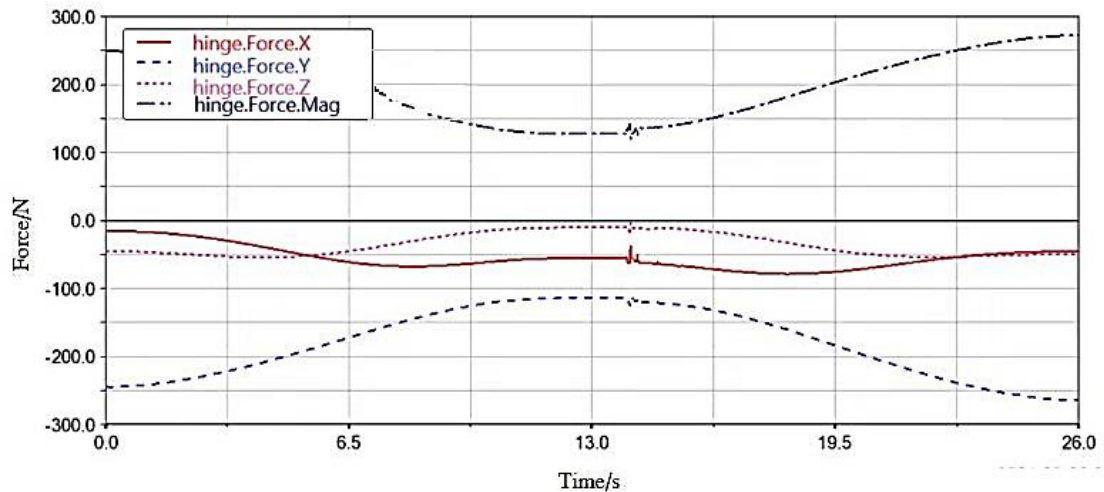


Fig. 6 - Variation in the force on the hinge connecting the upper arm and the lower arm

The robotic arm is constructed from 3 mm low-carbon steel plate. Force analysis indicates that the strength and stiffness of each component meet the necessary requirements. There is no significant deformation during operation, which effectively minimizes shaking and ensures accurate grasping.

Design of the picking claw

When manually picking morels, grasp the stem with the thumb, forefinger, and middle finger, then use a blade to cut it at a specific distance above the ground. This study examines the physical characteristics of morels and simulates the manual harvesting process. Compared to the double-finger structure, the three-finger end effector offers advantages such as high reliability, smooth movement, and resistance to detachment. Although the four-finger structure demonstrates effective grasping capabilities, it is difficult to control, complex in structure, and more expensive (Zhao et al., 2024; Chen et al., 2024). Based on a comprehensive analysis, this study adopts a three-finger structure. The picking claw comprises fingers, links, sliders, and blades, as shown in Figure 7.

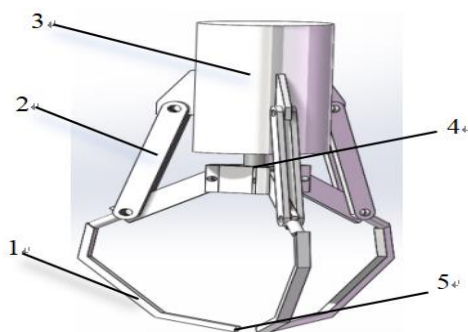


Fig. 7 - Schematic of the picking claw
1-finger; 2-link; 3-frame; 4-slider; 5-blade

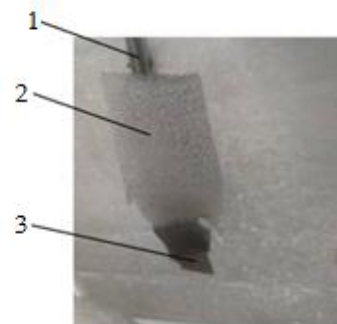


Fig. 8 - Composition of the picking finger
1-finger; 2-elastic foam; 3-blade

The frame of the picking claw is equipped with three fingers arranged uniformly at 120°. A servo motor is utilized to control the movement of these fingers. A power source simultaneously operates the fingers through a wire-pulling mechanism and a four-bar linkage, facilitating both closure and separation. When the servo motor rotates counterclockwise, the contraction of the cable drives the slider upward, causing the fingers to close. Conversely, when the servo rotates clockwise, the cable relaxes, and the fingers separate due to the action of a reset spring.

The reset spring is installed between the frame and the slider, featuring an elasticity coefficient of 1 N/cm, and a stretch of 3 cm. The fingers have a weight of 0.3 kg, while the other components collectively weigh

0.2 kg. The rotation speed of the servo is 120 °/s, and the required servo torque can be calculated to be 15 kg·cm. The selected servo model is the TD-8130MG, which has a torque rating of 29.5 kg·cm, thereby meeting the operational requirements.

The fingers are constructed from 45 steel. To accommodate morels of various sizes and prevent clamping damage, elastic foam was applied to the fingers as a buffer material. A triangular blade with a tip angle of 60 ° was selected and installed at the end of the finger, as illustrated in Figure 8.

The process of picking morels using the fingers was simulated. The variation in fingertip velocity was obtained, as shown in Figure 9. The labels “fingertip.Velocity.X”, “fingertip.Velocity.Y” and “fingertip.Velocity.Z” in the label represent the component velocity along the x, y, and z axes respectively. The label “fingertip.Velocity.Mag” represents the resultant velocity.

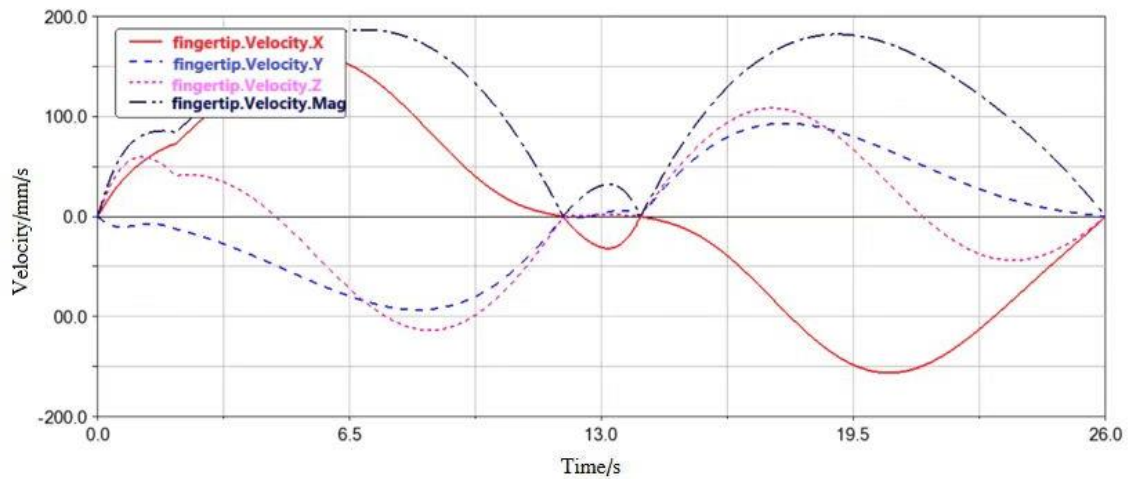


Fig. 9 - Variation in fingertip velocity

From Figure 9, it can be observed that at 12.5 seconds, the picking claw approaches the morel, and the velocity in each coordinate axis direction drops to zero, causing the picking claw to halt at the designated picking position. Between 12.5 and 13 second, the velocities along the y-axis and z-axis of the picking claw remain relatively constant, while the absolute value of the x-axis velocity increases. This indicates that the picking claw is performing a grasping operation on the morel in the x-axis direction. During the interval from 13 to 13.5 seconds, the absolute value of the x-axis velocity decreases, and the picking claw approaches the root of the morel at a reduced velocity for cutting operations. At 13.5 seconds, the velocity drops to zero, signifying the completion of the cutting and grasping actions. Throughout the entire picking process, the velocity of the picking claw changes relatively smoothly, with two brief pauses occurring when approaching the morel and after the cutting is completed. The impact generated by the fingertip is relatively small, which helps to reduce the damage rate of the morel.

Design of the mobile platform

Taking into account the planting environment of morels, the arrangement of all components, and the picking process, the mobile platform was designed to be 1140 mm long, 800 mm wide, and 600 mm high. The platform features a four-wheel support structure, with the front two wheels serving as the driving wheels and the rear two wheels functioning as the driven wheels. A DC motor transmits power through a chain drive to the output shaft, enabling the platform to move forward or backward (Wang et al.,2021). The following formula can be used to calculate the motor power.

$$P_e = \frac{1}{\eta} \left(\frac{mgfv}{3600} + \frac{mgiv}{3600} + \frac{C_d A v^3 m}{76140} + \frac{mga\delta v}{3600} \right) \tag{4}$$

where, P_e represents the motor power, kW; g represents gravitational acceleration, 9.8 N/kg; m represents the full load mass of the mobile platform, 100 kg; f represents the rolling resistance coefficient, 0.6; I represents the ground gradient; A represents the windward area in the forward direction, 1.2 m²; a represents the acceleration of the platform, with a maximum value of 0.5 m/s²; C_d represents the driving resistance coefficient, 0.7; v represents the platform velocity, 3 km/h; η represents the transmission efficiency, 0.9; δ represents the mass conversion coefficient of the platform, 1.2.

When the mobile platform ascends a slope with a gradient of 5% at a constant velocity of 3 km/h, the required motor power is 0.62 kW. When the platform accelerates at a rate of 0.5 m/s², the required motor power is 1.21 kW. Consequently, a brushless DC motor with a power of 1.5 kW was selected.

Prototype experiments

Experiments were carried out at a morel planting facility in Fushun, Liaoning Province, China. The diameter of a mature morel cap ranges from 30 to 60 mm, while the length of the cap varies between 40 and 100 mm. The diameter of the stem measures 20 to 40mm, and the stem length is typically between 50 and 70 mm. The mass of the morel is approximately 15 to 25 g. The experimental site is shown in Figure 10. The purpose of the experiment is to verify whether the robotic arm can accurately position the picking claw to the predetermined picking location, and to determine the optimal length of the blade mounted at the end of the picking finger. A 48V battery served as the power supply for the machine. The control system of the machine consists of a remote control, a receiver, an electronic speed controller, a motor, two electric push rods, and a steering engine. The remote control emits a 2.4GHz signal, which is then received and converted into a PWM (Pulse Width Modulation) signal by the receiver. The electronic speed controller achieves the start, stop, speed regulation of the motor, push rods and steering engine based on the received PWM signal. As a result, the position of the rotating mechanism, the upper arm, the lower arm can be adjusted to realize the picking process. The prototype is illustrated in Figure 11.



Fig. 10 – Experimental site



Fig. 11 – Experimental prototype

The primary factor affecting the picking efficiency is the blade length of the picking claw. If the blade is too short, it becomes challenging to cut the stem; conversely, if the blade is too long, it may inadvertently damage other immature morels. Consequently, four blade length levels were selected: 0 mm, 10 mm, 15 mm, and 20 mm. The index for the experiment included the picking success rate, the damage rate of mature morels, and the damage rate of immature morels. The calculation formulas are as follows:

$$\eta_c = n_c / n \quad (4)$$

$$\eta_d = (n_s + n_a) / n_c \quad (5)$$

$$\eta_z = n_j / n_z \quad (6)$$

where, η_c represents the picking success rate; η_d represents the damage rate of mature morels; η_z represents the damage rate of immature morels; n represents total number of picks; n_c represents the number of successful picks; n_s represents the number of morels with stem damage; n_a represents the number of morels with cap damage; n_j represents the number of damaged immature morels.

RESULTS

During the experiment, 15 mature morels were selected as a group at each level to calculate the experimental index values, with 4 groups being repeated. The damage to the morels caused by mechanical picking is shown in Figure 12.

The picking success rates at different levels are shown in Figure 13. When the picking claw is not equipped with blades, the claw's fingertip is unable to cut through the morel. In this case, the morel is grasped by the picking fingers and extracted from the soil by the robotic arm, leading to a lower success

rate. However, after the installation of the blades, the picking claw can effectively cut the root of the morel, resulting in a significant improvement in the picking success rate. Conversely, if the blade is excessively long, it may cause the picking claw to occupy more workspace, which can hinder smooth grasping movements and lead to a slight decrease in the picking success rate.



Fig. 12 - Morel damage

The damage rates of morels at different levels are shown in Figure 14. When the picking claw is not equipped with blades, the morel tends to break under tension, necessitating that the picking fingers exert additional pressure, which can easily lead to damage. Conversely, after the blades are installed, the morel can be severed with less force, significantly decreasing the damage rate. However, if the blade is excessively long, interference between the blade tips may occur when the claw is closed, potentially increasing the damage rate.

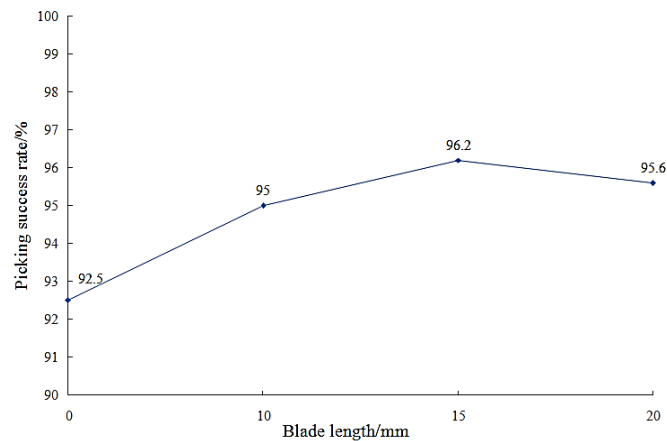


Fig.13 - Picking success rate at different blade lengths

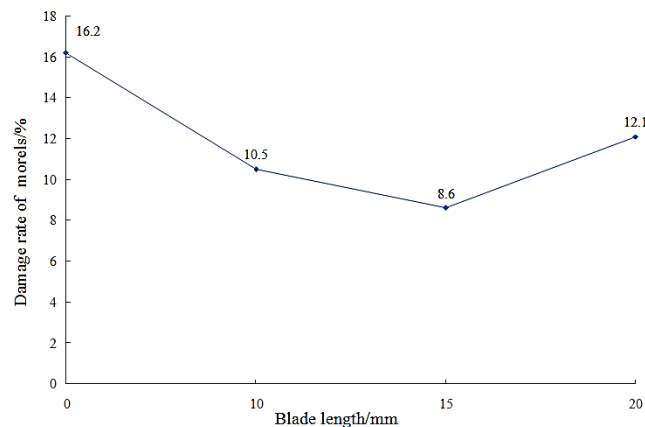


Fig. 14 - Damage rate of morels at different blade lengths

The damage rates of immature morels at different levels are shown in Figure 15. Immature morels are more fragile than mature ones and are typically found near mature morels, making them more susceptible to contact with the picking claw. In the absence of blades, the picking claw lacks sharp edges, which reduces the likelihood of damaging the surrounding immature morels. However, due to the complex and variable picking environment characterized by the irregular distribution of morels and the positional accuracy errors of the robotic arm, the blades are more prone to inadvertently contacting the immature morels during the cutting process, thereby increasing their damage rate.

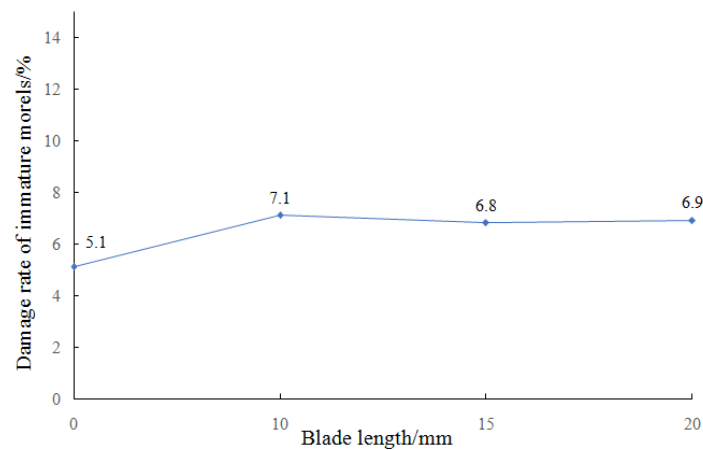


Fig. 15 - Damage rate of immature morels at different blade lengths

According to the experimental data, when the blade length at the end of the picking finger is set to 15 mm, the average picking success rate is 96.2%, the damage rate of morels is 8.6%, and the damage rate of immature morels is 6.8%. The picking machine can effectively grasp morels while maintaining a low damage rate, thereby meeting the requirements for morel picking operations.

CONCLUSIONS

The motion and force of the robotic arm and the picking claw during the picking process were analysed using Adams software. The simulation results proved the correctness of the theoretical model. The robotic arm adopts a three-degree-of-freedom structure, which can achieve precise positioning of the picking claw. The picking machine can perform positioning, cutting, and collection actions within 25 seconds. The picking claw is close to the ground when cutting the morel stem, ensuring the picking quality. The strength and stiffness of each component of the robotic arm meet the necessary requirements, ensuring both motion and grasping accuracy. The picking claw pauses briefly twice: once when approaching the morel and again after cutting. Furthermore, the velocity variation throughout the entire picking process is relatively smooth, which helps minimize damage to the morel.

Through single-factor experiments, the effect of the blade length of the picking finger on the picking success rate, the damage rate of morels, and the damage rate of immature morels was investigated. The results demonstrated that when the blade length was 15 mm, the picking success rate was 96.2%, the damage rate of morels was 8.6%, and the damage rate of immature morels was 6.8%. The picking machine ensures efficient picking operations while minimizing damage to both the picked morels and surrounding immature ones, thereby meeting the requirements for morel picking operations. However, this machine is just a prototype which requires manual operation. In future research, when combined with a visual recognition system for morels, it can work autonomously.

REFERENCES

- [1] Chen, J., Li, H., Liu, L., Jia, J., Zhao, R.; Wu, C. (2024). Design and experimental optimization of split tool type end-effector for picking famous tea (分体刀具式名优茶采摘末端执行器设计与试验优化). *Transactions of the Chinese Society of Agricultural Machinery*, 55(01), 39-46+195.
- [2] Ding, J., Liu, G., Yang, W. (2013). Design and simulation analysis of a fruit picking end-effector (一种果实采摘末端执行器设计与仿真分析). *Journal of Agricultural Mechanization Research*, 5(1), 112-115.
- [3] Gu, B., Ji, C., Wang, H., Tian, G., Zhang, G., Wang, L. (2012). Design and test of intelligent mobile fruit picking robot (智能移动水果采摘机器人设计与试验). *Transactions of the Chinese Society of Agricultural Machinery*, 43(6), 153-160.
- [4] Huang, L., Shang, X., Jiao, S. (2022). Warm-house planting technology of morel mushrooms in Central Plains (中原地区羊肚菌温棚种植技术). *Agricultural Science and Technology Newsletter*, 12(9), 218-221.
- [5] Huang, M., Yang, X., Zhang, C., Li, H., Wu, H., Wang, F. (2023). Study on the picking dynamics of *Agaricus bisporus* and its picking manipulator design (双孢菇采摘动力学研究及其采摘机械手设计). *Journal of Chinese Agricultural Mechanization*, 44 (12), 66-70+98.

- [6] Jun, J., Kim, J., Seol, J., Son, H. I. (2021). Towards an efficient tomato harvesting robot: 3d perception, manipulation, ended-effector. *IEEE Access*, 9,17631-17640.
- [7] Li, G., Ji, C., Zhai, L. (2014), Research progress and analysis of end-effector for fruit and vegetable picking robot (果蔬采摘机器人末端执行器研究进展与分析). *Journal of Chinese Agricultural Mechanization*, 35(5), 231-236+240.
- [8] Liu, W., Zhang, Y., Cai, Y. (2017). Current status and trend of the development of the morel mushroom industry in China (中国羊肚菌产业发展的现状及趋势). *Medicinal Mushroom*, 25(2), 77-83.
- [9] Safeea, M., Neto, P., Bearee, R. (2019). Robot dynamics: A recursive algorithm for efficient calculation of Christoffel symbols. *Mechanism and Machine Theory*, 142, 103589-103589.
- [10] Wang, X., Wu, P., Feng, Q. (2016). Design and test of tomato picking robot system (番茄采摘机器人系统设计及试验). *Journal of Agricultural Mechanization Research*, 38(4), 94-98.
- [11] Wang, X. (2019). *Harvesting tool for morel mushroom (羊肚菌采收工具)*. China, Patent, No.208572865A
- [12] Wang, X., Yuan, S., Shi, Y., Wei, Y., Tao, M. (2021). *A kind of morel mushroom picking and collecting device (一种羊肚菌采摘收集装置)*. China, Patent, No.214628683 A.
- [13] Wang, S. (2021). *A kind of simple morel mushroom harvesting equipment (一种简易羊肚菌采收设备)*. China, Patent, No.215074378 A.
- [14] Wang, C., Wu, W., Liu, J. (2021). Research on motion control system of magnetically guided four rudder wheel heavy-duty AGV (磁导式四舵轮重载 AGV 运动控制系统研究). *Construction Machinery and Equipment*, 52(12), 24-29.
- [15] Yang, Q. (2020). *Research on key technology of target recognition and localization control for flat mushroom picking robot (平菇采摘机器人目标识别与定位控制关键技术研究)*. [Doctoral dissertation, Suzhou University].
- [16] Yoshida, T., Onishi, Y., Kawahara, T., Fukao, T. (2022). Automated harvesting by a dual-arm fruit harvesting robot. *ROBOMECH Journal*, 9:19.
- [17] Yu, H., Zhao, J., Liu, X., Bian E. (2022). *A kind of harvesting tool for morel mushroom (一种羊肚菌采收工具)*. China, Patent, No. 216254377 A.
- [18] Zhao, Q., Huang, Y., Xu, Z., Li, R. (2009). Analysis of the present situation of the cultivation on morels (羊肚菌栽培研究现状). *Journal of Yunnan Agricultural University*, 24(6), 904-907.
- [19] Zhou, Z., Wang, J. (2012). Structural design and parameter optimization of tomato picking robot arm (番茄采摘机器人机械臂结构设计与参数优化). *Anhui Agricultural Science*, 40(22), 11520-11522.
- [20] Zhang, J., Ji, C., Gu, B., Shen, Z., Dong M. (2015), Ontology design of three-degree-of-freedom apple picking robot (三自由度苹果采摘机器人本体设计). *Computer Engineering and Applications*, 51(23), 251-257.
- [21] Zhang, B. (2019). *Research on the control system of Agaricus bisporus picking machine (双孢菇采摘机控制系统研究)*. [Doctoral dissertation, Hebei University of Technology].
- [22] Zhang, J. (2019). *Design of intelligent mushroom picking robot for factorized brown mushroom cultivation (面向工厂化褐菇种植的智能蘑菇采摘机器人设计)*. [Doctoral dissertation, Nanjing Agricultural University].
- [23] Zhang, J., Wang, G., Yuan, X. (2020). A comprehensive evaluation study of design options for omnidirectional mobile robots (全向移动机器人设计方案的综合评价研究). *Mechanical Design and Manufacturing*, (10), 273-275.
- [24] Zhao, X., Zhang, H., Fu, H., Xu, Y., Chen, J. (2024). Design and test of end-effector for picking fresh artichoke peppers (鲜食朝天椒采摘末端执行器的设计与试验). *Transactions of the Chinese Society of Agricultural Machinery*, 10(13), 1-12.

STATISTICS AND ANALYSIS OF PHYSICAL PARAMETERS OF ADZUKI BEAN SEEDS

红小豆种子物理参数统计及分析

Guoqiang DUN^{*1)}, Luhan WANG²⁾, Huiwen XUE¹⁾, Xinxin JI^{1,2)}, Quanbao SHENG²⁾, Xinming LI²⁾,
Chaoxia ZHANG¹⁾, Yuhan WEI¹⁾

¹⁾ Harbin Cambridge University, Intelligent Agricultural Machinery Equipment Engineering Laboratory, Harbin / China;

²⁾ Northeast Forestry University, College of Mechanical and Electrical Engineering, Harbin / China;

Tel: +86 13836027042; E-mail: dunguoqiangpaper@163.com

DOI: <https://doi.org/10.35633/inmateh-75-37>

Keywords: Mechanical seed-metering device; Adzuki bean seeds; Physical parameters; Seed shape

ABSTRACT

To address the issue of seed filling in mechanical seed meters for different varieties of adzuki beans and to provide a basis for designing the shape and size of seed metering plate holes, a statistical analysis of the physical parameters of seeds from 10 adzuki bean varieties with significant morphological differences was conducted. The three-axis dimensions (length, width, and thickness) and the equivalent diameter of the seeds were found to approximately follow a normal distribution. The distribution and dispersion of each physical parameter were analyzed. A linear correlation analysis was performed between the equivalent diameter and the hundred-seed weight, showing a consistent overall trend. By measuring the hundred-seed weight, the relative equivalent diameter was determined, which was then used to select the appropriate seed metering plate diameter. The linear correlation coefficient analysis of the three-axis dimensions of different varieties indicated that, when modeling adzuki bean seeds for simulation, either the width or thickness could be selected as the primary dimension based on specific conditions.

摘要

为解决红小豆机械式排种器对不同品种红小豆的充种问题, 提供排种盘型孔结构设计参数依据, 选取形态差异较大的10种红小豆种植品种的种子物理参数进行数据统计分析。种子的三轴尺寸长、宽、厚及均径均近似服从正态分布, 分析确定了各物理参数的分布离散情况, 均径与百粒重整体变化趋势基本一致并进行线性相关分析, 通过测量百粒重得出相对均径从而选择排种盘直径, 不同品种三轴尺寸间线性相关系数分析结果表明, 仿真红小豆种子建模时可根据具体情况选取宽或厚作为主尺寸。

INTRODUCTION

Adzuki Bean, or Vermillion Beans, is the leguminous family's annual semi-twining herbaceous plant. The taste of the adzuki bean is sweet, and it is planted all over China. The stability of its production is of great significance in ensuring China's food security. Adzuki bean has a purple-red surface, plump grains, and is rich in protein, vitamins, and carbohydrates (Li et al., 2023), so consumers deeply favor it. Adzuki bean breeding technology (Liu et al., 2024) is an essential means of variety improvement and grain production increase. The adzuki bean mechanical plot breeding experiment (Dun et al., 2022) is the best method for breeding high-quality and high-yield new varieties, which is focused on the research and development of seeding machinery and equipment (Shang et al., 2021).

At present, the filling problem of the mechanical seed-metering device is still the core technical problem, which mainly studies the internal relationship between the hole of the seed metering plate and the adzuki bean seeds. Different varieties of adzuki bean seeds are sown in the breeding test field in the same region, and these seeds have different geometric dimensions and seed grain shapes. Therefore, it is necessary to measure and statistically analyze the geometric dimensions of different varieties of adzuki beans in the same region as a reference for the design of the hole shape of the seed-metering device (Lan et al., 2022). Domestic and foreign scholars have researched the physical properties of various agricultural materials. Dun Guoqiang et al., (2024), conducted EDEM discrete element simulation on the seed filling characteristics of the double swing plate type seed metering device of different soybean varieties and simulated the seeding process; Zheng Xiaoshuai et al., (2024), from Qingdao Agricultural University analyzed the geometric shape and size parameters of *Cyperus esculentus* seeds, measured the precise outline of *Cyperus esculentus* seeds by using the cross-sectional circular runout method, and established a discrete element simulation particle model of the

seeds. They also performed parameter calibration and seeding simulation through simulation experiments, data analysis, and fitting. Based on the geometric characteristics of pumpkin seeds, *Yu Yaxin et al., (2024)*, from Zhejiang Sci-Tech University calibrated the discrete element simulation contact parameters of pumpkin seeds and seed metering device, and determined the range of negative pressure and the number of holes in the seed metering plate through single factor tests. *Zhang Shengwei et al., (2022)*, used the Hertz-Mindlin with bonding model to establish a seed simulation model and calibrated the simulation parameters between mung bean seeds and contact materials to further optimize seed planting components. *Yan Jianwei et al., (2023)*, from Guizhou University took white radish seed particles as the research object, establishing a discrete element model of white radish seed particles using 3D scanning reverse modeling technology and EDEM software. They calibrated simulation parameters through physical tests and virtual simulation experiments. *Li Qichao et al., (2021)*, established a discrete element model of vegetable seeds and a seed-metering device model based on the physical parameters of three different types of small-particle vegetable seeds. Using discrete element software EDEM, they analyzed the seeding performance and examined the movement behavior of vegetable seeds during the seed filling process.

Wenxin Zhang et al., (2022), determined the basic physical parameters, contact parameters and angle of repose of germinated American ginseng seeds through physical experiments, and through the steepest climbing test, the optimal range of the significance parameter values was determined. *Ma Wenpeng et al., (2023)*, used the discrete element method to simulate and analyze the mechanized seeding process of sesame seeds. The contact parameters of sesame seeds were calibrated by combining the actual seed drop test and the simulated seed drop test. *Xu Bing et al., (2021)*, calibrated the simulated discrete element parameters of buckwheat seeds in combination with the simulation optimization design test and physical test. *Karaiev Oleksandr et al., (2021)*, mathematically modeled the calibration process of fruit stone culture seeds such as cherry, sweet cherry, cherry plum, almond, and apricot kernel, etc. *Xingye Chen et al., (2024)*, calibrated the contact parameters of the bean pod pepper seeds, took the repose angle as the response value, and simulated the discrete element model of the bean pod pepper seeds by using reverse engineering reconstruction technology. *Tianyue Xu et al., (2023)*, took ellipsoidal seeds such as soybeans, adzuki beans, and kidney beans as research objects and analyzed their size and shape. The results showed that the normal distribution can approximate the size dispersion, and thus a method of modeling ellipsoidal seeds as particles based on the multi-sphere method was proposed.

In summary, previous studies have conducted in-depth research on the physical parameters, the model establishment, and simulation parameter calibration of agricultural materials. However, there is still room for research on the physical parameters, seed shape measurement, and statistical analysis of a certain number of multi-variety adzuki bean seeds. Since the shape and size of adzuki bean seeds are relatively irregular and small, to ensure the accuracy of the experiment, several adzuki bean seeds were selected as research objects. Their length, width, and thickness were measured, followed by statistical analysis and calculations of their triaxial dimensional relationships, average diameter, sphericity, length-to-width ratio, length-to-thickness ratio, volume, density, and 100-grain weight. This analysis provides a reference for designing the seeding plate hole of the adzuki bean mechanical seed-metering device.

MATERIALS AND METHODS

Determination of material properties of Pak Choi seeds

Ten adzuki bean varieties grown in China were selected, namely, Pearl Red, Xianfeng Extremely Early, Shouhe Acacia, Shengyou, Pangda Agricultural, Kyoto, Jin Wangjie, Red Pearl, Dazhi, and Dahongpao. 100 seeds of each variety were randomly selected, as shown in Figure 1. A digital display vernier caliper (range 200 mm, accuracy 0.01 mm) was used to measure the triaxial dimensions (length l , width w , thickness t) of each adzuki bean seed (*Wang et al., 2018*). An electronic analytical balance (range 100 g, accuracy 0.001 g) was used to measure the 100-grain weight of adzuki bean seeds. 100 seeds of each variety were respectively taken for measurement, and the average value was taken 5 times (*Bai et al., 2024*). The actual operation diagram is shown in Figure 2. The average diameter d , sphericity S_p , length-to-width ratio R_{lw} , length-to-thickness ratio R_{lt} , volume v , and density ρ of the adzuki bean seeds were calculated.

The specific calculation formula (*Dun et al., 2023*) is as follows:

$$d = \frac{l+w+t}{3} \quad (1)$$

$$S_p = \frac{\sqrt[3]{lwt}}{\max(l \cdot w \cdot t)} \tag{2}$$

$$R_{lw} = \frac{l}{w} \tag{3}$$

$$R_{lt} = \frac{l}{t} \tag{4}$$

$$v = \frac{1}{6} \pi lwt \tag{5}$$

$$\rho = \frac{m}{v} \tag{6}$$

where: l is the seed length, mm; w is the seed width, mm; t is the seed thickness, mm; m is the seed quality, g; ρ is the seed density, g/cm³; v is the seed volume, mm³; S_p is the seed sphericity; R_{lw} is the ratio of seed length to width; R_{lt} is the ratio of seed length to thickness.

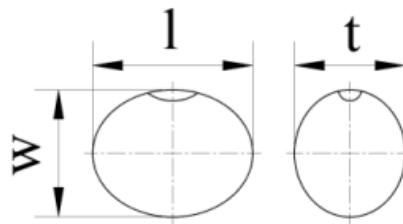


Fig. 1 - Triaxial dimensions of adzuki bean seeds



a) Adzuki bean seeds diagram; (b) Seed triaxial dimension measurement; (c) Seed quality measurement diagram

Fig. 2 - Measured physical parameters of adzuki beans

In order to analyze the population characteristic data of 100 seeds of each adzuki bean variety, the measured values and calculated values of the physical geometric parameters of the above varieties of seeds were calculated by mathematical statistics. The statistical parameters included each parameter's maximum, minimum, mean and coefficient of variation. The maximum and minimum values represented the distribution range limits of the parameter. The coefficient of variation is a commonly used statistic to measure the degree of data variation (Yang et al., 1993). The ratio of standard deviation to the mean value can eliminate the influence of measurement scale and dimension between different varieties of adzuki bean seeds. It is used to compare the dispersion degree of each parameter. The smaller the value, the more concentrated the overall distribution of the data, conversely, the larger the value, the more discrete the overall distribution. The statistical results of seed physical parameters of 10 kinds of adzuki bean seeds, such as Pearl red, Xianfeng Extremely Early and Shouhe Acacia, are shown in Table 1.

Table 1

Statistics of dimensions of adzuki bean seeds

Adzuki bean variety	Value	Length l/mm	Width w/mm	Thickness t / mm	Average diameter d / mm	Sphericity S _p	Length - width ratio R _{lw}	Length - thickness ratio R _{lt}	Volume v/ mm ³	Density ρ/g/cm ³	hundred-grain weight / g
Pearl red	Maximum value	7.37	5.94	5.78	6.18	0.98	1.37	1.54	121.6	2.402	

Adzuki bean variety	Value	Length l/mm	Width w/mm	Thickness t / mm	Average diameter d / mm	Sphericity S_p	Length - width ratio R_{lw}	Length - thickness ratio R_{lt}	Volume v/ mm^3	Density $\rho/g/cm^3$	hundred-grain weight / g
	Minimum value	5.02	4.70	3.99	4.80	0.79	0.98	1.04	56.58	0.635	
	Average value	6.05	5.29	4.86	5.40	0.89	1.15	1.25	82.017	1.427	
	Coefficient of variation	0.085	0.055	0.069	0.058	0.052	0.078	0.085	0.176	0.134	
	hundred-grain weight										11.597
Xianfeng Extremely Early	Maximum value	9.98	6.94	6.94	7.76	0.98	1.84	1.81	232.22	2.137	
	Minimum value	5.39	5.01	4.50	5.19	0.68	0.93	1.01	73.21	1.022	
	Average value	8.40	5.96	5.91	6.76	0.80	1.41	1.42	156.91	1.461	
	Coefficient of variation	0.104	0.076	0.077	0.075	0.065	0.098	0.098	0.214	0.104	
	hundred-grain weight										22.689
Shouhe Acacia	Maximum value	10.65	6.87	7.69	7.95	0.88	1.65	1.74	245.32	1.882	
	Minimum value	7.71	5.41	5.06	6.06	0.72	1.20	1.18	110.51	1.170	
	Average value	8.99	6.23	6.24	7.15	0.79	1.45	1.44	183.85	1.480	
	Coefficient of variation	0.072	0.049	0.062	0.051	0.046	0.067	0.074	0.144	0.067	
	hundred-grain weight										27.076
Shengyou	Maximum value	10.12	7.02	6.90	7.71	1.00	1.63	1.69	226.52	2.203	
	Minimum value	6.03	4.99	4.98	5.45	0.73	1.00	1.00	83.14	0.830	
	Average value	8.47	6.17	6.14	6.93	0.81	1.38	1.38	169.51	1.416	
	Coefficient of variation	0.089	0.065	0.068	0.062	0.061	0.087	0.089	0.176	0.098	
	hundred-grain weight										23.894
Pangda	Maximum value	10.04	6.94	7.08	7.88	0.93	1.70	1.69	242.71	2.261	
	Minimum value	5.12	5.10	4.94	5.70	0.70	0.82	0.83	95.53	1.228	
	Average value	8.36	6.04	6.03	6.81	0.81	1.39	1.39	160.85	1.514	
	Coefficient of variation	0.092	0.065	0.074	0.067	0.048	0.080	0.084	0.197	0.084	
	hundred-grain weight										24.175
Kyoto	Maximum value	8.57	7.72	6.80	7.16	0.96	1.61	1.64	186.74	2.061	

Adzuki bean variety	Value	Length l/mm	Width w/mm	Thickness t / mm	Average diameter d / mm	Sphericity S_p	Length - width ratio R_{lw}	Length - thickness ratio R_{lt}	Volume v/ mm^3	Density $\rho/\text{g}/\text{cm}^3$	hundred-grain weight / g
	Minimum value	4.81	4.22	4.44	4.76	0.73	0.88	0.97	56.20	0.709	
	Average value	7.31	5.71	5.66	6.23	0.84	1.29	1.30	125.23	1.410	
	Coefficient of variation	0.078	0.099	0.083	0.071	0.050	0.093	0.086	0.208	0.120	
	hundred-grain weight										17.535
	Maximum value	9.40	6.85	6.70	7.47	0.96	1.62	1.66	212.25	2.261	
Jin Wangjie	Minimum value	5.34	4.95	5.00	5.48	0.73	0.94	0.88	86.23	1.085	
	Average value	7.98	5.72	5.69	6.46	0.80	1.40	1.40	137.47	1.433	
	Coefficient of variation	0.083	0.071	0.071	0.065	0.046	0.077	0.077	0.195	0.106	
	hundred-grain weight										19.551
	Maximum value	10.00	8.68	6.90	7.75	0.92	1.72	1.78	232.88	1.689	
Red Pearl	Minimum value	6.26	4.96	4.96	5.47	0.70	1.00	1.11	83.94	1.001	
	Average value	8.24	5.91	5.86	6.67	0.80	1.40	1.41	151.16	1.504	
	Coefficient of variation	0.096	0.081	0.071	0.071	0.055	0.088	0.084	0.206	0.074	
	hundred-grain weight										22.606
	Maximum value	9.98	6.94	6.94	7.76	0.98	1.84	1.81	232.22	2.14	
Dazhi	Minimum value	5.39	5.01	4.50	5.19	0.68	0.93	1.01	73.21	1.02	
	Average value	8.40	5.96	5.91	6.76	0.80	1.41	1.42	156.91	1.46	
	Coefficient of variation	0.104	0.077	0.077	0.075	0.065	0.098	0.098	0.21	0.10	
	hundred-grain weight										22.689
	Maximum value	10.31	7.41	7.36	7.99	0.91	1.60	1.68	256.53	1.543	
Dahongpao	Minimum value	6.07	4.63	4.19	4.96	0.73	1.13	1.11	61.66	1.142	
	Average value	8.65	6.35	6.17	7.05	0.81	1.36	1.41	179.90	1.364	
	Coefficient of variation	0.095	0.075	0.090	0.079	0.046	0.066	0.080	0.216	0.058	
	hundred-grain weight										24.436
	Maximum value	10.31	7.41	7.36	7.99	0.91	1.60	1.68	256.53	1.543	

RESULTS

Single seed parameter analysis

First, taking Pearl Adzuki beans as an example, the triaxial dimensions and shape parameters of 100 seeds of this variety were statistically analyzed. The statistical results are shown in Table 1. The average values and coefficients of variation of length l , width w , thickness t , and average diameter d of Pearl Adzuki beans are 6.05 mm, 5.29 mm, 4.86 mm, 5.40 mm, and 0.085, 0.055, 0.069 and 0.058, respectively. The triaxial dimensions and average diameter approximately obeyed the normal distribution. The normal distribution of triaxial dimensions of seeds is shown in Figure 3. The length l , width w , thickness t , and average diameter d of Pearl Adzuki seeds showed leapfrog jumps in the first 20%, 16%, 21%, and 24%, and the changes in the last 80%, 84%, 79% and 76% of the seeds were more gradual, indicating that there were fewer small seeds and more large seeds in Pearl Red varieties. The distribution of seed length l , thickness t , and average diameter d was basically consistent and relatively discrete. The sizes were concentrated in 5.5 mm~7.0 mm, 4.5 mm~5.5 mm, and 4.9 mm~5.9 mm, respectively. The size ranges were 2.35 mm, 0.92 mm, and 1.38 mm, respectively. The sizes varied greatly, and a certain proportion of over-large and over-small sizes existed. The seed width w was more concentrated, with a size range of 0.65 mm. The overall distribution was too smooth and basically symmetrical. The coefficients of variation of seed length l , thickness t , and average diameter d were 0.085, 0.069, and 0.058, respectively, while the coefficient of variation of seed width w was 0.055, significantly smaller than the first three. The overall distribution was significantly concentrated. The sphericity S_p of Pearl Red seeds ranged from 0.79 to 0.98, with an average value of 0.89 and a coefficient of variation of 0.052. The average length-to-width ratio R_{lw} and length-to-thickness ratio R_{lt} of the seeds were calculated to be 1.15 and 1.25, respectively. The length l and width w were basically the same, but both were significantly larger than the seed thickness t . The length-width cross-section of the seed was an ellipse, the length-thickness cross-section was an ellipse, and the seed shape was an approximately ellipsoid of unequal diameters.

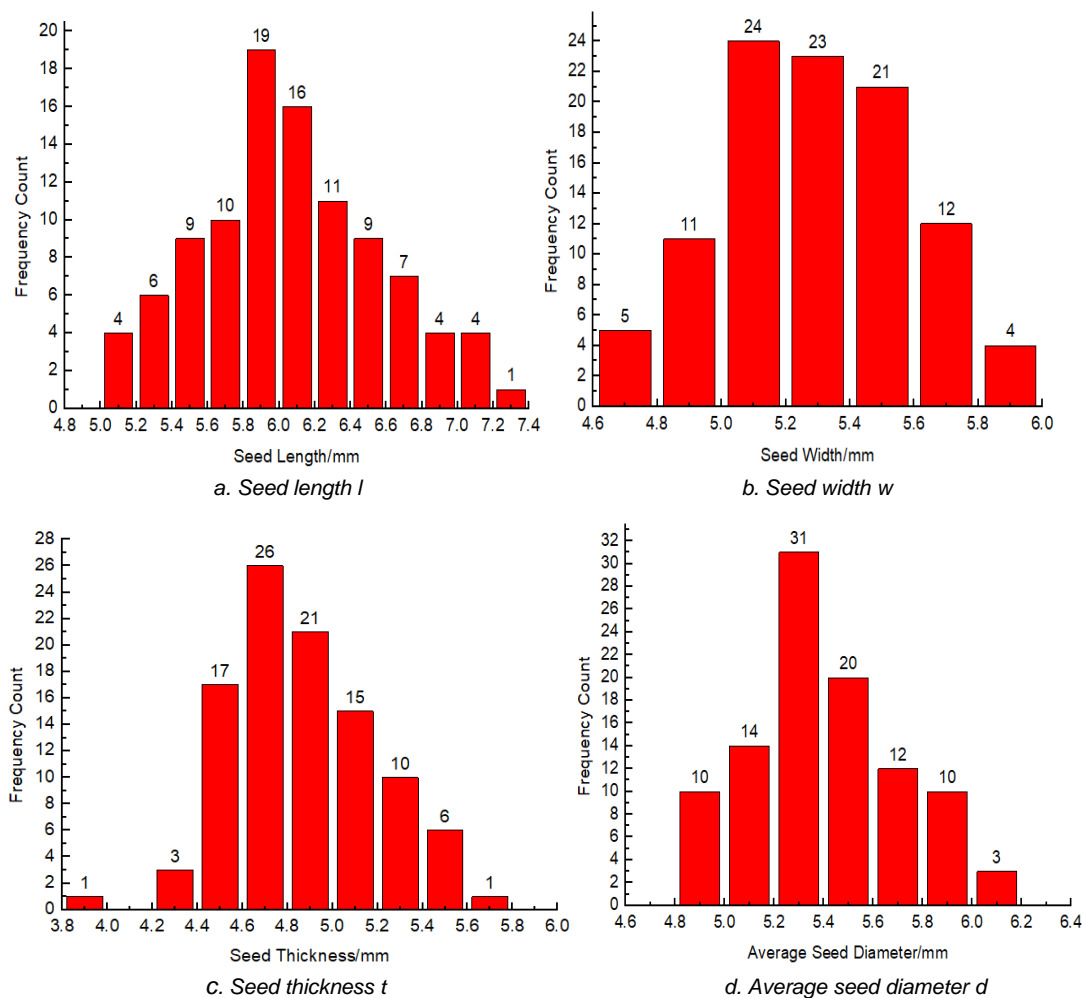


Fig. 3 - Seed grain triaxial and average diameter size distribution

In order to analyze the relationship between the length l , width w , and thickness t of adzuki bean seeds, origin 8.5 was used for parameter mapping (Chen *et al.*, 2024), and scatter plots of seed length and width, length and thickness, and width and thickness were drawn for linear fitting, as shown in Figure 4. The triaxial dimensions of adzuki bean seeds showed a linear positive correlation function relationship. The correlation coefficients of the linear fitting equations between the triaxial dimensions of length-width, length-thickness, and width-thickness were $R^2=0.1937$, $R^2=0.1567$, and $R^2=0.6424$. The Pearson coefficient between length-width and width-thickness was significantly greater than the linear correlation between length-thickness. Therefore, it can be determined that the width of the triaxial dimensions was the main dimension and the thickness was the secondary dimension. The seed width can be randomly generated according to the normal distribution during seed modeling, and the length and thickness dimensions can be calculated according to the functional relationship with the main dimension width. In this way, the size distribution of the adzuki bean seed population generated by simulation was closer to the actual situation.

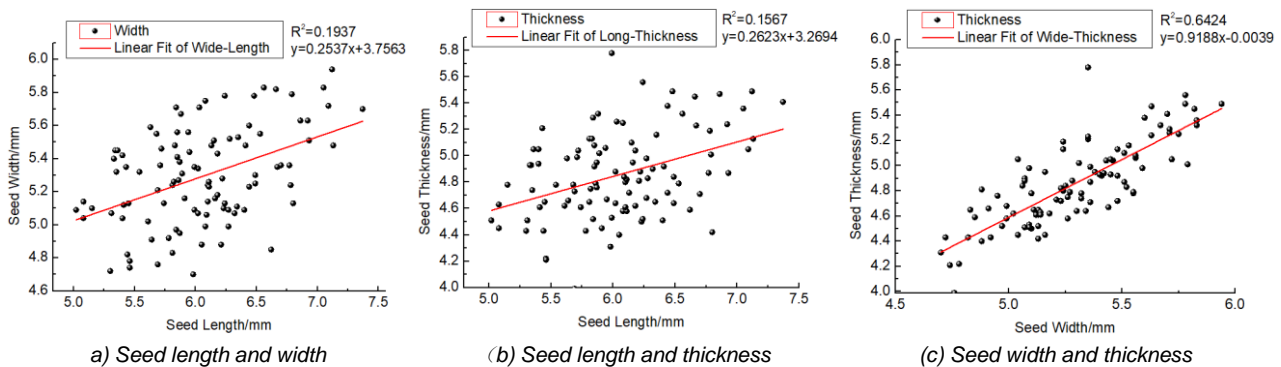


Fig. 4 - Scatter plot of the relationship between the triaxial dimensions of adzuki bean seed

Statistical analysis of different seed parameters

The measurement and statistical results of the parameters of a single variety of Pearl Red cannot represent the overall physical geometric parameters of adzuki bean seeds in the national planting area due to its variety of attributes and the particularity of regional environment planting. Therefore, as shown in Table 1, the physical parameters of 10 kinds of adzuki bean seeds were statistically analyzed. It can be seen from Table 1 that the physical parameters of 100 seeds in each adzuki bean variety obeyed the normal distribution. The coefficient of variation of length, width, thickness, and average diameter ranged from 0.049 to 0.104. The larger the coefficient of variation of the average diameter of adzuki bean seeds, the greater the degree of dispersion of the average diameter of seeds, the more irregular the seed shape, and the more it tends to be ellipsoidal. The coefficient of variation of sphericity ranged from 0.046 to 0.065, the coefficient of variation of length-to-width ratio and length-to-thickness ratio ranged from 0.066 to 0.098, the coefficient of variation of volume ranged from 0.144 to 0.216, and the coefficient of variation of density ranged from 0.058 to 0.134. The sphericity distribution was concentrated overall, followed by length-to-width and length-to-thickness ratios. The distribution of triaxial dimensions, average diameter and volume was relatively discrete, and the density distribution was the most discrete. The single-factor test method was adopted, and the experimental design expert software design-expert 8.0 was used. The adzuki bean varieties (10 kinds of adzuki bean seeds) and parameter values (maximum value, minimum value, average value) were used as experimental factors, and length, width, thickness, average diameter, sphericity, length-width ratio, length-to-width ratio, length-to-thickness ratio, volume, and density were used as experimental indicators. The statistical analysis of physical parameter tests was carried out, and the statistical results of the experimental indicators are shown in Table 2.

Table 2

Overall statistics of physical parameters of adzuki beans

Parameter	Minimum	Maximum	Average	Standard deviation	Coefficient of variation
Length / mm	4.81	10.65	8.08	1.082	0.134
Width / mm	4.22	8.68	5.93	0.516	0.087
Thickness / mm	3.99	7.69	5.85	0.575	0.098
average diameter / mm	4.76	7.99	6.62	0.658	0.099
Sphericity	0.68	0.997	0.81	0.052	0.064
Length-width ratio	0.82	1.84	1.36	0.141	0.103

Parameter	Minimum	Maximum	Average	Standard deviation	Coefficient of variation
Length-thickness ratio	0.83	1.81	1.38	0.132	0.085
Volume / mm ³	56.20	256.53	150.38	41.104	0.273
Density / g/cm ³	0.63	2.40	1.45	0.147	0.101

As shown in Table 2, the average length, width, thickness, average diameter, and variation range of the 10 kinds of adzuki bean seeds are 8.08 mm, 5.93 mm, 5.85 mm, 6.62 mm, 8.08±1.082 mm, 5.93±0.516 mm, 5.85±0.575 mm, and 6.62±0.658 mm, respectively. The seed length and width are close, and significantly larger than the seed thickness. The average diameter and the width of the seeds are close to each other. The coefficient of variation shows that the seed width distribution is relatively concentrated, and the seed length distribution is the most dispersed. In order to further explore the design structure of the seed metering plate hole, according to Tables 1 and 2, the factor index change trend chart was drawn using design-expert 8.0. The adzuki bean varieties were used as experimental factors, and the average diameter, 100-grain weight, and density of each variety were used as experimental indicators to analyze the changing trend of the adzuki bean seed average diameter, 100-grain weight and density parameters, as shown in Figure 5.

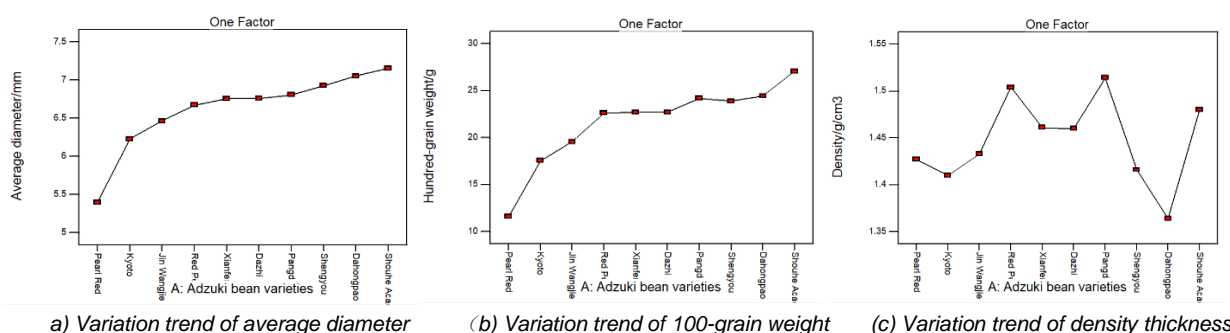


Fig. 5 - Variation trends of average diameter, 100-grain weight and density

As shown in Figure 5, the average diameter and 100-grain weight of different seeds have basically the same trend. The density of seeds of a few varieties (Shengyou, Dahongpao) is entirely opposite to the average diameter and 100-grain weight. The trends of seeds of other varieties (Kyoto, Red Pearl, Jin wangjie, Xianfeng Extremely Early, Dazhi, Pangda Agriculture, Shouhe Acacia) are basically consistent with their average diameter and 100-grain weight. Among them, the larger the average diameter of each adzuki bean variety, the larger the value of its 100-grain weight. Since the density range between the same beans is small, the density of specific varieties should be analyzed according to the specific variety combined with the average diameter and 100-grain weight. There is also a particular case in analyzing the average diameter and 100-grain weight trend. For example, although the average diameter of Shengyou's seeds is larger than that of Pangda Agriculture, the 100-grain weight is smaller than that of Pangda Agriculture, the floating trend of its value is not obvious. The main reason for this trend is that there are minimal exceptions in Shengyou adzuki bean seeds that lower the value of 100-grain weight, and it can be seen from the triaxial dimensions of the seeds and the range of the average diameter that the seed dimensions vary greatly.

The main parameters for designing the seed metering plate holes of the mechanical seed metering device are based on the average seed diameter increasing from 4.76 mm to 7.99 mm, with a variation of 3.23 mm. Therefore, the measured range of 100-grain weight is different, and the average diameter of each variety of seeds is calculated from the average length, width and thickness. The triaxial dimensions obey the normal distribution. Therefore, the external dimensions of adzuki bean varieties planted in the same area vary significantly, which puts forward necessary design requirements for the adaptability of the mechanical seed metering device to sowing varieties.

The seed metering plate with different hole sizes in the corresponding range can be accurately selected according to the 100-grain weight value in seed cleaning and replacement. As can be seen from Figure 6, there is a stable linear correlation between the 100-grain weight and the average diameter of adzuki bean seeds. Therefore, a linear equation was fitted between the 100-grain weight and the average diameter of 10 varieties of adzuki beans. The 100-grain weight of each variety of adzuki beans was set as the independent variable X, and the average diameter of each variety of seeds was set as the dependent variable Y.

Based on the principle of linear regression equation construction (Yu et al., 2024), the linear fitting equation was obtained as $y=0.1138x+4.1607$, and the Pearson coefficient R^2 was 0.9728. Therefore, when selecting the seeding plate, the 100-grain weight value x can be directly input to obtain the corresponding average diameter y , to select an appropriate seeding plate.

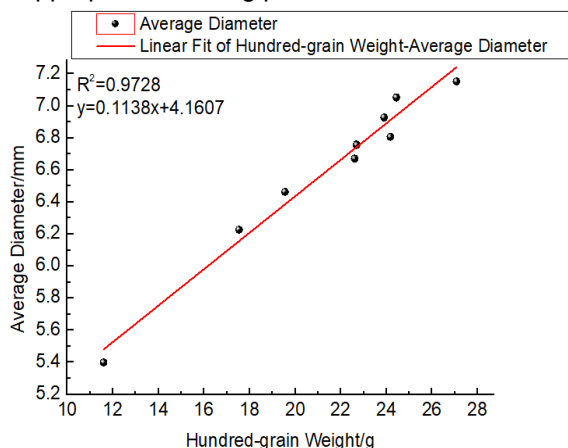


Fig. 6 - Linear fitting diagram of 100-grain weight-average diameter

Therefore, it will be very useful to study the overall statistical results of different seed physical parameters in the same region for the design of seed metering plate holes. Table 3 shows the results of the single-factor test ANOVA for physical parameters of different seed sphericity variation ranges.

Table 3

Packett-Burman test protocol and results

Shape parameters	Source of variance	mean square	F value	P value	Significance
Length / mm	Model	8.74	44.38	< 0.0001	**
	Adzuki bean variety	1.99	10.09	< 0.0001	**
	Parameter value	39.13	198.71	< 0.0001	**
	Error	0.20			
Width / mm	Model	2.50	11.93	< 0.0001	**
	Adzuki bean variety	0.28	1.33	0.2908	**
	Parameter value	12.49	59.66	< 0.0001	**
	Error	0.21			
Thickness / mm	Model	2.66	43.95	< 0.0001	**
	Adzuki bean variety	0.42	7.02	0.0002	**
	Parameter value	12.70	210.09	< 0.0001	**
	Error	0.060			
Average diameter / mm	Model	2.82	44.39	< 0.0001	**
	Adzuki bean variety	0.59	9.31	< 0.0001	**
	Parameter value	12.83	202.23	< 0.0001	**
	Error	0.063			
Sphericity	Model	0.026	37.51	< 0.0001	**
	Adzuki bean variety	1.979E-003	2.84	0.0282	**
	Parameter value	0.13	193.51	< 0.0001	**
	Error	6.959E-004			
Length-width ratio	Model	0.22	22.26	< 0.0001	**
	Adzuki bean variety	0.018	1.79	0.1412	**
	Parameter value	1.15	114.42	< 0.0001	**
	Error	0.010			
Length-thickness ratio	Model	0.23	46.91	< 0.0001	**
	Adzuki bean variety	0.012	2.52	0.0456	**
	Parameter value	1.19	246.70	< 0.0001	**
	Error	4.832E-003			
Volume/mm ³	Model	10753.12	34.73	< 0.0001	**
	Adzuki bean variety	2114.72	6.83	0.0003	**
	Parameter value	49625.89	160.27	< 0.0001	**
	Error	309.65			
Density / g/cm ³	Model	0.55	12.61	< 0.0001	**
	Adzuki bean variety	0.028	0.65	0.7434	**
	Parameter value	2.90	66.42	< 0.0001	**
	Error	0.044			

It can be seen from Table 3 that changes in the experimental factors, such as adzuki bean varieties, did not affect width, length-to-width ratio, or density ($P=0.237>0.01$, $P=0.1412>0.01$, $P=0.7434>0.01$). However, they had some effect on seed sphericity and length-to-thickness ratio ($0.01<P=0.0282<0.05$, $0.01<P=0.0456<0.05$), and an extremely significant impact on other physical parameters ($P<0.01$). The test factors had significant effects on all test indexes. In order to analyze the variation trends among the physical parameters of different varieties of adzuki beans, design-expert 8.0 was used to draw the variation trend diagram of factor indicators. The variation trend of the triaxial size and average diameter is shown in Figure 7.

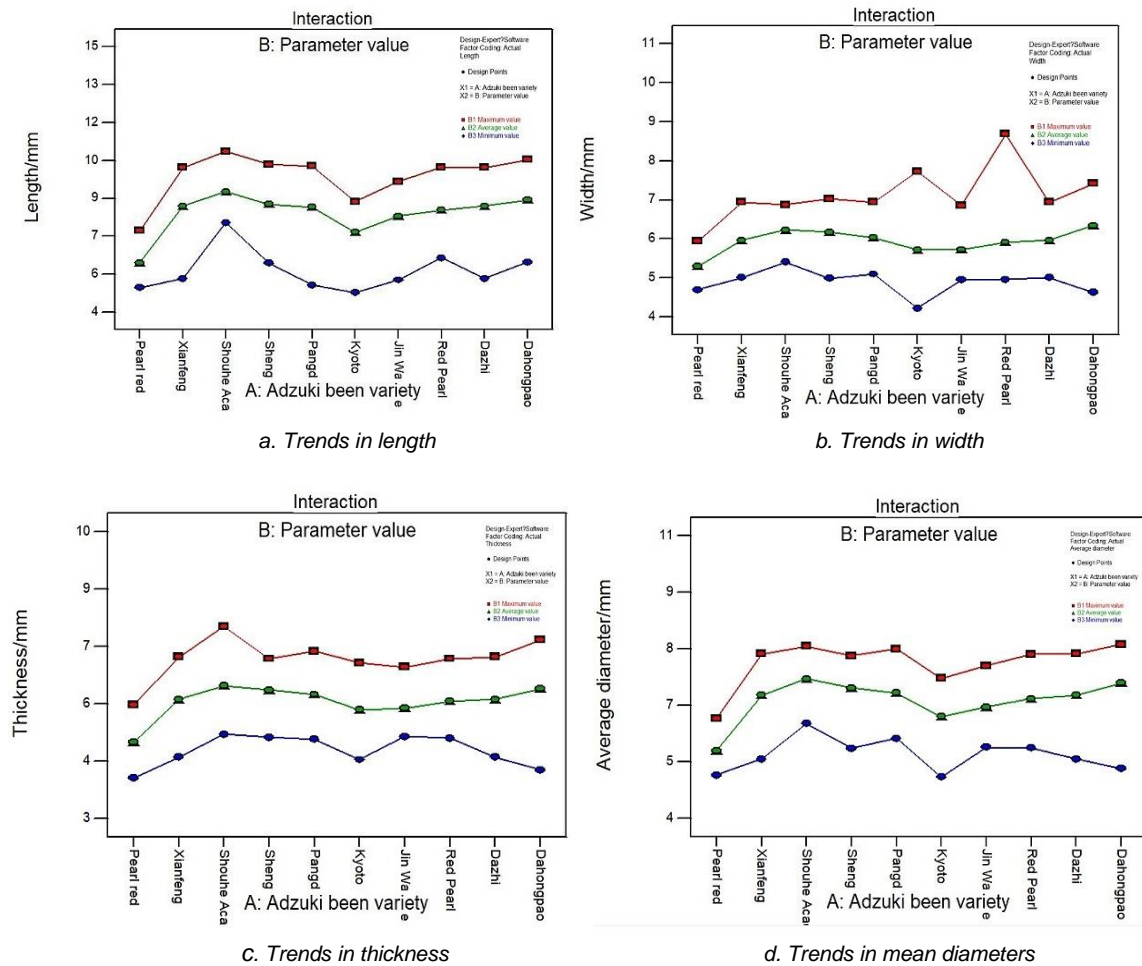


Fig. 7 - Variation trends diagram among different varieties

As can be seen from Figure 7, there are significant shape differences among different seeds. For each adzuki bean variety, the seed shape size parameter's mean value is basically equal to the mean value of the maximum and minimum values. However, there are some special cases, such as the average seed length of Shengyou, Pangda Agriculture, Kyoto and Jin wangjie tended to the maximum value. The average seed width of Kyoto, Red Pearl and Dazhi tended to the minimum value. The seed thickness of Xianfeng Extremely Early, Shouhe Acacia, Shengyou and Dahongpao tended to the maximum value, while the seed thickness of Jin Wangjie tended to the minimum value.

The main reason for this trend in triaxial size is that some parameters of the length, width and thickness of 100 seeds of each magenta adzuki bean seed obey asymmetric normal distribution. As shown in Figure 3, the length and thickness of Pearl Red seeds are asymmetrical. Seed width is a symmetrical normal distribution. The average diameter of seeds is the characteristic size of each seed population and the primary parameter of seed grain shape. It can be seen from Figure 7 that the overall change trend of the triaxial size of different seeds is basically the same, and the change trend of seed volume is also basically the same as that of the triaxial size, as shown in Figure 8.

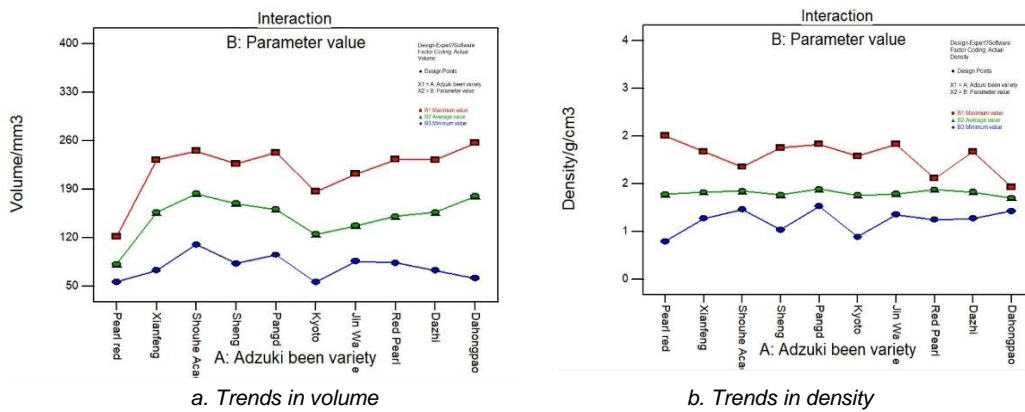


Fig. 8 - Variation trends diagram among different varieties

As shown in Figure 8, the volume of the 10 varieties of adzuki beans varies greatly. Except for Jinwangjie and Dahongpao, the average values are closer to the minimum value, and the volume change trend is basically consistent with the trend of the triaxial size change, with the average volume of 150.38 mm³ and the volume change range of 56.2 mm³–256.53 mm³. The coefficient of variation of the volume *v* of different varieties ranges from 0.052 to 0.216, the dispersion degree varies greatly, the greater the volume difference, the more comprehensive consideration is needed for the design of the seeding plate hole to determine the number of holes filled by the hole-direct seeding number of adzuki beans. The trend of adzuki bean seed density is entirely opposite to seed volume. The maximum and minimum density values are significantly different among different varieties, but the average value of seed density is very small, ranging from 1.364 g/cm³ to 1.514 g/cm³. Therefore, the influence of seed density on the seeding plate hole still needs to be considered in many aspects.

The variance analysis of the test results in Table 3 shows that the difference in sphericity among different varieties varies little, and its changing trend is shown in Figure 9.

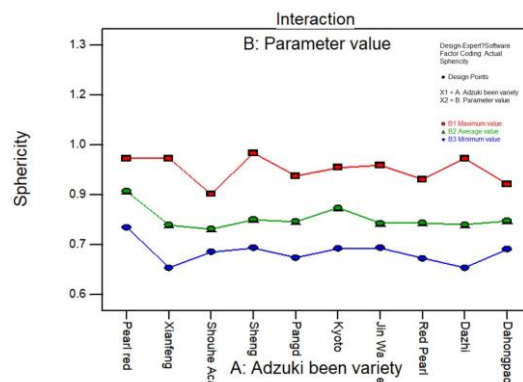


Fig. 9 - Sphericity variation trends among different varieties

It can be seen from Table 3 in Figure 9 that the average sphericity of 1000 seeds of 10 adzuki bean varieties is 0.81, and the sphericity range is 0.68–1.00. A small part of the seeds have a sphericity close to 1.00, which is a pure sphere, but most of them are non-equilinear ellipsoids and the maximum value of sphericity *S_p* is 1, with no significant change. The maximum and minimum values of sphericity *S_p* change gradually and obviously. The average value tends to the minimum direction. The variation coefficient of sphericity *S_p* for different varieties ranged from 0.046 to 0.065, and the dispersion degree changed little. The larger the sphericity, the more obvious the rolling effect of the seeds on the seed metering plate in the seed box, which is more conducive to filling the seed holes.

On the contrary, the smaller the sphericity, the lower the relative motion between seed particles, which is not conducive to filling the holes. For seeds filled into the hole, the smaller the sphericity, the better the seed storage and carrying effect of the hole. Therefore, the size of the seed sphericity requires some comprehensive and dialectical consideration for the design of the seed metering device. The stable state of the seed filling in the hole is the lowest center of gravity of the seed; that is, the smallest of the three axes is vertical, and the other two axes provide a reference for the diameter design of the hole to calculate the length-to-width ratio and length-to-thickness ratio of the seed, as shown in Figure 10.

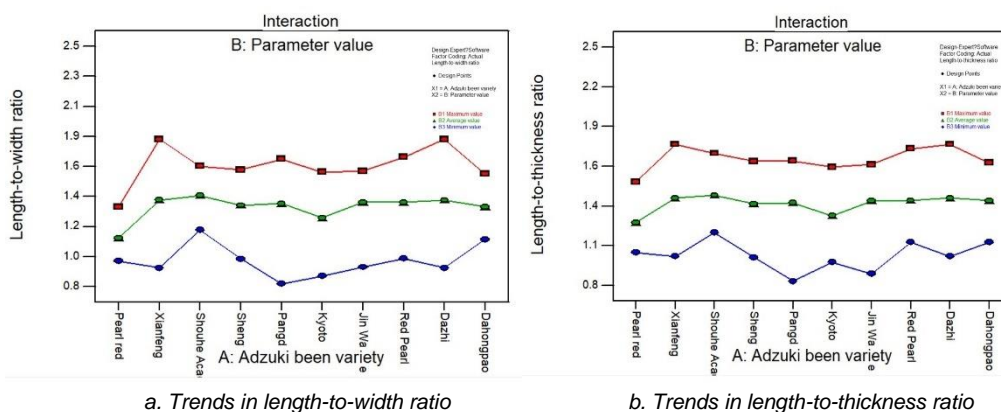


Fig. 10 - Variation trends diagram among different varieties

As shown in Figure 10, the average length-to-width ratio of the seeds of the 10 adzuki bean varieties is 1.36, the average length-to-thickness ratio is 1.38, the length-to-width ratio ranges from 0.82 to 2.21, and the length-to-thickness ratio ranges from 0.83 to 2.08. All unequal-diameter ellipsoid seeds appear in any shape, that is, the size of any axes of three axes has a maximum or minimum value, but each variety has its characteristics. For the length-to-width ratio of seeds, the overall average value is 1.36, and the length and width are basically equal. The minimum length-to-width ratio of Pearl Red, Xianfeng Extremely Early, Pangda Agriculture, Kyoto, Jinwangjie, and Dazhi Adzuki Bean is less than 1. The minimum values of the other varieties of adzuki beans are more significant than 1, but the maximum length-to-width ratio of all varieties of adzuki beans is greater than 1; For the length-to-thickness ratio of seeds, the average and maximum values are greater than 1 as a whole, and the minimum length-to-thickness ratio is less than 1 in some cases, such as Pangda Agriculture, Kyoto, and Jinwangjie Adzuki Bean, that is, the thickness of a small part of the seeds is greater than the length. In contrast, the length of all seeds of other varieties is greater than the thickness.

As shown in Figure 4, there is a stable linear correlation between the length, width and thickness of adzuki bean seeds. However, the Pearson coefficient R^2 of the fitted linear curve between different varieties' length, width and thickness are different. The fitting correlation coefficient R^2 of width-thickness of each variety is generally more significant than the fitting correlation coefficient of length-width and length-thickness. Most of the R^2 values of length-width are more significant than the R^2 values of length-thickness, and a small part is less than the R^2 value of length-thickness, such as Xianfeng Extremely Early, Kyoto, Red Pearl, and Dazhi Adzuki Bean. Therefore, the primary dimensions of the tri-axial dimensions calculated by different varieties are also different, directly affecting the model establishment of discrete element simulation seeds of the seed metering device. For this reason, the linear equations between the length, width and thickness of 10 kinds of adzuki beans are fitted, and the correlation coefficient R^2 is extracted as shown in Table 4. Except for Xianfeng Extremely Early, Kyoto, Red Pearl, and Dazhi Adzuki Bean, the main dimensions of other varieties are width. Seed modeling can be calculated according to the functional relationship with the actual main dimensions of adzuki beans, so that the size distribution of the simulated adzuki bean population is closer to the actual situation.

Table 4

Correlation coefficient R^2 of the linear equation of adzuki bean seeds

Correlation coefficient R^2 of linear equation				
Adzuki bean variety	Length-Width	Width-Thickness	Length-Thickness	Main dimension
Pearl Red	0.1957	0.6424	0.1567	Width
Xianfeng	0.2247	0.7200	0.2390	Thickness
Shouhe Acacia	0.1704	0.4571	0.1453	Width
Shengyou	0.1663	0.6262	0.1567	Width
Pangda Agricultural	0.2673	0.6363	0.2497	Width
Kyoto	0.1503	0.4986	0.2175	Thickness
Jin wangjie	0.2583	0.6557	0.2413	Width
Red Pearl	0.2178	0.4040	0.2784	Thickness
Dazhi	0.2356	0.7149	0.2395	Thickness
Dahongpao	0.5258	0.6979	0.3958	Width

CONCLUSIONS

(1) The physical characteristic parameters of seeds of 10 adzuki bean varieties were selected for statistical analysis. Length, width, thickness, average diameter, sphericity, length-to-width ratio, length-to-thickness ratio, volume, density, and 100-grain weight were statistically analyzed, and the maximum, minimum, mean, standard deviation and coefficient of variation of each parameter were obtained.

(2) The results of the analysis of the appearance parameters of Pearl Red Adzuki Beans showed that the triaxial dimensions of the seeds, length, width, thickness and average diameter all approximately obeyed a normal distribution. Subsequently, the statistical analysis of the seeds of multi-varieties adzuki beans, and the statistical test analysis results of different seed parameters showed that the average length and width of adzuki bean seeds of 10 varieties were basically the same and significantly greater than the average seed thickness, the analysis determined the discrete distribution of each physical parameter. Changes in adzuki bean varieties did not affect the width, the length-to-width ratio, or density. However, they had a significant impact on sphericity and the length-thickness ratio and had a very significant impact on other physical parameters. The overall change trend of the three-axis size was basically consistent with the 100-grain weight. For linear fitting of the 100-grain weight-average diameter, the equation and the Pearson correlation coefficient R^2 were obtained. The appropriate one can be directly selected according to the formula on the seeding plate. The volume change trend of seeds was basically consistent with the three-axis size, but the trend of both and density was basically consistent for the most part. There were also very few exceptions and a small part was completely opposite; this requires a specific design for the adzuki bean mechanical seed metering device to achieve the seed filling target of adzuki beans with different sizes. During the seed cleaning process, different hole sizes in the corresponding range can be selected based on the measured 100-grain weight value of the seeding plate.

(3) The average seed sphericity S_p was 0.89, and the average length-width and the length-thickness ratios of the seeds were 1.15 and 1.25, respectively. The length and width were basically the same, but both were significantly larger than the seed thickness t . The seed shape was an approximately ellipsoid of unequal diameters. The three-axis dimensions of the seed grains showed a linear positive correlation function relationship. The linear correlation of length-width was significantly greater than the linear correlation between length-thickness. However, the linear fitting correlation coefficients R^2 of length-width and length-thickness were relatively close. So, in practical applications, the primary size can be calculated based on the functional relationship of the actual size of adzuki beans so that the size distribution of the simulated adzuki bean population is closer to the actual situation.

REFERENCES

- [1] Bai Z., Meng H., Peng H., Qi J., Li Y. & Kan Z. (2025). Parameter calibration for discrete element simulation of Cistanche seeds (肉苁蓉种子离散元仿真参数标定). *Journal of Agricultural Mechanization Research* (02), 19-26+53.
- [2] Chen X., Wang X., Bai J., Fang W., Hong T., Zang N., Hong T. & Wang G. (2024). Virtual parameter calibration of pod pepper seeds based on discrete element simulation. *Heliyon* (11), 2405-8440.
- [3] Chen Y., Yang W., Tian J., Liao J., Zhao J. & Sun D. (2024). Simulation experimental study of green manure mixed seeder rower in Xinjiang orchard (新疆果园绿肥混合播种机排种器仿真试验研究). *Journal of Agricultural Mechanization Research* (09), 157-165.
- [4] Dnu G., Mao N., Liu W., Wu X., Zhou C. & Ji W. (2022). Design and experiment of four-bar translational seed metering device for soybean plot breeding (四杆平移式大豆小区育种排种器设计与试验). *Transactions of the Chinese Society for Agricultural Machinery* (04), 70-78.
- [5] Dun G., Wu X., Ji X., Zhang F., Ji W. & Yang Y. (2024). Simulation and optimization of soybean plot metering device with double swing plate (双摆盘式大豆小区排种器的仿真优化). *Journal of Agricultural Science and Technology* (06), 82-90.
- [6] Dun G., Liu W., Mao N., Wu X., Ji W. & Ma Y. (2023). Optimization design and experiment of alternate post changing seed metering device for soybean plot breeding (交替换岗式大豆小区育种排种器优化设计与试验). *Journal of Jilin University (Engineering and Technology Edition)* (01), 285-296.
- [7] Karaiev, O., Bondarenko, L., Halko, S., Miroshnyk, O., Vershkov, O., Karaieva, T., Shchur, T., Findura, P. & Pristavka, M. (2021). Mathematical Modelling of the Fruit-Stone Culture Seeds Calibration Process Using Flat Sieves. *Acta Technologica Agriculturae*. (3), 119-123.
- [8] Lan T. (2022). *Design and experimental study on horizontal disc seed metering device of Cyperus esculentus* (水平圆盘式油莎豆排种器的设计及试验研究). [Master's Thesis], Jilin Agricultural University.

- [9] Li Q. (2023). *Mechanism analysis and experimental study on scoop type precision seed metering device for small size vegetable seeds* (舀勺式小粒径蔬菜种子精量排种器机理分析与试验研究). [Doctor's Thesis], Northeast Agricultural University.
- [10] Li X., Liu Y. & Gong Y. (2023). Study on the technology of red bean and coix seed cake (红豆薏米蛋糕的工艺研究). *Farm Products Processing*, (22), 53-56.
- [11] Liu Z. (2024). High-yield and high-quality cultivation technology of adzuki beans in Muling (黑龙江穆棱红小豆高产优质栽培技术). *Special Economic Animals and Plants* (04), 96-98.
- [12] Ma W., Zhang S., Yin X. (2023). A Calibration of the Contact Parameters of a Sesbania Seed Discrete Element Model Based on RSM. *Processes*, (12).
- [13] Shang S., Wu X., Yang R., Li G., Yang X. & Chen D. (2021). Research status and prospect of plot-sowing equipment and technology (小区育种播种装备与技术研究现状与展望). *Transactions of the Chinese Society for Agricultural Machinery*. (02), 1-20.
- [14] Wang Y., Lv F., Xu T. & Yu J. (2018). Shape and size analysis of soybean kernel and modeling (大豆籽粒形状和尺寸分析及其建模). *Journal of Jilin University (Engineering and Technology Ed.)* (02), 507-517.
- [15] Xu B., Zhang Y., Cui Q. (2021). Construction of a discrete element model of buckwheat seeds and calibration of parameters. *INMATEH-Agricultural Engineering*. Vol. 64 (02), 175-184.
- [16] Xu T., Fu H., Liu M., Feng W., Zhang R., Wang Y. & Wang J. (2023). Ellipsoidal seed modeling and simulation parameter selection based on the discrete element method. *Materials Today Communication* s, 37, 2352-4928.
- [17] Yan J., Wei S., Zhang W. & Zhang F. (2023). Calibration of discrete element contact parameters for white radish seed particles (白萝卜种子颗粒接触参数标定). *Journal of Chinese Agricultural Mechanization*. (02), 1-11.
- [18] Yang Q. (1993). Significance test of the difference of coefficient of variation of two populations (两总体变异系数差异的显著性检验). *China Cattle Science* (01), 285-296.
- [19] Yu S., Feng G., Su X., Zhang X., Zuo S. & Zhang X. (2024). Multiple analysis of the relationship between agronomic traits and yield formation in 17 varieties/lines of lolium multiflorum (17份多花黑麦草品种(系)农艺性状与产量形成关系的多重分析). *Acta Agrestia Sinica*. (09), 2862-2874.
- [20] Yu Y., Wang Y., Zhou J. & Pan Y. (2024). Design and test of combined directional seed metering device for pumpkin seed (南瓜种子组合式定向排种器设计与试验). *Transactions of the Chinese Society for Agricultural Machinery*, 1-13.
- [21] Zhang S., Zhang R., Chen T., Fu J. & Yuan H. (2022). Calibration of simulation parameters of and mung bean seeds using discrete element method and verification of seed-metering test (绿豆种子离散元仿真参数标定与排种试验). *Transactions of the Chinese Society for Agricultural Machinery* (03), 71-79.
- [22] Zhang W., Wang F. (2022). Calibration of American ginseng seeds for discrete element simulation. *International Journal of Agricultural and Biological Engineering*, (06), 16-22.
- [23] Zheng X., He X., Shang S., Wang D., Li C., Shi Y., Zhao Z. & Lu Y. (2024). Calibration and experiments for discrete element simulation parameters of *Cyperus esculentus* seeds (油莎豆种子籽粒离散元仿真参数标定与试验). *Journal of Agricultural Mechanization Research* (02), 172-178.

RESEARCH ON DETECTION OF SPARTINA ALTERNIFLORA BASED ON SA-YOLO

基于SA-YOLO的互花米草识别算法研究

Chunqing WANG, Shuqi SHANG, Ruzheng WANG, Ziao YANG, Xiaoning HE, Dansong YUE^{*}

Mechanical and Electrical Engineering, Qingdao Agricultural University, Qingdao, Shandong 266109, China

Corresponding author: Dansong YUE

Tel: +86-13573820687; E-mail: 200501042@qau.edu.cn

DOI: <https://doi.org/10.35633/inmateh-75-38>

Keywords: *Spartina alterniflora*; YOLOv8; Ecological Protection

ABSTRACT

In view of the difficulty and high cost of monitoring the invasion of small aggregations of *Spartina alterniflora* in coastal wetlands, this study proposes a SA-YOLO detection model. First, by adopting a lightweight cascade attention mechanism as the feature extraction part of the network, the model's ability to extract features from *Spartina alterniflora* images is optimized. Secondly, the convolution layer with an improved adaptive attention mechanism is added to optimize feature extraction, dynamically adjust the weight of the feature map, and reduce the amount of calculation. Thirdly, the improved adaptive convolution network is used to optimize the original neck layer, improve the model's ability to integrate *Spartina alterniflora* image features, and reduce the amount of calculation. Finally, a *Spartina alterniflora* recognition system is independently built. The system effectively implements the proposed method and realizes the detection and recording of *Spartina alterniflora* information. This study successfully verifies the effectiveness of the proposed method by conducting experiments on the actual collected *Spartina alterniflora* dataset. The test results show that the recall rate and accuracy of the proposed SA-YOLO *Spartina alterniflora* detection model are 94.5% and 92.4%, respectively, both reaching a high level. It can be seen that the model can complete the identification and detection tasks of *Spartina alterniflora*, providing a solution for the identification and information collection of *Spartina alterniflora* in coastal areas.

摘要

针对滨海湿地小聚集互花米草入侵监测难度大、成本高的问题，本研究提出了SA-YOLO检测模型。首先，通过采用轻量级级联注意力机制作为网络的特征提取部分，优化模型对互花米草图像特征提取能力；其次，加入改进自适应注意力机制的卷积层优化特征提取，动态调整特征图权重，降低计算量；再者，采用改进的自适应卷积网络对原有的neck层进行优化，提高模型融合互花米草图像特征的能力，降低计算量。最后，自主搭建了互花米草识别系统。该系统有效实施了提出的方法，实现了互花米草信息的检测与记录。本研究通过在实际采集的互花米草数据集上进行实验，成功验证了所提方法的有效性。测试结果表明，所提出的SA-YOLO互花米草检测模型的召回率和准确率分别为94.5%和92.4%，均达到较高水平。可见该模型能够完成互花米草的识别检测任务，为沿海地区互花米草识别与信息采集提供了一种解决方案。

INTRODUCTION

Spartina alterniflora is an important coastal wetland plant and a typical invasive alien species. It was introduced into China in 1979 (Jin et al., 2024). *Spartina alterniflora* has a well-developed root system, mainly composed of underground stems and adventitious roots, which are widely distributed in the soil. On the one hand, this gives *Spartina alterniflora* good soil fixation and growth capabilities; on the other hand, it compresses the living environment of local species, easily causing damage to the local ecosystem and reducing species diversity. In addition, *Spartina alterniflora* has strong reproductive capacity and grows rapidly. One is sexual reproduction, through the random drift of seeds, it begins to take root and grow when it encounters a suitable environment; the other is asexual reproduction through rhizome diffusion, which allows *Spartina alterniflora* to expand its population in a short period of time. The growth and reproduction characteristics of *Spartina alterniflora* increase the difficulty and uncertainty of its prevention and control, and it is difficult to grasp its growth location, time and other factors (Feng et al., 2024). As shown in Figure 1, this is the growth and distribution map of *Spartina alterniflora* in China produced by the Key Laboratory of Biodiversity and Ecological

Engineering of the Ministry of Education of Fudan University.

The growth environment of *Spartina alterniflora* is mainly in coastal wetlands, including intertidal zones of coastal mudflats such as estuaries and bays, and river beaches affected by tides (Li *et al.*, 2024). These areas are complex and difficult to access, which facilitates the random growth of *Spartina alterniflora* (Zhang *et al.*, 2024). At the same time, it is also the growth environment of reeds and other aquatic herbs. *Spartina alterniflora* is similar to reeds in appearance, but there are also significant differences between the two (Qiu *et al.*, 2022). *Spartina alterniflora* has long leaf lines and rough edges. Because of its secretion characteristics, its leaf surface often has white powdery salt frost, so it has good salt tolerance (Ma *et al.*, 2010). Only by achieving effective monitoring and management of *Spartina alterniflora* can it be beneficial to maintain the local ecological balance and protect the coastal wetland environment. The development of drone technology and the rapid update of computer vision have provided high-quality methods for monitoring. Neural network recognition can reduce the influence of subjective factors, save costs, eliminate accurate positioning, and improve the accuracy of recognition results (Qiu *et al.*, 2022).

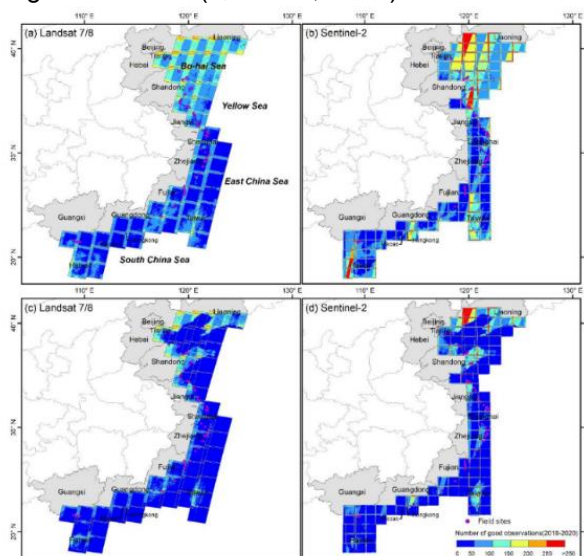


Fig. 1 – Distribution map of *Spartina alterniflora* in China

Tian *et al.* (2020) used the Zhangjiangkou National Nature Reserve in Fujian as the study area. Based on field surveys and drone aerial photography, they obtained training and validation samples of *Spartina alterniflora* for remote sensing image classification, and collected time series Sentinel-2 images of the start and end dates of the growing season in the study area from 2016 to 2018. Based on the spectral reflectance curves of different landform types in Sentinel-2 images, the vegetation index for extracting submerged *Spartina alterniflora* was established by using the characteristics of large differences in reflectance between submerged *Spartina alterniflora* pixels and pure water surface pixels in the red edge band. Then, an object-oriented random forest classification method was used to interpret *Spartina alterniflora* in the study area from 2016 to 2018. The seasonal expansion information of *Spartina alterniflora* was extracted, and the interpretation accuracy reached more than 92%. Li *et al.* (2024) conducted a hyperspectral inversion study on the functional traits of *Spartina alterniflora* in the Yancheng coastal wetland, confirming the great potential of hyperspectral technology in estimating functional traits. The accuracy and stability of the support vector machine constructed by selecting feature bands based on random forest importance score in inverting the functional traits of *Spartina alterniflora* leaves were verified. Zheng Hao *et al.*, (2023), used the Sentinel-2 NDVI dataset to obtain the vegetation phenology information of the study area in the core area of Yancheng Wetland Rare Bird National Nature Reserve, and identified the key phenological period for *Spartina alterniflora* extraction. Then, based on the multi-source and multi-temporal remote sensing data in the key phenological period, a feature set was constructed, and the landscape classification map was obtained by using five methods, ResNet18, MSRN2, CDCNN, SVM, and RF, and the accuracy was evaluated. Zhu *et al.*, (2020), combined deep learning with remote sensing data to achieve high-precision classification and dynamic monitoring of *Spartina alterniflora* in the coastal areas of Shandong Province.

Based on YOLOv8n, this study proposed an algorithm with high detection accuracy and fast detection speed, and actually deployed it on a self-built server to achieve timely monitoring and analysis of the growth of *Spartina alterniflora*, reduce the input of manpower and material resources, and provide solution experience

for the application of machine vision in the field of agricultural engineering.

MATERIALS AND METHODS

Data Acquisition and Pre-processing

The *Spartina alterniflora* dataset for this experiment was collected through web crawlers and field photography of some coastal wetlands, estuaries and river estuaries in Shandong Province. Images were collected from different angles, distances and time points. The collection equipment included mobile phones, Nikon Z30 micro-single cameras, etc. After screening and deletion, a total of 357 original images were obtained. In the actual dataset collection process, the image collection time was summer and autumn, so the dataset was divided into two categories of *Spartina alterniflora* in summer and autumn. The data set required for this experiment was enhanced by data enhancement and CutMix data processing under the Opencv library, and the original 357 images were enhanced to 1755 images by image translation, rotation, mirroring, and adjusting contrast and brightness, as shown in Figure 2.

After data enhancement, the Labellmg image annotation tool was used to annotate the images. They were divided into two major categories: summer *Spartina alterniflora* and autumn *Spartina alterniflora*, and the image annotation information file xml file was obtained, which was then converted into a txt format suitable for YOLO.

To meet the requirements for fast acquisition, processing, and recognition of *Spartina alterniflora*, this paper improves the original YOLOv8 network to achieve faster recognition and detection while improving detection speed and accuracy.

Spartina alterniflora recognition based on YOLOv8

The YOLOv8(*Github.com*) image recognition model consists of an input layer (Input), a backbone layer (Backbone), a bottleneck layer (Neck) and an output layer (Output). The image of *Spartina alterniflora* enters the Input and undergoes a batch resize operation to ensure the size consistency of the input image. The main network of SA-YOLO is used to extract features from images. The main network of the SA-YOLO model uses the cascaded attention mechanism EfficientVit (*Cai et al., 2022*) as the basic structure to complete the feature extraction of the *Spartina alterniflora* image. It mainly consists of four stages. The size of the feature map from input to output gradually decreases, forming a feature pyramid. First, the standard convolution layer performs upsampling preparation to extract the basic features of the *Spartina alterniflora* image; then, the image is subjected to deep convolution and weighted processing through a feature extraction module consisting of two MBConv modules, which helps capture the feature information of *Spartina alterniflora* in the image; finally, the image enters the two-layer EfficientVit Block module, which adopts a sandwich layout, uses MHSA (multi-head self-attention mechanism), and realizes channel information enhancement through parameter redistribution, strengthening the model's extraction of global information and local details of *Spartina alterniflora*. SPPF extracts the global feature information of *Spartina alterniflora* and performs global maximum pooling to enhance the receptive field. The feature fusion of the Neck part is enhanced, and the C2f convolution layer is optimized to DCNv4 (*Xiong et al., 2024*). This module has excellent expression and computing capabilities for complex backgrounds, and strengthens the model's feature expression and information extraction of *Spartina alterniflora* images. The SA-YOLO model structure is shown in Figure 2.

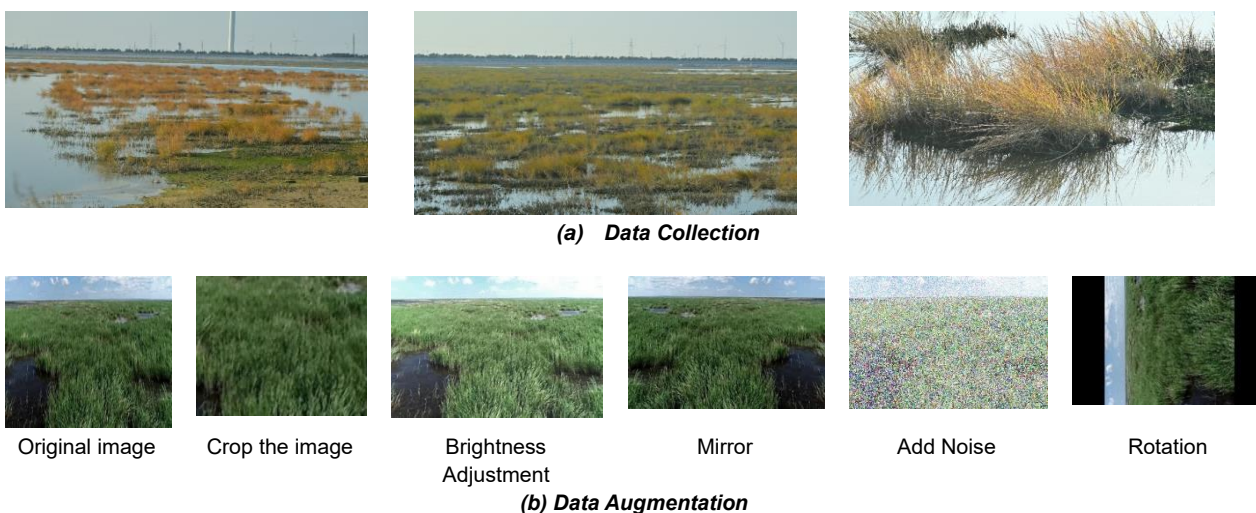


Fig. 2 - Dataset

SA-YOLO network improvement

This paper takes YOLOv8 as the basic model and proposes SA-YOLO for the growth environment and plant information elements of *Spartina alterniflora*. First, the lightweight EfficientViT network is used to replace the backbone to enhance the model's perception and feature extraction capabilities for higher-resolution images and expand the model's receptive field; when extracting features, the DCNv4 module is introduced to further reduce the model's computational workload while enhancing the model's feature fusion and expression capabilities, making the model more real-time and accurate while being lightweight. Compared with the original model, the improved SA-YOLO algorithm is not only lightweight, but also has higher computational efficiency and recognition accuracy.

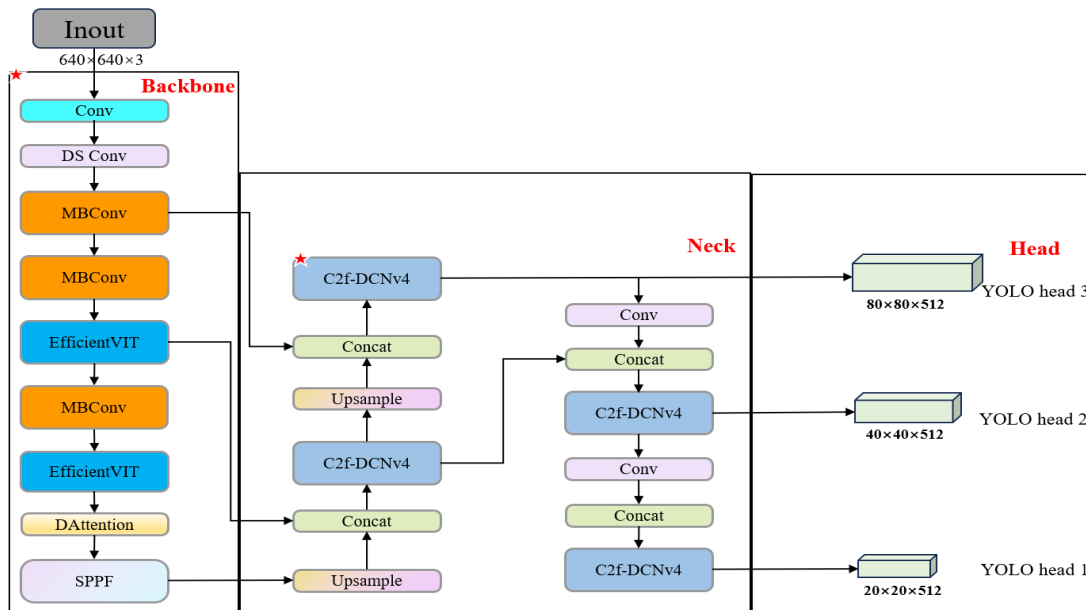


Fig. 3 -SA-YOLO Model structure

During the improvement process, the aim was to make the model have high-precision detection capability and strong feature extraction level for the input *Spartina alterniflora* images. The cascaded attention mechanism EfficientViT is introduced to replace the backbone network, so that the model has fast computing capabilities while maintaining high-precision detection. EfficientViT is a Vision transformer model for high-resolution dense prediction proposed by Cai et al., as shown in Figure 4 (a). By using ReLU linear attention to achieve global receptive field, lightweight and hardware-efficient operations can achieve the purpose of global receptive field and multi-scale learning.

EfficientViT uses EfficientViT block as the core module, as shown in Figure 4 (b), which consists of a sandwich structure (Sandwich Layout) and cascaded group attention (Cascaded Group Attention, CGA), that is, a lightweight MSA module and an MBCConv module. This basic module reduces the use of attention and alleviates the problem of memory access time consumption caused by attention calculation. At the same time, a layer of DWConv is added before each FFN as information interaction between local tokens and helps introduce inductive bias. The lightweight MSA module is mainly used to enhance the feature representation ability of the model, and plays an important role in the feature extraction and expression of *Spartina alterniflora* images in complex environments.

As shown in Figure 5, the lightweight MSA module (Rao et al., 2021) first performs multi-scale processing on the input *Spartina alterniflora* feature map to obtain feature representations of multiple scales, which cover different aspects from local details to global context information. Then, the ReLU linear attention mechanism is used to assign weights to these multi-scale features. After obtaining the weights, the lightweight MSA module applies these weights to the original multi-scale feature map for weighted fusion. Finally, the feature map processed by the lightweight MSA module will be sent to the subsequent network layer for further processing and prediction.

As shown in Figure 6, the MBCConv module (Mark et al., 2018) mainly consists of a 1x1 convolution layer (for dimensionality increase or decrease), a depthwise separable convolution, and a 1x1 pointwise

convolution. The 1x1 convolution layer in MBConv plays the role of dimensionality increase and dimensionality reduction.

As the core part of MBConv, the depthwise separable convolution applies a convolution kernel to each channel of the input feature map, and then fuses the information between channels of the output of the depthwise convolution through a 1x1 point-by-point convolution. Each convolution layer is usually followed by an activation function (ReLU6 (Mansuri et al., 2022) and a batch normalization layer. The activation function can increase the nonlinearity of the model and improve the expressiveness of the model, while batch normalization helps to accelerate the training process of the model and improve the stability of the model.

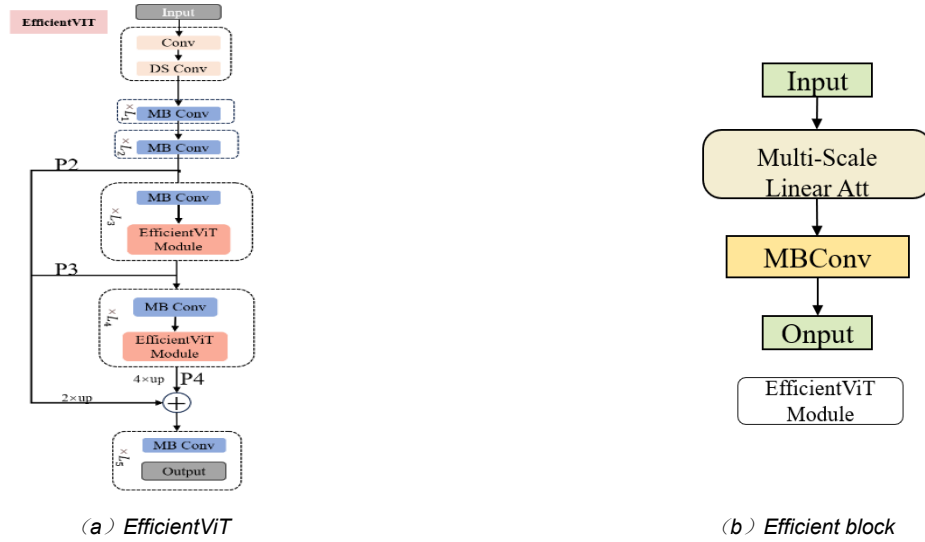


Fig. 4 - EfficientViT Model

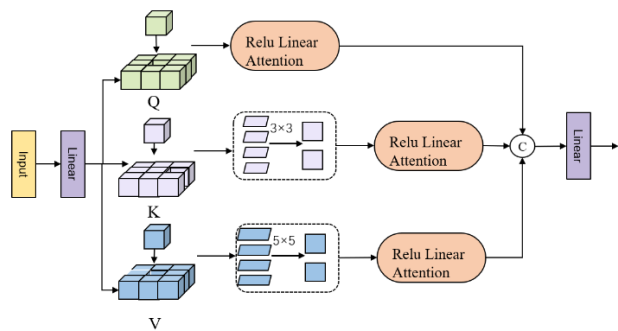


Fig. 5 -Lightweight MSA Module

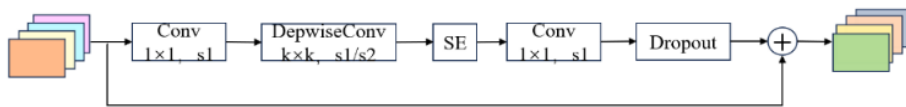


Fig. 6 - MBConv Model

C2f-DCNv4 convolution optimization

DCNv4 is a new type of deformable convolution network architecture. It adjusts the size of the convolution kernel by understanding different learnable offsets, so that the network focuses on the position and shape of *Spartina alterniflora* in the image. Compared with the previous generation, DCNv4 is optimized in two ways: when performing spatial aggregation, it no longer uses Softmax normalization processing and adopts a more flexible weight adjustment strategy; second, it adopts dynamic feature enhancement to convert the modulated scalar between 0 and 1 into an unbounded dynamic weight like convolution. The main structure of DCNv4 includes DCNv4Conv layer, batch normalization module and SiLU activation function (Jocher et al., 2021). After inputting the feature map, the channels are first grouped, where the input feature $x \in R^{(H \times W \times C)}$ (height H, width W and number of channels C), then each group is convolved to obtain the offset and weight, and finally the convolution results of all groups are spliced and output.

The output p_0 is calculated as follows:

$$y_g = \sum_{k=1}^k m_{gk} x_g(p_0 + p_k + \Delta p_{gk}) \tag{1}$$

$$y = \text{concat}([y_1, y_2, \dots, y_G]) \tag{2}$$

where: x_g and y_g represent the input features and corresponding output features of the g group respectively; m_{gk} represents the weight of the k -th sample point in the g group; p_k represents the k key node in the basic network; Δp_{gk} represents the offset relative to the basic network p_k ; concat represents the increase in the number of image feature descriptions.

The optimized structure of the C2f-DCNv4 module is shown in Figure 7. By introducing DCNv4 into C2f, the detection of *Spartina alterniflora* in complex growth environments is significantly improved, and it adapts to different changes in image sizes, thereby improving detection accuracy and robustness.

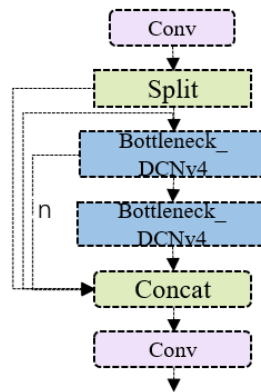


Fig. 7 - C2f_DVNV4 Model

Model deployment and hardware integration

This study conducted a field test on the proposed SA-YOLO model, and built a *Spartina alterniflora* recognition system based on the Flask framework and OpenCV to achieve real-time monitoring, target detection and statistical analysis of *Spartina alterniflora* in wetland environments.

This study tested non-dataset images collected in the field of *Spartina alterniflora*. Some of them were uploaded to the server locally after being taken by mobile phones and cameras, ensuring data security, preservation and reducing costs, and some were uploaded to the server in real time after being taken by drones. The server uses Flask as the backend framework and integrates the SA-YOLO model for target detection. During real-time uploading, in order to ensure efficient data transmission and real-time processing, data transmission supports Real Time Streaming Protocol (RTSP), which can push video streams to the server to achieve low-latency video processing and analysis.

As shown in Figure 8, the server receives the uploaded image. Subsequently, the system uses the SA-YOLO model for target detection. The processed detection results are re-encoded and pushed to the client through Flask's multipart/x-mixed-replace streaming transmission to achieve real-time monitoring and result display.

On the client side, users can view the identified video stream through a web browser and perform area annotation, target statistics, and parameter adjustments. In addition, the system provides historical data analysis and visualization functions, which can generate trend charts to analyze the growth distribution and changes of *Spartina alterniflora*, providing data support for ecological environment monitoring and governance.

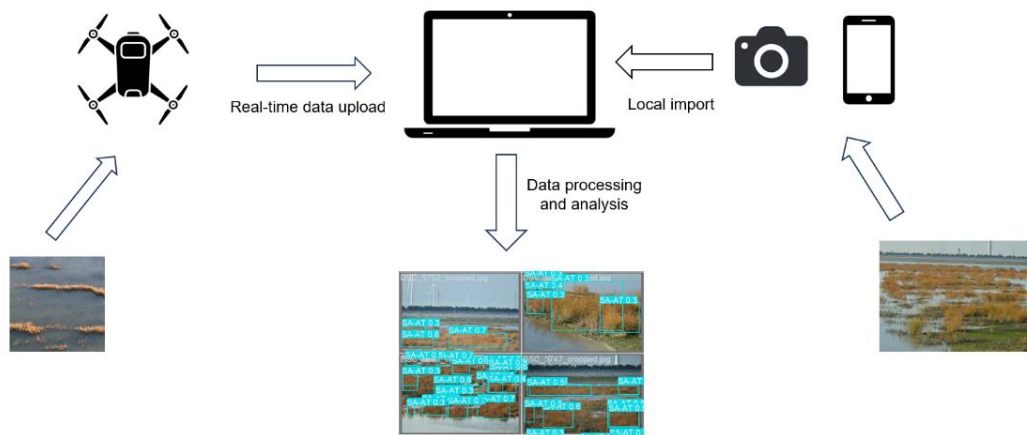


Fig. 8 - Working diagram of Spartina alterniflora identification system

RESULTS

The experiments and server deployments in this study were trained under the Windows 11 operating system. The CPU used was Intel i7-12600H, the GPU was NVIDIA RTX 3060 graphics card with 8 GB of video memory, the host memory was 16 GB, and the CUDA version was 11.8.

During the training process, according to the actual situation of the equipment, the batch size was set to 16, the number of process workers was set to 8, Adam with weight decay (AdamW) was used as the optimizer, the learning rate was set to 0.01, the momentum was set to 0.937, the weight decay coefficient was set to 0.1, and the number of training rounds was set to 300.

Model evaluation indicators

In order to fully verify the model's ability to identify and detect Spartina alterniflora, as well as the improved model's ability, precision *P* (Precision), recall *R* (Recall), and mean average precision (*mAP*) were used as indicators for evaluating the model.

The precision *P* represents the proportion of correctly predicted samples in all samples, as shown in Eq.(3):

$$P = \frac{T_P}{T_P + F_P} \times 100\% \tag{3}$$

The recall rate *R* represents the proportion of correctly predicted samples in all positive samples, as shown in formula (4):

$$R = \frac{T_P}{T_P + F_N} \times 100\% \tag{4}$$

The average precision *mAP* is the mean of the average precision (*AP*), and the average precision *AP* is the area of the *P-R* curve, as shown in formula (5):

$$mAP = \frac{\sum_{i=1}^N \int_0^1 P(R) dR}{N} \times 100\% \tag{5}$$

In the formula, *T_P* represents the number of correctly predicted positive samples, *F_P* represents the number of incorrectly predicted positive samples, *F_N* represents the number of incorrectly predicted negative samples, and *N* represents the number of categories. In this study, two categories of Spartina alterniflora are discussed, so *N*=2 at this time.

Ablation Experiment

In order to verify the model effect after replacing the backbone, the optimization degree of the model after adding the self-attention mechanism, and the effect of model feature fusion after adding deformable convolution, an ablation experiment was conducted.

Table 1

Ablation Experiment						
	EfficientVit	DAttention	C2f_DCNv4	<i>P</i> (%)	<i>R</i> (%)	<i>mAP</i> (%)
YOLOv8				89.3	87.1	90.2
1	√			90.4	89.6	92.1
2		√		88.1	86.9	90.5
3			√	89.6	88.2	91.8

4	√	√		89.7	88.6	91.7
5	√		√	91.3	90.7	92.6
6		√	√	91.5	90.8	92.2
SA-YOLO	√	√	√	92.4	94.5	93.1

Through ablation experiments, it can be seen that after replacing the backbone network, the accuracy, recall and average precision of the model in *Spartina alterniflora* recognition have all improved, indicating that the model has improved the feature extraction and receptive field of *Spartina alterniflora*. After replacing the deformable convolution, the model's detection ability has been further improved, as reflected in the accuracy and recall rates increased by 0.9% and 1.1% respectively, and the average precision value increased by 2.1%. Overall, the SA-YOLO algorithm proposed in this study is optimal.

Comparison of detection results by model

To verify the advantages of the improved model, it is compared with the original YOLOv8, YOLOv5, and YOLOv3. The performance comparison of different models is shown in Table 2.

Table 2

Model	Precision (%)	Recall (%)	mAP (%)
YOLOv8	89.3	87.1	90.2
YOLOv5	86.7	86.4	88.4
YOLOv3	85.1	85.3	87.6
SA-YOLO	92.4	94.5	93.1

As shown in Table 2, the accuracy and recall of the SA-YOLO model are both above 90%. In terms of accuracy, compared with the original YOLOv8, YOLOv5, and YOLOv3 networks, they are improved by 3.1%, 5.7%, and 7.3%, respectively. In terms of recall, SA-YOLO is 94.5%, which is improved to varying degrees compared with YOLOv8, YOLOv5, and YOLOv3, by 7.4%, 8.2%, and 9.2%, respectively. In terms of average precision, SA-YOLO is 2.9%, 4.7%, and 5.5% higher than YOLOv8, YOLOv5, and YOLOv3, respectively. From the comprehensive data, SA-YOLO has a significant improvement in the overall performance of the model, which is better than the other three models.

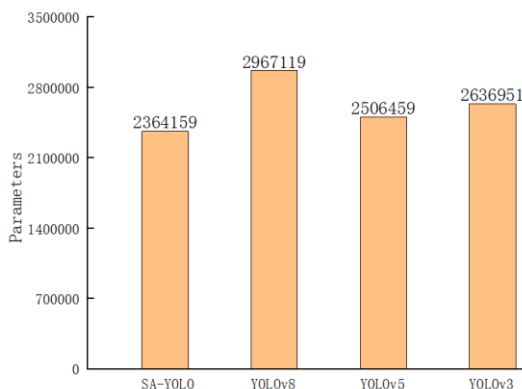


Fig. 9 - Comparison of parameters of each model

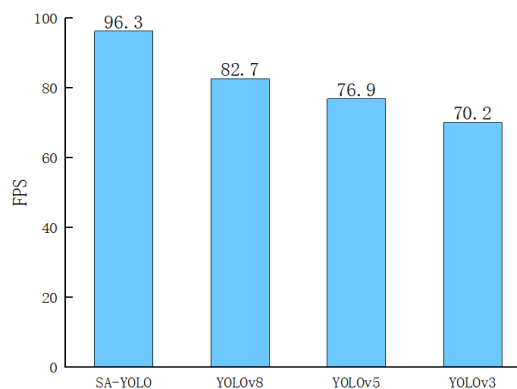


Fig. 10 – Comparison of detection speed FPS of each model

In Figures 9 and 10 the number of parameters and detection speed of different models in the process of detecting *Spartina alterniflora* is shown. Obviously, the SA-YOLO model generates fewer parameters during the detection process, but the detection speed and accuracy are far superior to other models. As shown in Figure 11, the detection results of *Spartina alterniflora* by the improved model have reached a higher level. Figure 12 shows the comparison of the recall rate and accuracy of YOLOv8 before and after the improvement.

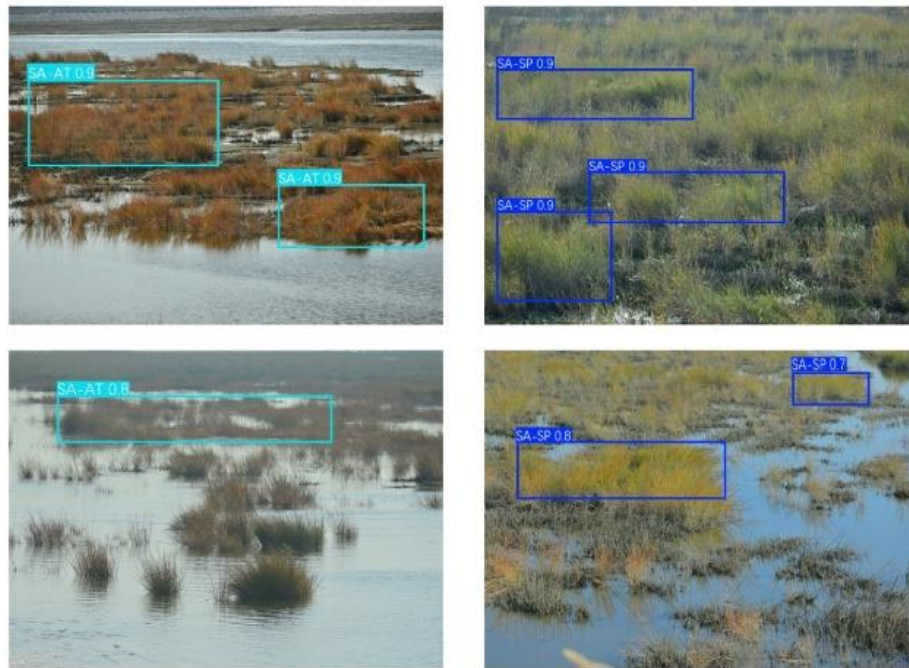


Fig. 11 –Some test results

The improved SA-YOLO model has better convergence ability and higher accuracy, which shows the effectiveness of the model improvement, especially after adding the cascaded attention mechanism and variable convolution, the model has better receptive field and recognition ability.

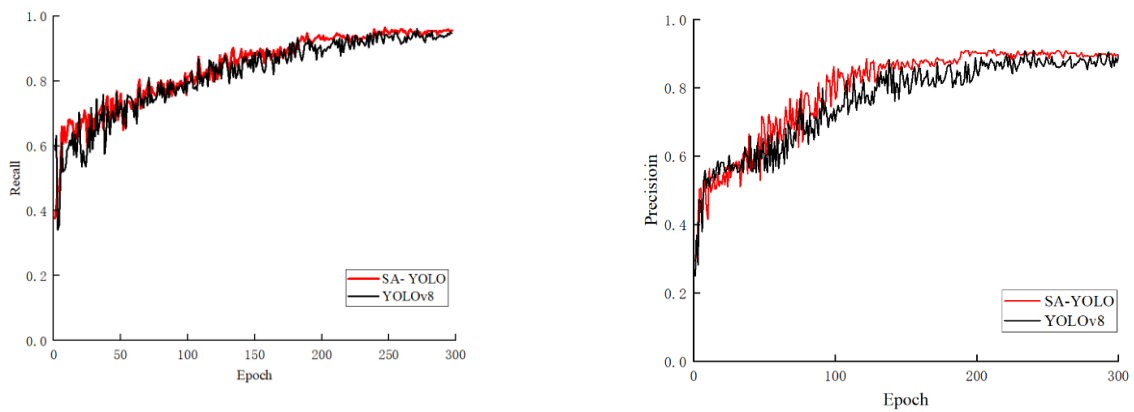


Fig. 12 – Recall and precision curve results

Comparison of the recognition and detection capabilities of each model for Spartina alterniflora in summer and autumn

As shown in Tables 3 and 4, the performance comparison of each model for the recognition of Spartina alterniflora in summer and autumn is shown.

Table 3

Detection Results of Different Models for Spartina Alterniflora in Summer			
Model	Precision (%)	Recall (%)	mAP (%)
YOLOv8	90.5	89.6	93.5
YOLOv5	87.3	88.7	90.2
YOLOv3	86.7	87.2	89.5
SA-YOLO	93.1	91.6	95.4

Table 4

Detection Results of Different Models for Spartina Alterniflora in Autumn			
Model	Precision (%)	Recall (%)	mAP (%)

YOLOv8	88.6	88.2	91.3
YOLOv5	87.5	89.1	89.3
YOLOv3	87.3	88.0	89.1
SA-YOLO	91.6	92.5	94.8

As shown in Tables 3 and 4, in the detection of data sets taken in different seasons but under the same weather conditions, the detection effects of each model for *Spartina alterniflora* in both seasons are good.

In the recognition of *Spartina alterniflora* in summer, the accuracy, recall rate and average detection precision of the SA-YOLO model are higher than those of the other three groups of models. The accuracy is 2.6%, 5.8% and 6.4% higher than YOLOv8, YOLOv5 and YOLOv3 respectively, and the recall rate is 2.0%, 2.9% and 4.4% higher respectively. The average precision is 1.9%, 5.2% and 5.9% higher respectively, which fully demonstrates that the proposed SA-YOLO model has the ability to detect *Spartina alterniflora*.

In the recognition of *Spartina alterniflora* in autumn, the expressiveness is not as good as that in summer, mainly because *Spartina alterniflora* grows more vigorously in summer, first of all, it has more characteristics in appearance, and secondly, it is also very different from the surrounding environment. In contrast, *Spartina alterniflora* in autumn is yellow in color and has sparse branches and stems, which is more integrated with the surrounding environment. However, SA-YOLO still has good recognition and detection capabilities. In terms of accuracy, it is 3.0%, 4.1%, and 4.3% higher than YOLOv8, YOLOv5, and YOLOv3, respectively. In terms of recall, it is 4.3%, 3.4%, and 4.5% higher, and in terms of average precision, it is 3.5%, 5.5%, and 5.7% higher.

System testing and effect evaluation

This study conducted multiple tests of the *Spartina alterniflora* information collection and identification system in November 2024 to verify the proposed SA-YOLO model for the *Spartina alterniflora* clusters in the coastal wetland area. As shown in Figure 13, it is an information image of *Spartina alterniflora* that was taken by a camera and uploaded locally by a computer.



Fig. 13 – Demonstration of the local upload effect of the *Spartina alterniflora* identification system

As shown in Figure 14, this study shows the effect of using drones to capture image pairs and achieve real-time uploading and processing. During the experiment, the drone and the computer were in the same Wi-Fi network to ensure the stability and real-time performance of data transmission.



Fig. 14– Real-time upload effect display of *Spartina alterniflora* identification system

CONCLUSIONS

The improved *Spartina alterniflora* detection model SA-YOLO based on YOLOv8 proposed in this study was trained and tested with a self-made dataset, which fully verified the effectiveness of the improvement. Multiple comparative tests were conducted, and the results showed that while SA-YOLO is lightweight, it has good performance in detection speed and accuracy of *Spartina alterniflora*. Its recall and accuracy reached 94.5% and 92.4%, and the mAP value of detection was 93.1%. Its comprehensive performance is higher than that of the original YOLOv8, YOLOv5, and Faster R-CNN.

In addition, this study also verified the actual deployment of the model, developed a *Spartina alterniflora* identification system, and conducted multiple field tests in stages. The results showed that both the *Spartina alterniflora* information images uploaded via the Internet and locally had good processing results and records.

Looking back at the entire research process, although the recognition and detection of *Spartina alterniflora* was achieved well, there is still room for improvement. First, the establishment of the *Spartina alterniflora* data set still needs further improvement; second, in terms of model deployment, there is a lot of room for server-side function expansion; third, you can try to combine the model with the *Spartina alterniflora* elimination machine.

This research is of great significance for the identification and detection of *Spartina alterniflora*, and is of great significance for future intelligent prevention and control of *Spartina alterniflora*, protection of the ecological environment and ecological diversity.

ACKNOWLEDGEMENT

This study was supported by the Key R&D Program of Shandong Province - Key Technology Research and Application Project for Alien Invasive Species Control (No. 2022CXGC010401).

REFERENCES

- [1] Cai H., Li J., Hu M., Gan C., Han S., MIT., Zhejiang University, Tsinghua University, MIT-IBM Watson., I Lab., (2022). EfficientViT: Lightweight multi-scale attention for on-device semantic segmentation. *arXiv preprint arXiv:2205.14756*.
- [2] Fan T, Gu J, Wang W., Zuo Y., Ji C., Hou Z., Lu B., Dong J. (2023). Lightweight honeysuckle recognition method based on improved YOLOv5s [J]. *Transactions of the Chinese Society of Agricultural Engineering*, 39(11): 192-200.
- [3] Feng H., Zhang T., Zhao H., Zhu Z., Geng Q., Yang W., Qiao Y., Zhao Y., Xia L., An S. (2024). Research progress on the impact of *Spartina alterniflora* control on coastal wetland ecosystems. *Wetland Science and Management*. (05), 2-6+12.
- [4] Jin H., Zheng M, Zhang Z., Wu H. (2024). Effects of *Spartina alterniflora* Invasion on Soil Mercury and Methylmercury in the Yellow River Delta Wetlands [J]. *Wetland Science*, (03), 376-386.
- [5] Jocher, G., Stoken, A., Borovec, J., NanoCode012., Stan Ch., Changyu, L., Laughing, T., YxNONG, Hogan, A., Lorenzomamma, AlexWang1900., Chaurasia, A., Diaconu, L., Marc., Wang H., MI5ah; Doug., Durgesh., Ingham, F., Frederik., Guilhen, Colmagro, A., Ye, H., Jacobsolawetz., Poznanski, J., Fang, J., Kim, J., Doan, K., Yu L, Lijun Y., (2021) ultralytics/yolov5: v4. 0-nn. SiLU () activations, *Weights & Biases logging, PyTorch Hub integration*. Zenodo.
- [6] Li M., Chen L., Li J., Yan D., Liu G., Wu C., Luan Z. (2024). Inversion of *Spartina alterniflora* Aboveground Biomass Based on Sentinel-2 Data [J]. *Marine Environmental Science*, (03), 386-397.
- [7] Li W., Zuo X., Liu Z., Nie L., Li H., Wang J., Dou Z., Cai Y., Zhai X., Cui L., (2024). Predictions of *Spartina alterniflora* leaf functional traits based on hyperspectral data and machine learning models. *European Journal of Remote Sensing*, 57(1), 2294951
- [8] Ma X., Lu Z., Lin T., et al. (2010) Ecological risk assessment of Yancheng coastal wetland [J]. *Marine Environmental Science*, 29(04):599-602.
- [9] Mansuri S., Gupta S.K., Singh D.P., Choudhary J. (2022). Modified DMGC algorithm using ReLU-6 with improved learning rate for complex cluster associations. In *2022 6th International Conference on Intelligent Computing and Control Systems (ICICCS)*. pp. 634-640. IEEE.
- [10] Qiu Z., Mao D., Feng K., Wang M., Xiang H., Wang Z. (2022). High-resolution mapping changes in the invasion of *Spartina Alterniflora* in the Yellow River Delta. *IEEE Journal of Selected Topics in Applied Earth Observations and Remote Sensing*, 15, 6445-6455.
- [11] Rao, R., Liu, J., Verkuil, R., Meier, J., Canny, J., Abbeel, P., Sercu T., Rives, A. (2021). MSA Transformer

- in *International Conference on Machine Learning* (PMLR).
- [12] Sandler, M., Howard, A., Zhu, M., Zhmoginov, A., Chen, L. Google Inc., (2018). Mobilenetv2: Inverted residuals and linear bottlenecks. In *Proceedings of the IEEE conference on computer vision and pattern recognition*, pp. 4510-4520.
- [13] Tian, Y., Jia, M., Wang, Z., Mao, D., Du, B., Wang, C. (2020). Monitoring invasion process of *Spartina alterniflora* by seasonal Sentinel-2 imagery and an object-based random forest classification. *Remote Sensing*, 12(9), 1383.
- [14] Wang C., Wang Y., Shang S., Zhang N. (2024). Research on chicken basic behavior recognition method based on YOLOv5x [J]. *Agricultural Equipment and Vehicle Engineering*, 62(04): 1-5.
- [15] Xiong, Y., Li, Z., Chen, Y., Wang, F., Zhu, X., Luo, J., Dai, J. (2024). Efficient deformable convnets: Rethinking dynamic and sparse operator for vision applications. In *Proceedings of the IEEE/CVF Conference on Computer Vision and Pattern Recognition*, pp. 5652-5661.
- [16] Zhang N., Mao D., Feng K., Zhen J., Xiang H., Ren Y. (2024) Classification of plant communities in the Yellow River Delta wetland based on GEE and multi-source remote sensing data. *Remote Sensing of Natural Resources*, 1-9.
- [17] Zheng H. (2023) *Remote sensing classification of the alien plant Spartina alterniflora based on deep learning* [D]. North China University of Technology.
- [18] Zhang, M., Schwarz, C., Lin, W., Naing, H., Cai, H., Zhu, Z. (2023). A new perspective on the impacts of *Spartina alterniflora* invasion on Chinese wetlands in the context of climate change: A case study of the Jiuduansha Shoals, Yangtze Estuary. *Science of the Total Environment*, 868, 161477.
- [19] Zhu Y. (2020) *Remote sensing monitoring and analysis of the alien invasive species Spartina alterniflora in Shandong Province based on deep learning classification method* [D]. First Institute of Oceanography, Ministry of Natural Resources.
- [20] ***Ultralytics/ultralytics: NEW - YOLOv8 in PyTorch > ONNX > OpenVINO > CoreML > TFLite (Github.com)

DETECTION AND COUNTING OF GRAZING CATTLE FROM AERIAL IMAGES USING CNN

CNN АШИГЛАН АГААРЫН ЗУРГААС БЭЛЧЭЭРИЙН МАЛЫГ ИЛРҮҮЛЭХ, ТООЛОХ

Hu GEJILETU¹⁾, Hishigdalai ULAANKHUU²⁾, Bat-Erdene NYANDAG^{3*)}

^{1,3)} Department of Computer Science, School of Applied Sciences, Mongolian University of Life Sciences, 17024, Ulaanbaatar, Mongolia

²⁾ School of Business, Mongolian University of the Humanities, 14200-0031 Ulaanbaatar, Mongolia

*Corresponding author, Email: baterdene@mul.s.edu.mn

DOI: <https://doi.org/10.35633/inmateh-75-39>

Keywords: deep learning, drone, object detection, yolov8

ABSTRACT

This study explores the use of deep neural networks for detecting and quantifying the cattle population in Mongolia using drone imagery, addressing the limitations of traditional methods that are labor-intensive and time-consuming. A custom dataset of aerial images featuring grazing cattle in Mongolia was developed, focusing on winter and spring seasons, to train and validate a model based on state-of-the-art object detection algorithms. Specifically, the You Only Look Once (YOLOv8) architecture was employed to detect cattle across diverse environmental conditions. Model performance was evaluated using widely accepted metrics, including precision, recall, F1 score, and the mean average precision (mAP). The findings demonstrate the effectiveness of the proposed approach, with the YOLOv8 model achieving a mAP of 97.3% at an IoU threshold of 0.5, highlighting its potential for efficient cattle detection and monitoring in Mongolia's unique environmental contexts.

ХУРААНГУЙ

Энэхүү судалгаа нь дроны зураг ашиглан Монгол дахь үхрийн тоо толгойг илрүүлэх, тоо хэмжээг тогтооход гүн мэдрэлийн сүлжээг ашигласан. Энэхүү ажил нь хөдөлмөр, цаг хугацаа их шаарддаг уламжлалт аргуудаас татгалзах боломжийг судалсан. Хамгийн сүүлийн үеийн объект илрүүлэх алгоритмд суурилсан загварыг сургаж, турших зорилгоор өвөл, хаврын улиралд анхаарлаа хандуулж, Монголын бэлчээрийн үхрийг харуулсан агаарын зургийн зорилтод өгөгдлийн багцыг боловсруулсан. Үүндээ YOLOv8 архитектурыг байгаль орчны янз бүрийн нөхцөлд үхэр илрүүлэхэд ашигласан. Загварын гүйцэтгэлийг нарийвчлал, санах ой, F1 оноо, дундаж нарийвчлал (mAP) зэрэг нийтээр хүлээн зөвшөөрөгдсөн хэмжигдэхүүнүүдийг ашиглан үнэлэв. Судалгааны үр дүн нь санал болгож буй аргын үр дүнг харуулж байгаа бөгөөд YOLOv8 загвар нь IoU-ийн босго 0.5-д 97.3%-ийн mAP-д хүрсэн нь Монгол орны байгаль орчны өвөрмөц нөхцөлд үхрийг үр дүнтэй илрүүлэх, хянах, тоолох боломжийг харуулсан.

INTRODUCTION

According to the preliminary results of the annual livestock census, by the end of 2023, Mongolia had 64.7 million head of livestock, including 5.4 million cattle (*National Statistics Office of Mongolia*). In the traditional setting, cattle farming typically occurs in a natural environment in Mongolia, where challenges like accidental drownings in rivers, snowbound or landslides may cause substantial damage and create serious challenges for cattle management (*Xu et al., 2020*). Consequently, monitoring cattle in Mongolia, including their behaviors and health, has emerged as a critical research area. The rapid progress in deep learning, particularly in methods involving convolutional neural networks (CNNs), offers effective solutions for detecting and classifying animals (*Radovic et al., 2017*).

Spanning the years 1980 to 2023 across all continents, a notable 71.4% of studies have been published since 2019, reflecting an increased focus on livestock detection in recent years (*Ocholla et al., 2024*). Furthermore, 69.2% of the studies relied on drones for detection and counting purposes, with alternative methods such as manned aircraft, satellites, and camera traps being used less frequently (*Ocholla et al., 2024*). The increasing popularity of drones is a result of innovations in embedded systems and electronic communication, which have reduced costs and enhanced their availability (*Olson and Anderson, 2021*).

Fig. 1 presents the distribution of studies on livestock detection and counting analyzed across various countries (*Ocholla et al., 2024*).

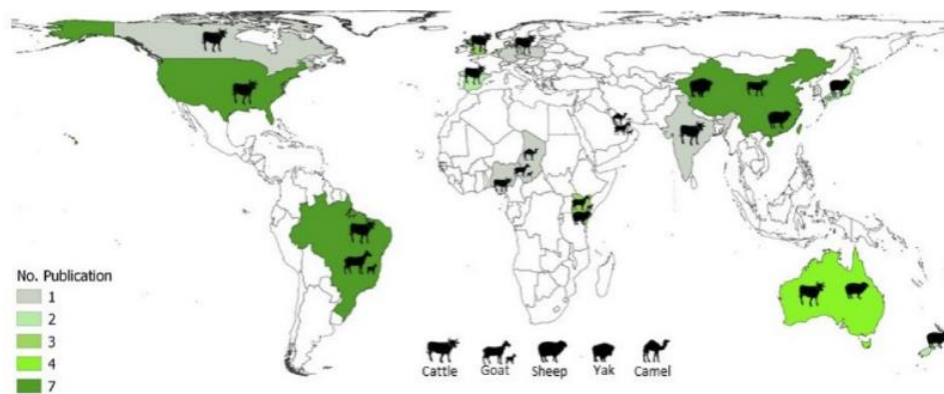


Fig. 1 - Country-wise distribution of studies on livestock detection and counting

Our research aims to leverage a cutting-edge object detection framework, specifically the YOLOv8 algorithm (Redmon *et al.*, 2016), to accurately detect and count grazing cattle in Mongolian grasslands using aerial images captured by drones.

Animal monitoring using remote technologies

Innovations in remote monitoring technologies have significantly improved data collection on animal behavior, enabling farmers to enhance meat quality, boost production efficiency, and ensure better health for livestock (Xu *et al.*, 2020). Farmers are employing wearable technologies, including RFID, GPS collars (Derek *et al.*, 2018), and smart ear tags (Kumar *et al.*, 2016), to track movement, behavior patterns, heart rate, body temperature, and other physiological indicators. These technologies play a crucial role in preventing illnesses and deaths among animals, thereby minimizing production losses (Xu *et al.*, 2020).

Motion-sensor cameras, commonly referred to as camera traps, offer a cost-effective method for recording animals' presence, locations, and activities (Verma and Gupta, 2018). These technologies collectively contribute to a more efficient and sustainable approach to animal monitoring and management in agricultural settings.

One significant drawback of existing ground-based techniques, such as smart ear tags and motion-sense cameras, is their constraint within large geographic areas and complex terrains, making it challenging to identify and track animals effectively (Gonzalez *et al.*, 2016). Combining drone technology with advanced machine learning models offers a promising approach to improving the management of livestock. Compared to traditional methods, drones demonstrate several unique advantages (Windrim *et al.*, 2019):

1. They are capable of operating at both low and extremely low altitudes.
2. They can acquire detailed, high-quality images even under varying weather conditions.
3. They can rapidly capture imagery across vast areas and challenging terrains that are otherwise difficult to access.

However, accurately and reliably counting animals in drone-captured imagery remains a crucial yet challenging task in intelligent livestock management (Wang *et al.*, 2021). The primary aim of this research is to explore deep learning approaches for the detection and quantification of animals, focusing on the automated analysis of cattle populations in drone-based images. Additionally, it highlights the potential of drone vision and object detection techniques to improve livestock management practices.

Drone-based animal detection and counting

CNNs (Lecun *et al.*, 2015) have proven to be an effective and reliable method for detection and counting tasks in image recognition, owing to its processing speed and accuracy. In recent years, advanced deep learning models such as Faster R-CNN (Ren *et al.*, 2015), Mask R-CNN (He *et al.*, 2017), and YOLO (Redmon *et al.*, 2016) have shown great promise in detecting and classifying objects across vast datasets, achieving higher accuracy, precision, and faster processing speeds.

Although these results are impressive, livestock monitoring still faces challenges in diverse and complex scenarios, including visual clutter (e.g., vegetation), strong lighting contrasts and shadows from farm structures, low target resolution, and high animal densities (e.g., tightly packed herds or feedlots) (Xu *et al.*, 2020). Therefore, a thorough evaluation of cattle-counting algorithms across various livestock farming environments in Mongolia is essential.

Deep learning algorithms for object detection are predominantly built on CNNs. These networks excel in image processing due to their capacity to extract hierarchical features directly from pixel-level data. These algorithms are specifically designed to identify and locate objects within images or videos (Lecun et al., 2015). Deep learning-based object detection methods can be classified into two categories: Two-Stage Detectors and One-Stage Detectors.

Two-Stage Detectors operate by initially generating potential regions of interest (Rois) within an image using techniques such as selective search or region proposal networks (RPNs). In the subsequent step, these Rois are classified, and their bounding boxes are adjusted for precision. Prominent examples of this category include R-CNN (Region-based Convolutional Neural Networks) (Girshick et al., 2014), Faster R-CNN (Ren et al., 2015), and Mask R-CNN (He et al., 2017). In contrast, One-Stage Detectors eliminate the need for a separate region proposal stage and directly predict bounding boxes along with class probabilities. Notable examples of this approach include YOLO (You Only Look Once) (Redmon et al., 2016) and SSD (Single Shot Multibox Detector) (Liu et al., 2016).

R-CNN and its variants, such as Faster R-CNN, are two-stage object detection frameworks known for their accuracy and detailed object localization but are slower and more computationally demanding. In contrast, YOLO is a single-stage algorithm optimized for real-time performance, making it ideal for applications requiring fast and efficient object detection, such as drone-based monitoring or video analysis (Xu et al., 2020).

Recent advancements in object detection methods have significantly enhanced the accuracy of monitoring livestock in pastures and open areas using drone-captured data.

The research done by João Vitor de Andrade Porto et al., (2021), highlights the application of Faster R-CNN for counting cattle in feedlots through aerial imagery, reporting an average precision of 89.7%.

Based on YOLOX, detection performance for counting cattle was improved through input resolution optimization, reaching a precision of 95.7% (Wang et al., 2023).

Mask R-CNN was applied to extract features and trained on drone-based imagery, achieving a classification accuracy of 96% for livestock (Xu et al., 2020).

Among the approaches discussed in the literature, YOLO stands out as a particularly promising method for cattle monitoring in real-time drone scenarios. The newer iteration, YOLOv8 (<https://ultralytics.com>), demonstrates significant improvements in speed, accuracy, and efficiency, making it a suitable benchmark for this study. This research aims to evaluate the feasibility and effectiveness of using YOLOv8 to detect and quantify cattle populations in diverse environmental conditions. The objectives of the study are as follows:

1. Apply the YOLOv8 model, pre-trained on the MS COCO dataset, to detect cattle in drone-captured images across various seasons.
2. Collect drone imagery of cattle during the winter and spring seasons to develop a custom dataset.
3. Train a custom YOLOv8 model using the collected dataset and evaluate its performance using standard metrics such as mAP, precision, recall, and F1 score.
4. Analyze cattle detection results across different seasons using the pre-trained and custom-trained models to validate the correctness and effectiveness of this research.
5. Offer insights into the applicability of deep learning object detection techniques for livestock monitoring and propose directions for future research in this domain.

Object detection techniques

Object detection is essential for this task, as it identifies and categorizes objects of interest by enclosing them within bounding boxes. The process typically involves two or three stages: generating bounding boxes to identify regions of interest, extracting features from these regions, and classifying objects to determine their categories. This study focuses on detecting a single class: cattle. In addition to detection, accurate localization of animals within images is crucial for effective counting and monitoring of livestock behavior.

Modern object detection models typically comprise two primary components: a backbone for feature extraction and a head for object classification and localization. The backbone processes input images and generates a feature map that supports the remaining network operations. The choice of backbone (e.g., VGG (Simonyan and Zisserman, 2015), ResNet (He et al., 2016), DenseNet (Huang et al., 2017), EfficientNet (Tan and Le, 2019)) depends on the detector's operating platform (CPU or GPU).

Object detection methods can be broadly categorized into two approaches: the two-stage approach, which employs region proposal algorithms, and the one-stage approach, which directly combines detection and classification tasks into a single step for real-time processing. This study focuses on the one-stage method



Fig. 4 - Drone-captured image of cattle in winter



Fig. 5 - Drone-captured image of cattle in spring

Many flight activities were conducted using the Potensic drone (www.potensic.com/atom.html), equipped with an integrated Sony camera, as shown in Fig. 6. The camera features a 1/2.3-inch CMOS image sensor capable of lateral and vertical rotation. It captures 4K videos and 12-megapixel photos with stabilization. Considering factors such as pixel resolution, photo capture delay, and operational convenience, videos were selected to create datasets of cattle in diverse scenes. The videos were recorded at 30 frames per second and saved in MOV format.



Fig. 6 - Image of the Potensic drone used for data collection

The drone performed 360-degree rotations above the cattle herd at altitudes ranging from 15 to 35 meters, capturing their posture from multiple angles. This approach significantly improved the accuracy of deep learning-based detection. Videos of varying lengths, up to 30 minutes, were recorded by the drone. However, as the YOLO training model requires image files, the OpenCV library was utilized in this study to extract frames from the videos. The most effective images for training were then carefully selected.

The winter dataset comprises 100 images containing a total of 1,563 cattle, with 70 images (1,376 cattle) allocated for training and 30 images (187 cattle) for testing. The spring dataset consists of 138 training images with 1,359 cattle, 17 testing images with 172 cattle, and 18 validation images containing 180 cattle. To ensure accurate labeling of ground truth data, the widely recognized image annotation and analysis platform Roboflow was utilized.

Our research is planned to continue over several years, with the aim of creating and sharing a benchmark drone-captured dataset of Mongolian livestock across all four seasons for scholarly purposes.

The Algorithm for detection and counting cattle

YOLOv8, developed by Ultralytics (<https://ultralytics.com>), is the newer version of the widely recognized model for real-time object detection and image segmentation. Leveraging advancements in deep learning and computer vision, YOLOv8 achieves exceptional performance in both speed and accuracy. Its optimized architecture enhances adaptability, enabling deployment across diverse applications and ensuring compatibility with a range of hardware environments, including edge devices and cloud-based systems.

YOLOv8 incorporates several key features that contribute to its high performance:

1. Mosaic Data Augmentation: This training technique merges four images into a single composite image, enabling the model to learn from varied object placements and contexts.
2. Anchor-Free Detection: This approach eliminates reliance on predefined anchor boxes by directly predicting object centers and bounding box dimensions, enabling more accurate and efficient object localization.
3. C2f Module: The C2f module enhances feature extraction by combining convolutional layers with feature fusion, thereby improving the model's accuracy in object detection.
4. Decoupled Head: YOLOv8 incorporates a decoupled head design that separates classification and localization tasks, enhancing both the model's efficiency and accuracy.

5. Loss Function: The model employs a modified loss function to optimize the training process and enhance object detection performance.

These features collectively enhance YOLOv8's advanced performance in fast and accurate object detection and image segmentation.

The implementation details

The YOLOv8 model was set up in a Python environment and initialized with a pre-trained model from the MS COCO dataset. Following the organization, formatting, and annotation of the collected cattle data, the model was trained on this dataset. The trained model was then tested and evaluated to measure its performance.

The training process was conducted on a 64-bit Windows 11 system equipped with an Intel Core i7-13620U CPU running at 2.4 GHz, 16 GB of RAM, and an NVIDIA RTX4050 GPU with 6 GB of dedicated memory.

To evaluate the performance of the proposed approach, precision, average precision (AP), and recall were utilized as evaluation metrics. Precision quantifies the ratio of true positive predictions to the total number of positive predictions (Equation 1), while recall measures the proportion of true positives relative to all actual positive instances (Equation 2). The precision-recall curve provides a comprehensive evaluation of the model's performance by analyzing the area under the curve across different IoU thresholds. Average precision, as defined in Equation 3, summarizes the precision-recall trade-off. IoU (Intersection over Union) quantifies the overlap between the predicted and ground-truth bounding boxes, expressed as the ratio of their intersection to their union, as specified in Equation 4.

$$P = \frac{\text{True Positives}}{\text{True Positives} + \text{False Positives}} \tag{1}$$

$$R = \frac{\text{True Positives}}{\text{True Positives} + \text{False Negatives}} \tag{2}$$

$$AP = \sum_{n=1}^N [R(n) - R(n - 1)] \times \max P(n) \tag{3}$$

where:

- N - the number of Precision-Recall (PR) points calculated;
- R(n) - the recall value at the n th point;
- P(n) - the precision value at the n th point.

$$IoU = \frac{A \cap B}{A \cup B} \tag{4}$$

RESULTS and DISCUSSIONS

The pre-trained Ultralytics YOLOv8 model is derived from the Microsoft COCO dataset, which predominantly features ground-level imagery. However, this model demonstrates limited suitability for detecting and counting objects in aerial images. An initial evaluation of the COCO-based pre-trained YOLOv8 model revealed inaccuracies, including misclassifications of cattle as birds in aerial imagery. As depicted in Fig. 8, these inaccuracies encompassed additional detections of shadows, missed cattle, and erroneous bird predictions, as further illustrated in Fig. 7.

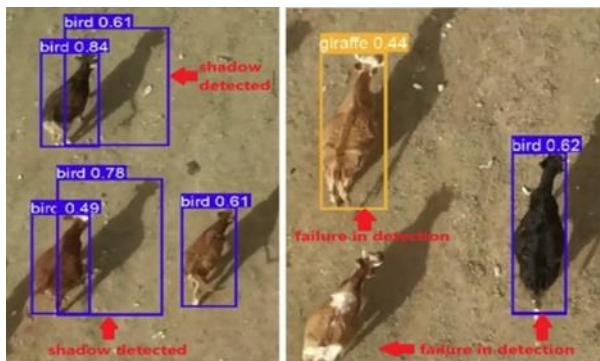


Fig. 7 - Examples of shadow and failure detections

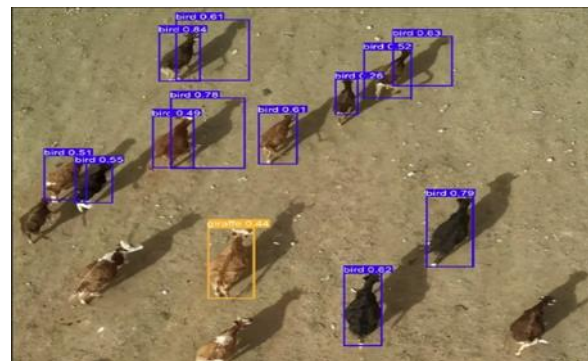


Fig. 8 - Predictions from the model pre-trained on the MS COCO dataset

The cattle detection model was trained on a custom-labeled dataset, resulting in high prediction accuracy. As demonstrated in Fig. 9, the custom-trained model accurately detected all cattle in the image with high confidence scores and no false positives, such as misclassifications involving shadows.

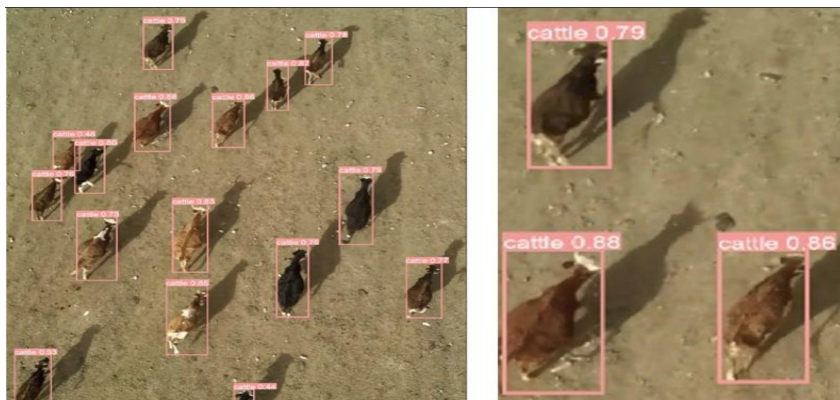


Fig. 9 - Prediction from the trained model with high confidence scores

Despite the blurriness of the images captured during winter, the trained model successfully detected cattle with high accuracy, as illustrated in Fig. 10.



Fig. 10 – Winter cattle detection results using the trained model

Comprehensively capturing a wide range of grazing cattle postures in natural environments is essential for deep learning-based object detection. In this study, low-altitude drones were employed to record 360-degree videos of cattle from multiple angles, ensuring the collection of diverse postural data. This approach was critical in achieving high model accuracy and reliable validation metrics. Unlike horses, which exhibit greater posture variability, cattle tend to graze in a more dispersed manner and display fewer postural variations due to their shorter necks, shorter legs, and robust bodies. These traits contributed to a more streamlined process for annotation, training, and validation in this research.

Accurate and comprehensive labeling of the full body of each cattle in the images, in addition to capturing diverse postures, is crucial for achieving effective object detection. This meticulous annotation process substantially contributes to improving the model's detection accuracy.

The performance of the trained model was assessed using evaluation metrics including mAP, precision, recall, and the F1 score. A comprehensive analysis of the results is presented in the following section.

1. Fig. 11 illustrates the Precision-Confidence Curve for the trained model. The plot indicates that the model achieves high accuracy beginning at a relatively low confidence threshold of 0.2 (20%), with precision generally improving as the confidence threshold increases. Precision attains its maximum value of 1.00 (100%) at a confidence threshold of 0.74 (74.0%), indicating a minimal occurrence of false positives at this level.

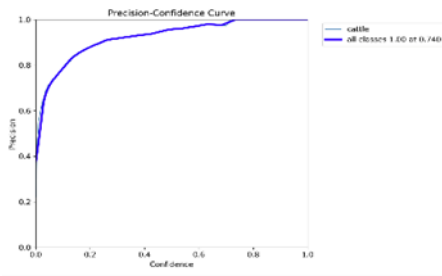


Fig. 11 - Precision-Confidence

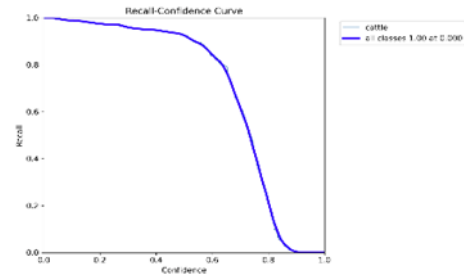


Fig. 12 - Recall-Confidence

- Fig. 12 presents the Recall-Confidence Curve for the trained model, highlighting its robust capability. Notably, the model achieves and sustains high recall levels at a confidence threshold of 0.7 (70%).
- Fig. 13 depicts the Precision-Recall Curve for the trained model. The metric 'All classes 0.973 mAP@0.5' indicates that the model achieves a mAP of 97.3% across all classes at an IoU threshold of 0.5 (50%), reflecting its overall detection performance.

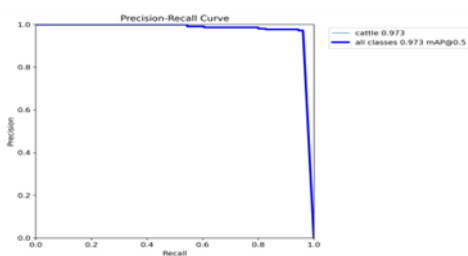


Fig. 13 - Precision-Recall

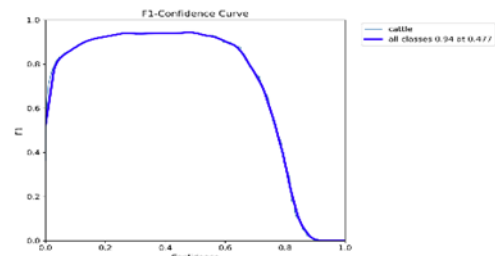


Fig. 14 - F1-Confidence

- Fig. 14 presents the F1-Confidence Curve for the trained model, highlighting its performance. An F1 score of 0.94 (94%) is achieved at a confidence threshold of 0.477 (47.7%), reflecting a well-balanced trade-off between precision and recall.

Upon completing the training phase, the YOLO validation function was employed to evaluate the model's performance. This validation process was conducted using 180 pre-annotated instances of cattle from 18 images in the dataset's validation set. The corresponding results are summarized in Table 1 below:

Table 1

Evaluation metrics of the trained model during validation

Class	Images [Number]	Instances [Number]	Precision [%]	Recall [%]	mAP@0.5 [%]	mAP@0.5:0.95 [%]
cattle	18	180	97.2%	96.1%	97.3%	59.9%

These metrics indicate excellent model performance, highlighted by high precision, recall, and an impressive mAP@0.5 score. The findings validate the model's effectiveness in accurately detecting and counting cattle in aerial images.

The confusion matrix for the single-class object detection model is depicted in the following figures. Fig. 15 presents the standard confusion matrix, while Fig. 16 illustrates the normalized version.

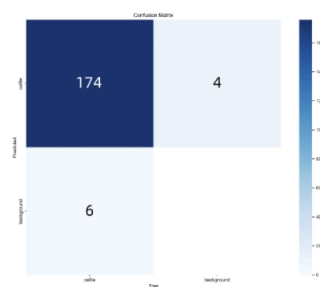


Fig. 15 - Standard confusion matrix



Fig. 16 - Normalized confusion matrix

CONCLUSIONS

The trained model achieved high performance metrics, validating the effectiveness of the proposed research methods and approach. This study demonstrates the feasibility of utilizing YOLOv8 for cattle detection and counting under diverse environmental conditions, contributing to advancements in livestock monitoring in Mongolia. Specifically, for counting large herds of livestock, this research provides robust evidence supporting a novel method that leverages deep learning-based object detection for high-precision identification in drone-captured images and accurate total counting.

Model predictions in this study indicate that the MS COCO-based model effectively learned the features of well-fed cattle during the summer but struggled to detect leaner Mongolian cattle in winter and spring. In contrast, the custom-trained model achieved high accuracy in identifying cattle across these seasons. This finding highlights the ability of deep learning approaches to capture significant feature variations associated with seasonal changes in cattle. Additionally, it underscores the potential of computer vision and deep learning to analyze the distinct characteristics of livestock under varying environmental conditions, offering valuable insights and methodologies to advance livestock research in Mongolia.

Mongolia's distinct four seasons-characterized by snow-covered winters, golden autumns, and lush green summers-combined with its varied terrain of rolling grasslands, alpine forests, and hills, pose unique challenges for cattle detection. Currently, the dataset comprises images collected and labeled during the winter and spring seasons. Over the next year, the dataset will be expanded through the collection of drone imagery capturing diverse cattle populations across all seasons and terrains in Mongolia. This initiative aims to develop a comprehensive aerial dataset of Mongolian cattle, facilitating the training of a high-accuracy detection and counting model optimized for diverse environmental conditions and landscapes throughout the country.

REFERENCES

- [1] Bailey, D., Trotter, M., Knight, C., Thomas, M. (2018). Use of GPS tracking collars and accelerometers for rangeland livestock production research. *Translational Animal Science*, Vol. 2, pp. 81–88, Oxford University Press US, <https://doi.org/10.1093/tas/txx006>.
- [2] Girshick, R., Donahue, J., Darrell, T., & Malik, J. (2014). Rich Feature Hierarchies for Accurate Object Detection and Semantic Segmentation. *In Proceedings of the IEEE conference on computer vision and pattern recognition*, pp. 580-587, CA/USA, <https://doi.org/10.1109/CVPR.2014.81>.
- [3] Gonzalez, L.F., Montes, G.A., Puig, E., Johnson, S., Mengersen, K., Gaston, K.J. (2016). Unmanned Aerial Vehicles (UAVs) and Artificial Intelligence Revolutionizing Wildlife Monitoring and Conservation. *Sensors*, Vol. 16 (1), pp. 97, <https://doi.org/10.3390/s16010097>.
- [4] He, K., Zhang, X., Ren, S., Sun, J., (2016). Deep residual learning for image recognition. *In Proceedings of the IEEE Computer Society Conference on Computer Vision and Pattern Recognition*, pp. 770–778, CA/USA.
- [5] He, K., Gkioxari, G., Dollár, P., & Girshick, R. (2017). Mask R-CNN. *In Proceedings of the IEEE International Conference on Computer Vision*, pp. 2961–2969, CA/USA.
- [6] Huang, G., Liu, Z., Van Der Maaten, L., & Weinberger, K. Q. (2017). Densely connected convolutional networks. *In Proceedings of the IEEE conference on computer vision and pattern recognition*, pp. 4700-4708, CA/USA.
- [7] João Vitor de Andrade Porto., Fábio Prestes Cesar Rezende., Gilberto Astolfi., Vanessa Aparecida de Moraes Weber., Marcio Carneiro Brito Pache., Hemerson Pistori. (2021). Automatic counting of cattle with Faster R-CNN on UAV images. *In Workshop de Visão Computacional (WVC)*, pp. 1-6, SBC, Português/Brasil, <https://doi.org/10.5753/wvc.2021.18880>.
- [8] Kumar, S., and S. K. Singh. (2018). Monitoring of pet animal in smart cities using animal biometrics. *Future Generation Computer Systems*, Vol. 83, pp. 553-563, doi.org/10.1016/j.future.2016.12.006.
- [9] LeCun, Y., Bengio, Y., & Hinton, G. (2015). Deep learning. *Nature*, Vol. 521, pp. 436–444, <https://doi.org/10.1038/nature14539>.
- [10] Liu, W., Anguelov, D., Erhan, D., Szegedy, C., Reed, S., Fu, C. Y., & Berg, A. C. (2016). SSD: Single shot multibox detector. *In Computer Vision–ECCV 2016: 14th European Conference*, pp. 21-37, Springer International Publishing.

- [11] Olson, D., & Anderson, J. (2021). Review on unmanned aerial vehicles, remote sensors, imagery processing, and their applications in agriculture. *Agronomy Journal*, Vol. 113, pp. 971-992, <https://doi.org/10.1002/agj2.20595>.
- [12] Ocholla, I. A., Pellikka, P., Karanja, F. N., Vuorinne, I., Odipo, V., & Heiskanen, J. (2024). Livestock detection in African rangelands: Potential of high-resolution remote sensing data. *Remote Sensing Applications: Society and Environment*, Vol. 33, 101139, <https://doi.org/10.1016/j.rsase.2024.101139>.
- [13] Ren, S., He, K., Girshick, R., & Sun, J. (2015). Faster RCNN: Towards real-time object detection with region proposal networks. *Advances in neural information processing systems*, Vol. 28, MA/USA.
- [14] Redmon, J., Divvala, S., Girshick, R., & Farhadi, A. (2016). You only look once: Unified, real-time object detection. In *Proceedings of the IEEE Conference on Computer Vision and Pattern Recognition*, pp. 779–788, CA/USA.
- [15] Radovic, M., Adarkwa, O., & Wang, Q. (2017). Object recognition in aerial images using convolutional neural networks. *Journal of Imaging*, Vol. 3, pp. 21. <https://doi.org/10.3390/jimaging3020021>.
- [16] Simonyan, K., Zisserman, A. (2015). Very deep convolutional networks for large-scale image recognition. *arXiv preprint*, arXiv:1409.1556, <https://doi.org/10.48550/arXiv.1409.1556>.
- [17] Tan, M., & Le, Q. (2019). Efficientnet: Rethinking model scaling for convolutional neural networks. In *International conference on machine learning*, pp. 6105-6114, PMLR.
- [18] Tsung-Yi Lin., Michael Maire., Serge Belongie., James Hays., Pietro Perona., Deva Ramanan., Piotr Dollár & C. Lawrence Zitnick. (2014). Microsoft coco: Common objects in context. In *Computer vision–ECCV 2014: 13th European conference*, Zurich, Switzerland, pp. 740-755, Springer International Publishing.
- [19] Verma, G. K., & Gupta, P. (2018). Wild Animal Detection Using Deep Convolutional Neural Network. In *Proceedings of 2nd International Conference on Computer Vision & Image Processing*, Vol. 2, pp. 327-338, Springer Singapore.
- [20] Windrim, L., Bryson, M., McLean, M., Randle, J., & Stone, C. (2019). Automated Mapping of Woody Debris over Harvested Forest Plantations Using UAVs, High-Resolution Imagery, and Machine Learning. *Remote Sensing*, Vol. 11, pp. 733, <https://doi.org/10.3390/rs11060733>.
- [21] Wang, D. L., Liao, X. H., Zhang, Y. J., Cong, N., Ye, H. P., Shao, Q. Q., & Xin, X. P. (2021). Real-time detection and weight estimation of grassland livestock based on unmanned aircraft system video streams. *Chinese Journal of Ecology*, Vol. 40, pp. 4099, <https://doi.org/10.13292/j.1000-4890.202111.008>.
- [22] Wang, Y., Ma, L., Wang, Q., Wang, N., Wang, D., Wang, X., Zheng, Q., Hou, X., Ouyang, G. (2023). A lightweight and high-accuracy deep learning method for grassland grazing livestock detection using UAV imagery. *Remote sensing*, Vol. 15, pp. 1593, <https://doi.org/10.3390/rs15061593>.
- [23] Xu, B., Wang, W., Falzon, G., Kwan, P., Guo, L., Chen, G., ... & Schneider, D. (2020). Automated cattle counting using Mask R-CNN in quadcopter vision system. *Computers and Electronics in Agriculture*, Vol. 171, 105300, <https://doi.org/10.1016/j.compag.2020.105300>.
- [24] Xu, B., Wang, W., Falzon, G., Kwan, P., Guo, L., Sun, Z., & Li, C. (2020). Livestock classification and counting in quadcopter aerial images using Mask R-CNN. *International Journal of Remote Sensing*, Vol. 41, pp. 8121-8142, United Kingdom, <https://doi.org/10.1080/01431161.2020.1734245>.
- [25] *** National Statistics Office of Mongolia, (2024), The total number of livestock reached 64.7 million decreased by 9.1% from the previous year, *NSO Livestock census*, M.Oyunjargal, B.Altansuvd, Mongolia.

RESEARCH ON GREENHOUSE PLANTING DENSITY OF LANDSCAPE FLOWERS IN COLD REGIONS BASED ON CFD SIMULATION

基于 CFD 模拟的寒冷地区景观花卉温室种植密度研究

Qibeier XIE ¹⁾, Jie REN ¹⁾,

¹⁾ School of Architecture, Inner Mongolia University of Technology, Hohhot, 010051, China

Corresponding author: Jie Ren

E-mail: rj881138@163.com

DOI: <https://doi.org/10.35633/inmateh-75-40>

Keywords: solar greenhouse; landscape flowers; planting density; with or without crops;

ABSTRACT

As an important facility structure in China, the solar greenhouse can provide a suitable environment for plant growth and development during winter, making it a viable structure for cultivating landscape flowers in cold regions. However, the impact of crop spacing in solar greenhouses on the thermal environment had received scant attention from researchers. Therefore, computational fluid dynamics (CFD) software was used to simulate the effect of crops on the thermal environment in solar greenhouses. The results of this study show that: the presence of crops in the greenhouse has a greater influence on the temperature in the solar greenhouse along the horizontal, vertical and longitudinal directions within the ranges of (3000, 8000 mm), (300 mm, at the film) and the distance from the inner surface of the east and west walls within the range of 10,000 mm; the presence of crops in the greenhouse has a greater influence on the internal temperature of the east wall, the west wall and the north wall; The influence of different planting densities of crops in the greenhouse on the internal temperatures of the solar greenhouse in the horizontal, vertical and longitudinal directions was within the ranges of (1000 mm, at the film), (600 mm, at the film), and the distance from the inner surface of the east and west walls was within the range of 6000 mm, respectively. This study can provide a theoretical basis for the cultivation and management of flowers in solar greenhouses in cold regions.

摘要

日光温室作为中国重要的设施结构，在冬季可提供植物生长发育的适宜环境，因此可在寒冷地区的日光温室中种植景观花卉。但是针对日光温室内花卉景观种植密度对温室热环境的影响较少，因此通过 CFD 模拟手段探究不同种植密度对温室湿热环境的影响。本研究结果显示：相对于无作物温室的温度，有作物温室的温度沿横向、竖向和纵向有较大变化的区域分别为 (3000,8000) mm、(300mm, 同跨度棚膜内表面高度处) 和距离东西墙体内部表面纵向距离为 10000mm 范围内；温室内作物不同种植密度对日光室内温度沿横向、竖向和纵向的影响范围分别为 (棚膜处,1000) mm、(600mm, 棚膜处) 和距离东西墙体内部表面距离为 6000mm 范围内。该研究可为寒冷地区日光温室花卉种植和管理提供理论依据。

INTRODUCTION

As the global population continues to grow, the demand for food shows a sharp upward trend, and facility horticulture, as a highly efficient agricultural production method, provides a highly promising solution to meet this challenge, while also helping to raise the income of the population (Cheng Weiwei., 2021). Among the many forms of facility horticulture, the development of solar greenhouses in China has been particularly remarkable, and they have become one of the key indicators of the level of agricultural modernization (Chen P et al., 2020). Daylight greenhouses, with their high-yield and high-efficiency production technology, have become an important way to improve crop yield and quality (Fu G.H. et al., 2016). However, the design and construction of solar greenhouses must fully consider the local climatic conditions, and China has a vast area with significant differences in climate. Therefore, an in-depth analysis of the thermal environment of solar greenhouses in Inner Mongolia can help promote the sustainable development of the greenhouse industry in this region (Hu Q.Q. et al., 2015).

The development of agricultural facilities and computer technology has led to the emergence of Computational Fluid Dynamics (CFD) as a powerful tool in the field of thermal environment index studies (He Z.G. et al., 2018; He Wei et al., 2022; Jia W.S. et al., 2016). Domenico et al., (2020), used TRNsys to perform simulations to select the best glazing for solar greenhouses considering different thermal phenomena, and the results showed that single pane glass/plastic materials are only recommended for tropical/hot climates, partially for dry (desert and semi-arid) climates and rarely for other climates. Li J.C., (2015), explored the effect of whether tomato was grown in the greenhouse on the microclimate environment in the solar greenhouse for the winter outdoor climatic conditions in Jinan, and found that the entrance wind speed had a small effect on the wind speed of the crop canopy, and that the temperature difference in the greenhouse was small and favourable to crop growth in the north-easterly winds, but did not consider the effect of transpiration. YU Wei et al., (2023), used CFD software for virtual identification and modelling of greenhouse temperature, and the results showed that the simulation results were in accordance with the temperature distribution law, indicating that the virtual and physical sensors can work together to monitor the greenhouse environment. Du Zhenyu et al., (2023), used CFD method to construct a numerical model of natural ventilation daylight greenhouse, explored the movement law of indoor airflow under the condition of natural ventilation and planting crops in spring, and the change rule of indoor temperature and humidity at different moments. The results show that: crops have a greater impact on the indoor airflow field, temperature and humidity field of the solarium; the temperature of the crop area in the solarium from 11:00 to 18:00 is too high, which does not satisfy the temperature range required by the 'four-stage variable temperature management'.

Most of the existing studies have focused on the environmental effects of the presence or absence of crops in solar greenhouses on the greenhouse environment, while few in-depth studies have been conducted on how different planting densities affect the greenhouse thermal environment, which was a key factor. In recent years, in order to improve the economic return of greenhouse cultivation, more and more greenhouse growers have begun to actively explore the landscape planting mode in traditional solar greenhouses (Shi L.J. et al., 2021). Taking the strawberry picking garden as an example, this model cleverly integrated the two major functions of crop cultivation and tourism, opening up a new development path for the greenhouse planting industry. However, under this innovative model, how to scientifically and reasonably plan the crop layout in the greenhouse (Sun B. et al., 2020), not only fully exploiting the utilisation potential of the greenhouse thermal environment to achieve efficient crop growth, but also ensuring that the tourists' sightseeing experience is not interfered with, and creating a comfortable and pleasant visiting environment, has become a key issue strengthening the further development of greenhouse planting industry. In this study, CFD simulation was used to accurately analyse the impact of different planting densities on the thermal environment in solar greenhouses, and to explore the intrinsic laws, with the aim of providing scientific, systematic and solid theoretical support for the optimization of greenhouse crop cultivation, and contributing to the sustainable development of greenhouse cultivation industry and the enhancement of its comprehensive benefits.

MATERIALS AND METHODS

Solar greenhouse geometry and grid model construction

Computational Fluid Dynamics (CFD) is a comprehensive discipline that integrates several fields such as mathematical modelling, fluid mechanics and computer science. It uses numerical analysis and fluid theory and other methods to carry out in-depth calculation, simulation and analysis of fluid objects, providing a powerful tool for solving complex fluid flow problems. The structure of CFD software consists of pre-processing, solver and post-processing. The pre-processing of CFD mainly includes the construction of the geometric model and mesh delineation, and a good pre-processing can greatly improve the accuracy of numerical simulation.

A geometrical model was constructed for a common solar greenhouse around the city of Hulunbeier in Inner Mongolia, China. The greenhouse was situated in a north-south orientation and measured 80 metres in length in the east-west direction. The dimensions of the greenhouse are as follows: a span of 10 metres, a ridge height of 5 metres, an earth wall on the north side of the building that was 4.5 metres high, and trapezoidal shapes on the north, east and west walls, with a lower base width of 8 metres and an upper base width of 2 metres. The intersection of the north wall, the west wall and the ground in the greenhouse was defined as the (0,0,0) point. SolidWorks modelling software was used for 1:1 three-dimensional modelling of the solar greenhouse, as shown in Figure 1.1.

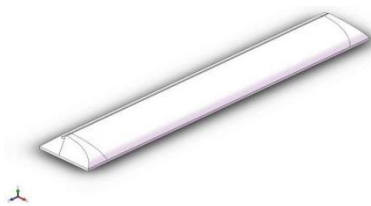


Fig. 1.1- 3D model of solar greenhouse

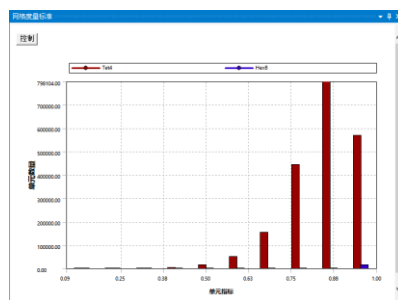


Fig. 1.2- Grid Quality

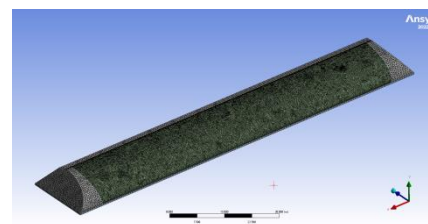


Fig. 1.3- Mesh Division

3D model meshing

Considering the boundary encryption and computational accuracy, a hybrid mesh is selected to process the model. The mesh size is 300 mm and the final mesh number was 1856226. The mesh quality is determined according to the mesh metric. The closer the mesh metric is to 1, the better the mesh quality. Grid division and grid quality were shown in Figure 1.2 and Figure 1.3.

CFD numerical modeling

Temperature change in a solar greenhouse is a dynamic and complex process influenced by factors such as construction, outdoor climate, growing conditions and internal ventilation. In order to improve the analysis efficiency and calculation accuracy, the CFD numerical model of temperature inside the solar greenhouse is reasonably simplified, assuming that the greenhouse is in a fully closed state except for the upper vent, ignoring the effect of humidity on the temperature, and that the parameters of each part of the material do not change with the temperature change.

Computational Fluid Dynamics (CFD) simulations are based on the three conservation laws of mass, momentum and energy, as well as the fundamental equations of fluid heat and mass transfer. In a confined space, the form of fluid flow is mainly affected by the Reynolds number (Re), which is manifested in two states: laminar and turbulent flow. In laminar flow, the fluid flows in layers, the flow velocity is stable, and the viscous force is dominant; while in turbulent flow, the fluid is in a disordered state, the flow velocity varies greatly, and the inertia force is dominant. The complex and dynamic fluid flow inside the solar greenhouse is usually regarded as turbulent flow. Therefore, turbulence models are widely used in the study of gas flow in greenhouses, among which the standard $k-\epsilon$ model is suitable for many scenarios and can obtain good results due to the assumption of turbulence isotropy.

In Fluent, radiation models include Rosseland model, P1 model, DTRM model, DO model, S2S model and solar radiation model. The simulation of the thermal environment of the solar greenhouse involves the radiative heat transfer processes such as the transmission of sunlight and the absorption and reflection of light by plants and soil, so the DO radiation model and the solar radiation model were preferred. In the simulation, the solar radiation calculator sets the solar orientation, irradiation intensity and material heat radiation parameters. The solar greenhouse is located at $49^{\circ}21'N$ latitude and $119^{\circ}25'E$ longitude, which is in the East 8 time zone. The solar radiation for this simulation was taken from the data at 17:00 on 26 January 2025 (a sunny day), the X-axis was reversed to due north, the Z-axis was reversed to due east in the coordinate system, the insolation coefficient was taken to be 1, and the light parameters were all set based on the solar calculator.

In CFD numerical simulation, porous media modelling is an effective tool for simulating the flow characteristics of fluids as they pass through complex regions containing solid particles or voids. In the simulation of the thermal environment of a solar greenhouse, considering the effect of the crop on air flow and heat transfer, it is a reasonable approximation to consider the crop as an isotropic porous medium. Considering the crop as a porous medium implies that structures such as the leaves and stalks of the crop are considered as a region with continuously distributed resistance. This treatment captures the crop's impedance to air flow, as well as the heat exchange process between the crop and the air.

Daylight greenhouses are subjected to differences in the distribution of solar radiation during the day, resulting in a temperature difference in the internal temperature, which leads to small changes in the air density inside the greenhouse. The Boussinesq assumption, which assumes that the air density varies so little in time and space that it can be approximated as a constant, simplifies the solution of the equations of hydrodynamics. The thermophysical parameters of the solarium envelope materials were shown in Table 1.

Boundary conditions and initial conditions

The setting of the boundary condition parameters has a great influence on the numerical simulation, and the boundary conditions and initial conditions are determined based on the experimental measured data and were set as follows:

(1) Setting of boundary conditions. The boundary conditions mainly include the setting of the boundaries of the front and rear roofs of the solar greenhouse, the east and west walls, the north wall and the soil. The interface between each part was set as a coupled wall. From 17:00 p.m. to 8:00 a.m. the next morning, the south roof was set as a layer of insulation.

(2) Setting of initial conditions. When constructing the thermal environment model of the solar greenhouse, the setting of initial conditions was a crucial step, which directly affected the accuracy and reliability of the simulation results. The experimental measurement data on 3 January 2024 were selected for model construction, and the initial temperature of the air inside the solar greenhouse was 16°C, respectively, and the outdoor temperature was applied to the outer surface of the greenhouse enclosure. In addition, the initial values of the north wall, soil, and crop surface temperatures were 22°C, 20°C, and 17°C, respectively.

Table 1

Material thermal property parameters of the solar greenhouse envelope

Parameters	PE	Wall	Soil	backward slope	Film	Crop
Densities[kg/m ³]	950	2000	1600	600	70	560
Specific heat capacity[J/(kg·K)]	1600	1050	1050	2500	1880	2100
Thermal conductivity[W/(m·K)]	0.34	0.8	0.75	0.29	0.04	0.19
Absorption coefficient	0.15	0.88	0.88	0.7	0.1	0.35
Scattering coefficient	0	0.12	0.12	0	0	0.1
Index of refraction	1.72	1.92	1.92	1.72	1.72	2.77

RESULTS AND DISCUSSION

Influence of the presence or absence of crops on the temperature distribution in solar greenhouse

Temperatures of greenhouses without crops and greenhouses with crop spacing of 1.5 m were selected for horizontal, vertical and longitudinal analyses, and temperatures of greenhouses with crop spacing of 1.5 m and 2 m were selected for horizontal, vertical and longitudinal comparisons.

Influence of the presence or absence of crops on vertical temperature changes in solar greenhouse

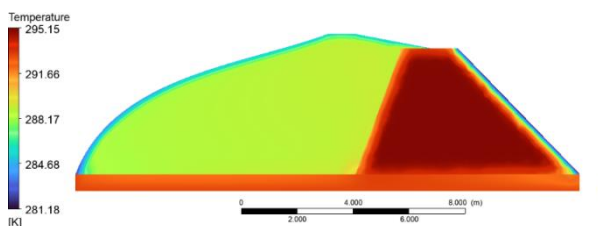


Fig. 3.1- Temperature cloud of X=36000mm north-south cross-section without crop

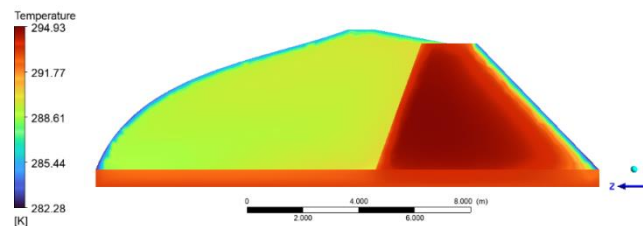


Fig. 3.2- Temperature cloud of X=36000mm north-south cross-section with 1.5m crop spacing

From Figures 3.1 and 3.2 above, in the specified parameters of $x=36000\text{mm}$, $z=0\text{mm}$, $y= (0, 5000)$ mm, the distribution law of vertical temperature was as follows: under constant working conditions, the temperature of the greenhouse with a crop greenhouse was higher than that of the greenhouse without a crop. In the range of $y=(0, 600)\text{mm}$, the temperature difference increased gradually, with a maximum temperature difference of 0.6°C , the minimum temperature difference was 0.06°C ; in the $y=(700, 4300)$ mm range, the temperature difference remained relatively stable, with a maximum temperature difference of 0.65°C ; in the $y=(4400, 4800)$ mm range, the temperature difference increased gradually, with a maximum temperature difference of 1.05°C and a minimum temperature difference of 0.65°C ; in the $y=(4900, 5000)$ mm range, the temperature difference decreased gradually, with a maximum temperature difference of 0.54°C and a minimum temperature difference of 0.04°C . The analysis indicated that the presence or absence of crops in the greenhouse exerted a negligible effect within the range of $y=(600, 4800)$ mm, yet it demonstrated a discernible effect within the ranges of $y=(0, 600)$ mm and $y=(4800, 5000)$ mm.

In the specified range of $x=36000$ mm, $z=5000$ mm, $y=(0, 3900)$ mm, the vertical temperature distribution law was as follows: under constant working conditions, the temperature of the greenhouse with crops was higher than that of the non-crop greenhouse. The temperature difference in the range of $y=(0, 100)$ mm gradually increased, and the maximum temperature difference was recorded at 0.49°C , while the minimum temperature difference was 0.06°C . In the range of $y = (200, 1200)$ mm, the temperature difference remains relatively smooth, with a maximum temperature difference of 0.48°C and a minimum temperature difference of 0.45°C . In the range of $y = (1300, 3500)$ mm, the temperature difference gradually increases, with a maximum temperature difference of 0.73°C and a minimum temperature difference of 0.46°C ; in the $y=(3600, 3900)$ mm range, the temperature difference decreased gradually, with a maximum temperature difference of 0.97°C and a minimum temperature difference of -0.12°C . The analysis indicated that the presence or absence of crops in the greenhouse exerted a negligible effect within the range of $y=(200, 3500)$ mm, yet it demonstrated a discernible effect within the ranges of $y=(0, 200)$ mm and $y=(3500, 3900)$ mm.

In the specified range of $x=36000$ mm, $z=9000$ mm, $y=(0, 1800)$ mm, the vertical temperature distribution law was as follows: under constant working conditions, the temperature of the greenhouse with a crop greenhouse temperature was indistinguishable from the temperature of the greenhouse without a crop. The temperature difference gradually increased in the range of $y = (0, 300)$ mm, with the maximum temperature difference of 0.55°C and the minimum temperature difference of 0°C . In the range of $y = (400, 900)$ mm, the temperature difference stayed relatively stable, with the maximum temperature difference of 0.66°C and the minimum temperature difference of 0.58°C . In the range of $y = (1000, 1800)$ mm, the temperature difference gradually decreases and the maximum temperature difference was 1.79°C and the minimum temperature difference was -0.13°C . From the above analysis, it can be seen that the presence or absence of crops in the greenhouse had a small effect in the range of $y = (300, 1000)$ mm, and a larger effect in the range of $y = (0, 300)$ mm and $y = (1000, 1800)$ mm.

As demonstrated in the preceding analysis, the presence or absence of crop temperature in the greenhouse exerted a lesser influence on the trellis at $x=36000$ mm and $y=300$ mm.

Effect of the presence or absence of crops on lateral temperatures in solar greenhouse

In order to explore the greenhouse, both with and without crops, the temperature along the transverse rule of change was to be analysed. For this purpose, the east-west span along the north-south cross-section was to be taken, with X set at 36000 mm, Y set at 0 mm, 1600 mm and 2400 mm, and Z set at $(-8000, 10000)$ mm on the temperature change curve.

From Figures 3.1 and 3.2 above, the change rule of temperature with crop temperature and without crop temperature at $y=0$ mm along the transverse direction was as follows: under the same working condition, the temperature of the greenhouse with crop was higher than the temperature of the greenhouse without crop; in the range of $z=(-8000,-6000)$ mm, the difference increased with the increasing of z , and the maximum difference was 0.6°C , and the minimum difference was 0.4°C ; in the range of $z=(-6000,2000)$ mm, the difference decreased with increasing z , the maximum difference was 0.8°C and the minimum difference was 0.07°C ; in the range of $z=(2000,10000)$ mm, the difference between the temperature of the greenhouse with crops and the temperature of the greenhouse without crops was maintained in the range of $(0.04, 0.07)^{\circ}\text{C}$. It can be seen that, considering the effect of the temperature difference of 0.5°C on the crop, the indoor crop had a greater effect on the internal temperature of the north wall, and a lesser effect on the temperature along the transverse direction at the soil surface of the indoor space.

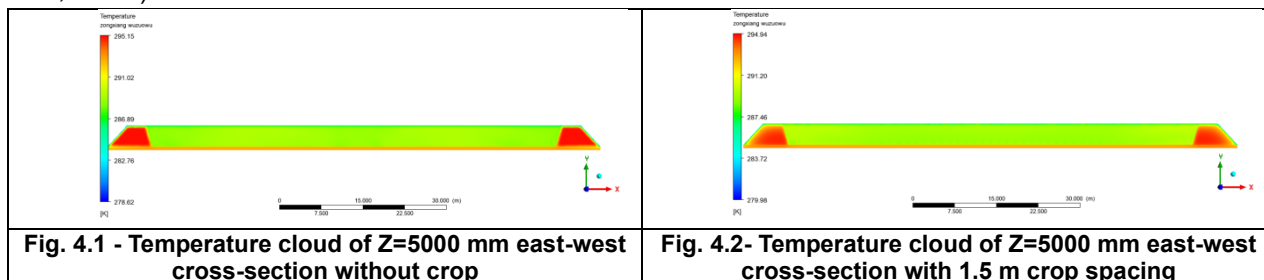
The change rule of temperature at $y=1600$ mm between the temperature with crop and the temperature without crop along the transverse direction was as follows: in the range of $z=(-6000, -2000)$ mm, the temperature of the greenhouse without crop was higher than the temperature of the greenhouse with crop; in the range of $z=(-6000, -5000)$ mm, the difference increased with the increased of z , and the maximum difference was 1.1°C , and the minimum difference was 1.0°C ; in the range of $z=(-5000, -2000)$ mm, the difference decreased with z , with a maximum difference of 0.6°C and a minimum difference of 0.3°C ; in the $z=(-1000, 9000)$ mm range, the temperature of the greenhouse with crops was higher than that of the greenhouse without crops; in the $z=(-1000, 0)$ mm range, the difference increased with z , with a maximum difference of 0.6°C and a minimum difference of 0.03°C ; in the range of $z = (0, 3000)$ mm, the difference decreased with increasing z , with a maximum difference of 0.62°C and a minimum difference of 0.45°C ; in the range of $z = (4000, 8000)$ mm, the difference stayed in the range of $(0.46, 0.64)^{\circ}\text{C}$ with increasing z ; in the range of $z = (8000, 9000)$ mm, the crop-free greenhouse temperature was higher than the temperature of the greenhouse with crops, with a temperature difference of 0.15°C . This shows that indoor crops had a greater effect on the interior of the wall at 5000 mm from the inner surface of the wall and on the interior space at 8000 mm from the inner surface of the wall.

The change rule of temperature at $y=2400$ mm between the temperature with crop and the temperature without crop along the transverse direction was as follows: in the range of $z=(-5000, -2000)$, the temperature of the greenhouse without crop was higher than the temperature of the greenhouse with crop, and the difference decreases with the increasing of z , with the maximum difference being 1.44°C and the minimum difference being 0.29°C ; in the range of $z=(-1000, 8000)$ mm, the temperature of the greenhouse with crop was higher than the temperature of the greenhouse without crop, in the range of $z=(-1000, 2000)$ mm, the difference decreased with increasing z , the maximum difference was 1.0°C , and the minimum difference was 0.53°C ; in the range of $z=(3000, 7000)$ mm, the difference was maintained in the range of $(0.60, 0.69)^{\circ}\text{C}$. In the range of $z=(7000, 8000)$ mm, the difference increased with increasing z and decreased with a maximum difference of 0.69°C and a minimum difference of 0.05°C . It was evident that indoor crops had a significant impact on the interior of the wall at 1000 mm from the inner surface of the wall and on the interior space at 7000 mm from the inner surface of the wall.

In summary, the presence or absence of crops in the greenhouse had a large effect on the temperature of the north side wall, and within the crop layer, the effect was larger at a distance of 3000 mm to 8000 mm from the inner surface of the north side wall.

Effect of the presence or absence of crops on longitudinal temperatures in solar greenhouse

To investigate the effect of crop presence on the longitudinal temperature distribution inside the greenhouse, an analysis was conducted along the east–west cross-section of the north–south span. Temperature variation curves were examined at $Z = 5000\text{mm}$, $y = 0$ mm, 1600 mm and 2400 mm, $x = (-8000, 80000)$ mm



As can be seen from Figure 4.1 and Figure 4.2, the change rule of temperature along the longitudinal direction of the greenhouse with and without crop temperature at $y=0$ mm was as follows: under the same working condition, the temperature of the greenhouse with crop temperature was higher than that of the greenhouse without crop temperature; within the range of $x=(-8000, -5000)$ mm, the temperature difference increased gradually with the increase of x , and the maximal temperature difference was 1.21°C ; within the range of $x=(-5000, 72000)$ mm range, the minimum temperature difference was 0.01°C , and the maximum temperature difference was 0.21°C ; in the $x=(72000, 78000)$ mm range, the temperature difference increased slowly as x increased, and the minimum temperature difference was 0.21°C , and the maximum temperature difference was 1.22°C ; in the $x=(78000, 80000)$ mm range, the temperature difference decreased gradually, the minimum temperature difference was 0.75°C and the maximum temperature difference was 1.22°C . It can be seen that, considering the effect of temperature difference of 0.5°C on the crop, the indoor crop has a greater effect on the temperature of the east and west walls, and a smaller effect on the temperature along the longitudinal direction at the soil surface of the indoor space.

The change rule of temperature at $y=1600$ mm along the longitudinal direction was as follows: in the range of width of the east and west walls, the temperature of the greenhouse without crops was higher than that of the greenhouse with crops; in the range of $x=(0, 72000)$ mm, the temperature in the greenhouse with crops was higher than that in the greenhouse without crops; in the range of $x=(0, 2000)$ mm, the difference of temperature was 1.2°C ; in the range of $x=(2000, 18000)$ mm range, the temperature difference gradually decreased, the maximum temperature difference was 1.2°C , and the minimum temperature difference was 0; in the $x=(18000, 34000)$ mm range, the temperature difference gradually increased, the maximum temperature difference was 0.51°C , and the minimum temperature difference was 0; in the $x=(34000, 40000)$ mm range, the temperature difference stayed constant, the temperature difference was 0.51°C ; in the range of $x=(40000, 56000)$ mm, the temperature difference decreased gradually, the maximum temperature difference was 0.51°C , and the minimum temperature difference was 0; in the range of $x=(56000, 72000)$ mm, the temperature difference decreased gradually, the maximum temperature difference was 1.45°C , and the

minimum temperature difference was 0. From the above analysis, it can be seen that, in the range of crop layers, the presence or absence of crops in the greenhouse has a greater effect on the temperature of the inner side of the east and west walls and on the temperature within the range of 10,000 mm from the longitudinal distance of the east and west walls.

The change rule of temperature at $y=2400$ mm along the longitudinal direction was as follows: in the range of the width of the east wall and the west wall, the temperature in the crop-free greenhouse was higher than the temperature in the crop greenhouse, and with the increase of the distance from the surface of the indoor wall, the temperature difference was gradually increasing, and the maximum temperature difference was 2.4°C , and the minimum temperature difference was 0.99°C ; in the range of $x=(0,72000)$ mm, the temperature in the crop greenhouse was higher than the temperature in the greenhouse without crops; in the range of $x=(0,18000)$ mm, the temperature difference gradually decreased, the maximum temperature difference was 1.3°C , and the minimum temperature difference was 0.07°C ; in the range of $x=(18000,22000)$ mm, the temperature difference stayed unchanged, and the temperature difference was 0.07°C ; in the range of $x=(22000,54000)$ mm, the temperature difference gradually increased, the maximum temperature difference was 0.66°C , the minimum temperature difference was 0.04°C ; in the range of $x=(54000,72000)$ mm, the temperature difference gradually decreased, the maximum temperature difference was 1.47°C , the minimum temperature difference was 0.04°C . From the above analysis, it can be seen that, the presence or absence of crops in the greenhouse had a greater impact on the temperature inside the east and west walls, and it has a greater impact on the temperature inside the wall at the longitudinal distance between the wall of 10000 mm and (34000,40000) mm range had a greater effect on the temperature.

Therefore, from the above analysis, it can be seen that the presence or absence of crops in the greenhouse had a greater effect on the temperature inside the east and west walls, and on the temperature within a distance of 10,000 mm from the surface of the wall, taking into account the effect of a temperature difference of 0.5°C on the crop.

Influence of different planting densities of crops on the temperature distribution in solar greenhouses

The study respectively simulated the temperature variation patterns in solar greenhouses with crop spacings of 1500 mm (actual) and 2000 mm. For the simulations, the temperature data at 17:00 on 26 January 2024 were selected as the initial boundary conditions. The temperature distribution maps at 08:00 were then analysed comparatively to assess the differences.

Influence on the vertical temperature of solar greenhouses

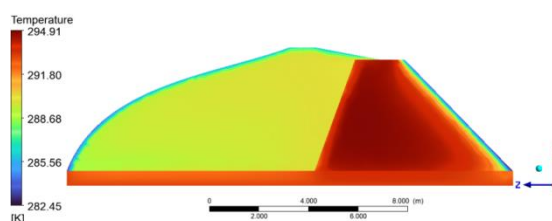


Fig. 5- Temperature cloud of $X=36000$ mm north-south cross-section with 2.0 m crop spacing

In order to investigate the vertical effect of different crop planting densities (1.5 m and 2 m, respectively) on the temperature in the greenhouse, $x=36000$ mm was taken in the greenhouse, and the difference in temperature between the crop planting density of 2 m and the temperature of the crop planting density of 1.5 m was analysed according to the difference in the height y when z was 0 mm, 5000 mm, and 9000 mm, respectively.

Taking $z=0$ mm, the temperature difference between the temperature at a crop planting density of 2 m and the temperature at a crop planting density of 1.5 m was analysed. Only when $y = (0, 800)$ mm, the temperature of crop planting density of 1.5 m was greater than the temperature of crop planting density of 2 m, the maximum difference was 0.2°C , and the minimum difference was 0.01°C ; when $y > 800$ mm, the temperature of crop planting density of 2 m was greater than the temperature of crop planting density of 1.5 m. The maximum temperature difference was 0.27°C and the minimum temperature difference was 0.15°C within the $y = (900, 4700)$ mm interval; when $y = (4800, 5000)$ mm, which is located in the vicinity of the film, the temperature difference gradually increases, and the maximum temperature difference was 0.69°C .

Taking $z=5000$ mm, the temperature difference between the temperature at a crop planting density of 2 m and the temperature difference at a crop planting density of 1.5 m was analysed. When $y = (0, 500)$ mm, the maximum difference in temperature between the two was 0.49°C ; when $y = (600, 1800)$ mm, the temperature difference between the two was more than 0.5°C , and the maximum temperature difference was 0.59°C ; when $y = (1900, 3400)$ mm, the maximum difference in temperature between the two was 0.49°C ; and when $y = (3500, 3900)$ mm, the maximum temperature difference between the two temperatures was 5.02°C and the minimum difference was 0.55°C .

Taking $z=9000$ mm, the temperature difference between the temperature at a crop planting density of 2 m and the temperature at a crop planting density of 1.5 m was analysed. When $y=(0, 1200)$ mm, the maximum temperature difference between the two temperatures was 0.3°C , and the minimum temperature difference was 0.23°C ; when $y=1300$ mm, the temperature difference between the two temperatures was the largest, which was 1.35°C ; when $y=1400$ mm, 1500 mm, the temperature of crop planting density of 1.5 m was greater than that of crop planting density of 2 m, and the difference in temperatures was 0.49°C respectively, 0.44°C ; when $y = (1600, 1800)$ mm, which was located in the vicinity of the film, the maximum difference in temperature was 0.59°C .

In summary, in the greenhouse when $x=36000$ mm, the temperature of crop planting density of 2 m was generally higher than the temperature of planting density of 1.5 m. However, there existed localized areas of contrast, where the temperature of crop planted at a density of 1.5 m was higher than the temperature of planted at a density of 2 m only at $z=0$ mm, $y<800$ mm, and at $z=9000$ mm, $y=1400$ mm, and 1500 mm. Further analysis showed that within the planting area, the effect of planting density on temperature was significant when $y>600$ mm, and the temperature difference could be up to 0.5°C or more. In addition, the effect of planting density on temperature was particularly pronounced in the area within 400 mm from the film, with lower temperatures near the film and larger temperature differences, especially at $z=5000$ mm, where the temperature difference at the film was the largest, reaching 5.02°C .

Influence on transverse temperature in solar greenhouses

The present study investigates the change rule of temperature along the transverse direction in the greenhouse with different planting densities. This study selected the data of different heights in the east-west spanning north-south direction in the greenhouse, and analysed the temperature within $z=(-8000, 10000)$ mm at $x=36000$ mm, $y=0$ mm, 1600 mm, and 2400 mm.

From the above figure, it can be seen that under the same working condition, in the greenhouse with crop planting densities of 2 m and 1.5 m respectively, the transverse temperature distribution pattern within $z=(-8000, 10000)$ mm at $x=36000$ mm and $y=0$ mm was as follows: the temperature difference within $z=(-8000, -5000)$ mm gradually increases, the maximum temperature difference was 0.1°C , and the minimum temperature difference was -0.02°C ; The difference in temperature values within $z=(-5000, -1000)$ mm remains unchanged, with a temperature difference of 0.05°C ; the temperature difference at $z=0$ mm was -0.26°C ; the difference in temperature values within $z=(0, 4000)$ mm remained unchanged, with a temperature difference of -0.06°C ; the difference in temperature values within $z=(4000, 8000)$ mm gradually increased, with a maximum temperature difference of 0.4°C ; the difference in temperature values within $z=(8000, 9000)$ mm gradually decreased, with a minimum temperature difference of 0.36°C ; and the temperature difference at $z=10000$ mm film was 0.72°C .

The change rule of temperature at $y=2600$ mm along the transverse direction was as follows: the temperature difference gradually decreased within $z=(-6000, -4000)$ mm, with the maximum temperature difference of -0.18°C and the minimum temperature difference of -0.01°C ; the difference in temperature values within $z=(-4000, -2000)$ mm stayed the same, with a temperature difference of 0.01°C ; the difference in temperature values within $z=(-2000, 3000)$ mm gradually increased, with the maximum temperature difference was 0.3°C ; the difference in temperature values within $z=(3000, 8000)$ mm gradually decreased, with a minimum temperature difference of 0.22°C ; and the temperature difference at $z=9000$ mm film was 0.58°C .

The change rule of temperature at $y=2400$ mm along the transverse direction was as follows: in $z = (-5000, -2000)$ mm within the temperature difference remained unchanged, the temperature difference was 0.03°C ; in $z = (-2000, 1000)$ mm within the difference in temperature values gradually increased, the maximum temperature difference was 0.29°C ; in $z = (1000, 7000)$ mm within the canopy gradually decreased, the minimum temperature difference was 0.21°C ; and the temperature difference at $z=8000$ mm film was 0.75°C .

In summary, the transversal air temperature distribution in the greenhouse was positively correlated with the planting density in the greenhouse, and the air temperature in the greenhouse with a planting density of 2

m was higher compared to the air temperature with a planting density of 1.5 m. The indoor air temperatures varied greatly in the range of 1 m near the film at the same height, with a difference value of more than 0.5°C; the wall temperatures varied greatly in the range of 1 m near the interior and exterior of the room, but with a difference of less than 0.25°C.

Impact on longitudinal temperature in solar greenhouses

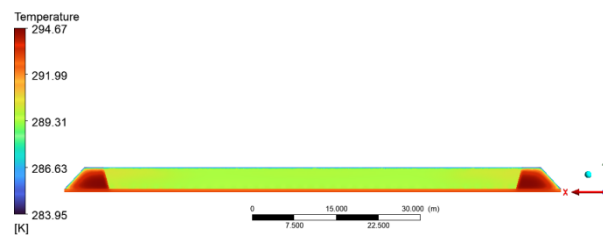


Fig. 6- Temperature cloud of Z=5000 mm east-west cross-section with 2.0 m crop spacing

In order to investigate the different crop spacing in the greenhouse on the indoor temperature along the longitudinal rule of change, the north-south span along the east-west cross-section was analysed, and the crop spacing of 2 m and 1.5 m, z=5000 mm, y=0 mm, 1600 mm, 2400 mm, x=(-8000,80000) mm at the temperature change curve was analysed.

From figures 4.2 and 6 above, under the same working condition, the greenhouse temperature of 2 m crop spacing and 1.5 m crop spacing at y=0 mm along the longitudinal rule of change was: in the range of east-west wall, the temperature of 2 m spacing was lower than 1.5 m spacing by 0.06°C on average; in the range of (1000,72000) mm, the temperature of 2 m spacing was higher than that of 1.5 m spacing, with the maximum temperature difference of 0.59°C and the minimum of 0.02°C. The temperature difference at 0 m was the largest at 3.19°C; in the range of (x=1000,72000) mm, the temperature difference was in fluctuation with the increase of x, with an average of 0.29°C, and the maximum was 0.59°C at 14000 mm, and the minimum was 0.02°C at 65000 mm; the temperature difference in the range of x=(73000,79000) mm did not vary much and averaged -0.07°C. Overall, crop spacing had a greater effect on temperatures in the range of 6000 mm and (10000, 16000) mm from the east-west wall and a smaller effect on temperatures within the wall.

The change rule of temperature along the longitudinal direction at y=1600 mm was as follows: in the range of east-west wall, the temperature of 2 m spacing was lower than that of 1.5 m spacing by 0.03°C on average; in the range of (0,73000) mm, the temperature of 2 m spacing was higher than that of 1.5 m spacing by 0.30°C on average. In the range of x=(0,73000) mm, the temperature difference was in a fluctuating state with an average of 0.30°C; in the range of x=(74000,79000) mm, the temperature difference decreased from -0.02°C to -0.07°C. Overall, crop spacing had a greater effect on the temperature within 6000 mm from the east-west wall and a lesser effect on the temperature within the east-west wall.

The change rule of temperature along the longitudinal direction at y=2400 mm was as follows: in the range of east-west wall, the temperature of 2 m spacing was lower than that of 1.5 m spacing by 0.03°C on average; the temperature difference increased with the increase of distance from the inner surface of the wall, and the maximum temperature difference was 0.29°C, and the minimum was 0.18°C. Within the range of x=(0,73000) mm, the temperature difference was in a fluctuating state, with an average difference of 0.24°C, and within the range of x=(74000,78000) mm range, the temperature difference increased from -0.04°C to -0.17°C. In conclusion, crop spacing had a small effect on the temperature inside the east-west wall and a large effect on the temperature within 5000 mm from the east-west wall.

Thus, from the above analysis, it can be seen that crop spacing has less effect on the temperature of the east and west walls, but more effect on the temperature within a distance of 6000 mm from the wall.

CONCLUSIONS

(1) The presence or absence of crops in the greenhouse has a greater influence on the temperature in the solar greenhouse along the horizontal, vertical and longitudinal directions within the ranges of (3000,8000) mm, (300 mm, at the film) and the distance from the inner surface of the east and west walls within the range of 10,000 mm;

(2) The presence or absence of crops in the greenhouse has a greater influence on the internal temperature of the east wall, the west wall and the north wall. The presence or absence of crops in the

greenhouse has a greater effect on greenhouse temperature than the density of crops grown in the greenhouse has on greenhouse temperature;

(3) The effect of different planting densities on the temperature of the greenhouse was less significant than that of different planting methods. The influence of different planting densities of crops on the internal temperatures of the solar greenhouse in the horizontal, vertical and longitudinal directions was within the ranges of (1000mm, at the film), (600 mm, at the film), and the distance from the inner surface of the east and west walls was within the range of 6000 mm, respectively.

ACKNOWLEDGEMENT

I am very grateful to Associate Prof. Jie Ren. I am very grateful to the School of Architecture, Inner Mongolia University of Technology, Hohhot. I am very grateful to the support of the project "Innovation and Entrepreneurship Training Programme for Undergraduates" of Inner Mongolia University of Technology for the year 2025. The project title is: Research on Landscape Ecological Environment Suitability and Application in Semi-Arid Areas.

REFERENCES

- [1] Cheng Weiwei (2021). *Study on thermal environment and marginal effect of sunken solar greenhouse (下沉式日光温室三维热环境及边际效应的研究)*. College of Agricultural Engineering, Shanxi Agricultural University.
- [2] Chen P., Wang Y.Z, Liu Q.Z., Zhang Y.T., Li X.Y, Li H.Q., Li W.H (2020). Phase changes of continuous cropping obstacles in strawberry (*Fragaria × ananassa* Duch) production[J]. *Applied Soil Ecology*, 155:103626.
- [3] Fu G.H., Liu W.K. (2016). Sunlight greenhouse pepper ridging embedded substrate cultivation root zone temperature variation characteristics (日光温室甜椒起垄内嵌式基质栽培根区温度日变化特). *Chinese journal of eco-agriculture*, 24(1):47-55.
- [4] Hu Q.Q., LI Y., Lu G.Q. (2015). Effect of high temperature smoking-shed technology on continuous cropping obstacle control of pepper greenhouse (高温闷棚技术对设施辣椒连作障碍防治效果的研究). *Journal of pepper science*, 13(1): 23-25.
- [5] He Z.G., Lou C.R., Dong H. (2018). Effects of straw returning on soil microhabitat and growth and development of tomato under continuous cropping (秸秆还田与高温闷棚对设施连作土壤微生境及番茄生长发育的影响). *Journal of Henan agricultural sciences*. 47(10):87-91.
- [6] He W., Luo W., Yu Z., Xu J., Sun X. (2022). Higher temperature Influence on the control effect of the root-knot nematode and soil microbial community structure of vegetables in the facility (高温闷棚对设施蔬菜根结线虫的防治效果及土壤微生物群落结构的影响). *Xinjiang Agricultural Science*, 59(1):179-189.
- [7] Jia W.S., Li M.N., Li Y. (2016). Application of Key Internet Thing Technologies in Facility Agriculture. *Journal of Food Safety and Quality*, 7(11):4401-4407.
- [8] Lal R. (2020). Home gardening and urban agriculture for advancing food and nutritional security in response to the COVID-19 pandemic, *Food Security*. 12 (4): 871–876.
- [9] Li J.C. (2015). *Effect of irrigated high temperature smothered shed on soil remediation of continuous cropping in greenhouse (灌水高温闷棚对温室连作土壤修复效果的研究)*. Xi'an: College of Horticulture, Northwest A&F University.
- [10] Yu W., Liu W., Bai Y., Ding X. (2023) Thermal environment simulation of a two-span solar greenhouse based on CFD[J]. *Journal of Agricultural Engineering*, 39 (16): 215-222.
- [11] Zhang Q., Du Z. (2023) Numerical simulation of temperature and humidity fields in spring solar greenhouse based on soil evaporation and crop transpiration[J]. *Journal of Taiyuan University of Technology*, 1-14.
- [12] Peng P., Liang L., Li H.L., Zhao G.S. (2019) Current situation, Problems and development suggestions of Facility agriculture in China (我国设施农业现状、问题与发展建议). *Northern Horticulture* (05):161-168.
- [13] Shi L.J., Sun J.Q., Cai C. (2021) Methods of swarming greenhouse in Shandong province and matters needing attention (山东地区常用的闷棚方法及注意事项). *Modern Agricultural Science and Technology* (17):88-89.

- [14] Sun B., Bai Z., Bao L., Xue L., Zhang S., Wei Y., Zhang Z., Zhuang G., Zhuang X. (2020). *Bacillus subtilis* biofertilizer mitigating agricultural ammonia emission and shifting soil nitrogen cycling microbiomes [J]. *Environment International*, 144: 105989.
- [15] Ghani S., Bakochristou F., El-Bialy E., Mahmoud S., Rashwan M., Abdel-Halim A., Ismail S. (2019). Design challenges of agricultural greenhouses in hot and arid environments – A review, *Eng. Agric. Environ. Food*. 12 (1):48–70.
- [16] Steven W., Van G., Thomas I. (2017). Energy Water and Nutrient Impacts of California-grown Vegetables Compared to Controlled Environmental Agriculture Systems In Atlanta, GA. *Resource, Conservation and Recycling*. 122:319-325.
- [17] Wang S.Q., Zhang Z.L., Hou W.N. (2012) Characteristics of soil temperature variation in southern marginal area of sunken solar greenhouse (下沉式日光温室南侧边缘区域土壤温度变化特征). *Transactions of the Chinese society of agricultural engineering*. 28 (8): 235-240.
- [18] Zhang L.H., Zhang F., Liu S., Xu L. (2010) Three-dimensional unsteady simulation of indoor temperature field of sunken earth wall greenhouse (下沉式土质墙体温室室内温度场的三维非稳态模拟). *Acta Solar Energy Sinica*. (31).

STUDY ON THE OPERATING EFFECT OF STRAW CRUSHING AND SPREADING DEVICES ON SINGLE AXIAL FLOW HARVESTERS

单纵轴流收获机装配秸秆粉碎抛撒装置作业效果问题研究

Jiang WANG¹⁾, Longjing LI¹⁾, Weiliang SHI¹⁾, Youqiang DING^{2)*}

¹⁾ College of Automotive Engineering, Zibo Vocational Institute, Zibo/China;

²⁾ Nanjing Institute of Agricultural Mechanization, Ministry of Agriculture and Rural Affairs, Nanjing/China

Tel: 18801239355; E-mail: dyq_cau@163.com

DOI: <https://doi.org/10.35633/inmateh-75-41>

Keywords: Single Axial Flow; Harvesters; Straw Crushing; Straw Spreading; operating effect

ABSTRACT

To identify the specific manifestations and influencing factors of the poor straw crushing and spreading effects in Northeast rice-growing areas, this paper focuses on the straw crushing and spreading device widely used on single axial flow harvesters. Experimental and theoretical analyses were conducted. The results indicate that the existing straw crushing and spreading devices, under different operating speeds and with various active blade types, exhibit crushing performance, spreading width, and spreading uniformity significantly below standard values. The primary issues are straw clumping, insufficient straw crushing, lateral bias in spreading, and inadequate spreading width. By establishing a theoretical model, the analysis reveals that the straw crushing effect is related to the characteristics of the straw itself, such as blade rotational speed, cutting angle, and support angle. In contrast, the spreading effect is associated with the motion direction of the straw leaving the threshing drum, straw ejection speed, and the arrangement of deflector plates. This paper clarifies the elements that need improvement in the operational effectiveness of the straw crushing and spreading devices attached to combine harvesters, providing a theoretical basis for subsequent enhancements.

摘要

为找到东北稻区秸秆粉碎抛撒效果差的具体表现形式及其影响因素, 本文以广泛使用的单纵轴流收获机装配的秸秆粉碎抛撒装置为研究对象, 开展试验和理论分析研究。试验表明, 现有秸秆粉碎抛撒装置在不同作业速度下, 采用不同动刀类型, 粉碎抛撒装置粉碎效果、抛撒幅宽和抛撒不均匀度都远低于标准值, 作业效果问题主要变现为: 秸秆成团、秸秆粉碎不充分、抛撒偏向一侧、抛撒幅宽不足。通过建立理论模型分析得出, 秸秆粉碎效果与秸秆自身特性, 粉碎刀转速、开刃角、支撑角有关; 抛撒效果与秸秆离开脱粒滚筒时运动方向、秸秆抛离速度、导流板布置有关。文章明确了联合收获机装配的秸秆粉碎抛撒装置作业效果需要提升的要素, 为后续改进提供理论依据。

INTRODUCTION

With the large-scale and intensive development of agriculture in China, single axial flow combine harvesters have become the mainstream products in the market due to their high efficiency and cost performance. These machines are particularly suitable for harvesting crops like rice (Gong et al., 2024; Zhang et al., 2021), which produce a substantial amount of straw and have gained significant usage in Northeast China (Wang et al., 2021). Returning straw to the fields can improve soil fertility, enhance soil structure, and increase grain yield (Wang et al., 2023; Zang et al., 2021), making it a critical measure for sustainable soil development (Wang et al., 2017). As a result, there is a growing demand for equipping combine harvesters with straw-crushing and spreading devices (Wang et al., 2022). However, in Northeast China's rice-growing areas, the ample and tough straw presents challenges, leading to poor crushing and spreading effects and unsatisfactory straw return quality (Sun et al., 2019).

Existing research on straw crushing and spreading (Jankauskas et al., 2023; Li et al., 2023; Sun et al., 2019; Vlăduț et al., 2023; Vlăduț et al., 2023; Wang et al., 2021; Wang., 2018; Wang., 2018) mainly focus on the design of the devices or the analysis of the product's application effects. There is a lack of detailed analysis of the causes of poor straw-crushing and spreading effects in this region.

More theoretical models must be developed to address these processes for the straw-crushing and spreading devices mounted on combine harvesters. This study conducts field experiments and theoretical analyses based on the original straw crushing and spreading devices of single axial flow combine harvesters. It aims to identify the specific problems and underlying causes in each stage of grinding and spreading while clarifying the aspects that need improvement, thus providing a foundation for future enhancements.

MATERIAL AND METHODS

Structure and Working Principle of the Straw Crushing and Spreading Device on Single Axial Flow Harvesters

The structure and spatial layout of the straw-crushing device mounted on this type of combine harvester are roughly illustrated in Fig.1. During operation, the straw crushing and spreading process can be divided into three stages:

(1) Straw Feeding Stage: Straw exits through the discharge opening of the threshing mechanism and slides down the collecting board to the entrance of the crushing device chamber.

(2) Straw Crushing Stage: After the straw enters the crushing device chamber, it is chopped up with the cooperation of the moving and fixed blades.

(3) Straw Spreading Stage: The crushed straw falls to the ground under the influence of the spreading device and its gravity.

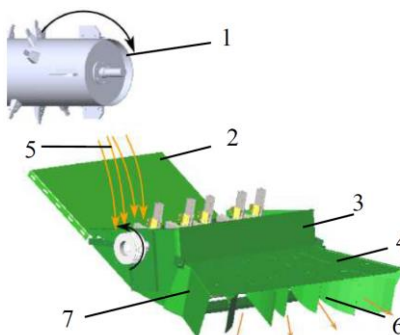


Fig. 1 - Schematic diagram of the spatial position of the single vertical axis flow harvester's straw crushing and spreading device

1. Threshing Mechanism; 2. Collecting Board; 3. Crushing Device; 4. Spreading Device; 5. Rice Straw; 6. Spreader Deflector Plate; 7. Spreader Housing

Experimental Design

Field experiments were conducted during the rice harvesting period using the John Deere C100 single vertical axis flow combine harvester to explore the factors affecting the performance of rice straw crushing and spreading operations, as shown in Fig.2. The stubble height was approximately 30 cm during the operation, as illustrated in Fig.3. The experiment was carried out at Experimental Field No. 36 in the Jian Sanjiang Farm of Heilongjiang Province, with the rice variety being Longjing 31. The average plant height was 94.62 cm, and the average panicle length was 15.94 cm, while the straw moisture content measured 33.01%.



Fig. 2 - John Deere C100 and Stubble height



Fig. 3 - Smooth blade and serrated blade



Fig. 4 - Field test image

The harvester's original straw crushing and spreading device uses a high-speed rotating swing knife and a single-row fixed knife. Both the fixed and moving knives have smooth blades (no serrations). The rotational speed of the knife shaft is 2600 r/min. The test compares the shredding and spreading effects of the moving knives, which are smooth-blade knives and serrated blades. As shown in Fig.3, the test-crushing moving knives use the original smooth blade and the serrated blade available on the market. After the smooth blade knife operation was completed, the knife shaft with the serrated knife was installed to replace the smooth blade knife shaft, and the test operation continued. The header width of the harvester was 4.5 m, and the feeding rate was 9 kg/s.

The test speed is based on the gear position of the harvester, and the first gear's low speed, the first gear's high speed, the second gear's low speed, and the second gear's high speed are selected. The corresponding speeds measured by the stopwatch are 0.95 m/s, 1.12 m/s, 1.21 m/s and 1.38 m/s.

The test used straw crushing qualified rate (crushing length <15 cm) y_1 , straw spreading width (harvesting width 4.5 m) d , and spreading unevenness F_b as evaluation indicators. Fig.4 is a field test image.

The straw spreading width measurement method is: 5 measuring points are taken at equal intervals within the harvesting stroke of the combine harvester, and the width is measured and recorded at each measuring point. The straw sampling method is: one point is taken within the two working strokes of the combine harvester, and 5 sampling frames with an area of 90 cm × 50 cm are placed in sequence at each measuring point parallel to the direction of the harvester header, and all the straw in the sampling frame is collected. The straw crushing qualified rate and spreading unevenness are calculated according to the requirements of GB/T 24675.6-2009 "Conservation Tillage Machinery Straw Crushers (GB/T 24675.6-2009-2009)". The calculation formulas for straw crushing qualified rate y_1 and spreading unevenness F_b are respectively:

$$y_1 = \frac{M_{ai} - M_{bi}}{M_{ai}} \times 100\%, \quad i = 1, 2, \dots, 10 \quad (1)$$

$$F_b = \frac{1}{M} \sqrt{\frac{1}{9} \sum_{i=1}^{10} (M_{ai} - \bar{M})^2} \times 100\%, \quad i = 1, 2, \dots, 10 \quad (2)$$

where M_{ai} is the total mass of the straw at the sampling point, g; M_{bi} is the mass of the straw with a length less than 15 cm at the sampling point, g; and \bar{M} is the average mass of the straw at each measuring point, g.

RESULTS

Test results and analysis

Fig.5 shows the changes in various test indicators with harvesting speed. Referring to the straw crushing qualification rate requirements in GB/T 24675.6-2009, it can be seen from Fig.5a that the operating results of different types of crushing knives are not ideal when crushing rice straw in Northeast China, all are far less than 85%, and the lowest operating speed is 0.95 m/s, the qualified rate of straw crushing with different crushing knife types is only 72.02% and 63.48%. At the same time, as the operating speed increases, the qualified rate of straw crushing also has a downward trend. Under the same operating conditions, the smooth-edged crushing knife has a higher straw crushing qualification rate than the serrated knife. Through actual observation of the shape of the straw after different knife types, it was found that the straw incision showed more tearing after being crushed by the serrated knife. Fig.5b reflects that the change of the blade of the movable knife has no significant impact on the throwing width. It is observed that the straw throwing width of the modified machine is significantly different from the harvesting width, and as the operating speed increases, the throwing width decreases. Fig.5c shows that the throwing unevenness of both knife types is poor, which is far from the standard requirement of less than 30%. As the speed increases, the throwing unevenness slightly increases. According to the test, the operating effect of this model's straw crushing and spreading device could be better, and it needs to continue to be improved to solve the critical technical problem of straw crushing and spreading that restricts the quality of straw return to the field.

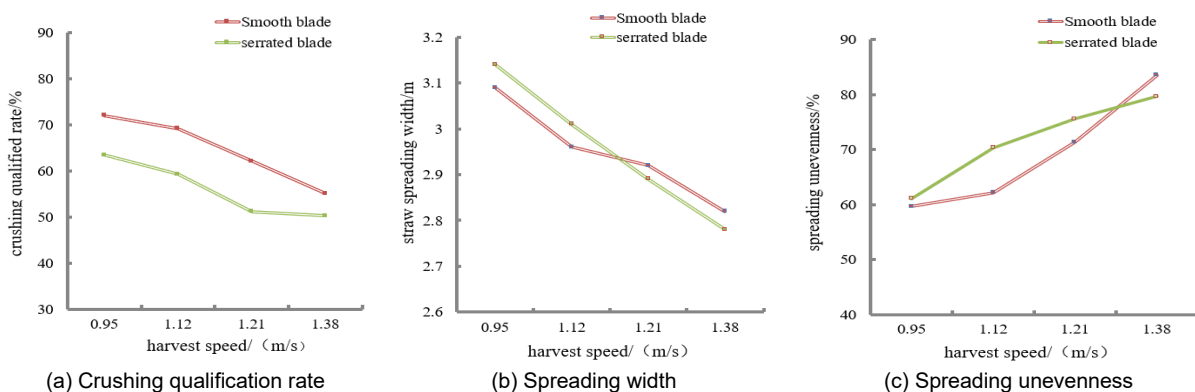


Fig. 5 - Variation of each test index with harvesting speed

Existing problems and theoretical analysis

Study on crushing problems

The straw scattered on the ground after the observation test is shown in Fig.6. After the observation operation, the straw mainly clumped together. As shown in Fig.6a, many straws were over 20 cm long, which severely impacted the subsequent straw burial and field return effectiveness (Sun et al., 2019). It was also found that the straw length did not meet the standard due to insufficient crushing. The straw shape exhibited one or more bends and damages along the straw shaft, as shown in Fig.6b. The main reason for this damage was that the moving and fixed knives failed to cut effectively into the straw. The excessive straw length also contributed to clumping.

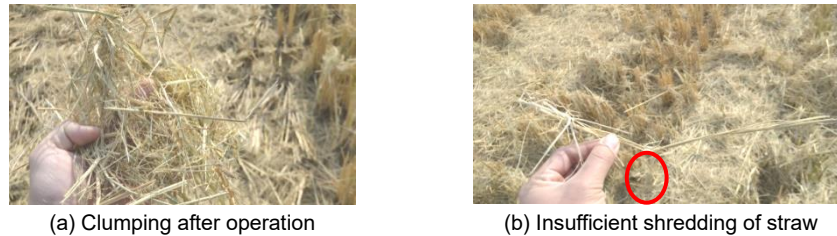


Fig. 6 - Straw scattered on the ground

(1) Analysis of straw cutting force

As an elastic body, straw undergoes two distinct stages during cutting: (1) the initial contact of the moving blade with the straw, leading to extrusion deformation, and (2) the continued movement of the moving blade, causing the straw to plastically deform before being cut. Effective straw cutting occurs in the second stage, making it crucial to study the force state of the moving blade during this phase. Establishing a mechanical model will aid in analyzing the key factors that influence the cutting effect in greater depth.

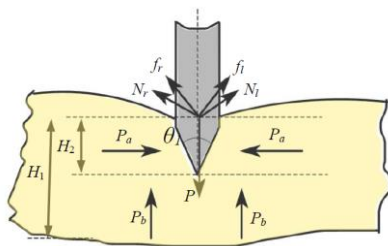


Fig. 7 - Model diagram of a moving knife cutting into a single straw

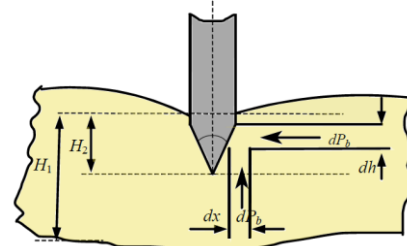


Fig. 8 - Schematic diagram of horizontal and vertical differential forces

As shown in Fig.7, a vertical cross-section model is established when the moving knife cuts into a single straw and the blade is sharpened on both sides. The force applied to the blade during the cutting process is analyzed. During the cutting process, the blade will be subjected to the extrusion force N_1 and N_2 of the straw stem on the blade, which is perpendicular to the sharpening surface in the opposite direction. Under the action of the extrusion force, friction forces f_1 and f_2 will be generated simultaneously. Because the sharpening is symmetrical, ignoring the differences in the microstructure inside the stalk, it can be assumed that $N_1=N_2$ and $f_1=f_2$. Therefore, it can be seen that the cutting force P on the straw at the moment the blade cuts in can be expressed as:

$$\begin{cases} P = 2(N_1 \sin \frac{\theta_1}{2} + f_1 \cos \frac{\theta_1}{2}) \\ f_1 = \mu N_1 \end{cases} \quad (3)$$

where θ_1 is the blade angle of the moving blade, °; μ is the friction coefficient of rice straw.

During the extrusion deformation process of the moving blade, the extrusion force N_1 acting on the grinding blade surface can be decomposed into the horizontal extrusion force P_a and the vertical extrusion force P_b of the straw on the blade (Koolen, 1994), so:

$$N_1 = P_a \sin \frac{\theta_1}{2} + P_b \cos \frac{\theta_1}{2} \quad (4)$$

To bring in factors related to straw characteristics, the extrusion pressure P_a and pressure P_b in the above formula can be obtained by integrating the differential forces in their respective directions (Zhao et al., 2015), as shown in Fig.8. As an elastic body, according to Hooke's law, the strain of straw after impact ϵ can be expressed as:

$$\varepsilon = \frac{\sigma}{E} = \frac{h_x}{H_1} \quad (5)$$

where σ is the stress when the straw is cut, N; E is the instantaneous elastic modulus of the straw when the knife cuts the straw; H_1 is the diameter of the straw before it is cut, mm; h_x is the thickness of the straw after it is squeezed, mm.

Therefore, the vertical squeezing force dP_b acting on the unit length of the straw can be expressed as:

$$dP_b = E\varepsilon \tan \frac{\theta_1}{2} dh_x \quad (6)$$

By integrating both ends of the above equation, the vertical extrusion force P_b can be obtained:

$$P_b = \frac{E}{H_1} \tan \frac{\theta_1}{2} \int_0^{H_2} h_x dh_x = \frac{E}{2H_1} H_2^2 \tan \frac{\theta_1}{2} \quad (7)$$

where H_2 is the thickness of the straw when it is plastically deformed by extrusion, mm.

Similarly, the horizontal extrusion force P_a can be obtained:

$$P_a = \frac{\nu E}{H_1} \int_0^{H_2} h_x dh_x = \frac{\nu E}{2H_1} H_2^2 \quad (8)$$

where ν is the Poisson's ratio of the straw.

Substituting equations 4, 7, and 8 into equations 3, the instantaneous cutting force P on the straw is obtained:

$$P = \frac{EH_2^2}{H_1} \left[\nu \left(\sin^2 \frac{\theta_1}{2} + \mu \sin \frac{\theta_1}{2} \cos \frac{\theta_1}{2} \right) + \tan \frac{\theta_1}{2} \left(\sin \frac{\theta_1}{2} \cos \frac{\theta_1}{2} + \mu \cos^2 \frac{\theta_1}{2} \right) \right] \quad (9)$$

When the instantaneous impact on the straw is more significant, the possibility of the knife cutting into the straw will be greater. According to Equation 9, the instantaneous cutting force on the straw is related to the characteristics of the straw itself. The friction coefficient of the straw and the resistance to bending of the straw impact the instantaneous force. The cutting angle of the moving knife also positively impacts the instantaneous force on the straw, so the cutting angle can be reasonably optimized when designing the blade. In addition, according to Formula 9, it can also be found that when the instantaneous extrusion thickness H_2 of the straw increases, the instantaneous cutting force of the straw increases significantly. Changes in the extrusion thickness H_2 are often related to the movable knife's rotational speed and the cutting blade's support angle. However, due to the straw's stable characteristics, when the movable knife's rotational speed reaches a specific value, the instantaneous extrusion thickness of the straw will not change. When the movable fixed knife supports cutting, increasing the straw cutting support angle can effectively prevent the movement of the movable knife caused by the poor bending strength of the straw, thereby obtaining a greater extrusion thickness. Therefore, when the cutting knife rotates at a certain speed, the straw support characteristics of the crushing knife can improve the straw-cutting effect.

Study on the spreading problem

The harvesting operation test found that the original straw crushing and spreading device had a poor operation effect, and the uneven spreading degree was significantly different from the national standard requirements. Through experimental observation, the main manifestations were: the straw spreading was biased to one side (along the left side of the operation direction), and the straw spreading power was insufficient, resulting in a small spreading width. As shown in Fig.9, the single longitudinal axial flow combine harvester had the phenomenon of straw spreading biased to one side during the crushing and spreading operation. During the operation, no straw was thrown on the right side of the spreading device (in the red frame of the Fig.9), so the straw after throwing was mainly distributed on the left side of the harvester center line, resulting in uneven spreading. As shown in Fig.10, the harvesting width of the entire harvester is D , m; the width of the thrown straw distributed on the left side of the harvester center line is expressed as d , m; in the actual operation process, it was observed that $d < D/2$ and the difference was significant, so the spreading width was small and insufficient to match the harvesting width.



Fig. 9 - Spreading to one side

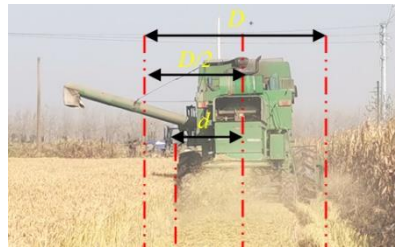


Fig. 10 - Spreading width is insufficient



Fig. 11 - Uneven straw feeding

(1) Study on the problem of spreading to one side

The movement of straw in the chamber of the crushing device is mostly tangential along the rotation of the crushing blade shaft (Mu, 2021). The spreading of straw to one side cannot be attributed to the axial movement of the straw during crushing. Instead, a possible cause is the uneven feeding of straw into the crushing device. To verify this hypothesis, the harvester crushing and spreading device was removed, and the straw flow state was observed after it left the threshing drum and before it entered the crushing device via the grass receiving plate. The straw flow direction is shown in Fig.11. It was observed that the straw flow was already biased to one side after leaving the drum and before entering the crushing device. The straw was not evenly distributed horizontally along the lower edge of the grass receiving plate, leading to the final uneven spreading of straw.

Considering that the straw crushing and spreading device equipped with the combine harvester operates on the straw discharged from the threshing device, the motion analysis of the state of the straw discharged from the threshing drum was carried out. Taking the straw flow with a specific volume as the research object, ignoring the entanglement, squeezing, and dragging effects caused by the continuous discharge between the straw flows, the surface velocity of the straw flow is decomposed. The x-axis direction is to the right in the width direction of the harvester; that is, the right direction is perpendicular to the forward direction of the harvester, and the z-axis direction is vertically upward. As shown in Fig.12, the straw flow will still maintain the tangential velocity v_1 rotating with the threshing drum and the movement velocity v_2 along the surface of the roller grass discharge board due to the centrifugal force of rotation and the support of the roller grass discharge board surface at the moment of separation. At the same time, the straw flow also accelerates a_0 due to its gravity at the moment of separation.

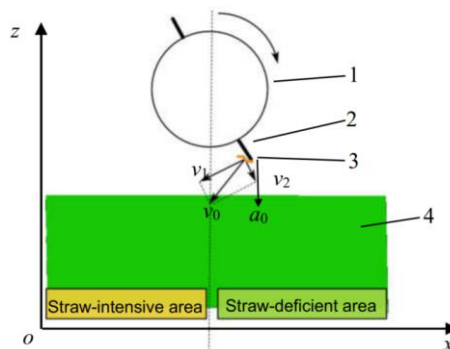


Fig. 12 - Kinematic analysis of the moment when the straw flow leaves the straw discharge plate

1. Threshing device; 2. Grass discharge board; 3. Straw flow; 4. Grass receiving board

Therefore, the instantaneous velocity v_0 of the straw flow leaving the roller straw discharge plate can be expressed as:

$$v_0 = \sqrt{v_1^2 + v_2^2} \quad (10)$$

In the formula, v_1 is the rotation speed of the threshing drum, m/s; v_2 is the movement speed of the straw along the surface of the drum discharge plate, m/s.

According to the literature (Chen et al., 2020; Li et al., 2021), it can be seen that the rotation speed of grain threshing equipment is generally 500~800 r/min, so the speed v_1 is larger than the speed v_2 . Therefore, according to the speed synthesis parallelogram rule, the direction of the speed v_0 is closer to the speed v_1 , which means that the discharged straw flow tends to move to the left.

Although there will be a vertical component force under the action of gravity during the period from when the straw flow breaks away from the straw discharge plate of the drum to when it starts to contact the crushing device and the straw plate, it will not significantly change the direction of the straw flow in a very short time. The continuous flow will form a dense area of straw on the left and a missing area of straw on the right at the bottom of the straw connecting plate of the crushing device. As shown in Fig. 12, this uneven straw feeding into the crushing device ultimately results in a deflected discharge, causing the crushed straw to be cast toward the left side.

From the above analysis, improving the uniformity of the transverse distribution of straw in the straw feeding and crushing device of a single longitudinal axis harvester is extremely important for reducing the unevenness of straw throwing. When optimizing the design, the direction of the straw falling off the drum can be guided, utilizing turbulence to counteract the tendency of the straw to move to the left. This approach helps ensure a more even distribution of straw when it is fed into the crushing device at the bottom of the straw plate.

(2) Research on the problem of insufficient throwing width

A dynamic model of the throwing width was established to study the factors influencing the throwing width of the straw crushing and throwing device assembled with the harvester. At the same time, it was assumed that the up and down rotation of the throwing device and the left and proper adjustment of the deflector did not affect the straw-throwing position. During the process of spreading straw in space, the right direction of the harvester width is used as the x-axis, the opposite direction of the working forward direction (i.e. backward) is used as the y-axis, and the vertical direction is used as the z-axis to establish a coordinate system and scatter the straw in the three-dimensional space. The motion is decomposed into *yoz* and *xoy* plane motions, as shown in Fig.13. v_c represents the operating direction and speed of the harvester, m/s; H_p is the height of the straw throwing point from the ground, m; w_c is the distance between the outermost deflector and the center line of the throwing device, m; w_b is the straw throw distance from the deflector. The movement distance along the x-axis after exiting, m; w_p is half of the width of the straw throwing width, m. The straw throwing speed is v_b , and the corresponding speeds decomposed into the x, y, and z axes are v_{b1} , v_{b2} , and v_{b3} .

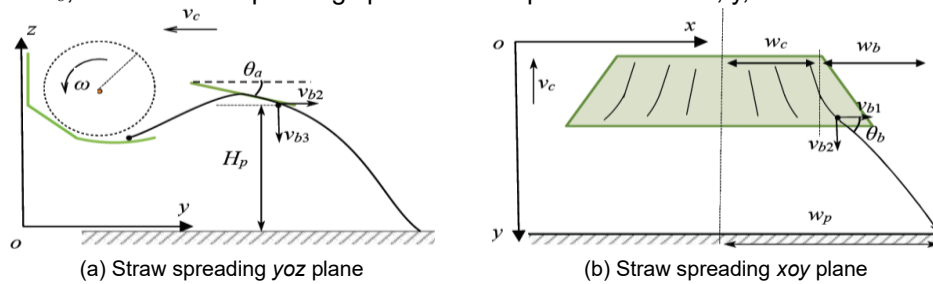


Fig.13 - Straw spreading trajectory of the straw crushing and spreading device

According to Fig.13b, the straw spreading width is twice w_p , and w_p can be expressed as:

$$w_p = w_c + w_b \tag{11}$$

From formula 11, it can be seen that the farthest distance determines the size of the straw spreading width. The straw is thrown under the guidance of the outermost guide plate. When the height H_p of the straw spreading point from the ground remains constant, the velocity v_{b1} of v_b along the x-axis determines the movement distance of the straw along the x-axis. The straw spreading motion can be analyzed using the theory of projectile motion. Referring to relevant literature (Brown, 2001), the motion equation of the straw along the x-axis during the spreading process is:

$$\begin{cases} \frac{d^2x}{dt^2} + k_a \left(\frac{dx}{dt}\right)^2 = 0 \\ k_a = \frac{\rho_a c_a A_a}{2m'} \end{cases} \tag{12}$$

where k_a is the air resistance factor; m' is the mass of the straw to be scattered, kg; ρ_a is the air density, kg/m³; c_a is the air damping coefficient; A_a is the resistance area caused by the shape and size of the straw, m².

To obtain the speed of the straw along the x-axis during the spreading process, equation 12 is integrated and solved. Assume that the initial conditions for spreading are: at spreading time $t=0$, $v_{bx}(0)=v_{b1}$, $x(0)=w_c$, and the speed of the straw along the x-axis at time t is solved as follows:

$$v_{bx}(t) = \frac{dx}{dt} = \frac{v_{b1}}{1 + k_a v_{b1} t} \quad (13)$$

The position coordinates of the straw along the x-axis during the spreading process can be expressed as:

$$x(t) = w_c + \int_0^t v_{dx}(t) dt = w_c + \frac{1}{k_a} \ln(1 + k_a v_{b1} t) \quad (14)$$

wherein, according to the spatial geometric relationship, the velocity v_{b1} along the x-axis can be expressed by the initial velocity of the straw spreading:

$$v_{b1} = \frac{\cot \theta_b}{\sqrt{1 + \tan^2 \theta_a + \cot^2 \theta_b}} v_b \quad (15)$$

Substituting equation 15 into equation 14, it can be obtained:

$$x(t) = w_c + \frac{1}{k_a} \ln\left(1 + \frac{k_a \cot \theta_b}{\sqrt{1 + \tan^2 \theta_a + \cot^2 \theta_b}} v_b t\right) \quad (16)$$

where θ_a is the installation angle of the spreading device, °; θ_b is the angle between the straw throwing speed and the x-axis, °.

Assuming that the time for the straw to fall to the ground after spreading is t_l , the value of w_c can be obtained by substituting it into the above formula. When the installation position of the spreading device is fixed, the installation angle is no longer adjusted, and external conditions remain constant due to the limited landing height, it can be considered that the straw landing time t and the air resistance factor k_a are fixed values. Under these conditions, the straw spreading distance w_p is only related to the throwing speed v_b and the angle θ_b between the throwing speed v_b and the x-axis. The magnitude of the straw throwing speed v_b is influenced by the airflow speed generated during the straw crushing process. The crushed straw will produce collisions and friction under the drainage action of the guide plate. This process can also increase the straw-throwing speed by reducing the kinetic energy loss. Therefore, a well-optimized guide plate layout angle can further enhance the spreading width.

CONCLUSIONS

Through an in-depth analysis of the problems existing in the operation of the original crushing and spreading device of the single longitudinal axial flow combine harvester, the factors requiring improvement in the straw feeding, crushing, and spreading stages were determined. The main conclusions of this study are as follows:

1. Through field test research, it was found that the problems existing in the operation of the straw crushing and spreading device equipped with the combine harvester in the rice-growing area of Northeast China were mainly manifested as straw clumping, insufficient straw crushing, spreading to one side, and insufficient spreading width.

2. A straw-crushing dynamics model was established, and the analysis revealed that the straw-crushing effect is influenced by the characteristics of the straw itself, the crushing knife speed, the blade angle, and the support angle. When the cutting knife operates at a certain speed, enhancing the support characteristics of the crushing knife on the straw can significantly improve the straw-cutting effect.

3. The kinematic models of the straw leaving the threshing drum and the guide plate were established respectively. The analysis showed that the straw flow discharged from the drum tended to move to the left, resulting in uneven straw feeding into the crushing device, which ultimately caused the crushed straw to be thrown to the left. When the installation position of the throwing device was fixed and the installation angle remained unchanged, the throwing width was influenced by the straw throwing speed and the installation angle of the guide plate.

ACKNOWLEDGEMENT

This research was funded by Funded by Shandong Postdoctoral Science Foundation (SDCX-ZG-202400013), National Key Research and Development Project (20106YFD0300909-3) .

REFERENCES

- [1] Brown M.C. (2001). *Velocity Measurements Near an Automotive Cooling Fan*, Master Thesis, University of Windsor.
- [2] Chen Y.P., Kang Y., Wang T.E., Ning X.J., Jin C.Q., Yin X. (2020). Distribution law of threshing material from longitudinal axial flow flexible threshing device of soybean harvester (大豆收获机纵轴流柔性脱粒装置脱出物分布规律). *Journal of China Agricultural University*, 25(09), pp. 104-111, DOI: 10.11841/j.issn.1007-4333.2020.09.11.
- [3] GB/T 24675.6-2009-2009 Conservation tillage machinery Straw crusher and return machine (保护性耕作机械 秸秆粉碎还田机).
- [4] Gong J.L., Luo Z.J., Zhang Y.F. (2024). Optimized design and simulation analysis of longitudinal flow corn cone threshing device. *INMATEH - Agricultural Engineering*, 73(2), pp.63-72, DOI: 10.35633/inmate-73-05.
- [5] Jankauskas V., Abrutis R., Žunda A., Gargasas J. (2023). Wear Study of Straw Chopper Knives in Combine Harvesters. *Applied Sciences*, 13(13), 7384, pp 1-19, <https://doi.org/10.3390/app13137384>.
- [6] Koolen A.J. (1994). Chapter 2 - Mechanics of Soil Compaction. *Developments in Agricultural Engineering*, 11, pp 23-44, DOI: 10.1016/B978 - 0 - 444 - 88286 - 8.50010 – 6.
- [7] Li H.B., Wang Q.H., Ma J., Yue D., Geng D. (2023). Design and experiment of transverse axial flow corn flexible threshing device. *INMATEH - Agricultural Engineering*, 69(1), pp. 461-470, DOI: <https://doi.org/10.35633/inmateh-69-43>.
- [8] Li X.P., Wang W.Z., Zhao G.Y., Sun C.C., Hu P.Z., Ji J.T. (2021). Design and Experiment of Rice Straw Chopping Device for Agitation Sliding Cutting and Tearing (纵轴流双柔性碾搓式谷子脱粒装置设计与试验). *Transactions of the Chinese Society of Agricultural Machinery*, 52(07), pp. 113-123, DOI: 10.6041/j.issn.1000-1298.2021.07.011.
- [9] Mu G.Z. (2021). *Study on Key Technologies and Devices of Crushing and Throwing in Ridge-Imitating Sweet Potato Vine Recycling Machine (仿垄式甘薯秧回收机粉碎抛送关键技术与装置研究)*, PhD dissertation, Shandong Agricultural University.
- [10] Sun N.N., Wang X.Y., Li. H.W., He J., Wang Q., Wang J., Liu Z., Wang Y. (2019). Design and experiment of differential sawing rice straw chopper for turning to field (差速锯切式水稻秸秆粉碎还田机设计与试验), *Transactions of the Chinese Society of Agricultural Engineering*, 35(22), pp. 367-276, DOI: 10.11975/j.issn.1002-6819.2019.22.032.
- [11] Vlăduț V., Biris S.Ș., Paraschiv G., Ungureanu N., Bungescu S.T., Voiceal I., Cujbescu D., Găgeanu I., Laza E., Popa L.D., Matel G., Atanasov A. (2023). Considerations regarding the effects of shocks and vibrations on operators of self-propelled agricultural equipment. *INMATEH - Agricultural Engineering*, 52(07), pp. 843–856, <https://doi.org/10.35633/inmateh-71-74>.
- [12] Vlăduț N.V., Ungureanu N., Biriș S.Ș., Voicea I., Nenciu F., Găgeanu I., Cujbescu D., Popa L.D., Boruz S., Matei G., Ekielski A., Teliban G.C. (2023). Research on the Identification of Some Optimal Threshing and Separation Regimes in the Axial Flow Apparatus. *Agriculture*, 13(4), 838, pp.1-17, <https://doi.org/10.3390/agriculture13040838>.
- [13] Wang J., Wang X.Y., Li. H.W., He J., Lu C., Liu D. (2021). Design and experiment of rice straw chopping device for agitation sliding cutting and tearing (水稻秸秆激荡滑切与撕裂两级切割粉碎装置设计与试验), *Transactions of the Chinese Society of Agricultural Machinery*, 52(10), pp. 28-40, <https://nyjxxb.net/index.php/journal/article/view/1243>.
- [14] Wang J., Wang X.Y., Li. H.W., Lu C.Y., He j., Wang Q.J., Liu D., Deng B., Zhang M.Y. (2022). Improvement of Straw Throwing Performance of Harvester Based on Matching Header Width. *Agriculture*, 12(9), 1291 pp. 1-20, <https://doi.org/10.3390/agriculture12091291>.
- [15] Wang J.W., Tang H., Wang J.F. (2017). Comprehensive Utilization Status and Development Analysis of Crop Straw Resource in Northeast China (东北地区作物秸秆资源综合利用现状与发展分析). *Transactions of the Chinese Society of Agricultural Machinery*, 48(05), pp. 1-21, DOI:10.6041/j.issn.1000-1298.2017.05.001.
- [16] Wang X. (2018). *Design and Test of Shredding and Scattering Machine for Longitudinal Axial Flow Rice and Wheat Combine Harvester (纵轴流稻麦联合收获机后切碎抛撒装置设计与试验)*, Master Thesis, Chinese Academy of Agricultural Sciences.

- [17] Wang X., Jin C.Q., Xu J.S., Ni Y.L. (2018). Research status and trend of the crop straws of combine harvester (联合收割机后秸秆切碎抛撒研究现状与趋势). *Journal of Chinese Agricultural Mechanization*, 39(01), pp. 1-6, DOI: 10.13733/j.jcam.issn.2095-5553.2018.01.001.
- [18] Wang Z.T., Ling J., Liu Z.X., Zhao D.Q., Li Z.X., Zhou S.L., Yuan X.M., Li X.H., Wen Y. (2023). Effect of straw return practices on soil physico-chemical properties and maize yield (秸秆还田方式对土壤理化性质和玉米产量的影响), *Chinese Journal of Eco-Agriculture*, 32(04), pp. 663-674, DOI: 10.12357/cjea.20230517.
- [19] Zhao F.Q., Wu C.Y., Huang M.S. (2015). Analysis of the cutting mechanism for straw chopper mounted on whole feeding combine harvester (全喂入联合收割机切碎装置茎秆切割机理分析). *Journal of Chinese Agricultural Mechanization*, 36(02), pp. 9-12, DOI: 10.13733/j.jcam.issn.2095-5553.2015.02.003.
- [20] Zhang H., Hobbie E.A., Feng P., Zhou Z., Niu L., Duan W., Hao J., Hu K. (2021) Responses of soil organic carbon and crop yields to 33-year mineral fertilizer and straw additions under different tillage systems. *Soil and Tillage Research*, 209, 104943, pp. 1-9, <https://doi.org/10.1016/j.still.2021.104943>.
- [21] Zhang Z.Z., Xie F.P., Tian L.Q., Liu D.W., Wang X.S., Li X. (2021). Current situation and development trend of threshing and separating system of international grain combine harvester (国外谷物联合收割机脱粒分离系统发展现状与展望). *Journal of Chinese Agricultural Mechanization*, 42(1), pp. 20-29, DOI: 10.13733/j.jcam.issn.2095-5553.2021.01.004.

DETERMINATION OF PHYSICAL PARAMETERS OF PELLETTED RICE SEEDS AND CALIBRATION OF DISCRETE ELEMENT SIMULATION PARAMETERS

丸粒化水稻种子物性参数测定与离散元仿真参数标定

Qianshu MA¹⁾, Tongjie LI¹⁾, Donghan XU¹⁾, Qingqing WANG^{*1)}

¹⁾Anhui University of Science and Technology, Bengbu, China

^{*)} Corresponding author E-mail: qqwang@ahstu.edu.cn; Tel: +86-13195519097

DOI: <https://doi.org/10.35633/inmateh-75-42>

Keywords: pelleted rice seeds; seed mechanics; simulation experiment; parameter calibration

ABSTRACT

The calibration of parameters for pelleted rice seeds (PR) is crucial for enhancing research on PR-related machinery and for executing high-speed precision hole sowing with unmanned aerial vehicles. This paper focuses on determining the fundamental physical and contact parameters of PR. A series of tests were conducted, including the Plackett-Burman test, the steepest ascent test, and the Box-Behnken test, using the stacking angle as the primary variable. These tests led to the identification of optimal combinations of simulation parameters. Specifically, the coefficients of rolling friction for the PR-PLA plate and PR-PR were measured at 0.137, while the coefficient of static friction for the PR-PLA plate was 0.336. This study provides a reference for calibrating simulation parameters of pelleted seeds and research on high-speed precision seeding.

摘要

丸粒化水稻种子的参数标定, 可以为丸粒化水稻相关机械的研究及无人机的高速精量穴播提供指导。本文以丸粒化的水稻为对象, 对其基本物性参数和接触参数开展测定。以堆积角为试验值进行 Plackett-Burman 试验、最陡爬坡试验和 Box-Behnken 试验, 获得最佳仿真参数组合 (丸粒化水稻种子-PLA 板滚动摩擦系数、丸粒化水稻种子-丸粒化水稻种子滚动摩擦系数及丸粒化水稻种子-PLA 板静摩擦系数分别为 0.137、0.137、0.336), 该研究能够为丸粒化种子的仿真参数标定及高速精量播种研究提供参考。

INTRODUCTION

Rice is one of the most vital food crops globally and serves as a crucial source of sustenance for over half of the world's population (Djavan. et al., 2025). It is not only a staple in many countries but is also used in a variety of recreational dishes (Ning, 2016).

Rice planting represents a crucial aspect of rice production, with the planting technology exerting a direct influence on yield (Cai. et al., 2023). Currently, three methods of mechanical planting are in use: potting transplanting, mechanical transplanting, and mechanized direct seeding. The first two of these require seedling transplanting, a relatively complex process that results in higher overall production costs for seedling transplanting (Xue et al., 2022). The mechanized direct seeding of rice has the potential to streamline the planting process, and it has gained significant traction in numerous countries and regions in recent years. The majority of existing rice direct seeding techniques employ the use of tractor-tractor seeders and drones. The method of tractor-tractor seeders is still primarily limited to strip seeding, with precision seeding also facing significant challenges, particularly in the precise separation of rice seeds from the population. Additionally, the use of ground machinery has been observed to have relatively low efficiency. While existing unmanned aircraft seeding is highly efficient, it remains primarily a sowing method with several limitations. These include the disorderly arrangement of seeds on the ground and the difficulty of rapidly and precisely separating them from the population. The unique physical characteristics of rice, including high flow resistance and adhesion, present a significant challenge to the rapid and precise separation of seeds from the population, which has been a key obstacle to the development of high-speed precision rice planting.

¹⁾ Qianshu MA, master degree; Tongjie LI, Prof. Dr. Master's Degree Tutor; Donghan XU, master degree; Qingqing WANG*, Dr, Lecturer.

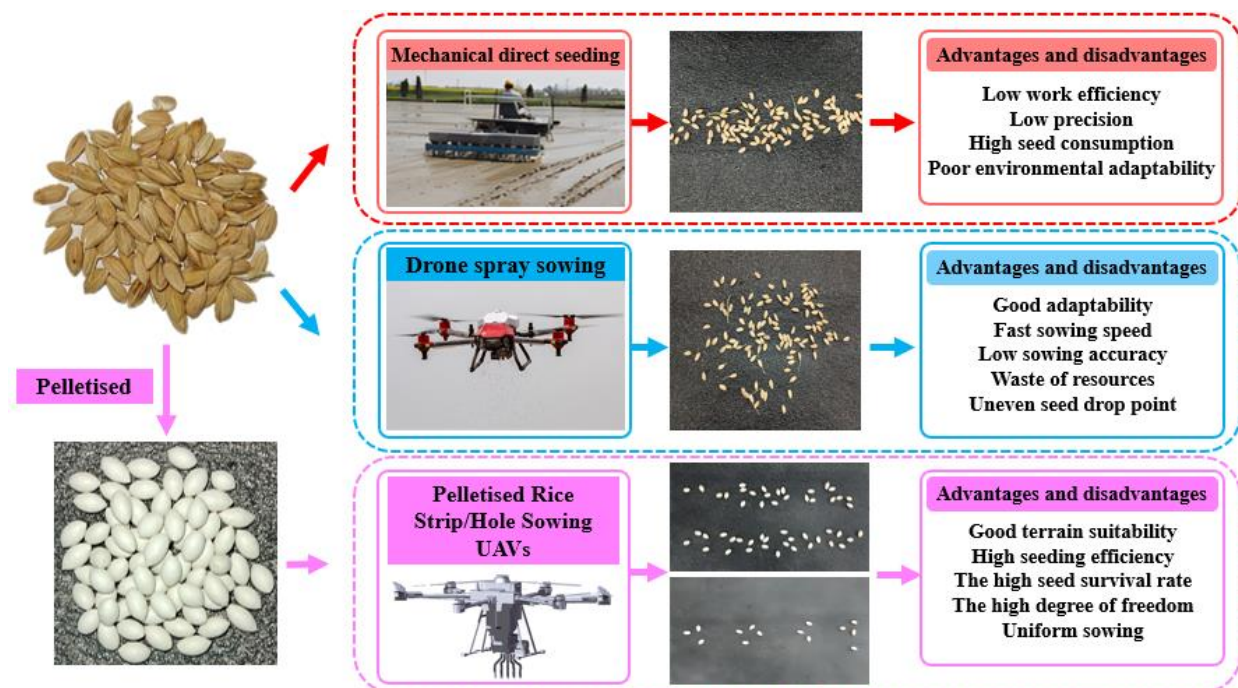


Fig. 1 - Comparison of direct seeding methods for rice

In light of the aforementioned considerations, our team proposed a method of pelleted rice seeds (PR), which can effectively solve the problem of rapid precision separation from the seed population, thus improving the sowing accuracy and sowing efficiency to carry out the subsequent high-speed precision planting of rice, as shown in Fig. 1, in the light of the characteristics of the physical structure of rice and planting needs. Seed pelleting treatment have been used in applications where germination, seedling emergence, resistance, and resistance to pests and diseases are improved (Ma et al., 2023; Yang et al., 2020; Wang et al., 2024). During the sowing process of PR, the forces between seeds and seeds and seeds and seed discharger are more complicated, and the parameter calibration of PRs can be carried out to find out their physical properties and promote the optimal design of pelleted seed discharger for precision hole sowing.

To date, researchers in both domestic and international settings have conducted simulations to calibrate discrete metamodelling about fertilizers, soils, seeds, and crops. In a previous study, Wen Xiangyu et al. (2020) proposed a friction factor calibration method based on the overall characteristics of granular materials. This method was then used to calibrate the discrete meta-simulation parameters between urea particles and PVC materials. This calibration was carried out according to the results of the analysis of variance (ANOVA) of different particle characteristics testing methods. In a further contribution to this field of study, Wang Xianliang et al. (2021) employed the Edinburgh Elasto-Plastic Adhesion nonlinear elastic-plastic contact model to calibrate the parameters of a discrete element simulation model of perennial no-tillage agricultural soil. Balevičius et al. (2011) conducted a sliding test to measure the static coefficient of friction between peas and Plexiglas. González-Montellano et al. (2012) investigated direct measurement methods for some parameters in discrete element simulation. Xuejie Ma et al. (2022) calibrated the contact parameters of alfalfa seed and coating powder as the main research objects and carried out the related discrete element simulation parameter calibration. Peng Zhang et al. (2022) simulated and determined the contact parameters such as stacking angle, collision recovery coefficient, static friction factor, etc., using Xinjiang cotton straw as the test material. As evidenced by the aforementioned research, the majority of discrete element simulation parameters have been calibrated for large seeds and soil. However, there is a lack of research on the calibration of discrete element simulation parameters for PR and other pelleted crop seeds.

In this paper, the discrete element simulation model of PR was calibrated and validated by combining physical tests with discrete element simulation. The angle of repose was used as the response variable. Furthermore, the Plackett-Burman test, the steepest-climbing test, and the Box-Behnken test were conducted sequentially. A two-sample t-test was conducted on the simulation results and experimental data using SPSS 23 software to ascertain the reliability of the simulation tests and identify the optimal combination of simulation parameters. This study serves as a reference for developing high-speed precision seeding of granular seeds, which aids in optimizing both the seeding equipment and the seed treatment process.

MATERIALS AND METHODS

Calibration of test materials and physical parameters

This paper is based on the study of early and mid-grain rice grown in large areas in southern and northern China. Hui Liangyu silk seed was used as an experimental subject to determine the external dimensions, thousand kernel weight, Poisson's ratio, and other basic physical properties of PR.

The PR exhibited an ellipsoidal shape, a compact texture, and a smooth surface. These characteristics could enhance the mobility and population separability of the seeds, as illustrated in Fig. 2. A total of 1,000 pill-PR were randomly selected and weighed using an electronic scale with an accuracy of 0.01 g to determine the thousand-grain weight. The seeds were divided into 10 groups and weighed separately, and the average value was calculated. The thousand-grain weight of the pill-PR was found to be 134.05 g. The external dimensions of the pill-PR were measured using a numerical vernier caliper (with an accuracy of 0.01 mm), as illustrated in Fig. 2. The mean diameter (D) and length (L) of the seeds were found to be 5.17mm×9.71mm, according to the measurement results.

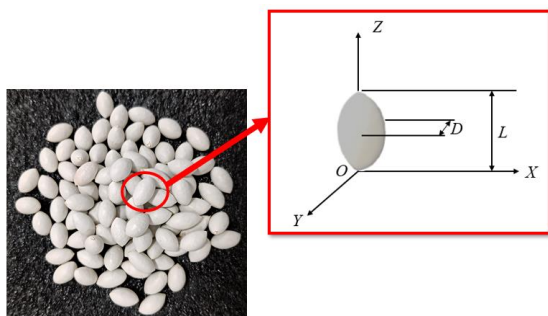


Fig.2 - Characteristic dimensions of PR



Fig.3 - Pressure deformation test of PR

One hundred PR were randomly selected and their original dimensions in radial (X-axis) and axial (Z-axis) directions were recorded. The compression deformation test of the PR was carried out using a universal material testing machine (UTM2501/50N, Shenzhen Sanshi Zongheng Technology), as shown in Fig. 3, with a test speed of 0.1 mm/min until the surface of the PR just broke (*Dun et al., 2024*). The radial deformation of the PR before and after the test was obtained using a universal material testing machine, and then the axial deformation of the PR was measured using electronic calipers (accuracy of 0.01 mm), and the Poisson's ratio of the PR was calculated to take the average value of 0.42.

A total of one hundred PR were randomly selected and their original dimensions in the radial (X-axis) and axial (Z-axis) directions were recorded. A universal material testing machine (UTM2501/50N, Shenzhen Sanshi Zongheng Technology) was employed to conduct pressure deformation tests on PR at a rate of 0.1 mm/min until the surface of the PR reached the point of rupture (*Dun et al., 2024*). The radial deformation of the PR was obtained using a universal material testing machine before and after the test. The axial deformation of the PR was then measured by electronic vernier calipers (accuracy of 0.01 mm), and the Poisson's ratio of the PR was calculated to yield an average value of 0.42.

Determination of exposure parameters

The contact parameters are primarily comprised of the static friction coefficient, rolling friction coefficient, collision recovery coefficient, and stacking angle (*Hou et al., 2020*). The contact parameters between the PR and the contact materials, as well as between the seeds themselves, represent crucial design parameters for a seed discharge device. In light of the engineering practice and the manufacturing materials of the seed discharger (*Xing et al., 2020*), this paper selects the contact parameters between the steel plate, the PLA material, and the PR, as well as the contact parameters between the PR.

Static Friction Coefficient Measurement Test

In this experiment, the static friction coefficients of PR were measured using the oblique method (*Cong, 2014*), which involved the use of steel plates and PLA plates. The coefficients were determined by observing the forces acting between the seeds, pellets, and plates. The test was conducted on a custom-built apparatus, and the dimensions ($L \times W \times H$) of the steel plate utilized for testing were 300mm×300mm×1mm, while the dimensions ($L \times W \times H$) of the PLA plate were 200mm×150mm×10mm, as illustrated in Fig. 4. The measurement will be taken along the long axis of the plate to be tested. The inclination angle of the plate will be increased

gradually until the PR begins to slide down its surface. This angle, which represents the sliding friction angle θ , will be recorded. Ten randomly selected PR seeds underwent three repetitions of the test to determine the tangent value of the sliding friction angle. This method was adopted to determine the static friction coefficient of the PR. The mean value of the static friction coefficient between the PR and the steel plate was 0.32, while the mean value of the static friction coefficient between the PR and the PLA plate was 0.34. To determine the coefficient of static friction between PR, the seeds were affixed to the PLA plate with tape, as illustrated in Fig. 4c. The resulting average value of the static friction coefficient between PR was 0.5.



Fig.4(a) - Test rig for coefficient of static friction between PR and steel plate



Fig.4(b) - Test rig for coefficient of static friction between PR and PLA plates



Fig. 4(c) - Test rig for inter-seed static friction coefficient of PR

Rolling Friction Coefficient Measurement Test

In this study, the side slope test method, as described by *Dun et al.*, (2024), was employed for the measurement of the variables under investigation. The underlying test principle is illustrated in Fig. 5. The apparatus comprises a PLA plate with a known inclination angle and a horizontal PLA plate. To conduct the rolling friction coefficient test between PR and the PLA plate, the PR is positioned on the inclined PLA plate, with an inclined rolling length of 30 mm. This allows the seeds to roll naturally under the influence of gravity, and the rolling distance of the seeds is then measured on the horizontal PLA plate. The rolling distance between the PR and the PLA plate is derived from the formula (1). The rolling friction coefficient between the PR and the PLA plate was determined through a series of 10 repetitions (*Wen et al.*, 2020). The resulting mean value was calculated to be 0.14.

$$mg \sin \theta \times h_0 = \mu_0 mg \cos \theta \times h_0 + \mu_0 mgh_1 \quad (1)$$

where:

m is the mass of PR, [Kg]; θ is the PLA plate tilt angle, [°]; h_0 is the rolling length of PR on an inclined PLA plate, [mm]; μ_0 is the coefficient of rolling friction between PR and PLA plates; h_1 is the rolling length of PR on a horizontal PLA plate, [mm].

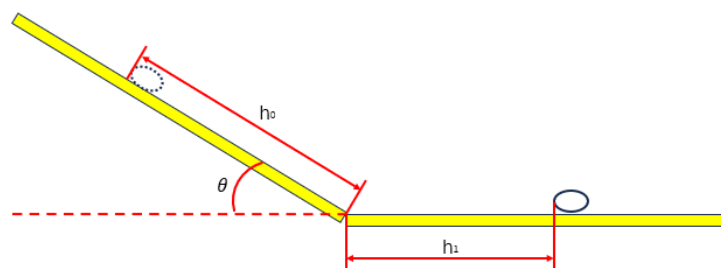


Fig.5 - Schematic diagram of side slope test

Replace the PLA plate in the above device with a steel plate, repeat the above test, and refer to the relevant literature (*Fan et al.*, 2024) to determine the rolling friction coefficient between the PR and the steel plate is 0.15.

In determining the rolling coefficient of friction between PR seeds, adhesive tape was used to uniformly fix the PR seeds onto two PLA boards. To account for the increase in rolling friction coefficient between the seeds, the angle of the inclined seed board was adjusted so that the sloping rolling length remained 30 mm. The above test was repeated 10 times, and following the relevant literature (*Wen et al.*, 2020), the average rolling coefficient of friction between PR seeds was determined to be 0.14.

Crash recovery factor

Mutual extrusion and collision are expected to occur between PR seeds and the seed discharger during the seed discharge process. To quantify this phenomenon, the interspecies collision recovery coefficient must be calculated (Hou *et al.*, 2020). This coefficient is defined as the ratio of the relative velocity of separation of two objects after a collision to their relative approach velocity before the collision. It is calculated using Equation (2) (Dun *et al.*, 2024). The collision recovery coefficient was determined through a free-fall test, the methodology of which is illustrated in Fig. 6. The distance between the funnel of the test bench and the PLA plate was set to 100 mm. The background plate had a spacing of 10 mm per frame, and a digital camera was used for high-speed photography, with the video slowed down by a factor of 10. The rebound height was measured after the seeds made contact with the PLA plate. Each set of data was tested 10 times, and the average value was calculated. The results yielded a collision recovery coefficient of 0.298 between PR and the PLA plate, 0.279 for interspecies collisions of PR, and 0.320 between PR and the non-steel plate.

$$e = \frac{|v_2 - v_1|}{|V_2 - V_1|} = \frac{|v_2|}{|V_2|} = \sqrt{\frac{h}{H}} \quad (2)$$

where:

V_1 is the initial velocity of the PR in free fall, i.e. $V_1 = 0 \text{ m/s}$; V_2 is the initial velocity of the PR before it touches the PLA plate, [m/s]; v_1 is the velocity of the PR when it bounces up at the highest point after colliding with the PLA plate, [m/s]; v_2 is the velocity of the PR after colliding with the PLA plate, i.e. $v_2 = 0 \text{ m/s}$; h is the height of the PR before free fall, [mm]; H is the highest height at which the PR bounces back from the free-fall collision with the PLA plate, [mm].

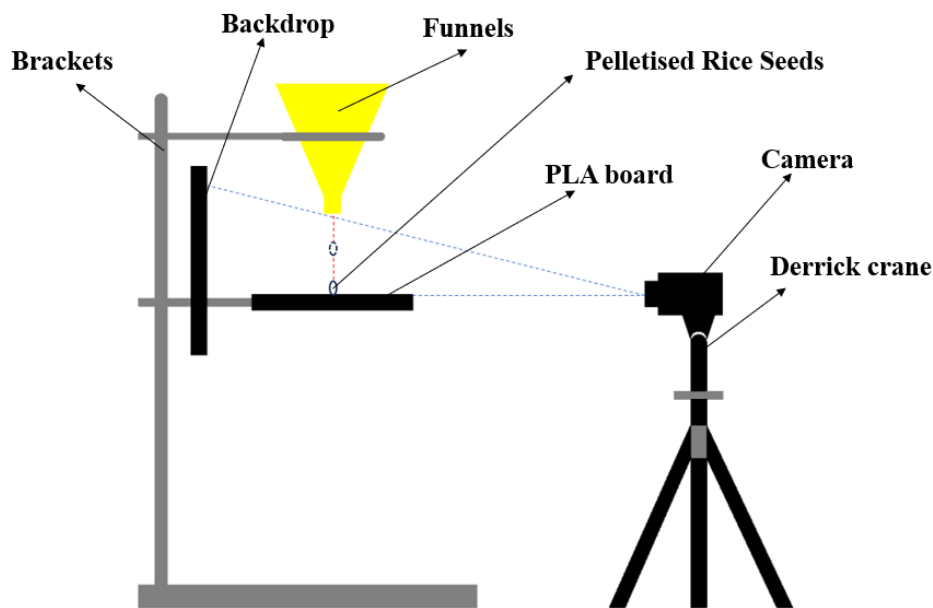


Fig. 6 - Schematic diagram of free fall test for PR

Stacking angle

The stacking angle is a macroscopic parameter that reflects the fluidity and friction characteristics of granular materials. Additionally, a seed stacking process occurs during the sowing of PR. To further verify the accuracy of the calibration parameters, the stacking angle was selected as a test index. In this experiment, the stacking angle was measured using the funnel method, as previously described in detail by Zhu *et al.*, (2022) and Al-Hashemi B.M.H. *et al.*, (2018). The test is shown in Fig. 7(a). The PR is placed into the funnel, where it falls into a pile on the PLA platform. The centerline of the camera is set to the same height as the PLA platform. Images of the PR stacking are captured using image processing software to measure the stacking angle, as illustrated in Fig. 7(b). This process is repeated 10 times to obtain an average angle, which represents the pill-PR stacking angle.

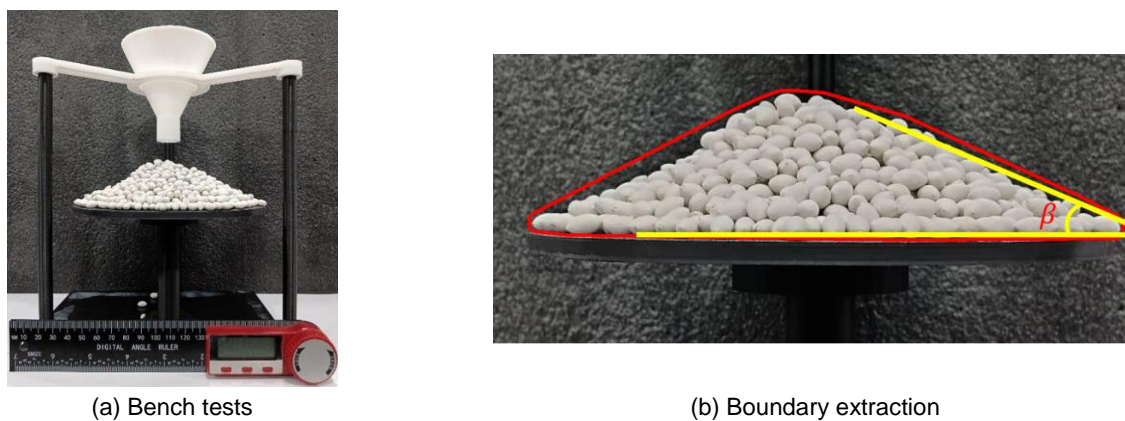


Fig. 7 - PR stacking angle test

Discrete elemental modeling of PR and calibration of simulation parameters

Development of a discrete meta-simulation model for PR

The external dimensions of the PR were determined through preliminary physical testing. Based on the test data obtained, the average dimensional values for each axis were calculated and then modeled using SolidWorks software. The generated models were saved in STL format and subsequently imported into EDEM software. As demonstrated in the related literature (Zhang *et al.*, 2017), the simulation modeling process is most significantly affected by the interaction between PR-PR, and PR-PLA plates, as well as the size and shape of the simulation model. The contour of the model, the rounded corners of the edges filled with PR, and the PR filled with spherical particles via EDEM software had minimal effect on the simulation results.

In the EDEM simulation test, the data obtained from the aforementioned test were inputted, and the stacking angle determination model was drawn according to the size of the actual stacking angle determination device, as illustrated in Fig. 8. A particle factory was constructed at the large aperture above the funnel for the dynamic generation of PR. The PR was generated in a fixed form (Hou *et al.*, 2020), with a generation rate of 1000 particles/s and a total of 600 particles. The grid size was three times the minimum particle radius (Hu, 2010). At the outset of the simulation, the PR was generated from the pellet plant situated above the funnel and subsequently descended under the influence of gravity. The seeds were generated in a continuous stream over 0.6 seconds, after which the simulation concluded at 2 seconds. The seeds coalesced into a seed pile on the chassis, and the stacking angle was subsequently determined through post-processing of the seed pile.

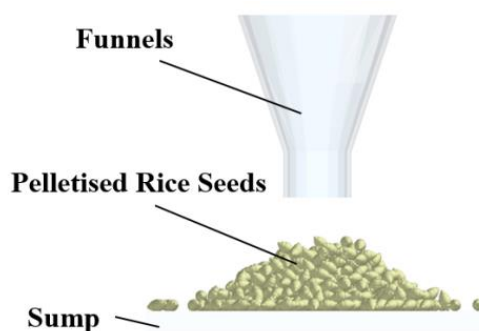


Fig. 8 - A simulation model for determining the stacking angle of PR

Discrete element simulation parameter calibration

Determination of the significant impact factor

The Design-Expert software was used in this study for the design of the Plackett-Burman experiment and data analysis. Plackett-Burman is a two-level design of experiments method that identifies significant parameters by comparing the difference between two levels of each parameter to the overall difference to determine the significance of the parameter (Bai *et al.*, 2023). The experimental parameters were identified based on the results of the physical tests described earlier. Parameters that had a significant effect on the response values were identified using the Plackett-Burman test (Li *et al.*, 2020). The maximum and minimum values of the seven test parameters listed in Table 1 were assigned +1 and -1, respectively. The Plackett-Burman test protocol and results are listed in Table 2.

Table 1

Plackett-Burman test parameter range table

Test parameters	Low level(-1)	High level(+1)
Poisson's ratio of PR (x1)	0.3	0.5
Rolling friction coefficient of PR-PLA plate (x2)	0.1	0.2
PR - Rolling Friction Coefficient of PR (x3)	0.1	0.2
Coefficient of static friction of PR-PLA plate (x4)	0.3	0.4
PR - Coefficient of static friction of PR (x5)	0.4	0.6
PR-PLA plate collision recovery coefficient (x6)	0.2	0.4
PR - Collision Recovery Coefficient of PR (x7)	0.2	0.4

Table 2

Plackett-Burman test program and results

Serial number	Test parameters							Stacking angle
	x1	x2	x3	x4	x5	x6	x7	
1	1	1	-1	1	1	1	-1	24.65
2	-1	1	1	-1	1	1	1	28.48
3	1	-1	1	1	-1	1	1	28.03
4	-1	1	-1	1	1	-1	1	25.77
5	-1	-1	1	-1	1	1	-1	23.31
6	-1	-1	-1	1	-1	1	1	17.63
7	1	-1	-1	-1	1	-1	1	18.10
8	1	1	-1	-1	-1	1	-1	19.05
9	1	1	1	-1	-1	-1	1	24.45
10	-1	1	1	1	-1	-1	-1	33.95
11	1	-1	1	1	1	-1	-1	34.61
12	-1	-1	-1	-1	-1	-1	-1	16.72

The data were imported into Design-Expert 13.0 software for analysis of variance (ANOVA) of the experimental results to determine the effect of each parameter. From the analysis, it was found that the coefficient of rolling friction of PR-PLA plate (X2), the coefficient of rolling friction of PR-PLA plate (X3) and the coefficient of static friction of PR-PLA plate (X4) had a significant effect on the stacking angle of PR, with P-values of 0.0726, 0.0024, and 0.0096, respectively. These values indicate a significant impact on the stacking angle, while the remaining parameters had relatively minor effects. Therefore, only the above three factors with significant effects were considered in the subsequent steepest climb test and Box-Behnken test.

Steepest climb test design

Based on the results of the Plackett-Burman test, the steepest climb test was conducted for the three selected significance factors (coefficient of rolling friction of PR-PLA plate, coefficient of rolling friction of PR-PLA seed, and coefficient of static friction of PR-PLA plate), and the relative error between the simulated stacking angle and the actual stacking angle was taken as the evaluation index to determine the optimum ranges of the above three test parameters (Liu et al., 2020). The design scheme and results of the steepest climb test are shown in Table 3.

For the simulation tests, all other insignificant parameters from the theoretical test results mentioned above were used: the PR Poisson's ratio 0.42, the PR-PR static friction coefficient 0.5, the PR-PLA plate collision recovery coefficient 0.298, and the PR-PR collision recovery coefficient 0.279.

Table 3

Steepest Climbing Test Design Options and Results

Serial number	x2	x3	x4	Stacking angle (°)	Relative error/%
1	0.1	0.1	0.3	15.82	0.323642582
2	0.12	0.12	0.32	20.22	0.135528003
3	0.14	0.14	0.34	25.3	0.081658829
4	0.16	0.16	0.36	27.24	0.164600257
5	0.18	0.18	0.38	29.24	0.250106883

According to the relative error results in Table 4, it can be seen that the rolling friction coefficient of PR and PLA plate and PR are both 0.14, and the static friction coefficient of PR-PLA plate is 0.34, the relative error between the simulated stacking angle and the actual stacking angle is small. It can be determined that the range of optimal intervals is in the vicinity of No. 3. Therefore, the follow-up will take No. 3 as the center point, and No. 2 and No. 4 as the low, high levels for subsequent Box-Behnken response surface tests.

Box-Behnken experimental design

In this paper, the Box-Behnken test design was performed using Design-Expert 13.0 software. This method fits a functional relationship between the parameters and response values to determine the interactions among the parameters. The solver is used to find the optimal values of the significant parameters (Bai et al., 2023). The Box-Behnken test for significance parameters was performed with No. 3 as the center point, No. 2 and No. 4 as the low (-1) and high (+1) levels, and all other parameters in the simulation test were set according to the parameters used in the steepest climb test. The test scheme and results are shown in Table 4.

Table 4

Box-Behnken experimental design scheme and results

Serial number	x2	x3	x4	Stacking angle (°)
1	-1	-1	0	23.77
2	1	-1	0	25.88
3	-1	1	0	25.54
4	1	1	0	27.62
5	-1	0	-1	24.81
6	1	0	-1	22.84
7	-1	0	1	23.45
8	1	0	1	26.71
9	0	-1	-1	24.98
10	0	1	-1	27.18
11	0	-1	1	26.89
12	0	1	1	27.16
13	0	0	0	23.57
14	0	0	0	23.15
15	0	0	0	23.90

The above test results were analyzed and fitted with multiple regression using Design-Expert 13.0 software to obtain the following second-order regression equations for the stacking angle of the PR simulation test:

$$\beta = 23.54 + 0.56A + 0.5675B + 0.575C - 0.2575AB + 1.31AC - 0.4325BC - 0.0687A^2 + 1.98B^2 + 0.9812C^2 \tag{3}$$

RESULTS

The results of Box-Behnken test ANOVA are shown in Table 5. From the analysis of the results in Table 5, it can be observed that factors A (x1), B (x2), C (x3), AC, B2, and C2 have a significant effect on the stacking angle, while the effect of AB, BC, A2 on the stacking angle is not significant. The p-value of this fitted model is 0.0013 (p<0.01), which indicates the relationship between the dependent and independent variables and its significance in the model; the lack-of-fit term P=0.5003>0.05, suggests that the model is well fitted. The coefficient of determination for the second-order regression equation of the stacking angle R^2=0.9775 and the adjusted coefficient of determination is R^2=0.9371, both of which are very close to one. In general, the

higher the coefficient of variation (CV), the lower the reliability of the test, In this test, the CV=1.56% which indicates that the fitted equation has a high degree of credibility and accurately represents real conditions, thereby verifying the test's reliability.

Table 5

Box-Behnken design Second order regression equation Analysis of variance

Source	Sum of squares	df	Mean Square	P-value
Model	33.2	9	3.69	0.0013
A (x1)	2.51	1	2.51	0.0098
B (x2)	2.86	1	2.86	0.0075
C (x3)	2.64	1	2.64	0.0088
AB	0.2652	1	0.2652	0.2446
AC	6.84	1	6.84	0.0011
BC	0.7482	1	0.7482	0.0777
A ²	0.0175	1	0.0175	0.749
B ²	14.49	1	14.49	0.0002
C ²	3.56	1	3.56	0.0048
Residual	0.7631	5	0.1526	
Lack of fit	0.4805	3	0.1602	0.5003
Pure Error	0.2826	2	0.1413	
Cor Total	33.96	14		
<i>R² = 0.9775; Adjusted R² = 0.9371; CV = 1.56%</i>				

In the data analysis optimization module of Design-Expert 13.0 software, the second-order regression equations were refined by averaging the results from 100 sets of optimal combinations. The coefficient of rolling friction between PR and PLA plates was found to be 0.137, reflecting the interaction of the PR on the surface of the PLA plate as well as among the seeds themselves. Meanwhile, the coefficient of static friction for the PR against the PLA plate was measured at 0.336, indicating the maximum frictional force encountered when the PR remains relatively stationary before rolling. The remaining parameters, which were considered insignificant, were averaged based on physical tests. To validate the accuracy of these optimal parameter combinations, simulation tests were performed using EDEM, as depicted in Fig.9. The stacking angles recorded from three replicates were 24.15°, 23.97°, and 22.97°. A t-test analysis comparing the simulation results with the actual test values, conducted using SPSS 23 software, produced a p-value of 0.481, which exceeds the 0.05 threshold. In statistical terms, a p-value greater than 0.05 typically indicates no significant difference between the two data sets. Consequently, this result confirms that the outcomes of the simulation tests align closely with the real physical test values, further demonstrating the accuracy and reliability of the optimal parameter combination.

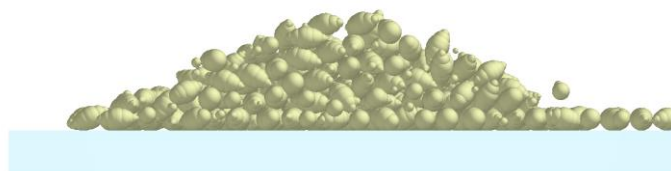


Fig. 9 - Validation of discrete element simulation of pile-up angle of PR

CONCLUSIONS

(1) The physical properties of the particulate material—including external dimensions, micrometric weight, and Poisson's ratio—along with the contact parameters, such as the static friction coefficient, rolling friction coefficient, and collision recovery coefficient, are established through physical testing. This process provides the essential parameters required for the discrete element simulation of the particle system.

(2) The Plackett-Burman test was performed according to the specified parameters to determine which factors most significantly affect the PR stack angle. The parameters under investigation include the rolling friction coefficient of the PR-PLA plate, the rolling friction coefficient of the PR-PR, and the static friction coefficient of the PR-PLA plate.

(3) The second-order regression equation for the stacking angle was derived using a Box-Behnken test. Following optimization and solving, the optimal simulation parameters identified are as follows: the rolling friction coefficient of the PR-PLA plate is 0.137, the rolling friction coefficient of the PR-PR plate is also 0.137, and the static friction coefficient of the PR-PLA plate is 0.336. Simulation experiments were conducted using these parameters, and a T-test analysis was performed to examine the correlation between the simulation results and the actual experimental values. The T-test analysis reveals no significant difference between the simulation results and the experimental values ($P > 0.05$), further confirming the authenticity and reliability of the simulation parameters after the experiments and calibration.

(4) This conclusion not only serves as a reference for research on PR and their high-speed precision sowing but also provides valuable insights for the practical application of these seeds in agriculture. This information can help optimize the seeding equipment design and seed handling process at a later stage, thus improving the efficiency and quality of agricultural production.

ACKNOWLEDGEMENTS

The authors would like to express their gratitude to the anonymous reviewers for their insightful comments. This research was funded by the Key Project of the Department of Education of Anhui Province (Grant No.2024AH050307), the Collaborative Innovation Project of Universities in Anhui Province (Grant No. GXXT-2023-042), and the Anhui University of Science and Technology Talent Introduction Project (Grant No. JXYJ202201).

REFERENCES

- [1] Al-Hashemi B.M.H., Al-Amoudi B.S.O. (2018). A review of the angle of repose of granular materials. *Powder Technology*, Vol. 330, pp. 397-417. <https://doi.org/10.1016/j.powtec.2018.02.003>
- [2] Bai J.Y., Xie B., Yan J.G., Zheng Y., Liu N., Zhang Q., (2023) Moisture content characterization method of wet particles of brown rice based on discrete element simulation. *Powder Technol.* Vol. 428, pp. 118775. <https://doi.org/10.1016/j.powtec.2023.118775>.
- [3] Cai M.Y., Ren X.Z. (2023). Current status and development characteristics of rice mechanized planting technology (水稻机械化种植技术现状及发展特征). *Use and Maintenance of Agricultural Machinery*, Vol. 317(1), pp. 99-102. <https://doi.org/10.14031/j.cnki.njwx.2023.01.029>. (in Chinese)
- [4] Cong J.L. (2014). *Research on the Mechanism and System of Pneumatic Precision Seed Metering for Rapeseed and Wheat* (油菜小麦兼用型气力式精量排种系统及其机理研究). [Doctoral dissertation, Wuhan: Huazhong Agricultural University]
- [5] Djavan De Clercq; Adam Mahdi. (2025). Modern computational approaches for rice yield prediction: A systematic review of statistical and machine learning-based methods. *Computers and Electronics in Agriculture*, Vol. 231, pp. 109852-109852. <https://doi.org/10.1016/J.COMPAG.2024.109852>
- [6] Dun G.Q., Wang L., Ji X.X., Jiang X.Y., Zhao Y., Guo N. (2024). Calibration and experimental verification of discrete element parameters for Jinxing purple garlic seeds (金乡紫皮蒜种离散元参数标定与试验验证). *China Agricultural Science and Technology Review*, Vol. 26(8), pp. 131-139. <https://doi.org/10.13304/j.nykjdb.2022.1023>. (in Chinese)
- [7] Dun G.Q., Wang L., Ji X.X., Jiang X.Y., Zhao Y., Guo N. (2024). Calibration and experimental verification of discrete element simulation model parameters for radish seeds (c). *Journal of Agricultural Mechanization Research*, Vol. 45(9), pp. 127-133. <https://doi.org/10.13733/j.jcam.issn.2095-5553.2024.09.019>. (in Chinese)
- [8] Fan C.S., He R.Y., Shi Y.Y., Wang J.L., Xu G.M. (2024). Study on parameter calibration method for organic-inorganic mixed fertilizer using discrete element method (有机无机混合肥料离散元参数标定方法研究). *Journal of Nanjing Agricultural University*, Vol. 47(2), pp. 402-413. (in Chinese)
- [9] Ge T., Jia Z.H., Zhou K.D. (2007). A theoretical model for calculating the restitution coefficient of point-contact collisions (计算点接触碰撞恢复系数的一种理论模型). *Journal of Mechanical Design and Research*, Vol. 3, pp. 14-15+22. <https://doi.org/10.13952/j.cnki.jofmdr.2007.03.019>. (in Chinese)
- [10] González-Montellano C., Fuentes J.M., Ayuga-Téllez E., Ayuga F. (2012). Determination of the mechanical properties of maize grains and olives required for use in DEM simulations. *Journal of Food Engineering*, Vol. 111(4), pp. 553-562. <https://doi.org/10.1016/j.jfoodeng.2012.03.017>
- [11] Hou Z.F., Dai N.Z., Chen Z., Zhang X.W. (2020). Determination of physical parameters of *Elymus nutans* seeds and calibration of DEM simulation parameters (冰草种子物性参数测定与离散元仿真参数标定). *Transactions of the Chinese Society of Agricultural Engineering*, Vol. 36(24), pp. 46-54. (in Chinese)

- [12] Hu G.M. (2010). *Discrete Element Method Analysis and Simulation of Granular Systems: Introduction to Industrial Applications of Discrete Element Method and EDEM Software* (颗粒系统的离散元素法分析仿真: 离散元素法的工业应用与 EDEM 软件简介). Wuhan: Wuhan University of Technology Press. (in Chinese)
- [13] Liu H.Y., Lu Q., Wang J.W., Zhou W.Q., Wang N.H. (2024). Rapid calibration method for discrete element simulation parameters of columnar granular organic fertilizer with variable moisture content. *Powder Technology*, Vol. 448 pp. 120354. <https://doi.org/10.1016/J.POWTEC.2024.120354>
- [14] Liu F.Y., Zhang J., Li B., Chen J. (2016). Analysis and calibration of discrete element parameters of wheat based on bulk density test (基于堆积试验的小麦离散元参数分析及标定). *Transactions of the Chinese Society of Agricultural Engineering*, Vol. 32(12), pp. 247-253. (in Chinese)
- [15] Li H.Q., Zhang G.C., Li X.C., Zhang H.B., Zhang Q., Liu W.B., Mu G. (2021). Calibration of the discrete element method parameters in living juvenile Manila clam (*Ruditapes philippinarum*) and seeding verification. *AgriEngineering*, Vol. 3(4), pp. 894-906.
- [16] Ma X.J., Hou Z.F., Liu M. (2022). Calibration of simulation parameters of coated particles and analysis of experimental results. *INMATEH-Agricultural Engineering*, Vol. 67(2), pp. 233-242. <https://doi.org/10.35633/inmateh-67-23>
- [17] Ma Y., Wang X.L., Wang Y.L., Ma Y.T., Cui H.P. (2023). Research progress on seed pelleting in the field of ecological restoration (生态恢复领域草种丸粒化研究进展). *Chinese Journal of Grassland*, Vol. 32(4), pp. 197-207. (in Chinese)
- [18] Ning X. (2016). *Research on Environmental Adaptation of China's Major Grain Crop Cultivation under Climate Change* (气候变化下我国主要粮食作物种植环境适应性研究). [Doctoral dissertation, Henan University]
- [19] R. Balevičius; I. Sielamowicz; Z. Mróz; R. Kačianauskas. (2011). Investigation of wall stress and outflow rate in a flat-bottomed bin: A comparison of the DEM model results with the experimental measurements. *Powder Technology*, Vol. 214(3), pp. 322-336. <https://doi.org/10.1016/j.powtec.2011.08.042>
- [20] Wang X.L., Zhong X.K., Geng Y.L., Wei Z.C., Hu H., Geng D.Y., Zhang X.C. (2021). Calibration of no-tillage soil parameters based on nonlinear elastic-plastic contact model in DEM (基于离散元非线性弹塑性接触模型的免耕土壤参数标定). *Transactions of the Chinese Society of Agricultural Engineering*, Vol. 37(23), pp. 100-107. (in Chinese)
- [21] Wang X.Q., Pi N.N., Weng Q.F. (2024). Seed pelleting and its research progress (种子丸粒化及其研究进展). *Hunan Agricultural Science*, Vol. 3, pp. 85-90. <https://doi.org/10.16498/j.cnki.hnnykx.2024.003.018>. (in Chinese)
- [22] Wen X.Y., Yuan H.F., Wang G., Jia H.L. (2020). Study on calibration method for friction coefficient in discrete element simulation of granular fertilizer (颗粒肥料离散元仿真摩擦因数标定方法研究). *Transactions of the Chinese Society for Agricultural Machinery*, Vol. 51(2), pp. 115-122+142. (in Chinese)
- [23] Xing X.P., Ma X., Chen L.T., Li H.W., Wen Z.C., Zeng G.Z. (2020). Experimental study on physical properties of solid granular fertilizers (固体颗粒肥料物理特性的试验研究). *Research on Agricultural Mechanization*, Vol. 42(9), pp. 125-130. <https://doi.org/10.13427/j.cnki.njyi.2020.09.022>. (in Chinese)
- [24] Xue K., Gao K., Kuang F., Zhang S., Liao J., Zhu D. (2022). Machinery-plant-paddy soil coupling model based numerical simulation method of mechanical transplanting process of big rice seedling. *Computers and Electronics in Agriculture*, vol.198, <https://doi.org/10.1016/J.COMPAG.2022.107053> (in Chinese)
- [25] Yang M.X., Zhang Y., Han L.P. (2020). Screening of pelleting formula for sorghum-sudangrass hybrid seeds (高丹草种子丸粒化配方的筛选). *Henan Agricultural Science*, Vol. 49(7), pp. 58-67. <https://doi.org/10.15933/j.cnki.1004-3268.2020.07.008> (in Chinese)
- [26] Zhang R., Han D.L., Ji Q.L., He Y., Li J.Q. (2017). Study on parameter calibration method of sand in discrete element simulation (离散元模拟中沙土参数标定方法研究). *Transactions of the Chinese Society for Agricultural Machinery*, Vol. 48(3), pp. 49-56. (in Chinese)
- [27] Zhang P., Zhang H., Li J., Tan C., Zhang J. (2022). Parametric calibration of cotton straw parameters in Xinjiang based on discrete elements. *INMATEH - Agricultural Engineering*, Vol. 67(2), pp. 314-322. <https://doi.org/10.35633/inmateh-67-32>
- [28] Zhu X.H., Fu S.K., Li X.D., Wei Y.Q., Zhao W. (2022). Research on general calibration method of discrete element parameters for sheep manure with different moisture contents (不同含水率羊粪离散元参数通用标定方法研究). *Transactions of the Chinese Society for Agricultural Machinery*, Vol. 53(8), pp. 34-41. (in Chinese)

RESEARCH ON ENVIRONMENTAL MONITORING AND COMPREHENSIVE EVALUATION SYSTEM OF PIG HOUSE BASED ON INTERNET OF THINGS TECHNOLOGY

基于物联网技术的猪舍环境监测与综合评价系统研究

Lihong RONG¹⁾, Junling FAN¹⁾, Xiaolong GUO²⁾, Zhimin TONG^{*1)}, Wenlong XU¹⁾, Yuexin PAN¹⁾, Shengzhang LI¹⁾, Weilong ZHANG¹⁾, Fang SUN¹⁾

¹⁾ College of Electrical and Mechanical Engineering, Qingdao Agricultural University, Qingdao/ China

²⁾ Shandong Hengji Agricultural and Animal Husbandry Machinery Co., Ltd., Weifang/ China

Tel: +8615845982569; E-mail: leicahit@qau.edu.cn

Corresponding author: Zhimin Tong

DOI: <https://doi.org/10.35633/inmateh-75-43>

Keywords: Pig house environment, Internet of Things, Data fusion, Weight calculation, Fuzzy evaluation

ABSTRACT

To address the issues of low precision and high cost in pig house environmental monitoring, an Internet of Things (IoT)-based pig house environmental monitoring system is proposed in this study. The system utilizes ESP32 as the main control chip of each sensor node, which is constructed in a star topology structure, realizing data transmission by using wireless communication technology. By incorporating the median filtering function and the Kalman filtering algorithm to perform data fusion of the same type of environmental parameters, the accuracy of the data is ensured. Based on the environmental suitability requirements of pigs, an evaluation index system for pig house environmental suitability is established, and comprehensive weight calculations are carried out by combining the entropy weight method and the improved analytic hierarchy process. Simulation experimental results demonstrate that the error of the temperature data after Kalman filtering fusion is merely 0.12%, fulfilling the monitoring accuracy requirements. The system can precisely evaluate the environmental suitability of pig houses, and it is applicable for monitoring pig house environments.

摘要

为解决猪舍环境监测精度低和成本高等问题, 本研究提出了一种基于物联网的猪舍环境监测系统。系统采用 ESP32 作为各传感器节点的主控芯片, 并通过星型拓扑结构搭建, 利用无线通信技术实现数据传输。通过引入中值滤波函数和卡尔曼滤波算法对同类型的环境参数进行数据融合, 确保数据准确性。基于猪只对环境的适宜度要求, 构建了猪舍环境适宜度评价指标体系, 并结合熵权法与改进层次分析法进行综合权重计算。仿真实验结果表明, 经过卡尔曼滤波融合后的温度数据误差仅为 0.12%, 满足监测精度要求。系统能够准确评价猪舍环境适宜度, 适用于猪舍环境监测。

INTRODUCTION

With the transformation of the agricultural industry structure, pig farming industry is evolving towards large-scale, intensive, and industrialized operations. This development is of great significance for optimizing the rural economic structure, improving agricultural efficiency, and increasing farmers' income (Han et al., 2010). However, currently, small and medium-sized pig houses still face challenges such as difficulties in implementing environmental monitoring technology and high monitoring costs. The quality of pig house environment is a crucial factor in ensuring the healthy breeding of pigs, directly influencing their growth, development, and reproductive ability (Spinka et al., 2017). It will lead to serious consequences, such as diseases and economic losses to farmers, if pigs grow in harsh environments for a long time (Chen et al., 2020; Li et al., 2023). Therefore, monitoring various parameters of the pigs' growth environment and improving the management level of pig farm environmental quality are of great significance for promoting the sustainable development of global pig farming industry (Li et al., 2024; Wang et al., 2024).

Numerous scholars have conducted research on the intelligent monitoring and control of pig house environmental quality to overcome existing problems. For example, Zeng et al., (2020), investigated a wireless multi-point, multi-source remote monitoring system for pig house environments, which can rapidly perceive the spatiotemporal distribution characteristics of pig house environmental parameters, providing valuable references for optimizing pig house environmental control.

Huang *et al.*, (2022), employed narrowband Internet of Things (IoT) and cloud platform technics to achieve remote monitoring and real-time regulation of multiple environmental factors such as temperature within pig house, effectively ensuring welfare of pigs and offering new design solutions for intelligent monitoring systems in pig farming. Nevertheless, these studies do not explore pigs' adaptability to pig house environment. Regarding the adaptability of pigs to pig house environment, many scholars have also carried out research (Xie *et al.*, 2024). For instance, Chen *et al.*, (2022), utilized an improved analytic hierarchy process combined with fuzzy comprehensive evaluation to establish a comprehensive evaluation system for pig house environment, which can evaluate the suitability of pig house environment in real-time and provide a good design solution for precise regulation and early warning of pig house environment. Wang *et al.*, (2023), applied a fuzzy comprehensive evaluation method to study an IoT-based environmental suitability evaluation system for fattening pig houses. This system can simultaneously collect data on multiple environmental factors in pig house and perform transmission, analysis, and display of these environmental data.

However, most of these studies typically adopt a single analytic hierarchy process (AHP) or entropy weight method for weight calculation, failing to comprehensively consider the deviation of subjective weight calculation methods and the one-sidedness of objective weight calculation methods (Xie *et al.*, 2016; Chi *et al.*, 2022; Xie *et al.*, 2024; Liu *et al.*, 2024).

To solve the aforementioned problem, this paper focuses on pig house environmental information monitoring as the research subject and combines Internet of Things (IoT) technology, wireless communication technology, and others to design an IoT-based pig house environment monitoring and application system (Gao *et al.*, 2016; Bai *et al.*, 2019; Zhou *et al.*, 2021; Wang *et al.*, 2024; Wang *et al.*, 2024). This system can remotely monitor environmental information such as temperature and relative humidity within pig house simultaneously. Additionally, to evaluate pig house environment more scientifically, the weight coefficient of the environmental evaluation index of pig house is calculated by integrating the subjective weight calculation method and the objective weight calculation method, thereby reducing the deviation and one-sidedness of the environmental evaluation. Finally, the fuzzy comprehensive evaluation method is utilized to assess the suitability of pig house environmental data. The suitability evaluation results can provide decision support for the precise regulation of pig house environment.

MATERIALS AND METHODS

Overall system plan

The experimental pig house is located at 11.32°E longitude and 37.19°N latitude. The internal view of the pig house is shown in Figure 1. The Internet of Things system for remote monitoring of the pig house environment mainly consists of three parts: the Information acquisition and perception layer, the Information wireless transmission layer, and the information processing and application layer. The overall structure of the system is illustrated in Figure 2. The pig house is monitored at 20 different points, each equipped with a set of sensor nodes. Thus, a total of 20 sets of sensor nodes and one set of sink node are installed in the monitoring area of the pig house.



Fig. 1 – Internal picture of pig house

Each set of sensor nodes is composed of the required environmental factor sensor, a data transmission interface, a main control chip and other structures, and it is powered by an independent power supply. These sensor nodes collect data on environmental factors within the pig house using their onboard main control chips and transmit the data via Wi-Fi to the sink node. The sink node performs data fusion on the received information from the sensor nodes and conducts corresponding evaluations based on a suitability evaluation model for the pig house environment, thereby enabling the analysis of environmental information throughout the entire pig house. Finally, the fused environmental factor data such as temperature and humidity are transmitted to the cloud platform via Wi-Fi, and the cloud platform uses the HTTP data transmission protocol to send this information to a WeChat mini-program, allowing users to view and access real-time environmental information about the pig house through either a PC or a mobile device.

ESP32 is used as the main control chip of the system. ESP32, which integrates a TCP/IP protocol stack enabling direct connection to Wi-Fi networks and also functioning as a hotspot, is utilized as the main control chip of this system. The sink node operates in softAP+Station mode, in this system. In this mode, the ESP32 main control chip can be used both as a terminal node and as a wireless access point, meeting the functional requirements of the sink node. Additionally, the ESP32 provides functions such as IIC interface, GPIO interface, UART serial port, and ADC interface, which can satisfy design requirements.

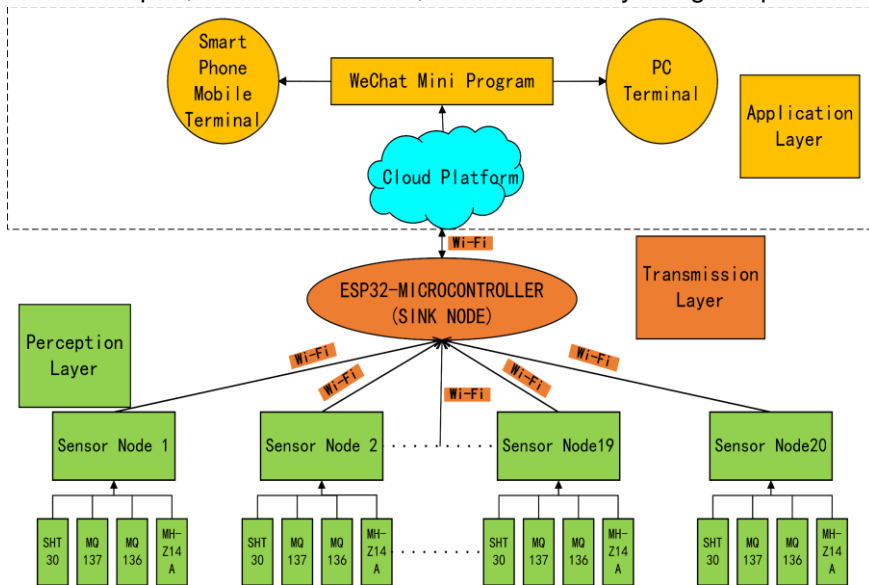


Fig. 2 – Overall system structure

System hardware design

(1) System sensor nodes hardware design

The temperature and relative humidity collection module adopts the SHT30 temperature and humidity sensor, which exhibits higher stability and reliability compared to other similar sensors. Its temperature measurement range is from -40°C to 125°C with an error margin of $\pm 0.2^{\circ}\text{C}$, and the relative humidity measurement range is from 0%RH to 100%RH with an error margin of $\pm 2\% \text{RH}$. It is connected to the ESP32 via an IIC interface. The ammonia gas collection module uses the MQ137 ammonia gas sensor, with a detection range of 5×10^{-6} to $5 \times 10^{-4} \text{ mg/m}^3$. The hydrogen sulfide collection module employs the MQ136 hydrogen sulfide sensor, with a detection range of 10^{-6} to 10^{-4} mg/m^3 . The carbon dioxide collection module utilizes the MH-Z14A carbon dioxide sensor, with a detection range of 0 to 10^{-2} mg/m^3 . The environmental information data within the pig house is processed by the ESP32 microcontroller and transmitted to the sink node via Wi-Fi. The connection circuit between the ESP32 MCU and the sensor is shown in Figure 3.

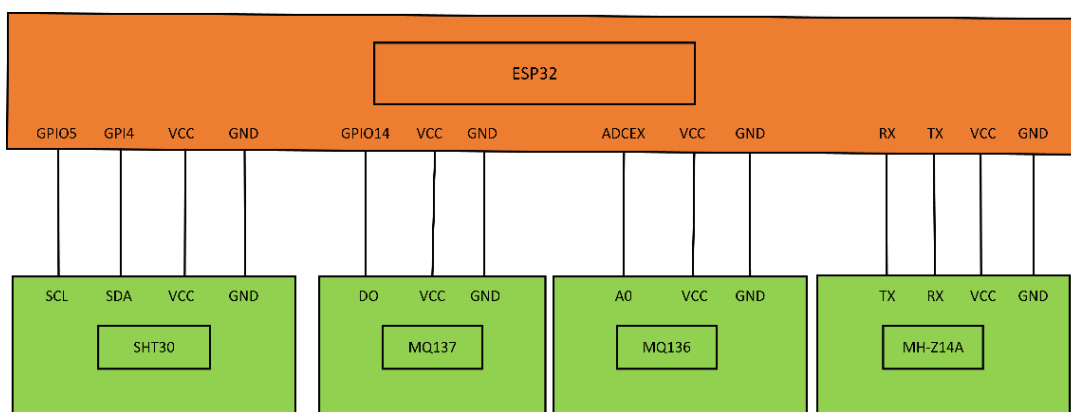


Fig. 3 – Interface between ESP32 and sensor

(2) System sink node hardware design

The main function of the sink node is to receive environmental information parameters collected from sensor nodes and it optimizes and fuses environmental data of the same type using a median filtering function and a Kalman filter algorithm. Meanwhile, it can display the current environmental information inside the pig

house and assess the current environment of the pig house in combination with a comprehensive evaluation model. The sink node adopts an ESP32 single-chip microcomputer along with an ILI9488 3.5-inch TFT display screen, allowing real-time viewing of the current environmental parameters on the display screen. The connection circuit between the ESP32 MCU and the TFT display is shown in Figure 4.

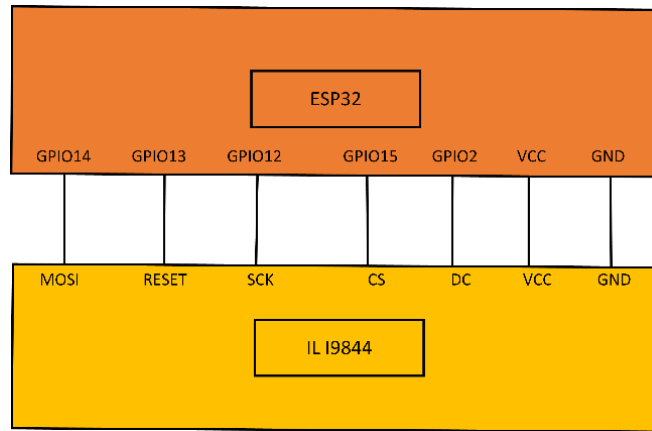


Fig. 4 – Schematic diagram of ESP32 MCU and ILI9488 display

Environmental parameter acquisition algorithm design

This paper's fusion algorithm is based on data collected by environmental parameter acquisition sensors, including temperature, humidity, ammonia gas concentration, hydrogen sulfide concentration, and carbon dioxide concentration. Before fusion, a median filter function is used to optimize the data and reduce the impact of random factors. Subsequently, a Kalman filter algorithm is applied to fuse the environmental data collected from the pig house. The main steps of the Kalman filter algorithm are as follows:

The system's current state prediction equation is as follows:

$$\hat{x}_{k/k-1} = A_{k-1/k-1} \hat{x}_{k-1/k-1} \quad (1)$$

where:

$\hat{x}_{k/k-1}$ is the predicted result of the system state at the current moment, $A_{k-1/k-1}$ is the system state transition matrix, and $\hat{x}_{k-1/k-1}$ is the optimal system state estimate from the previous moment.

There is a certain error between the predicted value and the true value, and the error covariance matrix equation is as follows:

$$P_{k/k-1} = A_{k-1/k-1} P_{k-1/k-1} A_{k-1/k-1}^T + Q_{k/k} \quad (2)$$

where:

$P_{k/k-1}$ is the system prediction state covariance matrix at the current moment, $P_{k-1/k-1}$ is the optimal prediction state covariance matrix from the previous moment, and $Q_{k/k}$ is the process noise covariance matrix.

The Kalman Gain equation is as follows:

$$K_{k/k} = P_{k/k-1} C_{k/k}^T (C_{k/k} P_{k/k-1} C_{k/k}^T + R_{k/k})^{-1} \quad (3)$$

where:

$K_{k/k}$ is the Kalman Gain, $C_{k/k}$ is the measurement matrix, and $R_{k/k}$ is the measurement noise covariance matrix.

The optimal state estimation equation for the system at the current moment is as follows.

$$\hat{x}_{k/k} = \hat{x}_{k/k-1} + K_{k/k} (y_{k/k} - C_{k/k} \hat{x}_{k/k-1}) \quad (4)$$

where:

$\hat{x}_{k/k}$ is the optimal state estimate at the current moment, and $y_{k/k}$ is the sensor measurement value at the current moment.

The covariance matrix update equation for the current moment is as follows:

$$P_{k/k} = [I - K_{k/k} C_{k/k}] P_{k/k-1} \quad (5)$$

where:

$P_{k/k}$ is the covariance matrix of the optimal state estimate at the current moment, and I is the identity matrix.

ENVIRONMENTAL SUITABILITY FUZZY COMPREHENSIVE EVALUATION MODEL

The comprehensive evaluation of the pig house is mainly carried out through sink node. The sink node receives data from sensor nodes and performs data fusion. Based on the fused values of various environmental parameters, a comprehensive weight calculation is performed by combining the entropy weight method and an improved analytic hierarchy process. Then, based on the data fusion values and weight set from the sink node, an evaluation of the suitability of the pig house environment is made.

Construction of the evaluation index system

The environmental factors that have the most significant impact on the growth, development, and reproduction of pigs include environmental temperature, relative humidity, ammonia gas concentration, carbon dioxide concentration, and hydrogen sulfide concentration. Therefore, this paper selects these five environmental parameters as the evaluation indicators for pig house environmental suitability. The degree of suitability is represented by 3 levels: Suitable (C), Relatively Suitable (M), and Unsuitable (B). Based on the environmental parameters of large-scale pig farms and the environmental management standards issued by the state, a pig house environmental evaluation index system is established, as shown in Table 1 (GB/T 17824.3-2008).

Table 1

Evaluation result set	Factor set				
	Temperature / °C	Relative Humidity/ %	Carbon dioxide / (mg·m ⁻³)	Ammonia gas / (mg·m ⁻³)	Sulfuretted hydrogen / (mg·m ⁻³)
Suitable	18~22	60~70	0~1000	0~2	0~2
Relatively suitable	16~18 or 22~27	50~60 or 70~80	1100~1200	5~10	4~6
Unsuitable	>27 or <16	>80 or <50	>1300	>20	>10

Evaluation modeling steps

The evaluation of pig house environmental suitability is conducted using a fuzzy comprehensive evaluation method that combines the entropy weight method, the improved analytic hierarchy process, and fuzzy set. The modeling steps are as follows:

- (1) Determine the factor set: Based on the established evaluation index system, determine the environmental factors that have the greatest impact on the healthy growth of pigs, and establish the evaluation factor set $I = \{u_1, u_2, u_3, u_4, u_5\}$. These include u_1 = temperature, u_2 = relative humidity, u_3 = ammonia gas concentration, u_4 = carbon dioxide concentration, and u_5 = hydrogen sulfide concentration.
- (2) Determine the evaluation result set: The evaluation result set is divided into three levels, denoted as $D = \{d_1, d_2, d_3\}$, where d_1 is Suitable (C), d_2 is Relatively Suitable (M), and d_3 is Unsuitable (B).
- (3) Establish the membership matrix and conduct single-factor evaluation: According to the evaluation standards for each indicator, determine the membership functions for each indicator. Use these membership functions to calculate the membership matrices for the five environmental factors: temperature, relative humidity, ammonia gas concentration, carbon dioxide concentration, and hydrogen sulfide concentration, corresponding to H_1, H_2, H_3, H_4 and H_5 . Combine these single-factor membership matrices to obtain the overall membership matrix H . Evaluate the pig house environment based on the maximum membership principle. The form of the membership matrix H is as follows:

$$H = \begin{bmatrix} H_1 \\ H_2 \\ H_3 \\ H_4 \\ H_5 \end{bmatrix} = \begin{bmatrix} h_{11} & h_{12} & h_{13} \\ h_{21} & h_{22} & h_{23} \\ h_{31} & h_{32} & h_{33} \\ h_{41} & h_{42} & h_{43} \\ h_{51} & h_{52} & h_{53} \end{bmatrix} = (h_{ij})_{5 \times 3} \tag{6}$$

where:

h_{ij} is the membership degree of the i -th evaluation indicator belonging to the j -th level.

- (4) The entropy weight method and an improved analytic hierarchy process (AHP) are used to determine the index weights. First, the collected data is standardized, and then the entropy values and information entropy redundancy of various environmental parameters within the pig house are calculated.

Based on this, the objective weight coefficient for each environmental parameter is derived. The improved AHP uses a 1-9 scales method for pairwise comparisons to obtain the importance ranking index of each environmental factor, establishing a comparison matrix. It then constructs an indirect judgment matrix and optimizes it to find the maximum eigenvalue and eigenvector, which are normalized to obtain the subjective weight coefficients. The subjective and objective weight coefficients are combined to obtain the comprehensive weight coefficient for each environmental factor. Finally, the comprehensive weight coefficient of each index is merged into a weight set ω .

(5) Fuzzy comprehensive evaluation. The comprehensive weight set ω calculated by entropy weight method and improved analytic hierarchy process is fuzzy synthesized with membership degree evaluation matrix H . By using a weighted linear transformation method, the fuzzy comprehensive evaluation result of the pig house environment is ultimately obtained.

$$Y = \omega \cdot H = \{y_1, y_2, y_3\} \tag{7}$$

where: Y is the comprehensive evaluation result matrix.

Consequently, the evaluation result matrix corresponding to the three suitability conditions of the pig house environment is obtained, and the suitability status of the pig house environment is determined based on the maximum membership principle.

Selection of membership function types

The key to evaluating the suitability of the pig house environment lies in determining the membership functions for the pig house environment. Based on the nature of the pig house environment evaluation factors, the functional relationship between membership degree and indicators needs to be constructed using continuous functions. In the evaluation of pig house environmental suitability, commonly used types of membership functions include ridge-shaped membership function, trapezoidal membership function, and triangular membership function. The ridge-shaped membership function optimizes the edges and corners of the trapezoidal membership function, which can reduce errors when calculating high membership degrees. Compared to the triangular membership function, the ridge-shaped membership function has better distinction between levels. Therefore, this paper uses the ridge-shaped membership function to calculate the membership degree matrix of evaluation factors such as temperature and humidity in the pig house environment. The expressions of the ridge-shaped membership function are shown in Formulas (8)-(10).

$$\text{Lower Type: } u(x) = \begin{cases} 1 & x \leq a \\ \frac{1}{2} - \frac{1}{2} \sin \frac{\pi}{b-a} \left(x - \frac{b+a}{2}\right) & a < x < b \\ 0 & x \geq b \end{cases} \tag{8}$$

$$\text{Middle Type: } u(x) = \begin{cases} 0 & x \leq a \\ \frac{1}{2} + \frac{1}{2} \sin \frac{\pi}{b-a} \left(x - \frac{b+a}{2}\right) & a < x < b \\ 1 & b \leq x \leq c \\ \frac{1}{2} - \frac{1}{2} \sin \frac{\pi}{d-c} \left(x - \frac{d+c}{2}\right) & c < x < d \\ 0 & x \geq d \end{cases} \tag{9}$$

$$\text{Upper Type: } u(x) = \begin{cases} 0 & x \leq a \\ \frac{1}{2} + \frac{1}{2} \sin \frac{\pi}{b-a} \left(x - \frac{b+a}{2}\right) & a < x < b \\ 1 & x \geq b \end{cases} \tag{10}$$

where: x represent the index values of the evaluation factors u_i , with its interval endpoints denoted as x_i 、 x_{i+1} . The membership degree of each evaluation level in the set of evaluation results is denoted as $u(x)$. The a , b , c , and d respectively represent the demarcation points in the set of evaluation results corresponding to various environmental factors in the pig house environment evaluation system. Each index value in the set

of evaluation factors has a corresponding fuzzy logical relationship. The ridge-shaped distribution membership functions of various environmental factors, established based on the pig house environment evaluation index system, are shown in Figure 5.

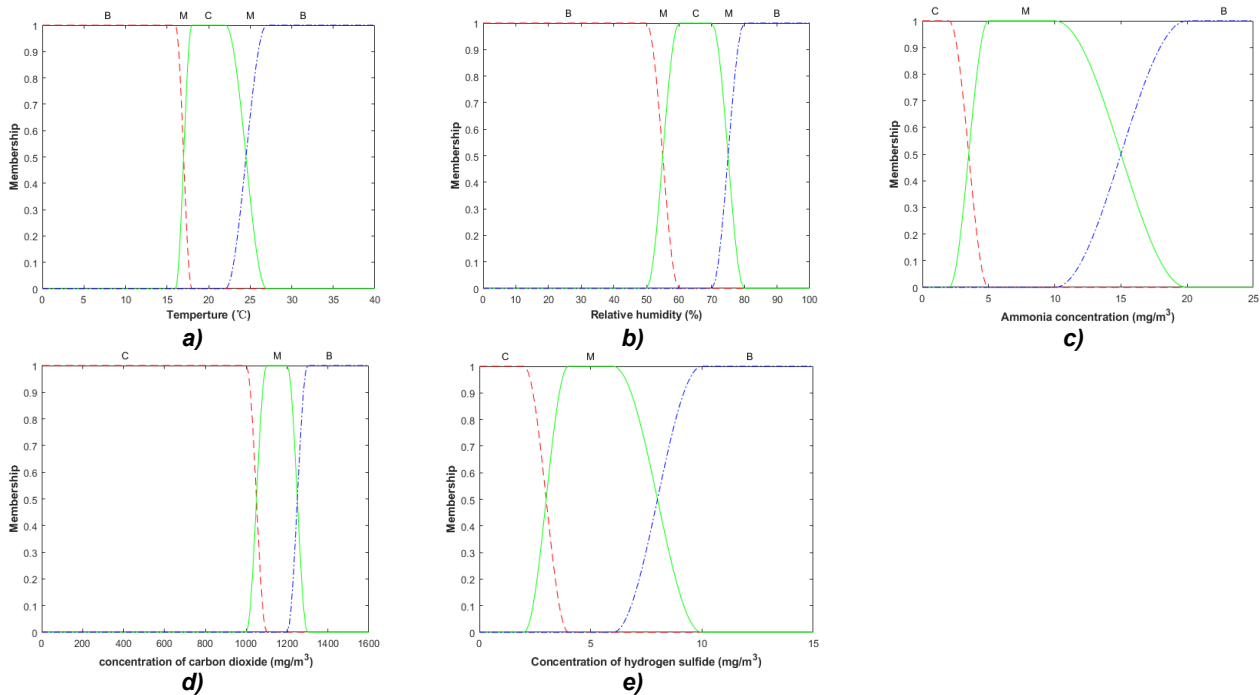


Fig. 5 – Membership function curves of each environmental factor
 a) Temperature; b) Relative humidity; c) Ammonia concentration;
 d) Concentration of Carbon dioxide; e) Concentration of hydrogen sulfide

In Figure a), b), c), d) and e), the three curves from left to right are the ring down type, the middle type and the ring up type.

Method for determining weight

(1) Weight calculation method based on the entropy weight method

Unlike the improved Analytic Hierarchy Process, which typically emphasizes subjective factors, the entropy weight method is a method of empowerment that objectively determines weight through observed values. The smaller the entropy value, the more disordered the information is, and thus its value in comprehensive evaluation is higher, resulting in a larger corresponding weight. For example, when there is a significant sudden increase in the temperature of the pig house, this algorithm will increase the weight of the temperature factor while reducing the weights of other factors with smaller changes. The algorithm process is as follows.

1) Standardize the data based on the following formula:

$$X'_{ij} = \frac{X_{ij} - \min(X_{1j}, X_{2j}, \dots, X_{nj})}{\max(X_{1j}, X_{2j}, \dots, X_{nj}) - \min(X_{1j}, X_{2j}, \dots, X_{nj})} + 1 \quad j = 1, 2, 3, \dots, m \quad (11)$$

2) Calculate the weight of the environmental parameter data for the j th item after standardization based on the following formula:

$$p_{ij} = \frac{X'_{ij}}{\sum_{i=1}^n X'_{ij}} \quad j = 1, 2, 3, \dots, m \quad (12)$$

3) Calculate the information entropy value of the environmental parameter for the j th item based on the following formula:

$$k = \frac{1}{\ln(n)} \quad (13)$$

$$e_j = -k \sum_{i=1}^n p_{ij} \ln(p_{ij}) \quad (14)$$

4) Calculate the information entropy redundancy of each environmental factor in the pig house based on the following formula:

$$f_j = 1 - e_j \tag{15}$$

5) Calculate the weight of each environmental parameter:

$$W_j^R = \frac{f_j}{\sum_{j=1}^m f_j} \quad j = 1, 2, 3, \dots, m \tag{16}$$

(2) Weight calculation method based on the improved analytic hierarchy process

Based on relevant research findings and the experience of livestock experts, the importances of evaluation indicators for multiple environmental factors in the pig house are determined as follows: environmental temperature, relative humidity, ammonia gas concentration, carbon dioxide concentration, and hydrogen sulfide concentration. The 1-9 scales method is used to compare these evaluation indicators with each other and construct a comparison matrix. The specific descriptions of the 1-9 scales method are shown in the table 2 below:

Table 2

Description of 1-9 scales	
Relative importance level	Scale significance
1	Equal importance
3	Slight importance
5	Obvious importance
7	Strong importance
9	Absolute importance
2, 4, 6, 8	The middle level of two adjacent levels

By conducting pairwise comparisons of environmental temperature (T), relative humidity (O), ammonia gas concentration (N), carbon dioxide concentration (E), and hydrogen sulfide concentration (HS), the importance of each factor is determined, resulting in a comparison matrix L . Then, the importance ranking index v_i for each factor is calculated, which are represented by the sum of each row in the comparison matrix L .

$$L = \begin{matrix} & T & O & N & E & HS \\ \begin{matrix} T \\ O \\ N \\ E \\ HS \end{matrix} & \begin{bmatrix} 1 & 2 & 3 & 4 & 3 \\ 1/2 & 1 & 2 & 3 & 2 \\ 1/3 & 1/2 & 1 & 3 & 2 \\ 1/4 & 1/3 & 1/3 & 1 & 1/3 \\ 1/3 & 1/2 & 1/2 & 3 & 1 \end{bmatrix} & \end{matrix} \quad i = 1, 2, 3, 4, 5 \tag{17}$$

where:

v_i is the importance ranking index for each factor indicator, and l_{ij} is the element in the i th row and j th column of the comparison matrix L .

Construct an indirect judgment matrix K reflecting the relative importance of each environmental factor. Let

$$q_m = \frac{v_{\max}}{v_{\min}} \tag{18}$$

where:

v_{\max} is the maximum ranking index, v_{\min} is the minimum ranking index, and q_m is the base point comparison scale. The indirect judgment matrix K is:

$$K = (k_{ij})_{5 \times 5} = \begin{cases} \frac{v_i - v_j}{v_{\max} - v_{\min}} (q_m - 1) + 1 & v_i - v_j \geq 0 \\ 1 / \left[\frac{v_i - v_j}{v_{\max} - v_{\min}} (q_m - 1) + 1 \right] & v_i - v_j < 0 \end{cases} \quad (i = 1, 2, 3, 4, 5) \quad (j = 1, 2, 3, 4, 5) \tag{19}$$

Transform the indirect judgment matrix K into an antisymmetric matrix S and then construct a quasi-optimal consistent matrix Z , the consistency requirement can be satisfied.

$$s_{ij} = \lg(k_{ij}) \quad (i = 1, 2, 3, 4, 5) \quad (j = 1, 2, 3, 4, 5) \tag{20}$$

where:

S is the antisymmetric matrix; s_{ij} is the element in the i th row and j th column of the antisymmetric matrix S ; k_{ij} is the element in the i th row and j th column of the indirect judgment matrix K .

$$z_{ij} = 10^{\frac{1}{n} \sum_{k=1}^n (s_{ik} - s_{jk})} \quad (i = 1, 2, 3, 4, 5) \quad (j = 1, 2, 3, 4, 5) \tag{21}$$

where:

z_{ij} is the element in the i th row and j th column of the quasi-optimal consistent matrix Z ; s_{ik} is the element in the i th row and k th column of the antisymmetric matrix S ; s_{jk} is the element in the j th row and k th column of the antisymmetric matrix S .

Finally, calculate the largest eigenvalue and the corresponding eigenvector of the quasi-optimal matrix Z , and normalize them as shown in equations (22) and (23) to obtain the required weight for each factor.

$$ZW = \lambda_{\max} W \tag{22}$$

$$W_j^A = \frac{W_j}{\sum_{j=1}^5 W_j} \tag{23}$$

where: λ_{\max} is the maximum eigenvalue of Z , and W is the relative weight vector.

After the aforementioned steps of the improved Analytic Hierarchy Process, the subjective weight of the evaluation index for each environmental factor is calculated, as shown in the table 3.

Table 3

Evaluation indicator weights of pig house environment	
Evaluation index	Weight
Temperature	0.4784
Relative humidity	0.2153
Ammonia gas	0.1468
Carbon dioxide	0.0562
Hydrothion	0.1033

(3) Combined weight calculation

Combine the subjective and objective weight values to obtain the combined weights. This calculation method can, to a certain extent, reduce the deviation of subjective weights and the one-sidedness of objective weights while leveraging their respective advantages, making the weight calculation more scientific. The comprehensive weights of the indices are calculated using the following formula:

$$\omega_j = \frac{W_j^A W_j^R}{\sum_{j=1}^n W_j^A W_j^R} \tag{24}$$

where:

ω_j is the comprehensive weight; W_j^A is the subjective weight calculated using the improved Analytic Hierarchy Process; W_j^R is the objective weight calculated using the entropy weight method. The comprehensive weights of the evaluation indicators are combined into a weight set ω , and ω satisfy $\omega = [\omega_T \ \omega_O \ \omega_N \ \omega_E \ \omega_{HS}]$.

RESULTS AND ANALYSIS

System data fusion effect test

Taking temperature as an example, the pig house temperature value measured by the precision temperature measuring instrument is used as the standard temperature.

During testing, each group of sensor node from 20 monitoring points in the pig house collected temperature data 10 times. The collected data from the sensor nodes are optimized using a median filtering function to reduce the influence of random factors. Subsequently, using MATLAB (2020a), the temperature data optimized by the median filtering function was compared with the temperature data processed by the algorithm discussed in this paper (a data fusion algorithm based on the median filtering function and Kalman filtering) and the standard temperature of 25.4 °C collected by a precision temperature instrument. The results are shown in Figure 6.

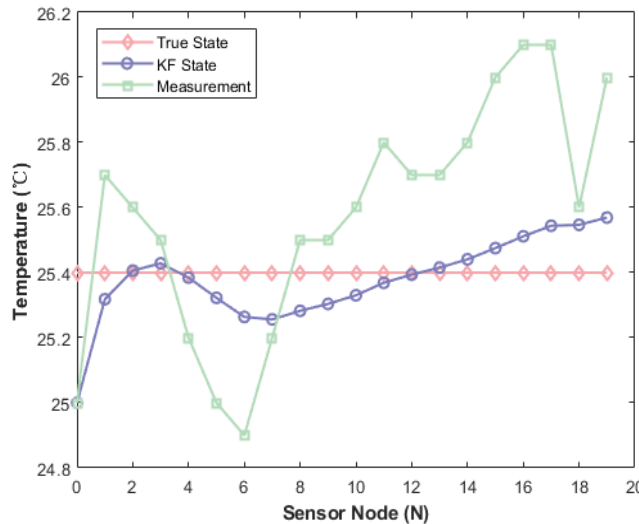


Fig. 6 – Comparison picture of the temperature values measured by three temperature measurement methods

From Figure 6, it can be seen that the average temperature measured by the 20 groups of sensor nodes is 25.57°C, while the average temperature after optimization by the fusion algorithm in this paper is 25.37°C, which is closer to the standard temperature of 25.4°C measured by the precision temperature instrument and the temperature data curve is smoother compared to that measured by the sensor nodes.

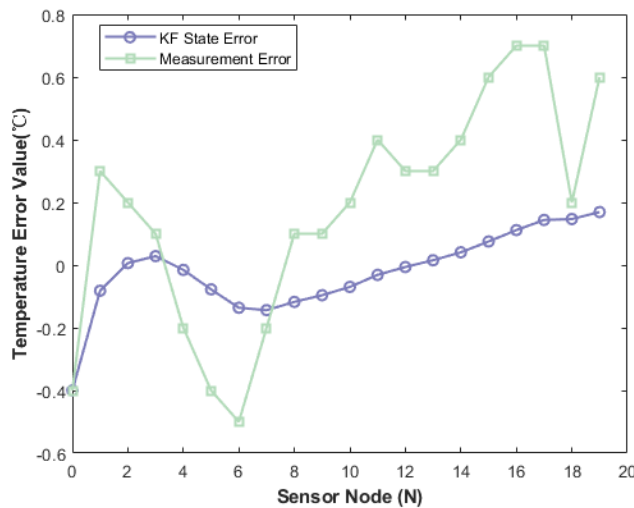


Fig. 7 – Error comparison results

From the error results comparison figure (Figure 7), it is evident that the measurement value error from the sensor nodes is 0.67% and the error range between -0.5°C and 0.7°C, indicating significant fluctuations. In contrast, the error value after applying the algorithm proposed in this paper is 0.12% and the error range is concentrated between -0.1°C and 0.2°C. The error comparison results demonstrate that the Kalman filtering data fusion algorithm proposed in this paper effectively improves the accuracy of sensor measurement data, indicating that the Kalman filtering algorithm meets the data processing requirements of this paper.

System operation test

The sensor nodes for collecting environmental information in the pig house are powered by an independent power source and use Wi-Fi for data transmission. Figure 8 show the historical data curves of pig house environment detection recorded every minute.

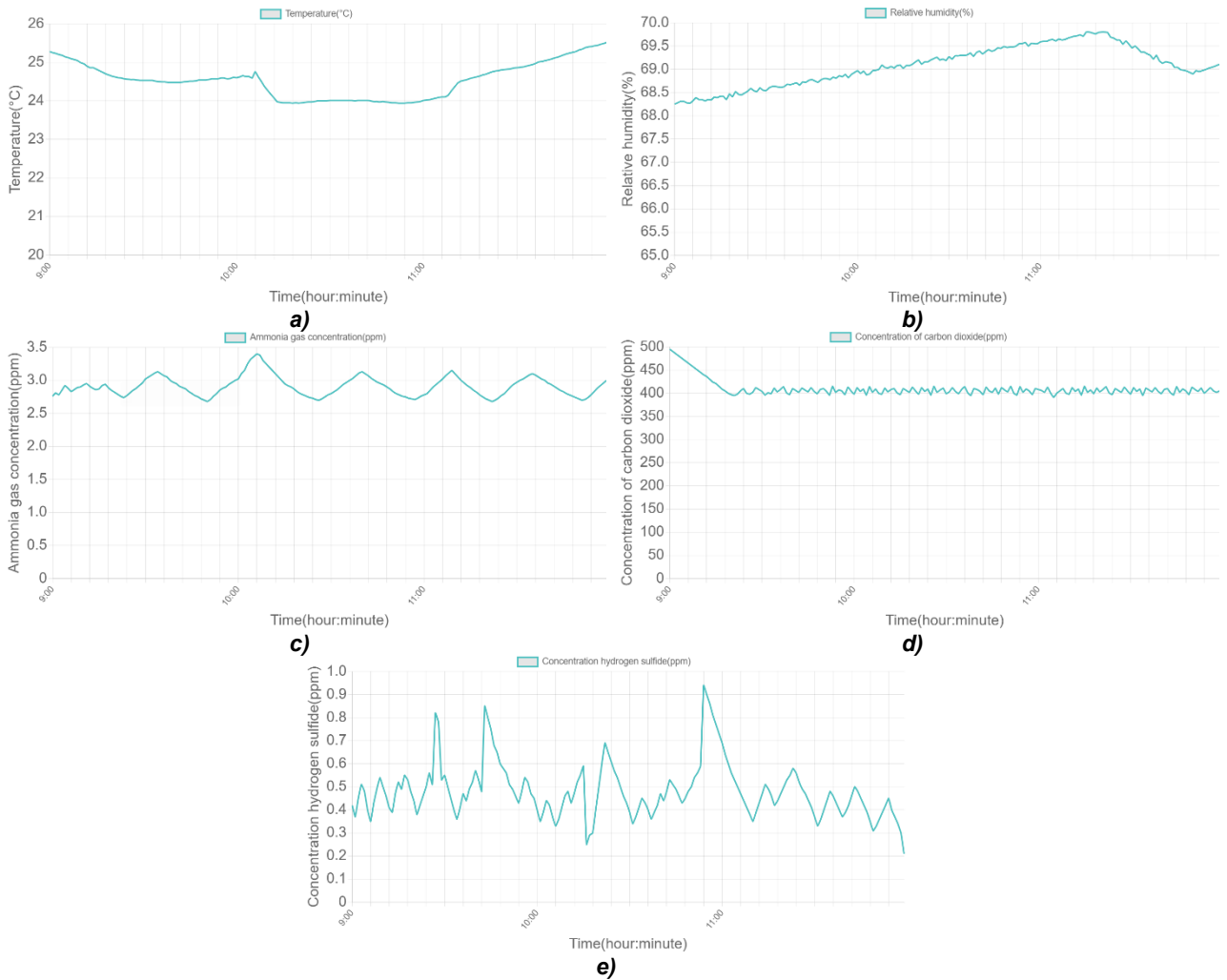


Fig. 8 – Historical data curves of environmental monitoring
 a) Temperature; b) Relative humidity; c) Ammonia concentration;
 d) Concentration of Carbon dioxide; e) Concentration of hydrogen sulfide

Environmental evaluation test

According to the collected 24h environmental factor data of pig house on October 11, 2024, the median filter function and Kalman filter data fusion algorithm were used to process these environmental data, and combined with fuzzy comprehensive evaluation, the membership curves of pig house environmental suitability evaluation at each time were obtained, as shown in Figure 9.

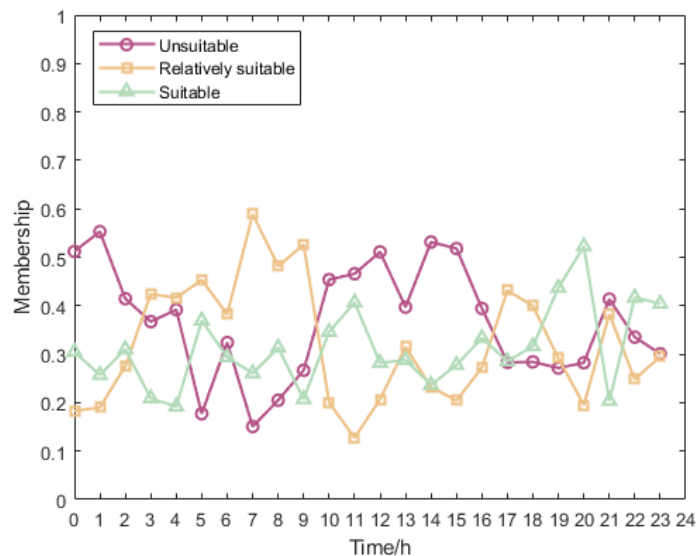


Fig. 9 – Membership degree curves of environmental suitability evaluation of pig house

From Figure 9, it can be seen that on this day, the combined proportion of suitable and relatively suitable conditions in the pig house environment is much greater than that of unsuitable conditions. The condition of the pig house environment is determined by multiple environmental factors and taking the data at 10:00 AM on a particular day as an example, the results after processing with the Kalman filter are as follows: temperature is 24.2°C, relative humidity is 66.82%, ammonia gas concentration is 5.3 ppm, carbon dioxide concentration is 1243 ppm, and hydrogen sulfide concentration is 0.05 ppm. By inputting these environmental factor data into the ridge-shape membership function, the membership matrix is obtained as shown in Eq. (25).

$$H = \begin{bmatrix} 0 & 0.59 & 0.41 \\ 0 & 1 & 0 \\ 0 & 1 & 0 \\ 0 & 0.61 & 0.39 \\ 1 & 0 & 0 \end{bmatrix} \tag{25}$$

Through the comprehensive weight calculation method, the weight set at this time is derived as $\omega = [0.4625, 0.2109, 0.1466, 0.0551, 0.1249]$. Combined with Equation (15), a fuzzy comprehensive evaluation of the suitability of the pig house environment is conducted, resulting in evaluation outcome $Y = [0.1249, 0.6640, 0.2111]$, which corresponds to respectively the evaluation result set $D = \{\text{suitable, relatively suitable, unsuitable}\}$. According to the principle of maximum membership, at this time, the proportion of "suitable" in the evaluation result set is 0.1249, "relatively suitable" has the highest proportion at 0.6640, and "unsuitable" is 0.2111. Therefore, it is determined that the pig house environment at this time is "relatively suitable." The evaluation results of the pig house environment can be displayed on the remote monitoring page, as shown in Figure 10 and Figure 11. The system client can display the environmental information of the current measurement area and provide the current environmental suitability status. The visual interface of the cloud platform is consistent with the data display results of the WeChat mini program, which proves that the performance of each unit of the system is stable, the operation is normal, and the design objectives are met.

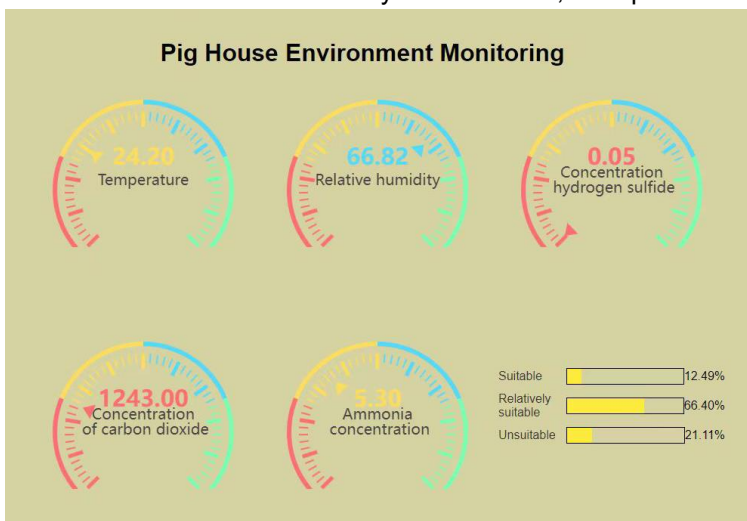


Fig. 10 – Cloud platform interface

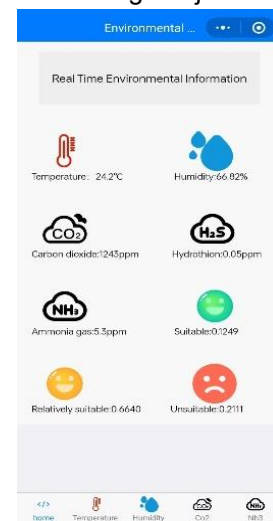


Fig. 11 – WeChat mini program page

CONCLUSIONS

This paper designs a pig house environmental monitoring system based on Internet of Things technology, which can monitor the environmental data in the pig house in real time. The Kalman filter data fusion algorithm is adopted in the system to ensure the accuracy of monitoring data, and this data fusion algorithm is implemented in the main control chip of the sink node. The test results of temperature data show that the error of Kalman filter algorithm is only 0.12%, which meets the monitoring accuracy requirement. In order to achieve an accurate evaluation of the pig house environment, a fuzzy comprehensive evaluation system for pig house is constructed, avoiding the one-sidedness of single environmental factor evaluation methods. The system combines subjective and objective weight calculation methods, reducing the deviation of subjective weights and the one-sidedness of objective weights to a certain extent, making the weight calculation more scientific. The field tests indicate that the system operates stably, and the cloud platform can display real-time environmental data and suitability evaluation results of pig houses, meeting the system requirements.

ACKNOWLEDGEMENT

The author has been supported by the “Qingdao Agricultural University Doctoral Start-Up Fund” (Project number: 1121005), the “Supported by the Open Project Program of Key Laboratory of Smart Agricultural Technology in Tropical South China, Ministry of Agriculture and Rural Affairs, P. R. China” (Project number: HNZHNY-KFKT-202206) and the “2023 Shandong Province Science and Technology based Small and Medium sized Enterprises Innovation Capability Enhancement Project” (Project number: 2023TSGC0741).

REFERENCES

- [1] Bai, X., Wang, Z., Sheng, L., & Wang, Z. (2019). Reliable data fusion of hierarchical wireless sensor networks with asynchronous measurement for greenhouse monitoring. [J]. *IEEE Transactions on Control Systems Technology*, Vol. 27(3): 1036-1046.
- [2] Chen, C., Liu, X., Liu, C., & Chang, R. (2020). Optimization of environmental comfort evaluation and prediction model for nursing female pig houses (哺乳母猪舍环境舒适度评价预测模型优化). *Chinese Journal of Agricultural Machinery*, (08), 311-319.
- [3] Chen, C., Liu, X., Duan, W., & Liu C. (2022). Assessment of the environmental comfort of lactating sows via improved analytic hierarchy process and fuzzy comprehensive evaluation [J]. *International Journal of Agricultural and Biological Engineering*, Vol. 15(2): 58-67.
- [4] Chi, Y., Guo, Y., Feng, H., Li, H., & Zheng, Y. (2022). Environmental quality evaluation method of pregnant pig houses based on multi-source information fusion (采用多源信息融合的妊娠猪舍环境质量评价方法). *Chinese Journal of Agricultural Engineering*, (18), 212-221.
- [5] Gao, H., Li, W., & Li, X. (2016). Design of the remote monitoring system for pigsty environment parameters based on the on IoT [J]. *International Journal of Earth Sciences and Engineering*, Vol. 9(5): 2256-2261.
- [6] Han, H., & Shu, L. (2010). Evolution trend and incentive analysis of China's pig industry (中国生猪产业演进趋势及诱因分析). *Chinese Journal of Animal Science*, (12), 7-12.
- [7] Huang, G., Hai, T., Yang, J., & Lin, G. (2022). Design of an intelligent monitoring system for pig house environment based on NB IoT and cloud platform technology (基于 NB-IoT 和云平台技术的猪舍环境智能监控系统设计). *Automation and Instrumentation*, (02), 18-24. doi: 10.19557/j.cnki. 1001-9944.2022.02.004.
- [8] Li, H., Li, B., Li, H., Song, Y., & Liu, Z. (2024). Three-Way k-Means Model: Dynamic optimal sensor placement for efficient environment monitoring in pig house [J]. *Animals: an open access journal from MDPI*, Vol. 14(3): 485.
- [9] Liu, Y., Wu, Y., Guo, Y., Li, D., Zhang, Z., Zuo, X., & Li, G. (2024). Design and implementation of real-time monitoring system for pig growth environment comfort (生猪生长环境舒适度实时监测系统设计与实现). *Chinese Journal of Animal Ecology*. (06), 76-81+96.
- [10] Li, Y., Li, J., Liu, Z., Bi, Z., Zhang, H., & Duan, L. (2023). Anomaly detection for herd pigs based on YOLOx [J]. *INMATEH-Agricultural Engineering*, Vol. 69(1), 88-98. DOI: <https://doi.org/10.35633/inmateh-69-08>
- [11] Spinka, M., Lawrence, A. B., & Newberry, R. C. (2017). 15–Positive welfare: What does it add to the debate over pig welfare? [J]. *Advances in Pig Welfare*, 415-444.
- [12] Wang, C., Ma, X., Dang, H., Fang, Z., Liang, C., & Wang, Y. (2024). Environmental quality evaluation of mixed vertical ventilation pig house in cold area (严寒地区混合垂直通风猪舍环境质量评价). *Chinese Journal of Agricultural Engineering*, (11), 204-211.
- [13] Wang, X., Zhang, X., Mu, Y., Sheng, Q., Yuan, Z., & Zheng, J. (2024). Environmental monitoring system of pig house based on Internet of Things (基于物联网的猪舍环境监测系统). *Modern Agricultural Equipment*, (03), 54-62.
- [14] Wang, S., Zhao, J., Chen, C., Gu, Chun., & Xu, G. (2023). Research and design of environment suitability evaluation system for fattening pig house based on Internet of Things (基于物联网的育肥猪舍环境适宜性评价系统研究与设计). *Software Guide*, (05), 91-96.
- [15] Wang, Z., Ying, S., Fang, Y., & Liu, Z. (2024). Design and implementation of Internet of Things system for pig intelligent breeding (生猪智慧养殖物联网系统设计与实现). *Chinese Journal of Agricultural Mechanization*. 1-8.

- [16] Xie, M., Li, H., & Zhan, K. (2024). Evaluation of summer chicken house environmental quality based on multivariate data and its impact on egg production performance (基于多元数据的夏季鸡舍环境质量评价及其对产蛋性能的影响). *Chinese Journal of Agricultural Engineering*. (8), 188-197.
- [17] Xie, Q., Li, J., Cao, S., Guo, Y., Liu, H., Zheng, P., Liu, W., & Yu, H. (2024). Study on comprehensive evaluation method of pig house environment based on time series (基于时序序列的猪舍环境综合评价方法研究). *Chinese Journal of Agricultural Machinery*. (12), 430-440.
- [18] Xie, Q., Su, Z., Ji, Q., Zheng, P., & Yan, L. (2016). Fuzzy comprehensive evaluation of environmental suitability of pig house (猪舍环境适宜性模糊综合评价). *Chinese Journal of Agricultural Engineering*. (16), 198-205.
- [19] Zhou, H., Rong, L., Liu, G., Tong, Z., Huo, J., & Chen, Q. (2021). Design of pig house environmental monitoring system based on agricultural Internet of Things (基于农业物联网的猪舍环境监控系统的设计). *Journal of Heilongjiang Bayi Agricultural University*. (02), 93-98.
- [20] Zeng, Z., Dong, B., Lu, E., Xia, J., Wu, P., & Shen, H. (2020). Design and experiment of wireless multi-point and multi-source remote monitoring system for pig house environment (猪舍环境无线多点多源远程监测系统设计与试验). *Chinese Journal of Agricultural Machinery*. (02), 332-340+349.
- [21] GB/T 17824.3-2008. *Environmental parameters and environmental management of large-scale pig farms (规模猪场环境参数及环境管理)* [S]. General Administration of Quality Supervision, Inspection and Quarantine of the People's Republic of China, Standardization Administration of China, 2008.

PRELIMINARY THERMODYNAMIC ASSESMENT OF A REFRIGERATION SYSTEM WITH A PCM BASED DEFROSTING

EVALUAREA TERMODINAMICĂ PRELIMINARĂ A UNUI SISTEM FRIGORIFIC CU DEGIVRARE PE BAZĂ DE PCM

Valentin APOSTOL¹⁾, Horatiu POP ^{*1)}, Tudor PRISECARU¹⁾, Claudia IONITA¹⁾, Jamal AL DOURI¹⁾
Adrian CHIRIAC^{*1,2)}, Cornel Constantin PAVEL¹⁾

¹⁾ Faculty of Mechanical Engineering and Mechatronics, National University of Science and Technology POLITEHNICA Bucharest / Romania.

²⁾ Academy of Romanian Scientists, Ilfov 3, 050044 Bucharest, Romania

Tel: +40744903488; E-mail: horatiu.pop@upb.ro; Tel: +40721882659; E-mail: gabriel.chiriac@upb.ro

Corresponding authors: Horațiu POP; Adrian CHIRIAC

DOI: <https://doi.org/10.35633/inmateh-75-44>

Keywords: vapor compression refrigeration, phase change material, evaporator, defrosting, thermal energy storage

ABSTRACT

This article presents a preliminary thermodynamic evaluation of a vapor compression refrigeration system (VCRS) using phase change materials (PCM) for defrosting. The objective of this study was to highlight the potential of heat recovery during the operation of the VCRS and its subsequent use in the defrosting process. The system was analyzed energetically, considering both the cooling and defrosting cycles using PCM-RT 35 HC. Input data are given, and they were experimentally measured on a VCRS installed in a freezing chamber located in the university campus. The analysis includes the following refrigerants: R32, R404A, R134a, R290, R600a, R600, R1234yf, and R1234ze(E). The results indicate that as the defrosting time increases, the refrigerant flow rate required for PCM-based defrosting decreases. Furthermore, it was observed that R600 requires the smallest refrigerant flow rate for the defrosting process, while R404A requires the highest to defrost the same mass of ice. The analysis revealed that R32 is the most suitable refrigerant for PCM-based defrosting, followed by wet or dry refrigerants (R404A, R134a, R290) and, finally, isentropic refrigerants (R600, R600a, R1234yf, R1234ze(E)). Additionally, it is noted that as the condensing temperature increased, the recoverable heat increased for R32, R404A, R134a, and R290, but decreased for isentropic refrigerants such as R600a, R600, R1234yf, and R1234ze(E). This analysis was conducted using a computational model implemented in the Engineering Equation Solver software.

REZUMAT

Acest articol prezintă o evaluare termodinamică preliminară a unui sistem frigorific cu comprimare mecanică de vapori (IFV) cu degivrare pe bază de materiale cu schimbare de fază (MSF). Scopul acestei lucrări a fost acela de a evidenția posibilitățile de recuperare a căldurii în timpul funcționării sistemului IFV și utilizarea ulterioară a acesteia în procesul de degivrare. Sistemul a fost analizat din punct de vedere energetic atât pentru ciclul de răcire cât și pentru cel de degivrare cu MSF-RT 35 HC. Datele de intrare au fost măsurate experimental pe un sistem IFV ce echipează o cameră de congelare existentă în campusul universitar. Sunt luați în considerare agenții frigorifici: R32, R404A, R134a, R290a, R600a, R600, R1234yf și R1234ze(E). Rezultatele arată că dacă timpul de degivrare crește, debitul de agent frigorific necesar degivrării cu MSF, scade. De asemenea, se observă că în cazul agentului frigorific R600 s-a utilizat cel mai mic debit de agent frigorific pentru degivrare iar în cazul lui R404A, cel mai mare debit, pentru a degivra aceeași masă de gheață. Din analiză se constată că freonul R32 se pretează cel mai bine în cazul degivrării cu MSF urmat de freonii umezi sau uscați: R404A, R134a, R290 și în final de freonii izentropici: R600, R600a, R1234yf, R1234ze(E). Se constată de asemenea că odată cu creșterea temperaturii de condensare crește căldura recuperată în cazul lui R32, R404A, R134a, R290a și scade în cazul agenților frigorifici izentropici: R600a, R600, R1234yf și R1234ze(E). Această analiză s-a realizat folosind un model computerizat în software-ul Engineering Equation Solver.

Valentin APOSTOL, Prof. Ph. D. Eng.; Horatiu POP Assoc. Prof. Ph.D.Eng; Tudor PRISECARU Prof. Ph. D. Eng;

Claudia IONITA, Assoc.Prof. Ph.D.Eng.; Jamal Al Douri. Ph.D. Student; Adrian CHIRIAC, Ph.D. Student; Cornel Constantin PAVEL, Ph.D. Student

INTRODUCTION

Significant greenhouse gas emissions are released into the atmosphere due to the extensive use of fossil fuels and industrial activities. Heating, ventilation, air-conditioning, and refrigeration (HVAC-R) systems that operate on the vapor compression refrigeration (VCR) cycle contribute substantially to these emissions. Depending on the country, HVAC-R systems account for 16% to 50% of a building's total energy consumption (Hepbasli, 2012) and approximately 33% of overall greenhouse gas emissions (Kharseh, et al., 2014). Greenhouse gas emissions from VCR systems can be divided into direct and indirect sources. Direct emissions, which result from refrigerant leaks, represent about 20% of the total, while indirect emissions, due to electricity consumption, equipment manufacturing, cooler production, defrost system, and material recycling, constitute the remaining 80% (Ragip, et al., 2023).

Refrigeration systems are a key component of the food industry. The most widely used refrigeration systems are the ones with vapor compression. A significant challenge for vapor compression refrigeration systems is the formation of ice on evaporator tubes, which poses a major operational issue. Ice formation begins when the surface temperature of the evaporator drops below both the freezing point of water and the dew point of the air, causing water vapor to condensate on the cold surface of the heat exchanger due to temperature differences. The water vapors that will eventually form the ice layer on the evaporator come from the food itself, from the moist air that enters the cold room when the door is opened or from other sources specific to each application. Relative humidity (RH) of the air inside the cold room also plays a crucial role in the ice formation process (Mohammed, et al., 2017).

The frost layer increases the thermal resistance between the air and the refrigerant, resulting in a decrease in cooling capacity. Additionally, the cooling capacity is further diminished due to a reduction in air-side volumetric flow. This occurs because the hydraulic diameter of the flow channel decreases while fan power remains constant (Le Gall et al., 1997). Consequently, both the refrigeration system's cooling capacity and its coefficient of performance (COP) are adversely affected (Al-Douri et al., 2024). Therefore, periodic defrosting is necessary.

As highlighted by Zhi-Ling et al., (2024), previous experimental studies evaluating defrosting heat supply in case of reverse cycle method indicate that 71% to 80% of the total heat required for defrosting is sourced from the indoor heat exchanger.

The most used defrosting methods for refrigeration systems have been detailed in the authors' previous research (Al-Douri et al., 2023). The defrosting method chosen for the given application has an influence on the air parameters (temperature, humidity) inside the refrigerating enclosure. The air parameters have a direct influence on the food products' quality. A defrost method based on a high operating temperature as electric defrosting for example, has as consequence a higher temperature inside the refrigerating enclosure at the end of the defrosting process. A defrosting method based on a low operating temperature like air defrosting for example has as consequence an increase in relative humidity inside of the refrigerating enclosure which can directly influence the quality of the food products. The PCM based defrosting method has a moderate operating temperature being suitable for applications from the food preservation industry. The current study focuses on an in-depth analysis of defrosting methods that employ phase change materials (PCM). Although most research in this field has been conducted at the level of heat pumps, the PCM approach has been investigated for its potential application to thermal energy storage (TES)-based defrosting methods in industrial refrigeration systems and beyond. According to the literature, TES-based defrosting methods are classified based on different energy sources into three categories: discharge heat storage, condensing heat storage, and subcooling heat storage.

For instance, to address the decline in heating capacity when the indoor heat exchanger is inactive, Wang et al. proposed operating the condenser and outdoor heat exchanger in parallel during defrosting mode. This configuration enables the PCM-HE to serve as a heat source for both space heating and defrosting. Zhang et al., (2014), demonstrated that heat dissipated from the compressor outlet of an air source heat pump, stored in the PCM-HE, can effectively melt frost on the outdoor coil. A similar discharge heat storage-based defrosting method has also been applied to air-cooled household refrigerators (Dobre et al., 2024; Zhongbao, et al., 2018).

In their work, Jian-kai et al., (2011), conducted an experimental comparison between the energy storage-based reverse cycle defrosting method and the traditional defrosting method for an air source heat pump. Under identical experimental conditions, the energy storage-based method reduced defrosting time by 60% and defrosting energy consumption by 48.1%.

Also, *Xin et al., (2021)*, reported that PCM-HEs could store sufficient energy during the heating phase and release it to melt and evaporate frost during the defrosting phase for a heat pump. Similarly, *Zhaozhong et al., (2023)*, demonstrated that for a split-air source heat pump (ASHP) unit utilizing phase change energy storage technology, the defrosting time could be shortened by 71.4–80.5%.

Zhang et al., (2014), also experimentally investigated the defrosting performance of a novel split-ASHP unit, where the compressor was encased in a PCM-HE to store dissipated heat. This innovative defrosting approach reduced energy consumption by 27.9% compared to the standard reverse cycle defrosting (SRCD) method (*Yang et al., 2019*).

Another experiment was conducted by *Miryam, et al., (2024)*, who utilized heat from the discharge of a heat pump compressor, stored in a PCM heat exchanger. During the defrosting process, the refrigerant passes through the PCM heat exchanger, vaporizes, and is then directed to the system's evaporator to remove the frost.

Zhongbao et al., (2017), performed an experimental study on defrosting methods using TES in a household refrigerator, comparing it with electric resistance defrosting. The experimental results demonstrated that the thermal storage defrosting system could reduce power consumption by 71% compared to the original electric heater defrosting method.

Overall, the energy storage defrosting method is one of the most promising ways to solve the frosting problem of the refrigeration systems.

MATERIALS AND METHODS

System description

The refrigeration system operates in cooling mode for 5,5 h. In this time interval a specific amount of ice is deposited on the evaporator coil. This amount of ice will be removed in the defrosting interval of 0,5 hours.

Functional parameters are presented in Table 1.

Table 1

VCRS characteristics			
Parameter	Value	Parameter	Value
Evaporating temperature t_o	-30°C	Cooling time $\tau_{cooling}$	5.5 hours
Condensing temperature t_c	33°C	Ice mass m_{ice}	1.4 kg
Cooling capacity \dot{Q}_o	4.5 kW	Heat storage capacity PCM RT 35-HC λ_{PCM}	240 kJ/kg
Defrosting time $\tau_{defrost}$	0.5 hours	Heat storage capacity Ice λ_{ice}	330 kJ/kg
Number of defrosts n	4	Pressure difference from p_8 to $p_6, \Delta p$	0.6 bar

The schematic and operating cycle of the VCRS are presented in Fig. 1 (a) and (b) respectively.

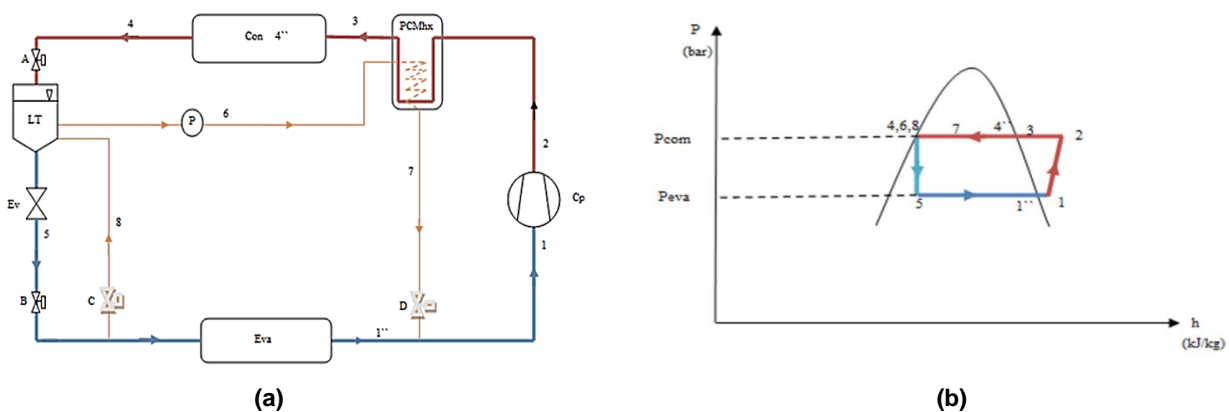


Fig. 1 - The schematic and operating cycle of the VCRS

(a) - Schematic view of the VCRS system with PCM; (b) - Thermodynamic cycle of the VCR system with PCM;

The authors' previous work (Al-Douri et al., 2023) presented an experimental study on the use of a PCM heat exchanger for defrosting the evaporator of a refrigeration system installed in the CG 005 room at the National University of Science and Technology POLITEHNICA Bucharest - Faculty of Mechanical Engineering and Mechatronics, Department of Engineering Thermodynamics. The study investigated the impact of several PCM types of SP 31, RT 35 HC, RT 54 HC, and SP 50 on the energy performance of the vapor-compression refrigeration system (VCR) for various refrigerants. The results demonstrated that RT 35 HC was the most suitable PCM, as the same amount of thermal energy was stored for a significantly smaller PCM mass compared to the other materials analyzed.

In the present work, the same refrigeration system with RT 35 HC-based PCM defrosting is analyzed, focusing on different aspects compared to the previous study.

Mathematical model

The evaporative pressure p_{eva} [bar], the condensing pressure p_{con} [bar], superheating degree Δt_{sh} are determined experimentally. With these values, the following thermodynamic states of the refrigerant can be determined:

$$\begin{aligned}
 \text{State 1''} &\rightarrow p_{eva}, \Omega, x=1 \rightarrow t_{1''}; h_{1''}; v_{1''}; s_{1''} \\
 \text{State 1} &\rightarrow p_{eva}, \Omega (t_1=t_{1''}+\Delta t_{sh}) \rightarrow h_1; v_1; s_1 \\
 \text{State 2} &\rightarrow p_{con}, \Omega (s_1=s_2) \rightarrow t_2; h_2; v_2 \\
 \text{State 3} &\rightarrow p_{con}, \Omega (t_3=t_c+\Delta t_{rec}) \rightarrow h_3; v_3; s_3 \\
 \text{State 4} &\rightarrow p_{con}, \Omega, x=0 \rightarrow t_4; h_4; v_4; s_4 \\
 \text{State 8} &\rightarrow p_{con}, \Omega, x=0 \rightarrow t_8; h_8; v_8 \\
 \text{State 6} &\rightarrow p_{con} + \Delta p, \Omega (h_6=h_8+|l_{8-6}|) \rightarrow t_6; h_6; v_6; s_6; p_6 \\
 \text{State 5} &\rightarrow p_{eva}, \Omega (h_5=h_6) \rightarrow t_5; v_5; s_5 \\
 \text{State 7} &\rightarrow p_{con} + \Delta p, \Omega, x_7=0.7 \rightarrow t_7; h_7; v_7; s_7
 \end{aligned} \tag{1}$$

where Δp is the rise of pressure from condensing pressure needed to circulate the liquid refrigerant on the defrosting loop, p_6 is liquid refrigerant pressure at the inlet of the PCMHx given by the defrost pump and p_{con} is the condensing pressure. Also, l_{8-6} represents the specific work of the defrost pump.

In eq. (1) the specific work required by the circulation pump is given by: $|l_{8-6}| = v_8 \Delta p$ and the refrigerant quality in state 7 is imposed $x_7=0.7$.

The mass flow rate of refrigerant \dot{m} can be written:

$$\dot{m} = \dot{Q}_0 / q_0 \tag{2}$$

$$q_0 = h_{1''} - h_5 \tag{3}$$

where: \dot{Q}_0 is the cooling capacity of the system and q_0 is the specific cooling capacity.

$$\tau_{\text{between defrost}} = (24 / n) \cdot 3600 \tag{4}$$

$$\tau_{\text{defrost}} = 30 \text{ min} \tag{5}$$

$$\tau_{\text{cooling}} = \tau_{\text{between defrost}} - \tau_{\text{defrost}} \tag{6}$$

where $\tau_{\text{between defrost}}$ is the time between 2 consecutive defrost cycles, τ_{defrost} is the time when the system is in defrost mode and τ_{cooling} is the time period when the system is in cooling mode, all three being in seconds.

In Eq. (4), n represents the number of defrosts that take place in 24 hours.

$$\dot{Q}_{\text{recovery}} = \dot{m} \cdot (h_2 - h_3) \tag{7}$$

$$Q_{\text{recovery}} = \dot{Q}_{\text{recovery}} \cdot \tau_{\text{cooling}} \tag{8}$$

$$\lambda_{\text{PCM}} = 240 \frac{\text{kJ}}{\text{kg}} \tag{9}$$

where $\dot{Q}_{recovery}$ is the heat flux that can be recovered from the refrigerant in the desuperheating process 2-3, $Q_{recovery}$ being the actual heat that can be recovered and λ_{PCM} is the heat storage capacity of PCM:

$$Q_{ice} = m_{ice} \cdot (c_{ice} \cdot (0 - t_{ice}) + \lambda_{ice}) \quad (10)$$

$$m_{ice} = 1.4 \text{ kg} \quad (11)$$

$$c_{ice} = 2.09 \text{ kJ/kg} \cdot \text{K} \quad (12)$$

$$t_{ice} = t_0 \quad (13)$$

$$\lambda_{ice} = 330 \text{ kJ/kg} \quad (14)$$

where Q_{ice} is the heat needed to melt the specific quantity of ice, (m_{ice}), c_{ice} is the specific heat of ice, t_{ice} represents the temperature of ice, which was taken equal to the evaporating temperature and λ_{ice} is the heat storage capacity for ice.

$$Q_{PCM} = m_{PCM} \cdot \lambda_{PCM} \quad (15)$$

$$Q_{PCM} = Q_{ice} \quad (16)$$

where Q_{PCM} is the heat that the mass of PCM (m_{PCM}) can absorb during defrosting period.

$$\dot{Q}_{ice} = Q_{ice} / \tau_{defrost} \quad (17)$$

$$\dot{Q}_{ice} = \dot{m}_{defrost} \cdot (h_7 - h_8) \quad (18)$$

where \dot{Q}_{ice} is the heat flux that can be absorbed in time $\tau_{defrost}$, h_7 and h_8 are the specific enthalpies at the exit and inlet of the evaporator during the defrost period [kJ/kg].

$$P_{cp} = \dot{m} \cdot (h_2 - h_1) \quad (19)$$

$$P_{p1} = |l_{8-6}| \cdot \dot{m}_{defrost} \quad (20)$$

$$|l_{8-6}| = v_8 \cdot \Delta p \quad (21)$$

where P_{cp} is the compressor power, h_2 and h_1 are the specific enthalpies at the exit and inlet of the compressor. P_{p1} is the power of the defrost liquid refrigerant circulation pump and v_8 is the specific volume of refrigerant after the evaporator exit on the defrost loop.

$$COP_{with\ pump} = \dot{Q}_0 / (P_{cp} + P_{p1}) \quad (22)$$

$$COP = \dot{Q}_0 / P_{cp} \quad (23)$$

where $COP_{with\ pump}$ represents the COP considering also the power of the defrost liquid refrigerant circulation pump and COP stands for the refrigeration cycle.

Based on the mathematical model presented before by Arora et al., (2008), Havelisky, (2000), Selbas, et al., (2006), a program has been developed in Engineering Equation Solver. Data resulted is expressed below for R600a, R600, R290, R32, R404a, R134a, R1234yf and R1234ze(E).

RESULTS

Figure 2 shows that when the defrosting time increases, the mass flow rate of defrosting refrigerant decreases for the same constant amount of ice ($m_{ice}=1.4$ kg), same evaporating temperature $t_0=-30^\circ\text{C}$ and the same quality $x_7=0.7$ at the exit of the PCMhx. Additionally, when defrost time is 30 minutes, refrigerant R600 displays the smallest refrigerant mass flow rate (0.0013 kg/s), while refrigerant R404A has the highest mass flow rate of roughly (0.0032 kg/s). For the defrosting time of 60 min increases the values of the defrosting refrigerant mass flow rate are much closer to each other compared to a defrosting time of 10 min.

Figure 3 and Table 2 show the COP values in function of the defrosting time for the analyzed refrigerants considering the same $t_0=-30^\circ\text{C}$ and quality $x_7=0,7$.

The coefficient of performance (COP) increases slowly with the increase of the defrosting time. It can be seen that the $COP_{with\ pump}$ of the refrigeration system with a PCM based defrosting is lower than the case of the refrigeration system without (COP). This is due to the fact that the power of the pump has a low value (see eq. 21 and eq. 22) which means that for both situations the coefficient of performance shows very close values.

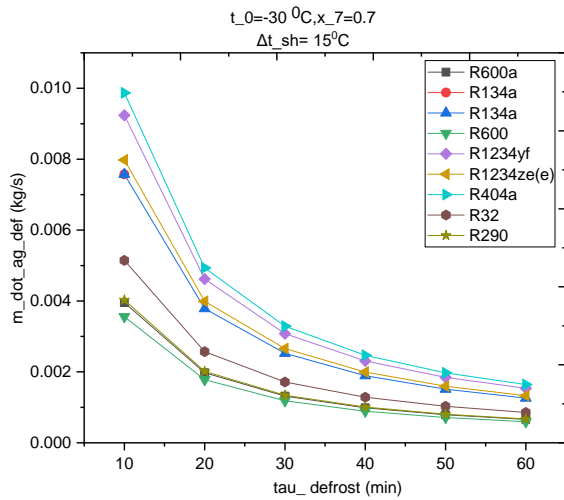


Fig. 2 – Mass flow rate of the defrosting agent versus defrost time

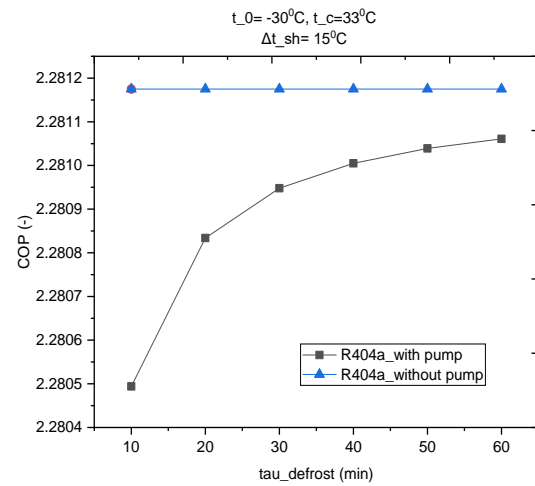


Fig. 3 - Comparison between COP with pump and COP without pump for R404a refrigerant

Table 2

Comparison between COP without pump and $COP_{with\ pump}$ for different refrigerants

Refrigerants	COP	$COP_{with\ pump}$	
		min	max
R600a	2.6743	2.6736	2.6742
R134a	2.6188	2.6182	2.6187
R600	2.7562	2.7556	2.7561
R1234yf	2.4059	2.4052	2.4058
R1234ze(E)	2.5684	2.5678	2.5683
R404A	2.2811	2.2804	2.2810
R32	2.5783	2.5778	2.5782
R290	2.5839	2.5831	2.5838

Table 2 shows that the influence of the defrosting time on the $COP_{with\ pump}$ and COP is the same with the specification that R600 has the highest coefficient of performance and R404A has the lowest for the same operating conditions: $t_0=-30^\circ\text{C}$, $t_c=33^\circ\text{C}$ and $x_7=0.7$.

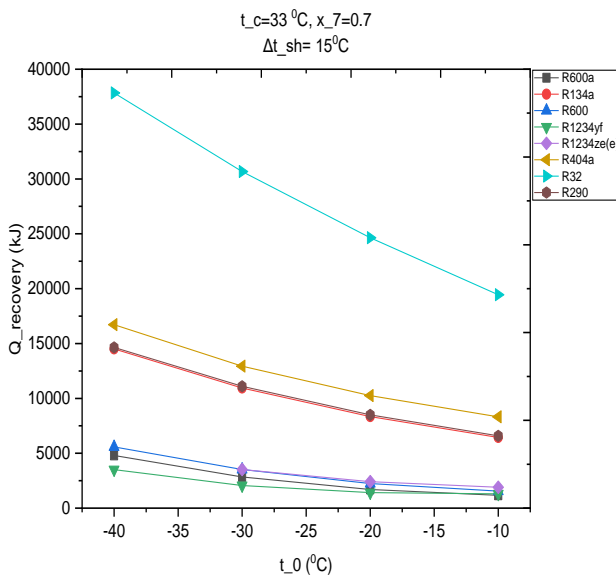


Fig. 4 – Variation of evaporation temperature with PCM heat recovery

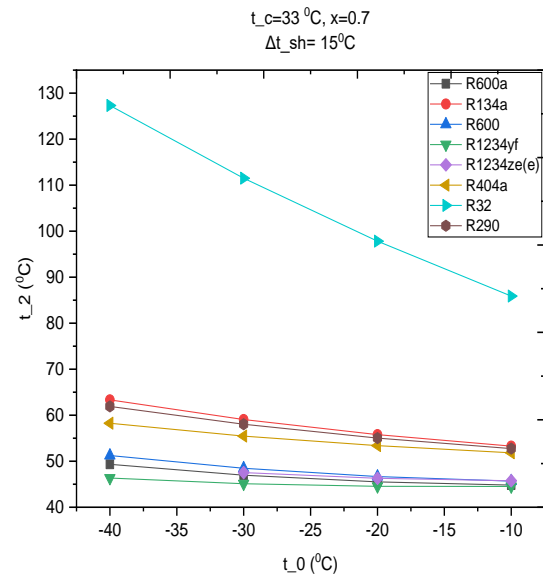


Fig. 5 - The correlation between discharge temperature t_2 and evaporation temperature t_0

Figure 4 shows the variation of the heat which can be recovered ($Q_{recovery}$) from the refrigerant depending on the evaporating temperature (t_0). The figure shows that increasing the evaporating temperature leads to a decrease of the recovered heat. Also, one can notice the heat recovered in the case when the refrigeration system operates at freezing temperatures (-15°C to -40°C) is higher compared to the case when it operates at refrigeration temperatures (-10°C to -15°C). This happens because when the evaporating temperature decreases the evaporating pressure decreases also which means higher compression ratio and as a result higher compressor discharge temperature t_2 (see Fig.5). It can be noticed that the highest heat recovery value can be achieved for R32 and the lowest one for R1234yf (see Fig.4).

The studied refrigerants fall into 3 groups: R32 with a $Q_{recovery}$ between 20000 kJ and 40000 kJ; R404A, R134a and R290 with a $Q_{recovery}$ between 7000 and 17000 kJ and R1234yf, R1234ze(E), R600 and R600a with a $Q_{recovery}$ between 1000 kJ and 5600 kJ.

As expected, the decrease in evaporating temperature results in an increase in discharge temperature t_2 as in the case of $Q_{recovery}$ (Fig 4). Three groups of refrigerants are distinguished: a) R32, b) R404A, R134a, R290 and c) R600, R600a, R1234yf, R1234ze(E). Group a) is characterized by the highest discharge temperatures (85°C-130°C), group b) between 55°C-65°C and group c) 45°C and 52°C. From the combined analysis of figures 4 and 5, it can be seen that R32 fits best to defrosting with PCM followed by groups b and c.

Table 3

Refrigerant $t_c=33°C; x_7=0,7, \Delta t_{sh}=15°C$	Q_{ice} (kJ)		$Q_{recovery}$ (kJ)	
	min(-10°C)	max(-40°C)	min(-10°C)	max (-40°C)
R600a	491,3	579	1165	4801
R134a	491,3	579	6439	14511
R600	491,3	579	1553	5579
R1234yf	491,3	579	1298	3504
R1234ze(E)	491,3	579	1898	3504
R404A	491,3	579	8323	16720
R32	491,3	579	19451	37839
R290	491,3	579	6593	14642

Data specified in Table 3 indicates that, for the operating conditions considered $t_0 \in [-10°C, -40°C]$, the recoverable heat is sufficient to achieve complete defrosting of the ice accumulated on the evaporator, even if the ice is subcooled and requires a greater amount of heat to melt.

Figure 6 shows that the increase of the condensing temperature t_c leads to an increase in the heat recovery. The influence of the condensing temperature on the recovered heat is different for the 3 groups of refrigerants. In figure 6 it can be observed that for R32 – from group a) and for group b), the increase in the condensing temperature leads to an increase of the heat that can be recovered. For instance, in the case of R32, it doubles from 30000 kJ to 60000 kJ, in case of R404A the increase being even greater. For group c), it can be seen that the recovered heat decreases while condensing temperature increases.

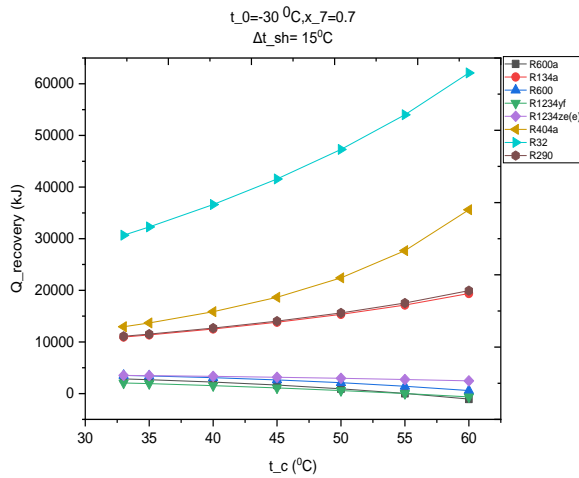


Fig. 6 - Variation of condensing temperature with PCM heat recovery

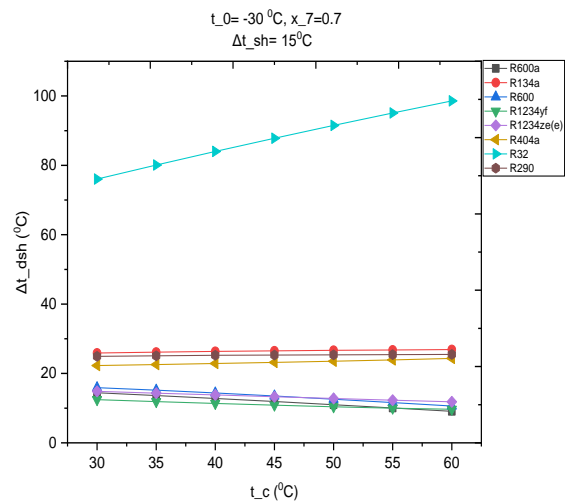


Fig. 7 - Influence of condensing temperature on the degree of desuperheating

According to Figure 7, for refrigerant R32, the desuperheating degree (Δt_{dsh}) increases with the condensing temperature, which justifies the results obtained in the case of heat that can be recovered (Fig. 6). The doubling of $Q_{recovery}$ is not only supported by the increase in Δt_{dsh} , but also by the properties of the refrigerant in terms of enthalpy values (h_2 and h_3). For refrigerants from group b), Δt_{dsh} is quasi-constant and the increase of $Q_{recovery}$ is generated by the enthalpy of the refrigerant. For group c), it is found that $Q_{recovery}$ is correlated with the decrease in Δt_{dsh} . It can be concluded that for certain refrigerants the increase in condensing temperature, in conditions of accumulation of a large amount of ice on the evaporator, can affect defrosting in the version with PCM.

It can be mentioned that the discharge temperature t_2 gives information about the type of PCM that can be used while Δt_{dsh} and $Q_{recovery}$ give information about the maximum amount of heat that can be recovered.

Table 4

Refrigerant $t_0=-30^{\circ}\text{C}; x_7=0.7,$ $\Delta t_{sh}=15^{\circ}\text{C}$	Q_{ice} (kJ)	$Q_{recovery}$ (kJ)			
		t_c (°C)	min	t_c (°C)	max
R600a	549.8	60	-1060	30	3036
R134a	549.8	30	10351	60	19377
R600	549.8	60	581.7	30	3648
R1234yf	549.8	60	-640.9	30	2248
R1234ze(E)	549.8	60	2475	30	3576
R404A	549.8	30	11947	60	35608
R32	549.8	30	28419	60	62103
R290	549.8	30	10497	60	19936

Upon careful analysis of Table 4, it is observed that for the group of refrigerants in category c), under tropical condensing temperatures, the recoverable heat decreases. For refrigerants such as R600a and R1234yf, the recoverable heat reaches negative values due to the fact that the refrigerants in category c) are isentropic. Consequently, the compression process leads to a discharge temperature t_2 lower than the condensing temperature, which means a reduction or even elimination of the desuperheating degree required for heat recovery. Under these conditions, it is no longer possible to recover heat from the refrigerant at the compressor discharge for the specified operating parameters.

Table 5

Refrigerant $t_0=-30^{\circ}\text{C}$; $x_7=0.7$, $\Delta t_{sh}=20^{\circ}\text{C}$	Q_{ice} (kJ)	$Q_{recovery}$ (kJ)			
		t_c ($^{\circ}\text{C}$)	min	t_c ($^{\circ}\text{C}$)	max
R600a	549.8	60	4334	30	6443
R600	549.8	60	5329	30	6807
R1234yf	549.8	30	6686	60	7934
R1234ze(E)	549.8	30	7344	30	8905

Table 5 presents the results obtained for a 20°C superheating degree. These results show a significant increase in recoverable thermal energy, thereby making PCM-based defrosting feasible for isentropic refrigerants.

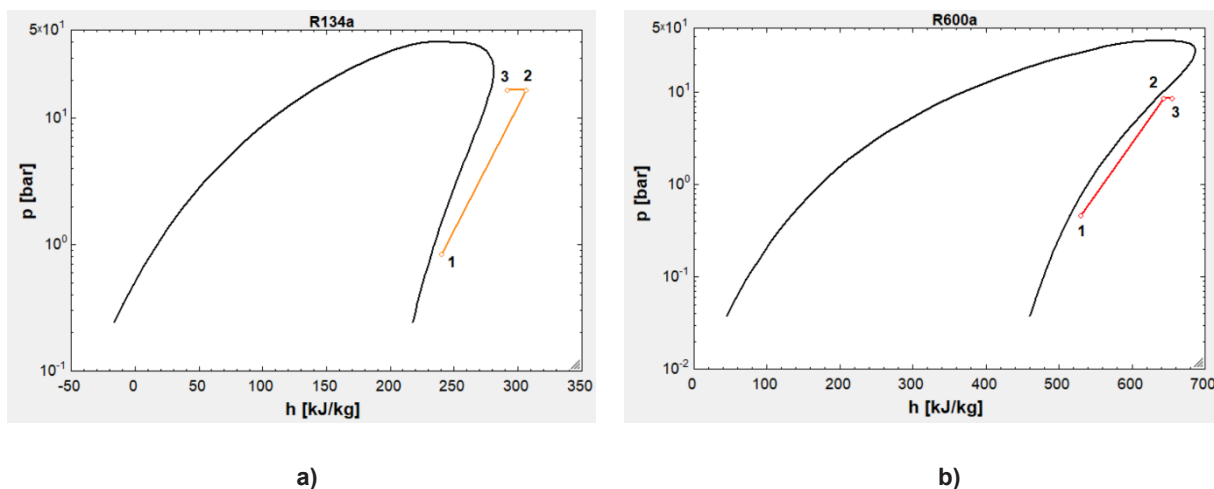


Fig. 8 – Compression and recovery processes for wet or dry refrigerants (a) and for isentropic refrigerants (b) in p-h diagram

Figures 8a and 8b illustrate two cases: (a) wet or dry refrigerants (e.g., R134a) and (b) isentropic refrigerants. The refrigerants R32, R404A, R134a, R290 from groups a) and b) are wet or dry. For these refrigerants the enthalpy in state 3 is lower than the enthalpy in state 2 making heat recovery possible. In Figure 8a and 8b the thermodynamic state 2 represents the state of the refrigerant at the compressor discharge and state 3 is the state of the refrigerant at the outlet of PCMhx.

In the case of isentropic refrigerants in group c): R600, R600a, R1234yf, R1234ze(E), the enthalpy of state 2 is lower than the enthalpy of state 3. Under these conditions, the possibility of recovering heat from the refrigerant at the compressor discharge is reduced to zero. Therefore, to enable PCM-based defrosting, it is necessary to increase the superheating degree before the compressor inlet.

Figure 9 shows the influence of the refrigerant quality over $COP_{with pump}$. From Figure 9 one can notice that for refrigerant quality values ranging from 0 to 0.1 the $COP_{with pump}$ increases abruptly and for values between 0.2 and 1 it increases much slower. The increase in $COP_{with pump}$ is attributed to the high-power input required by the liquid circulation pump during the initial phase of the defrosting process. As the liquid refrigerant circulates through the evaporator, its condensation rate progressively decreases, resulting in a gradually reduced flow rate of liquid refrigerant. Consequently, the power required to drive the pump decreases, leading to a slight yet linear increase in the $COP_{with pump}$.

Table 6 shows the effect of refrigerant quality on $COP_{with pump}$. It can be noticed that the refrigerant quality has a small impact on $COP_{with pump}$ and at the same time refrigerant R600 has the highest value out of all refrigerants analyzed in the present study. In Table 6 a higher number of digits have been used to point out the influence of the refrigerant quality (x_7) at the exit of the PCMhx on the $COP_{with pump}$. The influence of quality x_7 on $COP_{with pump}$ is not very strong and can be noticed after several digits depending on the refrigerant.

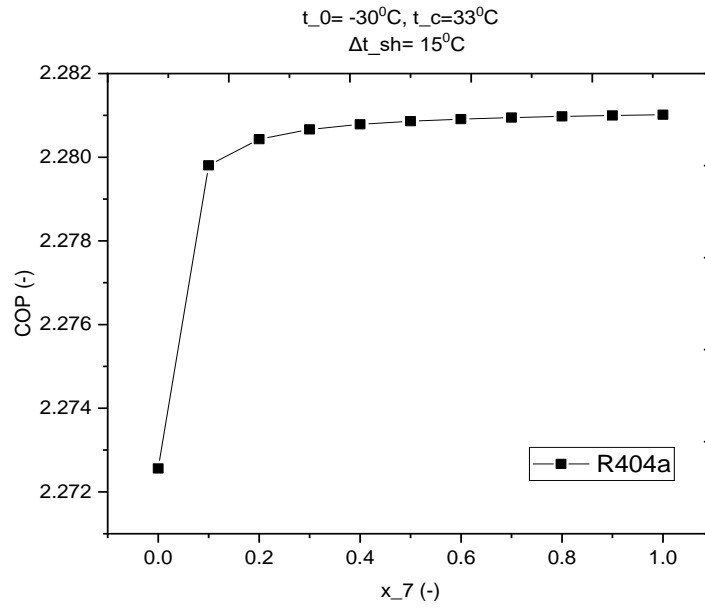


Fig. 9 - Influence of refrigerant quality over COP_{with pump}

Table 6

x ₇	COP _{with pump}							
	R600a	R134a	R600	R1234yf	R1234ze(E)	R404A	R32	R290
0	2.6698	2.6122	2.7527	2.4000	2.5633	2.2725	2.5654	2.5744
0.1	2.6731	2.6176	2.7551	2.4046	2.5672	2.2798	2.5772	2.5822
0.2	2.6736	2.6181	2.7556	2.4052	2.5677	2.2804	2.5777	2.5831
0.3	2.6738	2.6183	2.7558	2.4054	2.5679	2.2806	2.5779	2.5833
0.4	2.6740	2.6184	2.7559	2.4055	2.5680	2.2807	2.5780	2.5835
0.5	2.6740	2.6185	2.7559	2.4056	2.5681	2.2808	2.5781	2.5835
0.6	2.6741	2.6185	2.7560	2.4057	2.5681	2.2809	2.5781	2.5836
0.7	2.6741	2.6186	2.7560	2.4057	2.5682	2.2809	2.5781	2.5836
0.8	2.6741	2.6183	2.7560	2.4057	2.5682	2.2809	2.5781	2.5837
0.9	2.6742	2.6186	2.7561	2.4057	2.5682	2.2809	2.5781	2.5837
1	2.6742	2.6186	2.7561	2.4058	2.5682	2.2810	2.5782	2.5838

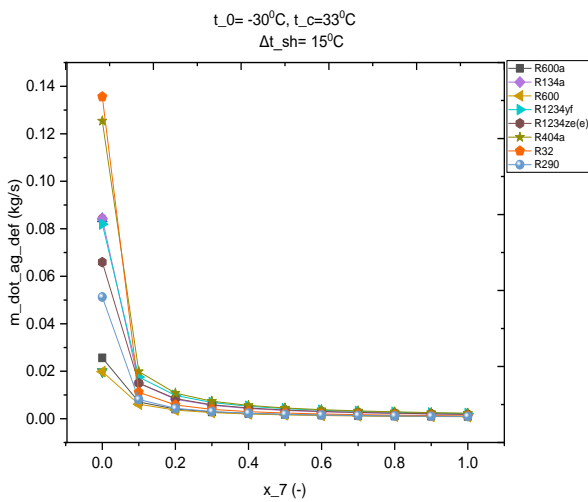


Fig. 10 - Effect of defrost refrigerant mass flow rate on refrigerant quality

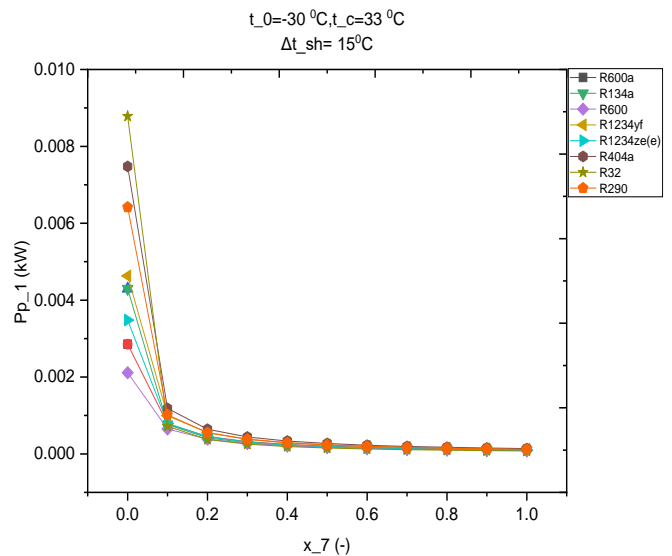


Fig. 11 - The relationship between pump power and refrigerant quality

Figure 10 shows the relationship between the mass flow rate of defrosting refrigerant and refrigerant quality x_7 . As expected, there is a significant correlation between these two parameters. The figure demonstrates that as the quality (x_7) increases, the mass flow rate of refrigerant required to maintain the same Q_{ice} decreases. This means that with a decrease in the mass flow rate of defrosting refrigerant the quality increases. Furthermore, the value of x_7 has an influence on the heat transfer from the PCMhx as well as on the power input of the pump, as shown in Figure 11.

Figure 11 shows the relationship between quality (x_7) and the power input of the defrost refrigerant pump. It shows that as x_7 increases from 0 to 1, the mass flow rate of defrost refrigerant decreases. This decrease leads to an increase in the work required to maintain the same pump power. This explains the fact that $COP_{with\ pump}$ of the refrigeration system with PCM based defrosting increases with the increase of x_7 , respectively the decrease of the defrosting refrigerant mass flow rate.

CONCLUSIONS

In this paper, the effect of using PCM heat storage for defrosting the evaporator of a refrigeration system was studied using different refrigerants. The impact of various refrigerants and system parameters on the energy performance of PCM-based defrosting was investigated under the same working conditions.

It was observed that as the defrosting time increases, the refrigerant flow rate required for PCM-based defrosting decreases. Among the refrigerants analyzed, R600 exhibited the lowest mass flow rate, while R404A the highest in order to defrost the same mass of ice.

Additionally, the $COP_{with\ pump}$ of the refrigeration system with PCM-based defrosting increases gradually with defrosting time, but it remains slightly lower than the system without defrosting, having comparable values in both cases.

The results indicate that an increase in the evaporating temperature leads to a decrease in the recoverable heat. However, for evaporating temperatures between -10°C and -40°C , the recoverable heat is sufficient to achieve complete defrosting of the ice accumulated on the evaporator.

In contrast, an increase in the condensing temperature improves the amount of recoverable heat for dry and wet refrigerants such as R32, R404A, R134a, and R290, but reduces it for isentropic refrigerants, including R600a, R600, R1234yf, and R1234ze(E).

Superheating plays a critical role in enhancing heat recovery. A higher superheating degree of significantly increases the recoverable heat, making PCM-based defrosting viable for isentropic refrigerants. Contrarily, the desuperheating degree varies with condensing temperature: it increases for R32, remains nearly constant for group b) refrigerants, and decreases for group c) refrigerants. This suggests that increasing the condensing temperature can influence the defrosting process differently depending on the refrigerant.

Previous analysis reveals that R32 is the most suitable refrigerant for PCM-based defrosting, followed by refrigerants in groups b) and c).

Additionally, the refrigerant quality at state 7 has a minimal influence on $COP_{with\ pump}$, with the highest value recorded for R600. As the refrigerant quality increases, the refrigerant mass flow rate required for defrosting decreases, resulting in lower power input for the circulation pump.

ACKNOWLEDGEMENT

This research was funded by the Romanian Ministry of Education and the National University of Science and Technology POLITEHNICA Bucharest through the PubArt Programme.

REFERENCES

- [1] Al Douri Jamal, Apostol V., Pop H., Prisecaru T., Pavel C.C., Uta I., Ioniță C., Popa L. (2023), Improving performance of cold room refrigeration system by desuperheating energy recovery using PCMs, *INMATEH - Agricultural Engineering*, Vol. 70 pp.549-556. DOI: <https://doi.org/10.35633/inmateh-70-53>
- [2] Al-Douri Jamal. (2024). Comparison between defrosting methods using different refrigerants, *U.P.B Scientific Bulletin*, Vol. 86, pp. 80-94.
- [3] Amer M., Wang C.C. (2017). Review of defrosting methods, *Renewable and Sustainable Energy Reviews*, Vol. 73(C), pp.53-74. DOI: 10.1016/j.rser.2017.01.120
- [4] Arora A., Kaushik S.C. (2008). Theoretical analysis of a vapor compression refrigeration system with R502, R404A and R507A. *International Journal of Refrigeration*, Vol.31, pp.998-1005.

- [5] Dobre C., Costin M., Constantin M. (2024). A Review of Available Solutions for Implementation of Small–Medium Combined Heat and Power (CHP) Systems. *Inventions*. Vol. 9:82. DOI: 10.3390/inventions9040082
- [6] Dong J.K., Jiank Y.Q., Yao Y., Zhang X.D. (2011). Operating performance of novel reverse-cycle defrosting method based on thermal energy storage for air source heat pump. *Journal of Central South University of Technology*, Vol. 18, pp. 2163-2169.
- [7] Essadik M., Hajabdollahi Ouderji Z., McKeown A., Lu Y. (2024), A multi-valve flexible heat pump system with latent thermal energy storage, *Energy & Buildings*, Vol. 321.
- [8] Havelský V. (2000) Investigation of refrigerating system with R12 refrigerant replacements, *Applied Thermal Engineering*. Vol.20, Issue 2, pp.133-140.
- [9] Hepbasli Arip (2012). Low exergy (LowEx) heating and cooling systems for sustainable buildings and societies. *Renewable and Sustainable Energy Reviews*, Vol. 16, pp. 73-104.
- [10] Jin Xin., Wu Fengping., Xu Tao, Huang Gongsheng, Wu Huijun., Zhou Xiaoqing, Wang Dengjia, Liu Yanfeng, Lai Alvin. (2021). Experimental investigation of the novel melting point modified Phase–Change material for heat pump latent heat thermal energy storage application. *Energy*, Vol. 216, 119191.
- [11] Kharseh M., Altorkmany, L., Al-Khawaj M., Hassani F. (2014), Warming impact on energy use of HVAC system in buildings of different thermal qualities and in different climates, *Energ. Conver. Manage.*, Volume 81, pp. 106-111.
- [12] Le Gall R., Grillot J.M., Jallut C. (1997), Modelling of frost growth and densification, *International Journal of Heat and Mass Transfer*, Vol. 40, Issue 13, pp. 3177-3187.
- [13] Li Zhi-Ling, Zhang Chun-Lu, Liu Hui-Ming, Wang Xi-Chun. (2024). Feasibility analysis of thermal storage defrosting method for air source heat pump: From energetic and economic viewpoints. *Applied Thermal Engineering*, Vol. 236(D), 121828.
- [14] Liu Zhongbao, Li Ao, Wang Qinghua, Chi Yuanying, Zhang Linfei. (2017). Experimental study on a new type of thermal storage defrosting system. *Applied Thermal Engineering*. Vol.118, pp.256-265. <https://doi.org/10.1016/j.applthermaleng.2017.02.077>
- [15] Liu Zhongbao, Zhao Fei, Zhang Lingfei, Zhang Ran, Yuan Meng, Chi Yuanying. (2018). Performance of bypass cycle defrosting system using compressor casing thermal storage for air-cooled household refrigerators. *Applied Thermal Engineering*, Vol.130, pp.1215-1223. <https://doi.org/10.1016/j.applthermaleng.2017.11.077>
- [16] Ning Zhaozhong, Zhang Xuelai, Ji Jun, Shi Yao, Du Fulin. (2023). Research progress of phase change thermal storage technology in air-source heat pump. *Journal of Energy Storage*. Vol. 64(5). DOI: 10.1016/j.est.2023.107114
- [17] Ragıp Y., Atta U., Akyuz A., Tuncer A.D. (2023). A new approach for environmental analysis of vapor compression refrigeration systems: Environmental impact index, *Thermal Science and Engineering Progress*. Vol. 42, p.101871. 10.1016/j.tsep.2023.101871
- [18] Selbaş R., Kızılkın Ö., Şencan A. (2006). Thermo-economic optimization of subcooled and superheated vapor compression refrigeration cycle, *Energy*, Vol. 31, pp.2108-2128.
- [19] Yang B., Dong J., Zhang L., Song M., Jiang Y., Deng S. (2019), Heating and energy storage characteristics of multi-split air source heat. *Applied Energy*. Vol. 238. pp. 303-310.
- [20] Zhang Long, Dong Jiankai, Jiang Yiqiang, Yao Yang. (2014). A novel defrosting method using heat energy dissipated by the compressor of an air source heat pump, *Applied Energy*, Vol.133, pp.101-111. <https://doi.org/10.1016/j.apenergy.2014.07.039>
- [21] ****Engineering Equation Solver Academic Professional*, V.10.836-3D #4487, (2020). Faculty of Mechanical Engineering, University POLITEHNICA of Bucharest, Romania.

DESIGN AND EXPERIMENT OF A DOUBLE LONGITUDINAL AXIAL-FLOW CORN THRESHING DEVICE FOR LARGE FEEDING CAPACITY

大喂入量双纵轴流玉米脱粒装置设计与试验

Mingrui LI^{1,3)}, Yanchun YAO^{1,2,3*)}, Yongkang ZHU^{1,3)}, Xibin LI^{1,3)}, Dong YUE¹⁾, Duanyang GENG¹⁾

¹⁾ College of Agricultural Engineering and Food Science, Shandong University of Technology, Zibo 255000, China;

²⁾ Opening Fund of National Key Laboratory of Agricultural Equipment Technology, Beijing 100083, China

³⁾ Institute of Modern Agricultural Equipment, Zibo 255000, China;

Tel: +86-15275906287; E-mail: ycyao2018@sdut.edu.cn

DOI: <https://doi.org/10.35633/inmateh-75-45>

Keywords: corn kernel harvest; double longitudinal axial flow; large feeding amount; threshing

ABSTRACT

Traditional corn threshing devices face issues of high unthreshed grain rate and high breakage rate under conditions of high feeding rates. To address this, a high-throughput double longitudinal axial flow corn threshing device was designed in this study. Based on a stress analysis of the interaction between threshing components and corn ears, an arc-shaped plate tooth structure was developed to progressively increase the squeezing force between the plate teeth and the ears. A combined threshing element, integrating arc-shaped plate teeth and round-headed nail teeth, was designed to improve threshing cleanliness and minimize grain breakage under high feed capacity conditions. The crucial parameters of the threshing cylinder were determined by theoretical analysis. Threshing bench experiments were conducted to investigate the effects of feed rate, threshing cylinder speed, and guide plate angle on the device's grain breakage rate and unthreshed grain rate. Based on the findings, the optimal parameter ranges were identified. An orthogonal test involving three factors at three levels each was conducted to determine the optimal working parameters of the device. The results indicated that the ideal conditions were a feed rate of 16 kg/s, a threshing cylinder speed of 400 r/min, and a guide plate angle of 26°. Under these parameters, the grain breakage rate was 5.02%, and the unthreshed grain rate was 0.171%. The operational performance met the actual harvesting requirements. This research could offer a reference for the design of large-feed-rate threshing devices and related harvesters.

摘要

当前传统的玉米脱粒装置在大喂入量条件下,存在籽粒未脱净率高、破碎率高的问题,对此本研究设计了一种大喂入量双纵轴流玉米脱粒装置。基于脱粒元件与玉米果穗的受力分析,本研究设计了弧形板齿结构,逐步增加板齿与果穗之间的挤搓力,有利于脱下不同脱粒难度的玉米籽粒;本研究设计了“弧形板齿+圆头钉齿”组合式脱粒元件,满足了大喂入量条件下装置实现高脱净率和籽粒破碎;通过理论分析的方法确定了脱粒滚筒的关键参数。通过台架试验研究了该装置中喂入量、滚筒转速和导流板角度对籽粒破碎率和未脱净率的影响规律,并确定了较优参数区间。通过三因素三水平正交试验,确定了该装置的最佳工作参数为:喂入量为 16kg/s、滚筒转速为 400r/min、导流板角度为 26°,此时籽粒破碎率为 5.02%,未脱净率为 0.171%,作业性能满足了实际收获需求。该研究可为大喂入量脱粒装置和相关收获机设计提供参考。

INTRODUCTION

Corn occupies the largest sown area among grain crops in China and ranks second globally in production (**China, 2024). Currently, the main methods of corn harvesting are ear harvesting and direct grain harvesting (Tao et al., 2019). Threshing is an essential link in the process of direct grain harvesting. The grain breakage rate and the unthreshed grain rate are important references for assessing the effect of the threshing device and exert significant influence on the threshing quality.

¹ Mingrui Li, M.S. Stud.; Yanchun Yao, Assoc.Prof.; Yongkang Zhu, M.S. Stud.; Xibin Li, M.S. Stud.; Dong Yue, M.S. Stud.; Duanyang Geng, Prof.

The current research on corn threshing devices mainly focuses on reducing the grain breakage rate, enhancing the threshed grain rate, and threshing corn with high moisture content. Scholars have introduced innovative designs by integrating threshing theory and bionic principles, including the corn thresher element resembling a chicken beak (Xinping et al., 2015), the rigid-flexible coupling bionic threshing unit (Li et al., 2021), and the thumb-type threshing element (Jiale et al., 2023) by studying corn threshing theory and applying bionic principles. To address issues like incomplete threshing in existing axial flow threshers, scholars have developed a segmented threshing device (Yuejiang et al., 2020), the combined "threshing bow teeth and movable nail teeth" thresher separation device (Youliang et al., 2022). To reduce grain breakage caused by rigid thresher elements, optimized design yields plate teeth with protrusions (Xiaopeng et al., 2003) and elastic short rasp bars as threshing elements (Duanyang et al., 2019). These structural improvements optimize impact effects during threshing. Regarding the issue of the difficulty in threshing corn with high moisture content, numerous scholars have achieved significant progress through structural enhancements and parameter optimizations (Yujie et al., 2023; Qing et al., 2024; Jinliang et al., 2024). Some researchers explored the influence of feed rate, threshing cylinder speed and other factors on the threshing effect through experiments, and constructed relevant mathematical models, which provided reference for deep understanding of the threshing mechanism and obtaining the best working parameters (Srison et al., 2016; Cujbescu et al., 2021; Vlădut N. et al., 2022; Vlădut N. et al., 2023). Some researchers have used sensors and optimized control algorithms, which in turn provide timely and effective regulation of threshing parameters to achieve better threshing results (Maertens et al., 2004; Maertens et al., 2005; Abdeen M., 2022). To improve harvesting efficiency further, grain combine harvesters are gradually evolving towards larger scales. Therefore, threshing devices that can handle larger feed rates are needed. Currently, the research mainly concentrates on threshing devices with feed rates less than 12 kg, and there is relatively scarce research on those with feed rates greater than 12 kg. Meanwhile, the traditional threshing devices, under the circumstance of large feed rates, have issues such as high grain breakage rate and high unthreshed grain rate.

In response to the above problems, this study presents the design of a double longitudinal axial-flow corn threshing device incorporating variable-height combined threshing elements consisting of arc-shaped plate teeth and round-head nail teeth, a conical drum body, and adjustable guide vanes. Through bench experiments, the influence patterns of feed rate, threshing cylinder speed, and angle of the guide plate on grain breakage rate and unthreshed grain rate were investigated. The optimal parameter combination was acquired. This provides a reference for designing the double longitudinal axial flow threshing device with a large feeding amount.

MATERIALS AND METHODS

The Overall Structure and Working Principle of the Threshing Device

The Overall Structure

The overall structure comprises a feeding inlet, threshing drum, upper cover plate, grid concave plate screens, deflector adjustment mechanism, frame, gearbox, and motor. Notably, the rotation direction of the threshing drum on both sides is reversed, as illustrated in Figure 1.

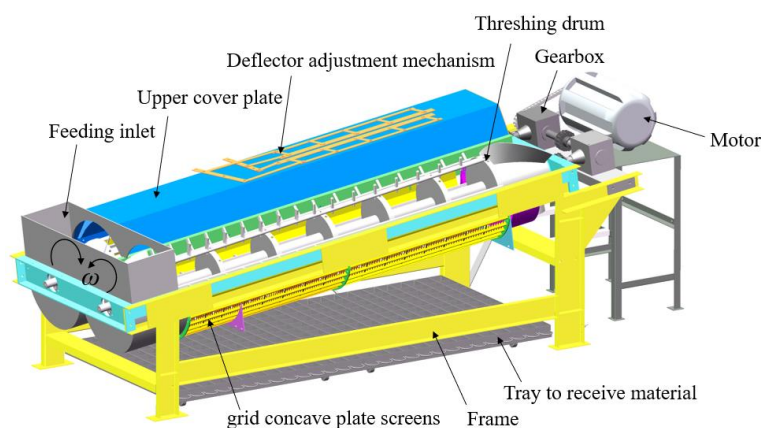


Fig. 1 - The Overall Structure of the Device

Under the harvesting condition of large feed-in volume, the double longitudinal axial-flow threshing drum has a lower rotational speed and a larger separation area than the single longitudinal axial-flow drum.

A lower rotational speed of the drum is conducive to reducing the impact force, thereby lowering the breakage of corn kernels. A larger separation area can decrease the thickness of the material layer, facilitating the timely separation of the threshed kernels out of the machine.

The Working Principle

During the threshing operation, corn ears are introduced through the feeding inlet and propelled into the threshing chamber on both sides of the double-longitudinal axial flow threshing device by the action of a screw feeding head. Under the combined influence of the threshing drum and upper cover plate, the corn ear moves toward the rear. It interacts with various components throughout this process, including threshing elements, conical drum bodies, grid concave plate screens, and striking and squeezing against other fruit ears to facilitate kernel separation from their cobs. The detached corn kernels are subsequently filtered through a grid of concave plate screens. At the same time, residual components such as cob cores and bracts are expelled via an outlet at the end of the threshing drum, thereby completing the threshing process.

The Design of Key Components

The design of the threshing drum

This paper designs a threshing drum of "variable-height threshing elements and conical roller body." The diameter of the addendum circle of the teeth at any cross-section of the threshing cylinder is a fixed value. The threshing components within the threshing cylinder combine arc-shaped plate teeth and round-headed nail teeth. The threshing drum is divided into four working zones based on its main functions: feeding, threshing, separation, and impurity discharge (Meizhou et al., 2020), as shown in Figure 2.

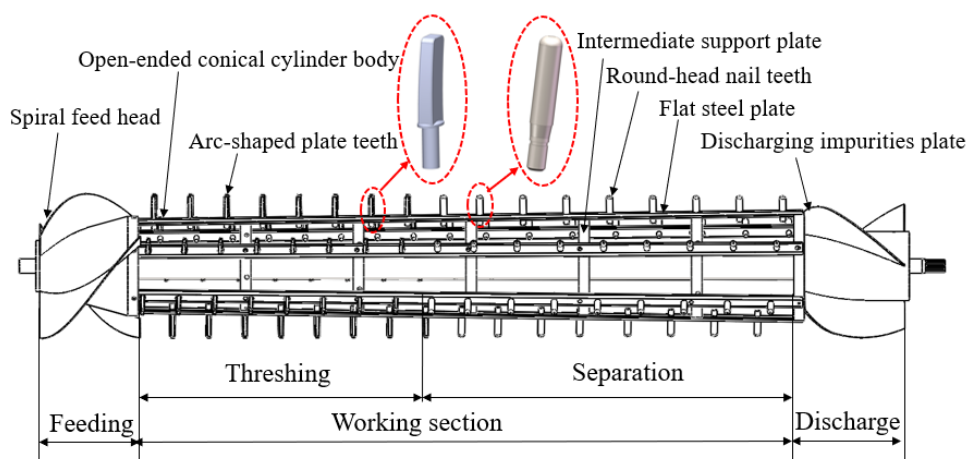


Fig. 2 - Structure diagram of threshing cylinder

Previous studies discovered that blockages mainly occurred in the first half of the threshing drum under significant feed rates. This paper employs a conical cylinder body to enhance the corn ears' accommodating capacity in the threshing cylinder's front half. Meanwhile, considering the relatively poor threshing effect at the front end of the conical cylinder body, longer threshing elements are installed at the small end of the conical cylinder body to improve the threshing capability at the front end of the conical cylinder body.

Most threshing and separation occur in the threshing section of the cylinder (Miu et al., 2008). Rigid threshing at this stage can cause a significant amount of breakage. Arc-shaped plate teeth let the cobs thresh under an oblique pushing force. This threshing action is conducive to reducing grain breakage. Round-headed nail teeth feature high efficiency, a high threshing cleanliness rate, and reduced losses due to the top gnawing of grains. When applied in the separation section of the threshing cylinder, they can guarantee the threshing cleanliness rate of the device under conditions of significant feed rates (Zheng et al., 2022). Meanwhile, the threshing section is designed to constitute 40% of the length of the working section, while the separating section makes up 60%. The threshing elements adopt a variable pitch arrangement that is dense at the front and sparse at the rear. In this paper, the spacing between the arc-shaped plate teeth is designed to be 138 mm, and the spacing between the round-headed nail teeth is 165 mm. The included angle between the flat steel and the axis of the roller is 30°. The distribution of the arc-shaped plate teeth and round-headed nail teeth is shown in Figure 3.

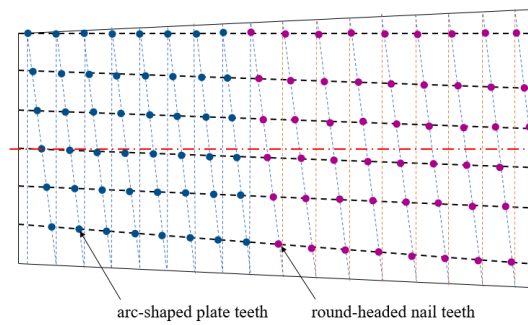


Fig. 3 - Schematic diagram of the arrangement of threshing elements on the threshing drum

The relationship between the length of the longitudinal axial flow threshing drum and the feed quantity is:

$$L = \frac{q}{q_0} \tag{1}$$

where: L denotes the working section length of the threshing drum, (m);

q represents the feeding amount of the threshing device, (kg/s);

q_0 represents the allowable feed rate per unit length in the threshing device, kg/(s·m). According to the recommendation in the "Agricultural Machinery Design Manual," q_0 is generally 3 to 4 kg/(s·m).

The unit is designed for a feed rate of 14~18 kg/s. Based on the calculation using formula (1), the value range of the unilateral threshing drum L is between 1.75 and 3.0 meters. Hence, the drum working section is designed to be 2.5 meters long.

The relationship between the diameter of the top circle of the threshing drum teeth D , the rotational speed n of the drum, and the linear speed v is as follows:

$$D = \frac{60v}{\pi n} \tag{2}$$

where: D is the diameter of the toothed top circle of the threshing drum, (m);

v is the threshing speed of the cylindrical axial roller, (m/s);

n is the rotational speed of the threshing drum, (r/min).

According to the recommendations in the "Agricultural Machinery Design Manual", the threshing speed of the cylindrical axial-flow drum (v) is 10 to 12 m/s and the threshing cylinder speed (n) ranging from 300 to 450 r/min, when substituted into Equation (2), the range of the top circle diameter of the threshing drum teeth is obtained as 430 to 760 mm. Hence, the design's top circle diameter D of the threshing drum is 550 mm. The threshing drum is a "constant-diameter drum," thus D is a fixed value.

The design of arc-shaped plate teeth and round-headed nail teeth

The corn cobs struck by the arc-shaped plate teeth will complete threshing under the continuously increasing squeezing and rubbing force, which is conducive to detaching corn kernels with different threshing difficulties. To guarantee the threshing cleanliness rate of the device, the round-headed spike teeth are designed to be arranged in the second half of the threshing drum. The structure of the arc-shaped plate teeth and the round-headed spike teeth is shown in Figure 4.

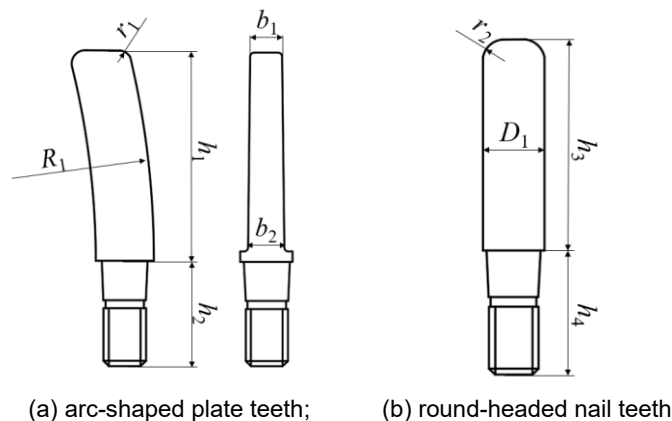


Fig. 4 - Threshing components structure

In Figure 4(a), h_1 is the working height of the arc-shaped plate teeth, taken as 75 to 95 mm; h_2 is the installation height; R_1 is the curve radius of the working surface of the arc-shaped plate teeth, taken as 344 mm; r_1 is the top fillet radius of the arc-shaped plate teeth, taken as 5 mm. b_1 is the top thickness of the arc-shaped plate teeth, taken as 12 mm; b_2 is the bottom thickness of the arc-shaped plate teeth, taken as 14 mm. In Figure 4(b), h_3 is the working height of the round-headed spike teeth, taken as 55 to 74 mm; h_4 is the installation height of the round-headed spike teeth; D_1 is the diameter of the round-headed spike teeth, taken as 20 mm; r_2 is the top fillet radius of the round-headed spike teeth. According to the theoretical research on the collision between the spike teeth and the corn cobs (Zhe, 2018), the calculation formula for the ball head radius is $R \geq 5$ mm. Therefore, in this paper, the top fillet radius r_1 of the arc-shaped plate teeth is designed to be 5 mm, and the top fillet radius r_2 of the round-headed nail teeth is 7 mm.

The threshing of corn cobs mainly occurs while moving from the upper cover plate to the bottom of the roller. During this process, the corn cobs struck by the arc-shaped plate teeth exist in two states: in contact with the concave screen or not in contact with the concave screen, as shown in Figure 5(a) and 5(b).

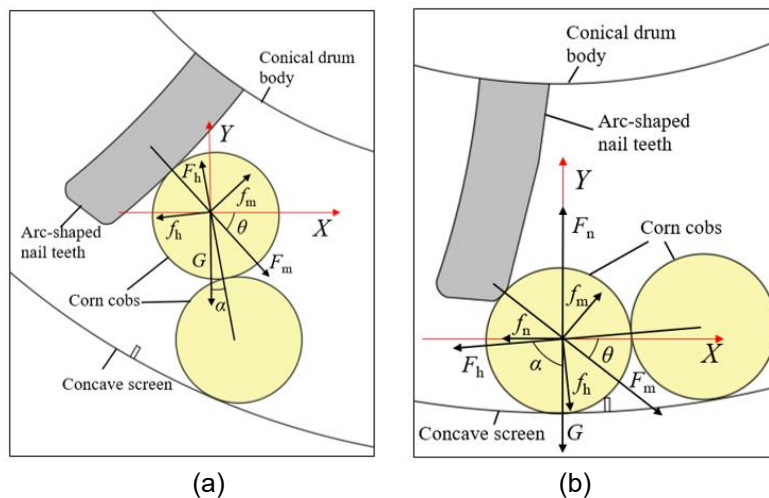


Fig. 5 - Force analysis diagram of corn cob

The force analysis of the corn cobs in these two states is carried out:

$$\begin{cases} F_{mx} = F_m \cos \theta \\ F_{my} = F_m \sin \theta \end{cases} \quad (3)$$

Figure 6(a) presents the schematic diagram of the state where the beaten ear of grain is not in contact with the concave sieve. Through the force analysis of it, the following can be obtained:

$$\begin{cases} F_x = F_{mx} + f_m \sin \theta - F_h \sin \alpha - f_h \cos \alpha \\ F_y = F_{my} - f_m \cos \theta - F_h \cos \alpha + f_h \sin \alpha + G \end{cases} \quad (4)$$

Figure 6(b) presents the schematic diagram of the contact state of the beaten ear of grain and the concave sieve. A force analysis of it yields:

$$\begin{cases} F_x = F_{mx} + f_m \sin \theta - F_h \sin \alpha - f_h \cos \alpha - f_n \\ F_y = F_{my} - f_m \cos \theta - F_h \cos \alpha + f_h \sin \alpha - F_n + G \end{cases} \quad (5)$$

where:

- F_m is the striking force of the arc-shaped nail teeth on the corn cob, (N);
- f_m - the friction force exerted on the corn cob by the arc-shaped nail teeth, (N);
- F_n - the supporting force of the concave plate screens on the corn cob, (N);
- f_n - the friction force of the concave plate screens on the corn cob, (N);
- F_h - the supporting force between the corn cobs, (N);
- f_h - the friction force between the corn cobs, (N);
- G - the gravity of the corn cob, (N);
- θ ($0^\circ < \theta < 90^\circ$) - the angle between the striking force of the arc-shaped nail teeth on the corn cob and the X-axis, ($^\circ$);
- α ($0^\circ < \alpha < 90^\circ$) - the angle between the supporting force between the corn cobs and the Y-axis, ($^\circ$).

When the corn cobs move from the upper cover plate to the bottom of the roller, affected by the impact force of the arc-shaped plate teeth and the gravity of the corn cobs, the relative position of the corn cobs and the threshing elements changes. During this process, θ gradually increases. As shown in Equation (3), the component force F_{mx} of the impact force of the arc-shaped plate teeth in the X-axis direction keeps decreasing, which slows down the axial movement speed of the corn cobs and enhances the rubbing contact between the corn cobs. At the same time, the component force F_{my} of the arc-shaped plate teeth in the Y-axis direction keeps increasing; that is, the downward pressure given by the arc-shaped nail teeth to the corn cobs gradually strengthens.

It can be inferred from Figure 5(a) and Equation (4) that to maintain the force equilibrium in the Y direction, F_h will constantly intensify, leading to a continuous increase in f_h . Combining Figure 5(b) and Equation (5), it is evident that F_h gradually strengthens, and consequently, f_h gradually rises. This rubbing and threshing process is gentle. Meanwhile, the arc-shaped plate teeth gradually squeeze the movable space of the corn cob. In this threshing process, the damage to the kernels is minor.

Design of conical drum body

The front end of the conical drum body has a smaller diameter, which enhances the grain accommodation capacity of the threshing device and strengthens the flexible contact among the corn cobs (Zhendong *et al.*, 2021). The threshing drum adopts an open type. The contact area between the open drum and the corn cobs is small, and the drum load is low, which is conducive to avoiding the problem of drum blockage caused by excessive feeding.

In this paper, the variation range of the working height of the threshing elements is designed to be 55 ~ 95 mm. As the length L of the threshing and separating section of the variable diameter open roller is 2.5 m, the taper β of the variable diameter roller body is:

$$\tan\beta = \frac{h}{L} \quad (6)$$

Hence, the taper of the conical drum body is 0.9° . This taper increases the gap at the feeding inlet by one layer of the thickness of the corn cobs compared to that at the discharge outlet, which is beneficial for smooth feeding and increasing the number of collisions between the corn cobs.

The design of the grid concave plate screens and the design of the adjustable upper cover plate with guide vanes

To prevent the uneven flow of corn cobs between the two threshing drums on both sides and influence the threshing effect, the threshing spaces of the two drums are not interconnected. Currently, the commonly used forms of concave plates include grid screens and punched screens. Grid screens have greater strength, and both the sieve porosity and separation efficiency are higher than those of punched screens. They are widely applied in existing combined harvesters. Therefore, this device employs a grid of concave plate screens. The double longitudinal axial flow grid concave plate screen is shown in Figure 6(a).

Adjusting the angle of the guide plate can control the axial movement speed of corn cobs and the material layer's thickness, significantly influencing the threshing effect. A combination guide plate with a fixed front section and an adjustable rear section is designed in the upper cover plate of the double longitudinal axial flow threshing cylinder. In this paper, the helix angle of the fixed guide plate is designed to be 24° . The helix angle range of the adjustable guide plate is designed to be 16° to 26° (Chen *et al.*, 2022). The structure of the unilateral upper cover plate is shown in Figure 6(b).

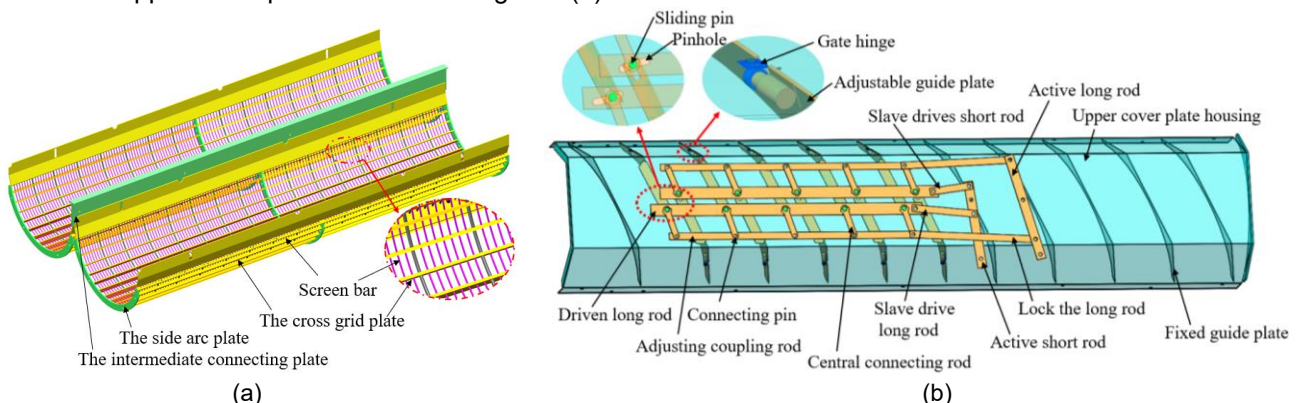


Fig. 6 - The Structural Diagram of the grid concave plate screens and the upper cover plate

One end of the adjustable guide plate is connected to the upper cover plate housing through a gate hinge, and the other end is connected to the driven long rod through a sliding pin. The other end of this driven long rod is connected to the active short rod. When the active short rod and the active long rod move simultaneously through force transmission, they cause a positional offset at one end of the adjustable guide plate. As a result, the angle of the adjustable guide plate changes, thereby controlling the axial movement speed of the corn cobs.

Experiment design

The existing research results (Chenlong *et al.*, 2022; Shulun *et al.*, 2024) indicate that the influences of the feed rate, the threshing cylinder speed, and the angle of the guide plate on the grain breakage rate are more significant than that of the threshing clearance. Hence, the feed rate, the threshing cylinder speed, and the angle of the guide plate were selected to research the device's threshing performance.

Test materials and conditions

In October 2024, a bench test was conducted at Shandong Tiankaizhongrui Machinery Technology Company Limited. The double longitudinal axial flow threshing roller was placed at an inclination of 7° to the ground, and the threshing clearance was 35 mm. The corn variety used in the experiment was "Liyuan296". The average moisture content of corn kernels was 31.3% using the LDS-1G model grain moisture detector. Thirty corn ears were taken for the physical characteristic experiments of the ears. The experimental data are as follows: the average ear length is 16.4 cm, the diameters at the middle and large ends are 49.7 mm, and the diameter at the small end is 46.9 mm. The test site is shown in Figure 7.



Fig. 7 - Testbed for double longitudinal axial flow with a large feeding amount

The threshing test of the corn threshing device

This paper conducts the corn threshing test by referring to GB/T 21961-2008 and GB/T 5982-2005. A platform scale weighs the corn cobs of the required weight and then spreads on the measurement area of the conveying device. After each test, the corn kernels in the receiving device are collected and thoroughly mixed for manual sampling, with each sample no less than 2 kg. The grain breakage rate Y_1 and the unthreshed grain rate Y_2 are calculated, and the calculation formulas are as follows:

$$Y_1 = \frac{m_s}{m_i} \times 100\% \quad (7)$$

$$Y_2 = \frac{m_j}{m_z} \times 100\% \quad (8)$$

where: m_s refers to the mass of broken grains in the sample, (g);

m_i is the total mass of grains in the sample, (g);

m_j represents the mass of unthreshed grains, (g);

m_z is the total mass of threshed grains, (g).

Single-factor test

The feed rate has a direct connection with the thickness of the material layer and thereby influences the threshing effect. The feeding quantities in this paper are set at levels 14 kg/s, 15 kg/s, 16 kg/s, 17 kg/s, and 18 kg/s respectively. The threshing cylinder speed is directly related to the striking force of the threshing components. Comprehensively considered, 300 r/min, 350 r/min, 400 r/min, 450 r/min, 500 r/min, 600 r/min, and 700 r/min were selected in this paper. The range of deflector angle adjustment for this device is 16 - 26°, and the deflector angles are horizontally set at 16°, 18°, 20°, 22°, 24° and 26° respectively.

Orthogonal test

According to the results of the single-factor experiments, the ranges of values for the test factors in the orthogonal experiments were determined. A quadratic orthogonal rotational combination experiment was carried out with three factors and levels. The three-factor level coding is presented in Table 1.

Table 1

Factors and levels of experiment			
Level	Experimental factor		
	Feed rate $X_1/(kg/s)$	Threshing cylinder speed $X_2/(r/min)$	The angle of the guide plate $X_3 / (^\circ)$
-1	15	350	22
0	16	400	24
1	17	450	26

RESULTS AND DISCUSSION

Bench tests were conducted under the experimental conditions set in this study. It was found that the unthreshed grain rate in each group was less than 0.3%, indicating a low level and demonstrating that the device performs well in terms of threshing cleanliness under these conditions. Therefore, the focus will subsequently shift to evaluating the corn grain breakage rate to further assess the threshing impact of the device.

The Results and Analysis of Single-Factor Experiment

The fixed values of the test parameters selected in this research are, respectively, the feed rate at 16 kg/s, the threshing cylinder speed at 400 r/min, and the angle of the guide plate at 16°. When carrying out the single-factor test of a certain factor, the parameters of the other two factors are selected as the fixed values. The experimental results are presented in Figure 8.

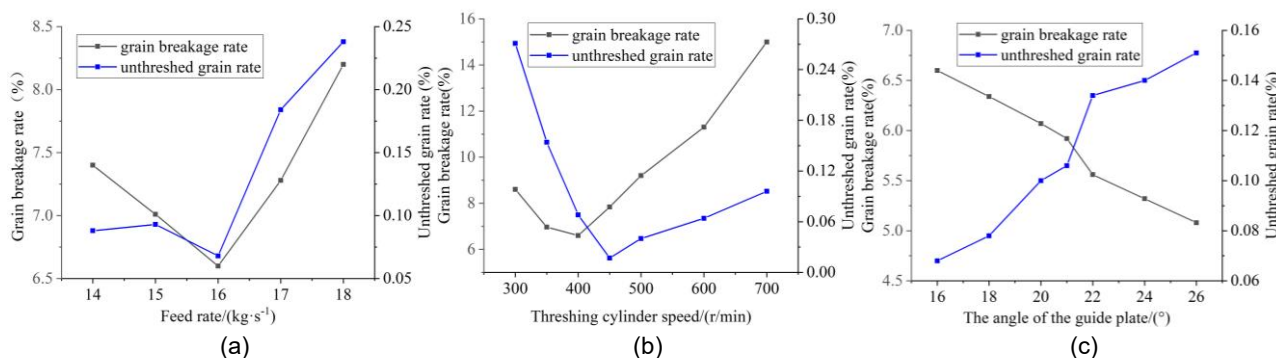


Fig. 8 - Diagram of the Results of the Single-Factor Experiment

In Figure 8(a) it is shown that with the increase in the feed rate, both the grain breakage rate and the unthreshed grain rate exhibit a trend of initially decreasing and then increasing. The reasons for this phenomenon are as follows: when the feed rate is relatively low, the corn cob being struck directly impacts the concave plate for rigid threshing, resulting in a higher grain breakage rate. Simultaneously, the axial movement speed increases rapidly upon impact due to less resistance. The threshing time is reduced, leading to a higher unthreshed grain rate. When the feed rate is relatively big, the material layer inside the roller is thicker. The threshed grains cannot be discharged from the machine in time, causing excessive impact. At the same time, it causes some corn cob to move to the impurity discharge section before the threshing is completed, resulting in a higher unthreshed grain rate.

In Figure 8(b) it is shown that as the threshing cylinder speed increases, both the grain breakage rate and the unthreshed grain rate demonstrate a trend of initially decreasing and then increasing. This is because when the threshing cylinder speed is low, the threshing time of the corn ears increases, and the number of strikes they receive increases, leading to a higher grain breakage rate. Meanwhile, the impact force of the threshing elements is small, causing some corn ears to be discharged from the machine before they are completely threshed, resulting in a higher unthreshed grain rate. At higher threshing cylinder speed, the threshing element strikes with high force, which results in higher kernel breakage and a rapid increase in the grain breakage rate. At the same time, it leads to a more incredible axial movement speed of the corn ears, causing some corn ears to be discharged from the machine before being completely threshed, resulting in a higher unthreshed grain rate.

It could be observed from Figure 8(c) that with the increase of the angle of the guide plate, the grain breakage rate shows a downward trend, while the unthreshed grain rate shows an upward trend. As the angle of the guide plate increases, the axial movement speed of the corn ears increases, which is conducive to the prompt discharge of the detached grains and avoids excessive impact, resulting in less grain crushing. Simultaneously, this behavior increases the probability of some corn ears being discharged from the machine before they are completely threshed, thereby increasing the unthreshed grain rate.

The Results and Analysis of the Orthogonal Experiment

Test Results and Analysis

The experimental scheme was designed based on the Box-Behnken module in the Design-Expert 13.0 software. With the grain breakage rate and the uncleaned grain rate as the experimental indicators, 17 experiments were carried out. The experimental scheme and results are presented in Table 2.

Table 2

Testing plan and results						
Experimental Number	Experimental Factors and Levels			Performance indicators		
	X_1 /(kg/s)	X_2 (r/min)	X_3 (°)	Y_1 %	Y_2 %	
1	16	350	22	6.21	0.252	
2	17	400	22	6.29	0.224	
3	16	400	24	5.41	0.143	
4	15	450	24	8.58	0.087	
5	15	350	24	7.49	0.274	
6	17	450	24	7.01	0.126	
7	16	400	24	5.32	0.194	
8	15	400	26	5.93	0.181	
9	16	400	24	5.62	0.092	
10	17	400	26	5.56	0.256	
11	16	400	24	5.23	0.154	
12	16	350	26	5.85	0.286	
13	16	450	26	6.73	0.046	
14	15	400	22	6.34	0.134	
15	16	400	24	5.54	0.178	
16	16	450	22	7.18	0.024	
17	17	350	24	7.72	0.246	

The data in Table 2 was analyzed for variance, and the results are presented in Table 3.

Table 3

Analysis of variance					
Source	df	Grain breakage rate Y_1		Unthreshed grain rate Y_2	
		F Value	P-value	F Value	P-value
Model	9	22.84	0.0002**	5.61	0.0166*
X_1	1	5.53	0.0510	2.19	0.1827
X_2	1	8.88	0.0205*	42.40	0.0003**
X_3	1	6.79	0.0351*	1.29	0.2940
$X_1 X_2$	1	11.57	0.0114*	0.63	0.4521
$X_1 X_3$	1	0.37	0.5644	0.032	0.8636
$X_2 X_3$	1	0.029	0.8698	0.020	0.8906
X_1^2	1	49.45	0.0002**	3.60	0.0997
X_2^2	1	112.76	<0.0001**	0.15	0.7132
X_3^2	1	5.44	0.0524	0.14	0.7202
Residual	7				
Lack of fit	3	5.17	0.0733	1.37	0.3735
Pure error	4				
Total error	16				

Note: *significant ($P < 0.05$), **very significant ($P < 0.01$)

It can be observed from Table 3 that X_1^2 and X_2^2 have an extremely significant effect on Y_1 ($P < 0.01$). X_2 , X_3 , and $X_1 X_2$ significantly influence Y_1 ($P < 0.05$). Other factors influencing Y_1 were insignificant ($P > 0.1$). Meanwhile, X_2 has an extremely significant influence on Y_2 ($P < 0.01$). Other factors influencing Y_2 are insignificant ($P > 0.1$). The $P < 0.05$ of the established regression model indicates that the relationship between the dependent variable of the regression model and the full set of independent variables is significant.

The P value of the lack-of-fit term is greater than 0.05, suggesting that the lack-of-fit is not significant, and the regression model fits the experimental results relatively well. Thus, the regression equation for the influence of each factor on Y_1 and Y_2 is obtained:

$$Y_1 = 5.97 - 0.22X_1 + 0.27X_2 - 0.66X_3 - 0.35X_1X_2 - 0.14X_1X_3 + 0.02X_2X_3 + 0.94X_1^2 + 1.27X_2^2 - 0.44X_3^2 \quad (9)$$

$$Y_2 = 0.11 + 0.019X_1 - 0.085X_2 + 0.04X_3 + 0.025X_1X_2 - 0.004X_1X_3 - 0.026X_2X_3 + 0.037X_1^2 - 0.016X_2^2 + 0.032X_3^2 \quad (10)$$

Response Surface Analysis

Through the data processing in the Model Graphs of the Analysis module, the interactive influences and influence rules of X_1 , X_2 , X_3 on the grain breakage rate are investigated. It can be known from Table 3 that the interaction effects of the three experimental factors on the unthreshed grain rate are not significant ($P > 0.05$). Thus, no further analysis is considered. The response surface results are presented in Figure 9.

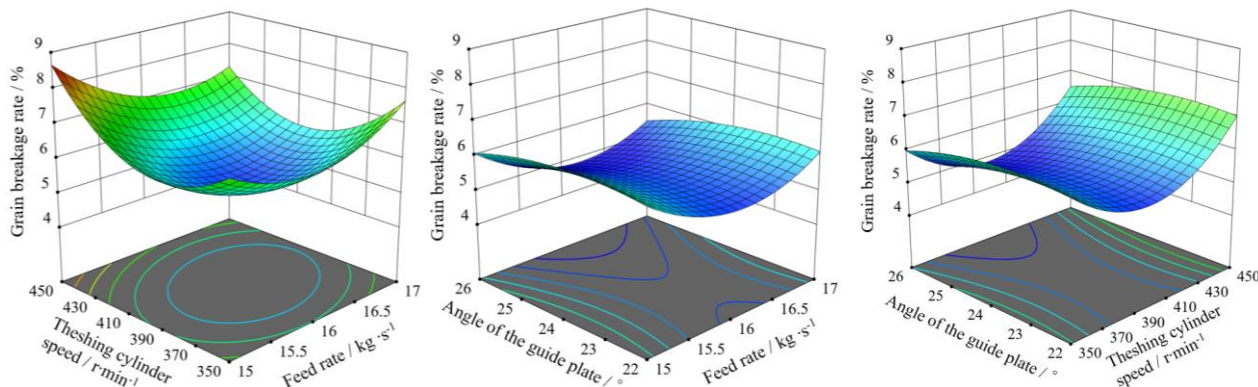


Fig. 9 - Response surface diagram of interaction factors

With the increase of the feed rate and the threshing cylinder speed, the grain breakage rate exhibits a trend of initially decreasing and then increasing, and the interaction effect of the two factors is significant. With the increase of the angle of the guide plate, the grain breakage rate shows a downward trend, while the interaction effect between the angle of the deflector plate and other factors is insignificant. This is because when both the feed rate and the threshing cylinder speed are at relatively low levels, the material layer of the corn ears is thin, and the axial movement speed of the corn ears is small. This circumstance results in, on the one hand, the impacted ears of grain directly hitting the concave screen for rigid threshing and, on the other hand, prolonging the threshing time of the ears of grain, leading to an increased breakage rate. When the feed rate and the threshing cylinder are both at relatively high levels, an overly thick material layer will impede the discharge of the detached corn kernels from the machine. Meanwhile, the excessive impact force endured by the corn ears causes the struck corn kernels to be directly crushed. Enlarging the angle of the guide plate enhances the materials' axial movement speed and reduces the material layer's thickness. This condition is conducive to the timely discharge of the already threshed corn kernels outside the machine, lowering the probability of excessive impact.

The Optimization of Threshing Parameters

The threshing effect was satisfactory. Hence, this paper's lowest grain breakage rate was taken as the optimization objective to optimize the threshing parameters. The multi-objective equation system was solved using the optimization solution module of Design Expert software. The optimal parameter combination was obtained: a feed rate of 16.057 kg/s, a threshing cylinder speed of 397.400 r/min, and an angle of the guide plate of 25.443°. The optimal parameters were simplified: a feed rate of 16 kg/s, a threshing cylinder speed of 400 r/min, and an angle of the guide plate of 26°. Multiple bench tests were carried out under this combination of parameters, and the average of the test results was taken. The actual grain breakage rate was 5.02%, and the unthreshed grain rate was 0.171%. The operational performance meets the actual harvesting requirements.

CONCLUSIONS

Existing threshing devices cannot meet the demand for large feeding volumes. This study focuses on three aspects - reducing impact force, increasing separation area, and controlling threshing time - to design a double longitudinal axial-flow corn threshing device suitable for large feeding volume conditions.

(1) Through the method of theoretical analysis, a threshing drum composed of a combined type of threshing elements of variable-height "arc-shaped plate teeth and round-head nail teeth" and a conical drum body was designed. The main structure and working process were analyzed, and the main structural parameters of the threshing drum were determined. This device satisfies the threshing requirements of high efficiency and low damage under the condition of large feed rates.

(2) The design of the arc-shaped plate teeth threshing element was based on a comprehensive analysis of the corn threshing process and mechanical considerations. It is capable of progressively increasing the squeezing and kneading force. An adjustable guide vane device was designed to control the axial movement velocity of corn cobs, thereby improving threshing performance.

(3) A large-capacity double longitudinal axial-flow threshing test rig was developed. The experiments indicate that the optimal parameter combination of this device is as follows: the feed rate is 16 kg/s, the rotational speed of the drum is 400 r/min, and the angle of the guide plate is 26°. At this point, the grain breakage rate is 5.02%, the unthreshed rate is 0.171%, and the operational performance meets the actual harvesting requirements.

ACKNOWLEDGEMENT

This work was supported financially by the Natural Science Foundation of Shandong (ZR2023ME149), the National Key R&D Program of China (2021YFD2000502), and the Opening Fund of the National Key Laboratory of Agricultural Equipment Technology (NKL2023007).

REFERENCES

- [1] Abdeen M.A., Xie G., Salem A.E., Fu J., Zhan G., (2022). Longitudinal axial flow rice thresher feeding rate monitoring based on force sensing resistors. *Scientific reports*, vol. 12, 1369, 369.
- [2] Chenlong, F., Dongxing, Z., Li, Y., Tao, C., Xiantao, H., Jiaqi, D., Huihui, Z. (2022). Power consumption and performance of a maize thresher with automatic gap control based on feed rate monitoring. *Biosystems Engineering*, vol.216, pp.147-164.
- [3] Chenlong, F., Dongxing, Z., Li, Y., Tao, C., Xiantao, H., Huihui, Z., Jiaqi, D. (2022). Development and performance evaluation of a guide vane inclination automatic control system for corn threshing unit based on feed rate monitoring. *Computers and Electronics in Agriculture*, vol.194, no.106745.
- [4] Cujbescu D., Găgeanu I., Iosif A., (2021). Mathematical modeling of ear grain separation process depending on the length of the axial flow threshing apparatus. *INMATEH-Agricultural Engineering*, vol. 65, no.3, pp.101-110.
- [5] Duanyang, G., Ke, H., Qian, W., Chengqian, J., Guohai, Z., Xiufeng, L. (2019). Design and experiment on transverse axial flow flexible threshing device for corn. Transactions of the Chinese Society of Machinery (横轴流式玉米柔性脱粒装置设计与试验). *Transactions of the Chinese Society of Machinery*, vol.50, no.3, pp.101-108; Shandong/China.
- [6] Jinliang, G., Zengjia, L., Yanfei, Z. (2024). Optimised design and simulation analysis of longitudinal flow corn cone threshing device. *INMATEH-Agricultural Engineering*, vol.73, no.2, pp.63-72.
- [7] Jiale, Z., Hainan, Z., Han, T., Xiaogeng, W., Yujun, Y. (2023). Bionic threshing component optimized based on MBD-DEM coupling simulation significantly improves corn kernel harvesting rate. *Computers and Electronics in Agriculture*, vol.212, no.108075;
- [8] Maertens K., Ramon H., Baerdemaeker J.D., (2004). An on-the-go monitoring algorithm for separation processes in combine harvesters. *Computers and Electronics in Agriculture*, vol.43, no.3, pp.197-207.
- [9] Maertens K., Babuška R., Baerdemaeker J.D., (2005). Evolutionary input selection for the non-linear identification of complex processes. *Computers and Electronics in Agriculture*, vol.49, no.3, pp.441-451.
- [10] Li, Z., Chengyu, L., Guozhen, H., Huimin, Y., Jianqun, Y., Qiang, Z. (2021). Design and experiment of bionic threshing part for high moisture content corn (高含水率玉米仿生脱粒元件设计与试验). *Journal of Chinese Agricultural Mechanization*, vol.43, no.2, pp.126-131; Jilin/China.
- [11] Meizhou, C., Guangfei, X., Chuanxu, W., Peisong, D., Yinping, Z., Guodong, N. (2020). Design and experiment of roller-type combined longitudinal axial flow flexible threshing and separating device for corn (纵轴流辊式组合玉米柔性脱粒分离装置设计与试验). *Transactions of the Chinese Society of Machinery*, vol.51, no.10, pp.123-131; Shandong/China.
- [12] Miu P.I., Kutzbach H.D. (2008). Modeling and simulation of grain threshing and separation in threshing unit—Part I. *Computers and Electronics in Agriculture*, vol. 60, no.1, pp.105-109.

- [13] Qing, T., Lan, J., Wenyi, Y., Jun, W., Gang, W. (2024). Design and experiment of high moisture corn threshing device with low damage. *INMATEH-Agricultural Engineering*, vol.74, no.3, pp.172-183.
- [14] Srison, W., Chuan-Udom, S., Saengprachatanarug, K., (2016). Effects of operating factors for an axial-flow corn shelling unit on losses and power consumption. *Agriculture and Natural resources*, vol.50, no.5, pp.421-425.
- [15] Shulun, X., Tao, C., Dongxing, Z., Li, Y., Xiaotao, H., Chuan, L., Jiaqi, D., Yeyuan, J., Wei, W., Chuankuo Z., Zhaohui D. (2024). Design and optimization for a longitudinal-flow corn ear threshing device of low loss and low energy consumption. *Computers and Electronics in Agriculture*, vol.226, no.109328.
- [16] Tao, C., Chenlong, F., Dongxing, Z., Li, Y., Yibo, L., Huihui, Z. (2019). Research progress of maize mechanized harvesting technology (玉米机械化收获技术研究进展分析). *Transactions of the Chinese Society for Agricultural Machinery*, vol.50, no.12, pp.1-13; Beijing/China.
- [17] Vlăduț N.-V., Biris, S.St., Cârdei, P., Găgeanu, I., Cujbescu, D., Ungureanu, N., Popa L.D., Perişoară, L., Matei, G., Teliban, G.-C., (2022). Contributions to the Mathematical Modeling of the Threshing and Separation Process in An Axial Flow Combine. *Agriculture*, vol. 12, no.10, 1520.
- [18] Vlăduț N.-V., Ungureanu, N., Biris, S. St., Voicea, I., Nenciu, F., Găgeanu, I., Cujbescu, D., Popa, L.-D., Boruz, S., Matei, G., Ekielski, A., Teliban, G.C., (2023). Research on the identification of some optimal threshing și separation regimes in the axial flow apparatus. *Agriculture*, vol. 13, no.4, 838.
- [19] Xiaopeng, H., Chenhe, L., Jianfang, S., Guangwan, W. (2003). Development of extruded and rolled corn sheller (挤搓式玉米脱粒机的研制). *Transactions of the Chinese Society of Agricultural Engineering*, vol.19, no.2, pp.105-108; Beijing/China.
- [20] Xinpin, L., Yidong, M., Xin, J., Lianxin, G. (2015). Design and test of corn seed bionic thresher (玉米种子仿生脱粒机设计与试验). *Transactions of the Chinese Society for Agricultural Machinery*, vol.46, no.7, pp.97-101; Henan/China.
- [21] Yujia, D., Guohai, Z., Aoqi, Z., Jitan, L., Jia, Y., Xin, W., Xiaohui, Y. (2023). Experimental analysis of threshing maize seeds with high moisture content. *INMATEH-Agricultural Engineering*, vol.69, no.1, pp.131-144.
- [22] Yuejiang, T., Chengqian, J., Yanpu, C., Peng, L., Xiang, Y., Enting, W., Kang, Y. (2020). Design and optimization of segmented threshing device of combine harvester for rice and wheat. *Transactions of the Chinese Society of Agricultural Engineering*, vol.36, no.12, pp.1-12; Shandong/China.
- [23] Youliang, N., Chengqian, J., Tingen, W., Lei, Z., Zheng, L. (2022). Design and experiments of the 4LZ-1.5 soybean combine harvester (4LZ-1.5 型大豆联合收获机设计与试验). *Transactions of the Chinese Society of Agricultural Engineering*, vol.38, no.22, pp.1-11; Nanjing/China.
- [24] Zheng, Z., Hongmei, Z., Mingtao, H., Hao, H., Liquan, Y., Wanzhang, W. (2022). Design and experiment on corn thresher with tangential-axial flow double-roller (切轴流双滚筒玉米脱粒试验台设计与试验). *Journal of Chinese Agricultural Mechanization*, vol.44, no.6, pp.45-52; Henan/China.
- [25] Zhe, Q. (2018). Research on combined maize threshing and separating device with low damage. PhD Thesis, China Agricultural University, Beijing/China.
- [26] Zhendong, W., Tao, C., Dongxing, Z., Li, Y., Xiantao, H., Zepeng, Z. (2021). Design and experiment of low damage corn threshing drum with gradually changing diameter (玉米收获机低损变径脱粒滚筒设计与试验). *Transactions of the Chinese Society of Machinery*, vol.52, no.8, pp.98-105; Beijing/China.
- [27] ***China Statistical Yearbook 2024, *Agriculture*, Available from: <https://www.stats.gov.cn/sj/ndsj/2024/indexch.htm>

CFD-DEM BASED DESIGN OF ELBOW LIFTING PIPE CONVEYANCE UNDER NEGATIVE PRESSURE AIRFLOW

基于 CFD-DEM 的负压气流下弯头提升管道输送设计

Lianglong ZHANG¹⁾, Yue SUN¹⁾, Fan Yang¹⁾, Yalin Sun¹⁾, Fangyan Wang^{1,3*)}; Xin Wang^{2*)}

¹⁾ College of Mechanical and Electrical Engineering, Qingdao Agricultural University, Qingdao 266109, China.

²⁾ College of Civil Engineering and Architecture, Qingdao Agricultural University, Qingdao 266109, China.

³⁾ Collaborative Innovation Center for Shandong's Main Crop Production Equipment and Mechanization, Qingdao 266109, China.

* Corresponding authors, Email: wfy66@163.com

DOI: <https://doi.org/10.35633/inmateh-75-46>

Keywords: chili cleaning, bend lift conveyor, conveying efficiency, CFD-DEM

ABSTRACT

To improve the material conveying efficiency in the elbow lifting transportation process under negative pressure airflow and to solve pipeline material blockage issues, a chili cleaning device was used as the core model. CFD-DEM coupled simulation was employed to analyze the lifting process of non-spherical chili materials in the elbow pipe. Key parameter optimization was carried out through experimental design, determining the optimal parameter combination as a pipeline curvature of 2.03 and an air-to-feed ratio of 4.571. This combination achieved a conveying efficiency 4.406 times higher than the lowest efficiency case, and the uniformity of material transport under optimal parameters was verified through simulation. This study lays a solid foundation for the design of pipeline bends and the optimization of material conveying analysis.

摘要

为提高负压气流下弯管抬升输送过程物料输送效率，解决管道物料堵塞。以辣椒清选装置为核心模型，采用 CFD-DEM 耦合模拟，分析非球形辣椒物料弯管的提升过程。通过试验设计进行关键参数优化，确定最佳参数组合为管道曲率 2.03 和气送比 4.571。该组合的输送效率是最低效率情况下的 4.406 倍，并通过仿真验证了最佳参数组合下物料输送的均匀性。这为设备弯管的设计和物料输送分析的优化奠定了坚实的基础。

INTRODUCTION

Pneumatic conveying originated in Britain in the late 19th century. Since then, it has been extensively applied in diverse industries. Pneumatic conveying systems enjoyed a global market of nearly 30 billion U.S. dollars in 2021 (Hentschel, 2011; Hilgraf, 2023). Compared to traditional conveying methods, pneumatic conveying is characterized by high efficiency and low cost. With the continuous advancement of the industry, the demands for its conveying efficiency and performance are constantly escalating. However, pipeline conveying is merely a simple component of the device, which, therefore, lacks sufficient attention. This oversight seriously impacts the overall efficiency and operational effectiveness (Afkhami et al., 2015; Cong et al., 2018; Ma & Zhao, 2018).

Pneumatic conveying technology did not attract scholars' attention until the 1950s, although it was developed earlier in overseas countries. During the continuous development of pneumatic conveying technology industry, pneumatic conveying can be mainly categorized into dilute-phase pneumatic conveying, dense-phase dynamic pressure pneumatic conveying, dense-phase hydrostatic pneumatic conveying, and cylinder pneumatic conveying, among which dilute-phase pneumatic conveying methods are currently the most widely adopted. The existing analysis is primarily focused on spherical particles, simply constrained to the theoretical analysis of horizontal conveying or lifting conveying. With the gradual development of equipment in the multi-level direction, pneumatic pipeline is no longer limited to horizontal conveying, so there is an urgent need to provide theoretical support for the design of vertical-horizontal lifting.

Lianglong Zhang, postgraduates; Yue Sun, postgraduates; Fan Yang, Lecturer, Ph.D.; Yalin Sun, postgraduates; Fangyan Wang, professor, Ph.D.; Xin Wang, Lecturer, Ph.D.

Traditionally, design mode requires a lot of human and material resources. The coupled fluid mechanics and discrete element simulation technique, on the other hand, help to reduce the consumption of resources and is able to track and analyze the motion state of materials under the action of fluid from a microscopic perspective, which, hence, has been widely used in various types of pneumatic research. For example, Li Zhengquan and Chen Huimin analyzed the force between particles and pipe wall and the scouring effect on the pipe wall in pipelines using fluid mechanics and discrete element method (Li *et al.*, 2024). Gu Fengwei and Zhao Youqun analyzed the conveying device of straw no-tillage planter with the help of CFD-DEM coupled simulation and improved the homogeneity of straw casting and crushing (Gu *et al.*, 2022). Combining computational fluid dynamics and discrete element method, Hemin Zhao and Yongzhi Zhao effectively simulated the motion state of particles in horizontal channel pneumatic conveying (Zhao & Zhao, 2020). In summary, the reliability and applicability of the coupled CFD-DEM simulation technique have been fully verified. However, vertical-horizontal lifting process is rarely explored, and most of the existing research focuses on regular particles and lacks actual data to provide a basis for pipeline design.

By constructing a CFD-DEM coupled simulation model using chili peppers and chili pepper stalks as particle models, this paper investigates the conveying process of vertical-horizontal lifting in depth from the laws of air flow field and the motion state of particles and studies the conveying effect of materials under different structures (Chen *et al.*, 2020; Uzi & Levy, 2018). Combined with the experimental design, the optimal structure parameters are identified through experiments and simulation verification (Drescher *et al.*, 2025). The research results of this paper will provide valuable reference for the subsequent material lifting and conveying system and its structural design.

MATERIALS AND METHODS

Installations and Critical Areas

On the basis of previous research on chili cleaning device, this paper analyzed bending and lifting pipe of the chili mixture. The device consisted of conveyor belt, rotary feeder, conveyor pipe, rotary unloader, settling pipe and other components, as detailed in Fig. 1. Among them, the specific gravity sorting area (Fig. 1 (a)) and the inertia sorting area (Fig. 1 (b)) played the most critical role in operation. The chili was transported through the vertical-horizontal lifting pipe and then mixed. The detailed analysis will be performed in this paper to maximize the conveying efficiency and ensure the uniformity of conveying.

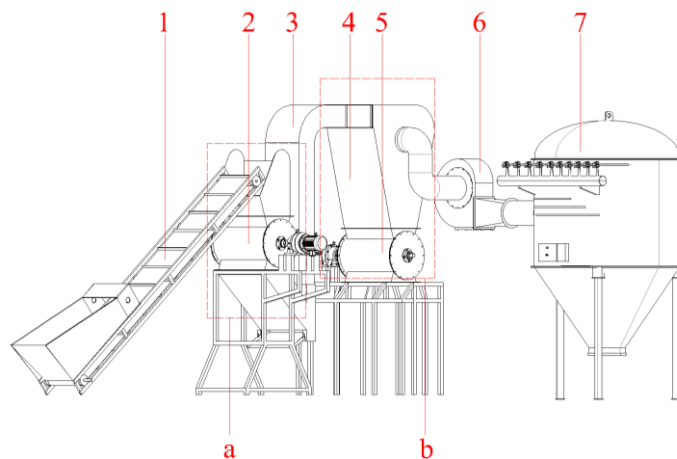


Fig. 1 - Chilli separator

1. conveyor belt; 2. rotary feeder; 3. lifting air duct; 4. sorting device; 5. rotary unloader; 6. centrifugal fan; 7. settling box
a. Specific gravity sorting area; b. Inertia sorting area

Theoretical analysis

The conveying pipeline needed to be rationally arranged, whose conveying efficiency would otherwise be affected, thereby potentially resulting in blockages, etc. Vertical - horizontal lifting pipelines are mainly divided into six types, as shown in Fig. 2 (a), where Pipeline 4 is the theoretically optimal route, which, however, is difficult to achieve in practice. Pipeline 2 is currently the most commonly used as it can be installed in a more standardized layout. Pipeline 2 has some single rounded corners designed into two rounded corners, which results in increased dissipation. Therefore, this paper presents an in-depth analysis and design of Pipeline 2.

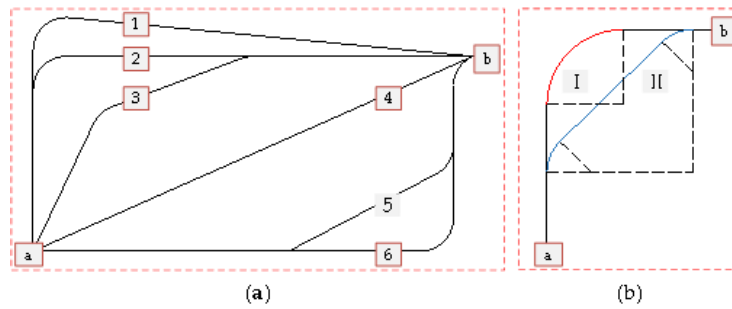


Fig. 2 - Pneumatic lifting conveying lines

a. Pneumatic lifting of the conveying pipeline arrangement; b. Schematic diagram of multiple corners of the pipeline

Conveying air velocity

Air velocity is one of the key parameters of chili cleaning device. According to the relevant provisions of the pipeline layout of the design institute, in the case of vertical or inclined pipe with elbows, the conveying air velocity should be 2.4 to 4.0 times the suspension velocity of the material. The floating speed of the material, V_p , was measured using suspension test bench provided by Qingdao Agricultural University (Gao et al., 2012; Ma Z. et al., 2011), as listed in Table 1.

Table 1

	Mixture material conveying speed		
	Overall dimensions [mm]	Suspension speed [m·s ⁻¹]	Conveying air velocity [m·s ⁻¹]
Chili	52.4~98.2	12.2-14.4	29.28~57.6
Chili stalks	21.5~43.1	9.1-10.5	21.84~42
Fractured stone	8~13	14.8~17.9	35.52~71.6

As the specific gravity sorting area is responsible for sorting out heavier impurities such as stones from the chili mixture, the conveying air velocity needs to be less than the minimum counterpart of stones and to meet the requirements in the conveying speed of chili peppers, stalk and other materials. Therefore, the optimal conveying air velocity of negative pressure at the inlet is 29.28~35.52 m·s⁻¹.

Curvature of bent pipe

The influence of the curvature generated in the material conveying process on the trajectory of the material was discussed.

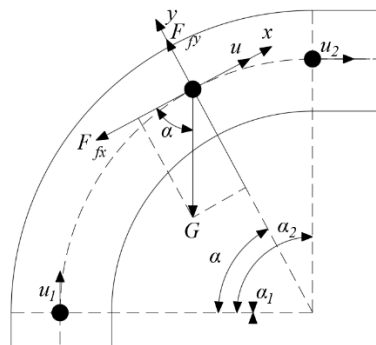


Fig. 3 - Material Bend Motion Analysis

The equations of motion are:

$$\begin{cases} -F_{fx} - G\cos\alpha = ma_x \\ F_{fy} - G\sin\alpha = ma_y \end{cases} \quad (1)$$

where F_{fx} , F_{fy} - airflow resistance components, (N); G - gravity, (N).

According to the boundary conditions, when particles were at Position 1, the angle of motion between the particles and the elbow was $\alpha_1=0^\circ$, and the velocity of the particles entering the bending phase was assumed to be $u=u_1$; when particles were at Position 2, the angle of motion between the particles and the elbow was $\alpha_2=90^\circ$, and the velocity of the particles entering the bending phase was assumed to be $u=u_2$.

The relationship between u_2 and α can be described as:

$$u_2^2 - e^{-f_w \alpha} u_1^2 = e^{-f_w \alpha} \frac{2gR}{4f_w^2 + 1} \{3f_w + e^{2f_w \alpha} [2(f_w^2 - 1) \sin \alpha - 3f_w \cos \alpha]\} \quad (2)$$

The final simplification of the above equation is obtained by combining the particles as they move from position 1 to position 2:

$$u_2 = e^{-\frac{\pi}{2} f_w} \sqrt{u_1^2 + \frac{2gR}{4f_w^2 + 1} [3f_w + e^{\pi f_w} (2f_w^2 - 1)]} \quad (3)$$

From eq. 3, it can be seen that the velocity of material movement is affected by the bending radius of the pipe.

Shape of Pipe

Pipes are commonly rectangular, circular and oval. Among them, circular pipes are more widely used for horizontal conveying. However, since the vertical-horizontal lifting process is very complex, this paper will examine and compare these three types of pipes in depth.

Gas-to-feed ratio

In the material conveying process, the material is vertically lifted and then horizontally conveyed through bending pipes. According to the relevant provisions about pipeline arrangement offered by the design institute, the air velocity of the material conveyed is mostly in the range of 12 m/s to 40 m/s, which is in line with the dilute phase pneumatic conveying speed conditions (Du et al., 2014; Huo et al., 2013). Under the condition of dilute-phase pneumatic conveying, gas-to-feed ratio is required to be between 1 and 5 (Hongxun, 1993), so as to meet the process requirements and performance indexes of the whole conveying system.

Experimental factors

Based on the above comprehensive analysis, the main factors affecting the material in the state of vertical-bend-horizontal conveying included pipe type, bend radius R, gas-to-feed ratio C. Curvature R/D was associated with elbow size, but was represented by radius R instead as the negative pressure of the pipe was constant and the cross-section size of the pipe had been determined. It will be further analyzed as a key influencing factor.

Simulation Settings

The simulation was coupled with ANSYS 2021r1 and EDEM 2020 software. The 'Mesh' module in ANSYS 2021r1 was used to delineate the mesh, and the Fluent module to analyze the flow field. In the Fluent module, the fluid medium was set to be air, and the k- ϵ model was employed to calculate the transient simulation method. The SIMPLE algorithm was used for computation. The material particles were generated and the mechanism was modelled using EDEM software. Data exchange between the two software packages was facilitated through a coupling plug-in, ensuring the accuracy and efficiency of the entire simulation (Alihosseini, Saegrov, & Thamsen, 2019; Zhao L. et al., 2016).

Simulation of particles and geometrical models

1) Particle physical parameters and contact parameters;

The physical properties of the chili mixture were measured based on the statistical principles of the physical parameters of the harvested chili mixtures. The characteristic properties of the material that could not be measured directly were obtained by EDEM calibration (Zhang et al., 2023). The parameters and contact coefficient of the material are listed in Table 2.

Table 2

Physical parameters of the material			
	Poisson's ratio	Shear modulus [MPa]	Density [kg·m ⁻³]
Chili	0.31	3.12	817.13
Chili handle	0.43	1.35	1024.45
Steel	0.29	79920	7860
	Coefficient of recovery	Coefficient of static friction	Coefficient of kinetic friction
Chili peppers-chili peppers	0.372	0.364	0.272
Chili peppers-chili stalks	0.277	0.452	0.341
Chili - steel	0.413	0.491	0.233
Chili stalk - chili stalk	0.362	0.682	0.578
Chili - steel	0.335	0.538	0.452

2) Particle modeling

In order to accurately simulate the actual working effect of the pipeline, particle modeling was conducted at a ratio of 1:1 between chili and chili stalk. By employing the SolidWorks finite element mesh module, the model was divided to generate node coordinates, and then the data was imported into EDEM software to construct the model for the particles of chili and chili stalk, as shown in Fig. 4.

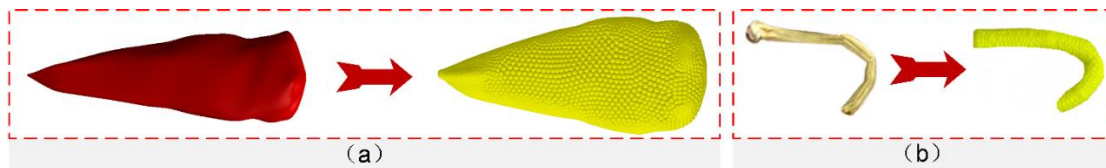


Fig. 4 - Particle-filled models
 a. Chili filler model; b. Chili stem filler model

3) Geometric modeling

A geometric model was established by SolidWorks software, and the mesh was delineated by the 'Mesh' module in Workbench, as shown in Fig. 5.

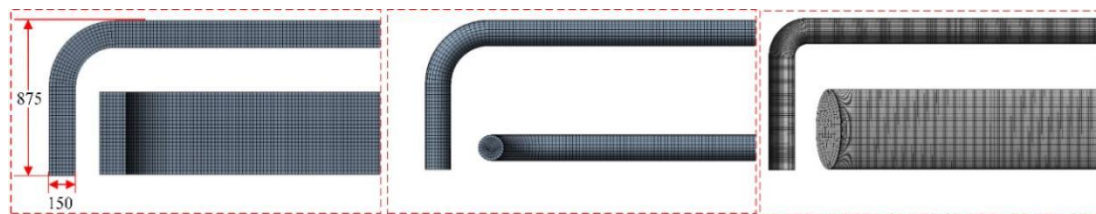


Fig. 5 - Geometric Modeling Mesh

Experimental

1) One-way test;

Using CFD-DEM coupled simulation technology and taking the uniformity of the airflow field, the stability of material conveying and the conveying efficiency as the evaluation indexes, this paper conducted the single-factor simulation analysis for the three key parameters, namely pipe type, curvature of elbow pipe R/D and air-to-feed ratio C . Among them, the pipe type included round, rectangular and oval; the curvature of elbow pipe R/D was set to be (1 ~ 5) because of common small curvature $R/D = 2$ and large curvature $R/D = 5$, and air-to-feed ratio C to be (1 ~ 5) according to the conditions of the rarefied-phase pneumatic conveying.

2) Orthogonal test;

According to the one-factor simulation results and agronomic requirements, curvature X_1 and air-to-feed ratio X_2 were taken as test factors, and material conveying efficiency Y as the evaluation standard (set 1s conveying 100 chilies as the unit efficiency). With the help of Design-Expert, two-factor three-level orthogonal test was performed (Cong et al., 2018).

The test factors are detailed in Table 3.

Table 3

Factor level coding table for chili pepper scavenging device test		
Encodings	Experimental factors	
	Curvature X_2	Gas to material ratio X_3
-1	1	1
0	2	3
1	3	5

In order to ensure the reliability of the CFD-DEM simulation, the optimal structural parameters were firstly obtained by simulation and experimental design analysis, and the pipe was processed according to the optimal combination of parameters to carry out the bending and lifting test on chili and chili stalk. During the test, the velocity at the key entrance and exit nodes was measured by a pipeline airflow speed transmitter, and compared with the velocity at the same locations obtained during the simulation to assess the reliability of the simulation results.

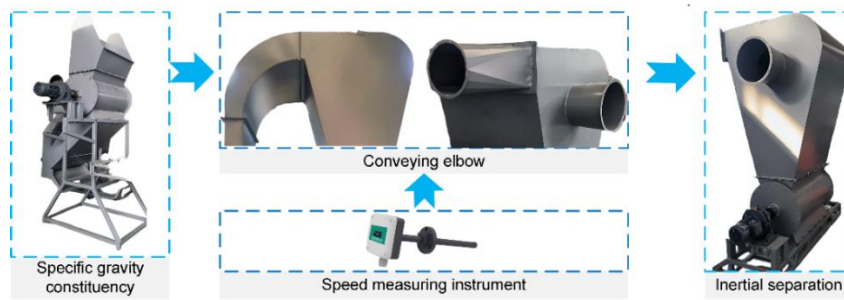


Fig. 6 - Of actual test setup

RESULTS

Analysis of the results of the one-way test

Analysis of pipe type simulation results

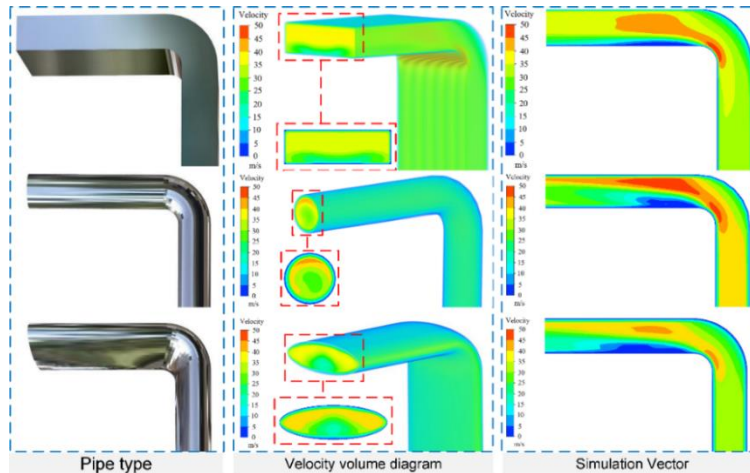


Fig. 7 - Pipeline fluid simulation volume diagram

As can be seen from the analysis of the cloud images for three types of elbow shown in Figure 7, airflow moved from the vertical area to the turning area in circular and elliptical elbows, mainly concentrating at the bottom and converging upward, which resulted in the turbulence in the horizontal area and therefore made it difficult to ensure the uniformity of material transportation (Liu et al., 2024; Wang et al., 2024; Zhang & Newell, 2024). In contrast, airflow movement in most areas remained unaffected when the airflow passed through the turning area in rectangular elbow due to the limitation of its own structure, so that airflow remained relatively stable in the material transportation process in the rectangular elbow, providing favorable conditions for the uniform and orderly transportation of the material.

Therefore, in terms of the airflow in the vertical and horizontal conveying processes, rectangular pipe was superior to oval and round ones. In the turning area, turbulence would not be produced in the rectangular pipe, which effectively ensured uniform airflow in the material conveying process and more stable airflow within the rectangular pipe from vertical to horizontal conveying.

Analysis of curvature simulation

The rectangular pipe was simulated, with air-to-feed set to be 2 and curvature R/D to be 1, 2, 3 and 4, respectively (Zhou et al., 2016). The simulation results are illustrated in Fig. 8.

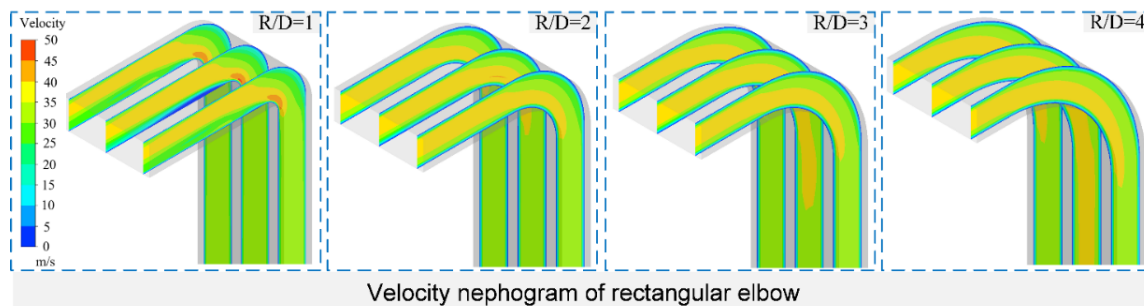


Fig. 8 - Curvature fluid simulation vector diagram

a. Velocity nephogram of rectangular elbow; b. Velocity nephogram of circular bend

As can be seen from Fig. 8, with the increase of the curvature R/D , the horizontal area of rectangular and round pipes did not change significantly, while the vertical area of high-velocity airflow area continued to expand towards the inlet.

As in the presence of negative pressure, when the airflow passes through the turning area, it would be attached to the lower wall of the turning area under the action of the Coanda Effect, thus generating adhesive flow. With the gradual increase of the curvature R/D , the turning trend of the airflow became more gentle and the adhesive flow of the steering process was cushioned. As a result, the high-velocity flow area was extended. Therefore, the larger the curvature R/D , the smoother the flow in the turning region.

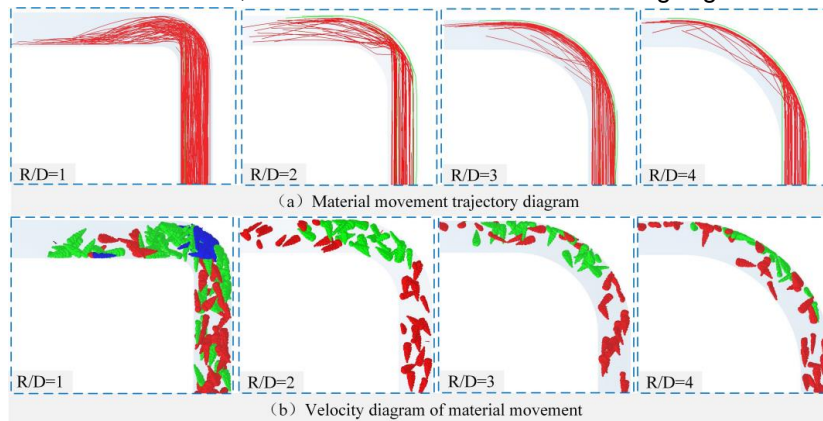


Fig. 9 - Particle coupling effect

a. Material movement trajectory diagram; b. Velocity diagram of material movement

As can be seen from Fig. 9, the larger the curvature R/D , the trajectory of the material was gradually concentrated at the top upon the completion of vertical and horizontal conveying. If a large number of materials were concentrated at the top of the pipe, then they would be unevenly distributed within the pipe, thus lowering the material conveying efficiency.

With the gradual increase of the curvature R/D , the number of collisions of material trajectory in the turning area obviously increased. The material would collide with the upper wall of the elbow under the action of the upward movement inertia when moving from the vertical area to the turning area. In addition, the turning area was enlarged, so that the materials would continue to collide repeatedly with the turning area following their initial collision, making the pipe very likely to be blocked.

For the sake of a comprehensive comparison, among the four common curvatures of rectangular pipes, the curvature $R/D = 2$ helped to ensure the uniform distribution of the materials in the pipe after they passed through the turning area and to effectively reduce the number of collisions between the materials as well as between the materials and the pipe wall, thus reducing the degree of damage to the materials.

Influence of air/feed ratio on conveying performance

A rectangular bend was simulated, with the curvature R/D being set to 2 and air-to-feed ratio to 1, 2, 3, 4 and 5, respectively (Ebrahimi & Crapper, 2017). The corresponding simulation results are shown in Fig. 10.

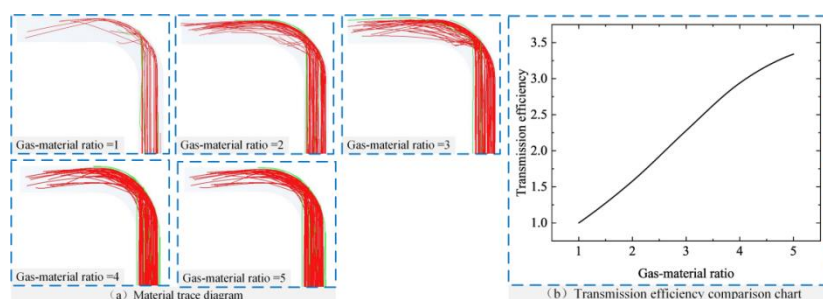


Fig. 10 - Particle coupling trace diagram

a. Material trace diagram; b. Transmission efficiency comparison chart

As seen in Fig. 10(a), increasing the air-to-feed ratio improved the uniformity of material conveying. With a higher air-to-feed ratio, the materials initially accumulated in the turning area, causing a reduction in speed. However, as the materials moved into the horizontal conveying section, they formed a more stable mass, leading to a more uniform trajectory.

As seen in Fig. 10(b), at a low air-to-feed ratio, the materials were not conveyed rapidly due to the occurrence of a winding phenomenon. As the air-to-feed ratio gradually increased, the cross-sectional area of the material exposed to the airflow became larger, enhancing the pulling force of the air on the material surface. This resulted in accelerated movement of the materials, thereby improving the efficiency of material conveying.

Analysis of orthogonal test

Experimental design and analysis were conducted using Design-Expert 13 software, with transportation efficiency as the evaluation indicator. The transportation efficiency of the least efficient combination was set as the baseline unit, represented as $Y_1=1$. The efficiency of the remaining combinations was then expressed as a multiple of the baseline according to the simulation results, i.e., $Y_1=n \times 1 (n \geq 1)$. The experimental results and ANOVA analysis are presented in Tables 4 and 5, respectively.

Table 4

Relationship between conveyor airflow speed and suspension velocity

Serial number	Factors		Performance indicators Gas to material ratio Y_1
	Curvature X_1	Gas-to-feed ratio X_2	
1	2	1	3.2
2	1	3	1.53
3	1	5	2.21
4	2	3	3.41
5	2	3	3.67
6	3	1	1.21
7	2	3	3.98
8	2	5	4.12
9	3	5	3.96
10	1	1	1
11	2	3	3.87
12	3	3	2.27

Table 5

ANOVA table for conveying efficiency

Source of variance	Square sum	Degrees of freedom	Mean square	F	P	Significance
Modelling	15.13	5	3.03	32.25	0.0001	Significant
X_1	1.21	1	1.21	12.95	0.0088	Significant
X_2	3.97	1	3.97	42.29	0.0003	Significant
X_1X_2	0.5929	1	0.5929	6.32	0.0402	Significant
X_2^2	8.15	1	8.15	86.82	< 0.0001	extremely significant
X_2^e	0.005	1	0.005	0.0529	0.8246	Insignificant
Residual	0.657	7	0.0939			
Lost proposal	0.4538	3	0.1513	2.98	0.1597	Insignificant
Inaccuracies	0.2032	4	0.0508			
Aggregate	15.79	12				

As shown in Table 6, the fit of the conveyor efficiency model was significant ($p < 0.1$), while the out-of-fit term was insignificant ($p = 0.1597$, $p > 0.05$). The terms X_1 , X_2 , and X_1X_2 had a significant effect on the chili clearing rate, with X_2^2 being extremely significant. After excluding the insignificant regression terms, the regression equation for conveying efficiency can be expressed as:

$$Y = 3.72 - 0.45X_1 - 0.8133X_2 - 0.3850X_1X_2 - 1.72X_1^2 \quad (4)$$

Air-to-feed ratio had a greater impact on material conveying efficiency than curvature. The interaction between air-to-feed ratio and curvature had a significant effect on conveying efficiency.

To determine the optimal levels of test factors, the optimization module of Design-Expert 13 software was used to establish a parameter optimization mathematical model. The model aimed to maximize conveying efficiency while considering the boundary conditions of each factor's test values. The objective function and constraints are as follows:

$$\begin{cases} \max Y(X1, X2) \\ \text{s. t } \begin{cases} 1 \leq X1 \leq 3 \\ 1 \leq X2 \leq 5 \end{cases} \end{cases} \quad (5)$$

According to the analysis, the optimal parameter combination was a curvature of 2.03 and an air-to-feed ratio of 4.571, resulting in a unit material conveying efficiency of up to 4.406.

Optimal combination of experimental and simulation results and comparison

Optimal simulation results

The simulation analysis results are shown in Fig. 11. As the materials were lifted from the vertical area to the turning area and then into the horizontal area, they were transported along the upper wall of the horizontal section due to changes in air resistance and gravity acting in the downward movement direction. Eventually, if the materials did not fall to the lower wall of the horizontal section, a uniform motion flow was formed, enabling stable horizontal conveying of the materials.

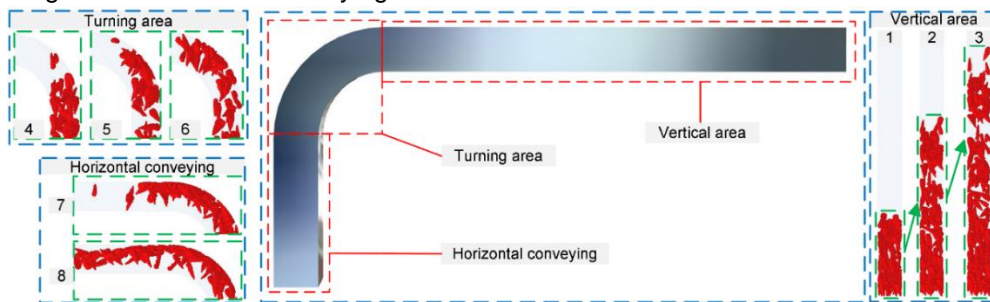


Fig. 11 - Schematic diagram of the motion state of the coupled simulated particles

Actual test results and simulation verification

The actual test was carried out in Jiaozhou, Qingdao, with a rectangular pipe shape, small curvature $R/D = 2.03$, and an air-to-feed ratio of 4.571. The materials used were chili peppers and chili stalks in the ratio of 10:1. The components of the test setup included an inertial sorting device, a centrifugal fan, and a curved conveying pipe.

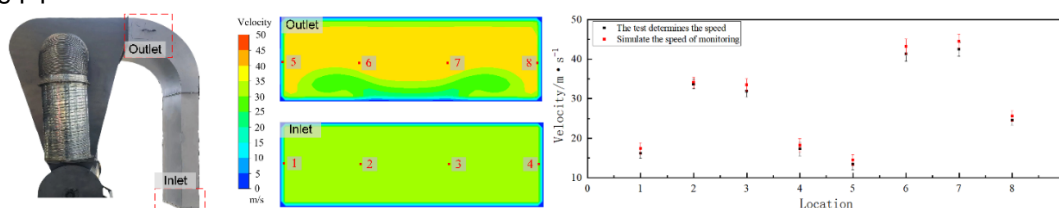


Fig. 12 - Comparison of actual test and simulation key position speed intention

As shown in Fig. 12, by comparing the simulation results of the velocity at the same positions at the inlet and outlet with the actual measurement results, it was found that the actual velocity was slightly lower than the simulated one. This deviation remained within a reasonable range due to the increasing energy consumption of airflow and material flow under the influence of external environmental factors in practical applications. Since the simulated speed closely matched the actual speed in both trend and magnitude, the simulation test results were proven to be highly accurate and reliable.

CONCLUSIONS

In this paper, the CFD-DEM coupled simulation technique was employed to simulate the material lifting and conveying state in a vertical-bend-horizontal pipeline. To achieve optimal material lifting and conveying efficiency, simulation analyses were conducted on pipe type, curvature, and air-to-feed ratio. Combined with

experimental design, the optimal pipe structure was determined to maximize material conveying efficiency. The following conclusions can be drawn:

- The comprehensive experimental design results indicate that material conveying efficiency is maximized when the curvature is 2.03 and the air-to-feed ratio is 4.571 for a rectangular pipe. Combined with the simulation results, this parameter combination ensures more uniform material transportation, meeting operational requirements.
- The CFD-DEM coupled simulation technique employed in this study significantly reduces design resource consumption while achieving ideal results. However, some deviations remain compared to actual tests. Nonetheless, the comparison of simulation and experimental speed measurements shows minimal errors at each point, effectively confirming the reliability of the simulation analysis.

REFERENCES

- [1] Afkhami, M., Hassanpour, A., Fairweather, M., & Njobuenwu, D. O. (2015). Fully coupled LES-DEM of particle interaction and agglomeration in a turbulent channel flow. *Computers & Chemical Engineering*, 78, 24-38. doi:10.1016/j.compchemeng.2015.04.003
- [2] Alihosseini, M., Saegrov, S., & Thamsen, P.U. (2019). CFD-DEM modelling of sediment transport in sewer systems under steady and unsteady flow conditions. *Water Science and Technology*, 80(11), 2141-2147. doi:10.2166/wst.2020.030
- [3] Chen, Q., Xiong, T., Zhang, X., & Jiang, P. (2020). Study of the hydraulic transport of non-spherical particles in a pipeline based on the CFD-DEM. *Engineering Applications of Computational Fluid Mechanics*, 14(1), 53-69. doi:10.1080/19942060.2019.1683075
- [4] Cong, H., Zhao, L., Meng, H., Yao, Z., & Wu, Y. (2018). Design and Test of Multilevel Collaborative Drying System for Crop Straws. *Acta Energetica Solaris Sinica*, 39(1), 163-169.
- [5] Drescher, E., Mohseni-Mofidi, S., Bierwisch, C., & Kruggel-Emden, H. (2025). A numerical assessment of different geometries for reducing elbow erosion during pneumatic conveying. *Powder Technology*, 449. doi:10.1016/j.powtec.2024.120357
- [6] Du, J., Hu, G., Fang, Z., & Fan, Z. (2014). Simulation of dilute pneumatic conveying with bends by CFD-DEM. *Journal of National University of Defense Technology*, 36(4), 134-139.
- [7] Ebrahimi, M., & Crapper, M. (2017). CFD-DEM simulation of turbulence modulation in horizontal pneumatic conveying. *Particuology*, 31, 15-24. doi:10.1016/j.partic.2016.05.012
- [8] Gao, L., Zhang, W., Du, X., Liu, X., & Yang, J. (2012). Experiment on aerodynamic characteristics of threshed mixtures of peanut shelling machine. *Transactions of the Chinese Society of Agricultural Engineering*, 28(2), 289-292.
- [9] Gu, F., Zhao, Y., Wu, F., Hu, Z., & Shi, L. (2022). Simulation analysis and experimental validation of conveying device in uniform rushed straw throwing and seed-sowing Machines using CFD-DEM coupled approach. *Computers and Electronics in Agriculture*, 193. doi:10.1016/j.compag.2022.106720
- [10] Hentschel, A. (2011). Pneumatic conveying and precise metering of dust. *Zkg International*, 64(10), 59-63.
- [11] Hilgraf, P. (2023). Direct scaling up of pneumatic conveying tests to industrial systems. *Zkg International*, 76(2), 42-51.
- [12] Hongxun, C. K. C. (1993). *Pneumatic conveying device*: Beijing: Machinery Industry Press.
- [13] Huo, Z., Zhang, D., Hu, Y., & Pei, X. (2013). Study on the Wear and Pressure Drop of The Pipe Bend in The Pneumatic Conveying of Grain Particles Dilute Phase. *Mechanical Science and Technology for Aerospace Engineering*, 32(11), 1680-1684.
- [14] Li, Z., Chen, H., Wu, Y., Xu, Z., Shi, H., & Zhang, P. (2024). CFD-DEM analysis of hydraulic conveying of non-spherical particles through a vertical-bend-horizontal pipeline. *Powder Technology*, 434. doi:10.1016/j.powtec.2024.119361
- [15] Liu, F., Li, H., Zhao, X., & Chen, Y. (2024). Study on the Spatiotemporal Evolution Pattern of Frazil Ice Based on CFD-DEM Coupled Method. *Water*, 16(23). doi:10.3390/w16233367
- [16] Ma, H., & Zhao, Y. (2018). Investigating the fluidization of disk-like particles in a fluidized bed using CFD-DEM simulation. *Advanced Powder Technology*, 29(10), 2380-2393. doi:10.1016/j.appt.2018.06.017

- [17] Ma, Z., Li, Y., & Xu, L. (2011). Testing and analysis on rape excursion components characteristics in floating, friction and wettability. *Transactions of the Chinese Society of Agricultural Engineering*, 27(9), 13-17.
- [18] Uzi, A., & Levy, A. (2018). Flow characteristics of coarse particles in horizontal hydraulic conveying. *Powder Technology*, 326, 302-321. doi:10.1016/j.powtec.2017.11.067
- [19] Wang, Z., Peng, G., Chang, H., Hong, S., & Ji, G. (2024). Investigation and Improvement of Centrifugal Slurry Pump Wear Characteristics via CFD-DEM Coupling. *Water*, 16(21). doi:10.3390/w16213050
- [20] Zhang, D., Zhang, X., Wu, D., Lin, S., Zhang, T., & Xu, W. (2023). Simulation of Pepper Cleaning Based on DEM-CFD Coupling. *Journal of Agricultural Science and Technology*, 25(07), 87-96. doi:10.13304/j.nykjdb.2022.0008
- [21] Zhang, X., & Newell, P. (2024). Simulation of Microcapsule Transport in Fractured Media Using Coupled CFD-DEM. *Water Resources Research*, 60(6). doi:10.1029/2023WR035728
- [22] Zhao, H., & Zhao, Y. (2020). CFD-DEM simulation of pneumatic conveying in a horizontal pipe. *Powder Technology*, 373, 58-72. doi:10.1016/j.powtec.2020.06.054
- [23] Zhao, L., Yu, Z., Zhu, F., Qi, X., & Zhao, S. (2016). CFD-DEM modeling of snowdrifts on stepped flat roofs. *Wind and Structures*, 23(6), 523-542. doi:10.12989/was.2016.23.6.523
- [24] Zhou, J.-w., Du, C.-l., Liu, S.-y., & Liu, Y. (2016). Comparison of three types of swirling generators in coarse particle pneumatic conveying using CFD-DEM simulation. *Powder Technology*, 301, 1309-1320. doi:10.1016/j.powtec.2016.07.047

DESIGN AND TESTING OF SMALL ELECTRIC DOUBLE-ROW LEEK HARVESTER

小型电动双行韭菜收获机设计与试验

Yuxin SHAN¹⁾, Yinping ZHANG^{*1)}, Hua ZHOU¹⁾, Jiasheng WANG²⁾, Qun MA³⁾¹⁾ College of Agricultural Engineering and Food Science, Shandong University of Technology, Zibo, 255000/China;²⁾ College of Mechanical and Electrical Engineering, Qingdao Agricultural University, Qingdao, 266109/China;³⁾ Shandong Dayi General Purpose Machinery Limited Company, Linyi, 276002/China.

Tel: +86-15165333108, Email: zhangyinping@sdut.edu.cn

DOI: <https://doi.org/10.35633/inmateh-75-47>**Keywords:** leek, harvesting machine, two rows, clamping conveying**ABSTRACT**

Aiming to address the limited space and the inapplicability of large harvesting equipment in Chinese greenhouses, a small electric double-row leek harvester was designed. This machine is capable of cutting, clamping, transporting, and collecting leeks simultaneously. A reciprocating cutting device was employed to accommodate varying row spacings. To make the machine suitable for small greenhouse environments, the parameters of the torsion clamping conveyor belt were optimized to reduce the overall size. Through theoretical analysis of the clamping and conveying system, the cutting mechanism, and the parameters for coordinated clamping-cutting operations, the structural design and working parameters were determined. A prototype was developed, and field experiments were conducted. The results showed that when the machine's forward speed was 0.3 m/s, the linear speed of the cutting knife was 0.66 m/s, and the conveyor belt speed was 0.42 m/s, the average damage rate was 4.87%, meeting the requirements for mechanized leek harvesting. This study provides a reference for the design of leek harvesters.

摘要

针对中国设施温室空间小、大型收获设备不适应等问题, 设计了小型电动双行韭菜收获机, 可一次性完成韭菜切割、夹持、输送、装框作业。采用往复式切割装置适应不同行距韭菜切割, 优化扭转夹持输送带参数, 减小整机尺寸, 适应温室小空间作业。通过对夹持输送装置、切割装置以及夹持-切割协同作业参数进行理论分析, 确定了夹持输送装置、切割装置的结构、工作参数。试制样机并进行了田间试验, 试验结果表明, 当机器前进速度为 0.3 m/s, 割刀线速度为 0.66 m/s、输送带速度为 0.42 m/s 时, 平均作业损失率为 4.87%, 满足韭菜机械化收获要求。本研究旨在为韭菜收获机的设计提供参考。

INTRODUCTION

Leek is native to China, with a perennial planting area of about 400,000 hm² and an annual output of about 2 million tons. Due to its special planting methods and different growth methods, it can be harvested at least 4–5 times a year (Gong *et al.*, 2018), but the mechanization level of leek harvest is low, mainly relying on manual sorting and boxing, which not only has low work efficiency, high labor intensity and high operating costs, but it is also difficult to guarantee the quality and efficiency of artificial harvest, affecting the development of leek industry (Zou *et al.*, 2022).

At present, the mechanical harvesting technology of leeks and other slender stalk leafy vegetables in foreign countries has been relatively mature (Wang *et al.*, 2021), such as the SLIDE TRAX SMALL parsley orderly harvesting machine from Hortech in Italy and the PO-335A leek harvester from ASA-LIFT in Denmark, which adopts a vertical clamping conveyor device with adjustable lifting and small clamping damage. However, the conveying device has a large structure and is not suitable for facility greenhouses (Liu *et al.*, 2019). The 4G-200 leek harvester of Korea Plant Company uses a twist clamping conveying belt to make leeks orderly spread in the same direction. The model is small and suitable for facility greenhouse operations, but it needs manual secondary sorting and boxing (Xu *et al.*, 2020). The mechanical harvesting technology of leek and other slender stalks of leafy vegetables in China is in the research stage. Some authors designed a leek harvesting machine with a two-stage conveying device (Feng *et al.*, 2023; Zhang *et al.*, 2022a; Liu *et al.*, 2023; Xin *et al.*, 2024; Xu *et al.*, 2024). The first-stage conveying device will transfer leek from vertical posture to horizontal posture, and the second-stage conveying device will transfer leek with horizontal posture to the collection device, which makes the leeks harvested this way more orderly. However, the overall length of the model is too long and the flexibility is poor.

Other researchers designed a small single-row leek harvester, which used a disc cutting knife and a twisting conveying belt to directly transport the cut leek to the ground behind the machine and lay it on the ground. The leek was manually picked up into the box (Zhao *et al.*, 2021; Zhang, 2024a). Su *et al.* (2020) extended the conveying distance of the conveyor belt and placed a collection box behind the machine to allow the leeks fall directly into the box. However, due to the significant height difference between the leeks and the box, the leeks tended to become disorganized after falling in.

Due to the long stems and leaves of leeks and the variation in row spacing, current leek harvesters primarily operate in a single row, using disc cutting knives and semi-cross torsion clamping conveyor belts, which result in low efficiency. Multi-row harvesters with high operation efficiency tend to be large in size and unsuitable for small plots in greenhouse facilities (Zhang *et al.*, 2024b). In this study, a small electric double-row leek harvester was designed. A reciprocating cutting knife was used, and the layout of the twisting clamping belt was optimized to shorten the clamping and conveying distance, thereby enabling double-row harvesting. The model is compact and offers high harvesting efficiency, making it suitable for greenhouse operations. The optimal structural parameters were determined through theoretical calculations of the clamping conveying device, cutting mechanism, and coordinated clamp-cutting operation. A prototype was developed, and field experiments were conducted to verify the rationality of the design parameters. This study provides a technical reference for the design of mechanized leek harvesters.

MATERIALS AND METHODS

Structure and Working Principle of the Harvester

The structure of the whole machine is shown in Fig. 1. It is mainly composed of a divider, a cutting device, a clamping conveying device, a collecting device, a travel device and a rack which can complete the cutting, clamping, conveying and boxing of leek at one time. The height of the reciprocating cutting knife can be adjusted up and down to meet the requirements of different cutting heights. Clamping conveying mechanism adopts double-row twisting clamping conveying mode to improve harvesting efficiency and orderliness. Conveying belt with sponge rubber strip is selected to reduce damage to leek. The main technical parameters of the machine are shown in Table 1.

Table 1

Main technical parameters of double-row electric leek harvester

Parameters	Unit	Values
Size of whole machine	mm	1800x900x880
Matched power	kW	0.5
Output Speed	r/min	330
Machine forward speed	m/s	0~0.75
Conveyor belt line speed	m/s	0~1.04
Working width	mm	660
Harvest height	mm	10~30

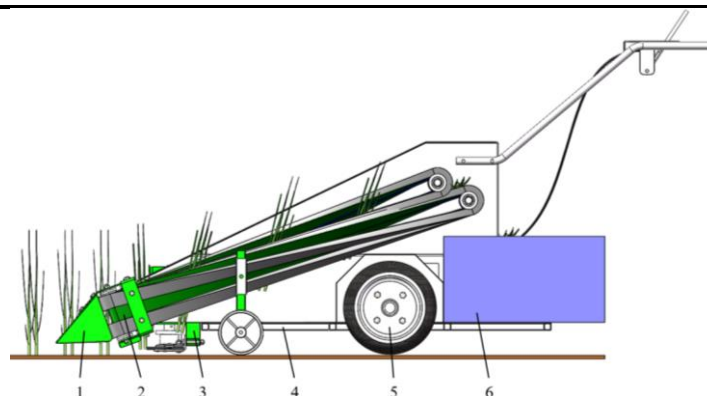


Fig. 1 - Structure diagram of double-row leek harvester

1 - Divider; 2 - Clamping conveying device; 3 - Reciprocating cutting device; 4 - Rack; 5 - Travel device; 6 - Collecting device

When the double-row leek harvester operates, the limiting wheel is first adjusted to align the divider of the harvester with the leek row, ensuring that the reciprocating cutting knife is parallel to the ground. During the machine's forward movement, the clamping conveyor first clamps the leek plant, and then the reciprocating cutting knife cuts the leek from the stem, and the clamping conveyor is transported backwards.

In the conveying process, to ensure the stability of the conveying and facilitate the subsequent collection, the clamping conveying belt is twisted, so that the state of the leek plant changes from vertical to horizontal, and the leek plants fall horizontally into the collection box in an orderly manner when it is transported to the end of the clamping conveying device.

Key component design

Clamping conveying device design

The clamping conveying device consists of two sets of torsion conveying mechanisms. Each mechanism is supported by two sets of belt rollers arranged at a 90-degree angle to each other, enabling the transition of the conveying direction from vertical to horizontal. Power is transmitted between the drive shaft and the driven shaft through a pair of spur gears with identical indexing diameters, ensuring synchronized rotation. The driven roller mounting rack can move forward and backward to adjust the tension of the conveyor belt, and left and right to adjust the belt gap. The structure of the clamping conveying device is shown in Fig. 2.

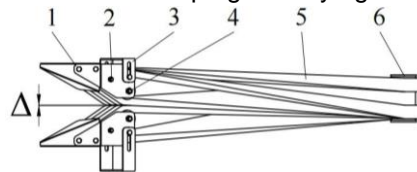


Fig. 2 - Structure diagram of clamping conveying device

1 - Driven roller guide roller holder; 2 - Guide roller; 3 - Fixed frame support frame; 4 - Driven roller; 5 - Conveying belt; 6 - Drive roller

During the conveying process, the gap between the upper and lower conveyor belts determines the size of the clamping force. Too large gap and too small clamping force will lead to misalignment or even dropping of the leeks during transport. Conversely, too small gap and too large clamping force will potentially cause damage to the leeks at the clamping point. To ensure orderly collection with minimal damage, the conveyor belt clearance was carefully designed. Experimental results on the physical characteristics of leeks showed that the diameter at the cutting position ranges from 5.09 to 7.76 mm. Mechanical property tests revealed that the critical compression force at which leeks become damaged is between 12.5 N and 18.95 N (Liu et al., 2022). Based on this, the initial gap between the upper and lower conveyor belts Δ was set to 3 mm, adjustable according to the planting density in a single row and stem diameter of the leeks during operation.

As shown in Fig. 3, to ensure reliable clamping and transportation of leek plants, the driving roller, driven roller, guide roller, and conveyor belt form a torsional clamping transport channel. Before the leeks enter the clamping conveying device, the gap between the upper and lower belts is small. As the leek plants enter the device, the sponges on the upper and lower conveyor belts are compressed and deformed by the leeks, causing the gap to widen. The leeks become "wrapped" by the sponge layers of the belts, which increases the number of contact points and improves clamping stability. This design effectively reduces damage to the leek plants.

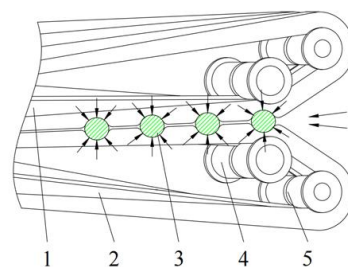


Fig. 3 - Schematic diagram of the transport process of the clamped part of leek plant

1 - Upper conveying belt; 2 - Lower conveying belt; 3 - Leek plant; 4 - Driven roller; 5 - Guide roller

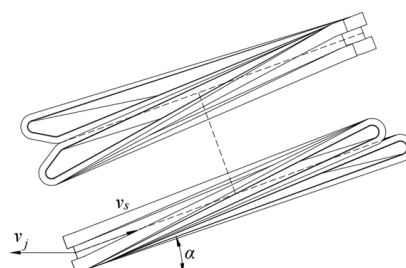


Fig. 4 - Speed analysis of transport process

To ensure smooth backward transmission of leeks and to prevent them from being pushed forward by the conveyor belt during harvesting, the belt speed must exceed the forward speed of the harvester (Li et al., 2023). Therefore, the conveyor belt speed and the machine's forward speed must satisfy the following condition:

$$v_s \cos \alpha > v_j \tag{1}$$

where:

α is the angle between the conveyor belt and the horizontal plane, ($^\circ$), $\alpha=20^\circ$ (Zhang et al., 2016); v_s is the conveyor belt speed, m/s; v_j is the machine's forward speed, m/s.

The minimum forward speed requirement for leek harvesting machinery is 0.2 m/s. According to equation (1), the speed of the driving roller must exceed 64 r/min. The designed speed range of the driving roller is 0~4495 r/min, corresponding to a conveyor belt speed range of 0~1.04 m/s. The design speed of the wheels is 0~55 r/min, corresponding to a forward machine speed of 0~0.75 m/s.

Cutting device design

Since the moisture content of the leek stem is as high as 84.5%, and considering the soft and easily damaged characteristics of the leek itself, this design selects a single-acting reciprocating cutting device, as shown in Fig. 5 (a). The cutting stroke $S=50$ mm, with a moving blade spacing $c=50$ mm, fixed blade spacing $c_0=50$ mm, top width $d=10$ mm, and edge height $h=55$ mm. The cutting knife length is 550 mm to meet the required harvesting width for leeks.

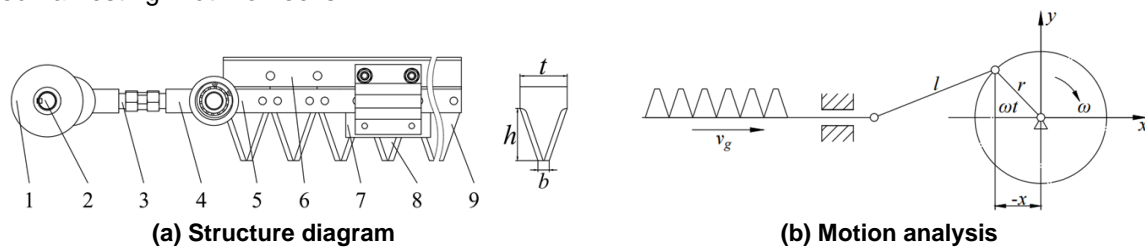


Fig. 5 - Cutting device

(a) 1 - Eccentric wheel; 2 - Power input shaft; 3 - Threaded connecting rod. 4 - Crank sleeve; 5 - Tool bar; 6 - Tool holder; 7 - Pressing edge plate; 8 - Moving blade; 9 - Fixed blade

Research indicates that as the angle θ increases, the cutting resistance will decrease, but if the angle θ exceeds a certain limit, the crop stems will slide out of the mouth of the moving and fixed blade, resulting in missed cutting or uneven stubbles (Shi et al., 2017). To reduce the above phenomenon and ensure that the reciprocating cutting device can cut normally at the moment of contact with the leek stem, the cutting process of the leek stem is analyzed, as shown in Fig. 6.

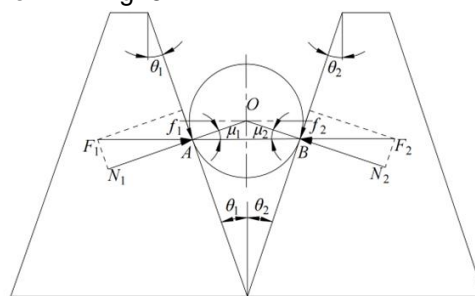


Fig. 6 - Force analysis diagram of blade clamping stem

As can be seen from Fig. 6., when the stems are clamped to maintain balance, the forces F_1 and F_2 must be equal in magnitude, opposite in direction, and on the same straight line:

$$\begin{cases} F_1 = N_1 \tan \frac{\theta_1 + \theta_2}{2} \leq N_1 \tan \mu_1 \\ F_2 = N_2 \tan \frac{\theta_1 + \theta_2}{2} \leq N_2 \tan \mu_2 \end{cases} \tag{2}$$

where: θ_1 - the cutting angle of the moving blade, ($^\circ$); θ_2 - the cutting angle of the fixed blade, ($^\circ$); μ_1 - the friction angle of the fixed blade to the stem, ($^\circ$); μ_2 - the friction angle of the moving blade to the stem, ($^\circ$); F_1 - the resultant force of the moving blade acting on the stem, N; F_2 - the resultant force of the fixed blade on the stems, N; N_1 - the normal force of the moving blade on the stems, N; N_2 - the normal force of the fixed blade on the stems, N;

After analysis, the following condition is obtained:

$$\theta_1 + \theta_2 \leq \mu_1 + \mu_2 \quad (3)$$

This inequality ensures the limiting condition for the clamping of the stem between the moving and fixed blades. Specifically, it means that the sum of the cutting angles θ_1 and θ_2 of the moving and fixed blade must not exceed the sum of the friction angles μ_1 and μ_2 between the blades and the stem. In this study, the values used were $\theta_1 = 19^\circ$, $\theta_2 = 18^\circ$.

During the operation of the cutting knife in the reciprocating cutting device, its absolute motion is a combination of reciprocating motion (as shown in Fig. 5. (b)) and linear motion:

$$\begin{cases} y = v_j t \\ x = r(1 - \cos \omega t) \end{cases} \quad (4)$$

where:

t is the time, s; y is the distance the machine travels in t time, mm; r is the crank radius, mm; x is the displacement of the moving blade in t time, mm.

The formula for calculating the forward distance of the moving blade is:

$$H = \frac{60v_j}{2n} = \frac{\pi}{\omega} v_j \quad (5)$$

where:

n is the rotational speed of the crank, r/min; H is the feed per revolution of the cutter, mm.

Based on geometric relations, the following equation can be derived:

$$y = \frac{H}{\pi} \arccos \frac{r-x}{r} \quad (6)$$

For leafy and stem vegetables like leeks, which require high cutting quality, a clean and smooth cut surface helps reduce damage and decay, extends shelf life, and enhances market value (Shan *et al.*, 2024).

The cutting diagram, drawn according to eq. (5), is shown in Fig. 7. I is the primary cutting area; III is the recutting area; b_1 is the average width of the fixed blade. The cutting device has no missed cutting zones and the repeated cutting area is relatively large, resulting in a neater and smoother cutting surface.

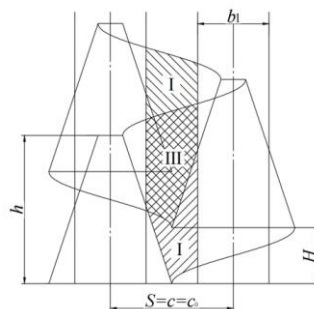


Fig. 7 - Cutting diagram of reciprocating cutting device

Clamping-cutting collaborative operation parameter design

Cutting leek plants while they are clamped is essential to ensure their orderly conveyance. After clamping and cutting, due to the combined effects of the machine's forward motion, the separation function of the divider, and the pulling action of the clamping conveyor belt, the leek plants may adopt unstable postures, such as leaning forward or backward in the direction of movement (Xin *et al.*, 2023). To ensure smooth clamping and transport after cutting, the relative positions of the clamping conveying device and the cutting device were carefully designed. Additionally, the postural changes of the leek plants in the forward direction of the machine were analyzed during the clamping-cutting process.

As the machine moves forward, the cutting knife contacts the clamped leek stems and performs a double-supported cutting action. For ease of analysis, a Cartesian coordinate system is established with the contact point O between the leek plant and the ground, at the clamping-uncut stage, as the origin. It is assumed that the clamping conveying device remains stationary relative to the ground, while the leek plant moves relative to the clamping conveying device at a speed v_j . The geometric relationship is illustrated in Fig. 8. Let the distance between the clamping point A and the front end of the cutting knife be l_g , the height of the cutting knife from the ground be h_1 , the height of the clamping point A from the ground be h_2 , the clamping-cutting time be t_1 , and the angles between the leek plant and the horizontal ground during clamping and cutting be β_1 and β_2 respectively.

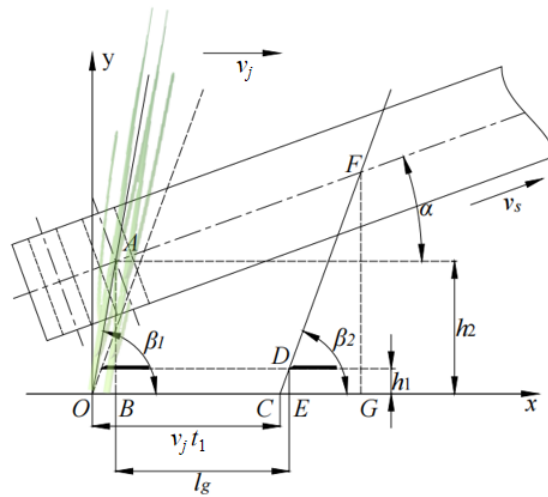


Fig. 8 - Analysis of the clamping-cutting process of leek plants

Since the motion of leek plant is the result of the combined movement of the harvester's forward speed v_j , and the clamping conveying speed v_s , the displacement equation of the clamping point F , during the clamping-cutting stage, relative to the clamping point A , in the clamping-uncut stage, is as follows:

$$\begin{cases} x_F = v_s t_1 \cos \alpha \\ y_F = v_s t_1 \sin \alpha \end{cases} \quad (7)$$

The clamping conveyor belt holds the leek stem at point A . To ensure the stem is securely clamped before cutting, it is necessary to determine the appropriate installation position of the cutting knife:

$$h_2 \cot \beta_1 \leq l_g \quad (8)$$

As shown in Fig. 9, during the clamping-cutting stage, the angle between leek plants and the ground satisfies the following trigonometric relationships in $\triangle CDE$ and $\triangle CFG$:

$$\begin{cases} \tan \beta_2 = \frac{h_1}{l_g + h_2 \cot \beta_1 - v_j t_1} \\ \tan \beta_2 = \frac{h_2 + v_s t_1 \sin \alpha}{h_2 \cot \beta_1 + v_s t_1 \cos \alpha - v_j t_1} \end{cases} \quad (9)$$

According to eq. (9), the angle between the leek plant and the ground in the clamping-cutting stage is:

$$\beta_2 = \arctan \frac{v_s t_1 \sin \alpha + h_2 - h_1}{v_s t_1 \cos \alpha - l_g} \quad (10)$$

According to eq. (10), the main parameters affecting the posture of leek plants during the clamping-cutting process are the linear speed of clamping conveying belt v_s , the height of cutting knife from the ground h_1 , the distance between clamping point A and the front end of the cutting knife l_g , and the angle between clamping conveying belt and horizontal plane α . Among them, the smaller the angle α between the clamping conveying belt and the horizontal plane. The smaller the inclination angle β_2 , the more inclined the clamping position of the clamping conveying belt relative to plant stems, the more unstable the clamping, and the greater the possibility of the clamping stem and leaf damage. If the angle α is too large, it may affect the overall height of the machine and interfere with the harvesting process (Hou et al., 2023). Research on the direction of stalk cutting showed that the cutting resistance and power consumption of skew cutting were reduced by 60% and 30% compared with perpendicular cutting. Using the skew cutting method at small angle to harvest vegetables with high water content such as leek can reduce damage to plants. In this study, the angle between the clamping conveying belt and the horizontal plane $\alpha = 20^\circ$, and the cutting knife installation position $l_g = 10$ mm, so as to ensure that clamping precedes cutting during harvester operation.

Field experiment

The prototype of double-row electric leek harvester was field-tested on July 22, 2024 at Shandong University of Technology in Zibo City, Shandong Province. The experiment equipment included the harvester, tape measure, stopwatch and other tools. The field experiment process is shown in Fig. 9.



Fig. 9 - Process of field experiment

This paper refers to the “Technical Specification for Quality Evaluation of Hand-held Stem and Leafy Vegetable Harvesters” (Ministry, 2020) and “Leafy Vegetable Harvesters” (Ministry, 2024), and related literature (Zhang *et al.*, 2022b; Kang *et al.*, 2020). Operation damage rate Z_s were used as performance evaluation experiment indexes of double-row electric leek harvester. The calculation formula is as follows:

$$Z_s = \frac{S_s}{S_j} \times 100\% \quad (11)$$

where: Z_s is the operation damage rate, %; S_s is the number of damaged leek plants; S_j is the number of effective clamping conveying leek plants.

According to preliminary experiments and theoretical analysis, machine's forward speed v_j , cutting speed v_g and conveying belt speed v_s , which affect operation damage rate, are selected as experimental factors. The experimental factors and levels are shown in Table 2.

Table 2

Experimental factors and levels				
Level	Machine's forward speed v_j (m/s)	Cutting speed v_g (m/s)	Conveying belt speed v_s (m/s)	
1	0.35	0.77	0.49	
0	0.3	0.66	0.42	
-1	0.25	0.55	0.35	

RESULTS

Design-Expert software was used to conduct a secondary rotary combination design experiment on the experimental data. The experimental schemes and results are shown in Table 3.

Table 3

Experimental schemes and results				
Number	v_j (m/s)	v_g (m/s)	v_s (m/s)	Z_s (%)
1	0.25	0.55	0.42	4.93
2	0.35	0.55	0.42	5.07
3	0.25	0.77	0.42	4.92
4	0.35	0.77	0.42	5.1
5	0.25	0.66	0.35	4.94
6	0.35	0.66	0.35	5.07
7	0.25	0.66	0.49	4.93
8	0.35	0.66	0.49	5.11
9	0.3	0.55	0.35	4.98
10	0.3	0.77	0.35	5.02
11	0.3	0.55	0.49	5.01
12	0.3	0.77	0.49	5.05
13	0.3	0.66	0.42	4.86
14	0.3	0.66	0.42	4.84
15	0.3	0.66	0.42	4.85
16	0.3	0.66	0.42	4.89
17	0.3	0.66	0.42	4.9

The experimental results were analyzed using Design-Expert software. The significance of the regression equation model was verified through analysis of variance and regression coefficient experiments. The results are presented in Table 4.

Table 4

Variance analysis of damage rate					
Source	Sum of Squares	Degree of freedom	Mean Square	F-value	p-value
Model	0.1251	9	0.0139	29.9	< 0.0001
v_j	0.0496	1	0.0496	106.69	< 0.0001
v_g	0.0013	1	0.0013	2.69	0.1451
v_s	0.001	1	0.001	2.18	0.1836
$v_j v_g$	0.0004	1	0.0004	0.8602	0.3845
$v_j v_s$	0.0006	1	0.0006	1.34	0.2843
$v_g v_s$	0	1	0	0	1
v_j^2	0.019	1	0.019	40.95	0.0004
v_g^2	0.0205	1	0.0205	44.05	0.0003
v_s^2	0.0251	1	0.0251	54.04	0.0002
Residual	0.0033	7	0.0005		
Lack of Fit	0.0006	3	0.0002	0.2861	0.8341
Pure Error	0.0027	4	0.0007		
Cor Total	0.1284	16			

According to Table 4, the regression equation for the damage rate Z_s was obtained by excluding the insignificant terms from the regression equation.

$$Z_s = 12.776 - 17.265v_j + 26.9v_j^2 + 5.764v_g^2 + 15.765v_s^2 \quad (12)$$

The interaction between any two factors and their effect on Z_s was analyzed by fitting the response surface, with any factor in eq. (12) set to the zero level, as shown in Figure 8.

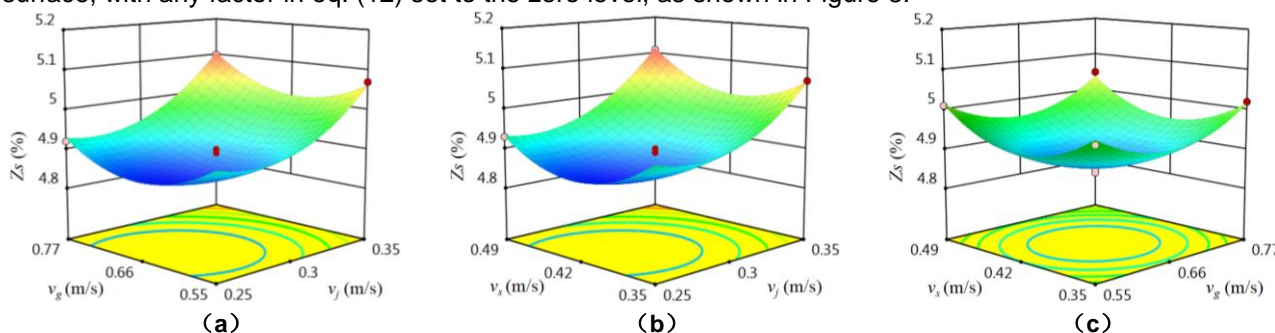


Fig. 8 - Response surfaces effect of factor interaction on experiment indicators

As shown in the response surface in Fig. 8, the factors affecting the operation damage rate from the largest to the smallest are machine's forward speed, cutting speed and conveying belt speed.

The Design-Expert software regression equation model was used to find the optimal parameters for the experiment impact factors: v_j at 0.3 m/s, v_g at 0.66 m/s, and v_s at 0.42 m/s. Under the optimal combination of parameters, the minimum operation damage rate Z_s was 4.84%.

The average operating damage rate was 4.87%, less than 5%, which meets the design requirements. The damage was mainly due to the tearing and breakage of the stubble, and the crushing damage caused by the plants detaching from the clamping conveying device at the end of the clamping conveying.

CONCLUSIONS

(1) Based on the agronomic and mechanized harvesting requirements of leek cultivation, a double-row electric leek harvester was developed. The machine primarily consists of travel, cutting, dividing, clamping, and conveying devices. It is capable of performing cutting, conveying, and collecting operations in a single pass, thereby reducing labor intensity and significantly improving harvesting efficiency.

(2) A clamping conveying device was designed, and the working conditions required to prevent leek plants from falling, clogging, or being crushed during the clamping and conveying process were analyzed. Based on this analysis, the structural parameters and conveying speed of the device were determined.

(3) A kinematic model of the single-acting reciprocating cutting device was established, and the structural parameters of the cutting mechanism were determined. The critical conditions required for smooth and complete cutting without omissions were analyzed, leading to the determination of the optimal working parameters for the cutting device.

(4) A field experiment and performance testing method were proposed, and the field experiment was successfully conducted. During both the harvesting operation and transfer process, the harvester met the operational and mobility requirements, demonstrating good power performance and passing ability. The results of the field experiment showed that the average operational damage rate was 4.87%, meeting the actual production and mechanized harvesting requirements for leek crops.

ACKNOWLEDGEMENT

This study was supported by grants from the Key R&D Program of Shandong Province, China (2022CXGC010611).

REFERENCES

- [1] Binxing Xu, Yongsheng Chen, Chunsong Guan, Feng Yu, Hua Chen, (2024), Design and experiment of disc-cutting device for leek harvester (韭菜收获机圆盘切割装置设计与试验), *Journal of Chinese Agricultural Mechanization*, vol.45, no.2, pp.79-83+100.
- [2] Dong Liu, Hongru Xiao, Yue Jin, (2019), Research status and development countermeasures of leaf vegetable orderly harvesting machinery (叶类蔬菜有序收获机械的研究现状及发展对策), *Jiangsu Agricultural Sciences*, vol.47, no.3, pp.27-31.
- [3] Dong Zhang, Dong Wei, Yufei Zhang, Zengchan Zhou, Tao Yao, Haowen Zhang, (2022a), Development and Application of Leek Harvester (韭菜收获机开发与应用), *Agricultural Engineering*, vol.12, no.10, pp.13-16.
- [4] Haitong Li, Tao Jiang, Zhuohuai Guan, Senlin Mu, Chongyou Wu, Min Zhang, (2023), Design and Experiment of Row following Rapeseed Stalks Orderly Harvester (对行式油菜茎秆有序收获机设计与试验), *Transactions of the Chinese Society for Agricultural Machinery*, vol.54, no.11, pp.92-101.
- [5] Jinji Zhao, (2021), Development of DC electric leek harvester (直流电动韭菜收割机研制), *Farm Machinery*, no.6, pp.88-89+96.
- [6] Jialin Hou, Chao Li, Zhilong Zhang, Tianhua Li, Yuqiang Li, Yanqiang Wu, (2021), Design and test of double-row walking garlic combine harvester, *Transactions of the Chinese Society of Agricultural Engineering*, vol.37, no.12, pp.1-11.
- [7] Jiwei Li, Lina Bian, Huanle Zhai, Guozheng Chang, (2021), Straightening Device Technology of Leek Harvester and Development of New Straightening Device (韭菜收割机扶禾装置技术及新装置研制), *Journal of Anhui Agricultural Sciences*, vol.49, no.21, pp.223-226+230.
- [8] Jing Zhang, Jun Wang, Dongdong Du, Sifang Long, Yongwei Wang, Xinrong You, (2022b), Design and Experiment of Crawler Self-propelled Single-row Harvester for Chinese Cabbage (履带自走式单行大白菜收获机设计与试验), *Transactions of the Chinese Society for Agricultural Machinery*, vol.53, no.12, pp.134-146.
- [9] Liangliang Zou, Xuemei Liu, Jin Yuan, Dong Xiaohua, (2022), Research progress in mechanized harvesting technology and equipment of leafy vegetables (叶菜机械化收获技术与装备研究进展), *Journal of Chinese Agricultural Mechanization*, vol.43, no.6, pp.15-23.
- [10] Lu Xin, Mei Zhang, Guisen Xun, Jiasheng Wang, (2024), Design and Test of Chinese Chives Combine Harvester (韭菜联合收获机的设计与试验), *Journal of Agricultural Mechanization Research*, vol.46, no.1, pp.96-100.
- [11] Ministry of Agriculture and Rural Affairs of the People's Republic of China (2020) *Technical specification of quality evaluation for hand-held stalk and leaf vegetable harvester*: NY/T 3664-2020. China Agriculture Press. <https://www.sdtdata.com/fx/fmrule/tsLibCard/182698.html>
- [12] Ministry of Agriculture and Rural Affairs of the People's Republic of China (2024) *Leaf vegetable harvester*: DG/T 249-2024. http://www.moa.gov.cn/govpublic/NYJXHGLS/202404/t20240430_6454721.htm
- [13] Na Liu, Jianfei Zhang, Hairong Jin, Wenyu Tong, Subo Tian, Xiaofeng Ning, (2023), Design and experiment on *Allium mongolicum* Regel harvester (蒙古韭收割机设计与试验), *Journal of Chinese Agricultural Mechanization*, vol.44, no.7, pp.33-39.
- [14] Qi Liu, Bin Chen, Songlin Sun, Mingtao Xiao, Chaoran Sun, (2022), Research on Mechanical Characteristics of Clamping Conveyor for Leafy Vegetables (叶类蔬菜有序收获夹持输送的力学特性研究), *Journal of Agricultural Science and Technology*, vol.24, no.4, pp.116-125.

- [15] Shanglong Xin, Wuyun Zhao, Linrong Shi, Fei Dai, Bin Feng, Zhibin Yan, Deyu Lyu, (2023), Design and experiments of the clamping and conveying device for the vertical roller type corn harvesting header (立辊式玉米收获割台夹持输送装置设计与试验), *Transactions of the Chinese Society for Agricultural Machinery*, vol.39, no.9, pp.34-43.
- [16] Weiqing Su, Panpan Yuan, (2020), Study on the Design of a Leek Harvester in Greenhouse (温室韭菜收割机设计研究), *Agricultural Science Technology and Equipment*, Hunan/China, no.2, pp.19-21.
- [17] Wei Wang, Xiaolan Lv, Shilin Wang, Daipeng Lu, Zhongyi Yi., (2021), Current status and development of stem and leaf vegetable mechanized harvesting technology (茎叶类蔬菜机械化收获技术研究现状与发展), *Journal of China Agricultural University*, vol.26, no.4, pp.117-127.
- [18] Wu Zhang, Xuefeng Song, Fengwei Zhang, Xiaoqing Cao, Panlou Yang, Qiang Xie, (2024a), Design and simulation analysis of leek harvester (手扶式韭菜收割机的设计), *Forestry Machinery & Woodworking Equipment*, vol.52, no.1, pp.64-70+75.
- [19] Wendong Zhang, Xueran Yang, Hongen Guo, Rui Sun, Yumeng Huo, Qinghai He, (2024b), Design and experiment of track-type and self-propelled chive harvester (履带型自走式韭菜收割机设计与试验), *Agricultural Equipment and Vehicle Engineering*, vol.62, no.11, pp.1-6+13.
- [20] Yongnian Zhang, Yinyan Shi, Xiaochan Wang, Odhiambo M., Guoxiang Sun, (2016), Design on flexible champing-conveying mechanism of orderly harvester for stems-leafy vegetables (茎叶类蔬菜有序收获机柔性夹持输送机构设计), *Journal of Chinese Agricultural Mechanization*, vol.37, no.9, pp.48-51.
- [21] Yinyan Shi, Man Chen, Xiaochan Wang, Yongnian Zhang, Odhiambo M., (2017), Dynamic Simulation and Experiments on Artemisia selengensis Orderly Harvester Cutter (芦蒿有序收获机切割器动力学仿真与试验), *Transactions of the Chinese Society for Agricultural Machinery*, vol.48, no.2, pp.110-116.
- [22] Yuanjuan Gong, Yulong Feng, Chuangye Li, Na Guo, Yufeng Liu, Xiaofeng Ning, (2018), Research Actuality of Leek Harvester and its Developing Countermeasures (韭菜收割机械研究现状及发展趋势), *Journal of Agricultural Mechanization Research*, vol.40, no.10, pp.262-268.
- [23] Yuewen Xu, Wei Xie, Di Liu, Teng Chen, Yang Zhang, Shangkun Dong, Haibo Deng, (2020), Status and Development of Stem leaf Vegetable Harvester (茎叶类蔬菜收获机的研究现状及发展对策), *Agricultural Engineering and Equipment*, Hunan/China, vol.47, no.1, pp.20-26.
- [24] Yulong Feng, Xuchao Yin, Hairong Jin, Wenyu Tong, Xiaofeng Ning, (2023), Design and experiment of a Chinese chive harvester, *International Journal of Agricultural and Biological Engineering*, vol.16, no.2, pp.125–131.
- [25] Yiyin Shan, Qingxi Liao, Xingyu Wan, Jiacheng Yuan, Lei Chen, Yitao Liao, (2024), Design and Experiment of Self-propelled Six-row Harvester for Oilseed Rape Shoot (油菜薹对行自走式收获机设计与试验), *Transactions of the Chinese Society for Agricultural Machinery*, vol.55, no.8, pp.93-104.

DESIGN AND SIMULATION ANALYSIS OF KEY COMPONENTS OF GRASS CRUSHER

牧草粉碎机关键部件设计与仿真分析

Tao CHEN¹⁾, Shu-juan YI^{*1)}, Song WANG¹⁾, Wen-sheng SUN¹⁾¹⁾College of Engineering, Heilongjiang Bayi Agricultural University, Daqing/P.R.China

Tel: +86-459-13836961877; E-mail: yishujuan_2005@126.com

Corresponding author: Shu-juan Yi

DOI: <https://doi.org/10.35633/inmateh-75-48>**Keywords:** Pasture; Grinding machine; Design; Simulation analysis**ABSTRACT**

In view of the problems of low efficiency, poor crushing quality and inapplicability to high water content forage, the cutter and crusher rotor of hammer type forage grinder was designed, the cutter and crusher process was analyzed theoretically, and the parameters of cutter and crusher rotor were determined. The modal analysis of the cutting and crushing rotor was carried out by ANSYS Workbench, to verify the rationality of the rotor structure. The alfalfa with water content of 65% was taken as the processing object, and the quadratic orthogonal rotation combination test was carried out with the output speed of motor, sieve diameter and feeding amount as the test factors, and the productivity and silking rate as the evaluation indexes. Through the analysis of variance and target optimization of the test results by Design-Expert 12.0 software, the regression equation between the test factors and the evaluation index was obtained. With the goal of maximizing the productivity and silking rate at the same time, the output speed of the motor, the diameter of the sieve and the feeding amount were solved by multi-objective optimization, and the optimal parameter combination was determined as follows: the output speed of the motor is 443.77r/min, the diameter of the sieve is 14mm, and the feeding amount is 1.27kg/s. The verification test shows that the productivity is 5065.98 kg/h, and the silk rates is 94.87%. The device has high crushing efficiency, good quality, and can crush high water content forage, which meets the design requirements of forage mill.

摘要

针对现有的牧草粉碎机效率低、粉碎质量差、对高含水率牧草不适用等问题,对锤片式牧草粉碎机的铡切和粉碎转子进行了创新设计,对铡切和粉碎过程进行了理论分析,确定了铡切和粉碎转子的参数。利用 ANSYS Workbench 对铡切和粉碎转子进行了模态分析,验证转子结构的合理性。将含水率为65%的苜蓿作为加工对象,进行了以电机输出转速、筛孔直径、喂入量为试验因素,以生产率和丝化率为评价指标的二次正交旋转组合试验。通过 Design-Expert 12.0 软件对试验结果进行了方差分析及目标优化,得到了试验因素与评价指标之间的回归方程,以生产率和丝化率同时最大化为目标,对电机输出转速、筛孔直径、喂入量进行多目标寻优求解,确定最优参数组合为:电机输出转速 443.77r/min、筛孔直径 14mm、喂入量 1.27kg/s,验证试验表明,生产率为 5065.98kg/h、丝化率为 94.87%;该装置粉碎效率高、质量好,而且能够粉碎高含水率牧草,满足牧草粉碎机设计要求。

INTRODUCTION

As one of the important links of grass processing, crushing quality has an important impact on processing cost and livestock digestion effect (Wu et al., 2022; Wang et al., 2017). Crushing is to cut off the grass and expose its internal nutrients, which can not only improve palatability, but also increase the contact area with the stomach juice of livestock, shorten the rumination and chewing time, and reduce the energy consumed by the chewing of livestock. The crushed grass is easy to chew and has a good taste, which promotes the absorption of nutrients by livestock (Fang et al., 2021; Huan et al., 2021). The length of forage required by ruminants is 30~50mm, and crushing too long or too short is not conducive to digestion and absorption. In order to prevent too short after stirring cutting, the length of the crushed grass should be 50~70mm (Fan et al., 2021; Zheng et al., 2016; Li et al., 2019).

¹⁾Tao Chen, Ph.D.; Shu-juan Yi, Prof. Ph.D.; Song Wang, Ph.D.; Wen-sheng Sun, Ph.D.;

Grass processing can be divided into shredding processing, crushing processing and kneading processing according to the crushing form, and the corresponding models are guilloff type mill, hammer type mill, kneading type mill, etc. (Zhang *et al.*, 2024; Liu *et al.*, 2019). The cut type crusher breaks the grass by cutting, although it has the advantages of simple structure, low power consumption and high productivity, but the processed broken grass is mostly round rod, and there are hard joints, which will lead to indigestion and palatability of livestock, which is not conducive to digestion and absorption of livestock (Jiang *et al.*, 2019). Hammer mill first crushed the grass to a certain extent through the impact of the hammer, and then the grass was thrown to the kneading board and sieve plate at a faster speed in the crushing room, which was further crushed by the collision of the kneading board and the rubbing of the sieve plate. The crushing efficiency was high and the adaptability was wide, but the crushed grass was too fine, which could not make its fiber better retained. As a result, it has a low volume and cannot be stored for a long time (Liu *et al.*, 2011). Under the kneading action of the high-speed rotating hammer and tooth plate, the crushed grass is broken into soft and fluffy filamentous segments, exposing nutrients, increasing the contact area with the digestive system of livestock, and promoting digestion and absorption (Ma *et al.*, 2016).

In terms of forage processing machinery, foreign countries have complete types, relatively perfect functions and mature technologies, but they are mainly used in large-scale farmland and pasture, and are not suitable for the miniaturization and convenience of forage processing machinery in small-scale breeding areas in China. Domestic scholars have been committed to the research of grass processing machinery, more and more new models continue to emerge. Wang Defu *et al.*, (2017), used high-speed camera technology to analyze the crushing mechanism of the hammer mill, and conducted experimental research on crushing performance. They found that the crushing forms of the hammer mill were mainly percussion crushing, impact crushing and rubbing crushing, and the impact crushing and rubbing crushing had a greater impact in the crushing process. It is concluded that the linear speed of the end of the hammer and the water content of the material have great influence on the crushing effect of the hammer mill. Wang Tiejun *et al.* (2021), designed a feeding-adjustable straw breaking and kneading machine to solve the problem that the existing machine could not adapt to the whole bundle manually packed and the small square bundle mechanically pressed corn straw simultaneously. Through the analysis of the force and movement of straw in each device of the machine, the key structure of the whole machine is designed and matched with the drive system, and the kneading performance test is carried out to realize the localized kneading treatment of scattered bale straw in the village. You Yong *et al.* (2021) designed a 4-row herringbone roller crushing device based on the agronomic requirements of king grass harvester crushing, combined with the characteristics of strong tillering ability, large biomass and high-water content of king grass. The main structure and parameters of the crushing device are determined by theoretical analysis and calculation. The test shows that the length of the king grass broken by the device is uniform and the qualified rate of the stalk broken is high, which can meet the requirements of the king grass broken during the harvest period. Although after years of painstaking research by many scholars, the kneading quality of forage grass has been improved to a certain length, due to the strong toughness of forage grass with high moisture content, the force required when it is broken by blows and other effects is greater, and the whole forage grass is easy to wrap around the rotor when it is crushed, causing blockage. Therefore, the existing grinding machine still has some problems, such as low efficiency, poor kneading quality, and not suitable for forage with large moisture content.

In this paper, taking alfalfa as the processing object, the cutting and crushing rotors of hammer forage crusher are innovated. The forage is cut before it is crushed, and it is cut into small segments of certain length by means of cutting rotor. Thus, the crushing quality and production efficiency can be improved, and the high-water content forage can be crushed.

MATERIALS AND METHODS

Structure and working principle

The cutting and crushing combined grass crusher is mainly composed of motor, frame, conveying mechanism, feeding mechanism, cutting mechanism, crushing mechanism, screening mechanism, transmission system and other parts. The structure is shown in Fig.1.

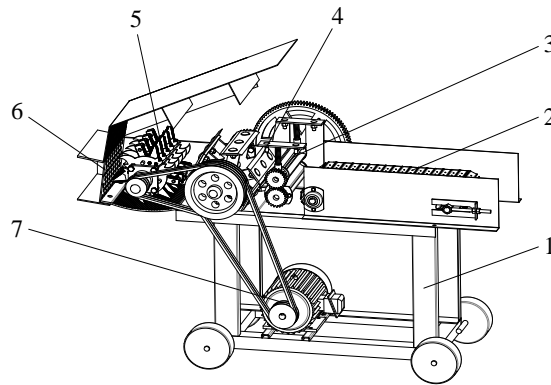


Fig.1 - Structure diagram of cutting and crushing cooperative grass crusher

1. Frame; 2. Conveying mechanism; 3. Feeding mechanism; 4. Cutting mechanism; 5. Crushing mechanism; 6. Sieve plate; 7. Motor

During operation, the whole grass is transported to the feeding mechanism through the conveying mechanism, and the feeding mechanism evenly feeds the grass into the cutting room to complete the feeding. The cutting mechanism breaks the grass into small segments of a certain length to complete the cutting. The crushing mechanism breaks the cut grass into filaments and completes the crushing. The crushed grass that meets the crushing length is thrown to the outside of the body through the screen plate through the dual action of the air flow generated by the rotation of the crushing rotor and the centrifugal force to complete the screening and throwing.

Force analysis and mechanism design of alfalfa during cutting process

The force analysis of alfalfa during cutting process is shown in Fig.2.

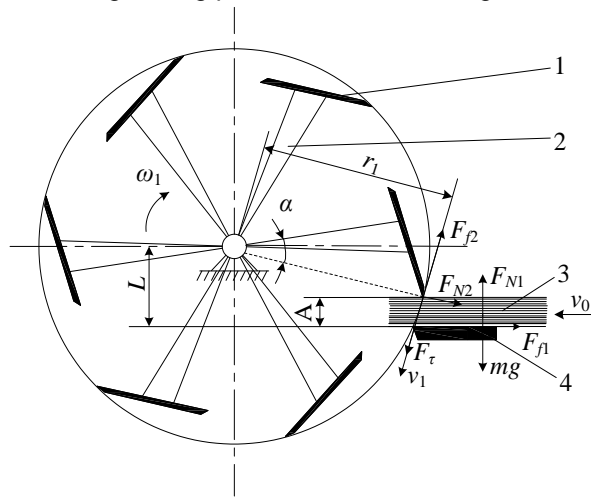


Fig. 2 - Analysis of the force and motion of alfalfa during the cutting process

1. Moving cutter; 2. Knife holder; 3. Alfalfa; 4. Fixed cutter

According to the cutting effect of moving and fixed knives on alfalfa, and the analysis of the force and movement of alfalfa in the process of cutting, the necessary conditions for cutting alfalfa are obtained:

$$F_{\tau} \sin \alpha \geq F_{f1} + F_{f2} \sin \alpha + F_{N2} \cos \alpha \tag{1}$$

It can be seen from Fig.2 that:

$$mg + F_{\tau} \cos \alpha + F_{N2} \sin \alpha = F_{N1} + F_{f2} \cos \alpha \tag{2}$$

$$F_{f1} = \mu_1 F_{N1} \tag{3}$$

$$F_{f2} = \mu_2 F_{N2} \tag{4}$$

where: α is the sliding cutting angle, ($^{\circ}$); m is alfalfa mass, kg; g is acceleration of gravity, m/s^2 ; F_{τ} is the cutting force of cutter on alfalfa, N; F_{N1} is the supporting force of cutter on alfalfa, N; F_{N2} is the positive pressure of a cutter on alfalfa, N; F_{f1} is the friction of cutter against alfalfa, N; F_{f2} is cutter friction on alfalfa, N; μ_1 is the friction factor between alfalfa and moving cutter; μ_2 is the friction factor between alfalfa and fixed cutter.

In this study, the design of the moving cutter and fixed cutter use the same material, the alfalfa and their friction factors are the same, that is, $\mu_1=\mu_2=\mu$, the joint vertical (1) ~ (4) can be obtained:

$$\mu + \frac{F_{N2} \cos(2\alpha) + mg \sin \alpha}{F_{N1} \cos \alpha} \leq \tan \alpha \tag{5}$$

$$\frac{F_{N2} \cos(2\alpha) + mg \sin \alpha}{F_{N1} \cos \alpha} \geq 0 \tag{6}$$

If formula (5) is established, the tangent value of alfalfa friction angle $\tan \varphi \leq \tan \alpha$ can be obtained, and the friction angle of alfalfa is generally $\varphi=24^\circ\sim 32^\circ$ (Chen et al., 2023), that is, $\alpha \geq 32^\circ$.

In order to facilitate the balanced sliding of alfalfa and reduce power consumption, the cutter should be inclined to install, but the inclination angle is too large to affect the dynamic balance and vibration, so the sliding angle is designed to be 32° , the circumferential interval of 60° is arranged with 1 blade cutter, the cutter shaft is arranged with 6 blades, guilloff cutter structure is shown in Fig.3.

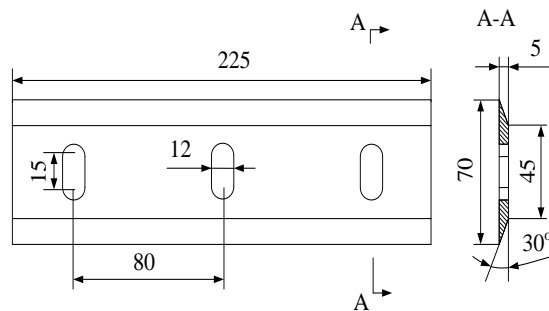


Fig. 3 - Structure diagram of the moving cutter

Force analysis and mechanism design of alfalfa in crushing process

The forces in alfalfa crushing process are shown in Fig.4.

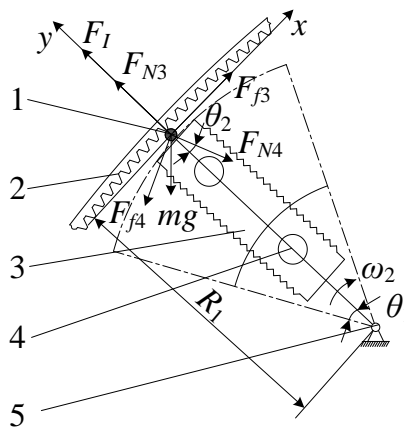


Fig. 4 - Stress Analysis of Alfalfa Silk Rolling Process
1. Alfalfa; 2. Kneading board; 3. Hammer; 4. Pin; 5. Crushing shaft

According to D 'Alembert's principle, alfalfa should meet the equilibrium state at the moment of crushing, and the equilibrium equation is established:

$$\begin{cases} \sum F_x = F_{f3} + F_{N4} \sin \theta_2 - F_{f4} \cos \theta_2 - mg \cos \theta_1 = 0 \\ \sum F_y = F_1 + F_{N3} - F_{N4} \cos \theta_2 - F_{f4} \sin \theta_2 - mg \sin \theta_1 = 0 \end{cases} \tag{6}$$

$$F_1 = m\omega_2^2 R_1 \tag{7}$$

$$F_{f3} = \mu_3 F_{N3} \tag{8}$$

$$F_{f4} = \mu_4 F_{N4} \tag{9}$$

Equations (6) ~ (9) can be obtained simultaneously:

$$\left\{ \begin{aligned} F_{f3} &= mg \cos \theta_1 + \left\{ \left[\mu_3 m \omega_2^2 R_1 + mg (\cos \theta_1 - \mu_3 \sin \theta_1) \right] \right. \\ &\quad \left. (\mu_4 \cos \theta_2 - \sin \theta_2) [(1 + \mu_3 \mu_4) \sin \theta_2 + (\mu_3 - \mu_4) \cos \theta_2]^{-1} \right\} \\ F_{f4} &= \mu_4 \frac{\mu_3 m \omega_2^2 R_1 + mg (\cos \theta_1 - \mu_3 \sin \theta_1)}{(1 + \mu_3 \mu_4) \sin \theta_2 + (\mu_3 - \mu_4) \cos \theta_2} \end{aligned} \right. \quad (10)$$

where:

ω_2 is the hammer angular velocity, rad/s; θ_1 - the horizontal angle between the alfalfa segment and the axis of the crushing shaft, ($^\circ$); θ_2 - the angle between the alfalfa segment and the axis of the kneading shaft and the direction of the kneading board's supporting force on the alfalfa, ($^\circ$); F_I - the centrifugal force in alfalfa section, N; F_{N3} - the supporting force of the hammer on alfalfa segment, N; F_{N4} - the support force of knead board on alfalfa segment, N; F_{f3} - the friction force of hammer against alfalfa segment, N; F_{f4} - friction force of kneading board on alfalfa segment, N; R_1 - alfalfa section turning radius, mm; μ_3 - friction factor between alfalfa segment and hammer piece; μ_4 - friction factor between alfalfa segment and kneading board.

Formula (10) shows that the friction force F_{f3} and F_{f4} during the grinding of alfalfa are related to the friction factor, position and angular velocity, etc. The trapezoidal teeth on the surface of the kneading plate near the hammer can increase the friction factor. The angular speed of the hammer is directly determined by the speed of the grinding shaft. When the machine power and transmission ratio are constant, the speed of the grinding shaft is mainly affected by the output speed of the motor. In order to clarify the influence of the output speed of the motor on the grinding effect of alfalfa, this paper optimizes it through experiments.

The hammer is designed as a rectangular zigzag shape, which increases the friction between the hammer and the material while striking and crushing the alfalfa, and can also produce better sliding and stabbing effects. The serrated knife is hexagonal, and the cutting edges on both sides of the knife are made into serrated edges to improve the strength and wear resistance of the blade. The structure of the hammer and serrated knife is shown in Fig.5.

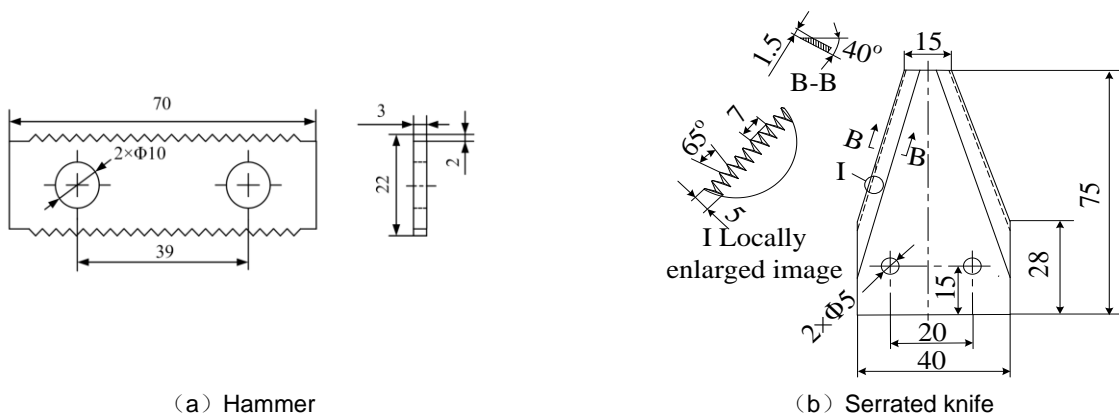


Fig. 5 - Structure diagram of hammer and serrated knife

Modal analysis

ANSYS Workbench software is used to analyze the mode of the cutting rotor and crushing rotor of the grinder, analyze its vibration characteristics and deformation, and ensure its reliability in the working process.

The modal analysis results of the cutting rotor are shown in Table 1 and Fig. 6.

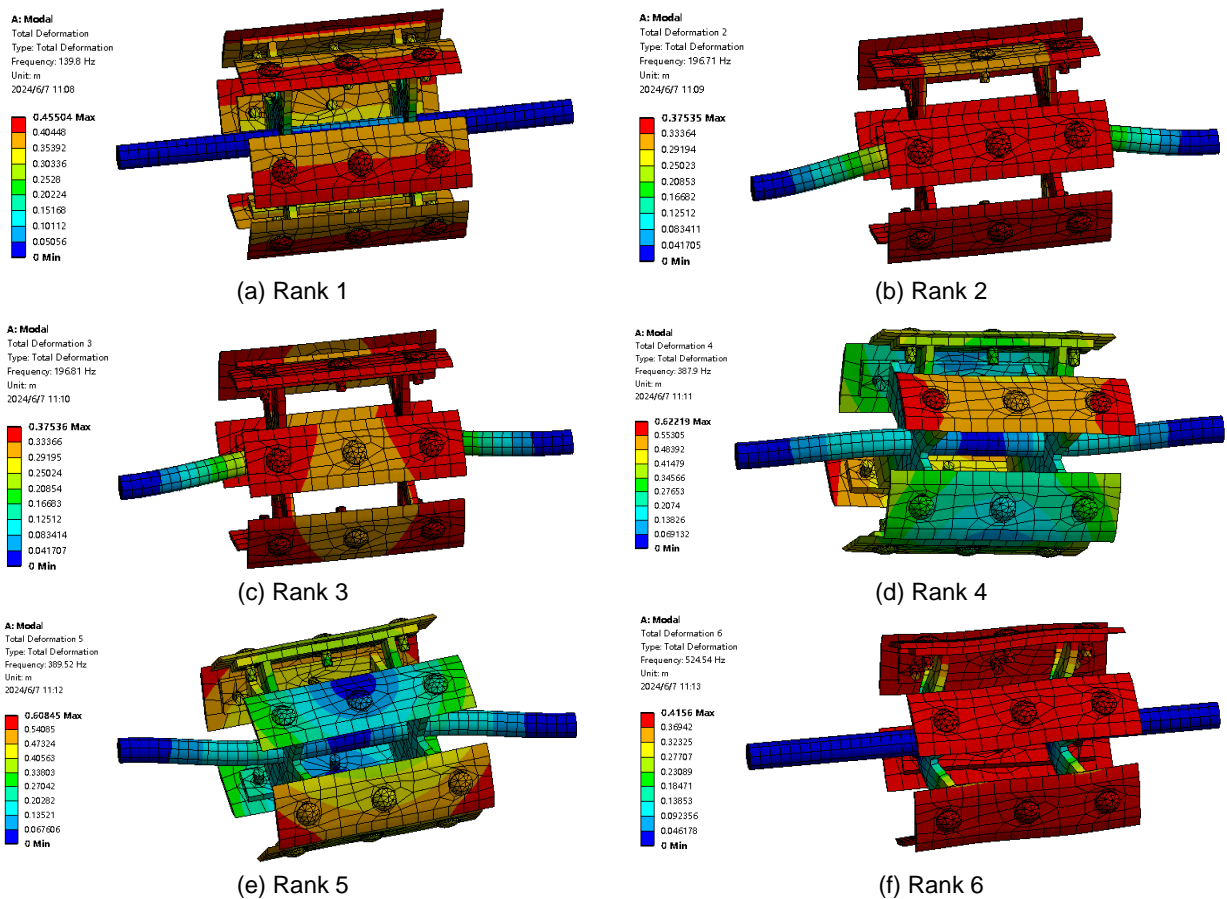


Fig. 6 - Cloud image of the first 6 modes of the cutting rotor

As can be seen from the Fig.6, the first-order vibration mode is represented by the deformation of the working edge surface of the cutter. The second order mode mainly shows the overall deformation of the rotor. The third order mode is mainly characterized by cutting tool deformation. The 4th-order mode mainly shows the deformation of cutting tool and tool holder. The 5th order mode is mainly tangential bending deformation. The 6th-order mode mainly shows the deformation of cutting tool and tool holder.

Table 1

Results of the first six modes of cutting rotor

Order	Intrinsic frequency/Hz	Maximum deformation/m	Main vibration mode
1	139.8	0.46	The working edge surface of the cutter is deformed
2	196.71	0.38	Integral rotor deformation
3	196.81	0.38	Cutter deformation
4	387.9	0.62	The cutter and tool holder are deformed
5	389.52	0.61	The cutting shaft is bent and deformed
6	524.54	0.42	The cutter and tool holder are deformed

In the process of rotor rotation, the excitation source mainly comes from self-rotation excitation. When the excitation frequency exceeds the natural frequency, the total performance of the rotor will have the risk of failure. The relation between the rotational speed of rotor and excitation frequency is

$$n = 60f \tag{11}$$

where: n is rotor assembly speed, r/min; f is rotary excitation frequency, Hz

The maximum working speed of the cutting rotor is 300r/min, and the maximum rotation excitation can be calculated to be 5Hz. Lower than the first order natural frequency 139.8Hz. Therefore, the designed cutter rotor can effectively avoid resonance phenomenon during high-speed rotation.

The modal analysis results of the crushed rotor are shown in Table 2 and Fig. 7.

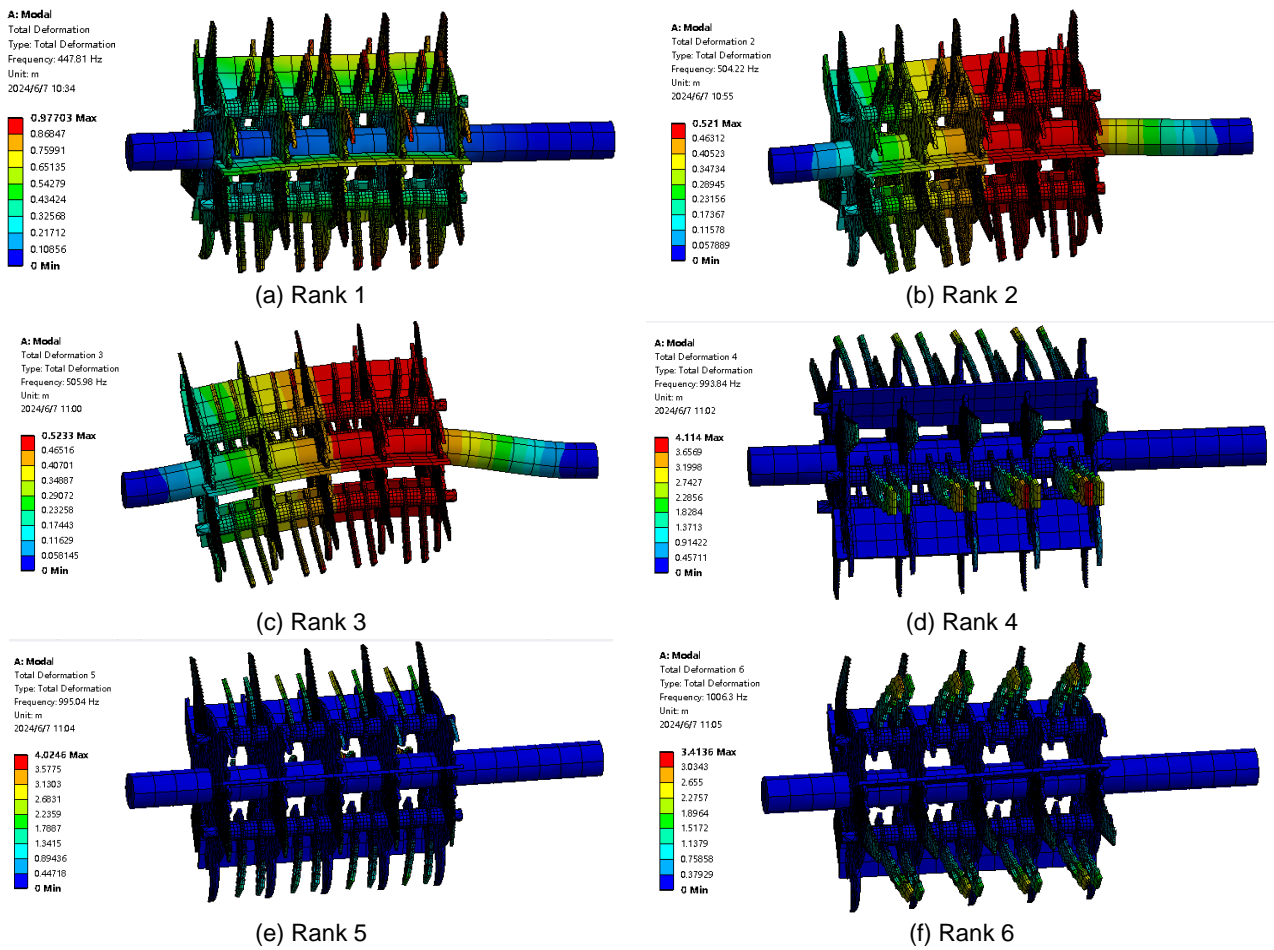


Fig. 7 - Cloud diagram of the first 6 orders of modal shapes of the crushing rotor

As can be seen from the Fig.7, the first-order vibration mode is manifested as the deformation of the outer edge of the hammer plate and the hammer frame plate. The second order mode mainly shows the deformation of rotor end and serrated knife. In the third order mode, the rotor is deformed as a whole. The fourth order vibration mode is mainly hammer deformation. The 5th order vibration mode is mainly hammer deformation. The 6-order vibration mode is mainly the hammer and serrated knife deformation.

Table 2

Results of the first 6 modes analysis of the crushed rotor			
Order	Intrinsic frequency/Hz	Maximum deformation/m	Main vibration mode
1	447.81	0.97	The edge of the hammer plate and the hammer frame plate is deformed
2	504.22	0.52	The rotor end and serrated knife are deformed
3	505.98	0.52	Integral rotor deformation
4	993.84	4.11	Hammer deformation
5	995.04	4.02	Hammer deformation
6	1006.3	3.41	Hammer and serrated knife deformed

The maximum rotational speed designed for the grinding rotor is 800r/min, and the maximum rotational excitation calculated by formula (11) is 13.33Hz. Lower than the first order natural frequency 447.81Hz. Therefore, the designed grinding rotor can effectively avoid resonance during high-speed rotation.

RESULTS AND DISCUSSIONS

The design of the kneading machine prototype was made and the performance test was carried out. Alfalfa was processed and collected at the dry grass planting base in Duerbert County, Daqing City, Heilongjiang Province. The alfalfa collected was free of diseases, pests and obvious mechanical damage. The average moisture content of alfalfa was determined by random sampling to be 65%. The test was carried out in the crop harvest Laboratory of Heilongjiang Bayi Agricultural University, as shown in Fig.8.



Fig. 8 - Test bench for cutting and crushing cooperative silk kneading machine

1. Crusher; 2. Feed conveyor belt

Productivity y_1

The weighed straw was fed, the time required to crush all the straw was recorded, and the productivity y_1 was calculated as:

$$y_1 = \frac{m}{t} \times 3600 \quad (12)$$

where: m is quality of straw for test, kg; t is test time, s.

Silking rate y_2

Samples were collected at the outlet at the same time interval for 3 times, each time no less than 200g. All samples were mixed and weighed. Qualified alfalfa silk was screened and weighed, and the silking rate y_2 was calculated:

$$y_2 = \frac{m_2}{m_0} \times 100\% \quad (13)$$

where: m_2 is quantity of alfalfa silk in sample, g; m_0 is alfalfa sample quality, g

The code of test factors is shown in Table 3, and the test scheme and results are shown in Table 4.

Table 3

Factor level coding			
Coding	Factor		
	Motor output speed x_1 (r/min)	The diameter of the screen x_2 /mm	Feeding quantity x_3 (kg/s)
1.682	500	20	2.0
1	449.3 (450)	18.8 (19)	1.8
0	375	17	1.5
-1	300.7 (300)	15.2 (15)	1.2
-1.682	250	14	1.0

Table 4

Test scheme and results						
Number	x_1	x_2	x_3	y_1 /kg·h ⁻¹	y_2 /%	
1	1	1	1	4590.21	95.84	
2	1	1	-1	4365.4	94.62	
3	1	-1	1	4952.07	94.53	
4	1	-1	-1	4757.15	96.56	
5	-1	1	1	4395.94	88.51	
6	-1	1	-1	4513.76	92.68	

Number	x_1	x_2	x_3	$y_1/\text{kg}\cdot\text{h}^{-1}$	$y_2/\%$
7	-1	-1	1	4582.55	83.41
8	-1	-1	-1	4588.32	91.62
9	1.682	0	0	4470.74	95.53
10	-1.682	0	0	4200.32	83.68
11	0	1.682	0	4390.6	93.87
12	0	-1.682	0	5149.43	93.35
13	0	0	1.682	5008.91	90.08
14	0	0	-1.682	4766.34	96.41
15	0	0	0	5137.16	91.63
16	0	0	0	5117.43	93.26
17	0	0	0	4974.76	91.85
18	0	0	0	5094.31	91.71
19	0	0	0	5070.22	91.64
20	0	0	0	5168.64	90.48
21	0	0	0	5171.6	90.15
22	0	0	0	5206.13	92.01
23	0	0	0	5095.08	92.23

The variance analysis results of the productivity and silk rate regression models were obtained, as shown in Table 5 and Table 6 respectively.

Table 5

Analysis of variance of productivity regression model

Source of variance	Sum of squares	Degree of freedom	Mean sum of squares	F	P
Model	2.24×10 ⁶	9	2.49E+05	39.15	< 0.0001
x_1	79053.77	1	79053.77	12.44	0.0037
x_2	3.84×10 ⁵	1	3.84×10 ⁵	60.46	< 0.0001
x_3	36300.18	1	36300.18	5.71	0.0327
x_2^2	30312.14	1	30312.14	4.77	0.0479
x_2^2	36899.58	1	36899.58	5.81	0.0315
x_2^2	843.78	1	843.78	0.13	0.7215
x_1x_2	1.29×10 ⁶	1	1.29×10 ⁶	202.62	< 0.0001
x_1x_3	2.73×10 ⁵	1	2.73×10 ⁵	42.95	< 0.0001
x_2x_3	1.27×10 ⁵	1	1.27×10 ⁵	20.02	0.0006
Residual error	82629.68	13	6356.13		
Lack of fit	45249.84	5	9049.97	1.94	0.1936
Error	37379.83	8	4672.48		
Sum total	2.32×10 ⁶	22			

Table 6

Analysis of variance for regression model of filamentization rate

Source of variance	Sum of squares	Degree of freedom	Mean sum of squares	F	P
Model	244.9	9	27.21	42.32	< 0.0001
x_1	149.99	1	149.99	233.27	< 0.0001
x_2	3	1	3	4.67	0.0499
x_3	41.6	1	41.6	64.7	< 0.0001
x_2^2	5.76	1	5.76	8.96	0.0104
x_2^2	16.73	1	16.73	26.02	0.0002
x_2^2	6.64	1	6.64	10.33	0.0068
x_1x_2	8.22	1	8.22	12.79	0.0034
x_1x_3	7.71	1	7.71	11.99	0.0042
x_2x_3	5.12	1	5.12	7.96	0.0144
Residual error	8.36	13	0.64		
Lack of fit	1.64	5	0.33	0.39	0.8426
Error	6.72	8	0.84		
Sum total	253.26	22			

As can be seen from Table 3, the productivity regression model ($P < 0.0001$) is significant, while the lack of fit ($P = 0.1936$) is not, indicating that the model has a good degree of fitting and no misfit phenomenon occurs. The determination coefficient $R^2 = 0.9644$, the correction determination coefficient $R_{adj} = 0.9398$, which is very close to 1, and the coefficient of variation is 1.66%, indicating that the test data is reliable. The predicted value of the regression equation has a significant relationship with the actual value obtained through the analysis of the test results. The regression equation of each factor and evaluation index obtained after removing the non-significant item is shown as follows:

$$y_1 = 5115.98 + 76.08x_1 - 167.75x_2 + 51.56x_3 - 61.56x_1x_2 + 67.92x_1x_3 - 10.27x_2x_3 - 284.7x_1^2 - 131.08x_2^2 \quad (14)$$

According to Table 4, the silk rate regression model ($P < 0.0001$) was significant, while the lack of fit ($P = 0.8426$) was not, indicating that the model had a good degree of fitting and no misfit phenomenon occurred. The determination coefficient $R^2 = 0.9670$, the correction determination coefficient $R_{adj} = 0.9441$, which is very close to 1, and the coefficient of variation is 0.85%, indicating that the test data is reliable. The predicted value of the regression equation has a significant relationship with the actual value obtained through the analysis of the test results. The regression equation of each factor and evaluation index obtained after removing the non-significant item is shown as follows:

$$y_2 = 93.66 + 3.31x_1 + 0.47x_2 - 1.75x_3 - 0.85x_1x_2 + 1.45x_1x_3 + 0.91x_2x_3 - 0.72x_1^2 + 0.7x_2^2 + 0.57x_3^2 \quad (15)$$

Parameter optimization and test verification

In order to obtain the optimal parameter combination of the operating performance of the kneading machine, the multi-objective optimization algorithm in the Design-Expert 12.0 software was used to establish an optimization mathematical model with the maximum productivity and maximum silking rate as optimization objectives, as shown in Equation (16).

$$\left\{ \begin{array}{l} \max y_1(x_1, x_2, x_3) \\ \max y_2(x_1, x_2, x_3) \\ s.t. \left\{ \begin{array}{l} 250r/min \leq x_1 \leq 500r/min \\ 14mm \leq x_2 \leq 20mm \\ 1kg/s \leq x_3 \leq 2kg/s \end{array} \right. \end{array} \right. \quad (16)$$

The optimal parameter combination of the machine is as follows: the output speed of the motor is 443.77 r/min, the diameter of the screen is 14mm, the feeding amount is 1.27kg/s, the predicted productivity is 5078.28kg/h, and the silk rate is 94.93%.

In order to verify the reliability of the optimization results, the output speed of the motor was rounded to 445r/min, the feed volume was rounded to 1.3kg/s, and the screen diameter was selected to 14mm. The optimization results were verified. Each group of tests was repeated five times, and the average value of the five test results was calculated as the actual value of the evaluation index under this condition. The measured productivity is 5065.98kg/h, the silk ratio is 94.87%. The relative errors with the optimization results are 0.24% and 0.06%, respectively, indicating that the established mathematical model and the optimization results are accurate and reliable, and the kneading machine has good working performance.

CONCLUSIONS

(1) The cutting and crushing process of grass crusher was analyzed theoretically, and the key components such as cutting knife, hammer blade and serrated knife were designed. The modal analysis of cutting rotor and crushing rotor was carried out using ANSYS Workbench software, and the first 6 natural frequencies and corresponding vibration modes were obtained. The vibration mode of each order is analyzed in detail to avoid the damage of the whole machine due to the resonance phenomenon in the working process.

(2) Aiming at the simultaneous maximization of productivity and silking rate, the output speed, screen diameter and feeding amount of the motor were optimized by multi-objective solution, and the optimal parameter combination was obtained as follows: output speed of the motor was 443.77 r/min, screen diameter was 14 mm and feeding amount was 1.27 kg/s. The verification test showed that the productivity was 5065.98kg/h and the silking rate was 94.87%, which met the requirements of crushing alfalfa with high water content.

ACKNOWLEDGEMENT

This work was supported by Heilongjiang Bayi Agricultural University Graduate Innovative Research Project (YJSCX2023-Z02).

REFERENCES

- [1] Bao, L., Li, Z., & Dongxing, Z. (2011). Force and motion states of hammer mill at unloaded running (锤片式粉碎机空载运行中锤片的受力及运动状态) [J]. *Transactions of the Chinese Society of Agricultural Engineering*, Vol.27, Issue 7, pp. 123-128. Henan/China.
- [2] Decheng, W., Changbin, H., Hongjian, W., Yong, Y., & Guanghui, W. (2017). Review of Alfalfa Full-mechanized Production Technology. *Transactions of the Chinese Society for Agricultural Machinery*, Vol. 48, Issue 8, pp. 1-25. Beijing/China.
- [3] Defu, W., Mo, W., & Liqiao, L. (2017). Mechanism Analysis and Parameter Optimization of Hammer Mill for Corn Stalk (锤片式粉碎机粉碎玉米秸秆机理分析与参数优化) [J]. *Transactions of the Chinese Society for Agricultural Machinery*, Vol.48, pp. 165-171.Heilongjiang / China.
- [4] Guoqiang, F., Zhongyu, W., Baoxing, W., Jinxing, W., Heyin, D., & Jian, H. (2021). Design and Experiment of Rotary Feed Tube Hammer Grinder (旋筒供料锤式饲草粉碎机设计与试验). *Transactions of the Chinese Society for Agricultural Machinery*, Vol. 52, Issue 12, pp.43-53. Shandong / China.
- [5] Haijun, Z., Yi, Q. & Haiqing, T. (2024). Design and Experimental Optimization of V-shaped Hammer for Hammer Mill. *INMATEH-Agricultural Engineering*, Vol. 73, Issue 2, pp.191-200.Zhengjiang/China.
- [6] Kun, W., & Yuepeng, S. (2022). Research Progress Analysis of Crop Stalk Cutting Theory and Method (农作物茎秆切割理论与方法研究进展分析) [J]. *Transactions of the Chinese Society for Agricultural Machinery*, (in Chinese). Vol.53, pp. 1-20. Shandong / China.
- [7] Mei, F., Zhihong, Y., Wenjie, Z., Weifeng, L., Zhenjiang, B., & Jinbao, S. (2021). Analysis and experiments of the movement process for the shredded material of disc knife chaff cutter (盘刀式铡草机粉碎物料运动过程分析与试验). *Transactions of the Chinese Society of Agricultural Engineering*, Vol. 37, Issue 7, pp.76-84. Inner Mongolia/China.
- [8] Qian, M., Fei, L., & Manquan. Z. (2016). Working mechanism and structure optimization of hammer of rubbing machine(揉碎机揉碎机理分析及锤片结构优化). *Transactions of the Chinese Society of Agricultural Engineering*, Vol. 32, Issue z2, pp. 7-15. Inner Mongolia/China.
- [9] Songyi, L. (2019). *Design and Performance Test of Corn Straw Crushing Device (玉米秸秆揉碎装置设计与性能试验研究)*. Hohhot: Inner Mongolia Agricultural University. Inner Mongolia/China.
- [10] Tao, C., Shujuan, Y., Yifei, L., Guixiang, T., Shanmin. Q. (2023). Establishment of Discrete Element Model and Parameter Calibration of Alfalfa Stem in Budding Stage (苜蓿现蕾期茎秆离散元模型建立与参数标定). *Transactions of the Chinese Society for Agricultural Machinery*, Vol. 54(5), pp.91-100. Heilongjiang/China.
- [11] Tiejun, W., Tieliang, W., Hongguang, C., Yuanjuan, G., Subo, T., & Ruili W. (2021). Design and Experiment of Adjustable Feeding Straw Bale-breaking and Rubbing Filament Machine (喂入调节式秸秆破包揉丝机设计与试验). *Transactions of the Chinese Society for Agricultural Machinery*, Vol. 52(6), Issue 6, pp.148-158. Liaoning/China.
- [12] Wei Z. (2016). *Design and performance test of 9RS-3 straw kneader (9RS-3 型秸秆揉丝机的设计与性能试验)*. Jinzhong: Shanxi Agricultural University. Shanxi/China.
- [13] Weigang, L. (2019). *Analysis of straw crushing characteristics and optimization of crushing equipment structure*. Guiyang: Guizhou University. Guizhou/China.
- [14] Xiaolong, H., Yong, Y., & Decheng, W. (2021). Optimization Design and Experiment on Small Cutting and Beating Machine of King Grass (小型组合式王草铡切打浆机优化设计与试验). *Transactions of the Chinese Society for Agricultural Machinery*, Vol. 52, Issue 3 pp. 117-126. Beijing/China.
- [15] Yajun, J., Yitao, L., & Qingxi, L. (2019). Design and Experiment on Cylinder-type Chopping Device of Harvester for Fodder Rapeseed in Winter and Spring (冬春鲜喂饲用油菜收获机滚刀式切碎装置设计与试验). *Transactions of the Chinese Society for Agricultural Machinery*, Vol. 50(2), pp.102-111. Hubei/China.
- [16] Yong, Y., Hongda, W., Xiaolong, H., Decheng, W., Chenchen, K., & Bingnan. Y. (2021). Design and Experiment of Roller Crushing Device of King Grass Harvester (王草收获机滚筒破碎装置设计与试验). *Transactions of the Chinese Society for Agricultural Machinery*, Vol. 52(4), pp.134-142. Beijing/ China.
- [17] Zhiqi, Z., Jin, H., Hongwen, L., Peisong, D., Qingjie, W., & Xiangcai, Z. (2016). Design and Experiment of Straw-chopping Device with Chopping and Fixed Knife Supported Slide Cutting (动定刀支撑滑切式秸秆粉碎装置设计与试验). *Transactions of the Chinese Society for Agricultural Machinery*, Vol. 47, Issue s1, pp.108-116. Beijing/China.

DESIGN AND EXPERIMENTAL STUDY OF CLEANING DEVICE FOR WHEAT HARVESTER BASED ON CFD-DEM

基于 CFD-DEM 的制繁种小麦收获机清选装置的设计与试验研究

Ranbing YANG^{1,2}, Shuai WANG¹, Zhiguo PAN¹, Guoying LI³, Yalong SHU¹,
Qi LIU¹, Zhen LIU¹, Yihui MIAO¹

¹ College of Electrical and Mechanical Engineering, Qingdao Agricultural University, Qingdao/ China

² College of Mechanical and Electrical Engineering, Hainan University, Haikou/ China

³ Qingdao Pulantech Machinery Technology Co., Ltd., Qingdao/ China

Tel: +8615318715305; E-mail: peter_panzg@163.com

Corresponding author: Zhiguo Pan

DOI: <https://doi.org/10.35633/inmateh-75-49>

Keywords: Wheat harvester, Seed production and propagation, Cleaning device, Coupled simulation

ABSTRACT

To address the issues of high admixture and loss rates during seed production and harvesting operations with combine harvesters, a low-loss, high-purity cleaning device suitable for wheat seed production and harvesting was designed. Considering the actual conditions of seed production and harvesting operations, the structure and dimensional parameters of key components were optimized. Through theoretical analysis, a motion model of wheat seeds on the cleaning sieve was established, identifying the main factors affecting the cleaning performance as fan speed, sieve amplitude, and vibration frequency. The CFD-DEM coupling method was used to simulate and analyze the sieving process under the influence of airflow within the cleaning chamber. A three-factor, three-level quadratic regression orthogonal combination simulation test was conducted to establish a response surface regression model for the seed admixture rate and the seed loss rate. Multi-objective comprehensive optimization of the factors indicated that the optimal operating parameters of the cleaning device are a fan speed of 1143 rpm an amplitude of 28 mm, and a vibration frequency of 9.4 Hz. Finally, field trial verification was conducted by setting the working parameters based on the coupled simulation test data. The operational results of the optimized cleaning device showed a seed admixture rate of 1.47% and a seed loss rate of 1.07%, with all results meeting the relevant standards. This study can provide valuable theoretical support for the development of wheat seed production and harvesting machines.

摘要

为解决联合收获机在进行制繁种收获作业时混杂率、损失率较高等问题，设计了一款适用于小麦制繁种收获作业的低损高净度清选装置。结合实际制繁种收获作业情况，优化了关键部件的结构及尺寸参数。通过理论分析，建立了小麦种子在清选筛上的运动模型，确定了影响清选效果的主要因素为风机转速、清选筛振幅和振动频率。采用 CFD-DEM 耦合方法对清选室内部气流作用下的筛分过程进行模拟分析，开展了三因素三水平二次回归正交组合仿真试验，建立了种子混杂率和种子损失率的响应面回归模型，对各因素进行多目标综合优化，结果表明：风机转速 1143 rpm、振幅 28 mm、振动频率 9.4 Hz，是清选装置的最优工作参数。最后，以耦合仿真试验数据为基础设置工作参数，进行田间试验验证，优化后的清选装置作业结果为：种子混杂率 1.47 %、种子损失率 1.07 %，结果各项均满足相关标准。本研究可为小麦制繁种收获机的研发提供有价值的理论依据。

INTRODUCTION

Seed multiplication, as a sophisticated integration of breeding technology and propagation techniques, plays an indispensable strategic role in meeting the urgent demands of agricultural production by cultivating high-quality, high-yield seeds. It significantly contributes to enhancing agricultural productivity, ensuring food security, promoting green development, and fostering economic prosperity, thus exerting a profound impact on the sustainable development of global agriculture (Mehta et al., 2019; Török et al., 2019; Krishna et al., 2023).

However, there is currently a severe scarcity of intelligent operational equipment specifically designed for seed multiplication harvesting. This deficiency directly affects the cost and efficiency of seed production, becoming a bottleneck that hinders the rapid development of the seed industry. Compared to field crop harvesting, seed multiplication harvesting faces more complex challenges: factors such as the diversity of

experimental varieties and the close proximity between adjacent seed plots make the process arduous (Lalghorbani *et al.*, 2022; Parihar *et al.*, 2023; Cheli *et al.*, 2024). At present, there is no dedicated machine type for wheat seed multiplication harvesting, and combine harvesters are typically used as substitutes. Although the mechanized operation technology in the wheat industry has matured, it still struggles to meet the stringent requirements of seed multiplication regarding key technical indicators such as loss rate, seed damage rate, and breakage rate, necessitating further optimization and enhancement at critical mechanisms and technical levels.

Delaney *et al.*, (2012), employed the EDEM method to study the impact of particle models on sieving motion, discovering that using single spherical particles in sieving motion simulations is insufficient to accurately simulate the actual flow and separation of non-spherical particles.

Ivan *et al.*, (2015), investigated factors influencing threshing capacity in conventional grain combine harvesters, providing a theoretical foundation for enhancing operational efficiency.

Buryanov *et al.*, (2019), designed a threshing device with adjustable concave spacing, effectively reducing loads on blowers and cleaning sieves.

Hevko *et al.*, (2019), established a mathematical model for the cleaning and conveying system of root/tuber crops, offering theoretical guidance for cleaner design.

Safranyik *et al.*, (2019), investigated the movement patterns of spherical particles during the cleaning process and determined the optimal operating parameters of the cleaning sieve using analytical methods, while also employing DEM to analyze the impact of interactions among multiple particles moving on the sieve surface.

Mircea *et al.*, (2020), developed an internal helical coil to optimize cyclone separator performance in cleaning systems.

Vlăduț *et al.*, (2022), proposed a mathematical model describing threshing-separation processes in axial-flow threshers, establishing theoretical principles for device design and optimization.

Vlăduț *et al.*, (2023), determined optimal operating parameters for cleaning-threshing systems during harvesting by analyzing key influencing factors.

Marin *et al.*, (2023), evaluated the impact of primary vibration sources in grain harvesters on operators, delivering theoretical insights for machine design refinement.

Wang *et al.*, (2024), adopted a CFD-DEM coupling approach to simulate operations under different field conditions, analyzing how various design parameters affect operational outcomes. They then validated their findings through experiments, thereby determining the optimal design scheme for a new type of wheat harvester.

This paper is based on the study of grain combine harvesters and addresses the issues of high seed contamination and loss rates during seed multiplication operations. It proposes a cleaning device specifically suitable for seed multiplication harvesting. Through an integrated method combining coupled simulation and field experiments, the key structures and parameters of the cleaning device are optimized, aiming to provide valuable insights for the research of cleaning devices in wheat seed multiplication harvesters.

MATERIAL AND METHODS

OVERALL STRUCTURE DESIGN OF THE CLEANING DEVICE

The use of conventional grain combine harvester cleaning devices results in a high residue of seeds, which easily leads to the mixing of different seed varieties, making it difficult to meet the requirements for seed multiplication. Traditional centrifugal fans tend to cause material accumulation in front of the sieve area, and when the wind speed is high, the loss rate increases; conversely, when the wind speed is low, the residue amount is substantial. To enhance cleaning efficiency and achieve the expected targets for seed multiplication harvesting, a cleaning device suitable for wheat seed multiplication harvesting has been designed, as shown in the figure 1.

The main functional components of the cleaning device include a centrifugal fan, cleaning sieve, shaking plate, and auger. During operation, the wheat threshed mixture falls through the concave sieve of the drum onto the shaking plate and cleaning sieve. Under the impetus of the centrifugal fan, the material becomes fluidized. Light impurities such as bran and short stalks are directly expelled from the cleaning chamber by the fan. Stalks are discharged from the debris outlet through the reciprocating motion of the fan and cleaning sieve. The wheat grains fall into the grain collection auger, while a small portion of the inadequately cleaned threshed mixture undergoes secondary cleaning through the debris auger.

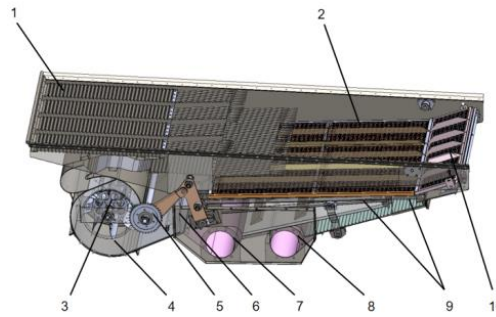


Fig. 1 – Overall structure of the cleaning device
 1. Shaking plate; 2. Cleaning sieve; 3. Fan impeller; 4. Fan volute; 5. Wind guide plate; 6. Eccentric rod gear;
 7. Grain-gathering dragon; 8. Miscellaneous dragon; 9. Baffle; 10. Tail sieve

DESIGN OF KEY COMPONENTS OF THE CLEANING DEVICE

Design of Dual Air Duct Centrifugal Fan

As the core component of the pneumatic conveying system, the performance of the fan affects the operational efficiency of the machine. Most grain combine harvesters use single-outlet centrifugal fans, which are characterized by simple structure, easy installation, and high wind pressure, performing well in high-resistance environments. However, existing research indicates that during wheat mechanical harvesting, the threshed mixture is unevenly distributed on the sieve surface, exhibiting a “V” shape with thicker material at the front and thinner at the back, as well as more material on the sides than in the center (Li et al., 2012; Fu et al., 2024) This suggests that the airflow of single-outlet centrifugal fans has coverage blind spots, making it difficult to cover the entire sieve surface, which is unfavorable for cleaning operations. Therefore, it is necessary to design a centrifugal fan suitable for seed breeding harvesting, taking into account the characteristics of seed breeding harvesting and the distribution pattern of the wheat threshed mixture, to achieve the desired objectives.

Design of Radial Dual-Fan Impeller

The impeller is the core component of a centrifugal fan, and its rotation drives the airflow throughout the cleaning chamber. Therefore, its structural and dimensional parameters have a decisive impact on the performance of the fan. Impellers can be classified into forward, radial, and backward types based on the blade exit angle. To meet the operational requirements of seed breeding harvesting, a radial blade dual-fan impeller has been designed. The main design parameters of the impeller include the outer diameter D_1 , inner diameter D_2 , blade length B , blade thickness t , and the number of blades. The structure and main parameters of the fan impeller are shown in the figure 2.

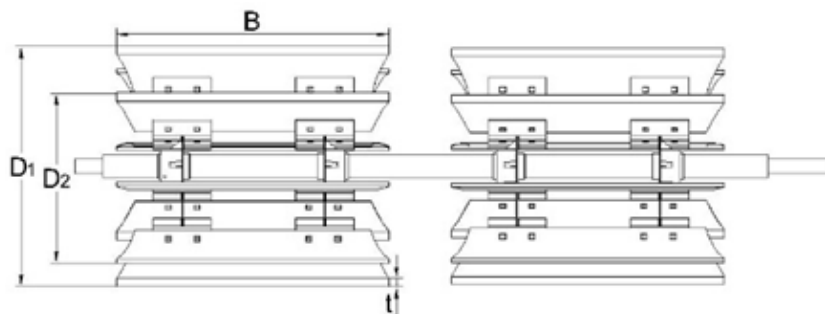


Fig. 2 – Fan Impeller Mode

Table 1

Fan Impeller Structural Parameters	
Parameter	Numerical value
Impeller diameter D_1 (mm)	400
Inner diameter of impeller D_2 (mm)	288
Blade length B (mm)	470
Blade thickness t (mm)	2
Blade quantity	8

Design of Blade Airfoil

The seed breeding and harvesting process is characterized by “tight schedules, heavy tasks, and high demands.” The fan in the cleaning system, which is responsible for sorting the mixture after threshing, must maintain stable operation for extended periods during the seed breeding and harvesting season. However, traditional straight blade designs often lead to unstable airflow separation and additional energy loss, directly resulting in decreased fan efficiency. To address this challenge, it is necessary to improve and upgrade the structural parameters of the fan blades (Zhang *et al.*, 2023). First, the blade bending angle should be adjusted. By utilizing fluid dynamics simulations and digital calculations, the optimal blade bending angle can be identified to ensure that airflow adheres more closely to the blade contour, thereby reducing flow separation and turbulence losses. Secondly, the leading edge of the blade has been modified to have a blunt angle. By optimizing the width ratio of the blade’s leading edge, pressure concentration is improved, and by adjusting the curvature of the blade’s leading edge to form a longer contraction passage, the range of efficient operating conditions for the blade is further expanded while ensuring stable operation under high-intensity conditions.

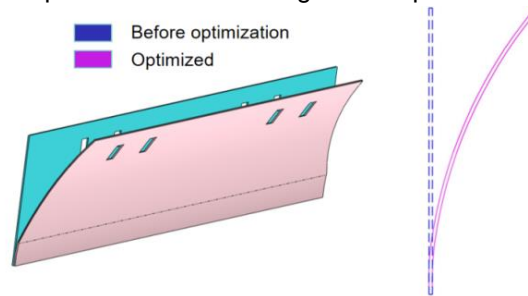


Fig. 3 – Comparison of Airfoil Before and After Optimization

Design of Fan Scroll Casing

The fan scroll casing serves the purpose of collecting and directing the accelerated airflow from the impeller, aiding in the circulation of airflow within the fan and converting part of the kinetic energy into static pressure energy. Due to the complex three-dimensional flow of gases inside a centrifugal fan, the scroll casing is filled with vortex structures of varying scales and intensities. Therefore, the scroll casing’s profile not only determines the guidance of airflow but also affects the flow loss within the fan, directly impacting the aerodynamic performance, output airflow, and pressure parameters of the entire fan. Currently, two widely used scroll profiles are the logarithmic spiral and the Archimedean spiral. The centrifugal fan scroll designed in this study is based on the Archimedean spiral, characterized by a smoothly curved equidistant spiral, which suppresses the formation of vortex regions within the scroll passage while maximizing airflow along the spiral. The main parameter calculations are shown in the table below, according to the Agricultural Machinery Design Manual:

Table 2

Fan Scroll Structural Parameters	
Parameter	Numerical value
Lower air outlet height L_1 (mm)	258
Upper air outlet height L_2 (mm)	84
Vertical distance H (mm)	186
Thread extension dimensions A	100
$R_1 = D_1/2 + (2/5)A$	240
$R_2 = D_1/2 + (9/10)A$	290
$R_3 = D_1/2 + (3/10)A$	230
$R_4 = D_1/2 + A/2$	250
$R_5 = D_1/2 + (4/5)A$	280

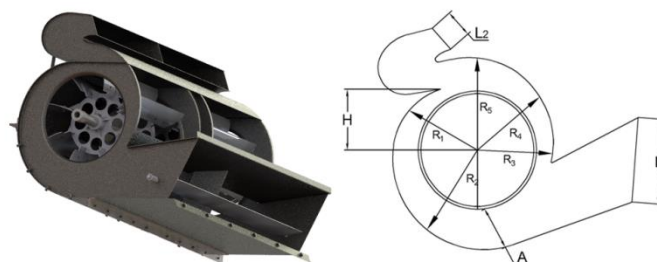


Fig. 4 – Fan Scroll Model

Design of Cleaning Sieve

As the core component of the cleaning device, the cleaning sieve plays a decisive role in the stratification and conveying movements of materials on the sieve surface. According to the shape and structure of the screen, cleaning sieves can be categorized into fish scale sieves, perforated sieves, bar sieves, etc. Among them, perforated sieves are mostly used for fine screening of small particles; bar sieves tend to experience hole blockage and beam fracture under high-intensity conditions; whereas fish scale sieves are composed of curved fish scale sieve plates with adjustable openings according to actual working conditions. They have a strong capability to convey residues without clogging easily, and the airflow on the sieve surface is uniform, which can meet the requirements of complex working conditions during seed production and harvesting.



Fig. 5 – Schematic Diagram of Cleaning Sieve

In cleaning operations, the mesh size is related to the feed rate. Referring to the "Agricultural Machinery Design Handbook," the formula for calculating the total length L of the sieve is:

$$L = \frac{F_z}{WF_s} \quad (1)$$

In the formula: F_z is the Machine feed rate; W is the Screen surface width; F_s is the feed rate that can be handled per unit area of the sieve.

Based on the actual feed rate and the actual grain quality on the sieve surface during the seed production and harvest process, the value of F_z is 4 kg/s, and the value of F_s is 2.4 kg/(s·m²). Considering the combination of the cleaning device with the frame and the single longitudinal axial flow drum threshing device, the sieve width is 1200 mm. Substituting these into the formula yields a value of L being 1390 mm. Taking into account that the mass of the material entering the cleaning device is approximately half of the drum's feed rate, the design of the cleaning sieve meets agronomic requirements.

Design of Eccentric Linkage Mechanism

The cleaning sieve achieves material stratification and movement towards the outlet through sieving motion. The specific motion process involves a deep groove ball bearing with an eccentric sleeve, which is positioned on the drive shaft using a shaft elastic retaining ring. The lower side of the connecting rod is fitted onto the deep groove ball bearing, while the upper side is hinged to the rocker arm with a bolt. The rocker arm is hinged to both the frame and the sieve base frame. A chain drive rotates the eccentric wheel at a constant angular velocity, and the connecting rod transmits this motion to the sieve frame, converting the rotational motion of the eccentric wheel into the reciprocating motion of the sieve frame. This motion pushes the material on the sieve surface towards the outlet and stratifies it. A schematic diagram of the structure is shown in the illustration.



Fig. 6 – Schematic Diagram of Eccentric Linkage Mechanism

Since the eccentric linkage mechanism is closed at both ends, it can be considered a closed-chain mechanism. Its degree of freedom analysis is as follows:

$$F = 3n - 2F_l - F_h \quad (2)$$

In the formula 2, F represents the degree of freedom of the mechanism; n represents the number of active components; F_l denotes the number of lower pairs; F_h represents the number of high pairs.

Analysis shows that there are 3 movable links, 4 lower pairs, and 0 higher pairs in this crank-link mechanism. Therefore, the degree of freedom is calculated as 1, meaning that only one input of power is required to enable the vibrating screen to achieve reciprocating motion.

MOTION ANALYSIS OF WHEAT SEEDS ON THE CLEANING SCREEN

After wheat seeds leave the shaking plate and enter the cleaning device, they move in the form of individual free particles. Therefore, when analyzing their forces in the airflow field, the focus should be on the individual behavior of wheat seed particles. When these particles fall onto the cleaning screen, the screen undergoes reciprocating motion, also known as simple harmonic motion, driven by a crank-rocker mechanism. During this process, the movement of materials on the screen surface primarily exhibits three states: forward sliding, backward sliding, and throwing. These movement states significantly affect the screening effect and separation efficiency of wheat from mixtures. Therefore, these motion characteristics must be fully considered in the design and optimization of cleaning devices.

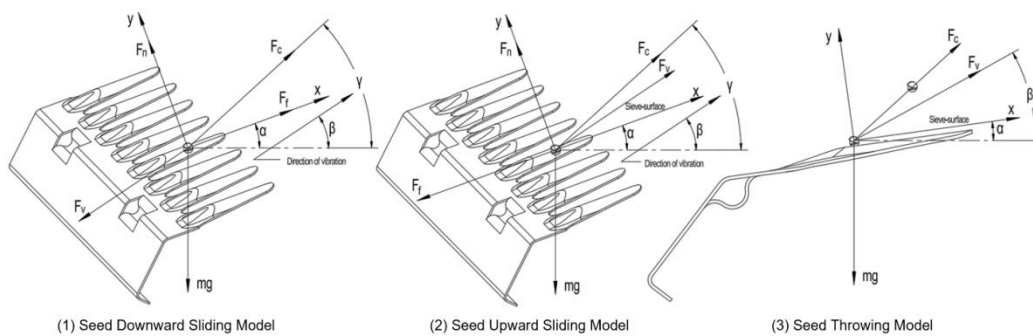


Fig. 8 – Analysis of Seed Motion States on the Cleaning Screen

Analysis of Seed Sliding Down the Screen Surface

According to D'Alembert's principle, when seeds are considered as rigid bodies and their motion on the screen surface is taken into account, a dynamic problem can be transformed into a static problem. By introducing inertial force, the main forces, constraint forces, and inertial forces of the particles formally constitute a system of equilibrium forces. In this context, a sliding motion model for the seeds can be established. When the seeds slide down the screen surface under the action of their inertial force and the direction of acceleration is positive, the motion model of the seeds can be described as follows:

$$F_c \sin(\gamma - \alpha) + F_n = mg \cos \alpha + F_v \sin(\beta - \alpha) \tag{3}$$

$$F_c \cos(\gamma - \alpha) + F_f = mg \sin \alpha + F_v \cos(\beta - \alpha) \tag{4}$$

In the formula, F_v denotes the inertial force; F_f denotes friction; F_c represents the wind power of the fan; α represents the inclination of the screen surface; β represents the vibration direction angle; γ indicates the airflow direction angle; φ denotes the friction angle.

Substituting the relevant parameters and performing rearrangement and simplification, the following is obtained:

$$\frac{\omega^2 r}{g} \cos \omega t = \left(\frac{V}{V_p}\right)^2 \cdot \frac{\cos(\gamma - \alpha + \varphi)}{\cos(\beta - \alpha + \varphi)} - \frac{\sin(\alpha - \varphi)}{\cos(\beta - \alpha + \varphi)} \tag{5}$$

In which, $\cos \omega t \leq 1$. The critical condition for the seeds to slide down the screen surface is:

$$\frac{\omega^2 r}{g} > \left(\frac{V}{V_p}\right)^2 \cdot \frac{\cos(\gamma - \alpha + \varphi)}{\cos(\beta - \alpha + \varphi)} - \frac{\sin(\alpha - \varphi)}{\cos(\beta - \alpha + \varphi)} \tag{6}$$

Analysis of Seed Sliding Up the Screen Surface

Similarly, when the seeds slide up the screen surface under the action of their own inertial force and the direction of acceleration is negative, the motion model of the seeds can be described as:

$$F_v \cos(\beta - \alpha) + F_c \cos(\gamma - \alpha) = F_f + mg \sin \alpha \tag{7}$$

$$F_n + F_c \sin(\gamma - \alpha) + F_v \sin(\beta - \alpha) = mg \cos \alpha \quad (8)$$

Substituting the relevant parameters and performing rearrangement and simplification, the following is obtained:

$$\frac{\omega^2 r}{g} \cos \omega t = \frac{\sin(\alpha + \varphi)}{\cos(\beta - \alpha - \varphi)} - \left(\frac{V}{V_p} \right)^2 \cdot \frac{\cos(\gamma - \alpha - \varphi)}{\cos(\beta - \alpha - \varphi)} \quad (9)$$

In which, $\cos \omega t \leq 1$. The critical condition for the seeds to slide up the screen surface is:

$$\frac{\omega^2 r}{g} > \frac{\sin(\alpha + \varphi)}{\cos(\beta - \alpha - \varphi)} - \left(\frac{V}{V_p} \right)^2 \cdot \frac{\cos(\gamma - \alpha - \varphi)}{\cos(\beta - \alpha - \varphi)} \quad (10)$$

Analysis of Seed Detachment from the Screen Surface

Analyzing the forces acting on seeds on the cleaning screen, it is evident that when the inertial force F_v is positive, and as the centripetal acceleration $\omega^2 r$ continuously increases, the support force F_n from the cleaning screen on the seeds decreases, gradually approaching zero.

At this point, the seeds, propelled by their own inertial force and the wind force from the cleaning fan, tend to be thrown off the surface of the cleaning screen. When the support force F_n exerted by the cleaning screen on the seeds equals zero, the seeds detach from the screen surface. Simultaneously, at the moment when the seeds begin to detach, sliding no longer occurs on the screen teeth, and the friction force disappears. At this moment, the motion model of the seeds can be described as:

$$F_N = mg \cos \alpha - F_v \sin(\beta - \alpha) - F_c \sin(\gamma - \alpha) \quad (11)$$

Substituting the relevant parameters and performing rearrangement and simplification, the following is obtained:

$$\frac{\omega^2 r}{g} \cos \omega t = \frac{\cos \alpha}{\sin(\beta - \alpha)} - \left(\frac{V}{V_p} \right)^2 \frac{\sin(r - \alpha)}{\sin(\beta - \alpha)} \quad (12)$$

In which, $\cos \omega t \leq 1$. The critical condition for the seeds to detach from the screen surface is:

$$\frac{\omega^2 r}{g} \geq \frac{\cos \alpha}{\sin(\beta - \alpha)} - \left(\frac{V}{V_p} \right)^2 \frac{\sin(r - \alpha)}{\sin(\beta - \alpha)} \quad (13)$$

In summary, the motion state of wheat seeds on the cleaning screen, apart from their own factors, is jointly determined by the airflow velocity and the acceleration ratio of the cleaning screen's motion (i.e., the fan speed and the vibration amplitude and frequency of the cleaning screen). To ensure cleaning performance, it is generally required that seeds can slide up and down on the screen surface while minimizing the occurrence of detachment from the screen. Therefore, finding the optimal combination of fan speed, amplitude, and vibration frequency is crucial for achieving good cleaning results. Due to the relatively complex motion patterns during the actual seed propagation and harvesting process, it is impossible to obtain accurate and effective dynamic data. Conducting numerical simulations of the airflow field in the cleaning chamber without material particles or vibration screening without airflow alone is incomplete. Therefore, it is necessary to use the coupled FLUENT and EDEM method, known as the CFD-DEM approach, to determine the optimal parameter range and combinations for key factors such as amplitude, airflow velocity, and airflow direction angle (Ding et al., 2022; Li et al., 2022).

RESULTS

RESEARCH ON THE MATERIAL MOVEMENT PATTERNS IN CLEANING DEVICES BASED ON CFD-DEM

To facilitate subsequent analysis, simulation models of the cleaning screen and the wheat threshing mixture were constructed using SOLIDWORKS and EDEM software. Orthogonal experiments were conducted with the seed impurity rate and seed loss rate as the main evaluation indicators, laying the foundation for further field trials and optimization of parameter combinations.

CFD Model of Cleaning Device

Firstly, considering the workload of coupled simulations and the computational capacity of the computer, a simplified 3D model of the cleaning chamber was constructed using SOLIDWORKS. Subsequently, the model in .STEP format from SOLIDWORKS was converted into a fluid domain model in .IGES format, which is recognizable by FLUENT, for meshing. The mesh was divided using a multi-module partitioning method, with the element size set between 0-1000 mm depending on the density. The total number of mesh elements was 45,422,210. The model after meshing is shown in the figure.

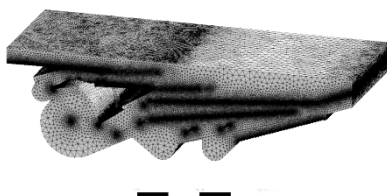


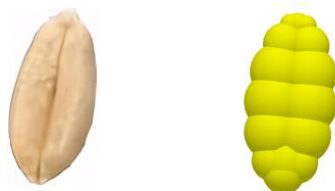
Fig. 9 – Schematic diagram of the cleaning room meshing

Then, the boundary conditions were set: both outlets of the centrifugal fan were assigned velocity-inlet boundary conditions, while the outlet was set as a pressure-outlet boundary. The fan impeller was configured with rotor-wall conditions, and the remaining areas were set as wall conditions. The k-epsilon model was chosen for the computational model, with the Standard Wall Function selected for the wall functions. The solution method employed was coupled, and the time step in FLUENT was set to 0.0004 s. After setting up, simulate the fluid domain model through simulation.

DEM Model of Wheat Threshing Mixture

Bags were placed at the grain outlet of the wheat harvester working in the field to collect the mixture threshed by the cleaning device. The proportions of wheat grains and stalks in the threshed mixture were measured to be 90.64% and 9.3%, respectively.

To construct a 3D model of wheat grains, 50 grains were randomly selected from the harvested wheat. Their average dimensions along the three axes were recorded using a vernier caliper, and the average values were calculated. Based on the results, the standard model dimensions for wheat grains were set to 6.76 mm×2.98 mm×2.88 mm. Using the obtained average dimensions of wheat grains, a 3D solid model was created with SOLIDWORKS software. The multi-sphere method was used in EDEM software to densely fill the 3D model, and a comparison between the filled particle model and actual wheat is shown in the figure.



(1) Wheat seeds (2) Discrete meta-model of wheat

Fig. 10 – Comparison Diagram of Wheat Seeds and Wheat Discrete Element Model

Similarly, 50 short stalks were randomly selected from the collected samples. After measuring their average dimensions along the three axes, the standard model dimensions for wheat stalks were determined to be a length of 23.54 mm, an outer diameter of 2.23 mm, and a wall thickness of 0.37 mm.

To ensure that the simulation experiments align with the actual conditions of seed production harvesting, mechanical properties and contact parameters between materials were determined by comprehensively referencing existing discrete element calibration literature for wheat grains and stalk particles, as well as data obtained from previous observations, measurements, and experimental studies. These parameters are shown in Tables 3 and 4.

Table 3

Material mechanical properties parameters			
Material	Poisson ratio	Shear modulus/pa	Density/kg-m ⁻³
Wheat seeds	0.3	2.6	1350
Short stalk	0.4	1	104
Cleaning sieve (Steel plate)	0.3	7800	7800

Table 4

Contact coefficient between materials			
Contact property	Restitution coefficient	Coefficient of static friction	Coefficient of rolling friction
Grain-Grain	0.2	1	0.01
Grain-Stem	0.3	0.5	0.01
Grain-Steel plate	0.45	0.35	0.01
Stem-Steel plate	0.3	0.36	0.01
Stem-Stem	0.22	0.5	0.01

The mass ratio measurement test was carried out on the mixture removed from the cleaning device obtained from the field. The mass ratio of each component of the mixture was 90.64 % of the grain mass and 9.3 % of the residual mass. Combined with the parameters of grain weight, grain and stem density, the number of particles generated in the simulation was calculated to be 4200 wheat grains and 450 wheat short stems, respectively. The particles were generated within 2.0 s.

Screening Simulation Process and Result Analysis

The figure below illustrates the cleaning states of the separation device at different time intervals, where the red spherical particles represent wheat seeds and the blue cylindrical particles represent short stalks.

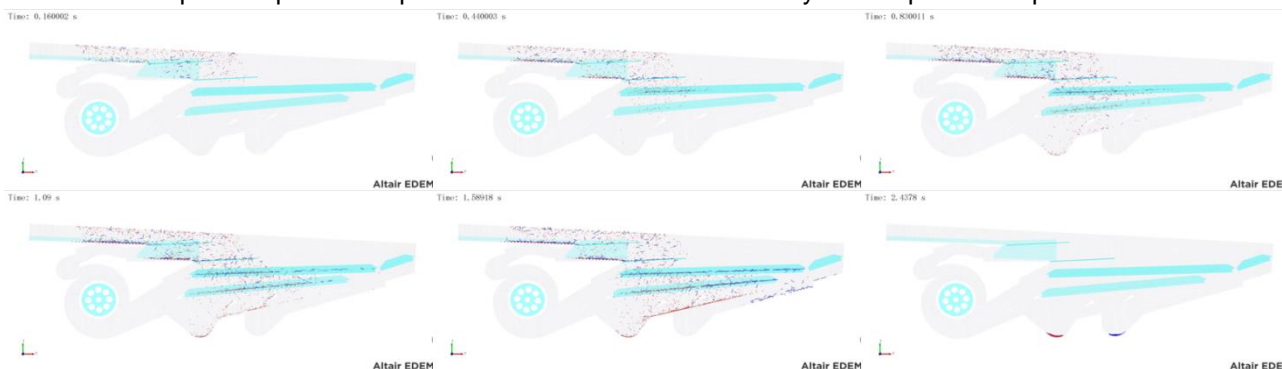


Fig. 11 – Simulation Time Frame Diagram of the Cleaning Chamber

Based on the illustration, it can be observed that at 0.16 seconds, the mixture particles begin to form in the particle generator and randomly fall onto the shaking plate. By 0.44 seconds, the particles come into contact with the cleaning screen and start moving towards the end of the screen due to the combined action of airflow and screening motion. At 0.83 seconds, some particles pass through the screen surface, and the wheat seeds, guided by the baffle plate, fall into the grain collection auger. By 1.09 seconds, a large number of mixture particles move towards the tail under the dual influence of airflow and screening motion, while light impurities are expelled out of the machine through the upper air outlet. At 1.58 seconds, the short stalks and light impurities are steadily discharged through the upper air outlet, and a large number of particles pass through the double-layer vibrating screen, guided by the baffle plates into the grain collection auger and the debris auger, respectively. By 2.4 seconds, the cleaning process is essentially complete; under the synergistic effect of airflow from the fan's dual outlets and screening motion, the vast majority of wheat seeds fall into the grain collection auger, with some entering the debris auger. These seeds, along with the debris, are transported by the auger above the vibrating screen for re-screening, with only a very small number of wheat seeds being expelled from the machine during the airflow and screening movements.

EXPERIMENTAL STUDY AND RESULT ANALYSIS OF WHEAT SEED SEPARATION AND CLEANING PERFORMANCE

Design of Experiments with Multiple Factors

To further investigate the combined effects of multiple factors on the performance of the cleaning device in wheat seed harvesting machines, the significance levels of various factors on the impurity rate and cleaning loss rate indicators are analyzed. This helps to determine the priority and influence order of each experimental factor on the test indicators and to identify the optimal parameter combinations. This analysis provides a theoretical basis for selecting factor levels in subsequent regression experiments. The experiment considers fan speed (X_1), amplitude (X_2), and vibration frequency (X_3) as experimental factors, and impurity rate (Y_1) and loss rate (Y_2) as the indicators of cleaning effectiveness, conducting a three-factor, three-level response surface experiment.

In the preliminary single-factor simulation experiments, impurity rate and loss rate were used as experimental indicators, while fan speed (900-1300 rpm), amplitude (10-50 mm), and vibration frequency (5-15 Hz) were considered as experimental factors. Specifically, when the fan speed was less than 1100 rpm material accumulation occurred, making it difficult for wheat seeds to pass through the sieve, resulting in an increased impurity rate. When the amplitude was less than 20 mm and the vibration frequency was less than 6 Hz, the separation effect between wheat seeds and short stalks was poor, leading to low cleaning efficiency. Conversely, when the amplitude exceeded 40 mm and the vibration frequency was greater than 10 Hz, there was significant fluctuation in the transport state of materials on the sieve surface, causing material splashing and a substantial increase in cleaning loss rate. Based on the analysis results of the single-factor experiments, the levels for fan speed were set at 1100 rpm, 1200 rpm, and 1300 rpm; the levels for cleaning sieve amplitude were set at 20 mm, 30 mm, and 40 mm; and the levels for vibration frequency were set at 6 Hz, 8 Hz, and 10 Hz. The coding table for experimental factor levels is shown in Table 5.

Table 5

Test code table			
Coding Level	Experimental factors		
	Fan speed X ₁ (rpm)	Amplitude X ₂ (mm)	Vibration frequency X ₃ (Hz)
-1	1100	20	6
0	1200	30	8
1	1300	40	10

Results and Analysis of Multi-Factor Experiments

The experimental setup and results are shown in the table. From the response surface experiment results, it can be seen that the range of seed admixture rate in this experiment is 1.15~1.96%, and the range of seed loss rate is 0.64~1.82%.

Table 6

Test design and results					
Experimental coding	Experimental factors			Hybridization rate of seeds Y ₁ /%	Losing seed rate Y ₂ /%
	Fan speed X ₁ (rpm)	Amplitude X ₂ (mm)	Vibration frequency X ₃ (Hz)		
1	1100	20	8	1.89	0.64
2	1300	20	8	1.29	1.02
3	1100	40	8	1.31	1.05
4	1300	40	8	1.17	1.92
5	1100	30	6	1.96	0.68
6	1300	30	6	1.34	1.23
7	1100	30	10	1.28	0.81
8	1300	30	10	1.21	1.74
9	1200	20	6	1.88	0.85
10	1200	40	6	1.29	1.36
11	1200	20	10	1.3	0.89
12	1200	40	10	1.15	1.82
13	1200	30	8	1.23	1.03
14	1200	30	8	1.19	0.99
15	1200	30	8	1.25	0.96
16	1200	30	8	1.27	0.94
17	1200	30	8	1.2	1.01

Perform a second-order multivariate regression fitting based on the simulation test data, and use Design-Expert 13 software to conduct regression analysis on seed admixture rate (Y₁) and seed loss rate (Y₂).

The regression equations for seed admixture rate (Y₁) and seed loss rate (Y₂) are:

$$Y_1 = 1.23 - 0.1788A - 0.18B - 0.1913C + 0.115AB + 0.1375AC + 0.11BC + 0.1148A^2 + 0.0723B^2 + 0.1047C^2 \tag{14}$$

$$Y_2 = 0.986 + 0.3412A + 0.3437B + 0.1425C + 0.1225AB + 0.095AC + 0.1050BC + 0.0283A^2 + 0.1433B^2 + 0.1007C^2 \tag{15}$$

To further analyze the impact of various experimental factors on the test indices, Design-Expert 13 software was used to obtain the response surface, as shown in the figure 12.

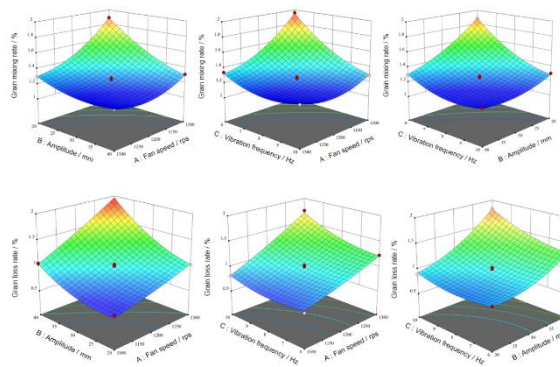


Fig. 12 – The response surface variation relationship of each factor to the test index

Experimental Optimization

In order to optimize the performance of the cleaning device and improve the effectiveness of seed harvesting, the fan speed, amplitude, and vibration frequency were subjected to parameter optimization design with the minimization of admixture rate and loss rate as the optimization objectives. The weight for admixture rate was set to five "+", and the weight for loss rate was set to three "+". The target values for the three factors were set within the optimization range, establishing a parametric mathematical model as follows:

$$\begin{cases} \min Y_1 \\ \min Y_2 \\ s.t. \begin{cases} 1100rps \leq X_1 \leq 1300rps \\ 20mm \leq X_2 \leq 40mm \\ 6Hz \leq X_3 \leq 10Hz \end{cases} \end{cases} \quad (16)$$

Using multi-objective parameter optimization in Design-Expert 13 software to analyze the mathematical model, the results indicate that the optimal operating parameters for the cleaning device are a fan speed (X_1) of 1143 rpm, an amplitude (X_2) of 28 mm, and a vibration frequency (X_3) of 9.4 Hz.

FIELD TEST

Building on the design of the cleaning device, its operating parameters were set according to the simulation test results and applied to the 4LX-1 wheat plot harvester. On June 22, 2024, a field trial was conducted at the Weifang Modern Agricultural Science and Technology Demonstration Park, harvesting the wheat variety "Zhengmai 113" at its optimal harvest time. The calculation formulas for seed admixture rate and seed loss rate are as follows:

$$P_z = \frac{M_z - M_m}{M_z} \times 100\% \quad (17)$$

$$P_s = \frac{M_b}{M_a + M_b} \times 100\% \quad (18)$$

In the formula: P_z represents the seed admixture rate, expressed as a percentage (%); M_z denotes the mass of the mixture in the grain collection auger, in g; M_m is the mass of seeds in the grain collection auger after impurities have been removed, in g; P_s represents the seed loss rate, expressed as a percentage (%); M_a is the harvested wheat seed yield per square meter, in g; M_b is the seed loss per square meter of wheat, in g.

Table 7

Serial number	Field test results	
	Low-loss and high-purity cleaning device	
	Hybridization rate of seeds/%	Losing seed rate/%
1	1.66	0.96
2	1.91	1.12
3	1.27	1.33
4	1.41	1.04
5	1.1	0.91
Mean value	1.47	1.07

The seed admixture rate and seed loss rate were calculated according to the formula, and the results are shown in the table. Under the optimal parameter combination of the optimized cleaning device, the average wheat admixture rate was 1.47%, and the average loss rate was 1.04%.

The operational results were similar to the simulation test results, with all indicators meeting the standards for seed production and harvesting. Therefore, the improved cleaning device is suitable for wheat seed production and harvesting operations.



Fig. 13 – Collection of Threshed Material and Field Test Diagram

CONCLUSIONS

(1) In this paper, a low-loss and high-purity cleaning device suitable for wheat breeding and harvesting operations was designed. The motion model of the sieve body and the material was established. It was determined that the operation effect of the cleaning device was affected by three important factors : fan speed, amplitude and vibration frequency.

(2) The CFD-DEM coupling simulation method was used to analyze the screening process of the separated mixture under the action of the fan, and the optimal structural parameters were obtained by combining the single factor test. The parameter combination was optimized with the minimum seed mixing rate and seed loss rate as the optimization objective, and the field verification test was carried out. The average mixing rate of wheat was 1.47 %, and the average loss rate was 1.04 %. The operation results were similar to the simulation test results, and all indicators met the relevant standards.

ACKNOWLEDGEMENT

The author was supported by the "National Key R&D Program" (2023YFD2000404-2) and "Mount Taishan Industrial Leading Talent Project in Shandong Province" (LJNY201804).

REFERENCES

- [1] Buryanov A., Chervyakov I. (2019). Using combines for cleaning grain crops by non-traditional technologies, *INMATEH – Agricultural Engineering*, 59(3), pp. 27-32.
- [2] Cheli, F., Abdelaziz, A. K. M., Arrigoni, S., Paparazzo, F., & Pezzola, M. (2024). Precision Agriculture Applied to Harvesting Operations through the Exploitation of Numerical Simulation. *Sensors*, 24(4), 1214.
- [3] Delaney, G. W., Cleary, P. W., Hilden, M., & Morrison, R. D. (2012). Testing the validity of the spherical DEM model in simulating real granular screening processes. *Chemical Engineering Science*, 68(1), 215-226.
- [4] Ding, B., Liang, Z., Qi, Y., Ye, Z., & Zhou, J. (2022). Improving Cleaning Performance of Rice Combine Harvesters by DEM–CFD Coupling Technology. *Agriculture*, 12(9), 1457.
- [5] Fu, J., Zhang, M., Cheng, C., Zhao, H., & Ren, L. (2024). Thickness monitoring of threshing mixture on the oscillating plate of corn grain harvester. *Computers and Electronics in Agriculture*, 227, 109485.
- [6] Gao, X., Cui, T., Zhou, Z., Yu, Y., Xu, Y., Zhang, D., & Song, W. (2021). DEM study of particle motion in novel high-speed seed metering device. *Advanced Powder Technology*, 32(5), 1438-1449.
- [7] Hevko R.B., Tkachenko I.G., Rogatynskiy R.M., Synii S.V., Flonts I.V., Pohrishchuk B.V. (2019). Impact of parameters of an after-cleaning conveyor of a root crop harvester on its performance, *INMATEH – Agricultural Engineering*, 59(3), pp. 41-48.
- [8] Ivan Gh., Vlăduț V., Ganea I. (2015). Improving threshing system feeding of conventional cereal harvesting combine, *Proceedings of the 43 International Symposium on Agricultural Engineering "Actual Tasks on Agricultural Engineering"*, pp. 431-440, Opatija – Croatia.
- [9] Krishna, T. P. A., Veeramuthu, D., Maharajan, T., & Soosaimanickam, M. (2023). The era of plant breeding: Conventional breeding to genomics-assisted breeding for crop improvement. *Current Genomics*, 24(1), 24-35.

- [10] Lalghorbani, H., & Jahan, A. (2022). Selection of a wheat harvester according to qualitative and quantitative criteria. *Sustainability*, 14(3), 1313.
- [11] Lenaerts, B., Aertsen, T., Tijsskens, E., De Ketelaere, B., Ramon, H., De Baerdemaeker, J., & Saeys, W. (2014). Simulation of grain–straw separation by Discrete Element Modeling with bendable straw particles. *Computers and Electronics in Agriculture*, 101, 24-33.
- [12] Li, H., Li, Y., Gao, F., Zhao, Z., & Xu, L. (2012). CFD–DEM simulation of material motion in air-and-screen cleaning device. *Computers and Electronics in Agriculture*, 88, 111-119.
- [13] Li, Y., Xu, L., Lv, L., Shi, Y., & Yu, X. (2022). Study on modeling method of a multi-parameter control system for threshing and cleaning devices in the grain combine harvester. *Agriculture*, 12(9), 1483.
- [14] Liang, Z. (2021). Selecting the proper material for a grain loss sensor based on DEM simulation and structure optimization to improve monitoring ability. *Precision Agriculture*, 22(4), 1120-1133.
- [15] Liu, P., Wang, XY., & Jin, CQ. (2022). Bench test and analysis of cleaning parameter optimization of 4 L-2.5 wheat combine harvester. *Applied Sciences*, 12(18), 8932.
- [16] Marin E., Cârdei P., Vlăduț V., Biriș S-Șt., Ungureanu N., Bungescu S.T., Voicea I., Cujbescu D., Găgeanu I., Popa L-D., Isitcioaia S., Matei Gh., Boruz S., Teliban G., Radu C., Kabas O., Caba I., Maciej J. (2023). Research on the influence of the main vibration-generating components in grain harvesters on the operator's comfort, INMATEH – Agricultural Engineering 74 (3), pp. 800-815.
- [17] Mehta, C. R., Chandel, N. S., Jena, P. C., & Jha, A. (2019). Indian agriculture counting on farm mechanization. *Agricultural Mechanization in Asia, Africa and Latin America*, 50(1), 84-89.
- [18] Mircea C., Nenciu F., Vlăduț V., Voicu Gh., Gageanu I., Cujbescu D. - Increasing the performance of cylindrical separators for cereal cleaning, by using an inner helical coil, *INMATEH – Agricultural Engineering*, vol. 62, no. 3 / 2020, pp. 249-258.
- [19] Parihar, D. S., Dogra, B., Narang, M. K., Javed, M., & Singh, D. (2023). Integrated seeding attachment for combine harvesters: a sustainable approach for conservation agriculture. *Environment, Development and Sustainability*, 1-21.
- [20] Safranyik, F., Csizmadia, B. M., Hegedus, A., & Keppler, I. (2019). Optimal oscillation parameters of vibrating screens. *Journal of Mechanical Science and Technology*, 33, 2011-2017.
- [21] Suardi, A., Stefanoni, W., Bergonzoli, S., Latterini, F., Jonsson, N., & Pari, L. (2020). Comparison between two strategies for the collection of wheat residue after mechanical harvesting: Performance and cost analysis. *Sustainability*, 12(12), 4936.
- [22] Török, K., Szentmiklóssy, M., Tremmel-Bede, K., Rakszegi, M., & Tömösközi, S. (2019). Possibilities and barriers in fibre-targeted breeding: Characterisation of arabinoxylans in wheat varieties and their breeding lines. *Journal of Cereal Science*, 86, 117-123.
- [23] Vlăduț N.-V., Biriș S.St., Cârdei P., Găgeanu I., Cujbescu D., Ungureanu N., Popa L.-D., Perișoară L., Matei G., Teliban G.-C. (2022). Contributions to the Mathematical Modeling of the Threshing and Separation Process in An Axial Flow Combine, *Agriculture*, 12(10), 1520.
- [24] Vlăduț N.-V., Ungureanu N., Biriș S.St., Voicea I., Nenciu F., Găgeanu I., Cujbescu D., Popa L.-D., Boruz S., Matei G., Ekielski A., Teliban G.C. (2023). Research on the identification of some optimal threshing și separation regimes in the axial flow apparatus, *Agriculture*, 13(4): 838.
- [25] Wang, L., Chai, X., Huang, J., Hu, J., & Cui, Z. (2024). Efficient and Low-Loss Cleaning Method for Non-Uniform Distribution of Threshed Materials Based on Multi-Wing Curved Combination Air Screen in Computational Fluid Dynamics/Discrete Element Method Simulations. *Agriculture*, 14(6), 895.
- [26] Wang, L., Zhang, S., Gao, Y., Cui, T., Ma, Z., & Wang, B. (2023). Investigation of maize grains penetrating holes on a novel screen based on CFD-DEM simulation. *Powder Technology*, 419, 118332.
- [27] Zhang, C., Geng, D., Xu, H., Li, X., Ming, J., Li, D., & Wang, Q. (2023). Experimental Study on the Influence of Working Parameters of Centrifugal Fan on Airflow Field in Cleaning Room. *Agriculture*, 13(7), 1368.

MASS FLOW DETECTION TECHNOLOGY FOR SEED AND FERTILISER PARTICLES AND ITS APPLICATION IN UAV-BASED SPREADING

种肥颗粒质量流量检测技术及其在无人机播撒中的应用建议

Yanshuang WANG^{1,2,3}, Cancan SONG^{*1,2,3}, Yongqi GAO^{1,2,3}, Yubin LAN^{1,2,3}, Guobin WANG^{1,2,3}, Rui MING⁴

¹) College of Agricultural Engineering and Food Science, Shandong University of Technology, Zibo / China;

²) Shandong University of Technology Sub-center of National Center for International Collaboration Research on Precision Agricultural Aviation Pesticide Spraying Technology, Zibo / China;

³) Research of Institute of Ecological Unmanned Farm, Shandong University of Technology, Zibo / China;

⁴) School of Computer and Big Data, Minjiang University, Fujian Provincial Key Laboratory of Information Processing and Intelligent Control, Fuzhou / China;

Tel: 8613424454257; E-mail: songcc@sdu.edu.cn

DOI: <https://doi.org/10.35633/inmateh-75-50>

Keywords: precision agriculture; solid particle; dense particle flow; mass flow detection; drone spreading; intelligent monitoring

ABSTRACT

The processes of sowing and fertiliser application represent a significant aspect of agricultural production. In order to achieve efficient and precise seeding and fertiliser application, mass flow detection of seed and fertiliser particles can facilitate real-time monitoring and precise decision-making for intelligent seeding and fertiliser application. However, the diversity of seed and fertiliser particle types and particle flow modes presents a challenge for existing detection methods, particularly in meeting the varying operational requirements, especially for particle mass flow detection in low-altitude and high-speed sowing operations of agricultural drones. In such cases, the overlap and flow rate will have a significant impact on the detection results due to the large displacement and the continuous high-throughput dense phase of the particle flow. This paper provides a summary of the existing seed and fertiliser particle mass flow detection techniques and their underlying working principles. It compares the direct detection based on mass with the indirect detection methods based on velocity and concentration, and analyses their respective advantages, disadvantages and applicability. It also explores the possibility of optimising the existing detection methods for the specific needs of agricultural UAVs and considers the potential introduction of cutting-edge science and technology in order to develop an efficient, accurate and convenient detection system to meet the growing market demand.

摘要

播种和施肥是农业生产中的重要环节。在实现高效和精准化播种和施肥作业中，种肥颗粒的质量流量检测能够为智能化播种和施肥提供实时监控和精准决策。然而由于种肥颗粒类型和颗粒流动方式的多样性，现有检测方法较难满足不同的作业需求，尤其是农用无人机低空高速播撒作业中的颗粒质量流量检测，由于排量较大，颗粒流为连续高通量密相，重叠度和流动速度会对检测结果产生较大影响。本文总结了现有的种肥颗粒质量流量检测技术及其工作原理，比较了基于质量的直接检测与基于速度和浓度的间接检测方法，分析了各自的优缺点及适用性。针对农用无人机的特定需求，探讨了优化现有检测方法的可能性，并展望了引入前沿科学技术以研发高效、精准、便捷的检测系统，以满足日益增长的市场需求。

INTRODUCTION

Taking information and knowledge as the core elements, through the cross-border integration of modern information technology and agriculture such as the Internet, Internet of Things, big data, artificial intelligence and intelligent equipment, smart agriculture, which realises information perception, quantitative decision-making, intelligent control, precise inputs, and personalised services in the whole process of agricultural production, has become the development trend of modern agriculture in the world (Zhao, 2019). As the premise and foundation of smart agriculture, precision agriculture in the new situation needs to achieve the goals of positioning, timing and quantification, and provide low-input, high-quality and sustainable agricultural production through the monitoring and feedback of each operational link.

¹ Yanshuang WANG, MS candidate, Student; ^{*2} Cancan SONG, PhD, MS supervisor; ³ Yongqi GAO, MS candidate, Student;

⁴ Yubin LAN, PhD, Professor; ⁵ Guobin WANG, PhD, Associate professor; ⁶ Rui MING, Research fellow;

Sowing and fertiliser application are indispensable in agricultural production, and seed and fertiliser particle mass flow detection is an important foundation for precision operations such as precision sowing, precision fertiliser application and yield estimation. The detection of the mass flow rate of seed and fertiliser particles not only helps to know the actual sowing and fertiliser application information in the region and reduce the loss, but also realises the closed-loop control of the discharge rate, which helps to improve the effect of the precision variables of sowing and fertiliser application (Mahmud *et al.*, 2020). Therefore, the mass flow detection of seeding and fertiliser particles can provide basic data for realising the whole monitoring and intelligent management of agricultural operations, which can help the precise perception and intelligent decision-making of the agricultural production process (Lee *et al.*, 2015).

In recent years, research on seed and fertiliser particle mass flow detection technology has progressed rapidly, resulting in the emergence of numerous types of solid particle mass flow detection technologies and methods. Ding *et al.*, (2019), discussed the mechanical electromechanical alarm detection method, machine vision detection method, photoelectric sensing detection method, capacitive sensing detection method, and piezoelectric sensing detection method in their summary of the research progress of small and medium-sized seed sowing detection technology. They also highlighted the advantages and disadvantages of different detection methods and combined these with the requirements of precision agriculture to propose sowing detection indexes for different sowing modes. The existing particle flow detection technology can be classified into two main categories: mass flow detection and volumetric flow detection. The former encompasses techniques such as particle weighing, impact detection, and the measurement of particle volume over a fixed period and fixed volume of particle emission time (Liu *et al.*, 2018). In the field of solid particle pneumatic conveying, scholars have investigated a range of detection methods based on mechanical, optical, acoustic, electrical and correlation techniques (Bergeijk *et al.*, 2001). A significant proportion of the aforementioned methodologies have been extensively utilized within the domain of agricultural seeding and fertiliser application. However, there is a paucity of research pertaining to the detection of high-throughput dense-phase particle flows exhibiting low void fraction. The mass flow detection of continuous high-throughput dense-phase particle flows is imperative, given that particle motion and deposition are influenced by numerous factors during unmanned aerial dispersal.

The objective of this paper is to provide a comprehensive overview of the existing seed and fertiliser particle mass flow detection techniques, analyse the fundamental principles and limitations of the various detection techniques and their viability in UAV broadcasting applications and suggest potential avenues for further research into particle mass flow detection techniques in agricultural UAV broadcasting.

MATERIALS AND METHODS

Mass flow measurement technology

Direct detection method

In the context of direct measurement, the mass flow rate of a solid particle stream is obtained through the detection of either the instantaneous mass change of the particle stream itself or a sensitive variable that is directly correlated with the aforementioned mass flow rate change. The most commonly employed methods are those based on weighing and Coriolis force.

Weighing method

The majority of weighing methods rely on pressure transducers and their associated accessories to directly obtain particle mass changes. Typically, pressure sensors are employed to directly detect the mass change of the material box, thereby obtaining the real-time mass flow rate of particles (Wu *et al.*, 2014). Alternatively, a combination of pressure sensors and springs is utilised (Figure 1) (Yu *et al.*, 2019). This detection method has been widely employed in the measurement of grain yield, pneumatic conveying and other mass flow detection of grain flow (Qu, 2017). The weighing detection method based on belt scales is, in fact, a calculation of the average value of the mass flow rate of particles passing through each cross-section perpendicular to the direction of belt movement per unit time. The method is straightforward to implement physically, has no specific requirements regarding the physical properties of the particles being measured, and is highly applicable. However, it is susceptible to the influence of the rotational speed of the belt pulley and the distribution of particles above the belt, which can result in cumulative errors (Zhou and Zhang, 2009). The deformation and buffering of the spring can serve to counteract the interference of external factors, such as machine vibration. To achieve real-time detection and automatic calibration of fertiliser application, Li Ang

(2001), combined a load cell with a strain force transducer to measure the weight and dynamic behaviour of a fertiliser applicator. This combined detection method represents a significant advancement over traditional weighing techniques, offering enhanced precision in measurement. The weighing type is primarily based on the conveyor belt and spring assembly, which is typically employed for quality inspection in indoor seeding quality inspection test beds and roller grain transport lines. However, it is less frequently utilised in actual field operations.

Coriolis method

The Coriolis method is achieved by establishing the relationship between the Coriolis force generated during the vibration or rotation of the component and the mass flow rate of the particles (Geng *et al.*, 2005). As shown in Figure 2, the linear relationship between the moment generated by the Coriolis force and the mass flow rate as the particles rotate on the rotating metering disc can be expressed by the equation:

$$M = q_m \omega R^2 \quad (1)$$

where, M is the moment of the Coriolis force relative to the centre of rotation, $N \cdot m$; q_m is the mass flow rate, kg/s ; ω is the measurement of angular velocity, rad/s ; R is the measuring wheel outer diameter, m .

Considering the movement of particles on the metering disc and the variation in instantaneous mass distribution, this method yields better detection results under conditions of constant angular velocity and stable instantaneous particle flow. Coriolis-based detection methods convert particle mass and indirectly measure the force and momentum changes generated by particle motion. However, these methods are highly influenced by the flow rate and velocity of grain particles. Accurately capturing these mechanical changes is both the key challenge and the focus for improving detection accuracy.

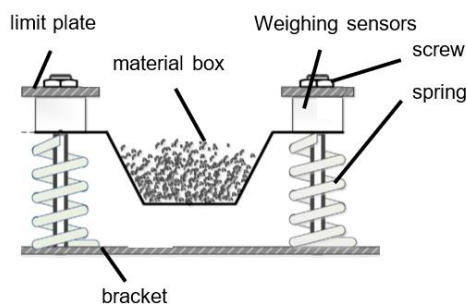


Fig. 1 - Weighing method based on pressure sensor

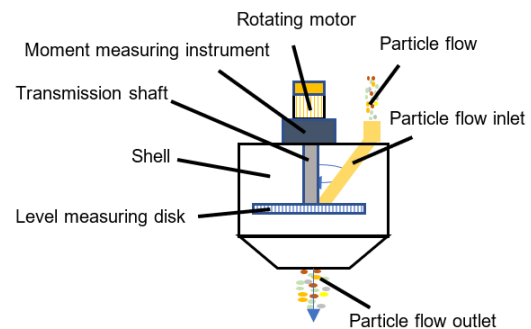


Fig. 2 - Coriolis force method based on rotation mode

Indirect detection method

Indirect measurement refers to determining the mass flow rate of particles by measuring the velocity or concentration of the solid particle stream. For a given particle, if its density and flow velocity are known, there is a correlation between the mass flow rate and the particle stream's concentration and velocity. Thus, the mass flow rate can be indirectly obtained by measuring these two parameters (Zheng and Liu, 2011; Zou Jing, 2015). In the following section, the correlation method is introduced taking into account two aspects: particle concentration detection and velocity detection.

Concentration-based detection method

Electrical method

This method mainly uses the charge change generated by the particle flow to obtain the particle concentration, including the capacitance method and the electrostatic method. The capacitance method refers to collecting the amount of output capacitance change generated when the particle flow passes between the poles of the capacitor and establishing the relationship between it and the particle flow rate according to the particle concentration to obtain the flow rate value (Zhou *et al.*, 2017).

The capacitance method has the advantages of stable operation, high reliability and strong resistance to dust contamination, but it has low sensitivity to the dense-phase particle flow with small concentration difference. In order to be able to accurately detect the capacitance variable generated by the dense-phase particle flow, the existing technology adopts new methods such as the differential capacitance principle or the construction of spiral capacitance sensors to improve the detection accuracy (Zhou *et al.*, 2014; Zhou L., 2014).

The electrostatic method is used to obtain the particle mass flow rate by detecting the amount of electrostatic charge generated by particle collision and friction and establishing the relationship between particle concentration and charge (Jia *et al.*, 2019; Wu *et al.*, 2019). In the actual pipe conveying particle flow, the collision between solid particles, the collision between particles and the pipe wall, and the friction between particles and the air flow generate a large amount of electrostatic charge.

The flow velocity of solid particles can be determined by inter-correlation velocimetry. The mass flow rate of solid particles can be calculated from their velocity and relative concentration (Qian *et al.*, 2012).

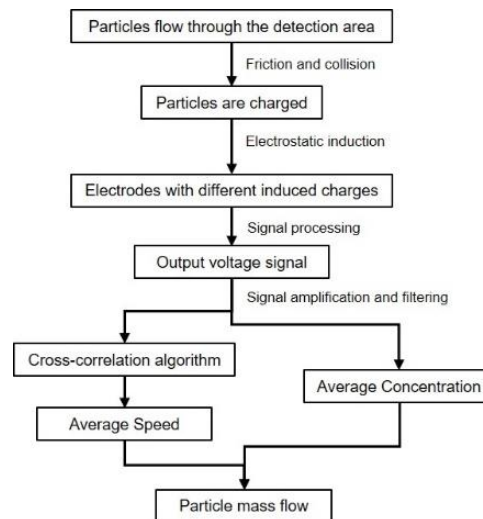


Fig. 3 - Electrostatic method

Research on detection technology based on this method has achieved some results. For example, Yan and Ma, (2000), used a pair of axially spaced metal rods mounted on the cross section of the pipe as electrostatic sensing elements and detected the mass flow rate by obtaining the alternating electrostatic signals caused by the particles flowing through the two rods in the pipe and developed a new type of detection instrument called 'StackFlow 2000', which can provide new opportunities for the application of electrostatic sensors. This method offers new possibilities for the development of electrostatic sensors. The distribution of the electrostatic sensing probes and the electrostatic response characteristics are the key factors affecting the detection results when using this method (Li Guanguan, 2016). Placement of multiple ring electrodes inside the particle flow tube to obtain the average flow velocity throughout the cross section of the measured tube area can improve the detection accuracy (Li *et al.*, 2014).

Volumetric concentration method

This method primarily utilizes the intermittent flow characteristics of particle streams. Changes in particle volume concentration are converted into voltage pulse signals, establishing a relationship between the number of voltage pulses and the number of particles. Based on this relationship, the particle mass flow rate can be calculated from the volume concentration. Common approaches under this method include the photoelectric method, piezoelectric method, and image-based method.

The photoelectric method primarily relies on the blocking effect of the particle flow on light intensity to detect changes in the light signal. A mapping relationship is established between the voltage pulses generated by light intensity fluctuations and the number of particles. Photoelectric sensors typically consist of a transmitter and a receiver, commonly using light-emitting diodes (LEDs) and phototransistors (Che *et al.*, 2017). During operation, as the particle stream passes between the transmitter and receiver, it causes variations in the light received, resulting in corresponding changes in the voltage signal. There is a clear correlation between the concentration of the particle stream and the voltage pulse signal. By counting these pulses, the number of particles can be estimated (Wu *et al.*, 2016; Qiu *et al.*, 2019; Karimi *et al.*, 2017). For continuous, dense, and high-throughput particle streams, the relationship between the induced voltage and flow rate can be established by constructing a distribution matrix of photoelectric sensors (Fig. 4) or dividing the particle channel into a grid (Fig. 5) to collect changes in multiple continuous voltage signals (Jiang *et al.*, 2021; Liu *et al.*, 2019). The relationship between induced voltage and flow rate can also be established by detecting changes in the thickness of the particle pile and using the relationship between the thickness of the particle pile and the mass

of the particles (Fig. 6) (Yin *et al.*, 2021), or by splitting a dense, high-throughput particle stream into multiple smaller streams using a discrete mechanism and detecting them in parallel with multiple sets of photoelectric sensors (Nong *et al.*, 2023; Xu *et al.*, 2022; Ding *et al.*, 2020). Swisher *et al.*, (2002), used a trapezoidal optical chamber to transmit laser light to an array detection unit composed of 32 photodiodes, allowing them to determine the instantaneous flow rate of fertiliser from an air-conveyor applicator based on the amount of light blocked by the granules. Regardless of the approach, whether using a photovoltaic line array or segmenting the granular stream, the key to improving this method lies in optimizing the photosensitive components (e.g., by using thin-faced lasers) and enhancing both the signal acquisition accuracy and the range of the photodiode sensors (Ding *et al.*, 2019; Ding *et al.*, 2021).

In the piezoelectric method, voltage pulse signals are generated by intermittent collisions between the particle stream and a piezoelectric element. These signals are detected and converted into particle counts. The frequency of collisions, and thus the number of voltage pulses, increases with the concentration of the particle stream. In other words, a higher particle concentration leads to more frequent impacts and a greater number of voltage signals. However, this method is less sensitive to particle streams with only slight changes in concentration. It also requires high-resolution detection capabilities to accurately respond to variations in particle concentration and to generate voltage pulse signals within an appropriate range.

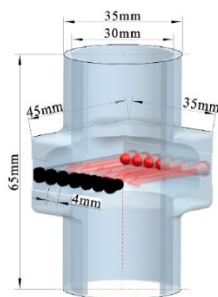


Fig. 4 - Mass flow detection method of continuous dense particle flow based on infrared sensor
(Jiang *et al.*, 2021)

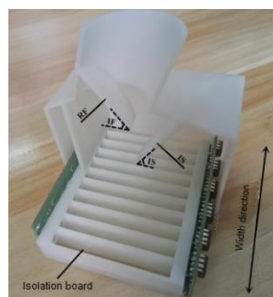


Fig. 5 - The dense particle flow is divided into a single row of small particle flow (Liu *et al.*, 2019)

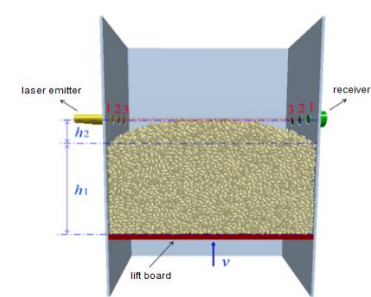


Fig. 6 - Photoelectric sensor array (Yin *et al.*, 2021)

The photoelectric and piezoelectric methods are relatively simple in principle and construction and have been widely used in fertiliser application and seeding (Jia *et al.*, 2018). Both methods essentially detect voltage pulse signals generated by the inductive element of the sensor and should be used in such a way as to ensure that a clear and stable signal is obtained as far as possible. For example, the detection accuracy of photoelectric sensors is susceptible to dust and other contaminants, and measures such as the installation of protective covers can be taken to ensure a clean detection environment (Ji *et al.*, 2016). Piezoelectric sensors are more sensitive to intermittent particle flow, and when detecting continuous particle flow, detection accuracy can be improved by using easily deformable materials (e.g. piezoelectric films), signal conversion and adaptive noise cancellation algorithms (Wang *et al.*, 2019; Xiong *et al.*, 2018).

The imaging method mainly uses high-speed camera technology to obtain images of the falling particle flow and counts the number of particles in unit space through image processing, which is also a volume concentration-based detection method (Back *et al.*, 2014). This method can obtain not only the particle flow information, but also the spatial motion trajectory of the falling particles (Yazgi and Degimencioglu, 2007). However, due to the high environmental requirements of this method, which requires a complex test bench to place the camera, light source, computer, etc., it is generally only used for laboratory testing (Lu *et al.*, 2019). In order to widen the scope of application, researchers have used a digital camera (Nikon, D70) and a charge-coupled device digital colour camera to capture images of seed and fertiliser particles, determine the number and size of particles, and experimentally verify the feasibility of these methods (Navid *et al.*, 2011; Back *et al.*, 2014).

The accuracy of image recognition is the basis of the image method. Since the image is mainly derived from the dynamic flow and static distribution of particles, and the number of particles is mostly used as the detection target, it will be affected by various factors such as light, vibration of the detection device, and overlapping of particle materials, and the detection error is relatively large. To improve the detection performance, neural networks and other image segmentation and feature extraction methods are also combined with image processing (Tan *et al.*, 2014; Zhao *et al.*, 2022).

In addition, to improve the detection accuracy of the existing detection system under the noise interference of field operations, the point cloud data collected by LiDAR has been used to characterise the geometric feature changes of particles as volume changes, and a related algorithm for calculating fertiliser emissions has been developed (Zhao *et al.*, 2021). This method requires processing and analysis of the point cloud data and is currently mostly used for indoor static particle flux detection platforms.

Attenuation method

This method mainly uses the principle that electromagnetic waves, sound waves, etc. are attenuated by the medium and the particle concentration is obtained by detecting the wave intensity before and after the emitted wave passes through the particle flow tube. Visible light, laser, microwave, X-ray, γ -ray and ultrasonic waves can be used as wave sources for the attenuation method. Using microwave as an example, the change in wave intensity through the particle flow can be characterised by the energy of the echo signal. By detecting the energy of the Doppler echo signal in the pipe, the density of the particle flow can be obtained, and then using the flow rate, the particle mass flow rate can be obtained (Isa and Wu, 2006). The traditional method of calculating the particle density is to use the power spectrum calculation to obtain the energy information of the signal. In the process of random signal acquisition, the power spectral density is commonly used to represent the distribution of the average power in the frequency domain, which can be used to obtain the total power P by integrating the operation over the entire frequency range, with the following equation:

$$P = \int_{f_{min}}^{f_{max}} s(f) d_f \quad (2)$$

where, P is the echo signal power; $s(f)$ is the power spectral density of the signal; f_{min} is the lower limit of the Doppler bandwidth; f_{max} is the upper limit of the Doppler bandwidth.

Power spectrum estimation methods include classical power spectrum estimation and modern spectrum estimation. Classical spectral estimation methods include the correlation function method (BT method) and the periodogram method, which is based on the FFT (Fast Fourier Transform) to estimate the power spectral density function, which is greatly affected by the transfer function and needs to be selected according to the actual situation (Deng *et al.*, 2014). Modern spectral estimation methods include AR model spectral estimation, MA model spectral estimation and ARMA model spectral estimation methods (Li Ying, 2015). When using this method, if the order of the parametric model is too low, it is difficult to accurately distinguish the frequency components, and if the order of the parametric model is too high, there is a possibility of distortion in the display of the true amplitude ratio, which affects the estimation of the true spectral peaks.

Velocity-based detection methods

Impulse momentum method

This method primarily utilizes the impact force generated by granule flow striking the force-measuring plate and force sensors, combined with the functional relationship between the impact force and the mass flow rate of granules, to determine the mass flow rate. The key to ensuring the detection accuracy of this approach lies in effectively extracting the valid deformation caused by the granule flow impact (Chen *et al.*, 2005; Zhou *et al.*, 2006). When the continuous particle flow passes through a fixed cross-section, the relationship between the cumulative particle mass W , the instantaneous mass flow rate m_i , the flow velocity v_i and the instantaneous flow rate Q_i is expressed as follows:

$$W = \sum_{i=1}^n Q_i(t) \Delta t = \sum_{i=1}^n m_i(t) v_i(t) \Delta t \quad (3)$$

If the continuous flow of particles hits the force plate continuously, the momentum of the moving particles will change after the collision with the force plate. Assuming that the velocity of the particles after the collision is zero, then the following formula is established:

$$I_i(t) = m_i(t) v_i(t) \quad (4)$$

From equation (4) it can be seen that if the particle collision momentum as well as the flow rate can be obtained, then the particle mass flow rate can also be obtained. The force plate deforms under the impact of the particle flow, the stress generated by the deformation is detected by strain sensors, and the relationship between the stress and the momentum can be determined by test calibration (equation 5).

$$I_i(t) = kU_i(t) \quad (5)$$

where, Δt is the timed sampling interval; $I_i(t)$ is the impulse of the particle flow, N·s; $m_i(t)$ is the mass of grain per unit length at any position on the conveyor belt at time t , kg; $v_i(t)$ is the instantaneous velocity of the grain at time t , m/s.

In order to resolve the issue of the test plate being vulnerable to a variety of factors, *Ding Yongqian (2009)*, investigated a pulse method based on velocity detection, which allows particles to flow through the test device by their own gravity and initial velocity without the need to maintain a constant velocity of motion. The method can calculate the particle flow rate based on the weight difference between two load cells and known structural parameters to determine the instantaneous mass flow rate and the total mass of particles to be detected. To improve the detection accuracy of the pulse method, *Fulton et al., (2009)*, simulated different field slopes experienced during field operations, investigated the effect of harvester traverse roll and pitch on the detection accuracy of existing mass flow sensors, and provided suggestions for optimising the detection method for different slopes. *Schrock et al., (1999)*, developed a new diaphragm grain mass flow sensor to isolate the grain from the load cell by using a flexible fabric-reinforced rubber diaphragm to reduce the possibility of cracking and entrapment of other contaminants behind the sensing element.

Pressure method

When faced with a continuous dense grain flow, the flow rate value can be obtained by collecting the continuously changing pressure generated by the grain flow acting on the pressure sensors and establishing the relationship between pressure and grain flow rate. As shown in Fig.7, multiple pressure sensors are arranged along the cross section of the particle flow between the two side walls of the deflector plate to establish the relationship between the instantaneous thickness of the particle flow and the pressure. Mathematical modelling methods are used to fit the thickness distribution equation of the cross section of the particle flow, and then the equation is integrated to obtain the instantaneous cross sectional area of the particle flow. The particle flow rate is used to establish the relationship between instantaneous mass and cross-sectional area, which in turn allows for the relationship between pressure and particle mass flow rate to be determined (*Geng et al., 2021*).

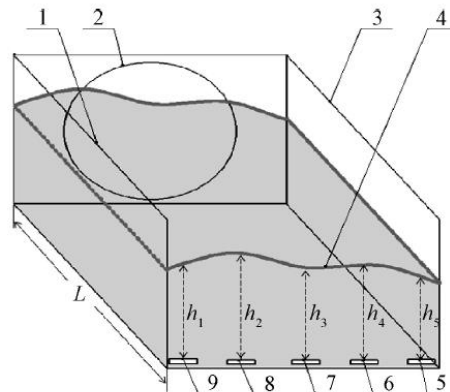


Fig. 7 - Schematic diagram of particle flow mass flow detected by piezoelectric sensor (*Xiong et al., 2018*)

1 - Right wall of the concave deflector plate; 2 - Tail of the grain collection elevator; 3 - Left wall of the concave deflector plate; 4 - Cross-section of grain flow; 5 - First reference position; 6 - Second reference position; 7 - Third reference position; 8 - Fourth reference position; 9 - Fifth reference position.

The method treats the flowing particle cluster as a solid mass of uniform density and establishes the relationship between particle flow pressure and flow velocity by detecting the force of the solid mass on the pressure sensor in real time, making it relatively friendly to dense phase particle flows and capable of obtaining large pressure signals. In addition to production measurement, the method can also be used in pneumatic conveying with a venturi to establish a relationship between the mass flow rate of solid particles by testing the difference in air flow pressure before and after gas-solid two-phase flow through the venturi (*Mailander and Moriasi, 2011*).

Doppler method

This method is a new non-destructive testing technique in which the measured element does not need to be in direct contact with the grain flow and there is no problem of corrosion and wear.

Moreover, in addition to microwaves, electromagnetic waves such as millimetre waves and lasers, as well as ultrasonic waves, can be used as the emitted wave source of this detection method (Yin Guang, 2012; Rafael et al., 2023). It has been widely used in grain particle flow detection (Penirschke et al., 2008). However, wave propagation is not only affected by the differential reflection caused by varying grain flow characteristics, but also by other factors that influence the reflected wave, which can interfere with the frequency shift (Pang et al., 2008). Developing appropriate detection structures and signal processing methods tailored to different grain characteristics is essential for ensuring the accuracy of this detection method.

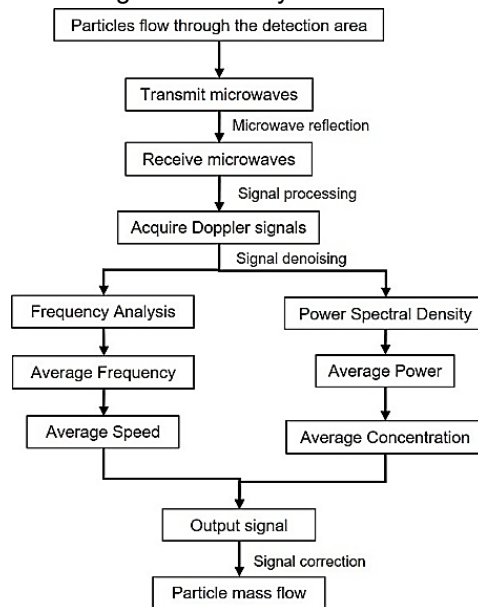


Fig. 8 - Microwave detection method based on doppler effect

Acoustic method

This method primarily involves acquiring acoustic signals generated by particle collisions and establishing their relationship with particle flow velocity, which is then used to calculate the mass flow rate (Wang et al., 2017). When the particle flow hits the steel plate during the free fall under gravity, the particle-particle collision and particle-steel plate collision can excite strong elastic waves, and the particle flow hitting the steel plate at different velocities will produce large differences in acoustic signals. Due to the damping effect of air and the relatively weak collisions between particles compared to collisions with a steel plate, acoustic signals are difficult to capture. However, an acoustic emission sensor can be used to detect the signals generated by the collision and friction of solid-phase particles with a steel plate (Wei et al., 2011). This method relies on acoustic signals produced during particle flow interactions, but when the particles are small or the collisions and friction are light, the resulting signals are weak and difficult to detect. Additionally, noise in the surrounding environment can further increase measurement errors. Therefore, accurately capturing and processing the effective acoustic signals generated by the particle flow is key to improving detection accuracy.

Summary of existing detection methods

The above detection methods obtain particle flow information from different angles, which can basically realise the detection needs in different scenarios, but they all have certain limitations (Figure 9). In the direct detection method, the detection element is in direct contact with the particles, which will definitely cause wear, corrosion and relaxation deformation of the sensor in the long run, and if it is in the pneumatic pipeline, it will also have a certain effect on the normal pressure drop in the pipeline, which will affect the efficiency of particle transport. In the indirect detection method, the concentration-based detection method is more sensitive to the particle concentration, and the light wave and acoustic wave are not only more demanding on the environment, which is affected by dust, impurities, temperature and humidity, but also the signal processing and analysis are relatively complicated. In particular, the detection of high-throughput dense-phase particle flow requires higher resolution and sensitivity of sensors, and the spatial distribution of sensors in the detection area as well as the post-signal processing techniques are more difficult than those of dilute-phase particle flow detection and require complex information conversion. The velocity detected by the velocity-based detection method is basically the average velocity of the particle flow, and the flow state and spatial distribution of the particles will directly affect the detection results, which can easily cause detection errors.

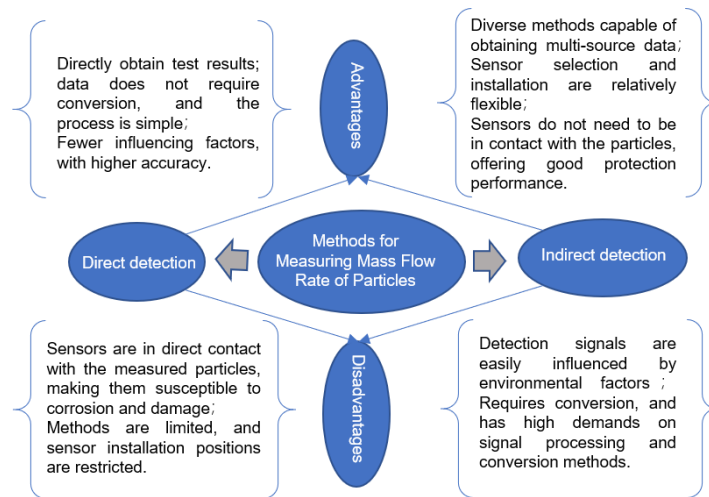
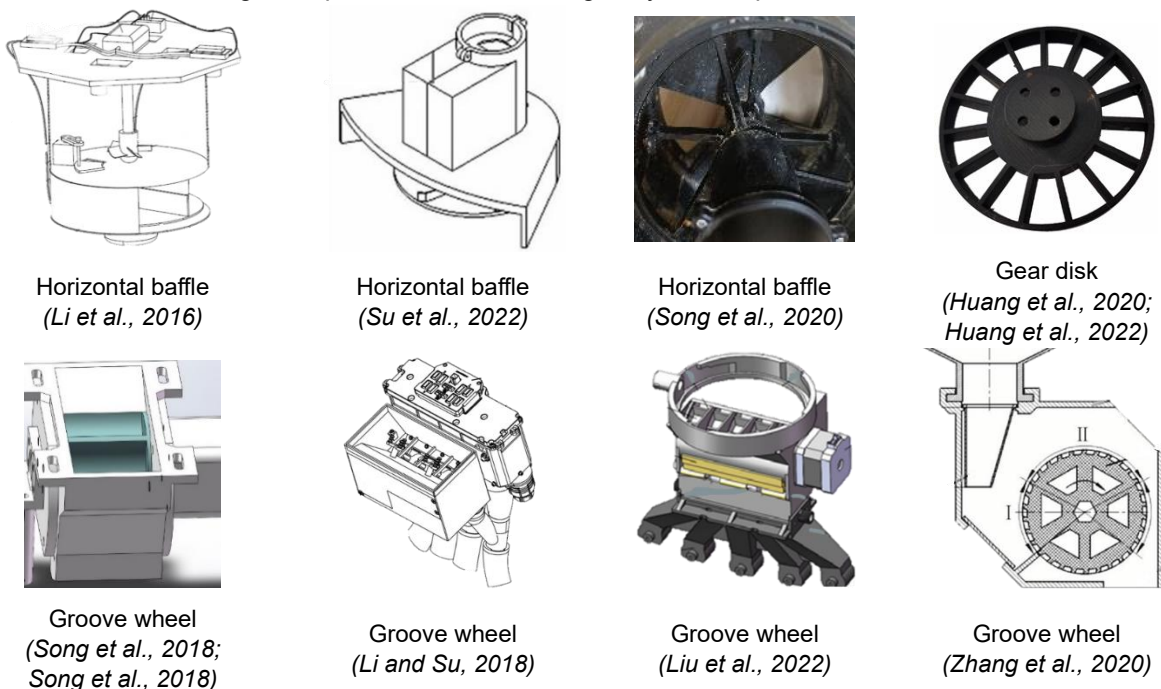


Fig. 9 - Comparison of different detection methods

In practice, the flow state and emission environment of seed and fertiliser particles are diverse, and there is still much room for improvement in the existing technology, and it is difficult to achieve good detection results using only the single method mentioned above. In order to improve the detection effect, researchers have attempted to fuse electrostatic sensors, differential pressure sensors and accelerometers, and constructed a data-driven model based on support vector machines to estimate the mass flow rate of a solid particle stream (Faisal et al., 2022). The machine vision system is characterised by its high precision, real-time capabilities, automation and intelligence. The image-based mass flow detection method of dense-phase particle flow is expected to yield significant achievements in the future (Liang Yongan, 2022; Wang Dingkan, 2022). The use of neural networks to model the relationship between the mass flow rate of solid particles and a variety of sensitive variables can also improve the detection effect (Ding Mingwei, 2022; Zhu Siqi, 2020).

Flow regulation and detection methods in drone seeding

The two main parts of the UAV spreading device are particle discharge and particle spreading, where the particle discharge method is related to the adjustable range of discharge and particle displacement adjustment, which mainly affects the particle discharge accuracy, and the particle spreading method is related to the particle diffusion trajectory and deposition range, which mainly affects the deposition width and uniformity (Song et al., 2020). Figure 10 shows the discharge mechanism in the existing UAV spreading device, which is mainly based on grooved wheels, horizontal baffles and centrifugal discs. It is typically installed at the bottom of the material box, having a simple structure and being easy to manipulate.



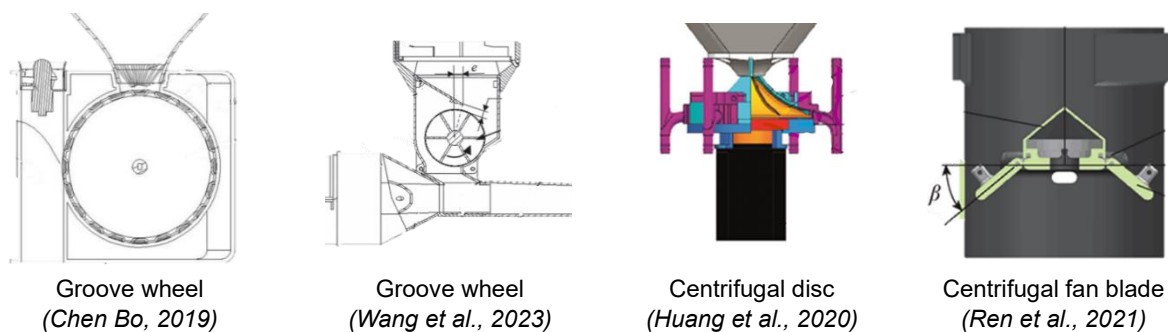


Fig. 10 - Method of displacement regulation and detection for UAV seeding

Song et al., (2021), designed a UAV variable fertiliser application system using an opposite laser sensor. The transmitting and receiving ends were fixed around the connecting pipe between the material box and the fertiliser discharger. Real-time detection of particle flow was achieved using the photoelectric principle, enabling mass flow detection of fertiliser particles. DJI Innovation employed a Hall sensor mounted on the agitator of the spreader. As the agitator rotates, the magnet on the Hall sensor interacts intermittently with magnetic strips on the side wall of the spreader. Variations in particle flow rate cause different levels of resistance as particles pass through the agitator, altering its rotation speed. These changes result in varying Hall sensor signals, which reflect the state of the particle flow (Huang and Zhang, 2020). To obtain more accurate detection results, Huang Junhao et al. developed a detection device based on differential weighing. The system uses multiple sensors to detect vibration noise and applies filtering techniques to improve detection accuracy (Huang et al., 2024).

RESULTS

Adaptation of different detection methods

The configuration of sensors, characteristics of detection components, and information processing techniques vary widely across different detection methods. Selecting an appropriate particle mass flow detection method tailored to specific discharge mechanisms is essential for accurately acquiring detection data and improving overall measurement precision. During UAV spreading operations, particle flow is highly susceptible to noise and vibration caused by the high-speed rotation of the rotors, which poses challenges to accurate mass flow detection. Additionally, conventional detection methods often fall short in terms of accuracy and resolution. Therefore, there is a pressing need to develop innovative detection technologies that offer strong anti-interference capability, high resolution, and rapid response time.

Table 1

Adaptation analysis of different detection methods applied to unmanned aerial dispersal

Detection Method	Feasibility	Limitations	Improvement Suggestions
Weighing Method	The feasibility is relatively strong. The load of the material box on the drone is limited and easy to plug and unplug. Pressure sensors can meet the requirements, allowing for real-time measurement.	This method mainly focuses on detecting changes in the weight of the material box, and the stress conditions of the material box have a significant impact on the detection results.	Multiple pressure sensors can be set up, using the differential principle to obtain the actual net load changes of the material box.
Coriolis Force Method	The feasibility is relatively poor. The size of the drone is limited, and most existing discharge mechanisms have compact structures, resulting in limited space for particle descent, making it difficult to generate Coriolis force.	The detection device is somewhat complex and has high installation requirements; it needs particle flow to generate Coriolis force for accurate detection.	/
Concentration-Based Method	The feasibility is relatively strong. During the drone's dispersal, the particle flow is substantial, and the signal changes based on particle volume concentration are significant and easy to obtain.	To acquire complete and accurate detection information when the particle flow is large, some methods require complex sensor arrangements, which can lead to signal redundancy and make signal processing difficult.	Improve signal processing methods and consider introducing deep learning algorithms to optimize the information processing process for faster and more accurate detection information.

Detection Method	Feasibility	Limitations	Improvement Suggestions
Velocity-Based Method	The feasibility is average. During the drone's dispersal, the distance from the material box to the dispensing mechanism is short, and the flow space for particles is limited, resulting in low speeds and making it difficult to generate noticeable signal changes.	Due to size constraints, the drone's discharge mechanism is small, and the range of particle speed variation is limited, making detection more challenging.	Optimize the signal detection circuit to amplify or convert the measured velocity-based signals to achieve significant signal changes.

Despite the existence of numerous existing seed and fertiliser particle flow quality flow detection methods, these are predominantly utilised in ground machinery with relatively slow operating speeds and small displacements. The response time and detection accuracy of these methods are generally adequate to meet requirements. However, when considering the implementation of these methods in the context of UAV seeding, it is evident that the response speed is inadequate. Furthermore, timely signal processing becomes challenging due to particle overlap and the rapid flow rate, which can result in incomplete information and increased error in the final calculated particle mass flow rate. In light of these challenges, this paper puts forward the following perspective:

1) In order to accelerate the realisation of unmanned precision operations, high-throughput dense-phase particle mass flow detection techniques applicable to agricultural UAV seeding need to be further optimised. For example, the existing unmanned aerial dispersal is divided into unconstrained diffuse dispersal and strip/shot dispersal with some constraints, and the corresponding discharge devices are mostly centralised and monolithic, which produce particle streams with different void ratios, and the installation location, mode, volume and weight of the sensors should be considered when performing the optimisation.

2) Existing sensors are typically designed for specific operating scenarios or particular types of particles, resulting in limited applicability. To address the diverse requirements of seed and fertiliser particle detection, it is necessary to explore innovative detection methods by integrating advanced technologies from various fields. For instance, flow tomography, such as X-ray imaging, can be used to obtain high-resolution, three-dimensional structural images by penetrating the material.

3) Current research has shifted from the development and performance optimisation of sensors to the integration of detection systems. How to use the existing detection information to develop an intelligent seed and fertiliser detection system and connect it to the management of smart agriculture to achieve a benign closed-loop operation system will be an important research topic in the field of smart agriculture in the future.

CONCLUSIONS

The application of unmanned aerial vehicle (UAV) spreading technology in seeding and fertiliser distribution plays a vital role in advancing agricultural precision. In precision operations, real-time information on particle mass flow is a fundamental prerequisite for effective particle displacement control and overall operation planning. Therefore, the study of high-throughput, dense-phase particle mass flow detection is crucial for achieving UAV-based precision seeding. This paper presents a comprehensive review of the principles, usage conditions, and adaptability of current mass flow detection methods for seed and fertiliser particle streams in UAV applications. The main conclusions are as follows:

Whilst the weighing and correlation methods are relatively simple to implement and have been used in UAV dispersal, the adaptability of other methods in this field remains to be investigated. For example, among the concentration-based detection methods, the electrical method is more sensitive to obvious signals. The short flow time and low velocity of particles in UAV dispersal produces relatively weak capacitance changes or electrostatic signals, which are not easily captured accurately and require signal amplification.

The application of volume concentration methods necessitates the consideration of detecting overlapping particles in high-throughput dense-phase particle flows, a consideration that extends to the expansion of the detection area of the sensor and the optimisation of the detection device. The employment of the image method requires the consideration of the accuracy of particle identification, whilst real-time image processing algorithms must be developed to meet the requirements of high-speed seeding by UAVs. The acoustic method utilised in the speed-based method primarily relies on the detection of particles impacting the detection plate sounding. However, in the context of UAV sowing operations, the high-speed rotation of the rotor wing generates significant vibrations, which can confound the distinction between particle impacts and

sound from the detection plate, thereby compromising the detection of the target signal. Consequently, the method is not particularly well-suited for utilisation in UAV sowing.

In the context of direct or indirect detection, any scenario that necessitates direct contact between the particle flow and the detection element is susceptible to damage to the detection element. Consequently, non-contact detection methods should be prioritised wherever feasible. The future of agriculture is unmanned, with intelligent seeding and fertiliser operations being a key development trend. In order to achieve this, existing mass flow detection technology needs to evolve beyond basic detection to include the ability to access data on the intelligent management platform. This will allow it to be integrated into a large database, facilitating accurate decision-making and providing data support.

REFERENCES

- [1] Back, S., Yu, S. H., Kim, Y., Chung, S. O., & Lee K. H. (2014). An image-based application rate measurement system for a granular fertilizer applicator. *Transactions of the American Society of Agricultural and Biological Engineers*, Vol.57, pp. 679-687, South Korea.
- [2] Vanbergeijk, J., Goenes, D., Willigenburg, L., & Speelman, L. (2001). PA—Precision Agriculture Dynamic weighing for accurate fertilizer application and monitoring. *Journal of agricultural engineering research*, Vol.80, pp.25-35, Hubei/China.
- [3] Che, Y. W., Li, G., Liu, X. T., Li, Z. I., & Wang, F. Z. (2017). Design and experiment of seeding quality infrared monitoring system for no-tillage seeder (免耕播种机播种质量红外监测系统设计与试验). *Transactions of the Chinese Society of Agricultural Engineering*, Vol.33, pp.11-16, Beijing/China.
- [4] Chen, S. R., Zhang, W. G., Li, X. P., Li, M. Z., & Huang, J. P. (2005). Experiment research of grain mass flow sensor based on impact (冲量式谷物流量传感器性能实验研究). *Transactions of the Chinese Society for Agricultural Machinery*, pp. 82-84, Jiangsu/China.
- [5] Chen, B. (2019). *Aircraft-mounted Pneumatic Seed Broadcasting Equipment and Sowing Drone*. China, Patent, NO. CN108715225A.
- [6] Ding, Y. Q. (2009). *Study on the methods for measuring mass flow rate of solid granular materials* (固体颗粒料质量流量检测方法的研究), PhD dissertation, *Nanjing Agricultural University*, Jiangsu/China.
- [7] Ding, M. W. (2022). *Research on temperature compensation technology of machine vision strain sensor* (机器视觉应变传感器温度补偿技术研究), MA dissertation, *Dalian University of Technology*, Liaoning/China.
- [8] Deng, Z. H., Liu, B. B., & Li, Y. L. (2014). Common power spectrum estimation method and MATLAB simulation (常见的功率谱估计方法及其Matlab仿真). *Electronic Science and Technology*, Vol.27, pp. 50-52, Shanxi/China.
- [9] Ding, Y. C., Zhu, K., Wang, K. Y., Liu, X. D. & Du, C. Q. (2019). Development of monitoring device for medium and small size seed flow based on thin surface laser-silicon photocell (薄面激光-硅光电池中小粒径种子流监测装置研制). *Transactions of the Chinese Society of Agricultural Engineering (Transactions of the CSAE)*, Vol.35, pp.12-20, Hubei/China.
- [10] Ding, Y. C., Wang, K. Y., Du, C. Q., Liu, X. D. & Chen, L. Y. (2020). Design and experiment of high-flux small-size seed flow detection device (高通量小粒径种子流检测装置设计与试验). *Transactions of the Chinese Society of Agricultural Engineering (Transactions of the CSAE)*, Vol.36, pp.20-28, Hubei/China.
- [11] Ding, Y. C., Chen, L. Y., Dong, W. J., Wang, W. C., & Liu, X. D. (2021). Design and experiment of the sowing monitoring system for a wide-width rapeseed planter (油菜宽幅播种作业监测系统设计与试验). *Transactions of the CSAE*, Vol.37, pp.38-45, Hubei/China.
- [12] Ding, Y. C., Wang, K. Y., Liu, X. D., Liu, W. P., Chen, L. Y., Liu, W. B., & Du, C. Q. (2021). Research progress of seeding detection technology for medium and small-size seeds (中小粒径种子播种检测技术研究进展). *Transactions of the Chinese Society of Agricultural Engineering (Transactions of the CSAE)*, Vol.37, pp.30-41, Hubei/China.
- [13] Fulton, J. P., Sobolik, C.J., Sheater, S. A., Higgins, S. F., & Burks, T. F. (2009). Grain yield monitor flow sensor accuracy for simulated varying field slopes. *Applied Engineering in Agriculture*, Vol.25, pp. 15-21, American.
- [14] Faosal, A., Wang, L. J., & Yan, Y. (2020). Mass flow rate measurement of solids in a pneumatic conveying pipeline in different orientations. *Measurement: Sensors*, Vol.27, 100021.
- [15] Geng, C. M., Man, Q. F., Xia, J. Q., & Nie, H. P. (2005). Analysis of Coriolis mass flow measurement principles for solid bulk materials (科里奥利固体散料质量流量测量原理分析). *Measurement Technology*, pp.33-34, Beijing/China.

- [16] Geng, D. Y., Tan, D. L., Su, G. L., Wang, Z. Y., Wang, Z. W., & Ji, X. Q. (2021). Optimization and experimental verification of grain yield monitoring system based on pressure sensors (压力式谷物产量监测系统优化与试验验证). *Transactions of the Chinese Society of Agricultural Engineering*, Vol.37, pp. 245-252, Shandong/China.
- [17] Huang, J. H., He, W. Z., Yang, D. S., Lin, J. Q., Ou, Y. Z., Jiang, R., & Zhou, Z. Y. (2024). Quantity monitor based on differential weighing sensors for storage tank of agricultural UAV. Vol.8, PP. 92-, Guangdong/China.
- [18] Huang, X. M., Xu, H. W., Zhang, S. Li, W.C., Luo, C. M., & Deng, Y. F. (2020). Design and experiment of a device for rapeseed strip aerial seeding (油菜成条飞播装置的设计与试验). *Transactions of the Chinese Society of Agricultural Engineering (Transactions of the CSAE)*, Vol.36, pp. 78-87, Guangdong/China.
- [19] Huang, X. M., Zhang, S., Luo, C. M., Li, W. C., & Liao, Y. T. (2020). Design and Experimentation of an Aerial Seeding System for Rapeseed Based on an Air-Assisted Centralized Metering Device and a Multi-Rotor Crop Protection UAV. *Applied Sciences*. Vol.10, PP. 8854-.
- [20] Huang, X. M., Zhang, S., Zhu, Y. Z., & Liu, Y. (2022). Seeding process analysis and test of the air conveying rapeseed aerial seeding device (气送式油菜飞播装置投种过程分析与试验). *Transactions of the Chinese Society of Agricultural Engineering (Transactions of the CSAE)*, Vol.38, pp. 31-41, Hubei/China.
- [21] Han, J. (2020). *Measurement system of mass flow rate of granular fertilizer based on microwave doppler effect* (基于微波多普勒效应的颗粒肥料质量流量测量系统研究), PhD dissertation, *Bayi Agricultural University*, Heilongjiang/China.
- [22] Huang, X. M., Zhang, C. (2020). Material detecting mechanism of sowing machine, sowing machine, AND unmanned aerial vehicle for protecting plants.US, Patent, NO. US20200137948A1.
- [23] Ji, C., Chen, X. G., Chen, J. C., Wang, S. G., & He, P. L. (2016). *Monitoring system for working performance of no-tillage corn precision seeder* (玉米免耕精量播种机排种质量监测系统). *Transactions of the Chinese Society for Agricultural Machinery*, Vol.47, pp.1-6, Xinjiang/China.
- [24] Jia, H. L., Wen, X. Y., Wang, G., Liu, H. L., & Guo, H. (2019). Design and experiment of mass flow Sensor for granular fertilizer (颗粒肥料质量流量传感器设计与试验). *Transactions of the Chinese Society for Agricultural Machinery*, Vol.51, pp.130-136, Jilin/China.
- [25] Jiang, M., Liu, C. I., Du, X., Huang, R. B., Dai, L., & Yuan, H. (2021). Research on continuous granular material flow detection method and sensor. *Measurement*, Vol.182, 109773.
- [26] Jia, H. L., Lu, Y., Qi, J. T., Zhang, Z., Liu, H. L., Li, Y., & Luo, X. F. (2018). Detecting seed suction performance of air suction feeder by photoelectric sensor combined with rotary encoder (光电传感器结合旋转编码器检测气吸式排种器吸种性能). *Transactions of the Chinese Society of Agricultural Engineering*, Vol.34, pp.28-39, Jilin/China.
- [27] Karimi, H., Navide, H., Besgaratu, B., Hossein, B., & Iraj, E. (2017). A practical approach to comparative design of non-contact sensing techniques for seed flow rate detection. *Computers and Electronics in Agriculture*, Vol.142, pp.165-172, Iran.
- [28] Li, W. C., Li, C. Y., Huang, X. M., Zhu, Y. Z., & Wang, W. Y. (2023). Operation quality control of rapeseed strip aerial seeding system via under-constrained seeding technique. *Computers and Electronics in Agriculture*. Vol.206, 107693.
- [29] Liu, W., Zhou, Z. Y., Xu, X. L., Guo, Q. Y., Zou, S. S., He, W. Z., Luo, X. W., Huang, J. H., Lin, J. Q., & Jiang, R. (2023). Evaluation method of rowing performance and its optimization for UAV-based shot seeding device on rice sowing. *Computers and Electronics in Agriculture*. Vol. 207, 107718.
- [30] Isa, M., & Wu, Z., (2004). Microwave radar sensor as solid flow counter. *High Frequency Postgraduate Student Colloquium, Piscataway NJ, IEEE*, 1360345.
- [31] Li, G. G. (2016). *Mass flow rate measurement of particles based on electrostatic sensors* (基于静电传感器的颗粒质量流量的测量), MA dissertation, *North China Electric Power University*, Beijing/China.
- [32] Li, J., Fu, F. F., Li, S., Xu, C. L., & Wang, S. M. (2014). Velocity Characterization of Dense Phase Pneumatically Conveyed Solid Particles in Horizontal Pipeline through an Integrated Electrostatic Sensor. *International Journal of Multiphase Flow*, Vol.76, pp.198-211.
- [33] Lee, W. S., & Ehsani, R. (2015). Sensing systems for precision agriculture in Florida. *Computers and Electronics in Agriculture*, Vol.112, pp.2-9, United States.
- [34] Liu, H. T., Ding, Y. Q., Yu, H. F., Jin, M. F., Jiang, Y. Z., & Fu, X. Q. (2018). Signal processing method and performance tests on weighting-sensor-based measuring system of output quantity for a seeding and fertilizing applicator. *IFAC-PapersOnLine*, Vol.51, pp.536-540, Nanjing/China.

- [35] Li, A. (2017). *Design and application of miniaturized multi-dimension force sensor* (小型多维力传感器设计及应用), MA dissertation, *Southeast University*, Jiangsu/China.
- [36] Isa, M., & Wu, Z. (2006). Microwave doppler radar sensor for solid flow measurements. *The 36th European Microwave Conference, IEEE*, pp. 1508-1510.
- [37] Wei, L., Hu, J. P., H., Zhao, X. S., Pan, H. R., Lakhari, I. A., & Wang, W. (2019). Development and experimental analysis of an intelligent sensor for monitoring seed flow rate based on a seed flow reconstruction technique. *Computers and Electronics in Agriculture*, Vol. 164, 104899.
- [38] Isa, M., & Wu, Z. (2006). Microwave Doppler Radar Sensor for Solid Flow Measurements. *Microwave Conference*. pp. 1508-1510, UK.
- [39] Li, Y. (2015). *Spectral estimation of random signals and its improvements* (随机信号的功率谱估计及其算法的改进), MA dissertation, *Tianjin University*, Tianjin/China.
- [40] Liang, Y. A. (2022). *Design and test of target spraying system based on machine vision* (基于机器视觉的对靶喷雾系统设计与试验), MA dissertation, *Jiangxi Agricultural University*, Jiangxi/China.
- [41] Li, J. Y., Lan, Y. B., Zhou, Z. Y., Zeng, S., & Zhu, Q. Y. (2016). Design and test of operation parameters for rice air broadcasting by unmanned aerial vehicle. *Int. J. Agric. Biol. Eng.* Vol.9, pp. 24-32.
- [42] Li, S., & Su, S. (2022). *A Material Spreading Device, a Drone, and a Material Spreading Method*, China, Patent, NO. CN110963039A.
- [43] Liu, W., Zou, S. S., XU, X. L., Gu, Q. Y., He, W. Z., Huang, J., Huang, J. H., Lin, J. Q., Zhou, Z. Y., Jiang, R., & Luo, X. W. (2022). Development of UAV-based shot seeding device for rice planting. *Int J Agric & Biol Eng*, Vol.15, pp. 1-7.
- [44] Lu, C. Y., Li, H. W., He, J., Wang, Q. J., Zhang, Y. F., & Huang S. H. (2019). Development of testbed for seeding performance test of drill metering device based on intermittent automatic sampling (间歇式自动取样条播排种器排种性能检测试验台研制). *Transactions of the Chinese Society of Agricultural Engineering*, Vol.35, pp. 10-19, Beijing/China.
- [45] Mahmud, M., Abidin M., Abiodun, E., & Hasan, H. S. (2020). Robotics and Automation in Agriculture: Present and Future Applications. *Applications of Modelling and Simulation*, Vol.4, pp.130-140, Malaysia
- [46] Mailander, M., & Moriasi, D. (2011). Test of pressure transducer for measuring cotton-Mass flow. *The Journal of Cotton Science*, Vol.15, pp. 137-143.
- [47] Nong, F., Xu, C. B., Li, Q., Wang, S., Long, T. M., & Ding, Y. C. (2023). Sequential parallel detection device for the granular fertilizer of rape mechanical direct seeding (油菜机直播颗粒肥分流有序并行检测装置设计与试验). *Transactions of the Chinese Society of Agricultural Engineering (Transactions of the CSAE)*, Vol.39, pp.18-28, Hubei/China.
- [48] Navid, H., Ebeahimian, S., Gassezadeh, H., & Mousavi Nia, M. J. (2011). Laboratory evaluation of seed 24metering device using image processing method. *Australian Journal of Agricultural Engineering*, Vol.2, pp. 1-4.
- [49] Penitschke, A., & Jakboy, R. (2008). Microwave mass flow detector for particulate solids based on spatial filtering velocimetry. *Transactions on Microwave Theory and Techniques*, Vol.56, pp. 3193-3199.
- [50] Pang, L., Shao, Y. J., Geng, C. M., Zhong, W Q., Liu, G. Y., Liu, L. H., & Tian, W. J. (2018). Measurement of solid mass flow rate by a non-intrusive microwave method. *Powder Technology*, Vol.323, pp. 525-532.
- [51] Qu, Z. L. (2017). *Design and test on weighting-based device for measuring sowing and fertilizing amount of seeder-fertilizer machine* (播种施肥一体机称重式播量检测装置的设计与试验), MA dissertation, *Nanjing Agricultural University*, Jiangsu/China.
- [52] Qian, C., Yan, Y., Shao, J., Wang, L., Zhou, H., & Wang, C. (2012). Quantitative characterization of pulverized coal and biomass-coal blended in pneumatic conveying pipeline using electrostatic sensor array and data fusion technology. *Measurement Science and Technology*, Vol.23, 085307.
- [53] Qiu, Z. M., Zhang, W. P., Zhao, B., Ji, J. T., Jin, X., & He, Z. T. (2019). Design and test of operation quality monitoring system for small grain electric seeder (小粒种子电动播种机作业质量监测系统设计与试验). *Transactions of the Chinese Society for Agricultural Machinery*, Vol.50, pp.77-83, Henan/China.
- [54] Rafael, B., Christopher, L., Matt, R., Jason, M., Bennie, B., & Yin, B. (2023). An mmWave radar-based mass flow sensor using machine learning towards a peanut yield monitor. *Computers and Electronics in Agriculture*, Vol.215, 108340, USA.
- [55] Ren, W. J., Wu, Z. Y., Li, M. L., Lei, X. L., Zhu, S. L., & Chen, Y. (2021). Design and Experiment of UAV

- Fertilization Spreader System for rice (水稻无人机撒肥系统设计与试验). *Transactions of the Chinese Society for Agricultural Machinery*, Vol.52, pp. 88-98, Sichuan/China.
- [56] Song, C. C., Zang, Y., Zhou, Z. Y., Luo, X. W., Zhao, L. L., & Ming, R. (2020). Test and Comprehensive Evaluation for the Performance of UAV-Based Fertilizer Spreaders. *IEEE Access*, Vol.8, pp. 53-63.
- [57] Su, D. X., Yao, W. X., Yu, F. H., Liu, Y. H., Zhen, Z. Y., Wang, Y. L., Xu, T. Y., & Chen, C. L. (2022). Single-Neuron PID UAV Variable Fertilizer Application Control System Based on a Weighted Coefficient Learning Correction. *Agriculture*, Vol.12, pp. 1019-1019.
- [58] Song, C. C., Zang, Y., Zhou, Z. Y., Luo, X. W., & Zang, Y. (2020). Test and Comprehensive Evaluation for the Performance of UAV-Based Fertilizer Spreaders. *IEEE Access*, Vol.8, pp. 53-63
- [59] Schrock, M., Oard, D. L., Taylor, R. K., Eisele, E. L., Zhang, N., & Pringle, J. L. (1999). A diaphragm impact sensor for measuring combine grain flow. *Applied Engineering in Agriculture*, Vol.15, pp. 639-642.
- [60] Swisher, D. W., Borgelt, S., Sudduth, K. A. (2002). Optical sensor for granular fertilizer flow rate measurement. *Transactions of the ASAE*, Vol.45, pp.881-888.
- [61] Song, C. C., Zhou, Z. Y., Jiang, R., Luo, X. W., He, X. G., & Ming, R. (2018). Design and parameter optimization of pneumatic rice sowing device for unmanned aerial vehicle (气力式无人机水稻撒播装置的设计与参数优化). *Transactions of the Chinese Society of Agricultural Engineering*, Vol.34, pp. 80-88+307, Guangdong/China.
- [62] Song, C. C., Zhou, Z. Y., Luo, X. W., Lan, Y. B., He, X. G., Ming, R., Li, K. L., & Shahbaz, G. H. (2018). Design and test of centrifugal disc type sowing device for unmanned helicopter. *International Journal of Agricultural and Biological Engineering*, Vol.11, pp.55-61, Hubei/China.
- [63] Song, C. C., Zhou, Z. Y., Zang, Y., Zhao, L. L., Yan, W. Y., Luo, X. W., Jiang, R., Ming, R., Zang, Y., Zi, L., & Zhu, Q. Y. (2021). Variable-rate control system for UAV-based granular fertilizer spreader. *Computers and Electronics in Agriculture*, Vol.180, 105832, Guangdong/China.
- [64] Tan, S. Y., Ma, X., Wu, L. L., Li, Z. H., & Liang, Z. W. (2014). Estimation on hole seeding quantity of super hybrid rice based on machine vision and BP neural network (基于机器视觉和BP神经网络的超级杂交稻穴播量检测). *Transactions of the Chinese Society of Agricultural Engineering*, Vol.30, pp. 201-208, Guangdong/China.
- [65] Wang, X. W., Jiang, R., Zhou, Z. Y., Song, C. C., Luo, X. W., Bao, R. F., Lyu, Z. C., Huang, J. H., & Lin, J. Q. (2023). Discharge rate consistency of each channel for UAV-based pneumatic granular fertilizer spreader. *Int J Agric & Biol Eng*, Vol.16, pp. 20-28.
- [66] Wang, D. K. (2022). *Research of agricultural UAV variable spraying system based on RBF neural network PID* (基于RBF神经网络PID的农用无人机变量喷施系统研究), MA dissertation, *Shenyang Agricultural University*, Jilin/China.
- [67] Wang, J. W., Zhang, Z., Wang, F., Jiang, Y. M.M & Zhou, W. Q. (2019). *Design and experiment of monitoring system for rice hill-direct-seeding based on piezoelectric impact method* (基于压电冲击法的水稻穴直播监测系统设计与试验). *Transactions of the Chinese Society for Agricultural Machinery*, Vol.50, pp. 74-84+99, Heilongjiang/China.
- [68] Wu, N., Lin, J., Li, B. F., & Zhou, Y. M. (2016). Design and test on performance monitoring system of no-tillage planter seed-metering device (免耕播种机排种器性能监控系统设计与试验). *Transactions of the Chinese Society for Agricultural Machinery*, Vol.47, pp.69-75, Jilin/China.
- [69] Wu, M. L., Yang, Y., Guan, C., Xiang, W., & Tao, Z. C. (2014). Design and test of a control system for rapeseed metering device based on pressure sensor for seed quantity control (基于压力传感器的油菜排种量控制系统的设计与试验). *Journal of Hunan Agricultural University (Natural Science Edition)*, Vol.40, pp.536-540, Hunan/China.
- [70] Wu, S., Yan, Y., & Qian, X. (2019). Experimental study on mass flow measurement of solid particles using electrostatic sensors (静电传感器测量固体颗粒质量流量实验研究). *Journal of Beijing University of Aeronautics and Astronautics*, Vol.45, pp.1575-1581, Beijing/China.
- [71] Wang, Z. C., Yuan, X. J., Wang, Y. M., & Li, H. G. (2017). Gas-solid two-phase mass flow rate and particle size measurement based on acoustic emission (基于声发射的气固两相流质量流率及粒径的测量). *Instrument Technique and Sensor*, Vol.7, pp. 93-96.
- [72] Wei, G. Y., Zhou, Y. F., Liao, Z. W., Wang, J. D., & Yang, Y. R. (2011). Detection of particle mass flowrate in high-speed fluidization based on acoustic emission technology (基于声发射信号测定高速流态化中的固体颗粒质量流量). *Acta Petrolei Sinica (Petroleum Processing)*, Vol.27, pp. 773-779.

- [73] Xiong, Y. J., Zhou, J., Wei, W., Shen, M. X., & Zhang, B. H. (2018). Design and experiment of grain mass flow sensor based on embedded system (嵌入式谷物流量传感器设计与试验). *Transactions of the Chinese Society of Agricultural Engineering*, Vol.34, pp. 9-46, Jiangsu/China.
- [74] Xu, C. B., Liu, J. Y., Su, Q. S., Jin, W., Wang, D. H., Wang, W. C., & Ding, Y. C. (2022). Design and experiment of the wheat seed flow multi-channel parallel detection device with thin-surface light refraction (薄面光折射式小麦种子流多通道并行检测装置设计与试验). *Transactions of the Chinese Society of Agricultural Engineering (Transactions of the CSAE)*, Vol.38, pp.81-91, Hubei/China.
- [75] Yin, G. (2012). *Study of ultrasonic flow measurement technique* (超声波流量测量技术研究), MA dissertation, Xi'an Shiyou University, Shanxi/China.
- [76] Yan, Y., & Ma, J., (2000). Measurement of particulate velocity under stack-flow conditions. *Measurement science & technology*, Vol.11, pp.59-65.
- [77] Yu, H., Ding, Y., & Fu, X. (2019). A solid fertilizer and seed application rate measuring system for a seed-fertilizer drill machine. *Computers and Electronics in Agriculture*, Vol.16, pp.836-844, Jiangsu/China.
- [78] Yin, J. J., Zhao, Z., Lei, C. P., & Yang, S. X. (2021). Improved optical-type measurement method of grain flow using array near-infrared photoelectric sensors. *Computers and Electronics in Agriculture*, Vol.183, 106075.
- [79] Yazgi, A., & Degimencioglu, A. (2007). Optimisation of the seed spacing uniformity performance of a vacuum-type precision seeder using response surface methodology. *Biosystems Engineering*, Vol.97, pp.347-356.
- [80] Zhao, J. L., Wang, X., Tian, H. L., Lu, W., Guo, C. J., & Liu, h. L. (2021). A fertilizer discharge detection system based on point cloud data and an efficient volume conversion algorithm. *Computers and Electronics in Agriculture*, Vol.185, 106131.
- [81] Zhao, Y. Y. Wu, W., Zhou, Y. Z., Zhu, B., Yang, T. L., Yao, Z. S., Ju, C. X., Sun, C. M., & Liu, T. (2022). A backlight and deep learning-based method for calculating the number of seeds per silique. *Biosystems Engineering*, Vol.213, pp. 182-194.
- [82] Zhou, J., Miao, Y., Zhang, F. C., & Liu, C. L. (2006). Field testing of parallel beam impact-based yield monitor (平行梁冲量式谷物质量流量传感器田间实验). *Transactions of the Chinese Society for Agricultural Machinery*, Vol.37, pp. 102-105, Jiangsu/China.
- [83] Zhu, S. (2020). *Research on image sensor correction algorithm based on neural network* (基于神经网络的图像传感器校正算法研究), MA dissertation, Harbin Engineering University, Heilongjiang/China.
- [84] Zhao, C. (2019). State-of-the-art and recommended developmental strategic objectives of smart agriculture (智慧农业发展现状及战略目标研究). *Smart Agriculture*, Vol.01, pp.1-7, Beijing/China.
- [85] Zhang, Q., Zhang, K., Liao, Q., Liao, Y. T., Wang, L., & Shu, C. X. (2020). Design and experiment of rapeseed aerial seeding device used for UAV (油菜无人机飞播装置设计与试验). *Transactions of the Chinese Society of Agricultural Engineering (Transactions of the CSAE)*, Vol.36, pp. 138-147.
- [86] Zhou, Z. Y., Ming, R., Zang, Y., He, X., Luo, X. W., & Lan, Y. B. (2017). Development status and countermeasures of agricultural aviation in China (中国农业航空发展现状及对策建议). *Transactions of the Chinese Society of Agricultural Engineering*, Vol.33, pp.1-33, Guangdong/China.
- [87] Zhou, L., & Zhang, X. (2009). Monitor System of Precision Seeder Based on Capacitive Sensor (基于电容测量的精密播种机监测系统研究). *Agricultural Mechanization Research*, Vol.31, pp.37-39, Beijing/China.
- [88] Zheng, Y., Liu, Q., (2011). Review of techniques for the mass flow rate measurement of pneumatically conveyed solids. *Measurement*, Vol.44, pp.589-604, Guangdong/China.
- [89] Zou, J. (2015). *Mass flow rate measurement based on microwave sensor* (基于微波传感器的质量流率测量), MA dissertation, Wuhan University of Technology, Hubei/China.
- [90] Zhou, L., Ma, M., Yuan, Y., Zhang, J., Dong, X., Wei, C. (2017). Design and test of fertilizer mass monitoring system based on capacitance method (基于电容法的施肥量检测系统设计与试验). *Transactions of the Chinese Society of Agricultural Engineering*, Vol.33, pp.44-51, Beijing/China.
- [91] Zhou, L., Li, S., Zhang, X., Wang, S., Yuan, Y., Dong, X. (2014). Detection of seed cotton mass flow based on capacitance approach (基于电容法的棉管籽棉质量流量检测). *Transactions of the Chinese Society for Agricultural Machinery*, Vol.45, pp.47-52, Beijing/China.
- [92] Zhou, L. (2014). *Research on detection of yield and seeding rate of cotton based on capacitive method* (基于电容法的棉花产量和播种量检测技术研究), PhD dissertation, China Agricultural University, Beijing/China.

DEVELOPMENT AND TESTING OF AN INTELLIGENT TOBACCO LEAF HARVESTING ROBOT BASED ON MACHINE VISION

基于机器视觉的智能烟叶采摘机器人开发与测试

YuPei LIN^{1,2}, GuoYong YAN³, Tao WANG³, Tao BAI³, Si TANG³, JunJie CHEN^{*1,2}, BaoLin ZHANG^{*3}

¹ Southwest University, College of Artificial Intelligence, Chongqing 400715, China

² National & Local Joint Engineering Research Center of Intelligent Transmission and Control Technology, Chongqing 400715, China

³ Qujing Tobacco Company of Yunnan Province, Yunnan 655000, China

Tel: +86 13887482855; E-mail: 1031730720@qq.com; 13887482855@139.com

DOI: <https://doi.org/10.35633/inmateh-75-51>

Keywords: Tobacco Leaf Harvesting, Machine Vision, Robotic arm, Biomimetic flexible gripper, Kinematic Model

ABSTRACT

The efficiency and quality of tobacco leaf harvesting are crucial for the economic performance of the tobacco industry. To enhance harvesting efficiency, a non-destructive tobacco leaf harvesting robot based on machine vision and robotics technology was developed. Experimental evaluations of key components demonstrated that the biomimetic flexible gripper based on the fin ray effect has good stiffness when the clamping force is 2.5 N, ensuring stable subsequent harvesting and collection of tobacco leaves. The introduction of a 6+1-axis robotic arm significantly expands the working range compared to the original 6-axis design, effectively covering the height of the tobacco stalk. The robotic arm's speed notably affects harvesting time ($P < 0.001$), with 1.2 m/s identified as optimal for balancing recognition efficiency and success rates. Additionally, exposure time plays a critical role in success rates ($P < 0.001$), achieving peaks of 90.00% in the morning and 83.33% in the afternoon at 40000 μ s. These advancements enhance tobacco harvesting technology and provide valuable insights for intelligent crop harvesting.

摘要

烟叶采摘的效率和质量对烟草行业的经济效益至关重要。为了提高采摘效率，基于机器视觉和机器人技术开发了一种无损烟叶采摘机器人。关键部件的实验评估表明，基于鳍条效应的仿生柔性夹爪在夹紧力为 2.5 N 时具有良好的刚度确保了后续烟叶采摘和回收的稳定性。引入的 6+1 轴机械臂相比原有的 6 轴设计，显著扩展了工作范围，有效覆盖了烟草柱的高度。机械臂的速度显著影响采摘时间 ($P < 0.001$)，1.2 m/s 的速度被确定为平衡识别效率和成功率的最佳值。此外，曝光时间对成功率也有关键作用 ($P < 0.001$)，上午和下午在 40000 μ s 时成功率分别达到 90.00% 和 83.33%。这些进展提升了烟叶采摘技术，并为农作物智能采摘提供了借鉴。

INTRODUCTION

Tobacco leaves represent a significant economic crop, with a vast global market for planting and consumption (Liu S. X. et al, 2015). Harvesting tobacco leaves is a critical process in the tobacco production chain, where efficiency and quality directly influence the economic benefits of the tobacco industry (Bu L. X. et al, 2020). Currently, tobacco leaf harvesting is predominantly manual, characterized by high labor intensity, long hours, and substantial costs. Moreover, variations in subjective awareness and technical skills among workers can easily lead to damage and contamination of the leaves, adversely affecting both quality and yield (Xu Y. C. et al, 2016). The introduction of automated harvesting machinery has greatly improved efficiency. Research in this field led Li Yang et al, (2022) to develop a semi-automated tobacco harvesting machine, in which optimal parameters for the harvesting mechanism were determined through experimental trials, resulting in improved efficiency. However, the damage rate still exceeds 20%. Similarly, Ma Sijie et al, (2024), focused on designing and optimizing the key structures of automated tobacco harvesting machinery, employing experimental design methods to establish optimal harvesting parameters and successfully reducing the damage rate to below 10%, though this figure remains relatively high.

YuPei LIN, Ph.D. Eng.; GuoYong YAN, M.S. Eng.; Tao WANG, SA. Eng.; Tao BAI, M.S. Eng.; Si TANG, M.S. Eng.; JunJie CHEN, M.S. Eng.; BaoLin ZHANG, M.S. Eng.

Overall, existing bulk automated harvesting solutions often result in significant damage to tobacco leaves, limiting their practical application in production.

The integration of machine vision and robotic technology presents a promising solution for tobacco leaf harvesting (Jin Y. *et al*, 2020). Machine vision enables rapid identification and localization of leaf maturity, while robotic technology allows for precise execution of harvesting actions. This combination not only enhances the success rate of harvesting but also significantly reduces damage to the leaves, achieving an intelligent and precise harvesting process. While these technologies have been widely applied in harvesting other agricultural products (Shu Y. F. *et al*, 2024), their implementation in tobacco leaf harvesting remains rare (Zhi H.E. *et al*, 2023). The primary challenges in applying machine vision and robotics to tobacco harvesting include: 1) ensuring harvesting stability and effectiveness, which necessitates designing actuators with good enveloping characteristics and appropriate stiffness for damage-free harvesting; 2) achieving seamless integration of agronomy and machinery, requiring an organic combination of maturity identification and harvesting procedures to enhance efficiency; 3) maintaining high visual recognition success rates in complex environments, which involves breakthroughs in recognition technology, improvements in recognition efficiency, and methods for actuator matching.

To address these challenges, this study develops an intelligent, damage-free tobacco harvesting robot based on machine vision. The focus is on innovatively designing the end-effector structure for tobacco leaves, optimizing the harvesting path of the robot in conjunction with agronomy, and fine-tuning key parameters of the vision system through field tests to achieve a comprehensive solution for an efficient and stable tobacco harvesting system. This research not only advances tobacco harvesting technology, enhancing both efficiency and quality, but also provides valuable insights for the intelligent harvesting of other crops, holding significant practical application value.

MATERIALS AND METHODS

Machine structure and workflow

Machine structure

The developed intelligent, non-destructive tobacco harvesting robot, shown in Fig. 1, features a tracked mobility system, a 6+1-axis robotic arm, an end-effector, a depth camera, and a control system. The tracked mobility system ensures excellent terrain adaptability for flexible movement in complex agricultural environments, enhancing operational efficiency. The 6+1-axis robotic arm adds a vertical degree of freedom, allowing seamless integration with tobacco harvesting operations to improve efficiency. The end-effector employs a novel soft-hard gripping structure designed to maximize precision and efficiency while minimizing leaf damage. The control system integrates path planning, obstacle avoidance, and multi-task coordination, dynamically adjusting the arm's trajectory based on real-time visual feedback to ensure safety and stability. Its compact, modular design facilitates maintenance and upgrades, automating harvesting operations and enhancing intelligence through integrated vision and motion control, demonstrating significant application potential.

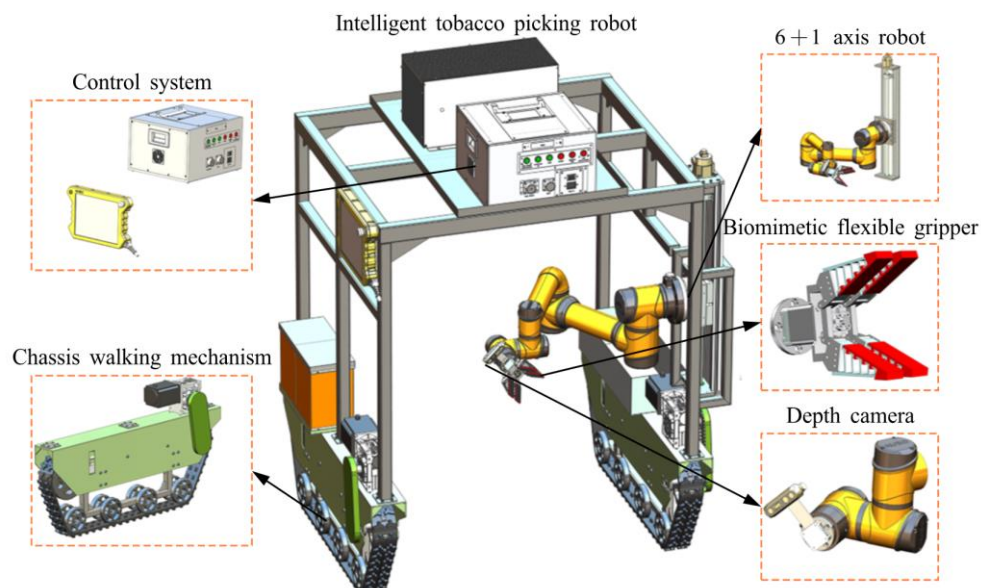


Fig. 1 – Machine Structure of the Tobacco Harvesting Robot

Workflow

The control system connects the end-effector, sliding device, robotic arm, and visual sensors via a central controller to facilitate automated and intelligent tobacco harvesting (Fig. 2). The process begins with program initiation, positioning the depth camera at the recognition point and issuing a recognition command. If obstructions are detected, the camera requests trajectory planning. The vision system identifies the petiole of the tobacco leaf, calculates the coordinates and angular orientation of the harvesting point, and transmits this data to the controller. The robotic arm then moves the end-effector to the harvesting point to complete the process. The system enters standby mode, ready to resume recognition and harvesting upon receiving new commands, concluding operations only when a stop command is issued.

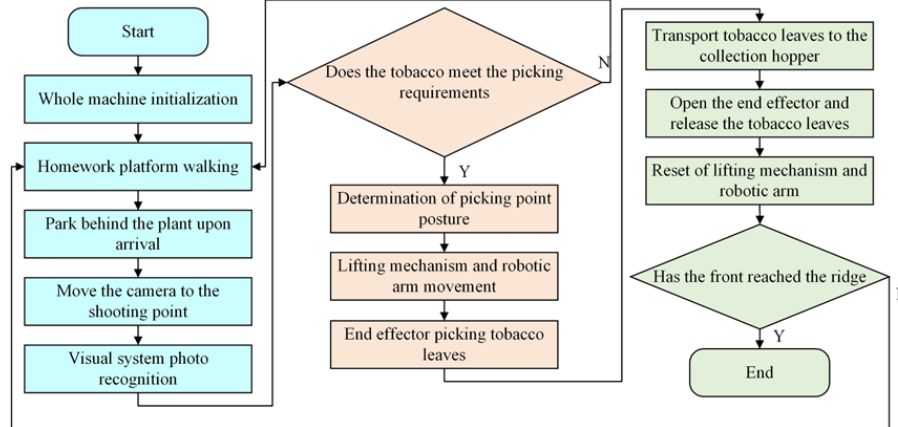


Fig. 2 – Workflow Diagram of the Tobacco Harvesting Robot

Design and Verification of the End Effector

Design of gripper structure

This study utilizes a gripper-style end-effector that combines gripping, harvesting, and transport functions. The design and optimization of the gripper structure are essential for effectively grasping and moving tobacco stems. After gripping and cutting the leaves, rapid transportation is needed, necessitating strong envelopment and structural rigidity. The fin-effect gripper must balance these functions through targeted design. An improved fin-effect gripper was developed, as illustrated in Fig. 3. The skeleton is made from thermoplastic polyurethane elastomer (TPU), which offers excellent elasticity and support, while the soft silicone contact surface securely envelops the tobacco leaves. The gripper features ribs that are thicker in the center and taper toward the edges, with outer joints designed to taper based on deformation needs and inner joints further thinned. This design aligns with the leaf stem's cross-sectional profile and the clamps' rigidity requirements.

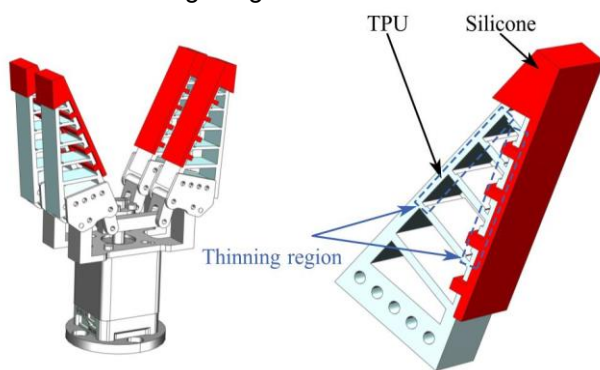


Fig. 3 – The structure design of fin gripper

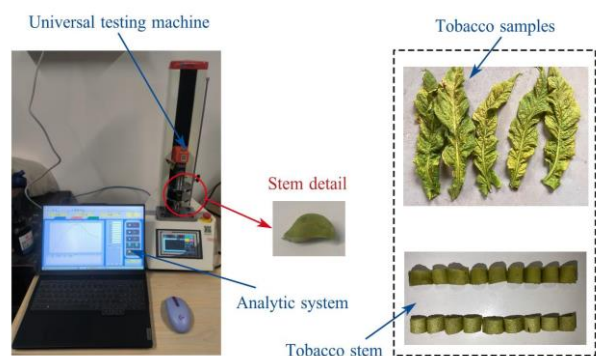


Fig. 4 – The physical properties testing of tobacco leaves and stems

The material model parameters of tobacco

The gripper structure is composed of two hyperelastic materials: TPU and silicone. The TPU material closely fits the second-order Mooney-Rivlin model, and its strain energy function is expressed as:

$$W = C_{10}(I_1 - 3) + C_{01}(I_2 - 3) \tag{1}$$

where W represents the strain energy, [MPa]; C_{10} and C_{01} are material parameters, [MPa]; I_1 and I_2 are the first and second strain invariants, respectively, with material parameters set as $C_{10}=2.101\text{MPa}$ and $C_{01}=0.105\text{MPa}$ (Guan Y. K. et al, 2023).

The second-order Yeoh model effectively characterizes silicone rubber, and its strain energy density function is expressed as:

$$W = C_{10}(I_1 - 3) + C_{20}(I_2 - 3)^2 \tag{2}$$

where C_{10} and C_{20} are material parameters set at 0.11 MPa and 0.02 MPa, respectively (Polygerinos P. et al, 2015).

The physical properties of tobacco leaf stems were determined through experimentation, with equipment and samples shown in Fig. 4. The tobacco leaves used in the experiment were collected from the Modern Tobacco Planting Demonstration Base in Malong District, Qujing City, Yunnan Province, China, and belong to the Yunyan 301 variety. Thirty mature and harvested tobacco leaves were randomly selected. The leaf blades were removed, retaining only the stems, which were cut into approximately 12 mm segments. Axial compression, radial compression, axial shear, and radial shear tests were conducted on the leaf stems using an electronic universal testing machine (ZQ-990). The density of the leaf stems was measured using the drainage method with an electronic balance (LQ-C20002) and a graduated cylinder. Due to slight variations in the shape and size of the test stems, each test was repeated 10 times, and the average value was calculated. The leaf stems were assumed to be transversely isotropic, meaning the radial and chord directions share the same modulus parameters. The final physical property parameters of the leaf stems are shown in Tab. 1, and Poisson's ratio was calculated using the following equations:

$$v_{xy} = \frac{E_x}{2G_{xy}} - 1 = v_{xz} \tag{3}$$

$$v_{yz} = \frac{E_y}{2G_{yz}} - 1 \tag{4}$$

Table 1

The physical property parameters of tobacco leaves and stems

Parameters	Elastic modulus [MPa]		Shear modulus [MPa]		Poisson's ratio		Density [kg·m ⁻³]
	E_x	E_y/E_z	G_{xy}/G_{xz}	G_{yz}	v_{xy}/v_{xz}	v_{yz}	ρ
Values	5.34	3.95	1.93	1.84	0.38	0.07	993.30

Finite element analysis of clamping force

Nonlinear static analysis was conducted using ANSYS Workbench. A simplified clamp model was imported, focusing on the clamping and wrapping behavior on the left side of the tobacco stem. Fillets and small step features were removed, and material connections were simplified to surface contact for enhanced computational efficiency. New materials were defined in the material library based on the given parameters and assigned to each part of the clamp. Friction contact was established between the silicone and the surface of the tobacco stem, while bonded contact was defined between the inner silicone surface and the TPU. A nonlinear meshing strategy was applied, generating first-order hexahedral elements to ensure computational efficiency and stability. To determine the optimal clamping force of the redesigned clamp, a fixed constraint was applied to the cylindrical hole of the clamp, while a lateral displacement constraint was added at the base of the stem. A clamping force was then applied on the opposite side of the stem, and the effects of clamping forces of 2 N, 2.5 N, and 3 N were explored. An integral solution method was used, accounting for large deformation, with nonlinear control implemented using the asymmetric Newton-Raphson method. The final solution met the force convergence criterion.

The displacement cloud diagrams of stable clamping under different forces are shown in Fig.5. It illustrates that as the clamping force increases, the enveloping capacity improves. Due to the large curvature of the outer contour of the leaf stem, achieving complete envelopment is challenging. Further modification of the clamp's size parameters to achieve full envelopment would result in excessive deformation and may cause the left and right jaws to collide. Therefore, this study improved the overall stiffness of the clamp while maximizing its envelopment of the leaf stem. Fig. 5 shows that under the studied clamping forces, the clamp envelops most of the outer edge of the leaf stem's left side, achieving overall good coverage. Additionally, because of the small transverse thickness of the leaf stem, excessive clamping force may cause the jaws to collide. At a clamping force of 2.5 N, the line connecting the top and bottom of the clamp passes through the long axis of the stem's cross-section, indicating the critical force at which the jaws might collide. Therefore, the clamping force should be kept at ≤ 2.5 N.

To further investigate the clamp’s stiffness, the equivalent strain cloud diagrams under different clamping forces were obtained, as shown in Fig.6. It illustrates that the equivalent strain distribution in the contact area is relatively uniform, with higher equivalent stress at each joint, reaching a maximum of 0.24 m/m under a 3 N clamping force. Additionally, the greater the clamping force, the larger the equivalent strain in the contact area between the clamp and the leaf stem, resulting in greater elastic recovery energy and improved clamp stiffness. Based on the maximum force limit from the above analysis, a clamping force of 2.5 N provides sufficient stiffness to ensure stable tobacco leaf harvesting and retrieval. Therefore, this clamping force of 2.5 N was selected for subsequent harvesting tests.

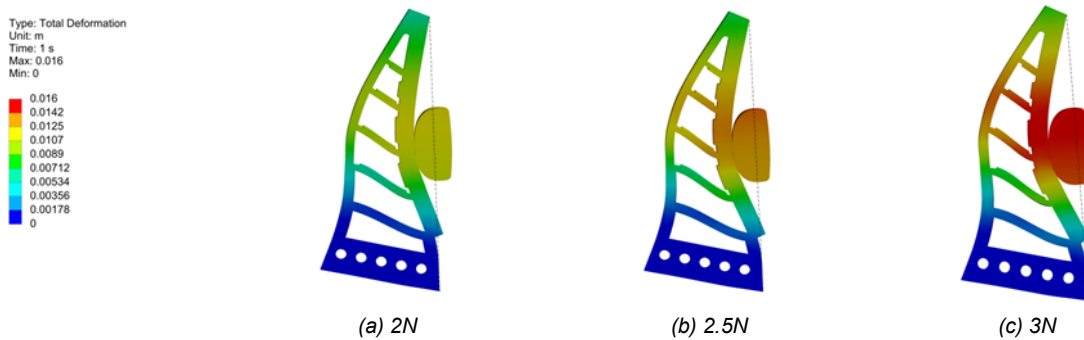


Fig. 5 – The displacement cloud diagrams of clamped leaf stems under different forces

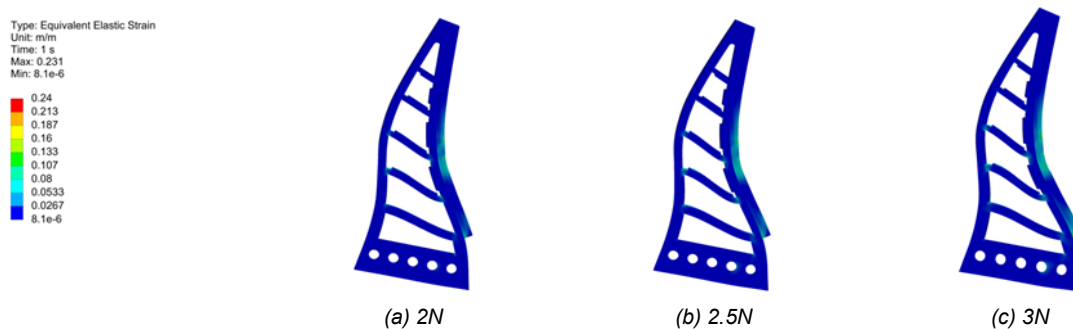


Fig. 6 – The equivalent strain cloud diagrams of clamped leaf stems under different clamping forces

The motion analysis of robotic arm

The structure and parameter design

The tobacco leaves harvesting robot uses the AUBO-I5 robotic arm, with its key parameters listed in Tab. 2. As shown in Tab. 2, the robotic arm has a working radius of 886.5 mm, while the average height of the tobacco leaves is approximately 1.5 m. Since tobacco plants mature gradually from top to bottom over 1-2 months, with only 2-3 leaves harvested at the same height during each picking cycle, a single robotic arm cannot meet agronomic needs. In this study, a 6+1 axis robotic arm solution was implemented, adding an 800 mm adjustable sliding platform at the base of the robotic arm. This setup allows the adjustment of the arm’s workspace to meet the agronomic requirements for layered tobacco leaf harvesting, while keeping the slide’s position fixed during the process.

Table 2

The parameters of the AUBO-I5 Robotic Arm

Max load	5 kg	Weight	< 24 kg	Free load ratio	< 4.8
Degrees of Freedom	6	Repeat positioning accuracy	±0.02 mm	Working radius	886.5 mm
Maximum velocity of each axis					
J₁	J₂	J₃	J₄	J₅	J₆
223 °/s	223 °/s	223 °/s	237 °/s	237 °/s	237 °/s

Workspace Analysis

The AUBO-I5 robotic arm features six degrees of freedom, with the first three controlling the end-effector’s position and the latter three its orientation. A fixed coordinate system was established for the links to describe each joint’s motion in three-dimensional space, with the joint posture represented by its coordinate system position. The kinematic model was derived using homogeneous coordinate transformation, employing the modified Denavit-Hartenberg (M D-H) method for the forward kinematic model.

$$\begin{aligned}
 {}^{i-1}T_i &= \begin{bmatrix} c\theta_i & -s\theta_i & 0 & a_{i-1} \\ s\theta_i c\alpha_{i-1} & c\theta_i c\alpha_{i-1} & -s\alpha_{i-1} & -s\alpha_{i-1}d_i \\ s\theta_i s\alpha_{i-1} & c\theta_i s\alpha_{i-1} & c\alpha_{i-1} & c\alpha_{i-1}d_i \\ 0 & 0 & 0 & 1 \end{bmatrix} & {}^0T_1 &= \begin{bmatrix} 1 & 0 & 0 & 0 \\ 0 & 1 & 0 & 0 \\ 0 & 0 & 1 & d_1 \\ 0 & 0 & 0 & 1 \end{bmatrix} & {}^1T_2 &= \begin{bmatrix} c_2 & -s_2 & 0 & 0 \\ 0 & 0 & -1 & -0.122 \\ s_2 & c_2 & 0 & 0 \\ 0 & 0 & 0 & 1 \end{bmatrix} \\
 {}^2T_3 &= \begin{bmatrix} c_3 & -s_3 & 0 & 0 \\ 0 & 0 & 1 & 0.1215 \\ -s_3 & c_3 & 0 & 0 \\ 0 & 0 & 0 & 1 \end{bmatrix} & {}^3T_4 &= \begin{bmatrix} c_4 & -s_4 & 0 & 0.408 \\ -s_4 & c_4 & 0 & 0 \\ 0 & 0 & -1 & 0 \\ 0 & 0 & 0 & 1 \end{bmatrix} & {}^4T_5 &= \begin{bmatrix} c_5 & -s_5 & 0 & 0.376 \\ -s_5 & -c_5 & 0 & 0 \\ 0 & 0 & -1 & 0 \\ 0 & 0 & 0 & 1 \end{bmatrix} \\
 {}^5T_6 &= \begin{bmatrix} c_6 & -s_6 & 0 & 0 \\ 0 & 0 & 1 & 0.1025 \\ -s_6 & -c_6 & 0 & 0 \\ 0 & 0 & 0 & 1 \end{bmatrix} & {}^6T_7 &= \begin{bmatrix} c_7 & -s_7 & 0 & 0 \\ 0 & 0 & -1 & -0.094 \\ s_7 & c_7 & 0 & 0 \\ 0 & 0 & 0 & 1 \end{bmatrix}
 \end{aligned} \tag{5}$$

where, s_i and c_i represent $\sin\theta_i$ and $\cos\theta_i$, respectively.

Multiplying the above matrices in sequence on the right yields the robot's forward kinematics expression.

$${}^0T_7 = {}^0T_1 {}^1T_2 {}^2T_3 {}^3T_4 {}^4T_5 {}^5T_6 {}^6T_7 \tag{6}$$

Fig.7(a) illustrates the model diagram and the coordinate systems for each joint, while Tab.3 lists the corresponding D-H parameters. The M D-H method provides the coordinate transformation matrix for the homogeneous transformation from coordinate system i to system $i-1$ (Peng J. et al., 2019).

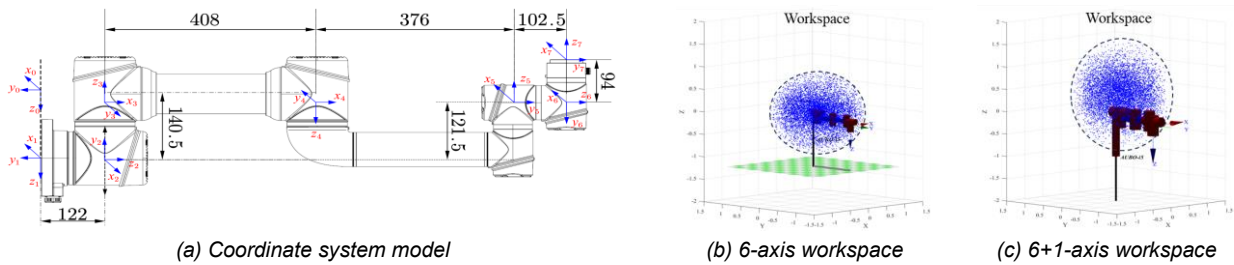


Fig. 7 – AUBO-I5 robot model and workspace

Table 3

The M D-H parameters of 6+1 axis robotic arm

Link i	a_{i-1} [mm]	α_{i-1} [°]	d_i [mm]	θ_i [°]	Variation range
1	0	0	d_1	0	0-800 mm
2	0	90	122	θ_1	$\pm 360^\circ$
3	0	-90	121.5	θ_2	$\pm 175^\circ$
4	408	180	0	θ_3	$\pm 175^\circ$
5	376	180	0	θ_4	$\pm 175^\circ$
6	0	-90	102.5	θ_5	$\pm 175^\circ$
7	0	90	94	θ_6	$\pm 360^\circ$

In Matlab, the Link and SerialLink functions were used to create a simplified model of the robotic arm's links. The simplified teaching model is shown in Fig. 7(a). The Monte Carlo method was used to simulate and analyze the robot's workspace, generating random values for each joint variable (Li J. et al, 2023):

$$\theta_i = \theta_{i_{\min}} + (\theta_{i_{\max}} - \theta_{i_{\min}}) \times \text{rand}(N,1) \tag{7}$$

Substituting the joint variables into the forward kinematics equation produces a point cloud map of the robot's workspace, as shown in Fig. 7(b) and 7(c). From the workspace point cloud, it is evident that without the sliding device, the workspace of the AUBO-I5 robotic arm is circular. With the 6+1 axis structure and the sliding device, the workspace becomes elliptical. This expanded workspace covers a larger area, meeting the height requirements for tobacco leaf picking by covering most of the plant's height. Additionally, the workspace analysis provides a theoretical basis for path planning and collision warning of the gripper.

Tobacco leaf recognition and positioning

The visual recognition system consists of an Intel RealSense D435i depth camera and an Nvidia Jetson Nano platform. The D435i camera, with a depth range of 0.1 to 10 m, captures tobacco leaf images, while the Jetson Nano, powered by a quad-core processor and CUDA GPU, handles deep learning tasks.



Fig. 8 – Visual system recognition and positioning

YOLOv7, a fast and accurate object detection algorithm, is used for real-time tobacco leaf recognition. The system captures images, processes them through YOLOv7's convolutional layers for feature extraction, and detects leaf stems using an Anchor-Free mechanism to generate bounding boxes. After non-maximum suppression, the system outputs the optimal coordinates for guiding the robot arm in precise picking. The method's high recognition accuracy and real-time performance make it suitable for complex field environments. To further enhance YOLOv7's accuracy, data augmentation, attention mechanisms, loss function refinements, and model integration were employed. The results of the visual recognition system are shown in Fig. 8.

RESULTS

Experimental conditions

The field test for tobacco leaf picking was conducted from August 14 to 16, 2024, in the modern tobacco leaf production demonstration area in Malong District, Qujing City, Yunnan Province. The test subjects were tobacco plants of the Yunyan 301 variety grown in the demonstration area. The test process is illustrated in Fig. 9.



Fig. 9 – Tobacco leaf harvesting field experiment

To evaluate the tobacco leaf picking performance of the entire machine, the time taken to fully pick a single leaf was used as a measure of overall picking efficiency. During preliminary testing, it was observed that jitter at the end of the robotic arm affected the recognition efficiency of the vision system. Therefore, the efficiency test was conducted at five speed levels: 20%, 40%, 60%, 80%, and 100% of the maximum movement speed of the robotic arm (the maximum linear speed and acceleration of the arm's end were 1.5 m/s and 1 m/s², respectively). The picking time at each speed level was recorded. To eliminate the effects of lighting variations, all tests were scheduled for the morning of the same day. Each speed level was tested by picking 10 tobacco leaves, and the average picking time was calculated over 50 tests. The picking success rate was used to evaluate the machine's reliability. Tests were conducted in both the morning and afternoon. Five camera exposure times—10000 μ s, 25000 μ s, 40000 μ s, 55000 μ s, and 70000 μ s—were selected as factors for exploration. At each exposure level, 30 tobacco leaves were picked, and the success rate was calculated over 150 tests.

Effect of robotic arm velocity on picking efficiency

The results of the tobacco leaf picking test at different robotic arm speeds are summarized in Tab. 4. As the robotic arm speed increased from 0.3 m/s to 1.5 m/s, the average picking time dropped significantly from 9.00 seconds to 2.47 seconds, indicating a clear downward trend. Variance analysis of the robotic arm speed revealed significant differences between groups ($P < 0.001$). Therefore, the speed of the robotic arm has a highly significant effect on the tobacco leaf picking time. As the robotic arm speed increases, the amplitude of vibrations at the arm’s end increases, potentially affecting the efficiency of the vision system's recognition. In practical picking, a balance must be struck between recognition efficiency and picking success rate. This is primarily because tobacco leaves near the plant may overlap or intertwine, and if the robotic arm moves too quickly, it could damage the surrounding leaves. Therefore, an efficient and relatively stable speed of 1.2 m/s was selected for subsequent experiments, ensuring maximum picking efficiency without compromising accuracy.

Table 4

The test results of tobacco leaf picking efficiency at different robot arm speeds

No.	Mechanical arm speed [m/s]	Average picking time [s]	Variance
1	0.3	9.00	0.37
2	0.6	6.75	0.13
3	0.9	5.22	0.03
4	1.2	3.71	0.01
5	1.5	2.47	0.04

Effect of exposure time on picking success rate

Exposure time is a crucial parameter for calibrating the visual recognition system. To investigate the effect of varying exposure times on picking success rates while accounting for changes in ambient light intensity during actual harvesting, experiments were conducted at 8 a.m. and 2 p.m., reflecting different ambient light conditions. The test data and pictures are shown in Tab. 5 and Fig. 10 respectively.

Table 5

Experimental results on tobacco leaf picking success rate under different exposure times

Exposure time [μs]	Picking success rate (a.m) [%]	Picking success rate (p.m) [%]
10000	33.67	43.33
25000	63.33	60.00
40000	90.00	83.33
55000	73.33	66.67
70000	53.33	46.67



Fig. 10 – Tobacco leaf harvesting picture under different exposure times

The results indicate that there are significant differences in picking success rates across various exposure times, regardless of the time of day. The variance analysis results show $P < 0.001$, indicating an extremely significant effect. In the morning, when the exposure time was set to 40000 μs, the picking success rate peaked at 90.00%. In the afternoon, under the same exposure time, the picking success rate also reached a peak of 83.33%. Overall, variations in ambient light intensity significantly influenced the picking success rates at the same exposure time. Under poor ambient lighting conditions, the upper limit of the picking success rate may be restricted. Therefore, selecting appropriate harvesting times and weather conditions is crucial. In conclusion, selecting an appropriate exposure time can significantly enhance the system’s ability to identify tobacco leaves, ultimately improving the picking success rate. The tobacco leaf picking robot system developed in this study, based on machine vision, demonstrates excellent picking performance.

CONCLUSIONS

This study developed an intelligent, non-destructive tobacco leaf picking robot utilizing machine vision. The research focused on the design and analysis of key components, with field experiments conducted to assess the machine's overall picking performance. This research yielded the following conclusions:

(1) The clamping jaw structure was redesigned based on the fin-ray effect. Finite element analysis revealed that increasing the clamping force improves the jaw's wrapping capability. To prevent collisions while maintaining sufficient rigidity and stability during tobacco leaf picking and collection, the clamping force was set to 2.5 N.

(2) The working space of the robot arm without the sliding table is circular, while the 6+1-axis arm with the sliding table has an elliptical workspace. This larger range covers most of the tobacco plant height, meeting the operational requirements for leaf picking.

(3) The speed of the robotic arm significantly impacts the picking time ($P < 0.001$). At 1.5 m/s, the average picking time was minimized to 2.47 seconds. A speed of 1.2 m/s was found to balance efficiency and picking success rate.

(4) Exposure time significantly affects the picking success rate ($P < 0.001$). A 40000 μs exposure achieved a peak success rate of 90.00% in the morning and 83.33% in the afternoon. Overall, changes in ambient light intensity noticeably impacted success under the same exposure conditions.

ACKNOWLEDGEMENTS

The study was funded by China National Tobacco Corporation Yunnan Provincial Company Project "Research and Application of Key Technologies for Automated Tobacco Leaf Picking and Editing Based on Image Recognition" (2023530000241021), Chongqing Education Commission Science and Technology Research and Technology Youth Fund Project (KJQN202400208) and Research Project of Beibei District, Chongqing (2024-05).

REFERENCES

- [1] Bu, L. X., Chen, C. K., Hu, G. R., Sugirbay, A., Chen, J., (2020). Technological Development of Robotic Apple Harvesters: A Review (苹果收获机器人技术发展综述). *INMATEH-Agricultural Engineering*, 61(2): 151-164.
- [2] Guan Y. K., Hou Z. G., Hu B., Cong X. P., Lyu C. L., (2023). Design and Experimental Research of Flexible Gripper Based on Fin Ray Effect (基于鳍条效应的柔性夹爪设计与试验研究). *Machine Tool & Hydraulics*, 51(04): 86-91.
- [3] He, Z., Ding, X. T., Li, K., Shi, Y. G., Cui, Y. J., (2023). Design and Experiment of End Effect for Kiwifruit Harvesting Based on Optimal Picking Parameters (基于最优采摘参数的猕猴桃采摘末端执行器设计与试验). *INMATEH-Agricultural Engineering*, 69(1), 325-334.
- [4] Jin Y. J., (2020). Recognition Technology of Agricultural Picking Robot Based on Image Detection Technology (基于图像检测技术的农业采摘机器人识别技术). *INMATEH-Agricultural Engineering*, 62(3): 191-200.
- [5] Li Y., Chu J. K., Yu J., (2022). Effect of Ditching on Seedling Quality and Mechanical Transplanting of Drill Seedlings Under Low Sowing Quantity (烟草收获机采摘机构对烟叶采收效果影响的研究). *Journal of Agricultural Mechanization Research*, 44(12): 170-174+181.
- [6] Liu, S., Wang, J., Mou, H., Fan, L., Fu, S., Zhu, C., (2020). Design and Experiment of Moving along Ridge Control System for Tobacco Picking Machine (烟叶采收机仿垄行走控制系统设计与试验). *Transactions of the Chinese Society of Agricultural Engineering*, 31(S2):83-87.
- [7] Li, J., Zhao, Q., Li, L. J., Wu, Z. C., Guo, X., (2023). Trajectory Planning of Camellia Oleifera Pollen Picking Manipulators Based on an Improved Particle Swarm Optimization Algorithm (基于改进粒子群算法的油茶花粉采摘机械臂轨迹规划). *Journal of Mechanical Transmission*, 47(2): 86-92.
- [8] Ma, S. J., Zhu, C. H., Zhang, C. C., Ran, Y. L., Li, B. Q., Wang, W. Z., (2024). Design and Experimental Research on Picking Mechanism of Self-propelled Tobacco Leaf Picking Machine (自走式烟叶采摘机采摘机构的设计与试验). *Journal of Agricultural Mechanization Research*, 46(03): 120-127.
- [9] Peng, J., Ding, Y., Zhang, G., Ding, H., (2019). An Enhanced Kinematic Model for Calibration of Robotic Machining Systems with Parallelogram Mechanisms. *Robotics and Computer-Integrated Manufacturing*, 59: 92-103.

- [10] Polygerinos, P., Wang, Z., Overvelde, J. T., Galloway, K. C., Wood, R. J., Bertoldi, K., Walsh, C. J. (2015). Modeling of Soft Fiber-Reinforced Bending Actuators. *IEEE Transactions on Robotics*, 31(3): 778-789.
- [11] Shu, Y., Zheng, W., Xiong, C., Xie, Z., (2024). Research on the Vision System of Lychee Picking Robot Based on Stereo Vision. *Journal of Radiation Research and Applied Sciences*, 17(1): 100777.
- [12] Yu Y. C., Wei F. D., Qin W. Y., Liu T., Zeng M., Ning W. Y., (2016). Technology Development of Tobacco Harvester (烟草收获机技术发展概述). *Journal of Agricultural Mechanization Research*, 38(02): 255-262.

OPTIMIZATION AND TESTING OF OPERATING PARAMETERS FOR THE AUTOMATIC SEEDLING PICKING DEVICE OF TOMATO POT SEEDLING TRANSPLANTER

番茄钵苗移栽机自动取苗装置作业参数优化与试验

Fukang ZHOU^{1,2)}, Mengqi ZHANG^{1,2)}, Weichen YAN^{1,2)}, Shijun SONG^{1,2)}, Yi NIU^{1,2)}, Tao FAN^{1,2)}, Bolong WANG^{1,2)}, Fangyuan LU^{1,2)}, Guohai ZHANG^{1,2*)}

¹⁾Shandong University of Technology, Collage of Agricultural Engineering and Food Science, ZiBo, China

²⁾Shandong University of Technology, Institute of Modern Agricultural Equipment, ZiBo, China

Tel: +8615965534882; E-mail: guohaizhang@sdut.edu.cn

Corresponding author: Guohai Zhang

DOI: <https://doi.org/10.35633/inmateh-75-52>

Keywords: agricultural machinery; tomato potting; vegetable transplanting; seedling removal device; response surface

ABSTRACT

This study focused on an in-depth analysis of the cam motion process of the seedling clamp within the automatic seedling-picking device for tomato pot seedlings. Key influencing factors, including spring stiffness coefficient, seedling needle holding angle, and seedling-picking frequency, were selected for investigation. Evaluation indicators included substrate loss rate, pot seedling drop rate, and seedling-picking success rate. A three-factor, three-level, second-order rotational orthogonal combination test was conducted. Using Design-Expert V13.0.5 software for data analysis, the theoretical optimal parameter combination was identified: a spring stiffness coefficient of 376.8 N/m, a seedling needle holding angle of 15.6°, and a seedling-picking frequency of 89 plants per minute. Under this parameter combination, the substrate loss rate was reduced to 3.94%, the pot seedling drop rate to 2.01%, and the seedling-picking success rate reached 94.05%. A verification test conducted on the seedling-picking device test bench showed that the experimental results closely aligned with the optimized theoretical values. These findings provide a valuable reference for the structural optimization and performance improvement of seedling-picking devices in fully automatic tomato transplanters and contribute significantly to the advancement of automation in tomato transplanting operations.

摘要

本研究聚焦于番茄钵苗自动取苗装置中的夹苗器凸轮运动过程展开深入分析。在研究过程中，选定弹簧刚度系数、苗针夹持角度以及取苗频率作为关键影响因素，并将基质损失率、钵苗脱落率和取苗成功率确定为评价指标，进而开展三因素三水平二次旋转正交组合试验。借助 Design-Expert.V13.0.5 软件对试验数据进行分析处理，最终获取理论上的最优参数组合，即弹簧刚度系数为 376.8 N/m，苗针夹持角度为 15.6°，取苗频率为 89 株/min。在该参数组合条件下，基质损失率低至 3.94%，钵苗脱落率仅为 2.01%，而取苗成功率高达 94.05%。随后，在取苗装置上进行验证试验，试验结果与优化所得理论结果基本相符。本研究所得的相关成果，能够为番茄全自动移栽机取苗装置的结构优化改进以及作业参数的精准控制提供有益的参考借鉴，对于推动番茄移栽作业的自动化发展具有重要意义。

INTRODUCTION

Ningxia serves as a pivotal production region for processing tomatoes in China. The tomato - related industry holds a place of considerable importance in Ningxia's agricultural production landscape (Niu et al., 2022). In recent years, Ningxia has predominantly employed seedling transplanting technology in tomato cultivation. With the continuous expansion of the planting scale, the annual demand for transplanting machinery during the spring season has also been on the rise (Liu et al., 2013). At present, the transplanting machinery in use is predominantly semi - automatic. The seedling-picking operation still needs to be completed manually, which is characterized by low automation, high labor intensity, low efficiency, and high operating costs.

Fukang Zhou M.S. Stud. Eng.; Mengqi Zhang M.S. Stud. Eng.; Weichen Yan M.S. Stud. Eng.; Shijun Song M.S. Stud. Eng.; Yi Niu M.S. Stud. Eng.; Tao Fan M.S. Stud. Eng.; Bolong Wang, As. Ph.D. Eng; Fangyuan Lu, As. Ph.D. Eng;; Guohai Zhang, Prof. Ph.D. Eng.

These factors are significantly hindering the advancement of seedling transplanting technology (Yu *et al.*, 2014; Zhang *et al.*, 2013; Hu *et al.*, 2014). Therefore, the automatic transplanting machine has become an inevitable development trend for achieving efficient and large-scale crop transplanting in Ningxia. It is imperative to advance the research and development of fully automatic transplanting machines equipped with automatic seedling-picking and seedling-dropping functions. The core of automatic transplanting machine research and development lies in automatic seedling picking technology. At present, both domestic and international research on mechanical automatic seedling-picking methods for automatic transplanting machines primarily focus on two approaches: the clamping (folder-picking) type and the ejecting type. Automatic transplanting machines developed using these two methods have already been applied in foreign countries (Dixit, 2010; Manjunatha *et al.*, 2009; Sakaue, 1996). Although this type of fully automatic transplanting machine offers high working efficiency and a high degree of automation, it is expensive, structurally complex, and primarily designed for bare-soil transplanting. As a result, it does not meet the agronomic requirements for transplanting on mulch film making it unsuitable for introduction and widespread adoption (Huang *et al.*, 2023). Domestic research on transplanting machinery started relatively late; however, several semi-automatic transplanting machine models have already been developed, applied, and promoted (Xue *et al.*, 2013; Jin, 2014). In recent years, several domestic universities and research institutes have conducted extensive research on automatic seedling extraction mechanisms, which are core components of automatic vegetable transplanters. Their work has focused on the mechanical properties of pot seedlings (Chen *et al.*, 2024; Hu *et al.*, 2023), the structural design of seedling extraction claws (Han *et al.*, 2013; Liang *et al.*, 2018; Han *et al.*, 2015), the optimization and simulation analysis of key components in the seedling extraction mechanism (Hai *et al.*, 2025; Wang *et al.*, 2015), and experimental studies on key parameters (Gao *et al.*, 2015; Zhang *et al.*, 2016; Zhang, 2014). However, despite this progress, no mature technology has yet been successfully applied in actual agricultural production.

This paper focuses on a tomato pot seedling automatic extraction device developed by the research group. A seedling extraction test bench was established to support experimental analysis. The seedling extraction mechanism employs a planetary gear-linkage system combined with an irregular slide drive to control the clamping motion and achieve the desired trajectory and posture for automatic seedling extraction. A cam-toggle mechanism is used to control the opening and closing of the seedling clamping needles, enabling both clamping and seedling releasing actions. Using the test bench and applying response surface method, the study optimizes key operating parameters of the device to enhance operational quality. The findings aim to provide a reference for the structural optimization and design improvement of automatic seedling extraction devices.

MATERIALS AND METHODS

Structure and working principle of automatic seedling picking device

The seedling extraction device is the core component of the automatic seedling extraction test bench. It is primarily composed of a rackmount, planetary gearbox, connecting rod, seedling needle, seedling pushing ring, cam, slide, etc., as illustrated in Fig. 1.

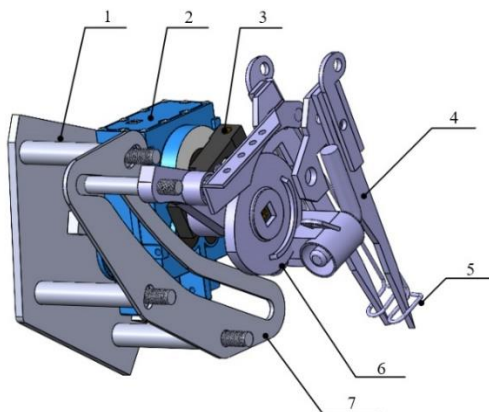


Fig. 1 – Overall system architecture Figure

Schematic diagram of tomato pot seedling automatic picking device

1. Rackmount; 2. Planetary gearbox; 3. Connecting rod; 4. Seedling needle; 5. Seedling pushing ring; 6. Cam; 7. Slide

According to the requirements of seedling picking and dropping operation (Li et al., 2015; Ye et al., 2014), the cam's working stroke is divided into four working phases: preparation for seedling picking, seedling clamping, seedling holding and seedling releasing, as shown in Fig. 2. To prepare the seedling clamping section AB, the two seedling needles are fully opened, the push ring slides upward along the seedling needles under the action of the cam, and the seedling needles approach the holes at a fixed angle. In the seedling clamping section BD, the seedling needles were inserted into the holes at a fixed angle, and when they reached point C, the distance between the tip points of the two seedling needles was gradually reduced to clamp the root plug, and the distance between the tip points of the seedling needles remained unchanged after the root plug was clamped. In the seedling holding section DF, the seedling needles vertically pull the pot seedling out from the tray holes. During this stage, the seedling pushing ring remains stationary. As the mechanism moves along the cam profile to point F, the seedling holding stage ends and the seedling needles begin to open. At this point, the pot seedling assumes a vertically downward posture. In the seedling release section FA, as the mechanism progresses to stage GA, the seedling pushing ring slides downward along the seedling needles. When it reaches point A, the pushing ring completes its stroke, pushing the seedling vertically downward to release it. Simultaneously, the seedling needles open and return to their initial angle, completing one full cycle of seedling extraction and release.

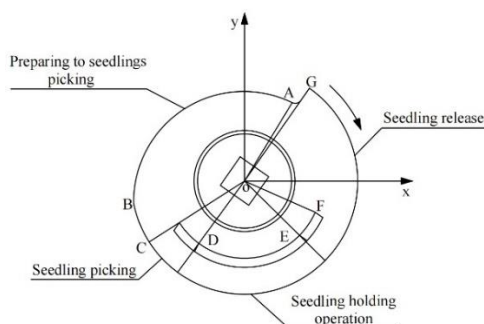


Fig. 2 – Cam working stroke

Principle of system operation

In order to investigate the effects of spring stiffness coefficient, clamping angle of seedling needle and seedling picking frequency on the performance of seedling picking device and the optimal combination of parameters, a three-factor and three-level quadratic rotary optimization experiment was carried out with the indicators of substrate loss, seedling shedding rate and seedling picking success rate. The spring stiffness coefficients X_1 were set at 300, 400 and 500 N/m, and the clamping angles X_2 were set at 14, 16 and 18°, respectively, the seedling picking frequency X_3 was set at 60, 90 and 120 plants/min. The quadratic rotary orthogonal combination scheme was designed, 20 groups of automatic seedling extraction device performance tests were conducted, each group of experiments was repeated three times and the average of the three test results was taken as the experimental results. Design-Expert.13.0.5 software was used to design the experimental scheme and analyze the results, as shown in Table 1.

Table 1

Experimental design and results						
No.	X_1	X_2	X_3	Substrate loss rate $Y_1/\%$	Pot seedling shedding rate $Y_2/\%$	Success rate of seedling picking $Y_3/\%$
1	-1	-1	-1	6.21	1.55	92.24
2	1	-1	-1	12.53	1.57	85.9
3	-1	1	-1	4.68	9.36	85.96
4	1	1	-1	6.94	5.49	87.57
5	-1	-1	1	10.21	5.48	84.31
6	1	-1	1	19.56	6.27	74.17
7	-1	1	1	5.48	9.41	85.11
8	1	1	1	12.52	7.83	79.65
9	-1.682	0	0	3.93	7.02	89.05
10	1.682	0	0	13.29	4.71	82
11	0	-1.682	0	14.07	2.35	83.58
12	0	1.682	0	5.43	9.37	85.2
13	0	0	-1.682	3.91	2.33	93.76
14	0	0	1.682	12.57	7.82	79.61
15	0	0	0	4.71	2.35	92.94
16	0	0	0	5.44	1.57	92.99

No.	X_1	X_2	X_3	Substrate loss rate Y_1 /%	Pot seedling shedding rate Y_2 /%	Success rate of seedling picking Y_3 /%
17	0	0	0	4.68	2.36	92.96
18	0	0	0	3.94	2.37	93.69
19	0	0	0	4.01	1.59	94.4
20	0	0	0	4.76	2.31	92.93

Experimental results and analyses

Quadratic polynomial regression models were established between spring stiffness coefficient, clamping angle of seedling-picking needle, frequency of seedling picking and substrate loss rate, pot seedling shedding rate and seedling picking success rate. The regression equations were obtained by eliminating the insignificant factors.

$$Y_1 = 4.57 + 2.98X_1 - 2.45X_2 + 2.34X_3 - 0.80X_1X_2 + 0.98X_1X_3 - 0.58X_2X_3 + 1.56X_1^2 + 1.96X_2^2 + 1.43X_3^2 \tag{1}$$

$$Y_2 = 0.21 - 0.62X_1 + 2.13X_2 + 1.48X_3 - 0.78X_1X_2 + 0.38X_1X_3 - 0.78X_2X_3 + 1.35X_1^2 + 1.34X_2^2 + 1.07X_3^2 \tag{2}$$

$$Y_3 = 93.34 - 2.36X_1 + 0.32X_2 - 3.82X_3 + 1.58X_1X_2 - 1.36X_1X_3 + 1.36X_2X_3 - 2.90X_1^2 - 3.30X_2^2 - 2.49X_3^2 \tag{3}$$

The results showed that the regression equation models for substrate loss rate, pot seedling shedding rate, and seedling removal success rate were $P < 0.0001$, indicating that the three regression equation models were significant, suggesting that the regression models fitted well within the experimental range.

Table 2

Variance analysis of regression models						
Indexes	Variance source	Sum of squares	Degree of freedom	Mean square	F value	P value
Y_1	Model	393.75	9	43.75	102.39	< 0.0001
	Residual	4.27	10	0.4273		
	Lack of Fit	2.74	5	0.5480	1.79	0.2697
	Pure Error	1.53	5	0.3066		
Y_2	Model	165.39	9	18.38	135.74	< 0.0001
	Residual	1.35	10	0.1354		
	Lack of Fit	0.5662	5	0.1132	0.7188	0.6370
	Pure Error	0.7877	5	0.1575		
Y_3	Model	635.07	9	70.56	100.16	
	Residual	7.05	10	0.7045		
	Lack of Fit	5.21	5	1.04	2.83	0.1389
	Pure Error	1.84	5	0.3677		

RESULTS

Effect of interaction factors on the substrate loss rate

The substrate loss rate's response surface is illustrated in Fig. 3. As shown in Fig. 3(a), when the seedling picking frequency is 90 plants/min, the substrate loss rate exhibits an upward trend with the increasing needle clamping angle, while it shows a downward trend with the rising spring stiffness coefficient. The response surface demonstrates a relatively rapid change in the direction of the needle clamping angle, whereas the change in the direction of the spring stiffness coefficient is relatively slow. At a certain seedling picking frequency, the impact of the needle clamping angle on the substrate loss rate is more pronounced than that of the spring stiffness coefficient. A lower substrate loss rate was observed at a spring stiffness coefficient of approximately 400 N/m and a needle clamping angle of around 16°.

As depicted in Fig. 3(b), when the clamping angle of the seedling needle is set at 16°, an increase in the spring stiffness coefficient leads to a higher rate of substrate loss. Similarly, as the frequency of seedling extraction rises, the rate of substrate loss also shows an upward trend.

The response surface analysis reveals that the substrate loss rate is more sensitive to changes in the spring stiffness coefficient, exhibiting a relatively rapid variation along this direction. In contrast, its change along the direction of seedling extraction frequency is comparatively slower.

As shown in Fig. 3(c), when the spring stiffness coefficient is fixed at 400 N/m, the substrate loss rate initially rises and then declines with increasing seedling extraction frequency, while it consistently increases with an increasing needle clamping angle. The response surface exhibits a more pronounced change in the direction of the needle clamping angle compared to the direction of the seedling extraction frequency. This indicates that, for a given spring stiffness coefficient, the needle clamping angle has a more significant impact on the substrate loss rate than the seedling extraction frequency.

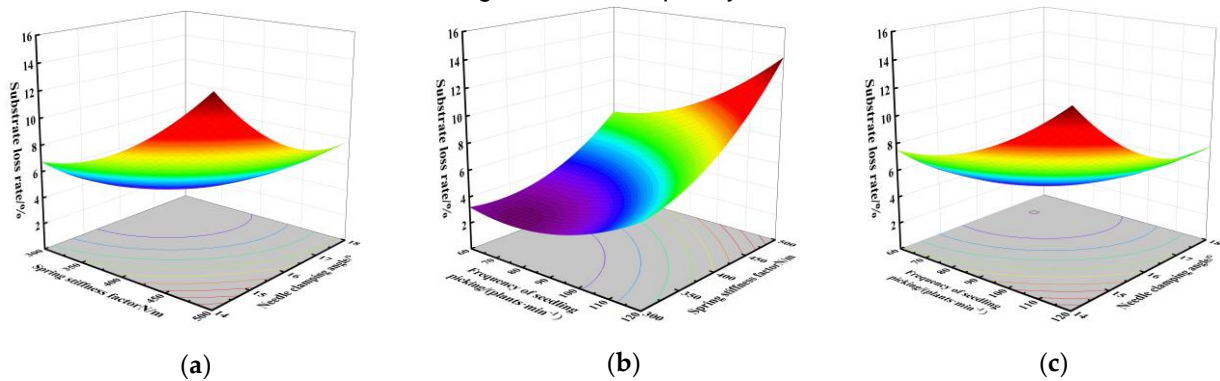


Fig. 3 – Effect of interaction factors on substrate loss rate

Effect of interaction factors on the pot seedling shedding rate

The response surface of the seedling shedding rate is presented in Fig. 4. As depicted in Fig. 4(a), when the seedling picking frequency is 90 plants/min, the seedling shedding rate increases with the increasing seedling needle clamping angle and first decreases and then increases with the rising spring stiffness coefficient. The response surface analysis indicates that the seedling shedding rate changes along the direction of the spring stiffness coefficient, but the rate of change is faster along the direction of the needle clamping angle. At a given picking frequency, the influence of the needle clamping angle on the seedling shedding rate is more significant than that of the spring stiffness coefficient.

As illustrated in Fig. 4(b), when the clamping angle of the seedling needle is 16°, the pot seedling shedding rate increases with the increasing spring stiffness coefficient. Meanwhile, it first decreases and then increases with the rising seedling picking frequency. The response surface exhibits a slower rate of change along the direction of seedling picking frequency and a faster rate of change along the direction of spring stiffness coefficient. When the seedling picking frequency is approximately 90 plants/min and the spring stiffness coefficient is around 400 N/m, the pot seedling shedding rate is relatively lower.

As depicted in Fig. 4(c), when the spring stiffness coefficient is approximately 400 N/m, the seedling shedding rate rises with the increasing seedling picking frequency and also increases with the increasing needle clamping angle. The response surface analysis indicates that the rate of seedling shedding varies more rapidly in the direction of the needle clamping angle and more slowly in the direction of the seedling picking frequency. Under a certain spring stiffness coefficient, the influence of the needle clamping angle on the seedling shedding rate is more significant than that of the seedling picking frequency.

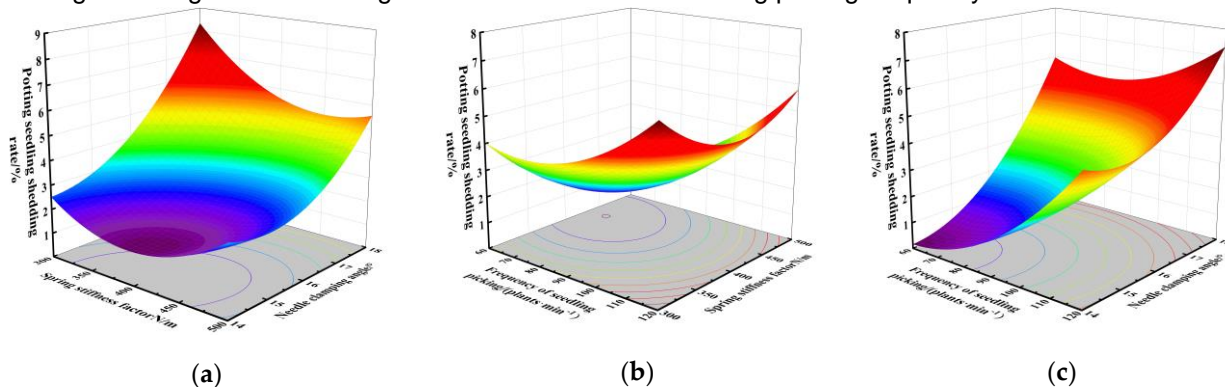


Fig. 4 – Effect of interaction factors on pot seedling shedding rate

Effects of interaction factors on seedling extraction success

The response surface of the seedling extraction success rate is presented in Fig. 5. As depicted in Fig. 5(a), when the seedling extraction frequency is 90 plants/min, the seedling extraction success rate decreases with the increasing seedling needle clamping angle and initially increases and then decreases with the rising spring stiffness coefficient. The response surface analysis reveals that the seedling extraction success rate exhibits a more rapid change along the direction of the spring stiffness coefficient and a relatively slower change along the direction of the needle clamping angle.

As shown in Fig. 5(b), when the clamping angle of the seedling needle is 16°, the success rate of seedling extraction increases with the increasing spring stiffness coefficient. Meanwhile, it initially increases and then decreases with the increasing seedling extraction frequency. The response surface analysis indicates a more rapid change in the direction of seedling extraction frequency and a relatively slower change in the direction of spring stiffness coefficient.

As depicted in Fig. 5(c), when the spring stiffness coefficient is set at 400 N/m, the success rate of seedling extraction initially increases and then decreases with the increasing seedling extraction frequency. Similarly, it first rises and then falls with the increasing needle clamping angle. The response surface analysis shows that the seedling extraction success rate varies gradually in the direction of the needle clamping angle, while it exhibits a relatively rapid change in the direction of the seedling extraction frequency. Given a certain spring stiffness coefficient, the impact of the seedling extraction frequency on the seedling extraction success rate is more pronounced than that of the seedling needle clamping angle.

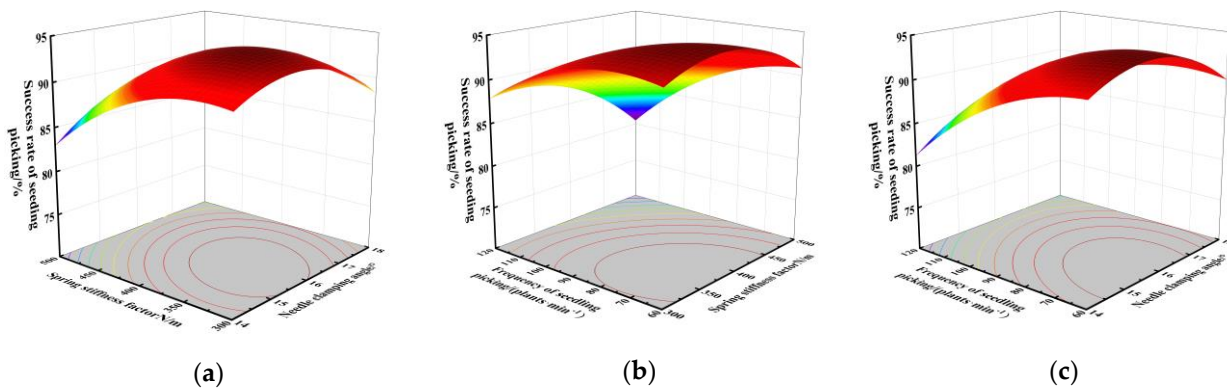


Fig. 5 – Effect of interaction factors on seedling extraction success

Parameter optimization

To enhance the operational performance of the seedling extraction device, an optimization of its working and structural parameters is conducted. This optimization is aimed at achieving three primary goals: reducing the substrate loss rate, decreasing the seedling dropout rate, and increasing the success rate of seedling extraction. The optimization process employs the Optimization-Numerical module in Design-Expert V13.0.5 software to determine the optimal parameter settings. The objective functions and constraints for this optimization are outlined as follows:

$$\begin{cases} \min Y_1 \\ \min Y_2 \\ \max Y_3 \\ X_1 \in [-1, 1] \\ X_2 \in [-1, 1] \\ X_3 \in [-1, 1] \end{cases} \quad (4)$$

The optimal parameter combinations were selected by the software Design-Expert.V13.0.5: spring stiffness coefficient of 376.81 N/m, a clamping angle of 15.6° and a seedling picking frequency of 89 plants/min. The model predicted the substrate loss rate of 3.94%, the pot seedling shedding rate of 2.01%, and a seedling-picking success rate of 94.05%.

Experimental validation

Using the optimized parameters (spring stiffness coefficient of 376.81N/m, seedling needle clamping angle of 15.6°, seedling picking frequency of 89 plants/min), the model validation experiments were carried out on the automatic seedling picking performance experimental table in the laboratory of agricultural machinery and equipment of Shandong University of Science and Technology, as shown in Fig. 6.

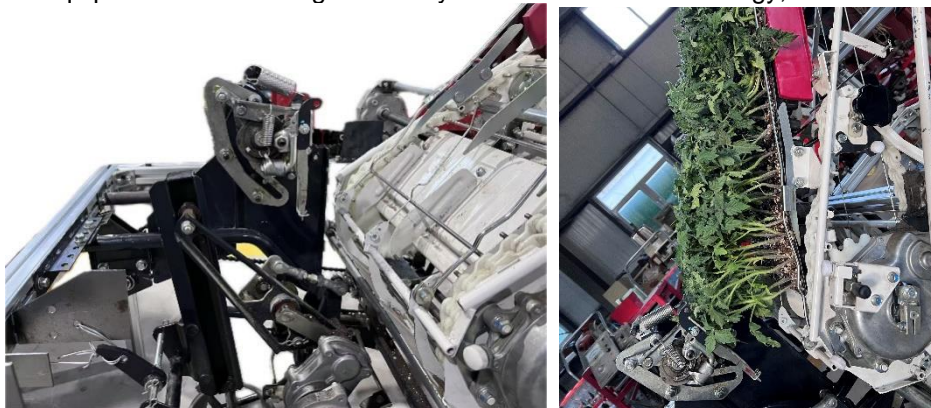


Fig. 6 – Automatic Seedling Picking Device Laboratory

To eliminate random errors and ensure the reliability of the results, five repeated tests were conducted, and the average values were calculated. Each test involved removing 72 seedlings from the entire tray, with the results summarized in Table 3. As can be seen, the average values of the substrate loss rate, pot seedling shedding rate, and seedling extraction success rate are 4.09%, 1.97%, and 93.94%, respectively. Notably, the error between the test value of the seedling extraction success rate and the optimized parameter value from the software is a mere 0.11%. This minimal discrepancy indicates that the selection of influencing factors on the quality of seedling extraction is reasonable and well - justified. Therefore, it can be concluded that the established performance optimization model of the automatic seedling picking device is correct and valid. Moreover, the obtained working and structural parameters fully meet the requirements for automatic seedling picking in tomato pot seedling machinery, ensuring both practical applicability and operational effectiveness.

Table 3

Results of seedling picking experiment under optimized conditions			
Test No.	Substrate loss rate $Y_1/\%$	Pot seedling shedding rate $Y_2/\%$	Success rate of seedling picking $Y_3/\%$
1	3.41	0.83	95.76
2	3.53	1.21	95.26
3	4.26	1.95	93.79
4	4.71	2.75	92.54
5	4.54	3.13	92.33
Average value	4.09	1.97	93.94

CONCLUSIONS

1) This study investigated the cam motion process of the seedling gripper in a tomato pot seedling automatic extraction device, enabling the precise determination of cam movement parameters. By conducting a theoretical analysis of the forces acting on the root plug during the seedling-picking process, combined with the planting frequency of duckbill planting, a one-factor experiment was carried out using spring stiffness coefficient, seedling needle clamping angle, and seedling-picking frequency as the variables. The results indicated that these parameters had significant effects on the substrate loss rate, pot seedling shedding rate, and seedling-picking success rate.

2) A second - order rotary orthogonal combination test was performed on the seedling - picking device. Regression models between each factor and index were established, and the parameters were optimized using the response surface methodology. The optimal parameter combinations for the automatic seedling - picking device were determined as follows: the spring stiffness coefficient was 367.8 N/m, the clamping angle of the seedling needles was 15.6°, and the picking frequency was 89 plants per minute. Under these parameter combinations, the average substrate loss rate was calculated to be 4.09%, the average pot seedling shedding rate was 1.97%, and the average seedling extraction success rate was 93.94%. The results of the bench - top validation test were found to be in close agreement with the optimization results.

ACKNOWLEDGEMENT

This research was funded by Modification and Development of Fully Automatic Vegetable Transplanter, project number 2023BCF01052.

REFERENCES

- [1] Chen L.T., Liu Z.X., Yu X.Y., & Mou X.W. (2024). Experimental Study on Potting Characteristics of Rice Seedling in Hole Tray (水稻穴盘秧苗钵体力学特性试验研究). *Agricultural Engineering, China*, 14(02), 39-47. DOI: 10.19998/j.cnki.2095-1795.2024.02.006.
- [2] Dixit J. (2010). Field performance and evaluation of manual paddy transplanter in Kashmir Valley. *Ama Agricultural Mechanization in Asia Africa & Latin America, Japan*, 41(1): 9-13.
- [3] Gao G.H., Feng T.F., & Li F. (2015). Optimization and experimental verification of working parameters for inclined-inserting transplanting manipulator for plug seedlings (斜入式穴盘苗移栽手爪工作参数优化及试验验证). *Transactions of the Chinese Society of Agricultural Engineering, China*, 31(24), 16-22.
- [4] Han L.H., Mao H.P., Miu X.H., Hu J.P., & Yang X.J. (2013). Design of an Automatic Seedling Picker End Effector Based on the Mechanical Properties of Plug Seedlings (基于穴盘苗力学特性的自动取苗末端执行器设计). *Transactions of the Chinese Society for Agricultural Machinery, China*, 44(11), 260-265.
- [5] Han L.H., Mao H.P., Yan L., Hu J.P., Huang W.Y., & Dong L.L. (2015). Pincette-type End-effector Using Two Fingers and Four Pins for Picking Up Seedlings (穴盘育苗移栽机两指四针钳夹式取苗末端执行器). *Transactions of the Chinese Society for Agricultural Machinery, China*, 46(07), 23-30.
- [6] Huang N.H., Tang Q., Song Z.W., Liu H., Wu Y., & Zhu T.W. (2023). Current Development Status and Trends of Seedling Picking Mechanisms for Dry Land Transplanting Machinery (旱地移栽机械取苗机构发展现状与趋势). *Journal of Intelligent Agricultural Equipment, China*, 4(04), 57-64.
- [7] Hu M.J., Yi W.Q., Hu F., & Qian Y. (2011). Development of an Automatic Seedling Removal Test System for Plug Seedlings (穴盘苗自动取苗试验系统的研制). *Journal of Nanjing Agricultural University, China*, 34(03), 122-126.
- [8] Hu S.Y., Hu M.J., Zhang W.Y., & Ge X.Y. (2023). Dynamics Analysis and Testing of the Transplanting Process of Pepper Plug Seedlings (辣椒穴盘苗取苗栽植过程动力学分析与试验). *Journal of Agricultural Machinery in China, China*, 44(07), 40-47+54. DOI: 10.13733/j.jcam.issn.2095-5553.2023.07.006.
- [9] Jin X. (2014). *Research on Automatic Transplanting Technology and Equipment for Vegetable Plug Seedlings (蔬菜穴盘苗自动移栽技术与装置的研究)*. China Agricultural University, China.
- [10] Li H., Cao W.B., Li S.F., Fu W., & Liu K.Q. (2015). Kinematic Analysis and Testing of an Automatic Seedling Picking Mechanism for Pepper Plug Seedlings (辣椒穴盘苗自动取苗机构运动学分析与试验). *Transactions of the Chinese Society of Agricultural Engineering, China*, 31(23), 20-27.
- [11] Liang X.F., Xiao X.Z., Zhu Y.J., Wang Y.W., & Wu C.Y. (2018). Design and Testing of an End Effector for Replanting Pot Seedlings at the Cotyledon Stage (.子叶期钵苗补苗末端执行器设计与试验). *Transactions of the Chinese Society of Agricultural Engineering, China*, 34(09), 49-57.
- [12] Liu Y., Li Y.X., Li B., Wang T., & Lu Y.T. (2013). Research Status of Crop Transplanting and Transplanting Machines in the Xinjiang Region (新疆地区作物移栽与移栽机研究现状). *Guangdong Agricultural Sciences, China*, 40(09), 189-191+196.
- [13] Manjunatha M. V., Reddy B. G., Masthana S., & Joshi V.R. (2009). Studies on the performance of self-propelled rice transplanter and its effect on crop yield. *Karnataka Journal of Agricultural Sciences, India*, 2285-387.
- [14] Niu Y., Wang X.J., Chen X., Yan Y., & Wang J.S. (2022). The current situation, problems and countermeasures of China's tomato industry development and the achievements of Ningxia's tomato industry development (中国番茄产业发展的现状问题和对策及宁夏番茄产业发展成效). *Heilongjiang Agricultural Science, China*, (12), 70-74.
- [15] Sakaue O. (1996). Development of seedling production robot and automated transplanter system. *Jarq Japan Agricultural Research Quarterly, Japan*, 30(4), 221-226.
- [16] Wang M.M., Song J.N., Liu C.L., Wang Y.L., & Sun Y.M. (2015). Design and Testing of a Crank and Rocker Type Seedling Clamping Mechanism for Vegetable Transplanters (蔬菜移栽机曲柄摆杆式夹苗机构的设计与试验). *Transactions of the Chinese Society of Agricultural Engineering, China*, 31(14), 49-57.

- [17] Xue D.Q., Hou S.L., & Zhang J.X. (2013). Research Progress and Development Trends of Dry Land Transplanting Machinery in China (我国旱地移栽机械的研究进展与发展趋势). *Journal of Agricultural Machinery in China*, CHINA, 34(05), 8-11.
- [18] Ye B.L., Li L., Yu G.H., Liu A., Cai D. (2014). Design and Testing of the Cam Mechanism for Seedling Arm of Vegetable Pot Seedling Transplanter (蔬菜钵苗移栽机取苗臂凸轮机构的设计与试验). *Transactions of the Chinese Society of Agricultural Engineering*, China, 30(08), 21-29.
- [19] Yu X.X., Zhao Y., Chen C.B., Zhou M.L., Zhang H., & Zhang Z.C. (2014). Development Status and Prospects of Transplanting Machinery(移栽机械发展现状与展望). *Journal of Agricultural Machinery*, China, 45(08).
- [20] Zhang M. (2014). *Research on the Fitting Gear Five-bar Rice Pot Seedling Transplanter Mechanism (拟合齿轮五杆水稻钵苗移栽机构的研究)*. Northeast Agricultural University, China.
- [21] Zhang Z.G., Cao W.B., Wang Q., & Zhang P. (2013). Current Development Status and Prospects of Automatic Transplanters for Plug Seedlings (穴盘苗自动移栽机的发展现状与展望). *Agricultural Mechanization Research*, CHINA, 35(05), 237-241. DOI:10.13427/j.cnki.njyi.2013.05.053.
- [22] Zhao Y., Zhu H.X., Xin L., Zhou M.L., Feng J., & Zhang M. (2016). Mechanism Analysis and Experiment of Transplanting Mechanism with Fitting Gear Five-bar for Rice Pot Seedling (拟合齿轮五杆水稻钵苗移栽机构的机理分析与试验). *Transactions of the Chinese Society of Agricultural Engineering*, China, 32(01), 12-21.
- [23] Zhai W.B., Li H.M., Dong A.H., Yang Y., Zhang B.Q., & Yuan Z.H. (2025). Design and Testing of the Seedling Picking Mechanism for Eggplant Pot Seedling Transplanter (茄子钵苗移栽机取苗机构设计与试验). *Journal of Agricultural Machinery in China*, China, 46(01), 30-35. DOI: 10.13733/j.jcam.issn.2095-5553.2025.01.005.

TOMATO MATURITY DETECTION BASED ON IMPROVED YOLOv8n

/ 基于改进 YOLOv8n 的番茄果实成熟度检测

JunMao LI, ZiLu HUANG, LingQi XIA, Hao SUN, HongBo WANG*

College of Mechanical and Electronic Engineering, Inner Mongolia Agricultural University, Hohhot / China

Tel: +86 13739981395; E-mail: wanghb@imau.edu.cn

DOI: <https://doi.org/10.35633/inmateh-75-53>

Keywords: tomato detection; YOLOv8n; fruit maturity detection; EMA attention mechanism; C2f-Faster module

ABSTRACT

The detection of tomatoes for automatic picking is challenging due to the dense distribution of fruit and severe occlusions. To address this, a dataset is developed using tomato images captured in a greenhouse environment, and an enhanced model for tomato fruit maturity detection based on YOLOv8n is proposed, which incorporates the EMA attention mechanism and the C2f-Faster module for multi-scale feature fusion. These additions not only improve detection accuracy but also enhance detection speed, thereby boosting the model's robustness and generalization ability. Experimental results demonstrate that the proposed ECF-YOLOv8n model achieves detection accuracies of 93.8%, 94.7%, 92.5% and 94.1% for immature, nearly mature, ripe tomatoes and mean average precision in a greenhouse setting, respectively. The model's size is 4.7 MB, with GFLOPs of 6.5G. Compared to advanced models like RT-DETR, YOLOv5, YOLOv7 and YOLOv11, the ECF-YOLOv8n model outperforms them in both detection accuracy and speed. This work provides valuable insights for the research, development and optimization of tomato picking robots.

摘要

针对目前番茄自动化采摘目标检测中因果实密集、遮挡严重等导致目标检测难度大的问题，本研究基于温室大棚环境下的番茄图像，构建了数据集，提出了一种基于 YOLOv8n 的番茄果实成熟度检测的改进模型，并添加引入了 EMA 注意力机制和 C2f-Faster 模块，以实现多尺度特征融合，在保证检测精度较高的情况下，有效提高了番茄果实检测速度，从而进一步提高了模型的鲁棒性和泛化能力。试验结果表明：提出的 ECF-YOLOv8n 模型对温室大棚环境下未成熟、将要成熟、成熟番茄检测精度和均值平均精度分别为：93.8%、94.7%、92.5% 和 94.1%，模型大小为 4.7 MB，GFLOPs 为 6.5G，与 RT-DETR、YOLOv5、YOLOv7、YOLOv11 等先进模型进行比较，该模型实现了较高的检测精度和更快的检测速度，本研究可为番茄采摘机器人的研发和优化提供重要参考。

INTRODUCTION

Tomato is one of the important economic crops in greenhouses. In recent years, the area of greenhouse tomato cultivation has continued to expand. However, tomato harvesting is still primarily carried out by humans, which is inefficient and costly. In addition, since the harvesting window for tomatoes is short, failing to pick the ripe fruits in time directly affects both fruit quality and economic benefits (Malik et al., 2018; Lawal et al., 2021). To achieve efficient and rapid automated tomato picking, accurate target detection is crucial. Target detection technology provides precise information for mechanized picking, enabling the automation of the harvesting process. Therefore, enhancing the accuracy of target detection is key to improving picking efficiency and reducing costs (Tsai et al., 2022; Li R et al., 2023; Miao, et al., 2023).

In recent years, convolutional neural networks (CNNs) based on deep learning have become a major research focus and have been widely applied to the identification of greenhouse tomatoes (Gao et al., 2022; Zeng et al., 2024). Target detection algorithms are generally categorized into two main types: one-stage and two-stage. Typical representatives of one-stage object detection algorithm include the YOLO series. The typical representative of the two-stage object detection algorithm is the RCNN series, including Fast R-CNN, Faster R-CNN and Mask R-CNN (Bai et al., 2024; Yin et al., 2024; Babu et al., 2024).

JunMao LI, M.S. Stud.; ZiLu HUANG, M.S. Stud.; LingQi XIA, M.S. Stud.; Hao SUN, Stud.;

HongBo Wang, Professor, Correspondent author

This algorithm first generates a series of candidate boxes for samples and then classifies the samples through a convolutional neural network. Compared with the one-stage algorithm, the two-stage algorithm has a slower detection speed, and a higher algorithm complexity.

In the field of fruit and vegetable maturity detection, numerous experts and scholars both domestically and internationally have conducted relevant research. In terms of one-stage algorithm, *Fengjun et al.*, (2024), addressed the issue of occlusion of *Camellia oleifera* fruits in natural environments by improving the original YOLOv7 model. They proposed a maturity detection method for *Camellia oleifera* fruits, providing a theoretical basis for the intelligent harvesting of these fruits. To improve the accuracy of surface defect detection in pinewood while maintaining detection speed, *Jiwen et al.*, (2024), proposed an improved RT-DETR model, RIC-DETR. Experimental results demonstrated that the RIC-DETR model achieved an accuracy of 95.4%, offering technical support for surface defect detection in pinewood. *Zheng et al.* (2022) constructed a new backbone network, R-CSPDarknet53, based on YOLOv4 by integrating a residual neural network to establish skip connections between the front and back layers, thereby preventing the loss of low-dimensional small target features. In addition, by replacing the maximum pool in the original SPP network with the deep separable convolution model, C-SPP is proposed to realize feature information reuse and multi-scale fusion. On this basis, a tomato detection model RC-YOLOv4 is constructed, which improves the detection accuracy of tomato in natural environment. The test results show that the tomato detection accuracy and recall rate of RC-YOLOv4 model in natural environment are 88% and 89% respectively, the average detection accuracy is 94.44%. *Appel et al.*, (2023), proposed an improved YOLOv5 tomato detection algorithm. By adding CBAM convolutional attention mechanism to the YOLOv5 model, feature extraction and target recognition were carried out to improve the accuracy of the model. Non-maximal suppression and distance union ratio (DIoU) were APPLIED to enhance the recognition of overlapping objects in the image. The results showed that the average accuracy of the CAM-YOLO algorithm for the detection of overlap and small tomatoes was 88.1%.

Li P. et al. (2023), based on the requirements of the tomato maturity grading task, adopted the MHSA attention mechanism to improve the YOLOv8 backbone, enhancing the network's ability to extract diverse features. The Precision, Recall, F1-score, and mAP50 of the tomato fruit maturity grading model constructed based on MHSA-YOLOv8 were 0.806, 0.807, 0.806, and 0.864. *Solimani et al.*, (2024), proposed a new data balancing method in order to overcome the problem of data imbalance. A squeezing and exciting (SE) block attention module is integrated into the head structure of YOLOv8 model, which significantly improves the algorithm's ability to detect objects of different sizes in complex environments, and can effectively detect flowers and fruits in tomato plants.

In terms of two-stage algorithm, *Gao et al.*, (2020), addressed the issue of occlusion in apples during the harvest period by applying the Faster R-CNN model for detecting occluded apples. Experimental results showed that the model achieved an average detection accuracy of 80%-90% for occluded apples. *Chen et al.*, (2022), integrated Gabor features into Faster R-CNN and proposed a two-stage training method based on a genetic algorithm and backpropagation to train a new Faster GG-R-CNN model, achieving an average precision of 94.57%. *Seo et al.*, (2021), developed a real-time robotic detection system based on Faster R-CNN, utilizing hue values to establish an image-based ripeness standard for tomatoes, with a recognition accuracy of 90.2%. *Fang et al.*, (2024), proposed a multi-target identification and localization method for tomato plants based on the VGG16-UNet model. The average intersection and pixel accuracies of the VGG16-UNet model after introducing the pretrained weights were 85.33% and 92.47%, respectively, which were 5.02% and 4.08% higher than those of the VGG16-UNet without pretrained weights, achieving the identification of main branches, side branches, and axillary bud regions.

In a greenhouse environment, factors such as lighting, occlusion, and the density of plants can complicate the accurate identification of tomato ripeness (*Huiqin et al.*, 2024), leading to low detection efficiency. To improve the detection accuracy and speed of tomato ripening in greenhouse, this study proposes an enhanced YOLOv8n object detection algorithm. By incorporating the EMA attention mechanism, the model reduces sensitivity to noise and outliers, while the C2f-Faster module enables multi-scale feature fusion, thus improving both detection accuracy and speed for tomatoes. To account for the complexity of greenhouse tomato scenes, images of tomatoes are captured under various weather conditions, lighting angles, and shooting perspectives, ensuring the dataset's richness and diversity. Additionally, preprocessing and image augmentation techniques are applied to enhance dataset quality, making it better suited for tomato fruit detection in greenhouse environments. This research provides valuable target information for tomato-picking robots and offers a theoretical foundation for automated harvesting.

MATERIALS AND METHODS

DATA SAMPLE COLLECTION AND DATASET CREATION

Data Sample Collection

The tomato image data were collected from a tomato picking garden located in the suburbs of Hohhot, where standardized cultivation techniques are applied. To ensure the diversity of the dataset, enhance the model's robustness, and improve its generalization ability, images of tomatoes were captured at different times of day, across various stages of ripeness, from different angles, at varying distances, and under different lighting conditions (Wang *et al.*, 2024). A total of 2,080 images, each with a resolution of 640×640, were selected for the dataset, as shown in Figure 1.



Fig. 1 - Images of tomatoes in a greenhouse in different scenes

Dataset Preparation

The creation of the dataset primarily involved two key processes: image annotation and dataset categorization. The Labellmg annotation tool was used for manual labelling of the image data, following the YOLO dataset annotation format. According to the national standard GH/T1193-2021, the maturity of tomatoes can be divided into unripe stage, green ripe stage, colour change stage, early red ripe stage, mid-red ripe stage and late red ripe stage. Specifically, tomatoes in the mid-red ripe stage and late red ripe stage have a red surface coverage of 40%-60% and 70%-100%, respectively. In the greenhouse, only mid-red and late-red ripe tomatoes are harvested (Zhao, 2024).

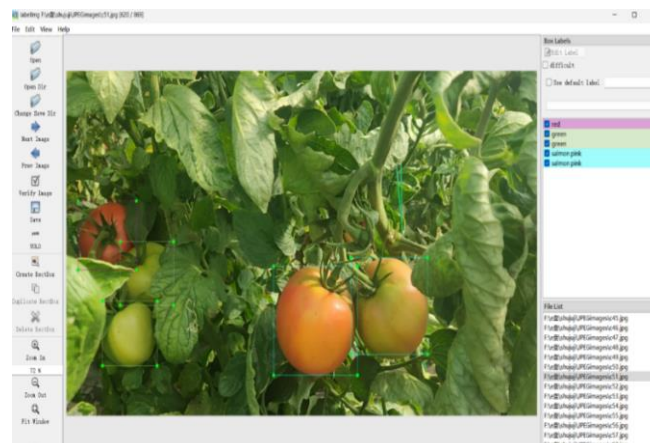


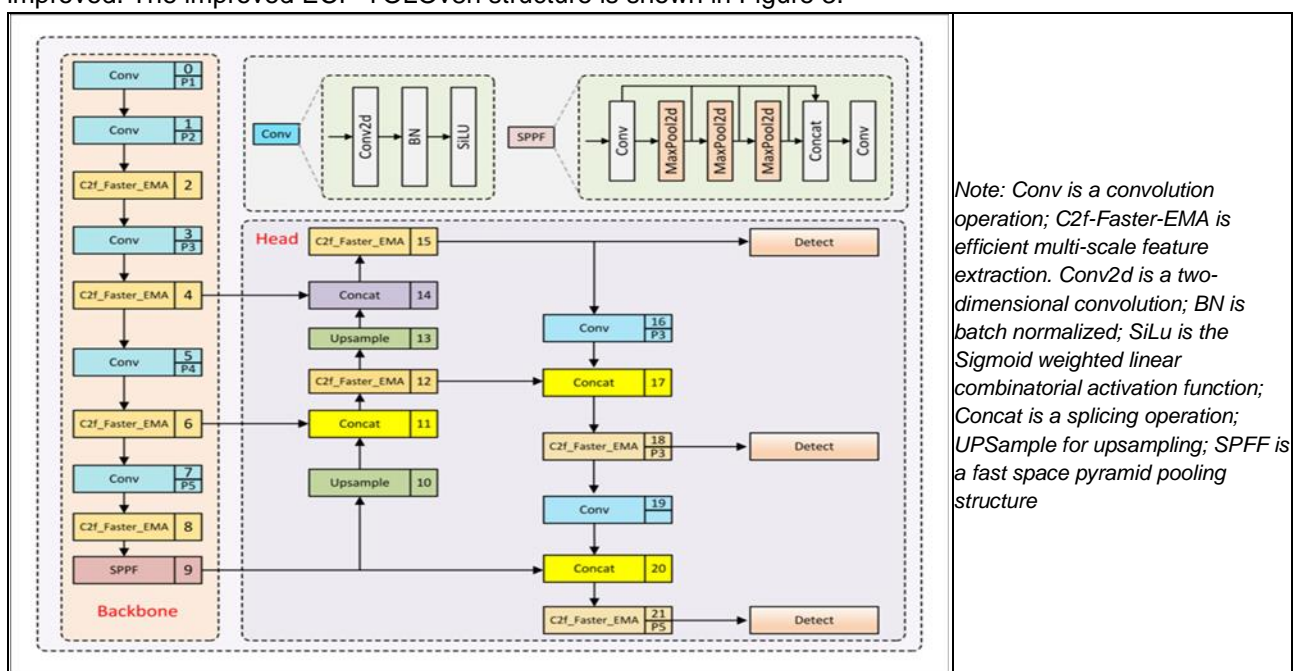
Fig. 2 - Tomato image annotation

In this paper, the labelled targets, i.e. the tomato fruits to be detected, are divided into three categories: Tomato fruits in the unripe, green-ripe, colour-changing, and early red-ripe stages, i.e. tomatoes with less than 40% red surface coverage, are classified as unripe and labelled as green; mid-ripe tomatoes with 40% to 60% red colouring on the fruit surface are classified as almost ripe and are labelled as salmon pink; late-ripe tomatoes with 70% to 100% red colouring on the fruit surface are classified as mature and labelled as red. The image annotations are illustrated in Figure 2. Upon completion of the annotation process, a corresponding text file (*.txt) for each image was generated, linking the image name with the txt file name. The labelled dataset was then split into training, validation, and test sets in a 7:1:2 ratio, with 1456 images for training, 208 images for validation, and 416 images for testing.

FRUIT MATURITY DETECTION MODEL OF TOMATO

YOLOv8 algorithm is the Yolo series target detection algorithm launched by Ultralytics. It is an upgrade based on the historical version of the Yolo series. The network composition of YOLOv8 mainly includes four parts: Input, Backbone, Neck and Head. Backbone is the network part used to extract image features in YOLOv8. It uses a series of convolution and deconvolution layers to extract features, and also uses residual connections and bottleneck structures to reduce the size of the network and improve performance. The neck part plays a role in feature fusion in YOLOv8. It uses multi-scale feature fusion technology to fuse feature maps from different stages of the backbone to enhance feature representation capabilities. The head part is responsible for the final target detection and classification tasks.

YOLOv8 has five different structures, namely YOLOv8m, YOLOv8l, YOLOv8x, YOLOv8n, and YOLOv8s. These models differ only in depth and width. The basic structure of these models is four parts. In order to meet the requirements of lightweight and real-time detection, while ensuring high detection accuracy and detection speed, YOLOv8n which has a relatively low complexity is chosen as the base model. It can achieve faster recognition speed and smaller storage occupancy while ensuring high detection accuracy, which is conducive to deployment on mobile devices (Hussain et al., 2023). Based on YOLOv8n, an improved ECF-YOLOv8n network model structure is proposed, and the EMA attention mechanism is introduced. By reconstructing some channels into batch dimensions and grouping the channel dimensions into multiple sub-features, the EMA attention mechanism can reduce information loss while keeping the tensor size unchanged, and enhance the model’s ability to capture spatial semantic features. The C2f-Faster-EMA module is also responsible for fusing feature maps of different scales to generate more representative feature representations. This feature fusion process may be achieved through upsampling, downsampling, splicing and other operations to ensure that the model can fully utilize multi-scale information to improve detection performance. While keeping the YOLOv8n model lightweight, the detection performance and speed of the model are improved. The improved ECF-YOLOv8n structure is shown in Figure 3.



Note: Conv is a convolution operation; C2f-Faster-EMA is efficient multi-scale feature extraction. Conv2d is a two-dimensional convolution; BN is batch normalized; SiLu is the Sigmoid weighted linear combinatorial activation function; Concat is a splicing operation; UPSample for upsampling; SPPF is a fast space pyramid pooling structure

Fig. 3 - Structural diagram of the improved YOLOv8n

EMA Attention Mechanism

EMA attention mechanism is a new type of efficient multi-scale attention method, which focuses on retaining information on each channel and reducing the amount of computation, as shown in Figure 4.

EMA is an attention weight descriptor that uses three parallel paths to extract grouped feature maps. Two of the parallel routes are located in the 1x1 branch, and the third parallel route is located in the 3x3 branch. In order to reduce the amount of computation and obtain the dependencies between channels at the same time, cross-channel information interaction is established in the channel direction.

In this structure, output represents the output plane of the input features, input represents the input plane of the input features, and k represents the kernel size. Accordingly, the G group is reshaped to the batch dimension and the input tensor is redefined as C//GxHxW. The two encoded features are connected in the height direction of the image and share the same 1x1 convolution without dimensionality reduction 1x1 branch (Xu et al., 2024). After decomposing the output of the 1x1 convolution into two vectors, two nonlinear sigmoid functions are used to fit the 2D Binomial distribution on the linear convolution. In order to realize the different cross-channel interaction features between the two parallel paths in the 1x1 branch, the attention maps of the two channels are aggregated within each group by a simple multiplication. On the other hand, the 3x3 branch captures the local cross-channel interaction through 3x3 convolution to expand the feature space. In this way, EMA not only encodes inter-channel information to adjust the importance of different channels, but also embeds the precise spatial structure information into the channel (Yang et al., 2024).

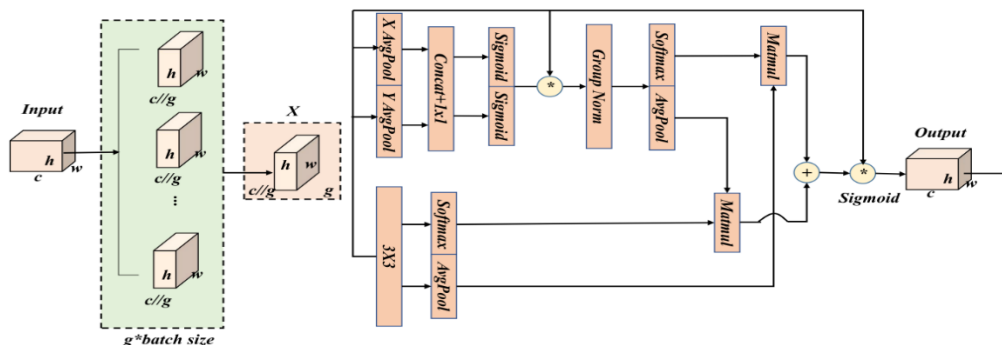


Fig. 4 - EMA module

C2f module

C2f module consists of a convolution block, which receives the input feature map and generates an intermediate feature map. The C2f module structure diagram is shown in Figure 5. The generated intermediate feature map is split into two parts, one part is directly passed to the final "Concat block", and the other part is passed to multiple "Bottleneck blocks" for further processing. The feature map input to the "Bottleneck block" is processed through a series of convolution, normalization and activation operations, and the final feature map is concatenated with the directly passed feature map in the "Concat block". In the C2f module, the number of "Bottleneck modules" is defined by the "depth multiple" parameter of the model, that is, the depth and computational complexity of the module can be adjusted according to the needs. The concatenated feature maps are input into a final convolutional block for further processing to generate the final output feature map.

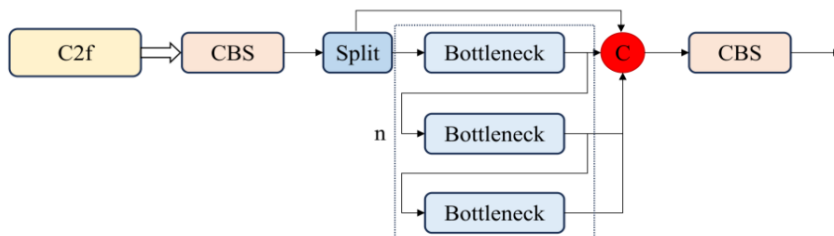


Fig. 5 - C2f module

C2f-Faster Module

In the target detection task, due to the relatively simple structure of the C2f module and the lack of a dedicated acceleration mechanism, it exhibits a low detection speed when processing large-scale data sets or performing real-time detection. In order to solve this performance bottleneck, a new neural network, FasterNet, was introduced. FasterNet has shown significant advantages in achieving fast target detection due to its excellent running speed and optimized design.

There is a new partial convolution (PConv) in the FasterNet module, as shown in Figure 6 (c). The core function of partial convolution (PConv) lies in its flexibility and adaptability to data missing. Compared with traditional convolution, partial convolution does not mechanically apply the same convolution kernel to all parts of the input data. Instead, it dynamically determines the scope of the convolution kernel based on the validity of the data, that is, whether the data points are missing or damaged.

When partial convolution (PConv) processes a convolution window, it first checks the data points within the window. For valid, non-missing data points, PConv applies the convolution kernel like a regular convolution operation. However, for missing or invalid data points, PConv will choose to ignore them and not include them in the convolution calculation. This flexibility means that the actual area of action of the convolution kernel may be different in each convolution window. This depends entirely on the completeness and distribution of the data in the window. In this way, partial convolution not only improves the robustness to missing data, but also more effectively extracts and utilizes the remaining valid information. By reducing redundant computation and memory access at the same time, spatial features can be extracted more efficiently. Each FasterNet (FasterBlock) module has a PConv layer followed by two Conv1x1 layers. Together, they are shown as an inverted residual block, where the intermediate layers have an expanded number of channels and shortcut connections are placed to reuse input features.

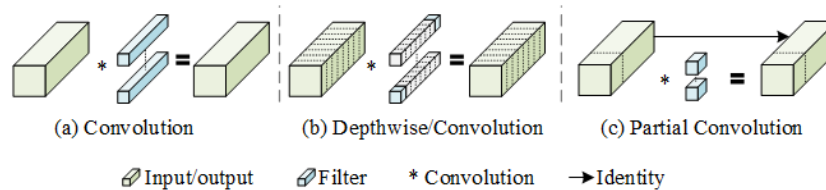


Fig. 6 - Three different convolution structures

The intermediate feature map generated by the fusion of the C2f module and FasterNet is split into two parts, one part is directly passed to the final Concat block, and the other part is passed to multiple FasterBlock blocks for further processing. The C2f-Faster module structure diagram is shown in Figure 7. The feature map input to the FasterBlock is further processed through a series of partial convolution, normalization and activation operations. At this time, the FasterBlock is more efficient and faster than the Bottleneck due to the existence of the partial convolution layer. The final feature map will be concatenated with the directly transmitted feature map in the Concat. The concatenated feature map will be input to a final convolution block for further processing to generate the final output feature map.

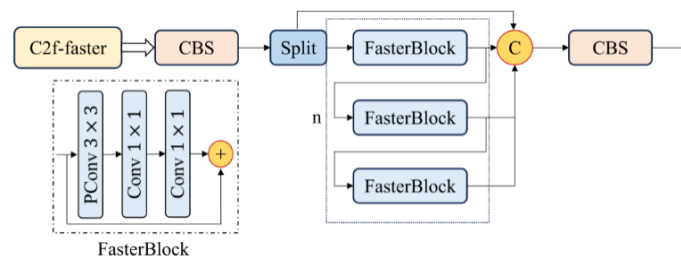


Fig. 7 - C2f-Faster module

C2f-Faster-EMA Module

Although C2f-Faster speeds up the detection speed, some convolution operations will cause some information loss, resulting in a decrease in detection accuracy, which cannot meet the requirements of tomato maturity detection in a greenhouse. Therefore, the EMA (Efficient Multi-scale Attention) attention mechanism is integrated in the C2f-Faster module, forming the C2f-Faster-EMA module, as shown in Figure 8.

The C2f-Faster-EMA module enhances the model's focus on key features, allowing it to more accurately identify target objects during detection, thereby improving overall detection accuracy. At the same time, the acceleration characteristics of FasterNet enable the C2f-Faster-EMA module to significantly reduce computational complexity and time consumption during target detection, speeding up the detection process. The FasterEMA module consists of a partial convolution layer (PConv) followed by a Sequential module comprising a multi-layer perceptron (MLP). This Sequential module includes a CBS module and a convolution layer (Conv2d). To further enhance the model's generalization ability and effectively prevent overfitting, DropPath regularization strategy is introduced. Specifically, DropPath randomly selects a subset of paths within each feature map and sets the weights of these paths to zero. This reduces the number of effective paths, thereby decreasing the model's parameter count and improving its robustness.

The Droppath operation can be applied to each feature map of every convolutional layer, with the pruning probability dynamically adjusted during training to control the extent of pruning. Finally, the EMA attention mechanism, incorporated into the C2f-Faster-EMA, enhances the feature fusion capability of the C2f module. By introducing a more complex network structure and attention mechanism, the model is able to learn more rich and comprehensive feature representations. These representations not only improve detection accuracy but also contribute to the model's robustness in more complex scenarios.

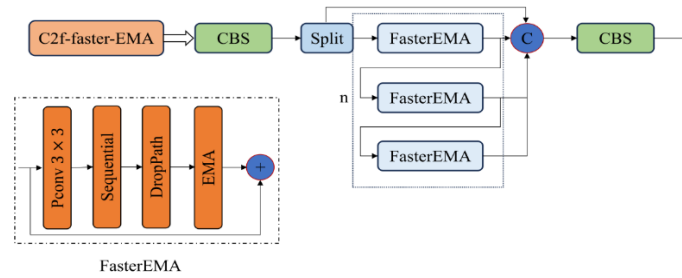


Fig. 8 - C2f-Faster-EMA module

Test environment

The operating system used for trial and training is Windows 11, the CPU is 12th Gen Intel(R) Core(TM) i5-12500H 3.10 GHz, the GPU is NVIDIA GeForce RTX 3060 Laptop GPU, and the running memory is 16G. CUDA version is 12.0, and is implemented using Python 3.10.14 under the PyTorch2.1.0 deep learning framework.

Evaluation indicators

Seven indicators were used to evaluate the maturity detection model of tomato fruit, namely precision (P), recall (R), average precision (AP), and mean average precision (mAP), model parameters, detection speed and memory usage. The calculation formulas of P, R, AP and mAP are as follows.

$$P = \frac{T_P}{T_P + F_P} \times 100\% \tag{1}$$

$$R = \frac{T_P}{T_P + F_N} \times 100\% \tag{2}$$

$$AP = \int_0^1 P(R) dR \tag{3}$$

$$mAP = \frac{\sum_{i=1}^m AP(n)}{3} \tag{4}$$

$$t = \frac{t_N}{N} \tag{5}$$

where, T_P represents the number of positive samples predicted as positive samples, that is, the number of correctly predicted tomato ripening levels; F_P represents the number of negative samples predicted as positive samples, that is, the number of falsely predicted tomato ripening levels; F_N represents the number of negative samples predicted as negative samples, that is, the number of tomato ripening level is incorrectly predicted; AP represents the P(R) curve made by using the Recall value as the X axis and the Precision value as the Y axis. The area of the measurement is the accuracy of identification of a certain category; mAP represents the average value of each category of AP, and measures the average quality of all categories.

RESULTS

IMPROVED TEST RESULTS OF YOLOV8N MODEL

In order to verify the effect of the improved YOLOv8n model, the accuracy P of the improved YOLOv8n model reached 93.7%, the recall R was 83.7%, and the average accuracy mean mAP was 94.1% for the 416 tomato fruit images divided into the test set. Some of the detection results are shown in Figure 9.



Fig. 9 - Improved YOLOv8n model detection results

COMPARISON OF IMPROVED YOLOV8N ABLATION EXPERIMENT PERFORMANCE

In order to better analyse the detection performance of the improved YOLOv8n model on tomato fruit maturity, ablation test was performed using YOLOv8n as the basic model to verify the optimization effect of each improved module. The optimization effect of each improvement point is evaluated using precision (P), recall (R), mean average precision (mAP), parameter quantity, floating point operations per second (FLOPs) and memory usage. The results of the ablation test are shown in Table 1.

Table 1

Model	Green mature (P)/%	Colour change (P)/%	Red mature (P)/%	MAP50 /%	Parameter quantity /M	FLOPs /G	Memory usage /MB
YOLOv8n	94.5	89.6	91.9	91.9	3.0	8.1	5.6
v8n-C2f-Faster	92.2	90.5	95	92.9	2.3	6.3	4.6
v8n-C2f-Faster-CGLU	93.2	92.7	87.1	93.2	2.2	6.2	4.5
v8n-C2f-Faster-EMA	93.8	94.7	92.5	94.1	2.3	6.5	4.7

The analysis results show that the proposed ECF-YOLOv8n model with the C2f-Faster-EMA module has significantly reduced the parameters, floating point operations amount and memory usage of the model compared with the YOLOv8n basic model, which improves the computing and storage efficiency. The detection precision (P) has also been increased, with the average of the mean average precision (mAP) increased by 2.2 percentage points, and the parameter quantity, floating point operations per second (FLOPs), and memory usage have been reduced by 23.33%, 19.75%, and 21.52%, respectively. This shows that the ECF-YOLOv8n model is maintaining high detecting rate, the model is lightweighted. Although the proposed ECF-YOLOv8n model with fusion C2f-Faster-EMA module has slightly increased the mean average precision (mAP) compared with the model with fusion C2f-Faster and C2f-Faster-CGLU. The average value has increased by 1.3 and 0.9 percentage points respectively, with a valuable increase, which can achieve accurate and efficient identification of tomato fruits by picking robots in greenhouse, and is more conducive to the picking of tomato picking robots.

COMPARATIVE TEST RESULTS OF IMPROVING YOLOV8N MODEL

In order to evaluate the detection effect of the ECF-YOLOv8n model proposed in this paper on tomato fruit maturity, three algorithms, YOLOv5, YOLOv7, YOLOv11, and RTDETR, were selected for performance comparison under the premise of consistent experimental conditions. The comparison results are shown in Table 2.

Table 2

Model	Precision (P) / %	Recall (R) / %	Mean average precision (mAP) / %	Frames per second (FPS)	Parameter quantity / M	FLOPs / G	Memory usage / MB
RT-DETR	87.5	82.1	87.6	87.0	19.9	56.9	40.5
YOLOv5	90.0	85.0	88.7	263.6	7.1	15.8	14.4
YOLOv7	91.5	87.2	94.3	145.8	37.9	104.1	73.8
YOLOv11	90.1	87.9	93.3	107.5	2.58	6.3	4.6
Ecf-YOLOv8n	93.7	83.7	94.1	335.1	2.3	6.5	4.7

As shown in Table 2, the ECF-YOLOv8n model achieved a precision (P) of 93.7%, a recall (R) of 83.7%, and a mean average precision (mAP) of 94.1%. Compared to other detection models, the ECF-YOLOv8n model demonstrates improved performance in greenhouse tomato maturity detection. Compared with the mean average precision (mAP), the RT-DETR, YOLOv5 and YOLOv11 models were improved by 6.5%, 5.4% and 0.8%. respectively, indicating that ECF-YOLOv8n has higher precision in the detection of tomato maturity in greenhouses. The ECF-YOLOv8n model has decreased by 0.2% compared with the YOLOv7 model in terms of the mean average precision (mAP), but the parameter quantity and memory usage of ECF-YOLOv8n are much smaller than that of YOLOv7, and the detection rate is faster.

The average frame of ECF-YOLOv8n reaches 335.1 frames/s, which is far higher than YOLOv7, showing that it has better efficiency and better real-time detection capabilities. Overall, ECF-YOLOv8n has shown balanced and excellent performance in detection performance, resource use and detection rate, and has better effect on the detection of tomato maturity in greenhouses.

Test verification

Owing to the constraints of test conditions, time, and other factors, a laboratory-based experiment was conducted to evaluate the detection performance of the enhanced ECF-YOLOv8n model for tomato maturity recognition. The results indicated that the average recognition accuracy of the improved ECF-YOLOv8n model for tomatoes reached 91%, which satisfies the requirements for greenhouse tomato harvesting. Future testing will be conducted in real-world greenhouse environments to improve the model's adaptability in complex scenarios, thereby better aligning it with the requirements of intelligent agriculture.

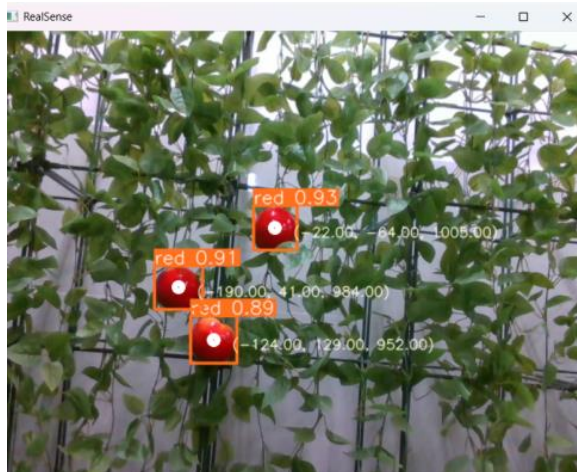


Fig. 10 - Tomato ripeness identification results

CONCLUSIONS

This paper improves the tomato maturity model based on the Yolov8n model, and realizes rapid and accurate detection of the tomato maturity in greenhouses. The main conclusions are as follows:

1) This paper proposes an ECF-YOLOv8n model based on the Yolov8n model. The precision (P) of this model for detecting the maturity of tomato is 93.7%, the recall (R) is 83.7%, and the mean average precision (mAP) is 94.1%. Through the ablation test results, it can be seen that the improved ECF-YOLOv8n model has a mean average precision (mAP) increase of 2.2% compared with the original YOLOv8n model, and has decreased by 23.33%, 19.75%, and 21.52% respectively in terms of parameter quantity, floating point operations per second (FLOPs), and memory usage, respectively. This indicates that the method proposed in this paper, which integrates the EMA attention mechanism and introduces the C2f-Faster module for multi-scale feature fusion, improves the speed of tomato maturity detection while maintaining high detection precision. It enables fast and accurate assessment of tomato maturity in greenhouse.

2) The C2f-Faster-EMA module is introduced into the backbone and head parts of the Yolov8n model to improve the network feature extraction capability. Compared with mainstream models such as RT-DETR YOLOv5 and YOLOv11 models, the mean average precision (mAP) is increased by 6.5%, 5.4% and 0.8%, respectively, and the experimental results show that the improved ECF-YOLOv8n model has a fast detection speed and high precision, which basically meets the real-time and efficient work of picking robots, and provides a theoretical basis for tomato picking technology.

3) In the laboratory environment, the detection performance of the enhanced ECF-YOLOv8n model for tomato ripeness identification was evaluated. The results demonstrated that the improved model achieved an average identification accuracy of 91%, meeting the requirements for greenhouse tomato harvesting.

ACKNOWLEDGEMENT

This research was supported by the Inner Mongolia Autonomous Region Science and Technology Innovation Guidance Project (Kcj1-202205) and Inner Mongolia Autonomous Region Science and Technology Plan Project (2022YFDZ0022, 2022YFDZ0032).

REFERENCES

- [1] Appe, S. N., Arulselvi, G., Balaji, G. N. (2023). CAM-YOLO: tomato detection and classification based on improved YOLOv5 using combining attention mechanism. *PeerJ Computer Science*, 9, e1463.
- [2] Bai, T., Luo, J., Zhou, S., Lu Y., Wang Y. (2024). Vehicle-type recognition method for images based on improved faster R-CNN model. *Sensors*, 24(8), 2650.
- [3] Babu, P., Habelalmateen, M. I., Srikanteswara, R., Reddy, R. A., Purushotham, N. (2024). Wafer Surface Semiconductor Defect Classification Using Convolution Neural Network Based Improved Faster R-CNN. In *2024 Second International Conference on Data Science and Information System (ICDSIS)* (pp. 1-4). IEEE.
- [4] Chen, M., Yu, L., Zhi, C., Sun, R., Zhu, S., Gao, Z., Zhang, Y. (2022). Improved faster R-CNN for fabric defect detection based on Gabor filter with Genetic Algorithm optimization. *Computers in Industry*, 134, 103551.
- [5] Fenghun, CHEN., Chuang, CHEN., Xueyan, ZHU., Deyu, SHEN., Xinwei ZHANG. (2024), Detection of Camellia oleifera fruit maturity based on improved YOLOv7 (基于改进 YOLOv7 的油茶果实成熟度检测). *Transactions of the Chinese Society of Agricultural Engineering*, 40(5), 177-186.
- [6] Gao, F., Fu, L., Zhang, X., Majeed, Y., Li, R., Karkee, M., Zhang, Q. (2020). Multi-class fruit-on-plant detection for apple in SNAP system using Faster R-CNN. *Computers and Electronics in Agriculture*, 176, 105634.
- [7] Gao, G., Wang, S., Shuai, C., Zhang, Z., Zhang, S., Feng, Y. (2022). Recognition and Detection of Greenhouse Tomatoes in Complex Environment. *Traitement du Signal*, 39(1).
- [8] Huiqin, Li., Zhaoming, Song, Cunxiang, Liu, Yatao, Xiao. (2024), Improvement of tomato fruit detection model based on YOLOv8n (基于 YOLOv8n 的番茄果实检测模型改进), *Journal of Henan Agricultural University*, doi:10.16445/j.cnki.1000-2340.20240511.002.
- [9] Hussain, M. (2023). YOLO-v1 to YOLO-v8, the rise of YOLO and its complementary nature toward digital manufacturing and industrial defect detection. *Machines*, 11(7), 677.
- [10] Jiwen, Hu, Guoliang, Zhang, Mingzhe, Shen, Wenhao Li. (2024), Detecting surface defects of pine wood using an improved RT-DETR model (面向松木表面缺陷检测的改进 RT-DETR 模型). *Transactions of the Chinese Society of Agricultural Engineering*, 40(7), 210-218.
- [11] Lawal, M. O. (2021). Tomato detection based on modified YOLOv3 framework. *Scientific Reports*, 11(1), 1447.
- [12] Li, P., Zheng, J., Li, P., Long, H., Li, M., Gao, L. (2023). Tomato maturity detection and counting model based on MHSA-YOLOv8. *Sensors*, 23(15), 6701.
- [13] Li, R., Ji, Z., Hu, S., Huang, X., Yang, J., Li, W. (2023). Tomato maturity recognition model based on improved yolov5 in greenhouse. *Agronomy*, 13(2), 603.
- [14] Li, X., Fang, J., Zhao, Y. (2024). A Multi-Target Identification and Positioning System Method for Tomato Plants Based on VGG16-UNet Model. *Applied Sciences*, 14(7), 2804.
- [15] Malik, M. H., Zhang, T., Li, H., Zhang, M., Shabbir, S., Saeed, A. (2018). Mature tomato fruit detection algorithm based on improved HSV and watershed algorithm. *IFAC-PapersOnLine*, 51(17), 431-436.
- [16] Miao, Z., Yu, X., Li, N., Zhang, Z., He, C., Li, Z., Sun, T. (2023). Efficient tomato harvesting robot based on image processing and deep learning. *Precision Agriculture*, 24(1), 254-287.
- [17] Seo, D., Cho, B. H., Kim, K. C. (2021). Development of monitoring robot system for tomato fruits in hydroponic greenhouses. *Agronomy*, 11(11), 2211.
- [18] Solimani, F., Cardelicchio, A., Dimauro, G., Petrozza, A., Summerer, S., Cellini, F., Renò, V. (2024). Optimizing tomato plant phenotyping detection: Boosting YOLOv8 architecture to tackle data complexity. *Computers and Electronics in Agriculture*, 218, 108728.
- [19] Tsai, F. T., Nguyen, V. T., Duong, T. P., Phan, Q. H., Lien, C. H. (2023). *Tomato Fruit Detection Using Modified Yolov5m Model with Convolutional Neural Networks*. *Plants* 2023, 12, 3067.
- [20] Wang, S., Shao, Z., Zhang, Y. (2024). Enhanced precision in greenhouse tomato recognition and localization: A study leveraging advances in Yolov5 and binocular vision technologies. *Quality Assurance and Safety of Crops & Foods*, 16(3), 67-81.
- [21] Xu, D., Xiong, H., Liao, Y., Wang, H., Yuan, Z., Yin, H. (2024). EMA-YOLO: a novel target-detection algorithm for immature yellow peach based on YOLOv8. *Sensors*, 24(12), 3783.

- [22] Yang, Ren, Xujun, Chen, Lei, Wang. (2024), Research on weakly supervised directed target detection algorithm based on cross-space multi-scale (基于跨空间多尺度的弱监督有向目标检测算法研究), *Laser Journal*, 45(7), 63-70.
- [23] Yin, X., Chen, L. (2024). Image object detection method based on improved faster R-CNN. *Journal of Circuits, Systems and Computers*, 33(07), 2450130.
- [24] Zeng, T., Li, S., Song, Q., Zhong, F., Wei, X. (2023). Lightweight tomato real-time detection method based on improved YOLO and mobile deployment. *Computers and electronics in agriculture*, 205, 107625.
- [25] Zhao, Z., Chen, S., Ge, Y., Yang, P., Wang, Y., Song, Y. (2024). RT-DETR-tomato: Tomato target detection algorithm based on improved RT-DETR for agricultural safety production. *Applied Sciences*, 14(14), 6287.
- [26] Zheng, T., Jiang, M., Li, Y., Feng, M. (2022). Research on tomato detection in natural environment based on RC-YOLOv4. *Computers and Electronics in Agriculture*, 198, 107029.

SEMI-SUPERVISED WHEAT EAR DETECTION ALGORITHM BASED ON THE MODIFIED YOLOv8

/ 基于改进 YOLOv8 的半监督麦穗识别算法

Yu ZHANG ¹⁾, Zihui XU ¹⁾, Fuzhong LI ¹⁾, Xiaoying ZHANG ^{*1)}, Xiao CUI ^{*1)}¹⁾ School of Software, Shanxi Agricultural University, Shanxi/China;Tel: +86-15803449361; E-mail: xiaoyingzhang@sxau.edu.cn; cuixiaocuilu@163.comDOI: <https://doi.org/10.35633/inmateh-75-54>**Keywords:** wheat spike, object detection, semi-supervised learning, YOLOv8**ABSTRACT**

In contemporary agricultural practices, the use of image and video acquisition technologies, such as drones and cameras, has become increasingly common for capturing and monitoring crop growth in agricultural fields. The reliance on visual data for analyzing farm management conditions and facilitating decision-making processes is gaining significant traction. However, in practical applications, image acquisition tools often face challenges in maintaining optimal distance and angle during data capture, which can negatively impact the detection accuracy of existing object detection methods. Semi-supervised learning plays a crucial role in improving object detection. In this study, a semi-supervised algorithm for wheat spike recognition was developed based on an optimized YOLOv8n model. The model incorporates SPDCConv and PSA attention modules after the SPPF layer, effectively reducing computational and memory demands while enhancing model performance. The proposed model achieved an accuracy of 94.2%, outperforming YOLOv5s, Efficient Teacher, and the baseline YOLOv8n by 10.9%, 4.5%, and 6.1%, respectively—demonstrating its strong potential for practical agricultural applications.

摘要

当今农业，使用无人机或摄像头这样的图像视频采集工具拍摄或监控农田作物生长情况变得常见，依靠这些图像分析农田管理情况和辅助决策也会变得越来越有市场。但在实际生产中，图像采集工具在拍摄时很难保持合理的距离和角度，这使得现有的目标检测方法检测精度低。而半监督学习对提高物体检测至关重要。我们开发了一种用于麦穗识别的半监督学习算法，使用了改进的 YOLOv8n，并在 SPPF 之后集成了 PSA 注意力机制和 SPDCConv。这些改进减少了计算和内存需求，提升了模型性能。我们的模型达到了 94.2% 的准确率，分别比 YOLOv5s、Efficient Teacher 和 YOLOv8n 高出 10.9%、4.5% 和 6.1%，展示了其实际潜力。

INTRODUCTION

Wheat, recognized as a globally cultivated food crop, has maintained its status as the third most extensively sown crop in terms of both area and total production since the 1940s. It serves as a staple food for approximately one-third of the global population and is cultivated across an estimated 224 million hectares, thereby supporting around 30 percent of the world's inhabitants (Eversole et al., 2014; Li et al., 2018a). Enhancing wheat yield per unit area remains a primary objective of contemporary breeding efforts. The implementation of automated detection and counting of wheat ears facilitates the rapid and precise assessment of ear numbers, which subsequently allows for the estimation of yield per plant, yield per unit area, and overall production. This advancement significantly aids researchers in optimizing breeding efficiency. With continuous advancements in artificial intelligence technologies, various approaches, including image processing, machine learning, and deep learning, are increasingly being applied to wheat yield prediction and phenotypic identification.

The methodologies employed for counting wheat ears through traditional image processing techniques can be broadly classified into three distinct categories (Fu Jingbo, 2021; Liu et al., 2019): curve fitting segmentation, image-based fractal segmentation, and pixel-based area estimation (Liu Tao, 2014). These approaches typically utilize color features or grain characteristics to extract images of wheat ears, followed by morphological operations such as corrosion expansion, cavity filling, and refinement processing. This sequence of operations facilitates the enumeration of wheat spike skeleton images through angular point detection methods. Moreover, Li et al., (2018b), implemented a technique that involved color space

transformation, utilizing a custom device to capture RGB images of wheat in natural field conditions, which were subsequently converted to HSV space.

The saturation component (S) was subjected to binary conversion, resulting in a binary image. An adhesion object segmentation algorithm was then applied to the wheat ear images, followed by the implementation of a concave point detection method for segmentation and counting, ultimately enabling the calculation of grain numbers and yield prediction. Furthermore, *Fernandez-Gallego et al., (2018)*, introduced a wheat ear counting method based on an enhanced K-means clustering algorithm, which relies on color feature clustering. In this approach, each sub-region identified through clustering is interpreted as representing a wheat ear, with the total number of sub-regions serving as an estimate of the wheat ear count. While traditional machine learning techniques for wheat ear counting significantly reduce the labor required compared to manual counting and enhance efficiency and accuracy to some extent, the complexity of field environments presents challenges in maintaining consistent image quality and limits the versatility of these methods.

The continuous advancements in deep learning within the domain of agricultural research have prompted certain scholars to integrate YOLOv5 with semi-supervised learning methodologies, culminating in the creation of a semi-supervised target detection algorithm that is applicable across various contexts. In their study, *Zhou et al., (2023)*, presented an innovative semi-supervised adaptive algorithm, named SSDA-YOLO, which combines a YOLOv5-based semi-supervised framework with a knowledge distillation approach. This algorithm enhances the quality of pseudo-labels through improved view refinement and global view filtering. Furthermore, *Lyu et al., (2022)*, reported a notable enhancement in the recognition accuracy of citrus bagging by incorporating a strip attention module into the YOLOv5 backbone and employing additional semi-supervised learning techniques.

Despite the advancements made in the aforementioned studies, which have enhanced the algorithm from various perspectives and yielded certain outcomes, significant challenges persist when applying these methods to single-stage target detection models, such as YOLO. In particular, the detection of wheat ears presents several critical issues. Firstly, there is an inconsistency in the scale of wheat spike targets. As wheat ears progress from the heading stage to maturity throughout their growth cycle, the size of individual wheat plants varies temporally. Additionally, certain weeds exhibit morphological similarities to wheat ears, thereby complicating the accurate differentiation and identification of these targets based solely on visual characteristics. Secondly, the samples of wheat spikes are frequently densely clustered. In areas where wheat plants are closely spaced, occlusion of wheat ears is a prevalent issue. The dataset contains a substantial number of samples, which not only affects the accuracy of target identification but also complicates the labeling process. Finally, the extensive volume of data within the wheat spike dataset results in high labor costs associated with large-scale annotation.

In response to the challenges previously outlined, this study proposes a semi-supervised algorithm for the detection of wheat spikes, which is based on an enhanced version of YOLOv8. The algorithm integrates Spatial Depth Conversion Convolution (SPDConv) to improve the detection of small objects in low-resolution images, thereby augmenting the feature extraction capabilities for such targets (*Sunkara and Luo, 2023*). Additionally, the PSA attention mechanism is incorporated to reduce the computational and memory demands associated with self-attention in visual tasks, ultimately resulting in enhanced detection accuracy. Furthermore, this paper presents improvements derived from the modified Efficient Teacher framework (*Xu et al., 2023*), which effectively increases the detection accuracy of the algorithm by utilizing valuable information from unlabeled images, all while preserving the model's original size.

MATERIALS AND METHODS

Data collection and data processing

To enhance the generalization performance of the model, this study employed two distinct datasets for training. One of these datasets, known as the Wheat Detect (WD) dataset, consists of images of wheat captured at the Yang Jia Zhuang Village experimental base of Shanxi Agricultural University. The specific wheat variety used for this dataset is Agricultural University 212. The images were systematically collected from April to June 2024, with a frequency of every three days, to comprehensively cover the filling and maturation stages of the wheat.

The shooting process involved a variety of weather conditions, encompassing both sunny and overcast scenarios. The iPhone 15 Pro Max was employed as the primary photographic equipment, leading to the

acquisition of over 6,500 images of wheat canopies, of which 3,011 were selected for further analysis. All images were stored in JPG format, ensuring a consistent resolution of 3648x2736 pixels.

The Labellmg software was utilized for image annotation, with the sole category label assigned being "wheat." The resulting annotation data were subsequently saved as "txt" files in the YOLO format.

The second data set is the Global Wheat Head Detection (GWHD) from the global wheat public database (David et al., 2021). This data set pooled 6,422 RGB images with a resolution of 1,0,24x1,024 pixels, and 275,187 labeled ears of wheat. The images were collected from Europe, North America and Asia, covering a variety of varieties, planting conditions, climate types, as well as collection methods, thus ensuring the diversity of the data set in terms of genotype and environment. These characteristics of GWHD data sets help improving the accuracy and reliability of wheat ear detection and positioning. Fig.1 shows some examples of images generated from data obtained from the Yang Jia Zhuang Experimental Base.



Fig. 1 - Images of wheat at different growth stages

YOLOv8ps structure

As depicted in Fig.2, Efficient Teacher, which is constructed on YOLOv5, introduces several enhancements to the network. Efficient Teacher proposes three modules to implement a scalable and effective SSOD framework. The Dense Detector module improves the quality of pseudo labels with dense input and offers better inference efficiency; the Pseudo Label Assigner module categorizes pseudo labels into two types to mitigate the issue of pseudo labeling.

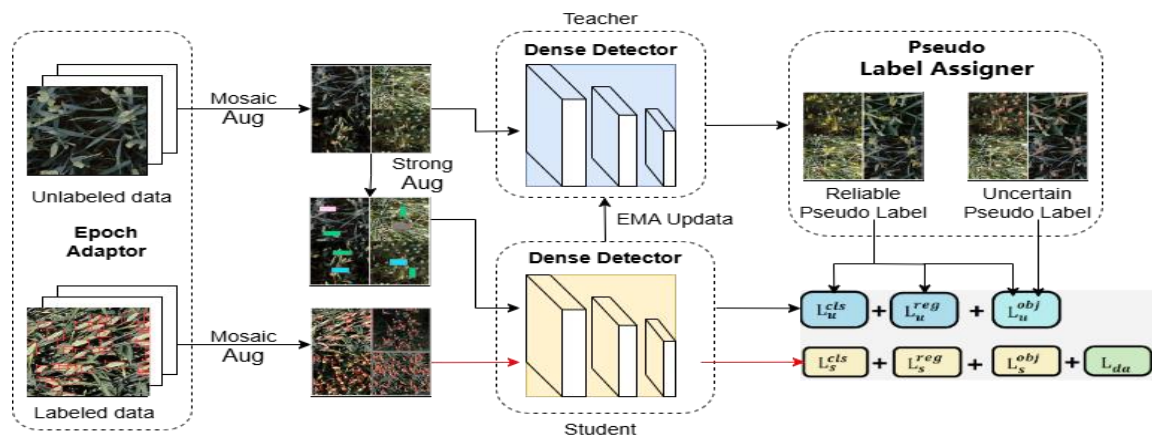


Fig. 2 - Semi-supervised training framework

Inconsistency problem, Epoch Adaptor reduces training time and the inconsistency of features. Although Efficient Teacher shows significant improvement in detection accuracy compared to SSOD and one-stage anchor-based detectors, it still faces significant challenges in the accuracy of small object detection. These challenges mainly stem from the fact that small objects occupy fewer pixels in images, making feature extraction difficult and thus affecting the accuracy of detection. To address these challenges, this study proposes a small object detection network architecture based on YOLOv8. The main innovations include: in the initial stage of the study, the YOLOv8ps model was proposed. By adopting this strategy, it was expected to capture the detailed features of small objects more accurately, thereby improving the overall detection performance. Subsequently, this study delved in to the efficiency of convolution (SPDCConv) within CNN architectures and introduced four layers of SPDCConv after the Conv layers in the YOLOv8 backbone network.

This method effectively maintains the detail information of the input image by transforming the spatial dimensions into depth dimensions, significantly enhancing the feature extraction performance for small objects.

Furthermore, to reduce the computational burden on the YOLOv8n network, Partial Self-Attention (PSA) was integrated, as proposed in YOLOv10. PSA addresses the high computational complexity and memory consumption associated with traditional self-attention mechanisms in visual tasks, thereby significantly enhancing the model's performance and capability.

As shown in Fig 3, the lightweight network architecture proposed in this study mainly consists of three core components: the backbone network, the neck structure, and the head module. The primary function of the backbone network is to extract feature information from the input image data and output feature maps at three different scales. During this feature extraction process, the study introduces the SPDConv module, which aims to take the feature maps produced by the previous convolution operation as input, process them through the SPD layer, and then perform further feature extraction through consecutive convolution layers. Additionally, the study integrates the PSA attention mechanism to address the inherent high computational complexity and significant memory consumption issues of traditional self-attention mechanisms in visual tasks.

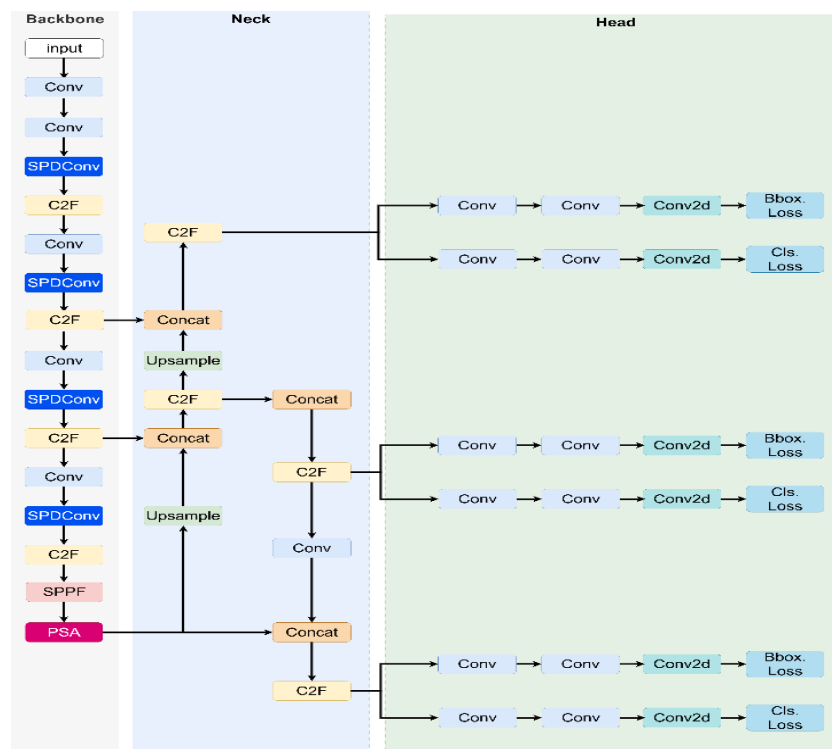


Fig. 3 - Network structure of improved YOLOv8 algorithm

The neck design of the network is used to enhance the ability to detect objects of different sizes by fusing feature maps from the backbone network at different scales, and then outputs three different scale feature maps. Similarly, both PSA and SPDConv are utilized for feature extraction and downsampling. Three independent and decoupled header structures are designed at the network's front, each responsible for predicting and analyzing feature maps of three distinct scales. This design allows each header structure to concentrate on processing feature information of a particular scale, thereby enhancing the network's capacity to capture and predict features across various scales. Consequently, this significantly improves the model's performance in visual tasks involving small objects. The darkened section in Fig. 3 represents the structural improvement module.

SPDConv The structure is composed of space to depth (SPD) layer and no convolutional step size (Conv) layer, replacing the pooling operation and convolution operation with step size in a similar way, and using scientific parameters to reduce the number of channels, which is suitable for a variety of convolutional neural network (CNN) architectures. In the traditional CNN architecture, the direct application of step convolution and pooling layer will lead to the gradual decrease of the spatial resolution of images with the deepening of the deepening of the network level, resulting in the loss of details of small objects, which makes the network encounter difficulties in accurately identifying these small objects. However, the combination of using SPD layers with step-free convolution layers enables the CNN to more effectively handle the challenges

posed by small objects and low-resolution images, thus improving the performance and robustness of the model in these complex scenarios.

For a specific feature plot X , the down sampling was performed by the scaling factor. Fig.4b shows the space-to-depth operation, where the spatial information is reorganized into the depth channel. When the scale factor is set to 2, the four feature subgraphs shown in Fig.4c can be obtained, and the shape of each subgraph is $(S/2, S/2, C)$, which realizes the effect of subsampling the feature graph X by 2 times. Subsequently, the four feature sub-maps are successively connected along the channel dimension to form the feature map in Fig.4d $(S/2, S/2, 4C)$. After completing the feature transformation in the SPD layer, the dimensions change from Fig. 4d $(D, 4C)$ to $(S/2, S/2, D)$. The detailed procedure is shown in Figure Fig.4.

In this study, four SPDConv layers were introduced after the Conv convolution layer. This move aims to take the feature graph generated by the convolution operation of the previous layer as input, and to transform the spatial dimension of the input image into depth dimension, so as to improve the depth of the feature graph without losing information. Subsequently, the convolution processing through the continuous Conv layer realizes the feature extraction without reducing the feature graph size, which effectively maintains the detailed information of the image. Compared with the traditional convolution operation, this insertion method is more efficient in retaining the information in the channel, which significantly enhances the feature extraction performance for small targets (Fig 3).

Despite the self-attention mechanism, its computational amount and memory footprint are high. To solve this problem, YOLOv10 proposed an efficient local self-attention mechanism (Wang et al., 2024), namely the PSA module. As shown in Fig.3, this module first divides the feature graph into two parts by channels after the convolution operation, one of which is sent to the N_PSA module composed of multi-head self-attention module (MHSA) and feedforward network (FFN). Subsequently, the two parts are reconnected and fused through a convolution operation. The PSA module is only placed after the lowest resolution stage, effectively avoiding the excessive consumption of resources caused by the squared computational complexity of the self-attention mechanism. Through this design, the PSA module can solve the high computational complexity and memory footprint problems faced by the self-attention mechanism in visual tasks, thus significantly improving the performance and capability of the model (Fig 5).

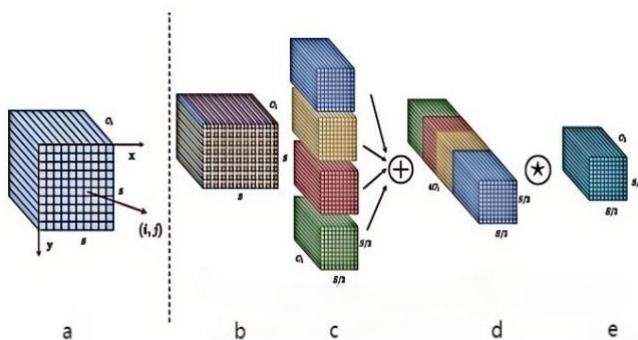


Fig. 4 - Illustration of SPDConv with a Scale Factor of 2

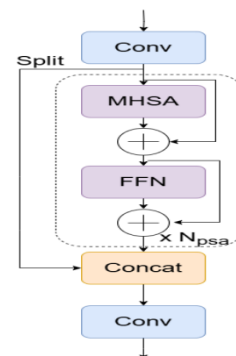


Fig. 5 - The partial self-Attention module (PSA)

Experimental Environment

The operating system used in this experiment is Windows 11, and the development environment of the model is Python 3.8, CUDA 11.1.0 and PyTorch 1.11.0. The training process was performed on the NVIDIA GeForce RTX 4060 graphics card. During the training process, YOLOv8n was used as the basic model, the size of the input image was set to 640×640 pixels, the batch size was set to 32, and the weight attenuation coefficient was set to 0.0005. In the fully supervised learning mode, the initial learning rate is set to 0.01, the minimum learning rate is set to 0.002, and the adjustment strategy of the learning rate adopts the cosine annealing method for a total of 40 training cycles (epochs). In the semi-supervised learning mode, the learning rate maintained a fixed value of 0.01, with a total of 300 training cycles.

Evaluation indexes of the model

A range of accepted evaluation measures in the field of target detection were used, including precision (Precision, P), recall (Recall, R), mean precision (mean Average Precision, mAP50) mAP50 at the IoU threshold of 0.5. Determine the integral of the precision-recall (P-R) curve.

In this study, only a single category of wheat ears was involved, with a sample size of $n=1$. Precision (P) is defined as the ratio of the number of correctly identified wheat ear samples to the total number of predicted

wheat ear samples, while Recall (R) is the ratio of the number of correctly identified wheat ear samples to the total number of actual wheat ear samples.

Model Detection Accuracy Analysis

In this research, a 50 cm x 50 cm plastic board was used to contain the samples during each shooting session, after which manual counting was performed. Subsequently, image capture was conducted, as illustrated in Figure 6. All images that had been manually counted were then utilized as a training set to assess the model's accuracy in identifying real-world scenarios and to compare it with other models.



Fig. 6 - Wheat image

RESULTS

In this study, our goal is to develop an efficient wheat spike detection algorithm by improving the original YOLOv8 network. These improvements include adjusting the network architecture of YOLOv8, incorporating SPDCConv and PSA attention mechanisms, and embedding them into a semi-supervised algorithm. To elucidate the impact of each improvement on the network, ablation experiments were conducted under the same training environment and hyperparameters. The YOLOv8n model served as the baseline, against which the previously mentioned improvements were sequentially implemented.

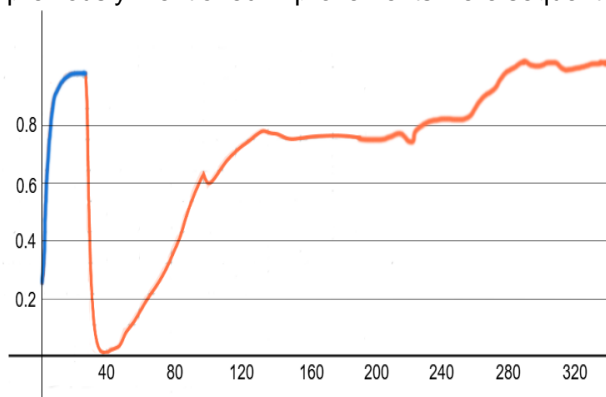


Fig. 7 - Changes in mAP50 metric during semi-supervised training stage

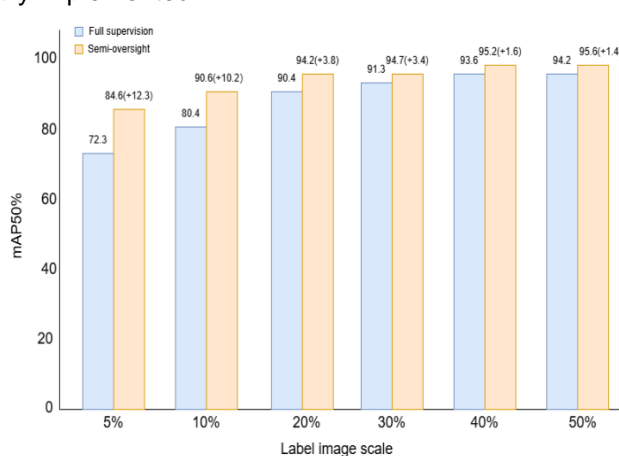


Fig. 8 - mAP50 metric of different annotation sample ratios

To verify the effectiveness of the proposed improvement strategy in improving the model accuracy, the ablation experiment was conducted based on the YOLOv8n algorithm. The experimental results are detailed in Table 1. Among them, A represents the introduced SPDCConv module, and B represents the PSA attention mechanism added after SPPF, while C represents the semi-supervised object detection method mentioned in this article.

According to the data in Table 1, the detection performance is significantly improved with the gradual integration of the improved module YOLOv8n. However, the proposed algorithm did not achieve the best performance in recall rates. The reason for this phenomenon is that the algorithm improves the extraction ability of the small target features, but also optimizes the computational complexity and memory footprint. Nevertheless, a slight decrease in recall is acceptable because the algorithm's accuracy and average accuracy have peaked, given the mutual constraints between accuracy (P) and recall (R).

Table 1

Results of the ablation experiment							
YOLOv8n	A	B	C	P	R	mAP50	mAP50:95
√				0.891	0.732	0.886	0.477
√	√			0.913	0.818	0.901	0.484
√		√		0.898	0.801	0.887	0.472
√			√	0.891	0.732	0.881	0.493
√	√	√		0.921	0.877	0.904	0.463
√	√		√	0.886	0.823	0.890	0.462
√		√	√	0.902	0.840	0.906	0.483
√	√	√	√	0.957	0.865	0.942	0.487

For the fully supervised training, a ratio of 0.2 and 1400 samples were used, after which 5600 images were introduced as unannotated samples to perform the semi-supervised training. Fig 7 illustrates the evolution of mAP50 values during fully supervised versus semi-supervised training. As can be seen from the figure, after the full supervised training, the mAP50 index of the algorithm has basically reached the fitting state, with the accuracy of 90.4%. Then, 3200 unlabeled samples were added for semi-supervised training. At this time, the mAP50 index of the model went through the process of first reducing and then rising, and finally achieved further improvement with an accuracy rate of 94.2%. The reason for the decrease lies in the early stage of the semi-supervised training, where the accuracy of the model is low and the quality of the pseudo-labels generated by the teacher model is not high. However, as the training continues, the quality of the pseudo-labels gradually improves, and the detection accuracy of the model is correspondingly enhanced.

Table 2

Comparative experiments on object detection algorithms						
Model	Size	P	R	mAP50	mAP50:95	
YOLOv5s	640	0.867	0.754	0.833	0.473	
YOLOv5l	640	0.899	0.776	0.825	0.466	
Faster R-CNN	640	0.898	0.846	0.910	0.486	
SSD	640	0.901	0.834	0.905	0.481	
YOLOv8n	640	0.891	0.732	0.881	0.493	
YOLOX	640	0.902	0.859	0.921	0.528	
Efficient Teacher	640	0.890	0.827	0.897	0.502	
V8	640	0.904	0.852	0.914	0.494	
V8ps	640	0.957	0.865	0.942	0.487	

Subsequently, this study compared the effects of fully supervised and semi-supervised training methods under different annotated sample proportions, and the experimental results are shown in Fig 8. In the figure, blue area on the left represents the mAP50 values obtained from the fully supervised training with the entire annotated samples, while the orange area on the right shows the mAP50 values obtained after the further semi-supervised training. Since the total number of samples used in the training is 7000, the annotated ratio of 20% corresponds to 1400 annotated samples and 5600 unannotated samples, and so on.

To further verify the performance advantages of the algorithm proposed in this paper on the wheat spike detection dataset, comparative experiments were conducted with other mainstream lightweight object detection models, including YOLOv5s (Jocher, 2020), YOLOv5l, Faster R-CNN (Ren et al., 2017), SSD (Liu et al., 2016), YOLOv8n, YOLOX (Z Ge et al., 2021) and Efficient Teacher. For fairness, their default resolutions were not adjusted. The experimental results are detailed in Table 2.

In this experiment, Efficient Teacher uses the YOLOv5s detector, while V8ps represents the semi-supervised training results with the improved YOLOv8n as the baseline model, and V8 represents the semi-supervised training results with YOLOv8n as the baseline model.

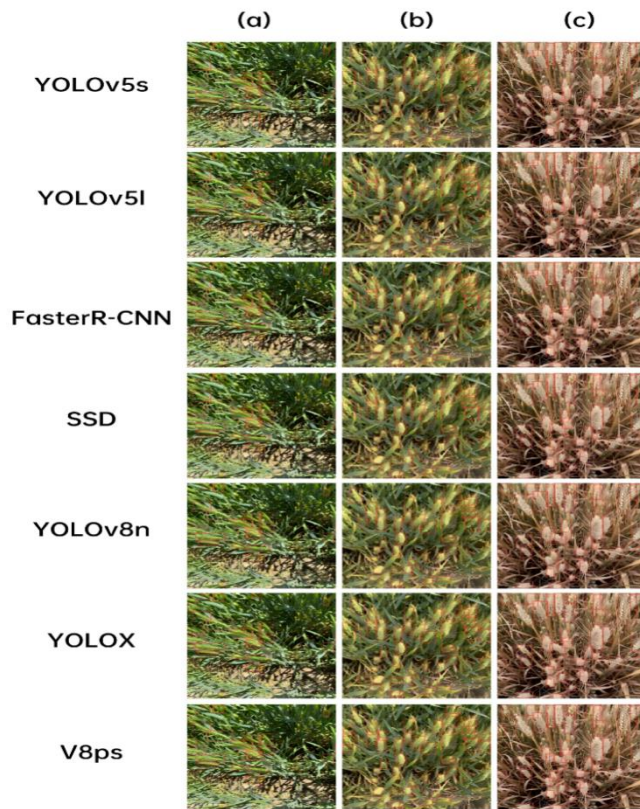


Fig. 9 - Comparison of V8ps and fully supervised models in wheat spike detection effectiveness

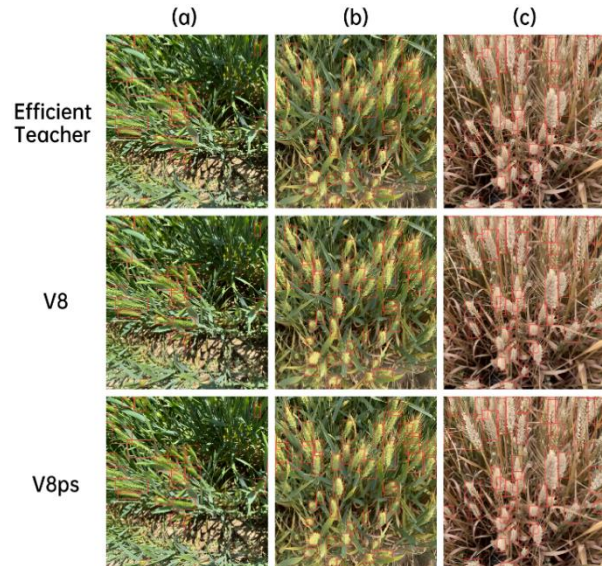


Fig. 10 - Comparison of V8ps and semi-supervised models in wheat spike detection effectiveness

The fully supervised target detection algorithms listed in the table were all obtained with 300 epochs without pre-training weights. According to the data in Table 2, using the improved YOLOv8n as the base model, the mean accuracy (mAP50) reached 94.2% under the semi-supervised training condition, and the performance improved by 4.5% compared with the semi-supervised base model Efficient Teacher. Its precision exceeds all other algorithms in the table compared to the fully supervised model. If the base model is changed from an improved YOLOv8n to an unimproved YOLOv8n, the improved YOLOv8n achieves a performance improvement of 2.8% on the mAP50 index.

Table 3

Comparative experiments on object detection algorithms					
Model	Manual count	Model count	Number of missed detection	Omission factor	Precision ratio
YOLOv5s	359	321	38	10.63%	89.37%
YOLOv5l	421	379	42	10.06%	89.94%
Faster R-CNN	433	391	42	9.68%	90.32%
SSD	217	196	21	9.59%	90.41%
YOLOv8n	189	172	17	9.15%	90.85%
YOLOX	285	259	26	8.98%	91.02%
Efficient Teacher	295	269	26	8.83%	91.17%
V8	311	285	26	8.28%	91.72%
V8ps	354	331	23	6.43%	93.57%

The manually counted images were randomly categorized into nine groups, each consisting of ten images, and the model was evaluated. As shown in Table 3, the enhanced model demonstrated significantly higher accuracy in real-world situations compared to other popular models, achieving a detection accuracy of 93.57% in the tests.

Furthermore, Fig.9 and Fig.10 respectively present a comparative analysis of the wheat spike detection effects of the improved model compared to the fully supervised model and the semi-supervised model at different growth stages. In these images, (a) represents Heading stage, (b) represents Filling stage, and (c) represents Harvesting period. Accordingly, it can be concluded that the improved model in this study is more suitable for the application scenario of wheat ear detection in the field.

CONCLUSIONS

To address the challenges of small target sizes, severe occlusion, and high annotation costs in wheat spike detection, a semi-supervised wheat spike detection algorithm, named YOLOv8ps, was proposed. It is based on YOLOv8. Our main contributions are summarized as follows: wheat spike images are sourced from wheat field environments and the global wheat public database. After annotating the images, data augmentation was performed to create the final dataset. YOLOv8ps was developed by integrating the SPDCConv module, which mitigates the adverse effects of processing small objects and low-resolution images, thereby enhancing the model's performance and stability in complex scenarios. Simultaneously, the introduction of the PSA attention mechanism further optimizes the model's performance. Ultimately, the combination of an improved semi-supervised learning method significantly enhances the model's detection accuracy. First, ablation experiments were conducted in a consistent training environment to analyze the independent impact of each improvement on the model. Subsequently, comparative experiments were carried out using both full-supervision and semi-supervision training methods under varying proportions of annotated samples to verify the effectiveness of the newly proposed YOLOv8ps in semi-supervised training. Finally, the model was compared with other existing models in terms of performance. Experimental results indicate that, compared to Efficient Teacher, the improved model's mean average precision (mAP50) increased by 4.5%, reaching 94.2%. In comparison to the full-supervision baseline model YOLOv8n, it increased by 6.1%, achieving excellent detection accuracy. Although model lightweighting and other optimization techniques have not yet been considered, future research will focus on expanding the dataset and exploring how to integrate these techniques with more advanced and efficient technologies to achieve a higher level of wheat detection performance.

ACKNOWLEDGEMENT

This work was supported by the Key R&D Program Project of Shanxi Province and Outstanding Innovation Project for Graduate Students in Shanxi Province under the topics are: Research on Precision Agriculture Intelligent Decision-making System [project number: 202202140601021]; and based on 5G three-dimensional intelligent cultivation system [project number:2023SJ120].

REFERENCES

- [1] David, E., Serouart, M., Smith, D., Madec, S., Velumani, K., Liu, S., Wang, X., Pinto, F., Shafiee, S., Tahir, I.S.A., Tsujimoto, H., Nasuda, S., Zheng, B., Kirchgessner, N., Aasen, H., Hund, A., Sadhegi-Tehran, P., Nagasawa, K., Ishikawa, G., Dandrifosse, S., Carlier, A., Dumont, B., Mercatoris, B., Evers, B., Kuroki, K., Wang, H., Ishii, M., Badhon, M.A., Pozniak, C., LeBauer, D.S., Lillemo, M., Poland, J., Chapman, S., de Solan, B., Baret, F., Stavness, I., Guo, W., (2021). Global Wheat Head Detection 2021: An Improved Dataset for Benchmarking Wheat Head Detection Methods. *Plant Phenomics* 2021. <https://doi.org/10.34133/2021/9846158>
- [2] Eversole, K., Feuillet, C., Mayer, K.F.X., Rogers, J., (2014). Slicing the wheat genome. *Science*. 345, 285–287. <https://doi.org/10.1126/science.1257983>
- [3] Fernandez-Gallego, J.A., Kefauver, S.C., Gutiérrez, N.A., Nieto-Taladriz, M.T., Araus, J.L., (2018). Wheat ear counting in-field conditions: high throughput and low-cost approach using RGB images. *Plant Methods*. 14, 22. <https://doi.org/10.1186/s13007-018-0289-4>
- [4] Ge Z., Liu S., Wang F., Li Z., Sun J., (2021). *YOLOX: Exceeding YOLO Series in 2021*.
- [5] Jingbo F., (2021), *Phenotypic Traits Extraction and Analysis of Potted Wheat Based on Deep Learning*. (基于深度学习的盆栽小麦表型性状提取与分析), PhD dissertation, Huazhong Agricultural University, Wuhan/China.
- [6] Jocher, Glenn R., Alex Stoken, Jiří Borovec, NanoCode, Ayushi Chaurasia, TaoXie, Changyu Liu, Abhiram, Laughing, tkianai, yxNONG, Adam Hogan, lorenzomamma, AlexWang, Jan Hájek, Laurentiu Diaconu, Marc, Yonghye Kwon, Oleg, wanghaoyang, Yann Defretin, Aditya Lohia, ml ah, Ben

- Milanko, Ben Fineran, D. P. Khromov, Ding Yiwei, Doug, Durgesh and Francisco Ingham. Ultralytics yolov5: v5.0 - YOLOv5 - P6 1280 models. *Zenodo* (2020). <https://doi.org/10.5281/zenodo.4154370>
- [7] Li, Y., Du, S., Yao, M., Yi, Y., Yang, J., Ding, Q., He, R., (2018). Method for wheatear counting and yield predicting based on image of wheatear population in field. (基于小麦群体图像的田间麦穗计数及产量预测方法) *Transactions of the Chinese Society of Agricultural Engineering* 34, 185–194.
- [8] Liu Tao, Sun Chengming, Wang Lijian., (2014). Wheat spike counting based on image processing technology. (基于图像处理技术的大田麦穗计数) *Transactions of the Chinese Society for Agricultural Machinery*, 2014, 45(2): 282-290.
- [9] Liu, W., Anguelov, D., Erhan, D., Szegedy, C., Reed, S., Fu, C.-Y., Berg, A.C., (2016). SSD: Single Shot MultiBox Detector. *European Conference on Computer Vision* (2015). pp. 21–37. https://doi.org/10.1007/978-3-319-46448-0_2
- [10] Liu, Z., Huang, W., Wang, L., (2019). Field wheat ear counting automatically based on improved K-means clustering algorithm. (基于改进 K-means 聚类算法的大田麦穗自动计数) *Transactions of the Chinese Society of Agricultural Engineering* 35, 174–181. <https://doi.org/10.11975/j.issn.1002-6819.2019.03.022>
- [11] Lyu, J., Li, S., Zeng, M., Dong, B., (2022). Detecting bagged citrus using a semi-supervised SPM-YOLOv5. (基于半监督 SPM-YOLOv5 的套袋柑橘检测算法) *Transactions of the Chinese Society of Agricultural Engineering*. 38, 204–211. <https://doi.org/10.11975/j.issn.1002-6819.2022.18.022>
- [12] Ren, S., He, K., Girshick, R., Sun, J., (2017). Faster R-CNN: Towards Real-Time Object Detection with Region Proposal Networks. *IEEE Trans Pattern Anal Mach Intell* 39, 1137–1149. <https://doi.org/10.1109/TPAMI.2016.2577031>
- [13] Sunkara, Raja and Tie Luo. No More Strided Convolutions or Pooling: A New CNN Building Block for Low-Resolution Images and Small Objects. (2022) *ArXiv abs 2208.03641*: pp. 443–459. https://doi.org/10.1007/978-3-031-26409-2_27
- [14] Wang, A., Chen, H., Liu, L., Chen, K., Lin, Z., Han, J., Ding, G., (2024). YOLOv10: Real-Time End-to-End Object Detection. (2024). *ArXiv abs 2405.14458*. <https://doi.org/10.48550/arXiv.2405.14458>
- [15] Xu, B., Chen, M., Guan, W., Hu, L., (2023). Efficient Teacher: Semi-Supervised Object Detection for YOLOv5. *ArXiv abs 2302.07577*. <https://doi.org/10.48550/arXiv.2302.07577>
- [16] Yang, G., Wang, J., Nie, Z., Yang, H., Yu, S., (2023). A Lightweight YOLOv8 Tomato Detection Algorithm Combining Feature Enhancement and Attention. *Agronomy* 13, 1824. <https://doi.org/10.3390/agronomy13071824>
- [17] Zhou, H., Jiang, F., Lu, H., (2023). SSDA-YOLO: Semi-supervised domain adaptive YOLO for cross-domain object detection. *Computer Vision and Image Understanding* 229, 103649. <https://doi.org/10.1016/j.cviu.2023.103649>

NUMERICAL SIMULATION OF AIR COOLING PROCESSES IN A POULTRY HOUSE WITH A TUNNEL-SIDE VENTILATION SYSTEM

Viktor TROKHANIAK¹, Oleksandr SYNYAVSKIY¹, Vadym TKACHUK¹, Tormi LILLERAND²,
Oleksandr SKLIAR³, Yevhen IHNATIEV^{2,3}, Jüri OLT²

¹National University of Life and Environmental Sciences of Ukraine, Ukraine

²Estonian University of Life Sciences, Institute of Technology, 56 Kreutzwaldi Str., EE 51006 Tartu, Estonia

³Dmytro Motornyj Tavsia State Agrotechnological University, 66 Zhukovsky Str., UA 69600 Zaporizhzhia, Ukraine

*Tel: +37253509822, e-mail: yevhen@emu.ee

DOI: <https://doi.org/10.35633/inmateh-75-55>

Keywords: CFD, tunnel ventilation system, cooling system, poultry house, heat exchange unit

ABSTRACT

During the warm season, when ambient temperatures exceed +28 °C, the tunnel ventilation system is predominantly used in poultry facilities. This system effectively removes excess heat from the environment. However, under conditions of high ambient temperatures and high humidity, specialized systems were required to cool the incoming air and create a controlled microclimate within the poultry house. In ventilation systems, various types of cooling methods are employed to reduce the temperature of incoming air during the summer. Most commonly, these involve water spray systems. The core objective of this study is to conduct theoretical research on regulating heat and mass transfer processes in poultry houses, considering both internal dynamics and interactions through external barriers. This study proposes an innovative approach to cooling incoming air in poultry house ventilation systems. The method utilized water sourced from underground wells and heat exchangers-recovery units (recuperators) to efficiently cool the incoming air. As a result of the numerical modeling, the temperature distribution within the service zone of the poultry house was determined. When heat exchangers were used, the inlet air temperature in the facility was maintained at +20 °C. The temperature increase along the length of the facility was clearly observed in the provided diagrams. The outlet temperature of the cooled air is +27.89 °C, which was attributed to heat generated by the poultry and the warming of the poultry house walls by external air. Thus, the air temperature within this cooling system did not exceed permissible limits. Analyzing the numerical modeling results at a height of 0.7 m from the floor level, it was concluded that no more than 2% of the poultry would experience discomfort under the proposed cooling system. The average air velocity was 0.83 m·s⁻¹, and the air temperature was +23.64 °C.

INTRODUCTION

A conventional method for maintaining a regulated microclimate in poultry houses is direct evaporative cooling (DEC) using cassette-type systems (Hoff, 2018; Liang et al., 2020; Boltyanska et al., 2022). However, this method has significant drawbacks, such as high aerodynamic resistance and installation costs. Another disadvantage is the clogging of cassette channels with dust during operation (Hui et al., 2018). Notably, mold formation on the clogged cassette surfaces can introduce harmful components into the incoming air, which, under high humidity conditions, may lead to various poultry diseases (Kim et al., 2008).

Direct evaporative cooling is a typical ventilation system used in poultry houses in hot climates (James, 2012; Czarick & Fairchild, 2014). As mentioned earlier, this cooling method becomes ineffective in conditions of relatively high humidity, resulting in reduced thermal comfort and degraded air quality for poultry.

Studies have examined two advanced ventilation systems designed for hot and humid climates to improve poultry housing conditions (Harrouz et al., 2021; Rozenboim et al., 2007). System I integrates a conventional direct evaporative cooler with an adsorption dehumidifier containing a packed bed, while System II combines a dew point indirect evaporative cooler with a packed-bed dehumidifier. These models were optimized using a genetic algorithm to evaluate and compare their performance. The findings revealed that System II met the heat and air quality requirements of poultry houses with 35% lower operational costs compared to System I over the entire cooling season.

One of the modern cooling systems that has gained attention in recent years and has proven to be a successful replacement for DEC is the indirect evaporative dew point cooler (IDPC) (Mahmood *et al.*, 2016). The IDPC is capable of significantly cooling the incoming air to its dew point without adding moisture (Tariq *et al.*, 2017). Many studies have examined the performance of IDPCs with various configurations of working airflow (in wet channels) and product airflow (in dry channels). They found that the crossflow IDPC has the lowest pressure drop, the lowest investment cost, and the highest energy efficiency ratio (Zhan *et al.*, 2011; Pandelidis *et al.*, 2019).

Al-Assaad *et al.* (2021) compared the performance of two cooling systems combining DEC or crossflow IDPC with tunnel ventilation for a poultry house in the hot and semi-arid climate of the Bekaa Valley in Lebanon. They demonstrated that the IDPC better met heat and air quality constraints while reducing system costs by 6.8%. This is due to the IDPC's ability to provide a lower supply air temperature, which reduces water consumption and, consequently, water and electricity usage.

All of the aforementioned cooling systems have their drawbacks, which ultimately lead to reduced productivity in poultry farms. Thus, the development of new and improved cooling systems for poultry houses remains a relevant issue. The aim of this study is to explore new ways to improve the poultry house cooling system by installing heat exchange equipment with evaporative cooling cassettes, as well as by implementing a non-traditional placement of exhaust fans on the side wall of the poultry house.

MATERIALS AND METHODS

A tunnel cooling system is proposed for poultry facilities during the hot season when the outside air temperature reaches +40 °C. The poultry house has dimensions of 120x21 meters and a height of 5.3 meters, the total volume of the poultry house is 5,234.4 m³. On the side walls, where evaporative cooling cassettes are typically located near the front end wall, heat exchange units are installed instead. The number of units is 3 pcs, each with dimensions of 5.3 × 1.0 m and a total capacity of 35.52 m³·s⁻¹ (42.8 kg·s⁻¹) for half of the poultry house. The heat exchangers for this system were developed in the study by Trokhaniak *et al.* (2023a). They ensure an outlet air temperature of +20 °C when the inlet air temperature is +40 °C. The warm outside air is cooled using water from underground wells.

Additionally, considering the authors' previous studies (Trokhaniak *et al.*, 2023b), exhaust fans are installed: 4 pcs on the side wall and 1 on the rear end wall, with a total capacity of 35.52 m³·s⁻¹ (42.8 kg·s⁻¹). This airflow volume is sufficient to remove excess heat from the poultry house.

The floor is made of concrete with a thickness of 0.1 m on the top and bottom, separated by a 0.05 m layer of polystyrene insulation. In areas 2 m from the walls, the thickness of the insulating material is increased to 0.1 m. The assumed temperature for the floor is +10 °C. The walls are constructed as three-layered structures, with concrete layers 0.06 m thick on both sides and a 0.1 m polystyrene layer in between. For simplification, the ceiling is modeled as a three-layer structure with concrete layers on both sides and an insulating material, Izovat 30, in between with a thickness of 0.1 m. For all external walls and the ceiling, third-kind boundary conditions (Fig. 1) were applied, with an external temperature of +40 °C and a heat transfer coefficient of 10 W·(m²·K)⁻¹, assuming low wind speeds were observed at the poultry house location.

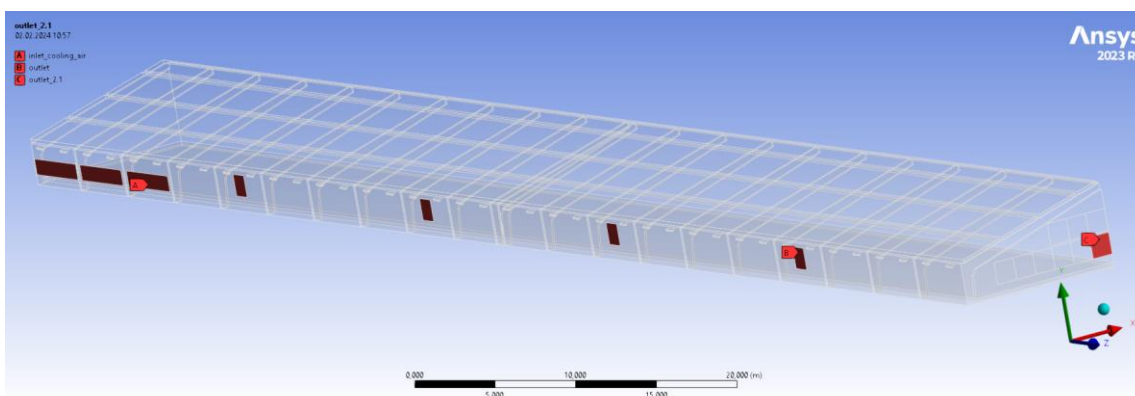


Fig.1 - 3D model of poultry house

The geometry of the poultry house was created using ANSYS Design Modeler 2023 R1, with boundary conditions applied. The geometry was then transferred to ANSYS Meshing 2023 R1 for mesh generation. The mesh was constructed using the CutCell method. The minimum face size was set to 0.015 m, and the maximum face size to 0.12 m. For the supply air inlets and exhaust fans, the mesh was refined with minimum element sizes of 0.01 m and 0.04 m, respectively. This refinement was implemented to achieve more accurate simulation results at the poultry house's inlet and outlet. As a result, the mesh quality indicator, orthogonal quality, was 0.214. The total number of elements was 4,485,116 pcs, and the total number of nodes was 4,854,992 pcs.

The numerical modeling was carried out directly in ANSYS Fluent 2023 R1. The model used the Navier-Stokes equations (Schneiderbauer & Krieger, 2014), the standard k- ϵ turbulence model, and the Discrete Ordinates radiation model (ANSYS, 2023). The tunnel effect of turbulent flows is also discussed in detail in Azhar *et al.*, (2022). The development of mathematical models in the technical field of crop and livestock farming is the focus of works by Bulgakov *et al.*, (2017, 2020a, 2020b), Ivanovs *et al.*, (2020). Specific aspects of the methodology presented in these works were used in the current study.

RESULTS AND DISCUSSION

In Fig. 2–3, the results of numerical modeling of the poultry house are shown at four locations along the length of the room: 10.25 m, 43.25 m, 74.75 m, and 109.25 m along the xy axis. The first location is the outlet of the second heat exchanger. The third is the third exhaust fan. The second and fourth are the third section of the poultry house and the end, respectively.

Fig. 2 shows the airflow lines in the poultry house at different locations. The airflow, exiting from the heat exchangers ($2.24 \text{ m}\cdot\text{s}^{-1}$, 3.080 Pa), covers a quarter of the poultry house's width and, due to heating, rises sharply upwards (Fig. 2a). Flowing over the ceiling, it meets the neighboring flow from the opposite side of the poultry house and descends towards the birds. A large air vortex is formed, which moves deeper into the poultry house. Such a gas-dynamic flow can be observed in Fig. 2b and 2d. As seen, the tunnel effect is formed. A similar phenomenon, but with more turbulent flows, can be seen in (Raza *et al.* 2020; Trokhaniak *et al.*, 2023b). In the middle at the top near the ceiling, a small stagnant air zone is formed. The average velocity in the poultry house is $0.58 \text{ m}\cdot\text{s}^{-1}$.

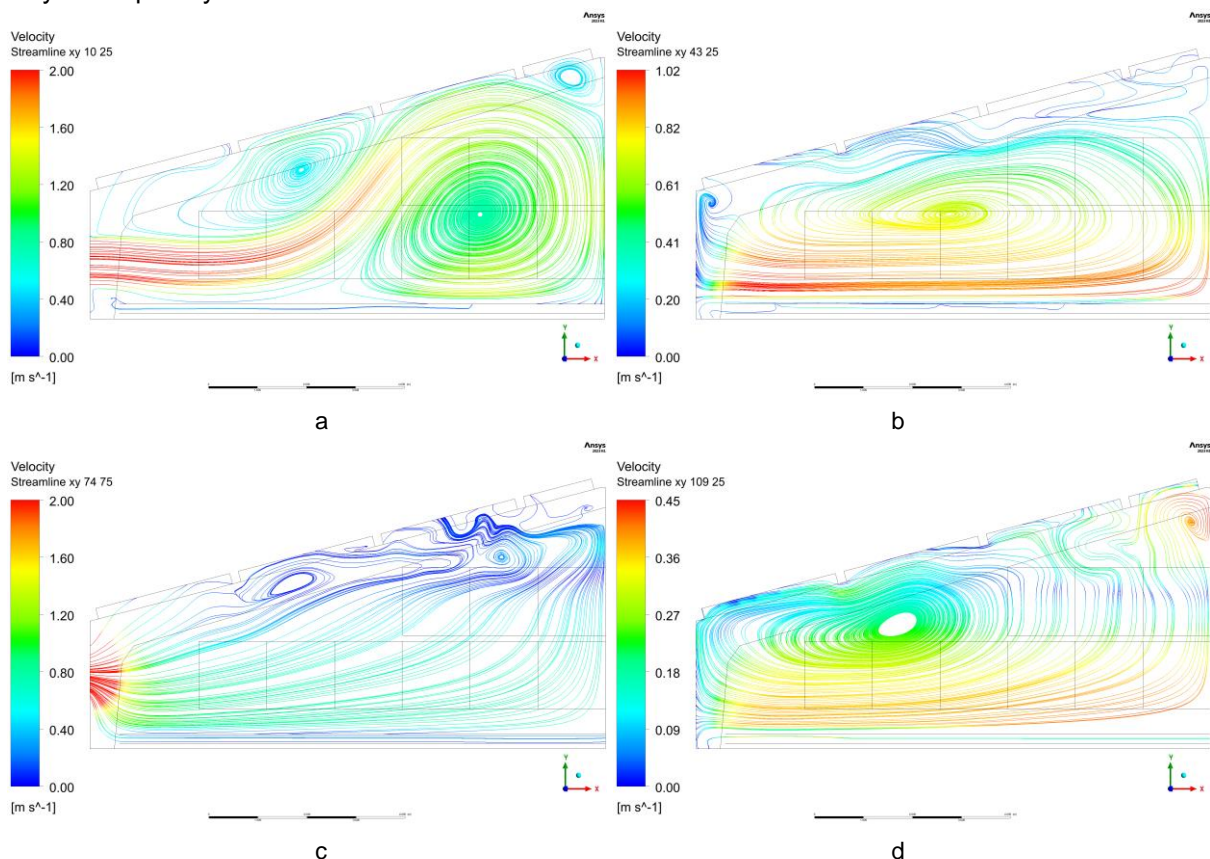


Fig. 2 - The air flow lines ($\text{m}\cdot\text{s}^{-1}$) in the poultry house along the xy axis at different distances from the front end wall

a – 10.25 m; b – 43.25 m; c – 74.75 m; d – 109.25 m

In turn, at the exhaust fans (Fig. 2c), located on the side wall, the air speed is $5.11 \text{ m}\cdot\text{s}^{-1}$. The air is evenly removed from the poultry house. The pressure at the outlet is -2.72 Pa . The fan on the rear end wall showed the following results: speed $-5.06 \text{ m}\cdot\text{s}^{-1}$; pressure -2.27 Pa .

Fig. 3 shows the temperature distribution in different sections of the poultry house. As seen, the cooled air from the heat exchangers, with a temperature of $+20 \text{ }^\circ\text{C}$ (Fig. 3a), enters the poultry house. After passing about 3.5 m and absorbing heat from the birds, the air heats up and rises. The average temperature in this section ranges from $+20 \text{ }^\circ\text{C}$ to $+22 \text{ }^\circ\text{C}$. Through the stagnant zones of the air flow at the top of the poultry house, the temperature increases, but as it approaches the birds, it cools down (Fig. 3b-3d). This thermal barrier has a size from 1.3 m to 1.6 m , with temperatures ranging from $+40 \text{ }^\circ\text{C}$ to $+24.1 \text{ }^\circ\text{C}$. Fig. 3c shows the temperature field at the level of the third exhaust fan. The temperature in this section is slightly higher, ranging from $+24.17 \text{ }^\circ\text{C}$ to $+25.83 \text{ }^\circ\text{C}$. This is due to the intense air mixing and high turbulence. The heated air enters the fan's exhaust field, where the temperature at the outlet is $+25.74 \text{ }^\circ\text{C}$.

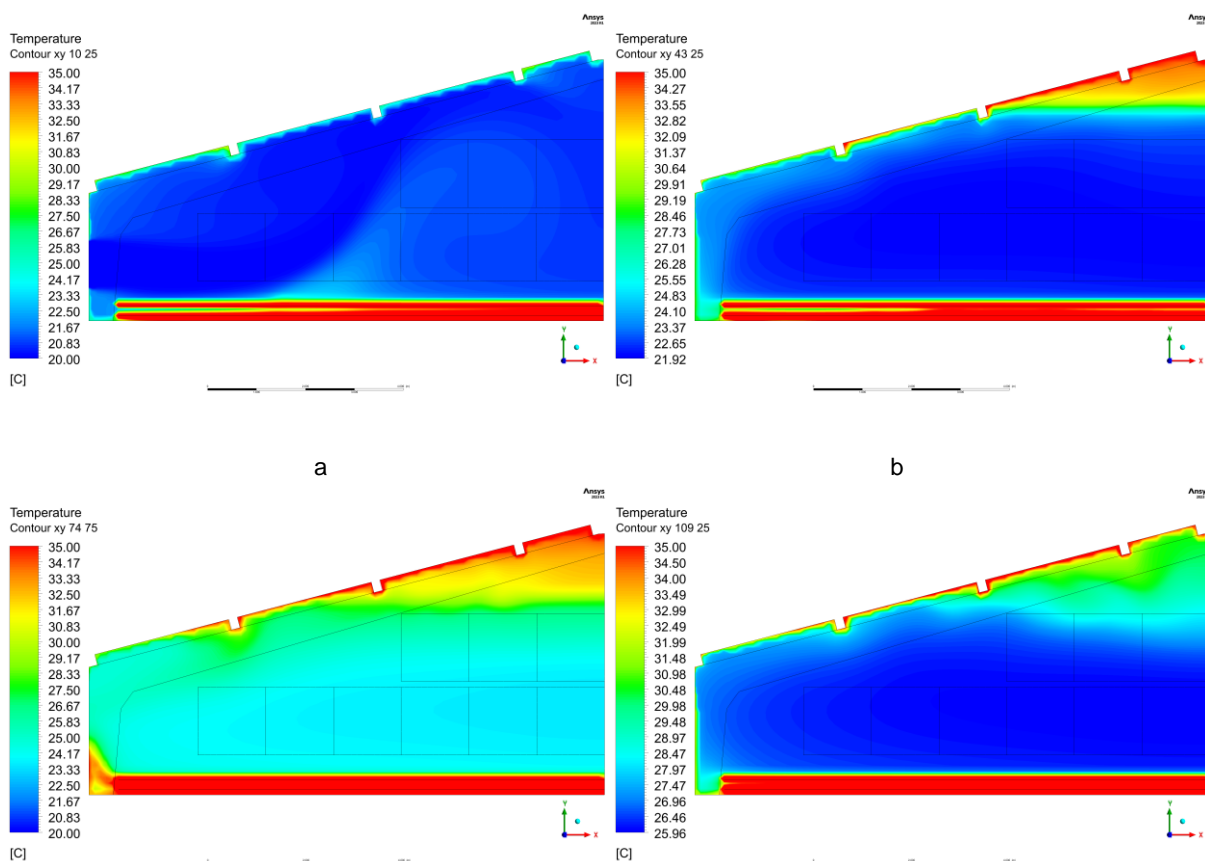


Fig. 3 - The air temperature field ($^\circ\text{C}$) in the poultry house along the xy axis at different distances from the front end wall

a – 10.25 m; b – 43.25 m; c – 74.75 m; d – 109.25 m

Fig. 4 shows the velocity field (Fig. 4a) and temperature field (Fig. 4b) at a height of 0.7 m from the floor level. These results are the most interesting and important, as the birds are kept on the floor. According to the technical norms for poultry housing, the air velocity near the birds should not exceed $2 \text{ m}\cdot\text{s}^{-1}$. As seen in Fig. 2a, the airflow from the heat exchangers enters the poultry house. It is slightly above $2 \text{ m}\cdot\text{s}^{-1}$, but this affects only 0.25% of the birds near the heat exchangers. An obvious and simultaneously interesting turbulent flow created by the first exhaust fan is also observed. Between the third heat exchanger and the first exhaust fan, a stagnant zone is observed (Fig. 4a). Due to this zone, an increase in temperature levels near the wall is noticeable (Fig. 4b). The model assumes that the birds are not placed within 0.5 m of the wall. Therefore, the birds will not experience discomfort. The average air velocity at a height of 0.7 m from the floor (Fig. 4a) is $0.83 \text{ m}\cdot\text{s}^{-1}$, and the pressure is 0.430 Pa .

The air temperature near the birds during the hot period of the year should not exceed +28 °C. Considering the results of the numerical simulation (Fig. 4b), the air temperature exceeding +28 °C occupies no more than 2% of the area. This indicates the sufficient effectiveness of the poultry house cooling system. On the rear side of the poultry house, where the exhaust fan is located, slightly higher air temperatures are observed, approaching +28 °C. This is due to the stagnant zone from the fourth exhaust fan on the side wall to the rear side of the poultry house. The average temperature across the entire area of the poultry house at a height of 0.7 m from the floor level is +23.64 °C.

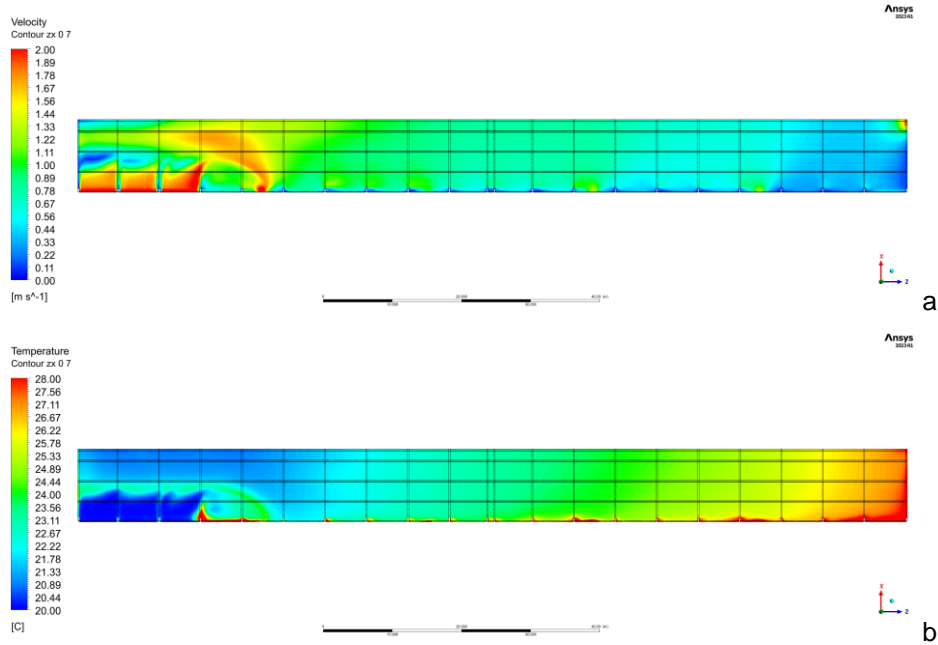


Fig. 4 - The air velocity field, m·s⁻¹ (a), and temperature field, °C (b), in the poultry house along the zx axis at a height of 0.7 m from the floor level

Fig. 5 shows the distribution of air temperature in the 3D poultry house, ranging from +20 °C to +35 °C. It can be seen that in the center of the poultry house, near the ceiling, the air temperatures are higher. With the tunnel-side ventilation system, the air gradually heats up along its length. As the air moves through the poultry house, part of it reaches the exhaust fan on the rear end wall with a temperature of +27.89 °C.

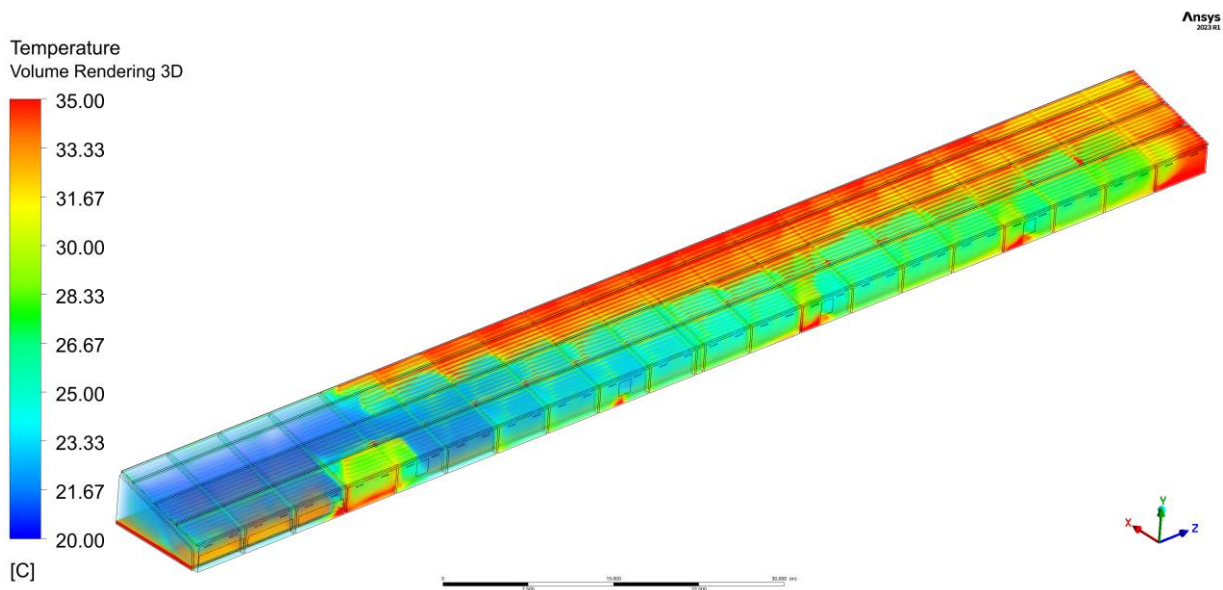


Fig. 5 - The visualization of the air temperature in the poultry house ranges from 20°C to 35°C

Considering Fig. 6, it can be concluded that due to the tunnel effect and the decrease in air velocity near the ceiling (Fig. 6a), the temperature rises in this area (Fig. 6b). To avoid such heat and mass transfer processes, the authors recommend relocating the exhaust fan on the rear wall of the poultry house, with its center positioned 4.45 m from the side wall. This would prevent stagnant airflow and thermal zones within the poultry house.

In the study by *Trokhaniak et al. (2024)*, the use of heat exchange equipment achieved a lower air temperature at the outlet (20 °C). However, this approach may require significant energy costs and the use of groundwater, which limits the applicability of this technology. In contrast, the system proposed in this article is less energy-intensive, ensuring uniform temperature and air velocity distribution with minimal discomfort for the poultry, though in some areas the temperature may slightly exceed 28 °C. Both studies confirm the effectiveness of the proposed cooling systems for poultry houses during the hot period of the year, but the approaches to implementing cooling are different.

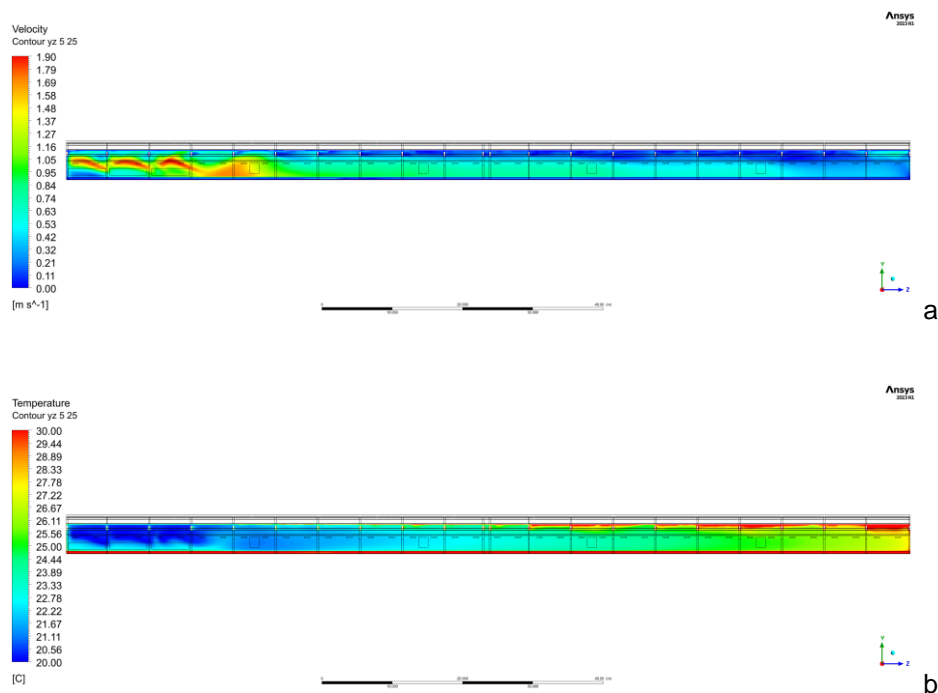


Fig. 6 - The air velocity field, m·s⁻¹ (a), and temperature field, °C (b), in the poultry house along the zy axis at 5.25 m from the side wall

Additionally, the study by *Trokhaniak et al. (2024)* demonstrated that with an air velocity of 14.36 m·s⁻¹ at the outlet of the ventilation openings, the airflow effectively reached the center of the room, ensuring uniform temperature distribution. In this case, the average air temperature in the poultry housing area was 26.56 °C, exceeding 28 °C only in certain locations. Discomfort was experienced by no more than 7.8% of the birds at an average air velocity of 0.74 m·s⁻¹. In this article, it is shown that the airflow velocity ensured uniform temperature distribution within a range that did not exceed critical values. Thermal comfort was achieved through the optimal placement of ventilation openings and the use of spoilers.

According to the numerical modeling results in the study by *Trokhaniak et al. (2024)*, the use of heat exchange equipment with groundwater as the cooling medium reduced the air temperature from 30 °C to 20 °C at the system outlet. This result demonstrates the high efficiency of the proposed cooling technology. In this article, the maximum temperature inside the poultry house did not exceed 28 °C, and the average temperature was within the range of 24.44–27.35 °C. These values confirm that the proposed cooling system also successfully maintains comfortable conditions for poultry during the hot period of the year. However, the cooling system relies on a combination of ventilation openings and directional elements (spoilers), which may require less energy compared to active heat exchange.

CONCLUSIONS

1. Using numerical modeling, the cooling system for the hot season with an outdoor air temperature of +40°C was investigated in 3D for half of the poultry house. A new cooling system for poultry houses is proposed, utilizing heat exchange equipment, with an outlet temperature of +20°C. Groundwater from underground wells is suggested as the cooling agent.
2. Air velocity fields were obtained at various sections of the poultry house. The effectiveness of the placement of heat exchange units and exhaust fans was demonstrated. The fresh air flow, exiting the heat exchangers with a speed of 2.24 m·s⁻¹ and a pressure of 3.08 Pa, passes a quarter of the width of the poultry house and, due to heating, rises sharply. The temperature in these sections averages from +20°C to +27.9°C, not exceeding the standard of +28°C during the hot season. Analyzing the results of numerical modeling at a height of 0.7 m from the floor level, it was concluded that no more than 2% of the birds would experience discomfort with the proposed cooling system. The average velocity is 0.83 m·s⁻¹, and the air temperature is +23.64°C.
3. To avoid the decrease in air velocities near the ceiling where the temperature rises, and similar heat and mass transfer processes, the authors recommend relocating the exhaust fan to the rear wall of the poultry house, with its center positioned 4.45 m from the side wall. This will prevent stagnant airflow and thermal zones in the poultry house.

ACKNOWLEDGEMENT

Supported by Education and Science of Ukraine projects of scientific works of young scientists (Kyiv), Project No. 110/1M-pr-2022.

REFERENCES

- [1] Al Assaad D.K., Orabi M.S., Ghaddar N.K., Ghali, K.F., Salam, D.A., Ouahrani D. (2021). A sustainable localised air distribution system for enhancing thermal environment and indoor air quality of poultry house for semiarid region. *Biosyst Eng*, 203,70–92.
- [2] ANSYS, (2023). *ANSYS Fluent Theory Guide*. Release 2023R1, Published in the USA, 1066 p.
- [3] Azhar Muhd & Ikegaya Naoki & Mohamad Mohd. (2022). Stochastic and statistical characteristics of artificially generated turbulent flow following Karman spectrum in a wind-tunnel experiment. *Journal of Wind Engineering and Industrial Aerodynamics*, 229, 105148. <https://doi.org/10.1016/j.jweia.2022.105148>
- [4] Boltyanska N., Podashevskaya H., Skliar O., Sklyar R., Boltianskyi O. (2022). Problems of implementation of digital technologies in animal husbandry. *CEUR Workshop Proceedings*, 3109, pp.75–82.
- [5] Bulgakov V., Adamchuk V., Ivanovs S., Ihnatiev Y. (2017). Theoretical investigation of aggregation of top removal machine frontally mounted on wheeled tractor. *Engineering for Rural Development*, 16, 273–280.
- [6] Bulgakov V., Nikolaenko S., Holovach I., Boris A., Kiurchev S., Ihnatiev Y., Olt J. (2020a). Theory of motion of grain mixture particle in the process of aspiration separation. *Agronomy Research*, 18 (Special Issue 2), pp. 1177–1188.
- [7] Bulgakov V., Sevostianov I., Kaletnik G., Babyn I., Svanovs S., Holovach I., Ihnatiev Y. (2020b). Theoretical Studies of the Vibration Process of the Dryer for Waste of Food. *Rural Sustainability Research*, 44(339), pp. 32–45.
- [8] Czarick M., Fairchild B. (2014). Plastic cooling pads are found to be less efficient comparing to paper cool pads. *Poultry Housing Tips* 24(8), College of Agricultural and Environmental Sciences, Georgia, USA, 64–69.
- [9] Harrouz J.P., Katramiz E., Ghali K., Ouahrani D., Ghaddar N. (2021). Comparative analysis of sustainable desiccant – Evaporative based ventilation systems for a typical Qatari poultry house. *Energy Conversion and Management*, 245, 114556. <https://doi.org/10.1016/j.enconman.2021.114556>
- [10] Hoff S.J. (2018). HVAC System. *InTech*. <https://doi.org/10.5772/intechopen.78785>.
- [11] Hui X., Li B.M., Xin H.W., Zheng W.C., Shi Z.X., Yang X., Zhao S.M. (2018). New control strategy against temperature sudden-drop in the initial stage of pad cooling process in poultry houses. *International Journal of Agricultural and Biological Engineering* 11(1), Beijing, China, 66–73. <https://doi.org/10.25165/j.ijabe.20181101.2479>

- [12] Ivanovs S., Bulgakov V., Nadykto V., Ihnatiev Ye., Smolinskyi S., Kiernicki Z. (2020). Experimental study of the movement controllability of a machine-and-tractor aggregate of the modular type. *INMATEH – Agricultural Engineering*, 61(2), 9–16. <https://doi.org/10.35633/inmateh-61-01>
- [13] James, O. Donald. (2012). *Technology of microclimate of broiler house*. Aviagen Brands. p.24, Huntsville, USA,.
- [14] Kim K., Yoon J.Y., Kwon H.J., Han J.H., Son J.E., Nam S.W., Lee I.B. (2008). 3-D CFD analysis of relative humidity distribution in greenhouse with a fog cooling system and refrigerative dehumidifiers. *Biosystems Engineering*, 100(2), San Diego, USA, 245–255.
- [15] Liang Y., Tabler G.T., Dridi S. (2020). Sprinkler technology improves broiler production sustainability: from stress alleviation to water usage conservation: A mini review. *Front Veterinary Sci*, 7, 689.
- [16] Mahmood M.H., Sultan M., Miyazaki T., Koyama S., Maisotsenko V.S. (2016). Overview of the Maisotsenko cycle – A way towards dew point evaporative cooling. *Renew Sustain Energy Rev*, 66, 537–555. <https://doi.org/10.1016/j.rser.2016.08.022>
- [17] Pandelidis D., Cichoń A., Pacak A., Anisimov S., Drąg P. (2019). Performance comparison between counter-and cross-flow indirect evaporative coolers for heat recovery in air conditioning systems in the presence of condensation in the product air channels. *Int J Heat Mass Transf*, 130, 757–777.
- [18] Raza H.M.U., Ashraf H., Shahzad K., Sultan M., Miyazaki T., Usman M. (2020). Investigating applicability of evaporative cooling systems for thermal comfort of poultry birds in Pakistan. *Appl Sci.*, 10(13), 4445. <https://doi.org/10.3390/app10134445>
- [19] Rozenboim I., Tako E., Gal-Garber O., Proudman J.A., Uni Z. (2007). The effect of heat stress on ovarian function of laying hens. *Poult Sci.*, 86 (8), 1760–1765.
- [20] Tariq R., Benarab F.Z. (2017). Mathematical Modelling and Numerical Simulation of Maisotsenko Cycle. *19th International Conference on Fluid Mechanics, Heat Transfer and Thermodynamics (ICFMHTT)*.
- [21] Schneiderbauer S., Krieger M. (2014). What do the Navier-Stokes equations mean?. *European Journal of Physics*, 35. 015020. [10.1088/0143-0807/35/1/015020](https://doi.org/10.1088/0143-0807/35/1/015020).
- [22] Trokhaniak V., Ivanovs S., Nasieka Yu., Chernysh O., Aboltins A., Ihnatiev Y., Synyavskiy O. (2023). Usage of CFD for research on lateral ventilation system in poultry house. *Engineering for Rural Development*, 22, 582-587. <https://doi.org/10.22616/ERDev.2023.22.TF120>
- [23] Trokhaniak V., Nasieka Y., Ihnatiev Ye., Synyavskiy O., Skliar O., Olt J. (2024) Study of heat exchange processes in the cooling system of a poultry house with side ventilation. *Agronomy Research*, 22(2), 1016–1025. <https://doi.org/10.15159/AR.24.084>
- [24] Trokhaniak V., Gorobets V., Shelimanova O., Balitsky A. (2023). Research of thermal and hydrodynamic flows of heat exchangers for different air cooling systems in poultry houses. *Machinery & Energetics*, 14(1), 68-78. <https://doi.org/10.31548/machinery/1.2023.68>
- [25] Zhan C., Duan Z., Zhao X., Smith S., Jin H., Riffat S. (2011). Comparative study of the performance of the M-cycle counter-flow and cross-flow heat exchangers for indirect evaporative cooling—paving the path toward sustainable cooling of buildings. *Energy*, 36 (12), 6790–6805.

EXPERIMENTAL INVESTIGATION ON THE SHEAR MECHANICAL PROPERTIES OF LICORICE ROOT

甘草根剪切力学特性的试验研究

Bintong ZHAO¹⁾, Zhu ZHAO²⁾, Zhongnan WANG^{*2)}, Ping ZHAO^{*1)}

¹⁾ College of Engineering, Shenyang Agricultural University, Shenyang / China

²⁾ Liaoning Agricultural Technical College, Yingkou / China

Corresponding author: Wang Zhongnan, Zhao Ping

Tel: +86-0417-7020545; E-mail: zhaosynd@163.com

DOI: <https://doi.org/10.35633/inmateh-75-56>

Keywords: Licorice root, Shear test, mechanical properties, physical and mechanical characteristics

ABSTRACT

The process of slicing is a vital component in the preliminary treatment of licorice roots. The physical properties and shear mechanical attributes of licorice root are of considerable importance for the development and optimization of machinery intended for slicing licorice root. In this research, four-year-old mature licorice roots were selected as the experimental specimens, and shear strength evaluations were conducted on these roots by means of a universal testing machine (Instron 3344 series). The experimental design utilizes a blend of univariate and multivariate orthogonal testing techniques. Within this design, moisture content, shear speed, and shear angle are identified as the independent variables, while the maximum cutting force is defined as the primary assessment criterion. The experimental results reveal that the primary and secondary factors influencing the shear strength of licorice root follow the order: moisture content > shear speed > shear angle. The optimal conditions for the slicing pretreatment process are identified as a moisture content of $50 \pm 2\%$, a shear speed of 0° , and a shear speed of $90 \text{ mm} \cdot \text{min}^{-1}$.

摘要

切片是甘草根预处理流程中的关键环节之一。甘草根的物理参数和剪切力学特性对于甘草根切片设备的研发和工艺优化具有重要意义。本研究选取四年生的成熟期甘草根作为试验材料，利用万能试验机（Instron3344系列）开展甘草根剪切性能试验。试验设计采用单因素和多因素正交试验，将含水率、剪切角度、剪切速度设定为试验因素，以最大剪切力作为评价指标。结果表明，影响甘草根剪切力的主次因素为：含水率>剪切速度>剪切角度。当含水率为 $50 \pm 2\%$ ，剪切角度为 0° ，剪切速度为 $90 \text{ mm} \cdot \text{min}^{-1}$ 时，进行切片预处理工序最为适宜。

INTRODUCTION

Licorice, alternatively known as Gan Cao, sweet grass, or sweet root, acquires its name due to the sweet flavor of its root. Licorice is taxonomically classified within the Fabaceae family, specifically residing in the subfamily Faboideae, the tribe Galegeae, and the subtribe Glycyrrhiza. It is a perennial herbaceous plant that is grouped under the genus Glycyrrhiza. Licorice, which is widely acknowledged as one of the earliest plant species enlisted in China's inventory of medicinal and edible resources, also serves as a significant natural resource in arid and semi-arid regions (He et al., 2024). Licorice is mainly distributed in arid and semi-arid areas around 40° north latitude. The major cultivation areas are concentrated in Central Asia, North America, and Eastern Europe. In China, licorice is one of the major economic crops. It has a relatively large cultivation area that is mainly spread across the northeastern, northern, and northwestern provinces. The key production areas encompass Xinjiang, Inner Mongolia, Ningxia, and Gansu (Li et al., 2015). The cultivation of licorice spans a period of two to four years from planting to harvesting. And it is generally necessary to conduct pretreatment on the roots prior to their utilization in medicinal applications. The cutting procedure is essential in the pretreatment stage, as it enhances the surface area interaction between the substrate and the solvent, thereby promoting the extraction of the drug and its subsequent delivery.

Shear strength, as one of the critical mechanical properties of agricultural materials, can provide theoretical foundations and effective parameters for the design, manufacturing, and optimization of licorice cutting devices and harvesting machinery.

¹ Zhao Bintong, Ph.D. Stud. Eng.; ²Zhao Zhu, Prof. Ph.D. Eng.; ²Wang Zhongnan, Lab.Techo. MA. Eng.; ¹Zhao Ping, Prof. Ph.D. Eng.

Currently, relevant research focuses on the shear mechanical properties of various plant organs and crops, covering the main roots of *Panax notoginseng* (Yang *et al.*, 2016) and the rhizomes of *Coptis chinensis* (Li *et al.*, 2023) as medicinal plants, the root systems of maize (Zhao *et al.*, 2021; Guo *et al.*, 2016) as a food crop, as well as common categories such as fruits (Wu *et al.*, 2022), seeds (Bao *et al.*, 2022; Huang *et al.*, 2021; Guo *et al.*, 2016), vegetables (Yang *et al.*, 2022) and crop stalks (Yang *et al.*, 2016; Li *et al.*, 2020). Moreover, the shear mechanical properties of tea tree new shoots (Wang *et al.*, 2022) also fall within the scope of research. In contrast, studies concerning the shear characteristics of *Glycyrrhiza uralensis* are notably scarce.

Therefore, this study opts for the roots of licorice harvested at the appropriate time as the research object, with cutting force serving as the evaluation criterion. It dissects the influences of moisture content, root diameter, shear speed, and other factors on the cutting force of licorice roots. Through the application of orthogonal experimental methodologies, the predominant influencing factors during the licorice cutting process are pinpointed, and the fluctuations in its shear mechanical properties are investigated. This offers a requisite theoretical groundwork for the design and optimization of the preliminary processing techniques and equipment for licorice.

MATERIALS AND METHODS

Materials

This study focuses on *Glycyrrhiza uralensis* as the principal experimental subject. The samples were obtained from a comprehensive demonstration practice base specialized in *Glycyrrhiza uralensis* cultivation in the Northeast region. The selected *Glycyrrhiza uralensis* plants were of four-year-old age and possessed a root system composed of both vertical and horizontal roots (as depicted in Figure 1). The vertical roots of the *Glycyrrhiza uralensis* (hereinafter denoted as *Glycyrrhiza uralensis* roots) had diameters spanning approximately from 1.5 to 3 cm, and their epidermis exhibited a coarse texture. Solely healthy *Glycyrrhiza uralensis* roots, demonstrating optimal growth status and being free from pests and diseases, were selected for this study. The lateral roots were trimmed and all residual debris was removed. The *Glycyrrhiza uralensis* roots are illustrated in Figure 2.

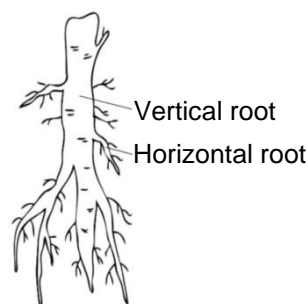


Fig. 1 - Schematic Diagram of the Structure of Licorice Root



Fig. 2 - *Glycyrrhiza uralensis* root

Equipment

The experimental apparatuses and implements employed in this study comprise a Model 101 electric blast drying oven (with a temperature range of 0 - 300°C and a voltage of 220 V), an Instron 3344 series microcomputer-controlled electronic universal testing machine, a stereo electron microscope (Nexcope NSZ606), a digital vernier caliper (having a measuring range of 150 mm and an accuracy of 0.01 mm), an electronic balance (with a capacity of 500 g and an accuracy of 0.001 g), an angle square, scissors, and sealing bags, among other items.

Experimental Methods

Determination of Physical Parameters and Tissue Structure

The simple random sampling method was adopted to randomly select samples of licorice roots for testing purposes. For each individual root, its length was measured three times, and then the average value was calculated. Subsequently, the licorice root was sectioned into five discrete portions, specifically designated as the upper, upper-middle, middle, lower-middle, and lower segments. The diameter measurements corresponding to each segment are presented in Figure 3. The average diameter of the licorice root was computed using Formula (1), which is as follows:

$$d_j = \frac{1}{6} \sum_{i=1}^2 (d_{1i} + d_{2i} + d_{3i}) \quad (1)$$

where:

d_j represents the mean diameter of the cross-sectional area of the licorice root, mm;

d_{1i} represents the length of the major axis of the cross-section of the licorice root recorded during the i -th measurement, mm;

d_{2i} represents the length of the minor axis of the cross-section of the licorice root recorded during the i -th measurement, mm;

d_{3i} represents the length of the shortest axis of the cross-section of the licorice root recorded during the i -th measurement, mm.

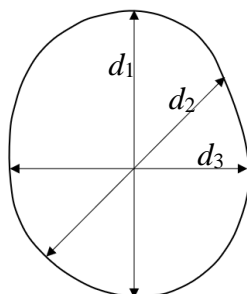


Fig. 3 - Schematic diagram of measurement positions for the diameter of licorice root cross-sections

Scissors and a scalpel were utilized to obtain cross-sectional specimens of licorice root with differing moisture content levels. The moisture content levels were adjusted by subjecting the licorice roots to different drying durations in a controlled environment. Subsequently, high-quality digital microscopy was employed to examine the tissue architecture within the cross-sections of the licorice root, focusing particularly on features such as the cell arrangement, vascular bundle structure, and parenchyma tissue morphology.

Determination of moisture content and density

The entire licorice roots were cut with scissors to determine of the moisture content of freshly harvested licorice and were then grouped accordingly. An electronic balance was employed to weigh each group of licorice roots separately, and the measurements were recorded. After weighing, the samples were placed in a drying box and then transferred into a vacuum drying oven, as depicted in Figure 4. The temperature was set at 110°C, and the weight was recorded every 2 hours until the mass stabilized with a relative change of less than 0.1% between consecutive measurements, indicating the end of the experiment. The average of the weights recorded every 2 hours during the drying process was calculated. Upon the completion of the drying process, the samples were weighed again to calculate the absolute moisture content using the following formula:

$$M = \frac{m_1 - m_2}{m_1} \times 100\% \quad (2)$$

where: M represents the moisture content of licorice root, %;

m_1 is the wet mass of the sample before drying, g;

m_2 is the dry mass of the sample after drying, g.



Fig. 4 - Licorice root drying test

The freshly harvested licorice roots were meticulously cleaned to remove any adhered soil and debris. After allowing the roots to air-dry for 30 minutes, until the surface appeared dry to the touch, a utility knife was used to cut the licorice roots into numerous small fragments. These fragments were then randomly divided into ten groups to ensure sample diversity and representativeness for subsequent measurements. The mass of each group was precisely measured using an electronic balance and denoted as M . A 500-milliliter beaker was selected, and 300 milliliters of water were initially added. The licorice root samples were then weighed and carefully placed into the beaker, ensuring complete submersion in the water. At this point, the change in water level was meticulously observed and recorded. The density of the licorice roots was subsequently calculated using formula (3), as follows:

$$\rho_g = \frac{M_g}{V_g} \quad (3)$$

where: ρ_g represents the density of licorice root, g/cm^3 ; M_g is the total mass of licorice root obtained through direct weighing, g; V_g is the total volume measured by the pycnometer method, mL.

Shear testing methodology

To explore the impacts of shear angle, shear speed, and moisture content of licorice root on its shear strength, based on preliminary investigations, licorice roots with a diameter of approximately 15 mm were selected and samples with a length of 80 mm were fabricated to ensure the representativeness and uniformity of samples for subsequent shear tests. Figure 5 clearly illustrates the schematic diagram of the sample.



Fig. 5 - Licorice root cutting test sampling

Single-factor experiment

The moisture content of the licorice root was adjusted to $(50 \pm 2)\%$, and the shear speed was set at 60 mm/s. The shear angles were arranged as shown in Figure 6, which were divided into 0° , 15° , 30° , 45° , and 60° . The 0° angle represents the shear test carried out on the transverse section of the licorice root. Five sets of repeated tests were performed for each shear speed, and the results were averaged.

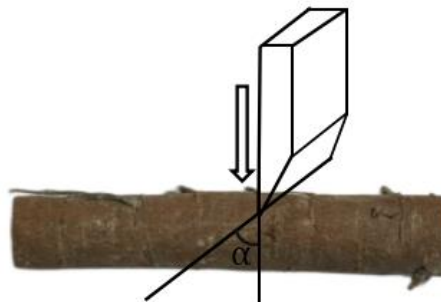


Fig. 6 - Cutting diagram

The shear speed was set to 60 mm/s and the shear angle to 0° . The moisture content of licorice was selected as $(50 \pm 2)\%$, $(40 \pm 2)\%$, $(30 \pm 2)\%$, $(20 \pm 2)\%$, and $(10 \pm 2)\%$ for the cutting tests. Five sets of replicated experiments were conducted for each moisture content, and the average of the results was obtained.

For licorice root with a moisture content of $(50 \pm 2)\%$ and a shear angle of 0° , the shear speeds were adjusted to 30 mm/min, 60 mm/min, 90 mm/min, 120 mm/min, and 150 mm/min for the cutting tests. Five sets

of replicated experiments were performed at each shear speed, and the average of the results was calculated. The cutting process is depicted in Figure 7.



Fig. 7 - Cutting process

Multifactorial experiment

By incorporating single-factor experiments, multifactorial orthogonal tests taking into account moisture content, shear angle, and shear speed were conducted. The multifactorial orthogonal test scheme is presented in Table 1.

Table 1

Experimental factors and levels

Test No.	Moisture content / %	Shear angle / °	Shear speed / (mm/min)
1	20±2	0	30
2	30±2	15	60
3	40±2	30	90
4	50±2	45	120

Evaluation indicators

During the experiment, the licorice root specimen was precisely positioned on the testing platform of a universal testing machine. The sampling frequency was meticulously set to 50 Hz, and the base span was accurately configured to 30 mm. A 1000 N sensor in conjunction with its corresponding shear fixture was employed, featuring a double shear surface. The research primarily focused on investigating the effects of shear angle, moisture content, and shear rate on the maximum cutting force of licorice root stems. The computer software interfaced with the testing machine automatically recorded the data and generated a cutting force - displacement curve.

RESULTS AND ANALYSIS

The physical parameters and structural characteristics

The mean length of four-year-old Ural licorice root was determined to be 41.78 mm, and the average diameter was measured as 15.054 mm. The direct measurements for each section are tabulated in Table 2.

Table 2

The physical parameters of Licorice root

Sampling location	Diameter / mm	Average diameter / mm	Average length / mm
Upper section	20.41	15.054	41.78
Upper-middle section	17.73		
Middle section	14.39		
Lower-middle section	12.72		
Lower section	10.02		

Figures 8 (a) and (b) depict the microscopic structural organization of licorice root under two distinct moisture content conditions, namely 52% and 11.6%. It is conspicuous that the principal constituents of the licorice root comprise the periderm, phloem rays, secondary phloem, xylem rays, secondary xylem, cambium, and fiber bundles. With a reduction in moisture content, the texture of the periderm becomes more pronounced and compact, the interstices between the phloem rays are marginally reduced, the secondary phloem displays

wrinkling, the xylem rays undergo a darkening in coloration, and the lignification of the secondary xylem is enhanced.

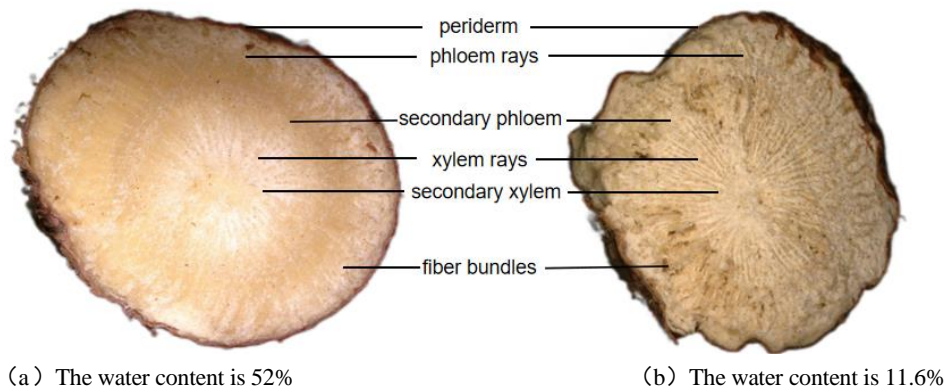


Fig. 8- Structure of cross-section of the internode of corn stalk

Moisture content and density

Based on the in-depth analysis of the experimental outcomes, the quality of ten groups of fresh licorice roots was found to stabilize subsequent to being dried for 12 hours at a temperature of 120°C. The initial moisture content of the fresh licorice roots was precisely measured and calculated, with a resultant moisture content of 52.36%. Moreover, the density of the licorice roots was ascertained by means of the specific gravity bottle method. Upon averaging the results, the final density of the fresh licorice roots was determined to be 1031 kg·m⁻³.

Analysis of the cutting process

When the moisture content was within the range of $(50 \pm 3)\%$, the loading speed was set at 60 mm/min, and the shear angle was 0°. The cutting force-displacement curve of licorice root is presented in Figure 9. The cutting process of licorice root can be categorized into three distinct phases. In the initial phase (segment OA), the licorice root is in a compressive state, and the cutting force displays an approximately linear increment with respect to the displacement. In the intermediate phase (segment AB), as the displacement continuously augments, the cutting force exhibits a fluctuating upward trend. With further progression of displacement, the load surges sharply, attaining a peak value, which signifies the critical state at which the licorice root is severed. In the final phase (segment BC), the licorice root stem is entirely severed by the tool, leading to a rapid attenuation in cutting force until it approaches zero. Research findings suggest that although substantial differences exist in cutting force under diverse moisture contents, loading rates, and shear angles, the overall tendency of the cutting force - displacement curve for licorice root invariably shows an initial increase, subsequent fluctuations, and ultimately a precipitous decrease.

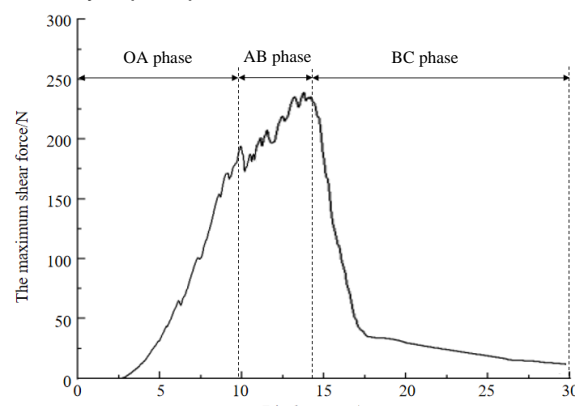


Fig. 9 - Cutting force-displacement curve

Analysis of Single-Factor Experimental Results

Analysis of the Influence of Moisture Content on the Maximum Shear Strength of Licorice Root

The variation in the impact of moisture content on shear strength is depicted in Figure 10. At a moisture content of $(50 \pm 2)\%$, the average maximum shear force was measured as 240.23 N. When the moisture content was adjusted to $(40 \pm 2)\%$, the average maximum shear force escalated to 312.87 N; at $(30 \pm 2)\%$, it

further augmented to 357.95 N. At $(20 \pm 2)\%$, the average maximum shear force attained 397.65 N, and at $(10 \pm 2)\%$, the maximum shear force peaked at 447.87 N.

These data show a trend of increasing shear force as the moisture content in licorice root decreases. It can be inferred that at a moisture content of $(50 \pm 2)\%$, the shear force reaches its minimum, indicating that this moisture level is optimal for preprocessing operations such as slicing and root trimming.

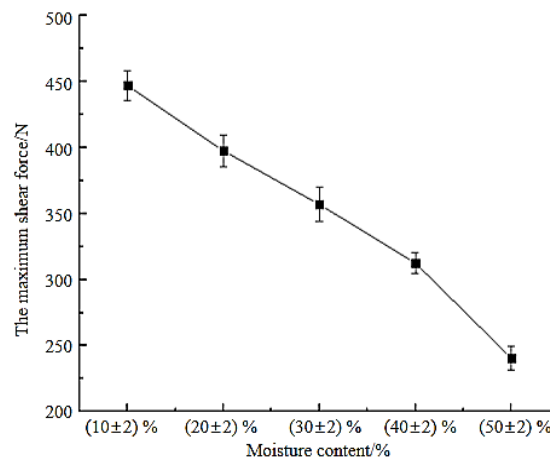


Fig. 10 - The effect of different moisture contents on cutting force

Analysis of the Influence of Shear Angle on the Maximum Shear Strength of Licorice Root

The variation in the impact of shear angle on shear strength is depicted in Figure 11. When the shear angle was set at 0° , the average value of the maximum shear force was measured as 292.398 N. Subsequently, when the shear angle was adjusted to 15° , the average value of the maximum shear force increased to 318.262 N. At a shear angle of 30° , the average value of the maximum shear force was 385.41 N. When the shear angle reached 45° , the average value of the maximum shear force was 426.366 N. And when the shear angle was set to 60° , the maximum shear force was 468.32 N. Within the range of shear angles from 0° to 60° , it was observed that the maximum shear force of licorice root exhibited a gradually increasing trend with the augmentation of the shear angle.

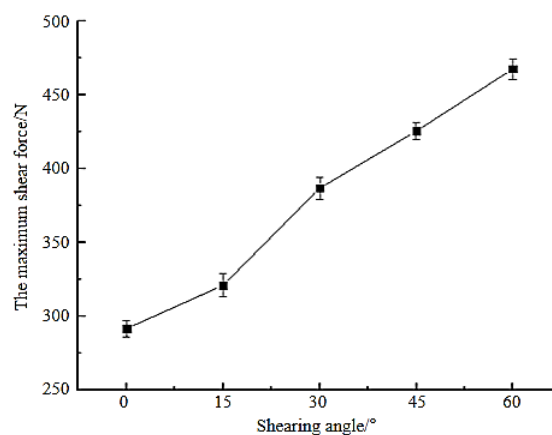


Fig. 11 - The effect of different shear angles on cutting force

Analysis of the Influence of Shear Speed on the Maximum Shear Strength of Licorice Root

The variation in the impact of shear speed on shear strength is depicted in Figure 12. When the shear speed was set at 150 mm/min, the average value of the maximum shear force of licorice root was measured as 290.398 N. Subsequently, when the shear speed was adjusted to 120 mm/min, the average value of the maximum shear force increased to 322.262 N. At a shear speed of 90 mm/min, the average value of the maximum shear force was 387.21 N. When the shear speed was reduced to 60 mm/min, the average value of the maximum shear force was 426.166 N. And when the shear speed was further decreased to 30 mm/min, the average value of the maximum shear force reached 476.32 N. It can be clearly seen that within the range

of shear speed s set in the experiment, the shear force of licorice root exhibited a decreasing trend with the increase of the shear speed.

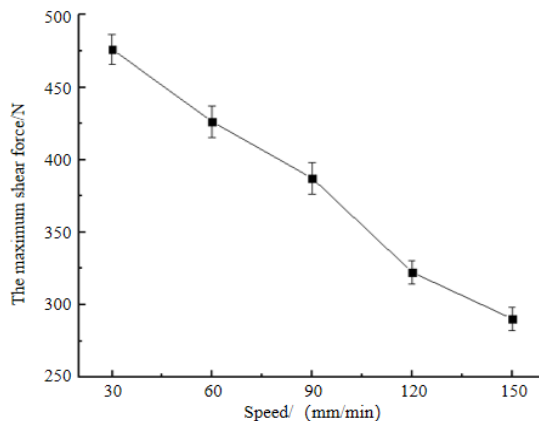


Fig. 12 - The effect of different shear speeds on cutting force

Multifactorial test analysis

After performing a univariate analysis of moisture content, shear angle, and shear rate, it is crucial to take into account the possible interactive effects among these factors, since they might have a cumulative influence on the shear strength of licorice root. Hence, combining these three factors for a multifactorial comprehensive analysis is justified. In this research, moisture content, shear angle, and shear rate were chosen as experimental variables, with the maximum shear strength as the experimental parameter. An orthogonal experiment was designed and carried out accordingly. The specific experimental protocol and corresponding results are shown in Table 3.

Table 3

Experimental factors and levels

Test No.	Moisture content A/%	shear angle B/°	shear speed C/(mm/min ⁻¹)	Maximum cutting Force /N
1	1	1	1	487.36
2	1	2	2	439.35
3	1	3	3	470.25
4	1	4	4	397.24
5	2	1	2	488.75
6	2	2	1	290.22
7	2	3	4	300.55
8	2	4	3	491.22
9	3	1	3	450.33
10	3	2	4	400.11
11	3	3	1	268.45
12	3	4	2	481.06
13	4	1	4	308.55
14	4	2	3	331.39
15	4	3	2	277.19
16	4	4	1	266.13

Analysis of variance, as an effective statistical method, allows for an in-depth examination of the fluctuations in experimental indicators caused by variations in the levels of experimental factors, thereby determining the significance of each factor's impact on the experimental outcomes. Data from Table 3 indicates that among the experimental factors considered in this study, the order of significance affecting the maximum shear force is as follows: moisture content, shear rate, and shear angle. The variation in moisture content of licorice has a highly significant effect on the shear force of licorice roots, dominating the entire influence framework. Additionally, the shear rate also significantly impacts the shear force of licorice roots, exhibiting a clear pattern of change with varying shear rates. In contrast, while the shear angle does have some effect on the shear force of licorice roots, its significance is relatively weak, suggesting a secondary role within the

multifactorial interaction system. Nevertheless, its influence should not be entirely disregarded when conducting precise analyses and optimizing the shear processing of licorice roots.

Table 4

Analysis of Variance						
Sources	SS	df	MS	F	P-value	Significance
Moisture content/A	49096.228	3	16365.409	7.704	0.018	*
shear angle/B	25835.984	3	8611.995	4.054	0.068	
shear speed/C	33104.015	3	11034.672	5.195	0.042	*
Error	12745.125	6	2124.188			
Total sum	120781.352	15				

Note: *, significance level $0.01 < P < 0.05$; **, significance level $P < 0.01$.

From Table 5, it can be observed that the influence of various experimental factors on the maximum shear force follows a descending order of significance: $A > C > B$, which translates to moisture content > shear rate > shear angle. The intuitive analysis results regarding the maximum shear force are in strong agreement with the results of the variance analysis.

Table 5

Intuitive analysis results			
Index	A	B	C
mean 1	448.6	433.7	328
mean 2	392.7	365.3	421.6
mean 3	400	329.1	435.8
mean 4	295.8	408.9	351.6
Range	152.7	104.6	107.8
Primary and secondary factors	$A > C > B$		
A relatively optimal combination	$A_4B_3C_1$		

For the determination of the optimal combination of factor levels, the present study endeavors to minimize the experimental index of maximum shear force. Via a visual analysis of the maximum shear force of licorice root, the level associated with the minimum value of the evaluation index was chosen. The optimal factor level combination with respect to maximum shear force was determined as $A_4B_3C_1$, which represents a moisture content of $50 \pm 2\%$, a shear angle of 0° , and a shear rate of $90 \text{ mm} \cdot \text{min}^{-1}$. This optimal factor level combination offers a critical reference for the optimization of the licorice root shearing process and bears substantial guiding significance for subsequent related research and practical applications.

CONCLUSIONS

This study systematically analyzes the physical parameters, structural organization, and shear characteristics of four-year-old licorice, thereby providing a theoretical foundation for optimizing post-harvest treatment and processing techniques. The specific conclusions are as follows:

(1) Measurements demonstrate that the average length of the roots of four-year-old Ural licorice is approximately 41.78 mm, with an average diameter of around 15.054 mm. The diameters at the upper, upper-middle, middle, lower-middle, and lower sections are approximately 20.41 mm, 17.73 mm, 14.39 mm, 12.72 mm, and 10.02 mm, respectively. Moreover, the moisture content of fresh licorice roots is determined to be 52.36%, and the density is $1031 \text{ kg} \cdot \text{m}^{-3}$.

(2) Shear tests on licorice roots disclose that the shear process mainly comprises three distinct stages: compression, shear, and unloading. This process reflects the mechanical response characteristics of licorice roots under shear forces, which is essential for a more profound understanding of their shear resistance.

(3) Results from single-factor experiments suggest that the shear force of licorice roots rises with increasing moisture content and shear angle, whereas it declines with a growing shear speed. Multi-factor experiments reveal the relative impact of various factors on the shear force of licorice roots in the following order: moisture content > shear speed > shear angle. The optimal combination of shear factors is identified as

A₄B₃C₁, corresponding to a moisture content of 50 ± 2%, a shear angle of 0°, and a shear speed of 90 mm·min⁻¹.

ACKNOWLEDGEMENT

This research was funded by the doctoral research project of Liaoning Natural Science Foundation in 2024(2024-BS-287), the "Enterprise Doctor Dual Innovation Plan of Yingkou City" project in 2023 (YKSCJH2023-015), and the scientific effort of Liaoning Agricultural Technical College (Lnz202216,Lnz202310).

REFERENCES

- [1] Bao, Y., Yi, S., Tao, G., Mao, X., Zhang, Z.,(2022), Experimental Study on the Material Properties and Mechanical Properties of Isatis Indigotica Seeds (板蓝根种子物料特性试验研究), *Journal of Agricultural Mechanization Research*, Vol.44, Issue 9, pp.202-208+216, Hei Longjiang / P.R.C;
- [2] Guo, Y., Cheng, Y., Ben, D., Yang, J., Wang, B., Dong, L., (2016), Experiment of longitudinal shear characteristics properties of corn straw (玉米秸秆纵向剪切特性试验), *Journal of Chinese Agricultural Mechanization*, Vol.37, Issue 2, pp.123-126, Ji Lin / P.R.C;
- [3] He, W., Zhang, Y., Xi, S., Huang, L., Jin, L., (2024), Construction and visual analysis of scientific knowledge graph of Glycyrrhizae Radix et Rhizoma from global perspective (全球视域下的甘草科研知识图谱构建及可视化分析), *Chinese Traditional and Herbal Drugs*, Vol.55, Issue 7, pp.2351-2365, Hai Nan / P.R.C;
- [4] Huang, X., Zhang, W., Zhang, K., Feng, S., Liu, Z., Yang, F., (2021), Design Study on Compression and Shear Mechanical Properties of Buckwheat Grain (荞麦籽粒的压缩和剪切力学特性研究), *Journal of Agricultural Mechanization Research*, Vol.43, Issue 5, pp.168-235, Shan Xi / P.R.C;
- [5] Li, H., Qing, M., Yu, J., (2015), Research progression of glycyrrhiza uralensis (甘草的研究进展), *Journal of Inner Mongolia Medical University*, Vol.37, Issue 2, pp.199-204, Neimenggu / P.R.C;
- [6] Li, L., Deng, G., Li, G., Zheng, S., Cui, Z., (2020), Test and analysis on shearing mechanical properties of fibrous roots of galangal (高良姜须根剪切力学特性试验研究), *Journal of Agricultural Mechanization Research*, Vol.41, Issue 8, pp.116-120, Guang Dong / P.R.C;
- [7] Li, Min., Yao, L., Chen, X., Gu, M., Zhao, S., Xie, S., (2023), Experimental Study on Physical and Mechanical Properties of Rhizomes of Coptis Chinensis (黄连根茎物理力学特性试验研究), *Journal of Southwest University (Natural Science)*, Vol.45, Issue 9, pp.153-161, Chong Qing/ P.R.C;
- [8] Wang, Qi., Lin, Hengchu., Liao, Peng., Wan, Jiaming., Zheng, Shuhe., (2022), Shearing mechanical properties of tea stem (茶叶茎秆剪切力特性), *Journal of Fujian Agriculture and Forestry University (Natural Science Edition)*, Vol.51, Issue3, pp.428-432, Fu Jian / P.R.C.
- [9] Wu, T., Zhang, Z., Du, H., Gao, W., Wang, S., He, J., Yang W., Wu X., (2022), Determination and Analysis of Mechanical Properties of Zanthoxylum (花椒力学特性的测定与分析), *Journal of Shanxi Agricultural Sciences*, Vol.44, Issue 9, pp.748-753, Shan Xi / P.R.C;
- [10] Yang, H., Wang, B., Gu, F., Wu, F., Zhang, Y., Hu, Z., (2022), Determination of some physical and mechanical properties of onion, *INMATEH-Agricultural Engineering*, Vol.68, Issue 3, pp.324-332, Bucharest / Romania;
- [11] Yang, W., Tan, J., (2016), Experiments on Mechanical Properties for Main Root of Yunnan Panax Notoginseng, *Journal of Kunming University of Science and Technology (Natural Science)*, Vol.41, Issue1, pp.75-81, Kun Ming / P.R.C;
- [12] Yang, Y., Liu, S., Lan, X., Gu, B.,(2016), Experimental study on compression and shear properties of peanut kernel damage (花生仁压缩及剪切特性试验研究), *Journal of Agricultural Mechanization Research*, Vol.37, Issue11, pp.81-84, Ji Lin / P.R.C;
- [13] Zhao, Y., Zhao, Y., Yang, Z., Fang, J., Tang, S., Yang, H., Sun, B., Zhao, W., (2021), Experimental study on the radial and axial shear characteristics of silage corn stalk (青贮玉米秸秆径向和轴向剪切特性试验研究), *Feed Research*, Vol.44, Issue17, pp. 93-96, Yun Nan / P.R.C;

OPTIMIZATION AND EXPERIMENT OF CONVEYING TURNOVER DEVICE BASED ON PEANUT PLANT CHARACTERISTIC PARAMETERS

基于花生植株特性参数的输送翻转装置优化与试验

Jiajun LIU¹⁾, Chenglin JIANG¹⁾, Penghui MAO¹⁾, Kuoyu Wang¹⁾, Shuqi SHANG¹⁾, Dongwei WANG²⁾, Ning ZHANG^{*1)}

¹⁾ College of Mechanical and Electrical Engineering, Qingdao Agricultural University, Qingdao / China

²⁾ Yellow River Delta Intelligent Agricultural Machinery Equipment Industry Academy, Dongying / China

Tel: +86-17860393079; E-mail: 17860393079@163.com

DOI: <https://doi.org/10.35633/inmateh-75-57>

Keywords: Peanut parameters; Peanut flip; Experiment; Simulation

ABSTRACT

Aiming at the problem that there are few studies on the turnover device in the current peanut laying operation equipment and lack of simulation parameters, this study measured the characteristic parameters of upright peanut plants and tested the feasibility of conveying the turnover device to flip the vine. By studying the mechanical properties of peanut plants, the suitable clamping height range of plants was determined. By studying the size, mass parameters and distribution of peanut plants, the possibility of plant flipping and falling was analyzed, and the main structure and working principle of the conveying flipping device were determined. Based on the RECURDYN-EDEM coupling, the joint simulation of the conveying and overturning device was carried out to complete the dynamic analysis of the plant conveying and overturning process, and the simulation parameters were further optimized. The test results show that the device can achieve 95.1 % plant turnover completion and improve the quality of field drying, which can meet the requirements of peanut laying and harvesting operation. It can provide a theoretical basis for the design of two-stage peanut harvesting device in the future.

摘要

针对目前花生铺放作业机具中翻转装置相关研究较少且缺乏仿真参数的问题，本研究对直立型花生植株特性参数进行测定，试验输送翻转装置翻转秧蔓的可行性。通过研究花生植株力学特性，确定植株适宜夹持高度范围；通过研究花生植株的尺寸、质量参数及其分布规律，分析植株翻转掉落的可能性，确定输送翻转装置的主要结构与工作原理。基于 RECURDYN-EDEM 耦合开展输送翻转装置联合仿真，完成植株输送以及翻转过程的动态分析，进一步优化了模拟参数。试验结果表明，该装置可实现植株翻转完成度 95.1%，田间晾晒质量提高，能够满足花生铺放收获作业要求，可为今后两段式花生收获作业装置的设计提供理论依据。

INTRODUCTION

Peanut is the most important oil crop and economic crop in China and even in the world (*China statistical yearbook, 2023*). At present, the mechanized harvesting methods of peanut are mainly divided into combined harvesting and two-stage harvesting (*Gao et al., 2017*). The first section of the two-stage harvest is mostly operated by digging and laying machines. After digging and removing the soil, the plants are laid in the field for drying for 3 to 5 days, and then the second section is collected. However, the field drying after the traditional two-stage harvest will result in a large difference in the moisture content of the upper and lower pods, which will greatly affect the subsequent picking and harvesting operations (*Chen et al., 2017*).

Domestic and foreign scholars have made some progress in the research of two-stage peanut harvester (*Guo et al., 2020*). *Bader et al., (2009)*, analyzed the mass distribution characteristics of peanut plants and the movement characteristics during the inversion of vines, and realized the inversion of the elevated peanut vines on the ground. AMADAS company developed belt and rod conveyor structure, through the combination of large conveyor and vibration table roller, to ensure the quality of the harvest, but for the domestic peanut planting mode and farmers purchasing power it does not match (*Amadas Industries, 2022*). Pearman company has produced a peanut harvester, which uses clamping chain to lift peanut plants to remove soil, and realizes inertial lateral laying by laying guide rods, but it has poor adaptability to peanut planting mode (*Pearman corporation, 2022*).

In recent years, the research progress of two-stage peanut harvesting in China has been rapid. Gao Lianxing *et al.* proposed the 'flip-sliding fence' type laying method and designed the flip laying device of chain-stick peanut picker, which realizes the orderly laying of peanut plants 'head-to-tail' through the flip wheel device and the sliding fence-type plant gathering device. This is conducive to the subsequent operation after drying in the field (Gao *et al.*, 2016). Zheng Jinsong, (2022), developed a peanut digging and inverted laying machine that uses a vibration digging mechanism, soil-conveying system, and turning-laying mechanism to complete the harvesting operation in a single pass. While the machine achieves a high degree of inverted placement, the harvested peanut plants contain more impurities, which can easily cause conveyor belt clogging and consequently reduce harvesting efficiency. Zhou Quan *et al.*, (2022), proposed a shovel-chain low-laying peanut picker and harvester, which employs an extruding and dialing roller at the end of the digging device to lift and transport the peanut plants. Soil is then removed through shaking and vibration, ultimately achieving longitudinal laying with the roots positioned behind the seedlings.

To achieve the placement of peanut pods above the leaves after harvest, Su, (2024), investigated the turning behavior of peanut plants by studying their physical and mechanical properties, combined with conveyor turning device bench tests and discrete element simulation experiments. The objective was to explore the key factors and influencing mechanisms involved in successful peanut plant turning. He *et al.*, (2024), further verified the optimal working performance of the conveyor turning device, aiming to provide a theoretical and technical reference for the development of two-stage peanut harvesting technology and equipment.

MATERIALS AND METHODS

Overall Structure and Parameters of The Test Rig

The overall structure of the conveying and tipping device is shown in Fig.1.



Fig. 1 – 3D Conveying and tipping device test platform model

The conveying and tipping device consists of components such as a rounding wheel, tensioning sprocket, vibrating wheel, guide grid, rounding grid, clamping chain, and others. During the clamping and lifting process, root-soil separation and final throwing of the peanut plants are achieved. The plants are first collected by the guide grid and then gradually lowered and laid down under their own weight as they pass through the collection grid.

Table 1

Main Technical Data	
Parameter	Value
Overall dimensions (length × width × height) (mm)	1940×540×710
Harvest method	Two-part
Horizontal inclination angle of clamping chain (°)	20°
Clamping height (mm)	140~170
Clamping and conveying speed (km·h ⁻¹)	1.4

Experiment Material Selection

The representative peanut variety "Huayu No. 25," commonly grown in Jiaozhou, Shandong Province, was selected as the experimental material. The crop was harvested in September 2024. The collected peanut plants were sealed in bags and brought back to the laboratory to prevent moisture loss. To better simulate the harvesting environment, the local planting pattern was measured, as shown in Fig.2.

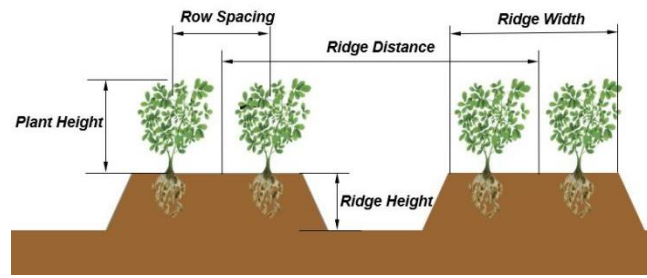


Fig. 2 - Peanut planting pattern diagram

Size parameters and their distribution rules

The three-axis size parameters of peanut plants are necessary for the motion analysis of peanut plants and the establishment of discrete element simulation models of peanut plants. The three-axis dimensions of 50 peanut test samples were measured using a ruler, as shown in Fig. 3, and processed through data analysis software. The results are shown in Table 1.

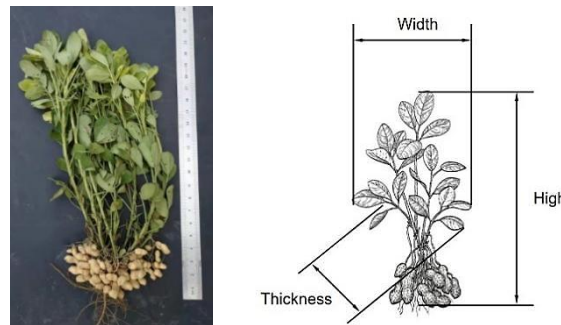


Fig. 3 - Three-axis dimension calibration of peanut plant samples

Table 2

Peanut sample three-axis size data statistics

Name	Average value	Standard deviation	95% confidence interval of mean		Minimum value	Medium number	Maximum value
			Upper limit	Lower limit			
Peanut plant height	464.79	3.15	465.69	463.9	457	463.35	482
Peanut plant width	262.24	9.77	265.02	259.46	232	261	287
Peanut plant thickness	78.92	7.31	81	76.85	65	77.43	96

The normal distribution diagram is obtained based on the measurement results, as shown in Fig.4.

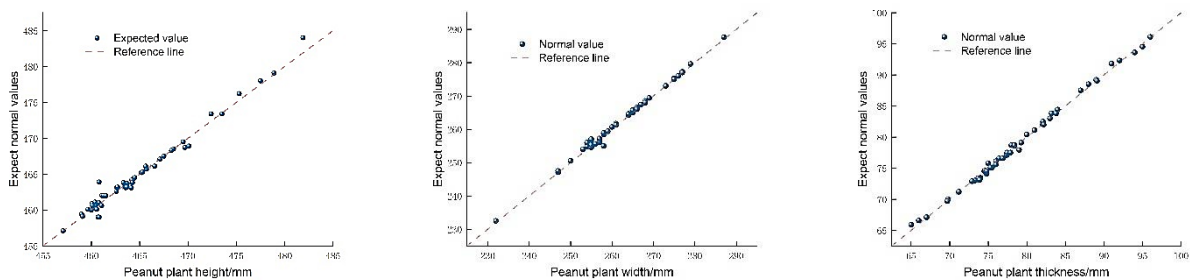


Fig. 4 - Size distribution rules of peanut plant samples

According to the above measurement results and statistical analysis, the height range of peanut plants is between 457 and 482 mm, with an average length of 464.79 mm. According to the statistical results, the standard deviation of the height of peanut plants is 3.15; the width of peanut plants ranges from 261 to 287 mm, with an average width of 262.24 mm. According to the statistics, the standard deviation of the width of peanut plants is 9.77; the thickness range of peanut plants is between 65 and 96 mm, with an average thickness of 78.92 mm. According to the statistics, the standard deviation of peanut plants is 7.31.

Study on the material characteristics of peanut plants

In order to study the flipping rules of peanut plants, it is necessary to analyze and determine the center of mass of peanut plants to provide data reference for the design of the conveying flip device.

Considering that in the actual peanut harvesting process, the peanut stalk, the pod, and the soil carried by the pod are a whole, a holistic study is conducted. In order to determine the position of the center of mass, the entire structure is assumed to be symmetrical, meaning the overall center of mass is located along the central axis of this symmetrical structure. The formula for calculating the centroid of peanut plants at harvest time was obtained, as shown in Figure 5.

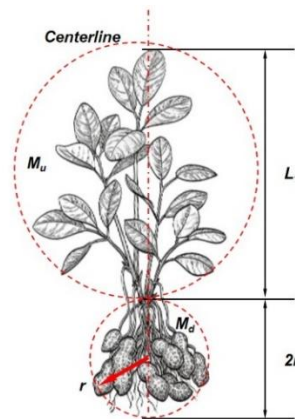


Fig. 5 - Schematic diagram of the overall center of mass of peanut plants

$$\bar{Y} = \frac{\sum M_n \cdot L_n}{\sum M_n} = \frac{M_u \cdot (L_1 + 2r) + M_d \cdot 2r}{M_u + M_d} \tag{1}$$

In the formula, \bar{Y} represents the distance from the root of the seedling to the center of mass along the central axis of the peanut plant during the harvest period. M_u denotes the mass of the above-ground portion, while M_d represents the mass of the underground portion. L_1 is the height of the above-ground part of the peanut plant, and r is the radius of the growth contour of the underground section of the plant.

In order to determine the above-ground part mass, underground part mass, above-ground part height and underground part growth profile radius during the harvest period, the sample needs to be measured multiple times to obtain an average value to explore the mass distribution of the above-ground peanut plants. The test results are shown in the Table 3.

Table 3

Peanut sample three-axis size data statistics

Sample serial number	L ₁ (mm)	M _u (g)	M _d (g)	r(mm)	\bar{Y} (mm)
1	342	335.6	290.1	59	301.43
2	338	340.3	298.4	56	292.09
3	324	320.8	291.5	63	295.75
4	360	352.1	315.6	50	289.83
5	346	327.5	322.7	52	278.28
Mean	342	335.26	303.6	56	291.48

Since the majority of a peanut plant's mass is concentrated in the underground portion, the center of mass is located closer to the rhizome. Based on the data in the table, the center of mass during the harvest period is found to be in the middle to lower part of the plant, near the rhizome. To ensure smooth flipping of the peanut plants when they come into contact with the bar, the seedling clamping height is controlled within the range of 140–180 mm.

Determination of friction coefficient of peanut seedlings

During the simulation analysis of the conveying and flipping motion of peanut plants, the friction coefficient plays a crucial role in determining the interaction between the peanut plants and both the clamping chain and the guide bar. The peanut plant serves as the primary subject of study; therefore, measuring its friction coefficient is of significant importance. (Liu, 2022).

The rolling friction and static friction of peanut seedlings characterize their friction properties when in contact with solid surfaces. In the study, the material in contact with peanut seedlings was Q235 steel. The rolling friction and static friction between the seedling vines and the guide bar were measured.

This test uses the inclined method to measure the friction coefficient of peanut seedlings, and the test diagram is shown in Fig. 6.

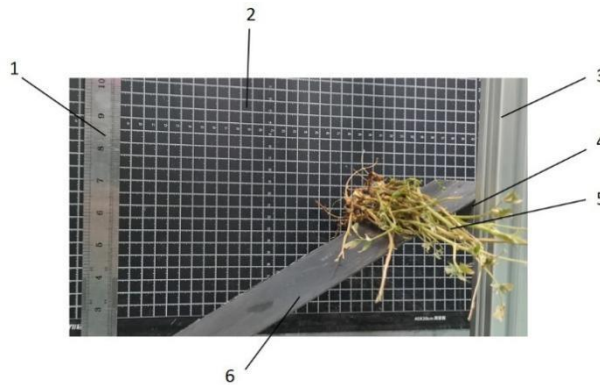


Fig. 6 - Friction coefficient bench test

1. Scale ruler; 2. Square scale board; 3. Bench frame; 4. Lift platform; 5. Peanut seedling sample; 6. Contact material

During the measurement test, the peanut seedlings are subjected to the support force F_1 , the static friction force f and their own gravity G that is obliquely facing the seedlings. When the component force along the inclined direction is greater than the static friction force it is subjected to, the stem slides down along the inclined surface. From this, the static friction factor μ_1 of the seedling and steel material can be obtained:

$$\mu_1 = \frac{f}{F_1} = \frac{G \sin \alpha_1}{G \cos \alpha_1} = \tan \alpha_1 \tag{2}$$

where α_1 is the inclination angle of the test material.

Similarly, when determining the static friction coefficient μ_2 between peanut seedlings, it is only necessary to replace the test material with peanut seedlings. Finally, the static friction coefficient μ_1 between the peanut seedlings and Q235 steel is 0.44, and the static friction coefficient μ_2 between peanut seedlings is 0.32.

Rolling friction coefficient determination

The tool used to measure the rolling friction coefficient of peanut seedlings is the same as that used for measuring static friction. The peanut seedling sample is approximated as a cylindrical object, and it is assumed that the resistance encountered during the rolling process arises solely from rolling friction. During rolling, the rolling friction torque M_1 is proportional to the normal force F_2 exerted on the contact surface. As the inclination angle of the slope gradually increases, the sample begins to roll. When rolling occurs, the stress conditions are illustrated in Fig. 7. The formula for calculating the rolling friction coefficient ε is:

$$\varepsilon = \frac{M_1}{F_2} = \frac{G_1 r_1 \sin \beta}{G_1 \cos \beta} = r_1 \tan \beta \tag{3}$$

where G_1 is the gravity of the peanut seedling sample, β is the angle at which the peanut seedling starts to roll on the contact material, and r_1 is the cross-sectional radius of the peanut seedling cross-section.

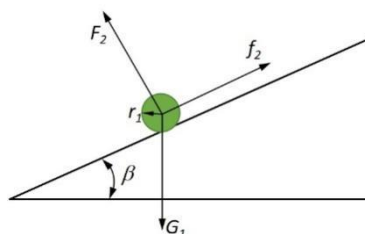


Fig. 7 - Schematic diagram of stress during rolling of seedlings and vines

The seedlings sample was placed on the inclined surface of the contact material of Q235 steel and the peanut seedlings for multiple tests, and the inclined angles β_1 and β_2 of the seedlings rolling were measured and recorded. The rolling friction between the peanut seedlings was calculated. The factor is 0.25, and the rolling friction coefficient between the peanut seedlings and steel is 0.13.

Determination of shear modulus and Poisson's ratio in peanut plants

A compression test was conducted using the XTC-18 Mass Composition Tester to determine the shear modulus and Poisson's ratio of peanut seedling samples. The test setup is shown in Fig. 8. The test parameters were as follows: test distance of 25 mm, loading speed range of 0.001~45 mm/s, test type set to downward pressure, trigger point type set to force, with a trigger point value of 5.000 gf. The target modes included pressure, displacement, and deformation. Prior to testing, the platform holding the sample was height-calibrated. The instrument was set to displacement mode, and the probe was programmed to press downward by a specified distance. After reaching the target value, the probe returned to its original position. The displacement value was set to exceed the height of the sample to ensure complete compression. A total of 30 peanut seedling samples were selected and divided into two groups of 15. One group was used for lateral compression tests, while the other group was used for longitudinal compression tests. Before testing, the transverse and longitudinal dimensions of all samples were measured and recorded.

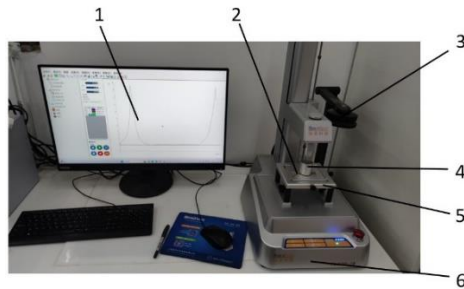


Fig. 8 - Test bench for mechanical properties of peanut seedlings

1. Program interface; 2. Seedling sample; 3. Sensor; 4. Planar probe; 5. Platform; 6. XTC-18 mass composition tester

The elastic modulus and Poisson's ratio calculation formulas of peanut seedling samples are:

$$\begin{cases} G_2 = \frac{E}{2(1 + \mu_3)} \\ \mu_3 = \left| \frac{\Delta \varepsilon_x}{\Delta \varepsilon_y} \right| = \left| \frac{\Delta d_x d_y}{\Delta d_y d_x} \right| \end{cases} \quad (4)$$

where: μ_3 is the Poisson ratio of peanut seedlings sample, G_2 is the shear modulus, ε_y is the longitudinal strain, d_y is the original longitudinal size, Δd_x is the lateral deformation, Δd_y is the longitudinal deformation, ε_x is the lateral strain, d_x is the original transverse size, and E is the elastic modulus.

The calculation method of elastic modulus of peanut seedlings is:

$$E = \frac{\sigma}{\varepsilon_y} \quad (5)$$

where σ is the stress of the peanut seedling sample.

The compression test of peanut seedlings was repeated 15 times, and the results were statistically analyzed and averaged. The shear modulus interval of peanut seedlings was 18.13~18.15 MPa, and the Poisson ratio interval of peanut seedlings was 0.33~0.35.

Dynamic simulation optimization analysis

According to the above analysis, the peanut plants were simulated and a geometric model was established for conveying and flipping device (Zhao et al., 2021). However, the actual structure of the device was relatively complex. In order to save simulation calculation time, components that did not affect the simulation operation results were omitted, as shown in Fig. 9a.

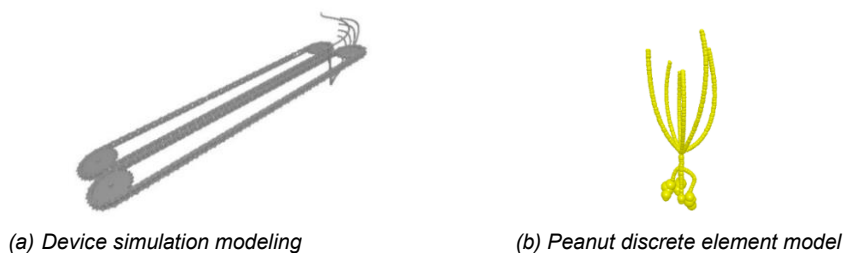


Fig. 9 - Emulation modeling

Through the RECURDYN-EDEM coupling simulation optimization analysis, the specific setting parameters are shown in Table 4. The peanut plant particles were generated in EDEM, and the particles were imported into RECURDYN software to set the position and speed, and then the flip process was simulated and analyzed by the device in RECURDYN. The plant model is shown in Fig. 9b (Zuo *et al.*, 2022).

Table 4

Peanut discrete element modeling simulation parameters					
Maximum feeding amount (kg/s)	Material generation rate (g/s)	Peanut plant height (mm)	Width (mm)	Result depth (mm)	Peanut plant size distribution
4	1.95	460	260	95	0.9 ~ 1.1

The Hertz-Mindlin (non-slip) contact model was adopted in order to study the regularities of peanut plant turnover and drop at the back end of the conveyor turnover device. During this process, peanut plant and peanut plant, peanut plant and clamp chain, peanut plant and guide rod were considered to be non-adhesive. (Hao *et al.*, 2021). The materials and contact mechanical parameters related to peanuts and conveying and flipping devices are shown in Table 5.

Table 5

Simulation material and mechanical parameters		
Item	Parameter	Numerical value
Peanuts	Shear modulus (Pa)	1.8×10^7
	Densities ($\text{kg} \cdot \text{m}^{-3}$)	450
	Poisson's ratio	0.35
Steels	Shear modulus (Pa)	7.9×10^{10}
	Densities ($\text{kg} \cdot \text{m}^{-3}$)	7865
	Poisson's ratio	0.3
Peanuts - Peanuts	Coefficient of restitution	0.5
	Static friction coefficient	0.32
	Rolling friction coefficient	0.25
Peanuts - Steel	Coefficient of restitution	0.42
	Static friction coefficient	0.44
	Rolling friction coefficient	0.13

The movement parameters of the conveying and flipping device include the conveying speed, the gripping height of the seedlings and the impact angle between the seedlings and the bar (Chen *et al.*, 2023). A one-factor test was performed on each motion parameter. The RECURDYN-EDEM coupling simulation process is shown in Fig.10. The impact angle between the seedlings and the bar is 18°, 19°, 20°, 21°, 22°; the conveying speed is 1.2, 1.3, 1.4, 1.5 and 1.6 m/s; the clamping height of the seedlings is 140 mm, 150 mm, and 160 mm , 170 mm and 180 mm.

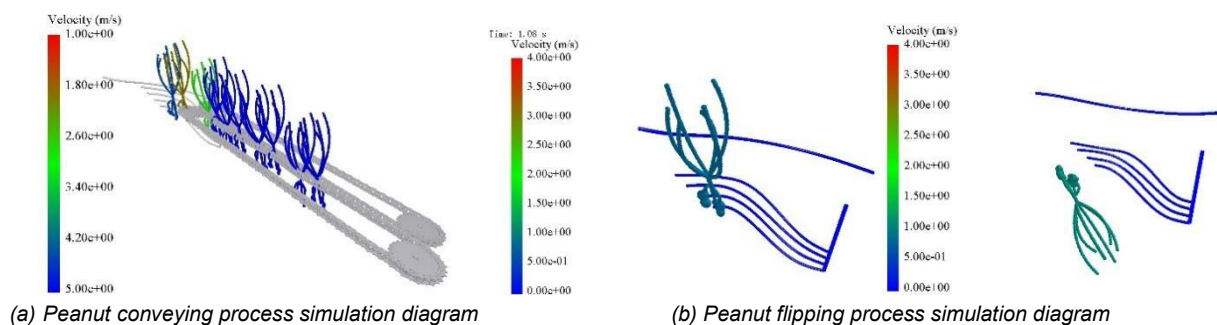


Fig. 10 - Directional turnover peanut harvest device simulation flow chart

Analysis of data results

According to the analysis of simulation process, the gripping height of peanut plant X1, the impact Angle of peanut plant X2 and the conveying speed X3 were tested by experimental factors. The degree of peanut flipping completion Y was used as the evaluation index. A 3-factor, 3-level orthogonal testing method was employed to design the experiments (Xie *et al.*, 2024). The factor coding is shown in Table 6.

Table 6

Test factor coding table			
Encodings	Factor		
	X ₁ (mm)	X ₂ (°)	X ₃ (m·s ⁻¹)
-1	140	18	1.2
0	160	20	1.4
1	180	22	1.6

The test scheme and results are shown in Table 7.

Table 7

Test factor coding table				
Encodings	Factor			Peanut flip completion
	X ₁ (mm)	X ₂ (°)	X ₃ (m·s ⁻¹)	
1	140	18	1.4	93
2	180	18	1.4	91.4
3	140	22	1.4	93.4
4	180	22	1.4	90.2
5	140	20	1.2	91.9
6	180	20	1.2	88.2
7	140	20	1.6	89.1
8	180	20	1.6	88.5
9	160	18	1.2	94.8
10	160	22	1.2	95.2
11	160	18	1.6	94.6
12	160	22	1.6	93.2
13	160	20	1.4	97.4
14	160	20	1.4	97.6
15	160	20	1.4	97.7
16	160	20	1.4	97.1
17	160	20	1.4	97.9

The response surface analysis of the test results was carried out by Design-Expert13.0.1.0 software, and the influence of each test factor on the completion degree of peanut flipping was obtained, as shown in Fig.11. It can be seen that when the clamping height is 156.8 mm, the conveying speed is 1.47 m / s, and the impact angle is 20.24 °, the peanut flipping completion degree is up to 98.1% (Zhang et al., 2024). With the increase of the impact angle between the vine and the grid, the chain clamping peanut vine is more unobstructed, which is convenient for the smooth turnover of the plant. With the increase of vine clamping height, the peanut flip completion degree showed a trend of increasing first and then decreasing, and the influence was the most obvious among the three factors. With the increase of conveying speed, the completion degree of peanut flipping showed a trend of increasing first and then decreasing (Zhang et al., 2022).

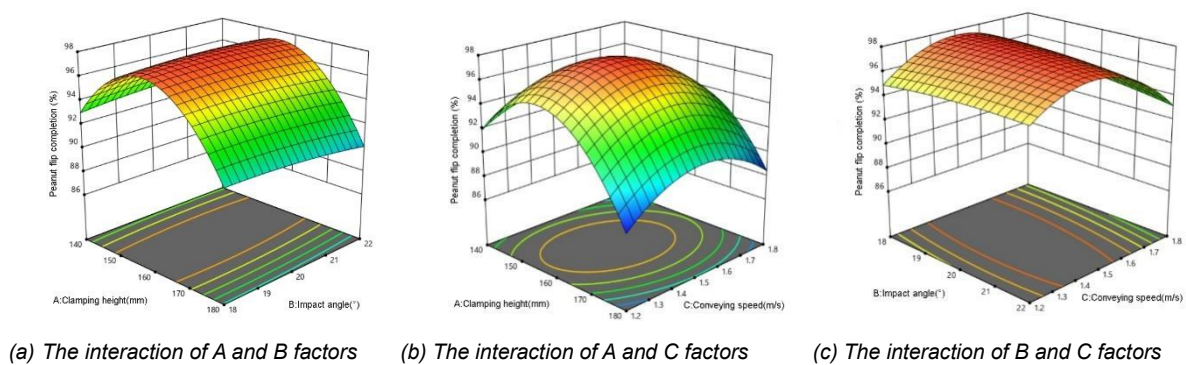


Fig. 11 - Response surface analysis of peanut turnover completion

According to the harvest demand of peanut turnover completion degree and the boundary of test factors, combined with the analysis results of related models, the constraints of the optimal solution are as follows:

$$\begin{cases} \min Y_1(x_1, x_2, x_3) \\ s.t \begin{cases} 140mm \leq x_1 \leq 180mm \\ 1.2m/s \leq x_2 \leq 1.6m/s \\ 18^\circ \leq x_3 \leq 22^\circ \end{cases} \end{cases} \quad (6)$$

Through the optimization scheme, when the clamping height is 160 mm, the clamping and conveying speed is 1.4 m/s, and the impact angle between the vine and the grid is 20°. It is the optimal combination parameter, and the peanut turnover completion degree is 96.1% (Zhang et al., 2022).

RESULTS

Field test of the device

The installation structure diagram of the conveying and flipping device bench is shown in Fig.12a.



Fig. 12 - Directional flipping peanut harvesting device test diagram

The feasibility of bench test design is established. After the data is optimized, it is installed on the whole machine for field testing, as shown in Fig. 12b. According to the theoretical prediction value of each factor and the actual operation situation, the vine clamping height was 160 mm, the conveying speed was 1.4 m/s, and the impact angle was 20°. Under the same test conditions of the quadratic multiple regression analysis test, three repeated tests were performed and the average value was taken. By counting the completion of peanut flipping and analyzing the moisture content of peanut pods in the field after flipping, the feasibility of peanut flipping and whether the quality of drying after flipping was improved were tested (Chen et al., 2024).

Compared with the traditional peanut unidirectional lateral orderly placement machine, it is better to realize the turnover and placement of peanuts on the ground after harvest, allowing for more thorough drying in the field. The higher the degree of peanut turnover, the better the field drying effect, and the lower the moisture content of peanut pods. The peanut flip completion degree and prediction results are basically the same as shown in Table 8, which is more in line with the requirements of two-stage peanut harvest.

Under identical drying conditions, the moisture content of peanut pods from the two different laying methods was compared after three days of drying.

Table 8

Comparison of peanut flipping completion	
Parametric	Peanut flip completion
Projected value	96.1%
Experimental value	95.1%

The peanut moisture content data of the experiment were visualized to form a line chart, as shown in Figure 13.

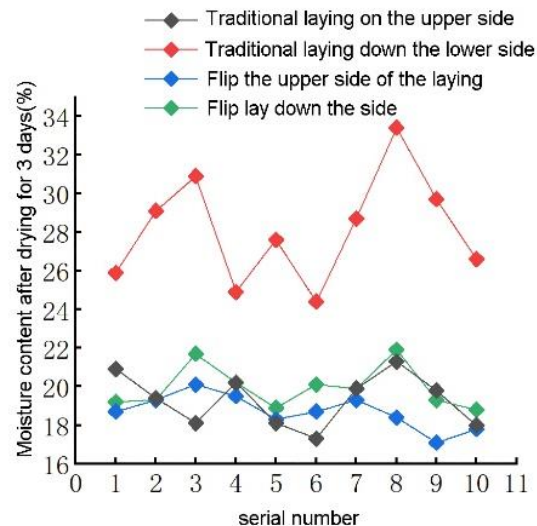


Fig. 13 - Peanut pod moisture content comparison chart

According to the experimental results, the highest value of peanut flip completion is 96.9 %, the lowest value is 92.7 %, and the average value is 95.1%. After 3 days of drying, the highest moisture content of the upper peanut pod was 19.8%, the lowest was 16.7%, and the average was 18.1%. After 3 days of drying, the highest moisture content of the lower peanut pod was 20.9%, the lowest was 18.5% and the average was 19.1%. Compared with the traditional peanut harvester, the harvesting efficiency and the drying quality of peanut in the field were further improved.

CONCLUSIONS

(1) Aiming at the problems of poor field drying quality and long harvest cycle of traditional two-stage peanut after harvest, an optimized laying method was proposed, and a conveying and turning device was designed. Peanut plants were turned down and laid on the ground to improve the quality of field drying.

(2) Through the analysis of the physical and mechanical properties of peanut plants, the feasibility of flipping was assessed. After the measured parameters were brought into the coupling simulation, the mathematical model of the relationship between test factors and indicators was established by Design-Expert software. The response surface method was used to study the law of peanut turnover completion.

(3) The performance of the equipment was tested. Under the optimal parameter combination, the harvest efficiency and harvest quality of the field experiment were tested.

ACKNOWLEDGEMENT

This research is supported by the national Natural Science Foundation of China Youth Science Foundation Project (52405278); Natural Science Foundation of Shandong Province Youth Science Fund Project (ZR2024QE377); funded by the National Key R & D Program (2022YFD2300100).

REFERENCES

- [1] Chen Z., Gao L., Chen Charles & Butts C L. (2017). Analysis of the status quo and development of peanut harvesting mechanization technology in China and the United States. *Journal of Agricultural Machinery*. (04), 1-21.
- [2] Gao L., Chen Z., Charles Chen & C.L. Butts. (2017). The evolution of peanut harvesting mechanization technology in the United States and its enlightenment to China. *Journal of Agricultural Engineering*. (12), 1-9.
- [3] Yu X., Guo H., Guo W., Xue S., Liu H. & Ye X. (2021). Research on tangential flow double drum peanut picking device based on two-stage harvesting. *Agricultural Mechanization Research*. (09), 83-87. doi:10.13427/j.cnki.njji.2021.09.015.
- [4] Bader M.J. (2009). *Peanut digger and combine efficiency*. Sumner P E. University of Georgia.
- [5] Chen, G., Li, F., Qu, F., Zhang, C. (2024) Parameter calibration and experiment of discrete element simulation of spherical-like soybean based on DEM. *INMATEH-Agricultural Engineering*, Vol. 74, No.3.

- [6] Chen T., Yi S., Li Y., Tao G., Qu S. (2023). Establishment of Discrete Element Model and Parameter Calibration of Alfalfa Stem in Budding Stage. *Transactions of the Chinese Society for Agricultural Machinery*, Vol. 54(5), pp. 91-100.
- [7] Gao L., Wang D., Dong H., Kong P., Li H & Liu Z. (2016). The design and test of the turning and laying device of the chain rod peanut harvester. *Journal of Shenyang Agricultural University*. (01), 57 - 63.
- [8] Hao J., Wei W., Huang P., Qin J., Zhao J. (2021). Calibration and experimental verification of discrete element parameters of oil sunflower seeds. *Transactions of the Chinese Society of Agricultural Engineering (Transactions of the CSAE)*, Vol. 37(12), pp. 36-44.
- [9] He X., Peng Q., Li G., Wang X., Zhang C. & Kang J. (2024). Determination of Restitution Coefficient of Peanut Seedling Root-Stem Collision. *Journal of Agricultural Machinery*. (S1), 156-164.
- [10] Liu Q., (2022). *Design and experiment of flexible clamping, conveying and cutting mechanism of Shanghai Green* (Master 's degree thesis), Hunan Agricultural University. <https://link.cnki.net/doi/10.27136/d.cnki.ghunu.2022.001115do>.
- [11] Su L., (2024). Design and test of seedling fruit directional laying peanut excavator (Master 's degree thesis), Henan Agricultural University. <https://link.cnki.net/doi/10.27117/d.cnki.ghenu.2024.000451>. doi:10.27117/d.cnki.ghenu 2024.000451.
- [12] Xie W., Ou Y., Jiang P., Meng D., Luo H. (2024). Calibrating and optimizing the discrete element parameters for clamping section stems during rape shoot harvesting. *Transactions of the Chinese Society of Agricultural Engineering (Transactions of the CSAE)*, Vol. 40(7), pp. 104-116.
- [13] Zhao H., Huang Y., Liu Z., Liu W., Zheng Z. (2021). Applications of discrete element method in the research of agricultural machinery: A review. *Agriculture*, Vol. 11(5), pp. 425.
- [14] Zhang D., Yi S., Zhang J., Bao Y. (2022). Establishment of millet threshing and separating model and optimization of harvester parameters. *Alexandria Engineering Journal*, Vol. 61(12), pp. 11251-11265, DOI: <https://doi.org/10.1016/j.aej.2022.04.048>
- [15] Zhang G., Chen L., Liu H., Dong Z., Zhang Q. (2022). Calibration and experiments of the discrete element simulation parameters for water chestnut. *Transactions of the Chinese Society of Agricultural Engineering (Transactions of the CSAE)*, Vol. 38(11), pp. 41-50.
- [16] Zhang H., Han X., Yang H., Chen X., Zhao G. (2024). Calibrating and simulating contact parameters of the discrete element for apple particles. *Transactions of the Chinese Society of Agricultural Engineering (Transactions of the CSAE)*, Vol. 40(12), pp. 66-76.
- [17] Zheng J., (2022). Design and experiment of peanut digging inverted placement machine based on two-stage harvest. *Research on Agricultural Mechanization*. (10), 133-139. doi:10.13427/j.cnki.njyi.2022.10.020
- [18] Zhou Q., (2022). *Development and transportation performance test of shovel chain type low laying peanut harvester* (Master's degree thesis), Jilin Agricultural University. <https://link.cnki.net/doi/10.27163/d.cnki.gjlnu.2022.000417>doi:10.27163/d.cnki.gjlnu.2022.000417.
- [19] Zuo B., Shang S., He X., Gao Z., Liu W, Zhang C., Ma Z., Wang D. (2022). Research and simulation analysis of peanut combined harvester excavating device. *INMATEH-Agricultural Engineering*, Vol.68, No.3.
- [20] ***Amadas Industries. *Machinery for Agriculture* [EB/OL]. (2021-12) [2022-1-9]. [https:// amadas.com/agriculture/#Peanuts](https://amadas.com/agriculture/#Peanuts).
- [21] ***National Bureau of Statistics of the People's Republic of China. (2023). China statistical yearbook. Beijing: China Statistics Press.
- [22] ***Pearman Corporation. Pearman peanut digger-shaker-inverter [EB/OL].(2013-12)[2022-1-9]. <http://pearmancorp.com>.

MULTIPLE PARAMETER OPTIMIZATION OF A LICORICE HARVESTER BASED ON ENSEMBLE MACHINE LEARNING AND IMPROVED GENETIC ALGORITHM

基于集成机器学习和改进遗传算法实现了甘草收获机的多参数优化

Jinyu SONG, Yonglei LI*, Xiaopei ZHENG, Lipengcheng WAN, Zongtian LIU

China Agricultural University, College of Engineering, Beijing / China

Tel: +86-13811692767; E-mail: liy0393@163.com;

Corresponding author: Yonglei Li

DOI: <https://doi.org/10.35633/inmateh-75-58>

Keywords: coupling simulation, parameter optimization, ensemble machine learning, response surface

ABSTRACT

Optimizing parameters is a crucial step in designing mechanical structures and a primary means of raising equipment efficiency. This paper proposes a multi-parameter optimization technique that combines an improved genetic algorithm (IGA) and ensemble machine learning (EML) to optimize a licorice harvester's work and structure parameters. The EML model is trained using a small sample dataset built on the coupled DEM-MBD (Multi-body Dynamics Coupled Discrete Element Method) simulation model. The impact of base learner diversity and quantity on the model's prediction accuracy is investigated. Using EML and IGA, the parameters of a licorice harvester are optimized. It is also contrasted with conventional response surface model (RSM) parameter optimization techniques. The study results show that the EML with KNN + lightGBM + catBoost as the base learner and linear as the meta-learner has an R^2 of 0.959, MAE of 0.048, and RMSE of 0.06. In comparison to the RSM, EML-IGA reduces resistance by 18.16% and specific power consumption by 21.33%; in comparison to the EML and Pre-improvement genetic algorithm (PIGA), it reduces resistance by 11.36% and specific power consumption by 11.19%. It provides a reference for intelligent parameter optimization methods.

摘要

参数优化是机械结构设计过程中必不可少的环节，也是提高机械工作效率的主要途径之一。本研究通过集成学习与改进遗传算法结合提出一种多参数优化方法对甘草收获机的结构和工作参数进行优化。基于 DEM-MBD 耦合仿真模型构建小样本数据集对集成学习模型进行训练，并探究基学习器的数量与多样性对集成学习模型预测精度的影响。利用集成学习结合改进遗传算法对甘草收获机的多个参数进行优化。并与传统的响应面参数优化方法进行对比。研究表明，以 KNN+lightGBM+catBoost 为基学习器，线性拟合为元学习器的集成学习模型，其 R^2 为 0.959，MAE 为 0.048，RMSE 为 0.06。其相较于改进前的遗传算法的优化结果，阻力降低 11.36%，比功耗降低 11.19%，相较于传统的响应面分析法，阻力降低 18.15%，比功耗降低 21.33%，为智能化参数优化方法提供参考。

INTRODUCTION

The main component of the licorice harvester is the digger device, whose work and structure parameters directly impact the machine's resistance and power consumption. Both domestically and internationally, researchers have conducted a great deal of study on the optimization of the parameters of the harvesting device for deep root crops to address the issues of high digging resistance and high power consumption in deep root crops. Zhang et al., (2024), optimized three working parameters of a residual film recycler using RSM to improve its pick-up rate. Awuah et al., (2022), optimized the parameters of the vibratory digging shovel based on DEM and RSM, significantly reducing the working resistance. The RSM utilized in the previously mentioned parameter optimization techniques is primarily useful for optimization variables fewer than or equal to 4. An excessive number of optimization variables might result in issues such as local optimal solutions and inaccurate fitting. As machine learning advances, more academics are using it to predict regression using multivariate inputs. Huang Lvwen et al, (2023), utilized 40 feature values as inputs into the LSTMED-MLP model to forecast the soluble solids content of apples. Ge et al., (2023), trained eight machine learning algorithms by multiple input features with different importance. It can be seen that machine learning is suitable for the nonlinear fitting of multivariate inputs for prediction.

However, most of the research has generally focused on the predictive performance of individual machine-learning models. Single models' limited adaptability makes them frequently unable to handle complex problems completely (Cao *et al.*, 2024).

On the other hand, by combining the benefits of several models, EML can successfully enhance the generalization performance of prediction models and lower prediction errors. Liu Tan *et al.* (2024), used EML to estimate the photosynthetic rate of greenhouse tomatoes, which increased the prediction's accuracy and stability. Zongquan, (1997), researched the predictive accuracy of Stacking's EML for cracking in reinforced concrete against that of a single machine learning model; it was discovered that the model performed better. Consequently, it is now worthwhile to research how to fully utilize the benefits of a single learner in order to enhance the model's generalization performance and prediction accuracy. Researchers have started combining machine learning and simulation modeling techniques to solve various real-world problems since numerical simulation techniques have become more popular. Yu *et al.*, (2023), trained BP neural networks using datasets obtained from numerical simulations. Liao *et al.*, (2021), combined DEM and deep learning methods to predict particle flow behavior in a wedge-shaped hopper.

An intelligent optimization technique, genetic algorithm (GA), is utilized to find the objective function's optimal solution (Aote *et al.*, 2023). Although it has a straightforward structure, it has limitations on local search capability and population variety. A few academics started enhancing GA. NING Fanghua *et al.* (2024), combined the NEH and random generation to produce high-quality first populations as an alternative to the conventional technique of randomly generating starting populations. Wei *et al.* (2024), introduced simulated annealing algorithm into the genetic algorithm, which improved the local search ability of the traditional genetic algorithm. The crossover and mutation probabilities of GA should be adjusted adaptively; however, this is rarely done by academics. Doing so would increase the genetic algorithm's capacity for global search and speed of convergence.

The EML model is trained using a small dataset built on the coupled DEM-MBD simulation model. The impact of base learner diversity and quantity on the model's prediction accuracy is investigated. EML-IGA was possible to predict licorice harvester performance indicators quickly and accurately. A uniform distribution of the initial population and adaptive adjustment of crossover and mutation probabilities are achieved by improving upon some of the shortcomings of conventional genetic algorithms. Subsequently, the optimization results of the response surface analysis method are compared with the EML - IGA to obtain a method suitable for complex multi-parameter optimization problems. The combination of structural and working parameters was also optimized to achieve the licorice harvester's minimum resistance and power consumption.

MATERIALS AND METHODS

Small sample dataset construction

- Physical structure of the licorice harvester

The structure of the licorice harvester is shown in Fig.1, which is mainly composed of digging device, suspension system, vibration system, excitation device and frame. Fig.2 shows the main structural parameters, digging inclination α , dispersal inclination β , dispersal length L , dispersal spacing D , and working width d . Working speed V , harvesting depth H , vibration frequency f , and crank amplitude A are the primary operating parameters.

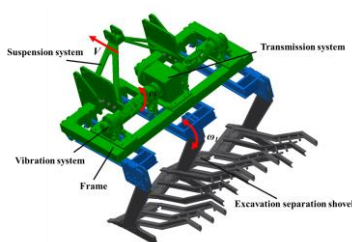


Fig. 1 - Physical structure of the licorice harvester

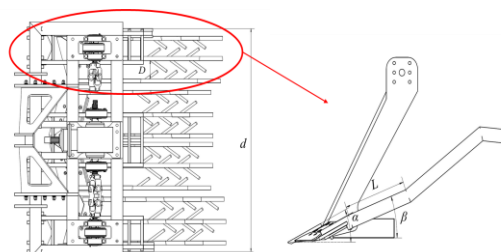


Fig. 2 - Main structural parameters of excavating shovel

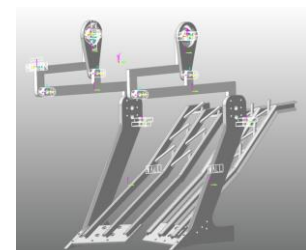


Fig. 3 - Multi-body dynamics simulation model of the licorice harvester

● MBD Simulation Model Building

The licorice harvester is first structurally simplified. Parts of the frame, gearbox, vibration system, etc. that do not affect the simulated motion setup are removed, and only half of the digging shovel structure of the original unit is retained. It accomplishes the objective of reducing the simulation time for model coupling and ensuring that the model moves by the working principle. The working width of the simplified unit is 840 mm. Fig. 3 shows the multi-body dynamics simulation model of the licorice harvester. Import the simplified 3D model into RecurDyn in .sat format and add motion and drives between parts. Two drives in total are added to the model. The first adds a forward drive with the drive function $V*time$ to the frame for linear motion. The other adds a vibration drive to the eccentric block for rotational motion with a drive function of $\frac{f*360}{57.3^\circ} * time$ ($time$ is the total simulation time).

● DEM simulation model construction

The soil's calibration and the soil particle interaction model selection are crucial to producing a DEM model. The soil samples calibrated were brown loam soils in Beijing. The density of the soil was 2130 kg/m^3 , shear modulus 0.96 MPa , Poisson's ratio 0.36 (Song Jiannong et al., 2021). The soil has a sticky texture and a high degree of bonding between soil particles. The Hertz-Mindlin with JKR Cohesion contact model was selected for parameter calibration because it takes the influence of bonding force into account and works well with cohesive soils with high adhesion forces (Junwei et al., 2019). The static repose angle of the soil served as an indicator for calibrating the target soil. The actual soil repose angle test was repeated five times and then averaged to obtain the actual soil repose angle $\theta = 31.42^\circ$. The natural soil static repose angle values were obtained by processing the raw photos of the static repose angle test using PyCharm software, which allowed for determining the soil repose angle. The processing is shown in Fig. 4.

Using soil-soil collision recovery coefficient $X1$, soil-soil static friction factor $X2$, soil-soil rolling friction factor $X3$, and JKR surface energy $X4$ as the test factors and soil repose angle as the test index, Box-Behnken simulation test was conducted to determine soil-soil contact parameters. The DEM model for the calibration test is shown in Fig. 5. The soil particles were defined as spherical, measuring 6 mm in size, and their distribution followed a conventional normal distribution with a 0.05 variance. Table 1 displays the range of JKR surface energies as well as the range of soil-soil contact coefficients needed for calibration, together with the organic glass intrinsic parameters needed for the tests and the soil-organic glass contact coefficients that have been observed in the literature (Fangping et al., 2020). The software Design-Expert 13 carried out the Box-Behnken simulation test program and optimized the results. Optimal parameter combinations of contact parameters are obtained: $X1=0.39$, $X2=0.4$, $X3=0.05$, $X4=7.22$. The combination of contact parameters is effective since the simulated value of the repose angle is 30.64° , and the relative error with the observed value is 2.48% , indicating the relative error is less than 5% . The digging shovel's material is 65Mn , its density is 7865 kg/m^3 , its Poisson's ratio is 0.3 , and its shear modulus is $7.9 \times 10^7 \text{ MPa}$ (Song Jiannong et al., 2021). The contact parameters of soil and digging shovel are as follows: the collision recovery coefficient e is 0.5 , the static friction factor μ_s is 0.3 , and the dynamic friction coefficient μ_r is 0.1 (Zhang et al., 2017).

For the excavation shovel to operate normally, the DEM simulation model needs to be configured as an earth slot since the shovel's real operating environment is a complete field. The length of the soil box was set at 3500 mm , the width at 950 mm , and the height at 800 mm , based on the excavation shovel's working width and speed.

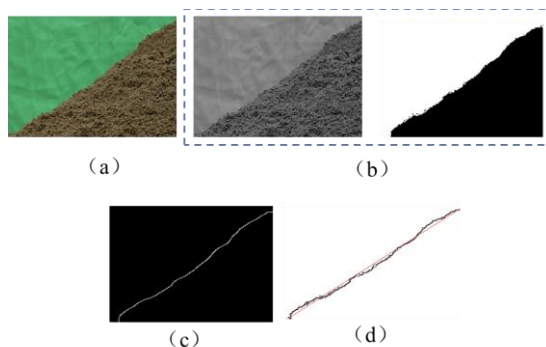


Fig. 4 - The process of soil repose angle processed by Pycharm

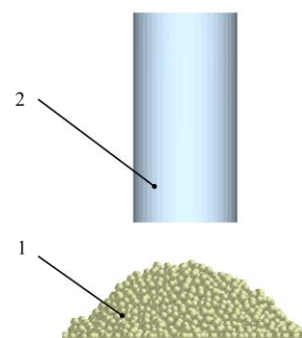


Fig. 5 - DEM model of calibration test

Table 1

Calibration model simulation parameters	
Parameter	Value
Poisson's ratio of soil particles	0.36
Density of soil particles /(kg/m ³)	2130
Shear modulus of soil particles /MPa	0.96
Poisson's ratio of organic glass	0.37
Density of organic glass/(kg/m ³)	2.5×10 ³
Shear modulus of organic glass /MPa	100
Soil-organic glass Recovery coefficient ball and steel	0.3
Soil-organic glass static friction coefficient<	0.41
Soil-organic glass rolling friction coefficient<	0.01
soil-soil collision recovery coefficient	0.35 ~ 0.7
Soil-soil static friction	0.4 ~ 1.1
Soil-soil rolling friction	0.05 ~ 0.25

● Coupled DEM-MBD simulation model of licorice harvester

The two digging shovels from the MBD simulation model are exported in WALL format and then loaded into the EDEM2020 software to establish the model. The time step of the MBD simulation was set to 15 samples per vibration cycle. In summary, the STEP design equation for the MBD model is $f^*15*time$, where time is the overall simulation duration. The DEM's time step is 20%, and the save interval is 0.005 s.

● Design of dataset construction methods

This study proposes using a small sample-based simulation dataset for machine learning training to increase design efficiency. The resistance F_q and the power consumption P_{wk} (power consumption per unit volume of soil handled by the licorice harvester) that the harvester experiences while in operation were utilized as optimization indications. F_q is extracted in the DEM model simulation results.

The driving torque T_q is extracted directly by the result function in RecurDyn. P_{wk} was calculated using Equation (1).

$$P_{Wk} = \frac{\bar{F}_q}{1000DBt} + \frac{\bar{T}_q R}{9550VDBt} \quad (1)$$

where:

\bar{F}_q is the average of resistance in the effective range, N;

\bar{T}_q is the average of driving torque with the value greater than 0, N.m;

R is the crank speed, r/min;

t is the working time, s;

V is the forward speed, m/s;

B is the working width, mm;

D is the digging depth, mm.

However, F_q and P_{wk} are calculated as a combined performance index Z utilizing linear weighting in accordance with the Entropy technique in order to simplify the genetic algorithm optimization. The entropy method is more objective, assigning weights based on sample data sets (de Blas et al., 2021). According to the calculations, the weight of P_{wk} is 0.757, and the weight of F_q is 0.243. The licorice harvester's primary structure and operating parameters have been described above. In this study, the parameters significantly affecting the composite indicator Z were screened by the Plackett-Burman test. Six design factors significantly impacted the composite index Z : vibration frequency f , crank amplitude A , harvesting depth H , operating speed V , digging inclination angle α , and dispersal inclination angle β . To summarize, this study generates a small sample dataset by utilizing the composite index Z as the optimization index and the licorice harvester's six structural and operating characteristics as the optimization variables. The dataset was produced by a 6-factor Box-Behnken test with 54 groups, created with the software Design-Expert 13.

Ensemble Machine Learning Model Building

● Building Methods for Ensemble Machine Learning

Ensemble Machine Learning (EML) is one of the more advanced machine learning paradigms (Ribeiro *et al.*, 2022). The main principle is to use one of the three strategies—Boosting, Bagging, or Stacking—to aggregate the prediction result of several learners (base learners) to achieve more excellent prediction performance than a single learner. Stacking has the flexibility to take full advantage of different base learners, as well as the ability to select meta-learners based on specific problems and samples. Therefore, a stacking integration strategy was selected for this study. There are two layers in the stacking integration model: Level 1, which comprises several base learners, each of which produces individual predictions. The meta-estimator, present in Level 2, used inputs of predictions from several base learners in Level 1 to learn more and generate the final integrated predictions. The base learner selects the eight machine learning models—Random Forest (RF), Decision Tree (DT), K Nearest Neighbors (KNN), Ridge Regression (RR), AdaBoost, lightGBM, catBoost, and XGBboost—that are commonly employed for regression prediction. The meta-learner selects a more straightforward linear regression to avoid overfitting and improve the model's generalization performance.

Evaluation index of Ensemble Machine Learning

The accuracy of the EML model is assessed in this work using three indices: the root mean square error (RMSE), the mean absolute error (MAE), and the coefficient of determination (R^2) (Wu *et al.*, 2022). The model's quality of fit is shown by the R^2 , which has a value range of 0 to 1. The closer the value is to 1, the better the model. The MAE and RMSE values represent the model's prediction error; the lower the number, the smaller the prediction error and the higher the model's fitting accuracy.

Improvement methods for genetic algorithms

● Improvements in initialization of populations

The population of the traditional genetic algorithm is not uniformly distributed and is initialized with a random distribution within the optimization range of the independent variables. This could lead to the algorithm finding a local optimum solution (Qiao *et al.*, 2022). Therefore, rather than using random distribution, Circle Chaotic Mapping is used in this work. Circle mapping can improve the algorithm's capacity for global search and offer a proper exploratory mechanism. The mapping form is indicated in Equation (2).

$$D_{i+1} = \text{mod}(D_i + a - \frac{b}{2\pi} \sin(2\pi D_i), 1) \quad (2)$$

where: D_i denotes the current mapping state value, located in the interval (0,1); D_{i+1} is the next state value. a and b are the control parameters, which usually take the values of $a=0.5$ and $b=0.2$. The mod function guarantees that the mapping's outcome stays inside (0, 1).

● Adaptive improvement for crossover and mutation probability

The Gompertz function is a mathematical model that Gompertz initially proposed. It is typically used to represent a system or process that increases in speed at the rate of the first fast change rule followed by a slow one (Yin *et al.*, 2021). The crossover, mutation probability, and function curve change rules are similar. Consequently, this study refines the Gompertz function to create an adaptive adjustment formula for the crossover and mutation probabilities. The general form of the Gompertz function is shown in Equation (3). An evolutionary coefficient R must be proposed to characterize the population's degree of evolution to satisfy the requirement that the probability of crossover mutation is by the population's degree of evolution. Individual fitness values are small and discrete during the early stages of genetic algorithm population evolution. However, as the population ages and approaches the ideal solution, its fitness values become more concentrated. The notions of expectation and variance are introduced to represent the change in fitness values. The population fitness value increases throughout the evolutionary process while the variance decreases. Therefore, the evolutionary coefficient R expression can be designed as Equation (4). To satisfy the adaptive features, the general form of the Gompertz function was combined with the evolutionary coefficients R to form the crossover and mutation probability adaptive adjustment formulas in Equation (5) and (6), where the a , b , and c coefficients are used to set the range of crossover mutation probability values and their trends.

$$f(x) = ae^{-be^{-cx}} \quad (3)$$

$$R = \frac{EX+1}{\sqrt{DX}} \quad (4)$$

$$f(x) = 0.9e^{-0.05e^{0.4R}} \tag{5}$$

$$f(x) = 0.1e^{-0.05e^{0.8R}} \tag{6}$$

where: x is the independent variable; a , b , c are positive real parameters. a denotes the maximum value; b controls the initial growth rate; and c controls the steepness of the growth curve. P_c is the crossover probability, ranging from (0,0.9); P_m is the variation probability, ranging from (0,0.1); and R is the evolutionary coefficient, ranging from (0, $+\infty$).

Design of multi-parameter optimization methods

Three optimizing strategies will be developed to optimize the licorice harvester's six structures and operating parameters. The first is based on traditional response surface analysis; the second is EML combined with a genetic algorithm for optimization; and the third is EML combined with the improved genetic algorithm for multi-parameter optimization. All three methods are based on the same dataset.

RESULTS

Exploration of the influence of structural working parameters on Z

To guide the actual design and optimization, the impact of operational and structure parameters on the performance indices was examined independently. Fig 6 shows the pattern of influence of single factors on Z. The remaining factors are at intermediate levels when examining the pattern of influence of individual components.

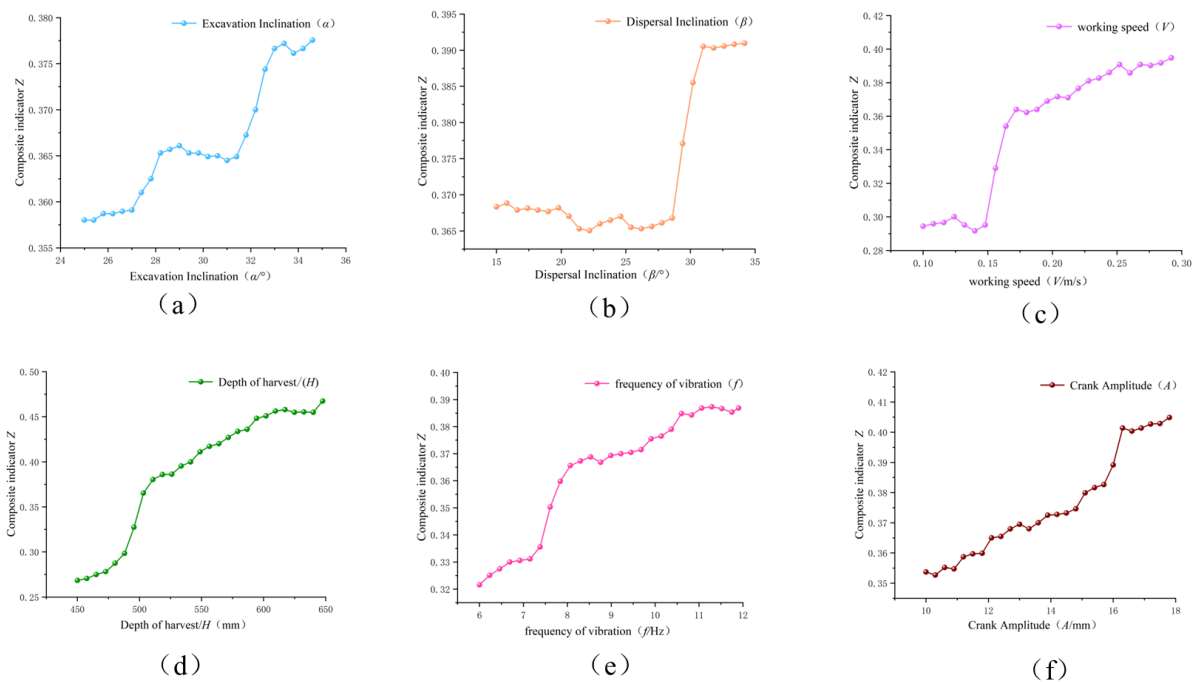


Fig. 6 - Single-factor influence pattern diagram

(a) Laws of influence of α on Z; (b) Laws of influence of β on Z; (c) Laws of influence of V on Z; (d) Laws of influence of H on Z; (e) Laws of influence of f on Z; (f) Laws of influence of A on Z

Fig. 6(a) shows the pattern of excavation inclination angle on Z. As α increases, Z is gradually increasing. However, when α is at $28-31^\circ$, Z is unchanged and tends to decrease slowly. Beyond 32° , Z increases rapidly before stabilizing. Thus, resistance and power consumption might quickly surge when the digging inclination is too high. Fig. 6(b) shows the law of β on Z. Z is nearly constant between 15 and 29° of β ; however, above 29° , Z climbs quickly to a higher level and then stays nearly constant. Consequently, the design of β should be smaller than 29° . Fig. 6(c) is the law of the effect of V on Z. When V exceeds 0.15 m/s, Z climbs quickly before rising slowly. In general, resistance and power consumption rise with V . Consequently, the deep-rooted crop harvester's working speed should be limited to roughly 0.15 m/s. The impact of H on Z is shown in Fig. 6(d). Resistance and power consumption rise with increasing H . 500 mm of H causes a spike in resistance and power consumption.

Therefore, not only will resistance and power consumption increase with increasing H (more than 500 mm), but the operation will also become increasingly challenging. (e) is the law of the effect of f on Z . There is an increase in power consumption with increasing f . Power consumption rises in proportion to the f . There is a spike in power consumption at 7.5 Hz. However, the power consumption is nearly constant and somewhat steady when the frequency is at 8-10 Hz. (f) is the law of A on Z . As the A increases slowly, the power consumption increases slowly.

In conclusion, there is a positive correlation between each factor's laws of impact over resistance and power consumption. It is important to keep each aspect within a narrow range when designing.

Comparative evaluation of different combinatorial basis learners' prediction effects for ensemble machine learning

The choice of base learners is the most crucial step in training ensemble machine learning models. This section investigates how the quantity and kind of base learners affect the model's prediction accuracy. Alternatives for the base learner, RF, DT, KNN, RR, AdaBoost, lightGBM, catBoost, and XGBboost, have been selected. Fig X displays the prediction results received after the model has been trained. As the Fig. 7 illustrates, all five of the prediction models—AdaBoost, lightGBM, catBoost, XGBboost, and RF—have good robustness, with R^2 values over 0.9 and RMSE and MAE errors hovering around 0.08, indicating excellent prediction accuracy. By comparison, R^2 was less than 0.8, and MAE and RMSE errors were more significant than 0.12, indicating lower prediction accuracy for KNN and ridge regression compared to the other models. The more accurate base learners—AdaBoost, lightGBM, catBoost, XGBboost, and RF—are chosen in order to guarantee the predictive capacity of ensemble machine learning. Because unlike the five model-building procedures mentioned above, KNN was also used as the primary learner to ensure the diversity of the underlying learners.

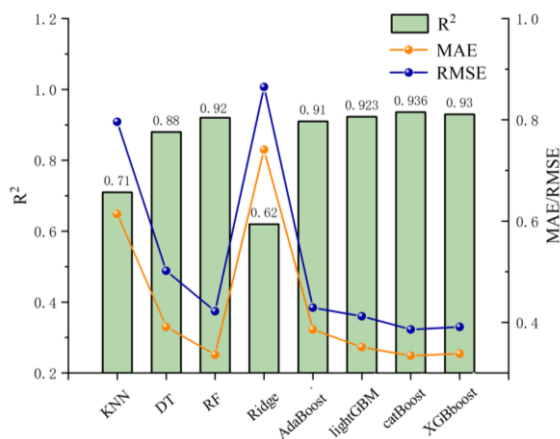


Fig. 7 - Base Learner Prediction Accuracy Graph

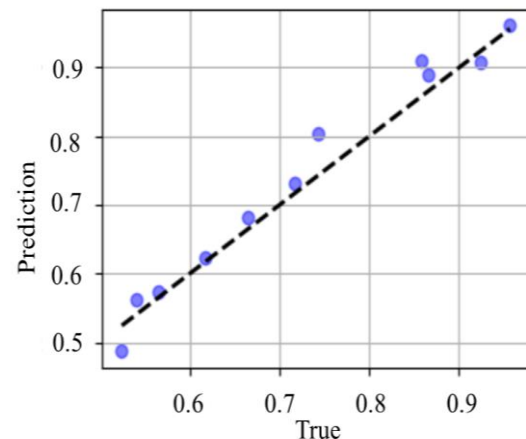


Fig. 8 - Robust graph of prediction accuracy

This study will use two-by-two, three-by-three, four-by-four, five-by-five, and six-by-six combinations to systematically analyze the impact of the set of base learners in different configurations on the model performance in order to investigate the impact of the number and diversity of base learners on the prediction accuracy of the integrated learning model. A linear model is used to fit the meta-learner in order to prevent the ensemble machine learning model from overfitting. Fig.9 displays the prediction accuracy of the ensemble machine learning using various base learner combinations. (a) displays the primary learner's two-by-two combination model's prediction performance. The model with the highest prediction accuracy is model 8-KNN+catBoost. The prediction performance of the three combined basic learner models is displayed in (b). Model 6-KNN+lightGBM+catBoost has the best robustness and lowest error. 0.959 is the R value, 0.048 is the MAE, and 0.06 is the RMSE. The prediction performance of the four combined basic learner models is displayed in (c). Models 4 and 5 both have an R^2 of 0.949, an MAE of 0.05, and an RMSE of 0.066, indicating higher accuracy and fewer prediction mistakes. The prediction performance of the five combined base learner models is displayed in (d). The three models have similar and strong prediction abilities. The error is approximately 0.066, and the R^2 approach is 0.95. The final model is a combination of six, and it has an RMSE of 0.068, an MAE of 0.052, and an R^2 of 0.939.

In conclusion, it was discovered that when the essential learners are merged two by two, the KNN+catBoost model performs best across all combinations. The models with three and four combinations have comparable predictive power, whereas those with six have less predictive power. Also, it was discovered that KNN models were included in the two-by-two model 8-KNN+catBoost, three-by-three model 6-KNN+lightGBM+catBoost, and four-by-four model 4-KNN+AdaBoost+lightGBM+catBoost combinations. Model KNN has the lowest predictive power R^2 , at just 0.71, as the preceding section has shown. This means that in addition to models with high individual predictive ability, models of various types are also needed to select base learners. Ensemble machine learning's prediction accuracy rarely increases appreciably once the base learner count reaches a certain point. Thus, the option of base learners is 2 or 3, given the combination of the arithmetic cost and the need for model prediction accuracy.

Therefore, in this study, ensemble machine learning with KNN+lightGBM+catBoost, which has the best prediction accuracy, as the base learner and linear fitting as the meta-learner was chosen as the prediction model for the performance index of the licorice harvester. As shown in Fig. 8, the prediction robustness plot of this model indicates its strong prediction ability.

Comparative analysis of optimization capabilities of different methods

From the above, the ensemble machine learning model identified in this study has KNN+lightGBM+catBoost as the base learner in the first layer and linear regression as the meta-learner. Pre- and post-improved genetic algorithms will be coupled with the ensemble machine-learning model to optimize the licorice harvester's operating and structure parameters. H was fixed at 600 mm during the optimization process, and the other parameters were optimized. The pre-improved optimization algorithm optimized the parameter combinations as $\alpha=26^\circ, \beta=27^\circ, V=0.1\text{ m/s}, f=6\text{ Hz}, A=11\text{ mm}$. The improved optimization algorithm optimized the parameter combinations as $\alpha=25^\circ, \beta=25^\circ, V=0.1\text{ m/s}, f=6\text{ Hz}, A=11\text{ mm}$. The findings of an ANOVA based on response surface analysis for Z optimization are displayed in Table 2. The response surface model's R^2 of 0.86 is less than the ensemble machine learning model's R^2 of 0.959, even though the response surface model is highly significant ($p < 0.01$) and the misfit term is not significant ($p > 0.05$). The response surface model was optimally solved with the same H of 600 mm. The optimized parameter combinations obtained were $\alpha=27^\circ, \beta=22^\circ, V=0.1\text{ m/s}, f=6\text{ Hz}$, and $A=13\text{ mm}$.

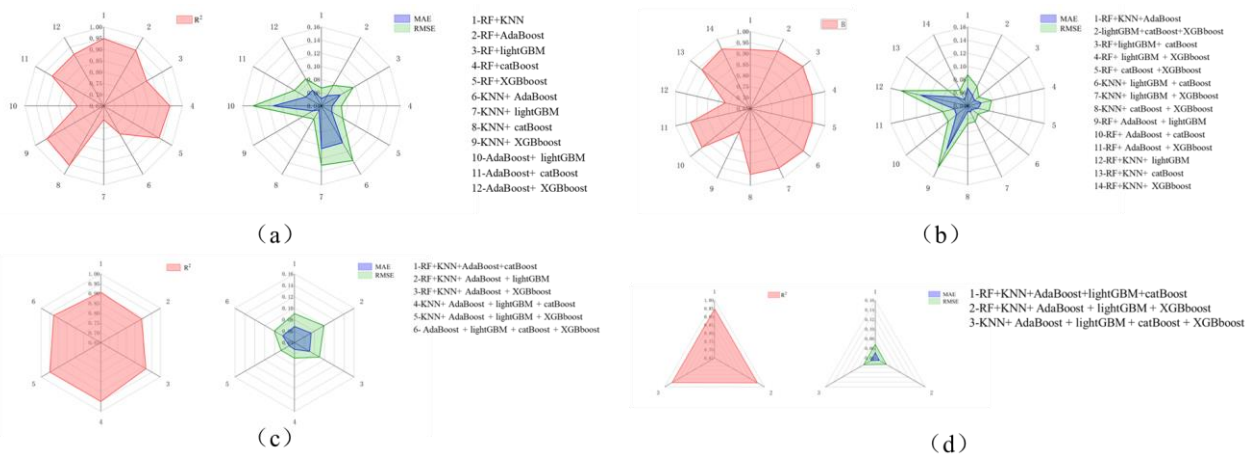


Fig. 9 - Analysis of the prediction accuracy of different combinatorial base learners' graph
 (a) two-by-two; (b) three-by-three; (c) four-by-four; (d) five-by-five

Table2

Response Surface Optimization ANOVA					
Variation source	Sum of squares	Degree of freedom	Mean square	F value	P value
Model	2.47	27	0.09	8.74	< 0.0001**
α	0.09	1	0.09	9.39	0.005**
β	0.05	1	0.05	5.30	0.0296*
V	0.05	1	0.05	5.33	0.0292*
H	0.30	1	0.30	29.25	< 0.0001**
f	0.95	1	0.95	91.07	< 0.0001**
A	0.08	1	0.08	8.23	0.0081**
αβ	0.06	1	0.06	4.45	0.04*

Variation source	Sum of squares	Degree of freedom	Mean square	F value	P value
αf	0.12	1	0.12	8.96	0.004**
V_f	0.12	1	0.12	8.84	0.004**
VA	0.17	1	0.17	12.53	0.001**
β^2	0.06	1	0.06	4.33	0.04*
V^2	0.02	1	0.02	1.69	0.2
f^2	0.1114	1	0.11	8.00	0.007**
Residual	0.5541	40	0.0139		
Lack of fit	0.5533	35	0.0158	20.81	0.15
Pure error	0.0037	5	0.0007		
Total sum	2.74	53			

Table 3 shows the performance results of the licorice harvester optimized by the three methods. The EL-IGA's optimization outcome considerably lowers resistance and power consumption. In comparison to the RSM, it reduces resistance by 18.16% and specific power consumption by 21.33%; in comparison to the EML-PIGA, it reduces resistance by 11.36% and specific power consumption by 11.19%.

In conclusion, RSM is less useful for solving intricate multi-parameter optimization issues, but the study's EML-IGA can efficiently locate the global optimal solution. The low-order data fitting method, which is prone to falling into local optimal solutions due to its inability to capture the complex relationship between the data, limits the RSM when solving most complex multi-parameter optimization issues. However, EML is good at fitting complex nonlinear relationships, providing an accurate, objective function for the ensuing genetic algorithm optimization, overcoming the limitations of traditional RSM methods, and providing high-precision fitting of design variables and performance metrics. Fast convergence in the optimization process is made possible by combining the IGA method, ensuring that the dominating populations down the population iteration are not killed while maintaining population variety.

Table3

Comparative analysis table of optimization results of different methods		
	Resistance /N	Power consumption /KJ
RSM	7411.99	74.4
EML-PIGA	6843.22	65.91
EML-IGA	6065.52	58.53

CONCLUSIONS

This paper uses DEM-MBD coupling simulation, ensemble learning, and an improved genetic algorithm to optimize the licorice harvester's structure and working parameters. It is found that the optimization results of EML-IGA are better than those of traditional RSM, which provides some ideas and methods for multi-parameter optimization.

(1) A coupled DEM-MBD simulation model of the licorice harvester was constructed, which could simulate the actual working condition of the licorice harvester in the soil. The correctness of the simulation model was demonstrated by the DEM model's error of 2.48%, with a relative error of less than 5%, when calibrated using the static soil accumulation angle.

(2) The EML model, trained using a small sample dataset from the simulation model, provides valuable insights into the impact of the quantity and variety of base learners on prediction accuracy. The findings suggest that a diverse range of base learners, in addition to a single model with strong predictive ability, can significantly enhance the predictive capacity of EML.

(3) With a model R^2 of 0.959, an MAE of 0.048, and an RMSE of 0.06, the model has the highest prediction accuracy and accurately represents the mapping relationship between the optimization variables and the optimization metrics when the first layer of the model is KNN + lightGBM + catBoost and the second layer is linear regression.

(4) In comparison to the RSM, EML-IGA reduces resistance by 18.16% and specific power consumption by 21.33%; in comparison to the EML-PIGA, it reduces resistance by 11.36% and specific power consumption by 11.19%. According to the study comparison, EML-IGA is appropriate for solving difficult multi-parameter optimization issues and addresses the shortcomings of RSM.

ACKNOWLEDGEMENT

This work was supported by the National Key Research and Development Program of China(2022YFD2002005).

REFERENCES

- [1] Aote, S. S., Pimpalshende, A., Potnurwar, A., & Lohi, S. (2023). Binary Particle Swarm Optimization with an improved genetic algorithm to solve multi-document text summarization problem of Hindi documents. *Engineering Applications of Artificial Intelligence*, 117. <https://doi.org/10.1016/j.engappai.2022.105575>
- [2] Awuah, E., Zhou, J., Liang, Z., Aikins, K.A., Gbenontin, B.V., Mecha, P., & Makange, N.R. (2022). Parametric analysis and numerical optimisation of Jerusalem artichoke vibrating digging shovel using discrete element method. In *Soil and Tillage Research*. Vol. 219. <https://doi.org/10.1016/j.still.2022.105344>
- [3] Cao, W., Zhang, Z., Fu, Y., Zhao, L., Ren, Y., Nan, T., & Guo, H. (2024). Prediction of arsenic and fluoride in groundwater of the North China Plain using enhanced stacking ensemble learning. *Water Research*, 259 (December 2023). <https://doi.org/10.1016/j.watres.2024.121848>
- [4] de Blas, C. S., Valcarce-Diñeiro, R., Sipols, A. E., Sánchez Martín, N., Arias-Pérez, B., & Santos-Martín, M. T. (2021). Prediction of crop biophysical variables with panel data techniques and radar remote sensing imagery. *Biosystems Engineering*, 205, 76–92. <https://doi.org/10.1016/j.biosystemseng.2021.02.014>
- [5] Fangping, X., Zhengyang, W., & Xiushan, W. (2020). Calibration of discrete element parameters of soils based on unconfined compressive strength test (基于无侧限抗压强度试验的土壤离散元参数标定) *Transactions of the Chinese Society of Agricultural Engineering*, 39-47.
- [6] Ge, J., Lei, G., Chen, H., Zhang, B., Chen, L., Bai, M., Su, N., & Yu, Z. (2023). Irrigation district channel dispatch flow prediction based on SHAP importance ranking and machine learning algorithm. *Nongye Gongcheng Xuebao/Transactions of the Chinese Society of Agricultural Engineering*, 39(13), 113–122. <https://doi.org/10.11975/j.issn.1002-6819.202304081>
- [7] Huang Lvwen, Tian Xu. (2023). Prediction of the soluble solid contents for apple fruit using electrical parameters [J]. *Transactions of the Chinese Society of Agricultural Engineering*.(基于电学参数的苹果可溶性固形物含量预测) *Transactions of the Chinese Society of Agricultural Engineering*, 252–259.
- [8] Junwei, L., Jin, T., Bin, H., Hubiao, W., & Chunyu, M. (2019). Calibration of parameters of interaction between clayey black soil with different moisture content and soil-engaging component in northeast China. *Transactions of the Chinese Society of Agricultural Engineering*, 14–15.
- [9] Liao, Z., Yang, Y., Sun, C., Wu, R., Duan, Z., Wang, Y., Li, X., & Xu, J. (2021). Image-based prediction of granular flow behaviors in a wedge-shaped hopper by combing DEM and deep learning methods. *Powder Technology*, 383, 159–166. <https://doi.org/10.1016/j.powtec.2021.01.041>
- [10] liu Tan, Zhu Hongrui, Y.Q. (2024). Prediction of Photosynthetic Rate of GreenhouseMulti-model Fusion Strategy Tomatoes Based on.(基于多模型融合策略的温室番茄光合速率预测方法) *Transactions of the Chinese Societyfor Agricultural Machinery*, 337-345.
- [11] Ning Fanghua, Huang Bingqi, Z. X. (2024). Hybrid Flow Shop Batch Scheduling Problem Solving Based on ImprovedGenetic Algorithm. *Software Guide*, 23(2).
- [12] Qiao, Y., Wu, N. Q., He, Y. F., Li, Z. W., & Chen, T. (2022). Adaptive genetic algorithm for two-stage hybrid flow-shop scheduling with sequence-independent setup time and no-interruption requirement. *Expert Systems with Applications*, 208(July). <https://doi.org/10.1016/j.eswa.2022.118068>
- [13] Ribeiro, M. H. D. M., da Silva, R. G., Moreno, S. R., Mariani, V. C., & Coelho, L. dos S. (2022). Efficient bootstrap stacking ensemble learning model applied to wind power generation forecasting. *International Journal of Electrical Power and Energy Systems*, 136(October 2021), 107712. <https://doi.org/10.1016/j.ijepes.2021.107712>
- [14] Song Jiannong, W. J., & Wan Lipengcheng, LI Yonglei, Su Chen. (2021). Simulation of soil tillage characteristics and influence analysis ofparticle sphere type based on EEPA contact model.(基于EEPA接触模型的土壤耕作特性模拟及颗粒球型影响分析) *Journal of China Agricultural University*, 193-206.

- [15] Wei, LIXinyu, W. K. (2024). Genetic simulated annealing algorithm for resource - constrained human - robot collaborative assembly line balancing problem. *Computer Integrated Manufacturing Systems*. <https://doi.org/10.13196/j.cims.2024.0192>
- [16] Wu, B., Xu, S., Meng, G., & Cui, Y. (2022). Research on structural parameter optimization of elliptical bipolar linear shaped charge based on machine learning. *Heliyon*, 8(10). <https://doi.org/10.1016/j.heliyon.2022.e10992>
- [17] Yin, F., Dong, H., Zhang, W., Wang, S., Shang, B., & Zhu, Z. (2021). Ability of anaerobic digestion to remove antibiotics contained in swine manure. *Biosystems Engineering*, 212, 175–184. <https://doi.org/10.1016/j.biosystemseng.2021.10.011>
- [18] Yu, Y., Yan, H., & Ye, C. (2023). Parameter optimization of rectification sill in the forebay of pumping station using BPNN-GA algorithm. (基于BPNN-GA的泵站前池整流底坎参数优化) *Nongye Gongcheng Xuebao/Transactions of the Chinese Society of Agricultural Engineering*, 39(14), 106–113. <https://doi.org/10.11975/j.issn.1002-6819.202303168>
- [19] Zhang, R., Han, D., Ji, Q., He, Y., & Li, J. (2017). Calibration Methods of Sandy Soil Parameters in Simulation of Discrete Element Methodn(离散元模拟中沙土参数标定方法研究) *Nongye Jixie Xuebao/Transactions of the Chinese Society for Agricultural Machinery*, 48(3), 49–56. <https://doi.org/10.6041/j.issn.1000-1298.2017.03.006>
- [20] Zhang, X., Kang, M., Shi, Z., Yan, J., Liu, X., Guo, L., & Wang, M. (2024). Design and experiments of a double drum surface residual film recycling machine after harvest. *Nongye Gongcheng Xuebao/Transactions of the Chinese Society of Agricultural Engineering*, 40(14), 1–13. <https://doi.org/10.11975/j.issn.1002-6819.202401037>
- [21] Zongquan, L. Z. (1997). Prediction Method for Reinforced Concrete Corrosion-induced Crack Based on Stacking Integrated Model Fusion. *Journal of Chinese Society for Corrosion and Protection*.

MILLET EAR DETECTION METHOD IN UAV IMAGES BASED ON IMPROVED YOLOX

/ 基于改进 YOLOX 的无人机图像谷穗检测方法

Fuming MA¹⁾, Shaonian LI^{*1)}, Juxia LI²⁾, Yanwen LI²⁾, Lei DUAN²⁾, Linwei LI²⁾, Jing TAN¹⁾, Yifan WANG¹⁾¹⁾ College of Energy and Power Engineering, Lanzhou University of Technology, Lanzhou, Gansu/ China²⁾ College of Information Science and Engineering, Shanxi Agricultural University, Jinzhong, Shanxi/ China

Tel: 0931-2973750; E-mail: Lsn19@163.com

Corresponding author: Shaonian Li

DOI: <https://doi.org/10.35633/inmateh-75-59>**Keywords:** YOLOX; CBAM; EIoU; millet ear detection; UAV; deep learning**ABSTRACT**

Rapid and accurate detection of millet ears is essential for yield estimation and phenotypic studies. However, traditional detection methods primarily rely on manual observation, which are both subjective and labor-intensive. To address this issue, this study employed Unmanned Aerial Vehicle (UAV) for image data collection of millet ears and proposed the YOLOX-CBAM-EIoU model to facilitate real-time detection, focusing on challenges such as small millet ears size, dense distribution, and severe occlusion in the dataset. Firstly, the Mosaic data augmentation technique was employed to enhance the diversity of the dataset. Subsequently, the CBAM attention mechanism was incorporated between the Neck and Prediction layers of YOLOX, enabling the reallocation of channel weights to enhance the extraction of fine-grained features and deeper semantic information. Additionally, EIoU Loss was utilized as the loss function for bounding box regression to mitigate missed detections in dense scenes. The improved model achieved an average precision (AP) of 90.30%, a 6.44 percentage point increase over the original YOLOX model, significantly enhancing detection performance for densely distributed millet ears. The improved model also demonstrated a Precision of 91.01%, Recall of 89.45%, and F1-score of 90.22, highlighting strong robustness and generalization capabilities. These findings substantiate the efficacy of the YOLOX-CBAM-EIoU model in improving detection performance under dense distribution and occlusion conditions, providing valuable technical reference for further UAV-based analyses of millet ears phenotypes and yield predictions.

摘要

小米穗的快速准确检测对于产量估计和表型研究至关重要。然而，传统的谷穗检测主要依靠人工观察，不仅主观性强且耗时耗力。为此，本研究通过无人机进行谷穗图像数据采集，主要针对数据集中谷穗体积小、分布密集、遮挡严重等问题提出了 YOLOX-CBAM-EIoU 模型对谷穗进行实时检测。该模型首先在 YOLOX 的颈部层和预测层之间引入了 CBAM 注意力模块，通过重新分配不同通道的权重，获得了更浅层的细粒度特征和更深层的语义信息，以提高对谷穗表型的特征提取能力；其次，采用 EIoU 函数作为回归损失函数，以改善密集场景下谷穗目标的漏检问题。结果表明，改进后的模型检测平均精度 (AP) 达到 90.30%，与原 YOLOX 模型相比提高了 6.44 个百分点，显著提高了密集分布的谷穗目标检测性能。改进后模型的精确率达到 91.01%，召回率达到 89.45%，F1 分数达到 90.22，表现出较强的鲁棒性和泛化能力。结果充分证明了 YOLOX-CBAM-EIoU 模型能显著提高谷穗在密集分布及遮挡条件下的检测效果，为进一步使用无人机分析谷穗表型和产量预测提供了技术参考。

INTRODUCTION

Millets are highly drought-resistant and can thrive in poor soils, making it an important coarse grain crop globally. China's millet planting area accounts for about 80% of the world, and its production accounts for about 90% of the world's total output (Li et al., 2021). Millet ears are crucial agronomic indicators for assessing yield and quality, playing a key role in breeding, nutritional diagnosis, and growth period monitoring. Therefore, research and management of millet ears could improve millets yield and quality, providing scientific basis for agricultural production.

¹⁾ Fumin Ma, M.S. Stud. Eng.; Shaonian Li, Prof. Ph.D. Eng.; Juxia Li, Prof. Ph.D. Eng.; Yanwen Li, Lecturer M.S. Eng.; Lei Duan, M.S. Stud. Eng.; Linwei Li, Lecturer M.S. Eng.; Jing Tan, M.S. Stud. Eng.; Yifan Wang, B.S. Stud. Eng.

The traditional method for detecting millet ears primarily relies on manual observation, which is labor-intensive, subjective and inefficient. In recent years, with the advancement of computer technology, the integration of computer vision technology with agricultural production has deepened, demonstrating significant application potential in the field of crop detection. *Zhao et al., (2014)*, proposed a method for wheat ear detection that integrated color information with the AdaBoost algorithm, achieving automated recognition and counting of wheat ears. *Liu et al., (2014)*, proposed a wheat ear counting method based on image analysis technology. By integrating color and texture features for image segmentation, the method achieved counting accuracies of 95.77% and 96.89% under broadcast and row-seeding conditions, respectively. *Li, (2016)* applied binarization and morphological processing to raw wheat images, incorporating the Harris corner detection algorithm to extract the wheat ear skeleton. This method effectively enabled the automatic assessment of wheat ear density per unit area. *Li et al., (2018)*, converted RGB images of wheat ears to binary images through color space transformation. They then applied boundary and regional feature parameters to identify fused regions. Subsequently, a line-matching technique based on concavity point detection was employed to segment these fused regions, enabling accurate quantification of the wheat ears. *Meng et al., (2019)*, utilized the improved K-means algorithm to cluster wheat texture features and achieve the recognition of wheat ears. When the traditional image processing methods shown above were used for target detection of cereal crops, it was found that the traditional methods had strong dependence on texture and color, making them highly susceptible to variations in background, lighting, and foliage. Additionally, these methods often required manual adjustment of feature thresholds, which could introduce subjective bias and lead to poor generalization across diverse environments and conditions.

Given the limitations of traditional machine learning technology, crop object detection methods based on deep learning technology have gradually emerged as the mainstream solution. Current research primarily concentrates on the application of deep learning to wheat, rice, and other crops, focusing on improving the accuracy and efficiency of detection models (*Yang et al., 2022; Huang et al., 2022; Liu et al., 2023; Xiong, 2018; Yang et al., 2021*). *Duan et al., (2018)*, proposed a rice panicle segmentation network model based on SegNet, which effectively addressed the challenges to segmentation accuracy posed by the irregular panicle edges, substantial variations in appearance across different rice varieties and growth stages, and occlusions. *Zhang et al.* proposed a convolutional neural network model for the identification of winter wheat ear. By incorporating non-maximum suppression technology, this model achieved the rapid and accurate detection of wheat ear in field conditions (*Zhang et al., 2019*). *Bao et al.* proposed a wheat ear recognition model based on convolutional neural network. This model incorporated an image pyramid to construct multi-scale sliding windows and utilized non-maximum suppression techniques to eliminate overlapping bounding boxes, ultimately achieving efficient counting of wheat ears (*Bao et al., 2019*). *Zhang et al., (2021)*, proposed an improved wheat ear detection method based on the feature pyramid network, which weighed the underlying high-resolution feature map to enhance the useful information channel. *Zhang et al., (2021)*, proposed a rice panicle detection model based on Faster R-CNN, which enhanced the model's performance in detecting small objects by incorporating dilated convolution. In 2023, *Bao et al.* proposed a wheat ear detection model based on TPH-YOLO, which effectively localized the wheat ear in high-density environments (*Bao et al., 2023*). In the same year, *Cai et al. (2023)*, made adaptive improvements to the YOLOv5l model to enable precise detection of rice panicles in field environments. By incorporating the Efficient Channel Attention mechanism before the spatial pyramid pooling layer of the original YOLOv5l model, this study effectively enhanced the model's accuracy and speed in detecting small targets. *Cai et al., (2023)*, proposed a method to reduce the training data for sorghum panicle detection through semi-supervised learning. The results indicated that this approach achieved performance comparable to supervised methods while using only 10% of the original training data.

However, the application of deep learning techniques in crop detection has primarily focused on wheat, rice, and other crops, while research on millet ear detection remained limited. On the other hand, the small size, dense distribution, and frequent occlusions of millet ears in field environments present significant challenges to accurate detection. To address these issues, this study employed UAV to capture images of millet ears in field environments and constructed a dataset of millet ears. Additionally, a millet ear detection model based on YOLOX was proposed. Specifically, (1) the CBAM attention mechanism was introduced to improve the YOLOX model's ability to extract detailed features of millet ears; (2) the original IoU loss function was replaced with the EIoU loss function, further improving the model's performance in detecting small, densely distributed millet ear targets.

MATERIALS AND METHODS

Data acquisition and processing

Data acquisition

The millet images used in this study were acquired from an experimental field located on the southern side of Shanxi Agricultural University, Jinzhong City, Shanxi Province (37°42'45" N, 112° 59' 27" E). The millet cultivar employed was Jingu21. Data collection was conducted between July and August 2022, during the heading stage of the millet. A DJI MAVIC AIR 2 portable UAV, equipped with a 48-megapixel visible light camera, was utilized for image acquisition. The camera was oriented vertically, at a 90° angle to the ground. The UAV was flown at an altitude of 3 m and a speed of 5 m/s during the image capture process. Representative images of the millet are presented in Fig. 1.



Fig. 1 - Images collected by UAV

Data Preconditioning

To ensure the high quality of the dataset, video footage was recorded under optimal conditions, specifically during clear weather and adequate lighting, between 9:30 AM and 10:30 AM. The raw videos were processed through frame extraction, with the elimination of images that were either highly similar or blurry, which culminated in the selection of 117 images, each with dimensions of 3840 pixels by 2160 pixels. However, the pixel proportion occupied by millet ears in these original images was found to be insufficient, presenting challenges for effective model training. Additionally, processing the original images at this resolution resulted in excessively long times. To address these concerns, each original image was subdivided into six smaller images using a 3×2 grid, yielding a total of 702 images, each with a resolution of 1280 pixels by 1080 pixels. An illustration of this image segmentation process is provided in Fig. 2.

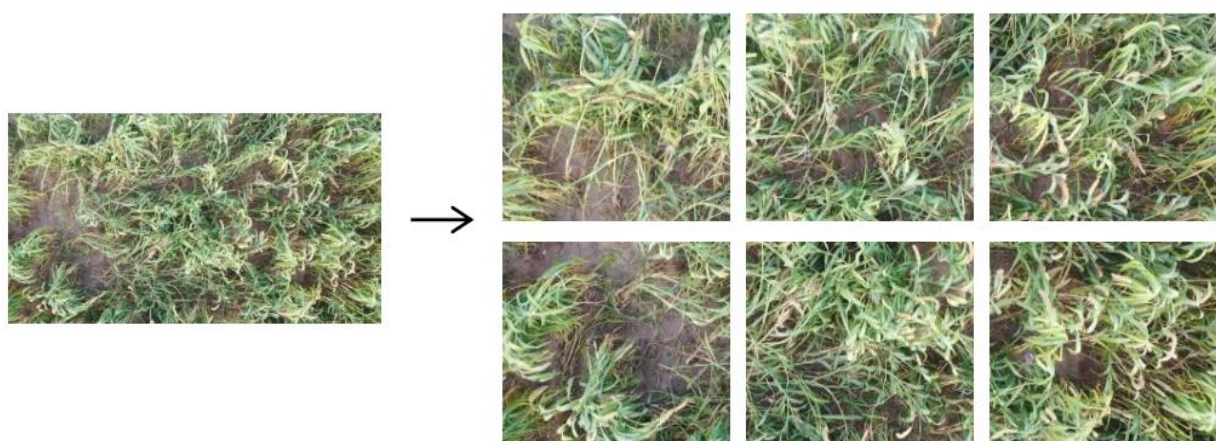


Fig. 2 - Image cutting example diagram

The millet ears in the images were annotated using Labeling software, and the annotation result is shown in Fig. 3.

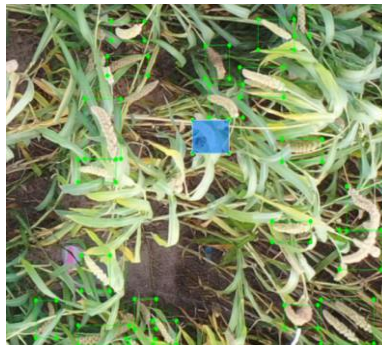


Fig. 3 - Data annotation results

In this study, the Mosaic data augmentation technique was employed to enhance the diversity of the dataset. The Mosaic data augmentation method involved a series of operations, including random scaling, rotation, and stitching. The newly generated image was created by stitching four original images after applying the transformations, as illustrated in Fig. 4. A total of 2,106 images of millet ears were obtained and divided into training, validation, and test sets in an 8:1:1 ratio.



Fig. 4 - Mosaic data enhancement

Algorithm introduction

YOLOX-CBAM-EIoU network architecture

In this study, an improved model named YOLOX-CBAM-EIoU was proposed for millet ear detection. Firstly, a Convolutional Block Attention Module (CBAM) was integrated between the Neck and Prediction layers of the YOLOX model. Secondly, the EIoU function was introduced as the model's loss function. These modifications were found to effectively improve the stability of the bounding box regression and mitigate the scattering of IoU loss during training, thereby improving the overall detection performance. The network architecture of the improved model is illustrated in Fig. 5.

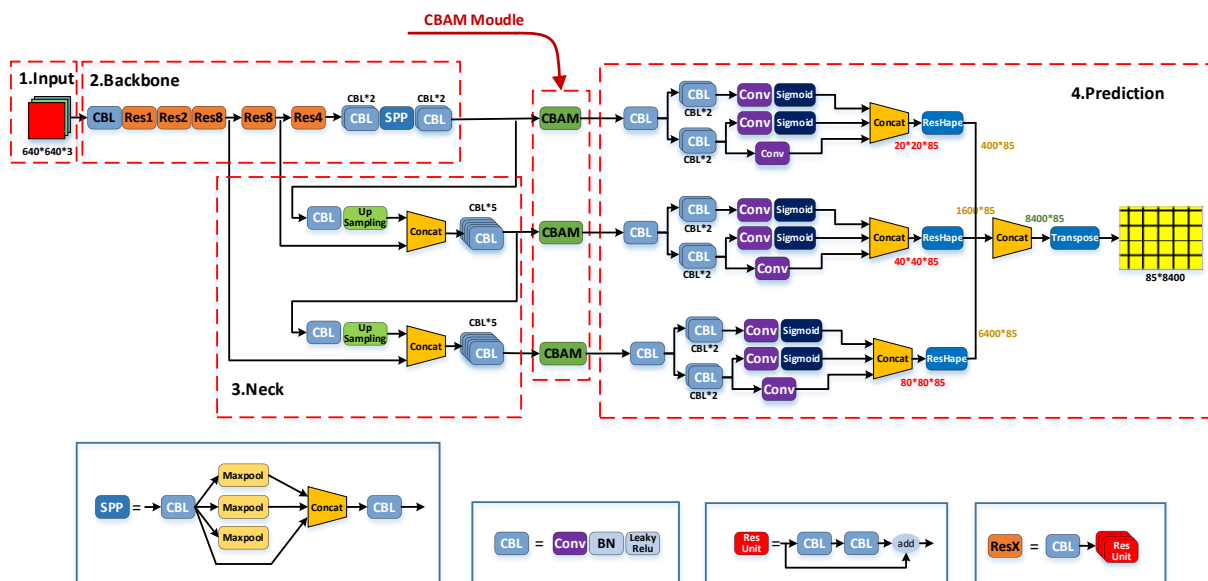


Fig. 5 - YOLOX-CBAM-EIoU network architecture

YOLOX network architecture

The YOLOX network architecture is mainly composed of four parts: the Input, the Backbone, the Neck, and the Prediction (Ge et al., 2021). In the Input stage, the image undergoes scaling, enhancement, and normalization processes to prepare it for further analysis. The Backbone utilizes CSPDarknet53 (Cross-Stage Partial Darknet53) for feature extraction, incorporating Spatial Pyramid Pooling (SPP) to effectively capture multi-scale feature information. The Neck component incorporates the Path Aggregation Network (PANet) structure, which enhances the generation of high-quality feature maps crucial for subsequent prediction tasks. In the Prediction stage, the network comprises three decoupled heads, each characterized by a unique configuration of convolutional layers and activation functions. This architecture provides a robust and efficient solution for object detection and localization across diverse scales and contexts.

CBAM attention mechanism

The CBAM is composed of a Channel Attention Module (CAM) and a Spatial Attention Module (SAM) (Woo et al., 2018). As illustrated in Fig. 6, the architecture of CBAM integrates two modules to enhance the network's representational power. Traditional convolutional neural network-based attention mechanisms primarily focus on channel-wise interactions, concentrating on the analysis of channel dimensions. In contrast, CBAM incorporates attention mechanisms in both channel and spatial dimensions, thus implementing a sequential attention structure that progresses from channel to spatial dimensions. The spatial attention mechanism enables the network to concentrate on pixel regions critical for image classification while disregarding less important areas. Simultaneously, the channel attention mechanism manages the distribution of channels within the feature maps. The synergistic combination of these two attention dimensions significantly improves the model's performance.

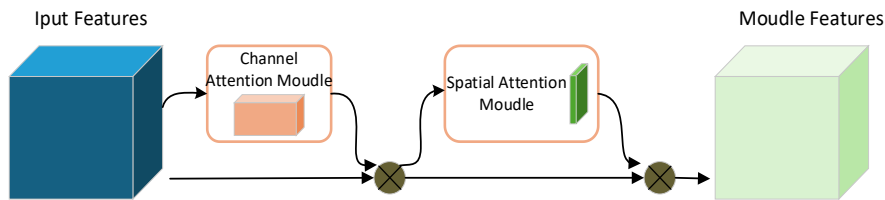


Fig. 6 - Structure of CBAM attention mechanism

EIoU loss function

In this study, the EIoU loss function (Zhang et al., 2022) was employed to replace the original IoU loss function in the YOLOX model. The definition of EIoU loss is shown in Equation (1):

$$L_{EIoU} = L_{IoU} + L_{dis} + L_{asp} = 1 - IoU + \frac{\rho^2(\mathbf{b}, \mathbf{b}^{gt})^2}{(w^c)^2 + (h^c)^2} + \frac{\rho^2(w, w^{gt})^2}{(w^c)^2} + \frac{\rho(h, h^{gt})}{(h^c)^2} \tag{1}$$

where:

\mathbf{b} and \mathbf{b}^{gt} denote the central points of anchor box and target box; $\rho^2(\cdot) = \|\mathbf{b} - \mathbf{b}^{gt}\|$ indicates the Euclidean distance; w and w^{gt} denote the weight of anchor box and target box; h and h^{gt} denote the height of anchor box and target box; w^c and h^c are the width and height of the smallest enclosing box covering the two boxes.

Evaluation indicators

In this study, the evaluation indicators for the model included Precision (P), Recall (R), F1-score, and Average Precision (AP). The formulas for these metrics are as follows:

$$P = \frac{TP}{TP + FP} \tag{2}$$

$$R = \frac{TP}{TP + FN} \tag{3}$$

$$F1 = 2 \times \frac{P \times R}{P + R} \tag{4}$$

$$AP = \int_0^1 P(R) dR \tag{5}$$

where:

P denotes accuracy; R denotes recall; FI denotes FI -score; AP denotes average precision; TP indicates the number of instances where the model correctly identifies the grain bounding box, matching the actual category label; FP denotes the number of instances where the model incorrectly identifies the grain bounding box, resulting in a mismatch with the actual category label; FN represents the instances where the model fails to detect any millet ears.

Parameter settings

The experimental equipment and configuration are shown in Table 1.

Table 1

Experimental Configuration	
Parameter	Configuration
Operating System	Windows 10
CPU	11th Gen Intel(R) Core (TM) i7-11800 H
GPU	RTX 3080 Ti
Memory	16 GB
Programming Language	Python 3.8
Development Environment	PyCharm
CUDA Driver	11.7

In the comparative experiments conducted in this study, all detection models were configured with identical hyperparameters and trained on the same dataset. Specifically, the training was conducted for 200 epochs, with a momentum of 0.9 and a weight decay regularization coefficient of 0.005. A learning rate decay strategy was adopted, with an initial learning rate set to 0.0001.

RESULTS AND ANALYSIS

Comparison of detection performance of different models

In this section, three comparative experiments were designed and conducted under identical experimental conditions to identify the millet ear detection model that yields the best performance. The details of the experimental procedures and the resulting analyses were presented below.

In the first set of comparative experiments, classical detection models including EfficientDet (*Tan et al., 2020*), YOLOv4 (*Bochkovskiy et al., 2020*), YOLOv5, and YOLOX were selected for millet ear detection. The detection results are presented in Table 2.

Table 2

Comparative experimental results of different models				
Model	Precision (%)	Recall (%)	F1 (%)	AP (%)
EfficientDet	78.11	52.04	62.46	70.50
YOLOv4	82.18	66.90	73.76	81.90
YOLOv5	83.13	62.73	71.50	81.76
YOLOX	88.07	54.95	67.68	83.86

Based on the comparison results presented in Table 2, it could be seen that the YOLOX model achieved an AP of 83.86%. Compared to the EfficientDet, YOLOv4, and YOLOv5 models, YOLOX demonstrated improvements in AP of 13.36%, 1.96%, and 2.1%, respectively. The results demonstrated the superior performance of the YOLOX model in millet ear detection tasks.

In the second set of comparative experiments, attention mechanisms including SE, BAM, NAM, and CBAM were selected to enhance the YOLOX model. These modified models were subsequently compared with the original YOLOX model to evaluate their performance improvements. The detection results are presented in Table 3.

Table 3

Results of attentional mechanism comparison experiments				
Model	Precision (%)	Recall (%)	F1 (%)	AP (%)
YOLOX	88.07	54.95	67.68	83.86

Model	Precision (%)	Recall (%)	F1 (%)	AP (%)
YOLOX-SE	81.59	79.95	80.76	85.66
YOLOX-BAM	83.79	76.24	79.84	84.63
YOLOX-NAM	84.75	75.38	79.79	85.37
YOLOX-CBAM	82.09	79.12	80.58	86.24

Based on the comparison results presented in Table 3, the introduction of CBAM significantly enhanced model performance compared to other attention mechanisms. Specifically, the YOLOX-CBAM model achieved a 12.9% improvement in the F1 and a 2.38% increase in AP relative to the baseline YOLOX model. Furthermore, in comparison to YOLOX models that incorporated SE, BAM, and NAM modules, the YOLOX-CBAM model demonstrated improvements in AP of 0.58%, 1.61%, and 0.87%, respectively. The superior performance of CBAM could be attributed to its dual-channel and spatial attention architecture, which enriched feature representations across both dimensions by integrating max pooling and average pooling. This design significantly enhanced the model's capacity to capture critical details in millet ear images. The results indicated that the integration of the CBAM attention mechanism into the YOLOX framework facilitated more accurate and reliable detection of millet ears.

In the third set of comparative experiments, the loss functions including GloU, CioU, DloU and EloU were employed to replace the IoU loss function in YOLOX. The detection results are presented in Table 4.

Table 4

Loss function comparison experiment results

Model	Precision (%)	Recall (%)	F1 (%)	AP (%)
YOLOX	88.07	54.95	67.68	83.86
YOLOX-GIoU	77.94	42.67	55.15	64.03
YOLOX-CIoU	79.93	49.52	61.15	69.43
YOLOX-DIoU	70.97	47.89	57.19	62.16
YOLOX-EIoU	92.04	56.56	70.06	86.06

Based on the comparison results presented in Table 4, the experiments demonstrated that the YOLOX-EIoU model exhibited superior performance over all other models, as evidenced by both AP and F1. Specifically, the F1 of the YOLOX-EIoU model surpassed that of the YOLOX, YOLOX-GIoU, YOLOX-CIoU, and YOLOX-DIoU models by 2.38%, 14.91%, 8.91%, and 12.87%, respectively. Additionally, the AP of the YOLOX-EIoU model surpassed that of the YOLOX, YOLOX-GIoU, YOLOX-CIoU, and YOLOX-DIoU models by 2.2%, 22.03%, 16.63%, and 23.9%, respectively. The results indicated that the EloU loss function serves as the optimal alternative to the IoU loss function in the original YOLOX model.

Ablative test performance comparison

To validate the improvement method proposed in this study, ablation experiments were conducted focusing on the CBAM and the EloU loss to assess the effectiveness of each enhancement. CBAM and EloU were sequentially integrated into the original YOLOX model while employing the same parameter configuration throughout the training process. The experimental results are presented in Table 5. The introduction of CBAM resulted in significant performance enhancement, with a 2.38% increase in AP. Furthermore, the utilization of both CBAM and EloU led to improvements in F1 and Recall, culminating in a 6.44% increase in AP. It could be concluded that the incorporation of the attention mechanism CBAM enabled the model to selectively emphasize informative features, thereby enhancing its representational capacity, as evidenced by the marked improvement in detection accuracy. Additionally, the EloU loss function enhanced sensitivity to the position and size of bounding boxes by introducing an extra penalty term, which further contributed to the improvement in detection precision.

Table 5

Results of ablation experiment

Model	Precision (%)	Recall (%)	F1 (%)	AP (%)
YOLOX	88.07	64.95	74.76	83.86
YOLOX-CBAM	82.09	79.12	80.58	86.24
YOLOX-EIoU	92.04	56.56	70.06	86.06
YOLOX-CBAM-EIoU	91.01	89.45	90.22	90.30

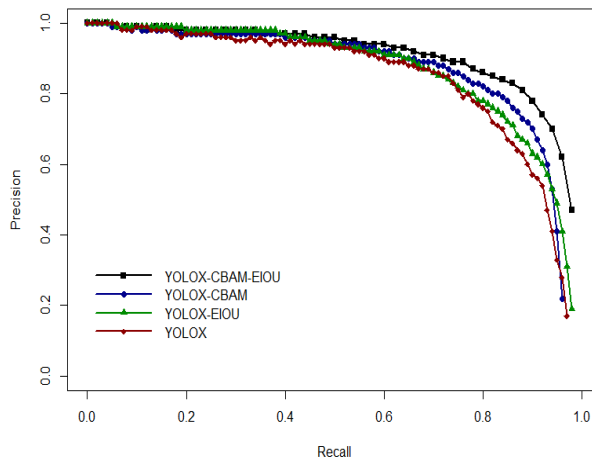
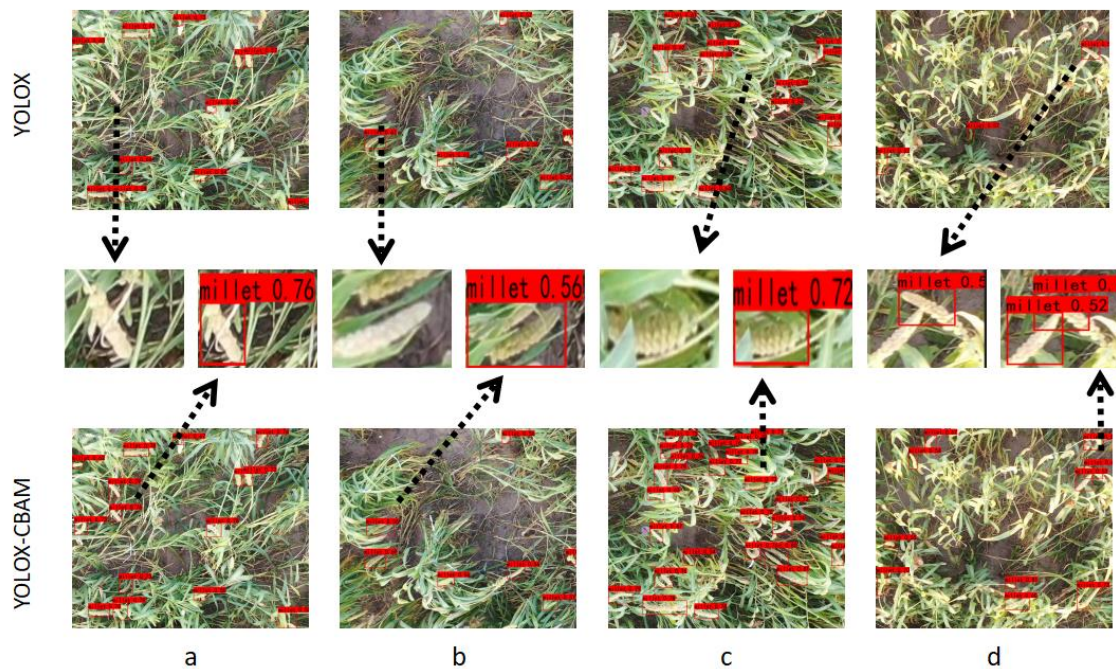


Fig. 7 - P-R curve of ablation experiment

To provide a more intuitive demonstration of the performance of the proposed YOLOX-CBAM-EIoU model, the P-R curves for the four different models mentioned in the ablation experiments were plotted, as shown in Fig. 7. In comparison to the other three models, the P-R curve of the YOLO-CBAM-EIoU model consistently lies at the top, and the area under the curve is the largest. The result indicates that the model achieves the highest AP, demonstrating superior performance in the task of millet ear detection.

Visualization analysis of detection results

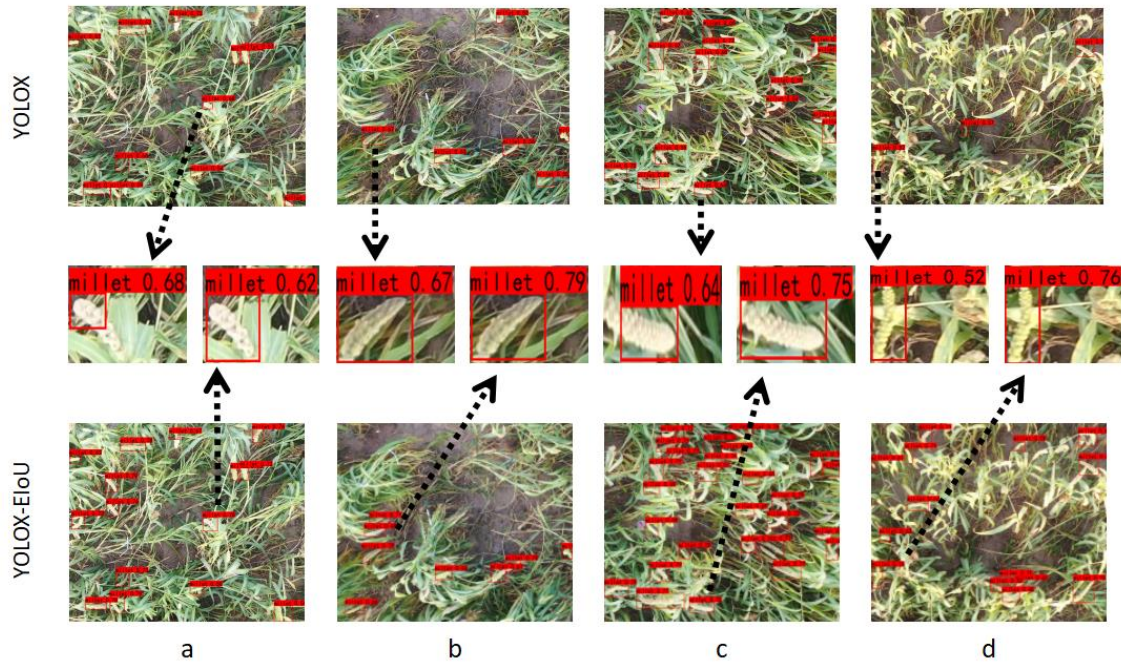
To provide a more intuitive evaluation of model performance, YOLOX, YOLOX-CBAM, YOLOX-EIoU, and YOLOX-CBAM-EIoU were tested and visually analyzed under identical experimental conditions. In the visualization results shown below, Fig. 8a and 8b represent cases where the millet ears are relatively dispersed, Fig. 8c and 8d correspond to cases where the millet ears are relatively dense and occluded. The red boxes in the figure indicate the detected millet ears.



(Note: the upper layer is YOLOX visualization result diagram; The middle layer is the enlarged image of the contrast effect; The lower layer is the YOLO-CBAM visual result chart)

Fig. 8 - Comparison of the detection performance before and after using the CBAM module

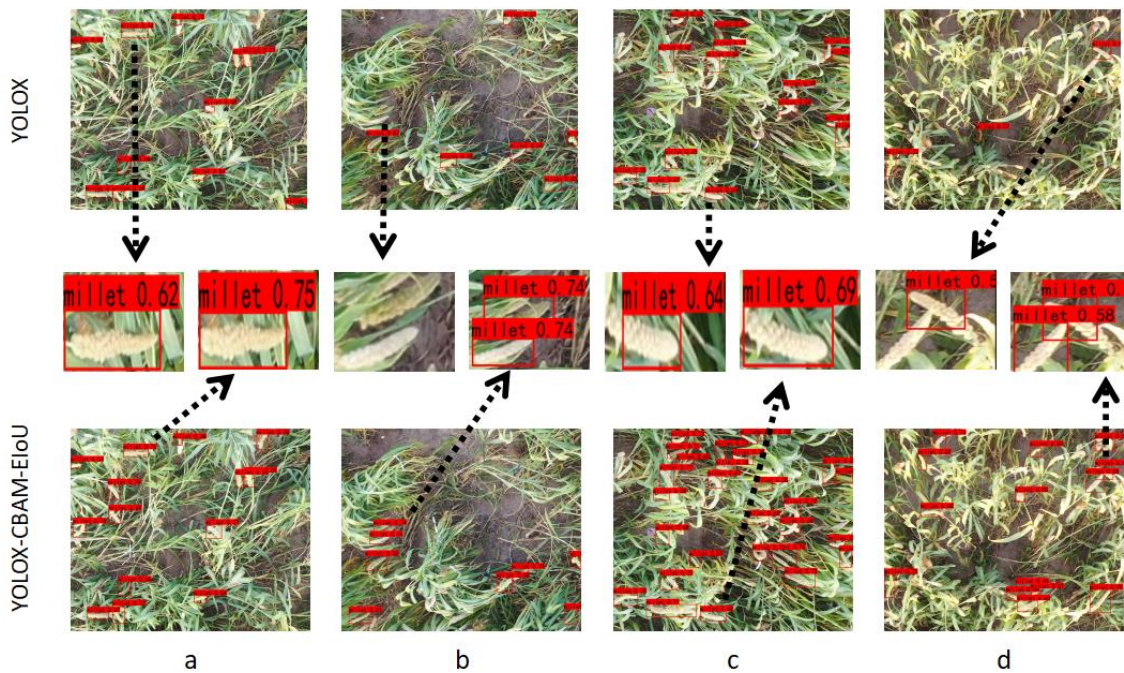
The detection results of the YOLOX-CBAM model are shown in Fig. 8. It can be observed that the millet ears in UAV images are small and subject to occlusion both among the ears and between ears and leaves. This causes considerably missed detection with the original YOLOX model. The incorporation of the CBAM attention mechanism can significantly reduce these missed detections, as evidenced in Fig. 8a and 8b. Moreover, the CBAM attention mechanism can effectively mitigate the issue of missed detection resulting from occlusion between millet leaves and ears, as shown in Fig. 8c and 8d.



(Note: the upper layer is the YOLOX visualization result diagram; The middle layer is the enlarged image of the contrast effect; Below is the YOLO-EIoU visualization result chart)

Fig. 9 - Comparison of detection performance before and after using the EIoU loss function

The detection results of the YOLOX-EIoU model are shown in Fig. 9. It can be observed that the YOLOX model exhibits instances of missing detections, along with relatively low confidence scores. Conversely, the improved YOLOX-EIoU model has fewer occurrences of missed detections, and a notable enhancement in the confidence of the predicted bounding boxes.



(Note: the upper layer is YOLOX visual result diagram; The middle layer is the enlarged image of the contrast effect; The lower layer is the YOLO-CBAM-EIoU visual result chart)

Fig. 10 - Comparison of detection performance before and after combining CBAM with EIoU

The detection results of the YOLOX-CBAM-EIoU model are shown in Fig. 10. It can be observed that our improved model can significantly reduce the occurrence of false negatives when detecting small-sized millet ear targets and partially occluded millet ear targets.

Furthermore, the discrepancy between the predicted bounding boxes and the actual bounding boxes is markedly minimized, with confidence levels achieving the highest standards among all tested models.

CONCLUSIONS

To address the current challenges in millet ear detection, such as the small size of millet ears, their dense distribution, and severe occlusion, this study proposed an improved model based on the YOLOX model. The proposed model achieved improvements of 2.94% in precision, 24.5% in recall, 15.46% in F1-score, and 6.44% in average precision. The following improvements were made in this study:

(1) CBAM attention mechanism was added to the neck of the YOLOX model to enhance its ability to extract detailed features of millet ears.

(2) The IoU loss function was replaced with the EIoU loss function. This refinement enhanced the precision of box dimensions and positions, leading to improved detection accuracy and reduced issues with low confidence and misalignment between ground truth and predicted boxes.

(3) The YOLOX-CBAM-EIoU model was proposed. Experiments demonstrated that integrating the CBAM attention mechanism with the EIoU loss function achieved the highest detection performance. The proposed improvement method could address issues observed in real-world application environments, including missed detections, false positives, significant discrepancies between ground truth and predicted boxes, as well as low confidence in detection boxes.

The experiment results demonstrate that this model could effectively solve the problem and accurately detect millet ears in the UAV image in the field environment, which provides a way for realizing intelligent management of large-scale millet planting. Furthermore, the model would be used in the planting and management of more cereal crops, and further research would be conducted on the calculation of crop density to provide a reference for the construction of intelligent farms.

ACKNOWLEDGEMENTS

This project is financially supported by the National Nature Science Foundation of China (52165006), Fundamental Research Program of Shanxi Province (202203021212450). The authors declare no competing interests.

REFERENCES

- [1] Bao L., Wang M., Liu J., Wen B., Ming Y., (2019), Estimation Method of Wheat Yield Based on Convolution Neural Network (基于卷积神经网络的小麦产量预估方法), *Acta Agriculturae Zhejiangensis*, 32(12), 2244-2252.
- [2] Bao W., Xie W., Hu G., Yang X., Su B., (2023), Wheat Ear Counting Method in UAV Images Based on TPH-YOLO (基于 TPH-YOLO 的无人机图像麦穗计数方法), *Transactions of the Chinese Society of Agricultural Engineering*, 39(01), 155-161.
- [3] Bochkovskiy A., Wang, C., Liao, H., (2020), Yolov4: Optimal Speed and Accuracy of Object Detection, *arXiv preprint arXiv: 2004. 10934*.
- [4] Cai, E., Guo, J., Yang, C., Delp, E., (2023), Semi-Supervised Object Detection for Sorghum Panicles in UAV Imagery, *In IGARSS 2023-2023 IEEE International Geoscience and Remote Sensing Symposium, CA/USA*, pp. 6482-6485.
- [5] Cai Z., Cai Y., Zeng F., Yue, X., (2023), Rice Panicle Recognition in Field Based on Improved YOLOv5l Model (基于改进 YOLOv5l 的田间水稻稻穗识别), *Journal of South China Agricultural University*, 45(01), 108-115.
- [6] Duan L., Xiong X., Liu Q., Yang W., Huang, C., (2018), Field Rice Panicle Segmentation Based on Deep Full Convolutional Neural Network (基于深度全卷积神经网络大田稻穗分割), *Transactions of the Chinese Society of Agricultura Engineering*, 34(12), 202-209.
- [7] Ge Z., Liu S., Wang F., Li Z., Sun J., (2021), YOLOX: Exceeding YOLO Series in 2021, *arXiv preprint arXiv: 2107. 08430*.
- [8] Han J., Yuan X., Wang Zhun., Chen Y, (2023), UAV Dense Small Target Detection Algorithm Based on YOLOv5s (基于 YOLOv5s 的无人机密集小目标检测算法), *Journal of Zhejiang University (Engineering and Technology)*, 57(06), 1224-1233.
- [9] Huang Z., (2022), *Research on Wheat Yield Estimation Based on Deep Learning Ear Recognition* (基于深度学习麦穗识别的小麦估产研究), MSc dissertation, Shandong Agricultural University, Shandong/China.

- [10] Li S., Liu F., Liu M., Cheng R., Xia E., Diao X., (2021), Current Status and Future Prospective of Foxtail Millet Production and Seed Industry in China (中国谷子产业和种业发展现状与未来展望), *Agricultural Sciences in China Scientia*, 54(03), 459-470.
- [11] Liu S., Ge H., Duan J., (2023), YOLOv5 Wheat Detection Algorithm with Lightweight Convolution and Attention Mechanism (结合轻量卷积和注意机制的YOLOv5 麦穗检测算法), *Modern Computer*, 29(09), 32-38.
- [12] Liu T., Sun C., Wang L., Sun Z., Zhu X., Guo W. (2014). In-field Wheat ear Counting Based on Image Processing Technology (基于图像处理技术的大田麦穗计数), *Transaction of the Chinese Society for Agricultural Machinery*, 45(02), 282-290.
- [13] Li Y., Du S., Yao M., Yi Y., Yang J., Ding Q., et al., (2018), Method for Wheat Ear Counting and Yield Predicting Based on Image of Wheat Ear Population in Field (基于小麦群体图像的田间麦穗计数及产量预测方法), *Transactions of the Chinese Society of Agricultural Engineering*, 34(21), 185-194.
- [14] Li Z., (2016), *Research on Wheat Spike Identification Based on Color Features* (基于颜色特征的麦穗图像识别算法研究), MSc dissertation, Henan Agricultural University, Henan/China.
- [15] Meng L., (2019), *Research on Field Wheat Ear Recognition Technology Based on Color and Texture Characteristics* (基于颜色和纹理特征的大田麦穗识别技术研究), MSc dissertation, Henan Agricultural University, Henan/China.
- [16] Tan M., Pang R., Le Q.V., (2020), EfficientDet: Scalable and Efficient Object Detection. *Proceedings of the IEEE/CVF Conference on Computer Vision and Pattern Recognition*, Seattle/United States, pp. 10781-10790.
- [17] Woo S., Park J., Lee J.Y., Kweon I.S., (2018), CBAM: Convolutional Block Attention Module. *Proceedings of the European Conference on Computer Vision (ECCV)*, Munich/Germany, pp. 3-19.
- [18] Xiong X., (2018), *Research on Field Rice Panicle Segmentation and Nondestructive Yield Prediction Based on Deep Learning* (基于深度学习的大田水稻稻穗分割及无损产量预估研究), PhD dissertation, Huazhong University of Science and Technology, Hubei/China.
- [19] Yang W., Duan L., Yang W., (2021), Deep Learning-based Extraction of Rice Phenotypic Characteristics and Prediction of Rice Panicle Weight (基于深度学习的水稻表型特征提取和穗质量预测研究), *Journal of Huazhong Agricultural University*, 40(01), 227-235.
- [20] Yang S., Wang S., Wang P., Ning Z., Xi Y., (2022), Detecting Wheat Ears Per Unit Area Using an Improved YOLOX (改进 YOLOX 检测单位面积麦穗), *Transactions of the Chinese Society of Agricultural Engineering*, 38(15), 143-149.
- [21] Zhang Q., Hu S., Shu W., Cheng H., (2021), Wheat Spikes Detection Method Based on Pyramidal Network of Attention Mechanism (基于注意力机制金字塔网络的麦穗检测方法), *Transactions of the Chinese Society for Agricultural Machinery*, 52(11), 253-262.
- [22] Zhang L., Chen Y., Li Y., Ma J., Du K., (2019), Detection and Counting System for Winter Wheat Ears Based on Convolutional Neural Network (基于卷积神经网络的冬小麦麦穗检测计数系统), *Transactions of the Chinese Society for Agricultural Machinery*, 50(03), 144-150.
- [23] Zhang Y., Xiao D., Chen H., Liu Y., (2021), Rice Panicle Detection Method Based on Improved Faster R-CNN (基于改进 Faster R-CNN 的水稻稻穗检测方法), *Transactions of the Chinese Society for Agricultural Machinery*, 52(08), 231-240.
- [24] Zhang Y., Ren W., Zhang Z., Jia Z., Wang L., Tan T., (2022), Focal and Efficient IOU Loss for Accurate Bounding Box Regression, *Neurocomputing*, 506, 146-157.
- [25] Zhao F., Wang K., Yuan Y., (2014), Study on Wheat Spike Identification Based on Color Features and AdaBoost Algorithm, *Crop Journal*, 2014(01), 141-144+161.

OPTIMIZATION OF VIBRATION TRANSMISSION SYSTEM BASED ON IMPLICIT PARAMETRIC MODELING OF SUGARCANE HARVESTER FRAME

基于机架隐式参数化建模的蔗秆切割损伤优化

Biao ZHANG^{1,2*}, Weimin SHEN¹⁾, Dan PAN¹⁾

¹⁾College of Mechanical Engineering, Guangxi University, Nanning, 530004, China;

²⁾Guangxi Key Laboratory of Environmental Pollution Control and Ecological Restoration Technology, Nanning 530007, China

* Correspondence: bzhang@gxu.edu.cn

DOI: <https://doi.org/10.35633/inmateh-75-60>

Keywords: sugarcane harvester, cutting damage, vibration transmission, dynamic optimization, parametric modeling

ABSTRACT

The hilly terrain where sugarcane harvesters travel, the harvest object of rough and tough stalks, and the perennial cultivation property are all different from those of other straw crops. In order to reduce the cutting damage of cane stalks caused by complex excitation in field conditions, a method for optimizing dynamic characteristics of vibration transmission system based on implicit parametric modeling of harvester frame was proposed. First, the impact damage effect of the cutter on the cut section of stalk was analyzed by high-speed images. Accordingly, the cutter amplitude RMS and impact velocity (V_I) were proposed as parameters to characterize the damage inducibility. Subsequently, a 5-DOF dynamic model of the whole machine was established covering 21 dynamic parameters. With the measured excitation of road spectrum, cane cutting force and engine, the virtual prototype simulation showed that the frame stiffness was the most sensitive to vibration response. Through topology optimization and implicit parametric modeling of such load-bearing frame, a high-rigidity design was derived to improve the vibration transmission characteristics. Comparison of testing results before and after frame optimization illustrated that the bending stiffness and torsional stiffness were increased by 1.95% and 2.84% respectively, and the RMS of operating frequency-response functions with road and engine as path sources were decreased by 21.7% and 27.2% respectively. As a result, the output amplitude RMS and impact velocity V_I were reduced by 35.9% and 5.9% respectively, implying corresponding improvements in the cutting quality of cane stalks. This study provided a reference for the development of harvester dynamic systems based on harvesting quality optimization.

摘要

甘蔗收获机的丘陵行进地形、粗韧茎秆割收对象及其宿根种植性状与其它秸秆作物条件不同。为降低蔗地工况复杂激励所致的蔗秆切割损伤，本文提出了一种基于机架隐式参数化建模对蔗秆切割损伤进行优化的方法。首先利用高速摄像图像剖析了刀盘-茎秆互作的冲击损伤效应。据此提出了采用刀盘振幅 RMS 和冲速 (V_I) 作为诱损性表征参量。随后，基于实测路谱建立了整机 5 自由度动力学模型，解析发现机架刚度对动力响应的敏感性最大。进而筛选出可映射机架承载式结构特征的 21 个设计变量，从而建立其隐式参数化模型，并通过拓扑优化衍生出机架高刚性的优化设计。优化前后的对比测试结果表明，其弯曲、扭转刚度分别提高 1.95% 和 2.84%，以路面、发动机为路径源的传振频响函数 RMS 各降低 21.7% 和 27.2%。综合引起致损振幅 RMS 和冲速 V_I 降低了 35.9% 及 5.9%，意味着蔗秆切割质量获得相应的改进。该研究可为收获机械的动力学系统开发及收割质量优化提供参考。

INTRODUCTION

Sugarcane is a perennial crop whose post-harvest residual stumps germinate, emerge and grow up at cane nodes under suitable environmental conditions (Liu *et al.*, 2018). At present, the planting area of ratoon sugarcane accounts for more than 70% of the total sugarcane area (Yang *et al.*, 2021; Wu *et al.*, 2022), so the germination rate directly affects the yield and efficiency of the next year. Since the main sugarcane-producing regions, such as Guangxi and Yunnan Provinces, are widely distributed across the hilly areas of South China, sugarcane harvesters often operate on uneven ridge-furrow terrain. Furthermore, due to the thick and highly fibrous nature of cane stalks, harvesters typically adopt a low-position cutting method, inserting the cutter deep into the soil to improve cutting efficiency (Mo *et al.*, 2013). The above compound working conditions are obviously different from the harvesting conditions of other straw crops such as corn and cotton, and have a

significant impact and instability on the key high-speed rotary cutter (Zou *et al.*, 2018). In the coupled environment of sugarcane fields, harvesters, and sugarcane plants, the harvester experiences vertical oscillations as it moves along uneven terrain. Influenced by multiple excitation sources, the cutting tool undergoes severe vibration, which can easily lead to damage of the budding nodes on the remaining cane stumps. These cutting quality issues significantly hinder the germination of ratoon sugarcane and have become a major bottleneck limiting sustainable and efficient sugarcane cultivation cycles.

So far, from the perspective of factors contributing to stalk cutting damage, Gupta *et al.* (1992), Razavi *et al.* (2010), and Wang *et al.* (2019) have experimentally analyzed the effects of structural and operational parameters - such as disc cutter configuration, blade layout, and rotational speed - on sugarcane harvest damage. Kroes *et al.* (1995) developed a model which described the base-cutter kinematics of the dual base-cutter sugarcane harvester. By using the model, the maximum permissible velocity ratio (forward speed/disc rotational speed) was calculated, which improved the cutting quality. Silva *et al.* (2008) evaluated the sugarcane root damage degree caused by cutting height differences through experiments. Peloso *et al.* (2021) studied effects of the cutter rotating speed and the sugarcane harvester moving speed on the cutting quality of sugarcane harvesters. Li *et al.* (2017) and Ma *et al.* (2006) analyzed the role relationship of system design elements on the cracking damage rate from perspectives of blade edge angle, travel speed and embedded depth. However, the cutting action of the blade is characterized by high speed, strong intermittent, short duration and invisible contact interface, making it difficult to use visual testing methods to effectively and accurately monitor the cutting process and damage evolution. In this regard, Liu *et al.* (2007) used high-speed cameras to experimentally test the splitting caused by the smooth blade cutting, and simulated the damage behavior of sugarcane under different load forms of tension, compression, bending and torsion (Liu *et al.*, 2007). Kroes *et al.* (1996) measured and predicted the force, energy, bending strength and splitting of sugarcane stalk during impact cutting. Mello *et al.* (2001) and Momin *et al.* (2017) studied the effects of the angle and serrated blades on the damage, force and energy and verified them by indoor high-speed camera and field test. In order to intuitively reveal the dynamic relationship and local structural characteristics of their interactions. Lv *et al.* (2008) and Yang *et al.* (2017) respectively established digital models of stem-plants based on structure-function, and simulated the damage process in the cutting motion by finite element method (FEM). The factors affecting the cutting state and extrusion of the cane head, as well as their interaction on the damage process, were quantitatively studied through virtual experiments.

Based on previous studies (Zhou *et al.*, 2017; Fan *et al.*, 2012), it has been confirmed that the cutting damage of sugarcane is significantly correlated with the amplitude of cutter, and the damage degree deepens as the amplitude increases. The vibration response output of the cutter is actually related to the imbalance caused by its own manufacturing and installation errors. It also interacts with the alternating loads on the whole vehicle generated by field road spectrum, engine, cutting force and other excitation sources. It itself is closely related to the dynamic characteristics of the vibration transmission system consisting of the frame, power gearbox, hydraulic lifting device, tires and other components. The system dynamics parameters involved include component mass and stiffness, connection stiffness and damping, power mounting position, etc. Therefore, from the perspective of a multi-source and multi-component coupled system, an in-depth analysis of the dynamic characteristics of such vibration transfer system from the excitation source to the response point is conducive to establishing the influence relationship between dynamic parameters and responses (Hou *et al.*, 2021; Xu *et al.*, 2017). Thus, the insensitive factors can be eliminated, the dynamical parameters of the dominant factors can be improved, and the characteristics of components can be optimized in terms of modal, lightweight and so on. Further, on the basis of considering the dynamic response, the forward design of the whole machine is guided to achieve the purpose of improving the sugarcane cutting quality.

Regarding the problem of cutting damage caused by vibration, this paper first analyzed the characteristics of excitation sources experienced by the sugarcane harvester under working conditions, and improved the response vibration evaluation from the perspective of cutting damage mechanism. Then, a dynamic analytical model of the vibration transmission system under action of multiple vibration sources was established. On this basis, a rigid-flexible coupling virtual prototype model was established to solve the nonlinear response, and the influence and correlation of multiple dynamic parameters on the response were analyzed. After screening, implicit parametric modeling and topology optimization design were carried out on the frame. Finally, the system dynamic characteristics were experimentally tested using the frequency-response function of the frame structure and the vibration characteristics of the response target to estimate the improved degree in sugarcane cutting damage.

MATERIALS AND METHODS

Principle of sugarcane cutting damage

Analysis of excitation Sources

Observation of damage morphology

During the operation of sugarcane harvester, the high-speed rotating cutterhead is subjected to various excitation in the process of cutting and conveying sugarcane, resulting in obvious axial vibration. Through observation, this vibration effect is usually accompanied by the splitting damage effect of ratoon cane stumps, as shown in Figure 1. The main forms of damage are penetrating tears and splitting notches along longitudinal stem-nodes. It is inferred that such damage is mainly attributed to the action of squeezing impact force when the blade comes into contact with cane material. Therefore, it is necessary to trace the sources of axial vibration of the cutter from the entire harvesting machine, including the forced vibration caused by field road spectrum, the second-order unbalanced inertial force of engine, and the self-excited vibration caused by sugarcane cutting.

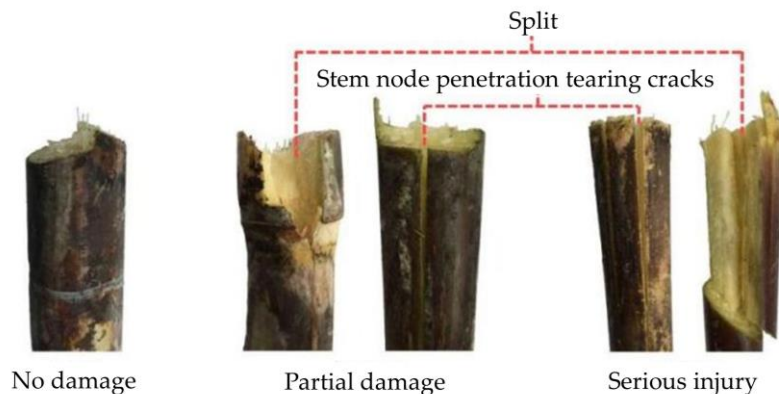


Fig. 1 - Cutting damage of sugarcane stubble

Measurement of field road spectrum

Using a portable data acquisition front end and PCB three-axis acceleration sensors, under a constant speed condition of $0.8 \text{ m}\cdot\text{s}^{-1}$, the Z-direction acceleration signal of a typical sugarcane field in the hilly area of Guangxi was collected as a road spectrum. The timing signal was then denoised through the MATLAB wavelet packet, and its amplitude-frequency curve was obtained using Fourier transform, as shown in Figure 2. It can be seen that road excitation is a low-frequency and high-amplitude displacement load, with frequencies concentrated within 10 Hz and the peak value appearing at 2.5 Hz.

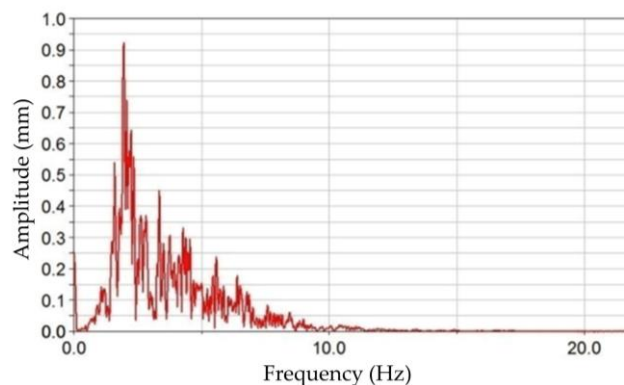


Fig. 2 - Amplitude-frequency curve of hilly field road spectrum

Calculation of engine excitation force

For the second-order reciprocating inertia force caused by the eccentricity of the engine cylinder, the calculation formula is as follows (Gu *et al.*, 2013):

$$F_{2nd} = 4 \cdot m_o \cdot r \cdot \omega^2 \left(\lambda + \frac{3}{2} \lambda^3 \psi^2 \right) \cos 2\alpha \quad (1)$$

where: m_o is the cylinder weight, kg; r is the crankshaft crank radius, m; ω is the angular velocity, rad/s; λ is the ratio of connecting rod; ψ is the eccentricity; α is the crank angle. In addition, the vertical vibration frequency of the engine follows:

$$f = \frac{Qn}{60} \tag{2}$$

where: Q is the proportional coefficient, which takes a value of 2 under the second-order inertia force; n is the engine speed, r/min.

Referring to the recorded cylinder parameters and the engine speed range of 1500~2000 rpm under working conditions (Zhou et al., 2018), it can be calculated that the excitation force from the engine is approximately 2493 N and the f is about 50~66.7 Hz.

Measurement of sugarcane cutting force

During the experimental sugarcane cutting process, a quartz three-phase dynamometer was used to collect the axial cutting force at a sampling frequency of 20 kHz. The data after using Matlab wavelet package to denoise the time-series signal is shown in Figure 3. At the same time, in order to understand the instantaneous cutting process of cane, an industrial camera was employed to focus on the cutting position of the stalk and record the frame images at four sequential cutting moments of the blade during cutting off a single cane, as shown in Fig. 4.

Based on Figure 3 and Figure 4, it can be seen that there were four equidistant peaks in the cutting force signal, indicating that the rotating blades of the cutter cut off a single cane after four repeated cuts. This was consistent with the results of high-speed photographic images. By calculating the sampling frequency and the number of sampling points, it was found that the cutting action time of single blade was extremely short, approximately 0.0023 s, and thus the cutting excitation frequency was about 434.8 Hz, which was a high-frequency self-excited vibration.

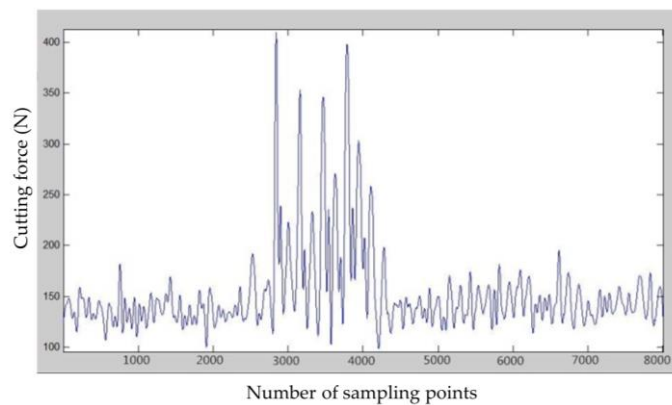
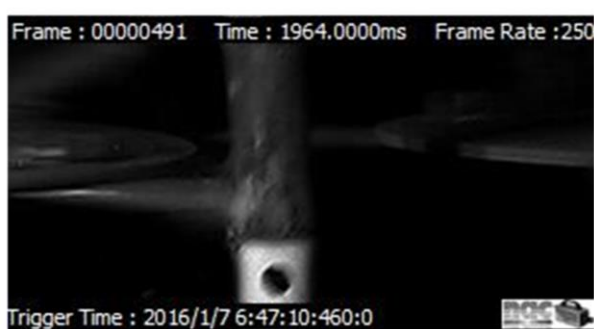
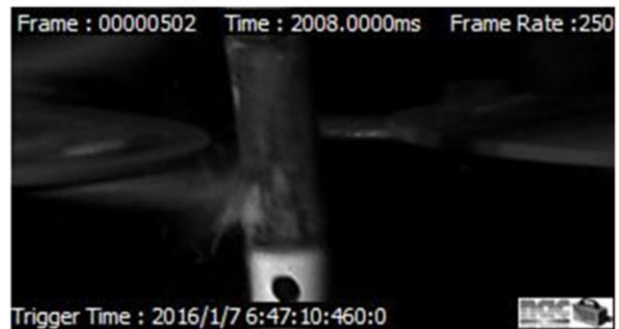


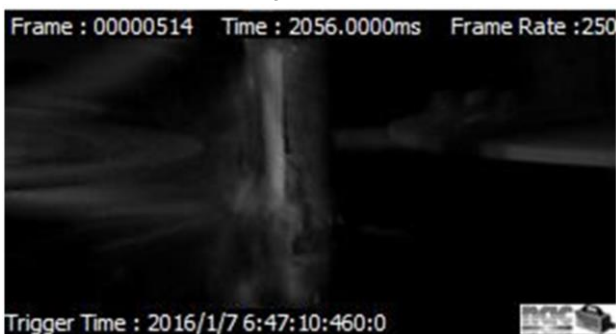
Fig. 3 - Cutting force pulse signal for cutting off single sugarcane



(a) Image at 1964 ms



(b) Image at 2008 ms



(c) Image at 2056 ms



(d) Image at 2100 ms

Fig. 4 - Sequential high-speed images of repeated cuts of a single stalk

Vibration evaluation index based on sugarcane damage process

Figure 5 shows the axial vibration of the working cutterhead sampled using a laser displacement sensor. Since the periodic displacement change of the cutter affects the cutting position of the stalk, the root mean square (RMS) of the amplitude was first used as the response index. In addition, within a single cutting duration of about 0.0023 s, a positive pressure (F_N) of about 246 N (taken from the average of the peak values in Figure 3) acted on the sugarcane cross-section, so the impulse (I) generated at the instant of cutting was calculated to be about 0.57 N·s, causing the cane material to crack. Further, since there was a certain interval of about 0.013 s between two consecutive cuts, as the cutting depth gradually increased, the second to fourth cuts can produce a certain bending moment (M), causing cracks to continue to expand:

$$M = F_N \cdot \Delta s \cdot i \quad (3)$$

where Δs is the feeding depth for a single cut, which is related to the harvester driving speed; $i=2, 3, 4$.

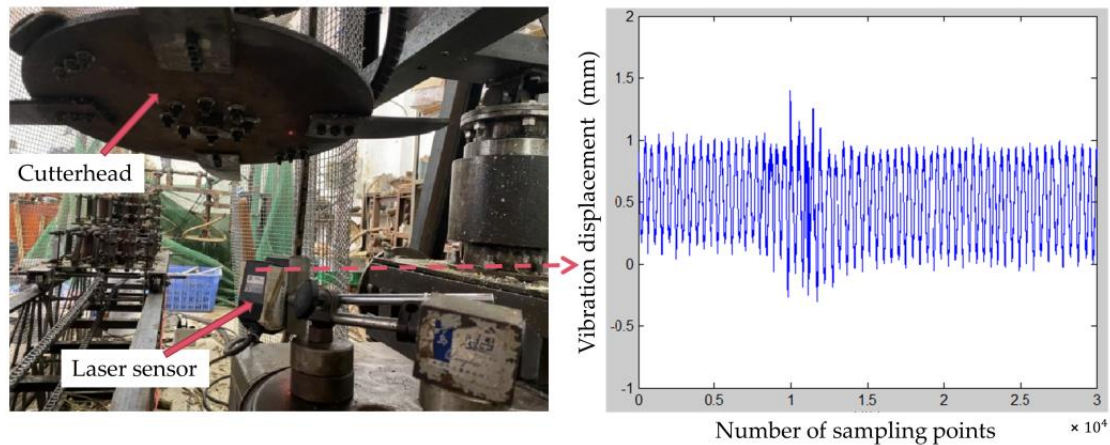


Fig. 5 – Cutter vibration signal measurement

Based on the above analysis, it can be known that the joint action of F_N , I and M lead to the damage of sugarcane nodes. Considering the spatial-temporal observation of instantaneous cutting, the single cutting time (Δt) of the blade is close to zero, and the corresponding axial relative displacement (Δu) is formed. Therefore, the impact velocity (V_I) can be defined to characterize the impact strength of the cutter on the section:

$$V_I = \lim_{\Delta t \rightarrow 0} \frac{\Delta u}{\Delta t} \quad (4)$$

In summary, based on the analysis of the damage mechanism of sugarcane cutting, the indicators of cutter amplitude *RMS* and impact velocity were proposed, thus forming a comprehensive response evaluation covering macroscopic vibration energy and local impact intensity. It was helpful to comprehensively evaluate the relationship between the cutter vibration responses and cutting damage.

Dynamic modeling of vibration transmission system

Dynamic model

The main vibration excitation devices installed on the frame include front guide wheels, rear drive wheels, cutting system and engine. Therefore, it is necessary to study the impact of the combined effects of ground roughness, engine cycle excitation force and cutting force on the dynamic characteristics of the whole machine, especially reflected in the impact on cutter vibration. The sugarcane harvester was simplified as a mass-spring-damping system (Mo et al., 2022), in which the four wheels were simplified into spring coupled damping. The dynamic theoretical model established is shown in Figure 6 (a). Based on the Z-direction sensitivity to cutting damage, this model only considered the degrees of freedom (DOF) in the three directions of vertical vibration (along the Z direction), transverse torsional vibration (around the Y-axis) and longitudinal torsional vibration (around the X-axis). Thus, the model contains 5-DOF, which are the vertical displacement of frame centroid (X_1), the rotation angle around X-axis (θ_1), the rotation angle around Y-axis (θ_2), and the vertical displacement of engine centroid (X_2) as well as the vertical displacement of cutting system (X_3).

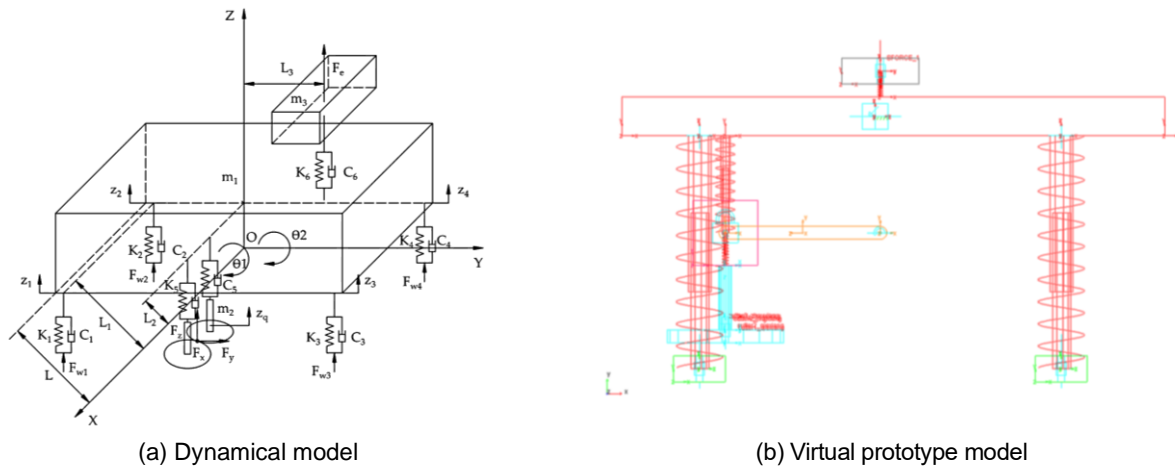


Fig. 6 - The frame model

Note: m_1 , m_2 and m_3 are masses of frame, power gearbox and engine, kg; K is stiffness, N/m; C is damping, N/(m/s); K_1 , K_2 , C_1 and C_2 are stiffness and damping of the front wheels; K_3 , K_4 , C_3 and C_4 are stiffness and damping of the rear wheels; K_5 and C_5 are stiffness and damping of the lifting hydraulic cylinder between gearbox and frame; K_6 and C_6 are stiffness and damping of the engine suspension; $F_{w1} \sim F_{w4}$ are road spectrum excitation loads on four wheels; F_e is vertical excitation force from the engine, N; F_x , F_y and F_z are respectively the radial, tangential and axial cutting force, N; L is half the length of frame, m; L_1 is the distance from front wheel or rear wheel to frame centroid, m; L_2 is the distance from gearbox to frame centroid, m; L_3 is the distance from engine to frame centroid, m; z_i is the vertical displacement of each wheel, m; z_q is the vertical displacement of cutting system, m.

Virtual prototyping simulation

Since the analytical model is a complex multi-DOF nonlinear system, the ADAMS 2020 software was used to establish a virtual prototype simulation model to solve the correlation coefficients between the above 21 dynamic parameters and the cutter vibration response (Zhang et al., 2023; Han et al., 2022). As shown in Figure 6 (b), a total of 11 components were created. The frame and engine parts were flexibly processed and then assembled with other rigid body parts, to reflect their stiffness characteristics, i.e. elastic modulus E_1 and E_2 respectively. Moreover, the required constraints, including global Y-direction translation, rotations around Z-direction and X-direction, were applied. The measured field road spectrum excitation (Fig. 2), the measured cane cutting force (Fig. 3) and the engine excitation force, modeled as a sine wave, were applied as loads to simulate real driving conditions.

Experimental testing of frame dynamic characteristics

Modal testing

The experimental bench model of the sugarcane harvester is shown in Figure 7, which includes the key operating assemblies.

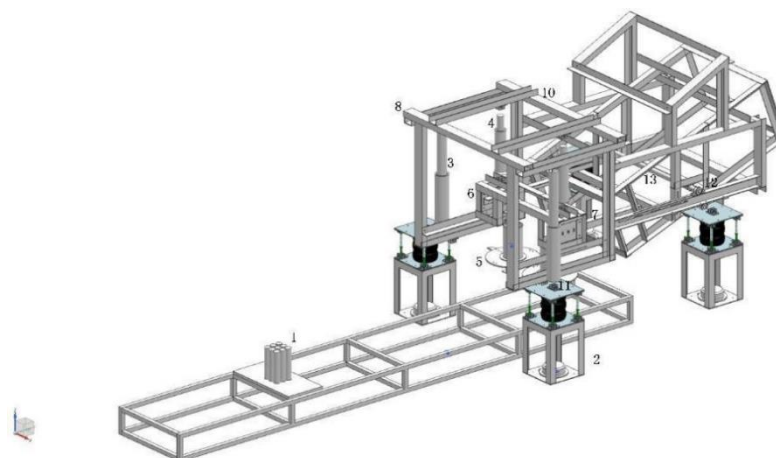


Fig. 7 - General assembly of the whole machine system

- 1- sugarcane clamping conveying device; 2- road spectrum exciter; 3- overall lifting hydraulic cylinder; 4- hydraulic cylinder for partial lifting of the cutting system; 5- cutter; 6- gearbox; 7- cantilever; 8- frame; 9- conveying rack; 10- motor for engine excitation; 11- exciter hinge; 12- logistics hinge; 13- pin shaft

The excitation devices involve mechanical road exciters, a triple-phase asynchronous motor, frequency converters and an infrared photoelectric speedometer for calibration. With these, low-frequency road excitation, engine excitation of 50 Hz and high-frequency cutting force excitation can be achieved in experiments. As the main rigid component that supports various parts of cane cutting system, the beam-structure frame bears the dynamic loads under working conditions. The purpose of modal analysis is to find the weak points of the frame under the excitation loads based on its natural vibration forms, so as to provide a reference for subsequent optimization.

The modal testing was performed using an LMS data acquisition system, PCB three-axis acceleration sensors, and an excitation hammer. With the single-point excitation and multi-point response method, the PCB sensors were arranged at 66 measuring points on the whole machine, as shown in Figure 8. In this way, constrained modal frequencies and vibration modes can thus be analyzed to search for locations of weak dynamic stiffness while avoiding frequency resonances.

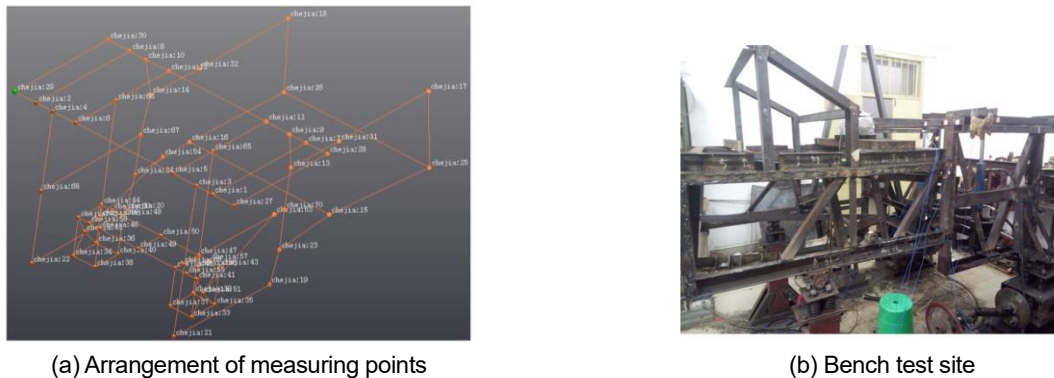


Fig. 8 - Modal Testing

Frequency-response function testing

Since the frame is the main transfer path from vibration sources to the cutter, it is necessary to test the vibration transfer function (VTF) before and after structural modifications. When the RMS of VTFs decreases and the peak frequency is far away from the excitation frequency, it means that the vibration isolation performance of the frame on the vibration transmission path is improved, and the response caused by the same excitation intensity is reduced. In addition, since the axial vibration of the cutter is most sensitive to the vertical vibration of the frame, the vertical VTF should be adopted.

With the road and engine vibration sources activated, a PCB acceleration sensor was arranged at the critical gearbox where the cutter was installed, as shown in Figure 9. Similarly, the LMS data acquisition system was employed to collect the response data of this target point of interest under multi-source vibration. Thus, the processed vertical frequency-response functions (FRF) from the two excitation sources to this response output location can be calculated as follows:

$$H(\omega) = \frac{t(\omega)}{f(\omega)} \tag{5}$$

where:

$t(\omega)$ is the frequency-related response at the target point, taking 0~100 Hz as the frequency analysis range; $f(\omega)$ is the hammer excitation force. In addition, the real time-domain signal of the cutter displacement before and after the frame optimization was also tested using the Laser vibration testing system, and its amplitude RMS was used as an indicator to verify the final optimization effect.

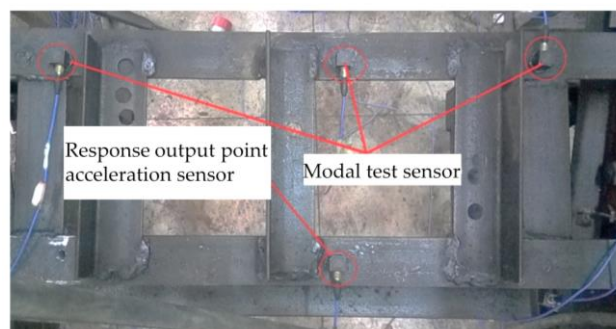


Fig. 9 - Response output signal acquisition

Optimized Design of Frame Structure

Multi-objective Topology Optimization

Considering the requirements of static Z-direction stiffness and dynamic vibration frequency, a comprehensive multi-objective optimization function combined compromise planning method with average frequency method was adopted for the frame structure (Liu et al., 2022):

$$\min F = \left\{ \omega^2 \left(\frac{C(\rho) - C_{\min}}{C_{\max} - C_{\min}} \right)^2 + (1 - \omega)^2 \left(\frac{\Lambda_{\max} - \Lambda(\rho)}{\Lambda_{\max} - \Lambda_{\min}} \right)^2 \right\}^{1/2} \tag{6}$$

where:

$C(\rho)$ and $\Lambda(\rho)$ are objective functions of flexibility and average frequency; ω is the weight of flexibility. Thus, the optimal material distribution capable of comprehensively improving stiffness and dynamic frequency can be suggested in the design domain to guide the frame shape design.

Besides, in ANSYS 14.5 software, the beam elements in the non-optimized region were set to SOLID92 and the shell elements in the optimized region were set to SHELL93. Dynamic single-step load conditions were applied simultaneously with the simple harmonic forces of the field road and the engine on the frame. Then, taking ω as 0.4, the iterative control of optimization objectives was implemented based on APDL language programming.

Implicit parametric modeling

In order to solve the problem of steel specification selection of the main load-bearing beams in the frame structure, an implicit parameter-based modeling of the frame was carried out to further obtain a better beam structure design scheme in terms of inherent dynamic characteristics (Chen et al., 2016). For the main force deformation forms of the beam, bending and torsion, its moment of inertia and polar moment of inertia depend on its cross-sectional shape and size. Hence, several stressed beams with large bending and torsion degrees were extracted based on the modal results, and their cross-sectional dimensions were used as parametric design variables (V_i). The ANSYS command flow was actually employed to create these beams to be optimized. The beam element used Beam188, which was a two-node three-dimensional linear element suitable for linear, large-angle or large-strain nonlinear analysis of slender to medium-thick short beam structures. As a result, an implicit parameterized model of the frame containing material properties, solder joints, constraints and other information was obtained, as shown in Figure 10.

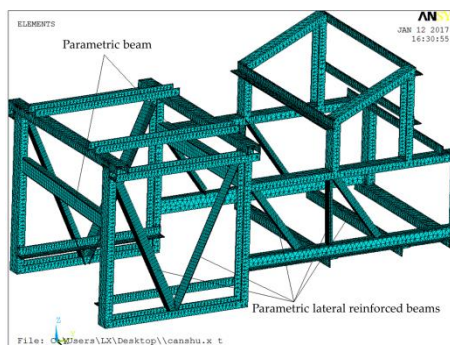


Fig. 10 – Implicit parametric model

Taking the reduction of the frame mass and moving the dangerous natural frequency out of the resonance frequency band as constraints, and aiming to increase the first to four-order natural frequencies as the goal, a mathematical model for beam section size optimization was established:

$$\begin{cases} \min F(V_i) = 1/f_{av} \\ s. t. \begin{cases} V_{i\min} \leq V_i \leq V_{i\max} \\ (50 - f_5) \cdot (66.7 - f_5) \geq 0 \\ m \leq m_o \end{cases} \end{cases} \tag{7}$$

where:

f_{av} is the low-order average frequency, Hz; V_i is the i -th design variable, $i=1,2...10$; f_5 is the 5th-order dangerous resonance frequency, Hz; m_o is the initial mass of frame, kg. Based on the conditions, a parametric optimization design was carried out using a zero-order algorithm with a maximum number of iterations of 30 (Yan et al., 2020).

RESULTS

Correlation analysis of cutter vibration

Under the joint action of road spectrum excitation, periodic excitation of engine and cane cutting pulse excitation, the simulated vibration response of the cutter is shown in Figure 11. It can be seen that the RMS of the cutter displacement response is 2.64 mm, and the RMS of the vibration velocity is 74.6 mm·s⁻¹. The average displacement during a single cutting is 0.17 mm, which can produce an impulse on the cut surface. The average displacement during the interval between two cuts is 0.97 mm, which could cause obvious bending moments to promote crack expansion.

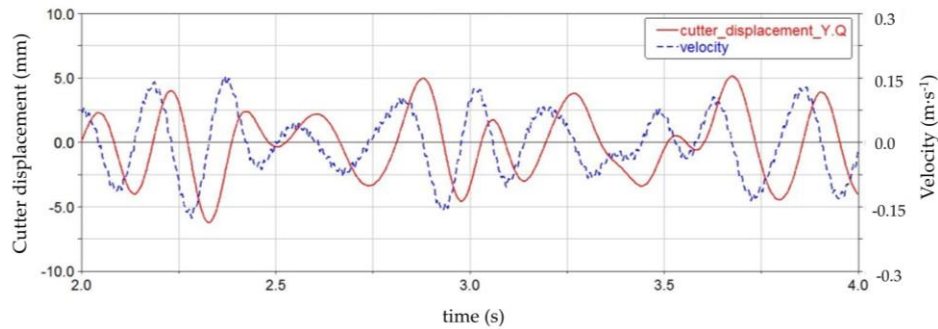


Fig. 11 - Nonlinear response of vibration

The correlation between dynamic parameters and cutter vibration was analyzed, and the results are shown in Table 1. It was found that the stiffness and mass (E_1 & m_1) of the frame had a higher impact on vibration, which was related to the fact that the frame structure accounted for the largest proportion and was the most widely distributed in the harvester. Therefore, the frame should be the main object of structural dynamics optimization where computing resources are concentrated.

Table 1

Correlation analysis results			
Dynamic parameters	Amplitude correlation	Impact velocity correlation	
m_1	-0.073	0.134	
m_2	0.022	-0.055	
K_1	0.051	-0.020	
K_3	-0.010	0.074	
K_5	-0.016	0.019	
K_6	0.009	-0.023	
L_1	0.026	-0.055	
L_2	0.006	-0.014	
L_3	-0.008	0.013	
E_1	0.168	-0.122	
E_2	0.091	-0.027	

Analysis of frame dynamic characteristics

The simulated and measured low-order frequency results below 50 Hz are shown in Table 2, and the corresponding vibration modes are shown in Figure 12. The errors between the finite element simulation results and the actual values are all less than 5%. Taking into account the errors in bench processing and assembly, it is believed that the accuracy requirements can be met. This suggests that further dynamic optimization can be carried out for the finite element model of frame. At the same time, it was found that the 5th-order natural frequency was close to the engine excitation frequency range, indicating that a dangerous resonance frequency currently existed.

Table 2

Comparison of modal results from finite element simulation and actual testing				
Order	Simulated frequency (Hz)	Tested frequency (Hz)	Description of vibration modes	
1	21.1	20.5	X-direction oscillation	
2	25.9	25.0	Z-direction oscillation	
3	40.0	38.6	X-direction first-order torsion	
4	47.6	45.3	Z-direction first-order bending	
5	53.0	51.2	X-direction second-order torsion	

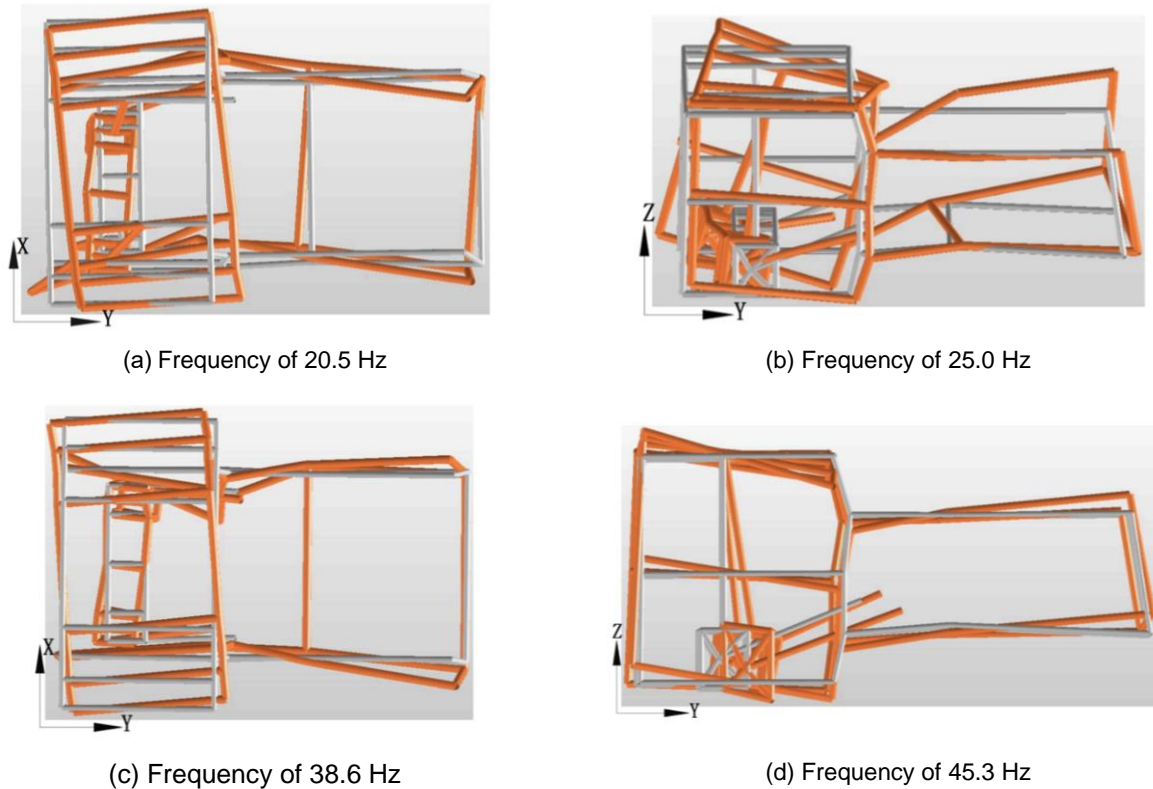


Fig. 12 - Vibration modes for modal testing

From the constrained modal results in Figure 12, the vibration modes and their frequencies were consistent with the finite element results. The combination of the four vibration modes showed that the dynamic stiffness of the frame was insufficient in the lateral and vertical directions, especially the open structure at the front end lead to severe lateral oscillations. Therefore, it was judged that the supporting structure located on the sides of the frame and the beam structures with right-angle bends were weak links and should be regarded as optimization focus.

Analysis of frame optimization

Figure 13(a) shows the density cloud diagram obtained by topology optimization of the frame under the condition of material removal rate of 50%. It has gradually evolved from the initial full-coverage plate-shell elements to a specific structural distribution composed of support beams. After extracting and simplifying the features of material-concentrated area, the reconstructed frame model is shown in Figure 13(b). The comparison results between the natural frequencies of the reconstructed model and the original values after topology optimization are shown in Table 3. The low-order frequencies have been increased by 17.91% to 86.37%, indicating that the dynamic characteristics have been further improved.

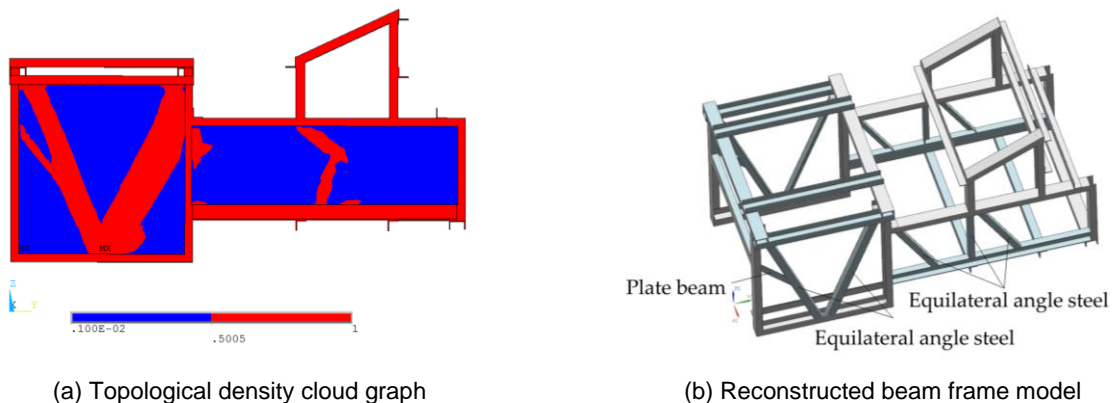


Fig. 13 - Multi-objective topology optimization results

Table 3

Comparison of natural frequencies before and after reconstruction

Natural frequency	Topology optimized	Reconstructed	Rate of change (%)
f_1 (Hz)	19.77	23.31	17.91
f_2 (Hz)	25.04	36.10	44.17
f_3 (Hz)	25.46	47.45	86.37
f_4 (Hz)	36.09	47.89	32.70

The initial values, constraints and parameter optimization results for parameterized variables and multi-objectives are shown in Table 4. Comparing the dynamic performance before and after optimization shows that without increasing the mass of the frame, the low-order frequencies of the frame were increased and the dangerous fifth-order natural frequency was moved out of the engine's resonance frequency band, achieving the expected optimization effect. Besides, the specification combination of steel dimensions for the main load-bearing beams was determined.

Table 4

Parameterized optimization results

Variables	Definition	Initial	Constraint	Optimized
V_1 (mm)	Front crossbeam channel steel width	80	50 ~120	85.3
V_2 (mm)	Front crossbeam channel steel height	43	35 ~55	48.9
V_3 (mm)	Front crossbeam channel steel thickness	5	4~6	4.3
V_4 (mm)	Middle crossbeam rectangular steel width	60	40~80	47.7
V_5 (mm)	Middle crossbeam rectangular steel height	90	70~120	70.8
V_6 (mm)	Middle crossbeam rectangular steel thickness	4	3~5	3.3
V_7 (mm)	Front side beam angle steel edge length	50	40~60	56.7
V_8 (mm)	Front side beam angle steel thickness	5	3~6	3.0
V_9 (mm)	Rear side beam angle steel edge length	40	30~50	46.2
V_{10} (mm)	Rear side beam angle steel thickness	5	3~5	3.2
m_1 (kg)	Frame mass	195.7	≤ 195.7	195.5
f_1 (Hz)	1 st -order frequency	28.5		29.2
f_2 (Hz)	2 nd -order frequency	31.1		32.7
f_3 (Hz)	3 rd -order frequency	38.9		39.2
f_4 (Hz)	4 th -order frequency	49.1		49.9
f_5 (Hz)	5 th -order frequency	58.3	≤ 50 or ≥ 66.7	66.9

Analysis of frequency-response characteristics

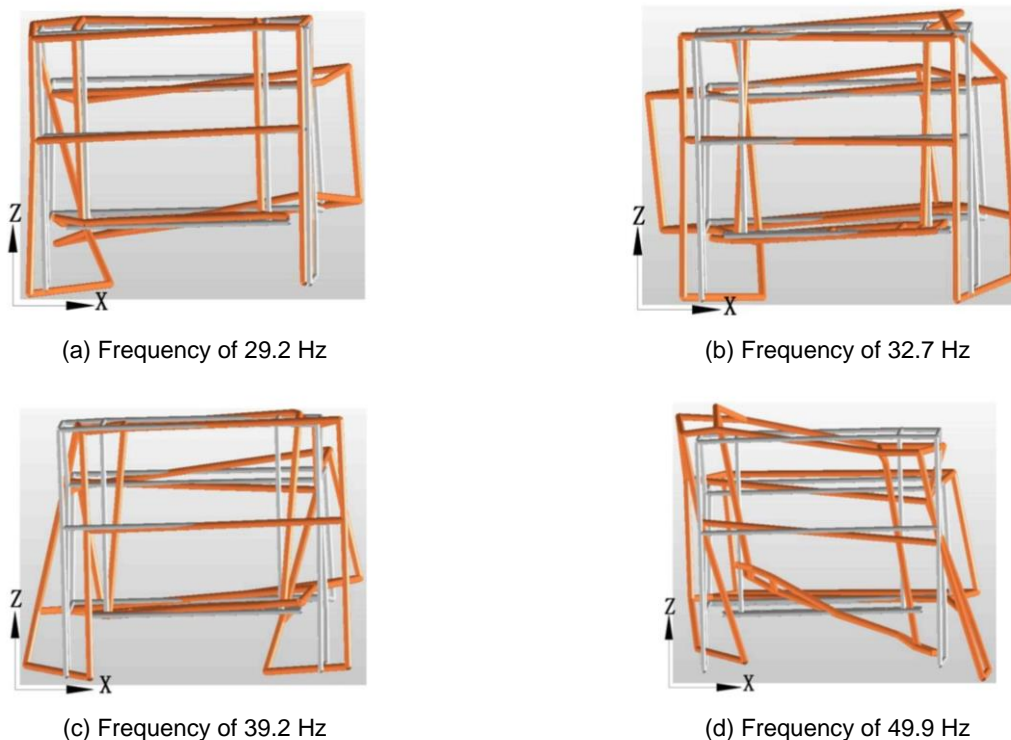


Fig. 14 - Vibration modes of optimized frame structure

It can be seen from the test results (Fig.14) that the vertical vibration mode of the optimized frame disappears, indicating that the vertical stiffness of the frame structure has been enhanced.

Figure 15 shows the vertical FRFs along different vibration transmission paths tested for the optimized frame. The frequency-response characteristics under multiple operating conditions can be extracted from it. In comparison, the response amplitude RMS ($2.3 \text{ e}^{-3}\text{g}\cdot\text{N}^{-1}$) excited by the road spectrum was larger than that ($2.2 \text{ e}^{-3}\text{g}\cdot\text{N}^{-1}$) of the engine. Among the two excitation sources, road excitation was the dominant factor. The peak value of frequency of excited by the road spectrum was close to the engine excitation frequency, which may cause dangerous resonance. The test results of the optimized frame were shown in Table 5. The response amplitude RMS excited by the road spectrum and engine were decreased by 21.7% and 27.2% respectively. In addition, the excitation frequencies that can produce significant amplitudes avoided two operating frequency ranges, i.e. 1~5 Hz for the road spectrum and 50~66.7 Hz for the engine.

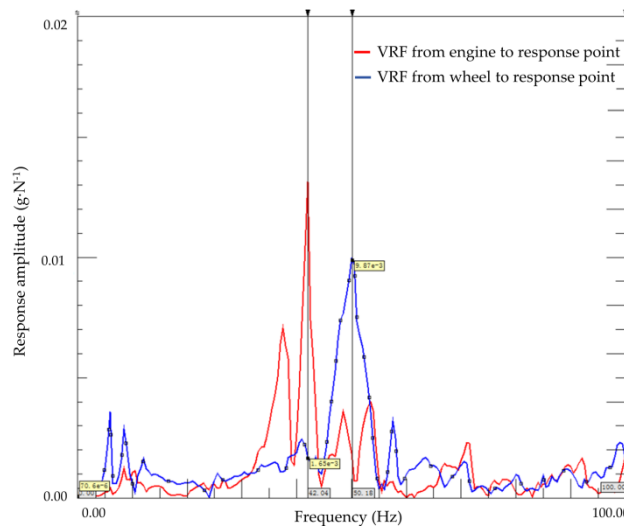


Fig. 15 - Tested frequency-response functions

Table 5 summarizes the comparison results extracted from the measured FRFs before and after frame optimization. It was found that bending and torsional stiffness of the optimized frame increased slightly, and throughout the range of 0~100 Hz, the amplitude RMS and variance values from the engine or road to the response point (P_e & P_r) were reduced to varying degrees (21.7%~46.6%), indicating that the response characteristics of these transmission paths have been improved and the system robustness has become more stable. It was comprehensively verified that the frame achieved dynamic characteristics optimization through topological and implicit parameter optimization processes. Moreover, the vertical vibration amplitude and VI output at the cutter position were ultimately reduced by 35.9% and 5.9% respectively. Based on the positive correlation between vibration response and cutting damage, the improvements of these two indicators were obviously beneficial to reducing the cutting damage level of sugarcane.

Table 5

Comparison of VRF index before and after frame optimization

FRF Index	Initial value	Optimized value	Rate of change
Bending stiffness ($\text{kN}\cdot\text{mm}^{-1}$)	11.80	12.03	1.95%
Torsional stiffness [$\text{kN}\cdot\text{m}\cdot(\text{N})^{-1}$]	11.98	12.32	2.84%
RMS of P_e ($\text{e}^{-3}\text{g}\cdot\text{N}^{-1}$)	2.2	1.6	-27.2%
Variance of P_e ($\text{e}^{-6}\text{g}^2\cdot\text{N}^{-1}$)	3.2	2.2	-31.3%
RMS of P_r ($\text{e}^{-3}\text{g}\cdot\text{N}^{-1}$)	2.3	1.8	-21.7%
Variance of P_r ($\text{e}^{-6}\text{g}^2\cdot\text{N}^{-1}$)	3.0	1.6	-46.6%
Vertical amplitude (mm)	0.64	0.41	-35.9%
V_l ($\text{mm}\cdot\text{s}^{-1}$)	101.2	95.2	-5.9%

CONCLUSIONS

(1) This paper presented a method for optimizing cutting damage of cane stalk based on implicit parametric modeling of frame. The excitation sources under the working conditions of sugarcane harvester were analyzed qualitatively and quantitatively by combining theory and experiment. Based on the analysis of the damage mechanism of sugarcane cutting, vibration amplitude and impact velocity were proposed as dynamic indicators to characterize damage inducibility.

(2) Through the constructed dynamic model and rigid-flexible coupled virtual prototype model, the parameters with the greatest influence on the nonlinear cutter response were selected from 21 dynamic parameters by correlation analysis. The results showed that the frame stiffness and mass had the greatest correlation with responses, which pointed out the target for subsequent optimization.

(3) Combined with topological and implicit parametric optimization, the dynamic characteristics of the frame were improved. Comparison of testing results before and after optimization showed that the bending and torsional stiffness were increased by 1.95% and 2.84%, and a dangerous natural frequency was moved out of the engine's operating frequency band. The RMS of FRFs with road and engine as path sources were reduced by 21.7% and 27.2% respectively, which comprehensively improved the frequency-response characteristics of such vibration system. Finally, the output amplitude RMS and impact velocity were decreased by 35.9% and 5.9% respectively, which was beneficial to reduce the level of damage to cane stalks. This study provided a reference for the development of harvester dynamic systems based on harvesting quality optimization.

ACKNOWLEDGEMENT

This research was funded by the Chinese Postdoctoral Science Foundation (Grant No. 2023MD734147), the Guangxi Major Science and Technology Special Project (Grant No. Guike AA22117004-1) and the Project of Guangxi Key Laboratory of Environmental Pollution Control and Ecological Restoration Technology (23-026-14).

REFERENCES

- [1] Chen X., Hu C., Ning, H., Wu Y., Wang S., Yang C. (2016). Implicit parameterization modeling and multi-performance lightweight optimization for SUV body-in-white (SUV 白车身隐式参数化建模及多性能优化轻量化), *Journal of Jilin University (Engineering and Technology Edition)*, vol.46, no.6, pp.1780-1785.
- [2] Gupta C P., Oduori M F. (1992). Design of the Revolving Knife-Type Sugarcane Basecutter, *Transactions of the ASAE*, vol.35, no.6, pp.1747-1752.
- [3] Fan Z., Li S., Ma F., Li W., Lai X., Xue B. (2012). Simulation analysis and experiment on influence of road spectrum of cane field on cutting quality (甘蔗地路谱对切割质量影响的仿真分析与试验), *Transactions of the Chinese Society of Agricultural Engineering*, vol.28, no.1, pp.37-41.
- [4] Gu D., Ding H., Qu Y., Zhang X., Shen H., Sun S., Hu A. (2013). Development of high-speed light diesel engine for forklift (叉车用轻型高速柴油机的开发), *Chinese Internal Combustion Engine Engineering*, vol.34, no.4, pp.83-91.
- [5] Han H., Sorokin V., Tang L., Cao D. (2022). Lightweight origami isolators with deployable mechanism and quasi zero stiffness property, *Aerospace Science and Technology*, vol.121, DOI: <https://doi.org/10.1016/j.ast.2021.107319>.
- [6] Hou J., Xu W., Wang J., Chen J., Zhang K., Li Y. (2021). Analysis of vehicle-bridge coupling vibration considering the influence of expansion joint (考虑伸缩缝参数影响的连续梁桥车-桥耦合动力响应研究), *Journal of Vibration and Shock*, vol.40, no.22, pp.151-160.
- [7] Kroes S., Harris H D. (1995). A kinematic model of the dual base cutter of a sugar cane harvester, *Journal of agricultural engineering research*, vol.62, no.3, pp.163-172.
- [8] Kroes S., Harris H D. (1996). Measuring and predicting force, energy, bending strength and splitting of sugar cane during an impact cut, *In: Z. EurAgEng' 96, Madrid*.
- [9] Li S., Chen Z., Zhou J., Mo H., Zhong J. (2017). Topological optimization design of sugarcane harvester cutter based on dynamic characteristics (基于动态特性的甘蔗收获机切割器拓扑优化设计), *Journal of Agricultural Mechanization Research*, vol.39, no.9, pp.25-30.
- [10] Liu F., Yang X., Fang X., Liu Y., Wu J., Zhao J. (2018). Design and experiment of chopper device in sugarcane harvester (甘蔗收获机切段装置设计与试验), *Transactions of the Chinese Society for Agricultural Machinery*, vol.49, no.9, pp.90-94.
- [11] Liu J., Luo L., Xiao X., Zhang C., Mi C. (2022). Multi-objectives topology optimization of frame in an electric mining dump truck based on fuzzy satisfaction variable weight coefficients method, *Journal of Mechanical Science and Technology*, vol.36, pp.3059-3069, DOI: 10.1007/s12206-022-0536-5.

- [12] Liu Q., Qu Y., Qin S., Huang S. (2007). High-speed photography analysis on the damage process in cutting sugarcane stalk with smooth edge blade (光刃刀片切割甘蔗茎秆破坏过程高速摄像分析), *Transactions of the Chinese Society for Agricultural Machinery*, vol.38, no.10, pp.31-35.
- [13] Liu Q., Qu Y., Qin S., Song C. (2007). Cutting force test of sugarcane stalk (甘蔗茎秆切割力试验), *Transactions of the Chinese Society of Agricultural Engineering*, vol.23, no.7, pp.90-94.
- [14] Lv Y., Yang J., Liang Z., Mo J., Qiao Y. (2008). Simulative kinematics analysis on the affecting factors of rate of broken biennial root of single base cutter of sugarcane harvester (单圆盘甘蔗切割器影响破头率的运动学仿真), *Transactions of the Chinese Society for Agricultural Machinery*, vol.6, no.4, pp.50-55.
- [15] Ma F., He Y., Li S., Liang S., Hu S. (2006). Analysis on fuzzy comprehensive evaluation and optimization of cutting performance of sugarcane harvester (甘蔗收获机切割性能的模糊综合评价与优化), *Transactions of the Chinese Society for Agricultural Machinery*, vol.37, no.12, pp.79-82.
- [16] Marin E., Cârdei P., Vlăduț V., Biriș S-Șt., Ungureanu N., Bungescu S.T., Voicea I., Cujbescu D., Găgeanu I., Popa L-D., Isitcioaia S., Matei Gh., Boruz S., Teliban G., Radu C., Kabas O., Caba I., Maciej J. (2023). Research on the influence of the main vibration-generating components in grain harvesters on the operator's comfort, *INMATEH – Agricultural Engineering* 74 (3), pp. 800-815, DOI: <https://doi.org/10.35633/inmateh-74-85>.
- [17] Mello, R. D. C., & Harris, H. (2001). Angled and serrated blades reduce damage, force and energy for a harvester basecutter. *Proc. Conf. Australian Soc. Sugar Cane Tech.* pp. 1212-1218.
- [18] Mo H., Qiu C., Li S., Ma S. (2022). Dynamic characteristic research on a simulated sugarcane field exciter for small sugarcane harvesters: simulations and experiments, *Journal of Vibroengineering*, vol.24, no.5, pp.806-823, DOI:10.21595/jve.2022.22015.
- [19] Mo J., Liu Q. (2013). Discussion on the mechanization technology of sugarcane harvesting in China (我国甘蔗收获机械化技术探讨), *Journal of Agricultural Mechanization Research*, vol.35, no.3, pp.12-18.
- [20] Momin M A., Wempe P A., Grift T E., Hansen A. (2017). Effects of Four Base Cutter Blade Designs on Sugarcane Stem Cut Quality, *Transactions of the ASABE*, vol.60, pp.1551-1560.
- [21] Pelloso M., Pelloso B F., de Lima A A., Ortiz A. (2021). Influence of harvester and rotation of the primary extractor speed in the agroindustrial performance of sugarcane, *Sugar Tech*, vol.23, pp.692-696, DOI: <https://doi.org/10.1007/s12355-020-00944-6>.
- [22] Razavi J., Kardany M., Masoumi A. (2010). Effects of some cutting blades and plant factors on specific cutting energy of sugarcane stalk. *17th World Congress of the International Commission of Agricultural Engineering (CIGR)*. Québec City, Canada June 13-17, 2010
- [23] Silva., Rouverson & Corrêa., Caio & Cortez. (2008). Statistical control applied in the process of mechanical sugar cane harvest. *Engenharia Agrícola*, vol.28, no.2, pp.292-304.
- [24] Vlăduț V., Biriș S.Șt., Bungescu T., Herișanu N. (2013). The influence of vibrations on the operator in the grain harvesters, *Applied Mechanics and Materials*, Vol. 430, pp 290-296, DOI: 10.4028/www.scientific.net/AMM.430.290.
- [25] Wang F., Zhang W., Di M., Wu X., Song Z., Xie B., Yang G., Ma S. (2019). Sugarcane Cutting Quality Using Contra-Rotating Basecutters, *Transactions of the ASABE*, vol.62, no.3, pp.737-747, DOI: 10.13031/trans.12716.
- [26] Wu J., Chen R., Qiu L., Fan Y., Li Y., Deng Y., Yan H., Zhou H., Zhou Z., Li A. (2022). Study on the effect of different reseeding methods on sugarcane (不同补种方法对宿根蔗的效果研究), *Sugarcane and Canesugar*, vol.51, no.4, pp.7-12.
- [27] Xu N., Ren Z., Li X., Cha H. (2017). Study on vertical vibration transmission and ride performance with the coupling effect between vehicle and suspended devices (车辆与吊挂设备耦合作用垂向系统振动传递及平稳性研究), *Journal of Vibration Engineering*, vol.30, no.6, pp.965-975.
- [28] Yan G., Shen X., Yu F., Zhu B., Liang W. (2020). Optimization design of frame structure of ROV based on ANSYS-Workbench (基于 ANSYS-Workbench 对水下机器人框架结构优化设计), *Manufacturing Automation*, vol.42, no.10, pp. 1-3+7.
- [29] Yang R., Zhou H., Liang Q., Tang S., Wang L., Gui Y., Huang H., Huang Z., Xian W., Lei J. (2021). Analysis of ratoon ability for sugarcane families (甘蔗家系宿根性分析), *Chinese Journal of Tropical Crops*, vol.42, no.7, pp.1932-1940.

- [30] Yang W., Wang E., Yang J., Li Y., Huang S., Liang Z. (2017). Test of the factors influencing the cutting quality of Case A8000 sugarcane combine (凯斯 A8000 甘蔗联合收割机切割质量影响因素的试验), *Journal of Agricultural Mechanization Research*, vol.39, no.5, pp.192-196.
- [31] Zou Z., Wu T., Gao Z., Zhang Z., Liu Q. (2018). Design and test of cut-off auto control system for sugarcane billet harvester (甘蔗收割机切割刀盘浮动控制系统的设计与试验), *Journal of Henan Agricultural University*, vol.52, no.1, pp.73-79.
- [32] Zhang Q., Xian Y., Xiao Q., Xu L., Li Z., Yi S., Li L. (2023). Backstepping sliding mode control strategy of non-contact 6-DOF Lorentz force platform, *Journal of Vibration and Control*, vol.29, no.5-6, pp.1061-1075.
- [33] Zhou J., Li S., Yang D., Zhong J., Mo H., Zhang B., Deng X. (2017). Influence of sugarcane harvester cutterhead axial vibration on sugarcane ratoon cutting quality (甘蔗收获机刀盘轴向振动对甘蔗宿根切割质量的影响), *Transactions of the Chinese Society of Agricultural Engineering*, vol.33, no.2, pp.16-24.
- [34] Zhou J., Li S., Mo H. (2018). Test on influence of sugarcane harvester's dynamic properties on the broken rate of ratoons (甘蔗收获机动态特性对宿根破头率影响的试验), *Journal of Agricultural Mechanization Research*, vol.40, no.2, pp.150-156.

A REVIEW OF INNOVATIVE DESIGN AND INTELLIGENT TECHNOLOGY APPLICATIONS OF THRESHING DEVICES IN COMBINE HARVESTERS FOR STAPLE CROPS

主粮作物联合收获机脱粒装置的创新设计与智能化技术应用研究综述

Fuqiang GOU^{1,2,3}, Jin WANG^{1,3}, Youliang NI¹, Zhenjie QIAN¹, Tengxiang YANG¹, Chengqian JIN^{*,1,4}

¹ Nanjing Institute of Agricultural Mechanization, Ministry of Agriculture and Rural Affairs, Nanjing, Jiangsu / China ¹

² Wenshan Advanced Technical School, Wenshan, Yunnan / China

³ Graduate School of Chinese Academy of Agricultural Sciences, Beijing / China

⁴ School of Agricultural Engineering and Food Science, Shandong University of Technology, Zibo, Shandong / China

Corresponding author: Chengqian JIN

Tel: +8615366092900; E-mail: jinchengqian@caas.cn

DOI: <https://doi.org/10.35633/inmateh-75-61>

Keywords: Grain combine harvester, threshing device, intelligent detection, intelligent control

ABSTRACT

This paper reviews the progress in innovative design and intelligent technology applications of threshing devices in combine harvesters for staple crops. To address the issues of poor adaptability and low intelligence in traditional threshing systems, researchers have significantly improved threshing performance by optimizing threshing components and drum structures. Meanwhile, machine vision and deep learning have achieved important breakthroughs in feed rate monitoring, breakage and impurity rate detection, and intelligent control. This review aims to provide a reference for research and applications in threshing system structural optimization and operational parameter control.

摘要

本文综述了主粮作物联合收获机脱粒装置的创新设计与智能化技术应用进展。针对传统脱粒装置适应性差和智能化程度低的问题，研究者通过优化脱粒元件和滚筒结构显著提升了脱粒性能。同时，机器视觉和深度学习在进料速度监测、破碎率与含杂率检测及智能控制方面取得了重要突破。综述旨在为脱粒系统结构优化、作业参数控制等研究与应用提供参考。

INTRODUCTION

With the rapid growth of the population and the increasing demand for food, food security plays a crucial role in economic and social development. Achieving efficient and low-loss mechanized harvesting is a key approach to increasing grain yield (Shahbazi et al., 2025). The combine harvester is a large-scale harvesting machine that integrates multiple functions (Fu et al., 2018; Ni et al., 2021; Yin et al., 2024), including cutting, threshing, and cleaning. While ensuring operator comfort (Marin et al., 2024; Vlăduț et al., 2023), the performance of the threshing system directly determines the quality and efficiency of grain crop harvesting. With the gradual application of emerging technologies such as sensor technology and automatic control in agricultural machinery for navigation (Xie et al., 2023; Yao et al., 2024), path planning (Chen et al., 2024), and operation quality monitoring (Guo et al., 2025), there is significant potential for the innovative design and intelligent upgrading of combine harvester threshing devices. These advancements lay the foundation for achieving clean, low-loss, and highly efficient intelligent harvesting with combine harvesters (Mandal et al., 2024).

The threshing system of a combine harvester primarily consists of a threshing drum, concave, transmission, and adjustment mechanisms (Miu et al., 2008b, 2008a). By adjusting operational parameters such as drum speed and feed rate, optimal threshing quality can be achieved (Vlăduț et al., 2023). Based on the different conveying directions of crops within the drum, various structural forms of threshing devices have been developed, including tangential threshing devices (Hussain et al., 2024), axial threshing devices (Srison et al., 2016; Vlăduț et al., 2022), and hybrid tangential-axial threshing devices (Chai et al., 2020).

¹ Fuqiang Gou, Stud. Eng.; Jin Wang, Stud. Eng.; Youliang Ni, Eng.; Zhenjie Qian, Associate Prof. Ph.D. Eng.; Tengxiang Yang, Eng.; Chengqian Jin, Prof. Ph.D. Eng.

Currently, threshing systems meet the requirements for harvesting various staple crops; however, challenges remain, including high grain breakage rates, high impurity and loss rates, and a lack of precise control (Guo *et al.*, 2019). In particular, under challenging harvesting conditions such as high humidity, threshing devices are prone to clogging and entanglement (Tang *et al.*, 2019). In terms of operational parameter and quality monitoring, installing quality detection sensors on key working components (Liu *et al.*, 2025) has enabled the monitoring of breakage rates and loss rates (Chen *et al.*, 2024).

However, due to environmental interferences such as vibration, dust, high humidity, and high temperatures, sensors often suffer from low real-time performance, stability, and accuracy (Li *et al.*, 2024; Liu *et al.*, 2024). Additionally, the lack of standardized communication protocols among various sensors and actuators leads to difficulties in integrating, sharing, and monitoring multi-source heterogeneous data (Qiu *et al.*, 2022). Furthermore, although machine learning- and deep learning-based operation quality detection methods (Hasan *et al.*, 2023) have achieved significant advancements, challenges remain in acquiring large-scale datasets, manual data annotation, and the high cost of training data (Ahmed *et al.*, 2025).

In terms of intelligent control strategies and algorithms, a state-space model of the threshing system has been established, and expert systems based on empirical rules have been integrated into the control module (Omid *et al.*, 2010). Additionally, associative models such as neural networks have been introduced to capture nonlinear relationships, while methods like fuzzy control (Craessaerts *et al.*, 2010) and adaptive regulation strategies (Zhu *et al.*, 2025) have been employed to achieve dynamic adjustment of operational parameters. However, due to limitations in sensor detection accuracy, the generalizability of algorithm models, and insufficient machine-wide coordination, modeling the complex, dynamic, and nonlinear relationships between operational parameters and crop attributes over time remains challenging. As a result, real-time responsiveness is poor, and the threshing control system lacks deep adaptive capabilities and multi-parameter decoupling (Zhang *et al.*, 2022a).

In summary, due to the variations in planting patterns and harvesting environments of different staple crops, existing data acquisition and information fusion methods still face challenges related to models and algorithms in practical applications. These issues significantly hinder the real-time control capability of threshing systems in adjusting operational parameters. Given this context, this study systematically reviews recent research progress in the structural design, operational performance optimization, and integration of intelligent technologies in combine harvester threshing devices for staple crops. Furthermore, potential future research directions and development trends are explored to provide insights and references for the continuous innovation and practical application of threshing devices.

INNOVATIVE DESIGN OF THRESHING DEVICE STRUCTURE

The primary operating targets of staple crop combine harvesters include maize, soybeans, and cereals (wheat and rice), necessitating the design of threshing devices tailored to the specific properties of different crops. Therefore, in the structural innovation of threshing devices, key operational components should be interchangeable and adjustable to accommodate various crop characteristics. Additionally, the combined application of multiple threshing structures, the flexibility of critical components, and lightweight design are fundamental principles in the innovative structural design of threshing devices (Dong *et al.*, 2023; Zhao *et al.*, 2023).

Corn Threshing Devices

For maize crops, the maize ear has a large volume, hard kernels, high adhesion strength between kernels and the cob, and a high moisture content. Therefore, maize grain harvesting requires a threshing system with sufficient throughput and high processing efficiency. To ensure low breakage while maintaining effective threshing, high-intensity impact or rubbing mechanisms are commonly employed (Qian *et al.*, 2017; Steponavičius *et al.*, 2023). By adjusting the threshing drum diameter, various variable-diameter and variable-speed threshing drum designs have been developed. For instance, Wang *et al.*, (2021), designed a conical variable-diameter threshing drum (Figure1), which enhances the ear-holding capacity in the threshing section, loosens the interaction forces between kernels and between kernels and the cob, and enables efficient threshing and conveying of maize ears with different diameters.

Traditional concaves in maize combine harvesters are typically designed with a fixed radius and are mostly rectangular or arcuate in shape, making it difficult to meet the diverse harvesting requirements of different crops and moisture levels. To address this limitation, Pužauskas *et al.*, (2017), proposed the concept of "inclined beam and variable-radius concaves" and found that when the working surface of the inclined beam was set at 45°, maize kernel separation efficiency, breakage rate, and threshing losses were optimized. By innovating the operational mechanism of threshing drums and the structural design of threshing components,

Hou et al., (2023), developed a novel low-damage, high-efficiency threshing drum. Additionally, Tang et al., (2024), designed a low-loss threshing device equipped with a "rotatable concave sieve" (Figure 2), in which the concave rotates in the opposite direction to the drum, significantly increasing the residence time of maize ears in the threshing space. The concave is designed as an adjustable structure, enabling high threshing efficiency without the need for a substantial increase in drum speed, while simultaneously reducing mechanical damage to the kernels.

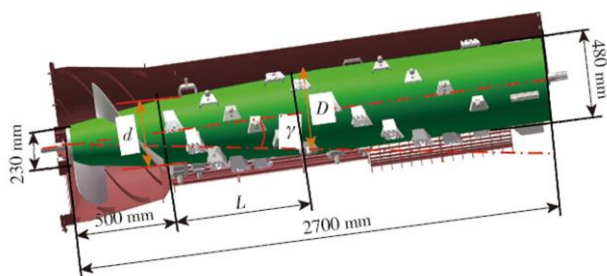


Fig. 1 - Variable diameter threshing drums (Wang et al., 2021)

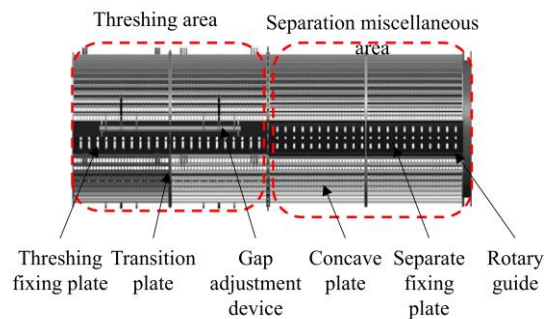


Fig. 2 - Schematic of rotary concave screen (Tang et al., 2024)

Traditional threshing devices typically employ rigid spike-tooth or short rasp-bar threshing elements, which often result in either "high impact and high breakage" or "insufficient threshing." Consequently, the concept of flexible threshing elements has been introduced. For instance, Li et al., (2020), found that rubber composite spike-tooth elements significantly improved the threshing performance of high-moisture maize ears. Similarly, Chen et al., (2020), demonstrated that a combination of "flexible spike-tooth and dual-torsion spring-loaded short rasp bars" effectively reduced impact damage to kernels. Building on these findings, Song et al., (2022), proposed a flexible threshing device featuring "front-end flexible spike-tooth elements and rear-end elastic short rasp bars with pressure springs" (Figure 3). This design balances maize ear grasping, helical conveying at the front end, and flexible impact and rubbing-based threshing at the rear end, thereby minimizing kernel damage.

For high-moisture maize threshing, Li et al., (2023), introduced a flexible threshing element composed of variable-stiffness conical springs and impact tooth bars, which can appropriately rebound or yield upon contact with maize ears. Similarly, Li et al., (2023), designed a novel threshing drum incorporating a combination of rasp bars, separation rods, and impurity-removal bars. Compared to conventional spike-tooth drums, the increased contact area between the rasp bars and kernels reduces impact and clamping-induced breakage, particularly under high-moisture conditions.

Additionally, Gong et al., (2024), drew inspiration from torsion spring structures to develop a variable-stiffness maize flexible threshing element composed of conical springs and short rasp bars. Furthermore, Xing et al., (2024), designed a threshing element with helically arranged rasp-bar blocks installed in the threshing section (Figure 4). The improvements in threshing elements mainly focus on the alternating arrangement of different threshing components or the adoption of novel flexible threshing elements to minimize maize kernel breakage.

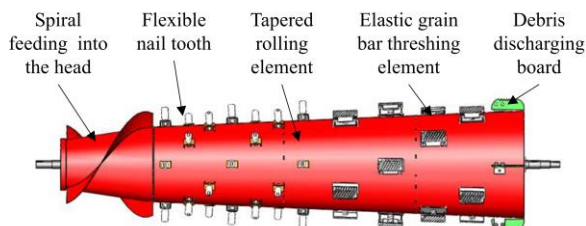
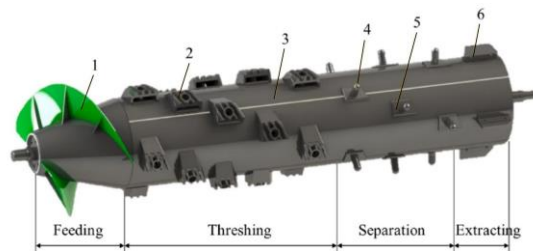


Fig. 3 - Flexible nail tooth and elastic grain bar threshing drum (Song et al., 2022)



1.Screw feeder; 2.Rasp bar threshing element; 3.Drum body; 4.Rod-tooth threshing element; 5.Installation base; 6.Exclusion board

Fig. 4 - Spirally arranged rasp bar threshing elements (Xing et al., 2024)

In summary, through concave adjustment, flexible improvements in threshing elements, and optimization of variable-diameter drum structures in maize threshing devices, the contradiction between incomplete threshing and high kernel breakage rates can be effectively mitigated. These advancements enhance the adaptability of threshing devices to varying feed rates and moisture conditions, thereby improving overall threshing efficiency and grain quality.

Grain threshing devices

For cereal threshing, the adhesion force between the grain and the husk (or pod) is relatively low, the grain size is small, and the moisture content is lower. Additionally, cereal crop stems are relatively thin and brittle. As a result, threshing elements in cereal harvesters predominantly utilize arc-tooth and spike-tooth structures to achieve threshing through friction and rubbing (Abdeen et al., 2021; Hu et al., 2024). For example, the application of a rigid-flexible coupled arc-tooth design has been shown to reduce stem clogging and decrease grain breakage rates.

For concave adjustment, the perforation design must ensure high screening efficiency, typically utilizing hydraulic or electronically controlled adjustment mechanisms (Su et al., 2020). For instance, Yuan et al., (2024), adopted a rod-tooth threshing drum (Figure 5) combined with an adjustable concave clearance design, demonstrating excellent adaptability to uneven wheat feeding and moist crops.

Based on the segmented axial-flow threshing and separation device for rice and wheat, Kang et al., (2022), designed a symmetrically adjustable concave, allowing for dual-sided threshing gap adjustments to enhance threshing performance across varying moisture conditions. Furthermore, Kang et al., (2025), developed an independently adjustable concave system comprising long concave sieves, short concave sieves, electric cylinders, and a control system. This system modifies the internal rubbing intensity of the material, thereby improving threshing efficiency.

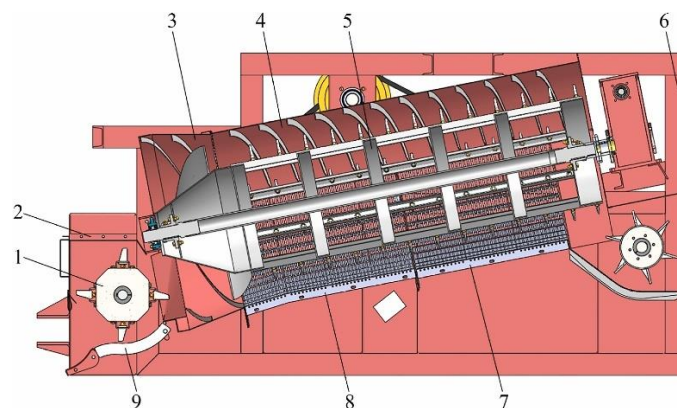


Fig. 5 - Tangential and longitudinal-axial threshing and separating unit (Yuan et al., 2024)

1. Tangential drum; 2. Tangential cover; 3. Conical cylinder; 4. Longitudinal axial cover; 5. Axial-flow drum;
6. Frame; 7. Rear axial concave; 8. Front axial concave; 9. Tangential concave

For the optimization of threshing drum structures, the primary approach involves using variable-diameter and variable-speed threshing drums to address the adaptability limitations of fixed-diameter drums in the threshing and separation zones. Typically, the threshing zone adopts a larger diameter, while the separation zone utilizes a smaller diameter conical drum. For instance, Abdeen et al., (2025), evaluated and optimized the performance of a longitudinal axial-flow threshing device using a conical threshing drum. Similarly, Zhang et al., (2022b), designed an axial threshing and separation device incorporating a front-end rasp bar and a rear-end spike-tooth structure, demonstrating that the combination of rasp bars and spike teeth meets the operational requirements for both threshing and separation.

Additionally, differential-speed threshing drums can be designed to enhance crop feed rate adaptability. Examples include a segmented threshing drum with an adjustable rotational speed difference between the front and rear sections (Kang et al., 2023) (Figure 6) and a coaxial differential-speed threshing drum with a spiral plate-tooth axial threshing system (Zhou et al., 2022). Furthermore, Wang et al., (2022), developed a combination threshing device with independently rotating inner and outer drums, effectively reducing grain breakage during threshing. For rice threshing, Liu et al., (2022), Wang et al., (2023), designed a variable-diameter rice threshing drum (Figure 7), which improves adaptability to varying feed rates and effectively reduces stem clogging issues.

In summary, the innovative design of cereal threshing devices enhances crop throughput capacity through concave adjustments, reduces grain breakage by incorporating flexible threshing elements, and improves multi-crop adaptability with variable-diameter and variable-speed drum designs. These advancements provide a critical foundation for enhancing the threshing performance and intelligent control of combine harvesters, offering significant engineering application value.

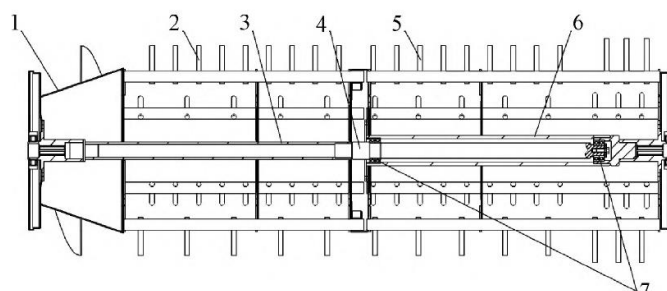


Fig. 6 - Structure diagram of differential threshing cylinder (Kang et al., 2023)
1. Feeding auger; 2. Front threshing cylinder; 3. Low speed hollow shaft; 4. Low speed solid shaft; 5. Latter threshing cylinder; 6. High speed hollow shaft; 7. Bearing

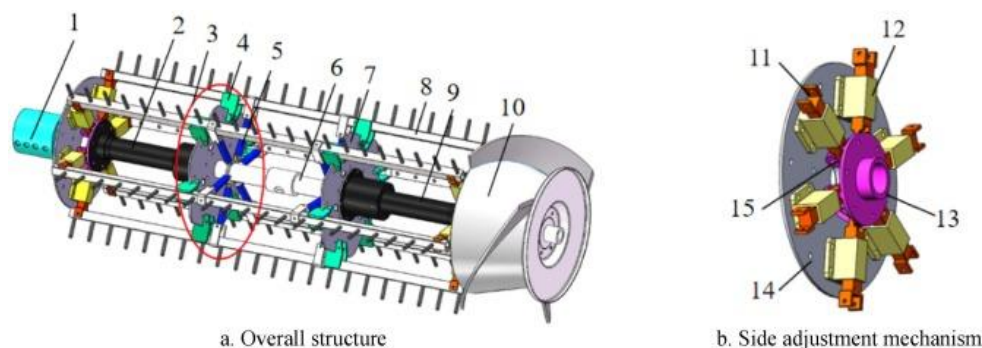


Fig. 7 - Schematic diagram of the variable-diameter threshing drum
(Liu et al., 2022; Wang et al., 2023)

1. Hydraulic rotary joint; 2. End hollow hydraulic cylinder; 3. Middle adjustment mechanism; 4. Baffle; 5. Tension spring; 6. Main shaft; 7. Middle support plate; 8. Threshing rod; 9. Feeding side hollow hydraulic cylinder; 10. Feeding wheel; 11. Connecting rod; 12. Sliding groove; 13. Guide rail push plate; 14. Side support plate; 15. Pin shaft.

INTELLIGENT TECHNOLOGY FOR THRESHING SYSTEMS

The primary objective of the intelligent technology applied to threshing and separation in combine harvesters is to enhance threshing efficiency, reduce loss and breakage rates, and ensure optimal operational quality across different crops and field conditions. This paper reviews research progress in key areas, including feed rate detection, breakage and impurity content monitoring, entrainment loss detection, and intelligent control. It explores the application of machine vision technology, deep learning models, and intelligent optimization algorithms in threshing systems, providing a reference for the integration of intelligent perception, decision-making, and control in threshing system operations.

Intelligent feed rate detection

In traditional combine harvesters, the grain feed rate is typically estimated based on the forward speed and cutting width, which results in low accuracy since the feed rate is influenced by multiple factors, including crop density, header height, cutting width, grain moisture content, and forward speed (Zhang et al., 2018). In recent years, with the application of sensor technology and deep learning in data detection, significant advancements have been made in grain feed rate detection technology. Furthermore, multi-sensor data fusion techniques have further improved detection accuracy.

Mechanical sensor detection technology

Mechanical sensor detection technology estimates the feed rate based on pressure variations as grain material passes through the auger, feeder house, and threshing drum. Typically, pressure sensors are installed on the feeder house bottom plate, while torque sensors are mounted on the auger drive shaft, concave, and drum bearings to measure pressure and torque fluctuations during harvesting. By integrating these measurements with the power consumption and operating speed of the threshing system, the feed rate can be calculated.

For instance, *Liang et al., (2013)*, developed an online monitoring system for feed rate estimation based on drum torque, rotational speed, grain flow, and the straw-to-grain ratio. However, the system exhibited a certain degree of data latency. To investigate the relationship between feed rate and header torque, *Zhang Z. et al., (2019)*, designed a feed rate monitoring system based on the torque of the header drive shaft, revealing a strong correlation between header torque and feed rate. *Abdeen et al., (2022)*, constructed a longitudinal axial-flow rice threshing platform and designed a threshing drum cover stress monitoring system using force-sensitive resistors. Their results showed that the force signals collected by the thin-film sensors were significantly correlated with drum rotational speed and feed rate. Additionally, by installing vibration acceleration sensors at the bottom of the inclined conveyor (Figure 8), *Liang et al., (2024)*, investigated the impact of feed rate on the vibration characteristics of the combine harvester's inclined conveyor.



Fig. 8 - Installation positions of the vibration acceleration sensor (*Abdeen et al., 2022*)
 (a) Position of the inclined conveyor in the combine harvester; (b) Sensor placement on the inclined conveyor

With the advancement of multi-sensor fusion technology, the integration of multiple parameters—such as header torque, inclined conveyor torque, and crop properties—has significantly improved the accuracy of feed rate detection. *Zhang et al., (2022)*, proposed a feed rate detection method based on multi-sensor decision-level fusion (Figure 9) and developed a feed rate monitoring system for grain combine harvesters. Their study analyzed the correlation between operating speed, crop density, auger torque, conveyor torque, and cylinder torque with feed rate. The results demonstrated that the proposed detection system exhibited high monitoring accuracy and stability.

To further enhance detection precision, *Sun et al., (2022)*, developed a neural network-based feed rate detection method by incorporating multiple parameters, including header drive shaft torque, header height, and grain moisture content. Among these approaches, torque and pressure measurements provide more direct and precise assessments. However, due to the distance between measurement points and the header, these methods exhibit a certain degree of data latency.

To address this issue, a feed rate monitoring system based on the reel force at the header position was developed (Figure 10). This system utilizes force sensors and angle sensors to detect variations in forward speed, reel rotational speed, header height, and plant bending force, enabling an accurate estimation of the combine harvester's feed rate (*Chen et al., 2025*).

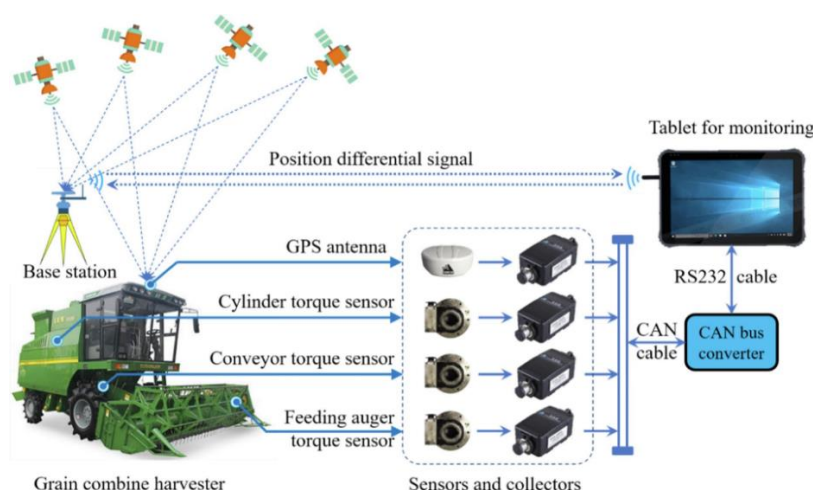


Fig. 9 - Multi-sensor fusion-based crop feed rate detection method (*Zhang et al., 2022*)

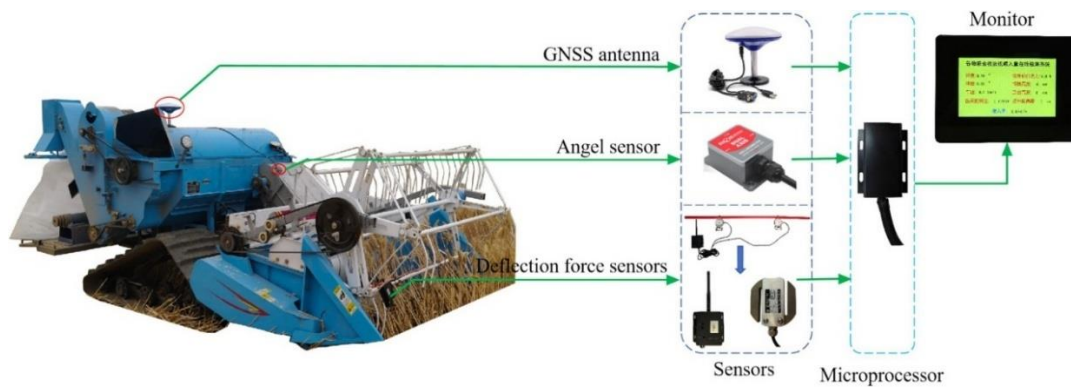


Fig. 10 - Design of the feed rate monitoring system (Chen *et al.*, 2025)

Intelligent detection technology

In addition to estimating feed rate based on material pressure measurements during harvesting, advanced intelligent detection technologies such as machine vision and LiDAR can be used for crop perception, enabling crop information collection and prediction. These technologies can estimate crop density and height, thereby indirectly predicting the relationship between crop feed rate and threshing performance.

The measurement principle of a LiDAR system is based on the constant speed of light to calculate the distance between the collision point and the emitted pulse (Rivera *et al.*, 2023). This allows for the determination of target object distance and depth, generating high-precision 3D point cloud data. Studies have shown that two LiDAR sensors can be used for real-time measurement of wheat crop density before harvesting with a combine harvester (Saeys *et al.*, 2009), as well as for analyzing the effects of LiDAR installation angle and height on crop height and density detection (Blanquart *et al.*, 2020).

To enhance LiDAR detection range and efficiency, LiDAR and spectral sensors can be mounted on unmanned aerial vehicles (Liu *et al.*, 2024), allowing for the integration of different data sources to develop a maize canopy height detection method. UAV-mounted spectral sensors offer the advantage of high-speed and efficient crop density detection; however, challenges remain, including high costs, blind spots in small target detection, and susceptibility to adverse environmental factors such as lighting conditions and dust.

With the continuous advancements in machine vision and deep learning technologies, deep learning is not only used for in-field crop and weed density detection (Adhinata *et al.*, 2024) but also for crop density assessment during the harvesting period. By equipping harvesters with machine vision technology, crop height and density data can be collected. Additionally, attention mechanisms can be introduced to optimize the backbone structure of neural networks, allowing for image segmentation and object detection of crops. This data, combined with field area measurements, can be used to estimate crop density. Zhang *et al.*, (2024), proposed a wheat crop density detection method based on an improved YOLOv5s model (Figure 11), which estimates the height of individual stubble-free wheat plants. Similarly, Sun *et al.*, (2024), developed a real-time rice panicle density detection method based on YOLOv5n (Figure 12). By applying coordinate transformation, this approach matches actual crop size with pixel area to calculate rice panicle density, thereby enhancing the harvester's crop state perception capabilities. Machine vision-based crop feed detection offers high accuracy and real-time performance; however, challenges remain, including the high computational cost of deep learning models, difficulties in field deployment, and the requirement for large-scale dataset training.



Fig. 11 - Visual data acquisition system for feed quantity (Zhang *et al.*, 2024)

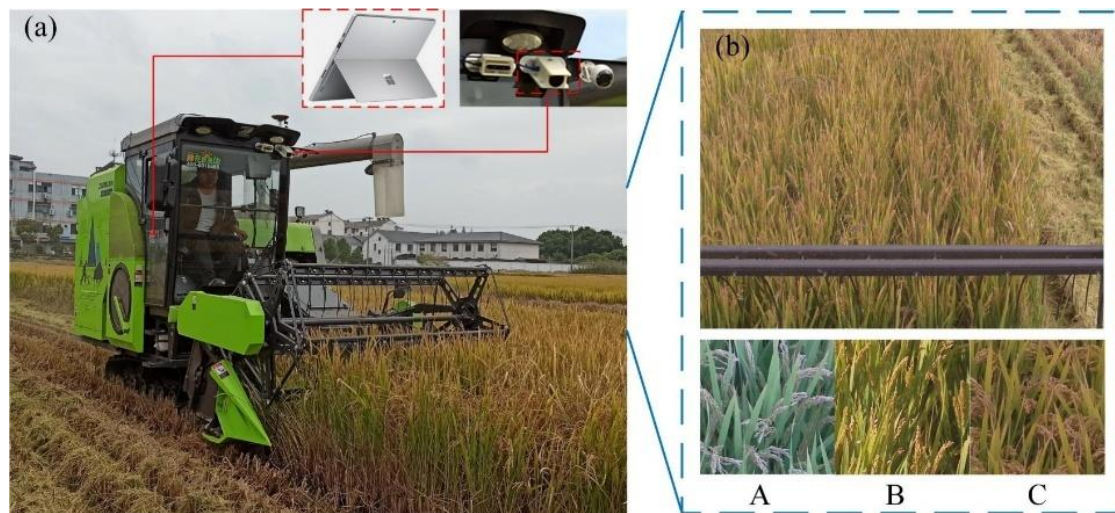


Fig. 12 - Real-time rice spike density detection image acquisition (Sun *et al.*, 2024)

(a) acquisition location; (b) sample

In summary, using mechanical sensors for indirect feed rate detection can provide insights into the material flow status within the harvester to a certain extent. However, the collected data lacks predictive capability, requires longer processing times, and is insufficient for providing real-time parameter adjustments for threshing operations. The integration of machine vision-based crop height and density detection methods with YOLO object detection models has proven effective in improving crop feed detection accuracy. Therefore, for crop feed rate detection, a multi-sensor fusion approach incorporating mechanical sensors, machine vision, and LiDAR can enhance environmental adaptability. Additionally, adopting lightweight neural network models combined with transfer learning techniques can reduce reliance on large-scale datasets, improve detection speed, and enhance model generalization capabilities.

Intelligent detection of breakage rate and impurity content

Traditional grain detection methods primarily rely on manual inspection, which is characterized by low efficiency, high error rates, and poor real-time performance. Machine vision and deep learning technologies, with their advantages of non-contact detection, high efficiency, and precise image recognition, provide new approaches for detecting grain breakage rate and impurity content. Machine vision analyzes grain morphological features based on image processing techniques, while deep learning, leveraging the powerful feature extraction capabilities of convolutional neural networks (CNN), integrates object detection, image segmentation, and classification regression methods. These approaches have demonstrated significant superiority in breakage rate and impurity content detection.

Machine vision-based intelligent detection

Machine vision-based grain breakage rate detection primarily relies on morphological, color, and texture feature extraction, as well as spectral imaging analysis, to distinguish between intact and broken grains. In terms of color feature extraction, image processing and feature extraction techniques have been used to calculate the impurity rate of maize kernels, cobs, and husks (Liu *et al.*, 2022). Similarly, Momin *et al.*, (2017), performed image segmentation and detection to identify different types of split soybeans, contaminated beans, defective beans, and stems/pods, achieving an identification accuracy of 96% for split beans, 75% for contaminated beans, and 98% for defective beans and stems/pods. Figure 13 illustrates the image processing workflow for grain and impurities in harvested soybeans.

To improve real-time breakage and impurity detection, Jin *et al.*, (2020), proposed an online rice breakage rate detection system for combine harvesters based on machine vision. This system identifies broken and intact grains by extracting the chromaticity of kernel images in the color space. Similarly, Chen *et al.*, (2021), developed a soybean image acquisition system based on machine vision, achieving a precision rate of 86.45% for breakage rate detection and 85.19% for impurity detection.

Regarding spectral imaging analysis, multi-spectral vision sensors have been employed to obtain spectral bands of pure maize kernels, husks, and straw based on pixel proportions (Wallays *et al.*, 2009). Additionally, by extracting impurity images and spectral features of wheat at different terahertz frequencies, a CNN classification model was developed to process and classify the imaging data, leading to the construction of the V2 CNN wheat image detection model (Shen *et al.*, 2021).



Fig. 13 - Image processing process of soybean harvested seeds with impurities (Momin *et al.*, 2017)

Machine vision-based impurity content detection primarily relies on object detection and classification, combined with hyperspectral imaging technology. By utilizing differences in reflectance between grains and impurities across the hyperspectral range, grain impurity detection can be effectively achieved. For instance, Liu *et al.*, (2023), introduced a standardized attention mechanism and employed the NAM-EfficientNetV2 network as the grain feature extraction structure. They applied fully convolutional pixel segmentation techniques to segment rice grains and impurities. Similarly, Zhang *et al.*, (2024), proposed a wheat breakage rate and impurity rate detection method based on the DeepLab-EDA semantic segmentation model and developed a wheat quality image acquisition system (Figure 14). The DeepLab-EDA model achieved mean intersection over union (MIoU), mean precision (MP), and mean recall (MR) values of 89.41%, 95.97%, and 94.83%, respectively, demonstrating a significant improvement in the accuracy of grain breakage and impurity segmentation.

Additionally, Chen *et al.*, (2025), integrated hyperspectral imaging with a random forest (RF) model to achieve rapid and accurate classification of soybean components. The RF classification model achieved optimal prediction accuracy during training, demonstrating its effectiveness in hyperspectral-based impurity detection.

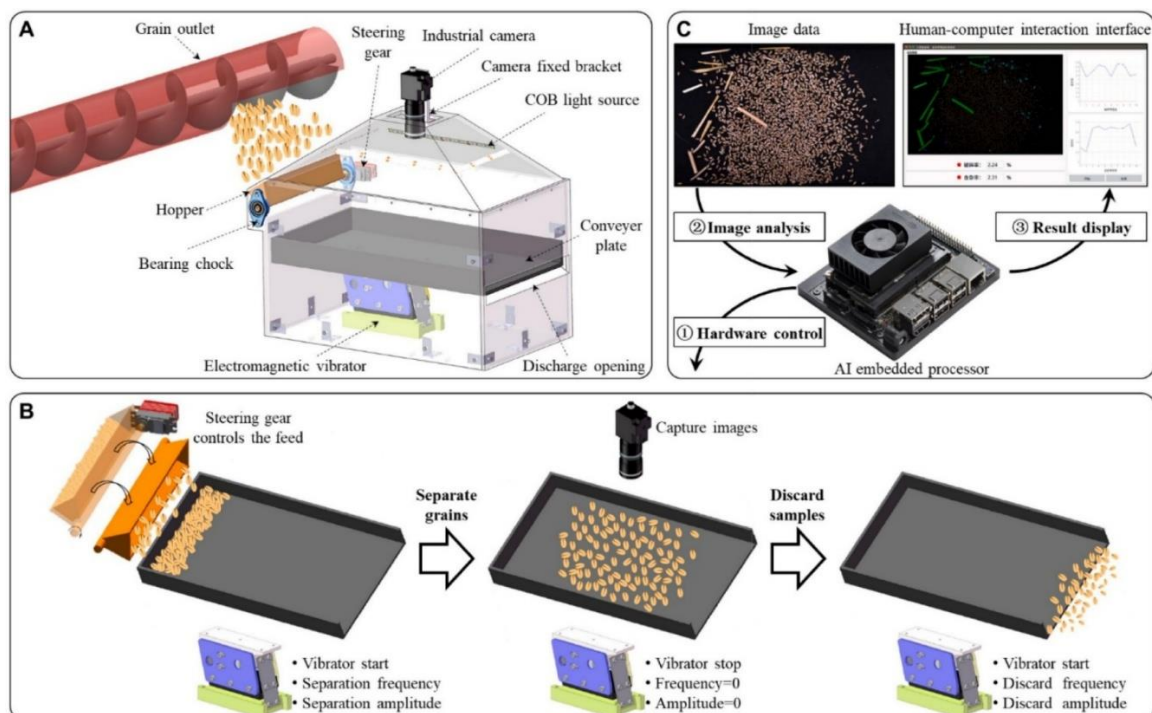


Fig. 14 - Wheat broken rate and impurity rate detection system (Qi *et al.*, 2024)

(A) wheat image acquisition device; (B) wheat grain sampling-discarding process; (C) system architecture

Deep learning-based intelligent detection

Deep learning-based grain breakage rate detection primarily utilizes YOLO or Faster R-CNN for object detection, U-Net or Mask R-CNN for image segmentation, and ResNet or VGGNet for feature extraction. These models are used to identify intact and broken grains, accurately segment breakage regions, and extract key features such as the edges, texture, and color of broken grains.

Traditional machine learning methods have relatively weak generalization capabilities for breakage detection. To address this, *Wu et al., (2022)*, proposed a maize impurity and breakage rate detection method using feature thresholds and a backpropagation (BP) neural network optimized with a genetic algorithm. The improved Mask R-CNN method demonstrated advantages such as fast detection speed and high accuracy, achieving a maize kernel breakage rate detection time of only 76 ms. *Wang et al., (2023)*, enhanced the YOLOv7 model by integrating a transformer encoding block and a coordinate attention mechanism, proposing the BCK-YOLOv7 model for maize kernel breakage detection. Similarly, *Fan et al., (2024)*, developed a breakage rate prediction model based on machine vision and machine learning algorithms. In another study, *Wang et al., (2025)*, utilized deep learning and sliding window techniques to propose a quantitative model for maize kernel breakage rate detection, named BCK-YOLOv7 (Figure 15). After model deployment, the system achieved a processing speed of 22 FPS, meeting the real-time detection requirements for maize kernel breakage rates. To reduce the computational complexity of detection models, *Wu et al., (2024)*, developed a lightweight impurity content and breakage rate detection system based on the Mask R-CNN model (Figure 16). The improved model increased segmentation accuracy for broken particles and impurities by 6.13% and 9.19%, respectively.

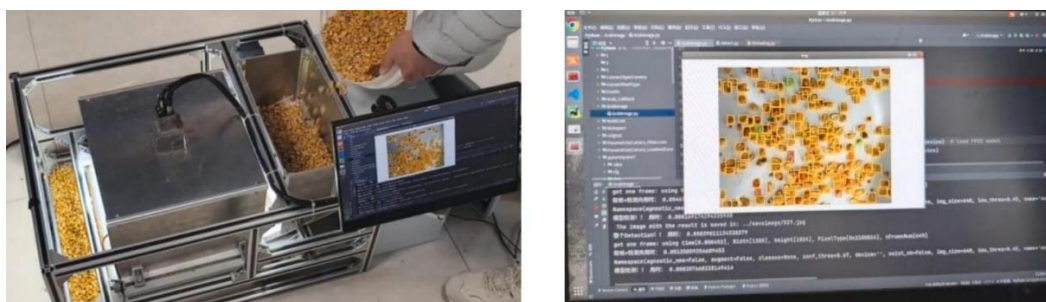


Fig. 15 - Dynamic detection of maize kernels based on BCK-YOLOv7 (*Wang et al., 2025*)

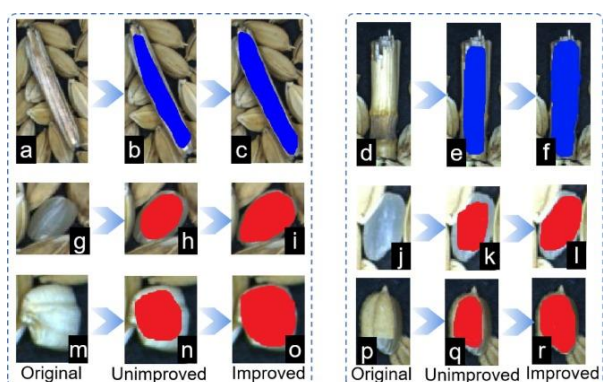


Fig. 16 - Comparison of Detection Performance Before and After Improvement Based on the Mask R-CNN Model (*Wu et al., 2024*)

Deep learning-based impurity content detection primarily employs ResNet or MobileNet for classification, combined with hyperspectral imaging and attention mechanisms to enhance impurity detection accuracy (*Yu et al., 2023*). *Zhang et al., (2023)*, evaluated rice impurity and breakage rates using an improved DeepLabv3+ and YOLOv4 model, achieving higher recognition accuracy compared to existing DeepLabv3+, YOLOv4, U-Net, and BP models. Similarly, *Niu et al., (2024)*, developed a lightweight YOLOv8 quality detection model to address issues of fine-grained information loss and low feature representation learning efficiency in YOLOv8, achieving an average recognition speed of 163.9 FPS per image, which is 5.2 FPS faster than the standard YOLOv8 model. *Zhang et al., (2024)*, proposed an improved YOLOv8n-based lightweight detection method tailored for small, high-density target detection, achieving impurity and breakage detection accuracies of 95.33% and 96.15%, respectively. Additionally, *Zhang et al., (2025)*, introduced a dual-attention diffusion model (DADM) based on a denoising diffusion probabilistic model, which demonstrated superior detection performance on maize, rice, and soybean datasets. This model effectively addresses challenges in agricultural image acquisition caused by seasonal, climatic, and environmental variations, further advancing the integration of deep learning applications in the agricultural sector.

In summary, significant progress has been made in grain breakage rate and impurity content detection using machine vision and deep learning. However, challenges remain, including high data annotation costs, poor real-time performance, and insufficient environmental adaptability. Future research should focus on lightweight deep learning models for integration into harvesters, enabling real-time processing. Additionally, the fusion of multimodal sensors should be explored to enhance the accuracy of grain and impurity recognition.

Intelligent detection of entrainment loss rate

The detection of entrainment loss in the threshing system is primarily used to evaluate threshing quality. Current research on entrainment loss monitoring mainly involves installing entrainment loss monitoring sensors beneath the threshing drum to analyze the correlation between the number of maize kernels detected by the sensors and the actual entrainment loss (Bomoi *et al.*, 2022). This approach enables indirect monitoring of entrainment loss. For entrainment loss detection, the YT-5L piezoelectric ceramic element is commonly used as a sensing component to develop grain loss monitoring sensors. The performance of these sensors is evaluated by analyzing the voltage amplitude and signal attenuation time of grain impact events. Additionally, operational parameters such as feed rate and drum speed influence the proportional relationship between sensor measurements and actual entrainment loss.

Liu *et al.*, (2023), designed an entrainment loss detection system for direct maize grain harvesting based on an embedded microcontroller. The system exhibited a maximum detection error of 9.96% and an average error of approximately 6.52%. Similarly, Dong *et al.*, (2024), symmetrically installed two entrainment loss monitoring sensors along the radial direction of the threshing drum and developed a maize entrainment loss monitoring model using a multiple linear regression machine learning algorithm. Figure 17 illustrates the structure and signal processing workflow of the entrainment loss monitoring sensor.

Furthermore, Dong *et al.*, (2024), designed another entrainment loss detection system (Figure 18) and implemented a random forest machine learning algorithm to construct a loss prediction model, significantly improving entrainment loss estimation accuracy. To further enhance detection precision and practical application, Yu *et al.*, (2025), identified that the optimal placement of the detection sensor was at the left tail end of the concave sieve, with a minimum distance of 58 mm between the sensor plate centerline and the concave sieve, and an installation angle of 65° relative to the horizontal plane, achieving the highest detection accuracy.

In summary, current entrainment loss detection models are relatively simplistic, often neglecting dynamic operating conditions such as feed rate and drum speed variations. This limitation results in significant fluctuations in sensor measurement errors, reducing detection accuracy. Additionally, the adaptability of sensor installation positions and structures remains insufficient, and the vibration characteristics of combine harvesters during field operations significantly impact sensor performance. With the accumulation of entrainment loss detection data, the integration of multi-sensor fusion and deep learning models can enhance noise suppression and real-time analysis capabilities, enabling the development of a more precise and reliable loss monitoring system.

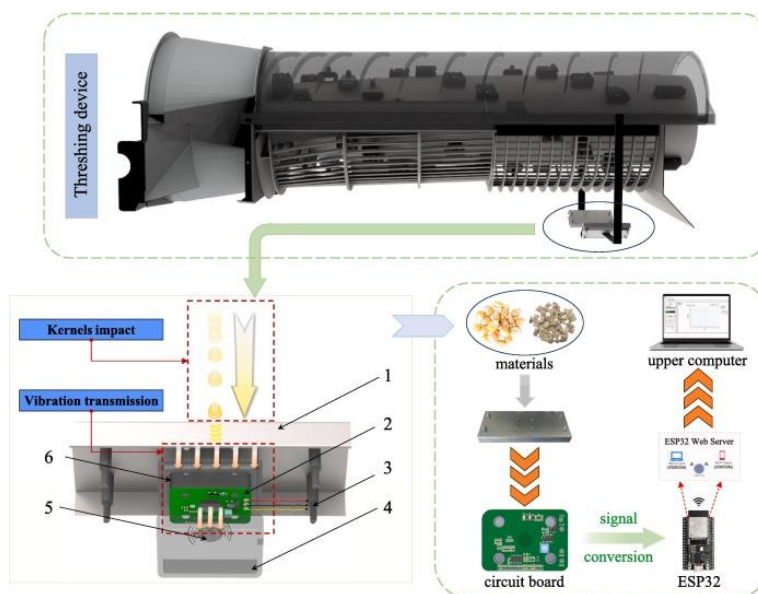


Fig. 17 - Structure and signal processing workflow of the entrainment loss monitoring sensor (Dong *et al.*, 2024)
1. Sensor sensitive plate; 2. Circuit board; 3. Sensor fixing bolt; 4. Circuit board protector; 5. Piezoelectric ceramic; 6. Damping material

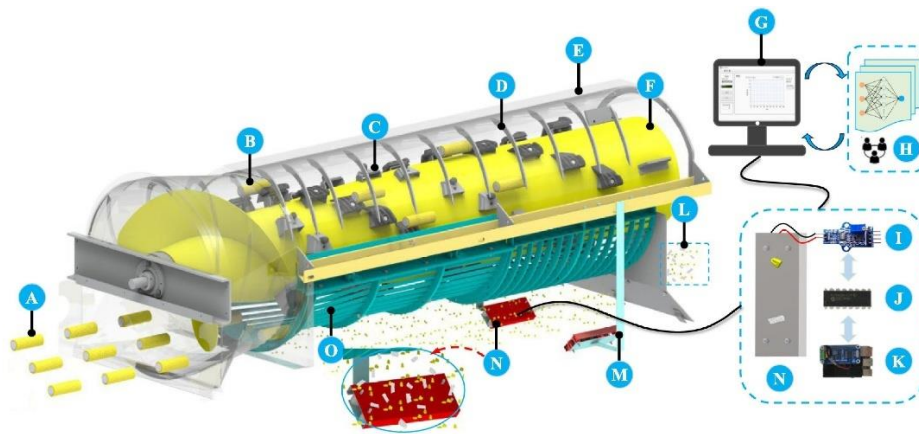


Fig. 18 - Schematic diagram of the entrainment loss monitoring system components (Dong et al., 2024)

(A) Maize Conveying; (B) Maize Threshing; (C) Threshing Elements; (D) Guide Vanes; (E) Threshing Cover; (F) Threshing Drum; (G) Display; (H) Classification Model; (I) Charge Amplification Module; (J) AD Converter Module; (K) Controller; (L) Entrainment Loss Material; (M) Sensor Mounting Bracket; (N) Sensor; (O) Concave Threshing Plate

Intelligent threshing control

Based on the structural innovations of threshing devices, the detection of operational parameters such as rotational speed, vibration, and torque, as well as machine vision-based detection of breakage rate and impurity content, a solid structural and data foundation has been established for intelligent control of the threshing system. Intelligent control technologies leverage algorithms such as fuzzy control, neural networks, and reinforcement learning to achieve dynamic adjustment of parameters including drum speed, concave clearance, and feed rate (Wang et al., 2025), thereby enhancing the threshing system's adaptability to multiple crops and improving threshing efficiency.

For intelligent control of maize threshing systems, the primary objective is to address the challenges of high grain breakage and entrainment loss rates during high-moisture maize harvesting under complex and time-varying operating conditions. Li et al., (2023), developed an automatic low-loss maize grain harvesting control system and optimized a control model for drum speed, concave clearance, and driving speed using an improved particle swarm optimization algorithm.

Additionally, some researchers have designed optimal control models based on feed rate and threshing gap. For instance, Fan et al., (2022), developed a threshing device equipped with an automatic gap adjustment system based on feed rate. Their results showed that the variable-gap threshing system outperformed fixed-gap systems in terms of efficiency under random feed rate fluctuations.

Moreover, variations in field conditions and crop density can cause fluctuations in the combine harvester's feed rate. To address this, Fan et al., (2023), proposed a multi-parameter maize threshing control structure and method based on feed rate (Figure 19). By applying intelligent algorithms, a control model was developed for drum speed, threshing gap, and cover vane angle, which enhanced the adaptability of the threshing system to different crop conditions.

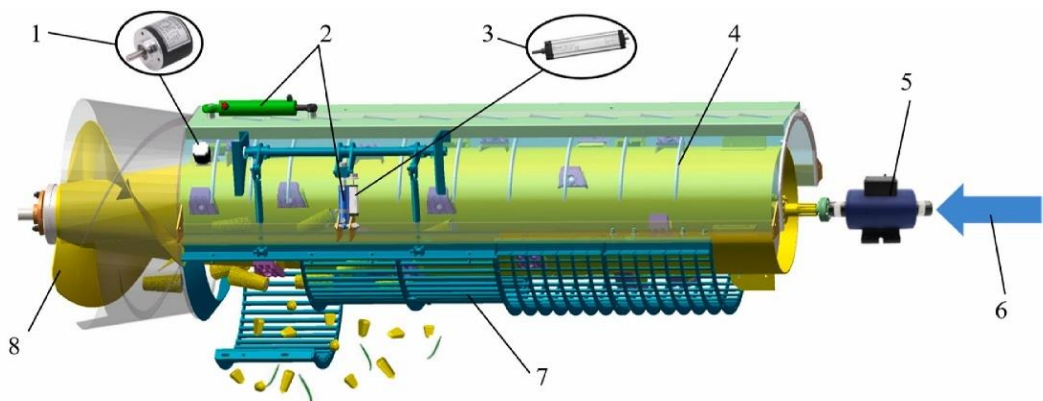


Fig. 19 - Hardware of the multi-parameter control system for maize threshing (Fan et al., 2023)

1. Angle sensor; 2. Hydraulic cylinder; 3. Displacement sensor; 4. Guide vane; 5. Dynamic torque sensor; 6. Hydraulic motor drive; 7. Concave; 8. Rotor

For intelligent control of cereal threshing systems, machine learning models have been applied to construct predictive models, effectively addressing the challenges of time variability, delay, and multi-parameter coupling in cereal threshing. These models provide a foundation for intelligent control of the threshing process. For example, *Ma et al., (2023)*, developed an artificial neural network (ANN) model to predict the performance of a flexible threshing device. Similarly, *Li et al., (2024)*, proposed a fusion approach combining particle swarm optimization and wavelet neural networks to optimize the state-space model of the threshing system. They employed model predictive control (MPC) to regulate multiple threshing parameters. The resulting state-space and adaptive control models demonstrated strong adaptability and stability for threshing system operation.

In summary, control technologies for intelligent threshing systems are developed based on structural innovations in threshing devices and the detection of operational parameters, providing both structural and data support for intelligent regulation. Methods such as fuzzy control and neural networks have been widely applied for the dynamic adjustment of threshing system operating parameters.

THRESHING SYSTEM DEVELOPMENT TRENDS

Multi-sensor fusion and intelligent detection

The multi-sensor fusion used for detecting operating parameters and operation quality in threshing systems still faces numerous challenges, including spatiotemporal synchronization, accuracy and robustness, real-time performance, and compatibility, making it difficult to provide stable and precise data. Therefore, for intelligent threshing systems, it is necessary to construct a multi-sensor fusion detection network utilizing various sensors such as infrared, laser, ultrasonic, and spectral sensors to enhance data accuracy.

Additionally, data synchronization mechanisms should be introduced, and intelligent filtering algorithms as well as deep learning methods should be applied to further improve data analysis and processing capabilities. Standardization of sensor data formats and communication protocols should also be established, along with the development of large-scale datasets for crop harvesting operations, to enhance the generalization capability of intelligent detection models.

Deep learning and intelligent algorithm optimization

Deep learning technology has demonstrated exceptional pattern recognition capabilities in the optimization of threshing operation parameters and quality detection. It significantly enhances the automation of key tasks such as grain loss prediction, breakage rate detection, impurity identification, and operational condition optimization. However, challenges remain, including limited availability of harvesting data samples, high data annotation costs, poor adaptability to different crops and field environments, and difficulties in integrating deep learning with threshing system control strategies.

Therefore, under the premise of multi-sensor fusion, the adoption of lightweight deep learning models is essential to enhance edge computing capabilities. In addition, the application of transfer learning and related techniques can promote the development of threshing operations toward higher precision, intelligence, and adaptability.

Intelligent control of threshing systems

Intelligent threshing control systems for combine harvesters still face core challenges such as difficulties in real-time control, poor crop adaptability, and complex multi-parameter coupling. Traditional control methods, including PID and fuzzy control, struggle to achieve precise regulation under complex and dynamically changing threshing conditions, often resulting in high levels of threshing loss, grain breakage, and impurity content.

Deep learning, through data-driven approaches, can predict optimal adjustment strategies for threshing parameters. When integrated with physical modeling, it enables the construction of reinforcement learning-driven intelligent adaptive control systems that autonomously adjust control parameters based on different crops and field environments. In the future, with the advancement of technologies such as digital twins, threshing control systems will become more precise and intelligent, further promoting the development of agricultural machinery toward unmanned operation and autonomous optimization.

CONCLUSIONS

The structural design of threshing devices in combine harvesters has been significantly optimized by fully considering crop characteristics and variations in operating conditions, resulting in enhanced multi-crop adaptability, improved threshing efficiency, and greater operational stability. At the same time, real-time monitoring technologies based on multi-sensor fusion, machine vision, and deep learning models have achieved major breakthroughs in key aspects such as feed rate detection, grain breakage rate analysis, impurity content assessment, and entrainment loss identification, providing high-precision data support for the intelligent regulation of threshing systems.

Moreover, adaptive control strategies based on fuzzy logic have laid the foundation for developing data-driven control systems with multiple inputs and outputs for threshing systems. Reinforcement learning methods are increasingly being adopted to enable real-time adjustment of threshing parameters in response to changing environmental conditions, ensuring that the system operates under optimal conditions—an emerging and important direction in the intelligent development of combine harvesters.

However, despite substantial technological progress, challenges remain in the online monitoring and dynamic regulation of threshing system operation parameters and quality indicators. In the future, with the further integration of artificial intelligence and deep learning into combine harvester threshing systems, the capabilities of intelligent perception, decision-making, and control will be significantly enhanced, ultimately enabling the construction of a low-loss, high-efficiency intelligent threshing system.

ACKNOWLEDGEMENT

We greatly appreciate the careful and precise reviews by the anonymous reviewers and editors. This research was funded by the National Key Research and Development Plan project (2021YFD2000503), the National Soybean Industry Technology System (CARS-04), the National Natural Science Foundation of China (No. 32171911), and the Central Public-interest Scientific Institution Basal Research Fund (S202411).

REFERENCES

- [1] Abdeen, M. A., Salem, A. E., & Zhang, G. (2021). Longitudinal Axial Flow Rice Thresher Performance Optimization Using the Taguchi Technique. *Agriculture*, 11(2), Article 2. <https://doi.org/10.3390/agriculture11020088>
- [2] Abdeen, M. A., Wu, W., Salem, A. E., Elbeltagi, A., Salem, A., Metwally, K. A., Zhang, G., & Elwakeel, A. E. (2025). The impact of threshing unit structure and parameters on enhancing rice threshing performance. *Scientific Reports*, 15(1), 6250. <https://doi.org/10.1038/s41598-025-91118-5>
- [3] Abdeen, M. A., Xie, G., Salem, A. E., Fu, J., & Zhang, G. (2022). Longitudinal axial flow rice thresher feeding rate monitoring based on force sensing resistors. *Scientific Reports*, 12(1), Article 1. <https://doi.org/10.1038/s41598-021-04675-w>
- [4] Adhinata, F. D., Wahyono, & Sumiharto, R. (2024). A comprehensive survey on weed and crop classification using machine learning and deep learning. *Artificial Intelligence in Agriculture*, 13, 45–63. <https://doi.org/10.1016/j.aiia.2024.06.005>
- [5] Ahmed, N., & Shakoor, N. (2025). Advancing agriculture through IoT, Big Data, and AI: A review of smart technologies enabling sustainability. *Smart Agricultural Technology*, 10, 100848. <https://doi.org/10.1016/j.atech.2025.100848>
- [6] Blanquart, J.-E., Sirignano, E., Lenaerts, B., & Saeys, W. (2020). Online crop height and density estimation in grain fields using LiDAR. *Biosystems Engineering*, 198, 1–14. <https://doi.org/10.1016/j.biosystemseng.2020.06.014>
- [7] Bomoi, M. I., Nawi, N. M., Abd Aziz, S., & Mohd Kassim, M. S. (2022). Sensing Technologies for Measuring Grain Loss during Harvest in Paddy Field: A Review. *AgriEngineering*, 4(1), Article 1. <https://doi.org/10.3390/agriengineering4010020>
- [8] Chai, X., Zhou, Y., Xu, L., Li, Y., Li, Y., & Lv, L. (2020). Effect of guide strips on the distribution of threshed outputs and cleaning losses for a tangential-longitudinal flow rice combine harvester. *Biosystems Engineering*, 198, 223–234. <https://doi.org/10.1016/j.biosystemseng.2020.08.009>
- [9] Chen, M., Chang, Z., Jin, C., Cheng, G., Wang, S., & Ni, Y. (2025). Classification and Recognition of Soybean Quality Based on Hyperspectral Imaging and Random Forest Methods. *Sensors*, 25(5), Article 5. <https://doi.org/10.3390/s25051539>

- [10] Chen, M., Jin, C., Ni, Y., Yang, T., & Xu, J. (2024). A dataset of the quality of soybean harvested by mechanization for deep-learning-based monitoring and analysis. *Data in Brief*, 52, 109833. <https://doi.org/10.1016/j.dib.2023.109833>
- [11] Chen M., Ni Y., Jin C., Xu J., & Zhang G. (2021). Online Monitoring Method of Mechanized Soybean Harvest Quality Based on Machine Vision(基于机器视觉的大豆机械化收获质量在线监测方法). *Transactions of the Chinese Society for Agricultural Machinery*, 52(1), 91–98. <https://doi.org/10.6041/j.issn.1000-1298.2021.01.010>
- [12] Chen, M., Xu, G., Wang, C., Xi, P., Zhang, Y., & Niu, G. (2020). Design and Experiment of Roller-type Combined Longitudinal Axial Flow Flexible Threshing and Separating Device for Corn(纵轴流辊式组合玉米柔性脱粒分离装置设计与试验). *Transactions of the Chinese Society for Agricultural Machinery*, 51(10), 123–131. <https://doi.org/10.6041/j.issn.1000-1298.2020.10.014>
- [13] Chen, T., Seok Ahn, H., Sun, W., Pan, J., Liu, Y., Cheng, J., & Xu, L. (2024). Optimizing path planning for a single tracked combine harvester: A comprehensive approach to harvesting and unloading processes. *Computers and Electronics in Agriculture*, 224, 109217. <https://doi.org/10.1016/j.compag.2024.109217>
- [14] Chen, X., Wu, S., Li, C., Liu, F., Yuan, L., & Wang, W. (2025). Design and experiment of feed rate monitoring system based on the action force of grain combine harvester reel. *Computers and Electronics in Agriculture*, 230, 109837. <https://doi.org/10.1016/j.compag.2024.109837>
- [15] Craessaerts, G., de Baerdemaeker, J., Missotten, B., & Saeys, W. (2010). Fuzzy control of the cleaning process on a combine harvester. *Biosystems Engineering*, 106(2), 103–111. <https://doi.org/10.1016/j.biosystemseng.2009.12.012>
- [16] Dong, J., Cui, T., Zhang, D., Yang, L., He, X., Xiao, T., Li, C., Xing, S., Jiang, Y., & Wang, H. (2024). Design and test of real-time monitoring system for maize entrainment loss based on piezoelectric signal classification. *Measurement*, 116050. <https://doi.org/10.1016/j.measurement.2024.116050>
- [17] Dong, J., Zhang, D., Yang, L., Cui, T., He, X., Jing, M., Li, C., Xing, S., & Jiang, Y. (2024). Research on monitoring model for maize entrainment loss sensor applicable to different operating parameters. *Computers and Electronics in Agriculture*, 220, 108854. <https://doi.org/10.1016/j.compag.2024.108854>
- [18] Dong, J., Zhang, D., Yang, L., Cui, T., Zhang, K., He, X., Wang, Z., & Jing, M. (2023). Discrete element method optimisation of threshing components to reduce maize kernel damage at high moisture content. *Biosystems Engineering*, 233, 221–240. <https://doi.org/10.1016/j.biosystemseng.2023.08.005>
- [19] Fan, C., Wang, W., Cui, T., Liu, Y., & Qiao, M. (2024). Maize Kernel Broken Rate Prediction Using Machine Vision and Machine Learning Algorithms. *Foods*, 13(24), Article 24. <https://doi.org/10.3390/foods13244044>
- [20] Fan, C., Zhang, D., Yang, L., Cui, T., He, X., Dong, J., & Zhao, H. (2022). Power consumption and performance of a maize thresher with automatic gap control based on feed rate monitoring. *Biosystems Engineering*, 216, 147–164. <https://doi.org/10.1016/j.biosystemseng.2022.02.015>
- [21] Fan, C., Zhang, D., Yang, L., Cui, T., He, X., Qiao, M., Sun, J., & Dong, J. (2023). A multi-parameter control method for maize threshing based on machine learning algorithm optimisation. *Biosystems Engineering*, 236, 212–223. <https://doi.org/10.1016/j.biosystemseng.2023.10.017>
- [22] Fu J., Chen Z., Han L., & Ren L. (2018). Review of grain threshing theory and technology. *International Journal of Agricultural and Biological Engineering*, 11(3), 12–20. <https://doi.org/10.25165/j.ijabe.20181103.3432>
- [23] Gong, J., Luo, Z., & Zhang, Y. (2024). Optimised Design and Simulation Analysis of Longitudinal Flow Corn Cone Threshing Device. *INMATEH - Agricultural Engineering*, 73(2), 63–72. <https://doi.org/10.35633/inmateh-73-05>
- [24] Guo, D., Du, Y., Wang, L., Zhang, W., Sun, T., & Wu, Z. (2025). Digital twin for monitoring threshing performance of combine harvesters. *Measurement*, 239, 115411. <https://doi.org/10.1016/j.measurement.2024.115411>
- [25] Guo, J., Du, Y., Wu, Y., & Mao, E. (2019). Research status and development trend of corn harvester threshing device. *2019 ASABE Annual International Meeting, July 7, 2019 - July 10, 2019*. <https://doi.org/10.13031/aim.201900701>
- [26] Hasan, A. S. M. M., Diepeveen, D., Laga, H., Jones, M. G. K., & Soheli, F. (2023). Image patch-based deep learning approach for crop and weed recognition. *Ecological Informatics*, 78, 102361. <https://doi.org/10.1016/j.ecoinf.2023.102361>

- [27] Hou, Y., Shang, S., Li, X., He, X., Zheng, H., Dong, T., Li, X., Liu, Z., Yang, S., & Wang, D. (2023). Discrete element method (EDEM) simulation and parameter optimization: Design and testing of a low-loss and high-efficiency corn threshing device. *INMATEH Agricultural Engineering*, 194–204. <https://doi.org/10.35633/inmateh-71-16>
- [28] Hu, Y., Tang, Z., Wang, S., Li, B., Guo, X., & Chen, S. (2024). The Influence of the Distribution Law and Uniformity of a Threshed Mixture with the Working Parameters of a Soybean Threshing Device. *Agronomy*, 14(7), 1581. <https://doi.org/10.3390/agronomy14071581>
- [29] Hussain, S., Jianjun, H., Yong, C., Ali, A., Song, H., Zheng, D., Farid, M. U., Ghafoor, A., & Ahmed, M. (2024). CFD study of self-cleaning system of multi-stage tangential roller threshing unit for precise buckwheat breeding. *Heliyon*, 10(5), e27180. <https://doi.org/10.1016/j.heliyon.2024.e27180>
- [30] Jin Chen, Yi Lian, Rong Zou, Shuai Zhang, Xiaobo Ning, & Mengna Han. (2020). Real-time grain breakage sensing for rice combine harvesters using machine vision technology. *International Journal of Agricultural & Biological Engineering*, 13(3), 194–199. <https://doi.org/10.25165/j.ijabe.20201303.5478>
- [31] Kang J., Wang X., Xie F., Hou J., Li Q., & Liu A. (2025). Design and test of the independently-adjustable concave plate screen for a multi-crop combine harvester (多作物联合收获机独立调节式凹板筛设计与试验). *Transactions of the Chinese Society of Agricultural Engineering*, 1–11. <https://doi.org/10.11975/j.issn.1002-6819.202406176>
- [32] Kang J., Wang X., Xie F., Luo Y., Li Q., & Chen Z. (2022). Design and experiment of symmetrical adjustable concave for soybean combine harvester. *Transactions of the Chinese Society of Agricultural Engineering*, 38(2), 11–22. <https://doi.org/10.11975/j.issn.1002-6819.2022.02.002>
- [33] Kang, J., Wang X., Xie F., Luo Y., Li Q., & Huang X. (2023). Experiments and analysis of the differential threshing cylinder for soybean with different maturities. *Transactions of the Chinese Society of Agricultural Engineering*, 39(1), 38–49. <https://doi.org/10.11975/j.issn.1002-6819.202206166>
- [34] Li, H., Wang, Q., Ma, J., Wang, Y., Yue, D., & Geng, D. (2023). Design and experiment of transverse axial flow corn flexible threshing device. *INMATEH Agricultural Engineering*, 461–470. <https://doi.org/10.35633/inmateh-69-43>
- [35] Li X., Du Y., Liu L., & Mao E. (2023). Design and experiment of the automatic control system for low damage corn grain direct harvesters(玉米低损籽粒直收机自动控制系统设计与试验). *Transactions of the Chinese Society of Agricultural Engineering*, 39(2), 34–42. <https://doi.org/10.11975/j.issn.1002-6819.202210210>
- [36] Li, X., Du, Y., Mao, E., Zhang, Y., Liu, L., Guo, D.(2023). Design and experiment of corn low damage threshing device based on DEM. *International Journal of Agricultural and Biological Engineering*, 16(3), 55–63. <https://doi.org/10.25165/j.ijabe.20231603.7042>
- [37] Li, Y., Hou, Y., Cui, T., Tan, D. S., Xu, Y., Zhang, D., Qiao, M., & Xiong, L. (2024). Classifying grain and impurity to assess maize cleaning loss using time–frequency images of vibro-piezoelectric signals coupling machine learning. *Computers and Electronics in Agriculture*, 227, 109583. <https://doi.org/10.1016/j.compag.2024.109583>
- [38] Li Y., Jiang J., Xu Y., Cui T., Su Y., & Qiao M. (2020). Preparation and Threshing Performance Tests of Rubber Composite Nail Teeth under Maize with High Moisture Content. *Transactions of the Chinese Society for Agricultural Machinery*, 51(11), 158–167. <https://doi.org/10.6041/j.issn.1000-1298.2020.11.017>
- [39] Li Y., Xu L., Li Y., Lv L., & Shi M. (2024). Modeling and control methods of a multi-parameter system for threshing and cleaning in grain combine harvesters. *Computers and Electronics in Agriculture*, 225, 109251. <https://doi.org/10.1016/j.compag.2024.109251>
- [40] Liang, X., Chen, Z., Zhang, X., Liguó, W., Li, W., & Che, Y. (2013). Design and Experiment of On-line Monitoring System for Feed Quantity of Combine Harvester(联合收获机喂入量在线监测系统设计与试验). *Transactions of the Chinese Society for Agricultural Machinery*, 44(S2), 1–6. <https://doi.org/10.6041/j.issn.1000-1298.2013.S2.001>
- [41] Liang, Z., Qin, Y., & Su, Z. (2024). Establishment of a Feeding Rate Prediction Model for Combine Harvesters. *Agriculture*, 14(4), Article 4. <https://doi.org/10.3390/agriculture14040589>
- [42] Liu, L., Du, Y., Chen, D., Li, Y., Li, X., Zhao, X., Li, G., & Mao, E. (2022). Impurity monitoring study for corn kernel harvesting based on machine vision and CPU-Net. *Computers and Electronics in Agriculture*, 202, 107436. <https://doi.org/10.1016/j.compag.2022.107436>

- [43] Liu, Q., Liu, W., Liu, Y., Zhe, T., Ding, B., & Liang, Z. (2023). Rice grains and grain impurity segmentation method based on a deep learning algorithm-NAM-EfficientNetv2. *Computers and Electronics in Agriculture*, 209, 107824. <https://doi.org/10.1016/j.compag.2023.107824>
- [44] Liu, T., Zhu, S., Yang, T., Zhang, W., Xu, Y., Zhou, K., Wu, W., Zhao, Y., Yao, Z., Yang, G., Wang, Y., Sun, C., & Sun, J. (2024). Maize height estimation using combined unmanned aerial vehicle oblique photography and LIDAR canopy dynamic characteristics. *Computers and Electronics in Agriculture*, 218, 108685. <https://doi.org/10.1016/j.compag.2024.108685>
- [45] Liu, X., Zhang, Z., Igathinathane, C., Flores, P., Zhang, M., Li, H., Han, X., Ha, T., Ampatzidis, Y., & Kim, H.-J. (2024). Infield corn kernel detection using image processing, machine learning, and deep learning methodologies under natural lighting. *Expert Systems with Applications*, 238, 122278. <https://doi.org/10.1016/j.eswa.2023.122278>
- [46] Liu Y., Li M., Wang J., Feng L., Wang F., & He X. (2023). Design and Test of Entrainment Loss Detection System for Corn Kernel Direct Harvester(玉米籽粒直收机夹带损失检测系统设计与试验). *Transactions of the Chinese Society for Agricultural Machinery*, 54(5), 140–149. <https://doi.org/10.6041/j.issn.1000-1298.2023.05.014>
- [47] Liu, Y., Li, Y., Dong, Y., Huang, M., Zhang, T., & Cheng, J. (2022). Development of a variable-diameter threshing drum for rice combine harvester using MBD - DEM coupling simulation. *Computers and Electronics in Agriculture*, 196, 106859. <https://doi.org/10.1016/j.compag.2022.106859>
- [48] Liu, Y., Li, Y., Ji, K., Yu, Z., Ma, Z., Xu, L., & Niu, C. (2025). Development of a hydraulic variable-diameter threshing drum control system for combine harvester part I: Adaptive monitoring method. *Biosystems Engineering*, 250, 174–182. <https://doi.org/10.1016/j.biosystemseng.2025.01.001>
- [49] Ma, L., Xie, F., Liu, D., Wang, X., & Zhang, Z. (2023). An Application of Artificial Neural Network for Predicting Threshing Performance in a Flexible Threshing Device. *Agriculture*, 13(4), Article 4. <https://doi.org/10.3390/agriculture13040788>
- [50] Mandal, S., Yadav, A., Panme, F. A., Devi, K. M., & Kumar S.M., S. (2024). Adaption of smart applications in agriculture to enhance production. *Smart Agricultural Technology*, 7, 100431. <https://doi.org/10.1016/j.atech.2024.100431>
- [51] Marin, E., Cardei, P., Vldu, V., Biri, S., Ungureanu, N., Bungescu, S. T., Voicea, I., Cujbescu, D., Gageanu, I., Popa, L.-D., Isticioaia, S., Matei, G., Boruz, S., Teliban, G., Radu, C., Kabas, O., Caba, I., & Maciej, J. (2024). Research on the influence of the main vibration-generating components in grain harvesters on the operator's comfort. *INMATEH - Agricultural Engineering*, 74(3), 808–823. <https://doi.org/10.35633/inmateh-74-71>
- [52] Miu, P. I., & Kutzbach, H.-D. (2008a). Modeling and simulation of grain threshing and separation in axial threshing units: Part II. Application to tangential feeding. *Computers and Electronics in Agriculture*, 60(1), 105–109. <https://doi.org/10.1016/j.compag.2007.07.004>
- [53] Miu, P. I., & Kutzbach, H.-D. (2008b). Modeling and simulation of grain threshing and separation in threshing units—Part I. *Computers and Electronics in Agriculture*, 60(1), 96–104. <https://doi.org/10.1016/j.compag.2007.07.003>
- [54] Momin, M. A., Yamamoto, K., Miyamoto, M., Kondo, N., & Grift, T. (2017). Machine vision based soybean quality evaluation. *Computers and Electronics in Agriculture*, 140, 452–460. <https://doi.org/10.1016/j.compag.2017.06.023>
- [55] Ni, Y., Jin, C., Chen, M., Yuan, W., Qian, Z., Yang, T., & Cai, Z. (2021). Computational model and adjustment system of header height of soybean harvesters based on soil-machine system. *Computers and Electronics in Agriculture*, 183, 105907. <https://doi.org/10.1016/j.compag.2020.105907>
- [56] Niu, S., Xu, X., Liang, A., Yun, Y., Li, L., Hao, F., Bai, J., & Ma, D. (2024). Research on a Lightweight Method for Maize Seed Quality Detection Based on Improved YOLOv8. *IEEE Access*, 12, 32927–32937. <https://doi.org/10.1109/ACCESS.2024.3365559>
- [57] Omid, M., Lashgari, M., Mobli, H., Alimardani, R., Mohtasebi, S., & Hesamifard, R. (2010). Design of fuzzy logic control system incorporating human expert knowledge for combine harvester. *Expert Systems with Applications*, 37(10), 7080–7085. <https://doi.org/10.1016/j.eswa.2010.03.010>
- [58] Pužauskas, E., Steponavičius, D., Jotautienė, E., Petkevičius, S., & Kemzūraitė, A. (2017). Substantiation of concave crossbar shape for corn ear threshing. *Mechanics*, 22(6), 553–561. <https://doi.org/10.5755/j01.mech.22.6.16370>

- [59] Qian, Z., Jin, C., & Zhang, D. (2017). Multiple frictional impact dynamics of threshing process between flexible tooth and grain kernel. *Computers and Electronics in Agriculture*, 141, 276–285. <https://doi.org/10.1016/j.compag.2017.07.022>
- [60] Qiu, Z., Shi, G., Zhao, B., Jin, X., & Zhou, L. (2022). Combine harvester remote monitoring system based on multi-source information fusion. *Computers and Electronics in Agriculture*, 194, 106771. <https://doi.org/10.1016/j.compag.2022.106771>
- [61] Rivera, G., Porras, R., Florencia, R., & Sánchez-Solís, J. P. (2023). LiDAR applications in precision agriculture for cultivating crops: A review of recent advances. *Computers and Electronics in Agriculture*, 207, 107737. <https://doi.org/10.1016/j.compag.2023.107737>
- [62] Saeys, W., Lenaerts, B., Craessaerts, G., & De Baerdemaeker, J. (2009). Estimation of the crop density of small grains using LiDAR sensors. *Biosystems Engineering*, 102(1), 22–30. <https://doi.org/10.1016/j.biosystemseng.2008.10.003>
- [63] Shahbazi, F., Shahbazi, S., Nadimi, M., & Paliwal, J. (2025). Losses in agricultural produce: A review of causes and solutions, with a specific focus on grain crops. *Journal of Stored Products Research*, 111, 102547. <https://doi.org/10.1016/j.jspr.2025.102547>
- [64] Shen, Y., Yin, Y., Li, B., Zhao, C., & Li, G. (2021). Detection of impurities in wheat using terahertz spectral imaging and convolutional neural networks. *Computers and Electronics in Agriculture*, 181, 105931. <https://doi.org/10.1016/j.compag.2020.105931>
- [65] Song, Z., Diao, P., Cui, P., Wei, M., Miao, H., & Yao, W. (2022). Design and experimental study of flexible threshing device for longitudinal axial flow corn. *INMATEH Agricultural Engineering*, 155–165. <https://doi.org/10.35633/inmateh-67-15>
- [66] Srison, W., Chuan-Udom, S., & Saengprachatanarak, K. (2016). Effects of operating factors for an axial-flow corn shelling unit on losses and power consumption. *Agriculture and Natural Resources*, 50(5), 421–425. <https://doi.org/10.1016/j.anres.2016.05.002>
- [67] Steponavičius, D., Kemzūraitė, A., Pužauskas, E., Domeika, R., Grigas, A., & Karalius, D. (2023). Shape Optimization of Concave Crossbars to Increase Threshing Performance of Moist Corn Ears. *Agriculture*, 13(5), Article 5. <https://doi.org/10.3390/agriculture13050983>
- [68] Su, Z., Li, Y., Dong, Y., Tang, Z., & Liang, Z. (2020). Simulation of rice threshing performance with concentric and non-concentric threshing gaps. *Biosystems Engineering*, 197, 270–284. <https://doi.org/10.1016/j.biosystemseng.2020.05.020>
- [69] Sun, J., Zhou, J., He, Y., Jia, H., & Toroitich Rottok, L. (2024). Detection of rice panicle density for unmanned harvesters via RP-YOLO. *Computers and Electronics in Agriculture*, 226, 109371. <https://doi.org/10.1016/j.compag.2024.109371>
- [70] Sun, Y., Liu, R., Zhang, M., Li, M., Zhang, Z., & Li, H. (2022). Design of feed rate monitoring system and estimation method for yield distribution information on combine harvester. *Computers and Electronics in Agriculture*, 201, 107322. <https://doi.org/10.1016/j.compag.2022.107322>
- [71] Tang, Q., Jiang, L., Yu, W., Wu, J., & Wang, G. (2024). Design and experiment of high moisture corn threshing device with low damage. *INMATEH Agricultural Engineering*, 172–183. <https://doi.org/10.35633/inmateh-74-15>
- [72] Tang, Z., Li, Y., Li, X., & Xu, T. (2019). Structural damage modes for rice stalks undergoing threshing. *Biosystems Engineering*, 186, 323–336. <https://doi.org/10.1016/j.biosystemseng.2019.08.005>
- [73] Vlăduț, N.-V., Biriș, S.-Ș., Cârdei, P., Găgeanu, I., Cujbescu, D., Ungureanu, N., Popa, L.-D., Perişoară, L., Matei, G., & Teliban, G.-C. (2022). Contributions to the Mathematical Modeling of the Threshing and Separation Process in An Axial Flow Combine. *Agriculture*, 12(10). <https://doi.org/10.3390/agriculture12101520>
- [74] Vlăduț, N.-V., Ungureanu, N., Biriș, S.-Ș., Voicea, I., Nenciu, F., Găgeanu, I., Cujbescu, D., Popa, L.-D., Boruz, S., Matei, G., Ekielski, A., & Teliban, G.-C. (2023). Research on the Identification of Some Optimal Threshing and Separation Regimes in the Axial Flow Apparatus. *Agriculture*, 13(4). <https://doi.org/10.3390/agriculture13040838>
- [75] Wallays, C., Missotten, B., De Baerdemaeker, J., & Saeys, W. (2009). Hyperspectral waveband selection for on-line measurement of grain cleanness. *Biosystems Engineering*, 104(1), 1–7. <https://doi.org/10.1016/j.biosystemseng.2009.05.011>
- [76] Wang, F., Li, Y., Liu, Y., Ji, K., Li, Z., Xu, X., & Xu, L. (2023). Design and Finite Element Analysis of Variable-Diameter Threshing Drum with Movable Radial Plates. *INMATEH - Agricultural Engineering*, 70(2), 539–548. <https://doi.org/10.35633/inmateh-70-52>

- [77] Wang, J., Shan, C., Gou, F., Qian, Z., Ni, Y., Liu, Z., & Jin, C. (2025). A Review of Key Technologies and Intelligent Applications in Soybean Mechanized Harvesting: Chinese and International Perspectives. *Journal of Biosystems Engineering*, 50(1), 79–104. <https://doi.org/10.1007/s42853-025-00254-3>
- [78] Wang, J., Yu, X., Zhang, J., Zhong, D., Li, Z., & Song, H. (2022). Design of Inner and Outer Roller Buckwheat Thresher and Field Test. *INMATEH - Agricultural Engineering*, 66(1), 111–120. <https://doi.org/10.35633/inmateh-66-11>
- [79] Wang, Q., He, Q., Yue, D., Li, D., Yin, J., Guan, P., Sun, Y., Geng, D., & Wang, Z. (2025). Dynamic real-time detection for corn kernel breakage rate based on deep learning and sliding window technology. *Computers and Electronics in Agriculture*, 232, 109926. <https://doi.org/10.1016/j.compag.2025.109926>
- [80] Wang, Q., Yang, H., He, Q., Yue, D., Zhang, C., & Geng, D. (2023). Real-Time Detection System of Broken Corn Kernels Based on BCK-YOLOv7. *Agronomy*, 13(7), Article 7. <https://doi.org/10.3390/agronomy13071750>
- [81] Wang Z., Cui T., Zhang D., Li Y., He X., & Zhang Z. (2021). Design and Experiment of Low Damage Corn Threshing Drum with Gradually Changing Diameter(玉米收获机低损变径脱粒滚筒设计与试验). *Transactions of the Chinese Society for Agricultural Machinery*, 52(8), 98–105. <https://doi.org/10.6041/j.issn.1000-1298.2021.08.009>
- [82] Wu, K., Zhang, M., Wang, G., Chen, X., & Wu, J. (2022). A Continuous Single-Layer Discrete Tiling System for Online Detection of Corn Impurities and Breakage Rates. *Agriculture*, 12(7), Article 7. <https://doi.org/10.3390/agriculture12070948>
- [83] Wu, Z., Chen, J., Ma, Z., Li, Y., & Zhu, Y. (2024). Development of a lightweight online detection system for impurity content and broken rate in rice for combine harvesters. *Computers and Electronics in Agriculture*, 218, 108689. <https://doi.org/10.1016/j.compag.2024.108689>
- [84] Xie, B., Jin, Y., Faheem, M., Gao, W., Liu, J., Jiang, H., Cai, L., & Li, Y. (2023). Research progress of autonomous navigation technology for multi-agricultural scenes. *Computers and Electronics in Agriculture*, 211, 107963. <https://doi.org/10.1016/j.compag.2023.107963>
- [85] Xing, S., Cui, T., Zhang, D., Yang, L., He, X., Li, C., Dong, J., Jiang, Y., Wu, W., Zhang, C., & Du, Z. (2024). Design and optimization for a longitudinal-flow corn ear threshing device of low loss and low energy consumption. *Computers and Electronics in Agriculture*, 226, 109328. <https://doi.org/10.1016/j.compag.2024.109328>
- [86] Yao, Z., Zhao, C., & Zhang, T. (2024). Agricultural machinery automatic navigation technology. *iScience*, 27(2), 108714. <https://doi.org/10.1016/j.isci.2023.108714>
- [87] Yin, Y., Ma, B., Meng, Z., Chen, L., Liu, M., Zhang, Y., Zhang, B., & Wen, C. (2024). Construction method and case study of digital twin system for combine harvester. *Computers and Electronics in Agriculture*, 226, 109395. <https://doi.org/10.1016/j.compag.2024.109395>
- [88] Yu, H., Li, Z., Guo, W., Li, D., Wang, L., & Wang, Y. (2023). An estimation method of maize impurity rate based on the deep residual networks. *Industrial Crops and Products*, 196, 116455. <https://doi.org/10.1016/j.indcrop.2023.116455>
- [89] Yu, Y., Cheng, Y., Fan, C., Chen, L., Wu, Q., Qiao, M., & Zhou, X. (2025). Automatic Control System for Maize Threshing Concave Clearance Based on Entrainment Loss Monitoring. *Processes*, 13(1), Article 1. <https://doi.org/10.3390/pr13010058>
- [90] Yuan, L., He, X., Zhu, C., Wang, W., Wang, M., & Wu, S. (2024). Design and test of tangential and longitudinal-axial threshing and separating unit for wheat. *Results in Engineering*, 21, 101774. <https://doi.org/10.1016/j.rineng.2024.101774>
- [91] Zhang, D., Yi, S., Zhang, J., & Bao, Y. (2022a). Establishment of millet threshing and separating model and optimization of harvester parameters. *Alexandria Engineering Journal*, 61(12), 11251–11265. <https://doi.org/10.1016/j.aej.2022.04.048>
- [92] Zhang, D., Yi, S., Zhang, J., & Bao, Y. (2022b). Establishment of millet threshing and separating model and optimization of harvester parameters. *Alexandria Engineering Journal*, 61(12), 11251–11265. <https://doi.org/10.1016/j.aej.2022.04.048>
- [93] Zhang, Q., Chen, Q., Xu, W., Xu, L., & Lu, E. (2024). Prediction of Feed Quantity for Wheat Combine Harvester Based on Improved YOLOv5s and Weight of Single Wheat Plant without Stubble. *Agriculture*, 14(8), Article 8. <https://doi.org/10.3390/agriculture14081251>
- [94] Zhang, Q., Hu, J., Xu, L., Cai, Q., Yu, X., & Liu, P. (2023). Impurity/Breakage Assessment of Vehicle-Mounted Dynamic Rice Grain Flow on Combine Harvester Based on Improved Deeplabv3+ and

- YOLOv4. *IEEE Access*, 11, 49273–49288. IEEE Access. <https://doi.org/10.1109/ACCESS.2023.3276450>
- [95] Zhang, Q., Wang, L., Ni, X., Wang, F., Chen, D., & Wang, S. (2024). Research on wheat broken rate and impurity rate detection method based on DeepLab-EDA model and system construction. *Computers and Electronics in Agriculture*, 226, 109375. <https://doi.org/10.1016/j.compag.2024.109375>
- [96] Zhang, S., Liu, L., Li, G., Du, Y., Wu, X., Song, Z., & Li, X. (2025). Diffusion model-based image generative method for quality monitoring of direct grain harvesting. *Computers and Electronics in Agriculture*, 233, 110130. <https://doi.org/10.1016/j.compag.2025.110130>
- [97] Zhang W., Du Y., Li X., Liu L., Wang L., & Wu Z. (2024). Online Detection Method of Corn Kernel Quality Based on FSLYOLO v8n(基于 FSLYOLO v8n 的玉米籽粒收获质量在线检测方法研究). *Transactions of the Chinese Society for Agricultural Machinery*, 55(8), 253–265. <https://doi.org/10.6041/j.issn.1000-1298.2024.08.023>
- [98] Zhang, Y., Chen, D., Yin, Y., Wang, X., & Wang, S. (2018). Experimental Study of Feed Rate Related Factors of Combine Harvester Based on Grey Correlation. *IFAC-PapersOnLine*, 51(17), 402–407. <https://doi.org/10.1016/j.ifacol.2018.08.188>
- [99] Zhang, Y., Yin, Y., Meng, Z., Chen, D., Qin, W., Wang, Q., & Dai, D. (2022). Development and testing of a grain combine harvester throughput monitoring system. *Computers and Electronics in Agriculture*, 200, 107253. <https://doi.org/10.1016/j.compag.2022.107253>
- [100] Zhang Z., Sun Y., Liu R., Zhang M., Li H., & Li M. (2019). Design and Test of Feed Rate Monitoring System for Combine Harvester(联合收获机喂入量监测系统设计与试验). *Transactions of the Chinese Society for Agricultural Machinery*, 50(6), 85–92. <https://doi.org/10.6041/j.issn.1000-1298.2019.06.009>
- [101] Zhao, J., Zhao, H., Tang, H., Wang, X., & Yu, Y. (2023). Bionic threshing component optimized based on MBD-DEM coupling simulation significantly improves corn kernel harvesting rate. *Computers and Electronics in Agriculture*, 212, 108075. <https://doi.org/10.1016/j.compag.2023.108075>
- [102] Zhou, X., Wang, Z., Tian, L., Su, Z., & Ding, Z. (2022). Innovative design and performance test of threshing-separating device for horizontal axial-flow combine harvester. *INMATEH Agricultural Engineering*, 497–508. <https://doi.org/10.35633/inmateh-67-49>
- [103] Zhu, Z., Chai, X., Xu, L., Quan, L., Yuan, C., Weng, S., Cao, G., & Jiang, W. (2025). Research on predictive control of a novel electric cleaning system for combine harvester based on data-driven. *Computers and Electronics in Agriculture*, 232, 110075. <https://doi.org/10.1016/j.compag.2025.110075>

WHEAT IMPURITY DETECTION ALGORITHM BASED ON IMPROVED YOLO v8

/ 基于改进 YOLO v8 的小麦杂质检测算法

Liqing ZHAO, Rui QIAN, Chuang LIU, Shuhao WANG, Junjie XIA

College of Electrical and Mechanical Engineering, Qingdao Agriculture University, Qingdao / China;

Tel: +86-13222725599; E-mail: 758128332@qq.comDOI: <https://doi.org/10.35633/inmateh-75-62>**Keywords:** Wheat Impurity Detection, YOLOv8, Multi-scale Feature Fusion, Lightweight Design**ABSTRACT**

To achieve fast and accurate detection of wheat impurities, this study proposes an improved YOLOv8-based algorithm that targets three typical impurity types: bran, straw, and spike. The original C2f module is replaced with the C2f_UIB structure from MobileNetV4 to reduce model complexity, and a High-level Screening Feature Pyramid Network (HS-FPN) is integrated to enhance multi-scale feature fusion. Additionally, a Generalized IoU loss function is adopted to improve detection robustness in dense impurity scenarios. The optimized model is deployed on an embedded Jetson Nano platform for real-time inference, coupled with an industrial camera and LED lighting system. To validate its practical effectiveness, an indoor experimental setup was constructed to simulate field conditions. A total of 30 wheat samples were tested, and results demonstrate high consistency between system detection and manual annotation, with minimal deviation across all impurity types. The proposed algorithm exhibits excellent accuracy, lightweight characteristics, and strong potential for deployment in intelligent agricultural equipment.

摘要

为实现对小麦杂质的快速准确检测, 本文提出一种基于改进 YOLOv8 的杂质识别算法, 主要针对三类典型杂质: 麦麸、秸秆和麦穗。该算法将 YOLOv8 中的 C2f 模块替换为 MobileNetV4 的 C2f_UIB 结构, 以降低模型复杂度, 并引入高级筛选特征金字塔网络 (HS-FPN) 以提升多尺度特征融合能力。此外, 采用广义 IoU 损失函数以增强高密度杂质场景下的检测鲁棒性。优化后的模型部署于 Jetson Nano 嵌入式平台, 并结合工业相机与 LED 面光源构建图像采集系统, 实现了模型的实时推理。为验证其实际应用效果, 搭建室内试验平台模拟田间作业环境, 对 30 组小麦样本进行了检测实验。结果显示, 系统识别结果与人工标注高度一致, 各类杂质检测误差极小, 表明所提算法具备良好的检测精度、轻量化特性及农业装备部署应用潜力。

INTRODUCTION

Wheat is one of the most important staple crops globally, playing a critical role in food security and economic development. However, the presence of impurities such as straw, wheat bran, and other foreign materials during the harvesting process significantly affects the quality and market value of wheat. Traditional methods for impurity detection rely heavily on manual labor, which is not only time-consuming but also prone to human error. With the aging agricultural workforce and rising labor costs, there is an urgent need for automated and precise impurity detection systems to improve the efficiency and quality of wheat harvesting.

In early research on visual impurity detection in agriculture, traditional image processing techniques such as color thresholding and morphological filtering were commonly used.

Chen *et al.* (2020) proposed a machine vision-based real-time impurity detection system for rice combine harvesters, employing decision tree algorithms to classify grain morphological features (A1-A6). The integrated lateral illumination system and decision tree model achieved 76% classification accuracy on training datasets, establishing a foundation for real-time parameter optimization in harvesting machinery.

Marjanović *et al.* (2018) developed a rainfall-triggered landslide prediction model using decision tree algorithms to analyze precipitation data from 2001-2014. Critical thresholds of 30 mm rainfall in 2-3 days and 140 mm cumulative rainfall over 30 days were identified, revealing dominant mechanisms of medium-term rainfall impacts on landslides in Western Serbia.

Ok *et al.* (2012) applied random forest with parcel-based analysis to SPOT5 imagery crop classification, achieving 85.89% overall accuracy (8% improvement over maximum likelihood methods), demonstrating superiority in multispectral interpretation.

Mavridou et al. (2019) systematically reviewed agricultural machine vision technologies across seven domains (fruit grading/yield estimation/disease detection), analyzing multi-sensor integration strategies to guide precision agriculture implementation.

These traditional methods are limited by their reliance on handcrafted features, low adaptability to complex environments, and difficulty in handling high-density impurity scenarios. In contrast, deep learning techniques have shown great potential by leveraging convolutional neural networks (CNNs) to automatically extract multi-level semantic features.

Deep learning overcomes these limitations by leveraging convolutional neural networks (CNNs) to automatically extract multi-level features.

Shen and Zhao (2021) proposed a lightweight YOLOv3-based detection model for peanut sorting systems, solving missed detection problems while ensuring real-time inference on CPUs.

Qi et al. (2023) designed a GhostNet-based pest detection model with attention-guided receptive field fusion, achieving high mAP and FPS under lightweight constraints.

Shi et al. (2023) developed a DCGA-YOLOv8 system for multi-crop navigation line extraction, achieving 98.9%-100% correct clustering rates for cabbage/kohlrabi/rice. The integration of threshold-optimized DBSCAN and B-spline curve modelling enabled safe agricultural machinery path planning.

Jia et al. (2024) proposed ADL-YOLOv8 for weed detection, incorporating AKConv networks and DySample upsampling. The model improved mAP@0.5 by 3.07% while maintaining 15.77% compression rate, providing lightweight high-precision solutions for smart weeding devices.

Zhang et al. (2024) built HR-YOLOv8 for crop growth monitoring using dual self-attention mechanisms and parallel feature fusion. The model enhanced detection accuracy by 5.2% for oil palm and 0.6% for strawberries, enabling high-resolution feature preservation.

Jiang et al. (2022) optimized YOLOv7 with CBAM attention modules for Muscovy duck flock counting, achieving 98.6% accuracy and 2.3% mAP@0.5 improvement over baseline models, supporting automated density monitoring in poultry farming.

Wang et al. (2022) streamlined YOLOv5s for real-time apple calyx/stem recognition via detection head search and channel pruning. The compressed model achieved 25.51 FPS on CPUs with 93.89% accuracy, enabling efficient automated sorting.

Mathew and Mahesh (2022) deployed YOLOv5 for bell pepper bacterial spot detection, implementing whole-image feature extraction to identify micro-lesions, providing early disease warnings for mobile agricultural systems.

These studies highlight that deep learning not only supports real-time multi-target recognition in complex scenes, but also enables flexible model design through end-to-end training.

In the domain of wheat impurity detection, several notable deep learning-based methods have emerged recently.

Zhou et al. (2023) proposed WheNet, an Inception-v3-based CNN that achieved 98.59% Top-1 accuracy for classifying wheat and five impurity types.

Li et al. (2023) combined terahertz 3D imaging with a metaheuristic RetinaNet model (AHA-RetinaNet-X), obtaining over 95% accuracy for impurity classification in non-destructive testing.

Chen et al. (2022) developed Ro-YOLOv5 based on rotated bounding boxes and Circular Smooth Labels, significantly improving impurity detection in wheat CT images.

However, many of these approaches rely on complex imaging systems (e.g., THz, CT), large-scale models, or lack the ability to run in real-time on resource-limited embedded devices. In addition, some methods focus on image classification rather than instance-level detection and localization, which limits their deployment in actual harvesting scenarios.

To address these challenges, this study proposes a lightweight wheat impurity detection algorithm based on an improved YOLOv8 architecture, integrating a Universal Inverted Bottleneck (UIB) module for computational efficiency, a High-level Screening Feature Pyramid Network (HS-FPN) for multi-scale fusion, and a GloU-based loss function for robust object localization. The model is deployed on a Jetson Nano embedded platform with industrial camera input, and validated through indoor experiments simulating real-world conditions. Compared with existing methods, our approach achieves high accuracy, fast inference, and low computational cost, making it highly suitable for intelligent agricultural equipment in modern farming environments.

MATERIALS AND METHODS

The wheat used in this study was provided by the Xizhai Agricultural Machinery Cooperative in Tianzhuang Town, Pingdu City, Qingdao, Shandong Province. The wheat was harvested using a combine harvester. The main impurity categories included wheat bran, straw, and spikes, which are the most common and representative types of impurities during the wheat harvesting process.

Wheat bran refers to fragments of the outer shell and germ produced during threshing. It is typically yellow or brown and has a regular shape. Straw is the residual stem of wheat plants with a smooth surface and varying thickness, appearing yellow or light yellow in color. Spikes are yellow or brown and usually consist of multiple unthreshed wheat kernels adhered together. Sample images of these impurities are shown in Figure 1.



Fig. 1 - Partial Wheat Impurity Samples

The image acquisition system used a Hikvision MV-CS060-10GC industrial camera equipped with a Hikvision MVL-HF0828-6MPE lens. The camera supported a maximum resolution of 3072×2048 pixels. During image capture, an acrylic tray was used to hold the wheat samples, and the shooting distance was fixed at 95 mm. The output image resolution was set to 2048×2048 pixels to ensure clarity and preserve the visual characteristics of the impurities. This also helped improve the precision of the subsequent labeling process. In total, 720 wheat images were collected.

The dataset was annotated using the X-AnyLabeling-GPU software and saved in YOLO format. To improve the model's generalization and robustness, the dataset was augmented through operations such as mirror flipping, 30° rotation, and brightness adjustment. A total of 2,140 images were selected for training, with the training and validation sets divided at a ratio of 8:2. The Mosaic augmentation function of YOLOv8 was also enabled during training to further enhance model robustness.

During wheat harvesting, the straw and spike impurities vary significantly in size and shape. Moreover, the relatively small sample size for these two categories makes accurate detection more difficult. While existing object detection algorithms can barely meet basic requirements, they often suffer from high complexity and large model parameters. Therefore, this study chose to improve the YOLOv8 model to better suit the task.

To enhance computational efficiency while maintaining accuracy and better utilize the computing power of the device, the Bottleneck module in the YOLOv8 C2f module was replaced with the Universal Inverted Bottleneck (UIB) module from MobileNetV4, forming a new structure named C2f_UIB. To improve the extraction of impurity features with diverse scales and shapes, the original PANet feature fusion network was replaced by the High-level Screening Feature Pyramid Network (HS-FPN). Compared with PANet, HS-FPN achieved better multi-scale feature fusion with fewer parameters. The network structure of the improved YOLOv8 model is illustrated in Figure 2.

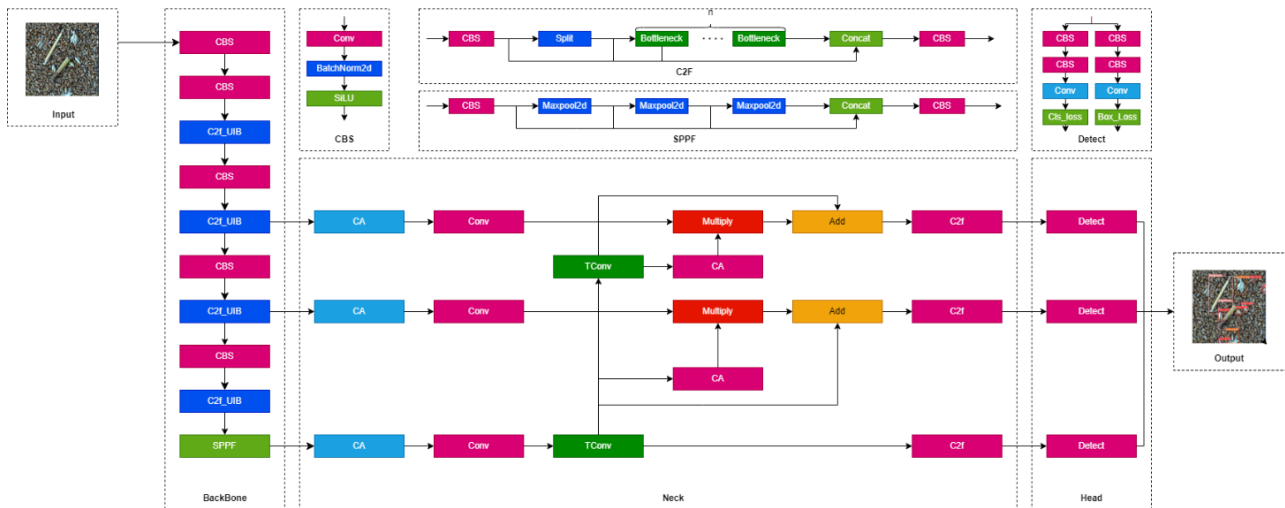


Fig. 2 - Improved YOLO v8 Lightweight Network Model

Universal Inverted Bottleneck

The Universal Inverted Bottleneck (UIB) was a lightweight network architecture introduced by MobileNetV4 to improve the efficiency of object detection (Qin et al., 2024). The UIB module significantly reduced the number of parameters and computational load by incorporating two optional depthwise convolutions (DW) into the Inverted Bottleneck (IB). Its core idea was to treat deep convolution as a variable structure by sharing common components such as pointwise expansion and projection. This design effectively reduced computational redundancy and optimized resource utilization efficiency.

Compared with the conventional Bottleneck structure used in the C2f module, the UIB module offered greater efficiency under limited computing resources. By replacing the Bottleneck in the C2f module with the UIB, an improved module named C2f_UIB was constructed. Experimental results demonstrated that the new module greatly reduced computation and memory usage without sacrificing performance. This improvement was of practical significance for large-scale deep learning tasks, especially in resource-constrained environments such as edge devices or mobile applications. The application of the C2f_UIB module further confirmed the potential and practical value of lightweight design for efficient object detection.

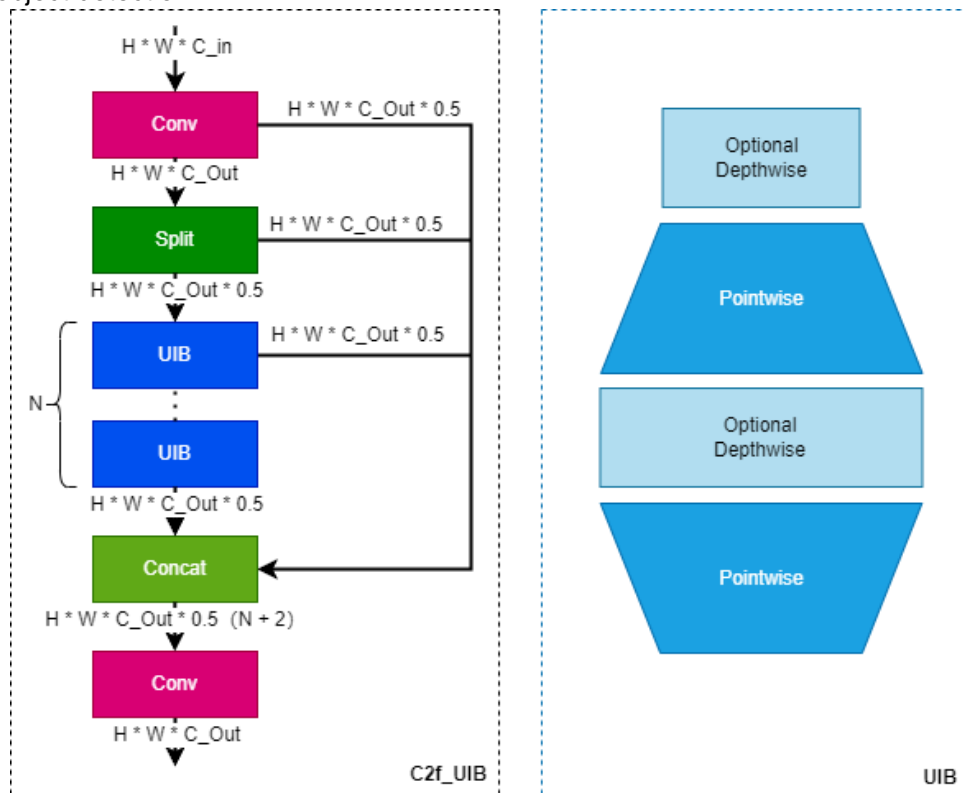


Fig. 3 - UIB Module Structure Diagram

Feature fusion network HS-FPN

The High-level Screening Feature Pyramid Network (HS-FPN) was a multi-scale feature fusion structure designed to enhance the attention and semantic understanding capabilities of the model when detecting impurities of different sizes, particularly straw and spikes. The HS-FPN framework consisted of two major components: a feature selection module and a feature fusion module (Chen et al., 2023). These modules worked together to aggregate features of varying semantic depths and spatial resolutions, thus providing more accurate and informative representations for impurity detection. The improved HS-FPN structure adapted to the YOLOv8 backbone is shown in Figure 4.

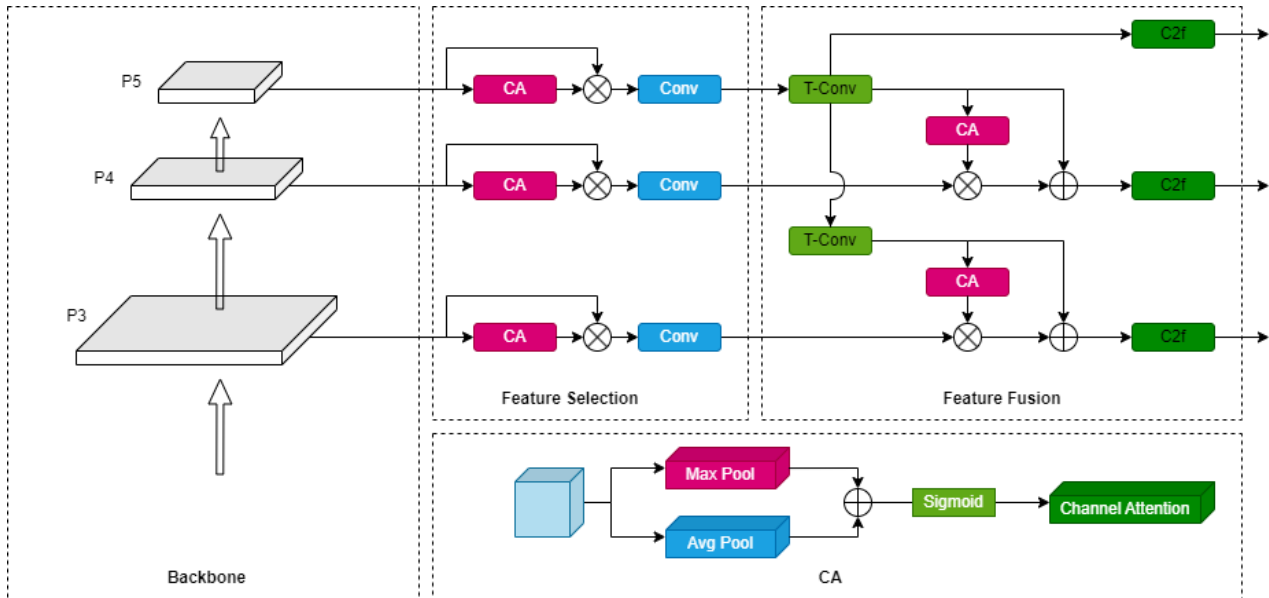


Fig. 4 – HS-FPN Structure Diagram

The feature selection module aimed to filter and reweight the multi-scale feature maps using a channel attention (CA) mechanism. As shown in the figure, the CA module first processed the input feature map using global average pooling and global max pooling to calculate the weights of each channel. These weights were then passed through a Sigmoid activation function to determine their importance. The weighted values were used to enhance the original feature map, emphasizing the most relevant feature channels for detection.

The feature fusion module served as the core component of HS-FPN. It combined feature maps of different resolutions to enhance the model's representational ability. Within this module, the Selective Feature Fusion (SFF) mechanism was used to selectively merge feature information.

The fusion process included two SFF blocks. Firstly, the high-level features with a size of $f_{high} \in R^{C \times H \times W}$ was up sampled via transposed convolution (T-Conv) to obtain $f_{high-T} \in R^{C \times 2H \times 2W}$ matching the scale of lower-level features. The channel attention module generated a weight vector $f_{CA} \in R^{C \times 1 \times 1}$, which was used to reweight the low-level feature f_{low} . The final fused feature output was calculated by the weighted addition of both:

$$f_{out} = f_{low} \times f_{CA} + f_{high-T} \quad (1)$$

This process enabled the model to leverage both detailed and abstract features. The transposed convolution and CA module jointly reconstructed the high-level features and facilitated their integration with low-level semantics. The optimization of this fusion strategy improved multi-scale feature utilization and overall detection performance.

Optimize loss function

The original YOLOv8 model employed the Complete IoU (CIoU) loss function for bounding box regression. However, CIoU suffered from ambiguity in aspect ratio representation and was not well-suited for high-density target detection. To overcome these limitations, this study adopted the Generalized IoU (GIoU) loss, which introduced the concept of an inclusion box.

GIoU not only measured the overlap between predicted and ground truth boxes but also quantified their spatial relationship when no intersection existed, thus providing richer gradient information for optimization (Zhang *et al*, 2022).

In high-density impurity scenes, GIoU utilized the surrounding region to enhance robustness under occlusion and tight target spacing. Moreover, its simplified formulation reduced normalization overhead and lowered computational complexity. These advantages made GIoU better suited for detecting varied-scale impurities under dense distribution, offering a more stable optimization path.

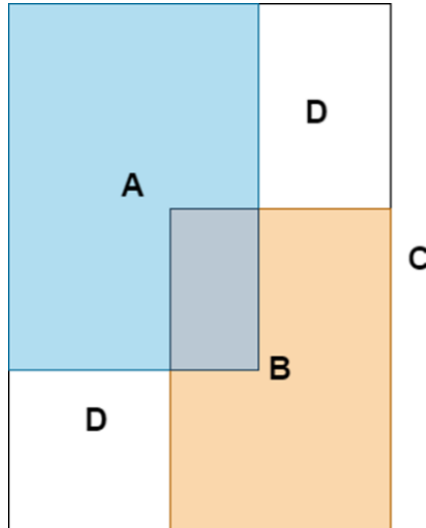


Fig. 5 – GIoU Loss Function

The GIoU is defined as:

$$GIoU = IoU - \frac{|C \setminus (A \cup B)|}{|C|} \quad (2)$$

where: $IoU = \frac{|A \cap B|}{|A \cup B|}$: represents the intersection and union ratio of the prediction box and the real box. C : It's the minimum closure rectangle containing the prediction box and the real box $|C \setminus (A \cup B)|$: It's the area in the closure rectangle that does not belong to the union of the prediction box and the real box. $|C|$: It's the area of the closure rectangle.

The corresponding GIoU-based loss function is:

$$L_{GIoU} = 1 - GIoU \quad (3)$$

This design not only reduced computational cost but also improved detection reliability in dense impurity scenarios.

Indoor Experimental Setup

To evaluate the proposed impurity detection model under practical conditions, an indoor experimental system was constructed to simulate the post-harvest wheat impurity collection environment. The system consisted of a sampling box, an industrial camera (Hikvision MV-CS060-10GC), a rectangular LED light source, and a Jetson Nano embedded processor for real-time inference, as shown in Figure 6.



Fig. 6 - Structure of the indoor impurity detection system.

The camera was fixed at a certain height above the observation window to ensure clear imaging of the wheat samples. The interior of the sampling box was coated with matte material to reduce light reflection and background interference. During each test, wheat samples were spread fully across the sampling area, and the system automatically captured images under stable lighting conditions. The collected images were then processed in real time by the YOLOv8 detection model deployed on the Jetson Nano platform.

This setup replicated key aspects of a combine harvester's impurity output environment and enabled controlled validation of the model's detection accuracy. A total of 30 samples were tested in this configuration, forming the basis for performance evaluation described in the Results section.

RESULTS

Test environments and parameter configuration

The experimental environment is Windows10 operating system, the CPU is AMD EPYC 7402 24-Core Processor, the main frequency is 2.79 GHz, the Python 3.9.7 development environment is used, the deep learning framework is Pytorch1.12.1, the GPU uses NVIDIA GeForce RTX 3090 for computing acceleration, and the GPU runs memory of 24 GB. The software environment is configured as CUDA12.2. The input image size is 640 pixels × 640 pixels, the training rounds are set to 300 rounds, the batch size is set to 16, and the optimizer is SGD.

Evaluating indicator

In the task of wheat impurity detection, it is essential to consider the model's accuracy, size, and deployment feasibility on edge devices. To objectively evaluate the performance of the target detection algorithms, this study employs a series of standardized evaluation metrics, including precision (P), recall (R), and mean average precision (mAP), alongside the model's memory usage and parameter count for a comprehensive performance comparison. These metrics collectively provide a thorough quantitative assessment of the model's precision, efficiency, and resource consumption in practical applications.

The calculation formula is as follows:

$$P = \frac{T_p}{T_p + F_p} \quad (4)$$

$$R = \frac{T_p}{T_p + F_n} \quad (5)$$

$$mAP = \frac{\sum_{i=1}^N AP_i}{N} \quad (6)$$

Precision measures the proportion of correctly predicted positive samples among all predicted positives, where T_p is the number of correctly detected positive samples and F_p is the number of false positives; Recall measures the proportion of actual positive samples detected by the model, where F_n is the number of missed positive samples; mean Average Precision is the average of the precision-recall curve area across all classes, with N being the total number of classes, and mAP comprehensively reflects the overall performance of the model in multi-class detection tasks.

Comparative test analysis of different algorithms

To evaluate the effectiveness of the proposed improved YOLOv8 model, it was compared with mainstream detection models, including Faster R-CNN, YOLOv5s, YOLOv7-Tiny, and the original YOLOv8n. As shown in Table 1, the improved model achieved the highest accuracy rate, recall rate, and average accuracy, outperforming all baseline models. Specifically, compared to YOLOv8n, the improved model increased accuracy by 1.0%, recall by 0.9%, and average accuracy by 1.3%. Notably, the model size was reduced by 46.7%, and parameter quantity decreased by 28.4%. This demonstrates that the lightweight design and multi-scale fusion effectively balance performance and efficiency. While YOLOv7-Tiny achieved comparable accuracy, its recall rate and average accuracy were inferior, and its parameter count remained higher. Traditional models like Faster R-CNN exhibited significantly lower performance and excessive resource consumption, highlighting the superiority of the proposed lightweight improvements.

Table 1

Models	Model Performance Comparison				
	accuracy rate	recall rate	average accuracy	model memory usage	parameter quantity
	[%]	[%]	[%]	[MB]	x 10 ⁹ [FLOPS]
Faster R-CNN	79.6	82.1	45.3	315.6	137.2
YOLOv5s	92.3	93.8	96.7	13.7	16.5
YOLOv7-Tiny	93.5	94.6	96.6	11.7	13.2
YOLO v8n	93.2	93.6	97.4	6.0	8.1
YOLO v8n+UIB+HSFPN+GIOU	94.2	94.5	98.7	3.2	5.8

Figure 7 shows the comparison between the improved model and YOLOv8n in terms of accuracy, recall and average accuracy. On the whole, our method performs better than YOLOv8n on all indicators.

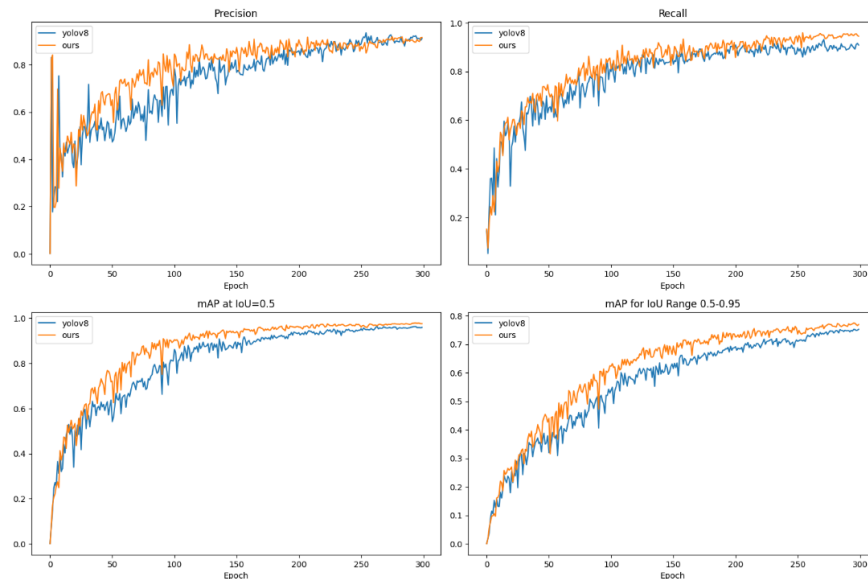


Fig. 7 – Performance curves of YOLOv8 model and improved YOLOv8 model

As demonstrated in Figure 8, the enhanced YOLOv8 model exhibits superior detection performance relative to the original architecture, with notable improvements in impurity recognition capability. The optimized model achieves reduced occurrence of both missed detections and false positives, while demonstrating higher confidence scores in accurate impurity identification.



Fig. 8 – Comparison of model detection effects

Ablation test

Ablation experiments were conducted to validate the contribution of each proposed improvement. As shown in Table 2, the baseline YOLOv8n achieved 93.2% accuracy, 93.6% recall, and 97.4% mAP. Introducing the UIB module alone slightly improved accuracy but reduced model memory usage by 11.7% and parameters by 13.6%. Replacing PANet with HS-FPN yielded more significant gains: accuracy increased to 93.7%, recall to 94.6%, and mAP to 97.8%, with a 33.3% reduction in memory. Using GloU loss alone improved recall and mAP without affecting model size. Combining UIB+HSFPN achieved 93.8% accuracy, 94.4% recall, and 98.3% mAP, while reducing memory to 3.2 MB. Finally, integrating all three improvements achieved optimal performance: 94.2% accuracy, 94.5% recall, and 98.7% mAP, confirming the synergistic effect of lightweight design, multi-scale fusion, and loss optimization.

Table 2

Models	Ablation experiment				
	Accuracy rate	Recall rate	Average accuracy	Model memory usage	Parameter quantity
	[%]	[%]	[%]	[MB]	$\times 10^9$ [FLOPS]
YOLOv8n	93.2	93.6	97.4	6.0	8.1
YOLOv8n+UIB	93.4	93.5	97.4	5.3	7.0
YOLOv8n+HSFPN	93.7	94.6	97.8	4.0	6.9
YOLOv8n+GIoU	93.6	94.3	97.7	6.0	8.1
YOLOv8n+UIB+HSFPN	93.8	94.4	98.3	3.2	5.8
YOLOv8n+UIB+HSFPN+GIoU	94.2	94.5	98.7	3.2	5.8

Indoor Test and Validation

To evaluate the practical performance of the proposed wheat impurity detection algorithm, an indoor test was conducted under simulated harvesting conditions. The experimental setup was described in detail in the Materials and Methods section.

A total of 30 wheat samples were tested. For each sample, the system automatically captured images and detected three impurity types: wheat spike, bran, and straw. The recognition results were displayed in real-time and recorded for statistical analysis. Figure 9 shows the indoor test platform, and Figure 10 presents representative detection results.

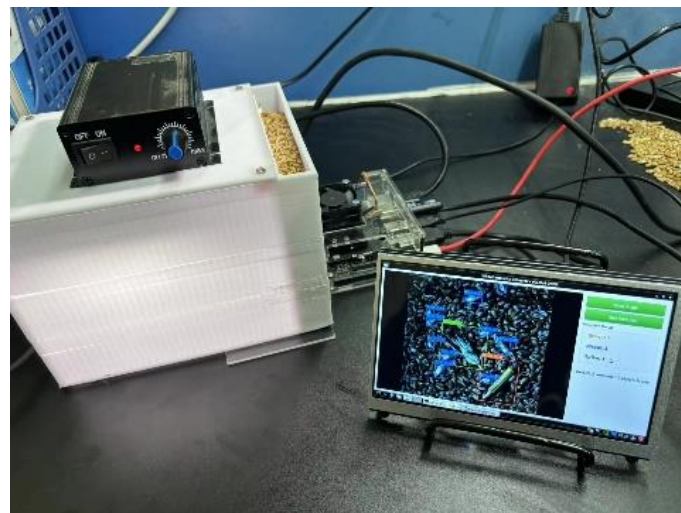


Fig. 9 – The indoor test

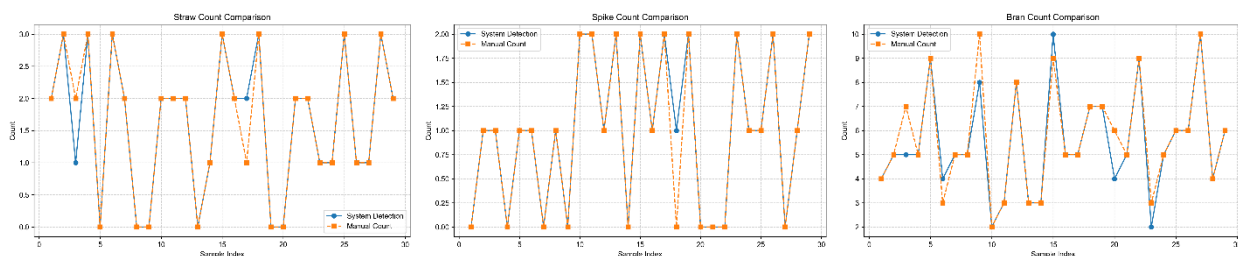


Fig. 10 – Comparison of impurity counts for systematic detection and manual annotation

According to the statistics, the model achieved high detection consistency. Only one sample had a single-object deviation in spike detection, and two samples had minor deviations in straw detection. Among the 162 bran targets, only six samples showed a one-object difference. These results validate the model's detection accuracy and robustness under realistic lighting and target distribution conditions.

The experimental outcomes further demonstrate the model's deployment potential in embedded platforms for intelligent agricultural equipment.

CONCLUSIONS

This study proposed an improved YOLOv8-based wheat impurity detection algorithm, focusing on lightweight design, multi-scale feature fusion, and enhanced loss function. By integrating the Universal Inverted Bottleneck (C2f_UIB), High-level Screening Feature Pyramid Network (HS-FPN), and GloU loss, the model achieved a significant reduction in computational cost while maintaining high detection accuracy.

The detection system was deployed on a Jetson Nano embedded platform and validated through indoor experiments simulating post-harvest impurity collection conditions. The experimental results demonstrated high recognition consistency and robustness, with most impurity categories exhibiting only minimal detection deviation.

Compared with existing mainstream detection models, the proposed approach offers a balanced trade-off between accuracy and efficiency, making it well-suited for real-time deployment in intelligent agricultural machinery. This work provides a practical reference for the application of deep learning in grain impurity detection, and lays a foundation for future field experiments and system integration.

ACKNOWLEDGEMENT

The author has been supported by the “National Natural Science Foundation of China” (No.32071911), the “National Key R&D Program of China” (No.2023YFD2000404), the “Shandong Province Modern Agricultural Industry Technology System Wheat Innovation Team” (No.SDIT-0-12).

REFERENCES

- [1] Chen, J., Lian, Y., & Li, Y. (2020). Real-time grain impurity sensing for rice combine harvesters using image processing and decision-tree algorithm. *Computers and Electronics in Agriculture*, 175, 105591.
- [2] Chen, J., Kao, S. H., He, H., Zhuo, W., Wen, S., Lee, C. H., & Chan, S. H. G. (2023). Run, don't walk: chasing higher FLOPS for faster neural networks. *Proceedings of the IEEE/CVF conference on computer vision and pattern recognition* pp. 12021-12031.
- [3] Chen, Y., Zhang, C., Chen, B., Huang, Y., Sun, Y., Wang, C., ... & Gao, Y. (2024). Accurate leukocyte detection based on deformable-DETR and multi-level feature fusion for aiding diagnosis of blood diseases. *Computers in biology and medicine*, 170, 107917.
- [4] Jia, Z., Zhang, M., Yuan, C., Liu, Q., Liu, H., Qiu, X., ... & Shi, J. (2024). ADL-YOLOv8: A Field Crop Weed Detection Model Based on Improved YOLOv8. *Agronomy*, 14(10), 2355.
- [5] Jiang, K., Xie, T., Yan, R., Wen, X., Li, D., Jiang, H., ... & Wang, J. (2022). An attention mechanism-improved YOLOv7 object detection algorithm for hemp duck count estimation. *Agriculture*, 12(10).
- [6] Li, G., Ge, H., Jiang, Y., Zhang, Y., Jiang, M., Wen, X., & Sun, Q. (2025). Research on wheat impurity identification method based on terahertz imaging technology. *Spectrochimica Acta Part A: Molecular and Biomolecular Spectroscopy*, 326, 125205.
- [7] Li, M., Zhang, Z., Lei, L., Wang, X., & Guo, X. (2020). Agricultural greenhouses detection in high-resolution satellite images based on convolutional neural networks: Comparison of faster R-CNN, YOLO v3 and SSD. *Sensors*, 20(17).
- [8] Li, P., & Zhu, C. (2024). Ro-YOLOv5: One new detector for Impurity in wheat based on Circular Smooth Label. *Crop Protection*, 184, 106806.
- [9] Liu, Q., Liu, W., Liu, Y., Zhe, T., Ding, B., & Liang, Z. (2023). Rice grains and grain impurity segmentation method based on a deep learning algorithm-NAM-EfficientNetv2. *Computers and Electronics in Agriculture*, 209, 107824.
- [10] Marjanović, M., Krautblatter, M., Abolmasov, B., Đurić, U., Sandić, C., & Nikolić, V. (2018). The rainfall-induced landsliding in Western Serbia: A temporal prediction approach using Decision Tree technique. *Engineering Geology*, 232, pp. 147-159.
- [11] Mathew, M. P., & Mahesh, T. Y. (2022). Leaf-based disease detection in bell pepper plant using YOLO v5. *Signal, Image and Video Processing*, pp. 1-7.
- [12] Mavridou, E., Vrochidou, E., Papakostas, G. A., Pachidis, T., & Kaburlasos, V. G. (2019). Machine vision systems in precision agriculture for crop farming. *Journal of Imaging*, 5(12), pp. 89.
- [13] Ok, A. O., Akar, O., & Gungor, O. (2012). Evaluation of random forest method for agricultural crop classification. *European Journal of Remote Sensing*, 45(1), pp. 421-432.

- [14] Patel, K. K., Kar, A., Jha, S. N., & Khan, M. A. (2012). Machine vision system: a tool for quality inspection of food and agricultural products. *Journal of food science and technology*, 49, pp. 123-141.
- [15] Qi, F., Wang, Y., Tang, Z., & Chen, S. (2023). Real-time and effective detection of agricultural pest using an improved YOLOv5 network. *Journal of Real-Time Image Processing*, 20(2), 33.
- [16] Qin, D., Leichner, C., Delakis, M., Fornoni, M., Luo, S., Yang, F., ... & Howard, A. (2024, September). MobileNetV4: universal models for the mobile ecosystem. In *European Conference on Computer Vision* pp. 78-96. Springer Nature Switzerland.
- [17] Redmon, J., Divvala, S., Girshick, R., & Farhadi, A. (2016). You only look once: Unified, real-time object detection. In *Proceedings of the IEEE conference on computer vision and pattern recognition*. pp. 779-788.
- [18] Ren, S., He, K., Girshick, R., & Sun, J. (2015). Faster R-CNN: Towards real-time object detection with region proposal networks. *Advances in neural information processing systems*, pp. 28.
- [19] Rezatofighi, H., Tsoi, N., Gwak, J., Sadeghian, A., Reid, I., & Savarese, S. (2019). Generalized intersection over union: A metric and a loss for bounding box regression. *Proceedings of the IEEE/CVF conference on computer vision and pattern recognition* pp. 658-666.
- [20] Shen, Y., Yin, Y., Zhao, C., Li, B., Wang, J., Li, G., & Zhang, Z. (2019). Image recognition method based on an improved convolutional neural network to detect impurities in wheat. *IEEE access*, 7, 162206-162218.
- [21] Shi, J., Bai, Y., Zhou, J., & Zhang, B. Multi-crop navigation line extraction based on improved YOLO-v8 and threshold-DBSCAN under complex agricultural environments. *Agriculture*. 2023; 14 (1): 45.
- [22] Wang, Z., Jin, L., Wang, S., & Xu, H. (2022). Apple stem/calyx real-time recognition using YOLO-v5 algorithm for fruit automatic loading system. *Postharvest Biology and Technology*, 185.
- [23] Zhang, J., Yang, W., Lu, Z., & Chen, D. (2024). HR-YOLOv8: a crop growth status object detection method based on YOLOv8. *Electronics*, 13(9), pp. 16-20.
- [24] Zhang, Y. F., Ren, W., Zhang, Z., Jia, Z., Wang, L., & Tan, T. (2022). Focal and efficient IOU loss for accurate bounding box regression. *Neurocomputing*, 506, pp. 146-157.
- [25] Zheng, Z., Wang, P., Ren, D., Liu, W., Ye, R., Hu, Q., & Zuo, W. (2021). Enhancing geometric factors in model learning and inference for object detection and instance segmentation. *IEEE transactions on cybernetics*, 52(8), pp. 8574-8586.

RESEARCH OF THE TECHNOLOGICAL PROCESS OF GRANULATION OF BULK AGRICULTURAL MATERIALS

ДОСЛІДЖЕННЯ ТЕХНОЛОГІЧНОГО ПРОЦЕСУ ГРАНУЛЮВАННЯ СИПКИХ СІЛЬСЬКОГОСПОДАРСЬКИХ МАТЕРІАЛІВ

Volodymyr BULGAKOV¹⁾, Adolfs RUCINS*²⁾, Yevhen IHNATIEV^{3,4)}, Serhiy STEPANENKO⁵⁾, Lucretia POPA⁶⁾, Simone PASCUZZI⁷⁾, Ivan HOLOVACH¹⁾, Oleksandra TROKHANIAK¹⁾

¹⁾National University of Life and Environmental Sciences of Ukraine / Ukraine;

²⁾Latvia University of Life Sciences and Technologies / Latvia;

³⁾Estonian University of Life Sciences / Estonia;

⁴⁾Dmytro Motorny Tavria State Agrotechnological University / Ukraine;

⁵⁾Institute of Mechanics and Automation of Agricultural Production of the National Academy of Agrarian Sciences of Ukraine;

⁶⁾National Institute of Research–Development for Machines and Installations Designed for Agriculture and Food Industry–INMA, Bucharest / Romania;

⁷⁾University of Bari Aldo Moro / Italy

*Corresponding author's E-mail: adolfs.rucins@lbtu.lv; vbulgakov@meta.ua

DOI: <https://doi.org/10.35633/inmateh-75-63>

Keywords: density, die, deformation, compaction, friction, resistance, granulation process, bulk materials

ABSTRACT

This research addresses the axisymmetric problem in the theory of granulation of porous bodies, with practical application in calculating the forces involved in the granulation of dispersed bulk materials such as chips, granules, and other agricultural and woodworking waste. For such materials, the shape of the particles (structural elements) is generally irregular and not geometrically well-defined. This characteristic served as the basis for adopting a continuum model of porous media. In this model, the material is treated as a continuous substance that fills all available layers of bulk space, allowing for the mechanical behavior of materials with internal pores or voids to be accurately described. The pores within the material are considerably smaller compared to other characteristic dimensions of the material's properties. In the continuum model, the mechanical characteristics of the material, such as stress, strain, and compaction, are described by mathematical equations that account for the material's physical properties and its behavior under loading. By reducing this model to a two-dimensional spatial form, a closed-form analytical solution was obtained using a general method for solving the differential equations of equilibrium along with the Huber–Mises energy condition for plasticity. The following assumptions were adopted as working hypotheses: radial and tangential stresses are equal, and the lateral pressure coefficient is equal to the proportional granulation density. Given that the problem is solved in a general form, the solution should be regarded as methodological, that is, it can be applied to any loading scheme exhibiting axial symmetry. Transcendental equations were derived to describe the deformation compaction process of a porous body. These equations account for both the ideal granulation process and the influence of contact friction forces. As a result of developing a solution method for these equations, dependencies were obtained for calculating the local characteristics of the stress state during granulation, as well as for integral parameters of the process, such as compaction and deformation work.

АНОТАЦІЯ

Дане дослідження присвячене вирішенню вісе-симетричної задачі теорії гранулювання пористих тіл з практичним застосуванням у вигляді силового розрахунку процесів гранулювання дисперсних сипучих матеріалів: стружкових, гранульованих та інших відходів сільськогосподарського виробництва і деревообробки. Для таких матеріалів форма частинок (структурних елементів) не є геометрично правильною або взагалі визначеною. Це служило підґрунтям для того, що в основу вирішення була покладена континуальна модель пористого тіла, яка дозволяє описувати механічну поведінку матеріалів, які мають пори або порожнини в своїй структурі. В даній моделі матеріал розглядається як неперервна речовина, що заповнює усі доступні шари сипкого простору. Пори у матеріалі вважаються невеликими в порівнянні зі значеннями інших властивостей матеріалу.

У континуальній моделі, механічні характеристики матеріалу, такі як напруження, деформація та тиск, описуються математичними рівняннями, що враховують фізичні властивості матеріалу та його поведінку під навантаженням. Ця модель застосовується для аналізу різних видів механічних деформацій та взаємодії матеріалів, включаючи стискання, розтягування, згин, обертання тощо. В результаті зведення даної моделі до двовимірної просторової моделі отримано замкнене аналітичне рішення методом спільного вирішення диференціальних рівнянь рівноваги та енергетичної умови пластичності Губера-Мізеса. В якості робочих гіпотез прийняті наступні припущення: радіальне і тангенціальне напруження рівні, коефіцієнт бічного тиску рівний пропорційній щільності гранулювання. З огляду на те, що задача вирішена у загальному вигляді, саме рішення слід розглядати як методологічне, тобто може бути використано для будь-якої схеми навантаження, яка виявляє осьову симетрію. Були отримані трансцендентні рівняння, які описують процес деформаційного ущільнення пористого тіла. Ці рівняння враховують як ідеальний процес гранулювання, так і вплив сил контактного тертя. Внаслідок розробки методу розв'язання цих рівнянь були отримані залежності для обчислення локальних характеристик напруженого стану в процесі гранулювання, а також для інтегральних параметрів цього.

INTRODUCTION

Porous bodies include materials that can be granular or other bulk substances (Pisarenko & Mozharovsky, 1981; Bertram, 2012; Hashiguchi & Yamakawa, 2012; Haupt, 2002; Lubliner, 1990; Zhou et al., 2021; Aruffo et al., 2024; Zheng et al., 2017; Uniyal et al., 2020). Zhou et al., (2021), present the shear strength behavior of glass beads with two particular sizes under the influence of 0-5% liquid and hydrated lime (HL) contents. Experimental work was performed to analyze the influence of liquid-powder mixture ratios on a wet granular system under various loading stresses. Hence, evaluating bulk density and shear resistance is crucial for assessing the growth and strength of agglomerated products (Aruffo et al., 2024; Zheng et al., 2017; Uniyal et al., 2020).

In the classification according to the physical and mechanical properties of particles (structural elements), these materials belong to the category of structurally heterogeneous (Landau, & Lifshits, 2013; Gurson, 1977; Bettinotti et al., 2017; Aruffo et al., 2022). Usually, the shape of the particles does not have a geometrically correct structure or may even be undefined, which casts doubt on the possibility of using the contact-discrete model of deformation compaction for such materials. In such situations it is more appropriate to use a model that treats the material as a compressible continuum and takes into account rheological characteristics, such as the yield strength (Lu & Li, 2017; Bratishko, 2020; Bratishko, 2014; Boltyanska, 2018; Salman et al., 2007; Probst & Ileleji, 2016).

Probst & Ileleji, (2016), presented a laboratory-scale batch drum granulation process used to produce granules from dried distillers grains with solubles (DDGS). This was achieved by adding condensed distillers solubles (CDS) as a binder to wet distillers grains (WDG), both of which are coproducts of the corn dry-grind ethanol process, under varying formulation and process conditions. A full factorial experimental design was employed to test all combinations of factor levels, including the amount of CDS binder, CDS solids content, screen size opening, and residence time. These characteristics allow for the assessment of the material's resistance to deformation.

Even though several studies have described the impact of granulation process parameters on granule size distribution, granules density, and flowability (Benali et al., 2009; Liu et al., 2013; Mangwandi et al., 2013), no systematic investigation has yet reported how these variables influence the granule hardness and compression properties of granules. Granule hardness could be one of the important properties in tablet formulation because granules having insufficient hardness are extremely fragile leading to compromise on quality. On the other hand, if the granules are extremely hard, this may compromise the compressibility. Meanwhile, compression behavior of granules might be altered by process variables. However, detailed studies are very limited on how process variables influence the compression behavior of granules. Heckle plot analysis can be commonly used for the analysis of compression behavior of pharmaceutical excipients. Therefore, one of the objectives of the present study was to investigate the impact of process variables on granule hardness and compression behavior of granules.

MATERIALS AND METHODS

The solution of the axisymmetric problem in the granulation theory of porous bodies involves determining the local characteristics of the stress state during granulation as a function of spatial coordinates, as well as key integral parameters such as compression, force, and deformation work (Pisarenko & Mozharovsky, 1981; Bertram, 2012; Hashiguchi & Yamakawa, 2012; Haupt, 2002; Lubliner, 1990). For modeling purposes, the porous body is represented as a solid, compressible, rigid-plastic material with a defined yield point. The granulation process of the porous material is carried out within a die, as illustrated in Fig. 1.

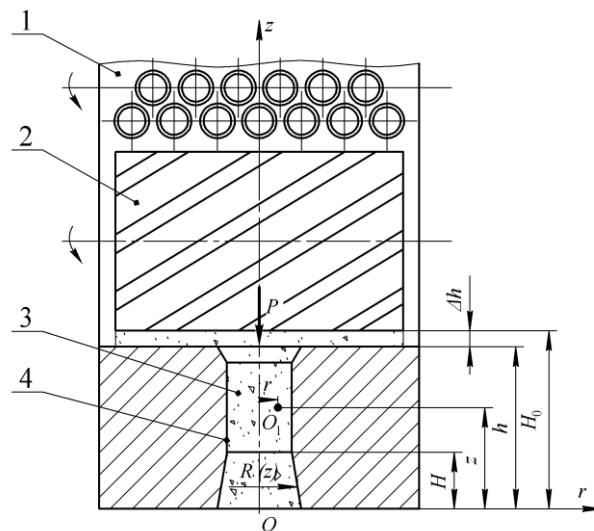


Fig. 1 – Technological scheme of granulation of a porous body in a die spinneret

1 – die; 2 – roller; 3 – porous material; 4 – spinneret

During the granulation process, the side surface of the die is modeled as a body of revolution. At any given moment under axisymmetric loading, it can be described by the equation $R=R(z)$. In the first stage of analysis, force calculations are performed without accounting for contact friction forces.

The following notations are used in this research: H_0, H – initial and final granulation height; h – current granule formation height; Δh – deformation path (compaction); R – radius of granule formation at a given section z ; ρ_0 – current material density; ρ_m – maximum material density (granules); $\mu = \rho_0/\rho_m$ – relative granule density; μ_0, μ_k – initial and final values of relative density; $\varepsilon = 1-\mu$ – relative porosity; σ_m – yield strength of the material; η – plasticity constant; f – coefficient of friction.

For any point in the deformation process the differential equations of equilibrium in cylindrical coordinates are written as follows (Pisarenko & Mozharovsky, 1981; Hashiguchi & Yamakawa, 2012; Landau & Lifshits, 2013; Bettinotti et al., 2017; Lu & Li, 2017):

$$\frac{\partial \sigma_R}{\partial R} + \frac{\partial \tau_{Rz}}{\partial z} + \frac{\sigma_R - \sigma_\varphi}{R} = 0 \tag{1}$$

$$\frac{\partial \tau_{zR}}{\partial R} + \frac{\partial \sigma_z}{\partial z} + \frac{\tau_{zR}}{R} = 0 \tag{2}$$

The plasticity condition is applied in the following form (Landau & Lifshits, 2013; Bratishko, 2020):

$$(\sigma_R - \sigma_\varphi)^2 + (\sigma_\varphi - \sigma_z)^2 + (\sigma_z - \sigma_R)^2 + 6 \cdot \tau_{Rz}^2 = 2 \cdot \sigma_m^2 \tag{3}$$

An elementary volume of a granule with the corresponding stress tensor components is shown in Fig. 2. Under axisymmetric loading conditions in meridional planes passing through the z -axis, the tangential stresses are zero, and the stress components are independent of the coordinate φ .

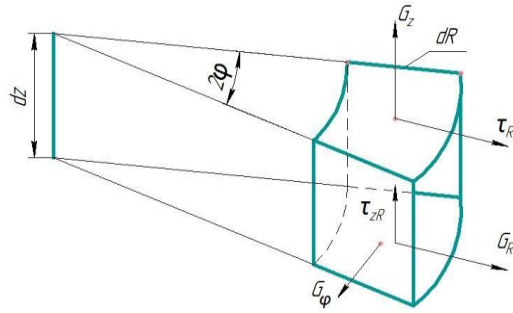


Fig. 2 – Schematic diagram of the elementary volume of the deformation element together with the components of the stress tensor during the granulation process

According to the Haar-Karman condition of full plasticity (Pisarenko & Mozharovsky, 1981; Salman et al., 2007; Payne et al., 2016), when the movement of the material in the radial direction is limited by the die wall, and tangential movement is kinematically prohibited due to the symmetrical separation of the surface in the planes φ, it can be assumed that $\sigma_\phi = \sigma_R$. In addition, the normal radial stress σ_R is directly proportional to the density of the material during the granulation process and within the limits $\mu = 1$ reaching value σ_z (Bratishko, 2014; Boltjanskaya, 2018; Pietsch, 2002):

$$\sigma_\phi = \sigma_R = \mu \cdot \sigma_z \tag{4}$$

Under conditions of fully-sided non-uniform compression, where the spherical component of the stress tensor significantly dominates the deviatoric component, a relationship is established between the normal axial (or radial) stress and the deviatoric stress. The relationship between the tangential and normal radial stresses is linear. In practice, the relative density of granules during the granulation process μ is approximately equal to the lateral pressure coefficient.

Relative density, as well as the deformation path or time, are common variables of the granulation process. However, for the studied fixed moment it is considered a constant when calculating the stress state.

Taking into account the proposed assumption (4), the law of paired tangential stresses $\tau_{Rz} = \tau_{zR} = \tau$ and the corresponding designation, $\sigma = \sigma_z$ the system of equations (1) – (3) can be expressed as follows:

$$\mu \frac{\partial \sigma}{\partial R} + \frac{\partial \tau}{\partial z} = 0 \tag{5}$$

$$\frac{\partial \tau}{\partial R} + \frac{\partial \sigma}{\partial z} + \frac{\tau}{R} = 0 \tag{6}$$

$$(1 - \mu)^2 \cdot \sigma^2 + 3 \cdot \tau^2 = \sigma_m^2 \tag{7}$$

The plasticity condition (Aruffo et al., 2024) establishes the following relationship between the components of the stress tensor:

$$\sigma = \varepsilon^{-1} \cdot (\sigma_m^2 - 3 \cdot \tau^2)^{0.5} \tag{8}$$

$$\tau = 0.58 \cdot (\sigma_m^2 - \varepsilon^2 \cdot \sigma^2)^{0.5} \tag{9}$$

For the following calculations we will create a table of derivatives of these expressions, using the concept, known in mathematics, of taking the derivative of an implicitly defined function and, taking into account (Lublinter, 1990), we will obtain:

For the subsequent calculations, a table of derivatives of these expressions will be will constructed using the mathematical concept of taking the derivative of an implicitly defined function. Taking into account the approach described in Lubliner (1990), it is obtained:

$$\dot{\sigma}_R = 3 \cdot \varepsilon^{-1} \cdot \tau \cdot \dot{\tau}_R \cdot (\sigma_m^2 - 3 \cdot \tau^2)^{-0.5} = -3 \cdot \tau \cdot \dot{\tau}_R \cdot \varepsilon^{-2} \cdot \sigma^{-1} = -\dot{\tau}_z \cdot \mu^{-1} \tag{10}$$

$$\dot{\sigma}_z = 3 \cdot \varepsilon^{-1} \cdot \tau \cdot \dot{\tau}_z \cdot (\sigma_m^2 - 3 \cdot \tau^2)^{-0.5} = -3 \cdot \tau \cdot \dot{\tau}_z \cdot \varepsilon^{-2} \cdot \sigma^{-1} \tag{11}$$

$$\dot{\tau}_R = -0.58 \cdot \varepsilon^2 \cdot \sigma \cdot \dot{\sigma}_R \cdot (\sigma_m^2 - \varepsilon^2 \cdot \sigma^2)^{-0.5} \tag{12}$$

$$\dot{\tau}_R = -0.58 \cdot \varepsilon^2 \cdot \sigma \cdot \dot{\sigma}_R \cdot (\sigma_m^2 - \varepsilon^2 \cdot \sigma^2)^{-0.5} = 0.33 \cdot \varepsilon \cdot \mu^{-1} \cdot \dot{\tau}_z \cdot \tau^{-1} \cdot (\sigma_m^2 - 3 \cdot \tau^2)^{0.5} \quad (17)$$

Equation (6) may be expressed as follows:

$$0.33 \cdot \varepsilon \cdot \tau^{-1} \cdot \mu^{-1} \cdot (\sigma_m^2 - 3 \cdot \tau^2)^{0.5} \cdot \frac{\partial \tau}{\partial z} - 3 \cdot \varepsilon^{-1} \cdot \tau \cdot (\sigma_m^2 - 3 \cdot \tau^2)^{-0.5} \cdot \frac{\partial \tau}{\partial z} + \frac{\tau}{R} = 0 \quad (18)$$

By performing the procedure of separation of variables and summing up the integration, the following is obtained:

$$0.6 \cdot \varepsilon \cdot \mu^{-1} \cdot \int \left(\frac{(0.3 \cdot \sigma_m^2 - \tau^2)^{0.5}}{\tau^2} \right) d\tau - 1.7 \cdot \varepsilon^{-1} \cdot \int (\sigma_m^2 - \tau^2)^{-0.5} d\tau + R_1^{-1} \cdot \int dz = 0 \quad (19)$$

$$0.33 \cdot \varepsilon \cdot \mu^{-1} \cdot \tau^{-1} \cdot (\sigma_m^2 - 3 \cdot \tau^2)^{0.5} + [0.58 \cdot \varepsilon \cdot \mu^{-1} + 1.73 \cdot \varepsilon^{-1}] \cdot \sin^{-1} [1.73 \cdot \tau \cdot \sigma_m^{-1}] - z \cdot R_1^{-1} = C \quad (20)$$

or considering (8):

$$\sigma \cdot \omega^{-1} \cdot \tau^{-1} + \chi \cdot \beta - z \cdot R_1^{-1} = C \quad (21)$$

where:

$$\chi = 0.58 \cdot \varepsilon \cdot \mu^{-1} + 1.73 \cdot \varepsilon^{-1}; \beta = \sin^{-1} [1.73 \cdot \tau \cdot \sigma_m^{-1}]; \omega = 3 \cdot \mu \cdot \varepsilon^{-2} \quad (22)$$

The integration constant C can be found by taking into account the initial and the limiting conditions. At the beginning of plastic deformation on the contact surface between the die and the roller during the granulation process, that is, at $z = h = H_0$ and $R = R_1$, the tangential stress reaches a value equal to the plasticity constant: $\tau = \eta = 0.58 \sigma_m$, and, taking into account condition (7), it is established that the normal stress becomes zero: $\sigma = 0$. Therefore:

$$C = 0.5 \cdot \chi \cdot \pi - H_0 \cdot R^{-1} \quad (23)$$

Then the solution (21) is expressed in the following way:

$$\sigma \cdot \omega^{-1} \cdot \tau^{-1} + \chi \cdot \beta - z \cdot R_1^{-1} = 0.5 \cdot \chi \cdot \pi - H_0 \cdot R^{-1} \quad (24)$$

By substituting $R = R(z)$ into expression (24), the marginal conditions can be satisfied. For a cylindrical die $R = \text{const}$, the value remains constant.

Equation (24) defines the equation of deformation compaction of a porous body, which connects all parameters of the process. To determine stresses σ and τ , this equation must be solved together with the plasticity condition (7), namely, by substituting expressions (8), (9):

$$(\sigma_m^2 - 3 \cdot \tau^2)^{0.5} \cdot \omega^{-1} \cdot \tau^{-1} \cdot \varepsilon^{-1} + \chi \cdot \beta - z \cdot R_1^{-1} = 0.5 \cdot \chi \cdot \pi - H_0 \cdot R^{-1} \quad (25)$$

$$1.73 \cdot (\sigma_m^2 - \varepsilon^2 \cdot \sigma^2)^{-0.5} \cdot \omega^{-1} \cdot \sigma + \chi \cdot \beta - z \cdot R_1^{-1} = 0.5 \cdot \chi \cdot \pi - H_0 \cdot R^{-1} \quad (26)$$

Equations (24)–(26) are transcendental, but functions $\sigma(z, R)$ and $\tau(z, R)$ are given implicitly. Their solution is possible only with the help of numerical methods. However, these equations are a closed solution for the problem of axisymmetric granulation theory of porous bodies under the condition of plasticity.

Let us represent the first term in equation (6) as function of σ and its derivative, using expressions (10), (12), (13):

$$\begin{aligned} \dot{\tau}_R &= -0.58 \cdot \varepsilon^2 \cdot \sigma \cdot \dot{\sigma}_R \cdot (\sigma_m^2 - \varepsilon^2 \cdot \sigma^2)^{-0.5} = \\ &= -0.58 \cdot \varepsilon^2 \cdot \sigma \cdot \dot{\tau}_z \cdot \mu^{-1} \cdot (\sigma_m^2 - \varepsilon^2 \cdot \sigma^2)^{-0.5} = \\ &= -0.33 \cdot \varepsilon^4 \cdot \sigma^2 \cdot \dot{\sigma}_z \cdot \mu^{-1} \cdot (\sigma_m^2 - \varepsilon^2 \cdot \sigma^2)^{-1}. \end{aligned} \quad (27)$$

Equation (6) can be rewritten as follows:

$$-0.33 \cdot \varepsilon^4 \cdot \sigma^2 \cdot \mu^{-1} \cdot (\sigma_m^2 - \varepsilon^2 \cdot \sigma^2)^{-1} \cdot \frac{\partial \sigma}{\partial z} + \frac{\partial \sigma}{\partial z} + \frac{\tau}{R} = 0 \quad (28)$$

Both parts of the equation are divided by τ , using the substitution of expression (9):

$$-0.33 \cdot \varepsilon^4 \cdot \sigma^2 \cdot \mu^{-1} \cdot \tau^{-1} \cdot (\sigma_m^2 - \varepsilon^2 \cdot \sigma^2)^{-1} \cdot \frac{\partial \sigma}{\partial z} + \tau^{-1} \cdot \frac{\partial \sigma}{\partial z} + R^{-1} = 0 \quad (29)$$

$$-0.58 \cdot \varepsilon \cdot \sigma^2 \cdot \mu^{-1} \cdot \left(\left[\frac{\sigma_m}{\varepsilon} \right]^2 - \sigma^2 \right)^{-1.5} \cdot \frac{\partial \sigma}{\partial z} + 1.73 \cdot \varepsilon^{-1} \cdot \left(\left[\frac{\sigma_m}{\varepsilon} \right]^2 - \sigma^2 \right)^{-0.5} \cdot \frac{\partial \sigma}{\partial z} + R^{-1} = 0 \quad (30)$$

By separating variables and integrating, it is obtained:

$$-0.58 \cdot \varepsilon \cdot \mu^{-1} \cdot \int \left[\sigma^2 \cdot \left(\left[\frac{\sigma_m}{\varepsilon} \right]^2 - \sigma^2 \right)^{-1.5} \right] d\sigma + 1.73 \cdot \varepsilon^{-1} \cdot \int \left(\left[\frac{\sigma_m}{\varepsilon} \right]^2 - \sigma^2 \right)^{-0.5} d\sigma + \int R^{-1} dz = 0 \quad (31)$$

$$-0.58 \cdot \varepsilon \cdot \mu^{-1} \cdot \left[\sigma \cdot \left(\left[\frac{\sigma_m}{\varepsilon} \right]^2 - \sigma^2 \right)^{-0.5} - \sin^{-1} \left[\varepsilon \cdot \sigma \cdot \sigma_m^{-1} \right] \right] + 1.73 \cdot \varepsilon^{-1} \cdot \sin^{-1} \left[\varepsilon \cdot \sigma \cdot \sigma_m^{-1} \right] + z \cdot R^{-1} = C \quad (32)$$

$$\left[0.58 \cdot \varepsilon \cdot \mu^{-1} + 1.73 \cdot \varepsilon^{-1} \right] \cdot \sin^{-1} \left[\varepsilon \cdot \sigma \cdot \sigma_m^{-1} \right] - 0.58 \cdot \varepsilon^2 \cdot \mu^{-1} \cdot \sigma \cdot (\sigma_m^2 - \varepsilon^2 \cdot \sigma^2)^{-0.5} + z \cdot R^{-1} = C \quad (33)$$

Or, taking into account (9) and (12):

$$\chi \cdot \alpha - \sigma \cdot \omega^{-1} \cdot \tau^{-1} + z \cdot R_1^{-1} = C \quad (34)$$

The constant of integration C can be determined using the initial and marginal conditions, for example, when $z = h = H_0$ and $R = R_1$. During the start of plastic deformation when $\tau = \eta = 0.58 \sigma_m$, $\sigma = 0$, the value of C will be equal to H_0 / R . The resulting solution (34) takes the following form:

$$\chi \cdot \alpha - \sigma \cdot \omega^{-1} \cdot \tau^{-1} + z \cdot R_1^{-1} = H_0 \cdot R^{-1} \quad (35)$$

Comparing Equations (24) and (35), it can be concluded that they essentially express the same equation, differing only in the angles α and β , as shown in (Fig. 3). By adding their left and right parts, the plasticity condition is obtained (7), which is expressed by the angles α and β :

$$\sin^{-1} \left[1.73 \cdot \tau \cdot \sigma_m^{-1} \right] + \sin^{-1} \left[\varepsilon \cdot \sigma \cdot \sigma_m^{-1} \right] = \alpha + \beta = \pi / 2 \quad (36)$$

Equation (35) can also be obtained from equation (24) by replacing β angle with angle $\alpha: \beta = \alpha - \pi / 2$.

The presence of trigonometric functions of angles in the equation of deformation compaction is a result of the relationship between normal and tangential stresses σ and τ according to the algebraic dependence (7).

To find stresses σ and τ using simple formulas, the specifics of axisymmetric loading are used. Let us turn again to Fig. 3. The nominal cross-section in the granulation channel, as well as the plasticity circle, have the shape of a circle with radius R . The point under consideration O_1 is located on a circle with radius R_1 . The section of this circle with diagonal OO_2 of triangle OO_2B_2 yields point O_1 that has the same coordinates z and R_1 , and is also in the same stress state as point O_1 . The projection of radius $R_1(OO_1)$ onto axis $\tau(R)$ forms segment $R_2(OB_1)$ and creates a coordinate triangle OO_1B_1 . Right triangles OO_2B_2 and OO_1B_1 with the same angles α and β have geometric similarities, that is:

$$\begin{aligned} \zeta = \sin \beta &= \frac{R_2}{R_1} = 1.73 \cdot \tau^{-1} \cdot \sigma_m^{-1} \\ \cos \beta &= \varepsilon \cdot \sigma \cdot \sigma_m^{-1} = \frac{\sqrt{R_1^2 - R_2^2}}{R_1} = \sqrt{1 - \left[\frac{R_2}{R_1} \right]^2} = \sqrt{1 - \zeta^2} \\ \sigma \cdot \tau^{-1} &= 1.73 \cdot \varepsilon^{-1} \cdot [\tan \beta]^{-1} \cdot 1.73 \cdot \varepsilon^{-1} \cdot \beta^{-1} \\ \sigma &= \sigma_m \cdot \varepsilon^{-1} \cdot \sqrt{1 - \zeta^2}; \quad \tau = 0.58 \cdot \zeta \cdot \sigma_m \end{aligned} \quad (37)$$

To calculate stresses σ and τ using formulas (37), it is sufficient to find the value of angle β and coefficient ζ . Let's substitute ratio σ/τ from formula (37) into (24), After minor transformations, a quadratic three-term equation is obtained, from which angle β is determined, and then coefficient ζ :

$$a \cdot \beta^2 + b \cdot \beta + c = 0; \beta_{1,2} = \frac{-b \pm \sqrt{b^2 - 4 \cdot a \cdot c}}{2 \cdot a}$$

where:

$$a = \chi \cdot \omega \cdot \varepsilon; b = -\eta \cdot \omega \cdot \varepsilon; c = 1.73; \eta = \chi \cdot \frac{\pi}{2} - \frac{H_0}{R} + \frac{z}{R_1}; \zeta = \sin\beta \quad (38)$$

The coefficient ζ is a complex function of the coordinates of the points within the elementary volume undergoing deformation, the relative density of the granules, and the yield strength of the material being deformed at a given temperature and granulation speed mode.

The system of equations (37), (38) is a closed analytical solution to the equation of deformation compaction of a porous body. In addition to calculations and analysis of local characteristics of the stress state of the granulation process, these equations allow determining the integral parameters of this process: of pressure, the force and deformation work.

The force calculation of the granulation process will be carried out by constructing force diagrams and determining the deformation work, which are related to the determination of the average integral value of pressure on the contact surface between the material and the die during the granulation process S at $z=h$, $R = R_1$. The average pressure, without taking into account the contact friction forces, is calculated using the following formula:

$$\begin{aligned} g_i &= \frac{1}{S_i} \cdot g_i(S) \cdot dS = \frac{1}{S_i} \cdot [\sigma_z + \tau_{zR}] \cdot dS = \frac{1}{\pi \cdot R_1^2} \int_0^R \left[\frac{\sigma_m}{\varepsilon} \cdot \sqrt{1-\zeta^2} + \frac{\zeta \cdot \sigma_m}{\sqrt{3}} \right] d(\pi \cdot R^2) = \\ &= \frac{2 \cdot \sigma_m}{R_1^2} \int_0^R \left[\frac{1}{\varepsilon} \cdot \sqrt{1-\zeta^2} + \frac{\zeta}{\sqrt{3}} \right] \cdot R \cdot dR. \end{aligned} \quad (39)$$

Based on the results of numerical integration (39), a diagram of the granulation process $g_i(\mu)$ is constructed, considering that $\varepsilon = 1-\mu$. It is important to note here that plastic deformation of the material does not occur at a zero value of the average pressure during the granulation process, calculated on the contact area. At the beginning of the process, the average pressure has a clearly defined value, which was taken into account when determining the initial and the marginal conditions and which can be calculated using formula (39).

The formula for the calculation of the force of the granulation process is as follows (Pisarenko & Mozharovsky, 1981; Bratishko, 2014; Bratishko, 2014):

$$P_i = g_i \cdot S_i = 2 \cdot \pi \cdot \sigma_m \cdot \int_0^R \left(\left[\varepsilon^{-1} \cdot \sqrt{1-\zeta^2} + \frac{\zeta}{\sqrt{3}} \right] \cdot R \right) dR \quad (40)$$

The impact of the contact friction forces is considered taking into account the efficiency of granulation processes of porous materials, which largely depends on the interaction of the lateral surface of granulation with the wall of the die, especially when the movement occurs. The speed of the movement of the material particles along the height of the spinneret during the granulation process decreases from the maximum value \mathcal{G} to zero, this means that the roller moves at a constant speed \mathcal{G} . This results in a lateral friction force that consistently counteracts the effective force exerted by the roller on the material during the granulation process. This interaction positively influences the process flow by reducing deformation resistance and lowering the energy required for deformation work.

The average value of the normal lateral pressure is calculated as (Zhou et al., 2021; Probst & Ileleji, 2016):

$$g_R = \frac{1}{h} \cdot \int_0^h [\sigma_R(z) + \tau_{Rz}(z)] dz = \sigma_m \cdot h^{-1} \cdot \int_0^h \left[\mu \cdot \varepsilon^{-1} \cdot \sqrt{1-\zeta^2} + \frac{\zeta}{\sqrt{3}} \right] dz \quad (41)$$

The Amonton-Coulomb law shows that the frictional force between the surfaces is proportional to the lateral pressure (Pisarenko & Mozharovsky, 1981; Bratishko, 2014; Bratishko, 2020):

$$\tau = f \cdot g_R = f \cdot \sigma_m \cdot h^{-1} \cdot \int_0^h \left[\mu \cdot \varepsilon^{-1} \cdot \sqrt{1 - \zeta^2} + \frac{\zeta}{\sqrt{3}} \right] dz \quad (42)$$

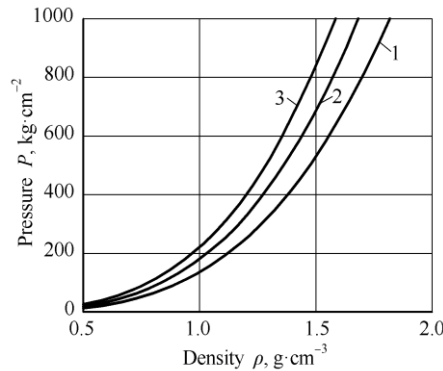


Fig. 4 – Dependence of specific pressing pressure P on the density of the material ρ for various values of the physical and mechanical properties of the material mixture

1 – $\delta = 141.4$; 2 – $\delta = 183.2$; 3 – $\delta = 220.6$

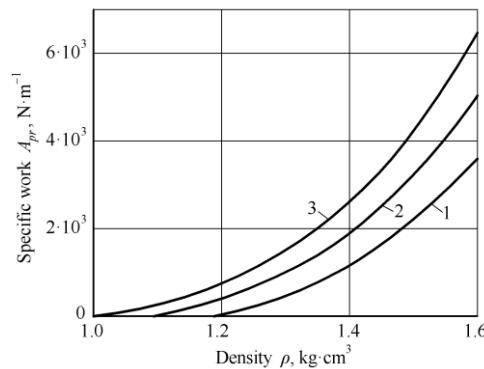


Fig. 5 – Dependence of the specific work A_{pr} of the granulation process on the density ρ of the material for various values of the physical and mechanical properties of the material mixture:

1 – $\delta = 141.4$; 2 – $\delta = 183.2$; 3 – $\delta = 220.6$

The lateral friction force is defined as the result of multiplying the specific friction force by the area of the lateral contact surface of the die during the granulation process. This ratio shows how the friction force depends upon the contact area and the magnitude of the specific friction force:

$$F_T = \tau \cdot S_R = 2 \cdot \pi \cdot R \cdot f \cdot \sigma_m \cdot \int_0^h \left[\mu \cdot \varepsilon^{-1} \cdot \sqrt{1 - \zeta^2} + \frac{\zeta}{\sqrt{3}} \right] dz \quad (43)$$

With this conclusion it can be claimed that the lateral friction force is determined by the contact area between the granulation surface and the bulk material that is supplied for granulation. This is of great importance in the analysis and calculation of the force parameters of the granulation process and the reduction of deformation resistance.

To take into account the impact of the contact friction forces during the granulation of a porous body in the moving die, the following calculation expression is used:

$$P = P_i - F_T = 2 \cdot \pi \cdot \sigma_m \cdot \left[\int_0^R \left(\left[\varepsilon^{-1} \cdot \sqrt{1 - \zeta^2} + \frac{\zeta}{\sqrt{3}} \right] \cdot R \right) dR - R \cdot f \cdot \int_0^h \left[\mu \cdot \varepsilon^{-1} \cdot \sqrt{1 - \zeta^2} + \frac{\zeta}{\sqrt{3}} \right] dz \right] \quad (44)$$

The displacement of deformation and the relative density of granules during the granulation process are related by the following relationship:

$$\Delta h = H_0 - H \cdot \mu^{-1} \quad (45)$$

Accordingly, the expressions for calculating the current value of the deformation work and the total work have the following form:

$$A_p = \int_0^{\Delta h} P(\Delta h) d(\Delta h) = \int_{\mu_0}^{\mu} P(\mu) d\mu \quad (46)$$

$$A_z = \int_0^{H_0-H} P(\Delta h) d(\Delta h) = \int_{\mu_0}^{\mu_k} P(\mu) d\mu \quad (47)$$

The above equations and formulas facilitate the calculations and analysis of the force parameters of the granulation process of porous bodies. They allow taking into account the impact of contact friction forces upon the process, which helps to determine the efficiency of the proposed process flow diagram and energy costs for deformation.

It should be noted that granulated materials have several advantages over the bulk materials. One of the main limiting factors for the widespread use of granulation is the low energy efficiency of the existing granulators. For example, the ring die granulators with a capacity of up to $1 \text{ t}\cdot\text{h}^{-1}$ are equipped with drive electric motors with a power of 90-110 kW.

Based on our calculations, innovative energy-efficient granulators are being developed from the original design of the press rollers and the annular die. A possibility to obtain granules from some types of both agricultural and wood processing raw materials has been experimentally proven. The research is carried out on a specially created experimental setup, which is shown in Fig. 6. Taking into account that the parameters of granulation processes influence a number of input factors, the granulation processes must be described by multifactorial dependencies that can be obtained on the basis of the theory of planning multifactorial experiments. To formulate the planning task correctly, it is necessary to conduct preliminary studies of the impact of individual factors.

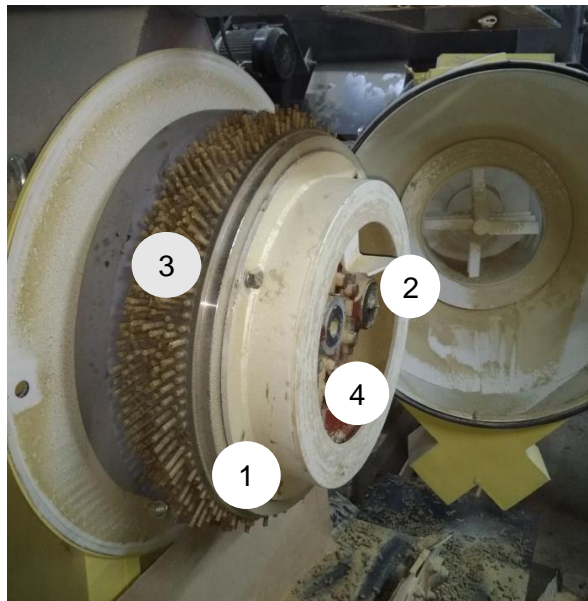


Fig. 6 – Experimental setup for granulating agricultural waste
1 – die; 2 – roller; 3 – granulate material; 4 – spinneret

During the experiments, the granulation system was used to process agricultural waste as well as wood-processing raw materials. The raw material was fed using a screw conveyor with adjustable drive shaft speed. The input parameters identified as influencing pellet quality and production efficiency were: temperature, raw material moisture content, the rotational speed of the gear transmission pinion, n , (rpm), and the screw shaft speed, n_w , (rpm). The raw material temperature was measured using a pyrometer-thermometer (model AZ-8838), and moisture content was measured with a Greisinger GMK100 non-contact moisture meter. The diameter of the die holes was 8 mm. Granulation productivity Q and pellet density ρ were selected as the main evaluation criteria. Productivity was determined using the well-known formula $Q = m \tau^{-1}$ ($\text{kg}\cdot\text{h}^{-1}$), where m is the mass of granules, obtained over time t .

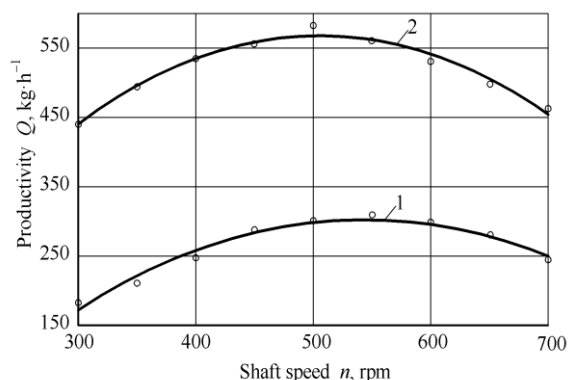


Fig. 7 – Dependence of granulation productivity of agricultural raw materials on the number of revolutions of granulator’s leading shaft ($d = 8 \text{ mm}$; $n_w = 20 \text{ rpm}$; $T = 14^\circ\text{C}$; $W = 34.8\%$)
 1 – two-roller granulation system; 2 – three-roller granulation system

Fig. 7 shows dependence of granulation productivity of agricultural raw materials on the number of drive shaft revolutions. It is evident that the dependencies have an optimum in the range of 500 – 550 rpm. In addition, it was found that when the material sticks to the die, the productivity decreases by 1.5-2.0 times. It is necessary to determine the factors that influence the nature of the free (without sticking) exit of granules through the holes of the die. During granulation of the raw materials its humidity and temperature were taken into account.

Fig. 8 presents the graphical dependence of the granulation productivity of woodworking raw materials on the number of revolutions of the granulator’s leading shaft.

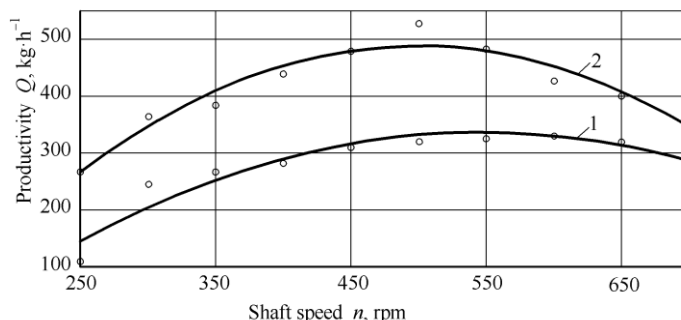


Fig. 8 – Dependence of granulation productivity of woodworking raw materials on the number of revolutions of the granulator’s leading shaft ($d = 8 \text{ mm}$; $n_w = 20 \text{ rpm}$; $T = 14^\circ\text{C}$; $W = 25.4\%$)
 1 – two-roller granulation system; 2 – three-roller granulation system

It has been established that dependence $Q(n)$ is also of an extreme nature. Maximum productivity (over $320 \text{ kg}\cdot\text{h}^{-1}$) is observed in the range of rotational speeds of the granulator’s leading shaft – from 600 to 700 rpm.

One of the key quality indicators of granules is their density, which was measured both immediately after production and after cooling. To determine granule density, samples with identical moisture content and temperature were taken, but produced at varying screw conveyor shaft speeds $n_w = 10 - 70 \text{ rpm}$, while maintaining a constant rotational speed of the granulator’s leading shaft $n = 500 \text{ rpm}$. The tests were conducted at different initial raw material moisture contents: 15.1%, 25.4%, and 34.8%.

The data, obtained during the experiment, are presented in Table 1.

Table 1

Density of granules of the agricultural raw materials depending on the number of revolutions of the screw conveyor "before cooling" / "after cooling" at different humidity of the raw materials

Number of screw revolutions n_w , rpm	Density of granules ρ , kg·m ⁻³ at various raw material moisture					
	15.1%		25.4%		34.8%	
	before cooling	after cooling	before cooling	after cooling	before cooling	after cooling
10	1252.2	1181	1140.3	1120.1	1011.2	951.8
20	1181.8	1123.4	1157.4	1120.9	1065.4	1023.2

Number of screw revolutions n_w , rpm	Density of granules ρ , kg·m ⁻³ at various raw material moisture					
	15.1%		25.4%		34.8%	
	before cooling	after cooling	before cooling	after cooling	before cooling	after cooling
30	1142.4	1078.9	1131.7	1102.6	1053.2	987.2
40	1210.2	1157.1	1110.2	1113.4	1034.4	974.5
50	1194.6	1078.5	1109.9	1100.5	1036.1	967.4
60	1248.3	1167.7	1134.4	1137.5	1011.5	996.6
70	1242	1185.9	1140.3	1120.4	1030.1	950.7

A graphical representation of the results of the experiment with a change in the granule density from the number of revolutions of the screw conveyor before and after cooling is shown in Fig. 9. It can be seen that the density remains almost constant, changing within 10%.

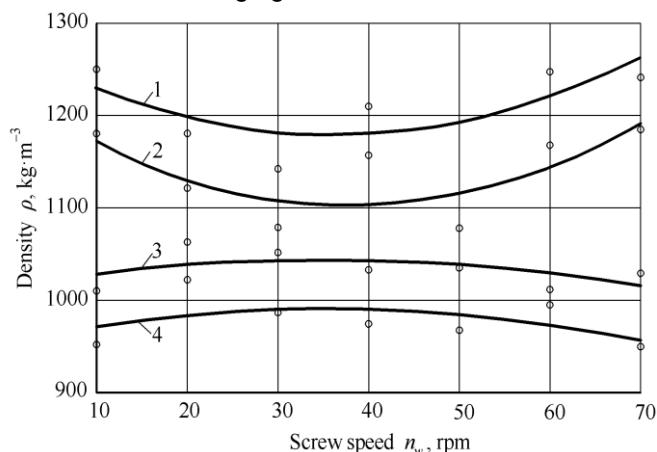


Fig. 9 – Graphic dependencies of the change of the granule density before and after cooling
 1 – granules before cooling; 2 – granules after cooling; ($d = 8$ mm; $T = 140^\circ\text{C}$; $W = 15.1\%$); 3 – granules before cooling;
 4 – granules after cooling; ($d = 8$ mm; $T = 140^\circ\text{C}$; $W = 34.8\%$)

The graphs presented in Fig. 9 show that the density of the granules, regardless of the initial moisture content of the raw material (from 15% to 35%), is practically independent of their cooling but depends on the feed rate of the raw material into the granulation zone. Thus, with an initial raw material moisture content of 34.8% an extreme value may be observed at the screw speed of $n_w = 20$ -30 rpm (Fig. 9).

Under the condition of lower initial raw material moisture content (15.1%) the granules obtained have a denser structure ($\rho \approx 1200$ kg m⁻³), and with high initial raw material moisture content (more than 35%), the density of the obtained granules decreases to $\rho \approx 950$ kg·m⁻³. In addition, it should be said that in the operating mode of the granulator ($n = 500$ rpm and $n_w = 50$ rpm), in which the highest productivity is observed, the density of the granules is the lowest.

A series of preliminary experimental studies showed that the selected input factors have a significant impact on the initial parameters of the granulation process, which allows constructing correctly a plan for conducting multifactorial studies and identifying mathematical dependencies that describe the granulation process.

CONCLUSIONS

The application of the continuum model to the force calculation of the granulation process of porous bodies made it possible to obtain a comprehensive analytical solution for an axisymmetric problem. Application of the continuum model to the force calculation of the granulation process of porous bodies made it possible to obtain a complex analytical solution for an axisymmetric problem. The obtained mathematical dependencies take into account the differential equations of equilibrium and the plasticity condition. Since this solution applies to bodies of revolution of general shape and setting, it can be used for any axisymmetric loading scheme.

Equations for deformation compaction of a porous body have been obtained, both for an ideal granulation process and taking into account the forces of contact friction.

A method has been developed for calculation of local parameters of the stress state during the granulation process, using the coordinates of the plastic deformation point, as well as integral process parameters, such as pressure, force and the deformation work.

It was established that under the conditions of initial raw material moisture content (15.1%), the granules obtained have a denser structure ($\rho \approx 1200 \text{ kg m}^{-3}$), and with high initial raw material moisture content (more than 35%), the density of the obtained granules decreases to $\rho \approx 950 \text{ kg m}^{-3}$. In addition, it should be said that in the operating mode of the granulator ($n = 500 \text{ rpm}$ and $n_w = 50 \text{ rpm}$), in which the highest productivity is observed, the density of the granules is the lowest.

REFERENCES

- [1] Aruffo, G.A., Michrafy, A., Oulahna, D., Michrafy, M. (2024). Experimental and numerical analysis of structural inhomogeneity of grooved compacts. *Powder Technology*. Vol. 445. 120140.
- [2] Aruffo, G.A., Michrafy, M., Oulahna, D., Michrafy, A. (2022). Modelling powder compaction with consideration of a deep grooved punch. *Powder Technology*. Vol. 395, pp. 681-694
- [3] Benali M., Gerbaud V., Hemati M. (2009). Effect of operating conditions and physico-chemical properties on the wet granulation kinetics in high shear mixer. *Powder Technol.* 190(1):160–169.
- [4] Bertram, A. (2012). *Elasticity and Plasticity of Large Deformations*. Springer. 345 p.
- [5] Bettinotti, O., Allix, O., Perego, U., Oancea, V. & Malherbe, B. (2017). Simulation of delamination under impact using a global-local method in explicit dynamics. *Fin Elem Anal Des*. Vol.125, pp.1-13.
- [6] Boltyanska, N. (2018). Ways to Improve Structures Gear Pelleting Presses. TEKA. *An International Quarterly Journal on Motorization, Vehicle Operation, Energy Efficiency and Mechanical Engineering*. Lublin-Rzeszow. Vol.18, No 2, pp.23- 29.
- [7] Bratishko, V. (2014). Coordination of structural parameters of feed screw granulator matrices by pressure and throughput (Узгодження конструкційних параметрів матриць гвинтових грануляторів кормів за тиском та пропускною здатністю). *Technology in agricultural production, industry engineering, automation*. Issue 27. pp. 187-191. (in Ukrainian)
- [8] Bratishko, V. (2020). *Mechanical and technological bases for the preparation of complete feed using screw granulators*. Thesis Phd. Glewaha, 397. <https://doi.org/10.6084/m9.figshare.12370349.v1> (in Ukrainian)
- [9] Gurson, A.L. (1977). Continuum theory of ductile rupture by void nucleation and growth. *J. Eng. Mater. Techn.* № 2. pp.69-78.
- [10] Hashiguchi, K. & Yamakawa, Y. (2012). *Introduction to Finite Strain Theory for Continuum Elasto-Plasticity*. Wiley. 417 p.
- [11] Haupt, P. (2002). *Continuum Mechanics and Theory of Materials*. Springer. 643 p.
- [12] Landau, L.D., Lifshits, E.M. (2013). *Fluid Mechanics: Landau and Lifshitz: Course of Theoretical Physics*, Volume 6. 2nd edition, 538. Amsterdam: Pergamon.
- [13] Liu H., Wang K., Schlindwein W., Li M. (2013) Using the Box-Behnken experimental design to optimise operating parameters in pulsed spray fluidised bed granulation. *Int J. Pharm.* 448(2):329–338. doi: 10.1016/j.ijpharm.2013.03.057.
- [14] Lu, J., Li, L. (2017). Determining the reference geometry of plastically deformed material body undergone monotonic loading and moderately large deformation. *Fin. Elem. Anal. Des*. Vol.130, pp.1-11.
- [15] Lubliner, J. (1990). *Plasticity Theory*. Macmillan Publishing. 528 p.
- [16] Mangwandi C., Albadarin A.B., Ala'a H., Allen S.J., Walker G.M. (2013) Optimisation of high shear granulation of multicomponent fertiliser using response surface methodology. *Powder Technol.* 238:142–150.
- [17] Payne, J., Rattink, W., Smith, T. & Winowski, T. (2001). *Pelleting Handbook*. Sarpsborg, Borregaard Lignotech. 73 p.
- [18] Pietsch, W.B. (2002) *Agglomeration Processes. Phenomena, Technologies, Equipment*. Weinheim, Wiley-vch. 614 p.
- [19] Pisarenko, G. & Mozharovsky, N. (1981). *Equations and boundary value problems of the theory of plasticity and creep. Reference manual*. Naukova Dumka: Kiev. 496 p.
- [20] Probst, K.V., Ileleji, K.E. (2016). The effect of process variables on drum granulation behavior and granules of wet distillers grains with solubles. *Advanced Powder Technology*. Vol. 27, No. 4, pp.1347-1359

- [21] Salman, A.D., Hounslow, M.J. & Seville, J.P.K. (2007). *Handbook of Powder Technology. Granulation*. Vol. 11. Oxford. Elsevier, 1402 p.
- [22] Uniyal, S., Gandarillas, L.P., Michrafy, M., Oulahna, D., Michrafy, A. (2020). Analysis of densification mechanisms of dry granulated materials. *Advanced Powder Technology*. Vol. 31. pp.351-358.
- [23] Zheng, Y.N., Lu, H.F., Guo, X.L., Gong, X. (2017). Study on the effect of nanoparticles on the bulk and flow properties of granular systems. *Fuel Processing Technology*. Vol.177, pp. 30-38.
- [24] Zhou, H., Dahri, M.W., Zhou, M.X., Lai, Z.Y. (2021). Examining the effects of liquid-powder binder concentration on the cohesion and friction of a granular bed. *Particulate Science and Technology*. Vol. 39, No.7, pp.832-843.

OPTIMIZATION OF PARTIAL HIGH-FREQUENCY QUENCHING TECHNIQUE PARAMETERS OF ROTARY TILLING BLADES

旋耕刀局部高频淬火工艺参数优化

Ruili WANG¹⁾, Xueyin BAI¹⁾, Fanbowen MENG¹⁾, Deshuai LI¹⁾, Zhengqing WANG¹⁾, Ke JIANG¹⁾, Wei WANG^{*1)},

¹⁾College of Engineering, Shenyang Agricultural University, Shenyang 10086, China

Corresponding authors. E-mail: syww@163.com

DOI: <https://doi.org/10.35633/inmateh-75-64>

Keywords: Rotary tilling blades, High frequency quenching, Hardness, Parameter optimization

ABSTRACT

The high-frequency quenching technique can enhance the surface hardness of 65Mn rotary tilling blades, thereby improving their wear resistance. This approach addresses common issues found in conventional rotary tilling blades, such as severe wear failure, short service life, and reduced operational efficiency due to frequent replacements. The quenching position was determined through finite element simulation. Based on orthogonal rotation combination tests using ternary quadratic regression, quenching temperature, tempering temperature, and tempering time were identified as key test factors. Using blade hardness as the evaluation index, the optimal parameters were determined to be a quenching temperature of 852 °C, tempering temperature of 171 °C, and tempering time of 85 minutes. Under these conditions, the blade hardness reached 57.5 HRC, meeting the national standard. Blades treated with these optimal quenching parameters were tested under actual soil conditions over a total operating area of 67 hm². The results showed that the average wear of the quenched blades was 11.9 g, and their wear resistance was 3.13 times higher than that of blades treated with conventional heat treatment. This represents a significant improvement in abrasion resistance and provides a solid experimental foundation for the reliability assessment of rotary tilling blades.

摘要

针对目前市面上旋耕刀工作过程中磨损失效严重, 使用寿命低, 耕作时需要频繁更换刀具影响作业效率等问题。采用高频淬火技术, 对 65Mn 旋耕刀表面进行强化处理从而提高其耐磨性。通过有限元仿真确定淬火位置, 基于三元二次回归正交旋转组合试验。确定了淬火温度, 回火温度和回火时间为关键试验因素, 以旋耕刀的硬度为试验指标, 得出最优试验参数淬火温度为 852 °C, 回火温度为 171 °C, 回火时间为 85min, 此条件下旋耕刀的硬度值为 57.5HRC, 符合国家标准。采用最优工艺参数对 65Mn 旋耕刀进行高频淬火, 在实际土壤环境中进行田间试验, 总作业面积 67hm²。结果表明: 经淬火处理后的旋耕刀平均磨损量为 11.9g, 与传统热处理后的旋耕刀相比耐磨性提高了 3.13 倍, 磨损程度得到极大改善, 为旋耕刀的可靠性研究提供了试验基础。

INTRODUCTION

With the rapid development of agricultural mechanization, the service life of the key parts of agricultural machinery and equipment is expected to get longer and longer (Hao *et al.*, 2021). Rotary tillers are essential agricultural machinery that significantly influence the quality and efficiency of soil tillage. Their supporting rotary tilling blades are responsible for critical operations such as ploughing, soil crushing, and land preparation, resulting in a flat and soft surface suitable for sowing (Xiao *et al.*, 2022). Therefore, the performance and service life of the blades directly affect the overall quality and effectiveness of the rotary tiller.

Most rotary tilling blades just operate in the open air, and interact with sand grains and crop stubble for a long time, resulting in serious wear and tear and a low service life, frequent failure and damage. According to incomplete statistics, more than 80% of the soil parts of agricultural machinery operation are scrapped due to the wear and failure of grinding particles, which not only increases the operation cost of agricultural machinery, but also seriously affects the operation quality and efficiency (Yadav *et al.*, 2020; Zhu *et al.*, 2022; Zhao *et al.*, 2024; Kaur *et al.*, 2011; Temesgen *et al.*, 2009; Valboa *et al.*, 2015; Sun *et al.*, 2022; Li, 2018).

In recent years, how to effectively improve the wear resistance and corrosion resistance of rotary tillage blade surface, reduce the energy consumption and reduce the loss is an urgent problem to be solved for agricultural machinery (Wang *et al.*, 2013; Shen *et al.*, 2022). In the past, to enhance the surface hardness of rotary tilling blades, many researchers both domestically and internationally have employed various coating preparation techniques to create wear-resistant layers on the blade surface, achieving significant research

outcomes (Xiao et al., 2013; Falalu et al., 2020; Wang et al., 2022; Xie et al., 2021; Dariusz et al., 2017; Huang et al., 2015; Lee et al., 2006; Satit et al., 2007). However, these methods often involve high equipment costs, complex procedures, and expensive materials, making them difficult to implement on a wide scale and limiting their practical applicability.

In order to reduce the cost, this study adopts partial high-frequency quenching technique, compared with the traditional heat treatment technique, which has the advantages of extremely fast heating speed, easy depth control of quenching layers, uniform heating and high production efficiency. Moreover, only the surface of a certain depth of the workpiece is reinforced, while the core parts basically maintain the organization and performance before treatment, so that the combination of high strength, high wear resistance and high toughness can be obtained. Because 65 Mn materials have better friction performance and better economy, the 65 Mn rotary tilling blades were selected to analyze the significance of the influence of each factor on the hardness of rotary tilling blades. Finally, the field test was carried out to verify the actual working effect of partial high frequency quenching, so as to provide a reference for improving the wear resistance of the surface of rotary blades.

MATERIALS AND METHODS

Partial high-frequency quenching technique of rotary tilling blades

High-frequency quenching is a rapid surface treatment technique characterized by controllable quenching depth and uniform heating. It selectively hardens the surface of the workpiece to a specific depth while preserving the original microstructure and mechanical properties of the core. As a result, it achieves an optimal combination of high strength, excellent wear resistance, and good toughness. Additionally, the method offers numerous advantages, including a high start-up success rate, high efficiency, precise control, smooth and continuous power adjustment (10–100% of rated power), reliable operation, advanced technological integration, and ease of operation.

The partial high-frequency quenching technique of rotary tilling blades is: first start the power supply, the machine begins to work; operate the partial high-frequency quenching device through the control panel of the equipment; hold the rotary tilling blades in the clamp device on the bench and clamp it; transfer the rotary tilling blades to the induction coil by the turntable automatically changing positions; heat the blade by moving the high-frequency induction coil to the blade position; use the infrared high-temperature sensor to collect the temperatures; and give feedback to the PLC control system. When heated to the set temperature range, the system automatically stops heating and returns to the original position; clamp the cylinder and loosen the blade; the return cylinder pushes the blade into the quenching fluid to cool it quickly; complete the quenching of a blade. Replace the rotary tilling blades in turn with the rotation of the turntable and repeat the high frequency quenching technique, as shown in Fig. 1.



Fig. 1 - Flow chart of high-frequency partial quenching technique of rotary tilling blades

Test materials and equipment

Type IT245 rotary tilling blade was selected, as shown in Fig. 2 below, the material is 65 Mn steel, and its chemical composition is shown in Table 1. According to the shape of the rotary tilling blade selected, the electromagnetic induction coil used was bent to a fixed shape, as shown in Fig. 3 below.

Table 1

65 Mn Steel Chemical Composition (wt.%)

C	Si	Mn	P	S	Cr	Ni	Cu
0.62~0.70	0.17~0.37	0.90~1.20	≤0.035	≤0.035	≤0.25	≤0.25	≤0.25



Fig. 2 - The rotary tilling blades of choice



Fig. 3 - Electromagnetic induction heating coils

The high frequency quenching device is used to quench the rotary tilling blade, and SX2-15-12 box resistance furnace to temper the blades, FLIR-T440 infrared thermal imager to measure the temperature, and HR-150A Roche hardness tester to measure the hardness.

The partial high-frequency quenching device is mainly composed of control system, cooling device, heating device, power supply, clamping device and working table, as is shown in Fig. 4.

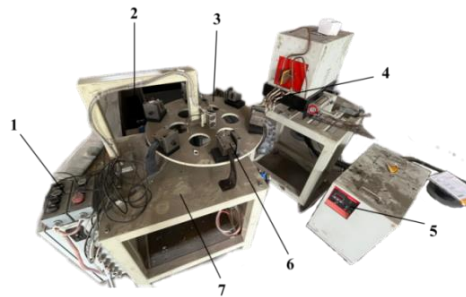


Fig. 4 - Rotary tilling blades high-frequency partial quenching device
 1 – Control system; 2 – Cooling device; 3 – Rotating disk; 4 – Heating device;
 5 – Power supply; 6 – Clamping device; 7 – Working table

Experiment indicators and methods

Each set of tests was conducted indoors with all doors and windows closed, maintaining a constant temperature of 15 °C. The rotary tilling blades underwent partial quenching. The quenching frequency was set to 20 kHz, resulting in an effective quenching depth of approximately 0.8–1.5 mm. After quenching, the blades were cooled using No. 20 mechanical oil at room temperature, then tempered in an SX2-15-12 box resistance furnace and allowed to cool to room temperature following tempering. The surface of each specimen was cleaned, and one side was polished using No. 800 corundum sander to remove the oxide layer. Hardness measurements were performed using an HR-150A Rockwell hardness tester. Each blade's surface hardness was measured three times, and the average was taken as its final hardness value. Each test level was repeated three times, and the average of these three repetitions was used as the final hardness value for that level.

Finite element simulation of rotary tilling blades

To determine the optimal partial quenching position of the rotary tilling blade, the blade was modeled in SolidWorks and analyzed using ANSYS Workbench. The test focused on the right-side machete blade of the IT245 rotary tiller. The 3D model was created in SolidWorks using operations such as stretching, bending, scanning and cutting, as illustrated in Fig. 5 and Fig. 6.

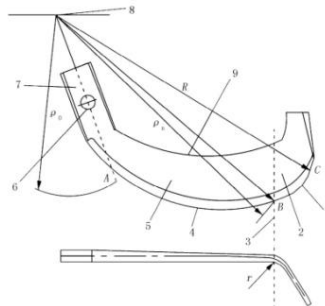


Fig. 5 - Schematic diagram of the structure of the rotary tilling blades
 1 – Positive cutting edge; 2 – Front cutting section; 3 – Bend lines; 4 – Side cutting edges; 5 – Side cutting section;
 6 – Mounting holes; 7 – Hilt; 8 – The center of rotation of the cutter roller; 9 – Back edge curve

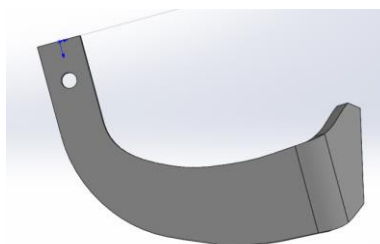


Fig. 6 - Geometric solid model

65 Mn is often adopted as the model material, and the main mechanical properties are shown in Table 2.

Table 2

65 Mn mechanical properties table

Material	Density / kg·m ⁻³	Elastic modulus / GPa	Poisson's ratio	Yield strength / MPa	Allowable stress / MPa
65Mn	7850	210	0.3	800	340

To improve the grid quality, the tetrahedral mesh was used to automatically divide the geometry, and the size of the grid was set to 6 mm to generate 2398 tetrahedral units, 10378 nodes, with a good grid quality of 0.7, as shown in Fig. 7.

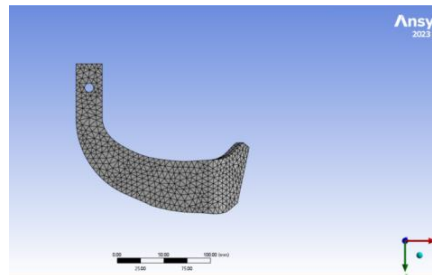


Fig. 7 - Meshing the model

Loads and boundary conditions were applied to the rotary tilling blades based on actual working conditions. Fixed constraints were assigned to the inner surfaces of the circular mounting holes. A force of 500 N, perpendicular to the surface, was applied to the side cutting edges, main cutting edges, and transition surface cutting edges for simulation and analysis.

Analysis of simulation results

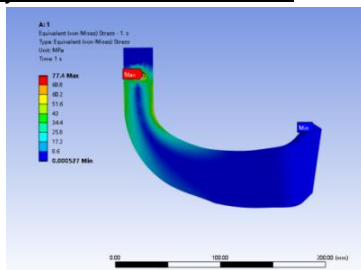


Fig. 8- Stress contour diagram

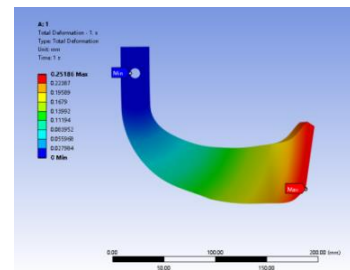


Fig. 9 - Total deformation contour diagram

Fig. 8 and Fig. 9 show the results of the static simulation analysis. The stress is concentrated at the mounting hole of the blade handle, as the rotary tilling blade acts as a single-degree-of-freedom rigid body. The section of the blade furthest from the constraint exhibits lower rigidity and greater deformation. Conversely, the area near the constraint, the handle, experiences the highest stress concentration due to the restriction at the tie point, with a maximum stress value of 77.4 MPa. The maximum displacement occurs at the main and side cutting edges and gradually decreases symmetrically toward both sides. The maximum total deformation is 0.25 mm, indicating that the simulation results meet the mechanical strength requirements for steel. Furthermore, the results are consistent with the actual fracture-prone areas observed in the field. Based on this analysis, the optimal quenching position is identified as the main cutting edge.

Analysis of influencing factors

Uni-variate test

The test aims to identify the factors that influence the wear resistance of the blade, specifically quenching temperature, tempering temperature, and tempering time. By varying one factor while keeping the others constant, the significance of each factor's impact on the test index can be assessed. If a factor has a significant effect, a reasonable value range is determined and later used as an input in the multi-factor optimization test. The quenching temperature is preset at 9 levels ranging from 800°C~880°C; the tempering temperature at 9 levels from 170°C~250°C; and the tempering time at 9 levels from 80 min~160 min.

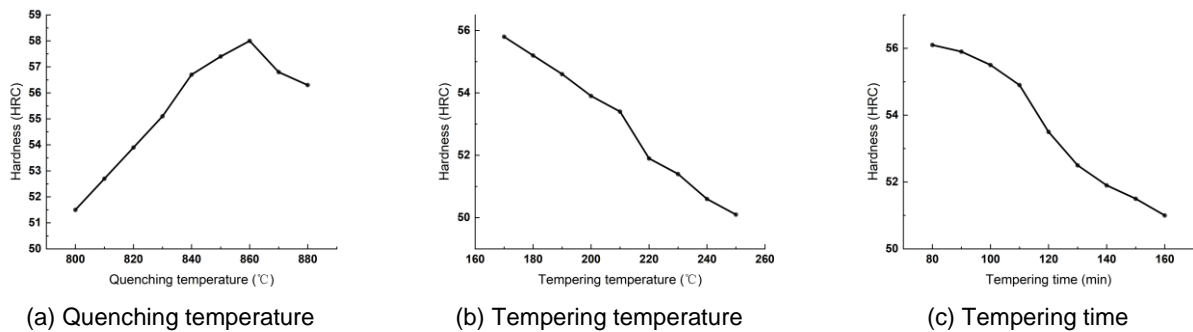


Fig.10 - Statistical graph of single factor examination results

With a tempering temperature of 210°C and a tempering time of 120 minutes, the rotary tilling blades were subjected to quenching to investigate the influence of quenching temperature on hardness. The results indicate that quenching temperature significantly affects the hardness of the rotary tilling blade, making it a critical parameter in the quenching process. According to the test data, a clear relationship between quenching temperature and hardness is observed (as shown in Fig. 10a). Specifically, the hardness of the rotary tilling blade initially increases with rising quenching temperature, reaches a maximum at 840°C, and then gradually decreases. As quenching temperature increases, the dissolution of carbon and alloying elements in the 65Mn steel into the austenite phase becomes more pronounced, promoting the formation of martensite during cooling. Since the hardness of quenched steel is primarily determined by the martensite content, this leads to a peak in hardness at the optimal temperature. However, higher temperatures do not always yield better results. Due to the high sensitivity of 65Mn steel to overheating, temperatures exceeding 840°C cause the austenite grains to coarsen, which diminishes the strength and toughness of the resulting martensite. This, in turn, leads to a reduction in quenching hardness and increased hardness loss during subsequent tempering.

The rotary blades were quenched at a quenching temperature of 840°C and a tempering time of 120 min. According to the test data, the tempering temperature and hardness relationship curves are shown in Fig. 10b. The hardness of rotary blades decreases with the increase of tempering temperature mainly because the tempering of 65 Mn steel is a diffusion and transition process from sub-stable martensite and residual austenite structure to ferrite and carbide. When the tempering temperature is low, the internal stress generated in the quenching process cannot be fully released, resulting in a slight hardness decrease. If the internal stress cannot be fully alleviated, cracking or deformation problems will arise. When the tempering temperature reaches 210°C, it is a more suitable tempering temperature for 65 Mn steel blades; within this temperature range, the internal stress can be effectively released and the hardness can be moderately reduced; customarily, a higher comprehensive hardness and toughness can be obtained, thus meeting the requirements of rotary blades. However, when the tempering temperature is too high, the martensite structure will be further decomposed (converting to bainite or ferrite). As a result, the hardness will be greatly reduced, which will also reduce the abrasive resistance and impact resistance of the blades.

The rotary blades were quenched at a quenching temperature of 840°C and a tempering temperature of 210°C. According to the test data, the relationship curves of tempering time and hardness are shown in Fig.10c. The change trends and principles of hardness with the tempering time are consistent with those of the tempering temperature. When the tempering time is too short, the internal stress cannot be released. The residual stress will affect the service life and safety of the blades. The hardness decrease is small, and the ideal comprehensive performance cannot be obtained. When the tempering time reaches 120 min, it can fully release the internal stress and reduce the hardness appropriately, which can maintain a high hardness level, but also improve the toughness and impact resistance of the blades. When the tempering time is too long, the martensite structure will be further decomposed to the more stable bainite or ferrite transition, which will not only lead to a great decrease in hardness, but also reduce the wear resistance and blade retention ability.

Combination trial

Based on the effects of the three factors (quenching temperature, tempering temperature and tempering time) on the hardness of rotary tilling blades, the test adopts Box-Behnken response surface trial design. With the quenching temperature being x_1 , tempering temperature being x_2 , tempering time being x_3 , the hardness response value being Y , the ternary quadratic regression orthogonal rotation combination test is carried out.

Regression analysis is conducted with Design-Expert 12.0 software, and significance verification test and variance analysis are performed on the basis of the test results. The levels of test factors and their coding are shown in Table 3.

Table 3

Level	Parameter		
	Quenching temperature	Tempering temperature	Tempering time
	[°C]	[°C]	[min]
-1	820	170	80
0	840	210	120
1	860	250	160

RESULTS

Test scheme and results

Based on a ternary quadratic regression orthogonal rotation combination test, a total of 17 test groups were conducted. Using blade hardness as the response variable Y , and quenching temperature x_1 , tempering temperature x_2 , and tempering time x_3 as influencing factors, a multiple regression analysis was performed. The regression equation for hardness Y was derived from the test data using Design-Expert 12.0 software, and its statistical significance was subsequently evaluated. The experimental design and corresponding results are presented in Table 4.

Table 4

Combined test protocols and results				
No.	Quenching temperature / [°C]	Tempering temperature / [°C]	Tempering time / [min]	Hardness / [HRC]
1	-1	-1	0	50.6
2	-1	1	1	57.6
3	1	0	1	47.4
4	-1	0	-1	53.1
5	0	1	-1	48.5
6	1	0	-1	56.9
7	0	0	0	48.7
8	1	0	-1	54.5
9	0	0	0	57.9
10	0	0	0	55.9
11	0	0	0	57.4
12	0	-1	1	52.3
13	0	0	0	55.5
14	-1	1	0	54.5
15	1	-1	0	54.7
16	0	0	0	54.5
17	0	1	1	54.1

The input data were analyzed using the Box-Behnken design in Design-Expert software to fit the regression model. Based on the results of the analysis of variance (ANOVA), a quadratic polynomial model was selected to best represent the relationship between the variables. The resulting regression equation describes the relationship between quenching temperature, tempering temperature, and tempering time with respect to blade hardness, and is given as follows:

$$\hat{Y} = 54.66 + 3.36X_1 - 1.85X_2 - 0.7875X_3 - 0.325X_1X_2 - 0.65X_1X_3 - 0.775X_2X_3 - 3.11X_1^2 + 0.62X_2^2 + 0.595X_3^2 \quad (1)$$

The significance test of the coefficients in the regression equation obtained the ANOVA results as shown in Table 4; the significance test coefficient of the hardness Y regression model being $p < 0.0001$, the equation can be deduced to be more significant. The regression equation can better reflect the practical problems. On account of $p = 0.4905 > 0.05$ of the mismatch term (Lack of Fit), the model fitting loss is not significant and fits well with the actual situation, which can be used to analyze and predict the optimal process parameters of high frequency quenching (Wang et al., 2024).

The coefficient of determination R^2 of the model was 0.9892, indicating that the model had high significance, while $R^2_{Adj} = 0.9754$ was able to explain 97.54% of the response value variation in the trial and was also close to the predicted correlation coefficient R^2_{pred} . Therefore, this model can better describe the relationship between hardness and each response factor, and this secondary regression model can be used to analyze and predict the optimal process parameters of high-frequency quenching.

As shown in Table 5, quenching temperature, tempering temperature, and tempering time (based on one-factor trials) all have significant effects on the hardness of the rotary tilling blade. The order of influence is as follows: quenching temperature > tempering temperature > tempering time. Regarding interaction effects between two factors, the following were found to significantly affect hardness: the interaction between quenching temperature and tempering time, tempering temperature and tempering time, as well as the quadratic terms of quenching temperature, tempering temperature, and tempering time. In contrast, the interaction between quenching temperature and tempering temperature did not show a significant effect on hardness.

Table 5

Analysis of variance of hardness

Source of variation	Sum of square	Degree of freedom	Mean square	F value	P value	Significance
Model	169.67	9	18.85	71.35	< 0.0001	**
X_1	90.45	1	90.45	342.34	< 0.0001	**
X_2	27.38	1	27.38	103.63	< 0.0001	**
X_3	4.96	1	4.96	18.78	0.0034	**
X_1X_2	0.4225	1	0.4225	1.6	0.2465	
X_1X_3	1.69	1	1.69	6.4	0.0393	*
X_2X_3	2.4	1	2.4	9.09	0.0195	*
X_1^2	40.59	1	40.59	153.64	< 0.0001	**
X_2^2	1.62	1	1.62	6.13	0.0425	*
X_3^2	1.49	1	1.49	5.64	0.0492	*
Residual	1.85	7	0.2642			
Lack of Fit	0.7775	3	0.2592	0.967	0.4905	
Pure Error	1.07	4	0.268			
Sum	171.52	16				

Note: $p \leq 0.01$ means highly significant (**); $0.01 < p \leq 0.05$ means significant (*); $p > 0.05$ means not significant.

Analysis and discussion of factor interaction

The images generated in the Model Graphs visually reflect the effects of each factor on the response value. The influence of each factor is clearly demonstrated through the changes in factor levels. To investigate whether the interaction between factors significantly affects the hardness of the rotary blades after quenching, response surface analysis was employed. This analysis involved fixing one factor and examining the interaction between the other two factors. Fig. 11 presents a three-dimensional graph of quenching temperature, tempering temperature, and tempering time, which provides a clear visual representation of how each factor influences the quenching performance of the rotary blades. It also demonstrates how these factors interact and jointly affect the evaluation indexes.

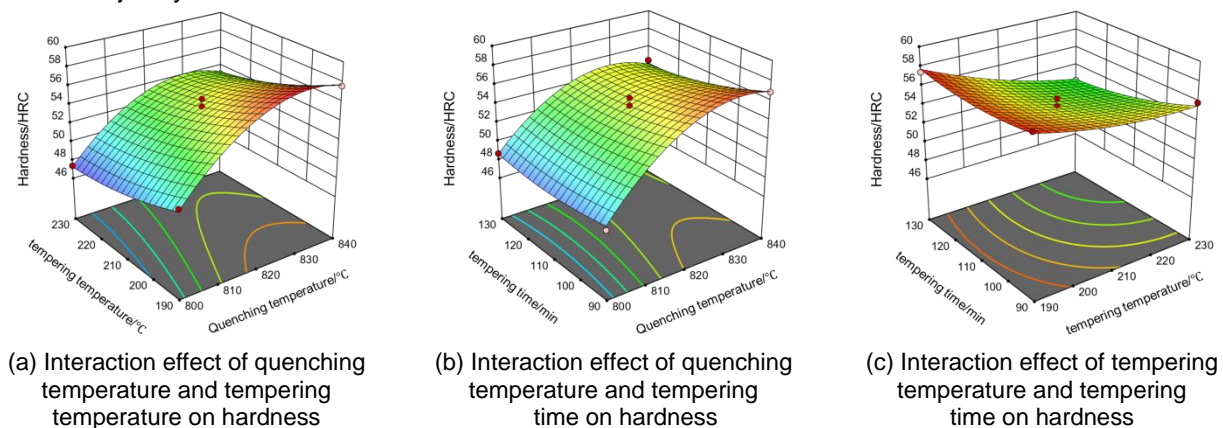


Fig. 11 - The effects of the interaction of various factors on the hardness of rotary tilling blades

Fig. 11a illustrates the response surface diagram showing the interaction effects between quenching temperature and tempering temperature on the hardness of rotary blades, with tempering time fixed at 120 minutes (0 level). The analysis reveals that when the quenching temperature is held constant at a low level, the change in hardness with increasing tempering temperature is minimal. However, at higher quenching temperatures, the hardness value decreases consistently as the tempering temperature increases. When the tempering temperature is held constant, the hardness response value increases within a certain range as the quenching temperature rises. However, once the quenching temperature reaches 840°C, any further increase leads to a gradual decline in the hardness of the rotary blades. This behavior is attributed to the growth of austenite grains: initially, the grains are fine, but as the quenching temperature increases, they begin to coarsen significantly. The higher the temperature, the more pronounced this grain growth becomes. In the case of 65Mn steel, excessive grain coarsening reduces the material's hardness, thereby diminishing the effectiveness of the heat treatment.

Fig. 11b presents the response surface diagram illustrating the interaction between quenching temperature and tempering time on the hardness of rotary blades, with tempering temperature fixed at 210°C (0 level). The analysis shows that within the tested range, when the quenching temperature is held constant, the effect of tempering time on hardness is not significant at lower quenching temperatures. However, at higher quenching temperatures, the hardness gradually decreases with increasing tempering time. Conversely, when tempering time remains constant (regardless of whether it is at a high or low level) the hardness initially increases as the quenching temperature rises, but then slowly goes down when the quenching temperature reaches 840°C. This is because the tempering process is a diffusion and transition process from sub-stable martensite and martensite and residual austenite tissues to ferrite and carbide. As tempering time extends, internal stresses are gradually relieved, leading to a moderate reduction in hardness.

Fig. 11c illustrates the response surface diagram showing the interaction effects between tempering temperature and tempering time on the hardness of rotary blades, with the quenching temperature fixed at 840°C (0 level). The analysis indicates that within the tested range, when the tempering temperature is held constant, the change in hardness with increasing tempering time is minimal at lower tempering temperatures. However, at higher tempering temperatures, the hardness gradually decreases as tempering time increases. Similarly, when tempering time is held constant (regardless of whether it is at a high or low level) the hardness decreases with increasing tempering temperature, with the decline being more pronounced at higher levels. This trend results from the interaction between tempering temperature and tempering time: during tempering, the transformation of martensite and retained austenite into ferrite and carbide occurs. The atomic diffusion along grain boundaries promotes grain growth, which increases the material's fracture toughness. However, this grain coarsening simultaneously leads to a reduction in hardness.

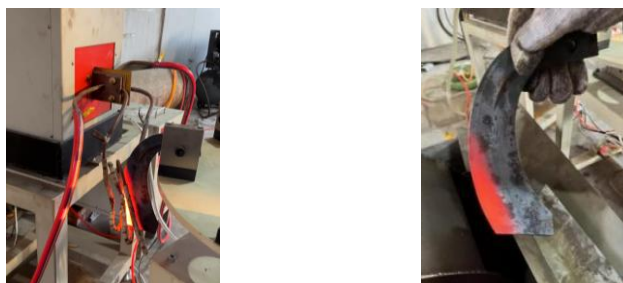
Parameter optimization and validation tests

The optimal combination of quenching process parameters was determined by analyzing the experimental data and optimizing the influencing factors. Based on the quenching performance requirements of rotary tilling blades and the boundary conditions of the key parameters, an optimization model was established. Using quenching temperature X_1 , tempering temperature X_2 , and tempering time X_3 as constraint variables, and hardness Y as the optimization target, a mathematical model for the rotary blade quenching process was developed. The computational method for this model is described in Equation (2) (Wang *et al.*, 2023).

$$\begin{cases} \max Y \\ 820 \leq X_1 \leq 860 \\ 170 \leq X_2 \leq 250 \\ 80 \leq X_3 \leq 160 \end{cases} \quad (2)$$

The target parameter was set to be maximized in the optimization module of Design-Expert 12.0 software. Each process variable was constrained within the ranges specified in Table 3. The optimized combination of process parameters was identified as follows: quenching temperature of 852.2°C, tempering temperature of 171.4°C, and tempering time of 84.7 min. Under this combination, the rotary tilling blade is predicted to achieve optimal quenching performance, with a hardness value of 57.9 HRC. To verify the reliability of the model, the optimized process parameters were tested under the same experimental conditions. The test specimens, both before and after quenching, are shown in Fig. 12.

For improved operability in practical applications, the optimized values were rounded to quenching temperature of 852°C, tempering temperature of 171°C, and tempering time of 85 min. Under these conditions, the measured average hardness was 57.5 HRC, with a relative error of only 0.81%, confirming the accuracy and credibility of the regression model and optimization analysis. It is worth noting that the optimized tempering temperature lies at the boundary of the test parameter range, indicating that low-temperature tempering effectively eliminates quenching stress while avoiding deformation or cracking. This ensures dimensional stability during operation and maintains the high hardness and wear resistance of the blade after heat treatment.



(a) Test site (b) Quenched samples
Fig. 12 - Test site and quenched rotary tilling blades samples

Field testing

When tilling with the rotary blades, the actual soil environment is often very complicated, as a result the soil tank test bench in the laboratory cannot fully simulate the field test conditions. In order to further verify the correctness of the above quenching test conclusions, the rotary blades are quenched under the above optimal process parameters to verify the wear resistance of the high-frequency quenching technique. Before the test, all the rotary blades were washed and dried, weighed with a balance with an accuracy of 0.1 g, and the original mass was recorded. The 10 rotary blades were quenched with the optimal parameter combination, and the other 10 were not treated, as shown in Fig.13.



(a) Unquenched rotary tilling blades (b) Quenched rotary tilling blades
Fig. 13 - Heat treatment before field trials

Then, the rotary blades quenched with the optimal combination parameters and the original blades without being quenched are installed on the shaft of the rotary blades alternately for a contrast test, as shown in Fig. 14. Field test site lies in the corn planting field of Yi County, Jinzhou City, Liaoning Province (Fig.15): the soil was sand soil, the average moisture content of the test soil was 19.8%, and the total working area was 67 hm². After the tillage, all rotary blades were removed and the surface soil was wiped off the friction loss was weighed and measured. The quality changes of rotary tilling blades before and after the field test are shown in Table 6.



Fig. 14 - Schematic diagram of rotary tilling blades installation



Fig. 15 - Field trials

Table 6

Title	The amount of wear and tear of the rotary tilling blades									
	Test blade number									
	1	2	3	4	5	6	7	8	9	10
The amount of wear on the rotary tilling blades after quenching/(g)	11.3	12.5	11.7	10.9	12.6	12.8	11.4	11.7	11.4	13.1
The amount of wear on the rotary tilling blades after not quenching/(g)	37.6	38.1	36.9	36.7	36.8	37.9	37.6	35.9	36.8	37.4

Discussion

From the table data, the average abrasion of 10 quenched blades is only 11.9 g, while the average abrasion of the other 10 without being quenched is as high as 37.2 g. In contrast, the wear resistance of the blades after being quenched increase by 3.13 times, which demonstrates that the high frequency quenching can effectively improve the wear resistance of the blades.

In order to improve the wear resistance of rotary tilling blades, many scholars at home and abroad used various coating preparation techniques to prepare wear resistance layer on the surfaces of rotary tilling blades. *Amardeep et al (2012)* compared three different kinds of explosive spraying coatings on high strength steel rotary tillers, namely WC-Co-Cr, Cr₃C₂NiCr and Stellite-21, and the following field tests showed that the three coated rotary blades show excellent wear resistance, helping to extend the service life of rotary tillers. *Zhan (2022)* prepared Fe/WC/CeO₂ stack welding layer on Q235 matrix by using plasma stack welding technology. In the field comparison test, it was found that the grinding crack of the cutting edge of the 65 Mn rotary tillers was dense and the abrasion was obvious, while the Fe/WC/CeO₂ stack welding layer carried no obvious wear marks, and the stack welding layer did not fall off, and the wear quality was reduced by about 65%. *Long et al (2022)* took 65 Mn rotary tillage blades as the matrix, selected BNi-2 brazing material and the carbide as the brazing coating material, studied the influence of heat treatment process after brazing coating on the tissue evolution and hardness of nickel base alloy, and the results showed that the hardness of the coating was high in the state of brazing coating. However, through comprehensive comparison, it is evident that although thermal spraying, plasma stack welding, and brazing coating technologies can enhance the microstructure of materials and improve the wear resistance of rotary tilling blades, these methods are associated with complex processes, high costs, and technical challenges. If not precisely controlled, the desired improvement in wear resistance may not be achieved, making these methods less practical for widespread application in agricultural settings. Compared with these surface strengthening processes, the high-frequency quenching technology adopted in this paper has the advantages of uniform heating, rapid heating-up and simple processing. The induction heating principle only heats the surface of the material to achieve the effect of hard outside and tough inside, which just meets the needs of rotary tilling blades.

CONCLUSIONS

In this study, 65 Mn steel, a commonly used material of rotary blades was selected, and based on the existing heat treatment research and combined with the characteristics of agricultural production, a partial high-frequency quenching technique with low cost and excellent performance was adopted to solve the wear and failure problem of 65 Mn rotary blades. In the quenching test, the hardness of rotary blades was taken as the technical index of partial high frequency quenching, and the appropriate parameter range of high frequency quenching was explored under the preliminary quantitative condition. Then, the following conclusions were drawn:

(1) The finite element static solution result shows that the maximum total deformation of rotary blades is 0.25 mm, located at the positive cutting edge position, and the maximum stress of rotary blades is 77.4 MPa, located at the upper half of the back edge curve. The solution result is in line with the actual situation, and the quenching position is determined. Single factor test preliminarily determined the value range of the parameters as follows: the quenching temperature is 820°C ~860°C, the tempering temperature is 170°C ~250°C, and the tempering time is 80min~160min; under these conditions, the hardness of the rotary blades is above 48, and the quenching effect is good.

(2) A regression model expressing the hardness of rotary blades was established by ternary quadratic regression orthogonal rotation combination test, and the influence pattern of each parameter was analyzed by using Design-Expert 12.0 software, and the fitting and significance tests were performed by ANOVA.

The effects of each factor on the hardness of rotary blades is as follows: quenching temperature>tempering temperature>tempering time. The interaction between quenching temperature and tempering time, between tempering temperature and tempering time both have a more significant effect. The optimized parameters bring about the best quenching conditions: quenching temperature 852°C, tempering temperature 171°C, and tempering time 85min, when the hardness of rotary blades is 57.5 HRC, which not only meets the national standard, has good wear resistance and corrosion resistance, but also provides a test basis for the study of high-frequency quenching technique and supporting equipment design.

(3) Through comparative analysis between the 10 blades quenched using the optimal quenching parameter combination and the 10 unquenched original blades, the average wear of the quenched blades was found to be only 11.9 g, whereas the unquenched blades exhibited an average wear of 37.2 g. This indicates that the wear resistance of the blades improved by 3.11 times after high-frequency quenching, thereby confirming the effectiveness and feasibility of the high-frequency quenching technique for enhancing the durability of rotary tilling blades.

(4) High-frequency quenching, as an emerging surface treatment technology, effectively enhances the surface wear resistance of metal components and offers considerable economic benefits. This study presents a preliminary investigation into the application of high-frequency quenching on 65Mn rotary tilling blades, demonstrating a notable improvement in their wear resistance. However, to further facilitate the adoption of this technique in agricultural production, more in-depth and systematic research is required. Importantly, the high-frequency quenching method is not limited to 65Mn steel; it holds promise for optimizing the surface treatment of other soil-contact parts in agricultural machinery. To expand its applicability, a comprehensive database of quenching parameters for various metal materials should be established, providing a valuable reference for enhancing the wear resistance of metallic components. It is worth noting that this study focused primarily on surface hardness and wear performance. To gain a more comprehensive understanding of the material behavior post-quenching, future research will explore the internal microstructural changes of the treated materials, thereby enabling more accurate and reliable evaluations of the high-frequency quenching process.

ACKNOWLEDGEMENT

This study was supported by Shenyang Science and Technology Plan Project of China (No.24-216-2-10)

REFERENCES

- [1] Amardeep, S. K., Jasmaninder, S. G., Deepak, J., Shivani, K. (2012). Wear behavior of thermal spray coatings on rotavator blades. *Journal of Thermal Spray Technology*, Vol. 21(2), pp. 355-359, India.
- [2] Bartkowski, D., Bartkowska, A. (2017). Wear resistance in the soil of Stellite-6/WC coatings produced using laser cladding method. *International Journal of Refractory Metals and Hard Materials*, Vol. 64, pp. 20-26, Poland.
- [3] Falalu, R. J., Zhang, B., Song, Y., Wang, R., Liu, S. (2020). Influence of plasma remelting conditions on quantitative graphite dissolution and modified surface characteristics in 500-12 ductile iron. *Materials Research Express*, Vol. 7(7), pp. 076502, Shenyang/China.
- [4] Hao, J., Zhan, Z., Hou, J., Zhao, J., Liu, J., Yin, C. (2021). Preparation and Microstructure of Fe/WC/CeO₂ Plasma Overlay Layer of Rotary Tillage (旋耕刀 Fe/WC/CeO₂等离子堆焊层制备及其组织性能). *Transactions of the Chinese Society of Agricultural*, Vol. 37(24), pp. 1-8, Baoding/China.
- [5] Huang, S., Sun, D., Wang, W., Xu, H. (2015). Microstructures and properties of in-situ TiC particles reinforced Ni-based composite coatings prepared by plasma spray welding. *Ceramics International*, Vol. 41(9), pp. 12202-12210, Changchun/China.
- [6] Kaur, R., Dhaliwal, I. S., Singh, A. (2011). Studies on the Wear Performance of Different Materials of Rotary Blades. *Journal of Research, Skuast Jammu*, Vol. 10 (1), pp. 24-32, India.
- [7] Lee, H. Y., Akira, I., Kim, S. H., Kim, K. B. (2006). The effects of induction heating rate on properties of Ni-Al based intermetallic compound layer coated on ductile cast iron by combustion synthesis. *Intermetallics*, Vol. 15(8), pp. 1050-1056, Korea.
- [8] Li, P. (2018). *Study on the failure rate model and selection optimization of rotary tillage knife in dryland soil (旱作土壤中旋耕刀失效速率模型及选型优化研究)*. China Agricultural University Master's dissertation, Beijing/China.

- [9] Long, W., Qin, J., Lu, Q., Liu, D., Wu, A. (2022). Heat treatment process of induction braze coating of rotary blades (旋耕刀感应钎涂层热处理工艺研究). *Materials Reports*, Vol. 36(07), pp. 98-102, Beijing/China.
- [10] Satit, K., Vilas, M. S., Panadda, N. (2007). Wear resistance of thermally sprayed rotary tiller blades. *Wear*, Vol. 263(1), pp. 604-608, Thailand.
- [11] Shen, B., Huang, H., Guo, S., Ni, H., Chang, Y., Wang, D., Ju, Y., Yuan, Z. (2022). Effect of carburizing process on wear resistance of high-speed hydraulic tipping plough components (渗碳工艺对高速液压翻转犁犁尖部件耐磨性的影响). *Transactions of the Chinese Society of Agricultural*, Vol. 38(14), pp. 35-42, Zhenjiang/China.
- [12] Sun, J., Liu, Q., Yang, F., Liu, Z., Wang, Z. (2022). Calibration of discrete element simulation parameters of interaction between soil and rotary tillage components on the slope of the Loess Plateau (黄土高原坡地土壤与旋耕部件互作离散元仿真参数标定). *Transactions of the Chinese Society for Agricultural Machinery*, Vol. 53(1), pp. 63-73, Xianyang/China.
- [13] Temesgen, M., Hoogmoed, W. B., Rockstrom, J., Savenjie, H. (2008). Conservation tillage implements and systems for smallholder farmers in semi-arid Ethiopia. *Soil and Tillage Research*, Vol. 104(1), pp. 185-191, Netherlands.
- [14] Valboa, G., Lagomarsino, A., Brandi, G., Agnelli, A. E., Simoncini, S., Papini, R., Pellegrini, S. (2015). Long-term variations in soil organic matter under different tillage intensities. *Soil and Tillage Research*, Vol. 154, pp. 126-135, Italy.
- [15] Wang, H., Zhao, Y., Yuan, X., Chen, K., Xu, R. (2013). Effects of Boronizing Treatment on Corrosion Resistance of 65Mn Steel in two Acid Mediums. *Physics Procedia*, Vol. 50, pp. 124-130, Zhenjiang/China.
- [16] Wang, Q., Li, Q., Zhang, L., Chen, D., Jin, H., Li, J., Zhang, J., Ban, C. (2022). Microstructure and properties of Ni-WC gradient composite coating prepared by laser cladding. *Ceramics International*, Vol. 48 (6), pp. 7905-7917, Anshan/China.
- [17] Wang, R., Li, D., Li, P., Bai, X., Wang, T., Wang, W., Zhao, Y. (2023). Optimum design for breaking device with double roller based EDEM. *INMATEH - Agricultural Engineering*, Vol. 70(2), pp. 570-582,
- [18] Wang, R., Li, D., Li, S., Ren, T. Bai, H., Jin, Y., Wang, W., Dev, S. (2024). Design and experiment on cutting and crushing device of side-sweeping straw returning machine. *INMATEH - Agricultural Engineering*, Vol. 72(1), pp. 589-600. DOI: <https://doi.org/10.35633/inmateh-70-56>
- [19] Xiao, B., Hong, M., De, Q., Li, Z., Zhang, R., Zheng, Z. (2013). Study on Surface Properties of Big Tilling Depth Rotary Blade for Laser Shock Peening. *Applied Mechanics and Materials*, Vol. 2659(395-396), pp. 973-97, Yangzhou/China.
- [20] Xiao, M., Niu, Y., Wang, K., Zhu, Y., Zhou, J., Ma, R. (2022). Design of self-excited vibrating rotary tillage and analysis of torsional and consumption reduction (自激振动旋耕刀设计与减扭降耗性能分析). *Transactions of the Chinese Society for Agricultural Machinery*, Vol. 53(11), pp. 52-63, Nanjing/China.
- [21] Xiao, W., Niu, P., Wang, P., Xie, Y., Xia, F. (2024). Simulation analysis and optimization of soil cutting of rotary blade by ANSYS/LS-DYNA. *INMATEH - Agricultural Engineering*, Vol. 72(1), pp. 22-32. DOI: <https://doi.org/10.35633/inmateh-72-02>
- [22] Xie, Z., Zhang, C., Wang, R., Li, D., Zhang, Y., Li, G., Lu, X. (2021). Microstructure and wear resistance of WC/Co-based coating on copper by plasma cladding. *Journal of Materials Research and Technology*, Vol. 15, pp. 821-833, Shanghai/China.
- [23] Yadav, A. K., Sharma, A. K. (2020). Studies on wear characteristics and surface modification techniques of rotavator blades. *International Journal of Agriculture Sciences*, Vol. 12(3), pp. 9531-9536, India.
- [24] Zhan, Z. (2022). Microstructure and Properties of Composite Coatings of Fe/WC/CeO₂ Prepared by Plasma Surfacing with Rotary Blade (旋耕刀等离子堆焊 Fe/WC/CeO₂ 复合涂层组织与性能). *Agricultural University Of Hebei Master's dissertation*, Baoding/China.
- [25] Zhao, X., Zhao, J., Zhao, J., Ma, Z., Li, J., Dai, B., An, M., Wang, J., Hao, J. (2024). Optimisation design and experimental analysis of rotary blade reinforcing ribs using DEM-FEM techniques. *Biosystems Engineering*, Vol. 249, pp. 1-17, Baoding/China.
- [26] Zhu, H., Wang D., He, X., Shang, S., Zhao Z., Wang, H., Tan, Y., Shi Y. (2022). Study on Plant Crushing and Soil Throwing Performance of Bionic Rotary Blades in *Cyperus esculentus* Harvesting. *Machines*, Vol. 10(7), pp. 562-562, Qingdao/China.

DESIGN AND EXPERIMENT OF GRAIN HARVESTER YIELD MONITORING SYSTEM BASED ON MULTI-SENSOR FUSION

基于多传感器融合的谷物收割机产量监测系统的设计与实验

Peng LIU ¹⁾, Shijun SONG ¹⁾, Wei LIU ¹⁾, Yuqian ZHAO ¹⁾, Weichen YAN ¹⁾, Guohai ZHANG ^{1,2*)}

¹⁾Shandong University of Technology, College of Agricultural Engineering and Food Science, Zibo, China

²⁾Shandong University of Technology, Institute of Modern Agricultural Equipment, Zibo, China

Tel: +86119862513808; E-mail: guohaizhang@sdut.edu.cn

Corresponding author: Guohai Zhang

DOI: <https://doi.org/10.35633/inmateh-75-65>

Keywords: Harvester yield monitoring system; Optical yield measurement; Weighing yield measurement; Self-feedback system

ABSTRACT

Precision agriculture requires accurate and efficient crop yield distribution information. However, both traditional field-based yield measurement methods and existing combine harvester yield monitoring systems face significant limitations. Traditional methods, such as direct weighing or sampling, are time-consuming and inefficient, and they only provide average yield values - insufficient for large-scale farming needs. Meanwhile, current monitoring systems often suffer from high measurement errors, low spatial resolution, and limited generalizability. For this reason, this study designs a new type of grain yield monitoring system, which corrects the photoelectric sensor data through the load cell data, realizes the calibration of the photoelectric sensor, avoids the influence of external factors, and improves the accuracy of measurement. Firstly, tests were carried out at three rotational speeds of 10 Hz, 20 Hz and 25 Hz of the motor inverter setting, respectively, to determine the positive proportionality coefficient between the photoelectric signal and the grain mass, and the overall error of the system was measured to be less than 6.44%. For the load cell, a model of the relationship between tilt angle and weighing accuracy was established and a compensation algorithm was proposed, the weighing error data in different directions and at different tilt angles were measured and analyzed, and a mathematical model between the corrected angle and the weighing error was established. Through the tilting experiment, the feasibility of the modified angle compensation model is verified, and the overall error after compensation is less than 0.25%, and the systematic error of measurement and production after the intervention of the feedback system is less than 0.74%. The experimental results demonstrate that the system significantly enhances the accuracy and stability of yield measurement. It holds substantial potential for widespread application, provides strong support for the advancement of precision agriculture, and is expected to drive agricultural production toward greater efficiency and sustainability.

摘要

精准农业需要准确且高效的作物产量分布信息，但传统的田间作物产量获取方法以及现有的联合收割机产量监测系统存在诸多问题。传统方法，如直接称重或抽样，不仅耗时且效率低下，而且只能获取平均产量，难以满足大面积种植的需求，而现有的系统测量误差大、空间分辨率低且通用性差。为此，本研究设计了一种新型的谷物产量监测系统，该系统通过称重传感器数据对光电传感器数据进行校正，实现了对光电传感器的校准，避免了外部因素的影响，提高了测量精度。首先，分别在电机变频器设定的10赫兹、20赫兹和25赫兹这三种转速下进行测试，以确定光电信号与谷物质量之间的正比例系数，经测量该系统的整体误差小于6.44%。对于称重传感器，建立了倾斜角度与称重精度之间关系的模型，并提出了一种补偿算法，测量并分析了不同方向和不同倾斜角度下的称重误差数据，建立了校正角度与称重误差之间的数学模型。通过倾斜实验，验证了修正后的角度补偿模型的可行性，补偿后的整体误差小于0.25%，反馈系统介入后测量和生产的系统误差小于0.74%。实验结果表明，该系统有效地提高了产量测量的准确性和稳定性，具有广泛的应用价值，为精准农业的发展提供了有力支持，有望推动农业生产朝着更高效、更可持续的方向发展。

INTRODUCTION

Precision agriculture, also known as smart agriculture, is an agricultural management method that integrates modern information technologies such as geographic information system (GIS), global positioning system (GPS), remote sensing technology, and Internet of Things (IoT) (Luo *et al.*, 2001; Maldaner *et al.*, 2021; Maldaner *et al.*, 2022; Price *et al.*, 2017; Sirikun *et al.*, 2021; Wang *et al.*, 2021; Yin *et al.*, 2024). It realizes precise control of the agricultural production process, including precise fertilization, irrigation, and harvesting, through real-time monitoring and data analysis of the farmland environment, crop growth, and soil conditions. In the process of crop cultivation and production management, obtaining the information of crop yield distribution in the farmland in an online, real-time, and effective method is the main starting point for the implementation of precision agriculture (Li *et al.*, 2004; Lou *et al.*, 2006). The traditional method of obtaining field crop yields is through direct weighing or sampling, which is not only time-consuming and inefficient, but also can only obtain the average yield of crops, so it is not suitable for obtaining the yields of field crops planted over large areas. The use of remote sensing technology to collect crop images or establish crop growth condition models are extracted crop characteristic values to establish the relationship with crop yield, but the collected data are affected by environmental factors (Choi *et al.*, 2018; Martello *et al.*, 2022; Taylor *et al.*, 2016). In field harvesting operations, real-time information on crop yield distribution in large fields can be accurately obtained through instantaneous yield monitoring of the combine harvester operation process. Through the drawn spatial distribution map of farmland yield, subsequent field management, rational use of agricultural resources, regulation of input-output ratio, improve yield, reduce pollution, is the basic guarantee of sustainable development of agricultural production (Wang *et al.*, 2021).

Currently, grain yield monitoring techniques mainly include impact measurement, volumetric measurement, dynamic weighing measurement, and radiation measurement, etc. Zandonadi *et al.*, (2009), verified the correlation between the tension on the tension side of the bin chain, shaft torque, and yield by setting a torque sensor in the bin of a harvester. The maximum error of the yield monitoring system designed in this way was 4.9%. Geng *et al.*, (2021), developed an on-line monitoring system for on-board grain yield based on the principle of grain flow pressure, guided by the mathematical model of grain yield and grain flow pressure. They built a grain yield monitoring test bed and investigated the effects of the number of sensors, the sensor installation position, and the horizontal inclination angle of the monitoring device on the yield measurement error of the grain yield monitoring system. The results showed that the indoor test error of the grain yield monitoring system was 3.27% and the field yield measurement error was 5.28%. Fang *et al.*, (2024), designed a convex surface grain mass flow sensor to compare the errors of different grain types and flow rates on the experimental measurements, and the measurement error was less than 5% after calibrating the zero point and coefficient of the sensor. Cheng *et al.*, (2023), constructed a corn seed yield model based on low-potential signals by adding three pairs of photoelectric sensors to a scraper—type elevator of a corn kernel harvester and achieved real-time monitoring of yield. The average error of the measured yield was 3.72%. Navid *et al.*, (2015), utilized a laser line scanner to measure material flow. In the system, the laser line scanner measures the distance between the sensor and the object according to the time-of-flight principle. Grain flows from a stationary bin, and a sliding door at the bottom of the bin is used to regulate the mass flow rate of grain. The results showed that the grain flow rate and the laser scanning signal are linearly related. This method is one of the yield measurement methods. Overall, the study shows that there is no significant difference in the measurement errors of different yield measurement methods, and the main sources of error include: non—calibration error, sensor response error, grain moisture content measurement error, and error due to uneven distribution of grain flow.

Existing combine harvester yield monitoring systems usually employ impact grain flow sensors, photoelectric volumetric flow sensors, or γ -ray technology-based grain photoelectric yield sensors. These sensors require continuous dynamic measurements and are affected by various factors, such as the moisture content of grains, species, yield differences, harvesting speed, and variations in flow rate due to vehicle adjustments at the ground level. These factors can lead to large measurement errors (De *et al.*, 2020; Jensen *et al.*, 2019; Sun *et al.*, 2022; Liu *et al.*, 2022). At the same time, these yield detection methods need to be calibrated before operation. Conventional calibration methods require correction by weighing on the ground for comparison. Moreover, with the change of time and space, frequent calibration is also necessary. Calibration difficulties cause detection inaccuracies. This system combines sensor strengths: load cells for large masses, photoelectric sensors for small ones. It calibrates photoelectric sensors with load cell data, improving per - unit yield measurement accuracy.

MATERIALS AND METHODS

Yield Monitoring System Principle

The principle of yield measurement using weighing method is to add a pressure transducer directly underneath the grain tank of the harvester and convert the weight of the grain applied to the transducer into an electrical signal (Hong *et al.*, 2019).

The working principle of the load cell is shown in Figure 1(b), where R_1, R_2, R_3 and R_4 are resistive strain gauges. When the load cell is subjected to gravity, it undergoes slight deformation. The strain gauges also deform under external force, leading to changes in their resistance values. These changes follow a specific relationship with the applied force. By measuring the variation in resistance, the magnitude of the external force can be accurately determined.

$$U = \frac{R_1 R_3 - R_2 R_4}{(R_1 + R_2)(R_3 + R_4)} U_0 \quad (1)$$

where U_0 is the DC supply voltage, and U is the output voltage. In the formula above, the resistance values of the four resistors are the same. When the sensor strain gauge is subjected to external forces, the resistance values change, and the output voltage will also change. Therefore, the amount of change in the voltage can be taken as an indication of the change in the resistance values, as a way to determine the force acting on the elastic element.

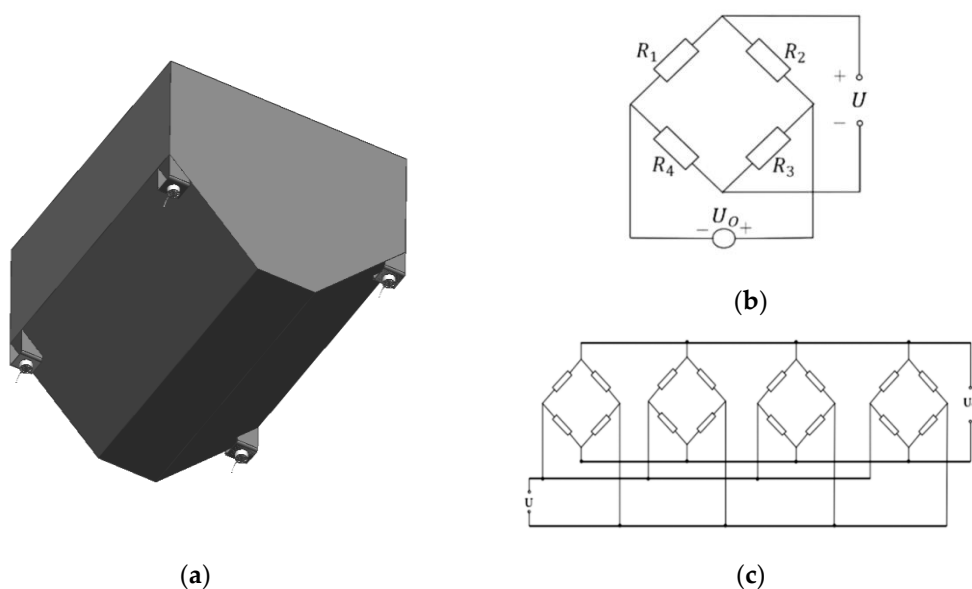


Fig. 1 - Installation position of the four load cells at the bottom of the grain tank

Designed according to the volume and shape of the harvester's grain tank, a weighing structure uses four load cells to measure the weight of the wheat in the tank. Each load cell needs to be placed on the same level during installation, otherwise the measurement quality will be inaccurate. Multiple load cells will output multiple signals, in order to streamline the wiring and the controller, a weighing structure only needs to collect one weighing signal, which can be connected to four load cells in series or in parallel (Marangoni *et al.*, 2017). Due to the poor stability of the series connection, the system uses the parallel connection for the 4 load cells, as shown in Figure 1(c). After connecting the pressure sensor with the transmitter, the RS485 to USB converter is used to connect the transmitter with the host computer, and the host computer data acquisition software receives, displays, stores and analyzes the collected data.

The light transmitter and light receiver of the opposed-radiation photoelectric sensor are on the same axis installed on both sides of the scraper lifter, respectively, and when the grain passes through the photoelectric path of the sensor, the photoelectric path is blocked, which causes the output voltage of the light receiver to change potentiometrically (Jin *et al.*, 2022). Therefore, the thickness of the grain on the scraper is determined by recording the duration of the output pulse signal of the photoelectric sensor, and the measurement of the grain mass is finalized based on the bottom area of the scraper and the grain capacity weight. The principle is shown in Figure 2(b).

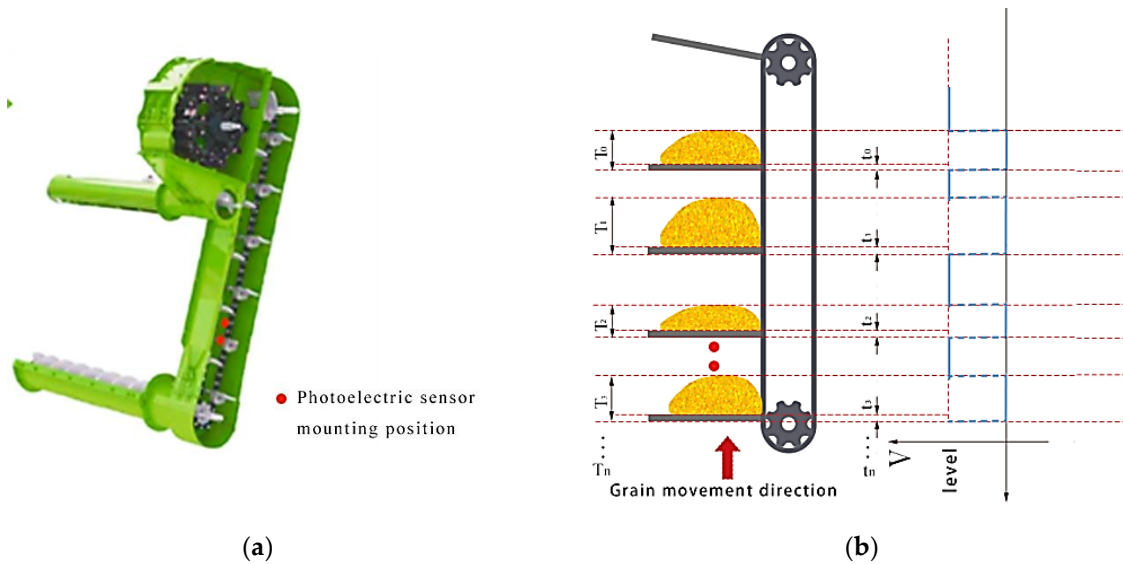


Fig. 2 - Photoelectric Sensor Yield Measurement Principle

where T_n is the time when the infrared rays of the opposed-beam photoelectric sensor are blocked by the grain and the scraper, and t_n is the time when the scraper blocks the sensor, and the sensor outputs a low-level signal. By counting the time of the low-level signal output from the opposed-beam photoelectric sensor, the yield estimation model constructed in this paper is used to obtain the weight of the grain entering the bin in the combine harvester.

When the combine harvester is operating under normal working conditions, the wheat yield M_1 is measured by the photoelectric yield monitoring system. Once it reaches the preset threshold, the load cell weighs the wheat in the grain tank to obtain M_2 , and the feedback unit calculates the calibration coefficient K .

$$K = \frac{M_2}{M_1} \tag{2}$$

where: K is the photoelectric metering calibration coefficient; M_1 is the mass measured by the photoelectric sensor; M_2 is the mass measured by the load cell. After the load cell weighs the grain in the tank, it calculates the new photoelectric metering coefficient. The system then updates the old coefficient with the newly calculated one and stores it for use in the next yield measurement.

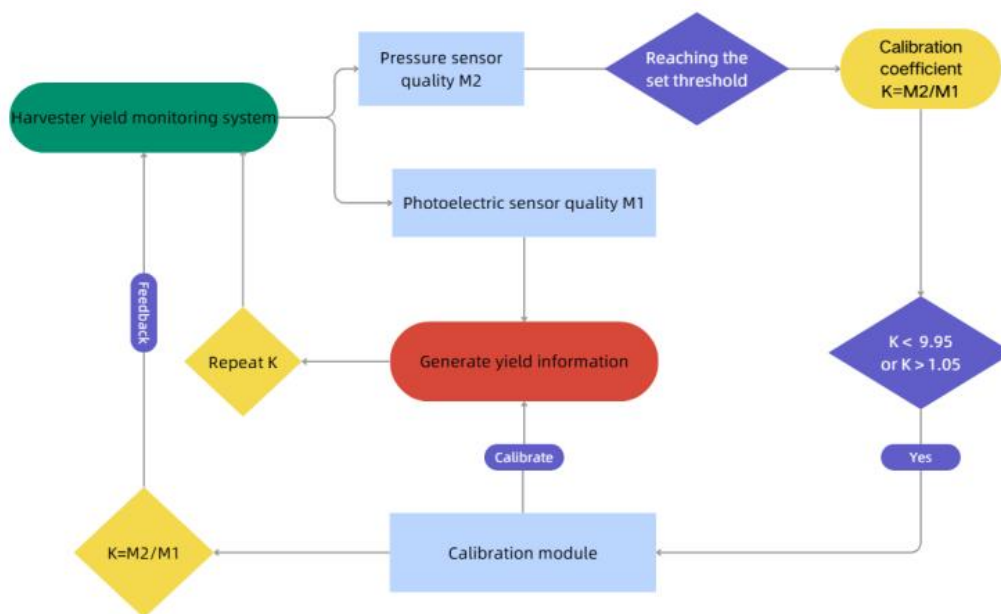


Fig. 3 - Workflow of the yield monitoring calibration system

Yield Monitoring System Hardware Selection

The yield monitoring system is installed on the grain combine harvester, which mainly collects crop yield information in real time. It mainly includes main control module, sensor module, data transmission module, digital signal processing and model conversion module, power supply module, data storage and display unit, etc., as shown in Figure 4.

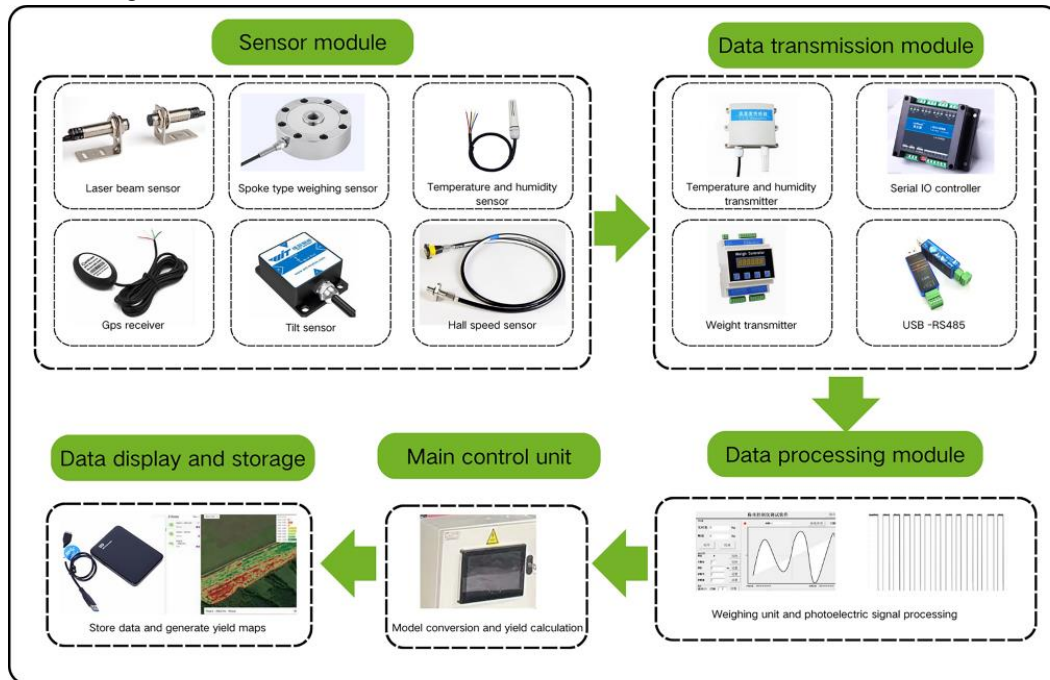


Fig. 4 - Schematic diagram of the harvester yield monitoring system

After passing through the harvester cleaning device, wheat grains are conveyed by a screw conveyor at the harvester's bottom to a scraper - type elevator. The scraper elevator, composed of a scraper, chain, and shell, uses the chain - moving scraper to lift grains to the harvester's grain tank. To study grain quality in the tank and the relationship between photoelectric sensor output and grain quality, a yield monitoring test bed was designed based on the 4YZL - 6S harvester elevator (Figure 5). The test bench includes a bottom screw conveyor, scraper elevator, top screw conveyor, grain tank, drive mechanism, and control system. The elevator is at a 72° angle to the ground. During operation, harvested wheat reaches the scraper elevator after cleaning. Photoelectric sensors at the elevator bottom estimate grain quality by recording pulse - signal durations from wheat shading, combined with scraper parameters. Pressure sensors under the grain bin convert grain weight to electrical signals, and data is sent to the host computer. When the photoelectric yield monitoring system reaches a set threshold, the pressure sensor weighs, calculates calibration coefficients, calibrates the photoelectric sensor, and generates yield information for real - time crop yield monitoring.

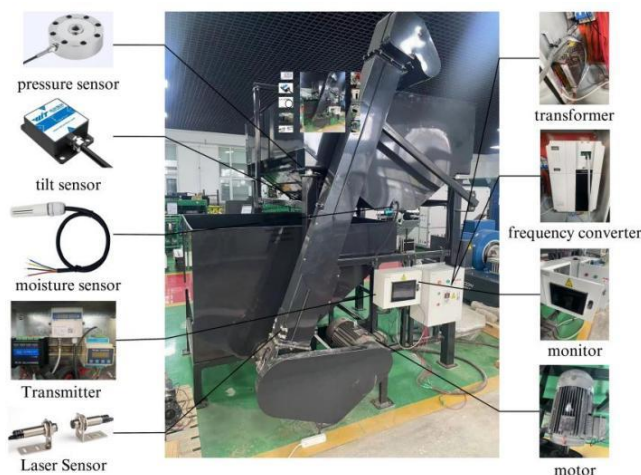


Fig. 5 - Yield monitoring system test bench structure

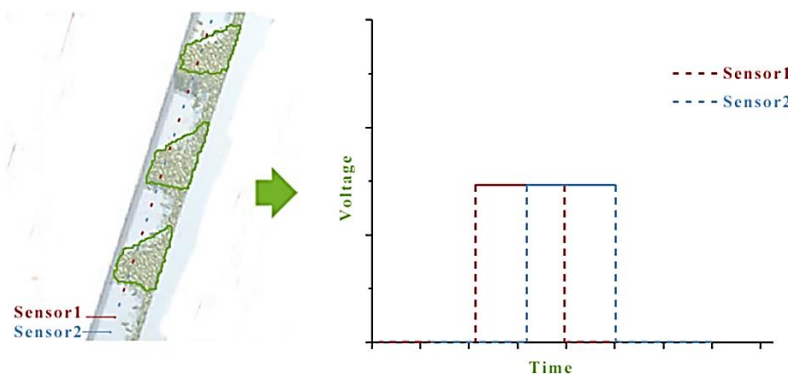
In order to obtain the relationship between the duration of photoelectric signal and the quality of grain, as well as the load pressure of the grain box on the counterweight sensor, this paper carries out the selection of hardware for the test bench. Two counter-reflective photoelectric sensors, specifically the E2F-20C2 (NPN) type, were selected and placed at the bottom of the scraper lifter. These sensors, manufactured by Wenzhou Mingxun Electronics Co., Ltd. (Wenzhou, China), have a supply voltage range of 6 – 36 V and a response time of ≤ 2 ms. The photoelectric sensors' data transmission module is selected to be the serial IO controller of LangHande, with a supply voltage of 9–24 V, and adopts the standard Modbus- RTU protocol of the relay. The load cell used is the SLLF-74 spoke-type load cell, manufactured by Shenglong Machinery Co., Ltd. (Wenzhou, China), with a measurement range of 1 T and a power supply requirement of 5–12 V. The load cell transmitter is the XSF4-channel digital transmitter from Bengbu Zhongnuo Sensors Technology Co., Ltd. (Bengbu, China), which operates with a 10–30 V power supply, has a sampling frequency of 500 Hz, supports the Modbus-RTU protocol, and offers an accuracy of 0.0003%. The transmitter is connected to the host computer via an RS-485 to USB converter. The power supply unit provides 12 V through a transformer to power both the sensors and the transmitters.

Photoelectric Sensor Yield Measurement Model

Since the photoelectric sensor cannot directly obtain the grain quality, it is necessary to construct the relationship between the photoelectric signal and the quality model. For NPN-type sensors, the transmitter emits light, and when an object enters the detection area to block the light, the amount of light received by the receiver changes, and the detection circuit produces an electrical signal change according to this change. When there is no obstruction, the sensor outputs a low level; when an object blocks the light, the sensor outputs a high level, thus realizing the detection of the object. Thus, the relationship between wheat volume and the photoelectric signal can be established by calculating the cumulative generation voltage time. In order to avoid the large error data generated by a single sensor, two photoelectric sensors were selected for the experiments in this paper. However, in the process of photoelectric sensors being blocked by wheat, the scraper of the grain bin will also block the photoelectric sensors at the same time, which will have an impact on the results of yield calculation, so the time of shielding wheat particles during the accumulation of photoelectric sensors eliminates the influence of the scraper on the total accumulation time, the calculated formula is:

$$T = \sum \left(\frac{T_{an} + T_{bn}}{2} - t_n \right) \tag{3}$$

The time at which photoelectric sensor No. 1 accumulates the generated potential is denoted as T_{an} , and the time at which photoelectric sensor No. 2 accumulates the generated potential is denoted as T_{bn} . The time at which the photoelectric sensor monitors the accumulation of each scraper is represented as t_n . Additionally, T signifies the average accumulated time during which the photoelectric sensor monitors the wheat. These time parameters are critical for analyzing the sensor's response and the accumulation process of the wheat. Looking at the analysis of the accumulation of wheat on the elevator by EDEM 2022.2 software, it can be approximated that the accumulation pattern of wheat on each scraper is close to a trapezoidal shape, as shown in Figure 6.



(a)

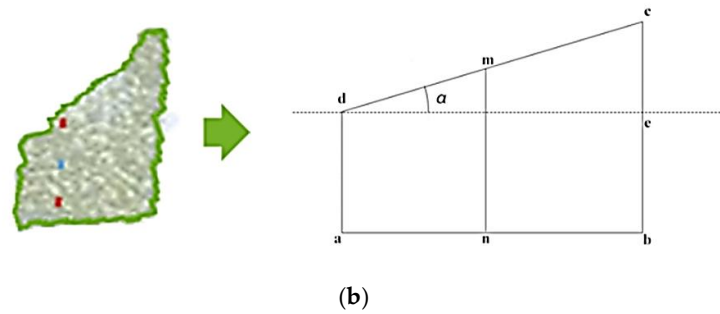


Fig. 6 - Relationship between wheat volume and potential

Since the scrapers are rigidly connected to the elevator chain, the spacing between each scraper is nearly identical. Given that the length and width of each scraper are fixed, a linear relationship exists between the volume of grain on each scraper and the stacking height of the grain. Therefore, the mass of grain on each scraper can be estimated by monitoring the duration for which the wheat obstructs the photoelectric sensors and combining this information with the elevator's speed. The volume of grain on a scraper is calculated as:

$$V = L_{ab}L_{mn} + \left(\frac{L_{nb}^2 \tan \alpha}{2} - \frac{L_{an}^2 \tan \alpha}{2} \right) L_1 \tag{4}$$

where L_{ab} is the width of the scraper, L_1 is the length of the scraper, L_{mn} is the photoelectric sensor monitoring line, which can be understood as the effective length of the grain that can be monitored by the photoelectric sensor during the scraper lifting process. L_{an} is the length from the sensor monitoring line mn to the upper edge of the scraper, L_{nb} is the length from the sensor monitoring line mn to the lower edge of the scraper, α is the angle of the top of the grain pile relative to the scraper. From Equation (5), it can be seen that there is a linear relationship between the stacked volume of grain and the measured value of photoelectric sensor L_{mn} under the ideal model. However, the yield monitoring system in this paper is calibrated to the thickness of the scraper after idling, when L_{mn} is 0 the volume V of the grain is also 0, and the value of the constant term in Equation (4) is 0. Therefore, the mass m of the grain measured in the system is positively proportional to the cumulative voltage time corresponding to L_{mn} and the mass of the wheat is given in the Equation (5):

$$m = kL_{mn} \tag{5}$$

where k is the coefficient of positive proportionality of the cumulative voltage generation time to m .

Weighing System Correction Model

To address errors from uneven terrain in field operations, a mathematical model between tilt angle and weighing error is established. Nonlinear regression fits experimental data, and a compensation algorithm for tilted grain bins is proposed. The photoelectric sensor data model is better calibrated by enhancing load cell stability. When the grain box is stationary on the ground (0°), the sensor output equals the actual wheat mass. When the grain box is tilted, the load cell is in a tilt - weighing state. As shown in Figure (7), the force on the sensor at this time is:

$$\begin{cases} F_2 = W_m \cos \alpha \\ F_3 = W_m \sin \alpha \end{cases} \tag{6}$$

where F_2 is the load of the load cell along the vertical direction of the grain tank, and F_3 is the load of the load cell along the horizontal direction of the grain tank, F_2 is the main direction force of the load cell, which is perpendicular to the pressure sensor and has a good linear relationship, while F_3 is the parallel direction force of the load cell, whose output is affected by the tilt direction of the grain tank, the mass of the wheat W_m , the angle of inclination α and other factors. From equation 7, the output of the load cell at this time is:

$$W_s = F_2 + f(F_3) = W_m \cos \alpha + f(W_m \sin \alpha) \tag{7}$$

where: W_s is the output value of the pressure transducer, $f(F_3)$ is the nonlinear function that affects the output of the pressure transducer. According to equation (6) and (7), it can be inferred that:

$$W_e = W_m - W_s = W_m(1 - \cos\alpha) - f(F_3) \tag{8}$$



Fig. 7 - Grain box force analysis

When the grain bin is at a certain angle to the ground, Equation (8) is decomposed by the Taylor's equation:

$$W_e = W_m \left(\frac{1}{2}\alpha^2 + o(\alpha^2) \right) - f(F_3) \tag{9}$$

In this equation, $o(\alpha^2)$ represents the second order infinitesimal quantity of α . Since the effect of $o(\alpha^2)$ in Equation (9) on the load weight value is very small, it can be neglected. Based on this, the weighing error compensation equation can be derived:

$$W'_m = W_s + W_e = W_m \left(1 + \frac{1}{2}\alpha^2 \right) - f(F_3) \tag{10}$$

where W'_m is the weight compensated according to the algorithm. Due to the complexity of the change of the force plane of the load cell and the insensitivity of the force F_3 in the horizontal direction of the sensor to the action of the load cell, Equation (11) can be simplified as follows.

$$W'_m = K_2 \cdot W_s \cdot \alpha^2 + B \tag{11}$$

where K_2 is the tilt compensation coefficient, B is the model correction value. Due to the insensitivity of the weighing pressure sensor to lateral stress. In this paper, simplifying the model, correcting the tilt direction according to the change of tilt angle of the load cell caused by the load of the grain tank, and then compensating the weighing accuracy according to the corrected tilt angle are considered.

RESULTS

Determination of the coefficient of proportionality

To get the positive coefficient k between cumulative potential generation time and wheat quality, experiments were done on a designed bench. Shandong Luzhong's Qimin 13 hulled wheat (moisture 12 - 14%, purity 98%) was used. Instruments included Yingheng T1 scale, Shandong Huali motor, and Shandong Shenchuan inverter. Test photos are shown in Figure 9.

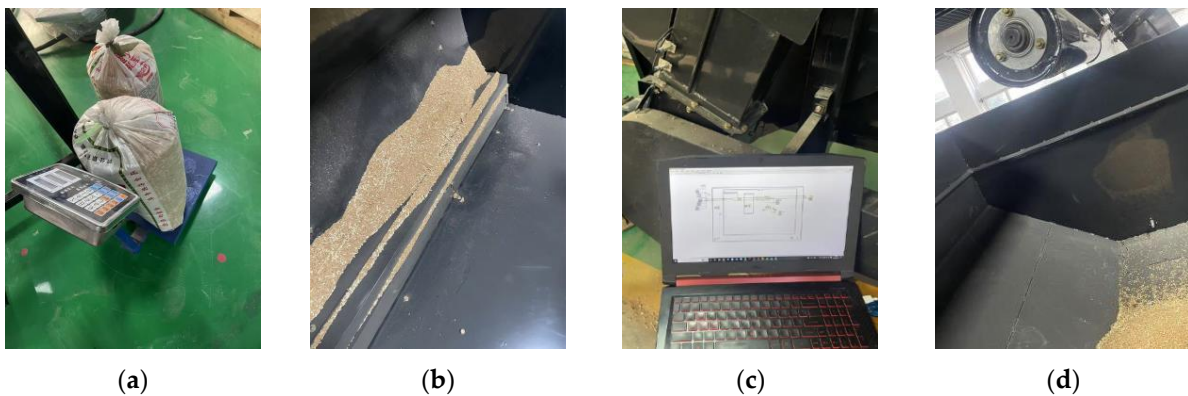


Fig. 8 - Indoor bench experiment site

To determine the proportionality coefficient under different scraper lifter speed conditions, 30 sets of tests were conducted at motor frequency converter settings of 10 Hz (approximately 150 r/min), 20 Hz (approximately 300 r/min), and 25 Hz (approximately 375 r/min). For each test, the system recorded the accumulated photoelectric signal duration along with the actual grain mass measured by a bench scale. The results are shown in Figure 9.

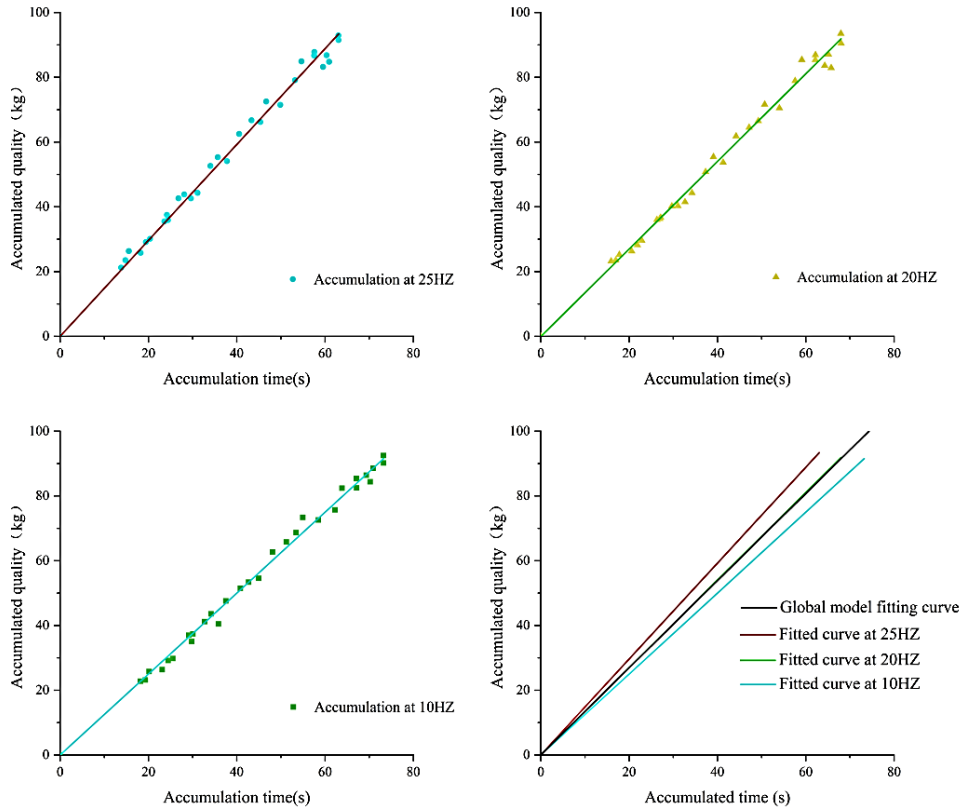


Fig. 9 - Fitted straight line between cumulative time and mass at different rotational speeds

Since the experiment has been calibrated for the cumulative time of the scraper pair in the unloaded state of the scraper lifter at each frequency, each frequency has the constraint that the constant term of the fitted curve is 0. Based on the experimental results, the cumulative time was fitted to the actual weighing mass of the grain by linear regression using Origin2024 software, and the following positive scale factors were obtained, respectively:

The positive proportionality coefficient at 25 Hz (approx.375 r/min) is:

$$M = 1.370(T_1 + T_2) \tag{12}$$

The positive proportionality coefficient at 20 Hz (approx.300 r/min) is:

$$M = 1.362(T_1 + T_2) \tag{13}$$

The positive proportionality coefficient at 10 Hz (approx.150r/min) is:

$$M = 1.349(T_1 + T_2) \tag{14}$$

Positive scale factor for global model:

$$M = 1.355(T_1 + T_2) \tag{15}$$

where $T_1 + T_2$ represents the total duration of the output signals from the two photoelectric sensors. Based on this relationship, the positive scale factor k is determined to be 1.355. The fitted model achieved correlation coefficients of 0.998, 0.992, 0.994, and 0.994.

Weighing error compensation

To study the impact of load cell weighing errors in the grain bin under different tilt angles, this research adjusted the yield test stand using a manual forklift to angles of 0.5°, 1°, and 1.5°. A total of 1000 kg of grain was loaded into the test stand, with sampling points set every 200 kg to calculate the error at each point. Before the experiment, the grain box was leveled using the HWT901B tilt angle sensor from Witte Intelligent Technology Co., Ltd. (Shenzhen, China). The motor frequency was set to 20 Hz, and 200 kg of wheat was added to the bottom grain bin. The cumulative time of the potential generated by the photoelectric sensor was recorded to determine the actual mass of wheat using a model conversion factor. After the wheat was transferred to the top grain bin, the mass measured by the load cell was collected. Due to gaps between the scraper elevator and screw conveyor, the measured mass was less than 200 kg, requiring manual replenishment until the load cell reading reached 200 kg.

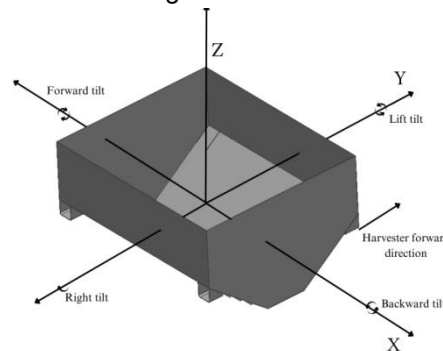


Fig. 10 - Schematic diagram of the adjustment direction of the laboratory bench

In practice, grain distribution in the bin is non-uniform. When the harvester tilts, the thickness of the grain pile and the position of the center of gravity shift in the left, right, or forward/backward directions. These variations, along with the mechanical structure of the harvester and sensor placement, influence the measurements. The harvester's structure may exhibit varying stiffness and flexibility in different directions, leading to differential deformation around the load cell when tilted. Additionally, despite precise mounting, slight variations in the sensitivity or response characteristics of the load cells in different directions may persist. These combined factors contribute to discrepancies in readings when tilted in various directions.

To address this, a forklift was used to fill the test stand from all four directions, adjusting it to the appropriate angles to collect weight and angle data from the grain bin. The weighing error under tilted conditions was determined by comparing the sensor-measured mass of wheat with the actual mass loaded. After completing the experiment at one sampling point, the process was repeated for the remaining points. The experimental results are presented in Figure 11.

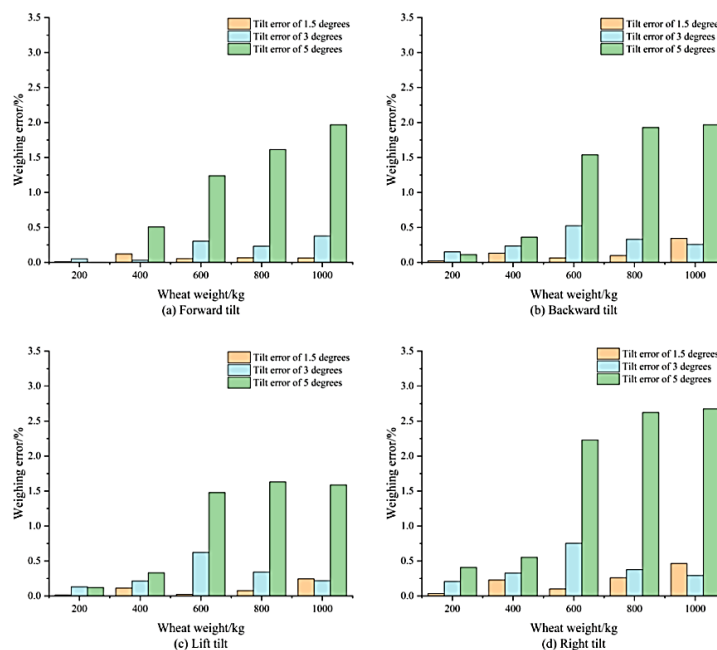


Fig. 11 - Weighing errors in different directions and at different angles of inclination

The experimental results show that the weighing error of the bin is almost negligible when the tilt angle is 0.5° . However, when the tilt angle reached 1.5° , the weighing errors in the four directions increased significantly, far exceeding the error levels of 0.5° and 1° . The analysis shows that the weighing accuracy of the bin under the left tilt condition is slightly higher than that of the other directions, which may be related to the inhomogeneity of wheat distribution in the bin. When the grain bin is tilted to the right, the grains on the left side may become more densely packed due to gravity, while the right side remains relatively loose. This causes the force on the right-side sensor to increase. Conversely, when the bin is tilted to the left, the inlet located on the right side promotes a more uniform grain distribution within the bin, thereby reducing the measurement error. For forward and backward tilts, the feeding port remains aligned with both directions, resulting in relatively similar errors in both cases. To improve weighing accuracy under inclined ground conditions, this paper proposes a corresponding error compensation algorithm for the grain bin.

To determine the tilt compensation coefficient K_2 and the model correction value in Equation (11), and to correct for the influence of inclination on the model, this study utilizes load cell weighing data collected under tilted conditions. The model parameters are fitted using the least-squares algorithm.

$$S = \sum_{i=1}^n (y_i - f(x_i))^2 \quad (16)$$

where S is the sum of squared errors, representing the total of the squared differences between the model's predicted value y_i and the true observed value $f(x_i)$. The objective of the least squares method is to minimize S in order to determine the optimal parameters of the model. Here, y_i is the observed value of the i -th sample, based on the model function f , when the input is the independent variable x_i of the i -th sample.

Considering that the measurement error is small and close to the accuracy error of the load cell itself when the tilt angle is 0.5° and 1° , this paper only compensates the weighing error for the weighing data with tilt angle of 1.5° under single-axis tilt condition. Where $K_2 = 0.44$, $B = -1.93$. The fitting accuracy is 0.818. In addition, the error plots for both corrected and uncorrected tilt angles are compared in this paper, as shown in Figure 12.

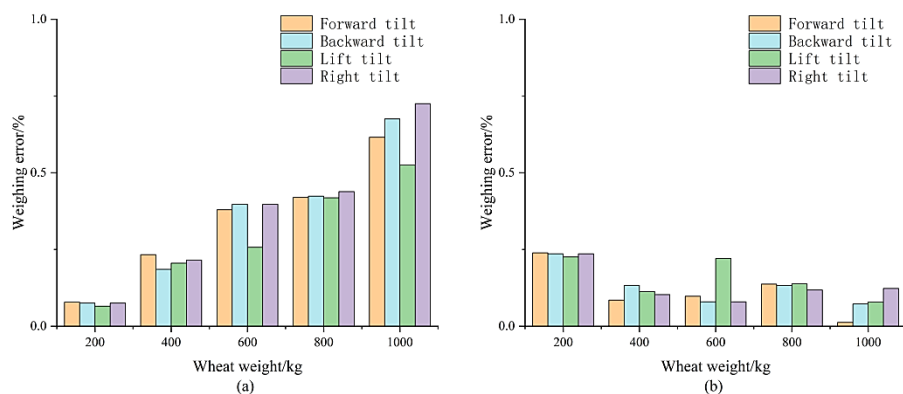


Fig. 12 - Plot of uncorrected model vs corrected model

From the comparison, it can be observed that the compensation accuracy and consistency of the model without tilt angle correction decrease as the loading load increases. In contrast, the compensation performance of the model with tilt angle correction improves progressively with increasing load. The overall error after compensation remains below 0.25%, and the accuracy of the corrected model consistently surpasses that of the uncorrected model. Overall, the compensation effect of the corrected model is significantly better than that of the uncompensated approach.

Experimental Results of a Self-Feedback Labor Monitoring System

In order to verify the accuracy of the model based on the improved photoelectric yield monitoring system, this paper simulates the harvester field operation by indoor bench test. The data of the photoelectric yield monitoring system and weighing system were obtained by manually inputting wheat into the bottom grain bin, and the test was conducted by inputting in batches of 200 kg into the grain inlet of the test stand. The calibration accuracy of the pressure sensing was set to 200 kg, and the yield quality corresponding to the global fitting coefficients was used to measure the yield. The excellence with the self-feedback system was contrasted, and the results of the experiments are shown in Table 1.

Table 1

Photogrammetric production data without the addition of a calibration system

Frequency /Hz	Quality of Inputs/kg														
	200			400			600			800			1000		
	Time /s	Mass /kg	Errors /%	Time /s	Mass /kg	Errors /%	Time /s	Mass /kg	Errors /%	Time /s	Mass /kg	Errors /%	Time /s	Mass /kg	Errors /%
10	146.92	196.88	1.56	306.66	410.92	2.73	466.71	625.39	4.23	629.34	843.32	5.42	794.29	1064.35	6.44
20	147.51	197.67	1.17	305.46	409.32	2.33	463.72	621.39	3.57	625.16	837.72	4.72	785.27	1052.26	5.23
25	146.40	196.17	1.91	306.00	410.04	2.51	464.42	622.33	3.72	625.98	838.82	4.85	788.25	1056.26	5.63

Table 2

Photometric data added to the calibration system

Frequency /Hz	Quality of Inputs/kg														
	200			400			600			800			1000		
	Time /s	Mass /kg	Errors /%	Time /s	Mass /kg	Errors /%	Time /s	Mass /kg	Errors /%	Time /s	Mass /kg	Errors /%	Time /s	Mass /kg	Errors /%
10	146.92	196.88	1.56	299.50	401.33	0.33	448.99	601.65	0.28	599.56	803.42	0.43	750.16	1005.21	0.52
20	147.51	197.67	1.17	299.21	400.94	0.23	449.25	602.00	0.33	598.78	802.37	0.30	749.38	1004.17	0.42
25	146.40	196.17	1.91	299.60	401.47	0.37	448.36	600.80	0.13	599.01	802.68	0.34	751.77	1007.37	0.74

The yield monitoring system with the addition of the self-feedback module is clearly shown by the experimental results to have a certain compensation effect at all three frequencies, and the before and after comparison with the error without the feedback module is shown in Figure 13.

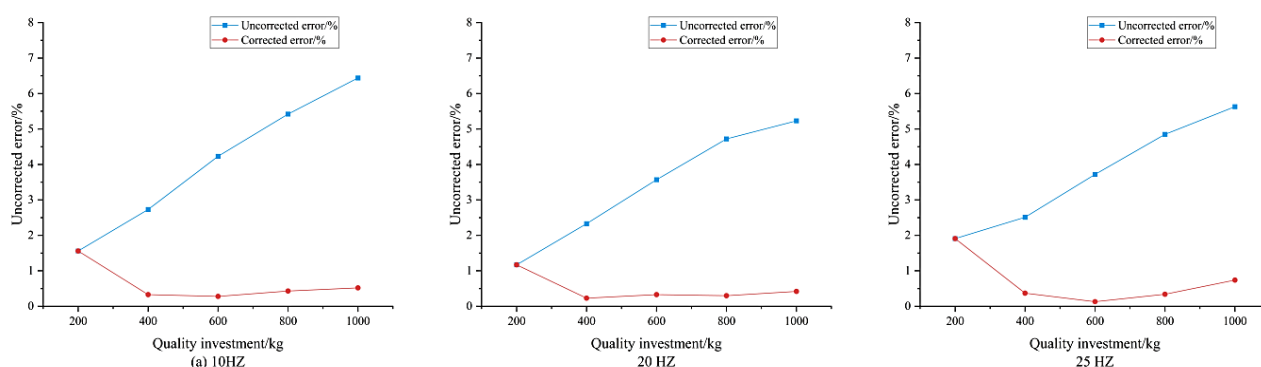


Fig. 13 - Comparison of yield data with and without calibration system

As shown by the results, the error is relatively large when the input is 200 kg. This is because the load cell's calibration accuracy is set for 200 kg, and the threshold for calibration had not yet been reached, meaning the feedback module had not been activated. At this stage, the photoelectric measurement coefficient remains at its initial value. Once the input reaches 400 kg, the system's self-feedback module begins functioning, correcting the photoelectric measurement coefficient. Observations from the 2nd to 5th tests show that the system's yield measurement error gradually stabilizes, with errors ranging from 0.23% to 0.74%. The optimal

calibration occurs at a frequency converter setting of 20 Hz, where the overall error remains below 0.42%, indicating strong accuracy and stability of the system. In contrast, the standalone photoelectric yield measurement system exhibits a larger error fluctuation range, between 1.17% and 6.44%, with a tendency for errors to increase over time. The self-feedback calibration system effectively performs dynamic calibration, keeping the error within a stable range. This significantly reduces system fluctuations and measurement errors, thereby ensuring the accuracy and stability of the system.

CONCLUSIONS

In this study, a multi-sensor fusion-based yield monitoring system for grain harvesters was successfully designed and validated, and a series of results of significant value were obtained. The positive proportionality coefficients between the photoelectric signal and the grain mass at different rotational speeds were determined through experiments, and the overall error of the system was less than 6.44% in the initial test. The established model of the relationship between tilt angle and weighing accuracy and the compensation algorithm were effective, with the overall error less than 0.25% after compensation and less than 0.74% after system intervention. The self-feedback calibration system played a key role in keeping the system error low under different loads, and the best calibration effect was achieved at 20 Hz, with the overall error less than 0.42%. The system provides an efficient and reliable yield monitoring solution for agricultural production, which strongly promotes the development of precision agriculture and helps to improve resource utilization efficiency and economic benefits. However, considering the complexity of practical applications, more field trials are needed in the future to further optimize the adaptability of the system to different environments and crops, and to improve the sensor parameters and algorithms, so as to give full play to the potential of the system in agricultural production and help agriculture achieve higher quality development.

ACKNOWLEDGEMENT

This article was supported by a grant from the Development of High Efficiency and Low Loss Single Longitudinal Axial Flow Threshing and Separation Technology and Intelligent Flexible Threshing Device Project, Grant No. 2021YFD200050204.

REFERENCES

- [1] Cheng S., Han H., Qi J., Ma, Q., (2023) Design and Experiment of Real-Time Grain Yield Monitoring System for Corn Kernel Harvester (玉米籽粒收获机实时谷物产量监测系统的设计与实验) *Agriculture*, Vol.13, 294. <https://doi.org/10.3390/agriculture13020294>
- [2] Choi, M.C., Lee, K.H., Jang, B.E., (2018) Grain Flow Rate Sensing for a 55 Kw Full-Feed Type Multi-Purpose Combine. *Int. J. Agric. Biol. Eng*, Vol. 11, pp. 206–210. <https://doi.org/10.25165/j.ijabe.20181105.2686>
- [3] De Queiroz, D.M., Coelho, A.L.D., Valente, D.S.M., Schueller, J.K. (2020) Sensors Applied to Digital Agriculture: A Review. *Rev. Cienc. Agron.* 51, e20207751.
- [4] Fang Y., Chen Z., Wu L., (2024) Design and Experiments of a Convex Curved Surface Type Grain Yield Monitoring System. (凸曲面型谷物产量监测系统的设计与实验) *Electronics*, Vol.13, 254. <https://doi.org/10.3390/electronics13020254>
- [5] Geng D., Tan D., Su G., (2021) Optimization and Experimental Verification of Grain Yield Monitoring System Based on Pressure Sensors. (压力式谷物产量监测系统的验证与优化) *Trans. Chin. Soc. Agric. Eng*, Vol.37, pp.245–252.
- [6] Hong, Y.D., Lee, B. (2019) Logarithmic Strain Model for Nonlinear Load Cell. *Sensors*, 19, 3486. <https://doi.org/10.3390/s19163486>.
- [7] Jensen, J.A., Garmendia, A.G. (2019) Comparison between Bin Tonnages and Yield Monitor Predictions. *Int. Sugar J.* Vol.121, pp. 272-277.
- [8] Jin C., Cai Z., Yang T. (2022) Design and Experiment of Yield Monitoring System of Grain Combine Harvester. (谷物联合收割机产量监测系统的设计与实验) *Trans. Chin. Soc. Agric. Mach.* Vol.53, pp.125–135.
- [9] Li M., (2004). The Technique of Crop Yield Monitor and Key Equipment Agric (作物产量监测技术及关键设备农业). *Agriculture Network Information*. pp. 34–38.

- [10] Liu R., Sun Y., Li M., (2022) Development and Application Experiments of a Grain Yield Monitoring System. (谷物产量监测系统的开发与应用实验) *Comput. Electron. Agric.*, Vol.195, 106851. <https://doi.org/10.1016/j.compag.2022.106851>.
- [11] Luo X., Zang Y., Zhou Z., (2006) Research Progress in Farming Information Acquisition Technique for Precision Agriculture (精准农业中农业信息获取技术的研究进展). *Trans. Chin. Soc. Agric. Engineering*, Vol. 22, pp. 167–173. Guangdong/China.
- [12] Luo X., Zhang T., Hong T. (2001). Technical System and Application of Precision Agriculture(精准农业的技术系统及应用). *Transactions of the Chinese Society for Agricultural Machinery*, Vol.32, pp. 103-106, Guangdong/China.
- [13] Maldaner, L.F., Canata, T.F., Molin, J.P. (2022). An Approach to Sugarcane Yield Estimation Using Sensors in the Harvester and Zigbee Technology. *Sugar Tech*, Vol.24, pp. 813–821.
- [14] Maldaner, L.F., Corrêdo, L.D., Canata, T.F., (2021). Predicting the Sugarcane Yield in Real-Time by Harvester Engine Parameters and Machine Learning Approaches. *Comput. Electron. Agric.* 181, 105945. SP/Piracicaba <https://doi.org/10.1016/j.compag.2020.105945>
- [15] Marangoni, R.R., Rahneberg, I., Hilbrunner, F., Theska, R., Fröhlich, T. (2017). Analysis of Weighing Cells Based on the Principle of Electromagnetic Force Compensation. *Measurement Science and Technology*. 28, 075101. <https://doi.org/10.1088/1361-6501/aa6bcd>
- [16] Martello, M., Molin, J.P., Bazame, H.C. (2022) Obtaining and Validating High-Density Coffee Yield Data. *Horticulturae*, Vol.8, 421. <https://doi.org/10.3390/horticulturae8050421>
- [17] Momin, M.A., Grift, T.E., Valente, D.S., Hansen, A.C. (2019) Sugarcane Yield Mapping Based on Vehicle Tracking. *Precis. Agric.*, Vol.20, pp.896–910. <https://doi.org/10.1007/s11119-018-9621-2>
- [18] Navid, H., Taylor, R.K., Yazgi, A., (2015) Detecting Grain Flow Rate Using a Laser Scanner. *Trans. ASABE*, Vol.58, pp.1185–1190.
- [19] Price, R.R., Johnson, R.M., Viator, R.P. (2017). An Overhead Optical Yield Monitor for a Sugarcane Harvester Based on Two Optical Distance Sensors Mounted above the Loading Elevator. *Appl. Eng. Agric.* Vol.33, pp. 687–693. <https://doi.org/10.13031/aea.12191>
- [20] Sirikun, C., Samseemoung, G., Soni, P., Langkapin, J., Srinonchat, J. (2021) A Grain Yield Sensor for Yield Mapping with Local Rice Combine Harvester. *Agriculture*, 11, 897. <https://doi.org/10.3390/agriculture11090897>
- [21] Sun Y., Liu R., Zhang M., Li M., (2022) Design of Feed Rate Monitoring System and Estimation Method for Yield Distribution Information on Combine Harvester. *Comput. Electron. Agric.*, 201, 107322. <https://doi.org/10.1016/j.compag.2022.107322>
- [22] Taylor, J.A., Sanchez, L., Sams, B., (2016) Evaluation of a Commercial Grape Yield Monitor for Use Mid-Season and at-Harvest. *J. Int. Sci. Vigne Vin*, Vol. 50, pp. 57–63.
- [23] Wang H., Bai X., Liang H. (2017) Proportional Distribution Method for Estimating Actual Grain Flow under Combine Harvester Dynamics. (联合收割机动态下实际粮食流量估算的比例分配方法). *Int. J. Agric. Biol. Eng.* Vol.10, pp.158–164. <https://doi.org/10.25165/j.ijabe.20171004.2732>
- [24] Wang S., Yu Z., Zang W., (2021) Review of Recent Advances in Online Yield Monitoring for Grain Combine Harvester (谷物联合收割机在线产量监测研究进展) *Trans. Chin. Soc. Agric. Eng.*, Vol. 37, pp.58-70.
- [25] Yin C., Zhang Q., Mao X., (2024) Research of Real-Time Corn Yield Monitoring System with DNN-Based Prediction Model (基于 DNN 的实时玉米产量监测系统研究). *Front. Plant Sci*, 15, 1453823. <https://doi.org/10.3389/fpls.2024.1453823>
- [26] Zandonadi, R.S., Stombaugh, T.S., Shearer, S.A., (2009) Laboratory Performance of a Mass Flow Sensor for Dry Edible Bean Harvesters. *Appl. Eng. Agric.* Vol. 26, pp.11–20.

RESEARCH ON A RICE FIELD METHANE DETECTION SYSTEM USING HOLLOW-CORE PHOTONIC CRYSTAL FIBRE BASED ON TDLAS TECHNIQUE

基于 TDLAS 技术的空心光子晶体光纤稻田甲烷气体检测系统研究

Bin LI* ¹⁾, Ruotong LIU¹⁾, Guangfei SHANG¹⁾, Lihui ZHANG¹⁾, Chenghao HAN²⁾, Yitong HUANG¹⁾ ¹

¹⁾ School of Electrical & Computer Engineering, Jilin Jianzhu University, Changchun 130012, P.R. China;

²⁾ School of Emergency Science and Engineering, Jilin Jianzhu University, Changchun 130012, P.R. China;

Tel: +86-043184566184; E-mail: libin@jlju.edu.cn; 870731919@qq.com;

DOI: <https://doi.org/10.35633/inmateh-75-66>

Keywords: Methane detection; rice field; DFB laser diode; infrared absorption

ABSTRACT

A methane gas detection system has been developed based on the infrared absorption method. The system can be deployed in dry rice field for real-time detection. It consists of self-developed circuits and essential optical parts. A distributed feedback laser has been chosen as the optical source of the system. Hollow-core photonic crystal fibre is also applied as a part of the gas cell. The major circuit boards include laser driver circuit, laser temperature control circuit, digital lock-in amplifier circuit and linear power circuit. The laser diode can be effectively controlled by using the above circuits. The laser driving current step is 1 mA and the temperature fluctuation is less than ± 0.02 °C. Based on the TDLAS technique, spectroscopy test shows that the proposed laser driving circuits has accurate control capability. The detection error is about 2.3% by performing the full-scale detection experiments. Further gas detection experiments using standard gas under 600 ppm also demonstrate the effectiveness and stability of the proposed system. By replacing the optical source and essential driving circuits of the system, the system can be applied to detect other trace gases.

摘要

开发了一种基于红外光谱吸收法的甲烷气体检测系统。研制的系统能够应用在早稻田中进行实时气体检测。它由自主开发的电路和相关光学部件组成。分布式反馈激光器作为光源，空心光子晶体光纤作为气室的一部分。系统中主要电路板包括激光器的驱动电路、激光器的温度控制电路、数字锁向放大器电路和线性电源电路。使用上述电路可以有效地控制激光二极管。激光驱动电流步长为 1 mA，其温度波动可以限制在 ± 0.02 °C 的范围内。基于 TDLAS 技术，光谱测试表明，所提出的激光驱动电路具有精确的控制能力。通过进行全量程的气体检测实验，检测误差约为 2.3%。进一步使用 600 ppm 以下的标准气体进行气体检测实验也证明了文章中提出系统的稳定性、有效性。通过更换系统的光源和基本驱动电路，该系统可以应用于其他痕量气体的检测。

INTRODUCTION

Rice as an important food crop is widely cultivated in China and many regions around the world. However, in recent years, the methane gas released from paddy fields has attracted the attention of many researchers (Jikun H. et al., 2014; Mujiyo M. et al., 2017; Xie B.H. et al., 2010). It is widely researched that CH₄ is a kind of important greenhouse gas and it is 28 times higher than carbon dioxide with a global warming potential (Ma J.L. et al., 2019; Palmer P.I. et al., 2021; Rajasekar P. et al., 2022; Rizzo et al., 2015). According to studies in the past years, the methane gas released from rice fields are increasing for numerous reasons (Bai Y. et al., 2023; Xu X.Y. et al., 2020). In this way, it is important to develop advanced and reliable sensors for monitoring methane gas in rice fields for purposes including environmental protection and sustainability.

Traditional methods of methane detection in rice field such as chamber technique has some drawbacks. The measurement accuracy of chamber technique is good. And this method is widely used for many years. However, it is not efficient in the real-time detection and monitoring of large areas of rice fields. Other traditional methods such as micrometeorological technique and isotope method, also have drawbacks including unstable accuracy and complex requirements in the sensing process (Arianti F.D. et al. 2023; Gao Z.R. et al., 2018; Zhang G.B. et al., 2014; Zhang G.B. et al., 2015). Therefore, it is essential to apply advanced methods for high-precision and large-scale monitoring of methane gas in rice fields.

¹ Bin Li, Prof.; Ruotong Liu, Stud.; Guangfei Shang, Stud.; Lihui Zhang, Prof.; Chenghao Han, Prof.; Yitong Huang, Stud.

The infrared spectral absorption method is an advanced optical technique to monitor trace gases which has been studied by many researchers. In 2021, Catia L. etc. proposed their work with an immunosensor for achieving fast and highly sensitive detection of cortisol based on plasmonic tilted fiber (Catia L. et al., 2021). In 2023, Maxime L. etc. proposed an electro-plasmonic biosensor for attracting cells and proteins by migration of controlled biomolecular. The sensor is on the surface of a probe linked with fiber (Maxime L. et al., 2023). Compared with traditional detection methods, the infrared spectral absorption method is characterized by high precision and rapid response. At the same time, this method has strong selectivity and is capable of monitoring specific gases for a long time in an open space. Different types of optical fibers are widely used in these detection systems (Bai Y.R. et al., 2021; Dar S.A. et al., 2020; Davis N.M. et al., 2016; Jiao Y.X. et al., 2021). Hollow-core photonic crystal fiber (HC-PCF) can be used not only for the transmission of optical signals but also as a part of the gas cell, enabling the target gas to come into contact with the light beam so as to achieve spectral absorption. It has been applied to replace gas chambers to achieve effective detection of target gas. Meanwhile, distributed feedback (DFB) laser diode has the characteristics of narrow linewidth and wavelength tunability. It can be linked with HC-PCF and commercial communication fiber to achieve the transmission of optical signals over long distances. Therefore, HC-PCF and DFB laser diode are suitable for the detection system based on infrared spectral absorption method.

In this paper, a highly integrated CH₄ sensing system is proposed. In the system, DFB laser diode and HC-PCF have been applied with other self-developed key modules. The TDLAS technique has been adopted as the core detection method in this system to perform gas sensing experiments. In this way, DFB laser diode has been chosen as the optical source in this system with other relevant optical parts such as fiber optic beam splitter and photodiodes. Compared to other commercial light sources such as QCL lasers, DFB laser diode has the advantage including effective tunable ability and lower heat generation. Therefore, remote detection of target gas can be achieved by its working features. The emitting light beam can be controlled and be modulated to meet the requirements of the TDLAS technique. Compared to our earlier research (Bin L. et al., 2018), the hardware part has been upgraded by using more powerful chips. And the software part has been upgraded by optimizing the control algorithm especially for laser temperature controlling circuit. This part has been updated in many ways. The photoelectric conversion circuit uses InGaAs photodiodes with a higher cost-performance ratio, which reduces the cost while ensuring the conversion performance. Meanwhile, second harmonic signals can be extracted for gas detection by using the technique of wavelength modulation spectroscopy (WMS). The proposed system can be deployed to perform CH₄ detection in large-scale rice fields remotely.

SYSTEM STRUCTURE AND DETECTION THEORY

System structure

The functional diagram of the proposed CH₄ sensing system is shown in Fig. 1. On the left side of Fig. 1 is the independently integrated detection system, which includes optical devices and electronic devices. The acrylic box on the right side of Fig. 1 is the gas cell of the detection system. It is placed in a dry paddy field for detection. Firstly, the detection system on the left side is integrated in an instrument case and can be placed near the measured area, and then communicates with the measured area through an optical fiber. This instrument has been proposed in our previous work. Then, the HC-PCF allows target gas spreads inside the fiber in order to be irradiated by the near infrared light beam. In this way, the gas absorption phenomenon can occur. The optical signal after coming into contact with the measured gas returns to the integrated detection instrument through the optical fiber, and the lost optical signal can be used to calculate the concentration of the gas.

The proposed detection instrument contains many key electrical and optical modules. All the calculation work is completed by the main control chip which is a Digital Signal Processor (DSP), including generating modulation signals, generating laser control instructions, and calculating the gas concentration, etc. The modulation signal includes ramp wave and sine wave. After the modulation signal of the laser is output by the DSP, the laser is driven by a ramp wave signal. It is generated by a high-performance Digital-to-Analog (DAC) chip which type is AD5541. Meanwhile, a Direct-Digital-Synthesizer (DDS) chip is applied to generate sine wave signal and the chip type is AD9851. With the signal modulation, a fiber optic beam splitter (FOBS) is used to divide the output signal of the DFB laser into two equal parts. One part enters the gas cell and undergoes an absorption reaction, and the other part has its light intensity reduced by an optical attenuator (OA). After photoelectric conversion which uses two InGaAs photodiodes, the difference between the two signals contains the information about the gas concentration. In this way, the subtraction of the absorbed signal

and the reference signal can be performed. In this system, it is sent digitally to the DSP by using an Analog-to-Digital (ADC) chip. Finally, the result of detection can be displayed or processed for further applications. The calculated data can be sent to a laptop via the UART port. And the gas information can be received by using software developed by LabVIEW to perform further analysis.

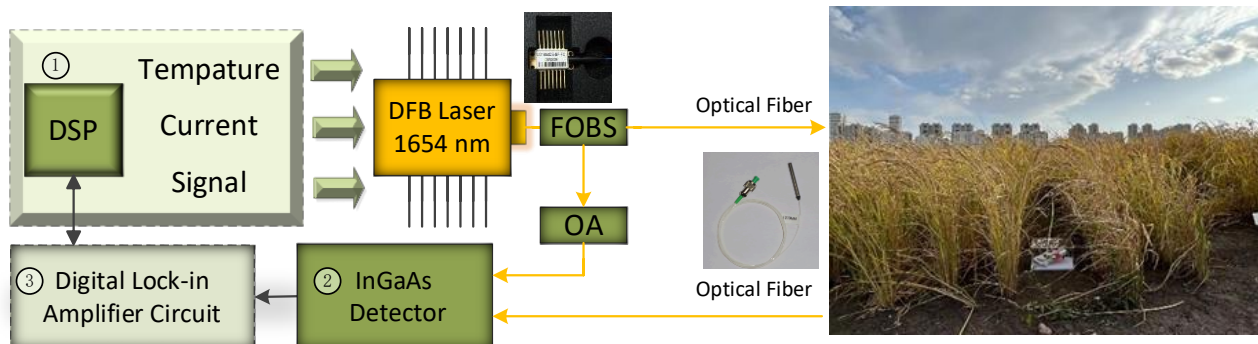


Fig. 1 - Block diagram of rice field methane gas detection system using TDLAS technique

Detection theory

Based on the TDLAS technique, the absorption line of CH₄ must be scanned across periodically in order to detect the optical loss. Fig. 2(a) shows the absorption spectrum of CH₄ around 1654 nm. And its absorption intensity is at the level of 10⁻²¹ cm⁻¹/(molecule cm⁻²). Therefore, in order to meet the requirement of detection, the selection of the laser is very important. In this system, a DFB laser is applied as the main light source of the detection system. Both DFB lasers and Quantum Cascade Laser (QCL) lasers are widely used in the field of gas detection. Compared with QCL lasers, DFB lasers are more likely to use optical fibers for long-distance signal transmission, which is applicable for the remote detection of methane gas in paddy fields. At the same time, DFB lasers are cheaper than QCL lasers, which also helps to carry out relevant experiments. The applied DFB laser has the center wavelength around 1654 nm as shown in Fig 2(d). In this infrared region, there are interfering gases such as H₂O and CO₂, which are also shown in Fig. 2 to demonstrate their absorption lines. It can be seen that their absorption intensity is much weaker than the intensity of CH₄. Their absorption intensity are 4 orders of magnitude lower than that of methane as shown in Fig. 2(b) and Fig. 2(c). Therefore, when detecting methane in this interval, water and carbon dioxide in the atmosphere hardly cause any interference. High selectivity is an advantage of the infrared spectroscopy method. When using traditional gas detection methods, it is very easy to be affected by interfering gases.

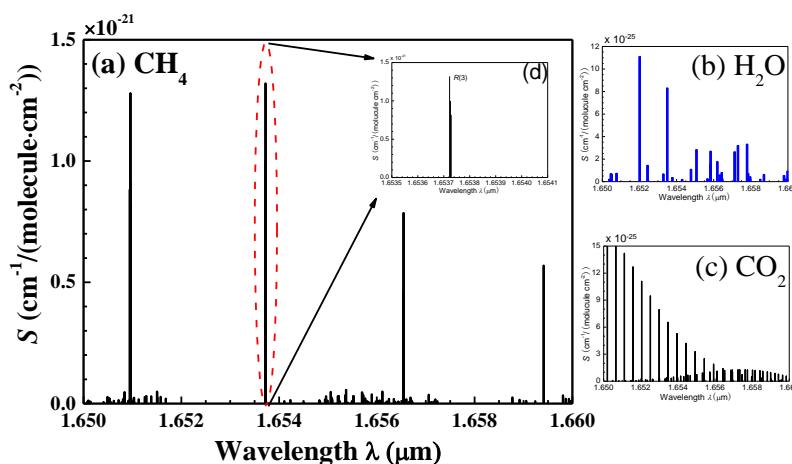


Fig. 2 - Absorption line selection of CH₄ (a) (d) and the absorption intensity of the interfering gas H₂O (b) and CO₂ (c) in this infrared region

The detection theory of absorption spectroscopy is governed by the Beer-Lambert law. The calculation is determined by the optical loss of spectral intensity (W/m²) while radiation interacts with gas molecules. The expression of the coefficient $\tau(\nu, t)$ is shown in Eq. (1). The transmitted intensity and the initial light intensity can be expressed as $I(\nu)$ and $I_0(\nu)$ respectively. The relationship can be seen as follows:

$$\tau(\nu, t) = \frac{I(\nu)}{I_0(\nu)} = \exp[-\alpha(\nu, t)LC] \tag{1}$$

where $\alpha(v, t)$ (cm^{-1}) in Eq. (1) is the absorption coefficient at frequency v (cm^{-1}). In this equation, C is the mole fraction of the target gas and L is the effective optical path length. Based on TDLAS and WMS technique, the DFB laser is tuned by a low-frequency repetitive ramp waveform with the period of T_{ramp} . Meanwhile, a high-frequency sine wave signal is added to the ramp wave. Its angular frequency is expressed as ω_{sin} . The expressions of the above signals and the strength of the light source can be represented in Eq. (2), Eq. (3) and Eq. (4), respectively:

$$u_{ramp}(t) = a + \frac{a}{T_{ramp}}(t - T_{ramp}) \quad (2)$$

$$u_{sin}(t) = b \sin(\omega_{sin}t) \quad (3)$$

$$I(t) = I_0[1 + mu_{ramp}(t) + mu_{sin}(t)] \quad (4)$$

In above equations, $u_{ramp}(t)$ and $u_{sin}(t)$ are the voltage of ramp signal and sine signal, a , b , m and T_{ramp} are the amplitude of ramp signal, the amplitude of sine signal, the intensity modulation coefficient and the cycle of ramp signal, respectively. The waveform of a standard ramp wave rises in a straight line, then falls sharply in one cycle period. In this paper, the cycle period of the modulating ramp wave was set as 10 Hz. The sine wave signal was set as 5 kHz. The sine wave signal is also set as the modulating signal and it is mounted on the ramp signal for modulation.

Therefore, the relationship of gas concentration and 2f harmonic signal of system can be calculated according to the equations. The ramp signal and the sine signal in above equations can be generated by DFB lasers which are under the control of the self-developed circuits.

MATERIALS AND METHODS

Laser driving circuit

According to the TDLAS technique, laser diode must be linearly controlled to scan across the gas absorption line. The driving current and operating temperature of laser diodes were precisely regulated using self-developed control circuits. Compared to the previous design, the main controller chip of the laser driving circuit was upgraded from TMS320F28335 to TMS320C28346. The main computing frequency reaches 300 MHz, with a cycle time of approximately 3.33 ns, resulting in a processing performance nearly twice that of the previous design. In this way, the floating-point performance has been enhanced and the algorithm for the detection system can be processed effectively especially for the digital lock-in part which involves complex real-time computing. Meanwhile, the TMS320C28346 also has abundant on-chip peripherals including six 32-bit timers, nine 16-bit timers, 258K 16-bit SARAM and serial port peripherals. However, there is also a problem of the new MCU in the system. Its package type is 256-ball plastic ball grid array (BGA) which is not convenient for hand soldering. After several attempts, the chip was successfully soldered on the board by using a hot air gun. The board has four layers as shown in Figure 3(a) which are top layer, bottom layer and two internal power layers. The completed board is shown in Figure 3(b).

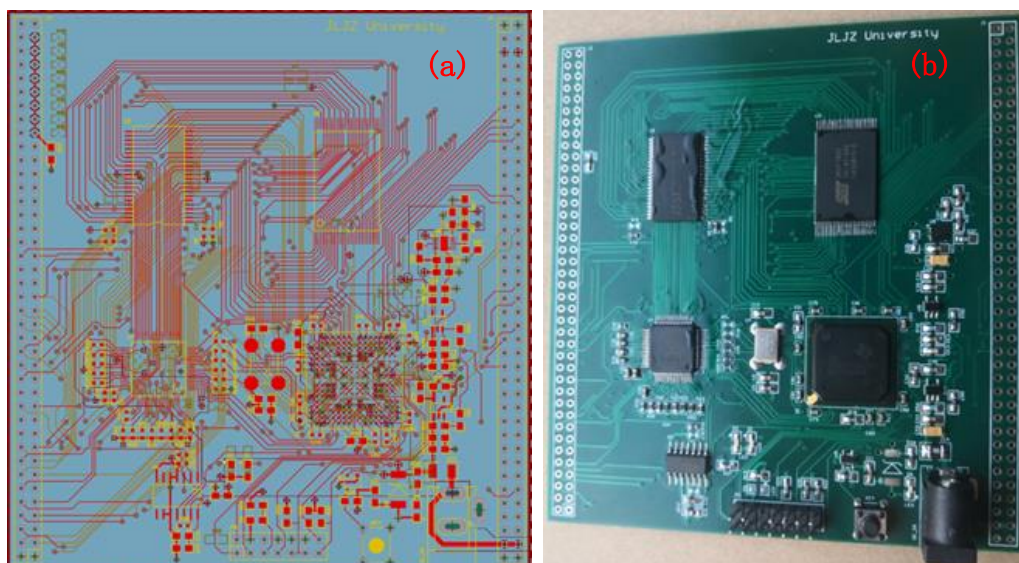


Fig. 3 – Self-developed PCB drawing (a) and soldered circuit board of the main controller

Laser temperature controller

The DFB laser has the characteristic that its output wavelength changes with the change of its operating temperature. Therefore, it is very important to control its operating temperature. On the one hand, if the temperature of the laser is too high, it may shorten its lifespan or cause damage to it. On the other hand, controlling the output wavelength of the laser by changing its temperature is very effective, especially in the detection system using TDLAS technology. Therefore, in this paper, a temperature control circuit for the DFB laser is developed based on the Thermoelectric Cooler (TEC) control circuit. The DFB laser used in the system has a built-in TEC module. Therefore, through the TEC control circuit, real-time and precise control of the laser's temperature can be achieved, thus enabling effective control of its output wavelength. The TEC control chip used in the system is the ADN8831. This chip can effectively control the TEC built into the laser based on the Analog PID algorithm. It can achieve a temperature fluctuation of no more than 0.01 degrees Celsius at the minimum. The photo of the developed circuit is shown in the figure. It is a four - layer PCB. The inner layer is the power layer, and the top and bottom layers are the signal layers. The compensation network of the laser diode is shown in Fig. 4. The resistors of R_{LOW} , R_{MID} and R_{HIGH} can be obtained in datasheet. The voltage V_{SET} , which decides the value of laser temperature, can be obtained by Eq. (5) - (8), as:

$$V_{SET} = \left(\frac{R_3}{R_{TH} + R_2} - \frac{R_3}{R_1} + 1 \right) \times \frac{V_{REF}}{2} \tag{5}$$

$$R_1 = R_{MID} + \frac{R_{MID}(R_{LOW} + R_{HIGH}) - 2R_{HIGH}R_{LOW}}{R_{HIGH} + R_{LOW} - 2R_{MID}} \tag{6}$$

$$R_2 = R_1 - R_{MID} \tag{7}$$

$$R_3 = \frac{R_1(R_1 + R_{LOW} - R_{MID})}{R_{LOW} - R_{MID}} \tag{8}$$

where V_{SET} is the output voltage for setting the temperature and it is can be set by DSP. The resistors of R_{LOW} , R_{MID} and R_{HIGH} set the temperature range which can be determined by specific characters of the laser diodes according to its datasheet, R_{TH} is the resistance of thermistor which is inside the DFB laser diode, V_{REF} is the reference voltage which is 2.5 V generated by the TEC controller chip, R_1 and R_2 are calculated by Eq. (6) and Eq. (7), R_3 represents the compensation resistor and can be calculated by Eq. (8). By using the above equations, as the resistors are chosen, the controlling voltage can be calculated and be generated to control the laser temperate.

The temperature controlling circuit is shown in Figure 4. In this circuit, the resistors and capacitors set the compensation network based on Analog PID. The temperature compensation network composed of these components can effectively approximate the actual value to the set value of temperature. The compensation network in the lower right corner can change the values of these resistors and capacitors by changing the jumper caps as shown in Fig. 4. The main controller chip of ADN8831 is placed on the center location of the board as shown in the photo. The left zone which is selected by the red lines is the temperature setting zone. The temperature value can be set by using serial resistors after calculation. The bottom area of the board is the compensation zone. The resistors and capacitors can be selected by using the jumper cap. According to the Analog PID algorithm, if the response time of the temperature controlling for DFB laser is extremely fast, the stability of the temperature fluctuation will be impacted. Therefore, it is necessary to achieve the balance of stability and response speed by adjusting the components.

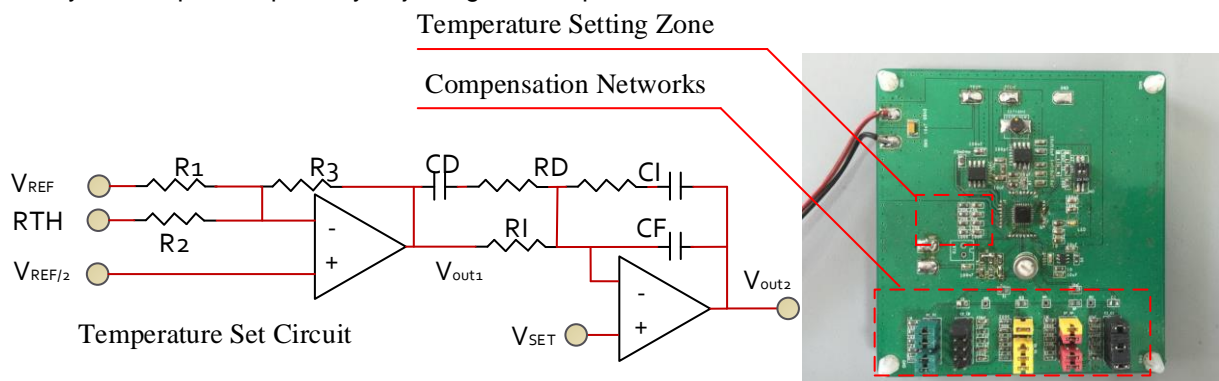


Fig. 4 – Temperature control circuit for DFB laser diode based on Analog PID algorithm

Experiments were carried out to investigate the temperature control performances by using the developed circuit. The stability test of the temperature control module is shown in Fig. 5.

The laser's temperature was stabilized at 24.55 °C within 15 hours. The laser temperature was sampled by an Analog-to-digital circuit. During the experiment, a random period of 100 minutes was selected to show the detailed fluctuation. Then, temperature data was transmitted by the serial port circuit from the DSP board to a computer. The fluctuation of temperature can determine the stability of the laser. The relationship between laser temperature and its output spectroscopy can be determined by carrying out experiments and be expressed as fitting formulas. The small temperature fluctuation within the range of ± 0.02 °C will not affect the stability of the output wavelength. Therefore, the fabricated laser temperature control circuit can effectively control the output wavelength of the laser.

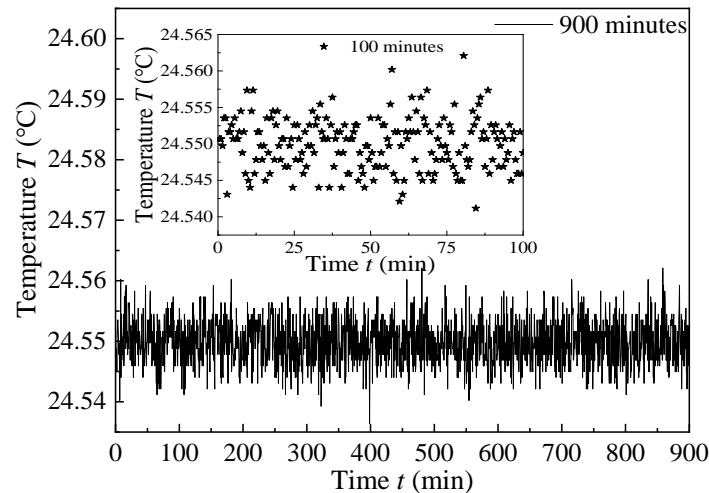


Fig. 5 – Temperature stability test of the proposed control circuit during 15 hours

HC-PCF characteristics

The Hollow-core photonic crystal is applied in this system. It can be used not only for signal transmission but also as a gas cell. The effective wavelength range of the HC-PCF used in the system is 1490-1680. Since the absorption peak of the gas to be measured in the system is around 1654 nm, the optical signal output by the laser can pass through the HC-PCF almost without loss. The transmission loss is only 25 dB/km. Its cross-section of the optical fiber is shown in Fig. 6(a). The center-to-center distance of the holes is 3.8 micrometers. Due to its 95% hollow structural characteristics, the gas to be measured can be filled inside, so that it can fully come into contact with the optical signal. The diameter of the fiber is about 70 μm . Its coating material is acrylate which has a single layer.

The gas diffusion performance of the HC-PCF has been tested in the system. Place the HC-PCF in a gas chamber with dynamic gas mixing, and inject methane gas with a concentration of 2000 ppm into the gas chamber through the method of dynamic gas mixing. Through observation, it can be seen that after approximately 69 minutes, the methane concentration inside the optical fiber is consistent with the external concentration. The speed of gas diffusion is acceptable for experiments such as long-term outdoor monitoring of methane. If it is necessary to increase the diffusion speed, laser drilling can be used to make holes in the outer sheath of the optical fiber. However, it is also necessary to re-evaluate the loss rate of its optical signal at the same time.

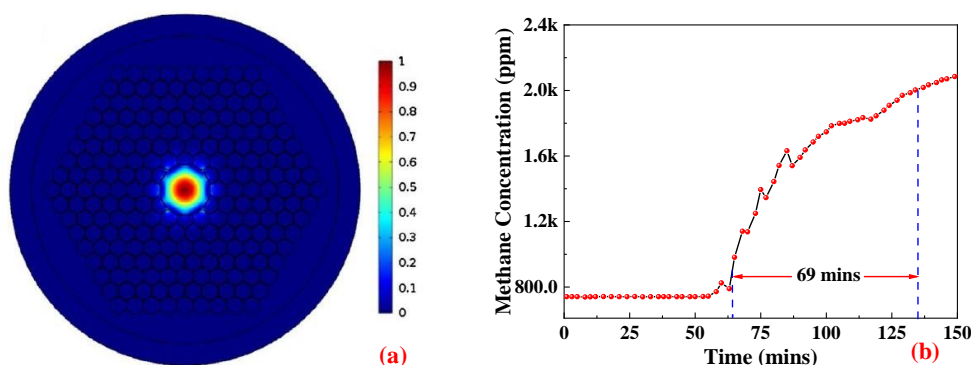


Fig. 6 – Simulation test of the optical structure (a) and the diffusion test of standard gas (b)

RESULTS AND DISCUSSIONS

Spectroscopy test

In order to meet the detection requirements of the detection system, the output spectrum of the laser must be stable and controllable. The output spectrum of the laser is determined by its control temperature and current. Therefore, it is important to evaluate the output spectral characteristics of the laser by changing its control temperature and driving current. The control temperature of the laser can greatly affect the output spectrum of the DFB laser, which is determined by the internal structure of the DFB laser. In contrast, the change in wavelength caused by the control current of the DFB laser is smaller than that caused by the control temperature. Therefore, during the experiment, it is usually the case that the output wavelength is first positioned at the absorption peak of the gas by changing the control temperature of the laser. Then, the wavelength position is finely adjusted by regulating the current of the DFB laser, so as to meet the requirements of the TDLAS detection technology.

In this paper, the proposed circuit controls the wavelength and the wavelength was tested by using an infrared spectrometer as shown in Fig.7. As can be seen in Fig.7(a), when the driving current of the laser is constant and the control temperature of the laser is changed, its central wavelength changes linearly. The injection current of the laser is set to 70 mA, and the adjustment coefficient between the temperature and the wavelength is approximately 0.115 nm/°C. In contrast, when the control temperature of the laser is kept constant, the driving current is changed, and the five sets of measured data are shown in Fig.7(b). The DFB circuit controls its current, which is increased from 40 mA to 80 mA with a step size of 10 mA. As shown in the figure, when the temperature of the laser is constant, the current of the laser is changed, and the adjustment coefficient between the current and the wavelength is measured to be approximately 0.014 nm/mA. Therefore, the control circuit proposed in this paper can effectively control the temperature and current of the laser, thus achieving effective control of its output wavelength and meeting the requirements of the detection system.

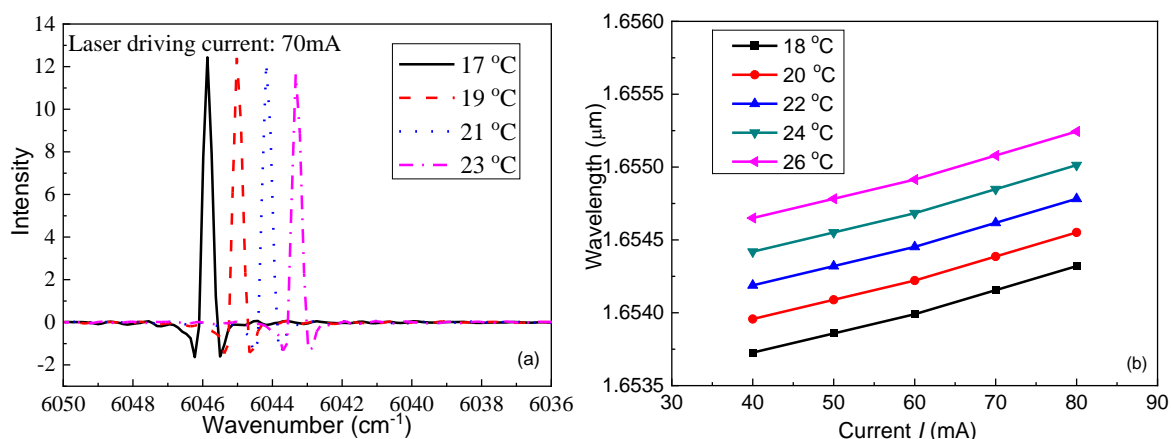


Fig. 7 – Spectroscopy test under the condition of constant temperature (a) and constant current (b)

Response time test

Since the detection and processing speed of infrared gas detection is very fast, the response time of the system is mainly determined by the volume of the gas chamber and the flow rate of the gas distribution. The detection system can detect the change of the concentration in the gas chamber in real time, so the data acquiring time of the DSP chip can be considered as the response time of the system. The calculation time of the DSP chip is very fast and the key signal which can be represent gas concentration can be obtained instantly. Compared to the traditional sensors, TDLAS technique has the advantage of fast response. This TDLAS based detection system performs an average calculation on the measured gas concentration, and the obtained average gas concentration is displayed on an LCD screen every 2 seconds. When the gas concentration in the gas chamber is changed, the fluctuation of the gas concentration will cause the detected second harmonic to fluctuate, as shown in Figure 8.

A gas mass flowmeter is applied in the system and it is required to manually adjust the knob to change the concentration during the process of gas detection. By adjusting the concentration, there is a certain slope at the rising edge of the concentration. Compared to the traditional method of gas distribution, dynamic gas distribution is the method that has better accuracy. The specific gravities of different gases need to be calculated and used to adjust the mass flowmeter in the experiment. When the target concentration is quickly

reached, the gas concentration in the gas chamber fluctuates as shown in Figure 8. Continuing to adjust the concentration when the concentration is not yet stable will cause the concentration of the gas chamber to oscillate. By measuring the Peak-to-Peak Voltage (PPV) value of the second harmonic, real-time fluctuations in gas concentration can be obtained.

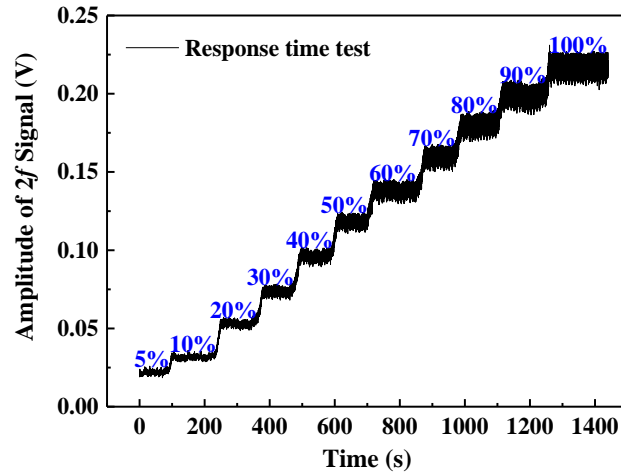


Fig. 8 – Response time test of the proposed detection system using 2f harmonic signal

Error test

The detection error of the detection system can be evaluated by using the dynamic gas mixing method. The dynamic gas mixing method can keep the gas concentration in the gas chamber approximately constant, and can change the gas concentration in the gas chamber within a short period of time. In the experiment, the high-concentration range and the low-concentration range were tested respectively, as shown in Fig. 9. For the experiments using high concentration of methane gas, the N₂ and pure CH₄ gas was mixed together after calculation of their relative height and volume. For the low concentration experiments, the pure liquid methane will be replaced by 1% standard gas to guarantee accuracy. In the high-concentration range, the error is relatively small, which is because the concentration inside the gas chamber using the dynamic gas mixing method is relatively stable, as shown in Fig. 9(a). In the low-concentration range, the error increases as shown in Fig.9(b). By calibrating the gas concentration with the second harmonic, the detection sensitivity can be further enhanced.

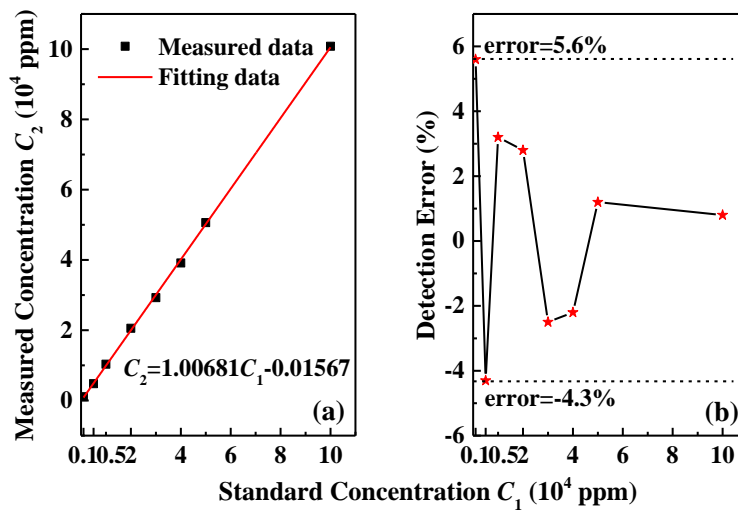


Fig. 9 – Error test of the measured methane gas using standard gas

Detection limit test

In combination with the WMS technology, detection sensitivity can be further improved. Through the sine wave and square wave of the same frequency and phase generated by the DDS, the first harmonic and the second harmonic after gas absorption can be obtained. Among them, the second harmonic can more effectively characterize the gas concentration, and the experiment carried out is shown in Fig.10.

In Fig.10(a), it can be seen that within the detection range, the second harmonic can be effectively extracted and is still clearly visible at 600 ppm. In Figure (b), when the gas chamber is filled with pure nitrogen, the fluctuation of the second harmonic can be evaluated, which is within the range of 1748 - 1754 mV. By increasing the effective absorption optical path, the detection lower limit of the system can be further reduced. In subsequent experiments, by using HC-PCF, the effective absorption optical path can be greatly increased, thereby improving the detection sensitivity of the system.

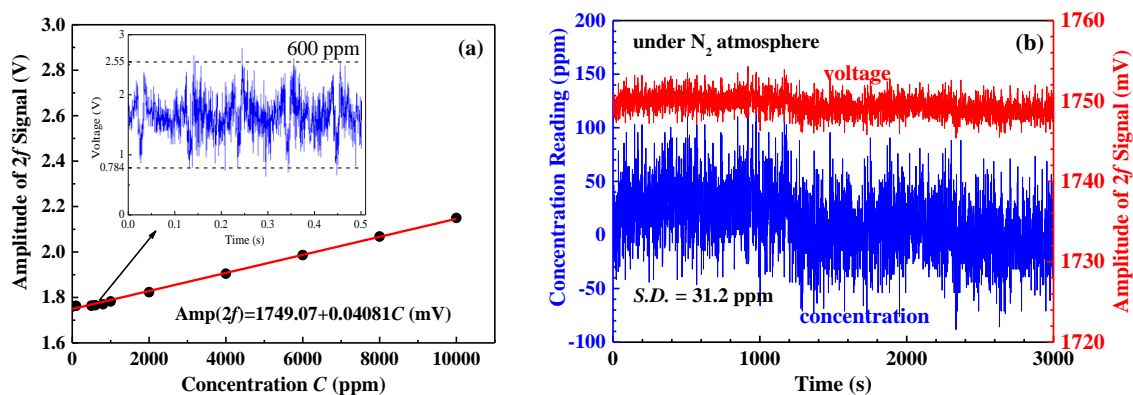


Fig. 10 – Detection limit test using 2f harmonic signal (a) and mixed standard gas (b)

CONCLUSIONS

The proposed methane detection system involves a DFB laser, InGaAs photodiodes, HC-PCF and updated circuits such as the DSP28346 circuit for laser controlling. By using the key components, the detection system has the ability to perform accurate remote detection of target gas. Through spectral testing, the stability of the laser's control temperature and driving current was verified, and the respective control coefficients were obtained. By conducting a variety of gas detection experiments, the effectiveness and stability of the detection system for detecting methane gas were developed. In subsequent research work, the use of HC-PCF will be increased to further improve the detection sensitivity of the detection system. Combined with this new type of optical fiber, the developed system can be used for large-scale methane gas monitoring in paddy fields.

ACKNOWLEDGEMENT

The authors wish to express their gratitude to Jilin Association for Higher Education (JGJX2020D246), the Education Department of Jilin Province of China (JKH20230334KJ), the Science and Technology Department of Jilin (20230203022SF, 20240302064GX), Changchun Development and Reform Commission (2022C045), and Undergraduate Innovation and Entrepreneurship Training Program Funding Project 2024 of Jilin Jianzhu University (S202410191078), for the generous support of this work.

REFERENCES

- [1] Arianti, F.D., Pertiwi, M.D., Triastono, J., (2023), Study of Organic Fertilizers and Rice Varieties on Rice Production and Methane Emissions in Nutrient-Poor Irrigated Rice Fields. *Sustainability*, vol.14, 5919. Switzerland; <https://doi.org/10.3390/su14105919>
- [2] Bai, Y.; Dai, Q.; Hai, J., Wang Q., Liao D., Liu G., Wang Y., Huang J., Zhang R., Siddig A. A. H., Bao W., Yang G., (2023), Manganese Slag Amendment Reduces Greenhouse Gas Emissions from Paddy Soil. *Atmosphere*, vol.14, 131. Switzerland; <https://doi.org/10.3390/atmos14010131>
- [3] Bai, Y.R., Yu H., He C., Miao Z., Rui D., Zhang Y., Lin X., (2021), A numerical simulation of a near-infrared three-channel trace ammonia detection system using hollow core photonic crystal fibre. *Optik*, vol.227, 166006, Germany; <https://www.sciencedirect.com/science/article/abs/pii/S0030402620318192?via%3Dihub>
- [4] Bin L., Shuocheng Z., Yaodan C., (2018), Development and Integration of a CO Detection System Based on Wavelength Modulation Spectroscopy Using Near-Infrared DFB Laser, *Journal of Spectroscopy*. vol.2018, 1707252, U.S.A.; <https://onlinelibrary.wiley.com/doi/10.1155/2018/1707252>
- [5] Catia, L., Sonia, O., P., Nelia, A., Maxime L., Mederic L., Florinda M. C., Joao L. P., Christophe C., Carlos M., (2021), Cortisol in-fibre ultrasensitive plasmonic immune-sensing. *IEEE Sensors Journal*, 21 (3), 3028-3034, U.S.A.; <https://ieeexplore.ieee.org/document/9201317>

- [6] Dar, S.A., Qazi, G, (2020), Investigation and comparison of sensitivity of LiDAR to laser physical parameters at 750 m using different detection techniques. *Optik*, vol.219, 165281, Germany; <https://www.sciencedirect.com/science/article/abs/pii/S0030402620311177?via%3Dihub>
- [7] Davis, N.M., Hodgkinson, J., Francis, D., Tatam R.P., (2016), Sensitive detection of methane at 3.3 μm using an integrating sphere and Inter-band Cascade Laser. *Optical Sensing and Detection IV*, vol.9899, 98990. Belgium; <https://www.spiedigitallibrary.org/conference-proceedings-of-spie/9899/1/Sensitive-detection-of-methane-at-33-%c2%b5m-using-an-integrating/10.1117/12.2227131.short>
- [8] Gao, Z.R., Ni, J.Z., Yan, J.Q., Jiang Q., (2018), Water-efficient sensing method for soil profiling in the paddy field. *International Journal of Agricultural and Biological Engineering*, vol.11(4), 207, China; <https://ijabe.org/index.php/ijabe/article/view/3593>
- [9] Jiao, Y.X., Fan, H.J., Gong, Z.F., Yang, K., Shen, F., Chen, K., Mei, L., Peng, W., Yu, Q., (2021), Trace CH_4 Gas Detection Based on an Integrated Spherical Photoacoustic Cell. *Applied Sciences*, vol.11, 4997, Switzerland; <https://www.mdpi.com/2076-3417/11/11/4997>
- [10] Jikun H., Yangjie W., (2014), Financing Sustainable Agriculture Under Climate Change. *Journal of Integrative Agriculture*, vol. 13, Issue 4, pp.698-712, China; <https://www.sciencedirect.com/science/article/pii/S209531191360698X?via%3Dihub>
- [11] Ma, J.L., Chen, W.Y., Niu, X.J., Fan Y.M., (2019), The relationship between phosphine, methane, and ozone over paddy field in Guangzhou, China. *Global Ecology and Conservation*, 17, U.S.A.; <https://www.sciencedirect.com/science/article/pii/S2351989418304955?via%3Dihub>
- [12] Maxime, L., Mederic, L., Marc, D., Karima C., Erik G., Christophe C., (2023), Electro-plasmonic assisted biosensing of proteins and cells at the surface of optical fibre. *Biosensors & Bioelectronics*, vol.220, 114867, England; <https://www.sciencedirect.com/science/article/abs/pii/S0956566322009071?via%3Dihub>
- [13] Mujiyo, M., Sunarminto, B.H., Hanudin, E., Widada J., Syamsiyah J., (2017), Methane production potential of soil profile in organic paddy field. *Soil Water Res*, vol.12(4), 212-219. Czech; https://www.agriculturejournals.cz/artkey/swr-201704-0004_methane-production-potential-of-soil-profile-in-organic-paddy-field.php?back=%2Fsearch.php?query%3DMethane%2Bproduction%2Bpotential%2Bof%2Bsoil%2Bprofile%2Bin%2Borganic%2Bpaddy%2Bfield%26sfrom%3D0%26spage%3D30
- [14] Palmer, P.I., Feng, L., Lunt, M.F., (2021), The added value of satellite observations of methane for understanding the contemporary methane budget. *Philosophical transactions of the royal society a-mathematical physical and engineering sciences*, vol.379, 20210106. England; <https://royalsocietypublishing.org/doi/10.1098/rsta.2021.0421>
- [15] Rajasekar, P., Selvi J.A.V., (2022), Sensing and Analysis of Greenhouse Gas Emissions from Rice Fields to the Near Field Atmosphere. *Sensors*, vol.22, 4141. Switzerland; <https://doi.org/10.3390/s22114141>
- [16] Rizzo, A., Boano, F., Revelli, R. (2015) Groundwater impact on methane emissions from flooded paddy fields. *Advances in water resources*, vol.83(Sep.), pp.340-350. U.S.A.; <https://www.sciencedirect.com/science/article/abs/pii/S0309170815001529?via%3Dihub>
- [17] Xie, B.H., Zhou, Z.X., Zheng, X.H., Zhang W., Zhu J.G., (2010), Modeling methane emissions from paddy rice fields under elevated atmospheric carbon dioxide conditions. *Advances In Atmospheric Sciences*, vol.27(1), 100-114, England, <https://link.springer.com/article/10.1007/s00376-009-8178-4>
- [18] Xu, X.Y., Zhang, M.M., Xiong Y.S., Yuan J.F., Shaaban M., Zhou W., Hu R.G., (2020), The influence of soil temperature, methanogens and methanotrophs on methane emissions from cold waterlogged paddy fields. *Journal Of Environmental Management*, vol.264, 110421. U.S.A.; <https://www.sciencedirect.com/science/article/abs/pii/S0301479720303558?via%3Dihub>
- [19] Zhang, G.B., Zhang, W.X., Yu, H.Y., Ma J., Xu. H., Yagi K., (2015), Fraction of CH_4 oxidized in paddy field measured by stable carbon isotopes. *Plant and Soil*, vol.389(1/2), pp.349-359, Netherlands; <https://link.springer.com/article/10.1007/s11104-014-2365-5>
- [20] Zhang, G.B., Ji, Y., Liu, G., Ma J., Xu H., (2014), Carbon isotope fractionation during CH_4 transport in paddy fields. *Science China - Earth sciences*, vol.57(07), pp.1664-1670, China; <https://link.springer.com/article/10.1007/s11430-014-4879-3>

OPTIMIZATION OF DAMAGED CORN KERNEL RECOGNITION ALGORITHM BASED ON A DUAL-LIGHT SYSTEM

基于双光系统的破损玉米籽粒识别算法优化

Yuchao REN¹⁾, Bin QI ^{*1,2)}, Xiaoming SUN^{*1,2)}, Jiyuan SUN¹⁾, Tengyun MA¹⁾, Yuanqi LIU¹⁾, Bohan ZHANG¹⁾, Qiong WU³⁾

¹⁾ College of Agricultural Engineering and Food Science, Shandong University of Technology/ China;

²⁾ School of Fine Arts and Design, Shandong University of Technology, Zibo City, China.

³⁾ Zibo Normal College/ China

Tel: +86-15966964198; E-mail: sdutid@163.com

Tel: +86-13581019376; E-mail: 3282110@qq.com

DOI: <https://doi.org/10.35633/inmateh-75-67>

Keywords: Corn Kernel, Object Detection, Light Angle, YOLOv8n

ABSTRACT

To enhance real-time detection of corn breakage rate under dim conditions, this study designed a dual-light (top/backlight) sampling system. By comparing four datasets (top-scattered, top-clustered, backlight-scattered, backlight-clustered), the algorithm optimized with backlight-scattered data achieved optimal accuracy (79.6%). A lightweight YOLOv8n_gcd model was proposed, integrating Ghost convolution in the backbone to reduce redundancy, attention mechanisms for feature enhancement, and depthwise separable convolutions in the neck. The optimized model reduced FLOPs by 24% and increased FPS by 165%, offering an efficient, low-cost solution for agricultural quality inspection with theoretical and practical value.

摘要

为了增强在昏暗条件下玉米破损率的实时检测，本研究设计了一种双光（顶部/背光）采样系统。通过比较四个数据集（顶光-籽粒分散、顶光-籽粒聚集、背光-籽粒分散、背光籽粒聚集），得出背光籽粒分散的数据优化的算法达到了最佳（79.6%）之后利用该数据集训练出一种轻量级的 YOLOv8n_gcd 模型，将 Ghost 卷积集成在骨干网中以减少冗余，将注意力机制用于特征增强，并在颈部进行深度可分离卷积。优化后的模型将 FLOP 降低了 24%，FPS 提高了 165%，为农业质量检测提供了一种高效、低成本的解决方案，具有理论和实践价值。

INTRODUCTION

Corn holds the position as the largest - scale grain crop in China (Cui *et al.*, 2019). With the progressive development of agricultural mechanization, the mode of corn harvesting in China is undergoing a significant transition from ear - based harvesting to direct kernel – harvesting (Li, 2017; Zhao *et al.*, 2020). This shift in the harvesting method represents a crucial step in modernizing corn production, enabling a more efficient and cost-effective approach. It has thus become an inevitable trend in the mechanized production of corn in the country (Zhu *et al.*, 2021). The operational quality of corn harvesting exerts a profound impact on both its yield and economic value. The breakage rate and impurity content serve as pivotal metrics for evaluating the performance of direct - kernel harvesters (Zhao *et al.*, 2025; Cui Y.S., 2024; Yang *et al.*, 2018). However, the traditional manual detection method is fraught with limitations. It is characterized by high labor intensity and low detection efficiency, which not only burdens the workforce but also fails to provide real-time and accurate feedback of the breakage rate and impurity content to the automatic control system of the harvester. As a result, timely adjustments to the operation parameters cannot be made, leading to potential substantial harvesting losses (Xu *et al.*, 2021; Wu *et al.*, 2024). This in turn has significantly impeded the advancement of intelligent harvesting technologies for domestic corn direct - kernel harvesters.

Convolutional Neural Networks (CNvolutional Neural Networks, CNNs) in deep learning have demonstrated exceptional performance improvements in cutting-edge fields such as object recognition, image classification, and image segmentation.

Yuchao Ren, M.S. Agr.; Bin Qi Assoc. Prof. Ph.D. Eng.; Xiaoming Sun, M.S. Eng., Lecturer; Jiyuan Sun, M.S. Agr.; Tengyun Ma, M.S. Agr.; Yuanqi Liu, M.S. Agr.; Bohan Zhang, M.S. Agr.; Qiong Wu, Senior Art and Craft Specialist.

Liu *et al.* showed significant advantages in training multi-scale image input models compared to single-scale scene classification strategies (Liu *et al.*, 2018). Since the introduction of ResNet, residual networks have successfully addressed the long-standing vanishing gradient problem enabling unrestricted network depth and garnering widespread attention in computer vision (He *et al.*, 2016). However, deep learning-based image classification tasks often suffer from excessive parameters and bulky models, posing challenges for deployment on mobile devices. To address this, Andrew *et al.* proposed MobileNets, a lightweight convolutional neural network that achieves efficient computation on mobile and embedded systems while reducing memory consumption, thereby streamlining model parameters and computational load (Howard *et al.*, 2017). However, this simplification comes at the cost of some accuracy loss. In MobileNetV2, Mark *et al.* introduced an inverted residual structure, achieving higher accuracy with the same computational cost while minimizing information loss (Sandler *et al.*, 2018).

In the field of damaged corn kernel identification, Velesaca *et al.* proposed a two-stage static detection algorithm for corn kernel breakage (Velesaca *et al.*, 2020). This method first segments individual kernels from clustered corn images using Mask R-CNN, then classifies them via a custom-designed network (CK-CNN). Han *et al.* introduced an independent component analysis (ICA)-based method for germ feature detection, selecting germ-representative components from RGB color space and integrating nine additional germ-area features, yielding a minimal area error of 0.7% compared to manual inspection (Han *et al.*, 2010). Li *et al.* developed an image acquisition device and an improved YOLOv4-tiny model for broken kernel detection, achieving 93.5% and 93% precision for intact and damaged kernels, respectively, with lower detection error than manual methods, demonstrating real-time applicability (Li *et al.*, 2021). Xu *et al.* selected corn varieties Denghai 518, Xundan 20, and Zhengdan 958, constructing a CNN model using the Keras deep learning framework, achieving an average recognition rate of 95.49% (Xu *et al.*, 2020). Quan *et al.* investigated corn kernel selection and classification, developing a lightweight convolutional neural network. By optimizing prototype parameters, they achieved optimal performance with a detection accuracy of 96.50% and an effective sorting rate of 97.51% for four categories of kernels (high-quality, rejected, germ-side, and endosperm-side) (Quan *et al.*, 2020).

As mentioned earlier, it is necessary to research an algorithm that is adaptable to dark conditions and is lighter and easier to deploy on mobile devices.

DUAL LIGHT DEVICE DESIGN

Lighting System Design

To address image acquisition challenges in low-light environments, this study designed a dual-light system with engineered multi-angle coordination (upper and lower illumination). Comparative experiments were conducted using datasets under distinct lighting conditions to evaluate optimal angles for image capture. Hybrid-angle lighting (simultaneous upper/lower illumination) was excluded to ensure experimental comparability. The core light source is the Leichu Lighting 600×600 direct-emitting LED panel which named Model LZ-600D, whose technical specifications are compared with industry standards in Table 1.

Table 1

Comparison of Main Light Source Technical Parameters and Industry Standards

Parameter	Light emission type	Rated power [W]	Luminous flux [lm]	Illuminance uniformity [%]	Color temperature [K]	Color Rendering Index (CRI)
Leichu 600×600 LED Panel	COB-integrated direct/edge-lit	80	9,600	92 (at 0.5 m distance)	6,500 ± 200	Ra ≥ 96
Industry Standard (Industrial Grade)	Direct/edge-lit	50–100	8,000–12,000	≥85	5,000–6,500 (recommended)	Ra ≥ 90 (for precision inspection)

Mechanical Structure and Optical Layout

A modular dark chamber (80 cm × 50 cm × 50 cm) was constructed to simulate post-threshing conditions (ambient light <10 lux). The chamber's interior was coated with black light-absorbing paint (reflectivity <2%), and labyrinthine light seals (attenuation >99%) were installed at joints to eliminate stray light interference. A circular aperture (8 cm diameter) was integrated at the top for imaging.

The lighting system comprised two configurations (Fig. 2):

Top Lighting: A ring-shaped array of 24 COB LED modules (3W each) with a three-layer homogenizing structure (diffuser plate, micro-prism film, anti-glare mesh) to reduce illuminance gradients to <5%.

Backlighting: An identical LED array and homogenizer positioned at the chamber base to create a planar light source.

A co-axial optical path (light source–camera–sample alignment) was implemented to minimize edge shadows and ensure accurate kernel morphology recognition.

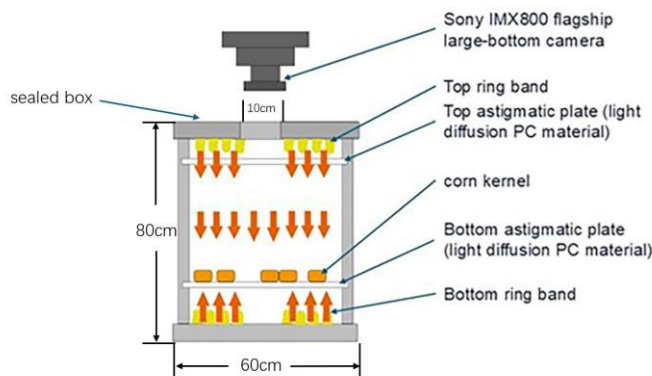


Fig. 2 – Schematic layout of the sampling device

Imaging System Design

The imaging system featured:

1) Camera: A Sony IMX800 image sensor (1/1.49", 54 MP) with 82% quantum efficiency at 550 nm, readout noise of $2.3e^-$, and dynamic range of 73 dB.

2) Lens: A Computar MLH-10X fixed-focus lens (25 mm focal length, f/2.8 aperture).

3) Stage: A three-axis precision stage with ± 50 mm horizontal range, <0.01 mm repeatability, and vertical electric focusing (0–100 mm travel). A laser rangefinder (0.1 mm accuracy) and dual-axis gimbal (15° pitch, 10° roll correction) were integrated to mitigate mechanical misalignment and vibration-induced imaging errors.

MATERIALS AND METHODS

Target Materials

The corn kernels harvested in the Northeast region of China during late September 2024 were chosen as the representative samples for this study. Two distinct types of corn kernels were the focus of detection: intact corn kernels, as illustrated in Fig. 3 (a), and damaged corn kernels, as shown in Fig. 3 (b).



Fig. 3 – Types of corn kernels

a) Complete corn kernels; b) Damaged corn kernels

During the corn - threshing process, kernel damage can occur due to multiple factors. Mechanically, the use of certain threshing machines, such as those equipped with round - headed spike - tooth mechanisms, can cause physical damage to the kernels. Additionally, improper operational practices, including sub-optimal moisture content levels (either too high or too low) and uneven feeding of corn materials into the threshing machine, can also contribute to kernel breakage.

Image Acquisition

Image collection was conducted within the established image - acquisition system. Initially, the enclosure of the system was opened, and the corn kernels designated for imaging were carefully placed inside. Subsequently, the enclosure was sealed to create a controlled, relatively dark environment that mimics the real-world conditions of post-threshing. Depending on the experimental setup, either the top - light or the back - light was activated. The height of the camera was then adjusted until the entire area of the corn kernels was within the field of view. For each batch of corn kernels, two images were captured: one with the top - light illumination and another with the back - light illumination. After image acquisition, the corn kernels were replaced, and the process was repeated. In total, 684 image pairs were collected.

Typically, the quality of the dataset significantly influences the predictive performance of subsequent deep - learning algorithms. To enhance the generalization and robustness of the network model, conventional data - augmentation techniques, such as noise injection, exposure adjustment, horizontal and vertical flipping, and random rotation, are often employed. However, in this experiment, the primary objective was to compare the efficacy of top - light and back - light illumination for detecting damaged corn kernels. Therefore, data - augmentation techniques were not applied to maintain the integrity of the original lighting - condition data.

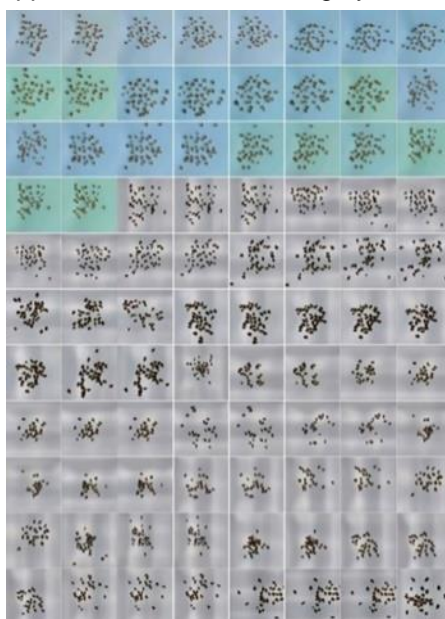


Fig. 4 – Sample images collected during the experiment

Image Calibration and Processing

After image acquisition, the datasets were categorized into four classes: top-scattered, top-clustered, backlight-scattered, and backlight-clustered. Subsequently, images within each subfolder were partitioned into training, validation, and test sets at a ratio of 6:2:2 to ensure balanced data distribution.

The images in each set were then imported into the Labelling software, a widely - used tool in the field of image recognition for manual annotation. In this study, the only objects of interest were intact and damaged corn kernels. Therefore, only these two types of kernels were annotated within the images, enabling the training of the subsequent detection algorithm.

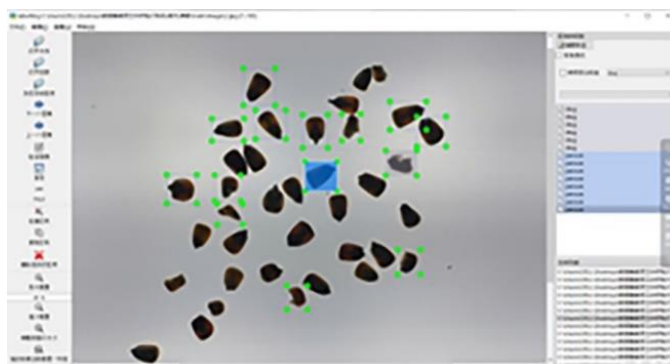


Fig. 5 – Example of an image being annotated in the Labelling software

ALGORITHM OPTIMIZATION AND TRAINING

YOLOv8 Model

Given the real-world application scenario of detecting damaged corn kernels, the YOLOv8n algorithm was selected for this study.

Renowned for its high - speed and efficient object - detection capabilities, YOLOv8n has found extensive applications across various domains. It is a component of the YOLOv8 network model, which supports multiple computer - vision tasks, including image classification, object detection, and instance segmentation. The YOLOv8 architecture consists of five main components: Input, Backbone, Neck, Head, and Output.

Compared to the full - scale YOLOv8 model, YOLOv8n has a more streamlined architecture with fewer model parameters and reduced computational requirements. This makes it particularly suitable for deployment in resource - constrained environments while still maintaining a relatively high detection speed. Despite its lightweight design, YOLOv8n can achieve competitive accuracy in object - detection tasks.

GhostNet

The backbone network architecture of the YOLOv8 model utilizes CSPDarknet. The significant depth and width of this backbone network, while suitable for high precision, incur high computational costs that degrade YOLOv8's overall detection speed. To address this limitation, this chapter introduces the lightweight network GhostNet, replacing the CSPDarknet in YOLOv8 with the hierarchical structure of GhostNet.

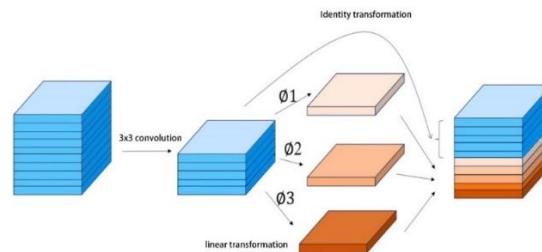


Fig. 6 – Ghost Convolution Process

CBAM Attention Mechanism

When detecting damaged corn kernels, the input images often contain not only the target objects but also substantial complex background information. The deep architecture of YOLOv8, after undergoing multiple convolutional layers, tends to neglect critical target feature information while disproportionately focusing on background features. To address this issue, this chapter integrates a spatial-channel combined attention mechanism—Convolutional Block Attention Module (CBAM) (Woo et al., 2018)—into the backbone network of YOLOv8. This mechanism aims to enhance the network's ability to precisely localize regions of interest (ROIs) and suppress the influence of background noise in remote sensing images. The core principle of the attention mechanism lies in dynamically amplifying the saliency of specific spatial and channel-wise features within input images, thereby refining the extraction of key discriminative features for improved detection accuracy.

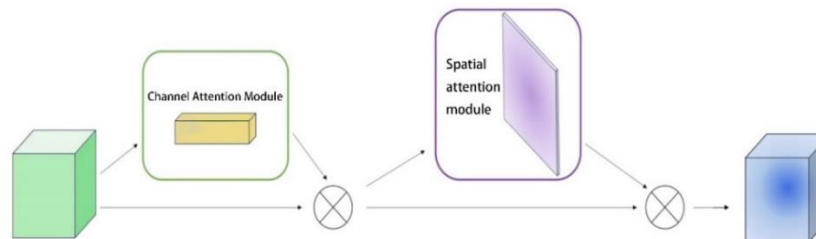


Fig. 7 – CBAM Attention Mechanism

Depthwise Separable Convolution

To further enhance the detection accuracy of the model, an attention mechanism can be introduced in the backbone of the original network. However, the attention mechanism may negatively impact inference speed. Therefore, Depthwise Separable Convolution (DWConv) is incorporated into the neck for localized optimization (Woo et al., 2018).

In the modified YOLOv8 model, standard convolutions in the backbone network are replaced with DWConv. The computation is divided into two steps: depthwise convolution (applying a single filter per input channel) followed by pointwise convolution (combining outputs across channels via 1×1 convolutions). Compared to standard convolutions, this approach drastically reduces computational complexity and accelerates model inference speed. The structure of this modification is illustrated in Fig. 8.

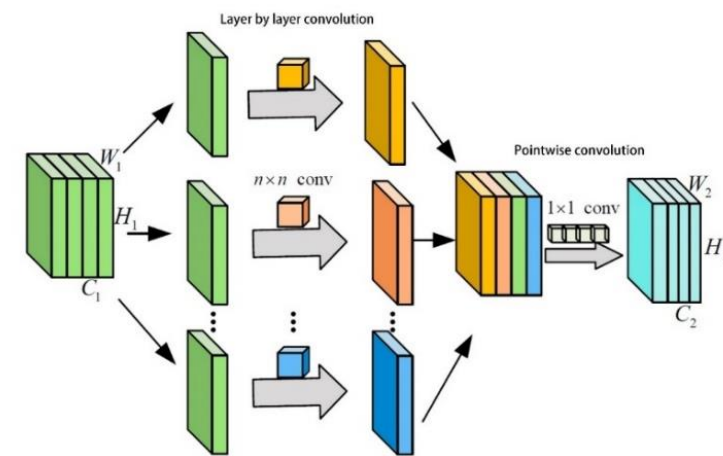


Fig. 8 – Depth Separable Convolutional Structure

MODEL TRAINING AND RESULT ANALYSIS

Training Environment

The experimental setup was configured with a 64-bit Windows 10 operating system. The hardware specifications included a 12th-generation Intel(R) Core (TM) i7-12700KF CPU operating at a base frequency of 3.61 GHz, 32 GB of RAM, and an NVIDIA 3080Ti graphics processing unit (GPU) with 12 GB of dedicated video memory. The deep-learning framework employed was Python 3.11.0, in conjunction with Cuda 12.4 for GPU-accelerated computations. Python 3.8.0 was used as the programming language, and the development environment was PyCharm Community Edition.

Evaluation Indicators

In the process of model training, two key performance indicators, precision and recall, play a vital role in assessing the algorithm's effectiveness. Precision measures the proportion of correctly identified positive samples among all samples predicted as positive, while recall represents the proportion of correctly identified positive samples among all actual positive samples. The mathematical formulas for calculating precision (P) and recall (R) are as follows:

$$P = \frac{TP}{TP+FP} \quad (1)$$

$$R = \frac{TP}{TP+FN} \quad (2)$$

where: *TP* (True Positive) refers to positive samples that are correctly classified as positive; *TN* (True Negative) represents negative samples that are correctly classified as negative; *FP* (False Positive) denotes negative samples that are incorrectly classified as positive; and *FN* (False Negative) indicates positive samples that are incorrectly classified as negative.

Mean Average Precision (*MAP*) is another crucial metric for evaluating the overall performance of the network model. It provides a comprehensive measure of the model's accuracy across different confidence thresholds. The formula for calculating *MAP* is as follows:

$$AP = \int_0^1 p(r) dr \quad (3)$$

$$MAP = \frac{\sum_{i=1}^k AP_i}{k} \quad (4)$$

where: *AP* (Average Precision) represents the average precision for a specific class of objects; and *k* is the total number of classes in the dataset.

In this experiment, four evaluation metrics were utilized to analyze the experimental results and compare them with the baseline network performance. These metrics include MAP_{b50 - 95}, MAP_{m50 - 95}, computational complexity, and inference time. The notation 50 - 95 represents the average MAP calculated at different Intersection over Union (IoU) thresholds, ranging from 50% to 95% with a step size of 5%.

Comparative experiment of datasets from different perspectives

To determine which lighting angle, top - light or back - light, is more suitable for detecting damaged corn kernels in real-world scenarios, the YOLOv8n algorithm was trained using four different datasets: top-scattered, backlight-scattered, top-clustered, and backlight-clustered. All training was conducted under identical experimental conditions, using the hyperparameters tuned from the original model and maintaining consistent training epochs and learning rates. The experimental verification results are presented in Table 2.

Table 2

Verification results of algorithms trained with different datasets

datasets	Precision/%	Recall/%	mAP _{0.5~0.95} (%)	FPS/F-s-1
<i>Top-scattered</i>	89.8	67	70.7	35
<i>Top-clustered</i>	76.6	77.7	61.4	39
<i>Backlight-scattered</i>	85.7	70.6	79.6	31
<i>Backlight-clustered</i>	80.6	74.1	75.4	30

As indicated by the data in Table 2, the Dispersal in the Backlight dataset performs the best, along with the fastest recognition speed. Through horizontal comparison, it was evident that discrete-kernel datasets were more conducive to training, resulting in more accurate models. Moreover, back-light-illuminated datasets generally outperformed top-light-illuminated datasets in terms of training efficiency and model accuracy. Therefore, backlight-scattered dataset was used to train the improved algorithm model.

Data Enhancement

After identifying the backlight-scattered dataset as the optimal training dataset, data preprocessing was performed to enhance sample diversity and enable the network to learn features from multiple perspectives before feeding it into the training pipeline. This process improves the model's ability to analyze feature data and strengthens its generalization capability. Data augmentation techniques—such as rotation, flipping, blurring, and brightness adjustment—were performed on the dataset samples, as illustrated in Fig. 9.

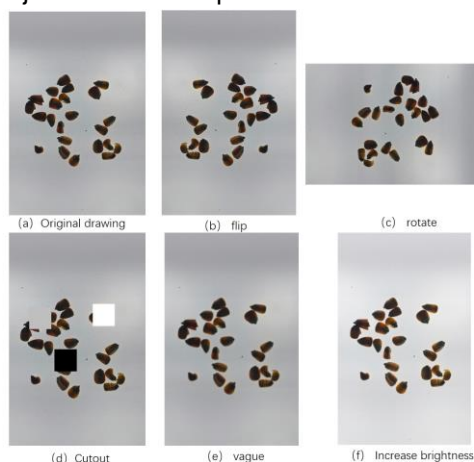


Fig. 9 – Data enhanced image

RESULTS

Ablation Experiment

To verify the effectiveness of the improvements proposed in this article, ablation experiments were conducted to validate the effectiveness of each part. The experimental results are shown in Table 3, where YOLOv8n_g represents the use of Ghost convolution on the basis of YOLOv8n, YOLOv8n_gc represents the use of attention mechanism on the basis of YOLOv8n_g, and YOLOv8n_gcd represents the addition of depthwise separable convolution on the basis of YOLOv8n_gc. Compared to YOLOv8n GFLOPS, YOLOv8n_g has decreased from 8.1 to 5.9, the model's accuracy mAP has decreased from 86.6% to 84.6%, and FPS has increased from 43 to 68. Although using Ghost convolution can significantly improve the model's detection efficiency, it will result in a loss of accuracy.

Compared to YOLOv8n_g, YOLOv8n_gc showed a 0.9 percentage point increase in accuracy and an 8% decrease in FPS with a 0.2 increase in GFLOPs. The attention mechanism can enhance the model's feature extraction ability for targets and improve detection accuracy. Compared to YOLOv8n_gcd, YOLOv8n_gcd reduces computational complexity by 7.97%, increases detection speed by 11fps, and reduces mAP value by 1.05%. Compared to YOLOv8n, YOLOv8n_gcw significantly improves FPS by 60% while slightly reducing model accuracy.

Table 3

Results of ablation experiment

Model	Ghost	CBAM	DWConv	GFLOPs	FPS	mAP
YOLOv8n	-	-	-	8.1	43	86.6%
YOLOv8n_g	√	-	-	5.9	68	84.6%
YOLOv8n_gc	√	√	-	6.1	60	85.5%
YOLOv8n_gcd	√	√	√	6.1	71	84.95%

The specific training dynamics of the YOLOv8n_gcw model are illustrated in Fig. 10. By observing the mAP@50 and mAP@50-95 metrics in Figure 10, it is evident that the model's average precision values stabilize around the 200th epoch, with no significant improvement thereafter. This indicates that the model has converged to its optimal state and does not benefit from further training iterations.

Concurrently, the evaluation metrics for Precision and Recall also exhibit stable and unchanging trends at this stage, suggesting that the model has achieved an optimal balance between detecting true positives and minimizing false positives/negatives. Therefore, additional training epochs are unnecessary, as they would not yield meaningful performance gains.

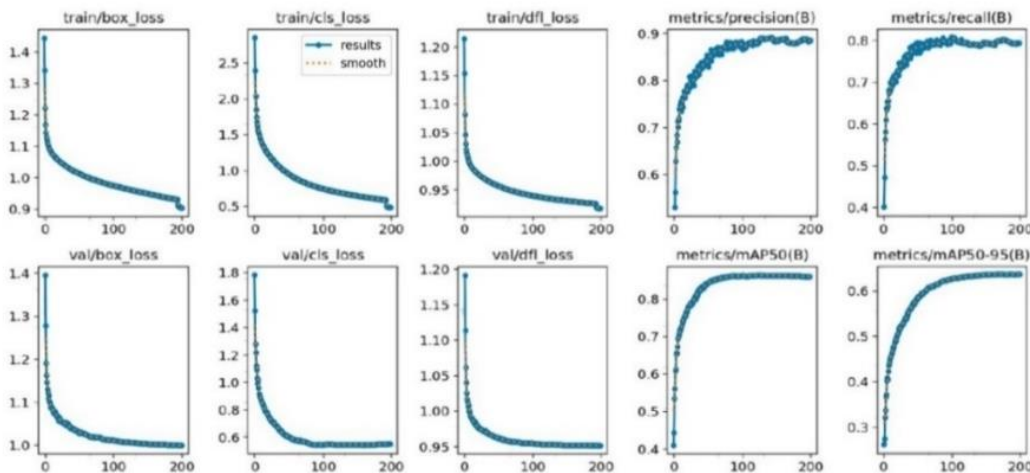


Fig. 10 – YOLOv8n_gcd Training Process Diagram.

Contrast Test

To further demonstrate the effectiveness of the algorithm presented in this chapter, comparative experiments were conducted against classical deep learning object detection algorithms, including Faster R-CNN, SSD, and YOLOv7 (Wang et al., 2023). The experimental results are shown in Table 4.

Table 4

Comparative experiment of different object detection algorithms

Model	GFLOPs	mAP@0.5	Precision	Recall
Faster-RCNN	227.8	80.6%	81.8%	74.6%
SSD	63.14	78.6%	79.1%	70.9%
YOLOv7	105.4	81.5%	82.4%	73.5%
YOLOv8n_gcd	6.1	84.95	84.8%	76.2%

The experimental results in Table 4 clearly demonstrate that the optimized model proposed in this study achieves significantly superior performance in reducing floating-point operations (FLOPs), with its FLOPs far lower than those of the other three benchmark models. In other aspects, compared to Faster R-CNN, SSD, and YOLOv7, the optimized model exhibits improvements in precision by 3%, 5.7%, and 2.4%, respectively; recall by 1.6%, 5.3%, and 2.7%, respectively; and mean average precision (mAP@0.5) by 4.35%, 6.35%, and 3.45%, respectively. Notably, the YOLOv8n_gcd model maintains a compact architecture with reduced computational demands, enabling rapid deployment on resource-constrained platforms. These enhancements collectively validate the superior performance and broad applicability of the proposed improved model in real-world applications.

CONCLUSIONS AND DISCUSSIONS

This study designed a dual-light device to collect datasets, generating four distinct datasets: top-lighting-dispersed, top-lighting-aggregated, backlighting-dispersed, and backlighting-aggregated, which were used to train the same algorithm. The results revealed that the backlighting-dispersed dataset achieved the highest accuracy and was most suitable for training. Building on this, an optimized YOLOv8-based model, termed YOLOv8n_gcd, was proposed. This model integrates Ghost convolutions into the backbone network to minimize redundant computations, incorporates attention mechanisms to enhance feature extraction for damaged regions, and replaces standard convolutions with depthwise separable convolutions in the Neck section. These localized optimizations achieve a balance between accuracy and lightweight efficiency. Comparative experiments demonstrated that the YOLOv8n_gcd model outperforms Faster R-CNN, SSD, and YOLOv7, with precision improvements of 3%, 5.7%, and 2.4%, recall improvements of 1.6%, 5.3%, and 2.7%, and mAP@0.5 gains of 4.35%, 6.35%, and 3.45%, respectively. Notably, the optimized YOLOv8s model retains a compact architecture with significantly reduced computational demands, enabling rapid deployment on resource-limited platforms. These advancements in precision, speed, and robustness validate the superiority and broad applicability of the proposed model in practical agricultural scenarios, offering a high-performance solution for real-time quality inspection tasks while maintaining adaptability to industrial constraints.

ACKNOWLEDGEMENT

This work was supported by the Shandong Province Science and Technology Minor Enterprises Innovation Ability Promotion Project (Project number: 2023TSGC1014), General Program of China Higher Education Association (23NL0406) and the Key Project of Undergraduate Teaching Reform Research in Shandong Province (Z2022263). The funders had no role in the study design, data collection and analysis, decision to publish, or preparation of the manuscript.

REFERENCES

- [1] Cui, T., Fan, C. L., Zhang, D. X., Yang, L., Li, Y. B., & Zhao, H. H. (2019). Research progress on mechanical harvesting technology of maize (玉米机械化收获技术研究进展分析). *Transactions of the Chinese Society for Agricultural Machinery*, Vol. 50(12), pp. 1–13, China.
- [2] Cui, Y. S. (2024). Technological progress of domestic corn combine harvesters in China (国内玉米联合收获机技术进展). *Agricultural Engineering*, Vol. 14(5), pp. 22-26, China.
- [3] Han, Z. Z., Zhao, Y. G., & Yang, J. Z. (2010). Corn embryo feature detection based on independent components of RGB kernel images (基于籽粒 RGB 图像独立分量的玉米胚部特征检测). *Transactions of the Chinese Society of Agricultural Engineering*, Vol. 26(03), 222–226+389, China.
- [4] He, K., Zhang, X., Ren, S., & Sun, J. (2016). Deep residual learning for image recognition. *Proceedings of the IEEE Conference on Computer Vision and Pattern Recognition* pp. 770–778. China.
- [5] Howard, A. G., Zhu, M., Chen, B., Kalenichenko, D., Wang, W., Weyand, T., Andreetto, M., & Adam, H. (2017). MobileNets: Efficient convolutional neural networks for mobile vision applications. *arXiv*. <https://doi.org/10.48550/arXiv.1704.04861>, China.
- [6] Quan, L. Z., Wang, J. Y., Wang, Q., Xiao, Y. H., & Feng, H. Q. (2020). Corn quality selection device based on electromagnetic vibration and convolutional neural network (基于电磁振动与卷积神经网络的玉米品质精选装置). *Journal of Jiangsu University (Natural Science Edition)*, Vol. 41(03), pp. 288-293+313, China.

- [7] Li, S. K. (2017). Factors influencing the quality of mechanical grain harvesting in corn and development directions of grain harvesting technology in China (我国玉米机械粒收质量影响因素及粒收技术的发展方向). *Journal of Shihezi University (Natural Science Edition)*, Vol. 35(3), pp. 265-272, China.
- [8] Li, X., Du, Y., Yao, L., Wu, J., & Liu, L. (2021). Design and Experiment of a Broken Corn Kernel Detection Device Based on the Yolov4-Tiny Algorithm. *Agriculture*, Vol. 11, pp. 1238, China
- [9] Liu, Y. F., Zhong, Y. F., & Qin, Q. Q. (2018). Scene classification based on multiscale convolutional neural network. *IEEE Transactions on Geoscience and Remote Sensing*, Vol. 56, pp. 7109–7121. China.
- [10] Sandler, M., Howard, A., Zhu, M., Zhmoginov, A., & Chen, L.-C. (2018). MobileNetV2: Inverted residuals and linear bottlenecks. *Proceedings of the IEEE Conference on Computer Vision and Pattern Recognition* pp. 4510–4520, US.
- [11] Velesaca, H. O., Mira, R., Suárez, P. L., Larrea, C. X., & Sappa, A. D. (2020). Deep learning based corn kernel classification. *2020 IEEE/CVF Conference on Computer Vision and Pattern Recognition Workshops (CVPRW)*, pp. 294–302. USA
- [12] Wang, C.-Y., Bochkovskiy, A., & Liao, H.-Y. M. (2023). YOLOv7: Trainable bag-of-freebies sets new state-of-the-art for real-time object detectors. *Proceedings of the IEEE/CVF Conference on Computer Vision and Pattern Recognition* pp. 7464–7475, China.
- [13] Woo, S., Park, J., Lee, J.-Y., & Kweon, I. S. (2018). CBAM: Convolutional block attention module. *Proceedings of the European Conference on Computer Vision (ECCV)*, pp. 3–19, South Korea.
- [14] Wu, Y. S., Li, A. H., Wan, Y. M., & Meng, T. C. (2024). Research progress on online detection technology of tobacco based on machine vision (基于机器视觉的烟草在线检测技术研究进展). *Laser & Optoelectronics Progress*, Vol. 61(8), pp. 49-62, China.
- [15] Xu, T. C., Wu, M., He, D. X., Zheng, Z. A., Xu, H. H., & Bao, J. Q. (2021). Application of machine vision in agricultural engineering (机器视觉在农业工程中的应用). *Agricultural Engineering*, Vol. 11 (8) , pp. 40-48, China.
- [16] Xu, Y., Liu, L., Li, Z. Y., Gao, Z., & Li, X. Z. (2020). Corn variety recognition based on convolutional neural network (基于卷积神经网络的玉米品种识别). *Journal of Jiangsu Agricultural Sciences*, Vol. 36(01), pp. 18-23, China.
- [17] Yang, J. Y., Song, B., Luo, Y. J., Zhang, J., Liu, J., Yang, C., & Duan, J. M. (2018). Quality evaluation and preliminary screening of identification indicators for mechanical grain harvesting of different corn varieties (不同玉米品种机械粒收质量评价及其鉴定指标初步筛选). *Journal of Henan Agricultural Sciences*, Vol. 47(11), pp. 25-31, China.
- [18] Zhao, B., Li, X. L., Zhou, M. L., Song, B., Lei, E., Li, Z., Wu, Y. W., Yuan, J. C., & Kong, F. L. (2020). Current status and influencing factors of kernel breakage rate in mechanical grain harvesting of corn in Southwest China (西南玉米机械粒收籽粒破碎率现状及影响因素分析). *Acta Agronomica Sinica*, Vol. 46(1), pp. 74-83, China.
- [19] Zhao, C. J., Ma, C., Li, J., & Wang, X. M. (2025). Research status and prospects of rice mechanization technology in hilly and mountainous areas (丘陵山地水稻机械化技术研究现状与展望). *Transactions of the Chinese Society of Agricultural Engineering*, Vol. 41(1), pp. 1-11, China.
- [20] Zhu, X. L., Chi, R. J., Du, Y. F., Deng, X. J., Zhang, Z., & Dong, N. X. (2021). Design and experiment of intelligent control system for low-loss threshing of high moisture corn (高含水率玉米低损脱粒智能控制系统设计与试验). *Transactions of the Chinese Society for Agricultural Machinery*. Vol. 52(S1), pp. 9-18, China.

SEMI-PHYSICAL SIMULATION RESEARCH ON THE CONTROL SYSTEM OF COMBINE HARVESTER CUTTING TABLE

联合收割机割台控制系统的半实物仿真研究

Yihu WANG¹⁾, Guohai ZHANG^{2*)}, Xipeng QIAN¹⁾, Qian DONG¹⁾

¹⁾ Shandong University of Technology, Zibo 255200, China;

²⁾ Institute of Modern Agricultural Equipment, Shandong University of Technology, Zibo 255200, China;

E-mail: guohaizhang@sdut.edu.cn

DOI: <https://doi.org/10.35633/inmateh-75-68>

Keywords: combined grain harvester, controller development testing, mathematical model, HIL

ABSTRACT

To address challenges in developing the rice-wheat harvester cutting platform controller—such as sensitivity to working conditions, long development cycles, and cumbersome performance testing—a semi-physical simulation platform is designed. Based on the functional requirements of the cutting platform, Simulink is used to build a mathematical model of the controller and its I/O hardware model. A hardware-in-the-loop simulation test platform is developed using the TC377ECU controller. By integrating the Whale Optimization PID algorithm, overshoot is reduced by 3.5%, and rise time improves by 0.303 s compared to conventional PID. Testing in both simulation and real environments shows a maximum absolute error of 10.58 mm for cutting height and a correlation coefficient of 0.9474. The rotational speed errors for the reel and auger have expectations of 0.106 rad/min and 0.101 rad/min, with standard deviations of 0.165 rad/min and 0.172 rad/min. This validates the controller's feasibility, shortens development time, and lowers costs.

摘要

针对稻麦收获机割台控制器开发过程受工况影响较大, 传统开发过程周期长, 测试控制器性能过程繁琐等问题, 设计了一套稻麦收获机割台自动调控系统半实物仿真平台。以稻麦收获机割台功能需求作为开发指标, 利用 simulink 搭建控制器数学模型以及 I/O 硬件模型, 基于 TC377ECU 控制器搭建硬件在环仿真测试平台。结合鲸鱼优化 PID 算法对控制策略进行了优化, 相较于普通 PID, 超调量降低了 3.5%, 上升时间提升了 0.303s。通过仿真平台与真实环境进行试验对比, 割台高度的最大绝对误差是 10.58mm, 相关系数为 0.9474; 拨禾轮和搅龙转速误差的数学期望依次为 0.106 rad/min 和 0.101 rad/min, 标准差为 0.165 rad/min 和 0.172 rad/min, 测试了控制器和仿真平台的可行性, 缩短了开发周期, 降低了开发成本。

INTRODUCTION

As one of China's major food crops, ensuring the production of rice and wheat is of primary importance. In 2024, 23,090.7 thousand hectares of wheat were sown, marking an increase of 31.7 thousand hectares, or 0.1%. With the growing prevalence of machine harvesting across the country, the automation level of agricultural machinery has reached a point where higher standards are required. This makes the development and optimization of agricultural machinery functions increasingly significant. To overcome the limitations of using joysticks for regulating the cutting platform parameters in traditional harvesters, researchers have increasingly focused on developing automatic regulation systems for the cutting platform of grain combine harvesters. Ji *et al.*, (2023), employed the polar filling method to model the rigid and flexible discrete elements of reed stalks, and conducted a three-point bending test in EDEM software to calibrate the bonding parameters. The optimal parameter combinations for the cutting table were identified through simulation analysis and later verified by field tests, confirming their alignment with the simulation results. Yao *et al.*, (2023), investigated the impact of harvester forward speed, transverse cutter cutting height, and longitudinal cutter cutting speed on the cutting table loss rate in rapeseed combine harvesting, addressing the issue of high loss rates. The analysis revealed that the significance order of these factors was: cutting speed > forward speed > cutting height. Optimal parameter combinations were determined through response surface analysis and regression model optimization, with the results experimentally verified for reliability.

Aiming to address the issues of low gripping capacity, poor cutting quality, and easy damage of existing harvester tools, *Zhao et al.*, (2024), designed a bionic knife blade inspired by the maxillary teeth of ants. They investigated the effects of parameters such as blade tooth pitch, constructed edge angle, and tilt angle on the stress field and deformation through finite element analysis. The results confirmed that optimizing the knife edge design significantly enhances its performance, providing a theoretical foundation for the design of harvester knives.

Chen et al., (2018), addressed the low automation levels in cutting platform parameter regulation by using a PLC as the controller to design an automatic adjustment device for the rice combine harvester's cutting platform. In their system, the response time for controlling the rotational speed of the reel was ≤ 0.8 s, with a control accuracy of 91.5%.

Liu et al., (2022), designed an adaptive profiling cutting table to ensure the stubble height remains within an optimal range during harvesting. The table could adjust its height and level adaptively, using a PLC controller and a fuzzy PID method for regulation. The cutting table's rising speed was 0.216 m/s, and its descending speed was 0.244 m/s.

Ji et al., (2022), aimed to improve harvesting quality by designing a cutting table with a response time of ≤ 0.8 s and control accuracy of 91.5%. They also developed a device to match the rotational speed of the reel with the forward speed using an STM32 controller and fuzzy PID control strategy. This system could adapt to different crops, with a rotational speed-to-vehicle speed ratio between 1.4 and 1.8, yielding better harvesting results.

Shi et al., (2024), designed an adaptive control system for the cutting platform to address the inefficiency and inaccuracy of manual adjustments. Using a PLC as the controller, the system achieved an average response time of 2.3 s for height control. These studies demonstrate that factors such as the height of the cutting platform, reel height, rotational speed of the reel, and auger speed directly affect the harvesting loss rate of rice and wheat. However, most of the research primarily focuses on optimizing the regulation process of the reel using fuzzy PID methods for height and speed control. The optimization of cutting platform regulation strategies remains under developed. Moreover, the process of controller development and testing requires numerous experiments for validation. This not only increases the risk of actuator burnout due to errors in control strategies but also raises testing costs and demands frequent mounting, dismounting, and optimization operations. Additionally, given the growth cycles of rice and wheat, continuous field experiments are necessary for verification, resulting in a lengthy development cycle. HIL simulation allows for effective testing of controllers by simulating realistic controlled objects. While HIL simulation has been widely applied in industries such as automotive and aviation, *Shahir et al.*, (2021), uses HIL to test complex algorithms in electric vehicle propulsion architectures, validating the correctness of the proposed theoretical concepts.

Abboush et al., (2024), applies semi-physical simulation techniques for fault injection, testing the safety of automobiles. *Klionovska et al.*, (2021), utilizes the HIL technique for spacecraft rendezvous simulation testing. Its application in agriculture has only emerged relatively recently, primarily for tractor steering control and gearshift simulation, *Hang et al.*, (2024), improves the steering control strategy for tractors and develop HIL testbeds. *Cevallos et al.*, (2022), applies the HIL technique to validate a hybrid control method for a greenhouse model.

Wu et al., (2023), uses HIL technology for an electric tractor seeding unit, building a hardware-in-the-loop simulation testbed to compare and validate proposed improvement strategies. *Zhu et al.*, (2022), applies the HIL technique to a corn harvester threshing unit, creating a low loss intelligent control simulation platform for corn.

Zhai et al., (2023), establishes a semi-physical simulation test platform for the tractor electro hydraulic suspension control system, verifying the performance of the designed controller in this system. It is evident that the introduction of semi-physical simulation technology has accelerated the development of automation in the agricultural sector, yet its application in the development of cutting table regulation systems remains limited.

Therefore, this paper aims to optimize the cutting platform's automatic regulation system, addressing the gap in current research regarding the optimization of cutting platform height control strategies. By combining the Whale Optimization Algorithm (WOA) with a PID based control strategy for height regulation, this approach reduces overshoot by 3.5% compared to traditional PID control, thereby enhancing system stability. Additionally, the rise time is improved by 0.303 seconds, which boosts the system's response speed. Agricultural automation systems are often influenced by environmental changes and the aging of equipment, which can impact response speed.

However, the WOA-optimized controller demonstrates strong adaptability to these variations, enhancing the system's robustness. In terms of reel and auger speed regulation, this study integrates findings from existing research to ensure that the speed ratio between the reel and vehicle speed remains within an optimal range. The TC377 is selected as the control center for the system, offering better compatibility with the harvester. To address the long testing cycles in traditional development processes, a semi-physical simulation platform for the cutting platform's automatic control system is constructed. The feasibility of the platform is evaluated in comparison with traditional methods, providing a solid foundation for the continued development of the cutting platform control system.

MATERIALS AND METHODS

Simulation platform overall structure

The overall structure of the simulation platform should have the function of simulating the environment of the real vehicle, so it is necessary to analyze the overall architecture of the cutting platform first; as shown in Figure 1, the whole simulation platform consists of on-board controllers, driver operating system, hydraulic model, actuator model, operation interface, information processing system, and power supply module, the on-board controller as the core component of the whole system. The simulation platform board issues its input to simulate the voltage signal of the sensor so that the controller mistakenly thinks that the current working environment is the real machine, to achieve the purpose of testing the controller function. The data transmission between the controller and the simulation platform is via I/O hardware. The CAN communication bus and the current value of each data can be monitored in real-time via telegrams. The operator interface interacts with the information processing system to send user operation data and controller feedback results. Its functional design mainly includes the working mode selection of the whole machine, the height of the cutting platform, the height of the reel, the speed regulation and monitoring of the reel, and the entire regulation process is realized by the controller sending out PWM pulse signals to control the openness of the solenoid valve.

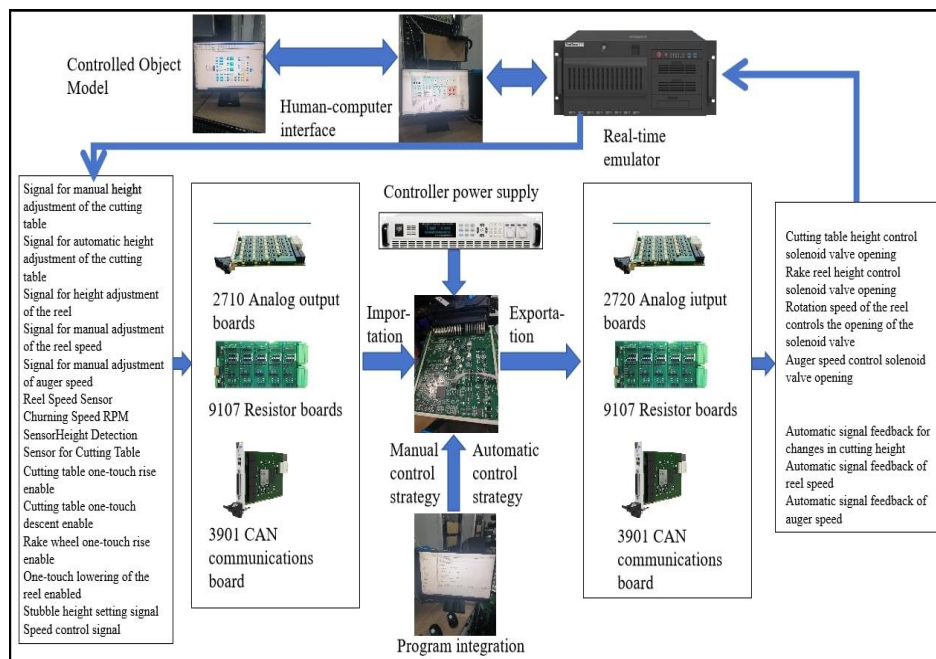


Fig. 1 - Block diagram of grain harvester cutting platform control system components

A complete grain harvester cutting table model is established using existing experimental data and formulas to create a realistic test environment for the controller. This includes simulating the conventional vehicle voltage signals required by the controller, the voltage signals from the cutter sensors, the control signals from the receiver controller, and the feedback status signals. The input and output signals of the entire system are regulated by the real-time simulator, and the regulation strategy is implemented based on the established I/O model. The controlled variables include the cutting platform height, the reel's height and rotational speed, and the auger's rotational speed. Modeling of the actuator based on the hydraulic system, with its schematic diagram shown in Figure 2.

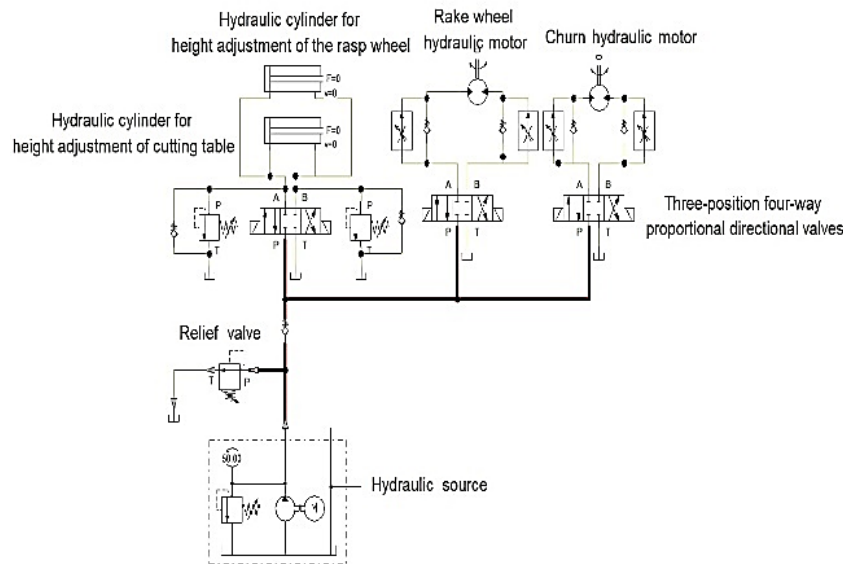


Fig. 2 - Hydraulic system schematic

The complete model must account for the following considerations: ①The hydraulic element’s power source is the pressure generated by fluid flow, requiring incorporation of the nonlinear relationship between flow rate and pressure. ②Assuming the hydraulic oil is compressible, the mechanical analysis must include the elastic resistance of the liquid. ③To ensure compatibility with the controller and minimize computational burden, the model must be discretized.

The height regulation of the cutting platform is primarily achieved by controlling the expansion and contraction of the hydraulic cylinder. The hydraulic cylinder’s power is derived from the conversion of hydraulic oil flow, and the displacement of the hydraulic cylinder is determined through the mathematical relationship between pressure and acceleration. A piston pump model is selected as the power source for the entire hydraulic system, with its displacement formula given by:

$$V = \frac{\pi}{4} d^2 D z \eta_v \tan \delta \tag{1}$$

where d is the plunger diameter, m; D is the diameter of the distribution circle of the plunger on the cylinder body, m; z is the number of plungers; η_v is the pump volumetric efficiency; δ is the inclination of the swashplate, rad.

Find the flow rate produced by the pump based on the displacement of the piston pump:

$$Q = nV \tag{2}$$

where:

Q is the output flow rate of the piston pump, m³/s; n is the engine speed of the piston pump, r/min; V is the displacement of the piston pump, L/rev.

Hydraulic oil exits the hydraulic pump, with one path flowing through the relief valve into the tank and the other passing through the check valve into the solenoid directional valve. During this process, a localized fixed capacity cavity is formed. Assuming the liquid is compressible, if the volume of the fixed-capacity cavity is V and the initial internal pressure is P_0 , then as the liquid continues to flow into the cavity at a changing rate of ΔQ , the pressure inside the cavity can be expressed as follows:

$$P = P_0 + B \int \frac{\Delta Q}{V} dt \tag{3}$$

where:

P is the hydraulic chamber pressure in Pa; P_0 is the initial pressure of the hydraulic chamber in Pa; B is the bulk modulus of elasticity of the hydraulic fluid in Pa; ΔQ is the amount of flow change in m³/s; V is the volume of a fixed volume in m³.

The hydraulic fluid output from the check valve serves as the input to the three-position four-way proportional directional valve. The position and opening of the proportional directional valve are controlled by a PWM signal from the controller. Given that the valve port opening is not strictly linear, the flow rate output from each valve port, based on the valve port characteristics, can be expressed as follows:

$$Q=C_d A_0 \sqrt{\frac{2\Delta p}{\rho}} \tag{4}$$

$$A_0 = \begin{cases} 0, & x < x_0, \\ Kx, & x > x_0. \end{cases} \tag{5}$$

C_d is the flow coefficient, dimensionless; A_0 is the cross sectional area of the hole, m^2 ; ρ is the density of the liquid, kg/m^3 ; Δp is the pressure difference between the inlet and outlet of the small hole, m^2 ; x_0 denotes the deadband flow rate, m^2 ; K is the gain coefficient, dimensionless.

The hydraulic oil output by the reversing valve flows to the hydraulic cylinder, and the flow of hydraulic oil realizes the reciprocating motion of the hydraulic cylinder push rod; according to the relationship between the force and acceleration can be calculated the displacement of the hydraulic bar, and its kinetic equation can be expressed as:

$$F_i - F_o - F_c - F_k - F_{load} = ma \tag{6}$$

F_i is the inlet chamber pressure, N; F_o is the outlet pressure, N; F_c is the liquid damping force, N; F_k is the liquid elastic force, N; F_{load} is the model load force, N; m is the mass of the piston rod, kg; a is the piston rod acceleration, m/s^2 .

The RPM model hydraulic circuit is similar to the height model, with the key difference being that the actuator in the RPM model is a hydraulic motor. This motor converts the pressure of the hydraulic fluid into mechanical energy to drive the rotation of the reel. The moment balance equation for the hydraulic motor and the load can be expressed as (Lu et al., 2023):

$$D_m(p_H + p_L) = J_t \frac{d^2\theta_m}{dt^2} + B_m \frac{d\theta_m}{dt} + G\theta_m + T_l \tag{7}$$

p_H and p_L are the hydraulic motor inlet chamber pressure and return chamber pressure, respectively, Pa; D_m is the displacement of the hydraulic motor, m^3/s ; J_t is the total inertia of the hydraulic motor and load, $kg \cdot m^2$; B_m is the viscous damping coefficient, kg/s ; G is the load spring stiffness, $N \cdot m$; T_l is any unintentional load moment acting on the hydraulic motor shaft, N; θ_m is the motor rotation angle, rad.

As the command processing center of the entire platform, the controller's control strategy plays a pivotal role, directly impacting the functionality of the cutting table and the overall effectiveness of the test. Among the various control tasks, height regulation of the cutting table is particularly critical. To achieve fast, stable, and precise control, a PID control strategy optimized using the Whale Optimization Algorithm (WOA) has been selected. WOA is an innovative bio-inspired intelligence algorithm modeled after the foraging behavior of humpback whales (NadimiShahraki et al., 2021; Miao et al., 2025; Wei et al., 2025). In the WOA optimization process, each humpback whale represents a candidate solution. These whales utilize a distinctive hunting technique known as the bubble-net predation strategy, which serves as the foundation for the algorithm's search and exploitation mechanisms.

In the encircling prey phase, the current best candidate solution is assumed to be the optimal solution for the target prey, or at least close to it (Yan et al., 2022). The humpback whale then moves around this best candidate solution, continuously updating its position. The mathematical model for this phase is represented as:

$$X(t+1) = X^*(t) - A \times |CX^*(t) - X(t)| \tag{8}$$

t is the number of iterations for the current update position, dimensionless; $X^*(t)$ is the current optimal position vector, m; $X(t)$ is the current position vector of the whale, m; A and C are position vector coefficients which operate as follows:

$$A = \frac{2T_{max}}{T_{max} + t} (2r_1 - 1) \tag{9}$$

$$C = 2r_2 \tag{10}$$

r_1 and r_2 is a random vector in the range (0,1), dimensionless; T_{max} is the iteration maximum, dimensionless.

During the prey search phase, humpback whales update their position in an upward spiral and keep approaching their prey, its hunting model is:

$$X(t+1) = X^*(t) + e^{bl} \cos(2\pi l) |X^*(t) - X(t)| \tag{11}$$

b is the whale spiral path coefficient and l is a (0,1) random number conforming to a uniform distribution, dimensionless.

From this, two behaviors of whales when catching prey are derived, assuming that the probability of both behaviors is the same.

$$X(t+1)=\begin{cases} X^*(t)-A\times|CX^*(t)-X(t)|, p<0.5 \\ X^*(t)+e^{bl}\cos(2\pi l)|X^*(t)-X(t)|, p\geq 0.5 \end{cases} \quad (12)$$

where p is the probability of the two behaviors, dimensionless.

When attacking the prey, the difference between the iteration value t and the maximum iteration value gradually decreases, causing the range of values of A to decline. When the value of A is within $[-1, 1]$, the next position of the whale can be any position between it and the prey, and at $A < 1$, the attack is launched at the prey.

To ensure that all humpback whales can perform a thorough search in the solution space, they must randomize their targets based on each other's positions. When the value of A is outside the range of $[-1, 1]$, the algorithm randomly selects a whale's position to modify the position vectors of other whales. This helps them locate suitable prey and enables global search capabilities.

$$X(t+1)=X_{random}(t)-A\times|CX_{random}(t)-X(t)| \quad (13)$$

where $X_{random}(t)$ is a vector of randomly selected whale positions, m .

Based on PID control of the cutting table elevation, the system error is used as the evaluation function for the whale optimization algorithm. The fitness function value is calculated, and the proportional, integral, and derivative parameters are adjusted according to the fitness to optimize the PID controller, thereby achieving optimal control.

To reduce the computational load of the simulation platform and facilitate test sampling, the model must be discretized. The Simulink tool is used to automatically solve the discrete model using the forward Euler method, which can be expressed as follows:

$$x(k+1)=x(k)+Tf(x(k),t(k)) \quad (14)$$

where $x(k)$ is the state variable at the current moment k , m ; $x(k+1)$ is the state variable at the next moment $k+1$, m ; T is the sampling time, s ; $f(x(k),t(k))$ is the derivative of the system, m/s .

RESULTS AND ANALYSIS

The simulation platform functionality test primarily includes the simulation function test of the controller signals and the hardware-in-the-loop (HIL) test.

Taking the cutting platform height regulation signal as an example, the controller adjusts the lift of the hydraulic cylinder based on the detection signal from the profiling device. The profiling device's source is the angle detected by the angle sensor, which sends out a voltage signal. This process can be used as the basis for analog signal testing. The voltage signal value can be set on the control panel, and a multimeter can be used to measure the voltage signal output from the corresponding board to conduct the test.

For the selection of an angle measurement sensor in a cutting table profiling device, the GT-B type Hall angle sensor is a suitable choice. This sensor features an output voltage range of 0-3.3 V, which corresponds linearly to an angular range of 0-360°.

The relationship between the measured angle and the simulated angle value follows the equation:

$$V=a\times\frac{3.3}{360} \quad (15)$$

where: V is the simulation platform voltage setting, V ; a is the angle value measured by the true angle sensor, °.

$$\theta=V\times\frac{360}{3.3} \quad (16)$$

where θ is the simulation platform angle analog input value, °.

Based on the measured angle value, the required voltage parameter V can be determined and set on the platform, allowing for the calculation of the corresponding angle input. A comparison between the measured sensor values and the platform's angle measurement values was conducted, with the test results presented in Table 1.

The results indicate that the maximum absolute error between the simulation platform and the measured sensor angle is 0.98°, while the maximum relative error is 0.08°. This discrepancy arises because, after setting the voltage parameter V , the board card outputs the voltage according to the set value, but minor deviations exist in the actual output. This conclusion is further validated by measuring the board card's output voltage using a multimeter.

Table 1

Sensor and simulation platform angle measurements

Experiment number	Measured angular value a	Simulation platform voltage setting value V	Simulation angle value θ	Absolute error	Relative error
	[°]	[V]	[°]	[°]	[-]
1	10.37	0.095	11.15	0.78	0.08
2	10.89	0.990	11.69	0.8	0.07
3	11.03	0.100	11.8	0.77	0.07
4	12.36	0.113	11.38	0.98	0.08
5	13.45	0.123	14.31	0.86	0.06
6	13.91	0.128	13.17	0.74	0.05
7	14.16	0.130	13.38	0.78	0.06
8	14.87	0.136	15.6	0.73	0.05
9	15.34	0.140	16.07	0.73	0.05
10	15.96	0.146	16.74	0.78	0.05

The CAN signal test uses VBA software to monitor real-time changes in message transmission data, assessing the accuracy and timeliness of signal transmission. Figure 3 displays the screen of real-time monitoring during the test. The CAN message monitoring screen displays real-time data transmission between the platform and the controller. The current value of each signal θ is updated in real-time, simulating an environment where CAN communication is active.

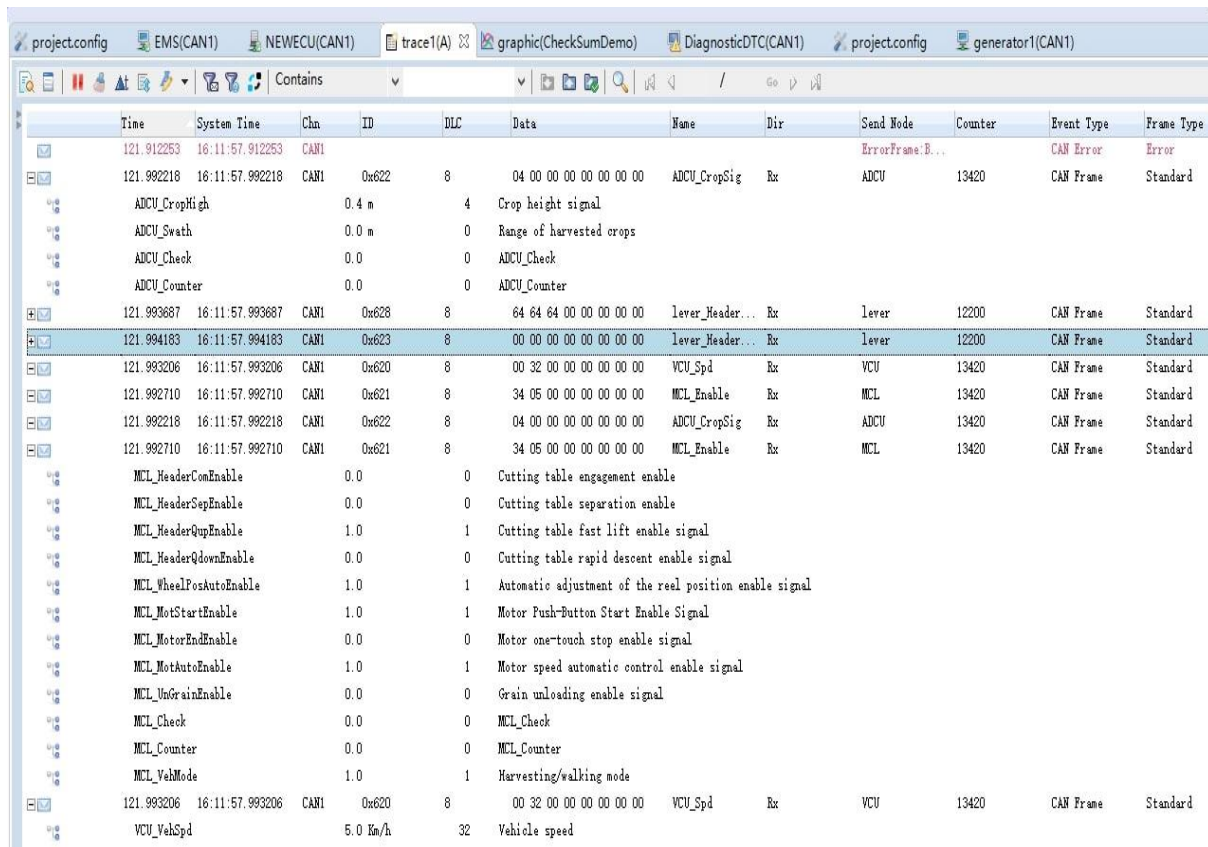


Fig. 3 - CAN communication real-time monitoring messages

To verify the optimization effect of the whale optimization PID and traditional PID control in regulating the lift of the cutting table, the dynamic response of the system will be observed. The mathematical transfer function for the lift of the cutting table is established. The opening of the reversing valve directly influences the speed of the hydraulic cylinder's lifting. The hydraulic cylinder's speed changes in accordance with the variation in the valve opening. The acceleration and deceleration, as well as the expansion and contraction of the hydraulic cylinder, are considered inertial elements (Qin et al., 2009). The transfer function for this process can be expressed as follows:

$$G(s) = \frac{1}{Ts+1} \tag{17}$$

where s is the Laplace operator, s^{-1} ; T is the hydraulic cylinder inertia constant, s , here take 0.83.

The simulation model of the control strategy is built in Matlab/Simulink environment and its model diagram is shown in Figure 4.

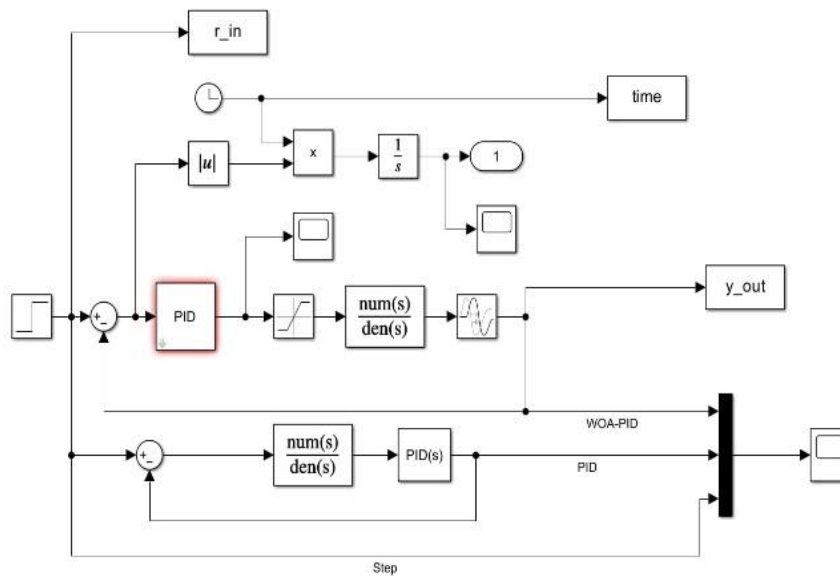


Fig. 4 - WOA-PID Simulink model

A step signal is used as the input to the system. After 10 iterations of the whale optimization algorithm, the optimal solution is obtained, yielding the corresponding values of K_p , K_i , and K_d . A comparison curve between the results of the optimized PID and the standard PID is then generated, and the resulting graph is shown in Figure 5.

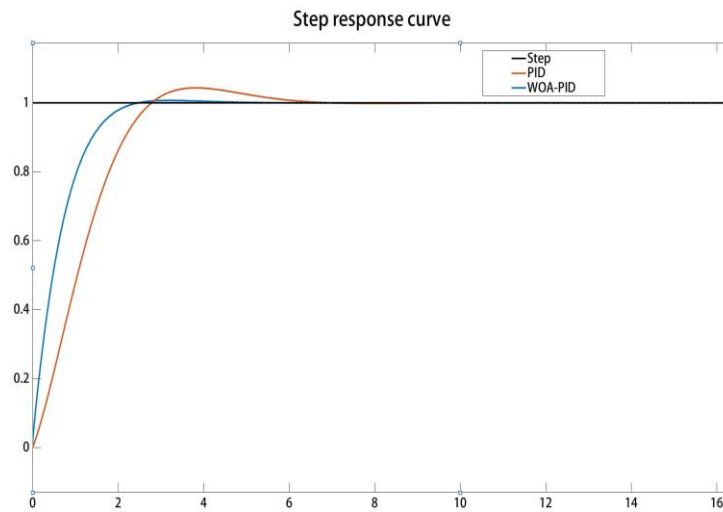


Fig. 5 - Control strategy step response comparison curve

From the dynamic response curve, it can be observed that the regulation effect of the whale optimized PID is significantly improved compared to the standard PID. The overshoot is reduced by 3.5%, and the rise time is improved by 0.303 seconds, enhancing the system's speed and stability.

To verify the feasibility of the semi-physical simulation platform for controller testing, a control experiment was conducted using the platform to simulate the working process of the rice and wheat harvester. The experimental indices included vehicle speed, cutting platform height, reel height and rotational speed, and auger rotational speed. These parameters were used to assess the accuracy and feasibility of the platform. The experiment was conducted in Junan County, Linyi City, Shandong Province, in a field of wheat to be harvested. The wheat had a grain height of approximately 450 mm, row spacing of about 300 mm, and a ground undulation of around 60 mm, with a uniform crop density across the field. The actual field measurements are shown in Figure 6. Based on the field conditions, the stubble height was set to 200 mm, and both the field experiment and semi-physical simulation platform experiment were carried out sequentially. According to the actual situation in the field, the stubble height was set to 200 mm, and the field experiment and semi-physical simulation platform experiment were carried out in turn.



Fig. 6 - Control strategy step response comparison curve

During field experiments, the harvester is set to harvesting mode, with the stubble height adjusted to 200 mm. The driving speed is increased to 12 km/h and maintained at a steady pace. As the terrain changes, the height of the cutting platform dynamically adjusts based on the detection values from the mimic device. The cutting platform's height is continuously recorded and using the mathematical relationship between the platform height and the angle sensor of the mimic device, the corresponding angle values are derived in response to terrain variations.

After harvesting a certain distance, the vehicle speed is reduced to 8 km/h. In harvesting mode, the rotational speeds of the reel and auger vary with the vehicle speed; therefore, the changes in rotational speed during acceleration and deceleration are recorded. The simulation platform parameters are configured based on the recorded angle values and vehicle speed from the field experiment. In the human-computer interaction interface, real-time monitoring is conducted to track the variations in cutting platform height in response to terrain changes, as well as the fluctuations in reel and auger rotational speeds corresponding to vehicle speed adjustments. The experimental results are presented in Table 2, Figure 7 and Figure 8.

As shown in Table 2, during the field test, the cutter height was recorded every 10 seconds from the actual vehicle and converted into the corresponding angular change as an input to the simulation platform. Throughout this process, the maximum absolute error in cutter height was 10.58 mm, which primarily resulted from conversion inaccuracies and voltage output errors from the platform. To evaluate the linear relationship between the actual cutter height and the simulated cutter height output from the platform, Pearson correlation analysis was conducted. The calculated Pearson correlation coefficient was 0.9474, indicating a strong correlation between the two. This result confirms that the simulation platform effectively replicates the cutter lifting and lowering process of the test vehicle.

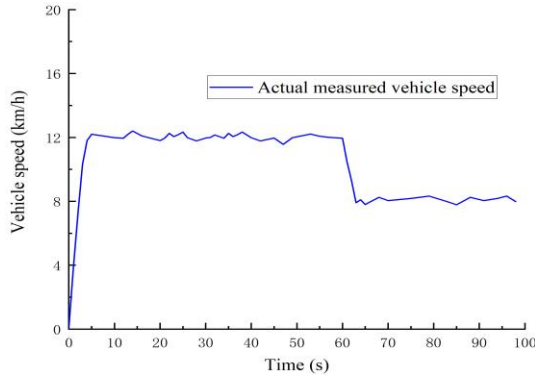
The experimental results show that the rotational speeds of the reel and auger vary with the vehicle speed. Directly adjusting their speeds through the platform alone cannot fully ensure consistency with field measurements. To accurately control a single variable, the vehicle speed curve is pre-sampled and used as an input to the control strategy. However, the output speed curve from the simulation platform is influenced by factors such as the simulation step length and refresh period. Therefore, the generated curve must be exported for comparison with the actual speed curve. Compared to the harvester, the mathematical expectation of the rotational speed error for the reel and auger is 0.106 rad/min and 0.101 rad/min, respectively, with standard deviations of 0.165 rad/min and 0.172 rad/min. These results indicate that the control strategy meets the actual harvesting requirements. Moreover, the simulation platform provides an accurate evaluation of the controller's functionality, making it a valuable reference for functional testing in the early stages of controller development.

Table 2

Sensor and simulation platform angle measurements

Experiment number	Calculated height of cutter trial	Calculated height of cutting table simulation	Absolute error in height above ground	Relative error in height above ground
	[mm]	[mm]	[mm]	[-]
1	203.0	205.1	2.1	0.010
2	201.3	200.5	0.8	0.003
3	205.7	207.2	1.5	0.007
4	200.9	200.5	0.4	0.002
5	197.4	198.9	1.5	0.008
6	201.3	200.2	1.1	0.005
7	204.6	205.1	0.5	0.002

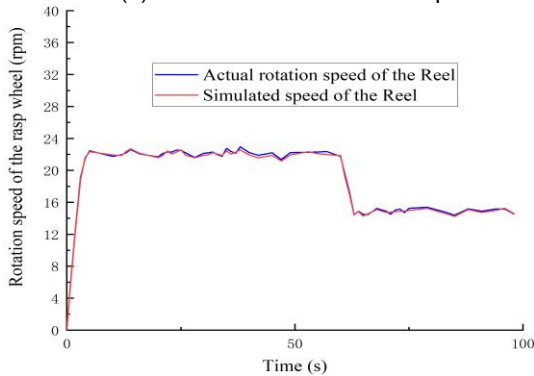
Experiment number	Calculated height of cutter trial	Calculated height of cutting table simulation	Absolute error in height above ground	Relative error in height above ground
	[mm]	[mm]	[mm]	[-]
8	202.4	201.5	0.9	0.004
9	193.3	193.6	0.3	0.002
10	204.8	203.4	1.4	0.007



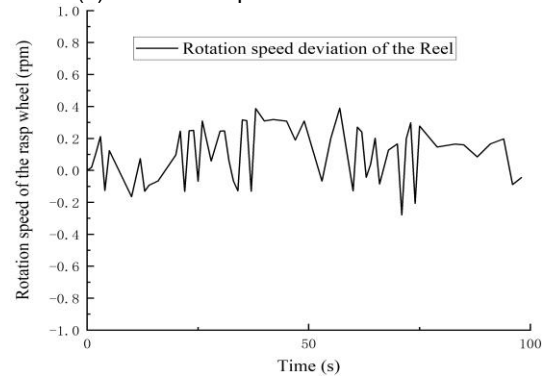
(a) Actual measured vehicle speed



(b) Simulated speed of the reel

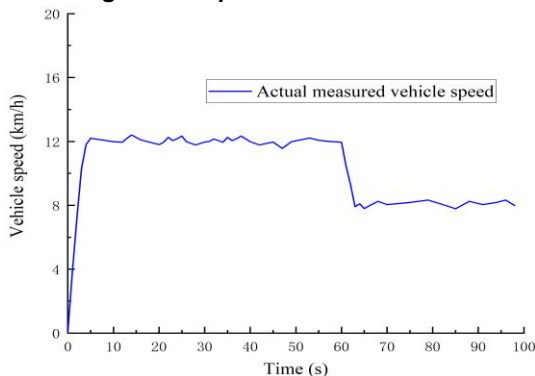


(c) Comparison of the reel speed



(d) Rotation speed deviation of the reel

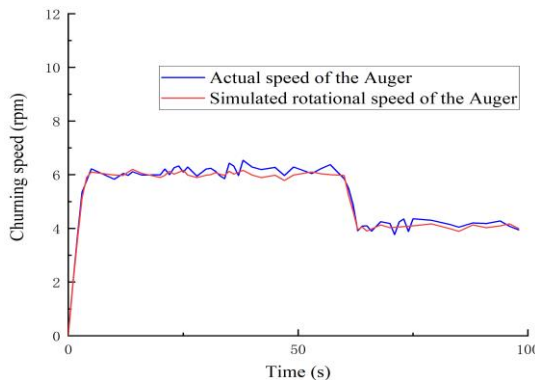
Fig. 7 - Comparison curve between simulation and actual rotation speed of the reel



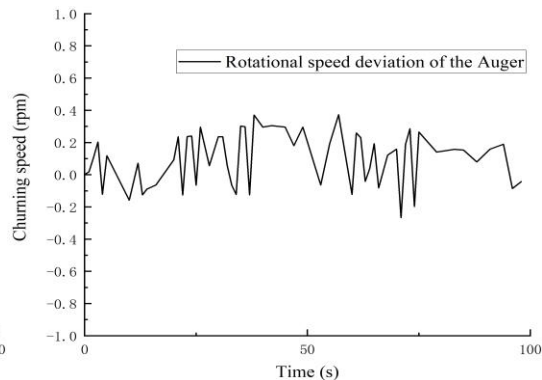
(a) Actual measured vehicle speed



(b) Simulated speed of the auger



(c) Comparison of the auger speed



(d) Rotation speed deviation of the auger

Fig. 8 - Comparison curve between simulation and actual rotation speed of the auger

CONCLUSIONS

(1) To enhance the output response characteristics of the cutter height regulation strategy, the cutter controller is optimized by combining the Whale Optimization Algorithm with PID control. The simulation results demonstrate that the optimized PID controller reduces the overshoot by 3.5% compared to the conventional PID controller and improves the rise time by 0.303 seconds. These improvements indicate that the optimized control strategy can effectively regulate the cutter height with both stability and rapidity.

(2) To effectively evaluate the controller's performance under real physical signals, hardware-in-the-loop (HIL) tests were conducted on a semi-physical simulation platform. Angle sensor variations caused by terrain undulations were used as input variables, while the output height values of the platform and the field-measured cutter height values served as comparison control experiments. The results showed that the maximum absolute error between the simulated and measured height variations was 10.58 mm. This indicates that the developed cutting platform model has a strong correlation with the actual cutting platform mechanism and can serve as a reliable basis for pre-testing the cutting platform controller.

(3) When testing control strategies for reel speed and auger speed, the speed values are influenced by the vehicle speed. First, the vehicle speeds, along with the corresponding reel and auger speeds, are recorded during the field experiment. These recorded speeds are then used as input variables for the semi-physical simulation platform, which outputs the corresponding reel and auger speeds. By comparing the deviation between the actual values and the output values of the platform under the same vehicle speed input, it is found that the mathematical expected error for the reel speed is 0.106 rad/min, and for the auger speed, it is 0.101 rad/min. The standard deviations are 0.165 rad/min and 0.172 rad/min, respectively. These results validate the reliability and feasibility of the simulation platform and provide a theoretical foundation for the development and testing of the cutting platform control system.

REFERENCES

- [1] Abboush, M., Knieke, C., & Rausch, A. (2024). A Virtual Testing Framework for Real-Time Validation of Automotive Software Systems Based on Hardware in the Loop and Fault Injection. *Sensors*, Vol. 24, pp. 3733, Germany.
- [2] Cevallos, G., Herrera, M., & Jaimez, R. (2022). A Practical Hybrid Control Approach for a Greenhouse Microclimate: A Hardware-in-the-Loop Implementation. *Agriculture*, Vol. 12, pp. 1916, Ecuador.
- [3] Chen, J., Wang, S., Lian, Y. (2018). Design and test of header parameter keys electric control adjusting device for rice and wheat combined harvester (稻麦联合收获机割台参数按键电控调节装置设计与试验). *Transactions of the Chinese Society of Agricultural Engineering*, Vol. 34, pp. 19-26, Jiangsu/China.
- [4] Hang, Q., Hu, C., & Li, R. (2024). Research on Distributed Dual-Wheel Electric-Drive Fuzzy PI Control for Agricultural Tractors. *Agriculture*, Vol. 14, pp. 1442, Shandong/China.
- [5] Ji, K., Li, Y., & Liang, Z. (2022). Device and Method Suitable for Matching and Adjusting Reel Speed and Forward Speed of Multi-Crop Harvesting. *Agriculture*, Vol. 12, pp. 213, Jiangsu/China.
- [6] Ji, K., Li, Y., Ji, B., Liang, Z., & Du, T. (2023). Discrete element method used to analyze the operating parameters of the cutting table of crawler self-propelled reed harvester. *INMATEH - Agricultural Engineering*, Vol. 71, pp. 345-355, <https://doi.org/10.35633/inmateh-71-30>
- [7] Klionovska, K., & Burri, M. (2021). Hardware-in-the-Loop Simulations with Umbra Conditions for Spacecraft Rendezvous with PMD Visual Sensors. *Sensors*, Vol. 21, pp. 1455, Germany.
- [8] Liu, W., Luo, X., Zeng, S. (2022). Performance test and analysis of the self-adaptive profiling header for ratooning rice based on fuzzy PID control (基于模糊 PID 控制的再生稻自适应仿形割台性能试验与分析). *Transactions of the Chinese Society of Agricultural Engineering*, Vol. 38, pp. 1-9, Guangdong/China.
- [9] Lu, K., Feng, G., & Ding, B. (2023). Robust H-Infinity Tracking Control for a Valve-Controlled Hydraulic Motor System with Uncertain Parameters in the Complex Load Environment. *Sensors*, Vol. 23, pp. 9092, Shenzhen/China.
- [10] Miao, F., Wu, Y., & Yan, G. (2025). Dynamic multi-swarm whale optimization algorithm based on elite tuning for high-dimensional feature selection classification problems. *Applied Soft Computing*, Vol. 169, pp. 112634-112634, Shanghai/China.
- [11] NadimiShahraki, M. H., Zamani, H., & Asghari, V. Z. (2021). A Systematic Review of the Whale Optimization Algorithm: Theoretical Foundation, Improvements, and Hybridizations. *Archives of Computational Methods in Engineering*, Vol. 30, pp. 106727, Australia.

- [12] Qin, Y., Zhao, D., Li, F. (2009). Constant Palstance Control of Combine Cylinder Based on RBF (基于RBF网络的联合收获机脱粒滚筒恒速控制). *Transactions of the Chinese Society for Agricultural Machinery*, Vol. 40, pp. 59-63, Jiangsu/China.
- [13] Shahir, F. M., Gheisarnejad, M., Sadabadi, M. S., & Khooban, M. H. (2021). A New Off-Board Electrical Vehicle Battery Charger: Topology, Analysis and Design. *Designs*, Vol. 5, pp. 51, Iran.
- [14] Shi, M., Li, Y., & Pan, Y. (2024). Design of an Adaptive Height Control System for Sugarcane Harvester Header. *Agronomy*, Vol. 14, pp. 1644, Guangxi/China.
- [15] Wei, F., Li, J., & Zhang, Y. (2023). Improved neighborhood search whale optimization algorithm and its engineering application. *Soft Computing*, Vol. 27, pp.17687-17709, China.
- [16] Wu, Z., Wang, J., & Xing, Y. (2023). Energy Management of Sowing Unit for Extended-Range Electric Tractor Based on Improved CD-CS Fuzzy Rules. *Agriculture*, Vol. 13, pp. 1303, Hubei/China.
- [17] Yao, J., Zhang, G., Wang, X., Lian, J., Liu, M., Qian, X., Wang, Y., & Liu, P. (2023). Harvest loss test and optimisation of key components of oilseed rape cutting tables. *INMATEH - Agricultural Engineering*, Vol. 71, pp. 429-440, <https://doi.org/10.35633/inmateh-71-37>
- [18] Yan, Z., Zhang, J., & Zeng, J. (2022). Three-dimensional path planning for autonomous underwater vehicles based on a whale optimization algorithm. *Ocean Engineering*, Vol. 250, pp. 111070, Harbin/China.
- [19] Zhao, Z., Shui, D., Liu, F., Zhao, B., & Wang, Z. (2024). Research regarding agricultural bionic blade development based on the mechanism of the cutting-sawing motion of the *Camponotus* mandible. *INMATEH - Agricultural Engineering*, Vol. 73, pp. 870-880, <https://doi.org/10.35633/inmateh-73-73>
- [20] Zhai, Z., Chen, Y., Zhu, S. (2023). Experiment on Electro-hydraulic Hitch Control System for Hilly and Mountainous Tractor Based on Semi-physical Simulation (基于半实物仿真的丘陵山地拖拉机电液悬挂控制试验). *Transactions of the Chinese Society for Agricultural Machinery*, Vol. 53, pp. 328-337, Beijing/China.
- [21] Zhu, X., Chi, R., Du, Y. (2022). Design of Hardware in Loop Simulation Platform for Intelligent Control System of Corn Kernel Harvester (玉米收获机低损脱粒智能控制系统半实物仿真平台设计). *Transactions of the Chinese Society for Agricultural Machinery*, Vol. 53, pp. 114-122, Beijing/China.

DESIGN AND PERFORMANCE EXPERIMENTS OF THRESHING AND SEPARATING DEVICE FOR HEAD-FEED COMBINE HARVESTER

半喂入联合收割机脱粒分离装置设计与性能试验

Liquan TIAN ^{*)}, Zhan SU, Zhao DING,

Intelligent Manufacturing College, Jinhua University of Vocational Technology.

^{*)} Corresponding author: E-mail: tlqbuct@foxmail.com

DOI: <https://doi.org/10.35633/inmateh-75-69>

Keywords: head-feed combine harvester, threshing and separating unit, segmented-differential, physical design, test study

ABSTRACT

To address the issues of incomplete threshing, separation loss, and grain breakage during the harvesting of super hybrid rice with conventional threshing and separating units in head-feed combine harvesters, a segmented-differential threshing and separating unit was developed. This unit mainly consists of a coaxial segmented-differential threshing drum and a rotary concave screen. Its structure and working principle are described in detail. A three-factor quadratic regression orthogonal rotation combination test was conducted, with the rotational speed of the segmented-differential drum, the linear velocity of the rotary concave screen, and the clamping chain speed as test factors. The grain loss rate, breakage rate, and impurity rate were taken as performance indicators. The test results were analyzed using Design-Expert 8.0.6 software to establish a mathematical model for the performance indicators and to determine the optimal combination of working parameters. Additionally, a comparative test was carried out between the segmented-differential unit and a conventional single-speed unit. The results showed that when the rotational speed of the low-speed/high-speed drum in the segmented-differential unit was 520/630 r·min⁻¹, the linear velocity of the rotary concave screen was 1.20 m·s⁻¹, and the clamping chain speed was 1.10 m·s⁻¹, the grain loss rate, breakage rate, and impurity rate were 1.95%, 0.20%, and 0.56%, respectively.

摘要

为解决半喂入联合收割机脱粒分离装置在超级杂交稻收获过程中脱粒不全、分离损失和断粒率的矛盾，研制了半喂入联合收割机分段差动脱粒分离装置。该装置主要由同轴分段-差动脱粒滚筒和旋转凹筛组成。阐述了分段式差动脱粒分离装置的结构和工作原理。以分段差动滚筒转速、旋转凹筛线速度、夹紧链速度为试验因素，以籽粒损失率、破碎率、杂质率为性能指标，进行三因素二次回归正交旋转组合设计试验。本文利用 Design-Expert8.0.6 软件对试验结果进行分析，建立脱粒分离装置性能指标数学模型，确定最佳工作参数组合。此外，本文还对分段脱粒分离装置与常规单速脱粒分离装置进行了对比试验。结果表明：当分段装置低速/高速滚筒转速为 520/630 r·min⁻¹，转凹筛线速度为 1.20 m·s⁻¹，夹紧链速度为 1.10 m·s⁻¹ 时，籽粒损失率、破碎率和杂质率分别为 1.95%、0.20% 和 0.56%。

INTRODUCTION

Rice is one of the main crops in China, accounting for about 65% of all the grain consumption (Xin et al., 2018). In recent years, the planting area of super hybrid rice has been gradually expanded, and the yield has been continuously increased. Compared with conventional rice, the biological characteristics of super hybrid rice are significantly different, such as high yield per unit area, thick stems, large grain-grass ratio, and high moisture content of stems (Xu et al, 2019; Hao et al, 2018; Wei et al, 2018). These characteristics bring new problems to the conventional threshing and separating unit for a head-feed combine harvester (Gao et al, 2017).

To improve operational efficiency and reduce losses, combine harvester manufacturers at home and abroad mostly take action to increase power, increase the threshing drum length and so on. The power of Kubota PRO888 head-feed combine harvester is 66.1 kW, its threshing drum length is 1000 mm, and its maximum operating efficiency is 0.67 hm²/h. The parameters of other foreign and domestic machines are similar.

These measures have improved the operational efficiency but failed to solve the problem that the super hybrid rice is incompletely threshed and has large losses during harvest. The current threshing and separating unit for the head-feed combine harvester is mostly composed of a single-speed drum with a fixed concave plate. For super hybrid rice or when feeding thick rice stalks, a low threshing drum speed results in insufficient threshing capacity, leading to incomplete threshing, separation losses, and even potential blockages within the drum. If the drum's rotation speed is increased, it may lead to a higher grain breakage rate and more broken stems, causing the operation quality to fall short of national standards for the three key indicators: loss rate, breakage rate, and impurity rate. To reduce incomplete threshing losses in super hybrid rice, *Wang (2016)* and *Chen et al. (2011)* studied the application of differential threshing drums for head-feed combine harvesters. *Wang, Xie & Li, (2019)*, designed a threshing drum with an adjustable diameter, enabling threshing clearance adjustment by varying the drum's diameter. Also, as a part of the combine harvester, the grid concave plate has a significant influence on the performance of the threshing and separating unit. *Wang et al., (2017)*, studied the threshing and separating units (with concave plate) of different structures and established the motion model of threshed materials. *Ding, (1987)*, established a mathematical model for the separation rate and hole size of grid concave plate. *Li et al, (2018)*, developed an adjusting mechanism for concave plate clearance to adjust the threshing clearance through a hydraulic cylinder. *Liu et al., (2018)*, studied a threshing and separating unit equipped with a single-speed drum and rotary concave plate. Its operational efficiency and performance were significantly improved compared to the unit with a fixed concave plate. However, the studies were limited to units with either a single-speed drum and fixed concave plate, or a single-speed drum combined with a rotary concave plate.

To address the issues of incomplete threshing, separation loss, and high grain breakage during the harvest of super hybrid rice using conventional threshing and separating units in head-feed combine harvesters, a segmented-differential threshing and separating unit was developed. This unit consists of a segmented-differential threshing drum and a rotary grid concave plate. This paper details the structure and working principle of the new unit, evaluates its performance through a multi-factor optimization experiment, and investigates its overall efficiency. The goal is to enhance threshing effectiveness and reduce losses, thereby providing a theoretical foundation for the innovative design of key components in head-feed combine harvesters.

MATERIALS METHODS

Main structure and working principle

The segmented-differential threshing and separating unit for a head-feed combine harvester is mainly composed of low-speed threshing drum, drum linkage, high-speed threshing drum, threshing drum shaft. The threshing drum consist of a leading-in spiral, rotary grid concave plate, belt wheel for high-speed drum, belt wheel for low-speed drum, and the driving wheel for grid concave plate, etc., as shown in figure 1 (the fairing cap on threshing and separating unit is not shown). The power of the machine is transferred from a driving wheel to each mechanism through a belt. In the segmented-differential threshing drum, the high-speed threshing drum and the low-speed threshing drum share the same draft and diameter. The high-speed and low-speed threshing drums are connected with the drum linkage and driven respectively by the belt wheel for high-speed/low-speed drums. The rotary grid concave plate is installed in the arc-shaped concave screen frame. The concave plate grid strips are also in the arc-shaped concave screen frame. They are driven by the driving wheel for the grid concave plate to rotate. Meanwhile, this guarantees the threshing clearance between the high-speed/low-speed threshing drum and the rotary concave plate to be 20 mm (*Wang & Ge, 1982*).

When the head-feed combine harvester operates, cut rice plants are clamped by the feeding chain into the threshing area through the leading-in spiral. The rice plants are firstly threshed and separated by carding and impact effect in the low-speed threshing drum, then threshed and separated by the high-speed threshing drum. The threshed grains afterwards fall onto the vibrating screen surface through the rotary grid concave plate, and will be put into subsequent cleaning operation. During the threshing process, most grains with small connection force are threshed and separated in the low-speed drum, which reduces the grain breakage rate. A few grains with large connection force are threshed and separated in the high-speed drum, which increases threshed rate and separation rate and reduces the grain loss rate. The rotary grid concave plate rotates, and the linear velocity direction of the upper grid surface is the same as that of the threshing drum. The rotary grid surface can thresh the ears of rice plants got to the grid concave plate and prevent blockage in the threshing drum.

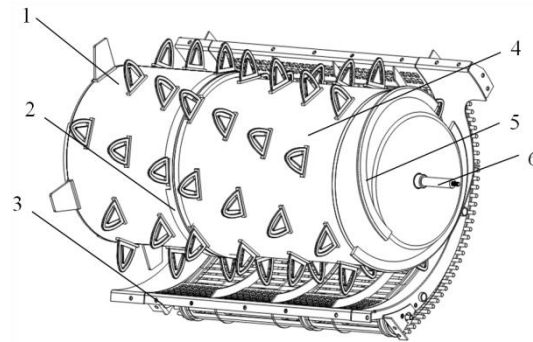


Fig. 1 - Segmented-differential threshing and separating unit

1. High-speed threshing drum; 2. Drum linkage; 3. Rotary grid concave plate; 4. Low-speed threshing drum;
5. Leading-in spiral; 6. Threshing drum shaft

Threshing drum

The structure of the threshing drum is closed, mainly composed of a coaxial straight high/low-speed threshing drum, drum linkage, threshing arcuate teeth, low-speed drum shaft, high-speed drum shaft, leading-in spiral, grass cutter, etc., as shown in figure 2. The leading-in spiral and the low-speed threshing drum are firmly attached, and two spiral guiding blades are set to comb and push the rice ears (Wang, Lv & Chen, 2017). The high-speed and low-speed threshing drums are connected by a linkage, which rotates with the low-speed threshing drum. The low-speed drum shaft is a hollow shaft, which is driven by the low-speed belt wheel and drives the low-speed threshing drum simultaneously. The high-speed drum shaft is set in the low-speed drum shaft through a bear, which is driven by the high-speed belt wheel and drives the high-speed threshing drum simultaneously. The high-speed and low-speed belt wheels are set on the left side of the drum shaft and driven respectively by the belt wheel of the machine power-output shaft with different drive ratios. The threshing arcuate teeth are helically arranged on the drum surface with an equal pitch, featuring a 4-start thread, a helical angle of 50°, and a total of 15 rows of threshing arcuate teeth.

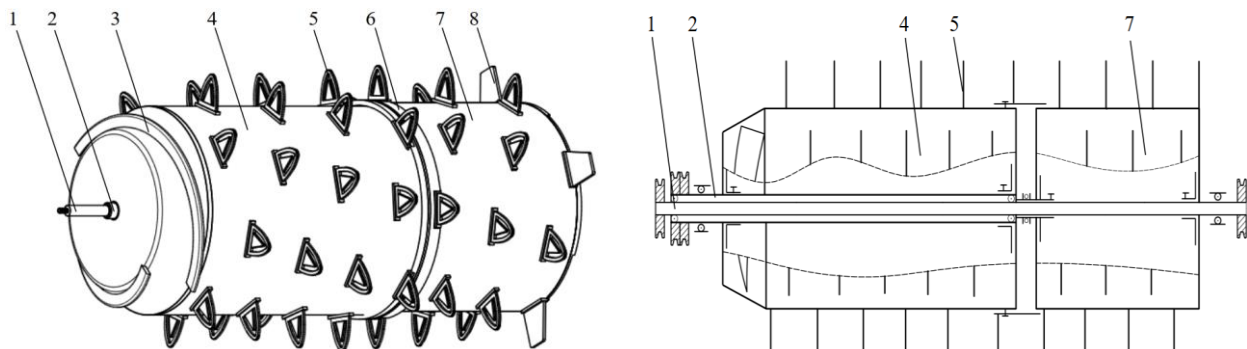


Fig. 2 - Threshing drum

1. High-speed drum shaft; 2. Low-speed drum shaft; 3. Leading-in spiral; 4. Low-speed threshing drum;
5. Threshing arcuate teeth; 6. Drum linkage; 7. High-speed threshing drum; 8. Grass cutter

The segmented-differential rotary threshing and separating unit for the head-feed combine harvester mainly utilize the carding and impact of threshing arcuate teeth on the ears of rice, so that the grains get the energy to fall off from the ears, thus achieving threshing and separation. Threshing drum length determines the threshing process. Generally, the longer the drum is, the longer the rice ears stay in the threshing chamber, and the longer the threshing arcuate teeth act on the rice ears, but it increases the threshing power consumption. According to the overall structure of the segmented-differential threshing and separating unit and the research results of the distribution law of threshed materials in the early stage (Peng et al, 2016), the total length of the threshing drum is determined to be 1000 mm, and the length of low-speed threshing drum (that is, the length of the grid concave plate in low-speed section) can be obtained from formula (1).

$$L = \frac{\varepsilon Q}{\eta \gamma R_1} \quad (1)$$

where: L – length of grid concave plate in the section of low-speed threshing drum (length of low-speed threshing drum), m; ε – ratio of the feeding rate undertaken by the low-speed threshing drum, taken as 0.85.

By substituting the relevant values into equation (1), L is 0.682 m, 2/3 (that is, 0.667 m) of the threshing drum length is taken as the low-speed threshing drum, and the remaining 1/3 is the high-speed threshing drum.

Rotary grid concave plate

The structure of the rotary grid concave plate is as shown in figure 3. Several grid strips are set in three groups of A12 type sleeve roller chain pin holes at two ends and the middle part to form a flexible screen surface consisting of grid strips. The two ends of the roller chain are connected to form a semicircular grid strip concave screen with a width of 800 mm. The width of each grid hole (that is, the spacing of grid strips) is 11 mm, and the length of grid holes is 50 mm. The inner core of the concave grid strip is a steel wire with a diameter of 5 mm, and fit together with steel tube with a diameter of 8 mm outside. The steel tube can rotate around the inner core. The screen surface can vibrate, making the threshed materials separate quickly and preventing blockage in the threshing drum. Concave plate grid strips use the upper and lower shaping platen as rotary track, using the threshing drum belt wheel to drive the grid concave plate driving wheel, and using a coaxial driving chain wheel with the driving wheel to drive the concave plate grid strip chain, so that the grid concave plate rotates around the driven chain wheel along the rotary track.

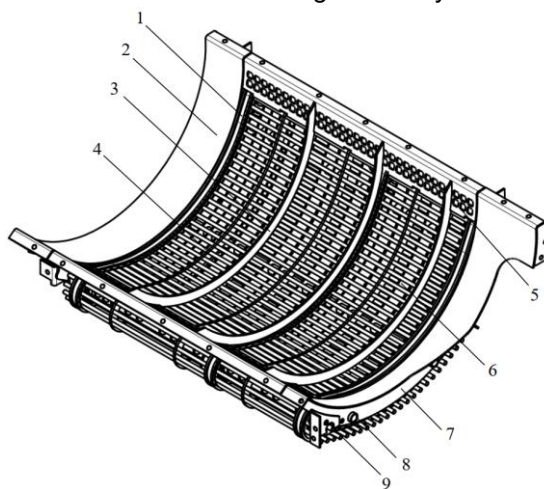


Fig. 3 - Rotary grid concave plate

1. Grid strip driving chain; 2. Concave screen frame; 3. Upper shaping platen; 4. Grid strip mounting chain;
5. Multi-hole side plate; 6. Lower shaping platen; 7. Grid strip; 8. Horizontal axis; 9. Driven shaft

The operation efficiency of the Segmented-differential rotary threshing and separating unit is related to the action area of the grid concave plate (the surrounding area of rotary grid concave plate) (Jin & Liu, 1980).

$$S = \frac{Q}{\eta} = E \cdot R_1 \cdot \gamma \quad (2)$$

where: S – surrounding area of rotary grid concave plate, m^2 ;
 η – productivity per unit area of grid concave plate, taken as $2.0 \text{ kg}/(m^2 \text{ s})$;
 Q – feeding quantity (i.e. working flow), taken as 1.5 kg/s ;
 E – width of head-feed grid concave plate, taken as 0.8 m ;
 R_1 – radius of rotary grid concave plate, taken as 0.295 m ;
 γ – wrap angle of rotary grid concave plate, rad.

By substituting the relevant values into equation (2), the surrounding area of the rotary grid concave plate is 0.75 m^2 , and the wrap angle is rounded to 180° .

TEST APPARATUS

Based on theoretical analysis and practical experience in the threshing and separating operations of head-feed combine harvesters, this study investigates how the working parameters of the segmented-differential threshing and separating unit, including the rotational speeds of the high-speed and low-speed threshing drums, the linear velocity of the rotary grid concave plate, and the clamping chain speed, affect the grain loss rate, breakage rate, and impurity rate. A segmented-differential threshing and separating test bench was designed for the head-feed combine harvester, and performance tests were conducted using a three-factor quadratic regression orthogonal rotation combination design.

Test bench

The segmented-differential threshing and separating test bench for the head-feed combine harvester includes: rice plants conveying platform, segmented-differential threshing and separating unit (high-speed/low-speed threshing drum, clamping chain, rotary grid concave plate, and cleaning vibrating screen), adjustable-speed motor and control box, etc., as shown in figure 4. The rice plant conveying platform consists of two conveyors connected in series, with adjustable height and a stepless variable conveying speed ranging from 0 to 2 m·s⁻¹. The power of the threshing drum adjustable-speed motor is 15kW, and the rotational speed of the high-speed/low-speed threshing drum is stepless speed changing. The power of the clamping chain driving motor is 7.5 kW, and the power of the rotary grid concave plate driving motor is 2 kW. The motor speed is adjusted by the frequency converter and the relevant data are recorded.

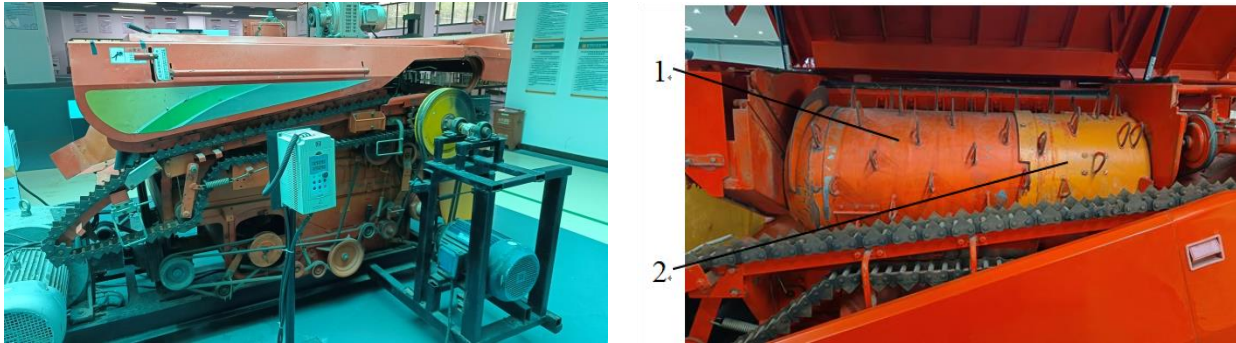


Fig. 4 - Threshing and separating test bench

1. Low-speed threshing drum; 2. High-speed threshing drum

Test material

The selected test material is "Yongyou 15#", which is widely planted in Zhejiang province, China. The basic characteristic parameters of rice are as shown in table 1.

Table 1

Basic characteristic parameters of rice	
Items	Parameters
Height of plants / cm	95 ~ 110
Length of ears / cm	18.5 ~ 25.5
Moisture content of grains / %	23.2~24.6
Moisture content of stems / %	66.4
Grain-grass ratio (stubble height 15 cm)	2.56:1
Thousand kernel weight / g	28.9
Yield per unit area / kg / ha	9890

RESULTS AND ANALYSIS

Performance indicators

Before the test, the conveyor speed was set according to the set feeding rate (working flow) of 1.5 kg/s. In each group of tests, rice plants were evenly spread in the designated range of conveyor. The lengthwise direction of rice plants was perpendicular to the conveying direction, and the rice ears were toward the threshing drum. Based on "Thresher-Testing method" (GB/T 5982-2017), the test was carried on.

According to the feeding rate and grain-grass ratio, the total grain weight obtained in each test was calculated and denoted as W . The total weight of grains sampled at the grain receiving port was denoted as W_1 . The broken grains and impurities were picked by hand and weighed respectively, and denoted as W_p and W_z . In the discharges collected at the cleaning chamber outlet and straw outlet, the broken ears containing grains and the unthreshed grains were picked and weighed, which were denoted as the cleaning loss W_q and separation loss W_j . Thus, the loss rate y_1 , breakage rate y_2 and impurity rate y_3 can be calculated by the following formulas.

$$y_1 = \frac{W_q + W_j}{W} \times 100\% \quad (3)$$

$$y_2 = \frac{W_p}{W_1} \times 100\% \quad (4)$$

$$y_3 = \frac{W_z}{W_1} \times 100\% \quad (5)$$

Test scheme

To explore how the parameters such as the rotational speed of high-speed/low-speed threshing drum, the linear velocity of rotary grid concave plate and the clamping chain speed influence the threshing and separating performance, the parameter variation range was controlled properly according to the production practice and single-factor test, and the three-factor quadratic regression orthogonal rotation combination design test was performed. The levels of individual factors are shown in table 2.

Table 2

Levels of test factors			
Coded value	Rotational speed of low-speed / high-speed drum	Linear velocity of rotary concave plate	Clamping chain speed
	$x_1 / (\text{r} \cdot \text{min}^{-1})$	$x_2 / (\text{m} \cdot \text{s}^{-1})$	$x_3 / (\text{m} \cdot \text{s}^{-1})$
-1.682	480/590	0.40	0.60
- 1	500/610	0.72	0.80
0	530/640	1.20	1.10
1	560/670	1.68	1.40
1.682	580/690	2.00	1.60

According to 23 groups of quadratic regression orthogonal rotation combination design tests, the test scheme and results are shown in table 3. Where y_1 is the loss rate, y_2 is the breakage rate and y_3 is the impurity rate.

Table 3

Test scheme and results						
Test no.	Test factors			Test indicators		
	Rotational speed of low-speed / high-speed drum $x_1 (\text{r} \cdot \text{min}^{-1})$	Linear velocity of rotary concave plate $x_2 (\text{m} \cdot \text{s}^{-1})$	Clamping chain speed $x_3 (\text{m} \cdot \text{s}^{-1})$	Loss rate $y_1 (\%)$	Breakage rate $y_2 (\%)$	Impurity rate $y_3 (\%)$
1	500/610	0.72	0.80	1.77	0.56	0.84
2	560/670	0.72	0.80	2.34	1.04	0.94
3	500/610	1.68	0.80	1.96	0.53	0.85
4	560/670	1.68	0.80	2.28	1.14	1.42
5	500/610	0.72	1.40	2.88	0.17	0.78
6	560/670	0.72	1.40	2.62	0.40	0.71
7	500/610	1.68	1.40	2.82	0.27	0.67
8	560/670	1.68	1.40	2.40	0.42	1.12
9	480/590	1.20	1.10	2.42	0.34	0.63
10	580/690	1.20	1.10	2.91	0.97	1.57
11	530/640	0.40	1.10	2.61	0.32	0.74
12	530/640	2.00	1.10	2.39	0.37	0.75
13	530/640	1.20	0.60	1.78	1.12	1.36
14	530/640	1.20	1.60	2.93	0.17	0.64
15	530/640	1.20	1.10	1.54	0.33	0.62
16	530/640	1.20	1.10	1.92	0.15	0.37
17	530/640	1.20	1.10	2.06	0.17	0.43
18	530/640	1.20	1.10	1.94	0.25	0.64
19	530/640	1.20	1.10	1.75	0.27	0.62
20	530/640	1.20	1.10	1.95	0.18	0.60
21	530/640	1.20	1.10	1.66	0.16	0.50
22	530/640	1.20	1.10	1.97	0.28	0.62
23	530/640	1.20	1.10	1.88	0.31	0.78

To apply the Expert8.0.6 software to the regression analysis of test data, the rotational speed of low-speed threshing drum x_1 , the linear velocity of rotary concave plate x_2 and clamping chain speed x_3 were selected as parameters, and the corresponding regression equation was obtained.

$$\begin{cases} y_1 = 70.31 - 0.28x_1 - 2.15x_2 + 9.24x_3 + 0.0003x_1^2 + 0.86x_2^2 + 1.63x_3^2 - 0.02x_1x_3 \\ y_2 = 41.54 - 0.16x_1 - 0.37x_2 + 0.82x_3 + 0.0002x_1^2 + 0.17x_2^2 + 1.64x_3^2 - 0.01x_1x_3 \\ y_3 = 60.23 - 0.21x_1 - 4.51x_2 - 3.93x_3 + 0.0002x_1^2 + 1.57x_2^2 + 0.009x_1x_2 \end{cases} \quad (6)$$

Test results and analysis

To intuitively analyze the relationship between individual parameters and the threshing and separating performance indicators, the Design-Expert8.0.6 software was used to obtain the response surface, as shown in figure 5.

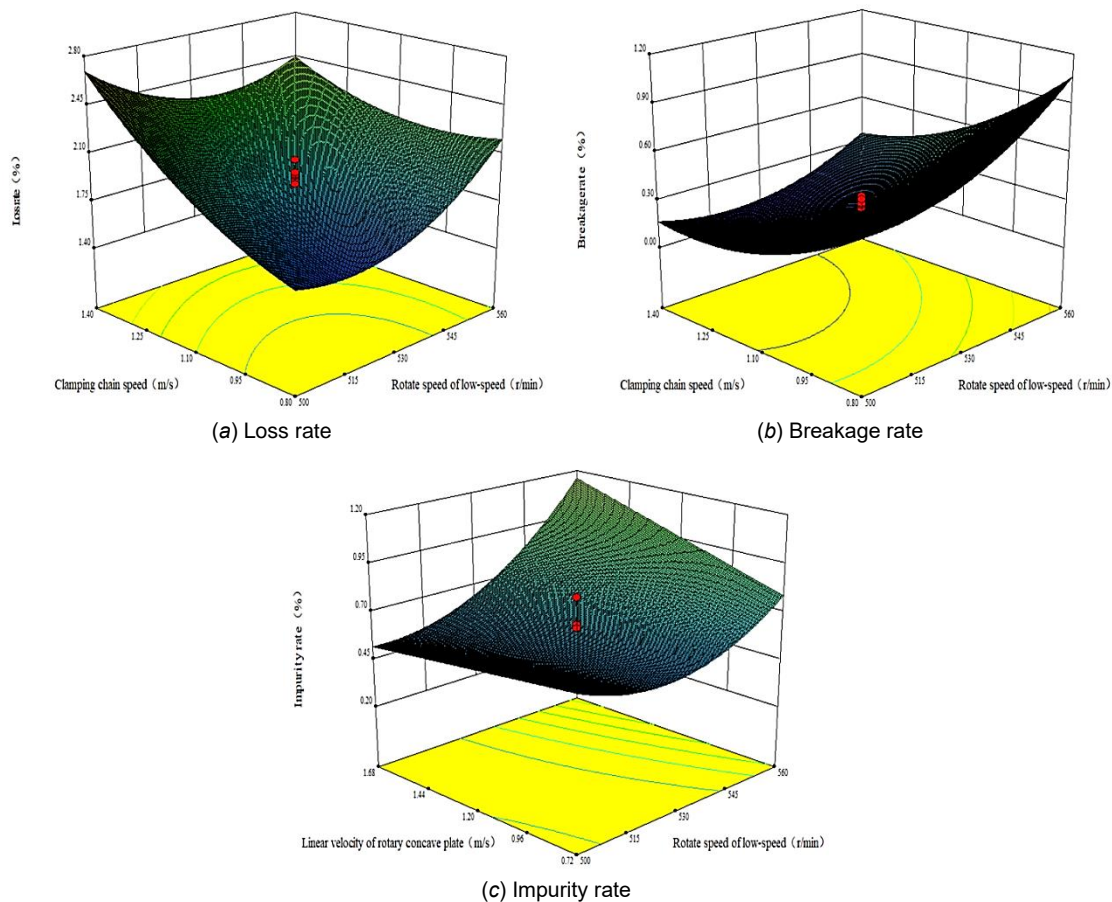


Fig. 5 - Response surfaces of individual factor's influence on performance indicators

According to the analysis of equation (6) and figure 5, it can be seen from figure 5(a) that in the interaction between the rotational speed of high-speed/low-speed threshing drum x_1 and clamping chain speed x_3 , the rotational speed of high-speed/low-speed threshing drum influences the loss rate more significantly. As the rotational speed of the high-speed/low-speed threshing drum increases, the clamping chain speed increases, and the loss rate of the threshing and separating unit increases gradually. It can be seen from figure 5(b) that in the interaction between the rotational speed of high-speed/low-speed threshing drum x_1 and clamping chain speed x_3 , both of them have a significant impact on the breakage rate of threshing and separating unit, indicating that when the clamping chain speed is low, the activation times of threshing drum on grains in rice ears increases, and the higher the rotational speed of the drum is, the higher the grain breakage rate is. It can be seen from figure 5(c) that in the interaction between the rotational speed of high-speed/low-speed threshing drum x_1 and the linear velocity of rotary concave plate x_2 , the rotational speed of high-speed/low-speed threshing drum has a significant impact on the impurity rate. As the rotational speed of the threshing drum increases, the broken stems and leaves in the threshing chamber increases, causing that the grain impurity rate gradually increases.

The grain loss rate, breakage rate and impurity rate are important indicators to evaluate the performance of the segmented-differential threshing and separating unit, and should be minimized under their individual constraint conditions. To obtain the optimal combination under the constraint conditions, the multi-objective variables optimization method is adopted to establish the nonlinear model by combining the boundary conditions of each factor, as follows:

$$\begin{cases} \min y_1 \\ \min y_2 \\ \min y_3 \\ \text{s. t. } (480/590)r/\text{min} \leq x_1 \leq (580/690)r/\text{min} \\ 0.4\text{ m/s} \leq x_2 \leq 2.0\text{ m/s} \\ 0.6\text{ m/s} \leq x_3 \leq 1.6\text{ m/s} \\ 0 \leq y_i(x_1, x_2, x_3) \leq 1 \end{cases} \quad (7)$$

Formula (7) was used to optimize multi-objective parameters based on the Optimization module of Design-Expert6.0.10 software. It was found that when the rotational speed of the high-speed/low-speed threshing drum was 518/626 r·min⁻¹, the linear velocity of rotary grid concave plate was 1.21 m·s⁻¹ and the clamping chain speed was 1.10 m·s⁻¹, the corresponding grain loss rate, breakage rate and impurity rate were 1.87%, 0.18% and 0.56%, respectively.

Discussion and analysis

To verify the performance of the segmented-differential threshing and separating unit and contrast it to the conventional single-speed threshing and separating unit, the boundary dimension and structure of the two units are basically the same, which are "two-speed drum (arcuate-tooth) + rotary concave plate" and "single-speed drum (arcuate-tooth) + fixed concave plate" respectively. The rice variety for the contrast test is YongyouNo.15, and the characteristic parameters are shown in table 1. The feeding rate of the two units is both 1.5 kg/s, which is artificial feeding. The rotational speed of the high-speed/low-speed threshing drum in the segmented-differential threshing and separating unit is set to 520/630 r·min⁻¹, and the rotational speed of the threshing drum in single-speed threshing and separating unit is set to 600 r·min⁻¹. After threshing, the threshed materials are collected and counted by a sampling tray. The sampling tray is divided into 6 grids along the axial direction of the threshing drum with each grid length of 167 mm, of which 4 grids are located under the low-speed threshing drum and 2 grids are located under the high-speed threshing drum.

Performance analysis of two kinds of threshing and separating units

In terms of the grain loss rate, breakage rate and impurity rate in the front 2/3 part of the threshing drum in the axial direction, the conventional single-speed threshing and separating unit was higher than the segmented-differential threshing and separating unit in the axial direction, indicating that the rotational speed of threshing drum had a significant influence on the three indicators of threshing and separating performance. In the back 1/3 part of the threshing drum in the axial direction, although the rotational speed of high-speed threshing drum is higher than that of single-speed threshing drum, the breakage rate and impurity rate of the conventional single-speed threshing and separating unit were still higher than those of the segmented-differential threshing and separating unit. The reason is that the broken grains produced in the forepart of the single-speed threshing and separating unit were mixed up with the stem layer to the posterior to separate. The impurities in the forepart of the conventional single-speed threshing and separating unit were not separated enough, which caused that the posterior impurity rate was higher than that of the segmented-differential threshing and separating unit. This also indicated that the posterior drum played an important role to threshing and separating.

Through determination, the contrast of performance indicators between the segmented-differential threshing and separating unit and the conventional single-speed threshing and separating unit is shown in table 4. It can be seen that the performance of the segmented-differential threshing and separating unit is significantly better than that of conventional single-speed threshing and separating unit.

Table 4

Comparison of grain breakage rate, impurity rate and loss rate

Threshing and separating unit	Breakage rate / %	Impurity rate / %	Loss rate / %
Single-speed drum + fixed concave plate	0.38	0.70	2.07
Two-speed drum + rotary concave plate (segmented-differential)	0.20	0.56	1.95

CONCLUSIONS

Taking the segmented-differential threshing and separating unit of a head-feed combine harvester as the research focus, a model describing the grain stress and movement within the unit was developed, and the structure and working principle of the unit were thoroughly analyzed. By effectively utilizing the dual-speed threshing drum and the rotary grid concave plate, the performance of the head-feed threshing mechanism and the operational efficiency of the head-feed combine harvester were significantly improved.

(1) With the rotational speed of high-speed/low-speed drum, the linear velocity of rotary grid concave screen, and the clamping chain speed as the test factors, the grain loss rate, breakage rate and impurity rate as the performance indicators, three-factor quadratic regression orthogonal rotation combination design method was used to establish the mathematical model between the factors and indicators. The results of the test were processed using the Design-Expert8.0.6 software and showed that the rotational speed of the high-speed/low-speed threshing drum was 518/626 r·min⁻¹, the linear velocity of rotary grid concave plate was 1.21 m·s⁻¹ and clamping chain speed was 1.10 m·s⁻¹. The grain loss rate, breakage rate and impurity rate were 1.87%, 0.18% and 0.56%, respectively.

(2) The loss rate is significantly affected by the rotational speed of the high-speed/low-speed threshing drum. The loss rate will increase gradually with the increase in the rotational speed of the high-speed/low-speed threshing drum. Both the rotational speed of the high-speed/low-speed threshing drum and clamping chain speed significantly affect the breakage rate. The grain breakage rate would increase when the clamping chain speed decreases or the rotational speed of the drum increases. The rotational speed of high-speed/low-speed threshing drum has a significant impact on the impurity rate. The grain impurity rate will gradually increase with the increase in the rotational speed of the threshing drum.

(3) The performances contrast test between the segmented-differential threshing and separating unit and the conventional single-speed threshing and separating unit showed that: the drum speed of the segmented-differential threshing and separating unit was 520/630 r·min⁻¹, the linear velocity of rotary grid concave plate was 1.20 m·s⁻¹ and clamping chain speed was 1.10 m·s⁻¹. The grain loss rate, breakage rate and impurity rate were 1.95%, 0.20% and 0.56%, respectively. The performance indicators were better than the regulations of the industry standard.

(4) This study was conducted using the Yongyou No.15 rice variety, with a moisture content ranging from 23.3% to 24.5%. Future research will evaluate the performance of the segmented-differential threshing and separating unit when processing other rice varieties. Additionally, the impact of higher throughput on the unit's threshing and separating performance will also be investigated.

ACKNOWLEDGMENTS

This work was supported by the National Natural Science Foundation of China (Grant No.32272002, 52275253) and Jinhua science and technology research project (Grant No.2023-2-025.2023-2-024).

REFERENCES

- [1] Chen, N., Yu, H.J., Chen, D.J., Gong, Y.J., & Zhang, Z.Z. (2011). Design and Test on Coaxial Differential Threshing Rotor of Head-feed Combine Harvester (半喂入联合收获机同轴差速脱粒滚筒设计与试验). *Transactions of the Chinese Society for Agricultural Machinery* 42(S): 39-42.
- [2] Gao, Z.P., Xu, L.Z., Li, Y.M., Wang, Y.D. & Sun, P.P. (2017). Vibration measure and analysis of crawler-type rice and wheat combine harvester in field harvesting condition (履带式稻麦联合收获机田间收获工况下振动测试与分析). *Transactions of the Chinese Society of Agricultural Engineering (Transactions of the CSAE)*. 33: 48-55, <https://doi.org/10.11975/j.issn.1002-6819.2017.20.006>.
- [3] Hao, S.R., Dong, B.H., Zhou, P., Pan, Y.C. & Wang, Z.X. (2018). The Effects of Water Stress on Growth and Resistance of Super Rice Against Loading (水分胁迫对超级稻生长发育和抗倒伏能力的影响). *Journal of Irrigation and Drainage*, 37: 1-8, <https://doi.org/10.13522/j.cnki.ggpps.20180118>.
- [4] Jin, C.L., Liu, G.H., (1980). Testing Analysis of Threshing and Cleaning Apparatuses of Head Feeding Combine (半喂入联合收割机的脱粒、清选机构试验分析). *Transactions of the Chinese Society for Agricultural Machinery*, 11: 87-98.
- [5] Liu, Z.H., Dai, S.J., Li, M.Q., Chen, N., Wang, Z.P., & Chen, D.J. (2018). Design and test of the head - feeding harvester's moving grate concave unit (半喂入联合收割机活动栅格凹板装置设计与试验). *Journal of Chinese Agricultural Mechanization*, 39: 9-14. <https://doi.org/10.13733/j.jcam.issn.2095-5553.2018.05.003>.

- [6] Liu, Z.H., Dai, S.J., Tian, L.Q., Chen, N., Wang, Z.M., & Chen, D.J. (2018). Design and Experiment on Rotary Grate Concave Threshing-Separating Unit of Head-feeding Combine Harvester (半喂入联合收获机回转式栅格凹板脱分装置设计与试验). *Transactions of the Chinese Society for Agricultural Machinery*, 49: 169-178. <https://doi.org/10.6041/j.issn.1000-1298.2018.05.019>.
- [7] Li, Y.M., Wang, J.P., Xu, L.Z., Tang, Z., Xu, Z.H., & Wang, K.J. (2018). Design and Experiment on Adjusting Mechanism of Concave Clearance of Combine Harvester Cylinder (联合收获机脱粒滚筒凹板间隙调节装置设计与试验). *Transactions of the Chinese Society for Agricultural Machinery*, 49(8): 68-75. <https://doi.org/10.6041/j.issn.1000-1298.2018.08.008>.
- [8] Peng, Y.X., Li, X., Liu, D.W., Xie, F.P., & Ren, S.G. (2016). Design and performance experiment of a threshing cylinder with longitudinal single axial flow (单纵轴流脱粒滚筒的设计与性能试验). *Journal of Hunan Agricultural University (Natural Sciences)*, 42: 554-560. <https://doi.org/10.13331/j.cnki.jhau.2016.05.017>.
- [9] Xin, L.J., Li, P.H., & Fan, Y.Z. (2018). Change of food consumption with population age structure in China (中国食物消费随人口结构变化分析). *Transactions of the Chinese Society of Agricultural Engineering (Transactions of the CSAE)*, 34: 296-302. <https://doi.org/10.11975/j.issn.1002-6819.2018.14.038>.
- [10] Xu, Y. D., Zhu, K.Y., Zhang, X.C., Wang, Z.Q., & Yang, J.C. (2019). Analysis in agronomic and physiological traits of green super rice. *Acta Agronomica Sinica*, 45: 70-80. <https://doi.org/10.3724/SP.J.1006.2019.82036>.
- [11] Wei, C.C., Li, Y.M., Xu, L.Z., Liang, Z.W., & Wang, J.P. (2018). Design and Experimental Study of Large Feed Quantity Crawler Full Feeding Rice Combine Harvester (大喂入量水稻联合收获机脱粒清选装置的设计与试验). *Journal of Agricultural Mechanization Research*, 8:70-74. <https://doi.org/10.3969/j.issn.1003-188X.2018.08.013>.
- [12] Wang, Z.M., Lv, P.M., Chen, N., & Ma, G., (2017). Study on distribution spectrum of grain connection force and differential-speed threshing device for combine harvester (水稻籽粒连接力分布频谱分析及联合收割机差速脱粒装置研究). *Journal of Zhejiang University (Agric.& Life Sci.)*. 43: 120-127. <https://doi.org/10.3785/j.issn.1008-9209.2016.07.271>.
- [13] Wang, Z.M., Lv, P.M., Zhou, X., Chen, N., & Chen, D.J. (2017). Performance of Threshing-separating-cleaning Unit of 4LZS-1.8 Combine-Harvester Based on Orthogonal Experiment (4LZS-1.8 型联合收割机脱分选系统性能正交试验). *Journal of Jilin Agricultural University*, 39: 360-365. <https://doi.org/10.13327/j.jjlau.2017.3361>.
- [14] Wang, Z.M., Lv, P.M., Chen, N., Li, H., Liu, Z.H., & Chen, D.J. (2016). Design and Experiment on Axial-flow Differential-speed Threshing Separating Cleaning Unit (横置差速轴流脱分选系统设计与试验). *Transactions of the Chinese Society for Agricultural Machinery*, 47: 53-61. <https://doi.org/10.6041/j.issn.1000-1298.2016.12.008>.
- [15] Wang, X.W., Xie, F.P., Li, X., Liu, D.W., & Wang, X.S. (2019). Design and experiment on threshing and separation device with adjustable concave clearance (可调间隙脱粒分离装置的设计与试验). *Journal of Hunan Agricultural University (Natural Sciences)*, 45: 205-211. <https://doi.org/10.13331/j.cnki.jhau.2019.02.017>.
- [16] Wang, Z. (2017). *Study on Work Mechanism and Design of Axial Flow Differential-speed Threshing-separating-cleaning Unit*. Chang'an University.
- [17] Wang, C.Z., & Ge, Y.J. (1982). A research on axial-flow threshing cylinder. *Transactions of the Chinese Society for Agricultural Machinery*, 13: 55-72.
- [18] Ding, H.D. (1987). Discussion on the hole theory design of axial flow drum separating concave plate(轴流滚筒分离凹板的孔格理论设计探讨). *Transactions of the Chinese Society for Agricultural Machinery*, 18: 80-84.

RESEARCH ON HYDRAULIC DRIVE CHASSIS OF TOBACCO HARVESTER IN SOUTHERN HILLY AREA

针对南方丘陵地区的烟叶收获机液压驱动底盘研究

Ting GUO¹⁾, Dandan ZHANG²⁾, Shuo LIN³⁾, Tao ZHANG⁴⁾, Mingduan LU^{*5)}

¹⁾ Hunan Tobacco Company Chenzhou Branch, Chenzhou 423000, China

²⁾ Guangdong Tobacco Company Shaoguan Branch, Shaoguan 512000, China

³⁾ Anhui Tobacco Company Wannan Branch, Wannan 242500, China

⁴⁾ Hunan Tobacco Company Changde Branch, Changde 415000, China

⁵⁾ College of Engineering and Technology, Southwest University, Chongqing 400715, China

Tel: +86-19562226905; E-mail: d15512606935@163.com

DOI: <https://doi.org/10.35633/inmateh-75-70>

Keywords: tobacco harvester, hydraulic drive, steering wheel control, chassis design

ABSTRACT

In order to solve the problems of inconvenient operation and easy loss of control levers in traditional tracked harvesters, this paper designs a hydraulic-driven chassis based on steering wheel control, and the structure and working principle of the chassis are described. The parameters such as track grounding length and drive wheel diameter are calculated; the design of the hydraulic drive system of the chassis is completed, and the driving control strategy is proposed. The test results show that the maximum speed of the chassis is 0.79 m/s, the minimum turning radius is 766 mm, and the failure rate tobacco rod clamping in field tests is only 4.37%. This design meets the needs of field operations, with high operability, stability, and ability, providing theoretical and practical basis for the development of tracked tobacco leaf harvesters.

摘要

为解决传统履带式收获机底盘操控不便、操纵杆易失位等问题, 本文设计了一种基于方向盘控制的液压驱动底盘, 并阐述了底盘结构、工作原理。对履带接地长度、驱动轮直径等参数进行了计算; 完成了底盘液压驱动系统的设计, 并提出了行驶控制策略。试验结果表明, 底盘最高速度为 0.79 m/s, 最小转弯半径为 766 mm, 田间试验烟杆夹持失效率仅为 4.37%。该设计满足田间作业需求, 具备较高操控性、稳定性和适应性, 为履带式烟叶收获机的发展提供了理论与实践依据。

INTRODUCTION

The tobacco industry occupies an important position in China's national economy (Liu et al., 2024), and the tobacco growing areas in China are mainly concentrated in 20 provinces and cities in the south (Tan et al., 2023). At present, the harvest of tobacco leaves mainly relies on manual labor, with high labor intensity, high cost and low operation efficiency, which restricts the rapid development of tobacco industry (Xue et al., 2024; Zhou et al., 2024). Therefore, the realization of mechanized tobacco harvesting is of great significance to the development of the industry.

Hydraulic crawler chassis is a key component of harvesting machinery (Wang B et al., 2024; Xi et al., 2024). Its outstanding advantages lie in strong traction and adaptability, low ground specific pressure, excellent obstacle crossing and load carrying capacity, and can work efficiently under complex conditions (Pan et al., 2024; Xiao et al., 2024; Du et al., 2023). By directly connecting the hydraulic pump and hydraulic motor, the hydraulic system eliminates transmission components such as transmission and differential, greatly improving transmission efficiency. Based on the growth characteristics of sweet sorghum, Wu L et al., (2018), designed a hydraulic driven harvester chassis, which uses dual pumps to drive the motor and can adjust the operation speed according to the density of plants. Wang P et al., (2022), designed 4CJZ-1000 self-propelled crawler tea picker. The crawler chassis controlled the power output of the gasoline engine through a pull-press joystick to realize movement and stopping. Xiao Wenying et al. (2023), designed a tractor hydraulic drive system and verified its applicability under large loads through field tests. Li et al., (2024), designed a fully hydraulic tracked power chassis, which uses a closed triple plunger pump to provide power for the driving and operating mechanism. Wang et al., (2023), designed a special chassis for the Chinese sugarcane harvester, and the hydraulic system realized the steering function by controlling the steering cylinder valve core.

At present, the variable pump displacement adjustment of most hydraulic systems is still achieved by turbine rack drive or joystick control valve, which has some problems such as inflexible control, out of position and unstable oil supply, which seriously affects the handling performance and safety of tracked vehicles.

Aiming at the above problems, a hydraulic driven tobacco leaf harvesting machine chassis is designed in this paper. The steering wheel control mechanism is used instead of the traditional joystick to realize the straight running and turning control of the chassis. Prototype production and performance verification were carried out to provide equipment support for tobacco leaf harvest in hilly and mountainous areas of South China.

MATERIALS AND METHODS

Structure of tobacco harvester

In order to meet the requirements for baking the upper leaf belt stalks after harvesting the lower leaves, the tobacco leaf harvester is primarily designed to perform two tasks: harvesting the upper leaves of the tobacco stalk and crushing the remaining stalk. The harvester consists of a chassis, control cabinet, soil excavation mechanism, clamping transmission mechanism, cutting mechanism, crushing and collection mechanism, guide collection mechanism, and collection box, as shown in Figure 1.

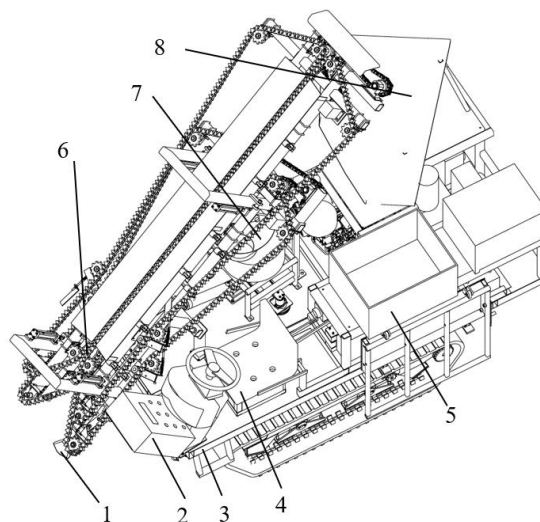


Fig. 1 - Schematic diagram of tobacco leaf harvester

1. Soil Loosening Mechanism; 2. Control Cabinet; 3. Rack; 4. Chassis; 5. Collection Box; 6. Clamping Conveying Mechanism; 7. Crushing Collection Mechanism; 8. Guiding Collection Mechanism

The tobacco harvester sequentially performs digging, conveying, cutting, crushing, and collecting of tobacco stalks. After starting the machine by pressing the control button on the control cabinet, the operator adjusts the position of the entire machine so that the tobacco stalks enter the feeding inlet of the clamping transmission mechanism. During operation, the stalks are excavated and pulled upward, moving backward and upward along the clamping chain. When the stalks reach the feed inlet of the crushing mechanism, the cutting mechanism separates the upper stalk (with leaves) from the lower root. The lower root falls into the crusher for crushing, while the upper stalk carrying the tobacco leaves continues to move backward and upward along the clamping chain. The staff on the platform assist in collecting the falling tobacco leaves and guide them into the collection box via the guide bend plate, completing the harvesting process.

Hydraulic drive chassis structure of tobacco leaf harvester

The hydraulic drive chassis structure of the tobacco leaf harvester is shown in Figure 2. The chassis is powered by a diesel engine, and the engine's output is distributed in two ways via a transfer box: one output is connected to a series variable piston pump to drive the tracked chassis for movement and steering; the other is connected to a gear pump to power the operational mechanisms. The output shaft of the travel hydraulic motor is directly coupled to the drive wheel, eliminating traditional transmission components such as the gearbox, clutch, and drive shaft. This design enables efficient power transmission and reduces energy loss. The vehicle body is also equipped with a complete power supply system, hydraulic oil tank, diesel tank, hydraulic seat valve, radiator, and a steering wheel control system.

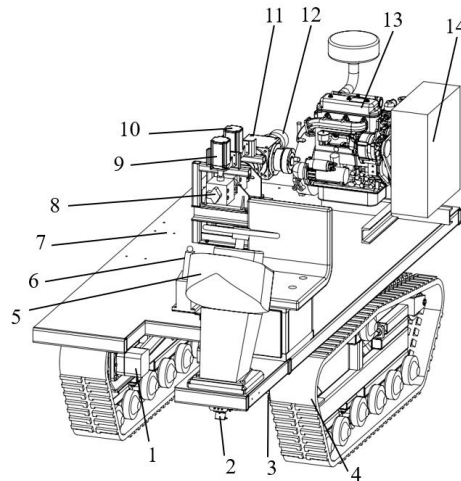


Fig. 2 - Schematic diagram of hydraulic drive chassis structure of tobacco harvester
 1. Hydraulic motor K1; 2. Angle encoder; 3. Hydraulic motor K2; 4. Track device; 5. Steering wheel;
 6. Shift handle; 7. Frame; 8. Series variable piston pump; 9. Stepper motor K1; 10. Stepper motor K2;
 11. Transfer box; 12. Gear pump; 13. Engine; 14. Fuel tank

Working principle of hydraulic drive chassis

The chassis of the tobacco harvester is hydraulically driven, powered by a diesel engine and a series variable piston pump. The series variable piston pump in this system is equipped with two valves and is connected to the stepper motors K1 and K2 by coupling. When operating the steering wheel, the Angle encoder monitors the steering Angle in real time and feeds the signal back to the STM32 microcontroller. According to the received Angle signal, the MCU controls the stepper motor to rotate at a predetermined Angle, thus adjusting the opening of the two valves of the plunger pump. The valve can be rotated to neutral, forward, or reverse positions. When the valve is in the neutral position, the hydraulic oil flows directly back to the tank. When the valve is shifted to the forward or reverse position, the direction of the hydraulic oil flow changes accordingly, thereby controlling the forward or reverse rotation of the hydraulic motor. The size of the valve opening determines the speed of the hydraulic motor, so as to achieve the forward, backward and steering of the tobacco harvester chassis. In addition, through the shift lever, the driver can switch between different gear positions to achieve high, medium and low speed conversion. The outline of the series variable piston pump is shown in Figure 3, and the overall technical parameters of the chassis are shown in Table 1.

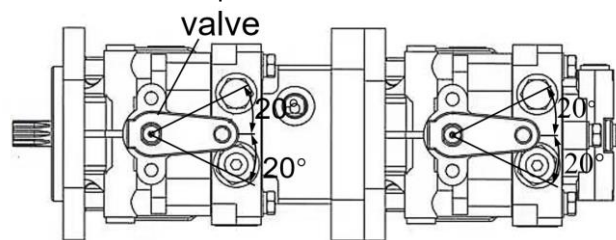


Fig. 3 - Outline of series variable piston pump

Table 1

Design parameters of hydraulic drive chassis of tobacco leaf harvester	
Parameters	Numerical value
Dimensions (Length x Width x Height) / mm	1500x3000x2500
Travel mode	Crawler type
Crawler width / mm	230
Crawler ground contact length / mm	1300
Full load weight / kg	2000
Engine power / kW	31
Steering method	Differential steering
Track gauge / mm	1200

Calculation of track parameter

Compared with the wheeled device, the crawler chassis shows better stability, obstacle crossing ability and smaller ground specific pressure when facing the undulating road surface and complex working environment. Therefore, the crawler type traveling device is selected and its key parameters are calculated.

The ratio of track grounding length L to track gauge B has an important effect on the driving performance of the chassis. When the L/B value is large, steering becomes more difficult; When the L/B value is small, the driving stability will be reduced (Wu et al., 2024; Chen et al., 2010).

The empirical formula for calculating the track grounding length is shown in equation (1):

$$L = (1.15 \sim 1.39) B \quad (1)$$

where L is the grounding length of the track, [mm]; B is the gauge, [mm].

The value range of the ratio of track width to ground length is shown in equation (2):

$$0.18 < \frac{b}{L} < 0.24 \quad (2)$$

where b is the width of the track, [mm].

The drive wheel diameter is calculated using the following formula:

$$D = \frac{t}{\sin(\pi/n)} \quad (3)$$

where D is the diameter of the drive wheel, [mm]; t is the track pitch, [mm]; n is the number of teeth on the drive wheel.

To ensure no rolling damage to the ridge body in tobacco fields, appropriately increasing the track width helps reduce ground pressure and enhances traction and adhesion performance (Ding et al., 2020; Li Qingjiang et al., 2024). Based on calculations and available market track specifications, the track grounding length was determined to be 1300 mm, the width 230 mm, and the pitch 72 mm. The diameter of the drive wheel is 270 mm.

Principle of hydraulic system

The chassis of the crawler tobacco harvester adopts a double pump (series variable piston pump) double motor drive scheme, and each hydraulic pump controls a hydraulic motor to drive a single track. In this way, the track can be independently driven on both sides, and the hydraulic oil circuits on both sides are independent of each other, effectively avoiding the interference and coupling phenomenon between the systems. Its single-side track hydraulic system is shown in Figure 4, and the engine drives a series variable plunger pump to provide pressure oil, converting the mechanical energy into the pressure energy of the hydraulic oil. The pressure oil rotates by driving the hydraulic motor, thus driving the movement of the track driving mechanism. The hydraulic system adopts volumetric speed regulation technology, which has high working efficiency and good load adaptability. The traveling hydraulic motor is a bidirectional variable motor, and the speed and rotation direction of the hydraulic motor can be controlled by adjusting the valve opening and direction of the plunger pump. The safety relief valve in the system plays a load protection role to ensure that the working pressure of the hydraulic system is always maintained within the safe range. Finally, the hydraulic oil flows through the loop back to the radiator for cooling and then back to the tank.

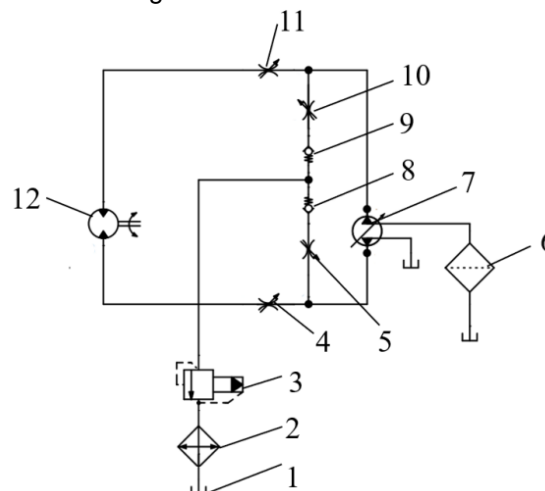


Fig. 4 - Schematic diagram of single-side pump-controlled hydraulic motor system

1. Fuel tank; 2. Air cooling; 3. Relief valve; 4, 5, 10, 11. Speed control valve;
6. Filter; 7. Plunger pump; 8, 9. Check valve; 12. Hydraulic motor

Selection of hydraulic motor

In the process of tobacco field operation, the chassis has the greatest resistance when running on the ramp, which mainly includes rolling resistance, slope resistance and acceleration resistance. In the tobacco leaf harvest operation, because the chassis is usually in a uniform motion state, the influence of acceleration resistance can be ignored. Therefore, the formula for calculating slope resistance is as follows:

$$F_a = Mgf \cos \alpha + Mg \sin \alpha \quad (4)$$

where F_a is the slope resistance, [N]; M is the mass of the whole machine, taken as 2000 kg; g is the acceleration of gravity, which is 9.8m/s^2 ; f is the operating resistance coefficient, which ranges from 0.08 to 0.12, and 0.12 is taken in this paper (Mei *et al.*, 2024). α is the climbing angle, which is 20° .

The torque of the traveling hydraulic motor is shown in equation (5):

$$T = \frac{F_a r}{k\eta_1} \quad (5)$$

where T is the required torque of a single traveling hydraulic motor, [N·m]; r is the radius of the drive wheel, which is 0.134m; k is the number of traveling hydraulic motors, 2; η_1 is the efficiency of the track travel device, which is 0.9.

The theoretical displacement of traveling hydraulic motor is shown in equation (6):

$$V_c = \frac{2\pi T}{P\eta_2} \quad (6)$$

where V_c is the displacement of the traveling hydraulic motor, [ml/r]; P is the maximum working pressure of the hydraulic system, taking 15 MPa; η_2 is the mechanical efficiency of the traveling hydraulic motor and is taken as 0.9 (Li *et al.*, 2024).

According to the driving speed of the chassis, the required speed of the hydraulic motor can be calculated, and the specific calculation formula is shown in equation (7):

$$n_c = \frac{1000v}{60 \times 2\pi r} \quad (7)$$

where n_c is the maximum speed of the traveling hydraulic motor, [r/min]; v is the maximum driving speed of the chassis, which is 3 km/h.

By substituting the relevant design parameters into equations (4)~(7), it is calculated that the maximum resistance of the whole machine is 8914 N, the torque of a single traveling hydraulic motor is 664 N·m, the theoretical displacement is 309 ml/r, and the required speed is 60 r/min. Since the output shaft of the traveling hydraulic motor is directly connected to the drive wheel, the hydraulic motor needs to bear radial, axial and impact loads from the drive wheel (Liu *et al.*, 2022), which puts higher requirements on the durability and torque capacity of the hydraulic motor. Therefore, after comprehensive evaluation, the BM5-400 hydraulic motor was finally selected. Its main technical parameters include: maximum displacement of 400 mL/r, output torque of 715 N·m, maximum output speed of 178 r/min, working pressure of 15 MPa, maximum input flow of 75 L/min.

Selection of hydraulic pump and engine

Hydraulic pump output flow is shown in equation (8):

$$Q_h = \frac{zKV_c n_c}{1000\eta_3} \quad (8)$$

where Q_h is the output flow rate of hydraulic pump, [L/min]; z is the number of hydraulic motors, taken as 2; K is the leakage coefficient of the hydraulic pump, taken as 1.1; η_3 is the volumetric efficiency of the traveling hydraulic motor, which is 0.9.

Hydraulic pump theoretical displacement is shown in equation (9):

$$V_h = \frac{1000Q_h}{n_h\eta_4} \quad (9)$$

where V_h is the theoretical displacement of hydraulic pump, ml/r; n_h is the speed of hydraulic pump, taken as 3000 r/min; η_4 is the volumetric efficiency of the hydraulic pump, which is 0.9.

By substituting the relevant parameters into equations (8) and (9), it is calculated that the output flow rate of the hydraulic pump is 46 L/min, and the theoretical displacement is 17 mL/r. According to the requirements of the system, two plunger pumps are installed in series, so the HAZE-21 series variable plunger pump is selected as the traveling hydraulic pump. The main technical parameters of the hydraulic pump include: maximum displacement of 21 mL/r, rated pressure of 17 MPa, rated speed of 3600 r/min. Each plunger pump will provide the required hydraulic energy for a traveling hydraulic motor.

According to the maximum flow required by the hydraulic system of the whole machine in the working process, the engine selection is further carried out. The calculation formula of engine power is as follows:

$$P_j = \frac{QP_h}{60\eta_s} \quad (10)$$

where P_j is the engine power, [KW]; Q is the required flow rate of the hydraulic system of the whole machine, [L/min]; P_h is the working pressure of the hydraulic pump, taken as 15 MPa; η_s is the engine mechanical efficiency, which is 0.9.

The total flow required by the machine's hydraulic system is the sum of the flow demands of both the driving mechanism and the working mechanism. Based on calculations, the hydraulic system requires a flow rate of 100 L/min under maximum working conditions. According to Equation (10), the required engine power P_j is 28 kW. Taking into account engine size and output performance, the 4L22B diesel engine from Shandong Huayuan Laidong Internal Combustion Engine Co., Ltd. was selected. This engine provides a good performance match, with a rated power of 31 kW and a rated speed of 3300 r/min.

Control structure

The steering wheel operation mechanism is illustrated in Figure 5. When the steering wheel rotates, it drives the pinion via the steering shaft, with the pinion and large gear engaging through meshing teeth. A limiting gear mounted on the large gear restricts the pinion's rotation to one and a half turns in both directions, thereby limiting the steering wheel's total rotation range to ± 540 degrees from the central position. As the steering wheel turns, the steering shaft and the angle encoder rotate synchronously, with the encoder capturing and transmitting the rotation angle data to the controller. The controller then calculates the required pulse count based on this angle data and adjusts the operation of stepper motors K1 and K2 accordingly. These stepper motors control the first and second flow control valves of the series variable piston pump, regulating the speed of hydraulic motors K1 and K2. The speed differential between the two motors enables the tracked vehicle to steer. The structure of the flow control valve mechanism is shown in Figure 6.

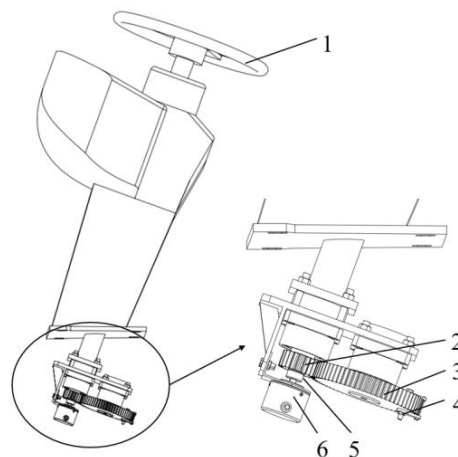


Fig. 5 - Structure diagram of steering wheel operating mechanism

1. Steering wheel; 2. Pinion; 3. Big gear; 4. Limit stop; 5. Steering shaft; 6. Angle encoder

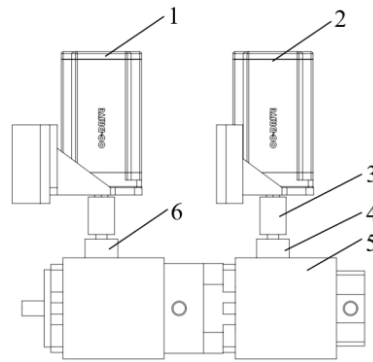


Fig. 6 - Flow control valve mechanism diagram

1. Stepping motor K1; 2. Stepping motor K2; 3. Coupling; 4. First class volume control valve; 5. Series variable piston pump; 6. Second flow control valve

Control System Integration

The steering wheel control system comprises a steering wheel, shift lever, stepper motors, and an angle encoder, as illustrated in Figure 7. The shift lever, adapted from an automotive automatic gear selector, includes five gear positions: forward fast (D3), forward medium (D2), forward slow (D1), park (P), and reverse (R). It is connected to the controller via five DuPont wires, transmitting five signals that enable the controller to synchronize the rotation angles of the two stepper motors. The angle encoder records the steering wheel’s rotation angle and updates the rotation of the stepper motors accordingly. The system’s controller is based on the STM32F103 core board, with the angle encoder connected through RS485 serial communication. A RS485-to-TTL chip is used to convert signals for compatibility. The controller’s GPIO pins are linked to the motor driver board, which receives PWM pulse signals to control the stepper motors’ movement. By adjusting the gear position and rotating the steering wheel, the chassis of the tobacco harvester can perform both linear and steering movements.

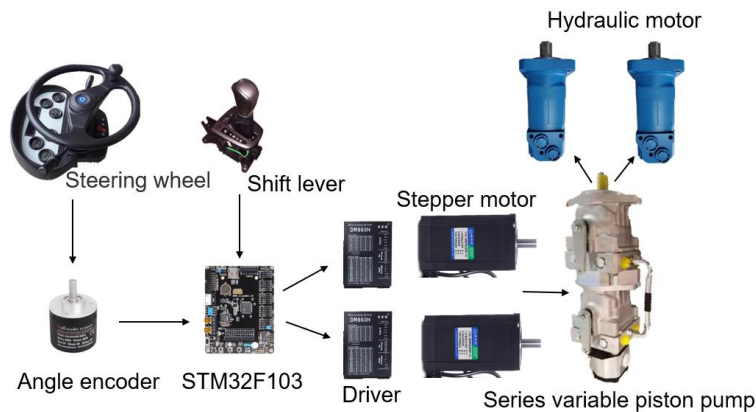


Fig. 7 - Schematic diagram of steering wheel system

Driving control strategy

(1) The controller determines the gear control signal of the straight-line operating mechanism:

The maximum rotation angle of the positive and negative direction of the flow control valve of the series variable piston pump is θ degree, and the number of pulses required by the rotation shaft of the motor to rotate 360 degrees is N , and the calculation formula is as follows:

$$N = \frac{360\partial}{\theta} \tag{11}$$

where θ is the step angle, measured in degrees; ∂ is a subdivision multiple and has no dimension.

The shift lever is equipped with n gears, each corresponding to a rotation angle α_n of the flow control valve (where $n = 1, 2, 3, \dots$, and $\alpha_n \leq \theta$). Each gear position is associated with an external interrupt in the controller, and each external interrupt triggers a specific interrupt function. The number of pulses generated by the interrupt function is calculated using the formula: $\alpha_n * N / 360$.

According to the selected gear position, the controller simultaneously sends the corresponding number of pulses to both the first and second stepper motors. These two motors respectively control the first volume control valve and the second flow control valve to rotate to a predetermined angle. At this point, both hydraulic motors rotate in the same direction and at the same speed, thereby enabling the chassis to move in a straight line.

(2) After determining the gear position in step (1), the controller evaluates the steering signal from the steering wheel control mechanism:

Set the maximum steering wheel rotation angle in both clockwise and counterclockwise directions from the center (neutral) position to the limit stop as β . Let the angle γ be the current rotation angle of the steering wheel from the center position, as detected by the angle encoder, where $\gamma \leq \beta$. For a given gear, the rotation angle of the flow control valve is α_n , corresponding to the steering wheel's rotation angle γ . Thus, for each 1° of steering wheel rotation from the center, the flow control valve must rotate by $\beta_n = 2\alpha_n/\beta$.

When the steering wheel is turned clockwise by γ degrees, the stepper motor K1 remains stationary, and the controller commands the stepper motor K2 to rotate in the opposite direction by $|\gamma\beta_n|$ degrees. When the steering wheel is returned to its neutral position by γ degrees, the stepper motor K1 remains stationary, and the controller commands the stepper motor K2 to return to its original position by $|\gamma\beta_n|$ degrees;

When the steering wheel is turned counterclockwise by γ degrees, the stepper motor K2 remains stationary, and the controller commands the stepper motor K1 to rotate in the opposite direction by $|\gamma\beta_n|$ degrees. When the steering wheel is returned to its neutral position by γ degrees, the stepper motor K1 remains stationary, and the controller commands the stepper motor K2 to return to its original position by $|\gamma\beta_n|$ degrees.

By controlling the stepper motors K1 and K2, a speed difference is generated between the hydraulic motors K1 and K2, thereby controlling the steering of the track vehicle.

Analysis of steering performance

During operation, the steering system of the track chassis achieves directional control through differential movement. In the steering process, the tobacco harvester turns with a specific turning radius toward the side with the lower track speed. The diagram of differential steering is illustrated in Figure 8.

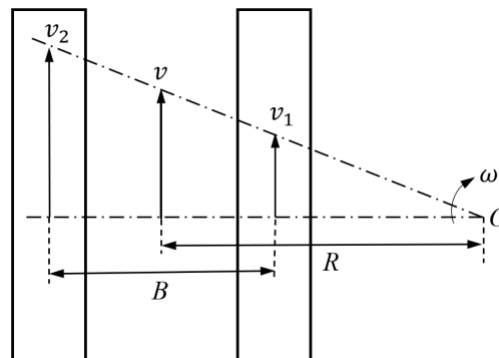


Fig. 8 - Diagram of differential right turn

Under ideal conditions, assuming that track slip and skid are negligible, the turning radius can be calculated using the following formula:

$$R = \frac{B(v_1 + v_2)}{2(v_2 - v_1)} \quad (12)$$

where R is the turning radius, [mm]; v_1 is the linear speed of the right track, [m/s]; v_2 is the linear speed of the left track, [m/s].

When the linear speeds of the right and left tracks are the same and in opposite directions, the tobacco harvester will achieve in-place turning of the chassis.

Test methods

The average plant spacing in the test field was approximately 400 cm, with row spacing ranging from 105 cm to 115 cm, and plant height ranging from 80 cm to 120 cm. The machine operated in slow gear mode, and three tobacco ridges were selected for harvesting, with each ridge having about 60 tobacco stalks. During the trial, the operation of the entire machine was observed, and the failure rate of tobacco stalk clamping for each ridge was calculated.

The calculation formula is as follows:

$$C = \frac{A_1}{A_2} \times 100\% \tag{13}$$

where C is the rate of tobacco rod clamping failure, [%]; A_1 is the number of tobacco rods not harvested in a single ridge; A_2 is the total number of tobacco rods in a single ridge.

RESULTS

Whole Machine Performance Test

The processing and trial production of the tobacco harvester chassis were completed at Guilin Maike Machinery Co., Ltd., and the upper working parts were successfully mounted. In order to comprehensively evaluate the performance and agronomic adaptability of the whole machine, performance tests were carried out in various aspects, mainly including driving speed test, steering performance test, and field harvesting effect test. The test instruments and equipment include tape measure, stopwatch, etc.

Driving Speed

The tobacco harvester is equipped with three forward speed gears, which are slow gear, medium gear, and fast gear, corresponding to the flow control valve rotation angles of 6 degrees, 12 degrees, and 20 degrees, respectively. The driving speed test was conducted according to the standard GB/T 10394.3-2002 “Feed Harvesters Part 3: Test Methods”, as shown in Figure 9(a). The test selected a flat field road with a length of more than 50 meters. The driver, by operating the gear shift lever, used a stopwatch to measure the time required for the machine to travel 50 meters at the highest speed in a straight line at different gears. Each gear measurement was repeated 3 times and the average was taken, and then the highest driving speed at different gears was calculated. The test results are shown in Table 2.



(a) Driving speed



(b) Turning radius

Fig. 9 - Steering turning test

Table 2

Test results for driving speed

Gear	Times	Time/s	Average time/s	Driving speed / (m·s ⁻¹)
Slow gear	1	200.69	198.79	0.25
	2	197.23		
	3	198.46		
Medium gear	1	105.16	105.44	0.47
	2	103.83		
	3	107.33		
Fast gear	1	62.36	63.37	0.79
	2	64.28		
	3	63.47		

As can be seen from Table 2, the driving speeds of the tobacco harvester at different gear settings are 0.25 m/s, 0.47 m/s, and 0.79 m/s, respectively, with the maximum driving speed being close to the predetermined target speed (3 km/h).

The machine is capable of driving at medium to high speeds in the field or on the road. Due to the power loss of the entire machine and the slippage of the track chassis on the field road surface (Wu *et al.*, 2024), the actual driving speed is slightly lower than the target speed.

Steering Test

The turning performance of the chassis is characterized by the turning radius. During the steering process, the maximum circular radius drawn by the track on the ground is the turning radius. When the steering wheel is fully turned to the left or right, the rotation angles of the two flow control valves of the series piston pump are the same but opposite in direction, causing the tracks to move at the same speed but in opposite directions, thus achieving the pivot turn of the tobacco harvester chassis. According to the standard GB/T 3871.5-2006 "Steering Circle and Passing Circle Diameter", the turning radius test was conducted on an open area of the processing plant. During the test, the machine was driven in slow gear, then the steering wheel was turned fully to the left or right, the machine rotated 360 degrees and the steering wheel was returned to the center, and then driven out of the test area. The diameters at the 0, 120, and 240-degree positions of the turning circle were measured, and the mean value and minimum turning radius were calculated. The test process is shown in Figure 9 (b), and the test results are shown in Table 3.

Table 3

Test results for minimum turning radius

Steering direction	Measurement location	Diameter/mm	Mean Diameter/mm	Turning radius/mm
Left turn	0°	1593	1552	776
	120°	1566		
	240°	1496		
Right turn	0°	1483	1532	766
	120°	1536		
	240°	1576		

As can be seen from Table 3, the minimum turning radius of the whole machine is 766 mm, which meets the design requirements for tobacco leaf operation and transfer. Compared with the track gauge, the measured value is slightly larger, mainly due to the overall weight of the machine and the presence of certain track slip and skid during turning.

Field experiment

To further verify the agronomic compatibility of the chassis, field harvesting trials were conducted at a tobacco planting base in Chenzhou, Hunan Province, as shown in Figure 10.



Fig. 10 - Field harvesting experiment

The experimental results indicate that the tobacco harvester operates smoothly with sufficient power. The failure rates for tobacco stalk clamping on three rows of tobacco were 4.91%, 3.38%, and 4.83% respectively, with a low overall clamping failure rate. The chassis has good agronomic compatibility and can complete the tobacco harvesting task relatively smoothly.

For the cases of tobacco stalk clamping failure, the analysis suggests that the cause may be related to the tobacco stalks being deeply rooted in the soil, which leads to the chisel-shaped spade of the soil loosening mechanism failing to effectively lift the stalks out of the soil. This affects the normal conveyance of the clamping chain, resulting in clamping failure. To further improve the success rate of clamping, subsequent optimizations to the design of the soil loosening mechanism will be made, enhancing the penetration power and soil adaptability of the spade head to ensure effective digging and clamping of tobacco stalks under various soil conditions. This will improve overall operational efficiency and the quality of tobacco leaf harvesting.

CONCLUSIONS

(1) To address the issues of difficult control and easy dislocation of control levers when tracked vehicles turn while traveling, this paper designs a tobacco harvester hydraulic drive chassis based on steering wheel control. This design can solve the problems of insufficient accuracy and complex operation inherent in traditional control methods. Through the design of the chassis structure and the selection of key components, and the performance test of the prototype, its applicability in tobacco harvesting has been verified.

(2) The chassis adopts a hydraulic drive system, with a power of 31 kW and a tracked drive mode. A steering strategy for straight steering control with the steering wheel is proposed, by adjusting the opening of the flow control valve of the series variable plunger pump, thus achieving control over the speed of the left and right tracks.

(3) The test results show that the tobacco harvester chassis can achieve three-speed gear shifting in actual work, with the highest travel speeds of 0.25 m/s, 0.47 m/s, and 0.79 m/s respectively, meeting different travel speed requirements; the minimum turning radius is 766 mm; field harvesting test results show that the machine runs smoothly during operation, the power system is sufficient, and can effectively cope with complex terrain and irregular crop planting environments. The average tobacco rod clamping failure rate is 4.37%, with a low overall clamping failure rate, meeting the requirements of field operations.

ACKNOWLEDGEMENT

Funding: This study was supported by the scientific research business fee fund (HN2023KJ06) of China National Tobacco Corporation Hunan Provincial Company.

REFERENCES

- [1] Chen Z., Guo X., Zhang C. (2010). The effect of the design of the ground aspect ratio on the driving performance of crawler vehicles [J]. *Research of Agricultural Mechanization*, 32(05): 112-4.
- [2] Ding Z., Li Y., Tang Z. (2020). Analysis of the compaction effect of wheeled and crawler vehicles on farmland soil [J]. *Transactions of the CSAE*, 36(05): 10-8.
- [3] Du X., Ning C., Yang Z., Ma C., He L., Han X. (2023). Design and Experiment of the Crawler Chassis Walking Hydraulic System for a Straddle-type Camellia Fruit Harvester [J]. *Transactions of the Chinese Society for Agricultural Machinery*, 54(03): 139-47.
- [4] Li M., Yang Q., Xie K., Wang Y., Xu D., Zhang Z. (2024). Design and experimental study on the hydraulic system of a self-propelled notoginseng combined harvester [J]. *Journal of Engineering Design*, 31(05): 670-80.
- [5] Li S., Chen H., Peng J., Men L., Zhang X., Li M. (2024). Design and test of a full hydraulic remote-controlled crawler power chassis for hilly and mountainous orchards [J]. *Transactions of the Chinese Society for Agricultural Machinery*, 55(02): 119-27+201.
- [6] Liu C., Li J., Wang H., Peng Z., Duan M., He W. (2024). Current situation and countermeasure analysis of tobacco leaf mechanical harvesting development [J]. *Southern Agricultural Machinery*, 55(10): 24-8+32.
- [7] Liu F. (2022). *Optimization of the crawler self-propelled potato harvester chassis* [D], Huazhong Agricultural University.
- [8] Li Q., Sun Z., Ren Q., Guo H., Zhang C., Luo S. (2024). Design and test of a self-propelled garlic harvester with continuous laying [J]. *Chinese Journal of Agricultural Mechanization*, 45(09): 1-7+14.
- [9] Mei S., Tang D., Shi Z., Song Z., Tian C., Zhou R. (2024). Design and test of the goji berry harvester based on arrayed vibration units [J]. *Transactions of the CSAE*, 40(23): 115-25.

- [10] Pan J., Xu L., Lu E., Dai B., Chen T., Sun W. (2024). Design and Experiment of an Unoccupied Control System for a Tracked Grain Vehicle [J]. *Sensors*, 24(9):2715. <https://www.mdpi.com/1424-8220/24/9/2715>
- [11] Tan S., Sun C., Li J., Xiao M., Ai W., Liu H. (2023). Current situation and countermeasure research on tobacco leaf mechanized harvesting in southern hilly areas [J]. *Southern Agricultural Machinery*, 54(14): 33-6.
- [12] Wang B., Zhu J., Chai X., Liu B., Zhang G., Yao W. (2024). Research status and development trend of key technology of agricultural machinery chassis in hilly and mountainous areas [J]. *Computers and Electronics in Agriculture*, 226: 109447.
- [13] Wang D., Zhao Y., You Y., Zhang X., Wang T., Li S. (2023). Design and test of the crawler self-propelled gentle slope grass harvester chassis [J]. *Transactions of the Chinese Society for Agricultural Machinery*, 54(09): 178-87.
- [14] Wang P., Yi W., Xiong C., Cheng F., Deng J., Zhou Y. (2022). Design and test of the 4CJZ-1000 self-propelled tea harvester [J]. *Journal of Southwest University (Natural Science Edition)*, 44(11): 228-33.
- [15] Wu L., Dong S., Liu T., Yahg J., Yan X. (2018). Design and test of a self-propelled sweet sorghum harvesting and spreading machine [J]. *Agricultural Engineering*, 8(10): 90-4.
- [16] Wu P., Sun W., Wang H. (2024). Design and Testing of an Inter-Toothed, Self-Propelled Digger for Deep-Rhizome Chinese Herbal Medicines [J]. *Agronomy*, 14(9):2024.
- [17] Wu Z., Chen L., Wang Y., Luo K., Lai X., Zhang X. (2024). Design and test of the track self-propelled tea harvester walking chassis passability [J]. *Transactions of the Chinese Society for Agricultural Machinery*, 56(01):474-483.
- [18] Xi C., Zhang F., Zheng L., Han Z., He C. (2024). Research on the design and collaborative control of the hydraulic system of agricultural power chassis in hilly and mountainous areas [J]. *Machine Tools and Hydraulics*, 52(20): 35-41.
- [19] Xiao M., Zhao Y., Wang H., Xu X., Zhu Y. (2024). Design and Test of Hydraulic Driving System for Undercarriage of Paddy Field Weeder [J]. *Agriculture*, 14(4):595.
- [20] Xiao W., Tong J. (2023). Design of the hydraulic drive system of the crawler tractor [J]. *Research of Agricultural Mechanization*, 45(11): 253-8.
- [21] Xue B., Li J., Jiao W., Li H., Liu X. (2024). Current situation and development trend of tobacco agricultural machinery and agronomy integration [J]. *Agricultural Equipment and Vehicle Engineering*, 62(02): 29-33.
- [22] Zhou Y., Wu J., Lin C., Deng J. (2024). Current situation and development suggestions of tobacco mechanization research in hilly and mountainous areas [J]. *Sichuan Agricultural Science and Technology*, (10): 121-5+39.

DESIGN AND EXPERIMENTATION OF ROOT-CUTTING DEVICE FOR HEAD-FORMING VEGETABLES

结球类蔬菜切根装置设计与实验

Yanjun LI^{1,2)}, Jianfei ZHANG^{*1,3)}, Fuxiang XIE^{*2)}, Yongtao YU²⁾

¹⁾ Key Laboratory of Modern Agricultural Equipment, Ministry of Agriculture and Rural Affairs, Nanjing/China;

²⁾ School of Machinery and Automation, Weifang University, Weifang/China;

³⁾ Nanjing Institute of Agricultural Mechanization, Ministry of Agriculture and Rural Affairs, Nanjing/China;

Tel: 17372778326; E-mail: zhangjianfei88@126.com

Correspondent author: Jianfei ZHANG, Fuxiang XIE

DOI: <https://doi.org/10.35633/inmateh-75-71>

Keywords: head-forming vegetables, root-cutting device, virtual simulation, experiment

ABSTRACT

In response to the current low level of mechanized harvesting for heading vegetables in China and the unsatisfactory harvesting results, this study focuses on the root-cutting operation during the harvesting process. A double-disk root-cutting device was designed to achieve low-power consumption and high-efficiency root cutting. Through LS-DYNA simulation experiments, the root-cutting process of the root-cutting device was simulated, and the cutting force and internal cutting energy of three different cutter combinations are compared. The simulation results show that the maximum cutting force of the double-serrated blade was the smallest, while the combination of a smooth blade and a serrated blade had the lowest internal cutting energy. Compared to smooth blades, serrated blades exhibited better clamping effects on the roots of head-forming vegetables. Considering both cutting force and internal cutting energy, the combination of a serrated blade and a smooth blade was found to be optimal. The quadratic rotary orthogonal combination test method was used to analyze the relationship between the main influencing factors of the root cutting device performance (rotational speed of the cutter, conveying speed, inclination angle of the cutter, and overlapping amount of the cutter) and the performance index (root cutting power) of the root cutting device. The bench test program was designed by applying regression analysis, response surface and multi-objective variable optimization methods. The bench test results show that the optimal parameter combination of the designed root cutting device were: cutter speed of 200 rpm, conveying speed of 0.3 m/s, cutter inclination angle of 10°, and cutter overlap of 20 mm. The predicted cutting power of the model was 51.19 W.

摘要

针对现阶段我国结球类蔬菜机械化收获水平低下，收获效果不理想等问题。本文重点研究结球类蔬菜收获过程中的切根作业，设计一种双圆盘切根装置，可实现低功耗、高效率切根。过 LS-DYNA 仿真实验，模拟了切根装置的切根工作过程并比较了三种切刀组合的切根力和切根内能，仿真实验结果双锯齿刀的最大切根力最小，光刀与锯齿刀的组合切根内能最小。光刀与锯齿刀相比，锯齿刀对结球类蔬菜根的钳持效果更好，综合切根力和切根内能，选择锯齿刀加光刀的组合更优。采用二次旋转正交组合试验方法，分析切根装置性能的主要影响因素（切刀转速、输送速度、切刀倾角、切刀重叠量）与性能指标（切根功率）的关系，应用回归分析、响应曲面和多目标变量优化方法设计了台架试验方案。台架试验结果表明，所设计切根装置的最优参数组合为：切刀转速 200r/min，输送速度 0.3m/s，切刀倾角 10°，切刀重叠量 20mm；模型预测的切根功率为 51.19W。

INTRODUCTION

Heading vegetables is one of the important vegetables consumed by the Chinese residents, which is important for ensuring the balanced supply of vegetable market, balancing the price of vegetables and ensuring the income of farmers (Sheng et al., 2021; Yan et al., 2024). The relevant agronomic data show that in the whole process of heading vegetable production, the harvesting operations accounted for more than 40% of the entire heading vegetable production operations (Li, 2020). At present, China's heading vegetable mechanized harvesting level is low, still completely rely on manual completion, harvesting process farmers need to constantly bend down and cut vegetables from the roots. Then remove the package and picking up the vegetable bulb. Finally load, with trucks. Thus, harvesting operations is a long time, labor-intensive process (Li et al., 2023; Wen et al., 2024).

Heading vegetables mechanized harvesting can reduce the labor intensity for vegetable farmers, eliminating the constantly bending over to cut and pick up of the manual processes. With the promotion of China's urbanization process and the rural labor force to the city to transfer, it is imperative to improve the level of mechanized harvesting for heading vegetables (Wang *et al.*, 2018; Zhou, 2013; Wang *et al.*, 2014).

Heading vegetables belong to a class of vegetables harvested without root, the quality of its cut root (whether the cut is flat, whether the cut is biased, whether there is damage, etc.) has a great impact on its subsequent storage. Therefore, many experts and scholars have conducted a lot of research on disk cutting device, most of them focus on the mechanical properties of crops, crop cutting mechanism, slip cutting theory, cutting device structure and other aspects of the study. (Jang *et al.*, 2021; Jing *et al.*, 2021).

El *et al.*, (2020), developed and tested a cabbage root cutting device and investigated the effects of cutter shape, cutter speed and cutter angle on the performance of the harvester. Xu *et al.*, (2009), investigated the shear characteristics of cabbage roots and stems using different conditions such as cutting speed, blade curve, blade thickness and blade smoothness. The effect of cutting speed, blade shape and blade smoothness on the shear force was tested. Li *et al.*, (2020), designed an adjustable root-cutting device, and obtained the influence law of individual factors on root-cutting reaction force through one-factor test and orthogonal test; then they conducted second-order orthogonal rotary combination multifactorial test to study the influence of cutter speed, cutting position, walking speed, cutter overlap and pitch angle on the maximum root-cutting reaction force, and at the same time, they used the response surface method for the optimization of the parameters to obtain the best parameter combination. Du *et al.*, (2017), carried out the cutting part test, cutting force orthogonal test, cutting and splitting breakage test and stem using the universal material testing machine. The test results showed that both the maximum cutting force and the average cutting force were linearly related to the crude fiber content, and the interval of 30-35 mm in diameter of kale rhizome was the optimal root cutting area.

Based on the above research, this paper designs a root cutting device for heading vegetables, applies LS-DYNA software to simulate and analyze the root cutting characteristics of different blade combinations, confirms the blade combinations according to the results, and optimizes the structure and working parameters of the root cutting device.

MATERIALS AND METHODS

Design of key components

Root cutting mechanism is an important part of the root cutting operation of heading vegetables. While operating, the root cutting mechanism needs to clamp and excise the roots of heading vegetables. Its performance will directly affect the results of the root cutting operation. Root cutting mechanism diagram is shown in Figure 1 and it mainly consists of: cutter, 4; cutter plate, 5; bracket, 1; cutter shaft, 6; universal joint coupling, 2; T-type commutator, 7; hexagonal shaft, 8 and hydraulic motor and other components, 3.

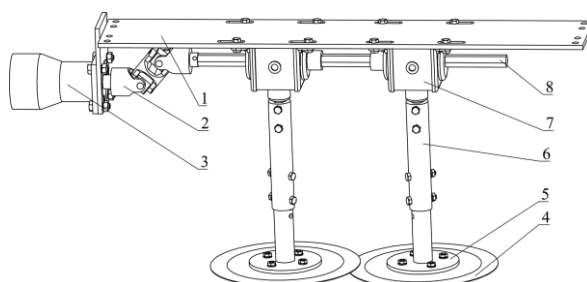


Fig. 1 – Structure diagram of heading vegetables root cutting mechanism

The design of the root cutting mechanism in this paper mainly focuses on the selection of the cutter and the design of the main parameters of the two cutters. There are generally two types of cutting mechanisms used for crop harvesting: the reciprocating type and the disk type. The reciprocating type is typically employed for harvesting crops with relatively fine stems, such as rice and wheat, while the disk type is commonly used for harvesting crops with thicker stems, such as sugarcane and cabbage. Since the roots of heading vegetables are relatively thicker, the type of cutter designed in this paper utilizes the disk type cutter.

According to the number of cutters used in the cutting process is divided into single disk cutting mechanism and double disk cutting mechanism.

Among them, the single disk cutting mechanism cutter needs a larger diameter, the rotational speed set is also relatively high. This situation can unbalance the force of the root cutting process; while the diameter of the double disk knife does not need to be too large, the rotational speed does not need to be too high, you can reduce the energy consumption in the work process, eliminate the force imbalance during root cutting. Therefore, the cutting mechanism designed in this paper selects double disk cutter. In order to ensure the integrity of the cut root, there is a certain overlap area between the double disk cutter. Common disk cutter shape mainly has a smooth edge type, serrated type and extra-blade type three types, as shown in Figure 2 (Li, 2018; Liu et al., 2021).

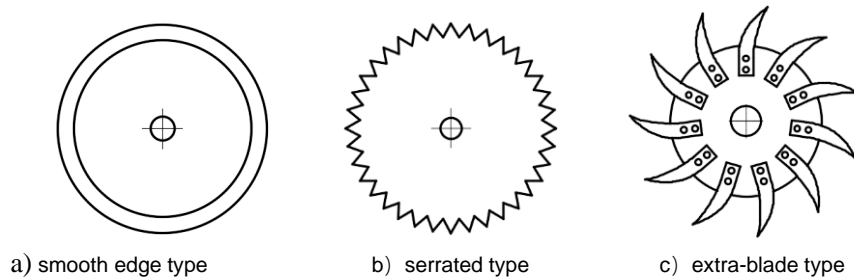


Fig. 2 – Different style cutters

Under the same working conditions, the cutting effect and power consumption of the disk cutter with different edges and structures are different. The smooth-edge cutter has the lowest power consumption and small force, while the extra-blade-type disk cutter is subject to the largest force and the highest cutting power consumption. Du Dongdong found that it was difficult to clamp cabbage roots for stable cutting by a separate smooth-edged disk cutter through mechanical analysis, therefore, this paper chooses the combination of smooth-edged and serrated cutter for root cutting (Du et al., 2011; Du et al., 2015; Du et al., 2017).

The root cutting device designed in this paper has overlapping upper- and lower-disk knives, and during the root cutting process, the double disk knives will clamp and cut off the heading vegetable roots. As the clamping force and shear force are in the rotating plane of the disk knives, only the force on the heading vegetable roots in the rotating plane of the disk knives is analyzed. The force on the heading vegetable roots is shown in the schematic diagram in Fig. 3:

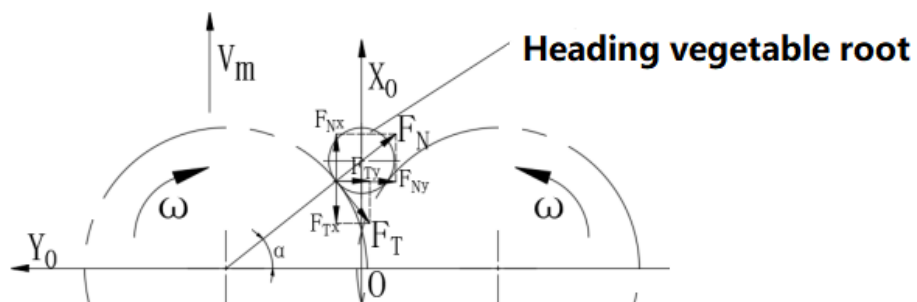


Fig. 3 – Stress analysis of heading vegetable root during root cutting process

The force analysis leads to the equation (1):

$$\begin{cases} F_C = F_{Ty} + F_{Ny} = F_T \sin \alpha + F_N \cos \alpha \\ F_S = F_{Tx} + F_{Nx} = F_T \cos \alpha - F_N \sin \alpha \\ F_T = f F_N \end{cases} \quad (1)$$

F_C - clamping force, N;

F_S - shear force, N;

F_N - normal reaction force of the disk cutter acting on the heading vegetable root, N;

α - angle between F_N and Y_0 axis direction, (°);

F_T - friction force of the disk cutter on the heading vegetable root, N;

f - friction coefficient between the disk cutter and the heading vegetable root, generally take 0.4~0.7.

From the force analysis, it can be seen that the disk cutter can clamp the heading vegetable root under the condition that: $F_T \cos \alpha > F_N \sin \alpha$, therefore, at $f > \tan \alpha$, the disk cutter can clamp the heading vegetable root.

$$\alpha = \sin^{-1} \frac{A_1/2}{(D+d)/2} = \arccos \frac{A_1}{D+d} \quad (2)$$

A_1 - center distance between two disk cutters, mm;

D - diameter of the disk cutter, mm;

d - diameter of cabbage root cutting place, generally take 25~35 mm.

When A_1 increases or D decreases, α decreases, which is beneficial for the two disk blades to clamp the root of heading vegetables for cutting. However, due to structural constraints such as the center distance A_1 between the two disk blades and the disk cutter diameter D , the angle α is typically limited to a range of 35° to 40°. Additionally, the friction coefficient f between the root of heading vegetables and the blade edge generally ranges from 0.4 to 0.7. As a result, it is difficult for two smooth-edged disk blades to effectively clamp the root of heading vegetables for cutting. In this paper, the ability of the cutter to clamp the root is improved by using a combination of a smooth-edged disk cutter and a serrated disk cutter.

According to the analysis results, in the case of the root cutting mechanism, conveying mechanism and frame do not interfere with each other, while meeting the requirements of the two pieces of the cutter have a partial overlap, the diameter of the outer end of the cutter is set to 270 mm, the diameter of the inner hole in the middle is set to 25 mm, and the design of the cutter parameters is shown in Figure 4.

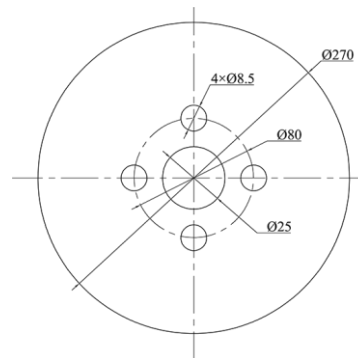


Fig. 4 – Design diagram of cutting tool structure

MATERIALS AND METHODS

Simulation experiment

In order to study the effect of different knife combinations on the maximum root cutting force and internal energy of root cutting, three knife combinations of double smooth-edged knife, double serrated knife and smooth-edged knife + serrated knife were simulated and analyzed using LS-DYNA software, and the root cutting characteristics of different knife combinations were analyzed according to the simulation results.

SolidWorks was used to establish three kinds of root cutting model, and then the model mesh was imported to Workbench/LS-DYNA in order to reduce the amount of calculation. In this study, the disk cutter will be defined as a rigid body. The mesh at the contact area between the roots of heading vegetables and the disk cutter in the root cutting process was finely divided, and the mesh size could be coarsened in other positions. The meshed root-cutting model is shown in Figure 10, and the number of nodes of the knotty vegetable root and disk cutter meshes are 42036 and 12960, the number of cells are 39510 and 6199, respectively.

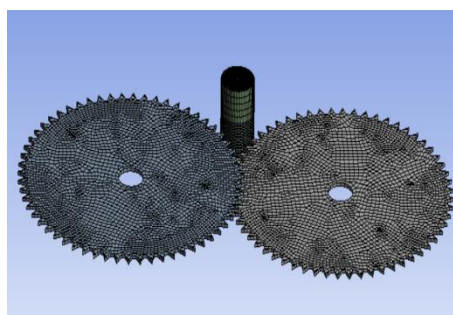


Fig. 5 – Grid division results

In the simulation model, the relative motion between the heading vegetable root and the cutter is used to simulate the actual root-cutting process. Select the upper end surface of the heading vegetables as fixed; the movement of the cutter is divided into forward motion and rotary motion around the axis, therefore, when constraining the cutter, it is necessary to set the X, Y, Z direction of the velocity component and X, Y, Z direction of the angular velocity component. The end time depends on the distance between the root of the heading vegetables and the cutter and the rotational speed of the cutter; the default safety factor of the time step is 0.9, and in the case of cutting simulation where the unit will be destroyed, it is possible to generate a negative volume, at this time, you can change the safety factor to a smaller one and set it to 0.6, and at the same time, the Minimum Time Step should be greater than 10^{-10} s (Li, 2013; Mohammad et al., 2019).

Bench Test

In order to optimize the key structural parameters and working parameters of the root cutting device, the root cutting performance test was carried out. The quadratic rotary orthogonal combination test method was adopted to analyze the relationship between the main influencing factors of root cutting performance (rotational speed of the cutter, conveying speed, inclination angle of the cutter, and the overlap amount of the cutter) and the performance index of the root cutting (cutting power). Regression analysis, response surface, and multi-objective variable optimization were applied to optimize the performance index of the root cutting device (cutting power).

The test is carried out on an independently designed double-disk heading vegetables root cutting test bench. This bench is mainly composed of double-disk cutting device, root cutting motor, clamping and conveying device, conveying motor, dynamic torque sensor, elastic pin coupling, frame, control and information acquisition system, etc. The test is carried out on a double-disk heading vegetables root cutting test bench. During the working process, the heading vegetable is stably clamped by the clamping and conveying device and conveyed in the direction of the cutting device, and the root of the heading vegetable is removed by the high-speed rotating double-disk cutter at the bottom.

Test Indicators

Referring to the national standard General Provisions on Measurement Methods for Test Conditions of Agricultural Machinery (GB/T 5262-2008) and the agricultural industry standards Test Methods for Sugar Beet Harvesting Machinery (JB/T 6276-2007) and Operational Quality of Sugar Beet Harvester (NY/T 1412-2007), the root cutting power P during the cabbage root cutting process was used as the test index.

$$P = \frac{(T_1 - T_0) \cdot n}{9550} \tag{3}$$

- P - cutting power, W;
- T_1 - total working torque, N·m;
- T_0 - idling torque, N·m.

Test Design

According to the previous experimental research, the factors that have a greater impact on the performance of root cutting mainly include the rotational speed of the cutter, conveying speed, inclination angle of the cutter, and overlap of the cutter. Therefore, in order to obtain a better combination of root cutting parameters, this experiment refers to the results of simulation tests and related literature, with the rotational speed of the cutter (A), conveying speed (B), cutter inclination (C) and the amount of overlap of the cutter (D) as the test factors, and with the root cutting power (R) as the response index, to carry out a four-factor, three-level quadratic rotary orthogonal test, the four factors of the Chinese cabbage cutting test level coding as shown in Table 1.

Table 1

Factors and level of orthogonal test				
Level	Factors			
	A. The rotational speed of the cutter (rpm)	B. Conveying speed (ms ⁻¹)	C. Cutter inclination (°)	D. Cutter overlap (mm)
1	200	0.3	5	15
2	300	0.4	10	20
3	400	0.5	15	25

RESULTS

Analysis of simulation test results

According to the above operation steps, the root cutting process in three types of cutting combinations was simulated and analyzed, and the root cutting process and the change curve of root cutting force were obtained through simulation analysis, as shown in Figure 6.

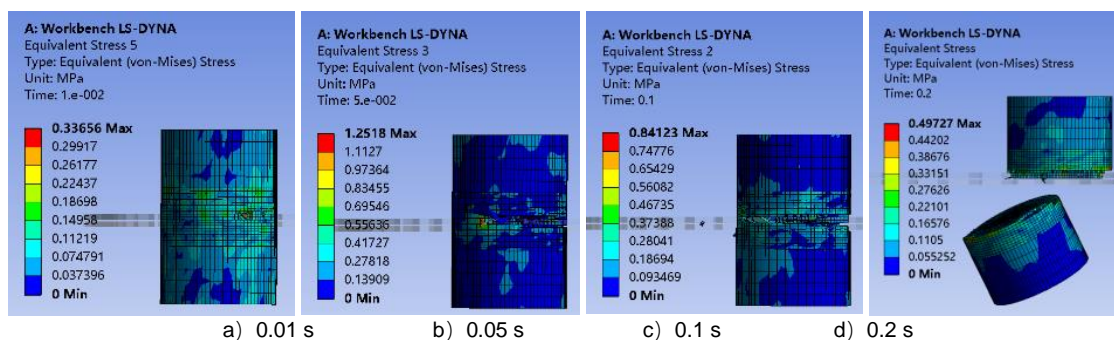


Fig. 6 – Simulation process of root cutting

The heading vegetables root and the cutter began to contact, the cutter approached the heading vegetables root and contacted the outer skin of the cabbage root, and the outer skin of the heading vegetables root was gradually deformed, as shown in Figure 6a. As the cutter continued to go deeper into the interior of the heading vegetables root, the cutter exerted a vertically acting cutting and friction force on the root resulting in the cutting of the root as shown in Figure 6b. The cutter continued to penetrate deeper into the root, and the root started to fracture, as shown in Figure 6c. Eventually, the cutter severed the cabbage root, as shown in Figure 6d.

The effects of different cutter combinations on the maximum root cutting force and internal energy of root cutting during root cutting were further analyzed and the statistical simulation results are shown in Table 2.

Table 2

Data of maximum root cutting force and internal energy under different cutter types		
Cutter types	Maximum root cutting force (N)	Internal energy (mJ)
Double smooth blade	22.797	1854.56
Double serrated blade	20.499	1751.4
Smooth + serrated blade	20.97	1653.53

From the data in Table 2, it can be concluded that the maximum root cutting force of the double serrated knife is the smallest, and the root cutting internal energy of the combination of smooth knife and serrated knife is the smallest. Compared to the smooth knife, the serrated knife has a better clamping effect on the cabbage root. The combination of serrated knife and smooth-edged knife is more optimal by combined analysis of the results of maximum root-cutting force and internal energy.

Analysis of bench test results

The experiments were designed in accordance with the BBD experimental design method, and the experimental program and results are shown in Table 3.

Table 3

Orthogonal test scheme and test results				
Factor				Response indicators
A (r/min)	B (m/s)	C (°)	D (mm)	R (W)
-1 (200)	-1 (0.3)	0 (10)	0 (20)	52.5
1 (400)	-1	0	0	90.8
-1	1 (0.5)	0	0	71.6
1	1	0	0	123.3
0 (300)	0 (0.4)	0	0	92.3
0	0	-1 (5)	-1 (15)	98.2
0	0	1 (15)	-1	92.2
0	0	-1	1 (25)	92.7

Factor				Response indicators
A (r/min)	B (m/s)	C (°)	D (mm)	R (W)
0	0	1	1	94
0	0	0	0	88.5
-1	0	0	-1	68.6
1	0	0	-1	102.3
-1	0	0	1	60.7
1	0	0	1	109.6
0	0	0	0	84.6
0	-1	-1	0	75.5
0	1	-1	0	107.6
0	-1	1	0	82
0	1	1	0	95.6
0	0	0	0	85.9
-1	0	-1	0	68.6
1	0	-1	0	107.7
-1	0	1	0	62.4
1	0	1	0	111
0	0	0	0	89.5
0	-1	0	-1	69
0	1	0	-1	101.5
0	-1	0	1	70.2
0	1	0	1	102.8

The quadratic polynomial response surface regression model of the root cutting power (R) on the rotational speed of the cutter (A), conveying speed (B), cutter inclination (C) and the amount of overlap of the cutter (D) was established by using Design-Expert 8.06 to fit the multivariate regression to test results in Table 4. In this table, df means degree of freedom. F-value is the ratio of the variance between the group means to the variance within the groups. A higher F-value indicates a greater difference between group means relative to the variation within the groups. The P-value is the probability of obtaining an F-value as extreme as the one calculated, assuming the null hypothesis is true. A small P-value (typically < 0.05) suggests that the observed differences between group means are statistically significant, leading to the rejection of the null hypothesis.

Table 4

Results of variance analysis of orthogonal test

Source	Root cutting power					
	Sum of Squares	df	Mean Square	F value	P value	Significant
Model	8324.53	14	594.61	63.97	<0.0001	**
A	5646.34	1	5646.34	607.45	<0.0001	**
B	2197.81	1	2197.81	236.45	<0.0001	**
C	14.30	1	14.3	1.54	0.2352	
D	0.27	1	0.27	2.9E-2	0.8671	
AB	44.89	1	44.89	4.83	0.0453	*
AC	22.56	1	22.56	2.43	0.1415	
AD	57.76	1	57.76	6.21	0.0258	*
BC	85.56	1	85.56	9.21	0.0089	**
BD	2.5E-3	1	2.5E-3	2.7E-4	0.9871	
CD	13.32	1	13.32	1.43	0.2511	
A2	73.92	1	73.92	7.95	0.0136	*
B2	19.04	1	19.04	2.05	0.1743	
C2	99.89	1	99.89	10.75	0.0055	**
D2	3.29	1	3.29	0.35	0.5617	
Residual	130.13	14	9.3			
Lack of Fit	93.3	10	9.33	1.01	0.5424	
Pure Error	36.83	4	9.2			
Cor Total	8454.66	28				

Note: ** indicates a highly significant effect ($P < 0.01$) and * indicates a significant effect ($P < 0.05$)

As can be seen from Table 4, the root cutting power regression model $P < 0.01$ and the misfit term $P > 0.05$, indicating a high degree of goodness of fit and a highly significant fitting effect.

From the value of F-value in Table 4, it can be seen that the factors affecting the root cutting power (R) of the root cutting device are, in order of priority: the rotational speed of the cutter (A), conveying speed (B), cutter inclination (C), the amount of overlap of the cutter (D). From the value of P in Table 3, it can be seen that the effect of A, B, BC, and C2 on the root cutting power is highly significant, the effect of AB, AD, and A2 on root cutting power is significant, and the rest of the items do not have a significant effect on the root cutting power.

In summary, the optimized regression fitting equation about root cutting power obtained after eliminating the insignificant terms is shown in equation (4), and the optimized model is reliable with $P < 0.01$ and the out-of-fit term with $P > 0.05$.

$$R = 87.61 + 21.69A + 13.53B - 1.09C - 0.15D + 3.35AB + 3.8AD - 4.63BC - 3.22A^2 + 4.08C^2 \quad (4)$$

Discussion

In order to further explore the factors affecting the experimental results and the degree of influence, this paper chooses to use the response surface method to analyze the influence of the rotational speed of the cutter (A), conveying speed (B), cutter inclination (C) and the amount of overlap of the cutter (D) on the root cutting power (R). The design of the root-cutting device is based on a set of objective function and constraints. By establishing the objective function and constraints, the optimal parameter combinations of the designed root cutting device are found.

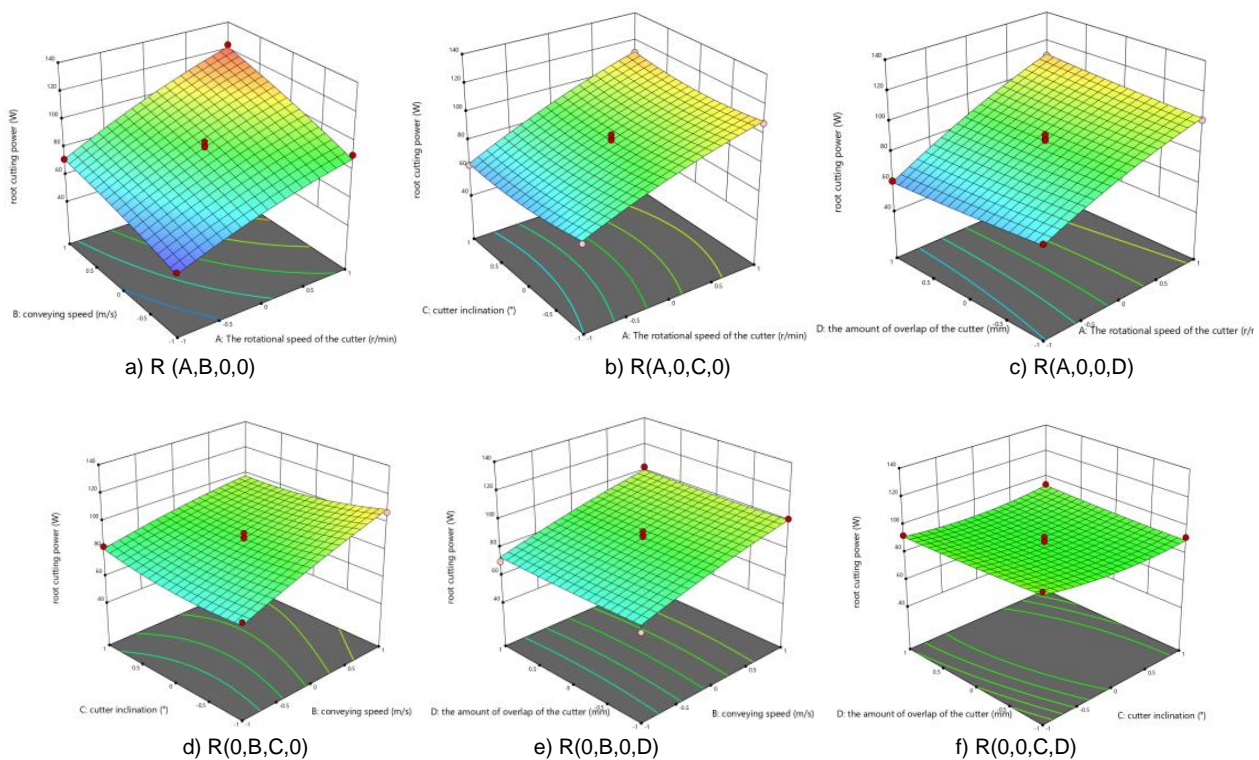


Fig. 7 – Three-dimensional response surface analysis of root cutting power interaction factors

As can be seen from Figure 7, the rotational speed of the cutter (A) and other factors response surface slope is larger, that is, the rotational speed of the cutter (A) on the root cutting power R has the greatest impact, conveying speed (B) is the next largest, while cutter inclination (C) and the amount of overlap of the cutter (D) on the root cutting power R has a smoother impact, that is, the interaction factors in the C and D have the smallest impact on the root cutting power.

In order to achieve low-power and high-efficiency root cutting, this paper takes the root cutting power as the optimization index, and carries out parameter optimization analysis on the influencing factors such as the rotational speed of the cutter, conveying speed, tilting angle of the cutter, and overlapping amount of the cutter. The regression model is optimized and solved using the optimization module in Design Expert 8.0.6 software, and the established optimization model is shown in equation (5).

$$\begin{aligned} & \min R \\ & s. t. \begin{cases} 200 \leq A \leq 400 \\ 0.3 \leq B \leq 0.5 \\ 5 \leq C \leq 15 \\ 15 \leq D \leq 25 \end{cases} \end{aligned} \quad (5)$$

CONCLUSIONS

(1) In order to improve the efficiency of mechanized harvesting of heading vegetables, a root cutting device for heading vegetables was designed. Through the LS-DYNA simulation experiments, the root cutting process of the root cutting device was simulated and the root cutting force and root cutting internal energy of three knife combinations were compared. The simulation results of the maximum root cutting force of the double serrated knife is the smallest, and the combination of the smooth-edged knife and the serrated knife has the smallest root cutting internal energy. Compared with the smooth-edged knife and serrated knife, the serrated knife has a better clamping effect on the heading vegetables root. The combination of serrated knife and smooth-edged knife is more optimal by combined analysis of the results of maximum root-cutting force and internal energy.

(2) In order to obtain the optimal structural parameters and operating parameters of the root cutting device, a quadratic rotary orthogonal combination test method was used to analyze the relationship between the main factors affecting the performance of the root cutting device (rotational speed of the cutter, conveying speed, inclination angle of the cutter, and overlap amount of the cutter) and the performance index (root cutting power), and the regression analysis, response surface, and multi-objective variable optimization methods were applied to design the bench test program. The results of the bench test showed that the optimal parameter combinations of the designed seed dispenser were: cutter speed of 200 rpm, conveying speed of 0.3 ms⁻¹, cutter inclination angle of 10°, and cutter overlap volume of 20 mm; and the model-predicted root-cutting power was 51.19W.

ACKNOWLEDGEMENT

The authors were funded for this project by the National Natural Science Foundation of China (Grant no. 52205273) and the Key Laboratory of Modern Agricultural Equipment, Ministry of Agriculture and Rural Affairs (2023007) .

REFERENCES

- [1] Du, D., (2017). *Research on crawler self-propelled kale harvester and development of weighing system (履带自走式甘蓝收获机研究及称重系统开发)*. MSc Thesis, Zhejiang University, Hangzhou/China;
- [2] Du, D., Fei, G., Wang, J., Huang, J., You, X., (2015). Design and test of self-propelled kale harvester (自走式甘蓝收获机的设计与试验). *Journal of Agricultural Engineering*, Vol.31, no.14, pp. 16-23;
- [3] Du, D., Wang, J., Qiu, S., (2014). Experimental study on optimization of cutting site and method of kale root and stem (甘蓝根茎部切割部位及方式优化试验研究). *Journal of Agricultural Engineering*, Vol.30, no.12, pp. 34-40;
- [4] El, D., El, S., (2020). Fabrication and Evaluation of a Cabbage Harvester Prototype. *Agriculture*, Vol.10;
- [5] Jang, B., Chowdhury, M., Ali, M., Islam, M., (2021). Stability and vibration analysis of a tractor-mounted Chinese cabbage collector. *Iop Conference Series: Earth and Environmental Science*, Vol.733, no.1, pp.7;
- [6] Jing, Z., Jun. W., Shuang G., (2021). Relaxation characteristics for quality evaluation of Chinese cabbage. *Journal of Food Engineering*, Vol.306, no.3, pp. 110635;
- [7] Li, H., (2018). Research and preliminary design of single row cabbage harvester (单行大白菜收获机的研究与初步设计). *Rural and Pastoral Mechanization*, Vol.5, pp. 15-18;
- [8] Li, X., (2020). Considerations for mechanized harvesting of Chinese cabbage and trends in research and development (大白菜机械化收获注意事项及研发趋势). *Agricultural Machinery Use and Maintenance*, Vol.3, pp. 2-3;
- [9] Li, M., Yi, F., Kang, N., Yan, W., Sheng, H., Kai, K., (2023). Analysis on root cutting mechanism of self-propelled Chinese cabbage harvester and optimisation of device parameters. *INMATEH-Agricultural Engineering*, Vol. 71, no.3, pp. 70-82;

- [10] Li, T., Meng, Zi., Ding, H., Hou, J., Shi, G., (2020). Mechanical analysis and parameter optimization of kale root cutting operation (甘蓝切根作业力学分析与参数优化). *Journal of Agricultural Engineering*, Vol.36, no.7, pp.63-72;
- [11] Li, X., (2013). Improvement design of 4YB-I type kale harvester(4YB-1 型甘蓝收获机的改进设计). *Gansu Agricultural University*;
- [12] Liu, F., Liu, L., Guo, J., Liu, Y., Di, M., (2021). Design and test of cutter disk inward tilting sugarcane root cutting device (刀盘内倾式甘蔗切根装置设计与试验). *Agricultural Engineering*, Vol.11, no.3, pp.95-101;
- [13] Mohammod, A., Ye-Seul, L., Md S., Kang, T., (2019). Kinematic analysis for design of the transportation part of a tractor-mounted Chinese cabbage collector. *Journal of Biosystems Engineering*, Vol.44, no.4, pp. 226-235;
- [14] Sheng, S., Pan, C., Jian, T., Meng, Q., (2021). Design and experimental study of flexible threshing unit for Chinese cabbage seeds. *INMATEH-Agricultural Engineering*, Vol. 65, no.3, pp. 333-344;
- [15] Wang, J., Du, D., Hu, J., Zhu, J., (2014). Vegetable mechanized harvesting technology and its development (蔬菜机械化收获技术及其发展). *Journal of Agricultural Machinery*, Vol.45, no.2, pp. 81-87;
- [16] Wang, W., Zhao, J., Sun, Y., Wang, L., Zhong, X., (2018). Status and development countermeasures of winter storage of Chinese cabbage (我国大白菜冬贮现状及发展对策). *Vegetables*, Vol.4, pp. 58-60;
- [17] Wen, Y., Yan, W., Sheng, H., Kang, N., Cheng, X., Li, M., (2024). Design and experiment of double-row wheel self-propelled Chinese cabbage harvester. *INMATEH-Agricultural Engineering*, Vol. 73, no.2, pp.702-720;
- [18] Xu, L., Yao, H., (2009). Research on shear characteristics of Chinese cabbage rootstalk. *Agricultural Mechanization in Asia, Africa & Latin America*, Vol.40, no.3, pp. 30;
- [19] Yan, J., Ning, Y., Fu, X., Yang, B., (2024). Seed discharge performance test of air suction seed discharger for small vegetable seeds. *INMATEH-Agricultural Engineering*, Vol. 73, no.2, pp. 721-730;
- Zhou, C., (2013) *Research on key technology and equipment for kale harvesting (甘蓝收获关键技术及装备研究)*. MSc Thesis, Northeast Agricultural University, Harbin/China.

DESIGN OF SEMI-PHYSICAL SIMULATION PLATFORM FOR GRAIN CLEANING AND REGULATING SYSTEM

谷物清选调控系统半实物仿真平台设计

Xipeng QIAN¹⁾, Yihu WANG¹⁾, Guohai ZHANG^{1 2)}

¹⁾Shandong University of Technology, College of Agricultural Engineering and Food Science, Zibo, China

²⁾Shandong University of Technology, Institute of Modern Agricultural Equipment, Zibo, China

Tel: +8615668066520; E-mail: guohaizhang@sdut.edu.cn

Corresponding author: Guohai Zhang

DOI: <https://doi.org/10.35633/inmateh-75-72>

Keywords: Grain harvesting, Cleaning device, Design, Semi-physical simulation system

ABSTRACT

To address the long development cycle of the grain air-screen cleaning device, a semi-physical simulation platform for the grain cleaning control system was designed. The platform was used to simulate the actual operational process, conducting both open-loop and closed-loop tests, with results compared to actual tests. In the open-loop test, the speed error had a mathematical expectation of 0.8387 rpm, with a standard deviation of 2.75 rpm, and the fish-scale sieve opening error had a mathematical expectation of -0.0117 mm, with a standard deviation of 0.038 mm. In the closed-loop test, the speed error had a mathematical expectation of 0.679 rpm, with a standard deviation of 1.815 rpm. The experimental results demonstrate that the simulation platform can effectively replicate the actual operating conditions of the grain cleaning device and validate the effectiveness of the TC377 controller's control algorithm, thereby improving the development efficiency.

摘要

针对谷物风筛式清选装置开发周期长的问题, 设计出一套谷物清选调控系统半实物仿真平台。利用半实物仿真平台模拟实际作业过程, 进行开环与闭环测试, 与实际测试进行对比。其中, 开环测试转速误差数学期望为 0.8387rpm, 标准差为 2.75rpm, 鱼鳞筛开度误差数学期望为 -0.0117mm, 标准差为 0.038mm。闭环测试转速误差数学期望为 0.679rpm, 标准差为 1.815rpm, 试验结果表明了该仿真平台能够模拟谷物清选装置的实际工况以及 TC377 作为控制器控制算法的有效性, 能够提高开发效率。

INTRODUCTION

China, as a major agricultural country, has high demands on the quality and efficiency of grain production due to its socio-economic context. During the processes of growth, harvesting, transportation, and storage, grains are susceptible to various adverse factors, leading to the presence of impurities, damaged kernels, and certain harmful substances. These factors not only impact the quality and nutritional value of the grains but may also pose potential health risks to consumers. Therefore, grain cleaning and sorting equipment plays an indispensable role in agricultural production (Qu et al., 2024; Wang et al., 2022).

The wind-sifting cleaning and sorting device is the primary equipment used by combine harvesters for grain cleaning operations. It offers advantages such as high cleaning efficiency and a high kernel cleaning rate. During operation, the wind-sifting cleaning device has multiple adjustable working parameters. The precision and automation of these adjustments are key factors that influence its cleaning efficiency and performance in field operations (Ning et al., 2018).

In the practical development of harvesting machine cleaning devices, limitations such as harvest season and test field conditions make it difficult to conduct extensive field trials under various operational conditions. Before conducting real-world vehicle tests, extensive iterative experimental research is required to obtain optimal test results, which, to some extent, impacts the development process of cleaning devices. Many research institutions have designed and manufactured various testing rigs, but these rigs are expensive, and the testing process requires large amounts of crops, which still presents certain constraints. Under these conditions, the concept of semi-physical simulation technology has been proposed (Jiang et al., 2022; Xu et al., 2024; Liu et al., 2018).

Semi-physical simulation technology is an important simulation technique, currently widely used in various fields such as aerospace engineering, military applications, automotive engineering, diesel engine electronic control systems, and medical applications (Cheng et al., 2022).

Hardware-in-the-loop simulation is a simulation method targeting specific research objects. Its core lies in introducing a portion of the simulation object system into the simulation environment in the form of a physical model, while the remaining components are described through mathematical modeling methods and further developed into corresponding simulation computation models. Based on this, leveraging the actual effects generated by the physical model, real-time joint simulation tests can be conducted, integrating the collaborative work of mathematical and physical models. At present, the semi-physical simulation technology is not widely used in the field of agricultural machinery, and it is mainly used for the steering control and gear shift simulation of tractors (Wu et al., 2023; Wu et al., 2019; Li et al., 2024). Semi-physical simulation technology provides strong support for the integration of control systems in the development of agricultural machinery. By combining virtual models with actual hardware, it allows for the validation of the system's overall performance at an early stage of agricultural machinery development, enabling the timely identification of potential issues and optimization of system design. Furthermore, this simulation technology can real-time simulate the performance of agricultural machinery during actual operation. Through interaction with physical hardware, developers can more precisely adjust control system parameters, thus optimizing the performance of the grain cleaning device and ensuring that the machinery operates efficiently and stably (Zhu et al., 2022).

Zhu Xiaolong et al. in China developed a semi-physical simulation platform for a low-loss threshing intelligent control system. Through signal simulation testing and automatic control strategy simulations, they demonstrated that the platform can be used for the development of intelligent control systems for corn grain harvesters. This platform has provided an experimental foundation for the development of intelligent control systems for corn grain harvesters. Through a comparison of simulation and experimental tests, the semi-physical simulation platform was successfully validated for the development of the intelligent control system, shortening the development cycle (Zhu et al., 2022). Xie Bin et al. designed the mechanical structure of the electric tractor's drive system and built a prototype, which was then downloaded to the controller for hardware-in-the-loop (HIL) experiments. Actual data from previous field tests on plowing and rotary tilling were used as the load for the HIL experiments, which were conducted on a personal computer. Through multiple simulations and experiments on the semi-physical simulation platform, the traditional drive system was successfully improved, enhancing ploughing and rotary tilling efficiency (Xie et al., 2022).

Therefore, this paper focuses on the development of a grain cleaning test bench and designs a semi-physical simulation platform, applying semi-physical simulation technology to the grain cleaning device. The aim is to address the issues of long development cycles and high development costs. By reviewing relevant literature and utilizing appropriate software, mathematical models of the key operating components of the grain cleaning system were established. The platform was equipped with various components that generated the necessary signals for the testing process, achieving the conversion between physical values and signal values, thereby enabling successful signal transmission between different circuit boards. Finally, before conducting actual experiments, the control effects were verified through simulation testing of the controller.

MATERIALS AND METHODS

The overall structure of the hardware-in-the-loop simulation platform is shown in Fig. 1. Its structure is mainly divided into three parts: the hardware platform, the up-per-level computer software, and the real-time simulation model.

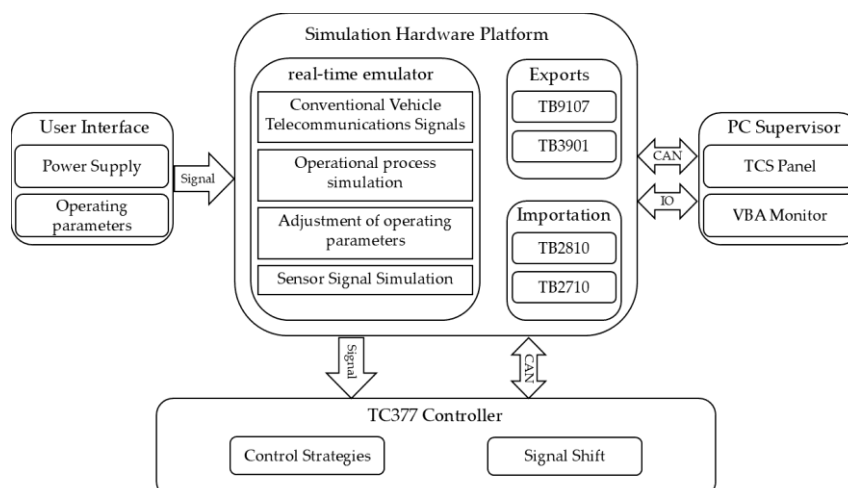


Fig. 1 - Overall Flow Chart

The specific requirements are as follows: (1) Simulate the electrical signals generated during the operation of the grain cleaning test bench, as well as the signals transmitted by the sensors. These signals are received through various boards located within the cabinet and transmitted to the controller via the ODU port. (2) It should be capable of simulating the actual working conditions, detecting variations in signals such as voltage and current during the control process, and performing data processing and transmission via hard-wire I/O signals and CAN communication. (3) Develop a model of the grain cleaning test bench and construct the mathematical model using the Simulink simulation platform. The controlled object receives the control signals from the controller and generates corresponding feedback signals to return to the controller, thus forming a complete closed-loop system. (4) The system is equipped with a human-machine interface, allowing for more intuitive and convenient adjustment and monitoring of the frequency variations of the inverter control cabinet, motor speed, fan speed, and other key components. The working status is monitored in real-time through CAN messages.

The components of the cabinet used for testing include devices such as PDU, programmable power supplies, regulated power supplies, PSM, function boards, general-purpose IO boards, and real-time processing systems, as shown in Fig. 2. The PDU primarily performs AC power control, distribution, and equipment protection functions. The real-time simulator ensures the simulation model operates in real-time, facilitates data interaction with the host-computer test software, and enables online parameter adjustment and monitoring. It also transmits the signals required by the controller through various IO boards and collects all signals transmitted by the controller.

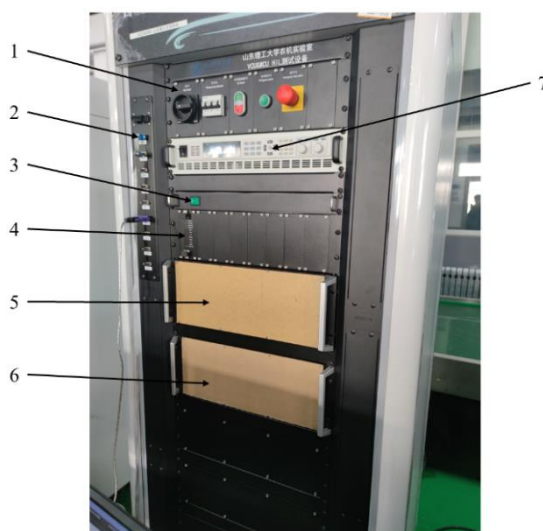


Fig. 2 - Cabinet Composition

1 - PDU Power Management, 2 - CAN interface, 3 - Signal conditioning power supply, 4 - Power switching, 5 - ODU connection draw box, 6 - Load draw box, 7 - Programmable power supply

The host computer software primarily includes Real-time Simulation Test Management Software (TCS), Automated Testing Software (TAE), Bus Monitoring Software (VBA), IO Model Generation Software (TB_IOModel_Gen), and Fault Injection Software (TB_EFI). The experimental management software oversees the management of model files and hardware resources. The bus monitoring software directly monitors messages on the CAN bus and functions as the bus monitor during the interaction between the HIL device and the controller. The fault injection software directly controls the fault injection board to introduce faults, thereby simulating real-world scenarios. The automation management software facilitates the invocation of the aforementioned software via the corresponding software interfaces, setting the execution sequence to achieve an automated testing process.

The drive motor selected is a squirrel-cage three-phase asynchronous motor, which drives the corresponding components through belt transmission. The motor speed is adjusted by varying the frequency using a frequency converter. A simulation model is built to simulate the corresponding frequency-controlled speed regulation system and output the corresponding motor speed. The motor speeds of the driving and driven wheels are detected by the VEMSEE speed sensor. Wind speed is measured by installing a wind speed sensor at the fan outlet and inside the sieve box. An impact plate sensor is used behind the sieve box to record the number of grains lost at the impurity discharge outlet during the grain cleaning process.

In actual operation, the size of the motor-driven load also affects the variation in motor speed. Therefore, to simplify the process, it is assumed that the motor's speed transmission is ideal. Mathematical models for the centrifugal fan, fish-scale sieve opening, spiral drill, and other components were established based on the agricultural machinery manual and relevant literature. The mathematical models were not optimized in this paper but are used to simulate the adjustment process of the test bench during actual operation. The physical values obtained during operation are converted into signal values and output through the circuit boards. The simulation of vehicle electrical signals and sensor signals is achieved through the IO conversion board and CAN communication board integrated into the simulation platform.

Table 1

The Main Technical Parameters of the Grain Cleaning Device	
Item	Parameter
Belt width	1000 mm
Feed motor speed	0~100 rpm
Fan speed	400~1200 rpm
Vibrating screen crank speed	0~280 rpm
Fish scale sieve opening	7~22mm
Rotating speed of the elevator	0~500rpm

This paper takes the air-screen grain cleaning device as the development object. The tuning ranges for the working components are based on the equipment settings provided by the grain cleaning device manufacturer, as well as the professional instructions from the training personnel. The tuning ranges comply with the manufacturer's technical specifications and usage recommendations, ensuring standardization and consistency during the experimental process. Additionally, the device was delivered at the end of last year and, under the guidance of trained personnel, the operational ranges for each component parameter were confirmed, thereby enhancing the reliability of the experiment.

The wind separation system of the grain cleaning device employs a volute centrifugal fan, consisting primarily of components such as the fan casing, air regulation plate, fan shaft, blade connection plate, and blades. This centrifugal fan features a relatively wide design, provides adequate airflow, and ensures a uniform distribution of air within the screening box, thereby meeting the cleaning and selection requirements. The airflow speed and direction within the system can be adjusted through the air regulation plate based on actual conditions, enabling the attainment of the desired cleaning and selection effect.

The cleaning airflow V is given by Equation (1).

$$V = \frac{\beta Q}{\mu \rho} \quad (1)$$

where: β is the proportion of impurities in the mixture, taken as $\beta=16\%$, for full feeding, the typical values for wheat range from 0.15 to 0.2, and for rice, from 0.1 to 0.15; for partial feeding, wheat typically ranges from 0.1 to 0.15, and rice from 0.08 to 0.12; Q is the machine's feeding rate, with a minimum value of 10 kg/s; μ is the concentration ratio of the airflow carrying impurities, taken as 0.25; ρ is the air density, taken as 1.29 kg/m³.

Outlet air velocity, v , is given by Equation (2).

$$v = \frac{V}{BH} \quad (2)$$

where B is the outlet width, mm; H is the outlet height, mm.

The variation in the fish-scale sieve opening corresponds to the vertical spacing between adjacent sieve plates is given by Equation (3). The airflow through the cross-sectional gap between adjacent sieve plates per unit time is given by Equation (4).

$$S_1 = l \cdot l_1 = l_0 \sin \alpha l_1 \quad (3)$$

$$N = 3600 S_1 v = 3600 l_0 \sin \alpha l_1 v \quad (4)$$

where: N is the airflow through the cross-sectional area of the gap between adjacent sieve plates per unit time, in m³/s; v is the airflow velocity, in m/s; S_1 is the cross-sectional area of the gap between adjacent sieve plates, in m²; l_0 is the length of the connecting plate between adjacent sieve plates, in m; l_1 is the width of the sieve plate, in m; l is the opening of the fish-scale sieve, in m.

v, l_0, l_1 is a fixed value, therefore, the change angle α of the sieve sheet determines the cross sectional ventilation N of the adjacent sieve sheet gap per unit time. From $l=l_0 \sin\alpha$, it follows that $0^\circ \leq \alpha \leq 90^\circ$, so $0 \leq \sin\alpha \leq 1$, when $\alpha = 90^\circ$, $\sin\alpha = 1$, at this point, the opening l of the fish scale sieve is at its maximum value and equal to l_0 .

The horizontal winch seed conveying speed is given by Equation (5).

$$v_{d1} = \frac{P_1 w_{d1}}{60\pi} \tag{5}$$

where v_{d1} is the axial conveying speed of the material, in m/s; p_1 represents the pitch of the helical blade, full-face blade $p_1 = 0.8D_1$, in m; D_1 represents the diameter of the helical blade, in m; w_{d1} represents the rotational speed of the screw shaft, in rpm.

Vertical winch seed conveying speed is given by Equation (6).

$$v_{d2} = \frac{w_{d2} R_{d2} \sin\alpha \sin\beta}{30 \sin(\alpha + \beta)} \tag{6}$$

where w_{d2} is the rotational speed of the screw shaft, in rpm; R_{d2} is the radius of the auger, in m; β represents the angle between the direction of grain movement and the horizontal, in degrees ($^\circ$); α represents the helical angle of the blade, in degrees ($^\circ$).

The simulation model built in MATLAB/Simulink consists of multiple modules. TestBaseIO: Cabinet Basic Control Module. This section primarily controls the output of the programmable power supply and its feedback. The programmable power supply is turned off by adjusting the high or low level of DO1. Additionally, the output voltage values of AO1 and AO2 are used to achieve the specified voltage and current settings in the model.

The IO model serves as the interface between the simulation model and external hardware. As shown in Fig. 3, the left-side module, MDL Data to Controller, transmits hard-wired signals from the model to the cabinet board, which are then sent to the controller. Conversely, the right-side module, Controller Data To MDL, collects hard-wired signals from the controller via the cabinet board and delivers them to the model.

In particular, the MDL Soft ECU Data to Bus module categorizes various messages, as shown in Fig. 4, which are centrally monitored and managed by VBA. Each signal is ultimately transmitted to the RTSE output interface, then forwarded to the CAN communication board, and finally sent to the controller under test.

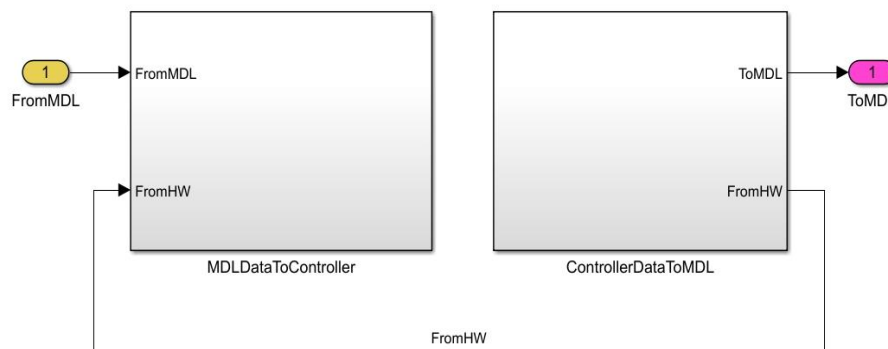


Fig. 3 - I/O model

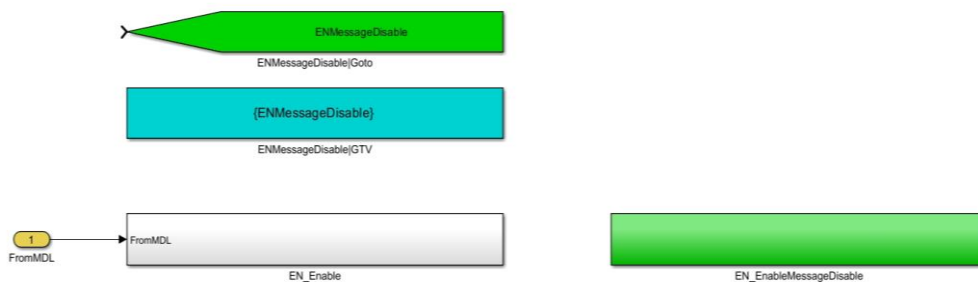


Fig. 4 - MDL Soft ECU Data to Bus

Test Bench Model: This model is used to simulate the virtual controlled object of the controller under test. The model is divided into three parts: the control cabinet, virtual controller, and test bench. The input to the model comes from signals transmitted by the IO model. The Maneuver module replaces the control cabinet and is primarily responsible for starting and stopping the test bench as well as regulating the motor speed. The virtual controller is not used in this model. The test bench model includes the motor model and the working components model. The specific setup is shown in Fig. 5.

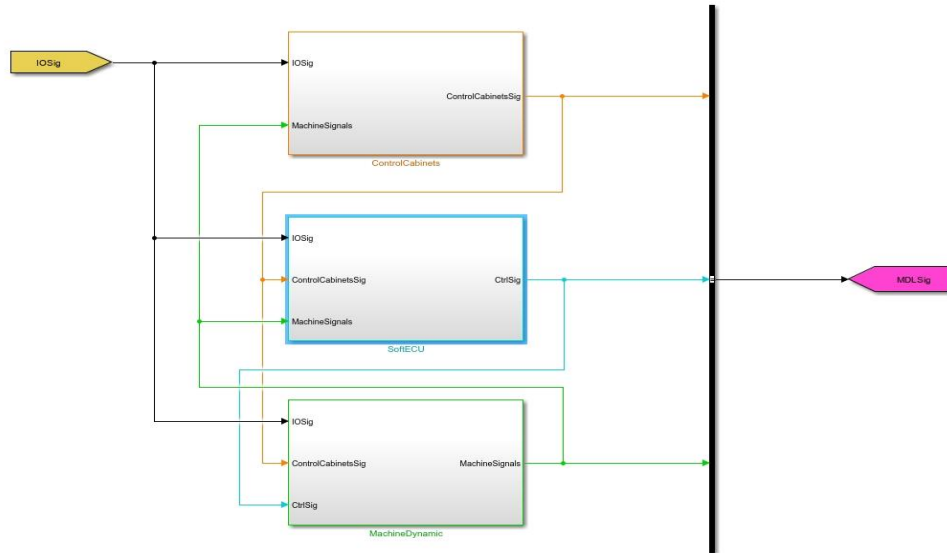


Fig. 5 - Test Bench Model

A 3D model of the grain cleaning test bench was built using SolidWorks software, based on the geometric and mass parameters of the working mechanism, as shown in Fig. 6 and Fig. 7. The model primarily includes components such as the shaker plate, vibrating screen, fan, and screw conveyor. The mass, moment of inertia, and connection parameters for each component are carefully set to ensure accuracy.

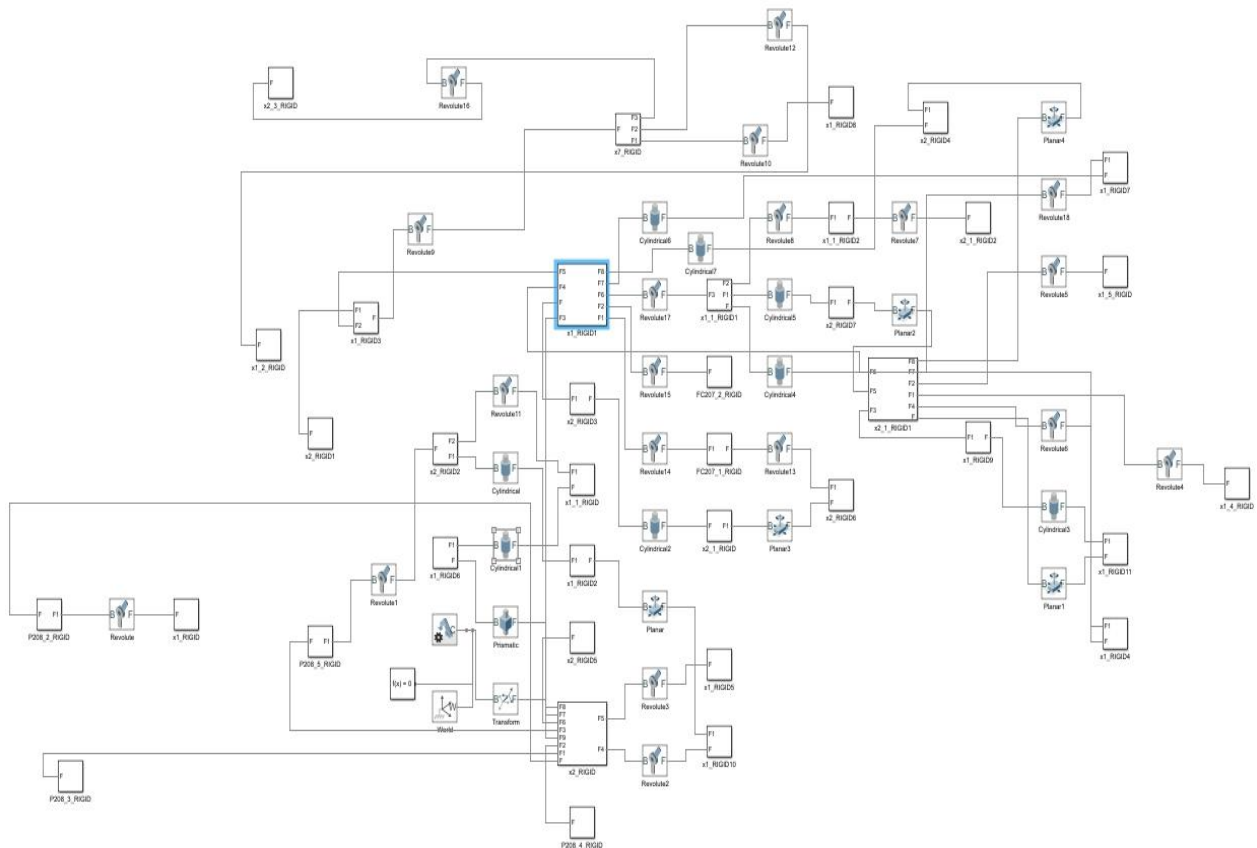


Fig 6 - Models in Simulink

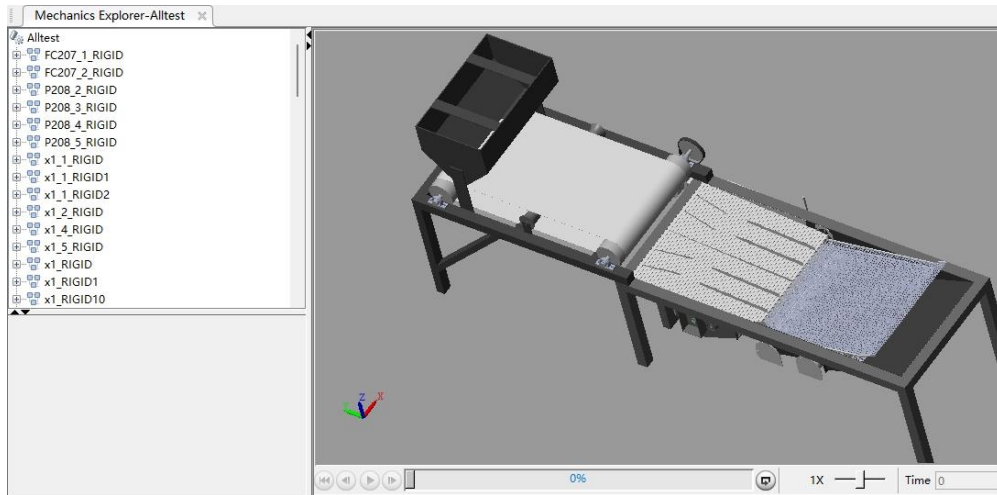


Fig. 7 - The mechanical operation diagram generated by Simscape

The TCS software control interface is shown in Fig. 8. The left side is configured for controlling the PDU and programmable power supply, enabling power cycling of the cabinet and controller as well as the corresponding voltage and current variations. The right side displays the operating parameters of each component, which need to be manually set. The basic control elements in the layout are connected to the relevant signals, reflecting the values detected by the sensors.

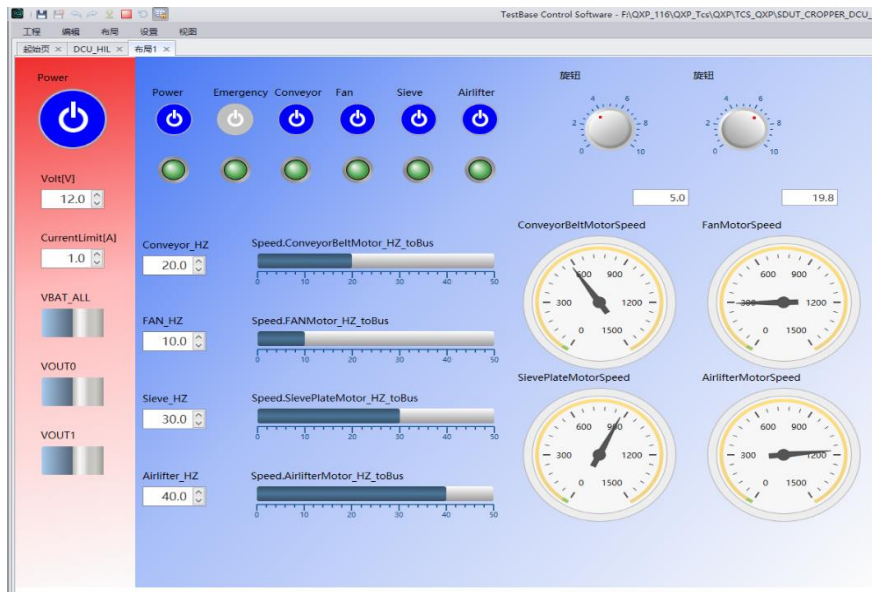


Fig. 8 - TCS Operator Interface

The VBA monitoring software is shown in Fig. 9. The cabinet is connected to the controller and successfully powered on. After running via TCS, the software reads the DBC file and displays multiple messages on the CAN bus. It intuitively shows whether the current components have started operating and the current operating frequency of the motor. The names assigned to these messages in the software provide a clearer view of the relationship between each message. This software effectively monitors whether CAN communication is running successfully.

21.481396	16:49:00.481396	CAN1	0x621	8	47 01 00 00 00 00 00 00	EN_Enable	Rx
		EN_PowerModules	1.0	1		Total Power Enable	
		EN_FanMotorSwitch	1.0	1		Fan motor enable signal	
		EN_ConveyorMotorSwitches	1.0	1		Conveyor belt enable signal	
		EN_EmergencyStopSwitches	0.0	0		Emergency stop enable signal	
		EN_AirlifterMotorSwitch	1.0	1		Cage lift enable signal	
		EN_SievePlateMotorSwitch	1.0	1		Screen box drive motor enable signal	
21.481893	16:49:00.481893	CAN1	0x623	8	00 0A 00 00 00 00 00 00	Speed_Motor	Rx
		AirlifterMotor_HZ	0.0	0		Fan speed adjustment signal	
		SievePlateMotor_HZ	0.0	0		Lifter speed adjustment signal	
		FANMotor_HZ	0.0	0		Screen box speed adjustment signal	
		ConveyorBeltMotor_HZ	10.0	A		Conveyor speed adjustment signal	
21.483021	16:49:00.483021	CAN1	0x624	8	E7 00 00 00 00 00 00 00	ECU_CtrlSig	Rx
		DCU1_SievePlateMotorState	1.0	1		Sieve box motor status signal	
		DCU1_PowerModulesState	1.0	1		Total power supply status signal	
		DCU1_AirlifterMotorState	1.0	1		Cage hoisting motor status signal	
		DCU1_ConveyorMotorState	1.0	1		Conveyor motor status signal	
		DCU1_EmergencyStopSwitchesState	1.0	1		emergency stop	
		DCU1_FanMotorState	1.0	1		Fan motor status signal	

Fig. 9 - VBA Monitor Interface

Automatic Control Strategy: An automatic control strategy is built within the controlled object model and the TC377 controller, with predefined goals to be achieved. During simulation, the TC377 controller periodically uses data feedback from sensors to assess the current operating status. By determining the deviation between the current state and the target parameters, it sends corresponding signals to drive the controlled object further, continuing until the parameters fall within the set range.

RESULTS

Operational parameter tests are conducted on both the simulation platform and the grain cleaning test bench. Under the assumption of no load, motor speed adjustment and fish-scale sieve opening adjustment experiments are carried out. The actual adjustment process of the operational parameters is compared with the simulation adjustment process to verify the effectiveness of the controlled object model within the simulation platform. To ensure that the control processes on both the simulation platform and the grain cleaning test bench are identical, the adjustment time and steps for both should be consistent during the experiments.

(1) Open-loop control test procedure:

Actual Test: Operate the control panel on the frequency converter control cabinet to adjust the motor's operating frequency to 41 Hz within 10 seconds. After the motor speed reaches 1200 rpm, it will continue to run, with detection and recording conducted through the speed sensor installed on the motor's drive wheel.

The adjustment range of the fish-scale sieve screen piece angle α is from 15° to 40°, and the screen opening l ranges from 7 mm to 22 mm. The fish-scale sieve adjustment device measures and records every 5° adjustment. The data record of the fish-scale sieve screen piece angle variation is presented in Table 2.

Table 2

Fish-Scale Sieve Screen Piece Angle Variation					
Angle of change	Fish Scale Sieve Opening	Emulate / mm Practice / mm		Relative error / mm	
α (°)	l / mm				
15	7	7.17	7.2	-0.4167	
20	10	9.56	9.6	-0.4167	
25	13	11.94	11.9	0.3361	
30	16	14.33	14.4	-0.4861	
35	19	16.72	16.7	0.1198	
40	22	19.11	19.1	0.0524	

Simulation platform test: Input the same control signals as those on the test bench into the upper-level TCS control interface, complete the input of the corresponding parameters and the adjustment of control knobs, and record the data generated by the controlled object during operation.

Comparison of the experimental results shown in Fig. 10 and Fig. 11 reveals that there is a discrepancy between the simulation results on the simulation platform and the actual test results of the grain cleaning machine. The main reason for this is the presence of numerous uncontrollable factors in the actual experiment, which cause deviations in the motor speed. In contrast, the simulation platform may experience voltage or current instability during transmission, leading to deviations in the simulated motor speed.

The actual measurement of the scalper screen opening contains errors due to manual measurement. The tool used was a standard vernier caliper with a precision of 0.1 mm. The mathematical expectation of the speed error is 0.8387 rpm, with a standard deviation of 2.75 rpm. The mathematical expectation of the speed error is positive, with the simulation results generally being 1 rpm higher than the actual measured results. Additionally, the motor speed does not remain completely stable at a specific value but exhibits some random fluctuations, which are caused by the instability in the actual measurements. The mathematical expectation for the fish-scale sieve is -0.0117 mm, with a standard deviation of 0.0380 mm. The measurement data shows some fluctuation, but the range of variation is small, which is within an acceptable range for the actual machine. Therefore, the controlled object model in the simulation platform can reasonably simulate the actual operating conditions of the grain cleaning test bench.

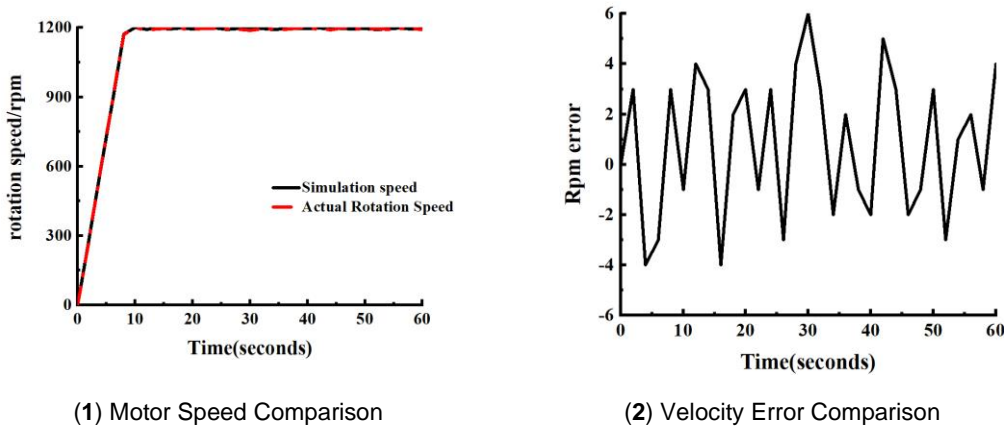


Fig. 10 - Open Loop Test Comparison and Error

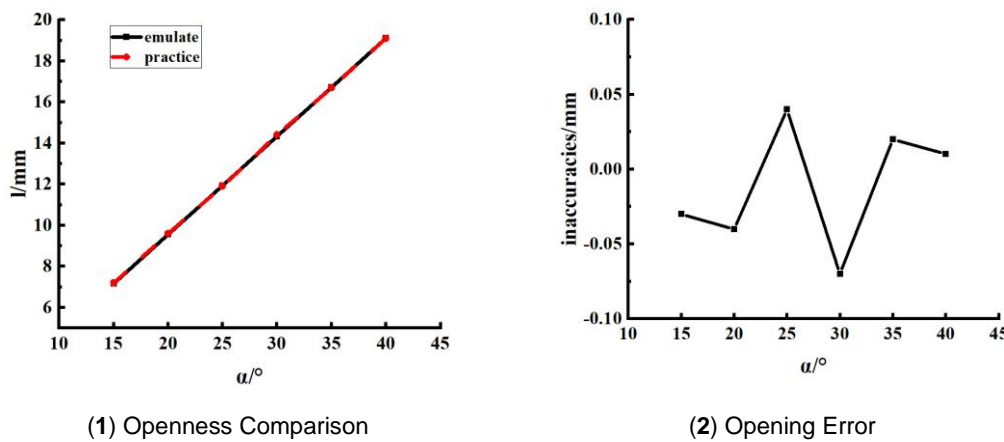


Fig. 11 - Fish Scale Sieve Opening Test Comparison

(2) Closed-loop control of the test process:

The TC377 development board, based on AutoSAR, is used as the controller. This controller is employed for both simulation and real-world experiments, with the results compared.

Actual test: Through the control panel on the frequency converter cabinet, the fan motor is stabilized to operate at around 400 rpm for a small amount of grain cleaning. After 20 seconds, the feeding rate is increased, and 20 seconds later, the initial feeding rate is restored. The experiment shows that the motor speed changes with the feeding rate. When the feeding rate suddenly increases, the controller receives the instruction for the change and sends a signal to increase the fan speed, thereby ensuring the normal operation of the cleaning process.

Simulation platform test: Design the same control signals as in the actual test. Adjust the input parameters in the initial state to stabilize the model at the corresponding speed. Then, increase the feeding rate by adjusting the control knob and restore the initial state after 20 seconds.

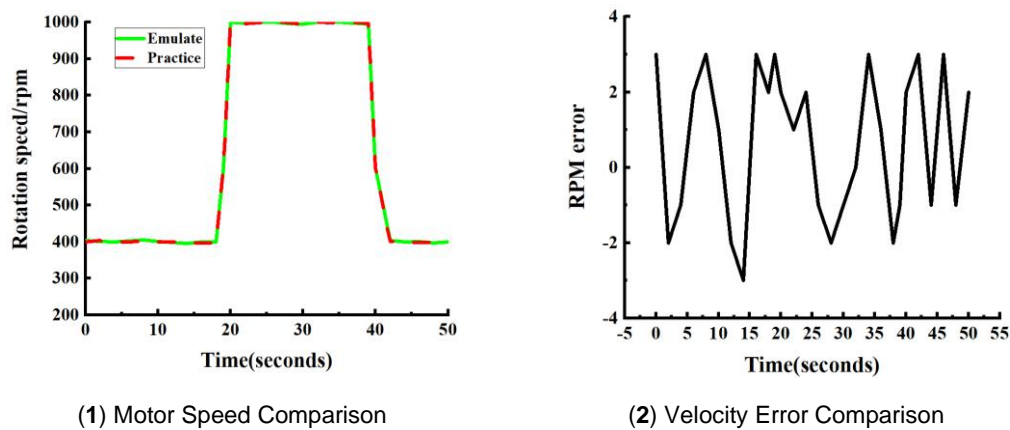


Fig. 12 - Closed Loop Test Comparison and Error

Due to deviations in the actual feeding weight and differences in bulk density, there is a slight error between the comparison tests. The experimental results are shown in Fig. 11. The mathematical expectation of the error during the speed adjustment process is 0.679 rpm. It can be observed that the simulation platform is capable of testing the controller and that the controller demonstrates strong control capability over the actual machine.

This paper takes the air-screen grain cleaning device, a common type of agricultural machinery, as the development object and applies semi-physical simulation technology to the grain cleaning device. By building a model on the semi-physical simulation platform, experimental results demonstrate that the simulation model can effectively replicate the actual operating conditions of the machine, with errors within an acceptable range. This provides a testing platform for the subsequent controller development, preventing potential damage to the grain cleaning device during the actual testing phase, and eliminating the need for multiple experiments, thus saving significant operational time.

CONCLUSIONS

(1) Due to the lengthy development process, cumbersome testing, and high development costs of the grain cleaning test bench, a hardware-in-the-loop simulation platform for grain cleaning control was designed. This platform is linked to the actual machine through the establishment of mathematical models for key components during operation. It provides the necessary hardware platform and corresponding upper-level control software for the development of the intelligent grain cleaning control system.

(2) Based on the practical influence of seasonal and site factors on the development of the grain cleaning device, a semi-physical simulation platform for the grain cleaning device control system was designed. This platform provides the hardware foundation and simulation test object for the development of the grain cleaning control system.

(3) The TC377 development board is used as the controller for both the actual machine and the controlled object on the simulation platform. A comparative experiment between simulation and real-world testing was conducted. The open-loop test verified the validity of the model and the successful transmission of signals, while the closed-loop test demonstrated the effectiveness of the controller algorithm and the actual control performance. This confirms that the simulation platform can significantly shorten the development cycle and reduce development costs.

(4) Hardware-in-the-loop simulation technology has achieved initial success in the field of grain cleaning. However, at present, its application objects are relatively simple, and there may be some errors in the development process. It is hoped that, in future development, improvements can be made to expand the applicability of this technology to various types of cleaning equipment.

ACKNOWLEDGEMENT

This research was supported by a grant from the Development of High Efficiency and Low Loss Single Longitudinal Axial Flow Threshing and Separation Technology and Intelligent Flexible Threshing Device Project, Grant No. 2021YFD200050204.

REFERENCES

- [1] Cheng, K., Wang, Q., Yang, D., Dai, Q., Wang, M. (2022). Digital-Twins-Driven Semi-Physical Simulation for Testing and Evaluation of Industrial Software in a Smart Manufacturing System. *Machines*. 10, 388, Guangzhou/China.
- [2] Jiang, Q., Wang, R. (2022). Simulation and Experiment of an Intelligent Control Model for the Cleaning of a Rice-wheat Combine Harvester (稻麦联合收获机清选智能调控模型仿真与试验). *Journal of System Simulation*. 34(11), 2485-2496. Anhui/China.
- [3] Kaven, L., Frehn, A., Basler, M., Jassmann, U., Röttgers, H., Konrad, T., Abel, D., Monti, A. (2022). Impact of Multi-Physics HiL Test Benches on Wind Turbine Certification. *Energies*. 15, 1336, Germany.
- [4] Li, Y., Zhang, X., Li, Y., Lv, L., Shi, M. (2024). Modeling and control methods of a multi-parameter system for threshing and cleaning in grain combine harvesters. *Computers and Electronics in Agriculture*. 225, 109251, Changzhou/China.
- [5] Lin, Z., Wang, W., Li, Y., Zhang, X., Zhang, T., Wang, H., Wu, X., Huang, F. (2023). Design and Experimental Study of a Novel Semi-Physical Unmanned-Aerial-Vehicle Simulation Platform for Optical-Flow-Based Navigation. *Aerospace*. 10(2):18, Fuzhou/China.
- [6] Liu, L., Yu, W., Yu, Z. (2018). Active Fault-tolerant Control Design for a Submarine Semi-physical Simulation System. *International Journal of Control, Automation and Systems*. 16, 2363–2372, Xiamen/China.
- [7] Ning, X., Jin, C., Yin, X., Liu, P., Li, Q. (2018). Research status and development trend of air-and-screen cleaning device for cereal combine harvesters (谷物联合收割机风筛式清选装置研究现状与发展趋势). *Journal of Chinese agricultural mechanization*. 39, 5-10, Zibo/China.
- [8] Qu, Z., Lu, Q., Shao, H., Le, J., Wang, X., Zhao, H., Wang, W. (2024). Design and Test of a Grain Cleaning Loss Monitoring Device for Wheat Combine Harvester. *Agriculture*, 14(5), 671, Zhengzhou/China.
- [9] Raikwar, S., Wani, L., Kumar, S. (2019). Hardware-in-the-Loop test automation of embedded systems for agricultural tractors. *Measurement, Volume 133*, Pages 271-280, German.
- [10] Wang, L., Liu, W., Li, Y., Yu, K. (2022). Research on Double-layer Jitter Plates with Holes in Large-feeding Mass Cleaning System of Maize Grain Harvester (大喂入量玉米籽粒收获机清选系统双层筛孔抖动板研究). *Transactions of the Chinese Society of Agricultural Machinery*. 53. 92-102, Heilongjiang/China.
- [11] Wang, X., Zhao, H., Le, J., Liu, Q. (2024). Investigation on Structural Design and Performance Analysis of the Grain Loss Monitoring System for Wheat Combine Harvester. *Journal of Agricultural Engineering*. 20(5), 24-35, Zhengzhou/China.
- [12] Wu, J., Tang, Q., Mu, S., Yang, X., Jiang, L., Hu, Z. (2023). Design and Test of Self-Leveling System for Cleaning Screen of Grain Combine Harvester. *Agriculture*. 13, 377, Nanjing/China.
- [13] Wu, Z., Xie, B., Chi, R., Ren, Z., Du, Yu., Li, Z. (2019). Driving torque management model for electric tractor in field cruise condition (电动拖拉机田间巡航作业驱动转矩管理模型). *Transactions of the Chinese Society of Agricultural Engineering*, 35(4): 88 – 98. Beijing/China.
- [14] Xie, B., Wang, S., Wu, X., Wen, C., Zhang, S., Zhao, X. (2022). Design and hardware-in-the-loop test of a coupled drive system for electric tractor. *Biosystems Engineering*. 216, 165-185, Beijing/China.
- [15] Xu, J., Guo, Y., Liu, F., Huang, H. (2024). Development and Experiment of Semi-Physical Simulation Platform for Space Manipulator. *Sensors*. 24, 4354, Qinhuangdao/China.
- [16] Zhou, J., Shen, L., Zhang, T. (2016). Modeling and HIL Simulation of Flight Conditions Simulating Control System for the Altitude Test Facility. *International Journal of Turbo & Jet-Engines*. 33, 319-328, Nanjing/China.
- [17] Zhu, X., Chi, R., Du, Y., Ban, C., Ma, Y., Huang, X. (2022). Design of Hardware in Loop Simulation Platform for Intelligent Control System of Corn Kernel Harvester (玉米收获机低损脱粒智能控制系统半实物仿真平台设计). *Transactions of the Chinese Society of Agricultural Machinery*, 53, 114-122, Beijing/China.

DESIGN AND EXPERIMENT OF A CORN INTER-PLANT WEEDING MACHINE BASED ON VISUAL RECOGNITION

基于作物株距信息识别的杂草精准清除机设计与试验

JingWen ZHANG^{1,2)}, QiangJi PENG^{3,4)}, JianMing KANG^{3,4)}, ZhiFeng DI^{3,4)}, ShaoWei WANG^{3,4)},
YingKai CHEN^{3,4)}, YuLong CHEN^{1,2*)}

¹⁾ School of Agricultural Engineering and Food Science, Shandong University of Technology, Zibo, China

²⁾ Institute of Modern Agricultural Equipment, Shandong University of Technology, Zibo/China

³⁾ Shandong Academy of Agriculture Machinery Sciences, Jinan, China

⁴⁾ Huang Huai Hai Laboratory of Modern Agricultural Equipment, Ministry of Agriculture and Rural Affairs, Jinan/China

E-mail: cy106471@sdut.edu.cn

Corresponding author: Yulong Chen

DOI: <https://doi.org/10.35633/inmateh-75-73>

Keywords: agricultural machinery, skeletonization, image stitching, corn interplant recognition

ABSTRACT

To address the challenges associated with high interrow weeding difficulty and seedling damage in corn fields, a weed removal machine based on crop spacing recognition was designed. It captures crop images at variable speed intervals, obtains corn seedling centroid coordinates via image stitching and skeleton extraction, calculates actual plant spacing through pixel-to-real coordinate transformation, and enables real-time control of the weeding device. Key components were analyzed for motion trajectories and critical parameters. Field tests revealed optimal performance at 0.45 m/s, namely, a 92.6% weed removal rate with 2.05% seedling damage, meeting operational requirements. This research provides technical and equipment support for interrow weeding.

摘要

针对大田玉米株间除草难度大、伤苗率高的问题，设计了一种基于作物株距信息识别的杂草清除机。依据车速信息变化间隔拍摄作物图像，通过图像拼接与骨架提取获取玉米苗质心坐标，结合像素坐标系与实际坐标系之间的转换原理计算出两作物实际株距，控制系统根据株距信息实时控制除草装置；对关键部件除草装置进行设计分析，分析除草运动轨迹，明确影响运动轨迹的关键参数。在设计分析的基础上进行田间试验，试验结果表明，当前进速度为0.45m/s时，除草效果较好，除草率为92.6%，伤苗率为2.05%，满足作业要求，该研究可为株间除草提供技术和装备支撑。

INTRODUCTION

Weeds compete with crops for nutrients and space for growth, severely affecting crop yield and quality (Uehleke et al., 2024; Zheng et al., 2024). Efficient weed control is a key link in agricultural production. At present, field weeding is performed via three main methods: manual weeding, chemical weeding, and mechanical weeding (Wang et al., 2021). Manual weeding is characterized by a high labor intensity, low efficiency, and high operating costs (Fang et al., 2022); chemical weed control poses problems such as environmental pollution and harm to the health of workers (Ji et al., 2023); and mechanical weeding has the advantages of reduced labor and high efficiency and is an inevitable choice for the development of modern agriculture (Lai et al., 2023). Improving the accuracy of crop center distance recognition in field operation environments is a key prerequisite for achieving interplant weed control operations.

Domestic and foreign scholars have conducted extensive research on interplant mechanical weed control for field crops. Pérez Ruiz et al. (2014) designed an interplant weed control device with a cylinder-driven opening and closing for hoes, which requires human-machine collaboration. Jiao et al. (2023) developed a device for weed control between rows in paddy fields and conducted field experiments.

Quan et al. (2021) designed a weed control mode based on corn root protection to address the problem of crop root damage in weed control with mechanical actuators. They also designed an intelligent plant weed control robot system to detect corn seedlings and weeds through YOLOv4 and conducted field experiments. The above research yielded several useful conclusions, but owing to issues such as work speed and performance limitations, there are currently no mature products available on the market (Xing et al., 2022).

A crop center recognition method is proposed to address the problems of high computational complexity and low efficiency in intelligent weed control algorithms. The proposed method uses machine vision to obtain the crop centroid and coordinate system transformation to obtain the actual distance between two crops. Image stitching technology is used to continuously obtain crop plant distance information, and the control system controls the rotation speed of the weed control device in real time on the basis of the plant distance information, thereby achieving interplant weed control in corn fields.

MATERIALS AND METHODS

Structure and working principle of the weed removal machine

The overall structure of the machine, which is shown in Figure 1, includes a self-propelled chassis, industrial cameras, weed control devices, etc. The overall structure is based on the self-propelled chassis, and the weed control device is installed at the lower middle position of the chassis.

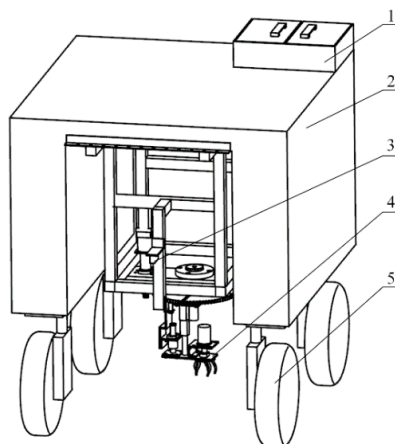


Fig. 1 - Structural diagram of the weed control device test prototype

1. Control system; 2. Self-propelled chassis; 3. Industrial camera; 4. Weed removal device; 5. Wheel hub motor

Table 1

Main technical parameters of the weed removal device

Parameters	Value
Size of whole machine (lengthxwidthxlength)/(mmxmmxmm)	1,000x800x400
Power/kW	25.2
Work speed/(m/s)	0.45
Control width/mm	240
Speed range of the weed removal device/(r/min)	30-40

Identification and localization methods for corn sprouts

The overall structure of algorithm used in the weed removal and machine plant spacing recognition system is shown in Figure 2. Plant images are taken at intervals on the basis of vehicle speed information, and a feature point matching mechanism and the fusion of different frequency bands are used to preserve details for image stitching. According to traditional machine vision methods, the image is processed, and the plant centroid is obtained by refining the skeleton and comparing the skeleton intersection points with the contour centroid. Finally, the plant spacing information is obtained by converting between the global coordinate system and the pixel coordinate system.

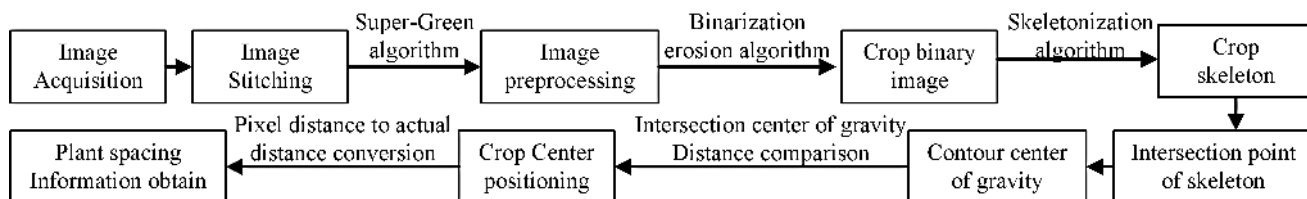


Fig. 2 - Overall algorithm structure

Original image acquisition

By continuously capturing images of seedlings through a vehicle-mounted industrial camera and adjusting the shooting time according to changes in vehicle speed, plant images are obtained, as shown in Figure 3.



Fig. 3 - Example seedling images captured with the device's camera

Image mosaicking

The scale-invariant feature transform (SIFT) algorithm is used to detect key points in the images and generate scale-invariant and rotation-invariant descriptors. A BFMatcher object is created, the KNN-Match method is utilized to match the feature descriptors between two images, the parameter $K=2$ is set, and the Euclidean distance for each feature point is returned.

$$d = v_1, v_2 = \sqrt{\sum_{i=1}^{128} v_{1i} - v_{2i}^2} \tag{1}$$

Here, v_1 and v_2 are 128-dimensional SIFT descriptor vectors.

A ratio test is applied to filter reliable matching points if the first-best match distance d_1 and the second-best match distance d_2 of a feature point satisfy:

$$\frac{d_1}{d_2} < 0.75 \tag{2}$$

In this case, the match is considered valid. Figure 4 shows the process of stitching two images together.

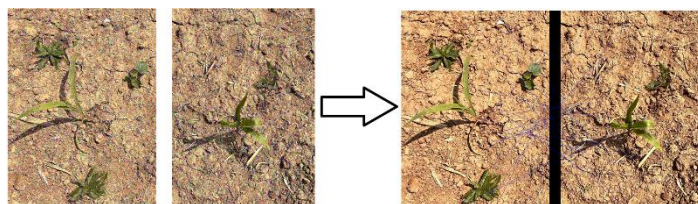


Fig. 4 - Stitching of two images

a. Feature points; b. Feature point matching

The homography matrix H is computed by matching point pairs, and the second image is projected to the coordinate system of the first image.

The homography transformation is defined as follows:

$$\begin{bmatrix} x' \\ y' \\ 1 \end{bmatrix} = H \begin{bmatrix} x \\ y \\ 1 \end{bmatrix} = \begin{bmatrix} h_{11} & h_{12} & h_{13} \\ h_{21} & h_{22} & h_{23} \\ h_{31} & h_{32} & h_{33} \end{bmatrix} \begin{bmatrix} x \\ y \\ 1 \end{bmatrix} \tag{3}$$

The optimal homography matrix H is iteratively estimated via the RANSAC algorithm by minimizing the reprojection error, defined as:

$$\arg \min_H \sum_i \|x_i - Hx_i\|^2 \tag{4}$$

After alignment is complete, the second image undergoes perspective rotation to match the angular orientation of the first image. The final image stitching result is shown in Figure 5.



Fig. 5 – Result of image stitching

Image preprocessing

Figure 6 shows the image preprocessing process for a single crop. The collected images are preprocessed via an ultragreen algorithm and area threshold segmentation. The corrosion algorithm is used for weed and plant seedling recognition, weed images are removed, and agricultural plant seedling images are extracted.

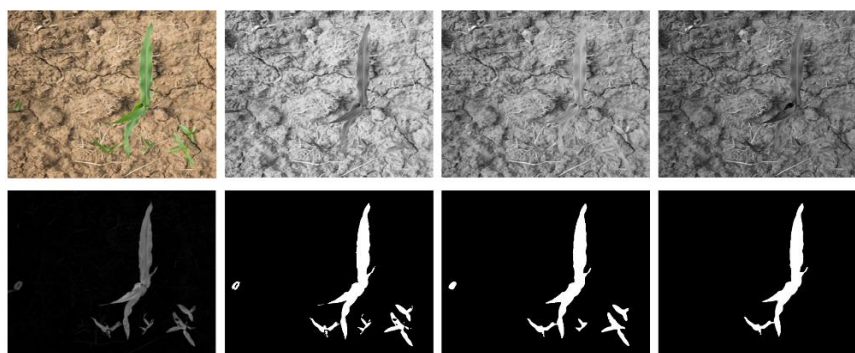


Fig. 6 - Image preprocessing

a. Original image; b. blue channel; c. green channel; d. red channel; e. excess green (ExG); f. binarization; g. morphological opening/closing; h. area threshold segmentation

Skeletonization

The principle of skeleton refinement is shown in Figure 7. First, the image is converted into a binary image by setting a threshold to retain only the contour regions of crop seedlings. The contour information is extracted via the findContours function in the OpenCV library, and the bounding box of each contour is calculated with its center coordinates expressed as:

$$c_x, c_y = \left(\frac{x_{\min} + x_{\max}}{2}, \frac{y_{\min} + y_{\max}}{2} \right) \tag{5}$$

where $(x_{\min}, x_{\max}, y_{\min}, y_{\max})$ are the extreme coordinates of the contour’s bounding box

Starting from the center, the radius is iteratively expanded in increments of ΔR to verify the tangency condition between the circle and the contour.

$$\sum_{(x,y) \in \partial M} \delta \left(\sqrt{x - c_x^2 + y - c_y^2} - R_k \geq 2 \right) \tag{6}$$

In the equation, δ represents the Dirac delta function, which is applied to determine the number of points on the contour where the distance equals the current radius R_k . At least two points must satisfy the tangency condition for this criterion to hold.

The process is further refined via the Zhang–Suen thinning algorithm (Wu et al., 2022) to iteratively erode edge pixels layer by layer, preserving a single-pixel skeleton. The pixel deletion conditions of the algorithm are as follows:

$$\begin{cases} N_p = \sum_{i=1}^8 p_i \text{ (Total number of pixels in the domain)} \\ B_p = \sum_{i=1}^8 |p_i - p_{i+1}| \text{ (Number of boundary transitions)} \end{cases} \quad (7)$$

If the following conditions are met,

$$2 \leq N(p) \leq 6 \text{ and } B(p) = 2 \quad (8)$$

the pixel p is deleted to preserve the centerline. All circles within the contour are detected, and their center coordinates are connected to ensure that the skeleton maintains a single-pixel width. The trajectory formed by linking these circle centers constitutes the crop contour skeleton.

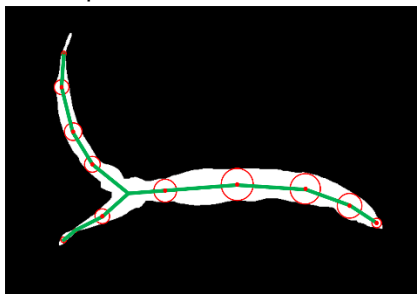


Fig. 7 - Skeleton thinning

Crop contour centroid acquisition

The matching process combines skeleton junction points and contour centroids. For each pixel $p(x,y)$ in the skeleton image, its 8 neighborhood pixels are examined, and the neighborhood coordinates are defined as:

$$\begin{cases} d_x = -1, 0, 1, 1, 1, 0, -1, -1 \\ d_y = 1, 1, 1, 0, -1, -1, -1, 0 \end{cases} \quad (9)$$

with 8-neighborhood traversal in a clockwise order.

A pixel p is identified as a junction point if its neighborhood contains at least three skeleton pixels. The mathematical condition is defined as follows:

$$\sum_{i=1}^8 S_{x+d_{xi}, y+d_{yi}} \geq 3 \quad (10)$$

In the equation, $S(x,y)$ represents the pixel value of the skeleton image at coordinates (x,y) , where 1 denotes the skeleton and 0 corresponds to the background.

The centroid coordinates (c_x, c_y) of the contour are calculated via image moments via the following formula:

$$c_x = \frac{M_{10}}{M_{00}}; c_y = \frac{M_{01}}{M_{00}} \quad (11)$$

where the image moment M_{pq} is defined as:

$$M_{pq} = \sum_x \sum_y x^p y^q I_{x,y} \quad (12)$$

In the equation, $I(x,y)$ represents the binary image, M_{00} corresponds to the contour area, and M_{10} and M_{01} are the first-order moments.

The skeleton junction point closest to the contour centroid is selected as the stem centroid. The Euclidean distance is calculated as follows:

$$d^* = \min_{x,y \in \text{set of Intersection Points}} \sqrt{(x_i - c_x)^2 + (y_i - c_y)^2} \quad (13)$$

The final localization result is illustrated in Figure 8.



Fig. 8 - Identification results for individual seedlings

a. Skeleton refinement results; b. junction points of the skeleton; c. contour centroid; d. plant centroid positioning results

Acquisition of plant spacing information

The camera is calibrated to obtain the intrinsic parameter matrix, which includes the focal length (f_x, f_y) and the principal point (C_x, C_y). The camera intrinsic parameter matrix is expressed as:

$$Z = \begin{bmatrix} f_x & 0 & C_x \\ 0 & f_y & C_y \\ 0 & 0 & 1 \end{bmatrix} \tag{14}$$

The centroid pixel coordinates of two corn plants are converted into coordinates in the image coordinate system. This conversion is based on the camera's intrinsic matrix and requires subtracting the principal point coordinates from the x and y values of the pixel coordinates and then dividing by the focal length to obtain the u and v values in the image coordinate system.

$$\begin{cases} u = \frac{x - C_x}{f_x} \\ v = \frac{y - C_y}{f_y} \end{cases} \tag{15}$$

where (x, y) represents the centroid's pixel coordinates and (u, v) represents the coordinates in the image coordinate system.

Furthermore, given that the depth information for the camera in the corn field is d , with d , the points in the image coordinate system are converted into points in the camera coordinate system, and the actual distance between the two corn plants in three-dimensional space is calculated. The coordinate calculation formula in the camera coordinate system is as follows:

$$\begin{cases} X = u \cdot d \\ Y = v \cdot d \\ Z = d \end{cases} \tag{16}$$

where d represents depth information, which is the distance from the camera to the corn plants in the vertical direction.

The actual distance between two corn plants is calculated via the distance formula between two points in three-dimensional space:

$$D_L = \sqrt{X_2 - X_1^2 + Y_2 - Y_1^2 + Z_2 - Z_1^2} \tag{17}$$

where (X_1, Y_1, Z_1) and (X_2, Y_2, Z_2) are the global coordinate sets of two adjacent seedlings.

The final positioning result is shown in Figure 9.

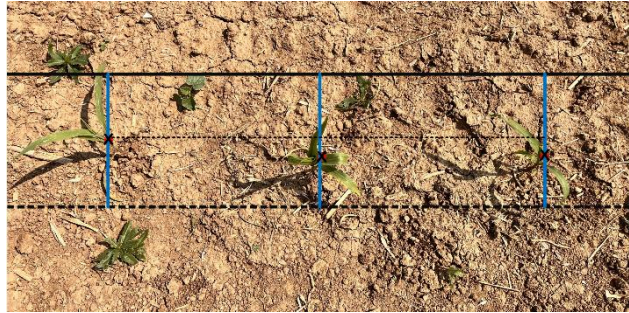


Fig. 9 - Results of interplant seedling identification and localization

Design and analysis of weeding devices

Weeding device design

The weeding device consisted of a support frame, a power transmission device, and a gear set, as shown in Figure 10. The weeding device is attached to the support frame, with the power transmission device acting as the core power provider for the weeding device. Power is transmitted to the small gear via coupling, and the small gear drives the large gear to rotate. The control system, which is based on the plant spacing information from the recognition system and the forward speed, controls the rotation speed of the weeding device in real time. Under the combined action of the rotation of the weeding device and the movement of the self-propelled chassis, the weeding tines form a cycloid trajectory on the ground (Huang *et al.*, 1979), ensuring that the center of the crop canopy is located at the center of a single cycloid trajectory, thus weeding without damaging the seedlings.

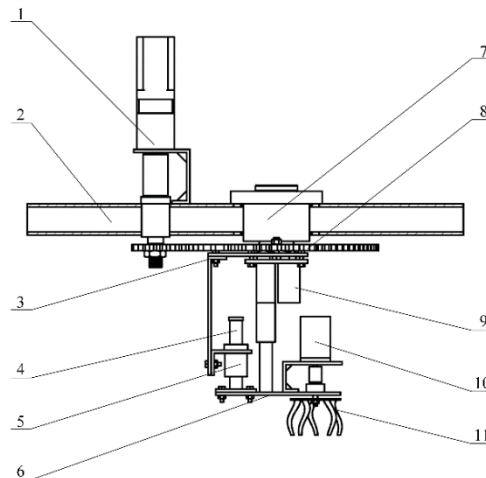


Fig. 10 - Schematic diagram of the rotating device structure

1. Power take-off; 2. Bracket support; 3. Support plate; 4. Optic axis; 5. Linear bearing; 6. Traditional support plate for weed removal; 7. Bearing housing; 8. Gear set; 9. Linear actuator; 10. Weed removal DC motor; 11. Weeding teeth

Weed removal trajectory analysis

The maximum major axis value L (defined as the distance between points A and B) and the maximum minor axis value S (defined as the distance between points C and D) were set to approximately 1. This configuration enabled effective prevention and removal of interrow weeds, and the trajectory variation of the cutting tool was the primary focus of the optimization analysis.

Optimization of parameter L

As shown in Figure 11, assuming that the intersection point of circle O and the y -axis is F , a perpendicular extension line passing through point F intersects the cycloid at point E , and a perpendicular extension line passing through point E intersects the x -axis at point E' . If the time taken for point E to complete a rotation is t , according to the theory of cycloids, the time required for point B to rotate is the same as that of point B' , and the time required for point B' to rotate is $t/2$.

Thus, it can be obtained:

$$t = \frac{2\pi R}{\lambda u_x} \Rightarrow \frac{t}{2} = \frac{\pi R}{\lambda u_x} \tag{18}$$

where t - rotation time of point F around the circle, [s];
 R - the radius of circle O , [mm];
 λ - the ratio of forward speed u to rotational speed v ;
 u_x —velocity of circle O in the x-axis direction, [m/s];

The abscissa value of point B is the same as that of point A' ; therefore,

$$l_{OA'} = u_x \frac{t}{2} = u_x \frac{\pi R}{\lambda u_x} = u_x \frac{\pi R}{\lambda} \tag{19}$$

The intersection circle O of BO and AO is connected to two points D and C . Let the arc length CK be l_1 and the arc length KD be l_2 . From the arc length formula, it can be obtained:

$$l_1 = \theta_1 R \Rightarrow \theta_1 = \angle COK = \frac{l_1}{R}, \left(0 < \theta_1 < \frac{\pi}{2}\right), \quad l_2 = \theta_2 R \Rightarrow \theta_2 = \angle KOD = \frac{l_2}{R}, \left(0 < \theta_2 < \frac{\pi}{2}\right) \tag{20}$$

According to the Pythagorean theorem:

$$AA' = l_{OA'} \cdot \tan \theta_1 = l_{OA'} \cdot \tan \left(\frac{l_1}{R}\right); \quad A'B = l_{OA'} \cdot \tan \theta_2 = l_{OA'} \cdot \tan \left(\frac{l_2}{R}\right) \tag{21}$$

Then,

$$AB = l_{OA'} \tan \theta_1 + \tan \theta_2 = l_{OA'} \left(\tan \left(\frac{l_1}{R}\right) + \tan \left(\frac{l_2}{R}\right) \right) \tag{22}$$

where

$$l_{OB} = \sqrt{l_{OA'}^2 + l_{OA'}^2 \tan^2 \theta_2} = \sqrt{l_{OA'}^2 (1 + \tan^2 \theta_2)}; \quad l_{OA} = \sqrt{l_{OA'}^2 + l_{OA'}^2 \tan^2 \theta_1} = \sqrt{l_{OA'}^2 (1 + \tan^2 \theta_1)} \tag{23}$$

Let $\theta_1 + \theta_2 = \theta_J$, ($0 < \theta_J < \pi$), and $AB=L$. According to the sine theorem:

$$L = \frac{l_{OB}}{\sin 90^\circ + \theta_2 - \theta_J} \tag{24}$$

Notably, L is an increasing function with respect to θ_J within $(0, \pi/2)$ and a decreasing function with respect to θ_J within $(\pi/2, 0)$.

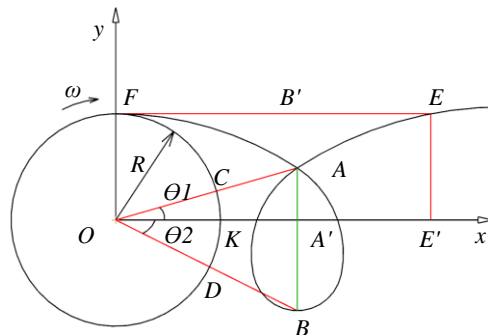


Fig. 11 - Optimization of parameter L

Optimization of parameter S

As shown in Figure 12, from $\omega t = \theta$ and $x = vt + R \sin \omega t$, it can be obtained:

$$x = \frac{v}{\omega} \theta + R \sin \theta \tag{25}$$

With respect to x , the derivative of θ is obtained:

$$\frac{dx}{d\theta} = \frac{v}{\omega} + R \cos\theta, \theta_J < \theta < \pi \tag{26}$$

When $dx/d\theta=0$, the extremum is:

$$\cos\theta_{\max} = -\frac{v}{\omega R} \tag{27}$$

$$\theta_{\max} = \arccos\left(-\frac{v}{\omega R}\right), \theta_J < \theta_{\max} < \pi \tag{28}$$

The maximum transverse chord value is as follows:

$$S = 2\left(\frac{v}{\omega}\theta_{\max} + R \sin\theta_{\max} - l\right) \tag{29}$$

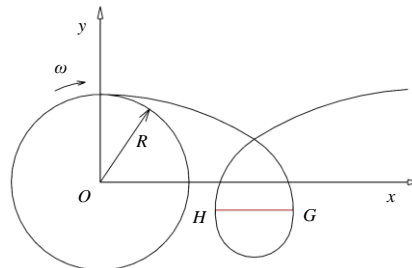


Fig. 12 - Optimization of parameter S

According to formulas (24) and (29), the values of parameters L and S are related to the turning radius, turning speed, and forward speed of the equipment. After image recognition analysis yields the plant spacing value, the turning speed and turning radius are adjusted in a timely manner in combination with the forward speed.

Design principles of the weed control machine control system

The controller detects the distance information between the weeding tines and the ground through a distance sensor and drives the weeding motor to ensure the high-speed rotation of the tines. A speed encoder and the NVIDIA Jetson TX2 microprocessor work in a loop to monitor the chassis travel speed and the crop center distance for the controller. After the relative position information of the seedlings is obtained, the controller adjusts the speed of the weeding device by controlling the stepper motor to achieve precise weeding.

Control system hardware and circuit design

The hardware circuit design of the control system is shown in Figure 13. The hardware circuit consists of encoders, STM32F103 microcontrollers, stepper motors, cameras, NVIDIA Jetson TX2 microprocessors, and other components.

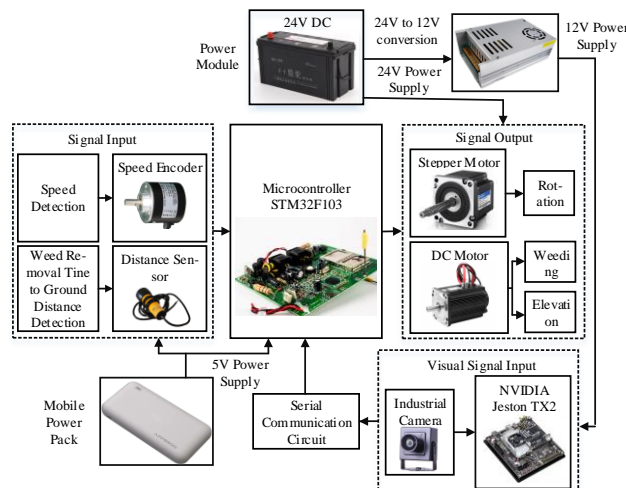


Fig. 13 - Hardware composition of the control system

The working process of the whole machine is as follows: as the chassis advances, the NVIDIA Jetson TX2 microprocessor begins to receive images captured by the camera and recognizes seedlings and weeds. The STM32F103 microcontrollers calculate the center coordinate position of the seedlings and the lateral and longitudinal deviations between the material center and the center of the weeding teeth in the pixel plane. When the seedlings are in the center position of the weeding teeth, the STM32F103 microcontrollers send a start signal to rotate the stepper motor. The microcontroller provides the alpha, beta, and gamma values of the host via a feedback loop on the basis of the recognition image and adjusts the speed of the stepper motor. After the hardware system was assembled, field experiments were conducted to verify the operation of all components of the entire machine.

RESULTS

Experimental conditions

The experiment was conducted on September 8, 2024, at the corn experimental base in Zhangqiu District, Jinan city, using a Nonghaha 2BYQF-3 air suction corn precision seeder with a row spacing of 0.65 meters. For the field performance test, corn seedlings at the 19-day-old and 3-4-leaf stage were selected, with an average stem thickness of approximately 16 mm and a plant height of approximately 25 cm. Five independent experiments were repeated at each forward speed (0.3, 0.4, 0.45, and 0.55 m/s), with a test area length of 16 m. Additionally, the weed control rate and seedling damage rate were recorded for each experiment.

Experimental indicators

In the experiment, weeding efficiency and the seedling damage rate were used as evaluation indicators.

$$P_C = \left(1 - \frac{R_S}{R_H}\right) \times 100\% ; P_D = \frac{R_D}{R_E} \times 100\% \quad (30)$$

In the formula, P_C represents the weed control rate, %; P_D represents the rate of seedling damage, %; R_S represents weeds that have not been removed after interplant weeding; R_H represents the total number of weeds before weeding; R_D represents the number of injured seedlings; and R_E represents the total number of experimental seedlings.

The experiment was set up with three test areas, each 20 m long. The forward speed of the self-propelled chassis was controlled at a constant speed with a remote controller, with the speed settings ranging from low to high. The starting preparation area was 2 m long, and the test area was 16 m long. The weeds in the test area included naturally occurring *Portulaca oleracea*, *Eleusine indica*, *Capsella bursa-pastoris*, etc. (Wang et al., 2021), with the depth of the weed roots being approximately 30 mm. Each test area was marked in advance with prepared signs, and the number of effective corn plants in each area was recorded. The experimental method refers to the "Practical Manual for Field Experiments of Crops," and the field experiment is shown in Figure 14.



Fig. 14 - Experimental scenario

1. Battery; 2. Laptop; 3. Self-propelled chassis; 4. Weeding unit; 5. Hub motor; 6. Weeding tines; 7. DC motor (weeding); 8. Lifting motor (DC); 9. Distance sensor; 10. Gear assembly; 11. Industrial camera; 12. Stepper motor (steering)

Analysis of experimental results

During the bench test analysis of the motion trajectory, a high seedling damage rate was observed. The analysis indicated that the cause was the jerking of the conveyor belt during operation, which led the control system to detect seedlings prematurely, causing a change in the speed of the weeding device and early entry to the weeding area, resulting in seedling damage. In the field test, flat land was chosen, and the self-propelled chassis was moved at a constant speed to avoid the aforementioned situation.

Table 2

Statistics for weeding performance indicators

Test No.	Forward speed/(m/s)	Weeding rate/%	SD (Weeding)	Seedling injury Rate/%	SD (Injury)
1	0.30	91.2 ± 1.5	1.5	2.21 ± 0.18	0.18
2	0.40	91.9 ± 1.2	1.2	2.15 ± 0.15	0.15
3	0.45	92.6 ± 0.9	0.9	2.05 ± 0.10	0.10
4	0.55	90.6 ± 0.9	1.8	2.35 ± 0.25	0.25

The field experiment results (Table 2) revealed that as the advancing speed increased from 0.3 to 0.55 m/s, the weed control rate first increased but then decreased, whereas the seedling damage rate gradually increased. At a speed of 0.45 m/s, the weed removal rate was the highest (92.6%), and the seedling damage rate was the lowest (2.05%). One-way analysis of variance (ANOVA) revealed that different forward speeds had a statistically significant effect on the removal of fast-growing seedlings ($F=4.32$, $p=0.023$) and the seedling injury rate ($F=3.89$, $p=0.035$) ($\alpha=0.05$). Multiple comparisons revealed that the weed control rate at a speed of 0.45 m/s was significantly greater than that in the other groups ($p<0.05$), whereas the seedling injury rate was not significantly different from that in the other groups ($p>0.1$). The variability analysis of the experimental data revealed that the standard deviation range of the weed control rate was 0.9–1.8%, and the standard deviation range of the seedling damage rate was 0.10–0.25%, indicating high repeatability of the control scheme. The coefficients of variation (CVs) at a speed of 0.45 m/s were 1.6% (weed control rate) and 7.8% (seedling damage rate), indicating stable and reliable machine performance under these operating conditions.

CONCLUSIONS

(1) A corn weeding machine was designed to meet the needs of weeding in corn fields. By using a camera to capture images of plants in the field and applying skeleton extraction algorithms and image stitching techniques to obtain real-time distances between plants, the control system accurately controls the speed of the weed control device on the basis of the distance information between plants.

(2) The key components of the weed control device were designed, and the motion trajectory of the cycloid of the weed control device was analyzed. The turning radius, turning speed, and forward speed were determined to be the key parameters affecting weed control.

(3) In field experiments, the chassis moved at a constant speed, and the results revealed that at a travel speed of 0.45 m/s, the weed control effect was good, with a weed control rate of 92.6% and a seedling damage rate of 2.05%, meeting the agronomic requirements for weed control in corn fields.

Future directions and applications:

To further enhance the practicality and impact of the proposed technology, future research could focus on the following tasks:

Algorithm Optimization: Deep learning models (e.g., convolutional neural networks) could be integrated into the proposed approach to improve real-time weed recognition accuracy under complex field conditions, including overlapping foliage and variable lighting.

Multi-crop adaptability: The system could be extended to other row crops (e.g., soybeans and cotton) by adjusting the plant spacing recognition algorithm and mechanical structure to accommodate diverse growth patterns.

These advancements could accelerate the adoption of intelligent weeding systems in sustainable agriculture, thus supporting the transition toward fully automated and eco-friendly farming practices while addressing global challenges related to food security and environmental conservation.

ACKNOWLEDGEMENT

This study was funded by the Shandong Science and Technology Innovation Project (CXGC2024A09) and the Provincial Science and Technology Innovation Development Project (2022SZX46). We would like to thank all the reviewers who participated in the review. We also want to thank the funders of this project. We sincerely thank you for all the support and assistance.

REFERENCES

- [1] Fang, H., Niu, M., Xue, X., Ji, C., (2022). Effects of mechanical-chemical synergistic weeding on weed control in maize field (玉米田间机械-化学协同除草的杂草防除效果). *Transactions of the Chinese Society of Agricultural Engineering*, 2022,38(06):44-51. Nanjing/China. DOI: 10.11975/j.issn.1002-6819.2022.06.005
- [2] Huang, Q., (1979). An Approximation Method for Finding the Intersection Point of a Cycloid and a Circle (求余摆线与圆的交点的一种逼近方法). *Mathematics in Practice and Theory*, vol. 1979, no. 2, pp. 6-12, Jilin/China.
- [3] Ji, J., He, Q., Zhao, L., Li, P., Liu, Y., Wang, X., (2023). Adaptive Fast Integrating Terminal Sliding Mode Tracking Control Technique for Weeding Robot (除草机器人自适应快速积分终端滑模跟踪控制技术). *Transactions of the Chinese Society for Agricultural Machinery*, vol. 54, no. 6, pp. 55-64, Sichuan/China. DOI: 10.6041/j.issn.1000-1298.2023.06.006
- [4] Jiao, J., Hu, L., Chen, G., Tu, T., Wang, Z., Zhang, Y., (2023). Design and experiment of an inter-row weeding equipment applied in paddy field (水田行间除草装置设计与试验). *Transactions of the Chinese Society of Agricultural Engineering*. 2023,39(24):11-22. DOI: 10.11975/j.issn.1002-6819.202306056
- [5] Lacroix, C., Pierreux, J., Brostaux, Y., Vandenberghe, C., Dumont, B., (2025). Assessing the combined effects of mechanical and chemical weeding on weed dynamics in winter wheat. *Weed Research*, 2025, 65(1): e12677. Gembloux/Belgium. DOI: 10.1111/WRE.12677
- [6] Lai, H., Zhang, Y., Zhang, B., Yin, Y., Liu, Y., Dong, Y., (2023). Design and experiment of the visual navigation system for a maize weeding robot. (玉米除草机器人视觉导航系统设计与试验). *Transactions of the Chinese Society of Agricultural Engineering*. 2023,39(01):18-27. Beijing/China. DOI: 10.11975/j.issn.1002-6819.202210247
- [7] Li, Y., Gans, N., (2017) Predictive RANSAC: Effective Model Fitting and Tracking Approach under Heavy Noise and Outliers. *Computer Vision and Image Understanding*, vol. 161, pp. 99-113. Dallas/America. DOI: 10.1016/j.cviu.2017.05.013
- [8] Li, Y., Guo, Z., Shuang, F., Zhang, M., Li, X., (2022). Key technologies of machine vision for weeding robots: A review and benchmark. *Computers and Electronics in Agriculture*, 2022, 196: 106880, Guangxi/China. DOI: 10.1016/J.COMPAG.2022.106880
- [9] Pérez-Ruiz, M., Slaughter, D. C., Fathallah, F. A., Gliever, C. J., Miller, B. J., (2014). Co-robotic intra-row weed control system. *Biosystems Engineering*, Vol. 126, pp. 45-55. DOI: 10.1016/j.biosystemseng.2014.07.009
- [10] Quan, L., Zhang, J., Jiang, W., Li, H., Yang, C., Zhang, X., (2021). Development and Experiment of Intra-row Weeding Robot System Based on Protection of Maize Root System. (基于玉米根系保护的株间除草机器人系统设计与试验). *Transactions of the Chinese Society for Agricultural Machine*. 2021,52(12):115-123. Heilongjiang/China. DOI: 10.6041/j.issn.1000-1298.2021.12.012
- [11] Uehleke, R., Plettenberg, L. V., Leyer, M., Hüttel, S., (2024). German sugar beet farmers' intention to use autonomous field robots for seeding and weeding. *Journal of Environmental Management*. 2024. PP 122472-122472. Germany. DOI:10. 1016/J. JENVMAN. 2024. 122472
- [12] Wang, J., Yan, D., Wang, Q., Tang, H., Wang, J., Zhou, W., (2021). Design and Experiment of Jet-type Paddy Field Weeding Device between Plants (射流式水田株间除草装置设计与试验). *Transactions of the Chinese Society for Agricultural Machinery*, vol. 52, no. 11, pp. 78-85+94, Heilongjiang/China. DOI:10.6041/j.issn.1000-1298.2021.11.008

- [13] Wang, J., Weng, W., Ju, J., Chen, X., Wang, J., Wang, H., (2021). Design and Test of Weeder between Rows in Rice Field Based on Remote Control Steering (基于遥控转向的稻田行间除草机设计与试验). *Transactions of the Chinese Society for Agricultural Machinery*, vol. 52, no. 9, pp. 97-105, Heilongjiang/China. DOI: 10.6041/j.issn.1000-1298.2021.09.011
- [14] Wang, S., Su, D., Wang, Z., Jiang, Y., Zhang, L., Tan, Y., (2021). Design and Experiments of the Cam Swing Rod Intra-row Weeding Device for Lettuce Farm (凸轮摆杆式生菜株间除草装置设计与试验). *Transactions of the Chinese Society of Agricultural Engineering*, vol. 37, no. 21, pp. 34-44, Beijing/China. DOI: 10.11975/j.issn.1002-6819.2021.21.005
- [15] Wu, Y., Wang, J., Wang, Y., (2022). Crop Stem Recognition and Localization Method Based on Skeleton Extraction Algorithm (基于骨架提取算法的作物茎秆识别与定位方法). *Transactions of the Chinese Society for Agricultural Machinery*, vol. 53, no. 11, pp. 334-340, Tianjin/China. DOI: 10.6041/j.issn.1000-1298.2022.11.034
- [16] Xing, Q., Ding, S., Xue, X., Cui, L., Le, F., Li, Y., (2022). Research on the development status of intelligent field weeding robot. *Journal of Chinese Agricultural Mechanization*, Vol. 43, No. 8, pp. 173. Nanjing/China. DOI: 10.13733/j.jcam.issn.20955553.2022.08.024
- [17] Zheng, H., Li, Z., Shan, Y., Zhu, Y., Xiao, M., (2024). Current and development trends of agricultural machinery weeding technologies and equipment (农田机械除草技术与装备研究现状与发展趋势). *Journal of Nanjing Agricultural University*. 2025,48(02):285-295. Nanjing/China. DOI: 10. 7685/jnau. 202404014

DESIGN AND TESTING OF SPIRAL CUTTER TOOTH TYPE FARMLAND STONE PICKER

螺旋刀齿式农田捡石机的设计与试验

Jia ZHANG^{1,2}, Heng QU², Ping XIAO¹, Shaoteng MA^{1,2}, Weisong ZHAO^{3,4*}

¹School of Mechanical and Electrical Engineering, Xinjiang Institute of Engineering, Urumqi, Xinjiang / China

²School of Mechanical and Electrical Engineering, Xinjiang Agricultural University, Urumqi, Xinjiang / China

³Western Agricultural Research Center, Chinese Academy of Agricultural Sciences, Changji, Xinjiang / China

⁴Nanjing Institute of Agricultural Mechanization, Ministry of Agriculture and Rural Affairs, Nanjing / China

Tel: +8613579297197; E-mail: zj34@xjje.edu.cn

Corresponding author: Weisong Zhao

DOI: <https://doi.org/10.35633/inmateh-75-74>

Keywords: agricultural stone picker, spiral cutter drum, EDEM, soil trench test

ABSTRACT

This study aimed to solve the inefficiency and high-energy-consumption problems of current agricultural stone pickers. It introduced a novel spiral cutter tooth design. Dynamic and kinematic analyses determined the key components' parameters and performance-influencing factors. With EDEM software, discrete element simulations using a three-factor, five-level quadratic regression orthogonal design were carried out. Stone-picking efficiency and power consumption were the evaluation metrics. Regression analysis and significance tests clarified the impact of forward speed, drum speed, and tilt angle. Multi-objective optimization of the regression model found the optimal parameters: 0.18 m/s forward speed, 260 rpm drum speed, and 30° tilt angle. Field tests with this setup achieved a 93.71% stone-picking rate and 4.63 kW stable power, validating the design's effectiveness. These results offer a theoretical basis and reference for stone picker design and optimization.

摘要

针对现有农田捡石机捡石效率低, 消耗功率大等问题, 提出了一种螺旋刀齿式农田捡石机, 通过动力学和运动学分析, 确定了关键部件的结构参数和运动参数范围, 以及影响工作性能的主要因素。利用 EDEM 软件开展了离散元仿真试验, 采用三因素五水平二次回归正交旋转中心组合试验方法, 以捡石效率和消耗功率为评价指标, 对机具前进速度、螺旋刀辊转速和螺旋刀辊侧倾角进行回归分析和显著性检验, 明确了各因素对评价指标的影响及主次顺序, 通过对回归模型进行多目标函数优化求解, 得出最佳参数组合为机具前进速度 0.18 m/s、螺旋刀辊转速 260 r/min、螺旋刀辊侧倾角 30°。使用最佳参数组合进行了土槽试验, 试验结果表明: 捡石效率为 93.71%, 稳定作业时的功率为 4.63 kW, 螺旋刀齿式捡石机作业稳定, 满足农田捡石作业要求。

INTRODUCTION

Arable land forms the cornerstone of agricultural development, with soil quality enhancement being paramount for sustainable farming practices (Zhan *et al.*, 2023). In northwestern China's newly developed Gobi farmlands, stony soils present a critical challenge. Elevated stone content restricts root proliferation, exacerbates soil desiccation, reduces seed germination rates, and ultimately compromises crop yields (Yu *et al.*, 2007; Zhang *et al.*, 2024). Furthermore, stone interference during mechanized operations accelerates equipment wear and impedes agricultural modernization.

Current stone removal strategies predominantly employ mechanical methods over manual collection (Li *et al.*, 2024; Bu *et al.*, 2022). Existing machinery—including comb-tooth shovels, tooth rakes, and shovel-chain systems—has been extensively studied. For example, Yu *et al.* developed a chain-tooth stone picker demonstrating high efficiency through dynamic analysis of soil-tool interactions, though limited by shallow excavation depth (Yu *et al.*, 2007). Ma *et al.* (2007) achieved shallow-layer stone removal (≤ 100 mm) using a wheel-tooth rake, yet faced challenges of excessive energy consumption and suboptimal collection rates. Niu *et al.*, (2007), advanced the field with a shovel-sieve design, employing discrete element modeling to analyze stone-soil separation dynamics. While functional, these systems universally exhibit energy inefficiency and inconsistent performance.

Jia Zhang, Assoc. Prof.; Heng Qu, Student; Ping Xiao, Assoc. Prof.; Shaoteng Ma, Lecturer; Weisong Zhao, Lecturer

To address these limitations, a novel spiral cutter tooth stone picker is introduced. Through kinematic analysis of stone-cutter interactions, critical operational parameters governing collection efficiency are identified. EDEM simulations and field trials validate the optimized design, demonstrating enhanced performance while reducing power demands. This work establishes a theoretical framework for advancing stone-picking technology, offering practical insights for agricultural equipment innovation.

MATERIALS AND METHODS

Overall structure and working principle

The spiral cutter tooth stone picker for agricultural fields primarily comprises a frame, gearbox, spiral cutter rollers, cutter teeth, and deflector plates. The spiral cutter rollers are symmetrically mounted on the frame at specific angles on either side, and the cutter teeth are arranged in a double helical line extending outward. The structure is illustrated in Fig 1.

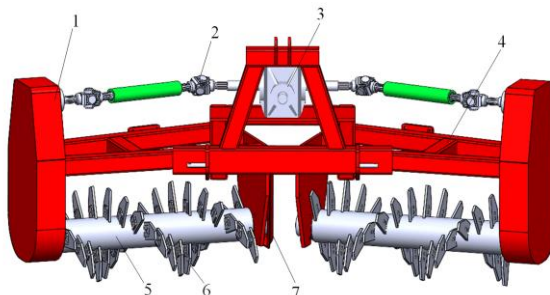


Fig. 1 – Schematic diagram of the overall structure
 1. transmission device; 2. universal shaft; 3. gearbox; 4. frame; 5. spiral cutter rollers;
 6. cutter teeth; 7. deflector plate

During operation, the machine connects to the tractor via a three-point hitch. The tractor provides power that is transmitted through the gearbox to the universal shaft and then through the internal transmission chains of the drive devices on both sides to the spiral blade roller. The rotational speed of the spiral blade roller aligns with the forward direction of the machine, effectively lifting stones from the surface and from certain soil depths. The lifted stones are conveyed toward the center, where the inner guide plates on the frame align them into rows, completing the stone-picking process. This machine not only picks stones but also tills and effectively loosens the soil. A schematic of the stone picker operation is shown in Fig. 2, and the main technical parameters are listed in Table 1.

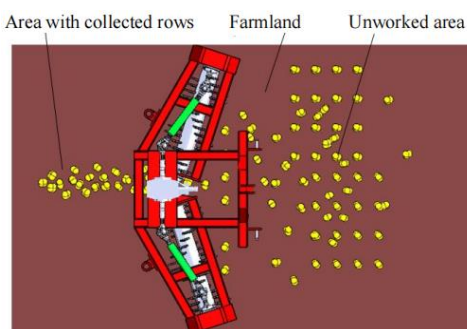


Fig. 2 – Schematic diagram of the operating principle of the stone picker

Table 1

Main technical parameters of the stone picker	
Parameter	Value
Connection type	Suspension type
Overall dimensions (lengthxwidthxheight) (mm)	2500x1105x1210
Working width (mm)	2100
Working depth (mm)	55
Spiral blade roller speed (r/min)	150~350
Traction power (kW)	≥40

Tooth structure design

The installation type of the teeth significantly affects the performance of the stone picker. Depending on the angle between the tangent at the point of contact between the tooth blade and the tooth shaft, the teeth can be classified as radial, forward-leaning, or backward-leaning. A force analysis is conducted at initial contact with the stone and when the stone is lifted off the ground for various tooth types to compare their effectiveness in stone picking. The force analysis for the three types of teeth is illustrated in Fig 3.

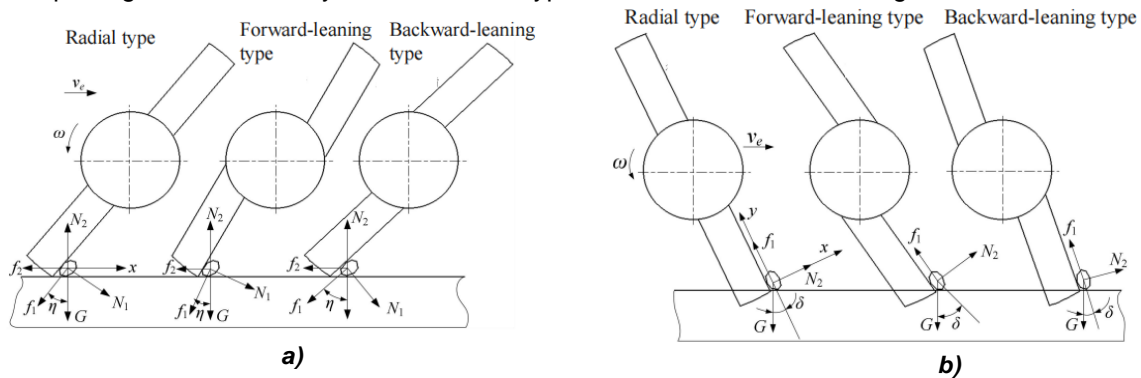


Fig. 3 – Force analysis of stones during operation

a) Force analysis of the stone at initial contact with the tooth; b) Force analysis of the stone during lifting by the tooth

As shown in Figure 3a, a coordinate system is established with the center of the stone as the origin, where the x-axis is parallel to the ground and the y-axis is perpendicular to it. When the tooth contacts the stone, there is no vertical movement relative to the ground; instead, the stone primarily undergoes horizontal displacement. The velocity along the x-axis is determined by the horizontal resultant force. The expression for this resultant force is given by:

$$F_{xa} = N_1 \cos \eta - f_1 \sin \eta - f_2 \tag{1}$$

where:

F_{xa} is the resultant force of the tooth in the horizontal direction, [N]; N_1 is the support force exerted by the tooth on the rock, [N]; η is the angle of entry into the soil, [°]; f_1 is the frictional force of the tooth on the rock, [N]; f_2 is the frictional force of the ground on the rock, [N]; G is the gravitational force of the rock, [N].

The derivative of equation (1) yields:

$$F'_{xa} = -N_1 \sin \eta - f_1 \cos \eta \tag{2}$$

where:

$$\eta < \pi/2 \tag{3}$$

This resultant force is derived from equations (2) to (3). The analysis reveals that as the entry angle η increases, the horizontal resultant force F_{xa} decreases, reducing the tooth's tendency to move forward at initial contact with the stone. Therefore, the preferred sequence for selecting tooth types is: forward-leaning, radial, and backward-leaning.

As shown in Figure 3b, a coordinate system is established with the center of the stone as the origin, where the direction perpendicular to the tooth contact surface serves as the x-axis and parallel to it serves as the y-axis. At the moment the tooth lifts the stone off the ground, no force is exerted on the stone by the ground. At this instant, the velocity in the direction perpendicular to the tooth contact surface is determined by the resultant force in that direction. The expression for the vertical resultant force acting on the working surface of the tooth is as follows:

$$F_{xb} = N_1 - G \sin \delta \tag{4}$$

where:

F_{xb} is the resultant force of the tooth in the direction perpendicular to the contact surface, [N]; δ is the angle of extraction from the soil, [°].

The derivative of equation (4) yields:

$$F'_{xb} = -G \cos \delta \tag{5}$$

where:

$$\delta < \pi/2 \tag{6}$$

Analysis of equations (5) to (6) reveals that as the extraction angle increases, the horizontal resultant force along the x-axis decreases, resulting in a reduced tendency for the stone to be lifted off the ground and diminishing the effectiveness of stone picking. When lifting the stone off the ground, the preferred sequence for selecting tooth types is: backward-leaning, radial, and forward-leaning teeth.

Balancing overall performance, radial teeth excel in continuously moving stones forward compared to backward-leaning teeth and are more effective in lifting stones off the ground than forward-leaning teeth. Therefore, selecting radial teeth maintains the stability of stone picking operations and can enhance the operational efficiency of the stone picker.

To facilitate the replacement of worn teeth, the teeth are designed to be detachable. The base of each tooth is curved to match the spiral blade roller, which enhances operational stability. To reduce soil resistance against the teeth, they are designed with a trapezoidal shape and sharpened tips. As shown in Fig. 4, the sharpened teeth have a reduced contact area at the tip, which lowers resistance during soil entry, enhances penetration ability, and reduces energy loss during contact (Gao *et al.*, 2023). When the tooth lifts the stone from the ground, the sharpened teeth cause the stone's weight and the angle of contact along the surface to decrease. Analysis of equations (5) and (6) shows that the sharpened teeth enhance the tendency to lift the stone off the ground along the tooth's vertical contact surface, thereby improving the stone-throwing effect.

The depth of stone extraction in farmland typically ranges from 0 to 50 mm below the surface; therefore, the chosen penetration depth for the teeth is set at 55 mm. The average profile length of stones is about 90 mm. To avoid excessive torque and power consumption from overly long teeth and inadequate stone-picking performance from overly short teeth, the length of the teeth is set at 140 mm. The diameter of the spiral blade roller is determined based on factors such as depth of penetration, size, and arrangement of the teeth. Considering all factors, the working diameter of the teeth (D) is set at 430 mm, while the diameter of the spiral blade roller (d) is 75 mm.

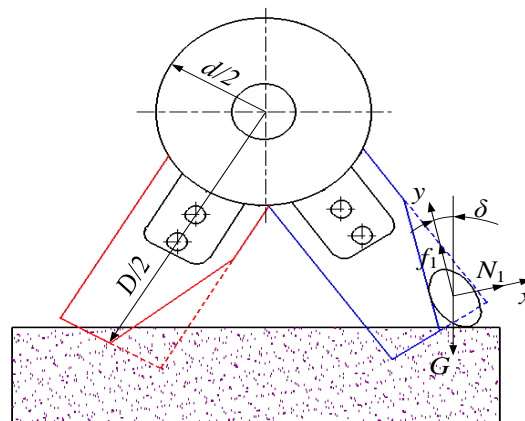


Fig. 4 - Comparison of tooth design before and after optimization

Design of tooth arrangement

An appropriate tooth arrangement can significantly enhance the stone-picking rate of the machine and reduce the occurrence of missed stones. Drawing on the principles of spiral cover implements (Zheng *et al.*, 2021; Yang *et al.*, 2023), the teeth are arranged in a spiral pattern. Increasing the number of spiral lines reduces the rotational speed of the spiral blade roller, which decreases the velocity and kinetic energy exerted on the stones, thus reducing their tendency to be thrown from the ground. To avoid issues such as excessively high rotational speeds with a single spiral head, excessive power consumption, and poor stone-picking performance with multiple spiral heads, a dual spiral line arrangement is employed.

Stones with a maximum profile length exceeding 50 mm can adversely affect crop growth; therefore, the spacing between two adjacent teeth on the spiral blade roller is set at 50 mm, and the pitch is set at 800 mm. The spiral rise angle (α) is calculated using formula (7) to be 30.5° . The spiral blade rollers on the left and right sides are installed in opposite directions, forming a symmetrical structure. An illustrative diagram of tooth installation and arrangement is shown in Fig. 5.

$$\alpha = \arctan \frac{P}{\pi d} \quad (7)$$

where:

α is the angle of the spiral ascent, [$^\circ$]; P is the pitch, [mm].

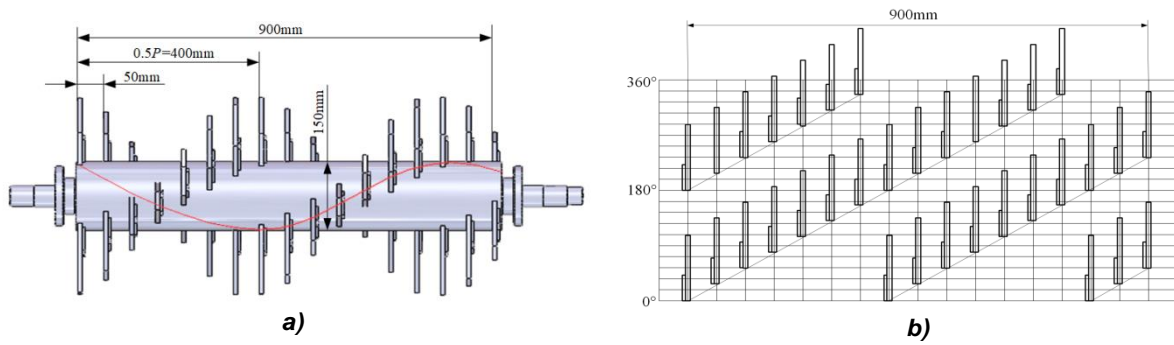


Fig. 5 – Schematic diagram of tooth installation and arrangement
 a) Tooth installation diagram; b) Double-helix arrangement diagram

Kinematic analysis of the tooth stone-picking process

When the stone picker moves at a uniform speed, the teeth rotate synchronously with the spiral blade roller. For analytical convenience, a spatial coordinate system O_{xyz} is established, as shown in Fig. 6. Here, the angle between the spiral blade roller and the x -axis is referred to as the side tilt angle γ . The x -axis indicates the direction of stone clearing, the y -axis is the forward direction of the equipment, and the z -axis is perpendicular to the ground. Using the centroid of the stone as the origin O_1 the component velocities of the tooth tip along the x , y , and z axes are as follows:

$$\begin{cases} v_x = R\omega \sin(\omega t) \sin \gamma \\ v_y = v_e + R\omega \sin(\omega t) \cos \gamma \\ v_z = R\omega \cos(\omega t) \end{cases} \quad (8)$$

where:

$$\omega = 2\pi n / 60 \quad (9)$$

v_e is the forward speed of the machinery, [m/s]; ω is the angular velocity of the spiral cutting roller, [rad/s]; n is the rotational speed of the spiral cutting roller, [r/min]; R is the radius of rotation of the tooth, [mm]; γ is the inclination angle of the spiral cutting roller, [°].

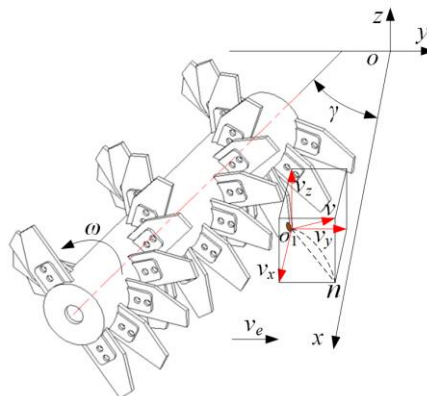


Fig. 6 – Kinematic analysis of the tooth

In the coordinate system O_{1xyz} , the absolute velocity of the tooth tip can be derived from equation (8):

$$|v| = \sqrt{v_x^2 + v_y^2 + v_z^2} = \sqrt{v_e^2 + R^2\omega^2 + 2v_eR\omega \sin(\omega t) \cos \gamma} \quad (10)$$

Based on equations (8) to (10), the factors affecting the absolute velocity of the tooth include the forward speed of the equipment v_e , the rotational speed of the spiral blade roller n , and the side tilt angle γ of the spiral blade roller. When the side tilt angle γ exceeds 45° , the lateral force on the tooth increases, making it prone to bending and damage, which reduces the effectiveness of the stone-picking operation. Therefore, the side tilt angle γ should be less than 45° . Since the lateral velocity v_{xy} and the dislodging velocity v_{yz} of the tooth directly affect the stone dislodgement distance and the soil disturbance coefficient (Yao *et al.*, 2022), the range for the side tilt angle γ is chosen to be between 20° and 40° . The operational process must ensure that the absolute velocity of the tooth is greater than the forward speed of the equipment v_e . The field operational speed of the stone picker v_e is set between 0.1 and 0.5 m/s. Through pre-experimental analysis, it was found that the stone-picking effect is optimal when the rotational speed n of the spiral blade roller is between 150 and 350 r/min.

Discrete element simulation analysis

EDEM simulation modeling

Establishing a realistic stone model is crucial for ensuring the accuracy of simulation data. Stones found in fields are typically rod-shaped, block-shaped, or slab-shaped, with particle sizes related to their shapes and contour lengths. Based on data from basic soil and stone experiments, stone particles are modeled using multi-sphere representations in the discrete element software. The average profile length is set at 90.0 mm, with stone sizes ranging from 50.0 mm to 120.0 mm. The size distribution parameter settings vary from 0.56 to 1.30, with a representative stone model illustrated in Fig. 7.



Fig. 7 – Discrete element model of the stone

During the operation of the stone picker, various contacts occur among tooth-soil particles, tooth-stone particles, soil-soil particles, soil-stone particles, and stone-stone particles. By combining initial parameter calibration with relevant literature, the physical and mechanical parameters of materials and the contact coefficients are determined (Deng et al., 2022; Chen et al., 2024; Hao et al., 2023). The mechanical characteristic parameters for each material particle, along with the contact coefficients for other objects, are detailed in Tables 2 and 3. The simulation models for soil-soil and soil-stone contacts are based on the Hertz-Mindlin with JKR model, while the Hertz-Mindlin (no slip) model is used for other contact types (Li et al., 2022; Shi et al., 2024; Zhang et al., 2022).

Table 2

Physical and mechanical parameters

Item	Soil particle	Stone	Tooth
Poisson's ratio	0.35	0.3	0.3
Density/kg·m ⁻³	2600	1600	7865
Shear modulus/Pa	2.5×10 ⁷	1×10 ⁷	7.9×10 ¹⁰

Table 3

Material contact parameters

Item	Parameter	Value
Soil -Soil	Coefficient of restitution	0.5
	Static friction coefficient	0.8
	Dynamic friction coefficient	0.23
	Surface energy/(J·m ⁻²)	5.5
Soil -Stone	Coefficient of restitution	0.06
	Static friction coefficient	0.5
	Dynamic friction coefficient	0.01
	Surface energy/(J·m ⁻²)	5.5
Soil -Tooth	Coefficient of restitution	0.2
	Static friction coefficient	0.3
	Dynamic friction coefficient	0.25
Stone-Stone	Coefficient of restitution	0.3
	Static friction coefficient	0.5
	Dynamic friction coefficient	0.01

Item	Parameter	Value
Stone-Tooth	Coefficient of restitution	0.2
	Static friction coefficient	0.5
	Dynamic friction coefficient	0.01

To simplify the EDEM simulation computation and considering the symmetry of the entire machine with no mutual influence, the simulation focuses solely on one side. The length of the single spiral blade roller is reduced to 530 mm and features 0.65 turns. A virtual soil trough model is established with dimensions of 1500 mm (length) × 1100 mm (width) × 160 mm (height). Due to the large size of the soil trough, soil particles are modeled as single spheres with a radius of 5 mm, while stones are placed on the surface of the soil.

Simulation parameter settings

Using SolidWorks software, the model is created to scale and saved in .stp format for import into EDEM for preprocessing, as shown in Fig. 8. The spatial coordinates of the initial motion state are aligned with those of the soil trough model. The penetration depth is set to 55 mm, along with the correct rotation direction, angular velocity, machine advance direction, and forward speed. Based on the forward speed, the simulation time is set, with a mixing timestep of 20% and a target save interval of 0.01 s.

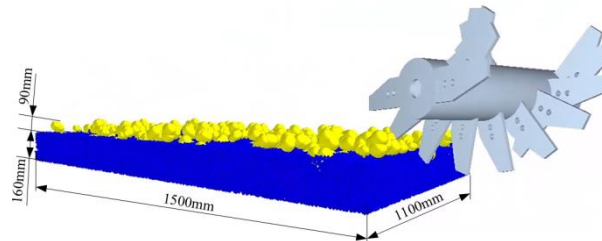


Fig. 8 – Modelling of stone-soil-knife-tooth interactions

Experimental design and methods

The method employed is a three-factor, five-level second-order regression orthogonal rotation central composite design. The experimental factors include the machine's forward speed, the rotational speed of the spiral blade roller, and the side tilt angle of the spiral blade roller, with the stone-picking rate and power consumption as the experimental indicators. The coding of the experimental factors is presented in Table 4.

Table 4

Experimental factors and codes

Coded Values	Factors		
	Forward speed/ (m·s ⁻¹)	Roller speed/ (r·min ⁻¹)	Roller side tilt angle/ (°)
1.682	0.5	350	40
1	0.42	321	36
0	0.3	250	30
-1	0.18	179	24
-1.682	0.1	150	20

Determination of Stone-Picking Rate: The stone-picking rate Y_1 is calculated using the Selection module in EDEM's post-processing analysis options. This module outputs the number of stones within the grid area before and after operation, as illustrated in Fig. 9. The formula for calculating the stone-picking rate Y_1 is as follows:

$$Y_1 = \left(1 - \frac{W_1}{W}\right) \times 100\% \tag{11}$$

where: W is the number of rocks in the soil trench before operation; W_1 is the number of rocks missed in the soil trench after operation.

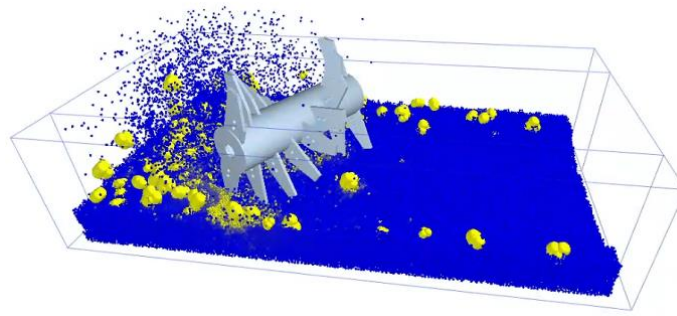


Fig. 9 – Simulation of the stone picker's operational process

Determination of Power Consumption: After the simulation is complete, torque data is exported using the EDEM post-processing module. The power consumption Y_2 of the spiral blade roller is calculated using the following formula:

$$Y_2 = P = \frac{T \times n}{9550} \quad (12)$$

where:

P is consumed power [kW]; T is the average torque of the spiral knife roller during operation [N·m].

Soil trough experiment

To validate the accuracy of the discrete element simulation results and the performance of the optimized stone picker, an indoor soil trough experiment was conducted on August 1, 2024, at the Key Laboratory of Intelligent Equipment at Xinjiang Agricultural University. The equipment used included the TCC-III computer-monitored soil trough test vehicle, stones, the spiral tooth-type stone picker, and a measuring tape.

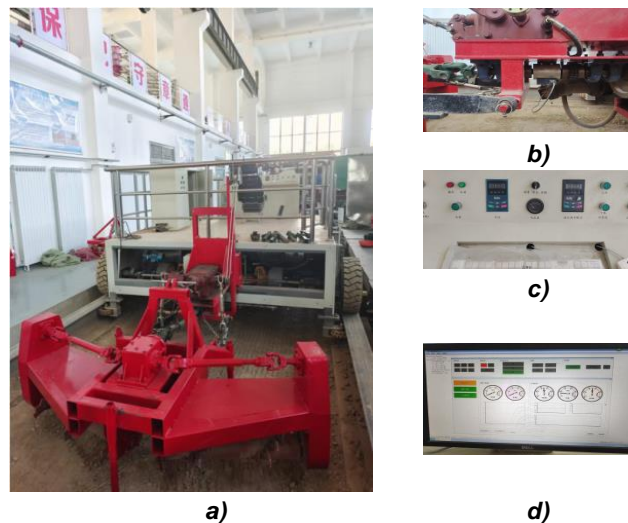


Fig. 10 – Soil trench test

a) Experimental prototype; b) Power monitoring sensor; c) Parameter adjustment system; d) Data monitoring system

The equipment was connected to the soil trough test vehicle via a three-point hitch. The experimental setup is shown in Fig. 10. The trough contained original sandy soil, with stones randomly placed on the 2m×10m soil surface before operation. Soil moisture and compaction were measured using a soil moisture meter and a soil compaction tester. The results indicated a soil moisture content of 12.7% and a compaction of 4094.57 kPa. Based on the simulation results, the experimental conditions were set as follows: roller speed $n=260$ r/min, forward speed $v_e=0.18$ m/s, tilt angle of 30° , and a working depth of 55 mm for a travel distance of 10 m in the soil trough.

RESULTS

Analysis of simulation experiment results

A total of 20 experiments were conducted, with the results presented in Table 5, where X_1 , X_2 and X_3 represent the coded values of the experimental factors.

Table 5

Experimental design and results					
Test No.	Factors			Response Value	
	X ₁	X ₂	X ₃	Y ₁ /%	Y ₂ /%
1	-1	-1	-1	87.27	2.17
2	1	-1	-1	84.46	3.44
3	-1	1	-1	93.31	4.03
4	1	1	-1	86.67	5.99
5	-1	-1	1	90.26	3.81
6	1	-1	1	87.54	4.91
7	-1	1	1	96.67	6.24
8	1	1	1	89.21	8.19
9	-1.682	0	0	96.88	3.06
10	1.682	0	0	88.02	5.67
11	0	-1.682	0	85.56	4.21
12	0	1.682	0	95.23	8.42
13	0	0	-1.682	86.15	3.18
14	0	0	1.682	92.74	6.24
15	0	0	0	91.21	3.64
16	0	0	0	92.84	3.79
17	0	0	0	92.31	3.81
18	0	0	0	92.57	3.78
19	0	0	0	93.66	3.45
20	0	0	0	93.27	3.92

The experimental data were processed using Design-Expert 13.0 to perform regression analysis and significance testing on the simulation results. Based on the analysis of variance (ANOVA), model significance, lack of fit, and correlation were evaluated, with results presented in Table 6. The ANOVA results indicate that both regression models for the stone-picking rate and power consumption are significant ($P < 0.01$), while lack-of-fit terms are non-significant ($P > 0.05$), demonstrating a good fit of the regression model equations. Thus, these models can be effectively used for the analysis and optimization of the experimental indicators. The order of influence of each factor on the stone-picking rate is as follows: machine forward speed, spiral blade roller rotational speed, and side tilt angle. For power consumption, the order of influence is: spiral blade roller rotational speed, side tilt angle, and machine forward speed. An F -test at a 0.05 confidence level was conducted, with non-significant terms removed to obtain the final regression model as follows:

$$\begin{cases} Y_1 = 92.68 - 2.53X_1 + 2.39X_2 + 1.69X_3 - 1.07X_1X_2 - 0.33X_1^2 - 1.05X_2^2 - 1.39X_3^2 \\ Y_2 = 3.74 + 0.78X_1 + 1.26X_2 + 0.93X_3 + 0.19X_1X_2 + 0.15X_1^2 + 0.84X_2^2 + 0.27X_3^2 \end{cases} \quad (13)$$

Table 6

Results of the ANOVA

Index	Variation source	Sum of squares	Degrees of freedom	Mean Square	F	P
Y ₁	Model	253.45	9	28.16	24.16	<0.0001**
	X ₁	87.31	1	87.31	74.90	<0.0001**
	X ₂	77.79	1	77.79	66.73	<0.0001**
	X ₃	38.91	1	38.91	33.38	0.0002**
	X ₁ X ₂	9.18	1	9.18	7.88	0.0186*
	X ₁ X ₃	0.067	1	0.067	0.057	0.8159
	X ₂ X ₃	3.6×10 ⁻³	1	3.6×10 ⁻³	3.1×10 ⁻³	0.9567
	X ₁ ²	1.54	1	1.54	1.32	0.2770

Index	Variation source	Sum of squares	Degrees of freedom	Mean Square	F	P
	X_2^2	16.00	1	16.00	13.72	0.0041**
	X_3^2	27.82	1	27.82	23.86	0.0006**
	Residual	11.66	10	1.17		
	Lack of fit	8.02	5	1.60	2.21	0.2028#
	Error	3.64	5	0.73		
	Total	265.10	19			
Y ₂	Model	52.86	9	5.87	102.48	<0.0001**
	X_1	8.34	1	8.34	145.45	<0.0001**
	X_2	21.66	1	21.66	378.00	<0.0001**
	X_3	11.75	1	11.75	204.98	<0.0001**
	X_1X_2	0.30	1	0.30	5.17	0.0462*
	X_1X_3	4.0×10^{-3}	1	4.0×10^{-3}	0.071	0.7958
	X_2X_3	0.21	1	0.21	3.69	0.0838
	X_1^2	0.31	1	0.31	5.39	0.0427*
	X_2^2	10.07	1	10.07	175.68	<0.0001**
	X_3^2	1.04	1	1.04	18.11	0.0017**
	Residual	0.57	10	0.057		
	Lack of fit	0.44	5	0.088	3.24	0.1113#
	Error	0.14	2	0.027		
	Total	53.43	19			

Note: **means extremely significant impact ($P < 0.01$), *means significant impact ($0.01 \leq P < 0.05$), # means no significant impact ($P > 0.05$).

Response surfaces were created to illustrate the effects of interactions among factors on the stone-picking rate and power consumption. Fig. 11a shows that, at a central level of the spiral blade roller's side tilt angle, the stone-picking rate is positively correlated with both the forward speed and the rotational speed of the spiral blade roller. When the roller's rotational speed is constant, an increase in forward speed results in a decrease in the lateral push speed of the tooth, which may prevent stones from being directed to one side within a limited distance. This increases the likelihood of missed stones and reduces the picking rate. Conversely, at a constant forward speed, increasing the roller speed enhances the lateral displacement of the stones and the frequency of stone lifting per unit time, thereby increasing the stone-picking rate.

Fig.11b indicates that, at a central tilt angle and constant forward speed, power consumption initially decreases and then increases with an increase in roller speed. Excessively high roller speeds lead to more frequent stone-lifting events, which ultimately increases power consumption. When the roller speed is constant, power consumption rises with increasing forward speed due to the increased contact distance between the teeth and the soil, which heightens resistance and increases operational torque. Increased power consumption reduces the lifespan of the teeth and raises strength requirements. To enhance stone-picking efficiency while minimizing power consumption, the structural and operational parameters of the equipment should be optimized.

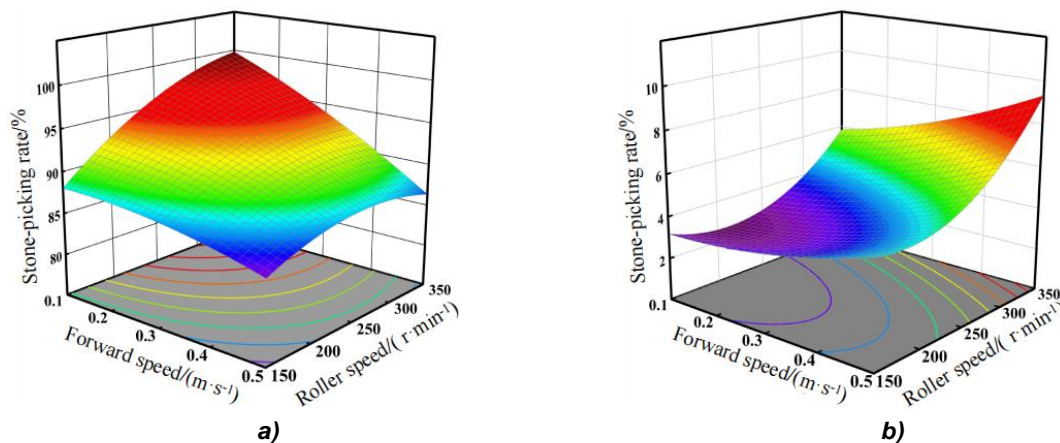


Fig. 11 – Response surface of the effect of factor interactions on each indicator

a) Effect of interaction factors on the stone-picking rate; b) Effect of interaction factors on power consumption

Parameter optimization

To achieve optimal performance, the Optimization module of Design-Expert software was used to perform constrained optimization of the regression model. The aim was to maximize stone-picking efficiency while minimizing power consumption. The objective function and constraints were defined as follows:

$$\begin{cases} \max Y_1(X_1, X_2, X_3) \\ \min Y_2(X_1, X_2, X_3) \\ \text{s.t.} \begin{cases} -1.682 \leq X_1 \leq 1.682 \\ -1.682 \leq X_2 \leq 1.682 \\ -1.682 \leq X_3 \leq 1.682 \end{cases} \end{cases} \quad (14)$$

When analyzing simulation parameters in the optimization module, the importance levels for the evaluation indicators were set, prioritizing the stone-picking rate as "+++" and power consumption as "+." The optimal parameter combination obtained was a forward speed of 0.18 m/s, a spiral blade roller speed of 274.71 r/min, and a side tilt angle of 30.28°. To account for the difficulty of setting exact speed ratios in the machine, the roller speed was rounded to 260 r/min and the tilt angle to 30°.

Analysis of the results of the soil trough experiment

Stone-picking rate measurement

The experiment included five repeat tests, with the average value taken as the verification result. The soil trough experiment setup is shown in Fig. 12. When operating under the optimal parameter combination, the average stone-picking rate achieved was 93.71%, with a deviation of 3.2% from the theoretical value. This indicates a close alignment between the experimental results and the model predictions. This outcome demonstrates that the designed stone picker performs well and meets the requirements for farmland stone-picking operations.



Fig. 12 – Prototype operation effect

Power consumption measurement

Once the equipment achieved stable operation, sensors recorded the real-time rotational speed and torque of the soil trough test vehicle’s output shaft. A dynamic torque sensor transmitted the torque data in real time to the digital display. Torque data for the 2–4 second interval is shown in Fig.13.

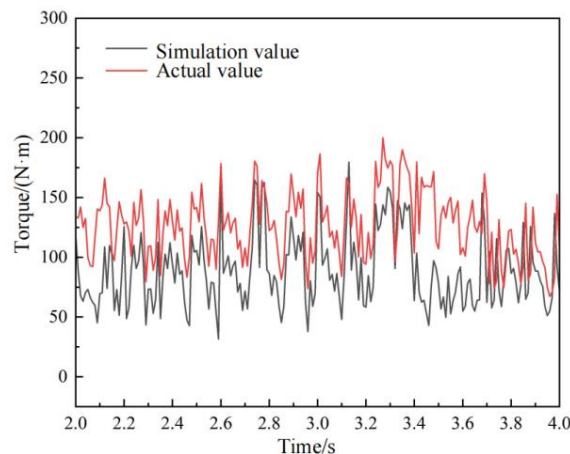


Fig. 14 – Power consumption verification

The average power consumption of the spiral blade roller was calculated using the torque formula. The average operational power consumption was 4.63 kW, which is slightly higher than the theoretical value. This discrepancy is likely due to the complex actual operating environment, the lower real speed compared to the theoretical speed, and the presence of numerous small stones.

CONCLUSIONS

(1) In response to the low stone-picking rate and high power consumption of existing stone pickers, a spiral tooth-type farmland stone picker was designed. A mechanical analysis of different tooth shapes for stone picking identified the optimal tooth type, followed by structural optimization of the teeth. A kinematic analysis of the stone-lifting process was conducted to establish the structural and operational parameters of the main components.

(2) Using EDEM discrete element simulation software, an interaction model among stones, soil, and teeth was developed. A three-factor, five-level, second-order regression orthogonal rotation central composite design was employed, with machine forward speed, spiral blade roller speed, and side tilt angle as factors, and stone-picking rate and power consumption as performance indicators. The effects of factor interactions on these performance indicators were analyzed.

(3) Design-Expert software was utilized to optimize the operating parameters of the stone picker. Optimal performance was achieved at a forward speed of 0.18 m/s, a spiral blade roller speed of 260 r/min, and a side tilt angle of 30°. Under these optimized conditions, the soil trough test demonstrated an average stone-picking rate of 93.71% and a power consumption of 4.63 kW. The spiral tooth-type stone picker exhibited stable operational performance, providing valuable insights and a reference framework for future optimization and design improvements of stone-picking machines.

ACKNOWLEDGEMENT

The authors were funded for this project by the Natural Science Foundation of Xinjiang Uygur Autonomous Region (Grant NO.2022D01A245).

REFERENCES

- [1] Chengzhi Deng, Shanwen Wang, Zhanpeng Li, Chong Chen, Zhiqiang Wei, Tingyi Duan. (2022). Optimization analysis of operation parameters of home plate in soil based on the discrete element method (基于离散元法的锄板入土作业参数优化分析). *Journal of Chinese Agricultural Mechanization*, Vol. 43, no.07, pp.188-196, Chongqing/China.
- [2] Chong Zhang, Xuhui Fan, Mingsen Li, Guang Li, Chunkai Zhao, Wenliang Sun. (2022). Simulation analysis and experiment of soil disturbance by chisel plow based on EDEM (基于EDEM的凿式犁铲土壤扰动仿真分析与试验). *Transactions of the Chinese Society for Agricultural Machinery*, Vol.53, no.S2, pp.52-59, Jilin/China.
- [3] Cong Niu, Yuting Xing, Chenggong Yan, Haochao Tan, Shuai Ma, Liming Xu. (2022). Simulation and experiment of shovel-screen type farmland stone picking and collecting machine (铲筛式农田石块捡拾收集机仿真与试验). *Journal of China Agricultural University*, Vol. 27, no.12, pp.221-233, Beijing/China.
- [4] Fang Ma, Lianxing Gao, Yuzhen Yu. (2007). Research on selecting picking equipment of surface harrow type rack rail rock picker's mechanism and parts (轮齿式浅耙型农田捡石机分捡装置研究). *Journal of Agricultural Mechanization Research*, no.5, pp.115-117, Shenyang/China.
- [5] Jia Zhang, Hong Wang, Chuanjiang Li, Jiayi Zhang, Yakun Du. (2024). Analysis on the development trend of farmland soil stone-picking mechanization technology based on patent bibliometrics (基于专利计量的农田土壤捡石机械化技术发展态势分析). *Journal of Chinese Agricultural Mechanization*, Vol.45, no.6, pp.250-256, Xinjiang/China.
- [6] Jicheng Li, Kunpeng Sun, Yonghua Zhang, Tianhui Zhang. (2023). Simulation of tillage behavior of double winged subsoiler based on discrete element method (基于离散元法的双翼深松铲耕作行为的仿真分析). *Journal of Inner Mongolia Agricultural University (Natural Science Edition)*, Vol.44, no.2, pp.67-75, Yunnan/China.

- [7] Kang Zheng, Yufei Li, Junfang Xia, Guoyang Liu, Jian Cheng, Qixin Kang. (2021). Design and experiment of land leveling blade roller of ditching and rotary tiller with gradual spiral angle (开沟旋耕机渐变螺旋升角轴向匀土刀辊设计与试验). *Transactions of the Chinese Society for Agricultural Machinery*, Vol.52, no.1, pp.63-73, Hubei/China.
- [8] Linrong Shi, Wuyun Zhao, Wei Sun. (2017). Parameter calibration of soil particles contact model of farmland soil in northwest arid region based on discrete element method (基于离散元的西北旱区农田土壤颗粒接触模型和参数标定). *Transactions of the Chinese Society of Agricultural Engineering (Transactions of the CSAE)*, Vol.33, no.21, pp.181-187, Gansu/China.
- [9] Mingjie Bu, Yangli Liu, Yuan Xu, Feng Wang, Yuchen Liu, Fengwei Zhang. (2022). Design and test of chain stone picker for reclaiming farmland (复垦农田链式捡石机的设计与试验). *Agricultural Equipment & Vehicle Engineering*, Vol.60, no.10, pp.31-35+41, Beijing/China.
- [10] Shengquan Li, Xiaogang Liu, Dongliang Li. (2024). Dynamic modeling and simulation of stress for farmland rock picker based on dynamic analysis (基于动力学分析的农田捡石机应力动态建模与仿真). *China Southern Agricultural Machinery*, Vol.55, no.11, pp.24-27, Gansu/China.
- [11] Weixiang Chen, Jibiao Qin, Chongcheng Chen, Yang Liu, Shuhe Zheng. (2024). Design and parameter optimization of trenching and soil-throwing blade for ecological tea garden by discrete element method (基于离散元法的生态茶园开沟抛土刀设计与参数优化). *Journal of Fujian Agriculture and Forestry University (Natural Science Edition)*, Vol. 53, no.1, pp.136-144, Fujian/China.
- [12] Wenwu Yang, Xiwen Luo, Zaiman Wang, Minghua Zhang, Shan Zeng, Ying Zang. (2016). Design and experiment of track filling assembly mounted on wheeled-tractor for paddy fields (轮式拖拉机水田轮辙覆土装置设计与试验). *Transactions of the Chinese Society of Agricultural Engineering (Transactions of the CSAE)*, Vol. 32, no.16, pp.26-31, Guangdong/China.
- [13] Wenyan Yao, Dianbao Zhao, Hequan Miao, Peide Cui, Maojian Wei, Peisong Diao. (2022). Design and experiment of oblique anti-blocking device for no-tillage planter with shallow plowing stubble clearing (免耕播种机浅旋清茬斜置式防堵装置设计与试验). *Transactions of the Chinese Society for Agricultural Machinery*, Vol. 53, no.8, pp.42-52, Shandong/China.
- [14] Xiaomei Zhan, Yali Li, Zhonghua Cao, Qinghui Yang, Jinbo Cui. (2023). Design of 1JS-100 soil stone picker (1JS-100 土壤捡石机的设计). *Journal of Agricultural Mechanization Research*, Vol.45, no.8, pp. 69-73, Chongqing/China.
- [15] Yuzhen Yu, Yucai Zheng, Lianxing Gao, Fang Ma. (2007). Kinematics analysis on chain tooth rock picker in the farmland soil (农田捡石机捡石机理研究). *Journal of Agricultural Mechanization Research*, no.3, pp.49-51, Hebei/China.
- [16] Yuzhen Yu, Lianxing Gao, Xiping Li, Fang Ma. (2007). Study of rock picker in farmland and the mechanism of rock picking (链齿式农田土壤捡石机栅条齿动力学分析). *Journal of Agricultural Mechanization Research*, no.5, pp.210-211, Hebei/China.
- [17] Yuzhen Yu, Lianxing Gao, Xiuli Ma, Fang Ma, Jinsheng Zhao. (2007). Research advance in the development of soil rock picker (土壤捡石机的研究进展). *Transactions of the Chinese Society of Agricultural Engineering (Transactions of the CSAE)*, no.11, pp. 274-279, Hebei/China.
- [18] Zhen Gao, Caiyun Lu, Xuyang Wei, Hongwen Li, Jin He, Qingjie Wang. (2023). Design and experiment of co-stirring combined corn strip straw cleaning device (协拨组合式玉米条带秸秆清理装置设计与试验). *Transactions of the Chinese Society for Agricultural Machinery*. Vol.54, no.10, pp.68-79, Beijing/China.
- [19] Zhihao Hao, Enlai Zheng, Xun Li, Haoping Yao, Xiaochang Wang, Shengyue Qian, Weixun Li, Min Zhu. (2023). Performance analysis of the soil-contacting parts for no-tillage planters and optimization of blade structure (免耕播种机旋耕刀耕作性能分析与结构优化). *Transactions of the Chinese Society of Agricultural Engineering (Transactions of the CSAE)*, Vol.39, no.2, pp.1-13, Jiangsu/China.

CALIBRATION AND OPTIMIZATION OF DISCRETE ELEMENT PARAMETERS FOR COTTON STALK-RUBBER BELTS INTERACTIONS

棉秆-橡胶带相互作用的离散元参数标定与优化

Yasenjiang BAIKELI ^{1,2}, Haodong XU ^{1,2}, Jiayi ZHANG ^{1,2}, Rensheng XING ^{1,2}, Yong YUE ^{*1,2}

¹⁾ College of Mechanical and Electrical Engineering, Xinjiang Agricultural University, Urumqi / China;

²⁾ Key Laboratory of Xinjiang Intelligent Agricultural Equipment, Urumqi / China

Tel: 8613999902318; E-mail: xndyueyong@xjau.edu.cn

Corresponding author: Yong Yue

DOI: <https://doi.org/10.35633/inmateh-75-75>

Keywords: Discrete element, Cotton stalks, Rubber belts, Parameter calibration, Harvesting efficiency

ABSTRACT

This study aims to accurately calibrate the interaction between cotton stalks and rubber belts in agricultural machinery using the Discrete Element Method (DEM). Through physical experiments, key parameters such as the collision recovery coefficient, static friction, and rolling friction were measured and validated through simulations in EDEM. Optimal values were identified as 0.446, 1.146, and 0.0194, respectively. Full-factorial analysis revealed significant effects on repose angle. Repeated trials confirmed a deviation of only 0.72% from experimental results, validating the calibration method. These findings provide a foundation for improving cotton stalk harvesting and transportation efficiency.

摘要

本研究旨在通过离散元法(DEM)准确标定棉秆与橡胶带在农业机械中的相互作用。通过物理实验,测得关键参数如碰撞恢复系数、静摩擦系数和滚动摩擦系数,并在EDEM中进行仿真验证,最佳值分别为0.446、1.146和0.0194。全因子分析显示这些参数对堆积角的影响显著。重复实验结果与实际实验值偏差仅为0.72%,验证了标定方法的准确性。本研究为优化棉秆收获和运输效率提供了理论基础。

INTRODUCTION

Cotton stalks, a major by-product of cotton production, hold significant value in industries ranging from bioenergy to materials manufacturing. In agricultural machinery, the interaction between cotton stalks and rubber belts is crucial, as these belts play a key role in efficiently pulling and transporting cotton stalks from the field during harvesting operations. However, calibrating key parameters like collision restitution, static friction, and rolling friction remains challenging, often leading to discrepancies between simulations and real-world performance, affecting key metrics such as uprooting efficiency, breakage rate, and missed uprooting rate, thereby causing inefficiencies in machine design.

The previous research on the calibration of cotton stalks has focused primarily on simulating individual mechanical properties or interactions with other materials. For instance, Zhang *et al.* (2022) and Zhang *et al.* (2024) advanced the calibration of cotton stalk parameters using Discrete Element Method (DEM) and response surface methods, improving the accuracy of simulations. Similarly, Jiang *et al.* (2023), expanded on this by incorporating cotton stalk-soil mixtures, enhancing the potential for improving harvesting performance. However, while these studies significantly improve the understanding of cotton stalk simulations, they still fall short of offering practical guidance for optimizing the design of flexible cotton stalk harvesting equipment.

Further contributions have come from studies that addressed the interaction between plant materials and rubber belts, such as Jin *et al.* (2022), who calibrated contact parameters between corn seeds and rubber belts, and Sun *et al.* (2019), who studied the contact parameters between wheat and conveyor belts. These studies helped enrich the field of plant-rubber belt interface research, yet they do not fully address the complexities involved in cotton stalk harvesting machinery design. Li *et al.* (2022) also conducted detailed DEM analyses to improve simulation accuracy in complex systems, but similar to the other studies, this

^{1,2} Yasenjiang Baikeli, M.S.Stud.Eng.; ^{1,2} Haodong Xu, M.S.Stud.Eng.; ^{1,2} Jiayi Zhang, Prof.Ph.D.Eng.; ^{1,2} Rensheng Xing, M.S.Stud.Eng.; ^{*1,2} Yong Yue, Prof.Ph.D.Eng.

research does not provide a complete framework for optimizing the design of rubber belt cotton stalk harvesting equipment. On the other hand, the calibration of rubber materials and their interactions with agricultural materials has received significant attention. *Rossow et al. (2021)* and *Zhao et al. (2023)* examined the interaction between rubber conveyor belts and various materials, contributing valuable insights into friction and wear behaviors. *Nattino et al. (2014)* also refined rubber material calibration through statistical models to improve predictive accuracy. While these studies do not directly address the optimization of rubber belt cotton stalk harvesting equipment, highlighting a clear gap in research.

Most existing studies have concentrated either on the mechanical properties of cotton stalks or on the contact characteristics of rubber with other materials. This study fills that gap by focusing on the dynamic interaction between cotton stalks and rubber belts, providing a more holistic view that directly contributes to the optimization of harvesting equipment.

MATERIALS AND METHODS

Test material

Cotton Stalks: The primary test material was Xinluzao 66 cotton stalks, sourced from Anning Town, Urumqi City (43°58'N, 87°30'E) in Xinjiang, China. The stalks were selected for uniform size and moisture content, crucial for accurate results. They were cut to 25 mm lengths, with key properties like density (1.08 g/cm³) and moisture content standardized using a drying oven at 105°C for 24 hours.

Rubber Belts: A standard EP100-640 × 3(4+2) rubber belt, widely used in agricultural machinery, was chosen for the tests. The belt measures 300 mm × 350 mm × 8 mm and features a polyester (EP) fabric core, providing high tensile strength and durability.

Test method

Contact coefficient calibration experiment: Physical experiments and EDEM 2022 software were used to calibrate the contact coefficient between cotton stalks and rubber belts, including collision recovery coefficient, static friction coefficient, and rolling friction coefficient. Single-factor experiments were employed to optimize each parameter, using average area count, slip angle, and rolling distance as metrics. Lastly, the Angle of Repose was measured using the Cylinder Lifting Method, which evaluated the pile angle of the cotton stalks on the rubber belts.

Full Factorial Experimental Design: A full factorial experimental design was implemented using Design Expert 10.0 to analyze the significance of the cotton stalk-rubber belt contact parameters and their interactions. This provided insight into both individual and combined parameter effects.

Box-Behnken test Design: The parameters were optimized through a Box-Behnken Design (BBD) and response surface analysis. A binary regression equation was derived, targeting the Angle of Repose, and the optimal parameter values were determined based on this analysis.

The coefficient of variation (CV) was 1.01%, indicating good reliability of the test, and the binary regression equation is shown in equation (2):

$$\theta = 43.04 + 0.8A + 0.225B - 1.25C - 0.625AB + 1.775AC + 0.375BC - 1.8325A^2 - 2.3325B^2 - 1.7825C^2 \quad (1)$$

By using the Design-Expert software constraint solving tool to find the minimum extreme value of the error point for equation (2), the angle of repose is used as the target to find the best value of parameters, and the collision recovery coefficient (A), static friction coefficient (B), and rolling friction coefficient (C) between cotton stalk and rubber belt are 0.446, 1.146, and 0.0197.

Cotton stalk-rubber belt contact parameter calibration experiment

Using EDEM 2022, contact parameters were simulated to enhance the accuracy of physical tests, focusing on single-factor experiments for optimal parameter isolation. The Hertz-Mindlin no-slip contact model was applied to simulate cotton stalk-rubber belt interactions during the angle of repose test, given the minimal bonding forces between particles (*Hu et al., 2022*). To replicate the cylindrical shape of cotton stalk shown in Figure 1(a), models were created with a diameter of 10 mm and lengths of 25 mm (*Zhang et al., 2024*), as shown in Figure 1(b), ensuring accurate calibration of the interaction.



Fig. 1 - Cotton stalk model

The results from the physical tests, combined with a review of relevant literature, provide the characteristic contact parameters for cotton stalks and rubber belts, as summarized in Table 1. A review of the literature (Zhang et al., 2024; Jiang et al., 2021) identified a range of values for the angle of repose, bending, and fracture characteristics, along with other key contact parameters for cotton stalks.

Table 1

Simulation parameters of materials in contact with cotton stalks

Materials	Parameter	Value	Units
Cotton stalk	Poisson's ratio	0.35	-
Cotton stalk	Shear modulus	0.69	GPa
Cotton stalk	Density	1080	kg/m ³
Rubber Belt	Poisson's ratio	0.48	-
Rubber Belt	Shear modulus	1 × 10 ⁹	GPa
Rubber Belt	Density	1.38	kg/m ³
Stalk-Rubber Belt	Collision recovery coefficient	0.35~0.5	-
Stalk-Rubber Belt	Static friction factor	0.5~1.5	-
Stalk-Rubber Belt	Rolling friction factor	0.015~0.025	-

Collision Recovery Coefficient

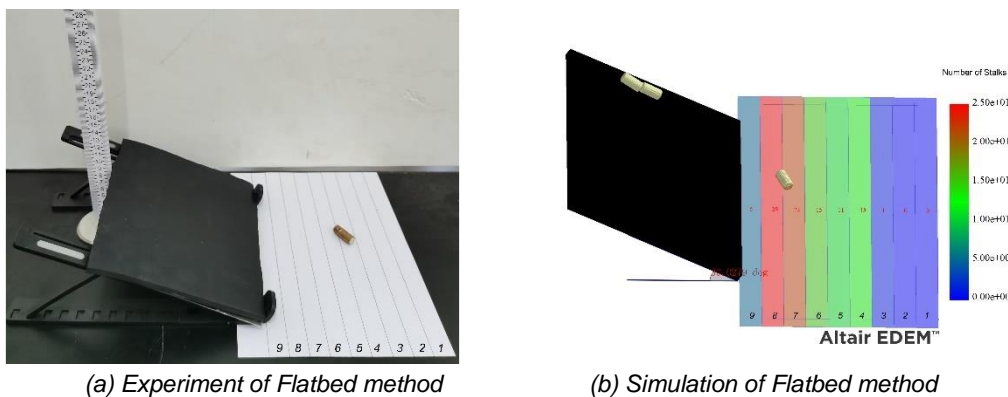


Fig. 2 - Measurement of Collision Recovery Coefficient for cotton stalk and rubber belt

To accurately measure the collision recovery coefficient between cotton stalks and a rubber belt using the Flatbed method (Zhang et al., 2024), a simple yet effective apparatus was designed as shown in Figure 2(a). The apparatus featured an inclined rubber belt plate, measuring 180 mm by 200 mm, set at a 30° angle. This setup allowed cotton stalk particles, each 25 mm in length, to be released from a height of 300 mm, enabling free fall onto the plate. Below the plate, a 9-grid paper with 25 mm spaced grids was placed to record the landing positions.

To facilitate the subsequent calculation of the area count, the method from (Niu et al., 2022) for measuring the collision recovery coefficient of feed was referenced. Using the average area as the target value and applying the equation as follow:

$$K = \frac{1}{N_{total}} \sum_{k=1}^n (kN_k) \tag{1}$$

where:

- K - the average number of areas;
- N_{total} - the total number of cotton stalk models;
- n - the total number of areas;
- N_k - the number of models in area k , where k is the area number.

The results of the collision recovery coefficient experiment are shown in Table 2. According to the aforementioned equation (1), the average area count was calculated to be 7.01. By measuring the average area count from particle landing positions, an accurate representation of the stalks' rebound behavior was obtained.

Table 2

Experimental Results of Collision Recovery Coefficient Measurement

Serial number	1	2	3	4	5	6	7	8	9
Number of stalks	0	0	2	2	5	16	37	35	3

To determine the optimal collision recovery coefficient between cotton stalks and the rubber belt in simulations, as shown in Figure 2(b), the coefficient was varied from 0.35 to 0.5, with a step size of 0.03. Six experiments, as shown in Table 3, were conducted to assess how changes in this coefficient affect the spatial dispersion of cotton stalks particles upon contact. The results in Table 3 showed that as the coefficient increased, the mean number of regions decreased, with the optimal value of 0.44 yielding the lowest error rate of 0.7%. This suggests that a coefficient of 0.44 most accurately replicates the interaction for further simulations.

Table 3

Simulation Results of Collision Recovery Coefficient Measurement

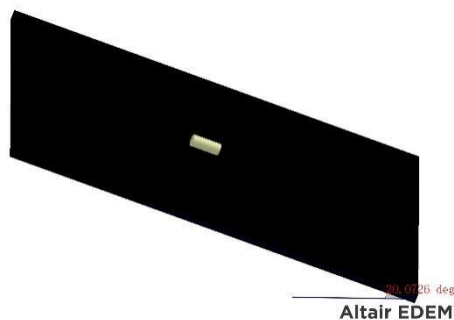
Serial number	Collision recovery coefficient	Mean number of regions	Error
1	0.35	7.85	12.0%
2	0.38	7.58	8.1%
3	0.41	7.53	7.4%
4	0.44	7.06	0.7%
5	0.47	6.76	3.6%
6	0.50	6.52	7.0%

Static Friction Coefficient

To measure the static friction coefficient between cotton stalks and the rubber belt, an inclined plane method was used (Du et al., 2012). A rubber belt (300 mm x 350 mm x 8 mm) was fixed onto a board, and a cotton stalk was placed on the belt, as shown in Figure 3(a). The belt was gradually lifted until the stalk began to slide, and the angle (θ) between the belt and the horizontal plane was measured. This process was repeated 10 times, as shown in Table 4, yielding an average θ of 53.7°.



(a) Experiment of Inclined Plane Method



(b) Simulation of Inclined Plane Method

Fig. 3 - Measurement of Static friction coefficient for cotton stalk and rubber belt

Table 4

Static Friction Measurement of Experimental Cotton Stalk Slip Angle

Serial number	1	2	3	4	5	6	7	8	9	10
1	69°	48°	45°	47°	74°	53°	61°	49°	46°	48°
2	64°	52°	47°	50°	65°	51°	52°	50°	49°	55°
3	44°	55°	46°	69°	54°	70°	44°	59°	49°	47°
Mean	59°	51.6°	46°	55.3°	64.3°	58°	52.3°	52.6°	48°	50°

A simulation experiment was conducted to measure the static friction coefficient between cotton stalks and the rubber belt using the inclined plane sliding test as shown in Figure 3(b). The collision recovery coefficient between the cotton stalks and the rubber belt was set at 0.4, while the dynamic friction coefficient was set to 0.

The static friction coefficient was tested over a range of 0.5 to 1.5, with a step size of 0.1, resulting in a total of 11 simulation experiments. The results of each simulation, along with the corresponding levels of the static friction coefficient, are summarized in the Table 5.

Table 5

Static Friction Measurement of Cotton Stalk Slip Angle Simulation

Serial no.	Coefficient of static friction	Slipping angle	Error
1	0.5	30.4°	43.4%
2	0.6	34.5°	35.6%
3	0.7	38.8°	27.7%
4	0.8	44.4°	17.3%
5	0.9	47.1°	12.3%
6	1.0	48.3°	10.1%
7	1.1	52.1°	3.0%
8	1.2	53.1°	1.1%
9	1.3	54.5°	1.5%
10	1.4	58.2°	8.4%
11	1.5	61.2°	14.0%

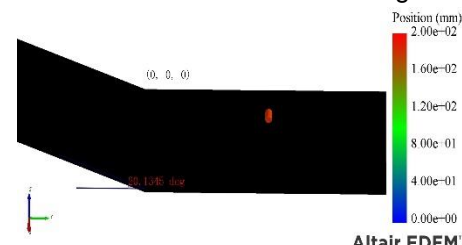
Based on the static friction measurement results shown in Table 5, the slipping angle of cotton stalks increases as the coefficient of static friction increases. The error percentage, however, decreases as the static friction coefficient increases, reaching its lowest point (1.1%) at a coefficient of 1.2. This suggests that a friction coefficient between 1.0 and 1.2 offers the most accurate prediction of the cotton stalk's slip angle in simulations, with minimal error.

The Rolling Friction Coefficient

To assess the rolling friction between cotton stalks and the rubber belt, the Oblique Rolling Method was employed (Liang et al., 2022), two rubber belt sections were mounted onto iron plates with dimensions of 350 mm x 300 mm x 8 mm and 600 mm x 500 mm x 8 mm, as shown in Figure 4(a). Preliminary tests revealed that when the angle of the first belt exceeded 25°, cotton stalks would bounce upon reaching the second belt, disrupting the smooth rolling motion. To prevent this, the belt was inclined at a consistent angle of 20°.



(a) Experiment of Oblique Rolling Method



(b) Simulation of Oblique Rolling Method

Fig. 4 - Measurement of Rolling Friction Coefficient for cotton stalk and rubber belt

During the main experiment, cotton stalks were released from a height of 100 mm above the second belt to measure the rolling distance on the horizontal section. If a cotton stalk rolled off the belt, the test was repeated to ensure accuracy.

After conducting 10 valid trials, the average rolling distance was found to be 190.5 mm, as shown in Table 6, indicating a smooth interaction between the cotton stalk and the rubber belt at the given conditions.

Table 6

Rolling friction determination of experimental cotton stalk rolling distance

Serial number	1	2	3	4	5	6	7	8	9	10	Mean
Rolling distance (mm)	138	249	218	204	198	181	219	134	153	211	190.5

Figure 4(b) shows the Simulation of Oblique Rolling Method in EDEM, the results of the rolling friction simulation experiment for cotton stalks are summarized in Table 7. In this experiment, the rolling friction coefficient was incrementally varied from 0.015 to 0.025, with a step size of 0.002. The findings demonstrate that as the rolling friction coefficient increases, the rolling distance of the cotton stalks decreases correspondingly. Notably, a coefficient of 0.019 was identified as the optimal value, yielding the smallest error of 1.6%, making it the most accurate for simulating the rolling motion of cotton stalks on the rubber belt. Consequently, this coefficient is recommended as the most suitable parameter for modelling cotton stalk-rubber belt interactions in discrete element simulations.

Table 7

Rolling friction determination of cotton stalk rolling distance simulation

Serial number	Rolling Friction Coefficient	Rolling distance (mm)	Error
1	0.015	212.6	11.6%
2	0.017	210.2	10.3%
3	0.019	193.6	1.6%
4	0.021	186.7	2.0%
5	0.023	163.6	14.1%
6	0.025	155.9	18.2%

Angle of Repose

The angle of repose is a macroscopic parameter that reflects the flow and friction characteristics of granular materials (Zhang et al., 2022), directly linked to contact parameters and the material's inherent physical properties. In this study, the angle of repose of cotton stalks on a rubber belt was measured to verify the accuracy of the contact parameters between the stalks and the rubber belt.

For the experiment, cotton stalks with diameters of 10 mm were cut to a uniform length of 25 mm, with 340 particles being used, as shown in Figure 5(a). A cylindrical rubber tube was placed vertically on the rubber belt, and the stalks were released at a uniform speed of 0.03 m/s (Wang et al., 2022), allowing them to naturally accumulate on the belt. The image of the cotton stalk's angle of repose was first binarized using MATLAB software to differentiate between the stalks and the background, as shown in Figure 5(b). Photoshop was then employed to extract the edge lines of the binarized image, as shown in Figure 5(c). Finally, the least squares method was applied to fit the boundary curve, as shown in Figure 5(d). In this figure, the x and y axes represent the width and heights of stalks, respectively. The experiment was repeated five times, with an average angle of repose measured at 43.04°.

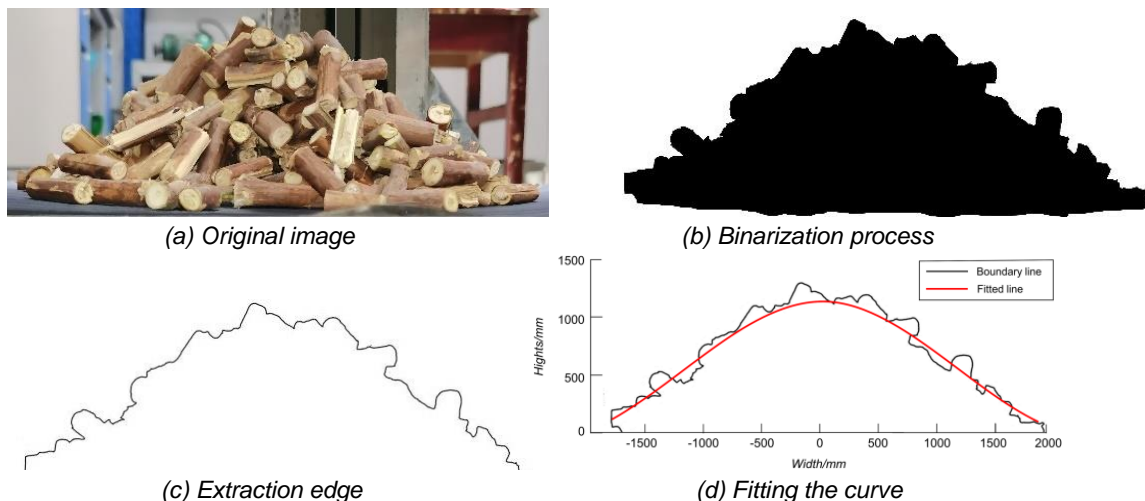


Fig. 5 - Image processing

In the EDEM simulation experiments, conducted under the same conditions as the physical tests, the Hertz-Mindlin contact model was utilized to simulate the interactions between particles. The particle factory, positioned 100 mm above the simulation base, generated cotton stalk particles at a rate of 114 particles per second, ensuring consistency with the stalk diameter. Figure 6(a) shows the static state of cotton stalk particles after generation, while Figure 6(b) shows the state of cotton stalk particles after the cylinder is lifted and the flow stops.

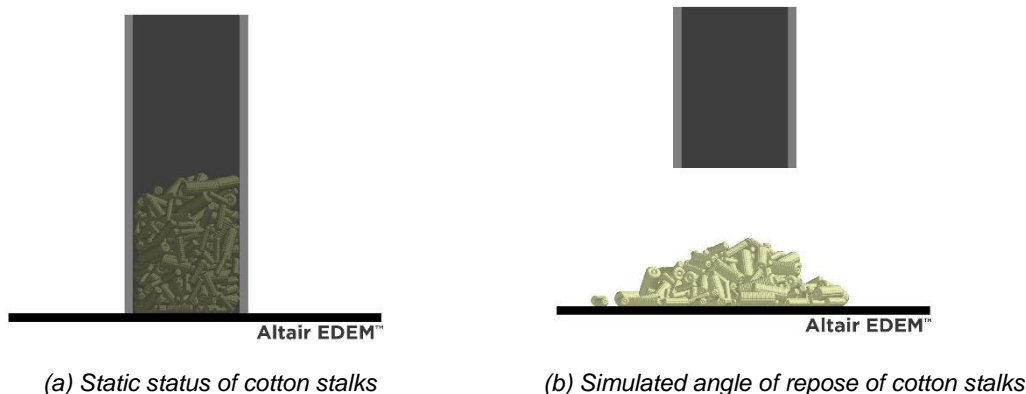


Fig. 6 - Cotton Stalks simulation stacking angle experiment

From these experiments, it was observed that the selected parameters closely replicated the physical behavior of the cotton stalks, providing reliable data for further analysis. Therefore, this setup and parameter configuration proved effective for accurately modeling the mechanical interactions of cotton stalk particles in discrete element simulations.

RESULTS AND ANALYSIS

A full factorial experiment was designed to investigate the factors affecting the angle of repose (θ) in the contact parameters between cotton stalks and the rubber belt. The experiment considered three factors: the collision recovery coefficient (A), static friction coefficient (B), and rolling friction coefficient (C), designed in Table 8. Since it was unclear whether each factor had a significant effect on the angle of repose, the experiment aimed to identify significant factors influencing θ .

The design also included three central points to ensure accuracy in the analysis. The levels of each factor are detailed in Table 9, with a total of 11 experimental designs established.

Table 8

Experimental factor level design

Experimental factor	-1	0	1
A	0.41	0.44	0.47
B	1.0	1.20	1.40
C	0.017	0.021	0.025

Table 9

Experimental design of contact parameters

Serial number	A	B	C	θ (°)
1	-1	-1	-1	40.9
2	1	-1	-1	41.2
3	-1	1	-1	42.8
4	1	1	-1	38.9
5	-1	-1	1	33.8
6	1	-1	1	40.7
7	-1	1	1	36.5
8	1	1	1	40.5
9	0	0	0	43.6
10	0	0	0	42.8
11	0	0	0	43.3

Table 10

Parameter significance analysis

Parameter	Effect	Sum of square	Mean square	F Value	P-Value	Significance ranking
A	1.825	6.66	6.66	37.15	0.009	3
B	0.525	0.55	0.55	3.07	0.178	6
C	-3.075	18.91	18.91	105.47	0.002	2
AB	-1.775	6.3	6.3	35.14	0.01	4
AC	3.625	26.28	26.28	146.57	0.001	1
BC	0.725	1.05	1.05	5.86	0.094	5

Based on the results shown in Table 10, a significance analysis of the parameters was conducted to evaluate their impact on the angle of repose. The interaction between the rolling friction coefficient and the static friction factor (AC) has the highest significance, as shown by its P-value of 0.001 and F value of 146.57, making it the most influential factor. In addition, the rolling friction coefficient (C) also plays a crucial role, with a P-value of 0.002 and an F value of 105.47, ranking second in significance. This highlights its strong independent effect on the angle of repose. Therefore, the analysis indicates that rolling friction (C) and its interaction with static friction (AC) should be prioritized for tuning in future simulations, as they exhibit the most significant effects on the simulation results, particularly in modeling the behavior of cotton stalks in discrete element simulations.

BBD response surface test results and analysis

To determine the optimal contact parameters between cotton stalks and the rubber belt, the Box-Behnken Design (BBD) was applied (Coetzee et al., 2017). In this study, A three-factor, three-level combination design test was established with 17 test simulations and five sets of tests at the central level in Table 11, and the BBD response surface test analysis of variance is shown in Table 12.

Table 11

BBD Response surface design

Serial number	A	B	C	$\theta(^{\circ})$
1	-1	-1	0	37.4
2	1	-1	0	40.0
3	-1	1	0	39.0
4	1	1	0	39.1
5	-1	0	-1	41.8
6	1	0	-1	40.1
7	-1	0	1	35.2
8	1	0	1	40.6
9	0	-1	-1	40.0
10	0	1	-1	39.8
11	0	-1	1	37.3
12	0	1	1	38.6
13	0	0	0	42.6
14	0	0	0	43.2
15	0	0	0	43.3
16	0	0	0	42.8
17	0	0	0	43.3

Table 12

BBD Response surface analysis of variance

Source	Freedom Degrees	Mean Square	F Value	P-Value Prob
Model	9	9.89	59.56	<0.0001
A	1	5.12	30.84	0.0009
B	1	0.41	2.44	0.1623

Source	Freedom Degrees	Mean Square	F Value	P-Value Prob
C	1	12.5	75.3	<0.0001
AB	1	1.56	9.41	0.0181
AC	1	12.6	75.92	<0.0001
BC	1	0.56	3.39	0.1082
A ²	1	14.14	85.18	<0.0001
B ²	1	22.91	138	<0.0001
C ²	1	13.38	80.59	<0.0001
Residual	7	0.17	-	-
Lack of Fit	3	0.25	2.43	0.257
Pure Error	4	0.1	-	-
Cor Total	13	-	-	-

Analysis of the response surface test variance data revealed that factors (B) and (BC) had no significant effect on the angle of repose. The regression model yielded a coefficient of determination R^2 of 0.9871, indicating a high level of model fit. Additionally, the lack-of-fit P-value was greater than 0.05, confirming that the model was statistically significant and the lack of fit was not significant.

Compared with other studies, this research advances calibration efforts beyond the traditional focus on isolated parameters, such as the mechanical properties of cotton stalks or individual interactions between rubber belts and materials, as seen in *Zhang et al. (2024)*, which improved the accuracy of simulations for chopped cotton stalks. Building on that foundation, this study incorporates a more comprehensive set of parameters, including the coefficients of collision recovery, static friction, and rolling friction. These parameters are further validated through real-world experimental data, enhancing the accuracy and realism of the simulation models. Regarding device design optimization, this study differs from works like those by *Zhang et al. (2023)* and *Li et al. (2022)*, which primarily concentrated on simulation accuracy and material-specific calibration.

This study provides a more refined, practical approach to simulating cotton stalk-rubber belt interactions, addressing a gap in the current literature by providing valuable insights for the optimization of flexible cotton stalk harvesting equipment. The innovation of this research lies in its practical application for optimizing the design of harvesting equipment.

CONCLUSIONS

(1) Through physical experiments, such as the flatbed method and the inclined plane method, the contact parameters between cotton stalks and rubber belts were calibrated. The flatbed method measured the average area count was calculated to be 7.01, while the inclined plane method yielded an average sliding angle of 53.7° and an average rolling distance of 190.5 mm for the cotton stalks. Using the average area count, sliding angle, and rolling distance as evaluation indicators, simulations of single-factor experiments based on EDEM 2022 software determined the optimal contact parameters between cotton stalks and rubber belts: a collision recovery coefficient of 0.44, a static friction coefficient of 1.2, and a rolling friction coefficient of 0.019.

(2) The full-factorial experimental analysis revealed that both the collision recovery coefficient and the rolling friction coefficient significantly affected the repose angle. Furthermore, the interaction between the collision recovery coefficient and the static friction coefficient, as well as between the collision recovery coefficient and the rolling friction coefficient, had a considerable impact on the repose angle.

(3) Using Design Expert 10.0 software, the response surface analysis, contour plots, and regression equations identified the optimal cotton stalk-rubber belt contact parameters: a collision recovery coefficient of 0.446, a static friction coefficient of 1.146, and a rolling friction coefficient of 0.0194. Repeated experiments (n=5) resulted in an average repose angle of 42.73°, with a deviation of 0.72% from the actual experimental results.

ACKNOWLEDGEMENT

This study was supported by the Xinjiang Uygur Autonomous Region Youth Science Fund (Grant No.2022D01B91) and the National Nature Foundation Project (Grant No. 52365038).

REFERENCES

- [1] Coetzee, C. (2017). Review: Calibration of the discrete element method. *Powder Technology*, 310: 104-142.
- [2] Du, X., & Wang, Y. (2012). Simulation and calibration of rubber materials for seals. *Tribology International*, 47: 23-29.
- [3] Du, X., Zeng, Y. W., Gao, R., Yan, J., & Zao, Y. (2012). Study on the influence of particle shape on friction mechanism by discrete element method (用离散元方法研究颗粒外形对摩擦机理的影响). *Journal of Southwest Jiaotong University*, 47(02): 252-257.
- [4] Hu, M., Xia, J., Zhou, Y., Luo, C., Zhou, M., & Liu, Z. (2022). Measurement and calibration of the discrete element parameters of coated delinted cotton stalk. *Agriculture*, 12(2): 286
- [5] Jiang, D., Chen, X., Yan, L., Gou, H., Yang, J., & Li, Y. (2023). Parameter calibration of discrete element model for cotton rootstalk-soil mixture at harvest stage in Xinjiang cotton field. *Agriculture*, 13(7): 1344.
- [6] Jin, X. N., Zhang, J. C., Xue, J. F., et al. (2022). Calibration of discrete element contact parameters between corn seeds and rubber belt (玉米种子与橡胶带离散元接触参数标定). *Journal of Agricultural Mechanization Research*, 44(07): 39-43.
- [7] Jiang, P., Li, Y., Li, J., Meng, H., Peng, X., Zhang, B., He, J., & Kan, Z. (2021). Experimental Research on the Bending and Fracture Characteristics of Cotton Stalk. *Transactions of the ASABE*, 64(6): 1771-1779.
- [8] Li, J., Lu, Y., Peng, X., Jiang, P., Zhang, B., Zhang, L., Meng, H., Kan, Z., & Wang, X. (2022). Discrete element method for simulation and calibration of cotton stalk contact parameters. *BioResources*, 18(1): 400-416.
- [9] Liang, R., Chen, X., Zhang, B., Wang, X., Kan, Z., & Meng, H. (2022). Calibration and test of the contact parameters for chopped cotton stems based on discrete element method. *International Journal of Agricultural and Biological Engineering*, 15(5): 1-8.
- [10] Niu, Z. Y., Kong, X. R., Shen, B. S., Li, H. C., Geng, J., & Liu, J. (2022). Calibration of discrete element simulation parameters for granular feed damage (颗粒饲料破损离散元仿真参数标定). *Transactions of the Chinese Society for Agricultural Machinery*, (07): 132-140+207.
- [11] Nattino, G., Finazzi, S., & Bertolini, G. (2014). A new calibration test and a reappraisal of the calibration belt for the assessment of prediction models based on dichotomous outcomes. *Statistics in Medicine*, 33.
- [12] Rossow, J., & Coetzee, C. (2021). Discrete element modelling of a chevron patterned conveyor belt and a transfer chute. *Powder Technology*, 391: 77-96.
- [13] Sun, Y. X. (2019). Experimental calibration of contact parameters between wheat and conveyor belt (小麦与输送机皮带接触参数的实验标定). *Transactions of the Chinese Society for Agricultural Machinery*, 50(12): 67-73.
- [14] Wang, R. L., Li, P. Y., Wang, T. J., et al. (2022). Calibration of discrete element parameters for round-bale corn stalks (圆捆玉米秸秆离散元参数标定). *Journal of Shenyang Agricultural University*, 53(03): 319-326.
- [15] Zhang, B., Chen, X., Liang, R., Wang, X., Meng, H., & Kan, Z. (2022). Calibration and test of contact parameters between chopped cotton stalks using response surface methodology. *Agriculture*, 12(11): 1851.
- [16] Zhang, H., Wen, Z., Chen, Y., Liu, J., Liu, H., Zhang, Z., & Zhang, X. (2023). Research on Cutting Angle Design Optimization of Rubber Cutter Based on Discrete Element Method. *Agriculture*, 13(10): 1894.
- [17] Zhang, J. X., Zhang, P., Zhang, H., et al. (2024). Calibration of discrete element simulation parameters for cotton stalks in Xinjiang (新疆棉花秸秆离散元仿真参数标定研究). *Transactions of the Chinese Society for Agricultural Machinery*, 55(01): 76-84+108.
- [18] Zhao, Y., Hou, Y., Li, X., Zhu, H., Cen, S., & Jin, H. (2023). Parameter calibration for the discrete element simulation of tire-soil interaction. *INMATEH Agricultural Engineering*, Vol.69(1). pp.693-702. DOI: <https://doi.org/10.35633/inmateh-69-67>

THE OPPORTUNITY OF ADVANCED TECHNOLOGIES UTILIZATION FOR DETECTING BASAL STEM ROT (BSR) IN PALM OIL PLANTATION: A REVIEW

PEMANFAATAN TEKNOLOGI CANGGIH UNTUK MENDETEKSI BUSUK PANGKAL BATANG (BSR) PADA PERKEBUNAN KELAPA SAWIT: REVIEW

Hasbi Mubarak SUUD¹⁾, Bayu Taruna Widjaja PUTRA^{2,3,*)}, Nazmi Mat NAWI⁴⁾,
Wahyu Nurkholis Hadi SYAHPUTRA^{2,3,5)}

¹⁾ Study Program of Agricultural Science, Faculty of Agriculture, Jember 68121, East Java, Indonesia

²⁾ Laboratory of Precision Agriculture and Geo-Informatics, University of Jember, Jember 68121, East Java, Indonesia

³⁾ Center of Excellence of Artificial Intelligence on Industrial Agriculture, University of Jember, Jember 68121, East Java, Indonesia

⁴⁾ Universiti Putra Malaysia, Malaysia

⁵⁾ Agrotechnology Study Program, Faculty of Agriculture, University of Jember, Jember 68121, East Java, Indonesia

Tel: +62811350512; E-mail: bayu@unej.ac.id

DOI: <https://doi.org/10.35633/inmateh-75-76>

Keywords: Basal Stem Rot, GIS, IoT, Machine Learning, Oil Palm Plantation, Remote Sensing, Automated Disease Detection

ABSTRACT

Basal Stem Rot (BSR) disease attacks in oil palm plantations are still the most significant cause of losses in oil palm plantations. The leading cause of BSR disease in oil palm plants is the *Ganoderma Boninense* fungus. The spread of BSR in an oil palm area can be massive due to transmission through root contact, airborne, and sporophores spread on the soil and in dead plant debris. The application of advanced technologies to mitigate and prevent the spread of BSR disease can be carried out considering that the nature of the spread and characteristics of this disease infection are well known. Advanced technologies such as the Internet of Things (IoT) are suitable for real-time monitoring of large areas. The key to successfully detecting BSR disease in oil palm plants is the selection of sensor technologies for monitoring and machine learning (ML) models used for segmenting and classifying infected plant characteristics. This paper comprehensively summarizes the spread of BSR disease and then describes various technologies and ML models for monitoring and preventing BSR disease in oil palm plantations. The use of ML can be potentially used for early detection of BSR. Finally, this paper can complement and provide a basis for developing technology to prevent the spread of BSR disease.

ABSTRAK

Penyakit Busuk Pangkal Batang (BSR) pada perkebunan kelapa sawit masih menjadi penyebab utama kerugian di perkebunan tersebut. Penyebab utama penyakit BSR pada tanaman kelapa sawit adalah jamur *Ganoderma boninense*. Penyebaran BSR pada area kelapa sawit dapat berlangsung masif karena penularannya melalui kontak akar, udara, dan penyebaran sporofor pada tanah serta sisa-sisa tanaman yang mati. Aplikasi teknologi canggih untuk mengurangi dan mencegah penyebaran penyakit BSR dapat dilakukan mengingat sifat penyebaran dan karakteristik infeksi penyakit ini sudah dikenal. Teknologi canggih seperti Internet of Things (IoT) sangat cocok untuk pemantauan secara real-time pada area yang luas. Kunci keberhasilan dalam mendeteksi penyakit BSR pada tanaman kelapa sawit adalah pemilihan teknologi sensor untuk pemantauan dan model pembelajaran mesin yang digunakan untuk segmentasi dan klasifikasi karakteristik tanaman yang terinfeksi. Makalah ini merangkum secara komprehensif penyebaran penyakit BSR, kemudian mendeskripsikan berbagai teknologi dan model pembelajaran mesin untuk pemantauan dan pencegahan penyakit BSR di perkebunan kelapa sawit. Diharapkan, artikel ini dapat melengkapi dan memberikan dasar bagi pengembangan teknologi dalam mencegah penyebaran penyakit BSR.

INTRODUCTION

Palm oil is a competitive and efficient commodity for vegetable oil production, particularly when considering production costs and the ratio of planting area to oil yield (Destiarni & Jamil, 2021). Apart from that, palm oil commodities have been proven to improve the welfare of small farmers if they follow the principles of correct cultivation methods (Thoumazeau et al., 2024). The economic prospects for palm oil commodities are increasing due to the diversification of derivative products in biomaterials, biofuels, and bioenergy, which can become a powerful new bioeconomic force (Sakai et al., 2022). The main derivatives of palm oil products are food ingredients such as margarine, spreads, ice cream, confectionery fats, emulsifiers, and vanaspati

(Ximenes *et al.*, 2022). Apart from that, methyl ester compounds from palm oil can be the primary alternative material for burning diesel engines. Even diesel fuel with a 20% mixture of palm oil (B20) has been proven to produce almost the same axial flame temperature as pure diesel fuel but with lower NO_x and CO₂ emissions (Pourhoseini *et al.*, 2021). Palm oil produces oil derivative products; even its leaves, stems, empty bunches, kernel shells, and mesocarp fibers can be used as asphalt hardeners and construction materials (Al-Sabaeei *et al.*, 2022). In developing countries like Indonesia, this commodity has proven to be an industrial sector that drives the economy by fostering entrepreneurship, enhancing village development, and supporting household income (Hariyanti *et al.*, 2024).

BSR disease reduces crop yields and destroys the lignin in cell walls. BSR disease symptoms are absent in the early stages and only emerge later. Although the infection develops slowly, it can spread across thousands of hectares of oil palm plantations (Naheer *et al.*, 2013). It also spreads very fast through contact with infected roots and basidiospores. This fungus can also spread and live in felled stems and remaining wood fibers in the soil (Rees *et al.*, 2012). BSR spreads rapidly, affecting oil palm of all ages but is most severe in plants over 25 years old. It is most prevalent in laterite, coastal, inland, and peat soils (Ibrahim *et al.*, 2020).

Currently, BSR detection in oil palm plantations relies on manual observation and laboratory analysis, as the fungi primarily inhabit the trunk and roots. Given its rapid and invasive nature, advanced technologies such as IoT, ML, and remote sensing offer faster detection. IoT integrates sensors, including soil, temperature, and leaf sensors, with single-board microcontrollers, aiding crop monitoring, irrigation, pest control, soil mapping, and disease detection, making it increasingly popular in agriculture (Rudrakar & Rughani, 2023). For large-scale plantations, remote sensing is the most effective method, with data acquired via satellites or UAVs in formats such as RGB images, spectroradiometer, multispectral, and hyperspectral data. Remote sensing has proven reliable for monitoring oil palm health (Santoso *et al.*, 2019), and advancements in imaging sensors with varying spatial, temporal, and spectral resolutions enhance its capabilities. Multispectral and hyperspectral imaging datasets enable detailed analysis of land cover changes, including plant canopy and soil characteristics, with prior studies confirming remote sensing's effectiveness in early plant disease detection (Abdullah *et al.*, 2023).

Early BSR detection requires fast, accurate data processing for timely decisions. Machine learning (ML) enhances disease detection accuracy, efficiently handling large datasets for data-driven decision-making. (Ennaji *et al.*, 2023). ML explores data by building estimation models and relationships between parameters. It processes structured datasets to predict trends. Supervised learning handles known classifications, while unsupervised learning finds patterns. Model development includes classification, regression, clustering, dimensionality reduction, reinforcement learning, and deep learning (Sarker, 2021). Applying ML in the agricultural sector usually goes through data extraction and classification stages to produce output (Kipli *et al.*, 2023). ML is widely used in agriculture for planting, harvesting, and post-harvest stages. It supports disease detection, soil analysis, plant age estimation, population counting, and yield classification (Meshram *et al.*, 2021).

This study aims to elucidate the opportunities for advanced technologies to detect BSR disease spreading in oil palm plantations. The presence of *G. Boninense* can be detected by the appearance of basidioma in the planting medium and changes in leaf color on oil palm seedlings under 1 year old. In addition, environmental factors such as temperature, duration, and intensity of rainfall, dew levels, soil temperature and water content, soil fertility, soil organic matter content, wind, herbicide history, and air pollution also influence the spread of pathogens. It also highlights the strengths and limitations of these technologies. By highlighting the strengths and limitations of existing technologies, this article proposes a novel approach that combines advanced sensor fusion with real-time processing to provide more reliable, cost-effective, and scalable solutions for early BSR detection in diverse environmental conditions.

MASSIVE DAMAGE DUE TO THE SPREAD OF BSR DISEASE IN OIL PALM PLANTATIONS

BSR is a severe threat to oil palm plantations and has been proven to cause severe economic losses for palm oil-producing countries. The fungus *Ganoderma boninense* (*G. Boninense*) is the main cause of BSR disease, which can result in economic losses of up to 43% over 6 months due to reduced oil palm yields (Assis *et al.*, 2016). BSR infection in oil palm plantations can reduce plant yields between 50% and 80% (Corley & Tinker, 2015). BSR disease is the biggest threat to oil palm plantations caused by the *Ganoderma Boninense* (*G. Boninense*) fungus which attacks the roots to the base of the plant stem. Without early detection or control, infected plants die within 6–12 months of symptom onset, with an 80% mortality rate in productive-age plants.

In Johor, Malaysia, the BSR infection rate rose from 1.51% in 1994 to 3.71% in 2009, averaging a 10.3% annual increase (Roslan & Idris, 2012).

Studies using the Bayesian Model Averaging (BMA) model approach show that the level of economic loss is estimated to reach 68% of the yield of all infected plants (Assis *et al.*, 2020). In 2009, BSR disease spread across 151,208 hectares in Malaysia, causing an estimated loss of US\$ 351 million (Parthiban *et al.*, 2016). By 2040, if uncontrolled, it could destroy 860,610 ha of productive oil palm plantations, leading to job losses and rising palm oil prices (Olaniyi & Szulczyk, 2020). Indonesia is also estimated to experience losses of US\$ 38 million for every 1% of oil palm plantation areas that experience BSR attacks based on calculations using commodity prices in 1996. It is estimated that losses due to oil palm plantations attacked by BSR in Southeast Asia could reach 500 million US\$ per year (Ahmadi *et al.*, 2017). The first convincing discovery of *G. Boninense* infection was in gardens owned by private corporations in North Sumatra, with an attack rate of 22% of the plant population per hectare in 2017 (Haryadi *et al.*, 2019). Losses due to the spread of BSR disease have not only hit Malaysia and Indonesia; in fact it was recently discovered that several oil palm plantations in Papua New Guinea experienced BSR infection rates of up to 50% (Murphy *et al.*, 2021). Statistics of losses due to BSR can be seen in Table 1.

Table 1

The summary on BSR-related losses

Metric	Value	Source
Yield losses	Can reduce yield by 50% to 80%	(Murphy <i>et al.</i> , 2021; Zakaria, 2022)
Annual economic losses	Estimated between US\$ 38 million to US\$ 351 million.	(Parthiban <i>et al.</i> , 2016; Paterson, 2023)
Environment Impact	CO ₂ and CH ₄ emissions from decomposition; soil pollution from chemical treatments.	(Jazuli <i>et al.</i> , 2022)
Agricultural Implication	Increased replanting costs; challenges in disease management.	(Paterson, 2023)

SPREAD OF BSR IN OIL PALM PLANTATIONS

The disease triangle concept highlights the interaction between the host, pathogen, and environment, all of which influence disease spread. Infectious diseases emerge when susceptible hosts, virulent pathogens, and favorable environmental conditions align (Mead *et al.*, 2022). Several types of ganoderma, such as *G. Boninense*, *G. Miniotacinctum*, *G. Chalceum*, *G. Tornatum*, *G. Zonatum*, and *G. Xylonoides*, can be the cause of the spread of BSR disease. However, *G. Boninense* is the main cause of BSR infection in oil palm plants (Zakaria, 2022). Several types of seeds are claimed to be more susceptible and more resistant to disease. Progenies from palm oil seeds PK 2724 and PK 2567 were detected as seeds that were susceptible to infection. AVROS oil palm seeds are also more vigorous than the Ekona and Calabar varieties (Chong *et al.*, 2012). In the latest study, 31 oil palm progenies had partial resistance to Ganoderma attacks in peatlands, but further confirmation and testing in the nursery were needed to ensure their performance (Amiruddin, 2022). Environmental factors can also influence pathogen behavior, such as germination speed, spread of inoculum, ability to survive and penetrate pathogens, and the potential for infection.

Stages Development of Ganoderma Boninense

The development phases of *G. Boninense* are the same as fungi in general as seen in Fig. 1(a). The mature fruiting body will produce basidiospores. Basidiospores can spread through the air or with the help of insects and then germinate into monokaryotic mycelia. This mycelium is not yet pathogenic to oil palm plants (Khoo & Chong, 2023). Pathogenic properties for oil palm plants only appear in dikaryotic mycelia after fusion or mating occurs. Dikaryotic mycelia are more commonly found on the surface of stems and roots than on the interior of oil palm stems (Pilotti *et al.*, 2018). The dikaryotic mycelia grows into mycelium, which eventually develops into an infectious inoculum. Mycelium will continue to develop into a fruiting body if it is infected with the suitable medium. The base of the stem of an oil palm plant that is injured or has been pruned is the medium most easily infected by mycelium *G. Boninense* (Jazuli *et al.*, 2022). This *G. Boninense* fungus colony has a characteristic white color on the surface and a dark color on the reverse side. On infected stems, fruiting bodies often appear to contain spores with layers varying in color from yellow to brown (Khoo & Chong, 2023).

Dikaryotic mycelia form rapidly in favorable conditions. *In vitro* studies show *G. boninense* spores germinate within 1–2 days in darkness. Monokaryotic mycelia grow 4–5 days after transfer to potato dextrose agar (PDA), with clamp cell formation observed 5–7 days post-mating, indicating successful fusion (Pilotti *et al.*, 2003). The development of dikaryotic mycelia, which infects the base of the oil palm stem, is characterized by the appearance of a slightly raised white button which changes shape into a dome structure within 2 days. This structure develops into a slender white column with a length of 1.1 cm and a width of 1.1 cm. Within 14 days, the structure of the column becomes harder and starts to turn brown, except for the apical tissue, which remains white. The apical tissue eventually stops growing and forms a growth cap. The longer it grows, the color of the cap becomes browner, and the size also increases. Its size can reach a length of 17.8 cm and a width of 14.6 cm at 14 weeks after infection (Ho & Nawawi, 1986a).

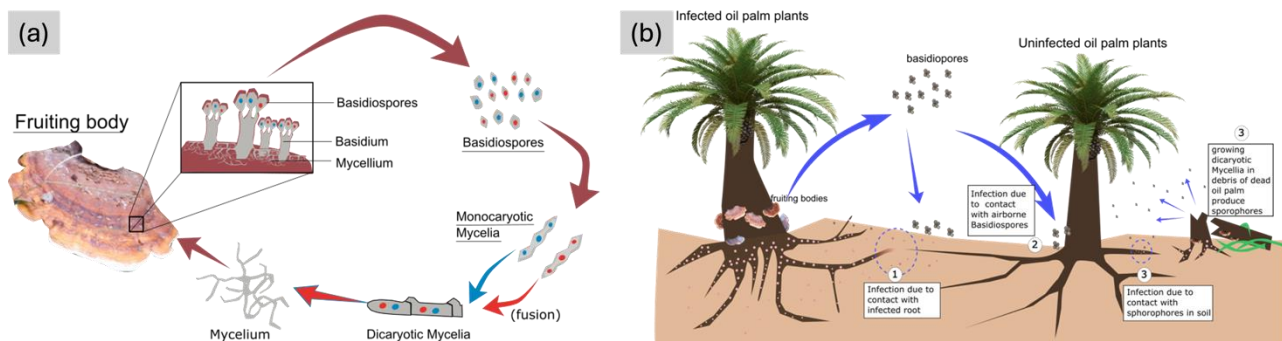


Fig. 1 - *G. boninense* and BSR transmission: (a) Life cycle of *G. boninense*. (b) Transmission via root-to-root contact, basidiospores, and free sporophores in debris and soil.

The spread of BSR in oil palm plants can be seen in Fig. 1(b). The spread of BSR is mainly due to the invasion of the *G. Boninense* pathogen in the roots. *G. Boninense* has the ability to spread through soil (soil-borne) and basidiospores in massive numbers with the help of wind or insects. The spread of *G. Boninense* basidiospores is not only influenced by one environmental factor but a combination of several factors (Ho & Nawawi, 1986b). Airborne basidiospores will develop on the surface of oil palm stems that are injured or have been pruned. Basidiospores that fall to the soil surface can be carried by water or insects, moving to the root area and colonizing oil palm roots. In addition, dikaryotic mycelia in the remaining roots and stems of dead oil palms can continue to grow and produce sporophores which can infect healthy plants (Pilotti *et al.*, 2018).

Symptoms of Infection in Oil Palm Plants

In the initial phase of the inoculum infecting oil palm plants, no symptoms can be observed directly with the naked eye (Siddiqui *et al.*, 2021). Based on recent observations, morphological symptoms on leaves only appear if the development of BSR disease on plants is severe or reaches 60-70% (Chong *et al.*, 2017). The initial characteristics of infected plant roots include changes in metabolism, characterized by the discovery of fatty acid compounds and steroidal compounds in large quantities in roots infected with *G. Boninense* (Isha *et al.*, 2020). The first morphological symptom that appears is chlorosis on oil palm leaves. This phase shows that *G. Boninense* has colonized the roots. Then, there is characteristic necrosis in the roots at the beginning of the infection, which then spreads to the base of the stem. Apart from that, stunted growth and curled leaves are symptoms in infected oil palm plants. This stage of infection indicates that the infection has reached the base of the oil palm plant stem.

Other symptoms that often appear on infected plants include the appearance symptoms of drought stress on the plant, spots appearing on the plant canopy on one side, a flat crown, many buds that should have opened but have not yet opened, the appearance of basidiocarp at the base of the lower stem, leaves unopened spears, and palm stems breaking and falling in cases of severe infection (Parthiban *et al.*, 2016). If fruiting bodies appear on oil palm plants, this indicates that the infection stage is severe. There has been massive degradation of plant stems. Old oil palm plants will die in 6 to 24 months, while young plants will die 2 to 3 years after the first symptoms of infection are detected (Siddiqui *et al.*, 2021).

Environmental Factors Support the Spread of BSR Disease

BSR disease can spread in various conditions and types of soil, even in oil palm plantations on peatlands, cases of BSR infection have been found (Midot *et al.*, 2019). Based on a survey conducted in

Malaysia, the most cases of BSR infection were found in lateritic soils and the least in peatlands. Lateritic soil is soil that has high aluminum and iron content. Usually, lateritic soils are formed in wet and hot tropical areas and are characterized by a red color (A. R. Mareddy, 2017). Land use history can also influence the spread of BSR infection. BSR disease can develop more massively in oil palm plantations located in coastal areas where the oil palm land was previously coconut plantation land. The spread of BSR disease has been shown to be more severe in areas with higher plant densities (Jazuli et al., 2024).

The chance of plants being infected with *G. Boninense* is greater in oil palm plantations that have undergone more than three replantings. Also, old plants have a greater chance of being infected than plants that have not yet produced fresh fruit bunches (Priwiratama et al., 2020). BSR infection can occur in various life cycles of oil palm plants. In cases found in Indonesia, the infection attack rate in 4 years old oil palm plants was between 1.42% and 4.28%. The attack rate on 17 years old oil palm plants is 50%. Meanwhile, in plantations with 33 year old oil palm plants, the infection rate was 0.71% (Lisnawita et al., 2016).

Tabel 2

The behavior of *Ganoderma Boninense* in each environmental parameter

No.	Parameter	Remarks
1.	Temperature	<ul style="list-style-type: none"> Optimal growth at 27–30°C; inhibited below 15°C and above 35°C; o growth at 45°C (Chong et al., 2017; Nawawi & Ho, 1990).
2.	Relative Humidity (RH)	<ul style="list-style-type: none"> Optimal at 50–60%; reduced growth above 60%.
3.	Soil pH	<ul style="list-style-type: none"> Best growth at pH 3–5.5 (Chong et al., 2017) pH 6 reduces BSR growth and supports seedlings (Rahman & Othman, 2020).
4.	Sunlight	<ul style="list-style-type: none"> Higher infection risk in shaded seedlings (Rees et al., 2007).

Molecular Testing Methods for BSR Disease

BSR infection can be detected by direct observation and molecular detection. The molecular detection approach is the fastest way to detect BSR infection (Bahari et al., 2024). Detection can also be done simpler, namely by observing pathogenic fungi directly at both macro and microscopic levels. However, this method takes a long time and has low resolution and sensitivity. Several molecular approaches to detect *G. Boninense* infection are real-time polymerase chain reaction (PCR) testing on fungal samples obtained in the field. The fruiting bodies or basidiomata part of the fungus is the most sensitive part for detecting the presence of pathogen DNA compared to the stem and root tissue of the fungus *G. Boninense* (Hilmi et al., 2022). Another commonly used early detection method for spreading BSR is a multiplex PCR-DNA kit using oil palm plants' root and stem tissue samples (Idris et al., 2010).

The enzyme-linked immunosorbent assay (ELISA) application can detect *G. Boninense* infection. This technique uses polyclonal antibodies to detect the presence of *G. Boninense* serologically. Detection can also be done by detecting the presence of typical ergosterol produced by the fungus *G. Boninense*. This method is carried out by making an extraction solution from samples suspected of being exposed to *G. Boninense* spores or mycelia. Ergosterol is detected if there is thin layer chromatography (TLC) in the extract solution and can then be quantified using high-performance liquid chromatography (Muniroh et al., 2014). However, this molecular method is quite complicated and expensive, so it is not appropriate to carry out in large areas with lots of samples (Siddiqui et al., 2021).

Many detection procedures can be done, but there is no truly effective way to stop the spread of BSR unless the biomarkers of *G. Boninense* have been detected (Mohd Hilmi Tan et al., 2023). Biomarkers are changes in cells, biochemistry, or molecules that can objectively measure normal biological processes, pathogenic processes, and pharmacological responses to treatment to control the development of infection. Biomarkers are technological tools that can help understand the causes, distribution status, diagnosis, and treatment response to a disease. The search for appropriate biomarkers to detect *G. Boninense* is currently being developed, but none are ready to be applied in the field. One of the biomarker developments being developed is the Oil palm extract medium (OPEM) model. This model is still being developed to produce a faster and non-invasive method for diagnosing *Ganoderma* in oil palm plantations (Santiago et al., 2023). The mRNA marker *EgPIN5* is a promising biomarker for early *G. Boninense* detection, identifying infection as early as 11 days post-inoculation before symptoms appear. LFA strips with ssDNA aptamers targeting *EgPIN5* RNA fragments offer a low-cost, visual detection method. While this approach shows potential, its sensitivity remains limited due to the low RNA copy numbers in field samples (Bahari et al., 2024).

Management of the Current Spread of BSR Disease

Management of the spread of *G. Boninense* can currently be done physically, chemically, and by biocontrol. Cleaning infected plantation areas must be done in detail. Clean clearing and windrowing procedures can be carried out to minimize the spread of inoculum. Infected oil palm plants must be chopped, crushed, and stacked between planting rows, although it cannot be guaranteed that the pathogen will not spread and infect healthy plants if this is done. Using fungicides to control the spread of *G. Boninense* is not very effective because this fungus is soil-borne. Fungicides will first be degraded in the soil before reaching their target. Injection of 90 ml of hexaconazole with 10 liters of water into the stems of infected oil palm plants can increase the survival rate by up to 70% and the ability to produce for several years to come (Mohammed et al., 2014). The use of biocontrol agents to control the spread of infection has been widely developed and shows reasonable success rates. Use of fungi *Trichoderma* spp., *Aspergillus* spp., and *Penicillium* spp. They were proven antagonistic to *G. Boninense* through in vitro experiments (Naher et al., 2013).

A mixture of *Trichoderma* spp, namely *Trichoderma aspergillum*, *Trichoderma harzianum*, and *Trichoderma virens*, as a biocontrol agent, can reduce symptoms of disease infection between 83% and 89%. The *Trichoderma* spp mixture can be applied in the nursery three months before planting the seeds (Musa et al., 2018). Application of *Trichoderma aspergillum* strain T76-14 is known to be able to respond to oil palm seedlings to control and limit pathogen colonization in host tissue and inhibit the distribution of *G. Boninense* in the soil (Samlkamnoed et al., 2023). Three bacterial strains, namely, *Pseudomonas aeruginosa* strain JQ-41, *Serratia marcescens* strain S16, and *Stenotrophomonas rhizophila* strain CASMBAUDAL2, together with one fungal strain, *Trichoderma* sp., and one actinomycetes strain, *Streptomyces* sp., have been proven to be able to prevent the growth of *G. Boninense* with inhibition levels between 70% - 88.5% (Rupaedah et al., 2024). Currently further studies are being carried out to formulate integrated control through a deeper understanding of the influence of physical, chemical and biological factors on the spread of *G. Boninense* infection. Temperature treatment, administration of boron and potassium, and application of the fungicide Manzoceb are known to reduce the specific metabolic rate of *G. Boninense* and have no effect on the development and metabolism of *Trichoderma virens* (Anothai et al., 2023).

THE POTENTIAL OF IoT UTILIZATION TO DETECT THE SPREAD OF BASAL STEM ROT DISEASE

Molecular infection testing can provide accurate confirmation of whether a plant has been infected with *G. Boninense* and how severe the infection is because it directly tests DNA sequences. However, this method requires complex lab tests, high expertise, is costly, and challenging for large-scale application. Therefore, advanced technologies like sensors and IoT have been developed for faster early detection of *G. Boninense* in oil palm fields. Imaging sensors, including RGB, multispectral, hyperspectral, thermal, fluorescence, and 3D, are widely used in precision agriculture. They can be applied in microscopes for cellular analysis, mounted on vehicles for plant imaging, deployed on UAVs for aerial monitoring, or placed on satellites for large-scale ecosystem assessment (Mahlein, 2016). High-resolution aerial images from UAVs can classify oil palm conditions based on tree crowns using image processing, ML, and deep learning. Hyperspectral imaging detects infection characteristics by combining absorption, reflectance, and fluorescence data into a hypercube (Vasefi et al., 2016). Non-imaging sensors like portable GC-MS, electronic noses, biosensors, and nuclear magnetic resonance (Wei et al., 2021). Table 3 summarizes sensor technologies tested for BSR detection in oil palms.

Table 3

Sensor Technology for BSR Detection in Oil Palm

Technology	Sensor	Measurement Technique	Pros	Cons	Ref.
Imaging	High-resolution RGB	UAV with 12.1 MP RGB camera	Low cost, easy to use	Sun bias, low infection correlation	(Izzuddin et al., 2019)
	Multispectral Imaging	UAV with multispectral camera	Full spectrum for classification, NIR effective for BSR	Accuracy depends on segmentation and sample size	(Ahmadi et al., 2022)
	Hyperspectral Imaging	Hyperspectral sensors on canopy	Detailed spectral-spatial models, low cost	Expensive instruments, complex data processing	(Kurihara et al., 2022)

Technology	Sensor	Measurement Technique	Pros	Cons	Ref.
	FLIR Thermal Imaging	FLIR cameras placed around trees	Easy to use, clear thermal stats	Narrow measurement spectrum, difficult infection suspicion	(Hashim et al., 2021)
Spectroscopy	Mid-infrared Spectroscopy	FTIR spectrometer in lab	High accuracy, detects biochemical compounds	Complicated sampling and analysis, expensive tools	(Liaghat et al., 2014)
	NIR Spectroscopy	NIRscan Nano spectrometer on leaves	Simple, rapid, non-destructive	Low sensitivity, complex calibration	(Mohd Hilmi Tan et al., 2023)
	Dielectric Spectroscopy	Measures dielectric properties of leaves	Rapid, detects health levels	Hard to pinpoint disease cause	(Khaled et al., 2022)
Satellite	WorldView-3 Satellite	Pixel value analysis of palm crown reflectance	Can classify infection symptoms	Requires expertise, accuracy depends on model selection	(Santoso et al., 2019)
	Sentinel-2 Satellite	Vegetation indices from multispectral data	Comprehensive data, low cost	No thermal band, influenced by cloud cover	(Handrian et al., 2022)
Sensor	Intelligent Electronic Nose	32 sensor elements detect compounds in soil, stem, and leaves	Classifies healthy and infected plants, estimates infection area	Reduced sensitivity in humid conditions, calibration challenges	(Markom et al., 2009)
	E-Nose MOS Gas Sensor	MOS sensors in the lab detect chemical properties	Quick detection, affordable	Sensitive to temperature/humidity	(Marhaenanto et al., 2025)
	Terrestrial Laser Scanning	3D laser scanning around oil palm trees	Effective at detecting unopened spears in infected plants	Time-consuming setup, requires trained staff for data extraction	(Husin et al., 2020)
	Electrical Resistance Sensor	Measures electrical resistance in stems/soil	Rapid, easy, and low-cost	Data highly influenced by temperature, humidity, and other factors	(Aziz et al., 2019)
Imaging with consumer-grade camera	Camera Canon 600D	Mounted to DJI phantom 3 to capture area	Low-cost, easy to use, large area	Data highly influenced by light intensity	(Hermantoro et al., 2023)
	Canon SX240 HS	Mounted to Turnigy 9XR Octocopter UAV	Low-cost, large area	Light-sensitive	(Bejo et al., 2018)

The IoT extends beyond sensor technology for data acquisition and can be developed into an integrated system for managing plant pests and diseases. This includes data traffic management, big data processing, sensor-CPU interfaces, and machine-user interaction design (Nayagam et al., 2023). Architectures integrating all components of an IoT system continue to evolve to simplify the integration of diverse systems and hardware. Lysis, a cloud-based architecture platform, has four key functions: integrating IoT with social networks, enabling virtual objects and device communication, storing sensor data while controlling sensor behavior, and allowing data requests from the same sensor across different IoT systems (Girau et al., 2016). The Lysis platform integrates sensors for real-time plant detection, classifies data using the Model Builder Micro Engine, and displays results via a smartphone app. The basic framework of the IoT layer architecture should have sensors and actuators, connectivity and communication paths, edge devices

and gateways, Cloud Platform, Data Analytics (machine and deep learning), mobile and web applications, decision support systems, and finally security and privacy (Dhaka et al., 2023). The IoT is not only limited to sensor technology for data acquisition but can also be developed into an integrated system for managing plant pests and diseases. This can include data traffic management, big data processing, sensor and CPU interfaces, and machine-user interaction design (Nayagam et al., 2023). Architectures that integrate all parts of an IoT system continue to evolve to bridge the complexity of integrating dissimilar systems and hardware. Lysis is an example of a cloud-based architecture platform that has 4 essential functions, namely social network integration with IoT, creating virtual objects and communication between devices, features for storing data from sensors and controlling sensor behavior, and the ability to request data from the same sensor but from different IoT systems. The Lysis platform can be developed into a plant detection system capable of connecting various collocated sensors and sending the data in real-time to a dataset management platform. The collected dataset is classified and modeled in the Model Builder Micro Engine, the results of which are displayed in the app on the user's smartphone (Delnevo et al., 2022). The basic framework of the IoT layer architecture should have sensors and actuators, connectivity and communication paths, edge devices and gateways, Cloud Platform, Data Analytics, mobile and web applications, decision support systems, and finally security and privacy.

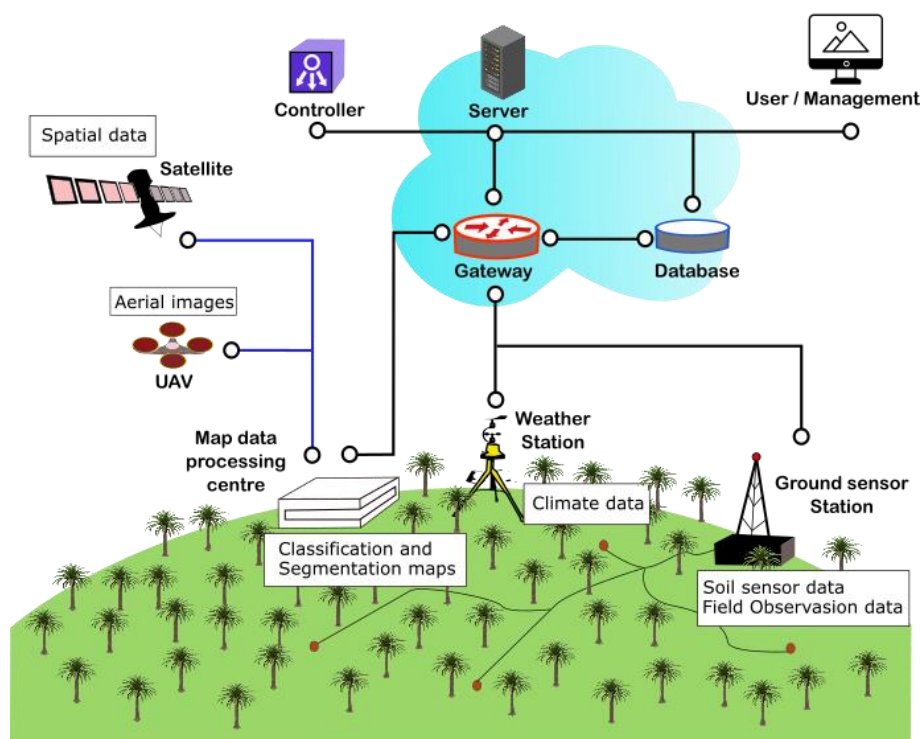


Fig. 2 - Concept of applying IoT for developing a BSR outbreak warning system

IoT technology makes it possible to apply it in building an early warning system for the spread of BSR disease in oil palm plantations. An initial overview of the concept of early warning for BSR disease using IoT can be seen in Fig. 2. Detection via imagery from UAVs and satellites can detect the characteristics of BSR infection, especially through monitoring the condition of the oil palm plant canopy. Satellite data containing multispectral information such as Sentinel-2, Landsat, and WorldView-3 are possible to use because they have many spectra to be analyzed either through modeling the spectral values or through converting the spectral values to obtain vegetative indices or surface temperature (Handrian et al., 2022). A UAV can capture aerial images for clearer analysis. Hyperspectral cameras offer high accuracy in segmenting and classifying BSR-infected oil palms but are costly. Monitoring often includes high-resolution aerial maps to enhance segmentation and classification. Hyperspectral data detects early BSR infection as mycelium develops on bark or fragile wood (Kurihara et al., 2022).

However, the characteristics of the plant canopy cannot wholly describe the spread of infection due to *G. Boninense* attacks the roots and base of oil palm plant stems. It has been proven with prior reports that the average accuracy of remote sensing in classifying the severity is around 80%, and in classifying healthy and

unhealthy trees is around 86.67% (Siddiqui *et al.*, 2021). So, field observations are still necessary to provide information about the presence of infected plants and confirm the monitoring result from remote sensing and sensors. These field observations can be carried out simultaneously with plant maintenance work. *G. Boninense* is also a fungus that can spread through airborne and direct contact, so it is also necessary to monitor environmental conditions by acquiring weather and climate data and soil conditions. Weather and climate data can be taken from weather stations, and soil condition data can be monitored using soil sensors or manual measurements. Meanwhile, data on soil electroconductivity distribution on land can be used to monitor soil conditions. Apart from carrying out analysis to predict disease outbreaks, steps to verify the results of predictions also need to be taken to control the spread of disease infections. Manual verification approaches and molecular detection can be carried out as further steps to verify the BSR outbreak warning system results. (Wang *et al.*, 2023). Manual verification approaches and molecular detection can be carried out as further steps to verify the BSR outbreak warning system results.

MODEL DEVELOPMENT FOR DETECTING BSR

Detection models are crucial factors other than data acquisition techniques and methods determining detection success. ML applications in precision agricultural systems can be used to detect plant pests and diseases. ML integrated into IoT is very powerful for real-time detection systems. ML has a role in predicting and detecting the spread of epidemics by studying datasets containing information about pathogen behavior, demographics, population, information about biology and biodiversity. Many models can be used to predict and detect the spread of disease infections, ranging from regression models neural networks to deep learning. Apart from that, the types of datasets used also vary, starting from spatial, epidemiological, meteorological, and remotely sensed data (Alfred & Obid, 2021). ML construction can be divided into several parts: dataset preparation, data preprocessing, data correlation analysis, determining the suitable model, and testing and verifying the selected model. The final stage is implementation (An *et al.*, 2024). Many statistical models and ML models can be used to prepare an early detection system for evaluating the spread of a disease. The model choice depends on the dataset type and the purpose of data processing. For example, if the goal is to obtain the relationship between spatial and temporal data in the spread of disease, spatio-temporal models can be used. If the goal is to detect climate data indicating what disease outbreak will occur, you can use Bayesian ML (Haque *et al.*, 2024). Several ML models that can be used to detect BSR disease in oil palm plantations are presented in Table 4.

Tabel 4

Several ML models for classifying the level of BSR disease infection in oil palm plants.

Models	Dataset Type	Purpose	Pros	Cons	Ref.
Kernel Naive Bayes	3D plot data from laser scans	Detect unopened spears, classify infection	Can classify with small datasets	Biased by poor data, not for continuous features	(Husin <i>et al.</i> , 2020)
ANN Backpropagation	VIS-NIR spectral data	Identify best wavelength for BSR	No parameter tuning, versatile	Sensitive to noise, slow training	(Ahmadi <i>et al.</i> , 2017)
PLS Discriminant Analysis	Hyperspectral images	Classify plant disease infection levels	Handles high variable-to-sample ratios	Requires deep statistical understanding	(Lelong <i>et al.</i> , 2010)
Support Vector Machine	Hyperspectral crown images	Classify infection using top fronds	Good for high-dimensional data	Needs large memory, struggles with large datasets	(Khaled <i>et al.</i> , 2018)
K-Nearest Neighbor	Hyperspectral frond samples	Classify BSR infection levels	Simple, no need for training model	Needs data smoothing, K-value affects accuracy	(Liaghat <i>et al.</i> , 2014)
Random Forest	Multispectral data from Sentinel 2A	Map plant infection distribution	Robust, handles imbalanced data	Complex interpretation, long prediction time	(Handrian <i>et al.</i> , 2022)
Multilayer-Perception NN	Hyperspectral drone images	Separate healthy/diseased plants	Handles non-linear problems	Slow computation, reliant on training data quality	(Lee <i>et al.</i> , 2022)

Models	Dataset Type	Purpose	Pros	Cons	Ref.
M-CR U-Net	Aerial RGB images	Classify infection severity via image segmentation	Robust for pixel-level segmentation	Downsampling reduces spatial accuracy, overfits on small datasets	(Win Kent <i>et al.</i> , 2023)

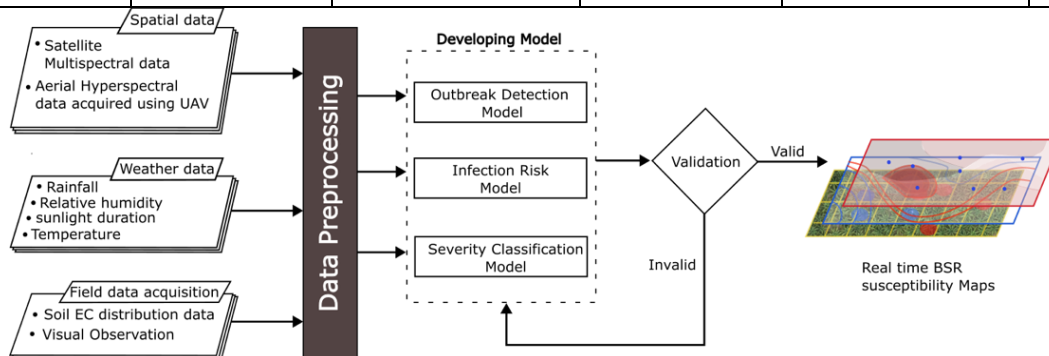


Fig. 3 - Proposed dataset and ML model development for real-time BSR susceptibility mapping

Models for segmentation and classification are not limited to those shown in Table 3, there are many more advanced models, especially deep learning models, which can be used for segmentation and classification but have not been widely used to detect the spread of BSR disease. For example, ML systems such as the YOLO (You Only Look Once) series can be used for image recognition and recognizing pest habitat environments. There are 3 models that can be developed to create a BSR outbreak warning system, namely the outbreak detection model, infection risk model, and severity classification model. The severity classification model aims to detect the presence of BSR infection in an oil palm plantation, which can classify infected and healthy plants and the level of infection. Meanwhile, the outbreak detection model is used to detect distribution patterns that may occur and need to be anticipated in the future. The resulting output is an integrated map that can show the existing and potential distribution of BSR infection, as shown in Fig.3. (Chen *et al.*, 2020). There are 3 models that can be developed to create a BSR outbreak warning system, namely the outbreak detection model, infection risk model, and severity classification model. The severity classification model aims to detect the presence of BSR infection in an oil palm plantation, which can classify infected and healthy plants and the level of infection. Meanwhile, the outbreak detection model is used to detect distribution patterns that may occur and need to be anticipated in the future. The resulting output is an integrated map that can show the existing and potential distribution of BSR infection, as shown in Fig. 3.

CONCLUSIONS

The Basal Stem Rot disease that attacks oil palm plantations is mainly caused by *Ganoderma Boninense*, a fungus that can spread via airborne spores, through root contact, or spread by its sporophores in the soil and plant debris. The ability of very fast and massive spread and transmission must be overcome quickly to reduce losses from the loss of potential fresh fruit bunch (FFB) harvests than they should. Advanced technologies can be a solution because of their ability to detect in real time through a precise classification and segmentation system and are able to cover large areas through geospatial data acquisition techniques either via satellite or drone. With the current advances in sensors, IoT, AI technologies, it is very possible to build a monitoring system and early warning system that integrates the results of data acquisition through direct observation, sensors, and dynamic and real-time geospatial data for the next future studies. The key to the success of this system lies in selecting a classification and segmentation model that can detect and assess the level of infection of *G. Boninense* on oil palm plants in oil palm plantations.

REFERENCES

[1] Abdullah, H. M., Mohana, N. T., Khan, B. M., Ahmed, S. M., Hossain, M., Islam, K. H. S., Redoy, M. H., Ferdush, J., Bhuiyan, M. A. H. B., Hossain, M. M., & Ahamed, T. (2023). Present and future scopes and challenges of plant pest and disease (P&D) monitoring: Remote sensing, image processing, and artificial intelligence perspectives. *Remote Sensing Applications: Society and Environment*, 32, 100996. <https://doi.org/10.1016/j.rsase.2023.100996>

[2] Ahmadi, P., Mansor, S., Farjad, B., & Ghaderpour, E. (2022). Unmanned Aerial Vehicle (UAV)-Based Remote Sensing for Early-Stage Detection of *Ganoderma*. In *Remote Sensing* (Vol. 14, Issue 5).

<https://doi.org/10.3390/rs14051239>

- [3] Ahmadi, P., Muharam, F. M., Ahmad, K., Mansor, S., & Seman, I. A. (2017). Early detection of ganoderma basal stem rot of oil palms using artificial neural network spectral analysis. *Plant Disease*, 101(6), 1009–1016. <https://doi.org/10.1094/PDIS-12-16-1699-RE>
- [4] Al-Sabaeei, A. M., Al-Fakih, A., Noura, S., Yaghoubi, E., Alaloul, W., Al-Mansob, R. A., Imran Khan, M., & Aliyu Yaro, N. S. (2022). Utilization of palm oil and its by-products in bio-asphalt and bio-concrete mixtures: A review. *Construction and Building Materials*, 337, 127552. <https://doi.org/10.1016/j.conbuildmat.2022.127552>
- [5] Alfred, R., & Obit, J. H. (2021). The roles of machine learning methods in limiting the spread of deadly diseases: A systematic review. *Heliyon*, 7(6), e07371. <https://doi.org/10.1016/j.heliyon.2021.e07371>
- [6] Amiruddin, M. D. (2022). Field Evaluation Of Oil Palm Genetic Materials For Partial Resistance In Ganoderma Hotspots Of Tropical Peat Soil. *Journal of Oil Palm Research*, 34(December), 657–667. <https://doi.org/10.21894/jopr.2022.0025>
- [7] An, H., Liu, Z., Sun, K., & Peng, B. (2024). A machine learning framework for intelligent prediction of ash fusion temperature characteristics. *Fuel*, 362, 130799. <https://doi.org/10.1016/j.fuel.2023.130799>
- [8] Anothai, J., Intara-anun, S., Samlikamnoed, P., & Chairin, T. (2023). Understanding factors influencing growth and lignocellulosic enzyme of Ganoderma for developing integrated control strategies for basal stem rot disease in oil palm. *Tropical Plant Pathology*, 48(2), 154–162. <https://doi.org/10.1007/s40858-022-00551-8>
- [9] Assis, K., Chong, K. P., Abu Seman, I., Darmesah, G., & Ho, C. M. (2020). Estimating the Yield Loss of Oil Palm Due To Ganoderma Basal Stem Rot Disease By Using Bayesian Model Averaging. *Journal of Oil Palm Research*, 33(March), 46–55.
- [10] Assis, K., Chong, K. P., Idris, A. S., & Ho, C. M. (2016). Economic loss due to Ganoderma disease in oil palm. *International Journal of Social, Behavioral, Educational, Economic, Business and Industrial Engineering*, 10(2), 604–608. <http://waset.org/publications/10003869>
- [11] Aziz, M. H. A., Bejo, S. K., Hashim, F., Ramli, N. H., & Ahmad, D. (2019). Evaluations of soil resistivity in relation to basal stem rot incidences using soil moisture sensor. *Pertanika Journal of Science and Technology*, 27(S1), 225–234.
- [12] Bahari, M. N. A., Abdullah, S. N. A., Sakeh, N. M., Ahmad, K., Shaharuddin, N. A., Abu Seman, I., & Osman, R. (2024). Devising a colorimetric aptasensor for detection of basal stem rot-associated RNA marker during early Ganoderma boninense infection in oil palm. *Physiological and Molecular Plant Pathology*, 129, 102209. <https://doi.org/10.1016/j.pmpp.2023.102209>
- [13] Bejo, S. K., Jalen, M., Husin, M. E., Khosrokhani, M., Muharam, F. M., Seman, I. A., & Anuar, M. I. (2018). Basal Stem Rot (BSR) Detection Using Textural Analysis of Unmanned Aerial Vehicle (UAV) Image. *EProceedings Chemistry*, 3(September), 40–45.
- [14] Chen, C.-J., Huang, Y.-Y., Li, Y.-S., Chang, C.-Y., & Huang, Y.-M. (2020). An AIoT Based Smart Agricultural System for Pests Detection. *IEEE Access*, 8, 180750–180761. <https://doi.org/10.1109/ACCESS.2020.3024891>
- [15] Chong, K. P., Dayou, J., & Alexander, A. (2017). *Pathogenic Nature of Ganoderma boninense and Basal Stem Rot Disease BT - Detection and Control of Ganoderma boninense in Oil Palm Crop* (K. P. Chong, J. Dayou, & A. Alexander (eds.); pp. 5–12). Springer International Publishing. https://doi.org/10.1007/978-3-319-54969-9_2
- [16] Chong, K. P., Markus, A., & Rossall, S. (2012). The susceptibility of different varieties of oil palm seedlings to Ganoderma boninense infection. *Pakistan Journal of Botany*, 44(6), 2001–2004.
- [17] Corley, R. H. V., & Tinker, P. B. (2015). The oil palm. In *Oil Crops: Growth, Uses, and Toxicity* (5th ed.). Wiley-Blackwell Publishing Ltd. <https://doi.org/10.1002/9781118953297>
- [18] Delnevo, G., Girau, R., Ceccarini, C., & Prandi, C. (2022). A Deep Learning and Social IoT Approach for Plants Disease Prediction Toward a Sustainable Agriculture. *IEEE Internet of Things Journal*, 9(10), 7243–7250. <https://doi.org/10.1109/JIOT.2021.3097379>
- [19] Destiarni, R., & Jamil, A. (2021). Price Integration Analysis of Crude Oil and Vegetable Oils. *Habitat*, 32(2), 82–92. <https://doi.org/10.21776/ub.habitat.2021.032.2.10>
- [20] Dhaka, V. S., Kundu, N., Rani, G., Zumpano, E., & Vocaturo, E. (2023). Role of Internet of Things and Deep Learning Techniques in Plant Disease Detection and Classification: A Focused Review. In *Sensors* (Vol. 23, Issue 18). <https://doi.org/10.3390/s23187877>

- [21] Ennaji, O., Vergütz, L., & El Allali, A. (2023). Machine learning in nutrient management: A review. *Artificial Intelligence in Agriculture*, 9, 1–11. <https://doi.org/10.1016/j.aiia.2023.06.001>
- [22] Girau, R., Martis, S., Atzori, L. (2016). A Cloud-Based Platform of the Social Internet of Things. In: Mandler, B., *et al.* Internet of Things. IoT Infrastructures. IoT360 2015. Lecture Notes of the Institute for Computer Sciences, Social Informatics and Telecommunications Engineering, vol 169. Springer, Cham. https://doi.org/10.1007/978-3-319-47063-4_7
- [23] Handrian, R. D., Trisasonoko, B. H., & Panuju, D. R. (2022). Discriminating the Severity of Basal Stem Rot Disease in Oil Palm (*Elaeis guineensis* Jacq.) Plantation Using Sentinel-2. *IOP Conference Series: Earth and Environmental Science*, 950(1). <https://doi.org/10.1088/1755-1315/950/1/012043>
- [24] Haque, S., Mengersen, K., Barr, I., Wang, L., Yang, W., Vardoulakis, S., Bambrick, H., & Hu, W. (2024). Towards development of functional climate-driven early warning systems for climate-sensitive infectious diseases: Statistical models and recommendations. *Environmental Research*, 249, 118568. <https://doi.org/10.1016/j.envres.2024.118568>
- [25] Hariyanti, F., Syahza, A., Zulkarnain, & Nofrizal. (2024). Economic transformation based on leading commodities through sustainable development of the oil palm industry. *Heliyon*, 10(4), e25674. <https://doi.org/10.1016/j.heliyon.2024.e25674>
- [26] Haryadi, D., Hendra, H., Singh Sidhu, M., Panjaitan, T., & Chong, K. P. (2019). The First Report on Basal Stem Rot Disease Causal Pathogen in Asian Agri Group, North Sumatra, Indonesia INDONESIA. 3 FGV Chair of Sustainable Oil Palm Management, Faculty of Sustainable Agriculture. *Asian Agri Research and Development Centre*, 6(2), 141–149. <http://tost.unise.org/>
- [27] Hashim, I. C., Shariff, A. R., Bejo, S. K., Muharam, F. M., & Ahmad, K. (2021). Classification of Non-Infected and Infected with Basal Stem Rot Disease Using Thermal Images and Imbalanced Data Approach. In *Agronomy* (Vol. 11, Issue 12). <https://doi.org/10.3390/agronomy11122373>
- [28] Hermantoro, Kurniawan, M. A., Trinugroho, J. P., Suparyanto, T., Isnain, M., Sudigyo, D., & Pardamean, B. (2023). Detecting Ganoderma Basal Stem Rot Disease on Oil Palm Using Artificial Neural Network Method. *Communications in Mathematical Biology and Neuroscience*, 2023, 1–16. <https://doi.org/10.28919/cmbn/7911>
- [29] Hilmi, N. H. Z., Idris, A. S., Maizatul-Suriza, M., Madihah, A. Z., & Nur-Rashyeda, R. (2022). MOLECULAR PCR ASSAYS FOR DETECTION OF Ganoderma PATHOGENIC TO OIL PALM IN MALAYSIA. *Malaysian Applied Biology*, 51(1), 171–182. <https://doi.org/10.55230/MABJOURNAL.V51I1.2201>
- [30] Ho, Y. W., & Nawawi, a. (1986a). Isolation , Growth and Sporophore Development of Ganoderma boninense from Oil Palm in Malaysia. *Development*, 9(1), 69–73.
- [31] Ho, Y. W., & Nawawi, A. (1986b). Diurnal Periodicity of Spore Discharge in Ganoderma boninense Pat. from Oil palm in Malaysia. *Spore*, 9(2), 147–150.
- [32] Husin, N. A., Khairunniza-Bejo, S., Abdullah, A. F., Kassim, M. S. M., Ahmad, D., & Aziz, M. H. A. (2020). Classification of Basal Stem Rot Disease in Oil Palm Plantations Using Terrestrial Laser Scanning Data and Machine Learning. In *Agronomy* (Vol. 10, Issue 11). <https://doi.org/10.3390/agronomy10111624>
- [33] Ibrahim, M. S., Seman, I. A., Rusli, M. H., Izzuddin, M. A. J., Kamarudin, N., Hashim, K., & Manaf, Z. A. (2020). Surveillance of ganoderma disease in oil palm planted by participants of the smallholders replanting incentive scheme in malaysia. *Journal of Oil Palm Research*, 32(2), 237–244. <https://doi.org/10.21894/jopr.2020.0024>
- [34] Idris, A. S., Rajinder, S., Madihah, A. ., & Wahid, M. B. (2010). Multiplex PCR-DNA kit for early detection and identification of. *MPOB Information Series*, june, 1–3.
- [35] Isha, A., Yusof, N. A., Shaari, K., Osman, R., Abdullah, S. N. A., & Wong, M.-Y. (2020). Metabolites identification of oil palm roots infected with Ganoderma boninense using GC–MS-based metabolomics. *Arabian Journal of Chemistry*, 13(7), 6191–6200. <https://doi.org/10.1016/j.arabjc.2020.05.026>
- [36] Izzuddin, M. A., Ezzati, ;, Nisfariza, ;, Idris, M. N. # ;, & Alias, A. S. (2019). Analysis of Red, Green, Blue (RGB) and Near Infrared (NIR) Images from Unmanned Aerial Vehicle (UAV) for Detection of Ganoderma Disease in Oil Palm. *Oil Palm Bulletin* 79, 79(November), 9–15.
- [37] Jazuli, N. A., Kamu, A., Chong, K. P., Gabda, D., Hassan, A., Abu Seman, I., & Ho, C. M. (2022). A Review of Factors Affecting Ganoderma Basal Stem Rot Disease Progress in Oil Palm. In *Plants* (Vol. 11, Issue 19). <https://doi.org/10.3390/plants11192462>
- [38] Jazuli, N. A., Kamu, A., Phin, C. K., Gabda, D., Hassan, A., Seman, I. A., & Mun, H. C. (2024). Evaluating

- the factors affecting the disease progress of Ganoderma basal stem rot disease in oil palm using OLS regression model and wild Bootstrap multiple regression. *AIP Conference Proceedings*, 2895(1), 90020. <https://doi.org/10.1063/5.0195411>
- [39] Khaled, A. Y., Abd Aziz, S., Bejo, S. K., Mat Nawi, N., & Abu Seman, I. (2022). Artificial intelligence for spectral classification to identify the basal stem rot disease in oil palm using dielectric spectroscopy measurements. *Tropical Plant Pathology*, 47(1), 140–151. <https://doi.org/10.1007/s40858-021-00445-1>
- [40] Khaled, A. Y., Abd Aziz, S., Bejo, S. K., Nawi, N. M., & Abu Seman, I. (2018). Spectral features selection and classification of oil palm leaves infected by Basal stem rot (BSR) disease using dielectric spectroscopy. *Computers and Electronics in Agriculture*, 144, 297–309. <https://doi.org/10.1016/j.compag.2017.11.012>
- [41] Khoo, Y. W., & Chong, K. P. (2023). Ganoderma boninense: general characteristics of pathogenicity and methods of control. *Frontiers in Plant Science*, 14(July), 1–17. <https://doi.org/10.3389/fpls.2023.1156869>
- [42] Kipli, K., Osman, S., Joseph, A., Zen, H., Awang Salleh, D. N. S. D., Lit, A., & Chin, K. L. (2023). Deep learning applications for oil palm tree detection and counting. *Smart Agricultural Technology*, 5, 100241. <https://doi.org/10.1016/j.atech.2023.100241>
- [43] Kurihara, J., Koo, V.-C., Guey, C. W., Lee, Y. P., & Abidin, H. (2022). Early Detection of Basal Stem Rot Disease in Oil Palm Tree Using Unmanned Aerial Vehicle-Based Hyperspectral Imaging. In *Remote Sensing* (Vol. 14, Issue 3). <https://doi.org/10.3390/rs14030799>
- [44] Lee, C. C., Koo, V. C., Lim, T. S., Lee, Y. P., & Abidin, H. (2022). A multi-layer perceptron-based approach for early detection of BSR disease in oil palm trees using hyperspectral images. *Heliyon*, 8(4), e09252. <https://doi.org/10.1016/j.heliyon.2022.e09252>
- [45] Lelong, C. C. D., Roger, J.-M., Brégand, S., Dubertret, F., Lanore, M., Sitorus, N. A., Raharjo, D. A., & Caliman, J.-P. (2010). Evaluation of Oil-Palm Fungal Disease Infestation with Canopy Hyperspectral Reflectance Data. In *Sensors* (Vol. 10, Issue 1, pp. 734–747). <https://doi.org/10.3390/s100100734>
- [46] Liaghat, S., Mansor, S., Ehsani, R., Shafri, H. Z. M., Meon, S., & Sankaran, S. (2014). Mid-infrared spectroscopy for early detection of basal stem rot disease in oil palm. *Computers and Electronics in Agriculture*, 101, 48–54. <https://doi.org/10.1016/j.compag.2013.12.012>
- [47] Lisnawita, Hanum, H., & Tantawi, A. R. (2016). Survey of Basal Stem Rot Disease on Oil Palms (*Elaeis guineensis* Jacq.) in Kebun Bukit Kijang, North Sumatera, Indonesia. *IOP Conference Series: Earth and Environmental Science*, 41(1). <https://doi.org/10.1088/1755-1315/41/1/012007>
- [48] Mahlein, A.-K. (2016). Present and Future Trends in Plant Disease Detection. *Plant Disease*, 100(2), 1–11. <https://doi.org/10.1007/s13398-014-0173-7.2>
- [49] Mareddy, A. R. (2017). 7 - *Impacts on soils and land environment* (A. R. B. T.-E. I. A. Mareddy (ed.); pp. 249–296). Butterworth-Heinemann. <https://doi.org/10.1016/B978-0-12-811139-0.00007-4>
- [50] Marhaenanto, B., Aningtyas, P. W., Putraa, B. T. W., Soedibyo, D. W., Syahputra, W. N. H. (2025). Estimating Flavonoid and Nitrogen Status of Guava Leaves Using E-Nose and SPAD Meter. *Agricultural Research*, 4. <https://doi.org/10.1007/s40003-025-00849-4>
- [51] Markom, M. A., Shakaff, A. Y. M., Adom, A. H., Ahmad, M. N., Hidayat, W., Abdullah, A. H., & Fikri, N. A. (2009). Intelligent electronic nose system for basal stem rot disease detection. *Computers and Electronics in Agriculture*, 66(2), 140–146. <https://doi.org/10.1016/j.compag.2009.01.006>
- [52] Mead, H. L., Kollath, D. R., Teixeira, M. de M., Roe, C. C., Plude, C., Nandurkar, N., Donohoo, C., O'Connor, B. L. W., Terriquez, J., Keim, P., & Barker, B. M. (2022). Coccidioidomycosis in Northern Arizona: an Investigation of the Host, Pathogen, and Environment Using a Disease Triangle Approach. *MSphere*, 7(5). <https://doi.org/10.1128/msphere.00352-22>
- [53] Meshram, V., Patil, K., Meshram, V., Hanchate, D., & Ramkteke, S. D. (2021). Machine learning in agriculture domain: A state-of-art survey. *Artificial Intelligence in the Life Sciences*, 1, 100010. <https://doi.org/10.1016/j.aillsci.2021.100010>
- [54] Midot, F., Lau, S. Y., Wong, W. C., Tung, H. J., Yap, M. L., Lo, M. L., Jee, M. S., Dom, S. P., & Melling, L. (2019). Genetic Diversity and Demographic History of *Ganoderma boninense* in Oil Palm Plantations of Sarawak, Malaysia Inferred from ITS Regions. In *Microorganisms* (Vol. 7, Issue 10). <https://doi.org/10.3390/microorganisms7100464>
- [55] Mohammed, C. L., Rimbawanto, A., & Page, D. E. (2014). Management of basidiomycete root- and stem-rot diseases in oil palm, rubber and tropical hardwood plantation crops. *Forest Pathology*, 44(6),

- 428–446. <https://doi.org/10.1111/efp.12140>
- [56] Mohd Hilmi Tan, M. I. S., Jamlos, M. F., Omar, A. F., Kamarudin, K., & Jamlos, M. A. (2023). Ganoderma boninense classification based on near-infrared spectral data using machine learning techniques. *Chemometrics and Intelligent Laboratory Systems*, 232, 104718. <https://doi.org/10.1016/j.chemolab.2022.104718>
- [57] Muniroh, M. S., Sariah, M., Zainal Abidin, M. A., Lima, N., & Paterson, R. R. M. (2014). Rapid detection of Ganoderma-infected oil palms by microwave ergosterol extraction with HPLC and TLC. *Journal of Microbiological Methods*, 100, 143–147. <https://doi.org/10.1016/j.mimet.2014.03.005>
- [58] Murphy, D. J., Goggin, K., & Paterson, R. R. M. (2021). Oil palm in the 2020s and beyond: challenges and solutions. *CABI Agriculture and Bioscience*, 2(1), 1–22. <https://doi.org/10.1186/s43170-021-00058-3>
- [59] Musa, H., Nusaibah, S. A., & Khairulmazmi, A. (2018). Assessment on trichoderma spp. mixture as a potential biocontrol agent of ganoderma boninense infected oil palm seedlings. *Journal of Oil Palm Research*, 30(3), 403–415. <https://doi.org/10.21894/jopr.2018.0035>
- [60] Naher, L., Yusuf, U. K., Ismail, A., Tan, S. G., & Mondal, M. M. A. (2013). Ecological status of Ganoderma and basal stem rot disease of oil palms (*Elaeis guineensis* Jacq.). *Australian Journal of Crop Science*, 7(11), 1723–1727.
- [61] Nawawi, A., & Ho, Y. W. (1990). Effect of temperature and pH on growth pattern of Ganoderma Boninense from oil palm in Peninsular Malaysia. *Pertanika Journal of Tropical Agricultural Science*, 13(3), 303–307.
- [62] Nayagam, M. G., Vijayalakshmi, B., Somasundaram, K., Mukunthan, M. A., Yogaraja, C. A., & Partheeban, P. (2023). Control of pests and diseases in plants using IOT Technology. *Measurement: Sensors*, 26, 100713. <https://doi.org/10.1016/j.measen.2023.100713>
- [63] Olaniyi, O. N., & Szulczyk, K. R. (2020). Estimating the economic damage and treatment cost of basal stem rot striking the Malaysian oil palms. *Forest Policy and Economics*, 116, 102163. <https://doi.org/10.1016/j.forpol.2020.102163>
- [64] Parthiban, K., Vanitah, R., Jusoff, K., Nordiana, A. A., Anuar, A. R., Wahid, O., & Hamdan, A. B. (2016). GIS Mapping of Basal Stem Rot Disease in Relation to Soil Series Among Oil Palm Smallholders. *American Journal of Agricultural and Biological Sciences*, 11(1). <https://doi.org/10.3844/ajabssp.2016.2.12>
- [65] Paterson, R. R. M. (2023). Future Climate Effects on Basal Stem Rot of Conventional and Modified Oil Palm in Indonesia and Thailand. *Forests* 2023, Vol. 14, Page 1347, 14(7), 1347. <https://doi.org/10.3390/F14071347>
- [66] Pilotti, C. A., Gorea, E. A., & Bonneau, L. (2018). Basidiospores as sources of inoculum in the spread of Ganoderma boninense in oil palm plantations in Papua New Guinea. *Plant Pathology*, 67(9), 1841–1849. <https://doi.org/10.1111/ppa.12915>
- [67] Pilotti, C. A., Sanderson, F. R., & Aitken, E. A. B. (2003). Genetic structure of a population of Ganoderma boninense on oil palm. *Plant Pathology*, 52(4), 455–463. <https://doi.org/10.1046/j.1365-3059.2003.00870.x>
- [68] Pourhoseini, S. H., Namvar-Mahboub, M., Hosseini, E., & Alimoradi, A. (2021). A comparative exploration of thermal, radiative and pollutant emission characteristics of oil burner flame using palm oil biodiesel-diesel blend fuel and diesel fuel. *Energy*, 217, 119338. <https://doi.org/10.1016/j.energy.2020.119338>
- [69] Priwiratama, H., Prasetyo, A. E., & Susanto, A. (2020). Incidence of basal stem rot disease of oil palm in converted planting areas and control treatments. *IOP Conference Series: Earth and Environmental Science*, 468(1). <https://doi.org/10.1088/1755-1315/468/1/012036>
- [70] Rahman, K. A., & Othman, R. (2020). Influence of pH levels on disease development in oil palm seedling roots infected with Ganoderma boninensis. *Rhizosphere*, 13, 100181. <https://doi.org/10.1016/j.rhisph.2019.100181>
- [71] Rees, R. W., Flood, J., Hasan, Y., & Cooper, R. M. (2007). Effects of inoculum potential, shading and soil temperature on root infection of oil palm seedlings by the basal stem rot pathogen Ganoderma boninense. *Plant Pathology*, 56(5), 862–870. <https://doi.org/10.1111/j.1365-3059.2007.01621.x>
- [72] Rees, R. W., Flood, J., Hasan, Y., Wills, M. A., & Cooper, R. M. (2012). Ganoderma boninense basidiospores in oil palm plantations: evaluation of their possible role in stem rots of *Elaeis guineensis*.

- Plant Pathology*, 61(3), 567–578. <https://doi.org/10.1111/j.1365-3059.2011.02533.x>
- [73] Roslan, A., & Idris, A. S. (2012). Economic Impact of *Ganoderma* Incidence on Malaysian Oil Palm Plantation-A Case Study. *Oil Palm Industry Economic Journal*, 12(1), 24–30.
- [74] Rudrakar, S., & Rughani, P. (2023). IoT based Agriculture (Ag-IoT): A detailed study on Architecture, Security and Forensics. *Information Processing in Agriculture*. <https://doi.org/10.1016/j.inpa.2023.09.002>
- [75] Rupaedah, B., Eko Prasetyo, A., Hidayat, F., Asiani, N., Wahid, A., Nurlaila, & Lutfia, A. (2024). Evaluation of microbial biocontrol agents for *Ganoderma boninense* management in oil palm nurseries. *Journal of the Saudi Society of Agricultural Sciences*, 23(3), 236–244. <https://doi.org/10.1016/j.jssas.2023.12.001>
- [76] Sakai, K., Hassan, M. A., Vairappan, C. S., & Shirai, Y. (2022). Promotion of a green economy with the palm oil industry for biodiversity conservation: A touchstone toward a sustainable bioindustry. *Journal of Bioscience and Bioengineering*, 133(5), 414–424. <https://doi.org/10.1016/j.jbiosc.2022.01.001>
- [77] Samlikamnoed, P., Anothai, J., & Chairin, T. (2023). Defense-related enzyme production in oil palm seedlings against basal stem rot pathogen *Ganoderma boninense* and its biological control by *Trichoderma asperellum*. *Physiological and Molecular Plant Pathology*, 128, 102154. <https://doi.org/10.1016/j.pmpp.2023.102154>
- [78] Santiago, K. A. A., Wong, W. C., Goh, Y. K., Tey, S. H., & Ting, A. S. Y. (2023). Metabolomics approach in identifying biomarkers from pathogenic *Ganoderma boninense* involved in early interactions with oil palm host. *Physiological and Molecular Plant Pathology*, 125, 101980. <https://doi.org/10.1016/j.pmpp.2023.101980>
- [79] Santoso, H., Tani, H., Wang, X., Prasetyo, A. E., & Sonobe, R. (2019). Classifying the severity of basal stem rot disease in oil palm plantations using WorldView-3 imagery and machine learning algorithms. *International Journal of Remote Sensing*, 40(19), 7624–7646. <https://doi.org/10.1080/01431161.2018.1541368>
- [80] Sarker, I. H. (2021). Machine Learning: Algorithms, Real-World Applications and Research Directions. *SN Computer Science*, 2(3), 1–21. <https://doi.org/10.1007/s42979-021-00592-x>
- [81] Siddiqui, Y., Surendran, A., Paterson, R. R. M., Ali, A., & Ahmad, K. (2021). Current strategies and perspectives in detection and control of basal stem rot of oil palm. *Saudi Journal of Biological Sciences*, 28(5), 2840–2849. <https://doi.org/10.1016/j.sjbs.2021.02.016>
- [82] Thoumazeau, A., Mettauer, R., Turinah, Junedi, H., Baron, V., Chéron-Bessou, C., & Ollivier, J. (2024). Effects of fertilization practices and understory on soil health and oil palm performances in smallholdings: An Indonesian case study. *Agricultural Systems*, 213, 103802. <https://doi.org/10.1016/j.agsy.2023.103802>
- [83] Vasefi, F., MacKinnon, N., & Farkas, D. L. (2016). Chapter 16 - Hyperspectral and Multispectral Imaging in Dermatology (M. R. Hamblin, P. Avci, & G. K. B. T.-I. in D. Gupta (eds.); pp. 187–201). Academic Press. <https://doi.org/10.1016/B978-0-12-802838-4.00016-9>
- [84] Wang, C.-X., Xiu, L.-S., Hu, Q.-Q., Lee, T.-C., Liu, J., Shi, L., Zhou, X.-N., Guo, X.-K., Hou, L., & Yin, K. (2023). Advancing early warning and surveillance for zoonotic diseases under climate change: Interdisciplinary systematic perspectives. *Advances in Climate Change Research*, 14(6), 814–826. <https://doi.org/10.1016/j.accre.2023.11.014>
- [85] Wei, X., Aguilera, M., Walcheck, R., Tholl, D., Li, S., Langston, D. B., & Mehl, H. L. (2021). Detection of Soilborne Disease Utilizing Sensor Technologies: Lessons Learned from Studies on Stem Rot of Peanut. *Plant Health Progress*, 22(4), 436–444. <https://doi.org/10.1094/PHP-03-21-0055-SYN>
- [86] Win Kent, O., Weng Chun, T., Lee Choo, T., & Weng Kin, L. (2023). Early symptom detection of basal stem rot disease in oil palm trees using a deep learning approach on UAV images. *Computers and Electronics in Agriculture*, 213, 108192. <https://doi.org/10.1016/j.compag.2023.108192>
- [87] Ximenes, L., Nurmalina, R., & Rifin, A. (2022). The Analysis of Competition for Indonesian Palm Oil Derivative Products in The Italian Market. *Jurnal Manajemen Dan Agribisnis*, 19(3), 437–451. <https://doi.org/10.17358/jma.19.3.437>
- [88] Zakaria, L. (2022). Basal Stem Rot of Oil Palm: The Pathogen, Disease Incidence, and Control Methods. *Plant Disease*, 107(3), 603–615. <https://doi.org/10.1094/PDIS-02-22-0358-FE>

DIGITAL ORCHARD CONSTRUCTION BASED ON NEURAL RADIANCE FIELD AND GEOREFERENCING TECHNOLOGY

基于神经辐射场与地理坐标配准技术的果树三维重建

Huiyan WANG¹⁾, Binxiao LIU²⁾, Jianhang WANG¹⁾, Changkun ZHANG¹⁾, Jinliang GONG²⁾, Yanfei ZHANG^{1*)}

¹⁾School of Agricultural Engineering and Food Science, Shandong University of Technology, Zibo 255000 / China

²⁾School of Mechanical Engineering, Shandong University of Technology, Zibo 255000 / China

Tel: +86-18265338441; E-mail: 1392076@sina.com

Corresponding author: Yanfei Zhang

DOI: <https://doi.org/10.35633/inmateh-75-77>

Keywords: Computer Vision; Fruit Trees; 3D Reconstruction; Neural Radiance Fields; Camera Pose Recovery; Georeferencing

ABSTRACT

This study aims to construct digital fruit trees with high-precision geolocation and high-quality canopy phenotypic details, supporting the development of digital fruit tree technology and the establishment of smart orchards. The Neural Radiance Fields (NeRF) theory was integrated with georeferencing technology. Firstly, multiple ground control points were placed around the tree, and their WGS-84 coordinates were recorded using an RTK surveying instrument. Next, a drone captured multi-view images of the fruit tree, recording the camera poses during the image acquisition. The multi-view fruit tree images undergo ray casting, hierarchical sampling, and high-frequency position encoding before being input into a Multilayer Perceptron (MLP). The MLP was then supervised through volume rendering to obtain a convergent radiance field that reflects the true form of the fruit tree, resulting in the generation of a fruit tree point cloud. Finally, by establishing correspondences between the points in the fruit tree point cloud and the ground control points in the real world, a rigid transformation matrix was computed to convert the point cloud from a local coordinate system to WGS-84 coordinates, yielding a geographically informed digital fruit tree. The experiments demonstrate that the constructed digital fruit tree exhibits excellent phenotypic details and accurately represents multi-scale characteristics. The accuracy of tree morphology indicators, such as tree height, crown length, and width, reached 99.12%, 99.34%, and 99.22%, respectively. Compared to point clouds generated by traditional Structure from Motion-Multi View Stereo (SfM-MVS) methods, the root mean square errors were reduced by 61.24%, 73.48%, and 62.32%, respectively. Additionally, the georeferencing accuracy achieved millimeter-level precision, with registration errors generally below 2 mm. The proposed method can construct digital fruit trees with high geolocation accuracy, detailed phenotypic information, and scale consistency, overcoming key barriers in the development of digital fruit tree technology. It can provide comprehensive data for various production operations in smart orchards.

摘要

本研究旨在构建具有高水平地理定位精度与高品质叶冠表型细节的数字果树，支持数字果树技术体系与智慧果园建设。将神经辐射场 (Neural Radiance Fields, NeRF) 理论与地理坐标配准 (Georeferencing) 技术相结合，以初果期的桃树作为研究对象。首先，在果树周围地面上布设多个地面控制点并通过 RTK 测量仪记录地面控制点中心位置的 WGS-84 坐标；其次，使用无人机环绕拍摄果树多视角图像并记录拍摄时相机位姿；然后，将多视角果树图像进行光线投射法分层采样和高频位置编码后输入多层感知机 (Multilayer Perceptron, MLP)，通过体积渲染 (Volume Rendering) 监督训练过程以获取收敛且能反映果树真实形态的辐射场并导出果树点云；最后，通过果树点云中与现实世界中地面控制点的对应关系，计算刚性变换矩阵，将果树点云从局部坐标系转换至 WGS-84 坐标系，得到具有地理信息的数字果树。试验表明，本研究构建的数字果树具有良好的表型细节，可准确表征果树多尺度表型细节。该方法构建的果树点云在树高、冠层长度与宽度等树形指标方面的精度分别达到 99.12%、99.34%、99.22%，相较于传统的运动恢复结构-多视图立体匹配 (Structure from motion-Multi View Stereo, SfM-MVS) 方法构建的果树点云，均方根误差分别减小 61.24%、73.48%、62.32%。同时，其地理坐标配准精度达到毫米级，配准误差普遍小于 2mm。该研究提出的方法能构建具有高地理坐标定位精度、高表型细节与高尺度一致性的数字果树，突破了制约数字果树技术体系发展的关键瓶颈，能够为智慧果园的数字化果树表型组学研究、数字化树形管理、数字化生长监测等领域提供关键技术支撑。

Huiyan Wang, M.S. Stud.; Binxiao Liu, M.S. Stud.; Jianhang Wang, M.S. Stud.; Changkun Zhang, M.S. Stud.; Jinliang Gong, Professor Dr.; Yanfei Zhang, Professor Dr.

INTRODUCTION

In the intelligent orchard production model of all-weather, all-process, and all-space unmanned operations, the digital fruit tree technology system plays a crucial role (Wu *et al.*, 2021). It provides comprehensive spatial perception capabilities for unmanned agricultural machinery, guiding autonomous tasks such as pruning (Yang *et al.*, 2017), thinning (Zhang *et al.*, 2020), and harvesting (Zhao, 2022). Simultaneously, in fields such as digital phenomics research (Hu *et al.*, 2019), digital tree management (Jiménez-Brenes *et al.*, 2017), and digital growth monitoring (Bdulridha *et al.*, 2019), the digital fruit tree finds extensive application, holding significant importance for the construction and management of smart orchards (Zhou *et al.*, 2019).

The acquisition of phenotypic information from fruit trees is a critical step in constructing digital fruit trees (Narvaez *et al.*, 2019). The main approaches for obtaining three-dimensional phenotypes of fruit trees are laser scanning systems (Zhang *et al.*, 2020; Colaço *et al.*, 2017) and stereo vision systems. Laser scanning provides high accuracy but is costly and lacks color information. In contrast, stereo vision systems, represented by the Structure from Motion-Multi View Stereo (SfM-MVS) method, have lower costs and can simultaneously capture both the structure and color information of fruit trees.

Notably, Dongyu Ren *et al.* achieved the reconstruction of peach tree branches and crowns using the Kinect v2 camera (Ren *et al.*, 2022),

Gatziolis *et al.* planned various aerial trajectories for SfM-MVS in tree 3D reconstruction (Gatziolis *et al.*, 2015), and Miller *et al.* reconstructed potted trees using handheld cameras (Miller *et al.*, 2015). However, for fruit tree canopies with complex topological structures and multi-scale high-frequency details, traditional stereo vision systems struggle to accurately capture their three-dimensional phenotypes, posing a critical scientific challenge to the development of digital fruit trees.

Mildenhall *et al.* introduced the theory of Neural Radiance Fields (NeRF) (Mildenhall *et al.*, 2021), an implicit neural rendering (Tewari *et al.*, 2022) for three-dimensional reconstruction. It achieves finer three-dimensional representations of complex phenotypes through sparse input image sets and a Multilayer Perceptron (MLP). With research and improvements to the NeRF theory, there has been a significant leap in both speed and quality (Barron *et al.*, 2021; Martin-Brualla *et al.*, 2021; Tancik *et al.*, 2023; Müller *et al.*, 2022).

The foundation of digital fruit trees lies in obtaining phenotypic information from fruit trees, and further applications rely on accurate geographical information (Zhang *et al.*, 2013). Geographical information supports automated agricultural practices in smart orchards and allows the integration of geographical, environmental, and meteorological data to build a comprehensive digital fruit tree management system. However, the fruit tree point clouds generated by stereo vision systems are limited to local coordinate systems, unable to provide global geographical information. Real-Time Kinematic (RTK) positioning systems, leveraging real-time differential GNSS technology, achieve centimeter-level high-precision geographical coordinate positioning. Therefore, combining the RTK positioning system with fruit tree point clouds allows for georeferencing, integrating digital fruit trees into a global geographical spatial framework. Extensive research has been conducted on the alignment and fusion of point clouds.

Nistér *D.*, (2004), extracted feature points from point cloud data for feature point matching after acquiring the data using a stereo camera, thereby efficiently solving the traditional five-point relative pose problem.

Konolige *et al.*, (2008) and Akbarzadeh *et al.*, (2006), utilized the ICP (Iterative Closest Point) algorithm to align point cloud data from multiple scenes. The ICP algorithm has shown considerable promise in recent years. However, the alignment in this study requires the matching and fusion of two ground point clouds with significant overlap, using image control points. For aligning fruit tree point clouds and georeferenced ground point clouds, this study refers to the four-point fast matching algorithm proposed by Aiger *D et al.*, (2008).

In addressing the challenges of stereo vision 3D reconstruction technology in accurately representing multi-scale complex phenotypic details of fruit trees and the lack of geographical location information in generated fruit tree point clouds, this study combined the Neural Radiance Fields theory with georeferencing technology. Focusing on peach trees, a method for constructing digital fruit trees based on the Neural Radiance Fields theory and georeferencing technology is proposed. The aim is to leverage the NeRF's excellent representation capabilities for high-frequency details and complex topological structures and the RTK's centimeter-level high-precision geographical coordinate positioning ability to build a digital fruit tree with high-level geospatial positioning accuracy and high-quality canopy phenotypic details.

MATERIALS AND METHODS

The experimental site for this study is the peach orchard at Shandong University of Technology, with the experimental subjects being individual peach trees in the early fruiting stage. Firstly, multiple ground control points were positioned around the fruit tree, and their WGS-84 coordinates were meticulously recorded using an RTK surveying instrument. Subsequently, a drone was employed to capture multi-perspective images of the fruit tree while simultaneously recording the camera poses during image acquisition. Following this, a Neural Radiance Field for the fruit tree was trained using image data augmented with additional pose information, and a point cloud was generated as an output. Lastly, through establishing correspondences between ground control points in the real world and points within the fruit tree point cloud, a rigid transformation matrix was computed. This facilitated the conversion of the fruit tree point cloud from local coordinate systems to the WGS-84 coordinate system, resulting in the generation of a geospatially informed digital fruit tree.

The equipment for fruit tree image acquisition and geographical coordinate measurement is illustrated in Figure 1. The image acquisition device utilized is the DJI "Mavic 2" unmanned aerial vehicle, while the geographical coordinate measurement device consists of the Qianxun SR2 high-precision Real-Time Kinematic (RTK) surveying instrument and ground control points.



Fig. 1 - Experimental equipment

1. Ground control point; 2. UAV; 3 RTK receiver 4. RTK display terminal; 5. RTK positioning rod

The individual peach tree selected for the experiment measured 2.18 m in height with a crown width of 2.17 m. The data collection was conducted between 4:30 and 4:45 p.m. under cloudy weather conditions, with a light breeze and no direct sunlight. The drone used for image acquisition operated with a focal length of 26 mm and a resolution of 1920 × 1080 pixels. The setup for fruit tree image acquisition and geographical coordinate measurement is shown in Figure 2. Four ground control points (GCPs) were placed around the tree, clearly marked at the base of the trunk, the top of the canopy, and along its edges. Using an RTK surveying instrument, the WGS-84 coordinates of these GCPs were recorded. Following the calibration of the intrinsic parameters of the UAV-mounted camera, the drone captured multi-view images by circling the tree along a spiral trajectory, also illustrated in Figure 2. The flight trajectory was designed based on the experimental protocol outlined by *Tewari et al. (2022)*, featuring a circumferential radius of approximately 3 m, a pitch of 0.5 m, and a rotation speed of around 2 RPM. This process resulted in the collection of 284 images with roughly 50% overlap. Finally, a 3D reconstruction dataset consisting of the fruit tree images and their corresponding camera pose data was compiled, serving as input for the subsequent neural radiance field-based 3D reconstruction of the fruit tree.

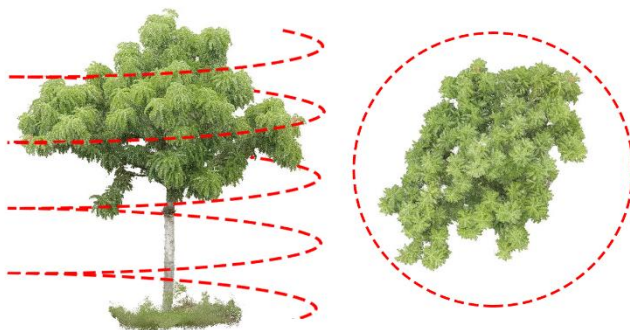


Fig. 2 - UAV aerial photography path

The Neural Radiance Fields (NeRF) were trained using two-dimensional fruit tree images and corresponding pose data to transform the two-dimensional images into a three-dimensional spatial structure of the fruit tree. The NeRF utilized an implicit function to record color and volume density information of sampled points in the scene. This function is approximated by a Multilayer Perceptron (MLP) and converges during the training iterations. The experimental hardware configuration for training included: CPU: i9-10850K; GPU: NVIDIA GeForce RTX3090; RAM: 64GB. The software programs used in the point cloud measurement and visualization process were Cloud compare and Metashape.

Initially, camera rays were projected from the camera origin toward specific pixel directions on the image plane using the ray casting method (Kajjya J et al., 1984). Each ray traverses the fruit tree scene to capture visual information along its path. The camera ray D , originating from the camera center and passing through a given pixel, can be mathematically expressed as:

$$D(m,n) = \frac{1}{\left\| K^{-1} \begin{bmatrix} m \\ n \\ H \\ 1 \end{bmatrix} \right\|_2} \begin{bmatrix} m \\ W \\ n \\ H \\ 1 \end{bmatrix} \tag{1}$$

The variable (m,n) represents the pixel coordinates through which the camera ray passes, with the pixel plane dimensions denoted as W for width and H for height. The camera intrinsic matrix is denoted as K .

Subsequently, sampling along the camera ray was conducted, where each sampled point was represented by a vector comprising five parameters: the coordinates of the points sampled along the ray (x,y,z) and the direction of the camera ray (θ,ϕ) . After encoding the sampled points, the vector was input into the Multilayer Perceptron (MLP). The MLP, a fully connected deep neural network, consisted of two parts, as illustrated in Figure 3. The first part of the MLP comprises eight fully connected layers with 256 dimensions each, taking the sampled point coordinates (x,y,z) as input. To address potential issues such as gradient explosion and vanishing gradients in deep neural networks, a residual connection structure (Rahaman N et al., 2019) is introduced in the fourth layer of the network. This involves concatenating the output of the fourth layer with the input signal (x,y,z) before inputting it into the fifth layer, thereby breaking network symmetry and enhancing the representational capacity of the MLP. The MLP outputs the volume density w and a 256-dimensional feature vector.

The second part, denoted as cMLP, takes the feature vector outputted by the w MLP and a 24-dimensional high-frequency signal representing the direction of the camera ray $f(\theta,\phi)$ as input. After concatenation, this combined input is passed through a 256-dimensional fully connected layer, and the output from the cMLP layer produces the color $C=(R,G,B)$.

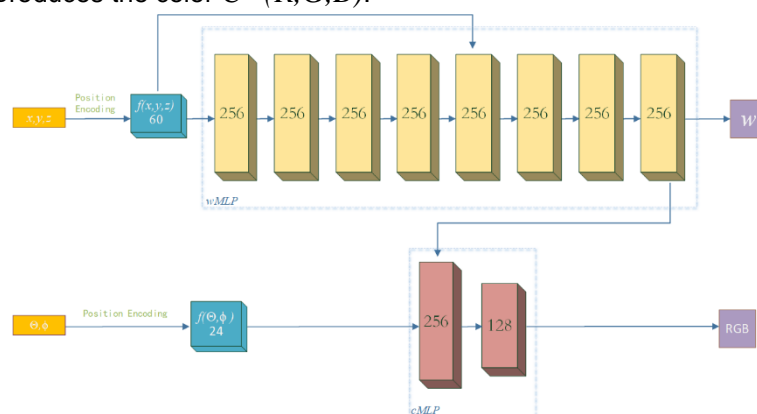


Fig. 3 - Neural radiance field MLP illustration

The fruit tree scene was approximated as a neural radiance field describing the volume density and color of all sampled points in the scene through the two components of the Multilayer Perceptron (MLP). The initial neural radiance field generated exhibits a discrete, cloud-like form, lacking accurate representation of the tree's morphology. Therefore, it is necessary to perform volume rendering on the volume density and color of the sampled points outputted by the MLP. Subsequently, the MLP's weights were updated in reverse to facilitate training.

Integral to this process is the direction along the camera ray, where each sampled point is integrated, and the volume density w serves as the weighting factor. Based on the volume density w , a weighted sum of colors C at each sampled point along the ray is computed. This calculation determines the color of the pixel point traversed by the camera ray. Higher volume density w corresponds to lower transparency, thus greater influence of the color C of the sampled point on the pixel color. This computation process is known as volume rendering, and the formula for the calculation is as follows:

$$\begin{cases} C_c(r) = \pi \int_{t_n}^{t_f} T(t)w(r(t))C(r(t), d)dt \\ T(t) = \exp(-\int_{t_n}^t w(r(s))ds) \end{cases} \quad (2)$$

The variable $C_c(r)$ represents the pixel color, $T(t)$ denotes the cumulative transmittance coefficient, $w(r(r(t)))$ is the volume density of the sampled point at position $r(t)$, $w(r(r(s)))$ is the volume density of the sampled point at position $r(s)$, $C(r(t))$ represents the color of the sampled point at position $r(t)$, t_n is the near point of the view frustum, and t_f is the far point of the view frustum.

Subsequently, to achieve high-quality rendering results with a reduced number of sampled points and simultaneously decrease computational complexity, coarse-fine two-level granularity stratified sampling and rendering were performed along the rays. This involves using the volume density distribution of coarse-grained sampled points as a reference to sample more fine-grained points in regions with higher volume density along the rays.

In the coarse-grained rendering phase, N_c points were uniformly sampled along the camera ray, input into the MLP, and subjected to coarse-grained volume rendering. The resulting coarse-grained rendering pixel color $\hat{C}_c(r)$ was obtained. Following this, N_f fine-grained sampled points, based on the volume density distribution of coarse-grained sampled points, are input again into the MLP for fine-grained volume rendering, yielding the fine-grained rendering pixel color $\hat{C}_f(r)$.

$$\begin{cases} \hat{C}_c(r) = \sum_{g=1}^{N_c} w_g C_g \\ \hat{C}_f(r) = \sum_{l=1}^{N_c+N_f} w_l C_l \end{cases} \quad (3)$$

The variables w_g and w_l represent the cumulative volume density of coarse-grained and fine-grained sampled points, respectively, while C_g and C_l denote the colors of coarse-grained and fine-grained sampled points. N_c and N_f are the respective quantities of coarse-grained and fine-grained sampled points.

After computing the coarse-grained rendering pixel color $\hat{C}_c(r)$ and the fine-grained rendering pixel color $\hat{C}_f(r)$, a comparison was made between each of them and the pixel color $C(r)$ at the pixel (m, n) traversed by the camera ray. This process results in the derivation of the training loss, followed by the computation of the squared sum of the L norm of the loss. Iterating over all pixels for a given viewpoint V , the loss function L for that viewpoint is obtained.

$$L = \sum_{r \in V} [\|\hat{C}_c(r) - C(r)\|_2^2 + \|\hat{C}_f(r) - C(r)\|_2^2] \quad (4)$$

The variables $\hat{C}_c(r)$ and $\hat{C}_f(r)$ represent the pixel colors computed through coarse-grained and fine-grained rendering, respectively, while $C(r)$ is the color of the pixel along the ray direction. O encompasses all pixels in a given view. Subsequently, the network weights of the MLP are updated in reverse based on the loss function, iteratively adjusting the scene to gradually approximate the real morphology of the tree. This process continues until convergence conditions are met, completing the training of the neural radiance field for the tree. The final outcome is the NeRF scene of the tree, which characterized the three-dimensional spatial structure and realistic color information. By mapping the coordinates and color information of each sampled point in the scene to the local coordinate system and recording it, the three-dimensional real-world point cloud of the tree is obtained, thus achieving the three-dimensional reconstruction of the tree.

The fruit tree point cloud obtained from the three-dimensional reconstruction exists in a local coordinate system. To establish a geospatially informed digital representation of the fruit tree, it is imperative to perform georeferencing on the fruit tree point cloud, thereby transforming it from the local coordinate system to the WGS-84 geographic coordinate system. In this study, ground control points (GCP) serve as registration benchmarks. Four ground control points were positioned around the fruit tree. Subsequently, using an RTK, the WGS-84 coordinates at the center of each ground control point were recorded. The simultaneous reconstruction of both the fruit tree and ground control points is illustrated in Figure 4, where the identification numbers of the ground control points are distinctly discernible in the point cloud.



Fig. 4 - Comparison of ground control point cloud and photo

Consider the point cloud representing the fruit tree as Point Cloud A. Select the coordinates of four ground control points' centers as matching points, and designate them as the Point Cloud B, with the WGS-84 geographic coordinates recorded by the RTK surveying instrument for these four ground control points as the corresponding matched points. For each matching point and its corresponding matched point, perform centering, and calculate the covariance matrix H using the decentered coordinates of the matching points.

$$\begin{cases} \Delta A_i = A_i - \phi A \\ \Delta B_i = B_i - \phi B \end{cases} \quad (5)$$

$$H = \sum_{i=1}^4 (\Delta B_i) \cdot (\Delta A_i)^T \quad (6)$$

Where ϕA represents the average coordinates of matching points in Point Cloud A, and ϕB represents the average coordinates of matching points in Point Cloud B. A_i and B_i denote the i -th matching points in Point Cloud A and B, respectively. ΔA_i and ΔB_i represent the decentered coordinates of the matching points. H stands for the covariance matrix. Subsequently, perform singular value decomposition on H and calculate the scaling factors. The calculation formula is as follows.

$$H = U \Sigma V^T = [u_1 \quad u_2 \quad u_3] \begin{bmatrix} \sigma_1 & 0 & 0 \\ 0 & \sigma_2 & 0 \\ 0 & 0 & \sigma_3 \end{bmatrix} \begin{bmatrix} v_1^T \\ v_2^T \\ v_3^T \end{bmatrix} \quad (7)$$

$$s = \frac{\sqrt{\sigma_1^2 + \sigma_2^2 + \sigma_3^2}}{\sigma_1} \quad (8)$$

Where U and V are the left and right singular vector matrices, respectively. Σ represents the singular value matrix, and u_i ($i=1,2,3$) denotes the column vectors of matrix U . Similarly, v_i ($i=1,2,3$) represents the row vectors of matrix V , and σ_i ($i=1,2,3$) denotes the singular values, indicating the scaling factors in different directions for the matching points. Through the left and right singular vector matrices and the scaling factor, calculate the rotation matrix R and translation vector t to transform Point Cloud A from the local coordinate system to the WGS-84 coordinate system. These components constitute the rigid transformation matrix that aligns Point Cloud A with Point Cloud B.

$$\begin{cases} R = VU^T \\ t = \phi B - s \cdot R \cdot \phi A \end{cases} \quad (9)$$

$$T = \begin{bmatrix} sR & t \\ 0 & 1 \end{bmatrix} \quad (10)$$

Where ϕA and ϕB represent the average coordinates of matching points in Point Cloud A and B , respectively. U and V are the left and right singular vector matrices, R is the rotation matrix, t is the translation vector, s is the scaling factor, and T is the rigid transformation matrix. Applying the rigid transformation matrix T to all points in Point Cloud A aligns Point Cloud A with the coordinate system of Point Cloud B . As a result, each point in the tree point cloud obtains its coordinates in the WGS-84 geographical coordinate system, establishing a digital tree with geographical coordinate information.

RESULTS AND ANALYSIS

The dataset for the three-dimensional reconstruction of the tree consists of a total of 284 images, with 21 images in the training dataset and 263 in the testing dataset. The training process of the tree NeRF scene spans 30,000 steps, taking 17 minutes and 16 seconds, with a generation rate of 1.14×10^5 training rays per second. As illustrated in Figure 5, after reaching 15,000 steps, the scene representation stabilizes, and parameters such as learning rate, training loss, distortion loss, RGB loss, among others, gradually converge. The learning rate is a critical component in the optimization of machine learning models. It is employed to regulate the step size of the update process, which is progressively reduced through the implementation of an exponential decay strategy. The training loss functions as the overarching objective function for model optimization, thereby guiding the direction of parameter updates. RGB loss serves as the primary supervisory signal of NeRF, reflecting the model's performance in color reconstruction and geometric rationality. Aberration loss, on the other hand, leads to a more rational volume density distribution, thereby enhancing geometric coherence and rendering quality.

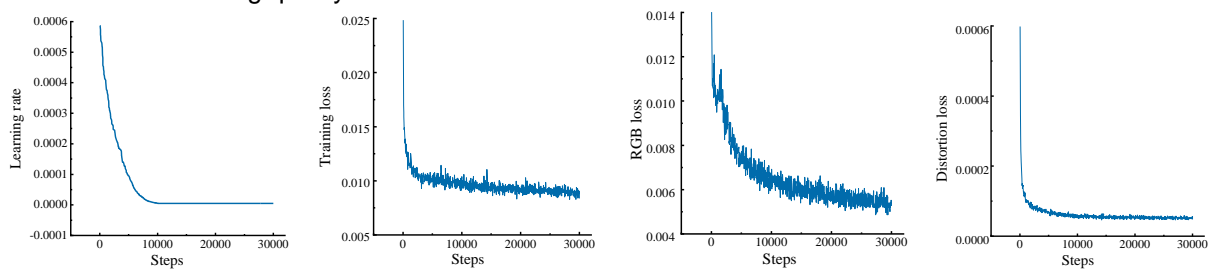


Fig. 5 - Neural radiance field training parameters

The reconstructed three-dimensional NeRF scene of the fruit tree is depicted in Figure 6, juxtaposed with corresponding depth maps and photographs of the fruit tree. The fidelity of the reconstructed fruit tree in terms of color and texture is exceptional, closely resembling the photograph of the fruit tree taken at the same pose, thereby achieving a representation effect at the level of real scenes. The contours of the canopy in the NeRF scene depth map are sharp and well-defined, with clear delineation of branches and leaf layers, providing distinct hierarchical depth information. This underscores the commendable three-dimensional representation efficacy of the NeRF scene.



Fig. 6 - Comparison between fruit tree photo and fruit tree NeRF scene and depth map

In order to assess the three-dimensional scene representation efficacy of the NeRF method, fruit tree images from the test dataset were compared with corresponding NeRF scene images captured at identical poses. Structural Similarity Index (SSIM) (Rahaman *N et al.*, 2019) and Learned Perceptual Image Patch Similarity (LPIPS) (Zhang *R et al.*, 2018) were introduced as two image quality assessment metrics to gauge the scene reconstruction capability of the NeRF method. Figure 7 illustrates the evolution of these evaluation metrics during the training process. The LPIPS metric stabilizes within the range of 0.2 to 0.3 after 25,000

steps, with a minimum value of 0.2050. The SSIM metric stabilizes within the range of 0.6 to 0.7 after 25,000 steps, reaching a maximum value of 0.7215.

Both evaluation metrics consistently reside within the high-quality range (Wang Z et al., 2004), indicating the NeRF method's proficient recovery capability for high-frequency detailed scenes.

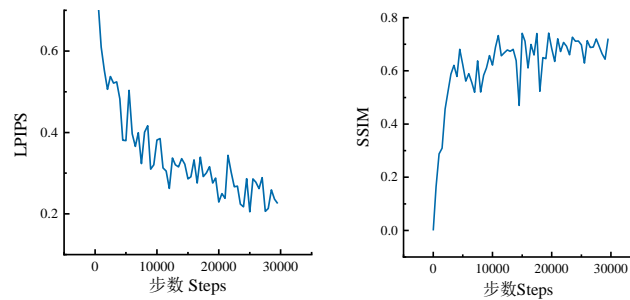


Fig. 7 - Neural radiance field quality assessment metrics

Due to the inherent nature of the NeRF scene for fruit trees, which is essentially a representation by an implicit function approximated using Multilayer Perceptrons (MLP), direct editing of the scene is not feasible. Consequently, it becomes imperative to convert the NeRF scene into a three-dimensional point cloud model for subsequent research and applications. The fruit tree point cloud model, derived from the NeRF scene, is depicted in Figure 8, where features such as the fruit tree, ground control points, and yellow markers at the base of the trunk are distinctly reconstructed within the point cloud model.



Fig. 8 - Comparison between NeRF scene of fruit tree and Point cloud model of fruit tree

The ground control points play a pivotal role as essential links establishing the connection between the local coordinate system and the WGS-84 coordinate system for the fruit tree point cloud. Four ground control points were deployed for this experiment, denoted as points 2, 13, 20, and 28. The centroids of these four points were utilized as matching points to compute the rigid transformation matrix. Consequently, the ground control points in the fruit tree point cloud model were aligned with their corresponding positions in the WGS-84 coordinate system. In the geospatial coordinate registration process of this experiment, the scaling factor s was determined to be 1.00809. The rigid transformation matrix T applied is expressed as follows:

$$T = \begin{bmatrix} 0.921 & -0.409 & 0.014 & 28.185 \\ 0.409 & 0.919 & -0.058 & -12.497 \\ -0.011 & -0.058 & -1.006 & 58.429 \\ 0 & 0 & 0 & 1 \end{bmatrix}$$

To validate the accuracy of geospatial coordinate registration, the right upper corner points of each ground control point and the vertices of the triangular yellow markers at the base of the trunk were selected as test points. An RTK surveying instrument was employed to measure the WGS-84 coordinates of these test points as actual values. Subsequently, the WGS-84 geographical coordinates at the corresponding positions in the fruit tree point cloud after registration were measured as experimental values. A comparison was then conducted between the measured and actual values. The geospatial coordinate registration accuracy, as depicted in Table 1, indicates registration errors within a 2 mm range, attaining accuracy at the millimeter level.

Table 1

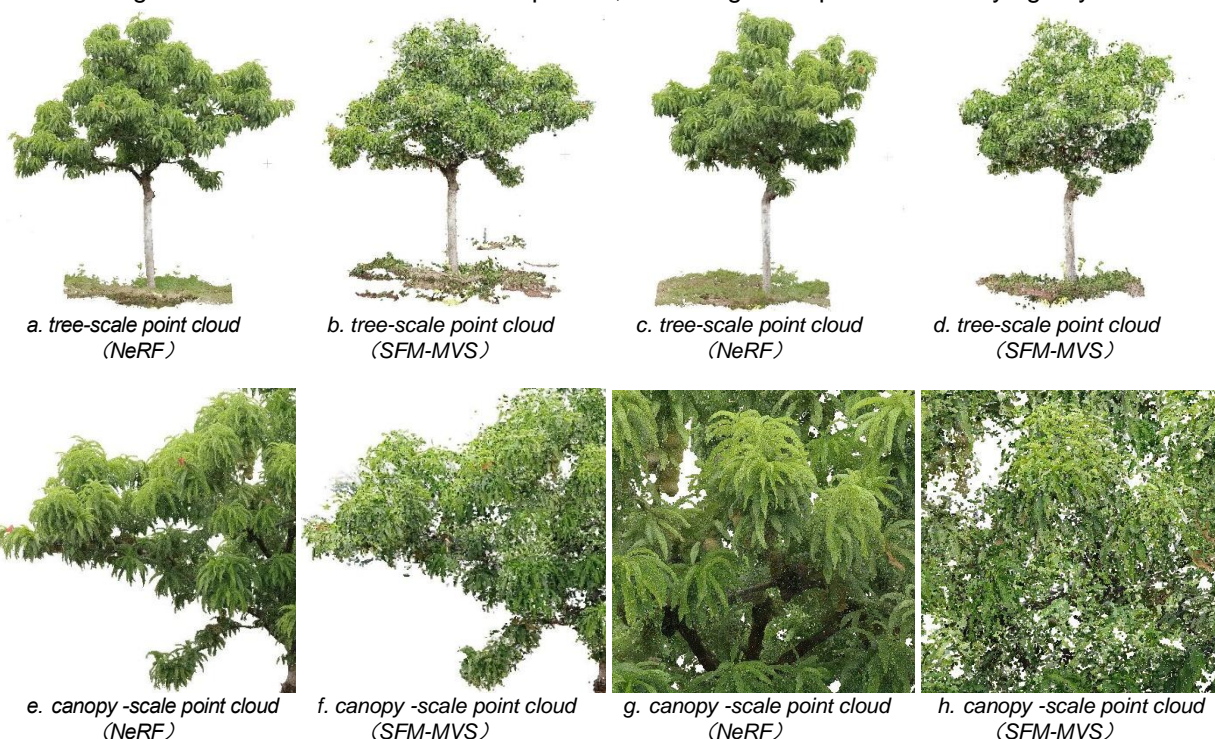
Georeferencing accuracy evaluation metrics

GCPs parameter	X-coordinate	Y-coordinate	Z-coordinate	Registration errors /mm
The measured value for GCP 2	588758.186722	4074069.579384	27.214424	—

GCPs parameter	X-coordinate	Y-coordinate	Z-coordinate	Registration errors /mm
The measured value for GCP 13	588760.144802	4074068.612587	27.178391	—
The measured value for GCP 20	588759.746929	4074066.781326	27.258263	—
The measured value for GCP 38	588757.133163	4074067.676079	27.354832	—
Measured value for trunk marker points	588758.619942	4074068.453690	27.209908	—
The tested value for GCP 2	588758.171104	4074069.567116	27.273319	1.2001
The tested value for GCP 13	588760.156357	4074068.628487	27.251610	1.9655
The tested value for GCP 20	588759.755337	4074066.795830	27.353138	1.6764
The tested value for GCP 38	588757.148190	4074067.669708	27.358818	1.8644
The tested value for trunk marker points	588758.608894	4074068.453888	27.345152	1.1049

To assess the quality of the NeRF fruit tree point cloud, a set of fruit tree point clouds was reconstructed using the classical stereo vision algorithm SFM-MVS as a control, based on the same dataset. A detailed analysis was conducted to compare the reconstruction effects and reconstruction scale consistency between the two types of fruit tree point clouds.

Regarding the reconstruction effects, as illustrated in Figure 9, a thorough comparison was made at the scales of tree, canopy, and organ for the phenotypic reconstruction of fruit trees using the two methods. At the tree scale, the NeRF method produced a fruit tree point cloud with sharp contours, clear crown textures, and well-defined branch hierarchy. In contrast, the SFM-MVS fruit tree point cloud exhibited blurred contours, abundant noise in the crown, and difficulties in texture recognition. At the canopy scale, the NeRF fruit tree point cloud accurately restored the morphology of branches and leaves. Details such as internal branches, clustered peach tree fruits, and diseased and withered leaves were clearly visible in Figure 9g, highlighting the NeRF method's outstanding recovery capability for high-frequency canopy details. In contrast, the SFM-MVS method at the canopy scale could hardly identify any fruit tree organs. At the organ scale, despite the clustering of immature peach fruits due to non-thinning, the NeRF method could still distinctly reconstruct each fruit, providing a clear, well-organized, and highly recognizable structure. This level of detail is sufficient to guide unmanned agricultural machinery in thinning and harvesting operations. Conversely, the SFM-MVS fruit point cloud at the organ scale exhibited a mosaic-like pattern, rendering it incapable of identifying any details.



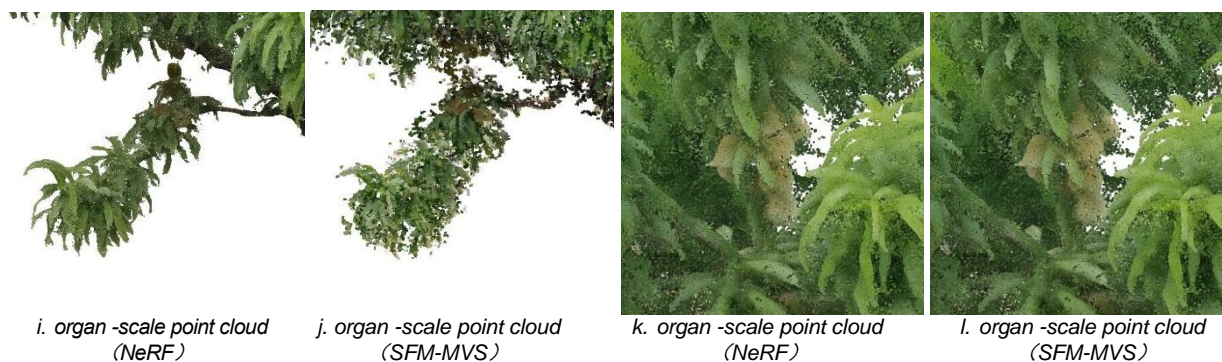


Fig. 9 - Comparison of NeRF fruit tree point cloud and MVS fruit tree point cloud

In terms of scale consistency, prior to the experiment, marker points were placed throughout the canopy of the fruit tree, as depicted in Figure 10. Tree height, crown length, and width were measured at these marker points and served as actual values. Additionally, the trunk diameter at 1.3 meters above the ground level was measured as an actual value for breast height.

Within the fruit tree point cloud, the distances were calculated for the corresponding measurement parameters by selecting marker points. Both actual and experimental values were measured 10 times, and the averages were taken as the true values.



Fig. 10 - Comparison between photo of tagged point and point cloud of tagged point

As indicated in Table 2, both methods exhibit comparable accuracy levels, with a root mean square error of 0.0047 m, when reconstructing the morphology of objects characterized by regular shape and simplicity, such as breast diameter. They both demonstrate a high-level reconstruction accuracy at the millimeter scale. However, in the reconstruction of the fruit tree canopy, which involves intricate details and complex phenotypic information, the reconstruction accuracy of the NeRF method significantly surpasses that of the SFM-MVS method. The scale consistency accuracy for tree height, crown major axis, and crown minor axis achieved by the NeRF method are 99.12%, 99.34%, and 99.22%, respectively. In comparison to the SFM-MVS method, the root mean square errors are reduced by approximately 61.24%, 73.48%, and 62.32%, respectively.

Table 2

3D Reconstruction scale consistency Evaluation Indexes

Parameter	measured value	NeRF tested value	NeRF Root Mean Square Error	NeRF Mean Accuracy	SFM-MVS tested value	SFM-MVS Root Mean Square Error	NeRF Mean Accuracy
Tree Height /m	2.1850	2.2030	0.0193	99.12%	2.1412	0.0495	97.73%
Canopy Length /m	2.1760	2.1845	0.0143	99.34%	2.1157	0.0637	97.07%
Canopy Width /m	1.6420	1.6456	0.0128	99.22%	1.6123	0.0340	97.93%
Breast Diameter /m	0.0680	0.0643	0.0047	93.09%	0.0645	0.0047	93.09%

CONCLUSIONS

This study, focusing on peach trees in the initial fruiting stage, addressed the scientific challenges associated with the limitations of stereoscopic vision-based 3D reconstruction techniques in representing multiscale complex phenotypic details of fruit trees and the absence of geographic information in generated

fruit tree point clouds. By integrating neural radiative fields with georeferencing technology, a digitally reconstructed fruit tree was successfully created with high-level geographic positioning accuracy and superior leaf canopy phenotypic details, thereby overcoming the technical bottlenecks that have hindered the development of the digital fruit tree technology system.

Experimental results demonstrated that Neural Radiance Fields (NeRF) could capture the intricate topological structure of fruit trees at multiple levels, including tree scale, canopy scale, and organ scale, accurately characterizing morphological features of tree branches, fruits, and even leaves. During the NeRF scene training process, the LPIPS metric reached a minimum value of 0.2050 and stabilized within the range of 0.2 to 0.3, while the SSIM metric achieved a maximum value of 0.7215 and stabilized within the range of 0.6 to 0.7. The scale consistency accuracy of NeRF fruit tree point clouds in tree height, canopy length, and width reached 99.12%, 99.34%, and 99.22%, respectively. Compared to Structure-from-Motion Multi-View Stereo (SFM-MVS) fruit tree point clouds, the root mean square errors were reduced by 61.24%, 73.48%, and 62.32%, respectively. The geographic coordinate registration accuracy of the fruit tree point cloud reached millimeter-level, with registration errors generally less than 2 millimeters.

The digitally reconstructed fruit tree established in this study possesses accurate geographic information and high-resolution phenotypic details at multiple scales. It can provide precise spatial data for unmanned agricultural machinery in the WGS-84 geographic coordinate system, endowing it with global perception capabilities to guide tasks such as pruning, thinning, and harvesting. Additionally, with its high-quality leaf canopy phenotypic details, the digitally reconstructed fruit tree lays a solid technical foundation for research in digital phenomics of fruit trees, digital lighting simulation, digital production management, digital yield estimation, digital growth monitoring, and digital agricultural technology training, thereby holding significant implications for the development of smart orchards.

ACKNOWLEDGEMENT

The authors thank the anonymous reviewers for their critical comments and suggestions for improving the manuscript. This work was funded by the Key Research and Development Program of Shandong Province (Major Innovative Project in Science and Technology) (2020CXGC010804), Natural Science Foundation of Shandong Province (ZR2021MC026).

REFERENCES

- [1] Akbarzadeh, A., Frahm, J.M., Mordohai, P., Clipp, B., Engels, C., Gallup, D., et.al. (2006). Towards urban 3D reconstruction from video[C] // *Third International Symposium on 3D Data Processing, Visualization, and Transmission (3DPVT'06)*. IEEE, pp. 1-8. <https://doi.org/10.1109/3DPVT.2006.141>. USA.
- [2] Aiger, D, Mitra, N.J., Cohen-Or, D. (2008). 4-points congruent sets for robust pairwise surface registration[M] // *ACM SIGGRAPH 2008 papers*.: 1-10. <https://doi.org/10.1145/1399504.1360684>.
- [3] Barron, J.T., Mildenhall, B., Tancik, M., Hedman, P., Martin-Brualla, R., & Srinivasan, P. P. (2021). Mip-nerf: A multiscale representation for anti-aliasing neural radiance fields. American. In *Proceedings of the IEEE/CVF international conference on computer vision*. pp. 5855-5864. USA.
- [4] Bdulridha, J., Batuman, O., Ampatzidis, Y. (2019). UAV-based remote sensing technique to detect citrus canker disease utilizing hyper spectral imaging and machine learning. *Remote Sensing*, 11(11): 1373-1395. <https://doi.org/10.3390/rs11111373>. USA.
- [5] Colaço, A. F., Trevisan, R. G., Molin, J. P., Rosell-Polo, J. R., & Escolà, A. (2017). A method to obtain orange crop geometry information using a mobile terrestrial laser scanner and 3D modeling. *Remote Sensing*, 9(8), 763. <https://doi.org/10.3390/rs9080763>. Brazil.
- [6] Gatzliolis, D., Lienard, J. F., Vogs, A., & Strigul, N. S. (2015). 3D tree dimensionality assessment using photogrammetry and small unmanned aerial vehicles. *PloS one*, 10(9), e0137765. <https://doi.org/10.1371/journal.pone.0137765>. USA.
- [7] Hu, W., Fu, X., Chen, F., Yang, W. (2019). A Path to Next Generation of Plant Phenomics. *Chinese Bulletin of Botany*, 54(5): 558–568. <https://doi.org/10.11983/CBB19141>. China.
- [8] Jiménez-Brenes, F. M., López-Granados, F., De Castro, A. I., Torres-Sánchez, J., Serrano, N., & Peña, J. M. (2017). Quantifying pruning impacts on olive tree architecture and annual canopy growth by using UAV-based 3D modelling. Spain. *Plant methods*, 13, 1-15. <https://doi.org/10.1186/s13007-017-0205-3>. Spain.
- [9] Kajiya, J. T., Vonherzen, B. P. (1984). Ray tracing volume densities. *ACM SIGGRAPH computer graphics*, 18(3): 165-174. USA.

- [10] Konolige K, Agrawal M. FrameSLAM: From bundle adjustment to real-time visual mapping[J]. IEEE Transactions on Robotics, 2008, 24(5): 1066-1077. USA.
- [11] Martin-Brualla, R., Radwan, N., Sajjadi, M. S., Barron, J. T., Dosovitskiy, A., & Duckworth, D. (2021). Nerf in the wild: Neural radiance fields for unconstrained photo collections. *In Proceedings of the IEEE/CVF conference on computer vision and pattern recognition*. pp. 7210-7219. USA.
- [12] Miller, J., Morgenroth, J., Gomez, C. (2015). 3D modelling of individual Tree using a handheld camera: Accuracy of height, diameter and volume estimates. *Urban Forestry & Urban Greening*, 14(4): 932-940. <https://doi.org/10.1016/j.ufug.2015.09.001>. New Zealand.
- [13] Mildenhall, B., Srinivasan, P. P., Tancik, M., Barron, J. T., Ramamoorthi, R., & Ng, R. (2021). Nerf: Representing scenes as neural radiance fields for view synthesis. *Communications of the ACM*, 65(1), 99-106. *Nerf in the wild: Neural radiance fields for unconstrained photo collections*. USA.
- [14] Müller, T., Evans, A., Schied, C., & Keller, A. (2022). Instant neural graphics primitives with a multiresolution hash encoding. *ACM transactions on graphics (TOG)*, 41(4), 1-15. USA.
- [15] Narvaez, F. Y., Reina, G., Torres-Torriti, M., Kantor, G., & Cheein, F. A. (2017). A survey of ranging and imaging techniques for precision agriculture phenotyping. *IEEE/ASME Transactions on Mechatronics*, 22(6), 2428-2439. <https://doi.org/10.1109/TMECH.2017.2760866>. Chile.
- [16] Nistér D. An efficient solution to the five-point relative pose problem[J]. IEEE transactions on pattern analysis and machine intelligence, 2004, 26(6): 756-770. USA.
- [17] Rahaman, N., Baratin, A., Arpit, D., Draxler, F., Lin, M., Hamprecht, F., ... & Courville, A. (2019, May). On the spectral bias of neural networks. *In International conference on machine learning*. pp. 5301-5310. PMLR.
- [18] Ren, D., Li, X., Lin, T., Xiong, M., Xu, Z., Cui, G. (2022). 3D Reconstruction Method for Fruit Tree Branches Based on Kinect v2 Sensor(基于 Kinect v2 传感器的果树枝干三维重建方法). *Transactions of the Chinese Society for Agricultural Machinery*, 53(S2): 197-203. <http://dx.doi.org/10.6041/j.issn.1000-1298.2022.S2.022>. China
- [19] Tewari, A., Thies, J., Mildenhall, B., Srinivasan, P., Tretschk, E., Yifan, W., & Golyanik, V. (2022, May). Advances in neural rendering. *In Computer Graphics Forum*. Vol. 41, No. 2, pp. 703-735.
- [20] Teunissen, P. J. G., Khodabandeh, A. (2015). Review and principles of PPP-RTK methods. *Journal of Geodesy*, 89.3: 217-240. Australia.
- [21] Wang, Z., Bovik, A., Sheikh, H., et al. (2004). Image quality assessment: from error visibility to structural similarity [J]. *IEEE transactions on image processing*, 13(4): 600-612. China.
- [22] Wu, S., Wen, W., Wang, C., Du, J., Guo, X. (2021). Research progress of digital fruit trees and its technology system (数字果树及其技术体系研究进展). *Transactions of the Chinese Society of Agricultural Engineering (Transactions of the CSAE)*, 37(9): 350-360. <http://www.tcsae.org/cn/article/doi/10.11975/j.issn.1002-6819.2021.09.039>. China.
- [23] Tancik, M., Weber, E., Ng, E., Li, R., Yi, B., Wang, T., ... & Kanazawa, A. (2023, July). Nerfstudio: A modular framework for neural radiance field development. *In ACM SIGGRAPH 2023 conference proceedings*. pp. 1-12. USA.
- [24] Yang, L., Zhang, D., Xie, R., Luo, J., Wu, C. (2017). Study on Pruning Simulation of Apple Trees at Initial Fruit Stage (初果期苹果树剪枝仿真研究), *Transactions of the Chinese Society for Agricultural Machinery*, 48(S1): 98-102+333. <http://dx.doi.org/10.6041/j.issn.1000-1298.2017.S0.016>. China.
- [25] Zhang, C., Yang, G., Jiang, Y., Xu, B., Li, X., Zhu, Y., Lei, L., Chen, R., Dong, Z., & Yang, H. (2020). Apple Tree Branch Information Extraction from Terrestrial Laser Scanning and Backpack-LiDAR. *Remote Sensing*, 12(21), 3592. <https://doi.org/10.3390/rs12213592>. China.
- [26] Zhao, J. (2022). *System research on robot apple picking path planning based on deep reinforcement learning (基于深度强化学习的机器人苹果采摘路径规划系统研究)* Zibo: Shandong University of Technology. China.
- [27] Zhang, G., Li, X., Cheng, S. (2013). Progress and Prospects of 3S Technology Application to Apple Orchard Informatization (3S 技术在苹果园信息化中应用研究的进展与展望). *Geomatics & Spatial Information Technology*, 36(08): 40-44. China.
- [28] Zhang, R., Isola, P., Efros, A. (2018). The unreasonable effectiveness of deep features as a perceptual metric. *Proceedings of the IEEE conference on computer vision and pattern recognition*. 586-595. China.
- [29] Zhou, G., Qiu, Y., Fan, J. (2018). Research progress and prospect of digital orchard techniques (数字果园研究进展与发展方向). *China Agricultural Informatics*, 30(01):10-16. <http://dx.doi.org/10.12105/j.issn.1672-0423.20180102>. China.

HUMAN LOWER LIMB MOTION PATTERN RECOGNITION BASED ON MULTI-SENSOR FUSION

基于多传感器融合的人体下肢运动模式识别

Cuihong LIU¹⁾, Yanbo HAN²⁾, Xiangwen SONG²⁾, Shipeng ZHANG¹⁾, Na HAN²⁾, Meng ZOU²⁾, Liyan WU^{*1)}

¹⁾College of Engineering, Shenyang Agricultural University, Shenyang, China;

²⁾Key Lab for Bionics Engineering of Education Ministry, Jilin University, Changchun, China

^{*}Corresponding author: Tel: 15942098712; E-mail: wly78528@syau.edu.cn

DOI: <https://doi.org/10.35633/inmateh-75-78>

Keywords: Human lower limb; Gait Mode Recognition; Plantar Pressure Measurement System; Inertial Measurement Units; Intelligent Prostheses

ABSTRACT

One of the essentials of intelligent prosthetics design is to recognize the wearer's movement intention, to provide the wearer with the corresponding control strategy and movement assistance. The 11 independent gait patterns and 5 transformed gait patterns are recognized by the self-designed human lower limb motion data measurement system. The human gait pattern is classified by the linear discriminant analysis (LDA) classifier, and the recognition accuracy is evaluated by K-fold Cross Validation(K-CV). The average recognition accuracy of independent gait patterns is 90.91%. In the independent gait pattern, the lowest recognition accuracy of DS1 gait phase is 90.53%, and the highest recognition accuracy of SS2 gait phase is 91.36%. The overall average recognition accuracy of the transformed gait pattern is 92.67%, the lowest recognition accuracy of DS1 gait phase is 91.93%, and the highest recognition accuracy of SS1 gait phase is 93.31%. The main reason affecting the recognition accuracy is that some gait patterns have similar motion characteristics. The method proposed in this study can accurately predict the wearer's locomotion mode and serves as a reference for gait pattern recognition, prediction, and control strategies in intelligent prosthetic devices.

摘要

智能假肢设计的关键之一是识别佩戴者的运动意图，为佩戴者提供相应的控制策略和运动辅助。通过自主设计的人体下肢运动数据测量系统对11种独立步态模式和5种变换步态模式进行识别。采用线性判别分析(LDA)分类器对人体步态模式进行分类，并采用K-fold交叉验证(K-CV)对识别精度进行评价。独立步态模式的平均识别准确率为90.91%。在独立步态模式下，DS1步态相位的识别准确率最低为90.53%，SS2步态相位的识别准确率最高为91.36%。变换步态模式的整体平均识别准确率为92.67%，DS1步态相位的最低识别准确率为91.93%，SS1步态相位的最高识别准确率为93.31%。影响识别精度的主要原因是某些步态模式具有相似的运动特征。本文提出的方法可以准确预测佩戴者的运动模式，为智能假肢的步态模式识别、预测和控制策略提供参考。

INTRODUCTION

Lower limb amputation affects daily life. Although passive prostheses can meet the basic daily use of amputees, the wearer presents asymmetrical gait patterns in performing daily activities (Zhu et al., 2014; Windrich et al., 2016; Dey et al., 2020). To compare with the able-bodied individuals, the amputees need to consume 20-30% extra metabolic energy in movement (Au et al., 2009). Intelligent prostheses, as a medical device that can simulate the human-machine relationship between amputee and prosthesis to the maximum extent, are attracting more and more attention (Tucker et al., 2015; Silva Júnior et al., 2015; Yang et al., 2016; Hernandez and Yu, 2022; Yue et al., 2023).

The study of locomotion mode is one of the important contents of intelligent prostheses. By collecting and analyzing relevant signals, the basic information of human movement can be extracted, and then different control strategies can be selected by judging the movement to ensure the smooth and labor-saving of the wearer. At present, the signals used for the study of locomotion mode are mainly divided into mechanical signals (such as gyroscopes, accelerometers, goniometers and magnetometers) (Bisio et al., 2016; Quintero et al., 2016) and bioelectric signals (electromyography (EMG) is a widely used bioelectric signal) (Bakina et al., 2018; Chen et al., 2015; Wang et al., 2016).

Cuihong Liu, Prof. Ph.D. Eng.; Yanbo Han, Xiangwen Song, Shipeng Zhang, Na han, M.S. Stud. Eng.; Meng Zou and Liyan Wu, Prof. Ph.D. Eng.

Nazarpour et al. recognized the locomotion mode based on EMG signals, utilized higher order statistics of EMG signal to classify four primitive motions, i.e., elbow flexion, elbow extension, forearm supination, and forearm pronation. The results indicated that the proposed approach provided higher identification rates (Nazarpour et al., 2007). Liu et al. collected the EMG signals of two able-bodied subjects and two unilateral transfemoral amputees during normal walking, compared and evaluated three kinds of adaptive classifiers off-line (Liu et al., 2017). The entropy-based adaptation was implemented for real-time human-in-the-loop prosthesis control. The online evaluation showed that the developed novel adaptive strategy may further enhance the reliability of neurally controlled prosthetic legs. Wang et al. proposed a wearable plantar pressure measurement system, which identified five locomotion modes through four force sensors mounted on insoles, and the average recognition errors of four phases of the five patterns were 19.6%, 12.6%, 5.2%, and 6.3% respectively (Wang et al., 2012). Young et al. used mechanical sensors to identify five motion modes of walking on level ground, ramp and stairs, with an overall accuracy of 93.9% (Young et al., 2013). Meng et al. collected EMG signals and linear acceleration of 10 able-bodied subjects in seven locomotion activities, such as sitting, standing and walking horizontally. By comparing four classifiers, the results show that the SVM model with a sliding window size of 80ms has the best recognition performance. EMG signal fusion not only improves the recognition accuracy of steady-state motion from 90% (only using acceleration data) to 98% (using data fusion), but also can predict the next steady-state motion (Meng et al., 2021).

EMG signal will change with the change of electrode conductivity, electrophysiology, space, user and other factors, and the myoelectric decoding algorithms is very demanding (Sensing et al., 2009; Jain et al., 2012; Young and Ferris, 2016; Fan et al., 2024). Compared with bioelectric signals, mechanical signals are more mature, smaller in size and highly integrated (Ambrozic et al., 2014; Gorsic et al., 2014; Yuan et al., 2017). The acquisition of mechanical signals is mainly through accelerometers, gyroscopes, pressure sensors and other devices (Adapala et al., 2013; Parri et al., 2017; Hussain et al., 2019). For example, Hartmann et al. proposed an online human activity recognition (HAR) system, in which wearable sensors (such as inertial measurement units) acquire data and identify activities through hidden Markov models (Hartmann et al., 2022). On the other hand, data provided by multiple sensors is superior to data provided by a single sensor in theory (Khaleghi et al., 2013). Multi-sensing technology can reduce the power consumption while achieving more abundant functions, because of the development of microcomputer system and electronic technology. Hartmann et al. proposed a multi-sensor data collector (CSL-SHARE) for HAR. sensors used include triaxial accelerometers, triaxial gyroscopes, sEMG sensors, biaxial electrogoniometer, and airborne microphone. The accuracy of the CSL-SHARE dataset reached 96.1% (Liu et al., 2021; Hartmann et al., 2022). Smart knee bandage is a new method, sensors are fixed inside knee bandages and socks, and evaluates the movement posture of patients through IMU and pressure sensors, so as to obtain the movement and rehabilitation of patients (Haladjian et al., 2017; Haladjian et al., 2018). It is worth noting that Hartmann et al. defined six High-Level Features of the subjects, obtained the information base by deploying different sensor carriers, and learned the relationship between the characteristic values of each activity and the sensor data through classification algorithms, so as to carry out pattern recognition. This method is a relatively advanced research content, and the recognition accuracy rate based on the CSL-SHARE and UniMiB SHAR datasets reaches 89.7% and 67.3%, respectively (Hartmann et al., 2023). In conclusion, the study of locomotion mode based on multi-sensor fusion has received more attention and development (Varol et al., 2010; Huang et al., 2011; Luo et al., 2023). Linear Discriminant analysis (LDA), also known as Fisher Linera Discriminant (FLD), is a classic algorithm for pattern recognition. It was introduced into the field of pattern recognition and artificial intelligence by Belhumeur in 1996. It is an effective feature extraction method. By this, the interclass dispersion matrix of projected pattern samples can be maximized, while the intra-class dispersion matrix is minimized (Tharwat et al., 2017). This method has been successfully applied to HAR. Hartmann et al. also compared the differences between the methods. The research showed that the poor recognition performance when it was used in a single read, but its transformation helped to improve the overall recognition performance, which was conducive to identifying most activities (Hartmann et al., 2021), and the evaluation performance of LDA based on HMM could be improved by 4 percentage (Hartmann et al., 2020). Therefore, the LDA method is adopted in this paper.

This study aims to accurately recognize human lower limb locomotion mode through the method of multi-sensor fusion. First a human lower limb motion data measurement system was developed. The measurement system consists of two inertial measurement units (IMUs) and a plantar pressure measurement system (PPS, containing three force sensors for each foot). The kinematic and dynamic parameters of the human motion are measured by IMU and PPS, respectively.

Linear discriminant analysis (LDA) was used to identify 11 independent gaits and 5 transformed gaits. Gait recognition helps to provide the right control strategy for the intelligent prosthesis, thus activating the corresponding drive mode to assist the amputee's movement. On the basis of ensuring the recognition accuracy, the number of motion patterns increased in this study. Outcomes covers the daily use of subjects, providing a reference for HAD and intelligent wearable devices.

MATERIALS AND METHODS

Human lower limb motion data measurement system

The key to accurately recognize locomotion mode is the reliability and stability of measurement system. The human lower limb motion data measurement system is presented, and its reliability and environmental adaptability is also verified.

The daily movement of human lower limbs includes the kinematic information of legs and the dynamic information between the sole and the ground. Only by collecting this information comprehensively, can the motion state of lower limbs be accurately described. The spatial motion information of human lower limbs is complicated, and it is difficult to cover the daily activity posture with a single sensor. Therefore, the composition of motion data measurement system designed in this paper needs two sensors, inertial measurement unit (IMU) and plantar-pressure measurement unit, which can make up for each other's shortcomings and facilitate us to analyze human lower limb gait more comprehensively. Secondly, due to the complexity of human movement, the data collected by the same type of single sensor can't completely reflect the information contained in the movement to a certain extent. To sum up, the composition of the human lower limb motion data measurement system is shown in Fig. 1. The system consists of two inertial measurement units (IMUs), six thin-film force sensors, an Analog to digital conversion module (A/D Mod) and a computer. The information detected by IMUs and plantar pressure sensors enables comprehensive analysis and recognition of lower limb gaits.

The IMU is an MTi-30 AHRS (Attitude and Heading Reference System) produced by Xsens of the Netherlands (fig. 1b). Motion capture of human lower limbs can be realized by IMU sensor. However, it is difficult for a single IMU sensor to accurately judge the movement with the gait cycle. Two IMU sensors are selected and fixed on the thigh and shank, which can reflect the complete information of the movement. The MT Manager software is used to display in real-time the three-dimensional motion information of the human lower limbs collected by the IMU, and it can also store the experimental data.

In this paper, the force sensor, FlexiForce A401, is a thin film sensor (fig. 1d), which is produced by Tek scan of America. This sensor integrates the measurement signal and processing circuit and obtains drift-free signal data through its built-in low-power processor.

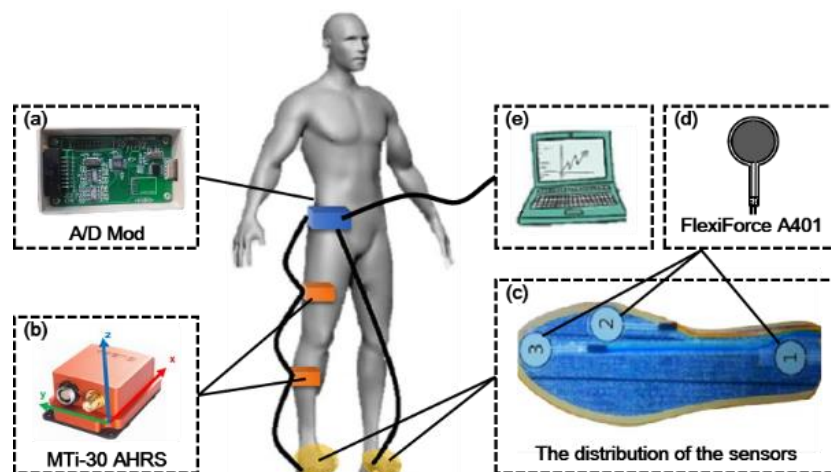


Fig. 1 - Human lower limb motion data measurement system

A single sensor cannot completely measure the pressure change of the entire plantar during the movement, and if the pressure sensing area is small or the location is inappropriate, it will inevitably cause the loss of the plantar pressure information. In this paper, the pressure test system (fig. 2a) is used to test the plantar pressure. In the experiment, three healthy volunteers walked through the plantar pressure test bench with bare feet. After collecting the data of the changes of plantar pressure, the plantar region was partitioned and the stress situation of each region was analyzed. The placement position of the plantar region sensor was determined by observing several zones with the largest strain (fig. 2b).



Fig. 2 - Position of the plantar region sensor
(a) Pressure test system; (b) Volunteer plantar pressure

Three sensors are attached to each insole to form a plantar pressure measurement system (PPS), the distribution of the sensors is shown in Figure 1c, the calcaneus tuberosity (sensor 1), the first metatarsal bone (sensor 2) and the hallux toe (sensor 3).

A/D Mod is installed on the waist of the wearer to process and convert the signals output by the sensor. To reduce the delay of data transmission, the transmission cable is used, and the computer is connected by USB to realize the transmission and storage of sensor data, and the analysis and visualization of IMU and force sensor data are realized.

Plantar pressure system calibration

IMU realizes data conversion through its built-in low-power processor. But the force sensor (FlexiForce A401) is a tiny thin force-sensitive resistor which varies with the vertical pressure. To ensure the accuracy of the value, it is necessary to carry out calibration.

Weight of 1-10 kg is used in the calibration. The weight is increased in increments of 1 kg and the corresponding force is 9.8 N. In the test, to ensure full contact between the weight and the force sensor, the weight is placed vertically, while the applied pressure value and the output value are recorded. The linear fitting was carried out by Matlab and the resulting calibration equation is shown in Equation 1:

$$V_{out} = 0.0028 \times F + 1.1128 \quad (1)$$

where V_{out} is the output value of the force sensor, F is the applied pressure. The residual norm of linear fitting is 0.0101, and the residual norm is < 0.05 . The results show that there is a good linear relationship between the output value and the applied pressure value (fig. 3). In order to identify various gaits more intuitively, the calibration equation was used to convert the voltage output of the sensors into the pressure value, and then the test results were analyzed.

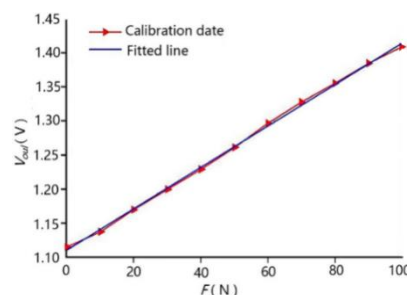


Fig. 3 - The fitting details

Adaptability to different ground surfaces

The contact force that is obtained by the plantar pressure measurement system may be affected by the type of surface. To ensure the output stability of different surfaces, the adaptability of 6 mm rubber floor, 3 mm carpet floor and 9 mm wood floor is carried out. The experiment process is described in Fig. 4.



Fig. 4 - The experiment process
(a) Rubber floor; (b) Carpet floor; (c) Wood floor

The experiment is carried out by an able-bodied subject, 25 years old, male, with weight of 75 kg and height of 1.72 m. The subject is asked to walk at a normal, comfortable pace across three different surfaces under laboratory conditions. The subject walks for 3 complete gait cycles each time, and the pressure between the foot and the ground is collected during the walking. The pressure data are shown in Fig. 5.

Fig. 5 shows the data collected by three force sensors of a plantar pressure measurement system, and data of different ground types are represented by curves of different colors. The maximum signal difference of each force sensor in three different ground types is 6.6%, 4.5% and 7.9%, respectively. And the maximum signal difference is always around the peak of the signal. These results indicate that the signals of three force sensors in different areas of the same foot have similarities on different ground. In other words, the plantar pressure measurement system adapts to different surfaces.

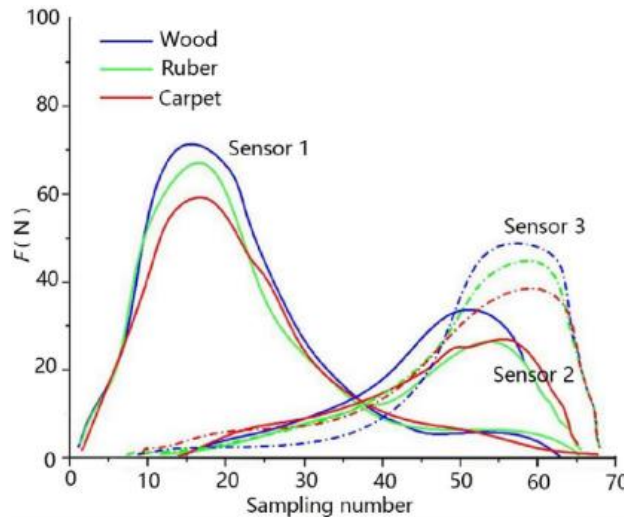


Fig. 5 - The pressure data on three surface types

The process of experiment

In our study, 10 able-bodied subjects are recruited. Their average age is 24.7 ± 1.4 years, average weight is 69.4 ± 10.7 kg, average height is 1.773 ± 0.054 m, and average foot size is 26.1 ± 0.5 cm. The positions of the sensors are shown in Fig. 1 10 able-bodied subjects are given adaptive exercises after wearing the device.

In this paper, 11 independent gait patterns and 5 transformed gait patterns are designed to study the locomotion mode. The number of experiment groups in each gait pattern is 15. The type of gait pattern and gait cycles are shown in Table 1.

Table 1

The number of trials for each pattern and gait cycles for each trial			
Type	Gait patterns	Trial number	Gait cycles
Independent gait patterns	Sitting (SI)	15	–
	Standing (ST)	15	–
	Level-Walking (LW)	15	5
	Level-Fast Walking (LFW)	15	5
	Soil Walking (SW)	15	5
	Stair Ascending (SA)	15	2
	Stair Descending (SD)	15	2
	Ramp Ascending (RA)	15	2
	Ramp Descending (RD)	15	2
	Soil Ramp Ascending (SRA)	15	2
	Soil Ramp Descending (SRD)	15	2
Transformed gait patterns	Level-Walking - Ramp Ascending (LW - RA)	15	4
	Level-Walking - Stair Ascending (LW - SA)	15	4
	Level-Walking - Stair Descending (LW - SD)	15	4
	Soil Walking - Soil Ramp Ascending (SW - SRA)	15	4
	Standing - Sitting (ST-SI)	15	–

The requirements of the test of independent gait are as follows. For the pattern of SI, the subjects are asked to sit on a 42 cm high chair in a normal, comfortable position (Fig. 6a). For the ST test, the subjects are asked to stand still on the ground, and the subjects are relatively relaxed, and maintain a steady body (Fig. 6b). The LW and LFW require subjects to walk 5 steps on a straight hard surface, the speed is scheduled walking speed and slightly higher than daily walking speed respectively (Fig. 6c). The walking conditions of SW are the same as LW.

The difference is that the road surface of SW is soft soil, and the soil needs to be turned over before and after walking (Fig. 6d). The test environment of SA and SD is four steps, the width of the step is 0.4 m, and the height is 0.15 m. The subjects need to walk at a comfortable pace and posture (Fig. 6e). RA and RD are tested on the hard floor on the ramp, and the slope on the hard floor slope is 5 m in length, 1 m in width and 18.5° in inclination angle. To maintain normal walking speed and posture (Fig. 6f). The difference between SRA and SRD and RA and RD is that the road surface of SRA and SRD is soft soil, the soil needs to be turned over before and after walking to ensure the soft soil (Fig. 6g).



Fig. 6 - Test of independent and transformed gait pattern

(a) SI; (b) ST; (c) LW and LFW; (d) SW; (e) SA and SD; (f) RA and RD; (g) SRA and SRD; (h) LW-RA; (i) SW-SRA

The requirements of the test of transformed gait are as follows. The walking conditions of LW-RA mode (Fig. 6h), LW-SA mode, LW-SD mode and SW-SRA mode (Fig. 6i) are consistent. The subjects are advised to walk 2 steps on each road. The difference between them is that the two types of pavements are different from each other. See independent gait for a detailed description. In ST-SI, the subjects stand up at first and then sit on a chair in a way that is normal for them.

During the experiment, 10 subjects perform only one gait pattern each time, and each gait pattern is done in 15 groups. After each group of experiments, subjects are given a certain rest time. This method eliminates the impact of muscle fatigue on the data.

Data filtering processing

The Matlab software is employed, and statistical analysis methods are utilized for data processing. Moreover, algorithms such as time-domain analysis and principal component analysis are applied for eigenvalue extraction and other processing.

One of the keys of preprocessing is to remove the noise in the acquisition and transmission stages from the data. The data information necessary for the test can be obtained by data filtering. The data information comes from IMU and force sensor. In this paper, the IMU has a built-in classical Kalman filtering algorithm to filter the signals in real time. Kalman filter is a common algorithm for sensor data processing in the navigation field. Based on the linear system state equation, the Kalman filter optimally estimates the current state of the system by updating the collected data and the previous state estimation data. Compared with other filtering algorithms, it can process data in the time domain. The filter algorithm can be directly used to process sensor data in the actual power assisted control, and the algorithm uses less storage space and is easy to implement in the system.

Take the ADC (Analog-to-Digital Converter) curve of the original pressure at the position of the first metatarsal bone (Fig. 1c-sensor2) from RD gait pattern as an example (Fig. 7). The subjects start walking downhill from a stationary state, the initial pressure value was about 28 N, and began to decline with the right foot gradually raised. With the heel landing again, the pressure tended to peak again, and then the value changed periodically.

There is noise impact in the data of Fig. 7 The noise source mainly has 3 aspects: One is the body shake, then because of the signal conversion process, the last one is the friction between the sole and the insole. To eliminate the periodic interference in the data and effectively suppress the high-frequency jitter, the ADC value of plantar pressure was filtered by Savitzky-Golay sliding filter in this paper.

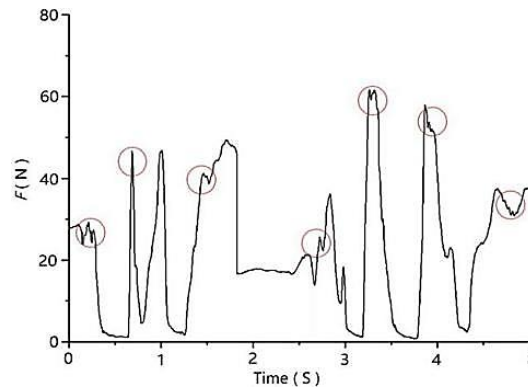


Fig. 7 - The value of the first metatarsal bone in RD gait patterns (before the filtering)

The core idea of Savitzky-Golay sliding filter is to fit the data in the window by the least squares method based on polynomials in the domain. Assume that the gait action data in a window of length p is $x(i)$, $i = -m, \dots, 0, \dots, m$, same as $2m+1=p$. In this window, K -order polynomials (Equation 2) are used to fit the original data.

$$f(i) = a_0 + a_1i + a_2i^2 + \dots + a_ki^k = \sum_{n=0}^k a_ni^n \tag{2}$$

The residual of the least squares fitting ε is calculated through Equation 3.

$$\varepsilon = \sum_{i=-m}^m (f(i) - x(i))^2 = \sum_{i=-m}^m \left(\sum_{n=0}^k a_ni^n - x(i) \right)^2 \tag{3}$$

To minimize the residual, the partial derivative of each polynomial coefficient needs to be 0, the derivative of it can be obtained through Equation 4.

$$\frac{\partial \varepsilon}{\partial a_r} = \sum_{i=-m}^m 2(f(i) - x(i))i^r = 0 \tag{4}$$

where $r=0, 1, \dots, k-1, k$.

The result after processing is shown in Equation 5.

$$\sum_{i=-m}^m \left(\sum_{n=0}^k a_ni^{n+r} \right) = \sum_{i=-m}^m x(i)i^r = \sum_{n=0}^k a_n \left(\sum_{i=-m}^m i^{n+r} \right) \tag{5}$$

where $r=0, 1, \dots, k-1, k$, The linear system of equations on the fitting coefficients can be obtained by derivation, which can be expressed by the following matrix (Equation 6).

$$A^T A a = A^T X \tag{6}$$

where, $a = [a^0, a^1, \dots, a^n]^T$, $X = [x(-m), \dots, x(0), \dots, x(m)]^T$,

The matrix A is defined as shown in Equation 7:

$$A = \begin{bmatrix} (-m)^k & (-m)^{k-1} & \dots & (-m)^0 \\ \dots & \dots & \dots & \dots \\ m^k & m^{k-1} & \dots & m^0 \end{bmatrix} \tag{7}$$

Finally, he result can be obtained as shown in Equation 8:

$$a = (A^T A)^{-1} A^T X \tag{8}$$

According to the coefficients, the results of k -order polynomial fitting to the original data can be obtained, and the filtering results can be obtained after discretization. After several tests, the best filtering effect with $p=6$ and $k=1$ is obtained. The ADC value of the first metatarsal bone in RD gait pattern after Savitzky-Golay filtering is shown in Fig. 8.

The gait segmentation

Gait Phase (GP) refers to the different states that a foot presents during a gait cycle. A gait cycle can be divided into several gait phases (Wang and Hou, 2007). Gait phase is usually composed of two parts: Stance Phase and Swing Phase (Fig. 9). The phases of the gait cycle are relatively fixed during normal motion. It is believed that the stance phase takes up 60 – 65% of the time in a gait cycle (Anwary et al., 2018).

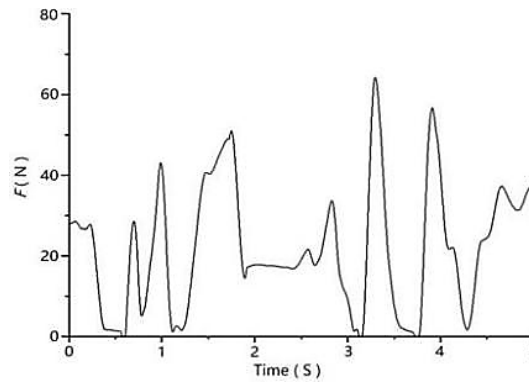


Fig. 8 - The value of the first metatarsal bone in RD gait patterns (after the filtering)

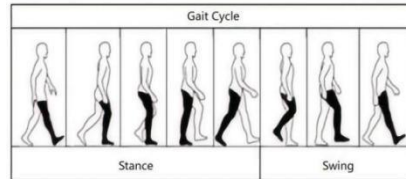


Fig. 9 - Gait cycle

If a gait cycle is effectively segmented, the effective and invalid data can be greatly reduced, and the real-time performance and accuracy of recognition can be obtained. In this paper, the plantar pressure and threshold are used to segment gait phase effectively. The threshold is finally determined as 1/3 of the pressure sum when the user stands still.

Based on previous research on gait, in this paper, two gait events are defined to divide the gait phase. The two gait events are Foot Contact (FC) and Foot Off (FO). FC is the gait event when the pressure rises below a defined threshold reaches the threshold; FO is a gait event when the pressure above the defined threshold drops to a threshold.

Take Fig. 10 as an example to explain a gait cycle. The black curve represents the sum of the three plantar pressure signals, dark blue represents Sensor 1, red represents Sensor 2, and light blue represents Sensor 3. When humans walk on flat ground, they start with the heel off the ground and move forward until the tip of the foot is off the ground. Through the proposed gait segmentation method, a complete gait cycle is divided into four stages by FC and FO: two-station 1 (DS1) and single-station 1 (SS1), two-station 2 (DS2) and single-station 2 (SS2). DS1 is the process of the left foot touching the ground to the right foot leaving the ground, DS2 is the opposite of DS1. SS1 is defined as when the sole of the left foot leaves the ground to when the sole of the left foot touches the ground. Again, SS2 is the opposite of SS1.

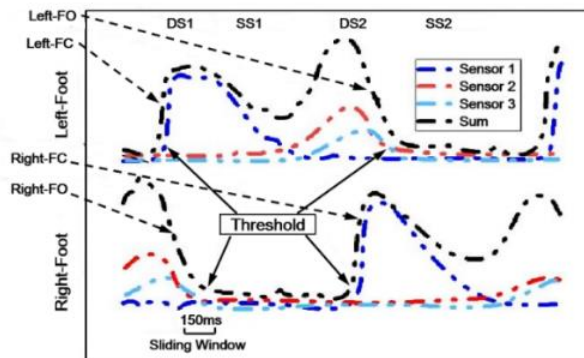


Fig. 10 - Gait segmentation in a gait cycle

Eigenvalue extraction and classifier

Signal eigenvalues are important parameters in locomotion mode recognition and are typically analyzed using window-based analysis and incremental steps. The detailed process is illustrated in Figure 11. During locomotion mode recognition, the eigenvalue of the signal is calculated within each analysis window of duration R. The window then shifts backward by a time interval t, and the eigenvalue for the next analysis window is computed.

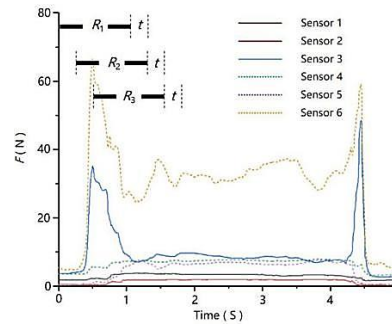


Fig. 11 - The process of eigenvalue extraction

In theory, the duration of the analysis window affects the length of recognition time and whether the current gait pattern is accurately reflected. The increment of the window will also affect the computation amount and recognition delay. The eigenvalue extraction of the signal is related to the sensor signals.

In this paper, a 150 ms sliding window is used to extract the eigenvalue of a total of 14 channels of sensing data (including two IMU sensing signals, each IMU has 4 channels) and pressure data (6 channels).

The sensor type in this paper is a mechanical sensor, the time-domain analysis method is used to extract signal eigenvalues. This method does not need signal transformation, and the calculation is easy and time-consuming. It mainly includes: maximum value, minimum value, mean value, standard deviation, and waveform length (the sum of absolute values of signal changes every 10 ms), where:

Waveform length (WL) is calculated by Equation 9.

$$l_0 = \sum_{k=1}^N |\Delta x_k| \tag{9}$$

Standard deviation (STD) is calculated by Equation 10.

$$STD = \sigma = \sqrt{\frac{1}{N-1} \sum_{k=1}^N (x_k - \bar{x})^2} \tag{10}$$

In summary, this paper constructs a sliding window of 15x14 matrix through Matlab and extracts the maximum value, minimum value, mean value, standard deviation and waveform length of each signal channel under this sliding window. LDA is a linear discriminant analyzer, which requires relatively low computational complexity and can better reflect the differences between samples by using prior knowledge of categories. Therefore, LDA is selected as the classification method.

The performance of LDA is the important target, its model is constructed and explained. In general pattern recognition, the goal of classification is to pursue the minimum error rate. By using the Bayes rule, the classification decision can be made to minimize errors. When the probability density in Bayes rule is a normal distribution condition, the expression of statistical decision-making is given in Equation 11.

$$P(x|c_i) = \frac{1}{(2\pi)^{d/2} |\Sigma_i|^{1/2}} \times e \left\{ -\frac{1}{2} (x - \mu_i) \Sigma_i^{-1} (x - \mu_i)^T \right\} \tag{11}$$

where $x = [x_1, x_2, \dots, x_d]$, x_i is the eigenvalue of the input, x is the corresponding feature vector, that is, the new sample formed after extracting the feature value from the original data. In this paper, the dimension of the feature vector is 1x30, that is, $d=30$. $\mu = [\mu_1, \mu_2, \dots, \mu_d]$, μ is the mean of the sample of eigenvalues, Σ_i is the covariance matrix of each class (symmetric nonnegative definite matrix).

For binary problems, it is only necessary to compare the numerator parts of the above formulas. If the two types of samples are separated, a decision surface exists, and the equation of the decision surface can be expressed as shown in Equation 12.

$$g(x) = \ln P(C_i|x) - \ln P(C_j|x) \\ g(x) = -\frac{1}{2} \left[(x - \mu_i) \Sigma_i^{-1} (x - \mu_i)^T - (x - \mu_j) \Sigma_j^{-1} (x - \mu_j)^T \right] - \frac{1}{2} \ln \frac{|\Sigma_i|}{|\Sigma_j|} + \ln \frac{P(C_i)}{P(C_j)} \tag{12}$$

Assuming that the covariance matrices of each class are equal, i.e., $\Sigma_i = \Sigma_j = \Sigma$, the decision surface equation $g(x)$ can finally be expressed as shown in Equation 13.

$$g(x) = \omega x^T + \omega_0 \\ \omega = (\mu_i + \mu_j) \Sigma^{-1} \\ \omega_0 = -\frac{1}{2} (\mu_i + \mu_j) \Sigma^{-1} (\mu_i - \mu_j)^T + \ln \frac{P(C_i)}{P(C_j)} \tag{13}$$

where ω and ω_0 are the model parameters. After obtaining the training model, they are directly used in the subsequent online identification test, and the model parameters do not change in the test.

Evaluation method

In our study, K-fold Cross Validation (K-CV) method is used to evaluate the recognition accuracy. In the K-CV method, 10-fold Cross Validation is used. The data of each gait pattern at each gait phase are divided into 10 parts, among which 9 parts are used for classifier training and the remaining one part is used for test data. This process is repeated 10 times to make the 10 parts used as one test data respectively.

Recognition Accuracy (RA) is defined by Equation 14.

$$RA = \frac{N_{cor}}{N_{total}} \times 100\% \tag{14}$$

where N_{cor} represents the number of correctly identified data groups, and N_{total} indicates the total number of test data groups.

To describe the recognition effect in more detail, a confusion matrix was used, as shown in Eq.15.

$$C = \begin{bmatrix} r_{11} & r_{12} & \dots & r_{1n} \\ r_{21} & r_{22} & \dots & r_{2n} \\ \dots & \dots & \dots & \dots \\ r_{n1} & r_{n2} & \dots & r_{nn} \end{bmatrix} \tag{15}$$

where each element is described as shown in Equation 16.

$$r_{ij} = \frac{n_{ij}}{n_i} \times 100\% \tag{16}$$

where n_{ij} is the number of gait patterns i recognized as j in the test. n_i denotes the number of gait patterns i in the test. r_{ij} represents the probability that gait pattern i is recognized as j . When $i=j$, r_{ij} represents the recognition accuracy of gait pattern i .

RESULTS AND DISCUSSIONS

Independent gait pattern recognition performance

The average recognition accuracy of the independent gait pattern is 90.91%, and the recognition accuracy of DS1, DS2, SS1 and SS2 are 90.53%, 91.18%, 90.59% and 91.36%, respectively. The independent gait pattern has 11 gaits pattern in total and contains gaits pattern with similar motion characteristics. Overall, the experimental results are satisfactory. It should be noted here that the SI and ST do not have gait phase, but they are lumped together for the brevity of the confusion matrix. The detailed results are shown in Fig. 12.

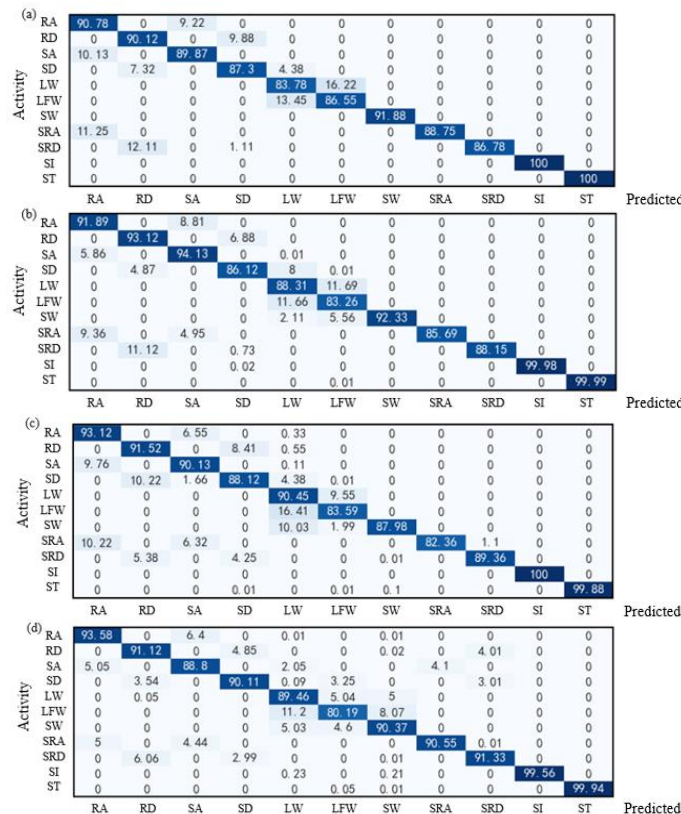


Fig. 12 - The detailed results of the independent gait pattern
 (a) DS1 phase; (b) DS2 phase; (c) SS1 phase; (d) SS2 phase

In the above results, the lowest recognition accuracy of the independent gait pattern is 80.19%, which is LFW in SS2 phase. Three flat walking modes are tested: LW, LFW, and SW. By comparing the curves of the plantar pressure system of the three gait patterns (Fig. 13), it can be seen that they have similar motion characteristics, which leads to the identification error. Although the recognition accuracy of LFW in SS2 phase is about 10% different from the average recognition accuracy, the accuracy of 80.19% is acceptable.

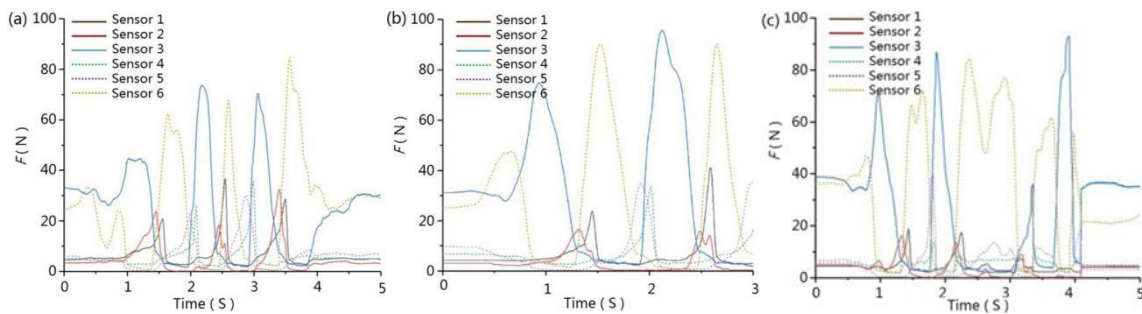


Fig. 13 - The curves of the plantar pressure system of the LW, LFW and SW
(a) LW; (b) LFW; (c) SW

Transformed gait patterns recognition performance

The results of the transformed gait pattern are similar to the independent gait pattern (Fig. 14). Its average recognition accuracy is 92.67%, and the recognition accuracy of DS1, DS2, SS1 and SS2 are 91.93% , 92.79%, 93.31% and 92.65%, respectively.

The lowest recognition accuracy is 85.47%, which is LW-SD in DS1 phase. In DS1, the two highest false recognition rates are LW-SA and SW-SRA, which are 7.20% and 4.02%, respectively. The three gaits pattern have similar motion characteristics. The higher false recognition rate is also due to these similar motion characteristics.

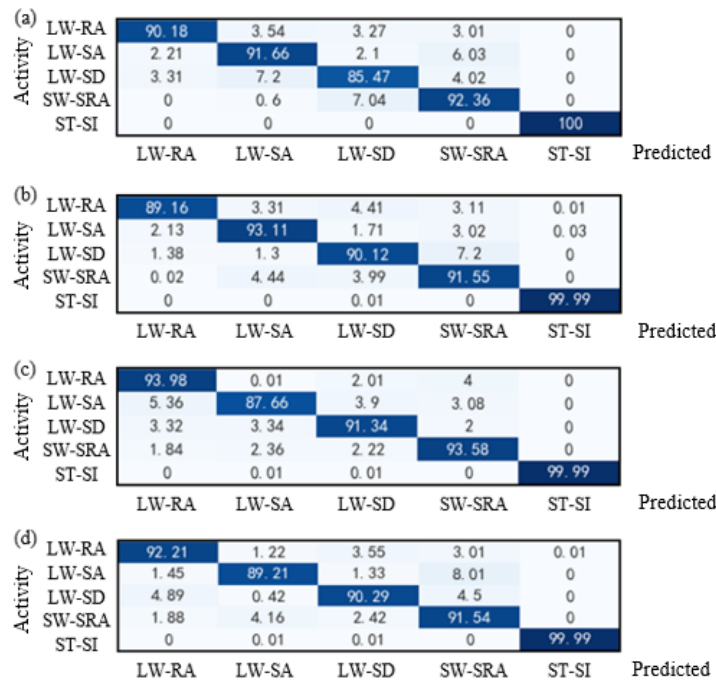


Fig. 14 - The detailed results of transformed gait pattern
(a) DS1 phase; (b) DS2 phase; (c) SS1 phase; (d) SS2 phase

Discussion

Independent gait has been studied relatively early, and the common human locomotion modes are: level walking, ramp ascent, ramp descent, stair ascent and stair descent. At present, the recognition rate of independent gait can reach above 95%. Compared with independent gait, the research time of transformed gait is relatively late, and the recognition is more difficult. At present, most types of gait recognition are less, about 5 – 8, and the road is mostly standardized (Table 2) (Gao et al., 2020; Liu et al., 2020; Young et al., 2013). Because the increase in the number of patterns will affect the recognition accuracy.

Table 2

Reference	Independent gait		Transformed gait	
	Number	Accuracy	Number	Accuracy
Gao et al. (2020)	5	98.46%	—	—
Liu et al. (2020)	5	95.8%	—	—
Young et al. (2013)	5	84.5%	8	93.9%
Our Method	11	90.91%	5	92.67%

In this paper, the number of locomotion modes has been increased. 11 independent gaits and 5 transformed gaits are studied. In addition, the road conditions are much closer to reality. The walking condition in the soil is added, which is more significant in application. The overall accuracy of pattern recognition for both independent and transformed gait is above 90%. This is a relatively satisfactory result.

At present, the main locomotion modes with similar motion curves have affected the accuracy. This may be related to the number of sensor and data processing. The increase in the number of sensor helps with pattern recognition, but it puts an extra burden on amputees' bodies and affects their movement. On the premise of ensuring the recognition accuracy, the use of sensors should be reduced. The recognition rate of the measurement system proposed in this work is above 90%, which achieves the expected goal.

CONCLUSIONS

In this paper, a human lower limb motion data measurement system, which has good environmental adaptability, was presented. Based on data filtering and gait segmentation, LDA classifier is used to analyze the data, and K-CV method is used to judge the accuracy of the results.

The average recognition accuracy of the independent gait pattern is 90.91%, and the highest accuracy of SS2 pattern is 91.36% among the four gait phases. The average recognition accuracy of the transformed gait pattern is 92.67%, and the highest accuracy among the four gait phases is 93.31% of SS1.

This method can accurately predict the locomotion mode of human lower limbs. Intelligent prostheses help lower limb amputees move by controlling joints, they can perform various activities more easily. Since the dynamics and kinematics required by the prosthesis are different in different locomotion modes, it is of great significance to accurately identify the user's locomotion mode for the operation of the prosthesis. Therefore, the method in this paper can provide a reference for the gait recognition, prediction and control strategy of intelligent prostheses.

ACKNOWLEDGEMENTS

This study was supported by the Basic scientific research project of Liaoning Provincial Department of Education (No. JYTMS20231271), China.

REFERENCES

- [1] Au, S. K., Weber, J., Herr, H., (2009), Powered ankle-foot prosthesis improves walking metabolic economy. *IEEE Transactions on robotics*, Vol. 25, pp. 51-66. <https://doi.org/10.1109/TRO.2008.2008747>
- [2] Adapala, R. K., Thoppil, R. J., Luther, D. J., Paruchuri, S., Meszaros, J. G., Chilian, W. M., Thodeti, C. K., (2013), TRPV4 channels mediate cardiac fibroblast differentiation by integrating mechanical and soluble signals. *Journal of molecular and cellular cardiology*, Vol. 54, pp. 45-52. <https://doi.org/10.1016/j.yjmcc.2012.10.016>
- [3] Ambrozic, L., Gorsic, M., Geeroms, J., Flynn, L., Lova, R. M., Kamnik, R., Munih, M., Vitiello, N., (2014), CYBERLEGs: A user-oriented robotic transfemoral prosthesis with whole-body awareness control. *IEEE Robotics & Automation Magazine*, Vol. 21, pp. 82-93. <https://doi.org/10.1109/MRA.2014.2360278>
- [4] Anwary, A. R., Yu, H. N., Vassallo, M., (2018), Optimal foot location for placing wearable IMU sensors and automatic feature extraction for gait analysis. *IEEE Sensors Journal*, Vol. 18, pp. 2555-2567. <https://doi.org/10.1109/JSEN.2017.2786587>
- [5] Bisio, I., Delfino, A., Lavagetto, F., Sciarrone, A., (2016), Enabling IoT for in-home rehabilitation: Accelerometer signals classification methods for activity and movement recognition. *IEEE Internet of Things Journal*, Vol. 4, pp. 135-146. <https://doi.org/10.1109/JIOT.2016.2628938>
- [6] Bakina, O. V., Fomenko, A. N., Korovin, M. S., Glazkova, E. A., Svarovskaya, N. V., (2018), An ICA-EBM-based sEMG classifier for recognizing lower limb movements in individuals with and without knee

- pathology. *IEEE Transactions on Neural Systems and Rehabilitation Engineering*. Vol. 26, pp. 675-686. <https://doi.org/10.1109/TNSRE.2018.2796070>
- [7] Chen, B. J., Wang, X. G., Huang, Y., Wei, K. L., Wang, Q. N., (2015), A foot-wearable interface for locomotion mode recognition based on discrete contact force distribution. *Mechatronics*, Vol. 32, pp. 12-21. <https://doi.org/10.1016/j.mechatronics.2015.09.002>
- [8] Dey, s., Yoshida, T., Schilling, A. F., (2020), Feasibility of training a random forest model with incomplete user-specific data for devising a control strategy for active biomimetic ankle. *Frontiers in Bioengineering and Biotechnology*, Vol. 8, pp. 855. <https://doi.org/10.3389/fbioe.2020.00855>
- [9] Fan, J. H., Jiang, X. Y., Liu, X. Y., Meng, L., Jia, F. M., Dai, C. Y., (2024), Surface EMG feature disentanglement for robust pattern recognition. *Expert Systems with Applications*, Vol. 237, pp.121224. <https://doi.org/10.1016/j.eswa.2023.121224>
- [10] Gorsic, M., Kamnik, R., Ambrozic, L., Vitiello, N., Lefeber, D., Pasquini, G., Munih, M., (2014), Online phase detection using wearable sensors for walking with a robotic prosthesis. *Sensors*, Vol. 14, pp. 2776-2794. <https://doi.org/10.3390/s140202776>
- [11] Gao, F., Liu, G. Y., Liang, F. Y., Liao, W. H., (2020), IMU-based locomotion mode identification for transtibial prostheses, orthoses, and exoskeletons. *IEEE Transactions on Neural Systems and Rehabilitation Engineering*, Vol. 28, pp. 1334-1343. <https://doi.org/10.1109/TNSRE.2020.2987155>
- [12] Huang, H., Zhang, F., Hargrove, L. J., Dou, Z., Rogers, D. R., Englehart, K. B., (2011), Continuous locomotion-mode identification for prosthetic legs based on neuromuscular–mechanical fusion. *IEEE Transactions on Biomedical Engineering*, Vol. 58, pp. 2867-2875. <https://doi.org/10.1109/TBME.2011.2161671>
- [13] Haladjian, J., Scheuermann, C., Bredies, K., Bruegge, B., (2017), A smart textile sleeve for rehabilitation of knee injuries. *The 2017 ACM International Joint Conference on Pervasive and Ubiquitous Computing and the 2017 ACM International Symposium on Wearable Computers*, pp. 49-52. <https://doi.org/10.1145/3123024.3123151>
- [14] Haladjian, J., Bredies, K., Brugge, B., (2018), KneeHapp textile: A smart textile system for rehabilitation of knee injuries. *IEEE 15th International Conference on Wearable and Implantable Body Sensor Networks (BSN)*, pp. 9-12. <https://doi.org/10.1109/BSN.2018.8329646>
- [15] Hussain, T., Maqbool, H. F., Iqbal, N., Khan, M., Salman, Dehghani-Sanij, A. A., (2019), Computational model for the recognition of lower limb movement using wearable gyroscope sensor. *International Journal of Sensor Networks*, Vol. 30, pp. 35-45. <https://doi.org/10.1504/IJSNET.2019.10020697>
- [16] Hartmann, Y., Liu, H., Schultz, T., (2020), Feature Space Reduction for Multimodal Human Activity Recognition. *Proc of the 13th International Joint Conference on Biomedical Engineering Systems and Technologies*, pp. 135-140. <https://doi.org/10.5220/0008851401350140>
- [17] Hartmann, Y., Liu, H., Schultz, T., (2021), Feature Space Reduction for Human Activity Recognition based on Multi-channel Biosignals. *Proc of the 14th International Conference on Bio-inspired Systems and Signal Processing*, pp. 215-222. <https://doi.org/10.5220/0010260802150222>
- [18] Hartmann, Y., Liu, H., Schultz, T., (2022), Interactive and Interpretable Online Human Activity Recognition. *2022 IEEE International Conference on Pervasive Computing and Communications Workshops and other Affiliated Events (PerCom Workshops)*, pp. 109-111. <https://doi.org/10.1109/PerComWorkshops53856.2022.9767207>
- [19] Hartmann, Y., Liu, H., Lahrberg, S., Schultz, T., (2022), Interpretable High-level Features for Human Activity Recognition. *Proc of the 15th International Joint Conference on Biomedical Engineering Systems and Technologies (BIOSTEC 2022)*, pp. 40-49. <https://doi.org/10.5220/0010840500003123>
- [20] Hernandez, I., Yu, W., (2022), Recent advances on control of active lower limb prostheses. *IETE technical review*, Vol.39, pp. 1225-1244. <https://doi.org/10.1080/02564602.2021.1994477>
- [21] Hartmann, Y., Liu, H., Schultz, T., (2023), Interpretable High-Level Features for Human Activity Recognition and Modeling. *Biomedical Engineering Systems and Technologies*, Vol. 1814, pp.141-163. <https://doi.org/10.5220/0010840500003123>
- [22] Jain, S., Singhal, G., Smith, R. J., Kaliki, R., Thakor, N., (2012), Improving long term myoelectric decoding, using an adaptive classifier with label correction. *In 2012 4th IEEE RAS & EMBS International Conference on Biomedical Robotics and Biomechanics*, pp. 532-537. <https://doi.org/10.1109/BioRob.2012.6290901>
- [23] Khaleghi, B., Khamis, A., Karray, F. O., Razavi, S. N., (2013), Multisensor data fusion: A review of the state-of-the-art. *Information fusion*, Vol. 14, pp. 28-44. <https://doi.org/10.1016/j.inffus.2012.10.004>

- [24] Liu, M., Zhang, F., Huang, H., (2017), An adaptive classification strategy for reliable locomotion mode recognition. *Sensors*, Vol. 17, pp. 2020. <https://doi.org/10.3390/s17092020>
- [25] Liu, Z. J., Lin, W., Geng, Y. L., Yang, P., (2017), Intent pattern recognition of lower-limb motion based on mechanical sensors. *IEEE/CAA Journal of Automatica Sinica*, Vol. 4, pp. 651-660. <https://doi.org/10.1109/JAS.2017.7510619>
- [26] Liu, H., Hartmann, Y., Schultz, T., (2021), CSL-SHARE: A Multimodal Wearable Sensor-Based Human Activity Dataset. *Frontiers in Computer Science*, Vol. 3, pp. 759136. <https://doi.org/10.5220/0010896400003123>
- [27] Luo, S. L., Shu, X. L., Zhu, H. X., Yu, H. L., (2023), Early prediction of lower limb prostheses locomotion mode transition based on terrain recognition. *IEEE Sensors Journal*, Vol. 23, pp. 27941-27948. <https://doi.org/10.1109/JSEN.2023.3320274>
- [28] Meng, L., Pang, J., Wang, Z. Y., Xu, R., Ming, D., (2021), The role of surface electromyography in data fusion with inertial sensors to enhance locomotion recognition and prediction. *Sensors*, Vol. 21, pp. 6291. <https://doi.org/10.3390/s21186291>
- [29] Nazarpour, K., Sharafat, A. R., Firoozabadi, S. M. P., (2007), Application of higher order statistics to surface electromyogram signal classification. *IEEE Transactions on Biomedical Engineering*, Vol. 54, pp. 1762-1769. <https://doi.org/10.1109/TBME.2007.894829>
- [30] Parri, A., Yuan, K. B., Marconi, D., Yan, T. F., Crea, S., Munih, M., Lova, R. M., Vitiello, N., Wang, Q. N., (2017), Real-time hybrid locomotion mode recognition for lower limb wearable robots. *IEEE/ASME Transactions on Mechatronics*, Vol. 22, pp. 2480-2491. <https://doi.org/10.1109/TMECH.2017.2755048>
- [31] Quintero, D., Villarreal, D. J., Gregg, R. D., (2016), Preliminary experiments with a unified controller for a powered knee-ankle prosthetic leg across walking speeds. *2016 IEEE/RSJ International Conference on Intelligent Robots and Systems (IROS)*, pp. 5427-5433. <https://doi.org/10.1109/IROS.2016.7759798>
- [32] Sensinger, J. W., Lock, B. A., Kuiken, T. A., (2009), Adaptive pattern recognition of myoelectric signals: exploration of conceptual framework and practical algorithms. *IEEE Transactions on Neural Systems and Rehabilitation Engineering*, Vol. 17, pp. 270-278. <https://doi.org/10.1109/TNSRE.2009.2023282>
- [33] Silva Júnior, W. C., Oliveira, M. A. V. D., Bonvent, J. J., (2015), Conception, design and development of a low-cost intelligent prosthesis for one-sided transfemoral amputees. *Research on Biomedical Engineering*, Vol. 31, pp. 62-69. <https://doi.org/10.1590/2446-4740.0647>
- [34] Tucker, M. R., Olivier, J., Pagel, A., Bleuler, H., Bourri, M., Lamercy, O., Millán, J. D. R., Riener, R., Vallery, H., Gassert, R., (2015), Control strategies for active lower extremity prosthetics and orthotics: a review. *Journal of NeuroEngineering and Rehabilitation*. Vol. 12, pp. 1-30. <https://doi.org/10.1186/1743-0003-12-1>
- [35] Tharwat, A., Gaber, T., Ibrahim, A., Hassanien, A. E., (2017), Linear discriminant analysis: A detailed tutorial. *AI communications*, Vol. 30, pp. 169-190. <https://doi.org/10.3233/AIC-170729>
- [36] Varol, H. A., Sup, F., Goldfarb, M., (2010), Multiclass real-time intent recognition of a powered lower limb prosthesis. *IEEE Transaction on Biomedical Engineering*, Vol. 57, pp. 542-551. <https://doi.org/10.1109/TBME.2009.2034734>
- [37] Wang, K. J., Hou, B. B., (2007), A survey of gait recognition. *Journal of Image and Graphics*, Vol. 12, pp. 1152-1160. <https://doi.org/10.3969/j.issn.1006-8961.2007.07.002>
- [38] Wang, X. G., Wang, Q. N., Zheng, E. H., Wei, K. L., Wang, L., (2012), A wearable plantar pressure measurement system: design specifications and first experiments with an amputee. *Intelligent Autonomous Systems 12: Volume 2 Proceedings of the 12th International Conference IAS-12(Jeju Island, Korea. Springer Berlin Heidelberg)*, pp. 273-281. https://doi.org/10.1007/978-3-642-33932-5_26
- [39] Windrich, M., Grimmer, M., Christ, O., Rinderknecht, S., Beckerle, P., (2016), Active lower limb prosthetics: a systematic review of design issues and solutions. *Biomedical Engineering Online*, Vol. 15, pp. 5-19. <https://doi.org/10.1186/s12938-016-0284-9>
- [40] Wang, Q. N., Zheng, E. H., Chen, B., J., Mai, J. G., (2016), Recent progress and challenges of robotic lower-limb prostheses for human robot integration. *Acta Automatica Sinica*. Vol. 42, pp. 1780-1793. <https://doi.org/10.16383/j.aas.2016.y000007>
- [41] Young, A. J., Simon, A. M., Hargrove, L. J., (2013), A training method for locomotion mode prediction using powered lower limb prostheses. *IEEE Transactions on Neural Systems and Rehabilitation Engineering*, Vol. 22, pp. 671-677. <https://doi.org/10.1109/TNSRE.2013.2285101>
- [42] Young, A. J., Simon, A. M., Hargrove, L. J., (2013), A training method for locomotion mode prediction using powered lower limb prostheses. *IEEE Transactions on Neural Systems and Rehabilitation*

- Engineering*, Vol. 22, pp. 671-677. <https://doi.org/10.1109/TNSRE.2013.2285101>
- [43] Young, A. J., Ferris, D. P., (2016), State of the art and future directions for lower limb robotic exoskeletons. *IEEE Transactions on Neural Systems and Rehabilitation Engineering*, Vol. 25, pp. 171-182. <https://doi.org/10.1109/TNSRE.2016.2521160>
- [44] Yang, J. Q., Yang, L., Ma, Y., (2016), Learning vector quantization neural network-based model reference adaptive control method for intelligent lower-limb prosthesis. *Advances in Mechanical Engineering*, Vol. 8, pp. 1-13. <https://doi.org/10.1177/1687814016647354>
- [45] Yuan, K. B., Wang, Q. N., Wang, L., (2017), Energy-efficient braking torque control of robotic transtibial prosthesis. *IEEE/ASME Transactions on Mechatronics*, Vol. 22, pp. 149-160. <https://doi.org/10.1109/TMECH.2016.2620166>
- [46] Yue, L., Lu, Z. X., Hui, D., Chao, J., Liu, Z. Q., Liu, Z. J., (2023), How to Achieve Human-Machine Interaction by Foot Gesture Recognition: A Review. *IEEE Sensors Journal*, Vol. 23, pp. 16515-16528. <https://doi.org/10.1109/JSEN.2023.3285214>
- [47] Zhu, J. Y., Wang, Q. N., Wang, L., (2014), On the design of a powered transtibial prosthesis with stiffness adaptable ankle and toe joints. *IEEE Transactions on Industrial Electronics*, Vol. 61, pp. 4797-4807. <https://doi.org/10.1109/TIE.2013.2293691>

APPLICATION OF MACHINE LEARNING MODELS FOR PREDICTIVE MAINTENANCE OF BIOTECHNICAL SYSTEMS

UTILIZAREA MODELELOR DE ÎNVĂȚARE AUTOMATĂ PENTRU MENTENANȚA PREDICTIVĂ A SISTEMELOR BIOTEHNICE

Adrian IOSIF¹, Edmond MAICAN¹, Sorin Ștefan BIRIȘ¹, Nicolae-Valentin VLĂDUȚ²

¹Faculty of Biotechnical Systems Engineering, University POLITEHNICA of Bucharest / Romania ²INMA Bucharest / Romania

E-mail: biris.sorinstefan@gmail.com

DOI: <https://doi.org/10.35633/inmateh-75-79>

Keywords: Predictive maintenance, Machine learning, Anomaly detection, Agricultural machinery, Hydraulic system monitoring, Multi-model voting framework, Sensor data analysis.

ABSTRACT

Ensuring the reliability and efficiency of agricultural machinery is critical for modern farming operations. Traditional maintenance strategies, including corrective and preventive approaches, often lead to unexpected downtime or excessive servicing costs. This study explores the application of machine learning-based predictive maintenance for agricultural equipment, focusing on the hydraulic system of a Massey Ferguson 7700 S tractor. Real-time sensor data was collected, with hydraulic pressure selected as the primary diagnostic metric for detecting early signs of mechanical degradation. A predictive maintenance framework was developed using seven machine learning models: Isolation Forest, One-Class SVM, KMeans, DBSCAN, Autoencoders, Convolutional Neural Networks (CNNs), and XGBoost. These models were individually applied to identify pressure anomalies indicative of potential failures. To enhance detection accuracy, a "Council of the Wise" ensemble approach was introduced, where an anomaly was validated only if at least four of the seven models agreed on its presence. This consensus-based method reduced false positives and improved fault identification reliability. Results demonstrated that integrating multiple models effectively distinguished significant anomalies from noise, capturing both transient mechanical instabilities and gradual wear-related failures. The findings highlight the potential of machine learning-driven predictive maintenance in optimizing maintenance schedules, reducing unplanned downtime, and extending equipment lifespan. This study establishes a scalable, data-driven maintenance approach that enhances the operational resilience of agricultural machinery, ensuring greater efficiency and sustainability in farming operations.

REZUMAT

Asigurarea fiabilității și eficienței utilajelor agricole este esențială pentru agricultura modernă. Strategiile tradiționale de mentenanță, inclusiv abordările corective și preventive, conduc adesea la perioade neprevăzute de indisponibilitate sau la costuri excesive de întreținere. Acest studiu investighează posibilitatea aplicării unui sistem de mentenanță predictivă pentru echipamentele agricole bazat pe învățarea automată, analizând date achiziționate din sistemul hidraulic al tractorului Massey Ferguson 7700 S. Datele au fost colectate în timp real, presiunea din instalația hidraulică fiind selectată ca parametru principal pentru detectarea timpurie a eventualelor defecțiuni. A fost dezvoltat un sistem de mentenanță predictivă bazat pe șapte modele de învățare automată: Isolation Forest, One-Class SVM, KMeans, DBSCAN, Autoencoders, Convolutional Neural Networks (CNNs) și XGBoost. Aceste modele au fost aplicate individual pentru a identifica anomaliile ale presiunii, fapt care ar putea scoate în evidență posibile defecțiuni. Pentru a îmbunătăți acuratețea detecției, a fost introdusă o abordare de tip „sfatul înțelepților”, în care o anomalie a fost validată doar dacă cel puțin patru dintre cele șapte modele au confirmat prezența acesteia. Această metodă bazată pe consens a redus numărul de alarme false și a îmbunătățit fiabilitatea identificării defecțiunilor. Rezultatele au demonstrat că integrarea mai multor modele a permis diferențierea eficientă a anomaliilor semnificative de zgomot, evidențiind atât instabilitățile mecanice tranzitorii, cât și degradările progresive. Concluziile evidențiază potențialul mentenanței predictive bazată pe învățarea automată în optimizarea programelor de întreținere, reducerea timpilor neplanificați de oprire și prelungirea duratei de viață a echipamentelor. Metoda propusă pentru mentenanța utilajelor agricole este scalabilă și poate îmbunătăți semnificativ reziliența operațională, eficiența și sustenabilitatea în sectorul agricol.

INTRODUCTION

Maintenance strategies in industrial and agricultural machinery have evolved to address operational reliability and cost efficiency. Traditional approaches include corrective maintenance, which involves repairing equipment only after a failure has occurred, often leading to unexpected downtime and high repair costs. Preventive maintenance seeks to mitigate these risks by scheduling routine inspections and servicing at fixed intervals, regardless of the actual condition of the equipment. While this approach reduces the likelihood of failures, it may result in unnecessary maintenance and higher operational costs.

Predictive maintenance, powered by machine learning and real-time data, proactively detects early signs of wear or malfunction, replacing fixed schedules and reactive repairs. By identifying subtle anomalies and degradation patterns, it optimizes maintenance scheduling, reducing unnecessary interventions while preventing costly breakdowns. Advanced algorithms enhance precision in fault detection, ensuring efficient resource allocation and extending equipment lifespan. Increasingly adopted in the agriculture and food industries, predictive maintenance improves equipment reliability, minimizes downtime, and lowers maintenance costs. Conventional methods, such as corrective maintenance, addressing failures after they occur, and preventive maintenance, based on predefined schedules, can lead to inefficiencies and unexpected failures. Machine learning models provide a more intelligent, data-driven approach, enhancing fault prediction accuracy and overall system performance.

This paper explores the application of machine learning (ML) models in predictive maintenance for biotechnical systems, evaluating their effectiveness in improving system reliability and efficiency. By examining the capabilities of various machine learning techniques in failure prediction and early fault detection, the study highlights the advantages of a data-driven approach in minimizing downtime and reducing maintenance costs. The potential of predictive maintenance extends beyond cost savings, it enhances operational resilience, ensuring that agricultural and food production systems remain sustainable and efficient in the face of growing industry demands (Lima *et al.*, 2021).

Agricultural machinery, such as the Massey Ferguson 7700 S tractor, operates under demanding conditions that require continuous performance monitoring to ensure efficiency and longevity. During various soil operations, including plowing, tillage, and planting, as well as harvesting corn or other crops, the hydromechanical systems of agricultural machinery, including the hydraulic system, engine, and drivetrain, experience dynamic mechanical stresses. Modern real-time condition monitoring systems integrated into such equipment collect high-frequency operational data, capturing parameters such as engine temperature, hydraulic pressure, vibration levels, fuel consumption, and mechanical load fluctuations. These data streams, when processed using machine learning models, allow for the early identification of potential failures, preventing costly breakdowns and minimizing downtime.

Ouadah *et al.* (2022) evaluates various supervised machine learning algorithms for predictive maintenance, focusing on their classification and regression capabilities. Key algorithms analyzed include Random Forest, Decision Trees, and k-Nearest Neighbors (KNN), tested on both real-world and simulation datasets. The findings indicate that:

- Random Forest and Decision Trees perform similarly in small datasets and excel in regression-based reliability prediction;
- KNN proves to be more effective for classification tasks, particularly in handling large volumes of data;
- the use of vibration analysis and reliability evaluation enhances failure detection accuracy, supporting early fault diagnosis in industrial equipment.

Furthermore, the study highlights vibration analysis as one of the most reliable PdM techniques, particularly for detecting faults in rotating machinery such as misalignment, imbalance, and bearing degradation. Additional monitoring methods include infrared thermography, acoustic analysis, lubricant analysis, and ultrasonic testing, all of which contribute to data collection for ML models. The results emphasize that PdM strategies, when combined with ML techniques, can reduce system downtime, optimize maintenance scheduling, and minimize costs. However, challenges such as data quality, model interpretability, and real-time deployment constraints remain critical factors in PdM implementation. The study concludes that while ML-based predictive maintenance provides a more dynamic and cost-effective approach than traditional methods, continued research is needed to refine models, improve scalability, and enhance real-time decision-making.

Predictive maintenance (PdM) is an essential component of modern industrial operations, aiming to optimize maintenance actions by predicting failures before they occur. Traditional PdM strategies rely on statistical models and machine learning (ML) techniques, but reinforcement learning (RL) has emerged as a promising approach for designing autonomous and adaptive maintenance strategies.

Siraskar et al. (2023) explores how reinforcement learning is applied to predictive maintenance across various industrial contexts, from early fault detection to health index modeling and maintenance scheduling. Unlike conventional ML techniques, which often require large amounts of labeled historical data, RL-based approaches learn optimal maintenance policies dynamically through interaction with the system.

A contribution of this work is the development of a taxonomy of RL-based predictive maintenance strategies, distinguishing between model-based RL, model-free RL, Markov Decision Processes (MDP), Partially Observable MDPs (POMDPs), and Semi-Markov Decision Processes (SMDPs). The paper highlights the advantages of RL over traditional PdM methods, including its ability to handle dynamic, non-stationary environments, optimize maintenance decisions in real time, and reduce overall maintenance costs. The review also outlines practical challenges in applying RL to PdM, including data quality issues, real-time deployment constraints, and the need for robust edge computing solutions. Additionally, the study emphasizes the importance of reward function design, exploration-exploitation trade-offs, and agent training efficiency in ensuring successful RL-based maintenance systems.

Meddaoui et al. (2024) focuses on remaining useful life (RUL) estimation, a key metric in predictive maintenance that determines the expected time before a component or system fails. Various ML models, including support vector machines (SVM), random forests (RF), k-nearest neighbors (KNN), and artificial neural networks (ANN), are evaluated to determine their effectiveness in predicting RUL. The findings indicate that:

- KNN and ANN models achieve the highest classification accuracy, with KNN reaching 95.92% accuracy in failure prediction;
- Random forests (RF) and principal component analysis (PCA) provide the best results for regression-based RUL estimation, demonstrating lower prediction error rates;
- feature engineering and data preprocessing techniques, including normalization, principal component analysis (PCA), and attribute selection methods, significantly impact model performance by reducing data dimensionality and improving predictive accuracy.

Recent advancements in artificial intelligence have revolutionized predictive maintenance strategies, enabling more efficient fault detection, failure prediction, and maintenance optimization (*O'Neil et al., 2022*). A study on deep learning-driven architectures for predictive maintenance highlights how machine learning techniques, particularly convolutional neural networks (CNNs), deep recurrent neural networks (DRNNs), stacked autoencoders (SAEs), and deep belief networks (DBNs), have evolved to address the complex challenges of reliability engineering in industrial systems. *Li et al. (2024)* systematically reviews deep learning-driven architectures applied to PdM, examining their advantages, limitations, and adaptability across various industrial scenarios.

The authors highlight how Industry 4.0 advancements and IIoT (Industrial Internet of Things) have enabled PdM models to process vast industrial datasets in real time. CNNs and autoencoders outperform traditional ML techniques by automatically extracting critical degradation patterns from raw sensor signals. LSTMs and DRNNs are particularly effective in failure prediction and RUL estimation, capturing long-term dependencies in machinery operations. Long Short-Term Memory (LSTM) networks, trained on historical operational data, provided fault predictions with an accuracy exceeding 95 percent. As a result, repair response time was reduced by 40 percent, and maintenance costs were lowered by 20 percent.

Serradilla et al. (2021) provide a comprehensive review of deep learning (DL) applications in predictive maintenance (PdM), addressing challenges in selecting suitable architectures for industrial use cases. Given the increasing volume of industrial data in the Industry 4.0 era, the study highlights how advanced DL techniques can optimize maintenance strategies by predicting failures before they occur, thus minimizing downtime and reducing costs. The authors categorize and analyze various state-of-the-art (SotA) deep learning architectures, including Self-Organizing Maps (SOM), One-Class Neural Networks (OCNN), and Generative Models, examining their adaptability to real-world industrial maintenance scenarios. The paper also systematically evaluates PdM data characteristics, reviews statistical and traditional ML techniques as baselines, and compares DL approaches against benchmark datasets. A key contribution of this work is the comparison of DL models on a turbofan engine degradation dataset, providing insights into performance, adaptability, and reproducibility in PdM applications.

Zhang et al. (2023) explores an optimized approach to configuring maintenance service vehicles for agricultural machinery operations. It presents a method for resource allocation that minimizes costs while enhancing the efficiency of maintenance services. Using a service coverage model, the research optimizes vehicle positioning and dispatch to ensure timely repairs while reducing overall operational expenses. An

improved genetic algorithm is implemented to address the challenge of optimizing service vehicle deployment, incorporating enhanced selection, crossover, and mutation techniques to refine resource distribution.

Wang et al. (2023) show that autoencoders, a type of neural network designed for unsupervised learning, can effectively extract meaningful fault-related features from large datasets. This approach enables the mapping of failure causes to observed fault phenomena, such as cutter winding, roller clogging, bridge blockage, chain wear, and excessive tool clearance. The results show that autoencoders outperform traditional rule-based and statistical models by dynamically learning complex patterns from sensor data, rather than relying on fixed analytical equations. A key advantage of ML-based predictive maintenance is its ability to identify anomalies before they lead to critical failures. For instance, when analyzing historical harvester failure data, an ML model trained on normalized and preprocessed sensor inputs achieved a prediction accuracy of over 93%, significantly outperforming support vector machines (SVMs), Bayesian classifiers, and sparse self-coding networks. The confusion matrix analysis confirmed that autoencoder-based models exhibited the lowest false-positive and false-negative rates, making them highly reliable for real-time predictive applications. In predictive modeling for refrigeration systems, sensor fusion techniques have been used to combine vibration, temperature, and pressure sensor data. ML algorithms process these multi-source inputs, allowing for early fault detection by recognizing subtle deviations from normal operating conditions. Experimental results indicate that deep learning models reduce false alarm rates by 27% compared to traditional threshold-based monitoring methods, providing a significant improvement in predictive accuracy.

To assess the effectiveness of ML models in predictive maintenance, Wang et al. (2023) have conducted comparative analyses of different approaches: self-coding neural networks (autoencoders), sparse self-coding networks, a variant of traditional autoencoders, and RotGBM, a hybrid gradient-boosting model.

Reliability is a fundamental concern in agricultural machinery, as failures in critical components can lead to significant productivity losses, increased maintenance costs, and operational inefficiencies. Traditional failure analysis methods rely on Failure Mode, Effects, and Criticality Analysis (FMECA) to identify high-risk components. However, these approaches often suffer from subjectivity and difficulty in data acquisition. By utilizing data mining techniques, researchers have been able to systematically analyze large datasets of operational faults, extract meaningful failure patterns, and enhance predictive maintenance strategies (Yang et al., 2022). The study of failure data collected from grain harvesters has identified the cutter component as the most failure-prone, with blade degradation being a dominant failure mode. Excessive clearance, misalignment, and improper installation contribute to high failure rates, requiring frequent inspections and maintenance interventions. Data-driven failure analysis has enabled the classification of failure causes into four primary categories: failures due to mechanical wear, accidental failures, operational errors, and failures caused by insufficient maintenance.

Risk assessment methodologies have been refined using machine learning models, allowing for a more precise evaluation of failure probabilities and severity. The use of risk matrix analysis, analytic hierarchy process (AHP), and FMECA data visualization has improved the accuracy of risk categorization. Machine learning models trained on failure history have successfully identified patterns in risk distribution, revealing that blockages in the header, speed mismatches between working parts, and cutter malfunctions pose the highest operational risks. The application of these models in predictive maintenance enables real-time fault detection, reducing downtime and optimizing repair schedules (Kammerer et al., 2021).

Challenges remain in implementing machine learning-based predictive maintenance at scale. The accuracy of predictions relies heavily on the quality and availability of sensor data, which can be affected by environmental conditions and sensor noise. Additionally, real-time decision-making requires low-latency processing, particularly in remote agricultural locations with limited connectivity. Advances in edge computing and federated learning are expected to address these limitations by enabling decentralized data processing, reducing dependence on cloud-based infrastructure.

Table 1 summarizes the key machine learning methods discussed in the recent studies, highlighting their specific applications in predictive maintenance and the advantages they offer in improving reliability, reducing downtime, and optimizing maintenance schedules.

Table 1

AI Methods for Predictive Maintenance

Method	Application in Predictive Maintenance	Advantages
Convolutional Neural Networks (CNNs)	Analyzes vibration and temperature data to detect faults like bearing degradation, misalignment, and lubrication failures.	Extracts both time-domain and frequency-domain features, improving predictive accuracy.

Method	Application in Predictive Maintenance	Advantages
Deep Recurrent Neural Networks (DRNNs)	Tracks component degradation over time, improving failure prediction in conveyor belts, gearboxes, and hydraulic systems.	Captures complex degradation trends that traditional methods miss.
Long Short-Term Memory (LSTM) & Gated Recurrent Units (GRUs)	Handles long-term dependency modeling, predicting remaining useful life (RUL) in time-series maintenance data.	Enables robust prediction of maintenance needs for systems requiring long-term analysis.
Stacked Autoencoders (SAEs)	Enhances feature extraction from high-dimensional sensor data, reducing reliance on manual feature selection.	Automates feature learning, enhancing predictive model efficiency.
Deep Belief Networks (DBNs)	Offers a probabilistic framework for modeling uncertainty in sensor-based failure prediction models.	Handles noisy sensor data effectively, increasing reliability of predictions.
Transfer Learning	Adapts models trained in one environment to new industrial conditions with minimal retraining.	Reduces the need for extensive labeled datasets, improving model adaptability.
Reinforcement Learning	Optimizes maintenance scheduling by dynamically learning from equipment performance data.	Continuously refines maintenance strategies based on real-time feedback.
Digital Twin Technology	Creates virtual representations of physical assets to simulate operational conditions and improve failure prediction accuracy.	Enhances predictive modeling by reducing reliance on physical testing, optimizing resource use.

Liu et al. (2024) provide a comprehensive overview of predictive maintenance, integrating Industry 4.0 concepts such as IoT, big data, and AI. The book highlights predictive maintenance as a key advancement over traditional methods, emphasizing real-time condition monitoring, fault diagnosis, and predictive analytics to enhance equipment performance and reliability. A major focus is the shift from conventional maintenance to AI-driven models using sensor data, digital twins, and machine learning for early fault detection. Digital twin technology enables real-time simulations and failure forecasting, while predictive algorithms optimize maintenance schedules, reducing unplanned downtime and improving spare parts management.

A case study on Vestas illustrates how SCADA systems and predictive maintenance enhance wind turbine performance through real-time data analysis. The book also explores applications in agriculture and food processing, where IoT-enabled sensors anticipate failures in farm machinery, irrigation systems, and food processing equipment. AI-driven monitoring of refrigeration units and conveyor belts ensures food safety and reduces spoilage risks.

Additionally, the book examines AI-based automation techniques, including genetic algorithms, particle swarm optimization, and neural networks, for optimizing repair schedules. Challenges such as multi-source data fusion and sensor integration are addressed, emphasizing the need for robust predictive models. The work underscores the role of Industry 4.0 in advancing predictive maintenance, making industrial systems smarter, more reliable, and cost-efficient. The Table 2 provides a summarized overview of key insights from Liu et al. (2024). This summary captures the essential aspects of predictive maintenance methodologies, including its integration with Industry 4.0, applications of AI and machine learning, the role of digital twins, sensor technologies, and industry-specific implementations in agriculture and food processing. Additionally, the table highlights the primary challenges and future directions of AI-driven predictive maintenance.

Table 2

Extended Summary of Intelligent Predictive Maintenance

Topic	Key Insights
Predictive Maintenance Concept	Transition from reactive and preventive maintenance to AI-driven predictive strategies.
Integration with Industry 4.0	Use of Cyber-Physical Systems (CPS), Industrial IoT (IIoT), and big data for real-time monitoring.
AI and Machine Learning Models	Implementation of deep learning, Bayesian networks, fault tree analysis, and neural networks for failure prediction.
Digital Twin Applications	Creation of virtual replicas for failure forecasting, operational simulations, and process optimization.
Sensor Technologies	Integration of vibration sensors, acoustic emission monitors, and temperature sensors for real-time anomaly detection.

Topic	Key Insights
Applications in Agriculture (Extended Insight)	Additional insights on predictive maintenance applications in farm equipment, including IoT-enabled sensors on combine harvesters, irrigation systems, and agricultural processing equipment, reducing failures and optimizing performance.
Applications in Food Industry (Extended Insight)	Beyond the book's scope: AI-driven predictive maintenance for monitoring refrigeration units, conveyor belts, and packaging automation, ensuring food safety, reducing spoilage, and minimizing production disruptions.
Challenges and Future Directions	Challenges in data integration, sensor reliability, and computational resource requirements; advancements in edge computing and federated learning proposed as solutions.

Bala et al. (2024) explore the integration of artificial intelligence (AI) with edge computing for predictive maintenance in industrial machines, addressing key challenges in data processing and model deployment. The study categorizes existing approaches into three main architectures: cloud-based training with edge deployment, edge-based training for enhanced data privacy, and hybrid cloud-edge training. The review highlights the advantages of edge computing, such as reduced latency and improved availability, while also acknowledging challenges like limited computational power and the need for lightweight AI models. Additionally, the paper discusses emerging research directions, including synthetic data generation, transfer learning applications, and secure communication protocols for edge AI. This work contributes to the evolving landscape of AI-driven predictive maintenance by assessing the trade-offs between centralized and distributed learning architectures.

Glock et al. (2024) introduce a novel unsupervised CPD framework, Predict and Compare (P&C), which integrates predictive machine learning models with statistical validation methods to improve anomaly detection reliability. Their approach aligns closely with ensemble-based strategies, such as the "Council of the Wise" framework employed in this study, which aggregates multiple model outputs to enhance detection accuracy. Using both deep learning models (LSTM) and statistical models (ARIMA), the Predict and Compare method successfully identifies structural shifts while mitigating false positives caused by long-term trend variations. The insights from *Glock et al. (2024)* reinforce the importance of combining predictive modeling with statistical validation in predictive maintenance applications. Their findings serve as a valuable reference point for enhancing multi-model anomaly detection frameworks, further supporting the scalability and adaptability of predictive maintenance strategies across diverse industrial settings.

MATERIALS AND METHODS

The predictive maintenance analysis was conducted using data collected from a Massey Ferguson 7700 S tractor, a widely used model in modern precision agriculture. Data acquisition took place in May 2023, focusing on the tractor's hydraulic system, which plays a crucial role in various agricultural operations, including plowing, lifting, and operating auxiliary implements. Given that hydraulic systems in agricultural machinery are subject to high operational loads and varying environmental conditions, they are critical components for predictive maintenance assessment.

The Massey Ferguson 7700 S series is known for its high-performance engine, advanced transmission options, and robust hydraulic capabilities, making it an ideal candidate for predictive maintenance analysis. This model is typically equipped with a 6.6L AGCO Power engine, delivering 140 to 280 horsepower, depending on the variant. Its Dyna-VT continuously variable transmission (CVT) allows for smooth and efficient power delivery, enhancing fuel efficiency and reducing mechanical stress. However, the hydraulic system is one of the most stressed components in the tractor, as it directly influences the performance of attached implements and overall machine efficiency (<https://www.masseyferguson.com/en/product/tractors/mf-7700-s.html>).

The hydraulic system of the 7700 S series operates within a pressure range of 140 to 200 bar, providing the necessary force for lifting and operating various implements. This system consists of variable displacement pumps, pressure relief valves, hydraulic cylinders, and control units that regulate fluid flow and pressure. Given that hydraulic failures are often attributed to fluid contamination, wear in seals and valves, pressure fluctuations, and overheating, predictive maintenance techniques are crucial in detecting early signs of degradation before failures occur.

This study evaluates predictive maintenance strategies in agriculture using AI-driven failure prediction and sensor-based diagnostics. By integrating these methodologies, the objective was to reduce unplanned downtime, optimize maintenance schedules, and enhance the operational lifespan of the tractor's hydraulic system, ultimately contributing to increased agricultural productivity.

The predictive maintenance framework for agricultural and food industry machinery, specifically for the Massey Ferguson 7700 S tractor's hydraulic system, operates through an integrated process of data acquisition, processing, analysis, and decision-making.

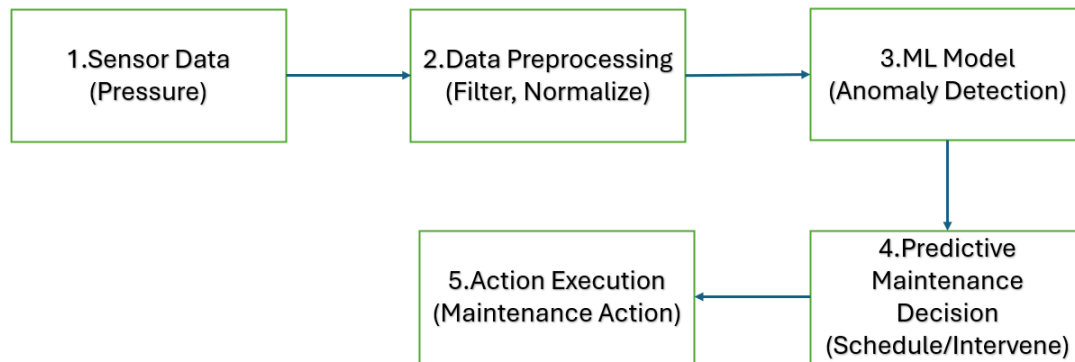


Fig. 1 - Data flow from sensor data collection through data preprocessing, ML model analysis (e.g., anomaly detection, failure prediction), maintenance decision-making, and action execution

The diagram in figure 1 follows a structured workflow that ensures early failure detection, optimizes maintenance scheduling, and improves equipment longevity.

1. **Sensor Data Collection.** The system begins with real-time data acquisition from multiple IoT-enabled sensors embedded in the hydraulic system of the tractor. These sensors continuously monitor key performance indicators (KPIs) such as:
 - hydraulic pressure fluctuations detect inefficiencies or valve blockages;
 - fluid temperature variations identify overheating risks or cooling inefficiencies;
 - vibration levels in hydraulic actuators and pumps indicates mechanical wear or imbalance;
 - operational workload and duty cycle variations determines stress levels on the system.
2. **Data Transmission and Preprocessing.** The collected sensor data is transmitted via wireless communication to an edge computing unit or cloud-based storage system. Here, the raw data undergoes preprocessing, including:
 - noise filtering – removes irrelevant fluctuations caused by environmental interference;
 - feature extraction – selects the most relevant sensor parameters for analysis;
 - data normalization – ensures consistency in input values across different operating conditions.
3. **Machine Learning Models for Anomaly Detection.** The processed data is then analyzed using machine learning (ML) models trained to recognize normal vs. abnormal operating patterns. Additionally, moving average and moving median filters were used as comparative statistical methods to smooth noisy sensor readings and identify abrupt fluctuations. While these are not machine learning techniques, they serve as baseline references to validate the anomaly detection models. Key AI techniques used include:
 - Time-Series Forecasting (LSTM, ARIMA – not applied in this study) to detect deviations from expected trends;
 - Isolation Forest and One-Class SVM for detecting anomalies by isolating rare and abnormal sensor readings;
 - K-Means and DBSCAN clustering to categorize different failure modes and identify outliers indicative of early-stage mechanical degradation;
 - Autoencoders for feature extraction and unsupervised anomaly detection, reconstructing normal operational states and identifying anomalies when deviations exceed a predefined threshold;
 - Convolutional Neural Networks (CNNs) to analyze spatial-temporal correlations in sensor data, particularly useful for identifying nonlinear relationships in hydraulic system degradation;
 - XGBoost for failure prediction, leveraging gradient-boosted decision trees to analyze feature importance and classify high-risk operational states.
4. **Predictive Maintenance Decision Making.** Based on the analysis, the system provides predictive alerts regarding potential failures before they occur. The maintenance strategy includes:
 - immediate alerts for critical failures when a component is on the verge of breakdown;
 - scheduled maintenance recommendations to address wear before it escalates;
 - spare parts inventory management ensuring the availability of necessary components based on predicted failure rates.

5. Action Execution and Maintenance Action Optimization. The system integrates with farm management software (FMS) or maintenance dashboards, allowing technicians to access real-time condition reports and historical performance logs. This enables:

- proactive intervention rather than reactive maintenance;
- minimized downtime by repairing components before catastrophic failure;
- cost reduction by avoiding unnecessary replacements and optimizing resource allocation.

To evaluate the performance of the hydraulic system, real-time sensor data was collected, encompassing pressure measurements, flow rates, temperature variations, and vibration levels. These parameters were continuously tracked to detect potential anomalies associated with seal wear, pump inefficiencies, valve obstructions, or hose degradation.

For this study, output pressure was selected as the primary diagnostic metric due to its critical role in assessing the health and efficiency of hydraulic pumps. Variations in pressure readings can reveal early signs of degradation, helping maintenance teams anticipate failures before they lead to system breakdowns. Several aspects of hydraulic pump performance can be inferred by closely monitoring pressure fluctuations, making it a valuable tool for predictive maintenance. One of the most critical insights that output pressure provides is an indication of internal component wear. A gradual drop in pressure over time may signal wear in essential components such as pistons, vanes, or gears, reducing overall efficiency and leading to performance losses. Additionally, monitoring pressure allows for the early detection of cavitation, a damaging condition where vapor bubbles form due to pressure inconsistencies and collapse violently, causing internal damage to the pump. While output pressure is an effective parameter for diagnosing hydraulic pump health, relying solely on it may not provide a complete picture of the system's condition. It is best used in combination with other parameters, such as flow rate, temperature, and vibration analysis, to create a more comprehensive predictive maintenance strategy. A multi-sensor approach helps improve diagnostic accuracy, allowing for a deeper understanding of the system's overall health and facilitating early anomaly detection (*Herrera-Granados et al., 2024*).

In this stage of the research, output pressure was selected as the primary health indicator of the hydraulic pump, with data recorded under constant torque conditions. The decision to maintain a constant torque setting provided a controlled operational environment, ensuring that any fluctuations in pressure readings could be attributed to internal factors within the pump or hydraulic system, rather than variations in external load or torque. By isolating pressure as the key variable, this study aimed to enhance the reliability of pressure-based diagnostics. Any deviations detected in the output pressure were more easily linked to specific mechanical issues such as component wear, cavitation, sealing degradation, or hydraulic resistance variations. These pressure anomalies act as early warning signals, allowing maintenance teams to take preventive action before critical failures occur.

The moving average is a widely used technique that smooths data by calculating the mean value over a predefined window of time. By averaging out short-term fluctuations, it provides a clearer representation of gradual changes in system behavior. For instance, if hydraulic pressure readings are recorded every second, applying a moving average over one minute interval can reveal long-term trends while minimizing the impact of transient noise. Large deviations from the moving average, such as sudden spikes or drops, can serve as early indicators of abnormal conditions. A sustained upward drift in temperature, for example, may suggest the gradual failure of a cooling system, while a sharp pressure drop could point to a hydraulic leak or valve malfunction. The moving median, in contrast, calculates the median value within a chosen time window, making it particularly effective at handling data sets with sudden, irregular spikes or short-lived anomalies. Unlike the moving average, which smooths all fluctuations evenly, the moving median focuses on the central tendency of the data, filtering out outliers that could distort the analysis. This property makes it highly valuable in predictive maintenance scenarios where sensor noise, electrical interference, or momentary load changes can create misleading spikes in the data. By emphasizing typical values rather than being influenced by extreme variations, the moving median helps in identifying genuine trends without overreacting to temporary fluctuations.

Combining the moving average and moving median offers a more comprehensive approach to anomaly detection. While the moving average is useful for identifying long-term trends and gradual deviations, the moving median ensures that brief, isolated spikes do not lead to false alarms. When applied together, these techniques provide a balanced perspective, helping maintenance teams distinguish between short-term disturbances and sustained changes that require intervention. This dual approach enhances predictive maintenance by allowing for early detection of subtle shifts in equipment behavior, ensuring that emerging faults can be addressed proactively before they lead to failures.

By incorporating both techniques into predictive maintenance strategies, organizations can optimize their ability to monitor system performance, improve failure prediction accuracy, and reduce the risk of unexpected breakdowns. These statistical smoothing methods serve as valuable tools in data preprocessing, supporting more advanced machine learning models by ensuring that input data remains stable, interpretable, and free from misleading noise. When integrated with real-time monitoring systems, moving averages and moving medians contribute to a more robust and reliable maintenance framework, ultimately improving operational efficiency and reducing downtime across industrial and agricultural applications.

One of the most valuable findings was that the most significant anomaly patterns were not necessarily extreme values, but rather subtle deviations that did not conform to typical operational trends. These nuanced anomalies, often overlooked by traditional threshold-based methods, reinforce the importance of leveraging multiple machine learning techniques to gain a more comprehensive perspective on system health. Given that no single model can be expected to detect every relevant anomaly with absolute accuracy, a more effective approach involves a form of ensemble learning inspired by the "wisdom of the crowd" principle.

This study proposes a method for estimating anomaly detection points, referred to as the "Council of the Wise." This approach relies on an ensemble decision-making system, where an odd number of models independently analyze incoming sensor data and "vote" on whether a given point should be classified as an anomaly requiring maintenance intervention. This method ensures a more balanced and reliable assessment, reducing the likelihood of false positives and false negatives. By aggregating the decisions of multiple diverse models, this ensemble approach enhances predictive accuracy and increases confidence in maintenance recommendations. For instance, if five out of the seven models flag a particular data point as anomalous, the system classifies it as an anomaly and triggers an alert for maintenance action. If only a minority of models detect an issue, the system may either discard the anomaly or mark it as a lower-priority concern for further observation. This voting mechanism mitigates the risk associated with the limitations of any single model, creating a more resilient and adaptive predictive maintenance framework.

By combining different models, each with distinct strengths in identifying various types of anomalies – whether based on density, clustering, reconstruction errors, or decision trees – the "Council of the Wise" approach maximizes the effectiveness of predictive maintenance. It reduces dependency on any single algorithm, ensuring a more robust and interpretable decision-making process. Ultimately, this proposed method enhances anomaly detection accuracy, optimizes maintenance scheduling, reduces downtime, and extends equipment lifespan, making it a valuable contribution to predictive maintenance strategies.

The "Council of the Wise" framework, where seven machine learning models independently analyze sensor data and "vote" to determine anomalies, shares conceptual similarities with the Digital Twin paradigm while serving a distinct function within predictive maintenance (*Pulcini and Modoni, 2024*). Both approaches leverage real-time data-driven decision-making and advanced computational models to enhance predictive accuracy and optimize system performance. A Digital Twin is a virtual replica of a physical system, continuously updated with sensor data to enable real-time monitoring, fault prediction, and operational optimization. In contrast, the "Council of the Wise" operates as an ensemble anomaly detection mechanism, where multiple machine learning models process the data independently and reach a consensus on potential failures. This ensemble approach enhances reliability by reducing false positives and ensuring that only significant deviations from normal operational patterns are flagged for maintenance interventions. Integrating the "Council of the Wise" within a Digital Twin framework could enhance predictive maintenance strategies by providing an additional decision-making layer. While the Digital Twin maintains a real-time simulation of system behavior, the ensemble-based "voting" mechanism would refine anomaly detection, improving failure prediction accuracy and ensuring more confident maintenance recommendations. This hybrid methodology would combine the benefits of continuous situational awareness and high-confidence anomaly detection, leading to proactive and precise intervention strategies, minimizing downtime, and optimizing resource allocation in industrial and agricultural applications.

In the field of predictive maintenance, accurately identifying early signs of mechanical degradation is essential to minimizing unplanned downtime and optimizing maintenance schedules. One of the key challenges in this domain is distinguishing genuine system anomalies from natural operational variations, particularly in complex industrial environments where data trends are influenced by multiple factors. Change point detection (CPD) techniques play a crucial role in this process, enabling systems to identify transitions between different operational states without being misled by normal fluctuations.

To develop a robust predictive maintenance framework, this study employed eight machine learning models: Isolation Forest, One-Class SVM, KMeans, DBSCAN, Autoencoders, Convolutional Neural Networks

(CNNs), XGBoost, and Gaussian Naïve Bayes. Each model was selected based on its ability to detect anomalies in hydraulic system pressure data, leveraging different approaches such as unsupervised learning, clustering, deep learning, and probabilistic classification. The following sections provide a detailed examination of how each model was applied and its effectiveness in identifying potential failures.

Isolation Forest is a powerful and efficient tool in predictive maintenance, particularly suited for detecting anomalies in systems where deviations in sensor data can indicate early signs of equipment wear, malfunction, or inefficiencies. It is an unsupervised machine learning algorithm designed to differentiate normal operating conditions from rare, abnormal events, making it highly effective in identifying potential failures before they escalate. Unlike One-Class SVM, which constructs a boundary around normal data points, Isolation Forest isolates anomalies by assessing how quickly a given data point can be separated from the majority of the dataset. This method works on the principle that anomalies are typically sparse and differ significantly from normal data, making them easier to isolate (Murphy, 2002; Xiao, 2022).

Isolation Forest is based on Isolation Trees (iTrees), which recursively divide data points by selecting random features and split values. For a given dataset X with n samples, an Isolation Tree is built using the following recursive function:

$$Partition(X) = \begin{cases} X, & \text{if } |X| = 1 \text{ (single point left)} \\ Partition(X_L) \cup Partition(X_R), & \text{otherwise} \end{cases} \quad (1)$$

where X_L and X_R are the left and right subsets after a random split on a randomly chosen feature. The height $h(x)$ of a data point x in an Isolation Tree represents the number of splits required to isolate x .

The key idea behind Isolation Forest is that anomalies are easier to isolate than normal points, so they tend to have shorter average path lengths in the Isolation Trees.

$$E(h(x)) = 2H(n-1) - \frac{2^{(n-1)}}{n} \quad (2)$$

where $H(n)$ is the harmonic number, approximated as:

$$H(n) \approx \ln(n) + 0.5772156649 \text{ (Euler - Mascheroni constant)} \quad (3)$$

Since anomalies tend to be isolated faster, their expected path length $E(h(x))$ is smaller than that of normal points.

To quantify how anomalous a point is, Isolation Forest computes an anomaly score $s(x)$ based on the path length:

$$s(x) = 2^{-\frac{E(h(x))}{c(n)}} \quad (4)$$

where $c(n)$ is an adjustment factor for normalizing path lengths:

$$c(n) = 2H(n-1) - \frac{2^{(n-1)}}{n} \quad (5)$$

The anomaly score $s(x)$ falls within the range $[0,1]$. If we have a high $s(x)$ ($s(x) \sim 1$) is likely an anomaly (isolated quickly). If we have a low $s(x)$ ($s(x) \sim 0$) is likely normal data (requires many splits to isolate). A typical threshold for anomaly classification is $s(x) > 0.6$ or $s(x) > 0.7$ based on empirical tuning.

One-Class Support Vector Machine (One-Class SVM) is a kernel-based anomaly detection model that learns a boundary around normal data and identifies points outside this boundary as anomalies. Unlike traditional SVMs used for classification, One-Class SVM is an unsupervised algorithm that operates on a single class of data (Murphy, 2002; Xiao, 2022).

One-Class SVM finds a hyperplane or hypersphere that best encloses normal data, separating it from potential outliers. The optimization problem is formulated as:

$$\min \frac{1}{2} \|w\|^2 + \frac{1}{\nu n} \sum_{i=1}^n \xi_i - \rho \quad (6)$$

where w is the normal vector defining the hyperplane, $\xi_i \geq 0$ are slack variables allowing some flexibility for soft margins, ρ is the decision boundary threshold, ν is the hyperparameter controlling the fraction of outliers allowed in the dataset (typically between 0 and 1), n is the number of training samples. The goal is to maximize the margin while allowing a small fraction of the training points to be considered anomalies.

Once trained, One-Class SVM uses the following decision function to classify new data points:

$$f(x) = \text{sign}(w \cdot \phi(x) - \rho) \quad (7)$$

where $\phi(x)$ is a feature transformation function (applied via a kernel), ρ is the threshold learned from the training data. A new point x is classified as normal if $f(x) \geq 0$ or anomalous if $f(x) < 0$.

One-Class SVM is a widely used tool in predictive maintenance, particularly effective for detecting anomalies in systems where normal operating behavior dominates, but occasional deviations may indicate potential faults, wear, or system degradation. Its ability to model normal conditions and identify unexpected variations makes it a valuable method for early fault detection, allowing maintenance teams to intervene before

minor issues develop into costly failures. In predictive maintenance applications, data is continuously collected from sensors monitoring critical parameters and other performance indicators. One-Class SVM is trained exclusively on this normal operating data, constructing a mathematical boundary that encapsulates expected values. Once trained, the model evaluates new sensor readings by determining whether they fall within or outside this learned boundary. Any data point that significantly deviates from the norm is flagged as an anomaly, signaling potential irregularities in the system.

KMeans is a widely used clustering technique that partitions data into a predefined number of clusters based on similarity. In predictive maintenance, this method is particularly effective for analyzing historical sensor data to identify typical operating states. By defining clusters that represent normal working conditions, KMeans can evaluate new data points in real-time. If a new observation falls significantly outside the boundaries of these predefined clusters, it is flagged as an outlier or anomaly. This approach is well-suited for relatively stable systems where operational patterns remain consistent (Murphy, 2002; Xiao, 2022).

The goal of K-Means is to minimize the total variance within clusters, defined as:

$$J = \sum_{i=1}^k \sum_{x \in C_i} \|x - \mu_i\|^2 \quad (8)$$

where J is the total sum of squared distances (cost function), k is the number of clusters, C_i is the set of points assigned to cluster i , x is a data point in cluster C_i , μ_i is the centroid of cluster i , $\|x - \mu_i\|^2$ represents the squared Euclidean distance between a point and its cluster center. The algorithm seeks to find the optimal centroids μ_i that minimize this cost function.

Each data point is assigned to the closest centroid using the Euclidean distance:

$$c(x) = \arg \min_i \|x - \mu_i\| \quad (9)$$

where $c(x)$ is the cluster index assigned to x . The function finds the centroid μ_i that minimizes the distance to x .

The algorithm iterates until centroids no longer change significantly or the decrease in cost function is below a threshold:

$$\mu_i^{(t+1)} - \mu_i^{(t)} < \epsilon \quad (10)$$

where t is the iteration index, ϵ is a small predefined tolerance level.

DBSCAN (Density-Based Spatial Clustering of Applications with Noise) offers a more flexible approach to anomaly detection by clustering data points based on density rather than predefining a fixed number of clusters. Unlike KMeans, which assumes that all data points should belong to a cluster, DBSCAN labels low-density points as noise or anomalies. This makes it particularly effective in handling complex sensor data where operating conditions may fluctuate, and anomalies do not necessarily conform to a fixed pattern (Xiao, 2022).

DBSCAN uses two important hyperparameter: ϵ (neighborhood radius) that defines the maximum distance within which points are considered neighbors and min_pts – minimum points – that defines the minimum number of points required within a neighborhood of radius ϵ for a point to be considered a core point.

To measure similarity between points, DBSCAN typically uses the Euclidean distance:

$$d(x_i, x_j) = \sqrt{\sum_{k=1}^d (x_{ik} - x_{jk})^2} \quad (11)$$

where $d(x_i, x_j)$ is the Euclidean distance between two points x_i and x_j , d is the number of dimensions, x_{ik} and x_{jk} are the k -th features of points i and j . Other distance metrics like Manhattan distance or Cosine similarity can be used depending on the application.

A point x in the dataset is classified into one of three categories:

- core point, if it has at least min_pts neighbors within distance

$$|\{x_j \in D \mid d(x_i, x_j) \leq \epsilon\}| \geq min_pts \quad (12)$$
- border point, if point lies within ϵ -distance of a core point but has fewer than min_pts neighbors;
- noise (outlier), if it is not a core point and does not lie within the ϵ -radius of any core point.

In predictive maintenance, DBSCAN is useful for identifying irregular or infrequent operating states that might not fit within predefined categories. For example, in rotating machinery, vibration readings often exhibit natural fluctuations due to varying loads and speeds (Laaradj et al., 2023; Popescu et al., 2022). DBSCAN can distinguish between expected variations and truly anomalous behavior, such as imbalance, misalignment, or excessive friction, by detecting low-density, outlier points in the data. Since DBSCAN does not require prior knowledge of the number of clusters, it is particularly advantageous for monitoring systems with variable operating conditions, where unexpected failures may arise in non-uniform patterns.

Both KMeans and DBSCAN contribute to a proactive maintenance strategy by enabling early detection of anomalies and potential faults. KMeans is best suited for systems with predictable and well-structured operational states, where deviations from established clusters can reliably indicate anomalies. In contrast, DBSCAN excels in complex and noisy environments where system behavior is more variable, allowing for greater adaptability in detecting rare but significant failures. By combining these clustering techniques with other anomaly detection methods, maintenance teams can improve predictive maintenance accuracy, optimize intervention timing, and extend the lifespan of critical machinery.

Convolutional Neural Networks (CNNs) are becoming increasingly valuable in predictive maintenance, particularly for detecting anomalies in sensor data that exhibit spatial or temporal patterns. While CNNs are traditionally known for their success in image processing, they have also proven to be highly effective in analyzing sequential data, making them a powerful tool for identifying irregularities in time-series sensor readings. Their ability to capture local dependencies within complex datasets allows them to recognize subtle variations that may indicate early signs of equipment degradation (Abo-Habaga et al., 2024; Subburaj et al., 2025; Yun et al., 2024; Zhang et al., 2024; Taner et al., 2024).

The fundamental operation in CNNs is convolution, which is applied between an input feature map and a set of learnable filters (kernels). Mathematically, the convolution operation for a 2D input (e.g., sensor data) is:

$$Z(i, j) = \sum_m \sum_n X(i - m, j - n)K(m, n) \quad (13)$$

Where:

$X(i, j)$ is input feature map (e.g., sensor data), $K(m, n)$ convolution kernel (filter), $Z(i, j)$ output feature map after convolution, (m, n) is kernel size (height and width). This convolution operation slides the kernel over the input and computes weighted sums, capturing local patterns like edges, trends, or changes in sensor data (Murphy, 2002; Xiao, 2022).

In predictive maintenance applications, CNNs are trained on historical sequences of normal operating data collected from sensors monitoring key parameters. By applying convolutional layers, CNNs extract patterns from these sequences, learning what constitutes normal fluctuations under different operating conditions. Unlike traditional anomaly detection methods that rely on manually defined thresholds, CNNs autonomously learn meaningful features from raw sensor data, enhancing their ability to detect deviations that signal emerging faults. Once trained, a CNN continuously processes new sensor data, comparing it to previously learned patterns. When it identifies abnormal trends – such as unexpected pressure spikes, sudden drops, or irregular variations in vibration frequency – it flags them as potential anomalies. These deviations may indicate developing issues such as wear in mechanical components, internal leaks in hydraulic systems, or imbalances in rotating machinery. By detecting these early-stage anomalies, CNNs enable maintenance teams to investigate and address potential failures before they escalate into severe damage or system downtime.

One of the primary advantages of CNNs in predictive maintenance is their ability to handle multidimensional data, making them particularly useful in systems where multiple sensor inputs need to be analyzed simultaneously. For example, in industrial machinery equipped with an array of sensors measuring different parameters, CNNs can correlate fluctuations across these variables, identifying complex patterns that may not be apparent through single-variable analysis. This capability allows for a more comprehensive assessment of equipment health, improving failure prediction accuracy.

Autoencoders, a specialized type of neural network, are highly effective in predictive maintenance for detecting anomalies in complex and nonlinear data patterns. Their primary function is to learn a compressed representation of normal operating data and then attempt to reconstruct it as accurately as possible. Any significant differences between the reconstructed output and the original data indicate deviations from expected patterns, which may signal the onset of equipment faults or mechanical degradation (Xiao, 2022).

An autoencoder aims to encode input data into a lower-dimensional representation and then reconstruct it as accurately as possible. It consists of two main parts: encoder that compresses input data into a latent space representation and decoder that reconstructs the original input from the latent space (Hajgató et al., 2022). Given an input x , an autoencoder learns two functions:

1. encoding function $z = f_{\theta}(x)$, where z is the latent representation (compressed encoding) and f_{θ} is the encoder function (usually a neural network with parameters θ);
2. decoding function $\hat{x} = g_{\phi}(z)$ where \hat{x} is the reconstructed input, g_{ϕ} is the decoder function (another neural network with parameters ϕ).

The goal of an autoencoder is to minimize the reconstruction error between x and \hat{x} .

Using XGBoost in combination with Isolation Forest creates a highly effective approach to anomaly detection in predictive maintenance, leveraging the strengths of both algorithms to enhance the accuracy and reliability of fault identification. This hybrid strategy takes advantage of Isolation Forest's ability to quickly isolate outliers while utilizing XGBoost's advanced pattern recognition to refine anomaly detection, reducing false positives and ensuring maintenance teams focus on critical system issues. Isolation Forest serves as the initial anomaly detection mechanism, analyzing historical sensor data – in this study, but could be also pressure, temperature, and vibration readings – to establish a model of normal operating behavior. By isolating outliers, it effectively flags deviations that may indicate potential failures. However, because Isolation Forest does not differentiate between minor fluctuations and critical anomalies, it can sometimes generate false positives, triggering unnecessary alerts. To refine these results, XGBoost is introduced as a second layer of analysis.

XGBoost optimizes a regularized loss function:

$$L = \sum_{i=1}^N l(y_i, \hat{y}_i) + \sum_{k=1}^K \Omega(f_k) \quad (14)$$

where $l(y_i, \hat{y}_i)$ is loss function (e.g., Log Loss for classification, MSE for regression), $\Omega(f_k)$ is regularization term to prevent overfitting, K number of trees, f_k prediction function for tree k .

Each XGBoost tree predicts the anomaly probability by using gradient boosting, where each new tree corrects the previous errors (Murphy, 2002):

$$g_i = \frac{\partial L}{\partial \hat{y}_i}, h_i = \frac{\partial^2 L}{\partial \hat{y}_i^2} \quad (15)$$

where g_i is gradient (first derivative of loss function), h_i is hessian (second derivative of loss function). These terms adjust tree weights for better classification of anomalies.

For each tree leaf, the new score is updated as:

$$w_j = -\frac{\sum g_i}{\sum h_i + \lambda} \quad (16)$$

where w_j is weight assigned to leaf j , λ is a regularization parameter.

The final anomaly score is a combination of Isolation Forest's anomaly score and XGBoost's refined classification probability:

$$S_{final}(x) = \alpha \cdot s_{IF}(x) + (1-\alpha) \cdot P_{XGB}(x) \quad (17)$$

where $s_{IF}(x)$ is Isolation Forest anomaly score, P_{XGB} is XGBoost probability of being an anomaly and α a weight parameter (controls importance of each method). A higher $S_{final}(x)$ means a higher likelihood of an anomaly.

Gaussian Naïve Bayes is a probabilistic classification model widely applied in predictive maintenance, particularly for anomaly detection and failure prediction in industrial systems. It operates based on Bayes' theorem, modeling each feature as following a Gaussian distribution (Murphy, 2002; Xiao, 2022).

The fundamental formula is:

$$P(C_k|X) = \frac{P(X|C_k)P(C_k)}{P(X)} \quad (18)$$

where $P(X|C_k)$ is the posterior probability of class C_k given the feature vector X , $P(X|C_k)$ is the likelihood, the probability of observing X given class C_k , $P(C_k)$ is the prior probability of class C_k , $P(X)$ is the marginal probability of the feature vector X , serving as a normalizing constant.

The assumption of Gaussian distribution allows the model to estimate the likelihood of different operating conditions based on historical sensor data, making it well-suited for systems where key parameters such as temperature, pressure, and vibration fluctuate within predictable ranges. Naïve Bayes assumes conditional independence of features, meaning:

$$P(X|C_k) = \prod_{i=1}^n P(X_i|C_k) \quad (19)$$

The predicted class is the one that maximizes the posterior probability:

$$C^* = \arg \max_{C_k} P(C_k|X) \quad (20)$$

Despite its strengths, Gaussian Naïve Bayes has limitations that must be considered when applying it to predictive maintenance. The model assumes independence between features, which may not always hold true in complex industrial systems where multiple variables interact. This simplification can lead to misclassifications, particularly when the underlying data distribution deviates significantly from a normal Gaussian pattern. Additionally, the model does not capture intricate dependencies between parameters as effectively as more advanced machine learning methods such as tree-based models or deep learning approaches.

Each of these eight machine learning models contributed with insights into anomaly detection, leveraging different mathematical approaches to identify deviations from normal operating conditions. Interestingly, some of the models identified similar patterns of abnormal behavior, reinforcing their reliability in predictive maintenance and suggesting consistency in detecting potential failures.

An important observation in this study was that Gaussian Naïve Bayes failed to detect any anomalies, making it unsuitable for inclusion in the final anomaly “voting” process. This is most likely due to the fact that Naïve Bayes relies on well-defined probability distributions and requires a larger dataset or extended training time to accurately learn the underlying patterns in the data. Given the complexity and variability of hydraulic pressure fluctuations, its assumptions about feature independence and Gaussian distribution may not have aligned well with the dataset, leading to an inability to effectively distinguish anomalies from normal operating conditions. This outcome underscores a broader challenge in artificial intelligence: the difficulty in predicting why certain models perform effectively in specific contexts while others fail to recognize meaningful patterns. Given its inability to identify anomalies in this dataset, Gaussian Naïve Bayes was excluded from the final decision-making process, ensuring that only models capable of reliably detecting deviations contributed to the “Council of the Wise voting” framework.

The implementation of all machine learning models was carried out using Python 3.9. The experiments were conducted using widely adopted open-source libraries, including Scikit-learn, TensorFlow, Keras, XGBoost, NumPy, and Matplotlib. Model training and evaluation were performed on a workstation equipped with an Intel Core i7 processor, 32 GB of RAM, and the Ubuntu 20.04 LTS operating system. This configuration provided sufficient computational resources to train the models efficiently and ensured the reproducibility of results in a controlled and stable software environment.

The dataset used in this study was recorded during real-life plowing operations in May 2023, using a Massey Ferguson 7700 S tractor equipped with a hydraulic pressure sensing system. In order to minimize external variability and isolate equipment behavior, an approximately constant torque level was maintained throughout the entire recording period, regulated by the onboard electronic control system. The dataset includes measurements sampled at a frequency of 20 Hz and later aggregated using harmonic means calculated over one-minute intervals, providing a stable temporal structure suitable for anomaly detection models. The models based on unsupervised learning, such as Isolation Forest, One-Class SVM, K-means, and Autoencoder, were trained using data presumed to represent normal system behavior, as no labeled anomalies were available at the time of analysis. For the deep learning models (Autoencoder and 1D CNN), the training was performed exclusively on segments of data identified as non-anomalous, with model evaluation conducted by observing reconstruction errors and deviation from learned representations. No separate validation dataset was required in the traditional supervised sense, as the focus of the analysis was on outlier and anomaly detection in time-series sensor data using models that learn from normal conditions. The detection results were cross-referenced with expert knowledge and system behavior to verify the correctness of anomaly localization.

The decision to average the pressure values was based on the operational characteristics of hydraulic systems, where most mechanical degradation processes and failure precursors evolve over extended periods rather than instantaneously. High-frequency fluctuations, while relevant in some cases, can introduce unnecessary noise in anomaly detection models, potentially leading to false positives. By computing one-minute mean values, we retained essential variations indicative of progressive component wear, valve inefficiencies, or pressure instabilities while minimizing the impact of momentary perturbations caused by sensor noise or minor operational transients. Additionally, reducing the data dimensionality improved computational efficiency. Despite this averaging process, the dataset still captured meaningful pressure variations associated with the hydraulic system’s health, ensuring that predictive maintenance insights were not compromised.

RESULTS

To comprehensively assess anomalies in the hydraulic system of the Massey Ferguson 7700 S tractor, seven machine learning models were applied: Isolation Forest, One-Class SVM, KMeans, DBSCAN, Autoencoders, CNNs, and XGBoost. Each of these models independently analyzed the sensor data, identifying deviations from normal operating conditions.

Figure 2 presents a comparative analysis between Moving Average, Moving Median, and the anomalies detected by Isolation Forest in the hydraulic pressure data. The Moving Average smooths out short-term fluctuations by averaging data points within a defined window, providing a clearer trend of pressure variations. Similarly, the Moving Median filters out transient spikes and noise, making it particularly effective in handling abrupt outliers that might distort the overall trend. A significant portion of the anomalies flagged by Isolation Forest aligns with points where the Moving Average and Moving Median exhibit noticeable deviations or sudden shifts, suggesting that the system experienced abnormal fluctuations in hydraulic pressure. However, while the Moving Average and Moving Median indicate general pressure trends, they do not inherently classify anomalies, unlike Isolation Forest, which explicitly isolates unusual patterns.

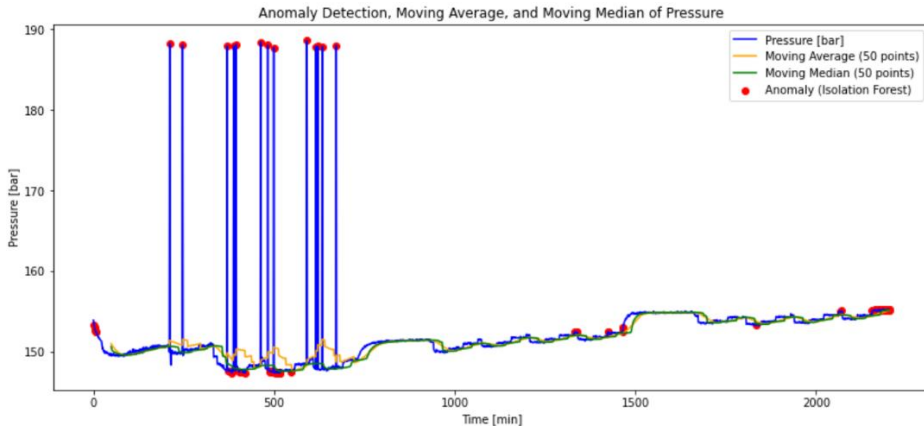


Fig. 2 – Moving Average and Moving Median compared with the anomalies detected by Isolation Forest in the hydraulic pressure data

This comparison highlights that statistical smoothing techniques like Moving Average and Moving Median can aid in visually interpreting pressure fluctuations, but they lack the ability to proactively detect anomalies with the same precision as machine learning-based models. The observed correlation between some of the Isolation Forest anomalies and deviations in the statistical trends reinforces the effectiveness of machine learning models in predictive maintenance, as they can effectively differentiate between normal system variations and potential faults.

The following figures (Figure 3 to 9) present the results of each machine learning model, showcasing their performance in detecting anomalies over time within the hydraulic pressure data. Each plot highlights pressure fluctuations and flagged anomalies, allowing for a comparative analysis of detection performance.

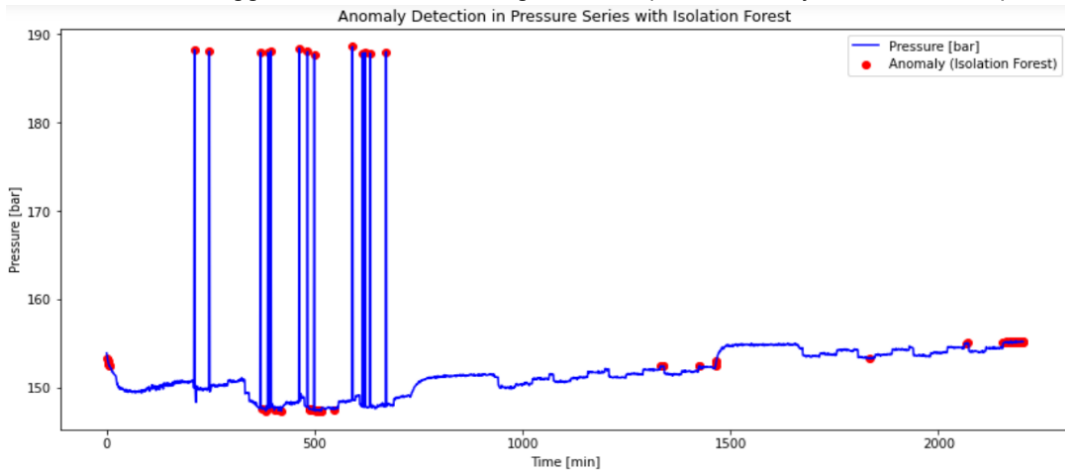


Fig. 3 – Isolation Forest results

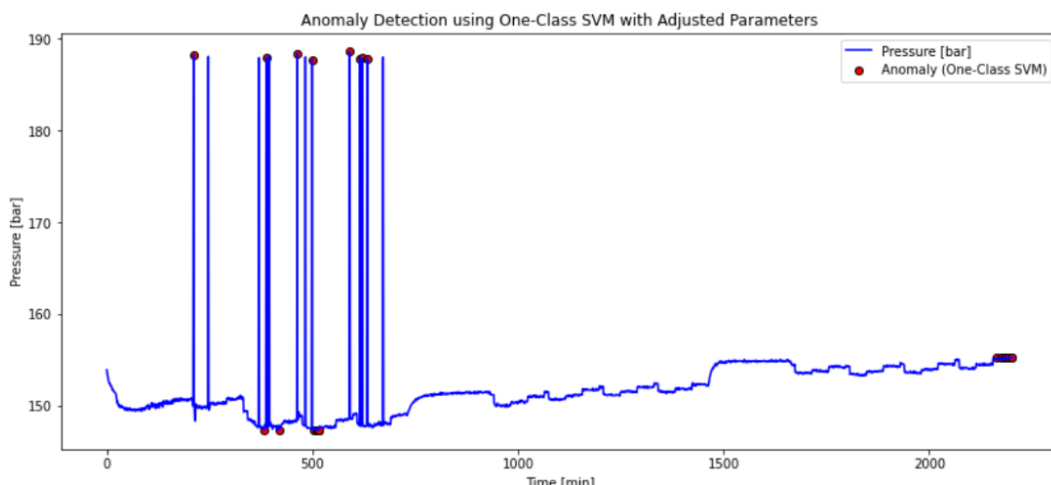


Fig. 4 – One-Class SVM results

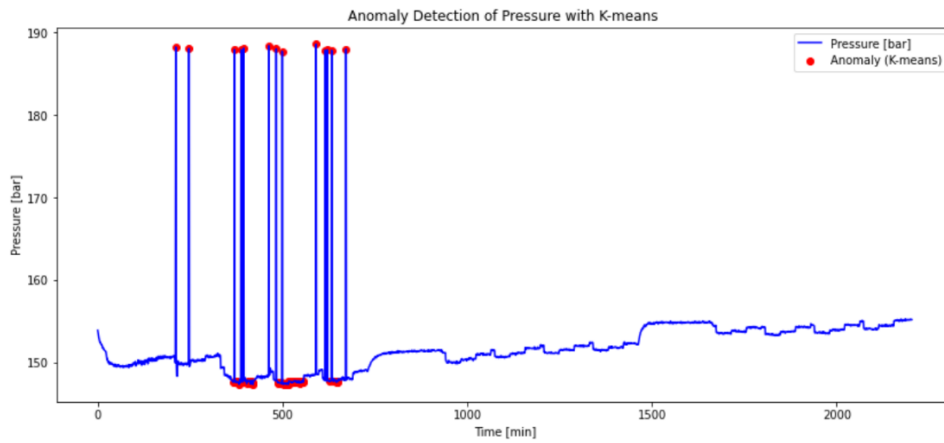


Fig. 5 – KMeans clustering results

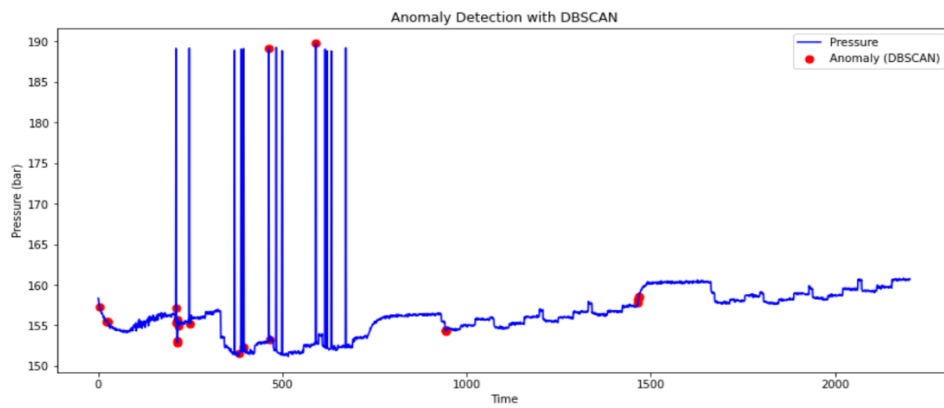


Fig. 6 – DBSCAN results

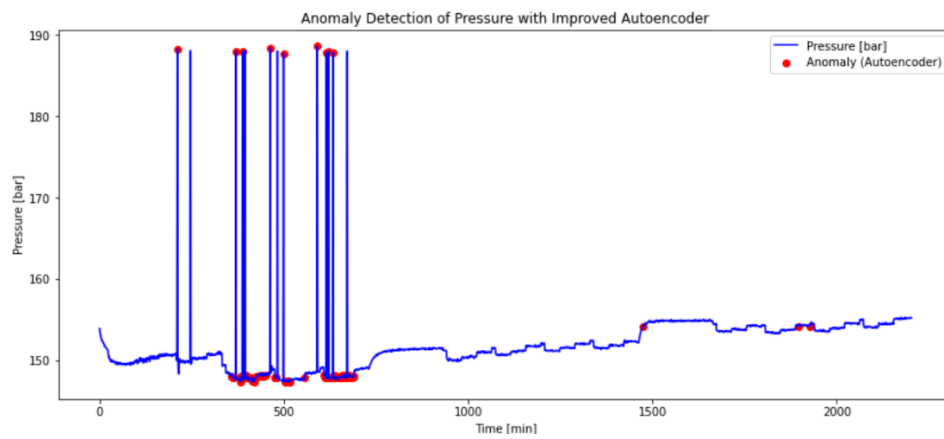


Fig. 7 – Autoencoder results

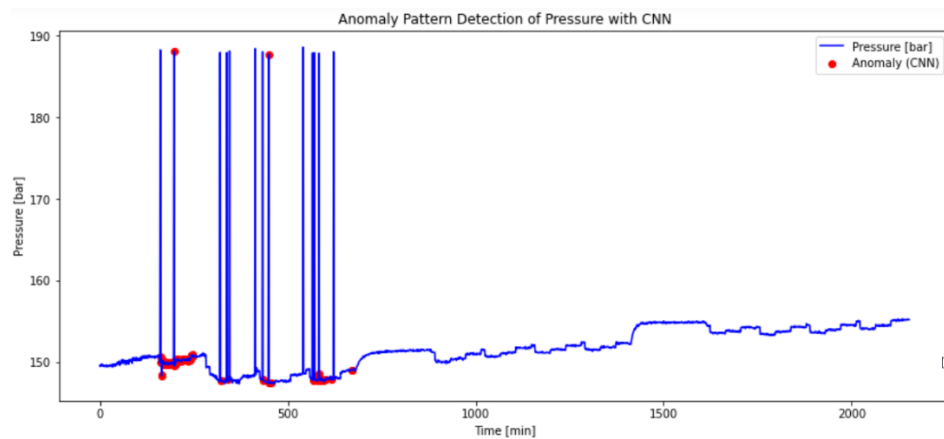


Fig. 8 – CNN results

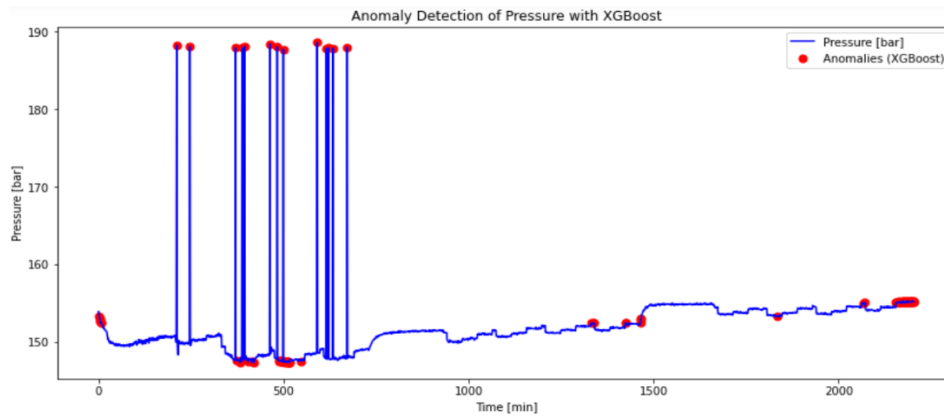


Fig. 9 – XGBoost results

Each figure provides a visual representation of how each algorithm performed in identifying anomalies, offering insights into their sensitivity, reliability, and potential limitations. The final anomaly decision (Table 3 and Figure 10), however, was determined using the "Council of the Wise" method, where an anomaly was validated only if at least four out of the seven models concurred on its presence. This consensus-based approach enhances the robustness of anomaly detection by reducing false positives and ensuring that flagged anomalies are significant deviations from normal operating conditions. By integrating these machine learning models, a robust anomaly detection framework was developed, ensuring greater accuracy in predictive maintenance. The results demonstrate that while some models are more sensitive, others provide a higher precision in detecting real faults.

Table 3 presents critical pressure anomalies identified through a consensus-based approach, where multiple machine learning models independently flagged specific points as outliers. These anomalies, identified under the specified experimental conditions, represent deviations from normal operational behavior in the hydraulic system of the Massey Ferguson 7700 S tractor. "The Council of the Wise" method, proposed in this study, combines the outputs of seven anomaly detection models (Isolation Forest, One-Class SVM, KMeans, DBSCAN, Autoencoders, CNNs, and XGBoost). Instead of relying on a single detection method, the approach ensures robustness by requiring that at least four models agree on an anomaly before it is classified as an outlier. This majority "voting" mechanism helps mitigate false positives and enhances detection accuracy.

Each entry in the table corresponds to a timestamp (Time, in minutes) and a recorded pressure value (Pressure, in bar), which has been identified as anomalous. These anomalies may indicate incipient mechanical degradation, hydraulic system inefficiencies, or potential faults, such as: valve malfunctions, leading to sudden pressure drops or spikes; cavitation or fluid instability, which can create short-term fluctuations in pressure; internal component wear, affecting system performance.

Since pressure variations in hydraulic systems are inherently dynamic, the use of this "voting"-based ensemble method significantly could improve reliability in predictive maintenance. These flagged anomalies warrant further inspection and maintenance intervention before they evolve into critical failures, thereby reducing downtime and improving system longevity.

Table 3

Final anomalies

Time (s)	Pressure (bar)
2164	151.71
2175	151.81
2186	151.81
2203	151.83
211	188.71
247	188.62
370	188.50
378	145.43
381	145.40
483	188.52
499	188.34
500	145.03
502	144.98
504	145.13
505	145.08
507	145.05
509	144.95
515	144.95
516	144.95
591	188.80
621	188.36
633	188.34
672	188.62

While this study focuses primarily on hydraulic pressure as a key indicator for predictive maintenance, additional sensor data – such as vibration, temperature, and load variation – were also collected during the experimental phase. However, to ensure clarity, reproducibility, and focus in this first phase of model evaluation, only pressure-based analysis was presented. These additional sensor signals are currently being processed and will be integrated into a multi-sensor anomaly detection framework in future work. The inclusion of multiple sensor streams is expected to enhance the robustness of the models and allow more nuanced fault detection and diagnostics.

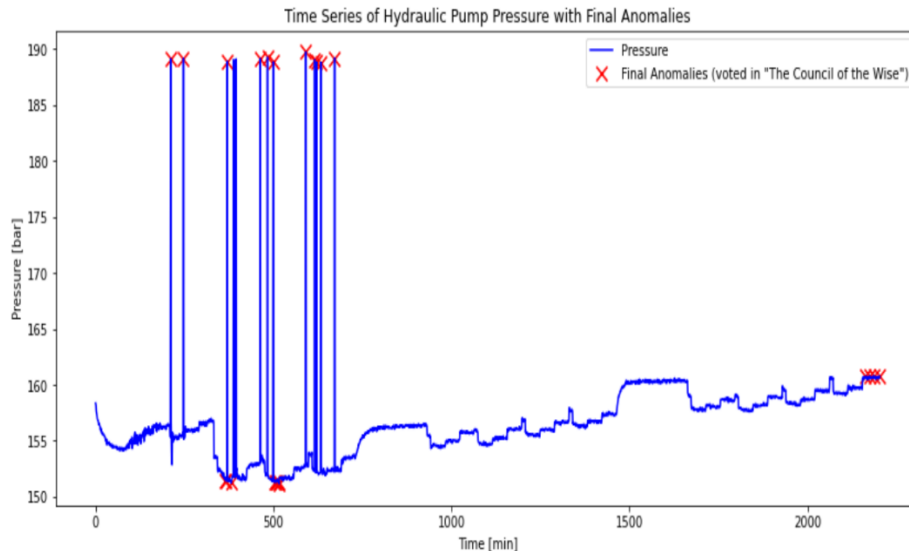


Fig. 10 – Final "voted" anomalies

CONCLUSIONS

The final results, summarized in Table 3, confirm the effectiveness of the "Council of the Wise" approach in identifying critical anomalies in the hydraulic system of the Massey Ferguson 7700 S tractor. The detected anomalies indicate significant deviations from normal operating conditions, with pressure values fluctuating beyond expected ranges. This validates the robustness of the multi-model "voting" framework, which successfully filtered out noise, reduced false positives, and preserved the most relevant anomalies.

The temporal distribution of anomalies reveals two key insights. Clusters of anomalies occurring within short intervals suggest transient mechanical instabilities, possibly due to sudden pressure surges, valve malfunctions, or localized hydraulic inefficiencies. In contrast, isolated anomalies at different time points indicate gradual wear or intermittent system irregularities that may not be detected by traditional threshold-based monitoring. By using seven machine learning models, this ensemble-based approach improves predictive maintenance reliability by incorporating diverse detection capabilities. The ability to reduce false alarms while capturing early indicators of mechanical degradation enhances its practical applicability for agricultural machinery maintenance. While this study highlights the potential of the approach, future research could further refine adaptive sampling techniques to enhance data utilization. Retaining raw high-frequency sensor data where beneficial, alongside dynamic aggregation methods, may improve both detection accuracy and computational efficiency. Additionally, optimizing the data preprocessing pipeline could help achieve a better balance between real-time responsiveness and long-term trend analysis. This study focused primarily on hydraulic pressure as an indicator, but incorporating additional sensor data – temperature fluctuations, vibration analysis, mechanical load variations, and fuel consumption metrics – could provide a more comprehensive failure prediction framework. Expanding monitored parameters would enhance fault detection accuracy, root cause analysis, and predictive capabilities.

It is acknowledged that under typical agricultural operations, torque is not constant and may vary due to factors such as soil resistance, implement load, or maneuvering dynamics. In the current experimental setup, torque was intentionally held approximately constant in order to isolate the effects of internal system behavior on hydraulic pressure, and to validate the ability of machine learning models to detect anomalies under controlled conditions. Future stages of this research will involve data collection under variable torque conditions, representing more realistic operating environments. This will allow the models to learn and adapt to fluctuations caused by load dynamics, and assess the robustness of anomaly detection under more complex field conditions.

Overall, these findings demonstrate that the multi-model “voting” framework is a promising predictive maintenance methodology, offering a reliable, automated, and proactive solution for identifying failures before they escalate into costly breakdowns. Future research should explore its adaptability to different agricultural machinery types and operational conditions, refining the approach through advanced AI techniques and real-time deployment.

REFERENCES

- [1] Abo-Habaga, M., Ismail, Z., Moustafa, N., Okasha, M., (2024), Developing an Automatic Precision Seeding Unit (APSU) for Pot Seed Planting, December 2024, *INMATEH Agricultural Engineering* 74(3), pp. 260-272, doi: <https://doi.org/10.35633/inmateh-74-22>.
- [2] Bala, A., Rashid, R.Z.J., Ismail, I., Oliva, D., Muhammad, N., Sait, S., Al-Utaibi, K., Amosa, T.I., Memon, K.A., (2024), Artificial intelligence and edge computing for machine maintenance-review, *Artificial Intelligence Review* 57:119, doi: <https://doi.org/10.1007/s10462-024-10748-9>.
- [3] Glock, A.-C., Sobieczky, F., Fürnkranz, J., Filzmoser, P., Jech, M., (2024), Predictive change point detection for heterogeneous data, *Neural Computing and Applications* 36, pp. 16071–16096, doi:<https://doi.org/10.1007/s00521-024-09846-0>.
- [4] Hajgató, G., Wéber, R., Szilágyi, B., Tóthpál, B., Gyires-Tóth, B., Hős, C., (2022), PredMaX: Predictive maintenance with explainable deep convolutional autoencoders, *Advanced Engineering Informatics* 54 101778, doi: <https://doi.org/10.1016/j.aei.2022.101778>.
- [5] Herrera-Granados, G., Misaka, T., Herwan, J., Komoto, H., Furukawa, Y., (2024), An experimental study of multi-sensor tool wear monitoring and its application to predictive maintenance, *The International Journal of Advanced Manufacturing Technology* 133, pp. 3415–3433, doi: <https://doi.org/10.1007/s00170-024-13959-0>.
- [6] Kammerer, C., Gaust, M., Küstner, M., Starke, P., Radtke, R., Jesser, A. (2021), Motor Classification with Machine Learning Methods for Predictive Maintenance, *IFAC PapersOnLine* 54-1, pp. 1059–1064, available online at www.sciencedirect.com.
- [7] Laaradj, S., Abdelkader, L., Mohamed, B., Mourad, N., (2023), Vibration-based fault diagnosis of dynamic rotating systems for real-time maintenance monitoring, *The International Journal of Advanced Manufacturing Technology* 126, pp. 3283–3296, doi: <https://doi.org/10.1007/s00170-023-11320-5>.
- [8] Li, Z., He, Q., Li, J., (2024), A survey of deep learning-driven architecture for predictive maintenance, *Engineering Applications of Artificial Intelligence* 133, 108285, doi: <https://doi.org/10.1016/j.engappai.2024.108285>.
- [9] Lima, A.L, da C. D., Aranha, V.M., Carvalho, C.J de L., Nascimento, E.G.S., (2021), Smart predictive maintenance for high-performance computing systems: a literature review, *The Journal of Supercomputing* 77, pp. 13494-13513, doi: <https://doi.org/10.1007/s11227-021-03811-7>.
- [10] Liu, M., Li, L., Yan, F., (2024), *Intelligent Predictive Maintenance*, Springer, ISBN 978-981-97-2676-9, doi: <https://doi.org/10.1007/978-981-97-2677-6>.
- [11] Meddaoui, A., Hachmoud, A., Hain, M., (2024), Advanced ML for predictive maintenance: a case study on remaining useful life prediction and reliability enhancement, *The International Journal of Advanced Manufacturing Technology* 132, pp. 323–335, doi: <https://doi.org/10.1007/s00170-024-13351-y>.
- [12] Murphy, K.P., (2022), *Probabilistic Machine Learning*, MIT Press, ISBN 978-0-262-04682-4, LC record <https://lccn.loc.gov/2021027430>.
- [13] O’Neil, R, Diallo, C., Khatab, A. (2022), A Novel Predictive Selective Maintenance, Strategy Using Deep Learning and Mathematical Programming, *IFAC PapersOnLine* 55-10, pp. 1207-1212, available online at www.sciencedirect.com.
- [14] Ouadah, A., Leila Zemmouchi-Ghomari, L., Salhi, N. (2022), Selecting an appropriate supervised machine learning algorithm for predictive maintenance, *The International Journal of Advanced Manufacturing Technology* 119, pp. 4277-4301, doi: <https://doi.org/10.1007/s00170-021-08551-9>.
- [15] Popescu, T., Aiordachioaie, D., Culea-Florescu, A. (2022), Basic tools for vibration analysis with applications to predictive maintenance of rotating machines: an overview, *The International Journal of Advanced Manufacturing Technology* 118, pp. 2883–2899, doi: <https://doi.org/10.1007/s00170-021-07703-1>.
- [16] Pulcini, V., Modoni, G., (2024), Machine learning-based digital twin of a conveyor belt for predictive maintenance, *The International Journal of Advanced Manufacturing Technology* 133, pp. 6095-6110, doi: <https://doi.org/10.1007/s00170-024-14097-3>.

- [17] Serradilla, O., Zugasti, E., Rodriguez, J., Zurutuza, U., (2021), Deep learning models for predictive maintenance: a survey, comparison, challenges and prospects, *Applied Intelligence* 52, pp. 10934-10964, doi: <https://doi.org/10.1007/s10489-021-03004-y>.
- [18] Siraskar, R., Kumar, S., Patil, S., Bongale, A., Kotecha, K., (2023), Reinforcement learning for predictive maintenance: a systematic technical review, *Artificial Intelligence Review* 56, pp. 12885–12947, doi: <https://doi.org/10.1007/s10462-023-10468-6>.
- [19] Subburaj, S.D.R., Eswaramoorthy, C., Latha, V.G., Chinnasamy, R.K.P., (2025), Efficient Pest Detection Through Advanced Machine Learning Technique, *Current Agriculture Research Journal* 12(3), pp. 1127-1134, DOI: <http://dx.doi.org/10.12944/CARJ.12.3.08>.
- [20] Taner, A., Mengstu, M.T., Selvi, K. Ç., Duran, H., Gür, I., Ungureanu, N., (2024), *Apple Varieties Classification Using Deep Features and Machine Learning*, *Agriculture*, 14, 252. doi: <https://doi.org/10.3390/agriculture14020252>.
- [21] Wang, X., Zhang, G., Yao, J., Lian, J., Yang, X., (2023), Fault Prediction Model of Corn Grain Harvester Based on Self-Coding Neural Network, *INMATEH - Agricultural Engineering* 70(2), pp. 221-231, doi: <https://doi.org/10.35633/inmateh-70-22>.
- [22] Xiao, P., (2022), *Artificial Intelligence Programming with Python*, Wiley, ISBN 978-1-119-82086-4, LC record <https://lccn.loc.gov/2022931189>.
- [23] Yang, X., Zhang, G., Yao, J., Lian, J., Xin Wang, X., Lv, D., Yujie Dend, Y., Zhang, A., (2022), Reliability Analysis of Grain Combine Harvesters Based on Data Mining Technology, *INMATEH - Agricultural Engineering* 67(2), pp. 211-220, doi: <https://doi.org/10.35633/inmateh-67-21>.
- [24] Yun, Y., Ma, Z., An, X., Li, D. (2024), *On-Site Intelligent Grading System for Fruits and Vegetables: Case Studies on Tomato and Apple*, pp. 61- 85, in Yun, Y., Sheng, W., Zhang, Z., (Editors), *Advanced Sensing and Robotics Technologies in Smart Agriculture*, Springer, ISBN 978-981-97-6440-2, doi: <https://doi.org/10.1007/978-981-97-6441-9>.
- [25] Zhang, C., Wang, N., Li, C., Sun, J., Jiang, Q., Han, X., Wang, J. (2024), Research on Defect Identification of Yu-Lu-Xiang Pears Based on Improved Lightweight Residual Neural Network Model, *INMATEH - Agricultural Engineering* 74(3), pp. 117-126, doi: <https://doi.org/10.35633/inmateh-74-10>.
- [26] Zhang, W., Zhao, B., Li, G., Zhou, L., Niu, K., Gao, S., (2023), Configuration Optimization Method of Agricultural Machinery Cluster Operation Maintenance Service Vehicle, *INMATEH – Agricultural Engineering* 69(1), pp. 537-548, doi: <https://doi.org/10.35633/inmateh-69-51>.

IMPROVED YOLOV8-ALGORITHM FOR SORTING FRESH WHITE TEA: COMBINING FEATURE ENHANCEMENT AND ATTENTION MECHANISM

改进的 YOLOv8 新鲜白茶分选算法：将特征增强与注意力相结合

Xuedong YU^{1,2}, Yadong NIU¹, Zhongyou ZHOU^{1,2}, Bo LU^{1,2}, Kaiqiang JIN^{1,2}, Rongyang WANG^{*1,2}

¹) College of Intelligent Manufacturing and Elevator Technology, Huzhou Vocational and Technical College, Huzhou, China

²) The Huzhou Key Laboratory of Robot System Integration and Intelligent Equipment, Huzhou, China

Tel: +8613957255852; E-mail: 2022024@huvtc.edu.cn

DOI: <https://doi.org/10.35633/inmateh-75-80>

Keywords: tea sorting; Dynamic Snake Convolution module; Multi-Head Self-Attention mechanism; YOLOv8

ABSTRACT

In this paper, an improved intelligent sorting algorithm for YOLOv8 white tea fresh leaves is proposed to solve the problems of unclear tea grades and uneven product levels caused by mechanical picking. The algorithm introduces the Dynamic Snake Convolution module (DsConv) for feature enhancement and adds an attention mechanism module, the Multi-Head Self-Attention mechanism (MHSA). Experiments show that the YOLOv8-DsConv-MHSA algorithm has an average accuracy of 96.4% and an average detection rate of 126.6 FPS per second, which is the best algorithm for white tea fresh leaf sorting in the comprehensive comparison. After deploying the proposed YOLOv8-DsConv-MHSA algorithm onto the developed tea sorting machine and conducting experimental comparisons with existing tea sorting machines, it is evident that the screening rate has been enhanced by 10.7%, and the operational efficiency has increased by 20%.

摘要

本文提出了一种改进的 YOLOv8 白茶鲜叶智能分拣算法，以解决机械采摘造成的茶叶等级划分不清和产品层次不齐的问题。该算法引入了动态蛇形卷积模块 (DsConv) 进行特征增强，并且添加了注意力机制模块--多头自我注意力 (MHSA)。实验表明：YOLOv8-DsConv-MHSA 算法的平均准确率为 96.4%，平均检测率为每秒 126.6 FPS，是综合比较中白茶鲜叶分选效果最好的算法。将所提出的 YOLOv8-DsConv-MHSA 算法部署到研发的茶叶分选机上，与现有茶叶分选机进行实验对比可知，筛分率提升了 10.7%，作业效率提升了 20%。

INTRODUCTION

Tea is an important economic crop in China, and the area under tea cultivation is one of the largest in the world, with a total production value of more than 600 billion yuan (\$86.6 billion). Scientific studies have shown that tea has great benefits for human health, and the demand for high-quality tea is gradually increasing (Ruxton *et al.*, 2013). Due to the huge production of tea, the picking method is gradually transitioning from labor to mechanization (Zheng *et al.*, 2011). The cost of tea picking through machinery has been greatly reduced, and the efficiency has been improved, but through the mechanical way of tea picking, the tea leaves picked will be mixed with leaf stems and debris, which need to be further sorted out to realize the tea grading of the high-quality fresh tea leaves (Yuan *et al.*, 2016).

Research on grading of machine-picked tea can improve the quality of machine-picked tea and is an effective way to solve the problem of high-quality tea picking. At present, most of the common tea grading devices are mechanized grading, mainly roller (Wang *et al.*, 2016), vibrating screen (Lv *et al.*, 2022), air flow sorting - mesh belt sieving (Wang *et al.*, 2019). These methods separate the normal tea leaves, broken buds and leaves, leaf stalks and other debris of fresh tea, but the grading effect is still a certain distance from the high-quality fresh tea. Achieving the standard of high-quality tea and improving the quality and economic value of tea is an urgent problem for the tea industry.

In recent years, with the continuous emergence of machine vision and artificial intelligence algorithms, it provides many new possibilities in the field of agricultural production and processing, and of course there are some scholars who have achieved research results in the intelligent sorting of fresh tea leaves.

Chen *et al.* (2010) from Nanjing Institute of Mechanical and Agricultural Research (NIMAR) applied BP neural network to classify fresh leaves of tea and achieved good results by extracting a variety of geometric features and texture parameters.

Liu et al. (2016) used artificial neural network to categorize and analyze the geometrical features and image characteristics of tea leaves, and identified them with various neural networks such as radial basis, BP neural network, Hopfield neural network, and so on. *Gao et al. (2017)* built a 7-layer convolutional neural network recognition model to realize automatic identification and sorting of fresh tea leaves by sharing weights and adjusting the learning rate. *Song et al. (2018)* took Keemun black tea as the research object, constructed an image acquisition system, extracted six absolute shape features and two relative shape features to construct a feature histogram, and identified it with various classification models such as BP neural network, Extreme Learning Machine (ELM), Support Vector Machine (SVM), Least Squares Support Vector Machine (LS-SVM), which provided experimental data and reference methods for the realization of the digital grade appraisal of tea leaves.

Zhu et al. (2019) designed a convolutional neural network (CNN) model with three convolutional layers, two pooling layers and one fully connected layer, the model recognized Huoshanhuangya tea correctly by 95.3% through the training and testing of real-time captured Huoshanhuangya tea images. *Yang et al. (2019)* proposed an improved (You Only Look Once) YOLO-v3 deep convolutional neural network algorithm for recognizing the picking point of young tea buds, which achieves end-to-end target detection and recognition of different poses of high-quality buds, taking into account both efficiency and accuracy. *Chen et al. (2020)* extracted the features of tea by determining the topology of the tea and used SVM to sort and recognize the tea with 94% recognition accuracy. *Gao et al. (2021)* constructed a tea sample dataset and completed the image recognition of tea by building a convolutional neural network, and the correct rate of the trained image recognition model was 96%.

Chen et al. (2021) designed a lightweight convolutional neural network model (MobileNetV2-Tea), and by improving the MobileNetV2 network, the MobileNetV2-Tea model obtained has 99% accuracy in fresh tea image recognition, with a model size of only 28.86M and an average recognition time of 45ms.

Gan et al. (2022) investigated feature classification methods using improved genetic algorithms to screen features with the best combination of three different classifiers with optimal dimensionality, and finally Support Vector Machines (SVMs) achieved 97% recognition accuracy on a 28-dimensional feature set.

Pi et al. (2023) applied YOLO-v5 to the task of intelligent detection of tea buds, and added the structure of bidirectional feature pyramid network (BiFPN) in Neck to optimize the structure of the network, which provided an effective detection model for the sorting of high-quality tea leaves.

Cao et al. (2023) proposed a novel fresh tea sorting system, which uses a tea recognition model based on YOLOv5 deep learning model for fast, high-precision multi-channel sorting of four grades of tea, with a model recognition accuracy of 88.8%. At the same time, the YOLO deep learning algorithm has demonstrated remarkable effectiveness in the detection of numerous crops, covering various types of crops such as cucurbits' fruits (*Zhao et al., 2022*), young apple fruits (*Du et al., 2024*), potato (*Pan et al., 2024*), grapes (*Tao et al., 2024*), wheat (*Bi et al., 2024*).

Although the above research has made some achievements in machine-picked fresh tea leaf sorting, there is still space for improvement in the precision and speed of sorting, especially considering the large-volume and larger-scale fresh tea leaf sorting scenarios. Therefore, this paper takes Anji white tea as the research object, and establishes a database of fresh tea samples containing one bud and one leaf, one bud and two leaves, one bud and three leaves, one bud and four leaves, broken leaves, and single bud in six forms. The state-of-the-art YOLOv8 deep learning algorithm is applied to the fresh tea leaf classification and recognition task to perform deep feature extraction and fresh tea leaf grade classification. On this basis, the Dynamic Snake Convolutional Kernel (DSConv) (*Qi et al., 2023*) is used to carry out the improved replacement of the convolutional kernel in the C2f module, and Multi-Head Self-Attention mechanism (MHSA) (*Vaswani et al., 2017*) is added to enhance the feature representation capability and extract more representative semantic information.

MATERIALS AND METHODS

Dataset collection

The fresh tea leaves dataset collected in this study was obtained from Anji County, Huzhou City, Zhejiang Province. The collected Anji white tea was brought back to the laboratory, video shooting was performed by Canon 6D II camera, and then the pictures of fresh tea leaves were serialized and extracted by frames, obtaining 2537 usable pictures of fresh tea leaves of different grades, which was used to obtain to the tea leaf sorting dataset. The details of the dataset are shown in Fig. 1.

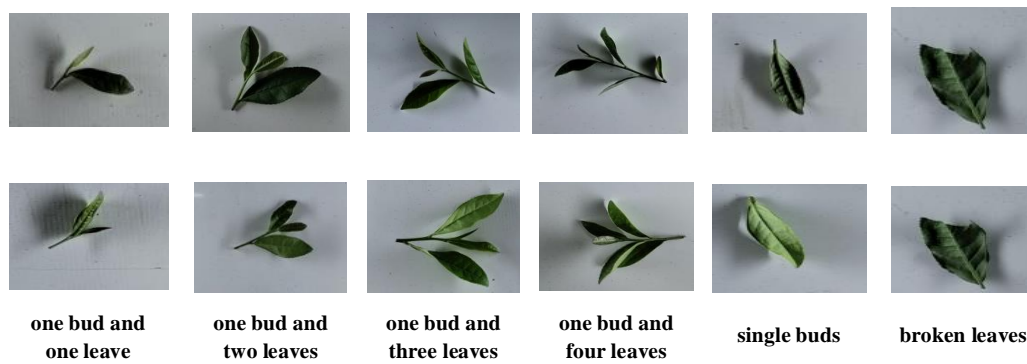


Fig. 1 - Specific types of fresh white tea leaves

Dataset expansion

The amount of data in the realistic fresh white tea leaf sorting scenario is huge. In order to adapt to the realistic demand as well as to meet the training requirements of the YOLOv8 deep learning algorithm, the fresh white tea leaves dataset is expanded to 18 times of the original dataset by rotating the angle, mirroring, sizing, changing the brightness, changing the chromaticity, changing the contrast, changing the sharpness, and so on. Fig. 2 shows a detailed illustration of the expansion of the fresh tea leaf dataset. The expanded dataset was obtained as 45,666 sheets, including 17,388 sheets of one bud and one leaf, 10,674 sheets of one bud and two leaves, 5,742 sheets of one bud and three leaves, 1,836 sheets of one bud and four leaves, 7,236 sheets of single buds, and 2,790 sheets of broken leaves. The fresh white tea leaf dataset of each category was divided into train and test sets in the ratio of 8:2, and the detailed dataset information is shown in Table 1.

Table 1

Number of specific images in the fresh white tea leaf dataset				
category	original	expansion	train	test
one bud and one leaf	966	17388	13910	3478
one bud and two leaves	593	10674	8539	2135
one bud and three leaves	319	5742	4594	1148
one bud and four leaves	102	1836	1469	367
single buds	402	7236	5789	1447
broken leaves	155	2790	2232	558

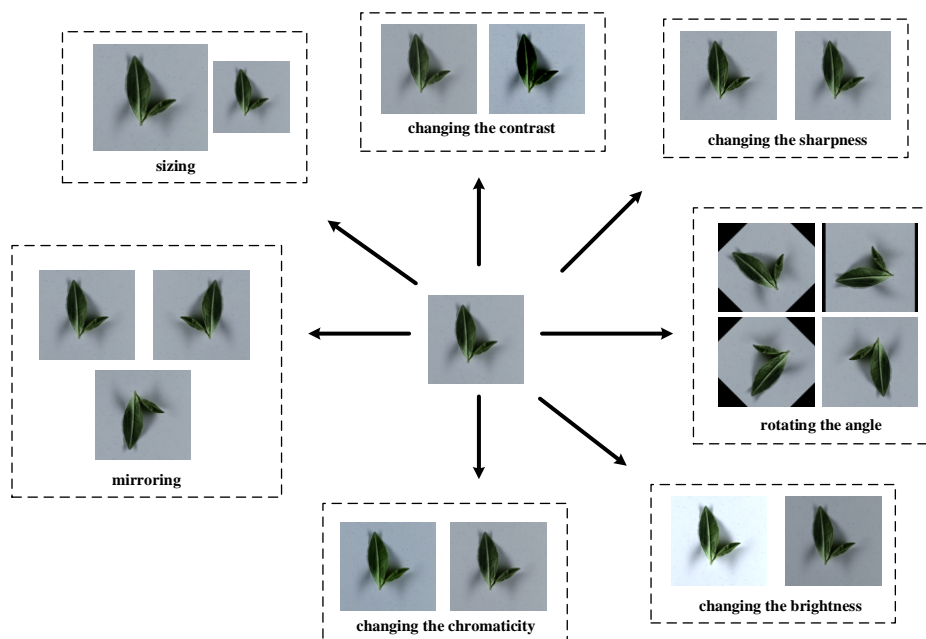


Fig. 2 - Example diagram of fresh white tea leaf dataset expansion

The YOLOv8 deep learning algorithm

The YOLOv8 model is a deep neural network-based target detection algorithm that supports tasks such as image classification, object detection and instance segmentation. Combining the YOLOv8 algorithm with fresh tea leaf sorting can quickly realize end-to-end intelligent grading of fresh tea leaves, which provides a good idea for fresh tea leaf sorting. The specific algorithm implementation process is as follows.

Firstly, from the captured video taken, fresh white tea leaf images are extracted by frame, and the fresh white tea leaf dataset is constructed according to multiple data expansion methods. Then the YOLOv8 deep learning network model is constructed. The recognition ability of the pre-trained YOLOv8 network model is mainly focused on the categories in the ImageNet dataset (the ImageNet dataset covers more than 1,000 image categories that are common in life), so the parameters of the YOLOv8 deep learning network model are dynamically adjusted according to the fresh tea leaves dataset. The model internally undergoes deep feature extraction and sorting, and is finally able to complete sorting of fresh tea leaves.

As shown in Fig.3, the YOLOv8 model applied to the intelligent sorting of fresh tea leaves mainly consists of a backbone network (Backbone) and a predictive output network (Head). The backbone network mainly uses the convolutional kernel to extract multi-scale features from the fresh white tea leaf contour, and operates the fresh tea leaf image layer by layer with multiple Conv, C2f and SPPT modules, so that the proposed features can be more representative. The predicted output network computes probability scores based on the extracted deep feature representations for intelligent sorting of different categories of fresh white tea leaves.

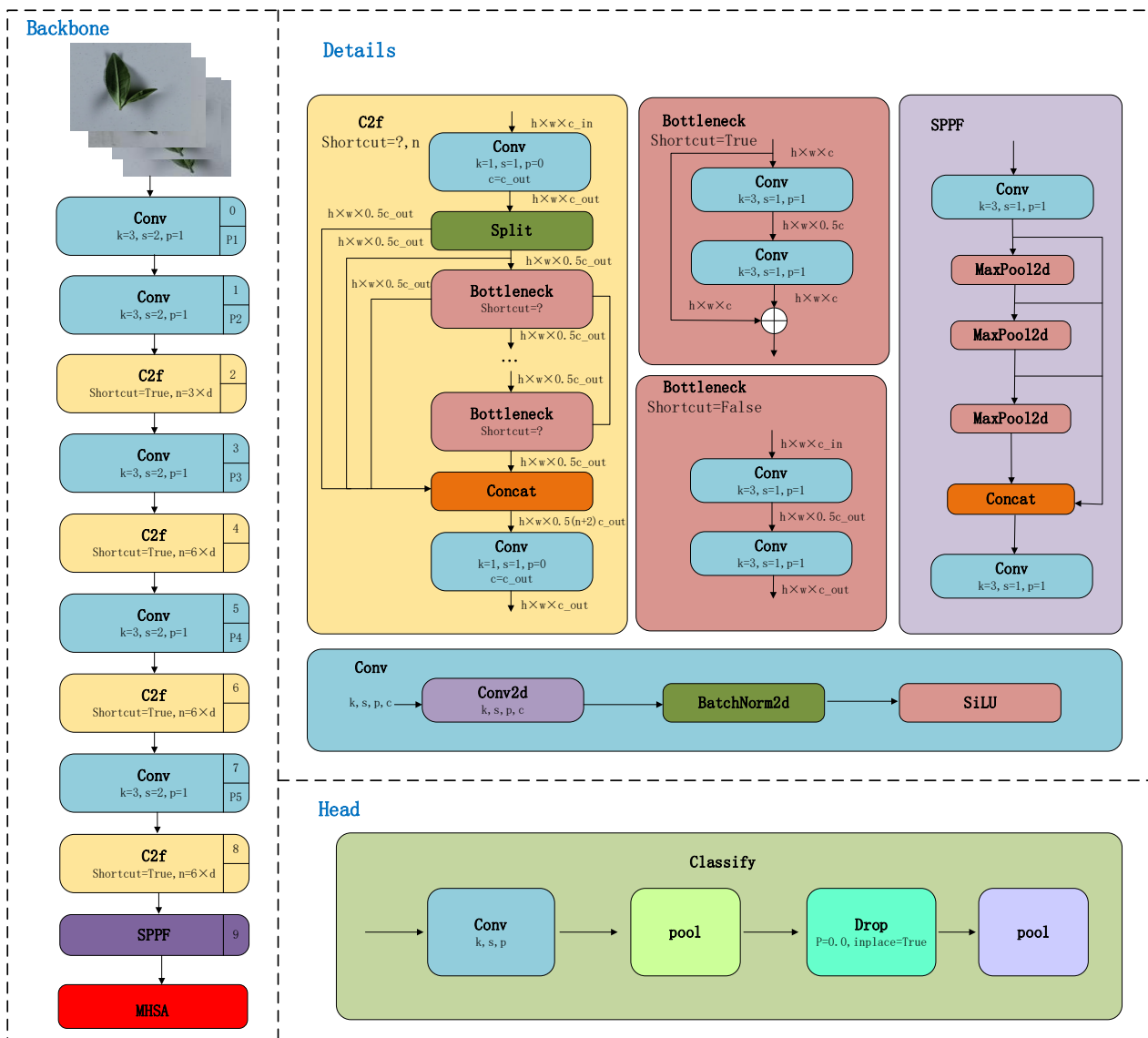


Fig. 3 - Flowchart of YOLOv8 sorting of fresh white tea leaves

Dynamic Snake Convolution Module (DSCConv)

The convolution Conv module in the YOLOv8 model performs convolutional computation for the entire region of the input fresh white tea leaf image, in order to be able to focus the convolution kernel on the target features of interest and reduce feature interference in the surrounding region, it is proposed that the dynamic snake convolution kernel (DSCConv) be introduced to the fresh white tea leaf feature extraction. The feature extraction process of the Dynamic Serpentine Convolution Kernel (DSCConv) is shown in Fig. 4. The next convolution position is calculated by extrapolating from the previous convolution position, starting from the center of the whole image $K_i=(x_i,y_i)$. By iterating continuously, it ensures that the extracted features are concentrated in the region where the fresh tea leaves are located, reduces the bias of the convolutional computation, and improves the accurate representation of the extracted features.

$$K_{i\pm c} = \begin{cases} (x_{i+c}, y_{i+c}) = (x_i + c, y_i + \sum_i^{i+c} \Delta y) \\ (x_{i-c}, y_{i-c}) = (x_i - c, y_i + \sum_{i-c}^i \Delta y) \end{cases} \quad (1)$$

The computational operation of convolution kernel actually starts from the center point and makes convolution computation in x-axis and y-axis directions sequentially, in x-axis direction, as shown in Equation (1), $K_{i\pm c}$ denotes any convolution computational position in the grid, $c=\{0,1,2,3,4\}$ denotes the distance from the center point, and the bias $\Delta=\{\delta|\delta\in[-1,1]\}$ is the offset of the next convolution position K_{i+1} relative to the previous one K_i . Since the convolution operation is a non-stop iterative process, \sum needs to be added outside the bias to perform a linear accumulation.

$$K_{j\pm c} = \begin{cases} (x_{j+c}, y_{j+c}) = (x_j + \sum_j^{j+c} \Delta y, y_j + c) \\ (x_{j-c}, y_{j-c}) = (x_j + \sum_{j-c}^j \Delta y, y_j - c) \end{cases} \quad (2)$$

Equation (2) represents the y-axis direction to do the convolutional computation operation.

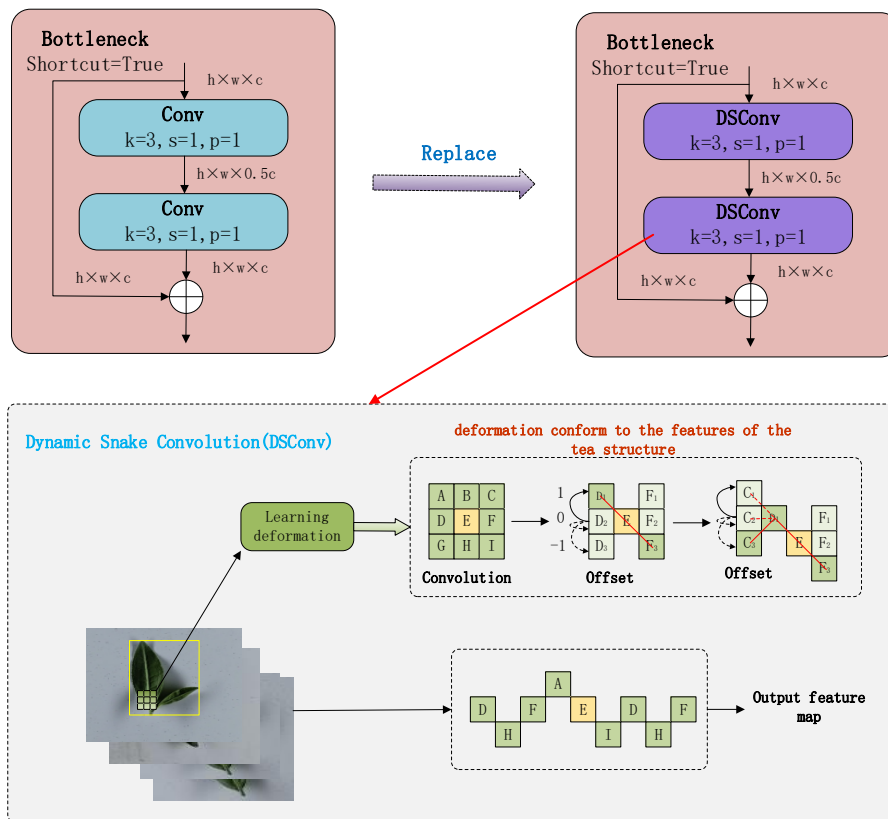


Fig. 4 - Flowchart of dynamic snake convolution kernel feature extraction

The Multi-Head Self-Attention mechanism (MHSA)

In the intelligent sorting of fresh tea leaves, the completeness of the extracted feature information is directly related to the subsequent performance of fresh tea leaves sorting and identification. To further enhance the feature representation capability, the multi-head self-attention mechanism (MHSA) is added to the YOLOv8 network model as a way to ensure the completeness and accuracy of the proposed features. As shown in Fig. 5, in the self-attention layer, all the keys K , values V , and query operations Q come from the feature parameters of the last fresh tea leaves, and the mapping calculation can make each position in the self-attention layer pay attention to all the positions in the previous layer, which increases the completeness of feature extraction. Each self-attention mechanism focuses on different subspace information of different positions, and the results of multiple attention mechanism calculations are fused and then linearly mapped to obtain the final feature representation.

$$A(Q, K, V) = \text{softmax}\left(\frac{QK^T}{\sqrt{d_k}}\right) V \tag{3}$$

where A denotes the Attention computation operation, d_k denotes the vector dimension computed by the input key and the query. The keys K , values V , and query operations Q computed from the previous layer are matrices.

$$MH(Q, K, V) = \text{Concat}(h_1, \dots, h_i) w^o \tag{4}$$

$$h_i = A(W_i^Q, KW_i^K, VW_i^V) \tag{5}$$

where $W_i^Q \in R^{d_{model} \times d_k}$, $W_i^K \in R^{d_{model} \times d_k}$, $W_i^V \in R^{d_{model} \times d_v}$, $W_i^O \in R^{hd_v \times d_{model}}$ are composed of parameter matrices of the corresponding dimensions. d_{model} denotes the unity parameter dimensions of the model, h denotes the number of attention heads, which is set to $h=4$ in this model. Multiple self-attention mechanisms are spliced and fused, where MH denotes multi-head self-attention mechanism and h_i denotes one of the $head_i$ attention mechanisms.

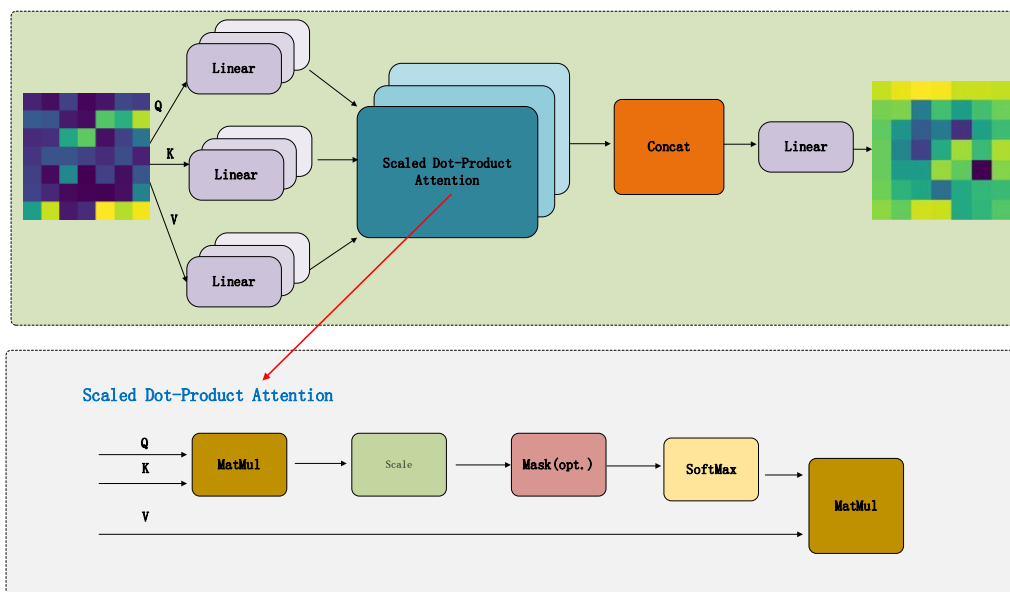


Fig. 5 - Flowchart of feature extraction for Multi-head Self-Attention Mechanism

Improving the network structure parameters of YOLOv8

The Dynamic Snake Convolution Module (DSConv) and Multi-head Self-Attention Mechanism (MHSA) are added into the YOLOv8 deep learning algorithm model to obtain the improved YOLOv8 model. In order to more clearly visualize the specific parameters of the model, the parameters of the improved YOLOv8 network structure are listed in Table 2.

Table 2

Network structure parameters of the improved YOLOv8						
Layers	From	n	Params	Module	Arguments	
0	-1	1	464	Conv	[3, 16, 3, 2]	
1	-1	1	4672	Conv	[16, 32, 3, 2]	

Layers	From	n	Params	Module	Arguments
2	-1	1	18888	C2f_DySnakeConv	[32, 32, True]
3	-1	1	18560	Conv	[32, 64, 3, 2]
4	-1	2	134800	C2f_DySnakeConv	[64, 64, True]
5	-1	1	73984	Conv	[64, 128, 3, 2]
6	-1	2	507024	C2f_DySnakeConv	[128, 128, True]
7	-1	1	295424	Conv	[128, 256, 3, 2]
8	-1	1	982088	C2f_DySnakeConv	[256, 256, True]
9	-1	1	164608	SPPF	[256, 256, 5]
10	-1	1	197376	MHSA	[256, 14, 14, 4]
11	-1	1	337926	Classify	[256, 6]
summary: 370 layers, 2735814 parameters, 2735814 gradients, 5.8 GFLOPs					

Experimental equipment and parameterization

The specific parameters of the computer used for the experimental training in this study are: the operating system is Windows 11, the CPU is i9, the GPU is NVIDIA RTX A4000, the deep learning modeling framework used is PyTorch 1.12.0, and the programming version is Python 3.9, and the specific parameter settings at the time of model training are shown in Table 3.

Table 3

Parameter settings for model training	
Parameters	Value
Image-size	224
Epochs	60
Batch	30
Momentum	0.937
Workers	8
Optimizer	Auto
Lr	0.01
Loss	VFL Loss

The improved YOLOv8 deep learning algorithm model built in this study is a classification problem, and the accuracy rate is mainly utilized as an evaluation metric when performing model evaluation (Li *et al.*, 2023).

$$ACC = \frac{TP+TN}{TP+TN+FP+FN} \quad (6)$$

$$mACC = \frac{\sum_{i=1}^N ACC_i}{N} \quad (7)$$

where ACC denotes accuracy, TP denotes the number of positive samples correctly identified, TN denotes the number of negative samples correctly identified, FP denotes the number of negative samples misreported, FN denotes the number of positive samples omitted, ACC_i denotes the accuracy of classification of the i th class of fresh white tea leaves, N denotes the type of fresh white tea sorting, which was six in this study, and $mACC$ denotes the mean accuracy.

RESULTS

Comparison of the impact of improved modules

In this study, the Dynamic Snake Convolution module (DSCConv) was replaced and the Multi-head Self-Attention Mechanism (MHSA) module was added in order to further improve the sorting of fresh white tea leaves. In order to validate the usefulness of the improvements that had been made, the test images were randomly selected from the database of fresh white tea leaves and experiments were conducted, and the extracted comparative plots are shown in Fig. 6.

As can be seen in Fig. 6, after replacing the dynamic snake convolution module in the C2f module, the features extracted from each channel are clearer and crisper. Taking the 10th channel as an example (as shown in the red box in Fig. 6), after the dynamic serpentine convolution module, the extracted features more closely match the contour map of fresh white tea leaves. This is due to the fact that the dynamic serpentine convolution kernel (DSCConv) is able to accurately extract adaptive features based on the overall external shape and structure of the tea leaves, focusing on the shape of the white tea fresh leaves themselves, which effectively improves the accuracy of the features.

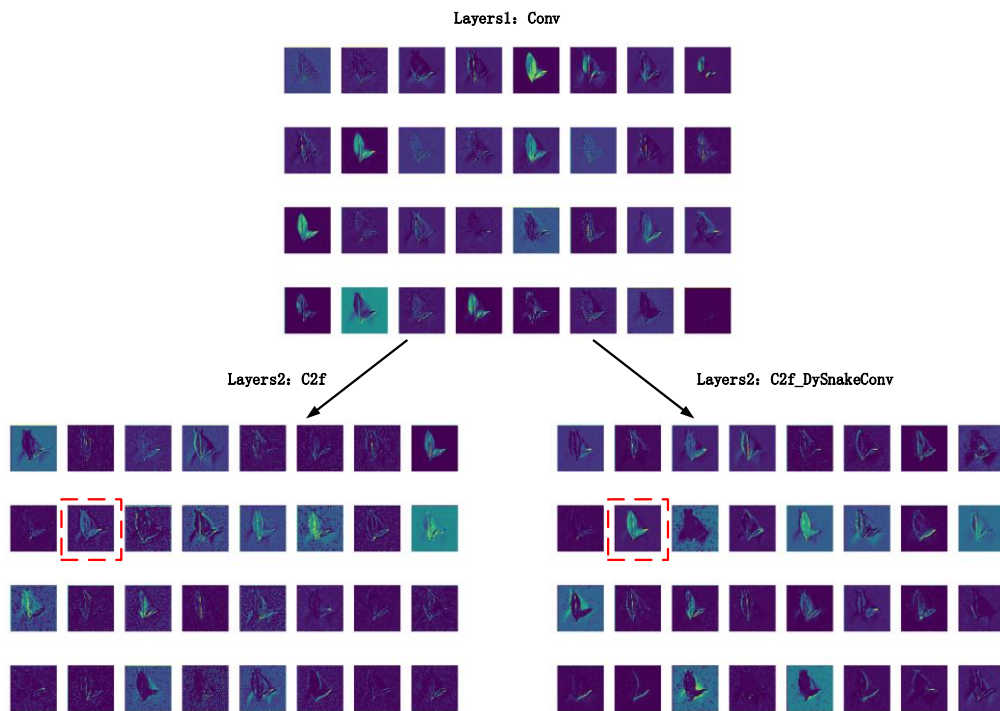


Fig. 6 - Comparison of features before and after replacing the dynamic snake convolution

In the YOLOv8 deep learning algorithm model, with the depth of the network layers, the deep network will focus more on abstract features, and for the Multi-head Self-Attention Mechanism (MHSA), it is added after the SPPF layer. As it can be seen from Fig.7, the multi-head self-attention mechanism (MHSA) focuses more on the detail region of fresh white tea leaves, which can effectively capture the robust features in the image of fresh tea leaves and realize the accuracy and completeness of the feature extraction, at the same time, it helps to further improve the recognition rate of the intelligent sorting of fresh white tea leaves.

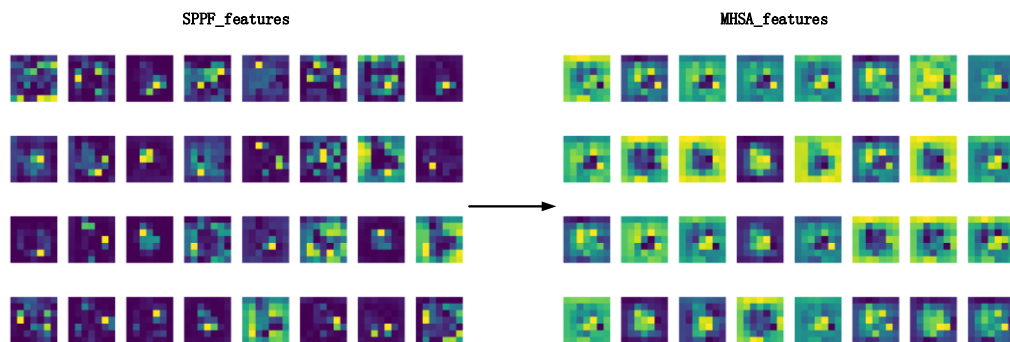


Fig. 7 - Comparison of features before and after the addition of the Multi-head Self-Attention Mechanism (MHSA) module

Comparison of Sorting Performance between Different Models

In this study, in order to verify the effectiveness of the proposed algorithms, YOLOv5, YOLOv7, YOLOv8, YOLOv8-DsConv, YOLOv8-MHSA and our algorithm (YOLOv8-DsConv-MHSA) are used in this study for comparative verification. In white tea fresh leaf sorting, the algorithm speed and sorting accuracy are two indicators that need to be considered in practical applications, so these two indicators are used for comparative analysis.

Table 4

Sorting effect of fresh white tea leaves with different algorithms

Model	ACC						mACC	FPS
	OL	TwL	ThL	FL	SiB	BrL		
YOLOv5	93.6	92.9	90.5	89.9	95.5	96.2	92.9	138.9
YOLOv7	94.1	93.4	90.9	90.6	95.2	96.5	93.4	147.1

Model	ACC						mACC	FPS
	OL	TwL	ThL	FL	SiB	BrL		
YOLOv8	95.2	94.6	93.5	91.8	96.2	97.1	94.6	161.3
YOLOv8-DsConv	96.5	95.7	94.1	93.2	97.9	97.5	95.7	137.0
YOLOv8-MHSA	96.3	96.1	94.9	93.6	97.3	97.4	95.9	140.9
Ours	97.4	96.4	94.9	94.8	97.0	97.8	96.4	126.6

As can be seen from Table 4, under the same experimental conditions, the YOLOv8-DsConv-MHSA algorithm proposed in this study is far ahead of the other algorithms in terms of accuracy, with an average of 96.4%, followed by the YOLOv8-MHSA algorithm with an average of 95.9%, the YOLOv8 algorithm, with an average of 94.6%, and the YOLOv8-DsConv algorithm with an average accuracy of 95.7%. From the processing speed of each model for white tea fresh leaves, YOLOv8 algorithm has the best recognition frame rate of 161.3 FPS, while YOLOv8-DsConv-MHSA algorithm has a certain degree of decline in recognition speed due to the increase in the parameters of the model, which is 126.6 FPS. Combining the results of the above data measured results, it can be seen that the proposed YOLOv8-DsConv-MHSA algorithm has the highest accuracy and the recognition speed of each fresh leaf can meet the requirements of practical applications. Among the various types of white tea fresh leaves, the sorting recognition effect of broken leaves is the best, up to 97.8%. The sorting effect of one bud and one leaf, one bud and two leaves, single bud is also more satisfactory, while the sorting effect of one bud and three leaves, one bud and four leaves is obviously poorer, which indicates that the task of recognizing the complex structure still has some difficulty.

Practical Application

Through continuous research and testing, our research team has successfully deployed the proposed algorithm model onto a developed tea sorting machine and conducted application debugging. The components of this tea sorting machine include sensors, a control cabinet, machine vision cameras, a server, robotic arms, and more. The implemented algorithm model is the proposed YOLOv8-DsConv-MHSA. First, the trained model is deployed on the server. When the tea leaves pass through the sensor on the conveyor belt, the sensor sends a signal to the control cabinet. The control cabinet then triggers the machine vision camera to capture an image. The captured image is transmitted to the server, where the fresh tea leaf image is input into the model to complete the sorting and recognition task. Subsequently, the robotic arm controls a vacuum suction cup to pick up the fresh tea leaves that do not meet the requirements and moves them to a parallel secondary conveyor belt for placement, thereby achieving automatic sorting of the fresh tea leaves.

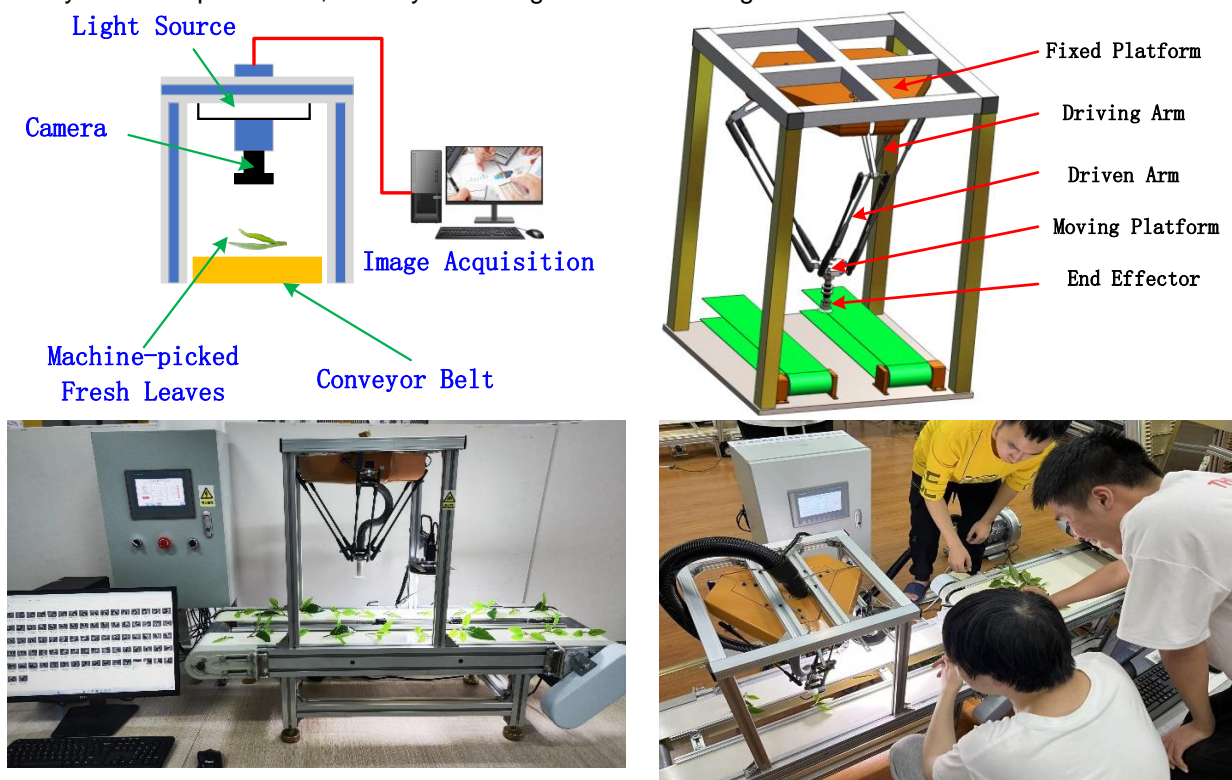


Fig. 8 - Research and Development Process of the Tea Fresh Leaf Sorting Machine

After the successful development of our tea sorting machine, a comparative analysis between the tea sorting machine developed by our team and existing tea sorting machines available on the market was conducted. Three tea sorting machines were identified for comparison: the YJY-2 developed by the Tea Research Institute of the Chinese Academy of Agricultural Sciences, the DJFJ developed by Zhejiang Sci-Tech University, and the 6CXF-70 developed by Zhejiang Chunjiang Tea Machinery Co., Ltd. Our analysis primarily focused on two key metrics: screening rate and operational efficiency. The screening rate is defined as the percentage of the weight of sorted tea leaves relative to the total weight of tea leaves, while operational efficiency refers to the amount of tea that can be processed per unit of time. As shown in Table 5, compared to the most advanced tea sorting machines currently available, our equipment achieved a 10.7% improvement in screening rate and a 20% increase in operational efficiency.

Table 5

Performance Comparison Analysis of Different Tea Sorting Machines				
Sorting Machine	YJY-2	DJFJ	6CXF-70	Ours
Sorting Grade	4	4	5	6
Screening Rate	62.4%	81.6%	76.5%	92.3%
Operational Efficiency	78kg/h	115kg/h	150kg/h	180kg/h

CONCLUSIONS

This paper investigates the problems encountered in sorting fresh white tea leaves and proposes an intelligent sorting algorithm for them using an improved YOLOv8. The algorithm introduces the DSConv and MHSA to enhance the accuracy of feature characterization and enable intelligent sorting of the established fresh white tea leaves dataset. The main results of this study are presented below:

1) A complete dataset of fresh white tea leaves and an improved YOLOv8 deep learning algorithm model were established. The accuracies for one bud and one leaf, one bud and two leaves, one bud and three leaves, one bud and four leaves, single bud, and broken leaves were 97.4%, 96.4%, 94.9%, 94.8%, 97.0%, and 97.8%, respectively, resulting in an average accuracy of 96.4%.

2) The comparison experiments demonstrate that the improved YOLOv8 deep learning model performs much better in intelligent sorting, with an improved average accuracy of 0.7% over YOLOv8-DsConv, 0.5% over YOLOv8-MHSA, 1.8% over YOLOv8, and 3.5% over YOLOv5;

3) In the improved YOLOv8 deep learning algorithm model, the DSConv is able to extract adaptive feature representations based on the shape structure of fresh white tea leaves, and the proposed features are concentrated in the region where the fresh white tea leaves are located, which reduces the bias of the convolutional computation, and improves the accurate representation of the extracted features;

4) In the improved YOLOv8 deep learning algorithm model, each self-attention mechanism in the MHSA focuses on different subspace information at different locations, and fuses the computation results of multiple attention mechanisms to make the captured image features of the fresh white tea leaves more robust, and to realize the accuracy and completeness of feature extraction.

5) The proposed YOLOv8-DsConv-MHSA was deployed on the server for the development of the tea sorting machine. Comparative analysis with existing tea sorting machines revealed that the screening rate improved by 10.7%, and the operational efficiency increased by 20%.

The experimental results show that the algorithm proposed in this study has broad application prospects in the intelligent sorting and recognition of tea leaves, providing a good solution for the subsequent sorting of mechanically harvested fresh white tea leaves. Additionally, the proposed YOLOv8-DsConv-MHSA was deployed on the server and the practical application development of the tea sorting machine was carried out. Of course, there are some limiting factors in the intelligent sorting of fresh tea leaves, such as mutual shading between tea leaves and the influence of light intensity. These issues need to be addressed in subsequent research, and the performance of the tea sorting machine should be further optimized.

ACKNOWLEDGEMENT

This work was supported by the National Natural Science Foundation of China (52105283), the Huzhou Public Welfare Application Research Project (2024GZ26,2021GZ27), and the teacher Professional Development Project for Domestic Visiting Scholars in Universities (FX2022113).

REFERENCES

- [1] Bi, Z., Li, Y., Guan, J., Zhang, X., (2024). Real-time wheat detection based on lightweight deep learning network RepYOLO model [J]. *INMATEH-Agricultural Engineering*, Vol. 72(1), pp-601-610, Romania. DOI: <https://doi.org/10.35633/inmateh-72-53>
- [2] Cao, J., Wu, Z., Zhang, X., Luo, K., Zhao, B., Sun, C., (2023). Sorting of fresh tea leaf using deep learning and air blowing. *Applied Sciences*, Vol. 13(6), 3551, Switzerland.
- [3] Chen, Y., Chang, C., Xiao, H., Song, W., Zhang, P., (2010). Application of artificial neural network technology in fresh tea leaf sorting. *Agricultural Network Information*, Vol. 7, pp. 37-40+43, China.
- [4] Chen, Z., He, L., Ye, Y., Chen, J., Sun, L., Wu, C., Chen, L., Wang, R., (2020). Automatic sorting of fresh tea leaves using vision-based recognition method. *Journal of Food Process Engineering*, Vol. 43(9), e13474, USA.
- [5] Chen, Z., Wang, D., Fang, H., Wang, G., Xie, B., (2021). Rapid identification method of fresh tea leaves based on lightweight model. In: *2021 IEEE International Conference on Real-time Computing and Robotics (RCAR)*. IEEE, pp. 1158-1163, USA.
- [6] Du, Y., Gao, A., Song, Y., Guo, J., Ma, W., Ren, L., (2024). Young apple fruits detection method based on improved YOLOv5 [J]. *INMATEH-Agricultural Engineering*, Vol. 73(2), Romania.
- [7] Gan, N., Sun, M., Lu, C., Li, M., Wang, Y., Song, Y., Ning, J., Zhang, Z., (2022). High-speed identification system for fresh tea leaves based on phenotypic characteristics utilizing an improved genetic algorithm. *Journal of the Science of Food and Agriculture*, Vol. 102(15), pp. 6858-6867, England.
- [8] Gao, M., Shi, M., Li, C., (2021). Research and implementation of image recognition of tea based on deep learning. In: *2021 21st ACIS International Winter Conference on Software Engineering, Artificial Intelligence, Networking and Parallel/Distributed Computing (SNPD-Winter)*. IEEE, pp. 63-68, USA.
- [9] Gao, Z., Wang, A., Liu, Y., Zhang, L., Xia, Y., (2017). Intelligent fresh-tea-leaves sorting system research based on convolution neural network. *Transactions of the Chinese Society of Agricultural Machinery*, Vol. 48(7), China.
- [10] Ruxton, C., (2013). Emerging evidence for tea benefits. *Nutrition Bulletin*, Vol. 38(3), pp. 287-301, England.
- [11] Li, P., Zheng, J., Li, P., Long, H., Li, M., Gao, L., (2023). Tomato maturity detection and counting model based on MHSA-YOLOv8. *Sensors*, Vol. 23(15), 6701, Switzerland.
- [12] Liu, Y., Li, H., (2016). Neural network image technology design of intelligent fresh tea leaf sorter principle research. *Fujian Tea*, Vol. 38(3), pp. 196-197, China.
- [13] Lv, H., Wu, C., Tu, Z., Chen, J., Jia, J., Chen, Z., Ye, Y., (2022). Optimization of grading parameters of vibratory classifier for machine-picked tea fresh leaves based on EDEM. *Journal of Tea Science*, Vol. 42(1), pp. 120-130, China.
- [14] Pan, Z., Zhang, H., Liu, Z., Yang, R., Su, Z., Li, X., Liu, Z., Shi, C., Wang, S., Wu, H., (2024). Potato appearance detection algorithm based on improved YOLOv8[J]. *INMATEH-Agricultural Engineering*, Vol. 74(3), pp.864-874, Romania. DOI: <https://doi.org/10.35633/inmateh-74-76>
- [15] Pi, W., Wang, R., Sun, Q., Wang, Y., Lu, B., Liu, G., Jin, K., (2023). White tea bud detection based on deep learning research. *INMATEH-Agricultural Engineering*, Vol. 70(2), Romania.
- [16] Qi, Y., He, Y., Qi, X., Zhang, Y., Yang, G., (2023). Dynamic snake convolution based on topological geometric constraints for tubular structure segmentation. In: *Proceedings of the IEEE/CVF International Conference on Computer Vision*, pp. 6070-6079, USA.
- [17] Song, Y., Xie, H., Ning, J., Zhang, Z., (2018). Grade recognition of Keemun black tea based on machine vision shape feature parameters. *Transactions of the CSAE*, Vol. 34(23), pp. 279-286, China.
- [18] Tao, S., Wen, S., Hu, G., Ge, Y., Wen, J., Cao, X., Chen, J., (2024). Improved YOLOv8N-based detection of grapes in orchards [J]. *INMATEH-Agricultural Engineering*, Vol. 74(3), pp.473-484, Romania. DOI: <https://doi.org/10.35633/inmateh-74-42>
- [19] Vaswani, A., Shazeer, N., Parmar, N., Uszkoreit, J., Jones, L., Gomez, A. N., Kaiser, Ł., Polosukhin, I., (2017). Attention is all you need. *Advances in Neural Information Processing Systems*, Vol. 30, USA.
- [20] Wang, C., Zhang, T., Zheng, Y., Chen, J., Hu, S., (2016). Simulation study of tea sieving by two degrees of freedom reciprocating tumbler screen. *Journal of Tea Science*, Vol. 36(6), pp. 613-620, China.
- [21] Wang, R., Wei, Y., Wu, C., Sun, L., Zheng, W., (2019). Numerical simulation of motion characteristics of flexible fresh tea leaf in Poiseuille shear flow via combined immersed boundary-lattice Boltzmann method. *International Journal of Modern Physics C*, Vol. 30(5), 1950038, USA.

- [22] Yang, H., Chen, L., Chen, M., Ma, Z., Deng, F., Li, M., Li, X., (2019). Tender tea shoots recognition and positioning for picking robot using improved YOLO-V3 model. *IEEE Access*, Vol.7, pp. 180998-181011, USA.
- [23] Yuan, H., Hua, J., Deng, Y., Jiang, Y., Wang, Y., Chen, G., Zhang, L., Yin, J., (2016). Optimization of grading and classification technology for machine-picking leaves based on YJY-2 type classifier. *Transactions of the Chinese Society of Agricultural Engineering*, Vol. 32(6), pp. 276-282, China.
- [24] Zheng, N., Wang, Z., (2011). Mechanization of tea picking: Break out the bottleneck of tea industry. *Chinese Country Technology and Science*, Vol. 12(9), pp. 14-17, China.
- [25] Zhu, Y., Fu, M., Shi, Y., (2019). Study on sorting technology of fresh tea leaves based on convolutional neural network model. *In: 2019 14th IEEE International Conference on Electronic Measurement & Instruments (ICEMI)*. IEEE, pp. 614-617, USA.
- [26] Zhao, F., Zhang, J., Zhang, N., Tan, Z., Xie, Y., Zhang, S., Han, Z., Li, M., (2022). Detection of cucurbits' fruits based on deep learning [J]. *INMATEH-Agricultural Engineering*, Vol. 66(1), pp.321-330, Romania. DOI: <https://doi.org/10.35633/inmateh-66-32>

APPLE FRUIT RECOGNITION METHOD BASED ON IMPROVED YOLOv5

/ 基于改进 YOLOV5 的苹果果实识别方法

Yang BAI¹⁾, Shengqiao XIE²⁾, Jian SONG^{*1)}, Cunyu ZHAO¹⁾, Fuxiang XIE¹⁾¹⁾School of Machinery and Automation, Weifang University, Weifang/China;²⁾ China National Heavy Duty Truck, Jinan/China

Tel: 13256361611; E-mail: 20210025@wfu.edu.cn

Correspondent author: Jian Song

DOI: <https://doi.org/10.35633/inmateh-75-81>**Keywords:** YOLOv5; Apple; Attention mechanism; Apple fruit recognition**ABSTRACT**

This study addressed the practical problems of complex picking environments, difficult image recognition, and low picking efficiency in apple harvesting, combined with China's agricultural requirements and picking systems. An improved apple fruit recognition method based on attention mechanisms and YOLOv5 was proposed. A dataset was created by collecting 3,600 apple images under front-light, side-light, and backlight conditions at different coloring stages in natural environments. The SENet and CBAM attention mechanisms were used to enhance YOLOv5's feature extraction network, and the model was trained to improve detection accuracy. Experimental verification showed that the YOLOv5x model embedded with the CBAM module achieved the highest mean average precision (mAP) of 98.3%. The CBAM module outperformed the SENet module. Actual tests of the apple-picking robot's vision system prototype showed that when the IOU threshold was set at 0.5 and 0.3, the average detection accuracy was over 85% in both cases. The results demonstrated that the improved YOLOv5 model exhibited robustness to light intensity variations. This approach provides a technical reference for developing apple picking robot vision systems.

摘要

针对苹果采摘存在采摘环境复杂、图像准确识别困难、采摘效率低下等实际问题，结合我国苹果采摘农艺要求及采摘体系。本文提出了一种基于注意机制和改进的 YOLOv5 的苹果果实识别方法。该方法通过收集 3600 张自然环境中顺光、侧光和背光的不同着色天数的苹果图像，创建了一个数据集，注意机制 SENet 和 CBAM 用于改进 YOLOv5 的特征提取网络，并对模型进行训练以提高模型的检测精度。经过实验验证，嵌入 CBAM 模块的 YOLOv5x 的平均检测精度最高，mAP 为：98.3%。CBAM 模块的性能优于 SENet 模块。结果表明：改进的 YOLOv5 模型对光强变化具有良好的鲁棒性。通过采摘机器人视觉识别系统样机的实际试验验证，当 IOU 阈值设为 0.5 和 0.3 时，该系统样机平均检测精度均在 85% 以上。改进后的 YOLOv5 模型可为苹果采摘机器人视觉系统的开发提供参考。

INTRODUCTION

China is the largest producer and consumer of apples, with a large cultivation area and high yield. However, the mechanization level of apple harvesting is relatively low (Lu et al., 2020). Apple-picking robots can improve harvesting efficiency and save costs, but the complex working environment and various uncertain factors make apple picking challenging. Rapid detection of fruits in complex natural environments is the primary task in research on apple-picking robots (Wang et al., 2021). Only when the visual system recognizes the target can the robotic arm and end effector be driven to complete fruit picking (Tian et al., 2020; Liu et al., 2019; Zhao et al., 2021). The accuracy of fruit recognition directly affects the efficiency and quality of robot harvesting.

Traditional target recognition methods for apple-picking robots mainly rely on the color and grayscale threshold of the fruits (Felzenszwalb et al., 2010). They require manual extraction of target features and are greatly influenced by natural light intensity, as well as branch and leaf occlusion. The robustness of the algorithm is poor. Target detection based on machine learning requires predetermined parameters, and the parameter size significantly affects the classification results.

Currently, deep learning-based detection algorithms are divided into single-stage algorithms and two-stage algorithms based on the different ways of predicting target categories and positions (Luo et al., 2020).

Since 2014, *Girshick et al., (2016)*, have successively proposed a series of two-stage algorithms, such as R-CNN, Fast R-CNN, Faster R-CNN, and Mask R-CNN.

The calculation area generation in the two-stage detection algorithm improves the detection accuracy, but increases the calculation amount, training difficulty and parameter quantity of the algorithm, reduces the prediction speed of the algorithm, and is difficult to meet the real-time detection requirements. To solve the problem of algorithm efficiency, *Redmon J et al., (2016)*, have successively proposed single-stage object detection algorithms represented by the YOLO series since 2016. Single-stage algorithms regress the position and class of bounding boxes in a single output layer, resulting in a significant improvement in detection speed compared to two-stage algorithms. Among them, the YOLOv5 algorithm is currently a more advanced object detection algorithm, surpassing YOLOv4 in both detection accuracy and speed. Therefore, this model has a significant advantage in hardware deployment and is suitable for rapid detection of apples in natural environments.

In this study, an improved YOLOv5 object detection method based on attention mechanisms is proposed to optimize the apple fruit detection process. The goal is to overcome errors and influences caused by environmental factors and enhance the detection performance of the visual system for fruits.

MATERIALS AND METHODS

Data acquisition and pre-processing

This study focuses on the Red Fuji apple in Yantai. The data collection was conducted at the Le Feng apple plantation in Linqu, Weifang. Figure 1 shows images of apples at different stages of maturity. Collecting images of apples at different coloring stages facilitates testing the impact of different maturity stages on the detection performance of the network model.



Fig. 1 – Apple images collected at different coloring periods

1. Coloring for 5 days; 2. Coloring for 10 days; 3. Coloring for 15 days



Fig. 2 – Images of an apple under different lighting angles

1. Front-lighting; 2. Side-lighting; 3. Backlighting

To ensure the diversity of collected image samples, apple images were captured under different weather conditions (sunny and cloudy) at the time range of 8:00-17:00. The captured images were taken in three lighting modes: front-light, side-light, and backlight. Figure 2 shows apple images captured under different lighting angles.

Data pre-processing

The labelling software was used to annotate the apple fruits in the collected 3600 images. Figure 3 shows the distribution of sample attributes in the dataset.

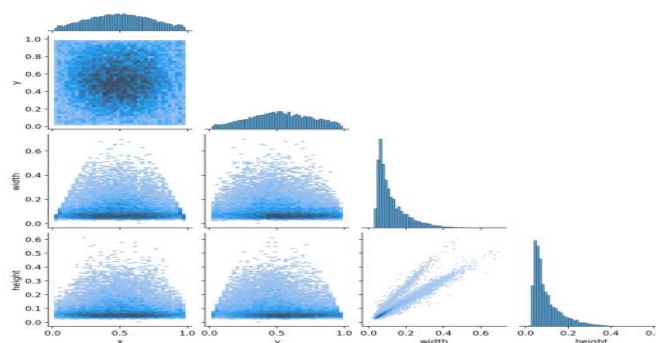


Fig. 3 – Distribution of sample attributes in the dataset

To ensure the randomness and rationality of dataset partition, manual partitioning was conducted on the collected apple images in this study. A total of 300 images were randomly selected from the original dataset to create Test Set 1, which consists of 100 images taken in front-lighting conditions, side-lighting conditions, and backlighting conditions, respectively. Additionally, Test Set 2 was created by randomly selecting 100 images of apples that were 5 days, 10 days, and 15 days old, respectively, while the remaining images were used as training data for the model. The number of samples in each dataset and the corresponding number of target boxes are shown in Table 1.

Table 1

Factors and level of orthogonal test						
Datasheet	Training sets		Test set 1		Test set 2	
	Number of pictures	Number of target boxes	Number of pictures	Number of target boxes	Number of pictures	Number of target boxes
Coloring for 5 days	1000	12038	100	1314	100	1328
Coloring for 10 days	1000	13117	100	1248	100	1196
Coloring for 15 days	1000	12864	100	1293	100	1159
Grand total	3000	38019	300	3855	300	3683

The 3600 original apple images collected in this study are not sufficient to cover all the factors such as lighting intensity, weather, noise, and clarity in natural environments. Therefore, data augmentation is performed on the original images to enhance the generalization ability of the object detection model and prevent overfitting. This study mainly adds random brightness, random contrast, random Gaussian noise, random saturation, and random flipping to the collected apple images to simulate various states of fruit trees in natural environments as much as possible. The augmented apple images are five times more than the original data. Figure 4 shows some examples of the apple images after augmentation.



1



2



3



Fig. 4 – Examples of image augmentation

1. Original Image; 2. Random Brightness; 3. Random Contrast; 4. Random Gaussian noise; 5. Random saturation; 6. Random rotation

Construct an apple recognition model based on improved YOLOv5

The YOLOv5 algorithm added modules such as image compression and Mosaic data augmentation at its input end (Yonghui et al., 2022). Mosaic utilized random scaling, cropping, and arrangement of four images to generate a new image, achieving data augmentation (Chen et al., 2022).

There were four different versions of the YOLOv5 algorithm: YOLOv5x, YOLOv5l, YOLOv5m, and YOLOv5s. The structural principles of the YOLOv5 versions were similar, with differences only in network width and depth (Liu et al., 2020, Yongpeng et al., 2024). The network structure of the YOLOv5 algorithm mainly consisted of modules such as Focus, CBL, CSP_1, CSP_2, and SPP, as shown in Figure 5.

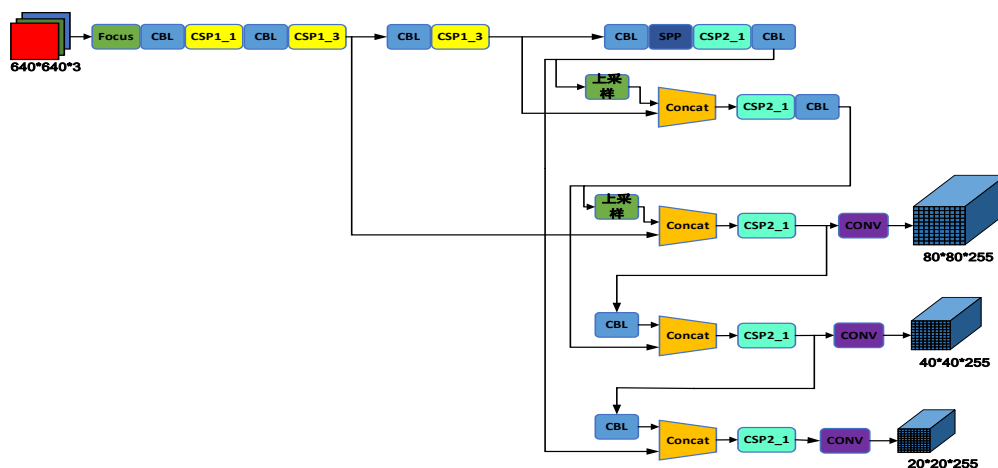


Fig. 5 – The network structure of YOLOv5

The CBL module consists of Convolutional layers, Batch Normalization (BN) layers, and Leaky ReLU (LR) layers. The CBL module plays a role in downsampling and helps reduce information loss in the downsampling process. The computational cost of the Focus module in YOLOv5 is approximately three times higher than that of downsampling with convolution, but it helps reduce information loss in the downsampling process.

The feature extraction network in the YOLOv5 algorithm consists of various functional modules such as Focus, CBL, CSP, and SPP. The deep network layers ensure the network's ability to extract features. The YOLOv5 algorithm utilizes convolutional operations to perform feature re-extraction on the output feature maps. The algorithm takes in input image data of size 640x640x3 and outputs three feature maps of sizes 80x80x18, 40x40x18, and 20x20x18, respectively. The feature map with a higher resolution is used for predicting smaller objects, while the ones with lower resolutions are used for predicting larger objects. Using feature maps of different resolutions helps improve the accuracy of object recognition for objects of different sizes.

Attention mechanism

The introduction of attention mechanisms in computer vision can effectively enhance the feature extraction capability of networks, thereby improving the accuracy of object recognition. Currently, widely used attention mechanisms in deep learning include SENet and CBAM.

SENet attention mechanism

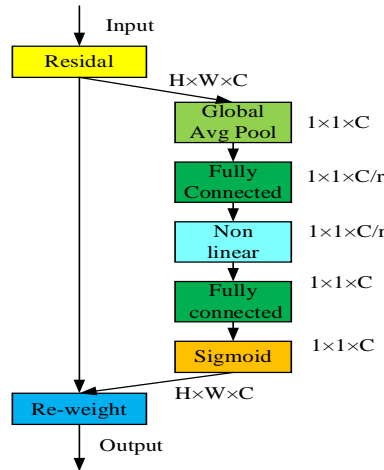


Fig. 6 – Schematic diagram of the seNet attention mechanism structure

Figure 6 shows the structure of the SENet network. The SENet takes an $H \times W \times C$ feature map as input, with C channels (Bai et al., 2022; Lin et al., 2021; Peng et al., 2022). First, the input feature map is globally average pooled, reducing the height and width of the feature map to 1×1 , as shown in Eq.(1). Then, two fully connected layers are applied, followed by the sigmoid activation function to normalize the values. This process obtains the weights for each channel in the input feature map. By multiplying these weights with the input feature map, a new calibration of the input feature map using channel attention is achieved, as shown in Eq.(2).

$$z_c = F_{sq}(u_c) = \frac{1}{H \times W} \sum_{i=1}^H \sum_{j=1}^W u_c(i, j) \tag{1}$$

$$\hat{X} = X \cdot \sigma(z) \tag{2}$$

- z_c : the c -th element of z ;
- H : the height of the feature map;
- W : the width of the feature map;
- $u_c(i, j)$: the (i, j) -th element of the c -th channel of u ;
- $\sigma(\hat{z})$: channel weight.

After passing through the first fully connected layer, the dimension of the feature map decreases, significantly reducing the model's parameters and computational complexity. After passing through the second fully connected layer, the dimension of the feature map is restored to the same as the input, establishing correlations between channels. This increases the weights of effective feature map channels and decreases the weights of other feature map channels, allowing the model to achieve better training performance.

CBAM attention mechanism

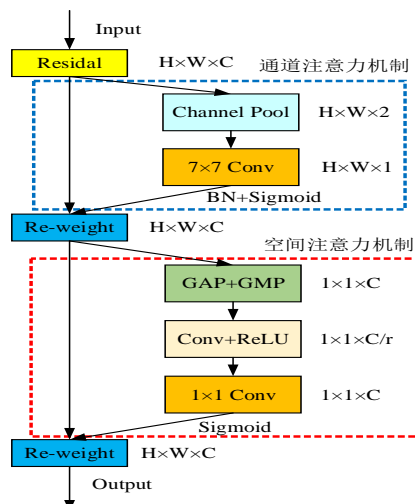


Fig. 7 – Schematic diagram of the structure of the CBAM attention mechanism

The structure shown in Figure 7 is the Convolutional Block Attention Module (CBAM), which consists of a Channel Attention Module and a Spatial Attention Module (Liu et al., 2021; Xia et al., 2023; Huang et al., 2021). The input feature map first goes through the Channel Attention Module, where the feature map's height and width are globally averaged and globally max-pooled. The resulting values are then passed through a Multi-Layer Perceptron (MLP) to obtain the channel attention weights. These weights are then added to the original input feature map through a multiplication and addition operation. This completes the calibration of the original input feature map using channel attention, as shown in Equation (3).

$$\begin{aligned} M_c(F) &= (MLP(AvgPool(F)) + MLP(MaxPool(F))) \\ &= \sigma(W_1(W_0(F_{avg}^c)) + W_1(W_0(F_{max}^c))) \end{aligned} \quad (3)$$

σ : Sigmoid function;

C : Number of channels;

W_1, W_0 : Input shared weights;

F_{avg}^c : Feature mapping generated by average pooling in space;

F_{max}^c : Feature mapping generated by maximum pooling in space.

After passing through the CBAM module, the feature map generates new feature maps with channel and spatial attention weights, enhancing the relationship between image features in both spatial and channel dimensions. This is beneficial for extracting typical features of the target (Su et al., 2021, Lingqing et al., 2024).

Loss function

In the target detection task, the loss function can better reflect the gap between the predicted value and the real value of the data, and then reflect the detection effect. The loss function used in this paper consists of three parts, they are Loss of confidence (L_{con}), Positioning loss (L_{GIOU}) and Classification loss (L_{class}). The total loss function (L_{total}) can be obtained by accumulating the three, as shown in Equation (4).

$$L_{total} = L_{con} + L_{GIOU} + L_{class} \quad (4)$$

In the formula, the confidence loss measures the confidence level of the prediction box, with the calculation shown in Equation (5). The calculation method of the function is cross entropy error, which determines whether the predicted bounding boxes contain the predicted target. If there is a predicted target in the current bounding box, the value of I_{ij}^{obj} is 1. If there is no predicted target in the current bounding box, the value of I_{ij}^{obj} is 0. The confidence values are weighted and summed to obtain the value of L_{con} .

$$\begin{aligned} L_{con} &= \lambda_{obj} \sum_{i=0}^{S^2} \sum_{j=0}^B I_{ij}^{obj} \left[-\hat{C}_i \ln C_i - \left(1 - \hat{C}_i\right) \ln \left(1 - \hat{C}_i\right) \right] \\ &\quad + \lambda_{no} \sum_{i=0}^{S^2} \sum_{j=0}^B I_{ij}^{no} \left[-\hat{C}_i \ln C_i - \left(1 - \hat{C}_i\right) \ln \left(1 - \hat{C}_i\right) \right] \end{aligned} \quad (5)$$

λ_{obj} : there is a target weight coefficient in the grid;

λ_{no} : no target weight coefficient in the grid;

S^2 : number of grids;

I_{ij}^{obj} : to determine whether the j -th bounding box in the i -th grid needs to be predicted,

I_{ij}^{no} : to determine whether the j -th bounding box in the i th grid has a target that does not need to be predicted,

C_i : predict the target confidence value;

\hat{C}_i : the actual target confidence value.

L_{class} is the classification loss, which is used to calculate the difference between the predicted value and the actual value of the category. The calculation is shown in Equation (6).

The calculation of L_{class} is similar to that of L_{con} . The values of I_{ij}^{obj} and I_{ij}^{obj} are the same as shown in Equation (7). The calculated probability value is weighted and summed to obtain the value of L_{class} .

$$L_{class} = \sum_{i=0}^{S^2} \sum_{j=0}^B \sum_{c \in class} I_{ij}^{obj} \left[-\hat{p}_i(c) - \ln \left(\hat{p}_i(c) \right) - \left(1 - \hat{p}_i(c) \right) \ln(1 - \hat{p}_i(c)) \right] \tag{6}$$

c : Boundary box prediction category;

$p_i(c)$: The probability that the target is predicted to be c in the i -th grid;

$\hat{p}_i(c)$: The actual probability that the target is c in the i -th grid.

In object detection tasks, IoU is often used to calculate the coordinate differences between predicted bounding boxes and ground-truth bounding boxes, and can more directly reflect the detection performance of the algorithm. The calculation formula is shown in (7) ~ (9).

$$IoU = \frac{A \cap B}{A \cup B} \tag{7}$$

$$GIoU = IoU - \frac{|C - (A \cup B)|}{|C|} \tag{8}$$

$$L_{GIoU} = \sum_{i=0}^{S^2} \sum_{j=0}^B (1 - GIoU) \tag{9}$$

A : Real box area;

B : Predicting box area;

C : A and B minimum circumscribed rectangle area.

RESULTS

The effect of adding attention mechanism on the test results

To verify the detection performance of the YOLOv5 algorithm after adding the attention mechanism module, a comparative experiment was conducted between the YOLOv5 algorithm with the added attention mechanism module and the original YOLOv5 algorithm. The performance was tested using a dataset composed of samples mixed from different maturity stages. Table 2 shows the experimental results of apple detection before and after adding the attention mechanism module to the YOLOv5 algorithm.

Table 2

Test results of Apple detection before and after the improvement of the YOLOv5 algorithm

Algorithm	Number of network parameters (MB)	Examination speed (ms)	mAP (%)
YOLOv5s	13.7 (0.00)	31.5 (0.00)	92.3 (0.00)
YOLOv5s-SENet	14.8 (+8.03%)	31.9 (+1.26%)	93.5 (+1.30%)
YOLOv5s-CBAM	15.1 (+10.22%)	32.1 (+1.9%)	94.2 (+2.06%)
YOLOv5m	40.2 (0.00)	80.2 (0.00)	93.1 (0.00)
YOLOv5m-SENet	42.8 (+6.47%)	81.4 (+1.50%)	94.4 (+1.40)
YOLOv5m-CBAM	43.6 (+8.46%)	82.3 (+2.62%)	95.6 (+2.69%)
YOLOv5l	88.5 (0.00)	148.3 (0.00)	95.6 (0.00)
YOLOv5l-SENet	92.8 (+4.86%)	149.8 (+1.01%)	96.9 (+1.36%)
YOLOv5l-CBAM	94.2 (+6.44%)	151.8 (+2.36%)	97.8 (+2.30%)
YOLOv5x	171.6 (0.00)	304.2 (0.00)	96.4 (0.00)
YOLOv5x-SENet	179.1 (+4.37%)	308.4 (+1.38%)	97.7 (1.35%)
YOLOv5x-CBAM	181.2 (+5.59)	311.7 (+2.47%)	98.3 (+1.97%)

According to Table 2, it could be seen that in the original YOLOv5 algorithm, YOLOv5x had an average detection accuracy of 96.4%, higher than the other three networks, but it had a longer detection time.

After separately embedding the SENet attention mechanism module, the average detection accuracy of YOLOv5s increased by 1.3% to 93.5%. YOLOv5m, YOLOv5l, and YOLOv5x also showed some improvements in average detection accuracy. The parameter count of YOLOv5s-SENet increased by 8.03% compared to the original version, resulting in a 1.26% increase in detection time. Compared to the original version, the parameter count of YOLOv5m-SENet, YOLOv5l-SENet, and YOLOv5x-SENet increased by 4.37% to 6.47%, with the highest increase being only 7.5MB. However, all versions achieved more than 1% improvement in accuracy, demonstrating good detection performance.

When the CBAM module was embedded in all four different network structures of the YOLOv5 algorithm, the parameter count of YOLOv5s, YOLOv5m, YOLOv5l, and YOLOv5x increased by 10.22%, 8.46%, 6.44%, and 5.59% respectively. The lighter the network, the greater the increase in parameter count. The actual detection results of YOLOv5 model before and after adding the attention mechanism modules were shown in Figure 7.

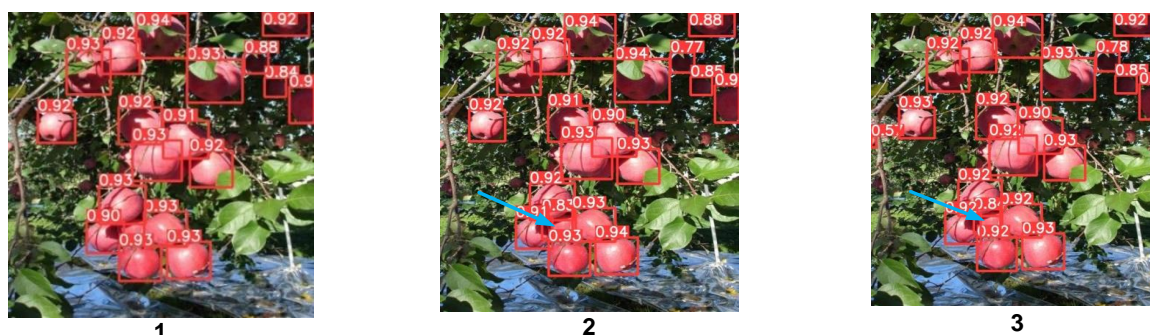


Fig. 8 – YOLOv5 test effect before and after improvement
1. Unimproved YOLOv5, 2. YOLOv5+SENet, 3. YOLOv5+CBAM.

From Figure 8, it could be seen that compared with Figure (a), the occluded fruits in Figure (b) and Figure (c) were successfully recognized, indicating that the YOLOv5 network model with the added attention mechanism module had improved accuracy in identifying small and occluded targets. Figure (c) showed that the improved YOLOv5-CBAM model successfully detected the small target fruit on the left, while the other two algorithms failed to detect this target. Taking into account various factors, embedding the attention mechanism module helped improve the model's accuracy in recognizing difficult samples, and the performance of the SENet module was slightly lower than that of the CBAM module.

Impact of different lighting intensity on experimental results

In natural environments, different lighting intensities have some influence on the brightness of captured images. Images captured in direct light are clearer, images captured in side-light have some variations in lighting and shadows, while images captured in backlight are darker, all of which can affect the accuracy of fruit detection. To further validate the detection performance of the proposed attention mechanism-based improved YOLOv5 algorithm, this section conducted relevant experiments using YOLOv5s, YOLOv5s-SENet, and YOLOv5s-CBAM as examples.

The test sets were then evaluated using different weight files before and after the addition of the attention mechanism, and the experimental results were shown in Table 3.

Table 3

Average detection accuracy at different light intensity datasets

Data set	YOLOv5s	YOLOv5s-SENet	YOLOv5s-CBAM
Front-lighting	94.3%	95.1%	95.6%
Side-lighting	92.6%	93.7%	94.3%
Backlighting	91.4%	92.5%	92.8%

According to Table 3, the average accuracy of the original YOLOv5s algorithm on the front-light dataset was 94.3%. The YOLOv5s - SENet and YOLOv5s - CBAM algorithms achieved average accuracies of 95.1% and 95.6%, respectively.

This indicated that embedding attention mechanism modules in the YOLOv5 algorithm improved the average detection accuracy across different lighting intensities, with the YOLOv5s - CBAM algorithm achieving the best detection performance. The YOLOv5s - CBAM algorithm achieved the highest average accuracy of 95.6% on the front-light dataset, which was 1.38% higher than that of YOLOv5s. Both the original and improved YOLOv5 algorithms achieved average accuracies above 94% on the front-light dataset. On the backlight dataset, YOLOv5s - CBAM achieved an average detection accuracy of 92.8%, while YOLOv5s achieved only 91.4%, a difference of 1.4%. Furthermore, the average accuracy of YOLOv5s - CBAM on the backlight dataset was 2.93% lower than that on the front-light dataset. This also explained why the average detection accuracy of both the original and improved YOLOv5 algorithms was lowest on the backlight dataset. On the side-lighting dataset, the average accuracy of YOLOv5s, YOLOv5s - SENet, and YOLOv5s - CBAM was 92.6%, 93.7%, and 94.3%, respectively, all of which fell between the average detection accuracy of the front-lighting and backlighting datasets.

The average accuracy of YOLOv5s on datasets with different lighting intensities differed by only 2.9%, indicating that both the original and improved YOLOv5 algorithms had good robustness to changes in lighting intensity. The detection results were shown in Figure 9.

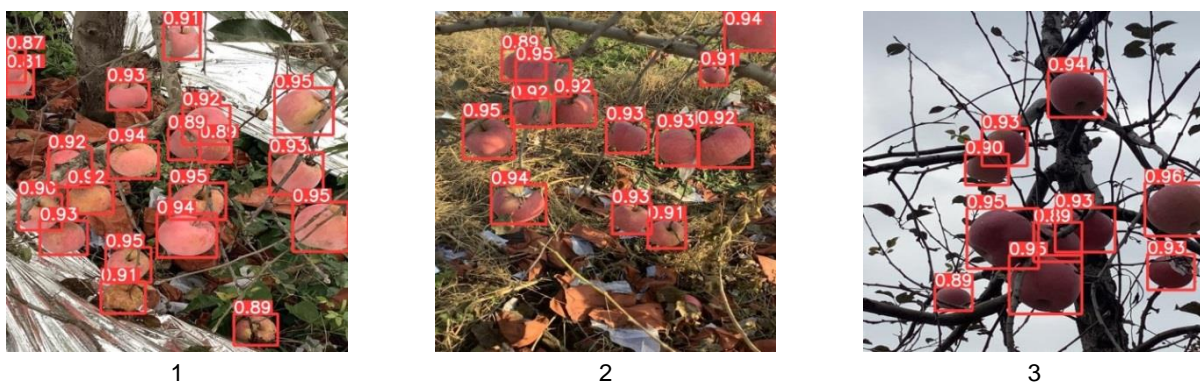


Fig. 9 – Detection effect at different light angles

1. Front-light; 2. Side-light; 3. Backlight

Prototype testing of a robotic target recognition system based on the proposed algorithm

As shown in Figure 9, the prototype of the vision recognition system for the picking robot was designed in this paper. The system was composed of a JETSON NANO embedded development board, a 5V4A power supply, a USB camera, and an HDMI touch display. Figure 9 presents the scene when the system prototype was functioning properly, with the recognition object being a simulated apple tree in a real - world scenario. As can be seen in Figure 9, the system could normally detect the fruit targets in the field of view, and the detection speed was stable at 30 frames per second.



Fig. 10 – Prototype of target recognition system for harvesting robot

Experimental verification showed that when the IOU threshold was set at 0.5 and 0.3, the average detection accuracy of the system prototype was over 85% in both cases, with a detection speed of 30 frames per second.



Fig. 11 – Actual testing results of Apple

CONCLUSIONS

This article proposed an apple detection method using attention mechanisms and improved YOLOv5 to facilitate picking robots' detection. Firstly, SENet and CBAM mechanisms enhanced YOLOv5's feature extraction network, improving model accuracy.

Experimental results showed that after embedding the attention mechanism module, the mAP of the YOLOv5m-CBAM model was 95.6%, which was improved by 2.69%, with an increase in detection time of 2.62%. Among the YOLOv5x models with embedded CBAM module, the average detection accuracy was the highest, with an mAP of 98.3%, and the performance of the CBAM module was superior to that of the SENet module. The improved YOLOv5s model achieved apple recognition accuracy ranging from 91.4% to 95.6% under different lighting conditions, with a difference in fruit recognition accuracy within 3% for the same model. These results demonstrated that the improved YOLOv5 model had good robustness to changes in light intensity. The improved YOLOv5 model could provide reference for the development of the visual system of apple picking robots. Actual tests of the apple-picking robot's vision system prototype showed that when the IOU threshold was set at 0.5 and 0.3, the average detection accuracy was over 85% in both cases.

REFERENCES

- [1] Bai Qiang, Gao Ronghua, Zhao Chunjiang, Li Qifeng, Wang Rong, Li Shuqin (2022). Multi-scale behavior recognition method for dairy cows based on improved YOLOV5s network (基于改进 YOLOV5s 网络的奶牛多尺度行为识别方法) [J]. *Transactions of the Chinese Society of Agricultural Engineering (Transactions of the CSAE)*, Vol. 38, no.12, pp. 163-172, doi: 10.11975/j.issn.1002-6819.2022.12.019.
- [2] Chen Yixiao, Alifu-Kurban, Lin Wenlong, Yuan Xu (2022). CA-YOLOv5 for Crowded Pedestrian Detection (面向拥挤行人检测的 CA-YOLOv5) [J/OL]. *Computer Engineering and Applications*: Vol. 52, no.2, pp. 1-10, doi:10.3778/j.issn.1002-8331.2201-0058
- [3] Du Yonghui, Gao Ang, Song Yuepeng, Guo Jing, Ma Wei, Ren Longlong (2022). Young Apple Fruits Detection Method Based on Improved YOLOv5 [J]. *INMATEH - Agricultural Engineering*, Vol. 73 no.2, pp. 84-93, doi: <https://doi.org/10.35633/inmateh-72-17>.
- [4] Girshick R, Donahue J, Darrell T, Malik J. (2016). "Region based convolutional networks for accurate object detection and segmentation", *IEEE transactions on pattern analysis and machine intelligence*, vol. 38, no. 1, pp. 142– 158;
- [5] Huang Linsheng, Luo Yaowu, Yang Xiaodong, Yang Guijun, Wang Daoyong (2021). Crop Disease Recognition Based on Attention Mechanism and Multi-scale Residual Network (基于注意力机制和多尺度残差网络的农作物病害识别) [J]. *Agricultural Machinery Journal*, Vol. 52, no.10, pp. 264-271, doi:10.6041/j.issn.1000-1298.2021.10.027
- [6] Lin Sen, Liu Meiyi, Tao Zhiyong (2021). Detection of underwater treasures using attention mechanism and improved YOLOv5 (采用注意力机制与改进 YOLOv5 的水下珍品检测) [J]. *Transactions of the Chinese Society of Agricultural Engineering (Transactions of the CSAE)*, Vol. 37, no.18, pp. 307-314, doi:10.11975/j.issn.1002-6819.2021.18.035.

- [7] Feng L., Liu Y., Jia Z., Yang H., Guan J., Zhu H., Ho Y. (2024). Detection of Apple Leaf Diseases Target Based on Improved YOLOv7[J]. *INMATEH - Agricultural Engineering*, Vol. 72. no.1, pp. 280-290, doi: <https://doi.org/10.35633/inmateh-72-26>.
- [8] Felzenszwalb P., Girshick R., McAllester D. (2010) Cascade object detection with deformable part models, *Computer vision and pattern recognition (CVPR), IEEE conference on. IEEE*, 2010, pp. 2241–2248.
- [9] Liu Fang, Liu Yukun, Lin Sen, Guo Wenzhong, Xu Fan, Zhang Bai (2020). Fast Recognition Method for Tomatoes under Complex Environments Based on Improved YOLO (基于改进型 YOLO 的复杂环境下番茄果实快速识别方法) [J]. *Journal of Agricultural Machinery*, Vol. 51, no.6, pp. 229-237, doi: 10.6041/j.issn.1000-1298.2020.06.024
- [10] Liu Xiaoyang, Zhao Dean, Jia Weikuan, Ruan Chengzhi, Ji Wei (2019). Fruit Segmentation Method Based on Superpixel Features for Apple Harvesting Robot (基于超像素特征的苹果采摘机器人果实分割方法) [J]. *Agricultural Machinery Journal*, Vol. 50, no.11, p.9, doi:10.6041/j.issn.1000-1298.2019.11.002.
- [11] Liu Mochen, Gao Tiantian, Ma Zongxu, Song Zhanhua, Li Fade, Yan Yinfa (2021). Target detection model of corn weeds in field environment based on MSRCR algorithm and YOLOv4 tiny (基于 MSRCR YOLOv4 tiny 的田间环境玉米杂草检测模型). *Transactions of the Chinese Society for Agricultural Machinery*, Vol. 53, No. 2, 246-255, 335, doi:10.6041/j.issn.1000-1298.2022.02.026
- [12] Lu Yiqiu, Yang Ye (2020). Study on the Development of Apple Harvesting Mechanization (苹果采摘机械化发展研究) [J]. *Southern Agricultural Machinery*, Vol. 51, no.14, pp. 2.
- [13] Luo Yuan, Wang Boyu, Chen Xu (2020). Research Progresses of Target Detection Technology Based on Deep Learning (基于深度学习的目标检测技术的研究综述) [J]. *Semiconductor Optoelectronics*, Vol. 41, no.1, pp. 1-10, doi:10.16818/j.issn1001-5868.2020.01.001
- [14] Peng Hongxing, Xu Huiming, Liu Huanai (2022). Model for identifying grape pests and diseases based on two-branch feature fusion and attention mechanism (融合双分支特征和注意力机制的葡萄病虫害识别模型) [J]. *Transactions of the Chinese Society of Agricultural Engineering*, Vol. 38, no.10, pp. 156-165, doi:10.11975/j.issn.1002-6819.2022.10.019
- [15] Redmon J., Divvala S., Girshick R., Farhadi A. (2016). You only look once: Unified, real-time object detection, *Proceedings of the IEEE conference on computer vision and pattern recognition*, pp. 779–788.
- [16] Su Baofeng, Shen Lei, Chen Shan, Mi Zhiwen, Song Yuyang, Lu Nan (2021). Multi-features Identification of Grape Cultivars Based on Attention Mechanism (基于注意力机制的葡萄品种多特征分类方法) [J]. *Agricultural Machinery Journal*, Vol.52, no.11, pp.226-233, 252, doi:10.6041/j.issn.1000-1298.2021.11.024.
- [17] Tian Bokai (2020). *Research on Apple Detection Classification and Location Technology in Complex Environment Based on Deep Learning* [D]. Tianjin University of Technology.
- [18] Wang Fang, Cui Dandan, Li Lin (2021). Target recognition and positioning algorithm of picking robot based on deep learning (基于深度学习的采摘机器人目标识别定位算法) [J]. *Electronic measurement technology*, Vol. 44, no.20, pp.6, doi:10.19651/j.cnki.emt.2107366
- [19] Xia Ye, Xiaohui Lei, Andreas Herbst, Xiaolan Lyu (2023). Research on Pear Inflorescence Recognition Based on Fusion Attention Mechanism with YOLOv5. *INMATEH-Agricultural Engineering*, Vol. 69, No.1, pp.11-20, doi: <https://doi.org/10.35633/inmateh-69-01>
- [20] Yongpeng Chen, Yi Niu, Weidong Cheng, Laining Zheng, Dongchao SUN (2024). Apple Detection Method in the Natural Environment Based on Improved YOLOv5[J]. *INMATEH - Agricultural Engineering*, Vol.72, no.1, pp. 183-192, doi: <https://doi.org/10.35633/inmateh-72-17>
- [21] Zhao Jun'ai (2021). Design and Experiment of Apple Picking Robot Based on Machine Vision (基于机器视觉的苹果采摘机器人的设计与试验) [J]. *Henan Science and Technology*, Vol. 0, no.20, pp.3, doi: 10.3969/j.issn.1003-5168.2021.20.017

DEVELOPMENT AND PERFORMANCE EVALUATION OF A NOVEL PEELING DEVICE FOR HIGH-MOISTURE CORN COBS

高含水率玉米果穗剥皮装置设计与试验

Bang Ji ^{1,3}, Long PAN ¹, Yusong XIE ¹, Hao ZHOU ¹, Yongkang LI ¹, Pu LI ^{*2}

¹ Hunan Agricultural University, College of Mechanical and Electrical Engineering, Changsha/China;

² Hunan Mechanical and Electrical Polytechnic, Changsha/China;

³ Hunan Key Laboratory of Intelligent Agricultural Machinery and Equipment, Changsha/China.

Tel: +86 17375860294; E-mail: 619741039@qq.com

Corresponding author: Pu Li

DOI: <https://doi.org/10.35633/inmateh-75-82>

Keywords: corn peeling, high-moisture corn cobs, high-speed camera, scratching device, friction peeling

ABSTRACT

To address the challenges of high moisture content and the difficulty of peeling corn cobs in certain regions during harvest, a novel peeling device was developed. The device uses directional friction to peel the cob after introducing scratches on the bracts. Mechanical and kinematic analyses were conducted to study the peeling process, along with the design of the scratching mechanism. High-speed camera technology was employed to observe the peeling process, confirming that the peeling rollers effectively gripped the bracts at the scratched points. A three-factor, three-level response surface optimization experiment was carried out, using peeling roller speed, pressing wheel speed, and the distance between the pressing wheel and the peeling roller as independent variables, with bract peeling rate and grain shedding rate as the response indicators. The results showed that at a peeling roller speed of $353.2 \text{ r}\cdot\text{min}^{-1}$, a pressing wheel speed of $81.42 \text{ r}\cdot\text{min}^{-1}$, and a distance of 37.16 mm between the pressing wheel and the peeling roller, the bract peeling rate reached 95.67% with a grain shedding rate of 1.45%. Validation tests under these conditions yielded a bract peeling rate of 93.33% and a grain shedding rate of 1.56%, meeting the operational requirements for efficient corn peeling.

摘要

针对部分地区大田玉米在收获时其含水率高剥皮困难等问题,设计了一款在果穗苞叶上划痕后定向摩擦去皮的剥皮装置。对果穗剥皮过程进行力学与运动学分析,并对划痕装置进行设计。采用高速摄像技术对果穗剥皮过程进行研究并验证了剥皮辊在苞叶划痕处能有效的抓取到苞叶。以剥皮辊转速、压送器转速和压送器距剥皮辊间距作为试验因素,以苞叶剥净率和籽粒损失率作为试验指标,进行三因素三水平响应曲面优化试验。结果表明:当剥皮辊转速为 $353.2 \text{ r}\cdot\text{min}^{-1}$ 、压送器转速为 $81.42 \text{ r}\cdot\text{min}^{-1}$ 、压送器距剥皮辊间距为 37.16mm 时,此时苞叶剥净率为 95.67%,籽粒损失率为 1.45%。在该条件下开展验证试验,得到苞叶剥净率、籽粒损失率分别为 93.33%、1.56%,满足玉米剥皮要求。

INTRODUCTION

In some regions, the high moisture content of corn cobs at maturity, generally ranging from 30% to 40%, is primarily due to the local climate and environmental conditions (Chen *et al.*, 2014; Li *et al.*, 2024). As a result, directly harvesting kernels often leads to a higher kernel breakage rate. Consequently, the standard method involves harvesting the entire cob, followed by drying, peeling, and threshing (Chen *et al.*, 2023). Given the high moisture content at harvest, if the cobs are not dried and peeled promptly, they are prone to deterioration and germination, which significantly affects their value (Zhao *et al.*, 2024; Barnwal *et al.*, 2012). Therefore, the development of an efficient method for peeling corn cobs with high moisture content is of paramount importance.

In recent years, numerous scholars have focused on improving the material properties of corn cobs and optimizing the structure of key components involved in the peeling process, to enhance the operational efficiency of peeling devices (Xie *et al.*, 2018; Liu *et al.*, 2020). Plett *et al.* (1994) conducted a study on various corn cob varieties to assess kernel crushing and found that the lowest kernel crushing rate occurred when the moisture content was between 16.7% and 22.1%.

Bang Ji, Lect. Ph.D.; Long Pan, M.S. Stud.; Yusong Xie, M.S. Stud.; Hao Zhou, M.S. Stud.; Yongkang Li, M.S. Stud.; Pu Li, Lect. M.S.

Li Zhenye *et al.* (2021) investigated the physical and tensile properties of corn cob bracts throughout the harvest period, developing a mathematical model that correlates bract tensile properties with moisture content and thickness.

Liu Lei *et al.* (2022) established a discrete element method (DEM)-based simulation model to analyze the corn peeling process, focusing on kernel crushing and shedding. Their study provided insights into the cob peeling process and highlighted the extent of kernel damage to light cobs during interaction with the peeling roller. The Kubota PRO1408Y-4 self-propelled corn cob harvester, produced by Kubota Agricultural Machinery Co., Ltd. in Japan, features an extended peeling roller (1.1 m in length), which ensures a high peeling rate even at elevated speeds. Additionally, the spacing between the pressing wheel and the peeling roller can be adjusted via a handle, allowing the device to accommodate different corn cob sizes (Shirly., 2015). Although these studies demonstrate effective peeling performance at low moisture content, they are less suited for high-moisture corn cobs. When corn cobs have high moisture content, the bracts and kernels bond more tightly, which prevents the peeling rollers from effectively gripping the bracts and performing an efficient peeling operation.

To address these challenges, the present study designs a peeling device specifically for the directional friction peeling of corn cob bracts after initial scratching. This design is based on an analysis of the physical properties and peeling requirements of the bracts from high-moisture corn cobs. Through theoretical analysis of the peeling process and the design of key components, the study also employs high-speed camera technology to verify that the peeling rollers can effectively grip and peel the bracts. Finally, through bench testing, relevant parameters are optimized to facilitate the efficient peeling of high-moisture corn cobs.

MATERIALS AND METHODS

Machine structure and working principle

The high-moisture-content corn cob peeling device consists of two main components: the scratching device and the peeling device, as illustrated in Fig. 1. During operation, the cob initially passes through the scratching device, where it is guided along a semi-circular rail. The rail is situated below the blade. As the cob progresses along the guide rail, it passes beneath the blade, which creates scratches on the bracts. Following this, the cob enters the peeling device. The rollers continuously grasp the bracts at the locations of the scratches (Zhao *et al.*, 2012).

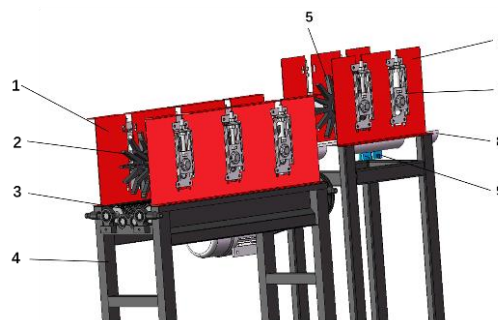


Fig. 1 – Three-dimensional structure of corn cob peeling device

1 - Peeling device; 2 - Pressing wheel; 3 - Peeling roller; 4 - Frames; 5 - Pressing wheels; 6 - Scratching devices; 7 - Height-adjustable bearing seats; 8 - Semi-circular guide rail; 9 - Knife holders.

Modeling of corn cob-mechanics

Cob bracts scratch force analysis

In the semicircular guide scratching process, the force conditions are illustrated in Fig. 2.

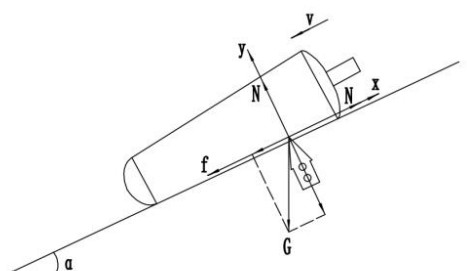


Fig. 2 – Force analysis diagram for cob bracts scratching process

When the cob is fed into the scratching device, it moves downward along the guide rail with a specified acceleration α , and the blade scratches the cob bracts under the action of the pressing force F . The force equation of the scratching process is given in Eq. (1) and (2).

$$mg \sin\alpha + f - F = ma \tag{1}$$

$$\begin{cases} N = mg \cos\alpha \\ f = \mu_1 N \end{cases} \tag{2}$$

From Equations 1 and 2, will result:

$$a = g(\sin\alpha + \mu_1 \cos\alpha) - \frac{2F}{m} \tag{3}$$

where:

m is the unpeeled cob mass, [kg]; g is the acceleration due to gravity, [$m \cdot s^{-2}$]; f is the frictional resistance of the guide rail acting on the cob, [N]; N is the support force of the guide rail on the cob, [N]; μ_1 is the friction factor between the guide rail and the cob; α is the guide rail inclination angle, [$^\circ$].

When the Corn cob moves within the guide rail at a uniform linear velocity, then:

$$S = v_0 t + \frac{1}{2} a t^2 \tag{4}$$

where:

S is the length of the guide rail, [m]; V_0 is the initial feeding speed of the corn cob [$m \cdot s^{-1}$]; t is the cob peeling time, [s].

Substituting Eq. (3) into Eq. (4), the required force F for cob scratching is obtained, as shown in Eq. (5).

$$F = \frac{m[gt^2(\sin\alpha + \mu_1 \cos\alpha) - 2(S - v_0 t)]}{2t^2} \tag{5}$$

Equation (5) shows that the scratching process is influenced by the inclination angle of the guide rail, α . Based on the peeling device's inclination angle, the value of α can range from 10° to 20° .

Conditions required for cob bracts peeling

As shown in Fig. 3, consider the peeling process of the bracts from point A to point B. The length of the bract from point A to point B is denoted as C. Treating the bract as an elastomer, a mechanical model for bract peeling is established to study the peeling process. During the bract peeling process, the action of the peeling force F on the bracts can be divided into three distinct components (Rivlin et al., 1997; Kendall et al., 1975).

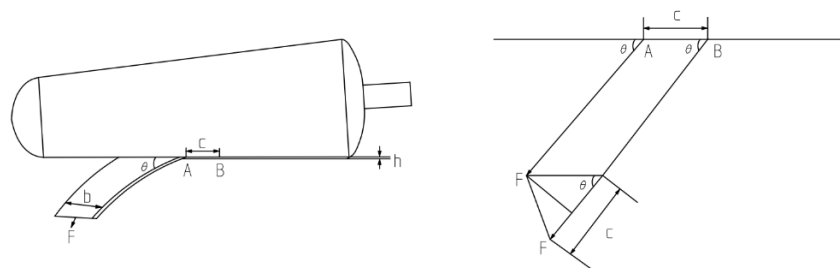


Fig. 3 – Schematic diagram of bracts peeling

Surface energy W_s refers to the energy generated when the peeling force F peels the upper bracts from the lower bracts as seen in Eq. (6):

$$W_s = -b c R \tag{6}$$

Potential energy W_p denotes the energy generated by the movement of the peeling force F from point A to point B as seen in Eq. (7):

$$W_p = c(1 - \cos\theta)F \quad (7)$$

Elastic potential energy: W_e refer to the energy produced by the peeling force F as it stretches the bracts. This energy comprises two components:

The first component is the work W_{e1} done by the constant force F in the stretching region:

$$W_{e1} = F \Delta c \quad (8)$$

It is known that $E = \frac{F/bh}{\Delta c/c}$, $\Delta c = \frac{Fc}{Ebh}$, thus:

$$W_{e1} = \frac{F^2 c}{Ebh} \quad (9)$$

The second component is the elastic strain energy W_{e2} :

$$W_{e2} = \frac{1}{2} F \Delta c \quad (10)$$

$$W_{e2} = \frac{F^2 c}{2Ebh} \quad (11)$$

where:

F is the peeling force of peeling bracts, [N]; E is the modulus of elasticity, [MPa]; θ is the peeling angle, [°]; b is the bract peeling width, [mm]; h is the bracts thickness, [mm]; R is the unit peeling energy, bract peeling energy consumption per unit area of bract peeling, [J].

According to the law of conservation of energy, the following equation is established:

$$-bcR + c(1 - \cos\theta)F + \frac{F^2 c}{2Ebh} = 0 \quad (12)$$

By solving this equation, the formula for the bract peeling force F is obtained as shown in Eq. 13:

$$F = Ehb \sqrt{\sqrt{(1 - \cos\theta)^2 + \frac{2R}{Eh}} + \cos\theta - 1} \quad (13)$$

From Eq. (13), it is clear that the peeling force F during bract peeling depends on several factors such as the peeling angle θ , the bract peeling width b , the bract thickness h , the bract elastic modulus E , and the energy consumption R required for peeling each unit area.

Design of the key components

Scratching device

When the moisture content of corn cobs is high, the pores of the bracts become saturated with water (Mandang et al., 2018), causing the bract layers to stack tightly and wrap around the bare cob. As a result, the peeling rollers cannot effectively grip the bracts, leading to difficulties in the peeling process. Scratching the surface of the bracts can cause them to split at the point of contact, as shown in Fig.4d, allowing the peeling roller to better grip the bracts at the scratched location.

The scratching device as illustrated in Fig.7. The blade is welded to the bottom of the guide rail through the knife frame. The blade extends approximately 2 mm into the notch, ensuring it scratches a sufficient depth into the bracts without damaging the seeds. The operation principle is as follows: the cob passes through the semi-circular guide rail, which is set at a certain angle, and slides down the guide rail due to its gravity and the force from the pressing wheel (Fig.7a).

When the cob reaches the tip of the blade, the pressing wheel exerts both downward and forward forces on the cob, causing the cob to move over the blade (Fig.7b).

This action effectively scratches the bracts (Fig.7c). Furthermore, the semi-circular guide causes the corn cob to enter the peeling device in a vertical orientation, reducing the likelihood of clogging within the peeling device. This improvement enhances both the peeling efficiency and overall working performance.

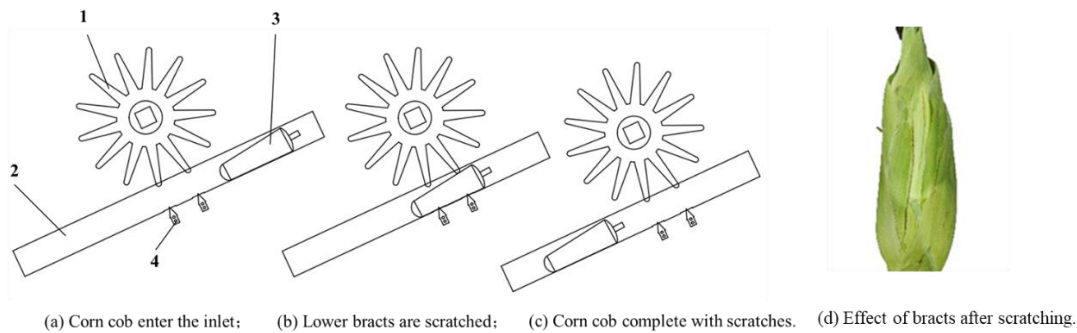


Fig. 4 – Schematic diagram of corn cob scratching and effect of bracts after scratching
 1 - Pressing wheel; 2 - Semi-circular guide rail; 3 - Corn cob; 4 Blade.

Peeling device

The peeling device is illustrated in Fig.5. During the corn cob peeling process, the peeling roller maintains continuous frictional contact with the bracts, which is a critical mechanism underlying the device’s operation (Fu et al., 2020; Gorad et al., 2019). The device's configuration incorporates both high and low rollers, making it particularly well-suited for cobs with tightly wrapped bracts. The surface of the peeling roller is designed with both fish scale rollers and double spiral rollers. The fish scale rollers, positioned as the high rollers, exert friction on the bracts, effectively gripping them. The low rollers are equipped with double spiral rollers, whose helical pattern promotes the cob's continuous forward movement. Furthermore, the height difference between the high and low rollers creates varying friction torques on the cob. This torque disparity not only aids in correcting the cob's position but also induces rotational motion around its axis, thus increasing the number of contact points between the bracts and the peeling roller (Yang et al., 2021).

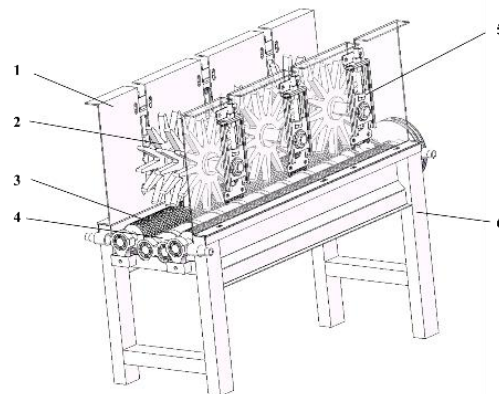


Fig. 5 – Peeling device
 1 - Fixed plate; 2 - Pressing wheel; 3 - Fish scale roller; 4 - Spiral roller; 5 - Height-adjustable bearing seat; 6 - Frame.

High-speed camera experiment design

To verify the ability of the peeling roller to effectively grasp and remove bracts during the peeling of corn cobs with high moisture content, a high-speed camera peeling test platform was constructed, consisting of a high-speed camera and the peeling device (Fig.6). Before the test, the shooting frame rate set to 3000 frames/s and resolution set at 1920×1080. (Zhu et al., 2015).



Fig. 6 – Test device
 1 - Peeling device; 2 - Fill light; 3 - Computer; 4 - High-speed camera.

Peeling performance test design

The test samples used in this study were the Denghai 605 corn variety and were harvested in Liuyang City, Hunan Province, China. Samples exhibiting optimal cob length and undamaged bracts were selected, with moisture content maintained at approximately 35%. The test materials and device are illustrated in Fig. 7.



Fig. 7 – Test materials and device

Based on a theoretical mechanical analysis of the corn peeling process and preliminary pre-tests, three primary factors—peeling roller speed, pressing wheel speed, and the distance between the pressing wheel and peeling roller—were chosen for response surface test. Following JB/T11907-2014 standards, two evaluation metrics were selected: the bract peeling rate (Y_1) and the grain shedding rate (Y_2). The respective calculation formulas are given below:

$$Y_1 = \left(1 - \frac{n_b}{n}\right) \times 100\% \quad (14)$$

$$Y_2 = \frac{G_s}{G + G_s} \times 100\% \quad (15)$$

where:

n is the total number of corn cobs of the measurement sample, [one]; n_b is the number of corn cobs without peeling bracts, [one]; G is the total mass of sample grains, [g]; G_s is the total mass of lost grains, [g].

Design of the one-way test

Based on both preliminary pre-tests and relevant research conducted by scholars domestically and internationally, the peeling roller speed was set within the range of 300–500 r·min⁻¹, the pressing wheel speed was set within the range of 40–120 r·min⁻¹, and the distance between the pressing wheel and peeling roller was set between 30 and 50 mm (Li, 2023). As detailed in Table 1.

Table 1

Single-factor test levels			
Level	Factor		
	The peeling roller speed [r·min ⁻¹]	The pressing wheel speed [r·min ⁻¹]	The distance between the pressing wheel and the peeling roller [mm]
1	300	40	30
2	350	60	35
3	400	80	40
4	450	100	45
5	500	120	50

Response surface test

Based on the results of the one-way test, the following parameter ranges were selected: peeling roller speed of 300–400 r·min⁻¹, pressing wheel speed of 60–100 r·min⁻¹, and the distance between the pressing wheel and peeling roller set at 35–45 mm. The factor levels are presented in Table 2.

Table 2

Factor coding of peeling test			
Encodings	Factor		
	Peeling roller speed [r·min ⁻¹]	Pressing wheel speed [r·min ⁻¹]	Distance between the pressing wheel and the peeling roller [mm]
-1	-1	-1	-1
0	0	0	0
1	1	1	1

RESULTS AND DISCUSSION

Results and analysis of the high-speed camera

Figure 8 presents the high-speed camera's capture of the cob bracts removal process post-scratching. Analysis of the high-speed footage revealed that the peeling process can be divided into two distinct stages: Firstly, due to the height difference between the high and low rollers, the friction torque acting on the cob varies, causing the cob to rotate around its axis. Simultaneously, the bracts' surface becomes puckered after being scratched. The pressing wheel intermittently applies pressure to the cob, which increases the friction between the peeling rollers and the scratched bracts. When this friction exceeds the bond between the layers of the bracts, the peeling rollers effectively grip the bracts (Fig. 8a–c). Secondly, once the peeling rollers grasp the bracts, they are continuously pulled. As the area of the bracts engaged between the two peeling rollers increases, the bracts break along the longitudinal veins, completing the peeling process (Fig. 8 d–f). Once the upper layer of bracts is peeled, the lower layers continue to be pulled by the combined forces of the peeling rollers and pressing wheel. Meanwhile, the cob continues to rotate around its axis, allowing each successive layer of bracts to be grasped and peeled until all the bracts are removed, as depicted in (Fig. 8 g–h). Thus, in the corn cob peeling process, increasing the friction between the peeling rollers and appropriately adjusting the difference in friction torque between the high and low rollers can facilitate the cob's rotation around its axis. This increases the contact time between the bracts and the peeling rollers, thereby improving the efficiency of bract removal.

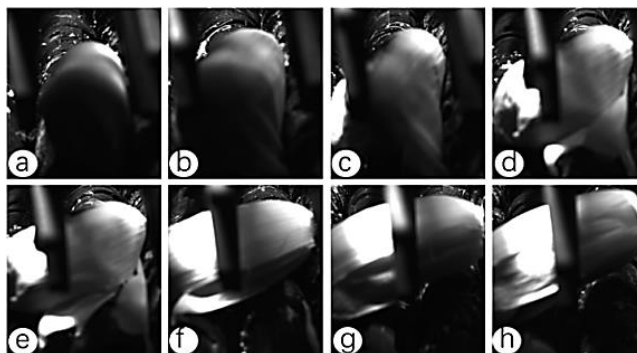


Fig. 8 – High-speed camera capture of bracts peeling process

Results and analysis of the one-way test

The results of the single-factor tests are presented in Fig. 9. As illustrated in Fig. 9, an increase in peeling roller speed, pressing wheel speed, and the distance between the pressing wheel and the peeling roller initially led to an increase in the bract peeling rate, followed by a subsequent decrease. In contrast, the grain shedding rate initially decreased and then increased. Specifically, when the peeling roller speed ranged from 300 to 400 r·min⁻¹, the maximum bract peeling rate reached 95%, and the minimum grain shedding rate was 1.45%. Similarly, when the pressing wheel speed varied between 60 and 100 r·min⁻¹, the maximum bract peeling rate increased to 96.67%, with a minimum grain shedding rate of 1.47%. When the distance between the pressing wheel and the peeling roller was adjusted to 35–45 mm, the maximum bract peeling rate was 95%, and the minimum grain shedding rate was 1.65%. Consequently, the optimal settings for the response surface test were determined to be a peeling roller speed of 300–400 r·min⁻¹, a pressing wheel speed of 60–100 r·min⁻¹, and a distance between the pressing wheel and the peeling roller of 35–45 mm.

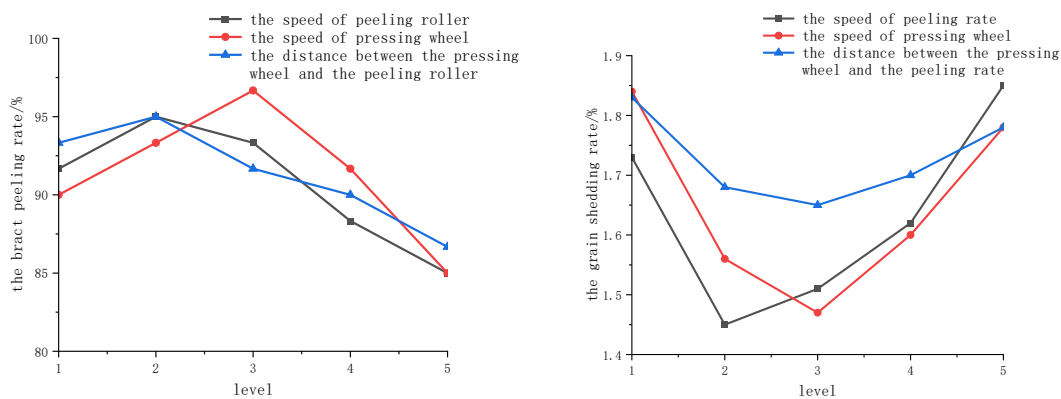


Fig. 9 – Single factor test results

Text results

Design-Expert 13 software was utilized for experimental design and data analysis, with the experimental design and results summarized in Table 3.

Table 3

Experiment scheme and results					
Test number	Factor			Y ₁ %	Y ₂ %
	X ₁	X ₂	X ₃		
1	0	0	0	95	1.45
2	1	0	-1	93.33	1.71
3	0	0	0	93.33	1.39
4	-1	1	0	88.33	1.88
5	0	0	0	95	1.53
6	0	0	0	95	1.48
7	1	0	1	91.67	1.69
8	0	1	-1	93.33	1.65
9	0	-1	1	90	1.83
10	0	-1	-1	91.67	1.63
11	-1	0	-1	91.67	1.69
12	0	1	1	88.33	1.79
13	1	1	0	93.33	1.99
14	-1	0	1	86.67	2.05
15	1	-1	0	86.67	1.71
16	-1	-1	0	88.33	1.92
17	0	0	0	96.67	1.49

Significance analysis

The analysis of significance for the bract peeling rate (Y₁) and grain shedding rate (Y₂) is shown in Table 4. Both regression models for Y₁ and Y₂ were found to be statistically significant, with P-values less than 0.01. This indicates that the models effectively describe the relationship between the experimental factors and the response variables. Moreover, the regression equations were not found to be significantly out of fit, suggesting a strong quadratic relationship between the test parameters and the factors within the tested range. The coefficients of determination (R²) for Y₁ and Y₂ were 0.9195 and 0.9558, respectively, demonstrating high consistency between the predicted and actual values. Based on the results, the regression terms X₃, X₁², and X₂² significantly influence Y₁ (P < 0.01). The interaction terms X₁, X₁X₂ and X₃² also showed a significant effect on Y₁ (0.01 < P < 0.05). Conversely, the regression terms X₂, X₁X₃, and X₂X₃ did not significantly affect Y₁ (P > 0.05). The corresponding regression equation for the bract peeling rate is provided in Eq. (16). For the grain shedding rate (Y₂), the regression terms X₃, X₁², and X₂² were found to have a very significant effect (P < 0.01). The interaction terms X₁, X₁X₂, X₁X₃, and X₃² were significantly associated with Y₂ (0.01 < P < 0.05). However, the terms X₂ and X₂X₃ had no significant impact on Y₂ (P > 0.05). The regression equation for the grain shedding rate is presented in Eq. (17).

$$Y_1 = 95 + 1.25X_1 - 1.67X_3 + 1.66X_1X_2 - 2.92X_1^2 - 2.92X_2^2 - 1.25X_3^2 \tag{16}$$

$$Y_2 = 1.47 - 0.055X_1 + 0.085X_3 + 0.08X_1X_2 - 0.095X_1X_3 + 0.2335X_1^2 + 0.1735X_2^2 + 0.0835X_3^2 \tag{17}$$

Table 4

Significance test result								
Source of variation	Sum of Squares	Y ₁			Y ₂			
		Degrees of freedom	F	P	Sum of Squares	Degrees of freedom	F	P
Mold	143.03	9	8.89	0.0044	0.5736	9	16.82	0.0006
X ₁	12.5	1	6.99	0.0332	0.0242	1	6.39	0.0394
X ₂	5.53	1	3.09	0.1221	0.0060	1	1.60	0.2469
X ₃	22.21	1	12.42	0.0097	0.0578	1	15.25	0.0059
X ₁ X ₂	11.09	1	6.2	0.0416	0.0256	1	6.75	0.0355
X ₁ X ₃	2.79	1	1.56	0.2519	0.0361	1	9.53	0.0177
X ₂ X ₃	2.77	1	1.55	0.2531	0.0009	1	0.2375	0.6409
X ₁ ²	35.81	1	20.03	0.0029	0.2296	1	60.57	0.0001
X ₂ ²	35.87	1	20.06	0.0029	0.1267	1	33.44	0.0007
X ₃ ²	6.57	1	3.67	0.0969	0.0294	1	7.75	0.0272
Residual	12.52	7			0.0265	7		
Lost								
Proposal	6.94	3	1.66	0.3113	0.0157	3	1.92	0.2682
Pure error	5.58	4			0.0109	4		
Aggregate	155.54	16			0.6002	16		
R ²	0.9195				0.9558			

Response surface analysis

Based on the regression equations and response surface analysis (see Fig. 10), an interaction was observed between the peeling roller speed, the pressing wheel speed, and the distance between the pressing wheel and the peeling roller. As the peeling roller speed increased, the bract peeling rate initially increased and then decreased, with the maximum rate observed in the range of 340~360 r·min⁻¹. Similarly, the bract peeling rate increases and then decreases with increasing pressing wheel speed, reaching its maximum in the range of 70~85 r·min⁻¹. Moreover, as the distance between the pressing wheel and the peeling roller increases, the bract peeling rate initially increases slowly and then decreases, with the maximum rate observed between 37 and 41 mm. In summary, the optimal bract peeling rate for corn cobs with high moisture content occurs when the peeling roller speed is between 340 and 360 r·min⁻¹, the pressing wheel speed ranges from 70 to 85 r·min⁻¹, and the distance between the pressing wheel and the peeling roller lies between 37 and 41 mm.

Based on the regression equation and response surface analysis (Fig. 11), an interaction was observed between the peeling roller speed, the pressing wheel speed, and the distance between the pressing wheel and the peeling roller. As the peeling roller speed increased, grain shedding initially decreased and then increased, with the minimum shedding rate occurring in the range of 340~360 r·min⁻¹. Similarly, grain shedding decreased and then increased with an increase in pressing wheel speed, with the minimum rate observed between 75 and 85 r·min⁻¹. Furthermore, as the distance between the pressing wheel and the peeling roller increased, grain shedding decreased and then increased, with the minimum shedding rate occurring within the interval of 35~39 mm. In summary, the optimum peeling rate for corn cobs with high moisture content was achieved when the peeling roller speed was between 340 and 360 r·min⁻¹, the pressing wheel speed was between 75 and 85 r·min⁻¹, and the distance between the pressing wheel and the peeling roller was between 35 and 39 mm, simultaneously minimizing the grain shedding rate.

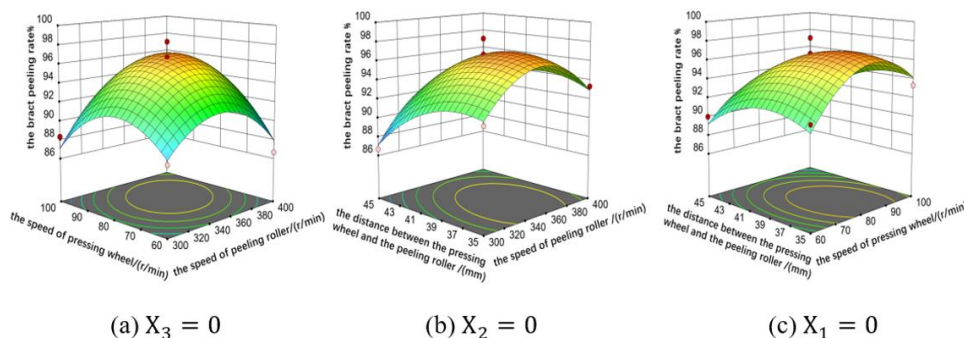


Fig. 10 – Effect of factor interactions on bract peeling rate

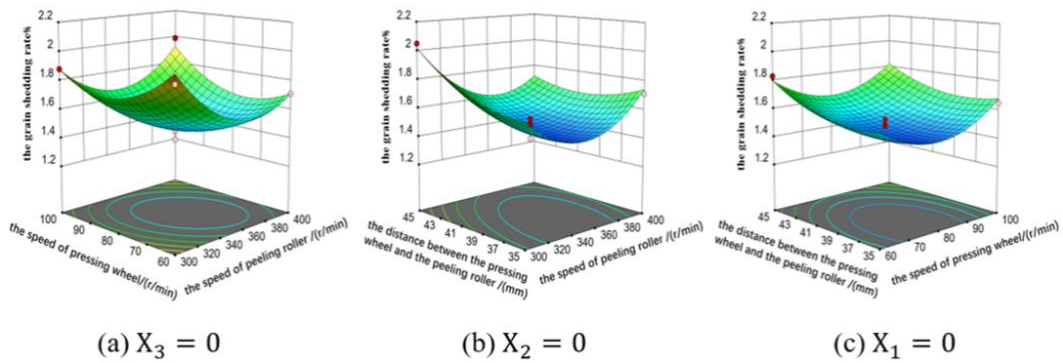


Fig. 11 – Effect of factor interactions on grain shedding rate

Validation test

Using the optimization module of Design-Expert 13 software, the quadratic regression models for Y_1 and Y_2 are optimized and solved, with the objective function and constraints defined as follows:

$$\left\{ \begin{array}{l} \max Y_1 \\ \min Y_2 \\ 300r \cdot \text{min}^{-1} \leq X_1 \leq 400r \cdot \text{min}^{-1} \\ 60r \cdot \text{min}^{-1} \leq X_2 \leq 80r \cdot \text{min}^{-1} \\ 35\text{mm} \leq X_3 \leq 45\text{mm} \end{array} \right\} \quad (18)$$

It led to the identification of the optimal parameter combination: peeling roller speed of 353.2 r·min⁻¹, pressing wheel speed of 81.42 r·min⁻¹, and a distance of 37.16 mm between the pressing wheel and the peeling roller. The bract peeling rate and grain shedding rate were found to be 95.67% and 1.45%, respectively.

The optimized test conditions were adjusted as follows: peeling roller speed of 353 r·min⁻¹, pressing wheel speed of 80 r·min⁻¹, and a distance between the pressing wheel and the peeling roller of 37 mm. To validate these conditions. Three repetitions were performed, resulting in an average bract peeling rate of 93.33% and an average grain shedding rate of 1.56%. These results, as presented in Table 5, fulfil the machine design specifications.

Table 5

Test validation results		
Test number	Bract's peeling rate	Grain shedding rate
1	95%	1.55%
2	90%	1.59%
3	95%	1.54%
Average value	93.33%	1.56%

CONCLUSIONS

(1) A peeling device was designed to remove the skin through friction, following the initial scratching of the surface of the cob bracts. Additionally, the design of the scratching mechanism ensured that the surface of the cob bracts was scratched to a specific depth without damaging the seeds. The semi-circular guide rail was incorporated to position the corn cob vertically as it entered the peeling device.

(2) A peeling test platform, comprising a high-speed camera and the peeling device, was established to investigate the cob peeling process and verify that the peeling rollers can effectively grip the bracts at the points where the surface was scratched.

(3) Using Design-Expert 13 software to process the experimental data, the optimal parameter combination for the peeling device was identified as follows: peeling roller speed of 353.2 r·min⁻¹, pressing wheel speed of 81.42 r·min⁻¹, and a distance of 37.16 mm between the pressing wheel and the peeling roller. Under these conditions, the bract peeling rate was 95.67%, while the grain shedding rate was 1.45%. In the verification test, the bract peeling rate was 93.33%, the grain shedding rate was 1.56%, and the device met the design requirements.

ACKNOWLEDGEMENTS

This work is financially supported by the Hunan Provincial Natural Science Foundation Project (2024JJ6248), the open Fund of State Key Laboratory of Agricultural Equipment Technology (SKLAET-202406) and the Hunan Agriculture Research System (HARS-02)

REFERENCES

- [1] Barnwal, P., Kadam D.M., Singh K.K. (2012). Influence of Moisture Content on Physical Properties of Maize. *International Agrophysics*, Vol. 26, pp. 331-334, Punjab/India.
- [2] Chen Qingwen, Zhi Chen, Han Zengde, Hao Fuping, Cui Junwei, Wu Hongxin, Feng Xiaochuan. (2014). Analysis and Prospects of the Corn Husker of Corn Harvester in China (我国玉米收获机剥皮装置的现状分析及展望). *Journal of Agricultural Mechanization Research*, Vol. 36, pp. 257-260, Beijing/China.
- [3] Chen Shun, Zhang Xinwei, Jiang Chunxia, Yi Kechuan, Wang Qingqing, Sha Xuemeng, Zhang Xiaolong. (2023). Experimental Study on the Peeling Fracture Effect of Fresh Corn Ear Based on High and Low Roller Peeling Equipment. *Agriculture*, Vol.13, pp.8, Chuzhou/China.
- [4] Fu Jun, Yuan Haikuo, Zhao Rongqiang, Chen Zhi, Ren Luquan. (2020). Peeling Damage Recognition Method for Corn Ear Harvest Using RGB Image. *Applied Sciences*, Vol.10, pp.10, Changchun/China.
- [5] Kendall K. (1975). Thin-film peeling-the elastic term [J]. *Journal of Physics D Applied Physics*, Vol. 8, pp.1449, Ibaraki/Japan.
- [6] Li Zhenye, Fu Jun, Luo Xiwen, Fu Qiankun, Chen Zhi, Ren Luquan. (2024). Determination of Friction Characteristics of Corn Ears at Varying Factors in Mechanical Peeling. *Journal of Food Process Engineering*, Vol. 47, pp. e14764, Jilin/China.
- [7] Liu J.J., Ye W., Zhang Z.H., Yu Z.L., Ding H.Y., Zhang C., Liu S. (2020). Vein distribution on the deformation behavior and fracture mechanisms of typical plant leaves by quasi in situ tensile test under a digital microscope. *Appl.Bionics Biomech*, Vol. 49, pp. 1643-1652, Huai'an/China.
- [8] Li Zhenye, Fu Jun, Luo Xiwen. (2021). Tensile Properties and Fracture Mechanisms of Corn Bract for Corn Peeling Device Design. *Agriculture*. Vol. 11, pp. 796, Jilin/China.
- [9] Liu Lei, Du Yuefeng, Li Xiao, Liu Lihan, Zhang Yan'an, Fan Y. (2022). Analysis and Experiment on Kernel Loss of Seed Corn during Peeling Based on DEM (基于离散元法的种子玉米剥皮过程籽粒损失分析与试验). *Transactions of the Chinese Society for Agricultural Machinery*. Vol. 53, pp. 28-38, Beijing/China.
- [10] Li Zhenye. (2023). *Research on key technologies and intelligent recognition for low-damaged-high-stripping peeling of corn ear harvester (玉米果穗收获机低损高净剥皮关键技术与智能识别研究)* (PhD dissertation, Jilin University, Jilin/China).
- [11] Mandang T., Sinambela R., Pandianuraga N. (2018). Physical and mechanical characteristics of oil palm leaf and fruits bunch stalks for bio-mulching [J]. *IOP Conference Series: Earth and Environmental Science*, Vol. 196, pp. 012015. 012015, Pertanian Bogor/ Indonesia
- [12] Plett S. (1994). Corn kernel breakage as a function of grain moisture at harvest in a prairie environment [J]. *Canadian Journal of Plant Science*, Vol. 74, pp. 543-544, Manitoba/Canada.
- [13] Rivlin R. (1977). *The Effective Work of Adhesion* [M]. New York: Collected Papers of R.S. Rivlin. Springer New York. pp.2611-2614. New York/ Britain
- [14] Shirly. (2015). Kubota 4YZB-3(PRO-1408Y) Self-propelled Corn Harvester. *Agricultural machinery*. Vol. 18, pp. 28.
- [15] Xie Fuxiang, Song Jian, Huo Hongpeng, Huo Xinxin. (2018). Experiment and Mechanical Characteristics on Bract Peeling of Corn Harvester (玉米苞叶力学性能与剥离试验). *Agricultural Mechanization Research*, Vol. 40, pp. 129-133, Qingdao/China.
- [16] Yang Ke, Jiang Chun-Xia, Zhang Wei, Zhang Dong-Mei, Liu En-Ke, & Guang-Gian, Z. (2023). Effects of Different Harvesting Time on the Mechanical Harvest Quality and Yield of Maize Grains (不同收获期对玉米子粒机械收获质量及产量的影响). *Journal of Maize Sciences*, Vol. 31, pp. 88-94, Taiyuan/China.
- [17] Yang Fan, Du Yuefeng, Fu Qiufeng, Li Xiaoyu, Zhu Zhongxiang. (2021). Design and testing of seed maize ear peeling roller based on Hertz theory. *Biosystems Engineering*, Vol. 202, pp. 165-178, Beijing/China.

- [18] Zhao Yiming, Dai Fei, Shi Ruijie, Chen Junzhi, Xin Shanglong, Zhao Wuyun, Fengwei, Z. (2024). Design and Experiment of Self-propelled Seed Corn Combine Harvester (自走式制种玉米联合收获机设计与试验). *Transactions of the Chinese Society for Agricultural Machinery*. Vol. 55, pp. 121-134, Lanzhou/China.
- [19] Zhao Chun Hua, Zhao Tao, Long H.B. (2012). Design and Experimental Study of the Multi-Function Corn Peeling Machine with Analysis of Segmented Metal Construction Materials. *Advanced Materials Research*, Vol. 600, pp. 144-147, Lanzhou/China.
- [20] Zhu Zhongxiang, Yue Xiaowei, Du Yuefeng. (2015). Dynamic simulation and high-speed photography experiment on corn-ear husking (玉米果穗剥皮的运动仿真与高速摄像试验). *Transactions of the Chinese Society of Agricultural Engineering*. Vol. 31, pp. 42-48, Beijing/China.

RESEARCH ON OPTIMIZING THE POWER BALANCE OF A PLOWING AGGREGATE COMPRISED OF A 180 HP TRACTOR AND A 5-MOLDBOARD PLOW

CERCETĂRI PRIVIND OPTIMIZAREA BILANȚULUI DE PUTERE AL UNUI AGREGAT DE ARAT FORMAT DINTR-UN TRACTOR DE 180 CP ȘI UN PLUG CU 5 TRUPIȚE

Constantin LĂCĂTUȘU¹⁾, Sorin-Ștefan BIRIȘ*¹⁾, Adrian IOSIF¹⁾, Nicolae-Valentin VLĂDUȚ²⁾,
Neluş-Evelin GHEORGHİȚĂ¹⁾, Edmond MAICAN¹⁾, Nicoleta UNGUREANU¹⁾

¹⁾National University of Science and Technology POLITEHNICA Bucharest, Faculty of Biotechnical Systems Engineering / Romania;

²⁾INMA Bucharest / Romania

Tel: 0744756832; E-mail: biris.sorinstefan@gmail.com

DOI: <https://doi.org/10.35633/inmateh-75-83>

Keywords: agricultural machine, tillage, traction force, mathematical modeling, power balance, optimization

ABSTRACT

Plowing is recognized as an essential agricultural task that cannot yet easily be substituted with alternative soil processing methods due to its significance. However, it is also one of the most fuel-intensive operations. The main objective of this paper is to determine the optimal operational parameters (working speed and working width) of a plowing aggregate composed of a 180 HP tractor and a 5-moldboard plow, which ensures the full utilization of the tractor engine's power and the use of the aggregate at its maximum working capacity, respectively, achieving an optimal power balance.

REZUMAT

Lucrarea de arat este recunoscută ca fiind una încă greu de înlocuit de alte lucrări de pregătire a patului germinativ datorită importanței și utilității acesteia. În același timp, lucrarea de arat este una dintre cele mai mari consumatoare de combustibil din întreg ciclul de cultivație. Obiectivul principal al lucrării constă în determinarea parametrilor de operare optimi pentru un agregat de arat compus dintr-un tractor de 180 CP și un plug cu 5 trupițe, care să asigure utilizarea în întregime a puterii motorului tractorului și folosirea agregatului la capacitatea maximă de lucru, respectiv, realizarea un bilanț de putere optimal.

INTRODUCTION

Plowing is a crucial agricultural operation that demands significant fuel consumption. To reduce the significant amount of fuel required for seedbed preparation operations, particularly for plowing, the tractor-implement aggregates must be properly configured, and the operating parameters must be selected to ensure the full utilization of the tractor engine's power (Șandru *et al.*, 1983; Croitoru *et al.*, 2017). Additionally, the soil processing equipment should operate at its maximum working capacity while maintaining an optimal power balance (Hunt, 1986).

Studies on soil-machine interaction aim to provide scientific insights into the dynamics between tillage tools, traction devices, and the terrain they operate on. Key variables examined include the forces needed to operate tillage tools, vertical and lateral forces acting on them, patterns of soil failure, displacement of soil particles, forces at the wheel-soil interface, wheel sinkage, rolling resistance, contact area of wheels, and soil stress at various depths (Ani *et al.*, 2018; Ghereș *et al.*, 2013).

The resistance force to the movement of agricultural aggregates arises from the friction between the wheels and the soil surface, the friction of the axles in the wheel bearings, and the deformation of the soil by the aggregate's wheels (Dobrescu, 1981). This force is influenced by the type and construction of the driving and supporting wheels, the weight of the aggregate, and the properties of the soil on which it operates. On loose, highly moist, or uneven soils, the resistance to movement is higher compared to operating on compacted, smooth-surfaced soils. Soil surface irregularities increase rolling resistance due to additional soil deformation, deviation of the machines in the aggregate from the forward direction, and the emergence of additional inertial forces (Gill, Vanden Berg, 1968; Kheiralla *et al.*, 2004).

Rolling resistance is also affected by the relaxation time of the soil and the tires after their mutual deformation at the point of contact. As relaxation time increases, soil deformation decreases, and vice versa (Koolen *et al.*, 1983). Low-pressure tires, typical for agricultural machines, have a larger contact area with the soil, resulting in lower specific pressure and reduced soil deformation. Consequently, rolling resistance on

deformable soil surfaces is lower, but the tires undergo more significant deformations, reducing their service life. On loose soils, aggregates equipped with low-pressure tires or tracks exhibit lower resistance to movement compared to those with metal wheels or high-pressure tires (Bennett et al., 2019; Jun et al., 2024).

The traction resistance of agricultural machines, like other aggregate parameters, exhibits a pronounced random nature (Ghereș et al., 2013). Several factors influence the variability characteristics, the most important being soil type, soil compaction, moisture, non-uniformity, texture, and structure of the processed soil, as well as certain variations occurring at the drive wheels and articulation points of the aggregate. These factors have a more pronounced effect on aggregates with high-powered tractors and at high working speeds (Abo et al., 2011; Biriș et al., 2017).

The variation in the working resistance of agricultural machines also leads to the tractor engine operating under unstable conditions. Depending on this variation and the engine load coefficient, power losses of up to 10-15% can occur. The load regime of the aggregate machines induces random dynamic processes in all aggregate components (Dobrescu, 1981; Md-Tahir et al., 2021).

The random nature of the engine torque further affects the tractor's traction characteristics. A negative impact can be observed on the adhesion force and the slippage of the driving wheels. At equal traction forces, higher dispersion in their value leads to increased tractor slippage. Additionally, when the frequency of traction resistance variation is high, significant power losses occur due to slippage (Md-Tahir et al., 2021; McKyes, 1985). The traction resistance value of agricultural machines considered in calculations is the average value obtained from statistical processing of traction diagrams recorded during operation (Trendafilov et al., 2023; Varani et al., 2023). As the working speed increases, the working resistance of agricultural machines also increases. The rate of this increase depends on the type of working parts of the machine and the nature of the working process (Cardei et al., 2023).

It is imperative to determine the optimal operating parameters for agricultural implements designed for seedbed preparation, ensuring full utilization of the tractor engine's power and operating the implement at maximum working capacity, thereby achieving an optimal power balance (Legay, 1988; Vlăduț et al., 2018). Currently, this can be accomplished using analytical and numerical calculation algorithms, which can be implemented on modern agricultural tractors and are presented within this study (Vlăduțoiu et al., 2017; Simionescu et al., 1995).

The main objective of the paper is to determine the optimal operational parameters of a plowing aggregate composed of a 180 HP tractor and a 5-moldboard plow, specifically: v - working speed and B - working width, which ensure the full utilization of the tractor engine's power and the use of the aggregate at its maximum working capacity. As will be further shown, the power balance equation can be used as an objective function for optimizing the power balance.

MATERIALS AND METHODS

The study presented in this paper was conducted for an aggregate consisting of a 180 HP tractor (A 1800-A) and a variable working width plough with 5 moldboards (PP5VM), designed to perform plowing operations on flat terrain or slopes with a maximum inclination of 6° (figure 1).



Fig. 1 - The 180 HP tractor and a plough with variable working width with 5 moldboards

The aggregate requires power for movement and power for performing the plowing operation. The tractor's drive wheels generate the power necessary to operate the aggregate. As a constraint, the coefficient of utilization of travel time, τ_d , can be considered, knowing that its level is proportional to the working capacity of the aggregate (Dobrescu, 1981).

The power balance of a plowing aggregate can be expressed by the following equation:

$$P_M \cdot \tau_M = \frac{f_l \cdot G \cdot v + f_v \cdot G \cdot v^2 + k \cdot a \cdot B \cdot v + \varepsilon \cdot a \cdot B \cdot v^3}{\eta_T \cdot (1 - \delta_p)} \quad (1)$$

where: P_M - is the power developed by the engine, (W); η_M - the engine power utilization coefficient, η_p - the efficiency of the transmission at the power take-off and the driving wheels; f_l - proportionality coefficient; f_v - coefficient of resistance increase due to speed growth, (s/m); δ_p - tractor slippage; G - the weight of the aggregate, (N); v - the working speed (m/s); B - the working width, (m); a - the working depth, (m); k - the resistance to deformation and crumbling of the soil furrow, (N/m²); ε - the coefficient characterizing the shape of the crown and the properties of the soil, (N·s²/m⁴).

The terms in the first fraction of equation (1) represent the power required for moving the aggregate, while the terms in the second fraction represent the power required for plowing. If the coefficient k is determined without considering the friction between the working parts and the furrow, then the last two terms correspond to Goriacichin's formula (Cardei et al., 2023). These frictions are accounted for when determining the coefficients f_l and f_v .

If it is considered that there is a relationship between the weight of the aggregate and the working width in the form of $G_B = \alpha \cdot B$, where α is the specific weight of the aggregate per working width, (N/m), the objective function becomes:

$$P_M \cdot \eta_M \cdot \eta_T \cdot (1 - \delta_p) = f_l \cdot \alpha \cdot B \cdot v + f_v \cdot \alpha \cdot B \cdot v^2 + k \cdot a \cdot B \cdot v + \varepsilon \cdot a \cdot B \cdot v^3 \quad (2)$$

The optimal parameters B and v are those that ensure maximum productivity at the engine power level. Since the technical productivity of plowing aggregates is related to the level of the time utilization coefficient of travel, τ_d , this constitutes the constraint:

$$\frac{v_g \cdot L}{v_g \cdot L + v \cdot (\Omega + m_l \cdot B)} - \tau_d = 0 \quad (3)$$

The optimal solution can be found using the Lagrange multiplier and the constraint (Simionescu et al., 1995):

$$\begin{cases} \frac{\partial P_M}{\partial v} + \lambda \cdot \frac{\partial \tau_d}{\partial v} = 0 \\ \frac{\partial P_M}{\partial B} + \lambda \cdot \frac{\partial \tau_d}{\partial B} = 0 \end{cases} \quad (4)$$

and the constraint:

$$\frac{m}{m + v \cdot (\Omega + m_l \cdot B)} - \tau_d = 0 \quad (5)$$

in which m and m_l are operating parameters dependent on the idle travel speed of the aggregate (v_g), the plot length (L), the length of the path travelled without working (S_g), the plot width (C), ($m = v_g \cdot L$, $m_l = S_g \cdot C$).

The terms in the system of equations (4) are determined using (Dobrescu, 1981):

$$\frac{\partial P_M}{\partial v} = f_l \cdot \alpha \cdot B + 2 \cdot f_v \cdot \alpha \cdot B \cdot v + k \cdot a \cdot B + 3 \cdot \varepsilon \cdot a \cdot B \cdot v^2 \quad (6)$$

$$\frac{\partial P_M}{\partial B} = f_l \cdot \alpha \cdot v + f_v \cdot \alpha \cdot v^2 + k \cdot a \cdot v + \varepsilon \cdot a \cdot v^3 \quad (7)$$

$$\frac{\partial \tau_d}{\partial v} = \frac{m \cdot (\Omega + m_l \cdot B)}{[m + v \cdot (\Omega + m_l \cdot B)]^2} \quad (8)$$

$$\frac{\partial \tau_d}{\partial B} = \frac{m_l \cdot m \cdot v}{[m + v \cdot (\Omega + m_l \cdot B)]^2} \quad (9)$$

A system of three equations with three unknowns is obtained:

$$\begin{cases} f_l \cdot \alpha \cdot B + 2 \cdot f_v \cdot \alpha \cdot B \cdot v + k \cdot a \cdot B + 3 \cdot \varepsilon \cdot a \cdot B \cdot v^2 - \lambda \cdot \frac{m \cdot (\Omega + m_l \cdot B)}{[m + v \cdot (\Omega + m_l \cdot B)]^2} = 0 \\ f_l \cdot \alpha \cdot v + f_v \cdot \alpha \cdot v^2 + k \cdot a \cdot v + \varepsilon \cdot a \cdot v^3 - \lambda \cdot \frac{m_l \cdot m \cdot v}{[m + v \cdot (\Omega + m_l \cdot B)]^2} = 0 \\ \frac{m}{m + v \cdot (\Omega + m_l \cdot B)} - \tau_d = 0 \end{cases} \quad (10)$$

The variable λ is eliminated by equating its value from the first equation of the system (10) with the value obtained from the second equation, resulting in:

$$3 \cdot v^2 + 2 \cdot v \cdot \left[\frac{m \cdot (1 - \tau_d)}{\tau_d \cdot \Omega} - \frac{\alpha \cdot f_v}{\varepsilon \cdot a} \right] + \frac{f_1 \cdot (f_v \cdot \alpha + k \cdot a \cdot \Omega)}{\varepsilon \cdot a \cdot \Omega} = 0 \tag{11}$$

from which the expression for the optimal speed is obtained:

$$v_{opt} = \frac{1}{3} \cdot \left[\frac{m \cdot (1 - \tau_d)}{\tau_d \cdot \Omega} - \frac{\alpha \cdot f_v}{\varepsilon \cdot a} + \sqrt{\left(\frac{\alpha \cdot f_v}{\varepsilon \cdot a} \right)^2 + \left(\frac{m \cdot (1 - \tau_d)}{\tau_d \cdot \Omega} \right)^2 + \frac{\alpha \cdot f_v \cdot m \cdot (1 - \tau_d)}{\varepsilon \cdot a \cdot \tau_d \cdot \Omega} - \frac{3 \cdot (\alpha \cdot f_1 + k \cdot a)}{\varepsilon \cdot a}} \right] \tag{12}$$

From the third equation of the system (10), it results:

$$B_{opt} = \frac{m \cdot (1 - \tau_d) - \tau_d \cdot \Omega \cdot v_{opt}}{\tau_d \cdot m_1 \cdot v_{opt}} \tag{13}$$

The productivity of the aggregate is:

$$U_{\tau_d} = v_{opt} \cdot B_{opt} \cdot \tau_d \tag{14}$$

The power required to operate the aggregate is calculated using the following equation:

$$P_{min} = f_1 \cdot \alpha \cdot B_{opt} \cdot v_{opt} + f_v \cdot v^2 \cdot \alpha \cdot B_{opt} + B_{opt} \cdot v_{opt} \cdot a \cdot k + \varepsilon \cdot a \cdot B_{opt} \cdot v_{opt}^3 \tag{15}$$

The above calculation can be applied when studying the parameters of a new implement or when forecasting the development of plowing aggregates.

For existing aggregates, the relationship between the weight of the aggregate and its components is established using the following formula:

$$G = G_0 + G_B = G_0 + \alpha \cdot B \tag{16}$$

where: G_0 - represents the constant weight of the aggregate (the weight of the tractor and the carrying device), and α - is the specific weight of the part that changes with the working width B .

In this case, the mathematical model takes the form of:

$$P_M \cdot \eta_M \cdot \eta_T \cdot (1 - \delta) = f_1 \cdot G_0 \cdot v + f_1 \cdot \alpha \cdot B \cdot v + f_v \cdot G_0 \cdot v^2 + f_v \cdot \alpha \cdot B \cdot v^2 + k \cdot a \cdot B \cdot v + \varepsilon \cdot a \cdot B \cdot v^3 \tag{17}$$

and:

$$\frac{m}{m + v \cdot (\Omega + m_1 \cdot B)} - \tau_d = 0 \tag{18}$$

By deriving the objective function and the constraints, the following is obtained:

$$\left\{ \begin{aligned} \frac{\partial P_M}{\partial v} &= f_1 \cdot (G_0 + \alpha \cdot B) + 2 \cdot f_v \cdot v \cdot (G_0 + \alpha \cdot B) + k \cdot a \cdot B + 3 \cdot \varepsilon \cdot a \cdot B \cdot v^2 \\ \frac{\partial P_M}{\partial B} &= f_1 \cdot \alpha \cdot v + f_v \cdot \alpha \cdot v^2 + k \cdot a \cdot v + \varepsilon \cdot a \cdot v^3 \\ \frac{\partial \tau_d}{\partial v} &= \frac{m \cdot (\Omega + m_1 \cdot B)}{[m + v \cdot (\Omega + m_1 \cdot B)]^2} \\ \frac{\partial \tau_d}{\partial B} &= \frac{m_1 \cdot m \cdot v}{[m + v \cdot (\Omega + m_1 \cdot B)]^2} \end{aligned} \right. \tag{19}$$

A system of three equations with three unknowns is formulated using the coefficient λ :

$$\left\{ \begin{aligned} f_1 \cdot G + f_1 \cdot \alpha \cdot B + 2 \cdot f_v \cdot v \cdot G + 2 \cdot f_v \cdot \alpha \cdot B \cdot v + k \cdot a \cdot B + 3 \cdot \varepsilon \cdot a \cdot B \cdot v^2 - \lambda \cdot \frac{m \cdot (\Omega + m_1 \cdot B)}{[m + v \cdot (\Omega + m_1 \cdot B)]^2} &= 0 \\ f_1 \cdot \alpha \cdot v + f_v \cdot \alpha \cdot v^2 + k \cdot a \cdot v + \varepsilon \cdot a \cdot v^3 - \lambda \cdot \frac{[m + v \cdot (\Omega + m_1 \cdot B)]^2}{m_1 \cdot m \cdot v} &= 0 \\ \frac{m}{m + v \cdot (\Omega + m_1 \cdot B)} - \tau_d &= 0 \end{aligned} \right. \tag{20}$$

By eliminating the variable λ and performing the simplifications, the following is obtained:

$$f_1 \cdot \alpha \cdot \Omega + f_v \cdot \alpha \cdot v \cdot \Omega + k \cdot a \cdot \Omega \cdot v^2 - f_1 \cdot G \cdot m_1 - 2 \cdot f_v \cdot v \cdot \Omega \cdot B \cdot m_1 - 2 \cdot \varepsilon \cdot a \cdot B \cdot v^2 \cdot m_1 = 0 \tag{21}$$

If B is replaced in the last equation of the system (20), the result is:

$$3 \cdot v^2 + 2 \cdot v \cdot \left[\frac{f_v \cdot (\alpha \cdot \Omega \cdot G \cdot m_1)}{\varepsilon \cdot a \cdot \Omega} - \frac{m \cdot (1 - \tau_d)}{\tau_d \cdot \Omega} \right] + \frac{f_1 \cdot (\alpha \cdot \Omega \cdot G \cdot m_1 + k \cdot a \cdot \Omega)}{\varepsilon \cdot a \cdot \Omega} - \frac{f_v \cdot \alpha \cdot m_1 \cdot (1 - \tau_d)}{\varepsilon \cdot a \cdot \tau_d \cdot \Omega} = 0 \tag{22}$$

from which the expression for the optimal speed results:

$$v_{opt} = \frac{1}{3} \cdot \left[\frac{m \cdot (1 - \tau_d)}{\tau_d \cdot \Omega} - \frac{f_v \cdot (\alpha \cdot \Omega \cdot m_1 \cdot G)}{\varepsilon \cdot a \cdot \Omega} + \sqrt{\left(\frac{m \cdot (1 - \tau_d)}{\tau_d \cdot \Omega} \right)^2 + \frac{f_v \cdot m \cdot (1 - \tau_d) \cdot (\alpha \cdot \Omega + 2 \cdot m_1 \cdot G)}{\varepsilon \cdot a \cdot \tau_d \cdot \Omega^2} \left(\frac{\alpha \cdot f_v}{\varepsilon \cdot a} \right)^2 - \frac{3 \cdot f_1 \cdot (\alpha \cdot \Omega \cdot m_1 \cdot G) + 3 \cdot k \cdot a \cdot \Omega}{\varepsilon \cdot a \cdot \Omega}} \right] \tag{23}$$

The optimal working width, B_{opt} , is determined by the relationship of the maximum working capacity of the aggregate:

$$B_{opt} = \frac{m \cdot (1 - \tau_d) - \tau_d \cdot \Omega \cdot v_{opt}}{\tau_d \cdot m_1 \cdot v_{opt}} \tag{24}$$

If the maximum loading of the tractor is desired, the following relation (25) results:

$$B_{opt} = \frac{P_a \cdot f_l \cdot G_0 \cdot v_{opt} \cdot f_v \cdot G_0 \cdot v_{opt}^2}{f_l \cdot a \cdot v_{opt} + f_v \cdot a \cdot v_{opt}^2 + k \cdot a \cdot v_{opt} + \varepsilon \cdot a \cdot v_{opt}^3} \quad (m) \quad (25)$$

If in equation (23) of the working speed, $G_B = \alpha \cdot B = 0$ is assumed, equation (12) is obtained. If it is assumed that the weight of the entire aggregate is constant, i.e., $\alpha = 0$, the following results:

$$v_{opt} = \frac{1}{3} \cdot \left[\frac{m \cdot (1 - \tau_d)}{\tau_d \cdot \Omega} + \frac{f_v \cdot m_l \cdot G}{\varepsilon \cdot a \cdot \Omega} + \sqrt{\left(\frac{m_l \cdot G \cdot f_v}{\varepsilon \cdot a \cdot \Omega} \right)^2 + \left(\frac{m \cdot (1 - \tau_d)}{\tau_d \cdot \Omega} \right)^2} + \frac{2 \cdot m_l \cdot G \cdot f_v \cdot m \cdot (1 - \tau_d)}{\varepsilon \cdot a \cdot \tau_d \cdot \Omega^2} + \frac{3 \cdot f_v \cdot m_l \cdot G \cdot 3 \cdot k \cdot a \cdot \Omega}{\varepsilon \cdot a \cdot \Omega} \right] \quad (26)$$

By applying equation (25) and the corresponding computational algorithm, a Python code was developed, allowing the calculation and plotting of the optimal values for the plow's total working width (figure 2.a), as well as the 3D generation of this dependency on the working speed and the utilization coefficient of the displacement time (τ_d) (figure 2.b).

```
import numpy as np
import matplotlib.pyplot as plt

m_1 = 45
m = 700
omega = 40

tau_d_values = [0.7, 0.71, 0.72, 0.73, 0.74, 0.75, 0.76, 0.77, 0.78]

v_opt = np.linspace(0.5, 2.5, 100)

plt.figure(figsize=(8, 6))

for tau_d in tau_d_values:
    B_opt = (m * (1 - tau_d) - tau_d * omega * v_opt) / (tau_d * m_1 * v_opt)
    # Filtrare pentru valorile B_opt in intervalul [0,8, 2]
    mask = (B_opt >= 0.8) & (B_opt <= 2)
    plt.plot(v_opt[mask], B_opt[mask], label=f"$\tau_d = {tau_d}$")

plt.title("Graph of $B_{opt}$ vs $v_{opt}$ for Different $\tau_d$")
plt.xlabel("$v_{opt}$ (m/s)")
plt.ylabel("$B_{opt}$ (m)")
plt.ylim(0.8, 2)
plt.axhline(0, color='black', linewidth=0.8, linestyle='--')
plt.legend()
plt.grid()

plt.show()
```

a)

```
import numpy as np
import matplotlib.pyplot as plt
from mpl_toolkits.mplot3d import Axes3D

m_1 = 45
m = 700
omega = 40

v_opt_values = np.linspace(0.5, 2.5, 50) # v_opt între 0.5 și 2.5
tau_d_values = np.linspace(0.7, 0.9, 50) # tau_d între 0.7 și 0.9

V_OPT, TAU_D = np.meshgrid(v_opt_values, tau_d_values)

B_OPT = (m * (1 - TAU_D) - TAU_D * omega * V_OPT) / (TAU_D * m_1 * V_OPT)

mask = (B_OPT >= 1) & (B_OPT <= 2)

fig = plt.figure(figsize=(10, 7))
ax = fig.add_subplot(111, projection='3d')

sc = ax.scatter(V_OPT[mask], TAU_D[mask], B_OPT[mask], c=B_OPT[mask], cmap='viridis', marker='o')

cbar = fig.colorbar(sc, ax=ax, shrink=0.5, aspect=10)
cbar.set_label("$B_{opt}$ (m)")

ax.set_title("3D Plot of $B_{opt}$ as function of $v_{opt}$ and $\tau_d$")
ax.set_xlabel("$v_{opt}$ (m/s)")
ax.set_ylabel("$\tau_d$")
ax.set_zlabel("$B_{opt}$ (m)")

ax.zaxis.label.set_rotation(90)
ax.view_init(elev=30, azim=140) # ROTIRE PENTRU VIZUALIZARE DIFERITĂ

plt.tight_layout()

plt.show()
```

b)

Fig. 2 – Python code for determining the optimal working width of a plow with 5 bodies

```
import numpy as np
import matplotlib.pyplot as plt

G_pl = 30000 # N
f_pl = 0.35
k_0 = 50000 # N/m^2
eps = 1000 # N/m^3
B = 1.5

a_values = np.linspace(0.05, 0.3, 100)

v_pl_values_fixed = [1, 1.5, 2, 2.5]

plt.figure(figsize=(8, 6))

for v in v_pl_values_fixed:
    R_pl_values = G_pl * f_pl + k_0 * a_values * B + eps * a_values * B * (v ** 2)
    plt.plot(a_values, R_pl_values, label=f"$v_{pl} = {v}$ m/s")

plt.title("Graph of $R_{pl}$ vs $a$ for Different Values of $v_{pl}$")
plt.xlabel("$a$ (m)")
plt.ylabel("$R_{pl}$ (N)")
plt.grid(True)
plt.legend()

plt.tight_layout()
plt.show()
```

a)

```
import numpy as np
import matplotlib.pyplot as plt

G_pl = 30000 # N
f_pl = 0.35
k_0 = 50000 # N/m^2
eps = 1000 # N/m^3

B_values = [1.25, 1.35, 1.45, 1.55, 1.65]

a_values = np.linspace(0.05, 0.3, 100)

v_pl = 2

plt.figure(figsize=(8, 6))

for B in B_values:
    R_pl_values = G_pl * f_pl + k_0 * a_values * B + eps * a_values * B * (v_pl ** 2)
    plt.plot(a_values, R_pl_values, label=f"$B = {B}$ m")

plt.title("Graph of $R_{pl}$ vs $a$ for Different Values of $B$")
plt.xlabel("$a$ (m)")
plt.ylabel("$R_{pl}$ (N)")
plt.grid(True)
plt.legend()

plt.tight_layout()
plt.show()
```

b)

Fig. 3 – Python code for determining the traction force of a plow with 5 plowshares

For the plowing work, the traction resistance force of the plow can be estimated using the following relation:

$$R_p = k_0 \cdot a \cdot B_l \quad [N] \quad (27)$$

in which: k_0 represents the specific soil resistance to plowing, $(2 - 10) \cdot 10^4$ [N/m²]; a is the working depth [m]; B_l is the total working width of the plow [m].

In figure 3.a, a Python code is presented that allows the calculation and graphical plotting of the dependency of the plow's draft resistance on the working depth for different working speeds, and in figure 3.b, the same dependency is shown, but for various total working widths of a plow with 5 plowshares and a variable working width.

In figure 4.a, a Python code is presented that allows the calculation and 3D plotting of the plow's traction resistance as a function of working depth and working speed for a single soil type, while in figure 4.b, the same dependence is shown for four soil types with different specific resistances to tillage in the case of a plow with 5 plowshares and a variable working width.

<pre>import numpy as np import matplotlib.pyplot as plt from mpl_toolkits.mplot3d import Axes3D G_pl = 30000 # N f_pl = 0.35 k_0 = 50000 # N/m^2 eps = 1000 # N/m^3 B = 1.5 # Constanta B (poți ajusta această valoare) v_pl_values = np.linspace(0.5, 3.5, 100) # Interval pentru v_pl a_values = np.linspace(0.1, 0.3, 50) # Interval pentru a V_PL, A = np.meshgrid(v_pl_values, a_values) R_pl_values = G_pl * f_pl + k_0 * A * B + eps * A * B * (V_PL)**2 fig = plt.figure(figsize=(10, 7)) ax = fig.add_subplot(111, projection='3d') surf = ax.plot_surface(V_PL, A, R_pl_values, cmap='viridis') cbar = fig.colorbar(surf, ax=ax, shrink=0.5, aspect=10) cbar.set_label("\$R_{pl}\$ (N)") ax.set_title("3D Surface Plot of \$R_{pl}\$ as function of \$v_{pl}\$ and \$a\$") ax.set_xlabel("\$v_{pl}\$ (m/s)") ax.set_ylabel("\$a\$ (m)") ax.set_zlabel("\$R_{pl}\$ (N)") plt.tight_layout() plt.show()</pre>	<pre>import numpy as np import matplotlib.pyplot as plt from mpl_toolkits.mplot3d import Axes3D from matplotlib.lines import Line2D import matplotlib.colors as colors G_pl = 30000 # N f_pl = 0.35 eps = 1000 # N/m^3 B = 1 # Constanta B v_pl_values = np.linspace(0.5, 3.5, 100) a_values = np.linspace(0.1, 0.3, 50) V_PL, A = np.meshgrid(v_pl_values, a_values) k_0_values = [30000, 50000, 70000, 90000] all_R_pl_values = [] for k_0 in k_0_values: R_pl = G_pl * f_pl + k_0 * A * B + eps * A * B * (V_PL)**2 all_R_pl_values.append(R_pl) min_val = min(np.min(R) for R in all_R_pl_values) max_val = max(np.max(R) for R in all_R_pl_values) fig = plt.figure(figsize=(12, 9)) ax = fig.add_subplot(111, projection='3d') norm = colors.Normalize(vmin=min_val, vmax=max_val) cmap = plt.get_cmap('viridis') surf_list = [] for i, k_0 in enumerate(k_0_values): R_pl_values = G_pl * f_pl + k_0 * A * B + eps * A * B * (V_PL)**2 surf = ax.plot_surface(V_PL, A, R_pl_values, cmap=cmap, alpha=0.6, norm=norm) surf_list.append(surf) custom_lines = [Line2D([0], [0], color=cmap(i / len(k_0_values)-1), lw=4) for i in range(len(k_0_values))] ax.legend(custom_lines, ["\$k_0\$ (N/m^2)" for k_0 in k_0_values], title="Values of \$k_0\$") cbar = fig.colorbar(surf_list[0], ax=ax, shrink=0.5, aspect=10) cbar.set_label("\$R_{pl}\$ (N)") ax.set_title("3D Surface Plot of \$R_{pl}\$ as function of \$v_{pl}\$ and \$a\$ for different \$k_0\$") ax.set_xlabel("\$v_{pl}\$ (m/s)") ax.set_ylabel("\$a\$ (m)") ax.set_zlabel("\$R_{pl}\$ (N)") plt.tight_layout() plt.show()</pre>
a)	b)

Fig. 4 – Python code for determining the 3D variation of the draft force of a plow with 5 plowshares

The power required to pull the plow during the plowing process is calculated:

$$P_t = k_0 \cdot a \cdot B_l \cdot v_l \quad [W] \quad (28)$$

where v_l represents the working speed of the tillage aggregate [m/s].

The energy consumption per unit of processed surface is calculated using the following relation:

$$E_{ha} = \frac{P_t}{S_h} \quad [Wh/ha] \quad (29)$$

where S_h represents the working capacity of the plowing aggregate [ha/h].

In figure 5.a, a Python code is presented which, based on relation (29), allows for the calculation and graphical plotting of the dependence of energy consumption per unit of worked surface for a plow with 5 moldboards with variable working width, for different working depths according to the specific resistance to plowing, and in figure 5.b, the same dependence is calculated and plotted in 3D.

<pre>import numpy as np import matplotlib.pyplot as plt B_l = 1.5 v_l = 2 W_h = 0.25 k_0_values = np.linspace(2e4, 10e4, 500) a_values = [0.15, 0.175, 0.2, 0.215, 0.25, 0.275, 0.3] plt.figure(figsize=(8, 6)) for a in a_values: P_t = k_0_values * a * B_l * v_l E_ha = P_t / W_h plt.plot(k_0_values, E_ha, label=f"a = {a}") plt.title("Graph of \$E_{ha}\$ vs \$k_0\$ for Different \$a\$ values") plt.xlabel("\$k_0\$ [N/m^2]") plt.ylabel("\$E_{ha}\$ [Wh/ha]") plt.legend() plt.grid(True) plt.show()</pre>	<pre>import numpy as np import matplotlib.pyplot as plt from mpl_toolkits.mplot3d import Axes3D B_l = 1.5 v_l = 2 W_h = 0.25 k_0_values = np.linspace(2e4, 10e4, 500) a_values = np.linspace(0.15, 0.3, 6) K0, A = np.meshgrid(k_0_values, a_values) E_ha = (K0 * A * B_l * v_l) / W_h fig = plt.figure(figsize=(10, 8)) ax = fig.add_subplot(111, projection='3d') surf = ax.plot_surface(K0, A, E_ha, cmap='viridis') ax.set_title("Graph of \$E_{ha}\$ vs \$k_0\$ and \$a\$") ax.set_xlabel("\$k_0\$ [N/m^2]") ax.set_ylabel("\$a\$ [m]") ax.set_zlabel("\$E_{ha}\$ [Wh/ha]") cbar = fig.colorbar(surf, ax=ax, shrink=0.5, aspect=5) cbar.set_label("\$E_{ha}\$ [Wh/ha]") plt.show()</pre>
a)	b)

Fig. 5 – Python code for determining the variation in energy consumption per unit area worked for a plow with 5 moldboards

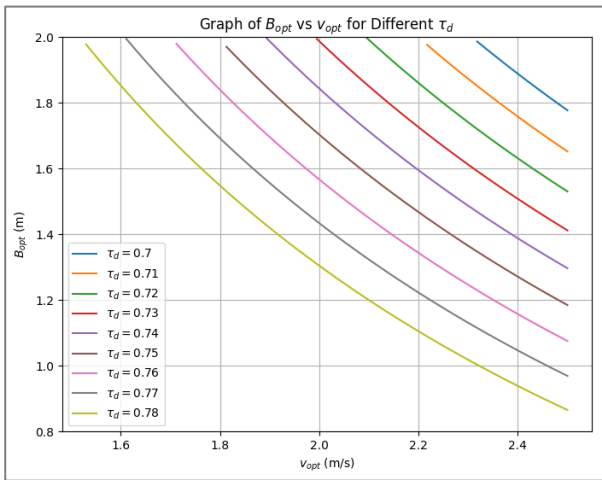
RESULTS

Through classical analytical calculation, applying the mathematical models embodied in equations (25) and (26), for a plowing unit operating under the conditions given in the first column of Table 1, the optimal parameters are obtained, which are found in the second column of the same table.

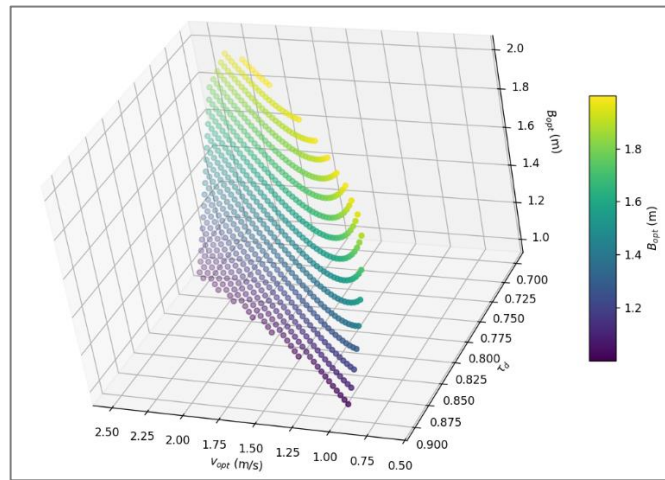
Table 1

The parameters resulting from the calculation for a plowing aggregate composed of a tractor A-1800 A and the PSP-5 (35) plow

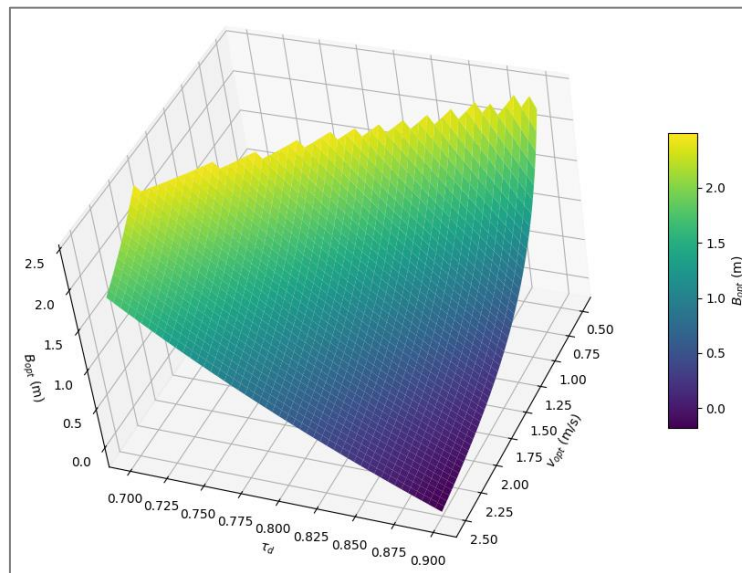
The conditions of the plowing aggregate formed by the A-1800 A tractor and the PSP-5 (35) plow.	The parameters of the plowing aggregate resulting from the calculation
The weight of the tractor: $G_t=97000\text{ N}$ The weight of the plow: $G_p=30000\text{ N}$ The weight of the aggregate: $G=G_t+G_p=127000\text{ N}$ $\tau_d=0.9$; $\Omega=40$; $m_I=10$; $k=35000\text{ N/m}^2$; $f_i=0.1$; $f_v=0.09$; $L=1000\text{ m}$; $v_g=0.5\text{ m/s}$; $a=0.25\text{ m}$; $\varepsilon=3000\text{ N}\cdot\text{s}^2/\text{m}^4$	$v_{opt}=2.03\text{ m/s}$ $B_{opt}=1.5\text{ m}$



a)



b)



c)

Fig. 6 – Graphical representation of the dependency of the optimal plowing width on the working speed and the travel time utilization coefficient for a plow with 5 moldboards

Using the calculation algorithms and Python codes presented in figure 2, the optimal values for the plow's total working width were calculated and plotted (figure 6.a), as well as the 3D variant of this dependency on working speed and the travel time utilization coefficient (τ_d) (figure 6.b). In addition, figure 6.c shows the 3D graph of the dependency of the optimal working width on the working speed - with values in the range of 0.5 - 2.5 m/s - and on the travel time utilization coefficient - with values in the range of 0.7–0.9.

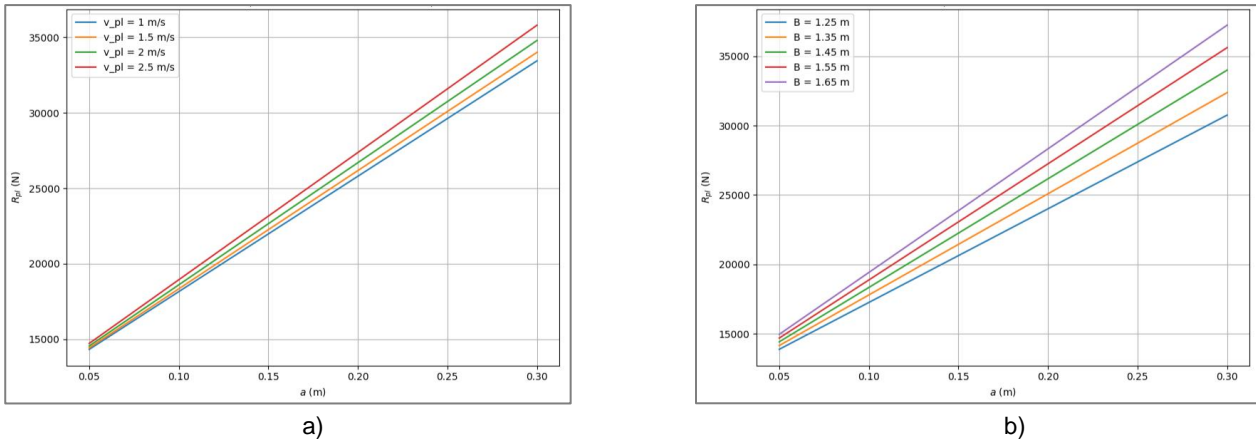


Fig. 7 – Graphical representation of the dependence of the draft force of a plow with 5 moldboards at working depth for different working speeds and different total working widths

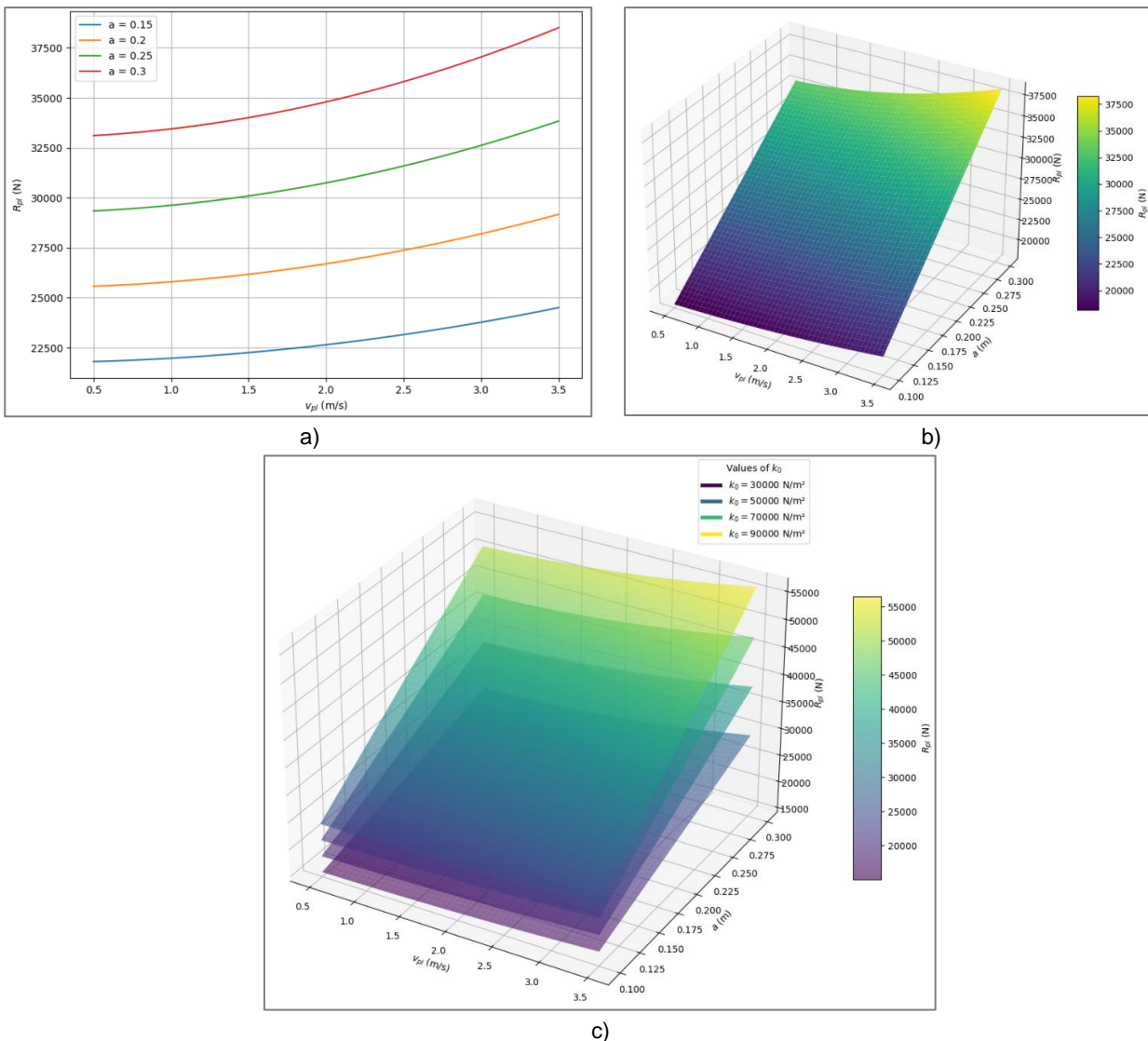


Fig. 8 – Graphical representation of the dependency of the traction force of a plow with 5 plowshares on working speed for various working depths and operating speeds

Using the calculation algorithms and Python codes presented in figure 3.a and figure 3.b, the dependence of the plow's draft resistance on working depth was calculated and plotted for different working speeds (figure 7.a), as well as the same dependence for various total working widths of a 5-furrow plow with variable working width (figure 7.b). It is easy to observe that the plow's draft resistance increases with the increase in working depth, for the different working speeds and various total working widths.

The draft force of the plow as its traveling speed increases, with the dependency $R_{pl}=f(v_{pl})$ being nonlinear (figure 8.a). The increase in draft force is smaller at lower speeds (0.5–2 m/s) and much more significant at higher working speeds (2–3.5 m/s).

In figure 8.b, the 3D graphical representation of the plows's draft force is shown, with working depth and working speed as the independent parameters, for a single type of soil. This was generated using the calculation algorithm and the Python program presented in figure 4.a. In figure 8.c, the same dependency is displayed, but for four different types of soil, using the calculation algorithm and Python code presented in figure 4.b.

Using the computational algorithms and the Python code presented in figure 5.a, the dependence based on relation (29) of the energy consumption per unit worked area for a plow with 5 moldboards of variable working width has been calculated and plotted, for different working depths as a function of the specific tillage resistance (different soil types) (figure 9.a). In figure 9.b, the 3D dependence of the energy consumption per unit worked area is presented as a function of the independent variables: working depth and specific tillage resistance, calculated and generated using the Python code presented in figure 5.b. The energy consumption per unit worked area for a plow with 5 moldboards of variable working width increases with an increasing working depth. The soil category and its physico-mechanical properties (specific tillage resistance) have a significant influence on the mechanical energy consumption.

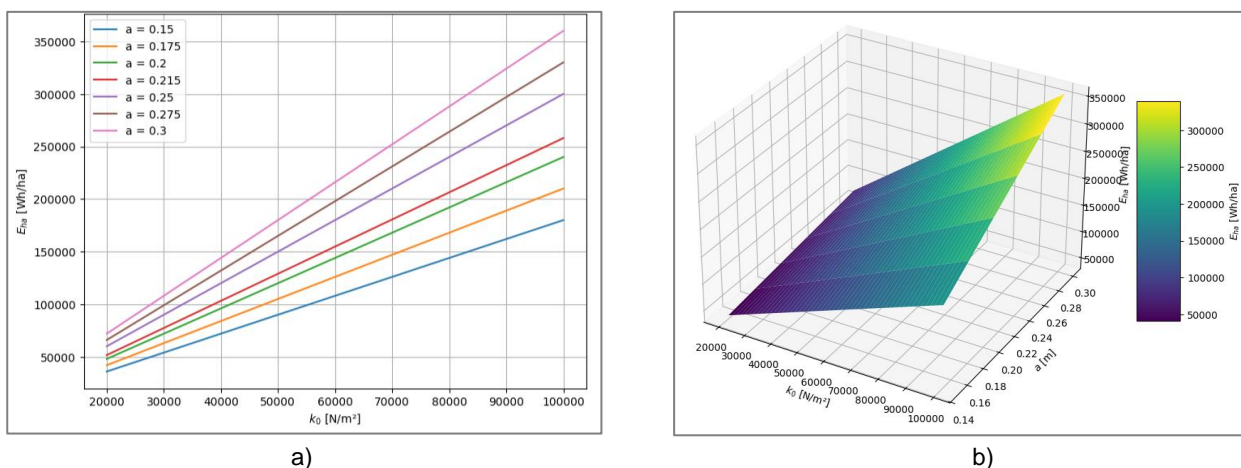


Fig. 9 – Graphical representation of the dependency of the traction force of a plow with 5 plowshares on working speed for different working depths and operating speeds

CONCLUSIONS

Optimal operation of the implements used for plowing is essential for efficient resource use and cost reduction. Fully utilizing the tractor's engine power and operating the plowing implement at its maximum capacity enables an optimal power balance. The optimal operating regime can be determined through numerical algorithms based on Lagrange multipliers, using computing programs (Python code in this case). To achieve maximum productivity at the engine power level, it is necessary to calculate the optimal working speed and optimal working width, depending on the coefficient of utilization of the plowing implement's transit time.

REFERENCES

- [1] Abo Al-Kheer A., Kharmanda M.G., El Hami A, Mouazen A.M., (2011), Estimating the variability of tillage forces on a chisel plough shank by modeling the variability of tillage system parameters, *Computers and Electronics in Agriculture*, Volume 78, Issue 1, Pages 61-70. <https://doi.org/10.1016/j.compag.2011.06.001>
- [2] Ani O. A., Uzoejinwa B. B., Ezeama A. O., Onwualu A. P., Ugwu S. N., Ohagwu C. J. (2018). Overview of soil-machine interaction studies in soil bins. *Soil and Tillage Research*, 175, pp. 13-27. <https://doi.org/10.1016/j.still.2017.08.002>
- [3] Bennett J. M., Robertson S. D., Marchuk S., Woodhouse N. P., Antille D. L., Jensen T. A., Keller T., (2019), The soil structural cost of traffic from heavy machinery in Vertisols. *Soil and Tillage Research*, 185, pp.85-93. <https://doi.org/10.1016/j.still.2018.09.007>

- [4] Biriş S. Şt., Ungureanu N., Gheorghită N. E., Maican E., Vlăduţ V., (2017), Theoretical research on enhancing the performance of cultivators working bodies, *Proceedings of the 45th International Symposium on Agricultural Engineering "Actual Tasks on Agricultural Engineering"*, pp.121-130, Opatija / Croatia; [CABI Record Number: 20173126969](#)
- [5] Cardei P., Constantin N., Persu C., Muraru V., Sfiru R., Niţu M. (2023). Analysis of the dependence of traction resistance force on forward speed for tractor-cultivator agregates. *INMATEH-Agricultural Engineering*, 70(2). <https://doi.org/10.35633/inmateh-70-57>
- [6] Croitoru Şt., Vladut V., Voicea I., Gheorghe Gh., Marin E., Vlăduţoiu L., Moise V., Boruz S., Pruteanu A., Andrei S., Păunescu D. (2017), Structural and kinematic analysis of the mechanism for arable deep soil loosening, *Proceedings of the 45th International Symposium on Agricultural Engineering "Actual Tasks on Agricultural Engineering"*, pp.207-216, Opatija / Croatia; [CABI Record Number: 20173126979](#)
- [7] Dobrescu C. (1981). *Optimization of agricultural machinery parameters for the purpose of reducing consumption (Optimizarea parametrilor agregatelor agricole în scopul reducerii consumurilor)*, Center for Teaching Materials and Agricultural Outreach, Bucharest, Romania
- [8] Ghereş M.I., Ghereş M., (2013), Research on determination of interaction tools-soil, *ProEnviroment*, vol.6, pp. 262-270. <http://journals.usamvcluj.ro/index.php/promediu>
- [9] Gill W.R., Vanden Berg G.E., (1968), Soil dynamics in tillage and traction, *U.S.A. Department of Agriculture*, Handbook 316, USA, Washington D.C.
- [10] Hunt R.D. (1986). *Engineering Models for Agricultural Production*. The Avi Publishing Co. Inc., Westport, Connecticut
- [11] Jun Guo, Enhui Sun Yue Yang, Jun Lu. (2024). Soil stress analysis at different depth after agricultural vehicle operation. *INMATEH-Agricultural Engineering*, 73(2). <https://doi.org/10.35633/inmateh-73-12>
- [12] Kheiralla A.F., Yaha A., Zohadie M., Ishakt W. (2004). Modelling of power and energy requirements for tillage implements operating in Serdang sandy clay loam, Malaysia. *Soil & Tillage Research*. 78 (2004), pp. 21-34. DOI: 10.1016/j.still.2003.12.011
- [13] Koolen A.J., Kuipers H., (1983), *Agricultural soil mechanics*, *Advanced Series in Agricultural Sciences*, Vol. 13. Springer, Heidelberg
- [14] Legay I.M. (1988). *Methods and models in the study of complex systems. For a diversified agriculture (Methodes et models dans l'etude des systemes complexes. Pour une agriculture divesifieé)*, L'Harmattan Publishing House, Paris, France
- [15] McKyes E., (1985), *Soil cutting and tillage*, Elsevier, Amsterdam-Oxford-New York-Tokyo
- [16] Md-Tahir H., Zhang J., Xia J., Zhou Y., Zhou H., Du J., Mamona H. (2021). Experimental investigation of traction power transfer indices of farm-tractors for efficient energy utilization in soil tillage and cultivation operations. *Agronomy*, 11(1), 168. DOI: 10.3390/agronomy11010168
- [17] Simionescu I., Dranga M., Moise V. (1995). *Numerical methods in engineering (Metode numerice în tehnică)*. Tehnică Publishing House, Bucharest, Romania
- [18] Şandru A., Cristea I., Neculaiasa V., Popescu S. (1983). *Operation of agricultural machinery (Exploatarea utilajelor Agricole)*. Didactică şi Pedagogică Publishing House, Bucharest, Romania
- [19] Trendafilov K., Tihanov G., Stoykova V., Shivacheva G. (2023). Algorithm for optimizing the movement of a mounted machine-tractor unit in the headland of an irregularly shaped field. *INMATEH-Agricultural Engineering*, 70(2). <https://doi.org/10.35633/inmateh-70-31>
- [20] Varani M., Mattetti M., Molari G., Biglia A., Comba, L. (2023). Correlation between power harrow energy demand and tilled soil aggregate dimensions. *Biosystems Engineering*, 225, pp. 54-68. DOI: 10.1016/j.biosystemseng.2022.11.008
- [21] Vlăduţ D.I., Biriş S-Şt., Vlăduţ V., Cujbescu D., Ungureanu N., Găgeanu I., (2018), Experimental researches on the working process of a seedbed preparation equipment for heavy soils. *INMATEH - Agricultural Engineering*, Volume 55, Pages 27-34.
- [22] Vlăduţoiu L., Cârdei P., Vlăduţ V., Fehete L., (2017), Modern trends in designing and selecting the machine/equipment for deep soil tillage, *16th International Scientific Conference "Engineering for Rural Development"*, pp.1415-1420, Jelgava / Latvia. DOI: 10.22616/ERDev2017.16.N320
- [23] ***CIGR Handbook of Agricultural Engineering, Plant Production Engineering. Volume III. (1999), *American Society of Agricultural Engineers*.

DESIGN AND EXPERIMENTAL STUDY OF HIGH-EFFICIENCY AND LOW-DAMAGE BIONIC PICKING DEVICE FOR TOBACCO LEAVES

高效低损伤烟叶仿生采摘装置的设计与试验研究

Chenhui ZHU¹⁾, Bingjie CHEN¹⁾, Bo LUO^{1, 3)}, Wanzhang WANG¹⁾, Bingjie LIU⁴⁾,
Baoshan WANG¹⁾, Liquan YANG^{*1, 2)}

- ¹⁾ School of Mechanical and Electrical Engineering, Henan Agricultural University, Zhengzhou 450002, China;
²⁾ Henan Province Engineering Research Center of Ultrasonic Technology Application, Pingdingshan University, Pingdingshan 467000, China;
³⁾ School of Intelligent Engineering, Zhengzhou College of Finance and Economics, Zhengzhou 450000, China;
⁴⁾ College of Information and Management Science, Henan Agricultural University, Zhengzhou 450002, China

Corresponding author: Liquan YANG
Tel: +8615038352581; E-mail: 2695@pdsu.edu.cn
DOI: <https://doi.org/10.35633/inmateh-75-84>

Keywords: agricultural machinery, tobacco leaf picking, bionic, low damage

ABSTRACT

To address the issues of high damage rate and low harvesting efficiency during the tobacco leaf picking process, this study analyzed the separation mechanics of tobacco stems and leaves. A low-damage bionic picking device was designed by imitating the manual method of harvesting tobacco leaves. Based on theoretical analysis of the device and its key components, the structure and parameters of the complete system were determined. The picking process was simulated using ADAMS software, focusing on the contact force between the rigid and flexible components at various picking rod speeds. This analysis yielded the optimal combination of structural and operational parameters. Field experiments were subsequently conducted, and a response surface mathematical model was established using Design-Expert software to evaluate the relationship between key factors and performance indicators. The optimal parameter combination was found to be: a picking rod speed of 0.8 m/s, a device inclination angle of 30°, a picking rod spacing of 90 mm, and a forward speed of 0.69 m/s. Under these conditions, the tobacco leaf damage rate was minimized, meeting the requirements for low-damage harvesting. Further experimental validation showed consistency with simulation results, confirming the model's reliability and demonstrating the practical feasibility of the device for tobacco field operations. This provides a valuable reference for the development of low-damage tobacco leaf harvesting equipment.

摘要

为解决目前烟叶采摘装置在采收过程中烟叶破损率高、采净率低的问题，对烟叶的茎叶分离进行分析，模仿人手采摘烟叶方式，设计了一种低损伤烟叶仿生采摘装置。通过对该装置及关键部位的理论分析，确定整体装置的结构和参数。利用 ADAMS 软件对烟叶采摘过程进行仿真，分析不同采摘手速度和茎秆送料速度下刚性结构与柔性缓冲结构之间的接触力，得到了最佳参数组合。最后进行了田间试验，使用 Design-Expert 软件，建立各因素与指标的响应面数学模型，分析了各因素与评价指标之间的关系，得到参数优化组合，采摘杆转速为 0.8m/s，装置倾斜角为 30°，采摘指间距为 90mm，前进速度为 0.69m/s，该组合下烟叶破损率最低，满足低损伤采摘的条件。结果基本与仿真结果一致，证明了模型的可靠性。最后进行了田间试验，试验结果表明此装置在实际烟叶田间采摘工作的可行性，为低损伤烟叶收获装置的研发提供了参考。

INTRODUCTION

In the tobacco harvesting process, picking is the most fundamental and challenging operation. The quality of harvested tobacco leaves directly influences the effectiveness of post-harvest grading. As the core component of the harvesting machinery, the picking device plays a crucial role. Therefore, the design of the tobacco leaf picking device is key to ensuring high-quality tobacco leaf harvesting.

¹⁾ Chenhui ZHU, Ph.D. Eng.; Bingjie CHEN, M.S. Stud. Eng.; Wanzhang WANG, Prof. Ph.D. Eng.; Baoshan WANG, Ph.D. Eng. Liquan YANG, Associate Prof. Ph.D. Eng.; Bo LUO, Ph.D. Stud.; ⁴⁾ Bingjie LIU, Ph.D. Eng.

Early tobacco leaf harvesting devices have been categorized into three primary types (Papusha S.K, 2022). The first type, a serrated harvesting device, employs a saw-toothed blade to sever the entire tobacco stalk at its base, achieving high operational efficiency. The second type, a chain-and-hole harvesting device, incorporates a series of spaced chains with apertures sized to accommodate the stalk diameter. During operation, the stalk is guided through these apertures, thereby completing the detachment process. Both serrated and chain-and-hole methods are exclusively suitable for fully matured tobacco plants. The third and most widely utilized type is the mechanical striking harvester, which induces leaf detachment by applying downward force on the petiole through controlled mechanical impact. Although these methods demonstrate operational efficiency, they exhibit elevated leaf damage rates (12–18%) and variable collection efficiency (67–82% across field trials). Further design refinements are therefore required to mitigate these limitations, particularly through enhanced stalk-gripping mechanisms and impact force modulation.

With the continuous advancement of modern agricultural technology, the mechanization and intelligentization of tobacco harvesting have become inevitable trends to enhance production efficiency and quality. In recent years, significant achievements have been made by scholars both domestically and internationally in the field of tobacco harvesting machinery and intelligent recognition. Sun C. (2024) and colleagues designed and tested key components of a comb-type tobacco harvester, providing valuable insights for optimizing tobacco harvesting equipment. Liu J. (2012) and Yu J. (2019) leveraged virtual manufacturing technology to design and simulate a tobacco harvesting system, further advancing the intelligence and automation of harvesting processes. Zhu H. (2014) developed a floating harvesting platform based on the advantages and disadvantages of tobacco leaf harvesting processes. This platform enables selective harvesting by determining the relative position of leaves and the harvesting device using sensor rods, while hydraulic systems control the platform's lateral movement and elevation. Gan W. (2018) and colleagues designed a tobacco leaf harvesting device featuring left and right curved blades connected via a rotating axis. This design effectively harvests mature leaves while protecting unripe ones, ensuring efficient and low-damage harvesting.

Bionic picking machinery is designed and improved by studying biological mechanisms and imitating the shape, structure, or function of organisms. Currently, bionic mechanical design has been widely applied in fields such as sensors and new materials, with numerous studies (Luo, Y. et al., 2024.) published in this area. Beyond developing cutting end effectors with low cutting resistance, bionic optimization of these effectors is achieved by mimicking the fingers and claws of natural organisms. Research in this field primarily focuses on crops such as fruits (Malekzadeh, 2019; He Z., 2022; Kurbah F., 2022), tea (Kurbah F., 2022; Nie Y.C., 2022) and vegetables (Du Z., 2021), with tomatoes (Gao J. et al., 2022; Gao J. et al., 2024; Guo T. et al., 2022; Hou Z. et al., 2021; Wang M. et al., 2022; Zhao L. et al., 2012) being the most extensively studied. For high-stalk crops like corn and tobacco, scholars have conducted significant research on bionic ear-breaking mechanisms for corn (Xu W.T. et al., 2018; Zhang L.P. et al., 2015). A notable example is the work of Zhang Liping and Chen Meizhou (Zhang L.P. et al., 2015. Chen M.Z. et al., 2018), who addressed issues such as high impurity rates in plate-type ear picking, gnawing in roller-type ear picking, and significant grain loss. They proposed a bionic ear-breaking hand-type mechanism for corn harvesting, providing valuable insights for the development of low-damage corn harvesting techniques. In contrast, research on bionic picking for tobacco leaves remains limited. Li Zhiguang (2016) designed a self-propelled intelligent bionic picking system for tobacco leaves. This system mimics the entire process of manual tobacco harvesting by controlling a bionic picking hand to perform actions such as extending, grasping, picking, releasing, and retracting, thereby reducing damage to both tobacco leaves and stems.

On the basis of drawing lessons from the existing automatic picking machinery of tobacco leaves and other crops, this paper intends to combine modern bionic technology, imitate the action of human hand picking, and apply force to tobacco leaves from top to bottom to make tobacco leaves fall. This paper verifies the possibility of low-loss harvesting of this bionic picking method, which can solve the problems of high crushing rate and low picking rate in the process of automatic picking of tobacco leaves, in order to provide theoretical basis and technical basis for low-damage automatic tobacco leaf picking technology.

ANALYSIS OF THE MANUAL HARVESTING PROCESS AND DESIGN OF BIONIC STRUCTURES

Analysis of Manual Harvesting Actions

Stem-leaf separation constitutes the initial critical stage in flue-cured tobacco harvesting. During mechanized operations, this process exhibits complex mechanical stress distributions due to heterogeneous stalk-foliage interactions.

Such dynamic force conditions frequently induce mechanical injuries to leaves, including surface abrasions, midrib fractures, and lamina tearing, as documented in field studies. Consequently, minimizing mechanical damage rates during automated stem-leaf separation has emerged as a pivotal technical challenge that must be resolved to enable fully mechanized tobacco production systems.

This paper analyzes the motion of manual tobacco leaf harvesting and designs a bionic harvesting device to achieve the purpose of reducing damage and increasing efficiency. Manual harvesting typically involves using the thumb and index finger (the "tiger mouth" position) to grip the leaf stem, pressing straight down until the leaf detaches from the stalk. The following Figure 1 is the manual harvesting process and the force diagram of tobacco leaves.

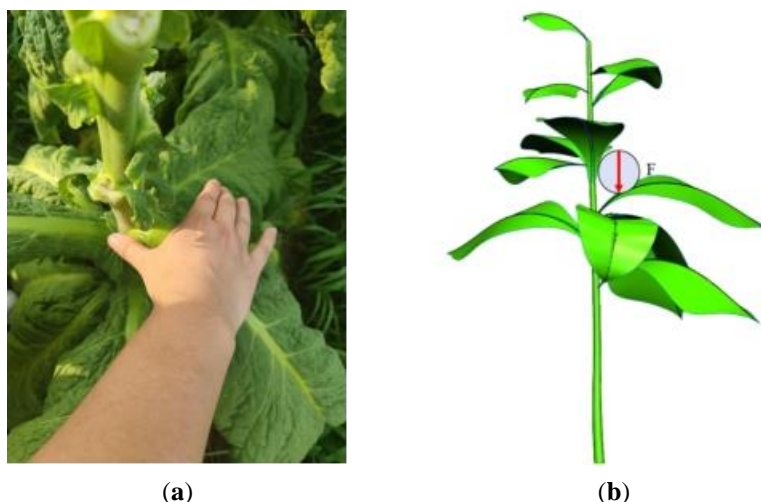


Fig. 1 - Manual harvesting action and force diagram of tobacco leaves
(a) Artificial harvesting method; (b) Harvesting force diagram.

Bionic Design Principles

The crucial part of the bionic tobacco leaf harvesting machine is the bionic picking rod, which acts as the executive mechanism to directly sever the leaves from the stem. The stability of the picking rod's operation directly impacts the performance of the harvester and the quality of the picked tobacco leaves. This study designs the bionic picking rod by mimicking the action of human fingers when picking tobacco leaves, considering that tobacco leaves grow in various directions around the stalk during their growth in the field. Auxiliary rods are therefore positioned vertically along the picking rod, and the two picking rods, in conjunction with the auxiliary rod, form a picking frame that ensures all leaves can be collected. The following Figure 2 is a bionic design.

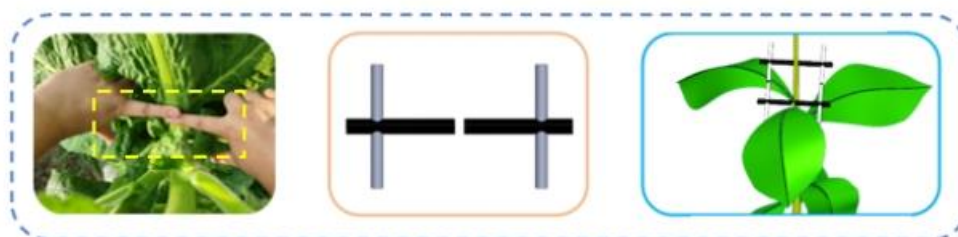


Fig. 2 - Bionic picking principle diagram

Design and Working Principle of Bionic Tobacco Leaf Harvesting Structure

The low-damage bionic tobacco leaf harvesting machine is structured vertically with a collection box at the top, followed by a transmission section, and a harvesting unit at the bottom, as shown in Figure 3. The harvesting unit consists of two oppositely positioned harvesting modules, with a gap reserved between them. The height and tilt angle of the harvesting unit are adjustable to accommodate tobacco plants of varying heights. The transmission section includes a series of rollers positioned below the harvesting unit and a conveyor belt that transports harvested leaves upward toward the collection box. The divider, designed in a triangular conical shape, is mounted at the front of the harvesting mechanism and positioned between two parallel bionic harvesting units, serving as the leading component of the entire apparatus.

This design can complete the layered mechanized picking of tobacco leaves, with low breakage rate and high harvesting efficiency. At the same time, it can greatly reduce the damage to tobacco plants and ensure the normal growth of tobacco plants in the future.

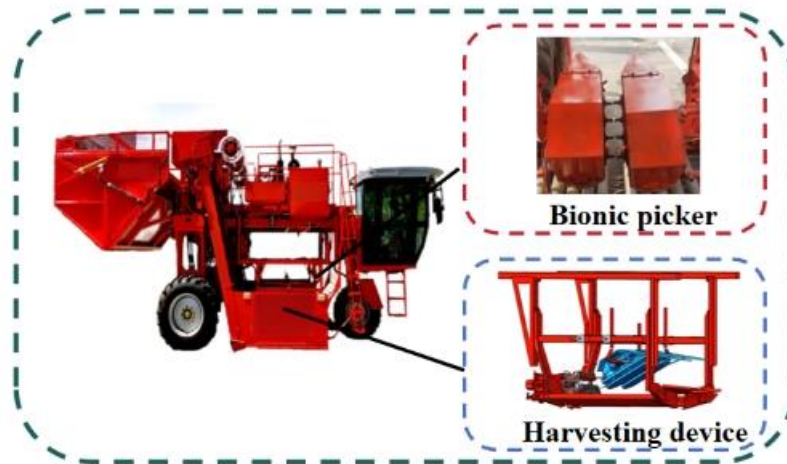


Fig. 3 - The overall structure of tobacco leaf harvester

Working Principle

When the tobacco leaf picking machine starts to harvest tobacco leaves, the tobacco plants are first introduced by the upper and lower pairs of dividers at the front end, and then the tobacco plants enter the bionic picking frame composed of picking rods and auxiliary rods on both sides. The picking frame is fixed on the chain and rotates around the picking frames on both sides, and the back end of the chain plane is tilted downward to ensure that the tobacco leaves within the preset height range can be harvested. The picking frame rotates downward and backward, and the picking machine moves forward. The petiole is subjected to a downward force. When the force is greater than the connection force between the tobacco leaf and the stem, the petiole breaks. After the tobacco leaves are removed, they fall on the conveyor belt below and are then transmitted to the collection box. The picking machine continues to move forward, and the flexible picking rod contacts and bends with the tobacco rod. The tobacco rod enters the next picking frame and carries out the tobacco leaf picking at the next height until the tobacco plant passes through all the picking frames to complete the tobacco leaf picking in the preset height range. The harvesting operation of the whole device imitates the action of rolling tobacco leaves down along the stem during manual picking through the motion synthesis of the picking frame and the whole machine, so as to realize the low-loss picking of tobacco leaves. The schematic diagram of the harvesting process is shown in Figure 4.

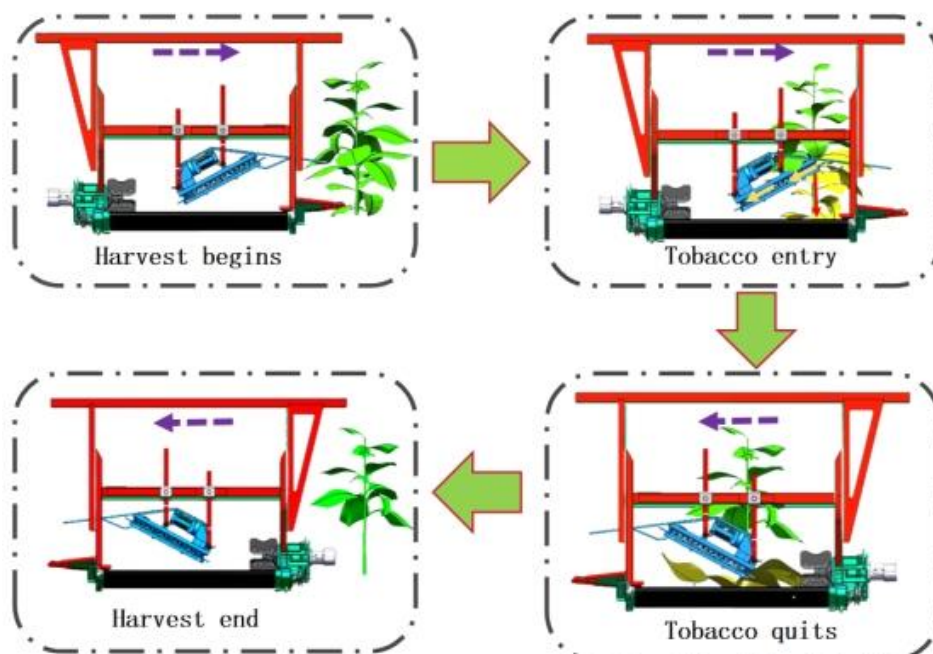


Fig. 4 - Tobacco leaf harvesting process

Analysis of Mechanical Properties in Tobacco Leaf Harvesting Process

Characteristics of Tobacco Leaf Harvesting

The growth characteristics of tobacco leaves and the connection strength of stems and leaves are important basis for the design of bionic picking device. The experiment was conducted in the tobacco fields of Xiangcheng County, Henan Province. The height of tobacco plant is moderate, the oil of tobacco leaf is large, the toughness is good, and it is suitable for mechanized harvesting. As shown in Figure 5, 20 tobacco plants were randomly selected as test objects, and steel ruler, electronic tension meter and protractor were used to measure the trait characteristics of tobacco leaves, the angle between petiole and stem, the position of picking force and the fracture force between stem and petiole. After removing extreme data, the average value of the measurement results was taken: length 58 cm, width 34 cm, stem diameter 3.6 cm, stem leaf angle 46°, petiole fracture force 34 N, which provided data support for the design of bionic picking device.



Fig. 5 - Measurement of tobacco leaf characteristics

Analysis of the Collision Process in Tobacco Leaf Harvesting

In the process of tobacco leaf picking, the collision between the picking device and the tobacco leaf will produce a large impact force. Assuming that the external force impulse is constant, the length of the collision time Δt will seriously affect the peak impact force. Prolonging the collision time can reduce the collision impact force, thereby reducing the damage rate of tobacco leaves. The tobacco leaf is regarded as a particle, and its collision process conforms to the impulse-momentum theorem:

$$I = \int_{t_0}^{t_0 + \Delta t} ma(t)dt \tag{1}$$

Where: I is the impulse of tobacco leaves, N·s; m is the quality of tobacco leaves, kg; a is acceleration, m/s²; t is time, s.

It can be seen from Equation (1) that the impulse of tobacco leaves during picking is not only related to its own weight, but also affected by collision time and collision acceleration.

Let y be the coordinate of the middle part of the tobacco leaf in the vertical direction, then the motion equation of the single degree of freedom system is:

$$m \ddot{y} + c \dot{y} + (k + k_o)y = 0 \tag{2}$$

$$y(0) = 0, \dot{y}(0) = v_0$$

In the case of underdamping, the solution of Equation (2) is:

$$y = Ae^{-\lambda \omega_i t} \sin \omega_s t \tag{3}$$

where:

$$\lambda = \frac{c}{2m\omega_i} \tag{4}$$

$$A = \frac{v_0}{\omega_s} \tag{5}$$

$$\omega_s = \sqrt{1 - \lambda^2} \omega_i \tag{6}$$

$$\omega_i = \sqrt{\frac{k + k_0}{m}} \quad (7)$$

In the formula, λ is viscous damping ratio, $\lambda < 1$; A is amplitude, mm; ω_s is damped natural frequency, Hz; ω_i is undamped natural frequency, Hz.

With an initial displacement of 0, the collision time is determined by the smallest positive root of Eq. (8):

$$f(t) = c \dot{y} + ky = 0 \quad (8)$$

The available collision time is:

$$\Delta t = \frac{\pi + \arctan \lambda_2}{\omega_i \sqrt{1 - \lambda^2}} \quad (9)$$

It can be seen from Equation (9) that the impact time is related to the tobacco leaves mass, picking mechanism stiffness coefficient, damping coefficient, and other parameters of the system, and these inherent parameters depend on its structure and materials.

As mentioned above, in the design of the next bionic picking device, the stiffness coefficient can be reduced and the damping coefficient can be increased by changing the structure and contact material of the picking mechanism, thereby reducing the collision acceleration, reducing the impact force at the moment of collision, and finally reducing the damage rate of tobacco leaves.

Bionic Harvesting Device Parameter Design

Harvesting Rod Parameter Design

The bionic picking rod and the auxiliary rod are fixed on the chain, and the chain and the motor are installed on both sides of the frame. The two chains are driven by the motor to rotate around the two sides of the frame. In the process of field operation, as the picking machine moves forward, the tobacco stem enters the picking frame composed of picking rod and auxiliary rod through the guidance of the front divider, as shown in the following Figure 6.

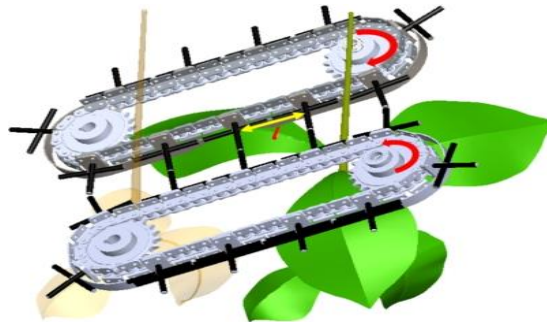


Fig. 6 - Picking rod structure diagram

If the picking frame is set too small, the stem pass ability is reduced, which is likely to cause damage to the stem and seriously affecting the picking effect; if the picking frame is too large, the torque of the tobacco leaves increases, and completing the picking operation requires greater force, resulting in an increase in the power consumption of the picking machine. Secondly, if the picking frame is too large, it will lead to the contact being not with the petiole but with the more fragile blade, resulting in an increase in the picking damage rate. Through field experiments, it has been determined that the distance between two adjacent picking rods on the same side of the transmission chain needs to be optimized:

$$l \times \cos \alpha = l_0 + d \quad (10)$$

where, l is the distance between the two picking rods in the same side, mm; α is the angle between the plane and the horizontal plane of picking rod, °; d is diameter, mm; l_0 is tobacco leaf picking position to the distance from the stem pole, mm.

According to the previous measurement and statistics of tobacco stems, d is 35 mm, the angle between the plane of the picking rod and the horizontal plane is 30, and the picking force of the tobacco petiole is tested. The distance from the picking force position to the stem is 70 mm, and it is reasonable to take 92 mm by calculation.

Harvesting Rod Rotation Speed Design

The picking rod rotates with the chain around the frame. It can be seen from the previous calculation that the greater the instantaneous speed of contact between the picking rod and the blade, the greater the impact force on the tobacco leaf, so the excessive speed of the chain will cause the damage rate of the tobacco leaf to increase. If the chain speed is simply reduced, the tobacco stem bent by the picking frame will cause damage to the tobacco stem because it does not pass through the flexible picking frame in time. According to the design principle of the picking device and the agronomic requirements of the layered picking of tobacco leaves, as shown in Figure 7, the speed of the picking frame needs to match the speed of the picking machine to achieve the expected effect of the picking rod relative to the downward movement of the tobacco stem. The speed of the two needs to meet:

$$v_1 = k \frac{v}{\cos \alpha} \quad (11)$$

where, v is picking machine forward operating speed, m/s; k is empirical coefficient; v_1 is the chain rotation speed of picking rod, m/s; α is the angle between the picking mechanism and the horizontal plane, °.

After many field experiments, the value of the empirical coefficient k is 1.0-1.1, the picking frame plane and the horizontal plane are 25°-35°, the integrity of the tobacco leaf is high, the damage to the tobacco stem is low, and the expected operation effect can be better realized. At the same time, in order to ensure the harvest efficiency of 1 to 1.3333 hectares per day, the operating speed v of the tobacco picking machine in the field is 1.5 km/h-4 km/h. When the angle α between the plane of the picking mechanism and the horizontal plane is set to 30°, substituting this value into Equation (11) yields a calculated range for the chain rotation speed v_1 of the picking rod between 0.48 m/s and 1.28 m/s.



Fig. 7 - Velocity relation diagram

Design of Grain Divider

The divider, as the core front-end component of the harvester, primarily serves to upright fallen tobacco plants and guide them into the harvesting mechanism while separating upper and lower leaves to prevent damage during harvesting. Its simple yet critical design directly impacts overall harvesting performance. Featuring symmetrical triangular-cone structures, the divider's effectiveness depends on its angle (β) and front height (l_1). Based on field data, it is designed to handle plants with up to 20° of lodging. For example, in central Henan, where mid-stem leaves grow 0.5–0.9 meters above ground, the front height (l_1) is calculated using the formula:

$$l_1 = 0.9 \cos \gamma \quad (12)$$

where, l_1 is the height of the front end of the layered device from the ground, cm; γ is tobacco lodging angle, °, $\gamma = 0 \sim 20^\circ$.

Because the maturity of tobacco leaves is from bottom to top, the design of the divider only considers the uppermost part of the picking layer. The distance from the front end of the divider to the ground is 84.5 ~ 90 cm, and the inclination angle of the divider should be satisfied.

$$\beta = \arcsin \frac{l_2 - l_1}{l_3} \quad (13)$$

where, β is angle of inclination of the divider, °; l_2 is the height from the rear end of the divider to the ground, cm; l_3 is length of divider, cm.

Through the comprehensive analysis of the characteristics of tobacco field planting in Henan and the agronomic requirements of picking, combined with the design experience, the distance from the front end of the divider to the mechanism is determined to be 46.5 cm, and the height from the connection position of the divider and the mechanism to the ground is 100 cm.

The data is brought into the formula (13) to calculate and sort out the value range of the inclination angle of the divider is about $12.4^\circ \sim 20.7^\circ$. The smaller the inclination angle of the divider, the better the effect of the divider and the passing ability. Considering that the picking machine needs to adapt to different heights of tobacco leaves, in order to ensure the picking effect, the inclination angle of the divider should be smaller on the basis of calculation. In summary, the inclination angle of the divider is 10° .

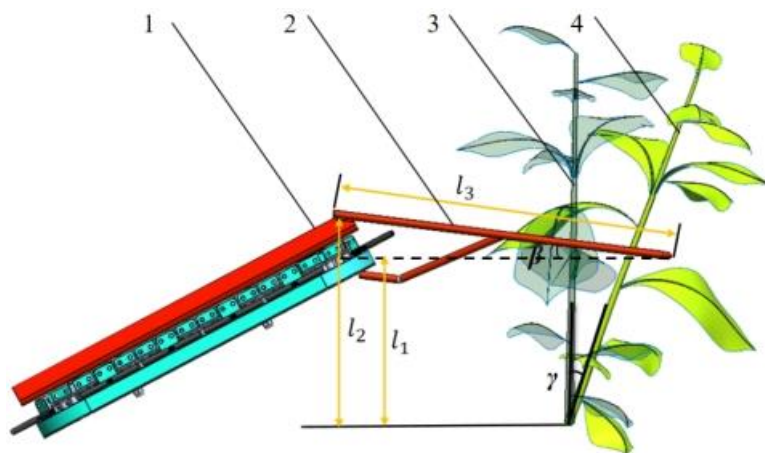


Fig. 8 - Schematic diagram of the staged righting process for lodged tobacco plants
(1) plucking device; (2) division mechanism; (3) uprighted tobacco; (4) lodged tobacco

Tobacco Harvest Simulation

Model Establishment

Based on field measurements of tobacco plant dimensions, the stalk height is set to 1700 mm, the stalk diameter to 4 mm, and the overall leaf dimensions to 600×350 mm. A thin-shell structure is created based on the leaf shape. As shown in Figure 9(a), a tobacco plant model is established using SolidWorks software. To clearly illustrate the harvesting process, the plant model is simplified, as shown in Figure 9(b). The simplified model consists of two components: the stalk and the leaf. The leaf is positioned 1000 mm above the ground, and the angle between the leaf stalk and the plant stalk is 50° .

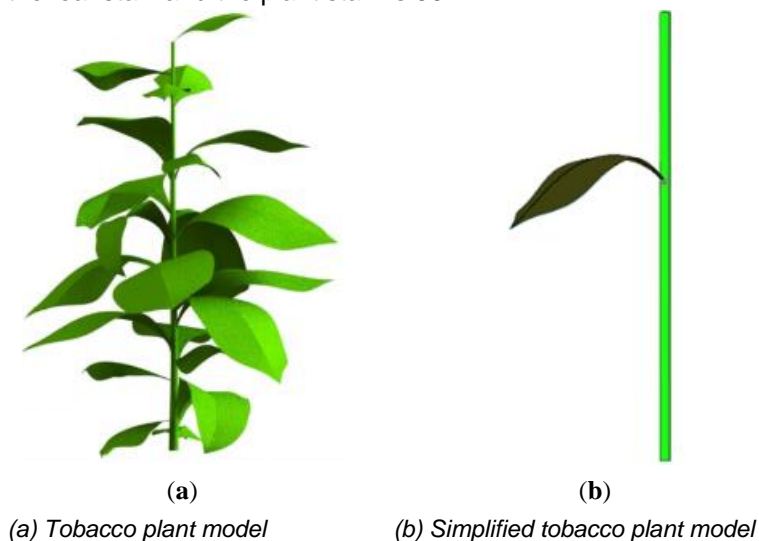


Fig. 9 - Whole tobacco and simplified model

Analysis of Tobacco Leaf Dropping Conditions

By applying an external force to the tobacco leaf, the change of the flexible connection force between the tobacco leaf and the tobacco stem under different forces is analyzed, so as to determine the condition of the

tobacco leaf falling from the tobacco plant, and lay the foundation for the simulation of the next tobacco leaf picking process.

Simulation Parameter Settings

The simplified tobacco plant model built in SolidWorks is imported into ADAMS. The file format is "Parasolid" format, which is relatively stable after conversion and is not easy to lose graphic information. Because the materials provided by the system do not meet the actual needs, the actual tobacco plant materials are created by inputting parameters such as tobacco plant density, tensile modulus and Poisson 's ratio. Combined with relevant literature (Zhang T. et al., 2018; Han M. et al., 2024; Zhang L., 2015) and data collected in the field, the model parameters of tobacco plants were selected in Table 1.

Table 1

Tobacco plant material parameters		
Density (Kg·mm ⁻³)	Tensile modulus (N·mm ⁻²)	Poisson's ratio
4.5E-0.7	1.1E+0.4	0.33

In order to accurately reflect the change rule of the flexible connection force between tobacco stems and tobacco leaves, it is necessary to add a fixed connection between tobacco stems and the earth to make it unable to move in any direction when analyzing the falling conditions of tobacco leaves in tobacco.

The connection between tobacco stems and leaves is modeled using a bushing force. Due to the numerous and complex parameters involved in flexible sleeve connections, there is currently limited literature and few relevant case studies available. Therefore, based on previously measured physical and chemical properties, as well as the shedding force of tobacco plants in the early stage (Qu Z. et al., 2024; Zhang H. et al., 2022), the parameters for the flexible sleeve force were defined as shown in Table 2. The central point at the junction between the tobacco stem and leaf was selected as the connection point for applying the flexible bushing force, labeled Bushing1.

Table 2

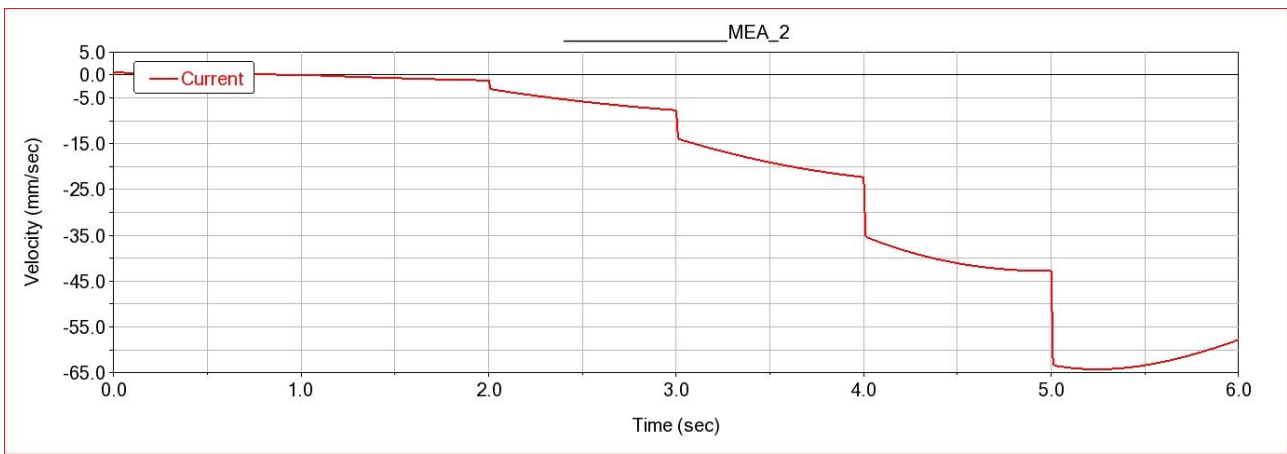
Flexible connection sleeve force parameters					
Connection force	Translation characteristics (x, y, z)		Rotation characteristics (x,y,z)		remark
	stiffness coefficient (N·mm)	damping coefficient (N·s·mm ⁻¹)	stiffness coefficient (N·mm/deg)	damping coefficient (N·mm·s/deg)	
Bushing 1	1.8	10	30	100	Connection between tobacco stem and leaf

Step function was used to apply increasing external load to tobacco leaves in ADAMS software, and the separation conditions of tobacco stems and leaves were analyzed. By referring to the relevant literature (Wen, B., 2010) and combining with the fracture force of tobacco petiole measured above, the external load range was set to 5-50 N, and the direction of external load was set along the negative direction of Y axis. The initial external load was set to 5 N, and then 10 N was added every 1 second. The functional equation is written as: + 5 + STEP (time, 1, 0, 1.01, 5) + STEP (time, 2, 0, 2.01, 10) + STEP (time, 3, 0, 3.01, 10) + STEP (time, 4, 4, 0, 4.01, 10) + STEP (time, 5, 0, 5.01, 10). The simulation time is set to simulate the falling process of tobacco leaf.

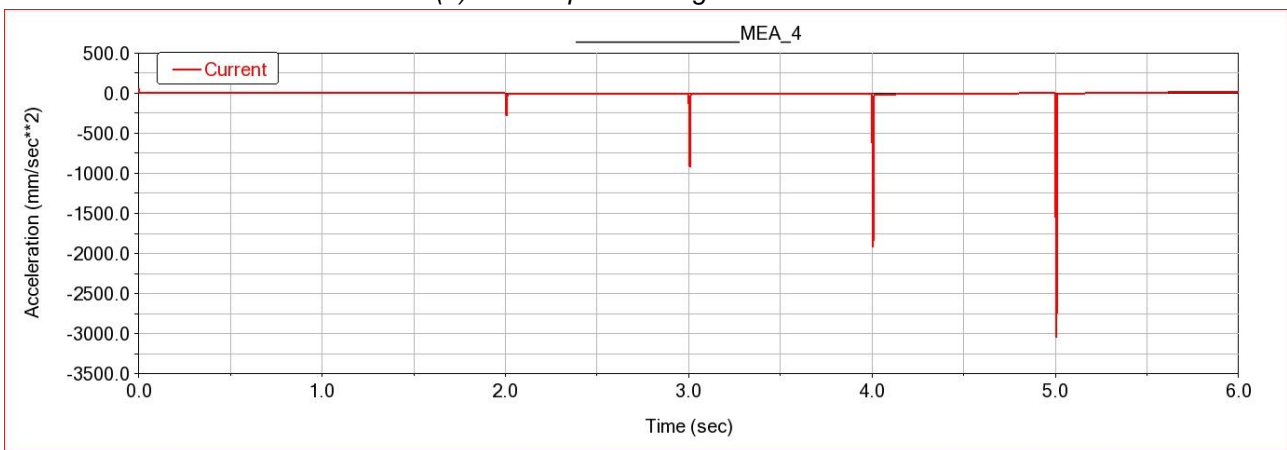
RESULTS AND DISCUSSIONS

Simulation Results Analysis

Figure 10 shows the velocity and acceleration curves of tobacco leaves in the X direction when subjected to external forces. As shown in the figure, since the tobacco leaves are only subjected to external loads in the negative Y direction, there is almost no velocity in the X direction, and the acceleration is also zero between 0s and 2 s. This indicates that when the external load is between 5 N and 15 N, the connection force (Bushing1) between the tobacco leaves and the tobacco stalk has not reached the breaking point. After 2 s, when the external load suddenly increases to 25 N, there is a significant change in velocity in the X direction, and the acceleration is no longer zero. This is because when the connection force reaches the breaking limit and the external load continues to increase, Bushing1 needs to transfer the received energy through lateral vibration. This shows that when the external force reaches 25 N, it has met the breaking condition of Bushing1.



(a) X axis speed change curve of leaf



(b) X axis acceleration curve of leaf

Fig. 10 - Curves of X-axis velocity and acceleration of tobacco leaf

The flexible connecting sleeve force Bushing1 between tobacco leaf and stem exceeded the bearing limit when the external force reached 25 N at the end of the second. Figure 11 illustrates the displacement curve of the flexible sleeve force. At the end of 2 seconds, the displacement of the Y axis reached 1.2981 mm. This indicates that the shedding condition for the tobacco leaf occurs when the Y-axis displacement of the flexible connection (Bushing1) reaches 1.2981 mm.

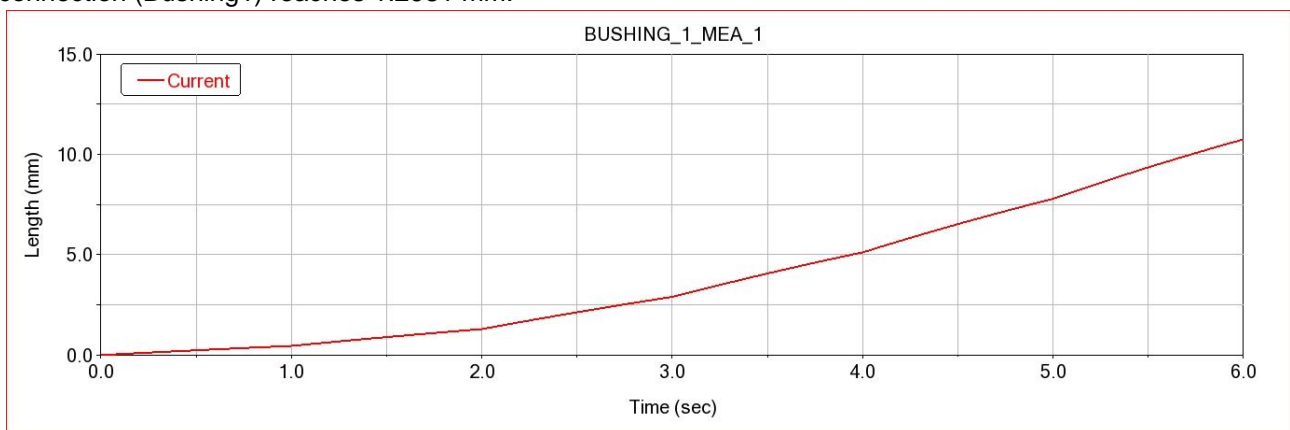


Fig. 11 - Flexible connection force displacement curve

Harvesting Process Simulation

The virtual prototype simulation analysis of the tobacco leaf picking process is to study the force change of the tobacco leaf during the picking process of the picking device, and to compare the force of the flexible picking mechanism and the rigid picking mechanism on the tobacco leaf. In this paper, the tobacco leaf picking device is taken as the research object. Because the picking process of a tobacco leaf is only affected by a picking rod, the number of picking rods is simplified to 1.

Import the model and set the material properties

The three-dimensional model of tobacco and picking rod is saved as "Parasolid" (*.x_t) format, and then imported into ADAMS to construct the simulation picking system of tobacco plant-picking rod. The relative position of picking rod and tobacco stem is adjusted. The axis direction of tobacco stem coincides with the Y axis, the vein of tobacco leaf is parallel to the X-Y plane, and the picking rod is parallel to the Z axis and placed above the tobacco leaf. The materials of picking rod are steel and rubber respectively. The relevant performance parameters of steel and rubber (Hou J. et al., 2022) are shown in Table 3.

Table 3

Physical performance parameters of picking rod			
Material type	Elastic modulus (N·mm ⁻²)	Density (Kg·mm ⁻³)	Poisson's ratio
Steel	2.06 E+05	7.85 E-06	0.3
Rubber	7.84	1.5 E-06	0.47

Adding Constraints, Drivers, and Sensors

Add constraints

The flexible connection between the two parts of the tobacco is still based on the data listed in Table 2. The picking rod is added with a negative moving pair relative to the earth along the Y axis, and the tobacco stem and the earth are fixed by a fixed pair.

Add driver

According to the previous calculation, when the rotation speed of the picking rod is 1.73 km/h ~ 5.08 km/h, the vertical downward combined speed is 0.865 km/h ~ 2.54 km/h, and the slip drive is added to the negative slip pair of the shaft to be 0.24 m/s, 0.4 m/s, 0.55 m/s and 0.71 m/s.

Define contact

The research on the contact parameters between tobacco and other materials in the literature is limited. Referring to the wood which is close to the physical and chemical properties of tobacco, combined with the relevant data measured above, and consulting the relevant references (Jin C. et al., 2023), the specific contact parameters are shown in Table 4.

Table 4

Contact parameters of different materials					
Material type	Stiffness coefficient (N·mm ⁻¹)	Force index	Damping coefficient (N·s·mm ⁻¹)	Static friction factor	Dynamic friction coefficient
Steel-Wood	2855	1.5	0.57	0.3	0.25
Rubber-Wood	2855	1.1	0.57	0.5	0.36

Define the sensor

Based on the previous analysis, Sensor1 is configured to monitor the displacement of the flexible connection bushing force (Bushing1) along the Y-axis. When the displacement exceeds 1.2981 mm, it is determined that the connection between the tobacco stem and leaf has fractured. At this point, both Sensor1 and Bushing1 are considered to have failed, indicating that the tobacco leaf has detached and fallen, completing the picking process. The sequence of the picking process is illustrated in Figure 12.

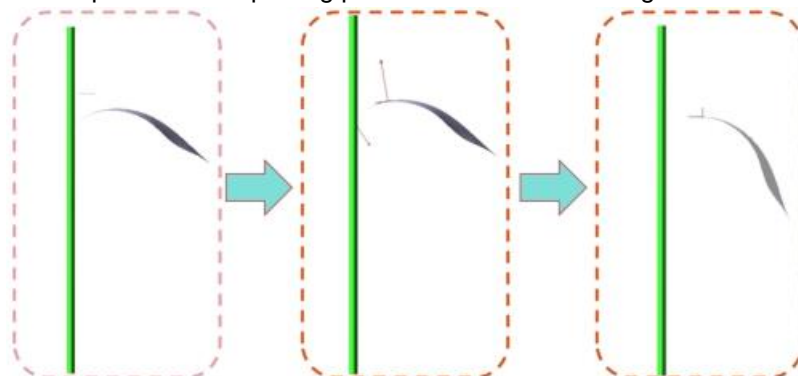
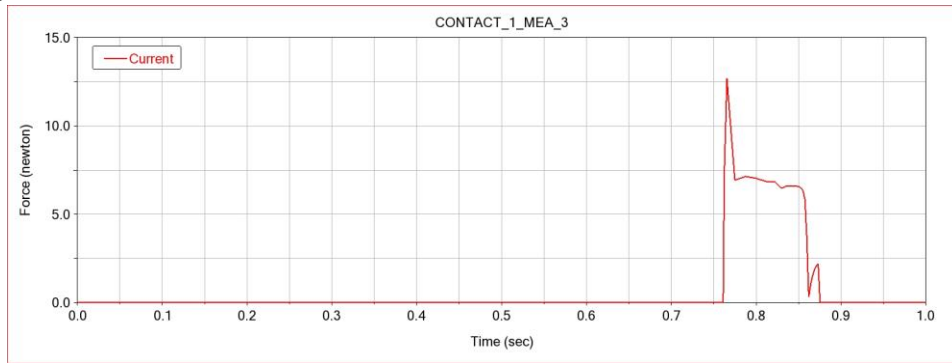


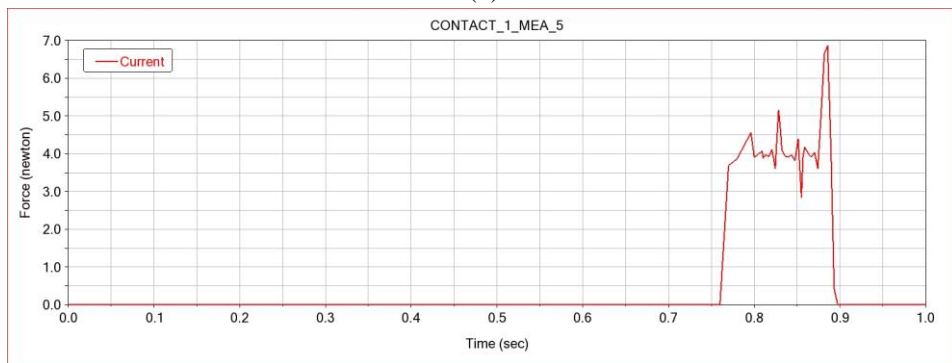
Fig.12 - Simulation of tobacco picking process

Simulation Results Analysis

The speed of the picking rod along the negative direction of the Y axis is 0.24 m/s, 0.4 m/s, 0.55 m/s, 0.71 m/s, respectively. As shown in Figures 13 ~ 16, the left side is the contact force change curve when the rigid picking rod collides with the tobacco leaf, and the right side is the contact force change curve when the flexible picking rod collides with the tobacco leaf.



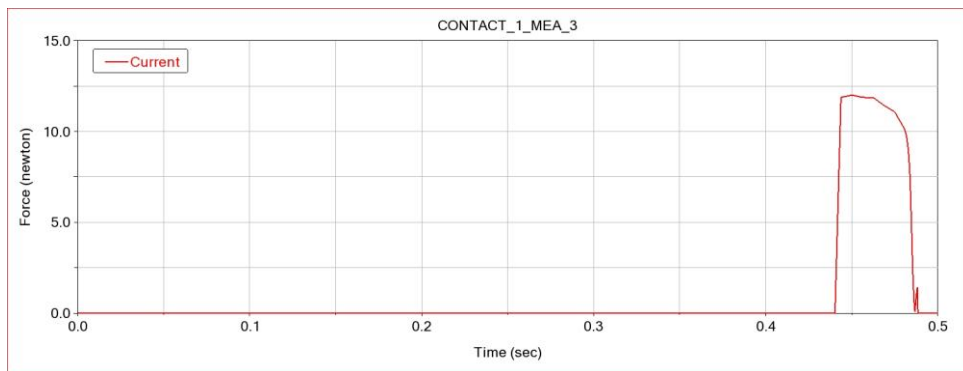
(a)



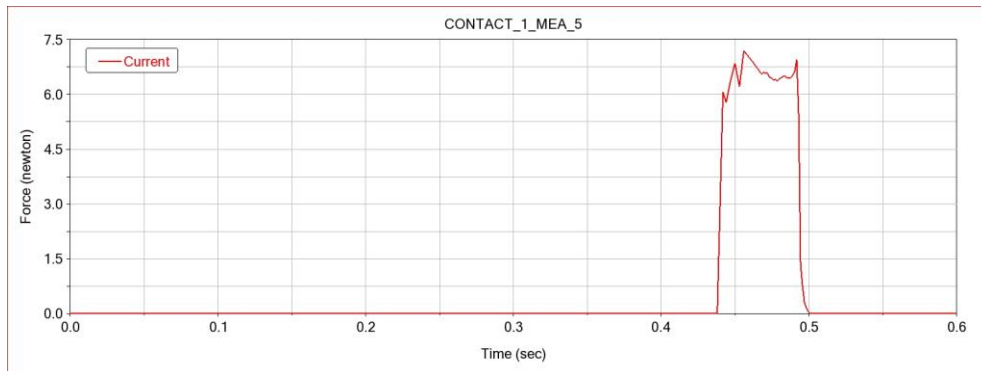
(b)

Fig. 13 - The collision force of tobacco leaves when the speed of picking rod is 0.24 m/s

(a) Rigid picking rod contact force; (b) Contact force of flexible picking rod



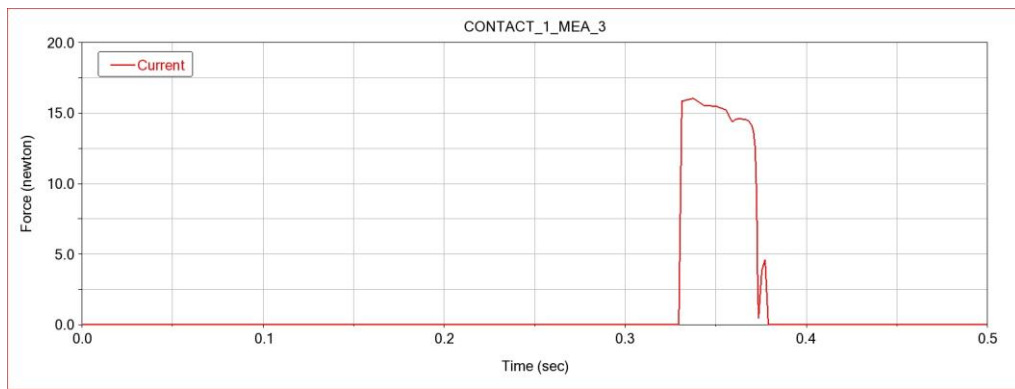
(a)



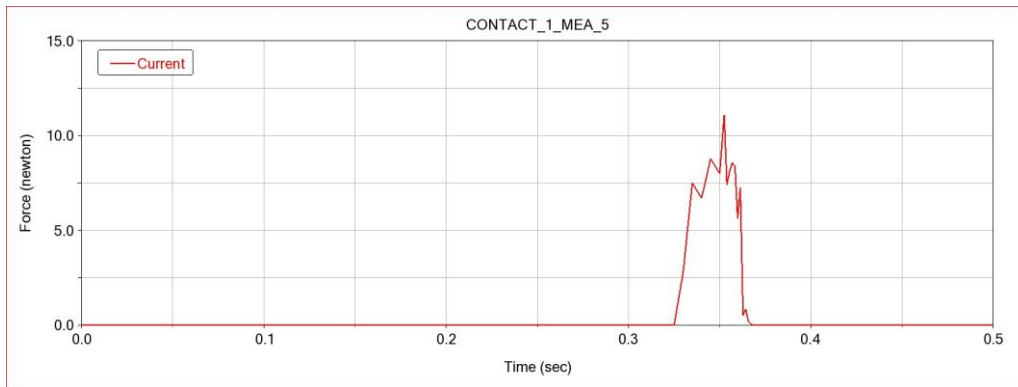
(b)

Fig. 14 - The collision force of tobacco leaves when the speed of picking rod is 0.4/s

(a) Rigid picking rod contact force; (b) Contact force of flexible picking rod



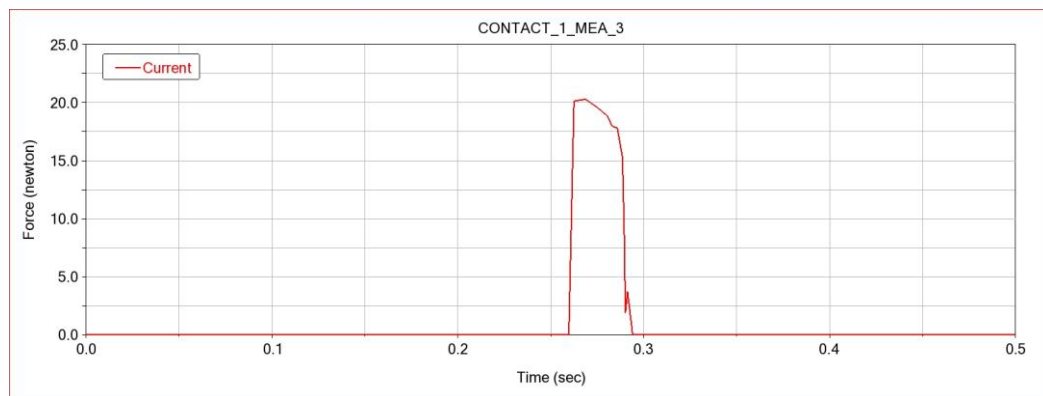
(a)



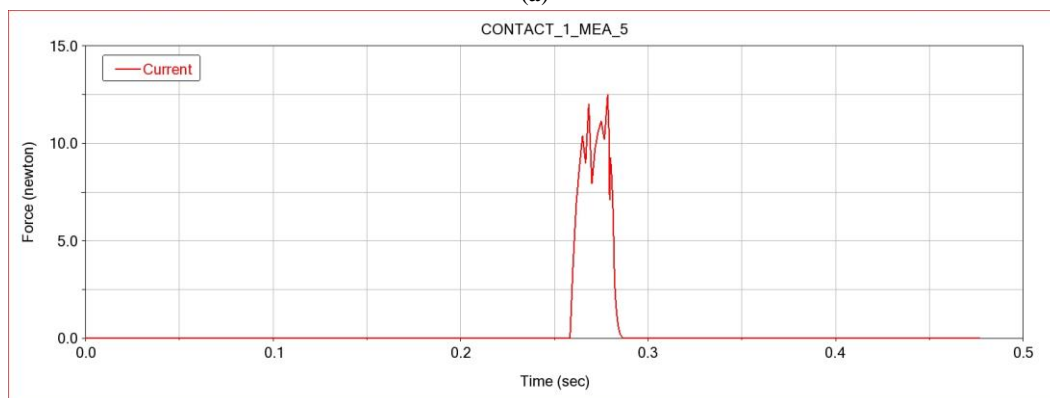
(b)

Figure .15 - Impact force on tobacco leaves when the speed of picking rod is 0.55 m/s

(a) Rigid picking rod contact force; (b) Contact force of flexible picking rod



(a)



(b)

Fig. 16 - Impact force on tobacco leaves when the speed of picking rod is 0.71 m/s

(a) Rigid picking rod contact force; (b) Contact force of flexible picking rod

The comparative analysis of test data shows that:

By comparing the simulation test data on the left and right sides, it is found that the change rule of the overall curve of the two is similar, but it is relative to the rigidity. For the picking rod, the action time of the flexible rubber picking rod on the tobacco leaves is prolonged, and the effect of reducing the collision force is obvious.

Comparing the four groups of different picking rod speeds, it is found that when the picking rod speed is 0.4 m/s, the corresponding flexible picking rod collision force in Figure 16(b) is the smallest.

In summary, combined with the comprehensive consideration of tobacco picking efficiency and collision damage, when the vertical speed of the picking rod is 0.4 m/s, the picking effect of the flexible rubber picking rod is the best.

Field Trials

Test Conditions and Equipment

The field experiment was conducted in a tobacco field located in Xuchang, Henan Province, focusing on the harvesting of middle-position tobacco leaves. The experimental setup is illustrated in Figure 17. The instruments and equipment used included the custom-built tobacco leaf bionic picking machine, a computer, and a high-speed camera system. This experiment was performed outdoors. During the trials, trained operators operated the bionic picking machine, adjusting its forward operating speed to perform straight-line picking operations under varying conditions.



Fig. 17 - Field experiment plot

Experimental Design

The test materials and contents are shown in Table 5. According to the working principle analysis and pre-experimental analysis of the tobacco simulation picking device, it is concluded that the rotation speed of the picking rod, the inclination angle of the picking plane, the spacing of the picking rod, and the material of the picking rod have a great influence on the efficiency and harvesting quality of the picking device. The damage rate and operating efficiency of tobacco leaves are selected as test indicators. Each test sample group consisted of two rows of tobacco plants, with a total length of approximately 150 m.

After each test group, the harvested tobacco leaves in the collection box were gathered for evaluation. Each leaf was examined to determine whether the main stem was broken and whether the area of leaf loss exceeded the predefined damage threshold. The classification criteria for harvested tobacco leaves are illustrated in Figure 18. The number of damaged and intact tobacco leaves was recorded separately, and the damage rate was calculated using the following formula.

Table 5

Tobacco plant material parameters				
Project	Test equipment	Test site	Experiment variables	Test metrics
elements	The processed tobacco leaf bionic picking machine, computer and high-speed camera system.	Xu chang, Henan Provinc	The picking rod, the inclinatio angle of the picking table and the picking rod spacing	The damage rate and operation efficiency



Fig. 18 - Classified tobacco leaves

$$Z_s = \frac{W_s}{W_i + W_s} \times 100\% \tag{14}$$

where: Z_s is the leaf damage rate, %; W_s is number of damaged tobacco leaves; W_i is number of intact tobacco leaves.

According to the ADAMS simulation results, the picking effect of the picking rod with flexible rubber material is better than that of the steel picking rod. The test factors were determined to be the rotation speed of the picking rod, the inclination angle of the picking table and the picking rod spacing, which were expressed by A, B and C respectively. The damage rate and operation efficiency of the test index tobacco leaves were expressed by W_1 and W_2 . The quadratic orthogonal rotation combination analysis method with three factors and three levels was used in the experiment. The factor coding was shown in Table 6, and a total of 17 groups were carried out. Design-Expert software was used to analyze the test results. The test results are shown in Table 7.

Table 6

Coding table of test factors

Codes	Factors		
	Picking rod speed	Picking table inclination	Picking pole spacing
	A (m/s)	B (°)	C (mm)
-1	0.6	25	80
0	0.8	30	90
1	1	35	100

Table 7

Test scheme and results

No.	Factors			W_1 Tobacco leaf breakage rate (%)	W_2 Operational efficiency (km/h)
	A Picking rod speed (m/s)	B Picking table inclination (°)	C Picking pole spacing (mm)		
1	0	1	1	25.94	2.360
2	0	-1	1	25.31	2.640
3	1	1	0	24.33	2.950
4	0	1	-1	25.11	2.380
5	-1	1	0	21.98	1.230
6	-1	0	0	23.34	1.562
7	1	0	0	24.54	3.130
8	0	0	0	18.34	2.505
9	-1	-1	0	21.64	1.638
10	1	0	-1	22.34	3.134
11	0	0	0	18.25	2.508
12	-1	0	-1	21.14	1.566
13	1	-1	0	22.84	3.280
14	0	-1	-1	24.74	2.620

No.	Factors			W ₁ Tobacco leaf breakage rate (%)	W ₂ Operational efficiency (km/h)
	A Picking rod speed (m/s)	B Picking table inclination (°)	C Picking pole spacing (mm)		
15	0	0	0	18.31	2.507
16	0	0	0	18.21	2.511
17	0	0	0	18.18	2.502

Experimental Results Analysis

The regression model of tobacco leaf breakage rate was established

The regression mathematical model of tobacco leaf damage rate W₁ was obtained by regression fitting of the test results:

$$W_1 = 18.26 + 0.74A + 0.35B + 0.73C + 0.29AB + 0.00AC + 0.065BC + 1.00A^2 + 3.44B^2 + 3.58C^2 \quad (15)$$

The determination coefficient of the regression equation is R² = 0.9892, and the fitting degree is high. The regression model was analyzed by variance analysis, and the results are shown in Table 8.

Available: P < 0.0001 of the model, indicating that the regression equation is significant; a, C, A², B², C² P < 0.01, the results were significantly affected; other factors and interaction terms P > 0.05, had no significant effect on the test index.

The significance of the influence of each factor on the damage rate of tobacco leaves is the rotation speed of the picking rod > the picking rod spacing > the inclination angle of the picking table. The interaction of each factor is shown in Figure 19.

Table 8

Test scheme and results Analysis of variance of tobacco leaf breakage rate						
Source	Sum of Squares	df	Mean Squares	F Value	P Value	
Model	127.65	9	14.18	71.20	<0.0001	
A	4.43	1	4.43	22.22	0.0022	
B	1.00	1	1.00	5.03	0.0599	
C	4.20	1	4.20	21.11	0.0025	
AB	0.33	1	0.33	1.66	0.2386	
AC	0.000	1	0.000	0.000	1.0000	
BC	0.017	1	0.017	0.085	0.7793	
A ²	4.23	1	4.23	21.23	0.0025	
B ²	49.75	1	49.75	249.75	<0.0001	
C ²	53.96	1	53.96	270.88	<0.0001	
Residual	1.39	7	0.20			
Lack of Fit	1.38	3	0.46	102.64	0.0003	
Pure Error	0.018	4	4.470E-003			
Cor Total	129.04	16				

Note: P<0.01 (extremely significant, **); p < 0.05 (significant, *)

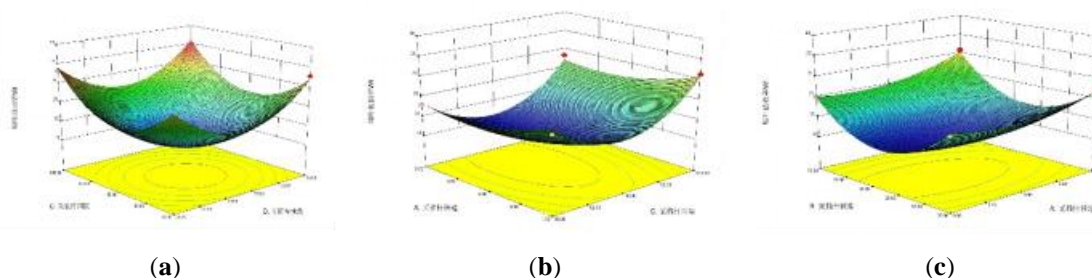


Fig. 19 - Effect of interaction of 21 factors on damage rate of tobacco leaf

- (a) The interaction between the picking rod spacing and the inclination angle of the picking table;
- (b) The interaction between the rotation speed of the picking rod and the picking rod spacing;
- (c) The interaction between the rotation speed of the picking rod and the inclination angle of the picking table.

When the rotation speed of the picking rod is fixed, the effect of the interaction between the picking rod spacing and the inclination angle of the picking table on the damage rate of tobacco leaves is shown in figure 19(a). When the interval of the picking table is fixed, the inclination angle of the picking table is too large or too small, it will lead to the increase of the damage rate of tobacco leaves. When the inclination angle of the picking table is constant, the damage rate of tobacco leaves increases with the increase of the picking rod spacing.

When the inclination angle of the picking rod is fixed, the influence of the interaction between the picking rod spacing and the rotation speed of the picking table on the damage rate of the tobacco leaf is shown in Figure 18(b). When the picking rod spacing is constant, the damage rate of tobacco leaves increases with the increase of the rotation speed of the picking rod. When the picking rod speed is constant, the damage rate increases slowly with the increase of the picking rod spacing.

When the picking rod spacing has a fixed value, the effect of the interaction between the inclination of the picking table and the rotation speed of the picking rod on the damage rate of tobacco leaves is shown in figure 18(c). When the rotation speed of the picking rod is constant, the inclination angle of the picking table is too large or too small, which leads to the increase of the damage rate of tobacco leaves. When the inclination angle of the picking table is constant, the damage rate of tobacco leaves increases slowly with the increase of the rotation speed of the picking rod.

Establishment of a regression model for working efficiency

The regression mathematical model of working efficiency W2 is obtained by regression fitting of the test results:

$$W_2 = 2.51 + 0.81A - 0.16B - 0.001C + 0.019AB + 0.0001AC - 0.01BC - 0.19A^2 - 0.04B^2 + 0.033C^2 \quad (16)$$

The coefficient of determination for the regression equation was R2 = 0.9978, indicating an excellent degree of fit. The regression model was evaluated using analysis of variance, with the results presented in Table 9. The model's P-value was less than 0.0001, confirming its statistical significance. The quadratic terms of variables A, B and A2 had P-values less than 0.01, indicating a significant influence on the results. Additionally, B2 had a P-value less than 0.05, suggesting it also had a significant effect on the response variable. Other factors and interaction terms had P-values greater than 0.05, indicating no significant effect on the test indices. The ranking of the factors based on their influence on operational efficiency was as follows: picking rod speed > picking table inclination > picking rod spacing. The interaction effects among these factors are illustrated in Figure 20.

Table 9

Analysis of variance of operation efficiency						
Source	Sum of Squares	df	Mean Squares	F Value	P Value	
Model	5.65	9	0.63	354.73	<0.0001	
A	5.28	1	5.28	2984.76	<0.0001	
B	0.20	1	0.20	111.87	<0.0001	
C	8.000E-006	1	8.000E-006	4.524E-003	0.9483	
AB	1.521E-003	1	1.521E-003	0.86	0.3846	
AC	0.000	1	0.000	0.000	1.000	
BC	4.000E-004	1	4.000E-004	0.23	0.6488	
A2	0.16	1	0.16	87.82	<0.0001	
B2	6.754E-003	1	6.754E-003	3.82	0.0916	
C2	4.711E-003	1	4.711E-003	2.66	0.1466	
Residual	0.012	7	1.768E-003			
Lack of Fit	0.012	3	4.111E-003	363.81	<0.0001	
Pure Error	4.520E-005	4	1.130E-005			
Cor Total	5.66	16				

Note: P<0.01 (extremely significant, **); p < 0.05 (significant, *)

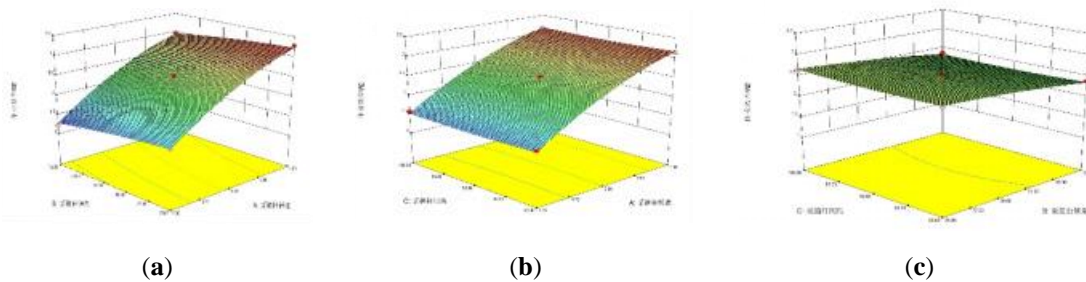


Fig. 20 - The effect of factor interaction on work efficiency

(a) The interaction between the rotation speed of the picking rod and the inclination angle of the picking platform;

(b) The interaction between the rotation speed of the picking rod and the picking rod spacing;

(c) The interaction between the inclination angle of the picking platform and the picking rod spacing.

When the picking rod spacing is a fixed value, the effect of the interaction between the picking rod speed and the inclination angle of the picking table on the operating efficiency is shown in Figure 20(a). When the inclination angle of the picking table is constant, with the increase of the rotation speed of the picking rod, the working efficiency gradually increases, and the change is more obvious. When the rotation speed of the picking rod is constant, the working efficiency increases with the decrease of the inclination angle of the picking table.

When the inclination angle of the picking table is fixed, the influence of the interaction between the picking rod speed and the picking rod spacing on the working efficiency is shown in Figure 20(b). When the picking rod speed is constant, the operating efficiency increases slightly with the decrease of the picking rod spacing, and the change is not obvious. When the picking rod spacing is constant, the working efficiency gradually increases with the increase of the rotation speed of the picking rod.

When the picking rod speed is constant, the influence of the interaction between the inclination angle of the picking table and the picking rod spacing on the working efficiency is shown in Figure 20(c). When the picking rod spacing is constant, the working efficiency gradually increases with the decrease of the inclination angle of the picking table. When the inclination angle of the picking platform is constant, the working efficiency increases slightly with the decrease of the picking rod spacing, and the change is not obvious.

In order to achieve better picking effect, the optimization module is used to optimize the regression model. By analyzing the constraints, the optimal parameter combination is obtained in the optimal combination of multiple parameters: picking rod speed 0.8 m/s, picking table angle 30° , picking rod spacing 90 mm, the tobacco leaf damage rate is 18.35%, the operation efficiency is 2.51 km/h, and the test index effect is the best.

The optimized parameter combination was tested and verified. The rotation speed of the picking rod was set to be 0.8 m/s, the inclination angle of the picking table was 30° , and the picking rod spacing was 90 mm. The average value of multiple tests was obtained. The damage rate of tobacco leaves was 18.32%, and the operating efficiency was 2.483 km/h, which verified the reliability of the model.

CONCLUSIONS

(1) To address the issues of low efficiency and high damage rates in the current tobacco harvesting process, the rotation speed of the picking rod, the dimensions of the picking frame, and the angle of the holding device were theoretically calculated and analyzed. Based on this analysis, a bionic tobacco leaf harvesting device was designed. The proposed device significantly enhances harvesting efficiency while effectively reducing the damage rate associated with mechanical picking.

(2) The tobacco leaf picking process was simulated using ADAMS software, focusing on analyzing the contact forces between rigid and flexible picking rods at different speeds. The optimal combination was identified as a vertical speed of 0.4 m/s using a flexible picking rod.

(3) Preliminary processing of the bionic harvester was completed, followed by field experiments to evaluate its performance. Design-Expert software was used to optimize and analyze the experimental data. The optimal combination of parameters for each experimental factor was determined as follows: the rotation speed of the picking rod was 0.8 m/s, the inclination angle of the picking table was 30° , and the picking rod spacing was 90 mm. Under these conditions, the tobacco leaf damage rate was 18.35%, and the operational efficiency reached 2.51 km/h.

(4) Using the optimized parameter combination, a follow-up harvesting test was conducted. The tobacco leaf breakage rate was 18.32%, with a relative error of only 0.1% compared to the predicted value. The operational efficiency reached 2.483 km/h, with a prediction error of 0.11%. These results confirm the reliability

of the optimized model. This study successfully achieved low-damage mechanized harvesting of tobacco leaves and provides a valuable reference for the development of bionic tobacco leaf harvesters designed to minimize leaf damage.

(5) The current harvesting equipment and experimental program are still in the preliminary stages of development, and the cost of the designed harvesting device remains relatively high. Future research will focus on investigating the effects of tobacco leaf surface properties on harvesting efficiency, with the aim of further optimizing the structural design to improve cost-effectiveness. Additionally, integration of a harvesting quality inspection system is planned to ensure consistent and reliable performance in real-world applications.

ACKNOWLEDGEMENT

This work is supported by Henan Provincial Science and Technology Research Project (222102110457, 242102111173); Henan Tobacco Company Science and Technology Special (2023410000240029, PYKJ202204); Henan Provincial Postdoctoral Funding Project (279456); China National Tobacco Corporation Tobacco Agricultural Machinery Research Project (110202301010); The Key Scientific and Technological Project of Henan Province Department of China (232102211087); Henan Province Science and Technology Research and Development Plan Joint Fund Project (232103810020).

REFERENCES

- [1] Chen, M.Z.; Cheng, X.P.; Jia, X.D.; Zhang, L.P.; Li, Q.Y. (2018). Optimization of operating parameter and structure for corn ear picking device by bionic breaking ear hand. *Transactions of the Chinese Society of Agricultural Engineering (Transactions of the CSAE)*. 34(5): 15-22. DOI.10.11975/j.issn.1002-6819.2018.05.003
- [2] Du, C.; Fang, W.; Han, D. (2024). Design and experimental study of a biomimetic pod-pepper-picking drum based on multi-finger collaboration. *Agriculture*. 14(2): 314. DOI.org/10.3390/agriculture14020314
- [3] Du, Z.; Hu, Y.; Lu, Y. (2021). Design of structural parameters of cutters for tea harvest based on biomimetic methodology. *Applied Bionics and Biomechanics*. 2021(1): 8798299. DOI: 10.1155/2021/8798299
- [4] Gao, J.; Zhang, F.; Zhang, J. (2022). Development and evaluation of a pneumatic finger-like end-effector for cherry tomato harvesting robot in greenhouse. *Computers and Electronics in Agriculture*. 197: 106879. DOI.org/10.1016/j.compag.2022.106879
- [5] Gao, J.; Zhang, F.; Zhang, J. (2024). Picking patterns evaluation for cherry tomato robotic harvesting end-effector design. *Biosystems Engineering*. 239: 1-12. DOI.org/10.1016/j.biosystemseng.2024.01.009
- [6] Gan, W.G.; Liang, W.; Yang, J.A. (2022). Tobacco leaf harvesting device. CN207604219U, 2018-07-13.
- [7] Guo, T.; Zheng, Y.; Bo, W. Research on the Bionic Flexible End-Effector Based on Tomato Harvesting. *Journal of Sensors*. 2022(1): 2564952. DOI.org/10.1155/2022/2564952
- [8] Han, M.; Li, M.; Duan, H. (2024). Rigid-flexible coupling simulation and experiment of plant stem clamping device based on ADAMS. *Transactions of the Chinese Society for Agricultural Machinery*. 55(02):109-117. DOI: 10.6041/j.issn.1000-1298.2024.02.010
- [9] He, Z.; Ma, L.; Wang, Y. (2022). Double-Arm cooperation and implementing for harvesting kiwifruit. *Agriculture*. 12(11): 1763. DOI.org/10.3390/agriculture12111763
- [10] Hou, J.; Xei, F.; Wang, X. (2022). Measurement of contact physical parameters of flexible rice straw and discrete element simulation calibration. *Acta Agriculturae Universitatis Jiangxiensis*. 44(03):747-758. DOI.org/10.13836/j.jjau.2022074
- [11] Hou, Z.; Li, Z.; Fadiji, T. (2021). Soft gras mechanism of human fingers for tomato-picking bionic robots. *Computers and Electronics in Agriculture*. 182: 106010. DOI.org/10.1016/j.compag.2021.106010
- [12] Jin, C.; Qi, Y.; Liu, G. (2022). Mechanism analysis and parameter optimization of soybean combine harvester reel. *Transactions of the Chinese Society for Agricultural Machinery*. 2023, 54(06):104-113. DOI: 10.6041/j.issn.1000-1298.2023.06.011
- [13] Kurbah, F.; Marwein, S.; Marngar, T. Design and development of the pineapple harvesting robotic gripper. *Communication and Control for Robotic Systems*. 437-454. DOI.org/10.1063/5.0099837
- [14] Li, X.; Zhang, W.; Xu, S. (2023). Low-damage corn threshing technology and corn threshing devices: A review of recent developments. *Agriculture*. 13(5): 1006. DOI.org/10.3390/agriculture13051006

- [15] Liu, J.; Ma, W.K. (2012). Design and simulation of tobacco harvesting system based on virtual manufacturing technology. *Key Engineering Materials*. 522: 736-739. DOI.org/10.4028/www.scientific.net/KEM.522.736
- [16] Luo, Y.; Li, J.; Yao, B. (2024). Research progress and development trend of bionic harvesting technology. *Computers and Electronics in Agriculture*. 222: 109013. DOI.org/10.1016/j.compag.2024.109013
- [17] Li, Z.G. (2016). Design and Development of a Self-Propelled Intelligent Bionic Tobacco Leaf Harvesting System [D]. *Henan Agricultural University*, 2016. DOI: 10.27117/d.cnki.ghenu.2016.000055.
- [18] Malekzadeh, M.S.; Queißer, J.F.; Steil, J.J. (2019). Multi-level control architecture for Bionic Handling Assistant robot augmented by learning from demonstration for apple-picking. *Advanced Robotics*. 33(9): 469-485. DOI:10.1080/01691864.2019.1587313
- [19] Nie, Y.C.; Chen, Y. (2022). Measurement of new shoot parameters and mechanical property analysis of plucking fingers for high-quality green tea. *Manuf. Autom.* 2022, 44: 83-86.
- [20] Papusha, S.K.; Kozhura, F.A.; Zhadko, V.V. (2021). Mechanization of tobacco harvesting. The state, problems and prospects of development. AIP Conference Proceedings. *AIP Publishing*. 2503(1): 030045. DOI:10.1063/5.0099837
- [21] Sun, C.; Tan, S.; Sun, S. (2024). Design and test of the key components for a combing-type tobacco harvester. *International Journal of Agricultural and Biological Engineering*. 17(1): 145-153. DOI: 10.25165/ij.ijabe.20241701.8324
- [22] Wang, M.; Yan, B.; Zhang, S. (2022). Development of a novel biomimetic mechanical hand based on physical characteristics of apples. *Agriculture*. 12(11): 1871. DOI.org/10.3390/agriculture12111871
- [23] Wen, B. (2010). Mechanical Design Manual, 5th ed.; *China Machine Press*: Beijing, China.
- [24] Xu, W.T.; Zhao, J.; Cui, X.; Li, Q.Y.; Jin, C.Q. (2018). The bionics design and analysis on device of corn picking with dragging and cutting stem. *Journal of Agricultural Mechanization Research*. 40(07): 81-86. DOI: 10.13427/j.cnki.njyi.2018.07.015.
- [25] Yu, J.; Chu, J.; Li, Y. (2020). Simulation Analysis on Key Mechanisms of the Automatic Tobacco Harvester Based on ADAMS. Recent Advances in Mechanisms, Transmissions and Applications: Proceedings of the Fifth MeTrApp Conference. *Springer Singapore*. 113-122. DOI.org/10.1007/978-981-15-0142-5_12
- [26] Zhang, H.; Chen, B.; Hu, J. (2024). Comparative experiment of fresh corn ear picking devices based on collision characteristics. *Journal of Henan Agricultural University*. 58(01):87-95. DOI: 10.16445/j.cnki.1000-2340.20231127.002.
- [27] Zhang, H.; Chen, B.; Li, Z. (2022). Design and simulation analysis of a reverse flexible harvesting device for fresh corn. *Agriculture*. 12(11):1953. DOI.org/10.3390/agriculture12111953
- [28] Zhang, L.P.; Li, Q.Y. (2015). Speed of bionic breaking corn ear hand and experiment on power consumption. *Transactions of the Chinese Society of Agricultural Engineering (Transactions of the CSAE)*. 31(19): 9-14. DOI: 10.11975/j.issn.1002-6819.2015.19.002
- [29] Zhang, T.; Liu, F.; Zhao, M. (2018). Determination of corn stalk contact parameters and calibration of Discrete Element Method simulation. *Journal of China Agricultural University*. 23(04): 120-127.
- [30] Zhang, L. (2015). Theoretical Analysis and Simulation Research on Novel Bionic Corn-ear Snapping Mechanism. *Jilin University*.
- [31] Zhu, H.J.; Wang, Z.M.; Bai, W.; Hu, G. (2014). Design of floating picking platform for tobacco leaf harvester. *Journal of Mechanical Research and Application*. 27(04):140-141. DOI: 10.16576/j.cnki.1007-4414.2014.04.074.

DEVELOPMENT OF A MULTI-DIMENSIONAL CLEANING SIEVE TO OPTIMIZE THRESHED OUTPUTS DISTRIBUTION AND EXPERIMENTS IN COMBINE HARVESTER

联合收获机多维均布清选装置开发与试验

Xiaoyu CHAI¹, Pengtao ZHANG¹, Xinting LIU², Lizhang XU¹, Liyuan CHEN^{1*}, Qiang LI³ and Longhai WANG⁴

¹ School of Agricultural Engineering, Jiangsu University, Zhenjiang, 212013, Jiangsu, China;

² Weichai Lovol Intelligent Agricultural Technology Co. Ltd, Weifang, 261000, Shandong, China;

³ Tongzhou District Agricultural Mechanization Technology Extension Station, Nantong, 226300, Jiangsu, China;

⁴ Institute of Process Equipment, College of Energy Engineering, Zhejiang University, Hangzhou, 310027, Zhejiang, China.

*Corresponding authors. Email: xfpaxy521123@163.com

DOI: <https://doi.org/10.35633/inmateh-75-85>

Keywords: multidimensional cleaning method; rapeseed; CFD-DEM; combined harvester

ABSTRACT

Searching for and identifying methods to reduce grain cleaning loss, grain impurity, and improve cleaning efficiency is crucial for processing threshed rapeseed outputs in uneven conditions. Leveling a single-degree-of-freedom cleaning sieve becomes particularly challenging under terrain undulations and limited cleaning space. Based on spiral theory and mechanical design principles, this study explores a multi-degree-of-freedom cleaning sieve capable of vertical movement along the horizontal plane and rotation around its center. This design allows the sieve to adjust its relative angle, enabling a more uniform distribution of threshed outputs. A CFD-DEM coupling method was used to simulate the movement of these outputs. The cleaning sieve inclined forward and to the right served as the experimental group, while a horizontal cleaning sieve functioned as the control group. Compared to the control, the experimental group showed a 14.6% reduction in grain loss and a 2.3% decrease in impurities. Furthermore, the centroid motion of the rapeseed was enhanced prior to sieving, facilitating more effective separation, while the movement speed of impurities outside the cleaning shoe increased, aiding impurity removal.

摘要

针对丘陵地区地形起伏，小型收获机清选空间有限的难题，多自由度的清选装置开发是相当具有挑战性的。文章基于螺旋理论和机械设计方法，探索了一种可以在水平方向上垂直移动并绕其中心旋转的多自由度清选筛。该清选筛通过调整筛面角度实现脱出物均布，实现清选性能和清选效率的提升。基于 CFD-DEM 耦合方法模拟脱出物运动，将清选筛前倾和向右倾斜状态设置为实验组，清选筛水平状态设置为对照组。结果表明，对比对照组，试验组籽粒损失和含杂分别减少了 14.6% 和 2.3%。同时，在筛分前，油菜籽、杂质的质心运动速度明显增强，这有利于去除含杂和提高筛分效率。该研究方法对于收获装备转型升级具有重要的实际意义。

INTRODUCTION

Rapeseed is the largest source of edible vegetable oil in China. Accelerating the development of rapeseed mechanization, supporting the upgrading of the oil industry, and reducing China's heavy dependence on imported raw materials for vegetable oil are among the country's most pressing priorities. Hilly and mountainous areas account for 1/3 of the country's crop cultivation area. Between the hills and low mountains there are many river valley basins. The four seasons are distinct, the land is fertile, suitable for rape planting. The primary crops of wheat and corn differ substantially in their agronomic and physical attributes compared to rapeseed (Zhao et al, 2022; Zhang et al, 2024; Li et al, 2024), making it impractical to directly apply their harvesting design methods and equipment to rapeseed. Hilly and mountainous regions typically experience abundant rainfall and sufficient sunshine, leading to robust rapeseed growth. In these areas, rapeseed plants usually range from 220 mm to 250 mm in height, and the grass-to-grain ratio is significantly higher than in the plains—often reaching as much as 4–5:1. After threshing and separation, the grain volume in the rapeseed material fed into the cleaning shoe accounts for only about 8%, while the volume of impurities is considerably higher. These impurities are diverse in composition, and the small, spherical rapeseed grains are mixed with various irregular residues.

¹ Xiaoyu Chai (Lecturer), Pengtao Zhang (M. Eng. student), Xinting Liu (Engineer), Lizhang Xu (Professor), Liyuan Chen (Doctor), Qiang Li (Engineer), Longhai Wang (Doctor).

This complex mixture makes stratification and separation difficult, resulting in a portion of the grains being discharged along with the impurities, thus increasing grain loss. Additionally, some impurities may fall into the grain auger, further raising the impurity content of the harvested product.

Unlike traditional field harvesting equipment, threshing and cleaning systems must account for variations in terrain (Vlăduț et al., 2023; Zhang et al., 2024). In hilly and mountainous regions, rapeseed suitable for mechanized harvesting is often cultivated on sloped lands, with inclines ranging from 6° to 15° in hilly areas and 15° to 25° on terraced slopes. For combine harvester manufacturers, incorporating components, or even designing entire machines, with the capability to adapt to uneven surface topography is essential for improving harvesting adaptability in these challenging environments. The IDEAL 10T combine harvesters (Fendt, 2025) are equipped with multiple guide strips and multi-layer vibrating sieves, enabling uniform material distribution during multi-crop harvesting. Technologies such as header contouring devices and 3D multi-layer vibrating sieves have been implemented (MF, 2025; Claas, 2025) to automatically adjust to varying slope angles, maintaining a level threshing and cleaning system. Experts and researchers have been actively engaged in developing small-scale harvesting machinery tailored for hilly and mountainous regions. To address the accumulation of threshed material on the sieve surface, caused by the topography of hilly and mountainous regions, technologies for threshed material dispersion and the analysis of particle movement trajectories have become particularly critical. A three-stage vibrating sieve equipped with guide strips and a cross-flow fan (Case, 2025) was employed to achieve more uniform airflow across the entire sieve, thereby improving the even distribution of materials on the sieve surface. The CFD-DEM coupling method has been increasingly applied to simulate two-phase flow performance in complex agricultural systems (Wang et al., 2024; Shen et al., 2024; Tanneru et al., 2024). Korn et al. utilized this method to simulate the separation process of threshed materials within the cleaning unit of a combine harvester. The CFD-DEM coupling method has been employed to simulate the movement of jojoba and flax threshing materials within an airflow-sieve cleaning device, enabling the prediction of grain separation performance under specific design conditions (El-Emam, 2021). Similarly, CFD-DEM has been used to study the movement of corn and rapeseed threshed outputs during the sieving process (Wang et al., 2021), helping determine optimal parameters such as sieve hole sidewall angle, airflow velocity, and airflow direction angle. These studies demonstrate that CFD-DEM simulations are highly effective for analyzing particle motion, offering clear insights into grain dynamics. As a result, the advantages of the CFD-DEM method will be applied in this study to enhance the analysis of threshed material behavior and cleaning performance.

Based on the above, current gas-solid coupling simulations in the cleaning process typically focus only on the primary components present on the cleaning sieve. However, in real-world conditions, particularly in hilly regions, rapeseed accumulation is often severe, and traditional simulations rarely account for the accumulation state of separated materials or the complex interactions between them. Furthermore, many simulations consider only a single particle type, overlooking the uneven distribution of different particle types across various regions. This simplification results in a significant deviation from the actual separation process. Therefore, it is essential to study the movement trajectories of separated particles under conditions of inclined accumulation and to further explore the underlying sieving mechanisms in order to enhance separation performance and overall cleaning efficiency.

MATERIALS AND METHODS

Multidimensional motion theory of the cleaning device

When a combine harvester operates in hilly and mountainous terrain, changes in surface topography can cause the entire cleaning device to tilt both in the forward-backward direction and the left-right direction. Moreover, the centrifugal force acting on threshed outputs in the longitudinal axial flow threshing and separation device typically causes the threshed outputs to distribute unevenly, with higher concentrations on both sides and lower concentrations in the middle (Liu et al., 2022; Li et al., 2022). This uneven distribution leads to threshed output accumulation on both sides of the sieve surface, negatively affecting the sieving efficiency. Therefore, it is necessary to develop a multidimensional cleaning device that can adapt to varying terrain conditions and dynamically regulate the distribution of threshed outputs. To minimize the impact of external factors such as terrain on the cleaning device, it is essential to eliminate the influence of forward-backward and left-right tilting on the cleaning system. Let the forward direction of the combine harvester be defined as the positive x-axis. In the following descriptions, "forward," "backward," "left," "right," "up," and "down" correspond to the positive x-axis, negative x-axis, positive y-axis, negative y-axis, positive z-axis, and negative z-axis, respectively.

The designed multidimensional cleaning device compensates for the effects of terrain on the cleaning shoe in both the forward-backward and left-right directions. This device features three degrees of freedom, including rotation around the x-axis and y-axis to adjust the uneven distribution of threshed outputs in the left-right direction.

Additionally, movement along the z-axis ensures that the relative position of the sieve surface remains constant within the adjustment range when the terrain has significant vertical undulations. The primary technical specifications are detailed in Table 1.

A combination of the SPS/RPS-UP parallel stable platform and the 2PSS-U parallel stable platform was selected to achieve multidimensional adjustment of the sieve surface within the confined space. The principle diagram of the multidimensional adjustment mechanism for the sieve surface is shown in Fig. 1.

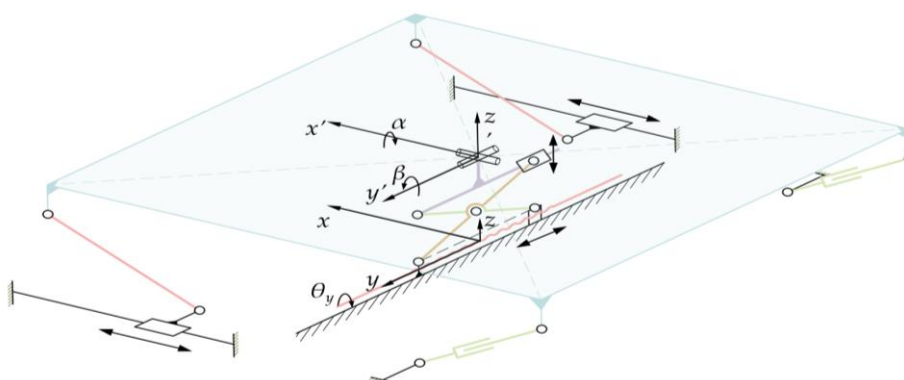


Fig.1 - Prototype of the multi-dimensional cleaning mechanism

The 2PSS-U parallel stable platform serves as the core of the design, with its U-branches modified to PU-branches. To accommodate the longitudinal movement, range of the mechanism, a retractable linear drive device is incorporated into the middle PU branch of the sieve surface. Additionally, two support points are added at the vertices of the platform to maintain dynamic stability during the adjustment process.

Table 1

Performance specifications of the multidimensional cleaning device

No.	Performance	Value	Remarks
1	Adjust the limit position around the x-axis	$+8^{\circ} \pm 0.5^{\circ}$, $-8^{\circ} \pm 0.5^{\circ}$	Angle with the horizontal direction
2	Adjust the limit position around the y-axis	$+8^{\circ} \pm 0.5^{\circ}$, $-8^{\circ} \pm 0.5^{\circ}$	Angle with respect to the horizontal direction
3	Range of longitudinal movement for the mechanism	≤ 65 mm	The limit position of the movement space must ensure a certain distance between the vibration plate and the fish scale sieve
4	Load capacity of the mechanism	≥ 2 kg	Mass flow rate of the threshed outputs stream
5	Rotation angle around the x-axis	$\leq 5^{\circ}$	Angle with the horizontal direction
6	Rotation angle around the y-axis	$\leq 5^{\circ}$	Angle with the horizontal direction

Structural design of multi-dimensional cleaning device

The multi-dimensional cleaning device, designed to adapt to terrain variations and the distribution state of separated materials, features a perforated sieve at its output end, positioned between the fish-scale screen and the vibrating plate. The structural principle of the adjustable cleaning device is illustrated in Fig. 1, while the designed multi-dimensional cleaning device is shown in Fig. 2. The system consists of a frame, an upper platform, a screw, a screw nut, connecting rods, and sliding blocks mounted on the upper platform. To enable folding motion, connecting rods with spherical joints at both ends are installed on either side of the upper sieve surface. At the center of the sieve, an "X"-shaped retractable cross-link mechanism serves as a linear actuator. The rotation of the screw, which is arranged along the y-axis, causes the screw nut to move along the y-axis. This screw also results in changes in the angle between the cross-links, which drives the upper platform to move up and down along the z-axis. At the two rear vertices of the platform, spherical joints and damping slide rods are used for connection. The damping slide rods are moving pairs with damping characteristics, and their other ends are connected to the frame via spherical joints.

These two damping slide rods act as driven components and enhance the stability of the mechanism's movement without affecting its degrees of freedom. Forward drive slider is fixed on the power guide rail on the side wall of the cleaning shoe, with a certain gap introduced between it and the spherical joint to reduce the probability of interference with the side wall during platform movement.

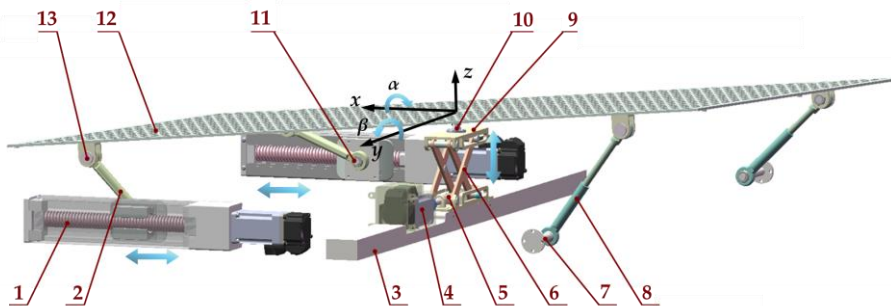


Fig. 2 - Schematic diagram of multi-dimensional cleaning device structure.

1. Screw sliding table; 2. Double spherical hinge connecting rod; 3. Support beam; 4. Lifting platform drive motor; 5. Drive screw; 6. Lifting platform connecting rod; 7. Damping rod support; 8. Damping rod; 9. Upper platform of the lifting platform; 10. Hook hinge; 11. Lower spherical hinge; 12. Movable screen surface; 13. Upper spherical hinge

The fixed end of the lifting platform is mounted to the bottom of the support beam, while its movable end is connected to the bottom of the hook joint. The center of the perforated sieve's rectangular envelope is attached to the top of the hook joint. At the four corners of the perforated sieve, four sets of positioning holes are symmetrically distributed, using the envelope's rectangular center as the origin. Four sets of positioning pins are employed to accurately position the four-fork frame bearing seats into the designated fixed holes.

The multi-degree-of-freedom sieving device is integrated into the cleaning shoe, as illustrated in Fig. 3. By combining the configurations shown in Fig. 1 and Fig. 2, a ball joint is mounted into the fork frame bearing seat of the multi-degree-of-freedom screening structure. A slider is affixed to the screw slide platform, and the central region of the slider incorporates a cylindrical structure designed to connect with the lower spherical joint. This design enables the lower spherical joint to move synchronously with the active end of the screw slide platform. The lower end of the damping rod is connected to a spherical joint on the damping rod support, while the upper end is linked to the fork frame bearing seat positioned behind the moving sieve. This configuration enables stable three-degree-of-freedom adjustment, even within the constraints of limited installation space.

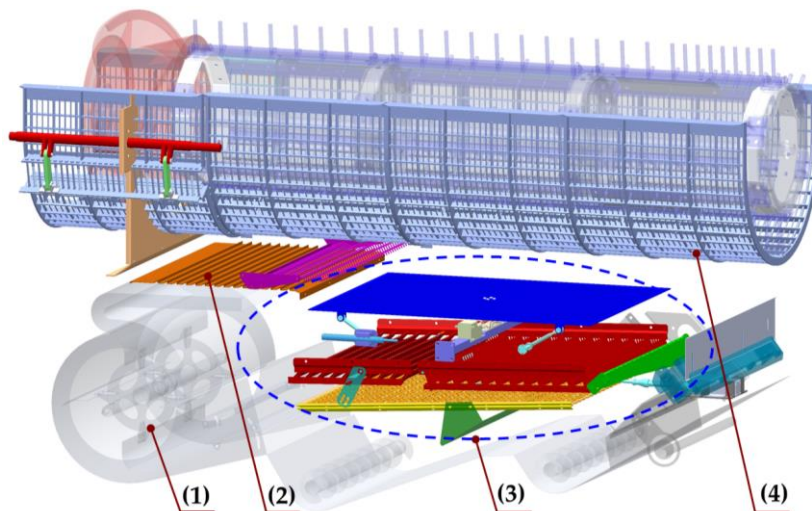


Fig. 3 -The multi-dimensional cleaning sieve in the cleaning shoe

(1) Longitudinal axial threshing cylinder; (2) Multi-dimensional perforated sieve; (3) Centrifugal fan; (4) Vibrating sieve.

Coupled simulation of threshed outputs in gas-solid two-phase flow

CFD and DEM coupled simulation model

To accurately reflect the cleaning process, it is necessary to analyze the combined effects of gas flow and vibrating sieves. In a gas-solid two-phase flow system, gas typically acts as the continuous phase, while the solid phase is dispersed as particles or clumps within the gas.

This study uses the computational fluid dynamics software Fluent (V15.0, CFD Inc., USA) to simulate the gas phase flow field, and discrete element method software EDEM (V2.7, DEM Solutions Ltd., UK) to analyze the motion and force states of solid phase particles. Through a coupling interface, CFD and DEM achieve real-time data exchange, including the transfer of mass, momentum, and energy, thus completing a bidirectional coupled numerical simulation of gas-solid two-phase flow. The advantage of this coupling technology is that it integrates the geometric characteristics of solid particles (such as shape and size) and physical properties (such as material properties and friction coefficients), providing a more accurate capture of the interactions and effects between the gas and solid phases (Tanneru et al, 2024).

The continuity equation and momentum equation for the gas phase can be represented as follows (Xu et al, 2020):

$$\frac{\partial \varepsilon \rho}{\partial t} + \nabla \cdot \rho \varepsilon u = 0 \quad (1)$$

$$\frac{\partial \varepsilon \rho}{\partial t} + \nabla \cdot \rho \varepsilon u \mu = -\nabla \rho + \nabla \cdot (\mu \varepsilon \nabla u) + \rho \varepsilon g - S \quad (2)$$

where:

ε represents the volume fraction term; ρ is the gas density, $\text{kg}\cdot\text{m}^{-3}$; u is the gas velocity, $\text{m}\cdot\text{s}^{-1}$; μ is the dynamic viscosity coefficient, $\text{Pa}\cdot\text{s}$, and S is the momentum sink, $\text{kg}\cdot\text{m}^2\cdot\text{s}^{-1}$.

The contact model forms the core basis of the Discrete Element Method (DEM). It essentially simulates the elastic-plastic mechanical behavior of particles under quasistatic conditions when in contact. Although the contact relationships between particles are nonlinear, approximate superposition principles are often used for analysis. In EDEM software, the default contact model is the Hertz-Mindlin model, also known as the "elastic-damping-friction contact mechanics model." This model takes into account the elastic deformation, damping effects, and frictional forces between particles during contact. Hertz-Mindlin model was employed to investigate the motion behavior of rapeseed particles in a multi-airflow cleaning device, the equations can be represented as follows (Ma et al, 2022).

$$F_{cni} = \frac{4}{3} E^* (R^*)^{1/2} \alpha^{3/2} \quad (3)$$

$$F_{dni} = -2 \sqrt{\frac{5}{6}} \beta \sqrt{S_n m^*} v_n^{rel} \quad (4)$$

$$F_{cti} = -S_t \delta \quad (5)$$

$$F_{dti} = -2 \sqrt{\frac{5}{6}} \beta \sqrt{S_t m^*} v_t^{rel} \quad (6)$$

where:

F_{cni} represents the normal contact force between particles, N; E^* is the equivalent elastic modulus, Pa; R^* is the equivalent particle radius, m; α is the normal overlap between the particles. F_{dni} represents the normal damping force between particles, N; β is the coefficient; S_n is the normal stiffness, $\text{N}\cdot\text{m}^{-1}$; m^* is the equivalent mass, kg; v_n^{rel} is the normal component of relative velocity, $\text{m}\cdot\text{s}^{-1}$. F_{cti} is the tangential contact force between particles, N; S_t is the tangential stiffness between the particles, $\text{N}\cdot\text{m}^{-1}$; δ is the tangential overlap between the particles. F_{dti} represents the tangential damping force between particles, N; v_t^{rel} is the tangential component of relative velocity, $\text{m}\cdot\text{s}^{-1}$.

Fluent - EDEM Gas-Solid Coupling Simulation

Establishment of flow channel model and boundary mesh division. After preliminary research and simulation of the airflow distribution on the sieve surface, it was found that a leaning forward and leaning right condition of the multidimensional cleaning sieve is most advantageous for the selection process in a combine harvester. Therefore, this configuration was selected as the basis for particle analysis and designated as the experimental group, while the condition with a horizontal sieve surface served as the control group. The Fluent-EDEM digital simulation method was employed to compare the movement of rapeseed threshed outputs under the influence of terrain and the movement of the threshing drum. The coupled flow path model of the experimental group is illustrated in Fig. 4.

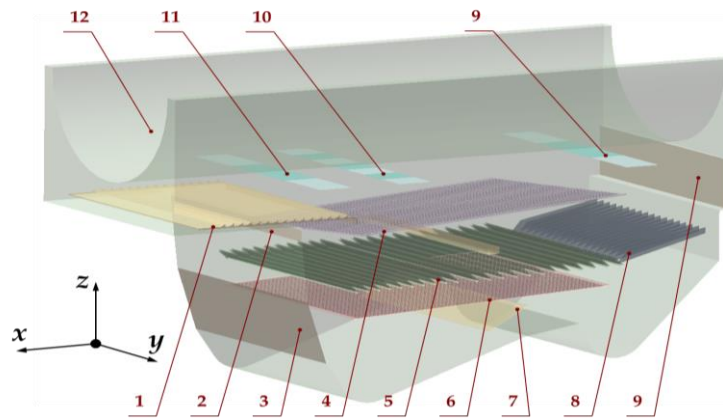


Fig. 4 - Coupled flow channel model of the cleaning shoe

- 1. Shaking plate; 2. Upper inlet; 3. Lower inlet; 4. Adjustable perforated sieve; 5. Fish scale sieve; 6. Woven sieve; 7. Guiding plate;
- 8. Tail sieve; 9. Outlet; 10. Threshing drum; 11. Concave sieve; 12. Particle factory ①-③;
- 13. Particle factory ④-⑩; 14. Particle Factory ⑪-⑬.

The flow path model was designed with an arcuate structure for the perforated plate sieve to facilitate observation of grain movement. The model includes upper and lower air inlets representing the fan's air outlets, with the airflow speed set to the average speed of the section. The meshing software was used to create a tetrahedral mesh for the cleaning shoe flow path model, resulting in a total of 6,021,268 mesh elements. The mesh file was saved as an MSH file and imported into both Fluent and EDEM software for simulation.

Establishment of EDEM environment and particle model. An experiment was conducted to observe the distribution pattern of the threshed outputs under the longitudinal axial threshing drum. This involved uniformly arranging 70 collection boxes, each with dimensions of 110×190×110 mm³, beneath the Longitudinal axial threshing drum, as illustrated in Fig. 5. In the EDEM software simulation, it is necessary to model the simulation objects. Therefore, the components of the output materials need to be categorized. The threshed output samples, collected from beneath the longitudinal axial-flow threshing device (as shown in Fig. 5), were manually sieved to identify four main types of threshed output components, as illustrated in Fig. 6.

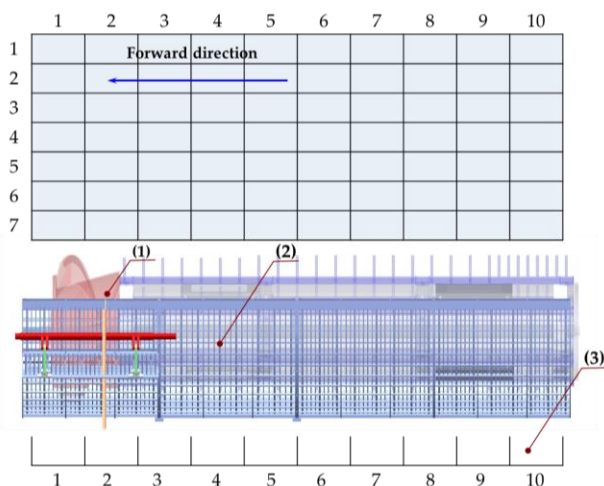


Fig. 5 - Longitudinal axial threshing drum and receiving box placement position

- (1) Longitudinal axial threshing drum; (2) Concave sieve;
- (3) Receiving box.

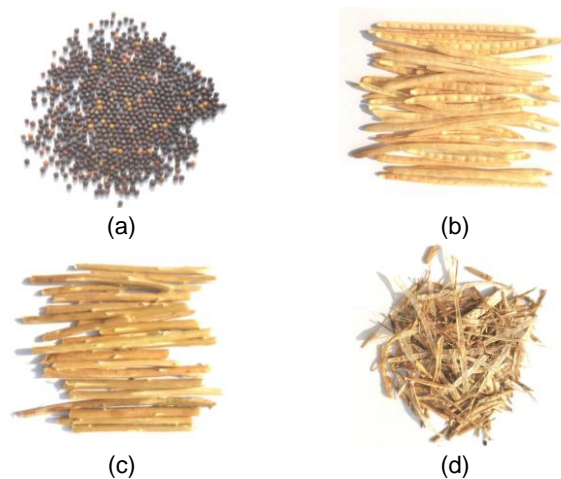


Fig. 6 - Main components of the rapeseed threshed outputs

- (a) Rapeseeds; (b) Pod shell; (c) Stem; (d) Light impurities.

In a gas-solid two-phase flow system, the dynamic behavior of different components under the influence of airflow within the cleaning shoe creates a complex multicomponent coupled simulation scenario. To conduct simulations in EDEM, these components must be modeled as particles. Due to limitations in EDEM's modeling capabilities, only spherical particles can be created. Therefore, a particle packing method is used to simulate the shape of the actual components by combining multiple spherical particles. The models of the four component types are shown in Fig. 7.

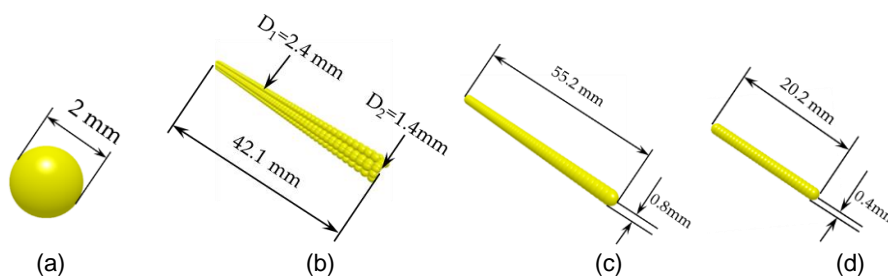


Fig. 7 - Particle filling model of the rapeseed threshed outputs
 (a) Rapeseed; (b) Pod shell; (c) Stem; (d) Light impurities

The shape of the rapeseeds is approximated as spherical, so a single spherical particle can satisfy the requirements. The pod shell can be approximated as a semi-cylindrical hollow structure, while the stems and light impurities can be approximated as cylindrical.

In EDEM software, it is necessary to input the mechanical properties of the threshed output particles, as well as their contact coefficients with other objects. According to relevant references, the contact coefficients and mechanical property parameters for the threshed outputs are set as shown in Tables 2 and 3.

Particle Factory Settings. In EDEM software simulations, it is essential to define the distribution state of the threshed outputs within the cleaning shoe. To achieve this, the mass of each threshed output component was measured. The mass of threshed outputs collected in each receiving box was recorded (Fig. 5), and the overall three-dimensional distribution trend of the threshed outputs in the cleaning shoe was analyzed, as shown in Fig. 8(a). The proportion of each component was determined, with the results depicted in Fig. 8(b).

Table 2

Contact coefficients between different materials

Parameter	Restitution Coefficient	Static Friction Coefficient	Rolling Friction Coefficient	Parameter	Restitution Coefficient	Static Friction Coefficient	Rolling Friction Coefficient
Rapeseed - Rapeseed	0.19	0.81	0.05	Pod shell- Light impurities	0.08	0.63	0.02
Rapeseed - Pod shell	0.15	0.76	0.03	Pod shell- Cleaning sieve	0.10	0.61	0.01
Rapeseed - Stem	0.20	0.80	0.03	Stem- Stem	0.12	0.72	0.03
Rapeseed- Light impurities	0.15	0.76	0.03	Stem- Light impurities	0.12	0.75	0.03
Rapeseed - Cleaning sieve	0.52	0.45	0.01	Stem- Cleaning sieve	0.10	0.66	0.02
Pod shell - Pod shell	0.08	0.63	0.02	Light impurities - Light impurities	0.50	0.50	0.01
Pod shell - Stem	0.12	0.75	0.03	Light impurities- Cleaning sieve	0.10	0.61	0.01

Table 3

Material mechanical properties parameters

Parameter	Poisson's ratio	Density / kg m ⁻³	Elastic Modulus / MPa
Rapeseed	0.28	960	15
Pod shell	0.35	250	8
Stem	0.4	205	20
Light impurities	0.40	120	10
Cleaning sieve	0.33	7800	7100

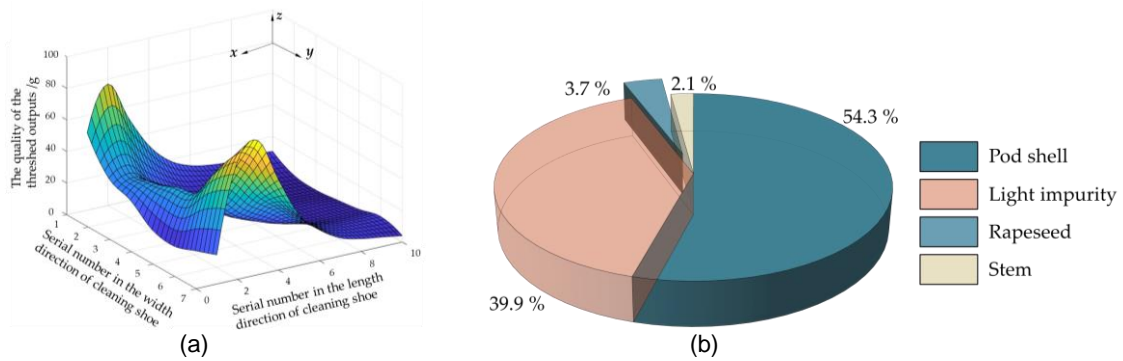


Fig. 8 - Distribution of rapeseed threshed outputs under the threshing drum
 (a) Distribution pattern of rapeseed threshing residue quality; (b) Proportion of threshed output components.

The cleaning efficiency and performance are directly related to the distribution of threshed outputs falling from the threshing device. To more accurately simulate real conditions, the generation and distribution of particles in the EDEM software are aligned with the actual distribution characteristics of the threshed outputs under the longitudinal axial flow threshing drum.

Based on the distribution patterns of the rape threshed outputs shown in Fig. 5 and Fig. 8 (b), three particle factory areas, slightly narrower than the width of the cleaning sieve and positioned 100 mm above the shaking plate, were established. These areas include a total of 13 particle factories, which are polygonal virtual regions in EDEM software used for particle generation. The total particle mass assigned to each particle factory corresponds to the mass distribution of threshed outputs shown in Fig. 8(a). The spatial distribution of the particle factory areas on the xy-plane is illustrated in Fig. 9.

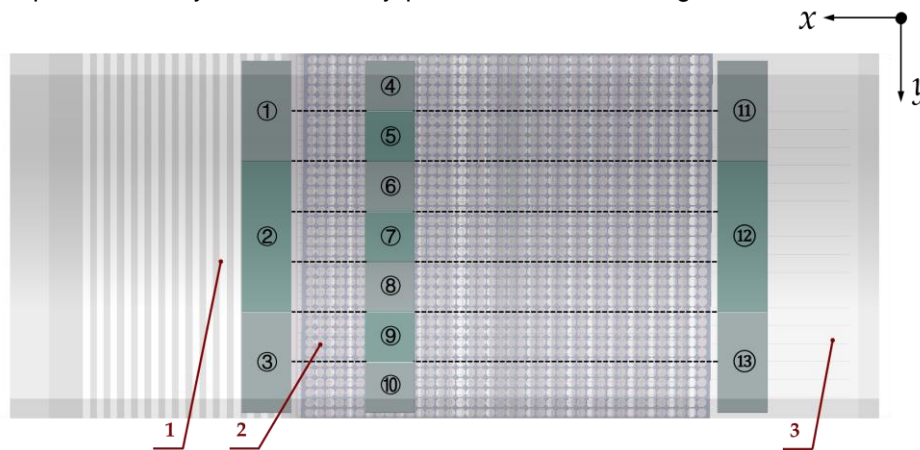


Fig. 9 - The particle factory distribution
 1. Vibrating plate; 2. Perforated sieve; 3. Tail sieve

The first particle factory area is located above the tail of the vibrating plate, its length in the x direction is 110 mm, and the length in the y direction is 770 mm, and the ratio of 2:3:2 in the y direction is divided into three particle factories ①~③, which are mainly used to simulate the effect of the shaking plate in front of the threshing drum. The second particle factory area is positioned above the middle part of the perforated sieve, with a length of 110 mm in the x direction and 770 mm in the y direction. It is divided into seven particle factories (④~⑩) along the y direction. This area is situated in the region where the threshed outputs from the vertical axis flow threshing drum falls most densely and is primarily used to simulate the effect of the perforated sieve on the threshed outputs. The third particle factory area is located above the front part of the tail sieve, its length in the x direction is 110 mm, the length in the y direction is 770 mm, and the ratio of 2:3:2 in the y direction is divided into 3 particle factories ⑪~⑬, which is mainly used to simulate the effect of the tail sieve on the threshed outputs.

Based on experimental measurements, the ratio of input to threshed outputs in the cleaning shoe of the combine harvester is 9:4. Considering the proportions of each component in the threshed outputs shown in Fig.8(b), along with the density and moisture content of each component, the required number of particles for each particle factory can be calculated.

With the input rate of the combine harvester set at 3 kg·s⁻¹, the differentiated settings of the particle factories allow for the creation of a distribution pattern in the cleaning shoe that is “more on the sides and less in the middle” along the y direction.

Coupling Simulation Settings. Import the MSH file format into Fluent to set up the numerical simulation parameters for the airflow phase. The standard κ - ϵ turbulence model was chosen to describe turbulent flow, and a pressure-based transient solver was employed. The environmental pressure was set to standard atmospheric pressure, and the direction of gravity acceleration was specified as the negative z-axis with a magnitude of 9.81 m·s⁻². Subsequently, the same MSH file was imported into EDEM for solid phase numerical simulation, with gravity acceleration also set as the negative z-axis, maintaining consistency. The boundary condition for the inlet was set as a velocity inlet, the airflow speed at inlet 1 was set to 17 m·s⁻¹, and at inlet 2, it was set to 14 m·s⁻¹. The model's outlet was set as a pressure outlet with a relative pressure of 0 Pa. The vibrating sieve includes a shaking plate, a fish-scale sieve, a tail sieve, and a woven screen. The opening of the fish-scale sieve was set to 45°, with an x direction displacement of 6 mm, and a z direction displacement of 17 mm. The vibration frequency was set to 6.5 Hz.

User-defined function (UDF) was used to establish coupling between Fluent and EDEM, utilizing the Eulerian-Eulerian model for numerical simulation of the gas-solid two-phase flow. During the coupling process, the time steps were synchronized, Fluent's time step was set to 5×10⁻⁵ s, and Rayleigh time step was set to 5×10⁻⁷ s. The total simulation duration was set to 1 s, with Fluent computational time being 100 times that of EDEM.

RESULTS AND DISCUSSION

Qualitative analysis of threshing outputs motion trends

The post-processing module in EDEM was used to export the movement trends of the particles. Distributions of the particles in the cleaning shoe at six representative time instances, 0.4 s, 0.6 s, 0.8 s, and 1 s, were selected to clearly observe the movement process of the particles, as shown in Fig. 10. Different colors were used to distinguish the components, black particles represent rapeseeds, green particles represent pod shells, yellow particles represent stems, and cyan particles represent light impurities.

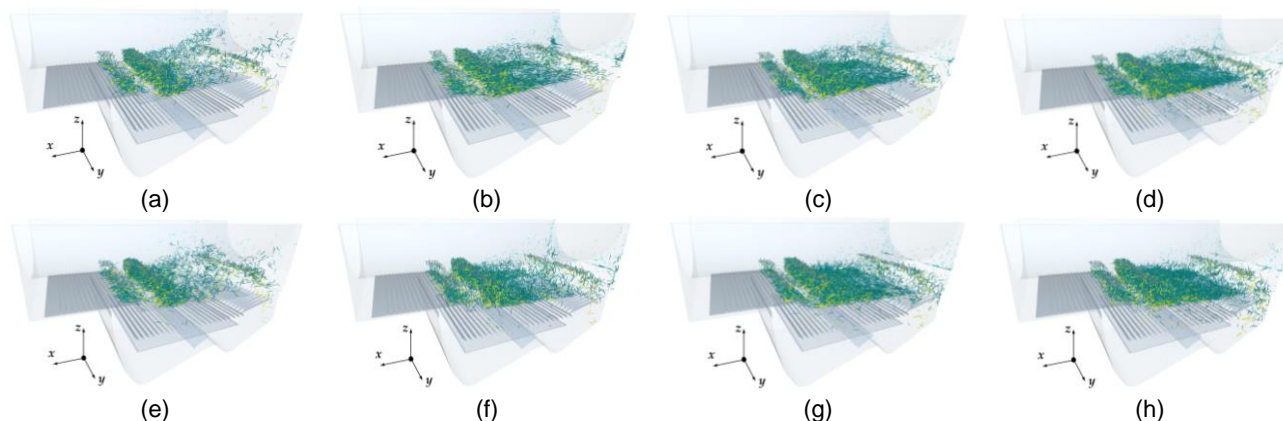


Fig. 10 - Distributions of the particles in the cleaning shoe

Figures (a), (b), (c) and (d) represent 0.4 s, 0.6 s, 0.8 s, and 1 s, respectively. The state of the cleaning sieve surface relative to the cleaning shoe is leaning forward and leaning right. Figures (e), (f), (g) and (h) represent 0.4 s, 0.6 s, 0.8 s, and 1 s, respectively. The state of the cleaning sieve surface relative to the cleaning shoe is horizontal.

In Fig. 10, these observations can be made, during the stage when the rapeseed threshed outputs fall from the particle factories to the perforated sieve (0–0.4 s), the particles of various components are influenced by the airflow from the fan's air duct, creating a waterfall-like descent. Rapeseed in both conditions begins to penetrate through the sieve, while threshed output components, excluding the rapeseeds, are driven by the airflow away from the sieve surface and towards the outside of the cleaning shoe. By this time, the threshed outputs passing through the perforated sieve is less than in the cleaning shoe horizontal condition.

In the period of 0.6–0.8 seconds, rapeseeds undergo further layering and sieving, with some rapeseeds having fallen onto the seed and impurities augers. In both conditions, along with rapeseeds falling through the perforated sieve, there are also impurities including pod shell, stem, light impurities.

By 0.8 seconds, the projectile motion trend of pod shells and light impurities gradually disappears. Pod shells that were suspended at relatively higher positions move to lower positions. At 1.0 second, the impurities particles above the perforated sieve move rapidly towards the outside of cleaning shoe in a flowing manner. The impurities exhibit a continuous outward movement trend. Additionally, there are more rapeseeds at the grain auger baffle in the cleaning sieve leaning forward and leaning right condition compared to the cleaning sieve horizontal condition.

Calculation of the rapeseed impurity rate and cleaning grain loss rate

After completing the numerical simulation, two key areas for counting the number of threshed output particles were defined in EDEM software, as shown in Fig. 11.

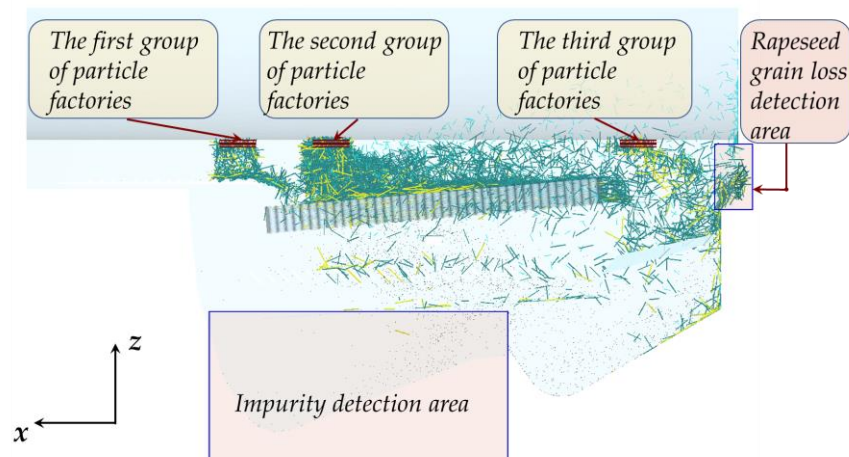


Fig. 11 - Schematic diagram of grain loss detection area and impurities detection area in the cleaning shoe

The first region is set near the grain auger and is used to count the number of rapeseeds, pod shells, stems and light impurities particles that pass through the cleaning sieve. This count is then used to calculate the impurity rate of the grains, which can be described by equation (7). The second statistical region is located at the outlet of the flow model and is intended to count the number of rapeseeds that are expelled from the cleaning shoe, thereby determining the cleaning loss rate. This rate can be calculated using equation (8).

$$P_1 = \frac{Q_1 M_1 + Q_2 M_2 + Q_3 M_3}{Q_1 M_1 + Q_2 M_2 + Q_3 M_3 + Q_4 M_4} \cdot 100\% \quad (7)$$

where:

P_1 represents the impurity rate of the grains, %; Q_1 represents the number of pod shells that pass through the perforated sieve and vibrating sieve, pieces; Q_2 represents the number of stems that pass through the perforated sieve and vibrating sieve, pieces; Q_3 represents the number of light impurities that pass through the perforated sieve and vibrating sieve, pieces; Q_4 represents the number of rapeseeds that pass through the perforated sieve and vibrating sieve, pieces; M_1 represents the mass of a single pod shell, g; M_2 represents the mass of a single stem, g; M_3 represents the mass of a single piece of light impurities, g; M_4 represents the mass of a single rapeseed, g.

$$P_2 = \frac{Q_5}{Q_4 + Q_5} \cdot 100\% \quad (8)$$

where:

P_2 represents the cleaning loss rate, %; Q_5 represents the number of grains that are expelled from the cleaning shoe, pieces.

Based on equations (7) and (8), the grain impurity rate and cleaning loss rate for both cleaning conditions can be calculated. The combined evaluation metric, defined as cleaning performance, is determined by weighted summation. Given the practical requirements, the cleaning loss rate is generally considered slightly more important than the grain impurity rate. Therefore, the weight for the cleaning loss rate is set at 0.6, and the weight for the grain impurity rate is set at 0.4. A lower combined evaluation value indicates better cleaning performance. The calculation results are shown in Fig. 12.

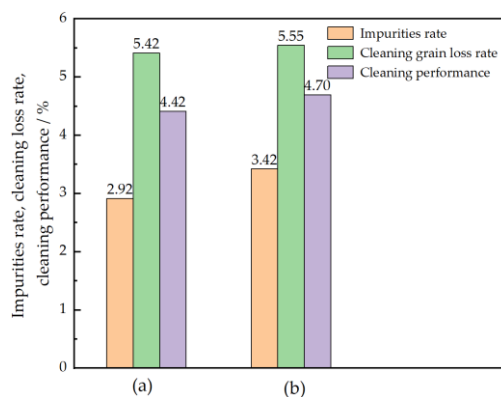


Fig. 12 - Comparison of cleaning performance

(a) The state of the cleaning sieve surface relative to the cleaning shoe is leaning forward and leaning right;
 (b) The state of the cleaning sieve surface relative to the cleaning shoe is horizontal

The grain impurity rate and cleaning loss rate for the control group are 3.42% and 5.5%, respectively. In contrast, in the experiment group, the grain impurity rate and cleaning loss rate are 2.92% and 5.42%, respectively. Both values are lower than those for the horizontal position. Specifically, the grain impurity rate decreases by 14.6%, the cleaning loss rate decreases by 2.30%, and the overall cleaning performance metric decreases by 5.9% in the experiment group. This indicates that the sieve in the leaning forward and leaning right condition is more favorable for the cleaning of the threshed outputs.

Field experiment

To evaluate the operational performance of the multi-dimensional cleaning sieve, a harvesting operation was conducted in a hilly area where rapeseed is grown. Field experiments were carried out at the Longxin Agricultural Machinery Cooperative in 2023, Jiangxi Province. The selected rapeseed variety was Ganyouza 8, with a yield of 186 kg, an average plant height of 1480 mm, a pod height of 720 mm, a pod layer diameter of 460 mm, a thousand-seed weight of 3.86 g, and a seed moisture content of 17.3%. The field experiment is shown in Fig. 13.



Fig. 13 - Combine harvester harvesting rapeseed in hilly and mountainous areas

Before the experiment, a 25 m test field was measured, and markers were placed at both ends. The cutting width of the combine harvester was 2.0 m, with a stubble height of 700 mm and a forward speed of $1.0 \text{ m}\cdot\text{s}^{-1}$. During the experiment, all material thrown out from the tail of the cleaning shoe was manually collected using mesh bag, rapeseed cleaning losses were manually separated from the tailings. The weight of the cleaning losses and the rapeseed grains in the grain tank was measured, and the impurity content in the grains was determined by sampling from the grain tank.

The rapeseed grain losses and impurity content under the conditions of the experimental group and the control group were compared, with each condition being repeated three times and the average value taken. The rapeseed grain loss and impurity content were calculated using the methods outlined in the Rapeseed Identification Guidelines. The cleaning loss rates for the experimental group and the control group were 1.41% and 2.03%, respectively, while the impurity contents were 2.18% and 2.64%, respectively. The experiment demonstrated that the rapeseed loss in the experimental group was reduced by 30.54% and 17.42%, proving that the designed multi-dimensional cleaning device effectively reduces field losses.

CONCLUSIONS

During the process of rapeseed harvesting in hilly and mountainous areas, terrain undulation and threshing device rotary operation lead to uneven threshed outputs distribution and on the sieve results in localized accumulation. This leads to poor airflow sieving efficiency and low cleaning efficiency in areas with higher threshed outputs concentration, while excessive airflow in areas with less threshed outputs causes grain-loss due to blowing rapeseeds out of the cleaning shoe. To address these issues, a multidimensional cleaning sieve design method is proposed. This method enables multi-degree adjustment within a limited space, enhancing both the uniformity of material distribution and the overall sieving efficiency.

The CFD-DEM gas-solid coupling approach was used to perform a detailed numerical simulation of a multi-degree-of-freedom cleaning device under specific feeding conditions. The grain impurity rate and grain loss rate were calculated for both the cleaning sieve leaning forward and leaning right condition (the experimental group) and the cleaning sieve horizontal condition (the control group). The comprehensive evaluation index of cleaning performance showed that, under the experimental group, the grain impurity rate decreased by 14.6% and the grain loss rate decreased by 2.3%.

This study not only deepens the understanding of the internal gas-solid two-phase flow characteristics within a multi-degree-of-freedom cleaning device but also provides important theoretical and technical support for improving the cleaning efficiency and operational performance of combine harvesters. By optimizing the sieve orientation, significant improvements in cleaning effectiveness can be achieved. Furthermore, this research provides a new measure to solve the problem of poor harvesting performance caused by the terrain of small harvesting machinery operating in hilly and mountainous areas.

ACKNOWLEDGEMENT

The work was supported by the National Natural Science Foundation of China (52405271), the Natural Science Foundation of Jiangsu Province (BK20230544) and the China Postdoctoral Science Foundation (310818).

REFERENCES

- [1] Case IH Axial-Flow 9250. (2025). Copyright©2025 CNH Industrial America LLC. <https://www.caseih.com/en-us/unitedstates/products/harvesting/axial-flow-250-series/axial-flow-9250>
- [2] Claas Lexion 8900. (2025). All content©CLAAS KGaA mbH. <https://www.claas.co.uk/products/combines/lexion-8900-7400>
- [3] El-Emam, M.A., Zhou, L., Shi, W.D., & Han, C. (2021). True shape modeling of bio-particulate matter flow in an aero-cyclone separator using CFD-DEM simulation. *Computational Particle Mechanics*, 8(4), 955-971. <https://doi.org/10.1007/s40571-020-00383-w>
- [4] Fendt IDEAL 10T. (2025). News Archive, Copyright©AGCO GmbH, 2019. <https://www.fendt.com/us/combines/ideal-10t-highlights>
- [5] Li, Y.M., Liu, Y.B., Ji, K.Z., & Zhu, R.H. (2022). A fault diagnosis method for a differential inverse gearbox of a crawler combine harvester based on order analysis. *Agriculture-Basel*, 12(9), 1300. <https://doi.org/10.3390/agriculture12091300>
- [6] Liu, Y.B., Li, Y.M., Dong, Y.H., Huang, M.S., Zhang, T., & Cheng, J.H. (2022). Development of a variable-diameter threshing drum for rice combine harvester using MBD-DEM coupling simulation. *Computers and Electronics in Agriculture*, 196, 106859. <https://doi.org/10.1016/j.compag.2022.106859>
- [7] Li X., Zhao Y., Zhao H., LiS., Diao P. (2024). Design and testing of a gap adjustable elastic low damage corn picking header based on ADAMS, *INMATEH - Agricultural Engineering* 74(3), pp. 388-400, DOI: <https://doi.org/10.35633/inmateh-74-34>
- [8] Ma, Z., Traore, S.N., Zhu, Y.L., Li, Y.M., Xu, L.Z., Lu, E., & Li, Y.F. (2022). DEM simulations and experiments investigating of grain tank discharge of a rice combine harvester. *Computers and Electronics in Agriculture*, 198, 107060. <https://doi.org/10.1016/j.compag.2022.107060>
- [9] MF BETA 7370. (2025). Copyright © AGCO Corporation and its subsidiaries and affiliates. https://www.masseyferguson.com/en_gb/product/combine-harvesters/mf-beta.html#modal-brochure
- [10] Shen, Z.H., Wang, W., Wang, G., Huang, D.R., & Jin, F. (2024). Interface velocity correction for improving resolved CFD-DEM simulation of two-phase flow in densely packed granular media. *Computers and Geotechnics*, 174, 106639. <https://doi.org/10.1016/j.compgeo.2024.106639>
- [11] Tanneru, Y.S., Finke, J.H., Schilde, C., Harshe, Y.M., & Kwade, A. (2024). Coupled CFD-DEM simulation of pin-type wet stirred media mills using immersed boundary approach and hydrodynamic lubrication force. *Powder Technology*, 444, 120060. <https://doi.org/10.1016/j.powtec.2024.120060>

- [12] Vlăduț N.-V., Ungureanu N., Biris S.St., Voicea I., Nenciu F., Găgeanu I., Cujbescu D., Popa L.-D., Boruz S., Matei G., Ekielski A., Teliban G.C. (2023). Research on the identification of some optimal threshing and separation regimes in the axial flow apparatus, *Agriculture* 13(4): 838, DOI: 10.3390/Agriculture13040838, Agriculture-2301663
- [13] Wang, H.Y., Huang, F.Y., Fazli, M., Kuang S.B., & Yu, A.B. (2024). CFD-DEM investigation of centrifugal slurry pump with polydisperse particle feeds. *Powder Technology*, 447, 120204. <https://doi.org/10.1016/j.powtec.2024.120204>
- [14] Wang, L.J., Chai, J., Wang, H.S., & Wang, Y.S. (2021). Design and performance of a countersunk screen in a maize cleaning device. *Biosystems Engineering*, 209, 300-314. <https://doi.org/10.1016/J.BIOSYSTEMSENG.2021.07.008>
- [15] Xu, L.Z., Li, Y., Chai, X.Y., Wang, G.M., Liang, Z.W., Li, Y.M., & Li, B.J. (2020). Numerical simulation of gas-solid two-phase flow to predict the cleaning performance of rice combine harvesters. *Biosystems Engineering*, 190, 11-24. <https://doi.org/10.1016/j.biosystemseng.2019.11.014tab>
- [16] Zhang J., Ding Y., Yang R., Pan Z., Mu J., Wang W., Liu Q, Wang S. (2024). Parameter calibration for discrete element simulation of cutting deck cleaning in small plot wheat combine harvester, *INMATEH - Agricultural Engineering* 72(1), pp.339-351, DOI: <https://doi.org/10.35633/inmateh-72-31>
- [17] Zhang Z., Jiang H., He X., Zhang F., Wang J., Wang D. (2024). Design and test of threshing and cleaning device for *Cyperus Esculentus* L. combine harvester, *INMATEH - Agricultural Engineering* 72(1), pp. 798-808, DOI: <https://doi.org/10.35633/inmateh-72-71>
- [18] Zhao Z., Yang X., Zhang G. (2022). Analysis and optimization test of operation process of cleaning device of corn seed harvester, *INMATEH - Agricultural Engineering* 68(3), pp. 211-220, DOI: <https://doi.org/10.35633/inmateh-68-21>

LOW HEAD MICRO-HYDRO TURBINES USED FOR EFFICIENCY INCREASE OF SOLAR POWERED IRRIGATION SYSTEMS

MICRO-HIDROTURBINE DE JOASĂ CĂDERE UTILIZATE PENTRU CREȘTEREA EFICIENȚEI SISTEMELOR DE IRIGAȚII ALIMENTATE DIN PANOURI FOTOVOLTAICE

Rareș-Andrei CHIHAIA¹⁾, Gabriela CÎRCIUMARU¹⁾, Sergiu NICOLAIE¹⁾, Lucia-Andreea EL-LEATHEY¹⁾,
Nicolae TĂNASE¹⁾, Constantin, DUMITRU¹⁾

¹⁾ National Institute for Research and Development in Electrical Engineering ICPE-CA Bucharest / Romania

*Tel: 0726637598, E-mail: rares.chihaia@icpe-ca.ro

DOI: <https://doi.org/10.35633/inmateh-75-86>

Keywords: low head turbines, irrigation systems, PV panels, energy efficiency, energy autonomy

ABSTRACT

This paper presents an improved solution for solar powered irrigation systems by integrating low-head micro-hydro turbines for energy recovery when discharging the water from the storage tank. The proposed solution is justified by the potential energy available when storing water in a tank using pumps powered by PV panels. This energy can be used to provide additional electricity when discharging the water, by placing a low-head micro-hydro turbine at the bottom of the tank. The energy produced can be used for pumping back a fraction of the consumed volume of water, or to ensure the pressure for longer distance irrigation networks. The energy surplus provided by the turbine is necessary especially when irrigating during mornings and evenings, when PV system power production is reduced. A low head micro-hydro turbine suitable for a small scale solar powered irrigation systems was tested on a dedicated testing stand in order to demonstrate its efficiency. The turbine was designed to generate 1 kW of power operating at 2.4 m head and 360 m³/h flow. The tested model reached a maximum output of 526 W at 2 m head and 240 m³/h flow. The rotor is made from thermoplastic by 3D printing, thus the flow through the turbine was limited to avoid damaging the blades. The experimental data was compared to the specific data of a small-scale solar powered irrigation system to determine the total efficiency of a hybrid irrigation system. The calculation takes into account the medium flow rate needed for turbine operation during irrigation phase, correlated with the electricity requirements of the pump for obtaining specific flows. The additional power output can increase the global efficiency of a solar powered irrigation system by feeding the electricity back to the pumping unit. For a PV power system that provides 20 kWh/day, the turbine can ensure around 22.5% of the energy needed for irrigation.

REZUMAT

Această lucrare prezintă o soluție îmbunătățită pentru sistemele de irigare cu energie solară prin integrarea micro-hidroturbinelor de joasă cădere pentru recuperarea energiei la golirea apei din rezervorul de stocare. Soluția propusă este justificată de energia potențială disponibilă atunci când se stochează apă într-un rezervor de acumulare, folosind pompe alimentate de panouri fotovoltaice. Aceasta poate fi valorificată prin amplasarea unei micro-hidroturbine de joasă cădere în partea inferioară a rezervorului. Astfel, turbina poate furniza energie electrică suplimentară la descărcarea apei. Energia produsă poate fi utilizată pentru pomparea înapoi a unei fracțiuni din volumul de apă consumat sau pentru asigurarea presiunii pentru rețele de irigare pe distanțe mai lungi. Surplusul de energie produs de turbină este necesar mai ales la irigarea dimineața și seara, când producția de energie a sistemului fotovoltaic este redusă. O microturbină pretabilă pentru sistemele de irigare de mică putere care utilizează energia solară a fost testată pe un stand dedicat pentru demonstrarea eficienței acesteia. Turbina a fost proiectată să genereze o putere de 1 kW funcționând la o cădere de 2.4 metri și un debit de 360 m³/h. Modelul de turbină testat a furnizat o putere maximă de 526 W la o cădere de 2 metri și un debit de 240 m³/h. Rotorul este realizat din termoplastice prin printare 3D; prin urmare, debitul prin turbină a fost limitat pentru a evita deteriorarea palelor. Datele experimentale au fost comparate cu datele specifice ale unui sistem de irigare la scară mică, alimentat din panouri fotovoltaice, pentru a determina eficiența totală a sistemului hibrid de irigare. Calculul ține cont de debitul necesar pentru funcționarea turbinei în faza de irigare, corelat cu necesarul de energie electrică pentru obținerea debitelor specifice. Energia electrică adițională obținută poate crește randamentul global al sistemului de irigare cu energie solară prin alimentarea pompei instalației. Pentru un astfel de sistem care furnizează 20 kWh/zi, turbina poate asigura până la 22,5% din energia necesară pentru irigare.

INTRODUCTION

The development of efficient and affordable PV systems is at hand for implementation in agriculture within solar powered irrigation systems. Moreover, some agricultural activities can be combined with solar systems, including crops, livestock, greenhouses and other agriculture domains that require electricity. Integrating renewable energy systems in agricultural infrastructure can be a promising solution for sustainable development. Moreover, considering that 70% from the world freshwater is used in agriculture (UNESCO, 2019; Garcia-Espinal et al., 2024), designing efficient technologies and equipment to be used for watering crops is of significant importance. For irrigation purposes, Lorentz solar water pumps provide special designed DC pumps suitable for operation in remote PV irrigation system. They can be used along with increased efficiency PV panels in portable systems that can be deployed wherever needed.

The pump can have a timer switch that offers the advantage of a time-controlled water-saving system. Precise timing must be set in accordance with the dependence of the solar cells power generation on the intensity of the sun radiation. The plants have to receive irrigation at the exact moment when the soil beneath is dry and needs watering the most. Water savings compared to general irrigation are achieved by using drip irrigation, thus avoiding watering unused areas and consequently weed growth (Jandova et al., 2022). The problem that arises when implementing PV systems for irrigation is that the timing of maximum power generation and the period needed for irrigation does not overlap. The solution for this issue is to use storage systems that can ensure the use of electricity at the time needed, when access to the grid is not possible. The most accessible solution is to use batteries for storing the energy during most active sunlight hours. Irrigation systems require reservoirs or tanks to be filled to ensure the proper flowrate when needed. Since potential energy is available when storing water in a tank, then a low-head micro-hydro turbine placed at the bottom of the tank can be added into the system to provide additional electricity when discharging the water. Considering that irrigation is performed during mornings and evenings, when the PV system power production is reduced, the energy surplus provided by the turbine is not only necessary, but makes the irrigation system more reliable and versatile. Among all types of irrigation systems, micro-irrigation is the most efficient way of irrigating crops according to Evans et al., 2018. The mentioned study shows that micro-irrigation has 60% less water waste comparing to the flood irrigation method. In this irrigation type, a water pump supplies water with pressure into the pipes and drippers. Although renewable energy-powered irrigation systems can improve the productivity of crops, the storage method to be used is still a challenge for large land areas (Rejekiingrum et al., 2021). Some studies have raised concerns about the water tank costs. Soenen et al., 2021 conducted a techno-economic comparison between battery and tank-based water pumping systems, concluding that the lifecycle cost (LCC) of tank-based systems is 22% higher than that of battery-based systems in terms of using domestic water supply. An optimization study carried out by A. Mazloumi et al. (2023) on a water tank storage-based solar-powered system showed that the cost of water supplied in the case of tank-based systems was lower compared to battery or diesel-based systems, but the tank size was limited to 10 m³. Therefore, the sizing of the tank can pose a challenge and the optimum storage volume must be identified. For example, building a 200 m³ water tank to meet water needs cannot be feasible given the required cost of construction, materials, and labour (Jahanfar et al., 2022). In another study, the cost of the tank-based systems increases twice that of the battery-based systems when scaling up (Attia et al., 2022).

Given the aspects mentioned above, if the envisaged project requires water storage tanks, then the use of complementary low-head micro-hydro turbine can be a solution for increasing the global efficiency of the PV irrigation systems. The downside of using the turbine is the impact of the hydraulic parameters, resulting in a reduced flow rate downstream. The hydraulic head, as the main flow parameter, is strongly modified by the presence of the turbine which causes the main head loss of the entire installation and hence the reduced flow. This happens because the turbine transforms most of the water pressure into mechanical energy, which the generator then converts into electrical energy. This drawback is not significant where reduced flow is needed, as the case of drip irrigation. Likewise, some irrigation systems already have regulating valves for adjusting the flow, in order to have a longer irrigation time with a limited flow, to avoid the quick discharge of the storage tank. If needed, the local pressure loss can be overcome by an increased head or by reducing the friction loss in pipes. The different opinions regarding the selection of suitable storage for PV irrigation systems have determined the development of various optimization models. The total efficiency of the system can be increased by using an intelligent system based on SCADA or IoT, like the one depicted in Kun et al., (2021).

Obstacles in expanding solar power generation to other purposes such as irrigations, involve the cost of solar cells and the dependency on weather conditions. The efficiency and performance of photovoltaic panels are tied to environmental variables, including climate factors.

Bălăceanu *et al.*, (2024), highlighted the influence of the environmental factors on the PV panel performance and proposed the use of simulation software to ensure the best results in terms of efficiency when placing the panels. Recent developments in electronics allowed the implementation of a network acquisition system based on multiple sensors for automatic irrigation and fertilization, which can reduce water consumption by 74.92% (Karunanithy *et al.*, 2020). Matheswaran *et al.* (2021) carried out a performance evaluation of standalone solar powered water irrigation system using DC pump. The good results recommend the system as a suitable candidate for the replacement of the existing grid connected pumping system. Few articles have been published on optimizing renewable energy-powered irrigation with battery or tank storage. The identified literature mostly uses the life cycle cost and either loss of load or loss of power supply probability as optimization criteria (Khatib *et al.*, 2021; Irandoostshahrestani *et al.*, 2023). Another approach of storage suitable for irrigation systems is to use compressed air that enhances the environmentally friendly and efficient operation of drip irrigation systems. Conventional storage methods commonly used in photovoltaic-powered drip irrigation systems, such as elevated tanks and batteries, have notable technological, economic, and environmental limitations. Thus, a group of researchers presents a novel photovoltaic drip irrigation technology (CAES-PVDI) that uses solar energy as the exclusive source of power, enabling stable and cost-effective high-quality drip irrigation using compressed air (Junjie *et al.*, 2024). The appropriate solution for storage must be customized depending on the project and takes into account many aspects such as: irrigated area, daily solar irradiation, investment and life-cycle cost, environmentally friendly solutions, environmental protection conditions. Each solution has advantages and disadvantages as stated by Jahanfar *et al.*, (2022), who performed a comparative study of solar water pump storage systems. The authors concluded that battery storage provide a constant power to pump, which results in a higher life span of the pump but has a significant replacement and maintenance cost. On the other hand, water tank storage has high life span, but presents challenges in building and installation of high-capacity water tanks.

None of the previous articles approaches the use of other means of producing electricity such as hydro-turbines connected within the PV irrigation system for increasing their efficiency. Clearly, some benefits can arise, as the global efficiency of the pumping system can be increased. However, a more in-depth analysis is required and will be performed in this paper, emphasizing the power output of water turbines operating in solar powered irrigation systems.

MATERIALS AND METHODS

The micro-hydro turbine suitable to use in a small scale solar powered irrigation system was tested on a dedicated stand specially designed for performing tests on low head turbines. These turbines are an environmentally friendly way to generate electricity by using a certain flow and a relatively low head of at least 1 meter, allowing water to pass through and be discharged at a lower level. Kaplan turbines offer good efficiency when operating at low head and despite their complexity, can be a suitable option for producing electricity within storage tank-based irrigation systems. Compared to other propeller or crossflow turbines, the Kaplan reaction turbine can be a solution at hand with sufficient performance even with fixed rotor blades and guide vanes. The turbine was designed, built and optimized using the methodology for conventional Kaplan turbines, noting that the installed flow rate and reduced head determined the optimization and adaptation of the rotor and stator according to recent parameters identified in literature (Różowicz *et al.*, 2019). The overall dimensions were correlated with the water drainage section at the bottom of the upper tank of the test stand as recommended by Peczkis *et al.*, (2021). The microturbine is made up of 3 main elements:

1. The base plate - consists of a lower flange (5) which performs two functions: at the lower part it ensures the sealing of the flange (4) glued to the transparent plexiglass tube (2) by pressing it against the bottom of the tank (3) using six screws (15). At the upper part, this plate constitutes the support for the guide vanes system which are fixed between the upper and lower plates, thus strengthening the entire assembly.

2. The upper plate (8) - has attached the hydrodynamic profiled cone with a set of screws (13), which consists of a core (7) that directs the flow towards the turbine rotor and has a glass bearing (11) at the bottom, where the shaft goes through. The plate has 16 holes through which the screws (14) that fix the guide vanes (6) are screwed into the base plate. At the top, another bearing is provided for the shaft (9). A conical housing (10) is also centrally placed using a set of screws (12) for supporting the pipe that ensures the connection with the mechanical testing assembly and through which the turbine shaft (9) passes.

3. The turbine rotor (1) - is placed as a continuation of the hydrodynamic profiled cone and has 4 blades with a NACA 2412 profile, having a diameter of 228 mm. The rotor is supported by the hydrodynamic cone and rotates inside the transparent plexiglass tube with an inner diameter of 230 mm.

The plexiglass tube is 2 meters long and is immersed at the bottom in the lower tank. The rotor is fixed to the transmission shaft by a transverse screw and thus the rotational movement is transmitted to the mechanical testing assembly. The basic drawing of the turbine is shown in figure 1.

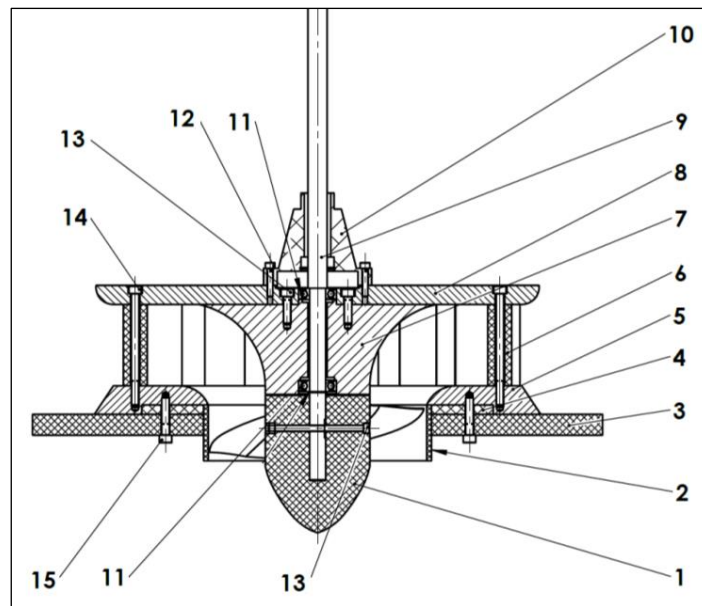


Fig. 1 – Low head micro-hydro turbine drawing

In order to calculate the rotor diameter, the statistical design method of Kaplan turbines can be used, based on the following relations according to *Anton, (1979)*:

$$D = a_D \frac{Q^{0.5}}{H^{0.25}} \quad a_D = 0,37 + \frac{270}{n_s} \quad n_s = 3,16n \frac{Q^{0.5}}{H^{0.75}} \quad (1)$$

where D – turbine diameter, a_D – coefficient expressed in relation with specific speed, Q – flow through the turbine, H – head of the turbine.

By applying the above formulas, resulted a rotor diameter of 228 mm and a specific speed n_s of 476. The hub diameter is recommended to respect a certain ratio between the total surface area exposed to the flow and the equivalent surface area where only the blades are exposed to flow. Therefore, according to *Anton, (1979)*, it is recommended that the ratio between the hub diameter and that of the rotor to be approximately 0.5 for a specific speed of approximately 500, resulting a hub diameter of 110 mm. Taking into account the distance of 1 mm between the tip of the blades and the wall of the draft tube, it results a 230 mm diameter of the plexiglass tube, around the rotor blades. The turbine draft tube is actually the transparent plexiglass tube that connects the two tanks of the testing stand. For the turbine model, a clear straight tube of plexiglass was chosen, although conical draft tubes with an opening angle of 10-12° contribute to a higher efficiency of the turbine (*Anton, 1979*). The straight clear tube was used in order to visualize the phenomena and considering that conical transparent tubes made from plexiglass were not available on the market. For the rotor blades design, the NACA 2412 hydrodynamic profile was chosen, which ensures good results in terms of lift coefficient. The rotor geometry was designed in 3D format and made of ABS on a 3D printer in the form of a compact part, with a transverse hole for the fixing screw. The overall drawing of the rotor in 3D view is shown in figure 2.

The guide vane system of the turbine is made of 16 blades that ensure de flow control and proper direction towards the rotor. In order to obtain maximum efficiency, the blade body must present minimal resistance to the current flow, resulting in a hydrodynamically optimized shape. The thickness of the profile must be large enough to withstand the water pressure in the completely closed position. The positioning angle α_D , between the tip of the trailing edge and the tangent to the circle drawn from centre and passing through its trailing edge must be precisely the angle α from the velocity triangle at the entrance of the rotor, in order not to cause sudden deviations of the current at the entrance. The dimensions of the guiding vanes system were chosen in such a way as to allow opening up to the maximum designed angle and closing to be done between the trailing edge of one blade and the inner surface of the next blade at a maximum of 0.25 of the chord length. For these blades, a symmetrical NACA 0018 profile was chosen that is slender enough to direct the water jet but with an adequate thickness to be securely in place with a M8 screw.

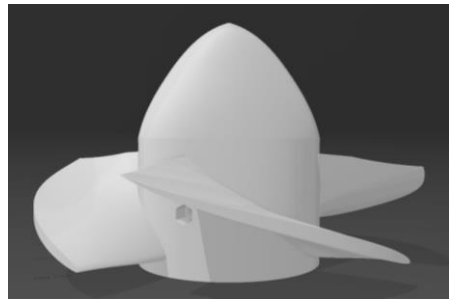


Fig. 2 – Rotor design for the low head micro-hydro turbine

The guide vanes are not adjustable during operation. Their position can be set at different angles before the turbine assembly. For the current testing, the placement angle was chosen to be 35° , according to the velocity triangle. The guide blade height is one of the parameters that, along with the angle α_b and the turbine speed, significantly influences the value of the flow rate Q and the circulation at the rotor entrance, respectively the energy conversion in the turbine (Anton, 1979).

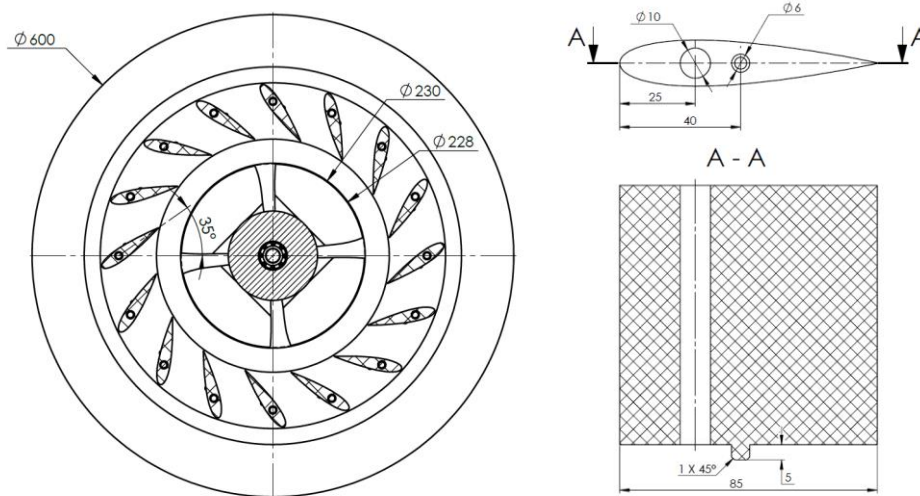


Fig. 3 – Guide vanes design of the turbine

The design of the guide vanes system is presented in figure 3. The base plate flange, the upper plate and the conical housing were made by CNC machining from aluminium. The rotor and the guide vanes were made from ABS using a 3D printer. Two glass bearings were used and the entire assembly was fitted using 16 screws (position 6 from figure 1). A rubber gasket was used to seal the bottom tank and was placed under the turbine assembly presented in figure 4.



Fig. 4 – Low head micro-hydro turbine assembly ready for testing

The turbine has a mechanical testing assembly attached to its upper part. It comprises of an assembly consisting of elastic couplings, a torque transducer and an electromagnetic brake and is capable of performing torque measurements up to 20 Nm and rotational speeds up to 4000 rpm. Figure 5 schematically shows the mechanical test assembly and the related components.

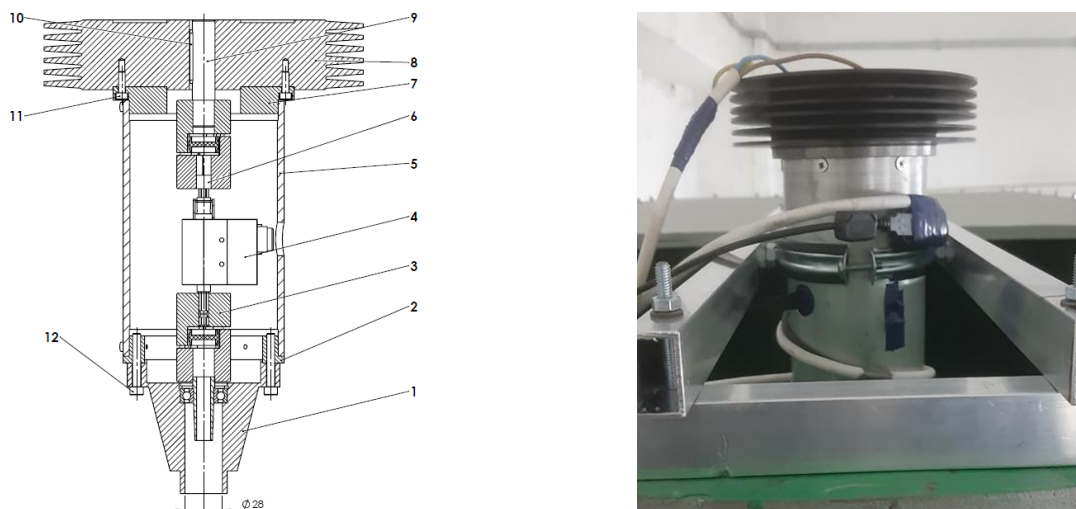


Fig. 5 – Mechanical testing assembly for the low head micro-hydro turbine

The assembly is mounted on the support rod using the conical part (1), which is connected to a plate (2) bolted into a cylindrical housing (5), on which an intermediate flange (7) is supported. This flange also represents the support for the electromagnetic particle brake (8). A shaft (9) transmits the movement from the turbine to this testing assembly through an elastic coupling (3) connected to the torque and speed transducer (4). At the top of the enclosure, the brake is also connected through an elastic coupling (6). The entire assembly is joined using a set of screws (11,12). The mechanical testing assembly is attached to the turbine and the entire assembly is lowered into the upper tank for integration into the hydraulic testing stand.

The turbine was designed to generate 1 kW of power operating at 2.4 m head and 360 m³/h flow. The tested model reached a maximum output of 526 W at 2 m head and 240 m³/h flow. The rotor is made from thermoplastic by 3D printing; thus, the flow through the turbine was limited to avoid damaging the blades. The turbine efficiency depends on the flow and head parameters. It can operate at partial load with reduced flow but the efficiency is highly affected where there is no adjustable blade system for the runner and the guiding vanes. Such a system is very complex, adds additional costs, is subject to more frequent wear and tear and requires periodic maintenance. Thus, it is not suitable for small scale microturbines due to the fact that the power increase is not significant in order to justify the additional cost of implementation and maintenance. The turbine can operate in water with sand or some small debris, but overtime, the turbine can be damaged. To avoid such issues, a screen can be fitted at the discharge pipe that supplies water to the reservoir; it can be cleaned or changed periodically, depending on the water quality.

TURBINE TESTING

The turbine was integrated into a specially designed testing facility. The testing stand comprises of a pumping unit with three pumps (7.5 kW, 120 m³/h) that circulates water between two overlapping tanks, the lower one with a volume of 3840 litres and the upper one with a volume of 2400 litres, located on a supporting metal structure (Popescu *et al.*, 2024). The pumping unit is connected using a hydraulic circuit made of pipes of 200 mm diameter, which has integrated an electromagnetic flow meter in order to permanently monitor the flow through the stand and turbine, respectively. The connection between the two tanks is ensured by a transparent plexiglass tube. The operation of the stand and data acquisition are performed using a programmable logic controller connected to a PC that can monitor the parameters and store them for further analysis. The low head micro-hydro turbine testing stand and its main components are presented in figure 6.

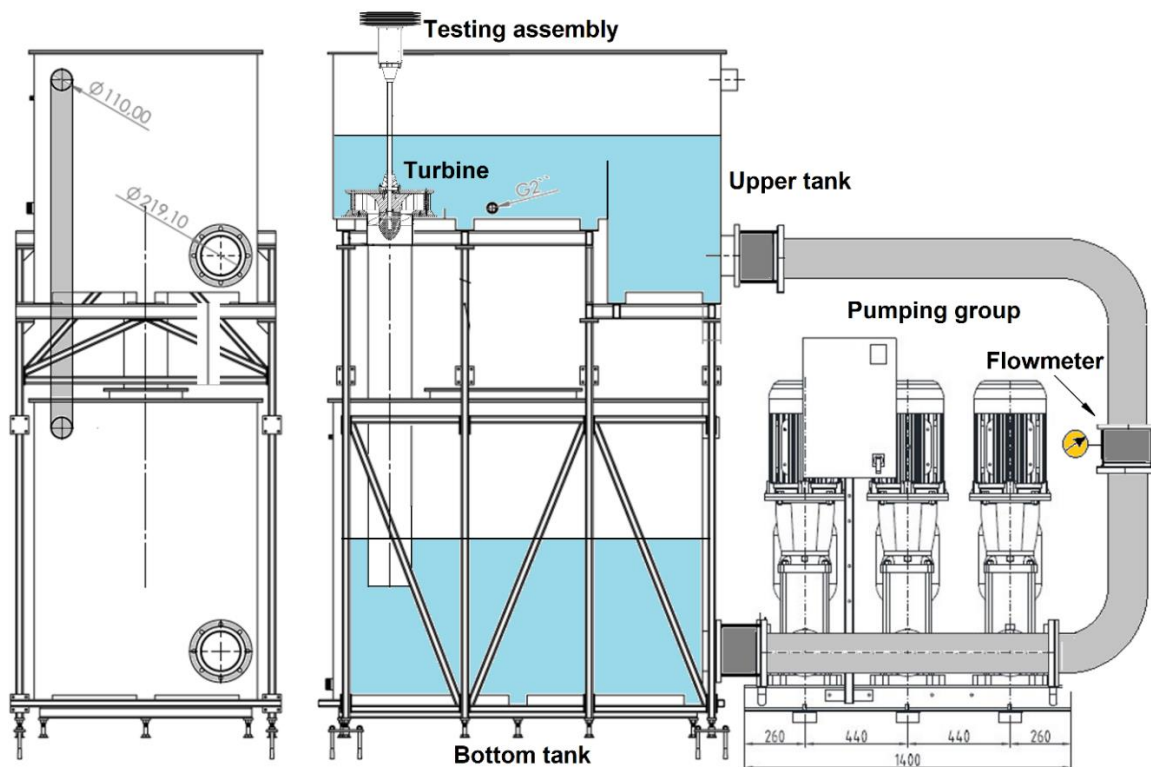


Fig. 6 – The testing stand of the low head micro-hydro turbine

The turbine was placed into position, according to figure 6, with the rotor aligned inside the transparent plexiglass tube. The testing procedure involved the following steps:

- Filling the lower tank to a maximum level, determined so that the volume of water ensures the filling of the entire installation (draft tube + pump + discharge pipe + buffer tank + vertical tube), providing a proper level in the upper tank of about 1 meter above the turbine;
- Setting the working flow rate and monitoring the rotational speed and torque of the turbine after stabilizing the flow regime; by slowly activating the brake, results a progressive increase in the useful torque at the rotor shaft;
- Progressively actuating the brake until the rotor stops and thus the maximum power of the turbine can be determined at a specific flow rate and head.

Figure 7 shows the turbine placed inside the tank, with the rotor protruding into the transparent tube, so that it can be observed during the experiments. In order to ensure a constant head for testing the turbine, the stand pumps are operated by an automatic flow rate adjustment system depending on the level set by the user, through a software application. To determine the energy parameters of the turbine, its shaft is coupled to an electronically adjustable electromagnetic brake and a torque/speed transducer. The recorded values are integrated into a data measurement and storage system in the form of a .csv database.

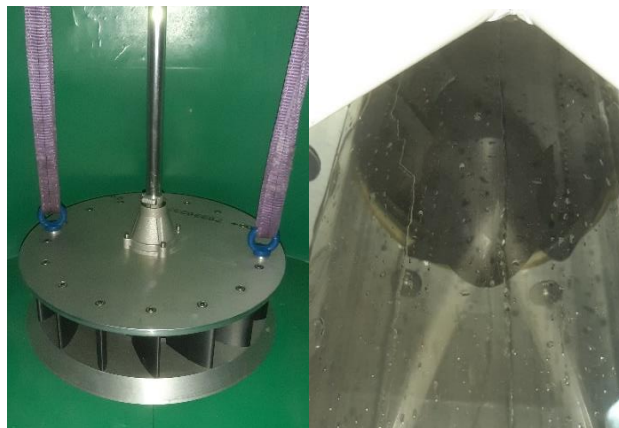


Fig. 7 – The low head micro-hydro turbine during mounting

Aspects from the turbine testing were captured in Figure 8 with details on the data acquisition system, the electromagnetic flow transducer and the transparent Plexiglas tube through which the wake caused by the rotor movement can be observed.

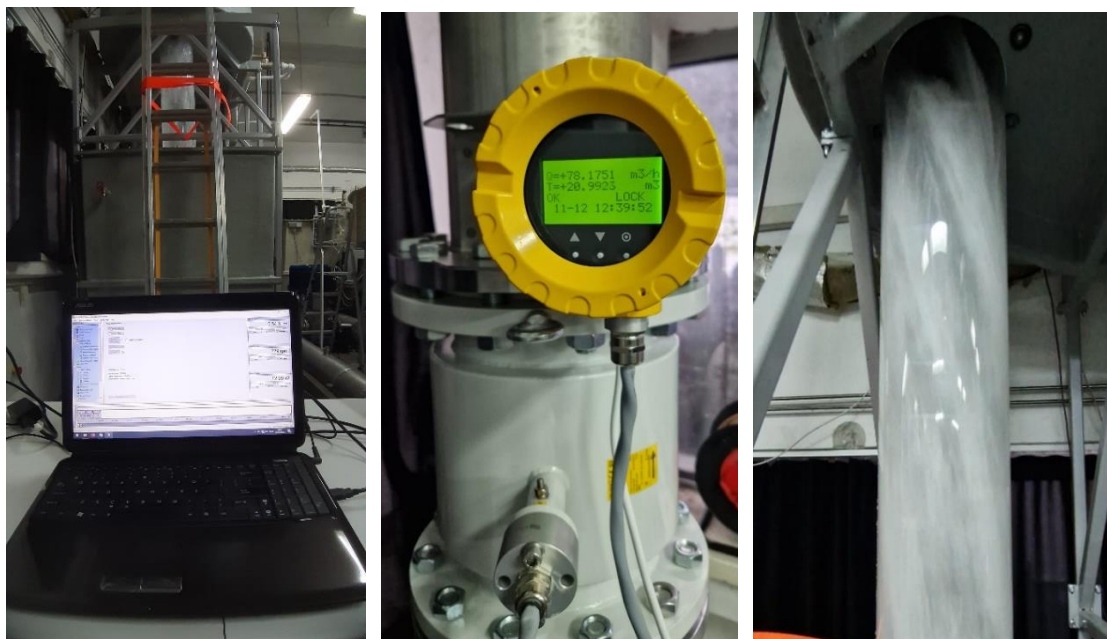


Fig. 8 – Testing of the integrated low head micro-hydro turbine

The rotor used for the experiments, made from ABS thermoplastic, withstood the tests without any damage. For evaluation purposes, this type of material can be used given the reduced operation time, but in real operating conditions, other materials must be considered, such as aluminium or stainless steel. Plastic rotors can be easily damaged by debris and are more prone to wear. The guide vanes and the draft tube should also be manufactured from strong, corrosion resistant materials. The draft tube of the testing stand was made from plexiglass in order to observe the flow around and after the rotor. This material is suitable only for laboratory conditions; for full-scale turbines, this tube must be replaced with a metal pipe.

RESULTS

The maximum flow considered when testing the turbine was of 240 m³/h, along with a head of 2 meters. The results demonstrated the importance of operating as close as possible to the design conditions, otherwise the efficiency can be greatly diminished. The objective of the tests was to study how the energy conversion occurs at the rotor level in order to improve its efficiency and determine how a low head micro-hydro turbine can be used for efficiency increase in solar powered irrigation systems. In addition to the hydraulic parameters that are critical for maximizing power, the resistant torque of the generator coupled to the turbine must be also taken into account.

The mechanical torque at the shaft resulting from the turbine-generator interaction determines a certain rotational speed and the optimal operating point must be identified through experimental tests. The high torque at the shaft breaks the rotor and a low rotational speed negatively influences the power output. On the other hand, the maximum speed is obtained at idle operating point and the generator load must be adapted to maintain a relatively high rotational speed, while maintaining a useful torque. Thus, such systems require a dedicated power converter unit based on a MPPT algorithm using perturb and observe method, integrating boost and buck converters for powering a considered load (*Chihai et al., 2020*). The robust power peak seeking control algorithm also presents a good option for attaining a high operating efficiency by achieving maximum power point tracking through a line search triggered by real-time measurements (*Naik et al., 2024*). These types of electronic controllers are also used for hydrokinetic turbines and have proven their functionality. The testing results of the turbine are synthesized in the diagram in figure 9, which shows the power output depending on the rotational speed of the rotor.

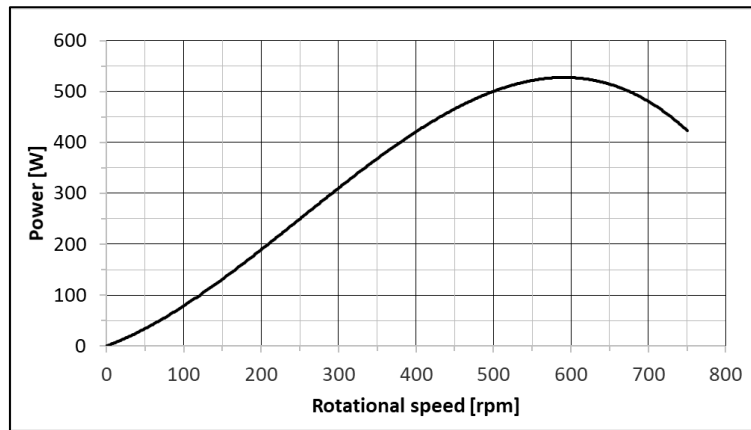


Fig. 9 – The power diagram of the micro-hydro turbine

The curve shows a peak of 526 W at around 600 rpm for the turbine tested at a 240 m³/h flow and 2 meters head. The efficiency varies depending on the available flow and head reaching up to 40% at the highest power value, as shown in figure 10.

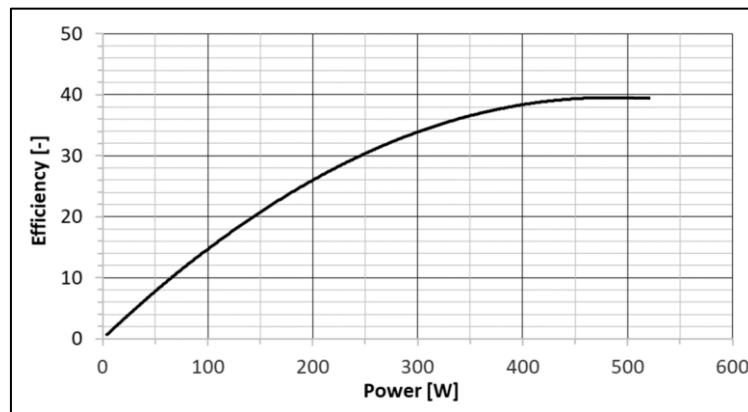


Fig. 10 – Efficiency curve of the micro-hydro turbine

The results demonstrate that a turbine can produce a power of around 500 W placed beneath a tank suspended at about 2 meters, where sufficient flow is ensured, as the case of irrigation systems using storage tanks. This power output can increase the global efficiency of a solar powered irrigation system feeding the electricity back to the pumping unit. In order to demonstrate the feasibility of the system, a reduced scale solar powered irrigation system with a turbine embedded can be designed and studied. The basic operating principle of such systems is presented in figure 11.

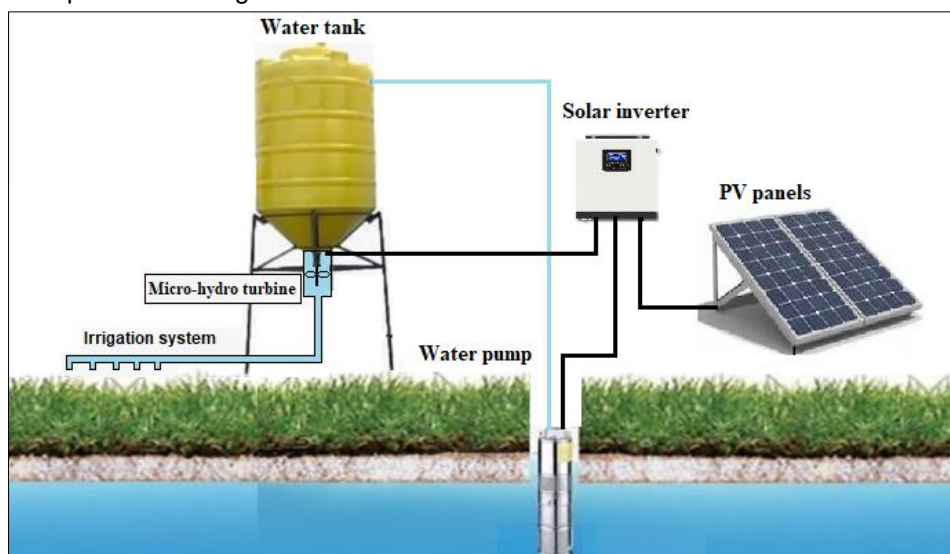


Fig. 11 – Reduced scale solar powered irrigation systems with embedded low head micro-hydro turbine

The water pump creates pressure that fills the tank when supplied with electricity from PV panels. The solar inverters manage the power received by the pump according to the power supplied by the panels, and the batteries state of charge (if the system is equipped with storage). The micro-hydro turbine is placed beneath the tank and supplies electricity when water flows for irrigation. It is also connected to the solar inverter and thus increases the overall efficiency of the system. In order to perform efficiency calculations for the proposed system, the parameters of the involved devices are presented below:

- **PV panels:** 5 x 500 W_{peak} , 2094 x 1134 x 35 mm, half-cut, monocrystalline cells, 21% efficiency;
- **Electric pump** CBM 303/A, 2.2 kW power, 42 m^3/h , head up to 22 meters, single-phase 230V. Another type of pump that can be used for DC application is Lorentz S1-700 model, with a maximum flowrate of 10 m^3/h and a power of 750 kW. In this case, 3 pumps can be deployed for ensuring 30 m^3/h at around 2.25 kW similar with the a.c. version.
- **Solar inverter/hybrid inverter:** 3200 W maximum power, off-grid type, single phase 230 Vac output, input from PV panels and hydro-turbine using a power controller and voltage stabiliser;
- **Micro-hydro turbine** of 1 kW maximum power, obtainable at 2.4 m head, with a flow rate of 360 m^3/h and a rotational speed of 850 rpm. The turbine will be connected to a permanent magnets synchronous electric generator with the rated power of 1 kW at 850 rpm, single phase output. Although the generator voltage will be around 230 Vac, due to the variation of the flow parameters, the turbine will have speed variations and thus the output voltage will be affected. To avoid any issues and to safely connect the solar inverter, a voltage stabilizer must be inserted in between in order to handle the voltage fluctuation in the range of 120 V-270 V ensuring a stable output of 230 Vac. If a DC system is considered, then the electric generator will have to comply with 24/48 Vdc voltage with a DC-DC buck-boost converter added to supply a constant voltage.

For an irrigation system, any type of PV panel is suitable as long as the string of panels are compatible in terms of voltage and current with the selected inverter. Lightweight PV panels are at hand because they are easy to handle and can be integrated into a mobile system. A renewable energy mobile containerized system can be deployed for off-grid application based on PV panels and micro-wind turbine in order to directly provide the energy via DC-DC power supply.

This type of application can be intended for irrigation and fertirrigation, in semi-dry and dry-sub-humid arid climates and was developed within a project that envisaged innovative technologies for crop irrigation, (Onose *et al.*, 2020).

In terms of energy balance, if a daily electricity production from PV panels of 20 kWh is considered, it results in approximately 9 hours operation time of the 2.2 kW pump. If the flow through the turbine is ensured in the range of 200 to 300 m^3/h flow and a minimum of 2 meters head, then the energy produced can be estimated to be around 4.5 kWh. Thus, across 24 hours, the turbine can ensure about 22.5% of the electricity needed for irrigation.

CONCLUSIONS

The work presented in this paper demonstrated the benefit of using low head micro-hydro turbines for increasing the efficiency of solar powered irrigation systems that use storage tanks. Testing performed with such a turbine in laboratory conditions using dedicated testing stand highlighted the fact that it can supply up to 526 W at 240 m^3/h and 2 meters head, making it a feasible solution for a small-scale irrigation system. The contribution of the turbine is useful because energy surplus is needed especially when irrigating during mornings and evenings, when the power production of the PV system is reduced. The additional power output can increase the global efficiency of a solar powered irrigation system, feeding the electricity back to the pumping unit. For a PV power system that provides 20 kWh/day, the turbine can ensure around 22.5% of the energy needed for irrigation. Given the aspects mentioned above, if the envisaged irrigation systems require water storage tanks, then the use of complementary low-head micro-hydro turbine can be a solution for increasing the global efficiency of the PV irrigation systems. The turbine converts the pressure energy of the stored water into mechanical energy and is suitable where reduced flow is needed, as the case for drip irrigation. Further research must be carried out in order to correlate a proper storage solution for a certain PV panel configuration used in an irrigation system. Renewable energy systems based on PV panels represent the best choice for powering a remote irrigation system without access to the grid. Improved solutions are being continuously developed worldwide and the work presented in this paper gives a new perspective on how to optimize the operation of solar powered irrigation systems in terms of energy efficiency.

ACKNOWLEDGEMENT

This work was supported by a grant of the Ministry of Research, Innovation and Digitization, CNCS/CCCDI - UEFISCDI, project number ERANET-ENERDIGIT-INFUSE-1, within PNCDI IV and by Scientific Programme NUCLEU contract no. 42N/2023, project no. PN 23140101/2023.

REFERENCES

- [1] Attia, A., Qureshi, A. S., Kane, A. M., Alikhanov, B., Kheir, A. M. S., Ullah, H., Datta, A., & Samasse, K. (2022). Selection of Potential Sites for Promoting Small-Scale Irrigation across Mali Using Remote Sensing and GIS. *Sustainability*, 14(19), 12040. <https://doi.org/10.3390/su141912040>
- [2] Anton I. (1979). *Hydraulic Turbines (Turbine hidraulice)*, Facla Publishing House, Timișoara
- [3] Bălăceanu, M., Popa, N.S., Nae, V., Târhoacă, M.-CR., Popescu, M.-O. (2024) The Influence of Environmental Factors on a Photovoltaic Panel – PVsyst Simulation. *Automatica (EEA)*, 72(2), pp. 03-12, ISSN 1582-5175.
- [4] Chihaiia, R.-A.; Vasile, I.; Cîrciumaru, G.; Nicolaie, S.; Tudor, E.; Dumitru, C. (2020). Improving the Energy Conversion Efficiency for Hydrokinetic Turbines Using MPPT Controller. *Applied Science*, 10(21), 7560. <https://doi.org/10.3390/app10217560>
- [5] Evans, J. P., Zaitchik, B.F. (2008). Modeling the large-scale water balance impact of different irrigation systems. *Water Resour.*, 44(8), doi:10.1029/2007WR006671
- [6] Garcia-Espinal, M. A., Pérez-Sánchez, M., Sánchez-Romero, F.-J., & López-Jiménez, P. A. (2024). Irrigation Distribution Network Design Parameters and Their Influence on Sustainability Management. *Water*, 16(8), 1131. <https://doi.org/10.3390/w16081131>
- [7] Irandoostshahrestani, M., & Rouse, R. D. (2023). Photovoltaic Electrification and Water Pumping Using the Concepts of Water Shortage Probability and Loss of Power Supply Probability: A Case Study. *Energies*, 16(1), 1. <https://doi.org/10.3390/en16010001>
- [8] Jahanfar, A.M.; Iqbal, T. (2022) A comparative study of solar water pump storage systems, *2022 IEEE 12th Annual Computing and Communication Workshop and Conference, CCWC*, Virtual conference 26th-29th January 2022, Las Vegas, USA;
- [9] Jandova, K & Stranak, R. (2022). Design and optimization of solar-powered irrigation system. *Journal of Physics: Conference Series*. (2382) 012012. doi:10.1088/1742-6596/2382/1/012012
- [10] Karunanithy, K., & Velusamy, B. (2020). Energy efficient Cluster and Travelling Salesman Problem based Data Collection using WSNs for Intelligent Water Irrigation and Fertigation. *Measurement*, 161, Netherlands;
- [11] Khatib, T. Muhsen, D.H. (2021). Intuitive and numerical sizing methods for photovoltaic water pumping systems, Book chapter in: *Photovoltaic Water Pumping Systems*, (pp.47-85)
- [12] Kun, T., Sanmin, S., Liangzong, D., & Shaoliang, Z. (2021). Design of an Intelligent Irrigation System for a Jujube Orchard based on IoT. *INMATEH-Agricultural Engineering*, 63(1),189-198. doi: 10.35633/inmateh-63-19;
- [13] Matheswaran, A., Ganesh babu, C., Lakshmi, K., Sivaranjani, P., Dhanuja, R.K., Nidhya Shree, M. (2021). Performance Evaluation of Standalone Solar Powered Water Irrigation System Using DC Pump. *IOP Conference Series: Materials Science and Engineering*. 1084(1).
- [14] Mazloumi, A., Poolad, A., Mokhtari, M. S., Altman, M. B., Abdelaziz, A. Y., & Elsis, M. (2023). Optimal Sizing of a Photovoltaic Pumping System Integrated with Water Storage Tank Considering Cost/Reliability Assessment Using Enhanced Artificial Rabbits Optimization: A Case Study. *Mathematics*, 11(2), 463. <https://doi.org/10.3390/math11020463>
- [15] Naik K., Valachovic H., Sun J. (2024). Robust Power Peak Seeking Control of Hydrokinetic Turbines, *IFAC-PapersOnLine*, 58 (20), Pages 452-457, ISSN 2405-8963, <https://doi.org/10.1016/j.ifacol.2024.10.095>
- [16] Onose B. A., Murgescu I., Sontea Ș. A. (2020). Hybrid RES Mobile Innovative System Optimized for DC-DC Applications, book chapter in: *Solar Energy Conversion in Communities*. *Springer Proceedings in Energy*. Springer, pp:141-156, DOI: [10.1007/978-3-030-55757-7_10](https://doi.org/10.1007/978-3-030-55757-7_10)
- [17] Peczkis, G., Wiśniewski, P., & Zahorulko, A. (2021). Experimental and Numerical Studies on the Influence of Blade Number in a Small Water Turbine. *Energies*, 14(9), 2604. <https://doi.org/10.3390/en14092604>
- [18] Popescu, T.C., Chiriță, AP., Nicolaie, S., Chihaiia, RA. (2025). Aspects Regarding the Design of a Low-Head Hydraulic Turbine Test Stand. *Machine and Industrial Design in Mechanical Engineering*. KOD

2024. *Mechanisms and Machine Science*, vol.174. Springer. https://doi.org/10.1007/978-3-031-80512-7_28;
- [19] Rejekiningrum, P., Apriyana Y. (2021). Design and implementation of solar pump irrigation systems for the optimization of irrigation and increase of productivity. *IOP Conf. Ser. Earth Environ. Sci.* (622) 012046. doi: 10.1088/1755-1315/622/1/012046
- [20] Różowicz, S., Goryca, Z., Peczkis, G., Korczak, A. (2019). Pico hydro generator as an effective source of renewable energy, *Przegląd Elektrotechniczny* . (95) 4, p200-204
- [21] Soenen, C., Reinbold, V., Meunier, S., Cherni, J. A., Darga, A., Dessante, P., & Quéval, L. (2021). Comparison of Tank and Battery Storages for Photovoltaic Water Pumping. *Energies*, 14(9), 2483. <https://doi.org/10.3390/en14092483>.
- [22] Zha, J., Ge, M., Tang, Z., Lei, J., Zhao, H., Zhang, Y. (2024). The incorporation of solar energy and compressed air into the energy supply system enhances the environmentally friendly and efficient operation of drip irrigation systems. *Agric. Water Manag.* 302, <https://doi.org/10.1016/j.agwat.2024.109019>.
- [23] ****UNESCO World Water Assessment Program*. The United Nations World Water Development Report 2019: Leaving No One Behind; UNESCO: Paris, France, 2019.

STUDY ON THE CHARACTERISTICS AND DISTRIBUTION OF DAMAGE RESISTANCE ON CORN KERNEL SURFACES

玉米籽粒表面抗损伤特性及分布研究

Qinghao HE¹⁾, Duanxin LI¹⁾, Jianning YIN¹⁾, Yipeng CUI¹⁾, Pengxuan GUAN¹⁾, Duanyang GENG^{*1)}, Wei GU²⁾

¹⁾ School of Agricultural Engineering and Food Science, Shandong University of Technology, Zibo/ China

²⁾ Starlight Agricultural Machinery Co., LTD, Huzhou/ China

Corresponding author: Corresponding author: Duanyang GENG

Tel: +8613668641238; E-mail: dygxt@sdut.edu.cn

DOI: <https://doi.org/10.35633/inmateh-75-87>

Keywords: Corn grains, damage, CDDRS-SCK, threshing damage

ABSTRACT

This study addresses the issue of corn grain damage, which limits the efficiency of mechanized corn harvesting. The characteristics and distribution of corn grain surface damage resistance (CDDRS-SCK) were investigated. The "vulnerable" surface of the corn grain was selected for damage testing. The results revealed significant variations in damage resistance across different surfaces and locations of the corn grains. A regression model for damage resistance strength, based on surface position, was developed. Additionally, the impact of grain damage resistance on threshing damage was compared and analyzed for different threshing devices, in accordance with their working principles. This research provides theoretical insights and data support for the development of corn mechanized threshing technology and equipment.

摘要

针对玉米籽粒损伤制约玉米籽粒机械化收获的问题。本文开展了对玉米籽粒表面抗损伤强度(CDDRS-SCK)的特征及分布研究。选取“易伤”表面进行损伤试验,结果表明玉米籽粒不同表面、位置的抗损伤强度具有显著差异性,构建了基于表面位置的籽粒抗损伤强度回归模型。结合不同脱粒装置工作原理,对比分析了籽粒抗损伤特性对不同装置脱粒损伤的影响规律。为玉米机械化脱粒技术与装置开发提供了理论指导与数据支持。

INTRODUCTION

Threshing is a critical stage in the corn harvesting process. High-moisture corn kernels are particularly susceptible to damage during direct harvest due to the interaction and friction between the kernels and threshing teeth (Kruszelnicka *et al.*, 2024). This damage not only affects the quality of the harvested corn but also compromises the secure storage of the grain (Li *et al.*, 2022). Research has shown that the majority of physical damage to corn kernels occurs during threshing, primarily as a result of random collisions (Petkevichius *et al.*, 2008). Consequently, minimizing threshing-induced damage has become a fundamental objective in the mechanical harvesting of corn.

Extensive research has been conducted on the characteristics of corn kernel damage, highlighting the influence of various factors on threshing outcomes. Corn variety and grain moisture content are significant determinants of the degree of threshing damage (Sehgal *et al.*, 1965). Studies have shown that as the moisture content increases, the damage ratio of corn kernels also rises (Yi *et al.*, 2016). Experimental findings further reveal that when corn kernels are positioned flat, moisture content exerts the greatest influence on the force required for kernel damage (Yu *et al.*, 2019). To investigate the mechanisms of corn kernel damage, research has focused on the stresses experienced by kernels during damage. The internal structural properties of kernels are a primary cause of damage (Dorsey-Redding *et al.*, 1990). Using electron microscopy, it was observed that fractures in maize subjected to high-temperature drying initially appeared in the silty endosperm and then rapidly propagated along the starch granule boundaries (Gunasekaran *et al.*, 1985). Compression experiments on corn kernels have demonstrated that their damage-resistance strength varies significantly under different stress conditions (Gao *et al.*, 2011; Yuan *et al.*, 1996).

Zhao further established the maximum tensile stress that can be sustained by different kernel surfaces (Zhao., 2012). The effects of threshing structures and operational parameters on maize damage have also been extensively studied. Waelti identified drum speed, threshing gap, and rasp bar structure as the primary factors contributing to threshing damage (Waelti, 1967). Arnold demonstrated that reducing drum speed is the most effective method to decrease the rate of corn kernel damage (Arnold et al., 1964). Additionally, Wu showed that plate-tooth threshing offers advantages over traditional pin-tooth threshing, including a higher threshing rate, lower kernel breakage, and reduced power consumption (Wu et al., 2006). Geng explored the application of the flexible threshing concept and proposed a novel strategy to mitigate maize damage during the threshing process (Geng et al., 2020).

In conclusion, extensive research has characterized corn damage resulting from various mechanical components and forces, leading to the development of threshing devices with diverse mechanical structures and operating principles. However, the characteristics and spatial distribution of damage-resistance strength on the surface of corn kernels (CDDRS-SCK) have not been thoroughly investigated. This knowledge gap limits the understanding of the mechanisms underlying corn kernel damage and hinders the establishment of a robust foundation for parameter optimization in threshing device design. This study aims to analyze the CDDRS-SCK and its contributing factors, and to evaluate its potential influence on the structural and operational design of threshing machinery.

MATERIALS AND METHODS

Test equipment

The experimental data were obtained through a surface damage experiment conducted on corn kernels. The experimental setup consisted primarily of corn kernels, a custom-designed indenter, and a WDS-5 liquid crystal display electronic universal testing machine (accuracy: 0.2% F.S.), which included a lifting table, guide rails, a lift controller, a compression head, and a display screen. The corn kernels used in this study were from the widely cultivated "Zhengdan 958" variety, commonly grown in the Huanghuaihai region of China. The experimental apparatus for corn kernel surface damage is depicted in Fig. 1.

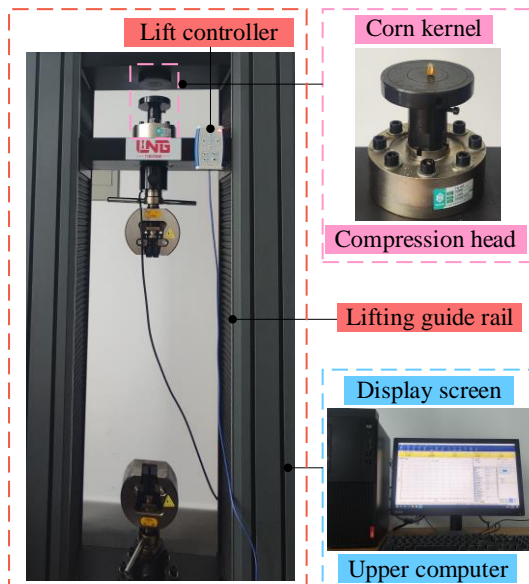


Fig. 1 - Corn kernel damage experiment device

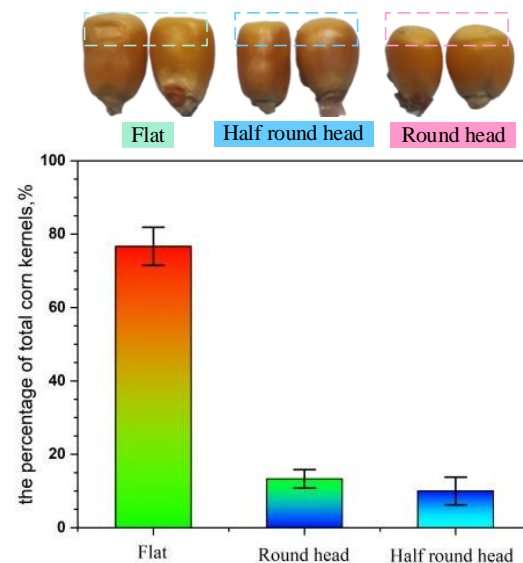


Fig. 2 - Corn kernel shape distribution map.

Selection of experimental corn kernels

Corn ears of the "Zhengdan 958" variety, with a moisture content of 24.5%, were harvested on September 26, 2024. Due to variations in component distribution and exposure to light, the head, middle, and tail sections of the corn ears exhibit distinct morphological characteristics. All corn kernels were manually peeled and categorized into three types based on their apex morphology: flat, round, and half-round. It was observed (Fig. 2) that approximately 80% of the kernels from the middle section of the corn ear are flat kernels.

Notably, flat kernels exhibit the lowest damage-resistance strength (DRS) among the three kernel types, as reported by (Vyn *et al.*, 1988). This implies that as long as the flat kernels remain intact during threshing, other kernel types are unlikely to be damaged. Consequently, flat kernels are representative of the DRS of corn kernels and were selected as the focus for investigating the characteristics and distribution of damage-resistance strength on the surface of corn kernels (CDDRS-SCK) in this study.

Test scheme

Definition of corn kernel test surface

The internal heterogeneity of corn kernels, as illustrated in Fig. 3, contributes to variations in the damage-resistance strength (DRS) across different kernel surfaces. This necessitates a comprehensive investigation of the DRS across all kernel surfaces. Preliminary damage testing of corn kernels revealed that the DRS of the left and right sides of the kernel is nearly identical, while the DRS of the main surface is significantly lower than that of the back surface. To accurately determine the characteristics and distribution of damage-resistance strength on the surface of corn kernels (CDDRS-SCK), it is critical to focus on surfaces most susceptible to damage, as these are the first to fail under repeated impacts from threshing elements. Therefore, the main surface, top surface, and left surface of corn kernels—referred to as "damage-susceptible" surfaces—were selected for this study.

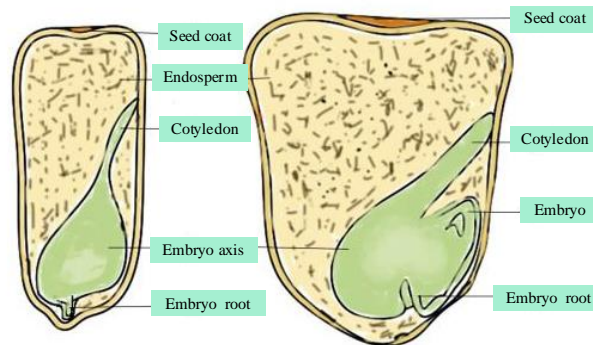


Fig. 3 - Corn kernel shape distribution map

Test procedure

A random sample of approximately 1000 hand-threshed corn kernels, with a moisture content of 24.3%, was selected for the study. To ensure uniform contact between the kernel surfaces and the indenter, the "damage-susceptible" surfaces of the experimental kernels were subjected to micro-grinding and marked using the point-marking method illustrated in Fig. 4. The marked points on each kernel surface were sequentially numbered from top to bottom and left to right. The indenter was carefully adjusted to align with a specific marked point on the corn kernel. Each marked point was then subjected to loading at a constant rate of 200 mm/min until the maximum damage-resistance force was recorded. To ensure reproducibility and statistical reliability, the average damage-resistance force F_i at each marked point was determined as the arithmetic mean of 20 repeated measurements, as expressed in equation (1):

$$F_i = \frac{1}{n} \sum_{j=1}^n F_{ij} \quad (1)$$

where F_i is the average force at point i ; F_{ij} is the j -th force measured at the same point, and $n=20$.

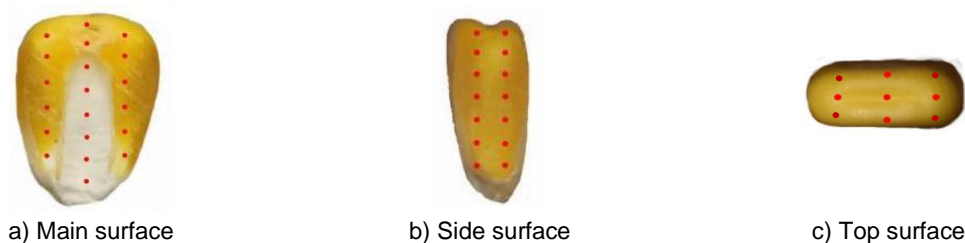


Fig. 4 - Different surface markers of corn kernels

Test evaluation index and calculation method

(1) Maximum damage-resistance force (F)

The maximum damage-resistance force (F) is defined as the highest force that can be applied to the surface of corn kernels before visible damage occurs. It corresponds to the maximum load sustained by the kernels under continuous application of pressure using a testing machine.

(2) Damage-resistance strength (DRS)

Damage-resistance strength (DRS) is defined as the maximum contact stress that corn kernels can endure without sustaining damage, serving as a critical parameter for evaluating their load-bearing capacity. To enhance the precision of DRS measurements across the surface of corn kernels, the concept of equivalent damage-resistance strength ($EDRS$) is introduced. The $EDRS$ is calculated as the mean DRS value derived from n experiments conducted at the same location on different corn kernels. The following formula is used to determine the $EDRS$:

$$\sigma_0 = \sigma_v = \frac{1}{n} \sum_{i=1}^n \frac{F_i}{A_0} \quad (2)$$

where, σ_0 represents the DRS at a specific location on the corn kernel, σ_v denotes the $EDRS$ at the same location, F_i is the maximum damage-resistance force recorded at the specific position across n repeated experiments on different kernels, A_0 is the contact area between the kernel and the custom-made indenter during the experiment, approximately 1 mm².

Test

The aforementioned testing protocol was applied to conduct loading tests at different locations on the same corn kernel until visible damage occurred. As illustrated in Fig. 5, the following tests were performed. For the main surface (a) of the corn kernel, two loading tests were conducted sequentially from left to right. For the side surface (b), a total of 14 loading tests were performed from left to right. For the side surface (c), nine loading tests were conducted, also from left to right. This systematic approach ensured comprehensive evaluation of the damage-resistance strength across multiple kernel surfaces.

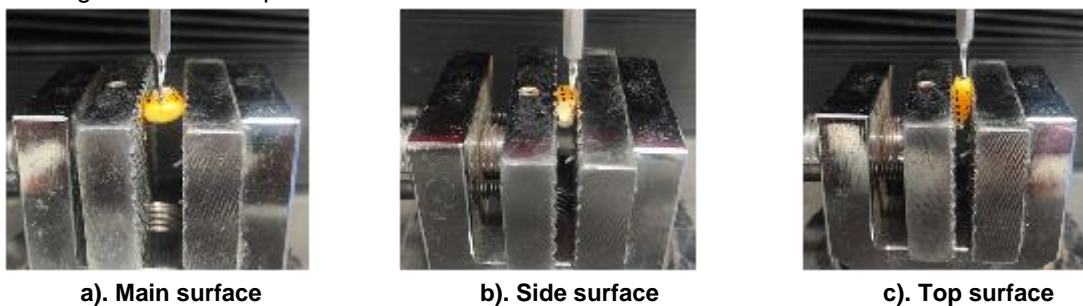


Fig. 5 - Surface loading test of different corn kernels

Based on the test sequence described above, a series of repeated experiments were conducted, as shown in Fig. 6. The resulting trends in the load-displacement curves were generally consistent. The average load-bearing capacity across different surfaces of the corn kernels exhibited a similar pattern: as the indenter displacement increased, the load on the kernel surface increased linearly until surface damage occurred, at which point the load-bearing capacity dropped abruptly. This behavior can be attributed to the elastic deformation of the kernels during the initial loading phase. Within this elastic deformation range, the stress on the kernel surface increases linearly with the indenter displacement. However, when the load exerted by the indenter exceeds the kernel surface's load-bearing capacity, the kernel surface fails, leading to a sudden decline in its carrying capacity. These findings highlight the importance of controlling the applied load during the mechanized harvesting of corn. Ensuring that the load remains below the kernel surface's carrying capacity is critical for maintaining harvest quality and minimizing kernel damage.

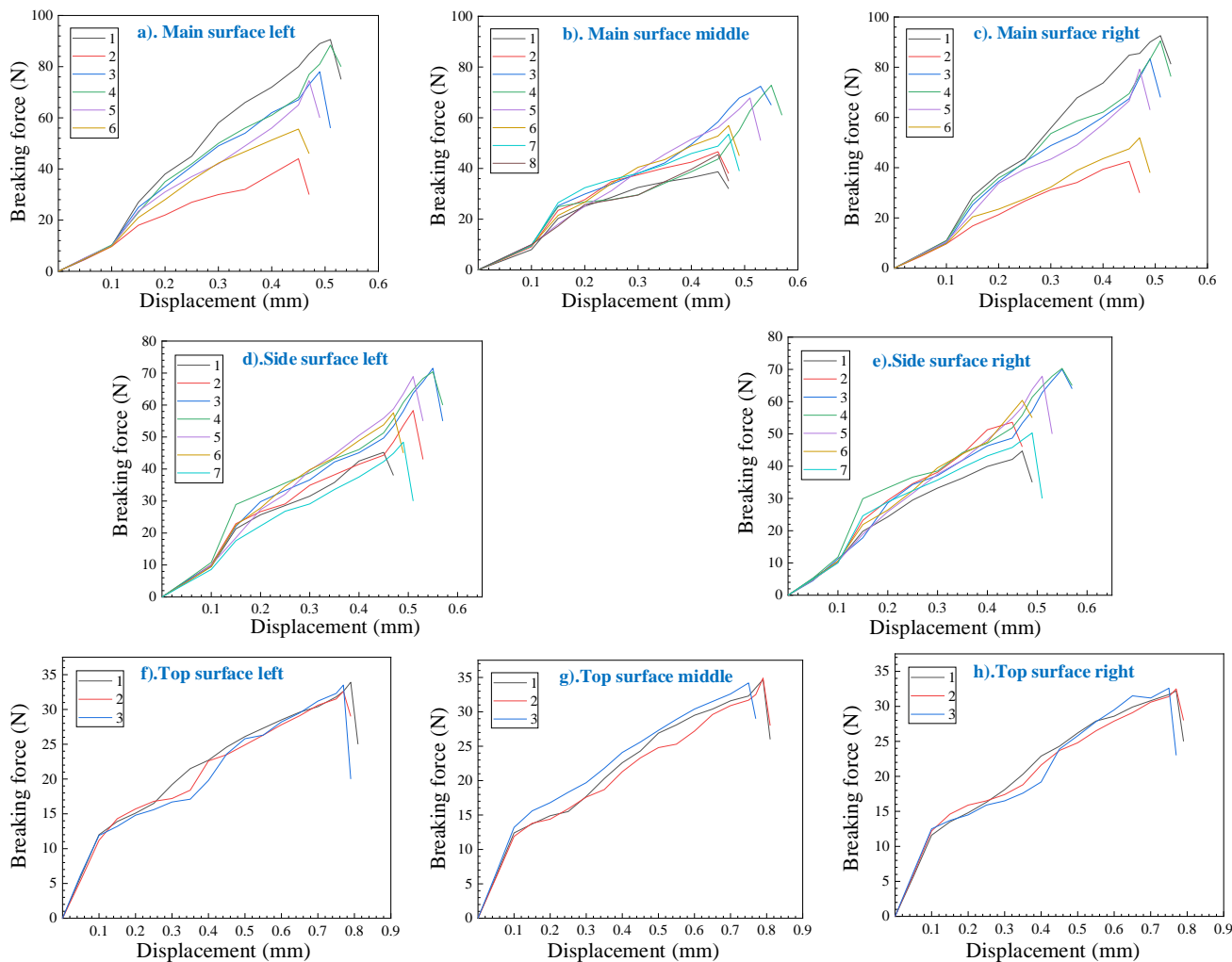


Fig. 6 - Grain surface stress curve

RESULTS AND DISCUSSIONS

Results

The results of the corn kernel damage experiment are summarized in Table 1, highlighting the maximum damage-resistance force for each surface. The data indicate that the main surface of the corn kernel exhibits the highest maximum damage-resistance force, while the top surface demonstrates the lowest. These findings suggest that during corn harvesting, kernel damage can be effectively minimized if the force applied by the threshing element remains below the maximum damage-resistance force of the top surface. This observation aligns with the conclusion that beak threshing results in reduced threshing damage, as reported by (Li et al., 2015).

Table 1

The damage test results of corn kernel (moisture content 24.3 %)

Surface		The damage-resistance force of marked points on corn grain (N)							
		1[*]	2[*]	3[*]	4[*]	5[*]	6[*]	7[*]	8[*]
Main	left	44.5±9.05 [†]	77.2±5.21	90.6±3.76	88.4±3.58	74.6±4.65	54.1±8.57	-	-
	middle	38.7±9.72	46.6±8.74	72.4±5.45	72.8±5.28	67.8±4.26	56.9±4.04	53.5±3.25	45.5±2.57
	right	42.5±7.22	79.2±4.64	92.5±2.83	90.5±3.05	83.4±4.25	51.9±5.12	-	-
Side	left	45.2±4.67	58.3±2.80	71.5±2.47	70.4±1.97	68.9±3.44	57.6±4.35	48.4±3.77	-
	right	44.7±4.36	53.6±3.29	70.3±3.15	70.0±2.37	67.9±3.20	60.4±4.17	50.3±4.56	-

Surface		The damage-resistance force of marked points on corn grain (N)							
		1[*]	2[*]	3[*]	4[*]	5[*]	6[*]	7[*]	8[*]
Top	left	33.9±1.88	32.6±2.17	33.5±1.57	-	-	-	-	-
	middle	34.7±1.76	34.9±1.85	34.2±2.46	-	-	-	-	-
	right	32.2±2.42	32.5±1.71	32.6±1.83	-	-	-	-	-

[*] The numbering of marked points follows the instructions in Fig 4. 44.5 ± 9.0 ; [†] represents the damage resistance force of the first marked point on the left side of the main surface of the corn kernel is 44.5 N and the mean square is 9.05.

While the damage-resistance force provides a partial measure of the relationship between applied force and corn kernel damage, failure theory indicates that a large applied force does not necessarily cause damage. Damage to the corn kernel surface or interior tissue occurs only when the externally applied load exceeds the material's inherent resistance strength. To better quantify this phenomenon, the equivalent damage-resistance strength (EDRS) at each marked point was calculated in this study. To visually represent the characteristics and distribution of damage-resistance strength on the surface of corn kernels (CDDRS-SCK), all calculated results were processed using the Origin software. The resulting contour maps of damage-resistance strength distribution across the three kernel surfaces are shown in Fig. 7. The analysis revealed distinct differences in the characteristics and distribution of damage-resistance strength across the three surfaces, as well as variations within each individual surface. These findings highlight the need for further investigation into the distribution and characteristics of damage-resistance strength on each kernel surface, with a focus on identifying the locations with the highest resistance to damage.

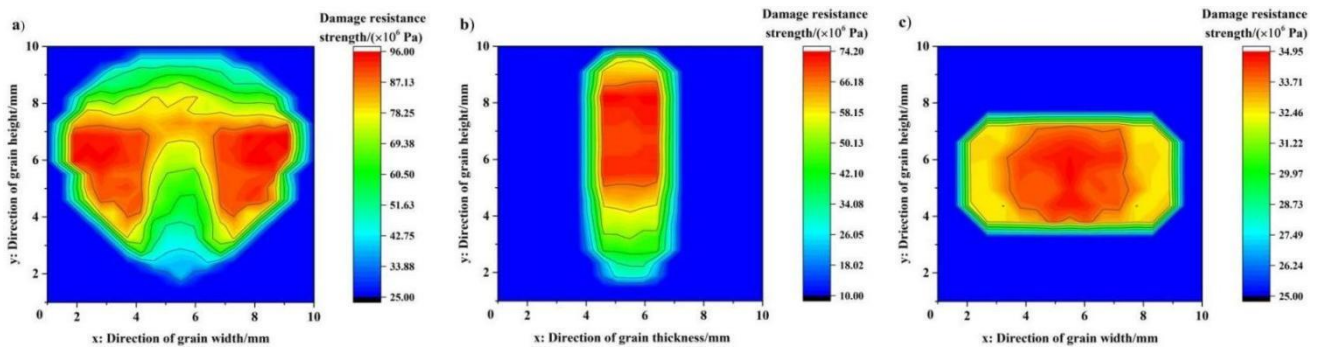


Fig. 7 - The distribution of damage-resistance on the a) main, b) side, and c) top surface of the corn kernel

Characteristics and distribution of damage resistance strength on the main surface of corn kernels

The characteristics and distribution of damage-resistance strength on the main surface of the corn kernel (CDDRS-MSCK) are shown in Fig. 8(a). The x-axis is defined along the lower boundary of the corn kernel, while the y-axis is defined along its left boundary. The CDDRS-MSCK is analyzed in both the width and height directions of the corn kernel. The distribution curve of damage-resistance strength in the horizontal direction at $y=6$ mm, which is symmetrically distributed along the width, is depicted at the top of Fig. 8(a). This curve represents the distribution and characteristics of damage-resistance strength along the width of the kernel's main surface. The results indicate that the damage-resistance strength in the middle of the kernel is approximately 74.5×10^6 Pa, while it symmetrically increases to about 97×10^6 Pa on both sides of the kernel. This pattern is attributed to the structural composition of the kernel in the width direction: the sides predominantly consist of endosperm deposits, whereas the central region mainly contains cotyledons, the germ, and the radicle, which are structurally weaker. Based on the CDDRS-MSCK findings, it is recommended that when the main surface is selected as the primary stress surface for threshing, the loading position should target the sides of the kernel while avoiding the central region. Additionally, to prevent the threshing load from concentrating on the kernel's center, the contact position between the threshing element and the kernel should span more than half the kernel's width.

The vertical directions $x = 3.5\text{mm}$, 5.5mm , and 7.5mm are chosen to evaluate the damage-resistance strength in the height direction at the right of Fig 6. The characteristics and distribution of damage-resistance strength at $x = 3.5\text{mm}$ and $x = 7.5\text{mm}$ are essentially identical in that the damage-resistance strength of the height direction range $y \in [4.2\text{mm}, 6.85\text{mm}]$ approaches $90 \times 10^6 \text{ Pa}$. While the damage-resistance strength decreases gradually in height direction between $y \in [0\text{mm}, 4.2\text{mm}]$ and $y \in [6.85\text{mm}, 10\text{mm}]$. This is because the region is predominantly endosperm and has a progressive maturation pattern. At a height of $x = 5.5\text{mm}$, the damage-resistance strength of the higher component is greater than that of the smaller lower portion. That's because, in the direction of height $x = 5.5\text{mm}$, the structures at the bottom are the radicle, germ, and hypocotyl, while the structures at the top are the endosperm structure. And during corn development, water is transferred from the radicle to the endosperm, and the kernel's aggregation leads the upper surface to lose more water than the lower section.

The vertical positions $x=3.5 \text{ mm}$, 5.5 mm , and 7.5 mm were selected to evaluate the damage-resistance strength in the height direction. The characteristics and distribution of damage-resistance strength at $x=3.5 \text{ mm}$ and $x=7.5 \text{ mm}$ are largely similar. In the height range $y \in [4.2 \text{ mm}, 6.85 \text{ mm}]$, the damage-resistance strength approaches approximately $90 \times 10^6 \text{ Pa}$. However, the damage-resistance strength decreases progressively in the height ranges $y \in [0 \text{ mm}, 4.2 \text{ mm}]$ and $y \in [6.85 \text{ mm}, 10 \text{ mm}]$. This reduction is attributed to the predominance of endosperm tissue in these regions, which exhibits a gradual maturation pattern. At $x=5.5 \text{ mm}$, the damage-resistance strength in the upper region is higher than in the lower region. This difference arises from the structural composition along this height direction: the lower portion predominantly contains the radicle, germ, and hypocotyl, whereas the upper portion consists mainly of endosperm tissue. During corn development, water transfer occurs from the radicle to the endosperm, leading to differential moisture loss. The upper region, composed primarily of endosperm, loses more water due to aggregation effects, resulting in greater resistance compared to the lower section.

When the main surface of the corn kernel is subjected to loading by the threshing element, it is recommended to select loading positions within the width range $x \in [2 \text{ mm}, 4.5 \text{ mm}] \cup [6.5 \text{ mm}, 9 \text{ mm}]$ and the height range $y \in [4.2 \text{ mm}, 6.85 \text{ mm}]$. This selection is expected to be more effective in reducing the corn kernel damage rate.

Characteristics and distribution of damage resistance on the side surface of corn kernels

As illustrated in Fig. 8(b), the characteristics and distribution of damage-resistance strength on the side surface of the corn kernel (CDDRS-SSCK) are presented. In the thickness direction, the damage-resistance strength exhibits a trapezoidal distribution. This pattern arises because the sides of the corn kernel predominantly consist of endosperm, which has a relatively homogeneous texture. Within a specific range, the damage-resistance strength remains largely uniform. However, as the edge of the kernel is approached, the resistance to damage decreases sharply due to stress concentration at the borders. Consequently, when the side of the kernel is subjected to loading by a threshing element, the loading position along the thickness direction has minimal impact on kernel damage. The damage-resistance strength along the vertical direction at $x=5.5 \text{ mm}$ follows an upward-sloping "bathtub" distribution. The maximum damage-resistance strength is observed in the height range $y \in [5.75 \text{ mm}, 8.1 \text{ mm}]$, while it decreases both above and below this range. The decline is more pronounced in the downward direction, as the middle and upper portions of the kernel are primarily composed of endosperm, with greater endosperm accumulation in the middle. In contrast, the lower portion consists mainly of radicle tissue, which exhibits lower resistance to damage.

Based on the analysis, selecting a threshing loading position within the height range $y \in [5.75 \text{ mm}, 8.1 \text{ mm}]$ along the side surface of the corn kernel is more effective in reducing the kernel damage rate during threshing.

Characteristics and distribution of damage resistance on the top surface of corn kernels

The characteristics and distribution of damage-resistance strength on the top surface of the corn kernel (CDDRS-TSCK) are analyzed along the width and thickness directions, as shown in Fig. 8(c). The damage-resistance distribution curve along the width direction at $y=5.5 \text{ mm}$ is illustrated in the upper curve of Fig. 8(c), which exhibits an "inverted bathtub" shape. This pattern arises because the top surface of the corn kernel primarily consists of endosperm, resulting in generally comparable damage-resistance strength. However, the longer endosperm precipitation time in the central region produces a smaller peak in the middle of the curve.

The curve further demonstrates that the damage-resistance strength on the top surface remains stable within the width range $x \in [2.1 \text{ mm}, 8.9 \text{ mm}]$ before rapidly decreasing. This decline is primarily attributed to the narrow upper and lower kernel structures and the stress concentration at the edges. In the thickness direction, the characteristics and distribution of damage-resistance strength, depicted on the right side of Fig. 10, resemble those observed in the thickness direction of the corn kernel's side surface. This similarity indicates that variations in loading positions along the thickness direction have minimal impact on threshing damage.

Therefore, to minimize the risk of corn kernel damage, the threshing element should target the width range $x \in [2.1 \text{ mm}, 8.9 \text{ mm}]$ on the top surface of the kernel.

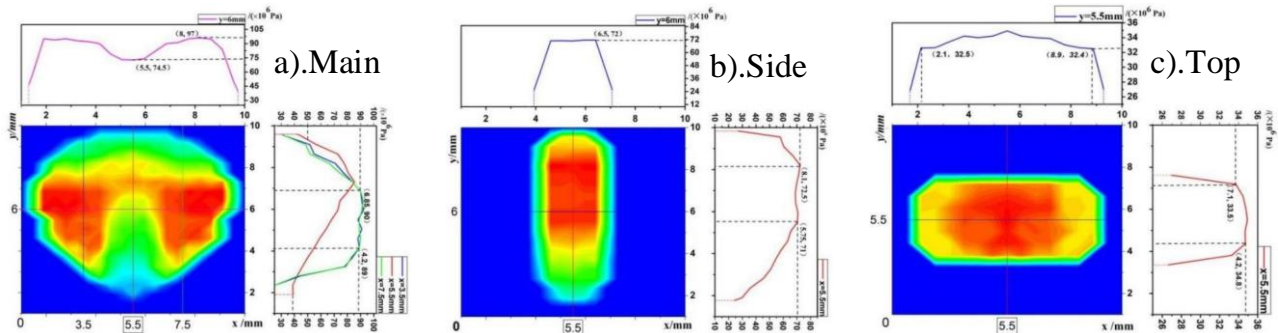


Fig. 8 - Distribution of Damage Resistance on the Surface of Corn Kernels

Discussions

Development of a damage resistance model for corn Kernels

Based on the test results and the distribution patterns of damage-resistance strength on the main, side, and top surfaces of the corn kernel, a spatial rectangular coordinate system was established. The origin was defined at the seed radicle. The Z-axis extends forward perpendicular to the top surface above the origin, the X-axis points leftward perpendicular to the side surface, and the Y-axis points outward perpendicular to the main surface. This coordinate system adheres to the right-hand rule. Using Design Expert software, response surface analysis was performed to construct a damage-resistance model for the typical surfaces of the corn kernel, as illustrated in Fig. 11. The nonlinear regression equation representing the damage-resistance strength of the corn kernel surface was established as follows:

$$\begin{cases} \sigma_z = -29.56x^2y^2 - 36y^3 - 0.85xy^2 + 22.39x^2y - 32.49y^2 + 13.4x^2 - 0.1xy + 39.77y + 0.27x + 74.6 & (z = \pm 2mm) \\ \sigma_x = 24.06y^2 - 0.12zy + 13.69y + 0.11z + 68.41 & (x = \pm 4mm) \\ \sigma_y = -0.42z^2 - 1.52x^2 + 0.098xz + 0.026z + 34.54 & (y = \pm 5mm) \end{cases} \quad (3)$$

In the established model, x denotes the width of the corn grain. y represents the height of the corn grain. z corresponds to the thickness of the corn grain. σ_z is the nonlinear regression equation representing the damage resistance strength of the principal plane of the maize kernel. σ_x is the nonlinear regression equation for the damage resistance strength of the side surface of the corn kernel. σ_y is the nonlinear regression equation for the damage resistance strength of the top surface of the corn kernel.

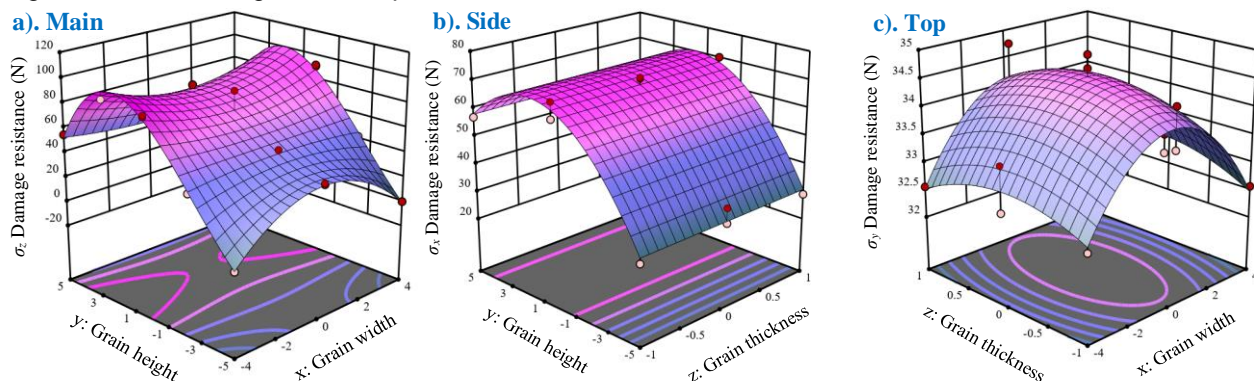


Fig. 11 - The damage resistance strength model of maize kernel typical surface

Among the models, the determination coefficients for the main plane and side surface damage strength were $R^2=0.9726$ and $R^2=0.9764$, respectively, with significance levels of the lack-of-fit terms $P>0.25$, indicating a strong fitting performance for these models. In contrast, the determination coefficient for the top surface damage strength model was $R^2=0.8170$, with a lack-of-fit significance level of $P>0.25$. This comparatively lower fitting accuracy is attributed to the stable distribution of damage strength on the top surface, which is less influenced by location variability. The models enable more accurate prediction of the damage strength of corn kernels across different surfaces and locations, providing valuable guidance for selecting optimal threshing loading positions and reducing threshing damage.

Effect of kernel damage resistance on mechanical threshing performance

Our findings reveal the characteristics and distribution of damage-resistance strength on the defined "damage-susceptible" surfaces of corn kernels. The distribution of damage-resistance strength varies across different kernel surfaces due to the influence of internal structural differences, yet follows specific patterns in certain directions. These distribution laws provide a basis for describing, analyzing, and optimizing the design, working principles, and application of corn harvesting equipment. Building on the analysis of the characteristics and distribution of damage-resistance strength on the surface of corn kernels (CDDRS-SCK), this section explores the influence of various threshing devices and threshing gaps on threshing-induced damage.

Corn kernel threshing primarily employs two methods: tangential flow and axial flow. The tangential flow threshing cylinder operates at rotation speeds ranging from 800 r/min to 1200 r/min (*Fu et al., 2018*), resulting in significant forces applied to the corn kernel surface. Previous analysis indicates that the surface of a corn kernel cannot withstand forces exceeding its maximum damage-resistance force. Under comparable conditions, the load exerted by tangential flow threshing is greater than that of axial flow threshing, leading to a higher rate of kernel damage. This observation aligns with practical experience and explains why most corn harvesters utilize the axial flow threshing technique. Axial flow threshing devices can be further categorized into two modes: transverse axial flow threshing and longitudinal axial flow threshing (*Tang et al., 2022; Wang, 2019*).

These methods differ significantly in the feeding mechanism and action process of the corn ears. In transverse axial flow threshing, the ears are fed radially and move along the axial direction of the drum, with the threshing element completing the process. During this procedure, the initial loading position of the corn kernels is on the top surface, which later transitions to the side surface as the direction of ear movement changes from radial to axial. According to the analysis in Table 1 and the section "The Characteristics and Distribution of Damage-Resistance Strength on the Top Surface of the Corn Kernel," the damage-resistance strength (DRS) of the top surface is the lowest, ranging between 33×10^6 Pa and 35×10^6 Pa. Consequently, this threshing method tends to cause more damage to kernels. In contrast, longitudinal axial flow threshing exerts force consistently on the side surface of the kernel, as the corn ears move entirely in the axial direction. The results from the section "The Characteristics and Distribution of Damage-Resistance Strength on the Side Surface of the Corn Kernel" reveal that the DRS of the side surface is significantly higher, ranging between 60×10^6 Pa and 70×10^6 Pa. This superior strength reduces the likelihood of kernel damage compared to transverse axial flow threshing. These findings align with practical threshing results, where longitudinal axial flow threshing is associated with a lower damage rate (*Wang et al., 2021*).

The influence of the threshing gap on mechanical threshing loss is analyzed theoretically based on the characteristics and distribution of damage-resistance strength on the surface of corn kernels (CDDRS-SCK). Proper regulation of the threshing gap is critical to minimizing threshing loss, as excessively small or large gaps can lead to undesirable outcomes (*Yang et al., 2021*). When the threshing gap is too small, the increased threshing load results in the threshing element acting on the top surface of the corn kernel, which has the lowest damage-resistance strength, or on the lower portions of the side and main surfaces, where the damage-resistance strength decreases gradually from approximately 55×10^6 Pa to 35×10^6 Pa. This inevitably exacerbates kernel damage. Conversely, when the threshing gap is too large, the threshing element primarily interacts with the top surface of the kernel, which also increases threshing loss. Therefore, an appropriate threshing gap is essential to reducing kernel damage, underscoring the need for adjustable threshing gaps in corn harvesters. According to previous studies, the threshing load is highest when processing the entire corn ear, and it decreases significantly as kernels are removed (*Li et al., 2017*).

Regardless of whether a tangential or axial flow threshing mechanism is used, a higher rotational speed of the threshing drum is required at the start of threshing to ensure the removal of kernels from the entire ear. During this initial phase, threshing damage is inevitable due to the mutually exclusive nature of effective threshing and damage prevention. However, as the structure of the threshing mechanism causes the corn ear to align parallel to the drum after partial threshing, the side surface of the corn kernel is subjected to greater stress. The findings in the section "The Characteristics and Distribution of Damage-Resistance Strength on the Side Surface of the Corn Kernel" indicate that the damage-resistance strength along the height direction of the side surface follows an upward-sloping "bathtub" distribution, whereas the strength along the thickness direction remains relatively uniform. Based on these results, it is recommended that the threshing gap be adjusted such that the threshing load is primarily exerted on the upper side of the corn kernel. For the "Zhengdan 958" corn variety studied here, it is advised that the action point of the threshing element be positioned approximately 2–4 mm from the kernel's top surface. While the proposed threshing position is specific to the "Zhengdan 958" variety, it is theoretically derived from experimental results and can serve as a valuable reference for analyzing and selecting optimal threshing positions for other corn varieties. Due to the variability among corn varieties, further adjustments may be necessary to adapt these recommendations to other cultivars.

CONCLUSIONS

This study addresses the issue of corn grain damage during the harvest of high-moisture corn using a combine harvester. A method for evaluating the surface damage load of corn grains is proposed. Multiple sets of loading tests were conducted, with the main, side, and top surfaces of the corn grains subjected to different loading conditions. The aim was to investigate the damage resistance of the various surfaces of the corn grains.

(1) Several groups of surface damage loading tests were conducted on different types of corn grains to investigate the distribution of damage resistance across the flat grain surface. The results revealed significant variations in the damage resistance of the "vulnerable" surface of the flat grain. Specifically, the surface exhibited the highest resistance, followed by the side surface, with the top surface showing the lowest resistance.

(2) By measuring the characteristics and distribution of damage resistance across different surfaces of corn grains, the variation in damage resistance on typical surfaces was determined. Based on the differences in the internal structure of corn grains, a distribution model of damage resistance for the typical surfaces was developed. The main factors influencing the variation in damage resistance were identified. This research provides a basis for selecting optimal threshing loads and positions in the mechanized threshing process of maize.

(3) Based on the characteristics and distribution of the surface damage resistance (CDDRS-SCK) of corn grains, the factors contributing to the lower damage rate observed in longitudinal axial flow threshing were analyzed. Theoretical analysis of the influence of the threshing gap on mechanical threshing was also conducted, and an optimal loading position for corn threshing was proposed. This study provides data support for the development of corn threshing technology and equipment, as well as for determining key operational parameters.

ACKNOWLEDGEMENT

The authors acknowledge the financial support provided by the National Key R&D Program of China (grant no. 2021YFD2000502), the Key Research and Development Plan Project of Shandong Province (grant no. NJYTHSD-202319), the Natural Science Foundation of Shandong Province (grant no. ZR202111290044), and the Modern Agricultural Industrial System of Shandong Province (grant no. SDAIT-02-12).

REFERENCES

- [1] Arnold R. E., & Lake J. R. (1964). Experiments with rasp bar threshing drums - Comparison of open and closed concaves. *Journal of Agricultural Engineering Research*. 9:250-251, United Kingdom.
- [2] Dorsey-Redding C., Hurburgh C. R., Johnson L. A., Fox S. R. (1990). Adjustment of maize quality data for moisture content. *Cereal Chemistry*. 67:292-295, United States.
- [3] Fu J., Zhi C., Lujia H., & Luquan Ren. (2018). Review of grain threshing theory and technology. *International Journal of Agricultural and Biological Engineering*. 11:12-20, China.

- [4] Gao L., Fei L., Xinwei Z., Yongli Z., Xin L., & Weipeng J. (2011). Mechanism of moisture content affecting threshing performance of seed corn (含水率对种子玉米脱粒性能的影响机理). *Transactions of the Chinese Society for Agricultural Machinery*, 42(12), 92–96, 42, Liaoning/China.
- [5] Geng D., Delei T., Xingrui Y., Guoliang S., Qian W., Xiufeng L., & Chengqian Jin. (2020). Design and test of corn flexible threshing cylinder element (玉米柔性脱粒滚筒脱粒元件设计与试验). *Journal of Jilin University (Engineering Edition)*. 50:1923-1933, Shandong/China.
- [6] Gunasekaran S., Deshpande S. S., Paulsen M. R., & Shove G. C. (1985). Size characterization of stress cracks in corn kernels. *Transactions of the ASAE*. 28:1668-1672, United States.
- [7] Kruszelnicka, W., Leda, P., Tomporowski, A., & Ambrose, K. (2024). Breakage behavior of corn kernels subjected to repeated loadings. *Powder Technology*, 435, 119372, Poland.
- [8] Li H., Rong Z., Tianyuan Y., & Zhiyou N. (2022). Experimental study on the impact breakage characteristics of maize kernels (玉米籽粒冲击破碎特性试验研究). *Transactions of the Chinese Society of Agricultural Engineering*. 38(7): 29-37, Hunan/China.
- [9] Li X., & Lei M. (2017). Analysis of finite element method on dynamic contact of corn ear (玉米果穗动力接触的有限元分析). *Journal of system simulation*. 29:67-75, Henan/China.
- [10] Li X., Yingdong M., Xin J., & Lianxing G. (2015). Design and test of corn seed bionic thresher (玉米种子仿生脱粒机设计与试验). *Journal of Agricultural Machinery*. 46:97-101, Henan/China.
- [11] Petkevichius, S., Shpokas, L., & Kutzbach, H.D. (2008). Investigation of the maize ear threshing process. *Biosystems engineering*, 99(4), 532-539, Germany.
- [12] Sehgal S. M., & Brown W. L. (1965). Cob morphology and its relation to combine harvesting in maize. *Iowa State Journal of Science*. 39:251-268, Italy.
- [13] Tang X., Chengqian J., Guohai Z., Zhen G., Nan Z., & Bei X. (2022). Research status of threshing and separating device for combine harvester in China (我国联合收获机脱粒分离装置的研究现状). *Agricultural Mechanization Research*. 44:1-9, Shandong/China.
- [14] Vyn T. J., & Moes J. (1988). Breakage susceptibility of corn kernels in relation to crop management under long growing season conditions. *Agronomy Journal*. 80:915-920, Canada.
- [15] Waelti H. (1967). Physical properties and morphological characteristics of maize and their influence on threshing injury of kernels. *Iowa State University*. Ames, Iowa, United States.
- [16] Wang X. (2019). *Study on threshing and separation system with adjustable concave clearance (脱粒间隙可调节的脱粒分离系统研究)*. [Ph.D.diss.], Hunan Agricultural University. Hunan/China.
- [17] Wu D., Feng X., & Changsheng Y. (2006). Performances comparison between plank-tooth corn shellers and nail-tooth corn shellers (板齿式与钉齿式玉米脱粒机的性能比较). *Agricultural mechanization research*. 10:78-80, Heilongjiang/China.
- [18] Wang J., Changsu X., Yanan X., Xin Q., Ziming L., & Han T. (2021). Vibration Analysis and Parameter Optimization of the Longitudinal Axial Flow Threshing Cylinder. *Symmetry*. 13:571, China.
- [19] Yang R., Dongquan C., Xiantao Z., Zhiguo P., & Shuqi S. (2021). Optimization design and experiment of ear-picking and threshing devices of corn plot kernel harvester. *Agriculture*. 11:904, China.
- [20] Yi K., Dewen Z., Xinwei Z., Zhihua Y., & Zheng L. (2016). Effect of moisture content on corn grain harvesting mechanization (含水率对玉米籽粒机械化直接收获的影响). *China Journal of Agricultural Machinery Chemistry*. 37:78-80, Anhui/China.
- [21] Yu S., Yaoming L., Zheng M., Jianting W., Biyou H., Lizhang X., & Zhong T. (2019). Study on damage of corn kernel and cob in corn kernel harvesting (玉米籽粒直收中籽粒及穗轴破损形态研究). *Journal of Agricultural Mechanization Research*, 10:208-212, Jiangsu/China.
- [22] Yuan Y., & Yuzhen L. (1996). Experimental investigation of mechanical properties for corn kernels (玉米籽粒力学性质的试验研究). *Journal of Jilin Agricultural University*. 04:78-81.
- [23] Zhao W. (2012). *Research on combined type of spiral bar tooth threshing mechanism for seed corn (组合式螺旋板齿种子玉米脱粒装置研究)*. [Ph.D.diss.], Northwest A&F University, Shanxi/China.

THE MULTIPLE APPLICATIONS OF INDUSTRIAL HEMP (*CANNABIS SATIVA L.*) IN THE CONTEXT OF SUSTAINABLE DEVELOPMENT

APLICAȚIILE MULTIPLE ALE CÂNEPILII INDUSTRIALE (*CANNABIS SATIVA L.*) ÎN CONTEXTUL DEZVOLTĂRII SUSTENABILE

Lorena-Diana POPA¹⁾, Simona-Florina ISTICIOAIA¹⁾, Nicolae-Valentin VLĂDUȚ²⁾, Gheorghe MATEI³⁾, Alexandra LEONTE¹⁾, Iuliana GĂGEANU²⁾, Florin NENCIU²⁾, Paula-Lucelia PINTILIE¹⁾, Andreea-Sabina PINTILIE¹⁾, Oana MILEA²⁾, Mihaela ROȘCA⁴⁾, Anca PANDA⁵⁾, Gabriel-Ciprian TELIBAN⁴⁾, Marian BURDUCEA^{4,6)}

¹⁾ Agricultural Research and Development Station Secuieni / Romania;

²⁾ National Institute of Research-Development for Machines and Installations Designed for Agriculture and Food Industry – INMA Bucharest / Romania; ³⁾ University of Craiova / Romania;

⁴⁾ "Ion Ionescu de la Brad" Iasi University of Life Sciences / Romania;

⁵⁾ Agricultural Research and Development Station Lovrin / Romania

⁶⁾ "Alexandru Ioan Cuza" University / Romania

Tel: 0232 20 1000; E-mail: mihaela.rosca@iuls.ro; marian.burducea@yahoo.com

DOI: <https://doi.org/10.35633/inmateh-75-88>

Keywords: industrial hemp, multifunctional crop, food and pharmaceutical products, hempcrete, biofuels and bioenergy, phytoremediation, sustainability

ABSTRACT

*This review explores the multiple directions of industrial hemp (*Cannabis sativa L.*) utilization at a global level, highlighting the importance of this crop as a renewable, sustainable, and environmentally friendly resource. While hemp has traditionally been employed for the production of fibers, seeds, and medicinal products, recent studies have expanded its applications into innovative fields such as eco-friendly construction materials (e.g., hempcrete and composite materials), automotive and aerospace industries, cosmetics, biofuels, and others. The remarkable properties of hemp, including low density, superior mechanical strength, carbon sequestration capability, and moisture regulation, helps reduce energy consumption and enhances the performance of construction materials, thereby providing competitive advantages in sustainability-oriented sectors. Moreover, hemp extracts and oils, rich in bioactive compounds (essential fatty acids, vitamins, antioxidants, and cannabinoids), have demonstrated therapeutic potential, reinforcing the role of hemp in the development of food, cosmetic, and pharmaceutical products. Additionally, hemp significantly contributes to phytoremediation by absorbing heavy metals and contaminants from the soil, and hemp fibers stand out for their durability and resistance, being valued in the textile industry for their ecological characteristics and superior performance. Industrial hemp stands out for its high versatility, and its valuable properties along with its favorable environmental impact support its integration into a wide range of sectors, opening promising perspectives for a more sustainable and environmentally responsible future.*

REZUMAT

*Această lucrare de sinteză explorează direcțiile multiple de utilizare ale cânepii industriale (*Cannabis sativa L.*) la nivel global, evidențiind importanța acestei culturi ca resursă regenerabilă, sustenabilă și cu impact ecologic redus. În timp ce cânepa a fost folosită tradițional pentru producția de fibre, semințe și medicamente, studiile recente au demonstrat extinderea aplicațiilor sale în domenii inovatoare precum construcțiile ecologice (de exemplu, betonul de cânepă și materialele compozite), industria auto și aeronautică, cosmeticele, biocombustibilii și altele. Proprietățile remarcabile ale cânepii, de la densitatea redusă și rezistența mecanică superioară la capacitatea de sechestrare a carbonului și de reglare a umidității, contribuie la reducerea consumului de energie și la îmbunătățirea performanțelor materialelor de construcție, oferind astfel avantaje competitive în sectoare ce pun accent pe sustenabilitate. Mai mult, extractele și uleiurile din cânepă, bogate în compuși bioactivi (acizi grași esențiali, vitamine, antioxidanți și cannabinoidi), au demonstrat potențial terapeutic, consolidând rolul acestei culturi în dezvoltarea produselor alimentare, cosmetice și farmaceutice. În plus, cânepa contribuie semnificativ la fitoremediere, absorbind metale grele și contaminanți din sol, iar fibrele textile de cânepă se remarcă prin durabilitate și rezistență, fiind apreciate în industria textilă pentru caracteristicile lor ecologice și performanțele superioare. Cânepa industrială se remarcă prin versatilitatea sa ridicată, iar proprietățile valoroase și impactul ecologic favorabil pe care îl are susțin integrarea acesteia într-o gamă largă de sectoare, deschizând perspective promițătoare pentru un viitor mai sustenabil și mai responsabil din punct de vedere ecologic.*

INTRODUCTION

Industrial hemp (*Cannabis sativa* L.) is a remarkably versatile plant, with significant social and economic value, being grown for a wide range of purposes, from the production of textile fibers, hurds, and seeds to the extraction of oils, with applications that include medicinal and recreational uses (Adesina et al., 2020; Cerino et al., 2021; EIHA Conference 2016–2023). Considered the ideal crop for the circular bioeconomy of the future, hemp is one of the oldest plants cultivated by humanity, with documented use dating back to around 8000 BCE, having played an essential role in the evolution of human agriculture (Cherney and Small, 2016; Promhuad et al., 2022). Central Asia is considered the birthplace of domesticated hemp, with the oldest evidence of hemp fiber use discovered in Taiwan (Manian et al., 2021). Starting around 2700 BCE, hemp began to be cultivated in China, becoming an important agricultural practice used to obtain various products (Mariz et al., 2024).

Industrial hemp can be harvested and valorized in multiple fields, being used in the production of food, feed, pharmaceutical and cosmetic products, construction materials, biodegradable plastics, textiles, paper, biofuels, and as energy source (Adesina et al., 2020; Cerino et al., 2021; Popa et al., 2021; EIHA Conference 2016–2023; Mariz et al., 2024). It is estimated that there are approximately 25,000 hemp-derived products, distributed across various industrial and commercial subsectors (Kraenzel et al., 1998). Its unique properties, especially its ecological benefits and high yield of natural technical fibers, make hemp a valuable crop for the development of a sustainable, biomass-based economy (Carus et al., 2013).

Hemp cultivation areas have shown an upward trend in recent years, both in Europe and globally. In fact, since the late 20th century, hemp cultivation has been revitalized and has emerged as one of the fastest-growing agricultural and industrial markets in recent decades (EIHA Conference 2016–2023).

Hemp is a multifunctional crop (Adesina et al., 2020), potentially addressing many existing climate and environmental issues. Its versatile nature could transform into billion-dollar markets, especially in the segments focused on reusable, recyclable, and compostable biomaterials. According to statistical evaluations (EIHA Conference 2023), the industrial hemp market has a potentially higher value (USD 350 billion) than the cannabis market (USD 233 billion).

Hemp has become a global billion-dollar business, and its market share in the industrial sector has reached new dimensions, with a growing number of publicly listed companies. According to a consumer behavior survey, the wholesale market value of hemp in the United States was estimated at over USD 700 million (Valizadehderakhshan et al., 2021; Malabadi et al., 2023). Globally, the industrial hemp market was valued at USD 4.13 billion in 2021, with forecasts indicating an annual growth rate of 16.8% for the period 2022–2030 (Malabadi et al., 2023). This expansion is supported by increasing demand from various industries using it, as well as by consumer interest in natural fibers, sustainable products, and hemp seed extracts/products (oil, press cakes, seeds, etc.) recognized for their nutritional and functional properties (EIHA Conference 2019; Malabadi et al., 2023).

In the United States, the market for hemp seeds and fiber is expected to grow at an annual rate of 17.1% between 2023 and 2030, reaching a value of approximately USD 16.75 billion (Khanal and Shah, 2024). In 2022, Canada was the world's largest producer of hemp seeds, with a total output of 32,988 tons (Čolić et al., 2024). Turkey, also considered a major global hemp producer, has recently increased its investments and support measures for this crop. The country's current strategy aims to expand production to meet the growing needs of various economic sectors (Aslan, 2024).

According to data from FAOSTAT, USDA, and TURKSTAT, the global production of hemp for fiber was estimated at 302,000 tons, cultivated on 79,000 hectares. This upward trend reflects not only the increasing demand for hemp-based products but also the ecological and economic advantages of this sustainable crop (Textile Exchange, 2023).

The aim of this paper is to analyze the multiple directions of industrial hemp (*Cannabis sativa* L.) utilization, in the context of its agricultural, economic, and ecological potential, highlighting both traditional uses, such as fiber, seed, and oil production, as well as innovative applications in biocomposites, bioenergy, and phytoremediation.

1. Use in human and veterinary medicine/pharmacy

Hemp (*Cannabis sativa* L.) represents a valuable source for medical and pharmaceutical applications due to its rich content of cannabinoids, the main active chemical compounds with unique pharmacological properties, as well as terpenes and flavonoids. This species contains over 100 cannabinoids, among the most important being THC (delta-9-tetrahydrocannabinol) and CBD (cannabidiol), each with distinct therapeutic

applications (Van Bakel et al., 2011; Andre et al., 2016; Aizpurua-Olaizola et al., 2016; Adesina et al., 2020; Seltzer et al., 2020; Malabadi et al., 2023).

THC, the main psychoactive cannabinoid, is approved in many European countries for medicinal uses, including the treatment of chronic pain, glaucoma, and disorders associated with multiple sclerosis (EIHA Conference, 2022). For example, the market dedicated to medicinal THC in Germany is showing an upward trend in both sales and the number of prescriptions issued. However, several challenges remain to be addressed, including an inconsistent and incoherent legal framework, ambiguous regulations, and regional disparities (EIHA Conference 2022), all of which limit the consistent use of this compound in medicine (Van Bakel et al., 2011).

CBD, the main non-psychoactive cannabinoid, is recognized for its anti-inflammatory, neuroprotective, and antioxidant effects (Sharma et al., 2014; Piomelli and Russo, 2016; Malabadi et al., 2023). Clinical studies have demonstrated its potential in treating inflammatory conditions, arthritis, diabetes, neurodegenerative diseases, cancer, drug-resistant epilepsy, and pain (Schultes, 1970; Izzo et al., 2009; Seltzer et al., 2020; Valizadehderakhshan et al., 2021; Malabadi et al., 2023). In addition, preclinical research suggests that CBD exerts a wide range of biological effects, including anticonvulsant, anxiolytic, anti-inflammatory, immunomodulatory, and antineoplastic activities (Cerino et al., 2021), potentially reducing inflammation and oxidative stress, with applications in the treatment of neurodegenerative diseases such as Alzheimer's and Parkinson's (Cassano et al., 2020; Bhunia et al., 2022).

Epidiolex, a drug approved by the European Medicines Agency (EMA) and the U.S. Food and Drug Administration (FDA), uses CBD to treat epileptic seizures associated with Lennox-Gastaut and Dravet syndromes (FDA, 2018). To date, the U.S. FDA has approved THC-based drugs such as nabilone and dronabinol for the treatment of chemotherapy-induced nausea and vomiting, sleep disorders, and weight loss regulation in HIV-AIDS patients. In Australia, Canada, and several European countries, nabiximol, a combined THC-CBD formulation, has been approved for the treatment of spasticity associated with multiple sclerosis, with positive results confirmed by recent studies (Mashabela and Kappo, 2024).

Recent studies explore the application of cannabinoids in oncology therapies, highlighting the potential of delta-9-tetrahydrocannabinol (THC) and cannabidiol (CBD) to inhibit tumor growth, alleviate the side effects of chemotherapy, and induce cellular processes such as autophagy and apoptosis, alongside significant anti-inflammatory effects (Mashabela and Kappo, 2024). Various preclinical studies have demonstrated potential anticancer properties of CBD and THC, which are experimentally used in the treatment of cancers such as prostate and breast cancer (EIHA Conference, 2022; Guggisberg et al., 2022). Researchers and medical professionals support the use of cannabis extracts in medical prescriptions, especially following the legalization of cannabis in numerous countries (Mashabela and Kappo, 2024).

Protein hydrolysates from hemp seeds have been studied for their antihypertensive and antioxidant properties, with promising results in both in vitro and in vivo studies on rats (Girgih et al., 2011). In addition, hemp is used in medicinal and therapeutic products, including pharmaceuticals for conditions such as prostate cancer, breast cancer, coronary heart disease, constipation, blood cholesterol reduction, and, experimentally, in the treatment of glaucoma, epilepsy, multiple sclerosis, dystonia, asthma, psychosis, Niemann–Pick disease, and topical infections (Găucă and Berea, 1997; Hazekamp and Fishedick, 2012).

McPartland and Russo (2001) emphasize the therapeutic potential of terpenes, describing their role in modulating cannabinoid receptors and regulating neurotransmitters such as serotonin, dopamine, and GABA. This synergistic interaction between terpenoids and cannabinoids opens new perspectives for the treatment of pain and mood disorders.

Essential oils extracted from hemp flowers are valued in the pharmaceutical industry due to their content of β -myrcene and limonene, recognized for their anti-inflammatory and sedative effects (Gurgel do Vale et al., 2002; Hazekamp and Fishedick, 2012). Additionally, hemp oils have demonstrated antimicrobial properties and the ability to accelerate wound healing following topical application (Callaway, 2004; Wylie et al., 2020). Other terpenes, such as β -caryophyllene, exert anti-inflammatory, analgesic, and anxiolytic effects, being beneficial in the management of conditions such as osteoarthritis, bronchial asthma, and colitis. Their efficacy is closely related to the interaction with inflammation-related receptor channels and the reduction of oxidative stress (Cerino et al., 2021).

Hemp is also gaining ground in veterinary medicine due to the therapeutic properties of cannabinoids, especially CBD. Hemp-based products are used to alleviate symptoms in animals, including anxiety, chronic pain, and inflammation (Wylie et al., 2020). Recent studies confirm the positive effects of CBD supplements on animals, focusing on reducing inflammation and improving quality of life, particularly for musculoskeletal,

neurological, or epileptic conditions (Gamble et al., 2018; McGrath et al., 2019; Garcia et al., 2022; Kosukwatthana et al., 2024).

A wide range of commercial cannabidiol (CBD)-based products are available for dogs and cats, used to manage conditions such as anxiety, depression, and chronic pain (Solcan et al., 2023). Studies conducted by Solcan (2017) and Solcan et al. (2002) recommend these products for the treatment of psychogenic dermatitis and chronic atopic dermatitis, as well as for managing anxiety and depression in companion animals (Falcă et al., 2011). Additionally, CBD can be used as palliative treatment in certain tumor diseases (Solcan et al., 2023).

2. Uses in human and animal nutrition

Applications in human nutrition

Industrial hemp represents a valuable resource for the food industry due to the exceptional nutritional profile of products derived from this crop. In Europe in particular, hemp has been considered for centuries a traditional source of nutritious food (Aladic et al., 2015), being used for the production of oils, flour, protein, dietary fibers, and other functional products such as hemp milk (Aladic et al., 2015; Lančaričová et al., 2021; Yano and Fu, 2023; Rizzo et al., 2023).

Various parts of the hemp plant, such as seeds and inflorescences, are valuable sources of food and ingredients for nutritional supplements. While hemp inflorescences are rich in terpenes, polyphenols, and non-psychoactive but biologically active cannabinoids such as cannabidiol (CBD), which exerts anxiolytic, spasmolytic, and anticonvulsant effects (Mechoulam et al., 2002), hemp seeds, with their high nutritional value and pleasant nutty flavor, are a valuable source of essential amino acids, fatty acids, minerals, vitamins, fiber, and high-quality protein essential for a balanced diet (Callaway, 2004; Carus and Sarmiento, 2016; Lančaričová et al., 2021; Montero et al., 2023). Additionally, hemp seed oil is a source of healthy polyunsaturated fatty acids, and hemp sprouts are rich in antioxidants (Cerino et al., 2021).

Hemp seeds are rich in high-quality, balanced, easily digestible, and sustainable proteins, containing between 20% and 30% protein, depending on variety and cultivation conditions. They provide all essential amino acids, including arginine, and present a unique protein profile consisting mainly of edestin and albumin (Callaway, 2004; Kolodziejczyk et al., 2012; Mihoc et al., 2012; Carus and Sarmiento, 2016; Montero et al., 2023; Yano and Fu, 2023). This protein profile makes hemp seeds suitable for use in energy bars, protein flour, and nutritional shakes. Studies show that these proteins may help lower blood pressure, cholesterol, and oxidative stress, having a positive effect on the cardiovascular system and supporting overall immune health (Callaway, 2004; Girgih et al., 2011a; Girgih et al., 2011b; Montero et al., 2023; Rizzo et al., 2023).

The benefits of using hemp seeds in food also derive from their valuable lipid composition, containing more than 80% polyunsaturated fatty acids, such as linoleic acid (ω -6) and alpha-linolenic acid (ω -3), in a 3:1 ratio, considered optimal for human health (Simopoulos, 2002; Oomah et al., 2002; Simopoulos, 2008; Pop et al., 2012; Rezapour-Firouzi et al., 2013; Lančaričová et al., 2021; Montero et al., 2023; Rizzo et al., 2023; Tura et al., 2023). In addition, hemp seeds are a valuable source of dietary fiber, vitamins, minerals, and contain 20–36% carbohydrates, along with other essential phytonutrients (Oomah et al., 2002; Callaway, 2004; Sirițanu and Sirițanu, 2007; Rezapour-Firouzi et al., 2013; Aladic et al., 2015; Popa et al., 2021; Yano and Fu, 2023).

Hemp seeds are also an important source of fat-soluble vitamins, especially vitamin E and vitamin A. Among the present tocopherol isomers (α -, β -, γ -, and δ -), γ -tocopherol is predominant and contributes to the oxidative stability of the oil, while α -tocopherol, though present in lower amounts, is the most biologically active. Moreover, hemp provides a wide range of essential macro- and microelements such as phosphorus, potassium, magnesium, calcium, iron, zinc, and copper, nutrients important for maintaining metabolic and physiological functions (Montero et al., 2023).

Due to the absence of gluten, lactose, and genetically modified organisms (GMOs), hemp products are suitable for special diets, including vegetarian, vegan, and paleo (EIHA Conference, 2016–2023; Wylie et al., 2020). Recognized for their nutritional value, hemp seeds have become an important source of nutrients, now integrated into current dietary trends and available in most European supermarkets in muesli, chocolate, and other products. These seeds can also be processed into beverages and yogurts similar to soy products (EIHA Conference, 2016–2023). In the form of protein flour, cold-pressed oil, dehulled and consumed raw or roasted, hemp seeds are a beneficial food, also having therapeutic applications for various ailments (Sirițanu and Sirițanu, 2007). Thanks to their nutty flavor, hemp seed flour is used to enrich bakery products (Adesina et al., 2020), helping to increase their protein and fiber content. Some studies suggest that the inclusion of hemp in products such as functional bread or nutritional bars may support digestive and metabolic health (Popa et al.,

2021; *EIHA Conference, 2016–2023*). Innovative food products developed from hemp highlight its role in a healthy and sustainable diet.

In recent years, public-private partnerships in Europe have focused on processing hemp protein into various food forms and textures and developing innovative products, with analyses revealing a very good and complete amino acid profile containing all essential amino acids (*EIHA Conference, 2023*).

High-quality hemp oil is obtained mainly by pressing industrial hemp seeds. This vegetable oil is 100% natural, with a greenish color and fine texture, and is commonly used unheated as a nutritional supplement or olive oil substitute, having a pronounced nutty aroma. Hemp seed oil is not recommended for cooking or frying at high temperatures due to its low smoke point (*Cherney and Small, 2016*). Cold-pressed, this oil stands out for its nutritional value thanks to its content of polyunsaturated fatty acids, phenols, flavonoids, and vitamin E, which give it significant antioxidant and anti-inflammatory properties by neutralizing free radicals (*Simopoulos, 2002; Cherney and Small, 2016; Cerino et al., 2021; Popa et al., 2021; Kaur and Kander, 2023*). Thanks to its distinctive flavor, hemp oil is frequently used in salads, canned goods, pastries, and confectionery, as well as a dietary supplement with benefits for skin and hair health (*Şandru et al., 1996; Cherney and Small, 2016; Gherasim, 2017; Popa et al., 2021; Kaur and Kander, 2023*).

Research conducted by IBA Bucharest highlighted that hemp seed cakes obtained by cold pressing are a valuable source of bioactive proteins, minerals, and total fiber, making them an ideal ingredient for the bakery industry (*Popa et al., 2021*). Thus, the use of these cakes allows for the creation of functional food products capable of supporting and improving health and positively impacting quality of life.

With proper quality management and marketing, the use of hemp seeds and oil in healthy human nutrition will continue to grow (*Carus and Sarmento, 2016*).

The use of hemp leaves provides a significant intake of calcium, magnesium, iron, vitamin E, flavonoids, phenols, chlorophyll, and other beneficial compounds, making them an exceptional natural and regional ingredient for teas, infusions, smoothies, or dietary supplements. They are an ideal source of minerals and nutrients in their natural form, especially recommended for vegans, without inducing psychotropic effects (*Simopoulos, 2002; Popa et al., 2021; Teleszko et al., 2022; EIHA Conference 2023*).

Besides its use in medicines, hemp is also used in the production of nutritional supplements such as CBD capsules and tinctures, which represent approximately one-third of the global \$1.34 billion CBD market (*Cerino et al., 2021*). These products are marketed for their benefits in reducing anxiety, improving sleep, and supporting the immune system (*EIHA Conference, 2023*). However, regulations regarding hemp-based supplements vary globally, limiting uniform access to these products (*Kaur and Kander, 2023*). In Europe, as a dietary supplement, CBD concentrate was classified as a novel food in January 2019 and therefore must undergo the approval process, which is cumbersome and expensive.

Hemp sprouts/microgreens can also be consumed as food. They are characterized by a high content of organic acids, amino acids, total polyphenols, flavonoids, etc., compounds known for their positive effects on cardiovascular and metabolic health (*Cerino et al., 2021; Montero et al., 2023; Popa et al., 2024*).

Applications in animal nutrition

Hemp plays an increasingly important role in animal nutrition, particularly through seeds and the oil obtained from pressing them. Hemp-based feed is becoming increasingly popular, being a sustainable and healthy alternative to conventional feed. It provides a natural source of protein and also offers essential fatty acids and fiber, contributing to a balanced diet with beneficial effects on animal health (*EIHA Conference, 2023*).

The main market for hemp seeds in animal nutrition is feed for birds and fish, which require high intakes of omega-3 and omega-6 for optimal development (*Carus and Sarmento, 2016*). Unhulled seeds and cakes resulting from oil extraction provide both valuable proteins and essential fatty acids with important nutritional benefits (*Oomah et al., 2002; Constantinescu, 2011; EIHA Conference, 2022*). Some studies also show that including these in laying hens' diets improves the omega fatty acid profile in eggs, thereby increasing the nutritional value of the final product (*Callaway, 2004*).

In the context of rising feed prices and supply challenges, hemp-based products represent a sustainable alternative, offering both economic and nutritional benefits (*EIHA Conference, 2022*).

Recent studies highlight that the inclusion of hemp-derived products in animal feed, including raw hemp oil as a valuable source of polyunsaturated fatty acids, may contribute to supporting overall health by improving cognitive function and reducing inflammation (*EIHA Conference, 2022; Haake et al., 2023; Puttharaksa et al., 2025*).

Against the backdrop of growing global demand for healthy and sustainable food, hemp emerges as a valuable nutritional resource suitable for both human and animal consumption. As the market for hemp-based food products expands, cereal bars, hemp seed butter, and plant-based beverages are gaining popularity in Europe and North America, reflecting the growing interest in natural and ecological diets (*Kaur and Kander, 2023*).

The economic potential of hemp in the food industry is estimated at billions of dollars, and the development of innovative products supports the transition to a more sustainable global food industry. In this context, the turnover in the hemp food segment and related raw materials is growing significantly. The increasing demand for natural food products has stimulated trade in hulled and unhulled seeds, hemp oil, protein powder, and leaves, visible both in retail and the industrial sector. Furthermore, collaboration among farmers, associations, and processors, focused on seed quality as a raw material, contributes to the sustainable consolidation of the hemp food market (*EIHA Conference 2016–2023*).

3. Use in the cosmetic industry

Industrial hemp has become increasingly used in the cosmetic industry due to its active compounds with multiple benefits for skin health, such as essential fatty acids, vitamins, and antioxidants.

Hemp-based cosmetic products, especially those made from cold-pressed seed oil, are appreciated for their ability to hydrate and soothe dry, irritated, or sensitive skin (*Cherney and Small, 2016*). The value of the oil is particularly due to its linoleic, α -linolenic, and γ -linolenic acid content, which have a significant impact on cellular membrane functions (*Vogl et al., 2004*). In addition to its role in restoring the skin's lipid barrier, hemp oil also helps prevent transepidermal water loss, maintaining optimal hydration (*Kaur and Kander, 2023*); it also contributes to the healing of skin inflammations and balancing acne conditions (*Vogl et al., 2004; Sapino et al., 2005*). Furthermore, hemp oil is used in personal care products such as soaps, lotions, and bath gels (*Şandru et al., 1996; Gherasim, 2017; Popa et al., 2021; Malabadi et al., 2023*), as well as in hair care products like shampoos and conditioners (*Adesina et al., 2020*), due to its ability to strengthen hair strands and moisturize the scalp. Vitamin E and essential fatty acids contribute to reducing hair loss and improving hair elasticity (*Popa et al., 2021*).

Cannabidiol (CBD), the main non-psychoactive compound in hemp, is increasingly used in the cosmetic industry due to its antioxidant, anti-inflammatory, anti-wrinkle, and brightening effects (*Karache and Singh, 2019; Chen et al., 2023*). The growing demand for natural and sustainable cosmetics has led to the integration of hemp into innovative formulations such as anti-aging creams, serums, deodorants, and facial masks (*Karache and Singh, 2019; Kaur and Kander, 2023*). Hemp extracts are appreciated for their antioxidant properties, helping to protect the skin against free radicals and reduce signs of premature aging (*Kaur and Kander, 2023*).

4. Use in the construction industry

Industrial hemp stands out as an ecological and sustainable solution in the construction industry due to its remarkable properties, such as thermal and acoustic insulation, durability (<https://www.carmeuse.com/ro-ro/aplicatii/materiale-de-constructii/hempcrete>; https://dumbrava47.ro/constructii_verzi/despre-proprietatile-ignifuge-ale-betonului-de-canepa-hempcrete/; *Kaboré et al., 2024*) and mechanical strength. Hemp-based construction materials include hempcrete, insulating panels, plasters, and composites for lightweight structures.

An interesting segment of the green materials market is the use of hemp shives (hurds) combined with lime for construction, a segment that holds approximately 16% market share (*Carus and Sarmiento, 2016*). Hempcrete, obtained by mixing hemp shives with hydrated lime, is an ecological material (<https://www.casadecanepa.org/betonul-de-canepa>), lightweight yet strong, used in wall, roof, and floor construction (*Asli et al., 2021; Kaboré et al., 2024*). Studies show that this material has a significantly lower environmental impact than conventional building materials (*Pretot et al., 2014*), due to its ability to absorb and store CO₂ and its low embodied energy (*Pretot et al., 2014; Adam, 2024; Kaboré et al., 2024*).

The favorable thermal properties of hempcrete (*Limam et al., 2016*) are due in part to its low thermal conductivity and good moisture regulation capacity, contributing to improved hygrothermal comfort and reduced energy demand (*Collet and Pretot, 2012; Palumbo et al., 2016*). Moreover, hempcrete is used in passive house construction thanks to its performance characteristics, being a recyclable, biodegradable, non-flammable, and mold- and pest-resistant material, making it ideal for green building projects (*Vogl et al., 2004; Asli et al., 2021; EIHA Conference, 2018*).

In the same vein, Romania has also successfully combined traditional raw materials, hemp and hydrated lime, with modern technologies for “green” construction and renovation. The resulting material, 100% sustainable and biodegradable, is naturally fire- and pest-resistant, allows water vapor permeability, and “breathes”; in this way, it regulates humidity by absorbing excess moisture and releasing it when levels drop below optimal (*EIHA Conference, 2018*). It is a carbon-negative material that continuously absorbs CO₂, making it ideal for those seeking to minimize environmental impact (<https://app.materlibrary.ro/ro/materiale/SHEMP-0001>).

The hemp shives resulting as a by-product of primary hemp processing can be used as a building material or as sound insulation between drywall panels (*Şandru et al., 1996*), while hemp fibers are used in the production of ecological insulation materials, which provide efficient thermal and acoustic insulation (*Kymäläinen and Sjöberg, 2008*). In 2015, hemp fiber insulation accounted for about 26% of total applications, being the second most important use (*Carus and Sarmento, 2016*). These materials are valued for their ecological properties, being biodegradable, non-toxic, offer high thermal performance, and have a long lifespan, thus contributing to reducing the carbon footprint of the final products (*Carus et al., 2013; Călăţan, 2018; Adam, 2024*). Romania, France, and Germany are among the pioneering countries in implementing eco-friendly materials, such as hemp fiber, in building insulation (*Călăţan, 2018*).

Beyond construction, other applications include the production of composite panels made from hemp fibers and natural resins for interior components, which are distinguished by their low weight, mechanical strength, and superior durability, being more resistant to rot, fire, fungi, and pests than wood (*Kymäläinen et al., 2005; Kymäläinen and Sjöberg, 2008; Călăţan, 2018; Popa et al., 2021*).

Using hemp in construction significantly contributes to reducing the carbon footprint of buildings, optimizing thermo-mechanical performance with minimal resources, and the fully recyclable nature of hemp-based materials supports the transition toward a circular economy (*Adam, 2024*).

5. Use in the automotive and aerospace industries

Industrial hemp is increasingly used in the automotive and aerospace industries due to its distinctive features such as low weight, mechanical strength, sustainability, and low production costs. These properties allow hemp to contribute to reducing the reliance on non-renewable resources and synthetic or petroleum-based materials, thus promoting a more environmentally friendly production model (*Faruk et al., 2012; Balakrishnan et al., 2016; Wellbrock et al., 2020; Balo and Sua, 2024*).

Significant advances in hemp research, supported by the European Commission and member states since the 1990s, have led to the identification of new applications for hemp fibers, such as biocomposites (*Carus and Sarmento, 2016*). In recent decades, the use of hemp fibers in composites as reinforcement material has increased considerably, meeting the demands for the development of biodegradable, sustainable, and recyclable materials (*Shahzad, 2012*).

Use of hemp fibers in the automotive industry

Natural fiber-reinforced biocomposites and/or biopolymers have seen significant development due to multiple advantages - processing efficiency, biodegradability, low cost, low density, high specific strength, and renewable nature (*Faruk et al., 2012; Wellbrock et al., 2020*).

Hemp, recognized as one of the most ecological and traditional natural fibers (*Shahzad, 2012*), has been integrated into the production of vehicle interior components, from door panels and dashboards to headrests, trunk linings, and spare wheel covers, due to its competitive mechanical properties and potential for carbon footprint reduction (*Carus et al., 2013; Carus and Sarmento, 2016; Wellbrock et al., 2020*), especially in mid- and high-class vehicles (*Karus et al., 2006*).

These biocomposite materials are durable and lightweight, have superior mechanical properties (*Karus et al., 2006; Faruk et al., 2012; Carus et al., 2013*), low density, and excellent energy absorption characteristics (*Carus et al., 2013*), thus contributing to energy savings (*Shahzad, 2012*) and improving fuel efficiency through vehicle weight reduction (*Sahib et al., 2023; https://www.energy.gov/eere/vehicles/lightweight-materials-cars-and-trucks*). They also offer favorable crash performance, a high proportion of biomass-based content, and competitive prices for high-quality interior designs (*Carus et al., 2013*). Life cycle assessments show that using hemp fibers as reinforcement can significantly reduce greenhouse gas emissions and increase the recyclability of vehicles (*Faruk et al., 2012; Shahzad, 2012*).

The European automotive industry, especially luxury manufacturers, have already adopted hemp fiber use in visible components like door panels, highlighting the potential of these materials to improve both technical performance and the sustainability of final products (*Shahzad, 2012; Wellbrock et al., 2020*).

Research shows that using hemp fibers as reinforcement in composites significantly improves the ecological characteristics of vehicles due to their low carbon footprint and high recyclability (*Faruk et al., 2012; Shahzad, 2012*).

Use of hemp in the aerospace industry

In the aerospace sector, adopting composites based on natural fibers, such as those derived from hemp, represents a promising strategy for reducing aircraft weight and enhancing sustainability. These materials are characterized by low density, excellent strength-to-weight ratios, and ecological properties (renewable, biodegradable, and recyclable), contributing to reduced fuel consumption and lower greenhouse gas emissions (*Mansor et al., 2019; Singh et al., 2023*).

A study by Balo and Sua (2024) highlights that using natural fibers, such as hemp, in combination with polymers, can significantly reduce the ecological impact of aircraft manufacturing, emphasizing the importance of optimal fiber and polymer matrix selection to enhance both mechanical performance and material sustainability. Moreover, Balakrishnan et al. (2016) demonstrated that fiber-based composite materials are increasingly used in the construction of aircraft and spacecraft due to their benefits, including weight reduction, increased specific strength, extended service life, and decreased corrosion problems.

The findings of these studies underline the significant potential of natural fiber composites in the aerospace industry, providing green solutions that, alongside improved mechanical performance, can support the development of future technologies in the field.

6. Use in agriculture

Industrial hemp is a versatile and environmentally friendly crop with numerous benefits for agriculture. It contributes to improving soil quality, reducing pesticide use, and increasing biodiversity, thus supporting the transition to sustainable agricultural practices. In Europe, hemp is among the few crops that can be cultivated conventionally without agrochemical inputs (*Carus and Sarmiento, 2016*). Compared to cotton, hemp requires less water and is less dependent on phytosanitary treatments, helping to reduce environmental impact (*Malabadi et al., 2023*).

Phytoremediation capacity

Hemp is known for its ability to regenerate depleted soils due to its deep root system, which improves aeration and reduces compaction, thereby optimizing soil structure and fertility (*Struik et al., 2000*).

Hemp also provides significant environmental benefits, being considered a hyperaccumulator, a plant capable of accumulating metals or other compounds (aromatic hydrocarbons, radioactive contaminants, etc.) in its tissues hundreds or thousands of times more than other species. Due to this characteristic, hemp can be used in phytoremediation processes (*Citterio et al., 2003; Reeves et al., 2017; Rhey et al., 2020; Malabadi et al., 2023; Sunoj Valiarambil et al., 2023*).

This plant can remediate contaminated soils by accumulating heavy metals such as lead (Pb), zinc (Zn), nickel (Ni), and cadmium (Cd) in its roots (*Linger et al., 2002; Ivanova et al., 2003; Adesina et al., 2020; Rhey et al., 2020; Sunoj Valiarambil et al., 2023; Visković et al., 2023; Guo et al., 2024*), allowing the plant to be harvested together with hazardous compounds (*Adesina et al., 2020*). A notable example is the use of hemp in 1986 for decontaminating soil in the area affected by the Chernobyl nuclear disaster (*Citterio et al., 2003*), demonstrating hemp's efficiency in phytoextraction. In this context, hemp has been repeatedly used to remediate polluted sites, particularly through phytoremediation targeting the accumulation of heavy metals such as copper (Cu), cadmium (Cd), chromium (Cr), cobalt (Co), zinc (Zn), iron (Fe), nickel (Ni), mercury (Hg), lead (Pb), arsenic (As), silver (Ag), and platinum (Pt), commonly found in contaminated areas (*Moscariello et al., 2021*).

Although hemp can accumulate heavy metals in roots and shoots, studies show that the stems and seeds used for fiber and biomass production contain low concentrations of inorganic contaminants, especially heavy metals, without reaching phytotoxic thresholds. Thus, these parts remain suitable for valorization, even when grown on contaminated soils (*Kurczyński and Wcisło, 2024*).

Carbon sequestration and CO₂ capture

A particularly important feature of hemp is its capacity to capture and store carbon. When used as an alternative to carbon-based raw materials, hemp enables the sequestration of substantial amounts of CO₂ in both the stem and the roots, through biosequestration (*Adesina et al., 2020; Popa et al., 2021*). Due to its rapid growth and development, hemp is one of the fastest carbon-to-biomass converters, one hectare of hemp can absorb up to 22 tons of CO₂ (*Adesina et al., 2020; Kurczyński and Wcisło, 2024*). Most of the carbon is stored in the harvested stem, and less in the roots and leaves (*Adesina et al., 2020*). On the other hand, in their study,

Finnan and Styles (2013) show that hemp has one of the highest CO₂ absorption rates among agricultural crops, with about 1.5–2.0 tons of CO₂ absorbed per hectare annually.

One potential application of hemp biomass is its conversion into biochar. According to Günther (2019), hemp cultivation can produce at least 13 tons of biochar per hectare per year. This biochar has the potential to increase soil carbon sequestration and reduce greenhouse gas emissions, thus contributing to climate change mitigation (Lehmann *et al.*, 2006).

The resulting biomass contributes to long-term carbon storage, especially when used in construction materials such as hempcrete (Arehart *et al.*, 2002; Jami *et al.*, 2016; Jami and Kumar, 2017; Kumar *et al.*, 2021; Sunoj Valiaparambil *et al.*, 2023).

Cover crop role

Hemp is frequently used as a cover crop due to its rapid growth and weed-suppressing capacity. This practice helps protect soil from erosion, retain moisture, and reduce the need for herbicides. Furthermore, after harvest, hemp biomass can be incorporated into the soil, enriching it with organic matter and essential nutrients (Linger *et al.*, 2002; Malabadi *et al.*, 2023).

Role in crop rotation

Including hemp in crop rotations helps reduce the incidence of pests and diseases specific to other crops. Studies show that this plant can reduce the need for pesticides (Adesina *et al.*, 2020) due to its natural weed-suppressing ability and disease resistance (Adesina *et al.*, 2020; Struik *et al.*, 2000). Vigorous hemp crops, with their fast growth rate, suppress weeds without chemical interventions, and the plant is not significantly affected by pests or diseases requiring pesticide use. Moreover, hemp adapts well to organic farming systems (Carus and Sarmento, 2016).

Mulch and compost production

Hemp stalks and leaves can be used for producing mulch and compost, providing an organic source of natural fertilizer. These materials improve soil water retention and add essential nutrients, reducing the need for chemical fertilizers (Struik *et al.*, 2000; Linger *et al.*, 2002; Carus *et al.*, 2013).

Animal bedding

Hemp stalks and hurds are frequently used as animal bedding due to their excellent absorbency. This natural material reduces moisture and odors in shelters, providing a healthier environment for animals. Moreover, hemp bedding is biodegradable and can later be composted, contributing to a sustainable agricultural cycle (Linger *et al.*, 2002).

Use for biofertilizers

Recent research highlights hemp's potential to be utilized in biofertilizer development, through microbial degradation of plant residues that support the growth of beneficial soil microorganisms (Donati *et al.*, 2025).

Use of residues in plant protection

Some residues from hemp processing can be valorized as botanical insecticides, miticides, or repellents, being integrated into ecological pest management programs (Adesina *et al.*, 2020; Benelli *et al.*, 2018). Hemp oil and plant residues can be used as natural insecticides and pesticides in organic agriculture (Hall *et al.*, 2014; Benelli *et al.*, 2018). Hemp also produces essential oils with insect-repellent properties and antifungal effects (Kurczyński and Wcisło, 2024).

Valorization in circular agricultural systems

Integrating hemp into circular agricultural systems is promoted through the reuse of residual biomass to produce natural fibers and other value-added products, thus reducing resource waste and supporting the transition toward a sustainable bioeconomy (Jayaprakash *et al.*, 2022).

7. Use in the textile industry

Industrial hemp is one of the oldest plants cultivated for textile fiber production, having been traditionally used in the textile industry. Due to its high mechanical strength, durability, and reduced environmental impact, hemp represents a sustainable alternative to synthetic fibers and cotton. Life Cycle Assessment (LCA) evaluations indicate that, compared to cotton and other natural fibers, hemp requires significantly less water and pesticides and has a lower environmental impact across most analyzed categories, especially when processing stages are optimized (Van der Werf and Turunen, 2008; Mariz *et al.*, 2024). Moreover, thanks to its high yield and low agricultural input requirements, hemp is also an economically viable option, with agricultural costs estimated to be more than 75% lower compared to cotton (Schumacher *et al.*, 2020).

Hemp fiber is recognized as one of the strongest and most durable natural fibers (Adesina *et al.*, 2020), exhibiting higher tensile strength than cotton, with values between 550–1110 MPa, compared to 287–800 MPa

for cotton (Mariz *et al.*, 2024). These properties make hemp suitable for a wide range of applications, from technical and coarse textiles to fine fabrics (Bălțeanu, 2001). Due to its high cellulose content (68–75%) and favorable mechanical properties such as tensile strength (310–900 MPa) and stiffness (Young's modulus of 30–80 GPa), hemp fiber is considered a viable option for durable textile applications (Elfaleh *et al.*, 2023). In addition, hemp exhibits natural antimicrobial properties, making it suitable for functional textiles such as sportswear or underwear (Mariz *et al.*, 2024).

To be effectively utilized in industry, fiber quality is assessed based on factors such as biochemical composition, mechanical properties, degree of processing and retting, performance under various stresses, morphological characteristics, and industrial spinnability (EIHA Conference, 2016–2023).

Modern technologies, such as enzymatic retting, allow for the production of finer and more flexible fibers capable of competing with cotton and other natural fibers. These advances have facilitated the integration of hemp into the fashion industry, including sustainable collections launched by well-known designers and brands (Carus *et al.*, 2013).

The combination of hemp fibers with other natural fibers, such as wool or silk, has opened new opportunities for producing premium textiles that blend the durability of hemp with the finesse and aesthetics of other materials (Shahzad, 2012).

The growing demand for sustainable textile products has stimulated the development of the hemp industry, particularly in Europe and Asia. Countries such as China, France, and Canada are leading in hemp fiber production and processing, while emerging markets are exploring innovative applications for this versatile resource (Faruk *et al.*, 2012).

8. Use in the energy industry

Climate change and the depletion of fossil resources make the identification of sustainable energy solutions a global priority. The increased energy demand in recent decades, along with the extraction and processing of conventional fuels, has caused significant negative environmental effects, including biodiversity loss and the acceleration of climate change (UNEP, 2020). In this context, innovative technologies and advances in green energy have opened new pathways for addressing these global challenges (Chang *et al.*, 2024). At the core of this energy transition lies the need to replace fossil fuels with renewable sources, with biomass energy emerging as a promising and versatile alternative (Liu and Huang, 2024).

One of the major global issues is represented by greenhouse gas emissions, especially carbon dioxide (CO₂) and nitrogen oxides (NO_x). CO₂ is primarily released during fossil fuel combustion, while NO_x is generated during high-temperature combustion processes (Zuo *et al.*, 2024). In this regard, the European Union has set the goal of achieving climate neutrality by 2050, with an intermediate objective of reducing emissions by at least 55% by 2030 compared to 1990 levels (European Commission, 2021).

According to the Production Gap Report, although most governments have committed to climate neutrality, projections indicate that by 2030, fossil fuel production will double the amount compatible with the 1.5°C threshold set by the Paris Agreement. Estimates suggest that by 2030, fossil fuel production could exceed the 1.5°C-compatible level by over 110% and the 2°C-compatible level by 69% (Achakulwisut *et al.*, 2023). In this context, lignocellulosic materials such as hemp are gaining recognition as low-carbon renewable resources, used not only for energy generation but also for the production of bioproducts and biofuels (Forfora *et al.*, 2024).

Hemp biomass as an energy resource

Hemp is a promising resource for energy production due to its high biomass yield and its capacity to generate biodiesel, biogas, bioethanol, and solid fuels (Kraszkievicz *et al.*, 2019; Rheay *et al.*, 2020). Currently, hemp biomass can be used to generate heat and electricity, produce vehicle fuel, and be compressed into briquettes or pellets (Prade *et al.*, 2012).

With a lignocellulosic composition rich in cellulose and lignin, hemp proves to be an excellent material for biochar (BC) and biofuel production, supporting the development of renewable energy applications (Minhas *et al.*, 2025). Its high cellulose content (50 - 70%) is comparable or even superior to that of other agricultural residues, such as wheat straw (35 - 45%) or *Miscanthus* (40 - 60%) (Roman, 2025).

Biogas from hemp waste

The plant residues resulting from hemp processing can be valorized through anaerobic digestion, a process that produces biogas while reducing methane emissions, thus having a positive environmental impact (Finnan and Styles, 2013). According to studies by Adamovics *et al.* (2014), hemp leaves have proven to be

the most efficient part of the plant for biogas production. In experiments on hemp biomass, hydrothermal pretreatment significantly increased methane yields compared to untreated material, as the process breaks down rigid cell structures, allowing anaerobic microbes better substrate access, stimulating enzymatic activity, and accelerating digestion (Mamimin *et al.*, 2024). The resulting methane-rich biogas (CH₄) can be used for producing electricity and heat or upgraded to biomethane suitable for gas grids or as an alternative fuel. The nutrient-rich digestate can be applied as natural fertilizer, supporting sustainable agricultural practices (Chang *et al.*, 2024).

Hemp harvested in autumn provides a higher biomass yield, and enzymatic treatment of the residues has been shown to enhance methane production (Prade *et al.*, 2012b; Asquer *et al.*, 2019). Although biogas/methane yields from hemp are lower than those from corn silage, the lower cost of hemp straw and its favorable behavior during anaerobic digestion make it an economically viable option (Asquer *et al.*, 2019).

Biofuels

Industrial hemp is a versatile source for producing various types of biofuels. These can be classified by physical state into solid (compressed biomass and biochar), liquid (bioethanol, biodiesel, bio-oil), and gaseous (biogas, biohydrogen, bio-syngas) fuels, all obtained from renewable feedstocks (Suhara *et al.*, 2024; Addison *et al.*, 2024). First-generation biofuels remain the most viable option in today's industry, ideal for large-scale production and commercialization due to the constant availability of raw materials (Suhara *et al.*, 2024).

Hemp bioethanol

Bioethanol is obtained by fermenting renewable biomass, followed by distillation and dehydration. While in the past the main raw materials were predominantly crops such as corn or sugarcane, nowadays agricultural waste and by-products, including those derived from hemp, are increasingly being used (<https://www.sterlingsihi.com/cms/ro/Romania/home/piete/sectorul-industrial/produse-alimentare/productia-de-biodiesel-si-bioetanol/produceria-bioetanolului.html>).

Hemp biomass has a high content of cellulose and glucans, which facilitates the production of fermentable sugars and, consequently, a higher bioethanol yield (Zhao *et al.*, 2020). Thus, hemp is considered one of the most valuable fiber sources, appreciated for its applications in the production of biochemicals, biogas, bioethanol, and biohydrogen (Brar *et al.*, 2024). Studies show that efficient pretreatment of the biomass and the use of conventional yeasts, such as *Saccharomyces cerevisiae*, can lead to good ethanol yields, which can subsequently be recovered through fractional distillation. The remaining solid fraction after fermentation can be used in thermochemical processes such as pyrolysis (Zhao *et al.*, 2020).

Bioethanol is produced by fermenting sugars extracted from biomass sources such as corn, sugarcane, agricultural residues, and wood. Yeasts or bacteria convert these sugars into ethanol, which can be used either on its own or blended with gasoline (Sartaj *et al.*, 2023). Biomass sources can be converted in various ways to serve as energy sources, thus contributing to reducing greenhouse gas emissions and replacing fossil fuels in sustainable energy generation (Chang *et al.*, 2024). In this regard, second-generation bioethanol, obtained from lignocellulosic materials, has become a promising alternative due to the availability and lower cost of raw materials (Viswanathan *et al.*, 2020).

Biodiesel production

Biodiesel can be obtained through several methods, including blending, micro-emulsification, thermal cracking and, most commonly, transesterification (Bhonsle *et al.*, 2025). This process involves the reaction of triglycerides (from vegetable oils, waste oils, or animal fats) with an alcohol, usually methanol, in the presence of a catalyst, resulting in biodiesel and glycerol (https://www.hielscher.com/ro/biodiesel_transesterification_01.htm). The feedstocks may come from first-generation sources (edible vegetable oils) or second-generation sources (waste oils, non-edible animal fats) (Sartaj *et al.*, 2023).

In this context, hemp seeds represent a promising resource for biodiesel production due to their oil content, which can be transformed through transesterification into a renewable, biodegradable, and non-toxic biofuel (Osman A. *et al.*, 2024). Hemp biodiesel is a viable alternative to conventional diesel, being non-flammable, low in emissions, and having excellent combustion properties, in compliance with international standards ASTM D6751 and EN 14214 (Prade *et al.*, 2011; Patel *et al.*, 2016; Sunoj Valiaparambil *et al.*, 2023).

According to recent literature, industrial hemp can produce up to 789 liters/ha of biodiesel, with a conversion rate of 75.9% (Parvez *et al.*, 2021; Abreu *et al.*, 2022), and increasing the lipid content to 10% could potentially double the output (Viswanathan *et al.*, 2020). It is also estimated that this crop could yield up to 3.95 million gallons of biodiesel annually (Visković *et al.*, 2024). Among the technical challenges is the high

viscosity of hemp oil, which can be effectively reduced through physicochemical pretreatments or ultrasonic processing (*Moscariello et al., 2021*).

A major advantage of biodiesel is that it can be used in existing diesel engines without significant modifications, making it a practical and sustainable solution for reducing fossil fuel dependence (*Singh et al., 2024*). Blends such as B5 (5% biodiesel, 95% diesel) and B20 (20% biodiesel, 80% diesel) are already widely used, helping to reduce carbon emissions and enhance energy sustainability (*Osman W. et al., 2024*). Tests conducted on hemp biodiesel revealed thermal efficiencies between 15.98% and 24.97%, lower carbon monoxide and hydrocarbon emissions, and performance comparable to commercial diesel (*Addison et al., 2024*).

Compared to bioethanol, biodiesel offers superior environmental benefits and greater energy efficiency (*Suhara et al., 2024*). In the study conducted by Ahmad et al. (2011), non-edible hemp oil was transesterified using a base catalyst, and the final product was analyzed using GC-MS, FT-IR, and NMR methods, revealing characteristics that comply with international standards and indicate good fuel quality.

Solid biofuels

The densification of hemp biomass plays a key role in the development of sustainable solid biofuels (*Roman and Grzegorzewska, 2024*). Dried hemp biomass can be compressed into briquettes or pellets without the need for chemical additives, as the lignin naturally present in the plant acts as a binder (*Kolodziej et al., 2012; Popa et al., 2021*). The energy properties of hemp are comparable or even superior to other solid biofuel sources such as cereal straw or wood (*Prade et al., 2012a*). Hemp briquettes have a calorific value of approximately 18,000 kJ/kg, higher than that of wood, and are characterized by rapid combustion and low sulfur emissions (*Kolodziej et al., 2012*).

Studies show that factors such as moisture content and particle size significantly influence processing efficiency and the quality of the final product. For example, briquettes exhibit higher vertical strength, while pellets are more durable during handling and transport. To obtain high-quality solid biofuels, it is essential to control moisture levels, analyze density, and conduct resistance tests (*Roman and Grzegorzewska, 2024*).

The compactness and durability of briquettes are influenced by different factors, especially lignin content. Thus, dioecious hemp, with its higher lignin content, is better suited for briquetting, particularly in northern regions (*Kraszkievicz et al., 2019*). Additionally, in the case of these biofuels, the presence of heavy metals does not pose a major risk, as long as the resulting ash is not used as fertilizer (*Alaru et al., 2013*).

Beyond its direct energetic benefits, the use of hemp in the bioenergy sector contributes to reducing greenhouse gas emissions, capturing carbon dioxide (CO₂) during the growth period, and improving soil quality, thus reinforcing the ecological value of this crop in the transition towards a sustainable energy system (*Citterio et al., 2003; Iványi and Izsáki, 2007; Adesina et al., 2020; Amaducci et al., 2015*).

9. Other uses

Hemp is a sustainable alternative to wood for paper production. Its long fibers provide high strength to the resulting paper, which can be used for documents, packaging, and industrial products. Hemp processing requires fewer chemicals and less water than wood-based paper production, thus reducing environmental impact (*Enarevba and Haapala, 2024*).

Hemp is also used in the production of industrial filters, carpets (*Tutek and Masek, 2022*), braids, fine fabrics, twine, sacks, mats, insulating materials, and other products (*Şandru et al., 1996; Gherasim, 2017; Leonte et al., 2022*).

CONCLUSIONS

Industrial hemp (*Cannabis sativa* L.) is increasingly emerging as a strategic crop in the context of the global transition toward sustainability, due to its remarkable versatility, economic value, and low environmental impact. The analysis of its various applications reveals significant potential that transcend traditional uses and extends into emerging fields such as green construction, renewable energy, the pharmaceutical industry, as well as environmental protection, through its phytoremediation capacity and contribution to carbon sequestration.

Through its ability to provide durable textile fibers, composite materials, biofuels, therapeutic products, and by contributing to soil regeneration and the reduction of greenhouse gas emissions, hemp offers coherent and sustainable solutions to today's economic, ecological, and social challenges. Its integration into sustainable agricultural systems and diversified value chains strengthens its strategic role in current policies aimed at combating climate change and advancing the transition toward a circular bioeconomy.

Future prospects include the development of a dedicated market for high-quality hemp-based products, with focus on health, innovation, and sustainability, as well as raising awareness among the public and decision-makers about the multifunctional nature of hemp and its role in delivering innovative solutions to current economic, social, and environmental challenges.

REFERENCES

- [1] Abreu, M., Silva, L., Ribeiro, B., Ferreira, A., Alves, L., Paixão, S.M., Gouveia, L., Moura, P., Carneiro, F., Duarte, L.C., Fernando A.L., Reis A., Gírio, F. (2022). Low indirect land use change (ILUC) energy crops to bioenergy and biofuels - A review. *Energies*, 15(12), 4348, <https://doi.org/10.3390/en15124348>.
- [2] Achakulwisut, P., Lazarus, M., Asvanon, R., Almeida, P. C., Fauzi, D., Ghosh, E., Nazareth A., Araújo, J. V. (2023). The Production Gap Report 2023: Phasing down or phasing up? Top fossil fuel producers plan even more extraction despite climate promises, <https://doi.org/10.51414/sei2023.050>.
- [3] Adam L. (2024). Contribuții la optimizarea performanțelor termo-mecanice ale betonului ecologic pe bază de cânepă. Teză de doctorat, Iași.
- [4] Adamovics, A., Dubrovskis, V., Platace, R. (2014). Productivity of Industrial Hemp and its Utilization for Anaerobic Digestion. *WIT Trans. Ecol. Environ.* 190, 1045–1055, doi:10.2495/EQ140982.
- [5] Addison, G., Milligan, K. A., Ohlig, S. (2024). Comparative analysis of ZnO and CeO₂ nanoparticle additives for the improvement of hemp biofuels as a sustainable biodiesel alternative: A comprehensive review. *Industrial Crops and Products*, 214, 118480, <https://doi.org/10.1016/j.indcrop.2024.118480>.
- [6] Adesina I., Bhowmik A., Sharma H., Shahbazi A. (2020). A review on the current state of knowledge of growing conditions, agronomic soil health practices and utilities of hemp in the United States. *Agriculture*, 10, 129; doi:10.3390/agriculture10040129;
- [7] Ahmad, M., Ullah, K., Khan, M. A., Zafar, M., Tariq, M., Ali, S., Sultana, S. (2011). Physicochemical analysis of hemp oil biodiesel: a promising non edible new source for bioenergy. *Energy Sources, Part A: Recovery, Utilization, and Environmental Effects*, 33(14), 1365-1374, <https://doi.org/10.1080/15567036.2010.499420>.
- [8] Aizpurua-Olaizola O., Soydaner U., Öztürk E., Schibano D., Simsir Y., Navarro P., Etxebarria N., Usobiaga A. (2016). Evolution of the cannabinoid and terpene content during the growth of *Cannabis sativa* plants from different chemotypes. *Journal of Natural Products*, 79, 2, 324–331, DOI: 10.1021/acs.jnatprod.5b00949.
- [9] Aladic, K., Jarni, K., Barbir, T., Vidovic, S., Vlastic, J., Bilic, M., Jokic, S. (2015). Supercritical CO₂ extraction of hemp (*Cannabis sativa* L.) seed oil. *Ind. Crop Prod.* 76, 472–478, <https://doi.org/10.1016/j.indcrop.2015.07.016>.
- [10] Alaru, M., Kukk, L., Astover, A., Lauk, R., Shanskiy, M., Loit, E. (2013). An agro-economic analysis of briquette production from fibre hemp and energy sunflower. *Industrial Crops and Products*, 51, 186-193, <https://doi.org/10.1016/j.indcrop.2013.08.066>.
- [11] Amaducci S., Scordia D., Liu F.H., Zhang Q., Guo H., Testa G., Cosentino S.L. (2015). Key cultivation techniques for hemp in Europe and China. *Industrial Crops and Products*, Volume 68, Pages 2-16, <https://doi.org/10.1016/j.indcrop.2014.06.041>.
- [12] Andre C. M., Hausman J. F., Guerriero G. (2016). *Cannabis sativa*: the plant of the thousand and one molecules. *Front. Plant Sci.* 7:19. doi: 10.3389/fpls.2016.00019;
- [13] Arehart, J.H., Nelson, W.S., Srubar III, W.V. (2002). On the Theoretical Carbon Storage and Carbon Sequestration Potential of Hempcrete. *J. Clean. Prod.* 266, 121846, <https://doi.org/10.1016/j.jclepro.2020.121846>.
- [14] Aslan, V. (2024). The analysis of classical, polynomial regression and cubic spline mathematical models in hemp biodiesel optimization: an experimental comparison. *Environmental Science and Pollution Research*, 31(6), 9392-9407, <https://doi.org/10.1007/s11356-023-31720-0>.
- [15] Asli, M., Sassine, E., Brachelet, F., Antczak, E. (2021). Thermal and Hygroscopic Study of Hemp Concrete in Real Ambient Conditions. *J. Build. Eng.* 44, 102612, <https://doi.org/10.1016/j.jobbe.2021.102612>.
- [16] Asquer, C., Melis, E., Scano, E. A., Carboni, G. (2019). Opportunities for green energy through emerging crops: biogas valorization of *Cannabis sativa* L. residues. *Climate*, 7(12), 142, <https://doi.org/10.3390/cli7120142>.

- [17] Balakrishnan P., John M.J., Pothan L., Sreekala M.S., Thomas S. (2016). Natural fibre and polymer matrix composites and their applications in aerospace engineering. *Advanced Composite Materials for Aerospace Engineering*, 365-383. <https://doi.org/10.1016/B978-0-08-100037-3.00012-2>.
- [18] Balo, F., Sua, L.S. (2024). Green Composites in Aviation: Optimizing Natural Fiber and Polymer Selection for Sustainable Aircraft Cabin Materials. *Textiles* 4, 561–581. <https://doi.org/10.3390/textiles4040033>.
- [19] Benelli, G., Pavela, R., Petrelli, R., Cappellacci, L., Santini, G., Fiorinin, D., Sut, S., Dall'Acqua, S., Canale, A., Maggi, F. (2018). The essential oil from industrial hemp (*Cannabis sativa* L.) by-products as an effective tool for insect pest management in organic crops. *Ind. Crop Prod.* 122, 308–315. <https://doi.org/10.1016/j.indcrop.2018.05.032>.
- [20] Bâlțeanu, Gh. (2001). *Crop Science (Fitotehnie)*, vol. 2. Ceres Publishing House, Bucharest, 147-169.
- [21] Bhunia S., Kolishetti N., Arias A.Y., Vashist A., Nair M. (2022). Cannabidiol for neurodegenerative disorders: A comprehensive review. *Front. Pharmacol.* 13:989717. doi: 10.3389/fphar.2022.989717.
- [22] Bhonsle, A. K., Kumar, A., Ray, A., Singh, J., Rawat, N., Atray, N. (2025). Biodiesel production from used cooking oil at room temperature using novel solvent—A techno-economic perspective, sensitivity analysis and societal implications. *Energy Conversion and Management*, 324, 119282, <https://doi.org/10.1016/j.enconman.2024.119282>.
- [23] Brar, K. K., Raheja, Y., Chadha, B. S., Magdoul, S., Brar, S. K., Yang, Y. H., Bhatia S. K., Koubaa A. (2024). A paradigm shift towards production of sustainable bioenergy and advanced products from Cannabis/hemp biomass in Canada. *Biomass Conversion and Biorefinery*, 14(3), 3161-3182, <https://doi.org/10.1007/s13399-022-02570-6>.
- [24] Callaway J.C. (2004). Hempseed as a nutritional resource: An overview. *Euphytica* 140, pg. 65 – 72. Kluwer Academic Publishers Netherlands;
- [25] Carus M., Sarmiento L. (2016). The European Hemp Industry: Cultivation, processing and applications for fibres, shivs, seeds and flowers. European Industrial Hemp Association (EIHA).
- [26] Carus M., Karst S., Kauffmann A., Hobson J., Bertucelli S. (2013). The European Hemp Industry: Cultivation, processing and applications for fibres, shivs and seeds. European Industrial Hemp Association (EIHA).
- [27] Cassano T., Villani R., Pace L., Carbone A., Bukke V. N., Orkisz S., Avolio C., Serviddio G. (2020). From *Cannabis sativa* to cannabidiol: promising therapeutic candidate for the treatment of neurodegenerative diseases. *Front. Pharmacol.* 11:124. doi: 10.3389/fphar.2020.00124.
- [28] Cerino P., Buonerba C., Cannazza G., D'Auria J., Ottoni E., Fulgione A., Di Stasio A., Pierri B., Gallo A. (2021). A Review of Hemp As Food and Nutritional Supplement. *Cannabis and Cannabinoid Research*, Volume 6, Number 1. DOI: 10.1089/can.2020.0001
- [29] Chang, J. H., Kumar, M., Selvaraj, S., Samuel, M. S., Ethiraj, S., Senthilkumar, A., Dong C.D., Shkir, M. (2024). Green energy breakthroughs: Harnessing nano-catalysts and enzymatic catalysts for bioenergy generation. *Industrial Crops and Products*, 215, 118527, <https://doi.org/10.1016/j.indcrop.2024.118527>.
- [30] Chen, X., Su, J., Wang, R., Hao, R., Fu, C., Chen, J., Li, J., Wang, X. (2023). Structural Optimization of Cannabidiol as Multifunctional Cosmetic Raw Materials. *Antioxidants* 12, 314. <https://doi.org/10.3390/antiox12020314>.
- [31] Cherney J.H., Small E. (2016). Industrial hemp in North America: Production, politics and potential. *Agron. J.*, 6, 58. <https://doi.org/10.3390/agronomy6040058>.
- [32] Citterio S., Santagostino A., Fumagalli P., Prato N., Ranalli P., Sgorbati S. (2003). Heavy metal tolerance and accumulation of Cd, Cr and Ni by *Cannabis sativa* L. *Plant Soil*, 256, 243–252. <https://doi.org/10.1023/A:1026113905129>.
- [33] Călățan G. A. (2018). *Ecological construction materials (Materiale ecologice pentru construcții)*. Doctoral Thesis, Cluj-Napoca.
- [34] Collet F., Pretot S. (2012). Experimental investigation of moisture buffering capacity of sprayed hemp concrete. *Constr. Build. Mater.*, vol. 36, pp. 58–65. <https://doi.org/10.1016/j.conbuildmat.2012.04.139>.
- [35] Constantinescu E. (2011). *Crop Science (Fitotehnie)*. Ștefan Marin Publishing house, Craiova.
- [36] Donati, L., Conti, A., Casagrande Pierantoni, D., Ruspi, C., Cerri, M., Emiliani, C., Cardinali, G., Corte, L. (2025). Spontaneous Bio-Recycling: Recovering Bioactive Molecules Through Endogenous Microbial Maceration of Hemp Residues. *Microorganisms*, 13, 455. <https://doi.org/10.3390/microorganisms13020455>.

- [37] Elfaleh I., Abbassi F., Habibi M., Ahmad F., Guedri M., Nasri M., Garnier C. (2023). A comprehensive review of natural fibers and their composites: An eco-friendly alternative to conventional materials. *Results in Engineering*, 19, 101271. <https://doi.org/10.1016/j.rineng.2023.101271>.
- [38] Enarevba, J., Haapala, K. R. (2024). The Emerging Hemp Industry: A review of Industrial Hemp Materials and Product Manufacturing. *AgriEngineering* 6, 2891–2925. <https://doi.org/10.3390/agriengineering6030167>.
- [39] European Commission. (2021). Delivering the European Green Deal: Factsheet. https://commission.europa.eu/strategy-and-policy/priorities-2019-2024/european-green-deal/delivering-european-green-deal_en (Accessed on April 7, 2025)
- [40] Falcă C., Solcan G., Moț T., Morar D., Papuc I., Vulpe V., Pop C., Vlăgioiu C., Giurgiu, G., Mircean M., Brăslau C.M. (2011). *Internal Medicine of Animals (Medicina internă a animalelor)*, vol. 2, Eurostampa Publishing House, Timișoara.
- [41] Faruk, O., Bledzki, A. K., Fink, H.-P., Sain, M.. (2012). Biocomposites reinforced with natural fibers: 2000–2010. *Progress in Polymer Science*, 37(11), 1552–1596. <http://dx.doi.org/10.1016/j.progpolymsci.2012.04.003>.
- [42] FDA. (2018). FDA Approves First Drug Comprised of an Active Ingredient Derived from Marijuana to Treat Rare, Severe Forms of Epilepsy. U.S. Food and Drug Administration.
- [43] Forfora, N., Azuaje, I., Vivas, K. A., Vera, R. E., Brito, A., Venditti, R., Kelley, S., Tu Q., Woodley A., Gonzalez, R. (2024). Evaluating biomass sustainability: Why below-ground carbon sequestration matters. *Journal of Cleaner Production*, 439, 140677, <https://doi.org/10.1016/j.jclepro.2024.140677>.
- [44] Finnan J., Styles D. (2013). Hemp: A more sustainable annual energy crop for climate and energy policy. *Energy Policy* 58, 152-162. <https://doi.org/10.1016/j.enpol.2013.02.046>.
- [45] Gamble L.-J., Boesch J.M., Frye CW, Schwark W.S., Mann S., Wolfe L., Brown H., Berthelsen E.S., Wakshlag J.J. (2018). Pharmacokinetics, Safety, and Clinical Efficacy of Cannabidiol Treatment in Osteoarthritic Dogs. *Front. Vet. Sci.* 5:165. doi: 10.3389/fvets.2018.00165.
- [46] Garcia G.A., Kube S., Carrera-Justiz S., Tittle D., Wakshlag J.J. (2022). Safety and efficacy of cannabidiol-cannabidiolic acid rich hemp extract in the treatment of refractory epileptic seizures in dogs. *Front. Vet. Sci.* 9:939966. doi: 10.3389/fvets.2022.939966.
- [47] Gherasim (căs. Leonte) A. (2017). *Research on Improving the Cultivation Technology of Monoecious Hemp for Fiber to Enhance Crop Efficiency (Cercetări cu privire la îmbunătățirea tehnologiei de cultivare a cânepii monoice pentru fibră în vederea eficientizării culturii)*. Doctoral Thesis. USAMV Iași;
- [48] Girgih A. T., Udenigwe C. C., Aluko R. E. (2011a). In Vitro Antioxidant Properties of Hemp Seed (*Cannabis sativa* L.) Protein Hydrolysate Fractions. *Journal of the American Oil Chemists' Society* 88:381–389, DOI 10.1007/s11746-010-1686-7.
- [49] Girgih A. T., Udenigwe C. C., Li H., Adebisi A. P., Aluko R. E. (2011b). Kinetics of enzyme inhibition and antihypertensive effects of hemp seed (*Cannabis sativa* L.) protein hydrolysates. *Journal of the American Oil Chemists' Society*, 88, pg. 1767–1774. <https://doi.org/10.1007/s11746-011-1841-9>.
- [50] Găucă C., Berea N. (1997). *Variation in Cannabinoid Content in Hemp Varieties and Populations from Romania. Scientific Papers (Variația conținutului în cannabinoid la soiurile și populațiile de cânepă din România. Lucrări științifice)*, vol. 40. Agronomy series – supplement, USAMV Iași;
- [51] Guggisberg J., Schumacher M., Gilmore G., Zylla D. M. (2022). Cannabis as an Anticancer Agent: A Review of Clinical Data and Assessment of Case Reports. *Cannabis and Cannabinoid Research* Volume 7, Number 1, DOI: 10.1089/can.2021.0045.
- [52] Guo, Y., Wen, L., Zhao, X., Xing, C., Huang, R. (2024). Industrial hemp (*Cannabis sativa* L.) can utilize and remediate soil strongly contaminated with Cu, As, Cd, and Pb by phytoattenuation. *Chemosphere*, 358, 142199. <https://doi.org/10.1016/j.chemosphere.2024.142199>.
- [53] Gurgel do Vale T., Couto Furtado E., Santos J.G., Viana G.S.B. (2002). Central effects of citral, myrcene and limonene, constituents of essential oil chemotypes from *Lippia alba* (Mill.) N.E. Brown. *Phytomedicine*, 9 (8), 709-714, <https://doi.org/10.1078/094471102321621304>.
- [54] Günther F. (2019). Carbon Sequestration for Everybody: Decrease Atmospheric Carbon Dioxide, Earn Money and Improve the Soil. Available online: https://terrapreta.bioenergylists.org/files/Terra%20pretav1_0.pdf.
- [55] Haake, J., Meyerhoff, N., Meller, S., Twele, F., Charalambous, M., Wilke, V., Volk, H. (2023). Investigating Owner Use of Dietary Supplements in Dogs with Canine Cognitive Dysfunction. *Animals* 13, 3056. <https://doi.org/10.3390/ani13193056>.

- [56] Hall, J., Bhattarai, S.P., Midmore, D.J. (2014). Effect of Industrial Hemp (*Cannabis sativa* L.) Planting Density on Weed Suppression, Crop Growth, Physiological Responses, and Fibre Yield in the Subtropics. *Renew. Bioresour.* 2, 1. DOI: 10.7243/2052-6237-2-1.
- [57] Hazekamp A., Fishedick J. T. (2012). *Cannabis* - from cultivar to chemovar. Drug testing and analysis, vol. 4, nr. 7 - 8, pg. 660 – 667; (wileyonlinelibrary.com) DOI 10.1002/dta.407.
- [58] Iványi I., Izsáki Z. (2007). Role of fibre hemp (*Cannabis sativa* L.) in sustainable agriculture. *Cereal Research Communications* 35, no. 2: 509–12. <http://www.jstor.org/stable/23790166>.
- [59] Ivanova, R., Angelova, V., Delibaltova, V., Ivanov, K. (2003). Accumulation of heavy metals in fibre crops flax, cotton and hemp. *J. Environ. Protect. Ecol.*, 4, 31–38.
- [60] Izzo, A.A., Borrelli, F., Capasso, R., Di Marzo, V., Mechoulam, R. (2009). Non-Psychotropic Plant Cannabinoids: New Therapeutic Opportunities from an Ancient Herb. *Trends Pharmacol. Sci.* 30, 515–527. DOI: 10.1016/j.tips.2009.07.006.
- [61] Kaboré, A., Maref, W., Ouellet-Plamondon, C.M. (2024). Hygrothermal Performance of the Hemp Concrete Building Envelope. *Energies* 2024, 17, 1740. <https://doi.org/10.3390/en17071740>.
- [62] Karche T., Singh M. R. (2019). The application of hemp (*Cannabis sativa* L.) for a green economy: a review. *Turk. J. Bot.* 43: 710-723. doi:10.3906/bot-1907-15.
- [63] Kaur G., Kander R. (2023). Sustainability of Industrial Hemp: A Literature Review of Its Economic, Environmental and Social Sustainability. *Sustainability* 15, 6457. <https://doi.org/10.3390/su15086457>.
- [64] Karus M., Ortmann S., Vogt D. (2006). Use of natural fibres in the German automotive industry.
- [65] Khanal, A., Shah, A. (2024). Techno-economic analysis of hemp production, logistics and processing in the US. *Biomass*, 4(1), 164-179, <https://doi.org/10.3390/biomass4010008>.
- [66] Kolodziej, J., Wladyka-Przybylak, M., Mankowski, J., Grabowska, L. (2012). Heat of combustion of hemp and briquettes made of hemp shives. *Renew. Energy Energy Effic*, 163-166.
- [67] Kolodziejczyk P., Ozimek L., Kozłowska J. (2012). The application of flax and hemp seeds in food, animal feed and cosmetics production. Handbook of natural fibres, Woodhead Publishing Limited;
- [68] Kosukwatthana, P., Rungsuriyawiboon, O., Rattanasrisomporn, J., Kimram, K., Tansakul, N. (2024). Cytotoxicity and Immunomodulatory Effects of Cannabidiol on Canine PBMCs: A Study in LPS-Stimulated and Epileptic Dogs. *Animals* 14, 3683. <https://doi.org/10.3390/ani14243683>.
- [69] Kraenzel D.G., Petry C., Nelson B., Anderson M.J., Mathern D., Todd R. (1998). Industrial hemp as an alternative crop in North Dakota. Agricultural Economics Report No. 402. The Institute for Natural Resources and Economic Development (INRED), North Dakota State University;
- [70] Kraszkiewicz, A., Kachel, M., Parafiniuk, S., Zapac, G., Niedziolka, I., Sprawka, M. (2019). Assessment of the possibility of using hemp biomass (*Canabis sativa* L.) for energy purposes: A case study. *Appl. Sci.*, 9(20), 4437, <https://doi.org/10.3390/app9204437>.
- [71] Kumar, V.G.; Ramadoss, R.; Rampradheep, G.S. (2021). A Study Report on Carbon Sequestration by Using Hempcrete. *Mater. Today Proc.*, 45, 6369–6371. <https://doi.org/10.1016/j.matpr.2020.11.012>.
- [72] Kurczyński, D., Wcisło, G. (2024). Producing and Testing the Properties of Biodiesel Sourced from Hemp Oil. *Energies*, 17(23), 5950, <https://doi.org/10.3390/en17235950>.
- [73] Kymäläinen H-R., Nykter M., Hautala M., Sjöberg A-M. (2005). Hygienic quality of stem fractions of mechanically processed fiber hemp and linseed. *Agricultural and Food Science*, vol. 14, nr. 2, pg. 143 – 153. DOI: 10.2137/145960605774825993.
- [74] Kymäläinen H-R., Sjöberg A-M. (2008). Flax and Hemp fibers as raw materials for thermal insulations. *Building and Environment*, vol. 43, nr. 7, pg. 1261 – 1269. <https://doi.org/10.1016/j.buildenv.2007.03.006>.
- [75] Jami, T., Rawtani, D., Agriwal, Y.K. (2016). Hemp Concrete: Carbon-Negative Construction. *Emerg. Mater. Res.* 5, 240–247.
- [76] Jami, T., Kumar, S. (2017). Assessment of Carbon Sequestration of Hemp Concrete. In International Conference on Advances in Construction Materials and Systems; RILEM: Chennai, India, pp. 665–673.
- [77] Jayaprakash, K., Osama, A., Rajagopal, R., Goyette, B., Karthikeyan, O.P. (2022). Agriculture Waste Biomass Repurposed into Natural Fibers: A Circular Bioeconomy Perspective. *Bioengineering*, 9, 296. <https://doi.org/10.3390/bioengineering9070296>.
- [78] Lančaričová A., Kuzmiaková B., Porvaz P., Havrlentová M., Nemeček P., Kraic J. (2021). Nutritional quality of hemp seeds (*Cannabis sativa* L.) in different environments. *Journal of Central European Agriculture*, 22(4), p.748-761. DOI: /10.5513/JCEA01/22.4.3198

- [79] Lehmann J., Gaunt J., Rondon M. (2006). Biochar sequestration in terrestrial ecosystems—A review. *Mitig. Adapt. Strateg. Glob. Chang.* 11, 403–427;
- [80] Leonte A., Isticioaia S. F., Pintilie P. L., Troțuș E., Naie M. (2022). Research on the effect of applying the Secuieni method to three varieties of monoecious hemp, in terms of production (seed, stems, fiber), in the pedoclimatic conditions of A.R.D.S. Secuieni. *Scientific Papers. Series A. Agronomy*, Vol. LXV, No. 2, 239 – 244.
- [81] Limam A., Zerizer A., Quenard D., Sallee H., Chenak A. (2016). Experimental thermal characterization of bio-based materials (Aleppo Pine wood, cork and their composites) for building insulation. *Energy Build.*, vol. 116, pp. 89–95.
- [82] Linger P., Mussig J., Fischer H., Kobert, J. (2002). Industrial hemp (*Cannabis sativa* L.) growing on heavy metal contaminated soil: Fibre quality and phytoremediation potential. *Ind. Crop Prod.*, 16, 33–42;
- [83] Liu, Y., Huang, Y. (2024). Assessing the interrelationship between fossil fuels resources and the biomass energy market for achieving a sustainable and green economy. *Resources Policy*, 88, 104397. <https://doi.org/10.1016/j.resourpol.2023.104397>.
- [84] Lučan Čolić, M., Jukić, M., Nakov, G., Lukinac, J., Antunović, M. (2024). Sustainable Utilization of Hemp Press Cake Flour in Ice Cream Production: Physicochemical, Rheological, Textural, and Sensorial Properties. *Sustainability*, 16(19), 8354. <https://doi.org/10.3390/su16198354>.
- [85] Malabadi R. B., Kolkar K. P., Chalannavar R. K., Lavanya L., Abdi G. (2023). Hemp helps human health: role of phytocannabinoids. *International Journal of Innovation Scientific Research and Review*, vol. 5, issue 4. pp.4340-4349.
- [86] Manian, A. P., Cordin, M., Pham, T. (2021). Extraction of cellulose fibers from flax and hemp: a review. *Cellulose*, 28(13), 8275-8294. <https://doi.org/10.1007/s10570-021-04051-x>.
- [87] Mamimin, C., Sompong, O., Reungsang, A. (2024). Enhancing biogas production from hemp biomass residue through hydrothermal pretreatment and co-digestion with cow manure: Insights into methane yield, microbial communities, and metabolic pathways. *Journal of Environmental Management*, 370, 123039. <https://doi.org/10.1016/j.jenvman.2024.123039>.
- [88] Mansor M.R., Nurfaizey A.H., Tamaldin N., Nordin M.N.A., (2019). Natural fiber polymer composites: Utilization in aerospace engineering. Biomass, Biopolymer-Based Materials, and Bioenergy. *Woodhead Publishing Series in Composites Science and Engineering*, 203-224.
- [89] Mariz, J., Guise, C., Silva, T. L., Rodrigues, L., Silva, C. J. (2024). Hemp: from field to fiber—a review. *Textiles*, 4(2), 165-182. <https://doi.org/10.3390/textiles4020011>.
- [90] Mashabela, M.D.; Kappo, A.P. (2024). Anti-Cancer and Anti-Proliferative Potential of Cannabidiol: A Cellular and Molecular Perspective. *Int. J. Mol. Sci.*, 25, 5659. <https://doi.org/10.3390/ijms25115659>.
- [91] McGrath S., Bartner L.R., Rao S., Packer R.A., Gustafson D.L. (2019). Randomized blinded controlled clinical trial to assess the effect of oral cannabidiol administration in addition to conventional antiepileptic treatment on seizure frequency in dogs with intractable idiopathic epilepsy. *J Am Vet Med Assoc.*, 254:1301–8. doi: 10.2460/javma.254.11.1301
- [92] McPartland, J.M., Russo, E.B. (2001). *Cannabis* and *Cannabis* Extracts: Greater than the Sum of Their Parts? *J. Cannabis Ther.* 1, 103–132.
- [93] Mechoulam R., Parker L.A., Gallily R. (2002). Cannabidiol: an overview of some pharmacological aspects. *J Clin Pharmacol.* 2002;42:11S–19S.
- [94] Minhas, R., Khoja, A. H., Kanwal, H., Hassan, M., Khan, A., Daood, S. S., Bahadar, A. (2025). Advanced characterization of hemp biomass pyrolysis: Bioenergy recovery and environmental implications. *Sustainable Chemistry and Pharmacy*, 45, 101989. <https://doi.org/10.1016/j.scp.2025.101989>.
- [95] Mihoc M., Pop G., Alexa E., Radulov I. (2012). Nutritive quality of Romanian hemp varieties (*Cannabis sativa* L.) with special focus on oil and metal contents of seeds. *Chemistry Central Journal*, vol. 6, nr. 1, pg. 122.
- [96] Montero L., Ballesteros-Vivas D., Gonzalez-Barrios A.F., Sánchez-Camargo Ad.P. (2023). Hemp seeds: Nutritional value, associated bioactivities and the potential food applications in the Colombian context. *Front. Nutr.* 9:1039180. doi: 10.3389/fnut.2022.1039180
- [97] Moscariello, C., Matassa, S., Esposito, G., Papirio, S. (2021). From residue to resource: The multifaceted environmental and bioeconomy potential of industrial hemp (*Cannabis sativa* L.).

- Resources, Conservation and Recycling, 175, 105864. <https://doi.org/10.1016/j.resconrec.2021.105864>.
- [98] Oomah B.D., Busson M., Godfrey D.V., Drover J.C.G. (2002). Characteristics of hemp (*Cannabis sativa* L.) seed oil. *Food Chemistry*, vol. 76, no. 1, pp. 33 – 43;
- [99] Osman, A. I., Nasr, M., Farghali, M., Rashwan, A. K., Abdelkader, A., Al-Muhtaseb, A. A. H., Ihara, I., Rooney, D. W. (2024). Optimizing biodiesel production from waste with computational chemistry, machine learning and policy insights: a review. *Environmental Chemistry Letters*, 22(3), 1005-1071. <https://doi.org/10.1007/s10311-024-01700-y>.
- [100] Osman, W. N. A. W., Rosli, M. H., Mazli, W. N. A., Samsuri, S. (2024). Comparative review of biodiesel production and purification. *Carbon Capture Science & Technology*, 13, 100264. <https://doi.org/10.1016/j.ccst.2024.100264>.
- [101] Palumbo M., Lacasta A. M., Holcroft N., Shea A., Walker P. (2016). Determination of hygrothermal parameters of experimental and commercial bio-based insulation materials. *Constr. Build. Mater.*, vol. 124, pp. 269–275.
- [102] Parvez, A. M., Lewis, J. D., Afzal, M. T. (2021). Potential of industrial hemp (*Cannabis sativa* L.) for bioenergy production in Canada: Status, challenges and outlook. *Renewable and Sustainable Energy Reviews*, 141, 110784. <https://doi.org/10.1016/j.rser.2021.110784>.
- [103] Patel, A., Arora, N., Sartaj, K. M., Pruthi, V., Pruthi, P. A. (2016). Sustainable biodiesel production from oleaginous yeasts utilizing hydrolysates of various non-edible lignocellulosic biomasses. *Renewable and Sustainable Energy Reviews*, 62, 836-855. <https://doi.org/10.1016/j.rser.2016.05.014>.
- [104] Piomelli D., Russo E.B. (2016). The *Cannabis sativa* versus *Cannabis indica* debate: An interview with Ethan Russo, MD. *Cannabis Cannabinoid Res.*, 1, 44–46;
- [105] Pop G., Alexa E., Laza A., Mihoc M., Militaru A., Pop D.A. (2012). Nutritional suitability of linseed and oil hemp from fatty acids profile perspective. *Planta Med.*; 78 - P1129. DOI: 10.1055/s-0032-1320816.
- [106] Popa L.-D., Vlăduț N.V., Buburuz Al.-A., Troțuș E., Matei Gh., Ungureanu N., Isticioaia S. F. (2021). *Hemp (Cannabis sativa L.) – From Cultivation to Utilization (Cânepa (Cannabis sativa L.) – de la cultivare la valorificare)*. Universitaria Publishing House, Craiova;
- [107] Popa L.-D., Teliban G.C., Buțerchi I., Burducea M., Isticioaia S. F., Nenciu F., Leonte A., Buburuz Al.-A., Pintilie A.S., Bodale I., Cojocar A., Lobiuc A., Stoleru V. (2024). Physiological, biochemical and agroproductive characteristics of hemp microgreens in different growing environments. *Scientific Papers. Series A. Agronomy*, Vol. LXVII, No. 1, 886 - 895.
- [108] Prade, T., Svensson, S. E., Mattsson, J. E. (2011). Biomass and energy yield of industrial hemp grown for biogas and solid fuel. *Biomass and Bioenergy*, 35(7), 3040-3049. <https://doi.org/10.1016/j.biombioe.2011.04.006>.
- [109] Prade, T., Finell, M., Svensson, S.E., Mattsson, J.E. (2012a). Effect of harvest date on combustion related fuel properties of industrial hemp (*Cannabis sativa* L.). *Fuel* 102, 592–604.
- [110] Prade, T., Svensson, S. E., Andersson, A., Mattsson, J. E. (2012b). Energy balances for biogas and solid biofuel production from industrial hemp. *Biomass and Bioenergy*, 40, 36-52. <https://doi.org/10.1016/j.biombioe.2012.01.045>.
- [111] Prétot S., Collet F., Garnier C. (2014). Life cycle assessment of a hemp concrete wall: Impact of thickness and coating. *Building and Environment*, vol. 72, 223-231.
- [112] Promhuad, K., Srisa, A., San, H., Laorenza, Y., Wongphan, P., Sodsai, J., Tansin, K., Phromphen, P., Chartvivatpornchai, N., Ngoenchai, P., Harnkarnsujarit, N. (2022). Applications of hemp polymers and extracts in food, textile and packaging: A review. *Polymers*, 14(20), 4274. <https://doi.org/10.3390/polym14204274>.
- [113] Puttharaksa, W., Charoensook, R., Tungtrakanpoung, R., Hoidokhom, N., Rungchang, S., Brenig, B., Numthum, S. A. (2025). Preliminary Evaluation of the Comparative Efficacy of Gel-Based and Oil-Based CBD on Hematologic and Biochemical Responses in Dogs. *Vet. Sci.*, 12, 342. <https://doi.org/10.3390/vetsci12040342>.
- [114] Reeves, R.D., Baker, A.J., Jaffré, T., Erskine, P.D., Echevarria, G., van der Ent, A. (2017). A Global Database for Plants that Hyperaccumulate Metal and Metalloid Trace Elements. *New Phytol.*, 218, 407–411. <https://doi.org/10.1111/nph.14907>.
- [115] Rezapour-Firouzi S., Arefhosseini S.R., Mehdi F., Mehrangiz E.M., Baradaran B., Sadeghihokmabad E., Mostafaei S., Fazljou S.M., Torbati M.A., Sanaie S., Zamani F. (2013). Immunomodulatory and therapeutic effects of Hot-nature diet and co-supplemented hemp seed, evening primrose oils

- intervention in multiple sclerosis patients. *Complementary Therapies in Medicine*. 21(5):473-80. doi: 10.1016/j.ctim.2013.06.006. PMID: 24050582.
- [116] Rheay, H.T., Omondi, E.C., Brewer, C.E. (2020). Potential of Hemp (*Cannabis sativa* L.) for Paired Phytoremediation and Bioenergy Production. *GCB Bioenergy*, 13, 525–536. <https://doi.org/10.1111/gcbb.12782>.
- [117] Rizzo, G., Storz, M.A., Calapai, G. (2023). The Role of Hemp (*Cannabis sativa* L.) as a Functional Food in Vegetarian Nutrition. *Foods*, 12, 3505. <https://doi.org/10.3390/foods12183505>.
- [118] Roman, K. (2025). The Estimation of the Possibility of Bioethanol Production from Hemp Cellulose Using the HWE Method. *Energies*, 18(6), 144. <https://doi.org/10.3390/en18061441>.
- [119] Roman, K., Grzegorzewska, E. (2024). The Comparison of Physical and Chemical Properties of Pellets and Briquettes from Hemp (*Cannabis sativa* L.). *Energies*, 17(9), 2210. <https://doi.org/10.3390/en17092210>.
- [120] Sahib dua, Khatri H., Naveen J., Jawaid M., Jayakrishna K., Norraahim M.N.F., Rashedi A. (2023). Potential of natural fiber based polymeric composites for cleaner automotive component production -a comprehensive review. *Journal of Materials Research and Technology*, Volume 25, pages 1086-1104, <https://doi.org/10.1016/j.jmrt.2023.06.019>.
- [121] Sapino S., Carlotti M.E., Peira E., Gallarate M. (2005). Hemp-seed and olive oils: their stability against oxidation and use in O/W emulsions. *International Journal of Cosmetic Science* 27 (6): 355. DOI: 10.1111/j.1467-2494.2005.00290_2.x.
- [122] Sartaj, K., Prasad, R., Matsakas, L., & Patel, A. (2023). Transforming recalcitrant wastes into biodiesel by oleaginous yeast: an insight into the metabolic pathways and multi-omics landscape. *Chemical Engineering Journal*, 474, 145625. <https://doi.org/10.1016/j.cej.2023.145625>.
- [123] Schultes R.E. (1970). *Random Thoughts and Queries on the Botany of Cannabis*. J and A Churchill: London, UK, 1970; pg. 11–33.
- [124] Seltzer E. S., Watters A. K., MacKenzie D. Jr., Granat L. M., Zhang D. (2020). Cannabidiol (CBD) as a Promising Anti-Cancer Drug. *Cancers*, 12, 3203; doi:10.3390/cancers12113203.
- [125] Sharma M., Hudson J. B., Adomat H., Guns E., Cox M. E. (2014). In Vitro Anticancer Activity of Plant-Derived Cannabidiol on Prostate Cancer Cell Lines. *Pharmacology and Pharmacy*, 2014, 5, 806-820. DOI: 10.4236/pp.2014.58091.
- [126] Schumacher, A. G. D., Pequito, S., Pazour, J. (2020). Industrial hemp fiber: A sustainable and economical alternative to cotton. *Journal of Cleaner Production*, 268, 122180. <https://doi.org/10.1016/j.jclepro.2020.122180>.
- [127] Shahzad, A. (2012). Hemp fiber and its composites - A review. *Journal of Composite Materials*, 46(8), 973-986. DOI: 10.1177/0021998311413623
- [128] Simopoulos A.P. (2002). The importance of the ratio of omega-6/omega-3 essential fatty acids. *Biomedicine and Pharmacotherapy*, vol. 56(8), pg. 365-379. DOI: 10.1016/s0753-3322(02)00253-6.
- [129] Simopoulos A.P. (2008). The Importance of the Omega-6/Omega-3 Fatty Acid Ratio in Cardiovascular Disease and Other Chronic Diseases. *Experimental Biology and Medicine*, 233(6):674-88, DOI: 10.3181/0711-MR-311.
- [130] Singh B., Ahmad K. A., Murugaiah M., Pai R., YK Ng E. (2023). Natural Fiber Reinforced Composites and Their Role in Aerospace Engineering. Book: *Green Hybrid Composite in Engineering and Non-Engineering Applications* Publisher: Springer Nature Singapore: Composites Science and Technology Series.
- [131] Singh, N., Saluja, R. K., Rao, H. J., Kaushal, R., Gahlot, N. K., Suyambulingam, I., Sanjay M.R., Divakaran D., Siengchin, S. (2024). Progress and facts on biodiesel generations, production methods, influencing factors, and reactors: A comprehensive review from 2000 to 2023. *Energy Conversion and Management*, 302, 118157. <https://doi.org/10.1016/j.enconman.2024.118157>.
- [132] Sirițanu V., Sirițanu C. (2007). *Research on the Performance of Certain Monoecious Hemp Varieties and Lines in Seed Cultivation. 45 Years of Scientific Activity (Cercetări privind comportarea unor soiuri și linii de cânepă monoică în cultura pentru sămânță. 45 de ani de activitate științifică)*. Anniversary model, "Ion Ionescu de la Brad" Publishing House, Iași.
- [133] Solcan G., Solcan C., Mitrea I.L. (2002). Psychogenic dermatoses in cats and dogs. Case reports- *Lucr. Șt. FMV Timioara*, 35, 309-311.
- [134] Solcan G. (2017). *Psychogenic Dermatitis in Companion Animals (Dermatitele psihogene ale animalelor de companie)*. *Romanian Journal of Veterinary Medicine and Pharmacology*, 2, 7, 258- 265.

- [135] Solcan Gh., Beșchea-Chiriac I.-S., Puiu I. (2023). Cannabinoids - toxicity and therapeutic uses in animals. *Rom J Vet Med Pharm.*, vol. VIII 42(4): 212-216.
- [136] Struik, P.C., Amaducci, S., Bullard, M.J., Stutterheim, N.C., Venturi, G., Cromack, H.T.H. (2000). Agronomy of fibre hemp (*Cannabis sativa* L.) in Europe. *Ind. Crop Prod.*, 11, 107–118. [https://doi.org/10.1016/S0926-6690\(99\)00048-5](https://doi.org/10.1016/S0926-6690(99)00048-5).
- [137] Suhara, A., Karyadi, Herawan, S. G., Tirta, A., Idris, M., Roslan, M. F., Putra, N.R., Hananto, A.L., Veza, I. (2024). Biodiesel sustainability: review of progress and challenges of biodiesel as sustainable biofuel. *Clean Technologies*, 6(3), 886-906. <https://doi.org/10.3390/cleantechnol6030045>.
- [138] Sunoj Valiaparambil S., J.; Dong, X.; Trostle, C.; Pham, H.; Joshi, M.V.; Jessup, R.W.; Burow, M.D.; Provin, T.L. (2023). Hemp Agronomy: Current Advances, Questions, Challenges, and Opportunities. *Agronomy*, 13, 475. <https://doi.org/10.3390/agronomy13020475>.
- [139] Șandru I., Paraschivoiu Rodica, Găucă C. (1996). *Hemp cultivation (Cultura cânepii)*. Helicon Publishing House, Timișoara;
- [140] Teleszko, M.; Zaj, A.; Rusak, T. (2022). Hemp Seeds of the Polish 'Bialobrzeskie' and 'Henola' Varieties (*Cannabis sativa* L. var. *sativa*) as Prospective Plant Sources for Food Production. *Molecules*, 27, 1448. <https://doi.org/10.3390/molecules27041448>.
- [141] Textile Exchange. (2023). Growing Hemp for the Future. <https://textileexchange.org/app/uploads/2023/04/Growing-Hemp-for-the-Future-1.pdf>.
- [142] Tura M., Mandrioli M., Valli E., Toschi T. G. (2023). Quality indexes and composition of 13 commercial hemp seed oils, *Journal of Food Composition and Analysis*, Volume 117, 105112. <https://doi.org/10.1016/j.jfca.2022.105112>.
- [143] Tutek, K.; Masek, A. (2022). Hemp and Its Derivatives as a Universal Industrial Raw Material (with Particular Emphasis on the Polymer Industry) - A Review. *Materials*, 15, 2565. <https://doi.org/10.3390/ma15072565>.
- [144] United Nations Environment Programme (UNEP). (2020). Sustainable trade in resources: Global material flows, circularity and trade. <https://wedocs.unep.org/bitstream/handle/20.500.11822/34344/STR.pdf?sequence=1&isAllowed=y>.
- [145] Valizadeherakhshan, M., Shahbazi, A., Kazem-Rostami, M., Todd, M.S., Bhowmik, A., Wang, L. (2021). Extraction of Cannabinoids from *Cannabis sativa* L. (Hemp) - Review. *Agriculture* 11, 384. <https://doi.org/10.3390/agriculture11050384>.
- [146] Van Bakel H., Stout J. M., Cote A. G., Tallon C. M., Sharpe A. G., Hughes T. R., Page J. E. (2011). The draft genome and transcriptome of *Cannabis sativa*. *Genome Biology*, 12:R102 <http://genomebiology.com/2011/12/10/R102>.
- [147] Van der Werf H.M.G., Turunen L. (2008). The environmental impacts of the production of hemp and flax textile yarn. *Industrial Crops and Products*, 27(1), Pages 1-10. <https://doi.org/10.1016/j.indcrop.2007.05.003>.
- [148] Visković, J., Zheljzkov, V. D., Sikora, V., Noller, J., Latković, D., Ocamb, C. M., Koren, A. (2023). Industrial hemp (*Cannabis sativa* L.) agronomy and utilization: A review. *Agronomy*, 13(3), 931. <https://doi.org/10.3390/agronomy13030931>.
- [149] Visković, J., Dunderski, D., Adamović, B., Jaćimović, G., Latković, D., Vojnović, Đ. (2024). Toward an environmentally friendly future: An overview of biofuels from corn and potential alternatives in hemp and cucurbits. *Agronomy*, 14(6), 1195. <https://doi.org/10.3390/agronomy14061195>.
- [150] Viswanathan, M. B., Park, K., Cheng, M. H., Cahoon, E. B., Dweikat, I., Clemente, T., Singh, V. (2020). Variability in structural carbohydrates, lipid composition, and cellulosic sugar production from industrial hemp varieties. *Industrial Crops and Products*, 157, 112906. <https://doi.org/10.1016/j.indcrop.2020.112906>.
- [151] Vogl C.R., Mölleken H., Lissek-Wolf G., Surböck A., Kobert J. (2004). Hemp (*Cannabis sativa* L.) as a resource for green cosmetics: yield of seed and fatty acid composition of 20 varieties under the growing conditions of organic farming in Austria. *Journal of Industrial Hemp*, vol. 9(1), pg. 51-68. https://doi.org/10.1300/J237v09n01_06.
- [152] Wellbrock W., Ludin D., Röhrlé L., Gerstlberge W. (2020). Sustainability in the automotive industry, importance of and impact on automobile interior - insights from an empirical survey. *International Journal of Corporate Social Responsibility* 5:10 <https://doi.org/10.1186/s40991-020-00057-z>.

- [153] Wylie S.E., Ristvey A.G., Fiorellino N.M. (2020). Fertility management for industrial hemp production: Current knowledge and future research needs. *GCB Bioenergy* 13:517–524. <https://doi.org/10.1111/qcbb.12779>.
- [154] Yano, H.; Fu, W. (2023). Hemp: A Sustainable Plant with High Industrial Value in Food Processing. *Foods*, 12, 651. <https://doi.org/10.3390/foods12030651>.
- [155] Zhao, J., Xu, Y., Wang, W., Griffin, J., Roozeboom, K., Wang, D. (2020). Bioconversion of industrial hemp biomass for bioethanol production: A review. *Fuel*, 281, 118725. <https://doi.org/10.1016/j.fuel.2020.118725>.
- [156] Zuo, Z., Niu, Y., Li, J., Fu, H., Zhou, M. (2024). Machine learning for advanced emission monitoring and reduction strategies in fossil fuel power plants. *Applied Sciences*, 14(18), 8442. <https://doi.org/10.3390/app14188442>.
- [157] ***<https://www.sterlingsihi.com/cms/ro/Romania/home/piete/sectorul-industrial/produce-alimentare/productia-de-biodiesel-si-bioetanol/producerea-bioetanolului.html>
- [158] productia-de-biodiesel-si-bioetanol/producerea-bioetanolului.html
- [159] *** 13th - 20th International Conference of the European Industrial Hemp Association (EIHA), June 2016 – 2023, Köln, Germany/Brussels, Belgium.
- [160] *** <https://www.casadecanepa.org/betonul-de-canepa>
- [161] *** <https://www.carmeuse.com/ro-ro/aplicatii/materiale-de-constructii/hempcrete>
- [162] *** https://dumbrava47.ro/constructii_verzi/despre-proprietatile-ignifuge-ale-betonului-de-canepa-hempcrete/
- [163] *** <https://app.materlibrary.ro/ro/materiale/SHEMP-0001>
- [164] *** <https://www.energy.gov/eere/vehicles/lightweight-materials-cars-and-trucks>
- [165] *** https://www.hielscher.com/ro/biodiesel transesterification_01.htm (Accessed at 8 April, 2025).

TOMATO LEAVES DISEASE IDENTIFICATION MODEL BASED ON IMPROVED MobileNetV3

基于改进 MobileNetV3 的番茄叶片病害识别模型

Cheng CHI^{1,2,3}, Lifeng QIN^{*1,2,3}

¹ College of Mechanical and Electronic Engineering, Northwest A&F University, Yangling, Shaanxi 712100, China

² Key Laboratory of Agricultural Internet of Things, Ministry of Agriculture and Rural Affairs, Yangling, Shaanxi 712100, China

³ Shaanxi Key Laboratory of Agricultural Information Perception and Intelligent Service, Yangling, Shaanxi 712100, China

Tel: +86 18009247416; E-mail: fuser@nwfau.edu.cn

DOI: <https://doi.org/10.35633/inmateh-75-89>

Keywords: tomato leaf disease; improved MobileNetV3; attention mechanism; dilated convolution

ABSTRACT

Aiming to address the issues of low accuracy and slow response in tomato leaf disease recognition models, an enhanced lightweight model for tomato leaf disease recognition was proposed. The SE attention module in the MobileNetV3-Large model was substituted with a CA attention module, and dilated convolution was incorporated to improve the model's recognition accuracy and response speed. The CA attention module enhances the perception and feature extraction capabilities of spatial coordinate information in images. Dilated convolution was introduced into the deep network architecture to expand the model's receptive field. The model was trained using a transfer learning approach that partially froze specific convolutional layers. Experimental results on a dataset comprising 10 common tomato leaf disease images and healthy leaf images demonstrated that the unimproved model achieved a recognition accuracy of 90.11% and an F1 score of 89.98%. After replacing the SE attention module with the CA attention module, the model's accuracy increased to 91.15%, with the F1 score rising to 91.08%. Furthermore, introducing the dilated convolution model improved the accuracy to 94.33% and the F1 score to 94.22%, while maintaining a parameter count of 2.79×10^6 and a validation set operation time of 11.76 seconds. Compared to other traditional lightweight models, this model exhibits significant advantages. The field test results show that the detection accuracy rate is 88.79% and the omission rate is 8.44%, which has practical application value. The DC-CA-MobileNetV3 tomato leaf disease recognition model proposed in this study can accurately and efficiently identify tomato leaf diseases, featuring a small number of parameters and ease of deployment in embedded systems.

摘要

针对番茄叶片病害识别模型的准确度低、响应速度慢的问题，提出了一种改进的轻量级番茄叶片病害识别模型，将 MobileNetV3-Large 模型中的 SE 注意力模块替换为 CA 注意力模块，并引入空洞卷积，以提高模型识别准确度与响应速度。利用 CA 注意力模块提高对图像空间坐标信息的感知能力和特征提取能力。在深层网络中引入空洞卷积模型，扩大模型感受野。使用只冻结部分卷积层的迁移学习方法对模型进行训练。在常见的 10 种番茄叶片病害图像与健康叶片图像构成的数据集上的实验结果表明，未改进的模型识别精准率为 90.11%，F1 值为 89.98%；改为 CA 注意力模块后，模型的精准率提高至 91.15%，F1 值提高至 91.08%；在此基础上引入空洞卷积模型后，精准率提高至 94.33%，F1 值提高至 94.22%，其模型参数量为 2.79×10^6 ，验证集运行耗时 11.76s，与其他传统轻量化模型相对比具有明显优势。在实际温室场地进行实地试验验证，检测准确率达 88.79%，漏检率为 8.44%，具有实际应用价值。本文提出的 DC-CA-MobileNetV3 番茄叶片病害识别模型可精准、高效地识别番茄叶片病害，同时具有参数量小、易搭载至嵌入式系统的优点。

INTRODUCTION

China ranks among the leading countries in global tomato production, and modern cultivation techniques such as greenhouse planting have significantly enhanced both the yield and quality of tomatoes. Nevertheless, during their growth cycle, tomatoes are susceptible to various diseases, including leaf mildew, yellow leaf curl virus, and powdery mildew. The absence of timely detection and intervention can severely compromise tomato yield and quality (Zhang et al., 2020).

Cheng Chi, M.S. Stud. Eng.; LiFeng Qin, Associate professor, Ph.D. Eng.

However, prompt identification of diseases and implementation of preventive and control measures can effectively mitigate disease propagation, which holds substantial significance for enhancing tomato yield and quality while minimizing economic losses (Tian *et al.*, 2021).

Vision-based technology for the detection and diagnosis of vegetable diseases has garnered significant attention. Xu developed an intelligent tomato disease diagnosis model using Bayesian optimization with LightGBM, preprocessed raw prescription data, and further extracted features from crop disease prescription data through a Wrapper-based recursive feature elimination method, achieving a comprehensive diagnostic accuracy of 89.11% (Xu *et al.*, 2022). Sladojevic employed a deep CNN model along with the Stanford background dataset to classify plant diseases, identifying 13 distinct types of plant diseases from healthy leaves and distinguishing plant leaves from their surrounding environment. The model's accuracy ranged between 91% and 98%, with an average accuracy of 96.3% for individual class tests (Sladojevic *et al.*, 2016). Brahim integrated AlexNet and GoogleNet models within a CNN framework, leveraging transfer learning and fine-tuning mechanisms to classify tomato leaf diseases, achieving accuracies of 98.66% and 99.18%, respectively (Brahimi *et al.*, 2017). Jiang utilized ResNet-50 to identify several tomato leaf diseases - primarily late blight, leaf mold, and yellow leaf curl virus - achieving a detection accuracy of 98% after multiple training iterations (Jiang *et al.*, 2020). Han employed infrared thermal imaging in conjunction with an improved version of YOLOv5 for the early detection of crop diseases. Their model achieved a mean Average Precision (mAP) exceeding 90% across various temperature gradients, enabling more precise and rapid identification of early-stage diseases (Han *et al.*, 2023). Ullah proposed the integration of EfficientNetB3 and MobileNet to detect tomato leaf diseases, achieving a detection success rate of 99.92% (Ullah *et al.*, 2023). Yang optimized the YOLOv5s-based crop yellowing and leaf bending detection model by applying trunk replacement, model pruning, and knowledge distillation techniques. Their approach reduced memory usage by 90% while maintaining an average accuracy reduction of less than 3% (Yang *et al.*, 2023).

The research on tomato leaf disease detection using deep learning models addresses the limitations of traditional manual inspection methods, significantly enhancing both the efficiency and accuracy of detection. However, several challenges remain. First, most deep learning models are characterized by their large size and complex architecture, requiring a substantial number of parameters to achieve high recognition accuracy. This results in heavy computational demands, poor real-time performance, and difficulties in deploying these models on embedded devices for practical applications. Second, given the diverse range of tomato leaf diseases and the similarity of symptoms among some conditions, there is still potential for improvement in the accuracy of existing recognition models.

To address the aforementioned issues, this paper proposes an enhanced algorithm based on the MobileNetV3 model, which is specifically designed for the detection of leaf diseases in tomato greenhouses. By leveraging transfer learning, the model is further optimized to extract both feature representations and their corresponding location information. This not only provides valuable data resources for subsequent inspection tasks but also effectively addresses the challenges of limited deployment on embedded devices.

MATERIALS AND METHODS

Data set construction

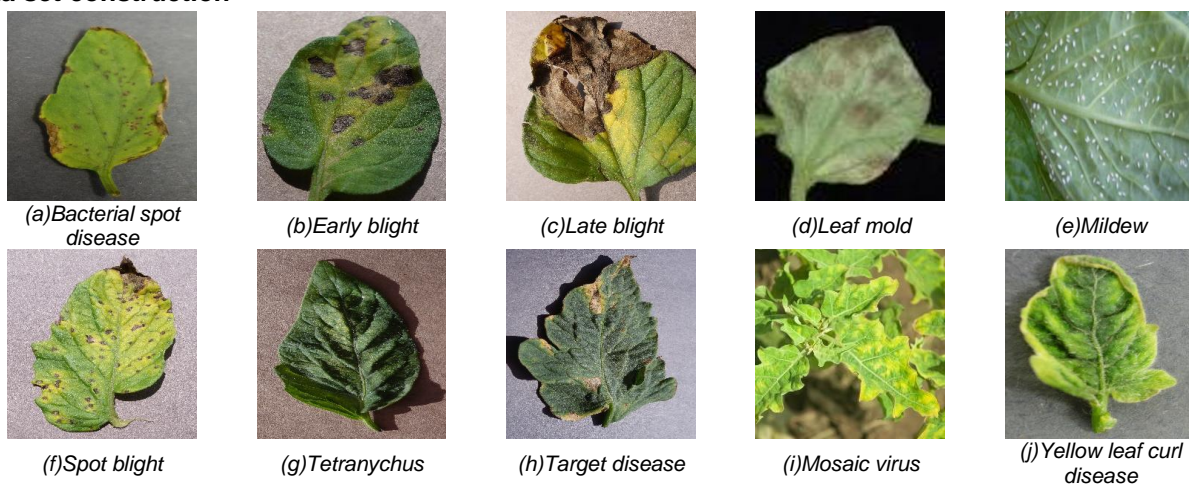


Fig.1 - Sample images of different tomato leaf diseases

In this study, tomato leaves were selected as the research subject, with healthy leaves and 10 common tomato leaf diseases chosen to construct a dataset. All images were sourced from a dataset published on Kaggle's official website. This dataset has been classified by domain experts, ensuring high reliability, which facilitates deep learning models in performing classification tasks effectively. Additionally, the original images underwent augmentation through rotation and mirroring techniques to expand the dataset size and enhance model generalization. Our dataset primarily comprises 10 types of tomato diseases, including bacterial spot, early blight, late blight, leaf mold, mildew, spot blight, spider mite damage, target spot, mosaic virus, yellow leaf curl virus, and healthy leaf images. A total of 32,534 images were split into training and validation sets at an 8:2 ratio. Disease names, corresponding labels, and sample counts are presented in Table 1, while partial image samples are illustrated in Figure 1.

Table 1

Label	Name of tomato leaf diseases	Number of sample images/piece
0	Healthy leaf	3856
1	Bacterial spot disease	3558
2	Early blight	3098
3	Late blight	3905
4	Leaf mold	3493
5	Mildew	1256
6	Spot blight	3628
7	Tetranychus	2182
8	Target disease	2284
9	Mosaic virus	2737
10	Yellow leaf curl disease	2537

Tomato leaf disease recognition model

(1) Lightweight network MobileNetV3 model

MobileNetV3 is a lightweight deep learning model introduced by the Google research team in 2019, and characterized by a reduced number of parameters, lower computational requirements, and shorter inference times (Shi *et al.*, 2024), which makes it particularly suitable for deployment on mobile and embedded devices. Building upon the MobileNetV2 architecture (Sandler *et al.*, 2018), MobileNetV3 incorporates the Squeeze-and-Excitation (SE) attention mechanism to enhance feature representation capabilities. Additionally, it introduces the h-swish activation function, which offers computational efficiency while maintaining high performance. The tail network structure has also been further optimized to improve overall accuracy (Howard *et al.*, 2020). MobileNetV3 provides two variants—MobileNetV3-Large and MobileNetV3-Small—to accommodate diverse hardware configurations and performance needs (Wu 2024). This study focuses on the MobileNetV3-Large model, with its structural parameters detailed in Table 2.

Table 2

Input	Operations	SE	Activation function	Stride
224 ² ×3	Conv2d	—	HS	2
112 ² ×16	Bneck,3×3	—	RE	1
112 ² ×16	Bneck,3×3	—	RE	2
56 ² ×24	Bneck,3×3	—	RE	1
56 ² ×24	Bneck,5×5	√	RE	2
28 ² ×40	Bneck,5×5	√	RE	1
28 ² ×40	Bneck,5×5	√	RE	1
28 ² ×40	Bneck,3×3	—	HS	2
14 ² ×80	Bneck,3×3	—	HS	1

Input	Operations	SE	Activation function	Stride
14 ² ×80	Bneck,3×3	—	HS	1
14 ² ×80	Bneck,3×3	—	HS	1
14 ² ×80	Bneck,3×3	√	HS	1
14 ² ×112	Bneck,3×3	√	HS	1
14 ² ×112	Bneck,5×5	√	HS	2
7 ² ×160	Bneck,5×5	√	HS	1
7 ² ×160	Bneck,5×5	√	HS	1
7 ² ×160	Conv2d,1×1	—	HS	1
7 ² ×960	Pool,7×7	—	—	1
1 ² ×160	Conv2d,1×1, NBN	—	HS	1
1 ² ×1280	Conv2d,1×1, NBN	—	—	1

(2) Improved MobileNetV3 model

Since the existing MobileNetV3 network model exhibits limited sensitivity to location information and insufficient feature learning capability for similar diseases, this paper proposes an enhanced approach for this network model. The improved network architecture is illustrated in Figure 2. First, the SE (Squeeze-and-Excitation) attention module in the bottleneck layer of the network is substituted with the CA attention module, enabling the network to better capture image location information, which facilitates further processing of such information. Second, dilated convolution is incorporated into the last two bottleneck layers, effectively expanding the receptive field without increasing computational complexity, thereby enhancing feature extraction.

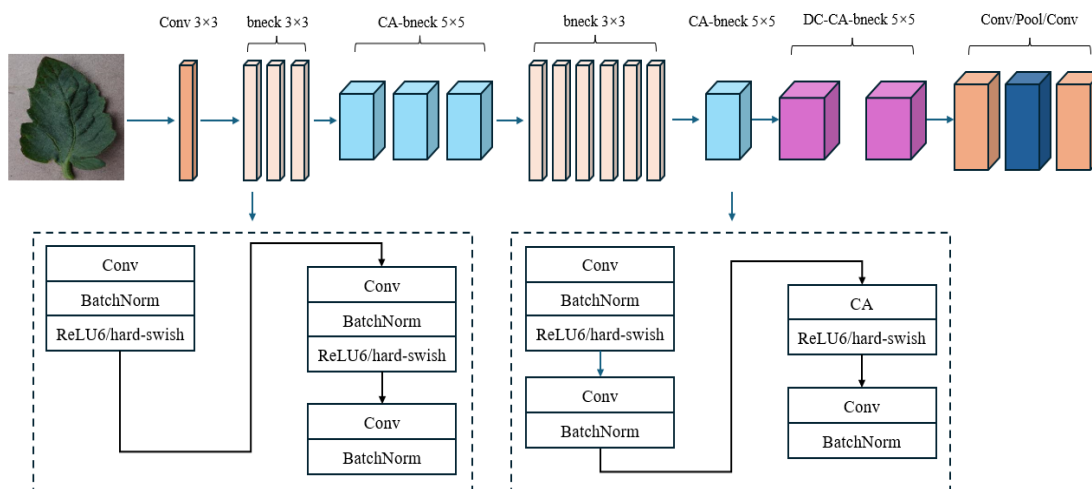


Fig. 2 - Structure diagram of improved MobileNetV3

Since the SE module primarily emphasizes the relationship between channels (*Li et al., 2020*) without accounting for spatial position information, its capability to acquire image information of tomato disease leaves is constrained. The CA attention module integrates decomposed coordinate coding to embed the diseased area's coordinate information into the feature map, thereby enhancing the model's spatial perception of the diseased region. Consequently, the CA attention module, which captures positional information, was employed to replace the SE attention module. This substitution only marginally increased the computing resources required and facilitated seamless integration into mobile inspection devices.

The CA attention mechanism effectively captures image features by modeling inter-channel relationships and long-range spatial dependencies (*Hou et al., 2021*). Specifically, channel attention is decomposed into two one-dimensional feature encoding processes. Global average pooling of input feature maps is performed along both the vertical and horizontal directions to generate perception maps in each direction. Subsequently, these perception maps are combined, and a series of convolutional layers along with nonlinear activation functions are employed to produce a pair of direction-aware and position-sensitive

attention maps. Ultimately, the generated attention maps are applied to the input feature maps via element-wise multiplication, thereby enhancing the representation of the object of interest while preserving accurate positional information (Zheng et al., 2024).

The calculation process of the CA attention mechanism primarily consists of three stages (Gu et al., 2025). Given an input feature map of size $C \times H \times W$, where C denotes the number of channels, H represents the height, and W indicates the width of the feature map, the CA module initially applies two pooling kernels, $(H,1)$ and $(1,W)$, to perform global average pooling along the horizontal and vertical directions, respectively. This operation yields two feature maps of dimensions $C \times H \times 1$ and $C \times 1 \times W$, which are subsequently concatenated to produce a feature map of size $C \times (H+W)$. The concatenated feature map is then transformed via 1×1 convolution, followed by batch normalization and a nonlinear activation function. Subsequently, the transformed feature map is split into horizontally and vertically independent feature maps, which undergo another 1×1 convolution operation. The resulting feature maps have the same number of channels as the input feature map. Finally, the Sigmoid activation function is applied to generate the attention map, which is used to emphasize feature regions through element-wise multiplication, thereby producing the final output feature map. Figure 3 illustrates the detailed calculation process of the CA attention module.

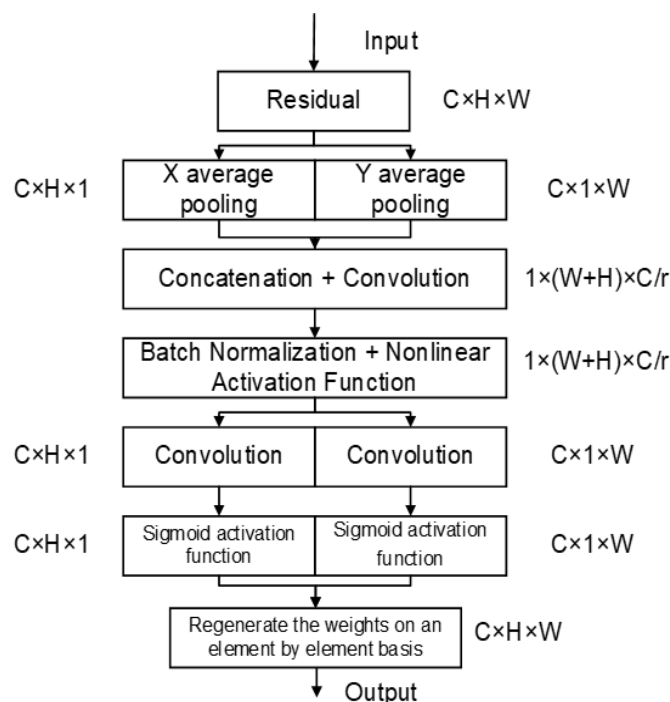


Fig. 3 - Flowchart of calculation of coordinate attention

Dilated Convolution is a technique that incorporates intervals into the convolution kernel, thereby expanding the receptive field of the kernel without increasing computational complexity or introducing additional parameters (Kumar et al., 2022). This facilitates more effective extraction of image features and enhances model learning and training. Given the diversity of tomato leaf diseases and the similarity among different diseases, it is crucial to preserve detailed texture information of disease spots. By leveraging its sparse sampling and resolution-preserving mechanism, dilated convolution effectively addresses detail loss issues caused by traditional down-sampling operations. Furthermore, it establishes correlations between the pathology of lesions and the entire leaf through a large receptive field, achieving a balance between detail enhancement and global perception in multi-scale feature fusion.

Figure 4 illustrates the cavity convolution expansion process. The critical aspect of this process involves the expansion coefficient r , which determines the number of intervals between elements within the convolution kernel. This mechanism enables the establishment of convolution kernels of varying sizes across different bottleneck layers, facilitating the extraction of image features at a deeper level and enhancing their alignment with the target object. In this study, cavity convolution is incorporated into the last two bottleneck modules of the MobileNetV3 network, with expansion coefficients r set to 2 and 4, respectively. The corresponding convolution kernels are also depicted in Figure 4.

Initially, cavities are inserted into the convolution kernel based on the specified expansion coefficient, followed by the computation of feature graph convolution. Finally, the resulting feature graph is output. The size of the feature map can be determined using the following formula:

$$o = \left\lceil \frac{i + 2p - (k - 1)r + 1}{s} \right\rceil + 1 \quad (1)$$

- o - Output the dimension (width or height) of the feature map.
- i -- Input the dimension (width or height) of the feature map.
- p --The extent of edge padding
- k --The size of the convolution kernel
- r --Coefficient of expansion
- s -- Stride. In a hollow convolution, the value is consistently set to 1.

The initial convolution kernel size is set to 3×3. When the expansion coefficient $r=2$, the convolution kernel expands to 5×5; when $r=4$, it further expands to 9×9. It is evident that as the expansion coefficient r increases, both the size of the convolution kernel and its receptive field grow significantly, without introducing any additional operational parameters.

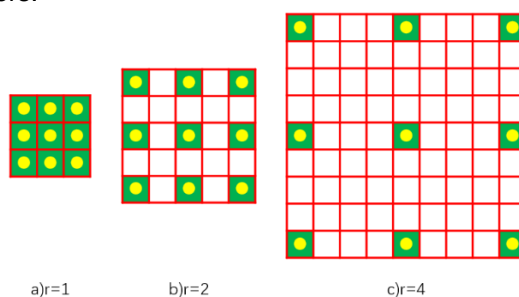


Fig. 4 - Schematic diagram of dilated convolution expansion

(3) Transfer Learning

Transfer learning (Jain *et al.*, 2021; Li *et al.*, 2023) is a machine learning technique that enables the adaptation of a pre-trained model to a new yet related problem, thereby enhancing the model's performance. By leveraging transfer learning, the amount of annotated data required for new tasks can be significantly reduced. In scenarios where existing data resources are limited, transfer learning can significantly boost model accuracy and generalization. This approach enables the model to leverage knowledge from related tasks, thereby learning more robust and transferable features. Consequently, this paper employs transfer learning to optimize the model for deployment and usage. Specifically, MobileNetV3 pre-trained on the ImageNet dataset serves as the source domain model, while the target domain is the tomato leaf disease dataset constructed in this study. To fine-tune the model, a transfer learning optimization strategy involving the freezing of selected convolutional layers is adopted.

The architecture of MobileNetV3 was optimized through techniques such as cavity convolution, coordinate attention module embedding, and other methods. Subsequently, the features of the ImageNet pre-trained model were transferred. The model was trained using a feature transfer approach based on freezing shallow common features and a model transfer approach involving fine-tuning of deep parameters. As a result, the tomato disease recognition model DC-CA-MobileNetV3 was developed.

RESULTS AND ANALYSIS

Experimental platform

The cloud platform provided by Featurize was utilized in this study. The hardware configuration comprised a 6-core Intel E5-2680 v4 processor, an NVIDIA RTX 3060 graphics card with 12GB of memory, and 32GB of system RAM. The software environment included Python 3.7 and the deep learning framework Tensorflow 2.7.

Performance index

Precision (P), Recall (R), mean Average Precision (mAP), and F1 Score (F1) (Sun *et al.*, 2025; Chen *et al.*, 2024) were employed as evaluation metrics to assess the performance of the DC-CA-MobileNetV3 model proposed in this study.

The formulae for precision (P) and recall (R) are:

$$P = \frac{TP}{TP + FP} \times 100\% \quad (2)$$

$$R = \frac{TP}{TP + FN} \times 100\% \quad (3)$$

In the context of mean Average Precision (mAP), P represents the accuracy rate, AP denotes the Average Precision for a single label (the average of the maximum precision values at each recall level), and mAP signifies the mean of the Average Precision across all labels.

The formula is as follows:

$$AP = \frac{\sum P}{N(\text{TotalImages})} \quad (4)$$

$$mAP = \frac{\sum AP}{N(\text{Classes})} \quad (5)$$

Taking bacterial spot disease as an example, TP denotes the count of samples that correctly identify bacterial spot disease among all samples; FP indicates the count of samples that erroneously classify another category or background as bacterial spot disease; FN refers to the count of bacterial spot disease samples misclassified as other categories or unidentified. AP represents the average of the highest precision values achieved for a single disease species across varying recall rates, while mAP signifies the mean value of AP across all disease categories.

The F1 score is a metric employed to comprehensively assess the performance of a classification model. It integrates the precision rate (P) and the recall rate (R), serving as their harmonic mean. This metric allows for the evaluation of model performance while maintaining equilibrium between precision and recall, and its calculation formula is as follows:

$$F1 = \frac{2PR}{P + R} \quad (6)$$

A Comparative Experiment on Transfer Learning Methods

Transfer learning can be categorized into three approaches, namely: Full Migration, which involves freezing all convolutional layers and training only the fully connected layer; Reuse Model, which employs only the model architecture without utilizing pre-trained parameters; and Fine-Tuning, which freezes only a portion of the convolutional layers (Cui et al., 2023). In this study, the Fine-Tuning method was adopted. To evaluate the effectiveness of the transfer learning approach used in this study, the improved MobileNetV3 model was employed as a benchmark, and the same experimental dataset was utilized. The three models were trained using the aforementioned transfer learning methods, respectively, and a tomato disease classification experiment was conducted. The results are presented in Table 3, while the training and validation accuracy curves for the three transfer learning methods are illustrated in Figure 5.

Table 3

Experimental results of test-set of the three migration methods			
Transfer Methodology	Precision/%	Recall/%	F1 Score/%
Fine tuning	94.33	94.12	94.22
Full migration	93.59	92.94	93.28
Reuse model	93.88	93.69	93.78

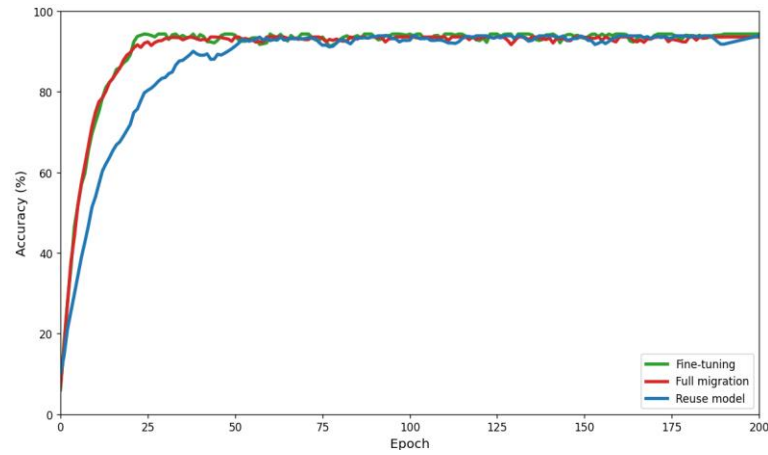


Fig. 5 - Comparison of accuracy of three migration methods

Ablation Study

To validate the effectiveness of the improvement measures, an ablation study was designed. Specifically, the CA attention module and cavity convolution techniques were integrated into the original model to enhance its performance. A classification experiment was subsequently conducted to compare the results, as detailed in Table 4.

Table 4

MobileNetV3-based ablation experiments

Serial Number	CA	DC	Precision (%)	Recall (%)	mAP (%)	F1 Score (%)
1			90.11	89.86	90.02	89.98
2	√		91.15	91.02	91.34	91.08
3		√	92.36	92.30	91.91	92.33
4	√	√	94.33	94.12	93.64	94.22

As shown in Table 4, the introduction of the CA attention module and the cavity convolution module individually led to a certain degree of improvement in model performance. When both methods were combined, the overall effect was optimal. The accuracy of tomato leaf disease identification reached 94.33%, and the F1 score reached 94.22%, surpassing the results obtained by either method alone as well as those of the unimproved model. Simultaneously, the improved model contains 2.79×10^6 parameters, enabling deployment on mobile devices. The increase in required training time is minimal, satisfying the demands for immediate application. In conclusion, the enhanced DC-CA-MobileNetV3 model demonstrates superior comprehensive performance compared to the original model.

A Comparative Study on Various Attention Mechanisms

In this study, the original SE module in MobileNetV3 was replaced with the CA module, which is capable of recognizing spatial positions. To compare and validate the performance of the CA module, MobileNetV3 models incorporating SE, ECA, and CA modules were evaluated under identical experimental data, model architecture, and training conditions. Under these consistent conditions, a fine-tuned transfer learning approach was employed for training over 200 epochs. Figure 6 presents the confusion matrix of classification results under different attention mechanisms, where the values on the main diagonal indicate the number of correctly classified samples. Detailed experimental data are provided in Table 5.

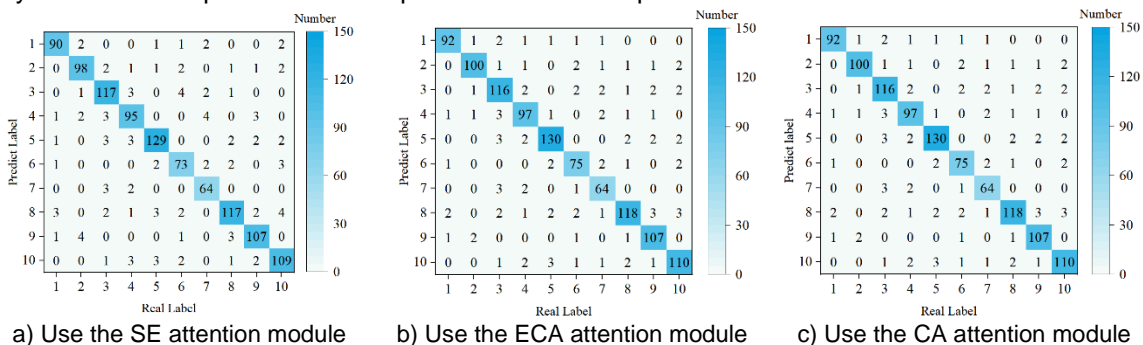


Fig. 6 - The confusion matrix of the MobileNetV3 model using different attention modules

Table 5

Comparison experiments of different attention mechanisms based on MobileNetV3

Methodology	P [%]	R [%]	mAP [%]	F1 Score [%]
SE	90.20	89.97	90.27	90.08
CA	91.15	91.02	91.34	91.08

Comparative experiment of different models

To validate the effectiveness and practicality of the model proposed in this study, comparative experiments were conducted with ShuffleNetV2 (Ma et al., 2018), AlexNet (Krizhevsky et al., 2012), VGG-16 (Simonyan et al., 2015), and ResNet-50 (He et al., 2014), respectively.

Among these models, ShuffleNetV2 is a classic lightweight convolutional neural network that shares similar applications with MobileNetV3. Additionally, AlexNet, VGG-16, and ResNet-50 have gained widespread recognition for their performance in visual classification tasks and thus provide valuable references for comparison. Under identical experimental datasets and model parameter configurations, the proposed model was evaluated against the four aforementioned models with the number of epochs set to 200. The results are presented in Table 6.

Table 6

Experiments of five models on test set

Name	Parameter number/number	Time / s	P / %	R / %	mAP / %	F1 Score / %
AlexNet	6×10^7	18.72	91.62	91.42	90.03	92.52
ShuffleNetV2	1.31×10^6	19.5	92.92	92.19	92.33	92.55
VGG-16	1.39×10^8	35.34	92.52	92.25	92.16	92.38
ResNet-50	2.21×10^7	24.12	93.56	93.28	93.27	93.42
Textual method	2.79×10^6	11.76	94.33	94.12	93.64	94.22

As shown in Table 6, the accuracy P of the enhanced MobileNetV3 network model proposed in this paper reaches 94.33%, which is respectively 2.71%, 1.41%, 1.81%, and 0.77% higher than that of the other four networks. This improvement can be attributed to the incorporation of CA (Coordinate Attention) and void convolution mechanisms, which enable the model to learn image features more effectively. The number of parameters in the model is only marginally higher than that of the lightweight ShuffleNetV2 model, while its recognition time is significantly shorter at 11.76 seconds, representing a reduction of 7.74 seconds compared to ShuffleNetV2. This performance ensures the real-time and high-efficiency requirements necessary for mobile devices and enables the processing of video stream image information. Additionally, the F1 score of the model's recognition capability reaches 94.22%, which is the highest among the compared models, indicating an excellent balance between precision and recall. In conclusion, the improved model presented in this study not only enhances recognition accuracy, but also maintains the characteristics of a lightweight architecture and fast response speed, thereby demonstrating its strong application potential.

Mobile Deployment and Experimentation of the Model

To verify the performance of the improved tomato leaf disease recognition model in practical scenarios, it was applied to the ROS framework and mounted on a patrol device to conduct a patrol experiment for tomato leaf diseases.

The ROS system selected the ROS2 Foxy version, where a workspace and module package were created, and a detection node was designed. The camera image topic /camera/image_raw was subscribed as the model input, and the labeled image /detection_results was used as the model output. The package.xml and setup.py and other dependency files were modified, and the module package was compiled using the colcon command.



Fig. 7 - Inspection device for field experiment drawing

In the experimental glass greenhouse in Wuquan Town, Yangling District, Xianyang City, Shaanxi Province, China, an Ackermann intelligent car equipped with a Raspberry Pi 4B development board was used as the patrol device, as shown in Figure 7.

A total of 121 tomato leaf images were collected to form the target detection validation set. The improved DC-CA-MobileNetV3 model combined with the SSD algorithm module was used to detect tomato leaf disease targets, and the results are shown in Figure 8, where only the rectangular boxes with a confidence level greater than 0.8 are retained. The comparison of the average detection accuracy and missed detection rate of the improved model and the original model on 121 images is shown in Table 7.

Table 7

Comparison of model detection results before and after improvement

Detection method	Precision / (%)	Omission Rate / (%)
Before improvement	84.55%	10.29%
After improvement	88.79%	8.44%



Fig. 8 - Model testing results in the actual scenario

CONCLUSIONS

In this study, we proposed an enhanced MobileNetV3-based model for tomato leaf disease recognition. Specifically, the CA attention module is integrated to replace the SE attention module in the original architecture, enabling more effective extraction of image target feature location information and facilitating subsequent localization tasks on mobile recognition devices. Additionally, dilated convolution is incorporated to expand the model's receptive field and improve its feature recognition capabilities. Experimental results demonstrate that the proposed DC-CA-MobileNetV3 model achieves a recognition accuracy of 94.33%, a recall rate of 94.12%, an average accuracy of 93.64%, and an F1 score of 94.22%, with a parameter count of 2.79×10^6 and an operation time of 11.76 seconds. These performance metrics indicate that the model satisfies the requirements for stability, rapidity, and accuracy, providing robust technical support for the development of intelligent monitoring and inspection systems for tomato leaf disease information. The model was deployed to mobile devices in a greenhouse environment. In actual environmental scenarios, the accuracy rate reached 88.75%, and the missed detection rate was 8.44%, demonstrating practical application value.

In practical application scenarios, factors such as illumination and occlusion can interfere with the performance of the tomato leaf disease recognition model. In future work, we will further optimize the model architecture by incorporating training with images captured under diverse complex conditions, thereby improving accuracy in real-world scenarios and enhancing network robustness.

ACKNOWLEDGEMENT

This research was supported by the Agricultural Science and Technology Innovation and Research Project of Shaanxi Province (Project No.: 2020NY-101 and 2024NC-ZDCYL-05-07).

REFERENCES

- [1] Brahim M., Boukhalfa K., Moussaoui A. (2017), Deep Learning for Tomato Diseases: Classification and Symptoms Visualization. *Applied Artificial Intelligence*, 31(4-6): 1-17. Algeria. DOI: 10.1080/08839514.2017.1315516.
- [2] Chen Z. C. (2024). *Research on tomato leaf disease recognition based on deep learning* (基于深度学习的番茄叶片病害识别研究) [Master's dissertation, Heilongjiang University];
- [3] Cui J. R., Wei W. Z., Zhao M. (2019). Rice disease recognition model based on improved MobileNetV3 (基于改进 MobileNetV3 的水稻病害识别模型). *Transactions of the Chinese Society for Agricultural Machinery*, 54(11): 217-224+276, Guangdong/China;
- [4] Gu R., Gu J. L., Song C. L., Qian C. H. (2019). Multi-scale lightweight apple leaf disease recognition model based on coordinate attention (基于坐标注意力的多尺度轻量级苹果叶片病害识别模型). *Chinese Journal of Agricultural Mechanization*, 46(02): 173-180+186, Jiangsu/China;
- [5] Han X., Xu Y. X., Feng R. Z., Liu T. X., Bai J. B., Lan Y. B. (2019). Early identification of crop diseases based on infrared thermal imaging and improved YOLO v5 (基于红外热成像和改进 YOLO v5 的作物病害早期识别). *Transactions of the Chinese Society for Agricultural Machinery*, Shandong/China, 54(12): 300-307+375.
- [6] He K., Zhang X., Ren S., Sun J. (2014). Spatial Pyramid Pooling in Deep Convolutional Networks for Visual Recognition. *IEEE Transactions on Pattern Analysis & Machine Intelligence*, 37(9): 1904-16. Shaanxi/China;
- [7] Hou Q., Zhou D., Feng J. (2021) Coordinate Attention for Efficient MobileNet work Design. *IEEE/CVF Conference on Computer Vision and Pattern Recognition*, Singapore, 13708-13717.
- [8] Howard A., Sandler M., Chen B., Wang W., Chen L. C., Tan M., Chu G., Vasudevan V., Zhu Y., Pang R. (2020). Searching for MobileNetV3. *IEEE/CVF International Conference on Computer Vision (ICCV)*, Korea (South), DOI:10.1109/ICCV.2019.00140.
- [9] Jain S., Gour M. (2021). Tomato plant disease detection using transfer learning with C-GAN synthetic images. *Computers and Electronics in Agriculture*, 187(2021), India; DOI: 10.1016/j.compag.2021.106279
- [10] Jiang, D.; Li, F.; Yang, Y.; Yu, S. (2020). A tomato leaf diseases classification method based on deep learning. *In Proceedings of the Chinese Control and Decision Conference*, 22–24 August, pp.1446–1450. Hefei/China;
- [11] Krizhevsky A., Sutskever I., Hinton G.E. (2012). Imagenet classification with deep convolutional neural networks. *Advances in neural information processing systems*, 25, USA;
- [12] Kumar V., Singh R., Dua Y. (2022). Morphologically dilated convolutional neural network for hyperspectral image classification. *Signal Processing: Image Communication*, 101: ID 116549. India; DOI: 10.1016/j.image.2021.116549
- [13] Li J., Wang C., Ma Z. Y., Wang G. W., Liao C. Y., Wang H.R., Guan .L. (2023). MobileNet-CAL: Classification of tomato pests and diseases based on transfer learning and attention mechanism (MobileNet-CAL: 基于迁移学习和注意力机制的番茄病虫害分类方法). *Journal of Jilin University (Engineering and Technology Edition)*, pp. 1-9, Jilin/China;
- [14] Li X., Shen X., Zhou Y., Wang X., Li T. Q. (2020). Classification of breast cancer histopathological images using interleaved DenseNet with SENet (IDSNet). *PLoS ONE*, 15(5), UK, DOI: 10.1371/journal.pone.0232127
- [15] Ma N. N., Zhang X. Y., Zheng H. T., Sun J. (2018). ShuffleNet V2: Practical Guidelines for Efficient CNN Architecture Design. *Springer, Cham*, Beijing/China. DOI:10.1007/978-3-030-01264-9_8.
- [16] Sandler M., Howard A., Zhu M., Zhmoginov A., Chen L. C. (2018). MobileNetV2: Inverted Residuals and Linear Bottlenecks. *IEEE/CVF Conference on Computer Vision and Pattern Recognition*, USA, DOI:10.1109/CVPR.2018.00474.
- [17] Shi B. M., He Y. X., Zhao X. (2024). Identification method of maize disease by migrating MobileNetV3 (迁移 MobileNetV3 的玉米病害识别方法). *Journal of Ningxia University (Natural Science Edition)*, Gansu/China, 1-8.

- [18] Simonyan K., Zisserman A. (2015). Very Deep Convolutional Networks for Large-Scale Image Recognition. *International Conference on Learning Representations. Computational and Biological Learning Society*, UK.
- [19] Sladojevic, S.; Arsenovic, M.; Anderla, A.; Culibrk, D. (2016), Stefanovic, D. Deep neural networks based recognition of plant diseases by leaf image classification. *Computational Intelligence and Neuroence*, Republic of Serbia, (3). DOI:10.1155/2016/3289801.
- [20] Sun S. S., Li X. K., Zhang H. L., He L., Zhao L. (2025). Tomato leaf pest detection model with embedded platform (嵌入式平台的番茄叶片病虫害检测模型). *Computer Engineering and Applications*, 1-12. Xinjiang/China;
- [21] Tian P. J., Li S. J., Zhang Y., Liu Y., Zhang S. B., Zhang D. Y.(2021), Detection and genetic variation analysis of leaf curl virus in infected tomato (侵染番茄的曲叶病毒检测及遗传变异分析). *Chinese Vegetables*, (05):28-32, Hunan/China;
- [22] Ullah, Z., Alsubaie, N., Jamjoom, M., Alajmani, S.H., Saleem, F. (2023). EffiMob-Net: A Deep Learning-Based Hybrid Model for Detection and Identification of Tomato Diseases Using Leaf Images. *Agriculture*, Kingdom of Saudi Arabia, 13, 737.
- [23] Wu X. X.(2024). *Research on rice disease image recognition method based on improved MobileNet* (基于改进 MobileNet 的水稻病害图像识别方法研究) [Master's dissertation, Heilongjiang Bayi Agricultural University].
- [24] Xu C., Ding J. Q., Zhao D. T., Qiao Y., Zhang L. X. (2022). Tomato disease diagnosis method based on LightGBM and prescription data (基于 LightGBM 和处方数据的番茄病害诊断方法). *Transactions of the Chinese Society for Agricultural Machinery*, 53(09):286-294, Beijing/China;
- [25] Yang J.H., Zuo H.X., Huang Q.C., Sun Q., Li S.E., Li L. (2023). Lightweight method of crop leaf disease detection model based on YOLO v5s (基于 YOLO v5s 的作物叶片病害检测模型轻量化方法). *Transactions of the Chinese Society for Agricultural Machinery*, 54(S1):.222-229 Beijing/China,.
- [26] Zhang C.C., Yuan S.K., Huo K.K. (2020). Factors affecting tomato production efficiency (影响番茄生产效率的因素). *Hubei Agricultural Mechanization*, (12):33-34, Henan/China;
- [27] Zheng C. J., Li S.B., Pu R.Q., Zhang T. (2019). Tomato leaf disease recognition based on lightweight convolutional neural network (基于轻量化卷积神经网络的番茄叶片病害识别). *Jiangsu Agricultural Sciences*, 52(11): 225-231, Guizhou/China.

DESIGN AND EXPERIMENT OF A PEANUT SEEDING DEVICE FOR SYNCHRONOUS HOLE FERTILIZATION AND DIRECTLY-ABOVE SEEDING

花生穴施肥同步正位播种装置设计与试验

Yi LIU¹⁾, Massoudibrahim SALEM²⁾, Haipeng YAN²⁾, Peng GUO²⁾, Chao XIA²⁾, Guangbao XIA³⁾,
Ahmed F. El-Shafie^{2,4)}, Dongwei WANG^{3,*)}

¹⁾College of Mechanical and Electrical Engineering, Qingdao Agricultural University, Qingdao/China

²⁾Yellow River Delta Intelligent Agricultural Machinery Equipment Industry Academy, Dongying/China

³⁾Industrial Research Institute of Saline and Alkaline High-Efficiency Agricultural Technology, Qingdao Agricultural University, Dongying/China

⁴⁾ Water Relations and Field Irrigation Department, National Research Centre, Cairo/ Egypt.

Tel: +86-459-13012532108; E-mail: w88030661@163.com

Corresponding author: Dongwei Wang

DOI: <https://doi.org/10.35633/inmateh-75-90>

Keywords: hole fertilization, fertilizer distributor, directly-above seeding, experiment, motion trajectory

ABSTRACT

To improve the utilization rate of fertilizers by peanut seeds, this study presents the synchronous hole fertilization and directly-above seeding of peanuts and designs a pneumatic horizontal disc hole fertilization device. A theoretical analysis of the ditching process of the fertilization furrow opener was carried out, and the height of the hole fertilization device from the ground was determined to be 40 mm. Through the analysis of the hole fertilization and directly-above seeding operation process, the time difference between seed metering and fertilizer metering was determined. Combining with theoretical analysis, EDEM-FLUENT coupling simulation tests and field tests were carried out on the device. The field test results showed that the error of the fertilization hole spacing ranges between 2.3-4.5%, the error of the hole fertilization depth is 3.2-5.1%, the seed - fertilizer distance is 64.8-67.2 mm, and the fertilizer distribution length is 99.3-107.5 mm. The test results meet the requirements specified in the sowing and fertilization standards.

摘要

为了提高花生种子对肥料的利用率, 本文以花生穴施肥同步正位播种为研究目标, 设计了这一种气吹式水平圆盘穴施肥装置。对施肥开沟器开沟过程进行了理论分析, 确定了穴施肥装置距离地面的高度为 40mm。通过对穴施肥及正位播种作业过程的分析, 确定了排种与排肥的时间差。结合理论分析对该装置进行了 EDEM-FLUENT 耦合仿真试验及田间试验, 田间试验结果表明施肥穴距误差为 2.3%-4.5%, 穴施肥深度误差为 3.2%-5.1%, 种肥间距为 64.8 mm-67.2 mm, 肥料分布长度为 99.3 mm-107.5 mm。试验结果满足播种施肥标准中规定的要求。

INTRODUCTION

Peanuts, an important oil crop and economic crop in China, play a crucial role in ensuring food security and supporting the agricultural economy (Tang et al., 2019; Shi et al., 2016). With the improvement of agricultural mechanization, peanut seeding technology is gradually evolving toward high efficiency and precision (Timilsena et al., 2015; Shang et al., 2016). Currently, traditional seeding operations still rely primarily on strip fertilization, which faces challenges such as low efficiency and poor fertilizer utilization (Liu., 2017;). Excessive use of chemical fertilizers is likely to lead to problems such as soil compaction, degradation, and environmental pollution (Parent et al., 2020). However, precision fertilization serves as an effective means of supporting the goals of sustainable agricultural development (Gyami et al., 2019). The peanut hole fertilization technique involves applying a fixed quantity of fertilizer in a hole-like pattern at a specific distance beside or directly beneath peanut seeds or plants. Studies have shown that this method enables quantitative and precise fertilization, thereby enhancing fertilizer use efficiency (Luo et al., 2016; Wang et al., 2016).

¹ Yi Liu, master degree; Massoudibrahim Salem, Prof. Ph.D.; Haipeng Yan, master degree; Peng Guo, Ph.D.; Chao Xia, Ph.D.; Guangbao Xia, Ph.D.; Ahmed El-Shafie, Prof. Ph.D.; Dongwei Wang, Prof. Ph.D.

Da Silva et al. designed a perforating and injecting device for liquid fertilizer, which combines soil perforation with liquid fertilizer injection to reduce disturbance to roots, crop residues, and soil, thereby improving plant fertilizer utilization (Da Silva et al., 2019); Martins et al. proposed a method for variable rate nitrogen fertilization in corn using optical sensors, providing data reference for variable rate fertilization decisions through a portable chlorophyll detector (Martins et al., 2020). Du Xin et al. designed an inclined trapezoidal hole-type hole fertilization distributor (Wang et al., 2018; Du et al., 2021) which achieves precision fertilizer filling through inclined trapezoidal holes with fixed volume and uses airflow assistance at the fertilizer discharge port to rapidly discharge fertilizers into holes. However, the distributor has a complex structure and requires replacing the fertilizer discharge adjustment plug to regulate the fertilization amount. Liu et al. designed an automatic seed-aligned fertilization system for corn based on a planetary gear system, which uses a rotary cavity disc hole fertilization device, which can detect in real-time the falling information of seeds and fertilizers, calculate their relative positions, and make real-time adjustments via a control motor (Liu et al., 2023).

To enhance fertilizer utilization rate and the yield per unit area of peanuts, this study focuses on the designed pneumatic horizontal disc hole fertilization device. By analysing the motion trajectories of seeds and clustered fertilizers, the phase difference between the seed metering disc and the fertilizer metering disc was determined. Moreover, field tests were carried out to evaluate the performance of hole fertilization and directly - above seeding performance of the synchronous hole fertilization and directly - above seeding device. The results are expected to provide both theoretical insights and practical references on the equipment for the advancement of precision fertilization technology in peanut cultivation.

MATERIALS AND METHODS

Overall structure and working principle of the synchronous hole fertilization and directly-above seeding device for peanuts

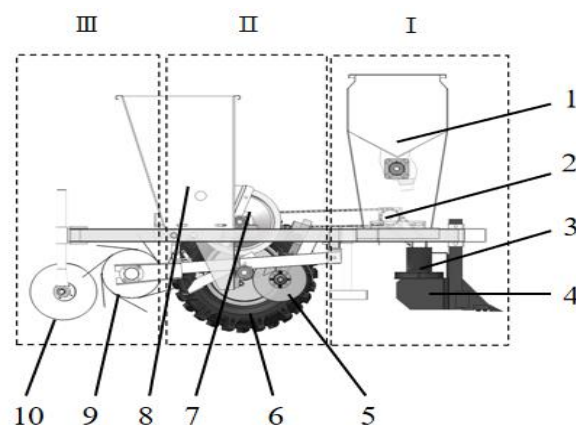


Fig. 1 - Overall structure of the synchronous hole fertilization and directly-above seeding device for peanuts

I - Fertilization unit; II - Seeding unit; III - Soil covering unit; 1 - Main fertilizer tank; 2 - Transmission device; 3 - Hole fertilization device; 4 - Fertilization furrow opener; 5 - Seeding opener; 6 - Ground wheel; 7 - Seed metering device; 8 - Seed box; 9 - Press wheel; 10 - Soil covering wheel.

The synchronous hole fertilization and directly-above seeding device for peanut planters is mainly composed of a seeding unit, a hole fertilization unit, and a motor control unit. The hole fertilization unit mainly includes a fertilization furrow opener, a hole fertilization device, a commutator, etc. During seeding operations, the hole fertilization device extracts fertilizer particles from the fertilizer box and forms clusters in the fertilizer cavity. These particles are transported by the fertilizer metering disc to the fertilizer discharge port, where they are discharged into the fertilization furrow in holes under the action of air flow. The seeding unit consists of a seed metering device, a disc-type furrow opener, a press wheel, a soil covering disc, etc., and uses a spoon-wheel precision seed metering device to achieve precise peanut seeding. The motor control unit is mainly composed of a microprocessor, a speed measurement device, a stepper motor, and a transmission system.

A speed sensor is installed on the ground wheel axle to detect in real-time and to calculate the travel speed, and regulate the motor rotation speed, ensuring that fertilizer particles are applied in holes along the fertilization furrow according to the peanut hole spacing. Meanwhile, the fertilizer metering disc shaft and the seed metering disc shaft maintain a fixed transmission ratio.

By analysing the motion relationship between seeds and hole-applied fertilizers, the phase difference between the seed metering disc and the fertilizer metering disc is determined to ensure that seeds are accurately placed directly above the fertilizers.

Design of hole fertilization device

The horizontal disc hole fertilization device is mainly composed of a fixed plate, housing, fertilizer metering disc, fertilizer quantity adjustment disc, fertilizer tank, motor, coupling, air inlet pipe, etc. According to the fertilizer metering workflow, the fertilizer metering disc can be divided into a fertilizer filling zone I, fertilizer transport zone II, fertilizer discharge zone III, transition zone IV, as shown in Figure 2.

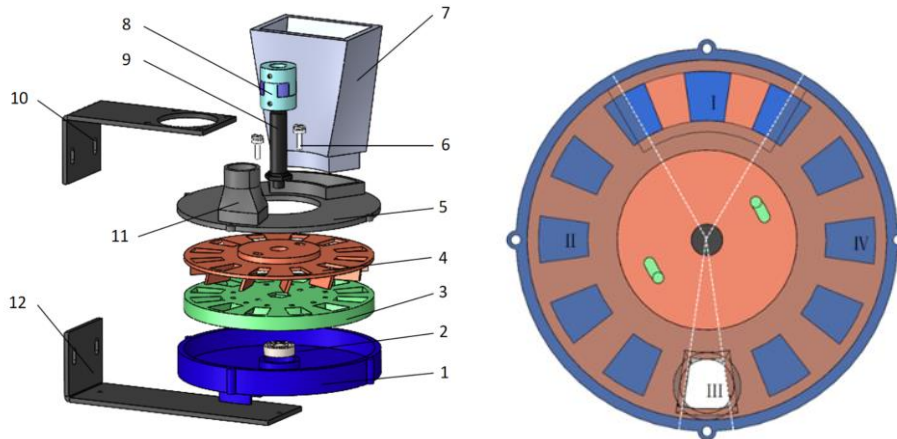


Fig. 2 - Structure of hole fertilization device and fertilizer metering disc zoning

1-Lower housing; 2-Bearing; 3-Fertilizer metering disc; 4-Fertilizer quantity adjustment disc; 5-Upper housing; 6- Fertilizer quantity adjustment bolt; 7-Fertilizer distributor tank; 8-Coupling; 9-Shaft; 10-Upper mounting plate; 11-Air inlet pipe; 12-Lower mounting plate; I -Fertilizer filling zone; II -Fertilizer transport zone; III-Fertilizer discharge zone; IV-Transition zone.

During fertilization, fertilizer particles fall from the planter's fertilizer box into the fertilizer distributor tank through the fertilizer discharge pipe, forming a fertilizer layer of a certain thickness. The fertilizer metering disc and the fertilizer quantity adjustment disc are fixed by fertilizer quantity adjustment bolts. By loosening these bolts and rotating the adjustment disc, the volume of the fertilizer cavities can be changed to regulate the filling amount. The fertilizer metering disc has multiple fertilizer cavities evenly distributed along its central axis. Driven by the shaft, the fertilizer metering disc and adjustment disc rotate counterclockwise in synchronization. As they pass through the fertilizer filling zone at a certain speed, fertilizer particles fill the cavities under gravity and the disturbance of the metering disc. Protected by the upper and lower housings and pushed by the metering disc, the clustered fertilizers travel through the fertilizer transport zone to the fertilizer discharge zone. An air inlet pipe is installed directly above the fertilizer discharge port, connected to a fan above. Under the action of positive pressure airflow and gravity, the fertilizer particles are rapidly discharged, forming holes in the field for application.

Analysis of the installation position of the hole fertilization device

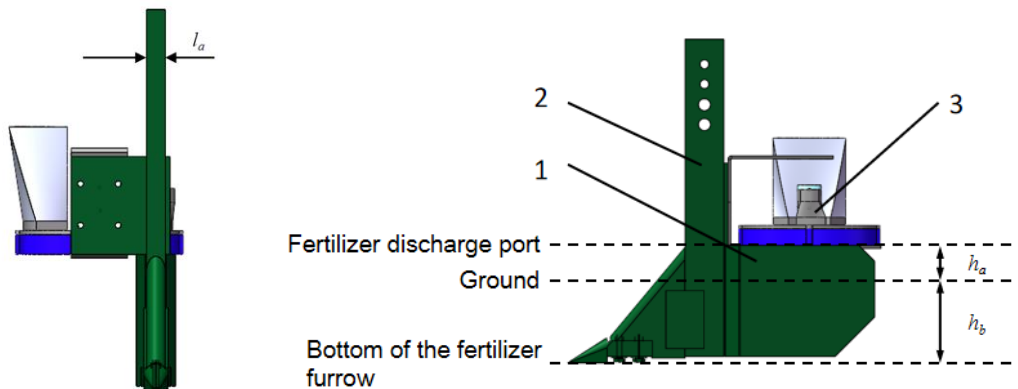


Fig. 3 - Schematic diagram of hole fertilization device installation position

1-Furrow opener wing; 2-Shovel column; 3-Hole fertilization device.

The hole fertilization device is fixed above the furrow opener wings, with the fertilizer discharge port located between the two wings, as shown in Figure 3. During fertilization operations, the furrow opener creates a fertilizer furrow in the soil. Hole-applied fertilizers are discharged from the fertilizer discharge port, fall into the furrow through the wings, and the extended wings on both sides prevent soil from collapsing on the sides of the furrow, maintaining a complete furrow shape.

To reduce the falling time of hole-applied fertilizers and to minimize bouncing and scattering caused by collisions with soil, the installation height of the fertilizer metering disc should be minimized to ensure low-position fertilization. The relative positions of the fertilizer distributor of the hole fertilization device with respect to the ground and the bottom of the fertilizer furrow are shown in Figure 3. During fertilization, the furrow opener lifts and throws part of the soil in the furrow to both sides, forming soil mounds on the edges of the furrow. To prevent excessive soil mounds from squeezing the fertilizer distributor, the installation height of the fertilizer discharge port must be analyzed and calculated. Assuming no soil compaction during furrowing and conservation of soil volume, the height h between the fertilizer discharge port and the ground satisfies the following condition:

$$l_a \cdot h_b \leq \frac{1}{2} h_a \frac{2h_a}{\tan \theta_t} \tag{1}$$

where: l_a is the width of the furrow opener shovel column, [m]; h_b is the height from the ground to the bottom of the fertilizer furrow, [m]; h_a is the height from the fertilizer discharge port of the fertilization device to the ground, [m]; θ_t is the soil angle of repose, [°].

The relational expression for the height from the fertilizer discharge port to the ground can be derived as:

$$h_a \geq \sqrt{l_a \cdot h_b \cdot \tan \theta_t} \tag{2}$$

The width of the furrow opener shovel column used in this study is 30 mm. According to relevant literature, the distance from the ground to the bottom of the fertilizer furrow is generally 90–110 mm, and the soil angle of repose is 31°. Calculations using Equation (2) show that the minimum height from the fertilizer discharge port of the fertilization device to the ground is 40 mm.

Motion analysis of clustered fertilizers

The synchronous direct-position seeding device for peanut hole fertilization first applies fertilizer particles in clustered form into the fertilizer furrow at the hole spacing required by peanut seeding agronomy, then places seeds directly above the fertilizers while maintaining a certain distance. The relative position between seeds and fertilizers directly affects peanut yield and fertilizer utilization efficiency. Here, h_j represents the vertical distance between seeds and fertilizers after seeding and fertilization, and the distribution of seeds and fertilizers is shown in Figure 4.

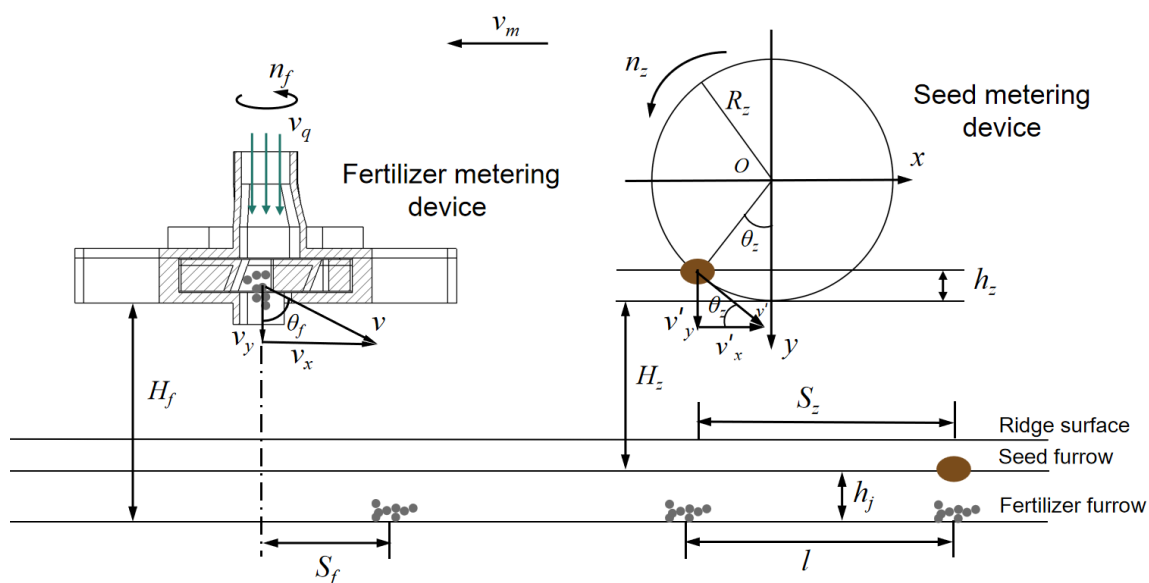


Fig. 4 - Analysis of motion trajectories of seeds and fertilizers

During fertilization, the fertilizer metering disc transports clustered fertilizer particles to the fertilizer discharge port. The fertilizers are discharged backward under the combined action of wind force and gravity, where v_m is the machine travel speed in the direction of machine movement. When the fertilizer distributor starts discharging at the fertilizer discharge port, the horizontal and vertical velocities of the clustered fertilizers when they leave the fertilizer cavities are:

$$\begin{cases} v_x = -v_m + v \cdot \sin \theta_f \\ v_y = v \cdot \cos \theta_f \end{cases} \quad (3)$$

where: v_x is the horizontal component velocity of hole-applied fertilizers when leaving the fertilizer cavity, [m/s]; v_y is the vertical component velocity of hole-applied fertilizers when leaving the fertilizer cavity, [m/s]; v_m is the machine travel speed, [m/s]; v is the resultant velocity of hole-applied fertilizers when leaving the fertilizer cavity, [m/s]; θ_f is the angle between the resultant velocity of hole-applied fertilizers and the vertical direction, [°].

When the hole-applied fertilizers leave the fertilizer cavity and fall into the fertilizer furrow, the distance they move in the vertical direction is:

$$H_f = v_y \cdot t_1 + \frac{1}{2} g t_1^2 \quad (4)$$

where: H_f is the distance from the fertilizer discharge port to the bottom of the fertilizer furrow, [m]; t_1 is the time for hole-applied fertilizers to fall from the fertilizer cavity to the furrow bottom, [s]; g is the gravitational acceleration, [m/s²].

From Equations (3) and (4), it results:

$$t_1 = \frac{-v \cdot \cos \theta_f + \sqrt{v^2 \cdot \cos^2 \theta_f - 2gH_f}}{g} \quad (5)$$

The horizontal displacement of hole-applied fertilizers when leaving the fertilizer cavity and falling into the fertilizer furrow is:

$$S_f = v_x \cdot t_1 \quad (6)$$

where: S_f is the horizontal moving distance of the fertilizer when it falls from the fertilizer cavity to the fertilizer trench during hole - application fertilization, [m].

Seed motion analysis

Peanut seeds start to detach from the seed metering disc at the position shown in [Figure 4](#) and fall into the seed furrow under the action of gravity. The horizontal and vertical velocities of peanut seeds when detaching from the seed metering disc are:

$$\begin{cases} v'_x = -v_m + v' \cdot \cos \theta_z \\ v'_y = v' \cdot \sin \theta_z \end{cases} \quad (7)$$

where: v'_x is the horizontal component velocity of seeds when detaching from the seed metering disc, [m/s]; v'_y is the vertical component velocity of seeds when detaching from the seed metering disc, [m/s]; v_m is the machine travel speed, [m/s]; v' is the resultant velocity of the peanut seed when it detaches from the seed - discharging disc, [m/s]; θ_z is the seed dropping angle, [°].

The distance travelled by peanut seeds in the vertical direction after detaching from the seed metering disc is:

$$H_z + h_z = v'_y t_2 + \frac{1}{2} g t_2^2 \quad (8)$$

where: H_z is the vertical distance from the bottom of the seed metering disc to the bottom of the seed furrow, [m]; h_z is the distance from the seed detachment position on the seed metering disc to the bottom of the seed metering disc, [m]; t_2 is the time for peanut seeds to detach from the seed metering disc and reach the seed furrow, [s].

Among these distances, distance h_z from the position where peanut seeds detach from the seed metering disc to the bottom of the seed metering disc is:

$$h_z = R_z (1 - \cos \theta_z) \tag{9}$$

where: R_z is the radius of the seed metering disc, [m].

From Equations (7), (8), and (9), it results:

$$t_2 = \frac{-v' \cdot \sin \theta_z + \sqrt{(v' \cdot \cos \theta_z)^2 + 2g[H_z + R_z(1 - \cos \theta_z)]}}{g} \tag{10}$$

The horizontal displacement of seeds, S_z , [m], when detaching from the seed metering disc and falling into the seed furrow is:

$$S_z = v'_x \cdot t_2 \tag{11}$$

The time difference between the falling of peanut seeds and fertilizers, Δt [s] is:

$$\Delta t = t_1 - t_2 \tag{12}$$

On the premise of ensuring the normal operation of the fertilizer metering device, its installation position should be as low as possible to reduce the scattering of hole-applied fertilizers and improve the hole-forming performance of the fertilizer metering device. According to the previous design, the installation height h_1 of the fertilizer metering device is 130 mm, which is lower than that of the seed metering device. Therefore, the falling time of seeds is longer than that of fertilizers, and the time difference between their descent must be considered to ensure that the seeds land directly above the hole-applied fertilizers.

Simulation model construction

The device model was established using SolidWorks software. To improve simulation efficiency and reduce simulation time, components without direct contact with fertilizer particles were simplified. A conveyor belt was added 130 mm below the fertilizer metering device to simulate the bottom of the fertilizer furrow for intuitive and quantitative analysis of the hole-fertilizing performance of the fertilizer metering device. The completed 3D model was saved in .STP format and imported into EDEM simulation software. A plane was added 40 mm below the seed discharge port to simulate the bottom of the seed furrow. Fertilizer particles were spherical with an equivalent diameter of 3.3 mm. Since there is no adhesive force between particles or between particles and the fertilizer metering device, the Hertz-Mindlin no-slip contact model was selected (Zhu *et al.*, 2020). The simulation models of the fertilizer metering device and fertilizer particles are shown in Figure 5, with model parameters listed in Table 1 and Table 2 (Ding *et al.*, 2019; Liu *et al.*, 2018; Ding *et al.*, 2018).

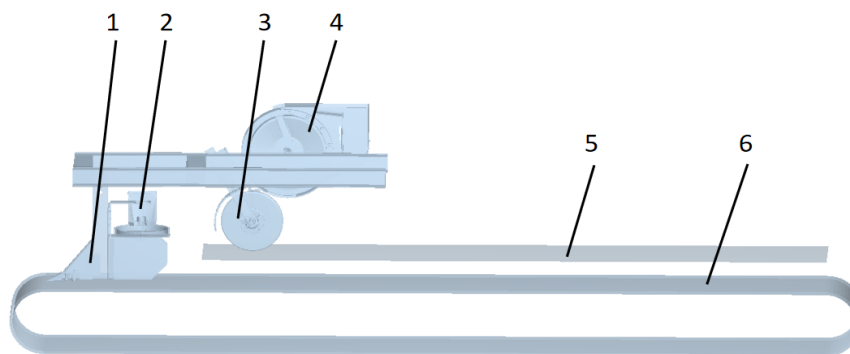


Fig. 5 - EDEM simulation model for synchronous hole fertilization and directly-above seeding device
 1-Fertilizer opener; 2-Hole fertilization device; 3-Seeding opener; 4-Seed metering device; 5-Seed furrow plane; 6-Conveyor belt.

Table 1

EDEM simulation parameters for fertilizer metering process

Item	Fertilizer particles	Fertilizer metering device	Soil	Peanut	Seed metering device
Poisson's ratio	0.25	0.41	0.31	0.30	0.35
Shear modulus/Pa	1.13×10^8	1.71×10^8	7.27×10^8	5.72×10^7	1.22×10^8
Density/kg·m ⁻³	1625	1150	2210	1300	1455

Table 2

Item	Contact parameters between materials				
	Fertilizer-fertilizer	Fertilizer-fertilizer metering device	Fertilizer-soil	Peanut-seed metering device	Peanut-soil
Coefficient of restitution	0.31	0.35	0.05	0.6	0.11
Static friction coefficient	0.33	0.26	1.27	0.34	1.17
Kinetic friction coefficient	0.13	0.21	1.21	0.04	0.92

The 3D model of the fertilizer metering device was imported into the Fluent module of Workbench in .STP format. The fluid domain model was extracted using the DesignModeler tool, and adjusted into three regions—air inlet pipe, fertilizer chamber, and fertilizer outlet—in SpaceClaim software. The adjusted fluid model was then imported into the Meshing module of Fluent for mesh generation (Sun et al., 2024). Polyhedral meshes were selected as the grid type, with interfaces set between the air inlet pipe and fertilizer chamber, as well as between the fertilizer chamber and fertilizer outlet. The air inlet and fertilizer outlet were set as pressure inlet and pressure outlet, respectively, as shown in Figure 6. In EDEM software, the time step was set to 3×10^{-6} s, while in Fluent software, the time step was 3×10^{-4} s. The total simulation duration was the time required for fertilizing 15 holes.

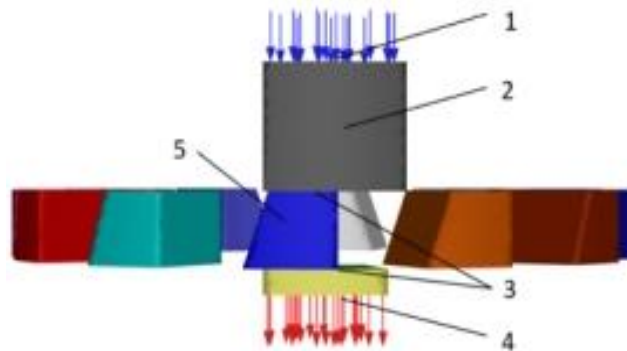


Fig. 6 - Airflow field simulation model
 1-Pressure inlet; 2-Air inlet pipe; 3-Interface; 4-Pressure outlet; 5-Fertilizer chamber.

Simulation of experimental design

The magnitude of airflow speed affects the fertilizer metering performance of the hole fertilization device. To obtain optimal airflow speed parameters and reduce the number of subsequent test combinations, a preliminary pre-experiment was first conducted. Specifically, when the machine's traveling speed was 4 km/h, the airflow speed was set from 0 to 16 m/s, and a single-factor test was carried out using the test indicators of fertilizer distribution length and accuracy of hole fertilization amount.

In the EDEM post-processing interface, Grid Bin Groups were added at the fertilizer metering disc and conveyor belt respectively (Liu et al., 2022), as shown in Figure 7.

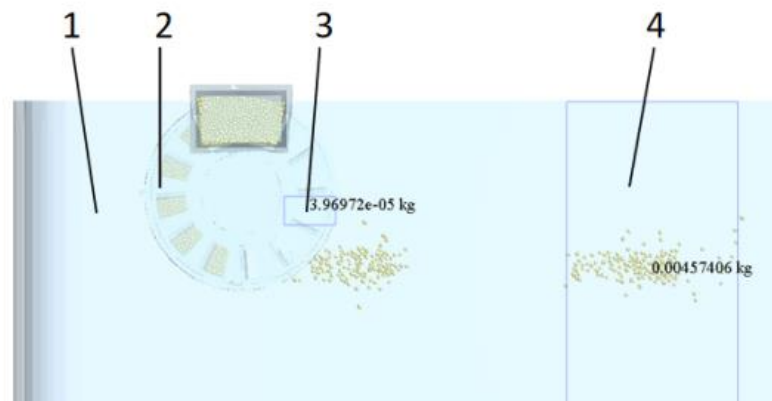


Fig. 7 - Grid cell group position
 1-Conveyor belt; 2- Hole fertilization device; 3- Grid cell group 1; 4- Grid cell group 2

The grid cell group on the fertilizer metering disc is located at two fertilizer chambers behind the fertilizer outlet, with a height of 30 mm and the same length and width as a single fertilizer chamber, used to count the mass of residual fertilizer in the chamber after metering. The grid cell group on the conveyor belt has its bottom on the same plane as the conveyor belt bottom, with a height of 40 mm and a width of 300 mm, used to count the mass of discharged fertilizer and the fertilizer distribution length. By adjusting the length of the grid cell group to match the fertilizer's distribution length, the desired fertilizer distribution length can be obtained.

Data for 15 fertilized holes were collected each time, and their average value was calculated to analyze the accuracy of hole fertilization amount and fertilizer distribution length. The calculation formula for the accuracy of hole fertilization amount is:

$$Y_1 = \frac{\sum_{i=1}^j \frac{m_i}{m}}{j} \times 100\% \quad (13)$$

where: Y_1 is the accuracy of hole fertilization amount, [%]; m is the standard fertilization mass per hole, [g]; m_i is the actual fertilization mass per hole, [g]; j is the number of fertilizer holes passing through the grid cell group.

The influence of airflow speed on the accuracy of hole fertilization amount and fertilizer distribution length is shown in Figure 8.

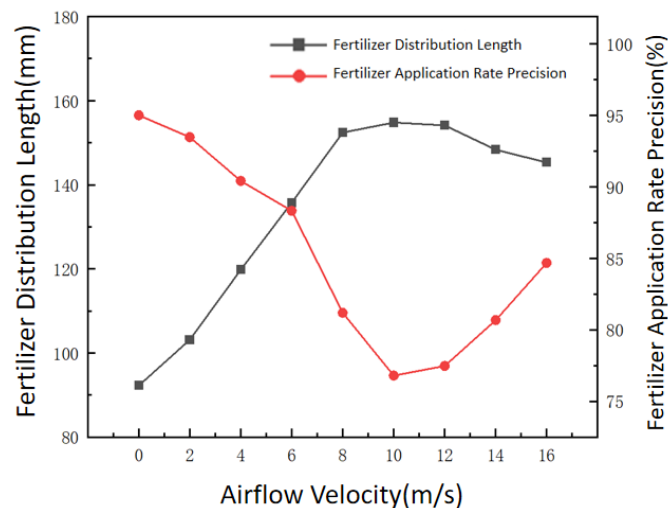


Fig. 8 - Effects of airflow speed on test indicators

When the airflow speed ranges from 0 m/s to 16 m/s, the accuracy of hole fertilization amount first increases and then decreases with the increase of airflow speed, though the decreasing trend is relatively slow. The fertilizer distribution length initially decreases and then increases, with both test indicators—fertilization amount accuracy and distribution length—reaching their optimal values at an airflow speed of 10 m/s. Under the conditions of a machine traveling speed of 4 km/h and a wall inclination angle of 70°, the hole fertilization performance of the fertilizer metering device is relatively stable when the airflow speed is approximately 10 m/s. The test results indicate that when the airflow speed is too low, the fertilizer metering device cannot discharge fertilizer from the chamber in time, reducing the accuracy of hole fertilization amount. When the speed is too high, although the fertilizer clearing rate of the metering device increases, the excessive velocity of fertilizer particles leaving the chamber causes splashing when they contact the conveyor belt, increasing the fertilizer distribution length. Therefore, the inlet airflow speed should be controlled between 8 m/s and 12 m/s.

RESULTS

Hole fertilization synchronous positioning seeding simulation test

Combining the results of single-factor tests, the airflow speed was designed to range from 8 m/s to 12 m/s, the machine traveling speed from 2 km/h to 6 km/h, and the hole spacing was set at 200 mm. Simulation tests were conducted with the longitudinal spacing between seeds and fertilizer, fertilizer distribution length, and hole spacing error in fertilization as test indicators.

The longitudinal spacing between seeds and fertilizer is defined as the distance between peanut seeds and the fertilizer distribution center in the machine's forward direction. The hole spacing in fertilization is taken as the distance between the centers of two adjacent fertilizer accumulations after fertilization, and the calculation formula for the hole spacing error is:

$$W = \frac{\sum_{i=1}^j |S - S_i|}{j S} \times 100\% \tag{14}$$

where: W is the hole spacing error in fertilization, [%]; S is the designed hole spacing for fertilization, [m]; S_i is the actual hole spacing at the i -th position during operation, [m]; j is the number of fertilizer holes passing through the grid cell group.

The results of the simulation test are shown in Figure 9, and the test results are presented in Table 3.

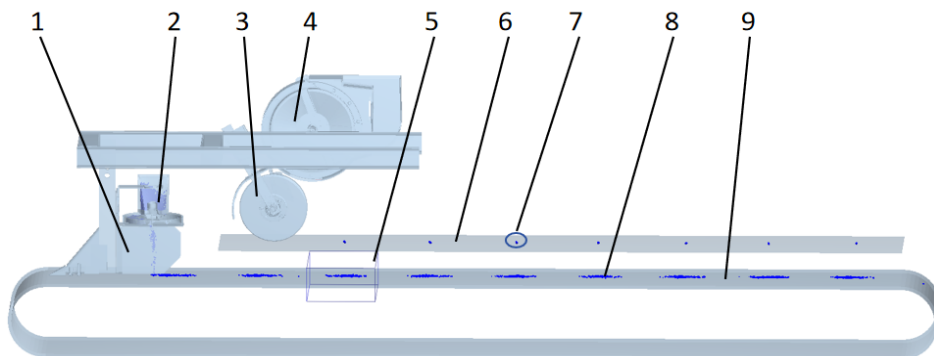


Fig. 9 - Synchronous positioning seeding simulation test for hole fertilization
 1-Fertilizer opener; 2-Hole fertilization device; 3-Seeding opener; 4-Seed metering disc; 5-Grid cell group; 6-Seed furrow plane; 7-Peanut seeds; 8-Clumped fertilizer; 9-Conveyor belt.

Table 3

Test results of synchronous positioning seeding for hole fertilization

Machine traveling speed [km·h ⁻¹]	Airflow speed [m·s ⁻¹]	Longitudinal spacing between seed and fertilizer [mm]	Fertilizer distribution length [mm]	Hole spacing error in fertilization [%]
2	8	6.8	93.3	3.6
	10	6.1	91.2	3.3
	12	7.7	92.9	3.9
4	8	7.3	91.7	4.9
	10	8.1	84.2	4.8
	12	8.7	85.6	5.1
6	8	10.2	98.5	5.2
	10	10.9	94.2	5.7
	12	11.7	95.7	6.0
Mean		8.6	91.9	4.7
Standard deviation		1.82	12.87	2.64

Data in Table 3 show that when the airflow speed is constant, the longitudinal spacing between seeds and fertilizer and the hole spacing error in fertilization show an increasing trend with the increase in machine traveling speed, with a mean longitudinal spacing between seeds and fertilizer of 8.6 mm and a mean hole spacing error of 4.7%. When the machine traveling speed is constant, the fertilizer distribution length shows a trend of first increasing and then decreasing, with a mean distribution length of 91.9 mm, and the minimum distribution length occurs at an airflow speed of 10 m/s. Considering the test data comprehensively, the airflow speed is determined to be 10 m/s.

Field experiment

The field experiment was conducted in Guangrao County, Dongying City, Shandong Province. The peanut variety used was Yuhua 18 and Luhua 10, and the fertilizer was granular slow-release compound fertilizer produced by Liuguo Chemical Industry Co., Ltd. Before the experiment, the soil was rototilled, leveled, and loosened to ensure that it meets the sowing conditions for peanuts.



Fig. 10 - Hole fertilization device and field experiment

Based on the widely used peanut fertilization amount in the region, we evaluated the hole fertilization performance and positioning seed metering performance of the device with reference to the *Technical Specifications for Quality Evaluation of Fertilizer Machinery* (NY/T 1003-2006) and *Operation Quality of Mulching Hole Seeding Machines* (NY/T 987-2006) (Hu et al., 2016; Geng et al., 2018). A 10 m operation length was selected as a test area, and field test data were analyzed using hole spacing error in fertilization, fertilization depth error, seed-fertilizer spacing, and fertilizer distribution length as test indicators. The test results are shown in Figure 11.



Fig. 11 - Field experiment data collection

Table 4 presents the field trial results for Yuhua 18 peanut seeds. When the machine travel speed ranges from 2 km/h to 6 km/h, the hole spacing accuracy rate can reach over 94.5%. The vertical distance between seeds and fertilizer is between 64.8 mm and 67.2 mm, and the fertilizer distribution length ranges from 95.7 mm to 107.5 mm.

Table 4

Field trial results of Yuhua 18 peanut seeds				
Machine traveling speed [km·h ⁻¹]	Hole spacing error [%]	Vertical spacing between seed and fertilizer [mm]	Fertilizer distribution length [mm]	Longitudinal spacing between seed and fertilizer [mm]
2	3.3	67.2	99.3	5.4
4	4.9	66.4	95.7	6.2
6	5.5	64.8	107.5	7.1

Table 5 presents the field trial results for Luhua 10 peanut seeds. The hole spacing accuracy rate can reach over 94.1%, the vertical distance between seeds and fertilizer ranges from 65.4 mm to 71.1 mm, and the fertilizer distribution length is between 91.1 mm and 105.8 mm.

Table 5

Field trial results of Luhua 10 peanut seeds				
Machine traveling speed [km·h ⁻¹]	Hole spacing error [%]	Vertical spacing between seed and fertilizer [mm]	Fertilizer distribution length [mm]	Longitudinal spacing between seed and fertilizer [mm]
2	3.7	71.1	101.3	6.2
4	4.6	68.7	91.1	7.7
6	5.9	65.4	105.8	10.1

Both sets of trials meet the requirements for simultaneous and correctly positioned hole fertilization and sowing.

CONCLUSIONS

(1) A hole fertilization device was designed, and its installation position was analysed to determine that the minimum distance between the fertilizer discharge port and the ground is 40 mm. The movement trajectories of seeds and fertilizer during the sowing and fertilization process were analysed to obtain the time difference between seed metering and fertilizer metering. Based on theoretical analysis, simulation tests were designed. The results of single-factor tests showed that the optimal hole fertilization performance occurs when the airflow speed is 8 m/s to 12 m/s. The two-factor test results indicated that the average values of the test indicators for the designed synchronous positioning seeding device with hole fertilization are as follows: longitudinal spacing between seeds and fertilizer of 8.6 mm, fertilizer distribution length of 91.9 mm, and hole spacing error in fertilization of 4.7%.

(2) A field experiment of the synchronous positioning seeding device with hole fertilization was carried out. The hole fertilization device was installed on a peanut seeding and fertilizing machine for two rows per ridge, and the transmission mode was changed simultaneously. The theoretical fertilization depth was set at 100 mm, the seeding depth at 30 mm, the theoretical hole spacing at 200 mm, and the machine traveling speed at 2 km/h to 6 km/h. The field trial results for Yuhua 18 peanuts showed a hole spacing error of 3.3% to 5.5%, a seed-fertilizer spacing of 64.8 mm to 67.2 mm, and a fertilizer distribution length of 99.3 mm to 107.5 mm. For Luhua 10 peanuts, the corresponding results were: 3.7% to 5.9% (hole spacing error), 65.4 mm to 71.1 mm (seed-fertilizer spacing), and 91.1 mm to 105.8 mm (fertilizer distribution length). The experimental results meet the requirements specified in the seeding and fertilization standards.

(3) Compared to the traditional strip fertilization, where the minimum fertilizer application rate is 450 kg/ha, the hole fertilization device used in this study achieves a minimum fertilizer application rate of 375 kg/ha, saving approximately 16.7% of fertilizer/ha and improving fertilizer utilization efficiency.

ACKNOWLEDGEMENT

The authors were funded for this project by the Innovation and Industrialization of Key Technologies for Combined Tillage and Sowing Equipment in Saline-alkali Land (2024CGZH14) and Creation of Key Components of High-efficiency Tillage and Land Preparation Equipment for Saline-alkali Land (Y20240055).

REFERENCES

- [1] Adu-Gyamfi, R., Agyin-Birikorang, S., Tindjina, I., Manu, Y., Singh, U. (2019). Minimizing nutrient leaching from maize production systems in northern Ghana with one-time application of multi-nutrient fertilizer briquettes. *The Science of the Total Environment*, Vol. 694. <https://doi.org/10.1016/j.scitotenv.2019.133667>
- [2] Ding, X., Cui, D., Liu, T., Wang, S., Zhao, L. (2019). Optimized design and test of precise variable fertilizer discharger structure (精准变量排肥器结构优化设计与试验). *Journal of Chinese Agricultural Mechanization*, Vol. 40, pp. 5-12. <https://doi.org/10.13733/j.jcam.issn.2095-5553.2019.01.02>
- [3] Ding, S., Bai, L., Yao, Y., Yue, B., Fu, Z., Zheng, Z., Huang, Y. (2018). Discrete element modelling (dem) of fertilizer dual-banding with adjustable rates. *Computers and electronics in agriculture*, Vol. 152, pp.8. <https://doi.org/10.1016/j.compag.2018.06.044>
- [4] Du, X., Liu, C., Jiang, M., Yuan, H., Dai, L. (2021). Design and experiment of inclined trapezoidal hole fertilizer point-applied discharging device (倾斜梯形孔式穴施肥排肥器设计与试验). *Transactions of the Chinese Society for Agricultural Machinery*, Vol. 52, pp. 43-53.

- [5] Da, S., Graziano, M. (2019) Modeling and design of an injection dosing system for site -specific management using liquid fertilizer. *Precision Agriculture*, Vol. 20, pp. 649-662. <https://doi.org/10.1007/s11119-018-9602-5>
- [6] Geng, R., Zhang, M., He, K., Li, Y., Xie, C., Jin, C. (2018). Design and test of tilted double circular hole disc type corn seed discharger (倾斜双圆环型孔圆盘式玉米排种器设计与试验). *Transactions of the Chinese Society for Agricultural Machinery*, Vol. 49, pp. 9. <https://doi.org/10.6041/j.issn.1000-1298.2018.01.008>
- [7] Hu, H., Li, H., Wang, Q., He, J., Zhang, Y., Chen, W., Wang, X. (2016). Design and testing of a deep fertilizer applicator for fixed-point latching between rows of corn (玉米行间定点扎穴深施追肥机的设计与试验). *Transactions of the Chinese Society of Agricultural Engineering*. Vol. 32, pp. 10. <https://doi.org/10.11975/j.issn.1002-6819.2016.24.004>
- [8] Luo, X., Liao, J., Hu, L., Zang, Y., Zhou, Z. (2016). Improving agricultural mechanization level to promote agricultural sustainable development (提高农业机械化水平促进农业可持续发展). *Transactions of the CSAE*, Vol. 32, pp. 1-11. <https://doi.org/CNKI:SUN:NYGU.0.2016-01-001>
- [9] Liu, C., Wei, D., Song, J., Li, Y., Du, X., Zhang, F. (2018). Systematic study on boundary parameters of discrete element simulation of granular fertilizer (颗粒肥料离散元仿真边界参数系统化研究). *Transactions of the Chinese Society for Agricultural Machinery*, Vol. 49, pp. 82-89. <https://doi.org/10.6041/j.issn.1000-1298.2018.09.009>
- [10] Liu, R., Liu, Z., Liu, L., Li, Y. (2022). Design and testing of a high-speed air-aspirated seed discharger for disturbance-assisted seed filling of corn (玉米扰动辅助充种高速气吸式排种器设计与试验). *Transactions of the Chinese Society for Agricultural Machinery*, Vol. 53, pp. 50-59. <https://doi.org/10.6041/j.issn.1000-1298.2022.09.005>
- [11] Liu, Z., Wang, X., Li, S., Huang, Y., Yan, X., Zhao, H. (2023). Design of Maize Automatic Hole Fertilization System Targeting at Seed Based on Planetary Gear Train (基于行星轮系的玉米穴施肥自动对种系统设计与试验). *Transactions of the Chinese Society for Agricultural Machinery*, Vol. 49, pp. 137-144. <https://doi.org/10.6041/j.issn.1000-1298.2023.03.006>
- [12] Liu, Q. (2017). Spatio-temporal changes of fertilization intensity and environmental safety threshold in China (中国化肥施用强度及环境安全阈值时空变化). *Transactions of the CSAE*, Vol. 33, pp. 214-221. <https://doi.org/10.11975/j.issn.1002-6819.2017.06.028>
- [13] Martins, R., Pinto, F., Moura, A., Siqueira, W., Villar, F. (2020). Nitrogen variable rate fertilization in corn crop prescribed by optical sensor. *Journal of Plant Nutrition*, Vol. 43, pp. 1681-1688. <https://doi.org/10.1080/01904167.2020.1729805>
- [14] Shang, J., Yin, X. (2016). Study on the present situation and reduction of fertilizer no n-point source pollution of China (中国化肥面源污染现状及其减量化研究). *Ecological Economy*, Vol. 32, pp. 196-199. <https://doi.org/10.3969/j.issn.1671-4407.2016.05>
- [15] Shi, C., Guo, Y., Zhu, J. (2016). Evaluation of over fertilization in China and its influencing factors (中国粮食生产中化肥过量施用评价及影响因素研究). *Research of Agricultural Modernization*, Vol. 37, pp. 671-679. <https://doi.org/10.13872/j.1000-0275.2016.0064>
- [16] Sun, W., Yi, S., Qi, H., Wang, S., Li, Y., Dai, Z. (2024). Design and Experiment of Twin Disks Intertwined Air-pressure High-speed Precision Seed-metering Device for Maize Delta-row Dense Plantings (双盘交错气压式玉米品字形密植高速精量排种器研究). *Transactions of the Chinese Society for Agricultural Machinery*, Vol. 55, pp. 168-179.
- [17] Serge, P., Wilffiend, D., Noura, Z., Michael, L., Gilles, T., Annie, P., Léon, P. (2020). Corn response to banded p fertilizers with or without manure application in eastern canada. *Agronomy journal*, Vol. 112, pp. 2176-2187. <https://doi.org/10.1002/agj2.20115>
- [18] Tang, H., Wang, J., Xu C., Zhou, W., Wang, J., Wang, X. (2019). Research progress analysis on key technology of chemical fertilizer reduction and efficiency increase (化肥减施增效关键技术研究进展分析). *Transactions of the Chinese Society for Agricultural Machinery*, Vol. 50, pp.1-19. <https://doi.org/CNKI:SUN:NYJX.0.2019-04-001>

- [19] Timilsena, Y., Adhikari, R., Casey, P., Muster, T., Adhikari, B., (2015). Enhanced efficiency fertilisers: a review of formulation and nutrient release patterns. *Journal of the science of food and agriculture*, Vol. 95, pp. 1131-1142. [https://doi.org/ 10.1002/jsfa.6812](https://doi.org/10.1002/jsfa.6812)
- [20] Wang, Yunxia., Liang, Z., Cui, Tao., Zhang, X., Qu, Z., Yang, L. (2016). Design and experiment of layered fertilization device for corn (玉米分层施肥器结构设计及试验). *Transactions of the Chinese Society for Agricultural Machinery*, Vol. 47, pp. 163 – 169. <https://doi.org/10.6041/j.issn.1000-1298.2016.S0.025>
- [21] Wang, J., Li, S., Zhang, Z., Li, J. (2018). Design and experiment of electrical drive side deep hill-drop fertilization system for precision rice hill-direct-seeding machine (水稻精量穴直播机电驱式侧深穴施肥系统设计及试验). *Transactions of the CSAE*, Vol. 34, pp. 43 – 54. [https://doi.org/ 10.11975/j.issn.1002-6819.2018.08.006](https://doi.org/10.11975/j.issn.1002-6819.2018.08.006)
- [22] Zhu, T., Cong, J., Qi, B., Wu, M., Peng, X., Wang, Y. (2020). Design and test of mechanical-pneumatic combined peanut precision seed discharger (机械气力组合式花生精量排种器设计与试验). *China Mechanical Engineering*, Vol. 31, pp. 9. <https://doi.org/10.3969/j.issn.1004-132X.2020.21.010>

DESIGN AND EXPERIMENTAL STUDY OF A CONTROL SYSTEM FOR SYNCHRONIZED CORN SEEDING AND HOLE FERTILIZATION

玉米播种和穴播施肥同步控制系统的设计与试验研究

Ziyu WANG¹, Hongchao WANG², Chunying LIANG^{*2}, Naichen ZHAO²

¹ College of Information and Electrical Engineering, Heilongjiang Bayi Agricultural University, Daqing 163319, China

² College of Engineering, Heilongjiang Bayi Agricultural University, Daqing/China

Tel: 13836961615; E-mail: liangchunying@byau.edu.cn

DOI: <https://doi.org/10.35633/inmateh-75-91>

Keywords: corn, hole fertilization, control system, experiment.

ABSTRACT

To solve the problems of slow system response speed and poor uniformity of seeding and fertilizer application, this paper designs a control system for synchronized corn seeding and precision hole fertilization. A sliding mode control method with integral variable structure and disturbance observer composite (ISMDO-SMC) is proposed. Furthermore, a three-factor, five-level quadratic orthogonal rotation combination experiment was conducted to develop a mathematical model for parameter optimization using a multi-objective variable optimization method. Simulation results from four algorithms were compared, revealing a regulation time of 0.42 seconds, a recovery time to steady state of 0.13 seconds, and a descending rotational speed of 2.5 r/min, which demonstrates the strongest dynamic response and stability. Moreover, the optimal parameter combination was determined to be the forward speed of 2.8 km/h, the fertilizer discharge shaft speed of 42 r/min, and the fertilizer discharger opening of 5.5 mm, resulting in the fertilizer application error of 1.7 g and the seed-fertilizer spacing error of 2.2 mm. The results of this study provide a theoretical basis for achieving efficient and stable seeding and fertilization operations.

摘要

为了解决系统响应速度慢和播种施肥均匀性差的问题, 本文设计了一种同步玉米播种与穴施肥的控制系统。提出了一种基于积分变量结构和扰动观测器复合的滑模控制方法。此外, 采用三因素五水平的二次正交旋转组合实验, 通过多目标变量优化方法建立了参数优化的数学模型。通过比较四种算法的仿真结果, 得出该系统的调节时间为 0.42 秒, 恢复稳态时间为 0.13 秒, 下降转速为 2.5 r/min, 表明其具有最强的动态响应和稳定性。进一步, 优化的参数组合为前进速度 2.8 km/h, 施肥轴转速 42 r/min, 施肥器开度 5.5 mm, 在此条件下, 施肥误差为 1.7 g, 种肥间距误差为 2.2 mm。该研究结果为实现高效稳定的播种施肥作业提供了理论依据。

INTRODUCTION

Corn is an important food and income crop that holds a significant position in global agriculture. In corn production, fertilizer application plays a crucial role in ensuring both high yield and high quality (Yu *et al.*, 2021). Traditional fertilizer application methods typically involve manual application or the use of fertilizer spreaders to distribute fertilizer across the ground surface (Vieira-Megda *et al.*, 2015). However, these methods increase production costs and result in low fertilizer utilization, preventing the achievement of spatially differentiated fertility replenishment (Zhang *et al.*, 2012). Irrational fertilizer application not only leads to environmental pollution but also negatively affects crop yield and quality (Qi *et al.*, 2024). Control systems that synchronize corn seeding with precision hole fertilization are an integral component of sustainable precision agriculture systems. These systems enhance fertilizer use and yield while reducing application rates and mitigating the environmental pressures caused by over-fertilization.

In recent years, variable fertilization techniques have gained increasing attention in several countries (Cheng *et al.*, 2022). Japan's Iseki Agricultural Machinery Co., Ltd. has developed a series of self-propelled variable spray fertilizer applicators for paddy fields. These machines are equipped with a variable fertilizer application system that collects real-time information on soil nutrients and crop characteristics through various sensors. The amount of fertilizer applied is adjusted by the controller to meet the specific requirements for crop growth (Shi *et al.*, 2019; Yu *et al.*, 2019; Chen *et al.*, 2019).

¹ Ziyu Wang, master degree; Hongchao Wang, Ph.D.; Chunying Liang, Prof. Ph.D.; Naichen Zhao, Ph.D.

To achieve refined operations, some researchers have extensively explored aspects such as fertilizer prescription decisions and variable control algorithms. Tola developed a fertilizer control system based on real-time fertilizer discharge sensors, which has reduced fertilizer application errors (Tola *et al.*, 2008). Bu proposed an optimization model for the fertilization control sequence based on a differential evolutionary algorithm, enabling online regulation of fertilizer application and improving fertilization performance (Bu *et al.*, 2022). The control system is the core of variable fertilizer application technology and plays a decisive role in the effectiveness of fertilizer application. A significant number of scholars have widely adopted the external grooved wheel fertilizer application method for variable fertilizer application, with fertilizer volume adjustment achieved by altering the rotational speed of the fertilizer discharge shaft. Sugirbay investigated the effect of groove wheel parameters on the stability of high-speed fertilizer discharging in external groove wheel fertilizer dischargers. They designed 25 groove wheel configurations and conducted bench tests to identify the optimal parameters and speed range (Sugirbay *et al.*, 2020). Alameen developed a variable-speed granular fertilizer application control system that uses cylinders to regulate the openings of all fertilizer dischargers. This system was able to accurately control the rate of granular fertilizer application, with an overall system error of less than 2.6% (Alameen, Al-Gaadi, & Tola, 2019). In summary, numerous scholars have conducted in-depth research on fertilizer application devices and control systems (Pramod *et al.*, 2023; Wang *et al.*, 2023). However, issues such as slow system response time and poor uniformity in seeding and fertilizer application during corn seeding and hole fertilization still require further investigation. Addressing these challenges is crucial for improving the overall performance and adaptability of fertilizer application devices, and for providing stronger technical support for the realization of precision agriculture.

The main objective of this study is to design a control system for synchronizing corn seeding and variable hole fertilization. An integral sliding mode variable structure controller was designed, and a novel convergence rate was introduced to significantly improve both the steady-state and dynamic performance of the control system. Additionally, the system incorporates an extended state observer to monitor perturbations caused by changes in motor parameters and load torque. The observed perturbation values are then fed into the sliding mode controller as feed-forward compensation, enhancing the system's ability to resist interference. Furthermore, the performance of the control system for synchronized variable hole fertilization during corn seeding was validated through a bench experiment.

MATERIALS AND METHODS

Machine Structure and Working Principle

The experimental bench primarily consists of a conveyor platform, a box, a corn hole application device, a seed discharger, a control system, and a photoelectric detection device, as shown in figure 1. The fertilizer and seed boxes are filled with fertilizer and seeds, respectively, and the conveyor belt moves at a constant speed once the power is turned on, simulating the relative motion between the locomotive and the field. Upon activating the system, the fertilizer discharge motor is first controlled to rotate, ensuring the preparation of fertilizer for the first hole application. The photoelectric sensor probe installed at the outlet of the seed discharger detects the seed, transmits the signal to the microcontroller, and controls the rotation of the fertilizer discharge tube stopper to a set angle, aligning the fertilizer discharge opening with the circular notch on the stopper to synchronize seeding and fertilizer application.

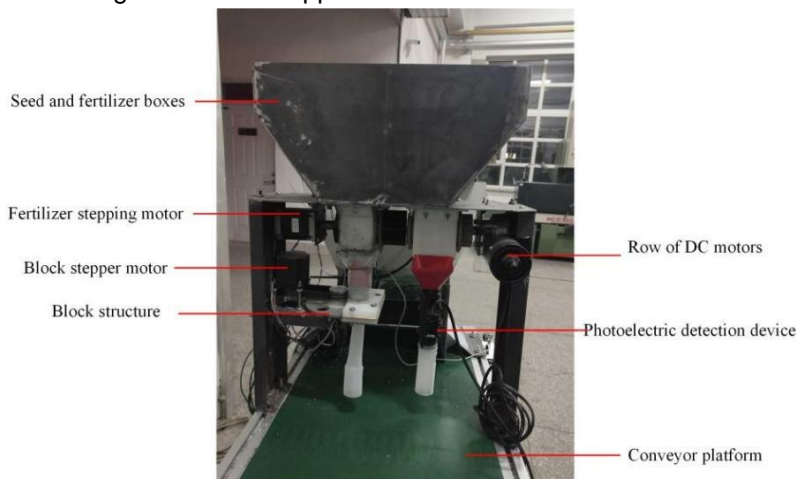


Fig. 1 - Experimental bench for synchronized corn seeding and precision hole fertilization

A disc stopper was designed to control the intermittency of the fertilizer discharge at the fertilizer discharge opening, using a non-corrosive plastic material. The stopper has three holes that are 120° apart from the center of the circle, the same size as the fertilizer pipe. The position of the baffle round hole coincides with the position of the mouth of the fertilizer discharge tube, allowing the fertilizer to fall through the round hole. The stopper is closed when the stopper round hole is turned 60°. The fertilizer builds up above the stopper, providing enough fertilizer for the next time the stopper switch is turned on. During this time the fertilizer discharged from the discharger is stored in the tube. The physical drawing of the stopper structure of the fertilizer discharge port is shown in figure 2.

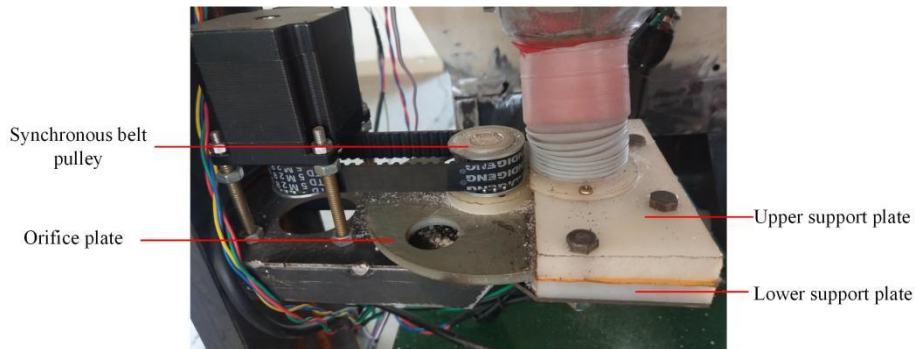


Fig. 2 - Physical drawing of the stopper structure of the fertilizer discharge port

Control System Design for Synchronization of Corn Seeding and Variable Hole Application of Fertilizer

The control system is an important part of the whole experimental bench, which is mainly composed of a data acquisition module, microcontroller control module, human-machine interface module, and actuator module, as shown in Fig. 3. The control system controls the fertilizer discharger by changing the motor speed for precise fertilizer discharge. The microcontroller chosen is the more commonly used STC15F2K60S2, which is simple to program, has a stable system, and lower cost. The single clock machine cycle of the microcontroller, the internal integration of high-precision R/C clock, and the highly reliable reset circuit make it a good option. The overall circuit diagram of the control system is shown in figure 4.

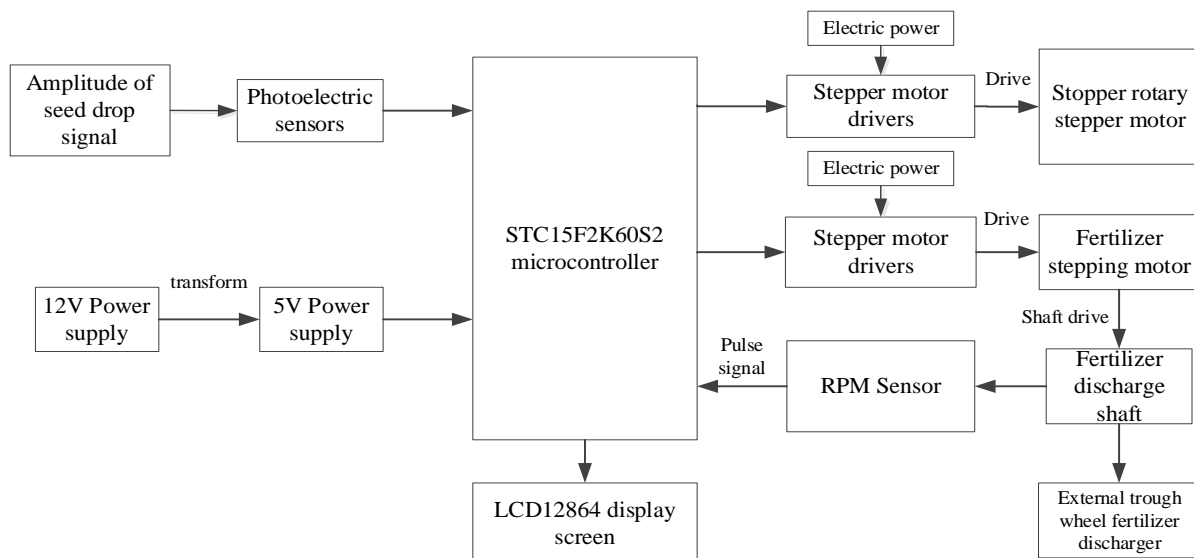


Fig. 3 - Hardware block diagram of the control system

After system initialization, the control system operates as in the flowchart is shown in figure 5. Initially, the motor controls the fertilizer spreader to rotate the corresponding number of slots, completing one fertilization cycle and waiting for the first seed to drop. Starting from the second fertilization cycle, when the photoelectric sensor detects a seed drop, it is necessary to determine whether the time interval since the previous drop is shorter than a predefined threshold. If the interval is shorter, it indicates a repeat drop, and the system returns to the waiting state.

Otherwise, it is considered a normal sowing cycle, and the corresponding pulse is immediately sent. The control flaps open and close at the corresponding angles to allow the prepared fertilizer to fall into the soil. After a delay, the flaps are closed at the specified angle, completing one cycle of hole fertilization, which repeats continuously. When no seed drop is detected, a missed sowing check is performed. If a missed sowing is detected, all interrupts are disabled, the fault code is displayed, and the system waits for a reset. Otherwise, it returns to continue waiting for the next seed drop.

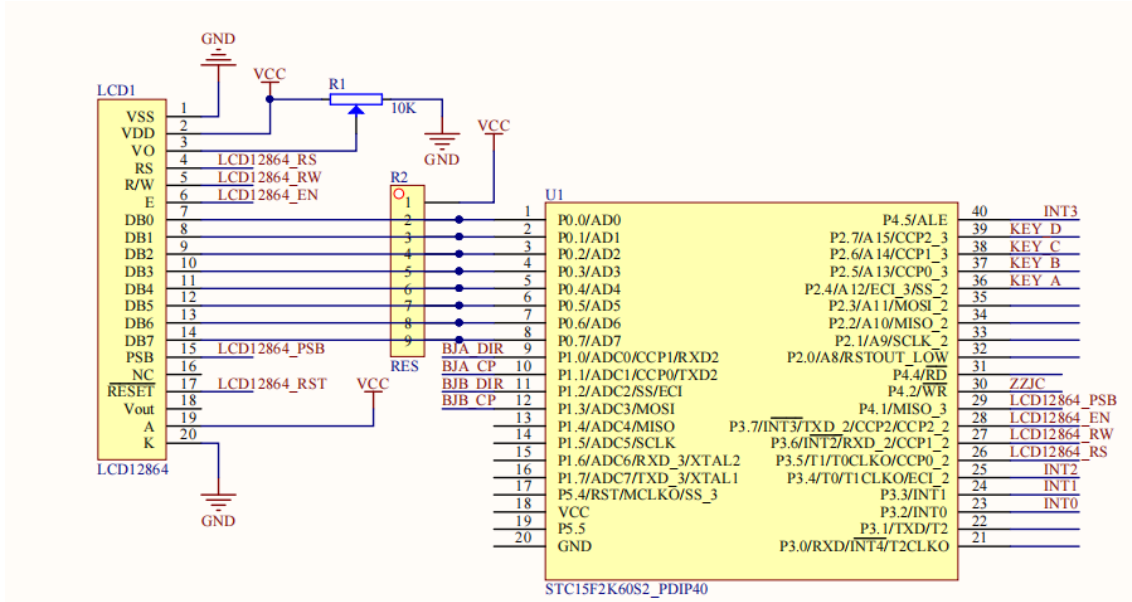


Fig. 4 - Overall circuit diagram of the control system

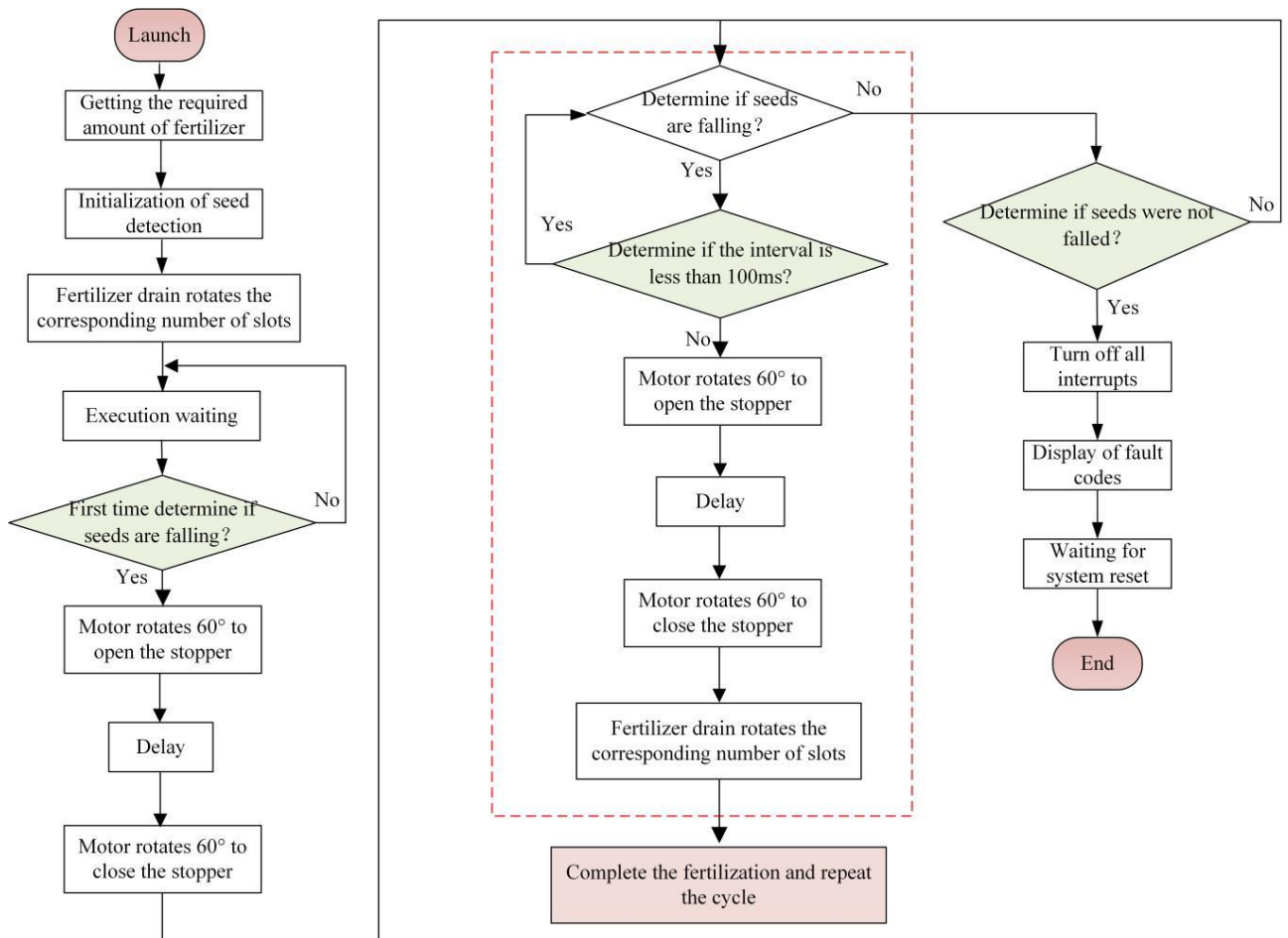


Fig. 5 - Control system flowchart

System Control Strategy

Mathematical Modeling of The Motor

Under the assumption of neglecting motor parameter variations and external disturbances, the mathematical model of the motor can be established, and the voltage equation is given by Equation (1).

$$\begin{cases} u_d = Ri_d + L_d \frac{di_d}{dt} - p\omega_m L_q i_q \\ u_q = Ri_q + L_q \frac{di_q}{dt} + p\omega_m L_d i_d + p\omega_m \psi_f \end{cases} \quad (1)$$

where:

u_d, i_d, L_d represent the voltage, current, and inductance on the d-axis, respectively;

u_q, i_q, L_q represent the voltage, current, and inductance on the q-axis, respectively;

R is the stator winding resistance; ω_m is the motor output speed; ψ_f is the magnetic chain;

p is the number of pole pairs.

Additionally, since the permanent magnet synchronous motor has $L_d = L_q$, the torque equation is given by equation (2), where T_e is the target torque.

$$T_e = \frac{3}{2} p \psi_f i_q \quad (2)$$

The equations of motion for the motor are given in Equation (3).

$$\frac{d\omega_m}{dt} = \frac{3p\psi_f}{2J} i_q - \frac{T_L}{J} - \frac{B}{J} \omega_m \quad (3)$$

where: B is the coefficient of viscous friction; J is the rotational inertia; T_L is the load torque.

Equation (4) is derived by considering the variation in system parameters and torque.

$$\frac{d\omega_m}{dt} = \left(\frac{3p\psi_f}{2J} + \Delta\alpha_1 \right) i_q - \left(\frac{T_L}{J} + \Delta\alpha_2 \right) - \left(\frac{B}{J} + \Delta\alpha_3 \right) \omega_m = \frac{3p\psi_f}{2J} i_q - \frac{B}{J} \omega_m + \beta \quad (4)$$

$$\beta = \frac{3p\psi_f}{2J} \Delta\alpha_1 i_q - \Delta\alpha_2 - \frac{B}{J} \Delta\alpha_3 \omega_m - \frac{T_L}{J} \quad (5)$$

where: $\Delta\alpha_1, \Delta\alpha_2, \Delta\alpha_3$ denote the values of parameter changes of the motor; β denotes the value of perturbation brought by the load torque and parameters.

Design Of Sliding Mode Controller

The motor state variable is given by Equation (6).

$$\begin{cases} x_1 = \omega_{ref} - \omega_m \\ x_2 = \dot{x}_1 \end{cases} \quad (6)$$

where ω_{ref} is the target speed; The derivation of Equation (6) leads to Equation (7).

$$\begin{cases} \dot{x}_1 = - \left(\frac{3p\psi_f}{2J} i_q - \frac{B}{J} \omega_m + \beta \right) \\ \dot{x}_2 = - \left(\frac{3p\psi_f}{2J} \dot{i}_q - \frac{B}{J} \dot{\omega}_m + \dot{\beta} \right) \end{cases} \quad (7)$$

The system sliding mode surface function is defined by Equation (8).

$$s = cx_1 + x_2 \quad (8)$$

Substituting Equation (6) into Equation (8) yields the following:

$$\dot{s} = c \dot{x}_1 - \frac{3p\psi_f}{2J} i_q + \frac{B}{J} \dot{\omega}_m - \dot{\beta} \tag{9}$$

In the actual motor control, the sliding mode control method suffers from high-frequency jitter. Therefore, it is necessary to select a suitable exponential convergence rate that can effectively attenuate the sliding mode jitter. To improve the system's performance, a novel, improved convergence rate will be introduced, as shown in Equation (10).

$$\begin{cases} \dot{s} = -\varepsilon|x_1| \operatorname{sgn}(s) - ks \\ \lim_{t \rightarrow \infty} |x_1| \end{cases} \tag{10}$$

where $\varepsilon > 0, k > 0$; $-\varepsilon|x_1| \operatorname{sgn}(s)$ is the isochronous convergence term; ks is the exponential convergence term.

As the error increases, the isochronous convergence term drives the system state variable toward the sliding mode surface, while the exponential convergence term reduces the system state variable to zero.

By combining Equations (9) and (10), the output equation of the controller is given by:

$$i_q^* = \frac{2J}{3p\psi_f} \int c \dot{x}_1 + \frac{B}{J} \dot{\omega}_m + \varepsilon|x_1| \operatorname{sgn}(s) + ks - \dot{\beta} dt \tag{11}$$

The Lyapunov function is chosen as shown in Equation (12):

$$V = \frac{1}{2} s^2 \tag{12}$$

According to the Lyapunov stability theorem, it is sufficient to prove that $V < 0$, in which case the system is asymptotically stable. Equation (13) can be derived from Equations (10) and (12).

$$\dot{V} = -\varepsilon|x_1| \operatorname{sgn}(s)s - ks^2 \tag{13}$$

where $\varepsilon > 0, k > 0$, and $\operatorname{sgn}(s)s > 0$: It follows that $V < 0$. Therefore, the system error can converge to 0 in a finite time, making the system stable. Meanwhile, the saturation function $\operatorname{sat}(s, \delta)$ is used instead of $\operatorname{sgn}(s)$, which can effectively suppress the jitter and further improve the robustness of the system. The saturation function $\operatorname{sat}(s, \delta)$ is selected as shown in Equation (14).

$$\operatorname{sat}(s, \delta) = \begin{cases} 1 & s > \delta \\ \frac{s}{\delta} & |s| < \delta \\ -1 & s < -\delta \end{cases} \tag{14}$$

Design of the Expansion Observer

The control law designed using the sliding mode surface accounts for motor parameter variations and load torque perturbations. Since the perturbation value cannot be measured, this paper designs a perturbation observer for estimation. In the actual motor speed control system, the system parameter perturbations change slowly, and the first-order derivative of the perturbation can be approximated as zero.

The system state-space equation is given by Equation (15).

$$\begin{cases} \dot{\omega}_m = \frac{3p\psi_f}{2J} i_q - \frac{B}{J} \omega_m + \beta \\ \dot{\beta} = 0 \\ y = \omega_m \end{cases} \tag{15}$$

Taking ω_m and β as the observation objects to establish the gain feedback for the speed estimation error e_1 , the extended disturbance observer is designed based on Equation (15), as shown in Equation (16).

$$\begin{cases} \dot{\hat{\omega}}_m = \frac{3p\psi_f}{2J} i_q - \frac{B}{J} \hat{\omega}_m + \hat{\beta} + \frac{\lambda_1}{\eta} e_1 \\ \dot{\hat{\beta}} = \frac{\lambda_2}{\eta^2} e_1 \\ e_1 = \omega_m - \hat{\omega}_m \end{cases} \quad (16)$$

where: $\hat{\omega}_m$ and $\hat{\beta}$ are the electrical angular velocity estimation, and load parameter uptake estimation, respectively; λ_1 , λ_2 , and η are positive real numbers. To achieve high gain, η is set to a small value. Using this observer allows not only the estimation of the disturbance terms $\hat{\beta}$ related to motor parameter variations and load torque, which can be used for feedforward compensation in the sliding mode control, but also ensures that $\hat{\beta}$ converges to β and $\hat{\omega}_m$ converges to ω_m .

From Equations (15) and (16), the error equation of the extended observer is given by Equation (17).

$$\begin{cases} \dot{e}_1 = \left(\frac{\lambda_1}{\eta} - \frac{B}{J} \right) e_1 + e_2 \\ \dot{e}_2 = \frac{\lambda_2}{\eta^2} e_1 \end{cases} \quad (17)$$

where e_1 denotes the speed estimation error; e_2 denotes the system parameters, and load torque estimation error.

The error equation of the state for the extended observer is shown in Equation (18).

$$\dot{e} = Ae + B\beta \quad (18)$$

$$\text{where } A = \begin{bmatrix} \frac{\lambda_1}{\eta} - \frac{B}{J} & 1 \\ \frac{\lambda_2}{\eta} & 0 \end{bmatrix}; B = \begin{bmatrix} 0 \\ 1 \end{bmatrix}; e = \begin{bmatrix} e_1 \\ e_2 \end{bmatrix}.$$

Substituting the observed perturbations and load torque uptake values into Equation (11), Equation (19) is obtained.

$$i_q^* = \frac{1}{D} \int c\dot{x}_1 + \frac{B}{J} \dot{\omega}_m + \varepsilon|x_1|sat(s) + ks - \dot{\beta} dt \quad (19)$$

From equation (19), it can be seen that parameter variations and load perturbations are used for feed-forward compensation. When both the load and motor parameters change, the controller can mitigate the effects of these perturbations on the system, thereby effectively improving system stability.

Experimental Methods

Simulation Experiments of the Control System

The simulation environment for the control system consists of 256GB of RAM, a 64-bit Windows 10 operating system, and MATLAB 2021b/Simulink as the simulation software. To verify the feasibility of the ISMDO-SMC algorithm proposed in this paper, simulation experiments were conducted on the control system. The control test groups include the Proportional-Integral-Derivative (PID) algorithm, the classical Sliding Mode Control (SMC) algorithm, and the Optimized Sliding Mode Control (OSMC) algorithm. The simulation setup of the control system is shown in figure 6.

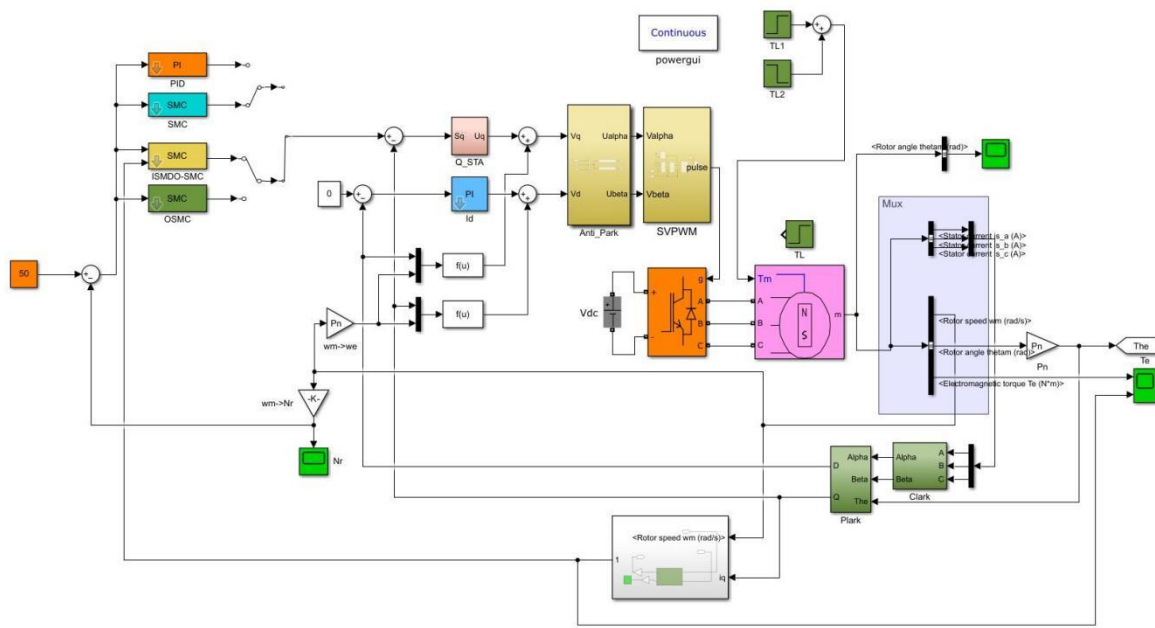


Fig. 6 - Simulation experiment of the control system

Bench Experiment

To investigate the fertilization precision of the control system, an experiment was conducted using a self-designed experimental setup, as shown in figure 7. The experimental material was “Siyu 335” corn seed, which was manually screened to ensure the purity of the seeds reached 100%. The moisture content of the corn seeds was $(11.4 \pm 0.2) \%$, and the mass of 1,000 kernels was $(323.0 \pm 0.3) \text{ g}$. The fertilizer used in this experiment was sulfur-containing, potassium-controlled slow-release urea. The experimental setup is based on the principle of relative motion, using the relative movement of the seed bed belt in relation to the device, thereby simulating the forward operation of the machine. Parameters such as the amount of fertilizer dispensed, the speed of the fertilizer discharge motor, and the hole spacing are controlled through the system. The fertilizer discharger opening was set to 10 mm, with rotational speeds of the fertilizer discharger at 30, 40, and 50 r/min. Four control strategies were tested in the experiment. The amount of fertilizer applied and the coefficient of variation of the grooved wheel’s rotation over one week were used as performance indexes to assess the impact of fertilizer application and variation on the stability of the control system.

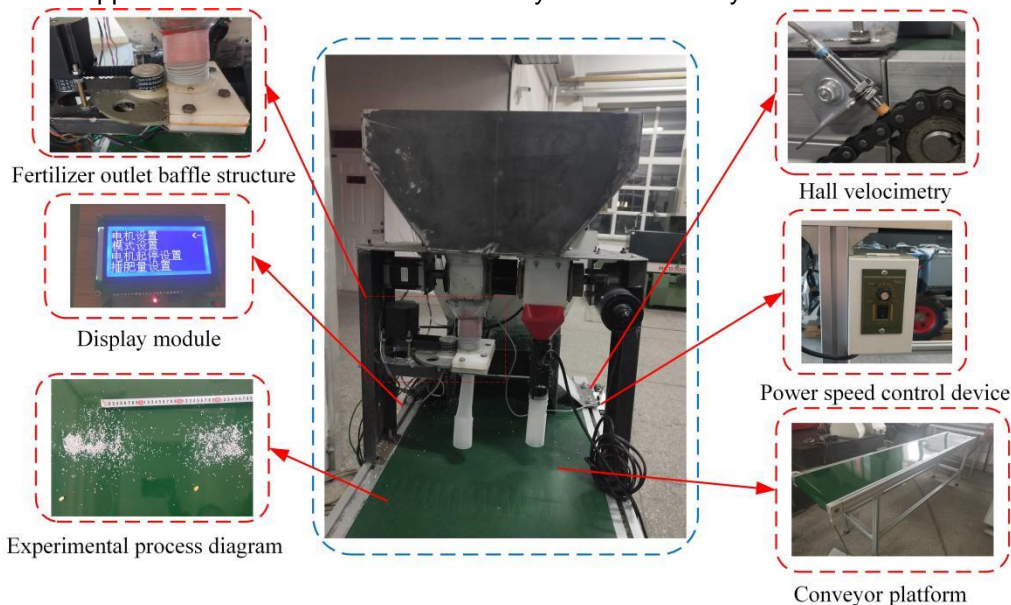


Fig. 7 - Self-designed experimental bench

The fertilizer discharger opening, fertilizer discharge shaft speed, and forward speed are key factors affecting the effectiveness of fertilizer application. These parameters interact with and constrain each other.

The difference between the sum of the actual fertilizer application rates and the theoretical fertilizer application rate in the stationary state for each group represents the fertilizer application error. A multifactor experiment was conducted, with the fertilizer application error and seed-fertilizer spacing error as performance indexes, to investigate their effects on the stability of the system under different operating parameters. The factor codes are shown in Table 1.

Table 1

Coded value	Factor		
	Forward speed x_1 (km/h)	Fertilizer discharge shaft speed x_2 (r/min)	Fertilizer discharger opening x_3 (mm)
1.682	3.6	50	25
1	3.28	45.9	20.9
0	2.8	40	15
-1	2.32	34.1	9.1
-1.682	2.0	30	5

RESULTS AND DISCUSSIONS

Stepper Motor Simulation Results Analysis

The target speed was set to 50 r/min, the DC side voltage to 311 V, and the initial load to 1 Nm. Figure 8 shows the speed response curves of the ISMDO-SMC, OSMC, PID, and SMC algorithms when a load of 10 Nm is abruptly applied at 0.75 s.

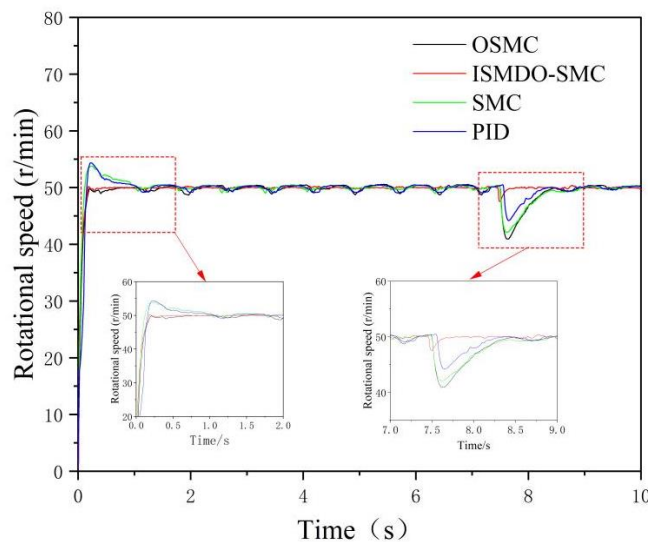


Fig. 8 - Speed response curves of the PID, SMC, ISMDO-SMC, and OSMC algorithms

From Figure 8, it can be observed that, during the starting phase, there are significant differences in the response time and the ability to follow the setpoint quickly across the four algorithms. The fast response and initial stability of the algorithms during startup affect the time required to reach the target speed. Large overshoot and oscillations typically occurred during the PID control startup phase, indicating that PID control produced significant fluctuations initially, which may cause the system to take a longer time to stabilize. The SMC algorithm performed slightly better than PID control, though some overshoot still occurred. The OSMC exhibited smoother performance at startup and was able to approach the target speed quickly with fewer fluctuations. The ISMDO-SMC showed almost no overshoot at the beginning and reached the set speed rapidly, demonstrating excellent control. After the sudden load addition, the PID, SMC, and OSMC all showed significant fluctuations and took a long time to return to a steady state. Among them, OSMC had the largest fluctuations and took the longest time to recover. In contrast, the ISMDO-SMC performed the best under sudden load changes, quickly suppressing the disturbances. In summary, the ISMDO-SMC reached the target speed faster and more smoothly during startup and exhibited superior resistance to disturbances with fast recovery after a sudden load change. In this study, the dynamic and anti-interference performance of four control algorithms (PID, SMC, ISMDO-SMC, and OSMC) were quantitatively analyzed and compared, as shown in Table 2.

The PID and SMC algorithms exhibited varying degrees of overshoot, 9% and 7.4%, respectively, and longer regulation times, 1.12 s and 1.03 s, respectively. The OSMC required 0.35 s more to regulate than the ISMDO-SMC algorithm, although it showed no overshoot. In terms of anti-jamming performance, the ISMDO-SMC algorithm demonstrated the best capability, with a descending speed of only 2.5 r/min and the shortest recovery time to steady state of 0.13 s. The OSMC algorithm had the longest recovery time of 0.85 s, with a descending speed of 9 r/min. In comparison, the PID and SMC algorithms had steady-state restoration times of 0.73 s and 0.75 s, respectively. The OSMC's performance was weaker, with a longer recovery time and higher descending speed. Overall, the ISMDO-SMC algorithm showed significant advantages in both dynamic and anti-interference performance. It achieved zero overshoot, with a peak time of 0.18 s and a regulation time of 0.42 s, both of which were significantly better than those of the other algorithms.

Table 2

Comparison of dynamic performance and anti-interference performance of PID, SMC, ISMDO-SMC, and OSMC algorithms

Algorithm	Overshoot	Peak time (t/s)	Regulation time (t/s)	Down speed (r/min)	Recovery of steady state time (t/s)
PID	9%	0.22	1.12	6	0.73
SMC	7.4%	0.25	1.03	8	0.75
ISMDO-SMC	0	0.18	0.42	2.5	0.13
OSMC	0	0.2	0.77	9	0.85

To verify that the designed expanding sliding mode observer exhibited good robustness to the system, the ISMDO-SMC algorithm was used to apply a torque of 10 Nm abruptly at 7.5 s and to unload the torque at 10.5 s. Figure 9 shows the comparison between the estimated and actual torque during sudden load addition and removal by the expanding observer. The actual torque curve in the steady-state phase showed jitter between 0 and 7.5 s, and between 10.5 s and 15 s, with an average magnitude of approximately ± 0.2 Nm. This jitter may have been caused by sensor noise or mechanical disturbances inside the motor. The estimated torque exhibited a significant step change near 7.5 s and 10.5 s, followed by a rise in the actual torque response, though with noticeable delays and overshoots. The peak value of the actual torque reached 1.1 times the set value at 7.5 s, corresponding to an overshoot of about 10%. This overshoot suggests that the control gain may have been set too high, leading to an over-response to the target torque. To reduce this overshoot, it may be necessary to lower the gain or mitigate the overshoot by introducing a derivative term. During sudden torque changes, the ISMDO-SMC algorithm provided a smoother torque estimation than the actual measured torque. Therefore, the perturbed values of estimated motor parameter variations and load torque, recorded by the expanding observer, can be effectively used in the sliding mode controller.

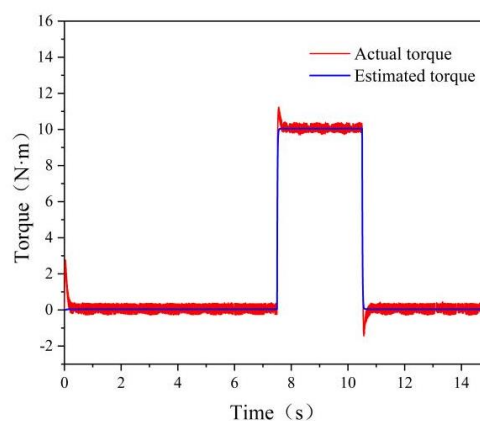


Fig. 9 - Comparison between the estimated and actual torque during sudden load addition and removal by the expanding observer

Fertilizer precision experiment

Figure 10 shows the distribution of fertilizer application amounts for the control algorithms (PID, SMC, ISMDO-SMC, and OSMC) at rotational speeds of 30, 40, and 50 r/min.

From the dynamic characteristics of the fertilizer application distribution, significant differences in stability performance were observed across the four control algorithms at different rotational speeds. The PID

algorithm exhibited large fluctuations in the amount of fertilizer applied, particularly at high rotational speeds (50 r/min), where both the fluctuation amplitude and extreme values increased significantly, indicating poor stability. The SMC algorithm improved the fluctuation amplitude compared to PID, resulting in a smoother distribution of the fertilizer application amount. However, it was still unable to completely eliminate the impact of large disturbances under complex working conditions. The OSMC algorithm significantly reduced the fluctuation amplitude by optimizing the sliding mode control, especially at high rotational speeds, where the distribution became more concentrated, demonstrating strong anti-disturbance capabilities. The ISMDO-SMC algorithm exhibited the smallest fluctuation amplitude and the smoothest distribution of fertilizer application at all rotational speeds. Even at the high speed of 50 r/min, the amount of fertilizer applied remained stable. Overall, the fertilization stability of the four control algorithms is ranked as follows: ISMDO-SMC > OSMC > SMC > PID. The ISMDO-SMC control algorithm significantly outperforms the others and is well-suited for scenarios that require high fertilization stability under complex working conditions.

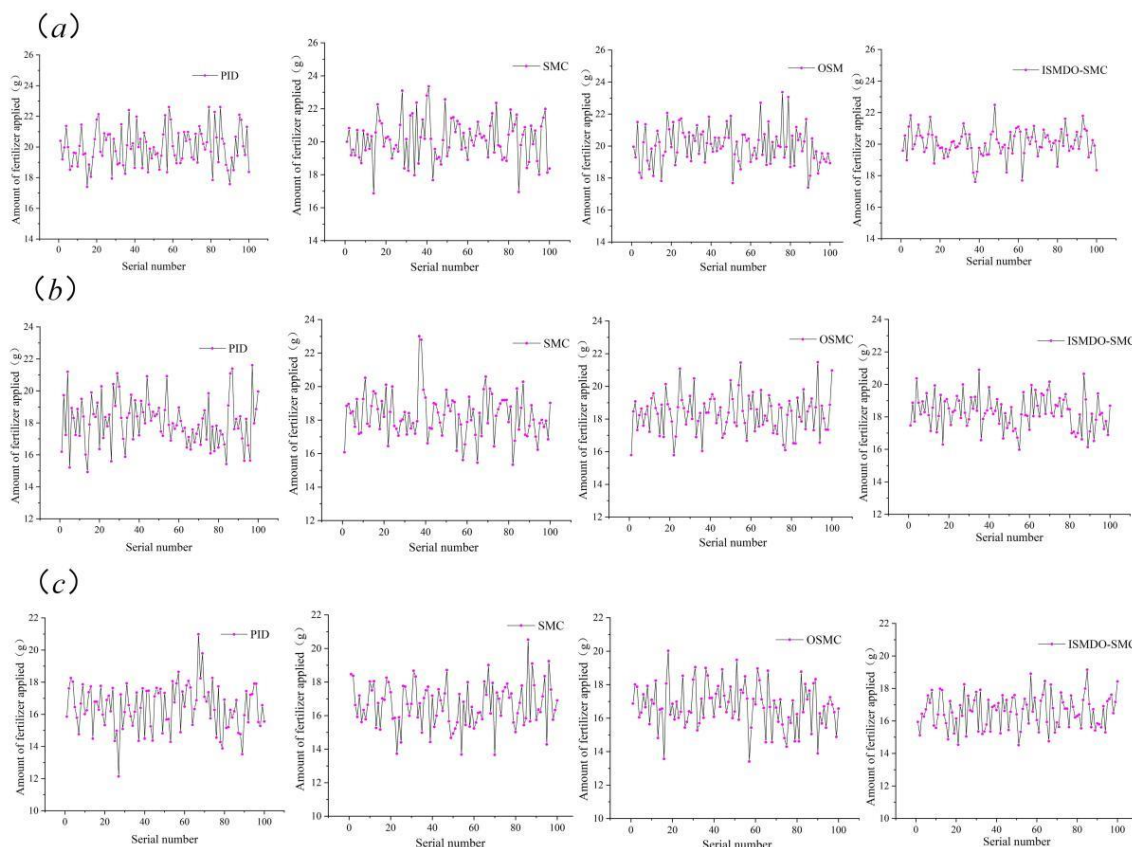


Fig. 10 - Distribution of fertilizer application amounts for the control algorithms (PID, SMC, ISMDO-SMC, and OSMC). (a) 30 r/min; (b) 40 r/min; (c) 50 r/min

Figure 11 shows the distribution of the coefficient of variation for the four control algorithms (PID, SMC, ISMDO-SMC, and OSMC) at rotational speeds of 30, 40, and 50 r/min. The coefficient of variation for the PID algorithm increased progressively with speed, from 6.50% at 30 r/min to 8.60% at 50 r/min, indicating poor performance in handling dynamic disturbances at high rotational speeds and a significant decrease in the stability of the fertilizer application system. The SMC algorithm partially compensated for the perturbations using sliding mode control, with coefficients of variation of 6.10%, 7.20%, and 8.20% at 30, 40, and 50 r/min, respectively. While this showed improvement over PID control, it did not completely resolve the issue of large fluctuations at high speeds. The OSMC algorithm further optimized sliding mode control, achieving coefficients of variation of 5.70%, 6.30%, and 7.60%, which were significantly lower than those of PID and SMC, demonstrating better robustness and anti-disturbance capability. The ISMDO-SMC algorithm exhibited the lowest coefficients of variation, at 4.90%, 5.70%, and 6.50%, respectively, and demonstrated the best stability across all rotational speeds. The dynamic disturbance suppression capability of the system was further enhanced by the intelligent optimization algorithm, effectively controlling fluctuations in the fertilizer application system. Therefore, based on the coefficient of variation, the stability of the four control algorithms is ranked as follows: ISMDO-SMC > OSMC > SMC > PID. The ISMDO-SMC algorithm significantly reduced the variability in fertilizer application, making it particularly suitable for scenarios that require high accuracy and stability in fertilizer application.

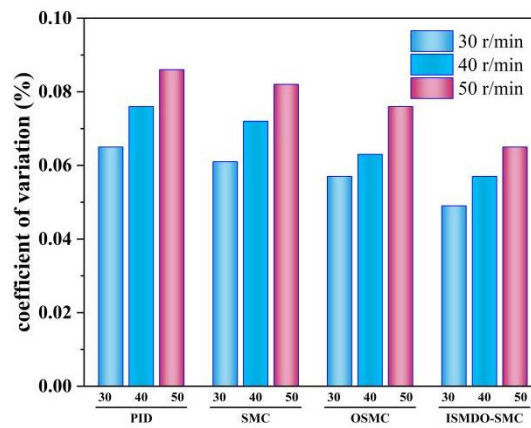


Fig. 11. Distribution of the coefficient of variation for the four control algorithms (PID, SMC, ISMDO-SMC, and OSMC)

Multi-factor Parameter Optimization Analysis

The experimental scheme and results are shown in Table 3. The regression equations for the factors influencing fertilizer application error and seed-fertilizer spacing error were obtained through multiple regression fitting using Design-Expert 8.0.6 software. The results of the analysis of variance (ANOVA) for the regression equations are shown in Table 4. The regression equations for both groups were highly significant ($P < 0.01$). The misfit P-value was not significant, indicating a good fit for the equation. The ANOVA results for fertilizer application error showed a P-value of 0.55 for the misfit term, indicating that no other factors affected the fertilizer application error. The ANOVA results for seed-fertilizer spacing error showed a misfit P-value of 0.06, indicating that no other factors influenced seed-fertilizer spacing error. After confirming that the models were significant and the misfit terms were not significant, the insignificant factors were removed, and the factor-coded regression equations (20-21) were developed.

$$y_1 = 140.92 - 4.03x_2 + 4.71x_3 + 15.23x_1^2 + 0.02x_2^2 \tag{20}$$

$$y_2 = 41.04 - 16.55x_1 - 0.69x_3 + 0.21x_1x_2 \tag{21}$$

where y_1 is the fertilizer application error, g; y_2 is the seed-fertilizer spacing error, mm; x_1 is the forward speed, km/h; x_2 is the fertilizer discharge shaft speed, r/min; and x_3 is the fertilizer discharger opening, mm.

Table 3

Experimental scheme and results

Experiment number	Forward speed x_1 (km/h)	Fertilizer discharge shaft speed x_2 (r/min)	Fertilizer discharger opening x_3 (mm)	Fertilizer application error y_1 (g)	Seed-fertilizer spacing error y_2 (mm)
1	1	1	1	3.46	4.6
2	1	1	-1	4.02	3.48
3	1	-1	1	18.67	2.76
4	1	-1	-1	6.32	2.16
5	-1	1	1	8.91	3
6	-1	1	-1	2.9	2.76
7	-1	-1	1	15.35	2.4
8	-1	-1	-1	4.25	3.6
9	-1.682	0	0	15.33	3.24
10	1.682	0	0	12.01	4.8
11	0	-1.682	0	19.87	3
12	0	1.682	0	3.89	3.36
13	0	0	-1.682	3.47	1.8
14	0	0	1.682	6	4.2
15	0	0	0	1.38	2.64
16	0	0	0	1.87	3.6
17	0	0	0	2.35	3.48
18	0	0	0	1.92	2.88
19	0	0	0	2.07	3.6
20	0	0	0	8.46	3.36
21	0	0	0	2.23	2.88
22	0	0	0	10.92	3.12
23	0	0	0	2.11	3.24

The experiment on the coefficients of the regression equations showed that the effects of the forward speed, fertilizer discharger opening, and fertilizer discharge shaft speed on fertilizer application error increased gradually. Fertilizer application error is an important indicator for assessing the performance of the fertilization system. Therefore, this paper focuses on analyzing the effects of interactions among various factors on fertilizer application error. To intuitively analyze the relationship between the test factors and fertilizer application error, Design-Expert 6.0.8 software was used to generate the response surface diagrams of the forward speed, fertilizer discharger opening, and fertilizer discharge shaft speed on the fertilizer application error indexes, as shown in figures 12-14.

Table 4

Results of the analysis of variance for the regression equations

Source of variance	Fertilizer application error (g)				Seed-fertilizer spacing error (mm)			
	Square sum	Degrees of freedom	F	P	Square sum	Degrees of freedom	F	P
Model	585.75	9	5.77	0.002**	7.99	9	4.00	0.012*
x_1	1.95	1	0.17	0.685	1.19	1	5.35	0.038*
x_2	204.92	1	18.16	0.001**	0.83	1	3.73	0.076
x_3	72.08	1	6.39	0.025*	1.93	1	8.70	0.011*
x_1x_2	11.81	1	1.05	0.325	1.44	1	6.50	0.024*
x_1x_3	3.54	1	0.31	0.585	0.90	1	4.04	0.066
x_2x_3	40.50	1	3.59	0.081	0.48	1	2.16	0.165
x_{12}	166.95	1	14.80	0.002**	0.89	1	3.99	0.067
x_{22}	111.27	1	9.86	0.008**	0.03	1	0.13	0.721
x_{32}	1.16	1	0.10	0.753	0.17	1	0.76	0.399
Residual	146.66	13			2.89	13		
Lost proposal	50.80	5	0.85	0.553	1.94	5	3.26	0.067
Errors	95.85	8			0.95	8		
Sum of all	732.41	22			10.88	22		

Note: * indicates significant ($P < 0.05$) and ** indicates highly significant ($P < 0.01$).

Figure 12 shows the effect of the interaction between x_1 and x_2 on the fertilizer application error when x_3 is 15 cm. When x_1 is certain, with the increase of x_2 , the error in the amount of fertilizer applied firstly decreases and then increases by a small margin. When x_2 is certain, the error in the amount of fertilizer applied decreases first and then increases with the increase of x_1 . However, in terms of magnitude, the magnitude of the fertilizer application error size influenced by the rotational speed exceeds the influence of the forward speed, so the appropriate speed of the fertilizer discharger can reduce the error.

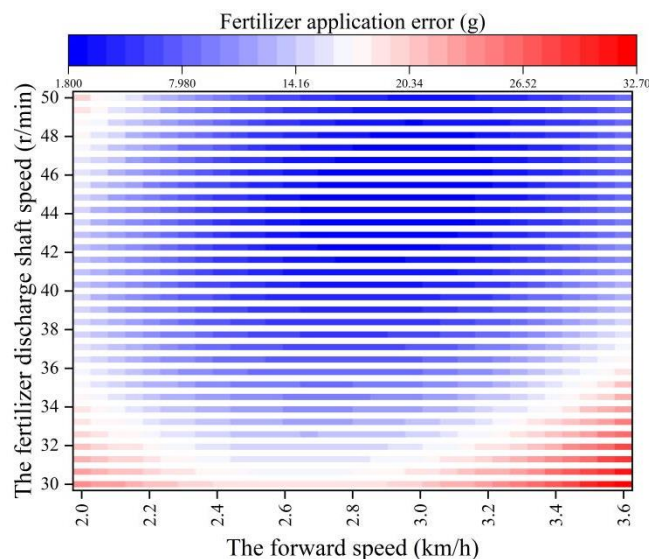


Fig. 12 - Interaction between forward speed and fertilizer discharge shaft speed on the fertilizer application error

Figure13 shows the effect of the interaction between x_1 and x_3 on fertilizer application error when x_2 is 40 r/min. At a fixed forward speed, the fertilizer application error gradually increases with the increase of x_3 . When x_3 is fixed, the fertilizer application error first decreases and then increases as forward speed increases. Therefore, selecting a smaller fertilizer discharger opening and driving at a moderate speed can effectively reduce the fertilizer application error.

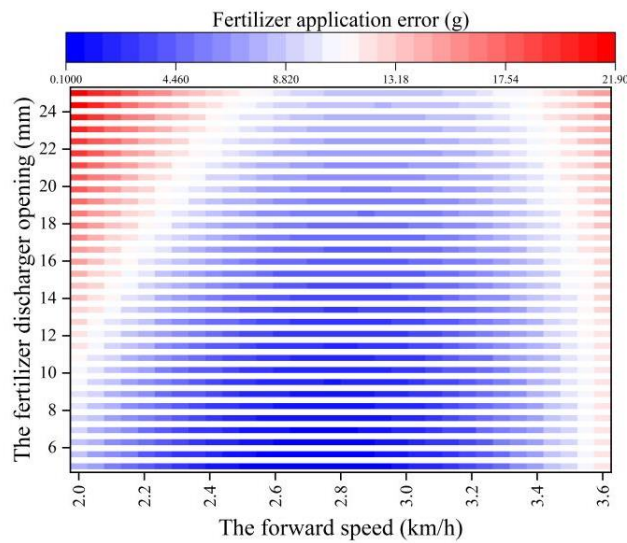


Fig. 13 - Interaction between forward speed and fertilizer discharger opening on the fertilizer application error

Figure 14 shows the effect of the interaction between x_2 and x_3 on fertilizer application error when x_1 is 2.8 km/h. When x_3 is larger, the fertilizer application error with x_2 gradually decreases, with a noticeable amplitude. When x_3 is smaller, the fertilizer application error first decreases and then increases with x_2 , with a smaller and less noticeable magnitude. When x_2 is fixed, the overall fertilizer application error increases gradually as x_3 increases.

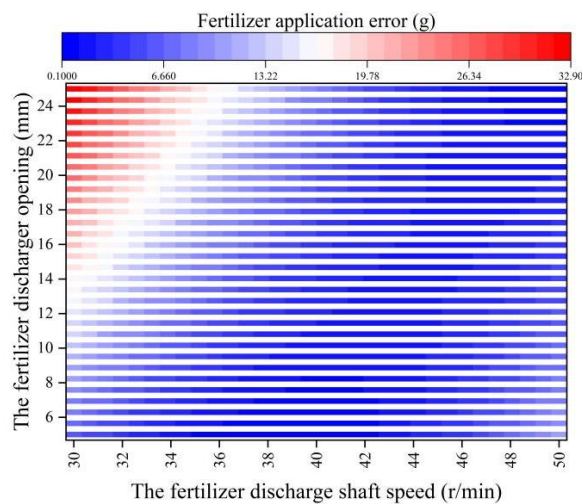


Fig. 14 - Interaction of fertilizer discharge shaft speed and fertilizer discharger opening on the fertilizer application error

Optimizing the best combination of parameters using the software requires setting the boundary conditions, and the mathematical model was developed as shown in equation (22).

$$\begin{cases} \min y_1 \\ \min y_2 \\ \text{s. t. } \begin{cases} 2 \text{ km/h} \leq x_1 \leq 3.6 \text{ km/h} \\ 30 \text{ r/min} \leq x_2 \leq 50 \text{ r/min} \\ 5 \text{ mm} \leq x_3 \leq 25 \text{ mm} \end{cases} \end{cases} \quad (22)$$

The optimization module in Design-Expert 8.0.6 software completed the parameter optimization. When the forward speed was 2.8 km/h, the fertilizer discharge shaft speed was 42 r/min, and the fertilizer discharger opening was 5.5 mm, the fertilizer application error and seed-fertilizer spacing error were minimized. Three sets of repetitive tests were conducted based on the optimized parameters, and the results showed that the error between the actual and optimized fertilizer application amounts was about 0.32, while the seed-fertilizer spacing error was 0.21. These results indicate that the optimized parameters effectively completed the fertilizer application operation. Under the condition of the optimal parameter combination, the fertilizer application error and seed-fertilizer spacing error in actual operation were 1.7 g and 2.2 mm, respectively.

CONCLUSIONS

(1) A control system for synchronizing corn seeding and precision hole fertilization was designed. The sliding mode controller with integral variable structure utilizes observed changes in motor parameters as feed-forward compensation, enabling the speed control system to respond quickly without overshoot. The jitter is minimal, and the regulation time is short under sudden load addition or removal, effectively suppressing the oscillations typically associated with sliding mode control.

(2) The mathematical model of the motor was established, and the controller was designed and simulated. The simulation results showed that the ISMDO-SMC algorithm had 0% overshoot, a peak time of 0.012 seconds, a regulation time of only 0.02 seconds, a steady-state recovery time of 0.02 seconds, and a descending rotational speed of 4 r/min, indicating the strongest dynamic response and stability. Additionally, the ISMDO-SMC algorithm demonstrated the lowest coefficient of variation for fertilizer application compared to the PID, SMC, and OSMC algorithms, with coefficients of variation of 4.90%, 5.70%, and 6.50% for rotational speeds of 30, 40, and 50 r/min, respectively.

(3) The regression equations of each factor on fertilizer application error and seed-fertilizer spacing error were obtained by fitting the experimental data with multiple regression. The mathematical model for parameter optimization was established through multi-objective variable optimization, yielding the optimal parameter combination. The optimal parameters were determined to be 1.7 g for fertilizer application error and 2.2 mm for seed-fertilizer spacing error, with the forward speed of 2.8 km/h, the fertilizer discharge shaft speed of 42 r/min, and the fertilizer discharger opening of 5.5 mm. These results demonstrate that the control system can significantly improve the stability and precision of fertilizer application and seeding, providing valuable insights for the development of fertilizer application control systems.

ACKNOWLEDGEMENT

This research was funded by the China Postdoctoral Science Foundation, grant number 2024MD763975; the School Orientation Training Research Initiation Fund Program, grant number XYB202307; the Heilongjiang Provincial Postdoctoral General Funding Project, grant number LBH-Z24250; the National Key Research and Development Program, grant number 2016YFD0200600.

REFERENCES

- [1] Alameen, A., Al-Gaadi, K., & Tola, E. (2019). Development and performance evaluation of a control system for variable rate granular fertilizer application. *Computers and Electronics in Agriculture*, 160, 31-39. <https://doi:10.1016/j.compag.2019.03.011>
- [2] Bu, H., Yu, S., Dong, W., Zhang, L., & Xia, Y. (2022). Analysis of the Effect of Bivariate Fertilizer Discharger Control Sequence on Fertilizer Discharge Performance. *Agriculture*, 12(11), 1927. <https://doi:10.3390/agriculture12111927>
- [3] Chen, H., Zheng, J., Lu, S., Zeng, S., & Wei, S. (2021). Design and experiment of vertical pneumatic fertilization system with spiral Geneva mechanism. *International Journal of Agricultural and Biological Engineering*, 14(3), 135-144. <https://doi:10.25165/j.ijabe.20211404.6575>
- [4] Cheng, B., He, R., Xu, Y., & Zhang, X. (2022). Simulation Analysis and Test of Pneumatic Distribution Fertilizer Discharge System. *Agronomy*, 12(10), 2282. <https://doi:10.3390/agronomy12102282>
- [5] Du, S., Wang, S., Wang, Y., Jia, L., Sun, W., & Liu, Y. (2023). Design of Sensorless Control System for Permanent Magnet Linear Synchronous Motor Based on Parametric Optimization Super-Twisting Sliding Mode Observer. *Electronics*, 12(12), 2553. <https://doi:10.3390/electronics12122553>

- [6] Pramod P., Madhukar Nalawade, S., Balasaheb Bhanage, G., Ashok Walunj, A., Bhaskar Kadam, P., G Durgude, A., & R Patil, M. (2023). Variable rate fertilizer application technology for nutrient management: A review. *International Journal of Agricultural and Biological Engineering*, 16(4), 11-19. <https://doi:10.25165/j.ijabe.20231604.7671>
- [7] Qi, Z., Liu, C., Wang, Y., Zhang, Z., & Sun, X. (2024). Design and Experimentation of Targeted Deep Fertilization Device for Corn Cultivation. *Agriculture*, 14(9), 1645. <https://doi:10.3390/agriculture14091645>
- [8] Shi, Y., Hu, Z., Wang, X., Odhiambo, M., & Ding, W. (2018). Motion analysis and system response of fertilizer feed apparatus for paddy Variable-Rate fertilizer spreader. *Computers and Electronics in Agriculture*, 153, 239-247. <https://doi:10.1016/j.compag.2018.08.021>
- [9] Sugirbay, A. M., Zhao, J., Nukeshev, S. O., & Chen, J. (2020). Determination of pin-roller parameters and evaluation of the uniformity of granular fertilizer application metering devices in precision farming. *Computers and Electronics in Agriculture*, 179, 105835. <https://doi:10.1016/j.compag.2020.105835>
- [10] Tola, E., Kataoka, T., Burce, M., Okamoto, H., & Hata, S. (2008). Granular fertiliser application rate control system with integrated output volume measurement. *Biosystems Engineering*, 101(4), 411-416. <https://doi:10.1016/j.biosystemseng.2008.09.019>
- [11] Vieira-Megda, M. X., Mariano, E., Leite, J. M., Franco, H. C. J., Vitti, A. C., Megda, M. M., Khan, S.A., Mulvaney, R.L., & Trivelin, P. C. O. (2015). Contribution of fertilizer nitrogen to the total nitrogen extracted by sugarcane under Brazilian field conditions. *Nutrient Cycling in Agroecosystems*, 101(2), 241-257. <https://doi:10.1007/s10705-015-9676-7>
- [12] Wang, J., Wang, Z., Weng, W., Liu, Y., Fu, Z., & Wang, J. (2022). Development status and trends in side-deep fertilization of rice. *Renewable Agriculture and Food Systems*, 37(5), 550-575. <https://doi:10.1017/s1742170522000151>
- [13] Wang, Y., Tan, Y., Wei, S., Liao, M., Zang, Y., & Zeng, S. (2023). Design and experimental study of the fertilizer applicator with vertical spiral fluted rollers. *International Journal of Agricultural and Biological Engineering*, 16(5), 80-87. <https://doi:10.25165/j.ijabe.20231605.7555>
- [14] Yu, C., Wang, Q., Cao, X., Wang, X., Jiang, S., & Gong, S. (2021). Development and Performance Evaluation of a Precise Application System for Liquid Starter Fertilizer while Sowing Maize. *Actuators*, 10(9), 221. <https://doi:10.3390/act10090221>
- [15] Yu, H., Ding, Y., Fu, X., Liu, H., Jin, M., Yang, C., Liu, Z., Sun, G., & Dou, X. (2019). A solid fertilizer and seed application rate measuring system for a seed-fertilizer drill machine. *Computers and Electronics in Agriculture*, 162, 836-844. <https://doi:10.1016/j.compag.2019.05.007>
- [16] Zhang, R., Zhao, C., Wang, X., Meng, Z., Chen, L., & Ma, W. (2012). A Variable-Rate Fertilizer Control System for Disc Fertilizer Spreaders. *Intelligent Automation & Soft Computing*, 18(5), 461-467. <https://doi:10.1080/10798587.2012.10643256>

GRAPE LEAF VARIETY RECOGNITION BASED ON THE AF-SWIN TRANSFORMER MODEL

基于 AF-Swin Transformer 模型的葡萄叶片品种识别

Changmei LIANG¹), Jiaxiong GUAN¹), Tongtong GAO¹), Juxia LI ^{*1}), Yanwen LI¹),
Qifeng ZHAO²), Pengfei WEN³), Zhifeng BI⁴), Fumin MA⁵)

¹) College of Information Science and Engineering, Shanxi Agricultural University, Jinzhong, Shanxi/ China

²) Shanxi Academy of Agricultural Sciences Polomogy Institute, Jinzhong, Shanxi/ China

³) College of Horticulture, Shanxi Agricultural University, Jinzhong, Shanxi/ China

⁴) Department of Basic Sciences, Shanxi Agricultural University, Jinzhong, Shanxi/ China

⁵) College of Energy and Power Engineering, Lanzhou University of Technology, Lanzhou, Gansu/ China

Tel: 15803446486; E-mail: lijxsn@126.com

Corresponding author: Juxia Li

DOI: <https://doi.org/10.35633/inmateh-75-92>

Keywords: Grape leaves; variety recognition; Swin Transformer; Focal Loss.

ABSTRACT

Aiming at the problem of differentiated cultivation strategies for different grape varieties, the AF-Swin Transformer model is proposed in this study. Firstly, Focal Loss is used to effectively tackle data imbalance in grape leaves. Secondly, the AdamW optimizer is selected to better control model complexity and improve generalization. The results show that the training accuracy of AF-Swin Transformer model is 7.87 percentage points higher than that of the original Swin Transformer model. Precision and recall improved by 4.4 and 4.3 percentage points, respectively. This study enables accurate automated variety monitoring within vineyard cultivation systems, assisting growers in implementing targeted cultivation strategies.

摘要

针对不同葡萄品种栽培策略存在差异化问题, 本研究提出了 AF-Swin Transformer 模型。首先, 引入 Focal Loss, 有效应对葡萄叶片数据不平衡, 其次, 选用 AdamW 优化器, 更好地控制模型复杂度并提高泛化能力。结果表明, AF-Swin Transformer 模型的训练集准确比原始 Swin Transformer 模型提高了 7.87 个百分点; 精准率和召回率分别提高了 4.4 和 4.3 个百分点。本研究能够在葡萄园中种植系统中实现准确的自动化品种监测, 帮助种植者实施有针对性的种植策略。

INTRODUCTION

Effective recognition of grape leaf varieties can assist grape growers in managing their crops more conveniently and making precise decisions (Cecotti *et al.*, 2020). During the development and maturation of grapes, they are susceptible to various diseases. Understanding the susceptibility of specific leaf varieties to certain diseases and their effective identification will enhance targeted prevention and treatment of grape diseases (Pereira *et al.*, 2019). Traditional methods for identifying grape varieties primarily depend on manual observation. While this method is straightforward, it is often affected by subjective factors and environmental changes, resulting in insufficient accuracy and stability in identification. Therefore, achieving automated identification of grape varieties through leaf image analysis will provide growers with more convenient management tools, helping them make more precise decisions and ultimately enhance the efficiency and competitiveness of the entire grape industry.

In recent years, the rapid development of deep learning technologies and computer vision has brought new solutions for plant leaf recognition (Patricio *et al.*, 2018). Convolutional Neural Networks (CNNs) such as AlexNet (Ni *et al.*, 2021), MobileNet (Zou *et al.*, 2024), and ResNet (Yang *et al.*, 2023) can automatically extract image features (Pushpanathan *et al.*, 2021) and have demonstrated superior performance in the classification tasks of different leaf varieties from the same plant. Deep learning has particularly become an effective tool for leaf feature extraction and variety recognition.

¹ Changmei Liang, Prof.; Jiaxiong Guan, M.Sc.Stu.; Tongtong Gao, Juxia Li, Prof. Ph.D. Eng.; Yanwen Li, Lecturer M.S. Eng.; Qifeng Zhao, Res.; Pengfei Wen, Prof.; Zhifeng Bi, Lec.; Fumin Ma, M.S. Stud. Eng.

Yin et al. employed the GoogLeNet model to recognize leaf images of 11 camellia plant varieties, achieving an overall accuracy of 94.1% (Yin et al., 2023). Lin et al. used ResNet50 for variety recognition of 9 types of Wuyishan Fujian tea leaves, with an accuracy rate reaching 96.04% (Lin et al., 2021). Sun et al. conducted research on the recognition of southern medicinal leaf varieties in complex backgrounds using an improved EfficientNetv2 model, achieving an accuracy rate of 99.12% (Sun et al., 2023). Chen et al. utilized a Multi-Attention Fusion Convolutional Neural Network (MAFNet) for recognizing apple leaf images, with the model achieving an accuracy rate of 98.14% (Chen et al., 2022). Tavakoli et al. applied Convolutional Neural Networks (CNNs) for the variety recognition of 12 types of legumes, where the model showed good recognition performance on a dataset of legume leaf back images, achieving an accuracy rate of 95.86% (Tavakoli et al., 2021). Dong et al. used an improved RegNet model to recognize varieties of 118 mature camellia leaves that grew under natural light conditions and achieved an overall accuracy of 93.7% (Dong et al., 2024). Su et al. used an improved ResNet50 to recognize datasets of 12 types of wine grape leaf images collected at different growth stages, achieving an accuracy of 88.75% (Su et al., 2021). Zhang et al. improved the YOLO-D1 model by integrating the YOLO object detection mechanism and proposed the YOLO-VOLO-LS method, which significantly enhanced the variety identification accuracy of lettuce at the early SP growth stage, achieving a test accuracy of 93.452% (Zhang et al., 2022). Islam et al. applied transfer learning based on the YOLO model to successfully recognize and localize Bangladeshi plant leaves, attaining a classification accuracy of 96% (Islam et al., 2019). Das et al. employed the YOLOv7 model to improve the identification and localization of medicinal plant leaves in complex environments, providing technical support for automated recognition in the herbal medicine industry (Das et al., 2024). Sennan et al. proposed a convolutional neural network (CNN) for spinach classification, achieving a classification accuracy of 97.5% on a dataset comprising four leaf categories (Sennan et al., 2022). Kaur et al. enhanced DenseNet-121 for grapevine variety identification, reaching 96% classification accuracy on high-resolution images of five grape leaf types (Kaur et al., 2024). Maulana et al. conducted a comparative analysis of various CNN models for grapevine leaf classification, with DenseNet and MobileNetV2 both achieving 99% accuracy, thereby improving classification precision and model robustness (Maulana et al., 2024).

Although the deep learning models mentioned above have achieved certain results in crop leaf variety recognition, research on grape leaf variety identification remains limited due to imbalanced sample sizes arising from varying rarity and collection difficulties, and the widely used YOLO model exacerbates this by requiring labor-intensive data annotation. This study focuses on mature grape leaves that have newly sprouted for 30 to 60 days in spring and addresses this issue by proposing the AF-Swin Transformer model. We utilize the AdamW optimizer, which incorporates weight decay. AdamW applies the weight decay term independently during parameter updates, separating it from the learning rate adjustments, which allows for a more precise implementation of weight decay. This approach effectively manages model complexity, reduces overfitting risk, and enhances stability. Moreover, the Focal Loss function is introduced to tackle the sample imbalance problem. Focal Loss mitigates the loss gradients of easily recognizable samples by introducing a modulation factor, encouraging the model to focus more on difficult-to-recognize samples. This enhances the model's ability to recognize rare varieties and improves its learning capacity for hard-to-identify samples, enabling the model to better recognize subtle differences and ultimately increase overall accuracy.

Therefore, the AF-Swin Transformer model proposed in this paper exhibits greater robustness and accuracy in recognizing grape leaf varieties, providing a scientific foundation for their identification.

MATERIALS AND METHODS

Sample dataset

All the leaf samples in this study were collected at the Fruit Tree Research Institute in Taigu District, Jinzhong City, Shanxi Province. A total of 5,516 images were collected using a Huawei Mate 40 smartphone, taken from various angles and time periods in a natural environment. The distribution of the number of samples for each variety is shown in Figure 1.

The leaves were collected from the upper-middle part of the grapevine branches, and they were healthy, mature leaves that had newly sprouted for 30 to 60 days in spring. At this stage, the leaves exhibit standard morphology, with clear leaf lobes, leaf shape, and visible venation structures. The image resolution is 3024x4032, the image format is JPEG, and the color mode is RGB.

Figure 2 displays sample images of 26 different grape varieties.

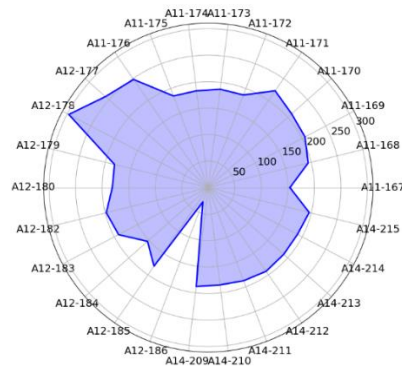


Fig. 1 - Distribution of the number of grape leaf varieties

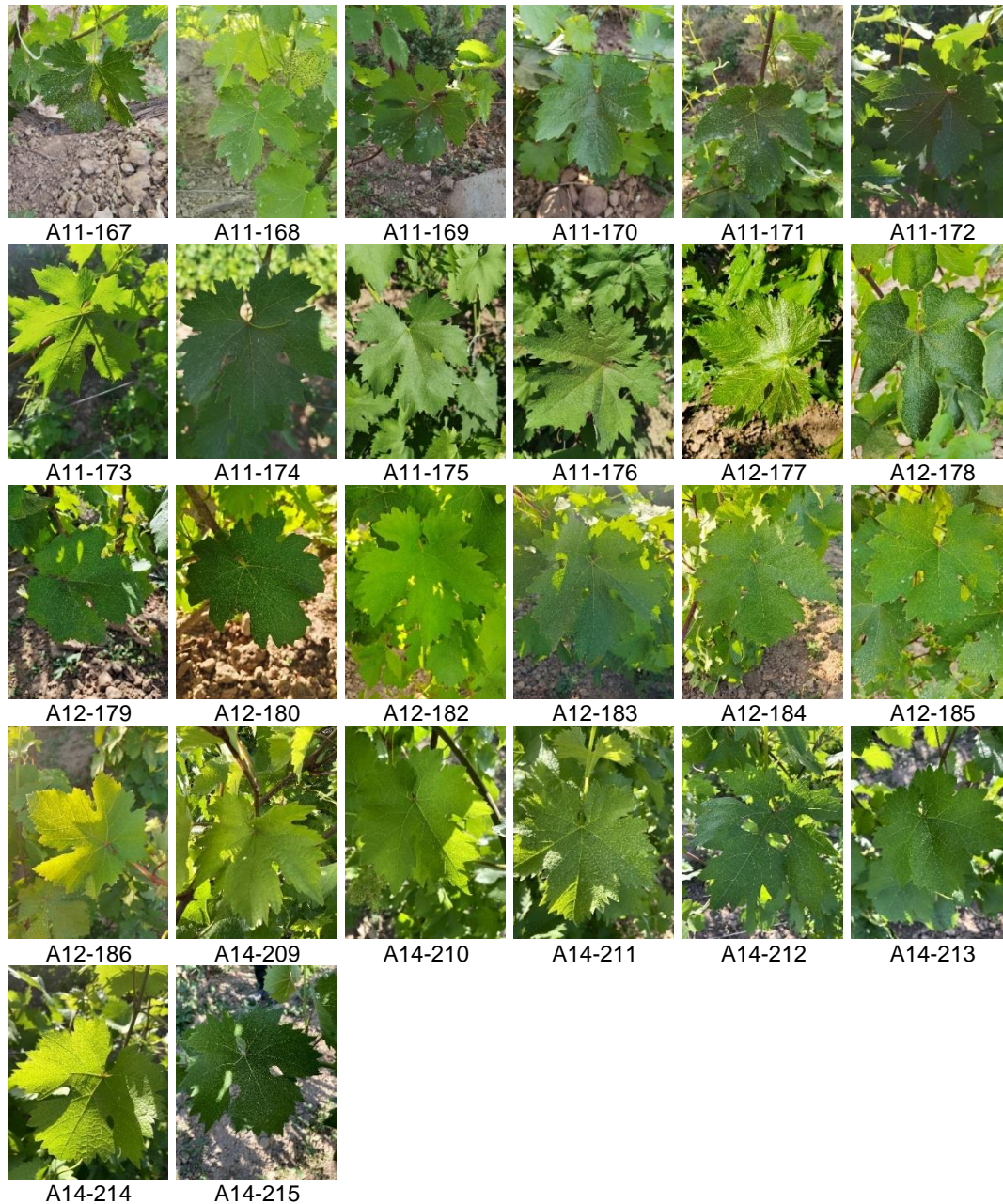


Fig. 2 - Examples of grape leaf samples from different varieties

Data augmentation

To enhance the recognition capability of the network model, four data augmentation methods—random rotation, flipping, brightness adjustment, and adding Gaussian noise—were randomly combined and artificially expanded during training to create a training dataset. The number of images for each variety after data augmentation is shown in Table 1.

This image augmentation technique is versatile and computationally efficient, effectively training deep learning models. The dataset was divided into training, validation, and testing sets in an 8:1:1 ratio. A schematic diagram of the grape leaf data augmentation (Lacate) is illustrated in figure 3. Figure 3(a) shows the original image, (b) displays the flipped image, (c) demonstrates the addition of Gaussian blur, (d) depicts an increase in brightness, (e) shows the rotated image, and (f) illustrates a decrease in brightness.

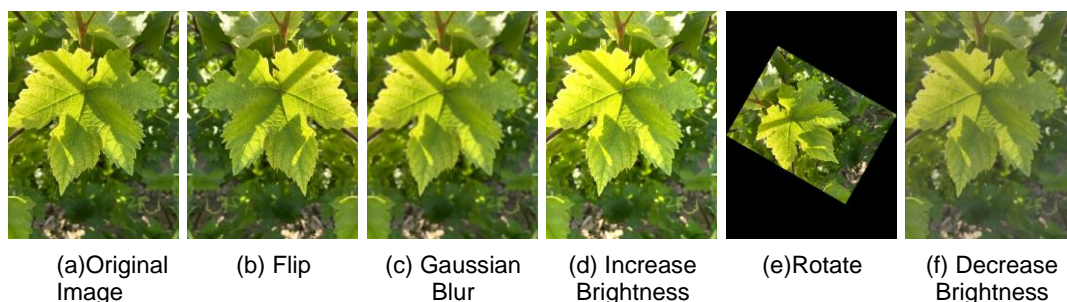


Fig. 3 - Data augmentation diagram (Lacate)

Table 1

Image dataset of grape leaf varieties					
Variety No.	Species	Total quantity	Training set	Validation set	Test set
A11-167	Suhaike	300	240	30	30
A11-168	Baolgal	380	304	38	38
A11-169	Australia Non-	410	328	41	41
A11-170	Baiyou Malake	420	336	42	42
A11-171	Bigqi Husa	440	352	44	44
A11-172	October	370	296	37	37
A11-173	Baisha Ani	370	296	37	37
A11-174	Calaido	360	288	36	36
A11-175	Saingiovese	370	296	37	37
A11-176	Delguri Mike	490	392	49	49
A12-177	Yiqikema	510	408	51	51
A12-178	Dalbash	590	472	59	59
A12-179	Aliwalne	360	288	36	36
A12-180	Bayangxilie	360	288		36
A12-182	Kalas Rose	390	312	39	39
A12-183	Victory	380	304	38	38
A12-184	Baiwujium	300	240	30	30
A12-185	Heisther	360	288	36	36
A12-186	Kalas	50	40	5	5
A14-209	Lacete	370	296	37	37
A14-210	Aibutri	370	296	37	37
A14-211	Su-38	370	296	37	37
A14-212	Shalele	380	304	38	38
A14-213	Baikakuer	380	304	38	38
A14-214	Dashlei	380	304	38	38
A14-215	Shabash	390	312	39	39

Improved swin transformer model

The Swin Transformer model addresses image tasks through a hierarchical design by dividing the input image into multiple windows, treating the elements within each window as independent tokens, and performing linear embedding to create initial feature representations. This mechanism not only enhances the model's capacity to process large images but also effectively avoids the computational and memory limitations that traditional Transformers face when dealing with high-dimensional inputs.

In several stages, the Swin Transformer blocks progressively extract features and adjust spatial resolution, with each stage further integrating information through a "Patch Merging" operation, which reduces computational load and increases the number of channels. The key aspect of the Swin Transformer is the combination of a sliding window multi-head self-attention mechanism (SW-MSA) and a multi-layer perceptron (MLP), which enhances the model's ability to learn local and global features. Additionally, layer normalization (LN) operations ensure the model's stability and training effectiveness.

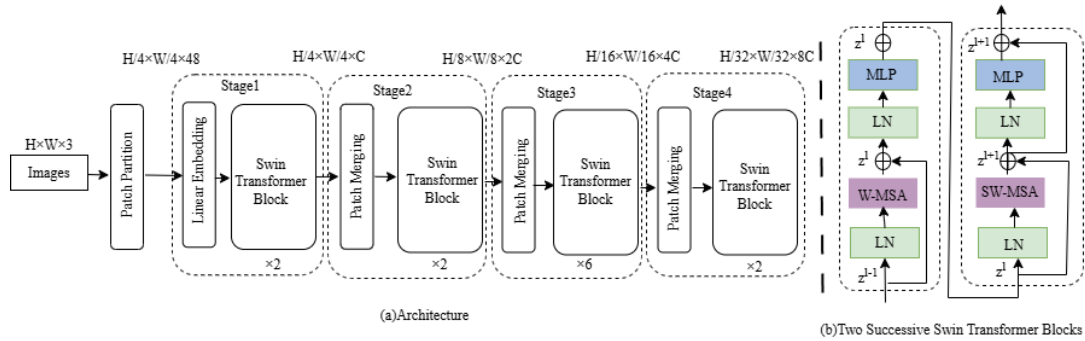


Fig. 4 - Structure diagram of the Swin Transformer model

Due to the imbalance of sample sizes among different grape leaf varieties, this study introduces the Focal Loss function. Focal Loss assesses the difficulty of each sample based on the model's predicted probabilities. It dynamically adjusts the model's focus by reducing attention to easily distinguishable samples during training, allowing the model to concentrate more on harder-to-distinguish samples. Unlike the cross-entropy loss function, Focal Loss introduces a tunable parameter that adjusts the model's focus between easily recognizable and difficult-to-recognize samples. When the value of γ is low, the model pays more attention to easily recognizable samples; when γ is high, the model focuses more on difficult-to-recognize samples. The formula for Focal Loss is as follows:

$$FocalLoss = -a_t (1 - p_t)^\gamma \log(p_t)$$

In the equation, the difficulty of recognition is reflected by p_t . When p_t is larger, it indicates a higher confidence level in identification, suggesting that the sample is easier to distinguish. Conversely, when p_t is smaller, it indicates a lower confidence level in identification, suggesting that the sample is more difficult to distinguish.

Experimental environment

The operating system was 64-bit Windows 10, using an Intel(R) Core(TM) i7-14650HX CPU@2.20 GHz processor with 32 GB of memory. The graphics card model was the NVIDIA GeForce RTX 4060. All CNN models are developed based on the PyTorch framework, with Python 3.8 used as the programming language for implementing network model training and testing. The training parameters included an initial learning rate of 0.00001, a stochastic gradient descent (SGD) optimizer, a weight decay coefficient of 0.05, and a batch size of 4. A cosine learning rate scheduler was utilized for a total of 50 epochs, ensuring a smooth adjustment of the learning rate to avoid sudden changes during training. After each iteration, the trained model was saved in a folder, and the training logs were recorded.

Model evaluation metric

To comprehensively evaluate model performance, several commonly used classification metrics were introduced, including Confusion Matrix, Accuracy, Precision, Recall, F1-score, ROC Curve, and AUC. The ROC Curve, plotted with the False Positive Rate (FPR) on the x-axis and the True Positive Rate (TPR) on the y-axis, represents each point corresponding to a potential classification threshold. The optimal classification threshold can be determined by selecting the point on the ROC Curve that is closest to the top left corner. Furthermore, the model's performance can be assessed using the Area Under the Curve (AUC), where a larger AUC indicates better performance. The formulas for each metric are as follows:

$$ConfusionMatrix = \begin{pmatrix} TP & FP \\ FN & TN \end{pmatrix} \quad (1)$$

$$Precision = \frac{TP}{TP + FP} \tag{2}$$

$$Recall = \frac{TP}{TP + FN} \tag{3}$$

$$Accuracy = \frac{TP + TN}{TP + FP + TN + FN} \tag{4}$$

$$F1 - score = \frac{2 \cdot Precision \cdot Recall}{Precision + Recall} \tag{5}$$

In the equation, *TP* represents the number of samples predicted as positive that are actually positive; *FP* represents the number of samples predicted as positive, but are actually negative; *FN* represents the number of samples predicted as negative, but are actually positive; *TN* represents the number of samples predicted as negative that are actually negative.

RESULTS AND ANALYSIS

Model training

This study evaluated the performance of four convolutional neural network models: Swin Transformer, MobileNetV2, MobileNetV3, and ViT for grape leaf recognition. The model training accuracy curves and loss change curves are shown in figures 5 and 6; the testing accuracy results are presented in Table 2.

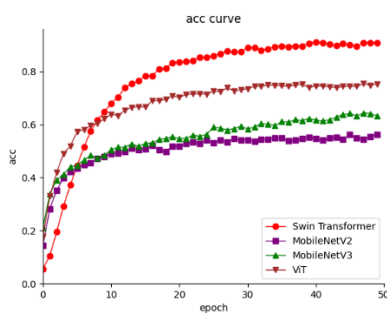


Fig. 5 - Training accuracy change curve

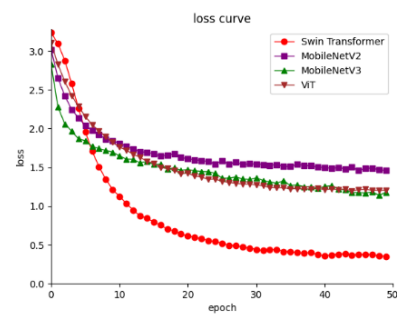


Fig. 6 - Training loss change curve

From the accuracy change curves, it can be observed that the Swin Transformer model achieves a faster improvement in accuracy, ultimately reaching approximately 90.85%. In comparison, MobileNetV2 and MobileNetV3 show relatively small changes in overall accuracy, with final accuracies of only 56.39% and 63.20%, respectively. Additionally, the Swin Transformer converges more quickly and stably than ViT. The loss change curve shows that the Swin Transformer model experiences a rapid decrease in loss during the first 30 training epochs and eventually stabilizes. In contrast, MobileNetV2, MobileNetV3, and ViT exhibit minimal loss reduction throughout the training process. Therefore, the Swin Transformer outperforms the other models in both training accuracy and loss, demonstrating strong robustness and performance advantages.

After model training, performance evaluation was conducted using a test dataset collected from real orchard environments, which included various natural conditions such as strong front lighting, backlighting, and different levels of occlusion.

Table 2

Recognition model testing accuracy

Class	Model1	Model2	Model3	Model4	Class	Model1	Model2	Model3	Model4
A11-167	0.967	0.867	0.967	0.5	A12-180	0.806	0.806	0.75	0.556
A11-168	0.947	0.842	0.868	0.711	A12-182	0.923	0.872	0.897	0.795
A11-169	0.927	0.878	0.878	0.488	A12-183	0.947	0.895	0.895	0.395
A11-170	0.929	0.786	0.976	0.667	A12-184	0.867	0.867	0.833	0.667
A11-171	0.932	0.614	0.932	0.227	A12-185	0.972	0.778	0.917	0.333
A11-172	0.946	0.919	0.838	0.432	A12-186	1.0	1.0	0.8	0.0
A11-173	0.919	0.622	0.973	0.162	A14-209	1.0	0.784	0.919	0.514
A11-174	0.972	0.75	0.917	0.306	A14-210	0.919	0.541	0.811	0.243

Class	Model1	Model2	Model3	Model4	Class	Model1	Model2	Model3	Model4
A11-175	1.0	0.865	0.973	0.324	A14-211	0.838	0.865	0.919	0.568
A11-176	0.837	0.857	0.878	0.571	A14-212	0.921	0.947	0.895	0.868
A12-177	1.0	0.922	1.0	0.627	A14-213	0.789	0.474	0.947	0.289
A12-178	0.966	0.864	0.966	0.847	A14-214	1.0	0.921	0.974	0.263
A12-179	1.0	0.833	0.861	0.194	A14-215	1.0	1.0	0.974	0.769

Note: In this paper, Model1 represents Swin Transformer, Model2 represents MobileNetV2, Model3 represents MobileNetV3, and Model4 represents Vision Transformer (ViT).

The experimental results show that the accuracy of the ViT and MobileNetV2 models is only 50.05% and 82.19%, respectively. The accuracy of the MobileNetV3 model is 90.61%, while the Swin Transformer model achieved 93.55%, the highest among the four models. It exceeds the accuracies of MobileNetV2, MobileNetV3, and ViT by 11.3, 2.94, and 43.50 percentage points, respectively.

Model parameter selection

Choose the Swin Transformer as the recognition model to test the impact of different training parameters on recognition performance. Keeping other parameters constant, four experimental sets (T1-T4) are established, with a batch size fixed at 4. The selected optimizers are SGD and AdamW, with initial learning rates of 0.0001 and 0.00001, respectively. The results of the experiments using different parameter selections are presented in Table 3.

Table 3

Test	Optimizer	Initial Learning Rate	Bach Size	Accuracy
T1	SGD	0.0001	4	90.85%
T2	SGD	0.00001	4	42.42%
T3	AdamW	0.0001	4	94.21%
T4	AdamW	0.00001	4	95.46%

The results indicate that, with the batch size held constant, the AdamW optimizer demonstrated better performance compared to SGD, particularly at the lower learning rate (0.00001), where model T4 achieved the highest accuracy of 95.46%. For models using the SGD optimizer, a higher learning rate (0.0001) contributed to improved model performance, as seen in model T1 with an accuracy of 90.85%, whereas the accuracy of model T2 with a lower learning rate significantly dropped to 42.42%. This suggests that for SGD, an appropriate increase in the learning rate may help enhance the model's training effectiveness. Overall, AdamW demonstrates greater robustness at low learning rates, likely due to its internal mechanisms, including momentum and adaptive learning rate characteristics. Therefore, it is recommended to prioritize the AdamW optimizer for similar tasks and adjust the learning rate appropriately to find the optimal configuration.

Based on this analysis, the Swin Transformer model demonstrates the best recognition performance with the AdamW optimizer, a batch size of 4, and an initial learning rate of 0.00001.

Improvement Of Loss Function

In this study, the loss function of the Swin Transformer model was improved by replacing the original standard loss function with the Focal Loss function. To validate the effectiveness of Focal Loss, comparative experiments were conducted with Cross-Entropy Loss and Label Smoothing Loss. Focal Loss increases the loss gradient for hard-to-classify samples, enhancing the model's learning ability for these challenging samples and effectively addressing class imbalance.

Table 4

Test	Loss	Accuracy	Precision	Recall
T5	Cross-Entropy Loss	93.55%	93.70%	93.60%
T6	Label Smoothing Loss	95.87%	95.87%	95.80%
T7	Focal Loss	98.64%	98.64%	97.90%

From Table 4, it can be observed that Focal Loss demonstrates the best performance in grape leaf variety recognition. In terms of accuracy, the model using Focal Loss achieved an accuracy of 98.72%, which is an improvement of 3.26 percentage points over the accuracy using Cross-Entropy Loss and 2.85 percentage points over Label Smoothing Loss.

In terms of precision, Focal Loss improved by 2.19 percentage points compared to Label Smoothing Loss and by 4.40 percentage points compared to Cross-Entropy Loss. Regarding recall, Focal Loss enhanced performance by 2.10 percentage points over Label Smoothing Loss and by 4.30 percentage points over Cross-Entropy Loss. This improvement can be attributed to Focal Loss's ability to dynamically adjust the loss gradient based on sample difficulty, enabling the model to focus more on samples prone to errors or from rare categories during training. In contrast, Label Smoothing Loss primarily enhances generalization by reducing the model's overconfidence in certain categories, but it does not address class imbalance directly like Focal Loss. Label Smoothing Loss may result in insufficient learning of easier categories, potentially impacting overall performance. In contrast, Focal Loss ensures balanced learning across all categories by focusing on hard-to-classify samples. This attention mechanism enhances the model's learning for difficult samples, thereby improving overall accuracy.

Confusion Matrix

To evaluate the performance of the improved AF-Swin Transformer network model, a test set that was not used in the training or validation phases was employed. The confusion matrix generated is shown in figure 7, where the shading indicates the magnitude of the values; lighter colors represent smaller values, while darker colors represent larger values. The horizontal axis represents the true labels, while the vertical axis represents the predicted labels. The diagonal elements indicate the number of correctly identified samples.

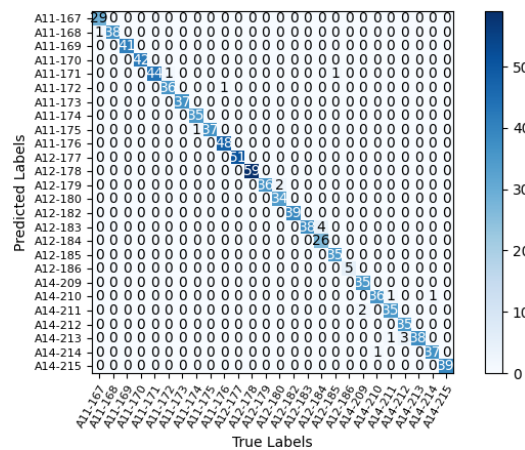
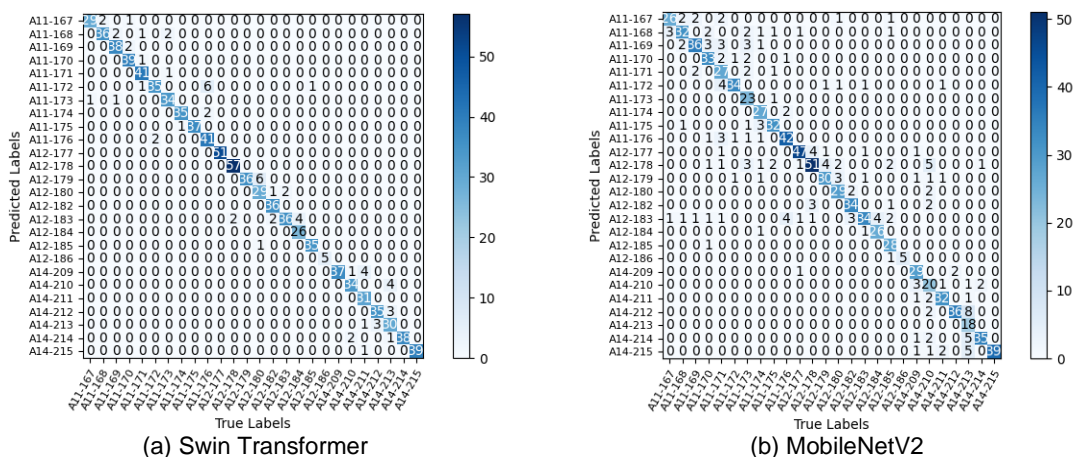


Fig. 7 - Confusion Matrix of AF-Swin Transformer Model

From figure 7, it can be observed that varieties A11-170, A11-171, and A11-172 exhibited no misidentification, indicating that their features are distinct. However, varieties A11-172 and A12-185 were misidentified as A11-171. This suggests that the recognition features for varieties A11-172 and A12-185 do not differ significantly from those of other varieties, making them susceptible to interference. This may also be influenced by shooting angles and lighting conditions.



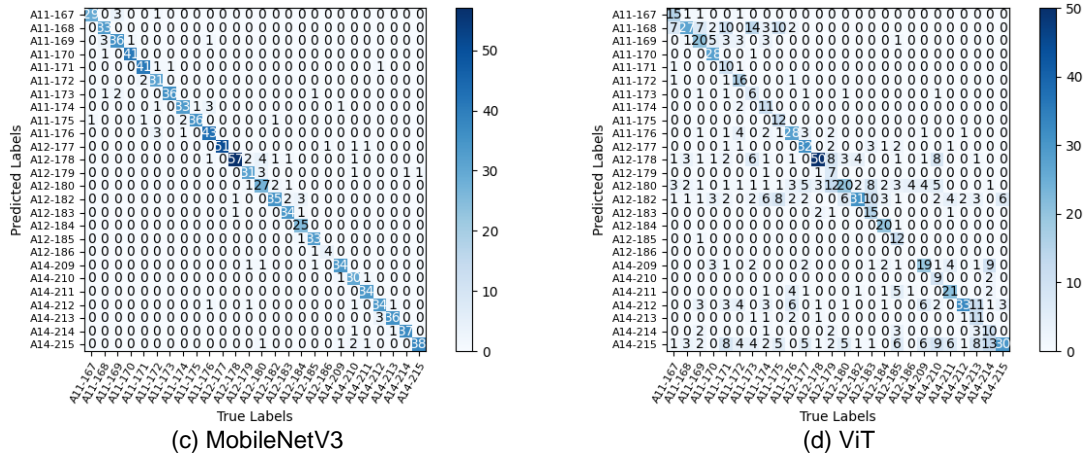


Fig. 8 - Confusion Matrix of Different Models

By comparing figures 7 and 8, which show the confusion matrices of the AF-Swin Transformer, Swin Transformer, MobileNetV2, MobileNetV3, and ViT models, it can be observed that the AF-Swin Transformer model correctly identifies varieties A11-169, A11-173, and A11-178, while the other models exhibit misidentifications for these varieties. This is primarily because Focal Loss enhances the model's ability to learn from hard-to-identify samples, addressing the issue of class imbalance, while the weight decay characteristics of the AdamW optimizer help improve the model's generalization capability, making it more precise when dealing with varieties that have subtle differences. These improvements provide the AF-Swin Transformer with a significant advantage in processing varieties with closely similar features. The above analysis demonstrates that the proposed improved model, AF-Swin Transformer, has strong robustness in recognizing grape leaf varieties.

Grad-CAM Visual Analysis

To understand the feature learning of grapevine leaf sample, this study used the Grad-CAM algorithm to output the gradient heatmap of the weights in the final convolutional layer and visualize the network model. As shown in figure 9, areas that are redder indicate that these features play a more critical role in class orientation.

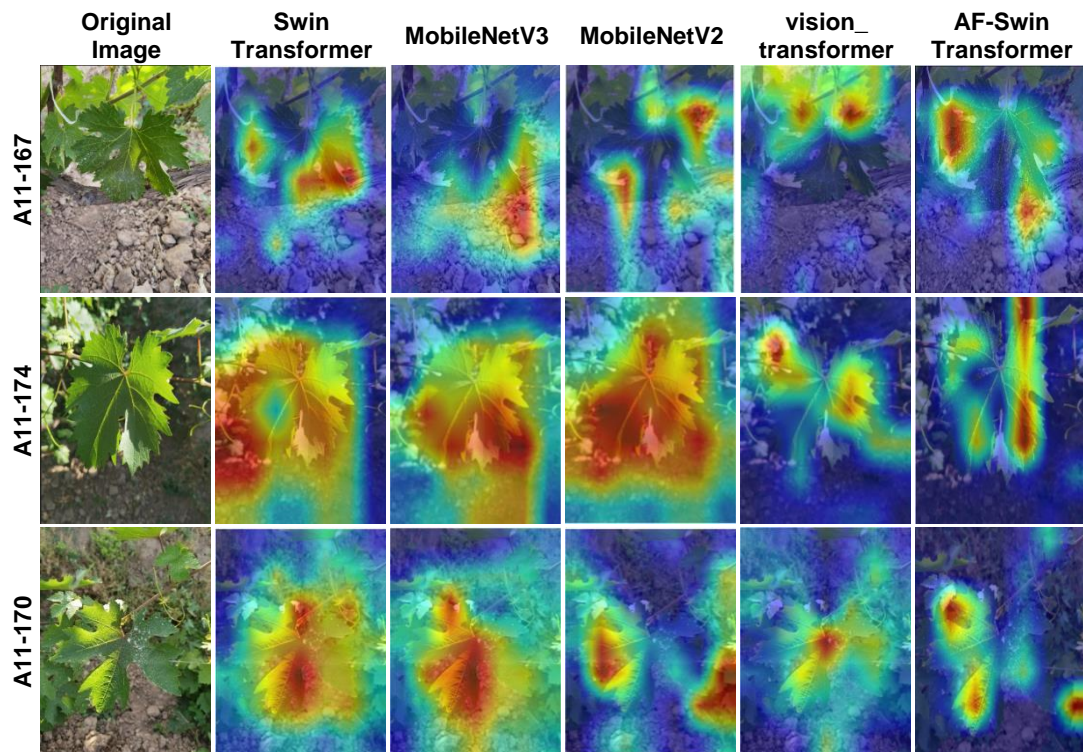


Fig. 9 - Grad-CAM Visualization of Recognition Results for Different Convolutional Neural Network Algorithms

Figure 9 compares the heatmaps of the Swin Transformer, MobileNetV2, MobileNetV3, ViT, and AF-Swin Transformer. The heatmap of the AF-Swin Transformer focuses on both the leaf veins and edges, with a broad distribution that covers a significant portion of the leaf area. In contrast, the heatmaps of MobileNetV2 and MobileNetV3 show higher activity only at the leaf edges, while the Swin Transformer and ViT heatmaps primarily focus on regions where leaf veins are located. Therefore, compared to the other four models, AF-Swin Transformer has a broader and more accurate recognition capability for grapevine leaves.

ROC Curve

To evaluate the recognition performance of the models comprehensively, ROC curves were analyzed. By comparing the area under the curve (AUC), we can intuitively assess the strengths and weaknesses of different models. The ROC curve for the AF-Swin Transformer is shown in Figure 10, while Figure 11 displays the ROC curves for the various models.

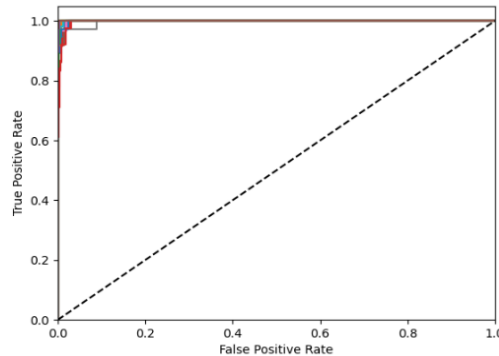


Fig. 10 - ROC Curve of AF-Swin Transformer

From figure 10, it can be seen that the AF-Swin Transformer model exhibits good distinguishing performance among different varieties.

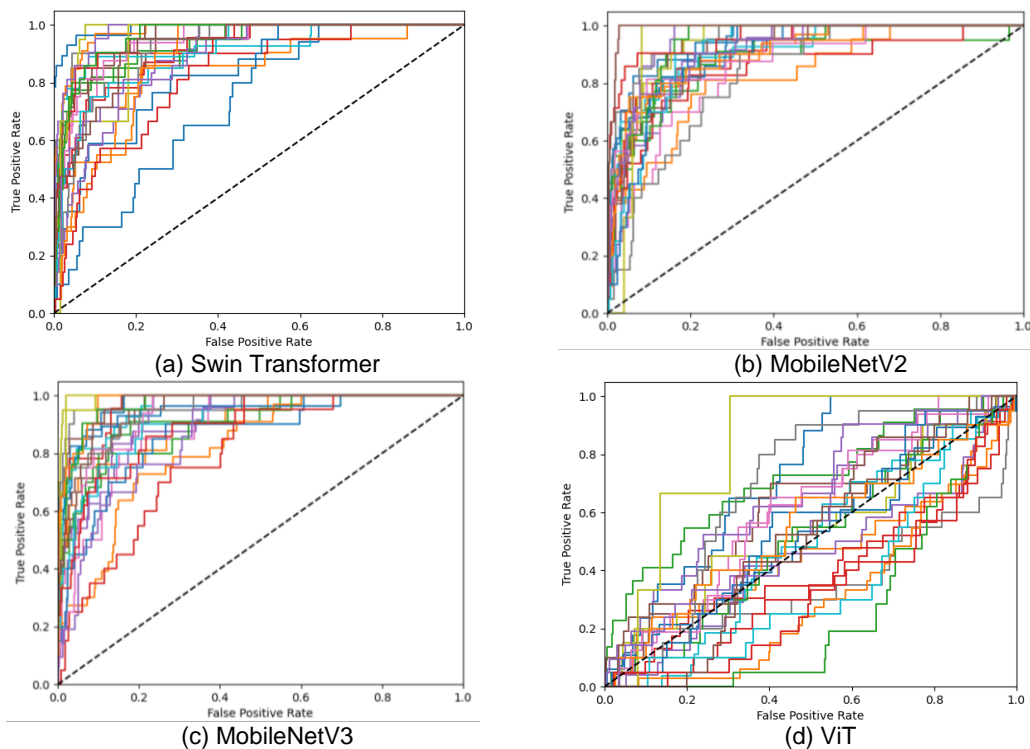


Fig. 11 - ROC Curves of Different Models

- Note: ■ A11-167 ■ A11-168 ■ A11-169 ■ A11-170 ■ A11-171 ■ A11-172 ■ A11-173 ■ A11-174 ■ A11-175
 ■ A11-176 ■ A12-177 ■ A12-178 ■ A12-179 ■ A12-180 ■ A12-182 ■ A12-183 ■ A12-184 ■ A12-185
 ■ A12-186 ■ A14-209 ■ A14-210 ■ A14-211 ■ A14-212 ■ A14-213 ■ A14-214 ■ A14-215

To further comprehensively evaluate the performance of the AF-Swin Transformer model, a comparative assessment was conducted using evaluation metrics such as precision, recall, F1-score, and AUC value for all the models used. As shown in Table 5:

Table 5

Evaluation Metrics of Different Models				
Models	Precision	Recall	F1 Score	AUC
Swin Transformer	0.937	0.936	0.934	0.910
MobileNetV2	0.811	0.798	0.795	0.918
MobileNetV3	0.859	0.863	0.856	0.932
ViT	0.626	0.474	0.478	0.520
AF-Swin Transformer	0.981	0.979	0.980	0.999

The table 5 shows that the AF-Swin Transformer achieves an overall precision of 0.981 in grapevine leaf variety identification, which is higher than that of the Swin Transformer, MobileNetV2, MobileNetV3, and ViT by 4.4, 17, 12.2, and 35.5 percentage points, respectively. The Recall value for the AF-Swin Transformer is 0.979, exceeding that of the Swin Transformer, MobileNetV2, MobileNetV3, and ViT by 4.3, 18.1, 11.6, and 50.5 percentage points, respectively. Additionally, the AF-Swin Transformer has the highest area under the ROC curve (AUC) among the models. The Focal Loss function reduces overfitting on simple samples compared to the cross-entropy loss function, enabling the model to concentrate on misclassified samples and effectively capture complex features and patterns. The AdamW optimizer maintains model stability during training and mitigates overfitting, particularly when handling complex datasets with subtle varietal differences. Therefore, the AF-Swin Transformer proposed in this study significantly outperforms other models in identifying grape leaf varieties and demonstrates clear advantages across various evaluation metrics.

CONCLUSIONS

This study focuses on recognizing grapevine leaf varieties and proposed the AF-Swin Transformer model, which efficiently identifies different grapevine leaf varieties despite sample imbalance conditions. The main conclusions are as follows:

(1) Compared to four other deep learning models, the AF-Swin Transformer model demonstrates better performance in grapevine leaf variety identification.

(2) To address the issue of sample imbalance among different grape leaf varieties, the Swin Transformer model's loss function was replaced with the Focal Loss function. Additionally, the AdamW optimizer was introduced to improve the model's generalization capability. The results show that the AF-Swin Transformer model demonstrates good stability in identifying grape leaf varieties.

This study identified only 26 grape leaf varieties, and future research will expand to include more varieties and further optimize the model. Additionally, exploration of data augmentation techniques and transfer learning methods will be undertaken to achieve efficient recognition of various plant leaves.

ACKNOWLEDGEMENTS

The data utilized in this study was provided by the National Grape Germplasm Resource Center (Pomology Institute, Shanxi Academy of Agricultural Sciences) and funded through Shanxi Agricultural University's Technology Innovation Improvement Project (CXGC2023046) and Youth Science & Technology Innovation Project (No.2019024).

REFERENCES

- [1] Cecotti H., Rivera A., Farhadloo M. (2020). Grape detection with Convolutional Neural Networks. *Expert Systems with Applications*, 159:113588. DOI:10. 1016/j.eswa.2020.113588.
- [2] Chen J., Han J., Liu C., Wang Y., Shen H., Li L. (2022). A deep learning method for the classification of apple varieties via leaf images from different growth periods in natural environment. *Symmetry*, 14(8):1-14.
- [3] Das S., Chatterjee M., Stephen R., Singh A. K., Siddique A. (2024). Unveiling the Potential of YOLO v7 in the Herbal Medicine Industry: A Comparative Examination of YOLO Models for Medicinal Leaf Recognition. *International Journal of Engineering Research & Technology (IJERT)*, Vol.13, Issue 11, Paper ID: IJERTV13IS110019
- [4] Dong Z., Yang F., Du J., (2024), Identification of varieties in *Camellia oleifera* leaf based on deep learning technology. *Industrial Crops and Products*, 216: 118635.

- [5] Islam M.K., Habiba S., Ahsa S.M.M. (2019). Bangladeshi plant leaf classification and recognition using YOLO neural network. *2nd International Conference on Innovation in Engineering and Technology (ICIET)*, pp. 1-5. IEEE.
- [6] Kaur A. (2024). Leaf Detectives: A Deep Learning Approach to Grapevine Varietal Identification with DenseNet-121. *In 2024 Global Conference on Communications and Information Technologies (GCCIT)*, pp. 1-5. IEEE.
- [7] Lin Lihui, Wei Yi, Pan Junhong (2021). Classification Method of Wuyi Rock Tea Leaves Based on Convolutional Neural Networks (基于卷积神经网络的武夷岩茶叶片分类方法). *Journal of Ningde Normal University: Natural Science Edition*, 33(4): 7.
- [8] Maulana F.A., Kertarajasa K., Yasa Y.S., Sari S.A., Sulistiyo M.D. (2024). Grapevine Leaves Classification Using Various CNN Model. *In 2024 11th International Conference on Information Technology, Computer, and Electrical Engineering (ICITACEE)*, pp. 224-229, IEEE.
- [9] Ni Jiangong, Yang Haoyan, Li Juan, Han Zhongzhi. (2021), Identification of Peanut Pod Varieties Based on Improved AlexNet (基于改进型 AlexNet 的花生荚果品种识别). *Journal of Peanut Science*, 050(004): 14-22.
- [10] Pereira C.S., Morais R., Reis M.J.C.S. (2019). Deep learning techniques for grape plant species identification in natural images. *Sensors*, 19(22): 4850.
- [11] Patricio I.R.R. (2018). Computer vision and artificial intelligence in precision agriculture for grain crops: A systematic review. *Computers and Electronics in Agriculture*, 153.
- [12] Pushpanathan K., Hanafi M., Mashohor S.I.W.F.F. (2021). Machine learning in medicinal plants recognition: a review. *Artificial Intelligence Review: An International Science and Engineering Journal*, 54(1):305-327.
- [13] Sennan S., Pandey D., Alotaibi Y., Alghamdi S. (2022). A Novel Convolutional Neural Networks Based Spinach Classification and Recognition System. *Computers, Materials & Continua*, 73(1).
- [14] Sun D.Z., Liu J.Y., Ding Z. (2023). A Multi-Variety Classification Method for Southern Medicinal Plant Leaves Based on the Improved EfficientNetv2 Model (基于改进 EfficientNetv2 模型的多品种南药叶片分类方法). *Journal of Huazhong Agricultural University*, 42(1): 258-267.
- [15] Su B.F., Shen L., Chen S. (2021). Multi-Feature Classification Method for Grape Varieties Based on Attention Mechanism (基于注意力机制的葡萄品种多特征分类方法). *Journal of Agricultural Machinery*, (011): 052.
- [16] Tavakoli H., Alirezazadeh P., Hedayatipour A. (2021). Leaf image-based classification of some common bean cultivars using discriminative convolutional neural networks. *Computers and electronics in agriculture*, 181: 105935.
- [17] Yang J., Run P., Zhang Y.Y. (2023). Research on Visual Recognition Methods of Chinese Herbal Medicine Plants Based on Deep Learning (基于深度学习的中草药植物视觉识别方法研究). *Chinese Journal of Stereology and Image Analysis*, 28(2): 203-211.
- [18] Yin X., Ji Y., Zhang R. (2023). Research on recognition of *Camellia oleifera* leaf varieties based on deep learning[J]. *Journal of Nanjing Forestry University*, 47(3): 29.
- [19] Zhang P., Li D. (2022), YOLO-VOLO-LS: a novel method for variety identification of early lettuce seedlings. *Frontiers in plant science*, 13, 806878.
- [20] Zou Wei, Yue Yanbin, Feng Enying. (2024). Identification of Anthracnose Disease in Chili Fruits Based on MobileNet V2 and Its Application (基于 MobileNet V2 的辣椒果实炭疽病识别及其应用). *Guizhou Agricultural Sciences*, 52(09): 125-132.

DESIGN AND EXPERIMENTAL STUDY OF A HIGH GROUND CLEARANCE WEEDING ROBOT CHASSIS

高地隙跨垄除草机器人底盘设计与试验

Wentao XU, Lei HAN, Yanhua MA, Tao LIU, Wen LIU

Inner Mongolia Agricultural University, College of Mechanical and Electrical Engineering, Inner Mongolia, China;

¹Tel: 0471-4309215; E-mail: hanlei@imau.edu.cn

Corresponding author: Lei Han; Tao Liu

DOI: <https://doi.org/10.35633/inmateh-75-93>

Keywords: high ground clearance weeding robot; inter-row chassis design; stability analysis; field test

ABSTRACT

This study addresses the inefficiency, high crop damage, and poor adaptability of traditional cornfield weeding machinery. A High-Clearance Inter-Row Weeding Robot Chassis was developed and tested through simulations and experiments. With a refined suspension and floating wheels, it achieves 800 mm ground clearance for dual-row weeding. Simulations show maximum chassis stresses of 124.7 MPa and 134.88 MPa under sharp turns and braking. Stability assessments indicate theoretical climb angles of 26.5° longitudinally and 35° transversely, with experimental test results of 22° and 32°, respectively. The robot operates at speeds exceeding 0.8 m/s, overcomes obstacles of up to 370 mm, and traverses trenches narrower than 350 mm or wider than 600 mm. Results confirm its stability, obstacle-crossing ability, and precision, offering a viable solution for intelligent weeding in complex fields.

摘要

本研究针对传统玉米田除草机械存在的低效率、高作物损伤率和适应性差等问题，研制并测试了一种高离地间隙的行间除草机器人底盘。通过设计浮动轮悬架结构，该底盘实现了 800 mm 的离地间隙，可用于双行除草。仿真结果表明，在急转弯和制动工况下，底盘的最大应力分别为 124.7 MPa 和 134.88 MPa。稳定性评估显示，理论纵向爬坡角为 26.5°，横向爬坡角为 35°，实际测试结果分别为 22° 和 32°。机器人运行速度大于 0.8 m/s，可跨越 370 mm 高的障碍物，并可通过宽度小于 350 mm 或大于 600 mm 的沟渠。结果表明，该机器人具备较高的稳定性、优异的越障能力和精确的作业性能，为复杂农田环境下的智能除草提供了一种可行方案。

INTRODUCTION

Weed infestation significantly impacts crop production by competing for resources such as water, nutrients, light, and space, especially during the seedling stage. Weeds hinder crop growth, reducing yields and potentially causing crop failure. While chemical weeding is effective, it poses risks to food security, and manual weeding is labor-intensive and inefficient. Intelligent weeding robots could provide a viable solution (Upadhyay et al., 2024; Yang, L. et al., 2023; Zhang, Z. et al., 2024).

Research on domestic weeding robots is mainly conducted by academic institutions. For example, Xin Li from Northeast Agricultural University designed a tracked weeding robot for paddy fields. Wei Li's team at China Agricultural University developed a tractor-drawn robot with crescent-shaped hoes and machine vision for efficient weeding. Liang'an Zhang from Anhui University of Technology created a four-legged laser weeding robot, offering better mobility and adaptability. Additionally, researchers at Nanjing Forestry University designed a robot for targeted pesticide application. However, most of these robots are limited to inter-row operation and have small payloads and short battery life (Bručienė et al., 2022; Guo, 2022; Hussain et al., 2023; Mao, 2020; Zhang L. et al., 2020).

To address labor intensity, plant damage, soil compaction, and the limitations of traditional methods, developing a high-clearance inter-row intelligent weeding robot is essential for improving precision in field operations.

MATERIALS AND METHODS

Suspension System Design

To enhance the robot's adaptability to complex operating environments and improve its off-road performance, the chassis suspension incorporates a front-and-rear cross-floating design. The two side wheels are mounted on a cross axle, and each wheel is equipped with an independent shock-absorbing damper, enabling vertical movement and rotational flexibility within a defined range around the cross axle. Furthermore, to prevent forward or backward tilting of the robot's body, the left and right cross arms are interconnected via linkages and a balance bar (Băzăvan and Ionita, 2024; Yao et al., 2023; Zhao et al., 2024). The installation configuration of the entire suspension system is presented in figure 1.

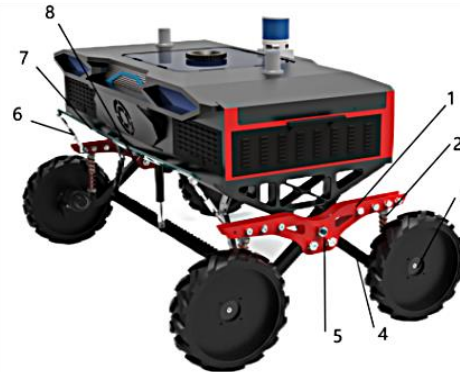


Fig. 1 – Installation position of the weeding robot suspension system

1. Side cross-arm; 2. Shock absorber; 3. Wheel; 4. Suspension lower arm; 5. Cross axle; 6. Connecting rod; 7. Balance bar; 8. Balance bar axle

Robot Chassis Stability Analysis

In SolidWorks, appropriate materials are assigned to each component of the robot, and their mass properties are analyzed to determine the robot's overall center of mass and center of gravity (Tao, 2024). Figure 2 illustrates the robot platform in a fully loaded state. The height of the center of gravity from the ground is approximately 730 mm. As shown in figure 3, the distance from the center of gravity to the front wheel axle is 370mm, while the distance to the rear wheel axle is 443mm.

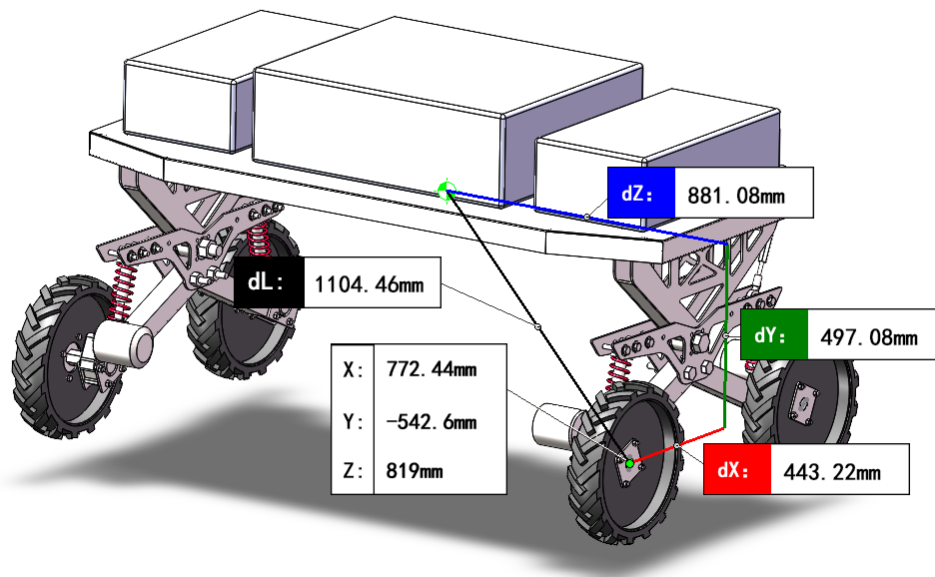


Fig. 2 – Relative position of the center of gravity and front axle under full-load conditions

Longitudinal stability analysis

When the robot operates on a field or roadway slope (moving along the slope), excessive slope angles may lead to longitudinal slip or overturning.

During actual operation, the robot's slow speed allows the effects of inertia, air resistance, and sliding resistance on its motion to be neglected (Mou et al., 2023; Zhou et al., 2024).

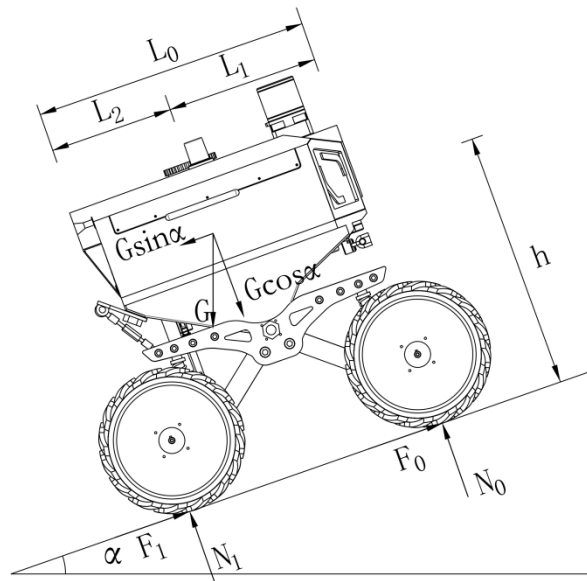


Fig. 3 – Schematic diagram of force distribution during longitudinal movement

As illustrated in figure 3, L_0 denotes the distance between the front and rear wheel axles of the high ground clearance, inter-row weeding robot; L_1 represents the distance from the robot's center of gravity to the front wheel axle center; L_2 is the distance from the center of gravity to the rear wheel axle center; G signifies the robot's weight; θ is the longitudinal slope angle; h is the height of the center of gravity; F_1 and F_2 are the tangential reaction forces at the contact points of the front and rear wheels, respectively; and N_0 and N_1 are the normal reaction forces at the contact points of the front and rear wheels, respectively.

(1) Conditions for Longitudinal Overturning

When the robot operates on a slope, the standard and tangential reaction forces acting on the front wheel are influenced by the terrain and slope angle. Longitudinal overturning occurs when these reaction forces reduce to zero ($N_0=0, F_0=0$), causing the robot to pivot around the rear wheel's contact point with the ground. The critical condition for longitudinal overturning is defined by the limit equilibrium equation at this point:

$$G \cos \alpha_1 \cdot L_2 - G \sin \alpha_1 \cdot h = 0 \tag{1}$$

Simplified, it becomes (2):

$$i_1 = \tan \alpha_1 = \frac{L_2}{h} \tag{2}$$

where:

G - Gravity acting on the robot; i_1 - longitudinal rollover stability; α_1 - slope angle, [°]; h - height of the center of gravity, [mm]; L_2 - distance from the robot's center of gravity to the rear axle along the direction of travel, [mm].

From the equation, both the height of the center of gravity and its distance from the wheel axles influence overturning stability. A greater distance between the center of gravity and the rear wheel axle increases the maximum climbing overturning angle, while a greater distance from the front wheel axle enhances the maximum descending overturning angle. When the longitudinal slope angle remains below the robot's overturning limit, the high ground clearance weeding robot maintains stability without overturning.

(2) Conditions for Longitudinal Sliding

During operation on a longitudinal slope, the robot may also experience wheel slip. The critical balance condition for longitudinal sliding is expressed as:

$$G \sin \alpha_2 - P_k \mu = 0 \tag{3}$$

where:

P_K - driving load on the robot's wheels, [N]; μ - road adhesion coefficient.

$$P_K = G \cos \alpha_2 \quad (4)$$

Substituting the values, it will result:

$$i_2 = \tan \alpha_2 = \mu \quad (5)$$

where:

i_2 - longitudinal slip stability; α_2 - critical angle for longitudinal slip, [°]; μ - adhesion coefficient.

According to the formula, longitudinal sliding stability depends on the coefficient of friction between the ground and the tires. When the slope angle is below the critical sliding angle, the robot operates normally. However, if the slope angle exceeds this critical value, the robot loses traction, leading to longitudinal sliding and reduced stability.

Transverse stability analysis

When the high ground clearance inter-row weeding robot operates transversely on a slope, a height difference may arise between its left and right sides, potentially resulting in transverse overturning or sliding. Neglecting the influences of air resistance, inertial resistance, and rolling resistance during the robot's motion, the force analysis of the robot moving transversely on a slope is illustrated in figure 4.

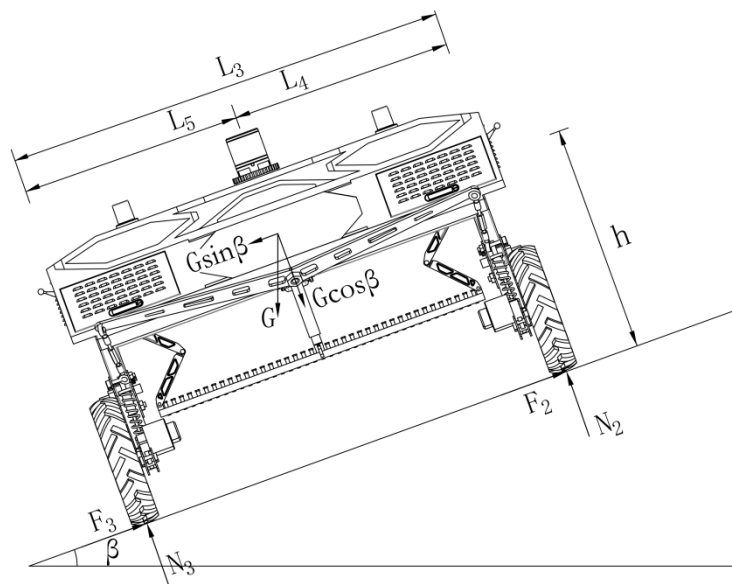


Fig. 4 - Schematic of transverse forces during travel

(1) Conditions for Transverse Overturning of the high ground clearance Inter-Row Weeding Robot

When the robot undergoes transverse overturning while traversing a slope, the standard and tangential reaction forces on the upper wheels reduce to zero. The robot will then rotate around the contact point between the lower wheel and the ground, leading to overturning. The critical balance equation for transverse overturning is as follows:

$$G \sin \beta_1 \cdot h - G \cos \beta_1 \cdot L_5 = 0 \quad (6)$$

Simplified, it becomes:

$$i_3 = \tan \beta_1 = \frac{L_5}{h} \quad (7)$$

where:

i_3 - denotes the transverse overturning stability; L_5 - represents the horizontal distance from the center of gravity to the lower wheel, [mm]; β_1 - indicates the slope angle, [°]; h - corresponds to the vertical distance from the center of gravity to the ground, [mm].

From the above equation, it is evident that both the height of the center of gravity and the horizontal distance from the center of gravity to the lower wheel significantly influence transverse overturning stability.

For a fixed track width, a lower center of gravity and a greater horizontal distance between the center of gravity and the lower wheel result in a larger critical angle for transverse overturning. Consequently, the risk of transverse overturning is reduced, thereby enhancing the robot's transverse stability.

(2) Conditions for Transverse Sliding of the high ground clearance Inter-Row Weeding Robot

In addition to the risk of overturning, transverse movement of the robot on slopes may also result in sliding. When the robot approaches the critical sliding condition, the limit equilibrium equation can be expressed as:

$$i_3 = \tan \beta_2 = \frac{L_5}{h} \tag{8}$$

Simplified, it becomes:

$$i_4 = \tan \beta_2 = \mu' \tag{9}$$

where:

i_4 - denotes transverse sliding stability; β_2 - represents the slope angle in degrees, [°]; μ' - transverse adhesion coefficient.

From this equation, it is evident that the robot can maintain normal transverse operation without slipping when the slope angle is smaller than the sliding angle.

Chassis Structural Strength Analysis

Analysis of Emergency Turning Conditions and Result Interpretation

During emergency turning maneuvers, transverse forces are exerted on the chassis frame components, generating transverse loads (Dharma et al., 2024; Dudescu et al., 2023; Kiran, 2024; Deulgaonkar et al., 2022). Given the robot's relatively low maximum speed, the centrifugal acceleration was set to 0.2g, based on its minimum turning radius and maximum operating speed. This results in transverse inertial forces acting on the chassis frame and its components. The load and constraints under steady-state driving conditions remain unchanged, with the inertial force applied in the direction of centrifugal force. The force magnitude is calculated as $F=0.2g$, where M represents the combined mass of the battery and water tank.

The analysis results for the emergency turning condition are shown in figure 5. The maximum stress of 124.7 MPa occurs at the contact point between the main beam of the platform's upper plate frame and the vertical side plate. The deformation contour map indicates a maximum deformation of 1.71 mm, which satisfies the strength requirements.

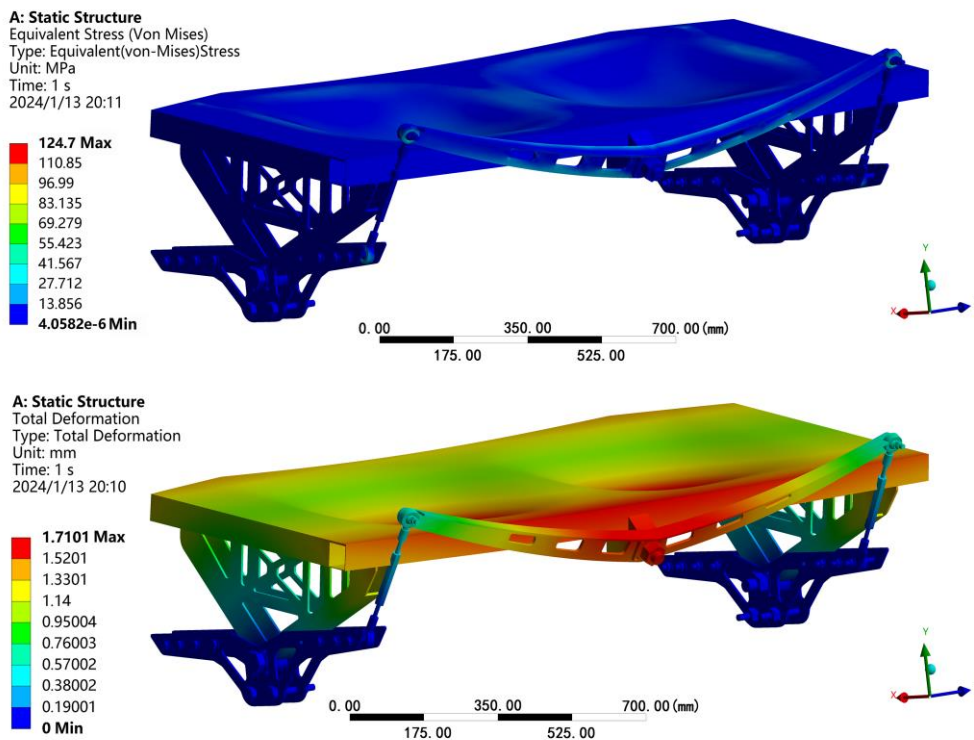


Fig. 5 - Analysis results of emergency turning conditions

Analysis of Emergency Braking Conditions and Result Interpretation

During field operations, the high ground clearance Inter-Row Weeding Robot may undergo emergency braking or reverse operation. In such scenarios, the chassis frame experiences significant inertial loads, acting in the direction opposite to the motion. The braking acceleration was estimated based on the robot's maximum speed, with the load and constraints under steady-state driving conditions remaining unchanged. The inertial force, applied to the upper components, acts opposite to the direction of motion. The braking acceleration was set to $0.4g$, and the inertial force magnitude was calculated as $F=0.4g$, where M represents the combined mass of the battery and water tank.

The analysis results for the emergency braking condition are shown in figure 6. The maximum stress of 134.88 MPa occurs at the connection between the tie rod and the middle balance connecting rod. The deformation contour map shows a maximum deformation of 4.52 mm on the upper plate of the chassis, primarily attributed to the large 125 l pesticide tank mounted on the upper side.

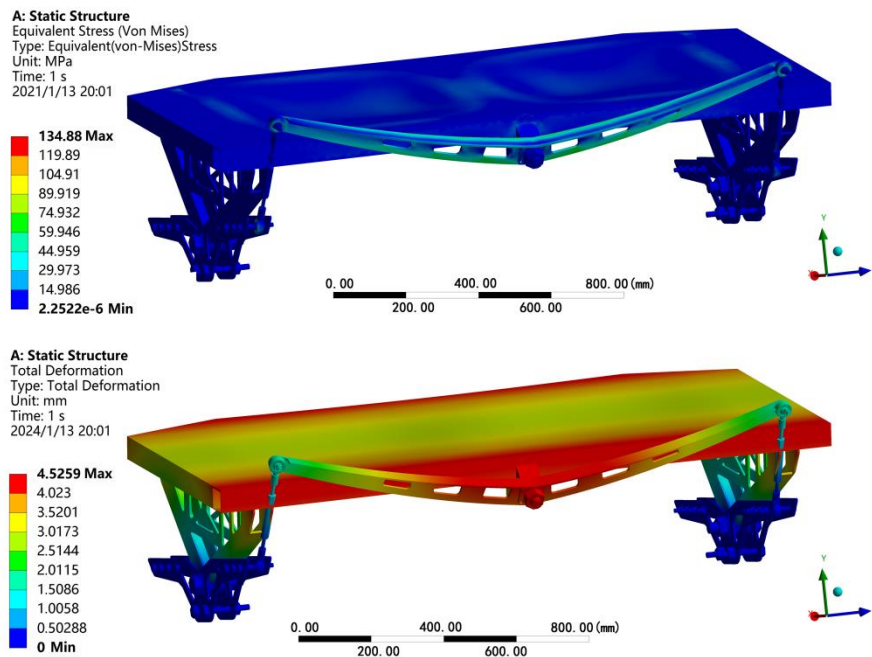


Fig. 6 - Analysis results of braking conditions

RESULTS

Weeding Robot Speed Test

Based on the theoretical design specifications, the high ground clearance Inter-row Weeding Robot achieves a speed exceeding 0.8 m/s on flat terrain. To validate whether the robot meets the theoretical speed requirements, a 50-meter test section on a flat farm road was selected. The robot's forward and reverse speeds were measured at both 50% and 100% throttle settings. The detailed testing procedure is illustrated in figure 7 (Cen, 2023; Jiang et al., 2023; Yang Z., 2023).



Fig. 7 - Test diagram of the weeding robot's deviation rate

Table 1

Test Results of the Weeding Robot's Speed on Field Terrain								
Test number	Forward				Reverse			
	50% Throttle		100% Throttle		50% Throttle		100% Throttle	
	Time of the experiment (s)	Speed (m/s)	Time of the experiment (s)	Speed (m/s)	Time of the experiment (s)	Speed (m/s)	Time of the experiment (s)	Speed (m/s)
1	84.3	0.593	56.8	0.880	85.2	0.587	55.4	0.923
2	83.5	0.600	57.4	0.871	84.8	0.590	56.8	0.880
3	83.8	0.597	55.1	0.907	86.9	0.575	56.4	0.887
Average	83.87	0.596	56.4	0.887	85.63	0.584	56.2	0.890

As presented in Table 1, the average forward speed at 50% throttle is 0.596 m/s, while the reverse speed is 0.584 m/s. At full throttle (100%), the average forward and reverse speeds increase to 0.887 m/s and 0.890 m/s, respectively. These results indicate that the weeding robot's operational speed on field roads complies with the design specifications.

Weeding Robot Obstacle-Crossing Performance Test

The high ground clearance Inter-Row Weeding Robot may encounter obstacles such as potholes or uneven terrain during field operations. To address these challenges, the robot is equipped with a specialized suspension system featuring independent suspension on all four wheels and cross arms on both sides. The four-wheel drive configuration ensures continuous ground contact for all wheels during obstacle traversal. To validate the effectiveness of this mechanism, the robot's obstacle-crossing performance must be experimentally evaluated to determine its maximum obstacle-crossing capacity.

(1) Single Wheel Vertical Obstacle Test

This test simulates scenarios where the robot encounters sudden obstacles, such as rocks or raised surfaces, as well as more considerable obstacles during regular operation. A brick is utilized to replicate these obstacles, with each brick having a thickness of approximately 50 mm. By stacking multiple bricks, obstacles of varying heights are simulated. The robot is gradually driven toward the vertical obstacle and attempts to traverse it. The height of the obstacle is incrementally increased until the chassis is no longer capable of crossing. The results are documented in Table 2.

Table 2

Single Wheel Vertical Obstacle Test		
Test number	Obstacle height [mm]	Crossing Result
1	53	Passed
2	106	Passed
3	159	Passed
4	212	Passed
5	265	Passed
6	318	Passed
7	371	Passed
8	424	Failed



Fig. 8 - Aspects from the experiment of crossing vertical obstacles with a single wheel of the weeding robot

(2) Single Wheel Trench Crossing Test

This experiment simulates scenarios in which the weeding robot encounters depressions or trenches in the field. The study evaluates the robot's trench-crossing capability by testing its performance on artificially dug trenches of varying widths. The trench width is incrementally increased until the robot fails to cross, and the corresponding data are recorded in Table 3.

Table 3

Single-Wheel Trench Crossing Experiment		
Test number	Trench width [mm]	Through the effect
1	200	Passed
2	250	Passed
3	300	Passed
4	350	Passed
5	400	Failed
6	450	Failed
7	500	Failed
8	550	Failed
9	600	Passed
10	650	Passed



Fig. 9 - Aspects from the experiment of the Weeding Robot's single-wheel trench crossing

The robot is capable of surmounting vertical obstacles with a maximum height of 371 mm. However, its trench-crossing performance varies depending on trench width: it can effectively traverse trenches narrower than 350 mm or wider than 600 mm. When the trench width is between 400 mm and 550 mm, the ditch width is close to the wheel diameter. When the wheels come into contact with the ditch walls, they are prone to slipping, resulting in temporary entrapment.

Experimental results demonstrate that the suspension system significantly improves the robot's obstacle-crossing capabilities by ensuring continuous ground contact for all four wheels during the traversal process.

Stability Test of the Chassis Platform of the Weeding Robot

During field operations, the high-ground clearance weeding robot encounters sloped terrain, an evaluation of its stability to determine the maximum operational angles and suitable working environments being necessary. To replicate real-world conditions, the robot was positioned on a slope board at various incline angles. The water tank was filled, and additional weights were applied to the battery compartment to simulate the actual load distribution during operation. The robot's tipping and slipping thresholds were recorded under these conditions, as illustrated in figure 10.



Fig. 10 - Stability test of the Weeding Robot

For the high-clearance Inter-Row Weeding Robot, the position of the center of gravity is shown in figure 2. After calculation, $i_1=0.602$, and the friction coefficient $\mu=0.5$. Thus, it is determined that $i_1 \geq i_2$. This indicates that when the robot travels on a slope, sliding occurs before overturning. The critical climbing angle is 26.5° . By calculation, $i_3=1.14$, and the typical dynamic friction coefficient is 0.71 . Thus, it is determined that $i_3 \geq i_4$. This indicates that sliding occurs first when the robot moves laterally on a slope, and the maximum operating angle is 35° .

The stability test results, summarized in Table 4, reveal that the maximum slope climb angle for longitudinal movement is 22° , while the robot can achieve up to 32° for transverse (horizontal) movement. A discrepancy exists between the measured values and theoretical calculations, primarily attributed to differences between the slope board surface and actual field conditions. Furthermore, theoretical analyses assume ideal conditions, such as rigid robot components and constant friction coefficients, which are seldom encountered in practical scenarios. As indicated in Table 4, the robot demonstrates a higher maximum climb angle during transverse (horizontal) movement compared to vertical (uphill) movement, highlighting its enhanced stability and reduced likelihood of slipping during field operations.

Table 4

Test Item	Stability Test Results		Instability Type
	Theoretical Value ($^\circ$)	Actual Value ($^\circ$)	
Longitudinal Climb Angle	26.5	22	Slipping
Transverse Climb Angle	35	32	Slipping

CONCLUSIONS

1. A high-clearance, floating-wheel weeding robot was developed for weed control in maize seedling stages under complex field conditions. The robot features a floating suspension, electric drive, and differential steering, with a wheelbase of 1,800 mm. It can cover two rows of crops in a single pass. Static analysis using Ansys revealed maximum stress values of 124.7 MPa during braking and 134.88 MPa during turning, with corresponding deformations of 1.71 mm and 4.52 mm. These results confirm that the chassis meets the required specifications.

2. A stability analysis was conducted on the high-ground-clearance cross-row floating wheel weeding robot chassis system. The theoretical maximum climb angles for longitudinal and transverse movement on slopes were determined to be 26.5° and 35° , respectively.

3. Field experiments were conducted to evaluate the chassis of the weeding robot. The results demonstrated an average field travel speed exceeding 0.8 m/s. The robot could overcome vertical obstacles up to 371 mm in height on a single wheel. Additionally, it successfully traversed ditches with widths below 350 mm and above 600 mm. Stability tests revealed maximum climb angles of 22° for longitudinal movement and 32° for transverse movement.

REFERENCES

[1] Băzăvan, A., & Ioniță, E.R. (2024). Versatile multi-axis chassis a solution for rescue operations and mobility. *Journal of Information Systems & Operations Management*, Vol. 18(1), Romania.

[2] Bručienė, I., Buragienė, S., & Šarauškus, E. (2022). Weeding effectiveness and changes in soil physical properties using inter-row hoeing and a robot. *Agronomy*, Vol. 12, pp. 1514, Switzerland.

- [3] Cen, H. (2023). Design and testing of a small agricultural robot for high-ridge and furrow environments (高垄畦沟小型农业作业机器人设计与试验). *Journal of Anhui Agricultural Sciences*, 51(23), 198–202, 237.
- [4] Dharma, MD, Bhavya, G., Nithin, R., Jagadeesh, Y., & Shashivardhan, G. (2024). Design and analysis of automotive chassis frame using finite element method. *International Journal of Mechanical Engineering Research and Technology*, Vol. 16(2), pp. 512-518, India.
- [5] Deulgaonkar, V. R., Deshpande, S., Bengle, A., & Dhanawade, P. (2022). Finite Element Analysis of Foldable Electric Vehicle. *International Journal of Vehicle Structures & Systems (IJVSS)*, 14(6).
- [6] Dulescu, M.C., Paul, B., & Neamțu, C. (2023). Structural analysis of an electric car chassis by numerical and experimental methods. *Acta Technica Napocensis-Series: Applied Mathematics, Mechanics, and Engineering*, Vol. 65(4S), Romania.
- [7] Guo, J.J. (2022). *Design and key technology research of a bow-shaped agricultural robot (弓腰式农业机器人设计及关键技术研究)*. Master's Thesis, Henan University of Science and Technology, Luoyang, China.
- [8] Hussain, A., Fatima, H. S., Zia, S. M., Hasan, S., Khurram, M., Stricker, D., & Afzal, M. Z. (2023). Development of cost-effective and easily replicable robust weeding machine—premiering precision agriculture in Pakistan. *Machines*, Vol. 11, pp. 287, Switzerland.
- [9] Jiang, W., Quan, L., Wei, G., Chang, C., & Geng, T. (2023). A conceptual evaluation of a weed control method with post-damage application of herbicides: A composite intelligent intra-row weeding robot. *Soil and Tillage Research*, Vol. 234, pp. 105837, Netherlands.
- [10] Kiran, B. N. (2024). Structural optimization of four-wheeler chassis. *International Journal of Mechanical Engineering and Technology (IJMET)*, Vol. 15(4), pp. 30-53, India.
- [11] Mao, T. (2020). *Design and experimental study of a walking platform for paddy field operation robots (水田作业机器人行走平台设计与试验研究)*. Master's Thesis, South China Agricultural University, Guangzhou, China.
- [12] Mou, X., Luo, Q., Ma, G., Wan, F., He, C., Yue, Y., ... & Huang, X. (2023). Simulation Analysis and Testing of Tracked Universal Chassis Passability in Hilly Mountainous Orchards. *Agriculture*, Vol. 13, pp. 1458, Switzerland.
- [13] Tao, Z. (2024). The design and research of collaborative robots based on Solidworks. *2024 IEEE 3rd International Conference on Electrical Engineering, Big Data and Algorithms (EEBDA)*, pp. 1174-1179, United States.
- [14] Upadhyay, A., Zhang, Y., Koparan, C., Rai, N., Howatt, K., Bajwa, S., & Sun, X. (2024). Advances in ground robotic technologies for site-specific weed management in precision agriculture: A review. *Computers and Electronics in Agriculture*, Vol. 225, pp. 109363, Netherlands.
- [15] Yang, T., Jin, C., Ni, Y., Liu, Z., & Chen, M. (2023). Path Planning and Control System Design of an Unmanned Weeding Robot. *Agriculture*, Vol. 13, Article 2001, Switzerland.
- [16] Yang, Z. (2023). Design and experimental study of an agricultural seeding robot (农业播种机器人的设计及试验研究). *Southern Agricultural Machinery*, 54(5), 59–61.
- [17] Yao, L., Yuan, H., Zhu, Y., & et al. (2023). Design and testing of a wheeled crop-growth-monitoring robot chassis. *Agronomy*, Vol. 13, pp. 3043, Switzerland.
- [18] Zhang, L.A., Tang, K., Zhao, Y.J., Wang, X.Y., Yu, D.Z. (2020). Optimization of leg structure parameters for a quadruped laser weeding robot (四足激光除草机器人腿部结构参数优化). *Transactions of the Chinese Society of Agricultural Engineering*, 36(2), 7–15.
- [19] Zhang, Z., He, W., Wu, F., Quesada, L., & Xiang, L. (2024). Development of a bionic hexapod robot with adaptive gait and clearance for enhanced agricultural field scouting. *Frontiers in Robotics and AI*, Vol. 11, pp.1426269, Switzerland.
- [20] Zhao, X., Yang, J., Zhong, Y., & et al. (2024). Study on chassis leveling control of a three-wheeled agricultural robot. *Agronomy*, Vol. 14, pp. 1765, Switzerland.
- [21] Zhou, L., Hu, C., Chen, Y., Guo, P., Liu, J., Chen, Y., & Cao, J. (2024). Research on a chassis stability control method for high-ground-clearance self-propelled electric sprayers. *Applied Sciences*, Vol. 14, pp. 7734, Switzerland.

INNOVATIONS IN SMALL WIND TURBINES: A COMPREHENSIVE REVIEW OF VERTICAL AXIS DESIGN AND EXPERIMENTAL FINDINGS

INOVAȚII ÎN DOMENIUL TURBINELOR EOLIENE DE MICI DIMENSIUNI: O REVIZIE CUPRINZĂTOARE A PROIECTĂRII TURBINELOR EOLIENE CU AX VERTICAL ȘI A REZULTATELOR EXPERIMENTALE

Bogdan Ovidiu DURAN^{*}, Adrian PANDELE, Dragos Mihail PREDA, Gheorghe VOICU^{*} ¹

National University of Science and Technology POLITEHNICA Bucharest, Romania

Tel: +40274715585; E-mail: ghvoicu_2005@yahoo.com; Tel: +40749995555; E-mail: bogdan.o.duran@gmail.com

DOI: <https://doi.org/10.35633/inmateh-75-94>

Keywords: SWT (small wind turbine), renewable energy, residential small wind turbine, Darrieus vs Savonius

ABSTRACT

This paper provides an overview of the recent developments on small wind turbines in terms of their distinguishing characteristics, experimental research and structural and operational development of small vertical axis wind turbines. Emphasizing their decentralized generation capability, cost savings, and sustainability, the first part discusses the characteristics of small wind turbines. Then the review paper goes through a synthesis process of experimental research work on small wind turbines to evaluate their performance, technological advancements evolved in line with actual world problems encountered. The paper also describes what was achieved by way of small vertical-axis wind turbine design, material problems, and aerodynamic theories that control their operation. Finally, the study provides a review of experimental research studies that were conducted on the performance of small vertical axis wind turbines. The study also shows the functioning methods of small vertical axis wind turbines examined by means of experimental research, which investigate their efficiency under different environmental circumstances and where they may be optimized. Emphasizing the interdependence between theory and practice, this paper examines answers wind turbine researchers have already looked at. A small part of international research data seeking to improve the efficiency and design of small wind turbines is collated here.

REZUMAT

Această lucrare oferă o imagine de ansamblu asupra dezvoltărilor recente ale turbinelor eoliene mici în ceea ce privește caracteristicile lor distinctive, cercetarea experimentală și dezvoltarea structurală și operațională a turbinelor eoliene mici cu ax vertical. Subliniind capacitatea lor de generare descentralizată, costuri și durabilitatea, în prima parte a lucrării sunt prezentate caracteristicile turbinelor eoliene mici. Analiza trece printr-un proces de sinteză a lucrărilor de cercetare experimentală asupra turbinelor eoliene mici pentru a evalua performanța acestora, progresele tehnologice evoluând în concordanță cu problemele reale întâlnite în timpul funcționării turbinelor. Lucrarea descrie, de asemenea, ceea ce s-a realizat prin proiectarea unei turbine eoliene mică cu ax vertical, problemele legate de selecția materialelor și teoriile aerodinamice care controlează funcționarea acestora. În cele din urmă, studiul oferă o trecere în revistă a studiilor experimentale de cercetare care au fost efectuate asupra performanței turbinelor eoliene cu ax vertical. Studiul arată, de asemenea, metodele de funcționare ale turbinelor eoliene cu ax vertical examinate prin cercetări experimentale, care investighează eficiența acestora în diferite circumstanțe de mediu și unde pot fi optimizate. Subliniind interdependența dintre teorie și practică, această lucrare examinează soluțiile existente la care cercetătorii de turbine eoliene au ajuns deja. O mică parte din datele cercetării internaționale care încearcă să îmbunătățească eficiența și proiectarea turbinelor eoliene mici este inclusă în lucrare.

¹ Bogdan Ovidiu DURAN, PhD Student; Adrian PANDELE, PhD Student; Dragos Mihail PREDA, PhD Student; Gheorghe VOICU, Prof. PhD. Eng,

INTRODUCTION

Wind power is currently among the most promising and sustainable sources of energy today. Wind turbines are essential in tapping into the use of natural resources to generate energy with the growing need for renewable energy sources. The technology in the devices is able to convert wind energy into electrical energy and present a clean source compared to fossil fuels, according to Brown et al. (Brown et al., 2015). Apart from reducing the use of non-renewable energy sources and greenhouse gas generation, wind power stands for environmental sustainability.

The main function of a wind turbine is to harness the energy of the wind and transfer it into the form of motion and afterwards into mechanical form and finally into electrical form. The principle on which it works is simple: the turbine's blades are pushed by the wind and rotated to create motion, as Ning et al. explained in their paper (Ning et al., 2014). Figure 1 shows the key components of a horizontal-axis wind turbine. The main components are the tower, nacelle, rotor, generator, and the blades. In the rotor's core is fitted the generator, which functions because the turbine's blades are spinning around it. The generated electrical power from the generator can be utilized on-site or transmitted through the power network.

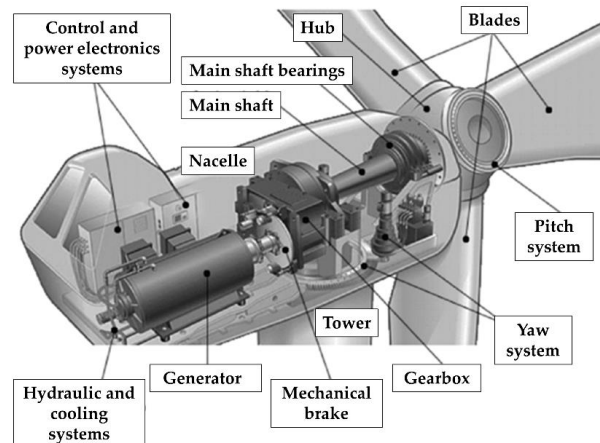


Fig. 1 - Diagram of key components of a wind turbine (Civera et al., 2022)

Designed to resemble the wings of an airplane in most instances, the blades capture the energy in the air (wind). The blades, along with the hub they are attached to, make up the rotor. The nacelle, the housing atop the tower, contains the generator and gearbox among the main components. The tower positions the turbine to elevated levels where the speed of the air is stronger and safer. The mechanical energy has to be transferred to electrical energy by the generator, as Enevoldsen et al. stated in their paper regarding the study of an extensive dataset consisting of 35 years of multi-megawatt wind turbine inventions (Enevoldsen et al., 2019). The wind delivers mechanical rotation energy in the form of spinning the blades around the rotor. A gear alters the speed in rotation after the mechanical energy is transferred to it via a shaft. The rotation is amplified to a functional speed with the aim of producing power. The mechanical energy is transferred from the gear to the generator, where electromagnetic induction is utilized to transform it into electrical energy. An interesting study belongs to Xiaohui et al., who presented in their paper an algorithm for calculating the magnetic transient effects in a wind turbine tower struck by lightning (Xiaohui et al., 2010).

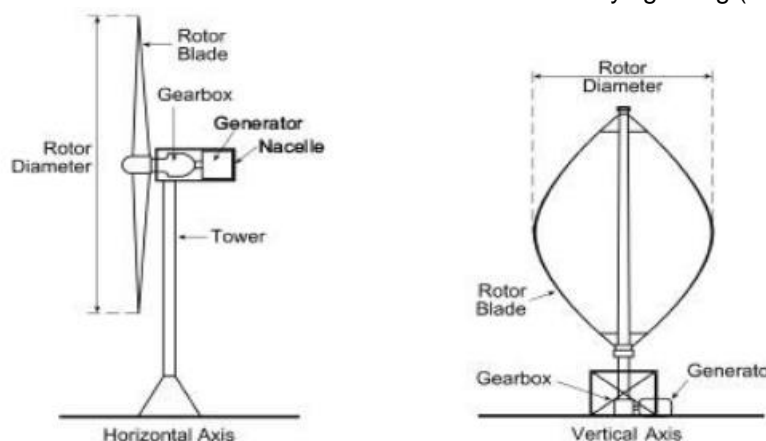


Fig. 2 - Horizontal axis wind turbine vs. vertical axis wind turbine (Salem et al., 2016)

HAWT (horizontal axis wind turbines) and VAWT (vertical axis wind turbines) are the two major types of wind turbines. In figure 2 are presented the resemblances between these two types. Although both are utilized to generate electricity from wind energy, they have different design, efficiencies, and applications. Eriksson et al. presented in their paper a comparative study of three wind turbines: a horizontal axis wind turbine and two vertical axis wind turbines; the Darrieus turbine and the H-rotor. Their study includes aspects like structural dynamics, control systems, maintenance, manufacturing and electrical equipment (Eriksson et al., 2008).

Just like propeller blades, the blades in the most prevalent type of turbine are mounted on a horizontal axis. Such turbines are mounted on tall towers in order to avail themselves of the stronger winds higher up in the air. They are suitable for onshore and offshore use due to high efficiency in high winds. However, they require a mechanism to alter the direction of the turbine so the blades may face the direction in which the wind blows, as also Elkodama et al. stated in their paper (Elkodama et al., 2023). The blades on vertical-axis wind turbines, on the other hand, rotate on a vertical axis. Such turbines are suitable for regions where the wind flows are turbulent or irregular because they neither require turning and can harvest the wind from any direction as Khammas et al. suggest in their paper (Khammas et al., 2015). Due to the fact that VAWTs are smaller and compact in nature, they may be utilized where there is limited space in urban areas or even within residential areas. Although they provide improved quietness and flexibility compared to HAWTs, they typically exhibit lower efficiency. They are utilized in ordinary-scale energy use; however, in the best conditions in terms of winds, they are less efficient in comparison to ordinary-scale large-size HAWTs.

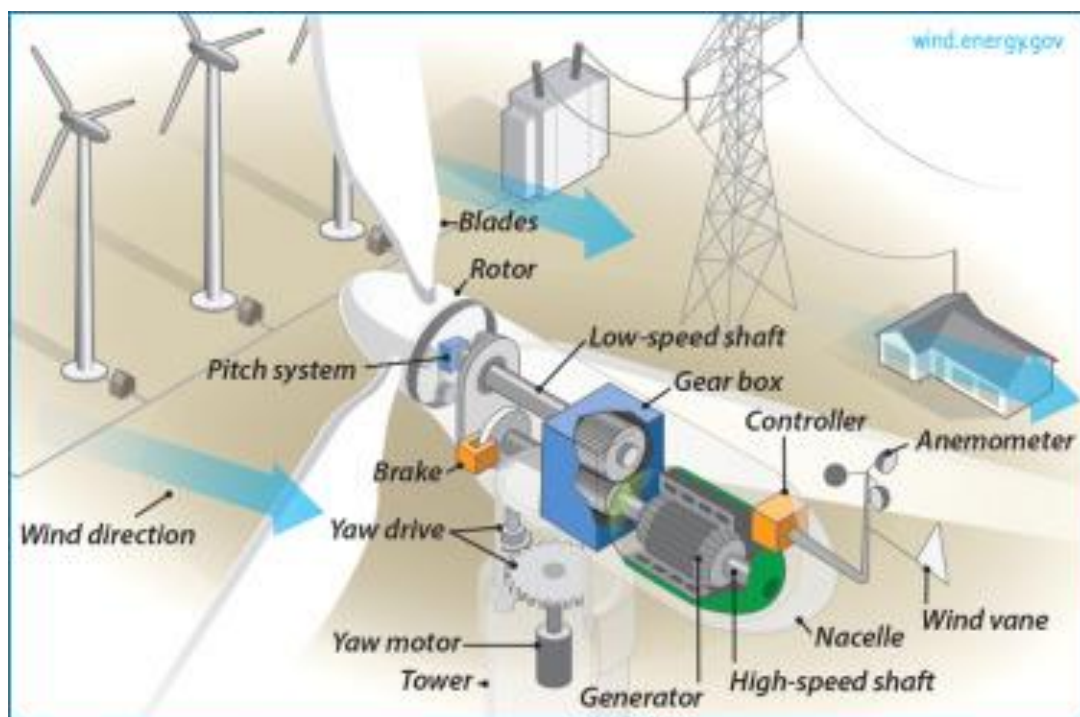


Fig. 3 - The process of generating energy through wind turbines
(Junginger et al., 2020)

There are several similarities and dissimilarities between the two categories, but the energy generation process is basically the same (as Figure 3 shows). HAWTs are efficient in energy conversion in regions with consistent and powerful winds. They are the turbines preferred for use in large-scale wind farms due to their long blades, which enable them to capture more energy (Adams et al., 2011). They would be difficult to service but are prone to wear and tear in extreme weather conditions. A very interesting study on the structural health monitoring of a HAWT was conducted by Adams et al., focusing on a Micon 65/13 horizontal-axis wind turbine.

Although VAWTs are less efficient in regions with powerful winds, they are suitable for use in residential or urban regions because they are compact and better suited to handle changes in the direction of the wind.

Having major components closer to the ground, they are easier to service. Kragten A. in his report presents the main advantages and disadvantages of a Darrieus wind turbine rotor and concludes that because of many disadvantages and only a few advantages, Darrieus is less efficient than a HAWT (Kragten A., 2004), and because of that, this type of wind turbine is not suitable for use in large-scale power production because they have low efficiency in energy conversion.

The graphic below depicts a categorization of the primary types of wind turbines based on their power coefficient at various tip speeds. Currently, the horizontal-axis wind turbine and vertical-axis wind turbine Darrieus type are more typical and widely employed on a large scale.

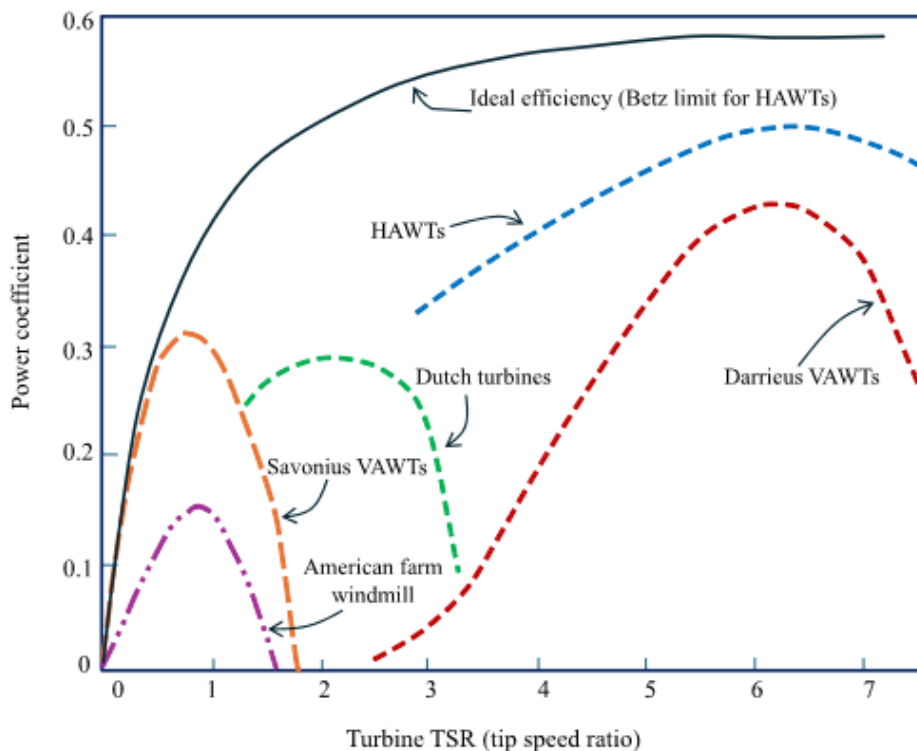


Fig. 4 - Comparison of HAWT and VAWT efficiency
(Abdolahifar et al., 2024)

Wind turbine technology in the last decades has seen tremendous improvement with advances in efficiency, design, and material technology. Wind turbine blades today are longer than 100 meters and much larger in size relative to the last generation (Winters et al., 2018). Low-speed winds are not a problem for such large-scale machines; now even at low wind speeds they produce a great amount of power. Apart from improving the durability of the turbine, advances in material technology in the form of light but strong composite material have reduced production costs. It is well known that the driving force behind the renewable energy revolution is represented by the wind farms. Figure 5 shows a wind farm where the horizontal-axis wind turbines are installed to replace fossil fuels with emissions-free electricity.

Advances in technology in offshore in the form of floating turbines allow it to be installed in the deep seas where the traditional fixed-based ones are no longer installable. Wu et al. present in their paper the state-of-the-art geotechnical and structural issues that affect offshore wind turbine foundations (Wu et al., 2019). The floating turbine expands the ability to produce power in areas previously inaccessible. Further, with the addition of smart grid technology, the wind turbine operates in the larger power network at optimal performance and enhances distribution and overall reliability in the network, aspects seen by Johnson et al. even from 1976 (Johnson et al., 1976). In Figure 6 three type of offshore floating wind turbine foundations are presented.



Fig. 5 - Wind farm (<https://drawdown.org/solutions/onshore-wind-turbines>)

Although they are promising, wind turbines are also detrimental. Possibly one of the greatest detriments is the fact that the wind is not always available. Wind speed is inconsistent, and there could be some locations where there are stretches of little or no wind at all, which generates intermittent energy generation. *Szlivka et al., (2017)*, presents the advantages and disadvantages of different types of wind turbines and their use in urban environments, with an emphasis on small wind energy systems that generate under 100 kW.

Storage facilities for the surplus energy generated during windy days, such as batteries or pumped hydro storage, are on the agenda as solutions. Environmental impact brought about by wind turbines is the other issue. They are thought to be cleaner than fossil fuels but can also impact wildlife in the immediate area, particularly birds and bats that may become entangled in the spinning blades. *Krijgsveld et al.* evaluated the collision rate of birds with contemporary, big 1.65 MW wind turbines for three months in fall and winter. They concluded that the collision rate was 0.08 birds per turbine per day on average (range 0.05-0.19) (*Krijgsveld et al., 2009*). The construction and upkeep of wind farms themselves also impact the immediate environments.

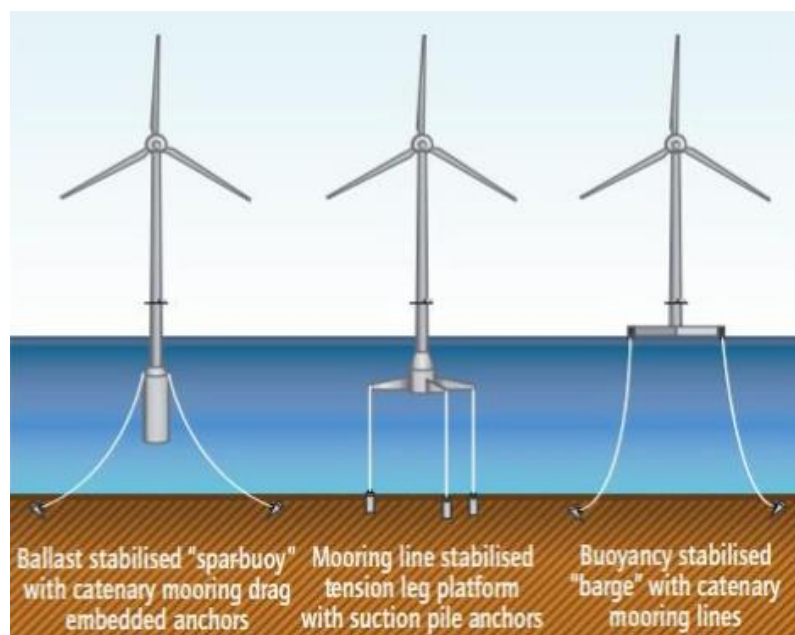


Fig. 6 - Offshore floating wind turbine
(*Wiser et al., 2011*)

The sound generated by the big wind turbines and their aesthetic effect are other issues. In his paper, Liu, (2017), reviews the aerodynamic and mechanical noise mechanisms of wind turbines, as well as de-noising methods used in health condition monitoring. The study concludes that new time-frequency analysis techniques in signal processing are still needed to effectively de-noise signals based on the unique characteristics of wind turbines. There has been opposition to the sight of wind farms in some areas, and the sound generated by the turbine blades can be bothersome to residents in the vicinity. While such concerns are contentious, technological advancements have made the noise levels less.

The installation of wind turbines can also involve high upfront costs, especially for large commercial farms. Wind turbines generally have low maintenance and operational costs; however, high initial costs in certain locations may pose a barrier to deployment. Sieros et al. investigated the cost-effectiveness of wind turbines with rotor diameters up to 250 m and hub heights over 150 m. Their conclusion was that the total optimization issue, including all additional expenses, had optimal solutions on a bigger scale (Sieros et al., 2012). Figure 7 depicts the cost history over 12 years and clearly shows a decline in cost per kW.

However, the future of wind turbines is promising. As research and development continue, wind turbines are increasingly economical, efficient, and environmental. Wind energy, along with other renewable sources such as solar energy, is expected to be a core component in global efforts to reduce dependence on fossil fuels and mitigate the effects of global warming. Badwawi et al., (2015), published a comprehensive review paper that summarizes major research on optimal sizing design, power electronics topologies, and control strategies. The paper also presents the state of the art for both grid-connected and stand-alone hybrid solar and wind energy systems.

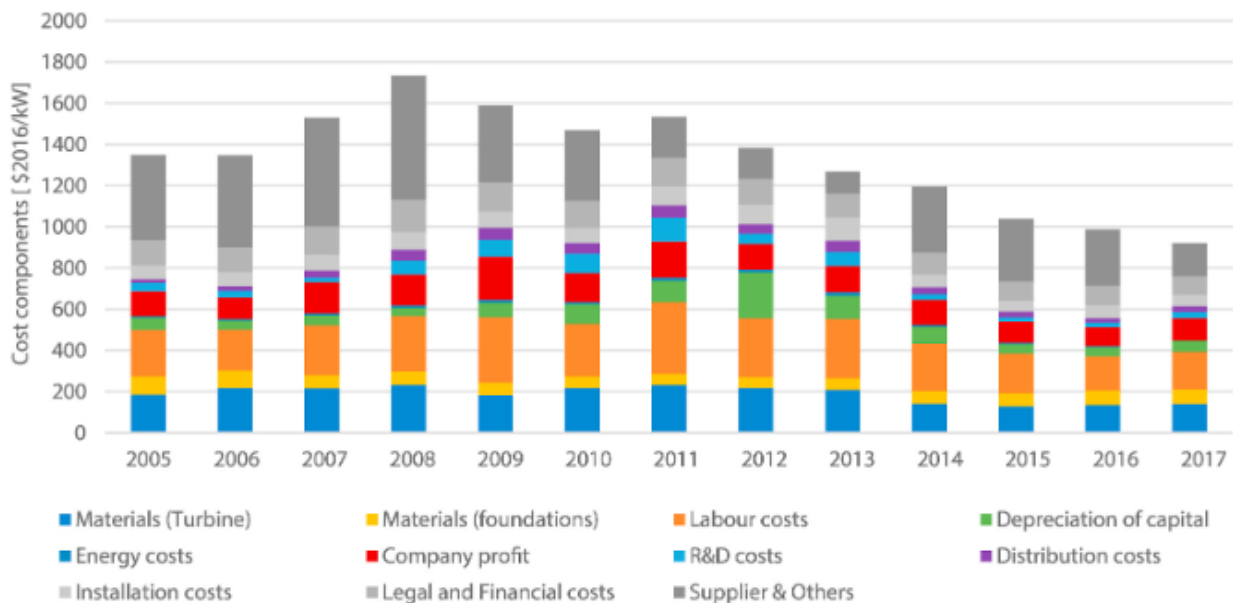


Fig. 7 - Cost comparison (initial investment vs. operating cost) (Elia et al., 2020)

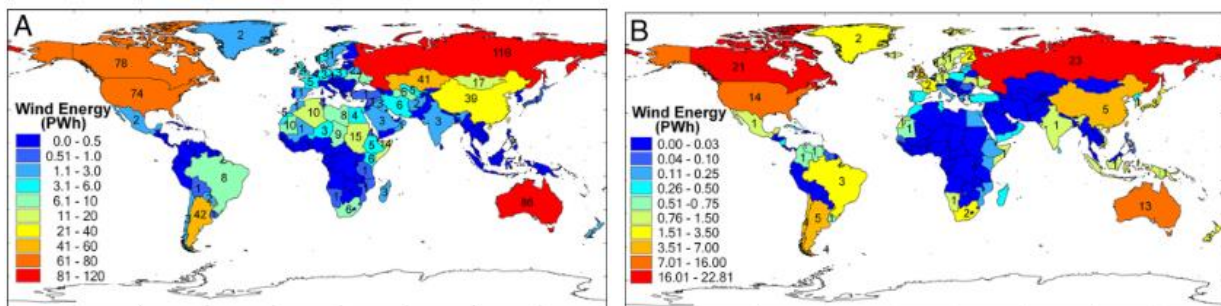


Fig. 8 - Global wind energy potential (A - Onshore. B - Offshore.) (Lu et al., 2023)

Wind turbines are among the most significant technologies supporting the transition from non-renewable to sustainable energy. As the ability to harness wind energy is a cornerstone of the renewable energy portfolio, both horizontal-axis and vertical-axis wind turbines are utilized, each offering distinct advantages. With ongoing technological advancements, wind turbines are expected to become more efficient and serve as a critical foundation in global efforts to mitigate climate change. Despite persistent challenges, such as the intermittency of wind power and its environmental impacts, the continued development of wind energy technology is projected to secure wind turbines a dominant role in clean energy production for the foreseeable future. However, location remains a crucial factor for the effective operation of wind energy systems. Figure 8 illustrates the global zones suitable for wind energy development, including both onshore and offshore applications.

Small wind turbines are increasingly being installed on farms as an inexpensive, clean source of energy. Farmers can reduce their consumption of grid electricity and decrease their energy bill by powering homes with electricity produced from a clean source. Small wind turbines have the capability of offering a stand-alone power source to drive farm lighting, irrigation (Figure 9), and machinery in rural or off-grid settings.

By harnessing wind power, an environmentally friendly and zero-hazardous pollutant-emitting source of power, small wind turbines conserve running expenses while promoting environmental efficiency. This serves to reduce the carbon footprint of farming activities. Small wind turbines can also be coupled with other renewable power systems, such as solar power, to make hybrid systems that can offer a round-the-clock power supply.

Small wind turbines are inexpensive since farmers themselves also get subsidized or encouraged by the government for using renewable technology. Apart from fulfilling the sector's energy requirement, farm wind power is helping to promote larger efforts to green the agricultural sector and mitigate the effects of climate change.



Fig. 9 - Small wind turbine in a farm

(<https://midwestwindmillcompany.com/product/small-farm-windmill>)

INTRODUCTION ON THE SPECIFICITY OF SMALL WIND TURBINES

Medium and small wind generators have attracted much excitement for application as an alternative energy source for small-scale off-grid scenarios. Small wind turbines convert wind into electricity as one step in achieving a more sustainable way of living: providing cleaner alternatives for traditional energy. An overview of challenges, solutions, and future needs in the wind energy domain is presented by Wallenius et al. in their paper (*Wallenius et al., 2016*). Small wind energy generation also offers numerous pros and few cons, in spite of becoming even more useful as concerns about climate change and energy security grow.

They all have that common principle: converting wind energy into mechanical energy, even at very small sizes. According to Bashir, the wind turbine is a promising technology because of its enormous energy potential, environmental friendliness, and minimal maintenance operation when compared to traditional energy generation, and future study on wind turbines should focus on the wind turbines' recycling capacity (Bashir, 2022).

As it is shown in figure 10, the wind turbines consist of three main parts: generator, rotor blades, and supporting structure (tower). The speed of the rotation of the blades is caught by the generator shaft. Then, through electromagnetic induction, it gets transformed into usable energy for homes or companies.

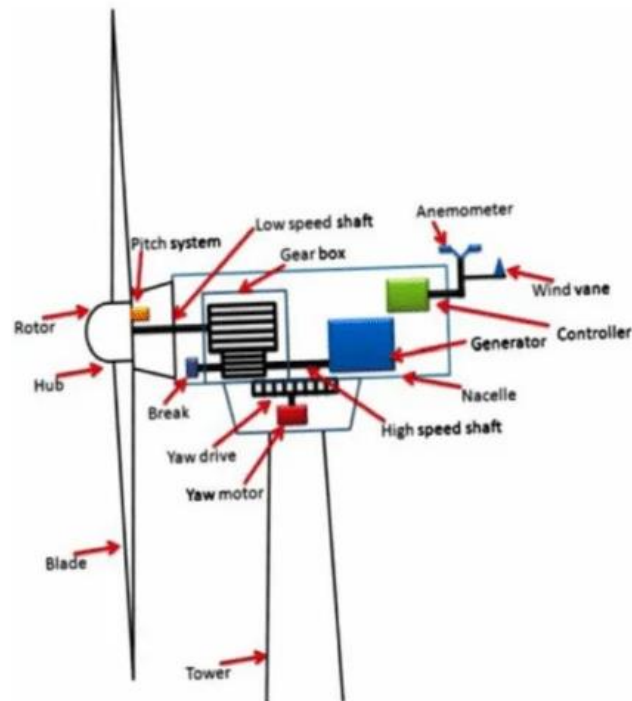


Fig. 10 - Basic components of a wind turbine

(<https://electricalsphere.com/wind-energy-basic-component-and-site-selection>)

Small-scale wind turbines are primarily classified, like all types of wind turbines, according to their axis of rotation, i.e., vertical-axis wind turbines (VAWTs) or horizontal-axis wind turbines (HAWTs). Typically, large installations as well as small ones most often go in for horizontal-axis wind turbines (HAWTs). Rotor blades of these wind turbines rotate in the horizontal plane, much like a normal aircraft propeller. The horizontal-axis wind turbines are specifically more effective in areas where the direction of the wind is relatively constant and predictable, such as open rural areas with ample space and high-speed wind, largely from farmland or coastal locations, as Kabak et al. specified in their paper, where an algorithm in order to determine the suitable regions where the wind turbines would be located was used (Kabak et al., 2022).

Vertical-axis wind turbines (VAWTs) can be more effective at collecting wind because they rotate their blades around a vertical axis and can thus take winds from any direction. Due to buildings and obstacles on the ground level, wind directions can be random at times in an urban setting, which is why such applications are suitable for VAWTs. Alqahtani, (2024), published an intriguing article in which the primary goal was to close the gap in process parameter optimization required to transform wind energy wake from highway traffic into electrical energy using vertical-axis wind turbines. VAWTs are not known to be as popular as HAWTs. However, they tend to be a lot more silent, smaller, and thus preferred for residential endeavors.

Both types of turbines have varied benefits based on the region and application, although they function on the same principle. Small wind turbines have a wide availability of application areas due to their adaptation and can be used to offer renewable energy in remote rural areas where small businesses and private homes can depend on it as a reliable alternative to normal energy sources. To back up this claim, Battisti et al. produced research in which they evaluated the effectiveness of small wind turbines in urban settings (Battisti et al., 2018). As a consequence, a new constraint for estimating the quantity of energy that a wind turbine will create in a certain location was proposed.

In a good wind resource area, a small wind turbine can provide a sufficient amount of electricity for the energy needs of a typical home. Normally, these systems are combined with solar panels to create a hybrid energy solution that optimizes energy production during both day and night. Hence, even if the sun or the wind doesn't provide the required power, homes can still be powered because of high power output resulting from both sources being harnessed. Small wind turbines will support the sustainable energy supply for remote or rural sites where grid connection is impossible or very expensive. The results of using a small wind turbine system to build environment lamps to comply with the green building approach can be found in Ozgener, (2006).

Besides, it can be proved beneficial for small businesses, particularly when they are stably and remotely located. For example, wind turbines can be installed at farms and small manufacturing sites to share the burden of energy expenses. It will help them reduce their dependency upon fossil fuels, which is particularly central since energy is costly and unreliable in certain areas. A review paper summarizing the different studies that have been carried out on the application of SWT technology in the built environment to study the inflowing wind characteristics, their performance, and to detect the knowledge gap, and also exploring the degree to which the international design standard of SWTs, IEC 41400-2, was written by Anup et al. (Anup et al., 2019).

Small wind turbines are the perfect choice for remote places where it is extremely expensive to have electricity lines installed. In places that are not part of the national power grid, a small wind turbine can be a power lifeline (Singh et al., 2013). Consider isolated villages, research facilities, homes, and even rescue missions after natural disasters—these all can use wind power to create electricity. For example, wind power can provide the energy required for daily living in coastal towns or mountain resorts or even remote research stations in distant corners of the Globe. By integrating energy storage devices with wind energy, isolated systems can be developed to ensure energy security in areas that would otherwise rely on costly and unreliable fuel supplies (Simic et al., 2013). A few examples of small wind turbines that are easily incorporated into urban settings because of their distinctive shapes and low noise pollution are shown in Figure 11.



Fig. 11 - Example of a residential small wind turbine installation

(<https://www.linkedin.com/pulse/does-small-wind-turbine-your-home-increase-thomas-vogel>)

A small vertical-axis wind turbine captures the wind energy naturally and can hence decrease reliance on fossil fuels. These types are essential for the reduction in carbon footprint and stopping climate change. The production of wind turbines as well as their installation is very low in carbon when compared to those emissions that have been produced in the very long term in coal, oil, or gas power plants. However, as Lenzen et al. stated in their paper, despite the fact that the construction and technology of most current wind turbines are rather consistent throughout a wide range of power ratings, existing life-cycle assessments of their energy and CO₂ intensity indicate significant variances (Lenzen et al., 2002).

Ultimately, reducing energy costs is one of the most attractive benefits of small wind turbines, although these wind turbine types, after being installed, require less maintenance and operation. The construction of residential systems can be quite costly; however, in the long run, the costs will be offset with savings on energy bills. For example, initial investment can be supported by subsidies, tax credits, and government incentives, thus making wind energy more affordable for consumers. The Global Framework for Climate Services (GFCS) is leading global initiatives to enhance the quality, availability, and application of climate data and forecasts to support renewable energy producers in decision-making processes (Terrado et al., 2017). Many households and companies will hence generate more of their own power, thereby decreasing their dependence on the utility system, and therefore saving up a considerable amount of money. Small wind turbines are expected to last for decades with very little maintenance, usually sporadic maintenance required by most systems, and an expected operating time of 20 to 30 years. Based on the power loss criterion of wind turbines, Hu et al., (2025), proposed a yaw system control strategy aimed at improving power output and extending turbine lifespan. When calculating the wind power loss threshold and delay time threshold, the proposed control strategy in their research uses historical data from the wind turbine. From this, they can directly control wind power loss and enhance wind turbine output.

Unlike solar panels, which might need some component repairs or routine cleaning, wind turbines rarely require frequent maintenance. Basic maintenance includes ensuring that the turbine remains aligned with the wind, noting the inspection of the electrical part of the system, as well as ensuring that the blades are clear of defects. Many small turbines tend to be built to withstand tormenting weather conditions, e.g., high winds, rain, and snow; hence, such turbines are strong and very suitable for many settings (Gonçalves et al., 2021). As Gonçalves et al. reported in their study, the highest values of wind energy output occurred on stormy days, implying that these high-impact storms had a favorable influence on wind energy production.

Small wind turbines indeed have their share of challenges, but they also come with their benefits. While they can prove to be cost-effective over time, a small wind turbine can be costly to construct at present, such as in the case of using a wind turbine system that also includes all mounting poles and electrical connections. Such systems are often financially out of reach for most businesses and homes. The most significant challenges are believed to be linked with social acceptance, transportation and installation logistics, and medium-term sustainability of the economic and political backing of wind energy as per McKenna et al. study (McKenna et al., 2016). In certain locations, however, these costs can be reduced through various incentives, tax credits, and rebates that make wind energy much more cost-effective.

The power output of small wind turbines has further dependence on wind speed at the site. Wind speed and direction are also the most important and of prime importance in determining the productivity of a turbine. In locations where there are very limited wind resources, the turbine will not generate enough power to make the project worthwhile. For this reason, the local wind conditions must be assessed prior to making a decision to install a turbine, as Mangos specifies in his doctoral dissertation (Mangos, 2024).

Despite all the advantages, the noise pollution is still created when it operates, especially in larger systems, though new wind turbines are typically quieter than their predecessors. People or businesses within residential areas may be disturbed by this. There are also visual issues, as some people may not prefer a wind turbine on their property because they do not want the appearance of it. Extensive research on the issues of noise pollution linked to the use of wind turbines was undertaken by Ruggiero et al. The paper concerns a predictive software program and experimental frequency spectrum and time history acoustic noise generated by wind turbines (Ruggiero et al., 2015).

A promising alternative for renewable energy production, small wind turbines are energy independent, cost-effective, and eco-friendly. With the improving technology, these systems are quieter, more efficient, and faster to install. The ability of small wind turbines to provide renewable power over a wide range of uses, from household use at home to rural regions, cannot be overstressed, even in the presence of issues such as installation costs and site location, aspects that are presented in Fingersh et al.'s report (Fingersh et al., 2006). Small wind turbines play a significant role in the global energy transformation as the world seeks cleaner alternatives to fossil fuels in creating a more sustainable and robust energy future.

SYNTHESIS OF EXPERIMENTAL RESEARCH ON SMALL WIND TURBINES

Small wind turbines (SWT) are very important units for producing decentralized renewable energy sources and are sustainable opportunities for rural and away-from-the-grid communities. Unlike the large turbine designs, these small wind turbines are designed to service small businesses and applications that are domestic and agricultural in nature, where the critical factors are reliability and efficiency (Glasberg et al.,

2024). Experimental testing is crucial to render these machines safe, long-lasting, and operationally efficient so as to fill the gap between theoretical designs and real-world performance. A typical example of the corresponding wind turbine class for each application can be seen in Figure 12. As Bianchini et al. suggested in the paper, a house requires a small wind turbine of around 1.5 kW, and one up to 15 kW can be used in a farm.

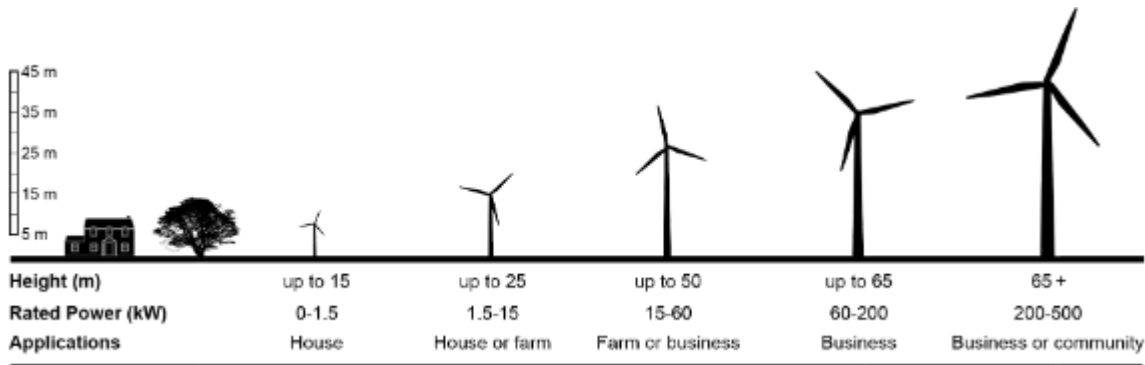


Fig. 12 - Small wind turbines vs large wind turbines (Bianchini et al., 2022)

In addition to maximizing turbine performance and compliance with regulation, experimental testing also ensures the validation of computer models. Environmental conditions commonly simplify computational fluid dynamics (CFD) and other theoretical models, and thus, a difference between predicted and actual performance exists (Dumitrescu et al., 2015). Experimental testing rectifies the gaps by providing empirical data in simulated and actual environments. In addition, such tests ensure turbines withstand turbulence, dynamic wind loads, and weather conditions for more extended periods, making them safer and more reliable. Representative research in the field belongs to Syawitri et al., who have conducted a flow field analysis to gain insight into the inherent flow physics, such as dynamic stall behavior, using hybrid RANS-LES turbulence models (Syawitri et al., 2021).

Field testing, hybrid approaches, and wind tunnel testing are the three broad categories into which small wind turbine test procedures are grouped. Torque, tip speed ratio (TSR), power coefficient (C_p), etc., are tested methodically. The models tend to be on a small scale, and sophisticated measuring devices such as particle image velocimetry (PIV) provide information about the air patterns surrounding the blades of the turbine. In their scientific paper, Edwards et al. used experimental PIV visualization in a wind tunnel on a three-bladed small vertical axis wind turbine experimental model to experimentally validate the CFD numerical simulation results (Edwards et al., 2015). An interesting experimental test was conducted by Nietiedt et al., which consists of using two optical measurement systems to simultaneously record fluid (PIV system) and deformation (photogrammetry system) information in one global coordinate system. Their setup can be seen in Figure 13.

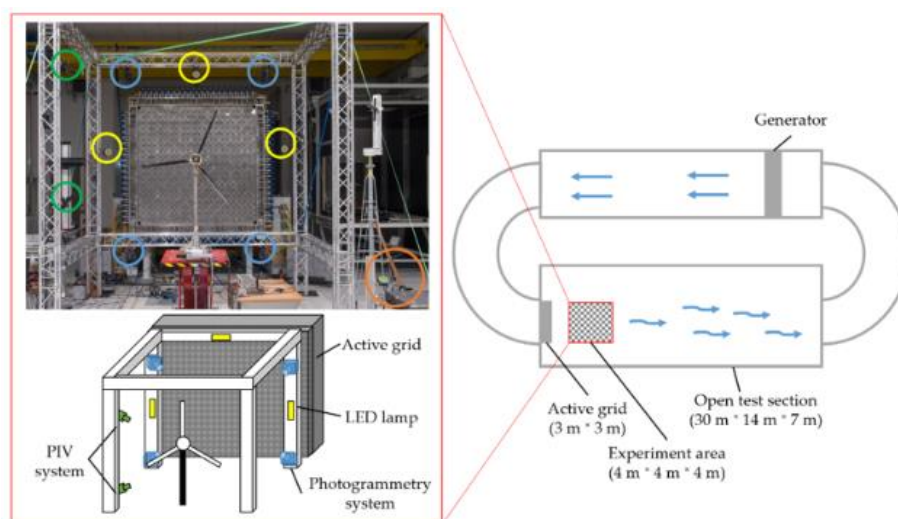


Fig. 13 - Wind tunnel with scale turbine models, airflow visualization (Nietiedt et al., 2022)

By placing turbines in their proper operating environments, field testing enhances wind tunnel research. This method takes into account variables such as wind direction, temperature changes, and environmental barriers such as trees or buildings. To evaluate material fatigue, erosion, and noise production under real-world operating conditions, long-term field experiments are crucial. The figure below depicts a stand-alone solution for this sort of study, which may be used practically anywhere on the globe. These solutions include a small wind turbine and a compact housing unit that contains all electronics, energy storage, data collection, and remote-control systems.



Fig.14 - Field test site with small wind turbines installed

(<https://nachhaltigwirtschaften.at/en/iea/technologyprogrammes/wind/iea-wind-task-27-workingperiod-2018-2019.php>.)

To offset individual limitations, hybrid test procedures—blending field testing with wind tunnel testing—are increasingly employed. Such procedures, economical and time-efficient, are accurate by utilizing wind tunnels for first-order parameter optimization and field testing for field validation without compromising on precision. In their paper, LeBlanc et al. report the procedures utilized in the development of a model of an H-type vertical axis wind turbine, which include physical measurement of the as-built form, experimental test updates to the models, and lastly, tests to model correlation on a component-by-component basis, as well as a completely assembled system, bringing in the ideas of "machine learning" and "digital twins" (LeBlanc et al., 2020). Emerging technologies, such as machine learning-based data analysis and digital twins, have further increased the strength of hybrid testing systems.

Yilmaz's work compares CFD simulation and experimental data to gain better knowledge of basic rotor aerodynamics principles for designing an aerodynamically efficient small wind turbine rotor by establishing the optimum design tip speed ratio (TSR) and number of blades. Figure 15 depicts part of his results.

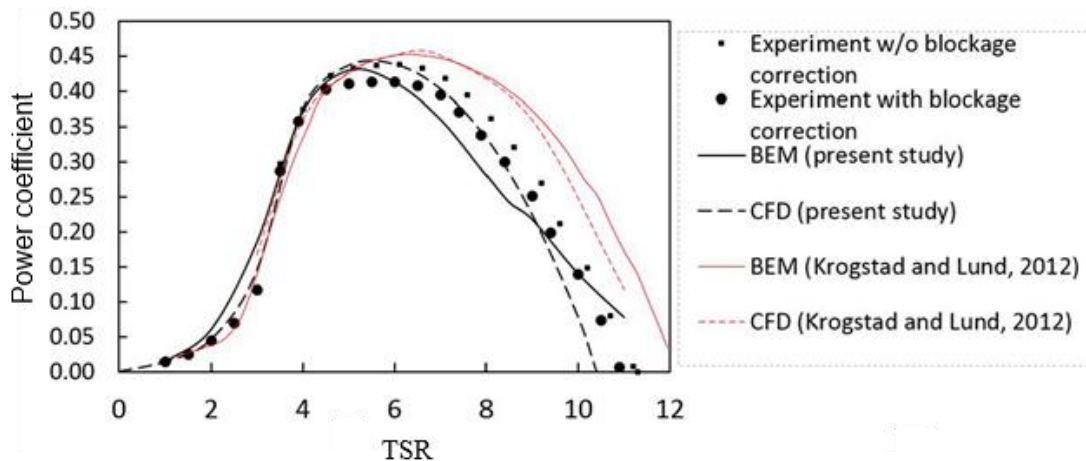


Fig. 15 - Power coefficient as a function of TSR (Yilmaz., 2022)

While it has its benefits, experimental testing has its disadvantages, such as very high costs, uncertain climatic conditions, and scaling issues. It requires a high cost to set up wind tunnels or test facilities in the field, and the cost is further increased through the use of high-accuracy sensors and data acquisition systems. The inhomogeneity in the field test condition makes it difficult to process data, and scaling issues in wind tunnel tests could lead to incorrect conclusions when applying the results to full-scale turbines.

High-definition sensors augment precise data, allowing real-time monitoring of important factors while the machine learning software detects patterns and anomalies from complex data sets, improving predictive modelling. Hybrid platforms, which combine virtual simulation and actual-world testing, such as digital twins, offer a cost-effective, scalable substitute for conventional practices (Pimenta et al., 2020).

A paper that examines the state-of-the-art of predictive digital twin platforms for wind energy systems based on a five-year review of literature, challenges, and limitations, and debates future research directions belongs to the Kandemir et al. They organize their review based on popular approaches like physics-based modeling, data-driven approaches, and hybrid modeling. Figure 16 is their depiction of a wind turbine development process that entails the digital twin technology.

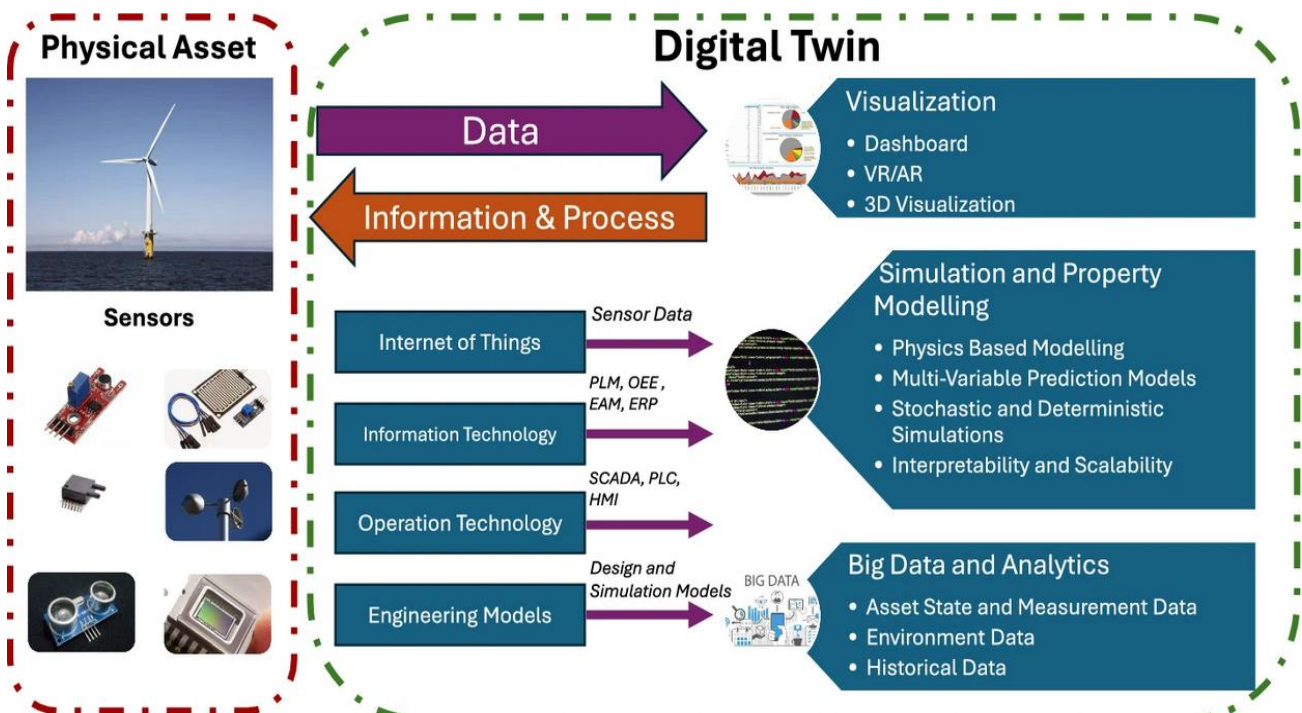


Fig. 16 - Wind turbine testing with digital twin technology (Kandemir et al., 2024)

The experimental testing of efficient and effective SWTs and their interaction with theory provides useful verification of theoretical expectations, guiding design improvements and performance limits consistent with safety and efficiency requirements across development stages. New technologies such as sensors, data analytics, and hybrid tests are changing the domain. These technologies could potentially be turning points for the sustainable future of human beings as they considerably increase the affordability and scalability of small wind turbines.

RESEARCH SYNTHESIS ON THE STRUCTURE OF SMALL VERTICAL AXIS WIND TURBINES

A couple of decades ago, wind power increased its popularity as an alternative and renewable energy compared to other energy resources. One of the most promising types of wind turbines is the vertical axis wind turbines (VAWTs), which are recommended for small-scale applications (Mălăeș et al., 2015). These turbines are the simplest to operate, require lower maintenance, and are the most environmentally friendly. Vertical-axis wind turbines can be located in residential and urban settings where wind and space conditions are less uniform due to their vertical axis.

The basic working principle of vertical-axis wind turbines is the same as that of horizontal-axis wind turbines, which is transforming wind energy into mechanical energy, which will then be used to generate electricity.

The major difference is noticed in the rotor direction. The VAWT turbine blades rotate around a vertical axis of rotation. There exist different VAWT designs, such as the Savonius and Darrieus (*Garmana et al., 2021*). For efficiency, the curved blades of the Darrieus turbine are comparable to the aerodynamic surfaces of an airplane wing. However, due to its simplicity and strength, the Savonius turbine—a semicircular blade with a simpler thrust design—is frequently used in low-wind conditions where other wind turbines struggle even to start. Figure 17 illustrates the principal types of vertical-axis wind turbines. They can gather wind from any direction and thus operate very efficiently with changing winds. Each type has its own advantages and applications, depending on the siting and intended energy output.

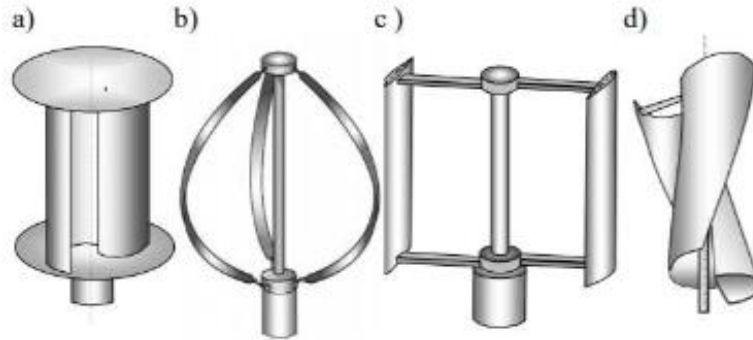


Fig. 17 - VAWT models: a) Savonius type, b) Darrieus type, c) H type, d) spiral type
(*Polak et al., 2006*)

Power rating, typically a few watts to a few kilowatts, defines small VAWTs. The turbines are utilized in domestic, rural, or off-grid applications. Small VAWTs can be inefficient, unreliable, and prone to structural issues - challenges highlighted in several recent studies (*Wood et al., 2011*) - particularly when their design does not align with the characteristics of the installation site. The efficiency and longevity of small VAWTs depend largely on their structural design. These turbines involve close attention to numerous parameters, ranging from material and blade shapes to aerodynamics. Of the most needed is the ability of the turbine to harness energy in low-speed wind, a condition that also comes in abundance for wind systems of small scales (*Clausen et al., 2023*).

The material and form of the blade on the turbine will have a direct impact on the mode of operation of the turbine. Darrieus turbine blades (Figure 18), for example, possess an airfoil cross-section and thus are more aerodynamically efficient and can provide more energy. Manufacturing such blades can be more expensive and complicated, though.

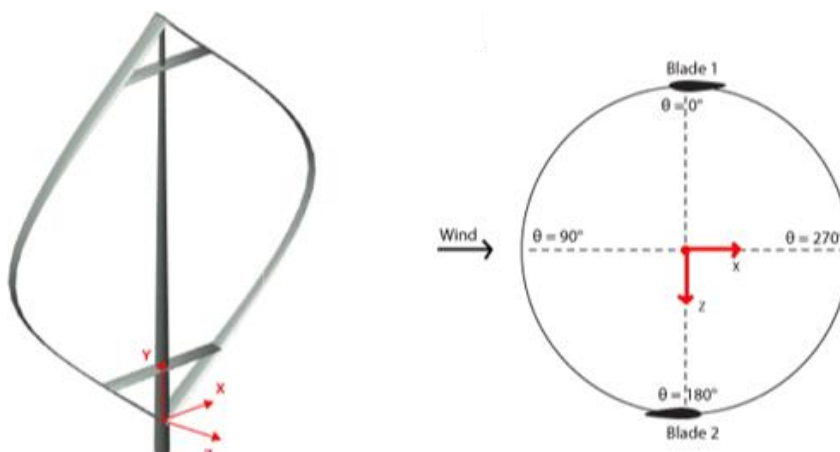


Fig. 18 - Cross-section of the aerodynamic profile of a Darrieus turbine blade
(*Sakib et al., 2021*)

The blade shape, rotor size, and blade number can affect the aerodynamics in small VAWTs. Three-bladed Darrieus turbines have been found to be a good balance between stability and efficiency. Due to its simplicity and ability to start rotating from low wind speeds, the Savonius type, despite its lower efficiency, is still predominantly used for small applications. The choice of material for the support frame of the turbine is also an important aspect in small VAWT design.

In addition to providing strength to withstand wind forces as well as other weather conditions, the blades, rotor, and support frame must also be light enough to allow for easy start-up and smooth running of the system. Fiberglass, composite, steel, and aluminum are the popular materials for manufacturing small VAWTs. Material science and aerodynamics research, as *Condruz et al. (2019)* have shown, and aerodynamics development have improved the vertical axis wind turbine efficiency. A comparison of materials for turbine blades is presented in Figure 19. Though the materials that can be used in the wind turbine blade manufacturing are composites, metals, wood, foams, and even polymers.

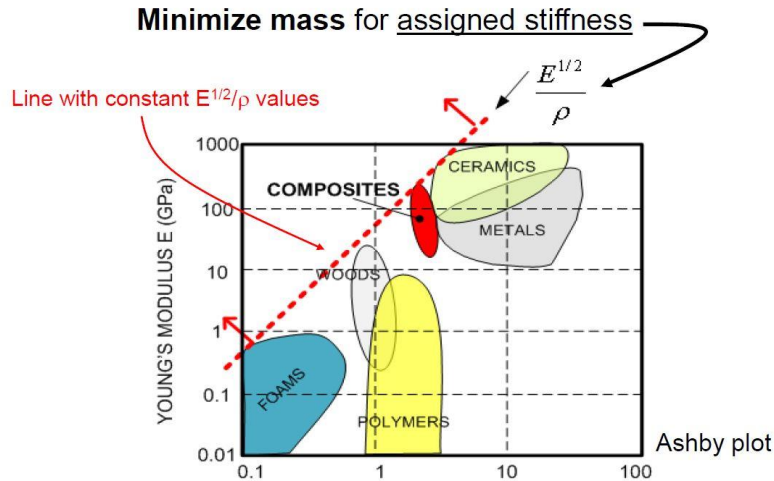


Fig. 19 - Comparison of materials for turbine blades: metal and composite materials
(<https://www.windfarmbop.com/why-wind-turbine-blades-are-made-of-composite-materials/>)

With its lightweight and corrosion-resistant properties, aluminum is very applicable for use on an urban scale on a small scale. On the other hand, steel is primarily used in large-scale developments due to its high strength, but it can also be employed in small VAWTs to meet stability requirements, provided that weight distribution is carefully managed. Their strength-to-weight ratios and resistance to environmental degradation also make fiberglass and composites increasingly sought after. Stability of turbine construction is vital, particularly as wind force changes fairly regularly in VAWTs. Computer-aided and advanced structural analysis techniques like finite element modelling (FEM) have been researched for their ability to optimize structural design. Such simulation makes it possible to accurately predict stress levels, vibration, and likely points of failure within the turbine structure. *Marzec et al., (2023)*, wrote a paper on structural topology optimization of the H-Rotor wind turbine coupled with the one-way Fluid Structure Interaction (FSI) approach. They aim to minimize the volume of the maximum stressed and deformed blades. The results consist of comprehensive information about unstable flow fields around the operating wind turbine coupled with the optimized topology of the interior of the blade without changing the external aerodynamic profile. Part of their results, blade deformations, are presented in Figure 20.

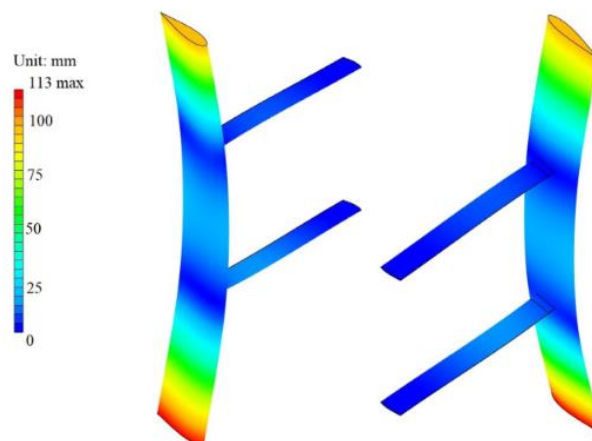


Fig. 20 - Finite element analysis of the VAWT rotor
(*Marzec et al., 2023*)

Small VAWTs' capacity to withstand the stresses of bending and torsion without malfunction is a major worry for engineers. One way to address that is by looking at hybrid turbine designs and multiple blades. The performance of a small vertical axis wind turbine depends on a few key factors: the wind conditions, the design of the turbine itself, and the control systems. To get the most out of small VAWTs, researchers have concentrated on boosting that power coefficient—the measure of how efficiently a turbine can turn wind energy into mechanical power. And that's because wind speeds in domestic and urban areas are notoriously unpredictable; there is a lot of turbulence and wind change in direction. That's why small VAWTs are designed to respond quickly. Savonius turbines, for example, may not produce as much power as Darrieus turbines, but they do operate efficiently at lower wind speeds—and that's a real advantage (Figure 21). A research study that aims to reveal the effect of the rotor radius ratio on the performance of the hybrid vertical axis wind turbine Savonius-Darrieus, using the Computational Fluid Dynamics methods, belongs to Irawan et al. Their results consist of the increase in the rotor radius ratio value causing an increase in the initial torque coefficient but a decrease in the maximum power coefficient value.

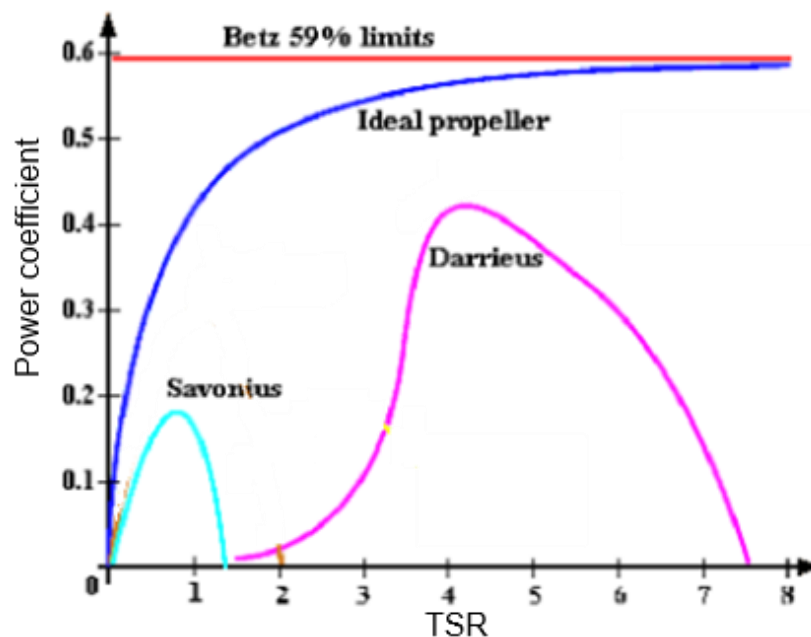


Fig. 21 - Darrieus vs Savonius efficiency

(Irawan et al., 2023)

Major design specifications of small vertical-axis wind turbines (VAWTs) include wind speed cut — the lowest speed at which the turbine starts to produce electricity. At this point, technologies like variable speed systems and pitch control come into play because these control systems maximize small VAWTs for a broader range of wind conditions. Small VAWTs generally aren't as efficient as large horizontal-axis wind turbines (HAWTs) because of the inherent aerodynamic losses of the vertical axis. Drag forces that build up as the blades rotate in the wind — especially when the wind speed isn't ideal — can reduce efficiency even further.

Researchers have been trying to drive efficiency up by pitching the blades, using hybrid designs (Malael et al., 2018), and implementing control strategies to cut down on drag resistance. Smart grid tech can be used to optimize turbine performance in real-time, based on the latest wind data. But one of the biggest challenges in designing a small VAWT is making sure the structure lasts a long time. That's because small turbines are most susceptible to the kind of mechanical fatigue that comes from variable loads and stresses—turbulence, wind gusts, and other environmental conditions. Blades, bearings, and other mechanical parts can break down and degrade over time. That's why ensuring durability is one of the biggest challenges in the development of small VAWTs. Ali et al. investigated structural optimization of sea-capable VAWTs designed for long-term reliable operation. Based on their analysis, the maintenance cost would be minimized with considerable savings without compromising structural integrity in the marine environment if their optimized combination is utilized. The outcomes of their structural fatigue analysis are demonstrated in the figure below.

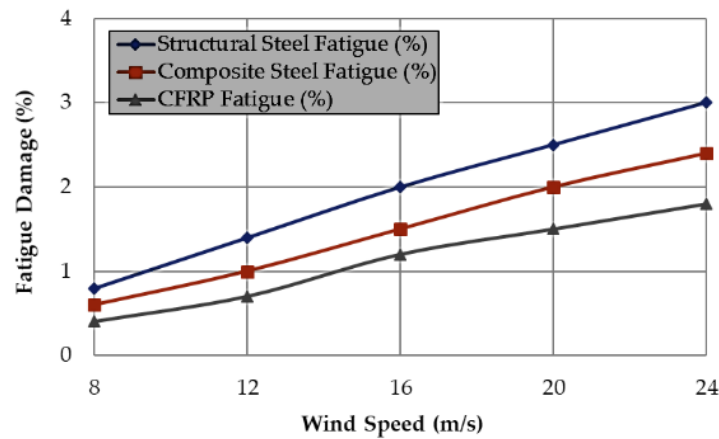


Fig. 22 - Structural fatigue analysis
(Ali et al., 2024)

Compact VAWTs depend on some pretty sophisticated bearing systems, vibration-damping technologies, and materials that can withstand fatigue much better. That's not the only thing driving adoption of these turbines in urban areas, though; aesthetics and noise pollution are just as much a factor. A major design challenge for urban wind turbines is the noise generated during operation. A study examining the power produced and noise generated by two small wind turbines that were tested inside a wind tunnel is one of Hays et al. Their suggested configuration showed a 9% increase in power generation and noise reduction of up to 7 dB(A) (Hays et al., 2019). Another paper that deals with the vertical axis wind turbine noise generation is Yue, (2023), in which URANS equations were used to numerically investigate the noise level for VAWT at three different wind speeds (Figure 23).

In residential areas, some of those compact designs — especially the ones with fewer blades — can be pretty loud. Engineers are refining those designs to reduce noise generation and adding features that do just that. And because in many places, people care deeply about how wind turbines look, aesthetics often ends up being a major factor in adopting small-scale wind turbines—especially in residential situations. Researchers are developing turbine designs that integrate seamlessly with their surroundings while maintaining high efficiency.

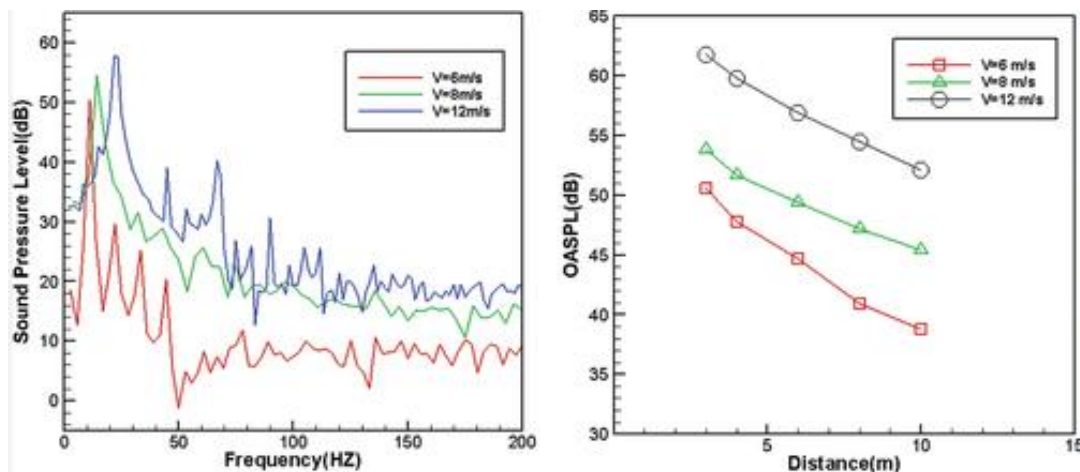


Fig. 23 - Noise levels for VAWT
(Yue., 2023)

Solving the problem of an increasing need for residential and off-grid energy, which can be renewable, is possible with the help of a small vertical-axis wind turbine. These turbines are still not the ultimate solution to generation without sporadic interference from the weather but are a step in the right direction that is reliable and can be efficient as well. Nevertheless, a whole lot of questions remain not only about the feasibility of their long-term use but also about whether they are a danger to the environment or not.

Currently, the possibilities of materials, aerodynamics, and control systems are being investigated as a means of overcoming these limitations and ensuring that the overall performance of small VAWTs gets better. The potential of small VAWTs in the renewable energy era, alongside innovation and consequent efficiency, especially in urban environments, which are normally characterized by inadequate wind speeds and little space, helps the situation to bounce back and take advantage of these possibilities. An interesting solution that can be integrated into the urban environment is presented in Figure 24. Three small wind turbine configurations can be easily mounted on a roof building.



Fig. 24 - Small vertical axis wind turbines installed in an urban area
(<https://www.cbc.ca/news/science/what-on-earth-wind-turbines-cities-1.6710512>)

SYNTHESIS OF EXPERIMENTAL RESEARCH ON THE WORKING PROCESS OF SMALL VERTICAL WIND TURBINES

The exponential growth of clean power generation has led to the widespread use of small wind turbines. These systems are present especially in places where the energy and space are limited, such as rural and urban areas. The vertical-axis wind turbine is among the most common wind turbine designs due to its straightforward construction, safety, low maintenance requirements, and ability to capture wind from all directions. The configuration also has several other advantages, particularly in urban areas where the wind can change its direction very often. In order to draw wind energy from any direction without a yaw system, VAWTs (*Mirecki et al., 2007*) represent a simplified solution due to their structural and mechanical structure. Energy conversion in VAWT is realized by using both drag and lift aerodynamic forces. The wind blows directly on the turbine blade's surface and causes the pressure reaction. The motion of the blades is resisted by drag, while lift is the force generated perpendicular to the wind direction, producing torque. An optimal turbine minimizes drag and maximizes lift, thereby achieving high efficiency. The balance between these two forces significantly impacts the energy capture efficiency of the turbine.

A famous example of most elementary turbines is the design of Savonius (Figure 25) turbines, which have the shape of cups, and the number of blades can be two or more (*Zemamou et al., 2017*). The most fitting use of these designs is the collection of energy from low wind rates. However, with the increase of wind velocities, its efficiency goes down as it highly depends on drag only.



Fig. 25 - A basic Savonius design (*Aboufares et al., 2015*)



Fig. 26 - Darrieus WT
(<https://en.wind-turbine-models.com>)



Fig. 27 - Helical wind turbine design (*Kumar et al., 2019*)

Similar to an airplane wing, the Darrieus turbine uses curved blades in a form like "egg beater" to create power. The more efficient this type of design is when there are stronger winds, the more advanced mechanical parts it requires to work effectively. The conventional structure of this type of turbine is seen in Figure 26. The benefits of Darrieus and Savonius forms are combined into a helical turbine (Figure 27) to demonstrate a balanced performance. Its helix-shaped blade structure makes the system go through minimal mechanical stress while maximizing efficiency over a wide range of wind speeds.

Because there is no need for complex components to direct the turbine towards the wind, VAWTs can collect wind energy from any direction. When the wind is irregular and turbulent, this is beneficial for the power production of these devices. The gearbox and generator, and other components, tend to be placed at the base of the turbine, so it is easier to perform maintenance and reduce downtime. For urban applications where space is limited, VAWTs are preferable since they are generally smaller and can be accommodated in small areas. Anup et al. in their paper elaborate on the diversified studies that have been conducted on the application of SWT technology in the built environment for the purposes of finding out about the inflowing wind characteristics, their performance, and establishing the knowledge gaps (Anup et al., 2019). Their paper also delves into the validity of the international design standard for SWTs, IEC 41400-2, for urban installations.

A test rig must mimic different wind conditions to be able to test the performance of a small vertical axis wind turbine. Tests may be done outdoors or in a controlled condition wind tunnel based on the resources available and the level of precision required. Both the direction and speed of the wind can be kept under controlled laboratory conditions at the wind tunnel. Even if a controlled environment like this would be expensive, it is very convenient for reproducible research. When the turbine is outside, natural wind is applied to the turbine. Performance is less predictable and less controllable even if results are more realistic. The detailed outdoor small wind turbine configuration test facility is illustrated by Figure 28. Such a facility has been used in the research work conducted by Mostafavi et al. Outdoor experimental testing under real conditions and without the use of a control environment presented difficult effects such as variability of rotor speed, generation of noise, overloads, and any external environmental influence.

An interesting research work paper that documents comprehensive wind tunnel test results data collected on six airfoils of applicability to small wind turbines is Selig et al., (2004). The authors used airfoils like E387, FX 63-137, S822, S834, SD2030, and SH3055. They used the NASA Langley Low Turbulence Pressure Tunnel as their experimental facility.

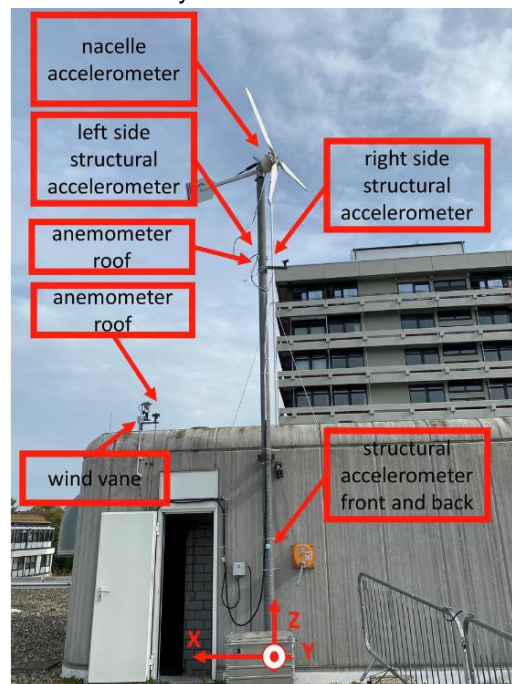


Fig. 28 - Small wind turbine - experimental setup (Mostafavi et al., 2024)

An anemometer is a very important measuring instrument used for assessing the turbine's efficiency under various conditions since it estimates the wind speed. Whereas an electrical output produced by the turbine is measured by a power meter, rotational torque transferred on the turbine shaft is measured by a

torque meter. Experiments are conducted in the laboratory with the help of a data acquisition system that stores and records data from an anemometer, a torque meter, and a power meter for post-processing afterwards. Torque, rotational speed, and power output are taken when the turbine is tested with changing wind conditions. The primary goal of experimental testing is to measure how effectively the turbine converts wind energy into electrical energy under different operating conditions (Migliore *et al.*, 2004).

Low (2 m/s) to high (15 m/s) wind speeds are employed to test the turbine. Test wind speed ranges are employed to determine the optimal wind speed to attain maximum turbine efficiency. Wind speed measurements are made progressively higher for torque and power output. Different blade configurations are employed to test to observe the impact on performance. Savonius, Darrieus, and helical blades are compared (Wakui *et al.*, 2005) under the same wind conditions to determine which of them is most appropriate for small-scale turbines. A comparison of Savonius, Darrieus, and the new configuration is done by Siddiqui *et al.* The results can be observed in the following graph in which the electrical power with respect to wind speed for each configuration is depicted.

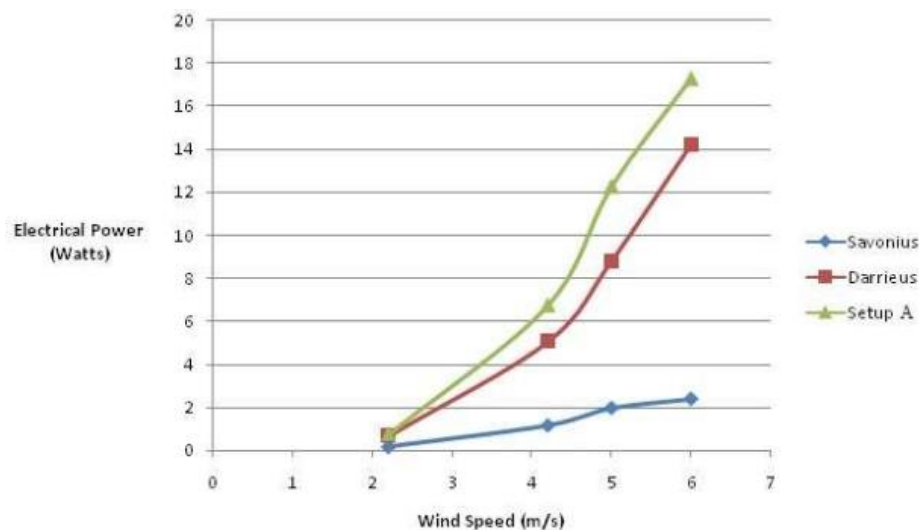


Fig. 29 - Performance comparison (Siddiqui *et al.*, 2016)

Performance curves are obtained from the analysis of experimental data and depict the relationship between wind speed and power generation. Efficiency is quantified by the power coefficient (C_p), or the ratio of actual power generated to the theoretical maximum power available from the wind. Conclusions about small vertical axis wind turbine performance can be drawn from experimental test data (Scungio *et al.*, 2016). Power output increases rapidly with rising wind speed to an optimum, a quite nonlinear relation between energy produced and wind speed. Performance is normalized after this because of aerodynamic and mechanical constraints.

At a moderate wind speed of about 8 to 12 m/s, the turbine is operating at its most efficient rate. The turbine can overspeed outside this range, decreasing its efficiency and possibly causing the system to be subjected to mechanical stress (Wood *et al.*, 2001). With higher wind speed, there is greater rotational speed and torque. The rotational speed of the turbine stabilizes as it approaches its mechanical limits, but at extremely high wind speeds. This implies that at higher speeds, the rotational speed is stable, but torque increases with the wind speed.

The mechanism of the drag-based Savonius turbine was connected to less efficiency at higher wind speeds, while that of the helical blade of the Darrieus turbine led to maximum efficiency for a wide range of wind speeds. The shape of the blade and the angle of attack contributed significantly towards the optimization of the maximum lift increment and the minimum decrement in drag, thereby maximizing the overall efficiency of the turbine. A typical power versus speed curve of a wind turbine is shown in Figure 30. It is the representation of Mittal *et al.*'s research and it shows how the power mechanically taken from wind is dependent on rotor speed. Small turbines have been observed to have lower energy conversion efficiency than large commercial turbines (Ozgener *et al.*, 2006), measured in terms of electrical power output to available wind energy. Small-scale systems are restricted, there are mechanical losses, and aerodynamic efficiency is poor. Notwithstanding this, small VAWTs are still very useful in decentralized power generation.

Experimental direct testing can provide vital information on the aerodynamic performance, performance parameters, and field applications of small vertical axis wind turbines. Since VAWTs with helical blades (Han et al., 2018), among others, feature a simple configuration, are easy to service, and can capture winds from any direction, they are an ideal choice for low to moderate wind speeds. Although they have lower energy conversion efficiency compared to large turbines, small VAWTs offer compact size and simple installation, making them well-suited for domestic applications and small-scale power generation in areas with fluctuating wind conditions.

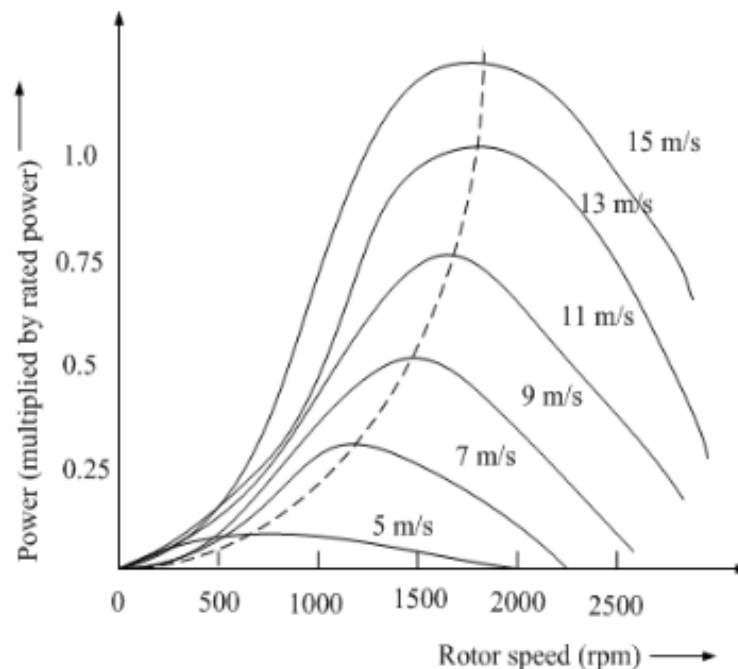


Fig. 30 - A typical power versus speed characteristic of a wind turbine (Mittal et al., 2011)

Research and development in small wind turbine technology will have to focus on improved blade design, reduction of mechanical losses, and use of optimized control systems in order to deliver optimum efficiency. On application of the advances, small vertical axis wind turbines can be an important part of the renewable energy industry that delivers sustainable energy solutions to urban and rural communities.

CONCLUSIONS

The paper is part of the documentation done for the PhD thesis, which has as the topic the research of a new wind turbine system integrated into the urban architecture. This review has highlighted the small wind turbine characteristics, including cost-effectiveness, environmental benefits, and suitability for various installation sites. The work is structured in four chapters that reveal the research done by the researchers in the field of small wind turbines. The first section belongs to the introduction on the specificity of small wind turbines with an accent on the advantages and disadvantages along with the challenges despite their benefits.

The synthesis of experimental research presented here highlights both the evolution and the barriers faced by small wind turbines in real-world applications. Issues such as energy conversion efficiency, reliability under various environmental conditions, and durability remain essential for optimizing small wind turbine systems. However, innovations in aerodynamic modelling, structural materials, and hybrid systems pave the way for improved performance in practical conditions.

Vertical-axis wind turbines offer clear advantages in urban areas and low-wind environments and are particularly well-positioned to play a leading role in these settings. With increasingly sophisticated design principles, new materials, and optimized work processes with ongoing research, small VAWTs can be more efficient and versatile in most areas of application. In the long term, ongoing improvement in small wind turbine technology is a giant opportunity for developing sustainable energy. The knowledge resulting from this review undoubtedly portrays areas to be investigated in the future, thereby giving ways for development and exploration in small wind energy systems.

REFERENCES

- [1] Abdolahifar, A., & Zanj, A. (2024). Addressing VAWT Aerodynamic Challenges as the Key to Unlocking Their Potential in the Wind Energy Sector. *Energies*, 17(20), 5052.
- [2] Aboufares, G. (2015). *Performance Characteristics of a Vertical Axis Wind Turbine Operating in Different Environmental Conditions* (Doctoral dissertation, University of Huddersfield).
- [3] Adams, D., White, J., Rumsey, M., & Farrar, C. (2011). Structural health monitoring of wind turbines: method and application to a HAWT. *Wind Energy*, 14(4), 603-623.
- [4] Ali, S., Park, H., & Lee, D. (2024). Structural Optimization of Vertical Axis Wind Turbine (VAWT): A Multi-Variable Study for Enhanced Deflection and Fatigue Performance. *Journal of Marine Science and Engineering*, 13(1), 19.
- [5] Alqahtani, M. (2024). Optimization of VAWT installation with spatial and temporal complexity considerations. *Frontiers in Energy Research*, 12, 1373586.
- [6] Andrew Ning, S., Damiani, R., & Moriarty, P. J. (2014). Objectives and constraints for wind turbine optimization. *Journal of Solar Energy Engineering*, 136(4), 041010.
- [7] Anup, K. C., Whale, J., & Urmee, T. (2019). Urban wind conditions and small wind turbines in the built environment: A review. *Renewable energy*, 131, 268-283.
- [8] Badwawi, R. A., Abusara, M., & Mallick, T. (2015). A review of hybrid solar PV and wind energy system. *Smart Science*, 3(3), 127-138.
- [9] Bashir, M. B. A. (2022). Principle parameters and environmental impacts that affect the performance of wind turbine: an overview. *Arabian Journal for Science and Engineering*, 47(7), 7891-7909.
- [10] Battisti, L., Benini, E., Brighenti, A., Dell'Anna, S., & Castelli, M. R. (2018). Small wind turbine effectiveness in the urban environment. *Renewable energy*, 129, 102-113.
- [11] Bianchini, A., Bangga, G., Baring-Gould, I., Croce, A., Cruz, J. I., Damiani, R., ... & Orrell, A. (2022). Current status and grand challenges for small wind turbine technology. *Wind Energy Science*, 7(5), 2003-2037
- [12] Brown, L. R. (2015). *The great transition: Shifting from fossil fuels to solar and wind energy*. WW Norton & Company.
- [13] Civera, M., & Surace, C. (2022). Non-destructive techniques for the condition and structural health monitoring of wind turbines: A literature review of the last 20 years. *Sensors*, 22(4), 1627.
- [14] Clausen, P. D., Evans, S. P., & Wood, D. H. (2023). Design, manufacture, and testing of small wind turbine blades. *Advances in wind turbine blade design and materials*. pp. 441-461. Woodhead Publishing.
- [15] Condruz, M. R., Malael, I., Vintila, I. S., & Cernat, M. P. (2019). Manufacturing of advanced composite wind turbine blades for counter rotating vertical wind turbine. *Mater. Plast*, 57, 45-56.
- [16] Dumitrescu, H., Cardos, V., & Malael, I. (2015). Boundary vorticity dynamics at very large Reynolds numbers. *INCAS Bulletin*, 7(3), 89.
- [17] Edwards, J. M., Danao, L. A., & Howell, R. J. (2015). PIV measurements and CFD simulation of the performance and flow physics and of a small-scale vertical axis wind turbine. *Wind Energy*, 18(2), 201-217.
- [18] Elia, A., Taylor, M., Gallachóir, B. Ó., & Rogan, F. (2020). Wind turbine cost reduction: A detailed bottom-up analysis of innovation drivers. *Energy Policy*, 147, 111912
- [19] Elkodama, A., Ismaiel, A., Abdellatif, A., Shaaban, S., Yoshida, S., & Rushdi, M. A. (2023). Control methods for horizontal axis wind turbines (HAWT): State-of-the-art review. *Energies*, 16(17), 6394.
- [20] Enevoldsen, P., & Xydis, G. (2019). Examining the trends of 35 years growth of key wind turbine components. *Energy for sustainable development*, 50, 18-26.
- [21] Eriksson, S., Bernhoff, H., & Leijon, M. (2008). Evaluation of different turbine concepts for wind power. *Renewable and sustainable energy reviews*, 12(5), 1419-1434.
- [22] Fingersh, L., Hand, M., & Laxson, A. (2006). Wind turbine design cost and scaling model (No. NREL/TP-500-40566). *National Renewable Energy Lab.(NREL)*, Golden, CO (United States).
- [23] Garmana, A., & Arifin, F. (2021). CFD analysis for combination Savonius and Darrieus turbine with differences in the number of Savonius turbine blades. In *2021 International Conference on Artificial Intelligence and Mechatronics Systems (AIMS)*. pp. 1-5. IEEE.
- [24] Glasberg, D., Stratila, S., & Malael, I. (2024). A Numerical Analysis on the Performance and Optimization of the Savonius Wind Turbine for Agricultural Use. *Engineering. Technology & Applied Science Research*, 14(1), 12621-12627.

- [25] Gonçalves, A., Liberato, M. L., & Nieto, R. (2021). Wind energy assessment during high-impact winter storms in southwestern Europe. *Atmosphere*, 12(4), 509.
- [26] Han, D., Heo, Y. G., Choi, N. J., Nam, S. H., Choi, K. H., & Kim, K. C. (2018). Design, fabrication, and performance test of a 100-W helical-blade vertical-axis wind turbine at low tip-speed ratio. *Energies*, 11(6), 1517.
- [27] Hays, A., & Van Treuren, K. W. (2019). A study of power production and noise generation of a small wind turbine for an urban environment. *Journal of Energy Resources Technology*, 141(5), 051202.
- [28] Hu, Y., Luo, P., Yao, W., Zhou, L., Shi, P., Yang, W., & Han, H. (2025). Power increase and lifespan extension control strategy of wind turbine yaw system based on power loss. *Sustainable Energy Technologies and Assessments*, 74, 104172.
- [29] Irawan, E. N., Sitompul, S., Yamashita, K. I., & Fujita, G. (2023). The effect of rotor radius ratio on the performance of hybrid vertical axis wind turbine Savonius-Darrieus NREL S809. *Journal of Energy and Power Technology*, 5(1), 1-12.
- [30] Johnson, C. C., & Smith, R. T. (1976). Dynamics of wind generators on electric utility networks. *IEEE Transactions on Aerospace and Electronic Systems*, (4), 483-493.
- [31] Junginger, M., Hittinger, E., Williams, E., & Wisser, R. (2020). Onshore wind energy. *Technological learning in the transition to a low-carbon energy system*. pp. 87-102. Academic Press.
- [32] Kabak, M., & Akalin, S. (2022). A model proposal for selecting the installation location of offshore wind energy turbines. *International Journal of Energy and Environmental Engineering*, 13(1), 121-134.
- [33] Kandemir, E., Hasan, A., Kvamsdal, T., & Abdel-Afou Alaliyat, S. (2024). Predictive digital twin for wind energy systems: a literature review. *Energy Informatics*, 7(1), 68.
- [34] Khammas, F., Hussein Suffer, K., Usubamatov, R., & Mustafa, M. T. (2015). Overview of vertical axis wind turbine (VAWT) is one of the wind energy applications. *Applied Mechanics and Materials*, 793, 388-392.
- [35] Kragten, A. (2004). The Darrieus rotor, a vertical axis wind turbine (VAWT) with only a few advantages and many disadvantages. *Report KD215. Engineering Office Kragten Design, Populierenlaan*, 51, 5492.
- [36] Krijgsveld, K. L., Akershoek, K., Schenk, F., Dijk, F., & Dirksen, S. (2009). Collision risk of birds with modern large wind turbines. *Ardea*, 97(3), 357-366.
- [37] Kumar, P. M., Sivalingam, K., Narasimalu, S., Lim, T. C., Ramakrishna, S., & Wei, H. (2019). A review on the evolution of Darrieus vertical axis wind turbine: Small wind turbines. *Journal of Power and Energy Engineering*, 7(4), 27-44.
- [38] LeBlanc, B., & Ferreira, C. (2020). Experimental characterization of H-VAWT turbine for development of a digital twin. *Journal of Physics: Conference Series*. Vol. 1452, No. 1, p. 012057. IOP Publishing.
- [39] Lenzen, M., & Munksgaard, J. (2002). Energy and CO2 life-cycle analyses of wind turbines—review and applications. *Renewable energy*, 26(3), 339-362.
- [40] Liu, W. Y. (2017). A review on wind turbine noise mechanism and de-noising techniques. *Renewable Energy*, 108, 311-320.
- [41] Lu, X., & McElroy, M. B. (2023). Global potential for wind-generated electricity. *Wind energy engineering*. pp. 47-61. Academic Press.
- [42] Malael, I., & Dragan, V. (2018). Numerical and Experimental Efficiency Evaluation of a Counter-Rotating Vertical Axis Wind Turbine. *Engineering, Technology & Applied Science Research*, 8(4).
- [43] Mălăel, I., Dragan, V., & Vizitiu, G. (2015). The vertical axis wind turbine efficiency evaluation by using the CFD methods. *Applied Mechanics and Materials*, 772, 90-95.
- [44] Mangos, O. (2024). *Contributions to the development of the wind energy potential of the Republic of Moldova (Contribuții la valorificarea potențialului energetic eolian al Republicii Moldova)* (Doctoral dissertation, Technical University of Moldova).
- [45] Marzec, Ł., Buliński, Z., Krysiński, T., & Tumidajski, J. (2023). Structural optimisation of H-Rotor wind turbine blade based on one-way Fluid Structure Interaction approach. *Renewable Energy*, 216, 118957.
- [46] McKenna, R., vd Leye, P. O., & Fichtner, W. (2016). Key challenges and prospects for large wind turbines. *Renewable and Sustainable Energy Reviews*, 53, 1212-1221.
- [47] Migliore, P., & Oerlemans, S. (2004). Wind tunnel aeroacoustic tests of six airfoils for use on small wind turbines. *J. Sol. Energy Eng.*, 126(4), 974-985.

- [48] Mirecki, A., Roboam, X., & Richardeau, F. (2007). Architecture complexity and energy efficiency of small wind turbines. *IEEE Transactions on Industrial Electronics*, 54(1), 660-670.
- [49] Mittal, R., Sandhu, K. S., & Jain, D. K. (2011). Grid voltage control of inverter interfaced wind energy conversion system (WECS). *International Journal of Environmental Science and Development*, 2(5), 337.
- [50] Mostafavi, A., & Friedmann, A. (2024). Wind turbine condition monitoring dataset of Fraunhofer LBF. *Scientific Data*, 11(1), 1108.
- [51] Nietiedt, S., Wester, T. T., Langidis, A., Kröger, L., Rofallski, R., Göring, M., ... & Luhmann, T. (2022). A Wind Tunnel Setup for Fluid-Structure Interaction Measurements Using Optical Methods. *Sensors*, 22(13), 5014.
- [52] Ozgener, O. (2006). A small wind turbine system (SWTS) application and its performance analysis. *Energy Conversion and Management*, 47(11-12), 1326-1337.
- [53] Pimenta, F., Pacheco, J., Branco, C. M., Teixeira, C. M., & Magalhães, F. (2020, September). Development of a digital twin of an onshore wind turbine using monitoring data. *Journal of Physics: Conference Series*. Vol. 1618, No. 2, p. 022065. IOP Publishing.
- [54] Polak A., Barański M. (2006). Wind turbines comparison. *Electrical Machines*, pp. 147-151
- [55] Ruggiero, A., Quartieri, J., Guarnaccia, C., & Hloch, S. (2015). Noise pollution analysis of wind turbines in rural areas. *International Journal of Environmental Research*, 9(4), 1277-1286.
- [56] Sakib, M. S., & Griffith, D. T. (2021). Parked and operating loads analysis in the aerodynamic design of multi-megawatt-scale floating vertical axis wind turbines. *Wind Energy Science Discussions*, pp. 1-28
- [57] Salem, M. E. M. (2016). Design of a pitch angle control system for a horizontal axis small wind turbine (Master thesis). Benha University. Benha Faculty of Engineering. Egypt
- [58] Scungio, M., Arpino, F., Focanti, V., Profili, M., & Rotondi, M. (2016). Wind tunnel testing of scaled models of a newly developed Darrieus-style vertical axis wind turbine with auxiliary straight blades. *Energy Conversion and Management*, 130, 60-70.
- [59] Selig, M. S., & McGranahan, B. D. (2004). Wind tunnel aerodynamic tests of six airfoils for use on small wind turbines. *J. Sol. Energy Eng.*, 126(4), 986-1001.
- [60] Siddiqui, A., Hameed, A., Mian, S. N., & Khatoun, R. (2016). Experimental Investigations of hybrid vertical axis wind turbine. *4-th International Conference on Energy, Environment and Sustainable Development (EEDS2016)*.
- [61] Sieros, G., Chaviaropoulos, P., Sørensen, J. D., Bulder, B. H., & Jamieson, P. (2012). Upscaling wind turbines: theoretical and practical aspects and their impact on the cost of energy. *Wind energy*, 15(1), 3-17.
- [62] Simic, Z., Havelka, J. G., & Vrhovcak, M. B. (2013). Small wind turbines—A unique segment of the wind power market. *Renewable Energy*, 50, 1027-1036.
- [63] Singh, R. K., & Ahmed, M. R. (2013). Blade design and performance testing of a small wind turbine rotor for low wind speed applications. *Renewable Energy*, 50, 812-819.
- [64] Syawitri, T. P., Yao, Y. F., Chandra, B., & Yao, J. (2021). Comparison study of URANS and hybrid RANS-LES models on predicting vertical axis wind turbine performance at low, medium and high tip speed ratio ranges. *Renewable Energy*, 168, 247-269.
- [65] Szlivka, F., Molnár, I., & Sándor, G. (2017). Advantages and disadvantages of different types of wind turbines and their usage in the city. *Wind Energy Harvesting*.
- [66] Terrado, M., González-Reviriego, N., Lledó, L., Torralba, V., Soret, A., & Doblas-Reyes, F. J. (2017). Climate services for affordable wind energy. *WMO Bull*, 66, 48-53.
- [67] Wakui, T., Tanzawa, Y., Hashizume, T., & Nagao, T. (2005). Hybrid configuration of Darrieus and Savonius rotors for stand-alone wind turbine-generator systems. *Electrical Engineering in Japan*, 150(4), 13-22.
- [68] Wallenius, T., & Lehtomäki, V. (2016). Overview of cold climate wind energy: challenges, solutions, and future needs. *Wiley Interdisciplinary Reviews: Energy and Environment*, 5(2), 128-135.
- [69] Winters, J., & Saunders, Z. (2018). The largest wind turbine ever. *Mechanical Engineering*, 140(12), 31-31.
- [70] Wiser, R. et al., (2011). *Wind Energy in IPCC Special Report on Renewable Energy Sources and Climate Change Mitigation*, Cambridge and New York: Cambridge University Press.

- [71] Wood, D. (2011). Small wind turbines. *Advances in wind energy conversion technology*. pp. 195-211. Berlin, Heidelberg: Springer Berlin Heidelberg.
- [72] Wood, D. H. (2001). A blade element estimation of the cut-in wind speed of a small turbine. *Wind Engineering*, 25(2), 125-130.
- [73] Wu, X., Hu, Y., Li, Y., Yang, J., Duan, L., Wang, T., ... & Liao, S. (2019). Foundations of offshore wind turbines: A review. *Renewable and Sustainable Energy Reviews*, 104, 379-393.
- [74] Xiaohui, W., & Zhang, X. (2010). Calculation of electromagnetic induction inside a wind turbine tower struck by lightning. *Wind Energy*, 13(7), 615-625.
- [75] Yilmaz, O. (2022). Increasing power coefficient of small wind turbine over a wide tip speed range by determining proper design tip speed ratio and number of blades. *Proceedings of the Institution of Mechanical Engineers, Part C: Journal of Mechanical Engineering Science*, 236(23), 11211-11230.
- [76] Yue, Q. (2023). Aerodynamic noise prediction and reduction of H-Darrieus vertical axis wind turbine. *Australian Journal of Mechanical Engineering*, 21(3), 1093-1102.
- [77] Zemamou, M., Aggour, M., & Toumi, A. (2017). Review of Savonius wind turbine design and performance. *Energy Procedia*, 141, 383-388.
- [78] ***<https://drawdown.org/solutions/onshore-wind-turbines>
- [79] ***<https://electricalsphere.com/wind-energy-basic-component-and-site-selection/>
- [80] ***<https://en.wind-turbine-models.com/turbines/93-dornier-darrieus-55>
- [81] ***<https://nachhaltigwirtschaften.at/en/iea/technologyprogrammes/wind/iea-wind-task-27-workingperiod-2018-2019.php>.
- [82] ***<https://www.cbc.ca/news/science/what-on-earth-wind-turbines-cities-1.6710512>
- [83] ***<https://www.linkedin.com/pulse/does-small-wind-turbine-your-home-increase-thomas-vogel/>
- [84] ***<https://midwestwindmillcompany.com/product/small-farm-windmill>
- [85] ***<https://www.windfarmbop.com/why-wind-turbine-blades-are-made-of-composite-materials/>

RESEARCH ON ROOT PRUNING METHODS APPLIED TO ORCHARD TREES

CERCETARI PRIVIND METODE DE TAIERE A RADACILOR POMILOR FRUCTIFERI

Ana ZAICA, Radu CIUPERCĂ, Vasilica ȘTEFAN, Alin-Nicolae HARABAGIU,
Elena-Melania CISMARU, Ștefan DUMITRU, Alexandru ZAICA
INMA Bucharest, Romania

Corresponding author: zaica_ana@yahoo.com

DOI: <https://doi.org/10.35633/inmateh-75-95>

Keywords: tree, roots characteristics, cutting resistance, cutting indices

ABSTRACT

Root pruning is a widely adopted practice in modern orchard management, with the primary goal of stimulating regeneration and optimizing annual fruit production. There are numerous researches on the architecture of the root system of trees, the volume and depth of root development, as well as the importance of cutting them in fruit growing. Also, the specialized literature presents different types of equipment intended for cutting roots, but there are few studies that address aspects related to the resistance forces encountered during this work. This paper presents research conducted using a specialized root-cutting implement equipped with a chisel-type blade. The study outlines the technical characteristics and performance indicators of the equipment, which was tested on various soil types to evaluate its working parameters. As a result of the experiments, the following were determined: the root cutting resistance at different working depths and across three soil categories - sandy, clayey, and loamy - as well as the corresponding working speeds required to maintain efficient operation under maximum tractor power conditions. Using the experimentally determined values, the variation diagrams of these indices were plotted, such as: the stress distribution diagram and the speed variation depending on the cutting resistance, the maximum total cutting resistances were identified, at the maximum depth of 50 cm, at the most unfavorable blade inclination angle of 45°. The maximum values determined for these were 768.5 daN for sandy soil, 1185.5 daN for clay soil and 1602.5 daN for loamy soil. These results highlight the influence of soil type and working parameters on the mechanical stresses of the blade during root pruning work in fruit plantations.

REZUMAT

Lucrarea de tăierea rădăcinilor pomilor este o lucrare des folosită în pomicultură, scopul acesteia fiind acela de a determina stimularea și regenerarea plantației în vederea gestionării producției anuale de fructe. Există numeroase cercetări privind arhitectura sistemului radicular al pomilor, volumul și adâncimea de dezvoltare a rădăcinilor, precum și importanța efectuării lucrării de tăiere a acestora în pomicultură. De asemenea, literatura de specialitate prezintă diferite tipuri de echipamente destinate tăierii rădăcinilor, însă sunt puține studii care abordează aspectele legate de forțele de rezistență întâmpinate în timpul acestei lucrări. Articolul prezintă cercetările efectuate cu un echipament de tăiat rădăcini prevăzut cu cuțit de tip daltă, pentru care sunt prezentate caracteristicile și indicii de performanță aferenți, testat pe diferite categorii de sol, în vederea determinării indicilor de lucru ai acestuia. În urma realizării experimentărilor s-au determinat: rezistența de tăiere a rădăcinilor, la diferite adâncimi de lucru, pe diferite tipuri de sol (nisipos, argilos și argilos), precum și vitezele de lucru în funcție de rezistența totală la tăiere, pentru utilizarea puterii maxime a tractorului. Utilizând valorile determinate experimental s-au trasat diagramele de variație ale acestor indici, precum: diagrama de distribuție a tensiunilor și variația vitezei în funcție de rezistența la tăiere, s-au identificat rezistențele totale maxime de tăiere, la adâncimea maximă de 50 cm, la cel mai nefavorabil unghi de înclinare a cuțitului de 45°. Valorile maxime determinate pentru acestea au fost de 768,5 daN pentru sol nisipos, 1185,5 daN pentru sol argilos și 1602,5 daN pentru sol lutos. Aceste rezultate evidențiază influența tipului de sol și a parametrilor de lucru asupra solicitărilor mecanice ale cuțitului în timpul lucrărilor de tăiere a rădăcinilor în plantațiile pomicole.

INTRODUCTION

The process stimulating and regenerating a tree involves removing some of the tree's surface roots to encourage the growth of deeper, stronger roots. Pruning shallow roots reduces the tree's need for water and nutrients and encourages the growth of deeper roots. These deeper roots are better able to absorb water and nutrients, which helps the tree grow and produce more fruit.

Pruning is usually done during the tree's dormant season, which is in the fall or spring, before active growth begins. It is important to do this carefully and avoid cutting too many roots to avoid damaging the tree's health too much (*Wade et al., 2020*).

The consequences of root cutting include root degradation, root structural depth, root location, root regeneration, drying of fine roots, formation of rounded roots, scorched roots, and root grafts (*Watson et al., 2014*). The root system architecture and a possible root orientation can be adapted for mechanical reinforcement (*Beier et al., 2020*).

The sizes and shapes of root systems for different plant growth forms vary depending on above-ground plant size, climate, and soil texture. With the exception of trees, root systems tend to be shallower and wider in dry, warm climates, and deeper and narrower in cold, wet climates. Shrubs are more shallowly rooted in regions with summer rainfall compared to those with winter rainfall (*Schenk and Jackson, 2002*).

A study on cherry trees aimed to examine the influence of root pruning on tree vigor, with the goal of managing the harvest through more compact canopies (*Perry, 2015*).

Tree roots play a crucial role in various aspects such as soil penetration, degradation, root architecture, root defects, available rooting space, regeneration, deep root structure, and root extension (*Watson et al., 2014*).

In other research, issues related to rooting depth, lateral root spread, and aboveground/belowground allometries of plants have been explored (*Schenk et al., 2002*). Additionally, studies have examined the effects of root pruning on leaf nutrient content, photosynthesis, and tree growth in a poplar plantation. These studies aimed to investigate the impact of root pruning on tree growth and physiology by quantifying the extent of root pruning through allometric analysis, taking initial steps toward developing a practical tool for arborists to support root management and care decisions (*Da-wei Jing et al., 2018; Jing DW et al., 2017*).

To stimulate growth, some researchers performed root pruning twice a year, 60 cm away from the trunk and 30 cm deep, as follows: the first pruning was done on one side of the row before autumn leaf fall, and the second in spring during flowering (*Mitre et al., 2012*).

Various methods of classifying individual roots have been documented. Based on their distribution, roots are categorized as either vertical or horizontal, while in terms of length and thickness, they are classified as either skeletal or fibrous. Horizontal roots grow more or less parallel to the soil surface, typically at a depth of about 30 to 100 cm, whereas vertical roots extend downward into the soil. Skeletal roots are characterized by their considerable length and thickness - ranging from a few centimeters to several meters long - and can reach several centimeters in diameter. In the management of mature trees, it is critical to assess the diameter at breast height (DBH) prior to any root pruning activity. Current guidelines recommend avoiding the cutting of roots located within a radial distance of less than five times the DBH from the trunk. For example, in a tree with a DBH of 12 inches, root pruning should be limited to areas beyond a 60-inch radius from the trunk. Younger trees exhibit greater resilience and may tolerate root cuts at a closer distance - approximately three times the DBH. Nevertheless, in all cases, root pruning should be conducted as far from the trunk as practicable to minimize physiological stress. When performed with care, root pruning can be compatible with tree health; however, imprecise or overly aggressive interventions may compromise structural integrity, disrupt water and nutrient uptake, and ultimately result in tree decline or mortality. The severity of damage caused by root pruning increases significantly with proximity to the trunk. It is generally recommended not to remove more than 25% of a tree's root system, as exceeding this threshold may result in tree decline, structural failure, or mortality. A recovery period of at least two years should be allowed between successive root pruning interventions. Additionally, root pruning should be avoided during the spring period following bud break (*Coffie, 2001*). Roots are commonly classified based on diameter into six main categories: very fine (< 0.5 mm), fine (0.5–2 mm), small (2–5 mm), medium (5–10 mm), large (10–20 mm), and very large (> 20 mm) (*Gliński and Lipiec, 1990*).

Most fine roots are concentrated within the surface layer of approximately 1 m² of medium-textured soil, with the majority of fine, non-woody roots located at a depth of about 15 cm. This distribution is largely influenced by genetic factors under favorable growth conditions in the topsoil (*Craul, 1993*).

Approximately 70% of roots are located within the humus layer of the soil profile (*Wasterlund, 1989*). Key morphological characteristics of individual roots include surface texture, color, and diameter (*Fitter et al., 1991*).

Several studies have sought to establish correlations between root parameters - such as number, diameter, and spatial orientation - and aboveground plant dimensions, including stem and crown diameter. Notably, highly significant positive correlations have been identified between stem diameter measured at 1.3 m above ground level and total root biomass (*Kuiper and Courts, 1992*).

Roots may be classified based on several criteria:

A - According to their growth orientation within the soil profile, roots are categorized as follows:

- horizontal roots - those that grow nearly parallel to the soil surface or form an angle between 60° and 90° with the vertical axis;
- oblique roots - those that form an angle between 30° and 60° with the vertical axis;
- vertical roots - those that grow at an angle of up to 30° relative to the vertical axis.

B - According to size, roots can be classified into the following categories:

- skeletal roots, these are roots longer than 30 cm and thicker than 3 mm, with diameters that can exceed 10–15 cm. The primary skeletal root is the taproot (or embryonic root);
- filling roots (also referred to as fibrous or transitional roots) - these roots occupy the spaces between skeletal roots and measure between 0.5 and 30 cm in length and 1–5 mm in diameter;
- absorptive roots characterized by their small size - 0.1 to 0.4 cm in length and 0.1 - 1 mm in thickness - these roots are typically white and have a short lifespan of 15 to 25 days. They are covered with numerous root hairs or, in certain species such as walnut, hazelnut, and currant, replaced by mycorrhizae, which fulfill the absorptive function (Cichi, 2011).

Two descriptive models are commonly used to characterize root system parameters: root density as a function of soil depth and root density as a function of horizontal distance from the plant (Van Noordwijk et al., 1996).

Modeling the mechanical reinforcement of soil by root networks is inherently complex and requires the application of advanced computational methods. One such method involves finite element analysis, which incorporates appropriate constitutive equations to simulate soil–root interactions. The finite element software PLAXIS - short for Plasticity Axisymmetric - is widely used for such analyses (Brinkgreve and Vermeer, 1998).

Trenches excavated closer to the trunk than the recommended tree protection zones did not compromise the stability of two commonly occurring tree species. Although *Tilia cordata* exhibited lower overall stability compared to *Acer platanoides*, neither species showed significant adverse effects even under the most severe trenching treatments (Pallafray et al., 2024).

Additionally, studies have quantified both the average and maximum vertical forces required to uproot stumps in a single piece. These investigations also considered the influence of soil type and uprooting techniques. It was hypothesized that increasing soil moisture content and employing preparatory treatments - such as the application of initial mechanical forces - would decrease the subsequent force needed for stump extraction (Lindroos, et al., 2010).

Various types of equipment for tree root cutting have been developed globally by renowned manufacturers. An Italian company has produced the *Root-cutting tool SHARK*, which features a lamellar blade with hydraulically adjustable working depth and operates without a pendulum mechanism. This equipment is designed to perform effectively in light soils free of stony inclusions (AGROFER). Additionally, a Dutch company has developed the *Root Pruner*, which incorporates a stability system based on a wheel train to enhance operational control (BORECO). However, neither manufacturer provides detailed information regarding the mechanical stresses acting on the cutting blades during operation, nor do they present comprehensive research on the equipment's performance across different soil types or under varying working conditions. This study presents the results of experimental research on the root pruning of fruit trees, carried out using a prototype device specifically designed for this purpose and tested under varying soil conditions.

MATERIALS AND METHODS

Based on the considerations outlined above, INMA Bucharest, developed an experimental root-cutting device for trees. This equipment was employed in the present study, and its main components are illustrated in Figure 1.

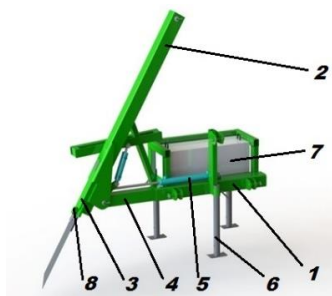


Fig. 1 - Schematic diagram of the experimental equipment for tree root cutting.

1. framework; 2. blade holder arm; 3. sliding pipe; 4. traverse; 5. hydraulic system;
6. foot support; 7. ballast block; 8. cutting force monitoring system.

During operation, the equipment should be positioned so that the cutting blade is aligned at the predetermined distance from the tree row, taking into account the age and size of the trees. The blade, actuated by a hydraulic system, is inserted into the soil to the specified depth, following the cutting protocol established by the operator. Once positioned, the tractor, coupled to the implement, is started, and the root-cutting operation is carried out.

Main technical characteristics:

- maximum working depth, 500 mm;
- maximum horizontal telescopic extension of the blade, 500 mm;
- adjustable blade inclination (working angle), 45°...70°;
- total equipment weight (including ballast), approximately 600 kg.

The equipment and measuring devices used for the experimental procedures consisted of the following components: a force transducer, a micro PLC 13, a force amplifier, and an operator terminal. An agricultural tractor with a rated power of 100 HP was employed as the energy source for operating the root-cutting implement.

Determination of root cutting resistance

The root-cutting operation, illustrated in Fig. 2, involves a sequence of mechanical actions performed by the cutting blade:

- Vertical soil penetration: the blade is inserted vertically into the soil to a predetermined depth, initiating the cutting process
- Horizontal soil displacement: As the blade moves forward, it deforms and displaces the surrounding soil laterally. The volume of displaced soil is defined by the difference between the physical volume of the blade and the volume of the deformed soil.
- Root severance: As the blade progresses, it encounters and severs tree roots located within its path.

This process is influenced by several factors, including soil type, moisture content, and root density. A clear understanding of these interactions is essential for optimizing the design and operation of root-cutting equipment.

The total resistance to root cutting R_t is calculated using relation (1):

$$R_t = R_c + R_d + R_f + R_{rc} \quad [\text{daN}] \quad (1)$$

in which:

R_c - resistance to soil cutting, [daN];

R_d - resistance to soil deformation, [daN];

R_f - frictional resistance between the coulter and the soil, [daN];

R_{rc} - resistance to root cutting, [daN];

To further explain the components of relation (1), the following expressions (2), (3), (4) and (5) were used, adapted from *Scripnic and Babiciu, (1979)*:

$$R_c = k_c \cdot l_c = k_c \cdot \frac{d_c}{\sin \beta} \quad (2)$$

$$R_d = k_d \cdot l_d \cdot l_c = k_0 \cdot \frac{t_c}{2} \cdot \frac{t_c}{\sin \alpha} \cdot \frac{d_c}{\sin \beta} \quad (3)$$

$$R_f = \mu_f \cdot G_c \quad (4)$$

$$R_{rc} = k_{rc} \cdot S_r \quad (5)$$

where:

k_c - specific resistance to soil cutting, [daN/cm];

k_d - specific resistance to soil deformation, [daN/cm²];

k_0 - volume coefficient of deformation, [daN/cm³];

d_c - working depth of the cutting blade, [cm];

l_c - contact length of the blade with the soil, [cm];

t_c - thickness of the cutting blade, [cm];

l_d - contact width of the blade with the soil in the cutting area, [cm];

α - sharpening angle of the cutting blade, [degrees];

β - penetration angle of the blade into the soil, [degrees];
 μ_f - coefficient of friction between the blade and the soil;
 G_c - portion of the equipment weight acting on the blade, [daN];
 k_{rc} – specific resistance to root cutting, [daN/cm²];
 S_r - total cross-sectional area of roots cut simultaneously, [cm²] (*Scripcic and Babiciu, 1979*).

Substituting (2), (3), (4), (5) into (1), the relation (6) results:

$$R_t = k_c \cdot \frac{d_c}{\sin \beta} + k_0 \cdot \frac{t_c}{2} \cdot \frac{t_c}{\sin \alpha} \cdot \frac{d_c}{\sin \beta} + \mu_f \cdot G_c + k_{rc} \cdot S_r, \text{ daN} \quad (6)$$

The resistances acting on the blade during operation are schematically illustrated in Fig. 2.

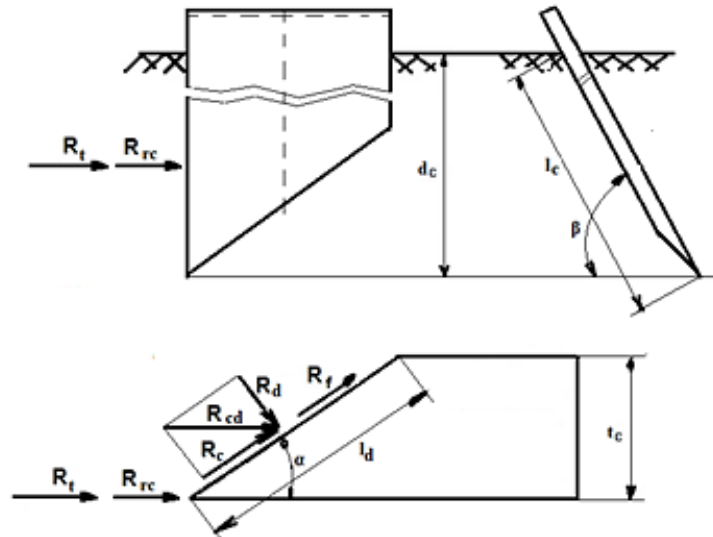


Fig. 2 - Schematic representation of the resistances acting on the cutting blade during operation

In the design of technical equipment for tree root pruning, two primary factors must be considered. First, the resistance encountered by the main cutting component, as defined in Equation (1), plays a critical role in determining the mechanical requirements of the system. Second, the type, condition, and characteristics of the soil, along with the tree species, must be taken into account, as these are governed by specific physical and chemical properties that influence root structure and resistance.

The working speed of the equipment, under specific operating conditions, is limited by factors such as the power of the tractor within the aggregate, the total resistance to root cutting, and the penetration angle of the blade into the soil. The relationship governing this limitation is expressed by Equation (7):

$$v = \frac{P}{R_t} \quad (7)$$

Where:

v - working speed of the equipment, [m/s];
 P - available working power, [W];
 R_t - total resistance to root cutting, [daN], (*Kepner et al., 1987*)

According to the fundamental principles of agricultural mechanics (*Kepner et al., 1987*), the working speed of an implement is directly proportional to the power developed and inversely proportional to the resistance exerted by the soil and biological material - in this case, tree roots.

RESULTS

The total resistance to cutting tree roots is influenced by several key factors, including:

- the type and condition of the soil;
- the distribution and development of roots within the soil profile;
- the working depth of the cutting blade and the penetration angle into the soil.

To evaluate the energy efficiency of the tractor-equipment aggregate during the root-pruning operation, it is necessary to calculate the total resistance encountered by the cutting mechanism. This resistance is determined using Equation (6).

The parameters and coefficients used in the calculation are as follows: $k_c = 5 \dots 10$ daN/cm; $k_0 = 1 \dots 2.5$ daN/cm³; $d_c = 50$ cm; $t_c = 1.5$ cm; $\alpha = 15^\circ$; $\beta = 45 \dots 70^\circ$; $\mu_f = 0.4 \dots 0.6$ soil/metal (Scripnic and Babiciu, 1979); $G_c = 100$ daN, measured by weighing; $R_{rc} = 60 \dots 75$ daN, resistance to cutting an apple tree root with $S_r = 1$ cm², the average value adopted in calculations was 67.5 daN.

The cutting resistance of the root R_{rc} was determined experimentally using a custom-designed cutting device equipped with a force transducer. This device was developed by the authors and manufactured within the institution where the research was conducted. By substituting both the known values and those determined experimentally into equations (2) through (5), the resulting resistances acting on the cutting blade were calculated for different soil types. These results, presented in Table 1, correspond to a maximum cutting depth of 50 cm and a blade inclination angle of 45°.

Table 1

Resistances on the root cutting blade, $d_c = 50$ cm, $S_r = 1$ cm², $\beta = 45^\circ$

Soil type	R_c [daN]	R_d [daN]	R_r [daN]	R_{rc} [daN]
Sandy soil $k_c = 5$ daN/cm; $k_0 = 1$ daN/cm ³ ; $\mu_f = 0.4$	354	307	40	67.5
Loamy soil $k_c = 7.5$ daN/cm; $k_0 = 1.25$ daN/cm ³ ; $\mu_f = 0.5$	530	538	50	67.5
Clay soil $k_c = 10$ daN/cm; $k_0 = 2.5$ daN/cm ³ ; $\mu_f = 0.6$	707	768	60	67.5

Since the experimental equipment for cutting tree roots allows for the adjustment of both cutting depth and blade penetration angle, and is designed to operate across various soil types with differing characteristics, it is equipped with a monitoring system that records real-time values of total cutting forces. This feature enables the selection of optimal working parameters while ensuring that the resistance does not exceed the mechanical strength limit of the blade.

The diagram presented in Figure 3 illustrates the variation in total root cutting resistance as a function of cutting depth for three different soil types. This graphical representation supports the selection of an appropriate tractor for the implement, ensuring that the machine provides sufficient traction force to achieve the required working depth.

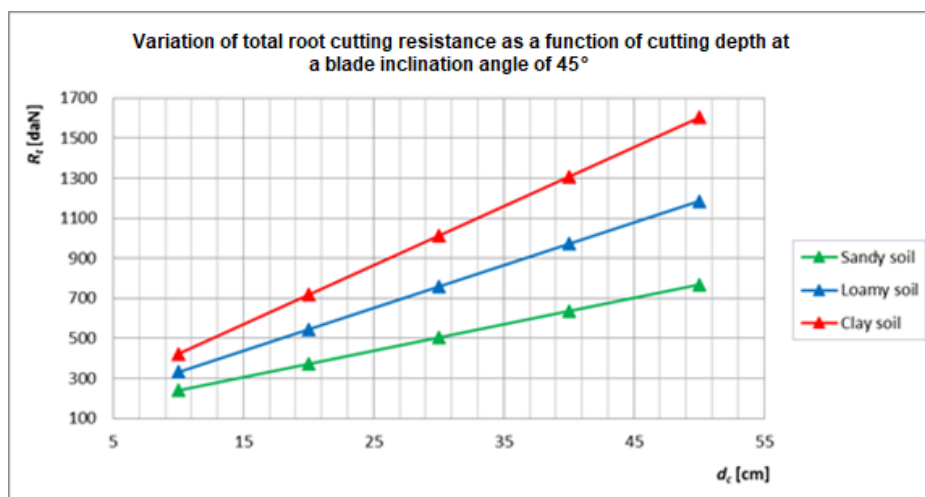


Fig. 3 - Variation of total root cutting resistance as a function of the working depth

Figure 4 illustrates the variation of total root cutting resistance as a function of the inclination angle of the cutting blade during operation, for the three soil types evaluated. The values obtained from this analysis can be used to adjust the cutting process according to the age and structural characteristics of the trees, ensuring that the operation aligns with the parameters defined by the established root pruning technology.

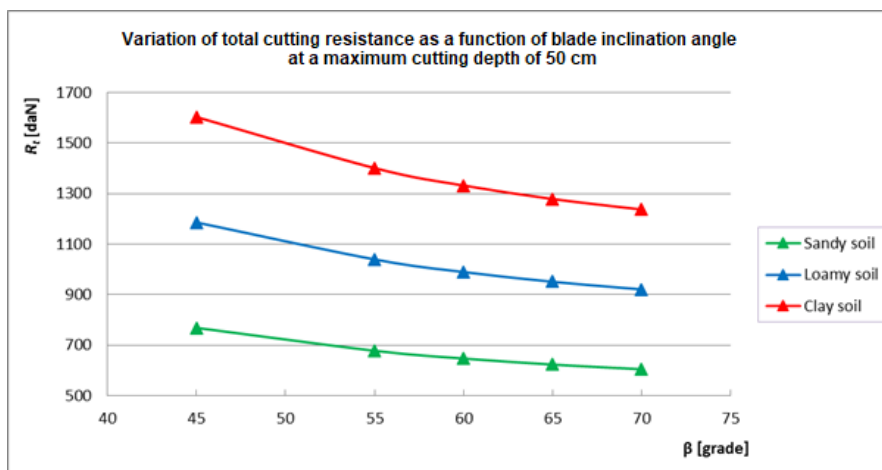


Fig. 4 - Variation of total cutting resistance as a function of blade inclination angle

The variation of working speed as a function of root cutting resistance, at different blade inclination angles, is presented in Figure 5.

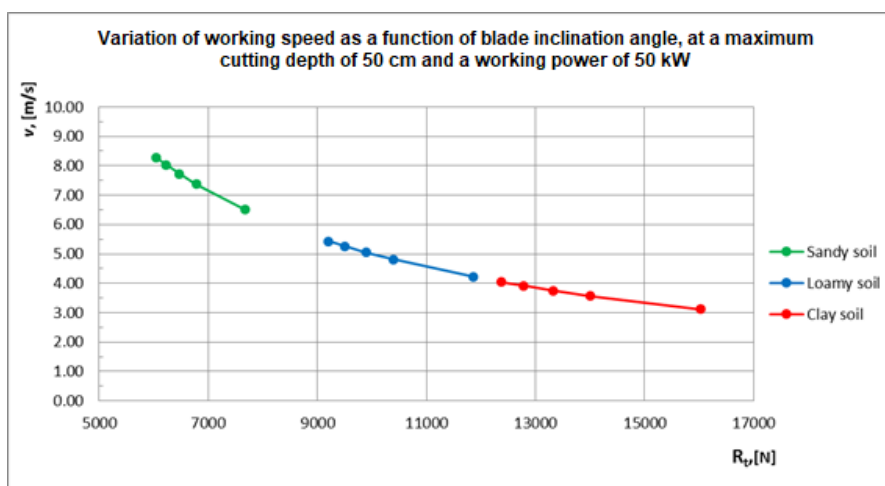


Fig. 5 - Variation of working speed as a function of total resistance to root cutting

This diagram provides practical guidance for operators who, based on the available tractor power and the resistance values presented in Figures 3 and 4, can determine the optimal working speeds for root cutting operations.

CONCLUSIONS

Root pruning is a valuable technique in pomology, aimed at improving tree health and enhancing annual fruit production.

The performance indicators of the experimental equipment were evaluated. The total resistance to root cutting varied with working depths from 10 to 50 cm, with values ranging as follows: 235...768 daN for sandy soil; 310...1185.5 daN for loamy soil; 405...1602.5 daN for clayey soil. The maximum achievable working speed, at a blade inclination angle of 50° and tractor power of 50 kW, ranged between: 6.5...8.5 m/s for sandy soil; 3...4 m/s for loamy soil; 4...5.5 m/s for clayey soil.

Equipping the device with a cutting resistance monitoring system allows for real-time adjustment of working parameters, ensuring the operation remains within mechanical safety limits. The findings of this study are significant both for the design of efficient root pruning equipment for fruit trees and for advancing research toward the development of intelligent, adaptive pruning technologies.

ACKNOWLEDGEMENT

This work was supported by a project of the Ministry of Research, Innovation and Digitization, through Program NUCLEU - Project: PN 23 04 01 05 - Innovative technology for the maintenance of fruit plantations, contract no. 9N/ 01.01.2023.

REFERENCES

- [1] Beier M. P., Tsugawa S., Demura T., Fujiwara T. (2020). Root shape adaptation to mechanical stress derived from unidirectional vibrations in *Populus nigra*, *Plant Biotechnology*. 37, DOI: 10.5511/plantbiotechnology.20.0813a, pp.423–428.
- [2] Brinkgreve, R.B.J. and Vermeer, P.A. (1998). *PLAXIS 8.2 Finite Element Code for Soil and Rock Analysis*, Version 8.2., Eds. Rotterdam, the Netherlands.
- [3] Cichi, M. (2011). *Pomiculture (Pomicultură)* - Universitaria, Craiova / Romania. ISBN 978-606-14-0084-3;
- [4] Cofie, P. (2001). *Mechanical properties of tree roots for soil reinforcement models*, Dissertation Wageningen University, Dutch, ISBN 90-5808-333-0.
- [5] Craul, P. J. (1993). Urban Soil in Landscape Design, *Journal of Plant Nutrition and Soil Science*, Volume156, Issue 5, pp. 457-457, <https://doi.org/10.1002/jpln.19931560513>.
- [6] Da-wei Jing, Zhen-yu Du, Ming-you Wang, Qing-hua Wang, Hai-lin Ma, Fang-chun Liu, Bing-yao Ma, Yu-feng Dong. (2018). Regulatory effects of root pruning on leaf nutrients, photosynthesis, and growth of trees in a closed-canopy poplar plantation, *PMCID*: PMC5962049, *PMID*: 29782538, doi: 10.1371/journal.pone.0197515 M.
- [7] Fitter, A. H., Stickland T. R., M. L. Harvey, G. W. Wilson. (1991). Architectural analysis of plant root systems, *New Phytologist*, Volume118, Issue 3, pp. 375-382, <https://doi.org/10.1111/j.1469-8137.1991.tb00018.x>.
- [8] Gliński, J. and Lipiec, J. (1990). *Soil physical conditions and plant roots*. CRC Press, Florida.
- [9] Jochen Schenk, H., Jackson R. B. (2002). Rooting depths, lateral root spreads and below-ground/above-ground allometries of plants in water-limited ecosystems, *British Ecological Society Journal of Ecology*, <https://doi.org/10.1046/j.1365-2745.2002.00682.x>.
- [10] Jing, D.W., Du, Z.Y., Wang, M.Y., Wang, Q.H., Ma, H.L., Liu, F.C., Ma, B.Y., Dong, Y.F. (2017). Effects of root pruning on the physicochemical properties and microbial activities of poplar rhizosphere soil. *PloS One*, <https://doi.org/10.1371/journal.pone.0187685> *PMID*: 29117215.
- [11] Kepner, R.A., Bainer, R. and Barger, E.L. (1982). *Principles of Farm Machinery*. 3rd Edition, AVI Publishing, INC., Westport.
- [12] Kuiper, L.C. and Coutts, M.P. (1992). Spatial disposition and extension growth of the structural root system of douglas-fir, *For. Ecol. Manage*, 47: pp.111-125.
- [13] Lindroos, O., Henningsson, M., Athanassiadis, D.& Nordfjell, T. (2010). Forces required to vertically uproot tree stumps. *Silva Fennica* 44(4): www.metla.fi/silvafennica ·ISSN 0037-5330, *The Finnish Society of Forest Science*. The Finnish Forest Research Institute, pp.681–694.
- [14] Mitre V., Mitre I., Sestras A. F., Sestras R. E. (2012). Effect of Roots Pruning upon the Growth and Fruiting of Apple Trees in High Density Orchards, *Bulletin UASVM Horticulture*, 69(1), Print ISSN 1843-5254; Electronic ISSN 1843-5394.
- [15] Pallafray C., Sivarajah S., Ruel J.C. (2024). Impact of Root Cutting on *Acer platanoides* and *Tilia cordata* Tree Stability in Urban Parks, A Case Study in Quebec City, Canada, *Forests*, Vol.15(6), 1041.
- [16] Perry R.A. (2015), *Renewed interest in root pruning*, Department of Horticulture, Michigan State University Extension.
- [17] Scripnic V., Babiciu P., (1979), *Agricultural Machinery (Maşini Agricole)*, Ed. Ceres, Bucharest, 35, 45;
- [18] Van Noordwijk, M., Lawson G., Soumare A., Groot J. JR. and Hairiah K. (1996). Root distribution of trees and crops: competition and/or complementarity. In: C.K. Ong and P. Huxley (eds), *Tree-crop interactions: a physiological approach*, University Press, Cambridge, U.K., pp. 319-365.
- [19] Wade G. L., Midcap J. T. (2020). Pruning Ornamental Plants in the Landscape, Bulletin 961 *Extension Horticulturists*, University of Georgia, Reviewed by Bodie Pennisi.
- [20] Watson G.W., Hewitt A.M., Custic M., Marvin Lo, (2014), The Management of Tree Root Systems in Urban and Suburban Settings II: A Review of Strategies to Mitigate Human Impacts, *Arboriculture & Urban Forestry*, 40(5), [http](http://www.arboriculture.com). 249-271, DOI: 10.48044.
- [21] Wasterlund, I., (1989), Strength components in the forest floor restricting maximum tolerable machine forces. *Journal of Terramechanics*, Vol. 26, No. 2: pp.177-182.
- [22] ***AGROFER, <https://www.agrofer.it/project/movimento-terra-tagliaradici-shark/>
- [23] ***BORECO, <https://agri-com.nl/fruiteelt/wortelsnijder/Wortelsnijder-met-schuinsnijframe-wielstel-gewichtendrager>

DESIGN AND EXPERIMENTAL STUDY OF THE SUPPLY SYSTEM FOR GRASS SEED PELLETIZATION COATING MACHINE

草种丸粒化包衣机供给装置设计与研究

Liying CHEN¹⁾, Zhanfeng HOU^{1,2,3)}, Haiyang LIU¹⁾, Bingyan LI¹⁾, Liyang BAO¹⁾, Zhimin WANG¹⁾

¹⁾ Inner Mongolia Agricultural University, College of Mechanical and Electrical Engineering, Inner Mongolia, China

²⁾ Inner Mongolia Engineering Research Center of Intelligent Equipment for the Entire Process of Forage and Feed Production, Hohhot, 010018, China

³⁾ Inner Mongolia Engineering Research Center for Intelligent Facilities in Prataculture and Livestock Breeding, Hohhot 010018, China
Tel: +86-0471-4309215; E-mail: njau-hzf@163.com

Corresponding author: Zhanfeng HOU

DOI: <https://doi.org/10.35633/inmateh-75-96>

Keywords: Pelletization Coating, Small-sized Forage Grass Seeds, Electronic Control System, Microcontroller Unit, Bidirectional Thyristor Circuit, Precision Dosage Control.

ABSTRACT

To address the challenges of low automation, insufficient precision in seed-powder-liquid ratio control, and suboptimal coating quality in current domestic small-sized forage grass seed pelletization coating equipment, this study designed and developed a fully automated pelletization coating system. The system employs a Microcontroller Unit as the core controller, integrates an ATFC101 serial touchscreen for human-machine interaction, and combines programming and electronic control technologies to achieve precise regulation of material and liquid supply, enabling fully automated and quantized coating operations. The hardware of the feeding system adopts a bidirectional thyristor circuit, while the software implements a hierarchical switching control strategy to ensure high precision and stable material delivery. Experimental trials using Caragana seeds and pelletization powder demonstrated that the integrated electro-control system achieved full automation, with seed dispensing deviation controlled within 1.2 g and powder deviation within 0.32 g, significantly improving dosing accuracy. This research provides critical theoretical and technical insights for optimizing automated pelletization coating equipment for small-sized forage grass seeds.

摘要

针对当前国内小粒牧草种子丸化包衣设备存在的自动化程度低、种粉液比例控制精度不足及包衣质量欠佳等问题,本研究设计并开发了一种小粒牧草种子全自动丸化包衣设备,系统以单片机为核心控制器,采用ATFC101串口屏作为人机交互界面,结合编程与电控技术,实现了供料与供液量的精确调控,进而达成全自动精量化包衣操作。供料系统硬件部分采用双向晶闸管电路,软件采用分层切换控制策略,确保了供料的高精度与稳定性。以柠条种子及丸粒化粉料为试验对象,研究结果表明,该电控系统与丸化包衣设备的集成实现了全自动操作,其中落种偏差控制在1.2g以内,落粉偏差控制在0.32g以内,显著提升了精确落料性能。本研究为小粒牧草种子全自动丸化包衣设备的设计与优化提供了重要的理论依据与技术参考。

INTRODUCTION

Seed pelletization coating technology is a processing method that uniformly encapsulates seeds with powdered agents, liquid binders, and other nutritional or protective materials to form small, spherical pellets with consistent size and shape. This technology not only significantly improves seed precision in mechanical precision seeding but also enhances seed resilience against biotic and abiotic stresses (Jarrar *et al.*, 2023; Paravar *et al.*, 2023; Yi, 2020). This technique has been widely applied in grassland ecological restoration projects to rehabilitate degraded and desertified grasslands through aerial seeding. By increasing seed size and mass, pelletization effectively mitigates the impact of wind speed and direction on seed dispersal, improves landing stability, and ensures better soil surface embedding, thereby substantially enhancing aerial seeding quality (Pedrini *et al.*, 2023; Zheng *et al.*, 2024). These benefits are particularly pronounced for small-sized forage grass seeds, which exhibit markedly improved germination rates and ecological adaptability post-treatment (Javed *et al.*, 2022).

Pelletization coating technology originated internationally in the 1940s. Over nearly 80 years of advancement, equipment development has evolved from rudimentary mechanical operations to intelligent and precision-driven modern systems. For instance, Denmark's HEID Corporation produces the CC-type rotary seed coater, which utilizes automated control systems to precisely coordinate the metering of materials and coating agents, effectively minimizing human error and enhancing coating uniformity and pelletization quality. Canada's Ohara Technologies developed the HVCC3015 continuous coater, featuring a zone-controlled, multi-angle spray nozzle design that optimizes spray angles and chemical dosage, significantly reducing coating dead zones and improving uniformity, efficiency, and final product quality. With dynamic metering and modular design, Niklas Germany has developed W.N.14 continuous coating machine, which realizes precise proportioning and automated operation through metering roller linkage and PLC control to enhance coating uniformity, reduce pharmaceutical waste and improve production efficiency (Ma *et al.*, 2023). In contrast, domestic research on pelletization in China began relatively late, transitioning from manual operations in the 1990s to fully automated systems. Chinese scholars have designed and tested pelletizers for diverse seed types while continuously optimizing their electro-control systems. Examples include the 5BY-5.0V Seed Coater by Jiuquan Okay Seed Co., which ensures precise chemical-to-seed ratios and thorough mixing. Yang *et al.* (2014) developed an intelligent control system to enhance coating quality and synchronize seed-chemical delivery. Sang *et al.* (2015) integrated advanced detection and control systems into the BY-150 coater, significantly improving dosing accuracy for both seeds and liquid agents. The 5BYR-100 Seed Coater, designed by the Guangdong Provincial Agricultural Machinery Research Institute, was optimized for batch coating of vegetable seeds. Despite these advancements, existing equipment predominantly targets vegetable and crop seeds, with limited options for small-sized forage grass seeds, and automation levels remain suboptimal. While researchers have improved pelletization quality through mechanical refinements, critical factors such as seed-powder-liquid ratios - key determinants of coating efficacy - are often inadequately addressed in current studies.

To address the aforementioned challenges, this study designed a fully automated pelletization coating system for small-sized forage grass seeds, achieving precise control over seed, powder, and liquid supply, alongside fully automated coating operations. Centered around a microcontroller unit and integrated with a closed-loop control strategy, the system enables intelligent regulation and stable operation throughout the entire process. This innovation aims to enhance the quality and efficiency of seed pelletization coating, providing robust technical support for forage cultivation and ecological restoration projects.

MATERIALS AND METHODS

Overall Structure and Operational Principle

System Architecture

The grass seed pelletization coating equipment consists of a powder feeding device, seed feeding device, liquid feeding device, pelletization coating device, and control system. Its structure is shown in Fig.1.

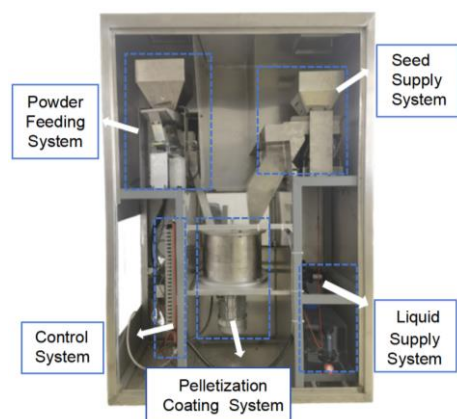


Fig. 1 – Schematic diagram of the overall system structure

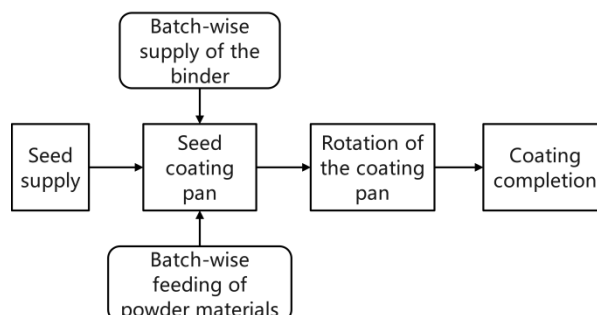


Fig. 2 – Flow chart of the pelletization process

The operational workflow of the pelletization coating equipment is as follows: First, the seed feeding device delivers seeds into the pelletization coating drum. After initiating drum rotation, the seeds are evenly distributed within the drum.

The liquid supply system then activates, injecting the coating solution into the drum. The drum continues rotating in an idle state to ensure thorough wetting of the seed surfaces. Subsequently, the powder feeding device supplies powdered material into the drum, followed by another idling phase to achieve uniform powder coating. Throughout the process, the liquid coating agent is supplied in quantitatively controlled batches, with powder dosing always synchronized after the liquid application. The batch-wise liquid and powder supply sequence is illustrated in Figure 2, operating in a cyclic "liquid supply-idling-powder supply-idling" mode until the preset pelletization criteria are met (Pasha et al., 2017). Finally, the drum idles for an extended period to enhance the compressive strength and surface smoothness of the coated pellets, completing one full coating cycle.

Control Workflow Overview

Based on the operational workflow of the pelletization coating equipment, the overall control flowchart of the system was designed, as illustrated in Figure 3. After system startup, initialization is completed first. Subsequently, operational parameters are configured via the touchscreen, and the equipment is activated. The system initiates seed feeding and enters an idle operation state once the seed quantity reaches the preset value. After the idle operation time meets the set duration, the liquid supply process is triggered. When the liquid supply volume reaches the single-cycle target, the system halts the liquid supply and re-enters idle operation. Following this, the powder supply process is activated, succeeded by another idle phase. The system operates cyclically in the "liquid supply-idle operation-powder supply-idle operation" sequence until the predetermined number of cycles is achieved, after which it transitions to the pelletization phase. During pelletization, the system runs for the set duration, concluding the process. The equipment then stops, marking the completion of a full coating cycle.

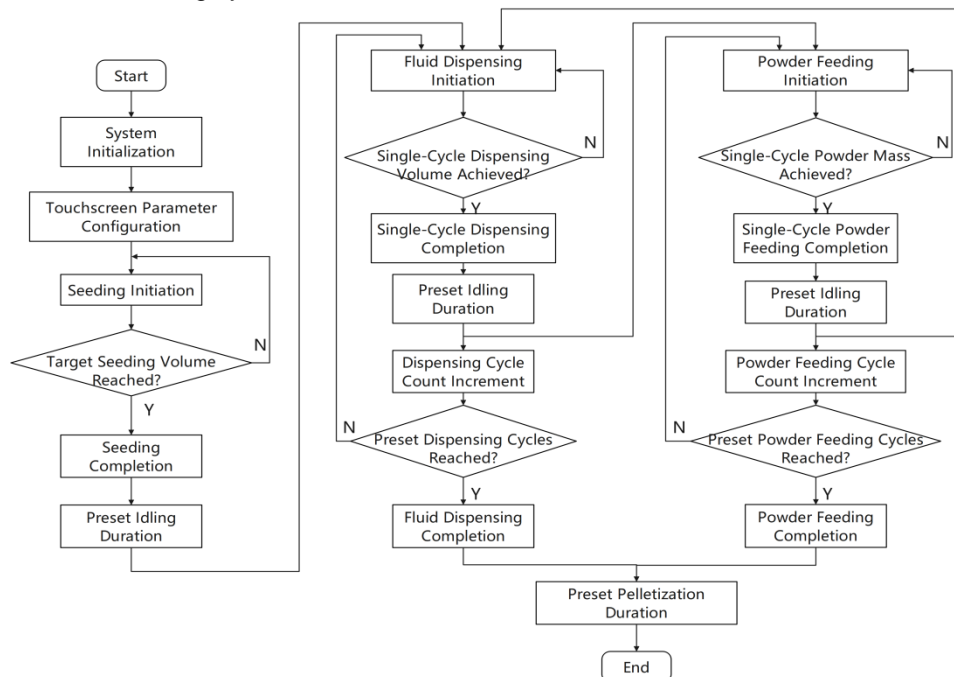


Fig. 3 – Control system flow diagram

Design of the Seed Supply Device Structure and Working Process

A seed metering device was ultimately designed by integrating a load cell, servo motor, and weighing hopper into the electromagnetic vibratory feeder. The structure of the feeder, as shown in Figure 4, comprises a material trough, leaf springs, an electromagnetic vibratory exciter, a base frame, and vibration isolation springs (Afzal et al., 2020). The electromagnetic exciter consists of critical components such as an electromagnet (coil with iron core) and an armature. In the alternating current (AC)-driven electromagnetic vibratory feeder, the operational principle relies on the coupling of electromagnetic forces and mechanical vibrations. When AC flows through the electromagnet coil, an alternating magnetic field is generated, producing periodic electromagnetic forces. During the positive half-cycle of the AC, current energizes the coil, creating an electromagnetic force that attracts the armature to the iron core. This action drives the trough backward while deforming the leaf springs to store elastic potential energy. During the negative half-cycle, the current direction reverses, weakening or eliminating the electromagnetic attraction.

The leaf springs then release stored energy, propelling the armature and iron core in the opposite direction, thereby moving the trough forward. With a standard AC frequency of 50 Hz, the feeder completes 50 reciprocating vibrations per second, equivalent to 3,000 cycles per minute (Mucchi *et al.*, 2013). This process converts electrical energy into mechanical energy through electromagnetic forces, enabling periodic vibrations of the trough to achieve material conveyance.

The feeding capacity of an electromagnetic vibratory feeder is influenced by multiple critical factors, including the mechanical index, trough inclination angle, and material properties (particle size, density, and moisture content). Among these, the mechanical index (K), defined as the ratio of the trough's maximum acceleration to gravitational acceleration, serves as a core parameter that directly governs material conveying speed and uniformity (Despotović *et al.*, 2017; Chandravanshi *et al.*, 2017).

$$K = 4\pi^2 f^2 a/g \quad (1)$$

In the formula: f - vibration frequency, [Hz];

a - amplitude, [m];

g - gravitational acceleration, [m/s²].

In this study, the vibration frequency was set to 3,000 cycles per minute (50 Hz). By adjusting the vibration amplitude (a), the feeding capacity was optimized to accommodate the conveying requirements of diverse materials, thereby improving operational efficiency and precision. Building on this foundation, the electromagnetic vibratory feeder was enhanced and an intelligent seed feeding device was designed. This device enables two operational modes-high-speed and low-speed-by modulating the exciter's amplitude: high-speed mode prioritizes feeding rate for rapid material delivery, while low-speed mode minimizes feeding error to ensure precise quantitative dosing.

During system operation, the seed supply system drives the trough vibration via the electromagnetic vibratory exciter in high-speed mode, conveying seeds to the weighing hopper. The Microcontroller Unit monitors the real-time seed weight in the hopper through feedback from the load cell. When the feeding rate reaches the switching point (expressed as a percentage of the total seed quantity), the Microcontroller Unit switches the exciter to low-speed mode to enhance dosing precision (Zhang *et al.*, 2021; Campos *et al.*, 2012). Upon achieving the preset seed quantity, the Microcontroller Unit halts the exciter's vibration and controls the servo motor to rotate at a specified angle, thereby opening the discharge gate to deposit the quantified seeds into the pelletization coating drum. The process flowchart is illustrated in Figure 5.

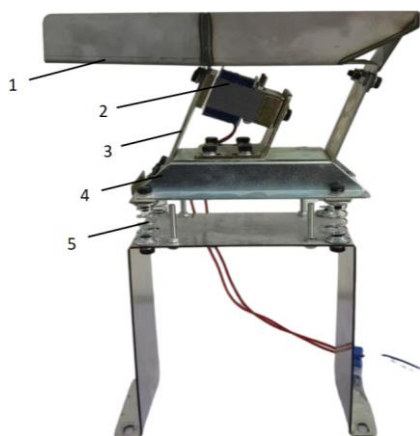


Fig. 4 – Structural diagram of the electromagnetic vibration feeder

1. material trough; 2. electromagnetic vibratory exciter;
3. leaf spring; 4. base frame; 5. vibration isolation spring

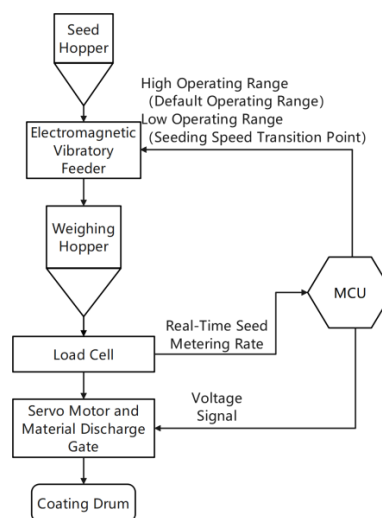


Fig. 5 – Process flow chart of the seed supply system

Hardware Design

The hardware components of the seed-feeding device primarily consist of a load cell, electromagnetic vibrator, and servo motor. To ensure precise seed delivery, the system employs a high-precision parallel cantilever load cell with a 0-2 kg range and 0.02 g accuracy. This load cell features a composite error of <0.02% F.S., an operational temperature range of -20 to +75°C, sensitivity of 1±0.03 mV/V, a power supply voltage of 5-12 V, and an overload capacity of 150% F.S., offering high accuracy, user-friendly operation, and strong anti-interference capability. Since the load cell's output signal is weak and susceptible to interference, the system incorporates an HX711 module to amplify and convert the analog signals.

This module integrates a high-precision 24-bit A/D converter with a 2.6-5.5 V operating voltage range, delivering low-noise, high-resolution performance for stable digital output, making it ideal for high-accuracy weighing applications.

The amplitude regulation of the electromagnetic vibrator is achieved through a TRIAC-based voltage control circuit (shown in Figure 6). This circuit connects the mains power to the signal input terminal, with the output terminal linked to the electromagnetic vibrator. The circuit configuration includes: Q1 as the bidirectional thyristor (TRIAC), D1 as the bidirectional trigger diode (DIAC), RX/R2/C2 forming the phase-shift network, and C1/R1 composing the snubber circuit to suppress voltage transients during switching operations and protect circuit components. By adjusting the resistance value (RX) in the phase-shift network, the circuit controls the charging time of capacitor C2 until it reaches the DIAC's trigger voltage (32 V), thereby modulating the TRIAC's conduction phase angle. This directly varies the output RMS voltage, enabling the electromagnetic vibrator to operate at two distinct speed settings (high/low) for seed feeding applications.

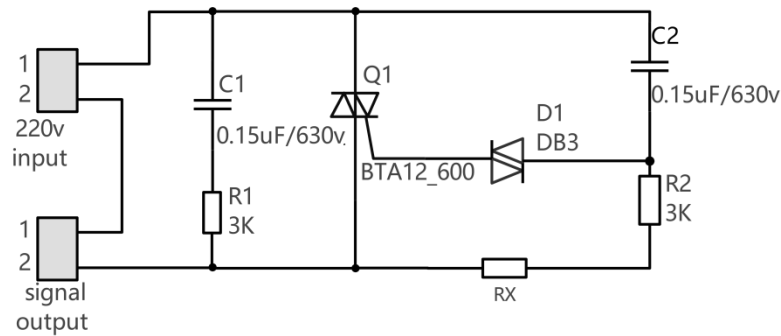


Fig. 6 –TRIAC voltage regulating circuit

The system employs a metal-gear micro servo with a 0.4413 N·m torque and a 180° controllable rotation range, featuring a no-load speed of 0.14s/60° at a 6V operating voltage. This servo provides precise angular positioning while maintaining excellent wear resistance and operational stability, ensuring consistent performance during prolonged high-frequency operation for rapid and accurate gate control in the feeding process. The servo is controlled through PWM signals with pulse widths ranging from 500 μs to 2500 μs (0.5-2.5 ms), where smaller pulse widths correspond to smaller rotation angles and larger pulses produce proportionally greater angles. This enables smooth 0-180° rotation for fine-tuned gate positioning, meeting the precise angular control requirements of the feeding system.

Design of the Powder Feeding Device

Although the material hoppers and specifications of the weighing system (hopper dimensions and weighing hopper capacity) differ between the powder feeding device and the seed feeding device, their mechanical structures, operational workflows, and hardware designs remain highly consistent. The process flowchart of the powder feeding system is illustrated in Figure 7.

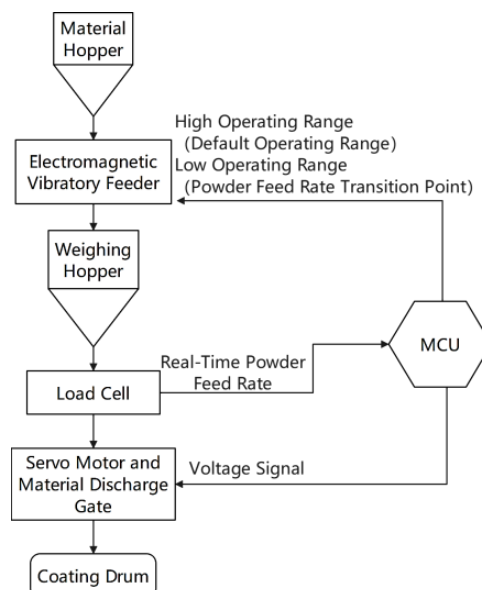


Fig. 7 – Process flow chart of the powder supply system

Design of the Liquid Delivery Device

Structure and Working Process

The liquid feeding system comprises a medicinal solution tank, a liquid supply pump, a flow meter, and an electromagnetic valve. The flow meter monitors the liquid flow rate in real-time and transmits the data to the Microcontroller Unit, enabling precise measurement and control of the liquid supply volume. The operational workflow is as follows: the liquid supply pump delivers the medicinal solution through a pipeline to the pellet coating pot, while the flow sensor continuously collects flow rate data and sends it back to the Microcontroller Unit. When the detected value reaches the preset threshold, the Microcontroller Unit immediately triggers a shutdown command to the electromagnetic valve, terminating the current liquid supply cycle. The process flow diagram of the liquid feeding system is illustrated in Figure 8.

Hardware Design

The hardware components of the liquid feeding system primarily consist of a liquid supply pump, flow meter, and solenoid valve. To ensure accurate flow measurement, the system employs a Digma flow meter with a measurement range of 0.05-0.82 L/min and an accuracy of $\pm 0.5\%$ F.S. This flow meter has a total error of less than 0.5% F.S., an operating temperature range of -10 to +60°C, output signals of 4-20mA or pulse, a power supply voltage of 12-24V DC, and an overload capacity of 120% F.S. With advantages such as high measurement accuracy, fast response speed, and strong resistance to medium contamination, it is particularly suitable for fluid control applications requiring low flow rates and high precision.

In the liquid feeding system, a normally closed DC 12V solenoid valve is installed at the outlet of the liquid supply pump to prevent backflow. Coupled with its dedicated driver circuit (shown in Figure 9), this solenoid valve allows for real-time, precise control of liquid flow. The driver circuit utilizes a high-response configuration consisting of a transistor-relay combination for accurate flow regulation. The control mechanism operates via the Microcontroller Unit's I/O port, which is connected to the solenoid valve driver circuit. When the I/O port outputs a high-level signal, the transistor enters saturation, energizing the relay to open the solenoid valve and initiate liquid flow. Conversely, a low-level signal from the I/O port drives the transistor into cutoff, de-energizing the relay to close the solenoid valve and stop the liquid flow. This switching mechanism provides reliable on/off control, with response times under 15ms, as confirmed through experimental testing.

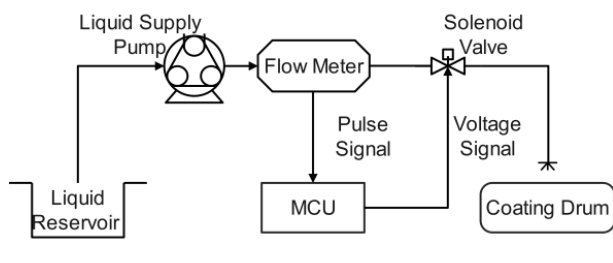


Fig. 8 – Process flow chart of the liquid supply system

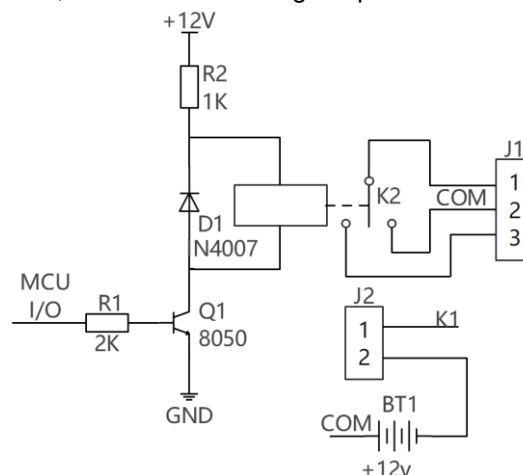


Fig. 9 – Driving circuit of the solenoid valve

Overall Control System Design

The small grass seed pelleting and coating equipment consists of a feeding device and a pelleting-coating unit. The pelleting-coating unit includes a speed sensor, frequency converter, AC motor, and coating drum. Based on closed-loop control principles, this study designed both the feeding device and pelleting-coating unit, with the closed-loop control system structure shown in Figure 10 (Upasan et al., 2013; Gai et al., 2013). In this system, sensors continuously collect controlled variables (such as flow rate, rotational speed, weight, etc.) from the controlled object and send the detected signals back to the controller. The controller compares the feedback values with setpoints to calculate deviation errors, then generates corresponding control signals based on preset control algorithms. Upon receiving the control signals, actuators adjust control variables (such as valve opening, motor speed, vibration frequency, etc.) to affect the controlled object, dynamically driving the controlled variables toward their setpoints. This process achieves automatic system regulation and precise control (Fowler et al., 2013).

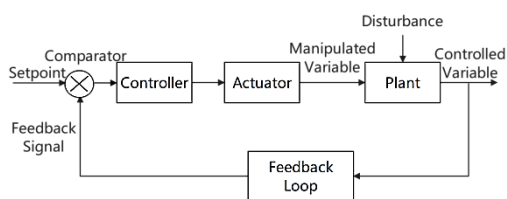


Fig. 10 – Block diagram of the closed-loop control system

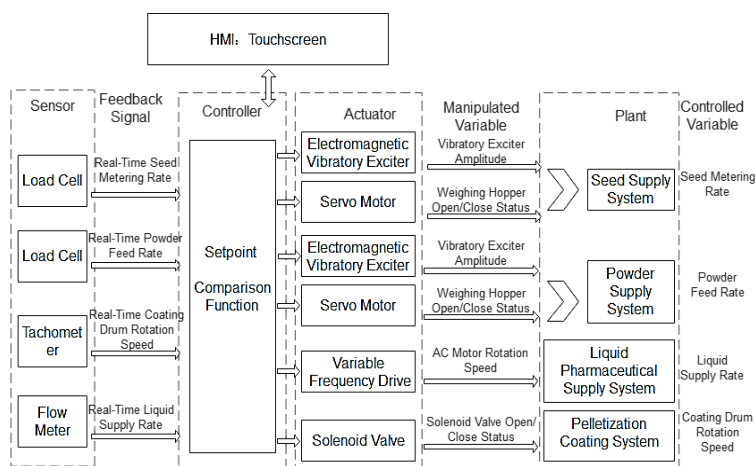


Fig. 11 – Schematic diagram of the control system

Based on the structural characteristics and operational workflow of the feeding device and pelleting-coating unit, the overall control system architecture was developed, as shown in Figure 11. This architecture includes a human-machine interface (touch screen), a controller (Microcontroller Unit), sensors (load cell, flow meter, speed sensor), actuators (electromagnetic vibrator, servo motor, solenoid valve, frequency converter), and controlled objects (seed feeding system, powder feeding system, liquid feeding system, and pelleting-coating system). The system achieves coordinated multi-subsystem control and integrated operation (Du et al., 2025).

RESULTS AND DISCUSSION

Experimental Study on the Seed Supply Device

In this study, using Caragana seeds as test specimens, the focus was on analyzing the seeding speed and accuracy of the testing equipment. The experiment required the determination of two key parameters: resistance values corresponding to high/low seeding speeds and the optimal speed switching point (expressed as a percentage of the total seed quantity). The high-speed mode primarily enhances throughput, while the low-speed mode improves dosing accuracy. The speed switching point represents a critical control parameter for error reduction: excessively high values may cause airborne seeds to exceed the remaining quantity before switching, compromising accuracy; excessively low values prolong the process duration due to slower low-speed discharge of substantial residual seeds.

To analyze the seed feeding rate and error, the resistance (R_X) in Figure 6 was adjusted from 0 to 1000 k Ω , with resistance values partitioned at 40 k Ω intervals. At each resistance setting, five replicate speed measurements were performed, and the mean value was calculated to generate the seed feeding rate variation curve corresponding to different resistance values, as illustrated in Figure 12.

As demonstrated by the test results in Figure 12, the seed feeding rate exhibited a downward trend with increasing resistance values. Within the resistance range of 0 to 440 k Ω , the feeding rate remained relatively stable above 50 g/s. Considering the maximum uniform coating capacity of the pelletization coating drum (200 g of seeds), the resistance value corresponding to the high-speed mode was selected as 480 k Ω , yielding a feeding rate of 42.61 g/s. This configuration balances rapid seed delivery and operational stability, effectively meeting the demands of high-throughput pelletization processes.

To mitigate seed feeding error by selecting resistance values in the low-speed mode, a focused investigation into error characteristics at high resistance values was conducted. A resistance range of 920 k Ω to 1000 k Ω (corresponding to seed feeding rates of 1.18 g/s to 4.33 g/s) was tested. The resistance values were partitioned at 10 k Ω intervals, with five replicate measurements performed at each interval. The mean value of these measurements was adopted as the error result for the respective resistance value. This methodology yielded the error variation curve corresponding to different resistance values, as shown in Figure 13.

As demonstrated by the experimental results in Figure 13, the error exhibited a decreasing trend with increasing resistance values. Combined with the seed feeding rate data from Figure 12, at a resistance value of 1000 k Ω , the corresponding seed feeding rate was 1.18 g/s with an error of 1.32 g. Both the feeding rate and error at this resistance value met the design requirements. Therefore, 1000 k Ω was selected as the optimal resistance value for the low-speed mode.

To investigate the influence of different seed feeding rate switching points on dosing accuracy, resistance values of 480 k Ω (high-speed mode) and 1000 k Ω (low-speed mode) were selected for a 200 g seed dosing error test. The switching points were set at 75%, 80%, 85%, 90%, and 95% of the target seed quantity. At each switching point, five replicate measurements were conducted. The mean error and standard deviation for each switching point were calculated, yielding the error variation curve corresponding to different switching points, as shown in Figure 14.

According to the experimental results shown in Figure 14, the seeding error reaches its minimum value with the smallest standard deviation when the seed feeding speed switching point is set at 90% of the total seed feeding amount, indicating optimal seeding stability under this condition. Therefore, 90% of the seed feeding amount is selected as the optimal switching point for seed feeding speed adjustment.

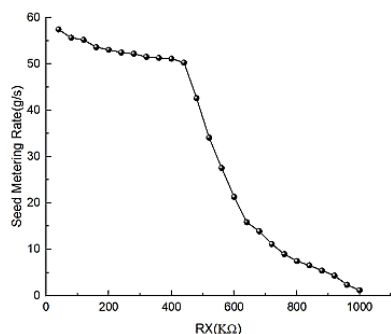


Fig. 12 – Variation curves of seed feeding speed under different resistance values

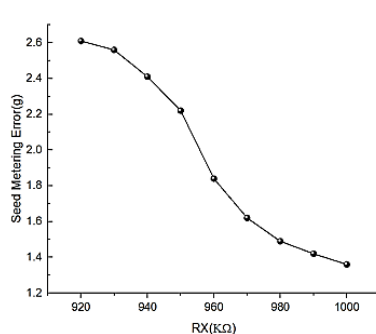


Fig. 13 – Variation curves of seed feeding error under different resistance values

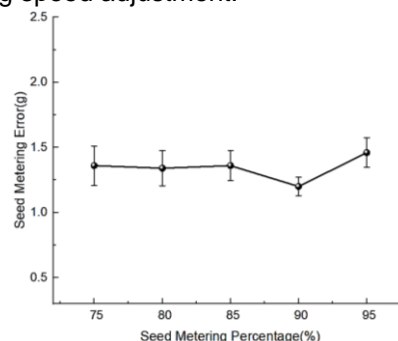


Fig. 14 – Variation curves of seed feeding error at different speed switching points

Experimental Study on the Powder Supply Device

Given the identical hardware design between the powder feeding device and the seed feeding device, the parameters requiring determination in the experiments are the same: the resistance value (RX) of the phase-shifting network and the powder feeding speed switching point (percentage of powder feed amount). To analyze the relationship between feeding speed and error, RX was set within the range of 260-680 k Ω , with resistance values partitioned at 20 k Ω intervals. For each resistance value, five speed measurements were conducted, and the average values were calculated to derive the powder feeding speed variation curve corresponding to different RX values, as shown in Figure 15.

As evidenced by the experimental results in Figure 15, the powder feeding speed exhibits a declining trend with increasing resistance values. When the resistance exceeds 520 k Ω , the rate of speed reduction accelerates markedly. Considering the total powder supply amount of 30 g in this study, the resistance value corresponding to the high-speed setting was selected as 260 k Ω , where the feeding speed reaches 2.41 g/s, thereby fulfilling the requirement for rapid powder delivery.

To reduce powder feeding errors by selecting resistance values under the low-speed setting, a focused investigation into error characteristics at high resistance values was conducted. Resistance values ranging from 920 k Ω to 1000 k Ω (corresponding to feeding speeds of 0.17 g/s to 0.46 g/s) were systematically tested. The resistance values were partitioned at 10 k Ω intervals, and five repeated measurements were conducted at each resistance value, with the average value adopted as the representative error result. This methodological framework yielded the powder feeding error variation curve corresponding to different resistance values, as illustrated in Figure 16.

As demonstrated by the experimental results in Figure 16, the powder feeding error exhibits a declining trend with increasing resistance values. Combined with the seed feeding speed data from Figure 15, at a resistance value of 600 k Ω , the corresponding powder feeding speed is 0.28 g/s, with a feeding error of 0.29 g. Both the feeding speed and error at this resistance value meet the design requirements. Therefore, 600 k Ω is selected as the optimal resistance value under the low-speed setting.

To investigate the influence of different powder feeding speed switching points on feeding accuracy, resistance values of 260 k Ω (high-speed setting) and 600 k Ω (low-speed setting) were selected for 30 g powder feeding accuracy tests. The switching points were set at 75%, 80%, 85%, 90%, and 95% of the total powder feeding amount. Five repeated measurements were conducted at each switching point. The average error values and standard deviations were calculated for each switching point, yielding the powder feeding error variation curve corresponding to different switching points, as shown in Figure 17.

As evidenced by the test results presented in Figure 17, the powder feeding error reaches its minimum value when the speed switching point is set at 85% of the total powder feeding amount. Notably, this configuration also yields the smallest standard deviation, demonstrating optimal feeding stability under these conditions. Based on these findings, 85% of the total powder feeding amount was determined to be the optimal speed switching point for the system.

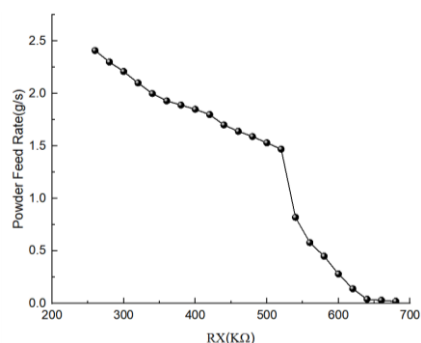


Fig. 15 – Variation curves of powder feeding speed under different resistance values

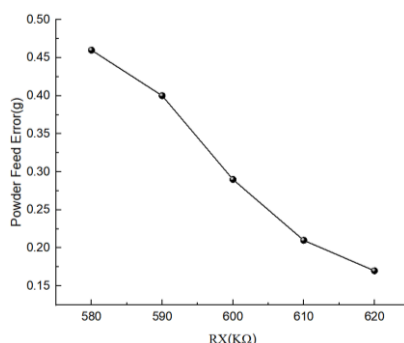


Fig. 16 – Variation curves of powder feeding error under different resistance values

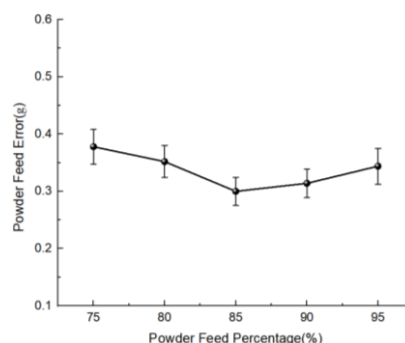


Fig. 17 – Variation curves of powder feeding error at different speed switching points

Error Test Testing

To verify whether the designs of the seed-feeding and powder-feeding devices meet the error requirements for coating operations, error analysis tests were conducted for both systems. The results of the seed-feeding error test are presented in Table 1, while the results of the powder-feeding error test are shown in Table 2.

Table 1

Seed Metering Error Test Value			
SEED METERING QUANTITY [G]	NUMBER OF TRIALS	AVERAGE SEED DISPENSED [G]	ABSOLUTE ERROR [G]
100	5	101.2	1.2
150	5	151.16	1.16
200	5	201.16	1.16
250	5	251.1	1.1
300	5	301.18	1.18

Table 2

Powder Feeding Error Test Value			
POWDER FEEDING QUANTITY [G]	NUMBER OF TRIALS	AVERAGE POWDER DISPENSED [G]	ABSOLUTE ERROR [G]
20	5	20.32	0.32
25	5	25.31	0.31
30	5	30.29	0.29
35	5	35.3	0.3
40	5	40.3	0.3

Based on the statistical calculations of the experimental data (n=5 trials), the systematic errors showed a gradual decrease with the increase of material quality. Specifically, the seed supply error gradually decreased from 1.2% to 0.39% (100-300 g interval), and the flour supply error decreased from 1.6% to 0.75% (20-40 g interval). Compared to the existing state-of-the-art systems, the maximum seed supply error in this study was reduced by 32% (from 1.8% to 1.2%) and the powder supply error was reduced by 53% (from 2.0% to 0.75%) compared to the benchmark study by Zhang et al. (2022). The team reported seed supply/powder supply errors of 1.25-1.8% vs. 1.6-2.0%, respectively, under the same working conditions. The above performance improvement is due to the optimized layered switching control strategy, which effectively suppresses the inertial drop of the airborne residual material after the load cell triggers the closing of the drop plate.

CONCLUSIONS

This study developed a fully automated intelligent control system that integrates seed feeding, powder feeding, liquid supply, and coating functions to meet the specific process requirements of small grass seed pelleting and coating. The modular design of the system enables real-time monitoring and segmented adjustment of coating parameters through multi-sensor data fusion and hierarchical switching control, significantly enhancing the consistency of quality and the controllability of the pelleting and coating process for small seeds.

1) The study designed the seed-feeding and powder-feeding devices using a dual-mode control strategy, while employing a closed-loop control approach for the liquid-feeding device. The design was optimized to enhance the feeding accuracy of both the seed and powder delivery systems.

2) This study successfully integrated the control system with the pellet coating equipment and performed systematic performance validation tests. The experimental results show that the system achieves a seed feeding accuracy error of ≤ 1.2 g and a powder feeding accuracy error of ≤ 0.32 g, both of which meet the design specifications.

In order to further expand the application value of the system, the subsequent research can focus on the following directions:

1) optimization of multi-species adaptability: verify the system's adaptability to the coating of quinoa, sesame and other seeds with ultra-small particle sizes ($\Phi < 1$ mm), and develop parameter self-matching algorithms.

2) industrialization expansion research: design modular expansion interface, support multi-machine cooperative operation and flexible capacity configuration (50-500 kg/h), to adapt to the needs of large-scale production lines.

This technology can also be extended and applied in the field of precision powder engineering, such as pharmaceutical micro-pill coating, functional fertilizer preparation, etc., to provide technical support for the upgrading of agricultural intelligent manufacturing equipment.

ACKNOWLEDGEMENT

The authors were funded for this project by the Development and Research on Key Technologies and Equipment for Degraded Grassland Restoration Based on Coated Forage Seed Hydroseeding (No. 2023YFDZ0006) and the Science and Technology Research Project of Inner Mongolia Autonomous Region Higher Education Institutions (No. NJZZ23046).

REFERENCES

- [1] Afzal, I., Javed, T., Amirkhani, M., & Taylor, A. G. (2020). Modern Seed Technology: Seed Coating Delivery Systems for Enhancing Seed and Crop Performance. *Agriculture*, Vol. 10(11), pp. 110526. <https://doi.org/10.3390/agriculture10110526>
- [2] Campos, N., & Sanchez, A. (2012). Towards the Formal Implementation of Hierarchical Discrete-event Controllers in Automated Manufacturing Systems. *IFAC Proceedings Volumes*, Vol. 45, Issue 6, pp. 224-229. <https://doi.org/10.3182/20120523-3-RO-2023.00138>
- [3] Chandravanshi, M. L., & Mukhopadhyay, A. K. (2017). Dynamic analysis of vibratory feeder and their effect on feed particle speed on conveying surface. *Measurement*, Vol. 101, pp. 145-156. <https://doi.org/10.1016/j.measurement.2017.01.031>
- [4] Despotović, Ž. V., Urukalo, D., Lečić, M. R., & Ćosić, A. (2017). Mathematical modeling of resonant linear vibratory conveyor with electromagnetic excitation: simulations and experimental results. *Applied Mathematical Modelling*, Vol. 41, pp. 1-24. <https://doi.org/10.1016/j.apm.2016.09.010>
- [5] Du, Z., Yang, L., Zhang, D., Cui, T., He, X., Xie, C., Jiang, Y., Zhang, X., Mu, J., Wang, H., Xiao, T., & Li, H. (2025). Design and experiment of a soil organic matter sensor-based variable-rate seeding control system for maize. *Computers and Electronics in Agriculture*, Vol. 229, pp. 109752. <https://doi.org/10.1016/j.compag.2024.109752>
- [6] Fowler, A. G., Rakotondrabe, M., & Moheimani, S. O. R. (2013). Closed-Loop Control of a Novel 2-DOF MEMS Nanopositioner with Electrothermal Actuation. *IFAC Proceedings Volumes*, Vol. 46, Issue 5, pp. 391-398. <https://doi.org/10.3182/20130410-3-CN-2034.00115>

- [7] Gai, W., & Wang, H. (2013). Closed-loop dynamic control allocation for aircraft with multiple actuators. *Chinese Journal of Aeronautics*, Vol. 26, Issue 3, pp. 676-686. <https://doi.org/10.1016/j.cja.2013.04.031>
- [8] Jarrar, H., El-Keblawy, A., Ghenai, C., Abhilash, P. C., Bundela, A. K., Abideen, Z., & Sheteiwy, M. S. (2023). Seed enhancement technologies for sustainable dryland restoration: Coating and scarification. *Science of the Total Environment*, Vol. 904, pp. 166150. <https://doi.org/10.1016/j.scitotenv.2023.166150>
- [9] Javed, T., Afzal, I., Shabbir, R., Ikram, K., Saqlain Zaheer, M., Faheem, M., Haider Ali, H., & Iqbal, J. (2022). Seed coating technology: An innovative and sustainable approach for improving seed quality and crop performance. *Journal of the Saudi Society of Agricultural Sciences*, Vol. 21, Issue 8, pp. 536-545. <https://doi.org/10.1016/j.jssas.2022.03.003>
- [10] Ma, X., Liu, M., Hou, Z., Gao, X., Bai, Y., & Guo, M. (2023). Numerical simulation and experimental study on the pelletized coating of small grain forage seeds (小粒牧草种子丸粒化包衣数值模拟与试验). *Transactions of the Chinese Society of Agricultural Engineering*, Vol. 39, Issue 2, pp 43-52. DOI: 10.11975/j.issn.1002-6819.202211002
- [11] Mucchi, E., Di Gregorio, R., & Dalpiaz, G. (2013). Elastodynamic analysis of vibratory bowl feeders: Modeling and experimental validation. *Mechanism and Machine Theory*, Vol. 60, pp. 60-72. <https://doi.org/10.1016/j.mechmachtheory.2012.09.009>
- [12] Paravar, A., Piri, R., Balouchi, H., & Ma, Y. (2023). Microbial seed coating: An attractive tool for sustainable agriculture. *Biotechnology Reports*, Vol. 37, pp. e781. <https://doi.org/10.1016/j.btre.2023.e00781>
- [13] Pasha, M., Hare, C., Ghadiri, M., Gunadi, A., & Piccione, P. M. (2017). Inter-particle coating variability in a rotary batch seed coater. *Chemical Engineering Research and Design*, Vol. 120, pp. 92-101. <https://doi.org/10.1016/j.cherd.2017.01.033>
- [14] Pedrini, S., Webber, Z., D'Agui, H., Dixon, K., Just, M., Arya, T., & Turner, S. (2023). Customise the seeds, not the seeder: Pelleting of small-seeded species for ecological restoration. *Ecological Engineering*, Vol. 196, pp. 107105. <https://doi.org/10.1016/j.ecoleng.2023.107105>
- [15] Sang, J., Zhao, C., & Zhu, C. (2015). Design of detection and control system for BY-150 seed coating machine (BY-150 型种子包衣机检测控制系统设计). *Transactions of the Chinese Society of Agricultural Machinery*, 37(3), 83-86. <https://doi.org/10.13427/j.cnki.njyi.2015.03.020>
- [16] Upasan, A., & Kumsuwan, Y. (2013). Closed Loop Speed Control of Induction Generator with Scalar-control Inverters. *Energy Procedia*, Vol. 34, pp. 371-381. <https://doi.org/10.1016/j.egypro.013.06.765>
- [17] Yang, W., Zhao, W., & Yang, M. (2014). Development of intelligent seed coating machine control system based on expert system (基于专家系统的智能化种子包衣机控制系统研制). *Journal of Chinese Agricultural Mechanization*, Vol. 35, Issue 1, pp. 216-219+248
- [18] Yi, L. (2020). Problems and countermeasures of grass seed coating technology (草种子包衣技术存在问题及对策). *Chinese Journal of Animal Husbandry and Veterinary*, vol. 12, pp. 193-194
- [19] Zhang, X., Huang, Y., Wang, S., Jiang, L., Li, G., & Xie, Y. (2021). Hierarchical autonomous switching control of a multi-modes omnidirectional mobile robot. *Mechatronics*, Vol. 80, pp. 102692. <https://doi.org/10.1016/j.mechatronics.2021.102692>
- [20] Zheng, X., Huang, J., Li, Y., Wan, L., Ma, X., Song, J., & Liu, Z. (2024). Numerical simulation method of seed pelletizing: Increasing seed size by powder adhesion. *Powder Technology*, Vol. 444, pp. 119991. <https://doi.org/10.1016/j.powtec.2024.119991>
- [21] Zhang, X., Hou, Z., & Dai, N. (2022). Design of an Electric Control System for Seed Coating Based on LabVIEW (基于 LabVIEW 的种子包衣电控系统的设计). *Journal of Chinese Agricultural Mechanization*, Vol. 44, Issue 7, pp. 112-117. DOI:10.13427/j.cnki.njyi.2022.07.019.

PAME-YOLO: A MODEL FOR APPLE LEAF LESION DETECTION IN COMPLEX ENVIRONMENTS BASED ON IMPROVED YOLOv8s

PAME-YOLO: 一种适用于复杂环境的基于改进 YOLOv8s 的苹果叶片病斑检测模型

Yuansheng BING¹⁾, Xiao YU^{*1,2)}, Zeqi LIN¹⁾, Feng YU¹⁾

¹⁾ School of Computer Science and Technology, Shandong University of Technology, Zibo, Shandong/China

²⁾ Institute of Modern Agricultural Equipment, Shandong University of Technology, Zibo, Shandong/China

Tel: +8613163680678; E-mail: neaufish@sdut.edu.cn

Corresponding author: Xiao Yu

DOI: <https://doi.org/10.35633/inmateh-75-97>

Keywords: YOLOv8s, apple leaf lesions, target detection, attention mechanism, complex environments

ABSTRACT

The detection of apple leaf lesions in complex environments is hindered by several factors, such as the small size of lesion areas, variability in lighting conditions, and occlusions caused by overlapping leaves. These issues significantly limit the performance of existing detection models. Therefore, an enhanced detection algorithm for apple leaf lesions, termed PAME-YOLO, is proposed in this study, building upon the YOLOv8s framework. First, the main convolutional module is reconstructed using the Parallelized Patch-Aware Attention Module (PPA) while fusing Efficient Multi-Scale Attention (EMA). This effectively strengthens the model's capacity to localize small target lesions in complicated environments. Second, an Attention-based Intra-scale Feature Interaction (AIFI) is introduced into the feature extraction network to replace the Spatial Pyramid Pooling-Fast (SPPF) module, which better captures the subtle features of apple leaf lesions. Next, the downsampling enhancement module is designed to mitigate information loss during the original downsampling process, which contributes to a significant improvement in detection precision. Finally, the Efficient Head is designed, a lightweight and efficient detection head that lowers parameter count and computational intricacy without sacrificing accuracy. Compared with YOLOv8s, the proposed model delivered a notable enhancement in performance, with precision (P) increasing by 0.8 points and recall (R) by 1.5 points. The mAP@0.5 achieved 91.4%, which is 1.5 percentage points higher than that of YOLOv8s. Meanwhile, the mAP@0.5:0.95 rose to 56.4%, reflecting an increase of 1.4 percentage points. The improved model realizes the accurate detection of apple leaves lesions in complicated surroundings, offering reliable technical assistance for disease prevention and contributing to the development of the apple industry.

摘要

在复杂环境中，苹果叶片病斑的检测受到诸多因素的影响，如病斑区域尺寸较小、光照条件变化以及叶片重叠造成的遮挡等问题。这些因素严重限制了现有检测模型的性能。为此，本文在 YOLOv8s 算法的基础上提出了一种称为 PAME-YOLO 的苹果叶片病斑检测算法。首先，本文使用并行补丁感知注意力模块同时结合高效多尺度注意力机制对主干卷积模块进行重构，这有效增强了模型在复杂环境中对小目标病斑的定位能力。其次，本文在特征提取网络中引入基于注意力的尺度内特征交互模块，来替换原有的快速空间金字塔池化模块，以更好地捕捉苹果叶片病斑的细微特征。随后，本文设计了新的下采样增强模块，以弥补原有下采样过程中的信息丢失，从而显著提高检测精度。最后，我们设计了一种轻量高效的检测头 Efficient Head，该检测头能够在保持精度的同时降低模型参数和计算复杂度。与 YOLOv8s 相比，所提出的模型在性能上取得了显著提升，精确率 (P) 提高了 0.8 个百分点，召回率 (R) 提高了 1.5 个百分点，mAP@0.5 达到了 91.4%，比 YOLOv8s 高出了 1.5 个百分点，同时 mAP@0.5:0.95 达到了 56.4%，提高了 1.4 个百分点。综上所述，改进后的模型实现了在复杂环境下对苹果叶片病斑的精准检测，为病害防控提供了可靠的技术支持，助力了苹果产业的可持续发展。

INTRODUCTION

Apple is a major cash crop that is widely consumed across the globe (Bai *et al.*, 2021). However, it is susceptible to diseases, particularly those affecting the leaves. Leaf infections can significantly disrupt physiological metabolism and photosynthesis, directly impairing apple growth and harvest. Consequently, prompt and precise identification of apple leaf diseases is essential for effective orchard management. This not only enables growers to prevent the spread of diseases and improve fruit quality and yield but also contributes to substantial economic and environmental benefits.

In earlier years, manual observation was the primary method for identifying apple diseases in most orchards and farms. However, this approach is time-consuming, prone to misdiagnosis, and increasingly inadequate for meeting the demand for fast and accurate disease identification. As artificial intelligence continues to evolve, object detection techniques powered by deep learning (Yann *et al.*, 2015) have found increasing application in the agricultural situations. According to the processing pipeline, models for object detection are typically categorized into two distinct groups: two-stage and one-stage detectors. The most representative example of a two-stage detection method is R-CNN (GIRSHICK *et al.*, 2014). Gong *et al.*, (2023) suggested an improved Faster R-CNN algorithm. This algorithm has an average accuracy of 63.1% on an annotated apple leaf disease dataset, which surpasses other target detecting techniques. Zhang *et al.*, (2021) presented a soybean leaf disease detection model named MF3R-CNN, which employs skip connections between multiple layers in the feature extraction network to facilitate multi-feature fusion, thereby effectively fulfilling the necessities of object detection tasks. Despite the great detection accuracy provided by two-stage algorithms, their training and inference processes are time-consuming, which limits their suitability for deployment in intelligent agricultural equipment.

Compared to two-stage detectors, one-stage detection methods are more appropriate for practical applications due to their better scalability and faster inference speed. Among the most well-known one-stage detection methods is the YOLO series, which has gained widespread deployment in the agriculture industry. Abulizi *et al.*, (2024) integrated lightweight dynamic Sampling (DySample) to enhance small lesion feature extraction and employed Margin Penalty Distance Intersection over Union (MPDIoU) for precise localization of overlapping lesion boundaries. These enhancements achieved higher accuracy in tomato leaf disease recognition. To identify apple leaf diseases, Li *et al.*, (2023) proposed an improved YOLOv5s model by introducing a Bi-Directional Feature Pyramid Network (BiFPN), a Transformer module, and the Convolutional Block Attention Module (CBAM) to reduce background interference. The model achieved an average detection accuracy of 84.3% in natural environments. Gao *et al.*, (2024) replaced the traditional convolution and C2f structure with GhostConv and C3Ghost, respectively. They also incorporated the Global Attention Mechanism (GAM) and a BiFPN to enhance the detection of small apple leaf lesions in complicated environments.

Although the studies described above have made some progress, several problems in detecting apple leaf diseases remain unresolved. First, some disease spots are small, and different diseases may exhibit similar features, resulting in the model struggling to detect the lesions accurately. Additionally, in real-world cultivation environments, factors such as leaf occlusion and uneven lighting can reduce the model's capability to concentrate on diseased areas, limiting detection performance. Moreover, some studies have placed excessive emphasis on improving precision, while overlooking the increased model intricacy and computing expenses.

To overcome these issues, PAME-YOLO was developed, an enhanced YOLOv8s-based model for detecting apple leaf disease spots. The following contributions were made by this paper:

1. The C2f-PE module is designed by incorporating the PPA (Xu *et al.*, 2024) module and the EMA (Ouyang *et al.*, 2023) attention mechanism to further enhance the capability of identifying small lesions and differentiating similar features.
2. The SPPF module is substituted with the scale interaction module AIFI (Zhao *et al.*, 2024), which strengthens the high-level feature extraction, improves detection performance, and reduces redundant computation.
3. The downsampling enhancement module MPC is designed to improve the model's attention to small lesions in complex backgrounds, enabling it to better preserve key contextual information and enhance detection accuracy.
4. Aiming at the problem of high computational and large parametric quantities of the original detection head, the Partial Convolution (PConv) (Chen *et al.*, 2023) was employed to design the Efficient Head detection head, which increases detection efficiency while lowering computing costs and model complexity.

MATERIALS AND METHODS

Dataset

The raw images of the apple leaf disease in this research are acquired by the publicly available dataset AppleLeaf9 (Yang et al., 2022). Approximately 94% of the images in this dataset were taken in field settings, which ensures that the collected image data meet the requirements for complex backgrounds. From the dataset, 1,607 images of three common apple leaf spot diseases—Alternaria leaf spot, rust, and grey spot—were selected as the original image data. To address the limited original dataset, the data augmentation was applied to increase the images to 8952. After that, the augmented images were separated into training, validation, and test sets at a proportion of 8:1:1, with disease locations and categories annotated using the Labeling annotation tool.

YOLOv8

YOLOv8 is a strong visual recognition framework made to handle a range of computer vision tasks, including object detection, image classification, and instance segmentation (Wang et al., 2025). Compared to its predecessors YOLOv5 and YOLOv7, YOLOv8 delivers improved recognition precision along with accelerated inference performance. Its architecture comprises three primary components: the backbone, the neck, and the detection head (Tian et al., 2024). In feature extraction and fusion stages, YOLOv8 substitutes the C2f structure for the C3 module that was utilized in YOLOv5, facilitating richer gradient flow and improving feature representation. The classification and detection tasks are separated in the head by YOLOv8's decoupled structure, enhancing detection performance. Furthermore, it replaces the anchor-based mechanism of YOLOv5 with an anchor-free approach, giving the model greater flexibility and efficiency in identifying objects of different sizes and forms.

Improved YOLOv8 Algorithm

To address challenges such as the small size of disease spot features, high similarity among different lesions, reduced detection accuracy in complicated cultivation environments, and the extensive parameters, this study suggests an improved model based on YOLOv8s, named PAME-YOLO, as illustrated in Fig. 1.

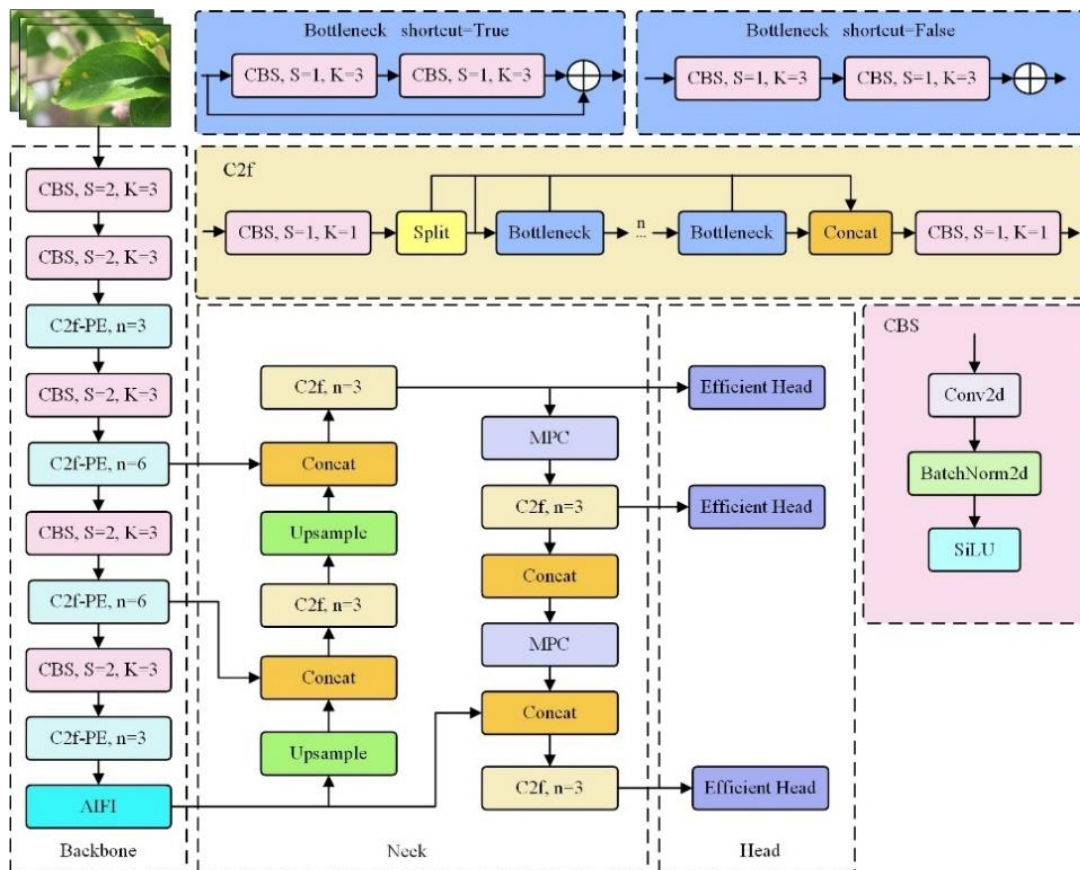


Fig. 1 - Overall architecture of the PAME-YOLO

C2f-PE

The C2f module can enable multi-scale feature extraction and fusion. Its multi-branch design strategy enhances the network's adaptability and representation capability. However, its ability to detect small targets and distinguish similar features remains limited. Therefore, this study redesigns and enhances the C2f module by integrating the PPA module and the EMA attention mechanism. The enhanced C2f-PE module is displayed in Fig. 2.

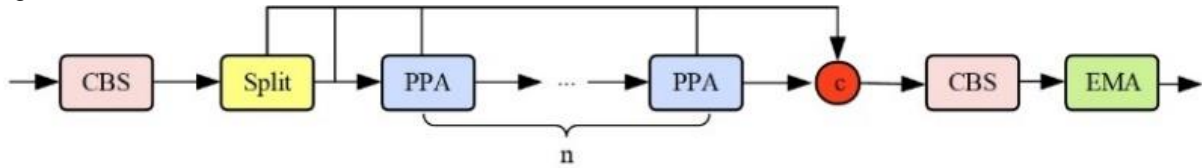


Fig. 2 - Structure of C2f-PE Module

Multiple downsampling operations can lead to the loss of details about small targets and missed detections. To make the model better at locating small disease spots, this paper incorporates the PPA module from the context fusion network HCF-Net into the C2f module. As illustrated in Fig. 3, the PPA module is made up of two essential parts: a multi-branch feature extraction architecture and an attention mechanism. The main benefit of PPA is its multi-branch feature extraction strategy. This method effectively increases the accuracy of detecting tiny disease spots on apple leaves by employing parallel branches, which extract features at different sizes and levels. The initial step in the feature extraction procedure is to convert the input tensor $F \in \mathbb{R}^{H \times W \times C}$ into $F' \in \mathbb{R}^{H \times W \times C'}$ using point-wise convolution. Then, F' is handled through three distinct parallel paths, which respectively generate the local feature tensor $F_{local} \in \mathbb{R}^{H \times W \times C'}$, the global feature tensor $F_{glocal} \in \mathbb{R}^{H \times W \times C'}$, and the linear feature tensor $F_{conv} \in \mathbb{R}^{H \times W \times C'}$. Lastly, the fused feature map $\tilde{F} \in \mathbb{R}^{H \times W \times C'}$ is obtained by adding the three tensors. After multi-branch feature extraction, an attention module is applied to produce the final output. The attention module is constituted by a sequence of channel attention (Wang et al., 2020) and spatial attention mechanisms (Woo et al., 2018). This design is particularly effective for detecting small disease spots on apple leaves and suppressing background noise, leading to improved accuracy and robustness of the model. The parameter p, which defines the patch size, serves to differentiate local and global branches, thereby promoting spatial feature fusion and displacement encoding (Bi et al., 2025).

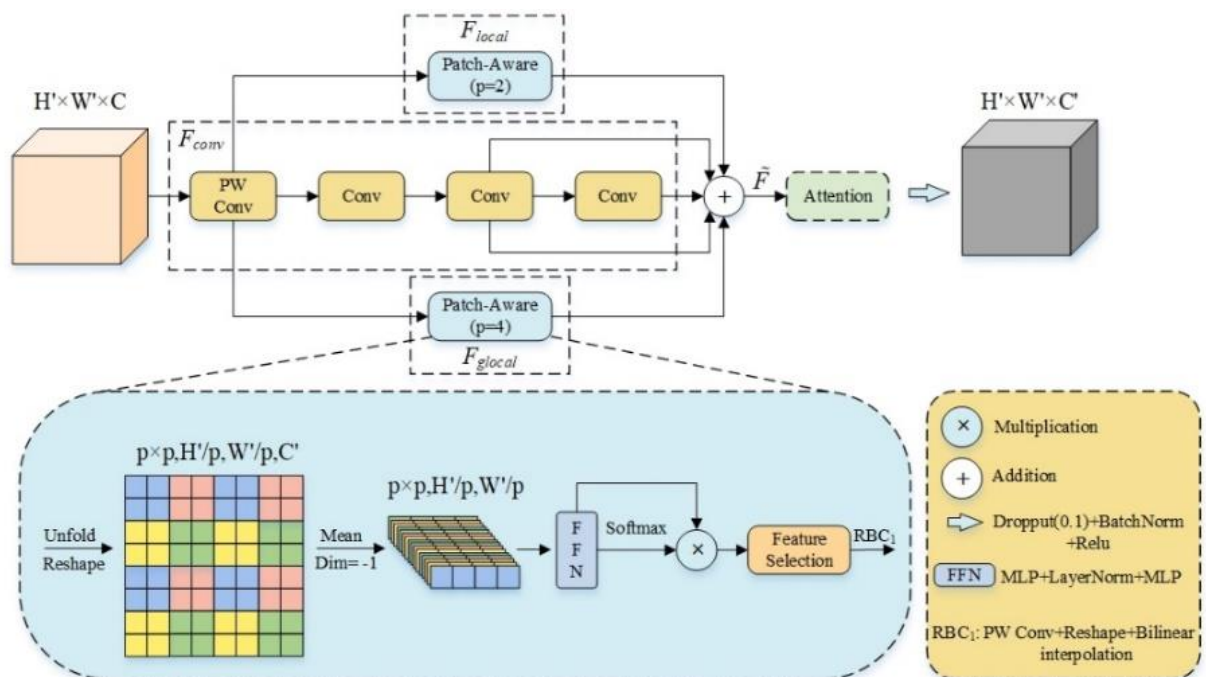


Fig. 3 - Parallelized Patch-Aware Attention Module

A certain degree of feature similarity exists both among different types of disease spots and between disease spots and surrounding objects, which can result in false detections. This issue is related to the limitation in the model feature extraction capability or the insufficient ability to select extracted feature information. To strengthen the model's feature extraction capacity, this paper also incorporates the EMA attention mechanism after the C2f module.

Fig. 4 presents the EMA module, which adopts cross-spatial learning to achieve efficient scale-aware attention. It reshapes part of the channels into the batch dimension and applies grouping in the channel dimension without requiring dimensionality reduction. This successfully stops channel feature information from being lost while reducing computational cost, and it features high accuracy and a low parameter count.

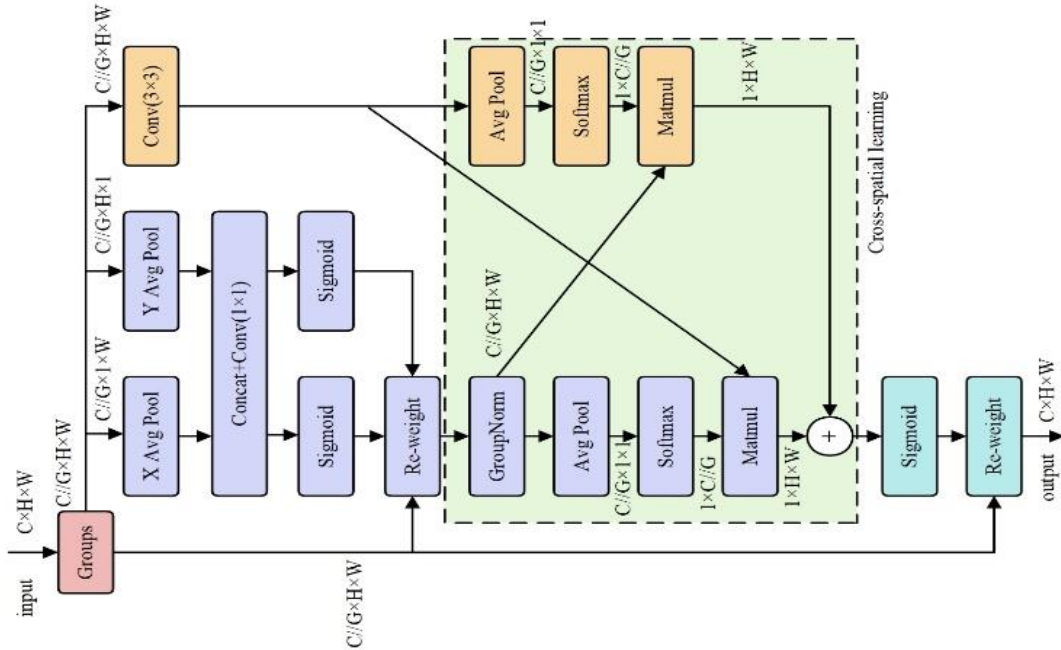


Fig. 4 - EMA attention mechanism framework diagram

AIFI

The SPPF module is an essential component of YOLOv8, enabling multi-scale feature fusion to enhance contextual information capture. However, it incurs a high cost of calculation. To mitigate this problem, the SPPF module is substituted with the AIFI module, which focuses on processing advanced image features. This contributes to enhanced detection accuracy while lowering computational cost. Compared to traditional multi-scale feature fusion methods, AIFI employs a single-scale Transformer encoder to focus feature fusion within the same scale. This helps capture finer-grained information and reduces the computational cost. Advanced features contain richer semantic content compared to low-level features, which have limited contribution due to insufficient semantic representation. As a result, the intra-scale interactions of lower-level features are redundant.

As seen in Fig. 5, the AIFI firstly linearizes the input 2D picture S_5 , converting it into a one-dimensional vector by arranging the rows sequentially. Then, a multi-head attention mechanism is employed, enabling the model to gather information from different spatial locations in the sequence, which strengthens its capacity to model long-range dependencies in the feature representation. The processed sequence is then combined with the original input for layer normalization. Afterward, the output undergoes a feed-forward network (FFN) for non-linear transformation and feature extraction. Finally, the FFN output is added to the previously normalized result and undergoes an additional layer of normalization. The one-dimensional vector is then reshaped back into its 2D form, F_5 , for further processing in the subsequent network. The specific process can be described by Equations (1) and (2).

$$Q = K = V = Flatten(Input) \tag{1}$$

$$Output = Reshape(FNN(MultiHead(Q, K, V))) \tag{2}$$

Here, Flatten refers to the flattening operation, Q , K , and V are the results of applying the flattening operation on the 2D image, MultiHead denotes the multi-head attention mechanism, Reshape stands for the reshaping operation, and FFN represents the feed-forward network operation.

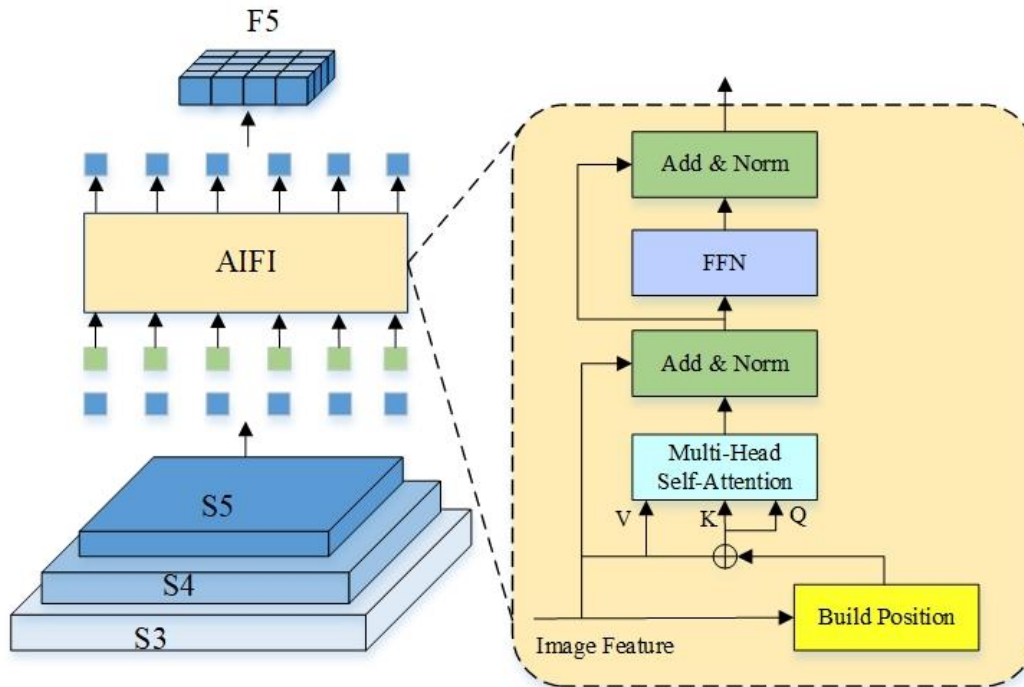


Fig. 5 - Structure of AIFI module, S3, S4, S5 represent different scale feature maps

Thanks to the Multi-Head Self-Attention and the FFN network, AIFI realize a scale-level interactions between advanced features, which helps the network better represent the connections of conceptual entities in the picture. This leads to improved extraction of subtle features of apple leaf spots, enhancing the detection performance and reducing false detections. Meanwhile, due to the feature fusion within the scale in AIFI, the computational cost of the detection model is reduced.

MPC Downsampling Enhancement Module

Downsampling techniques facilitate the processing of feature maps at different scales and objects by reducing the spatial size of feature maps. However, they also lead to information loss and a reduction in resolution. To address the partial loss of leaf spot information during downsampling, this study designs an improved downsampling module called MPC, as visualized in Fig. 6. The MPC downsampling is designed to strengthen the model's concentration on small lesion details in complex backgrounds, effectively preserving crucial contextual information and improving detection accuracy. The main components of the MPC are a 1x1 convolution, a Maxpool2d operation, a PConv, and a 3x3 convolution.

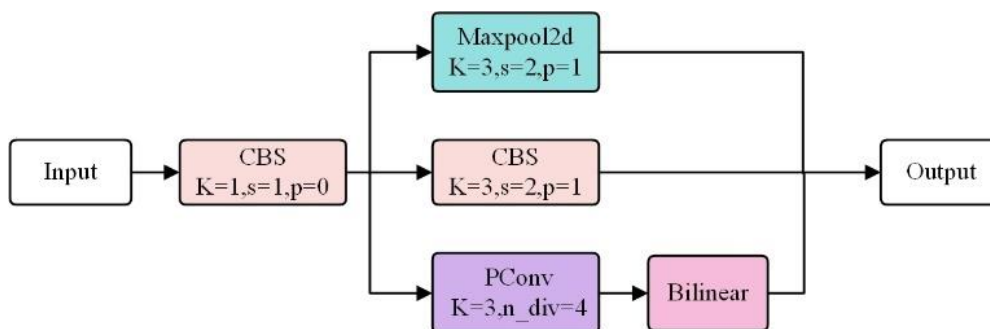


Fig. 6 - Structure of MPC module

Traditional downsampling in YOLOv8 uses a standalone 3x3 convolution module. While this module captures key features from the input data through filtering operations on the feature map, it also reduces the resolution of the feature map, impairing the capability to capture subtle patterns. To overcome this difficulty and improve the model's effectiveness and lightweight design, this study integrates PConv into the downsampling process. A comparison of the convolution operations between partial convolution and standard convolution is shown in Fig. 7.

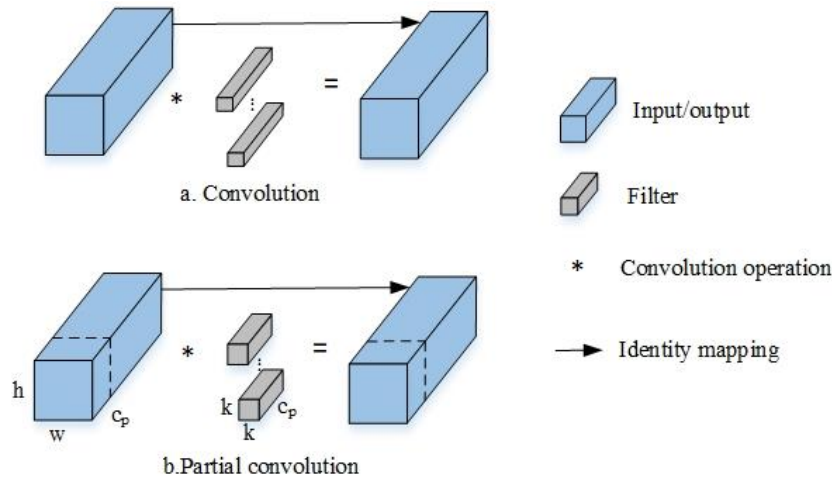


Fig. 7 - Convolutional operation comparison diagram

PConv leverages the inherent redundancy of feature representations by selectively performing standard convolution on a portion of the input channels without influencing the transformations of the remaining channels (Fu et al., 2024). Here, h , w represent the input height and width dimensions, respectively; c is input channels count; c_p refers to used convolution channels count; k denotes the kernel size used for the partial convolution; and r indicates the ratio of used convolution channels. The Floating Point Operations (FLOPs) after using partial convolution can be represented by Equation (3).

$$F_{PConv} = h \times w \times k^2 \times c_p^2 \tag{3}$$

$$r = \frac{c_p}{c} \tag{4}$$

Given the default participation ratio r set to 1/4, PConv achieves only 1/16 of the computational complexity compared to standard convolution, significantly reducing the time and memory required for convolution operations.

During the downsampling enhancement process, MPC integrates PConv with Maxpool2d to better balance computational efficiency and information integrity. Partial convolution extracts spatial features by applying convolution operations to only a portion of channels, keeping the other channels unaltered during feature processing. This strategy enables the model to efficiently process complex input images while demonstrating excellent capability in extracting disease spot features in complex backgrounds. Furthermore, it keeps the model from obsessively concentrating on irrelevant information, such as the background, thus reducing unnecessary computational overhead. As a result, both detection precision and computing efficiency in leaf spot detection are improved.

Efficient Head

Compared to the coupled structure of the detection head in the YOLOv5 model, the YOLOv8 head design employs a decoupled structure, in which classification and regression operation are processed separately, as presented in Fig. 8. Specifically, each branch comprises a 3x3 convolutional and a 1x1 convolutional, with each branch designed to focus on its respective task.

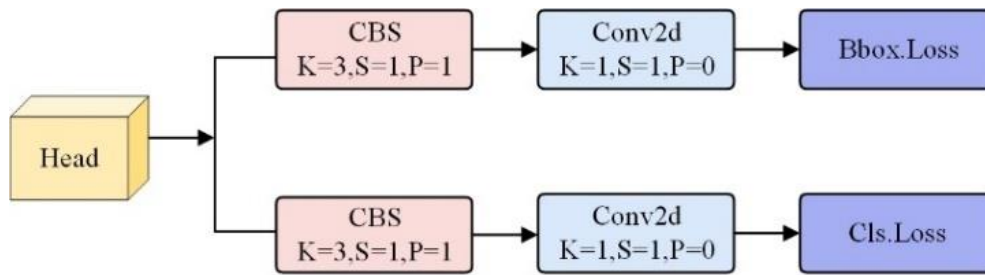


Fig. 8 - Structure of YOLOv8 Detection Head

To lessen the computational overhead and the parameter quantity while improving both detection speed and accuracy, this paper redesigns the Efficient Head based on the concept of parameter sharing, as shown in Fig. 9. The idea of merging first and then splitting is adopted, replacing the original two 3×3 convolutional blocks with a combination of the fast and efficient PConv and a 1×1 convolution. This improvement lowers parameter quantity and computing load while enabling more efficient feature extraction.

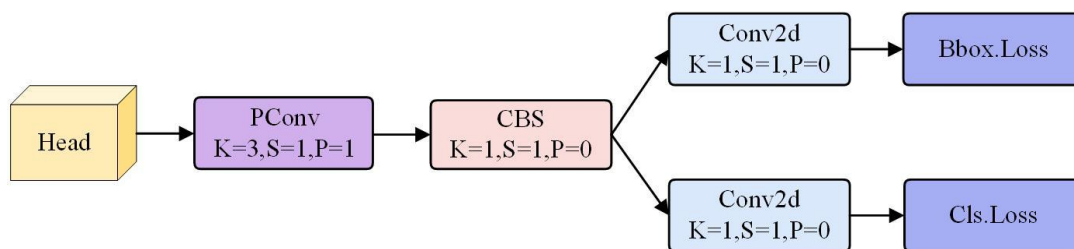


Fig. 9 - Structure of Efficient Head

RESULTS

Experimental Environment

The experimental environment comprised CUDA 11.7 on Ubuntu 18.04, using PyCharm as the development platform, PyTorch 2.0. as the deep learning framework, Python 3.8.10. An NVIDIA RTX 3060 GPU (12 GB) provided hardware acceleration. The training process spanned 150 epochs, adopting the Stochastic Gradient Descent (SGD) optimizer, an initial learning rate of 0.01, a batch size of 16, an initial learning rate of 0.01, with a patience parameter of 50.

Evaluation Metrics

To evaluate the model's performance impartially, frequent object detection metrics are employed, including Precision (P), Recall (R), mean Average Precision (mAP), and FLOPs. The formula is used for calculating P and R can be expressed by Equations (5) and (6).

$$P = \frac{TP}{TP + FP} \tag{5}$$

$$R = \frac{TP}{TP + FN} \tag{6}$$

Here, TP represents the quantity of diseases that the algorithm successfully recognized; FP represents the quantity of diseases that the algorithm incorrectly identified; FN represents the quantity of diseases not identified.

Although precision and recall are commonly used performance metrics, there is an inherent trade-off between them—optimizing one metric often comes at the expense of the other. Therefore, relying solely on either precision or recall fails to present a thorough and intuitive assessment of overall performance of a model. In contrast, mAP integrates characteristics of both metrics by calculating the average precision across varying recall levels, offering a more holistic evaluation. Furthermore, mAP more accurately reflects a model's performance under different detection difficulty levels, making it a more representative metric. The expression used to compute mAP is provided below:

$$AP = \int_0^1 P(R)dR \tag{7}$$

$$mAP = \frac{1}{c} \sum_{i=1}^c AP_i \quad (8)$$

Here c represents the count of classes in the dataset, i stands for the class index, and AP represents the area under the P-R curve for a single class.

Ablation Experiment

To evaluate the effectiveness of the suggested improvements in apple leaf lesion detection, ablation experiments were conducted on each improved method, as illustrated Table 1. All experiments were conducted without the use of transfer learning to ensure a fair and accurate evaluation of the proposed model's performance. A "√" marks that the improved method was applied in the experimental group.

Table 1

Results of ablation experiments										
No.	C2f-PE	AIFI	MPC	Efficient Head	P/%	R/%	mAP@0.5/%	mAP@0.5:0.95/%	FLOPs/G	
1	x	x	x	x	90.5	80.8	89.9	55.0	28.4	
2	√	x	x	x	90.1	81.1	90.9	55.7	33.3	
3	x	√	x	x	91.5	81.3	90.9	56.1	28.3	
4	x	x	√	x	90.1	81.2	90.3	55.3	29.4	
5	x	x	x	√	89.8	81.7	90.5	55.2	21.5	
6	√	√	x	x	89.6	82.4	91.1	56.2	33.2	
7	√	√	√	x	91.6	82.0	91.2	56.1	34.1	
8	√	√	√	√	91.3	82.3	91.4	56.4	27.2	

In Experiment 2, the C2f-PE module was substituted for the C2f module, which leads to a 1.0% improvement in mAP@0.5 relative to the Experiment 1. This result confirms that the C2f-PE module can strengthen the model's capacity for localizing small disease spots, but it also increases the model's computational cost by 14.7%. Experiment 3 replaced the SPPF layer with the AIFI module, resulting in improvements of 0.5% in recall, 1.0% in mAP@0.5, and 1.1% in mAP@0.5:0.95. This demonstrates that the model benefits from intra-scale feature interaction, which enables better extraction of fine-grained features of apple leaf spots and enhances overall detection accuracy. In Experiment 4, the downsampling enhancement module MPC was added, resulting in a 0.4% improvement in mAP@0.5. This confirms that incorporating the MPC module can help the feature extraction process better preserve contextual information and make up for the information lost due to downsampling. After the Efficient Head was introduced in Experiment 5, the model's average precision improved by 0.6%, while its floating-point operations were reduced by 24.3%. This verifies the efficiency and lightweight characteristics of the Efficient Head. In Experiment 7, the ablation results demonstrated a 1.3% improvement in mAP@0.5 and 1.1% and 1.2% increases in precision and recall, respectively, compared with the baseline model. This improved detection performance but also increased the computational cost by 16.7%. Finally, the PAME-YOLO algorithm, which integrates four improvement methods, was compared to the baseline model. The improved PAME-YOLO demonstrated performance gains of 0.8%, 1.5%, 1.5%, and 1.4% in Precision, Recall, mAP@0.5, and mAP@0.5:0.95, respectively, while achieving a 4.2% reduction in computational load. Through a succession of experiments and comparative analysis, the improvements suggested in this paper has been effectively validated.

Detection Head Comparison

This study designs a novel lightweight detection head to enhance the detection efficiency and precision. In comparison experiments, several schemes were tested: (a) sharing two 3×3 convolutions; (b) sharing two 3×3 grouped convolutions; (c) sharing one 1×1 convolution and one 3×3 convolution; (d) sharing one PConv and one 1×1 convolution. Table 2 illustrates the comparison results of four schemes.

Table 2

Comparison experiment of different detection heads					
Plan	P/%	R/%	mAP@0.5/%	FLOPs/G	Parameters/M
(a)	91.5	81.9	91.0	37.5	18246403
(b)	89.9	82.9	91.0	27.0	12311299
(c)	91.2	82.2	91.2	32.5	15493891
(d)	91.3	82.3	91.4	27.2	12589955

From the Table, it can be seen that although schemes (a) and (c) achieve higher mAP values, their computational cost and parameter count are too large, resulting in lower detection efficiency. Scheme (b), while exhibiting lower computational costs and fewer parameters, achieves the lowest precision among all schemes. Scheme (d) effectively balances detection precision with model complexity, delivering a high mAP value alongside a reduction in model parameters. Therefore, scheme (d) is selected as the detection head for the improved model to enhance detection efficiency.

Comparison with Current Advanced Algorithms

A comparison between the PAME-YOLO and other mainstream methods is conducted under the same condition and the same dataset. As presented in Table 3, the PAME-YOLO outperforms other mainstream object detection algorithms in terms of recall, mAP@0.5, and mAP@0.5:0.95. Specifically, the recall is higher than RT-DETR-L, YOLOv5s, YOLOv5m, YOLOv7-tiny, YOLOv8n, YOLOv8s, and YOLOv10s by 6.2%, 3.6%, 2.6%, 2.1%, 4.3%, 1.5%, and 0.4%, respectively, while the mAP@0.5 is higher by 5.2%, 3.0%, 2.0%, 3.4%, 2.8%, 1.5%, and 0.7%, respectively. The YOLOv5m model achieves the highest detection precision, but its parameter and computational requirements are too large. This means it requires higher computational resources and larger storage space to operate, making it unsuitable for real-time tasks. Considering all metrics, PAME-YOLO demonstrates higher detection precision, recall, and stability than other algorithms, with a reasonable model size and computational complexity, allowing it more appropriate for agricultural applications.

Table 3

Model	P/%	R/%	mAP@0.5/%	mAP@0.5:0.95/%	Parameters/M	FLOPs/G
RT-DETR-L	87.1	76.1	86.2	51.9	31989905	103.4
YOLOv5s	91.5	78.7	88.4	54.0	7018216	15.8
YOLOv5m	92.3	79.7	89.4	54.5	20861016	47.9
YOLOv7-tiny	87.2	80.2	88.0	51.6	6020400	13.2
YOLOv8n	89.9	78.0	88.6	54.2	3006233	8.1
YOLOv8s	90.5	80.8	89.9	55.0	11126745	28.4
YOLOv10s	90.6	81.9	90.7	54.5	8037282	24.5
PAME-YOLO	91.3	82.3	91.4	56.4	12589955	27.2

Comparison of different diseases under YOLOv8s and PAME-YOLO

A comprehensive comparative analysis of precision, recall, and mAP@0.5 was conducted for each type of leaf disease using the YOLOv8s and PAME-YOLO models. In Table 4, PAME-YOLO achieves notable improvements in all three metrics relative to the original YOLOv8s. This implies that the model possesses a stronger ability to recognize diseases and can effectively reduce the occurrence of missed detections and false positives, particularly for small target lesions.

Table 4

Class	YOLOv8s			PAME-YOLO		
	P/%	R/%	mAP@0.5/%	P/%	R/%	mAP@0.5/%
Alternaria leaf spot	91.6	69.7	85.8	92.4	71.2	86.7
Grey spot	89.1	82.4	88.4	89.5	85.1	91.6
Rust	90.8	90.4	95.5	92.0	90.5	95.9

Heatmap Visualization

In the apple leaf disease detection task, the Grad-CAM (Selvaraju et al., 2017) method was used to visually highlight the regions of interest and the areas where the model concentrates its attention during object detection, further enhancing the comprehension of the decision-making process. In the heatmap, darker pixels indicate a greater contribution to the prediction result, while lighter pixels indicate a smaller contribution. The heatmaps before and after model improvement are displayed in Fig. 10. It is evident that the PAME-YOLO model pays less attention to irrelevant information such as the background, and focuses more on the disease spots, making it better suited for complex orchard environments.

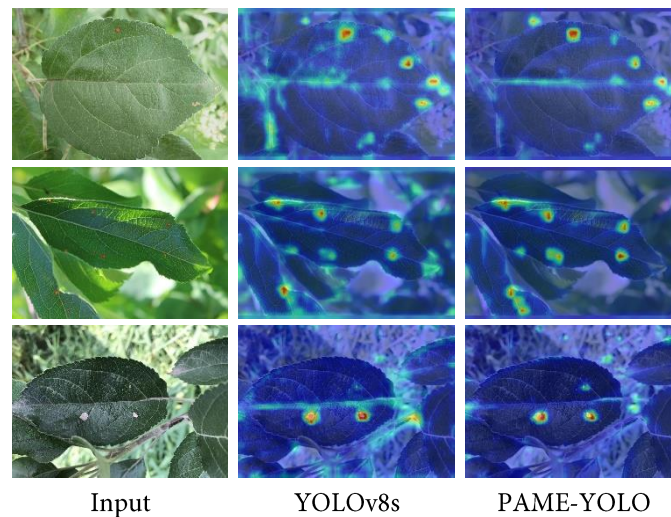


Fig. 10 - Visualization results of a heatmap

Visualization of Detection Results

Several images of leaves affected by Alternaria leaf spot, grey spot, and rust diseases were randomly selected to present detection results. As illustrated in Fig. 11, YOLOv8s shows suboptimal performance in detecting small spots on leaves in complex backgrounds. Specifically, it fails to detect some instances of Alternaria leaf spot and rust disease when the targets are small. In contrast, PAME-YOLO enhances the localization capability for small lesions by introducing the C2f-PE module, enabling accurate detection of spots without missed cases. Additionally, when detecting grey spot disease, the baseline model mistook the photographer's finger at the bottom left of the image for a lesion, resulting in a false detection. In contrast, PAME-YOLO correctly distinguished the actual spots from irrelevant objects, avoiding false detections and demonstrating higher robustness. In the figure, the yellow box represents a missed target, the blue box represents an error detection target.

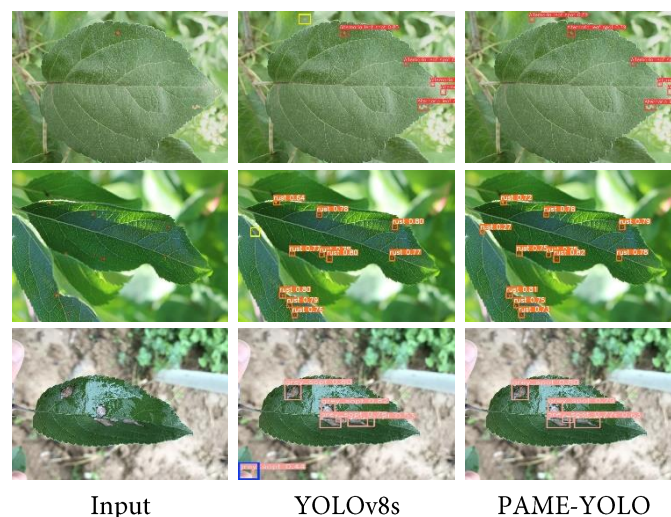


Fig. 11 - Detection effect comparison diagram

Model Deployment and Application Implementation

As illustrated in Fig. 12, the trained model for apple leaf disease spot detection was quantized using the NCNN inference framework and it was deployed to a mobile platform, based on which an application named Apple Leaf Disease Detector was subsequently developed. To ensure cross-platform compatibility, the user interface was developed using uni-app. The application was then compiled into an APK file via Android Studio and subsequently installed and tested on a smartphone running Android 13. The main interface of the application includes an image preview panel, a button for uploading images from the gallery, a camera button for real-time capture, and a detection button.

Users are provided with the option to either import apple leaf images from the device gallery or acquire them in real time via the built-in camera. After the image is uploaded or captured, the user can click the "Detection" button to initiate model inference. The detection results are displayed on the image in the form of bounding boxes, along with disease category labels and confidence scores. As can be observed from Fig. 13, this app can accurately detect apple leaf lesion across different categories even in challenging orchard environments.

The deployed application is lightweight and responsive, supporting accelerated inference via NCCN. This enables efficient, low-latency identification of apple leaf diseases in the field, offering strong practical value for fruit growers.

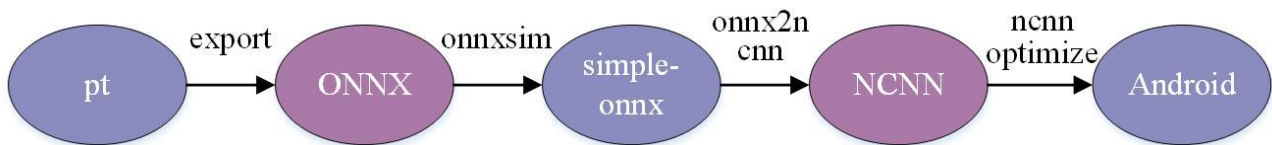


Fig. 12 - Model quantization and conversion pipeline



Fig. 13 - Detection of Apple Leaf Diseases on Mobile Platforms

CONCLUSIONS

This study proposed an enhanced object detection algorithm called PAME-YOLO that focused on the issues of low detection accuracy and the susceptibility to overlooking small lesion targets in apple leaf disease diagnosis under complicated backgrounds. Specifically, the C2f-PE feature extraction module was designed to improve the model's detection accuracy for small lesion targets. In addition, an intra-scale feature interaction mechanism was introduced to capture more fine-grained lesion information and reduce false detections. The downsampling enhancement module, MPC, was designed to ensure that critical contextual information was comprehensively preserved at the feature extraction stage. Lastly, a lightweight and efficient detection head was employed to reduce model parameters and computational cost, thereby enhancing both detection efficiency and accuracy. The outcomes of the experiment demonstrate that, compared with the YOLOv8s baseline, the improved algorithm yields an increase of 1.5% in recall, 1.5% in mAP@0.5, and 1.4% in mAP@0.5:0.95. Relative to other mainstream algorithms, the proposed algorithm shows exceptional detection performance under complicated conditions, highlighting its advantages for practical applications. This provides important technical assistance for the early control and management of apple leaf diseases, helping to reduce crop loss and improve orchard health. In subsequent research, the dataset will be further expanded by incorporating a greater diversity of apple leaf disease images, aiming to strengthen the model's generalization capability and practical usefulness.

ACKNOWLEDGEMENT

The author has been supported by the National Social Science Foundation of China (No. 24BTQ031).

REFERENCES

- [1] Abulizi, A., Ye, J., Abudukelimu, H., Guo, W. (2024). DM-YOLO: improved YOLOv9 model for tomato leaf disease detection. *Frontiers in Plant Science*, 15, 1473928. DOI: <https://doi.org/10.3389/fpls.2024.1473928>.
- [2] Bai, X., Li, Z., Li, W., Zhao, Y., Li, M., Chen, H., et al. (2021). Comparison of Machine-Learning and CASA Models for Predicting Apple Fruit Yields from Time-Series Planet Imageries. *Remote Sensing*, 13(16), 3073. DOI: <https://doi.org/10.3390/rs13163073>.
- [3] Bi, J., Li, K., Zheng, X., Zhang, G., Lei, T. (2025). SPDC-YOLO: An Efficient Small Target Detection Network Based on Improved YOLOv8 for Drone Aerial Image. *Remote Sensing*, 17(4), 685. DOI: <https://doi.org/10.3390/rs17040685>.
- [4] Chen, J., Kao, S., He, H., Zhuo, W., Wen, S., Lee, C. (2023). Run, Don't Walk: Chasing Higher FLOPS for Faster Neural Networks. In *2023 IEEE/CVF Conference on Computer Vision and Pattern Recognition (CVPR)*, pp.12021-12031, Vancouver, BC, Canada. DOI: <https://doi.org/10.1109/CVPR52729.2023.01157>.
- [5] Fu, C., Ren, L., Wang, F. (2024). Recognizing beef cattle behavior under automatic scene distinction using lightweight FABF-YOLOv8s (自动化场景区分下 FABF-YOLOv8s 轻量化肉牛行为识别方法). *Transactions of the Chinese Society of Agricultural Engineering*, 40(15), 152-163. DOI: <https://doi.org/10.11975/j.issn.1002-6819.202404073>.
- [6] Girshick, R., Donahue, J., Darrell, T., Malik, J. (2014). Rich Feature Hierarchies for Accurate Object Detection and Semantic Segmentation. In *2014 IEEE Conference on Computer Vision and Pattern Recognition*, pp.580-587, Columbus, OH, USA. DOI: <https://doi.org/10.1109/CVPR.2014.81>.
- [7] Gong, X., Zhang, S. (2023). A High-Precision Detection Method of Apple Leaf Diseases Using Improved Faster R-CNN. *Agriculture*, 13(2), 240. DOI: <https://doi.org/10.3390/agriculture13020240>.
- [8] Gao, L., Zhao, X., Yue, X., Yue, Y., Wang, X., Wu, H., et al. (2024). A Lightweight YOLOv8 Model for Apple Leaf Disease Detection. *Applied Sciences*, 14(15), 6710. DOI: <https://doi.org/10.3390/app14156710>.
- [9] LeCun, Y., Bengio, Y., Hinton, G. (2015). Deep learning. *Nature*, 521(7553), 436–444. DOI: <https://doi.org/10.1038/nature14539>.
- [10] Li, H., Shi, L., Fang, S., Yin, F. (2023). Real-Time Detection of Apple Leaf Diseases in Natural Scenes Based on YOLOv5. *Agriculture*, 13(4), 878. DOI: <https://doi.org/10.3390/agriculture13040878>.
- [11] Ouyang, D., H, S., Zhang, G., Luo, M., Guo, H., Zhan, J. (2023). Efficient Multi-Scale Attention Module with Cross-Spatial Learning. In *ICASSP 2023-2023 IEEE International Conference on Acoustics, Speech and Signal Processing (ICASSP)*, pp.1-5, Rhodes Island, Greece. DOI: <https://doi.org/10.1109/ICASSP49357.2023.10096516>.
- [12] Selvaraju, RR., Cogswell, M., Das, A., Vedantam, R., Parikh, D., Batra, D. (2017). Grad-CAM: Visual Explanations from Deep Networks via Gradient-Based Localization. In *2017 IEEE International Conference on Computer Vision (ICCV)*, pp.618-626, Venice, Italy. DOI: <https://doi.org/10.1109/ICCV.2017.74>.
- [13] Tian, Y., Zhao, C., Zhang, T., Wu, H., Zhao, Y. (2024). Recognition Method of Cabbage Heads at Harvest Stage under Complex Background Based on Improved YOLOv8n. *Agriculture*, 14(7), 1125. DOI: <https://doi.org/10.3390/agriculture14071125>.
- [14] Wang, H., Zhang, Y., Zhu, C. (2025). DAFPN-YOLO: An Improved UAV-Based Object Detection Algorithm Based on YOLOv8s. *Computers, Materials & Continua*, 83(2), 1929-1949. DOI: <https://doi.org/10.32604/cmc.2025.061363>.
- [15] Wang, Q., Wu, B., Zhu, P., Li, P., Zuo, W., Hu, Q. (2020). ECA-Net: Efficient Channel Attention for Deep Convolutional Neural Networks. In *2020 IEEE/CVF Conference on Computer Vision and Pattern Recognition (CVPR)*, pp.11531-11539, Seattle, WA, USA. DOI: <https://doi.org/10.1109/CVPR42600.2020.01155>.
- [16] Woo, S., Park, J., Lee, JY., Kweon, IS. (2018). CBAM: Convolutional Block Attention Module. In *Proceedings of the European conference on computer vision (ECCV)*, p.3-9, Munich, Germany. DOI: https://doi.org/10.1007/978-3-030-01234-2_1.
- [17] Xu, S., Zheng, S., Xu, W., Xu, R., Wang, C., Zhang, J., et al. (2024). HCF-Net: Hierarchical context fusion network for infrared small object detection. In *2024 IEEE International Conference on Multimedia and Expo (ICME)*, pp.1-6, Niagara Falls, ON, Canada. DOI: <https://doi.org/10.1109/ICME57554.2024.10687431>.

- [18] Yang, Q., Duan, S., Wang, L. (2022). Efficient Identification of Apple Leaf Diseases in the Wild Using Convolutional Neural Networks. *Agronomy*, 12 (11), 2784. DOI: <https://doi.org/10.3390/agronomy12112784>.
- [19] Zhang, K., Wu, Q., Chen, Y. (2021). Detecting soybean leaf disease from synthetic image using multi-feature fusion faster R-CNN. *Computers and Electronics in Agriculture*, 183, 106064. DOI: <https://doi.org/10.1016/j.compag.2021.106064>.
- [20] Zhao, y., Lv, W., Xu, S., Wei, J., Wang, G., Dang, Q. (2024). DETRs Beat YOLOs on Real-time Object Detection. In *2024 IEEE/CVF Conference on Computer Vision and Pattern Recognition (CVPR)*, pp.16965-16974, Seattle, WA, USA. DOI: <https://doi.org/10.1109/CVPR52733.2024.01605>.

POINTNET++LR3D: AN IMPROVED POINTNET++ MODEL FOR INDIVIDUAL IDENTIFICATION OF PIG BACK POINT CLOUD

POINTNET++LR3D: 一种改进的 POINTNET++ 模型用于猪背点云个体识别

Yongshuai YANG¹⁾, Yaqi YAN¹⁾, Yuhang LI¹⁾, Jiarui ZHANG¹⁾, Xiaochan GAO¹⁾, Jie HU¹⁾, Juan LIU^{*2)}

¹⁾ College of Software, Shanxi Agricultural University, Taigu, Shanxi / China;

²⁾ College of Liberal Arts and Sciences, Shanxi Agricultural University, Taigu, Shanxi / China;

Corresponding authors: Juan LIU; Tel: +86-18335463280; E-mail: liujuannk@sxau.edu.cn

DOI: <https://doi.org/10.35633/inmateh-75-98>

Keywords: Individual identification; 3D point cloud; PointNet++; local context fusion; bilinear regularization

ABSTRACT

Individual pig identification is a key technology to realize fine farming management, which is of great value in the fields of animal behavior tracking and health monitoring. Aiming at the limitations of traditional 2D vision methods in stereo feature extraction, this study uses pig back point cloud to effectively capture deep 3D features such as back contour and skin texture and proposes an improved PointNet++ model for pig individual identification, which explicitly captures the local geometric and feature differences through two-stream differential coding, refines the feature distribution by using low-rank bilinear decomposition and residual sharpening strategies, and then establish the two-way dependency between channel and space to generate the global perceptual map, and finally combine with Mish activation function to enhance the nonlinear feature extraction. The experiment takes the hybrid long white pig as the research object and uses the Intel D435i depth camera to collect data and construct the segmentation and identification model. The results show that the improved model PointNet++LR3D achieves an overall accuracy of 97.11% in the individual identification task, which is an improvement of 1.9% compared to the base PointNet++MSG model. In addition, extended tests on the ModelNet40 dataset show an improvement in classification accuracy to 93.1%, validating the generalization ability of the architectural improvements. This study provides an efficient solution for non-contact pig identification based on point cloud, demonstrating the potential for application in fine-tuned farming.

摘要

猪只个体识别是实现精细化养殖管理的关键技术，在动物行为追踪、健康监测等领域具有重要价值。针对传统二维视觉方法在立体特征提取上的局限性，本研究使用猪背点云有效捕捉背部轮廓和皮肤纹理等深度三维特征，提出了一种改进的 PointNet++ 模型用于猪只个体识别，通过双流差分编码显式捕捉局部几何与特征差异，利用低秩双线性分解和残差锐化策略细化特征分布，进而建立通道与空间的双向依赖关系生成全局感知图，最后结合 Mish 激活函数增强非线性特征提取。实验以杂交长白猪为研究对象，使用 Intel D435i 深度相机采集数据，构建分割与识别模型。结果表明，改进模型 PointNet++LR3D 在个体识别任务中整体准确率达 97.11%，相比基础 PointNet++MSG 模型提升 1.9%。此外，在 ModelNet40 数据集上的扩展测试显示分类准确率提升至 93.1%，验证了架构改进的泛化能力。本研究为基于点云的非接触式猪只识别提供了高效解决方案，展现了在精细化养殖中的应用潜力。

INTRODUCTION

In modern agriculture and animal management, individualized management and fine monitoring have become the key factors in improving breeding efficiency and animal welfare (Neethirajan *et al.*, 2024). Individual identification is the key technology to realize individual tracking of health data (Vidal *et al.*, 2021), which provides the necessary support for various aspects of precision management, health monitoring, fine feeding, behavioral monitoring and analysis, breeding selection, and automated management (Su *et al.*, 2024; Krampe *et al.*, 2024).

The traditional animal individual identification technology mainly has two major categories: physical tag identification and radio frequency identification (Ruiz *et al.*, 2011); currently applied in the breeding industry is still the most used in the physical tag using ear tags or collars to distinguish each body, however, the physical tags are prone to wear and tear, loss and damage, but also requires manual operation close contact with the animal, which increases the human cost as well as the risk of animal stress (Martínez *et al.*, 2016).

With the rapid development of computer vision and deep learning technologies (Wang *et al.*, 2022), vision-based individual identification methods have gradually become a research hotspot, which significantly improves the flexibility and robustness of identification mainly by capturing the external features of pigs, such as their faces, body sizes, or back contours (Saleem *et al.*, 2021; García *et al.*, 2020). However, 2D images are still unresolved due to factors such as light, angle and occlusion, which make it difficult to fully capture the three-dimensional morphological features of pigs, especially in dynamic scenes, and the stability of the identification effect still needs to be improved. In contrast, 3D point cloud technology (Guo *et al.*, 2020) obtains three-dimensional information about pigs through depth sensors (Yu *et al.*, 2024), which can more comprehensively describe the dorsal contour, curvature, and spatial structural features of pigs (Shuai *et al.*, 2020), and has become a hot spot of research by its advantage of being able to obtain three-dimensional depth information of pigs.

In recent years, significant progress has been made in applying point cloud technology in livestock individual identification. Zhou and others first proposed an individual identification method based on the pig back point cloud, utilizing PointNet++ for back point cloud segmentation and constructing a pig individual identification model based on the improved PointNet++LGG algorithm by increasing the adaptive global sampling radius, deepening the network structure, and increasing the number of features, with accuracy reaching 95% (Zhou *et al.*, 2023). Similarly, Kyaw *et al.* used the PointNet++ algorithm to detect and segment the dorsal surface region of a cow from a point cloud image, providing applications for individual cow identification, lameness detection, and body condition scoring (Kyaw *et al.*, 2024). These studies achieved non-contact and high-precision individual identification through 3D point cloud technology, overcoming traditional methods' limitations and providing technical support for fine farming.

Inspired by the above studies, this study notes that the application of point cloud technology in livestock individual identification is still in its infancy and that most of the current improvements of PointNet++ focus on the feature extraction stage, especially on enhancing the expression of local features by optimizing the grouping of points such as multi-scale grouping or dynamic grouping (Luo *et al.*, 2024; Nong *et al.*, 2023). However, fewer studies have systematically improved the characterization ability of point cloud features by starting from the fusion mechanism of local and global features. Therefore, this study proposes a new improvement strategy based on this, constructing an innovative module of local context fusion and global bilinear regularization, integrating it into the network architecture of PointNet++, explicitly modeling geometric and feature differences within the framework of PointNet++, and refining the feature distributions through global sensing, and utilizing low-rank bilinear decomposition and residual sharpening strategies to refine the feature distributions. Feature distributions to establish the bidirectional dependence between channel and space. This approach not only enhances the model's sensitivity to the local details of the pig back point cloud, such as curvature and edges, but also improves the feature differentiation through global regularization, thus achieving higher accuracy and robustness in the task of livestock individual identification in dynamic scenes.

MATERIALS AND METHODS

Introduction of experimental pig data

The data on the pigs used in this experiment were collected from Huifeng Breeding Professional Cooperative in Guangling County, Datong City, Shanxi Province, and the experimental pigs were labeled and approved by the pig farm. The pig farm features a semi-enclosed structure, and the experimental data were collected under two natural conditions: with sunlight and without sunlight. In order to increase the robustness of the experiment, no external lights were used throughout the collection, and point cloud data were collected from the backs of ten pigs, all of which were crossbred long white pigs and pigs with similar age, weight, and body hair color were selected as the collection objects.

Data Acquisition

In this study, the following acquisition plan was developed during the acquisition process, as shown in Fig.1. The depth camera Intel D435i was used to collect the depth information of the pig's back, the D435i adopts a dual-camera design and calculates the depth information based on binocular stereo vision (Servi *et al.*, 2024; Zhang *et al.*, 2022), which generates high-resolution depth data by capturing the parallax images from both cameras. In order to capture individual pigs in multiple postures, the recorded video was used to capture depth information and RGB color images simultaneously from the upper part of the pig's back.

To verify whether different camera heights and angles affect identification accuracy, the camera positions were intentionally varied. The cameras were mounted on the top of a telescopic pole, which was handheld to capture approximately one minute of video from each angle of the pig's back. The videos were recorded at a resolution of 468 × 828 pixels and a frame rate of 30 Hz. In total, 10 video recordings in the BAG format were collected.



Fig. 1 - (a) Environment of the pig house and Acquisition of pig back point cloud data

Data pre-processing

(1) Depth image to point cloud image conversion

Each BAG file stores the depth and RGB color information of the ten pigs. Additionally, the camera's intrinsic parameters (focal lengths f_x , f_y and principal point coordinates C_x , C_y) are recorded within each file. These parameters are extracted by parsing the BAG files.

First, the BAG files are parsed frame by frame using Intel RealSense to extract depth and color frames. Depth images are manually filtered with the assistance of corresponding color images; only those with poor-quality back data are removed to ensure the reliability of the experimental dataset. Since the objective of this experiment is to assess whether individual pigs can be accurately identified based on body features - such as the contours and curvature of the back - rather than color features, only the depth images are retained after filtering. These retained depth images are subsequently converted into point cloud representations.

The depth value of each pixel in the depth image is converted to the actual 3D coordinates by combining the camera's internal reference, assuming that the pixel coordinates are U and V , and the actual depth is Z . The 3D coordinates (X, Y, Z) of the point can be expressed as:

$$X = \frac{(U - C_x) \cdot Z}{f_x}, \quad Y = \frac{(V - C_y) \cdot Z}{f_y}, \quad Z = \text{depth_image}(U, V) \quad (1)$$

where: $(U - C_x)$ and $(V - C_y)$ denote the horizontal and vertical distances of the pixel point relative to the center of light, and the X Y coordinates of the pixel point in the actual 3D space can be obtained by multiplying the distance by the depth value of the point, Z , and dividing by the focal length, f_x or f_y .

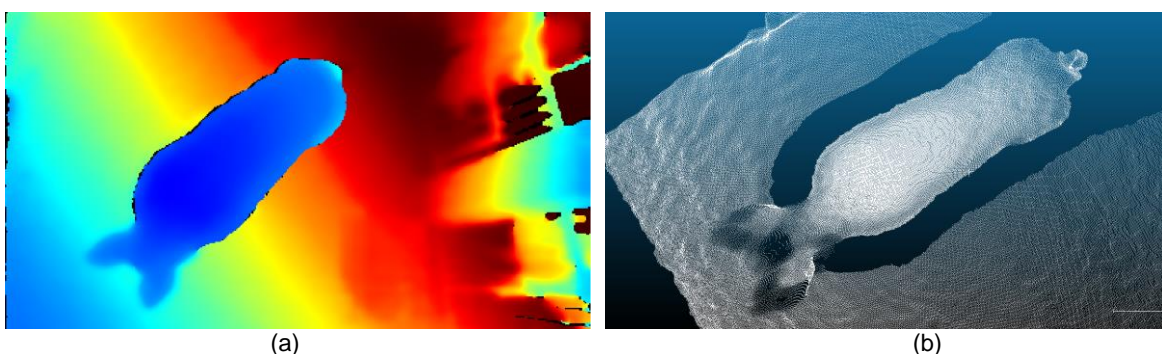


Fig. 2 - Depth images converted to point cloud images

(a) Pig depth image (b) Pig point cloud image

(2) Pig back point cloud labeling

The generated dorsal point cloud data not only has the pig body point cloud but also includes a large number of background point clouds, using CloudCompare software to label the point clouds as pig dorsal point clouds and background point clouds because the pig is in a low head posture most of the time and the head bobbing is more obvious, most of the captured head point cloud images are incomplete and badly adhered to the ground and walls, in order to avoid the interference of the head point cloud, the head is labeled as the background point when labeling the point clouds, only the dorsal point cloud is retained as the segmentation target. As shown in Fig. 3, the pig has two main postures, standard standing and twisted body, and the two points with the most considerable curvature changes between the neck and the back of the pig are segregated for labeling.

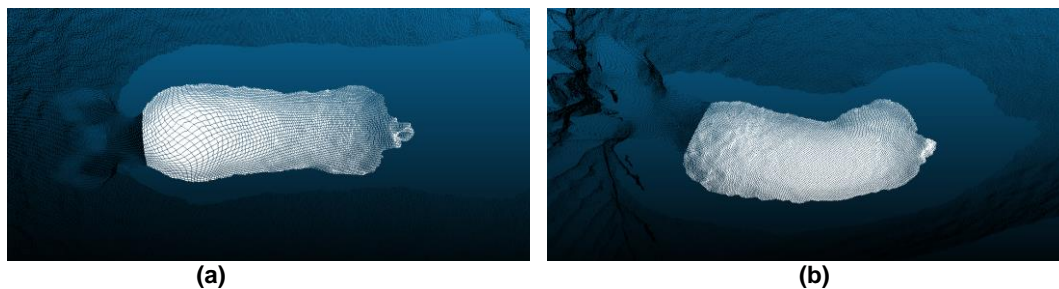


Fig. 3 - Pig back point cloud labelling in two poses
 (a) Splitting of a pig in standard standing position (b) Segmentation of a pig with twisted body

Segmentation and identification Modelling

The process of pig individual identification based on pig back point cloud is mainly composed of two parts: segmentation model construction and identification model construction. First, the collected raw data are converted into point cloud images, then the background and head are removed by the segmentation model. Finally, the segmented pig back point cloud is input into the individual identification model, and the specific number of the pig is output.

Back - background point cloud segmentation

(1) Segmentation method

The PointNet family of networks are neural networks specialized in point cloud data processing that directly manipulate irregular point cloud data without the need to convert the point cloud data into regular grids or voxels (Qi *et al.*, 2017). The segmentation problem in this study is relatively simple, with only two parts, the back and the background, but the data used in this study is a dynamic moving image of a pig, and the posture of the pig at the neck is severely deformed when it is moving. Compared with PointNet, PointNet++ extracts local features layer by layer through the process of 'sampling-grouping-feature extraction-feature propagation,' which is more delicate processing of local features, so the PointNet++ network is chosen to build the segmentation model in this study.

(2) Segmentation model based on PointNet++MSG

As shown in Fig. 4, the segmentation network chooses the PointNet++ Multiscale Grouping Feature Learning (PointNet++MSG) framework, which includes four parts: two-layer sampling, multiscale grouping, feature extraction downsampling and feature propagation upsampling (Qi *et al.*, 2017).

Due to the vast number of points in the original point cloud, random sampling of the original point cloud is required, and the network receives the randomly sampled globally uniformly sampled points containing xyz coordinates and normal vectors. Feature extraction is performed by three Set Abstraction (SA) layers downsampling step by step: SA1 receives the 6-dimensional point cloud input, extracts 64-, 128-, and 128-dimensional features and splices them in [0.1,0.2,0.4] triple radius on 512 sampling points; SA2 generates 256-dimensional features in [0.4,0.8] double radius on 128 sampling points; SA3 generates 256-dimensional features by global pooling to generate 1024-dimensional global features. Feature propagation is performed by Feature Propagation (FP) with layer-by-layer upsampling: FP3 fuses global and SA2 features, FP2 reconstructs the mid-level geometry, and FP1 splices the original point coordinates with labels to recover fine-grained features. The classification head uses a two-layer convolutional network to output semantic category probability distributions for pig back and background.

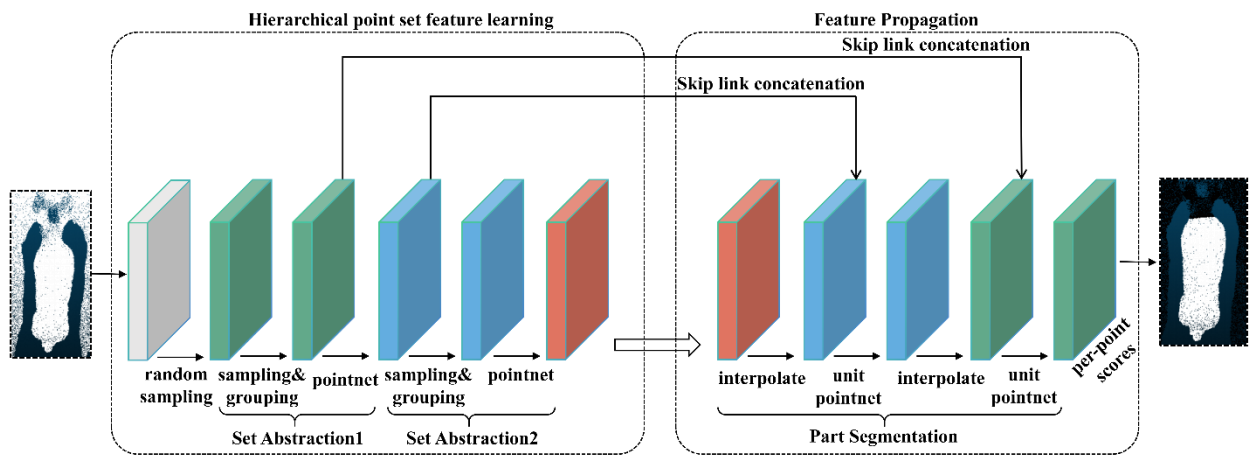


Fig. 4 - Segmentation model for pig back based on PointNet++MSG

Individual identification of pigs

(1) Individual identification method

Compared with segmentation, the identification task needs to focus on local and global feature extraction. In this study, individual identification models for pigs are developed based on the single-scale (SSG) and multi-scale (MSG) grouping strategy algorithms of PointNet and PointNet++, respectively, as the baseline model for individual identification. An improved model PointNet++LR3D with local context fusion as well as global bilinear regularization is proposed, which significantly improves the characterization of high-dimensional features of pig dorsal point clouds by means of dual-stream differential coding of geometries and features, low-rank bilinear decomposition and residual sharpening strategies.

(2) Individual pig identification model based on PointNet++MSG

As shown in Figure 5, the individual pig identification model and segmentation model are similar in principle, except that compared to the segmentation task, the individual identification only has 'sampling-grouping-feature extraction' without the process of feature propagation, and the 1024-dimensional global features obtained after three-layer SA feature extraction are directly input into the classification layer, and the classification layer outputs the category of each pig through a three-layer full connection. The classification layer outputs the class distribution probability of each pig.

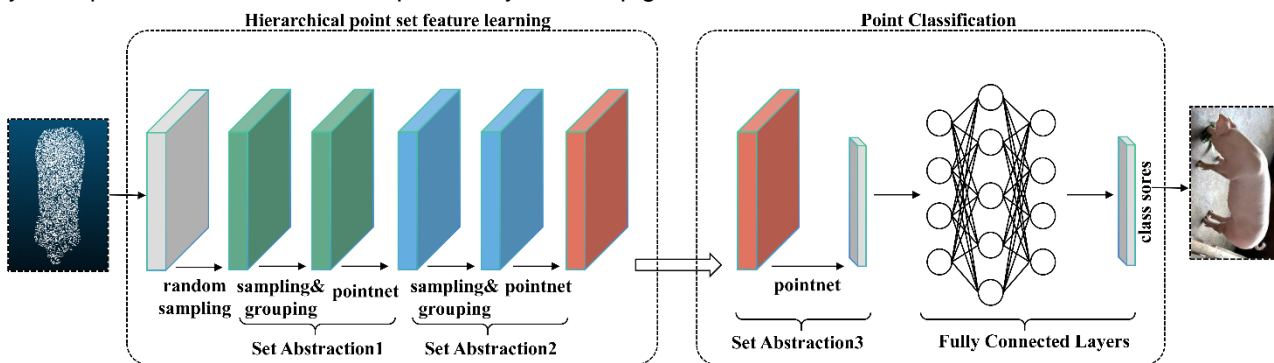


Fig. 5 - Individual identification model for pigs based on PointNet++MSG

Local Context Fusion with Bilinear Regularization Strategies for LR3D Modules

In traditional point cloud data processing networks, PointNet++ only aggregates MLP-encoded features in local coordinates, ignoring differences in features between neighboring points, and PointNet++'s Set Abstraction aggregates local features through farthest-point sampling and grouping and extracts features only through MLP stacking, does not explicitly model point-neighborhood relationships, and lacks the sensitive capture of geometric differences such as curvature and regular vector changes. EdgeConv, on the other hand, mainly performs dynamic graph convolution based on neighborhood point feature differences without directly modeling 3D geometric coordinate relationships. As shown in Figure. 6, this study uses a CNN-based model to learn feature maps, proposes dual-stream differential coding to model both geometric and feature differences to capture local structural changes explicitly, and enables geometric and feature contexts to be encoded separately through shared MLP and asymmetric pooling using split aggregation to avoid confusion between coordinate and feature information and enhance interpretability.

(1) Local context fusion strategy for two-stream feature splicing

To construct the local context for each point, the k-nearest neighbor (KNN) algorithm is employed to identify its neighborhood, which is a widely used neighborhood finding method in point cloud processing. The KNN algorithm calculates the 3D Euclidean distances from all points in the point cloud to a target point p_i and selects the k closest points as its neighbors: $\mathcal{N}(p_i) = \{p_{i1}, p_{i2}, \dots, p_{ik}\} \in \mathcal{N}(p_i)$, by combining the edge $\forall p_{ik} \in \mathcal{N}(p_i)$ between p_i itself and its k neighbors, the local geometric map in 3D space is: $\tilde{p} = [p_i; p_{ik} - p_i] \in \mathbb{R}^{k \times 6}$, where p_i is the current point, and $p_{ik} - p_i$ is the coordinate difference reflecting the local geometric structure. Thus, the local geometric map of all points P is denoted as $\tilde{P} = [p_1, p_2, \dots, p_i, \dots, p_N] \in \mathbb{R}^{N \times k \times 6}$. Finally, the local geometric map is encoded by shared MLP, and the local geometric context encoding is aggregated by applying the Max Pooling function to k neighbors:

$$P = \max_k \left(MLP_{\theta}(\tilde{P}) \right), P \in \mathbb{R}^{N \times \frac{C}{2}} \quad (2)$$

Meanwhile, the local feature map of f_i in C-dimensional space can be formed: $\tilde{f} = [f_i; f_{ik} - f_i] \in \mathbb{R}^{k \times 2C}$, where f_{ik} is the corresponding feature of $p_{ik} \in \mathcal{N}(p_i)$, and $f_{ik} - f_i$ is the feature difference, which reflects the semantic difference. Therefore, the local feature map of a feature map F is represented as $\tilde{F} = [f_1, f_2, \dots, f_i, \dots, f_N] \in \mathbb{R}^{N \times k \times 2C}$. The local feature context encoding is obtained by following a similar operation in Equation (2):

$$F = \max_k \left(MLP_{2\theta}(\tilde{F}) \right), F \in \mathbb{R}^{N \times \frac{C}{2}} \quad (3)$$

Where $MLP_{2\theta}$ is another shared MLP encoding the local feature map, finally the local geometric context and the local feature context() are concatenated as the output of the final local context fusion block:

$$\mathcal{F}_L = \text{concat}(P, F), \mathcal{F}_L \in \mathbb{R}^{N \times C} \quad (4)$$

Compared with EdgeConv operations, the method proposed in this study defines and constrains both local geometric context and feature context and has inherent 3D geometric relationships that can directly reflect local surface geometric changes and semantic differences. In addition, local context fusion blocks can be flexibly deployed at different point cloud resolutions and CNN layers, which benefits most existing point cloud networks.

(2) Global bilinear regularization

In addition to collecting more local details for the feature representation of each point, the global bilinear regularized blocks proposed in this study aim to refine the feature maps by considering the global perception of the entire point cloud. In conventional self-attention mechanisms, global perception is estimated as long-range dependencies between point features, i.e., cosine similarity, which consumes significant memory. In contrast, the global perception in this study is computed as element-wise dependencies between feature maps based on global channels and point descriptors, and through a low-rank decomposition strategy, the memory consumption is significantly reduced.

In order to encode the global channel descriptor, firstly, the input features are linearly transformed by applying the weight matrix $W_C \in \mathbb{R}^{C \times \frac{C}{r}}$, where r is the reduction factor to reduce the dimension of the fused output $\mathcal{F}_L \in \mathbb{R}^{N \times C}$; then, the ReLU function is utilized to not only provide the nonlinearity after linearly mapping with W_C but also to satisfy the requirement of non-negativity in Equation (7); lastly, through the average pooling operation on the N elements along the spatial axis, the spatial information can be compressed into the global channel descriptor g_c . The above operation is as follows:

$$g_c = \text{avg}_N \left(ReLU(\mathcal{F}_L W_C) \right), g_c \in \mathbb{R}^{\frac{C}{r}} \quad (5)$$

Where ' $\mathcal{F}_L W_C$ ' is the matrix product between \mathcal{F}_L and W_C , and 'avg' denotes the average pooling along the spatial dimension N with a reduction factor satisfying $r \geq 2$. Furthermore, $g_c = [\mu_1, \mu_2, \dots, \mu_j, \dots, \mu_{\frac{C}{r}}]$, where μ_j represents the global response of the j -th channel in the whole point cloud feature map.

The global point-by-point descriptor g_p can also be generated using a similar approach in the context of another weight matrix $W_p \in \mathbb{R}^{C \times \frac{C}{r}}$, the ReLU function, and an average pooling operation on the $\frac{C}{r}$ elements along the channel axis:

$$g_p = \text{avg}_{\frac{C}{r}} \left(ReLU(\mathcal{F}_L W_p) \right), g_p \in \mathbb{R}^N \quad (6)$$

In addition, $g_p = [\lambda_1, \lambda_2, \dots, \lambda_i, \dots, \lambda_N]$, where λ_j is the global response of the i -th point in the whole point cloud feature map.

Unlike the use of Hadamard product between vectors, the geometric mean $\sqrt{\lambda_i \mu_j}$ captures the higher-order interactions of the channel with the space, providing a more robust global response than arithmetic averaging, and captures the low-rank global bilinear response by taking the square root of the outer product of g_p and g_c :

$$G = \text{sqrt}(g_p \otimes g_c), G \in \mathbb{R}^{N \times \frac{C}{r}} \tag{7}$$

where the element η_{ij} located in the i th row and j th column of G is mathematically computed as:

$$\eta_{ij} = \sqrt{\lambda_i \mu_j}, \eta_{ij} \in \mathbb{R} \tag{8}$$

The synthesis of the global bilinear response of all elements according to the corresponding point-by-point and channel descriptions in Equation 6 can be interpreted as an effective and efficient method in the following way. For each element, λ_i and μ_j are the arithmetic mean of the i th point and j th channel, respectively, and η_{ij} is the geometric mean of λ_i and μ_j . Firstly, taking the square root enhances the numerical stability, and secondly, it captures the bi-directional dependence of the channel on the space and provides a higher-order averaged response based on the spatial and channel-related information.

(3) Residual Sharpening Feature Recovery

After restoring the channel dimensions using a shared MLP, a residual connection is employed to preserve local features. Finally, the channel dimensions are fully recovered, and a full-size global perceptual map is generated:

$$\mathcal{F}_G = \text{MLP}(G + \mathcal{F}_L W_C + \mathcal{F}_L W_p), \mathcal{F}_G \in \mathbb{R}^{N \times C} \tag{9}$$

The average pooling operations in Equations 4 and 5 are used to compress global information from the point cloud and channel space, respectively; however, average pooling, as a conventional method for feature map compression, tends to generate smooth global representations that may weaken the uniqueness and representativeness of the features. To this end, this study proposes a more effective global-aware feature exploitation strategy to enhance feature differentiation in point cloud analysis. Specifically, to sharpen the learned features, the uniqueness of local features is emphasized by subtracting the global perceptual feature \mathcal{F}_G from the local context fusion output \mathcal{F}_L . This subtraction effectively filters out redundant patterns originating from the global average vectors g_p and g_c , thereby reinforcing the distinctiveness of local features. The use of the Mish activation function further enriches the final output feature map by introducing additional nonlinear transformations.

$$\mathcal{F}_{out} = \text{Mish}(\mathcal{F}_L - \mathcal{F}_G), \mathcal{F}_{out} \in \mathbb{R}^{N \times C} \tag{10}$$

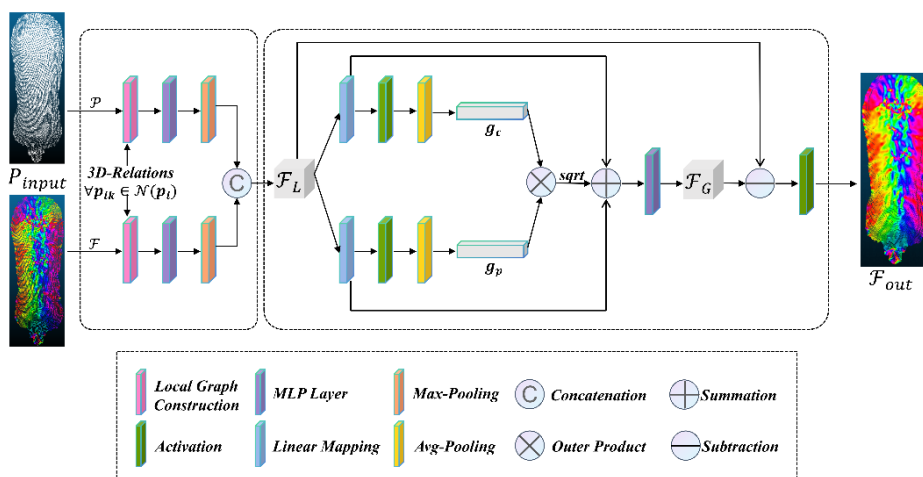


Fig. 6 - LR3D module introducing local context fusion and bilinear regularization

Integration of LR3D module in PointNet++MSG network

The LR3D (Local-Regional 3D) module proposed in this study is a novel point cloud feature extraction mechanism that enhances point cloud feature representation through two key components: local context fusion and global bilinear regularization. The LR3D module is integrated into the PointNet++(MSG) network architecture, and feature enhancement is mainly performed at two key layers, as shown in Figure 7, in the Set

Abstraction (SA) layer of PointNet++(MSG), by inserting the LR3D module after the SA1 and SA2 layers, respectively, with the following improvement strategies:

The LR3D module is introduced after the SA1 layer to explicitly capture local geometric and feature differences through a two-stream differential coding strategy for local context fusion. Local context encoding \mathcal{F}_L is generated using a shared MLP with asymmetric pooling, while the global perceptual map \mathcal{F}_G is produced via a global bilinear regularization block applied to the dual feature streams. This process refines the feature distribution using low-rank bilinear decomposition and a residual sharpening strategy, establishing a bidirectional dependency between channel and spatial dimensions. As a result, the network gains a stronger understanding of the relationship between global structures and local details in the pig back point cloud. The final output feature map \mathcal{F}_{OUT} undergoes nonlinear transformation through the Mish activation function, further enhancing the model's robustness and generalization capability in complex point cloud scenarios, such as distortions caused by pig movement and variations in height. This approach strengthens the SA1 layer's ability to capture low-level local structures (e.g., back edges and body contours), addressing the limitation of traditional PointNet++ architectures that rely solely on stacked MLPs, and improves both global consistency and individual differentiation. The LR3D module is subsequently applied after the SA2 layer to further integrate the high-dimensional features extracted by SA1. Finally, the feature stream enhanced by the two LR3D modules is passed through a third Set Abstraction (SA3) layer for global feature aggregation, followed by classification via a multilayer perceptron (MLP).

This staged integration approach makes full use of the multi-scale grouping properties of the SA1 and SA2 layers, enabling the LR3D module to optimize the local and global representation capabilities in the feature extraction stages at different resolutions, respectively. The experimental results show that after adding the LR3D module after the SA1 and SA2 layers, the model's accuracy in the individual pig identification task is significantly improved while maintaining the balance of computational efficiency, which fully verifies the effectiveness of this improvement strategy.

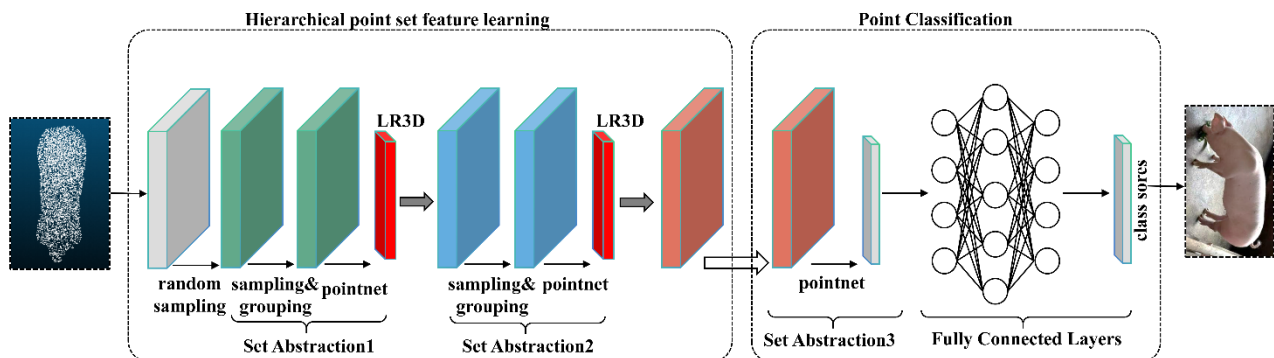


Fig. 7 - PointNet++ MSG classification model incorporating LR3D module

Experimental Sample Setting

This experiment collected 8,300 point cloud images from 10 pigs and processed them to obtain the experimental dataset for 10 pigs. The dataset was divided into training, validation, and test sets in a ratio of 7:1.5:1.5. The training set was used for model learning, the validation set was used for parameter adjustment and performance evaluation, and the test set was used to verify the model's generalization ability.

Experimental parameter settings

The operating system used in this experiment is Ubuntu 20.04, the CPU is Intel Xeon Platinum 8270 2.70GHz, the memory is 64GB, the GPU is NVIDIA GeForce RTX 4090 D, the video memory is 24GB, and the deep learning frameworks are PyTorch 2.4.1 and Python 3.8.

Considering the impact of segmentation and identification speed, the initial sampling and target point numbers for the segmentation model are set to 1024 and 5000, respectively, while the sampling point number for the identification model is set to 2048. The batch size (Batch Size) is set to 8 for both models. The total number of training iterations (Epochs) for the segmentation and identification models is set to 100 and 200 cycles, respectively. The initial learning rate is set to 0.001, using the Adam optimizer with a weight decay rate of $1e-4$. The learning rate is adjusted via a StepLR scheduler, decreasing to 0.7 of the original value every 20 cycles. The loss function employs negative log-likelihood loss (NLL Loss). The experiment is run on a single GPU, with data loading using 10 worker threads to enhance efficiency.

RESULTS

Experimental evaluation indexes

In the segmentation test, six metrics, namely, overall accuracy (OA), mean intersection and merger ratio (mIoU), precision, recall, F1 score, and average segmentation time (AvgTime) for pig back categories, were used to evaluate the segmentation performance of the model for pig back and background. In the identification (classification) test, the six metrics of OA, Precision, Recall, F1, Top-3 Accuracy, and Average identification Time (AvgTime) were used to evaluate the model's identification performance for individual pigs.

In the segmentation test calculation process, four key metrics are primarily used: true positive (TP), false positive (FP), true negative (TN), and false negative (FN). True positive (TP) represents the number of points predicted as pig back that are actually pig back. False positive (FP) represents the number of points predicted as pig back that are actually background. True negative (TN) represents the number of points predicted as background that are actually pig back. False Negative (FN) represents the number of points predicted as background but actually being pig back. In the identification test, TP represents the number of pigs correctly identified as belonging to a specific pig category, FP represents the number of pigs incorrectly identified as belonging to that category, TN represents the number of pigs correctly identified as belonging to the category but not actually belonging to it, and FN represents the number of completely incorrect identifications.

$$\begin{aligned}
 \text{Over Accuracy} &= \frac{TP + TN}{TP + FP + TN + FN} \\
 \text{IOU} &= \frac{TP}{TP + FP + FN} \\
 \text{Precision} &= \frac{TP}{TP + FP} \\
 \text{Recall} &= \frac{TP}{TP + FN} \\
 \text{F1 - score} &= \frac{2(\text{Precision} * \text{Recall})}{\text{Precision} + \text{Recall}}
 \end{aligned} \tag{11}$$

Pig back-Background Segmentation Model training results

In the pig back-background segmentation experiment, this study trained three models on the training and validation sets. Each model's validation accuracy and loss changed during training, as shown in Figure 8. All models' accuracy and loss values steadily increased and decreased with the increase in training iterations and gradually stabilized and converged after approximately 40 iterations. Among them, the PointNet++ MSG and PointNet++ SSG models performed well, with validation accuracy reaching approximately 99.8% and loss values tending towards 0, while the PointNet model performed slightly worse. Therefore, no significant overfitting was observed during training in the models. Overall, PointNet++ MSG achieves the best segmentation performance under the multi-scale grouping strategy, effectively capturing the local geometric features of pig back point clouds, thereby demonstrating stronger robustness and stability in segmentation tasks.

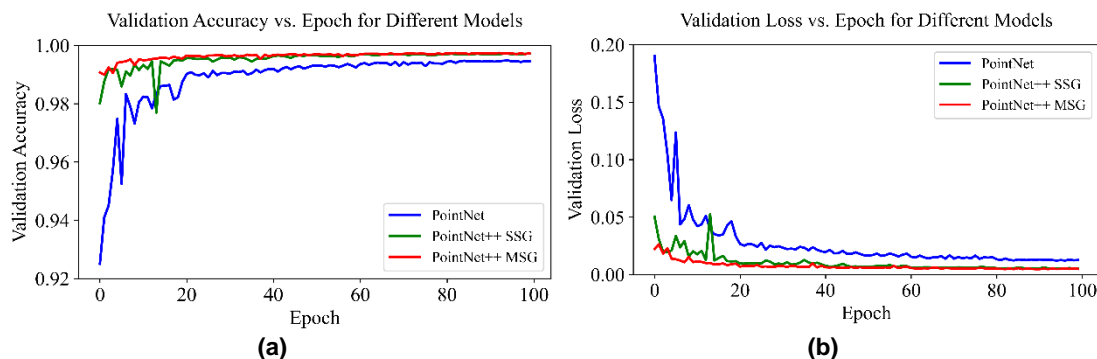


Fig. 8 - Segmentation model validation results

(a) Validation accuracy curves (b) Validation loss curve

Pig back-Background Segmentation model test results

To further explore the segmentation performance of the models on unfamiliar datasets, the segmentation performance of the three models was evaluated using a test set, and the results are shown in Table 1.

PointNet++ MSG achieved 99.83% in Overall Accuracy (OA), which is an improvement of 0.03% to 0.30% compared to the other models. In terms of mean intersection and merger ratio (mIoU), PointNet++ MSG achieved 99.35%, which is 0.10% to 1.05% higher than other models, showing stronger segmentation consistency. In terms of Precision, Recall, and F1 scores, PointNet++ MSG achieved 99.38%, 99.53%, and 99.46%, respectively, which were 0.15% to 1.25%, 0.03% to 0.55% and 0.10% to 0.90% higher than the other models, indicating that it has a significant advantage in reducing misclassification and missed classification with significant advantages. Considering the real-time task requirements of individual identification, in terms of segmentation time (AvgTime), PointNet has the fastest inference speed of 0.004 s/sample but performs relatively poorly regarding segmentation accuracy. Although the inference time of PointNet++ MSG is slightly higher than the other two models at 0.071 s/sample, it still meets the real-time requirements.

In summary, PointNet++ MSG shows excellent performance in the pig back-background segmentation task. This task effectively deals with the complex geometric changes in the dynamic point cloud data and provides a high-quality segmentation basis for the subsequent individual identification task.

Table 1

Segmentation model test results						
Model	OA	mIoU	Precision	Recall	F1	AvgTime
	[%]	[%]	[%]	[%]	[%]	[s/pig]
PointNet	99.53	98.30	98.13	98.98	98.56	0.004
PointNet++SSG	99.80	99.25	99.23	99.50	99.36	0.064
PointNet++MSG	99.83	99.35	99.38	99.53	99.46	0.071

Individual Pig Identification Model training results

In order to evaluate the performance of different models in the pig back point cloud individual identification task, the validation loss and accuracy of the base models (PointNet, PointNet++SSG, PointNet++MSG) and the improved PointNet++LR3D model were compared during the training process. The trend of the validation accuracy and loss of each model is shown in Figure 9. The experimental results show that the loss of all models decreases rapidly at the beginning of training and then levels off. At the same time, the accuracy increases rapidly and stabilizes at the end of training. The base PointNet model has the worst performance with higher test loss and lower accuracy; PointNet++SSG and PointNet++MSG have reduced loss and improved accuracy through hierarchical feature extraction. The improved PointNet++LR3D model performs best with the lowest test loss and highest accuracy. This excellent performance is attributed to the LR3D module's significant improvement in feature extraction through bilinear regularization of geometry and features, which better captures the complex geometric properties of pig dorsal point cloud data and provides a more efficient solution for individual identification tasks.

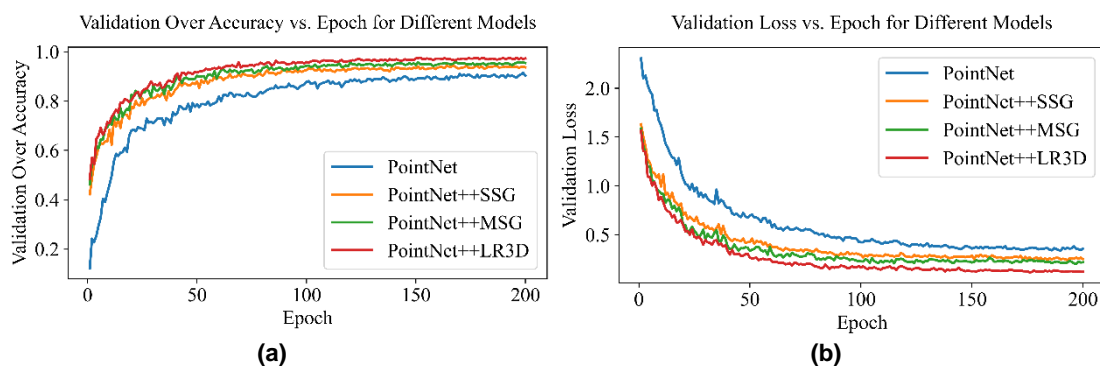


Fig. 9 - Individual Identification model validation results

(a) Validation accuracy curve (b) Validation loss curve

Individual Pig Identification model testing results

In order to further verify the performance of different models in the pig dorsal point cloud individual identification task, the optimal training models were selected to test the PointNet, PointNet++SSG, PointNet++MSG, and the improved PointNet++LR3D models.

The overall performance indexes of each model in the individual identification task and the accuracy of individual identification for 10 pigs are shown in Tables 2 and 3.

The experimental results show that the basic PointNet model has an overall accuracy of 88.92% and an average identification time of 0.0015 s, which exhibits very high computational efficiency. However, its accuracy ranges from 75.89% to 95.24% from Pig1 to Pig10, with large fluctuations, and some individuals are poorly identified, especially Pig7 (75.89%), reflecting PointNet's limited ability to extract pig dorsal point cloud features. PointNet++SSG and PointNet++MSG through hierarchical feature extraction significantly improved the performance, where the overall accuracy of PointNet++SSG was 92.93% and that of PointNet++MSG was further improved to 95.42%, and the individual identification accuracies of the two were more balanced, ranging from 88.46% to 96.67% and 92.73% to 99.17%, respectively, and the individual identification accuracies of both were more balanced, ranging from 88.46% to 96.67% and 92.73% to 99.17%, respectively, due to the hierarchical feature extraction layer is introduced, the identification time grows to 0.0529 s and 0.0540 s. The improved PointNet++LR3D model proposed in this study performs the best, with the highest overall accuracy of 97.11%, a precision rate of 97.04%, a recall rate of 97.09%, an F1 score of 97.06%, and a Top-3 accuracy rate of 99.44%, the best performance in all indicators, and its accuracy on 10 pigs ranges from 95.38% to 99.21%, with the slightest fluctuation and the most stable identification effect. Due to the inclusion of the two-layer LR3D module, although the average inference time is slightly elevated to 0.0576 seconds, it still meets the real-time time requirement of the individual identification task. The LR3D module proposed in this study significantly enhances the model's ability to fine-grain feature extraction from point cloud data through geometric and feature bilinear regularization. Although the inference time of PointNet++LR3D is slightly higher than that of the other models, it strikes a good balance between performance enhancement and computational efficiency. It provides a better solution for the individual identification task in pigs.

Table 2

Overall test results of the different models under the individual identification task

Model	OA	Precision	Recall	F1	Top-3	AvgTime
	[%]	[%]	[%]	[%]	[%]	[s/pig]
Pointnet	88.92	89.04	88.82	88.74	97.51	0.0015
PointNet++SSG	92.93	92.97	92.96	92.88	98.31	0.0529
PointNet++MSG	95.42	95.49	95.42	95.42	98.47	0.0540
PointNet++LR3D	97.11	97.04	97.09	97.06	99.44	0.0576

Table 3

Individual identification accuracy of each pig under different models

Model	Accuracy									
	[%]	[%]	[%]	[%]	[%]	[%]	[%]	[%]	[%]	[%]
pig	Pig1	Pig2	Pig3	Pig4	Pig5	Pig6	Pig7	Pig8	Pig9	Pig10
Pointnet	95.24	86.81	87.69	90.15	94.12	93.20	75.89	87.30	83.64	94.17
PointNet++SSG	93.33	93.06	88.46	91.67	92.44	94.56	90.18	92.86	96.36	96.67
PointNet++MSG	95.24	94.44	94.62	94.70	95.80	95.92	95.54	96.03	92.73	99.17
PointNet++LR3D	97.14	95.83	95.38	97.73	98.32	97.96	95.54	99.21	95.45	98.33

Confusion Matrix

In order to more intuitively assess the performance of the different models in the pig dorsal point cloud individual identification task, a classification confusion matrix was constructed for the four models, as shown in Figure 10. The horizontal axis of the confusion matrix represents the predicted labels, the vertical axis represents the actual labels, and the values on the diagonal indicate the number of correctly predicted samples. In contrast, the off-diagonal values indicate the number of misclassified samples. The results show that all models have high identification performance on most individuals, with correctly predicted samples mainly concentrated on the diagonal and fewer misclassified samples, verifying the effectiveness of the pig dorsal point cloud in the individual identification task.

By comparing the confusion matrices of the four models, it can be found that the base model has significant confusion in some categories. Among them, PointNet performed relatively poorly, with multiple misclassifications to other classes for pig2, 8, 9, and 6 misclassifications to pig4 for the predictions of pig3, pig7, and pig8, and bidirectional confusion between pig5 and pig9, with the error numbers of 7 and 4, respectively.

PointNet++SSG was significantly optimized by a single-scale grouping of the categorical purity of pig3, pig7, and pig8 and eliminated the one-way confusion of misclassification of pig9 to pig5. However, there were still four misclassifications of pig5 to pig9. PointNet++MSG further reduced the confusion of some categories by introducing multiscale grouping, significantly reduced the occurrence of misclassification of pig2, and further eliminated the two-way confusion between pig5 and pig9 bi-directional confusions.

In contrast, the improved model PointNet++LR3D shows significant advantages, with an average improvement of 10.7% in the number of correct diagonal predictions and a reduction in the maximum single-class error from 9 to 3 in PointNet. In particular, the bi-directional confusion between the confusing pig5 and pig9 is almost eliminated. Experiments show that the introduced local context and bilinear regularization strategy effectively enhances the ability to distinguish fine-grained feature differences and significantly reduces the misclassification rate between similar individuals.

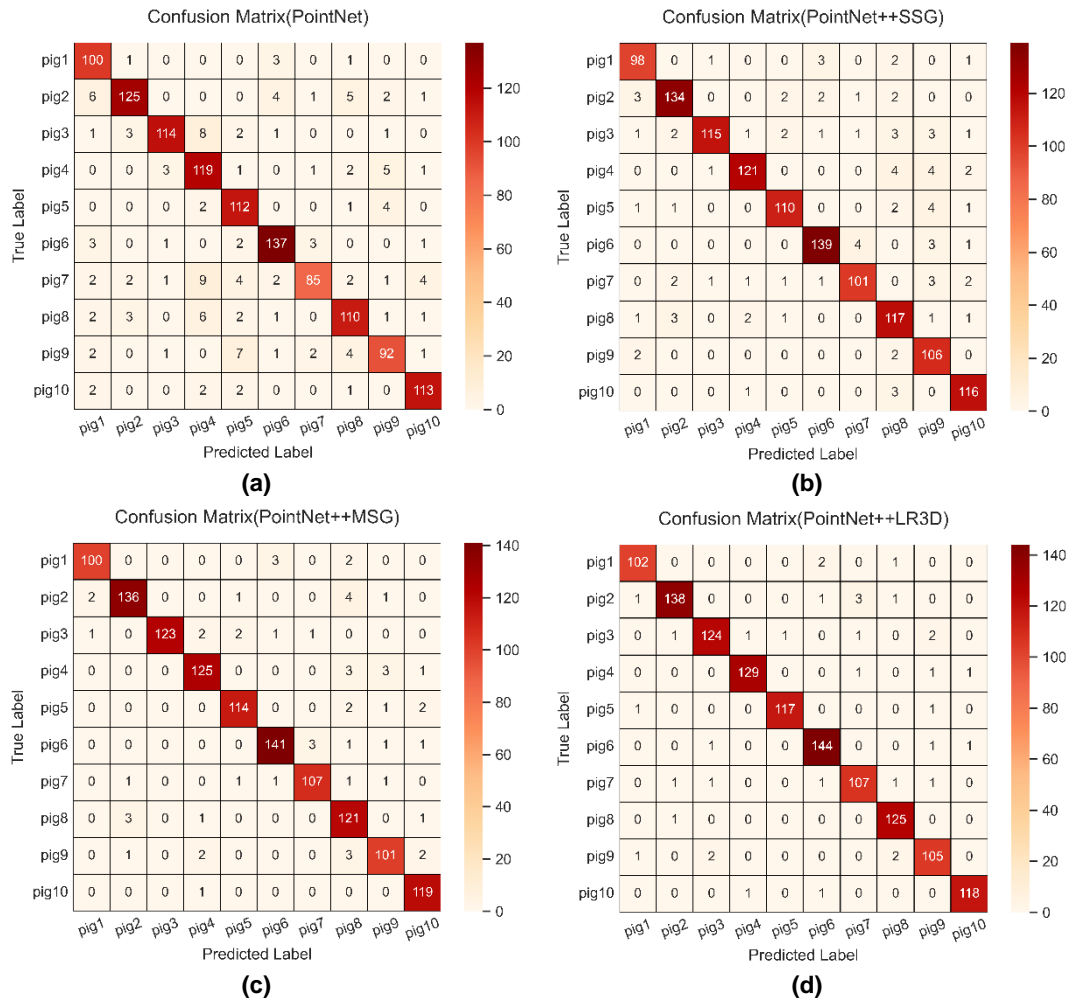


Fig. 10 - Classification confusion matrix for the ten pigs

(a) PointNet classification confusion matrix (b) PointNet++SSG classification confusion matrix (c) PointNet++MSG classification confusion matrix (d) PointNet ++LR3D classification confusion matrix

Discussion

Since the classification performed in this experiment and that performed in the ModelNet40 dataset are fundamentally different, the classification task in ModelNet40 is to classify different objects with significant differences in shape features, while the pig individual identification task performed in this experiment is to classify similar individuals within the same species, which inherently increases the classification difficulty.

To further validate the feasibility of the innovative LR3D bilinear regularization module introduced in this study for individual pig back point cloud identification, extended tests were conducted on the ModelNet40 public point cloud dataset, a classic benchmark for point cloud multi-classification tasks. Testing on this public dataset aims to evaluate the generality and robustness of the proposed method and verify its performance across different point cloud data scenarios.

The test results show that the improved PointNet++ model proposed in this study, by incorporating two LR3D modules, achieves an overall accuracy (OA) and average accuracy (macc) of 93.1% and 91.0% on the ModelNet40 dataset, representing improvements of 2.4% over the original PointNet++ model's 90.7% and 87.6%, respectively. This demonstrates that the proposed improved model enhances classification performance across diverse point cloud data scenarios.

CONCLUSIONS

This study proposes an individual identification method for pig back point cloud data based on the improved PointNet++ model. By introducing local context fusion and a global bilinear regularized LR3D module, the model's ability to extract and classify dynamic pig point cloud features is significantly enhanced. Experimental results demonstrate that the improved model achieves an identification accuracy of 97.11% in the individual identification task, performing the best among all methods. Furthermore, extended testing on the ModelNet40 public dataset further demonstrates the generality and effectiveness of the proposed method.

The LR3D module proposed in this paper significantly enhances the geometric sensitivity and semantic expressiveness of point cloud feature extraction through the local context fusion strategy of dual-stream differential coding and the global bilinear regularization mechanism, providing an efficient solution for analyzing complex 3D scenes. Its modular design gives LR3D excellent flexibility, enabling it to adapt easily to various point cloud processing network architectures, including PointNet++, DGCNN, and other mainstream models. It is seamlessly deployed at different feature extraction stages and CNN layer resolutions. LR3D effectively captures rough geometric structures in the low-resolution layer, such as edges and curvature changes; in the high-resolution layer, its ability to refine local features further enhances semantic differentiation. Experiments show that LR3D significantly improves the model accuracy in the classification task of similar individual identification while maintaining the balance of computational efficiency, demonstrating strong robustness and versatility. Looking ahead, the LR3D module can be widely applied to tasks such as point cloud segmentation and detection, providing a solid feature enhancement framework for 3D vision research.

Compared with traditional physical tags and RFID identification, this study achieves non-contact and high-precision pig individual identification using 3D point cloud technology, which overcomes the problems of fragile tags, the high cost of manual operation, and environmental interference. It provides an efficient solution for individual tracking, health monitoring, and behavioral analysis in fine-tuned farming. However, there are still some limitations in this study: the experimental sample size is small, with only 10 pigs and a single pig breed, and the model can be extended to a larger and multi-breed pig population to verify the generalization ability in the future. In addition, the dynamic point cloud data acquisition is limited by the camera view and the moving speed of the pigs, and the data acquisition process needs to be further optimized. This study provides innovative ideas and technical support for animal individual identification based on point cloud, which has high theoretical value and application prospects.

ACKNOWLEDGEMENT

This work has been supported by the Shanxi Province Basic Research Program (Free Exploration Category) (202303021222066), the 'Middle-aged and Young Elite Innovative Talent Cultivation Project' (SXAU KY2024002).

REFERENCES

- [1] García, R., Aguilar, J., Toro, M., Pinto, A., & Rodríguez, P. (2020). A systematic literature review on the use of machine learning in precision livestock farming. *Computers and Electronics in Agriculture*, 179, 105826.
- [2] Guo, Y., Wang, H., Hu, Q., Liu, H., Liu, L., & Bennamoun, M. (2020). Deep learning for 3d point clouds: A survey. *IEEE transactions on pattern analysis and machine intelligence*, 43(12), 4338-4364.
- [3] Krampe, C., Ingenbleek, P. T., Niemi, J. K., & Serratosa, J. (2024). Designing precision livestock farming system innovations: A farmer perspective. *Journal of Rural Studies*, 111, 103397.
- [4] Kyaw, P. P., Tin, P., Aikawa, M., Kobayashi, I., & Zin, T. T. (2024). Cow's Back Surface Segmentation of Point-Cloud Image Using PointNet++ for Individual Identification. In *International Conference on Genetic and Evolutionary Computing*. pp. 199-209. Singapore: Springer Nature Singapore.
- [5] Luo, J., Zhang, D., Luo, L., & Yi, T. (2024). PointResNet: A grape bunches point cloud semantic segmentation model based on feature enhancement and improved PointNet++. *Computers and Electronics in Agriculture*, 224, 109132.

- [6] Martínez-Miró, S., Tecles, F., Ramón, M., Escribano, D., Hernández, F., Madrid, J., ... & Cerón, J. J. (2016). Causes, consequences and biomarkers of stress in swine: an update. *BMC veterinary research*, 12, 1-9.
- [7] Neethirajan, S., Scott, S., Mancini, C., Boivin, X., & Strand, E. (2024). Human-computer interactions with farm animals—enhancing welfare through precision livestock farming and artificial intelligence. *Frontiers in Veterinary Science*, 11, 1490851.
- [8] Nong, X., Bai, W., & Liu, G. (2023). Airborne LiDAR point cloud classification using PointNet++ network with full neighborhood features. *Plos one*, 18(2), e0280346.
- [9] Qi, C. R., Su, H., Mo, K., & Guibas, L. J. (2017). Pointnet: Deep learning on point sets for 3d classification and segmentation. In *Proceedings of the IEEE conference on computer vision and pattern recognition* (pp. 652-660).
- [10] Qi, C. R., Yi, L., Su, H., & Guibas, L. J. (2017). Pointnet++: Deep hierarchical feature learning on point sets in a metric space. *Advances in neural information processing systems*, 30.
- [11] Ruiz-Garcia, L., & Lunadei, L. (2011). The role of RFID in agriculture: Applications, limitations and challenges. *Computers and electronics in agriculture*, 79(1), 42-50.
- [12] Saleem, M. H., Potgieter, J., & Arif, K. M. (2021). Automation in agriculture by machine and deep learning techniques: A review of recent developments. *Precision Agriculture*, 22(6), 2053-2091.
- [13] Servi, M., Profili, A., Furferi, R., & Volpe, Y. (2024). Comparative Evaluation of Intel RealSense D415, D435i, D455 and Microsoft Azure Kinect DK Sensors for 3D Vision Applications. *IEEE Access*.
- [14] Shuai, S., Ling, Y., Shihao, L., Haojie, Z., Xuhong, T., Caixing, L., ... & Hanxing, L. (2020). Research on 3D surface reconstruction and body size measurement of pigs based on multi-view RGB-D cameras. *Computers and electronics in agriculture*, 175, 105543.
- [15] Su, J., Tan, B. E., Jiang, Z., Wu, D., Nyachoti, C. M., Kim, S. W., ... & Wang, J. (2024). Accelerating precision feeding with the internet of things for livestock: From concept to implementation. *Science Bulletin*, 69(14), 2156-2160.
- [16] Vidal, M., Wolf, N., Rosenberg, B., Harris, B. P., & Mathis, A. (2021). Perspectives on individual animal identification from biology and computer vision. *Integrative and comparative biology*, 61(3), 900-916.
- [17] Wang, S., Jiang, H., Qiao, Y., Jiang, S., Lin, H., & Sun, Q. (2022). The research progress of vision-based artificial intelligence in smart pig farming. *Sensors*, 22(17), 6541.
- [18] Yu, S., Liu, X., Tan, Q., Wang, Z., & Zhang, B. (2024). Sensors, systems and algorithms of 3D reconstruction for smart agriculture and precision farming: A review. *Computers and Electronics in Agriculture*, 224, 109229.
- [19] Zhang, K., Ren, W., Luo, W., Lai, W. S., Stenger, B., Yang, M. H., & Li, H. (2022). Deep image deblurring: A survey. *International Journal of Computer Vision*, 130(9), 2103-2130.
- [20] Zhou, H., Li, Q., & Xie, Q. (2023). Individual pig identification using back surface point clouds in 3D vision. *Sensors*, 23(11), 5156.

PATH PLANNING STUDY OF INTELLIGENT GRAIN TRANSPORTER BASED ON GRAIN DEPOT SCENARIO

基于粮库场景下智能粮食转运车的路径规划研究

Boqiang ZHANG¹, Genliang YANG¹, Liang LI²*, Chenglong ZHANG¹, Xun ZHANG¹,
Xuemeng XU¹, Xiaoling WU²

¹ School of Mechanical and Electrical Engineering, Henan University of Technology, Zhengzhou 450001 / China;

² YUTONG BUS CO.,LTD. Zhengzhou 450061 / China;

Tel: 15981863085; E-mail: pretty510@163.com

Corresponding author: Liang LI

DOI: <https://doi.org/10.35633/inmateh-75-99>

Keywords: Grain depot scenario, Hybrid A* algorithm, Dynamic node extension, KD-Tree, Path planning

ABSTRACT

To address the problems of low search efficiency, long time-consuming planning and poor adaptability to narrow passages of the original Hybrid A* algorithm in path planning for intelligent grain transfer vehicles in grain depot scenarios, a Hybrid A* algorithm with variable resolution and variable step size is proposed. First, the dual-heuristic function and the cost function with steering and reversing penalties are reasonably designed to ensure that the algorithm can search for a derivable path. Second, the distance cost based on the KD-Tree algorithm is combined into the node extension, and the node extension is performed using variable resolution and variable step size according to the change of the distance cost to improve the node search efficiency. Then, Reeds-Shepp curve search fitting is used to pinpoint the target point pose. The simulation validation results show that the improved Hybrid A* algorithm reduces the number of search nodes by 83% and the planning time by 37% in simple maps, while the number of search nodes and the planning time are reduced by 80.6% and 56.6%, respectively, in complex maps, which improves the path search efficiency. After the real-vehicle test, the improved Hybrid A* algorithm reduces by 52.9% and 61.4% in terms of the number of search nodes and planning time consumed, respectively, and there is a significant improvement in the planning efficiency, which enhances the operational efficiency of the grain transfer vehicle.

摘要

针对粮库场景中智能粮食转运车辆在路径规划时原始 Hybrid A*算法存在搜索效率低、规划耗时长及狭窄通道适应性差等问题,提出一种变分辨率和变步长的 Hybrid A*算法。首先,合理设计双启发函数与含有转向和倒车惩罚的代价函数,保证算法能够搜索到一条可行驶的路径。其次,将基于 KD-Tree 算法的距离代价结合到节点扩展中,根据距离代价的变化使用变分辨率和变步长进行节点扩展,提高节点搜索效率。然后,采用 Reeds-Shepp 曲线搜索拟合精确定位目标点位姿。仿真验证结果表明,在简单地图中,改进 Hybrid A*算法的搜索节点数量缩短了 83%,规划耗时缩短了 37%;在复杂地图中,搜索节点数量和规划耗时分别缩短了 80.6%, 56.6%,提高了路径搜索效率。经过实车试验,改进 Hybrid A*算法在搜索节点数量和规划耗时方面分别缩短了 52.9%、61.4%,规划效率有明显提升,从而提升了粮食转运车辆的运行效率。

INTRODUCTION

Granaries are a critical component of food storage (Nayak et al., 2020). However, traditional grain depots face several challenges in the processing and transfer of residual grain. These include narrow passages, complex environments with numerous grain piles, and reliance on manually operated vehicles for transportation, which results in low efficiency and high operational costs. In order to overcome this problem, intelligent grain transfer vehicle has gradually become a research hotspot (Teng et al., 2023). By integrating advanced sensors, high-precision positioning system and intelligent decision-making module (Peng et al., 2021), the intelligent grain transfer vehicle can quickly and accurately sense the obstacles in the known surrounding environment and make obstacle avoidance decisions.

Boqiang ZHANG, Senior engineer Ph.D. Eng.; Genliang YANG, M.S. Stud. Eng.; Liang LI, Engineer ;

Chenglong ZHANG, M.S. Stud. Eng.; Xun ZHANG, Lect. Ph.D. Eng.; Xuemeng XU, Prof. Ph.D. Eng.; Xiaoling WU, Engineer

The movement of the intelligent grain transporter is inseparable from the path planning, and a good path planning algorithm can improve the efficiency of the transporter and reduce the waste of grain. At the same time, the application of automatic driving technology to the residual grain transfer in grain depot scenarios is of great significance in guaranteeing the quality of grain and the construction of smart grain depots (Tang et al., 2024).

Path planning, as one of the key technologies in autonomous driving technology, is to generate optimal paths that satisfy collision avoidance constraints, kinematic constraints (e.g., minimum turning radius and speed constraints), and dynamic constraints such as acceleration constraints, deceleration constraints in structured roads (e.g., urban roads) or unstructured road scenes (e.g., harbors, grain warehouses, etc.) (Xiong et al., 2020), which is of great significance to improve vehicle driving safety and the efficiency of residual grain transfer in grain warehouses. At present, the commonly used path planning algorithms include three major categories: ant colony algorithm (Wu et al., 2023) based on machine learning method, PRM algorithm (Huang et al., 2024) and RRT algorithm (Yin et al., 2023) based on sampling method, and Dijkstra algorithm (Dijkstra, 2022) and A* algorithm (He et al., 2022) based on graph search method. However, none of these path planning algorithms consider vehicle kinematic characteristics when planning paths, resulting in limitations of the planned paths in grain depot scenarios. For this reason, Dolgov et al. proposed the Hybrid A* algorithm that considers satisfying the vehicle kinematic characteristics, which is able to plan a driving path close to the global optimum due to its novel node extension, but its planned paths will suffer from the problems of curvature not being able to maintain continuity, poor quality of the paths, and inefficient searching, which is still difficult to satisfy the practical needs (Dolgov et al., 2010). Therefore, some scholars are attracted to study the Hybrid A* algorithm. Aiming at the problems that the curvature of the paths planned by Hybrid A* algorithm cannot be kept continuous, the path quality is poor and the search efficiency is low, scholars carry out the improvement research from the aspects of path quality and search efficiency.

In the realm of path quality enhancement, diversified methodologies have been proposed to address trajectory optimization. Deng et al. (Deng et al., 2022) implemented a segmented spline curve optimization framework based on quadratic programming, while Zhang (Zhang, 2024) investigated the motion trajectory of warehouse robots by deriving spatial kinematic equations and introducing an enhanced Ant Colony Optimization-Dynamic Window Approach (ACO-DWA) algorithm. Ren et al. (Ren et al., 2022) innovatively designed a variable-radius Reeds-Shepp curve, integrating it with segmented Bessel curves and gradient descent techniques to ensure path smoothness. Concurrently, Tang et al. (Tang et al., 2021) synergized the artificial potential field method with the Hybrid A* algorithm, collectively mitigating discontinuities in curvature and improving navigational safety. Regarding search efficiency optimization, Tian et al. (Tian et al., 2023) augmented the heuristic function through distance field mapping, whereas Cao et al. (Cao et al., 2023) refined heuristic value acquisition by incorporating bidirectional path search strategies. Qin et al. (Qin et al., 2024) introduced collision risk cost into node extension mechanisms, and Li (Li, 2024) proposed an obstacle feature extraction method via raster map preprocessing to optimize ant colony algorithms. Furthermore, Sedighi et al. (Sedighi et al., 2019) enhanced path exploration efficiency by integrating Voronoi diagrams with the Hybrid A* framework. Although the Hybrid A* algorithm has made significant progress in both path quality and search efficiency, the existing methods still face challenges in grain depot scenarios. Especially in the complex environment of narrow aisles and many obstacles in the grain depot, the existing methods are still deficient in dynamically adjusting the resolution and the linkage between the step size and the distance to the obstacles.

The original Hybrid A* algorithm has the problems of low node search efficiency, long time consumption and poor adaptability to narrow channels when planning paths in the grain depot scenario. In this paper, a Hybrid A* algorithm with variable node resolution and variable step size is proposed, which mainly makes reasonable design of the heuristic function, the actual cost function and reasonable improvement of the node extension method. Among them, the dynamic node extension method is evaluated with the distance cost based on the KD-Tree algorithm, which changes the static extension into the dynamic extension with variable resolution and variable step size, and improves the path search efficiency.

MATERIALS AND METHODS

Hybrid A* algorithm

The Hybrid A* algorithm is a graph search algorithm improved from the A* algorithm, and its planned path takes into account the kinematic constraints of the vehicle, so that a path close to the global optimum can be planned.

The idea of Hybrid A* algorithm is the same as that of A* algorithm, both are heuristic search. The cost function of Hybrid A* algorithm is as follows:

$$f(n) = g(n) + h(n) \tag{1}$$

In equation (1), the defining domains of the cost function $f(n)$, the actual cost $g(n)$, and the heuristic function $h(n)$ are all the nodes N in the search space, and the value domain R is a non-negative real number; where n is the current node, $g(n)$ is the actual generation value from the starting node to the current node, and $h(n)$ is the heuristic generation value from the current node to the goal point, and $f(n)$ integrates the actual cost from the starting point to the current point and the estimated cost to the goal point.

The Hybrid A* algorithm searches as described below:

First, the Hybrid A* algorithm (Cao, 2023) receives the start position, end position, and a 2D raster map containing vehicle position coordinates and heading angle information. It performs path planning within this static 2D raster map (Elfes, 1989), which includes obstacle data and passable areas. The algorithm initializes an empty Open list and Closed list to manage the search nodes and inserts the start node into the Open list. Next, the algorithm selects the current node for expansion based on the heuristic cost to the target point, choosing the node with the lowest cost function value $f(n)$ from the Open list. It then checks whether this node can be connected to the goal using an obstacle-free Reeds-Shepp curve (Reeds & Shepp, 1990). If a valid connection is found, the curve is accepted as the final path, and the algorithm terminates. If no direct connection is possible, the current node is moved to the Closed list and treated as a parent node. Child nodes are generated based on vehicle kinematic constraints, and the cost function $f(n)$ is calculated for each. These child nodes are then added to the Open list. The process repeats, expanding nodes, checking for connections, and updating the Open and Closed lists, until either a valid path is found or the Open list is empty. The overall workflow of the algorithm is illustrated in Fig. 1.

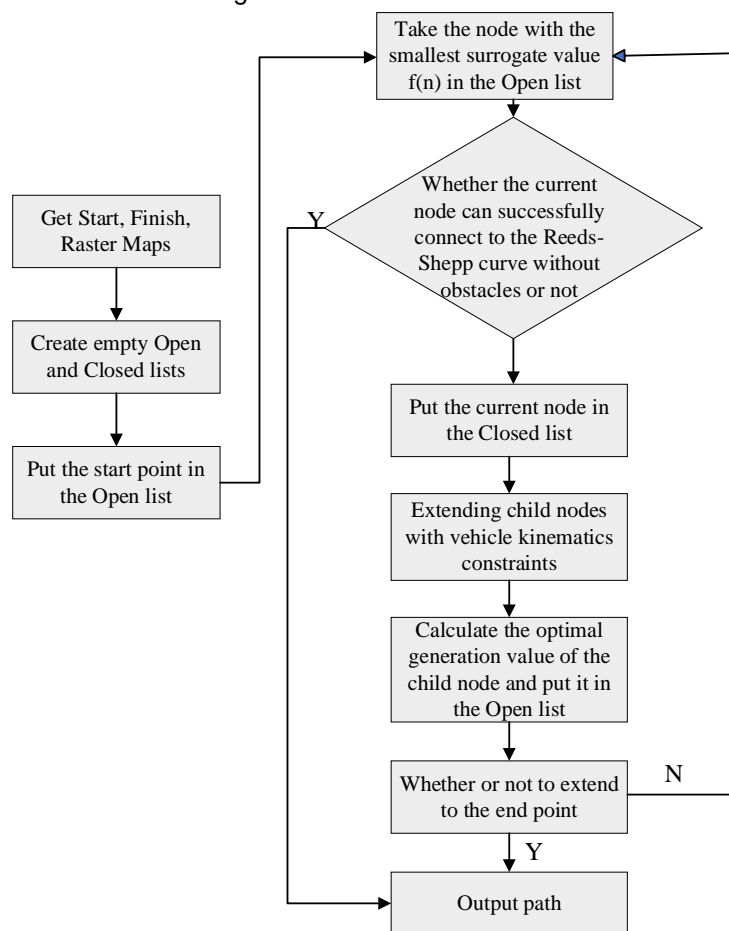


Fig. 1 - Flowchart of Hybrid A* algorithm

Improvements to the Hybrid A* algorithm

In order to solve the problems of low search efficiency and high time consumption in the original Hybrid A* algorithm when applied to complex grain depot scenarios with narrow aisles and numerous obstacles, an improved Hybrid A* algorithm is proposed.

Firstly, a more effective design of the heuristic function and the actual cost function is implemented to enhance the accuracy and relevance of the path planning. Secondly, the KD-Tree algorithm (Ram & Sinha, 2019) is used for nearest neighbor and distance range search to compute the distance to the nearest obstacle. When multiple points have the same calculated distance and surrogate value, to ensure the smoothness and safety of the driving path, priority is given, based on the calculation results, to the point with a smaller angle relative to the current driving direction, or to the point that is farther away from the obstacle. At the same time, the calculated obstacle distance cost is fused into the node expansion process. Based on this distance, dynamic expansion with variable resolution and variable step size is applied, improving the efficiency of path searching. Finally, the Reeds-Shepp curve (Reeds & Shepp, 1990) is used to generate the final path, ensuring it meets vehicle motion constraints and is optimal for driving. Combined with the vehicle schematic shown in Fig. 2, the Hybrid A* algorithm is specifically improved in the following ways:

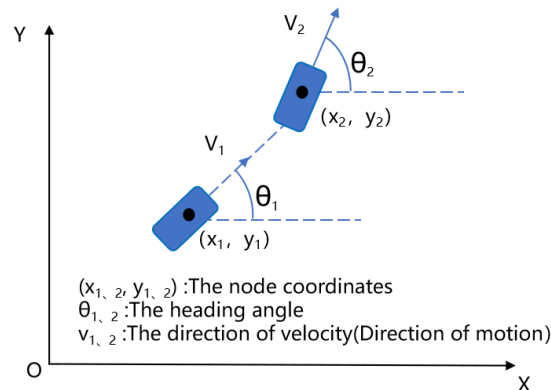


Fig. 2 - Schematic diagram of the vehicle

Heuristic function design

In Hybrid A* algorithm, the heuristic function plays a key role to estimate the heuristic generation value from the current node to the goal point to help the path search. To satisfy the vehicle kinematics and environmental constraints, two heuristic functions are used in parallel and the larger value of the two is selected as the heuristic search value as shown in equation (2).

$$h(n) = \max\{h_1(n), h_2(n)\} \quad (2)$$

In equation (2), the domain of definition of $h_1(n)$ and $h_2(n)$ is the set N of all nodes in the search space, where each node $n \in N$ contains the position coordinates (x, y) and the heading angle θ , and the value domain R is a nonnegative real number; where $h_1(n)$ is the first heuristic function that considers the kinematic constraints of the vehicle while ignoring the environmental obstacle constraints. When considering the kinematic constraints of the vehicle, it is necessary to incorporate factors such as minimum turning radius and speed into the heuristic function. This ensures that the planned path aligns with the vehicle's actual motion capabilities and avoids generating infeasible trajectories. Typically, this is achieved by using Reeds-Shepp curves to compute the shortest feasible path from the current node (x_n, y_n, θ_n) to the goal point (x_g, y_g, θ_g) . The length of this path serves as the first heuristic function, denoted as $h_1(n)$. The second heuristic function, $h_2(n)$, takes into account environmental obstacle constraints while ignoring the vehicle's kinematic limitations. To enable obstacle avoidance, an obstacle distance field is introduced into the heuristic. The A* algorithm is used to evaluate the distance between the path and surrounding obstacles, where greater distances yield higher heuristic values. This steers the path away from obstacles, generating a safer route from the current node (x_n, y_n, θ_n) to the goal point (x_g, y_g, θ_g) . The length of this path defines the value of the second heuristic function, $h_2(n)$. Here, n represents the current node, g is the goal point, (x, y) are the node coordinates, and θ is the heading angle.

$h_1(n)$ incorporates the feasible steering range of the Reeds-Shepp curve, helping to avoid dead ends where the vehicle cannot turn around. In contrast, $h_2(n)$ performs a search on the raster map using the A* algorithm, enforcing obstacle avoidance by utilizing obstacle grid markers. The combination of these two heuristics ensures that the planned path remains clear of hazardous areas. As a result, the final driving path not only complies with the vehicle's kinematic constraints but also effectively navigates around environmental obstacles.

Cost function design

In order to avoid unnecessary steering and reversing of the vehicle, it is necessary to ensure the continuity of the search path. In this paper, a penalty term is added for steering and reversing in the cost function to make the planned path more continuous.

The actual cost of each child node $n_i(x_i, y_i, \theta_i)$ in the search path of the Hybrid A* algorithm is shown in equation 3; where the child node n_i is a new node generated by expanding from the current node through vehicle kinematics constraints.

$$\begin{cases} g_i(n) = g_p(n) + g_{turn}(n) \times \omega_1 + g_{reverse}(n) \times \omega_2 \\ g_{turn}(n) = |\theta_i - \theta_p| \\ g_{reverse}(n) = L \end{cases} \quad (3)$$

In equation (3), $g_i(n)$ is the generation value of child node n_i , $g_p(n)$ is the generation value of parent node n_p , $g_{turn}(n)$ is the vehicle steering penalty coefficient, $g_{reverse}(n)$ is the vehicle reversing penalty coefficient, L is the length of the variable step length, θ is the heading angle, and ω_1, ω_2 are the weighting coefficients. Through several experiments, the parameters are adjusted according to the needs of vehicle driving in different scenarios, usually $\omega_1 > 1$ and $\omega_2 > 1$ (Wilt & Ruml, 2012).

In the designed cost function, $g_{turn}(n)$ represents the penalty associated with changes in the heading angle at a path point - that is, the angle between the vehicle's direction of movement and the X-axis of the global coordinate system. This change reflects a shift in the vehicle's actual trajectory. By applying a penalty for turning, the number of steering actions is reduced, thereby improving the smoothness of the planned path. The corresponding weight ω_1 can be flexibly adjusted based on the specific application scenario; for instance, if frequent steering is undesirable, a higher value of ω_1 can be used. Similarly, $g_{reverse}(n)$ represents the penalty for reverse driving. This is combined with the variable step length L to reduce the number of backward steps in the path, thereby encouraging forward motion. The weight ω_2 can also be flexibly adjusted; for example, if reversing is permitted but should be minimized, a higher value of ω_2 can be applied. By designing the cost function in this way, the planned path can be adapted to meet different driving requirements, balancing between path smoothness, forward motion preference, and scenario-specific constraints.

Node Extension Method Design

Although the original Hybrid A* algorithm satisfies vehicle kinematics and can generate extended trajectories based on these constraints, it expands nodes using a fixed resolution and fixed step size. This approach limits the diversity of path options, making it difficult to approximate optimal paths, reduces the flexibility of the search process, and results in high computational cost. Consequently, the node expansion process - where the current node generates a series of potential new nodes based on vehicle kinematics and the algorithm's search strategy - becomes time-consuming and inefficient. To address these issues, the node expansion method is improved by incorporating the distance $d_{nearest}(n)$ from the current node to the nearest obstacle, calculated using the KD-Tree algorithm. A dynamic node expansion strategy is proposed, which adjusts both the resolution and step size according to $d_{nearest}(n)$. This enhancement increases the flexibility of node expansion in the Hybrid A* algorithm and reduces extension time.

KD-Tree is a tree-based data structure designed for storing and efficiently retrieving points in k-dimensional space, enabling fast nearest neighbor searches (Bi et al., 2022). When using conventional methods to calculate the nearest distance (i.e., the minimum distance from the current node to an obstacle), it is necessary to compute the distance to each obstacle and compare the results, which is inefficient and yields poor performance. To address this, obstacles in the map are structured into a 2D KD-Tree, allowing both nearest neighbor and range searches between the current node and surrounding obstacles. By applying the KD-Tree algorithm within the 2D raster map, the nearest distance from an expanding node to nearby obstacles can be quickly determined, significantly improving the efficiency and safety of the path search.

In this context, obstacles refer to static objects that obstruct vehicle movement, and their positions in the 2D raster map are represented as coordinate points (i.e., obstacle coordinates).

The nearest distance between a node and an obstacle is calculated using the Euclidean distance formula: $\sqrt{(x_2 - x_1)^2 + (y_2 - y_1)^2}$ which represents the straight-line distance between two points. The implementation process is illustrated in the flowchart shown in Fig. 3.

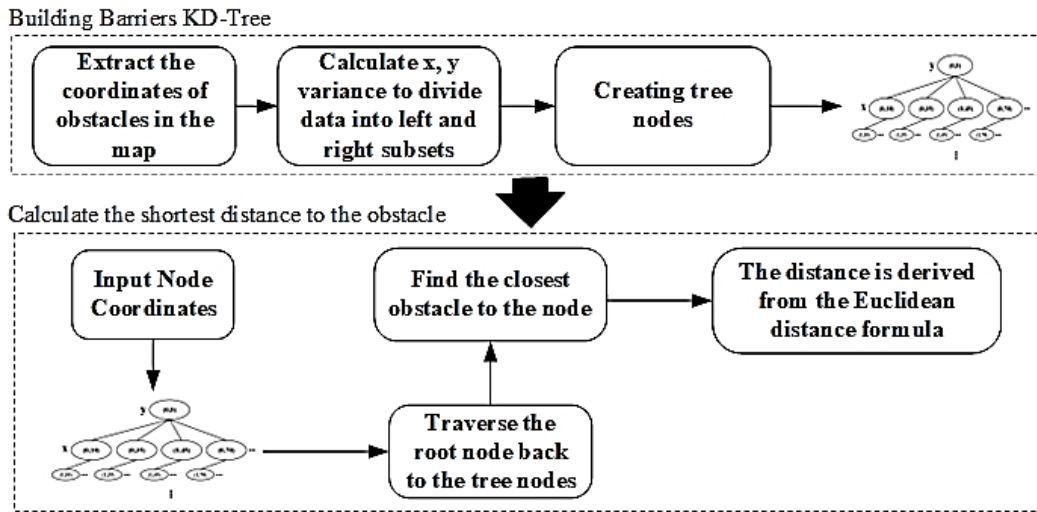


Fig. 3 - Flowchart of KD-Tree algorithm implementation

Based on the nearest distance $d_{nearest}(n)$ between the current vehicle node and the nearest obstacle, calculated using the previously constructed 2D KD-Tree of the obstacle data, the raster map can be globally partitioned into different regions according to d_{max} and d_{min} . Specifically, when $0 < d_{nearest}(n) < d_{min}$, the node is considered to be within a collision region, as illustrated in Fig. 4.

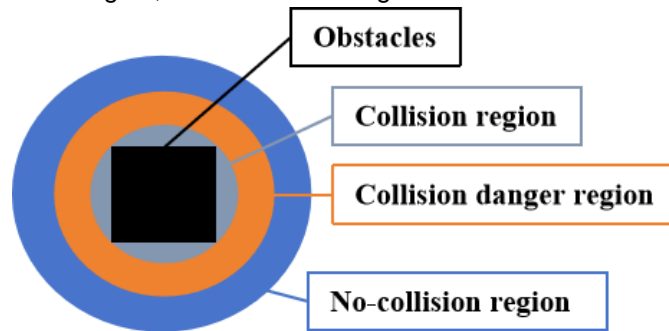


Fig. 4 – Schematic diagram of the region

The value of $d_{nearest}(n)$ is used to determine which region the vehicle occupies along the planned path. Simultaneously, the variable resolution K and variable step length L are linked to the nearest obstacle distance $d_{nearest}(n)$, enabling a dynamic adjustment of the node expansion strategy. As $d_{nearest}(n)$ changes, the search mode for node expansion is dynamically modified. Upper and lower bounds are defined for both the resolution and step length, and their values are adjusted in real time using Equations (4), (5), and (6). This adaptive approach allows the algorithm to select the most suitable node expansion mode based on the surrounding environment, significantly enhancing the efficiency of the path search.

$$K = \begin{cases} K_{min} & , \quad d_{max} \leq d_{nearest}(n) \\ K_{min} + a_1 \times b_1 & , \quad d_{min} \leq d_{nearest}(n) \leq d_{max} \\ K_{max} & , \quad 0 \leq d_{nearest}(n) \leq d_{min} \end{cases} \quad (4)$$

$$L = \begin{cases} L_{max} & , \quad d_{max} \leq d_{nearest}(n) \\ L_{min} + a_2 \times b_2 & , \quad d_{min} \leq d_{nearest}(n) \leq d_{max} \\ L_{min} & , \quad 0 \leq d_{nearest}(n) \leq d_{min} \end{cases} \quad (5)$$

where the values of a_1 , a_2 , b_1 , b_2 are shown in equation (6):

$$\begin{cases} a_1 = K_{max} - K_{min} \\ a_2 = L_{max} - L_{min} \\ b_1 = \frac{d_{max} - d_{nearest}(n)}{d_{max} - d_{min}} \\ b_2 = \frac{d_{nearest}(n) - d_{min}}{d_{max} - d_{min}} \end{cases} \quad (6)$$

In the above, d_{min} is the minimum safe distance from the obstacle and d_{max} is the maximum safe distance from the obstacle. In equation (5), K_{max} is the maximum discretization level of the variable resolution during node expansion and K_{min} is the minimum discretization level. Similarly, in Equation (6), L_{max} and L_{min} represent the maximum and minimum values, respectively, of the variable step length used during node expansion.

Therefore, after obtaining the vehicle position in the path, the algorithm determines whether the vehicle collides with the obstacle through $d_{nearest}(n)$. If in the collision-free region, the algorithm uses the resolution of the minimum discretization and the step size of the maximum length for node extension, and the resolution and step size of the node extension process if the obstacle is encountered in the search path will be changed with the change of the nearest distance $d_{nearest}(n)$. Fig. 5 shows the schematic diagram of dynamic extension, in which black squares are obstacles, green circles are collision-free regions, and red circles are dangerous collision regions. Fig. 6 shows the comparison diagram before and after the improved node extension, in which the blue box is the starting point of the vehicle, the red box is the end point of the path, the black square is the obstacle, the white grid part is the passable area, and the red track is the node trajectory. This improved node extension method can reduce the collision probability and improve the path accuracy by increasing the resolution discretization of the search path and decreasing the step length in the narrow channel and complex environment of the granary; in the normal environment of the granary, it can reduce the number of nodes to be searched and accelerate the search speed by decreasing the resolution discretization of the search path and increasing the step length. This not only improves the search efficiency of the Hybrid A* algorithm, but also ensures that the vehicles search over long distances and narrow aisles, further guaranteeing the safety of the path.

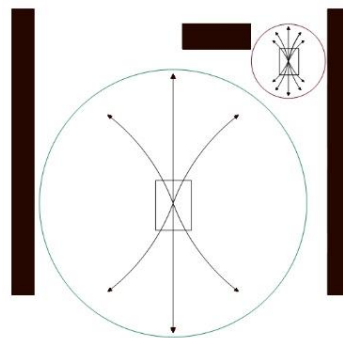


Fig. 5 - Schematic diagram of dynamic node extension

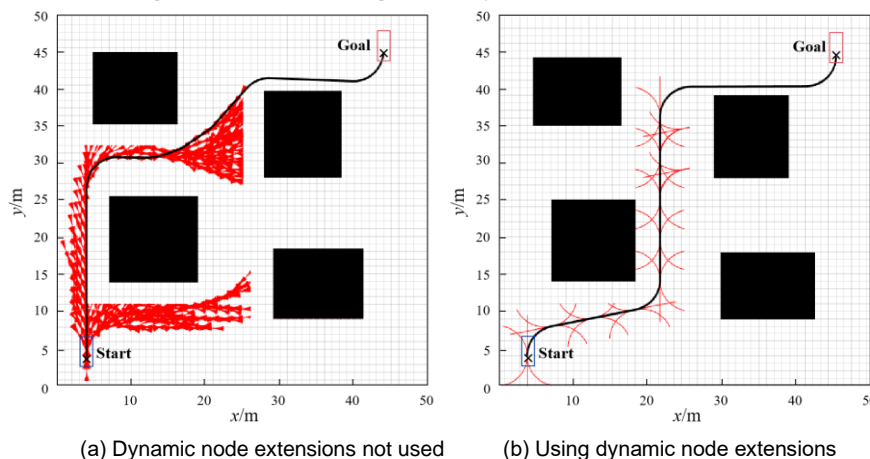


Fig. 6 - Comparison of planning before and after improving the way of extension nodes

Table 1

Comparison of dynamic node extension data

Title	Dynamic node extensions not used	Using dynamic node extensions
Number of nodes/piece	843	49
Search time/s	1.95	0.62

From the comparison data in Table 1, it can be concluded that the use of dynamic extension nodes reduces the number of search nodes by 94% and the search time by 68% compared to not using dynamic extension. The path search efficiency of the improved Hybrid A* algorithm can be improved by using dynamic extension nodes.

Search Path Fitting

It may not be possible to search the exact target point pose by the improved node extension approach, and in this paper, the Reeds-Shepp curve, which takes into account the vehicle kinematics constraints, is used for the final path search fitting. As shown in Fig.7, the blue box is the starting point, the red box is the end point, the black square is the obstacle, and the red dashed line is the Reeds-Shepp search curve. When the Hybrid A* algorithm is extended to the current node and the target point, it will use the Reeds-Shepp curve for path search; if there is no collision with obstacles during the path fitting process, the fitted path is a valid path to stop searching; otherwise, it continues to use the Hybrid A* algorithm to conduct path searching until a drivable path is obtained.

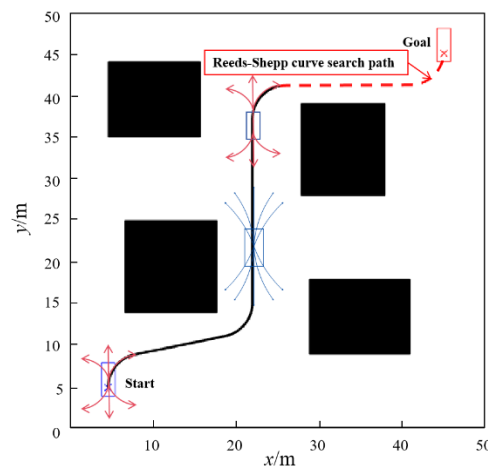


Fig. 7 - Schematic diagram of Reeds-Shepp curve path search fitting

RESULTS

Algorithm Testing

To verify the effectiveness and feasibility of the proposed algorithmic improvements, two types of obstacle distribution maps, simple and complex, were carefully designed within environment maps featuring diverse topologies. These maps included narrow passages and multi-obstacle layouts typical of grain depot scenarios. Based on these two simulated grain depot environments, the performance of the original Hybrid A* algorithm and the improved version proposed in this study was evaluated. The comparison focused on two key indicators: search time and number of search nodes, allowing for a comprehensive analysis of algorithmic performance. The experiment was conducted using MATLAB R2020a. The simulated vehicle parameters are as follows: a length of 4.0 m, a width of 1.6 m, a wheelbase of 2.75 m, and front and rear overhangs of 1.0 m each. The maximum turning angle of the front wheels is 0.6 rad. The simulation environment is a 50 m × 50 m raster map. The vehicle's starting position and orientation, as well as the distribution of obstacles, are illustrated in Fig. 8 and Fig. 9. In the figures, the blue box indicates the vehicle's starting position, the red box marks the target position, black squares represent obstacles, white grids denote traversable areas, and the red line shows the trajectory through the path nodes. According to the obstacle layout, Fig. 8 represents a simple map with a sparse and regular distribution of obstacles, while Fig. 9 depicts a complex map characterized by a high density and irregular distribution of obstacles. The simulations were performed on a Windows 10 platform with an Intel i5-1135G7 processor and 16 GB of RAM. MATLAB R2020a was used to simulate the proposed algorithm in the context of two grain depot environments. In both scenarios, the starting and target positions remained fixed, and the obstacle configuration was unchanged. Under these conditions, the generated path trajectories were largely consistent across multiple runs. Performance metrics such as the number of nodes, search time, and path length were evaluated based on the average results from more than ten simulation trials.

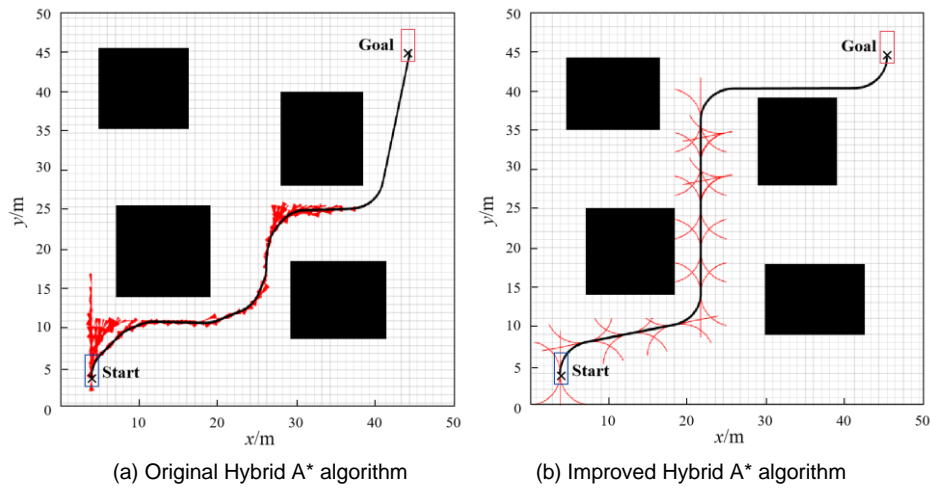


Fig. 8 - Comparison of simple map path planning

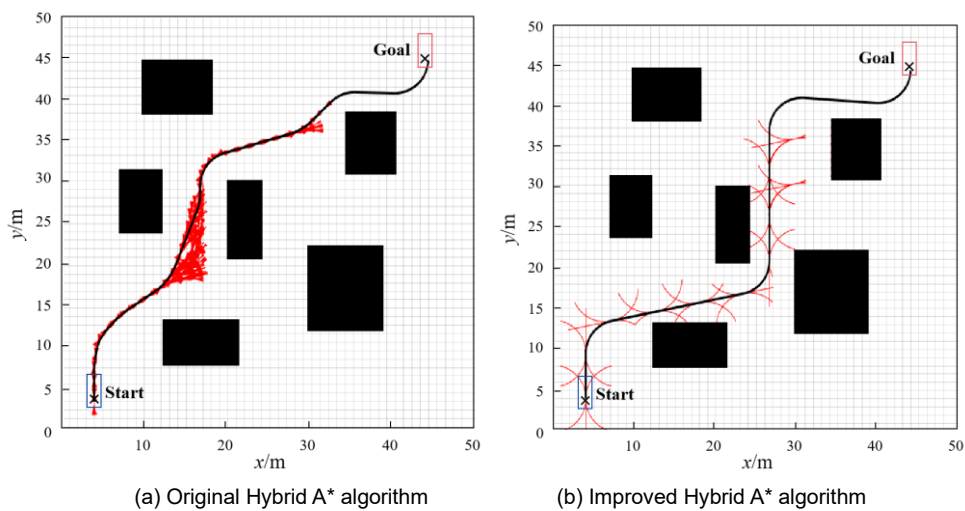


Fig. 9 - Comparison of complex map path planning

Table 2

Simple map simulation test data comparison

Algorithm	Number of nodes/piece	Search time/s	Path length/m
Original Hybrid A*	301	0.99	66.2
Improved Hybrid A*	49	0.62	71.4

Table 3

Complex map simulation test data comparison

Algorithm	Number of nodes/piece	Search time/s	Path length/m
Original Hybrid A*	191	1.66	64.1
Improved Hybrid A*	37	0.72	71.5

As shown in Table 2 and Fig. 8, in the setup of simple grain depot map, the improved Hybrid A* algorithm reduces by 83% and 37% in the number of search nodes and path search time, respectively, compared to the original Hybrid A* algorithm. As shown in Table 3 and Fig. 9, the improved Hybrid A* algorithm reduces the number of search nodes and path search time by 80.6% and 56.6%, respectively, compared with the original Hybrid A* algorithm in the setup of complex grain depot maps. The simulation results show that the improved Hybrid A* algorithm has a significant improvement in the number of search nodes and the search path time compared to the original Hybrid A* algorithm in the setup of two kinds of maps of grain depot environments, but in terms of path length, the improved algorithm takes vehicle kinematics constraints and collision avoidance into consideration when planning paths and chooses paths more in line with the driving requirements, so there is no substantial enhancement. The efficiency order of the original and improved algorithms may be different under different grain depot obstacle topologies.

When the distribution of obstacles is sparse and the shape is regular, the performance of the two algorithms may be similar; however, when the distribution of obstacles is dense and the shape is complex, the improved algorithm may show higher efficiency.

Real-vehicle Verification

In order to further verify the effectiveness and feasibility of the improved Hybrid A* algorithm, the test vehicle used in this paper is an intelligent grain transfer vehicle conforming to the Ackermann steering model (Ren et al., 2009), with a vehicle length of 4.0 m, width of 1.6 m, height of 2.2 m, wheelbase of 2.75 m, a minimum turning radius of 5.5 m, and a maximum turning angle of 0.54 rad at the front wheels, and is equipped with 16-wire LIDAR. RTK inertial guidance, millimeter wave radar and other sensors are shown in Fig.10 (a). Tested using the ROS operating system under Ubuntu 18.04, the original planning algorithm in the ROS system was replaced with the improved Hybrid A* algorithm and the original Hybrid A* in the form of the ROS plugin, and then experimental testing was carried out. The map used for navigation is constructed by RTK inertial guidance acquisition of road boundary points, and is processed into the raster map needed in the ROS system through image processing. The experimental results are shown in Fig. 10, the blue line area in (b) is a selected part of the grain depot scene, the black part in (c) and (d) is the obstacle, the green square is the starting point, the blue square is the end point, and the yellow line is the planned trajectory. As can be seen in Fig. 9, both Hybrid A* algorithms can plan a drivable path. In terms of search time, the original Hybrid A* algorithm takes 25.34s and the improved Hybrid A* algorithm takes 9.76s, and the improved algorithm improves 61.4% compared to the original one. In terms of the number of search nodes, the original algorithm searches for 34 nodes and the improved algorithm searches for 16 nodes, which is 52.9% higher compared to the original algorithm. In terms of the path length, the original algorithm and the improved algorithm plan a length of 80.85m and 80.73m, respectively, with no significant improvement. The results show that the improved Hybrid A* algorithm proposed in this paper is effective in improving the path search efficiency and safety in the presence of narrow aisles and the complex environment of the grain depot scenario.

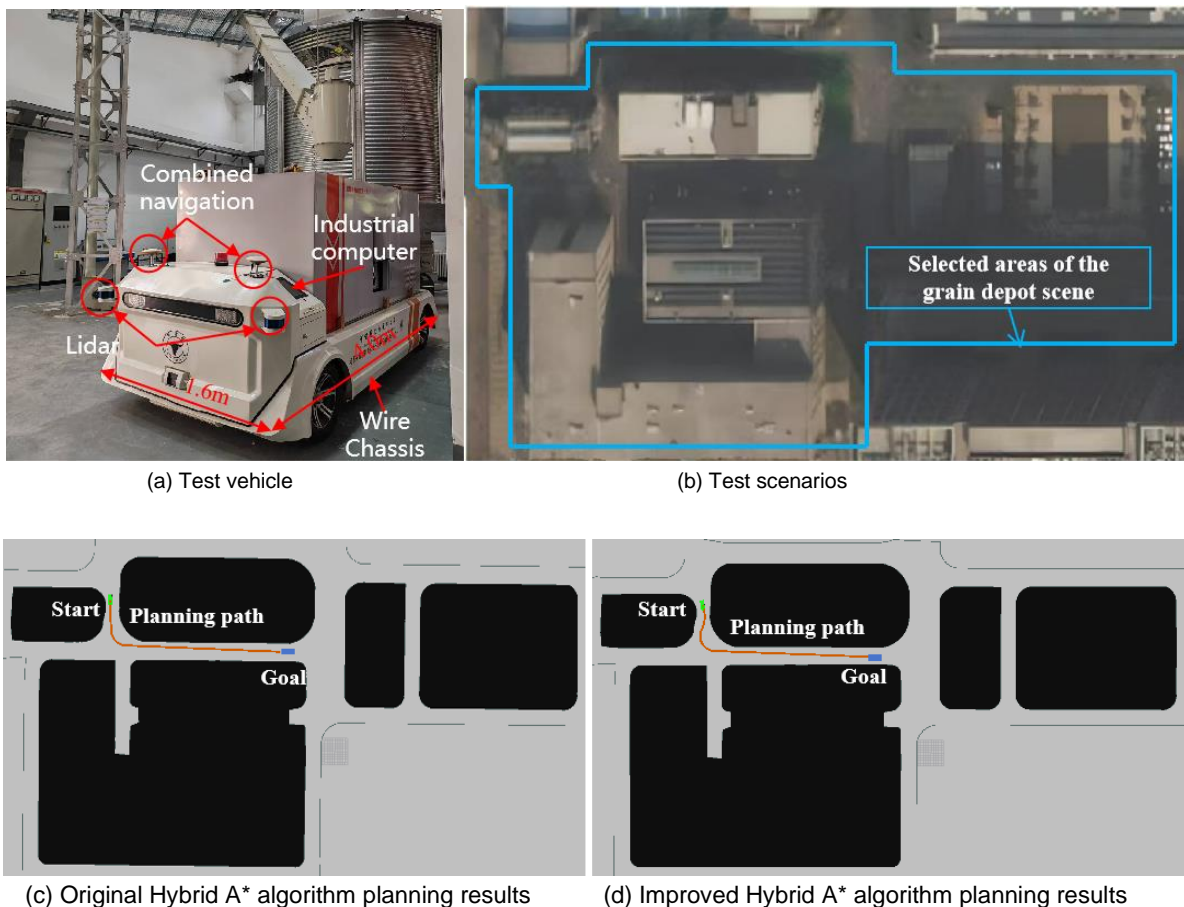


Fig. 10 - Real vehicle validation results

CONCLUSIONS

In this paper, a Hybrid A* algorithm based on variable resolution and variable step size is proposed for the deficiencies of the original Hybrid A* algorithm in the grain depot scenario. Firstly, by introducing weight coefficients and penalty terms, the heuristic function and cost function are reasonably designed to reduce the number of times that the vehicle turns and reverses in path planning. Secondly, combining KD-Tree to calculate the distance cost between nodes and obstacles, the resolution and step size are dynamically adjusted to realize the flexibility of node extension. Finally, in order to accurately locate to the target position, Reeds-Shepp curves are used for path search fitting to ensure the accuracy of the planned path. Simulation results show that the improved Hybrid A* algorithm reduces 83% and 37% in simple maps compared to the original Hybrid A* algorithm in terms of the number of search nodes and planning elapsed time, respectively. In complex maps, the reduction is 80.6% and 56.6%, respectively. The results of the real-vehicle experiments show that the improved Hybrid A* algorithm reduces the number of search nodes and planning time by 52.9% and 61.4%, respectively, compared with the original Hybrid A* algorithm. In summary, the improved Hybrid A* algorithm proposed in this paper significantly improves the path search efficiency of the intelligent grain transporter in the grain depot scenario by dynamically adjusting the resolution and step size, combining the KD-Tree distance cost with the Reeds-Shepp curve search fitting, which further validates the feasibility of the improved algorithm. Future research topics may include improving the adaptability of the algorithm for real-time planning in dynamic obstacle environments as well as conducting experiments in obstacles with different topologies to expand the scale and diversity of the experiments, while considering vehicle travel time and energy consumption to enhance the effectiveness of the improved algorithm. At present, although the improved algorithm has been experimentally validated, its in-vehicle validation needs further improvement. At this stage, the research focuses on being able to improve the search efficiency when planning paths in grain depot scenarios, and subsequent research will be further expanded on this basis.

ACKNOWLEDGEMENT

The authors thank the anonymous reviewers for their constructive comments. This study was partially supported by the National Key Research and Development Program of China [Grant No. 2022YFD2100201], the Key Research, Development and Promotion Project of Henan Province [Grant No. 231111241100], Supported by Cultivation Project of Tuoxin Team in Henan University of Technology [Grant No. 2024TXTD16], and the Science and Technology Tackling Project of Henan Province [Grant No. 252102241052].

REFERENCES

- [1] Bi, W. H., Ma, J. W., Zhu, X. D., Wang, W. X., & Zhang, A. (2022). Cloud service selection based on weighted KD tree nearest neighbor search. *Applied Soft Computing*, Netherlands, 131, 109780.
- [2] Cao, Y., Yan, J., Li, X., & Cao, L. (2023). A Method of Path Search for Automatic Parking System Based on Improved Hybrid A*Algorithm (基于改进混合 A*算法的自动泊车系统路径搜索方法), *Automobile Technology*, Changchun/China, 6(06), 37-41. <https://doi.org/10.19620/j.cnki.1000-3703.20230268>
- [3] Cao, L., (2023). *Research on Automatic Parking Path Planning Algorithm Based on Hybrid A** (基于 Hybrid A*的自动泊车路径规划算法研究), MSc dissertation, Dalian University of Technology, Dalian/China.
- [4] Dijkstra, E. W. (2022). A note on two problems in connexion with graphs. *Numerische Mathematik*, Germany, 1(1), 287-290. <https://doi.org/10.1007/BF01386390>
- [5] Dolgov, D., Thrun, S., Montemerlo, M., & Diebel, J. (2010). Path Planning for Autonomous Vehicles in Unknown Semi-structured Environments. *International Journal of Robotics Research*, England, 29(5), 485-501. <https://doi.org/10.1177/0278364909359210>
- [6] Deng, M., Lin, Y., Huang, J., & Luo, Y. (2022). Research on Hybrid A*Based Path Optimization of Unmanned Mine Truck (基于混合 A*算法的无人驾驶矿用卡车路径优化研究), *Control and Information Technology*, Zhuzhou/China, 5(05), 60-67. <https://doi.org/10.13889/j.issn.2096>
- [7] Elfes, A. (1989). Using occupancy grids for mobile robot perception and navigation. *Computer*, USA, 22(6), 46-57. <https://doi.org/10.1109/2.30720>
- [8] He, Z. B., Liu, C. G., Chu, X. M., Negenborn, R. R., & Wu, Q. (2022). Dynamic anti-collision A-star algorithm for multi-ship encounter situations. *Applied Ocean Research*, Netherlands, 118, 102995. <https://doi.org/10.1016/j.apor.2021.102995>
- [9] Huang, Y. Z., Wang, H., Han, L., & Xu, Y. Q. (2024). Robot path planning in narrow passages based on improved PRM method. *Intelligent Service Robotics*, Germany 17(3), 609-620.

- [10] LI, S. (2024). Multi-UAV Task Allocation and Path Planning Method for Agricultural Patrol Scenes. *INMATEH-Agricultural Engineering*, Romania, 74, 582-591. <https://doi.org/10.35633/inmateh-74-52>
- [11] Nayak, M. K., Daglish, G. J., Phillips, T. W., & Ebert, P. R. (2020). Resistance to the Fumigant Phosphine and Its Management in Insect Pests of Stored Products: A Global Perspective. In A. E. Douglas (Ed.), *Intelligent Service Robotics*, Germany, 65, 333-350. <https://doi.org/10.1146/annurev-ento-011019-025047>
- [12] Peng, Y., Jiang, M., Ma, Z., & Zhong C. (2021). Review on development of key technology for autonomous vehicle (汽车自动驾驶关键技术研究进展), *Journal of Fuzhou University(Natural Science Edition)*, Fuzhou/China, 49(05), 691-703. <https://doi.org/10.7631/issn.1000-2243.21272>
- [13] Qin, D., Zhang, W., Wang, T., & Chen, J. (2024). A Path Planning Method for Parallel Parking in Constrained Parking Channels (受限泊车通道下自动驾驶平行泊车的路径规划方法), *Journal of Zhengzhou University(Engineering Science)*, Zhengzhou/Chian, 45(05), 1-7.
- [14] Ren, X., & Cai, Z. (2009). Using the Ackerman principle for kinematic modeling of wheeled mobile robots (基于阿克曼原理的车式移动机器人运动学建模), *CAAI Transactions on Intelligent Systems*, Haerbin/China, 4(06), 534-537. <https://doi.org/10.3969/j.issn.1673-4785.2009.06.011>
- [15] Reeds, J. A., & Shepp, L. A. (1990). Optimal Paths for a Car That Goes Both Forwards and Backwards. *Pacific Journal of Mathematics*, USA, 145, 367-393. <https://doi.org/10.2140/PJM.1990.145.367>
- [16] Ren, B., Wang, X., Deng, W., & Nan, J. (2022). Path Optimization Algorithm for Automatic Parking Based on Hybrid A* and Reeds-Shepp Curve with Variable Radius (基于混合 A*和可变半径 RS 曲线的自动泊车路径优化方法), *China Journal of Highway and Transport*, Xian/China, 35(07), 317-327.
- [17] Ram, P., & Sinha, K. (2019). Revisiting kd-tree for nearest neighbor search. *Paper presented at the Proceedings of the 25th acm sigkdd international conference on knowledge discovery & data mining*, USA, 1378-1388. <https://doi.org/10.1145/3292500.3330875>
- [18] Sedighi, S., Nguyen, D.-V., Kapsalas, P., & Kuhnert, K.-D. (2019). Implementing Voronoi-based Guided Hybrid A* in Global Path Planning for Autonomous Vehicles. *2019 IEEE Intelligent Transportation Systems Conference (ITSC)*, Auckland/New Zealand, 3845-3851. <https://doi.org/10.1109/ITSC.2019.8917427>
- [19] Tang, F., & Li, Y. (2024). Current Status and Recommendations for the Development of Smart Grain Depot Construction in China (中国智慧粮库建设发展现状及建议), *Science and Technology of Cereals, Oils and Foods*, Beijing/China, 32(05), 35-41+257. <https://doi.org/10.16210/j.cnki.1007-7561.2024.05.005>
- [20] Teng, S. Y., Hu, X. M., Deng, P., Li, B., Li, Y. C., Ai, Y. F., . . . Chen, L. (2023). Motion Planning for Autonomous Driving: The State of the Art and Future Perspectives. *IEEE Transactions on Intelligent Vehicles*, USA, 8(6), 3692-3711. <https://doi.org/10.1109/TIV.2023.3274536>
- [21] Tian, Y., Lin, S., Fang, D., & Jiang, J. (2023). Path Planning of Robot with Nonholonomic Constraint based on Improved Hybrid A* algorithm (基于改进 HybridA*的非完整约束机器人路径规划算法研究), *Machinery*, Chengdu/China, 50(03), 63-71. <https://doi.org/10.3969/j.issn.1006-0316.2023.03.010>
- [22] Tang, B., Hirota, K., Wu, X., Dai, Y., & Jia, Z. (2021). Path Planning Based on Improved Hybrid A* Algorithm. *Journal of Advanced Computational Intelligence and Intelligent Informatics*, Japan, 25(1), 64-72. <https://doi.org/10.20965/jaciii.2021.p0064>
- [23] Wu, L., Huang, X. D., Cui, J. G., Liu, C., & Xiao, W. S. (2023). Modified adaptive ant colony optimization algorithm and its application for solving path planning of mobile robot. *Expert Systems with Applications*, England, 215, 119410. <https://doi.org/10.1016/j.eswa.2022.119410>
- [24] Wilt, C., & Ruml, W. (2012). When does weighted A* fail. *Paper presented at the Proceedings of the International Symposium on Combinatorial Search*, USA, 3(1),137-144. <https://doi.org/10.1609/socs.v3i1.18250>
- [25] Xiong, L., Yang, X., Zhuo, G., Leng, B., & Zhang, R. (2020). Review on Motion Control of Autonomous Vehicles (无人驾驶车辆的运动控制发展现状综述), *Journal of Mechanical Engineering*, Beijing/China, 56(10), 127-143. <https://doi.org/10.3901/JME.2020.10.127>
- [26] Yin, J. H., Hu, Z., Mourelatos, Z. P., Gorsich, D., Singh, A., & Tau, S. (2023). Efficient Reliability-Based Path Planning of Off-Road Autonomous Ground Vehicles Through the Coupling of Surrogate Modeling and RRT. *IEEE Transactions on Intelligent Transportation Systems*, USA, 24(12), 15035-15050.
- [27] Zhang, K. (2024). Obstacle Avoidance Path of Wheeled Agricultural Handling Robots in Warehouse Based on Improved ACO-DWA Algorithm. *INMATEH-Agricultural Engineering*, Romania, 74, 571-581. <https://doi.org/10.35633/inmateh-74-51>

DESIGN OF IOT-BASED GREENHOUSE MONITORING AND CONTROL SYSTEM USING ADAPTIVE PARTICLE SWARM OPTIMIZED FUZZY PID CONTROLLER AND VISUALIZATION PLATFORM

/

基于自适应粒子群优化模糊 PID 控制器和可视化平台的物联网温室监控系统设计

Peiyu LIN ^{1,2,3)}, Rui XU ^{1,2,3)}, Haifang WANG ⁴⁾, Jingcheng HUANG ^{1,2,3)}, Zhen GUO ^{1,2,3)}, Xia SUN ^{1,2,3)},
Ibrahim A. DARWISH ⁵⁾, Yemin GUO ^{*1,2,3)}, Jicheng ZHAO ^{*1,2,3)}

- ¹⁾ College of Agricultural Engineering and Food Science, Shandong University of Technology, No. 266 Xincun Xilu, Zibo, Shandong 255049, China;
²⁾ Shandong Provincial Engineering Research Centre of Vegetable Safety and Quality Traceability, No. 266 Xincun Xilu, Zibo, Shandong 255049, China;
³⁾ Zibo City Key Laboratory of Agricultural Product Safety Traceability, No. 266 Xincun Xilu, Zibo, Shandong 255049, China
⁴⁾ Wangjing Hospital, China Academy of Chinese Medical Sciences, Beijing 100102, China;
⁵⁾ Department of Pharmaceutical Chemistry, College of Pharmacy, King Saud University, P.O. Box 2457, Riyadh 11451, Saudi Arabia

*Corresponding authors: Professor Yemin GUO and Jicheng ZHAO

Tel: +86-533-2786398; E-mail: gym@sdut.edu.cn; zhaojicheng@sdut.edu.cn

DOI: <https://doi.org/10.35633/inmateh-75-100>

Keywords: internet of things, fuzzy PID control, adaptive particle swarm optimization algorithm, smart agriculture, greenhouse control

ABSTRACT

Traditional greenhouse management often suffers from slow responsiveness and limited adaptability due to its reliance on manual operations. This study proposes a greenhouse environment monitoring and control system that integrates Internet of Things (IoT) technologies with a fuzzy PID controller optimized through an Adaptive Particle Swarm Optimization (APSO) algorithm. A real-time monitoring platform was developed based on a WebSocket-enabled front-end/back-end separation architecture. Environmental parameters, such as temperature and humidity, were collected by sensors and transmitted in real time to the platform via the MQTT protocol, enabling data visualization and anomaly detection. The APSO algorithm was employed offline to optimize the fuzzy PID parameters, and the resulting controller was implemented on a microcontroller to achieve real-time control. Compared with conventional PID control, the APSO-optimized controller reduced overshoot by 72.1% and shortened the settling time by 20%. Experimental results demonstrated that the system was less susceptible to external environmental disturbances, maintaining temperature fluctuations within 0.3°C. This study provides a robust and effective solution for smart greenhouse management.

摘要

由于依赖人工操作，传统的温室管理往往存在响应速度慢、适应性有限等问题。本研究提出了一种温室环境监测和控制系统，该系统将物联网（Internet of Things, IoT）技术与通过自适应粒子群优化（Adaptive Particle Swarm Optimization, APSO）算法优化的模糊 PID 控制器相结合。提出基于 WebSocket 的前端/后端分离架构，开发了一个实时监控平台。温度和湿度环境参数由传感器收集，并通过 MQTT 协议实时传输到平台，从而实现数据可视化和异常检测。采用 APSO 算法离线优化模糊 PID 参数，并在微控制器上实现控制器的实时控制。与传统的 PID 控制相比，APSO 优化控制器将过冲降低了 72.1%，并将稳定时间缩短了 20%。实验结果表明，该系统不易受外部环境干扰的影响，能将温度波动保持在 0.3°C 以内。本研究为智能温室管理提供了一个稳健有效的解决方案。

INTRODUCTION

In recent years, advancements in agricultural production technologies have become increasingly critical due to the continuous growth of the global population and the rising demand for food. Predictions indicate that by 2050, the global population will reach approximately 8.52 billion, reflecting a 10.6% increase from 7.7 billion in 2020 (Akaev, 2022). Correspondingly, global food demand is expected to rise by nearly 60% (van Dijk et al., 2021). However, the agricultural sector faces escalating challenges, including limited arable land, water scarcity, and environmental concerns.

A significant portion the world's freshwater resources is used for agricultural irrigation, while a large proportion of greenhouse gas emissions can be attributed to the global food production system (*Hemathilake and Gunathilake, 2022, Khondoker et al., 2023*). In addition, climate change has led to an increased frequency of extreme weather events, further complicating agricultural production and heightening its unpredictability (*Kumar et al., 2022*). Therefore, improving agricultural efficiency and sustainability has become imperative.

Smart agriculture, which integrates information technology, automated control, and agricultural science, has emerged as a promising solution to these challenges (*Goli et al., 2024*). Among its various applications, greenhouse cultivation plays a pivotal role in enhancing crop yield and quality by providing controlled environmental conditions (*Atia and El-madany, 2017*). Globally, over 470,000 hectares of land worldwide are dedicated to greenhouse cultivation, yielding approximately ten times more per unit area compared to open-field cultivation (*Zhou et al., 2021*). Many crops grown in greenhouses (e.g. tomatoes, strawberries, etc.) require stable temperature and humidity levels to promote optimal flowering, fruit set and ripening. Temperature deviations can adversely affect fruit quality and yield, while high humidity may increase the risk of fungal diseases. Therefore, precise microclimate control is essential for successful crop cultivation. However, traditional greenhouse control systems often struggle to maintain precise environmental regulation due to fluctuating external conditions and complex parameter interactions. Many conventional approaches lack the responsiveness and precision required for modern agricultural standards (*Katzin et al., 2022*). In particular, traditional control methods face challenges such as response delays and insufficient adjustment precision in regulating key environmental parameters like temperature and humidity concentration, making it difficult to meet the high standards of modern agriculture.

The concept of the Internet of Things (IoT) can be traced back to the 1990s (*Chin et al., 2019, Schoder, 2018*). With advancements in technology and the expansion of its applications, IoT holds the potential to revolutionize various fields, including supply chain management, logistics tracking, intelligent transportation, and environmental monitoring (*Fadhel et al., 2024*). In agriculture, IoT has emerged as a key emerging technology driving agricultural development, with widespread applications in cultivation, livestock farming, and agricultural product traceability, playing a crucial role in promoting agricultural advancement (*Gatkal et al., 2024, Mohamed et al., 2022, Omasa et al., 2022*). Wang *et al.* (2018) developed an IoT-based intelligent greenhouse control system that can effectively monitor the greenhouse environment. However, the cloud platform lacks analysis and algorithm control and cannot achieve accurate environmental control.

Fuzzy logic control, with its advantages in handling nonlinear and uncertain systems, has become an effective method for greenhouse environment control. Unlike traditional control methods, fuzzy logic control does not require precise mathematical models and can achieve flexible control of complex systems through fuzzy rules and fuzzy inference, making it particularly suitable for the multi-variable and highly coupled environment of greenhouses (*Cheng, 2020, Wang and Zhang, 2018, Thomopoulos et al., 2024*). Marco A. Márquez-Vera *et al.* (2016) developed an internal temperature control system for greenhouses based on an inverse fuzzy model. The fuzzy partitions for each climate variable used two membership functions, which enhanced the model's accuracy and response speed. The model was tuned using batch least squares and updated with recursive least squares to optimize control performance. Adaptive Particle Swarm Optimization (APSO) is an improved algorithm that introduces an adaptive mechanism to the traditional Particle Swarm Optimization (PSO) algorithm (*Zhang et al., 2014*). Different from the standard PSO algorithm, APSO dynamically adjusts the key parameters of the algorithm and automatically optimizes them based on feedback information during the search process. This improves the global search capability and helps avoid convergence to local optima. Through this adaptive mechanism, APSO can better balance global exploration and local exploitation, and enhance the convergence and search efficiency of the algorithm, which is especially suitable for complex, multi-peaked, nonlinear, and high-dimensional optimization problems (*Zheng et al., 2023*).

Based on the aforementioned background, this paper develops and tests a small greenhouse control system that integrates fuzzy PID control optimized by an APSO algorithm and an intelligent monitoring platform. The system design includes data collection from a network of sensors, parameter adjustment via a fuzzy controller, and seamless integration with the intelligent monitoring platform. The overall cost of the system is lower compared to traditional greenhouse methods, which not only improves the accuracy of environmental regulation, but also provides significant economic benefits. It can accurately control greenhouse temperature, reducing energy consumption, and the use of sensors and low-maintenance communication equipment helps to lower design costs. Furthermore, the intelligent monitoring platform minimizes manual intervention, improving management efficiency and reducing labour costs.

MATERIALS AND METHODS

Hardware equipment

In a small-scale greenhouse control system for smart agriculture, sensors are critical components for achieving real-time monitoring and control of environmental parameters (Lee *et al.*, 2019). The system described in this paper utilizes a variety of devices to monitor key environmental data in the greenhouse, as shown in Table 1. The soil sensor (Model: VMS-3001-TR-*) and air sensor (Model: VMS-3002-WS) were sourced from VEMSEE flagship store (Address: Hangzhou, Zhejiang Province, China). The 8-channel RS485 hub supports multi-channel input and can connect up to 8 RS485 signal inputs, thereby enabling centralized management of data from multiple sensor devices. The system gateway was obtained from the PUSER flagship store. Its main function is to receive RS485 signals from the hub, convert them into JSON format, and then transmit the converted JSON data to the control system using the MQTT protocol.

In terms of actuators, the system is equipped with PTC heaters and semiconductor coolers to adjust the temperature. To optimize the circulation of cold and warm air, the heater is installed in the lower part of the greenhouse, while the cooler is installed in the upper part. In addition, ventilation fans are included to provide effective air circulation. To control the air humidity in the greenhouse, the system is equipped with an ultrasonic humidifier, supplemented by fans to enhance the humidification effect. The fan installed next to the humidifier helps to evenly distribute the misted moisture throughout the greenhouse, ensuring uniform humidity.

Table 1

Hardware Equipment		
Equipment	Models	Producers
soil sensor	VMS-3001-TR-*	VEMSEE Flagship Store
air sensor	VMS-3002-WS	VEMSEE Flagship Store
hub	HM-RS485-16-JX	eMybos
gateway	USR-M100	PUSER Flagship Store
heater	DJR	Kunli Electric
cooler	12V Semiconductor Chiller	ZeJie
humidifier	SHILU-12568	ShiLu
fan	15050-17251	SanXie

Greenhouse structure

The greenhouse frame is shown in Figure 1. It is constructed from 3-mm thick acrylic panels, providing good light transmission for plant growth. The greenhouse was designed in a square shape with a length of 800 mm, a width of 600 mm and a height of 700 mm. Ventilation openings with a diameter of 150 mm are provided on both sides to facilitate air circulation. The top of the greenhouse is provided with three square holes 47 mm long to hold the cooler and the bottom is provided with mounting holes 5 mm in diameter for the heater. To further ensure temperature stability, an insulating film was added to the exterior of the greenhouse to improve thermal efficiency and minimize heat loss.

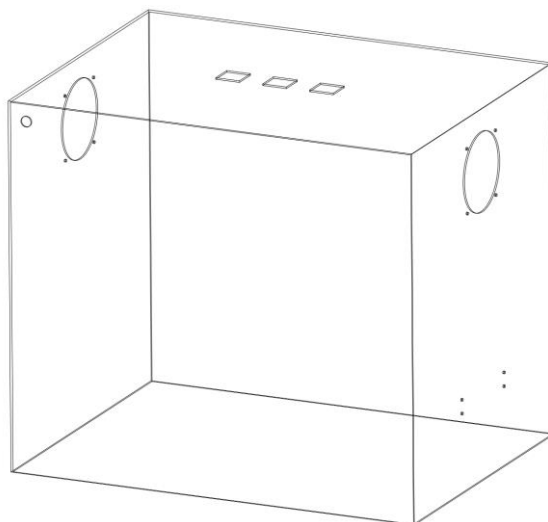


Fig. 1 - Greenhouse frame

System architecture

The overall conceptual diagram of the proposed system is shown in Figure 2. The system architecture consists of three main components: an environmental monitoring system, a control system and a data visualization platform. The primary function of the environmental monitoring system is to collect, transmit and initially process environmental data. The system comprises six RS485 sensor nodes and one edge gateway.

Each sensor is connected to the hub via an RS485 interface and communicates with the edge gateway through a serial port. The edge gateway is responsible for receiving environmental data from the hub performing initial processing and converting the data format. First, it receives sensor data such as temperature and humidity from the hub via a pre-configured interface, encapsulates the data into JSON format, and sends the JSON data to the specified MQTT topic via the MQTT protocol. The system utilizes the ESP8266 Wi-Fi module to connect to the MQTT server and subscribe to the topic to receive the environmental data. The received JSON data is transferred through serial communication to STM32F103ZET6 microcontroller, which is responsible for processing and analysing the received data. It compares the real-time data with the pre-set parameters to determine if the environmental conditions are within the expected range. Based on the comparison results, the control system adjusts the duty cycle of the PWM (pulse width modulation) signal to fine-tune the system's response. By modulating the PWM signal, the switching state of the electromagnetic relay is controlled, which in turn regulates actuators such as fans, heaters, coolers, etc., ensuring real-time monitoring and fine-tuning of environmental parameters.

The data visualization platform adopts MVVM (Model- View - ViewModel) separation framework for the front-end and back-end, which ensures the modularity and efficiency of the system. The back-end is implemented using the Django Channels framework, which is mainly responsible for processing the data received from the edge gateway and facilitating real-time communication with the front-end via WebSocket (*Fuentes et al., 2024*). The front-end is implemented using a JavaScript framework, which receives the data pushed from the back-end via WebSocket and updates the display interface in real time. The data is finally stored in a MySQL database for post-processing and analysis. The whole system is designed to be efficient and reliable, ensuring that users can monitor environmental data in real time and respond in a timely manner.

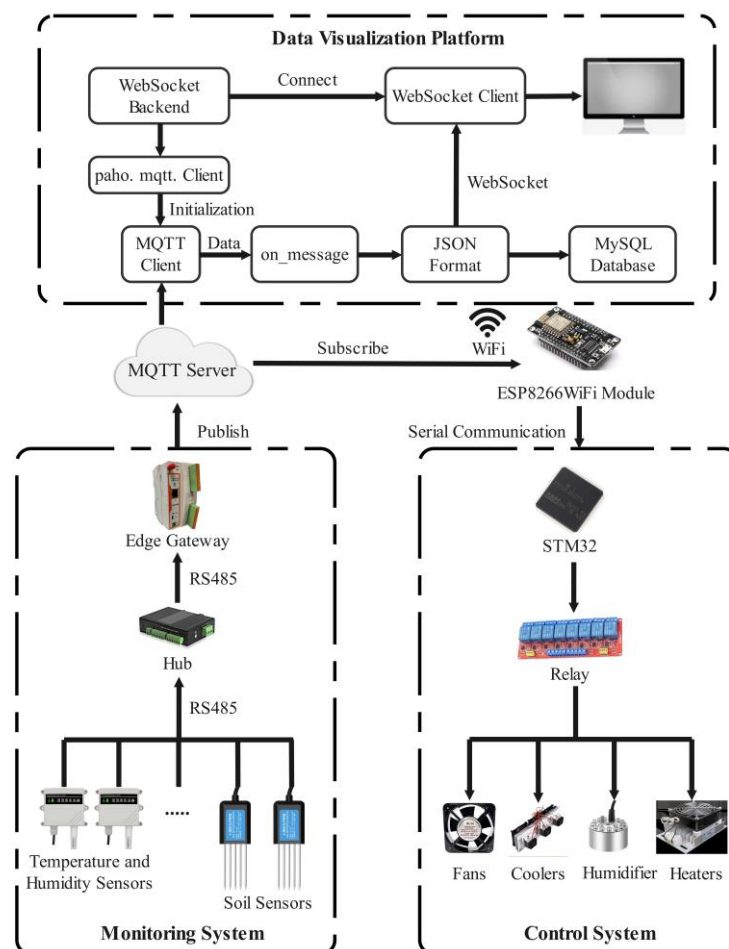


Fig. 2 - System framework

Optimization of fuzzy PID control parameters based on APSO

PSO is a global optimization algorithm that simulates the foraging behaviour of a flock of birds and searches for an optimal solution by updating the positions and velocities of each particle in the population. PSO relies on fixed parameter settings (e.g., inertia weights and learning factors), which are adjusted by the guidance of the individual optimums and global optimums during the search process (Chen and Chi, 2010). In a traditional PSO, the formula for updating the velocity and position of each particle is:

$$v_i(t+1) = w \cdot v_i(t) + c_1 \cdot r_1 \cdot (pdest_i - x_i) + c_2 \cdot r_2 \cdot (gbest - x_i) \quad (1)$$

$$x_i(t+1) = x_i(t) + v_i(t+1) \quad (2)$$

where:

v_i is the velocity of particle i ; x_i is the position of particle i ; w is the inertia weight, which is used to control the velocity of the particle; c_1, c_2 is the learning factor; r_1, r_2 is a random number in the range of [0,1]; $pdest_i$ is the historical optimal position of particle i ; and $gbest$ is the historical optimal position of the whole particle.

However, traditional PSO is prone to fall into local optimal solutions and is sensitive to parameter settings (Pan et al., 2020). The APSO algorithm introduces a dynamic adjustment mechanism on this basis, which automatically adjusts the inertia weights, learning factors and other parameters according to the current search stage, making the algorithm more flexible in balancing the global and local searches, improving the search efficiency and robustness of the algorithm, and reducing the probability of falling into a local optimum (Weng et al., 2024). In optimizing the parameters of the fuzzy PID controller, APSO can accurately adjust the proportional (KP), integral (KI), and differential (KD) coefficients, which makes the controller more adaptable and robust in the face of complex, nonlinear, and time-varying systems (Liu, 2016).

First, the position and velocity of the particle swarm are initialized. The initial position of each particle represents a set of PID control parameters. The velocity of the particle determines the step size and direction of its search, and the initial velocity is typically set to a random value. The position and velocity of the particle are respectively:

The position and velocity of the particle are given by:

$$x_i = (KP, KI, KD) \quad (3)$$

$$v_i = (v_{KP}, v_{KI}, v_{KD}) \quad (4)$$

where: i denotes the number of the particle.

APSO primarily enhances the search ability of particle swarms and optimizes the convergence speed by dynamically adjusting inertial weights and learning factors, thereby improving the search efficiency of the global optimal solution and reduces the likelihood of falling into the local optimal solution.

The inertia weight controls the relationship between the particle's current speed and its previous speed, and determines the particle's "inertia". The inertia weight is generally reduced during the iteration process so that particles can conduct extensive searches in the early iterations and then focus their searches in the later iterations to converge to the global optimal solution.

The calculation formula is as follows:

$$W = w_{max} - \frac{(w_{max} - w_{min})}{T_{max}} T \quad (5)$$

where:

w_{max} is the initial inertia weight; w_{min} - minimum inertia weight; T_{max} - maximum number of iterations; T - current number of iterations.

The learning factor controls the speed at which particles approach their personal optimal solution and the global optimal solution, determining the dependency of particle search. Usually, the PSO algorithm uses two learning factors: one is the individual learning factor and the other is the group learning factor. The individual learning factor controls how the particle depends on its own historical experience, that is, how the particle adjusts its current speed according to the optimal position it has reached.

The group learning factor controls how the particle depends on the global experience of the group, that is, how the particle adjusts its current speed according to the optimal solution in the group.

The specific adjustment formula is:

$$c_1(t) = c_{1,\max} - \frac{(c_{1,\max} - c_{1,\min})}{T} \cdot t \quad (6)$$

$$c_2(t) = c_{2,\max} - \frac{(c_{2,\max} - c_{2,\min})}{T} \cdot T \quad (7)$$

where:

$c_{1,\max}$, $c_{2,\max}$ - maximum value of the learning factor; $c_{1,\min}$, $c_{2,\min}$ - minimum value of the learning factor; t - current number of iterations; T - maximum number of iterations.

The standard random number in PSO can lead to search restrictions in the particle update process, increasing the likelihood of falling into local optimal solution, especially when the solution space is complex and the dimension is high. After the introduction of Levy flight, a random term with heavy-tail distribution is usually used to replace the original random numbers r_1 and r_2 , so that the particle position update is no longer determined only by uniform random numbers, but a "heavy-tail jump" mechanism is introduced. The update formula is as follows:

$$v_i(t+1) = w \cdot v_i(t) + c_1 \cdot L_1 \cdot (pdest_i - x_i) + c_2 \cdot L_2 \cdot (gbest - x_i) \quad (8)$$

where:

L_1 and L_2 are random numbers generated based on Levy distribution, following a heavy-tailed distribution. These random numbers are usually generated through the distribution formula of Levy flight, which is characterized by occasional large jumps to help particles perform global search.

RESULTS

Model identification

A PTC heater was installed at the base of the small-scale greenhouse, complemented by fans mounted symmetrically at the top. Temperature and humidity sensors were positioned at different locations within the greenhouse, and different target temperatures are set to simulate the operational process of the greenhouse and infer its transfer function model. In the closed greenhouse model, the ambient temperature is approximately 25.4°C, and the target temperature is set to 30.0°C. When the ambient temperature has not reached the target value, the heater will continue to operate; if the temperature exceeds the target value, the ventilation fan will be activated to cool the environment. Temperature data is recorded once per second over a period of 750 seconds.

To identify the system model, the recorded sample data was imported into the MATLAB/Simulink environment to determine the system's transfer function. The System Identification Toolbox in MATLAB, employing the nonlinear least squares method, is used for this process. The best fit value is calculated using the following formula: after importing the collected temperature data into MATLAB, the System Identification Toolbox in Simulink applies the least squares method to analyse and identify the system's transfer function.

The model's best fit R^2 is calculated using the following equation:

$$R^2 = 1 - \frac{\sum (y - y_m)^2}{\sum (y - \bar{y})^2} \quad (9)$$

where:

R^2 represents the model's best fit, y is the actual recorded temperature data, y_m is the predicted temperature data based on the identified transfer function model, and \bar{y} is the mean of the actual temperature data.

This equation evaluates the model's accuracy by calculating the ratio between the sum of the squared errors between the predicted values and the actual measurements (numerator) and the total variance of the actual measurements from their mean (denominator). If the R^2 value approaches 100%, it indicates that the identified transfer function model fits the actual data well; conversely, a lower R^2 value suggests a poorer fit. As shown in Figure 3, the output temperature of the greenhouse system and the fitted curve are presented.

The resulting fitted curve is as follows:

$$G(s) = \frac{4.87}{151s + 1} e^{-30s} \tag{10}$$

the fit of the curve is: 94.54%

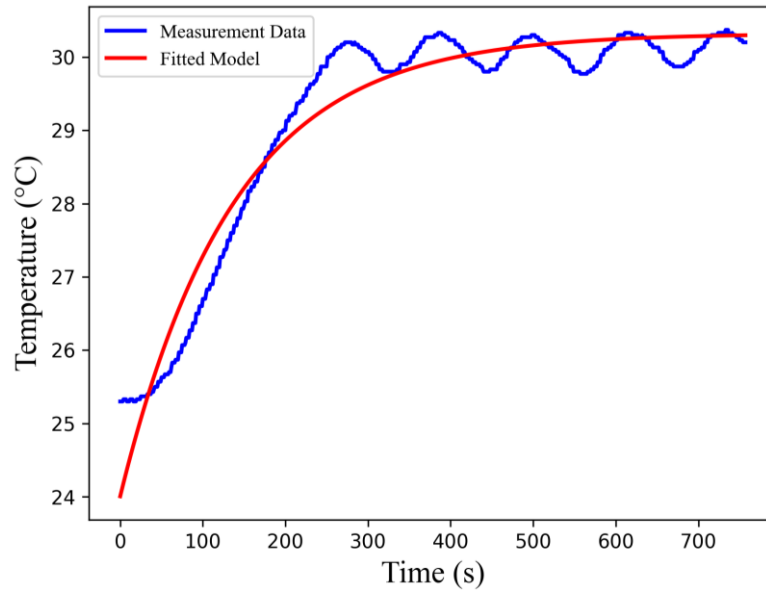


Fig. 3 - Real-time temperature parameters and fitted curves

Fuzzy control strategy and rules

In accordance with the principles of the fuzzy PID control algorithm, the inputs to the fuzzy PID controller are the error and the rate of E and the rate of error Ec . These inputs are crucial for the controller to assess the system's deviation from the desired setpoint. The outputs of the fuzzy PID controller correspond to the adjustments of the proportional, integral, and derivative gains, represented as ΔKP , ΔKI , and ΔKD . As shown in Table 2, the fuzzy domains for E , Ec , KP , KI , KD are $[-6, 6]$, $[-6, 6]$, $[-3, 3]$, $[-0.3, 0.3]$, and $[-0.3, 0.3]$, respectively. The fuzzy subsets are PB, PM, PS, ZO, NS, NM, and NB. The membership functions for the inputs E and Ec are shown in Figures 4 (a) and (b), while the membership functions for the outputs ΔKP , ΔKI , and ΔKD are depicted in Figure 4(c), (d), and (e), respectively.

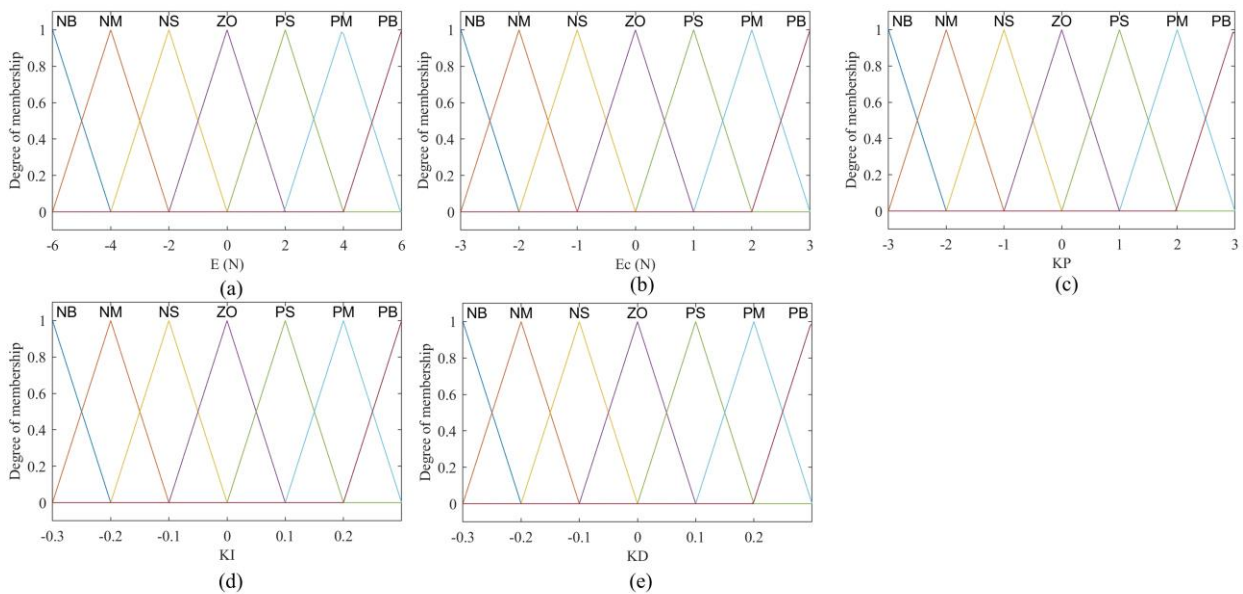


Fig. 4 - Domain and membership function of (a) E , (b) Ec , (c) ΔKP , (d) ΔKI and (e) ΔKD

Table 2

Fuzzy quantization parameters for input and output quantities

Variable	E	Ec	KP	KI	KD
Fuzzy discourse domain	[-6,6]	[-6,6]	[-3,3]	[-0.3,0.3]	[-0.3,0.3]
Fuzzy subset	PB, PM, PS, ZO, NS, NM, NB				
Membership function	Trimf				

The fuzzy rule base is composed of several "if-then" rules, where each rule is designed for specific input conditions and corresponding outputs. The input variables— E and Ec —are fuzzified into different linguistic variables, while the output variables represent adjustments to the PID controller parameters. Based on different combinations of error E and error rate Ec , 49 strategies and rules have been developed for adjusting ΔKP , ΔKI , and ΔKD in the fuzzy PID control system, as shown in Table 3. The input-output characteristic surfaces are presented in Figure 5 (a), (b), and (c).

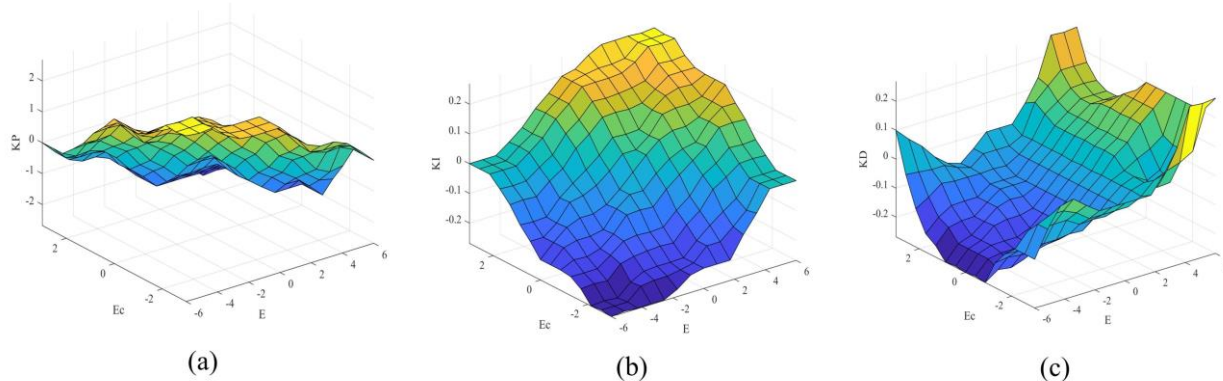


Fig. 5 - Input and output characteristic surfaces of (a) ΔKP , (b) ΔKI , (c) ΔKD

Table 3

Fuzzy control rules

E	Ec						
	NB	NM	NS	ZO	PS	PM	PB
NB	PB, NB, NS	PB, NB, NS	PM, NM, NB	PM, NM, NB	PS, NS, NB	ZO, ZO, NM	ZO, ZO, PS
NM	PB, NB, NS	PB, NB, NS	PM, NM, NB	PS, NS, NM	PS, NS, NM	ZO, ZO, NS	NS, ZO, ZO
NS	PM, NB, ZO	PM, NM, NS	PM, NS, NM	PS, NS, NM	ZO, ZO, NS	NS, PS, NS	NS, PS, NS
ZO	PM, NM, ZO	PM, NM, NS	PS, NS, NS	ZO, ZO, NS	NS, PS, NS	NM, PM, NS	NM, PM, ZO
PS	PS, NM, ZO	PS, NS, ZO	ZO, ZO, ZO	NS, PS, ZO	NS, PS, ZO	NM, PM, ZO	NM, PB, ZO
PM	PS, ZO, PB	ZO, ZO, NS	NS, PS, PS	NM, PS, PS	NM, PM, PS	NM, PB, PS	NB, PB, PB
PB	ZO, ZO, PB	ZO, ZO, PM	NM, PS, PM	NM, PM, PM	NM, PM, PS	NB, PB, PS	NB, PB, PB

Simulation and experimental results

The structure of the APSO fuzzy PID controller is shown in Figure 6. The APSO algorithm is executed to optimize the three parameters of the fuzzy PID controller, and the resulting optimization curve is presented in Figure 8 (a) - (e).

The optimization process illustrates the trend of each parameter across multiple iterations. As the number of iterations increases, the parameters gradually stabilize, indicating that the APSO algorithm effectively adjusts the particle swarm's search strategy and quickly finds the optimal control parameters. The fitness variation curve is shown in Figure 8 (f). From the curve, it can be observed that the APSO algorithm performs a global search in the initial stage, identifies a better solution within a short time, and then gradually converges to the optimal solution.

During the system simulation, the initial temperature of the greenhouse was set to 30°C, and the simulation time was set to 750 seconds. The performance of APSO fuzzy PID control, fuzzy PID control, and traditional PID control were compared. As shown in Figure 7, during the dynamic response phase, the APSO-optimized fuzzy PID control method significantly reduces the oscillation amplitude and frequency compared to the PID and fuzzy PID methods. This effectively improves the dynamic characteristics of the system and ensures that the response curve meets the control requirements.

By analysing the fluctuation curves of the simulation experiments using a MATLAB oscilloscope, the time domain performance metrics can be derived and the results are shown in Table 4. Compared to fuzzy PID and PID, APSO fuzzy PID reduces overshoot by 22.8% and 72.1%, respectively; the adjustment time is reduced by 9% and 20%, respectively; and the system's stability is significantly improved. By observing the oscilloscope waveform, it is evident that the optimized controller can quickly identify and effectively suppress the influence of disturbances, allowing the system output to return to a stable state in a short time. This demonstrates that the fuzzy PID controller optimized by APSO has strong anti-disturbance capability, enabling the system to maintain high control accuracy and robustness under interference.

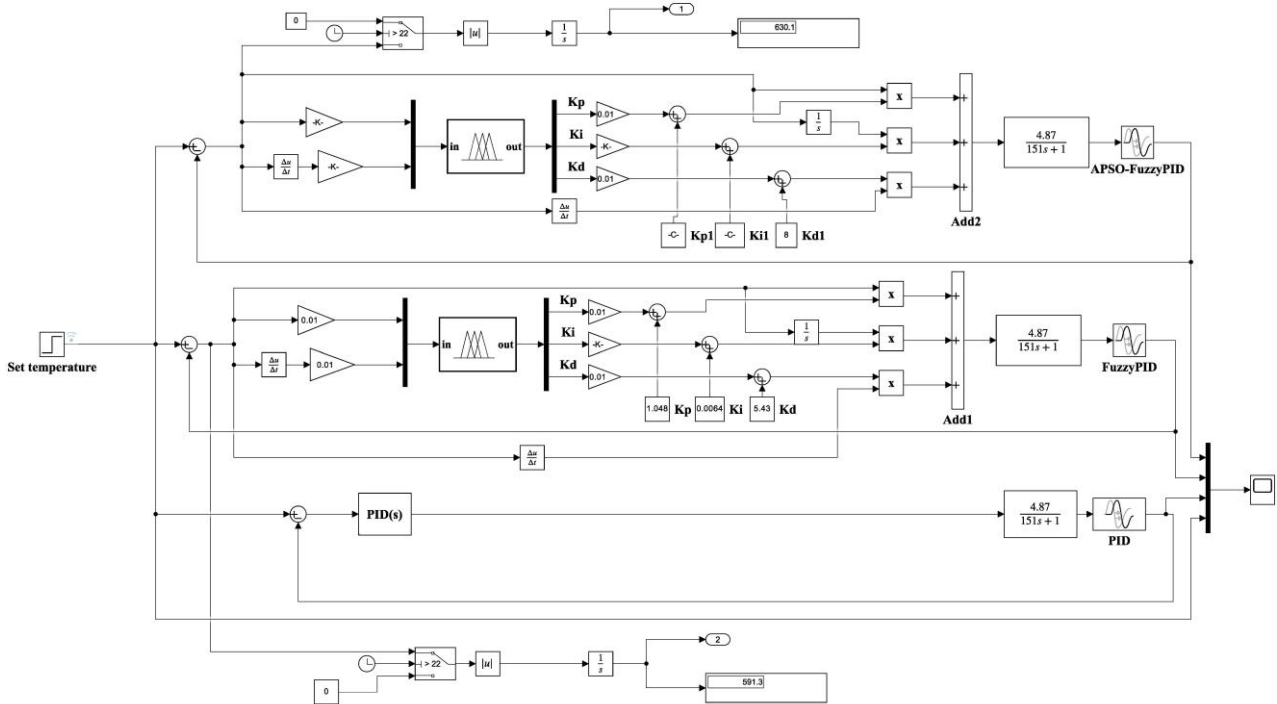


Fig. 6 - System controller

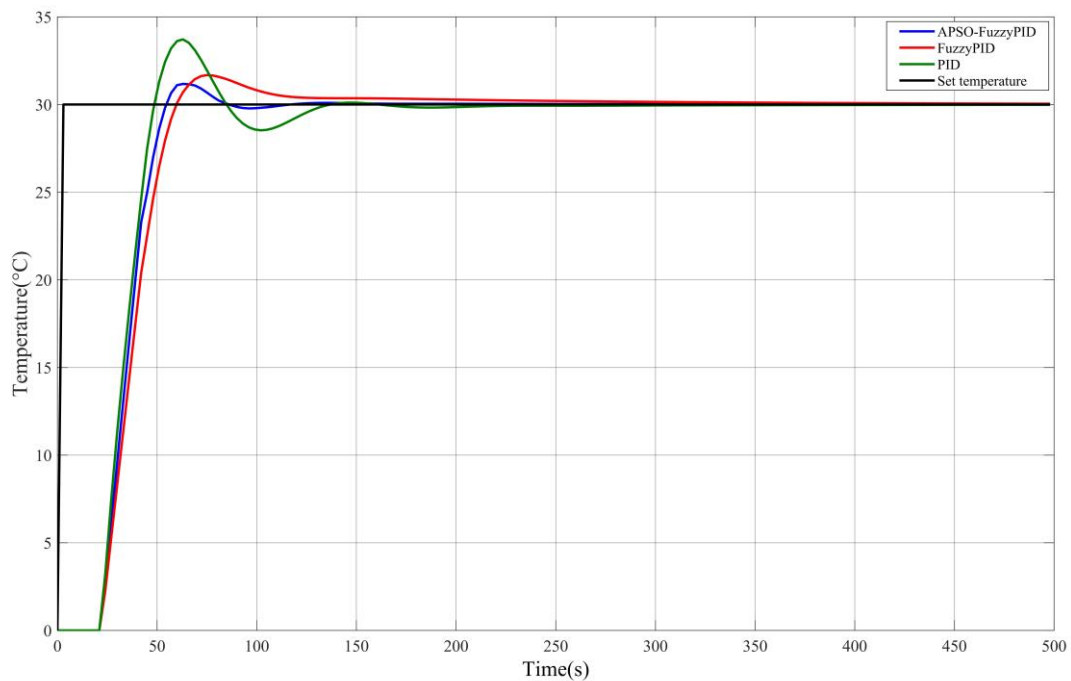


Fig. 7 - Simulation result

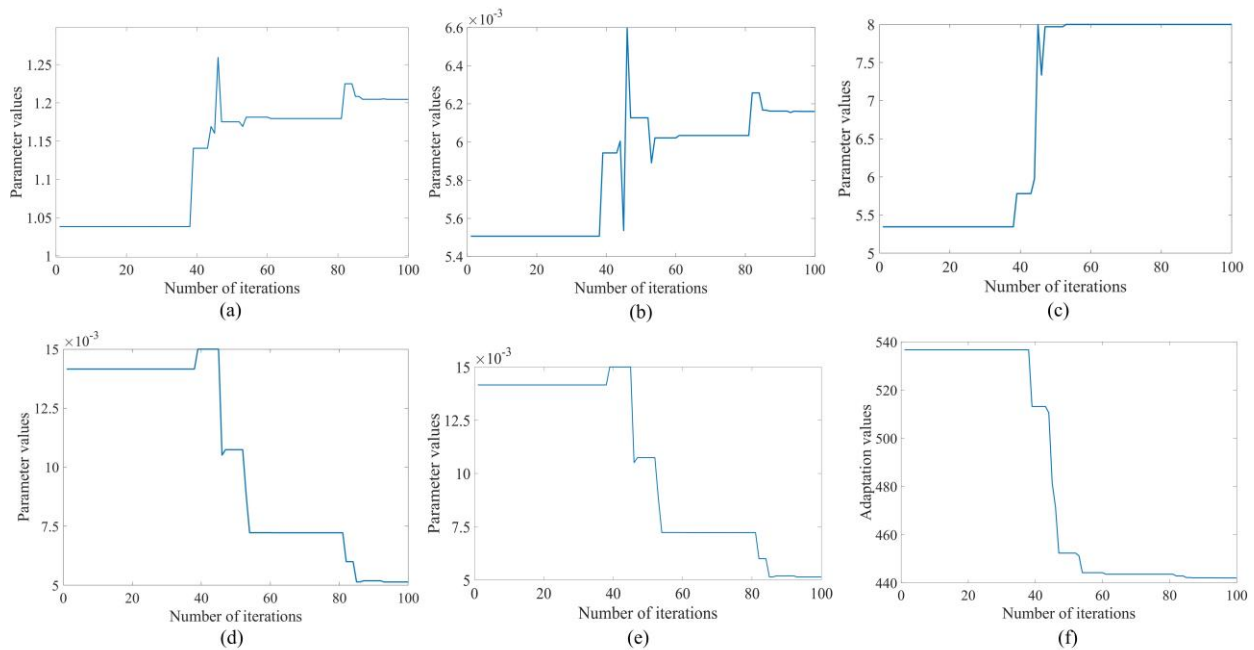


Fig. 8 - (f) Adaptation changes curves; parameter optimization results (a): KP, (b): KI, (c): KD, (d): Ke, (e): Kec. Table 4

Analysis of simulation results

Performances	Methodologies		
	APSO Fuzzy PID	Fuzzy PID	PID
Rising time t_r/s	23.8	27.7	20.6
Overshoot $\sigma/\%$	3.65%	4.73%	13.07%
Adjustment time t_s/s	110.1	121	137.5

The structural layout of the greenhouse is depicted in Figure 9. Three air temperature and humidity sensors were placed around the greenhouse to monitor the overall temperature, while a soil parameter sensor was embedded in the soil to monitor soil conditions. Two fans were symmetrically installed to facilitate air circulation, and the heater and cooler were installed in the upper and lower parts of the greenhouse, respectively, to control the temperature.



Fig. 9 - Greenhouse structure

In this experiment, the effectiveness of the greenhouse control system was tested at set temperatures of 24°C, 28°C, and 30°C, as shown in Figure 10 (a), (b), and (c). Throughout the experiment, the internal temperature of the greenhouse was continuously adjusted and monitored in real time using a precise environmental control system. The results showed that the temperature control system in the greenhouse responded quickly and remained near the set point, with fluctuations within 0.3°C. This demonstrates the system's strong temperature regulation capability, effectively maintaining the required temperature range and ensuring the stability of the greenhouse environment. In terms of humidity control, the greenhouse humidity was regulated using direct control methods, as ambient humidity decreases slowly. The experimental results are shown in Figure 10 (d).

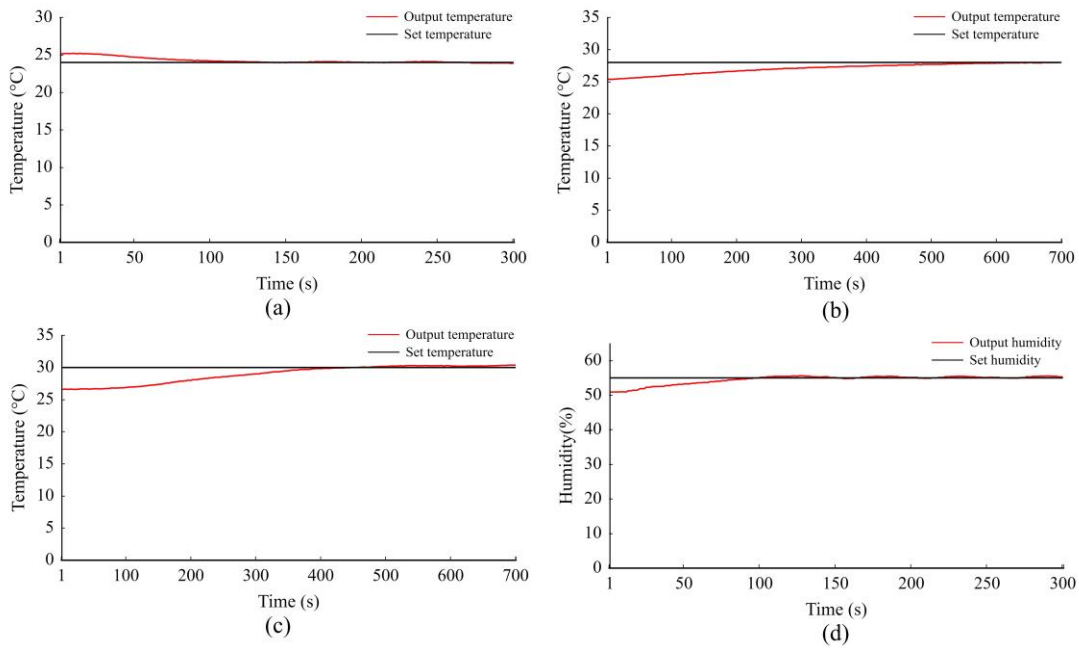


Fig. 10 - Temperature control curves at (a) 24°C, (b) 28°C, (c) 30°C, (d) 55% Humidity

The performance tests of the system at outside temperatures of 22°C and 17°C are shown in Figure 11 (a) and (b), respectively. The test results revealed that as the ambient temperature decreased, the system's response time extended accordingly; however, this did not affect the overall control effectiveness. To evaluate the system's performance under varying humidity conditions, tests were conducted at greenhouse humidity levels of 30%, 40%, 50%, and 60%, with the results displayed in Figure 11 (c), (d), (e), and (f). The results showed that the different humidity levels had almost no effect on the system's responsiveness or its stabilizing effect.

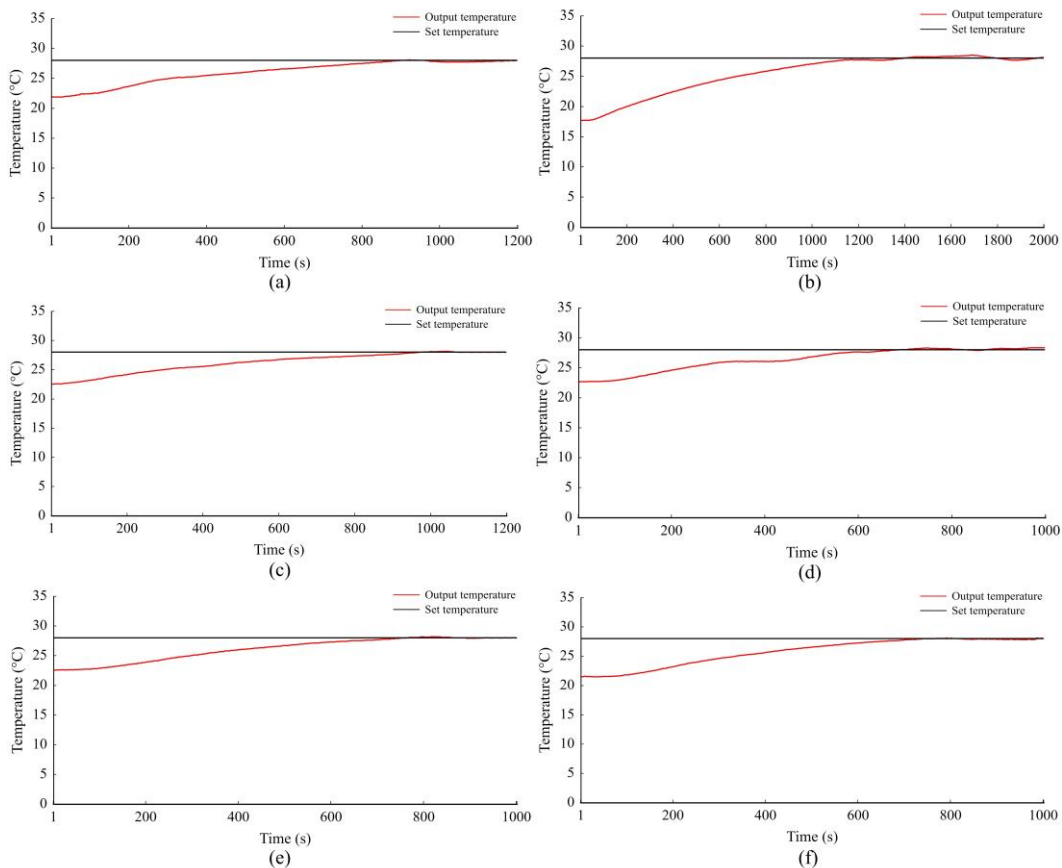


Fig. 11- Control effect at different ambient temperatures: (a) 22°C, (b) 17°C; control effect at different humidity: (c) 30%, (d) 40%, (e) 50%, (f) 60%

The configured data visualization platform, shown in Figure 12, clearly displays various environmental parameters within the greenhouse, including temperature, humidity, soil salinity, and pH. The platform is also equipped with an anomaly alert function, which automatically triggers an alarm when any environmental parameter exceeds the preset safety range, prompting the user to take timely action. Figure 13 shows the developed MySQL database, which allows different data to be stored for later analysis and processing.



Fig. 12 - Data presentation platform

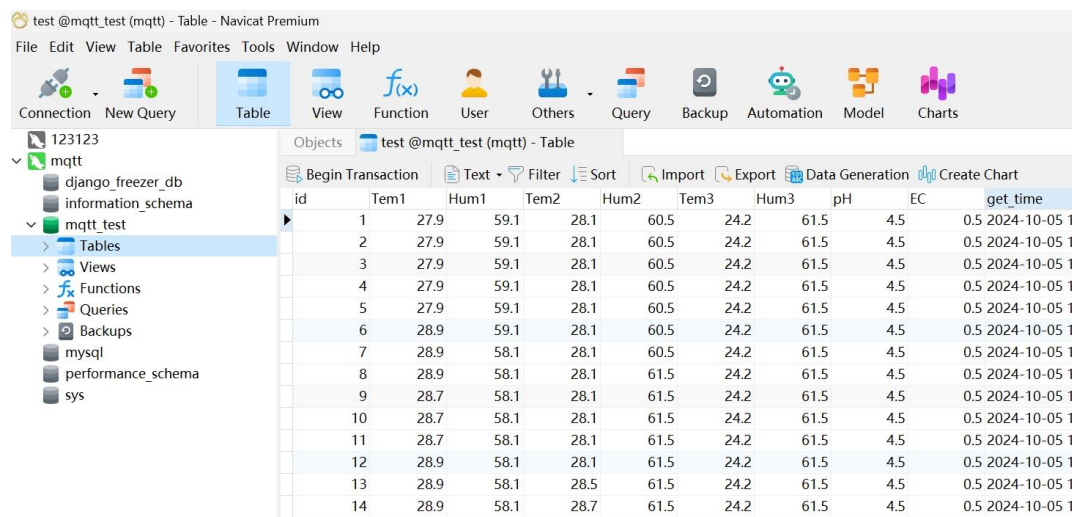


Fig. 13 - MySQL database

CONCLUSIONS

This study focused on the design and implementation of a greenhouse environmental control system, with an in-depth investigation of a fuzzy control-based temperature regulation strategy and the integration of an intelligent display platform for environmental monitoring. Through experimental validation, the greenhouse environment achieved stable and precise control under different temperature settings, confirming the effectiveness of the fuzzy control method in managing complex nonlinear systems. In addition, the constructed big data display platform successfully collected and visualized greenhouse parameters such as temperature and humidity in real time, providing managers with intuitive and detailed environmental information. Moreover, the platform included an anomaly alert feature that could promptly identify and notify users of potential environmental risks, thereby enhancing the safety and automation of greenhouse management.

Future work will focus on optimizing the control algorithms for broader deployment, integrating more diverse environmental sensors, and enhancing the robustness of the platform under varying network conditions. This study not only validated the efficacy of fuzzy control in greenhouse environmental management but also demonstrated the broad application potential of intelligent display platforms in agricultural management.

The system ensures the stability of the crop growth environment while simplifying management processes and reducing the need for manual intervention, providing strong support for the intelligent and precise development of modern agriculture.

ACKNOWLEDGEMENT

This work was supported by the National Natural Science Foundation of China (32372438, 31772068, 31872909, 32111530291, 32281240407), Funding Project for the Central Government to Guide the Development of Local Science and Technology (YDZX2022163), Technological Innovation Guidance Project of Department of Science & Technology of Gansu Province (22CX8NA023). The authors also extended their appreciation to the Researchers Supporting Project number (RSPD2025R944), King Saud University, Riyadh, Saudi Arabia, for funding this work.

REFERENCES

- [1] Akaev A. (2022). Phenomenological models of the global demographic dynamics and their usage for forecasting in 21st century. *Applied Mathematics*, 13(7), 612-49. <https://doi.org/10.4236/am.2022.137039>
- [2] Atia D. M., El-madany H. T. (2017). Analysis and design of greenhouse temperature control using adaptive neuro-fuzzy inference system. *Journal of Electrical Systems and Information Technology*, 4(1), 34-48. <https://doi.org/10.1016/j.jesit.2016.10.014>
- [3] Chen T. Y., Chi T. M. (2010). On the improvements of the particle swarm optimization algorithm. *Advances in Engineering Software*, 41(2), 229-39. <https://doi.org/10.1016/j.advengsoft.2009.08.003>
- [4] Cheng Y. (2020). Research on intelligent control of an agricultural greenhouse based on fuzzy PID control. *Journal of Environmental Engineering and Science*, 15(3), 113-18. <https://doi.org/10.1680/jenes.19.00054>
- [5] Chin J., Callaghan V., Allouch S. B. (2019). The Internet-of-Things: Reflections on the past, present and future from a user-centered and smart environment perspective. *Journal of Ambient Intelligence and Smart Environments*, 11(1), 45-69. <https://doi.org/10.3233/AIS-180506>
- [6] Fadhel M. A., Duhaim A. M., Albahri A., Al-Qaysi Z., Aktham M., Chyad M., Abd-Alaziz W., Albahri O., Alamoodi A., & Alzubaidi L. (2024). Navigating the metaverse: unraveling the impact of artificial intelligence—a comprehensive review and gap analysis. *Artificial Intelligence Review*, 57(10), 264. <https://doi.org/10.1007/s10462-024-10881-5>
- [7] Fuentes J. M., Silva M., Muñoz C., Reyes H., Bustamante-Encina R., & Gatica G. (2024). Georeferenced environmental platform for kindergarten monitoring based on internet of things and websockets. *Procedia Computer Science*, 231, 629-35. <https://doi.org/10.1016/j.procs.2023.12.172>
- [8] Gatkal N. R., Nalawade S. M., Sahni R. K., Bhanage G. B., Walunj A. A., Kadam P. B., & Ali M. (2024). Review of IoT and electronics enabled smart agriculture. *International Journal of Agricultural and Biological Engineering*, 17(5), 1-14. <https://doi.org/10.25165/j.ijabe.20241705.8496>
- [9] Goli I., Kriauciūnienė Z., Zhang R., Bijani M., Kabir Koohi P., Rostamkalaei S. A., Lopez-Carr D., & Azadi H. (2024). Contributions of climate smart agriculture toward climate change adaptation and food security: The case of mazandaran province, Iran. *Trends in Food Science & Technology*, 104653. <https://doi.org/10.1016/j.tifs.2024.104653>
- [10] Hemathilake D., Gunathilake D. (2022). Agricultural productivity and food supply to meet increased demands. *Future Foods*, 539-53. <https://doi.org/10.1016/B978-0-323-91001-9.00016-5>
- [11] Katzin D., Van Henten E. J., Van Mourik S. (2022). Process-based greenhouse climate models: Genealogy, current status, and future directions. *Agricultural Systems*, 198, 103388. <https://doi.org/10.1016/j.agsy.2022.103388>
- [12] Khondoker M., Mandal S., Gurav R., & Hwang S. (2023). Freshwater shortage, salinity increase, and global food production: A need for sustainable irrigation water desalination—A scoping review. *Earth*, 4(2), 223-40. <https://doi.org/10.3390/earth4020012>
- [13] Kumar L., Chhogyel N., Gopalakrishnan T., Hasan M. K., Jayasinghe S. L., Kariyawasam C. S., Kogo B. K., & Ratnayake S. (2022). Climate change and future of agri-food production. *Future Foods*, 2022, 49-79. <https://doi.org/10.1016/B978-0-323-91001-9.00009-8>
- [14] Lee S. Y., Lee I. B., Yeo U. H., Kim R. W., & Kim J. G. (2019). Optimal sensor placement for monitoring and controlling greenhouse internal environments. *Biosystems Engineering*, 188, 190-206. <https://doi.org/10.1016/j.biosystemseng.2019.10.005>

- [15] Márquez-Vera M. A., Ramos-Fernández J. C., Cerecero-Natale L. F., Lafont F., Balmat J.-F., & Esparza-Villanueva J. I. (2016). Temperature control in a MISO greenhouse by inverting its fuzzy model. *Computers and electronics in Agriculture*, 124, 168-74. <https://doi.org/10.1016/j.compag.2016.04.005>
- [16] Mohamed T. M. K., Gao J., Tunio M. (2022). Development and experiment of the intelligent control system for rhizosphere temperature of aeroponic lettuce via the Internet of Things. *International Journal of Agricultural and Biological Engineering*, 15(3), 225-33. <https://doi.org/10.25165/j.ijabe.20221503.6530>
- [17] Omasa K., Ono E., Ishigami Y., Shimizu Y., & Araki Y. (2022). Plant functional remote sensing and smart farming applications. *International journal of agricultural and biological engineering*, 15(4), 1-6. <https://dx.doi.org/10.25165/j.ijabe.20221504.7375>
- [18] Pan Y., Chen J., Yuan Z. (2020). Research on intelligent ship path planning optimization based on chaos particle swarm optimization. *International Core Journal of Engineering*, 6, 407-16. [https://doi.org/10.6919/ICJE.202012_6\(12\).0057](https://doi.org/10.6919/ICJE.202012_6(12).0057)
- [19] Schoder D. (2018). Introduction to the internet of things. *Internet of Things A to Z: Technologies and Applications*. Wiley.
- [20] Thomopoulos V., Tolis F., Blounas T.-F., Tsipianitis D., & Kavga A. (2024). Application of fuzzy logic and IoT in a small-scale smart greenhouse system. *Smart Agricultural Technology*, 8, 100446. <https://doi.org/10.1016/j.atech.2024.100446>
- [21] van Dijk M., Morley T., Rau M. L., & Saghai Y. (2021). Systematic review and meta-analysis of global food security projections to 2050. *Research Square*. <https://doi.org/10.21203/rs.3.rs-530565/v1>
- [22] Wang L., Zhang H. (2018). An adaptive fuzzy hierarchical control for maintaining solar greenhouse temperature. *Computers and electronics in agriculture*, 155, 251-56. <https://doi.org/10.1016/j.compag.2018.10.023>
- [23] Weng H., Zhu W., Wu J. (2024). Multi mode coordinated control algorithm for DC near-field photovoltaic based on adaptive mutation particle swarm optimization. *Ain Shams Engineering Journal*. 103168. <https://doi.org/10.1016/j.asej.2024.103168>
- [24] Zhang Z., Jiang Y., Zhang S., Geng S., Wang H., & Sang G. (2014). An adaptive particle swarm optimization algorithm for reservoir operation optimization. *Applied Soft Computing*, 18, 167-77. <https://doi.org/10.1016/j.asoc.2014.01.034>
- [25] Zheng W., Meng F., Liu N., & Huang S. (2023). A game model for analyzing wireless sensor networks of 5G environment based on adaptive equilibrium optimizer algorithm. *Sensors*, 23(19), 8055. <https://doi.org/10.3390/s23198055>
- [26] Zhou D., Meinke H., Wilson M., Marcelis L. F. M., & Heuvelink E. (2021). Towards delivering on the sustainable development goals in greenhouse production systems. *Resources, Conservation and Recycling*, 169, 105379. <https://doi.org/10.1016/j.resconrec.2020.105379>

INSTRUCTIONS FOR AUTHORS

Article Types

Three types of manuscripts may be submitted:

1. **Regular articles:** should describe new and carefully confirmed findings, and experimental procedures should be given in sufficient detail for others to verify the work. The length of a full paper should be the minimum required to describe and interpret the work clearly (max.10 pages). *Additional pages will be supplementary charged.*
2. **Review articles:** must contain at least three basic elements: an introduction or background information section; the body of the review containing the discussion of sources; and, finally, a conclusion and/or recommendations section to end the paper. The length of a full paper should be the max. 20 pages (if the number of references is 80-100) and max. 45 pages (if the number of references is over 300). *Additional pages will be supplementary charged.*

Manuscripts should be written in English (American or British usage is accepted, but not a mixture of these) and submitted directly on the journal website. The 2nd, 3rd and the next versions can be sent by e-mail, at the following address: inmatehjournal@gmail.com, mentioning the registration number (N...).

Please be sure to include your full affiliation and e-mail address (see Sample manuscript)

The authors are responsible for the accuracy of the whole paper and references.

There are allowed 2 papers by each first author.

The text layout should be in single-column format. To avoid unnecessary errors, it is strongly advised to use the "spell-check" and "grammar check" functions of your word processor.

Review Process

All manuscripts are reviewed by 2 members of the Scientifically Review Office.

Decisions will be made as quickly as possible, and the journal strives to return reviewer comments to authors within 3 weeks to 4 months, depending on the reviewers' responses. The editorial board will re-evaluate manuscripts that are accepted pending review.

NOTE:

Submission of a manuscript implies: that the work described has not been published before (excepting as an abstract or as part of a published lecture or thesis) that it is not under consideration for publication elsewhere.

1. REGULAR ARTICLES

- Manuscripts should be concise, in **1.15 line spacing**, and should have 2 cm all over margins. The font should be **Arial 10 pt.** Ensure that each new paragraph is clearly indicated, using TAB at 1 cm.
- Title will be **Arial 12 pt.** and explicit figures will be **Arial 9 pt.**
- Text will be written in English.
- Chapters' titles are written by **Arial 10 pt, Bold, Uppercase** (e.g INTRODUCTION, MATERIAL AND METHODS), between chapters is left a space for 10 pt. At the beginning of each paragraph, leave a tab of 1 cm.
- The paper body will be written in **Arial 10 pt., Justify alignment.**

TITLE **Arial 12 pt., Uppercase, Bold, Center** (in English language) and **Bold Italic** (in native language).

Should be a brief phrase describing the contents of the paper. Avoid long titles; a running title of no more than 100 characters is encouraged (without spaces).

AUTHORS: **ARIAL 9, Bold, Centre alignment (Max. 6 authors)**

Under the paper's title, after a space (enter) 9 pt., write **authors' name and surname** and **affiliations** (**Arial 8 pt.-Regular**)

When the paper has more than one author, their name will be followed by a mark (Arabic numeral) as superscript if their affiliation is different.

Corresponding author's name (next row), (**Arial 8 pt.**). Should be added also: phone, fax and e-mail information, for the paper corresponding author (**font: 8 pt., Italic**).

If the authors wish, academic positions can be added in the Footnote, by Times New Roman, Italic, 9pt.

KEYWORDS (*In English*) about 4 to 7 keywords that will provide indexing references should be listed (*title: Arial 10pt, bold italic, text Arial 10 pt., italic*).

A list of non-standard *Abbreviations* should be added. In general, non-standard abbreviations should be used only when the full term is very long and used often. Each abbreviation should be spelled out and introduced in parentheses the first time it is used in the text. Standard abbreviations (such as ATP and DNA) need not to be defined.

ABSTRACT (*in English and Native language, Arial 10 pt.*), the title *bold*; the text of abstract: *italic*) should be informative and completely self-explanatory, briefly present the topic, state the scope of the experiments, indicate significant data, and point out major findings and conclusions. The Abstract should be max.250 words. Complete sentences, active verbs, and the third person should be used, and the abstract should be written in the past tense. Standard nomenclature should be used and abbreviations should be avoided. No literature should be cited.

INTRODUCTION (*Arial 10 pt.*) should provide a clear statement of the problem, the relevant literature on the subject, and the proposed approach or solution. It should be understandable to colleagues from a broad range of scientific subjects. We should refer to the current stage of researches performed in the field of the paper to be published, by quoting up-to-date specialty studies, preferably published **in the last 10 years**, excepting certain referential specialty books/studies, especially papers issued in magazines/journals/conferences/ISI quoted symposia or in other international data bases, which are well known and available.

It is imperative to incorporate references from a diverse range of countries globally, rather than limiting sources to those from the native country.

MATERIALS AND METHODS (*Arial 10 pt.*) should be complete enough to allow experiments to be reproduced. However, only truly new procedures should be described in detail; previously published procedures should be cited, and important modifications of published procedures should be mentioned briefly. Methods in general use need not be described in detail.

RESULTS (*Arial 10 pt.*) should be clarity presented. The results should be written in the past tense when describing findings in the authors' experiments. Results should be explained, but largely, without referring to the literature. Discussion, speculation and detailed interpretation of data should not be included in the Results, but should be put into the CONCLUSIONS section.

CONCLUSIONS (*Arial 10 pt.*) The main conclusions drawn from results should be presented in a short Conclusions section. Do not include citations in this section.

Formulae, symbols and abbreviations: Formulae will be typeset in Italics (preferable with the Equation Editor of Microsoft Office or MathType) and should be written or marked as such in the manuscript, unless they require a different styling. They should be referred to in the text as Equation (4) or e.g. (4). The formulae should be numbered on the right side, between brackets (*Arial 10 pt.*):

$$P = F \cdot v \quad (1)$$

Terms of the equation and the unit measure should be explained, e.g.

P is the power, [W];

F – force, [N];

v – speed, [m/s]

SI units must be used throughout.

Equation terms in text, must be written using the same style as in Equation.

Tables should be self-explanatory without reference to the text. The details of the methods used in the experiments should preferably be described in the legend instead of in the text. The same data should not be presented both in table and graph form or repeated in the text.

Table's title will be typed *Arial 9 pt, Bold, Centered*.

In the table, each row will be written *Arial 9 pt*, single-spaced throughout, including headings and footnotes.

The table should be numbered on the right side, between brackets (*Arial 10 pt*):

Figure (*Arial 9 pt., Bold, Center*) should be typed in numerical order (Arabic numerals). Graphics should be high resolution (e.g.JPEG). Figure number is followed by what represent the figure or graph e.g.:

Fig. 1 - Test stand

Legend: (*Arial 8 pt., Italic, Center*), e.g.

1 - plansifter compartments; 2- break rolls; 3 – semolina machines; 4 – reduction rolls; 5 – flour

ACKNOWLEDGMENTS (*Arial 10 pt.*) of people, grants, funds etc should be brief (*if necessarily*).

REFERENCES (*Arial 10 pt.*)

(*In alphabetical order, in English and in the original publication language.*)

Minimum 20 references, from which minimum 3 references from the last 3 years

It is imperative to incorporate references from a diverse range of countries globally, rather than limiting sources to those from the native country.

The number of self-cited papers should not exceed 10% of the total references !

It can be used "References" tool from the *Word Editor*.

References should be cited in the text in brackets as in the following examples:

(*Babiciu P., Scripcnic V., 2000*)

All references must be provided in English with a specification of original language in round brackets.

Authors are fully responsible for the accuracy of the references.

References should be alphabetically, **automatically numbered or without numbering**, with complete details, as follows:

Examples:

Books: Names and initials of authors, year (between brackets), title of the book (Italic), volume number, publisher, place, pages number or chapter, ISSN/ISBN:

[1] Vlăduț V., (2009), *Study of threshing process in axial flow apparatus (Studiul procesului de treier la aparatele cu flux axial)*, vol.1,"Terra Nostra", Publishing House, ISSN/ISBN, Iași/Romania;

Journal Article: Names and initials of authors, year (between brackets), full title of the paper, full name of the journal (Italic), volume number, publisher, place, page numbers, DOI or URL:

[1] Li Q., Feng J., (2024). Design and experimental analysis of rotary spoon soybean precision seeder (转勺式大豆精密排种器设计与试验分析), *INMATEH Agricultural Engineering*, vol.74, no.3, pp.13-24, Bucharest/Romania. DOI: <https://doi.org/10.35633/inmateh-74-01>

Conference or Symposium: Names and initials of authors, year (between brackets), full title of the paper (Regular), full name of the conference/symposium (Italic), volume number, publisher, place, ISSN, page numbers

[2] Bungescu S., Stahl W., Biriș S., Vlăduț V., Imbrea F., Petroman C., (2009), Cosmos program used for the strength calculus of the nozzles from the sprayers (Program Cosmos folosit pentru calculul de rezistență la zgomet al aparatelor de distribuție), *Proceedings of the 35 International Symposium on Agricultural Engineering "Actual Tasks on Agricultural Engineering"*, pp.177-184, Opatija / Croatia;

Dissertation / Thesis: Names and initials of authors, year (between brackets), full name of the thesis (Italic), specification (PhD Thesis, MSc Thesis), institution, place;

[3] Matache M.G., (2016). *Researches regarding testing in simulated and accelerated regime of agricultural machinery resistance structures (Cercetări privind încercarea în regim simulat și accelerat a structurilor de rezistență ale mașinilor agricole)*, PhD dissertation, POLITEHNICA University, Bucharest/Romania.

Patents: Names and initials of authors, year (between brackets), patent title (Italic), patent number, country:

[4] Grant P., (1989), *Device for Elementary Analyses*. Patent, No.123456, USA.

Legal regulations and laws, organizations: Abbreviated name, year (between brackets), full name of the referred text, document title/type (Italic), author, place:

[5] *** EC Directive, (2000), Directive 2000/76/EC of the European Parliament and of the Council of 4 December 2000, on the incineration of waste, Annex V, *Official Journal of the European Communities*, L332/91, 28.12.2000, Brussels.

Web references: The full URL should be given in text as a citation, if no other data are known. If the authors, year, and title of the documents are known and the reference is taken from a website, the URL address has to be mentioned after these data:

The title of the book, journal and conference must be written in Italic.

The title of the article must be written Regular.

Citation in text

Please ensure that every reference cited in the text is also present in the reference list (and vice versa). Do not cite references in the abstract and conclusions. Unpublished results, personal communications as well as URL addresses are not recommended in the references list.

Making personal quotations (one, at most) should not be allowed, unless the paper proposed to be published is a sequel of the cited paper. Articles in preparation or articles submitted for publication, unpublished, personal communications etc. should not be included in the references list.

Citations style

Text: All citations in the text may be made directly (or parenthetically) and should refer to:

- **single author:** the author's name (without initials, unless there is ambiguity) and the year of publication: "as previously demonstrated (*Brown, 2010*)".

- **two authors:** both authors' names and the year of publication: (*Adam and Brown, 2008; Smith and Hansel, 2006; Stern and Lars, 2009*)

- **three or more authors:** first author's name followed by "et al." and the year of publication: "As has recently been shown (*Werner et al., 2005; Kramer et al., 2000*) have recently shown"

Citations of groups of references should be listed first alphabetically, then chronologically.

Units, Abbreviations, Acronyms

- Units should be metric, generally SI, and expressed in standard abbreviated form.
- Acronyms may be acceptable but must be defined at first usage.

2. REVIEWS

Reviews and perspectives covering topics of current interest in the field, are encouraged and accepted for publication. A review must have **at least 80 references**.

It might give a new interpretation of old material or combine new with old interpretations. Or it might trace the intellectual progression of the field, including major debates. And depending on the situation, the literature review may evaluate the sources and advise the reader on the most pertinent or relevant.

Literature reviews must contain at least three basic elements: an introduction or background information section; the body of the review containing the discussion of sources; and, finally, a conclusion and/or recommendations section to end the paper.

The following provides a brief description of the content of each: Introduction: Gives a quick idea of the topic of the literature review, such as the central theme or organizational pattern. Body: Contains your discussion of sources and is organized either chronologically, thematically, or methodologically. Conclusions / Recommendations: Discuss what you have drawn from reviewing literature so far.



Edited by: INMA Bucharest

6, Ion Ionescu de la Brad Blvd., sect. 1, Bucharest, ROMANIA

Tel: +4021.269.32.60; Fax: +4021.269.32.73

[https:// inmateh.eu](https://inmateh.eu)

e-mail: inmatehjournal@gmail.com

